2008

MRR 2008 Proceedings of the 30th Monitoring Research Review: Ground-Based Nuclear Explosion Monitoring Technologies

To view these Proceedings online, visit
https://na22.nnsa.doe.gov/gnem/mrr2008.

Vol. I

# MRR 2008

## Proceedings of the 30th Monitoring Research Review: Ground-Based Nuclear Explosion Monitoring Technologies

## September 23–25, 2008

## Portsmouth, Virginia

## Volume I

Seismic Regional Characterizationand Wave Propagation
Seismic Event Detection and Location
Seismic Identification and Source Characterization

Approved for Public Release; further dissemination unlimited.

National Nuclear Security Administration

AIR FORCE RESEARCH LABORATORY

LA-UR-08-05261

## ACKNOWLEDGEMENTS

The National Nuclear Security Administration (NNSA) and the Air Force Research Laboratory (AFRL) gratefully acknowledge the important contributions of the following people for their work to produce the ***MRR 2008 Proceedings of the 30th Monitoring Research Review: Ground-Based Nuclear Explosion Monitoring Technologies.***

***Authors*** of papers for excellent research, technical documentation, and cooperation with electronic submission processes.

***Dr. Anton M. Dainty, Mr. Robert J. Raistrick, Dr. Frederick R. Schult***, AFRL/VSBYE, and ***Ms. Doris Richards***, ESC/PAM, for review and clearance of abstracts and papers related to AFRL contracts.

***Dr. Mark T. Woods***, Air Force Technical Applications Center (AFTAC)/TTR, for review and clearance of abstracts and papers related to AFTAC contracts.

***Dr. Stanley D. Ruppert***, Lawrence Livermore National Laboratory (LLNL), for assistance in ensuring that the CDs could be read on a variety of platforms and for burning the CDs.

***Mr. Marvin A. Wetovsky***, Los Alamos National Laboratory (LANL), for overall coordination of the Proceedings development, for techn***ical edit***ing and formatting of abstracts and papers, and for design of the CD label.

***Ms. Eileen F. Patterson***, LANL, for supplementary on-line editing and formatting of papers.

***Ms. Deidre´ A. Plumlee***, LANL, for composition and format of the electronic submissions of the Proceedings covers.

***Ms. Jody Benson***, LANL, for taking care of submissions to office of classification.

***Ms. Marie D. Arrowsmith***, LANL, for numerous technical consultations.

***Ms. Sandra Valdez***, LANL, for labeling the CDs.

***Mr. Geoff G. Miller, Ms. Karen E. LaRue, Ms. Diana J. Hollis, Mr. Leo W. Beckstead, Ms. Sandra L. Bonchin, Mr. Burton J. Krohn***, and ***Mr. Randy Drake***, LANL, for classification review of compiled papers.

***IRM-RMMSO,*** LANL, for color printing and binding of the hard copies.

***Ms. Leslie A. Casey***, NNSA, for review and clearance of abstracts and papers related to NNSA contracts and for NNSA overall support of the Proceedings.

***Mr. Steven T. Eacret***, Space and Missile Defense Command (SMDC), for review and clearance of abstracts and papers related to SMDC contracts. Additional thanks to ***Mr. Mark S. Pickens***, SMDC lead.

***Ms. Mary L. Girven***, Sandia National Laboratories (SNL), for making everyone's job easier with web-based technology for abstract and paper submission, on-line review and approval tools, and creation of the master files for the hardcopy, CD, and website versions of the Proceedings.

***Ms. Guadalupe (Lupe) Massoth***, SNL, for providing assistance to Mary Girven on website development and help in creating the master files.

***Dr. William R. Walter***, LLNL; ***Dr. Stephen C. Myers***, LLNL; ***Dr. W. Scott Phillips***, LANL; ***Mr. Ward L. Hawkins***, LANL; ***Dr. Dale N. Anderson***, Pacific Northwest National Laboratory (PNNL); Ms. Laura Wilhelm, PNNL; Mr. Martin E. Keillor, PNNL; ***Dr. Ted W. Bowyer***, PNNL; ***Mr. J. Mark Harris***, SNL; and ***Dr. Christopher J. Young***, SNL, for a myriad of internal management and technical reviews of NNSA abstracts and papers.


## Previous Proceedings

| Year | Title of the Proceedings |
|---|---|
| 2007 | Proceedings of the 29th Monitoring Research Review: Ground-Based Nuclear Explosion Monitoring Technologies |
| 2006 | Proceedings of the 28th Seismic Research Review: Ground-Based Nuclear Explosion Monitoring Technologies |
| 2005 | Proceedings of the 27th Seismic Research Review: Ground-Based Nuclear Explosion Monitoring Technologies |
| 2004 | Proceedings of the 26th Seismic Research Review - Trends in Nuclear Explosion Monitoring |
| 2003 | Proceedings of the 25th Seismic Research Review - Nuclear Explosion Monitoring: Building the Knowledge Base |
| 2002 | Proceedings of the 24th Seismic Research Review - Nuclear Explosion Monitoring: Innovation and Integration |
| 2001 | Proceedings of the 23rd Seismic Research Review: Worldwide Monitoring of Nuclear Explosions |
| 2000 | Proceedings of the 22nd Annual DoD/DOE Seismic Research Symposium: Planning for Verification of and Compliance with the Comprehensive Nuclear-Test-Ban Treaty (CTBT) |
| 1999 | Proceedings of the 21st Seismic Research Symposium: Technologies for Monitoring the Comprehensive Nuclear-Test-Ban Treaty |

# Table of Contents - Volume I


**1. Seismic Regional Characterization and Wave Propagation** 1

1-01 **Bergman, E., E. Engdahl, M. Ritzwoller, and S. Myers**
*Crustal Structure of the Iran Region from In-Country and Ground-Truth Data* 3

1-02 **Bonner, J., A. Stroujkova, and K. Mayeda**
*Predicting Explosion-Generated Sn and Lg Coda Using Synthetic Seismograms* 10

1-03 **Bungum, H., M. Pasyanos, J. Faleide, and S. Clark**
*Development and Tuning of a 3-D Stochastic Inversion Methodology for the European Arctic* 20

1-04 **Ferris, A., D. Reiter, and A. Stroujkova**
*Improved Phase Characterization of Far-Regional Body Wave Arrivals in Central Asia* 30

1-05 **Fisk, M. and S. Taylor**
*Applications of a Constrained Inversion and an Enhanced Kriging Method to Improve Source, Path, and Site Corrections for Regional Seismic Phases* 40

1-06 **Ford, S., D. Dreger, W. Phillips, W. Walter, K. Mayeda, and L. Malagnini**
*Attenuation Tomography of Northern California and the Yellow Sea / Korean Peninsula from Coda-Source Normalized and Direct Lg Amplitudes* 50

1-07 **Gerstoft, P., J. Zhang, W. Kuperman, N. Harmon, K. Sabra, M. Fehler, and S. Taylor**
*Estimating Local and Near-Regional Velocity and Attenuation Structure from Seismic Noise* 57

1-08 **Gritto, R., J. Siegel, and W. Chan**
*Structure of the Korean Peninsula from Waveform Travel-Time Analysis* 67

1-09 **Gritto, R., M. Sibol, J. Siegel, H. Ghalib, Y. Chen, R. Herrmann, G. Alequabi, H. Tkalcic, B.S. Ali, B. Saleh, D. Mahmood, O. Shaswar, A. Mahmood, S. Abdullah, F. Ibrahim, R. Zand, B. Ali, L. Omar, N. Aziz, N. Ahmed, T. Al-Nasiri, A. Ali, A. Taqi, and S. Khalaf**
*Crustal Structure of North Iraq from Receiver Function Analyses* 79

1-10 **Julia, J., A. Nyblade, R. Gök, W. Walter, L. Linzer, and R. Durrheim**
*Developing and Exploiting a Unique Seismic Dataset from South African Gold Mines for Source Characterization and Wave Propagation* 87

1-11 **Lay, T., X. Xie, and X. Yang**
*Development of Regional Phase Tomographic Attenuation Models for Eurasia* 98

1-12 **Levshin, A., M. Barmin, X. Yang, and M. Ritzwoller**
*Toward a Rayleigh Wave Attenuation Model for Asia and Surrounding Regions* 108

1-13 **Mackey, K.**
*Analysis of Digitized Seismograms from Russian Geophysical Survey Stations of Soviet Peaceful Nuclear Explosions* 118

1-14 **Mackey, K., L. Steck, K. Fujita, H. Hartse, and R. Stead**
*Seismic Characterization of Northeast Asia* 122

1-15 **Martin, R., M. Krasovec, E. Vergino, and M. Toksöz**
*Extension of the Caucasus Seismic Information Network Study into Central Asia* 132

1-16 **Mellors, R., R. Gök, M. Pasyanos, G. Skobeltsyn, U. Teoman, T. Godoladze, and E. Sandvol**
*High-Resolution Seismic Velocity and Attenuation Models of the Caucasus-Caspian Region* 142

1-17 **Minaya, E., E. Lázaro, P. Aliaga, M. Gonzalez, and W. Cano**
*Synthetic Seismogram Study of the Eastern Central Andes* 151

1-18 **Morozov, I.**
*PNE Coda Attenuation and Scattering Parameters in Northern Eurasia* 159

1-19 **Ni, S., R. Chu, H. Thio, A. Pitarka, and D. Helmberger**
*Synergy Between Remote Sensing and Seismic Methods: Path Calibration* 170

1-20 **Nowack, R., W. Chen, and T. Tseng**
*Frequency-Dependent Nature of Pn in Western China: Gaussian Beam Modeling of Data from the Hi-CLIMB Experiment* 180

1-21 **Nyblade, A., A. Adams, R. Brazier, Y. Park, and A. Rodgers**
*Ground Truth, Magnitude Calibration, and Regional Phase Propagation and Detection in the Middle East and the Horn of Africa* 190

1-22 **Pitarka, A., D. Helmberger, and S. Ni**
*Analyses and Simulation of 3D Scattering due to Heterogeneous Crustal Structure and Surface Topography on Regional Phases, Magnitude Discrimination* 201

1-23 **Reiter, D. and W. Rodi**
*A New Regional 3-D Velocity Model for Asia from the Joint Inversion of P-Wave Travel Times and Surface-Wave Dispersion Data* 213

1-24 **Ritzwoller, M., Y. Yang, and M. Pasyanos**
*Short Period Surface Wave Dispersion from Ambient Noise Tomography in Western China* 222

1-25 **Rodgers, A., E. Matzel, M. Pasyanos, A. Petersson, B. Sjogreen, C. Bono, O. Vorobiev, T. Antoun, I. Lomov, W. Walter, and S. Myers**
*Seismic Simulations Using Parallel Computing and Three-Dimensional Earth Models to Improve Nuclear Explosion Phenomenology and Monitoring* 231

1-26 **Romanowicz, B., A. Cao, P. Cupillard, L. Stehly, A. Kim, M. Pasyanos, and D. Dreger**
*Calibration of 3D Upper Mantle Structure in Eurasia Using Regional and Teleseismic Full Waveform Seismic Data* 241

1-27 **Rowe, C., M. Maceira, M. Begnaud, L. Steck, and W. Phillips**
*Geophysical Modeling in Eurasia: 2D Crustal P and Lg Propagation; Upper-Mantle Shear Wave Propagation and Anisotropy; and 3D, Joint, Simultaneous Inversions* 251

1-28 **Savage, B., A. Rodgers, J. Tromp, and B. Covellone**
*Initial Steps Toward Next-Generation, Waveform-Based, Three-Dimensional Models and Metrics to Improve Nuclear Explosion Monitoring in the Middle East* 261

1-29 **Song, X., X. Sun, S. Zheng, Z. Xu, Y. Yang, and M. Ritzwoller**
*Surface Wave Dispersion Measurements and Tomography from Ambient Seismic Noise Correlation in China* 268

1-30 **Srinivasan, C., Y. Willy, and C. Sivakumar**
*Strong Motion Studies in the Mines of Kolar Gold Fields* 279

1-31 **Stump, B., R. Zhou, T. Kim, Y. Chen, Z. Yang, R. Herrmann, R. Burlacu, C. Hayward, and K. Pankow**
*Shear Velocity Structure in NE China and Characterization of Infrasound Wave Propagation in the 1-210 Kilometer Range* 287

1-32 **Young, C., S. Ballard, J. Hipp, M. Chang, G. Barker, M. Begnaud, W. Phillips, L. Steck, and C. Rowe**
*A 3D Tomographic Model of South Central Asia Based on Pn Travel Times from GT Events* 297

1-33 **Zhang, H., K. Mackey, K. Fujita, C. Thurber, L. Steck, C. Rowe, S. Roecker, and M. Toksöz**
*Three-Dimensional Seismic Imaging of Eastern Russia* 306

1-34 **Zhang, W., Y. Shen, L. Zhao, and X. Yang**
*Refined Local and Regional Seismic Velocity and Attenuation Models from Finite-Frequency Waveforms* 316

**2. Seismic Event Detection and Location** 327

2-01 **Abramovich, I. and T. Zhu**
*Next Generation Robust Low Noise Seismometer for Nuclear Monitoring* 329

2-02 **Ballard, S., C. Young, J. Hipp, G. Barker, and M. Chang**
*Implementation of a Pseudo-Bending Seismic Travel-Time Calculator in a Distributed Parallel Computing Environment* 338

2-03 **Ballard, S., J. Hipp, and C. Young**
*Robust, Extensible Representation of Complex Earth Models for Use in Seismological Software Systems* 347

2-04 **Begnaud, M., X. Yang, R. Stead, W. Phillips, C. Rowe, and L. Steck**
*Location Improvements in East Asia: Tomographic Model Analysis and Utilizing Public Data for Ground Truth Identification* 356

2-05 **Brogan, R., S. Nava, J. Coyne, and Y. Jia**
*Seismicity of Central Asia as Observed on Three IMS Stations* 366

2-06 **Carr, D., G. Bogart, S. Goodman, P. Baldwin, and D. Robinson**
*A Laser Interferometric Miniature Seismometer* 376

2-07 **Chang, S., M. Flanagan, S. van der Lee, E. Matzel, and M. Pasyanos**
*Evaluation of Regional Travel-Time and Location Improvement Along the Tethyan Margin Using a New Three-Dimensional Velocity Model* 385

2-08 **Engdahl, E., E. Bergman, S. Myers, and F. Ryall**
*Improved Ground Truth in Southern Asia Using In-Country Data, Analyst Waveform Review, and Advanced Algorithms* 395

2-09 **Fourguette, D., M. Ötügen, L. Larocque, and T. Ioppolo**
*Optical MEMS-Based Seismometer "WhiGS"* 403

2-10 **Helmberger, D., A. Rodgers, S. Ni, S. Wei, and J. Tromp**
*Advanced Waveform Simulation for Seismic Monitoring* 408

2-11 **Leugoud, R.**
*Seismic Detection Using Mini Seismometer* 419

2-12 **Myers, S., S. Ballard, C. Rowe, G. Wagner, M. Antolik, W. Phillips, A. Ramirez, M. Begnaud, M. Pasyanos, D. Dodge, M. Flanagan, K. Hutchenson, G. Barker, J. Dwyer, and D. Russell**
*A Model and Methods for Regional Travel-Time Calculation* 425

2-13 **Pinsky, V., E. Husebye, T. Matveeva, and Y. Fedorenko**
*On the CTBT Monitoring Potential of Using Lg-Phase Arrival Times at Local and Regional Distance Ranges* 435

2-14 **Ren, Y., W. Zhang, T. Yang, Y. Shen, and X. Yang**
*Finite-Frequency Seismic Tomography of Body Waves and Surface Waves from Ambient Seismic Noise: Crustal and Mantle Structure Beneath Eastern Eurasia* 445

2-15 **Ringdal, F., D. Harris, T. Kvaerna, and S. Gibbons**
*Expanding Coherent Array Processing to Larger Apertures Using Empirical Matched Field Processing* 455

2-16 **Ringdal, F., S. Gibbons, and D. Harris**
*Adaptive Waveform Correlation Detectors for Arrays: Algorithms for Autonomous Calibration* 465

2-17 **Rodi, W. and S. Myers**
*Modeling Travel-Time Correlations Based on Sensitivity Kernels and Correlated Velocity Anomalies* 475

2-18 **Rodi, W., D. Reiter, and S. Myers**
*A Unified Approach to Joint Regional/Teleseismic Calibration and Event Location with a 3D Earth Model* 485

2-19 **Standley, I. and W. Pike**
*Initial Results on Rugged Low Power Compact Silicon MEMS Sensors for Use in Nuclear Explosion Monitoring* 494

2-20 **Toksöz, M., R. Van der Hilst, Y. Sun, L. Gülen, D. Kalafat, H. Kuleli, C. Li, and H. Zhang**
*Seismic Tomography of the Arabian-Eurasian Collision Zone and Surrounding Areas* 504

2-21 **Yin, L., M. Erdtmann, L. Domash, and J. Zhao**
*Three-Axis Seismometer* 514

**3. Seismic Identification and Source Characterization** 523

3-01 **Abercrombie, R., K. Mayeda, W. Walter, G. Viegas, and K. Murphy**
*Seismic Source Scaling and Discrimination in Diverse Tectonic Environments* 525

3-02 **Anderson, D., D. Fagan, S. Taylor, and T. Mercier**
*Discrimination Calibration Analysis Methods for Regional Stations* 535

3-03 **Arrowsmith, M., S. Arrowsmith, B. Stump, and M. Hedlin**
*A Suite of Discriminants for Ground-Truth Mining Events in the Western U.S. and its Implications for Discrimination Capability in Russia* 544

3-04 **Bonner, J., B. Stump, W. Walter, X. Yang, and M. Leidig**
*Empirical and Theoretical Seismic Energy Partitioning from Explosions Under Different Confinement and Media Conditions* 554

3-05 **Bonner, J., M. Leidig, K. Murphy, S. Dougherty, and R. Martin**
*Explosion Source Characteristics in Frozen and Unfrozen Rock* 563

3-06 **Bonner, J., R. Herrmann, M. Pasyanos, H. Benz, and D. Harkrider**
*Improving $M_S$ Estimates by Calibrating Variable-Period Magnitude Scales at Regional Distances* 573

3-07 **Fisk, M., S. Taylor, H. Patton, and W. Walter**
*Applications of a Next-Generation MDAC Discrimination Procedure Using Two-Dimensional Grids of Regional P/S Spectral Ratios* 583

3-08 **Ford, S., D. Dreger, and W. Walter**
*Identifying Isotropic Events Using a Regional Moment Tensor Inversion* 593

3-09 **Franks, J., B. Pope, R. Reed, M. Jezard, G. Kraft, S. Motlagh, S. LeClaire, M. Antolik, A. Henson, and K. Hutchenson**
*Extension of $M_S$(VMAX) to Global Paths* 603

3-10 **Hall, N.**
*Micro-Seismometers Via Advanced Mesoscale Fabrication* 610

3-11 **Hartse, H., G. Randall, and S. Arrowsmith**
*Regional Event Identification Research in Asia* 615

3-12 **Hong, T. and J. Rhie**
*Investigation of Regional Source Properties of the Underground Nuclear Explosion in North Korea* 625

3-13 **Leidig, M., P. Boyd, R. Martin, J. Lewkowicz, D. Richter, R. Garfield, J. Reid, and J. Bonner**
*Quantification of Rock Damage from Small Explosions and its Effect on Shear-Wave Generation: Phase I—Homogenous Crystalline Rock* 630

3-14 **Mayeda, K.**
*Small-Event Yield and Source Characterization Using Local P and S-Wave Coda Source Spectra* 640

3-15 **Patton, H.**
*Explosion Source Model Development in Support of Seismic Monitoring Technologies: New Models Accounting for Shock-Induced Tensile Failure* 649

3-16 **Salzberg, D.**
*Semi-Empirical Yield Estimates for the 2006 North Korean Explosion* 658

3-17 **Sammis, C., R. Biegel, and A. Rosakis**
*An Experimental Study of S Wave Generation by Fracture Damage in Underground Nuclear Explosions* 666

3-18 **Stead, R., H. Hartse, W. Phillips, and G. Randall**
*mb Bias and Regional Magnitude and Yield* 672

3-19 **Stevens, J. and H. Xu**
*Wave Propagation from Complex 3D Sources Using the Representation Theorem* 682

3-20 **Stevens, J., H. Xu, and G. Baker**
*Shear Wave Generation by Decoupled and Partially Coupled Explosions* 692

3-21 **Walter, W., M. Pasyanos, E. Matzel, R. Gök, J. Sweeney, S. Ford, and A. Rodgers**
*Regional Seismic Amplitude Modeling and Tomography for Earthquake-Explosion Discrimination* 702

# Seismic Regional Characterization and Wave Propagation

# CRUSTAL STRUCTURE OF THE IRAN REGION FROM IN-COUNTRY AND GROUND-TRUTH DATA

Eric A. Bergman[1], Eric R. Engdahl[1], Michael H. Ritzwoller[1], and Stephen C. Myers[2]

University of Colorado[1] and Lawrence Livermore National Laboratory[2]

Sponsored by Air Force Research Laboratory[1] and National Nuclear Security Administration[2]

Contract No. FA8718-08-C-0020[1] and DE-AC52-07NA27344[2]
Proposal No. BAA08-69

## ABSTRACT

We are investigating the crustal and upper mantle structure of the Iran region using in-country data sets of seismic phase arrival times, supplemented by ground-truth data sets developed from our previous research efforts. Other data sets from global, regional, and national bulletins in the region are being integrated as well. The in-country data sets, covering approximately the last 10 years of seismicity in the region, are being carefully reviewed for quality control, selectively re-picked, and combined with ground truth and other data sets for careful relocation of all seismic sources with magnitudes of approximately 2.5 and larger. Using these relocated sources with well-characterized uncertainties and the associated phase readings for crustal and regional phases, we perform forward modeling and tomographic inversion, under the assumption of isotropic velocities, to study the velocity structure and variability of the crust and upper mantle in this region. The resulting models and datasets will provide a well-characterized baseline for more detailed studies in the future. We are continuing efforts to discover and develop new ground truth data sets in this region.

We present some of the currently available data sets for this effort, along with preliminary tomographic inversion results based on them. We present a strategy for tomography based on ray-tracing in a region for which substantial variations in crustal thickness are expected, and using datasets that have different characteristics than those normally employed for this type of study. Through relative event relocation, clusters of events have very strong constraints on relative location, depth, and origin time. For each cluster, then, there will be only a single set of free parameters addressing uncertainty in location, depth, and origin time of the cluster's hypocentroid, rather than independent parameters for each event in the cluster. This dramatically reduces the number of free parameters in an inversion. Furthermore, we have a large dataset (~500) of events in calibrated clusters that qualify as GT5 or better. Arrival-time data from subsets of these events can be set aside for use in validation of models derived from tomography.

## OBJECTIVES

This research has the goal of developing in-country data sets that can be used to improve ground-based monitoring capabilities in the Iran region, by providing information needed to develop and test more accurate travel time models for seismic phases that propagate in the crust and upper mantle. The main data set to be produced is a bulletin of earthquakes in the region at magnitudes of 2.5 and higher, associated with readings from seismograph stations operating in-country for the period 1995–2005. These events and readings will be integrated with the best available catalog of regional seismicity for that period that includes associated regional and teleseismic phase-arrival times. All events will be relocated, carefully reviewed, and calibrated, where possible, with ground-truth data. We will conduct preliminary modeling experiments with these data, using Pn/Sn tomography to image broad-scale features of the crust and upper mantle in the region. The resulting data sets and model results will provide a solid foundation for further research.

## RESEARCH ACCOMPLISHED

We have only recently begun work on this project, but we have made progress in several areas related to data acquisition and using tomographic studies as a quality control method.

### ISC Data

We have begun integrating the latest International Seismological Centre (ISC) data release, from early 2004 through early 2006, with our existing catalog (Engdahl et al., 2008) of earthquakes in the study region. The ISC data add a large amount of data at far regional and teleseismic distances for events for which we previously held mainly in-country data. The expanded data set (Figure 1) will make it feasible to form new clusters of earthquakes for analysis with a multiple event relocation method that has been specialized for location calibration work. It also adds many Pn raypaths for events and/or station that are at the margins of our study area, which nevertheless add important coverage of the study area.

A

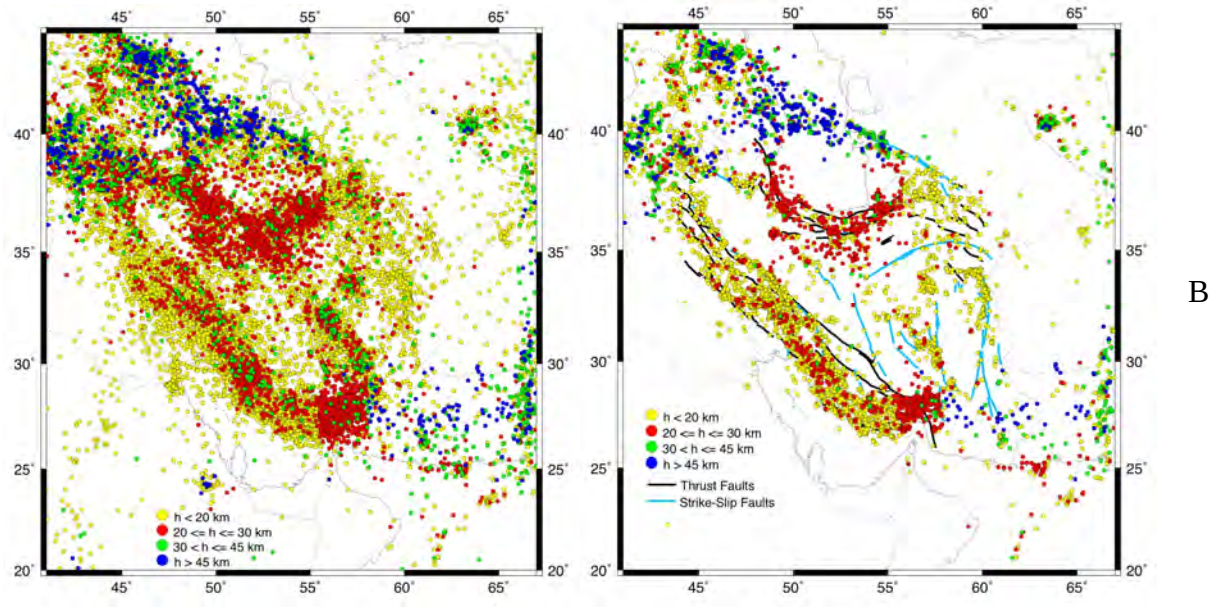


B

**Figure 1. A) Seismicity map (25,661 events from 1923-2008, M ≥ 2.5) of the study region color coded by depth, based on the new catalog of Engdahl et al. (2008). B) 7,592 events meeting a constraint on secondary azimuth gap (<180°, applied to stations at all distances), which greatly reduces location bias.**

For location calibration and tomographic research, we concentrate on events with better azimuthal coverage. In the study region, 7,592 events meet a criterion of having a secondary azimuth gap of less than 180° (stations at all distances), and these will be of the greatest use in our project (Figure 1B). The distribution of seismic stations is also of great importance to provide good azimuthal coverage for tomography (Figure 2). Station coverage in the eastern

(especially southeastern) part of the study region is still problematic, but new stations have been installed recently (or are planned) that should improve the coverage somewhat through the course of this project.

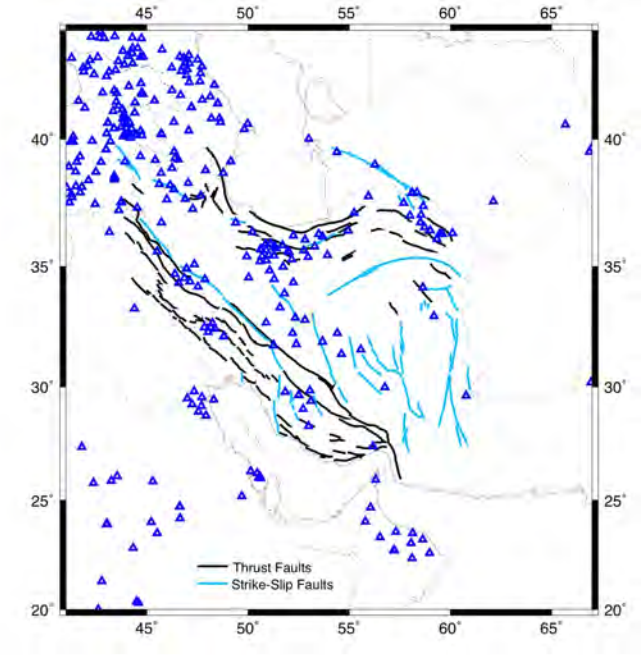


**Figure 2. Seismic stations for which we have phase readings in the study area.**

### In-Country Data

One of us (Bergman) traveled to the study region in June 2008 and acquired several data sets of relevance to this project. These include the full set of phase picks made for earthquakes in 2006, 2007, and early 2008 by in-country analysis for all events with a magnitude of 3.5 and larger, 809 events in all. We also acquired a data set of phase readings for earthquakes in the study area that were made at stations of the Oman seismograph network for 2004–2007. These data will provide very strong improvements in azimuthal coverage for seismic events in the southern portion of the study area.

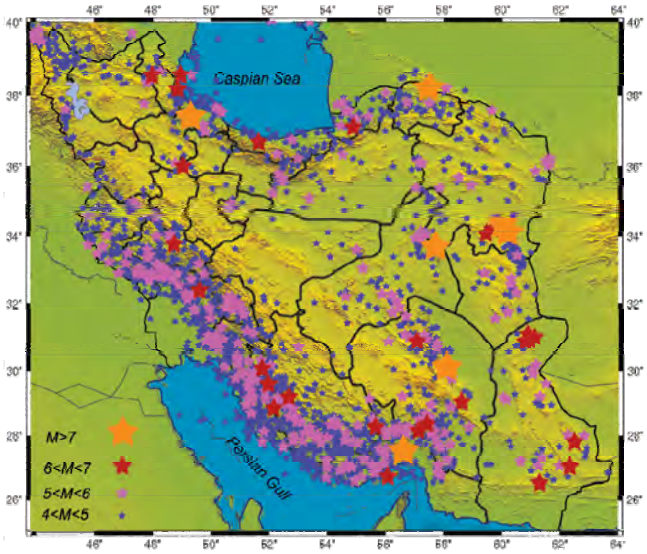


**Figure 3. Data from 2,760 events are available from a network of accelerometers. In almost all cases (except the largest events), the presence of data implies that an accelerometer station was within a few tens of kilometers of the event.**

We have also gained access to data from a network of ~1,000 accelerometers covering much of the study region, going back several decades (Figure 3). Because it is common for these stations to be found close to earthquakes of interest, these data provide exceptional depth resolution, and we expect this new data set to help greatly with our location calibration studies. Most of the accelerometer data has been recorded with uncalibrated timing systems, but we have successfully used S-P times to constrain the distance of events from the station. Since the stations are typically within a few tens of kilometers of recorded events, they provide a strong constraint on depth.

## Pn Tomography

We have begun developing our existing code for Pn tomography (Barmin et al., 2001) to meet the needs of the current project. As part of this process, we have conducted a preliminary inversion of our data set of Pn readings, which has been augmented by the recently-added ISC data for the period 2004–2006. We restrict the data set to raypaths between 2° and 9° to avoid complications with diving rays at greater epicentral distances. The distribution of stations and events used for this exercise is shown in Figure 4. The raypaths and raypath density distribution are shown in Figure 5. The central part of the study region is very well covered. Because of the scarcity of stations, the southeastern part of the study region is the least sampled.

A

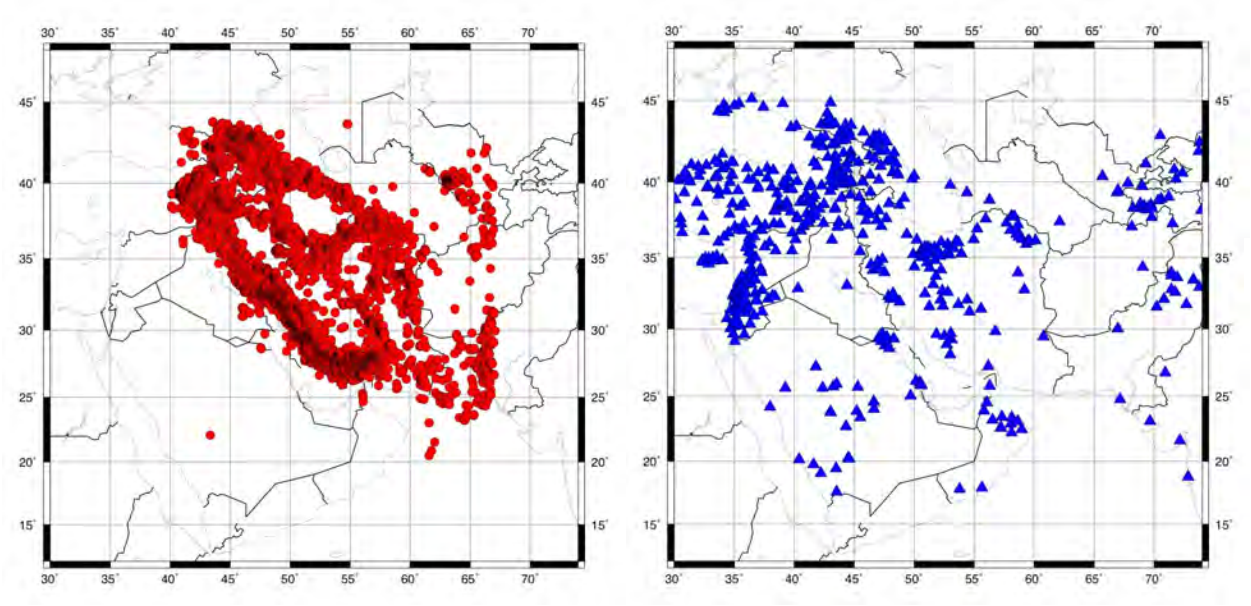

B

**Figure 4. 6,037 events (A) and 603 stations (B) used in a preliminary tomographic inversion using Pn phase readings with path lengths between 2° and 9°.**

The starting model for Pn tomography was CRUST5.1 (Mooney et al., 1998). Using a grid size of 0.5°, we solved for the best-fitting Pn velocity, holding crustal thickness fixed. The results are shown in Figure 6, compared to the results of Pn tomography for the same region by Ritzwoller et al. (2002), extracted from a larger-scale study that covered most of Eurasia. The latest tomographic study (Figure 6A) benefits from far more data from in-country stations than was available for the earlier study, and it is not surprising to see velocity variations at much shorter wavelengths in the new study. The velocity anomolies seen in the 2002 study are also seen in the recent study, but with higher resolution, and additional anomalies are revealed. It is likely, however, that much of the signal in Figure 6A is due to unmodelled variations in crustal thickness. This will be a central focus of our research.

A

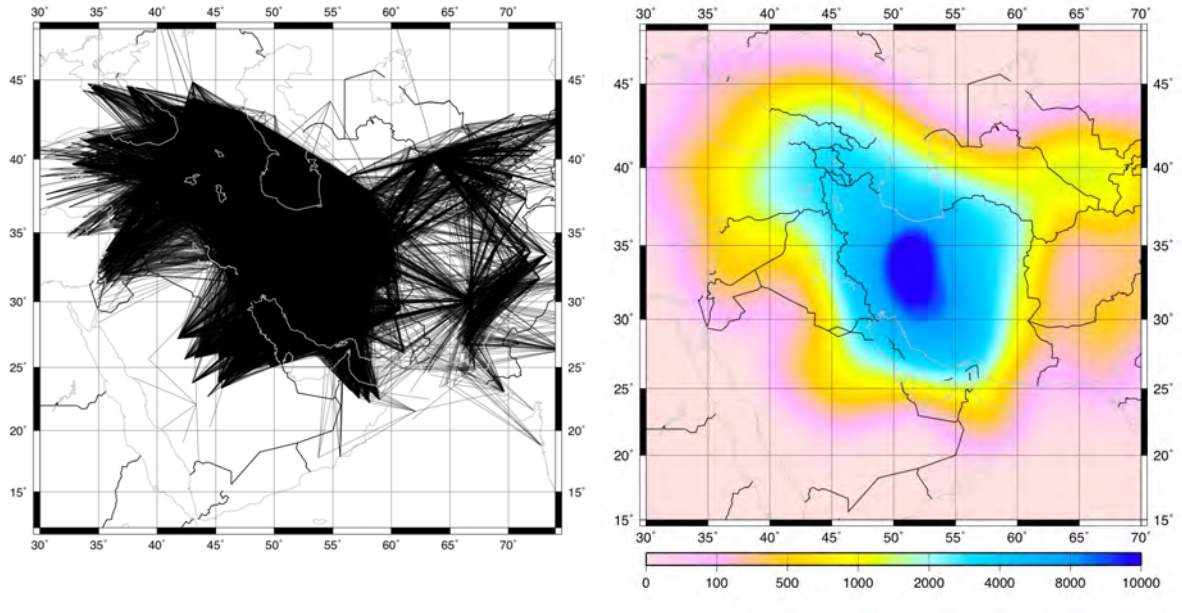


B

**Figure 5. A) 59,213 raypaths used in the preliminary Pn tomographic study. B) Ray path density.**

**Independent Constraints on Crustal Thickness**

For our Pn tomography it will be very useful to have independent information on crustal thickness in the study region. It is known that crustal thickness varies substantially across the region, and these variations are a major cause of variations in the travel times of seismic phases.

The effects of the continental collision between the Arabian Peninsula and Asia are evident in the heterogeneity of crustal structure in and around the study region. Recent studies report crustal thickness in the Arabian shield ranging from 32–37 km, thickening to 43–45 km in the foredeep basin of the Zagros Mountains (Gok et al., 2008). The increase in crustal thickness is attributed to the sediment load and downward flexure of the crust. To the northwest of the foredeep, folding and faulting in the Zagros Mountains is exposed at the surface and surface elevation steadily increases. However, crustal thickness remains relatively constant from the foredeep to the main Zagros thrust fault (Paul et al., 2006). From the main Zagros thrust to ~50-90 km northwest of the main Zagros thrust, the crust abruptly thickens to approximately 70 km, before returning to a thickness of ~42 km further to the northwest (Paul et al., 2006). Jackson et al. (2002) report even more dramatic variations in crustal thickness in the vicinity of the south Caspian basin. The crust in the south Caspian Basin proper is relatively thin (~30 km), but to the west and east the crust thickens dramatically to 60 km and 45+ km, respectively.

In our recent trip to the study region we consulted researchers who have assembled substantial data sets related to estimates of crustal thickness in the region (e.g., Mokhtari et al., 2004), and these data will be utilized in our Pn tomography both as constraints and for validation of tomographic results.

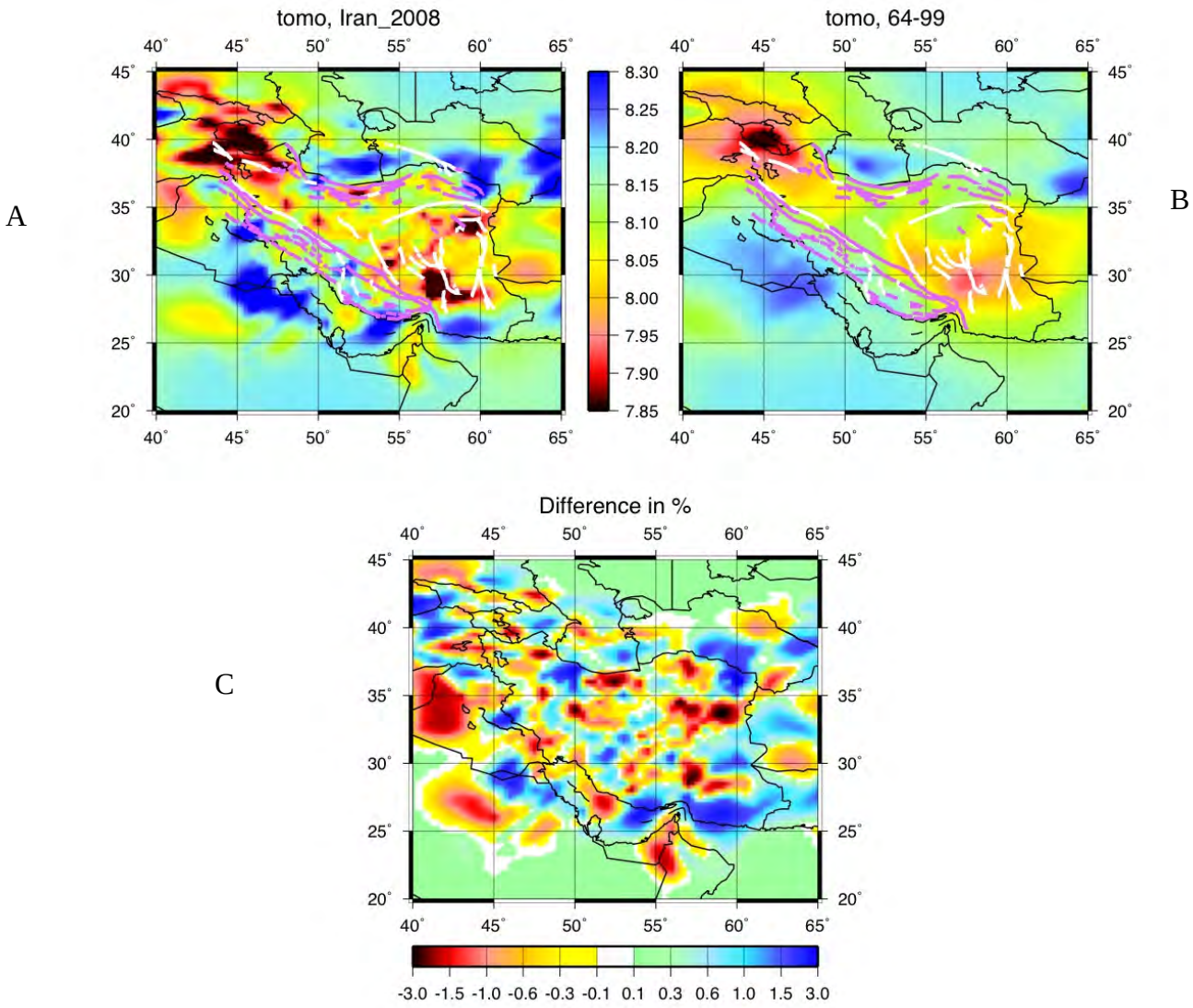


**Figure 6. A) Results of preliminary Pn tomography using our most recent data set, with crustal thickness fixed according to the CRUST5.1 model (Mooney et al., 1998). B) Result of Pn tomography by Ritzwoller et al. (2002), using a data set taken from the EHB catalog for the years 1964–1999, containing few in-country data. C) Difference (in percent) between the tomographic results shown in A and B.**

Our tomographic studies under this project will be most focussed on their use as a means of grooming the data set of earthquake locations and phase readings, for application to a variety of research strategies. However we also hope to make progress towards a better understanding of the variations of crustal thickness and velocities in the crust and upper mantle.

**Ground-Truth Studies**

We have recently completed a comprehensive study of ground-truth locations for earthquakes in the study area (Engdahl et al., 2008). The data set of more than 500 earthquakes with calibrated (at GT5 or better) locations and origin times will be of great value in the current study for validating our tomographic results. During the course of this project, we will continue to expand the ground truth database as the opportunity occurs, with special emphasis placed on acquiring ground truth in regions which are as yet poorly sampled. Access to new sets of in-country data,

as discussed above, and the ongoing occurrence of seismic activity in an increasingly more-densely instrumented region will ensure that such opportunities exist.

## CONCLUSIONS AND RECOMMENDATIONS

We have already had significant success in acquiring the in-country data on which this project is most dependent. In fact we have already acquired data with which we would be able to satisfy the technical requirements of this project. Nevertheless, with the continued development of working relationships with in-country seismologists and institutions we are optimistic of further progress and expect to continue acquiring important new data sets and auxilliary data that will further improve the data set available for studying the crustal and upper mantle structure of this complext region. We are planning a return trip to the study region in the fall of 2008 for this purpose.

## REFERENCES

Barmin, M. P., M. H. Ritzwoller, and A. L. Levshin (2001). A fast and reliable method for surface wave tomography, *Pure Appl. Geophys.* 158: 1351–1375.

Engdahl, E. R., E. A. Bergman, S. C. Meyers, and F. Ryall (2008). Improved ground truth in southern Asia using in-country data, analyst waveform review, and advanced algorithms, these Proceedings.

Jackson. J., K. Priestley, M. Allen, and M. Berberian (2002). Active tectonics of the South Caspian Basin, *Geophys. J. Int.* 148: 214–245.

Paul, A., A. Kaviani, D. Hatzfeld, J. Vergne, and M. Mokhtari (2006). Seismological evidence for crustal-scale thrusting in the Zagros mountain belt (Iran), *Geophys. J. Int.* 166**:** 227–237

Gok, R., H. Mahdi, H. Al-Shukri, and A. Rodgers (2008). Crustal structure of Iraq from receiver functions and surface wave dispersion: implications for understanding the deformation history of the Arabian-Eurasian collision**.** *Geophys. J. Int.* 172: 1179–1187.

Mokhtari, M., A. M. Farahbod, C. Lindholm, M. Alahyarkhani, and H. Bungum (2004). An approach to a comprehensive Moho depth map and crust and upper mantle velocity model for Iran, *Iranian Int. J. Sci.* 5: 2, 223–244.

Mooney, W.D., G. Laske, and T.G. Masters (1998). CRUST 5.1: A global crustal model at 5° × 5°, *J. Geophys. Res.* 103: 727–747.

Ritzwoller, M. H., M. P. Barmin, A. Villaseñor, A. L. Levshin, and E. R. Engdahl. (2002). Pn and Sn tomography across Eurasia to improve regional seismic event locations, *Tectonophysics* 358: 39–55.

# PREDICTING EXPLOSION-GENERATED *Sn* AND *Lg* CODA USING SYNTHETIC SEISMOGRAMS

Jessie L. Bonner, Anastasia Stroujkova, and Kevin M. Mayeda

Weston Geophysical Corporation

Sponsored by National Nuclear Security Administration

Contract No. DE-AC52-05NA26610
Proposal No. BAA05-59

## ABSTRACT

Recent examinations of the characteristics of coda-derived *S* and *Lg* spectra for yield estimation have shown that the spectral peak of Nevada Test Site (NTS) explosion spectra is depth-of-burial dependent, and that this peak is shifted to higher frequencies for Lop Nor explosions at the same depths. To confidently use coda-based yield formulas, we need to understand and predict coda spectral shape variations with depth, source media, velocity structure, topography, and geological heterogeneity.

We are in the final year of a synthetic seismogram study to evaluate the characteristics of *Lg* coda generated from explosions and earthquakes. To meet our objectives, we have developed a deterministic model for the western United States and the NTS. In order to generate coda in our 2D and 3D pseudospectral simulations, heterogeneity was added in the crust and/or upper mantle. Three parameters—correlation length, Hurst number (H), and fractional velocity perturbation of the heterogeneities—are used to construct different realizations of random media. We have estimated the heterogeneity parameters for the NTS using available seismic and geologic data. Lateral correlation, variance and coherence measures between seismic traces are estimated from clusters of nuclear explosions and well-log data. The horizontal von Karman correlation length estimated for nuclear explosion *Lg* phases is between 0.4–1.1 km, with Hurst numbers between 0.3 and 0.6. A dominant heterogeneity dimension of 0.5–1.8 km results in best *Lg* coda coherence at frequencies between 1 and 4 Hz.

Examples of the *Lg* and *Lg* coda synthetics produced by these models resemble NTS earthquake and explosion waveforms; however, there is a considerable non-uniqueness problem that must be addressed. We investigated methods for quantifying our synthetics in order to assure that simulated waveforms have similar characteristics as observed coda and direct *Lg*. One such characteristic is that the Q estimates for direct *Lg* and its coda are typically observed to be near equivalent in many tectonic settings. For example, near the NTS, $Q_{Lg}$ (direct) and $Q_{Lg}$ (coda) typically range between 200–300. Thus, we have compared the Q values of synthesized *Lg* coda and direct *Lg* from models with different attenuation structures. These structures range from constant shear wave Q (e.g., $Q_{\beta}$=200 or 500) throughout the crust to published, depth-dependent models for the Basin and Range. We examined the effect of the location of the stochastic variations (e.g., within the entire crust, above the middle crust, or only in the upper crust) on the $Q_{Lg}$ (direct) and $Q_{Lg}$ (coda) estimates obtained from the synthetics. The comparison of the variations in Q estimates for different source types (e.g., earthquakes and explosions) at different depths suggests that our stochastic models produce realistic 1 Hz estimates of $Q_{Lg}$ (direct) and $Q_{Lg}$ (coda) for published Basin and Range attenuation models. Estimates for the frequency dependence of the synthetic coda are relatively high compared to observed data.

We are currently using these calibrated stochastic models to generate regional-distance synthetics for monopole explosions at depths ranging from 0.1 to 1 km for all test site models. We have superposed secondary source effects, such as a compensated linear-vector dipole (CLVD) source, on the monopole synthetics. We are now deriving *Sn* and *Lg* coda spectra from the synthetics, estimating moments and yields from these spectra, and comparing them to observed data from NTS. If successful, this synthetic method may be used to estimate the *S* and *Lg* coda properties for yield estimation of explosions at either historical test sites or for broad, uncalibrated regions where we will likely have little information on velocity structure.

## OBJECTIVES

We are attempting to determine why the current mechanisms for *Sn* and *Lg* generation from explosions often produce stable coda magnitudes that are transportable between test sites. We aim to understand and predict *Lg* and *Sn* coda spectral shapes with variations in source depth, material properties, velocity structure, and geological heterogeneity.

Our investigation objectives include the following:

1) Compilation and parameterization of seismic velocity models consisting of deterministic material models with stochastic perturbations;

2) Estimation of the effect of deterministic and stochastic model parameters on *Lg* propagation using synthetic waveforms generated by the Generalized Fourier Method (GFM) (Orrey, 1995);

3) Calibration of stochastic variations at each test site using nearby earthquake data; and

4) Calculation of 2D/3D synthetics for composite explosion source models of varying depths and moments for each test site.

During the past year, we have worked on all four of our above objectives and are near completion of the project. If these methods prove to be successful for explaining the characteristics of explosion-generated direct *Lg* and *Lg* coda at the NTS, we plan to test the transportability of these modeling techniques at the Shagan, Degelen, Novaya Zemlya, and Lop Nor test sites.

## RESEARCH ACCOMPLISHED

### Modeling Direct *Lg* and *Lg* Coda Q in the Basin and Range

The objective of our research is to determine if numerical modeling of *Lg* and its coda can replicate the depth-dependent spectral peaking observed at the NTS (Murphy et al., in review). In order to complete this task, we have developed a velocity and attenuation model for the NTS and are currently calibrating the stochastic parameters of the model.

**Velocity Model.** The background deterministic velocity structure for NTS (Figure 1) is based on a regional model for the Basin and Range similar to the model developed by Benz et al. (1991). The velocities in the upper crust are based on borehole data, geologic and gravity data, refraction studies and seismic experiments (McLaughlin et al. 1983; Stump and Johnson, 1984; Ferguson et al., 1994; Stevens et al., 1991). We have used various techniques to estimate stochastic parameters for the Basin and Range. This includes using previous well-located nuclear explosions to estimate correlation lengths for scattering of the *Lg* phase (Tibuleac et al., 2005, 2006). These results suggest that the horizontal correlation (Ay) lengths for a von Karman stochastic model range between 0.5 - 1 km with smaller vertical correlation (Az) lengths. The H numbers are related to the fractal dimension of the medium and range between 0.3 and 0.6. Figure 1 shows the results of converting the deterministic velocity model for the NTS region into a stochastic model for generating direct *Lg* and its coda.

**Attenuation Models.** We have considered different intrinsic background attenuation models in our numerical modeling exercises, ranging from constant shear wave Q models to published Q models for the western United States. Bonner et al. (2007) measured $Q_{Lg}$ (direct) and $Q_{Lg}$ (coda) from synthetics propagated through a constant shear wave Q model (e.g., $Q_\beta$ = 200 or 500) for the entire crust. Their modeling suggested that $Q_{Lg}$ (direct) typically ranged between the values of $Q_\beta$ and $Q_a$ for models without stochastic variations. Stochastic variations lowered the apparent $Q_{Lg}$ (direct); however, it was troubling that the measured $Q_{Lg}$ (direct) and $Q_{Lg}$ (coda) were never approximately the same. A comparison of regionalized Q maps often shows the near-equivalence of these two estimates of attenuation.

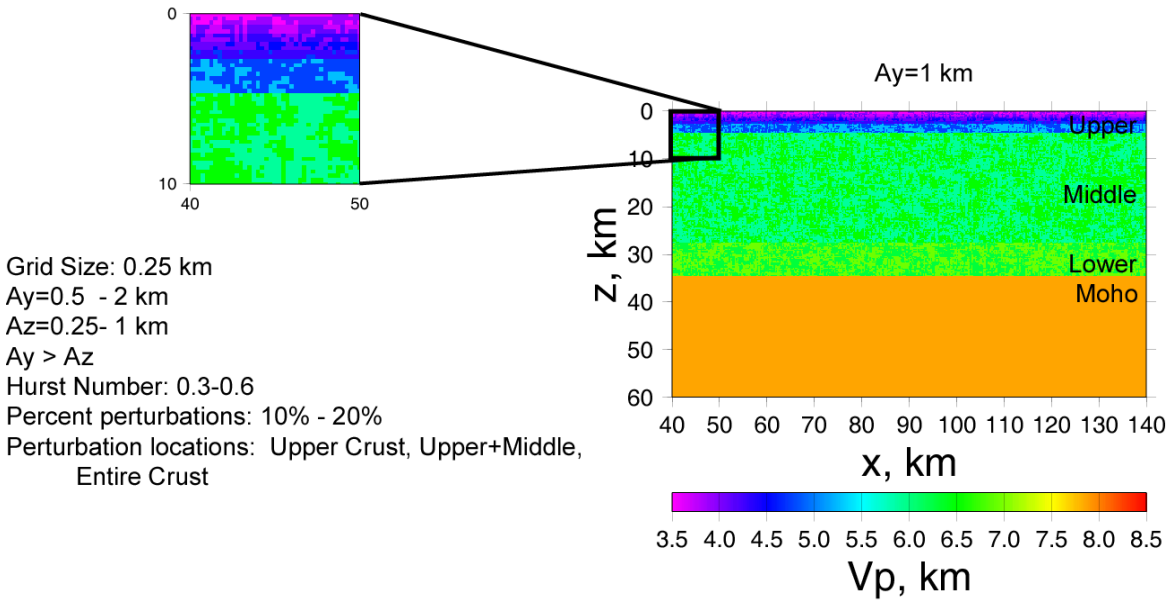


**Figure 1. Example of a 2D stochastic model for the NTS used to model $Q_{Lg}$ (direct) and $Q_{Lg}$ (coda) in this study. Also listed are the variations in Ay, Az, Hurst number, and perturbation magnitude and location used to make different models for testing.**

In this paper, we examine synthetics propagated through two published Q models for the Basin and Range. The Patton and Taylor (PT) (1984) model is characterized by low $Q_\beta$ (85–172) throughout the entire crust. Similarly, the Mitchell and Xie (MX) (1994) model has low $Q_\beta$ in the upper crust (50–80); however, they suggest high $Q_\beta$ in the middle to lower crusts (400–1000). We incorporated these two Q models into our deterministic and stochastic models (Figure 1) for the NTS and computed synthetics for earthquakes using the GFM (Orrey, 1995).

**Methodology.** Record sections of GFM synthetic waveforms generated by four different perturbations of our NTS model are shown in Figure 2, including deterministic (e.g., without stochastic heterogeneity) and stochastic (Ax = 1, Az = 0.5) versions for both the PT and MX attenuation models. The appearance of the synthetics with stochastic variations compares favorably with observed waveforms from earthquakes and explosions in the Basin and Range (see Tibuleac et al., 2005, 2006 for additional examples).

**Direct *Lg* Q Estimation.** We windowed the direct *Lg* arrivals between 3.6 and 3.0 km/sec and estimated the spectral amplitudes A at each station at distance *R*. We used a cosine taper and smoothed the spectra in order to reduce the variance between the stations. For each frequency *f* we used the following equation (Mitra et al., 2006):

$$\log_{10} A + 0.5 \log_{10} R = \log_{10} S - \frac{\pi f \log_{10} e}{vQ} \qquad (2)$$

to solve for *Q(f)*. For each frequency, we plotted $\log_{10} A + 0.5 \log_{10} R$ versus *R* and performed a linear regression to determine Q. We used a velocity (v) of 3.5 km/sec for the direct *Lg* arrival. Plots of the Q as a function of frequency are then used to estimate the Q at 1 Hz ($Q_o$) and the frequency dependence (η) (see Figure 3). Because of the grid size and velocities in our models, our simulations are only valid at frequencies less than 2–3 Hz.

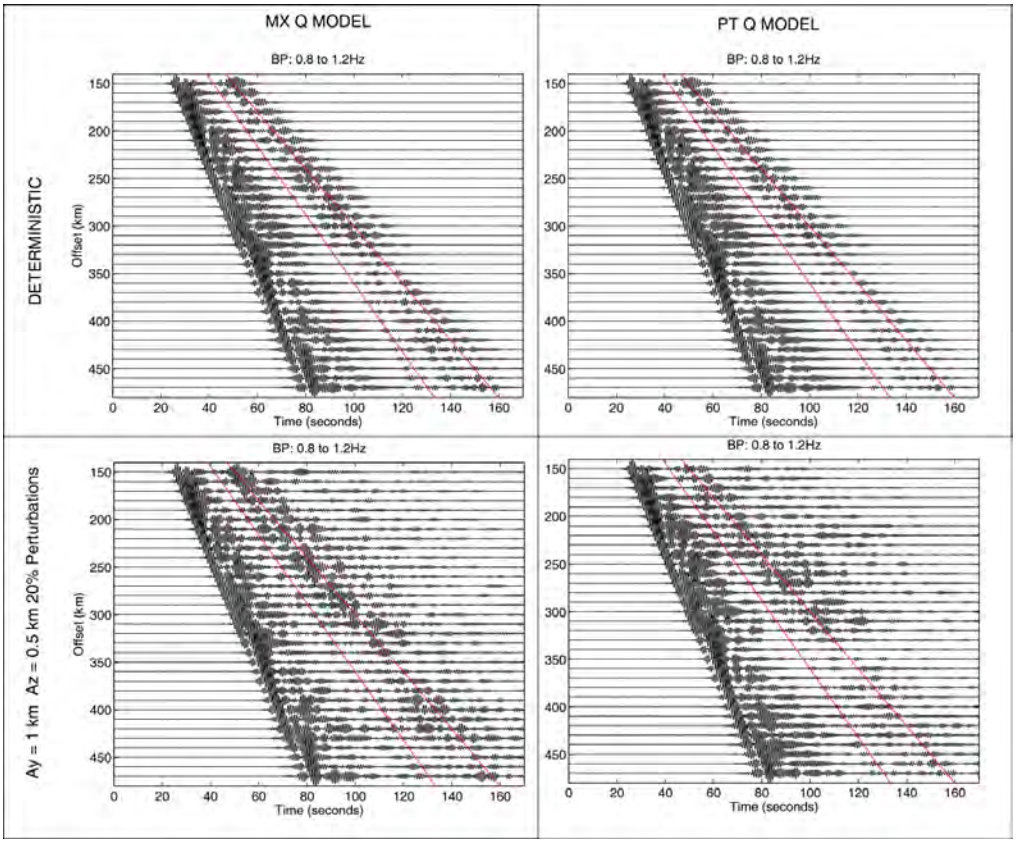


**Figure 2. GFM Synthetic waveforms filtered near 1 Hz for deterministic (Top Row) and stochastic (Bottom Row) models for the NTS. Synthetics in the left column were propagated through the Mitchell and Xie (1994) Q model while the Patton and Taylor (1984) Q model was used to attenuate the synthetics in the right column.**

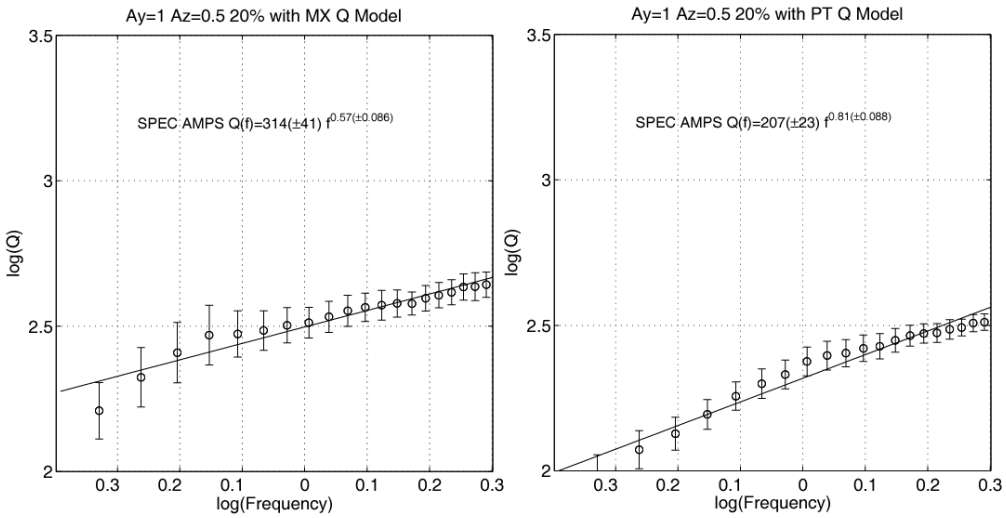


**Figure 3. Estimating $Q_{Lg}$ (direct) from synthetics. (Left) Regression of log Q versus frequency for *Lg* propagated through a stochastic NTS model with the Mitchell and Xie (1994) shear-wave Q model. (Right) Same as left except for use of Patton and Taylor (1984) Q model. There appears to be two different trends (above and below 1 Hz); however, for this study, we can fit most of the data plus error with a single line.**

Given the non-uniqueness associated with synthetic modeling efforts similar to this, we decided to determine if our GFM synthetics have similar characteristics as observed coda and direct *Lg*. In the remaining sections, we compute the apparent $Q_{Lg}$ (direct) and $Q_{Lg}$ (coda) values for the synthetics using different Q models for comparison to observed estimates in the Basin and Range.

***Lg* Coda Q Estimation.** To estimate $Q_{Lg}$ (coda) , we used the stacked spectral ratio (SSR) method of Xie and Nuttli (1988). In this method, amplitude spectra for windows at different times within the synthetic coda are used to form spectral ratios. The ratios are corrected for velocity and geometrical spreading, stacked, and regressed versus frequency to determine the coda Q at 1 Hz ($Q_o$) and the frequency dependence ($\eta$). Examples of the SSR analysis on synthetic data are shown in Figure 4.

**Results.** Table 1 provides measured $Q_{Lg}$ (direct) and $Q_{Lg}$ (coda) in the Basin and Range from previous studies. These results suggest that both the direct and coda Q for the *Lg* phase recorded in this region should range between 200-300 with $\eta$ between 0.40 and 0.80. Table 2 and Figure 5 show the results of measuring the direct *Lg* Q and *Lg* coda Q for synthetics propagated through our different deterministic and stochastic models for the Basin and Range. Without the presence of stochastic variations, GFM synthetics in an XM Q model do not produce $Q_{Lg}$ (direct) values that match the measured estimates for the Basin and Range. However, with 20% stochastic variations added to the model, the XM Q model produces synthetics with $Q_{Lg}$ (direct) and $Q_{Lg}$ (coda) that fall within the range of observed data. The synthetic $Q_{Lg}$s (direct) for all PT models were within the measured range; however, adding 20% variations resulted in $Q_{Lg}$ (coda) estimates that were slightly below observed. Unfortunately, our synthetics do not reproduce the observed $Q_{Lg}$ (coda) frequency dependence $\eta$ no matter which Q model is used. In the coming months, we hope to determine the reason for this discrepancy, which could include the effects of using 2D versus 3D models as well as possible need for frequency-dependent intrinsic attenuation in the model.

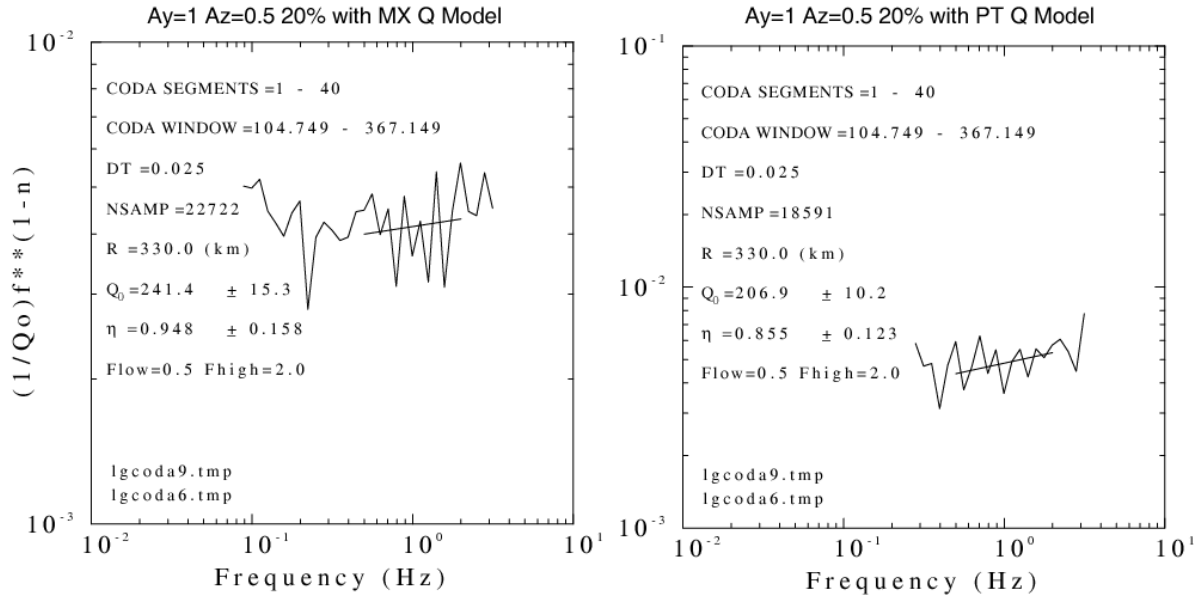


**Figure 4. SSR method (Xie and Nuttli, 1988) applied to synthetic waveform data for *Lg* coda Q estimation for a stochastic model with Mitchell and Xie (left) and Patton and Taylor attenuation (right).**

**Table 1. Observed $Q_{Lg}$ (direct) and $Q_{Lg}$ (coda) for the Basin and Range**

| Q Study | $Q_{Lg}$ (direct) | $Q_{Lg}$ (coda) | *Lg* $Q_o$ (direct) | η |
|---|---|---|---|---|
| Singh and Herrmann (1983) | | 200-300 | | 0.40-0.60 |
| Chavez and Priestley (1986) | 214 ± 15 | | | 0.54 |
| Xie and Mitchell (1990) | 267 ± 56 | 275 ± 26 | | |
| Baqer and Mitchell (1998) | | 250-300 | | 0.40-0.60 |
| Benz et al. (1997) | 235 ± 11 | | | 0.56 ± 0.04 |
| Aleqabi and Wysession (2006) | | | 234-312 | 0.40-0.80 |

**Table 2. Synthetic $Q_{Lg}$ (direct) and $Q_{Lg}$ (coda) for Basin and Range models**

| | $Q_{Lg}$ (direct) | | | | $Q_{Lg}$ (coda) | | | | Stochastic Parameters | | | |
|---|---|---|---|---|---|---|---|---|---|---|---|---|
| MODEL | Lg $Q_o$ | Error | η | Error | CODA $Q_o$ | Error | η | Error | Q Model | Ay | Az | Percent |
| 1 | 225 | 22 | 1 | 0.05 | 214 | 13 | 1.1 | 0.1 | PT | 1 | 0.5 | 10% |
| 2 | 207 | 23 | 0.81 | 0.09 | 195 | 12 | 0.92 | 0.09 | PT | 1 | 0.5 | 20% |
| 3 | 253 | 26 | 0.9 | 0.05 | 208 | 16 | 1.16 | 0.1 | PT | 1 | 0.25 | 10% |
| 4 | 207 | 21 | 0.96 | 0.03 | 197 | 9 | 0.88 | 0.08 | PT | 1 | 0.25 | 20% |
| 5 | 267 | 22 | 1.3 | 0.21 | --- | -- | ---- | ---- | PT | --- | ---- | --- |
| 6 | 385 | 51 | 0.69 | 0.04 | 263 | 25 | 1.11 | 0.11 | XM | 1 | 0.5 | 10% |
| 7 | 314 | 41 | 0.57 | 0.07 | 237 | 20 | 0.84 | 0.11 | XM | 1 | 0.5 | 20% |
| 8 | 370 | 59 | 0.98 | 0.07 | 251 | 20 | 1.17 | 0.1 | XM | 1 | 0.25 | 10% |
| 9 | 310 | 31 | 1.1 | 0.06 | 233 | 13 | 0.91 | 0.1 | XM | 1 | 0.25 | 20% |
| 10 | 632 | 127 | 1 | 0.05 | --- | -- | ---- | ---- | XM | --- | ---- | --- |

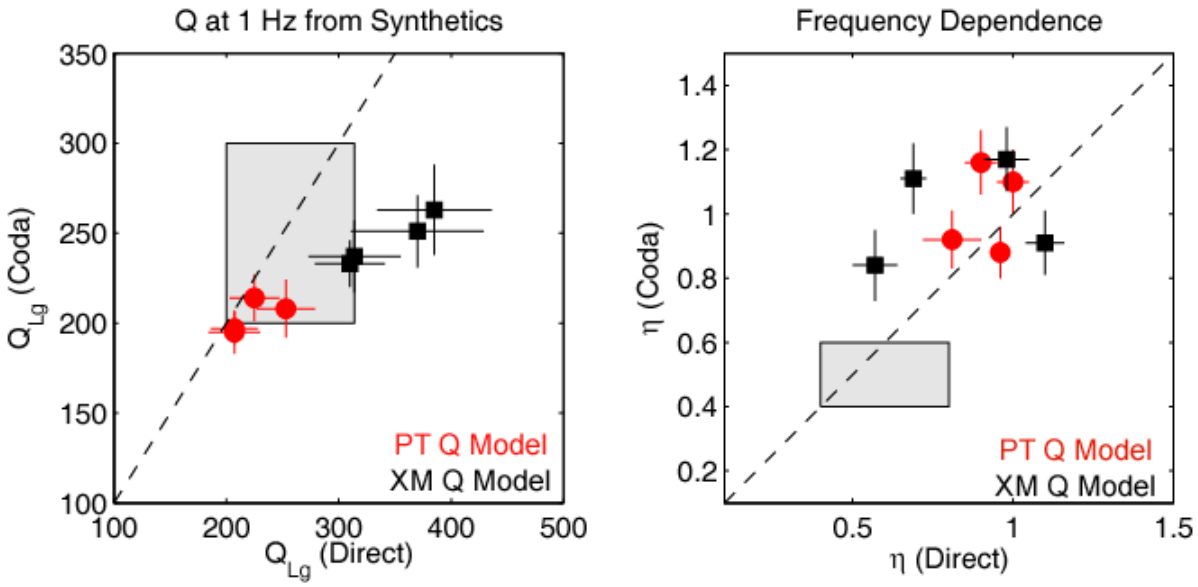


**Figure 5. $Q_o$ (left) and η (right) determined for *Lg* synthetics from Basin and Range stochastic models compared to observed estimates (shaded regions).**

**Modeling NTS Explosion-Generated Coda.** The earthquake simulations using the Patton and Taylor (1994) Q model for the Basin and Range together with various stochastic perturbations provide $Q_{Lg}$ (direct and coda) estimates that best match observed data (Table 2). We generated explosion synthetics for PT models 1-4 and

compared them to NTS nuclear explosions recorded at station MNV (distance ~230 km). Figure 6 shows a comparison of the MNV recordings of the NTS event Brie compared with synthetics for Model 1. Model 1 consists of the PT Q model and stochastic variations up to 10% with correlation distances of 1.0 to 0.5 km. The synthetics and observed data were normalized to their maximum *Pg* amplitudes. Brie was detonated a depth of less than 250 meters (Murphy et al., in review); therefore, we placed our monopole explosion source at a depth of 250 meters in order to compute the synthetics. The synthetics are valid at frequencies less than 2-3 Hz, and both the observed and synthetic waveforms in Figure 6 have been bandpass filtered between 0.1 and 2 Hz.

A quick glance of the waveforms in Figure 6a might suggest good agreement between the observed and synthetic arrivals. The *Pn* and *Pg* arrivals show very good correlation in both relative amplitude and arrival times. We note that the *Lg* arrival (green box) is not as pronounced in the synthetic waveform as it is in the observed data, and that the synthetic coda (blue box) has higher frequency content and more rapid amplitude decay than the observed data. This is also shown by the coda spectra in Figure 6b which shows a large amplitude peak near 0.9 Hz in the observed data that is missing from the synthetic coda.

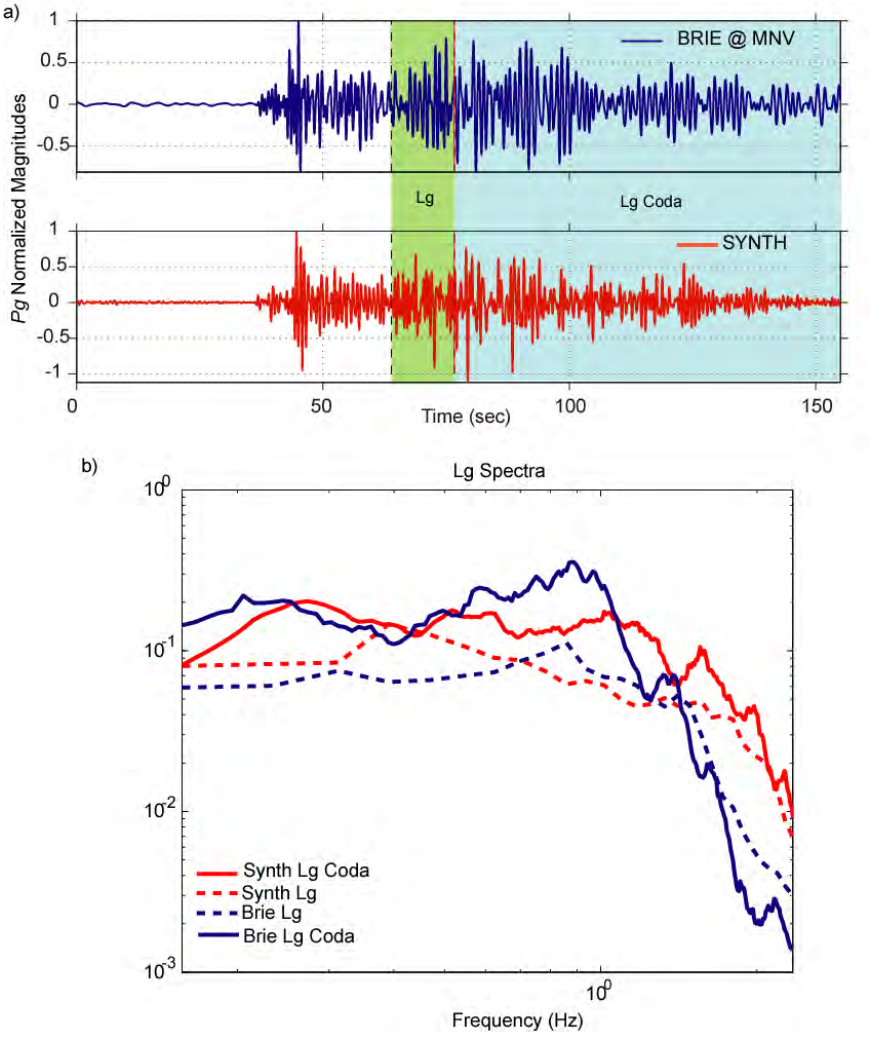


**Figure 6. Explosion synthetics and data. a). Comparison of observed waveforms for the NTS explosion Brie recorded at NTS compared to GFM synthetics for the explosion using Model 1 from Table 2. The time windows for *Lg* and *Lg* coda (green and blue boxes, respectively) were used to compute spectra (b).**

The correlation distances for the Model 1 perturbations were 1 and 0.5 km, and the results shown in Figure 6 suggest that coda energy at frequencies less than 1 Hz was being scattered too rapidly when compared to observed data. By decreasing the correlation distance from 0.5 to 0.25 km, we should decrease the rapid scattering below 1 Hz. This is confirmed in the seismograms and spectra for simulations using Model 4 (Figure 7). The simulations for Model 4 have increased energy near 1 Hz in the first 25 seconds of the coda analysis window compared to the synthetics shown in Figure 6. We note peaks in the synthetic and observed spectra between 0.9 and 1 Hz (Figure 7b). These synthetics provide an excellent comparison to the observed data for the *P*, *P* coda, direct *Lg*, and early coda arrivals. Our synthetics do not do an adequate job of modeling the observed coda at periods less than 0.7 Hz at onset times greater than 120 seconds (see Figure 8), which may be the result of reaching the limit of our 2D coda modeling methods. The later arriving coda may be multi-pathing from structures away from the direct path, which can not be effectively modeled using only 2D profiles. In the remaining months of the project, we will also add a CLVD source to the monopole explosion to see if the addition of more short-period surface-wave energy could improve the match between observed and synthetic coda.

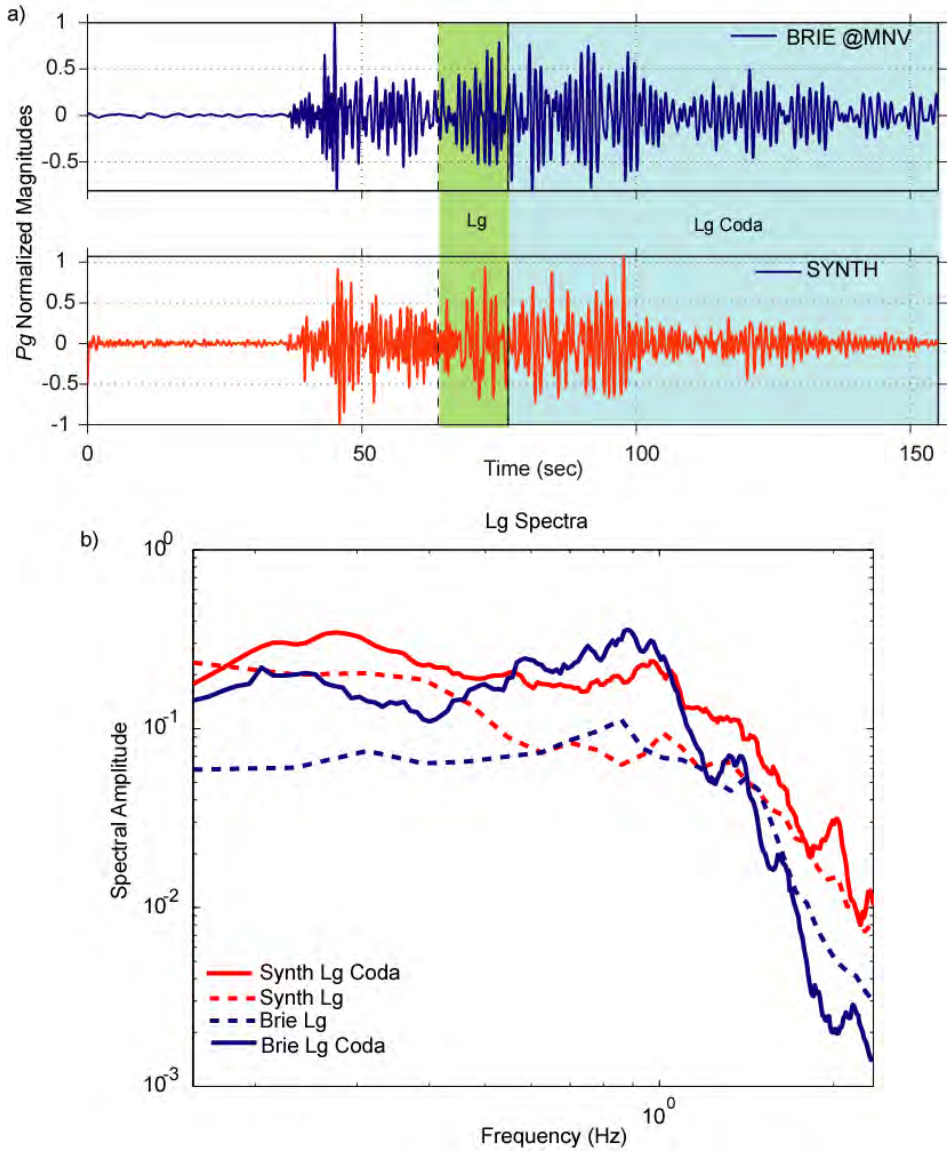


**Figure 7. Explosion synthetics and data. a) Comparison of observed waveforms for the NTS explosion Brie recorded at NTS compared to GFM synthetics for the explosion using Model 4 from Table 2. The time windows for *Lg* and *Lg* coda (green and blue boxes, respectively) were used to compute spectra (b).**

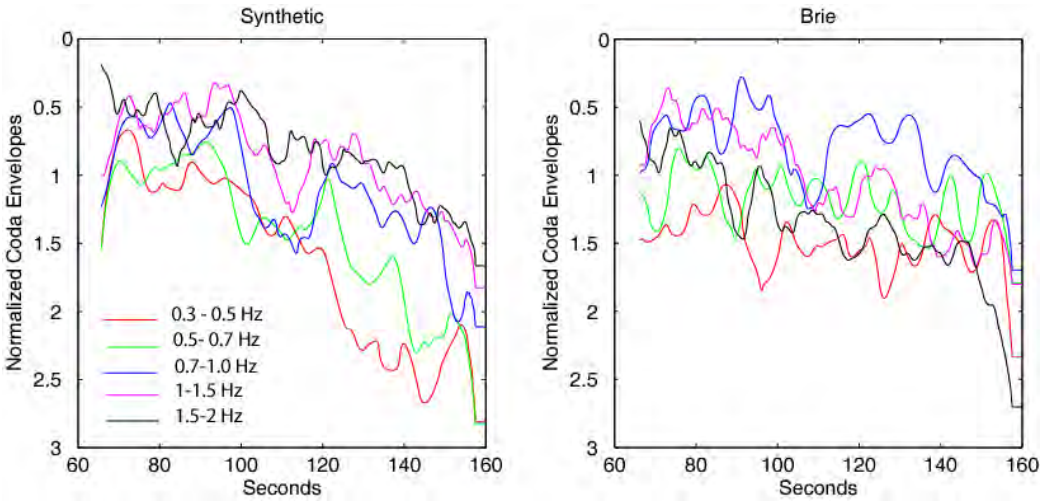


**Figure 8. A comparison of the coda envelopes for the Model 4 synthetics (left) and observed explosion seismograms (right) for five narrow bands between 0.3 to 2 Hz.**

## CONCLUSIONS AND RECOMMENDATIONS

Our objective is to try to develop synthetic seismograms for *S*-wave coda from explosions. The ability to accurately model direct *Lg* and *Lg* coda using accurate earth models (both velocity and attenuation) will be important for regions in which explosion calibration data do not exist. Our results for NTS suggest we can numerically model direct *Lg* and *Lg* coda that have similar attenuation and propagation characteristics as observed data. We can do so using literature-based velocity and attenuation models and standard estimates for correlation lengths. We also have modeled explosion-generated coda that have attributes such as peak frequency and relative amplitudes that sometimes closely match observed nuclear explosion data, especially for the early onset arrivals in the coda windows.

Currently, our models do not produce realistic estimates of the frequency dependence for *Lg* coda in the Basin and Range. Aki (1969) described the coda as the result of backscattered waves from numerous heterogeneities distributed randomly and uniformly in the crust and upper mantle within an ellipse. Based on his definition, the scattering that creates the coda is from 3D phenomena; this suggests our initial modeling in 2D may never provide us with a perfect match between observed and synthetic coda. In order to achieve a model where the synthetic coda matches the observed, we may have to consider 3D models; however, this will ultimately either increase the computation time greatly or decrease the resolvable frequency bandwidth to below 1 Hz. Example synthetics for *Lg* and *Lg* coda from our first attempts at incorporating 3D stochastic models are shown in Figure 9.

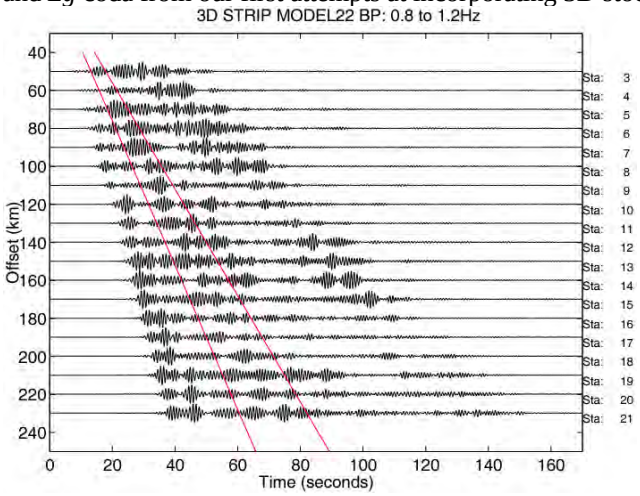


**Figure 9. GFM synthetics in a 3D stochastic velocity model. The *Lg* group velocity window is outlined using the red lines.**

## REFERENCES


Aki, K. (1969). Analysis of seismic coda of local earthquake as scattered waves, *J. Geophys. Res*. 74: 615–631.

Aleqabi, G.I. and M.E. Wysession (2006). $Q_{Lg}$ distribution in the Basin and Range province of the western United States. *Bull. Seism. Soc. Am*. 96: 384–354.

Baqer, S., and B. J. Mitchell (1998). Regional variation of *Lg* coda *Q* in the continental United States and its relation to crustal structure and evolution, *Pure Appl. Geophys.* 153: 613–638.

Benz, H. M., Unger, J. D., Leith, W. and V. Ryaboy (1991). The Norilsk DSS Profile in Northern Siberia: Interpretation of the velocity structure and comparison with Basin and Range and New England profiling results, Abstracts of the 13th Annual PL/DARPA Seismic Research Symposium: 85–100.

Benz, H. M., A. Frankel, and D. M. Boore (1997). Regional *Lg* attenuation for the continental United States, *Bull. Seism. Soc. Am.* 87: 606–619.

Bonner, J. L., K. Priestley, I. Tibuleac, and A. Stroujkova (2007). Estimating *Lg* coda Q on synthetic seismograms, Abs. *Seism. Res. Letts.* 78: 307.

Chavez, D. E., and K. F. Priestley (1986). Measurement of frequency dependent *Lg* attenuation in the Great Basin, *Geophys. Res. Lett.* 13**:** 551–554.

Ferguson, J.F., A.H. Cogbill, and R.G. Warren (1994). A geophysical-geological transect of the Silent Canyon caldera complex, Pahute Mesa, Nevada, *J. Geophys. Res.* 99: 4323–4339.

McLaughlin, K.L, L. R. Johnson, and T.V. McEvilly (1983). Two-dimensional array measurements of near-source ground accelerations. *Bull. Seism. Soc. Am.* 73: 349–375.

Mitchell, B.J., and J. Xie (1994). Attenuation of multiphase surface waves in the Basin and Range province, part III: Inversion for crustal anelasticity, *J. Geophys. Int*. 116: 468 -484.

Mitra, S. K. Priestley, V.K. Gaur, and S.S. Rai (2006). Frequency-dependent *Lg* attenuation in the Indian platform, *Bull. Seism. Soc. Am*. 96: 2449 -2456.

Murphy**,** K. R., K. Mayeda**,** and W. R. Walter (in review). Coda Spectral Peaking for Nevada Nuclear Test Site Explosions, submitted to *Seism. Soc. Am.*

Orrey, J. L. (1995). A generalized Fourier pseudospectral method for elastodynamics . Ph. D. Thesis. University of Colorado, Boulder.

Patton, H. J. and S. R. Taylor (1984). Q structure of the Basin and Range from surface waves, *J. Geophys. Res.* 89: 6929–6940

Singh, S. K., and R. B. Herrmann (1983). Regionalization of crustal coda *Q* in the continental United States, *J. Geophys. Res.* 88**:** 527–538.

Stevens, J. L., T. G. Berker, S. M. Day, K. L. McLaughlin, N. Rimer, and B. Shkoller (1991). Simulation of teleseismic body waves, regional seismograms, and Rayleigh wave phase shifts using two-dimensional, nonlinear models of explosion sources, *Explosion Source Phenomenology, Geophysical Monograph* 65: American Geophysical Union: 239–252.

Stump, B. W., and L. R. Johnson (1984). Near-field characterization of contained nuclear explosions in tuff, *Bull. Seism. Soc. Am.* 74: 1–26.

Tibuleac, I. M., A. Stroujkova, J. L. Bonner and K. Mayeda (2005). Predicting explosion generated *Lg* and *Sn* using synthetic seismograms, in *Proceedings of the 27th Seismic Research Review: Ground-Based Nuclear Explosion Monitoring Technologies*, LA-UR-05-6407, Vol. 1, pp. 214–221.

Tibuleac, I. M., A. Stroujkova, J. L. Bonner, K. Mayeda, and J. Britton (2006). Predicting explosion generated *Lg* and *Sn* using synthetic seismograms, in *Proceedings of the 28th Seismic Research Review: Ground-Based Nuclear Explosion Monitoring Technologies*, LA-UR-06-5471, Vol. 1, pp. 283–294.

Xie, J. and O. Nuttli (1988). Interpretation of high-frequency coda at large distance: stochastic modeling and method of inversion, *Geophys. J.* 95: 579–595

Xie, J., and B. J. Mitchell (1990). Attenuation of multiphase surface waves in the Basin and Range Province, part I, *Lg* and *Lg* coda, *Geophys. J. Int.* 102:121–137.

# DEVELOPMENT AND TUNING OF A 3-D STOCHASTIC INVERSION METHODOLOGY FOR THE EUROPEAN ARCTIC

Hilmar Bungum[1], Michael E. Pasyanos[2], Jan Inge Faleide[3], and Stephen A. Clark[3]

NORSAR[1], Lawrence Livermore National Laboratory[2], and University of Oslo[3]

Sponsored by National Nuclear Security Administration

DE-AC52-08NA28651[1,3], and DE-AC52-07NA28116[2]
Proposal No. BAA08-38

## ABSTRACT

High-resolution seismic models are a critical component of calibrating earth structure for improved seismic monitoring. We will in this study develop the Markov Chain Monte Carlo (MCMC) inversion method into an even stronger tool for deriving reliable three-dimensional seismic models of the crust and upper mantle, based on multiple types of geophysical data sets. This will be done by tuning the method to the European Arctic through development of a probabilistic geophysical model. While a new and much improved model (BARENTS3D) recently has been developed for this region (Ritzmann et al., 2007), stochastic models have a potential to better represent our state of knowledge (and uncertainty) about geophysical structure because deterministic models do not express well the tradeoffs inherent in the data. Stochastic inverse methods also allow a more systematic exploration of the model space to help avoid the trap of falling into local minima. Finally, stochastic models allow prediction of observable distributions (and through them observable uncertainties).

In this project, we will use multiple data types, notably (i) surface-wave group velocities, (ii) regional body-wave travel times, (iii) gravity data, (iv) compiled 1D velocity models, and (v) thickness relationships between sedimentary rocks and underlying crystalline rocks, to develop the model by comparing predictions of the proposed models to the observed data. The Barents Sea region is ideally suited for such development and tuning of stochastic inversion techniques because: 1) multiple data types have already been assembled and much knowledge is available about the uncertainties in these data, 2) an excellent S-wave velocity model is available which can serve as a starting model (http://www.norsar.no/seismology/barents3d/) and as a foundation for the base sampler, 3) an ongoing UiO project on the Barents Sea region will provide additional a priori constraint on the starting model as well as a wider geologic context by which to assess the stochastic inversion results, and 4) the region encompasses test sites and several seismic stations and arrays, making it suitable to invest in more sophisticated forms of modeling. In the process of developing and implementing a new inversion methodology, the primary outcome of this study will be an improved seismic model with rigorously quantified uncertainties in parameters and observables.

## OBJECTIVES

The main purpose of this study is to develop further the Markov Chain Monte Carlo (MCMC) methodology as applied to lithospheric velocity models. The stochastic MCMC approach is especially powerful for two reasons: it has the capability to utilize widely different types of data, such as seismological data and gravity in one inversion process; and it treats uncertainties in an advanced way, significantly improving upon conventional Monte Carlo and other inversion methods. In this study we will use the MCMC method on a variety of geophysical data sets to map the posterior probability distribution of the solution space of the model, with special emphasis on the joint inversion of gravity data and data from seismic methods such as group velocity maps.

The study area is the European Arctic, including the Barents Sea and surrounding regions such as the Norwegian-Greenland Sea, the southern Eurasian Basin, Novaya Zemlya and the southern Kara Sea, the East-European lowlands and the Kola Peninsula. Sediment thicknesses, crustal velocities, crustal thicknesses and upper mantle velocities vary widely across the area, leading to very complicated propagation of regional waves in the crust and upper mantle. By mapping the variation in seismic velocities in the region, we can calibrate the region for travel-time predictions and more accurate event locations, account for phase blockage and amplitude variations in phase association, and eventually model waveforms for template-matching analysis.

While 3D seismic velocity models for the greater Barents Sea region have been developed under previously funded studies (http://www.norsar.no/seismology/barents3d/), the emphasis in this effort is to use stochastic methods to characterize the model uncertainties and the uncertainties on predicting observables, such as the travel time of regional seismic phases. By capturing the model uncertainties and (importantly) their correlations, we will be able to reliably propagate the uncertainties into parameters derived using this model, such as seismic event locations using model-based travel times. While the information that each of these data sets are able to contribute individually will be used, they will also be combined in order to best determine the seismic structure of the whole region, and to provide reasonable uncertainty estimates on the structure. By implementing an MCMC methodology in the greater Barents Sea region, we will also produce a stronger tool for many other regions that are less well covered by data.

The main research objective of this study is therefore to further develop and tune the probabilistic MCMC inverse technique in a region that is well covered by multiple high-quality datasets, in particular, group velocity maps, travel-time data, and crustal-scale deep seismic data. A new high-resolution (ca. 50 km grid size) geophysical model for the European Arctic will then be a parallel product from this research. While a good velocity model already exists (Levshin et al., 2007), a mantle density dilemma, characterized by a high-velocity anomaly that is not seen in the gravity data, has revealed complex velocity-density relations in the upper mantle (Ritzmann and Faleide, 2008), that can only be solved by joint inversion of gravity and seismological data. The MCMC technique incorporates a variety of data sets, and through testing of thousands of models it allows a critical examination of the tradeoffs among model parameters.

Particular attention within this study will be given to the variability of models that are reasonable when fitting multiple data sets, and we will put emphasis on the assessment of the error bounds and the relative influence of the different data sets and their uncertainties. Such a rigorous assessment can only be quantified through extensive model testing. From a variety of possible models, we will carefully assess the interdependence of input parameters and establish the consequences for seismic event detection and event discrimination. Finally, the achieved knowledge will be transferred to other regional geophysical models (such as the Yellow Sea-Korean Peninsula region) aimed at elaborating their reliance on the basis of the backup constraints used. The region and the data sets selected for this study have been chosen because of their uniqueness, diversity, and high quality, which will allow us to develop the method further, in particular, by characterizing the ability of the method to capture both model and observable uncertainties.

## RESEARCH ACCOMPLISHED

Since the present study has not yet started at the time of writing, this paper will essentially be based on the proposal, supplemented with some new data and results that have become available since the writing of the proposal.

### Methodology and Approach

In this study we will be utilizing an advanced inversion technique to generate a well-constrained seismic model of the crust and upper mantle of the European Arctic, specifically, a stochastic inversion using the MCMC algorithm

(Figure 1). The stochastic method inverts data by probabilistically sampling the model space along one or more Markov Chains, comparing the observations predicted by the proposed model to the observed data, and preferentially accepting models that produce a good fit, thus generating a posterior distribution of models. The likelihood is mapped through a series of stages comparing proposed models to data, with Bayes' Theorem relating the prior and posterior distributions.

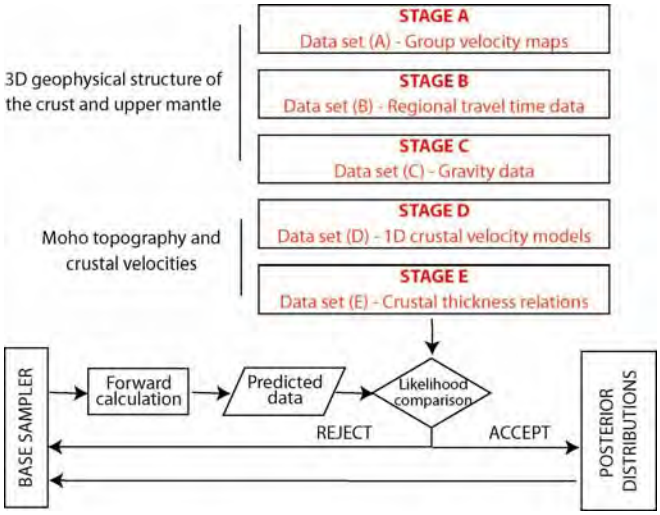


**Figure 1. Schematic diagram of the stochastic MCMC inversion methodology, showing the algorithm for a multi-stage problem as intended in this study.**

Each stage in the MCMC algorithm compares the proposed model to a different data type than the previous stages and, by properly ordering the stages, we can most efficiently search our parameter space. As the Markov Chains sample the model space, the posterior probability density function of the parameter space is mapped out. The stochastic method is able to produce a model that is able to reliably predict observations for a variety of geophysical data types.

The MCMC approach is a derivative of the Metropolis algorithm (Metropolis et al., 1953) as described by Mosegaard and Tarantola (1995). While specifics of the methodology can be found in Pasyanos et al. (2006), a brief outline is provided here. The first task in this methodology is to develop a "base sampler," a program that selects a proposed model, given the model parameterization and set of constraints that we can provide. This proposed model is a random (Monte Carlo) perturbation from the current state in the model space. Based on fits to the data (discussed below), the proposed model is either accepted or rejected. If a model is rejected, then we return to the previous model. If the model is accepted, however, then the base sampler will select the next model as a perturbation to the newly accepted model. In this way, we construct a Markov Chain to search the model space.

Whether or not we accept a model is based in part on how well predictions of the model compare to observations for a variety of data sets. If we always accepted a proposed model, then we would simply be sampling from our prior distribution. Instead, we base the acceptance on the fit of a proposed model to the observed data. For each data type, we use a likelihood function that includes the data predicted for a given model, a vector containing the observed measurements, and the estimated data uncertainty, based on an L2 norm. We decide whether or not to accept a model by comparing the respective likelihoods of the current and proposed models. After the Markov Chains have adequately sampled the model space, we are left with the distribution of models that is consistent with our observables and the uncertainties in our observables.

### Geologic Setting

The study region (Figure 2) encompasses old cratonic crust, continental shelf regions, and oceanic crust. The oldest rocks, of Archean/Proterozoic ages, are found on the Kola Peninsula and nearby regions and occur within a patch of ancient terrains. The Caledonian Orogen extends along western Norway and is subdivided into four tectonic nappes. Obduction started in the Vendian to Middle Cambrian and lasted until the Silurian.

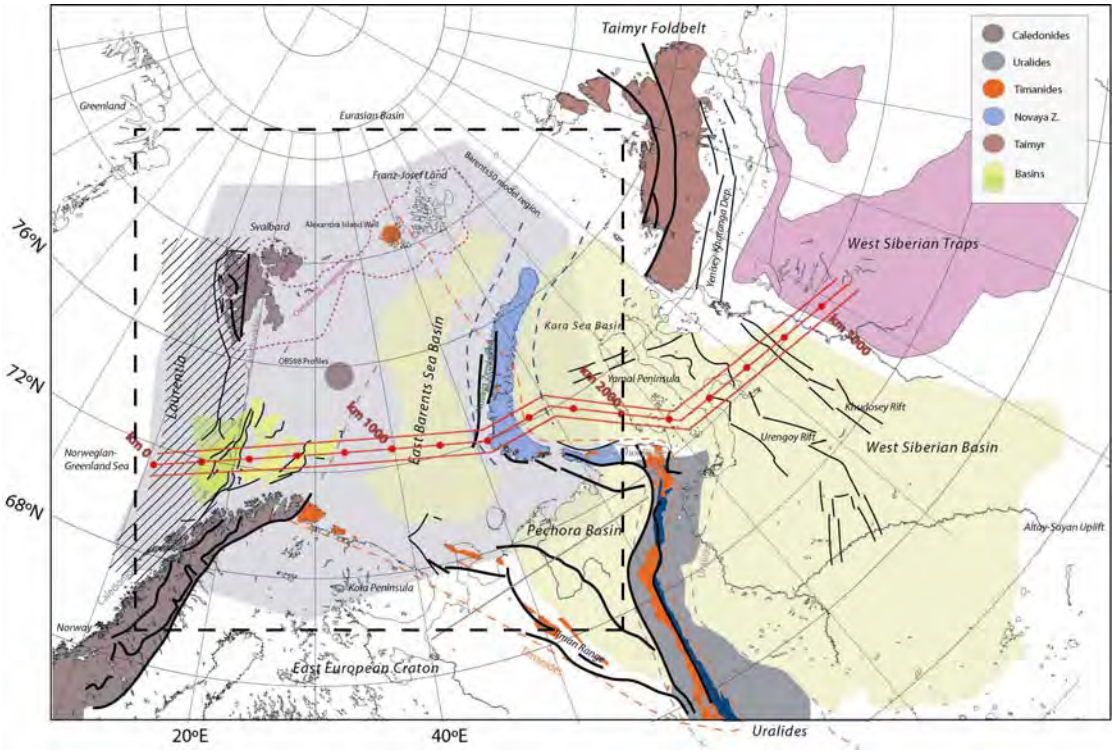


**Figure 2. Map of the greater Barents region with main geological features (after Ritzmann and Faleide, 2008). The black dashed box indicated the target region for this study. Thick red lines show the location of the transect in Figure 3.**

Caledonian main thrusts, striking N and NE, are also revealed in the western Barents Sea (Ritzmann and Faleide, 2007). After the Caledonian orogenic collapse, the western Barents Sea experienced widespread Paleozoic- and Mesozoic/Paleocene rifting along the N/NE-trending Caledonian basement grain. During the Early Cretaceous rift phase, some of the basins in the western Barents Sea region subsided more than 12 km, leading to a total sedimentary succession at present of more than 20 km. Similar deep sedimentary basins are observed in the eastern Barents Sea, to the west of the (most likely) Late Triassic-Early Jurassic Novaya Zemlya Fold Belt.

The nature of the underlying crystalline crust and upper mantle in the eastern Barents Sea basins is still a matter of debate, since some authors propose an oceanic crustal nature. Generally, the deformation style in the western (more brittle) and eastern (more flexural) Barents Sea is very different. Cretaceous magmatism is evident to the east of the Svalbard Archipelago. Seafloor spreading in the Norwegian-Greenland Sea and the Eurasian Basin started in Early Eocene times. The western continental margin of today consists of a series of sheared and rifted margin segments. A comprehensive and referenced geological overview can be obtained from Ritzmann et al. (2007).

Recent results established a high-velocity body in the upper mantle below the eastern Barents Sea Basin, Novaya Zemlya, and the Kara Sea (Figure 3). The high-velocity body has about a 100-km thickness and reveals a slight dip towards the east. Early interpretations regarded this structure as a remnant of a subducted slab (Levshin et al., 2007). However, seismic velocities of peridotite mantle rocks, along a standard continental geotherm, are considerably lower than those observed here (Cammarano et al., 2003). Seismic velocity anomalies within the upper mantle are predominantly caused by temperature variations, rather than compositional effects (Goes et al. 2000). This, in turn, leads to the assumption that the eastern Barents Sea is underlain by a cold cratonic keel similar to the Siberian Craton (Ritzmann and Faleide, 2008).

This concept gets additional support from simple 2D gravity modeling. Neither the free-air gravity, nor the geoid, show a pronounced, long-wavelength (ca. 1,000 km) anomaly across the eastern Barents Sea (Ebbing et al., 2007; Ritzmann and Faleide, 2008), suggesting a simple, horizontally layered mantle density structure. Density contrasts due to temperature variations below cratons are presumed to be entirely compensated by Al/Fe depletion

(weight loss), and hence no lateral density variations are observed at cratonic boundaries. The upper mantle density structure of BARMOD (Levshin et al. 2007) and CUB1.0 (Shapiro and Ritzwoller, 2002) is calculated from seismic velocities, using fixed heterogeneity ratios. This technique violates significantly the findings from the gravity modeling, since velocity changes are obviously not simply proportional to density changes (Ritzmann and Faleide, 2008). Thus, the joint inversion of seismological data and gravity data planned in this study is essential to achieve a reasonable upper mantle geophysical and compositional structure.

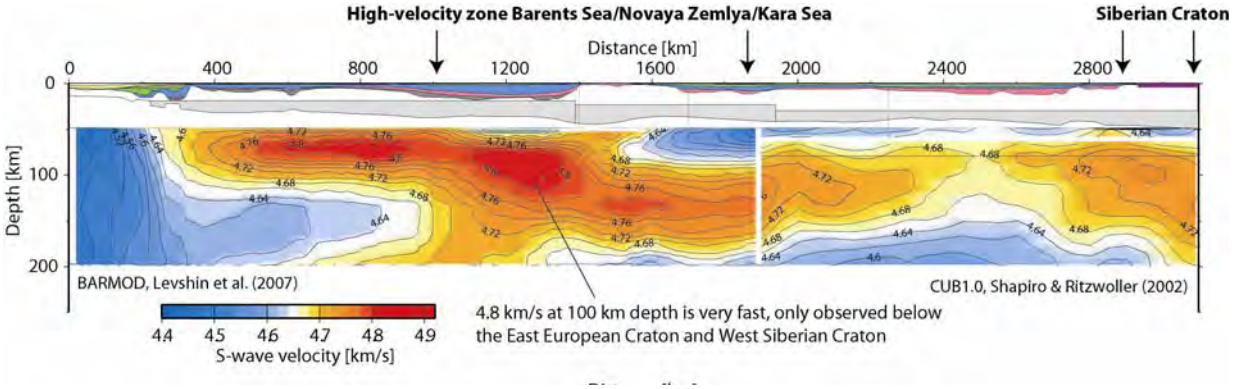


**Figure 3. West-East transect from the Norwegian-Greenland Sea (left) across the Barents Sea to Novaya Zemlya (km 1,500) and the Siberian Craton (right). The panel shows absolute S-wave seismic velocities (Levshin et al., 2007). Profile location shown in Figure 2.**

**Model Development**

The Barents Sea–Novaya Zemlya region is interesting both from a geophysical and a seismic verification point of view. A largely DOE funded study was completed in 2005 in which 3D seismic velocity models both for the crust (BARENTS50) and the upper mantle (BARMOD) were developed, using a grid density of 50 km and one degree, respectively (Levshin et al., 2007; Ritzmann et al., 2007). Figure 4 shows a Moho map of the BARENTS50 crustal model, which will be used as a starting model in this study.

Levshin et al. (2007) searched for new surface wave data set in the European Arctic and retrieved observations from regional data archives in Norway, Finland, Denmark, and Russia in addition to data from the data centers of IRIS and GEOFON. Rayleigh and Love wave group velocity measurements between a 10 and 150 s period were combined with existing data provided by the University of Colorado at Boulder. This new data set was inverted for maps showing the 2D group-velocity distribution of Love and Rayleigh waves for specific periods. Using a Monte Carlo inversion technique (Shapiro and Ritzwoller, 2002), they constructed a new 3D shear-velocity model of the upper mantle using the crustal BARENTS50 model as a backup constraint.

The basic principle of the model development is to stochastically propose a 3D geophysical structure and compare this subsequently to available data sets. Generally, we acquired the following data sets: (A) group velocity maps based on a comprehensive set of recordings, (B) regional travel time data, (C) gravity data, (D) 1D crustal velocity models (sampled from 2D profiles), and (E) regionally dependant thickness relations between the sediment and crystalline crustal thickness. Sets (A) to (C) constrain the entire lithosphere, while (D) and (E) explicitly constrain the local crustal structure.

All of our compiled data sets are independent of each other. We can use the group velocity maps and the gravity data to infer the geophysical parameterization (velocity, density) while we use the thickness relation and regional travel time data to map more locally the crust-mantle boundary topography, which can cause travel time differences of up to several seconds. In the following sections, we will describe the different data sets that we plan to use in producing the model. The exact order of the data sets in the inversion will be optimized to increase the efficiency of the stochastic inversion. Our next step is then comparing the observations of proposed models to data.

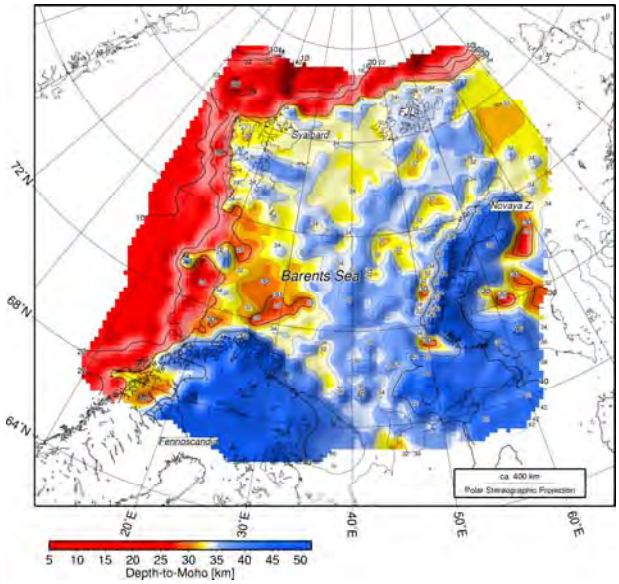


**Figure 4. Moho depth map for the main target area in the greater Barents Sea region (Ritzmann et al., 2007).**

*Set (A): Comparison with group velocity data*

The first set of parameters we will employ are measurements of surface-wave dispersion. We actually have two sets of group velocity measurements available for use in this region. The first one of these is from a study based on a combined University of Colorado and NORSAR data base that resulted in the BARMOD model (Levshin et al., 2007), based on Love and Rayleigh wave data between 1970 and 2005. The data cover periods between 10 and 150 s, and there are around 2,500 paths at a period of 30 s. Figure 5 shows group velocities from the combined NORSAR and Universities of Colorado (CU), Oslo, and Paris study (Levshin et al., 2007).

The surface-wave data are a very good indicator of average velocity structure, although, unlike some of the body-wave phases, surface-waves are not particularly sensitive to pronounced velocity/density gradients. Surface waves are also very good at covering aseismic regions or non-instrumented regions that are not similarly well covered by body-wave phases. Since our target region is located offshore, a regional body-wave tomography model would require the deployment of an ocean-bottom seismometer grid, which is not planned nor expected within the near future.

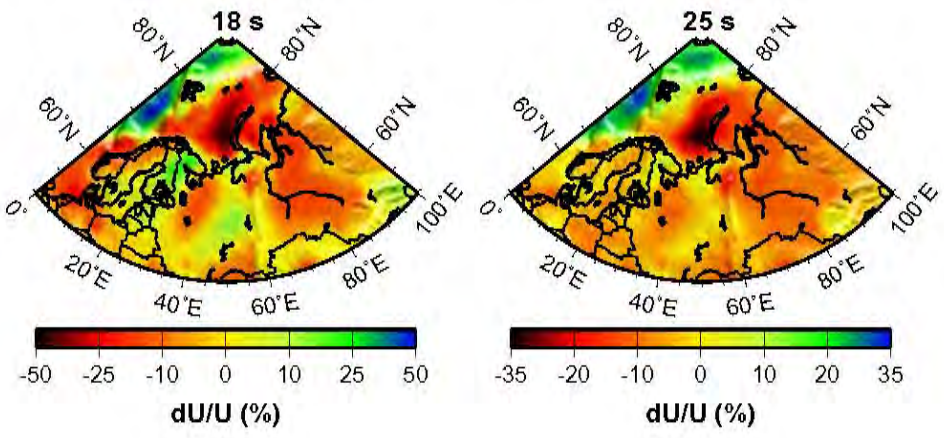


**Figure 5. 2-D distribution of inverted group velocities, presented as deviations from the average velocity, for periods of 18 and 25 s (Levshin et al., 2007).**

*Set (B): Comparison with regional travel time data*

Data set B, chosen for comparison of proposed models with constraints, consists of travel time data from analyst picks, and here we have two different datasets. The primary set of such data includes a comprehensive collection of reference events, including GT (ground truth) events, collected and analyzed by NORSAR (Maercklin et al., 2007). Besides *Pn* and *Pg* readings, the database also contains a comprehensive collection of *Sn* and *Lg* phases, and these will be used in this study.

For some of these data there are quality problems related in part to epicenter precisions but also to timing errors at the seismic stations. One of the advantages with the stochastic inversion methodology is, however, that the uncertainties in the input data can be properly accounted for. Many active seismic experiments have been additionally observed by the International Monitoring System auxiliary array SPITS (e.g., Schweitzer, 2000), and these absolute travel time observations will be added as GT-0 observations to the database.

*Set (C): Gravity data*

After passing the likelihood comparison for the lithospheric P-and S-wave velocity structure (group velocity maps and travel-time data) the subsequent test targets the density structure. The regional gravity field will be calculated on the basis of the stochastically proposed 3D density structure and compared to the observed gravity field.

Gravity data (free-air) are freely available from various recent projects, such as the Arctic Gravity Project (http://earth-info.nga.mil/GandG/wgs84/agp/) and the GRACE experiment (gravity recovery and climate experiment; Tapley et al. 2005). The free-air gravity anomalies in the Barents Sea/Kara Sea region are mostly very smooth (-50 to +20 mgal; Figure 6). Notable exceptions are the up to 20-km-deep sedimentary basins and adjacent basement highs in the western Barents Sea, which provide gravity signals of up to 100 mgal. Interestingly, the 20 km deep East Barents Sea Basin (east of 40°E) is not characterized by a broad regional gravity low, suggesting a deeper-seated local compensation.

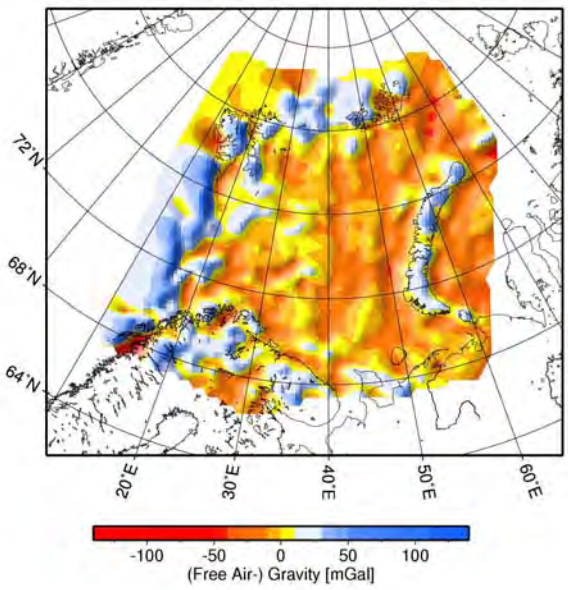


**Figure 6. Free air gravity data in the target region (http://earth-info.nga.mil/GandG/wgs84/agp/).**

Again we mention the misleading concept that density is proportional to seismic S-wave velocity below the eastern Barents Sea. As stated earlier, the thermal state of the upper mantle in the target region is likely to be cold and possibly cratonic (Ritzmann and Faleide, 2008). This infers high seismic velocities and low densities due to chemical depletion. Any amplitude modeling performed with existing models (1D-BAREY, 3D-BARMOD) are thus based on overestimated densities causing excessively high impedance contrasts, for example, at the crust-mantle boundary or at the lithosphere-asthenosphere boundary. The joint inversion of the density structure is therefore a very important part of this project.

*Set (D): 1D crustal velocity profiles*

In this study we will use vertical 1D velocity profiles compiled from 2D models (Figure 7) to constrain the velocity structure directly beneath and in close vicinity to seismic stations. In all, there are 620 1D velocity-depth profiles comprising the existing database (Ritzmann et al., 2007). While most of the profiles are for P-wave velocities, some S-wave profiles are also included. The data constraint derives from deep seismic reflection profiles as well as wide-angle OBS surveys.

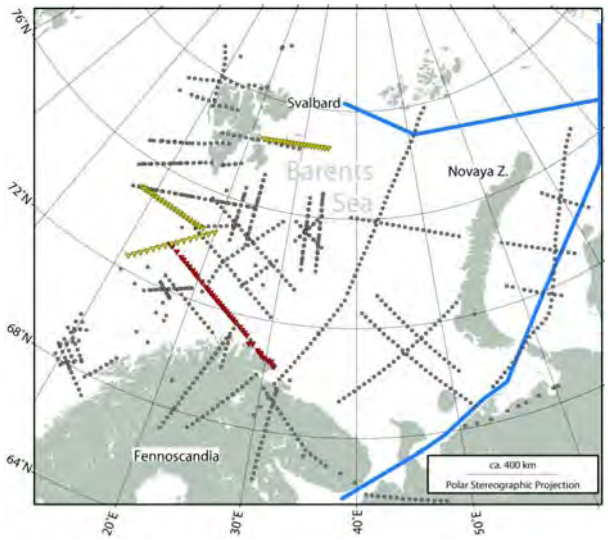


**Figure 7. Distribution of 1D seismic profiles for the crustal column used as constraint in the BARENTS50 3D model (grey circles; after Ritzmann et al., 2007). New deep seismic surveys providing additional constraint were recently published (blue), acquired in 2007 (red), or planned for 2008 (yellow).**

*Set (E): Regionally dependent thickness relations*

A crucial observation during the construction of the BARENTS50 crustal model (Ritzmann et al., 2007) was the regional dependence of sediment thickness relative to the thickness of the crystalline crust (Figure 8). On the basis of the state-of-the-art geological knowledge of the Barents Sea, separate geological provinces were defined. These provinces are local and regional sedimentary basins, basement horsts, or units overprinted by volcanic activity. The 620 1D velocity profiles were assigned to these provinces, and the sediment thickness was plotted against the thickness of the crystalline crust. Figure 8 shows the result for eight of these provinces.

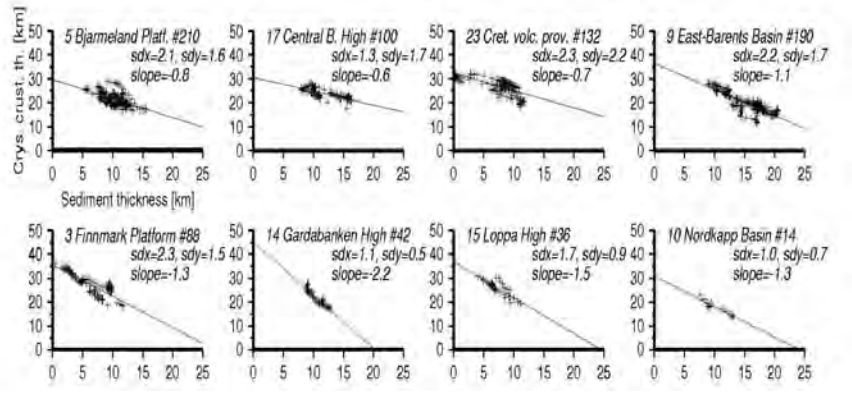


**Figure 8. Eight characteristic examples of thickness relations in the Barents Sea region. The x-axis shows the sediment thickness, while the y-axis shows the crystalline crustal thickness.**

The data can be sufficiently fitted by linear regressions with province-dependent slopes and intercepts (Figure 8). Since a regional sediment thickness map is available (compiled in Ritzmann et al., 2007), we were able to infer the crystalline crustal thickness from the sediment thickness at any node in the model. This is especially important in regions with limited data constraint, such as the northeastern Barents Sea. Here, the characteristic relationships help to infer the probable Moho depth by summation of the sediment thickness and the remaining 'crystalline' thickness inferred by using the regression parameter. In turn, all MCMC-proposed (crustal) models that are not in accordance with this observation fail the test. These data will be employed in a manner similar to the 1D velocity profiles, by assessing the misfit of proposed models to the depth-to-basement data and regression parameters.

*Uncertainty considerations*

One important component of this study is in assessing uncertainties on both the seismic models and on observables. The MCMC stochastic inversion methodology makes it relatively easy to assess the uncertainties of seismic models, since the technique maps out the probability distribution of the models. Uncertainties on observable parameters, such as travel times, can be assessed by calculating the travel times through all of the models in the posterior distribution, or some fraction of the models.

Each phase has a range of travel times associated with them, some of which appear to be skewed rather than simply normally distributed. While the overall distribution of travel times for each phase would ideally be used in locations, if necessary, the distributions could in some cases be approximated by a normal distribution or a sum of normal distributions. We would like to assess whether the uncertainties of the observables predicted from the model are consistent with the uncertainties of our input data sets. This assessment can only be accomplished with the high quality travel time data available in this project.

**New Data and Results Available from the Barents Sea**

As part of the recently launched Petroleum-related studies of the Barents Sea Region (PETROBAR) project coordinated by UiO, new wide-angle seismic profiles have been and will be acquired in the boreal summer seasons of 2007 and 2008. In 2007 an OBS survey was carried out along an existing deep seismic reflection profile in the SW Barents Sea (Figure 7, red profile). Planned for 2008, another PETROBAR OBS profile will be acquired east of Svalbard, as well as two OBS profiles across the western Barents Sea margin adjacent to Bear Island (Figure 7, yellow profiles) as part of an International Polar Year project coordinated by NORSAR.

Further, wide-angle seismic data were recently acquired and published by several Russian researchers (e.g., Ivanova et al., 2006; Sakoulina et al., 2007; Roslov et al., 2008; for locations, see Figure 7, blue profiles). Therefore we will be able to extend the database for 1D profiles continuously and enable an even better crustal profile coverage than was available for the BARENTS50 model.

## CONCLUSIONS AND RECOMMENDATIONS

In conclusion, the MCMC stochastic inversion method seems to be a promising way of building seismic models and quantifying uncertainties in the European Arctic, with potential for wider application in other locations. We look forward to implementing this methodology on our unique dataset for the region and presenting our results at future meetings.

## ACKNOWLEDGEMENTS

Due to the late start-up of the project, the present paper has been written largely on the basis of the proposal. As such, we are indebted to a number of people who took part in that process. First of all, Oliver Ritzmann, from the University of Oslo (UiO), was a key person in the earlier (2003-2005) DOE Barents Sea study, and was a driving force behind the present proposal. We also appreciate very much that data and results from an ongoing UiO Barents Sea study (PETROBAR), funded by the Research Council of Norway and StatoilHydro, has already been made available for the present study.

## REFERENCES

Cammarano, F., Goes, S., Vacher, P., and Giardini, D. (2003). Inferring upper mantle temperatures from seismic velocities, *Phys. Earth. Planet. Int.* 138: 197–222.

Ebbing, J., Braitenberg, C. and Wienecke, S. (2007). Insights into the lithospheric structure and the tectonic setting of the Barents Sea region by isostatic considerations. *Geophys. J. Int.* 171: 1390–1403, doi: 10.1111/j.1365-246X.2007.03602.x.

Goes, S., Govers, R., and Vacher, P. (2000). Shallow mantle temperature under Europe from P and S wave tomography, *J. Geophys. Res*. 105: (B5), 11153–11169.

Ivanova, N. M., Sakoulina, T. S., and Roslov, Yu.V. (2006). Deep seismic investigations across the Barents-Kara region and Novozemelskiy Fold Belt (Arctic Shelf). *Tectonophysics* 420: 123–140, doi: 10.1016/j.tecto.2006.01.011.

Levshin, A., Schweitzer, J., Weidle, C., Shapiro, N., Maercklin, N., and Ritzwoller, M. (2007). Surface wave tomography for the Barents Sea and Surrounding Regions, *Geophys. J. Int*. 170: 441–459, doi:10.1111/j.1365-246X.2006.03285.x.

Maercklin, N., Ritzmann, O., Bungum, H., and Faleide, J.I. (2007). A seismic velocity model for the greater Barents Sea region: Reference events and travel time modeling. Unpublished manuscript.

Metropolis, Rosenbluth, N.A., Rosenbluth, A., Teller, A., and Teller, E. (1953). Equations of state calculations by fast computing machines, *J. Chem. Phys*., I, 1087–1092.

Mosegaard, K. and Tarantola, A. (1995). Monte Carlo sampling of solutions to inverse problems, *J. Geophys. Res*., 100, 12,431–12,447.

Pasyanos, M. E., Franz, G. A., and Ramirez, A. L. (2006). Reconciling a geophysical model to data using a Markov Chain Monte Carlo algorithm: An application to the Yellow Sea-Korean Peninsula region, *J. Geophys. Res.* 111: B03313, doi:10.1029/2005JB003851.

Ritzmann, O., Maercklin, N., Faleide, J. I., Bungum, H., Mooney, W. D., and Detweiler, S. T. (2007). A 3D geophysical model for the crust in the greater Barents Sea region: Model construction and basement characterization. *Geophys. J. Int*. 170: 417–435, doi: 10.1111/j.1365-246X.2007.03337.x.

Ritzmann, O. and Faleide, J. I. (2007). Caledonian basement of the western Barents Sea. *Tectonics* 26: TC5014, doi:10.1029/2006TC002059.

Ritzmann, O. and Faleide, J. I. (2008). The crust and mantle lithosphere in the Barents Sea/Kara Sea region. *Tectonophysics*, TECTO 124236, doi: 10.1016/j.tecto.2008.06.018.

Roslov, Yu.V., Sakoulina, T. S., and Pavlenkova, N.I. (2008). Deep seismic investigations in the Barents and Kara Seas. *Tectonophysics*, TECTO 124225, doi: 10.1016/j.tecto.2008.05.025.

Sakoulina, T. S., Verba, M. L., Ivanova, N. M., Krupnova, N. A. and Belyaev, I. V. (2007). Deep structure of the northern part of the Barents-Kara region along the transect 4-AR (Taimyr Peninsula-Franz Josef Land Arch. In: "*Models of the earth's crust and upper mantle*", papers of the International Symposium, St. Petersburg 18–20 September 2007, VSEGEI-Press, 197–200 (in Russian).

Tapley, B., Ries, J., Bettadpur, S., Chambers, D., Cheng, H., Condi, F., Gunter, B., Kang, Z., Nagel, P., Pastor, R., Pekker, T., Poole, S., and Wang, F. (2005). GGM02 - An improved Earth gravity field model from GRACE", *J. Geodesy*, doi:10.1007/s00190-005-0480-z.

# IMPROVED PHASE CHARACTERIZATION OF FAR-REGIONAL BODY WAVE ARRIVALS IN CENTRAL ASIA

Aaron Ferris, Delaine Reiter, and Anastasia Stroujkova

Weston Geophysical Corp.

Sponsored by Air Force Research Laboratory

Contract No. FA8718-06-C-0002
Proposal No. BAA06-86

## ABSTRACT

At far-regional and near-teleseismic distances the early body-wave coda contains information that is potentially useful to monitoring seismologists. However, waveforms from this distance range are typically under-utilized because of propagation complexities that cause significant difficulties in seismogram interpretation. For example, the first ~20 seconds of a far-regional seismogram often include multi-pathed arrivals caused by the interaction of the wavefield with upper mantle discontinuities at 220 km, 410 km and 660 km depth. Depth phases (e.g., *pP, pP410, sP, sP410,* etc.) also add complexity to the early part of the seismogram since they can constructively or destructively interfere with the primary phase arrivals. Array observations from earthquakes in central Asia regularly exhibit a variety of complex phase phenomena, such as back-azimuth anomalies, emergent or late-arriving first arrivals, large amplitude secondary arrivals, and interference phenomena between upper mantle arrivals and depth phases.

We have developed array-based methods to improve the characterization of primary and early coda phase arrivals observed at far-regional and near-teleseismic distances. These techniques include improved signal processing to accurately measure the delay times ($\tau$'s) and slownesses ($p$'s) of primary and secondary phases from small-aperture arrays. We use these $\tau$–$p$ measurements to develop representative crust and mantle velocity-depth profiles and suites of synthetic seismograms through those models. Then we use the processed array beams to derive 'wavefield templates'; i.e., grouped observations with similar phase characteristics. We analyze these wavefield templates by comparing them with synthetics, looking for quantitative explanations for the phase behaviors we observe.

Our approach results in a methodology that improves phase characterization and yields earth models that more accurately predict the succession of expected arrivals. We have applied our techniques to observations from two regional small-aperture arrays in Kazakhstan (MKAR and KKAR), and find that our results provide insight into wavefield behaviors that are regularly observed on the MKAR and KKAR arrays.

## OBJECTIVE

The objective of our research is to enhance the usefulness of regional, small-aperture arrays by developing array-based methods that can more accurately characterize far-regional (14˚-29˚) seismic wavefield structure. Far-regional (14˚–29˚) seismograms are particularly interesting because of the strong influence upper-mantle heterogeneity has on the early *P* coda arrival structure (< 20 secs). The suite of observed phases often includes multi-pathed arrivals and their depth phase counterparts, generated from wavefield interaction with upper mantle discontinuities at 220 km, 410 km, and a 660-km depth. The P-coda arrivals can be closely spaced in time (1–2 sec) and have similar ray parameters that range between 8–11 sec/degree. Further wavefield complexity arises from interference between depth-phase multiples and near-receiver scattered arrivals with the primary arrivals. These complexities can be region and earthquake specific.

The regional seismic arrays that have been built in the last fifteen years should be a rich data source for the study of far-regional phase behavior. The arrays are composed of high-quality borehole seismometers that make high-fidelity, low-noise recordings. However, beyond regional distances, the small apertures of these arrays (< 5km) limit their usefulness beyond first-arrival P- and S- onset picks. At these distances standard array methods (e.g., slant-stacking and frequency-wavenumber analysis) cannot resolve the arrival times and slownesses of primary and secondary arrivals, making the proper identification and classification of far-regional arrivals quite difficult. We are overcoming this limitation by applying refined array processing techniques in conjunction with straightforward wavefield generalization methodologies. Our goal is to characterize the commonly observed early coda arrivals that propagate from the different seismic regions of central Asia, utilizing recordings from the Makanchi (MKAR) and Karatau (KKAR) small-aperture arrays in Kazakhstan (Figure 1). This research will improve the usefulness of small-aperture arrays by increasing their ability to classify small-magnitude events that may be poorly recorded regionally and teleseismically.

## RESEARCH ACCOMPLISHED

We have developed array-based methodologies to characterize the *P* coda of far-regional events using small aperture arrays. Our methodology includes several components: 1) improved small-aperture array processing to measure delay-times (τ) and slownesses (*p*) of primary and secondary arrivals; 2) construction of region-specific velocity-depth profiles derived from the τ-*p* measurements (i.e., τ-*p* transformations), as well as models derived from wavefield continuation methods, and 3) the derivation of 'wavefield templates' from clustering of array beams to capture the commonly observed arrival structure. These methods employ both theoretical and empirical techniques to reduce a large waveform data set (~600 earthquakes; Figure 1) into a smaller set of robustly observed wave phenomena. We then attempt to explain these phenomena using well-accepted, straightforward techniques. The separate components of our methodologies are discussed below.

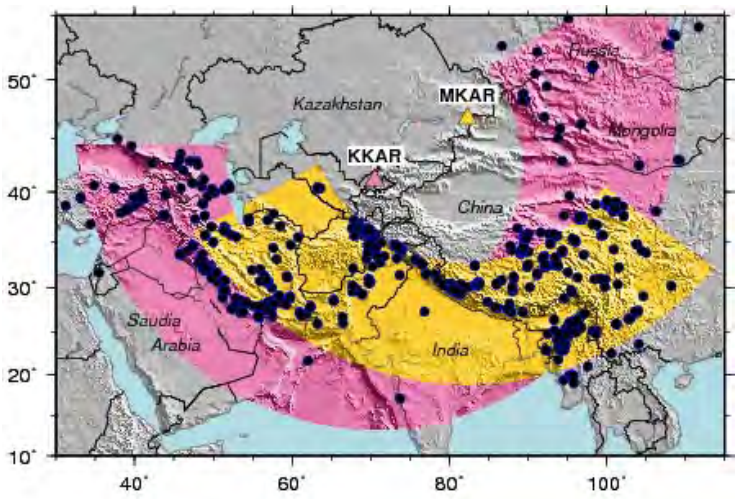


**Figure 1. Map of central Asia showing the location of the Makanchi (MKAR) and Karatau (KKAR) arrays in Kazahkstan, as well as earthquakes (circles) used in this study. Colored bands mark the 14˚–29˚ distance range from each array.**

**Improved Small-Aperture Array Processing**

Our objective for the array processing is to compile a set a phase delay times (τ), slowness measurements (*p*) and array beams for our waveform data set of 600 central Asian earthquakes. The small aperture (< 5 km) of many of the newer arrays installed for nuclear monitoring purposes presents a serious challenge for typical array processing methods. However, we have developed and applied improved velocity spectra analysis (*vespa*) and phase-weighted stacking methods (PWS; Schimmel and Paulssen, 1997) to improve phase identification at small-aperture regional arrays. Our results indicate that in many cases we can detect closely-spaced arrivals by their slowness values in a time window that includes the direct *P* arrival, depth phases and arrivals from upper-mantle discontinuities (Ferris and Reiter, 2007).

In Figure 2 we show an example of applying phase-weighted stacking to a typical regional event recorded by the MKAR array. At a distance of 14.33˚ and depth of 17 km, a series of arrivals are predicted to occur within the first 16 seconds of this seismogram. In addition to the main *P* branch, the reference model iasp91 (Kennett and Engdahl, 1991) predicts the *pP* and *sP* depth phases at a delay time of ~4 seconds and ~7 seconds, respectively, relative to the first arrival. These depth phases are followed by their multi-pathed counterparts that bottom at the 410 km discontinuity and have a delay time of ~12 and ~14 seconds for *pP410* and *sP410*. When compared to the decomposed wavefield (represented by the phase coherence vespagram in Figure 2), it is not clear how these predicted arrivals correspond to the observations. Even the main *P410* arrival, which should be near the caustic of the travel-time branch and thus amplified, is not obviously identifiable. However, there may be interference between the *P410* and *sP* phase, as they are predicted to arrive within 0.3 seconds of each other. If the earthquake depth is decreased to 10 km, the *pP* and *sP* arrivals agree better with the observations. However, a change in focal depth does not account for all the observed arrivals, especially the coherent later arrivals near 15 seconds, or explain the ambiguity in the *P410* arrival.

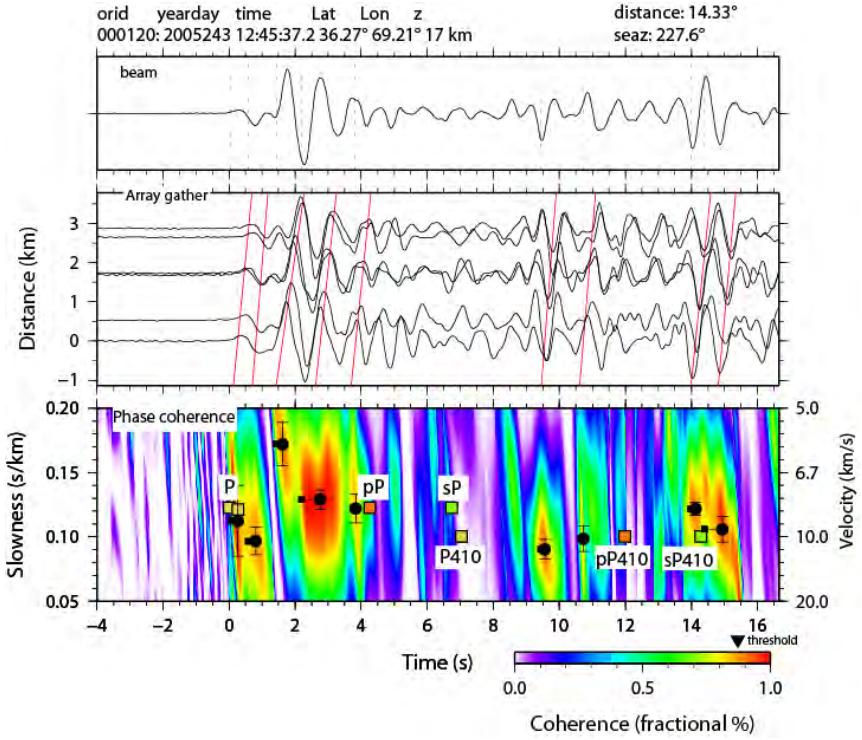


**Figure 2. Example of phase-weighted array processing for an earthquake recorded by the MKAR array at an epicentral distance of 14.3. The top panel shows the array beam, computed using the slowness of the first arrival. Dashed lines mark the computed onset times. The middle panel shows the array gather and move-out curves for detected arrivals. The bottom panel shows the phase-weighted coherence vespagram. Black circles mark arrivals with phase coherence greater than 85% (i.e., detections); black squares mark the computed onset time. Colored squares show the iasp91 predicted arrivals (yellow = *P* branch , orange = *pP* depth phases, green = *sP* depth phases).**

This exercise of comparing our array measurements to those predicted from global reference models illustrates the need for more region-specific models. The next component of our improved phase characterization scheme is to use our array measurement and array beams to derive models that can more accurately match the observations. Our methodologies to accomplish this and preliminary results are discussed in the following sections.

**Regional Velocity Depth Profiles**

To address the need for more applicable earth models and to generalize our array observations, we are developing two separate methods to derive velocity-depth profiles for the specific regions monitored by the MKAR and KKAR arrays. Both methods are based on $\tau$-$p$ (i.e., delay-time/slowness) techniques that decompose wavefields into their components parts. The first method involves directly inverting array-based delay-time and slowness measurements to solve for a velocity-depth function (e.g., Carbonell and Smithson, 1994). The second method applies wavefield continuation techniques to array-beam record sections to accomplish the same goal (e.g., McMechan, 1984). While these methods are not new, they are not typically applied to small-aperture array data, but rather to data from long linear arrays of seismometers (e.g., Morozov et al., 2005). Since we apply these methods to multiple events records, a main challenge is accounting for the effects of differing source parameters (origin time, event depth, and focal mechanism), which may be unknown or poorly constrained. While our methods are under active development, preliminary results show that we are able to extract reasonable models for specific regions in our study area. The two methods, direct inversion and wavefield continuation, are discussed below.

*Direct Inversion of Array-Based Delay-Time and Slowness Measurements*

Figure 3 illustrates how we prepare array-based delay-time and slowness measurements for velocity-depth inversion. In this example we groom the outliers from data set of measurements made at MKAR, consisting of 110 earthquakes ranging from 14°–29° epicentral distance, which includes earthquakes extending from the Hindu Kush region of Pakistan/Afghanistan to the Makran coast and Zagros Mountains of Iran. The grooming removes everything outside the 8.0–14.5 (sec/deg) slowness range, to help eliminate measurements from *P*-to-*S* scattered signals and coherent noise. We also discard measurements that exhibit significant slowness smearing (i.e., measurement uncertainties) during the PWS processing. Once the groomed measurements (Figure 3a) have been collected, we reduce them to a single $\tau$-$p$ curve by computing the error-weighted-mean $\tau$ value within evenly spaced slowness bins (Figure 3b), excluding bins with only a few measurements. Averaging the $\tau$'s within a common slowness bin acts to correct for errors in focal depth by accounting for the $\pm\tau$ offset between *P* and *pP*. While this is not a perfect correction due to missed phases in the array processing, the inclusion of *sP* arrivals, and measurement error, we have found it more effective and feasible than correcting $\tau$ on an event basis using catalog depths, which typically have large uncertainties. The averaged $\tau$-$p$ curves are the observations that are input into the velocity-depth inversions. The curve shown in Figure 3b generally agrees with the iasp91 $\tau$-$p$ curve; however, it is not as smooth, which may be partially caused by measurement error and inadequate averaging, not just differing earth structure.

Figure 4 shows a preliminary velocity profile determined from the MKAR $\tau$-$p$ data shown in Figure 3. There are many ways to parameterize this inverse problem, and the results in Figure 4 represent one solution. To derive the model we solved for the thicknesses of a sequence of layers that best fit the $\tau$-$p$ observations, using a damped least-squares formulation. For this particular inversion, we linearized the problem by assigning each slowness $p$ to the layer representing its maximum depth of penetration (i.e., the ray turning point), which depends on the initial velocity-depth profile and is updated after each inversion iteration. The under-determined system of equations we invert is $\tau = G \cdot h$, where $\tau$ is a vector of our zero-offset time observations and $h$ is vector of model layer thicknesses. Each row of $G$ is composed of the vertical slowness through each layer up to the turning depth for each $p$ observation. While linearizing the inversion allows a direct estimation of model uncertainties, the final results tend to be strongly influenced by the initial model. We are currently examining other algorithms to better understand model non-uniqueness, as well as other parameterizations of the linear inverse problem.

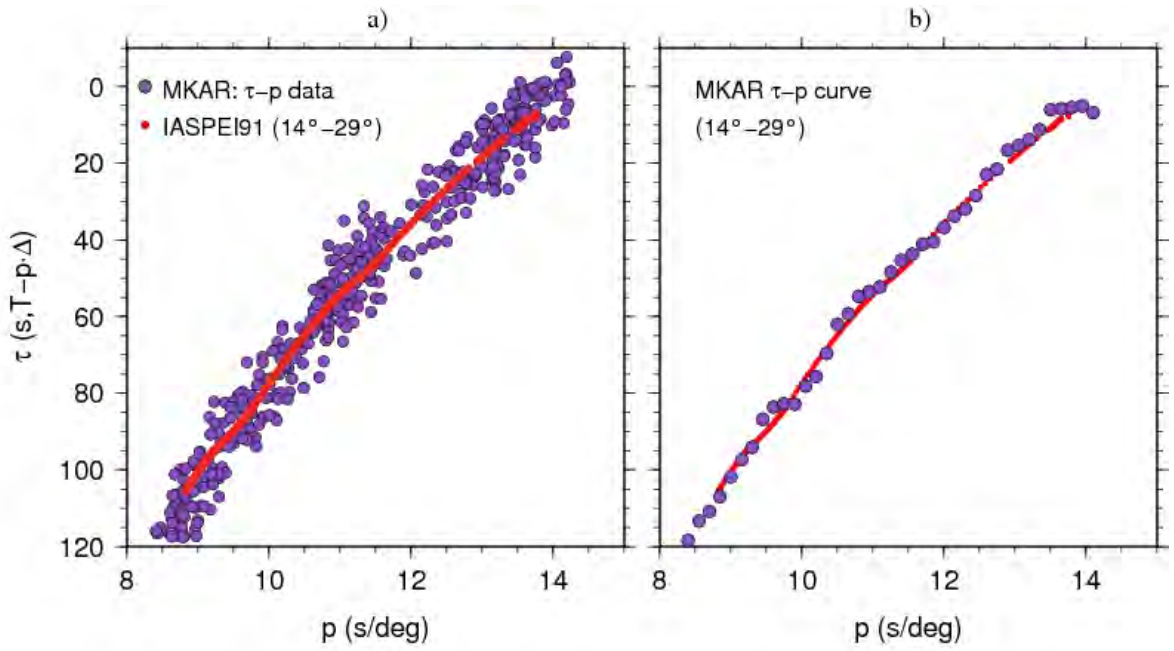


**Figure 3. Sample *τ-p* data from the MKAR array. a) The groomed MKAR data (blue circles); red dots show the iasp91 *τ-p* curve for a surface-focus source. The range in *τ* for a particular slowness is caused by the difference in *τ* for earthquakes at different depths, rather than just measurement error. b) The averaged *τ-p* curve from the groomed data, evenly sampled in slowness at 0.15 sec/deg.**

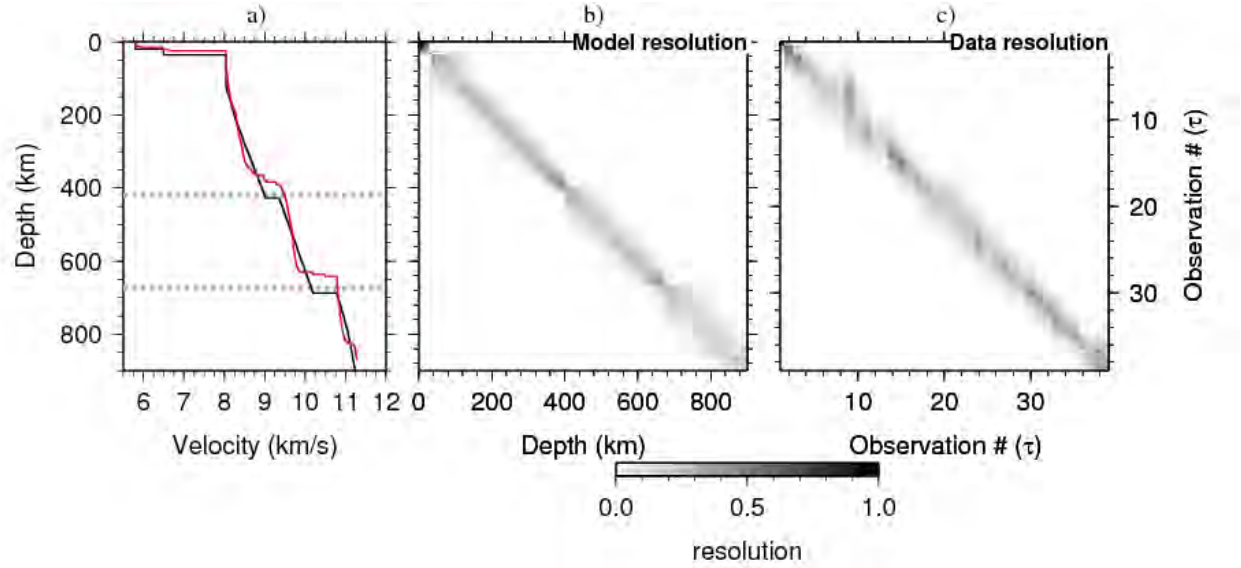


**Figure 4. Preliminary *τ-p* inversion for a 1-D velocity profile of the MKAR data shown in Figure 3. a) final model (red) compared to the starting model (black); b) the model resolution matrix; and c) the data resolution matrix.**

*Wavefield Continuation Analysis using Array Beams*

Wavefield continuation (e.g., Clayton and McMechan, 1981) is commonly used to extract velocity profiles from record sections recorded by long linear arrays of sensors. In our case, array beams form the record sections. We

arrange the beams according to their epicentral distance and align them based on the first arrivals (Figure 5a). Arrivals are aligned relative to a reference model, a time shift that acts as an event-based static correction. The correction tries to account for the differences in earthquake depth and origin time. This is a simplistic correction and does not correctly account for the time shifts of secondary phases (i.e., pre-critical arrivals from the major discontinuities), whose arrival times relative to the first arrival depend on earthquake depth. However, some type of correction needs to be made to each array beam in order to get a reasonable $\tau$-$p$ transformation. To account for the difference in source mechanism, we perform the wavefield continuation calculations on the envelopes of the beams rather than the raw amplitude records. This acts as a low-pass filter, reducing the resolution of the resulting velocity-depth profile.

The wavefield continuation method consists of two linear transformations of the wavefield record sections. First, record sections are slant stacked, transforming them from the distance-time domain into the $\tau$-$p$ domain (Figure 5b). This is followed by a downward continuation, or depth migration, of the wavefield to transform the $\tau$-$p$ data to the slowness-depth plane. This second step is an iterative process, where the $\tau$-$p$ data are repeatedly migrated until the slowness-depth image converges to the input velocity model (Figure 5c). There are several ways to update the velocity model between iterations. We are currently using a scheme that picks the maximum amplitude at each depth from the slowness-depth image and then computes the weighted average between it in the input velocity model. This scheme performs adequately; however, noise in the initial $\tau$-$p$ transformation can cause artifacts in the final velocity-depth profile. We are currently working on methods to improve the iterative migration procedure.

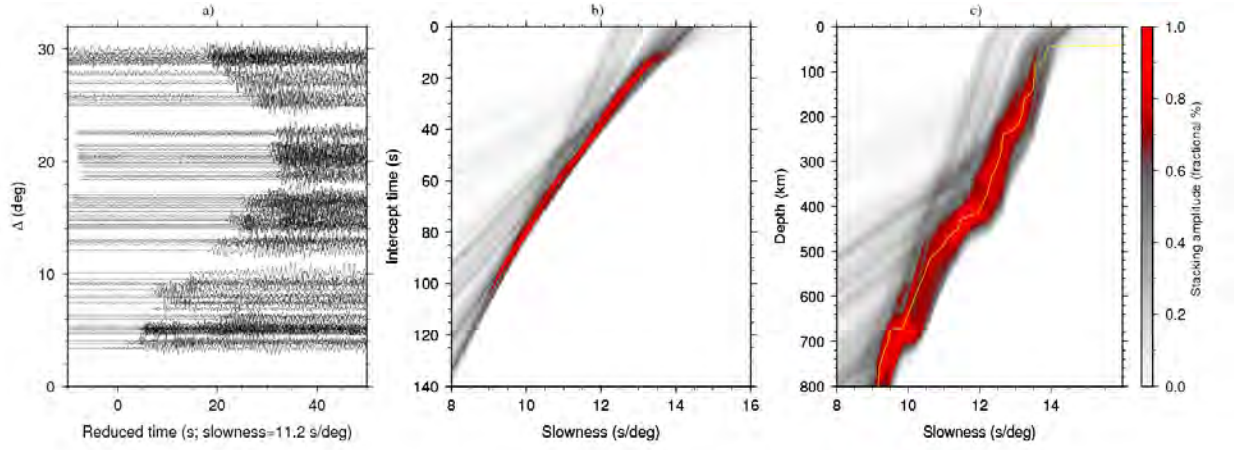


**Figure 5. Example showing the transformation of a record section (a) to the $\tau$-$p$ domain (b) and the downward continuation to the slowness-depth domain (c). Array beams are from 104 earthquakes that extend from the Hindu Kush region of Pakistan/Afghanistan to the Makran coast and Zagros mountains of Iran.**

Figure 6 shows a comparison of our preliminary velocity-depth profile derived from the wavefield continuation procedure to the iasp91 model. Below 400 km depth, our model exhibits moderately slower velocities than iasp91, and a gradient zone at the 410 km rather than a sharp discontinuity (Figure 6a). A comparison of the slowness vs. distance curves for the predicted *P* arrivals for each model are shown in Figure 6b. Here the differences are more apparent, where our derived model shows more structure above the 410 km discontinuity (slowness < ~12 sec/deg), and a significant difference in the caustic points of both the 410 km (termination of B-C branch in Figure 6b) and 660 km discontinuity (termination of D-E branch). While our model is preliminary, some of the features we observe may be related to an inadequate distance sampling of our array beams, as well as the windowing procedure used in the initial $\tau$-$p$ transformation. Both of these would explain the initial appearance of the predicted 410 km and 660 km triplicate arrivals at greater distances (18° and 20°, respectively) in our derived model than the iasp91 model, where they appear at 14° and 18°, respectively.

.

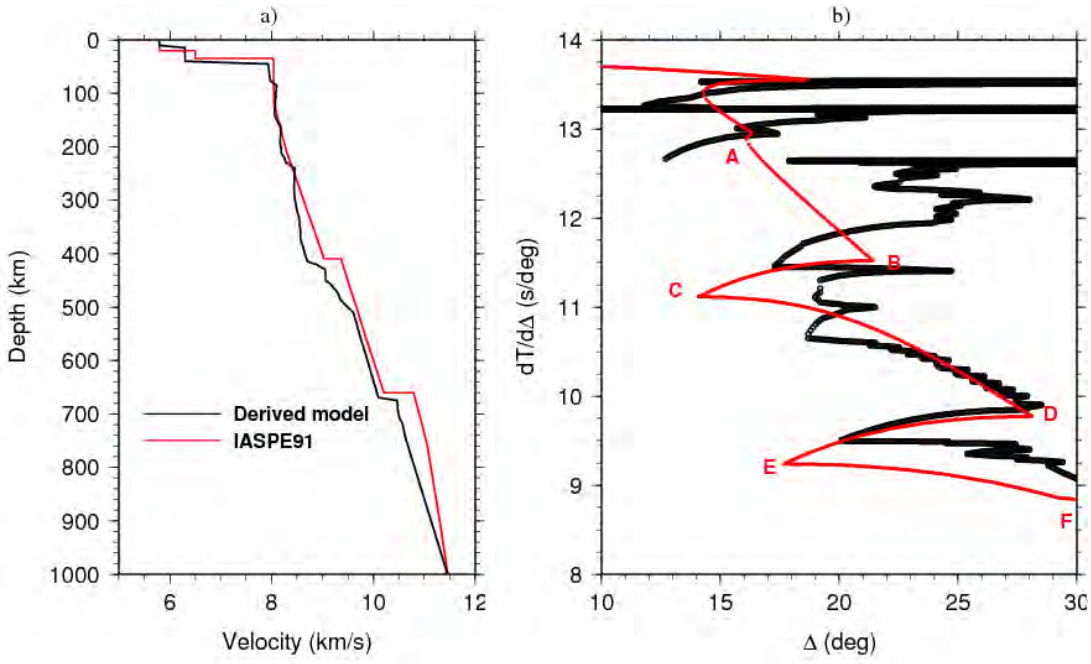


**Figure 6. Comparison of the velocity-depth profile from wavefield continuation to the iasp91 reference model: (a) derived model (black) and iasp91 model (red). (b) Slowness vs. distance comparison between the derived model (black) and the iasp91 model (red) for predicted *P* arrivals.**

**Waveform Templating for Groups of Like Waveforms**

Another component of our phase characterization methodology is the analysis of the array beams using clustering techniques. In addition to the arrival times and slowness of the coda phase arrivals, phase-weighted stacking analysis yields array beams, which are then input to a waveform clustering algorithm. The algorithm is based on 'fuzzy clustering' to form groups of beams that exhibit similar characteristics; it has been used widely in pattern recognition applications (Bezdek, 1981). Clusters are defined by assigning each beam a cluster membership value, which is a quantitative measure that incorporates a distance measure between each array beam and a representation of the cluster centers. We have experimented with distance measures involving *L1* and *L2* norms, as well as waveform semblance, with varying degrees of success that depend on data noise levels. From each cluster of similar beams, we derive a template waveform using a stacking process that weights each cluster member by its degree of membership to that particular cluster. The 'fuzziness' of the method allows a single beam to be a member of more than one cluster group. The objective behind the waveform clustering is to reduce the database of observations to a set of representative waveforms that exhibit consistent phase-arrival behavior. Sometimes the clustering is geographic, but there are other wave phenomena that can also produce groupings of similar waveforms

Figure 7a shows the cluster group and its associated wavefield template that results from applying our waveform clustering algorithm to the set of 100 events shown in Figure 7b. These beams are derived from seismograms recorded by the MKAR array in the 14°–29° distance range that extends from northern Pakistan to the Makran coast in Iran. In this example, the algorithm clusters the events into 5 groups, with 12–24 members per group. We applied an *L2*-norm distance measure and aligned the array beams prior to clustering using multi-channel cross correlation (VanDecar and Crosson, 1990), applied to the first four seconds of each beam signal. We have found the alignment of the beams to be beneficial to the clustering procedure. However, the length of the cross-correlation window is an important variable. For example, if the window is too long, the array beams align on the maximum amplitude signal in the record. For some beams, the maximum amplitude arrival may occur early in the seismogram, while for others it occurs much later. This can result in some unusual clustering of events that seems counter-intuitive. For this reason, we find clustering methods based strictly on cross correlation, as used in other types of studies (e.g., Menke 1999; Ferretti et al., 2005; Barani et al., 2007) are not suitable for our particular needs.

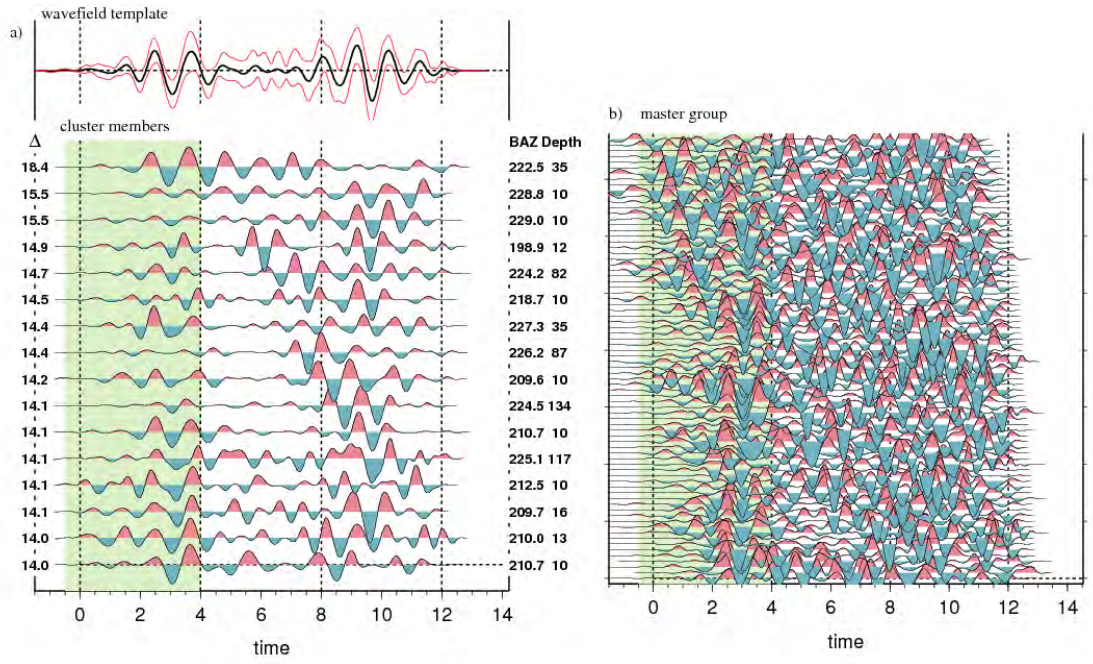


**Figure 7. Example of wavefield clustering to generate a wavefield template. (a) The bottom panel shows the cluster members sorted by epicentral distance (shown on the left). The green band highlights the time band of cross correlation. The top panel shows the computed wavefield template (black) and 1-$\sigma$ deviation (red). (b) A record section of all 100 earthquakes input to the clustering algorithm.**

For the example shown in Figure 7, the resulting cluster members include earthquakes that are near the 14.3° distance range, but some more distant earthquakes are also included. The earthquake depth range is also variable, but may be due to poorly constrained catalog depths. In general, the cluster members show consistent waveform structure in the cross-correlated portion of the signal. Later arrivals show more variability between the cluster members, but still appear to align well at approximately 8 seconds and later. The most variability occurs between 4 and 8 seconds delay time, where some records show large amplitude arrivals while other show little signal. Some of this variability is likely due to differences in earthquake distance, triplicated arrivals, and the presence of depth phases. We continue to refine and improve the wavefield clustering algorithm.

**Phase Characterization Analysis**

To characterize observed phase arrivals, we calculate different misfit measures between our suite of body-wave synthetic seismograms and the observed wavefield templates. Since the synthetic waveforms are generated from models derived from the $\tau$-$p$ data, arrival times of the wavefield templates should be well matched. We note that to derive meaningful measurements, we must account for frequency content and amplitude variations.

Figure 8 provides an example of how we fit the synthetic seismograms to the wavefield template shown at the right of Figure 7. We computed synthetics using a test model (CRUST2.0 over AK135) for focal depths ranging from 0–60 km and event distances between 14° and 30°. Then we calculated the *L2* root-mean-square (RMS) residual of the differences between the wavefield template and each synthetic seismogram. The left panel in Figure 8 shows the results of this exercise, with a black cross denoting the distance (15.4°) and depth (32 km) at which the minimum RMS value occurs. In general, the best-fitting synthetic fits the overall structure of the template, even though the method is fairly crude. However, a portion of the wavefield template does not fit well (between 7–8 s), and this may be due to a number of causes. For instance, the test model we used to generate the synthetics may be inaccurate. Also, the focal mechanism or the misfit measure we employed in the comparisons could be inadequate.

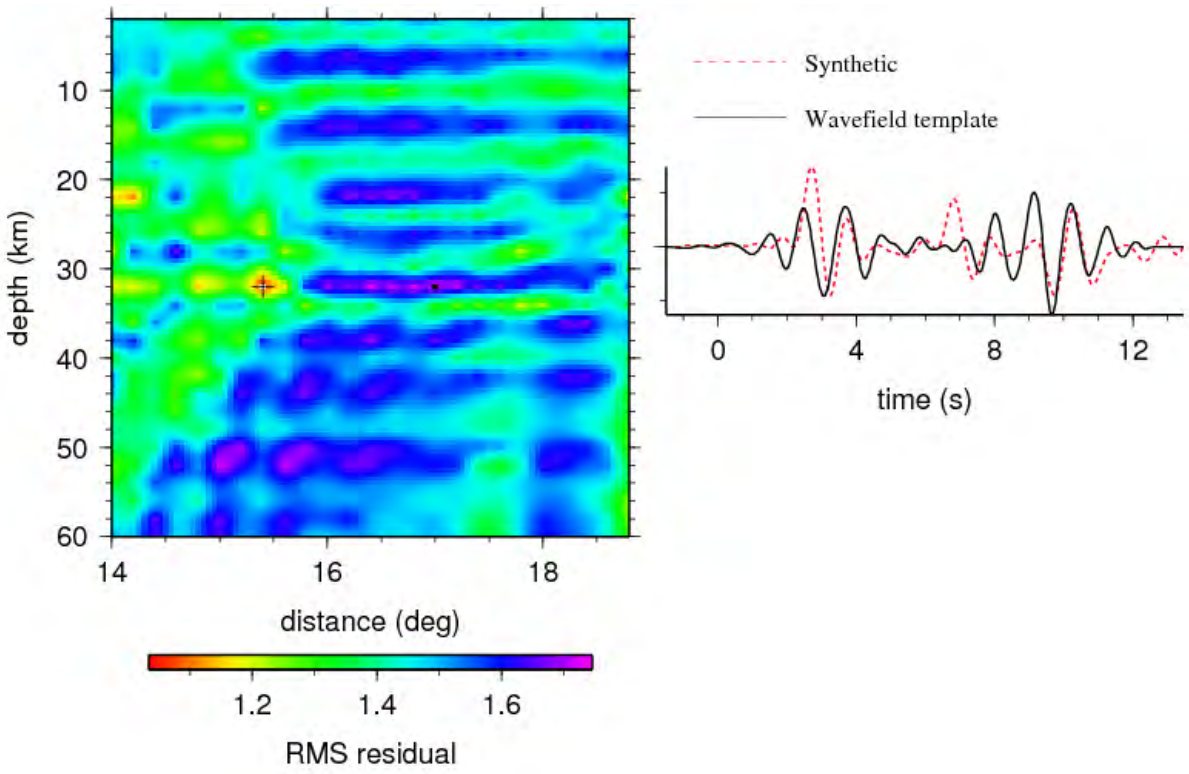


**Figure 8. Example of fitting synthetic seismograms to an empirical wavefield template. Right panel shows the wavefield template (black) and the best-fitting synthetic (red). The left panel shows an image of the root mean-square residual between the wavefield template and a suite of synthetics computed for varying event distance and depth. The best-fitting synthetic for this wavefield template corresponds to a distance of 15.4° and an event depth of 32 km (black cross).**

## CONCLUSIONS AND RECOMMENDATIONS

Regional seismic arrays that have been recently installed for nuclear monitoring are under-utilized in the study of far-regional arrivals. The small aperture of many of these arrays (< 5km) restricts their usefulness at these distances beyond first arrival onset picks of *P* and *S* waves. However, our research is overcoming this limitation by applying refined array processing techniques in conjunction with $\tau$-*p* and wavefield templating analysis methods. Our methodology improves the characterization of primary and early coda-phase arrivals observed at far-regional and near-teleseismic distances. Our approach is to distill the wide variety of seismicity we observe to subsets of commonly and robustly observed phase-arrival phenomena. We are then using well-accepted modeling and inversion techniques to explain these phenomena. Our aim is to explain as much of the phenomena as we can with simple and straightforward techniques, leaving the anomalies for future research.

We are developing and applying our techniques to central Asian earthquakes recorded on the MKAR and KKAR arrays in Kazahkstan. Our results indicate that we can differentiate between the numerous arrivals of the early coda. However, global reference models cannot capture the phase succession and arrival-time behavior we observed from the complex tectonic regions of central Asia. To address this, we are developing regional 1-D models directly from the array measurements (delay-times, slowness, and beams). Since these models are derived from the data, they should better explain the phase behavior we observe from specific regions. To test these models and further improve phase characterization, we are constructing 'wavefield templates' through cluster analysis to generalize the waveform structure from the different seismic regions. The templates are then used in a waveform fitting analysis to gain a better understanding of the phase phenomenon observed from the complex seismic regions of central Asia.

## REFERENCES

Barani, S., G. Ferretti, M. Massa, and D. Spallarossa (2007). The waveform similarity approach to identify dependent events in instrumental seismic catalogues. *Geophs. J. Int*. 168: 100–108.

Bezdek, J. C. (1981). Pattern recognition with fuzzy objective function algorithms, Plenum Press, New York.

Carbonell, R. and S. B. Smithson (1994). Inversion of reflected *PP*, *SS*, and converted *PS*/*PP* travel times for crustal structure, *Bull. Seism. Soc. Am.*, 84, 1889–1902.

Clayton, R. and G. McMechan (1981). Inversion of refraction data by downward continuation, *Geophysics* 46: 6, 860–868.

Ferretti, G., M. Massa, and S. Solarino (2005). An improved method for the recognition of seismic families: Application to the Garfagnana-Lunigiana Area, Italy. *Bull. Seism. Soc. Am*. 95: 1903–1915.

Ferris, A. and D. Reiter, (2007). Using small-aperture arrays to identify far-regional P-wave arrivals, in *Proceedings of the 29th Monitoring Research Review: Ground-Based Nuclear Explosion Monitoring Technologies*, LA-UR-07-5613, Vol. 1, pp. 14–23.

Kennett B. L. N. and E. R. Engdahl (1991). Travel times for global earthquake location and phase identification, *Geophys. J. Int.* 105: 429–465.

McMechan, G. A. (1984). Inversion of a refraction wavefield by imaging in the p-x and v-z planes, *Geophys. J. R. Astr. Soc.* 78: 723–733.

Menke, W. (1999). Using waveform similarity to constrain earthquake location, Bull. *Seism. Soc. Am.*, 89, No. 4, 1141–1146.

Morozov, I. B., E. A. Morozova, S. B. Smithson, P. G. Richards, V. I. Khalturin, and L. N. Solodilov (2005). 3D First-arrival regional calibration model of northern Eurasia, *Bull. Seism. Soc. Am.* 95: 951–964.

Schimmel N. and H Paulssen (1997). Noise reduction and detection of weak, coherent signals through phase weighted stacking, *Geophys. J. Int.* 130: 497–505.

VanDecar, J. C., and R. S. Crosson (1990). Determination of teleseismic relative phase arrival times using multi-channel cross-correlation and least squares, *Bull. Seis. Soc. Am.* 80: 1, 150–159.

# APPLICATIONS OF A CONSTRAINED INVERSION AND AN EXTENDED KRIGING METHOD TO IMPROVE SOURCE, PATH, AND SITE CORRECTIONS FOR REGIONAL SEISMIC PHASES

Mark D. Fisk[1] and Steven R. Taylor[2]

Alliant Techsystems[1] and Rocky Mountain Geophysics, LLC[2]

Sponsored by National Nuclear Security Administration

Contract No. DE-AC52-06NA27321
Proposal No. BAA06-19

## ABSTRACT

Objectives of this project are to develop and apply two methods to improve source and path corrections for regional seismic phases. In the first, we estimate and constrain source parameters using Brune (1970) model fits to relative spectra of regional seismic phases for event pairs with similar locations and focal mechanisms, but different seismic moments. We then use the source-corrected spectra to estimate geometrical spreading, Q, and site terms for Pn, Pg, Sn, and Lg in Eurasia. This constrained approach eliminates a fundamental trade-off, thereby improving estimates of source and distance corrections. We performed a preliminary study using waveform cross-correlations from Dr. Schaff for events prior to 2000 in Eurasia to find suitable pairs. We extended the analysis to event pairs in Eurasia from 2000 to 2006. Using the Preliminary Determination of Epicenters (PDE) catalog, we formed a list of candidate pairs, acquired a very large volume of regional data from the Incorporated Research Institutions for Seismology (IRIS), and computed waveform cross-correlations to find pairs of similar events. We computed and fit network-median relative spectra for almost 3,600 pairs. We automated these processing steps and finished reviewing and refining the results. We merged these results with our previous ones to obtain more extensive estimates of source corner frequencies versus moment and stress-drop parameters for Eurasia. We generated kriged grids of stress drop and associated uncertainties. We further fit the combined distance and site terms to the source-corrected spectra, showing that robust estimates of these effects are possible by first constraining source terms. We describe further work to separately constrain Q, geometrical spreading, and site parameters.

The second method, an extension to Bayesian kriging, provides robust path corrections and uncertainties for regional phase amplitudes, that properly treats localized calibration events that may have anomalous, correlated amplitudes. Clusters of anomalous reference events can significantly bias kriged amplitude corrections and uncertainties, if this correlation is not treated. Fisk and Taylor (2007) demonstrated the problem for a cluster of Rock Valley earthquakes at the Nevada Test Site (NTS) that have very high Pn/Lg values, leading to miscategorization of some NTS explosions. To address this issue, Fisk and McCartor (2008) developed a fundamental improvement to the kriging methodology, incorporating an additional correlation length to treat similar focal mechanisms, and tested the method on the NTS datasets and on large samples of underground nuclear explosions (UNEs) and earthquakes worldwide. Application to the worldwide datasets indicates that the power of the hypothesis test to reject earthquakes as explosions is marginally reduced, without miscategorizing any known explosions and providing a robust treatment of clustered data.

## OBJECTIVES

We have been developing and testing two methods to improve magnitude and path corrections for regional seismic phase amplitudes. Objectives of the first method, a constrained inversion approach, are to improve estimates of geometrical spreading and Q models for Pn, Pg, Sn, Lg in Eurasia, by eliminating trade-offs with source corner frequencies, and to improve source parametrizations in Eurasia, in terms of grids of stress drop and corner frequency scaling. The objective of the second method, an extension to Bayesian kriging, is to provide robust path-specific corrections and uncertainties for regional phase amplitudes, that properly treat localized calibration events that may have anomalous, correlated amplitudes. This project has three main tasks: (Task 1) Assemble multiple datasets of regional seismic recordings of earthquakes throughout broad areas of Eurasia; apply waveform cross-correlation techniques to determine nearby pairs/clusters of events; and assemble spectral amplitude measurements of Pn, Pg, Sn, and Lg for the events. (Task 2) Implement a technique to estimate corner frequencies and scaling parameters by fitting relative spectra of a Brune model to data for pairs of nearby earthquakes of different moments; compute grids of stress drop and earthquake corner-frequency scaling with moment for Eurasia; use spectral amplitude data for regional phases and constrained source parametrizations to perform a robust inversion for geometrical spreading and Q-model parameters; and test and evaluate resulting magnitude and distance corrections on events in Eurasia, using cross-validation methods. (Task 3) Investigate clusters of earthquakes to assess the potential for events with anomalous, correlated mechanisms to bias kriged amplitude correction grids beyond existing uncertainty estimates; develop a technique to quantify the correlation of regional phase amplitudes within clusters; extend a Bayesian kriging method to incorporate these correlation measures in the computation of amplitude correction and uncertainty grids; and test and evaluate the methods on events in Eurasia, using cross-validation techniques. We plan to deliver the techniques, parametrizations of stress drop, corner frequency scaling, geometrical spreading and Q models, and kriged amplitude correction and uncertainty grids for stations in Eurasia.

## RESEARCH ACCOMPLISHED

### *Constrained Inversion Technique*

We have implemented and applied an approach to constrain the source parameters for earthquakes throughout Eurasia, using Brune (1970) model fits to relative spectra of regional phases for nearby event pairs/clusters with similar mechanisms, but different seismic moments. We assembled and processed very large datasets for this effort. We have further estimated fits of the combined distance and site terms, which show that robust estimates of these effects may now be obtained by first constraining and removing the source scaling. Following Sereno et al. (1988) and Taylor and Hartse (1998), the amplitude spectrum for a given phase and station, for event i, may be modeled by

$$A_i(f) = S_i(f, f_c) G(r_i, r_0) \exp\left(-\frac{\pi f}{Q(f) v} r_i\right) P(f), \qquad \text{(EQ 1)}$$

where $S_i(f, f_c)$ is the source spectrum with corner frequency $f_c$, $r_i$ is the epicentral distance, $v$ is the group velocity, $P(f)$ is the site term, $Q(f) = Q_0 f^{\hat{\gamma}}$ is the frequency-dependent attenuation, $G(r, r_0)$ is the frequency-independent geometrical spreading, taken to be inversely proportional to distance to a power $\eta$, beyond a reference distance $r_0$. Taylor et al. (2002) and others have used the logarithm of Equation (1) in a grid search to simultaneously estimate all of the parameters. However, significant trade-offs among the parameter estimates are well known and difficult to constrain by standard techniques and available data (e.g., Taylor and Hartse, 1998). This has led to grossly inaccurate corrections of regional amplitudes for distance and magnitude. Fisk and Taylor (2006) discuss examples.

Instead of performing a grid search for all parameters simultaneously, we use relative spectra for event pairs with similar locations and focal mechanisms (assessed by waveform cross-correlations), but different moments, to factor

out path and station effects and obtain reliable estimates of the source parameters. That is, for a pair of nearby earthquakes with similar radiation patterns, the model relative spectra for a given phase type is given by

$$\frac{A_1(f)}{A_2(f)} = \frac{S_1(f)}{S_2(f)} = \frac{M_0^{(1)}[1 + (f/f_c^{(2)})^2]}{M_0^{(2)}[1 + (f/f_c^{(1)})^2]}. \qquad \text{(EQ 2)}$$

For a Brune (1970) dislocation source, the corner frequency for seismic phase type $\xi$ is given by

$$f_c(\xi) = c_\xi v_s(\xi)\left(\frac{\sigma_b}{M_0}\right)^{1/3}, \qquad \text{(EQ 3)}$$

where $\sigma_b$ is the stress drop, $v_s(\xi)$ is the source medium velocity for P or S waves, and $c_\xi$ is a constant that can depend on phase type. Walter and Taylor (2002) allow for non-constant stress drop by defining the apparent stress drop for a given seismic moment, $M_0$, as

$$\sigma_b = \sigma_b^{(0)}\left(\frac{M_0}{M_0^{(0)}}\right)^{\psi}, \qquad \text{(EQ 4)}$$

where $\sigma_b^{(0)}$ is the stress drop at reference moment $M_0^{(0)}$. Using pairs of localized earthquakes, we fit $\sigma_b^{(0)}$ and $\psi$ to empirical relative spectra of regional phases. Figure 1 illustrates the network-averaged relative spectra and model fits for an earthquake pair in Kyrgyzstan during 1997. The relative spectra are quite similar for the various phases, although over different frequency ranges because of phase-dependent signal-to-noise limitations. Hence, the model fits, and estimated corner frequencies are very similar. This appears to be a fairly common and important phenomenon for the earthquakes analyzed.

Using waveform cross-correlations for 4,236 events in Eurasia prior to 2000 (*cf.* Schaff and Richards, 2004) to find a subset of event pairs in the Los Alamos National Laboratory (LANL) database, we acquired seismograms from IRIS, added and refined regional phase picks, computed the spectra, averaged relative spectra over stations, and fit the model for each phase, and for all available phases simultaneously, as in Figure 1. We allowed the relative moments to be estimated from the relative spectra or to use moment magnitudes ($M_W$) from LANL. We performed three types of fits in which the apparent stress-drop scaling parameter, $\psi$, is a free parameter or fixed at 0.0 or 0.25. The latter two cases correspond, respectively, to corner frequency scaling as $M_0^{-1/3}$ (Brune, 1970) or as $M_0^{-1/4}$ (Nuttli, 1983; Cong et al., 1996; Walter and Taylor, 2002). We computed kriged grids of stress drop for these three cases.

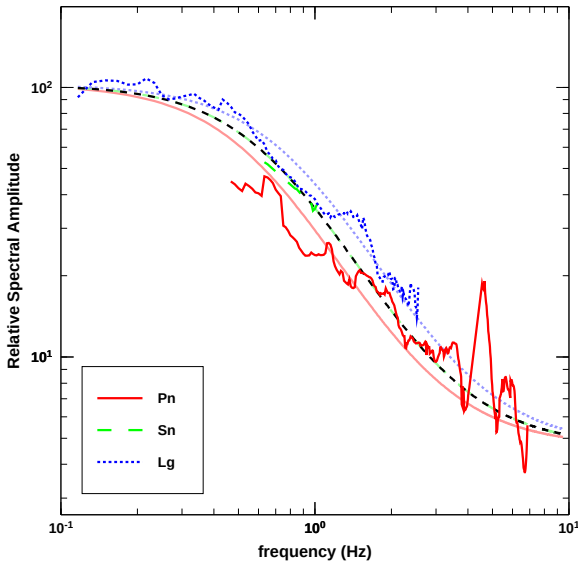


**Figure 1. Example of relative spectra for a pair of $M_W$ 6.0 and 4.7 earthquakes in Kyrgyzstan. Model fits for each phase are represented by corresponding line types. The black dashed curve shows the model fit using relative spectra for all available phases.**

Figure 2 shows corner frequency estimates versus log moment for Pn, Sn, and Lg for events in Eurasia, fixing $\psi = 0$ in this case. Linear fits are shown with (dashed) and without (solid) the slopes fixed at –1/3. Considering the amount of scatter due to spatial and other variations, the fits are remarkably consistent for all phases, and the slope estimates are all close to –0.33, although the slope estimates depend on the explicit treatment of $\psi$. Figure 3 shows that Pn and Lg corner frequencies are fairly similar for most of the earthquakes in diverse areas of Eurasia, comparable to findings by Walter and Taylor (2002) for western U.S. earthquakes. This is important for two reasons. First, it helps explain why P/S ratios discriminate more effectively at higher frequencies, in most areas examined (provided path and station effects are properly treated). That is, as shown by Fisk (2006, 2007) the frequency dependence of P/S discrimination performance depends on the ratio of P- and S-wave corner frequencies squared. This ratio is significantly larger for explosions than earthquakes at all sites examined. Thus, P/S ratios exhibit less frequency

dependence for earthquakes than explosions. Second, this result allows more robust fitting of Brune source parameters, using a broader range of frequencies, by combining relative spectra of regional P and S phases for earthquakes (e.g., the black dashed curve in Figure 1).

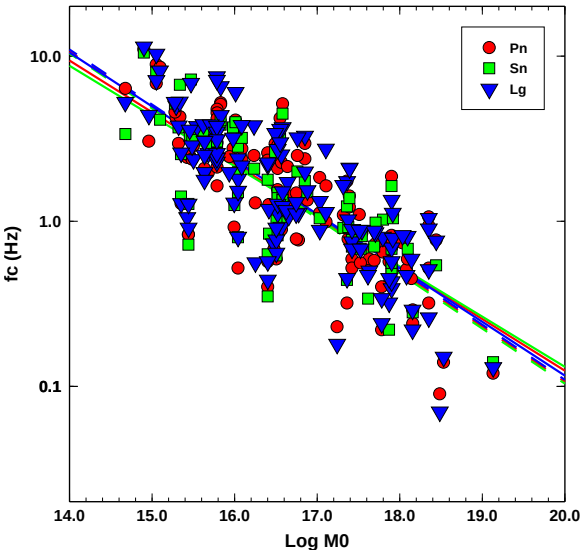


**Figure 2. Corner frequency estimates of Pn, Sn, and Lg spectra versus log moment for events in Eurasia. Linear regression fits (lines) are shown, indicating scaling with source size.**

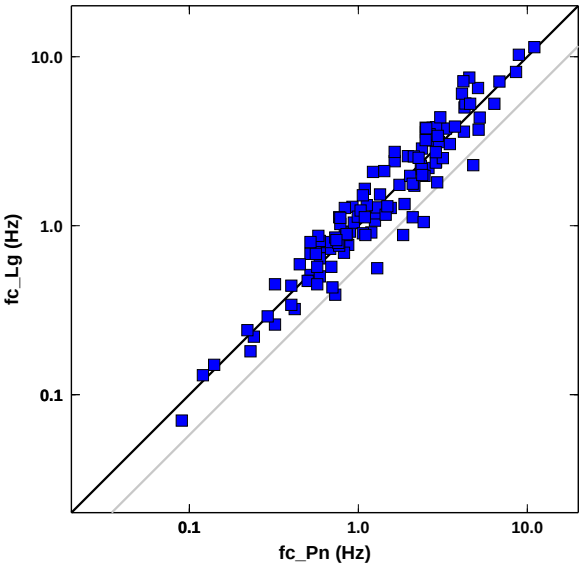


**Figure 3. Estimated Lg versus Pn corner frequencies, indicating similar values for most of the earthquakes. Black and gray lines represent ratios of 1.0 and 1.73 (*cf.* Madariaga, 1976; Choy and Boatwright, 1995).**

Figure 4 shows preliminary kriged stress-drop grids based on Lg (left) and Pn (right) data. The grids are very similar, indicating similar stress-drop estimates from Lg and Pn. There are concerns that stress-drop estimates by other approaches are biased due to trade-offs with Q (e.g., Phillips et al., 2008, discuss stress drop bias in low Q regions). Such bias is not present in our analysis because we use relative spectra that factor out Q effects.

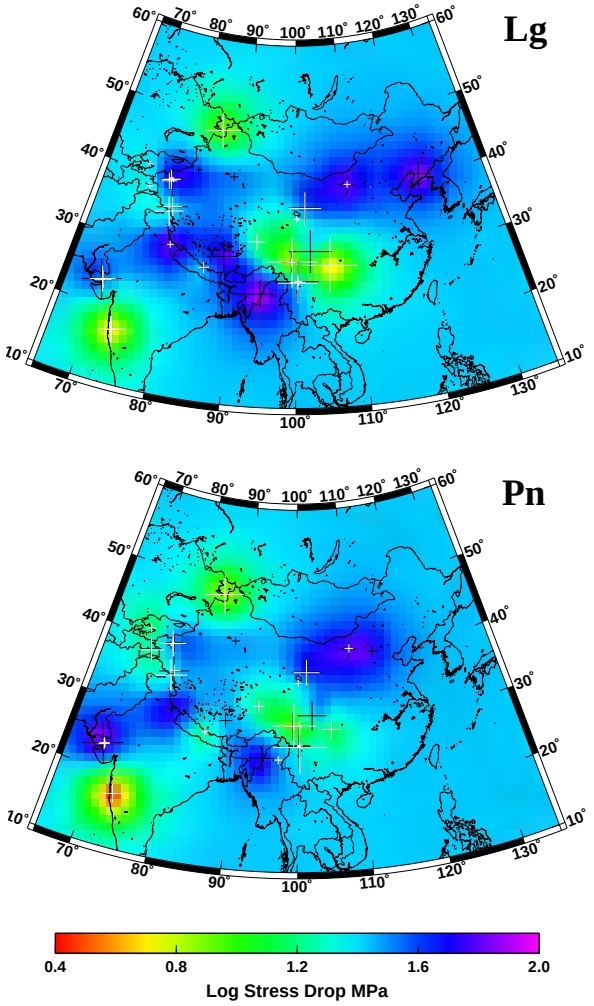


**Figure 4. Initial kriged grids of stress drop based on estimates from Lg (top) and Pn (bottom) relative spectra. The size and color of the markers indicate the absolute residual and sign relative to the grid.**

We extended our analysis of relative spectra to event pairs in Eurasia from 2000 to 2006 (see Figure 5). Using the PDE catalog, we formed a list of candidate pairs, based on proximity and relative mb or $M_W$ values in the PDE, and acquired a very large volume of regional data

from the IRIS Data Management Center (DMC) for the events. We then computed waveform cross-correlations to find similar event pairs, like the analysis by Schaff and Richards (2004). We computed and fit network-median relative spectra for almost 3600 pairs of events. We have automated all of these processing steps, although it is still necessary to review and refine the results. In the Brune model-fitting analysis, we fix the moment of the larger event of the pair (in the numerator), assuming it is better recorded and, hence, has a more reliable moment estimate. We then estimate the moment of the smaller event, based on the network-median relative spectra.

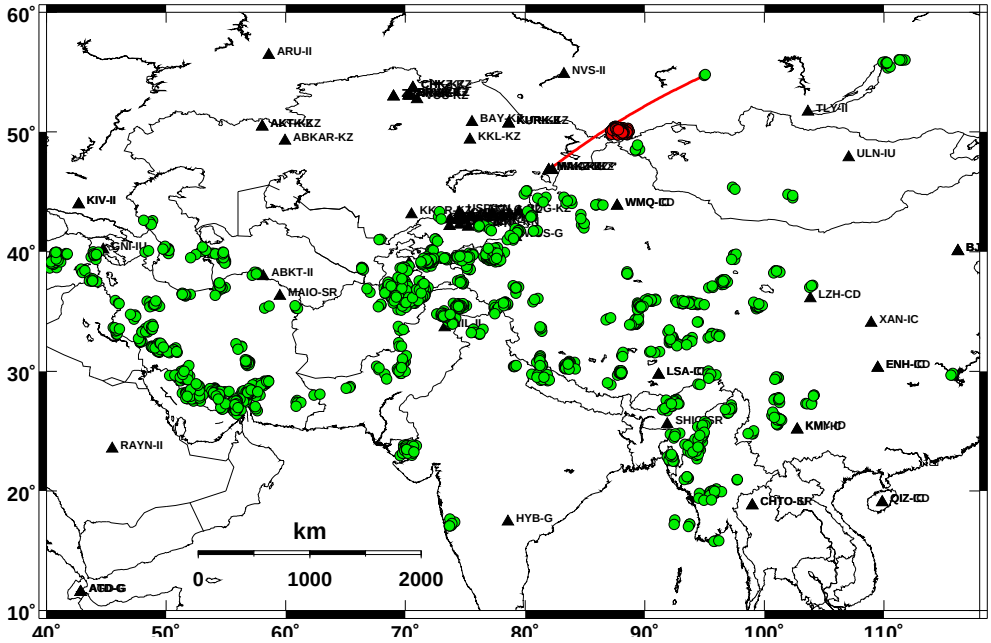


**Figure 5. Events and stations used to process relative spectra and fit corner frequencies and stress drops. The cluster highlighted in red and the great-circle path along two clusters to MAKZ are discussed below.**

We have finished reviewing and refining the automatic processing and Brune model-fitting results, completing a major and important quality control (QC) effort. Figure 6 shows an example for one event pair associated with the highlighted cluster in Figure 5. Figure 7 shows the corner frequency estimates for all pairwise combinations using three large master events (circles, diamonds, and squares), the median value for each event (triangles), and the scaling relation with log moment (line) for this cluster. These plots indicate the degree to which the source parameters may be constrained by our approach. We have merged these results with our previous results (that were processed purely manually, including phase picks, spectral processing, network averaging, and model fitting) to obtain more extensive estimates of corner frequencies versus moment and stress-drop parameters for Eurasia. We have generated kriged grids of stress drop and the associated uncertainties for Eurasia (Figure 8).

We have used the estimated Brune source terms (corner frequencies and stress drops) to correct the spectra for source scaling. We generally find that the source-corrected spectra are quite similar for events in a given cluster, indicating that the source corrections are very consistent, based on our Brune model fitting of the relative spectra. Using these instrument- and source-corrected spectra, we have estimated the combined effects of Q, geometrical spreading, and site effects. Under the standard model of Equation (1), geometrical spreading is a constant (i.e., independent of frequency) for a cluster at a fixed distance from a given station. This allows the frequency-dependent Q and site terms to be fit to the corrected log spectra versus log frequency. The constant of this fit involves geometrical spreading and a constant site factor. We use the median of the corrected spectra for a given cluster/station, which is more robust to outliers than the average. Results of these fits to various clusters have been very encouraging.

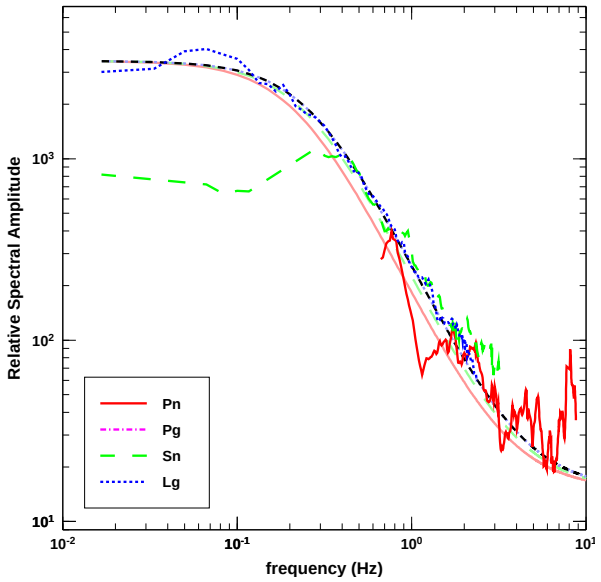


**Figure 6. Network-median relative spectra of Pn, Sn, and Lg for a pair of events in the cluster depicted by red markers in Figure 5. Also shown are the Brune relative source model fits (smooth curves).**

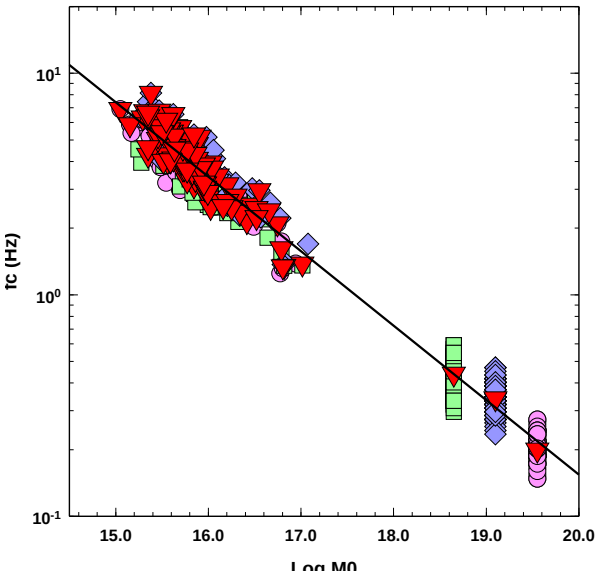


**Figure 7. Corner frequency versus log moment for the cluster highlighted by red markers in Figure 5, estimated by fitting the combined relative spectra of Pn, Sn, and Lg, as in Figure 6. Shown are estimates for all pairwise combinations using three large master events (circles, diamonds, squares), the median value for each event (triangles), and the scaling relation with log moment (line) for this cluster.**

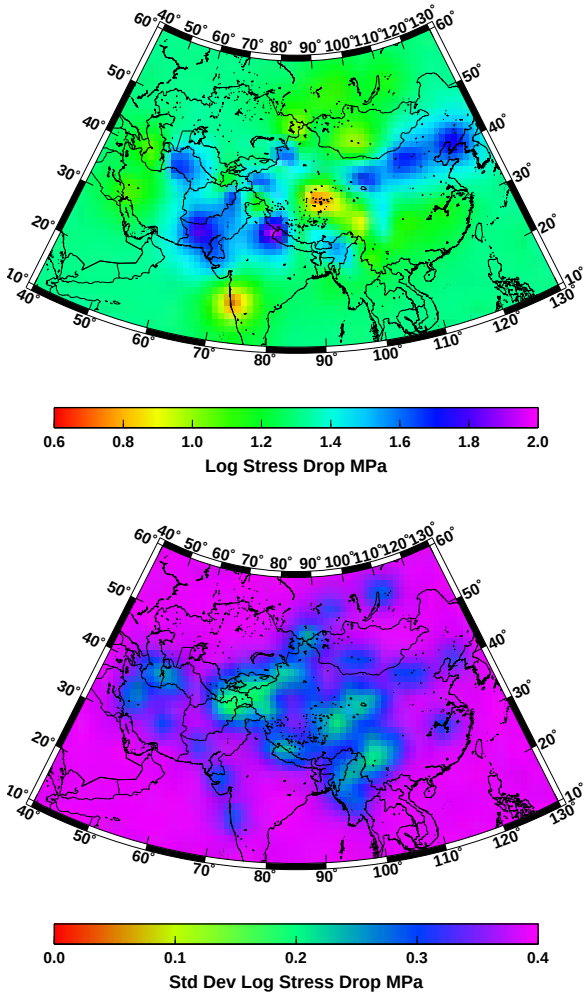


**Figure 8. Updated kriged grids of stress drop (top) and calibration standard deviation (bottom) using combined relative spectra of Pn, Sn, and Lg and merging our initial and recent processing results.**

For example, Figure 9 shows the source-corrected Lg spectra at BRVK (Borovoye, Kazakhstan) for the cluster depicted by red circles in Figure 5. It illustrates several important aspects of our analysis. First, the light blue curves show the corrected Lg spectra for each event that was recorded by BRVK. Overall, the curves are fairly similar in shape and relative amplitude offset, indicating that the corrections for source terms (moments and corner frequencies) are effective and consistent. There are modest departures at low and high frequencies, where noise effects bias the spectra. Second, the median corrected Lg spectrum (red curve) for the cluster is robust to outliers. For example, the lowest blue curve is

due to a bad BRVK BHZ recording that slipped through the automated QC criteria. Although such cases are rare, they can significantly impact the mean, if used instead of the median. Third, the fit (black curve) to the median spectrum illustrates very good agreement over a wide range of frequencies. We have generated comparable results for all of the recording stations and for other clusters (i.e., paths) with various numbers of events.

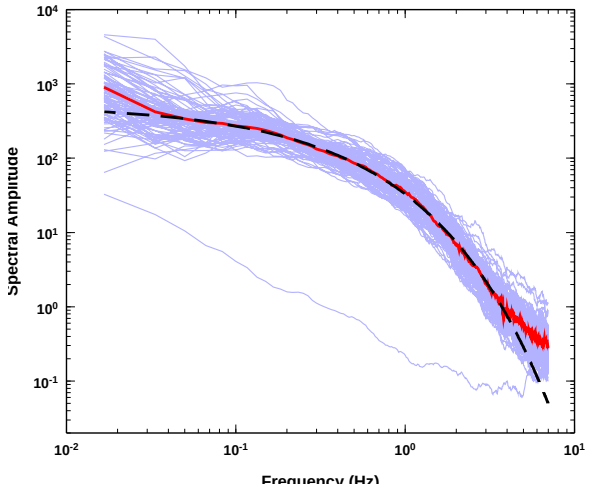


**Figure 9. Source-corrected Lg spectra at BRVK for all events in the cluster (blue), the median (red), and a model fit of the combined distance and site effects (black dashed).**

The black dashed curve provides excellent calibration over a wide range of frequencies for all of the combined non-source-related physical effects (Q, spreading, and site terms) for this path/station. For an isolated cluster, these fits do not provide independent, reliable estimates of the individual path and site parameters. For example, to estimate accurate Q parameters ($Q_0$ and $\gamma$), we need to separate their frequency dependence from that of the site term. One option is to use all available source-corrected spectra to perform a large inversion for these remaining parameters. This will give distinct parameter estimates but, based on experience, these quantities will still have trade-offs that are not well constrained.

We have also been investigating alternative, more innovative analyses to constrain the remaining trade-offs and separate the path and site effects that do and do not depend on frequency and distance. Separating these terms is important and beneficial for several reasons. First, it allows physical interpretation and comparison of estimated model parameters to other results. Second, it allows more reliable interpolation of spatially-varying physical parameters (e.g., $Q_0$). Third, it allows merging results we obtain with existing models at LANL. Note that the constant term of the model fit to the source-corrected spectrum (e.g., the offset of the black curve in Figure 9) depend only on geometrical spreading and a constant site term. Since the former term depends on distance and the latter does not, we can use the constants of the fits for all clusters/pairs of events recorded by a given station at different distances to separately constrain them. Once we estimate these terms, the only remaining parameters to be resolved are $Q_0$, $\gamma$, and one that governs the frequency dependence of the site term. We have investigated various approaches for this final step. One is to insert the spectra for all of the events in our datasets, now corrected for all but these two terms, into a grid search for three parameters. This is a much smaller parameter space than the full space associated with Equation (1). As in separating the spreading and constant site terms, $Q_0$ and $\gamma$ can be separated from the frequency-dependent site term by distance.

Another approach that imposes an additional constraint on these last 3 parameters is to use the relative median spectra for clusters with similar paths, but at different distances from a station, to factor out the site term and obtain a robust estimate of Q for that path. This estimate of Q has no trade-off with source, site, or geometrical spreading effects. Figure 10 illustrates this approach. It shows the ratio of the median spectra at station MAKZ (Makanchi, Kazakhstan), already corrected for source terms, for the two clusters along the great-circle path in Figure 5. This relative spectrum factors out the site term. The geometrical spreading terms for these two clusters are different constants, i.e., independent of frequency. Mathematically, assuming Q is relatively constant over a path, the ratio of source-corrected, median spectra for the two clusters is simply given by

$$\log(\bar{A}_1/\bar{A}_2) = \frac{\pi f^{1-\gamma}}{Q_0 v}\Delta r, \qquad \text{(EQ 5)}$$

where $\Delta r$ is the separation of the clusters. Fitting this expression to empirical spectral ratios gives constrained estimates of $Q_0$ and $\gamma$ (e.g., Lg $Q_0 = 546$ for the path depicted in Figure 5 and associated with Figure 10).

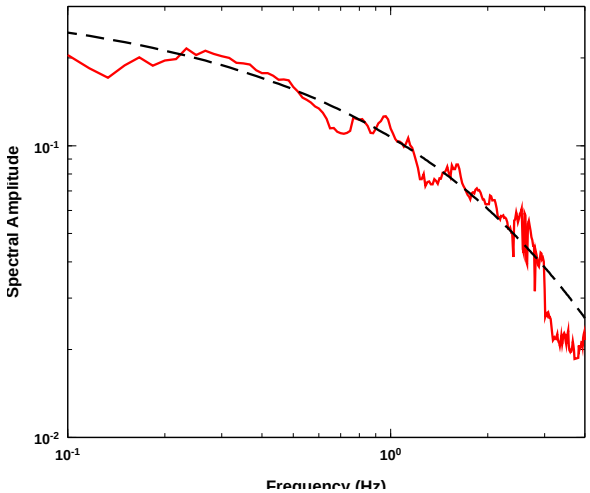


**Figure 10. Ratio of source-corrected median spectra at MAKZ for two clusters along the great-circle path in Figure 5. The relative spectrum factors out the site term and allows a robust estimate of Q for this path.**

Correcting the source-corrected spectra of these clusters now for Q, the remaining frequency dependence is due to site effects. Once this is done for at least one path, the frequency-dependent site term may be estimated and fixed, under the assumption of the standard model that $P(f)$ is independent of azimuth. We can then estimate Q for all paths with available data. The other assumption is that a suitable path exists for a given station along which Q is fairly constant. We need to investigate its validity for stations of interest. Although this research would require some effort, the potential payoff is substantial to constrain and improve Q models in Eurasia. We refer to the overall approach as a stepwise, iterative procedure to constrain all of the parameters of the standard model, using our available source-corrected spectra and preliminary model fits (as in Figure 9) as a starting point.

### *Treatment of Correlation for Clustered Reference Data in Kriging Regional Seismic Discriminants*

As a separate study, we also investigated the effects of anomalous regional phase amplitudes (from events with abnormal mechanisms, depths, and/or paths) on kriged amplitude corrections and uncertainties, and the impact on discrimination errors. We demonstrated the problem using a cluster of Rock Valley (RV) earthquakes at NTS that have very high Pn/Lg values. In the worst case, using only RV earthquakes to calibrate station KNB, 11 of 88 NTS UNEs are miscategorized as *earthquake-like*. The reason for this error rate is that the RV events have very high Pn/Lg values at KNB ($2.6\sigma$ above the global average), biasing the kriged corrections at NTS, and the posterior calibration uncertainty computed by the old kriging method (Bottone et al., 2002) is small, treating the 11 RV events as independent. Since all of the RV events have similar mechanisms (Smith and Brune, 1993) and highly correlated waveforms (e.g., Figure 11), it is invalid to treat their Pn/Lg values as independent in the kriging analysis.

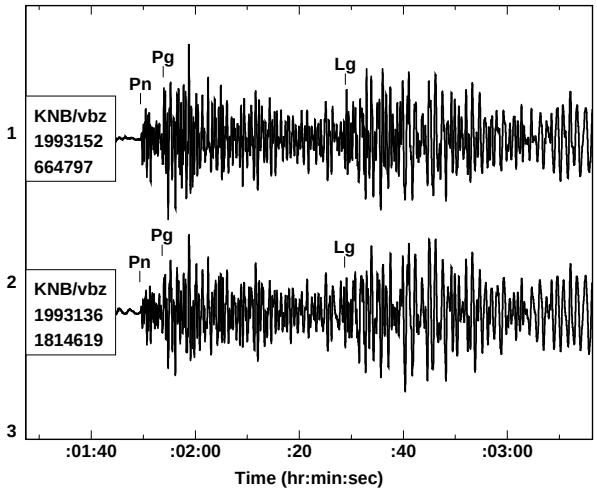


**Figure 11. Seismic recordings (0.5–5.0 Hz) of two RV events by KNB, showing their similarity.**

To ameliorate this problem, Fisk and McCartor (2008) extended the Bayesian kriging method of Bottone et al. (2002), incorporating an additional correlation length. The original correlation length treats regional path variations, estimated to be about 5 to 6 degrees for Pn/Lg and Pn/Sn in various region types (Bottone et al., 2002). The new correlation length treats events with similar focal mechanisms that typically occur on much shorter distance scales of faulting zones (e.g., a few km for the RV events). Treating this correlation limits the effective number of reference data for clustered events. It keeps the corrections from weighting such data too heavily and the posterior calibration variance from being too small. Fisk and McCartor (2008) showed that no NTS UNEs are miscategorized by the new method, even replicating the entire set of RV events 20 times. Many events are *undetermined* by the new procedure for the KNB/RV

case, but this is appropriate, given the very anomalous RV reference data. Fortunately, such cases are rare (i.e., less than 1% for values $2.6\sigma$ above the global average). The fact that a large fraction of events are *undetermined* for rare and anomalous cases should not be alarming. In fact, application to global datasets shows that the power of the test to reject earthquakes as being explosions at the 99.5% confidence level did not degrade much from the original screening rate of 78%, even for relatively large values of the new correlation length, $\alpha_r$ (Figure 12).

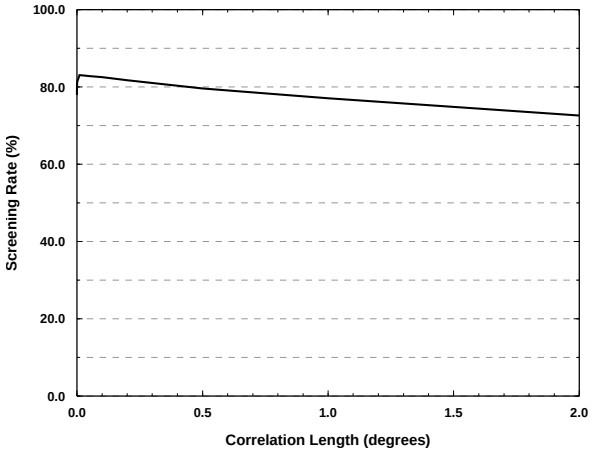


**Figure 12. Percentage of earthquakes worldwide that are rejected as *explosion-like* at the 0.005 significance level as a function of the correlation length $\alpha_r$.**

## CONCLUSIONS AND RECOMMENDATIONS

We developed and tested two methods to improve source and path corrections for regional seismic phases. The first estimates and constrains source parameters using Brune model fits to relative spectra of regional phases for event pairs with similar mechanisms, but different moments. We applied it to two very large datasets in Eurasia. We automated the various processing steps, including assessment of event pairs from waveform cross-correlations, computing network-median of relative spectra (large over small events), and fitting the Brune model to estimate corner frequencies and stress drop. We used kriging to compute grids of stress drop for Eurasia. Using spectra corrected for source terms, we have fit the combined distance and site effects for the various events and stations in our dataset, showing that good calibration of non-source-related physical effects (distance and site terms) may be obtained over a wide range of frequencies for paths with data.

We also investigated ways to constrain remaining trade-offs among Q, geometrical spreading, and site terms that have different dependencies on distance and frequency. We advocate a stepwise, iterative procedure to constrain all parameters of the standard model. Starting with our source-corrected spectra and the model fits (e.g., shown in Figure 9), the procedure would separate the spreading and constant site terms, apply those corrections, and then resolve Q and frequency-dependent site terms. This is expected to provide more accurate estimates of all of the physical parameters of Equation (1) than currently exist. In the future, we would also like to incorporate coda measurements and methods (1) to augment the source terms estimated using spectra of direct phases, relaxing the restriction on event pairs with similar mechanisms; and (2) as a way to independently estimate site terms.

Second, we extended the Bayesian kriging method of Bottone et al. (2002), introducing a second correlation length to treat clusters of correlated reference events. This limits the effective number of samples for such clusters. We have shown that the new method does not miscategorize any NTS UNEs, even replicating the set of RV events many times. Thus, the extended method is very robust. Although many events were *undetermined* for this case, this is appropriate for the anomalous RV reference data. Fortunately, such cases are rare. In fact, application to global datasets shows that the power of the test to reject earthquakes as explosions does not degrade much, even for fairly large values of $\alpha_r$. Thus, a practical solution is available, using a conservative value of $\alpha_r$, with little impact on overall performance. This is also encouraging because location estimates in most realistic situations may not have sufficient precision to allow use of smaller values of $\alpha_r$. Further work is needed to estimate $\alpha_r$. Although this does not seem necessary for the global case, application to specific sites may improve significantly by using site-specific values. Treatment should include how the data are explicitly correlated, especially for areas where various numbers of clusters with distinct mechanisms occur, e.g., in terms of correlations of waveforms or amplitude data.

## ACKNOWLEDGMENTS

We thank Gary McCartor and Steve Bottone for many useful discussions, Bill Walter and Ward Hawkins for providing seismic data, and David Schaff for providing waveform cross-correlation values. We acknowledge the IRIS DMC for seismic data used in this study.

## REFERENCES

Bottone, S., M. D. Fisk and G. D. McCartor (2002). Regional seismic event characterization using a Bayesian formulation of simple kriging, *Bull. Seism. Soc. Am.* 92: 2277–2296.

Brune, J. N. (1970). Tectonic stress and the spectra of seismic shear waves from earthquakes, *J. Geophys. Res.* 75: 4997–5009.

Choy, G. L. and J. L. Boatwright (1995). Global patterns of radiated seismic energy and apparent stress, *J. Geophys. Res.* 100: 18,205–18,228.

Cong, L., J. Xie and B. J. Mitchell (1996). Excitation and propagation of Lg from earthquakes in central Asia with implications for explosion/earthquake discrimination, *J. Geophys. Res.* 101: 27,779–27,789.

Fisk, M. D. (2007). Corner frequency scaling of regional seismic phases for underground nuclear explosions at the Nevada Test Site, *Bull. Seism. Soc. Am*. 97: 977–988.

Fisk, M. D. (2006). Source spectral modeling of regional P/S discriminants at nuclear test sites in China and the Former Soviet Union, *Bull. Seism. Soc. Am*. 96: 2348–2367.

Fisk, M. D. and G. D. McCartor (2008). Treatment of correlation for clustered reference data in kriging regional seismic discriminants, *Bull. Seism. Soc. Am*. 98: in press.

Fisk, M. D. and S. R. Taylor (2006). Robust magnitude and path corrections for regional seismic phases in Eurasia by constrained inversion and enhanced kriging techniques, in *Proceedings of the 28th Seismic Research Review: Ground-Based Nuclear Explosion Monitoring,* LA-UR-06-5471, Vol. 1, pp. 15–24.

Fisk, M. D. and S. R. Taylor (2007). Robust magnitude and path corrections for regional seismic phases in Eurasia by constrained inversion and enhanced kriging techniques, in *Proceedings of the 29th Monitoring Research Review: Ground-Based Nuclear Explosion Monitoring,* LA-UR-07-5613, Vol. 1, pp. 24–33.

Madariaga, R. (1976). Dynamics of an expanding circular fault, *Bull. Seism. Soc. Am.* 66: 639–667.

Nuttli, O. W. (1983). Average seismic source-parameter relations for mid-plate earthquakes, *Bull. Seism. Soc. Am.* 73: 519–535.

Phillips, W. S., R. J. Stead, G. E. Randall, H. E. Hartse and K. Mayeda (2008). Source effects from broad area network calibration of regional distance coda waves, in *Scattering of Short Period Waves in the Heterogeneous Earth*, H. Sato and M. C. Fehler, Editors, in press.

Schaff, D. P. and P. G. Richards (2004). Repeating seismic events in China, *Science* 303: 1176–1178.

Sereno T. J., S. R. Bratt and T. C. Bache (1988). Simultaneous inversion of regional wave spectra for attenuation and seismic moment in Scandinavia, *J. Geophys. Res.* 93: 2019-–2035.

Smith, K. D. and J. N. Brune (1993). A sequence of very shallow earthquakes in the Rock Valley fault zone; southern Nevada test site, *EOS Suppl.* 74: 417.

Taylor, S. R., and H. E. Hartse (1998). A procedure for estimation of source and propagation amplitude corrections for regional seismic discriminants, *J. Geophys. Res.* 103: 2781–2789.

Taylor, S. R., A. A. Velasco, H. E. Hartse, W. S. Phillips, W. R. Walter, and A. J. Rodgers (2002). Amplitude corrections for regional seismic discriminants, *Pure and Appl. Geophys., Special Edition on Monitoring the Comprehensive Nuclear-Test-Ban Treaty: Seismic Event Discrimination and Identification* 159: 623–650.

Walter, W. R., K. M. Mayeda, and H. J. Patton (1995). Phase and spectral ratio discrimination between NTS earthquakes and explosions. Part I: Empirical observations, *Bull. Seism. Soc. Am.* 85: 1050–1067.

Walter, W. R. and S. R. Taylor (2002). A Revised Magnitude and Distance Amplitude Correction (MDAC2) Procedure for Regional Seismic Discriminants: Theory and Testing at NTS, UCRL-ID-146882, LA-UR-02-1008.

# ATTENUATION TOMOGRAPHY OF NORTHERN CALIFORNIA AND THE YELLOW SEA/KOREAN PENINSULA FROM CODA-SOURCE NORMALIZED AND DIRECT LG AMPLITUDES

Sean R. Ford[1,3], Douglas S. Dreger[1], William S. Phillips[2], William R. Walter[3], Kevin Mayeda[4], and Luca Malagnini[5]

Berkeley Seismological Laboratory[1], Los Alamos National Laboratory[2], Lawrence Livermore National Laboratory[3], Weston Geophysical[4], and Instituto Nazionale di Geofisica e Vulcanologia[5]

Sponsored by National Nuclear Security Administration

Contract No. DE-FC52-06NA26605
Proposal No. BAA08-39

## ABSTRACT

Inversions for regional attenuation (1/*Q*) of *Lg* are performed in two different regions. The path attenuation component of the *Lg* spectrum is isolated using the coda-source normalization method, which corrects the *Lg* spectral amplitude for the source using the stable, coda-derived source spectra. Tomographic images of Northern California agree well with one-dimensional (1-D) *Lg Q* estimated from five different methods. We note that there is some tendency for tomographic smoothing to increase *Q* relative to targeted 1-D methods. For example, in the San Francisco Bay Area, which contains high attenuation relative to the rest of the region, *Q* is overestimated by ~30. Coda-source normalized attenuation tomography is also carried out for the Yellow Sea/Korean Peninsula (YSKP), where output parameters (site, source, and path terms) are compared with those from the amplitude tomography method of Phillips et al. (2005), as well as with a new method that ties the source term to the magnitude and distance amplitude corrections (MDAC) formulation (Walter and Taylor, 2001). The source terms show similar scatter between coda-source corrected and MDAC source perturbation methods, whereas the amplitude method has the greatest correlation with estimated true-source magnitude. The coda-source better represents the source spectra compared to the estimated magnitude and could be the cause of the scatter. The similarity in the source terms between the coda-source and MDAC-linked methods shows that the latter method may approximate the effect of the former, and therefore could be useful in regions without coda-derived sources. The site terms from the MDAC-linked method correlate slightly with global Vs30 measurements. While the coda-source and amplitude ratio methods do not correlate with Vs30 measurements, they do correlate with one another, which provides confidence that the two methods are consistent. The path $Q^{-1}$ values are very similar between the coda-source and amplitude ratio methods except for small differences in the Da-xin-an-ling Mountains, in the northern YSKP. However. there is one large difference between the MDAC-linked method and the others in the region near stations TJN and INCN, which point to site-effect as the cause for the difference.

## OBJECTIVES

Understanding of regional attenuation $Q^{-1}$ can help with structure and tectonic interpretation (e.g., Frankel, 1990), and correcting for the effects of attenuation can lead to better discrimination of small nuclear tests (e.g., Baker et al., 2004; Mayeda et al., 2003; Taylor et al., 2002). Present threshold algorithms for event identification rely on $Q$ models that are derived differently, and the models can vary greatly for the same region. In previous work (Ford et al., 2008), we compared 1-D methods to measure $Q_{Lg}$ and attempted to assess the error associated with the results. The assessment showed the possible influence of lateral attenuation, and in order to understand its importance, we perform inversions for 2-D attenuation in the previous study region of Northern California and extend the analysis to the Yellow Sea/Korean Peninsula (YSKP). In the same spirit as the comparison of 1-D methods, we compare three 2-D methods using the YSKP. The comparison is made for the output site, source, and path parameters.

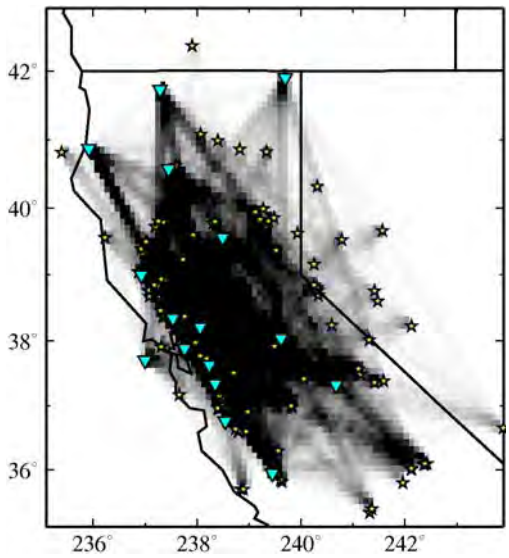


**Figure 1. Northern California region with events (yellow stars), stations (blue triangles), and path density.**

## RESEARCH ACCOMPLISHED

### Northern California

The Northern California dataset consists of 158 earthquakes recorded at 16 broadband (20 sps) three-component stations of the BDSN between 1992 and 2004 (Figure 1). Using this data, we implement the amplitude tomography method of Phillips et al. (2005), which assumes the *Lg* spectrum ($A_{Lg}$) can be represented as

$$\ln(A_{Lg}) = \ln(S(f)) + \ln(P(f)) - \frac{\pi f}{U}\int_s Q^{-1} ds,$$

where $U$ is the phase velocity, and the inversion solves for $S(f)$ and $P(f)$, the source and site terms, respectively, as well as $Q^{-1}$ along the path, $s$, in a damped least-squares sense. This method will be referred to as Amp. We also employ an altered form of this method where the source term is corrected using the stable, coda-derived source spectra in order to isolate the path attenuation component of the *Lg* spectrum (Walter et al., 2007). This method will be referred to as CS. Source spectra derived from the coda are calculated via the methodology of Mayeda et al. (2003) and from the northern California study of Mayeda et al. (2005). Figure 2 compares the two methods for

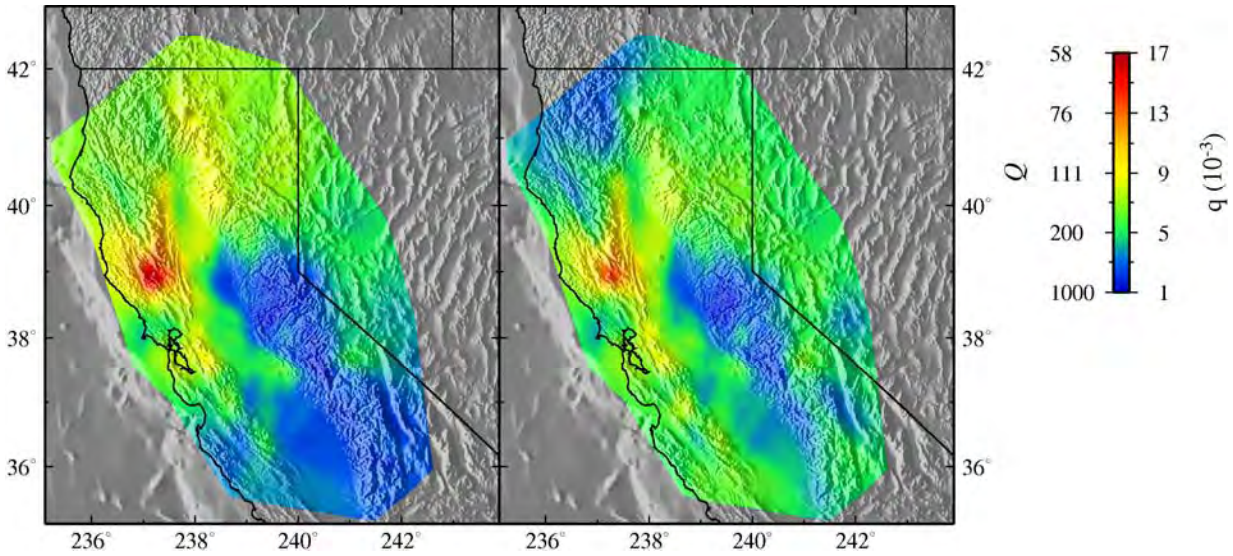


**Figure 2. $Q_{Lg}$ at 1 Hz. Left, using the standard amplitude method of Phillips et al. (2005). Right, using the coda-source corrected method.**

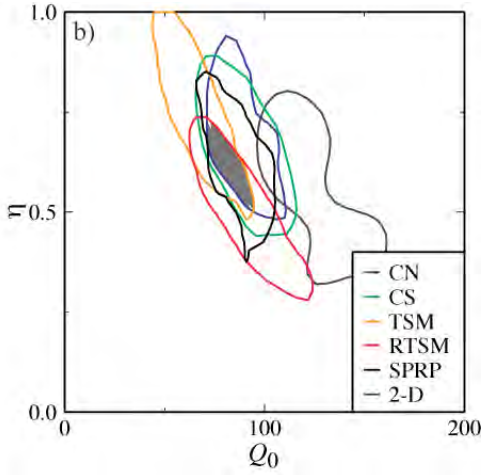


**Figure 3. 2-D *Q* and power-law dependence distribution (grey line) compared with those from various 1-D analyses for the Bay Area. See text for method descriptions.**

Northern California. The CS method seems to better constrain path *Q* when there are few paths, as is the case in the southern section of the Great Valley. The CS-derived tomogram more closely resembles that of Phillips and Stead (2008), which confines the high *Q* region to the Sierras.

In previous work, we applied the coda normalization (CN), two-station (TS), reverse two-station (RTS), source-pair/receiver-pair (SPRP), and the new coda-source normalization (CS) methods to measure *Q* of the regional phase, *Lg* ($Q_{Lg}$), and its power-law dependence on frequency of the form $Q_0 f^{\eta}$. The CN method is implemented in the time domain for paths leading to a common station, and it returns a stable *Q* measurement when the region near a station is homogenous. The CS method uses previously calculated coda-derived source spectra to remove the source term in the frequency domain and is best suited to calculate an effective *Q* for a given path. The TS and RTS methods are implemented in the frequency domain, and the calculated *Q* is more stable due to the extraction of the source term. The RTS method produces a power-law *Q* with less error than the TS method due to its additional extraction of the site terms, though it is more restrictive in its data requirements. The SPRP method is the RTS method with a relaxation of the data requirements and is implemented in the time domain here.

In an attempt to normalize the dataset used for each method, we restricted the data to lie in a small region along the Franciscan block. We implemented all five methods to calculate $Q_0 f^{\eta}$ in the region. The populations are then smoothed to produce an empirical distribution so that the 95% confidence region can be estimated. We can compare the 1-D results with those of this 2-D analysis via calculation of the power law parameters for the same region for the CS method by fitting a least-squares line to the *Q* estimated for each frequency band at the midpoint of the band in the log domain. We extract the power-law parameters at points within the subregion and, as above, we produce an empirical distribution. Figure 3 compares the distributions. The range in $\eta$ and variance of $Q_0$ are similar between the 1-D and 2-D results, but the mean of the $Q_0$ distribution is shifted by about 30. This may be due to some regularization effects. This analysis shows that some of the variability in the 1-D analysis is due to the 2-D structure.

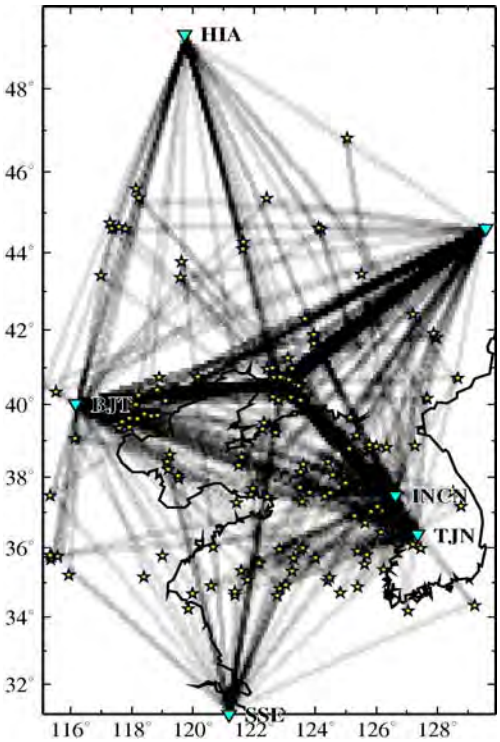


**Figure 4. YSKP region with events (yellow stars), stations (blue triangles), and path density.**

**Yellow Sea/Korean Peninsula (YSKP)**

The YSKP dataset consists of 146 earthquakes recorded at 6 broadband (20 sps) three-component stations of the glonal seismographic network (GSN) and OHP-Japan (station TJN) networks (Figure 4). $Q_{Lg}$ at 1 Hz is calculated using the CS method and we compare it to previous results to see if this method can produce similar results. The comparison is made in Figure 5 and this study agrees well with previous work, which captures the high attenuation (low *Q*) in Bohai Bay and the Songliao Basin and low attenuation (high *Q*) near northern South Korea and in the Changbai Mountains to the east and the Da-xin-an-ling Mountains to the north.

We implement the same two tomographic methods described above, as well a new one (Pasyanos et al., 2008, in preparation) that formulates the source term in terms of the MDAC

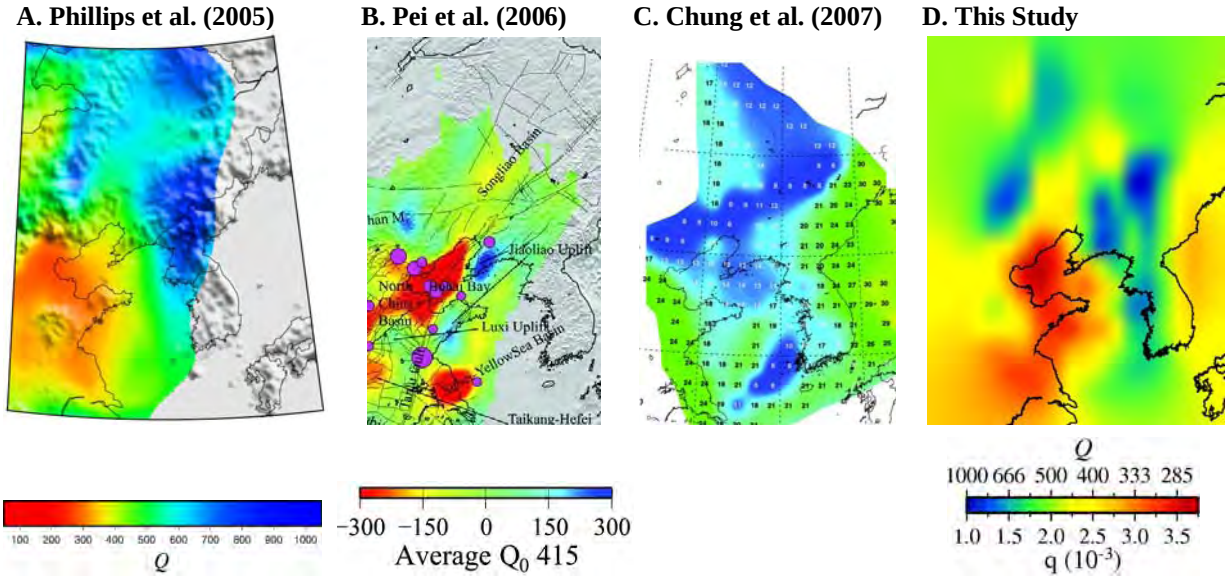


**Figure 5. Attenuation tomography comparison for the YSKP. The numbers in Panel C are $1/Q$ (q) × $10^4$, blue is low q (attenuation), and green is high q. Panel D shows the coda-source-corrected amplitude tomography results from this study.**

(Walter and Taylor, 2001) source. In this way, the output source terms are perturbations to the original source, and this perturbation can be tuned (see Walter et al., these Proceedings). This method will be referred to as the dM method. We can now make a preliminary comparison between the source and site terms (Figure 6) and the path $Q$ (Figure 7) from all three methods.

When the site and source terms are compared with database $M_W$ (first row of Figure 6), the Amp method produces an excellent match, whereas the coda sources used in the CS method and the output $M_W$s from the dM method produce similar scatter in the source terms. The coda-sources are superior measurements of the source spectra, and the fact that the dM method produces a similar relationship gives high confidence that the source terms from the dM method are reliable. In the dM method, the source terms are expressed directly as a small change to the initial moment making them easier to interpret physically and more easily used for event identification, since they are tied to the MDAC formalism.

When site terms are compared with Vs30 values for each station taken from the topography-derived database of Wald and Allen (2008) (first column of Figure 6), there is no correlation for the Amp and CS methods, but there is a slight correlation for the dM method. However, we are encouraged that the CS and Amp methods produce consistent site terms.

There is little correlation between sediment depth and $Q$ calculated by all three methods (first row and column of Figure 7). Path $Q$ from the CS and Amp methods are highly correlated and differ only along the Da-xin-an-ling Mountains to the north, where the Amp method predicts higher $Q$ than the CS method. This may be a similar effect as what is seen in Northern California for the Great Valley, and therefore the path $Q$ for the CS method is assumed to be more robust, though the difference is slight. Beside the mountain region mentioned earlier, the dM method differs greatly from the other two methods off the coast of Korea (bottom row of Figure 7). This region contains two of the six stations used in the analysis (TJN and INCN), so this difference may be due to a site effect difference. In fact if we look at the comparison between site terms of the CS and dM methods (Figure 6, lower right), one can see that TJN and INCN are the most inconsistent of all the methods.

## CONCLUSIONS AND RECOMMENDATIONS

The attenuation tomography methods employed here have difficulty representing extreme attenuation structure, though the lateral variation agrees well with 1-D methods. Initial work with the coda-source corrected amplitude tomography shows that it compares nicely with previous methods and may be able to better constrain $Q$ in regions

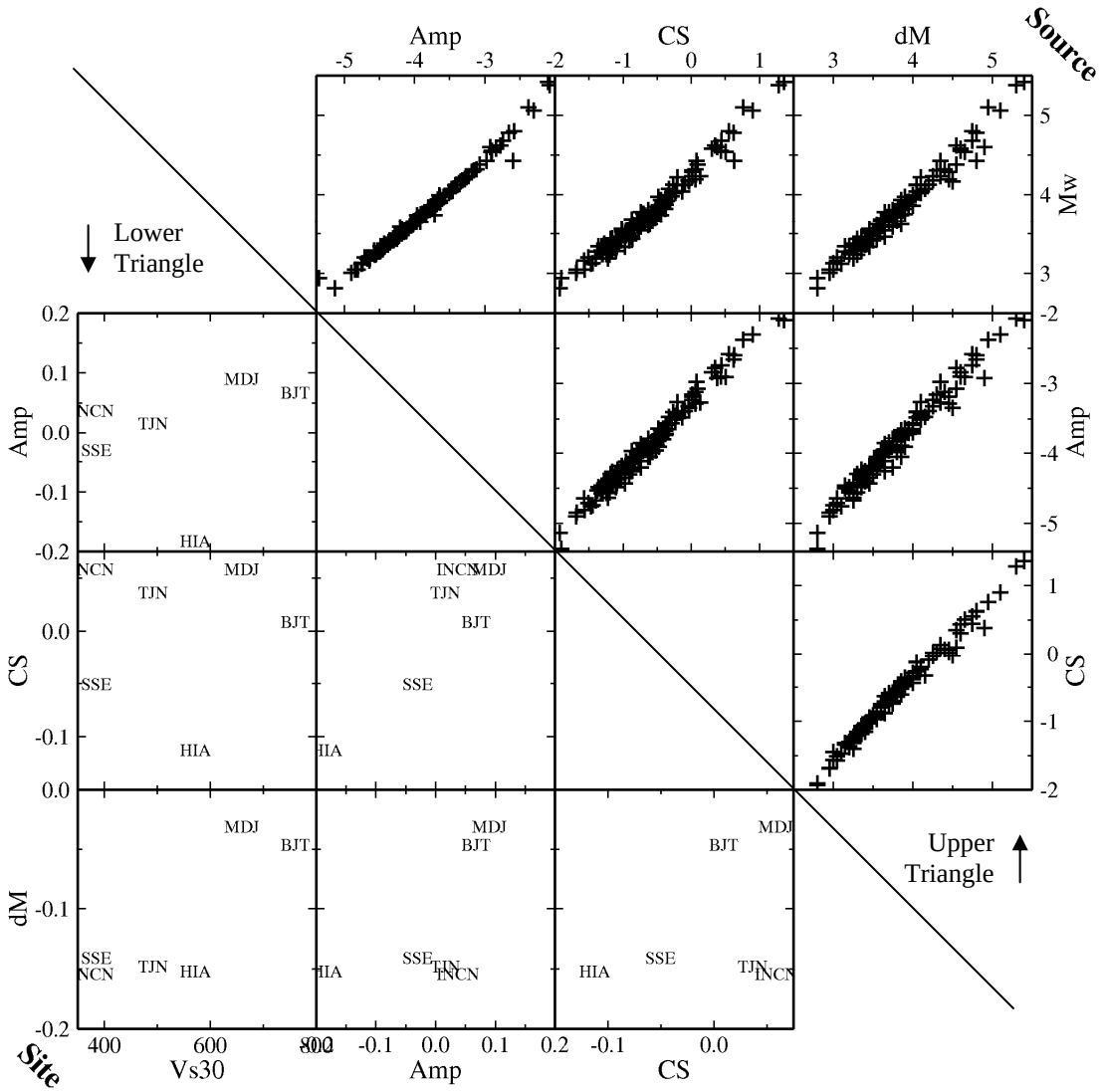


**Figure 6. Source and site term comparison for the amplitude tomography method (Amp), coda-source corrected version of that method (CS), and MDAC-formulated method (dM). Source comparison is shown the upper triangle where $M_W$ is from the MDAC database, dM is in units of $M_W$, CS is in log amplitude of the source spectra, and Amp is in arbitrary log amplitude from the inversion. Note that the dM method can easily be tied to a physical MW. Site comparison is the lower triangle where Vs30 are values from Wald and Allen (2008) and points are given by station names. Values are in arbitrary log units.**

with fewer paths. Also, this method can take advantage of larger data sets than the Amp method because the latter is restricted to events recorded at more than one station. A new attenuation tomography method that is tied to the source formalism used in MDAC analysis has the ability to produce output parameters that can be used by MDAC to correct for source and path amplitudes. Preliminary tests of this method show that calculated source terms agree well with the coda-sources and that path *Q* is similar to standard amplitude tomography.

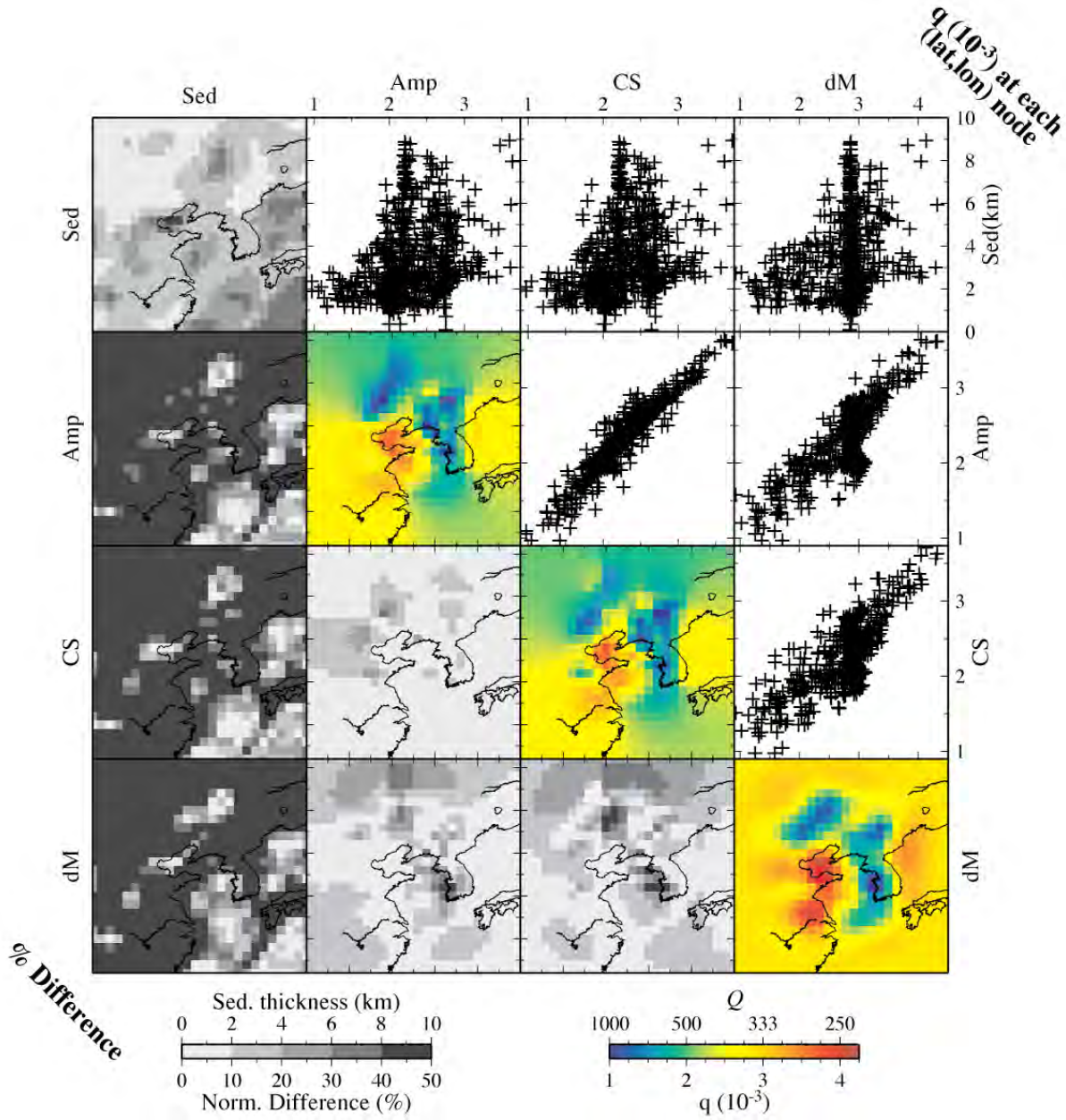


**Figure 7. Path *Q* comparison for the various methods used in this study (see text or Figure 6 for explanation). Diagonal shows attenuation for the YSKP region where Sed is the 1° sediment thickness. Comparison at each node is shown in the upper triangle where values are given in q ($1/Q \times 10^{-3}$) and Sed (sediment thickness) is in km. Spatial comparison in percent difference is shown in the lower triangle.**

**ACKNOWLEDGEMENTS**

We thank Mike Pasyanos for making his initial tomography results available. This is LLNL contribution LLNL-CONF-405553.

**REFERENCES**

Baker, G. E., J. Stevens, and H. M. Xu (2004). Lg group velocity: A depth discriminant revisited, *Bull. Seism. Soc. Am.* 94: 722–739.

Chung, T. W., M. H. Noh, J. K. Kim, Y. K. Park, H. J. Yoo, and J. M. Lees (2007). A study of the regional variation of low-frequency $Q_{Lg}^{-1}$ around the Korean Peninsula, *Bull. Seism. Soc. Am.* 97: 2190–2197.

Ford, S. R., D. S. Dreger, K. Mayeda, W. R. Walter, L. Malagnini, and W. S. Phillips (2008). Regional attenuation in northern California: A comparison of five 1-D Q methods, *Bull. Seismol. Soc. Am.*, in press.

Frankel, A. (1990). Attenuation of high-frequency shear waves in the crust: Measurements from New York State, South Africa, and Southern California, *J. Geophys. Res.* 95: 17441–17457.

Mayeda, K., A. Hofstetter, J. L. O'Boyle, and W. R. Walter (2003). Stable and transportable regional magnitudes based on coda-derived moment-rate spectra, *Bull. Seis. Soc. Am.* 93: 224–239.

Mayeda, K., L. Malagnini, W. S. Phillips, W. R. Walter, and D. Dreger (2005). 2-D or not 2-D, that is the question: A northern California test, *Geophys. Res. Lett.* 32: L12301.

Pei, S., J. Zhao, C. A. Rowe, S. Wang, T. M. Hearn, Z. Xu, H. Liu, and Y. Sun (2006). $M_L$ amplitude tomography in North China, *Bull. Seism. Soc. Am.* 96: 1560–1566.

Phillips, W. S., H. E. Hartse, and J. T. Rutledge (2005). Amplitude ratio tomography for regional phase *Q*, *Geophys. Res. Lett.* 32: L21301.

Phillips, W. S. and R. J. Stead (2008). Attenuation of Lg in the western US using the USArray, *Geophys. Res. Lett.* 35: L07307, doi:10.1029/2007GL032926.

Taylor, S., A. Velasco, H. Hartse, W. S. Philips, W. R. Walter, and A. Rodgers (2002). Amplitude corrections for regional discrimination, *Pure. App. Geophys*. 159: 623–650.

Wald, D. J. and T. I. Allen (2008). Topographic slope as a proxy for seismic site conditions and amplification, *Bull. Seism. Soc. Am.*, in press, http://earthquake.usgs.gov/research/hazmaps/interactive/vs30/

Walter, W. R., K. Mayeda, L. Malagnini, and L. Scognamiglio (2007). Regional body-wave attenuation using a coda source normalization method: Application to MEDNET records of earthquakes in Italy, *Geophys. Res. Lett.* 34: L10308.

Walter, W. R. and S. R. Taylor (2001). A revised magnitude and distance amplitude correction (MDAC2) procedure for regional seismic discriminants, Lawrence Livermore National Laboratory report UCRL-ID-146882.

# ESTIMATING LOCAL AND NEAR-REGIONAL VELOCITY AND ATTENUATION STRUCTURE FROM SEISMIC NOISE

Peter Gerstoft[1], Jian Zhang[1], William A Kuperman[1], Nick Harmon[1], Karim G. Sabra[2], Michael C Fehler[3], and Steven R Taylor[4]

University of California, San Diego[1], Georgia Institute of Technology[2], Massechusetts Institute of Technology[3], Rocky Mountain Geophysics, LLC [4]

Sponsored by Air Force Research Laboratory

Contract No. FA8718-07-C-0005
Proposal No. BAA07-70

## ABSTRACT

This paper investigates the utility of computing Time-Domain Green's Functions (TDGF) to be used for estimating velocity and attenuation structure for the purposes of nuclear explosion monitoring over local and near-regional distances. Our objective is to extend and apply the methodology of deriving TDGF for propagation between two receivers by cross correlation of seismic noise and/or coda of earthquakes observed at the receivers and concentrates on the following four tasks:

1. The specific noise spectrum of the ocean microseism needs to be accounted for and compensated for in order to be able to measure group velocities across a wider bandwidth. The use of robust time-frequency analysis of the extracted coherent waveforms from seismic noise provides a means to obtain broadband estimates of group velocities up to 0.5 Hz for seismic stations located in coastal regions.
2. We are investigating methods to obtain spatial variations in attenuation using ambient noise. We assume that surface waves generated by atmospheric pressure fluctuations act as a forcing function on a damped harmonic oscillator system. The forcing function is adaptively updated from the network beam as a function of time. The relative attenuation at each site can be estimated from the width of the resonance peak relative to the driving forcing function.
3. Mean-phase velocity-dispersion curves are calculated for the TUCAN seismic array in Costa Rica and Nicaragua from ambient seismic noise using two independent methods, noise cross correlation and beamforming. The noise cross correlation and beamforming methods are compared and contrasted by evaluating results from the TUCAN array. The results of the two methods as applied to the TUCAN array agree within 1%, giving good confidence in the phase velocities extracted from noise.
4. From a data set recorded by a small-scale array (~4 km aperture), unbiased surface-wave Green's functions for short-periods of less than 2 s have been extracted, as evidenced by a good match of noise-based impulse response with the borehole shot records sharing common paths. Beamforming has been used to identify specific directional noise, which may generate fast P-wave arrivals, and thus needs to be analyzed with care. Such noise-based P-wave response and its reflections have turned out to be information-rich as well, revealing the lateral structure anomaly of the studied area.

## OBJECTIVES

Our objective is to extend and apply the methodology of deriving time-domain Green's functions (TDGF) for propagation between two receivers by cross-correlation of seismic noise and/or coda of earthquakes observed at the receivers. We have previously shown that it is possible to obtain travel-time information for short-period surface waves (around 6 s) by cross-correlating seismic noise at local and regional scales. We propose to add the following improvements to the TDGF method: (1) modifying to better handle cases having nonisotropic noise; (2) implementing a system identification approach for obtaining reliable amplitude information for the TDGF, allowing for the estimation of attenuation along paths between receivers, and (3) extracting TDGF from Lg or Sn coda.

## RESEARCH ACCOMPLISHED

### Improving Surface-Wave Group-Speed Measurements Using Time-Frequency Analysis

We have previously shown that estimates of the TDGF can be extracted from seismic noise cross-correlation (Sabra et al., 2005a, 2005b). This can to be used for measuring local velocity and attenuation structure for the purposes of nuclear explosion monitoring over local and near-regional distances. Using 18 days of seismic noise recording in Southern California, we were able to obtain travel-time information for short-period surface waves (around 7.5 s) by cross-correlating seismic noise at local and regional scales. However, being able to measure broadband estimates of the Rayleigh wave group velocity can potentially provide a means to better constrain the inversion procedure about crustal velocity structure.

We have investigated signal-processing tools to improve the measurements of group-speed estimates from the cross-correlation waveforms. Surface waves are dispersive, and their associated dispersion curves can be used to invert for shear velocity profiles with depth. The main challenge with using surface waves is the complexity of the required data processing and interpretation of the results. Our goal is to show how robust time-frequency analysis of the extracted coherent waveforms from seismic noise improves the precision of group velocity measurements of surface waves. In particular, it is important to reduce the uncertainty of the dispersion-curve measurements in order to minimize the number of acceptable earth models.

Group velocities are typically measured by computing spectrograms or the moving-window method. In seismology they are often estimated using multiple filter banks. All these techniques result from Fourier transforms and thus create a large smearing in the time–frequency domain as a result of the Gabor-Heisenberg inequality (Gabor, 1946). An additional issue is the biases caused by the seismic signals' being nonstationary and strongly varied in spectral amplitude. To mitigate those limitations, various time–frequency methods have been developed (Cohent, 1989). The Wigner-Ville transform $WV_{lm}(t,f)$ yields a time-frequency energy distribution of the cross-correlation $C_{lm}(t)$ (with analytic representation noted $\tilde{C}_{lm}$ [Auger and Flandrin, 1995]) computed between two seismic noises recorded at sensors #l and #m:

$$WV_{lm}(t,f) = \int_0^T \tilde{C}_{lm}(t+\tau/2)\tilde{C}^*_{lm}(t-\tau/2)\exp(-i2\pi f\tau)d\tau \quad . \qquad (1)$$

We tested his approach on the cross-correlation waveform obtained from seismic noise recorded southwest of the Hawaiian Islands (Laske, 1999). Seismic months of seismic noise (June 1997 to December 1997) were recorded on a pair of OBS sensors, 342 km apart, and sampled at 25 Hz. The seismic cross-correlation was computed following the methodology described in (Sabra et al. 2005a). We computed the Wigner Ville transform using the algorithm described in (Auger and Flandrin, 1995). In order to ease the visual interpretation of the signal's time-frequency structure, a smoothed version can be computed by a two-dimensional (2D) low-pass filtering of the Wigner-Ville transform in order to reduce the interference of cross terms and noise artifacts (Figure 1.a). Selecting the arrival times along the maxima contours of the $WV_{lm}(t,f)$ yields an estimate of the change of the group velocity $V_g$ vs. frequency $f$, of these coherent seismic waves between sensor pairs. As a complement to this smoothing, a reassigned representation of $WV_{lm}(t,f)$ is performed that essentially increases the concentration of the signal components (Figure 1.b) (Auger and Flandrin, 1995), thus improving estimates of $V_g$. Extracting reliable and high-resolution measurements of

$V_g$ are essential for the estimation of the earth velocity structure. Robust time-frequency analysis of the extracted coherent waveforms from seismic noise, appear to provide broadband estimates of group velocities up to at least 0.25 Hz for seismic stations located in coastal regions.

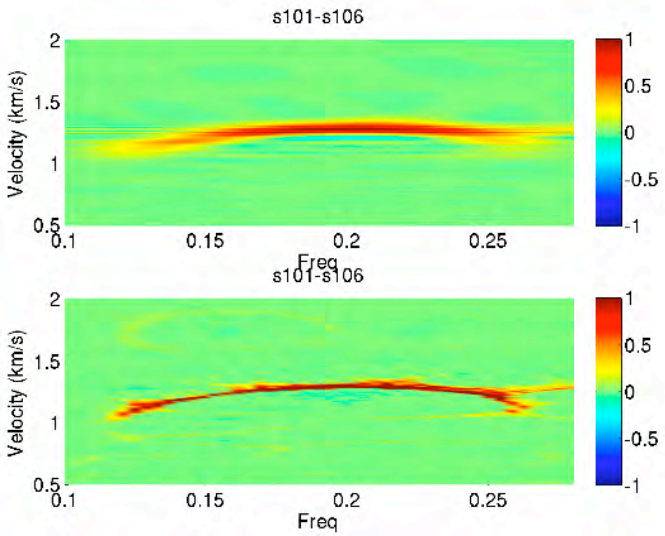


**Figure 1. Time-frequency analysis of the extracted coherent between a pair of OBS senors located 343 km apart southwest of the Hawaiian Islands: (a) smoothed Wigner-Ville transform and (b) Wigner-Ville transform after energy reassignment processing.**

**Extracting Attenuation from Noise**

We have been using ambient seismic noise to construct attenuation maps beneath a network of stations. The approach we are looking at is to estimate the *Q* on a site-by-site basis as opposed to taking a tomographic approach (e.g., Matzel, 2008). The idea is to treat time-varying frequency-wavenumber (F-K) beams of the ambient noise field as a forcing function beneath a network of stations. Each station responds differently to the forcing function, depending on the site structure and attenuation. We use the differential equation for a forced, damped, harmonic oscillator to simulate the response of each station to the forcing function given by

$$\ddot{x} + \gamma \dot{x} + \omega_0^2 x = \frac{1}{m} F(t), \tag{1}$$

where $F(t)$ is the forcing function, $m$ is the mass, $x$ is the sensor displacement response to the forcing function, $\gamma$ is the viscous damping term, and $\omega_0$ is the natural frequency of the oscillator. The power spectrum of the sensor response (where $m = 1$) is given by

$$P_x(\omega) = \frac{P_F(\omega)}{\left[\left(\omega_0^2 - \omega^2\right)^2 + (\gamma\omega)^2\right]}. \tag{2}$$

As will be further described below, we estimate the power spectrum of the forcing function from the array beam on the maximum power of the ambient noise field. For light damping, $\gamma << \omega_0$, the power spectrum for a particular site relative to that of the forcing function is given by

$$P_{xF}(\omega) = \frac{P_x(\omega)}{P_F(\omega)} = \frac{1}{\omega_0^2\left[4\left(\omega_0^2 - \omega^2\right)^2 + \left(\frac{\omega}{Q}\right)^2\right]}, \tag{3}$$

where $\gamma = \omega_0/Q$. For each station, it is then possible to do a grid search over a range of $\omega_0$ and $Q$ values to match the observed resonance peaks.

To find the power spectrum of the forcing function, $P_F(\omega)$, we first compute the time varying F-K spectrum of the ambient noise impinging upon a network of stations. To test the methodology, we examined one day's worth of noise for a subset of 54 stations from the Southern California Seismic Network (SCSN). We computed the F-K spectrum for two-hour window lengths, an example of which is shown in Figure 2.

The noise predominantly arrives from the west and southwest for this particular time block. The black cross in Figure 2 shows the point having the maximum energy for the F-K spectrum, and we computed a beam from this point. In future work, we will examine the possibility of integrating a semicircle of beams from the F-K spectrum spanning a wider range of azimuths. In our preliminary study, we have computed the beams from the maximum F-K point for each of the two-hour time windows and computed the median power for the day as a power spectral estimate of the forcing function. Using the F-K beam and the median power appears to eliminate the necessity of one-bit normalization commonly used to remove earthquakes from ambient noise-time series.

Figure 3 shows the observed power spectral ratio, $P_{xF}(w)$, at a hard-rock (CHF) and soft-rock (BRE) site. Note that the resonance curve for the soft-rock site is broader than that from the hard-rock site indicating higher attenuation at the soft-rock site. The solid line in Figure 3 shows the predicted resonance peak for a single oscillator frequency (Equation 4). The prediction appears to be too peaked, suggesting that a more general absorption band model (e.g., Liu, 1976) may be necessary to fit the observed resonance peaks.

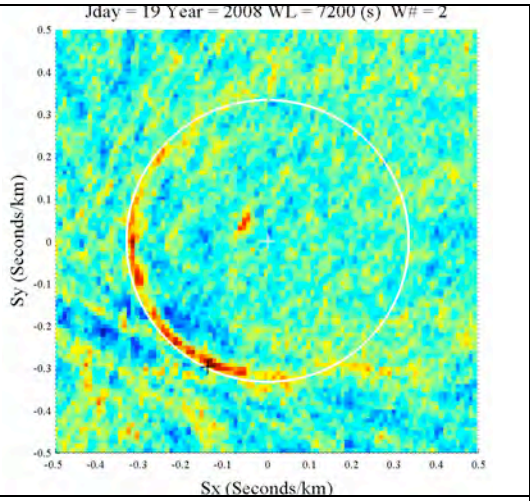


**Figure 2. F-K spectrum for a two-hour sample of ambient noise for a subset of 54 stations from the SCSN. White circle corresponds to a phase velocity of 3 km/s. Black cross indicates beam point.**

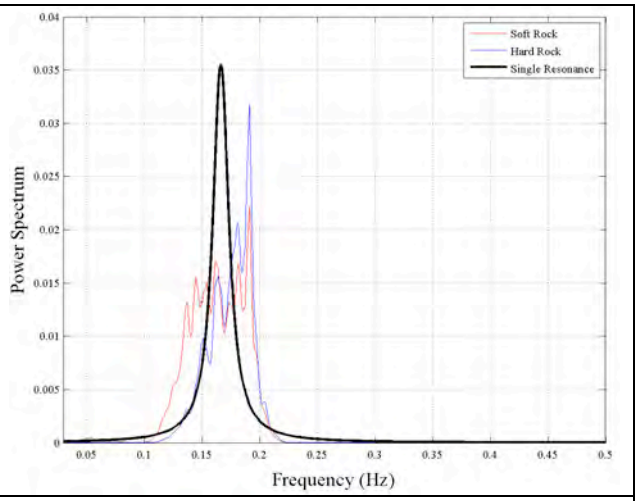


**Figure 3. Power spectral ratio, $P_{xF}(w)$, observed at a hard rock and soft rock site. Black line is prediction of power spectral ratio for a single resonance peak (Equation 3).**

**Midscale Seismic Beamforming and Noise Cross-Correlation**

We determined phase velocities using 593 days (July 2004 to March 2006) of station-to-station noise cross-correlation function (NCF) for the vertical components of the 49 stations of the TUCAN seismic array (Figure 4c) using a method similar to Harmon et al. (2007). Variations from Harmon et al. (2007) include removing the instrument responses from the signals (the TUCAN contains different sensor types), decimation to 1-s sampling, a root mean square (RMS) clipping scheme for the daily time series (Sabra et al., 2005) and signal whitening by normalizing the Fourier coefficients by their respective magnitude, both to create a single broadband NCF. Then we cross-correlated hourly time series segments for all station pairs and stacked the resulting correlograms. The NCF phase dispersion was determined by unwrapping the phase of the stacked NCF and applying a $\pi/4$ correction. We determined the cycle ambiguity by matching the average phase velocity determined from teleseismic events at 20-s periods (Abers el al., 2007). The mean teleseismic phase velocity estimates were determined using the method of Yang and Forsyth (2006),

with 95 events with good azimuthal coverage. We calculate the mean phase dispersion curve and its standard error of the mean by station-to-station distance-weighted averaging. A station-to-station NCF phase velocity estimate was used to calculate the mean phase dispersion curve if (1) the NCF had signal-to-noise ratio >10, (2) the temporal average of ~4-month NCF stacks had a standard deviation of <.1 km/s, and (3) the station-to-station path was greater than 3λ after Lin et al. (2008). Distance weighting was chosen since longer paths should be more representative of average structure. For 15–29-s periods, the teleseismic and NCF mean phase velocity estimates were within 1%, except at 18 s, where they were within 2%.

For station-to-station paths perpendicular to the Pacific coast, the NCFs are dominated by 6–10-s microseisms coming from the coast. This can be seen by comparing NCFs with comparable path lengths and different orientations such as N1–N13 and B4–N11 (Figure 4f, e). A high-frequency signal owing to the Pacific microseisms is seen at negative lag (from southwest) for the path perpendicular to the Pacific coast whereas no high-frequency signal is seen at positive lag for this path (Figure 4f) or for positive and negative lags of the coast parallel paths (Figure 4d, e). The amplitudes and frequency contents of the NCFs suggest that the noise distribution changes with period.

For periods between 10 and 22 s, the Beamformer output in Figure 5, there is a nearly continuous ring maximum with surface wave slownesses, suggesting that surface waves dominate the signal in this period range, which is consistent with the 2D model of noise distribution. Above a 18-s period, there is little signal from the Pacific (180°–240°), while in the secondary microseism band (6–10-s period) the dominant source direction is 180°–240° azimuth with little energy coming from other directions, which is consistent with what was observed in the NCF.

For periods greater than 6 s, both NCF and beamformer average phase-velocity estimates are within an error of each other (Figure 6). For the best-resolved periods (7–20 s), the phase velocity from beamforming agrees within 1% with the NCF estimates. The agreement is best in this band because this is where the microseisms are strongest (see Figure 5). Below a 6-s period, the agreement between the two estimates begins to erode due to aliasing, as the beamformer output no longer resolves any coherent surface waves, and the errors in the NCF estimates increase. The NCF estimate is more stable due to the inherent averaging in the frequency domain caused by windowing in the time domain. The station geometry requirements for the two methods are different. The NCF method requires only two stations. Beamforming, on the other hand, requires an array of stations. We choose the NCF station spacing to be at least 3λ at a 20-s period to avoid near-field effects and to allow distinct phases to emerge (Bensen et al., 2007). Data selection requirements of the NCF limit the number of station pairs to 270 out of 1149 at 20 s. For beamforming array aperture larger than 1λ is required to resolve the longest periods of interest and station spacing < λ/2 to prevent spatial aliasing at shortest periods for a regularly spaced array, but for irregular arrays it can be relaxed somewhat. For the TUCAN array, which consists mainly of two regularly-spaced line arrays pointing southwest, beamforming aliasing manifests itself as a straight-line beamformer output (perpendicular to the line-array directions) rather than a point for sources coming from the southwest, as shown in the 7-s band in Figure 5. For shorter periods, the beamformer aliasing becomes more severe, making it difficult to extract phase velocities. In the 7–20-s bands, the phase slowness can be resolved, but aliasing does contribute to the errors in the phase-slowness estimates. Overall, the aliasing at the periods of interest, 7–20 s, is minor, while it dominates at periods of less than 7 s.

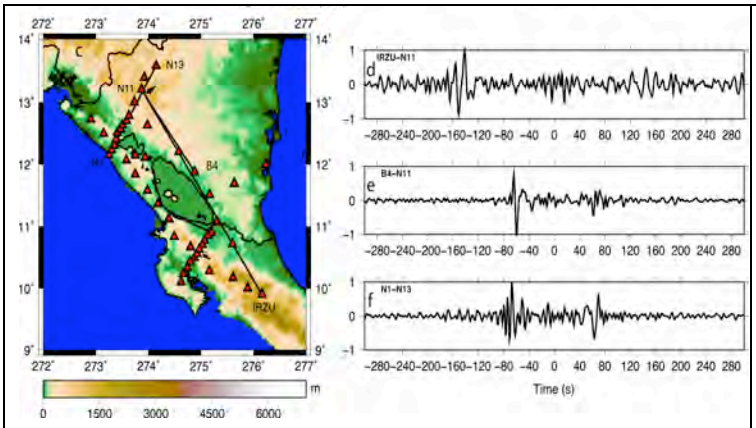


**Figure 4. Station locations (red triangles) and topography (from ETOPO2) of the TUCAN array. The time series show the normalized bandpass filtered (5–33 s) NCF between stations (d) IRZU-N11, (e) B4-N11, and (f) N1-N13. Positive lags correspond to waves traveling from N11 and N13.**

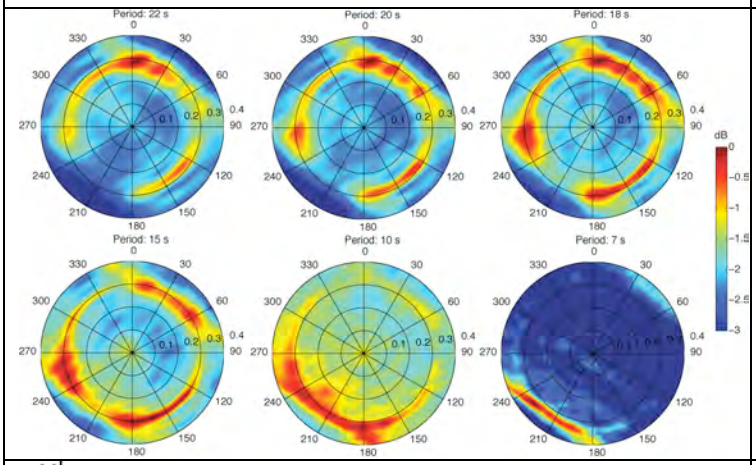


**Figure 5. Azimuth vs. phase slowness plots of 593-day stack of beamformer output (dB) of the TUCAN array for 7-, 10-, 15-, 18-, 20-, and 22-s periods. Slowness is the radial distance on the polar plots from 0.00–0.4 s/km.**

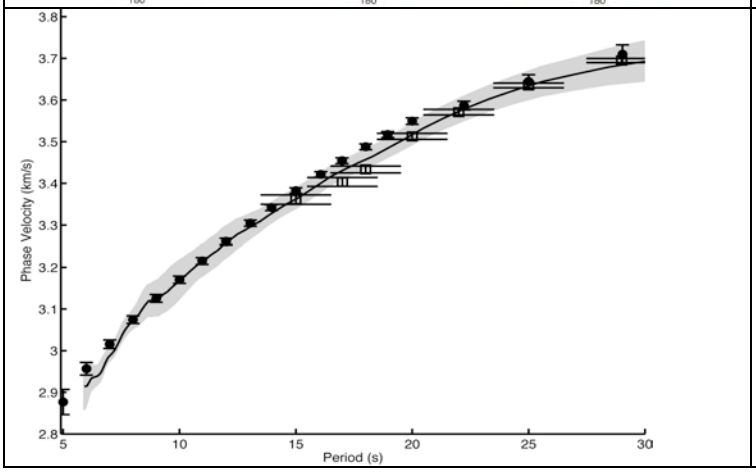


**Figure 6. Phase-velocity estimates from beamforming (solid black line), with 3× standard error of the mean (grey region), noise correlation methods (circles), with 3× standard error of the mean bars and teleseismic phase-velocity estimates (open squares), with 3× standard error of the mean.**

**Local-Scale Seismic Noise Cross-Correlation from the Calico Fault Experiment**

In this work we present the seismic noise cross-correlation (NCC) results from a dataset recorded by a dense array (~5-km aperture, see Figure 7a) along the Calico fault in California's Mojave desert. The dataset is unique for NCC study in terms of (1) local scale (a few km), (2) long recordings (~6 months), and (3) the common site of a sensor and a borehole shot, allowing direct comparison of the noise-based Green's functions with the shot records. Our goal is to demonstrate the successful retrieval of reliable Green's functions from a noise field with a strong P-wave component and the application of seismic NCC for revealing fault zone structures.

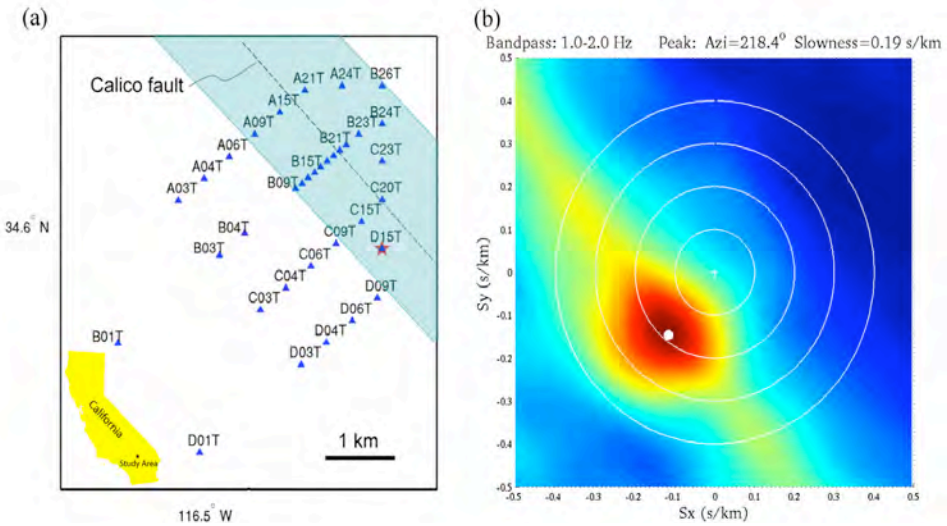


**Figure 7. (a) Map of the Calico fault area, showing stations (blue triangles), a borehole shot (red star), the Calico fault trace (dashed), and the fault zone (light blue); (b) Slowness-azimuth distribution of the noise field from beamforming, stacked over a frequency band of 1–2 Hz.**

Over broadband, the major part of the noise in southern California are microseisms mainly coming from the Pacific ocean (e.g., Gerstoft and Tanimoto, 2007). Here we focus on the frequency band of 0.5–3.0 Hz, in which microseisms may not be predominant. Using vertical-component noise records, we show in Figure 7b a 1-day beamforming output stacked over 1.0–2.0 Hz. Clearly the noise field is dominated by a coherent energy coming from the SW, at an apparent speed of ~5 km/s. Such slowness-azimuth pattern holds for all the other days within the 6-month period, indicating that this incident energy is temporally and spatially stable. Given the apparent speed of ~5 km, it is too fast to be a surface wave. We further suggest that it is a P wave as it is strongest on the vertical component.

From beamforming results, apparently a plane wave arrives at the array from the lower crust or upper mantle. We then expect to see a peak in the NCC output of a pair of sensors, of which the time lag from zero corresponds to the effective interreceiver distance along the direction of the incident wave, rather than the one along the surface. The time when the peak emerges would be a cosine function of the difference between the azimuths of the station-pair axis and the incident wave. Note, that for the case of a body wave, such a peak is no longer related to neither surface-wave nor body-wave Green's function. However, we still expect to see surface-wave Green's functions in the NCC outputs, as long as a diffusive wavefield (at least partially) coexists.

Indeed, we observe both a fast- and a slow-wave packet in the NCC output of each pair. Both appear propagating from the record section (not shown) of the NCC traces having directions roughly along NE–SW. The fast wave packet has a speed of about 5 km/s (getting faster for station pairs with azimuths away from NE–SW, e.g., arriving at zero along NW–SE), confirming that it is originated from the ballistic body wave observed from beamforming. The slow one turns out to be a packet of surface-wave Green's functions, as verified by a good match, for a range of distance and azimuth, respectively, of the noise-based impulse responses (the derivative of NCC outputs) with the records of a borehole shot sharing common paths (Figure 8). This comparison is a particular advantage of our experiment as we deployed a sensor (D15T in Figure 7a) at essentially the same site as the shot (red star in Figure 7a).

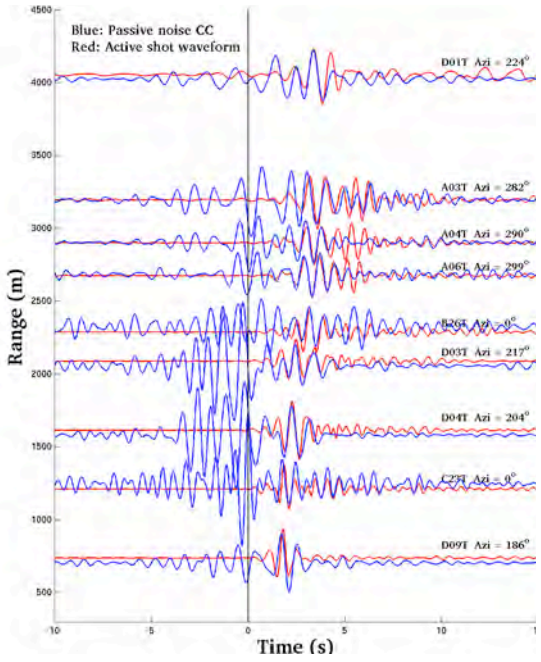


**Figure 8. A good match of noise-based surface-wave Green's functions (blue) with the borehole shot records sharing common paths.**

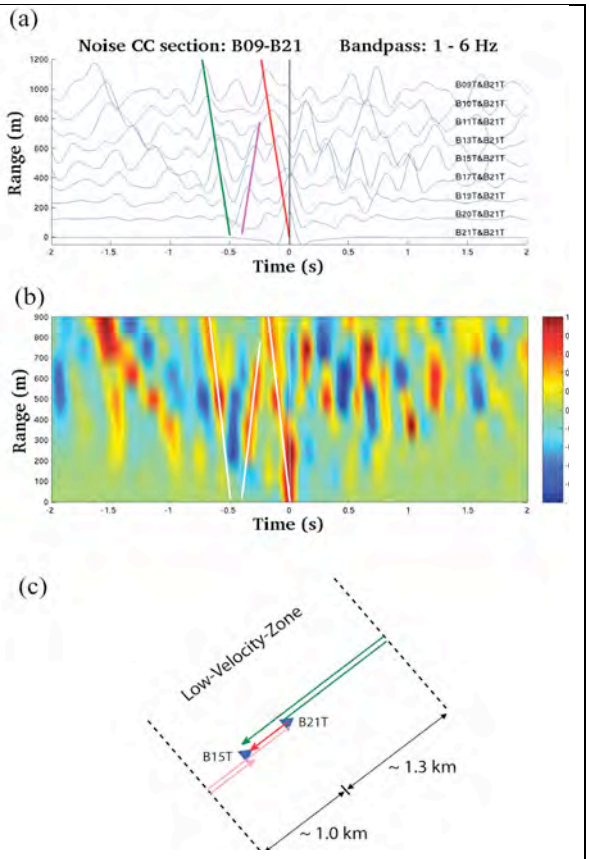


**Figure 9. (a) Record section of the NCC, for the profile B09T-B21T. Lines of red, purple, and green mark the direct arrival and its reflections from the side walls of LVZ, respectively. (b) Same as in (a), except the amplitude of the signals shown in color scale. (c) An LVZ model showing an example of the corresponding virtual arrivals from B21T to B15T.**

Our results indicate that the NCC technique is feasible and robust in converging Green's functions even for the noise field dominated by strong ballistic waves. However, caution is needed to distinguish body-wave Green's functions from plane-wave generated impulse responses. Although the case we provided is for near-field, i.e., scales less than a few wavelengths, which means that specific modes of surface waves are not well developed yet, Green's functions emerged from noise may still find their applications in exploration, engineering, and explosion monitoring fields, e.g., surface-wave isolation/removal.

The P-wave noise identified in our experiment provides a stable natural source for studying the structures along the Calico fault. By performing NCC for pairs of sensors along a profile (B09T-B21T, see Figure 7a), we construct a virtual record-section (Figure 9a) as if a plane-wave source with an apparent speed of 5 km/s were placed at the site of B21T. Interestingly, as seen in Figure 9a and 9b, besides the direct arrival of the virtual event (marked by a red line), another two arrivals with the same absolute speed show up (marked by a purple line and a green line, respectively). Indeed, these three arrivals can be interpreted by a low-velocity-zone (LVZ) model shown in Figure 9c. Thus, the wave from a virtual source at B21T will be reflected back from both sides of the boundaries of LVZ. From the direct arrival and its reflections in the record-section, our inversion of the distance from B21T to the reflectors (i.e., side walls of LVZ) amounts

to 1.0 km and 1.3 km, respectively. Thus, we estimate that the width of the Calico fault LVZ to be about 2.3 km, which agrees favorably with other evidences (Radiguet, unpublished material).

## CONCLUSIONS AND RECOMMENDATIONS

(1) Using time-frequency analysis methods, more-robust estimates of the surface-wave group velocity can be obtained.

(2) Seismic attenuation near a station can be extracted from noise by assuming that the ambient noise obtained from a time-variable F-K beam acts as a forcing function on a damped harmonic oscillator system.

(3) Beamformer output provides valuable information about noise distribution through time. We show that from 7–20-s period seismic noise in clipped seismograms for 18 months of data is dominated by surface waves and is consistent with a 2D model of noise distribution, having good azimuthal coverage from 10–22-s period. Beamforming provides an accurate, independent estimate of the mean phase-velocity dispersion across a seismic array that is within 1% of NCF and teleseismic estimates. Thus, beamforming can potentially resolve the cycle ambiguity in NCF phase-velocity estimates without a complementary teleseismic study.

(4) We provide results of a local-scale (~ 5 km × 5 km) seismic NCC experiment at a frequency band of 0.5 Hz and above. By applying beamforming, we identify a strong P wave in the noise field, suggesting that a careful analysis of the noise distribution and wave type is needed in the efforts of extracting P-wave Green's functions. By comparing the noise-based surface-wave Green's functions with the borehole shot records sharing common paths, we obtain a good match and thus verify the robustness of the NCC technique for a noise field dominated by a body wave. We then find that the NCC can turn the ballistic P-wave noise into a virtual record-section of a profile of sensors. From the direct arrival and its reflections shown in the record section, we invert the width of the Calico fault LVZ to be ~2.3 km.

## REFERENCES

Abers, G. A., K. M. Fischer, M. Protti, and W. Strauch (2007). The TUCAN broadband seismometer experiment: Probing mantle melting in the Nicaragua-Costa Rica subduction zone, *IRIS Newsletter* 1: 10–12.

Auger, A. and P. Flandrin (1995). Improving the readability of time-frequency and time-scale representations by the reassignment method, *IEEE Trans. Sig. Process.* 43: 1068–1089.

Bensen, G. D., M. H. Ritzwoller, M. P. Barmin, A. L. Levshin, F. Lin, M. P. Moschetti, N. M. Shapiro, and Y. Yang (2007). Processing seismic ambient noise data to obtain reliable broadband surface wave dispersion measurements, *Geophys. J. Int.* 169: doi: 10.1111/j.1365-1246X.2007.03374.x.

Cohen, L. (1989). Time-frequency distribution—A review, *Proc. IEEE* 77: 941–981.

Gabor, D. (1946). Theory of communication, *J. Inst. Electron. Eng*. 93: 429–457.

Gerstoft, P. and T. Tanimoto (2007). A year of microseisms in southern California, *Geophys. Res. Lett.* 34: L20304, doi:20310.21029/22007GL031091.

Harmon, N., D. Forsyth, and S. Webb (2007). Using ambient seismic noise to determine short-period phase velocities and shallow shear velocities in young oceanic lithosphere, *Bull. Seis. Soc. Am*. 97: 2024–2039.

Laske, G., J. Phipps Morgan, and J. A. Orcutt, (1999). First results from the Hawaiian SWELL pilot experiment: *Geophys. Res. Lett.* 26: 3397–3400, doi: 10.1029/1999GL005401.

Lin, F., M. P. Moschetti, and M. H. Ritzwoller (2008). Surface wave tomography of the western United States from ambient seismic noise: Rayleigh and Love wave phase velocity maps, *Geophys. J. Int.*, doi:10.1111/j1365-1246X.2008.03720.x.

Liu, H. P., D. L. Anderson, and H. Kanamori (1976). Velocity dispersion due to anelasticity: Implications for seismology and mantle composition, *Geophys. J. R. Astron. Soc*. 47: 41–58.

Matzel, E. M. (2008). Attenuation tomography using ambient noise correlation, *Seism. Res. Lett.* 79: 358.

Sabra, K., P. Gerstoft, P. Roux, W. A. Kuperman, and M. Fehler (2005a). Extracting time-domain Green's function estimates from ambient seismic noise, *Geophys. Res. Lett.* 32.

Sabra, K., P. Gerstoft, P Roux, W.A. Kuperman, and M. Fehler (2005b). Surface wave tomography from microseisms in Southern California, AGU *Geophys. Res. Lett.* 32: L14311, doi:10.1029/2005GL023155.

Yang, Y. and D. W. Forsyth (2006). Regional tomographic inversion of amplitude and phase of Rayleigh waves with 2-D sensitivity kernels, *Geophys. J. Int.* 166: 1148–1160.

# STRUCTURE OF THE KOREAN PENINSULA FROM WAVEFORM TRAVEL-TIME ANALYSIS

Roland Gritto[1], Jacob E. Siegel[1], and Winston W. Chan[2]

Array Information Technology[1] and Harris Corporation[2]

Sponsored by Air Force Research Laboratory

Contract No. FA8718-06-C0006

## ABSTRACT

Seismic waveform data of the Korean Meteorological Administration (KMA) have been analyzed to perform 3-D tomographic travel-time inversions to produce high-resolution 3-D crustal P- and S-wave velocity models for the South Korean peninsula. In a first step, waveform data from 2001 through May 2008 have been analyzed to map the Moho discontinuity below South Korea using refracted Pn travel times. Phase-arrival information from both velocity and accelerometer sensors was collected. The analysis included 270 events throughout the region producing 8,860 phase picks of Pg, Pn, Sg/Lg, and Sn phases. A total of 5,090 P-wave and 3,770 S-wave phases were identified. Using the combination of all available velocity and accelerometer data from the 119 KMA stations, it was possible to estimate depth locations for 226 KMA events. The hypocenters were subsequently used to derive travel-time distance curves based on 1-D velocity models to appraise the quality of the travel-time picks. The analysis produced, respectively, crustal P- and S-wave velocities of 6.13 km/s and 3.57 km/s and upper mantle velocities of 8.02 km/s and 4.48 km/s. The travel-time distance curves were used to determine static corrections for all station locations. After applying static corrections to all observed travel-times, refracted P-wave phases along the Moho boundary were selected from the dataset to estimate the depth and topography of the Moho discontinuity beneath South Korea. The resulting Moho topography reveals a relatively flat interface with depth variations from 28 to 34 km. The shallowest parts are below the Yellow Sea and below the Sea of Japan, while the deepest structure is located below the Yeongnam Massif. Joint inversion for hypocenters and velocity structure was performed to derive 3-D P- and S-wave velocity models for the crust. The inversion was constrained by the depth of the Moho interface derived in the previous step. Using analyst phase picks, it was possible to reduce the variance between observed and calculated travel times by 77%. Compared to preliminary event locations based on the 1-D velocity model, the relocated events indicate crustal seismicity deeper than 20 km beneath the peninsula. Additionally, a gradual decrease in depth of seismicity is observed beneath the Yellow Sea. The obtained 3-D velocity distribution is not correlated with the geologic terrains of the peninsula. The velocity distribution is relatively homogeneous corroborating the good fit of the 1-D velocity model. Upper crust velocity values are estimated at 6.2 km/s and 3.6 km/s for P- and S-waves respectively. These values increase beneath 25 km to 7 km/s for P- and 4.3 km/s for S-waves. Mantle velocities are encountered below 32 km depth reaching 8.5 km/s and 4.8 km/s for P- and S-waves, respectively, corroborating the results of the Moho topography study. Finally, 35 GT5 events were selected from the 270 relocated events using Bondár's criteria (Bondár et al., 2004). The 35 events are well located within the dense KMA network as required by Bondár's criteria.

## OBJECTIVES

The primary objective of this research is to produce high-resolution 3-Dcrustal P- and S-wave velocity models of the South Korean Peninsula. The structure of the crustal model will be supplemented by the derivation of a 3-D Moho interface below the peninsula. The resulting velocity and structural models will provide valuable information for regionalization and relocation studies.

## RESEARCH ACCOMPLISHED

Waveform data from the Korean Meteorological Administration (KMA) were analyzed for the years 2001 through May 2008 to determine the phase arrival of body waves from local and regional events. The KMA operates a dense seismic network consisting of 138 stations with velocity and accelerometer sensors. The analyzed data consist of triggered waveforms recorded for local and regional events throughout the Korean Peninsula. Phase arrival information of P- and S-waves was subsequently used to delineate the structure of the Moho interface between crust and mantle.

### Korean Meteorological Administration (KMA) Waveform Data

The KMA of the Republic of Korea (ROK) operates a dense network of seismic stations throughout the country. The network consists of 138 stations comprised of velocity and accelerometer sensors. Station configurations include combinations of velocity and accelerometer sensors as well as single sensor sites. The analyzed data included triggered waveforms of local and regional events from 2001 through May 2008. For stations with single sensor configuration, the analyzed data were obtained from either velocity or accelerometer data, while both velocity and accelerometer data were obtained for those stations with dual sensor configuration. The intention is to improve the significance of data for stations where travel-time data from more than one instrument are available.

### Travel-Time Analysis of KMA Waveform Data

The analysis of the KMA waveform data produced a total of 8,860 phase picks from 270 events located throughout the Korean Peninsula. The number of located events amounts to a seismicity rate of approximately 32 events per year and confirms previous estimates for this region. Identified phases included Pg, Pn, Sg/Lg, and Sn. The number of individual identified phases amounted to 5,090 P-wave and 3,770 S-wave phases. Because the accelerometer data contain higher frequency information, epicentral distances from the events to the accelerometer stations were generally shorter than those associated with velocity stations, which helped to constrain the depth of the events. Furthermore, this approach decreased the uncertainty of the hypocenter location. Using the combination of velocity and accelerometer data, it was possible to estimate depth locations for 230 of the KMA events.

Quality control of the data was performed using travel-time-distance curves. The phase picks of the KMA data from January 2001 – May 2008 are shown in Figure 1. The travel-time of P- and S-wave phases is plotted as a function of hypocentral distance to assess the quality of the selected phase picks. The diamond-shaped symbols represent the P- and S-wave phases determined from the waveform data. The short black horizontal lines at each data point represent the relative location error for each hypocenter estimate associated with that phase pick. For each hypocenter, a relative error is calculated separately for the x-, y- and z-direction. In order to facilitate the presentation of this uncertainty, we take the relative errors for the three directions and calculate a single resulting vector, which represents the radius of a sphere around each hypocenter estimate indicating the uncertainty in its location. Therefore, the short black horizontal lines in Figure 1 represent the length of the radius of the error sphere for each hypocenter estimate. In contrast, the short black vertical lines at each data point represent the relative timing error for the event time associated with that phase pick. Considering all phase picks from velocity and accelerometer data, the average hypocentral error was reduced by 17% relative to the original hypocenters published by the KMA. The colored solid lines in Figure 1 represent the best linear fit, in a least-squares sense, through the cloud of travel-time picks. It can be seen that the fit is very good for hypocentral distances below 400 km. Although the number of events decreases for hypocentral distances beyond 400 km, the linear fit is still good at greater distances. The velocity values listed in Figure 1 are averaged P- and S-wave velocities of the crust and upper mantel as determined from the slope of the travel-time distance curves. These values are in good agreement with published estimates for the Korean Peninsula (i.e., Chang and Baag, 2006). If the model of a single-layered crust is employed to determine average crustal thickness from the travel-time curves in Figure 1, a value of 32 km is obtained. In comparison, Chang and Baag (2006) conducted receiver function studies based on teleseismic body wave data. They report a distribution of crustal thicknesses from 28 km in the eastern part to 35

km in the south-western part of South Korea. Therefore, the average value of 32 km, determined from the phase picks of the KMA data, appears to be a good estimate for crustal thickness, giving confidence in the obtained arrival times. A separate method to estimate Moho topography is presented below.

**KMA GT5 Events**

GT events are important benchmarks to test earthquake location techniques and validate velocity models. We applied Bondár's criteria (Bondár et al., 2004) to the database of 230 KMA events with depth locations requiring that each potential GT5 event is located:

(a) by at least 10 stations, all within 250 km distance from the epicenter;
(b) with an azimuth gap of less than $110^o$;
(c) with a secondary azimuth gap of less than$160^o$; and
(d) by at least one stations within 30 km distance from the epicenter.

Forty-four events were identified that matched these criteria, each one having a cumulative location error δe of less than 5 km. The cumulative location error is defined as:

$$\delta e = \sqrt{\delta x^2 + \delta y^2 + \delta z^2}$$

where δx, δy, and δz are location errors in longitude, latitude and depth, respectively. Figure 2 shows GT5 events identified from the KMA hypocenter database. They are well located within the dense network of KMA stations as required by Bondár's criteria.

**Estimation of 3-D Moho Structure from Refracted P-waves**

Two important parameters that define crustal structure are the depth and topography of the Moho boundary between crust and mantle. The topography of this interface can help to explain crustal tectonics and consequently the kinematics of wave propagation through the crust. Refracted P-wave phases along the Moho boundary can be used to estimate the depth of this interface. As can be seen in Figure 1, refracted Pn phases were observed between hypocentral distances from 130 km to 650 km. In total, 810 Pn phases were collected from the KMA data from January 2001–May 2008.

Before the depth and topography of the Moho could be estimated, near-station effects due to inhomogeneities in the near subsurface had to be removed from the Pn travel times. These static corrections prevent travel-time anomalies from near surface inhomogeneities to be mapped into anomalies of Moho elevation at depth. The static corrections were estimated using a least-squares approach minimizing the misfit between observed and calculated Pg travel times. The least-squares approach jointly inverted for a homogenous crustal velocity model and static correction terms at each recording station. These static corrections were subsequently subtracted from the Pn travel times before they were used to estimate Moho topography.

Several approximations have to be considered when estimating depth from travel times of refracted waves. The most important is that of a one-dimensional velocity model of a layer over a half space. In the current case, the velocity estimates for the crust and upper mantle derived from the linear fits in Figure 1 are utilized. Furthermore, it is assumed that the Moho interface is piece-wise flat over the propagation distance of each refracted phase along this boundary, while dip of the flat segments is allowed. A sketch indicating the geometric assumptions is presented in Figure 3. With these approximations, ray theory and the principles of refraction seismology were applied to determine Moho depth and topography. For each refracted ray path, two depth-estimates for the Moho interface below the hypocenter and recording station were calculated together with the dip of the Moho interface between these two points. A maximum-likelihood approach was applied to the results of a grid search over a two dimensional depth-and-dip space to minimize the misfit between observed and calculated Pn travel times. Once the depth and dip of the Moho interface was determined below each hypocenter and recording station, the data were interpolated using an adjustable-tension continuous-curvature surface-gridding approach (Wessel and Smith, 1995). The result of the gridding is shown in Figure 4, which displays a 3-D surface plot of the Moho interface below South Korea. The emerging pattern reveals a slightly undulating interface with a mean depth of 31 km. The Moho appears elevated extending from the north-east through the center to the south-west at a depth of approximately 29 km. To the north and south of this structure, the interface dips down to about 34 km, while it

appears to be elevated below the Yellow Sea and the Sea of Japan. The mean depth of the Moho interface will be used to constrain the inversion for 3-D velocity structure presented in the next section.

**Three-Dimensional Crustal Velocity Structure**

The number of phase picks obtained from waveform analysis between January 2001 and May 2008 amounted to 8,400. However, not all of these phase picks can be utilized during the velocity inversion as the implemented ray tracing is based on the eikonal solver by Podvin and Lecomte (1991), which considers first arrivals only. Therefore, Pg- and Sg-phases will only be considered for distances shorter than their respective crossover distances, while Pn- and Sn phases will be used beyond these distances. The ray density of all P-wave phases is presented in Figure 5, where it is superimposed on the Korean peninsula. The green circles and blue triangles denote, respectively, the epicenters of the events and the locations of the seismic stations. The red circles represent the node spacing implemented during the inversion.

The P-wave velocity estimates resulting from travel-time tomography produced homogeneous values of about 6 km/s for the upper crust, which suggest that these measurements cannot be used to differentiate the geologic terrains (refer to Figure 6). Below 25 km depth, the velocity increases to typical lower-crust values of about 7 km/s. At a 32-km depth, the transition from crustal- to mantle velocities can be observed. Variations in velocity range from 6.5 to 8.5 km/s, with the latter representing upper mantle velocities. The pattern of high- and low-velocity regions at 32 km depth correlates to some degree to the pattern of the Moho topography in Figure 3. The brown color in Figure 4 represents an elevated Moho, which indicates the presence of mantle material and thus higher velocities (blue color in Figure 6). In contrast, the blue color in Figure 4 represents a depressed Moho, which indicates the presence of crustal material and thus lower velocities (green colors in Figure 6).

The S-wave velocity estimates, presented in Figure 7, corroborate the results of the P-wave inversion to a certain degree. The velocity distribution is relatively smooth in the upper crust with values of 3.5 km/s. Variations in velocity, which could indicate the presence of different geologic terrains, are not apparent. The velocity values appear to decrease in the lower part of the crust. However, this may be an artifact caused by the poor ray coverage at this depth range, due to the lack of sufficient Sn phase arrivals at longer distances.

## CONCLUSIONS AND RECOMMENDATIONS

To interpret the Moho topography, it is necessary to incorporate the crustal tectonics of the Korean Peninsula. Although the pattern of Moho topography reveals a northeast/southwest trend, a correlation to the general trend of the major geologic terrains of the Korean Peninsula is only weakly developed. Nevertheless, the Moho coincides to a certain degree with surface topography. The central depression of the Moho interface is co-located with the Yeongnam Massif, which may indicate isostatic compensation for this mountain range (Kwon and Yang, 1985; Choi and Shin, 1996). This feature is common in most investigations of crustal structure in this region.

Analysis of phase information derived from KMA waveform data points to a relatively homogenous crust below South Korea. The good linear fit through the travel-time distance data in Figure 1, as well as the homogenous velocity distribution obtained from 3-D velocity inversions indicates crustal structure with little variation with respect to seismic velocities. Therefore, the geologic terrains, observed at the surface cannot be separated by seismic velocities at depth. The results derived in this study for the Moho topography are corroborated by the work of Chang and Baag (2006) and Yoo et al. (2007), who mapped the Moho interface using surface-wave dispersion and receiver-function analyses. In both studies, a pattern of the Moho interface, similar to the one displayed in Figures 3 was found. The fact that the results of our refraction study, which was based on a 1-D velocity model, match the results of these previous studies, indicate that a 1-D velocity model is an acceptable approximation, at least for the upper half of the crust below South Korea.

## ACKNOWLEDGEMENTS

The figures and maps throughout this document were created using the Generic Mapping Tools by Wessel and Smith (1995).

## REFERENCES

Bondár, I., S.C. Myers, E. R. Engdahl and E.A. Bergman (2004). Epicenter accuracy based on seismic network criteria, *Geophys. J. Int* 156: 483–496.

Chang, S. J. and C. E. Baag (2006). Crustal Structure in South Korea from Joint Analysis of Broadband Waveforms and Travel Times, *Bull. Seis. Soc. Am*. 96: 856–870, doi:10.1785/0120040165.

Choi, K. S. and Y. H. Shin (1996). Isostasy in and around the Korean Peninsula by analyzing gravity and topography data, *J. Geol. Soc. Korea* 32: 407–420.

Kwon, B. D. and S. Y. Yang (1985). A study on the crustal structure of the southern Korean Peninsula through gravity analysis, *J. Korean Inst. Mining Geol*. 18: 309–320.

Podvin, P. and I. Lecomte (1991). Finite difference computation of travel times in very contrasted velocity models: A massively parallel approach and its associated tools, *Geophys. J. In*t. 105: 271–284.

Wessel, P. and Smith, W. (1995). New version of the generic mapping tools released. *EOS Trans. AGU* 76: 329.

Yoo, H. J., R. B. Herrmann, K. H. Cho, and K. Lee (2007). Imaging the three-dimensional crust of the Korean Peninsula by joint inversion of surface-wave dispersion and teleseismic receiver functions, *Bull. Seism. Am.* 97: 3, 1002–1011, doi: 10.1785/0120060134.

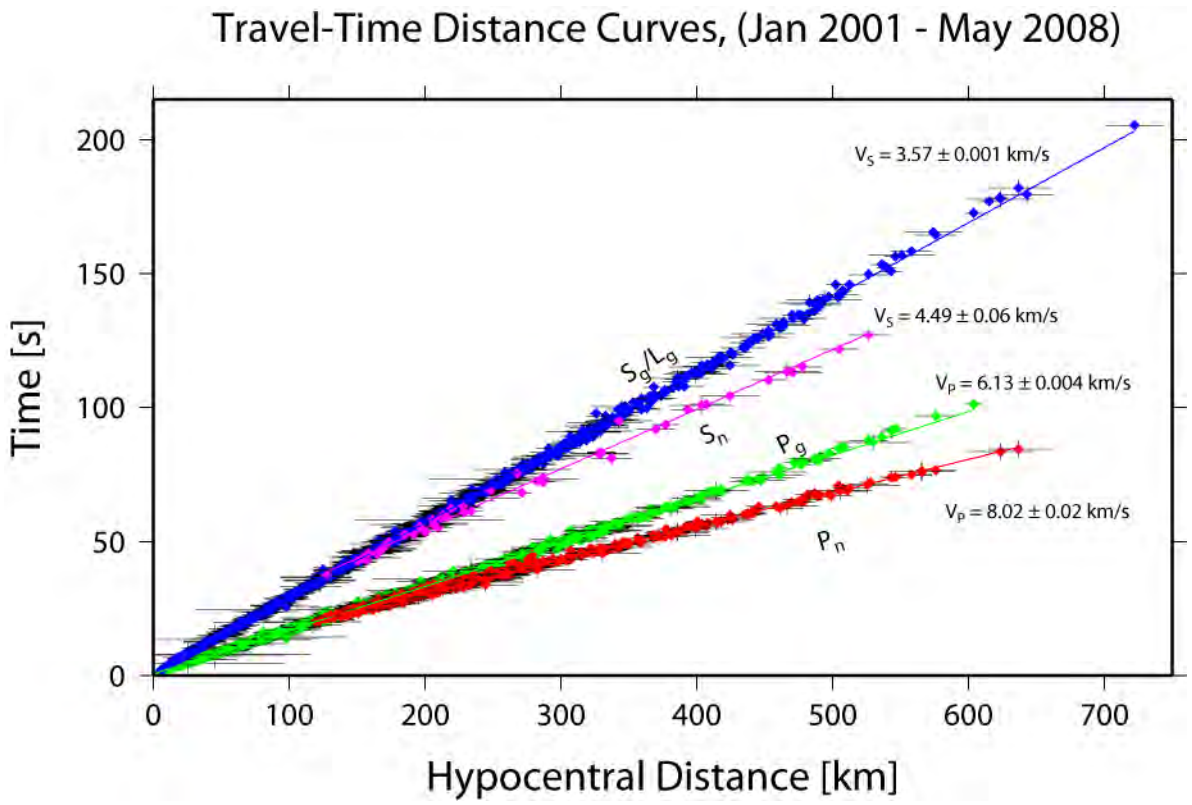


**Figure 1. Travel time as a function of hypocentral distance for the P- and S-wave phase picks as determined from KMA waveform data for the period January 2001- May 2008. The phase picks are indicated by colored diamonds, while the solid colored lines represent their best least-squares fit resulting in the velocity values as noted. The short black horizontal lines at each data point represent the relative location error for each hypocenter estimate associated with that phase pick. The short black vertical lines at each data point represent the relative timing error for event time associated with that phase pick.**

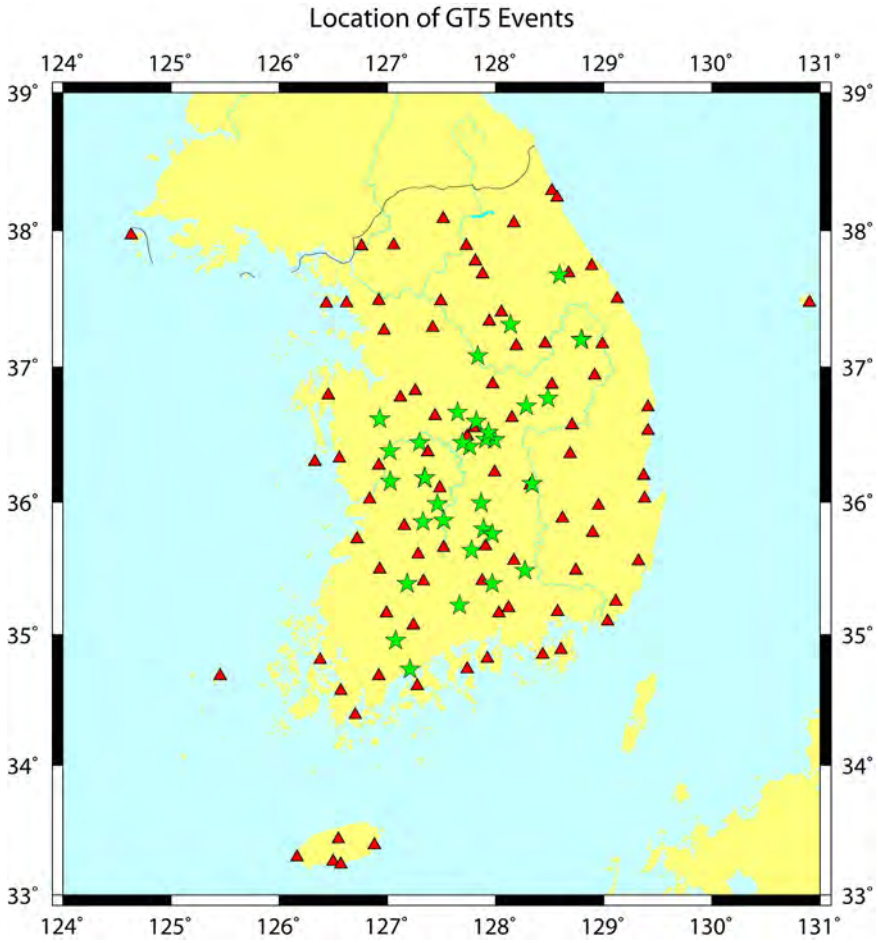


**Figure 2. GT5 events identified from a database of 230 events with depth location derived from KMA waveform data from January 2001 – May 2008. Green starts denote epicenter of GT5 events, while the red triangles represent the KMA stations.**

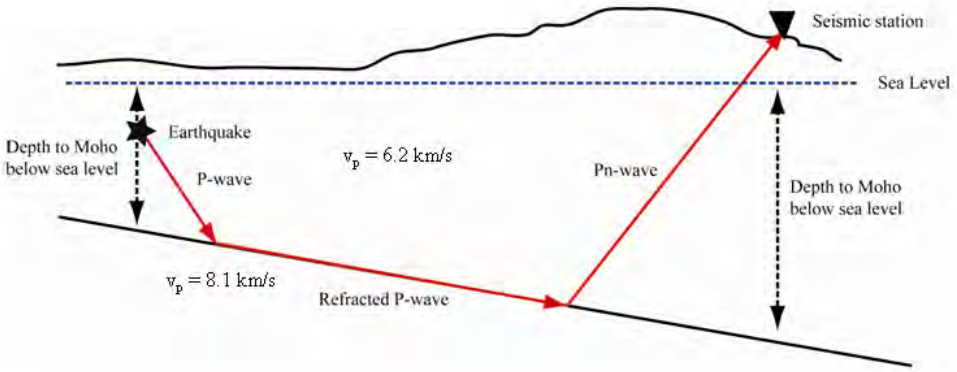


**Figure 3. Sketch indicating the geometry for calculating theoretical travel times for refracted waves**.

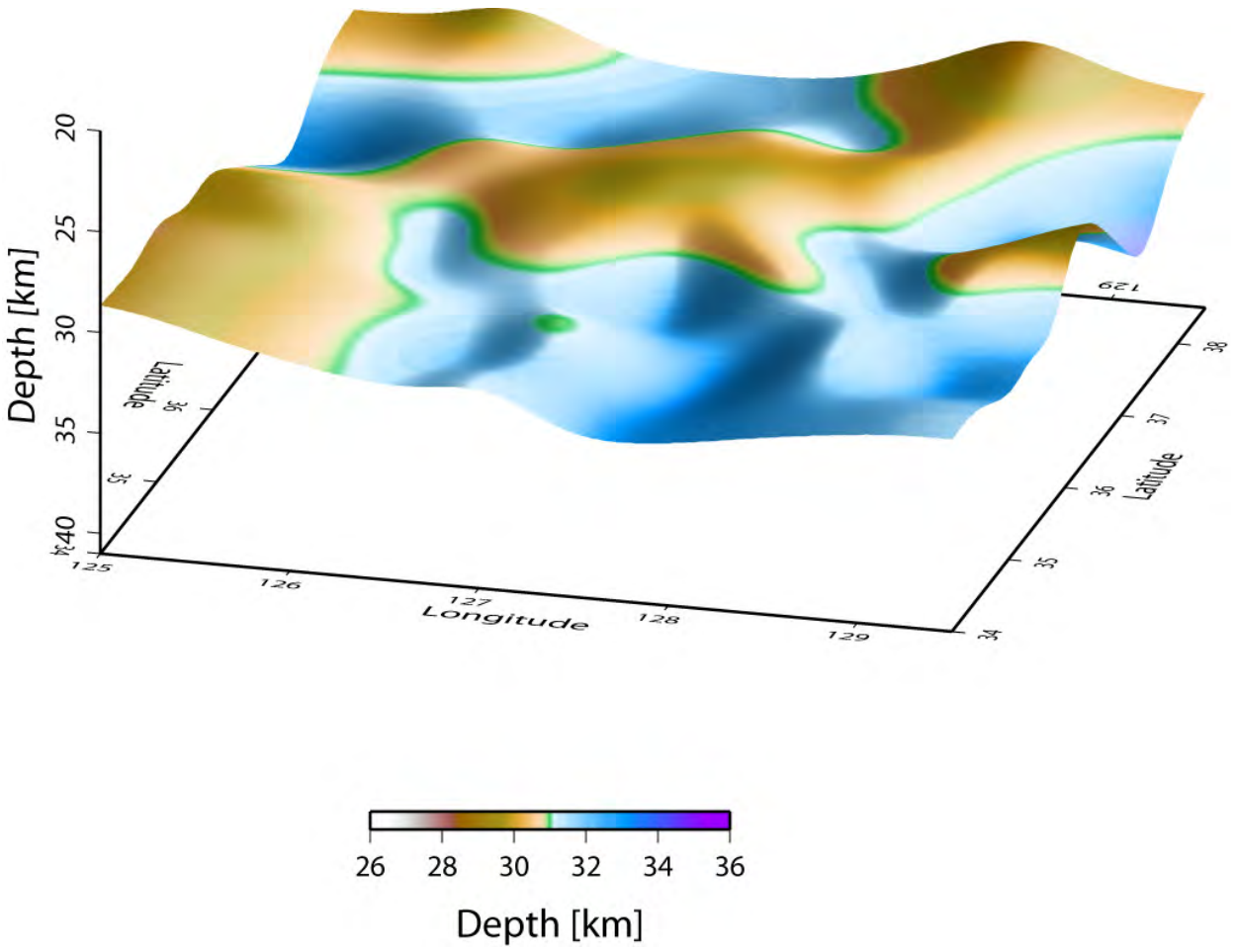


**Figure 4. Three-dimensional surface plot of the Moho discontinuity below South Korea based on depth estimates below each KMA station and each recorded earthquake.**

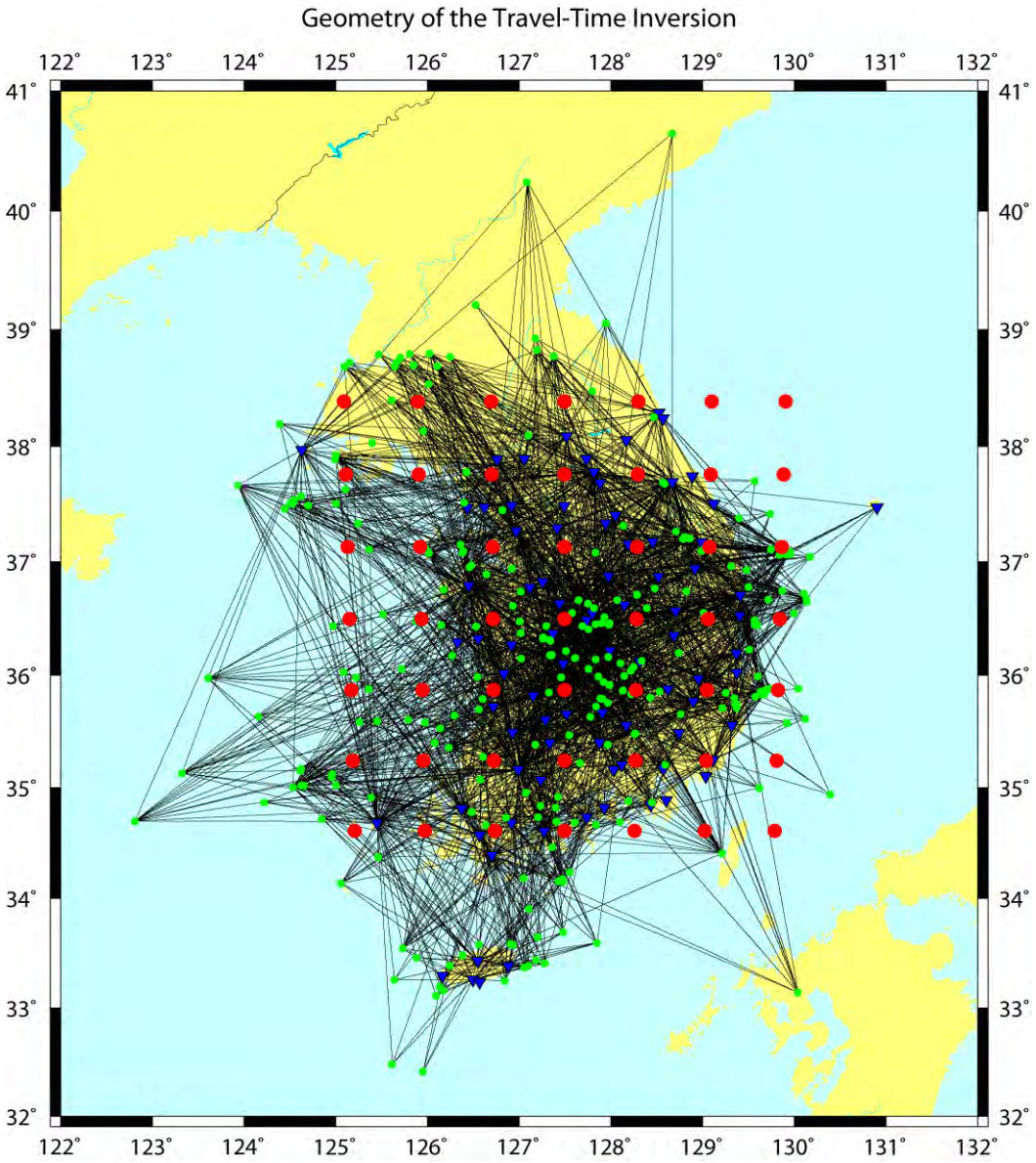


**Figure 5. Geometry of the inverse problem. The P-wave (Pg and Pn) ray density is projected onto the surface, while the red circles indicate the nodes used during the inversion. Green circles and blue triangles indicate epicenters and seismic stations, respectively.**

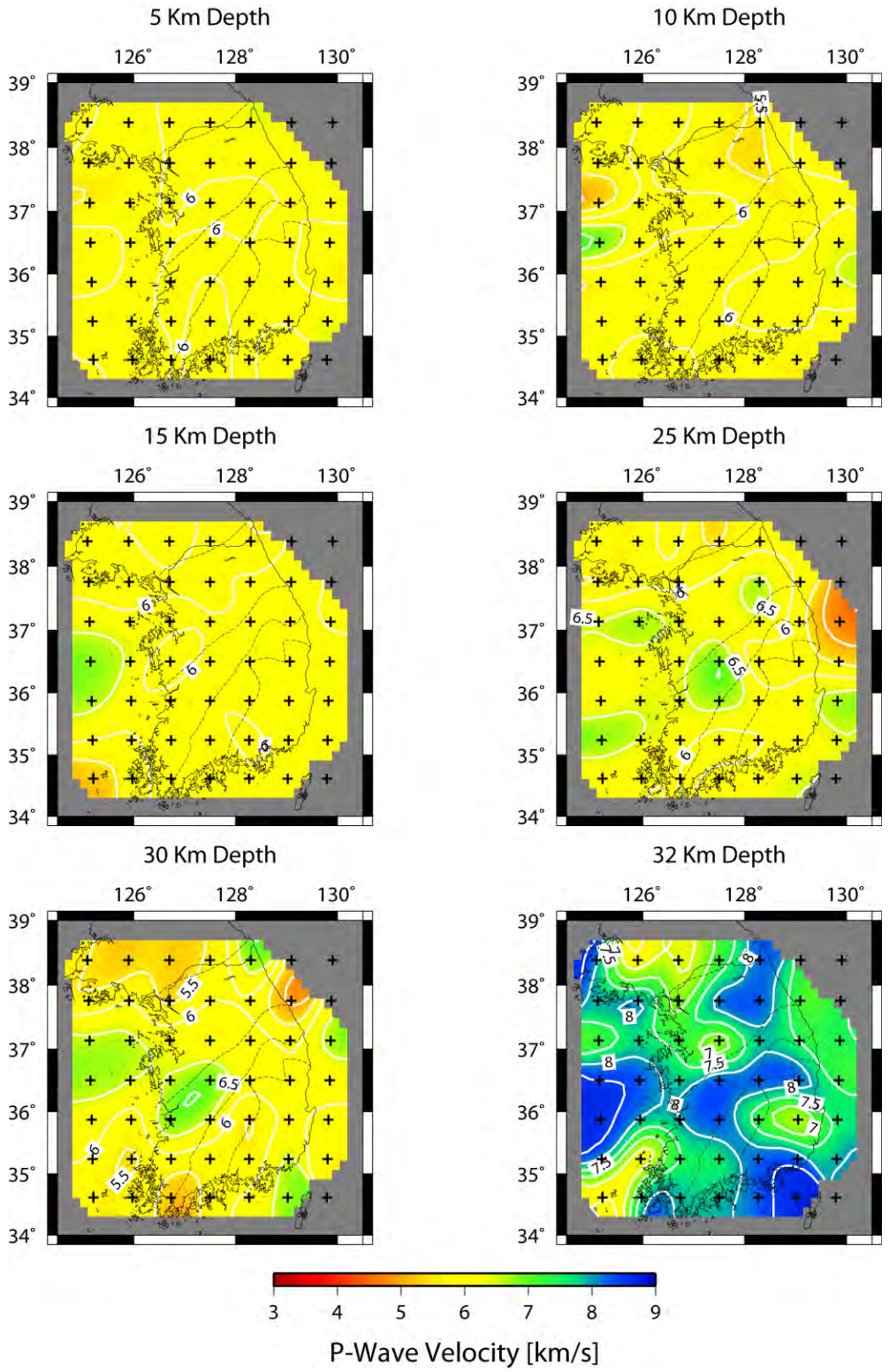


**Figure 6. Horizontal cross-sections of P-wave velocity distribution as a function of depth derived from 3,315 Pg and Pn phases and 270 earthquakes distributed across South Korea.**

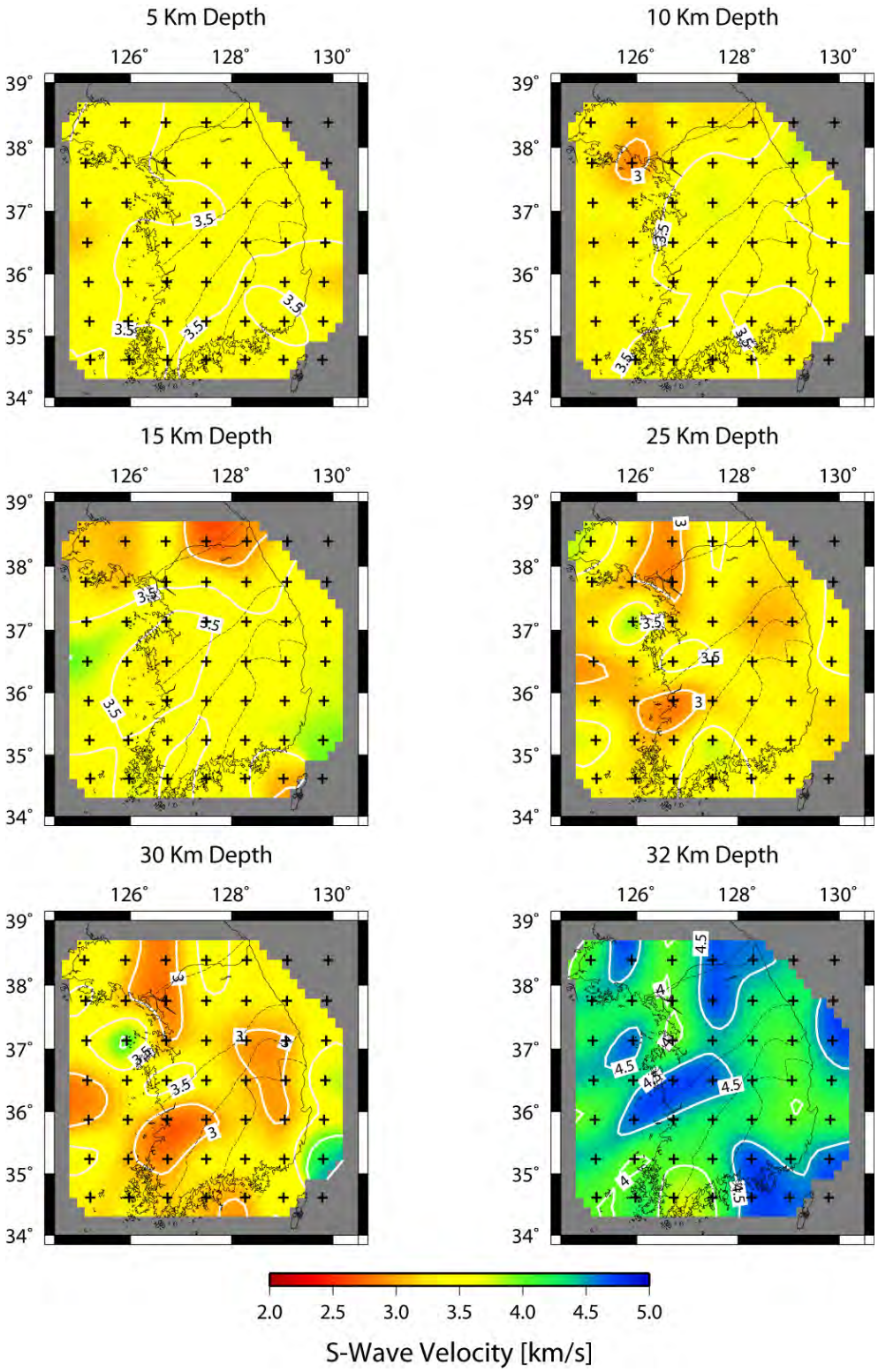


**Figure 7. Horizontal cross-sections of S-wave velocity distribution as a function of depth derived from 2,279 Sg and Sn phases and 270 earthquakes distributed across South Korea.**

# CRUSTAL STRUCTURE OF NORTH IRAQ FROM RECEIVER FUNCTION ANALYSES

Roland Gritto[1], Matthew S. Sibol[1], Jacob E. Siegel[1], Hafidh A. Ghalib[1], Youlin Chen[1], Robert B. Herrmann[2], Ghassan I. Alequabi[3], Hrvoje Tkalcic[4], Bakir S. Ali[5], Borhan I. Saleh[5], Dawood S. Mahmood[6,7], Omar K. Shaswar[9,10], Aras Mahmood[5], Shaho Abdullah[5], Fadhil Ibrahim[8], Rashid Zand[8], Basoz Ali[5], Layla Omar[5], Nokhsha I. Aziz[5], Nian H. Ahmed[5], Talal Al-Nasiri[10], Ali A. Ali[7], Abdul-Karem A. Taqi[7], and Samira R. Khalaf[7]

Array Information Technology[1], Saint Louis University[2], Washington University in Saint Louis[3], Australian National University[4], Sulaimaniyah Seismological Observatory[5], Iraq Meteorological Organization[6], Baghdad Seismological Observatory[7], Erbil Seismological Observatory[8], Sulaimaniyah University[9], and University of Baghdad[10]

Sponsored by Air Force Research Laboratory

Contract No. FA8718-07-C-0008
Proposal No. BAA07-59

## ABSTRACT

A primary objective of this project is to estimate the local and regional seismic velocity structures of north and northeastern Iraq, including the northern extension of the Zagros collision zone. Furthermore, earthquake source mechanisms will be investigated once a velocity model is derived for this region. Thus far, global seismic network coverage is poor throughout the region and extrapolated velocity models found in the literature lack sufficient accuracy to permit events to be located with significant precision. Ten three-component broadband stations composing the North Iraq Seismographic Network (NISN) were installed in late 2005. At present, waveforms from 290 teleseismic events, from November 30, 2005 through March 31, 2007, have been processed for P-wave receiver functions (RFs). Based on the USGS Preliminary Determination of Epicenters (PDE) bulletins, the epicentral distances of these teleseismic events to NISN stations range from 30º to 90º while their magnitudes equal or exceed 5.5. Results obtained to date indicate a lower-than-average shear wave velocity when compared to other crustal regions of the Earth. Additionally, Moho depths appear slightly shallower below the stations located along the foothills compared to the stations at higher elevation in the Zagros mountains. The Moho below the foothills is estimated at 40-50 km depth, while it dips down to a depth of 45-55 km below the northern extension of the Zagros zone. Common among the receiver functions is the presence of a significant velocity discontinuity at a depth of 15 km and 20 km for the stations below the foothills and Zagros mountains, respectively. The increase in velocity across this discontinuity lead to the observation of mid-crustal refracted body waves throughout NISN. Evaluation of the resulting models will be performed through relocation of recorded events, synthetic waveform analysis, and correlation with available geophysical and geological information.

## OBJECTIVE

The objective of the current paper is to estimate the seismic velocity structure beneath the stations of the North Iraq Seismographic Network (NISN) based on RFs inversion techniques. This effort will subsequently be supplemented by the determination of crustal structure from surface wave dispersion analyses. The two methods are complementary and provide valuable constraints on estimating seismic velocity structures. Evaluation of the resulting models will be performed through relocation of recorded events, synthetic waveform analysis, and correlation with available geophysical and geological information.

In November 2005 and in cooperation with the Sulaimaniyah, Erbil, Baghdad, and Mosul seismological observatories (SSO, ESO, BSO and MSO, respectively) the first eight stations of NISN were deployed, followed by stations BHD in Baghdad and MSL in Mosul in April 2006. Figure 1 shows a generalized diagram of the seismotectonic framework of the Arabian plate. NISN stations (white triangles) are located along the northeast boundary of the plate where the Zagros thrust zone and the Bitlis suture zone converge. This region is characterized by a high level of seismic activity, as evidenced by the large number of local and regional events recorded by NISN (Ghalib et al., 2006) and by the teleseismically located earthquakes reported by the United Stated Geological Survey (USGS) bulletins. A close up of the geographic location of NISN is presented in Figure 2. The NISN stations, located parallel to the strike of the Zagros fold belt, are divided in two groups; one along the foothills and the other at higher elevation in the Zagros mountains. Since December 2005, Array IT has collected over 760 GB of data from NISN including local, regional and teleseismic events. The data consist of high-quality, continuous, three-component broadband recordings collected at a rate of 100 sps. Although the seismicity rate of the Zagros fold and thrust zone alone is relatively high, it may have gone mostly undocumented in the past. One explanation is that many of the unreported events are small and may not have been detectable by the regional stations in Turkey and Iran. Second, degradation of Iraq Seismological Network (ISN) capability has significantly impacted monitoring events in this region. Also, noteworthy to mention is that many of the events reported by the USGS and ISC seem to cluster around the local stations in Iran and Turkey that reported their parameters, leaving a major section of the Zagros, its foothills and fold belt to be covered by NISN in an effective and comprehensive manner. The average seismicity rate for local and regional earthquakes recorded by NISN is approximately 150 events per month, resulting in an unprecedented dataset available for research under this effort.

## RESEARCH ACCOMPLISHED

RFs are reflection time-series computed from three-component seismograms that represent the relative response of seismic waves to the earth structure near a receiver (Ammon, 2006). The RF methodology has been extensively used by seismologists. While the overall method is straightforward to define, the computation of reliable receiver functions can be problematic due to the non-uniqueness of RF inversions and has been the subject of many studies, including Burdick and Langston (1977), Langston (1977), Ammon (1991), Cassidy (1992), Ligorría and Ammon (1999), Park and Levin (2000), and Helffrich (2006). The current approach is based on the techniques by Zhu and Kanamori (2000), Julià et al. (2000), and Ammon (2006) to determine RFs and invert for crustal seismic velocity models.

A search of the USGS PDE bulletins for the period from 30 November 2005 to 31 March 2007 resulted in a long list of teleseismic events at various azimuths and epicentral distances in the range of 30–90 degrees from NISN. Corresponding searches of NISN for events exceeding magnitude 5.5 resulted in about 290 events available for analysis. The azimuthal distribution of these events relative to NISN is presented in Figure 3. The distribution of events is not symmetric, as most epicenters are located along the western rim of the pacific region from the Aleutian Islands to the north-east to Indonesia to the south-east. In contrast, events to the west are located along the Mid-Atlantic ridge, while events to the south are grouped along the Southwest Indian Ridge and the East-African Rift Zone. The variation of RFs at each station with respect to azimuth and ray parameter of the incoming waves was investigated. It was found, however, that this variation is not very significant.

An example of teleseismic waveform data recorded at stations KSBB, KSSS, and KSWW is shown in Figure 4. The event occurred in the Kuril Islands on 22 June 2006 with a magnitude (Mw) of 6.0. The quality of observed P-waves was assigned a grading scale (A, good, through D, poor) to reflect the minimum signal-to-noise level

which still produced stable and reliable receiver functions. The grading helped to understand the impact of signals with low signal-to-noise ratios on the RFs and resulting models. In the final data processing, only good-quality waveforms (grade A and B) were used.

In order to fit the observed RFs we use an iterative linearized inversion technique (Ammon, 2006), which strongly depends on the starting model. The best starting model is estimated using the method by Zhu and Kanmori (2000), which generates a three-layered model over a half space providing an initial Moho depth and $v_p/v_s$-ratio beneath each station. The result of the initial search is presented in Table 1.

**Table 1: Summary of initial search results for Moho depth and $v_p/v_s$-ratio beneath the stations of NISN**

| Station | Available events | Used events | Moho Depth [km] | $v_p/v_s$ |
|---|---|---|---|---|
| KDDA | 112 | 29 | 52.3+/-0.8 | 1.62+/-0.05 |
| KEHH | 127 | 55 | 49.8+/-1.4 | 1.55+/-0.06 |
| KEKZ | 131 | 15 | 44.7+/-0.8 | 1.80+/-0.06 |
| KESM | 94 | 46 | 39.1+/-0.9 | 1.83+/-0.07 |
| KSBB | 136 | 42 | 48.6+/-1.3 | 1.70+/-0.06 |
| KSJS | 123 | 32 | 48.9+/-1.2 | 1.73+/-0.08 |
| KSSS | 103 | 53 | 52.3+/-0.8 | 1.85+/-0.05 |
| KSWW | 134 | 65 | 54.2+/-0.7 | 1.71+/-0.06 |

A cross correlation approach was subsequently used to determine the most coherent RFs at each station before they were stacked to generate the final observed RF.

In preparation for the inversion process, the Moho depths and $v_p/v_s$-ratio obtained from Table 1 were used to generate a simple multi-layered initial compressional- and shear-velocity model which followed the general characteristics of the models derived by Ghalib (1992). The thicknesses of the crustal layers varied from 0.5 km at the top to a maximum of 10 km at the bottom, representing a gradual increase with depth. In the upper mantle, the layer thicknesses ranged from 10 to 100 km.

The resulting one-dimensional shear-wave velocity models for stations KESM, KEHH, KSWW, KSSS, KDDA, KEKZ, KSJS, and KSBB are presented in Figure 5. The best fit of these RFs ranged from 60% to 93%, while the back-azimuth to these events ranged from 20 to 120 degrees. Common among the eight models are the relatively low shear-wave velocities of the layers in comparison to other regions of the Earth and the presence of a significant positive velocity discontinuity between upper and lower crust. The results of the RF inversion suggest a slightly shallower Moho below the foothills at 40-50 km depth, while it dips down to 45-55 km below the Zagros mountains. All crustal models indicate the presence of a significant positive velocity discontinuity at about 15 km and 20 km depth for the stations below the foothills and Zagros mountains, respectively. The increase in velocity across this discontinuity resulted in the observation of mid-crustal refracted body waves throughout NISN. These results are consistent with previous observations made by, among others, Aleqabi et al. (2007), Pasyanos et al. (2004), and Ghalib (1992).

## CONCLUSIONS AND RECOMMENDATIONS

The presented results are part of an ongoing effort to estimate the seismic velocity structure beneath eight of the NISN three-component broadband stations. The presented models were exclusively estimated from the inversion of PFs of teleseismic P wave seismograms. Most significant about these models is that they consistently reflect lower-than-average velocities, as has previously been observed, which seems to characterize the crustal structure of this region.

Continuous data collection and processing of teleseismic P- and surface-wave data is currently under way for refinement of the presented results and simultaneous inversion. These data will help generate more-reliable models

that can withstand the test of relocating events with higher precision and synthetic waveform modeling that matches well with the observed seismograms.

## ACKNOWLEDGEMENTS

The figures and maps throughout this document were created using the Generic Mapping Tools by Wessel and Smith (1998).

## REFERENCES

Aleqabi, G., M. Wysession, H. A. A. Ghalib, M. Sibol, B. Saeed Ali, B. Saleh, A. Mahmood, S. Abdullah, L. Omar, N. Aziz, N. Ahmed, D. Mahmood, N. Alridaha, T. Alnasiry, O. Shaswar, A. Ali, A. Taqi, S. Khalaf, and F. Ibrahim (2007). Seismic velocity structure of Iraq and surrounding regions from surface-waves waveform inversion, *Seism. Res. Lett.* 78: 310**.**

Julià, J., C. J. Ammon, R.B. Herrmann, and A. M. Correig (2000). Joint inversion of receiver function and surface wave dispersion observations, *Geophys. J. Int.* 143: 1-19.

Zhu, L. and H. Kanamori (2000). Moho depth variation in southern California from teleseismic receiver functions, *J. Geophys. Res.* 105: 2969–2980.

Ammon, C. J. (1991). The isolation of receiver effects from teleseismic P waveforms, *Bull. Seism. Soc. Am.* 81: 2504–2510.

Ammon, C. J. (2006). Receiver-Function Analysis, Pennsylvania State University, Web page: http://eqseis.geosc.psu.edu/~cammon/HTML/RftnDocs/rftn01.html

Burdick, L. J. and C. A. Langston, (1977). Modeling crustal structure through the use of converted phases in teleseismic body-wave forms, *Bull. Seism. Soc. Am.* 67: 677–691.

Cassidy, J. F. (1992). Numerical experiments in broadband receiver function analysis, *Bull. Seism. Soc. Am.* 82: 1453–1474.

Ghalib, H. A. A., G. I. Aleqabi, B. S. Ali, B. I. Saleh, D. S. Mahmood, I. N. Gupta. R. A. Wagner, P. J. Shore, A. Mahmood, S. Abdullah, O. K. Shaswar, F. Ibrahim, B. Ali, L. Omar, N. I. Aziz, N. H. Ahmed, A. A. Ali, A.-K. A. Taqi, and S. R. Khalaf (2006). Seismic characteristics of northern Iraq and surrounding regions, in *Proceedings of the 28th Seismic Research Review: Ground-Based Nuclear Explosion Monitoring Technologies*, LA-UR-06-5471, Vol. 1, pp. 40–48.

Ghalib, H. A. A. (1992). Seismic velocity and attenuation of the Arabian plate, Ph.D. dissertation, Saint Louis University, 1–314.

Helffrich, G. (2006). Extended-time multitaper frequency domain cross-correlation receiver-function estimation, *Bull. Seism. Soc. Am.* 96: 344–34.

Langston, C. A. (1977). The effect of planar dipping structure on source and receiver responses for constant ray parameter, *Bull. Seism. Soc. Am.* 67: 1029–1050.

Ligorría, J. P. and C. J. Ammon (1999). Iterative deconvolution and receiver-function estimation, *Bull. Seism. Soc. Am.* 89: 1395–1400.

Park, J. and V. Levin (2000). Receiver functions from multiple-taper spectral correlation estimates, *Bull. Seism. Soc. Am*. 90: 1507–1520.

Pasyanos, M. E., W. R. Walter, M. Flanagan, P. Goldstein, and J. Bhattacharyya (2004). Building and testing a priori geophysical model for western Eurasia and North Africa, *Pure Appl. Geophys*. 161: 235–281.

Wessel, P. and W. H. F. Smith (1998). New, improved version of Generic Mapping Tools released, *EOS, Trans. AGU* 79: 579.

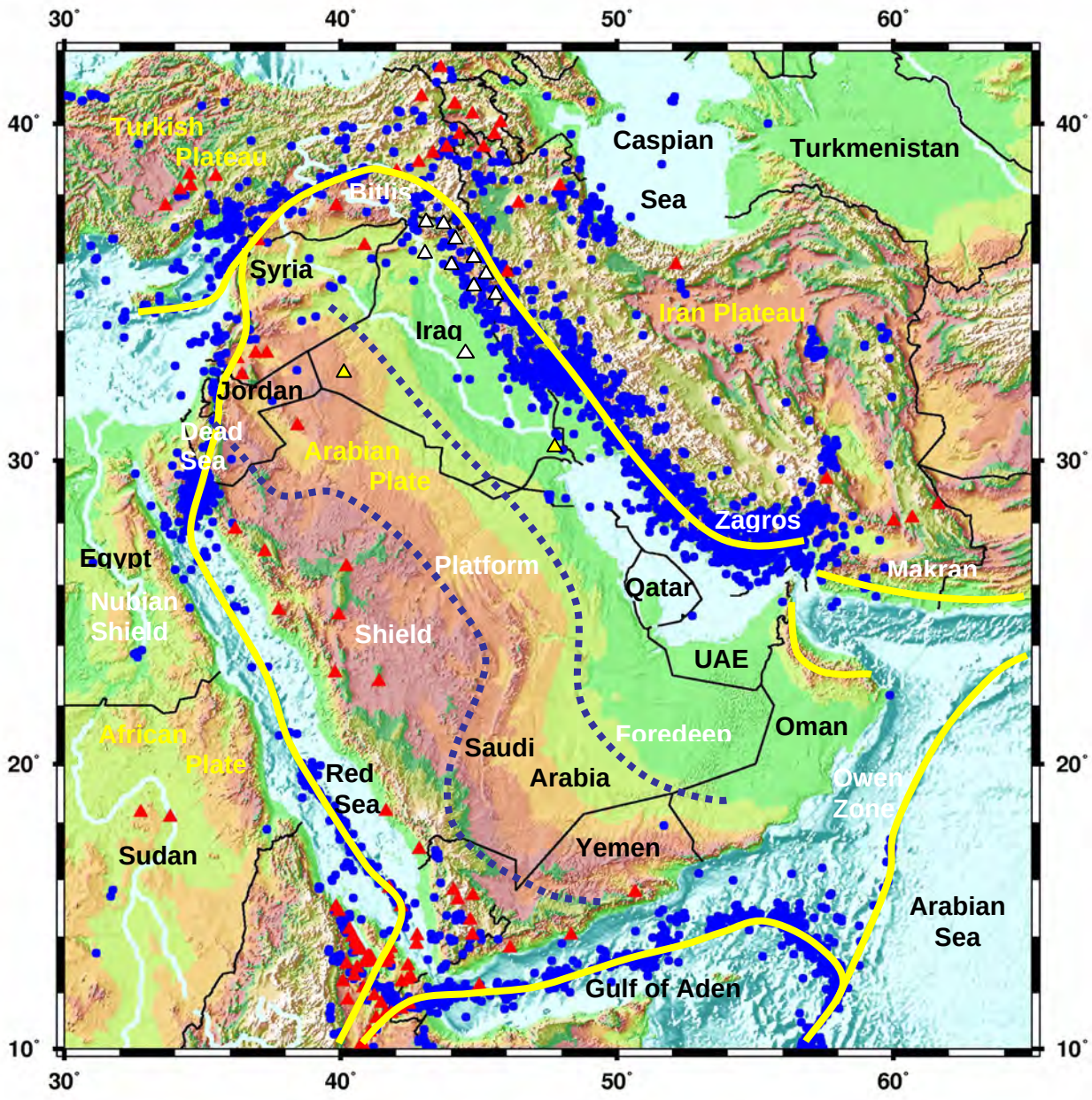


**Figure 1:** Map of the Arabian Peninsula and surrounding regions. The major geographic, tectonic and geologic features are labeled. The plate boundaries are marked with yellow lines. Earthquakes and volcanoes are shown as blue circles and red triangles, respectively. White triangles represent the 10 stations that comprise North Iraq Seismological Network (NISN). The yellow triangles reflect the location of some of Iraq Seismological Network (ISN), but are currently not operational.

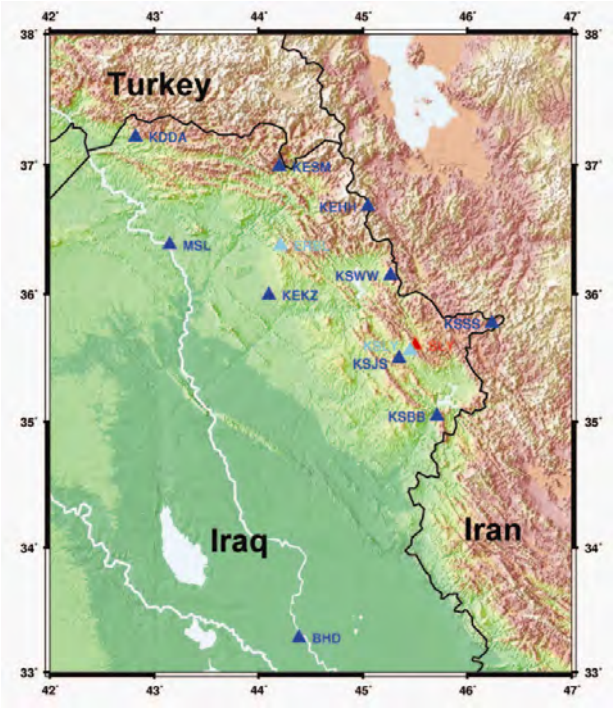


**Figure 2. Geographic location of the North Iraq Seismic Network (NISN). Ten PASSCAL stations (blue triangles) are currently operational throughout north-eastern Iraq. Light blue triangles indicate temporary sites of two stations (ERBL and KSLY). The red triangle (SLY) signifies the original location of one of Iraq Seismological Network (ISN) original five stations.**

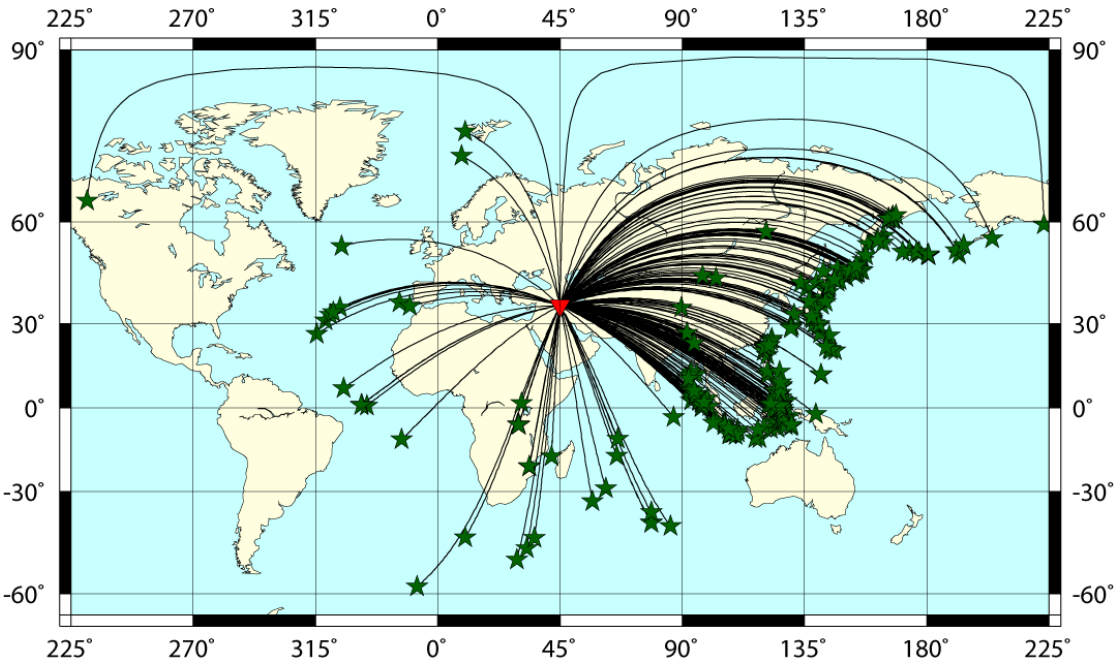


**Figure 3. Global distribution of events (Mb > 5.5, from November 2005 to March 2007). Green stars denote earthquake epicenters, black lines the great-circle paths of the waves from the events to the network and the red triangle the location of NISN.**

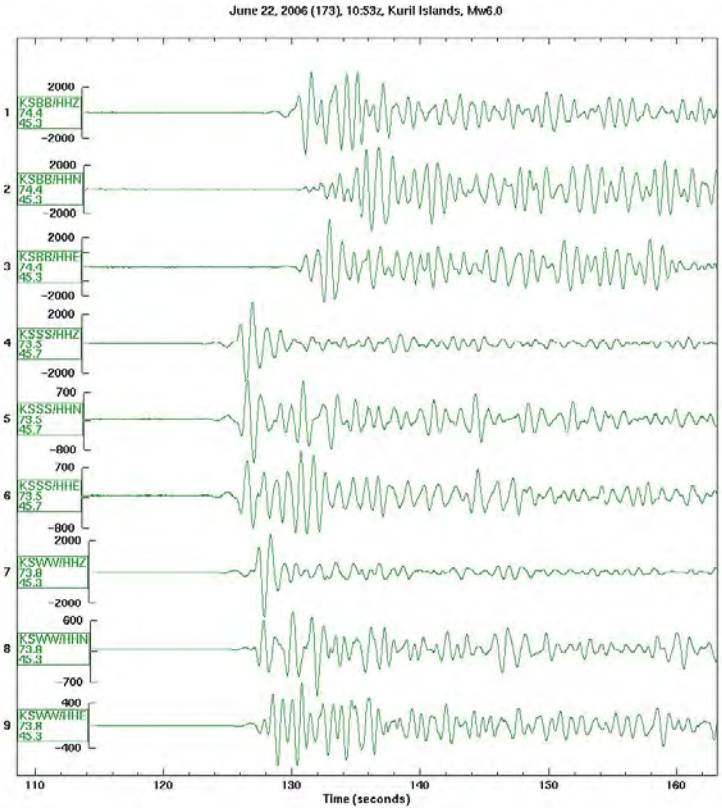


**Figure 4. Broad-band seismogram records of teleseismic P-waves of a Mw 6.0 event located in the Kuril Islands. Waveforms were recorded at three NISN stations (KSBB, KSSS, and KSWW) and subsequently used in RF inversion.**

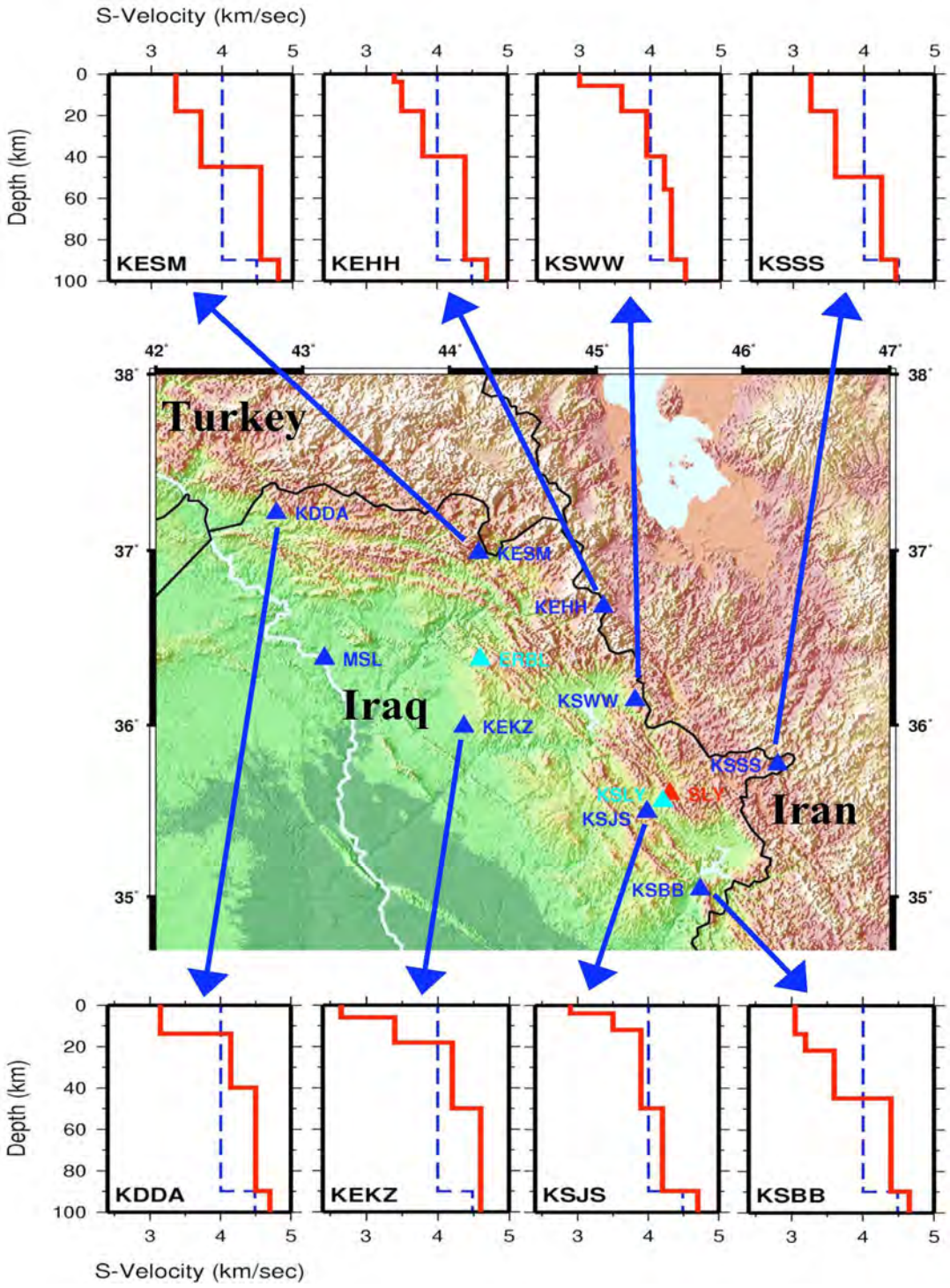


**Figure 5.** **Locations of NISN stations (blue triangles) and associated shear-wave velocity models obtained from RF inversion. Moho depths beneath the stations in the foothills appear shallower than those beneath the stations in the Zagros mountains. Similarly, a mid-crustal velocity increase appears at shallower depth below the foothills (~ 15 km depth) compared to the Zagros mountains (~ 20 km depth). Station ERBL and KSLY (aqua triangles) are the temporary stations. Station SLY (red triangle) belongs to ISN.**

# DEVELOPING AND EXPLOITING A UNIQUE SEISMIC DATASET FROM SOUTH AFRICAN GOLD MINES FOR SOURCE CHARACTERIZATION AND WAVE PROPAGATION

Jordi Julià[1], Andrew A. Nyblade[1], Rengin Gök[2], William R. Walter[2], Lindsay Linzer[3], and Ray Durrheim[3]

Penn State University[1,] Lawrence Livermore National Laboratory[2], and
Council for Scientific and Industrial Research[3]

Sponsored by National Nuclear Security Administration

Contract Nos. DE-FC52-06NA27320 and DE-AC52-07NA27344
Proposal No. BAA06-06

## ABSTRACT

In this project, we are developing and exploiting a unique seismic dataset to address the characteristics of small seismic events and the associated seismic signals observed at local (<200 km) and regional (<2000 km) distances. The dataset is being developed using mining-induced events from three deep gold mines in South Africa recorded on in-mine networks (<1 km) composed of tens of high-frequency sensors, a network of four broadband stations installed as part of this project at the surface around the mines (1–10 km), and a network of existing broadband seismic stations at local/regional distances (50–1000 km) from the mines. After a year of seismic monitoring of mine activity (2007), over 10,000 events in the range –3.4 < ML < 4.4 have been catalogued and recorded by the in-mine networks. Events with positive magnitudes are generally well recorded by the surface-mine stations, while magnitudes of 3.0 and larger are seen at regional distances (up to ~600 km) in high-pass filtered recordings.

We have analyzed in-mine recordings in detail at one of the South African mines (Savuka) to (i) improve on reported hypocentral locations, (ii) verify sensor orientations, and (iii) determine full moment tensor solutions. Hypocentral relocations on all catalogued events have been obtained from P- and S-wave travel-times reported by the mine network operator through an automated procedure that selects travel times falling on Wadati lines with slopes in the 0.6–0.7 range; sensor orientations have been verified and, when possible, corrected by correlating P-, SV-, and SH-waveforms obtained from theoretical and empirical (polarization filter) rotation angles; full-moment tensor solutions have been obtained by inverting P-, SV-, and SH-spectral amplitudes measured on the theoretically rotated waveforms with visually assigned polarities. The relocation procedure has revealed that origin times often necessitate a negative correction of a few tenths of a second and that hypocentral locations may move a few hundreds of meters. The full moment tensor determination has revealed that the most common focal mechanism (47 out of 82 solutions for events in the 0.2 < ML < 4.1 range) consists of a similar percentage of isotropic (implosive) and deviatoric components, with a normal fault-type best double-couple (DC).

We have also calibrated the regional stations for seismic coda-derived source spectra and moment magnitude using the envelope methodology of Mayeda et al. (2003). We tie the coda Mw to independent values from waveform modeling. The resulting coda-based source spectra of shallow mining-related events show significant spectral peaking that is not seen in deeper tectonic earthquakes. This coda peaking may be an independent method of identifying shallow events and is similar to coda peaking previously observed for Nevada explosions, where the frequency of the observed spectral peak correlates with the depth of burial (Murphy et al., 2008).

## OBJECTIVES

The main objective of this project is to develop and exploit a unique seismic data set from mine-related events recorded at in-mine (<3 km), local (3–10 km), and regional (>100 km) distances (Figure 1). The in-mine recordings are being obtained through three in-mine seismic networks consisting of a few tens of high-frequency geophones (natural frequencies of 4.5 Hz, 14 Hz, and 28 Hz), which are routinely used to monitor seismic activity in the mines. The local recordings are being acquired through four broadband seismic stations (three Guralp CMG-3T and one Guralp CMG-40T feeding 24-bit RefTek data loggers) deployed under this project and located on the surface of the mining area. And the regional recordings are being acquired mostly through the AfricaArray stations in South Africa and surrounding countries. The dataset that we are assembling is unique in that it contains (1) events spanning several orders of magnitude, (2) events from a range of source depths, and (3) events from a variety of source types (e.g., pillar collapses, tensile fractures, normal and strike-slip faulting, and sources with a significant volumetric component).

We plan to exploit this dataset by using the mining events in 10 related areas of research aimed at improving U.S. operational capabilities to monitor for low-yield nuclear tests: (1) create an event catalog with accurate origin times and locations; (2) determine seismic moment, radiated energy, corner frequency, and stress drop; (3) obtain focal mechanisms from moment tensor inversion; (4) define several categories of event types (shear slip, tensile failure with volumetric component, explosions, pillar collapse) using focal mechanisms and in-mine observations; (5) define and calibrate a coda Mw scale for southern Africa; (6) using calibrated coda techniques, determine Mw for all cataloged events; (7) investigate the effects of depth and source mechanism on the coda-derived source spectra and evaluate the potential of using coda spectral peaking as a depth discriminant; (8) define and calibrate local-to-regional phase (direct P and S, Pn, Pg, Sn and Lg) propagation characteristics, including the use of the MDAC technique to determine appropriate geometrical spreading and frequency dependent Q values for the region; (9) characterize relative P and S excitation and source apparent stress resulting from variations in source parameters, including magnitude, mechanism, depth, rock characteristics, and source type; (10) define regional phase ratios that can discriminate between the different source categories, and compare these discriminants and their performance with ongoing work done for other types of mining events, such as in Scandinavia and the western U.S.

The first surface-mine broadband station was deployed in January 2007, and three more stations were deployed during the remainder of 2007, which have been operating continuously after installation. High-frequency recordings from the in-mine networks at Savuka, Mponeng, and TauTona have been already assembled for 2007 (January through December). The assembled data set contains tens of thousands of events spanning ~8 orders of magnitude (11,224 events in the -3.4 < ML < 4.4 magnitude range for Savuka), as catalogued by Integrated Seismic Systems International (ISSI), with high-quality broadband recordings at local distances (surface-mine network) for positive magnitudes (ML > 0) and regional distances for magnitudes above ML ~3.5. During this year, we have concentrated on quality control of the data (seismic locations and sensor orientations), as well as analyzing the in-mine recordings to develop a “ground-truth” database of robustly constrained locations, origin times, and full moment tensor solutions. We have devised automated procedures that check the inner consistency of the event associations provided by ISSI as well as the orientation of the in-mine sensors. We have also implemented an automated procedure to measure spectral amplitudes of P-, SV-, and SH-phases. We are now testing procedures to relocate seismic sources with the in-mine network and to obtain full moment tensor solutions from the spectral amplitudes. The procedures have been tested on the data set collected for 2007 at Savuka mine and are detailed in the next section.

In the coming year, we will continue assembling a similar data set for 2008 and applying the quality check (QC) procedures to all the in-mine data. We will refine the relocation and moment tensor inversion procedures and build a catalog of “ground-truth” seismic locations and moment tensors by comparing our seismic location and moment tensor solutions to detailed mine plans.

## RESEARCH ACCOMPLISHED

### Hypocentral Locations and Origin Times

Hypocentral locations for mine-related seismic events are routinely determined and reported by ISSI from manually picked P- and S-wave travel times on the in-mine recordings. Any event with at least four P-wave travel times and four S-wave travel times will be located by ISSI; otherwise, the event is rejected and not saved in the system. The locations are determined by inverting the picked travel-times after assuming a constant seismic velocity between the station and the seismic source; this velocity, however, can vary among stations for the same event in an attempt to

account for site effects within the mine. The inverted hypocentral locations and origin times are routinely reported by ISSI, along with basic source parameters such as P- and S-wave scalar moment, energy, and corner frequency.

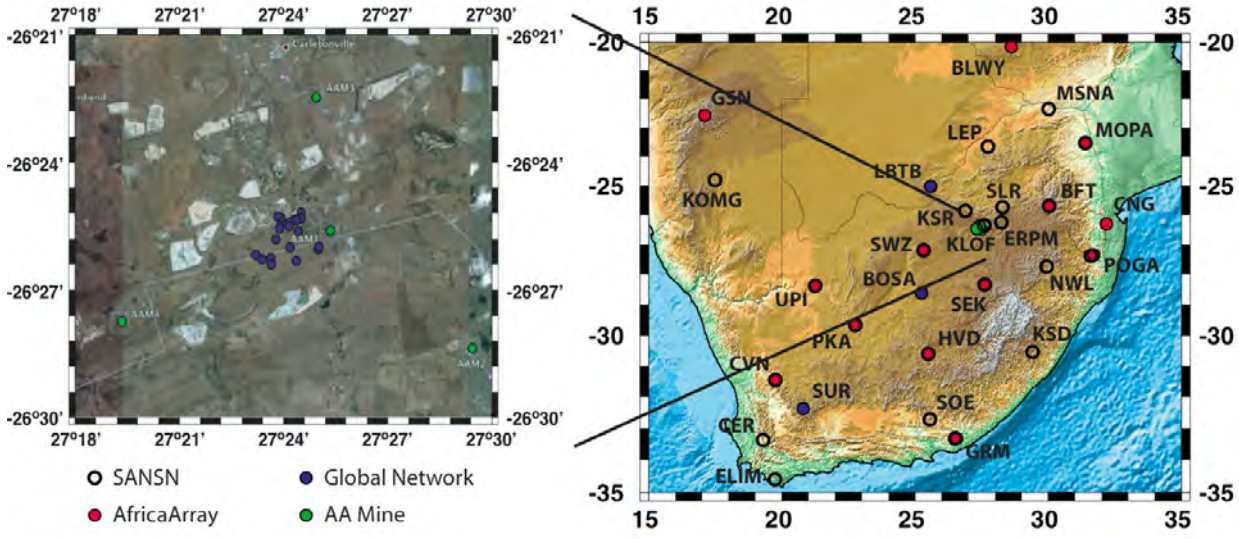


**Figure 1. (left) Satellite image from Google Earth showing the Carletonville mining area where the three mines contributing to this project are located. The blue dots are the surface projection of the Savuka in-mine network, while the green dots are the surface broadband stations deployed under this project. (right) Map of broadband stations in South Africa. The red dots are the AfricaArray stations, which are shared with the South Africa National Seismic Network (SANSN), shown as open circles. The blue dots are the three permanent global seismographic network (GSN) stations.**

In a recent visit to ISSI, we learned that the "dumping" command in their home-grown software erroneously writes the trigger time of the first seismic waveform recorded by the system in place of the event origin time. In order to obtain proper origin time estimates, we constructed Wadati diagrams for all the catalogued events. Wadati diagrams are plots of $t_S$-$t_P$ versus $t_P$, where $t_P$ and $t_S$ are the P- and S-wave travel times, respectively. Under the assumption of a medium of constant velocity, it can be shown that

$$t_S - t_P = (V_P/V_S - 1)(t_P - t_o) ,$$

where $t_0$ is the origin time, and $V_P$ and $V_S$ are the P- and S-wave velocities, respectively. This is the equation of a straight line with a slope directly related to the $V_P/V_S$ ratio of the propagating medium and which intersects the abscissa at the origin time.

Interestingly, we found that many times some ($t_S$-$t_P$,$t_P$) pairs did not fall on the Wadati line (see Figure 2). The travel-time differences are in general too large to be attributed to variations in seismic velocity, and are more likely caused by erroneous S-wave travel-time picks, false GPS locks or drifts in the timing system, phase misidentification, or erroneous event associations. The Wadati diagrams showed promise in successfully identifying these inconsistencies, and we devised an automated filter that extracts the largest subset of ($t_S$-$t_P$,$t_P$) pairs that follow a straight line (i.e., regression coefficient of 0.9 or larger) with an associated $V_P/V_S$ ratio between 1.60 and 1.70. After applying this Wadati filter to the 11,224 catalogued event, a total of 2,508 were rejected. Those were mostly small events, generally with local magnitudes below 1.0, recorded at just a few stations (a minimum of 3 points are required in the Wadati filter to fit a straight line).

The results of this Wadati filter prompted us to relocate the events that passed the filter. We followed a very simple scheme in which the selected P- and S-wave travel times were inverted, assuming a whole space of $V_P$ = 6.1 km/s and a $V_P/V_S$ = 1.64. The forward problem is expressed as

$$t_P = t_0 + d/V_P \text{ and}$$

$$t_S = t_0 + d/V_S ,$$

where d is the hypocentral distance, and the relocation is done iteratively through the linearized scheme described by

$$\begin{pmatrix} \Delta t_1 \\ \Delta t_2 \\ : \\ \Delta t_N \end{pmatrix} = \begin{pmatrix} 1 & -(x_1-x_0)/d_1V & -(y_1-y_0)/d_1V & -(z_1-z_0)/d_1V \\ 1 & -(x_2-x_0)/d_2V & -(y_2-y_0)/d_2V & -(z_2-z_0)/d_2V \\ : & : & : & : \\ 1 & -(x_N-x_0)/d_NV & -(y_N-y_0)/d_NV & -(z_N-z_0)/d_N \end{pmatrix} \begin{pmatrix} \Delta t_0 \\ \Delta x_0 \\ \Delta y_0 \\ \Delta z_0 \end{pmatrix}$$

The iterative process was stopped when the change in the rms error was less than 1% or when the number of iterations was equal to 10. The latter situation occurred only for 22 events, which were rejected.

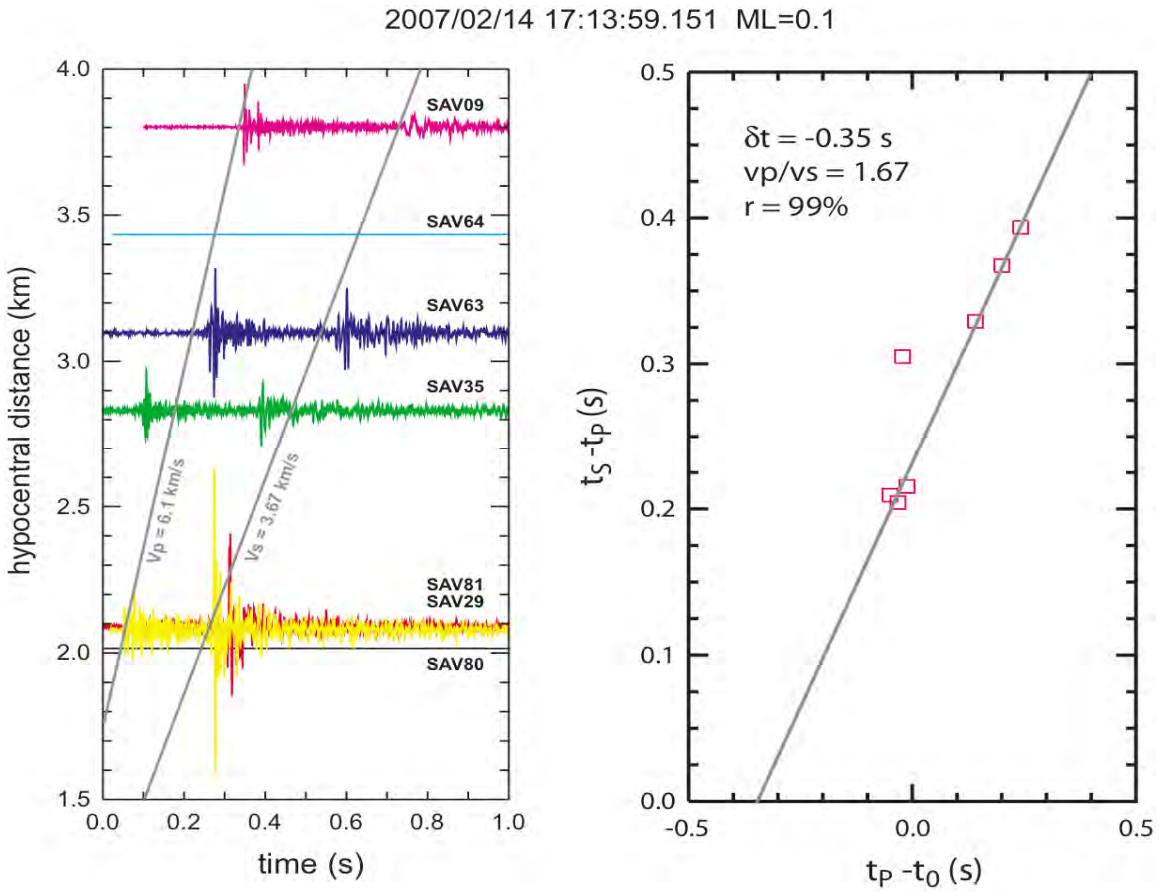


**Figure 2. (left) Record section for a ML = 0.1 event (vertical traces) as recorded at the Savuka mine. Note that some traces (SAV64, SAV80) have a failed component and the time shift of trace SAV35. (right) Wadati diagram for the same event. Note how the point for SAV35 plots outside the Wadati line. The grey line is the LSQ fit to the points and has an associated Vp/Vs of 1.67, a correlation coefficient of 0.99, and an origin time correction of –0.35 s.**

Figure 3A shows the distribution of rms differences between observed and predicted travel times before and after the relocation. The multimodal appearance of the "before" distribution is likely due to the trigger times erroneously reported as "origin times" by ISSI. Figures 3B–D display a few histograms summarizing the relocation procedure described above and show that, in general, the hypocenters migrated just a few hundred meters from the original ISSI location and that the original "origin times" needed a negative correction of a few tenths of second. Finally, note that origin time corrections were also obtained from the Wadati diagrams. Figure 3E shows that the corrections independently obtained through the Wadati diagrams and the relocation scheme are equivalent.

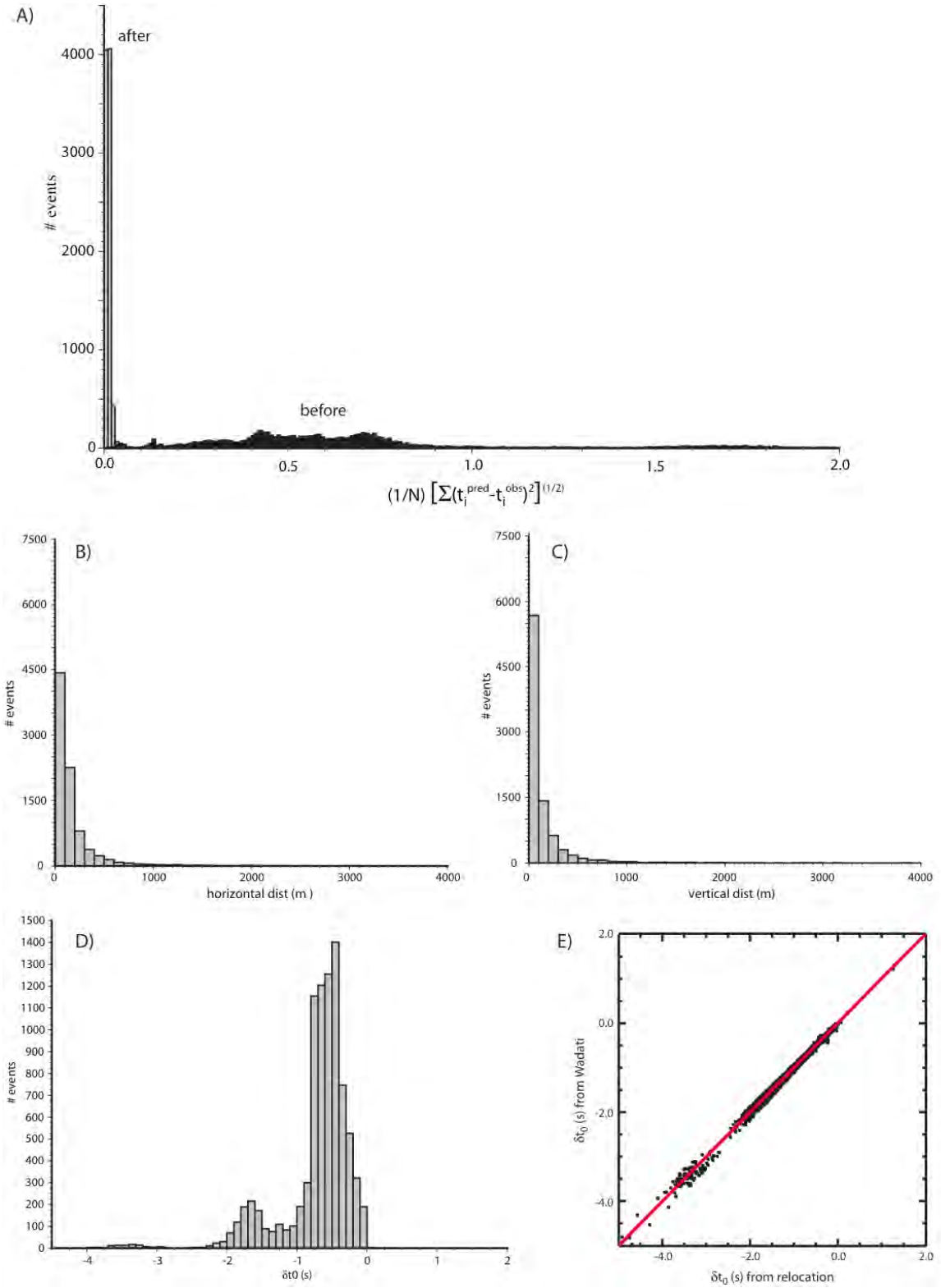


**Figure 3. (A) Comparison of the distribution of travel-time residuals before and after relocation. (B) Histogram showing horizontal migration of hypocenters after relocation. (C) Histogram showing vertical migration of hypocenters after relocation. (D) Histogram showing origin time corrections after relocation. (E) Comparison between origin time corrections from the relocation scheme and from the Wadati diagrams.**

**Sensor Orientations**

Seismic waveforms are originally recorded by the high-frequency geophones in the West, South, Down coordinate system. As a preliminary step to moment tensor inversion, the original traces must be rotated into the local ray-coordinate system (i.e., P, SV, SH). Such a rotation can be easily achieved from known hypocentral ($x_0$,$y_0$,$z_0$) and station locations ($x_S$,$y_S$,$z_S$) through

$$\text{tg } \varphi = (x_S - x_0)/(z_S - z_0)$$

$$\cos \theta = (z_S - z_0)/[(x_s - x_0)^2 + (y_S - y_0)^2 + (z_S - z_0)^2]^{1/2},$$

where x is North, y is East, and z is Up, and θ and φ are the take-off angle and azimuth, respectively. Due to the difficulties in installing and maintaining an in-mine network, however, half of the 20 high-frequency geophones making up the Savuka in-mine network had at least one failing component and could not be rotated (and used to constrain the moment tensor solutions). Moreover, many times the theoretical rotation lead to counter-intuitive results where most of the P-wave energy is polarized in the SH component, suggestive of a sensor misalignment.

The rotation angles can also be obtained empirically from the eigenvectors associated to the eigenvalues in the covariance matrix (Montalbetti and Kanasewich, 1970) defined as

$$\begin{pmatrix} \text{Var}[x] & \text{Cov}[x,y] & \text{Cov}[x,z] \\ \text{Cov}[x,y] & \text{Var}[y] & \text{Cov}[y,z] \\ \text{Cov}[x,z] & \text{Cov}[y,z] & \text{Var}[z] \end{pmatrix}$$

where,

$$\text{Var}[x] = \Sigma\,(x_i - x)^2/(n-1),\ \text{Cov}[x,y] = \Sigma\,[(x_i - x^*)(y_i - y^*)]/(n-1)\ ,$$

where $^*$ denotes the average within the P-wave window on the in-mine recordings. Realize that this "polarization filter" successfully finds the directions of the P-, SV-, and SH-axis (Figure 5) but cannot resolve the sense of motion, due to the symmetry of the covariance matrix with respect to reflections about the origin of coordinates.

In any case, we systematically computed the correlation coefficients (absolute value) between the empirically and theoretically rotated P-, SV-, and SH-waveforms for each of the 8,000 relocated events. The results are displayed in Figure 4 and show that only 4 of the 9 stations are correctly oriented. We explored the possibility of a sensor misalignment due to a rotation about the vertical channel, and found that a clockwise rotation of ~55$^o$ for SAV35, a rotation of 180$^o$ for SAV34, and a clockwise rotation of 90$^o$ for SAV77 and SAV79 led to the expected correlation coefficients between empirically and theoretically rotated waveforms. Unfortunately, no corrections could be found for SAV08 and SAV27.

We also checked sensor orientations for the surface-mine stations by comparing recordings of teleseismic waveforms with those recorded at the nearby GSN station LBTB, and found that station AAM3 had a rotation about the vertical channel of ~180$^o$.

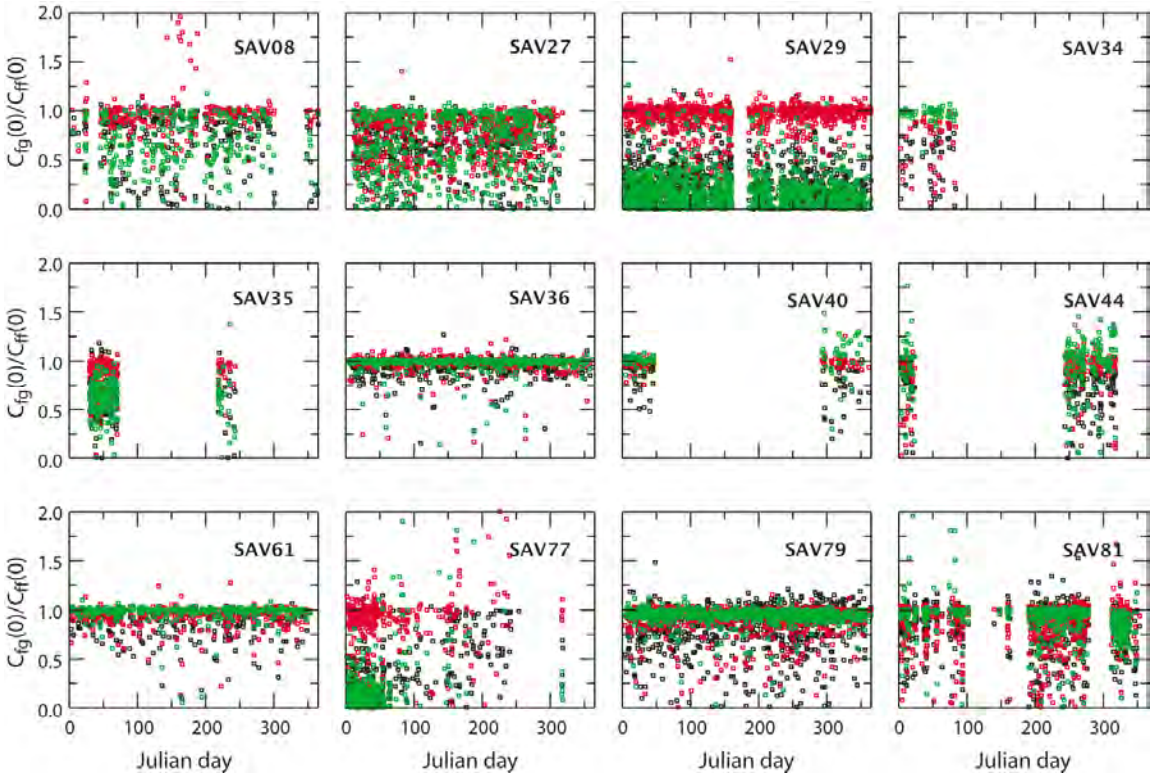


**Figure 4. Correlation coefficients between theoretically and empirically rotated waveforms (green, SH; red, SV; black, P). Note that only stations SAV36, SAV40, SAV61, SAV79, and SAV81 show coefficients close to 1 in all three components.**

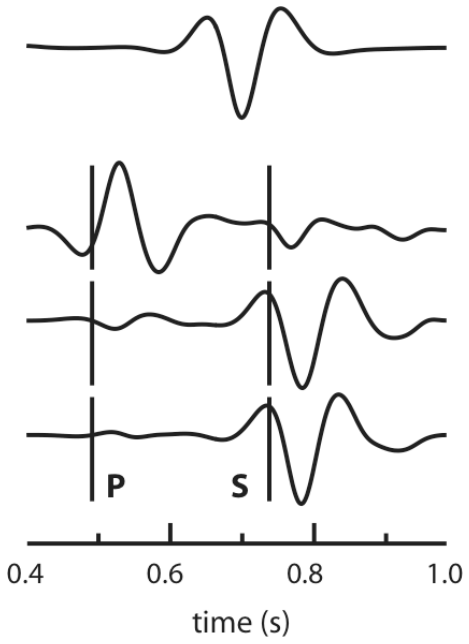


**Figure 5. Impulse response for a 4.5-Hz instrument in the time-domain (top) and P-, SH-, and SV- recordings (bottom) of a mine-related event from station SAV29. Polarities can be assigned as negative (P), positive (SH), and positive (SH) after a visual comparison of the traces with the impulse response.**

**Moment Tensor Solutions**

Full moment tensor solutions are being obtained from P-, SV-, and SH-spectral amplitudes. We assume a medium of uniform velocity ($V_P$ = 6.1 km/s, $V_P/V_S$ = 1.64), so that the displacements can be expressed as (e.g., Udías, 2000):

$$u_i = G_{ij,k} m_{jk} \quad i,j,k = 1,2,3 ,$$

where

$$G_{ij,k} = (1/4\pi\rho v^3 R)\, \gamma_i\gamma_j\gamma_k\, \delta'(t-R/v) \quad \gamma_i = x_i/R ,$$

where $\rho$ is density, v is the P- or S-wave velocity, and R is the hypocentral distance. The forward problem is then written by rotating the displacements into the ray-coordinate system and Fourier transforming the resulting equation to obtain spectral amplitudes. This defines a linear problem that is inverted by calculating the natural inverse (e.g., Menke, 1989) through a singular value decomposition of the forward problem's matrix.

Spectral amplitudes from the in-mine recordings are obtained through the time-domain procedure of Urbancic et al. (1996). This procedure evaluates the spectral plateau of the P- or S-wave spectrum by computing the ratio

$$\Omega_o = 4(S_{D2})^{3/2}(S_{V2})^{-1/2} ,$$

where

$$S_{D2} = 2\int D^2(t)\, dt \quad S_{V2} = 2\int V^2(t)\, dt ,$$

and D(t) and V(t) are the displacement and velocity, respectively. Following Trifu et al. (2000), the integrals extend between the P- and S-wave travel-times, for the P-wave amplitude, and twice the S-P time after the S-wave travel time for the SV and SH amplitudes.

The polarity of the spectral amplitudes is assigned visually for each measurement. An impulse response is first generated in the time-domain for the sensor recording the amplitudes and then both the impulse response and the data are low-pass filtered at 10 Hz (or higher frequency for the 14-Hz and 28-Hz sensors). Due to the narrow frequency band of the resulting signal the side lobes are significant, but the final pulse shapes are generally good enough for assigning polarities (Figure 5).

Figure 6 (left) shows an example of a full moment tensor inversion for a Mw = 1.0 event recorded by the Savuka in-mine network. The moment tensor solution has a significant volumetric component (~60% implosive) and a deviatoric component that splits in similar amounts between double-couple (DC) and compensated linear vector dipole (CLVD) contributions. The best-fitting DC is of normal-fault type. Figure 6 (right) compares the low-pass filtered waveforms with synthetic waveforms for a whole space, to ensure the consistency between the time-domain and the frequency-domain amplitude measurements both in size and polarity. Even though we did not invert the waveforms in the time domain, the agreement is generally excellent.

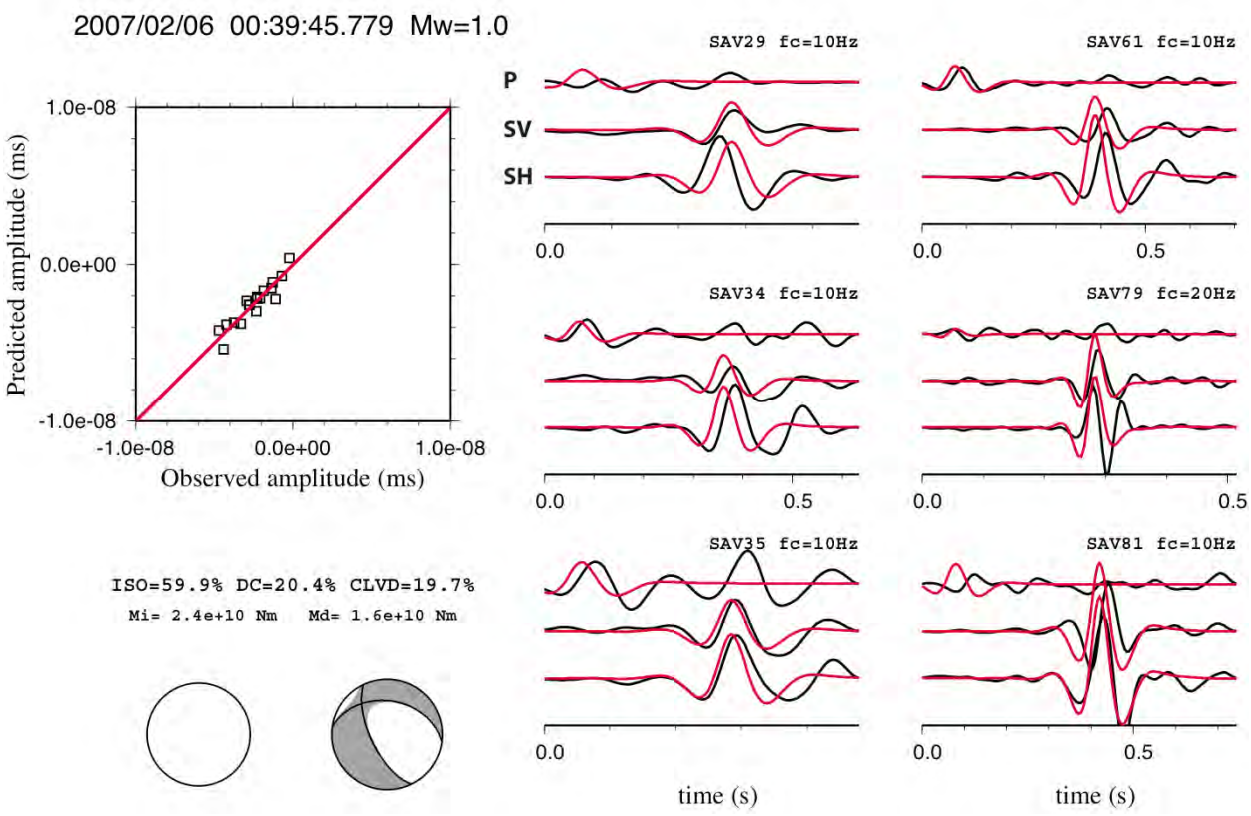


**Figure 6. Moment tensor inversion results for a Mw=1.0 event recorded at Savuka mine. (left) Comparison between observed and predicted spectral amplitudes and isotropic and deviatoric "beach balls" for the moment tensor. (right) Comparison of observed (black) and predicted (red) waveforms. Realize the inversion was done with spectral amplitudes, not waveform inversion.**

## Regional Coda Magnitudes and Spectra

We have also been looking at the seismic coda from regional events, both natural earthquakes and mine-related, that are recorded at regional stations across South Africa. Regional coda envelopes are useful to establish a calibrated moment magnitude scale for the area and to study source spectra of events using the methodology of Mayeda et al. (2003). To calibrate the stations, we first examined the coda from events that are known to be natural earthquakes. In 2006 there was a magnitude 7.2 earthquake in Mozambique, just northeast of South Africa, that had a good sequence of aftershocks. We used this sequence and a few other earthquakes to determine the coda path and shape correction factors. By waveform modeling some of the largest events at intermediate periods, we obtained calibration moments and were able to derive the source spectra shown on the left hand side of Figure 7. These coda parameters can now be used to obtain moment magnitudes for any event recorded at one of the calibrated regional stations.

When we applied the coda technique to the mining-related events, we found unusual shaped source spectra with a peak amplitude near 1 Hz, as shown on the right hand side of Figure 7. Our working hypothesis is that the peaking is related to strong Rg excitation for the shallow mine-related events. We are working to better quantify these observations by looking at the good ground-truth location and depth mine events. This South African observation is similar to coda peaking previously observed for Nevada explosions, where the frequency of the observed spectral peak correlates with depth of burial (Murphy et al., 2008). These observations appear to indicate that coda spectral peaking might be used to identify shallow events and discriminate them from more-typical-depth earthquakes.

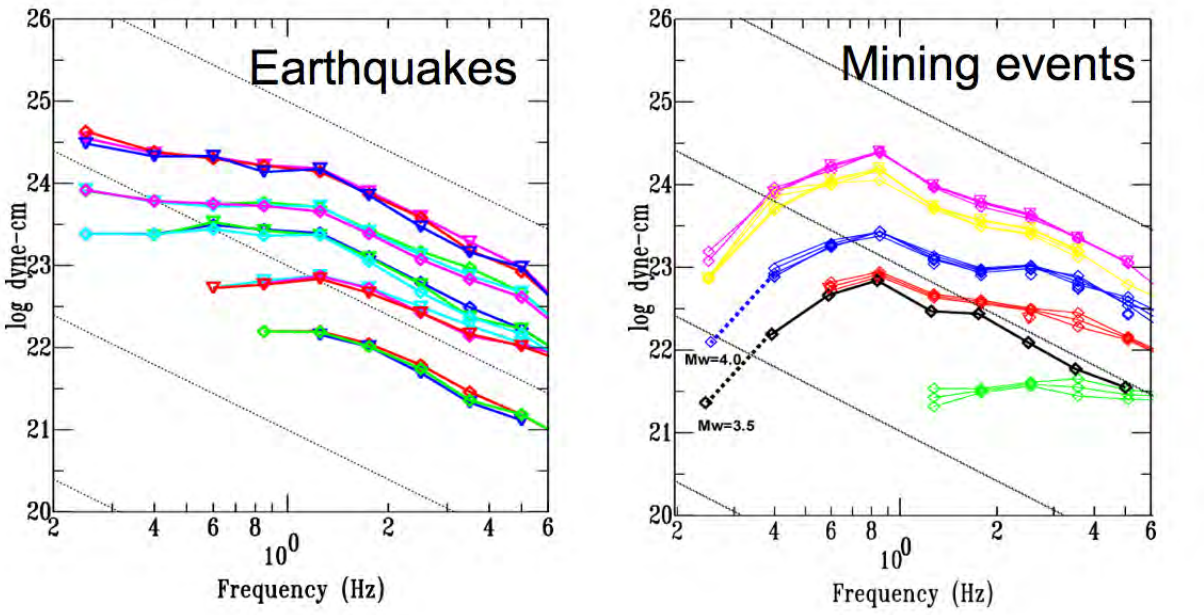


**Figure 7. Coda derived source spectra from earthquakes (left) and mining induced events (right). The earthquakes have the usual shape: a near constant proportional to the moment at long periods and falling of as frequency$^{-2}$ at the high frequencies. Coda based Mw's for any event can be determined from the long period level. In contrast the mine events show an unusual peaked shape, which may be an indicator of shallow depth due to Rg excitation and scattering into the coda. The lowest frequency points shown with dashed lines come from long period waveform modeling.**

## CONCLUSIONS AND RECOMMENDATIONS

1. The comparison between our event relocations and the original ISSI event locations (Figures 4b and 4c) suggest our estimates might be correct within a few hundred meters. ISSI claims their locations are accurate within ~50 m, but the outliers usually present in the Wadati diagrams suggest the accuracy could be lower. We are working with scientists at the Council for Industrial and Scientific Research (CSIR) in South Africa to implement a hybrid relocation scheme to produce more accurate locations (Spottiswoode and Linzer, 2003). In any case, an accuracy of a few hundreds of meters (i.e., ground truth 1, GT1) for the mine-related events is good enough for most of the areas of research aimed in this project.
2. The trigger times of the first recording stored in the in-mine network were erroneously reported as event origin times reported by ISSI. We have obtained consistent corrections from Wadati diagrams and a simple relocation scheme.
3. We have identified a few sensor misalignments for both in-mine and surface-mine stations. Corrections could be obtained for most of them by comparing empirical and theoretical rotations to the local ray-coordinate system, but some in-mine sensors still remain uncorrected.
4. Measurement of spectral amplitudes in the time domain has been successfully automated, but assigning polarity to the amplitudes is still done visually. We are still working on a procedure to automatically assign polarities.
5. We have obtained 111 moment tensor solutions for which 82 show a good match between observed and predicted amplitudes. The majority of these solutions (47 out of 82) have similar percentages of volumetric (implosive) and deviatoric component, in good agreement with the stress field expected from mining practices.

6. We have requested mine plans for 2007 for Savuka, Mponeng and TauTona. The mine planes will be critical in providing a "ground truth" check for our hypocentral locations and moment-tensor solutions.
7. Coda derived source spectra may provide a means of identifying shallow events and discriminating them from more normal-depth earthquakes. We are working to better understand and quantify this observation.

## ACKNOWLEDGEMENTS

We thank ISSI and Anglo Gold Ashanti for providing the seismic data and mine plans from the Savuka, Mponeng and TauTona mines. We also thank ISSI and the Council for Scientific and Industrial Research for assisting with event locations and solving other technical issues concerning the in-mine data, and we thank the Council for Geoscience for installing and operating the four broadband stations of the surface mine network. The IRIS data management center has provided assistance with archiving and distributing data from the permanent AfricaArray seismic stations, including data used in this study.

## REFERENCES

Mayeda, K., A. Hofstetter, J. O'Boyle, and W. R. Walter (2003). Stable and transportable regional magnitudes based on coda derived moment-rate spectra, *Bull. Seism. Soc. Am*. 93: 224–239.

Menke, W. (1989). *Geophysical Data Analysis: Discrete Inverse Theory*. Academic Press.

Montalbetti, J. M. and E. R. Kanasewich (1970). Enhancement of teleseismic body waves with a polarization filter, *Geophys. J. R. Astr. Soc.* 21: 119–129.

Murphy, K. R., K. Mayeda, and W. R. Walter (2008). Lg-coda methods applied to Nevada Test Site events: Spectral peaking and yield estimation, submitted to *Bull. Seism. Soc. Am.*

Spottiswoode, S. and L. Linzer (2003). Improved seismic event locations, *ISRM 2003: Technology Roadmap for Rock Mechanics* 1–6.

Trifu, C. I., D. Angus, and V. Shumila (2000). A fast evaluation of the seismic moment tensor for induced seismicity, *Bull. Seism. Soc. Am.* 90: 1521–1527.

Udías, A. (2000). *Principles of Seismology*. Cambridge University Press.

Urbancic, T. I., C. I. Trifu, R. A. Mercer, A J. Feustel, and J. A. G. Alexander (1996). Automatic time-domain calculation of source parameters for the analysis of induced seismicity, *Bull. Seism. Soc. Am.* 5: 1627–1633.

# DEVELOPMENT OF REGIONAL PHASE TOMOGRAPHIC ATTENUATION MODELS FOR EURASIA

Thorne Lay[1], Xiao-Bi Xie[1], and Xiaoning (David) Yang[2]

University of California, Santa Cruz[1] and Los Alamos National Laboratory[2]

Sponsored by National Nuclear Security Administration

Contract No. DE-FC52-05NA26606[1]and DE-AC52-06NA25396[2]
Proposal No. BAA05-23

## ABSTRACT

We are developing regional-phase (*Pn*, *Pg*, *Sn*, *Lg*) tomographic attenuation models for Eurasia. The models will be integrated into the National Nuclear Security Administration (NNSA) Knowledge Base and used in the Magnitude and Distance Amplitude Correction (MDAC) station calibration for the development of regional seismic discriminants. Our current focus is on *Pn*, an extremely important phase in seismic event identification.

Accurately accounting for regional-phase geometric spreading is critical for the development of useful attenuation models. It is particularly important for *Pn* and *Sn* waves because the propagation mode of these waves makes them more susceptible to upper mantle velocity structures and the Earth's sphericity, which in turn causes the geometric spreading of *Pn* (and *Sn*) to be dependent on frequency as well as on range in a complicated way. We conduct numerical simulations to quantify *Pn* and *Sn* geometric spreading in a spherical Earth model with constant mantle velocities. Based on our simulation results, we have presented new *Pn* and *Sn* geometric spreading models in the form $G(r, f) = [10^{n_3(f)} / r_0](r_0 / r)^{n_1(f)\log(r_0/r)+n_2(f)}$ and $n_i(f) = n_{i1}\left[\log(f / f_0)\right]^2 + n_{i2}\log(f / f_0) + n_{i3}$, where $i$ = 1, 2, or 3; $r$ is epicentral distance; $f$ is frequency; $r_0$ = 1 km and $f_0$ = 1 Hz. We derive values of coefficients $n_{ij}$ by fitting the model to computed *Pn* and *Sn* amplitudes for a spherical Earth model having a 40-km-thick crust, generic values of *P* and *S* velocities and a constant-velocity uppermost mantle.

We applied the new spreading model to observed data in Eurasia to estimate average *Pn* attenuation, obtaining more reasonable results compared to using a standard power-law model. Our new *Pn* and *Sn* geometric-spreading models provide generally applicable reference behavior for spherical Earth models with constant uppermost-mantle velocities.

We have extended numerical modeling of *Pn* behavior in the presence of laterally varying structure in both the Moho discontinuity and fine-scale structure of the uppermost mantle lid. Observations of *Pn* show larger path variance than for other regional phases, and we find that even weak heterogeneities in the lid can produce large scatter in *Pn* amplitudes and significant deviations from the ideal geometric spreading relation shown above. Statistical influences of random heterogeneities are established by many models, and implications for the attenuation inversions are considered.

## OBJECTIVE

The objective of this project is to develop 1-Hz, two-dimensional, regional-phase (*Pn, Pg, Sn* and *Lg*) tomographic attenuation models for Eurasia. The models will be used in MDAC for improved event identification.

## RESEARCH ACCOMPLISHED

### *Pn* geometric spreading

Accurately accounting for geometric spreading is critical for the development of meaningful regional-phase attenuation models. This is particularly true for *Pn* and *Sn* waves because the nature of their wave propagation renders them acutely sensitive to upper mantle velocity structure and the Earth's sphericity. Even simple one-dimensional (1D) velocity models can produce geometric spreading of *Pn* and *Sn* that is strongly dependent on frequency and range (e.g., Sereno and Given, 1990). If frequency dependence of the geometric spreading actually occurs and is neglected, the attenuation model will acquire incorrect frequency dependence. Similar arrival times of *Pg* and *Pn* phases and *Pn* and *P* phases at their respective crossover distances result in rapidly changing *P*-wave amplitudes, difficulty in phase isolation and identification, and uncertainty in appropriate specification of the propagation path and geometric spreading at these distances. Lateral variation of Moho topography and upper-mantle lid velocity and fine-scale heterogeneity of the lower crust and/or mantle lid further introduce 2D and 3D complexities into *Pn* and *Sn* spreading.

In our previous modeling efforts, primarily based on the reflectivity method and earth flattening transform (EFT) of the spherical model under consideration, we generate complete synthetic seismograms within a specified slowness range for 1D, plane-layered velocity models. The EFT transformations of velocity $v$ and depth $z$ are (Chapman, 1973; Müller, 1977)

$$v_f = \frac{R}{R - z_r} v_r \quad \text{and} \quad z_f = R \ln\left(\frac{R}{R - z_r}\right), \tag{1}$$

where $R$ is the radius of the Earth. Subscript $r$ designates values in the spherical (radially symmetric) model and subscript $f$ designates values in the plane (flat) model. The density $\rho$ transformation is

$$\rho_f = \left(\frac{R}{R - z_r}\right)^m \rho_r, \tag{2}$$

which is not unique since $m$ can take any value between -5 and 1. For regional body-waves, the choice of $m$ is not critical (Müller, 1977). We choose $m$ = -1 for *P*/*SV* simulations (Müller, 1977) and $m$ = -5 for *SH* simulations (Chapman, 1973). We experimented with different values of $m$, and the results were basically unchanged. Finally, the transformation of amplitudes calculated from plane-model simulations back to corresponding amplitudes in the spherical model is

$$A_r = \left(\frac{\Delta}{\sin\Delta}\right)^{1/2} \left(\frac{R}{R - Z_r}\right)^{\frac{m+5}{2}} A_f, \tag{3}$$

where $Z_r$ is the depth of the source in the spherical model and $\Delta$ is epicentral distance in radians.

We approximate the velocity gradient resulting from the EFT (Equations 1 and 2) with homogeneous layers in the plane Earth model, as is required by the reflectivity method. The thickness of these layers affects the accuracy of the approximation, with thinner layers yielding more accurate results. We set the thickness of these layers to be about 0.4 of the minimum wavelength of the waves to be modeled, which appears to be more than adequate. Further reducing the ratio (e.g., from 0.4 to 0.2 of the minimum wavelength) does not alter the results appreciably. The total thickness of the gradient zone is set to be more than 100 km larger than the maximum penetration depth of the direct wave in a homogeneous spherical model recorded at the longest epicentral distance considered. This thickness guarantees that no *Pn* or *Sn* waves observed within the distance range of interest are affected by the lower boundary of the gradient zone. Below the gradient zone, the velocity is constant.

We use the same generic spherical Earth model considered by Sereno and Given (1990) as the Base Earth Model for our simulations and use the synthetics from the simulation to derive parameters of the *Pn* and *Sn* geometric-spreading models that we develop. The Base Earth Model consists of a 40-km-thick outer layer, representative of an average continental crust, with a constant-velocity mantle underneath (Figure 1). The model has no anelastic attenuation. The simplicity of this model allows us to isolate the effects of the sphericity on *Pn* and *Sn* geometric spreading. We use an isotropic point source for *Pn* simulations. The source for *Sn*(*SH*) simulations is a fundamental fault vertical strike-slip source and the source for *Sn*(*SV*) simulations is a dip-slip source. For all source types in our main calculations, a delta function is used as the source time function; source depth is 15 km and source strength is $10^{15}$ N m. Three-component synthetic ground displacements are computed at 33 locations distributed log-evenly along a linear profile from 200 km (1.8°) to 2,500 km (22.5°). The Nyquist frequency of the seismograms is 20 Hz.

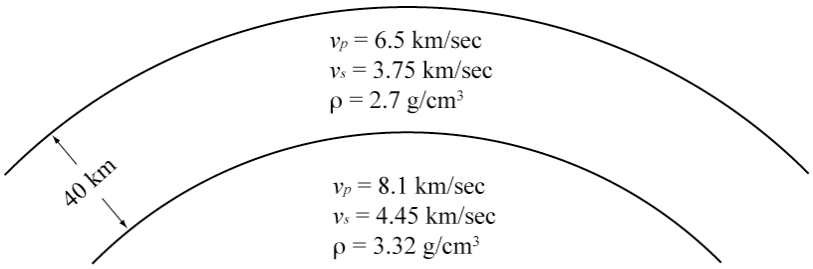


**Figure 1. Base Earth model used for *Pn* and *Sn* simulations and the development of new *Pn* and *Sn* geometric-spreading models. Quality factor *Q* is infinite throughout the model.**

We cut *Pn* and *Sn* portions of the synthetic seismograms using fixed-velocity windows. The velocities that we use to define the widths of *Pn* windows are 7.6 km/sec and 8.2 km/sec and those for *Sn* windows are 4.0 km/sec and 4.7 km/sec (Hartse, et al., 1997). The windows are centered at the peaks of the phases. We also tested a fixed-window-width method, and the results remained essentially the same. We window *Pn* and *Sn*(*SV*) from vertical-component seismograms and *Sn*(*SH*) from transverse-component seismograms. After *Pn* and *Sn* seismograms are windowed, we taper the seismograms with small tapers (between 2% to 20% depending on the length of the signal relative to the window length) and Fourier transform the seismograms to obtain the amplitude spectra. We make spectral-amplitude measurements at 100 frequencies log-evenly distributed between 0.75 and 13 Hz. Amplitude at each frequency $f_i$ is calculated by taking the average of the amplitudes between frequencies $f_i/\sqrt{2}$ and $\sqrt{2}\, f_i$.

### *Pn* Modeling Results for the Base Earth Model

To visualize the *Pn* amplitude decay in a spherical Earth model, we plot 10-Hz *Pn* amplitudes for the base model in Figure 2. We extend the epicentral-distance range to between 135 km (1.2°) and 8,000 km (71.9°) for this particular simulation in order to better depict the evolution of *Pn* waves. Amplitudes at distances beyond about 20° are measured from the direct wave that has been completely separated from the interference head waves. The amplitudes are corrected for the free-surface effect, which is only important at teleseismic distances. Also plotted in the figure are the amplitude decay of a conical head wave in a plane one-layer-over-half-space model (Aki and Richards, 2002; Eq. 6.26) and the amplitude decay of infinite-frequency direct wave in a spherical Earth model from ray tracing. At distances close to the critical distance, *Pn* geometric spreading behaves like that of a conical head wave. As distance increases, *Pn* spreading starts to deviate from that of the head wave and at about 5°, *Pn* amplitudes begin to increase. Ten-Hz direct-wave energy separates from the rest of the interference head wave at about 10°. It is seen from the figure that this separation is manifested in a change in the smoothness of the *Pn* amplitude variation followed by a reduced rate of amplitude increase. In the range beyond the critical distance and before the direct-wave separation, *Pn* evolves from a wave similar to a conical head wave to the interference head wave, which is a superposition of multiple waves reflected from the Moho. As the epicentral distance approaches teleseismic distances, the direct-wave spreading approaches that of the infinite-frequency wave from ray tracing results, as expected. The direct wave dominates the whole *Pn* wave packet at long distances. We do not see any significant difference between spectral amplitudes obtained by windowing the whole *Pn* wave packet and those obtained by just windowing the direct wave

after its separation from the packet. This is consistent with theoretical predictions (Červený and Ravindra, 1971).

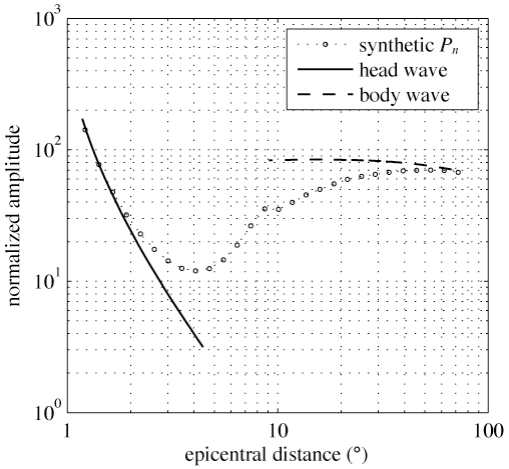


**Figure 2. 10-Hz synthetic *Pn* amplitude decay in a spherical Earth model with constant mantle velocities. The solid line depicts the theoretical amplitude decay of a conical head wave in a plane one-layer-over-half-space Earth model. The dashed line is the amplitude decay of infinite-frequency direct wave in a spherical homogeneous Earth model from ray-tracing calculations.**

*Pn* geometric spreading in a spherical Earth model is not only different from that of a head wave as is shown in Figure 2, but also frequency dependent. Figure 3 shows the *Pn* amplitude-variation surface as a function of distance and frequency for the base model. The strong frequency dependence of the amplitudes is apparent. Amplitudes at higher frequencies are affected more by the sphericity than are lower-frequency amplitudes.

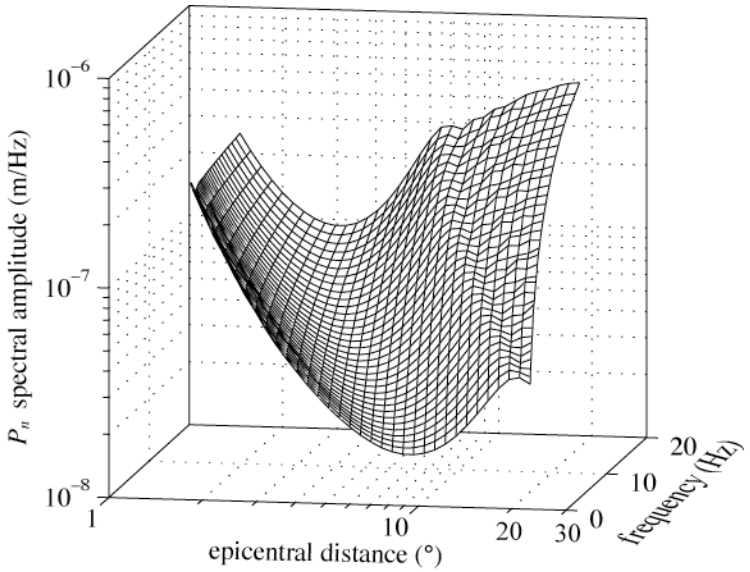


**Figure 3. Synthetic *Pn* amplitudes as a function of epicentral distance and frequency.**

In last year's report, and as published in Yang et al. (2007) we presented a parameterized description of *Pn* geometric spreading for this simple reference model. The amplitude spectrum of *Pn* can be parameterized as:

$$A(r,\theta,f) = K(f)M_0R(\theta)G(r,f)\exp\left(-\frac{\pi f}{Q(f)v}r\right)S(f) \quad (4)$$

with the new geometric-spreading model expressed as

$$G(r,f) = \frac{10^{n_3(f)}}{r_0}\left(\frac{r_0}{r}\right)^{n_1(f)\log\left(\frac{r_0}{r}\right)+n_2(f)} \qquad (r_0 = 1 \text{ km}) \quad (5)$$

and

$$n_i(f) = n_{i1}\left[\log\left(\frac{f}{f_0}\right)\right]^2 + n_{i2}\log\left(\frac{f}{f_0}\right) + n_{i3} \qquad (i = 1, 2, 3;\ f_0 = 1 \text{ Hz}). \quad (6)$$

In Equation 4, $K$ is a frequency-dependent scaling factor; $M_0$ is source moment; $R$ is source radiation pattern; $Q$ is *Pn* quality factor; $v$ is *Pn* velocity; $S$ is receiver site response; $r$ is epicentral distance; $\theta$ is azimuth angle and $f$ is frequency. $r_0$ and $f_0$ are included in Equations 5 and 6 in order for the new model to have the same dimension as standard power-law models (e.g., Sereno et al., 1988). The main differences between the new geometric-spreading model (Equations 5 and 6) and the standard frequency-independent power-law model are the addition of the first term in the exponent and the frequency dependence of parameters $n_i$. In the logarithm domain, the new model is a quadratic function of log-distance, whereas the power-law model is linear. The reason for choosing a log-quadratic function is to keep the parameterization as simple as possible while providing a good fit to the synthetics. The adoption of a quadratic functional form for $n_i$ (Equation 6) is based on the behavior of $n_i$ versus the frequency obtained by fitting Equation 6 to synthetic *Pn* amplitudes at individual frequencies.

If we take common logarithm of Equation 5, substitute Equation 6 into the result and let $r_0$ and $f_0$ equal one, we obtain

$$\begin{aligned}\log[G(r,f)] = {} & n_{11}(\log f)^2(\log r)^2 + n_{12}\log f(\log r)^2 + n_{13}(\log r)^2 \\ & -n_{21}(\log f)^2\log r - n_{22}\log f\log r - n_{23}\log r \\ & +n_{31}(\log f)^2 + n_{32}\log f + n_{33}\end{aligned}, \quad (7)$$

where $r$ is in kilometers and $f$ is in hertz. To derive coefficients $n_{ij}$, we fit Equation 7 to synthetic *Pn* amplitudes shown in Figure 3 in a least-squares sense. *Pn* amplitudes are corrected for $M_0$ used in the simulation ($10^{15}$ N m) and $K$ before the fitting. This yielded the coefficients in Table 1.

**Table 1 Coefficients of the new *Pn* geometric-spreading model**

| $n_{11}$ | $n_{12}$ | $n_{13}$ | $n_{21}$ | $n_{22}$ | $n_{23}$ | $n_{31}$ | $n_{32}$ | $n_{33}$ |
|---|---|---|---|---|---|---|---|---|
| -0.217 | 1.79 | 3.16 | -1.94 | 8.43 | 18.6 | -3.39 | 9.94 | 20.7 |

Similar processing provided an *Sn* geometric spreading model for the Base Earth Model structure.

### *Pn* Spreading Sensitivity to Mantle Velocity Gradients

The velocity structure of the mantle lid is seldom well-constrained. The most direct constraint is provided by the shape of the *Pn* travel time curve as a function of distance over a wide-enough distance range for reliable measurement, and even when there is an apparent travel time branch curvature, it is difficult to distinguish between a smooth gradient with depth versus constant velocity layering with small step increases. Receiver function methods and surface wave dispersion inversions sometimes indicate gradients in the lid structure, but resolution tends to be poor, especially for *P*-velocity. As a result, reference velocity structures often assume constant or near-constant velocity in the mantle lid by default, so our Base Earth Model is not a bad starting point in many cases. However, there are regions where the lid velocity appears to increase or decrease with depth. The effects of positive *P*-velocity gradients in the mantle lid on the frequency-dependent spreading of *Pn* are illustrated in Figure 4. The basic shape of the spreading behavior is preserved, but the distance-behavior shifts systematically to shorter distances, with overall higher *Pn* amplitudes as the gradient increases. It is possible to determine appropriate coefficients for a spreading representation like Equation (7) for any specific gradient, but this is only warranted if there are a priori constraints on the specific model in the region for which the spreading is to be utilized. Of course, the use of an inappropriate spreading relationship will directly map into any inferred frequency-dependent

attenuation structure, so it is clear that precise knowledge of the lid gradient is essential for robust attenuation estimation. This non-linear sensitivity of the spreading to the velocity model is a formidable issue for *Pn* and *Sn* attenuation determination that has not been widely appreciated.

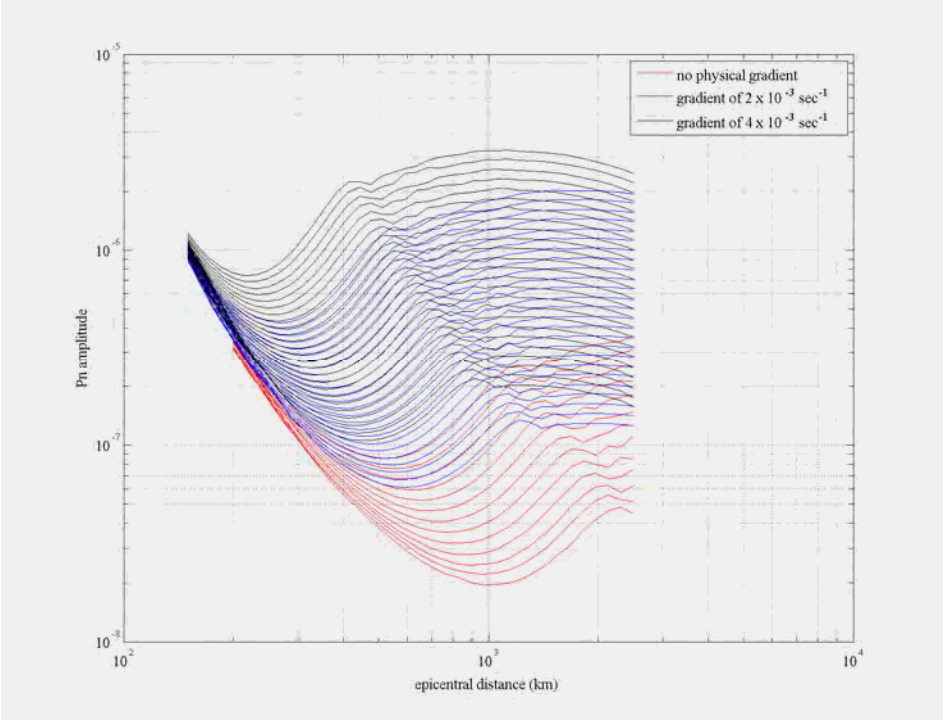


**Figure 4. *Pn* amplitude versus distance curves similar to Figure 3, but for the Base Earth Model (red curves, for no physical gradient in the lid) and for two models with mild positive gradients in the mantle lid. The suite of curves for each case corresponds to frequencies ranging from 0.75 Hz (lowest curve) to 12 Hz (highest curve).**

### *Pn* Spreading Sensitivity to Lateral Mantle Velocity Heterogeneity

Given the disconcerting sensitivity of *Pn* spreading to a typically poorly-constrained attribute of the reference velocity model (the velocity gradient in the uppermost mantle lid), the prospect of robust attenuation determination for the uppermost mantle appears limited. Most standard seismological practices assume rather simple reference models, known to be gross approximations of the real structure, under the assumption that errors in the reference model produce only mild biases in other properties such as attenuation. This is simply not the case here, given the non-linear sensitivity of the *Pn* and *Sn* whispering gallery arrivals for 1D structures. But the non-linearity itself raises the following question: how stable is the precise behavior in the presence of lateral heterogeneity? Clearly the actual mantle lid has multi-scale lateral heterogeneities; does their presence weaken the acute sensitivity of *Pn* spreading to the reference structure?

We explored the effects of lateral heterogeneity in the mantle lid velocity structure using a 2D finite-difference code (Xie and Lay, 1994) in which we impose random lateral velocity fluctuations characterized by rms velocity fluctuations of a particular strength and horizontal and vertical averaging functions with different length scales. This allows us to consider 2D random heterogeneity models like that shown in Figure 5.

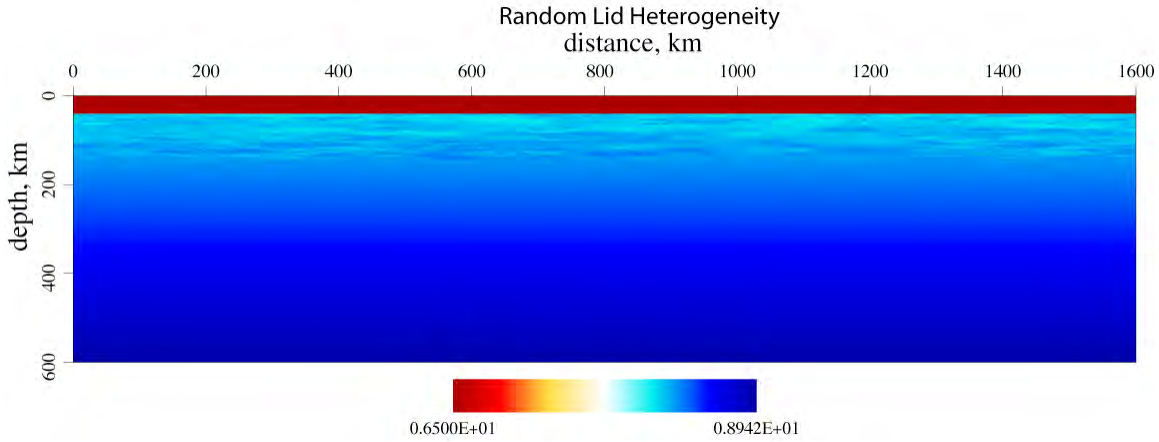


**Figure 5. Visualization of the 2D velocity model with 0.5% (rms) *P*-velocity heterogeneity in the upper 100 kilometers of the mantle lid. The background model is the EFT version of the Base Earth Model, so there is a slight positive velocity gradient across the crust and mantle.**

The 2D finite-different modeling approach cannot achieve the very high frequencies of the 1D wave-number integration method, as the synthetics are limited to about 1 sec dominant period. Tests with simple 1D models indicate that the basic behavior of *Pn* spreading is accurately reproduced, as shown in Figure 6.

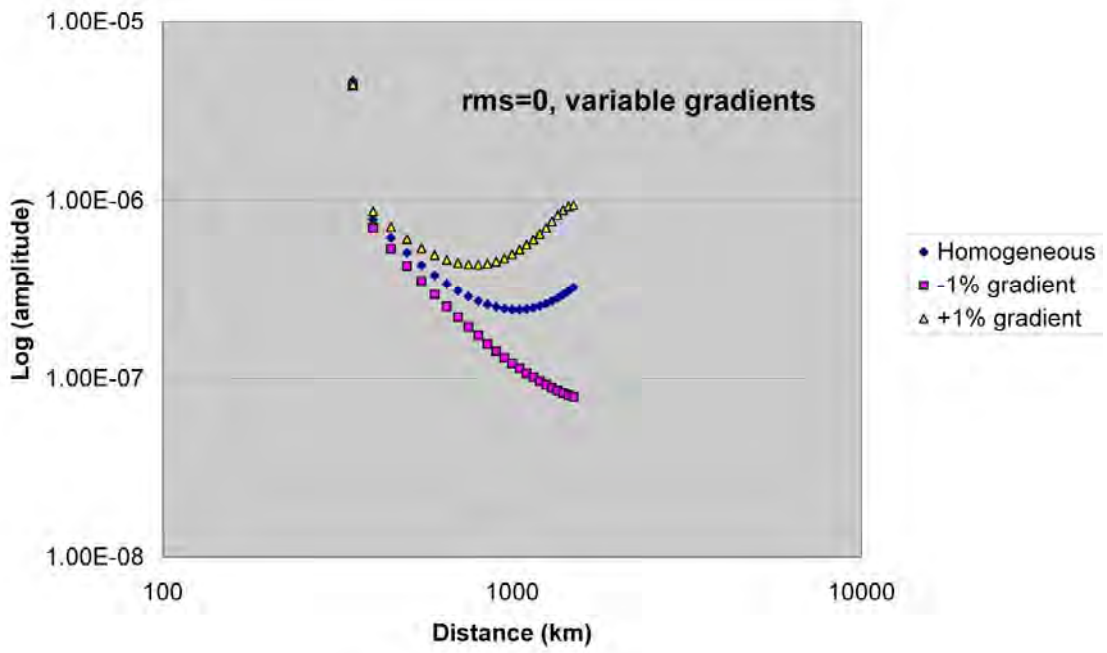


**Figure 6. *Pn* amplitude versus distance for the 1D Base Earth Model (Homogeneous) and for models with negative and positive gradients, from synthetics computed by the 2D finite difference method. The dominant period is about 1 sec. The amplitudes are corrected to 3D spreading, but not for the $(\Delta/\sin(\Delta))^{1/2}$ conversion to spherical spreading.**

Analysis of effects of random heterogeneity requires a statistical sampling of the effects associated with different realizations of the random-velocity parameters. Many models have been run for various statistical properties of the mantle lid structure, with complete synthetic seismograms being computed.

Figure 7 shows the synthetic *Pn* amplitudes for five realizations of a heterogenous structure with 0.5% rms P-velocity fluctuations with anisotropic averaging lengths of 40 km horizontally and 3 km vertically, along with an average of the ensemble, which can be directly compared to the result for the Base Earth Model.

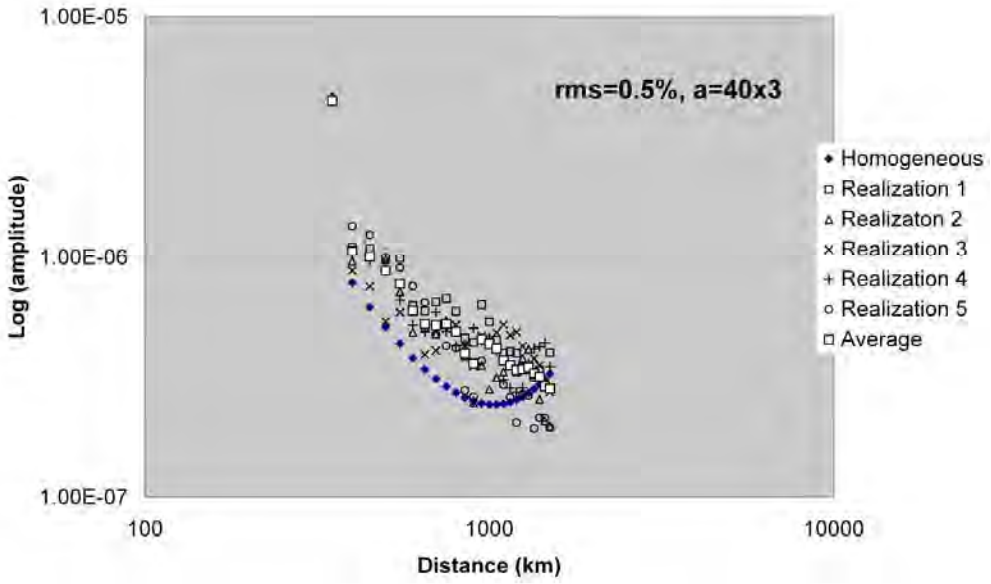


**Figure 7. *Pn* amplitudes for five realizations of random velocity models with 0.5% velocity heterogeneity, 40 km horizontal averaging length and 3 km vertical averaging length. The average amplitude (white boxes) can be compared with results for the Base Earth Model.**

An interesting behavior in Figure 7 is that the presence of velocity fluctuations affects the basic shape of the spreading, and can be represented well by a power-law type behavior at this frequency. This suggests that the 1D spreading behavior is rather delicate, with modest heterogeneity disrupting the specific interference that gives rise to the complex shape. Similar ensembles of simulations for variable aspect ratios, from isotropic heterogeneities to horizontally elongated heterogeneities (Figure 8), show that the change in spreading from the Base Earth Model to something closer to a power-law behavior increases with the degree of anisotropy (i.e., the minimum in the spreading curve is progressively eliminated as the heterogeneities become more pancake-like). For a specific heterogeneity aspect ratio (40 km x 3 km), the effect of variable rms velocity level is shown in Figure 9. As the strength of the velocity functions increases, there is progressive reduction of curvature of the amplitude-distance trend, and the overall amplitude behavior is increasingly power-law like.

These results present something of a conundrum; the simple 1D velocity structures are very simple, but produce complex geometric spreading behavior that is non-linearly sensitive to the model parameters, while 2D models with geologically realistic lateral heterogeneities produce relatively simple geometric spreading behavior. It is likely that 3D effects will further enhance the tendencies manifested in the 2D calculations. In essence, prior efforts that have assumed simple power-law geometric spreading behavior, which is not a realistic form of spreading for any known 1D velocity model, may actually be reasonable results to the extent that the specific power law corresponds to a viable level of uppermost mantle velocity heterogeneity. Of course, the precise spectrum and statistical distribution of real mantle lid heterogeneities is not known for any specific path, just as the precise 'best' 1D lid velocity gradient is not known. Thus, propagating uncertainties in the geometric spreading model into uncertainties in attenuation model estimates remains very difficult. The effects of the heterogeneities on shorter period signals have not been assessed, and doing so presents formidable computational challenges for long-range *Pn* and *Sn*: the overall frequency-dependent behavior remains to be characterized. The effects of rough Moho structure and deep crustal heterogeneity also need to be evaluated before settling on a procedure for attenuation estimation.

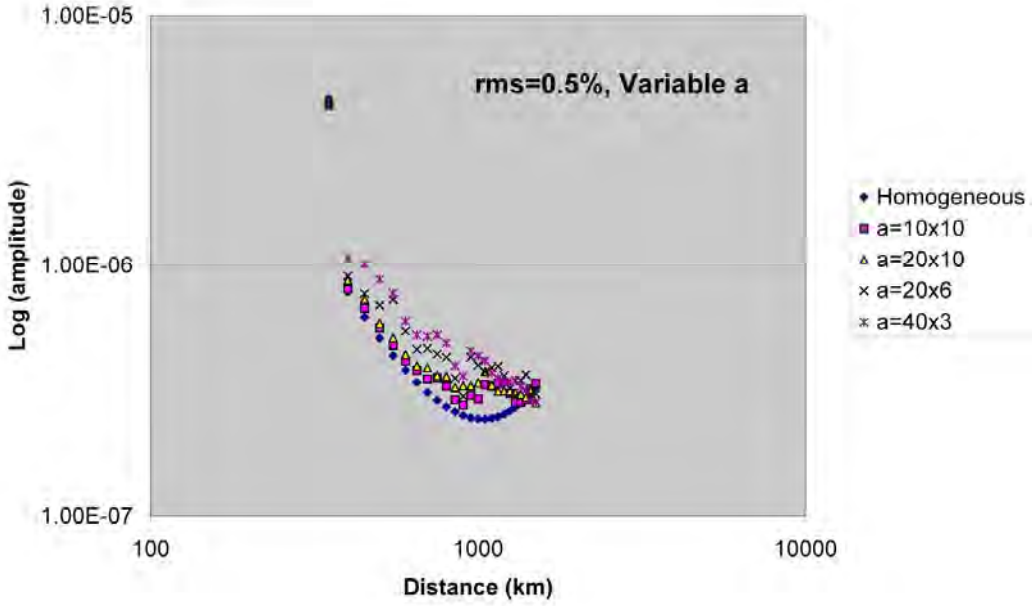


**Figure 8. *Pn* amplitudes for averages of ensembles of five realizations for random velocity models with 0.5% rms velocity heterogeneity, with 10 to 40 km horizontal averaging lengths and 10 to 3 km vertical averaging lengths.**

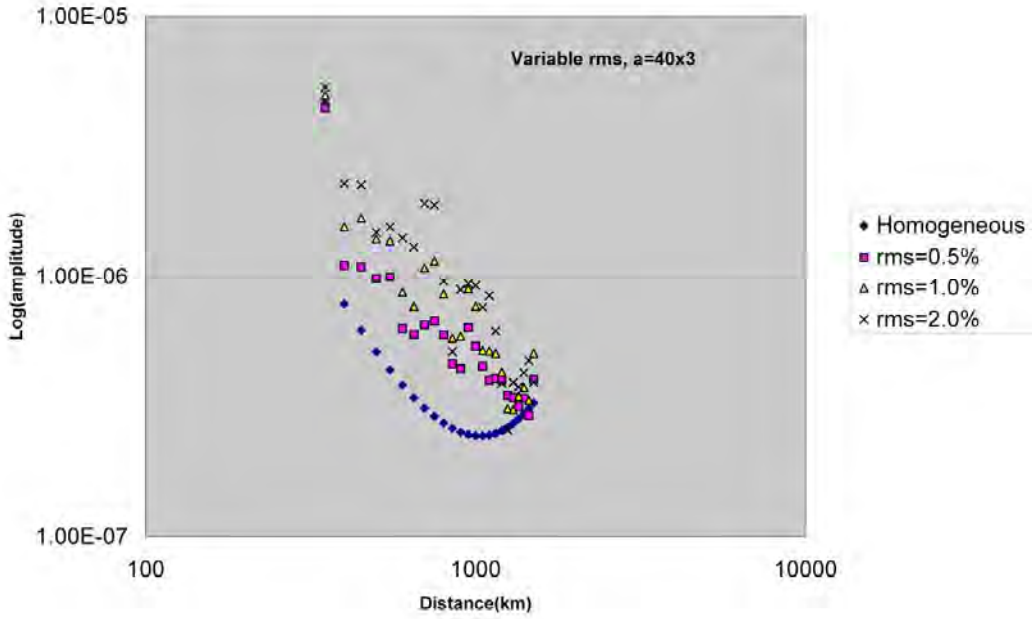


**Figure 9. *Pn* amplitudes for averages of ensembles of five realizations for random velocity models with varying 0.5 to 2.0% rms velocity heterogeneity, with 40 km horizontal averaging length and 3-km vertical averaging length.**

## CONCLUSIONS AND RECOMMENDATIONS

The behavior of geometric-spreading for *Pn* and *Sn* is surprisingly subtle and complex, even for simple 1D reference models (e.g., Menke and Richards, 1980; Sereno and Given, 1990). As anticipated in our report last year, the effects of variable 1D mantle lid gradients have been shown to preserve the basic function form of the frequency-dependent complexity of the constant-velocity mantle lid model, but the effects are so strong that new coefficients would need to be determined for the spreading model to be adequate. Indeed, the sensitivity to gradient is non-linear, raising questions about the choice of spreading model given typical situations where there is little or no information on the local lid velocity gradients. Of course, if the data for a given region are sufficient to constrain the lid velocity gradient (this may be the case across the Russian platform, for example), specific spreading computations can clearly provide a reference behavior relative to which attenuation estimates can be performed. In detail, even this is not going to be easy, given the degenerate nature of layered versus gradient model fits to first arrival times.

Computations with lateral heterogeneities in the mantle lid add an additional, possibly mitigating complexity to the problem of *Pn* and *Sn* geometric spreading. 2D finite-difference simulations indicate that the precise shape of the geometric spreading behavior for 1D models is quickly disrupted by even moderate levels of lateral heterogeneity, and the behavior for 1-sec period waves moves toward a power-law representation as the level of heterogeneity increases and as the horizontal/vertical aspect ratio of the heterogeneities increases. This behavior needs further quantification and exploration of its frequency dependence, but may provide a basis for using a conventional power-law-type geometric spreading with new recognition that the associated model for which it is approximating the amplitude decay is not a conventional 1D constant velocity mantle model or even a constant lid-gradient model, but is intrinsically a statistically heterogeneous model with some form of power-law heterogeneity, akin to those for very complex, multiple-arrival phases such as *Lg*. While specifying the preferred power law is still going to be difficult given the very limited knowledge of actual lid heterogeneity on any given path or in any given region, some understanding of trade-offs with attenuation model inferences may prove possible. Further modeling with rough Moho, crustal heterogeneity, and broader band seismograms is required before final recommendations and attenuation models can be achieved.

## REFERENCES

Aki, K., and P. G. Richards (2002). *Quantitative Seismology*, 2nd edition, University Science Books, Sausalito, California.

Červený, V., and R. Ravindra (1971). *Theory of Seismic Head Waves*, University of Toronto Press, Toronto.

Chapman, C. H. (1973). The Earth flattening transformation in body wave theory, *Geophys. J. R. astr. Soc.* 35: 55–70.

Hartse, H. E., S. R. Taylor, W. S. Phillips, and G. E. Randall (1997). A preliminary study of regional seismic discrimination in central Asia with emphasis on western China, *Bull. Seism. Soc. Am.* 87: 551–568.

Menke, W. H., and P. G. Richards (1980). Crust-mantle whispering gallery phases: a deterministic model of teleseismic *Pn* wave propagation, *J. Geophys. Res.* 85: 5416–5422.

Müller, G. (1977). Earth-flattening approximation for body waves derived from geometric ray theory—improvements, corrections and range of applicability, *J. Geophys.* 42: 429–436.

Sereno, T. J., and J. W. Given (1990). *Pn* attenuation for a spherically symmetric Earth model, *Geophys. Res. Lett.* 17: 1141–1144.

Sereno, T. J., S. R. Bratt, and T. C. Bache (1988). Simultaneous inversion of regional wave spectra for attenuation and seismic moment in Scandinavia, *J. Geophys. Res.* 93: 2019–2035.

Xie, X.-B., and T. Lay (1994). The excitation of *Lg* waves by explosions: A finite-difference investigation, *Bull. Seism. Soc. Am.* 84: 324–342.

Yang, X., T. Lay, X.-B. Xie, and M. S. Thorne (2007). Geometric spreading of *Pn* and *Sn* in a spherical Earth model, *Bull. Seism. Soc. Am.* 97: 2053–2065, doi:10.1785/0120070031.

# TOWARD A RAYLEIGH WAVE ATTENUATION MODEL FOR ASIA AND SURROUNDING REGIONS

Anatoli L. Levshin[1], Mikhail P. Barmin[1], Xiaoning Yang[2], and Michael H. Ritzwoller[1]

University of Colorado at Boulder[1] and Los Alamos National Laboratory[2]

Sponsored by National Nuclear Security Administration

Contract Nos. DE-FC52-05NA26608[1] and DE-AC52-06NA25396[2]

## ABSTRACT

We report on the progress toward the development of attenuation models for short-period (12–22 sec) Rayleigh waves in Asia and surrounding regions. These models are defined by maps of attenuation coefficients across the region of study in the specified period band. These models are designed to calibrate the regional surface-wave magnitude scale and to extend the teleseismic surface-wave magnitude—body-wave magnitude (*Ms-mb*) discriminant to regional distances.

In order to obtain accurate attenuation estimates, we must first measure surface-wave amplitudes reliably. Taking advantage of certain characteristics of Rayleigh waves, such as the dispersion and the elliptical particle motion, we employed a suite of techniques in making accurate fundamental-mode Rayleigh-wave amplitude measurements. We first analyze the dispersion of the surface wavetrain using a spectrogram. Based on the characteristics of the data dispersion, we design a phase-matched filter by using either a manually picked dispersion curve, or a model-predicted dispersion curve, or the dispersion of the data, and apply the filter to the seismogram. Intelligent filtering of the seismogram and windowing of the resulting cross-correlation based on the spectrogram analysis and the comparison between the spectrum of phase-match filtered data and raw-data and source spectra effectively reduces amplitude contaminations from surface-wave higher modes, multipathing, body-wave energy and other noise sources, and results in reliable amplitude measurements in many cases. We implemented these measuring techniques in a graphic-user-interface tool called Surface Wave Amplitude Measurement Tool (SWAMTOOL). Using the tool, we collected and processed waveform data for 200 earthquakes occurring throughout 2003–2006 inside and around Eurasia. The records from 135 broadband permanent and temporary stations were used.

After obtaining surface-wave amplitude measurements, we analyzed the attenuation behavior of the amplitudes using source- and receiver-specific terms calculated from the three-dimensional (3D) velocity model CUB2 of the region. Based on the results, we removed amplitudes that yielded negative average attenuation coefficients, and included an additional parameter in the inversion to account for the possible bias in Harvard Centroid Moment Tensor (CMT) (Dziewonski et al., 1981) scalar moments. We used the tomographic inversion to obtain surface-wave attenuation-coefficient maps from 12 to 22 seconds for Asia and surrounding regions. The inverted attenuation maps are consistent with geological features of Asia. We observe low attenuations in stable regions such as eastern Europe, the Siberian platforms, the Indian Shield, the Arabian platform, the Yangtze Craton, and others. High attenuation is observed in tectonically active regions such as the Himalayas, the Tian Shan, Pamir and Zagros mountains. Finally, we conducted the calibration of a new *Ms* formula (Russell, 2006) for the same region using 3D group-velocity models.

## OBJECTIVES

The objectives of this study are 1) to develop short-period (12–22s), two-dimensional (2D) Rayleigh-wave attenuation maps for Asia and surrounding regions along with associated uncertainty statistics through a tomographic approach, and 2) to calibrate Russell's (2006) *Ms* formula with these maps for the same region.

Knowledge of the seismic-energy loss during the propagation of surface waves from the source to receivers is essential for the accurate estimation of the surface-wave magnitude *Ms* and the seismic moment of the source. This is especially important for nuclear-explosion monitoring, in which *Ms* is used in the most robust seismic discriminant, the *Ms-mb* discriminant. In order to apply this discriminant to regional-distance monitoring, a modified *Ms* formula using shorter-period (< 20 s) surface-wave amplitudes is required (e.g., Marshall and Basham, 1970; Russell, 2006). At regional distances, seismic-wave propagation is strongly influenced by the lateral heterogeneity of the crust and upper-mantle material properties. Short-period, 2D surface-wave attenuation maps developed from observed amplitude data used to correct for the propagation effects in calculating *Ms* hold the potential to reduce station-magnitude scatter and network-magnitude bias. In this paper, we describe the surface-wave amplitude collection and measurement, the development of the attenuation models, and the Russell (2006) *Ms* calibration results.

## RESEARCH ACCOMPLISHED

### Surface-Wave Data Collection and Amplitude Measurement

Surface-wave amplitudes could be contaminated by a variety of sources such as multipathing, focusing and defocusing, body wave, higher-mode surface wave, and other noise sources. In order to obtain accurate attenuation estimates, we must measure surface-wave amplitudes reliably by reducing the contamination as much as possible. Taking advantage of certain characteristics of Rayleigh waves, such as the dispersion and the elliptical particle motion, we employed a suite of techniques in making accurate fundamental-mode Rayleigh-wave amplitude measurements. We first analyze the dispersion of the surface wavetrain using a spectrogram. Based on the characteristics of the data dispersion, we design a phase-matched filter by using either a manually picked dispersion curve, or a model-predicted dispersion curve, or the dispersion of the data, and apply the filter to the seismogram. Intelligent filtering of the seismogram and windowing of the resulting cross-correlation based on the spectrogram analysis and the comparison between spectrum of phase-match filtered data and raw-data and source spectra effectively reduces amplitude contaminations from surface-wave higher modes, multipathing, body-wave energy and other noise sources, and results in reliable amplitude measurements in many cases.

We implemented these measuring techniques in a graphic-user-interface tool called Surface Wave Amplitude Measurement Tool (SWAMTOOL). Figure 1 is a computer-screen snapshot of SWAMTOOL. The tool consists of four panels showing the seismograms (upper right), a map (lower right), the data spectrogram (upper left), and the spectra of the source, the data and the noise (lower left). The surface-wave segment is first isolated with the guidance of nominal group-velocity marks, shown as red vertical dashed lines in the top figure of the seismogram panel, and the dispersion characteristics predicted by 2D group-velocity models (Ritzwoller and Levshin, 1998; Levshin and Ritzwoller, 2003; Stevens et al., 2001; Levshin et al., 2003), depicted as open red circles in the spectrogram panel. A phase-matched filter is then constructed with a dispersion curve (red line in the spectrogram panel) determined by analyzing the surface-wave spectrogram and the dispersion predicted by the group-velocity models. Depending on the characteristics of the data dispersion, we use either a manually determined dispersion curve, or the dispersion curve of the data, or the dispersion curve predicted by the group-velocity model to construct the phase-matched filter. Surface-wave spectral amplitudes (red line in the spectrum panel) are measured after the seismogram is processed with phase-match filtering and windowing. We use theoretical source spectrum (green line in the spectrum panel) as a reference for windowing the cross-correlation resulting from the phase-match filtering (middle figure in the seismogram panel), taking into account the source-depth uncertainty (black lines bracketing the green region in the spectrum panel.) We also calculate the backazimuth of the incoming Rayleigh wave and compare it with the great-circle backazimuth. The result is displayed at the lower left of the map panel. Other information displayed in the tool includes the average Q between the source and the station at 10, 15, and 20 s (in the spectrum panel), noise spectrum (blue line in the spectrum panel), and source and path information in the map panel. Finally, the usable frequency band of the measured spectrum is determined by the yellow region in the spectrum panel.

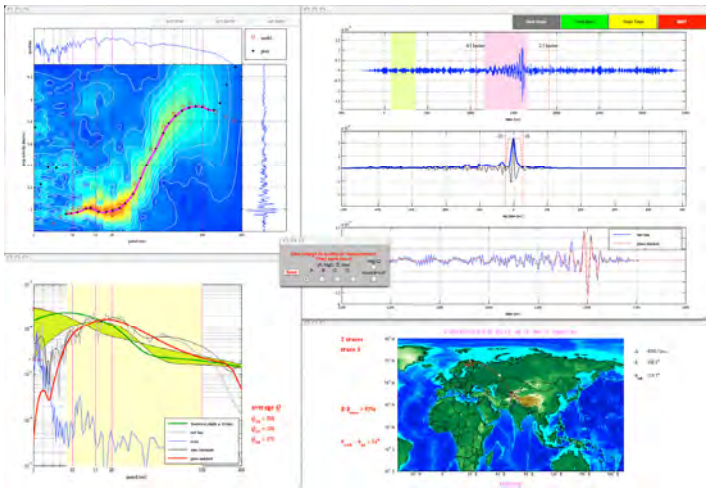

**Figure 1. A computer-screen snapshot of SWAMTOOL. It shows an example where the medium between the source and the receiver is relatively simple with weak lateral heterogeneities. The seismogram possesses well-behaved dispersion characteristics, which are also predicted by the group-velocity model. The spectrum of phase-match filtered data does not differ significantly from the spectrum of the raw data.**

Figure 1 shows an example where the medium between the source and the receiver is relatively homogeneous. Figure 2 gives an example illustrating how multipathing is treated. An example showing the reduction of noise from body waves and other sources using the tool is given in Figure 3.

We collected and processed waveform data for 200 earthquakes occurring throughout 2003–2006 in and around Eurasia. The magnitudes of these events range from 5 to 6. Source depths are less than 70 km. Data from 135 broadband permanent and temporary stations were used. Using SWAMTOOL, we made both two-station amplitude

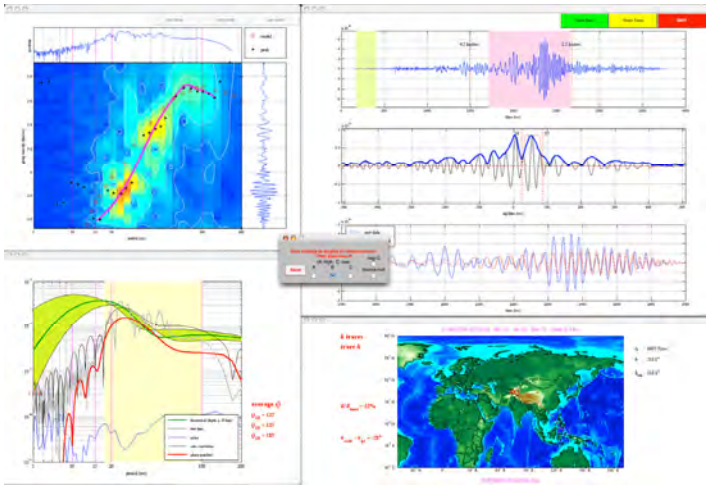

**Figure 2. This example illustrates how the effects of multipathing and focusing are mitigated by using SWAMTOOL. In this example, the surface wave from the source traverses the Tarim Basin, resulting in surface-wave packets traveling along different paths and arriving at the receiver at slightly different times. The cross-correlation from phase-match filtering shows two peaks corresponding to the two surface-wave packets, although they are difficult to distinguish in the spectrogram due to the similarity of their travel times. Windowing of the cross-correlation removes one of the surface-wave packets and reduces the effects of multipathing and focusing.**

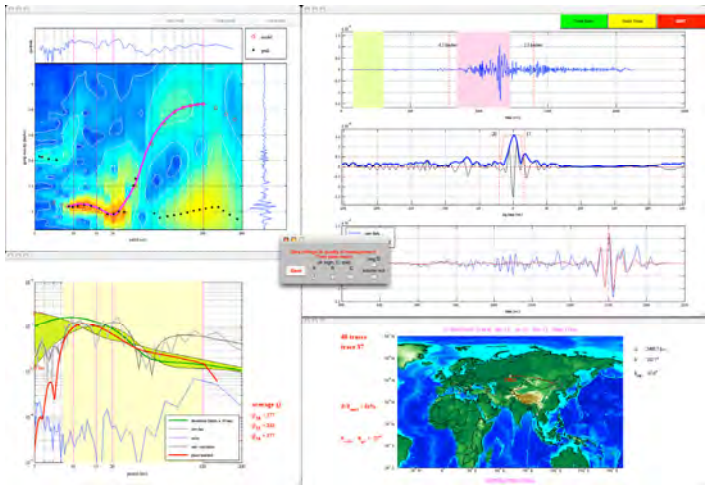

**Figure 3. This figure is an example in which the surface-wave signal is contaminated by body waves and signals from other sources. The spectrogram shows strong signals from other sources, in addition to the fundamental-mode surface wave. Because signals from sources other than the surface wave have different dispersion characteristics, the application of phase-matched filter and windowing can effectively remove these signals partly because they appear as signal packets in the cross-correlation at different lag-times from that of the surface wave.**

ratio and single-station spectral-amplitude measurements, but only single-station amplitudes are used in later tomographic inversions. Figure 4 shows the path coverage of single-station amplitude measurements at different periods.

**Amplitude Selection Based on Average Attenuation Analysis**

Before using measured amplitudes in the tomographic inversion, we estimated the average attenuation between sources and receivers from the measurements. Measurements that yielded negative attenuation coefficients were rejected. We used the theoretical surface-wave amplitude formula for a heterogeneous Earth (Woodhouse, 1974; Levshin, 1985; Levshin et al., 1989) to estimate the average attenuation. For a laterally heterogeneous medium, the spectral amplitude of a surface wave can be expressed in an asymptotic form as

$$A(\omega) = S(\omega, h, \varphi)P(\omega)B(\omega), \tag{1}$$

where $\omega$ is circular frequency; $h$ is source depth and $\varphi$ is station azimuth. $S$, $P$ and $B$ are source, path and station terms respectively. $S$ and $B$ depend on the medium structures and properties at the source and receiver locations, which are generally different in a heterogeneous Earth. The path-dependent term $P$ has the form

$$P = \frac{\exp\left(-\omega \int_L \frac{dl}{2U(\omega,l)Q_R(\omega,l)}\right)}{\sqrt{k(\omega)r_0 \sin\Delta}} = \frac{\exp\left(-\int_L \gamma_R(\omega,l)dl\right)}{\sqrt{k(\omega)r_0 \sin\Delta}}, \tag{2}$$

where $\Delta$ is the epicentral distance; $r_0$ is Earth's radius; $U$ is the group velocity of the surface wave; $k$ is the wavenumber; $Q_R$ is the quality factor; and $\gamma_R$ is the attenuation coefficient. The integral is taken along the great-circle path between the source and the receiver. It represents the average attenuation of the path.

To obtain the average attenuation from measured amplitudes, we calculated theoretical source and receiver terms $S$ and $B$ using the 3D velocity model CUB2 (Shapiro and Ritzwoller, 2002) and CMT solutions. We then removed the source and receiver terms calculated for the specific source and receiver locations from measured amplitudes. Source- and receiver-corrected amplitudes were used to estimate the average attenuation.

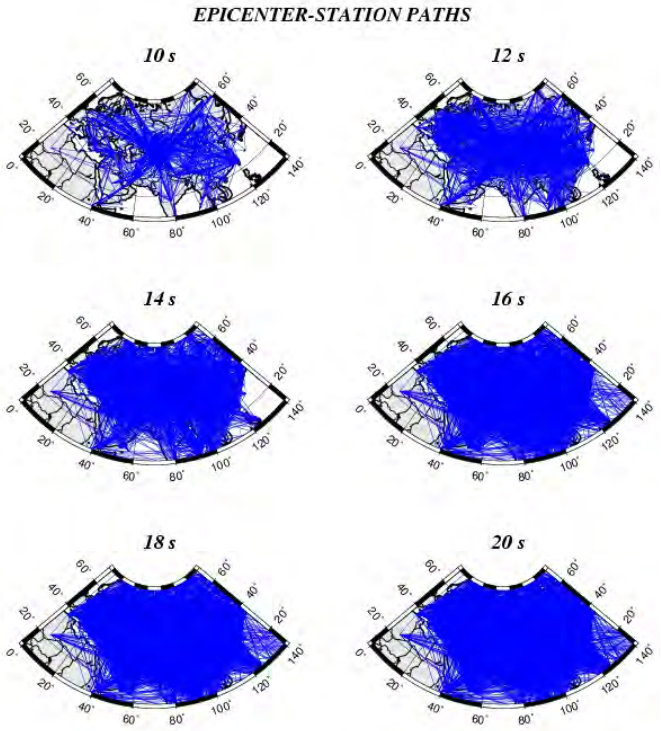


**Figure 4. Path coverage of single-station amplitude measurements at different periods.**

Figure 5 plots the logarithm of corrected amplitudes, indicative of the average attenuation, as a function of epicentral distance at 12, 16, and 20 seconds. The offset from zero of the least-squares-fitted line at zero distance indicates that there is a possible bias in CMT source parameters, consistent with the observation of Yang et al., (2004). In addition, some of the estimated attenuation coefficients are negative, which is not physical. There are several possible explanations for obtaining negative attenuation coefficients. They include un-modeled site response, remaining contamination in the measured amplitudes, errors in the source parameter and inadequate description of the wave propagation by the ray theory (Equation 2). We then removed the amplitudes that resulted in negative average attenuation coefficients from the subsequent tomographic inversion.

**Attenuation-Coefficient Tomographic Inversion**

We used the selected source- and receiver-corrected amplitudes in the attenuation-coefficient tomographic inversion to obtain attenuation-coefficient models for Asia and surrounding regions at periods between 12 and 22 seconds. We used a modified version of the inversion algorithm described by Barmin et al. (2001). The algorithm inverts for the attenuation-coefficient models by minimizing the functional

$$F(T) = \frac{1}{N}\sum_{ij}(d_{ij})^2, \tag{3}$$

at period $T$, where $N$ is the total number of paths and $d_{ij}$ is the amplitude residual between source $i$ and station $j$:

$$d_{ij} = q_{ij}^{obs} - q_{ij}^{0} = \int_{ij} m(\mathbf{r})dl + \ln(\delta M_i)\,., \tag{4}$$

where $q_{ij}^{abs}$ is the value of the integral in Equation 2 from measured amplitude. $q_{ij}^{0}$ is the value of the integral from the attenuation model that we invert for, and $m(\mathbf{r})$ is the model perturbation from a reference model $m_0(\mathbf{r})$. The additional unknown parameter $\delta M_i$ is included to account for the possible CMT moment bias.

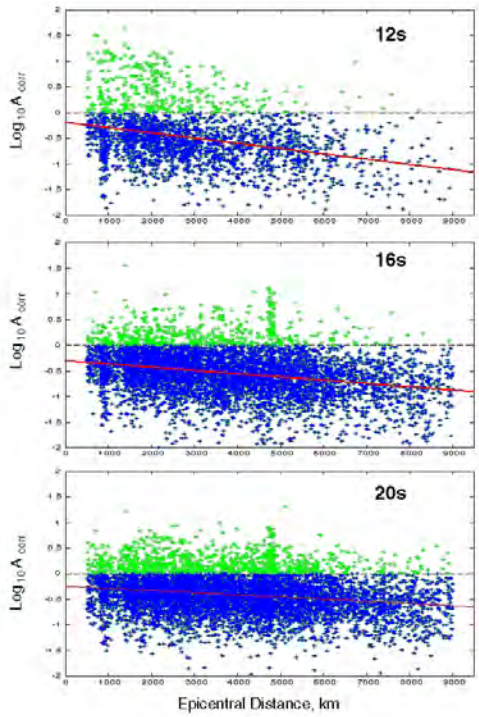


**Figure 5. Source- and receiver-corrected single-station spectral amplitudes plotted against epicentral distance. The red line is the least squares fit of the data. Green dots are data rejected from the tomographic inversion.**

We minimized $F(T)$ using least squares and several damping parameters described in Barmin et al. (2001) with an additional damping parameter for $\delta M_i$. Equations 3 and 4 were used in the inversion of 18-s amplitudes to obtain $\delta M_i$. The resulting $M_{0i} = M_0 + \delta M_i$, where $M_0$ is the CMT scalar moment, was then used to correct the amplitudes for the source term at other periods, and $\delta M_i$ was removed from the inversions. Numerous experiments with different values of damping parameters yielded the optimal inversion results. We also experimented with inversions in which we included $\delta M_i$ for all the periods ("free" scalar-moment inversion.) The results are similar. The resulting tomographic models of attenuation coefficients $\gamma_R$ for Asia and surrounding regions are shown in Figure 6. The attenuation models are consistent with geological features of Asia. We observe low attenuations in stable regions such as eastern Europe, the Siberian platforms, the Indian Shield, the Arabian platform, the Yangtze Craton, and others. High attenuation is observed in tectonically active regions such as the Himalayas, the Tian Shan, Pamir, and Zagros mountains.

We estimated variance reductions achieved with our tomographic models by comparing their residual statistics with those of homogeneous models. For periods between 12 and 22 seconds, variance reduction is between 30% and 40% (Figure 7). Including a moment correction term $\delta M_i$ in the inversion did further reduce the variance.

**Calibration of Russell's (2006) *Ms* Formula for Asia**

Russell (2006) describes a new formulation of surface-wave magnitude using time-domain and Butterworth band-pass filtered amplitude. The new *Ms* is applicable for amplitudes measured at arbitrary periods and is not affected by the dispersion characteristics, including Airy-phase anomalies, of the surface waves because of the band-pass filtering. The ability of the Russell (2006) *Ms* to use amplitudes at variable periods is important in calculating regional surface-wave magnitude because at regional distances in continental regions, surface waves usually peak at

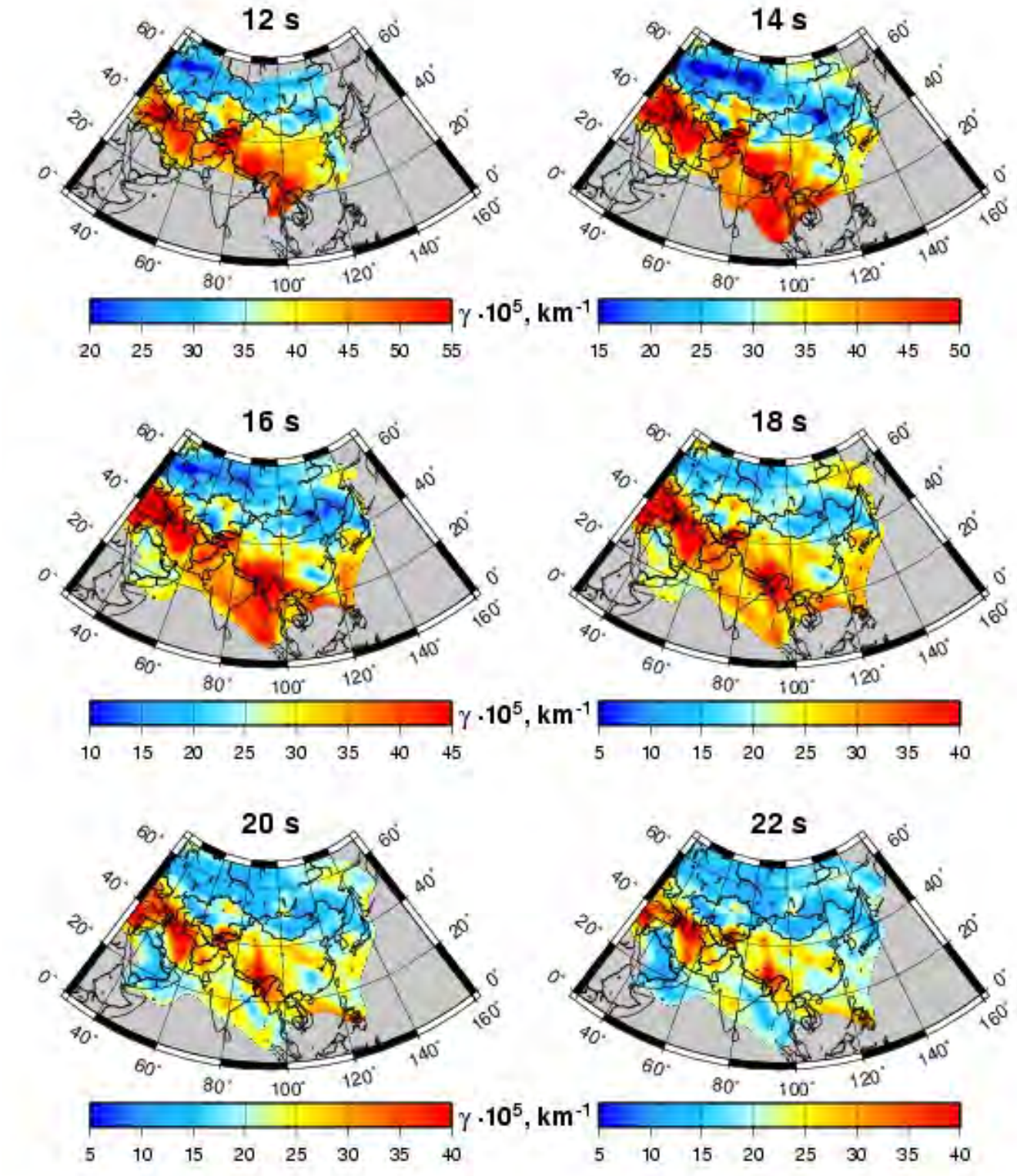


**Figure 6. Tomographic models of attenuation coefficients across Asia and surrounding regions. Grey color corresponds to areas where the path density is less than 20 paths across an equatorial cell of $2^o \times 2^o$.**

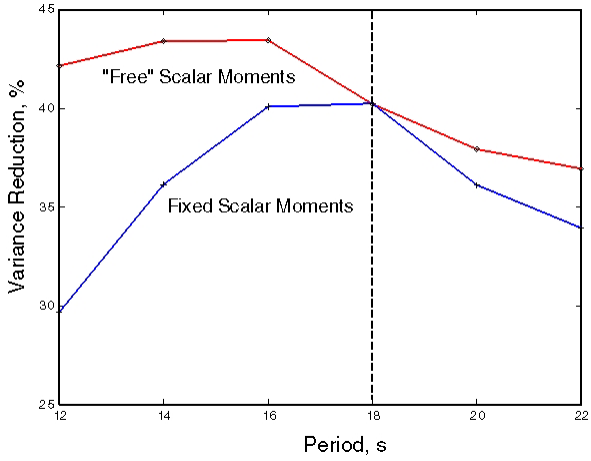


**Figure 7. Variance reduction of tomographic attenuation-coefficient models compared with homogeneous models. In "fixed-scalar-moment" inversions, $\delta M_i$ obtained from the inversion of 18-sec amplitudes was used to correct the amplitudes for the source terms at other periods. In "free-scalar-moment" inversions, $\delta M_i$ was included in inversions of amplitudes at all periods.**

periods that are shorter than 20 seconds, at which traditional surface-wave magnitudes are defined. The Russell (2006) *Ms* is defined as

$$M_{S(b)} = \log_{10}(a_b) + \frac{1}{2}\log_{10}(\sin\Delta) + B_{att}\Delta - 0.66\log_{10}\left(\frac{20}{T}\right) - \log_{10}(f_c) + C_b \qquad (5)$$

and

$$f_c \le \frac{G_{\min}}{T\sqrt{\Delta}},$$

where $a_b$ is the time-domain, Butterworth band-pass filtered amplitude; $\Delta$ is the epicentral distance in degrees; $B_{att}$ is related to the attenuation of the surface wave; $T$ is the period of the amplitude; and $f_c$ is the half width of the Butterworth-filter pass band. $G_{\min}$ is the minimum value of $G$ where

$$G = \frac{U}{\pi b_n \sqrt{\left|\frac{dU}{dT}\right|\kappa}}. \qquad (6)$$

$U$ and $dU/dT$ are the surface-wave group velocity and its derivative with respect to a period for the region of interest; $b_n$ is related to the order of the Butterworth filter; and $\kappa$ is the degree-to-km converting factor. For typical continental regions, Russell (2006) found that $G_{\min} = 0.6$ is adequate. $C_b$ in Equation 5 also depends on $G$.

To make the new *Ms* consistent with traditional formulae such as Rezapour and Pearce's (1998) *Ms*, Russell (2006) equated Equation 5 with traditional formulae and derived formulae for $B_{att}$ and $C_b$:

$$B_{att} = B_0\left(\frac{20}{T}\right)^{1.8} \text{ and } C_b = C + \log_{10}\left(\frac{G_0}{400}\right). \qquad (7)$$

In the above formulae, $C$ is the constant in traditional *Ms* formulae. $G_0$ is $G$ at 20 seconds. Adopting the formulation of von Seggern (1977), Russell (2006) obtained a $B_0$ value of 0.0031 and a $C$ value of 2.2 for $a_b$ in nanometers. Using nominal values of $U$ and $dU/dT$ at 20 seconds for continental regions, Russell (2006) derived a $C_b$ value of -0.42 for a 6$^{th}$-order Butterworth filter.

Bonner et al. (2006) developed a new amplitude measuring technique to be used along with the Russell (2006) *Ms* formula. They first band-pass filter the seismogram between 8 and 25 seconds using a bank of Butterworth filters.

From among the filtered data, they then find the time-domain amplitude that maximizes the ratio $a_b/f_c$, thus giving the maximum *Ms* (Equation 5). The technique yields station magnitudes with significantly reduced scatter (Bonner et al., 2006).

To calibrate Russell (2006) *Ms* for Asia, we collected seismograms from 98 events that occurred from 2002 to 2003 in Asia. We used Bonner et al.'s (2006) technique to measure the surface-wave amplitudes. We then calculated Russell (2006) *Ms* with Equation 5 using the nominal parameter values derived by Russell (2006). We also calculated Prague *Ms* (Vaněk et al., 1962) and Rezapour and Pearce (1998) *Ms* using amplitudes with periods in the band from 18 to 22 seconds. The Rezapour and Pearce (1998) *Ms* is currently used at the International Data Centre (IDC) as the standard *Ms* measurement. The Russell (2006) *Ms* that we calculated using the nominal parameter values with this dataset is, on average, about 0.12 magnitude unit (mu) larger than the Rezapour and Pearce (1998) *Ms* calculated with the same dataset. The mean station-magnitude variance of the Russell (2006) *Ms* is, on the other hand, 19% smaller than that of the Rezapour and Pearce (1998) *Ms* and 58% smaller than that of the Prague *Ms*, consistent with the conclusion of Bonner et al. (2006).

To derive the parameter $C_b$ in Equation 7 that is specific to Asia, we utilized the surface-wave group-velocity models developed by Levshin et al. (2003). We first converted velocity to slowness. We then took the arithmetic mean of the slowness for all model nodes as the average slowness for the whole region. The average group velocity and its derivative (Equation 6) were then derived from the average slowness. From the average group velocity and its derivative at 20 seconds, we obtained a $G_0$ value of 0.72. Using this $G_0$ in Equation 7, we obtained an Asia-specific $C_b$ of -0.54. This value is 0.12 mu smaller than the nominal value of -0.42 derived by Russell (2006). If we use this value in Equation 5 to calculate the Russell (2006) *Ms* with the dataset that we collected, the average *Ms* will be the same as the average of Rezapour and Pearce (1998) *Ms* from the same dataset.

Another parameter in the Russell (2006) *Ms* formula, which is also region-dependent, is $G_{\min}$ in Equation 5. We found $G_{\min}$ for a particular path from among the $G$ values along the path calculated from the group-velocity model of Asia. We then use the smaller of $G_{\min}$ and 0.6, a value suggested by Russell (2006), to define the bandwidth $f_c$ of the Butterworth filters used in filtering the data and in the *Ms* calculation. The Russell (2006) *Ms* calculated using the Asia-specific $G_{\min}$ has an even smaller station-magnitude variance. The mean station-magnitude variance of the Russell (2006) *Ms* is now 24% smaller than that of the Rezapour and Pearce (1998) *Ms*. The Russell (2006) *Ms* itself is increased by 0.04 mu on average.

## CONCLUSIONS AND RECOMMENDATIONS

We developed a surface-wave amplitude-measuring tool to make reliable amplitude measurements. The tool incorporates techniques such as phase-match filtering and backazimuth calculation in order to reduce the noise contamination of fundamental Rayleigh-wave amplitudes. With the tool, we made surface-wave spectral-amplitude measurements for Asia and surrounding regions in the frequency band between 12 and 22 seconds. Using the amplitude measurements, we conducted tomographic inversions and developed 2D surface-wave attenuation-coefficient models from 12 to 22 seconds for the region.

We calibrated the Russell (2006) surface-wave magnitude *Ms* using the 2D group-velocity model for Asia (Levshin et al., 2003). Russell (2006) *Ms* calculated with Asia-specific parameters reduces the station-magnitude variance. The average magnitude is more consistent with the Rezapour and Pearce (1998) *Ms* used by IDC. We plan to conduct further calibration study of Russell (2006) *Ms* using the attenuation models that we developed.

## ACKNOWLEDGEMENTS

Seismograms used in this study are from the Incorporated Research Institutions for Seismology, Data Management Center. Some of the figures in this paper were plotted using the Generic Mapping Tool (Wessel & Smith, 1995). We also thank Jessie Bonner for valuable Butterworth filter information gleaned from personal communication.

## REFERENCES


Barmin, M. P., M. H. Ritzwoller, and A. L. Levshin (2001). A fast and reliable method for surface wave tomography, *Pure Appl. Geophys*. 158: 1351–1375.

Bonner, J. L., D. R. Russel, D. G. Harkrider, D. T. Reiter, and R. B. Herrmann (2006). Development of a time-main, variable-period surface wave magnitude measurement procedure for application at regional and teleseismic distances, *Bull. Seism. Soc. Am*. 96: 678–696.

Dziewonski, A., Chou, T.-A., and Woodhouse, J. H. (1981). Determination of earthquake source parameters from waveform data for studies of global and regional seismicity, *J. Geophys. Res*. 86: 2825–2852.

Levshin, A. L. and M. H. Ritzwoller (2003). Discrimination, detection, depth, location, and wave propagation studies using intermediate period surface waves in the Middle East, Central Asia, and the Far East, Technical Report DTRA-TR-01-28, Defense Threat Reduction Agency, 120 pp.

Levshin, A. L., J. L. Stevens, M. H. Ritzwoller, D. A. Adams, and G. E. Baker (2003). Improvement of detection and discrimination using short period (7s-15s) surface waves in W. China, N. India, Pakistan and Environs, Final Report, submitted to Defense Threat Reduction Agency, 49 pp.

Levshin, A. L. (1985). Effects of lateral inhomogeneities on surface wave amplitude measurements., *Ann. Geophys.* 3: 4, 511–518.

Levshin, A. L., T. B. Yanovskaya, A. V. Lander, B. G. Bukchin, M. P. Barmin, L. I. Ratnikova, and E. N. Its (1989). *Seismic Surface Waves in Laterally Inhomogeneous Earth*. (Ed. V.I. Keilis-Borok), Kluwer Publ. House.

Marshall, P. D. and P. W. Basham (1972). Discrimination between earthquakes and underground explosions employing an improved Ms scale, *Geophys. J. R. astr. Soc*. 28: 431–458.

Rezapour, M. and R. G. Pearce (1998). Bias in surface-wave magnitude *Ms* due to inadequate distance corrections, *Bull. Seism. Soc. Am*. 88: 43–61.

Ritzwoller, M. H. and A. L. Levshin (1998). Eurasian surface wave tomography: group velocities, *J. Geophys. Res.* 103: 4839–4878.

Russell, D. R. (2006). Development of a time-domain, variable-period surface wave magnitude measurement procedure for application at regional and teleseismic distances, Part I: Theory, *Bull. Seism. Soc. Am*. 96: 665–677.

Shapiro, N. M. and M. H. Ritzwoller (2002). Monte-Carlo inversion for a global shear-velocity model of the crust and upper mantle, *Geophys. J. Int*. 151: 88–105.

Stevens, J. L., D. A. Adams, and G. E. Baker (2001). Improved surface wave detection and measurement using phase-matched filtering with a global one-degree dispersion model, in *Proceedings of the 23rd Seismic Research Review: Worldwide Monitoring of Nuclear Explosions*, LA-UR-01-4454, Vol. 1, pp. 420–430.

Vaněk, J., A. Zatopek, V. Karnik, N. V. Kondorskaya, Y. V. Riznichenko, E. F. Savarensky, S. L. Solov'ev, and N. V. Shebalin (1962). Standardization of magnitude scales, *Bull. Acad. Sci. USSR, Geophys. Ser*., No. 2, pp. 108–111 (in English).

von Seggern, D. H. (1977). Amplitude-distance relation for 20 second Rayleigh waves, *Bull. Seism. Soc. Am.* 67: 405–411.

Wessel, P. A. and W. H. Smith (1995). New version of the generic mapping tools released, *EOS, Trans. Amer. Geophys. Un.* 76: Suppl., 329.

Woodhouse, J. H. (1974). Surface waves in a laterally varying layered structure, *Geophys. J. Roy. Astr. Soc*. 37: 461–490.

Yang, X., S. R. Taylor, and H. J. Patton (2004). The 20-s Rayleigh wave attenuation tomography for Central and Southeastern Asia, *J. Geophys. Res*. 108: B12304, doi:10.1029/2004JB003193.

# ANALYSIS OF DIGITIZED SEISMOGRAMS FROM RUSSIAN GEOPHYSICAL SURVEY STATIONS OF SOVIET PEACEFUL NUCLEAR EXPLOSIONS

Kevin G. Mackey

Michigan State University

Sponsored by Air Force Research Laboratory

Contract No. FA8718-08-C-0018

## ABSTRACT

Throughout the 1970s and 1980s, the permanent seismic stations of the Soviet Union recorded over 100 Peaceful Nuclear Explosions (PNEs) detonated within the Soviet Union. These records have not been analyzed using modern digital methods and remain in Russian Archives. We have started a new initiative in collaboration with the Institute of Petroleum Geology and Geophysics (IPGG) of the Siberian Branch of the Russian Academy of Sciences (RAS) in Novosibirsk to assemble the records of these historic PNEs recorded at the permanent stations of the Russian regional networks. Most of these PNEs were detonated to conduct long-range Deep Seismic Sounding (DSS) profiles throughout much of the former Soviet Union in the 1970s and 1980s. The seismograms from the stations deployed for the DSS profiles are well known and continue to be studied. However, the seismograms from the permanent seismic stations have not been included in DSS studies. Collectively, there are several thousand records obtainable that will yield previously unused ray paths through the seismically more complex fold belts and accretionary zones, in particular in the Russian Far East beyond the eastern extent of the DSS profiles. We are collecting seismograms from the various seismogram archives in Russia, focusing initially on the Far East. The photopaper records are being scanned at high resolution (600 dpi) and then digitized and rectified. Test seismograms have been processed and have yielded good results. Record sections representing different geologic settings will be assembled to better understand crustal and velocity structure.

## OBJECTIVES

This study seeks to obtain, scan, digitize, and analyze seismograms from Soviet permanent seismic station networks of Soviet Peaceful Nuclear Explosions (PNEs). The analysis seeks to better resolve the crustal and velocity structure of Russia, particularly the Russian Far East where Deep Seismic Sounding (DSS) profiles using the PNEs were not conducted.

## RESEARCH ACCOMPLISHED

Long-range DSS profiles were conducted in the Soviet Union from 1971 to 1988 using PNEs (Figure 1) as sources (e.g., Benz et al., 1992). These profiles have been extensively analyzed using the original profile data both in Russia (e.g., Belousov et al., 1991) and more recently reprocessed in the west (e.g., Morozov et al., 2005). These PNEs were recorded using instruments deployed along the profiles at distances of 100–200 km spacing. These PNE profiles have been used to study a wide range of seismological phenomena, including attenuation, lithospheric and upper mantle structure, and scattering (e.g., Egorkin et al., 1987). Given that most of the PNEs were detonated in stable, cratonic areas, while the regional networks were located in the seismically active periphery, study of the PNEs recorded at the regional network stations will add a great number of previously unused ray paths through the seismically more complex fold belts and accretionary zones, in particular in eastern Russia and along the Russian border with China.

These PNEs were recorded at analog seismic stations operated by the regional networks resulting in over 7,800 seismograms (GS RAS, 2001) from the permanent Russian seismic stations. Only one systematic study (GS RAS, 2001) has been conducted with these records, basically consisting of P- and S-phase time picks for calibrating Russian Geophysical stations for Comprehensive Nuclear-Test-Ban Treaty (CTBT) monitoring. Although broad in scope, the study did not include any waveform analysis. Many seismograms were digitally scanned but are of poor quality and low resolution and thus of little use beyond the picking of basic arrival times. The study did not address stations in the former Soviet republics besides Russia.

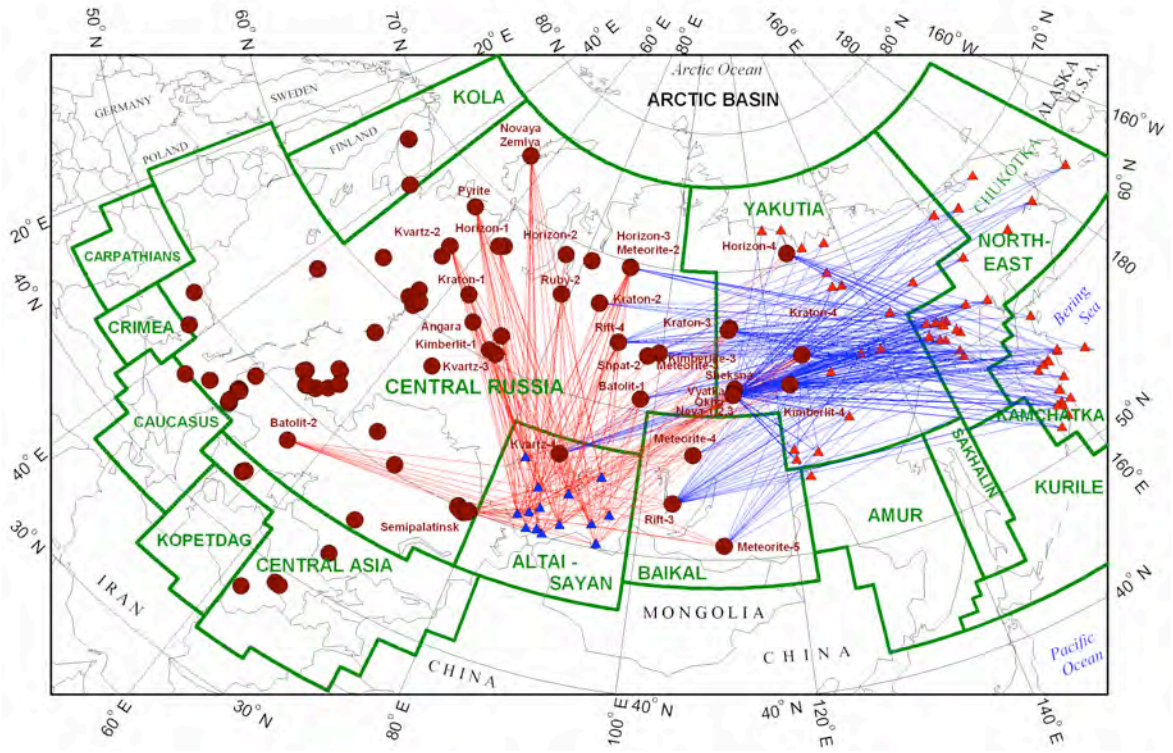


**Figure 1. Current status of PNE seismograms collected by the joint Michigan State University (MSU)-Novosibirsk digitization and analysis project. Blue lines are paths of MSU's current holdings. and red lines are Novosibirsks holdings of high-resolution scans of PNE recordings at geophysical stations (triangles). PNEs are denoted by red circles.**

We recently began working with the seismology group at IPGG to begin assembling, digitizing, and analyzing records from the regional networks of Russia. Figure 1 shows the raypaths of seismograms already scanned or

digitized in this study. IPGG has developed software to digitize these analog records and convert them into useable form. The photopaper records are scanned at high resolution (600 or 1200 dpi) in either gray scale or color to preserve faint traces. Figure 2 shows a sample seismogram scan and digitized waveform of the Neva 2-2 (a.k.a. Neva 3) PNE as recorded by the seismic station Kulu in the Magadan network. The digitization process is manual, with as many points along the trace entered as needed to create an unaliased waveform. The digitized seismogram is then resampled at a user-specified sample rate. For each seismogram, we will scan all three components, but initially digitize only vertical components. Selected horizontal components will later be digitized to compute various phase-amplitude ratios. We will compare the resulting PNE phase ratios with those of selected tectonic earthquakes analyzed in the same manner.

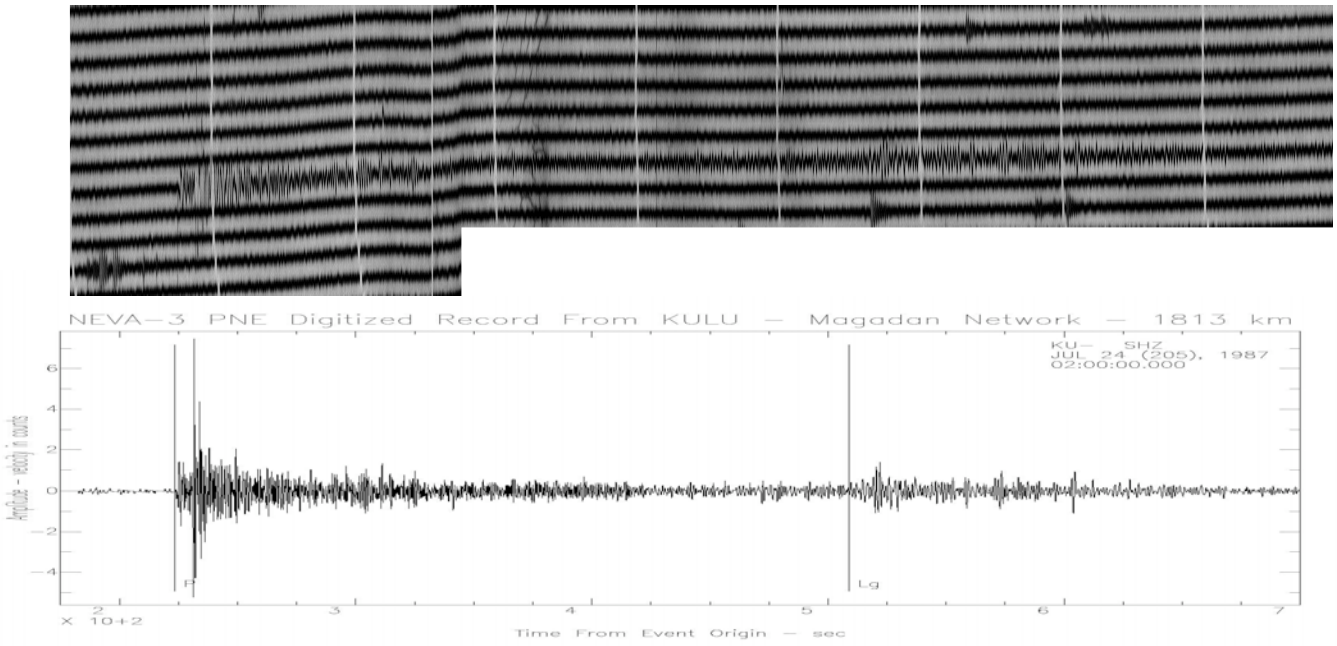


**Figure 2. Top, scanned photopaper Z component seismogram from station Kulu in the Magadan network of the Neva 2-2 PNE. Bottom, digitized version of the Neva 2-2 (a.k.a. Neva 3) PNE, as recorded at Kulu. The horizontal and vertical scales are approximately the same in both figures. The instrument is a short-period SM-3, z comp. Figure 3 shows a better image of the P arrival.**

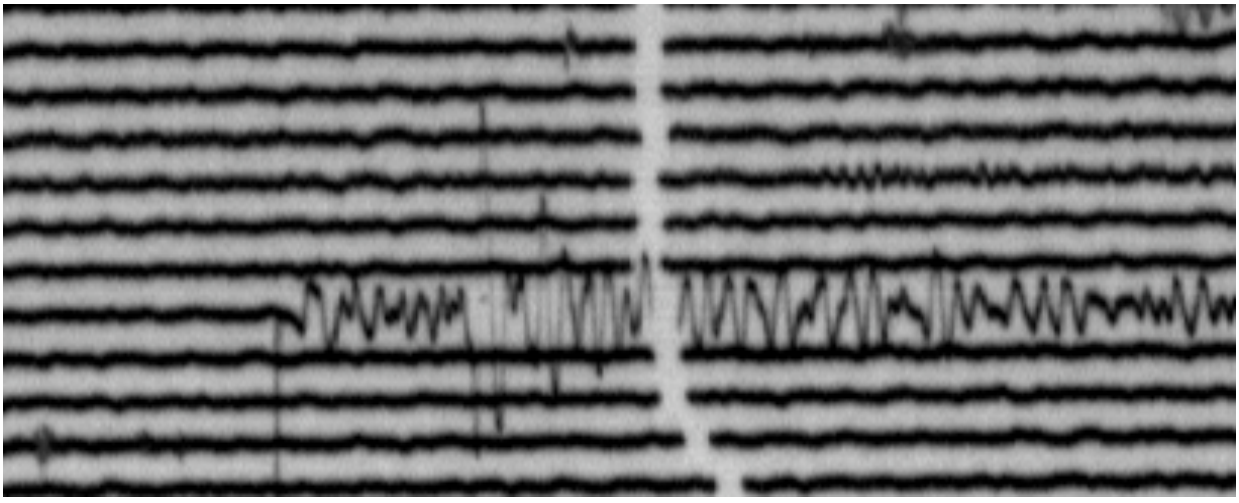

**Figure 3. Close-up of high-resolution seismogram scan from Figure 2 showing the P arrival.**

Digitized waveforms will be used to construct record sections of different regions (not necessarily linear profiles). Record sections will be analyzed for phase identification, crustal structure, and velocity structure. A sample record section using east Siberian craton PNEs, as recorded by seismic stations in the Altai-Sayan network (Figure 1), is shown in Figure 4. Our results will be compared with those of Morozov et al. (2005) where appropriate. In many cases, our records will complement the existing profiles, either being perpendicular to or reversing them, or extending into regions not previously sampled.

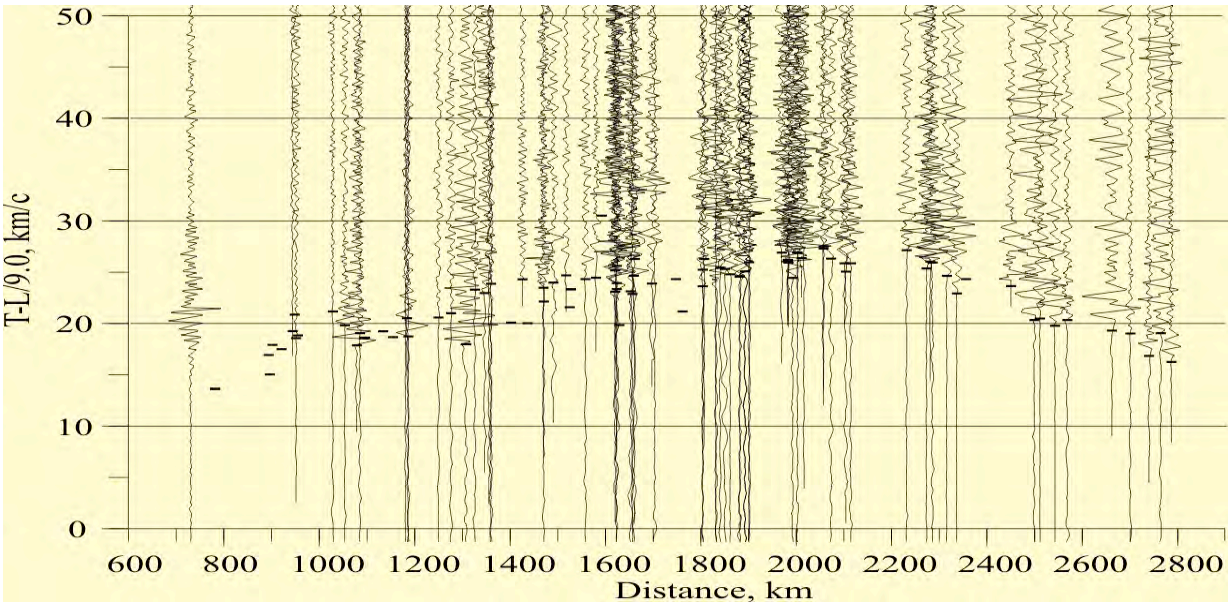


**Figure 4. Record section showing digitized seismograms of East Siberian Craton PNEs, as recorded in the Altai Sayan network. A reduction velocity of 9.0 km/s has been applied. Figure courtesy of V. Suvorov.**

## CONCLUSIONS AND RECOMMENDATIONS

Throughout the 1970s and 1980s, the permanent seismic stations of the Soviet Union recorded over 100 PNEs detonated within the Soviet Union. These records have not been analyzed using modern digital methods and remain in Russian Archives. Our digitization and analysis of these records will greatly complement the earlier DSS profile studies and extend ray-path coverage into eastern Russia.

## REFERENCES

Beloussov, V. V., N. I. Pavlenkova, and G. N. Kvyatkovskaya (1991). *Deep Structure of the USSR*, Nauka, Moscow, 224 pp. (in Russian).

Benz, H. M., J. D. Unger, W. S. Leith, W. D. Mooney, L. Solodilov, A. V. Egorkin, and V. Z. Ryaboy, 1992, Deep seismic sounding in northern Eurasia, *Eos Trans. Am. Geophys. Union* 73: 297, 300.

Egorkin, A. V., S. K. Zuganov, N. A. Pavlenkova, and N. M. Chernyshev (1987). Results of lithospheric studies from long-range profiles in Siberia, *Tectonophys.* 140: 29–47.

GS RAS, 2001. Calibration of the seismic stations of the Russian Academy of Sciences for CTBT seismic monitoring purposes, annual technical report SAIC-02/3029.

Morozov, I. B., E. A. Morozova, S. B. Smithson, P. G. Richards, V. I. Khalturin, and L. N. Solodilov (2005). 3D first arrival regional calibration model of northern Eurasia, *Bull. Seismol. Soc. Am.* 95: 951–964.

# SEISMIC CHARACTERIZATION OF NORTHEAST ASIA

Kevin Mackey[1], Lee Steck[2], Kazuya Fujita[1], Hans Hartse[2], and Richard Stead[2]

Michigan State University[1] and Los Alamos National Laboratory[2]

Sponsored by National Nuclear Security Administration

Contract Nos. DE-FC52-2004NA25540[1] and DE-AC52-06NA25396[2]

## ABSTRACT

Our project of seismic characterization of northeast Asia has continued on a multi-faceted approach concentrating on eastern Russia, including field deployments, data synthesis and interpretation, database integration, and travel-time tomography.

For field efforts, we deployed four remote seismic stations in the Seimchan-Buyunda basin in the Magadan region to get a better idea of baseline seismicity. Several events per day were recorded over approximately 40 days of station operation; the detection threshold for events was an order of magnitude higher than that of base stations in the cities. Suspected faulting-related geomorphological features observed in satellite images were also field checked along the Ulakhan Fault, a major earthquake generating feature, in this area. Fault scarps and sag ponds were identified cutting across a major alluvial fan. These dramatic features were previously undocumented and represent part of a major, but poorly understood fault system. This fault likely represents ground truth locations of earthquakes in the area.

For data analysis efforts, we completed interpretation of earthquake records from seismic stations deployed in the Stanovoi Range in 2006, including the determination of a composite focal mechanism. Other data analysis included extending our focal mechanism compilation of eastern Siberia to northeast Kamchatka, and analysis of seismicity and mechanisms in the Karaginsky Island area. Finally, we also updated focal mechanism and seismicity compilations for the Chersky Range.

Our Siberia database enhancements for this past year include: (1) addition of new origin information for earthquakes and explosions (and associated phase data and amplitudes), from the Irkutsk, Yakutsk, and Magadan networks., (2) additional catalog information from Siberia and the Far East in Russian language (Cyrillic) spread sheets covering years 1998-2004, and (3) and the inclusion of United States Geological Survey Earthquake Data Reports and International Seismological Centre magnitudes for larger events where Russian network operators did not report a K-class or a magnitude estimate.

We have been using Pn, Pg, and Lg tomography to obtain crustal and upper-mantle velocities in northeast Asia. Pn velocities are higher beneath the Siberian Platform and generally lower under the tectonically active regions in the central and eastern portions of our study area. Pg velocities show a similar geographic trend, and our results agree closely with Pg results from earlier studies. Pg velocities beneath Sakhalin Island are anomalously low and we are working to understand this observation. Lg velocities are high beneath the Siberian Platform, the Chersky Range and the Verkhoyansk Foldbelt. Low Lg velocities are found beneath Sakhalin Island. In general, average Vp/Vs ratios of 1.73 to 1.75 are found throughout the study region. Travel-time correction surfaces will be developed from the tomographic maps, and these will be compared to correction surfaces currently being developed from the raw travel-time data.

## OBJECTIVES

The main objective of our research is to improve the overall seismic characterization of northeastern Asia. To accomplish this we seek to develop a complete seismicity database and to use this database to discriminate industrial explosions, develop velocity models, and understand the relationship between the sizes, sources (both seismologic character and tectonics), and locations of events.

## RESEARCH ACCOMPLISHED

**Source Characteristics and Active Faulting**. Understanding the exact location and character of faults is beneficial for ground truth (GT) studies as it makes it possible for events to be tied to specific faults, as well as t0 understand expected event types. The source characteristics of earthquakes in northeastern Asia have generally been poorly determined. In certain areas (northeast Kamchatka, Stanovoi Range, central Chersky Range), several events have occurred since the general application of centroid moment tensor (CMT) analysis; in others no sizable events have occurred. While the general stress regime has been known for several decades (e.g., Cook et al., 1986; Parfenov et al., 1988), the details in many areas remain unclear. We discuss several aspects of active faulting and source characterization in eastern Russia.

The Ulakhan fault is the primary candidate fault for the edge of the North American plate in eastern Yakutia and the Magadan region (Figure 1) and thus can be expected to be one of the primary active faults in the region. The fault can be traced for nearly 900 km, extending from northwest of the Indigirka River in the north to the southern end of the Seimchan-Buyunda Basin in the south; it is nearly comparable in length to the San Andreas fault. Although most of the Ulakhan fault has never been surveyed on the ground, much of the fault is very clear on satellite images, where clear scarps, offset rivers, sag ponds, etc., are apparent (Figure 2). Geomorphology and consistent offsets in the river drainage system indicate a minimum left-lateral movement along the fault of about 24 km (Fujita et al., 2004) since the river network was established in about the Pliocene. Focal mechanisms also indicate a left-lateral motion on the fault. Analysis of the northern section of the primary branch of the Ulakhan fault shows a series of en-echelon basins in the vicinity of, and west of, the Indigirka River. The Indigirka River, other rivers, geology, and topography all reflect the proposed 24-km left-lateral offset. In Figure 3, we show two images of the northern section of the Ulakhan fault. The upper image is the present day, while the lower shows restored topography and alignment of rivers after cutting the image and removing 24 km of offset. Note that on the restored image, it is difficult to see the cut used for the restoration as river valleys, topography, and rock structure match almost perfectly.

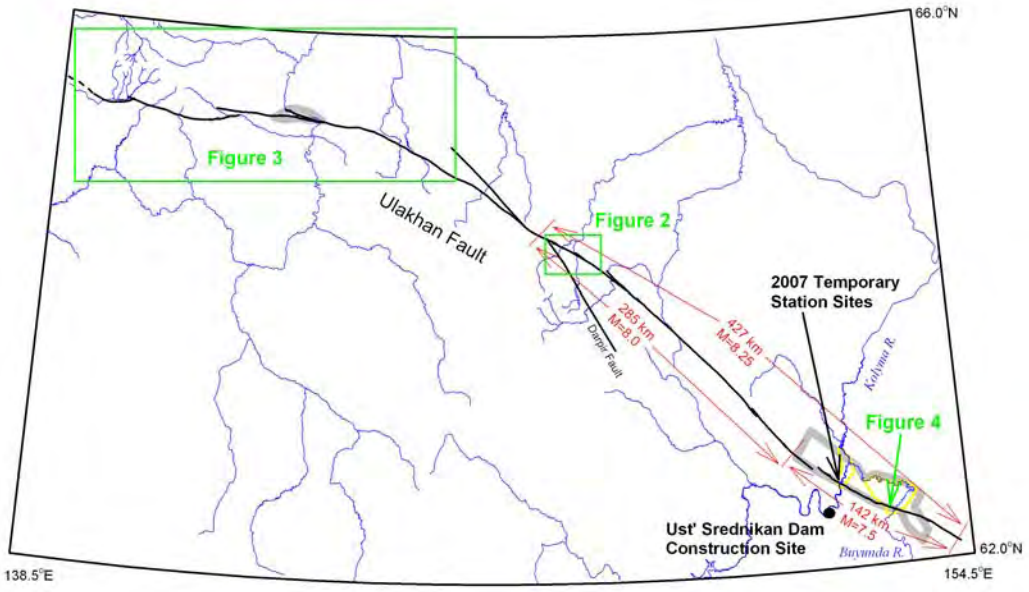


**Figure 1. The Ulakhan fault in the Magadan and Yakutsk regions. Figures as described in the text and below are indicated in green. Red indicates possible fault segments and expected magnitudes if the entire segment slips. The grey region indicates the Seimchan-Buyunda Basin.**

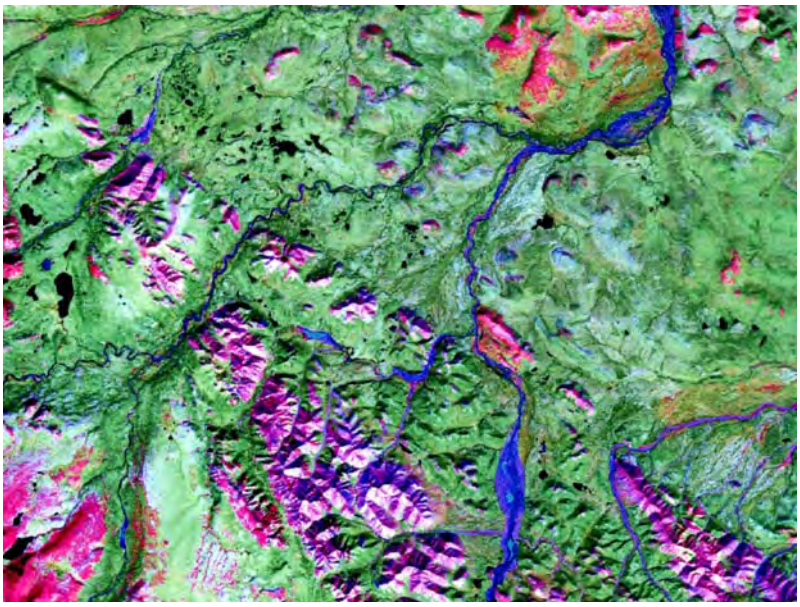

**Figure 2. Satellite image of the central Ulakhan fault. The fault extends from upper left to lower right. Note the clear lineation, scarps, offset rivers, and abandoned stream channels.**

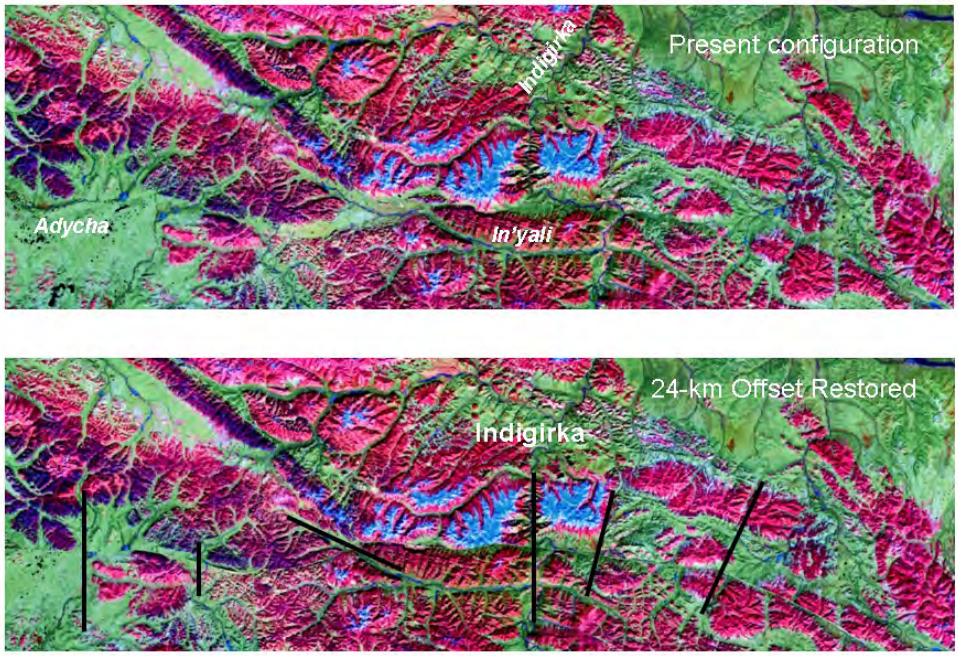


**Figure 3. The northern section of the Ulakhan fault in the Yakutsk region. The upper image is the present day, while the lower shows restored topography and alignment of rivers after cutting the image and removing 24 km of offset. Black lines indicate areas of river/valley alignment after restoration.**

We surveyed a section of the Ulakhan fault in the southern portion of the Seimchan-Buyunda Basin, where the fault crosses the abandoned alluvial fan of the Buyunda River. Along a 4-km section of the fault, we found a series of 12 well-developed sags connected by pressure ridges and/or scarps (Figure 4a). The scarps have a maximum of about 3 m of vertical offset, with the basin (north) side being lower. We also note that the sags axes are preferentially oriented slightly more east-west than the sections defined by scarps or pressure ridges, consistent with left-lateral motion on the fault. Figure 4b shows one of the well-developed sags. The observed geomorphology is

consistent with the Ulakhan being a significant Strike-Slip fault system. Given the observed fault length, the Ulakhan may be capable of generating great earthquakes. Using relationships proposed by Wells and Coppersmith (1994), the southern segments of the Ulakhan fault may be capable of generating earthquakes in the Magnitude-8 range (Figure 1). It must be stated, however, that the true character of ruptures on the Ulakhan is unknown. No research has been conducted to establish if the fault slips in large, but infrequent, earthquakes, nor what the recurrence interval might be. Seismic hazards on the Ulakhan fault are of particular importance to the Ust' Srednikan Hydroelectric dam on the Kolyma River that is under construction only 27 km from the fault. Additional seismicity studies, field surveys, and geologic research must be conducted to understand the Ulakhan fault and the seismic characteristics of the area.

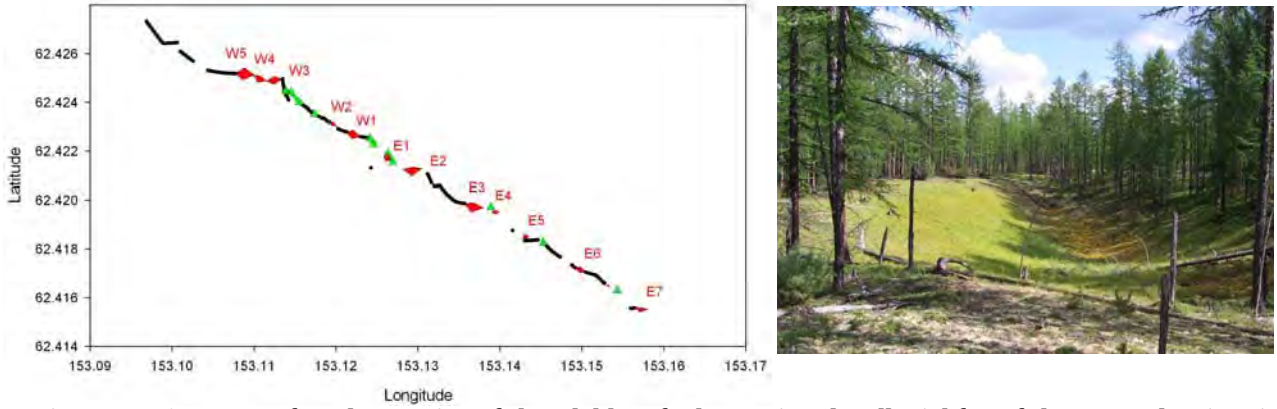


**Figure 4. A.) Survey of a 4 km section of the Ulakhan fault crossing the alluvial fan of the Buyunda River in the Seimchan-Buyunda Basin. Sags are shown in red, pressure ridges in green and scarps in black (left). B.) Photo of well-developed sag E7 on A (right).**

We conducted a small seismic deployment in the Seimchan Basin along the Ulakhan Fault. Previous temporary deployments in the vicinity of the Ulakhan fault lasted only a few days at most. In these deployments, high seismicity levels were observed, with up to ten local events per day. We conducted a more extensive deployment to verify the levels of seismic activity in the vicinity of the Ulakhan. Two short-period seismic stations were deployed a few kilometers off the main Seimchan highway and within the basin. Both stations were within 15 km of the Ulakhan fault. Although these stations were not ideally situated from a noise perspective, we recorded 84 local earthquakes (distances less than the Pn/Pg crossover distance, which is about 120 km for this area) in 33 days, with the stations having a 92% operational data collection rate. A sample seismogram of a local event is shown in Figure 5.

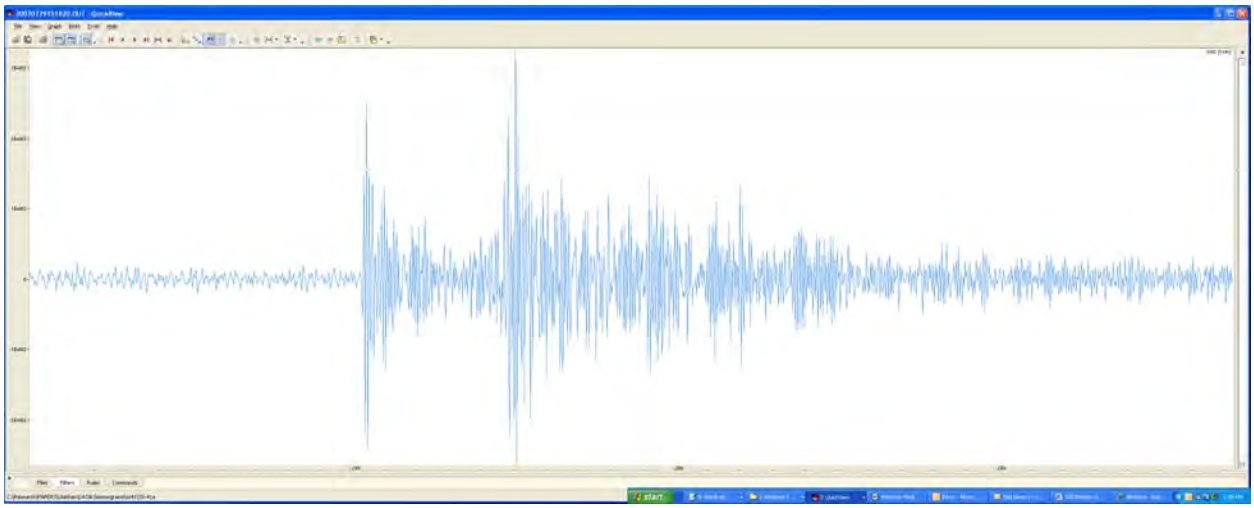

**Figure 5. Sample seismogram from one of the temporary stations deployed along the Ulakhan fault in the fall of 2007. The S-P time for this local event is about 4.5 seconds.**

In theory, the Ulakhan fault system should extend to the southeast, eventually intersecting and crossing the isthmus of Kamchatka. We have expanded our focal mechanism catalog to include northeast Kamchatka, including events in Shelikhov Bay and the enigmatic zone of seismicity north of the Kamchatka-Aleutian arc-arc junction (Figure 6).

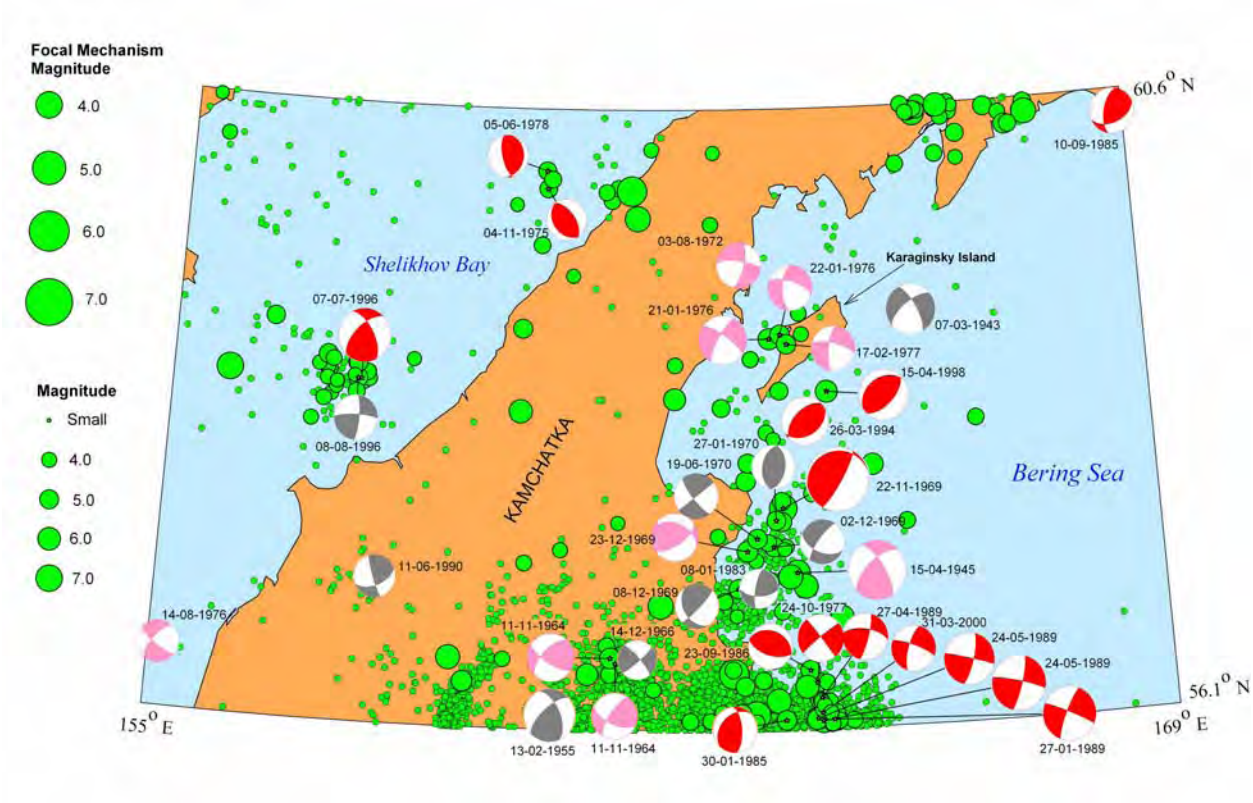


**Figure 6. Previously determined focal mechanisms presented in the literature for northeast Kamchatka. Focal mechanisms are lower hemisphere projections with compressional quadrants solid. Red mechanisms are reliable (CMT, synthetic, or well-constrained first motions), pink mechanisms are unreliable, and grey mechanisms are those for which the raw data are not available. Epicenters and focal mechanisms are scaled by magnitude.**

The distribution of seismicity and the previously determined focal mechanisms have been interpreted as representing strike-slip faulting along the Kommandorsky Islands in the southeast (Pacific-Bering plate motion), a convergence between Bering and Okhotsk north of the arc-arc junction to Karaginsky Island, thrusting between Bering and North America in the northeast, and transpression between Okhotsk and North America in the northwest (e.g., Fujita et al., 1990; Mackey et al., 1997; Pedoja et al., 2006).

Of particular interest is the cluster of events on the west side of Karaginsky Island and on the adjacent Kamchatka Isthmus. The mechanisms for this cluster shown in Figure 6 are taken from McMullen (1985) and suggest transtension—possibly with two different orientations. The Karaginsky Island sequence occurred in 1976–1977 (Zobin and Matvienko (1991) and is presumed to have had a northeast-southwest-trending rupture based on the aftershock sequence (McMullen 1985; Zobin and Matvienko, 1991). Three distinctly different mechanisms have been proposed for the events of this sequence, the transtensional mechanism (Figure 7; McMullen, 1985), a dip-slip mechanism with an approximately east-west striking nodal plane (Savostin et al., 1983; Zobin and Matvienko, 1991), and a thrust mechanism with northeast-southwest compression (Koz'min, 1984). To supplement the generally teleseismic data used in these determinations, additional first-motion data were obtained from the Alaska and Kamchatka regional networks.

The first motions are the clearest for the February 17, 1977, aftershock, and worst for the January 21, 1976, mainshock. The mainshock has an extremely emergent or precursory arrival and the first motion is extremely weak,

and probably lost at lower gain stations. Data obtained for the February 17, 1977, aftershock are more impulsive and indicate compressional first motions across Kamchatka as well as Alaska. These observations are consistent with the McMullen (1985) mechanism, however, it should be noted that the teleseismic first motions from the World Wide Standardized Seismographic Network (WWSSN) are very poor, and it is possible that the dilatational first motions in the center of the focal sphere, being at greater distances, miss the true first arrival.

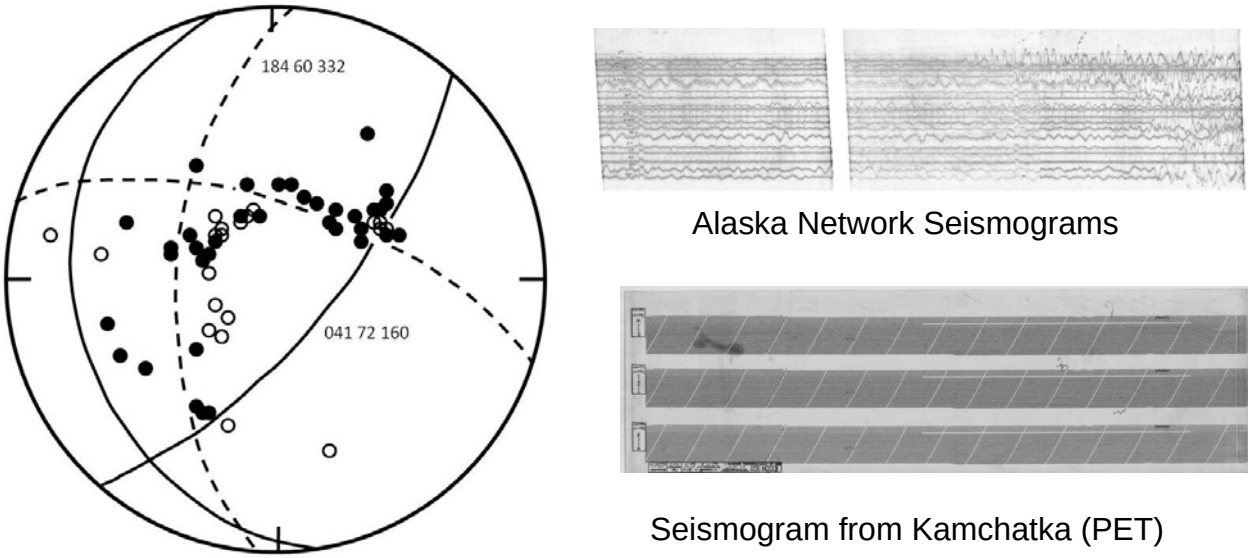


**Figure 7. Lower hemisphere projection first motion focal mechanism for the January 22, 1976, event. Solid circles are compressions, open circles are dilations. Most of the first motions are taken from the ISC bulletin except those to the southwest (Kamchatka network) and at the extreme east (Alaska network) which have been re-read (see inset for sample records). The dashed lines show the solution of McMullen (1985), while the solid lines show an alternative thrust mechanism discussed in this paper.**

Figure 7 shows the first motion focal mechanism for the January 22, 1976, aftershock. Based on the first motions, both the McMullen (1985) solution (dashed lines) and a thrust solution with northwest-southeast directed thrusting (solid lines) are possible. The thrust solution is similar to that of the large Mw 7.3 event of November 22, 1969, located just to the south. Given that the dilatations that support the transtensional solution of McMullen (1985) are from the most distant stations in Europe and south Asia, the possibility exists that the true first arrival was missed due to low-gains or attenuation. Selected WWSSN records for this event yielded no reliable first motions. Thus, the possibility that these events are subduction zone-like thrust events must be re-considered.

The first arrivals for the January 21, 1976, mainshock are complicated due to precursory arrivals (observed both on Kamchatka and Alaska regional network records) which may represent an extremely slow initiation to rupture or small, precursory events. As a result, first motion-based mechanisms for this event should be viewed with caution for this event. However, if all of the events of the Karaginsky sequence of 1976–1977 are assumed to have the same mechanism, then the data from the Kamchatka and Alaska regional networks preclude the dip-slip and thrust solutions of Savostin et al. (1983), Zobin and Matvienko (1991), and Koz'min (1984) for the January 21, 1976, mainshock. Further analysis, including waveform modeling, is planned to distinguish between the two other solutions (McMullen, 1985, and low-angle thrust) discussed here.

We have updated our general focal mechanism catalog for the Chersky Range both with new mechanisms, as well as corrected epicenters and magnitudes. In particular, we note that the January 7, 2001, earthquake west of Magadan, previously associated with the Chelomdzha-Yama fault, apparently lies on a smaller fault visible in satellite imagery (Figure 8). This, along with other aspects of the seismicity suggest that the Chelomdzha-Yama fault is not as important a structure as previously thought (e.g., Imaev et al., 2000) and may not be active in the present day.

This has significant implications for the sources of earthquakes and active faulting along the northern coast of the Sea of Okhotsk.

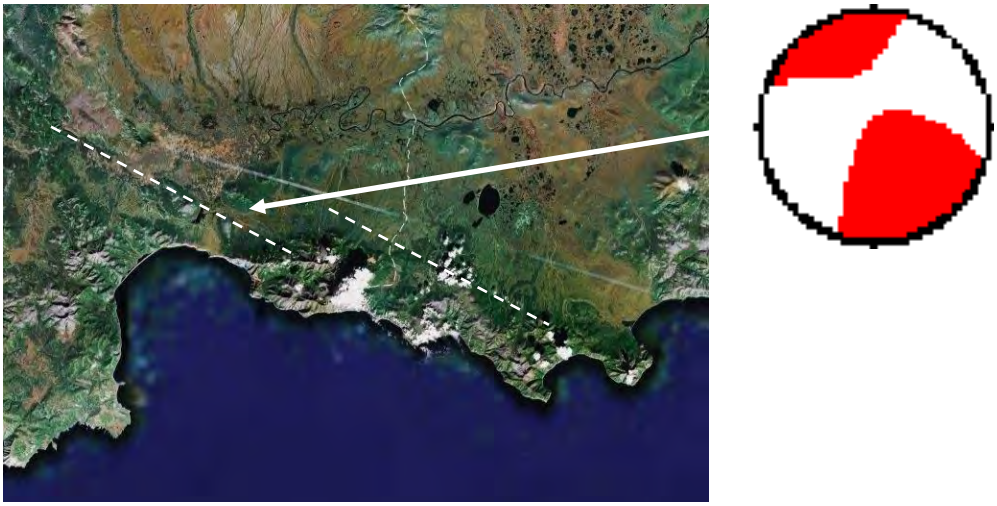

**Figure 8. Satellite image of epicentral region of January 7, 2001, earthquake showing WNW-ESE trending faults which parallel one of the nodal planes of the earthquake. The Global Moment Tensor solution is shown at right (Google Earth image).**

In a previous report (Mackey et al., 2007), observational evidence was presented for thrusting near the Stanovoi volcanic field. Although not enough data were available to determine a first-motion focal mechanism for any individual events, a composite focal mechanism was determined using Pg first-motions from local events recorded during the summer, 2006, deployment. Data from events located in clusters to the southeast of the volcanic field were tabulated separately from events elsewhere. The data from clusters southeast of the volcanic field are consistent with the focal mechanism (105 38 134) from first motion data for the mb 4.6 event of April 27, 1979, determined by Koz'min (1984). Use of all data yields a pure thrust focal mechanism of 110 37 090 (Figure 9), which is consistent with the orientation of the thrusts seen from the air. It should be noted that only a limited number of events were available for first motion data and crustal structure (and therefore take-off angles) was uncertain.

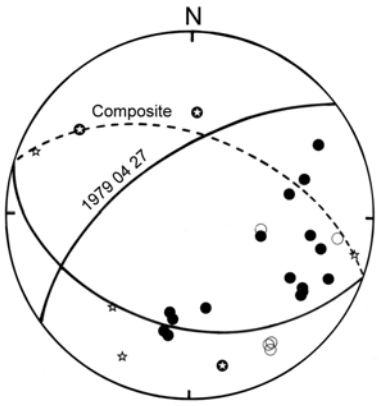


**Figure 9. Composite focal mechanism from the 2006 Stanovoi deployment. Lower hemisphere projection; compressions are solid, dilatations are open. Circles denote data from southeast of the volcanic field; stars represent other data. The solid lines show the mechanism for the April 27, 1979, event determined by Koz'min (1984), while the dashed line shows the second plane using all data from our deployment.**

**Crustal Velocities** We have extended our analysis of the eastern Russia database to conduct crustal velocity tomography for the region. Using the eastern Russia seismicity database, the epicentral ground truth of each event was evaluated using the Bondar et al. (2004) criteria and about 10–20% of our events were identified as having GT25 epicenters, that is, known to within at least 25 km of the true epicenter. GT events tend to be the largest events with highest signal-to-noise ratios and the clearest phase identifications. To invert this dataset, we used a method analogous to Pn tomography, whereby we assume a great circle path between source and receiver. Events were restricted to depths of less than 33 km, and stations were constrained to be at distances between 0.5 and 14º from the

epicenter for Pg, and 0.7 and 25º for Lg. To accommodate depth uncertainty and near-receiver velocity effects we solved for both an event term, e, and a site term, r, and we damped the site term sum to zero. The travel time for the $i^{th}$ event to the $j^{th}$ station is expressed as

$$t_{ij} = \Sigma\, \delta x_l s_l + e_i + r_{j,} \qquad (1)$$

where the $\delta x_l$ are path segments and the $s_l$ are slownesses for those segments. The summation is taken over the n segments of the great circle path. In our solution, we employ first difference regularization over a 1º by 1º grid, and solve the set of equations using the LSQR conjugate gradient method (Paige and Saunders, 1982). We invert for slowness over a region spanned by latitudes from 45 º to 75º N and longitudes from 90 º to 200ºE. Tests were run for checkerboards with 2 º, 4 º, and 10º squares with velocities alternating between ±10% perturbations. Coverage with good resolution is better for Lg than for Pg largely due to the longer ray paths of Lg phases. For Lg, good resolution is obtained using 4º-grids for much of Northeastern Russia while Pg resolution is reduced.

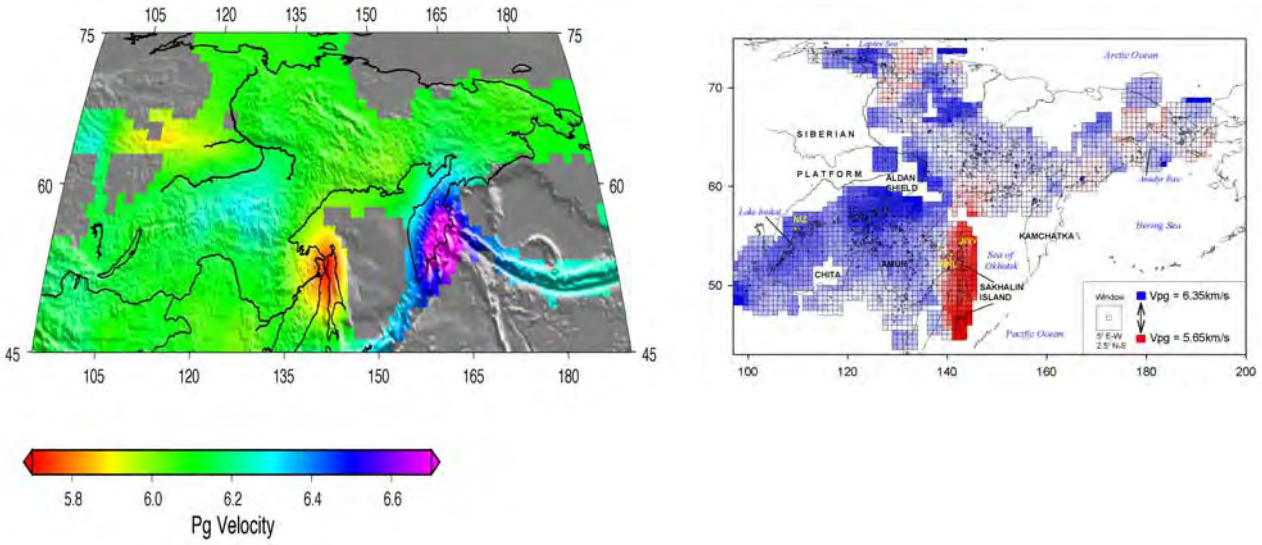


**Figure 10. Left. Pg velocities of eastern Russia determined by tomography in this study. Right. Comparison of crustal velocity as determined by Mackey et al. (2003) using an independent method.**

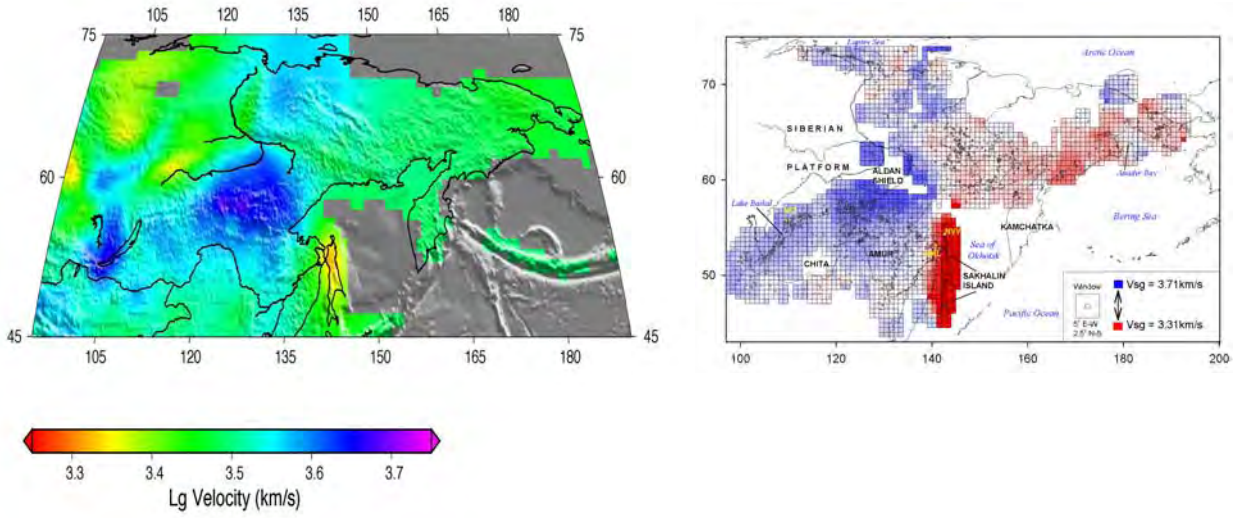


**Figure 11. Left: Sg (Lg) velocities of eastern Russia determined by tomography in this study. Right: Comparison of crustal velocity as determined by Mackey et al. (2003) using an independent method.**

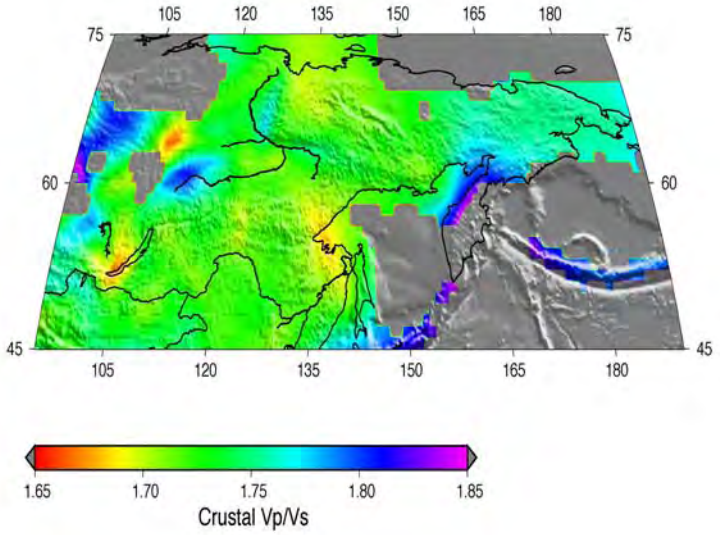


**Figure 12. Crustal Vp/Vs ratio for eastern Russia.**

Inversion results for Pg and Lg are shown in Figures 10 and 11. Obvious trends in velocities are observed: 1) regions with convergent tectonics, i.e., the Pacific Rim, particularly associated with Kamchatka, exhibit faster than average apparent Pg velocity. 2) Sakhalin Island, where low velocities are observed. 3) The Siberian Craton (Aldan Shield), where elevated velocities are also observed, consistent with an old, thick, cold crust. We also compute Vp/Vs ratios by taking the ratio of the Pg and Lg velocity maps (Figure 12).

The tomography results can be compared with crustal velocities for eastern Russia determined several years ago by Mackey et al. (2003; Figures 10 and 11) using a method that jointly solved for seismic velocities and hypocenters while minimizing residuals. General patterns of velocity anomalies are consistent with a few exceptions. Anomalies associated with Sakhalin Island and the Aldan Shield are nearly identical in both magnitude and extent. The low velocity anomaly associated with the Laptev Sea Rift is not apparent in the tomography.

## CONCLUSIONS AND RECOMMENDATIONS

Traditional interpretations of faults and faulting in the area have been challenged by reanalysis of historical data and satellite image interpretation. Analysis of active faulting in conjunction with reanalysis of historical seismicity and current deployments are allowing us to improve our understanding of the nature and location of natural seismicity sources in eastern Russia. Due to the relatively low occurrence of earthquakes amenable to CMT analysis, use of historical and smaller events are critical to determining the nature of the earthquake sources. First motion data from the regional networks provide constraints which can be applied to waveform modeling and other techniques. Temporary networks provide additional information on active faulting and, as they tend to be located outside of towns, yield much lower detection thresholds.

Two independent methods have now been applied to determine Pg velocities throughout northeast Russia. While they are in general agreement, several discrepancies continue to exist and need further study. The low velocities in Sakhalin, however, have been consistent among several models and have been noted by workers of the Russian Sakhalin network as well. Careful analysis of data we are currently obtaining from Kamchatka, in particular, should improve our models of the northern Sea of Okhotsk and the northern end of the subduction zone.

The continued expansions of, and enhancements to, the MSU Siberia Seismicity database remain critical in improving both velocity models and source analysis.

## ACKNOWLEDGEMENTS

We would like to thank our many colleagues from the Geophysical Survey, Russian Academy of Sciences, for assistance with both data collection and fieldwork that is necessary for the continuation of this work.

## REFERENCES

Bondar, I, S. C. Myers, E. R. Engdahl, and E. A. Bergman (2004). Epicenter accuracy based on seismic network constraints, *Geophys. J. Int*. 156: 483–496.
Cook, D. B., K. Fujita, and C. A. McMullen (1986). Present-day plate interactions in northeast Asia: North American, Eurasian, and Okhotsk plates, *J. Geodyn*. 6: 33–51.

Fujita, K., D. B. Cook, H. Hasegawa, D. Forsyth, and R. Wetmiller (1990). Seismicity and focal mechanisms of the Arctic region and the North American plate boundary in Asia, in Grantz, A., G. L. Johnson, and J. F. Sweeney, J. F., eds., *The Geology of North America, v. L., The Arctic Region*, Geological Society of America, Boulder, 79-100.

Fujita, K., G. Sella, K. G. Mackey, S. Stein, K.-D. Park, V.S. and Imaev (2004). Relationships between seismicity and GPS determined velocities in northeast Asia: *Eos Trans. Am. Geophys. Un.* 85: (47), Supplement: F667.

Imaev, V. S., L. P. Imaeva, and B. M. Koz'min (2000). *Seismotectonics of Yakutia*, GEOS, Moscow, 226 pp. (in Russian).

Koz'min, B. M. (1984). *Seismic Belts of Yakutia and the Focal Mechanisms of Their Earthquakes*, Nauka, Moscow, 126 pp. (in Russian).

Mackey, K. G., K. Fujita, K., L. V. Gunbina, V. N. Kovalev, V. S. Imaev, B. M. Koz'min, and L. P. Imaeva (1997). Seismicity of the Bering Strait region: Evidence for a Bering Sea block, *Geology* 25: 979–982.

Mackey, K. G., K. Fujita, L. K. Steck, and H. E. Hartse (2003). Seismic regionalization of eastern Russia, in *Proceedings of the 25th Seismic Research Review—Nuclear Explosion Monitoring: Building the Knowledge Base*, LA-UR-03-6029, Vol. 1, pp. 73–82.

Mackey, K. G., H. E., Hartse, L. K. Steck, R. J. Stead, C. A. Rowe, K. Fujita, and L. Gutirrez, (2007). Seismic characterization of northeast Asia, in *Proceedings of the 29th Monitoring Research Review:Ground-Based Nuclear Explosion Technologies*, LA-UR-07-5613, Vol. 1, 123–132.

McMullen, C. A. (1985). *Seismicity and Tectonics of the Northeastern Sea of Okhotsk*, M.S. Thesis, Michigan State University, East Lansing, 107 pp.

Paige, C. C., and M. A. Saunders (1982). Algorithm 5583, LSQR: Sparse linear equations and least-squares problems, *Trans. Math. Software*, 8: 195-209.

Parfenov, L. M., B. M. Koz'min, O. V. Grinenko, V. S. Imaev, and L. P. Imaeva (1988). Geodynamics of the Chersky seismic belt, *J. Geodyn.* 9: 15–37.

Pedoja, K., J. Bourgeois, T. Pinegina and B. Higman (2006). Does Kamchatka belong to North America? An extruding Okhotsk Block suggested by coastal neotectonics of the Ozernoi Peninsula, Kamchatka, Russia, *Geology* 34: 353–356.

Savostin, L., L. Zonenshain, and B. Baranov (1983). Geology and plate tectonics of the Sea of Okhotsk region, *Am. Geophys. Un., Geodynamics Ser.* 11: 189–221.

Wells, D. L., and K. J. Coppersmith, (1994). New Empirical Relationships among Magnitude, Rupture Length, Rupture Width, Rupture Area, and Surface Displacement, *Bulletin of the Seismological Society of America*, 84: 974–1002.

Zobin, V. M., and Y. D. Matvienko (1991). Karaginsky earthquake of 21(22) January, 1976, *Vulkanologiya i Seismologiya*, 13(1): 93–103. (in Russian)

# EXTENSION OF THE CAUCASUS SEISMIC INFORMATION NETWORK STUDY INTO CENTRAL ASIA

Randolph Martin[1], Mary L. Krasovec[1], Eileen Vergino[2], and M. Nafi Toksöz[3]

New England Research[1], Lawrence Livermore National Laboratory[2],
and Massachusetts Institute of Technology[3]

Sponsored by National Nuclear Security Administration

Contract Nos. DE-AC52-04NA25612[1], DE-AC52-07NA27344[2], and DE-AC52-04NA25612[3]

## ABSTRACT

The Central Asian Seismic Research Initiative (CASRI) is an extension of the Caucasus Seismic Information Network (CauSIN). Both projects seek to promote cooperation, transparency, and stability in these highly seismically active regions of strategic interest to the U.S. by working with the countries to improve the monitoring and hazard assessment. Building knowledge bases of geological, geophysical, and seismic information in the respective regions, utilizing modern crustal modeling techniques to create a combined model of the regions, and applying modern hazard assessment techniques will aid these countries in improving their seismic monitoring capacity. The CauSIN project was completed in 2007; the CASRI is currently in its final stages, though work in the area will be continued in a separate project.

Over the past three years, a great deal of tectonic, geologic, geophysical, seismic event catalog, waveform, and phase arrival data from local networks in the CASRI region (Kazakhstan, Kyrgyzstan, Tajikistan, and Uzbekistan) have been collected. The historical catalog contains nearly 11,000 events from 500 AD through the present. The modern seismic catalog (from the digital instrumental period) includes 469 events from 1991 to 2005.

In the past year, a large number of phase arrival time picks have been collected from stations of the local networks in Kazakhstan and Kyrgyzstan. (Uzbekistan and Tajikistan do not currently have operating digital stations.) Kyrgyzstan has a ten-station digital network (KNET) that began operations in September 1991 as the result of a cooperative project sponsored by the Incorporated Research Institutions for Seismology (IRIS) university consortium and the Kyrgyz government. The National Nuclear Center of Republic of Kazakhstan (NNC RK) operates thirteen digital stations that have been brought online in various stages since the summer of 1994. This includes three IRIS monitoring stations and seven arrays, the newest of which was installed in 2004.

The local time pick database from Kazakhstan and Kyrgyzstan includes over 6,000 P phase picks and 2,500 S phase picks from more than 400 events. Following a process similar to that used in the CauSIN project, the local time pick database is combined with time picks from the Engdahl, van der Hilst, and Buland (EHB) database in preparation for a rigorous crustal tomography calculation. Together, these data provide coverage of the seismically active southern portion of the CASRI study region, but almost no coverage in the quiescent shield area to the north. However, explosion events provide some coverage in this gap. Newly digitized waveform data have been received for nuclear tests at the Semipalatinsk test site in Kazakhstan, Lop Nor in China, Pokharan in India, and Chagai in Pakistan, as well as for several peaceful nuclear explosion (PNE) events scattered throughout Turkmenistan, Uzbekistan, Kazakhstan, and southern Russia.

## OBJECTIVES

The primary goal of this project is to develop a database of new waveform data, geology, and active tectonics in the Caucasus and Central Asian regions. With this new database, we will be able to improve earthquake locations and identify potential "ground truth" (GT) events, aiding in the monitoring of these regions of strategic interest to U.S. national security. The dense network, calibration events (mining and quarry blasts), improved models, and better location algorithms (including multiple-event grid search, and double difference) will improve the event locations. Scientists at collaborating countries are very eager to assist with this task, since improved locations will aid in the identification of active faults and help them to improve their hazard assessments and building codes for the region, better protecting public safety and stability for their countries.

With the ground truth events to serve as validation, we will obtain a detailed crust/upper mantle structure in Central Asia, using data from newly installed seismic stations as well as the Global Seismic Network (GSN) and other stations operated as part of the national networks.

## RESEARCH ACCOMPLISHED

### 1.0 Local Networks

Recent meetings with seismologists from the participating CASRI nations have led to the sharing of detailed information about the local networks, most of which have been undergoing a period of recovery and expansion since the breakup of the Soviet Union. Reviews of the full status of the networks in Kazakhstan, Kyrgyzstan, Uzbekistan, and Tajikistan follow.

### 1.1 Kazakhstan

The NNC RK and the Institute of Seismology have been the main body operating seismic networks in Kazakhstan. The networks of the NNC RK operated nearly continuously throughout the tumultuous early 90s, focusing primarily on meeting treaty monitoring obligation, while the Institute of Seismology was operating mainly analog networks during this period, with a focus on earthquake monitoring, The network included both analog and digital weak-motion stations (KazNET) as well as strong motion instruments.

The main installations of the NNC RK were the Geophysical Observatories at Aktyuinsk, Borovoye, Kurchatov, and Makanchi, which were created during the Soviet times for monitoring worldwide nuclear explosions and passed to the Institute of Geophysical Research at the NNC RK in 1994. At that time, a Joint Seismic Program (JSP) between the NNC RK and IRIS in the U.S. was established, with the goal of making effective use of Kazakhstan's monitoring capabilities. Eight broadband 3-component stations (AKT, BRV, ZRN, VOS, CHK, KUR, MAK and TLG) equipped with STS-2 and CMG-3 seismometers and IRIS/PASSCAL 16 and 24-bit digital data acquisition systems were installed in July and August 1994, and a unique 24-element Kurchatov seismic "cross array" began operating in October.

Between 1994 and 1996, 3-component broadband IRIS stations were installed at the Borovoye and Kurchatov observatories and in Makanchi, and the Borovoye and Kurchatov arrays received equipment updates. All of these stations are part of the GSN and used in joint experiments with the Lamont-Doherty Earth Observatory of Columbia University in the U.S.

In 1996, Kazakhstan signed the Comprehensive Nuclear-Test-Ban Treaty (CTBT), and five facilities located on Kazakhstan territory were included in the newly created International Monitoring System. These include the Makanchi seismic array (PS23), which is a primary IMS seismic station, seismic arrays Borovoye (AS057), Kurchatov (AS058), and the Aktyubinsk 3-component seismic station (AS059), which are auxiliary seismic network stations, and the Aktyubinsk infrasound station (IS31).

Since April 1997 NNC RK had carried out several projects which have expanded their network, continuing to add modern acquisition equipment and satellite communication systems to existing stations and adding seismic arrays such as those in Makanchi, Borovoye, and Makanchi which operate as part of the IMS.

In sum, NNC RK now operates thirteen digital stations (see Figure 1A), which include 3 IRIS monitoring stations and 7 arrays. NNC RK sends data out to several groups, including the IDC, USA NDC, IRIS, EMSC, ISC, the Institute of Seismology of Kazakhstan, GS RAS, NORSAR, and SEA/DASE. (More information is available at http://www.kndc.kz). Additionally, the Institute of Seismology is in the process of upgrading their weak-motion network, adding digital three-component weak-motion and strong-motion stations for earthquake monitoring.

### 1.2 Kyrgyzstan

Kyrgyzstan operates a 10-station broadband seismic network called KNET, which became operational in September 1991 (see Figure 1). So far in its lifetime, with IRIS sponsorship and JSP funding, it has survived the economic and political turbulence from the breakup of the former Soviet Union and the formation of the Republic of Kyrgyzstan, as well as the 19 August 1992, magnitude-7.4 Suusamyr earthquake, located under the network station Almayashu (AML). KNET is operated by the Kyrgyz Institute of Seismology (KIS) and the Institute of High Temperature Physics of the Russian Academy of Sciences (IVTAN). IRIS participants in this project have included the University of California at San Diego, Indiana University, Rennselear Polytechnic Institute, and the University of Colorado. The University of California San Diego had responsibility for collecting and processing KNET data most recently in 2002.

KNET utilizes Streckeisen STS-2 sensors with PASSCAL dataloggers, which are combined with advanced digital telemetry and data processing techniques to provide high-dynamic-range (24-bit), broadband (0.008–50 Hz.) seismic data. The geometry of the network was dictated by the need to maximize earthquake monitoring capability within line-of-sight telemetry constraints. Since this network has broadband sensors, it may also be used as a long-period array, which will enhance signals with apparent wavelengths in the range of 10 to 100 kilometers.

In addition to the triggered data set, over five years of continuous network data are presently available. All data, along with several technical reports, are available through the IRIS Data Management Center in Seattle (http://eqinfo.ucsd.edu/deployments/knet.php).

### 1.3 Uzbekistan

The seismic network of the Institute of Seismology, Academy of Sciences, Uzbekistan, has been actively pursuing sources of funding to upgrade its analog seismic to digital or to install all new stations. In 2002, China installed 5 broadband digital stations in Uzbekistan, but it has been very difficult for the country to utilize the data received, and today none of the stations are operational. At the present time, therefore, there are no operational digital stations.

### 1.4 Tajikistan

Tajikistan once operated a network of 49 analog stations, but the civil war of 1992 resulted in a great deal of damage, and much of the seismic data collected in the previous several decades was lost. At present, the network still does not function, but efforts are underway to recover existing hardware and upgrade it to digital where possible (http://www.smnt.tj). Working with a group of Swiss seismologists, they have recently added several new digital seismic stations; they have some records from the last three years only.

## 2.0 Seismic Data: Event Catalogs

The past year has seen addition to our database of the earthquake catalog from CASRI scientists. The catalog is shown in Figure 2, split into events in the historical period before 1922, when the Soviet era began; the Soviet era; and the years since 1991, after the Soviet era.

### 2.1 Seismic Data: Phase Arrivals

Phase arrival tables have been received from CASRI participants (Kazakhstan, Kyrgyzstan, Tajikistan, and Uzbekistan). Figure 3 shows that ray paths are focused in the southern portion of the study area, since very little seismic activity takes place in the stable shield to the north. P wave paths, shown in the top figure, extend toward the Caspian Sea, while S wave paths in the western part of the study region are sparser.

These data are being combined with time picks from the EHB database in preparation for tomography studies.

### 2.2 Seismic Data: Nuclear Explosions

Another aspect of the data collected in the CASRI project is time pick and waveform data from explosion events in central Asia, specifically waveform data not previously available. Figure 3 shows events for which waveform data have been received. These include nuclear tests at the Semipalatinsk test site in Kazakhstan, Lop Nor in China, Pokharan in India, and Chagai in Pakistan, and several peaceful nuclear explosion (PNE) events scattered throughout Turkmenistan, Uzbekistan, Kazakhstan, and southern Russia. Data from the PNE events will be especially helpful to the tomography studies discussed in the next section, since they provide ray paths in the seismically inactive stable shield region of northern Kazakhstan.

Data from several nuclear explosions, shown in Figure 4, provide ray paths in the seismically quiescent region of northern Kazakhstan and provide ground truth in tomography studies. Figures 5 and 6 show waveforms for a nuclear explosion at the Semipalatinsk Test Site in northeast Kazakhstan and for a peaceful nuclear explosion (PNE) in southern Russia.

**A. Kazakhstan Network**

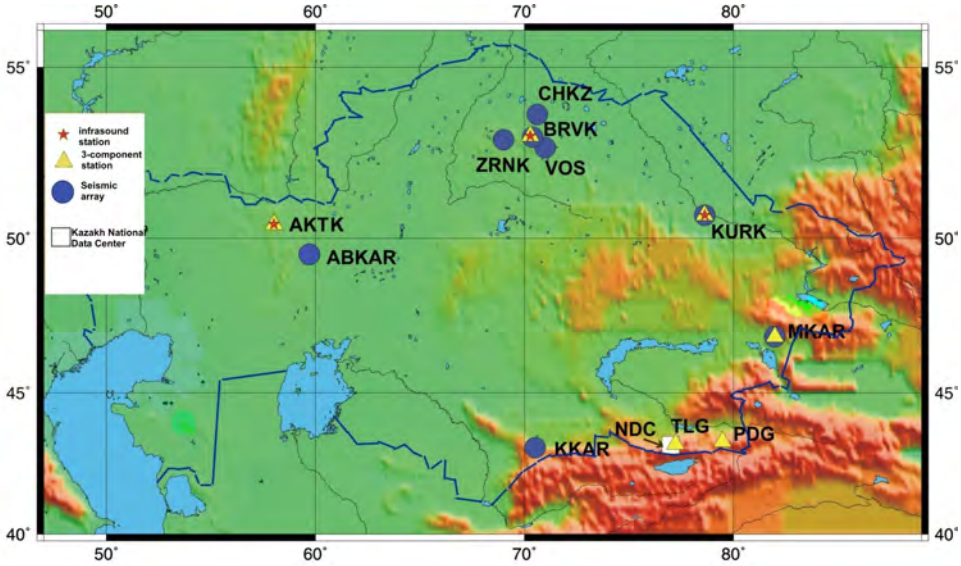


**B. Kyrgyzstan Network**

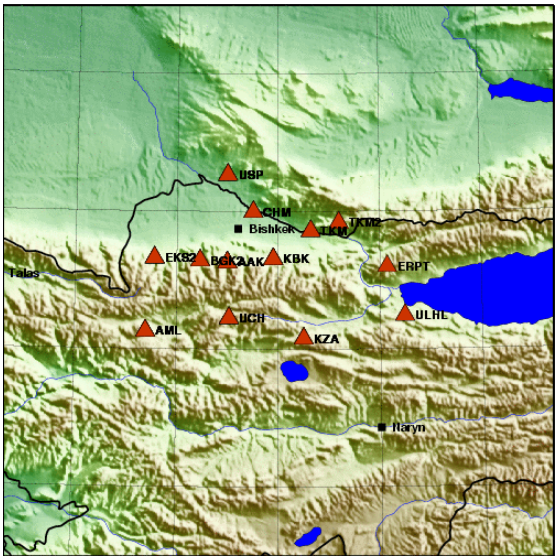


**Figure 1. Maps of local seismic networks discussed in sections 1.1 and 1.2.**

**A. Historical events: pre-1922**

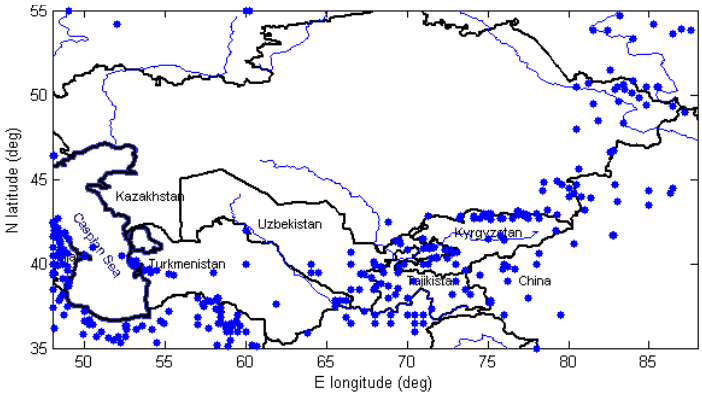


**B. Soviet-era data: 1922–1991**

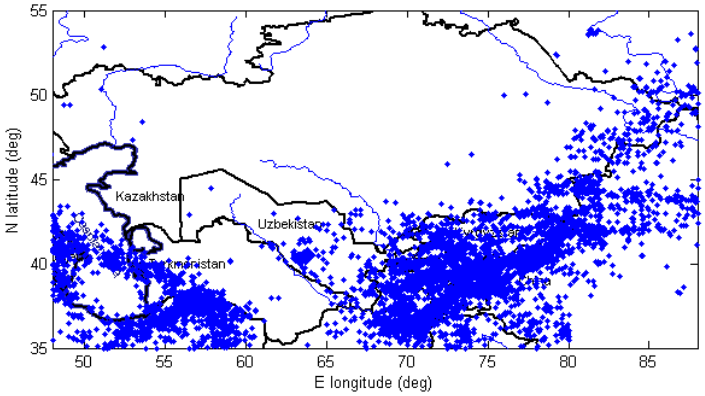


**C. Post-Soviet events: 1992–present**

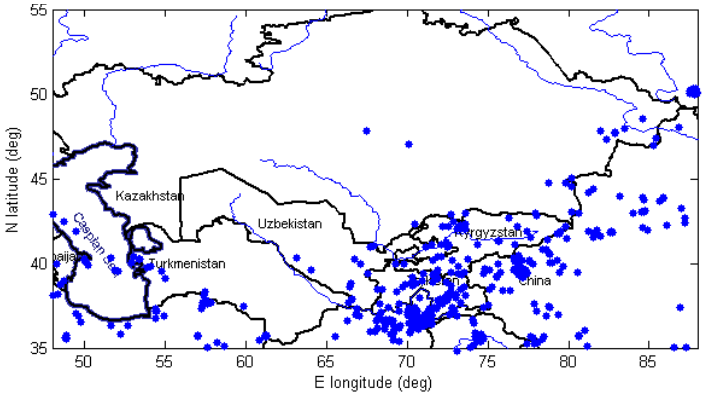


**Figure 2. Event catalog, split into three eras: pre-Soviet Union, including events back to 2000 BC; the Soviet era; and 1992–present.**

**P pick raypaths from local CASRI networks**

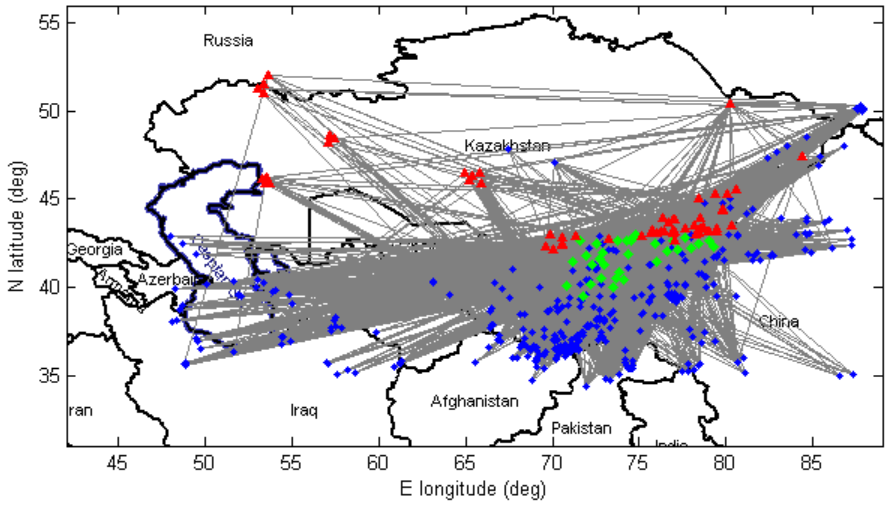


**S pick raypaths from local CASRI networks**

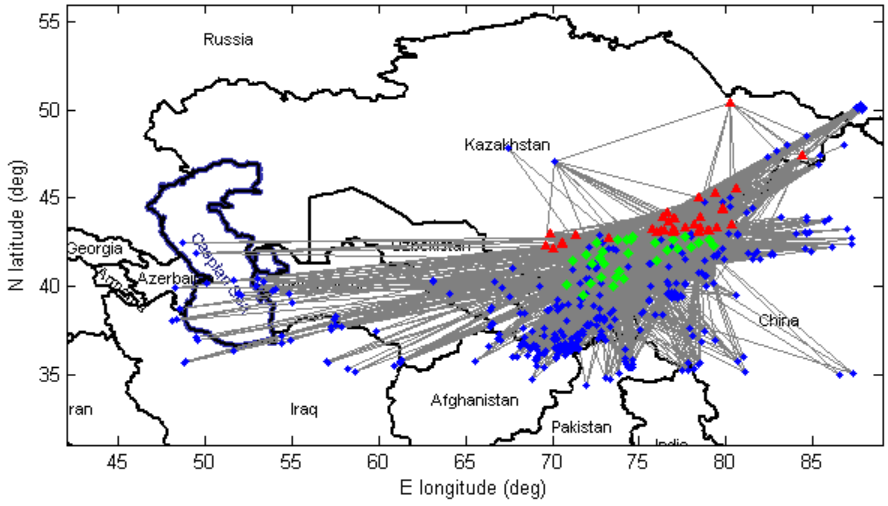


**Figure 3. Ray paths to stations in Central Asia from local and regional earthquakes for which arrival times are available.**

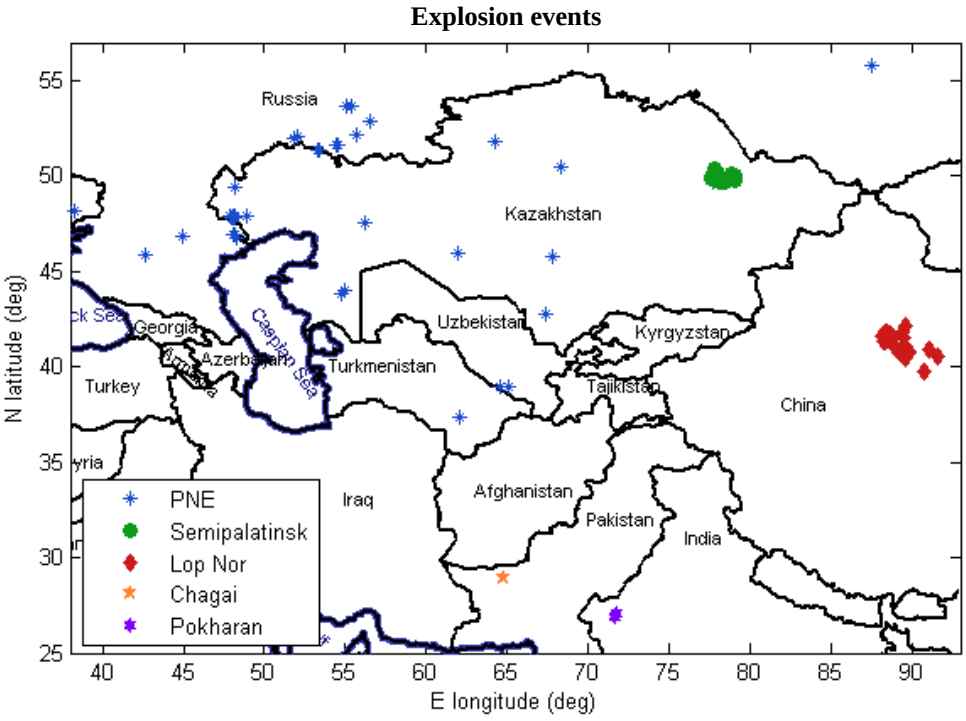


**Figure 4. Event locations for explosion data collected during the CASRI project. Data from peaceful nuclear explosion (PNEs) will provide ray paths in the seismically quiet north Kazakhstan region.**

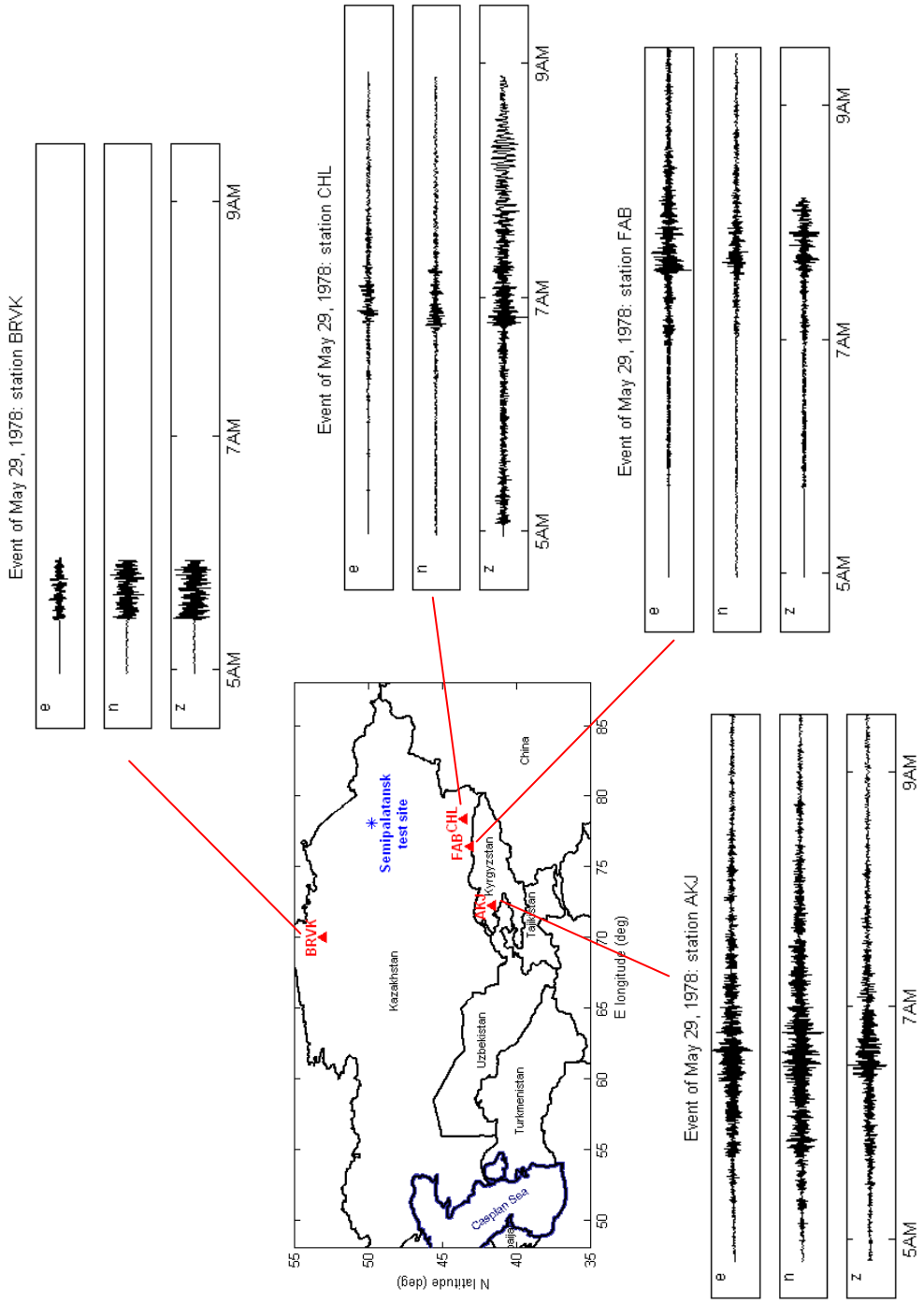


**Figure 5. A nuclear test carried out at the Semipalatansk test site on May 29, 1978, recorded at four stations in Kazakhstan and Kyrgyzstan. The data provide ground truth in tomographic studies of the crust, since the exact position of the source is known.**

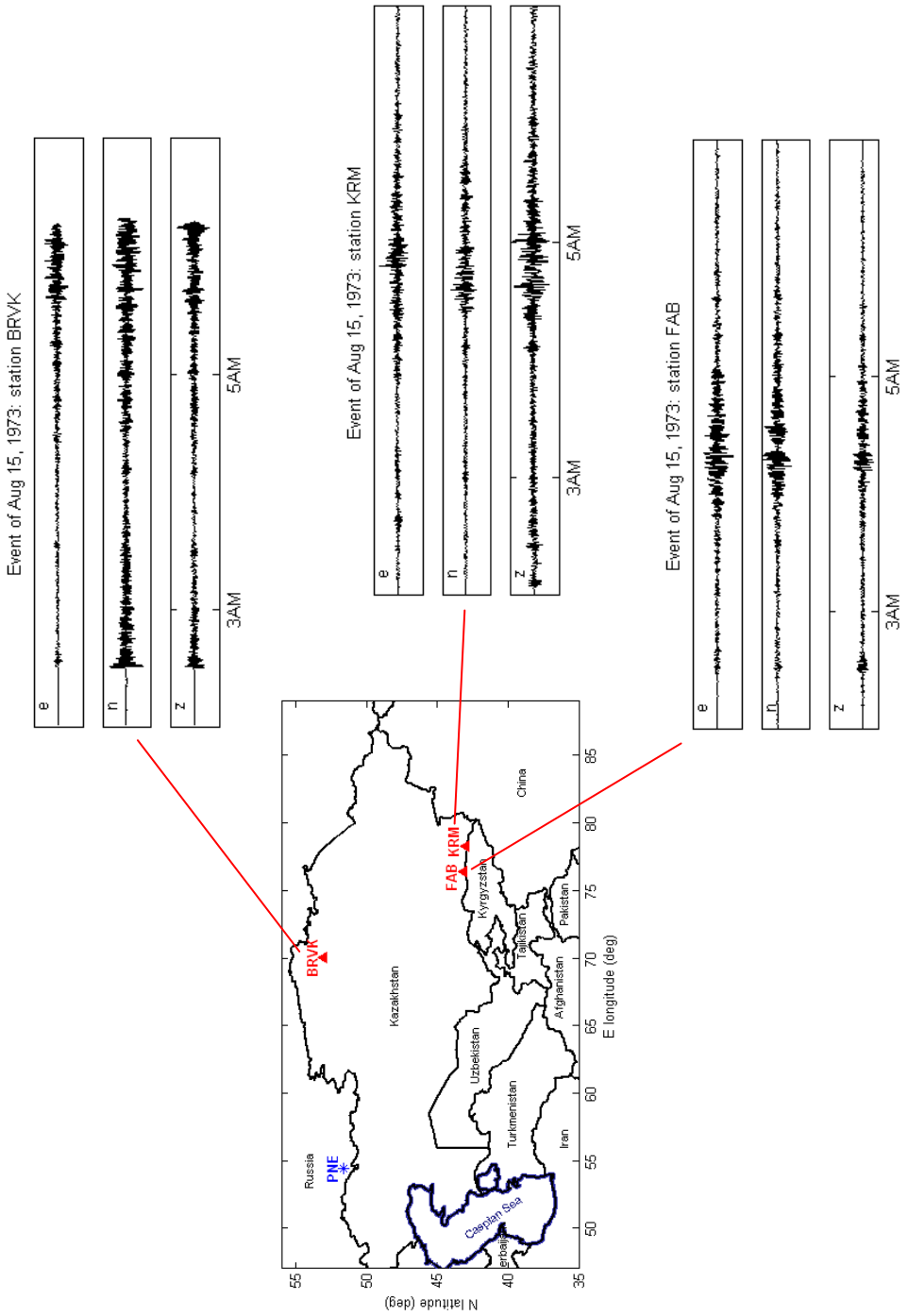


**Figure 6**. **A peaceful nuclear event (PNE) carried out in southern Russian on August 15, 1973, recorded at three stations in Kazakhstan. In addition to providing ground truth, PNE data include ray paths in the seismically quiescent area of northern Kazakhstan.**

# HIGH-RESOLUTION SEISMIC VELOCITY AND ATTENUATION MODELS OF THE CAUCASUS-CASPIAN REGION

Robert Mellors[1], Rengin Gök[2], Michael Pasyanos[2], Gleb Skobeltsyn[3],
Ugur Teoman[4], Tea Godoladze[5], and Eric Sandvol[3]

San Diego State University[1], Lawrence Livermore National Laboratory[2], University of Missouri[3], Kandilli Observatory and Earthquake Research Institute, Turkey[4], and Seismic Monitoring Center, Georgia[5]

Sponsored by Air Force Research Laboratory

Contract Nos. FA8718-07-C-0007 and DE-AC52-07NA27344
Proposal No. BAA07-18

## ABSTRACT

The southwest edge of Eurasia is a tectonically and structurally complex region that includes the Caspian and Black Sea basins, the Caucasus Mountains, and the high plateaus south of the Caucasus. Using data from 25 broadband stations located in the region, new estimates of crustal and upper mantle thickness, velocity structure, and attenuation are being developed. Receiver functions have been determined for all stations. Depth to Moho is estimated using slant stacking of the receiver functions, forward modeling, and inversion. Moho depths along the Caspian and in the Kura Depression are in general poorly constrained using only receiver functions due to thick sedimentary basin sediments. The best fitting models suggest a low velocity upper crust with Moho depths ranging from 30 to 40 km. Crustal thicknesses increase in the Greater Caucasus with Moho depths of 40 to 50 km. Pronounced variations with azimuth of source are observed indicating 3D structural complexity and upper crustal velocities are higher than in the Kura Depression to the south. In the Lesser Caucasus, south and west of the Kura Depression, the crust is thicker (40 to 50 km) and upper crustal velocities are higher. Work is underway to refine these models with the event-based surface wave dispersion and ambient-noise correlation measurements from continuous data. Regional phase (*Lg* and *Pg*) attenuation models as well as blockage maps for *Pn* and *Sn* are being developed. Two methods are used to estimate Q: the two-station method to estimate inter-station Q and the reversed, two-station, two-event method. The results are then inverted to create *Lg* and *Pg* Q maps. Initial results suggest substantial variations in both *Pg* and *Lg* Q in the region. A zone of higher Pg Q extends west from the Caspian between the Lesser and Greater Caucasus, and a narrow area of higher *Lg* Q is observed.

## OBJECTIVES

The Caucasus-Caspian region is an area of complex structure accompanied by large variations in seismic wave velocities and attenuation (e.g., Ritzwoller and Levshin, 1998; Murphy et al., 2005; Mitchell 1997). In such areas, accurate geophysical models are fundamentally important to nuclear monitoring. In particular, the great thickness and irregular geometry of the low-velocity and low-density sediments in the Caspian and Black Sea basins (e.g., Laske and Masters, 1997) creates profound effects on seismic waveforms, especially on surface waves and regional phases. These effects are compounded by variations in crustal structure in the Caucasus and by high attenuation under the East Anatolian plateau (Al-Lazki et al., 2003; Sandvol et al., 2001). Because regional models based on widely spaced stations may suffer from insufficient spatial sampling, we are developing comprehensive velocity and attenuation models using new broadband data that have become available in this area.

The primary focus is the Caucasus-Caspian region, which is roughly defined as lying between 40 and 55 E longitude and between 37 and 44 N latitude (Figure 1). A unified upper mantle/crustal velocity model will be developed using multiple techniques. In addition, the same data will be used to construct detailed maps of regional phase attenuation (Lg, Pg, Pn, and Sn). Finally, the results will be compared and validated using the various algorithms as well as independent datasets (local and regional events and active source studies).

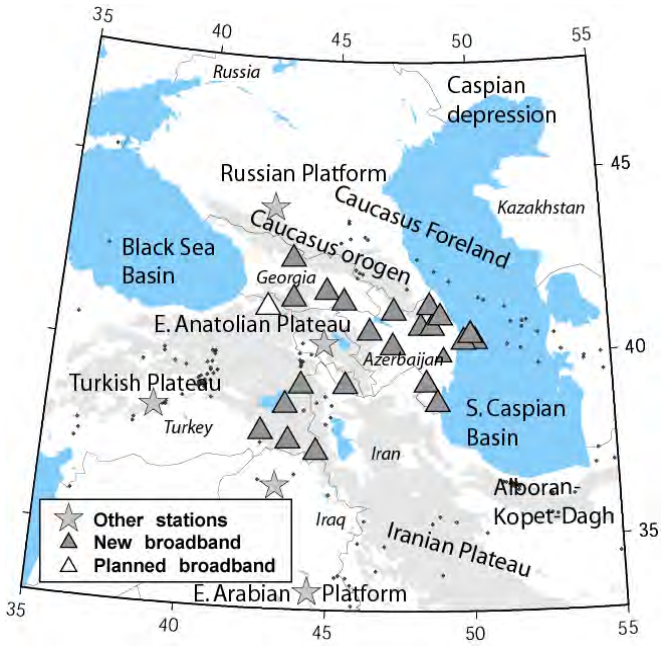


**Figure 1. Regional map showing newly available broadband stations (triangles) and two years (2003-2004) of earthquakes from the PDE catalog (small circles) to show distribution of regional events. Names and locations of geophysical regions are from Sweeney and Walter (1998).**

### Previous work

The region shows considerable spatial variability in travel times and phase propagation throughout the area (Table 1). Myers and Schultz (2000) noted errors of 42 km when locating events in the Caucasus Mountains with sparse regional stations and a standard model (prior to application of an empirical correction). They also noted that arrivals at regional distances are “strongly affected by upper-mantle-discontinuities.” Regional phase variations have been documented on a regional basis by a number of studies, but reliable direct-phase Q measurements are still lacking, mainly because of sparse station coverage and irregular distribution of earthquakes (e.g., Kadinsky-Cade et al., 1981; Rodgers et al., 1997a; Mitchell, 1997; Cong and Mitchell, 1998; Sarker and Abers, 1998; Baumgardt, 2001; Sandvol et al., 2001; McNamara and Walter, 2001; Gök et al., 2000; Gök et al, 2003). Here we summarize the regions and relevant seismic characteristics, where known.

The South Caspian and the Black Sea basins are thought to be underlain by oceanic crust, although it is possible that the South Caspian may simply be thinned continental crust overlain by thick sediments (Mangino and Priestly, 1998; Baumgardt, 2001). The great thickness (up to 20 km) of sediments in the South Caspian strongly affects surface waves as well, but efforts to resolve the situation by modeling higher frequency surface waves were inconclusive due to possible 3D effects (Priestley et al., 2001). Improved coverage and the use of ambient noise tomography should be useful in resolving this question. *Lg*, which is critical for discrimination purposes, is blocked by both the Black Sea and South Caspian basins. *Sn* does propagate through the South Caspian (Rodgers et al., 1997b; Sandvol et al., 2001). A large amount of active source data have been collected, which is useful for constraining the shallow velocity structure and depth of the sedimentary cover (Neprochnov et al., 1970; Belousov et al., 1992, Davies and Stewart, 2005; Knapp et al., 2004).

West of the Caspian in the Caucasus orogenic belt and foreland, events (Myers and Schultz, 2000) are subject to substantial travel-time anomalies at regional distances. It is unclear whether the *Lg* blockage observed in the South Caspian extends into the Greater Caucasus, as the available studies disagree. Rodgers et al. (1997b) and McNamara and Walter (2001) infer partial blockage of *Lg* in a belt extending from the Black Sea to the South Caspian. Alternatively, Sandvol et al. (2001) observe relatively efficient *Lg* propagation in the Caucasus and Central Caspian and attribute most of the attenuation to raypaths that cross the Anatolian plateau. Baumgardt (2001) reports unblocked *Lg* from Caucasus events to stations in Iran but blockage in the Caspian depression. The discrepancies among studies may reflect the poor station coverage with resulting poor resolution of ray paths. The crustal structure of this region still remains unclear given the lack of the data in the region. The boundary between the South Caspian and the Central Caspian is called the Absheron-Balkhan sill, an area of high seismicity and possibly of incipient subduction (Jackson et al., 2002; Brunet et al., 2003).

The South Caspian blends into the southern Caucasus in the Kura depression, a sedimentary basin with uncertain structure (i.e., is it an onshore extension of the South Caspian or is it underlain by continental crust?). Poor *Sn* propagation is evident throughout the Anatolian Plateau. The southern Caucasus (or Lesser Caucasus) differs from the Greater Caucasus to the north due to extensive Quaternary volcanism. Near the South Caspian, the southern Caucasus merges into the Alborz Mountain belt, an area of clear *Lg* propagation as well as *Pg* and *Pn*.

Until now, little broadband data has been available for the region. Relevant global stations exist in the S. Caucasus (GNI), Eurasian platform (KIV), east of the Caspian (ABKT) and to the south (MSL and BHD). A broadband array was temporarily installed in 1992 at ABKT and a broadband network was installed in the Caucasus from 1991 to 1994. A limited amount of broadband data was collected from a temporary deployment of broadband stations at three sites (LNK, BAK, and SHE) occupied during the two year Caspian Seismic Deployment. However, data return from these sites was limited and Mangino and Priestley (1998) presented receiver functions only from one station (LNK). Recently, permanent broadband stations have been deployed across the region as part of various national networks. Much of this data remains under the control of various institutes, and we are working with these institutes to analyze the data.

**Methods and data**

The work consists of four basic tasks: data collection, regional phase analysis, velocity model development, and model validation.

Regional phase analysis will define crustal and upper mantle propagation and attenuation within the region. By using the relatively dense coverage of broadband stations, we intend to construct a detailed map of regional phase propagation in and around the region (*Pg*, *Pn*, *Lg*, and *Sn*). The primary questions are: What is the lateral extent of *Lg* blockage in the South Caspian and Black Sea? How far and to what degree does it extend into the Caucasus? What are the boundaries of *Sn* propagation? Do we see effects due to the Central, North, and Pre-Caspian basins on *Lg*? Two methods will be used to isolate the regional wave path: the two-station method for measuring inter-station Q and the reversed two-station, two-event spectral-ratio method (Chun et al., 1987; Zor et al., 2007). This method has the advantage that we should be able to isolate the relative station response without having to assume that our response information is reliable. Once *Lg* Q has been measured, the results will be inverted to create *Lg* Q tomography maps, as is required for a regional phase-Q model. The rapid changes in *Lg* in the region require dense station spacing. The two-station methods will also be used to measure *Pg*, *Pn*, and *Sn* Q. Laterally varying *Pn* Q models are more difficult to develop than *Lg* or *Pg* Q models because *Pn* is observed only in a limited distance range (between ~2–14°), thus reducing the number of Pn paths available and making inversion difficult. However, it is

expected that the resulting blockage maps will be superior to existing maps. We will further refine our existing blockage maps for *Sn* (e.g., Sandvol et al., 2001) and then use to these to estimate a maximum allowable Q for those regions with *Sn* blockage.

In parallel with the attenuation work, crustal and upper mantle velocity structure will be determined using surface wave and receiver functions modeling. Results from the surface wave work and receiver functions will be jointly inverted for a unified model (Gök et al., 2006). Both phase and group velocities will be measured. The phase velocities will be event based (Forsyth et al., 1998). The ambient noise correlation will be measured using continuous data (Shapiro and Campillo, 2004). Pasyanos and Walter (2002) performed a study of surface wave group velocity dispersion across Western Eurasia and North Africa and a larger-scale study across Eurasia, North Africa, and the surrounding regions (Pasyanos, 2005) using 30,000 Rayleigh and 20,000 Love wave paths. We will be adding group velocity measurements to existing Rayleigh and Love measurements. Receiver functions are a well-established technique (e.g., Langston, 1979; Ammon et al., 1990; Zhu and Kanamori, 2000) that use teleseismic *P* (or *S*) phases to estimate crustal and upper mantle velocity structure in the vicinity of the seismometer. Mangino and Priestley (1998) applied receiver function analysis to the Caspian Seismic Experiment station LNK (near the current broadband station LKR) and found "considerable variation over fairly short horizontal distances." Their results under LNK showed a thinner crust and approximately 13 km of sediment over a high velocity mid to lower crust. As receiver functions are effective at identifying discontinuities, combining receiver function analysis with surface wave data is a powerful technique. The joint inversion method of Julia et al. (2000) will be used.

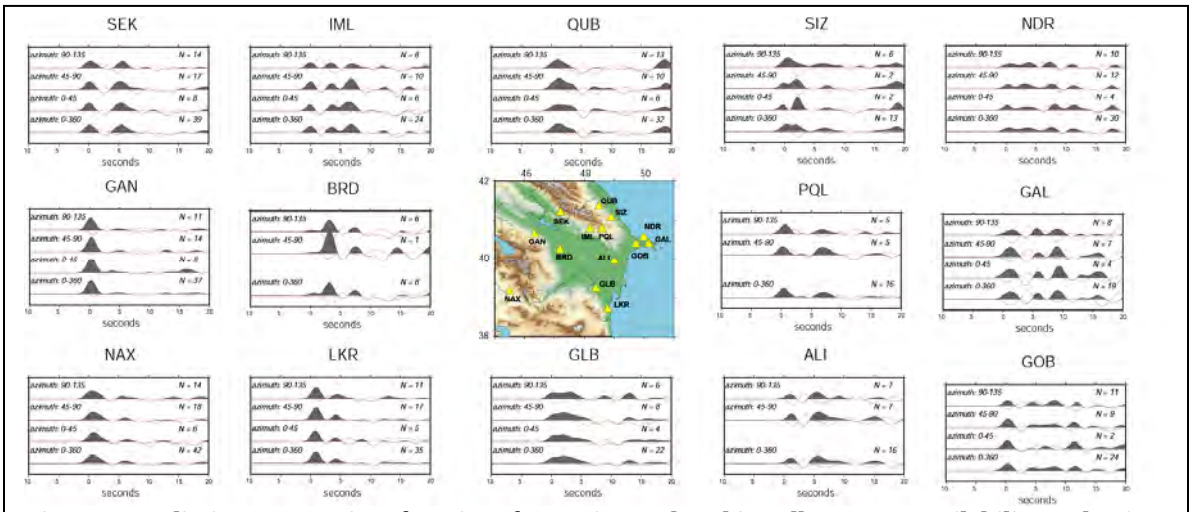


**Figure 2. Preliminary *P* receiver functions for stations colored in yellow. Data availability and noise levels vary from station to station, which results in varying numbers of events. Note great variability in phases and hence crustal structure across the region. Red line is tangential component.**

## RESEARCH ACCOMPLISHED

### Data collection

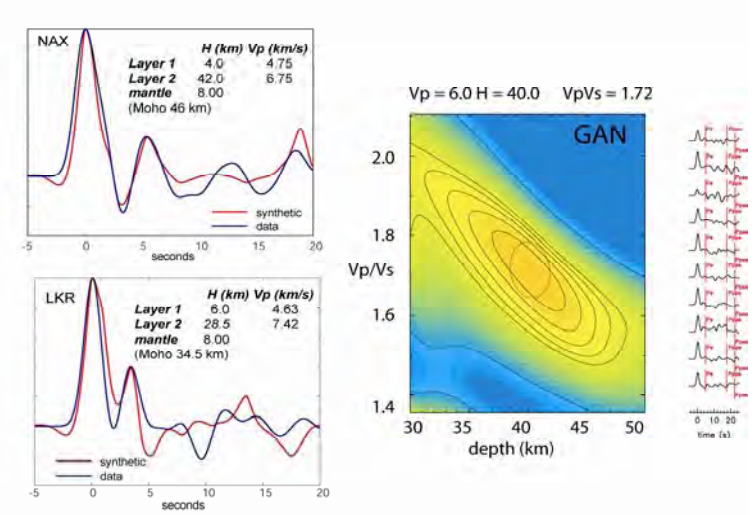


**Figure 3. Example of techniques used to estimate depth to Moho and crustal velocities. Upper right shows the depth/VpVs stack for station GAN. The figures on the left show the observed data (black) and results of a forward model (red).**

Both event data (triggered and windowed) have been collected for the years 2006 and 2007 for stations in all three networks. The data have a number of different sample rates and seismometer types. We have been working to reliably remove the instrument response for all stations in the KOERI, Azeri, and Georgian networks. The event data are used for receiver functions and surface wave analysis. The continuous data are collected for ambient noise tomography.

### Receiver functions

Receiver functions have been calculated for all stations (Figures 2 and 3). Teleseismic events with magnitude greater than 5.2 and at distance between 30 and 90 degrees were selected. Iterative deconvolution and a variety of filter windows were applied. Slant stacking (e.g., Zhu and Kanamori, 2000) was applied to all data to provide an estimate of the depth to Moho and VpVs ratio. In general, stations in areas with thick sediments and high noise levels (such as those near the Caspian) the PS converted phase at the Moho is not as clear and our slant-stacking process is not as well resolved. This is most likely due to the interference of multiples phases with the sedimentary basin.

Figure 4 shows the results of our slant stacking analysis. We plan to reduce the uncertainties and improve the reliability of the slant stacking with additional data from 2008 as well as adding results from the eastern portion of the Kandilli (KOERI) seismic network in eastern Turkey. We will also be adding new results from several of the broadband stations in Georgia. Overall our results seem to suggest that there is only a modest root beneath the Lesser Caucasus, similar to that observed in eastern Turkey (e.g., Zor et al., 2007). Our results also suggest that there may be a significant root beneath the Greater Caucasus; however, we only have a few stations on the southern edge of this mountain range.

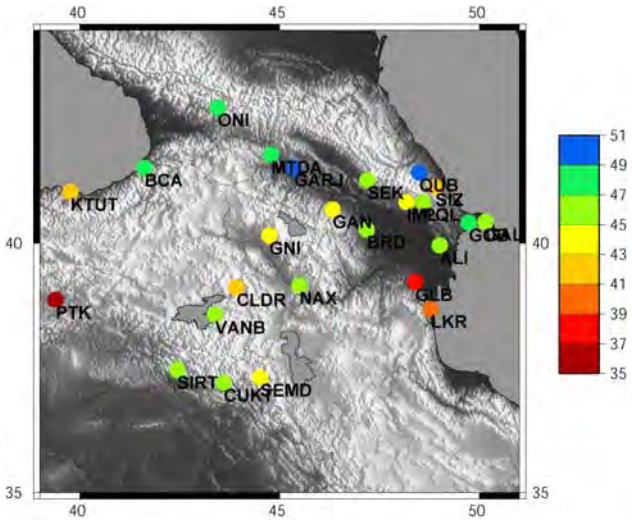


**Figure 4. Stations and estimated depths to Moho based on the stacking technique of Zhu and Kanamori (2000). These results include data from both the Kandilli and Azeri networks as well as the few Global Seismographic Network stations in the region.**

### Surface Wave Analysis

In addition to the receiver function analysis, we are analyzing surface waves in order to create a three dimensional

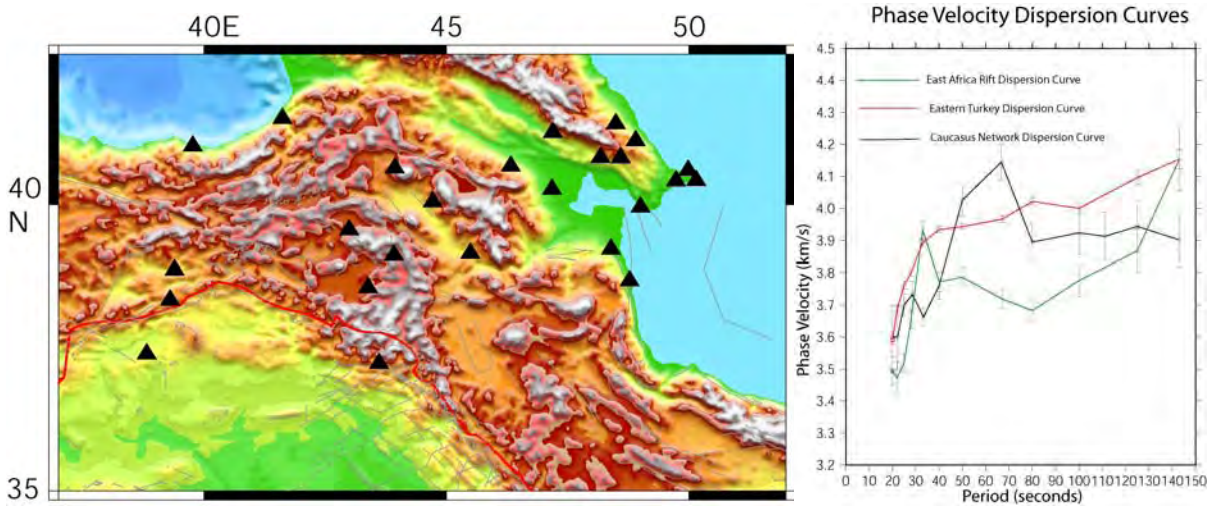


**Figure 5. The broadband seismic stations used in our initial surface wave analysis and the resulting optimal one-dimensional phase-velocity dispersion curve. This curve was generated using 15 teleseismic events and approximately 18 stations throughout eastern Anatolia and the Lesser Caucasus. These very preliminary results suggest the presence of a mantle lid beneath the Lesser Caucasus in contrast with the lack of a mantle lid observed in eastern Turkey (red curve).**

region velocity model for this region (Figure 5). We have measured phase velocities of Rayleigh waves in the period band 30–150 s using the two plane wave approach of Forsyth et al. (1998) and Yang and Forsyth (2006). Our initial data inversions for Rayleigh wave phase velocity used a grid with roughly 50 km spacing. This very preliminary model has a relatively high error because we have only analyzed approximately 6 months of data (15 events) recorded by both the Azeri and Kandilli networks. Despite the higher errors and the relatively few events analyzed, we have found preliminary evidence for an uppermost-mantle lower-velocity zone at about a 75-second period. This is in strong contrast with our phase-velocity measurements in eastern Turkey which do not show any evidence of a lithosphere-asthenosphere boundary.

### Regional Wave Attenuation

We have continued to update our *Lg* Q model using new two station paths from new stations in Azerbaijan and eastern Turkey and imposing a much more restrictive maximum and minimum distance requirement (Figure 6). Our updated frequency dependent Q models for both *Lg* and *Pg* have included approximately 4,000 waveforms from approximately 200 events recorded by 10 permanent and temporary networks throughout the Middle East.

We have found, similar to the previous models, efficient *Lg* propagation throughout much of the Arabian plate. We continue to find the lowest Qo values in the East Anatolian plateau (~70 to 100) and the East Anatolian Fault Zone (~80 to 120). The frequency dependent exponent for Lg is less than that of Pg in the Middle East. Resolution tests for Q tomography in our work indicate that we have very good resolution throughout much of the Anatolian Plateau. We also continue to observed evidence of modest-to-low Q throughout most of the lesser Caucasus. Our preliminary model is limited due to the elimination of events that cross the south Caspian Sea basin, thus blocking *Lg*. We do however observe some inefficient *Lg* paths that we are able to use to estimate *Lg* Q's in the Lesser Caucasus

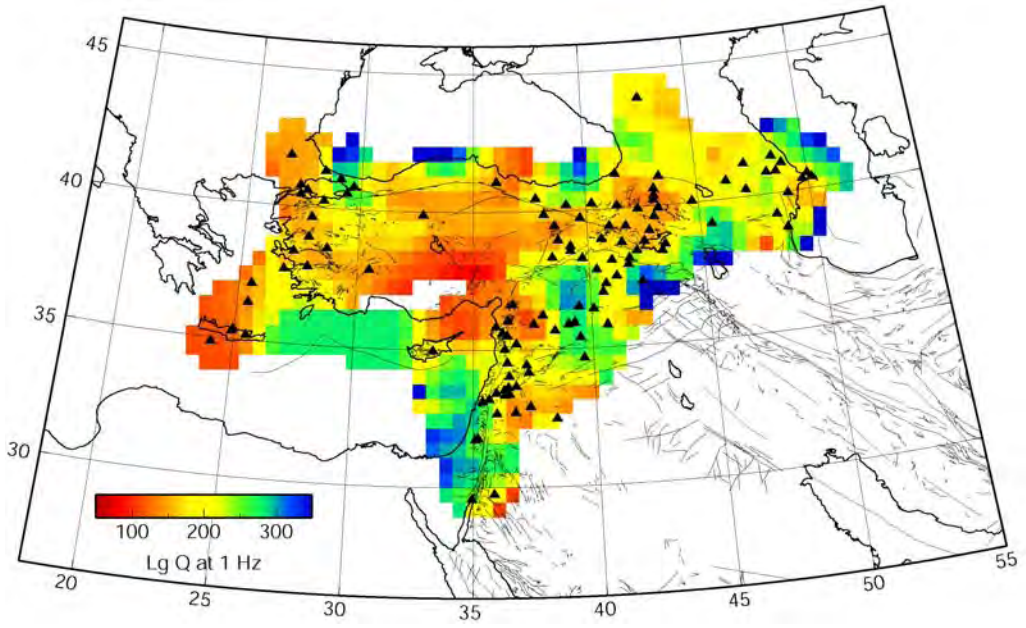


**Figure 6. Our updated two station *Lg* Q model for the Middle East using the new paths from eastern Turkey and Azerbaijan. The very high Q measurements (*Lg* Q > 300 are probably largely an artifact of a few unreliable paths crossing the northern Zagros and Caspian Sea regions.**

mountains. Additional paths are needed, however, as our model is still relatively unstable in northwestern Iran and the Caspian Sea. This can be seen by the relatively high *Lg* Q values that we are currently obtaining.

We have also made progress on estimating reliable *Lg* and *Pg* geometrical spreading terms by calculating high frequency synthetic seismograms in a 1D velocity structure using the finite difference and reflectivity methods. We used the synthetics to compute the geometrical spreading terms for a uniform Q crust.

## CONCLUSIONS AND RECOMMENDATIONS

Preliminary analysis of receiver functions shows clear consistency between events and the outlook is promising for this technique despite the complex structure and basin sediments. Results for station LKR are similar to those from the Mangino and Priestley (1998) study, which was situated near the same site. The uppermost mantle structure looks similarly very complex. The very different looking surface wave phase velocities that have been seen in eastern Turkey (Sandvol et al., 2004) compared with our initial results suggest that there is a change in lithospheric thickness from easternmost Anatolia to the Lesser Caucasus. The *Lg* attenuation also suggests a strong lateral variation in crustal attenuation from eastern Anatolia to the Lesser Caucasus. Our measurements suggest that the highest attenuation ($Q_{Lg}$ < 100) is restricted to easternmost Anatolia.

## ACKNOWLEDGEMENTS

R. Herrman, C. Ammon, and J. Julia provided software used in the analysis of this data.

## REFERENCES

Al-Lazki, A.I.,D. Seber, E. Sandvol, E.,N. Turkelli, R. Mohamad, and M. Barazangi (2003). Tomographic Pn velocity and anisotropy structure beneath the Anatolian plateau (eastern Turkey) and the surrounding regions, *Geophys. Res. Let.* 30: (24).

Ammon, C., J., G. E. Randall, and G. Zandt, (1990). On the nonuniqueness of receiver function inversions, *Jour. Geophys. Res.* 95: (10), 15,303–15,318.

Baumgardt, D. R. (2001). Sedimentary basins and the blockage of Lg wave propagation in the continents, *Pure Appl. Geophys*. 158: 1207–1250.

Belousov, V. V., N. I. Pavlenkova, and G. N. Kvyatkovskaya (1992). Structure of the crust and upper mantle of the [Former] USSR, *International Geology Review* 34: (3), 213-338.

Brunet, M.F., M. V. Korotaev, A. V. Ershov, and A. M. Nikishin (2003). The South Caspian Basin; a review of its evolution from subsidence modeling, *Sedimentary Geology* 156: 1–4; 119–148.

Chun, K.-Y., G. F. West, R. J. Kokoski, and C. Samson (1987). A novel technique for measuring Lg attenuation; results from Eastern Canada between 1 to 10 Hz, *Bull. Seismo. Soc. Am*. 77: (2), 398–419.

Cong, L. and B. Mitchell, (1998). Lg coda Q and its relation to the geology and tectonics of the Middle East. *Pure and appl. Geophys*, 153: 2-4, 563–585.

Davies, R. J. and S. A. Stewart (2005). Emplacement of giant mud volcanoes in the South Caspian Basin: 3D seismic reflection imaging of their root zones, *Jour. of the Geo. Soc*. 162: 1, pp. 1–4(4).

Forsyth, D. W., Webb, S. C., Dorman, L. M., Shen, Y. (1998). Phase velocities of Rayleigh waves in the MELT experiment on the East Pacific Rise, *Science* 280: 1235–1238.

Gök, R., N. Turkelli, E. Sandvol, D. Seber, and M. Barazangi, (2000). Regional wave propagation in Turkey and surrounding regions, *Geophys. Res. Let*. 27: 3, 429–432.

Gök R., E. Sandvol, N. Türkelli, D. Seber, and M. Barazangi (2003). Sn attenuation in the Anatolian and Iranian plateau and surrounding regions, *Geophys. Res. Lett*. 30: 24, 8042

Gök, R., M. E. Pasyanos and E. Zor (2006). Lithospheric Structure of the Continent-Continent Collision Zone: Eastern Turkey, submitted to *J. Geophys. Res*.

Jackson, J., Priestley, K., M. Allen, and M. Berberian (2002). Active tectonics of the South Caspian Basin, *Geophys. J. Inter*. 148: (2), 214–245.

Julia, J., C. Ammon, R. Herrman, and A. Correig, (2000). Joint inversion of receiver function and surface wave dispersion observations, *Geophys. Jour. Int*. 143: 1, 99–112.

Kadinsky-Cade, K., Barazangi, M., Oliver, J., and Isacks, B.(1981). Lateral variations of high-frequency seismic wave propagations at regional distances across the Turkish and Iranian plateaus, *J. Geophys. Res*. 86: 9377–9396.

Knapp, C., J. Knapp, and J. A. Connor (2004) Crust-scale structure of the South Caspian Basin revealed by deep seismic reflection profiling, *Marine and Petro. Geology* 21: 1073–1081.

Langston, C. A., (1979). Structure under Mount Rainier, Washington, inferred from teleseismic body waves. *J. Geophys. Res.* 84: 4749–4762.

Laske, G. and G. Masters (1997). A Global Digital Map of Sediment Thickness, EOS Trans. AGU: 78, F483.

Mangino, S and K. Priestley (1998). The crustal structure of the southern Caspian region, *Geophys. J. Inter*. 133: (3), 630–648.

McNamara, D. and W. Walter, (2001), Mapping crustal heterogeneity using Lg propagation efficiency throughout the Middle east, Southern Europe, and Northern Africa. *Pure Appl. Geophys*. 158: 1165–1188.

Mitchell, B. (1997). Lg coda variation across Eurasia and its relation to crustal evolution, *J. Geophys. Res* 102: (10), 22,767–22,779.

Murphy, J. R., W. Rodi, M. Johnson, D. Sultanov, T. Bennett, M. Toksoz, V. Ovtchinnikov, B. Barker, D. Reiter, A. Rosca, and Y. Shchukin, (2005), Calibration of International Monitoring System (IMS) Stations in Central and Eastern Asia for Improved Seismic Event Location. *Bull. Seismo. Soc. Am.* 95: (4): 1535–1560.

Myers, S. C., and C. A. Schultz, (2000), Improving sparse network seismic location with Bayesian kriging and teleseismically constrained calibration events, *Bull. Seismo. Soc. Am.* 90: (1), 199–211.

Neprochnov, Y. P., Kosminskaya, I. P., and Malovitsky, Y. P., (1970). Structure of the crust and upper mantle of the Black and Caspian seas, T*ectonophysics* 10: (5-6), 517–538.

Pasyanos, M.E., and W.R. Walter, (2002), Crust and upper mantle Structure of North Africa, Europe, and the Middle East from inversion of surface waves, *Geophys. J. Int*. 149: 462–480.

Pasyanos M.E., (2005), A variable resolution surface wave dispersion study of Eurasia, North Africa, and surrounding regions, .*J. Geophys. Res*. 110, B12301, doi: 10.1029/2005JB003749.

Priestley, K., H. Patton, and C. Schultz (2001), Modeling anomalous surface-wave propagation across the southern Caspian Basin, *Bull. Seismo. Soc. Am*. 91: (6), 1924–1929.

Ritzwoller, M.H. and A.L. Levshin (1998). Eurasian surface wave tomography: Group velocities, *J. Geophys. Res.* 103: 4839–4878.

Rodgers, A. J., T. Lay, W. Walter, K. M. Mayeda, (1997a). A comparison of regional-phase amplitude ratio measurement techniques, *Bull. Seismo. Soc. Am.* 87: (6), 613–1621.

Rodgers, A. J., J. F. Ni, T. M. Hearn, (1997b). Propagation characteristics of short-period Sn and Lg in the Middle East, *Bull. Seismo. Soc. Amer*. 87: (2), 396–413.

Sandvol E., Seber, Barazangi, M., Vernon, F., Mellors, R., and Al-Amir, A.,(1998). Lithospheric velocity discontinuities beneath the Arabian Shield, *Geophys. Res. Lett*. 25: 2873–2876.

Sandvol, E., K. Al-Damegh, A. Calvert, D. Seber, M. Barazangi, Mohamad, R, R. Gök, N. Turkelli, and C. Gurbuz, (2001). Tomographic imaging of Lg and Sn propagation in the Middle East, *Pure. App. Geophys.* 158, 1121–1163.

Sarker, G. and G. A. Abers (1998). Deep structures along the boundary of a collisional belt: attenuation tomography of P and S waves in the Greater Caucasus. *Geophysical Journal International* 133 (2), 326-340. doi: 10.1046 j.1365-246X.1998.00506.x,.

Shapiro, N. M. M. Campillo, L. Stehly, and M. H. Ritzwoller (2005). High resolution surface wave tomography from ambient seismic noise, Science, 307(5715), 1615-1618.Sweeney, J., and W. R. Walter, 1998, Preliminary definition of geophysical regions for the Middle East and North Africa, UCRL-ID-132899 Lawrence Livermore National Laboratory Report, 38 pp.

Sweeney, J. and W. R. Walter (1998), Preliminary definition of geophysical regions for the Middle East and North Africa, UCRL-ID-132899, LLNL (http://www.llnl.gov/tid/lof/documents/pdf/235042.pdf).

Yang, Y. And Forsyth, D., (2006). Regional tomographic inversion of the amplitude and phase of Rayleigh waves with 2-D sensitivity kernels, *Geophys. J. Int*. 168: 1148–1160.

Zhu, L., and H. Kanamori (2000). Moho depth variation in Southern California from teleseismic receiver functions, *J. Geophys. Res*. 105: (2), 2969–2980.

Zor, E., E. Sandvol, J. Xie, N. Türkelli, B. Mitchell, A. Gasanov, and G. Yetirmishli.,(2007). Crustal Attenuation within the Turkish Plateau and Surrounding Regions, *Bull. Seism. Soc. Am.* 97: 151–161.

# SYNTHETIC SEISMOGRAM STUDY OF THE EASTERN CENTRAL ANDES

Estela Minaya, Evanz Lázaro, Percy Aliaga, Magaly Gonzalez, and Wilfredo Cano

Observatorio San Calixto

Sponsored by the Air Force Research Laboratory

Contract No. FA8718-07-C-0009

## ABSTRACT

Along the South American coast, there have been several earthquakes of great magnitude—between 7.5 and 9.5 Mw, with ruptures 50 km to 950 km long, producing maximum intensities between VII and X (MM)—particularly in two seismic gaps located in southern Peru and northern Chile. In these places, two large earthquakes occurred in the 19th century, in 1868 and in 1877, establishing the possibility of the seismic gap hypothesis: *earthquake hazard increases with the time since the last large earthquake of long rupture length occurred, forming a seismic gap at whose ends will occur seismic activity of small magnitude and minor rupture length* (Kelleher, 1972). In 1995, 2001, and 2007, earthquakes occurred within the limits of both gaps. They were felt and had light effects in cities in western Bolivia, especially in La Paz. Of major magnitude, they occurred within the limits of gaps located in the coupling zone of the Nazca and the South American plates.

The above-mentioned earthquakes were here used to generate the characteristics of the 19th-century earthquakes. The effects of such an earthquake today would be catastrophic for the city of La Paz, situated in a basin with rugged topography, abrupt slopes, a geology of slightly compacted and highly eroded soils, and a complex hydrology of surface and underground rivers. Completing the picture are expanding, disorganized demographics. The city could be highly vulnerable to an earthquake with characteristics of the 19th-century events.

The EGF method (Empirical Green Function, Irikura, 1986) was applied to an earthquake in Peru on 15/08/2007 and an aftershock on 16/08/2007, registered at the LPAZ station. Numerical analyses of the synthetic and principal seismograms (short period) show a correlation for frequencies lower than 10 Hz and predominance between 0.05 and 2.5 Hz.

## OBJECTIVES

To estimate, from synthetic seismograms, the effects in the Central Andes of earthquakes that have taken place at intermediate depths on the coast of Peru and Chile, and specifically to estimate local intensities in the most vulnerable areas. To verify through this research estimates of attenuation. To increase understanding, and capacities for regional monitoring, of earthquakes in the Central Andes and surrounding areas.

## RESEARCH PERFORMED

The area of study is located in the Eastern Central Andes, in the region where the Nazca Plate subducts at 30º dip the South American Plate (along the trench). The area is characterized by Morpho-tectonic variations transversal to the coastline summarized by the following Morpho-tectonic units: Forearc, Western Cordillera, Altiplano, Eastern Cordillera, Sub Andean, and Foreland (Lamb et al., 1997; Gregory-Wodzicki, 2000). See Figure 1.

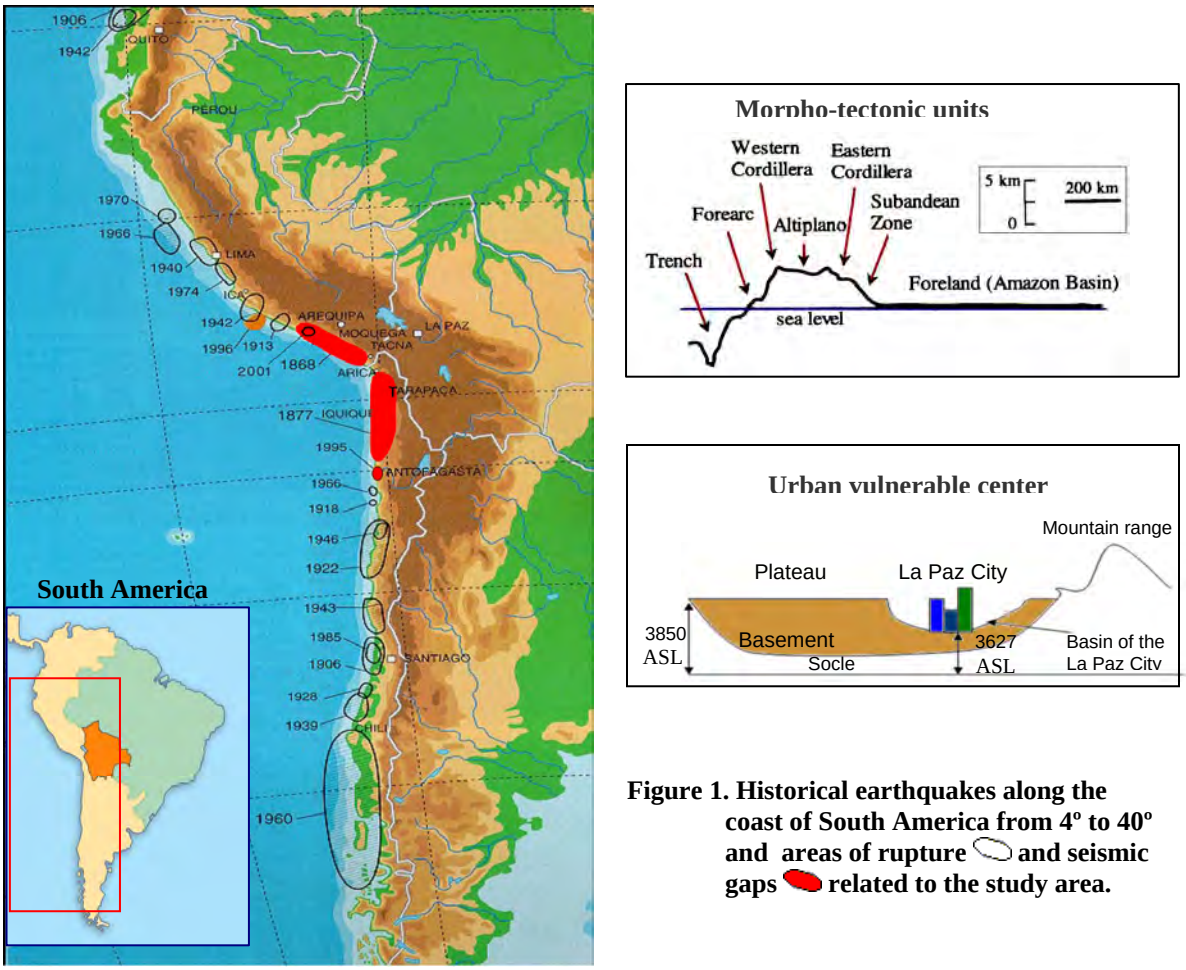


**Figure 1. Historical earthquakes along the coast of South America from 4º to 40º and areas of rupture and seismic gaps related to the study area.**

The seismic history of the South American coast between 4º and 40º south reveals the relative frequency of occurrence for earthquakes of magnitudes 7.5 to 9.5 Mw, lengths of rupture between 50 km and 950 km, and maximum intensities near epicenter of VII to X (MM). In some zones, moreover, it is possible to apply the seismic gap hypothesis: *the hazard of an earthquake increases with the time since the last large earthquake produced a very long rupture within which seismic activity of small magnitude and short rupture length will occur at the ends* (Kelleher, 1972). It is possible to apply this hypothesis to two earthquakes that occurred in the 19th century, in 1868 and in 1877, the main earthquakes in this study (Figure 2).

Earthquakes occurred on 30/07/1995 and 23/06/2001 at the ends of the gaps of the earthquakes previously mentioned that reinforce the probability of the hypothesis that great earthquakes could occur in each seismic gap with characteristics similar to the 19th century earthquakes, and whose effects in the urban centers of Bolivia's western region could be catastrophic. This evaluation of the geological conditions of urban centers in the Eastern Central Andes permitted selection of one of the more vulnerable cities, La Paz (Figure 1).

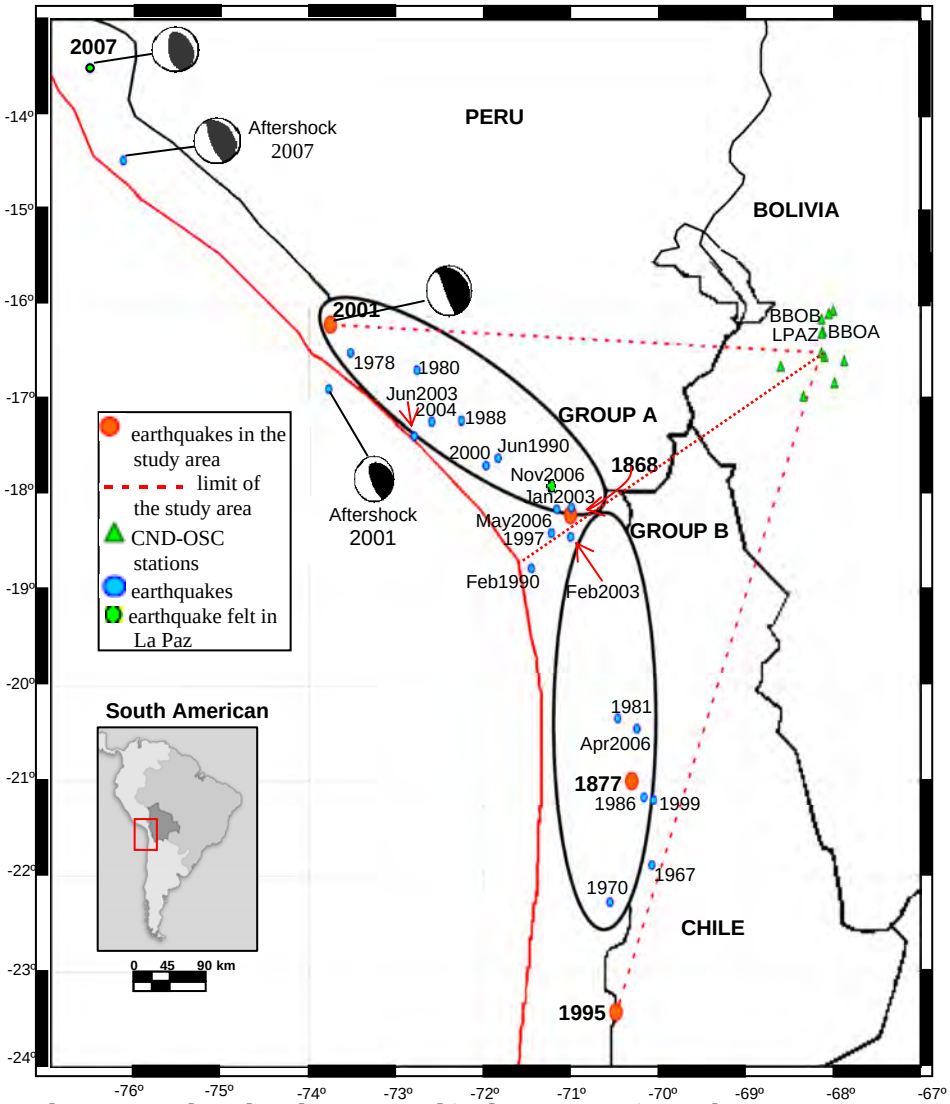


**Figure 2. Study area: earthquakes that occurred in the two gaps, in southern Peru (group A) and in northern Chile (group B); earthquakes felt in La Paz. See Table 1.**

**Geological Conditions of La Paz**

The city of La Paz,, situated between the Altiplano and the Western Cordillera, occupies an erosion basin formed by intense glaciation processes. These processes have generated topography that is highly sloped and, in some places, very rugged. See Figure 3.

Soils in La Paz are heterogeneous sediments, poorly consolidated, classified into three types of rocks: a base level formed by Paleozoic (Devonian) and Mesozoic (Cretaceous) rocks; a layer above of lacustrine sediments of the La Paz Formation (1.8–0.01 Ma); and sediments produced by four processes of glaciation that correspond to the Miraflores Formation (Figure 3). The basin is crossed by approximately 200 rivers and tributaries, whose flows have generated the high slopes (Figure 3).

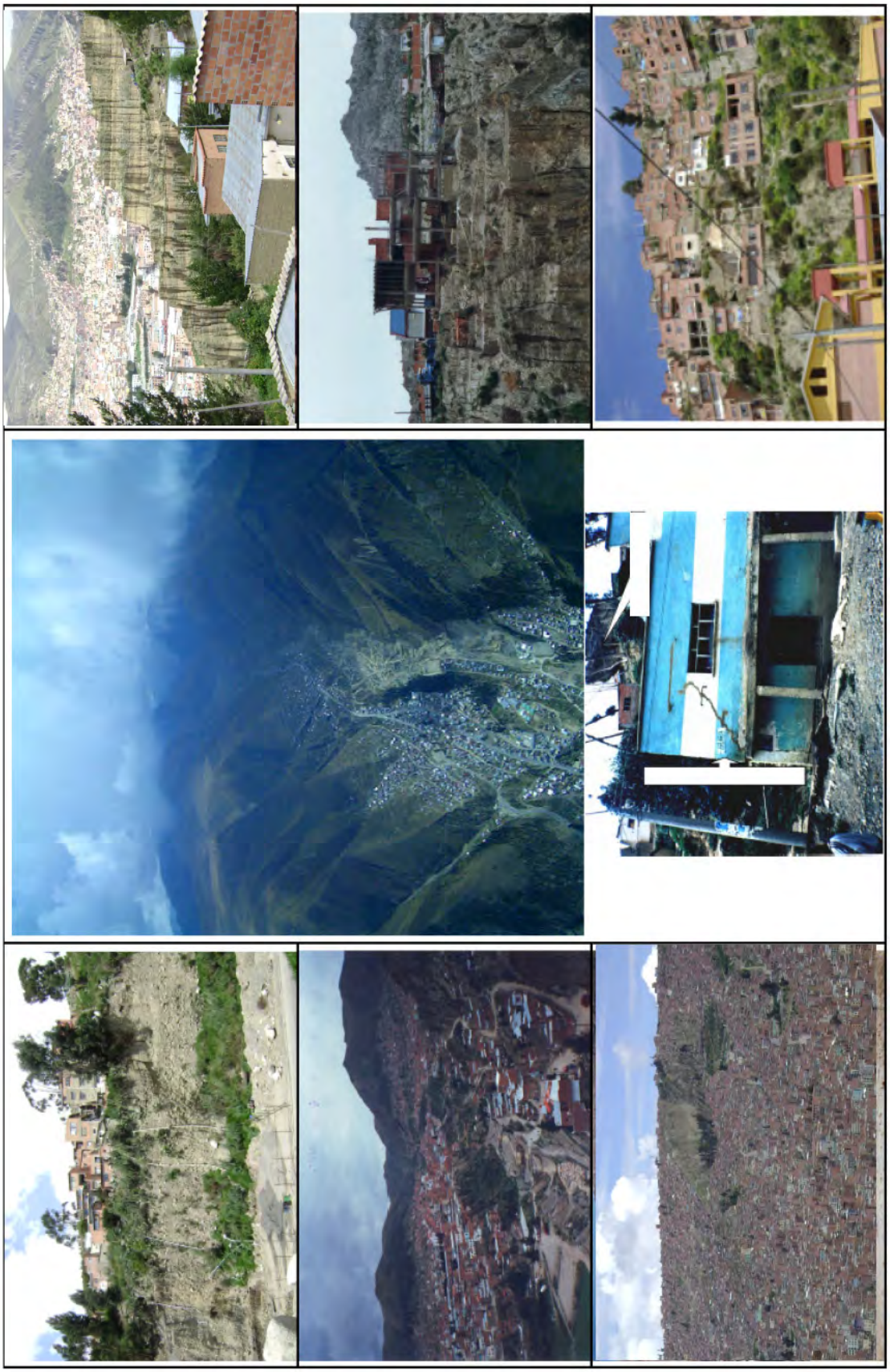

**Figure 3. Geological conditions of La Paz.**

These geological, hydrogeological, and geomorphological conditions increase the vulnerabilities generated by excessive urban expansion with few controls on construction and human settlements.

**Data Selection**

Groups A and B in Table 1 and Figure 2 correspond to the earthquakes that occurred in the southern Peru and northern Chile gaps, respectively. Selection corresponded to meeting the following criteria: an interplate earthquake; a seismic event of major magnitude (≥4.5 Mw); and effects felt in La Paz, as occurred during the 2007 earthquakes.

The first part of the evaluation was to characterize the differences and similarities between the earthquakes of groups A and B and the earthquakes of major magnitude of 23/06/2001 and 30/07/1995, using records of the LPAZ and BBOA stations belonging to CND-OSC. The results, shown in Figure 4, correspond to the evolution over time of the frequency content (spectrogram) and FFT (Fast Fourier Transform), specifying the predominant frequencies associated with the source and trajectory of the seismic waves.

To apply Irikura's methodology, we selected the major earthquakes of 23/06/2001 and 15/08/2007 and their aftershocks of 25/06/2001 and 08/08/2007 (Table 1). Records from the BBOB and LPAZ stations were considered for both earthquakes.

**Table 1. Earthquakes occurring in the seismic gap and felt in La Paz, with aftershocks.**

| Group | Date | Time | Latitude [°] | Longitude [°] | Depth [km] | Mw |
|---|---|---|---|---|---|---|
| A | 13/08/1968 | 22:00:00.00 | -18.00 | -70.50 | 25 | 9 |
| | 15/04/1978 | 13:49:30.80 | -16.50 | -73.52 | 39 | 5.3 |
| | 07/03/1980 | 8:25:09.30 | -16.68 | -72.76 | 53 | 5.9 |
| | 12/04/1988 | 23:19:55.40 | -17.21 | -72.25 | 30 | 6.9 |
| | 08/06/1990 | 13:49:22.70 | -17.60 | -71.83 | 25 | 5.6 |
| | 13/04/1997 | 23:20:33.90 | -18.39 | -71.22 | 37 | 5.5 |
| | 03/08/2000 | 19:22:08.10 | -17.68 | -71.97 | 7 | 5.8 |
| | 23/06/2001 | 20:33:14.10 | -16.27 | -73.64 | 30 | 8.4 |
| | 25/06/2001* | 6:38:47.90 | -16.88 | -73.77 | 38 | 5.7 |
| | 03/06/2003 | 23:58:02.80 | -17.37 | -72.79 | 33 | 5.9 |
| | 09/01/2003 | 7:02:57.70 | -18.12 | -70.99 | 32 | 5.3 |
| | 16/09/2004 | 14:48:52.70 | -17.22 | -72.59 | 47 | 5.4 |
| | 25/05/2006 | 20:48:05.41 | -18.14 | -71.16 | 34 | 5.6 |
| | 20/11/2006 | 14:38:15.00 | -17.92 | -71.22 | 35 | 5.5 |
| | 15/08/2007 | 23:40:57.89 | -13.39 | -76.60 | 39 | 8 |
| | 16/08/2007* | 11:35:41.79 | -14.29 | -76.21 | 35 | 6 |
| B | 10/05/1877 | - | -21.00 | -70.30 | 40 | 9 |
| | 21/12/1967 | 2:25:21.00 | -21.89 | -70.07 | 20 | 6.0 |
| | 19/06/1970 | 10:56:13.50 | -22.28 | -70.55 | 44 | 6.1 |
| | 21/06/1981 | 10:30:00.90 | -20.34 | -70.46 | 35 | 5.3 |
| | 20/02/1986 | 9:16:03.80 | -21.17 | -70.16 | 55 | 5.5 |
| | 10/02/1990 | 3:34:32.00 | -18.76 | -71.45 | 37 | 4.6 |
| | 30/07/1995 | 05:11:23.60 | -23.34 | -70.29 | 46 | 8.0 |
| | 17/02/1999 | 21:58:54.30 | -21.20 | -70.05 | 30 | 5.6 |
| | 20/02/2003 | 20:07:05.10 | -18.43 | -71.00 | 29 | 5.6 |
| | 09/04/2006 | 20:50:46.02 | -20.45 | -70.24 | 34 | 5.8 |

* Aftershocks

Parameters: ISC until 2004 and NEIC until 2007

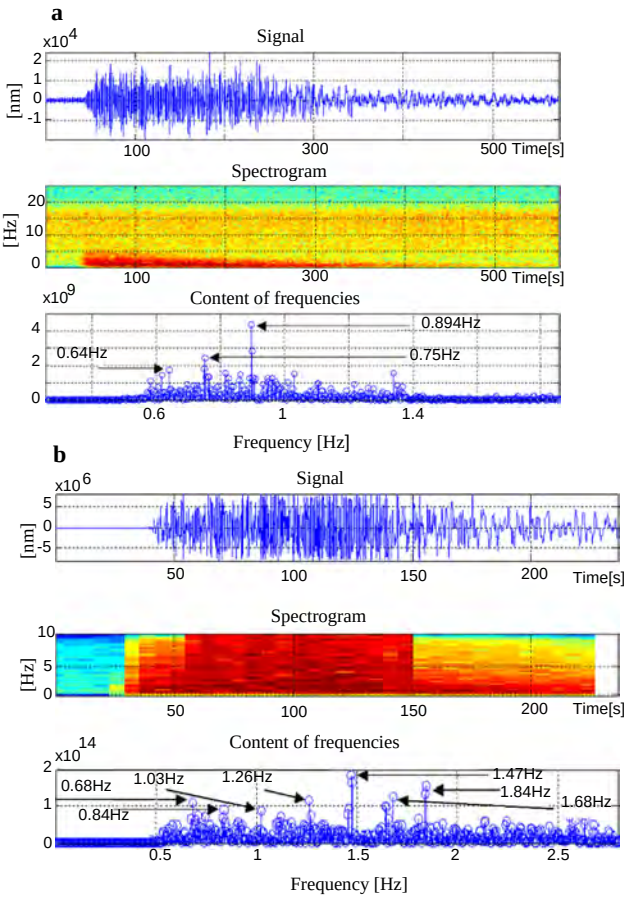


**Figure 4. (a) The 07/30/1995 main shock recorded at station BBOA CPZ-D: top, seismogram; middle, spectrogram; bottom, content of frequencies. (b) The 06/23/2001 main shock recorded at the LPAZ station: top, seismogram; middle, spectrogram; bottom, content of frequencies.**

**Generation of Synthetic Seismogram**

The methodology applied in this study was developed by Irikura (1986). The main idea is to use a Green Function on a small earthquake (aftershock or foreshock) to generate a synthetic seismogram corresponding to the main earthquake. This methodology has the advantage over other methods that it does not require numerical treatment of propagation and site effects (Kamae and Irikura, 1998). The aftershock must meet two requirements to be selected: first, it must be near the main earthquake's hypocenter; and second, it must have a focal mechanism similar to that of the main earthquake. The small earthquake is named the **element,** and its record plays the role of the Green Function.

Because earthquakes of the 19th century were not recorded, this methodology is applied to earthquakes with minor characteristics occurring in the gaps, and the results allow us to generate records of these earthquakes.

The earthquake element broken out is a small area called the subfault. An NxN array of subfaults generates an area of the same dimensions as the main earthquake fault, and each subfault generates a synthetic signal. Using the law of scaling and an omega-square model, it is possible to superimpose all these subfault signals to generate synthetic signals for the main earthquake.

The methodology applies the following relations (Irikura, 1986):

$$s(t) = C\sum_{i=1}^{N}\sum_{j=1}^{N}\left(\frac{r}{r_{ij}}\right)F\left(t - t_{ij}\right) * u(t), \quad t_{ij} = \frac{r_{ij} - r_o}{\beta} + \frac{\xi_{ij}}{V_R} \qquad (1)$$

where *u(t)* is the record of the earthquake element, C is a constant obtained from the spectral relation between the main and element earthquakes, $r_{ij}$ is the distance from the subfaults (i,j) to station, $r$ is the distance from the element earthquake to station, $t_{ij}$ is the time delay, $r_o$ is the distance from the start point of the rupture to the station, $\xi_{ij}$ is the distance between the subfaults (i,j) considering one of them as a start point, $\beta$ is the velocity of the shear wave , and $V_R$ is the rupture velocity. *F(t)* is defined as

$$F(t) = \delta(t) + \frac{1}{n}\sum_{k=1}^{(N-1)n}\delta\left(t - \frac{(k-1)\tau}{(N-1)n}\right), \qquad \tau = \frac{16\,S^{1/2}}{7\pi^{3/2}\beta} \qquad (2)$$

where $\delta(t)$ is the Dirac delta function, *n* is an integer selected to displace the fictitious period $\tau/(N-1)$ to a level out of range of the frequencies of interest, k is the subindex of the summation, N is the number of subfaults (Figure 5), $\tau$ is the rise time associated with the stress accumulated before the rupture (Géller, 1976), $\beta = 3.7\ [km/s]$ is the velocity of the shear wave (theoretical value), and S is the area of the rupture.

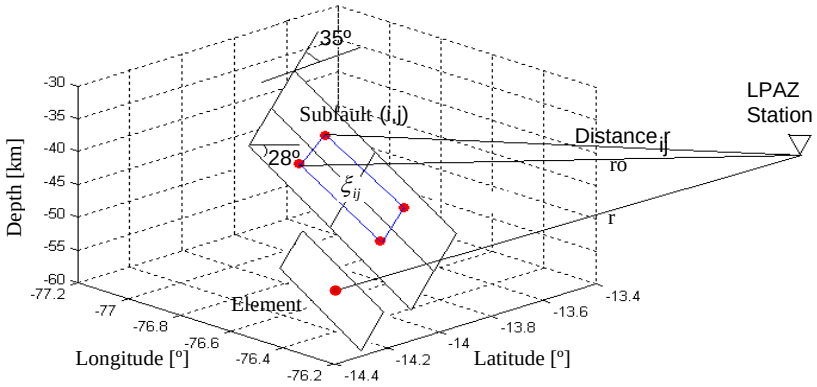


**Figure 5. Geometric array of NxN subfaults and fault parameters.**

An initial test of this methodology was applied to the main earthquake of 23/06/2001 and its aftershocks of 25/06/2001 using earthquake records at the BBOB station, whose record was saturated for the main earthquake and

did not allow us to generate a synthetic seismogram. The earthquake will be analyzed with records at the LPAZ station in the future. Table 2 presents fault parameters and results.

The second earthquake treated occurred on 15/08/2007, with aftershocks on 16/08/2007. Registered at the LPAZ station, the earthquake was located outside and to the north of the gap in Peru; it was considered because it was felt in La Paz and could allow validation of the Irikura methodology. Fault parameters and results are shown in Table 2 and Figures 6 and 7.

**Table 2. Fault parameters and results.**

| Fault parameters | | |
|---|---|---|
| **Earthquakes:** | **23/06/2001** | **15/08/2007** |
| Strike | 310 [º] | 325 [º] |
| Dip | 18 [º] | 28 [º] |
| Rupture Length | 320 [km] | 150 [km] |
| Velocity S | 3.7 [km/s] | 3.8 [km/s] |
| Rupture Velocity | 2.96 [km/s] | 1.43 [km/s] |
| Time Rise | 25.1 [s] | 16 [s] |

| Results | | |
|---|---|---|
| **Earthquakes:** | **23/06/2001** | **15/08/2007** |
| Subfaults Array | 16 | 4 |
| Corner Frequencies | 1.5 Hz, (Main)<br>3.92 Hz (Element) | 156 Hz (Main)<br>2.97 Hz (Element) |
| N | 4 | 2 |
| C | 235 | 2.3 |

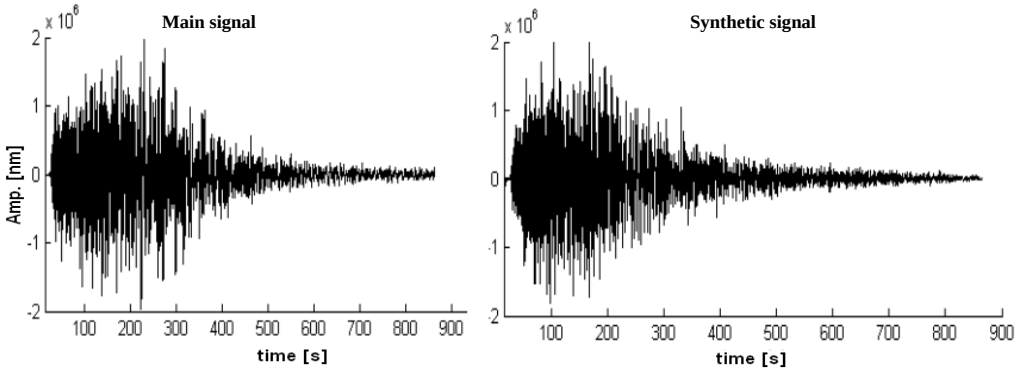


**Figure 6. Signal of the main earthquake recorded in SHZ at LPAZ station and the synthetic signal for the earthquake.**

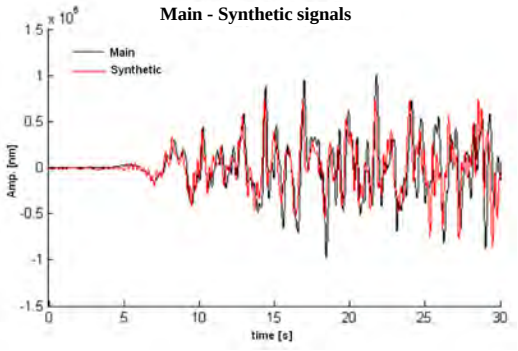


**Figure 7. Extended window of 30 [s] to correlate the synthetic and main signals.**

## CONCLUSIONS

The earthquakes of 30/07/1995 and 23/06/2001 that occurred at the ends of the gaps confirm part of the seismic gap hypothesis.

The La Paz basin has rugged topography and poorly consolidated soils, with uncontrolled human settlement and unregulated construction significantly contributing to increased vulnerability.

Differences in frequency content between the earthquakes of 30/07/1995 and 23/06/2001 are 0.5–1.4 Hz and 0.5–7 Hz. Spectral analysis shows greater frequency dispersion in the earthquake of 23/06/2001 (Peru), which corresponds to a more complex trajectory than the 1995 earthquake (Chile).

To model a synthetic signal with characteristics associated with the 19th-century earthquakes, we tested the method of EGF developed by Irikura (1986), a robust tool that helps solve problems of trajectory and site response, using aftershocks in the Green Function. This methodology was first applied to the earthquake of 23/06/2001, but the results are incomplete.

The second application was to the 15/08/2007 earthquake, recorded over a short period at station LPAZ. Seismograms of the main earthquake and the synthetic seismograms have the same correlations for frequencies less than 10 Hz and frequency predominance between 0.05 and 2.5 Hz.

## REFERENCES

Geller R.J., (1976). Scaling relations for earthquake source parameters and magnitudes. *Bull. Seismol. Soc. Am*. 66: 5, 1501–1523

Gregory-Wodzicki K. M., 2000. Uplift history of the Central and Northern Andes, *Review Geol. Soc. Am. Bull.* 112: 7, 1091–1105.

Irikura, K., (1986). Prediction of strong acceleration motion using Empirical Green's Functions, Pto 7th Japan Eartq. Eng. Symp, pp. 151–156.

Kamae, K., and K. Irikura, (1998). Source model of the 1995 Hyogo-Ken Nanbu earthquake and simulation of near-source ground motion, *Bull. Seismol. Soc. Am*. 88: 400–412.

Kelleher, J.A. (1972). Rupture zones of large South American earthquakes and some predictions, *J. Geophys. Res.* 77: 2087–2103.

Lamb, S., L. Hoke, L. Kennan, and J. Dewey (1997). Cenozoic evolution of the Central Andes in Bolivia and northern. *Geological Society Special Publication*, 121: 237–264.

# PNE CODA ATTENUATION AND SCATTERING PARAMETERS IN NORTHERN EURASIA

Igor B. Morozov

University of Saskatchewan

Sponsored by National Nuclear Security Administration

Contract No. DE-FC52-05NA26609
Proposal No. BAA05-52

## ABSTRACT

Magnitude-yield calibration of Northern Eurasia can be improved by using the large chemical and Peaceful Nuclear Explosion (PNEs) seismic datasets acquired by the Soviet Deep Seismic Sounding (DSS) program. Currently, we are using inversion and numerical modeling to analyze the coda amplitude parameters and *P*-wave travel times from numerous DSS explosions, which would lead to a detailed empirical mapping of seismic properties within northern Eurasia.

In this report, PNE *Lg* coda amplitudes from seven profiles are inverted to produce maps of the following new coda parameters: 1) frequency-dependent scattering intensities, 2) geometrical parameter ($\gamma$), and 3) effective quality ($Q_e$). The $\gamma$ and frequency-independent $Q_e$ parameters replace the traditional frequency-dependent $Q(f) = Q_0(f/f_0)^{\eta}$ parameterization and provide stability, independence of assumptions of a background model, and convenience in interpretation. As we have shown before, parameter $\gamma$ also yields itself to independent numerical waveform modeling, correlates with crustal tectonic types, and may be a portable attribute valuable for coda regionalization. All three maps show notable correlations with regional tectonics and with recently derived maps of phase amplitude ratios and *Lg Q*.

## OBJECTIVES

The correct and transportable measurement of attenuation parameters is critical in coda magnitude studies. Recently (Morozov et al., in press) we showed that short-period coda attenuation of regional arrivals can be interpreted in terms of the geometrical spreading ($\gamma$) and effective attenuation ($Q_e$) parameters. Taken together, they represent the generalized attenuation coefficient: $\alpha(f) = \gamma + \pi f/Q_e$. This model removes the commonly observed ambiguity of the frequency-dependent $Q(f)$, and parameter $\gamma$ becomes most useful for interpretation. Modeling of *P*-wave coda at regional distances and analysis of two Peaceful Nuclear Explosions in Russia in terms of this concept showed a remarkable agreement, particularly in the values of $\gamma$.

In this report, we apply the same parameterization to the inversion of spatially-variable surface-consistent *Lg* coda parameter $\alpha(f)$ from five PNE profiles in Siberia. Minimalistic model parameterization and the Constrained Simultaneous Iterative Reconstruction Technique (SIRT) are used for unbiased inversion. The resulting map of the geometrical parameter ($\gamma$) is in excellent agreement with both modeling and inversion in Morozov et al. (in press). The values of $\gamma$ differentiate between the crustal tectonic types within the study area and are also in agreement with a summary of over forty worldwide studies (Morozov, in press). In addition, scattering amplitudes are found to be highly variable and strongly correlate with geological structures. Coda $Q_e^{-1}$ values also show pronounced correlations with geological structures, although these values may also be somewhat overestimated compared to two detailed PNE point studies by Morozov et al. (in press).

## RESEARCH ACCOMPLISHED

### Rationale

Geophysical characterization of the Earth's lithosphere broadly consists of descriptions of its velocity, density, and attenuation structures. Combinations of these parameters are used in a broad range of applications, from providing structural and rheological constraints for geodynamics to event location, discrimination of seismic events, calibration and regionalization. For the first two of these parameters, a variety of precise methods have been developed, but *in situ* attenuation remains notoriously difficult to measure and interpret. In particular, while quality parameter ($Q$) often showing strong frequency dependence, characterization of such frequency-dependent attenuation ($Q(f)$) may be ambiguous and dependent on model assumptions and inversion methods.

Morozov (in press) recently proposed a new technique for measuring attenuation without the use of the ambiguous $Q(f)$ and illustrated it on a number of examples. In this study, we employ this method to invert coda $Q$ values from five Peaceful Nuclear Explosion (PNE) profiles in Russia and to map the frequency-dependent attenuation across a broad area of Siberia (Figure 1).

Different types of attenuation (body, surface, *Lg*, and coda waves) are often presented in the following power-law form of frequency-dependence:

$$Q(f) = Q_0\left(f \big/ f_0\right)^{\eta}, \qquad (1)$$

where $Q$ is the apparent quality parameter, and $f_0$ is some reference frequency often taken to equal 1 Hz (Aki, 1980). However, as argued by Morozov (in press) and Morozov et al. (in press), parameters of such a power-law dependence may be strongly influenced by the observation process, and in particular by the assumptions made about the geometrical spreading of scattered (in the case of coda $Q$) or other waves. Parameters $Q_0$ and $\eta$ trade off with each other through the uncertainty of the assumed geometrical spreading. The geometrical spreading (GS), in its turn, cannot be considered constant within large areas, and ~10% uncertainties in it can account for much of the observed frequency dependence of the apparent $Q$ (Morozov, in press). Unconstrained variations of GS also make it difficult to correlate attenuation parameters from different regions, and also to link them to lithospheric properties. In seismic calibration and nuclear test monitoring studies, uncertainties in $Q_0$, $\eta$, and geometrical spreading are particularly undesirable, because they prevent the construction of consistent, seamless models of large areas, and complicate magnitude calibration.

Numerical waveform coda modeling (Morozov et al., in press) showed that for a layered 1-D model with a constant, frequency-independent crustal attenuation, the observed coda $Q(f)$ exhibited a strong dependence on frequency. Although such dependence is often observed in coda $Q$ and $Lg$ $Q$ data (e.g., Der et al., 1986; Campillo, 1987, 1990; Frankel, 1990; Mitchell and Cong, 1998; Benz et al., 1997; Mitchell et al., 1997; McNamara et al. 1996; McNamara, 2000; and Erickson et al., 2005), this modeling shows that it may relate to the crustal structure (particularly to layering) and not necessarily to its rheology, fracturing, or fluid content. Similar observations were made earlier by Anderson et al. (1965) for long-period surface waves and by Mitchell (1991) for $Lg$ waves in the Basin and Range. Strictly speaking, because the values of $Q$ and $\eta$ trade off with the imprecisely known velocity/density structures, these parameters are not necessarily be associated with attenuation properties and may not reliably correlate with geological structures or with the variations of the physical state of the lithosphere. However, the potential association of the widespread observations of frequency-dependent $Q(f)$ with variations of the structure still has not been examined , and values of $Q$ are typically interpreted as related to rheology, physical state, or fluid content of the lithosphere (e.g., Mitchell et al., 1997).

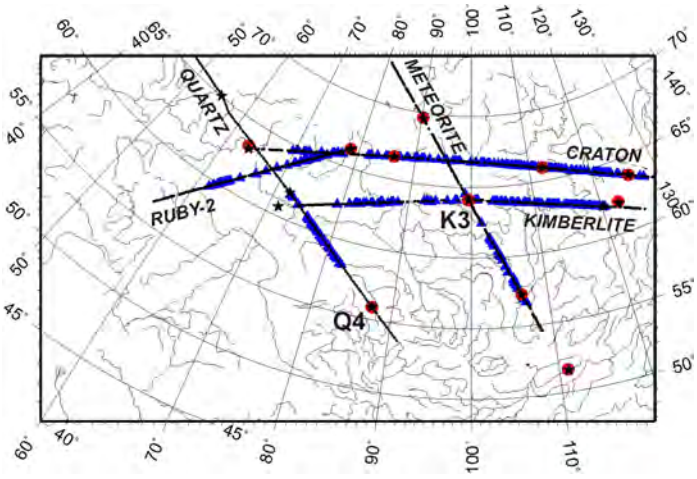


**Figure 1. Sources (red circles) and receivers (blue triangles) with measured frequency-dependent coda *d*ln(Amplitude)/*dt* derivatives. Black stars are the PNEs, and small black triangles – 3-component receiver locations. Only 3° grid cells containing sources or receivers were used in the inversion. Two PNEs used in Part I are indicated: Q4 - Quartz-4, and K3 – Kimberlite-3 (see also Figure 2).**

In the practice of $Q(f)$ interpretations, and in particular in $Lg$ coda $Q$ studies (such as coda magnitude calibration), the sensitivity of coda $Q$ to the frequency is usually overcome by referencing the coda $Q(f)$ dependence to some common frequency level, such as 1 Hz, in all comparisons (e.g., Mitchell et al. 1997; Phillips et al., 2004). However, this still does not resolve the problem of $Q(f)$ ambiguity, as such referencing process depends on the velocity structure through parameter $\eta$, making the resulting values less portable. Note that because of the inherent dependence of the results on unconstrained GS, changes in inversion approaches sometimes also lead to updated values of $Q_0$ and $\eta$ (for example, indicated by Xie et al. (2006) in relation to Mitchell et al. (1997) or Xie (2002) in relation to McNamara et al., (1996)). Thus, the interplay of the assumed forms of GS and power-law $Q(f)$ in dependence (1) creates a difficult environment for measurements and interpretation of attenuation.

In many coda $Q$ and $Lg$ $Q(f)$, and particularly in nuclear test monitoring studies, $Q$ is treated as a sort of coda-shape or spectral-amplitude shape parameter. When used strictly for matching the observed time-frequency dependent amplitudes, the above model works even with imprecise or even arbitrary GS. However, the ability of matching the amplitudes still does not prove that the propagation model is correct and can be used to constrain the crustal and mantle properties. This problem is well-known in the inversion theory – under-constrained (or over-parameterized) models tend to fit the data perfectly while leaving ambiguities in the solution (Menke, 1989). When interpreting such solutions and comparing them to each other, it is important to avoid using parameter combinations that are related to the unconstrained degrees of freedom. Unfortunately, both $Q_0$ and $\eta$ in eq. (1) are such parameters, which co-vary with the unconstrained GS.

To resolve this difficulty of intermixed GS and attenuation effects and the resulting apparent character of $Q(f)$, we proposed (Morozov, in press, and Morozov et al., in press) to incorporate a geometrical spreading parameter $\gamma$ in the following equation for coda amplitude decay:

$$A(t, f) = A_0(f) t^{-\nu} e^{-\alpha(f)t} = A_0(f) t^{-\nu} e^{-(\gamma+\kappa f)t}, \qquad (2)$$

where $\kappa = \pi/Q_e$, and $\nu$ is the theoretical GS exponent corresponding to the type of scattered wave modes that is considered as predominant. Arguments for form (2) based on the scattering theory were given by Morozov

(unpublished); however, this expression can also be viewed as a purely empirical approximation (Morozov et al., 2006; Morozov, in press). The subscript "*e*" in $Q_e$ indicates the "effective" character of the quality parameter, in which we do not differentiate between the intrinsic attenuation and small-scale (Rayleigh- and Mie-type) scattering. Note that parameter $\kappa$, and consequently also $Q_e$, can be frequency-dependent. However, no indications of such dependence were found in several published examples of *Lg*, and body-wave data (Morozov, in press), and also in surface-wave and normal-oscillation data (Morozov, unpublished).

In parameterization (2), the two parameters ($Q_0$, $\eta$) of the power law (1) are replaced with three: $\nu$, $\gamma$ and $\kappa$. Within the typical errors of spectral observations, there is little room for seeking frequency-dependent $\gamma$ or $\kappa$, and they can therefore be considered frequency-independent. Morozov (in press and unpublished) re-examined several surface-, body-, *Lg*-, and coda-wave studies and showed that model (2) was invariably applicable to all of them. In most cases, this resulted in significant increases of the reported values of *Q*.

Parameter $\nu$ significantly trades off with $\gamma$, and therefore it is acceptable to use amplitudes $A(t, f)$ corrected for geometrical spreading with fixed $\nu$ values determined from theoretical considerations, as it is commonly done in $Q(f)$ studies. In such cases, parameter $\gamma$ describes the spatial variations of uncompensated geometrical spreading. In the case of regional *Lg* coda *Q* of this study, we use a model of cylindrically-propagating coda waves generated within the near-surface. In this case, the spreading area of scattering surrounding the source and/or receiver compensates the geometrical spreading of coda waves, and $\nu$ can be set equal to 0 (Morozov and Smithson, 2000). However, this is only a simplified model, and, for example, diving and reflected scattered waves, deeper, or multiple scattering would change the $t^{-\nu} \approx 1$ law, and make it regionally variable. Our objective in this study is to measure these variations, in the form of a spatially-variant $\gamma$.

Parameter $\gamma$ was found to correlate with lithospheric types and ages; in particular, the value of $\gamma_D = 0.008$ s$^{-1}$ appeared to clearly separate the tectonically stable ($\gamma < \gamma_D$) and active areas ($\gamma > \gamma_D$; Morozov, in press). In addition, numerical modeling of the regional *P*-wave coda conducted in several PNE-based models (Morozov et al., in press) showed that the modeled $\gamma$ was in a close agreement with the measurements from PNE data, and coda *Q* could be related to the S-wave crustal $Q_S$. Therefore, it is particularly interesting to look for correlations of $\gamma$ with geological structures across a large contiguous area like the PNE profiling area of this study.

From the viewpoint of the classical scattering theory (e.g., Chernov, 1960, p.53; Nikolayev, 1968), parameterization (2) is merely a return to the traditional frequency-dependent attenuation coefficient $\alpha(f)$ instead of the "scattering quality" parameter $Q_s$ introduced by Aki (1980). Dainty (1981) gave a justification for expression (2) as describing scattering of 1-30-Hz *S*-wave on larger scatterers. In coda *Q* studies, such scattering could occur by means of diving, reflected, and mode-converted waves propagating through the crust. Note that such processes mostly involve deterministic effects, such as ray bending in crustal velocity gradients and reflections from major lithospheric structural contrasts, and therefore the use of $Q_s$ leads to undesirable connotation of random scattering and loss of correlation with the structure. Therefore, instead of using $Q_s$, we prefer using the uncompensated GS, which simply represents the frequency-independent part of the attenuation coefficient: $\gamma = \alpha(f=0)$.

Preliminary analysis of two PNEs (Figure 1; Morozov et al., in press) suggested that $\gamma$ values could be remarkably stable, even in the case of surprisingly strong frequency dependence ($\eta \approx 1$) within the Siberian Craton. The observed values of $\gamma$ also agreed well with those derived from waveform synthetics computed for the study area. We argued that $\gamma$ could potentially provide a stable and transportable criterion for correlating the observations of attenuation with crustal tectonic types.

In this paper, we further apply the approach arising from parameterization (2) to mapping the short-period attenuation structure in central Siberia by using several PNE datasets (Figure 1). Detailed descriptions of the PNE profiles and geological setting of the study area were recently given by Li et al. (2007 and submitted to BSSA) and are not repeated here. The resulting $\gamma$ and $Q_e$ maps show good stability and correlations with velocity structures and tectonics. Because the parameters being mapped are directly related to crustal and upper mantle properties, they should also provide a good basis for comparisons to other studies and for incorporation into forward modeling.

## Data

The dataset consists of log-amplitude coda amplitude readings from the PNE explosion records from five Deep Seismic Sounding profiles in Russia (Figure 1). Figure 2 shows an example of transverse-component (relative to the

source-receiver direction) record from PNE Kimberlite-3 (labeled K3 in Figure 1) located near the edge of the Siberian Craton. Note the high density of recordings (10-15 km spacing) and the differences in the wavefield propagating within and beneath the West Siberian Basin (west of the PNE) and the Siberian Craton (Figure 2).This PNE was also used in detailed studies by Morozov et al. (in press).

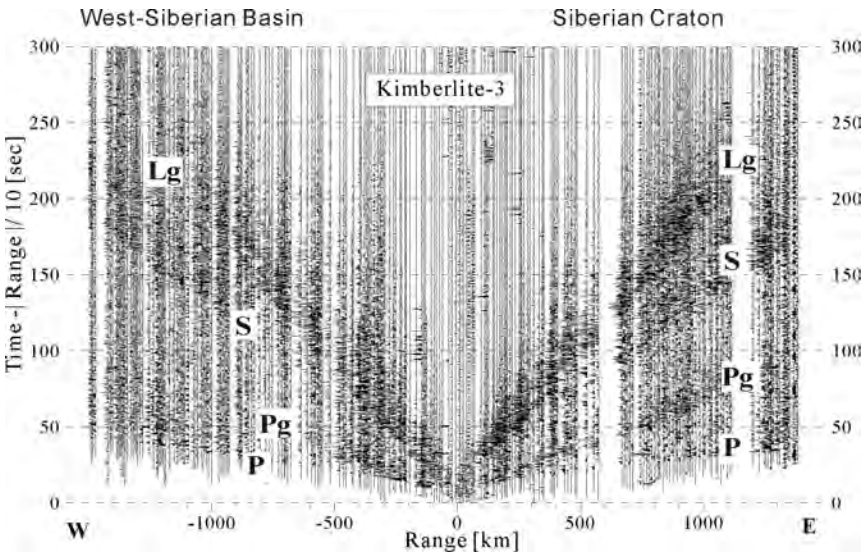


**Figure 2. Transverse-component record from PNE Kimberlite-3 (K3 in Figure 1), filtered within 0.5 - 8.0 Hz pass-band. The regional phases (labeled *P*, *Pg*, *S*, and *Lg*) are clear and observed to far source-receiver distances. Note the difference between the branches of *Lg* in two directions from the PNE.**

The data were carefully edited by removing poor and clipped records, and all regional arrivals were identified and picked. The *Lg* distance ranges and time windows were selected interactively from all PNE record sections. Coda windows started 20 sec after the picked *Lg* onsets and extended for 50 – 100 sec. Pre-*Lg* noise windows (i.e., the *P*- and *S*-wave coda; cf. Morozov and Smithson, 2000) were also picked. By using these windows, *Lg* to pre-*Lg* amplitude ratios were calculated, and traces with these ratios below 1.1 were discarded.

Edited records were further band-pass filtered within four overlapping frequency bands of 1–2, 1.5–3, 2–4, and 3–5 Hz. Within each band, three-component trace envelopes were formed, and $d\ln(Amplitude)/dt$ derivatives and their standard error estimates were measured by using the "robust fit" technique in Matlab. The resulting values of frequency-dependent log-amplitude coda slopes were saved in a database which was used in the subsequent analysis.

## Surface-Consistent ($\lambda$,$\gamma$, $Q_e$) Inversion Method

The power and utility of the $\alpha(f)$ model is in its direct link to the observations (Morozov, in press). In the case of regional coda attenuation, coda $\alpha_c(f)$ simply becomes the negative time derivative of the logarithm of coda amplitude (2):

$$\alpha_c(f) = -\frac{d\ln A(t, f)}{dt}, \tag{3}$$

which can be measured by fitting the coda envelopes in each individual record. Because of the source-receiver reciprocity, the observed coda amplitude (2), and consequently $\alpha_c(f)$, contain contributions from scattering near the source and receiver. Spatial separation of these two areas and the corresponding differences in their $\alpha(f)$ values could be significant for mapping, particularly in the case of the long-range PNE sources. Thus, we need to invert the observed $\alpha_c(f)$ for spatial variations in $\alpha(f)$. To accomplish this, we use the surface-consistent approach, and represented $\alpha(f)$ as functions of the coordinates and frequency. The surface-consistent model implies that for the collocated source and receiver, the values of $\alpha(f)$ should be the same, and for spatially close locations, $\alpha(f)$ values are close.

To derive a model for the observed $\gamma$ and $Q_e$, we use an approximation for the event-energy envelope by Morozov and Smithson (2000), in which the intensity (energy density) of the primary event was described by a short pulse of parabolic shape arriving at time $t_0$, with amplitude $P_0$ and duration $\tau$. The coda of this arrival was described by exponentially decaying amplitude following the pulse:

$$P_{\text{coda}}(t,\lambda,\alpha)=\begin{cases}0, & t<t_0,\\ \lambda(f)P_0\pi e^{-2\pi f(t-t_0)/Q}=\lambda(f)P_0\pi e^{-2\alpha(f)t}, & t\ge t_0,\end{cases} \quad (4)$$

where $\lambda(f)$ is the scattering efficiency factor (the relative coda intensity at the time of the primary event). In general, this parameter may also depend on the frequency.

From PNE Quartz-4 records (Q4 in Figure 1), the duration of the primary onsets was estimated as $\tau = 1.25$ s for the teleseismic *P*, and $\lambda = 0.22$ for all events (Morozov and Smithson, 2000). The relative coda intensity at the time of the primary event was $\lambda\tau \approx 0.27$ (Equation [4]), which can be considered as significantly smaller than 1. Therefore, the total wavefield intensity at the receiver:

$$P_{SR}(t)=\left[P_{primary}(t)+P_{coda}(t,\lambda_S,\alpha_S)\right]*\left[P_{primary}(t)+P_{coda}(t,\lambda_R,\alpha_R)\right], \quad (5)$$

(quantities with subscripts *S* and *R* correspond to the source and receiver locations, respectively, and the asterisk denotes time convolution) can be approximated to the first order in $\lambda$:

$$P_{SR}(t)=P_{primary}(t)*P_{primary}(t)+P_{primary}(t)*\left[P_{coda}(t,\lambda_S,\alpha_S)+P_{coda}(t,\lambda_R,\alpha_R)\right]. \quad (6)$$

The resulting coda intensity is given by the second term in this expression:

$$P_{SR,coda}(t)\propto\lambda(x_S,y_S,f)e^{-2\alpha(x_S,y_S,f)t}+\lambda(x_R,y_R,f)e^{-2\alpha(x_R,y_R,f)t}, \quad (7)$$

where we also assumed surface consistency of $\lambda$. From eq. (2), $\alpha(x,y,f)$ is further approximated by a linear function of frequency:

$$\alpha(x,y,f)=\gamma(x,y)+\kappa(x,y)f, \quad (8)$$

Taking into account the source and receiver site effects, the coda intensity (7) is further approximated as:

$$P_{SR,coda}(t)\approx\zeta(f)e^{-2\alpha_c t}, \quad (9)$$

where $\zeta(f)$ is a time-independent amplitude normalization factor of the specific seismic record. With these approximations, eq. (9) leads to the following system of non-linear equations:

$$d_{n,t,f}=\lambda_S(f)e^{-2[\alpha(x_S,y_S,f)-\alpha_c]t}+\lambda_R(f)e^{-2[\alpha(x_R,y_R,f)-\alpha_c]t}-\zeta_n(f)=0 \quad (10)$$

for all *t*, *f*, and record numbers *n*. Solving equations (10) is equivalent to minimizing the following objective function:

$$\Phi(\gamma,\kappa,\lambda,\zeta)=\frac{1}{2}\sum_f\sum_n\int_{T_n}\left[\lambda_S(f)e^{-2[\alpha(x_S,y_S,f)-\alpha_c]t}+\lambda_R(f)e^{-2[\alpha(x_R,y_R,f)-\alpha_c]t}-\zeta_n(f)\right]^2dt, \quad (11)$$

where $T_n$ is the coda observation time window. The summation in eq. (11) takes place over all records and frequencies of interest, and the minimization is performed in terms of parameters $\gamma$, $\kappa$, $\lambda(f)$, and $\zeta(f)$. In this study, to improve the stability of the inverse, we did not consider the dependence of $\kappa$, $\lambda$, and $\zeta$ on frequency, and solved for variations of $\gamma$, $\kappa$, and $\lambda$ as functions of spatial coordinates only.

To define the spatial inversion grid for parameters $\gamma$, $\kappa$, and $\lambda$, care needs to be exercised in order to not over-parameterize the model excessively. To achieve a "minimalistic" parameterization, we defined a spatial grid with increments of 3° in both latitudes and longitudes covering the entire area of profiling. Only cells containing the actual source or receiver points (Figure 1) were included in the inversion, which resulted in 53 cells. For each of these selected grid cells, a bilinear basis function (finite element) $\psi_i(x,y)$ was defined (*x* was the longitude, *y* is the latitude, and *i* is the cell number), such that $\psi_i(x,y) = 1$ in its center and $\psi_i(x,y) = 0$ at the centers of all other cells.

"Blocky" basis functions typical in travel-time tomography (with $\psi_i(x,y) = 1$ within the entire cell) were also tried, with no significant differences in the results.

With properly defined basis functions, the following identity holds at any point ($x$, $y$):

$$\sum_i \psi_i(x, y) = 1, \tag{12}$$

where the summation includes all cells. With the help of this functional basis, values of $\gamma$, $\kappa$, and $\lambda$ at any point ($x$, $y$) can be expressed through the corresponding values ($\gamma_i$, $\kappa_i$, $\lambda_i$) at the nodes; for example, for $\gamma$:

$$\gamma(x, y) = \sum_i \psi_i(x, y)\gamma_i \,. \tag{13}$$

Within the class of functions given by the finite-element functional basis (13), the objective function (11) becomes a non-linear function of model parameters: $\Phi(\gamma_i, \kappa_i, \lambda_i, \zeta_n)$. However, unconstrained degrees of freedom are still present in this parameter space, such as an arbitrary scaling of parameters $\lambda$ and $\zeta$ in eq. (11) and source-receiver trade-off caused by non-uniform sampling of the model. These degrees of freedom are typically removed by regularization, which is performed by adding constraint terms to the objective function (11), for example:

$$\tilde{\Phi}(\gamma_i, \kappa_i, \lambda_i, \zeta_k) = \Phi(\gamma_i, \kappa_i, \lambda_i, \zeta_k) + \sum_k w_k \Psi_1(\gamma_i, \kappa_i, \lambda_i), \tag{14}$$

where functions $\Psi_1(\gamma_i, \kappa_i, \lambda_i)$ penalize various undesirable types of instabilities. However, this method of regularization requires a non-trivial selection of weights $w_k$ and biases the solution from minimizing the objective function (11) and satisfying equations (10). Most importantly, properties of the resulting constraints may be difficult to assess in order to evaluate their effects on the interpretation. Therefore, a simpler regularization scheme with readily interpretable constraints would be preferable.

In order to obtain a stable solution without being unbiased from the minimum of $\Phi(\gamma_i, \kappa_i, \lambda_i, \zeta_n)$, we utilized the iterative nature of the SIRT (Simultaneous Iterative Reconstruction Technique) solver that we employed. After each iteration, the solution was corrected to satisfy the following criteria:

1) $\lambda_i \geq 0$ and $\kappa_i \geq 0$ at all points. These constraints correspond to non-negative scattering amplitude and $Q$, respectively. Note that unlike $\kappa_i$, $\gamma_i$ can take both negative and positive values.

2) $\sum_i \lambda_i = N_{\text{grid}}$, where $N_{\text{grid}}$ is the total number of grid points involved in the inversion. This constraint was enforced by rescaling all values of $\lambda_i$ and removing the scaling invariance of the minimum of expression (11).

3) $\left|\lambda_i - \lambda_i^{\text{smooth}}\right| < \beta\lambda_i^{\text{smooth}}$, where $\lambda_i^{\text{smooth}}$ is the smoothed value of $\lambda_i$ derived by averaging the adjacent points (and excluding the $i$-th one), and $\beta$ is the tolerance parameter selected equal to 0.05 in our inversion. This criterion guaranteed that adjacent cells differ by no more than $\beta$ in terms of $\lambda_i$. Similar constraints were implemented for $\gamma_i$ and $\kappa_i$.

4) Additionally, similar constraints, for example: $\left|\lambda_i - \lambda_i^{\text{apriori}}(x, y)\right| < \beta' \lambda_i^{\text{apriori}}(x, y)$, could be added to keep the solution in the vicinity of some *a priori* model. Such constraints could be useful to remove instabilities at isolated points near the circumference of the model, or for extrapolation of the solution outside of the area of coverage. The *a priori* model can be parameterized at user-specified sets of support points between which the values of $\lambda^{\text{apriori}}(x, y)$ are linearly interpolated by using a Delaunay triangulation. However, we did not use such constraints in the solution presented below.

To invert for $\gamma_i$, $\kappa_i$, $\lambda_i$, and $\zeta_n$ numerically, we used the SIRT method by applying it directly to Equation 10. For a small parameter perturbation, these equations become:

$$d_{f,n,t} = d^0_{f,n,t} + \delta d_{f,n,t} = d^0_{f,n,t} + \left[\delta\lambda_S - 2t(\delta\gamma_S + f\delta\kappa_S)\right]e^{-2(\alpha_S - \alpha_c)t} + \left[\delta\lambda_R - 2t(\delta\gamma_R + f\delta\kappa_R)\right]e^{-2(\alpha_R - \alpha_c)t} - \delta\zeta_n = 0. \tag{15}$$

Quantities $\delta\gamma$, $\delta\kappa$, and $\delta\lambda$ evaluated at the source and receiver locations are further expressed as combinations of the corresponding values at the nearest grid nodes by using equation 13. By combining all parameter perturbations $\delta\gamma_i$, $\delta\kappa_i$, $\delta\lambda_i$, and $\delta\zeta_n$ into one model vector **p**, the resulting equations form a linear system:

$$\mathbf{A}\delta\mathbf{p} - \mathbf{B} = \mathbf{0}\,, \tag{16}$$

which was over- or mixed-determined (Menke, 1989; 7,986 data points and 885 unknowns in our inversion). Its approximate solution in the least-squares sense is:

$$\delta\mathbf{p} = \left(\mathbf{A}^T\mathbf{A}\right)^{-1}\mathbf{A}^T\mathbf{B}\,, \tag{17}$$

where $T$ denotes the matrix transpose. In SIRT (and related back-projection methods), the diagonally-dominant $\mathbf{A}^T\mathbf{A}$ matrix is replaced in this equation with its diagonal, whose inverse can be easily calculated:

$$\delta\mathbf{p} \approx c\left[diag\left(\mathbf{A}^T\mathbf{A}\right)\right]^{-1}\mathbf{A}^T\mathbf{B}\,. \tag{18}$$

This method requires the storage of only two vectors: $\mathbf{A}^T\mathbf{B}$ and the diagonal of $\mathbf{A}^T\mathbf{A}$, and consequently it can be efficiently applied to very large problems. In our study, the inverse (18) was calculated during iterative scanning through the entire $s_c(f)$ dataset, and was terminated when model updates became sufficiently small. Between the iterations, "trimming" operations were applied to the model in order to make it satisfy the constraints above. Our final model (Figure 3) resulted in ~90% data error reduction from the starting model with $\gamma_i = 0$, $\kappa_i = 0$, and $\lambda_i = 1$. To suppress parameter oscillations during this process, a scaling factor $c < 1$ ($c = 0.5$ in our inversion) was applied during stepping (18) and was gradually reduced when data error increases were detected.

## Results

The resulting maps of $\lambda$, $\gamma$, and $\kappa$ within the area of *Lg* coda *Q* data coverage from five PNE profiles are shown in Figure 3.To produce continuous maps, we used linear interpolation within a Delaunay triangulation constructed on the centers of the 53 grid cells that were used in the inversion (Figure 1). This explains the shapes of some of the features located near the edges of the coverage area (such as the Baikal Rift zone and the Urals; Figure 3).

As expected, the scattering amplitudes, $\lambda$, show strong variations which remarkably well correlate with tectonic areas (Figure 3a). High $\lambda$ values are found in the Uralian and in the Sayan-Baikal (labeled BR in Figure 3b) fold belts which could potentially be related to stronger surface topography and complex crustal structures due to folding. High scattering amplitudes are also present in the western part of the Siberian Craton. By contrast, the eastern part of the Siberian Craton (the Minusisk-Aldan High; Figures 3a and b) and most of the West Siberian Basin show low $\lambda$.

The geometrical spreading exponent, $\gamma$, also correlates with tectonics (Figure 3b). Note that the level of $\gamma_D = 0.008$ s$^{-1}$ (purple color in Figure 3b, marked) separates the stable cratonic areas (with $\gamma < \gamma_D$) from the tectonically active Baikal Rift, for which $\gamma$ is distinctly higher than $\gamma_D$. As Morozov et al. (in press) showed by numerical modeling, such a difference could be caused by generally higher level of contrasts within the tectonically active crust, potentially with presence of relatively thin attenuative zones. As these authors also suggested, within stable parts of the study area, $\gamma$ varies only moderately, from about 0.004 to 0.007 s$^{-1}$ (Figure 3b).

The effective surface-consistent coda $Q_e^{-1}$ values, defined as $Q_e^{-1} = \kappa/\pi$, also show a distinct correlation with tectonic structures and reasonable stability within the study area (Figure 3c). Coda $Q_e$ is low in the Baikal Rift zone ($Q_e \approx 100$) and near the Urals ($Q_e \approx 130$) but higher within the Siberian Craton ($Q_e \approx 300$). Within the eastern part of the West Siberian Basin, the attenuation is the lowest ($Q_e \approx 1000$). However, although indicating a reasonable correlation with the geological structures, the values of $Q_e^{-1}$ appear somewhat over-estimated (could be to a factor of about 2) compared to detailed measurements performed on two individual PNEs (Morozov et al., in press). Potential reasons for such an overestimation will be considered in future research.

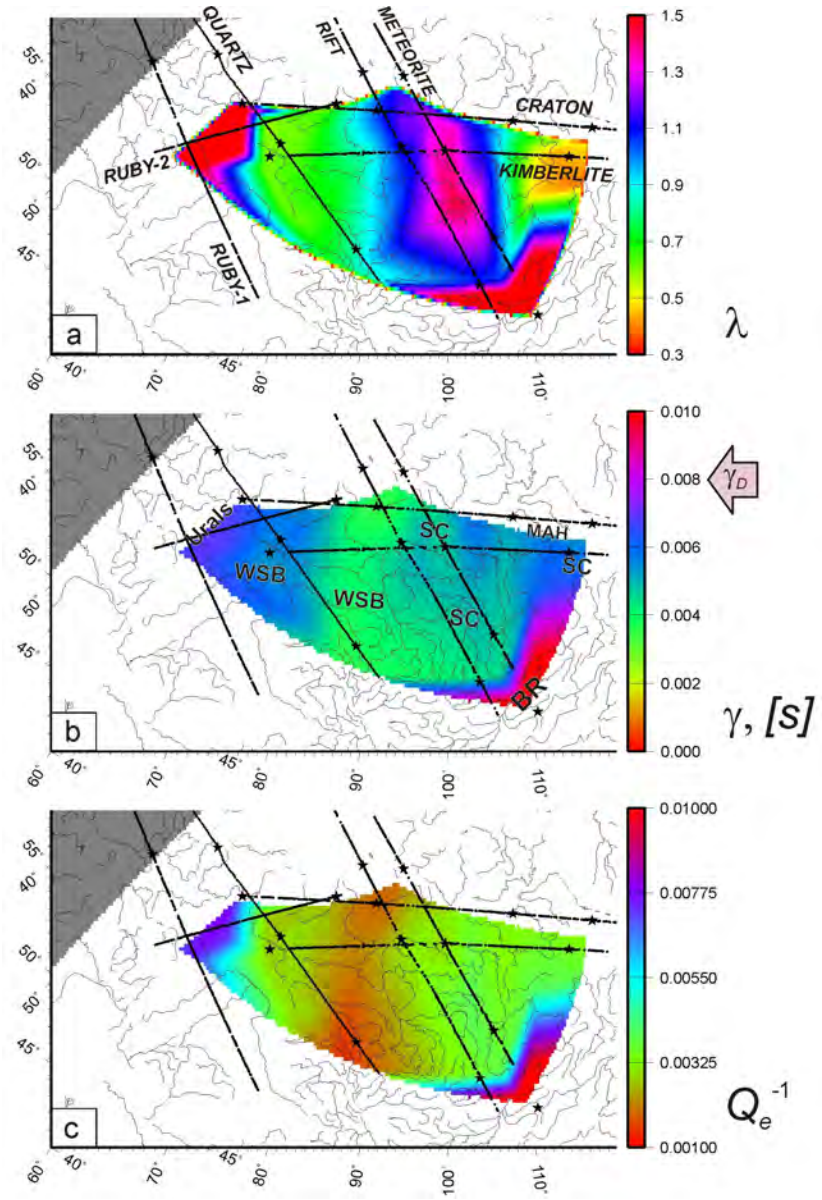


**Figure 3. PNE *Lg* coda *Q* inversion results: a) coda scattering amplitude $\lambda$; b) uncompensated geometrical spreading $\gamma$; 2) effective coda attenuation $Q_e^{-1} = \kappa/\pi$. In plot b), note the level of $\gamma_D = 0.008$ s$^{-1}$ which was suggested to discriminate between stable and active tectonic areas (Morozov, in press). Major tectonic regions are indicated in plot b): BR – Baikal Rift; SC – Siberian Craton; MAH – Minusinsk-Aldan High; WSB – West Siberian Basin PNE profiles are labeled in plot a).**

## CONCLUSIONS AND RECOMMENDATIONS

Morozov et al. (in press) demonstrated that short-period coda attenuation of regional arrivals can be interpreted as a combination of uncompensated geometrical spreading ($\gamma$) and effective attenuation ($Q_e$). Taken together, these parameters represent the generalized attenuation coefficient: $\alpha(f) = \gamma + \pi f/Q_e$, which in many cases can be measured directly from the data. Parameter $\gamma$ removes the common ambiguity of the $Q(f)$ and is most useful for correlating different study areas and tectonic types. Modeling of *P*-wave coda at regional distances and analysis of two Peaceful Nuclear Explosions in Russia in terms of this concept showed a remarkable agreement, especially in $\gamma$ values.

In this report, we applied the same parameterization to the inversion of spatially-variable surface-consistent *Lg* coda parameters from five PNE profiles in Siberia. The resulting map of the geometrical parameter ($\gamma$) is in excellent agreement with both modeling and inversion in Part I, and also with a summary of over forty worldwide studies (Morozov, in press). In addition, scattering amplitudes were found to be highly variable and strongly correlate with geological structures. Coda $Q_e^{-1}$ values also showed pronounced correlation with geological structures, although these values also appeared somewhat overestimated compared to the detailed point studies in Morozov et al. (in press).

## REFERENCES


Aki, K. (1980). Scattering and attenuation of shear waves in the lithosphere, *J. Geophys. Res.* 85: 6496–6504.

Anderson, D. L., A. Ben-Menahem, and C. B. Archambeau (1965). Attenuation of seismic energy in the upper mantle, *J. Geophys. Res*. 70: 1441-1448.

Benz, H., A. Frankel, and D. Boore (1997). Regional *Lg* attenuation in the continental United States, *Bull. Seism. Soc. Am.* 87, 600–619.

Campillo, M. (1987). *Lg* wave propagation in a laterally varying crust and the distribution of the apparent quality factor in central France, *J. Geophys. Res.* 92: 12604–12614.

Campillo, M. (1990). Propagation and attenuation characteristics of the crustal phase *Lg*, *PAGEOPH,* 132, 1–17.

Chernov, L. A., *Wave Propagation in a Random Medium,* pp. 35–57, McGraw-Hill, New York, 1960.

Dainty, A. M. (1981). A scattering model to explain seismic *Q* observations in the lithosphere between 1 and 30 Hz, *Geophys. Res. Lett*. 8: 1126–1128.

Der, Z. A., A. C. Lees, and V. F. Cormier (1986). Frequency dependence of *Q* in the mantle underlying the shield region of Eurasia, Part III: The *Q*-model, *Geophys. J. R. Astr. Soc.* 87: 1103–1112.

Erickson, D., D. E. McNamara, and H. Benz (2005). Frequency-dependent Lg Q within the continental United States, Bull. Seism. Soc. Am. 94: 1630–1643.

Frankel, A., A. McGarr, J. Bicknell, J. Mori, L. Seeber, and E. Cranswick (1990). Attenuation of high-frequency shear waves in the crust: measurements from New York State, South Africa, and southern California, *J. Geophys. Res*., 95; 17441–17457.

McNamara, D. E. (2000). Frequency-dependent Lg attenuation in south-central Alaska, Geophys. Res. Lett. 27: 3949–3952.

McNamara, D. E., T. J. Owens, and W. R. Walter (1996). Propagation characteristics of *Lg* across the Tibetian Plateau, *Bull. Seism. Soc. Am*. 86: 457–469.

Menke, W., 1989. Geophysical data analysis: Discrete inverse theory, Academic press, San Diego, CA, p. 35-60.

Mitchell, B. J. (1991). Frequency dependence of $Q_{Lg}$ and its relation to crustal anelasticity in the Basin and Range Province, *Geophys. Res. Lett*. 18: 621–624.

Mitchell, B. J., and Cong, L. (1998). *Lg* coda *Q* and its relation to the structure and evolution of continents: a global Perspective, *Pure Appl. Geophys*. 153: 655–663.

Mitchell, B. J., Pan, Y., Xie, J., and Cong, L. (1997). *Lg* coda *Q* variation across Eurasia and its relation to crustal evolution, J. Geophys. Res. 102: 22767–22779.

Morozov, I. B. and Smithson, S. B. (2000).Coda of long-range arrivals from nuclear explosions, *BSSA* 90: 929–939.

Morozov, I. B. (*Geophys J. Int*., in press). Geometrical attenuation, frequency dependence of *Q*, and the absorption band problem, manuscript available at: http://seisweb.usask.ca/downloads/Papers/Q_2008/Morozov_Qf_GJI_Apr2008.2.pdf

Morozov, I. B., C. Zhang, J. N. Duenow, E. A. Morozova, and S. Smithson, (*Bull. Seism. Soc. Am., in press*). Frequency dependence of regional coda *Q*: Part I. Numerical modeling and an example from Peaceful Nuclear Explosions, Manuscript available at: http://seisweb.usask.ca/downloads/Papers/Coda_Q_Modeling_2007/Morozov_et_al_Coda_Q.2.pdf

Morozov, I., Morozova, E., Zhang, C. Chubak, G., Phillips, W.S. and Lipovetsky, I. (2006). Magnitude-yield and travel-time calibration of northern Eurasia using deep seismic sounding datasets, in *Proceedings of the 28th Seismic Research Review*: *Ground-Based Nuclear Explosion Monitoring*, LA-UR-06-5471, Vol. 1, pp. 130–140.

Nikolayev, A. V. (1968). Seismic properties of weakly heterogeneous media (Engl. Transl.) *Acad. Sci. USSR Phys. Solid Earth*, 83–87.

Phillips, W.S., H.J. Patton, S.R. Taylor, H.E. Hartse, and R.E. Randall, (2004). Calibration for coda based magnitude and yield, in *Proceedings of the 26th Seismic Research Review*: *Trends in Nuclear Explosion Monitoring*, LA-UR-04-5801, Vol. 1, pp. 449–456.

Xie, J. (2002) *Lg Q* in the eastern Tibetan Plateau, *Bull. Seism. Soc. Am.* 92: 871–876.

# SYNERGY BETWEEN REMOTE SENSING AND SEISMIC METHODS: PATH CALIBRATION

Sidao Ni[1], Risheng Chu[2], Hong K. Thio[1], Arben Pitarka[1], and Donald V. Helmberger[2]

URS Group, Inc.[1] and California Institute of Technology[2]

Sponsored by National Nuclear Security Administration

Contract No. DE-AC52-03NA99505
Proposal No. BAA03-72

## ABSTRACT

In previous reports, we have concentrated on validating ground truth locations by modeling extended faults with combined Interferometric Synthetic Aperture Radar (InSAR) and waveform inversions and using various combinations of seismic data at all ranges. The final task of this project involves combining the ground-truth (GT) events from the community to validate paths at all distances for regions of interest. These calibrations can then be used to address higher order source parameters (directivity) and low yield explosions. As the recent Korean shot demonstrated, we can probably expect to have a small set of teleseismic, far-regional and regional data to analyze in estimating the yield of an event. Since stacking helps to bring signals out of the noise, it becomes useful to conduct comparable analyses on neighboring events, explosions or earthquakes. If these auxiliary events have accurate locations, moments, and source descriptions, we have a means of directly comparing effective source strengths.

We now have over 30 events with well determined locations, by cluster analysis, local arrays, and/or INSAR, and source parameters. Many of these events have the Cut-And-Paste (CAP) methodology applied, where sections of synthetic seismograms are allowed to shift in time relative to the data in order to account for path corrections. The method has been shown to be greatly improved at higher frequency (2 to .5 Hz) by adding amplitude corrections, CAP+, and constructing site-responses. We demonstrate that both far-regional containing triplications and teleseismic waveform data can be used effectively to retrieve source parameters with such corrections. These corrections can be larger than 10 at many stations which has prevented the inversion of small events in the past. Moreover, certain paths prove difficult to calibrate because of rapidly varying waveforms while some prove stable, i.e., ABKT, and ANTO. We present calibration results for both 1D and 3D models for these selected paths where source parameters are demonstrated to agree with regional results.

## OBJECTIVES

The International Monitoring System has been concentrating on locating and estimating source parameters by following two strategies; (1) calibration-based and (2) model-based. The first relies on path calibration from well-located events while the second attempts to estimate the source properties from a well-developed 3D earth models. The focus of this report is to use our GT events in conjunction with efforts from our colleagues to establish a master-set of simple events with well determined source mechanisms and P-wave segments sampling the upper mantle transition zone. This collection can then be used effectively to calibrate specific paths or refine 3D earth structures in Southeast Asia.

## RESEARCH ACCOMPLISHED

The importance of triplications or natural focusing produced by the earth is easily observed by examining observations from the recent Korean test and neighboring earthquakes, Kim (1995), as displayed in Figure 1. Note that the explosion signal is well above the noise that is predicted by synthetics, although the true nature of this sample of the mantle is not well known with only a prediction given here. Similarly, the PKP triplication again displays a strong signal for the explosion. The core phases are well known relative to the upper mantle triplications where individual arrivals prove difficult to isolate.

Although there have been many attempts at performing such tasks, they have not been very successful because of the complexity involved with seismograms at distances of less than 30°. Thus, most global tomography studies use P-data beyond 30° and PP beyond 60°, etc. It appears that the main difficulty is that depth phases from crustal events arrive on top of the triplications and make it difficult to identify secondary arrivals when only a collection of individual events are assembled into a record section. Fortunately, dense arrays display very clear triplications, Figure 2, and allow some systematic approaches to be developed in refining structures and establishing path corrections. The first is that we must have clear identifications of depth phases and accurate source characterization, and second, we must either correct for complicated source histories or eliminate such events from consideration.

We started with 1,720 events with CMTs Mw > 5 within our study area, Figure 2A, and examined their teleseismic waveforms as in Figure 2B. After testing forward synthetics, we only accepted those events that allowed clear depth phases pP and sP at several stations at different azimuths. If the Harvard centroid moment tensor (CMT) had roughly the right mechanism, we simply adjusted the depth determination to fit the deconvolved records as displayed in Figure 2B. Only 504 events remained after this analysis, which we will refer to as Master Events. A comparison of these depths is given in Figure 3 along with maps of CMT and National Earthquake Information Center (NEIC) depths as color coded (Figure 4). Note that many of the events in the region of Iran have been relocated at shallower depths. This means that their origin times need to be adjusted when developing travel time correction surfaces.

The source durations were deconvolved and stored along with the other source parameters to establish a master set. Next, we collected a large sample of P-wave recordings at all ranges of less than 30° (over 21,000 30s segment for these events). We used a library of triplication models to identify turning depths of the various arrivals. After relocation by gathering GT information from the community, we can test existing 3D earth models and perform tomographic images of individual triplication branches. With refined triplication models we can attempt source inversion using the CAP (Cut and Paste) methodology to all ranges.

### Mapping Triplications

Next, we examined the recording of these Master Events at more than 300 stations in the ranges less than 30°, including those from the global seismological network, KNET, KZNET, and CNDSN (Chinese National Digital Seismic Network). We also included all the PASSCAL-type data; Sino-US (XC), INDEPTH II & III (XR), Nanga Parbet (XG), GHENGIS (XW), Tarim (XM), HIMNT (YL), BHUTAN (XA), Namche Barwa (XE), MIT-China (YA) and the Sochuan (XS). Over 20,000 P-waves were collected.

Record sections were assembled from this collection with common depth points as displayed in Figure 5, and some preliminary 1D modeling, Chu (2008). Even though these synthetics involve several different mechanisms and depths, the triplicated branches become apparent as indicated by the dotted lines. The fast structure above the 410 km discontinuity is interpreted as a flat lying slab, Chu and Zhu (2008).

**Regional Travel-Time Samples**

The upper-mantle samples from the entire collection is displayed in Figure 6A with travel-time depth anomalies plotted in Figure 6B displaying the large variation along an India-Tarim Basin cross-section AB. The AB line is denoted in Figure 7A. Note that negative travel-time residuals (blue) indicate that the velocities around the turning points are faster than those in iasp91, while positive residuals (red) suggest slow velocity anomalies. Negative residuals above the 410 appear to dominate most of the cross-section except beneath the northern edge of the Tibetan Plateau. A sharp boundary appears at the northern edge of the Tarim Basin at depths greater than 200 km, but ends at the 410 discontinuity. This structure is similar to detached slab segments that have been imaged beneath the Western United States. A relatively slow patch occurs at about Lon (85°), Lat (36°) which appears to be a localized up-welling, which is also seen in receiver functions, Kind et al (2002).

Travel-time residuals below the 410 km are relatively small beneath the entire region, except directly beneath the Southern edge of the Tibet. This feature can be seen in some of the tomographic images (Li et al., 2006), but is weaker in our data set.

## CONCLUSIONS AND RECOMMENDATIONS

In this study, we have refined the source properties over 500 events by modeling P, pP and SP at teleseismic distances. Multiple arrivals on these records have been identified, delineating distinct travel paths. Then pulses can be used directly in comparing neighboring events or assembled to refine existing 3D earth models. The timing delays can be used directly in tomographic style and added to existing files or waveform segments matched against 3D synthetics.

Unfortunately, most of the recent events studied by means of InSAR, cluster analysis and local arrays have not been included in the above dataset. Over 30 events in IRAN now have well determined locations. Many of these events have the CAP methodology applied, where sections of synthetics seismograms are allowed to shift in the time relative to the data in order to a recount for path corrections. We recommend that all these events be added to the above collections. Moreover, we recommend performing the CAP analyses at all distances including the above collection where site-corrections are applied (CAP +, Tan and Helmberger, 2006). This will allow source estimations using a complete set of waveforms. Moreover, solutions become possible even with a sparse network (Thio et al, 1999).

## REFERENCES

Chu, R (2008). Upper mantle velocity structure beneath the Tibetan Plateau from triplicated seismic P waveforms, *PhD Thesis*, Saint Louis University.

Chu, R. and L Zhu (2008). Detached Eurasian mantle lithospheric remnants beneath the Tibetan plateau inferred from triplicated P waveforms, *JGR, in preparation.*

Chu, R., S Ni and D.V. Helmberger (2008). Mapping lateral variation in upper mantle triplications beneath the Eastern Pacific Margins, *in preparation.*

Kim, S. K., 1995. A study on the crustal structure of the Korean Peninsula (in Korean), *J. Geol. Soc. Korea* 31: 393–403.

Kind, R., Yuan, X., Saul, J., Nelson, D., Sobolev, S. V., Mechie, J., Zhao, W., Kosarev, G., Ni, J., Achauer, U., Jiang, M. (2002). Seismic images of crust and upper mantle beneath Tibet: evidence for Eurasian plate subduction, *Science* 298: 5596, 1219–1221.

Li, C, R.D. van der Hilst, and N.M. Toksoz (2006). Constraining spatial variation in P wave velocity in the upper mantle beneath SE Asia, *Phys. Earth Planet. Inter.* 154: 180–195.

Ni, S., Ding X. and D.V. Helmberger (2000). Constructing synthetics from deep earth tomographic models, *Geophys. Journ. Int.* 140: (1), 71–82.

Ni, S., Cormier V. and D.V. Helmberger (2003). A comparison of synthetic seismograms for 2D structures: Semianalytical versus numerical, *Bull. Seis. Soc. Am.* 93: (6), 2752–2757.

Ni, S., A. Pitarka, D.V. Helmberger, (2008). Short-period Synthetics for 3D models, Numerical vs. Analytical, *Seis. Res. Lett.* 79: .2, p. 298.

Tan, Y and D.V. Helmberger (2007). A new method for determining small earthquake source parameters using short-period P waves, *Bull., Seism. Soc. Am*. 97: 1176–1195.

Thio, H. K., Song, X, Saikia, C. K., Helmberger, D. V., and Woods, B.B. (1999). Seismic source and structure estimation in the western Mediterranean using a sparse broadband network, *Journ. Geophys. Res.* 104:(B1) pp. 845–861.

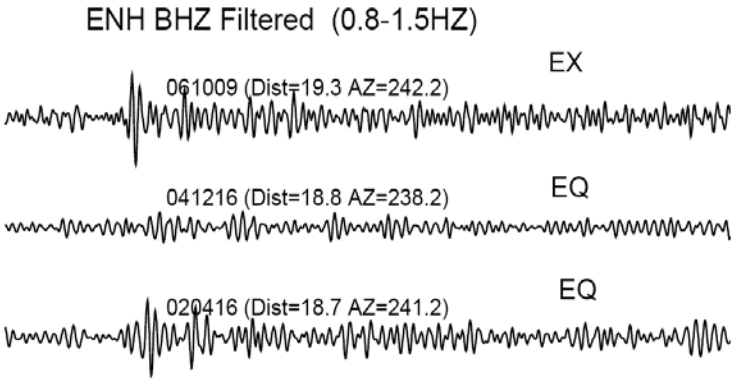


**Figure 1A. P waves at upper mantle triplication distances recorded at station ENH for three events. Event 041216 shows weaker amplitude probably due to its source mechanism.**

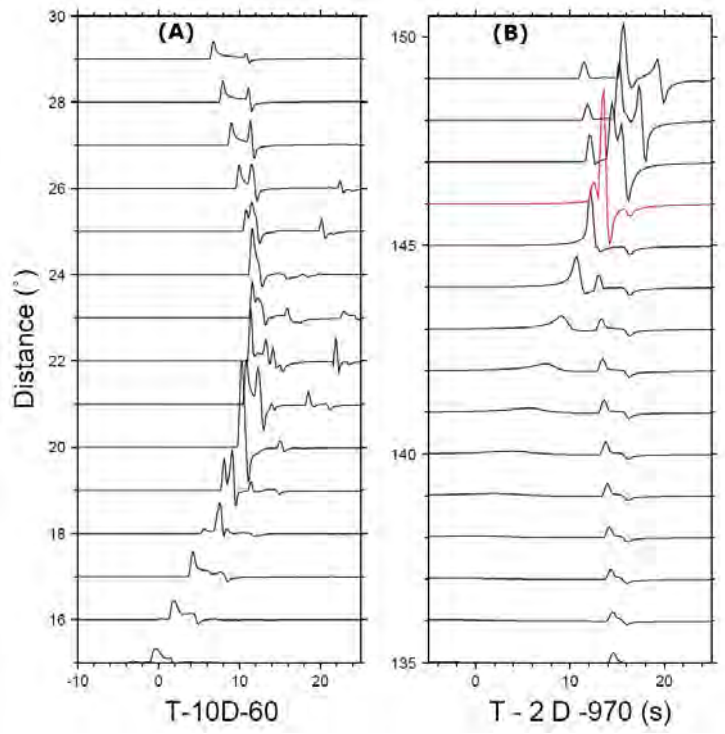


**Figure 1B. (A) Synthetic P waveforms at upper mantle triplication distances based on 3D tomography model by Grand (2002) with the WKM algorithm (Ni et al., 2000). Around distances of 19-20 degrees, P waves are substantially stronger because of constructive interference of various triplication branches. (B) Synthetic PKIKP/PKPab/bc waveforms for PREM. Note that PKP is very strong around 146 degrees (green trace) since it is close to B-caustic.**

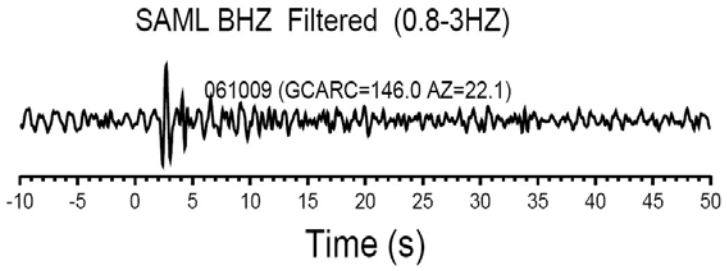


**Figure 1C. The 061009 explosion observed at station SAML at a distance of 146 degrees.**

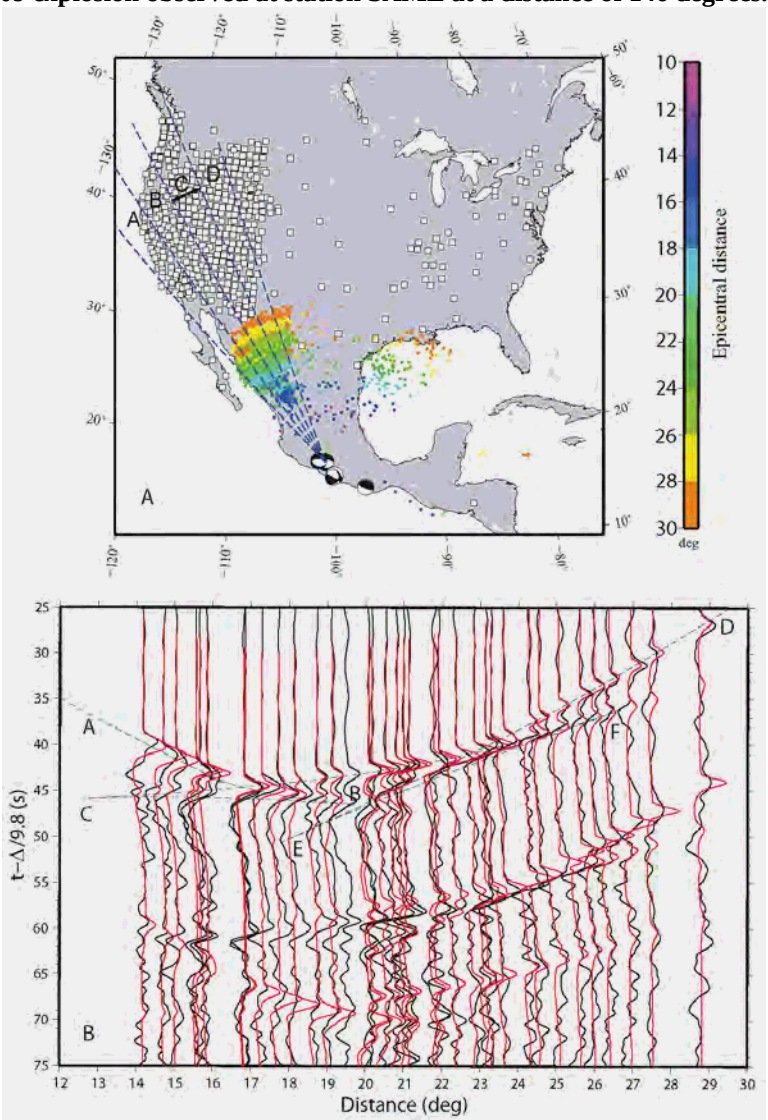


**Figure 2. Upper-mantle triplications observed on the US Array of an event beneath Mexico (top). The model is a modification of GCA (Chu and Helmberger, 2008). The event is at a depth of 65 km so that the depth phases are apparent. For shallow events, their depth phases interfere with the various branches of the two triplications caused by the 410 and 660 km discontinuities, respectively. In this case, the P-wave portion is isolated, so that we can easily identify the AB branch which is the first arrived at distances less than 17°, the CD branch from 18° to 22°, and the EF branch beyond 24°, as denoted by the dotted lines (bottom).**

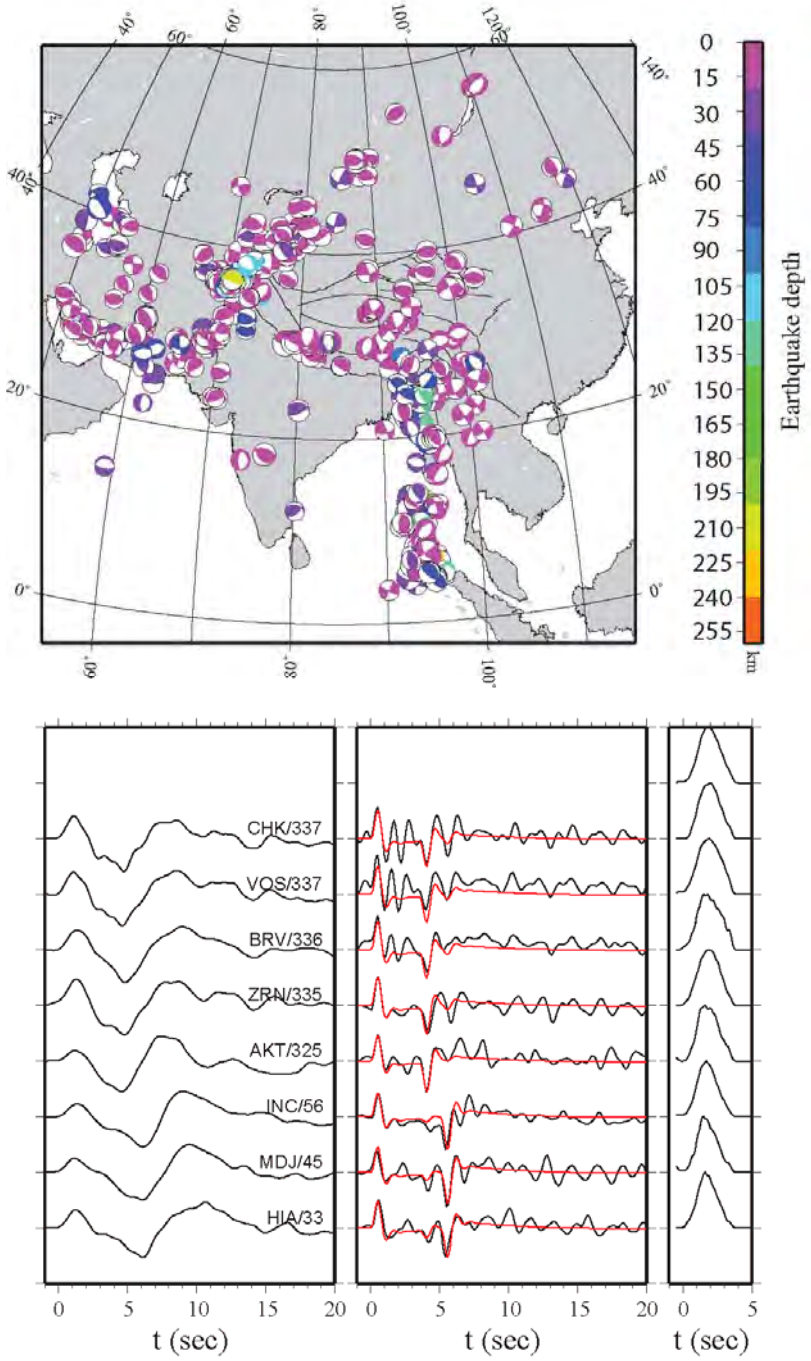


**Figure 3. Master events with the verified mechanisms and refined depths using teleseismic modeling (top). Only events shallower than 250 km are plotted in color-code. The bottom panel shows an example of modeling depth phases for a shallow event (d=11km) and derived source time function obtained by deconvolutions [Chu et. al, 2008]. Note that the bottom three traces display a strong sP relative to those above.**

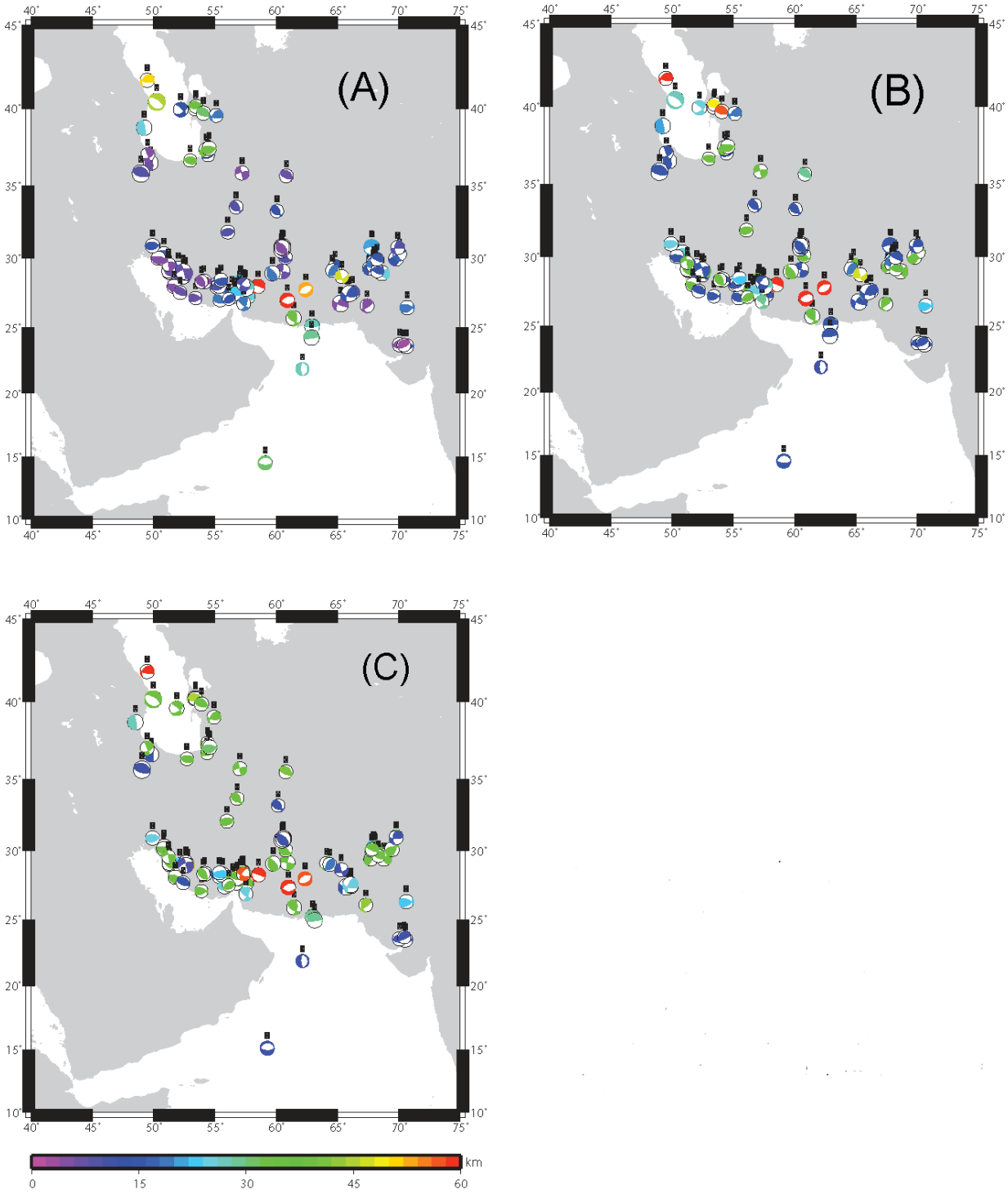


**Figure 4. Comparison of the earthquake depths estimated for the region of Iran using the technique by Chu et al. (2008). Note that most of the events in the interior of Iran are distinctly shallower in our results (A) vs. the depths from the CMT (B) and NEIC catalogs (C), although some of the events beneath the Captain Sea are deeper.**

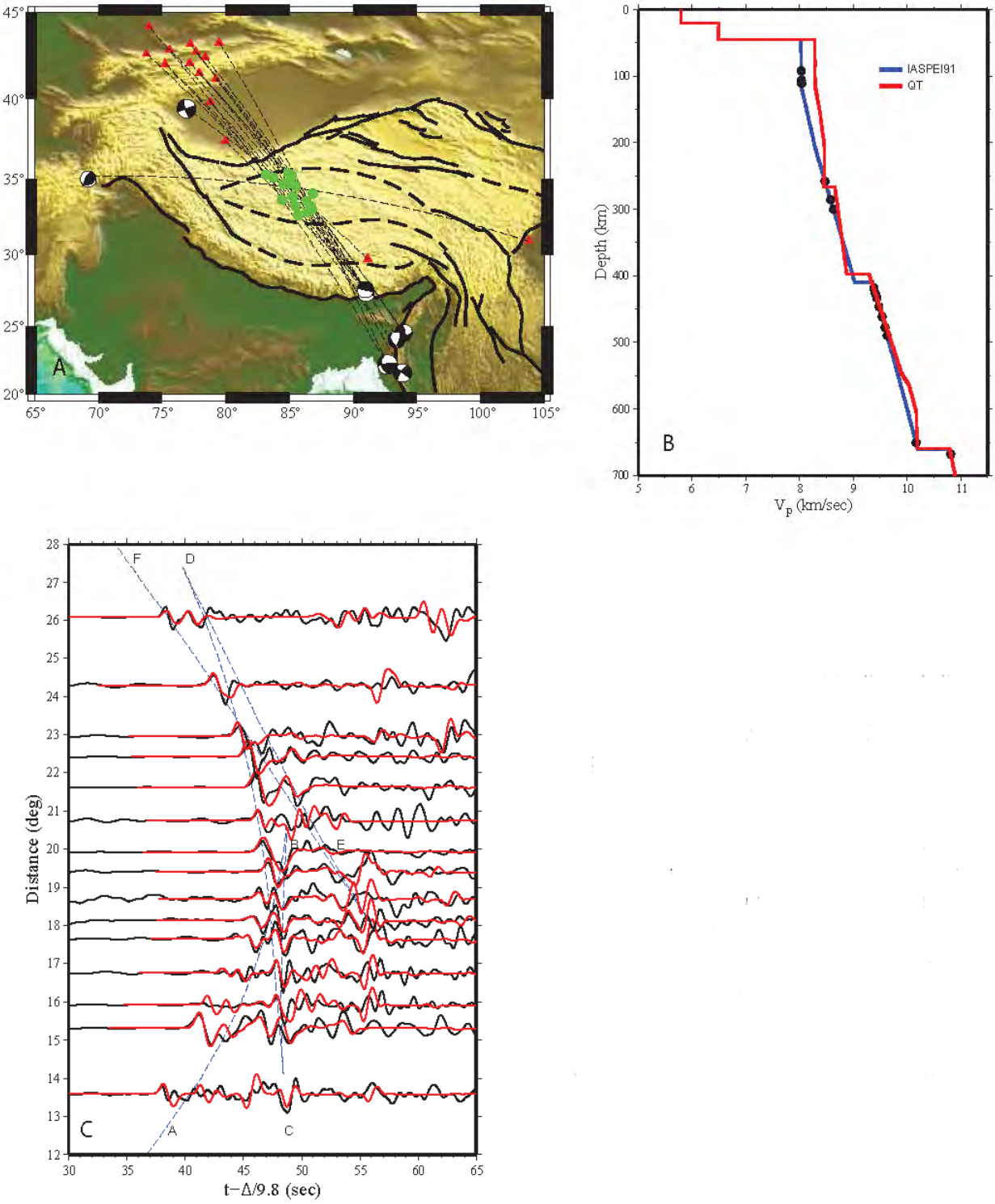


**Figure 5. Modeling triplications at a common depth sampling the upper mantle beneath the Qiangtang province of Central Tibet. Figure 5A shows the event-station pairs and turning points (green dots) of seismic rays in Figure 5C. The black dots in Figure 5B represent the bottoming depths of the various ray paths assuming a 1D model (iasp91). Thus, the nearest event provides the smallest range (13.7 deg) while the most distant event (26.1 deg.) produces the deepest sample. The best fitting model (QT) is displayed in Figure 5B in red with the associated waveform fits in Figure 5C. The various traces involve individual source parameters.**

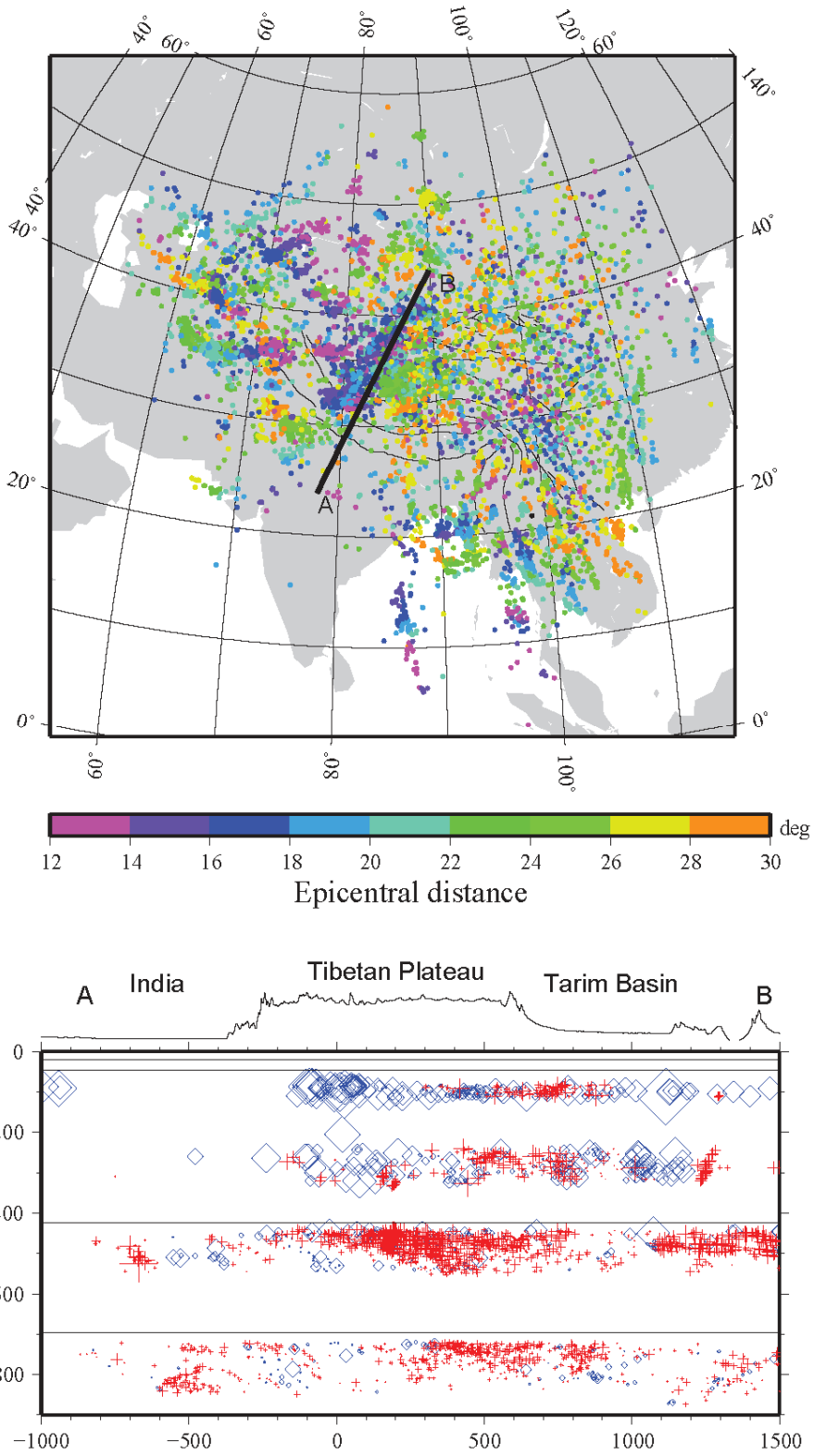


**Figure 6. A map displaying the mid-points between each event-station pair involving 11,306 samples (top). The color scale shows the epicentral distance for each sample, which corresponds to its turning depth. The profile AB is a cross section in western Tibet. Travel time residuals relative to iasp91 along AB (bottom) with negative values (blue) indicating relatively fast paths (high velocities). See Figure 7 for scale of differential times.**

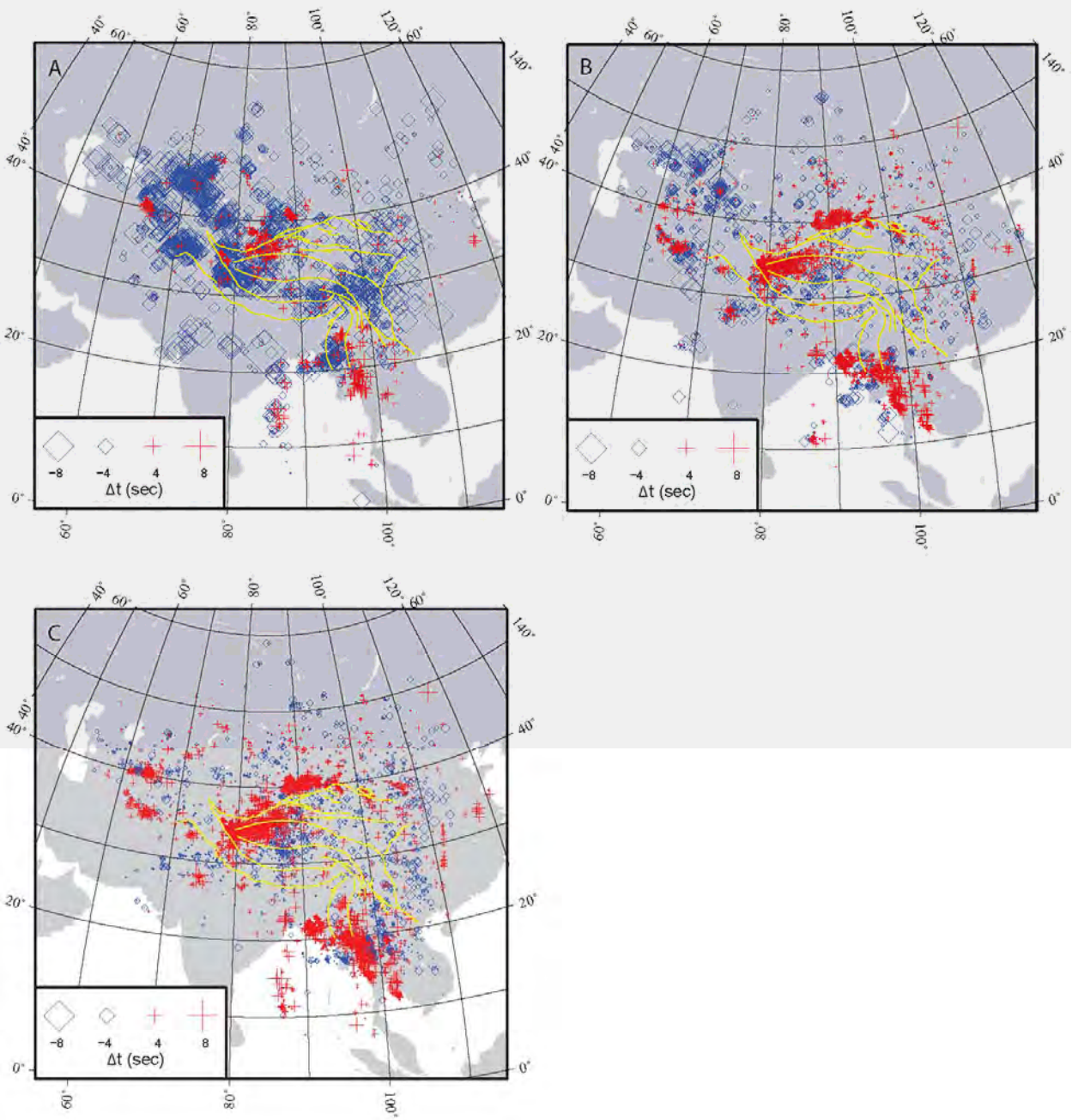


**Figure 7. Display of travel time anomalies at various depths beneath Southeast Asia. The delays are plotted relative to branch's. Figure 7(A) shows the delays for those rays sampling above the 410 km discontinuity. The CD branch sampling in the transition zone, 410 to 660 km, are presented in Figure 7(B) and below 660 km given in Figure 7(C).**

# FREQUENCY-DEPENDENT NATURE OF *Pn* IN WESTERN CHINA: GAUSSIAN BEAM MODELING OF DATA FROM THE HI-CLIMB EXPERIMENT

Robert L. Nowack[1], Wang-Ping Chen[2], and Tai-Lin Tseng[2]

Purdue University[1] and University of Illinois[2]

Sponsored by Air Force Research Laboratory

Contract No. FA8718-08-C-0025
Proposal No. BAA08-42

## ABSTRACT

In realistic models of the crust and the upper mantle where vertical gradients in wave speeds and major interfaces are present, propagation of *Pn*, an important seismic phase at regional distances, involves complex effects of interference. Such effects can result in wave-trains whose frequency-contents and amplitudes vary with distance in counter-intuitive ways. In this new project, we are investigating the propagation of *Pn* beneath western China using data from Hi-CLIMB (An Integrated Study of the Himalayan-Tibetan Continental Lithosphere during Mountain Building). This experiment is one of the largest broadband seismic experiments to date, with more than 210 deployments at close station-spacing of 3–8 km over a distance of 800 km. The linear array is complemented by a regional array of comparable aperture, producing an unprecedented dataset for Eurasia. For the current project, which just began in May of 2008, we are organizing a dataset for regional seismic events recorded by the Hi-CLIMB arrays and will show examples of long seismic profiles over apertures of 500 km from several different azimuths. We are also investigating methods of modeling and inversion based on Gaussian beams (GB), which offer several distinct advantages. First, GB modeling can be applied both for interference waves, which have caustics, and for pure head waves. Second, GB modeling can handle laterally varying media, an important aspect that cannot be investigated by standard methods such as reflectivity. Third, GB is computationally efficient, suitable for analyzing large datasets. We will illustrate our approaches with data from an earlier experiment using explosions. Based on numerous events recorded by the Hi-CLIMB array, we will investigate frequency-dependent propagation of *Pn* over a large region in western China using GB and also finite-difference schemes. Attributes of seismic wave-trains, including arrival times, amplitudes of signal-envelopes, and instantaneous pulse frequencies will be used to constrain how structures in the crust and the upper mantle affect the propagation of *Pn*. The objective is to achieve self-consistent models of *Pn* propagation in western China which are free from assumptions such as a frequency-independent factor for geometric spreading. To this end, our results should advance efforts in isolating effects of frequency-dependent propagation from those of pure-inelastic attenuation (Q), leading to improved methodologies for discrimination and yield estimates at regional distances.

## OBJECTIVES

In this new project, which started in May 2008, we are analyzing the propagation of regional *Pn* waves recorded by Hi-CLIMB (An Integrated Study of the Himalayan-Tibetan Continental Lithosphere during Mountain Building) in Tibet. Considering the dense station-spacing (3 to 8 km) and large aperture (800 km) of the Hi-CLIMB seismic experiment, our objective is the use these densely recorded data to construct a self-consistent model of *Pn* propagation over a large region in western China. In turn, a better understanding of frequency-dependent effects of propagation from data inversion/modeling will improve frequency dependent attenuation models of regional *Pn* phases, leading to a clearer separation of inelastic from elastic effects in a laterally varying crust and upper mantle, eventually eliminating the assumption of a simplified, frequency-independent geometric spreading component.

To account for the intricate nature of *Pn* propagation, we are applying the Gaussian beam (GB) method, an asymptotic approach. GB is stable at caustics and can be used for the diving waves, pure head-waves, and interference waves by choosing suitable beam parameters (Nowack and Stacy, 2002). A major advantage of GB is that it works well in laterally varying media. In contrast, alternatives such as the reflectivity method, are restricted to one-dimensional media. When compared with purely numerical simulations for laterally varying media, such as the finite difference method, GB is computationally efficient in facilitating modeling and inversion of large datasets—tasks in which a large number of forward calculations are required. However, for small scale scattering, hybrid methods or full finite difference modeling may still be required. As a practical measure, essential features of *Pn* waveforms will be distilled into seismic attributes such as arrival times, envelopes of wave amplitudes, and instantaneous pulse frequencies for modeling and inversion.

## RESEARCH ACCOMPLISHED

The Hi-CLIMB seismic array was deployed between 2002 and 2005, in three phases, over 210 broadband sites at a station-spacing of 3-8 km (for the main, linear array). The main, north-south trending linear array is complemented by an east-west expanding regional array. The overall the aperture is about 800 km by 800 km (Figure 1). A unique feature of Hi-CLIMB is that it is the only seismic profile that crosses the highest portions of the Himalayas, linking baseline measurements of the Indian shield, in a pristine state prior to its involvement in active deformation, with data in the interior of Tibet. There are abundant, high quality data from numerous events at regional distances from the array. Figure 2 shows a preliminary plot of regional events with magnitudes greater than 4.6 over the time period of the Hi-CLIMB deployment.

Figure 3 shows a preliminary seismic profile from a single event with a magnitude of 4.6 located to the west of the array (located by the star in Figure 2) and recorded by central and northern portions of the Hi-CLIMB array. Clear arrivals of both *Pn* and *Pg* phases are observed to epicentral distances of more than 550 km, with *Pn* overtaking *Pg* as the first arrival at distances near 300 km. The first arrivals are marked by the dotted line, and the *Pn* arrival becomes a first arrival after about 325 km. By comparing the signals marked by box A near 350 km with a dominant frequency of about .5 Hz with box B near 560 km where the pulse frequency is higher at about .7 Hz, this increase in dominant frequency with distance suggests complex interference effects for *Pn* propagation in this region. A preliminary profile from a second event with a magnitude of 4.8 with a location just south of the middle and northern portions of the array is shown in Figure 4. Here, the *Pn* becomes the first arrival after about 290 km. The character of the *Pn* is more complicated for this profile than for the profile for the first event, and this suggests that there is significant lateral variability in the region that will need to be addressed in this study.

To interpret first arrival *Pn* data recorded from regional events by the Hi-CLIMB array, the Gaussian beam method will be used for larger scale features in the model. The Gaussian beam method (GB) is an asymptotic approach for the computation of high-frequency wavefields in laterally varying media by the summation of paraxial beams, each surrounding a central ray-path and having a Gaussian distribution in amplitude away from the central ray (Popov, 1982; Cerveny et al., 1982; Nowack and Aki, 1984). Reviews of the method are given by Babich and Popov (1989) and more recently by Nowack (2003) and Popov (2002). There are several advantages in using GB. First, individual beam components have no singularities along their paths. Thus the summation of beams is also regular everywhere, in contrast to ray methods. Second, GB naturally introduces some smoothing and therefore is not as sensitive to model parameterizations as ray-methods. Third, GB does not require the added computation of two-point ray tracing.

New approaches are being developed to perform two parameter beam summations based on initial position and angle of individual beam components. The advantage of these new approaches is that a wider range of beam parameters can be used for the each individual beam solution, but the trade-off is in speed of computation (Lugara et al., 2003; Nowack, 2003; Nowack et al., 2006; Nowack et al., 2007a; Nowack, 2008).

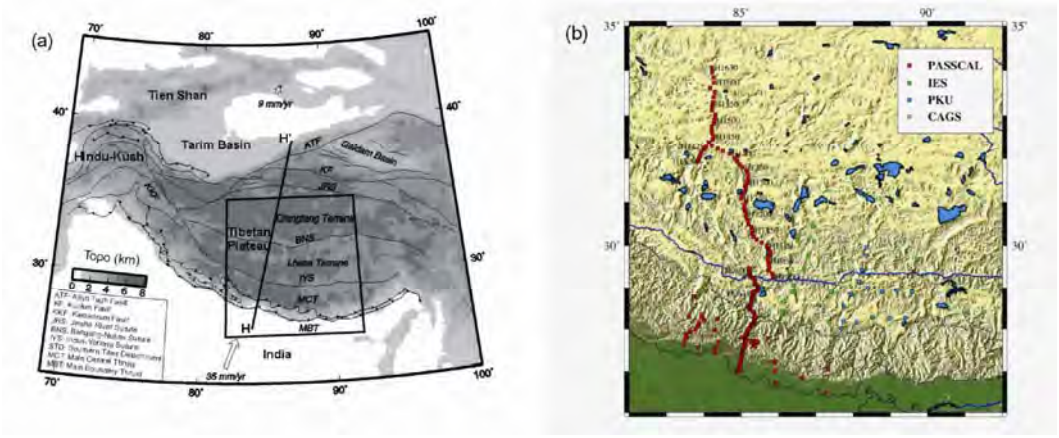


**Figure 1. Map showing geologic setting and configuration of Project Hi-CLIMB. (a) Grey-scale topographic map showing overall setting of the Himalayan-Tibetan collision zone. Two open arrows show ground velocity with respect to stable Eurasia. The box shows the region depicted in panel (b). Thin, solid curves show major geological boundaries. (b) Topographic map showing the full configuration of the Hi-CLIMB broadband seismic array. Notice a large aperture of 800 km by 800 km and the dense spacing of stations along the main, linear array. In addition to the IRIS/PASSCAL pool, instruments also came from several other participating institutions (see legend).**

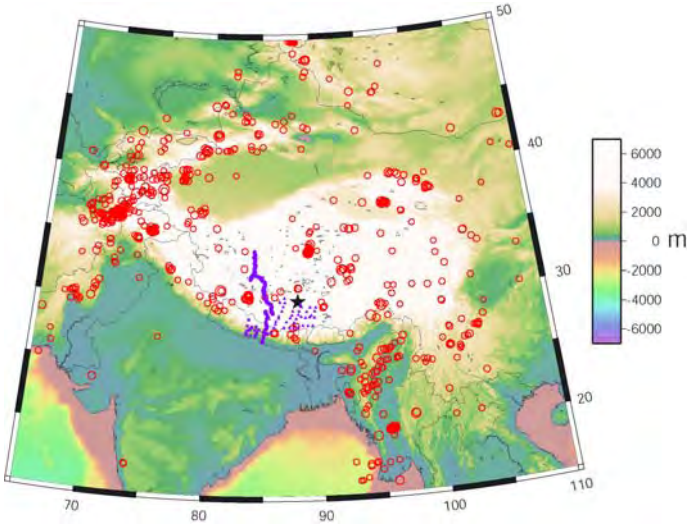


**Figure 2. A color-coded topographic map, showing epicenters of large to moderate-sized earthquakes ($m_b$ 4.6 or above; open red circles) recorded by the Hi-CLIMB array (purple triangles). The asterisk marks the epicenter of a Tibetan earthquake ($m_b$~4.8) which serves as the seismic source of the preliminary profile shown in Figure 4.**

To efficiently describe essential features of a complex waveform, it is useful to identify key attributes of the data. Procedures for extracting such attributes include complex trace analysis, and the general approach of wavelet analysis (e.g., Daubechies, 1992; Mallat, 1999). The approach described here is the former, in which an analytic signal is constructed from a seismogram. From the analytic signal, its envelope and instantaneous frequency can be

determined. Applications of complex trace analysis to seismic data have been described by Taner et al. (1979), and an application to estimate seismic attenuation by matching observed values of instantaneous frequency was

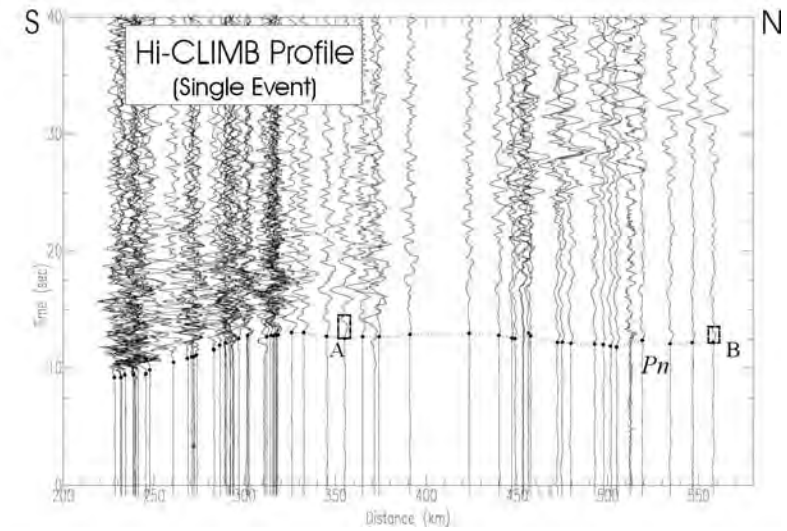


**Figure 3. An example of seismic profile from a single event (marked by the star in Figure 2) recorded by central and northern portions of the Hi-CLIMB main array, showing clear arrivals of *Pn* (marked by the dotted curve) which become the first arrival at distances beyond about 325 km. Notice the dominant frequency of *Pn* actually can increase with distance: Compare signals marked by box A, about 0.5 Hz near 350 km; and box B, about 0.7 Hz near 550 km. Solid circles mark first arrivals at selected seismograms. The time-scale is reduced by a wave speed of 8.0 km/s.**

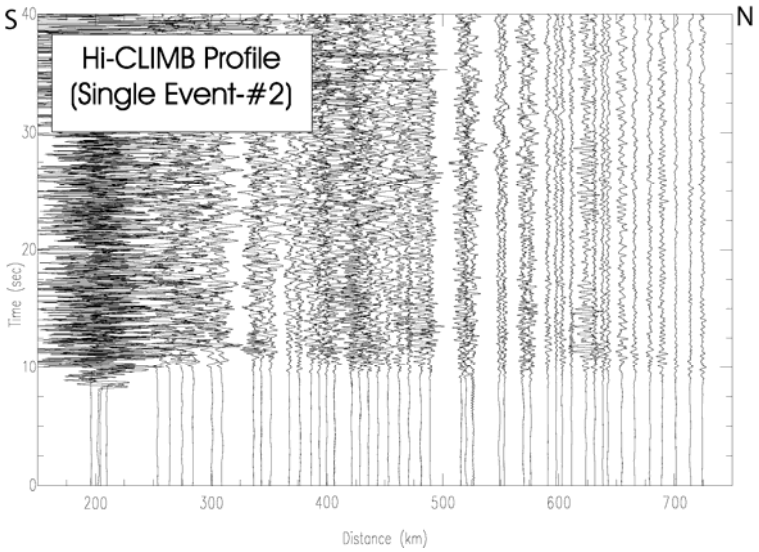


**Figure 4. A second example of a seismic profile from a single event with a magnitude of 4.8 located directly south of the middle and northern sections of the Hi-CLIMB array. The *Pn* becomes the first arrival at distances beyond about 290 km. The time-scale is reduced by a wave speed of 8.0 km/s.**

performed by Matheney and Nowack (1995). It is important to recall that the instantaneous frequency is generally not equivalent to the spectral frequency. However, an appropriate weighted average of the instantaneous frequency

converges to an average of positive spectral frequencies. Figure 5 shows an example of results from this procedure. For a seismic phase of interest, one can extract amplitudes from its envelope, timing of the seismic phase, and instantaneous frequencies as a function of time. For estimating seismic attenuation, one can match instantaneous frequencies between observed and attenuated reference pulses (Matheney and Nowack, 1995). More general inversions of all seismic attributes for selected seismic phases are also feasible, including previous work by Nowack and Matheney (1997) and Matheney et al. (1997).

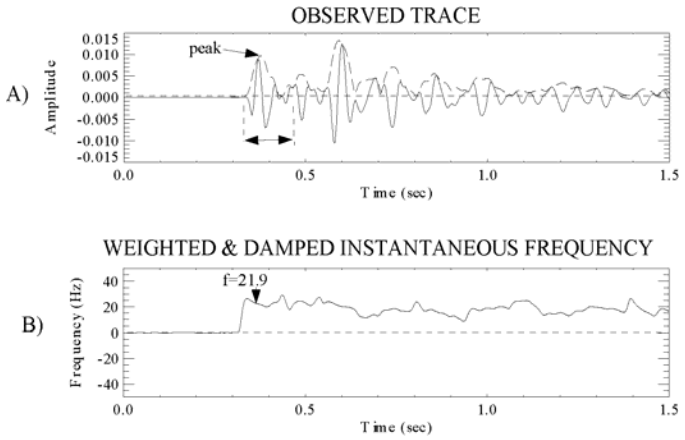


**Figure 5. An example of extracting attributes from seismic data. A) Comparison of observed seismogram (solid trace) and its envelope calculated based on the Hilbert transform of data (dashed curve). The peak amplitude of the Hilbert envelope for the first pulse is marked. B) Damped and smoothed instantaneous frequency as a function of time (from Matheney and Nowack, 1995).**

*Pn* is not a simple head-wave but is comprised of complex sets of interfering waves when there is a positive velocity gradient with respect to depth below the Moho interface (Cerveny and Ravindra, 1971; Hill, 1971; Menke and Richards, 1980). These interfering waves can simply result from the spherical nature of the earth (Hill, 1973; Sereno and Given, 1990; Yang et al., 2007), an effect equivalent to a velocity gradient in the corresponding flattened model. How observed amplitudes of refracted arrivals change over distance supports the interpretation that these

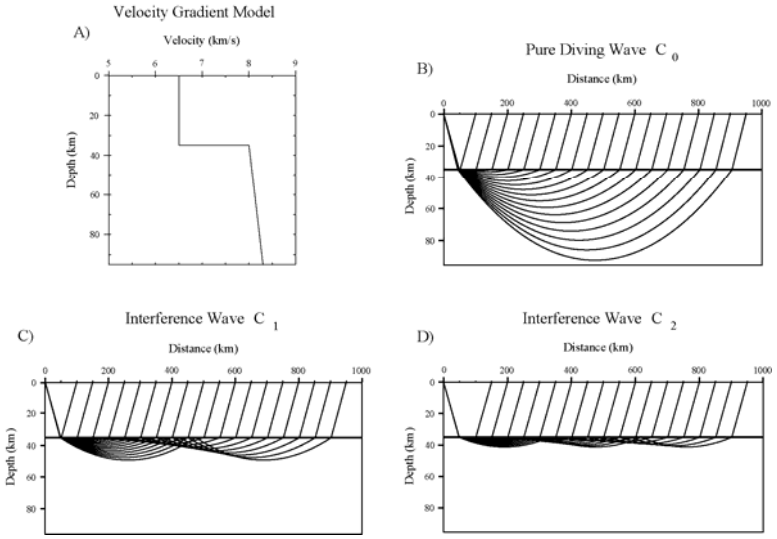


**Figure 6. Illustration showing how a positive gradient in wave velocity beneath the Moho can affect the propagation of *Pn*. A) The model for *P*-wave speeds. The linear gradient beneath the Moho can simply arise from the spherical nature of the earth. B) Paths of the primary, diving rays (pure head waves are not shown). C) Paths of the first set of sub-Moho interference wave. D) Paths of the second set of sub-Moho interference wave (from Nowack and Stacy, 2002).**

arrivals are comprised of diving and interference waves, instead of only a pure head wave (Braile and Smith, 1975). Figure 6 shows an example of how a positive upper mantle gradient can effect the propagation of Pn waves by forming a set of interference waves at the Moho (from Nowack and Stacy, 2002).

In the last several years, there has been a debate on the effects of small scale scattering in the upper mantle on the propagation of teleseismic *Pn*. Ryberg et al. (1995, 2000) and Tittgemeyer et al. (1996) favored a model in which scattering in the upper mantle can account for many of the characteristics of teleseismic *Pn*. In contrast, Morozov et al. (1998) and Morozov and Smithson (2000) advocated a model with a positive upper mantle gradient forming an interference head wave along with crustal scattering to explain teleseismic *Pn*. However, the recent analysis of Nielson and Thybo (2003) supports the model that the *Pn* phase travels as an upper mantle whispering gallery and that the origin of its long coda at teleseismic distances is due to crustal scattering. For our study, we will model the first arrival *Pn* phase as an interference wave at regional distances using Gaussian beam modeling. At greater distances, a hybrid approach or the direct use of finite difference modeling may be required to model the characteristics of teleseismic *Pn* as a combination of upper mantle gradients and small scale scattering in the crust or upper mantle.

Nowack and Stacy (2002) compared expansions of interference waves using Gaussian beams and the reflectivity method, which is restricted to one-dimensional velocity structures. The fact that GB expansions are non-singular at caustics is essential for multiple underside reflections ,which are associated with caustics and pseudo-caustics, and for these cases finite-sized beams are used. Meanwhile, broad beams are used to represent wide-angle reflections, including the pure head-wave (Nowack and Aki, 1984). In both cases, beams are specified by effective planar phase-fronts at the receiver, providing stable results during summations.

Figure 7 shows comparisons of results from GB and reflectivity, where the reflectivity modeling includes multiples from the free surface which were not included in the GB modeling. In general, these two methods yield comparable results: Notice the good agreement between the two methods in key crustal and *Pn* seismic attributes at all distances. In Fig. 7C, the envelope amplitudes of the first arriving pulses are shown following the procedure of Mathaney and Nowack (1995). The gap near 125 km corresponds to the cross-over distance between the direct crustal arrival and *Pn*. Fig. 7D shows the instantaneous pulse frequencies for the first arrival. At distances less than 100 km, instantaneous pulse frequencies are for the direct, crustal arrivals. At greater distances, the values are for *Pn*. For this particular velocity model, instantaneous frequencies ($f_I$) initially drop just beyond the cross-over distance, mainly reflecting properties of the pure head-wave. Subsequently, $f_I$ starts recovering as diving and interference waves begin to emerge. $f_I$ continues to increase with distance and eventually overshoots beyond values of direct arrivals seen at close-in distances, an effect resulting from interference of different sets of underside reflections below the Moho. This result is confirmed by analyzing centroid-frequencies of the amplitude spectra of the relevant pulses (Nowack and Stacy, 2002). A similar trend in $f_I$ was reported by Cerveny and Ravindra (1971) using asymptotic analysis. These pure-elastic effects in regional body-waves must be accounted for in order to obtain meaningful estimates of attenuation.

It should be emphasized again that unlike reflectivity, GB is valid for laterally varying media. This is an essential feature to study regional body-waves in areas such as western China where laterally varying structure is most likely to be prevalent in the lithosphere. To this end, we will further validate GB in laterally varying earth models by comparing with other methods which generates complete wavefields, such as the finite difference method (Virieux, 1988). The advantage of using the Gaussian beam method is primarily in its computational speed, a necessary feature for inversion or modeling of massive datasets where a large number of forward simulations must be performed.

The discussed methodologies to be used for Hi-CLIMB were previously applied to data from the Deep Probe/SAREX project by Stacy and Nowack (2002). SAREX (Southern Alberta Refraction Experiment) was designed to provide detailed information on crustal structures along the Canadian portion of the combined Deep Probe/SAREX profile (Clowes et al., 2002; Gorman et al., 2002). To interpret the observations, Stacy and Nowack (2002) computed synthetic seismograms using GB; whose attributes were then compared with those extracted from the data. The resulting features in the amplitudes and the instantaneous frequencies were found to be more complicated than that shown in Figure 7. In addition, a model for Q was simultaneously determined, resulting in a self-consistent representation of both elastic and inelastic effects of wave propagation over a large range of

distances. When modeling Pn propagation beneath Hi-CLIMB in western China, it is anticipated that more complicated *Pn* propagation characteristics will also be found.

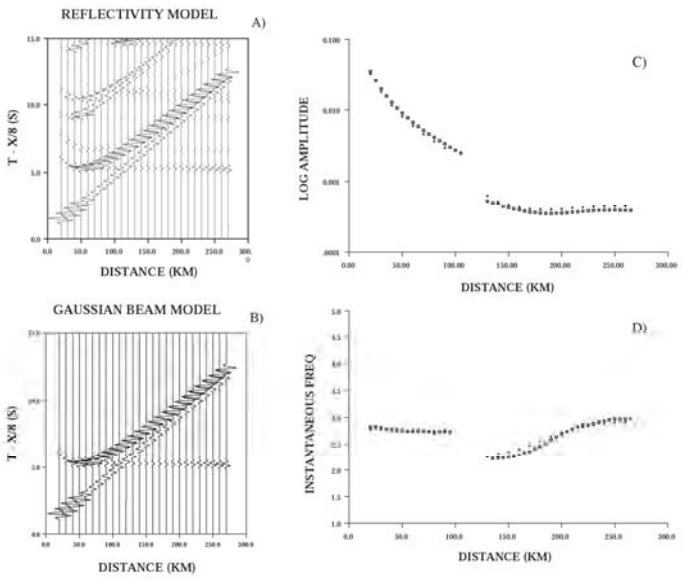


**Figure 7 Synthetic seismograms and associated seismic attributes from the simple layer over a gradient model. A) Synthetic seismograms using the reflectivity method. B) Synthetic seismograms using the Gaussian beam method. C) Amplitude of the envelope of the first arriving pulse as a function of distance. Notice that there is a sudden drop in amplitudes near distances of 100 km. Results from Gaussian beam modeling (pluses) and those from reflectivity (squares) are similar. D) Instantaneous frequency of the first arrival pulse as a function of distance. Beyond distance of about 120 km, instantaneous frequency actually increases with increasing distance. Again, results from Gaussian beam modeling (pluses) and those from reflectivity (squares) are similar. The source pulse is a Gabor wavelet with a dominant frequency of 2.77 Hz. To isolate elastic effects of wave propagation, a constant Q value of 2000 was assumed (from Nowack and Stacy, 2002).**

A major initial task of the project is to first make a comprehensive database of regional events recorded by the Hi-CLIMB array. The database will include full waveforms, instrument responses, a catalog of events and other important information such as uncertainties of locations and focal mechanisms. Meissner et al. (2004) used earthquake data recorded by the INDEPTH III array in central Tibet to study regional phases and concluded that errors in epicenters of up to 15 km are negligible for *Pn* and would only slightly affect *Pg* at close-in distances. So errors in epicenter do not appear to be a major concern. Nevertheless, we plan to quickly assess such errors by comparing event catalogs based on global (Engdahl, et al., 1998) and regional datasets, both of which are available in the public domain (the latter is available at the China Earthquake Networks Center, CENC). In terms of focal depths, it has been known for some time that most events are shallow in Tibet, between 5 to 10 km (Molnar and Chen, 1983; Chen and Molnar, 1983; Langin et al., 2003). Nonetheless, if necessary, relocations will be performed using a combination of regional data from the Hi-CLIMB array and teleseismic data. One possibility is to adopt a simplified relocation approach, as used by Zhu et al. (2006) for regional events in Tibet.

If necessary, for larger events, $m_b$ of 5.5 and above, we can obtain precise results of source parameters from the inversion of waveforms recorded at teleseismic distances. Similarly, for smaller events, their source parameters can be retrieved from inversion of regional waveforms (Zhu et al., 2006). Both procedures are routinely performed by Chen's group (e.g., Kao et al., 2002; Chen and Yang, 2004). Meanwhile, there are a number of models reported in the literature for the crust and upper mantle of Tibet (e.g., Hearn et al., 2004; Liang et al., 2004, 2006; Sun and Toksoz, 2006, Li et al., 2006), sufficient for constructing preliminary background models. Also, a recent study by Phillips et al. (2007) used *Pn* travel-times to invert for upper mantle velocities and gradients in the region.

Once a suitable set of events, with precise locations of epicenters, depths, and focal mechanisms, is assembled, we will bring together a starting velocity model from published results, including those from recent *Pn* travel-time tomography and seismic refraction studies. In addition, we will incorporate our own results from migration imaging using teleseismic data from the Hi-CLIMB array (Nowack et al., 2007b). We shall then build a large number of seismic profiles based on these chosen events. In the first example (Figure 3), an increase of frequency for *Pn* with propagation distance is already apparent (cf. Boxes A and B in Figure 3), suggesting that the *Pn* from this region is being influenced by interference effects. The next step is to extract seismic attributes from each seismic profile so that quantitative analysis and modeling can be carried out.

The modeling of these attributes involves matching observed envelope-amplitudes and instantaneous pulse frequencies with those calculated, mainly using Gaussian beams. To minimize effects of seismic source-time functions, one strategy is to match pulses observed at close-in distances with theoretical ones and normalize the rest of the data accordingly. Alternatively, the normalization can be performed by deconvolution of all data with an appropriate reference signal. The reference can be a *P*-pulse observed at teleseismic distance, if the event is large enough ($m_b$ above ~5 or 5.5). Otherwise, a pulse observed at close-in distances could be appropriate. Once the seismic attributes are normalized, we will then perform systematic modeling using Gaussian beams. The final product will be several laterally varying velocity and attenuation models over a large region of western China, since numerous regional earthquake from different azimuths were well-recorded by the Hi-CLIMB array (Figure 2).

## CONCLUSIONS AND RECOMMENDATIONS

For the first year of this new project, we are building a comprehensive database of regional events recorded by the Hi-CLIMB array. The starting point of this database will be relevant global and regional catalogs of seismicity, followed by relocation of selected events and inversion for source depths and focal mechanisms, if required. The major deliverable will be the database, including the catalog of events with precise locations of epicenters, focal depths, and focal mechanisms. Further validation of the Gaussian beam method is being conducted to efficiently and precisely calculate *Pn* propagation in laterally varying crustal and upper mantle structures. We will carefully compare results from different methods, including those from finite difference algorithms. The comparisons will also include extraction of relevant seismic attributes.

In the second phase of the project, we will construct seismic profiles across the Hi-CLIMB array for a selected set of relocated regional events. Normalization and deconvolution of seismic profiles by various reference signals in order to remove effects of the source-time function will be performed. Extraction of key seismic attributes will then be performed from observed seismic profiles, and detailed modeling/inversion of seismic attributes using Gaussian beams will be conducted in order to build self-consistent models for propagation of *Pn* beneath the Hi-CLIMB array in western China.

## REFERENCES

Babich, V. M. and M. M. Popov (1989). Gaussian summation method (review), Radiofizika 32: 1447–1466 (translated in *Radiophysics and Quantum electronics* 32: 1063–1081, 1990).

Braile, L. W. and R. B. Smith (1975). Guide to the interpretation of crustal refraction profiles, *Geophys. J.R. Astr. Soc.* 40: 145–176.

Cerveny, V., M. M. Popov, and I. Psencík (1982). Computation of wavefields in inhomogeneous media—Gaussian beam approach, *Geophys. J.R. Astr. Soc.* 70: 109–128.

Cerveny, V. and R. Ravindra (1971). *Theory of Seismic Head Waves*, Univ. of Toronto Press.

Chen, W.-P., and P. Molnar (1983). Focal depths of intracontinental and intraplate earthquakes and their implications for the thermal and mechanical properties of the lithosphere, *J. Geophys. Res.* 88: 4183–4214.

Chen, W. P. and Z. H. Yang (2004). Earthquakes beneath the Himalayas and Tibet: evidence for strong lithospheric mantle, *Science* 304: 1949–1952.

Clowes, R. M., M. J. Burianyk, A. R. Gorman and E. R. Kanasewich (2002). Crustal velocity structure from SAREX, the Southern Alberta Refraction Experiment, *Can. J. Earth Sci.* 39: 351–373.

Daubechies, I. (1992). *Ten lectures on wavelets*, SIAM, Philadelphia.

Engdahl, E.R., R.D. van der Hilst, and R.P. Buland (1998). Global teleseismic earthquake relocation with improved travel times and procedures for depth determination, *Bull. Seism. Soc. Am.* 88: 722–743.

Gorman A. R., R. M. Clowes, R. M. Ellis, M. J. Burianyk, E. R. Kanasewich, I. Asudeh, Z. Hajnal, G. D. Spence, T. J. Henstock, A. R. Levander, G. R. Keller, and K. Miller (2002). Deep Probe—maging the roots of western North America, *Can. J. Earth Sci.* 39: 375–398.

Hearn, T. M., S. Wang, J. F. Ni, Z. Xu, Y. Yu, and Z. Zhang (2004). Uppermost mantle velocities beneath China and surrounding regions, *J. Geophys. Res.* 109: B11301, doi:10.1029/2003JB002874.

Hill, D. (1971). Velocity gradients and anelasticity from crustal body-wave amplitudes, *J. Geophys. Res.* 76: 3309–3325.

Hill, D. (1973). Critically refracted waves in a spherically symmetric radially heterogeneous earth model, *Geophys. J.R. astr. Soc.* 34: 149–177.

Kao, H., Y.-H. Liu, W.-T. Liang, and W.-P. Chen (2002). Source parameters of regional earthquakes in Taiwan (1999–2000) including the Chi-Chi earthquake sequence, *Terr. Atmos. Ocean. Sci.* 13: 279–298.

Langin, W. R., L. D. Brown, and E. A. Sandvol (2003). Seismicity of central Tibet from Project INDEPTH III seismic recordings, *Bull. Seism. Soc. Am.* 93: 2146–2159.

Li, S., W. D. Mooney, and J. Fan (2006). Crustal structure of mainland China from deep seismic sounding data, *Tectonophysics* 420: 239–252.

Liang, C. and X. Song (2006). A low velocity belt beneath northern and eastern Tibetan Plateau from Pn tomography, *Geophys. Res. Lett.* 44: L22306, doi:10.1029/2006GL027926.

Liang, C., X. Song, and J. Huang (2004). Tomographic inversion of *Pn* travel times in China, *J. Geophys. Res.* 109: B11304: doi:10.1029/2003JB002789.

Lugara, D., C. Letrou, E. Shlivinski, E. Heyman, and A. Boag (2003). Frame-based Gaussian beam summation method: theory and applications, *Radio Science* 38: 8026.

Mallat, S. (1999). *A wavelet tour of signal processing*, 2nd edition, Academic Press, San Diego.

Matheney, M. P. and R. L. Nowack (1995). Seismic attenuation values obtained from instantaneous frequency matching and spectral ratios, *Geophys. J. Int.* 123: 1–15.

Matheney, M. P., R. L. Nowack, and A. M. Trehu (1997). Seismic attribute inversion for velocity and attenuation structure, *J. Geophys. Res.* 102: 9949–9960.

Meissner, R., F. Tilmann, and S. Haines (2004). About the lithospheric structure of central Tibet, based on seismic data from the INDEPTH III profile, *Tectonophysics* 380: 1–25.

Menke, W. H. and P. G. Richards (1980). Crust-mantle whispering gallery phases: a deterministic model of teleseismic Pn wave propagation, *J. Geophys. Res.* 85: 5416–5422.

Molnar, P., and W.-P. Chen (1983). Depths and fault plane solutions of earthquakes under the Tibetan plateau, *J. Geophys. Res.*, 88: 1180–1196.

Morozov, I., E. A. Morozova, S. B. Smithson, and L. N. Solodilov (1998). On the nature of the teleseismic Pn phase observed on the ultralong-range profile Quartz Russian, *Bull. Seismol. Soc. Am.*, 88: 62-73.

Morozov, I. and S. B. Smithson (2000). Coda of long-range arrivals from nuclear explosions, *Bull. Seism. Soc. Am.* 90: 929–939.

Nielsen, L. and H. Thybo (2003) The origin of teleseismic Pn waves: Multiple crustal scattering of upper mantle whispering gallery phases, *J. Geophys. Res.* 108: doi:10.1029/2003JB002487.

Nowack, R. L. (2008). Frame-based Gaussian beam summation and seismic head waves, in *Proceedings of the Project Review*, Geo-Mathematical Imaging Group, Purdue Univ. West Lafayette IN, Vol. 1, 113–119.

Nowack, R. L. (2003). Calculation of synthetic seismograms with Gaussian Beams, *Pure Appl. Geophys.* 160: 487–507.

Nowack, R. L. and K. Aki (1984). The two-dimensional Gaussian beam synthetic method: testing and application, *J. Geophys.* 89: 7797–7819.

Nowack, R. L. and M. P. Mathaney (1997). Inversion of seismic attributes for velocity and attenuation structure, *Geophys. J. Int.* 128: 689–700.

Nowack, R. L. and S. M. Stacy (2002). Synthetic seismograms and wide-angle seismic attributes from the Gaussian beam and reflectivity methods for models with interfaces and velocity gradients, *Pure Appl. Geophys.* 159: 1447–1464.

Nowack, R. L., W.-P. Chen, U. E. Kruse, and S. Dasgupta (2007a). Imaging offsets in the Moho: Synthetic tests using Gaussian beam with teleseismic waves, *Pure Appl. Geophys.* 164: 1921–1936

Nowack, R. L., W.-P. Chen, T. L. Tseng, and the Hi-CLIMB Imaging Team (2007b). Imaging the crust and upper mantle beneath the Hi-CLIMB seismic array in Tibet using Gaussian beam migration of radial receiver functions, Fall 2007 Am. Geophys. Un. Meeting, San Francisco.

Nowack, R. L., S. Dasgupta, G. T. Schuster, and J. M. Sheng (2006). Correlation migration using Gaussian beams of scattered teleseismic body waves, *Bull. Seism. Soc. Am.* 96: 1–10.

Phillips, W. S., M. L. Begnaud, C. A. Rowe, L. K. Steck, S. C. Myers, M. E. Pasyanos, and S. Ballard (2007). Accounting for lateral variations of the upper mantle gradient in Pn tomography studies, *Geophys. Res. Lett.* 34: L14312, doi:10.1029/2007GL029338.

Popov, M. M. (1982). A new method of computation of wave fields using Gaussian beams, *Wave Motion* 4: 85–97.

Popov, M. M. (2002). *Ray theory and Gaussian beam method for geophysicists*, Universidade Federal da Bahia, Brazil, 172 pp.

Ryberg, T., K. Fuchs, A. V. Egorkin, and L. Solodilov (1995). Observation of high frequency teleseismic Pn waves on the long-range Quartz profile across northern Europe, *J. Geophys. Res.* 100: 18,151–18, 163.

Ryberg, T., M. Tittgemeyer, and F. Wenzel (2000). Finite difference modeling of P-wave scattering in the upper mantle, *Geophys. J. Int.* 141: 787–800.

Sereno, T. J. and J. W. Given (1990). Pn attenuation for a spherically symmetric earth model, *Geophys. Res. Lett.* 17: 1141–1144.

Stacy, S.M. and R. L. Nowack (2002). Modeling of wide-angle seismic attributes using the Gaussian beam method, *Studia Geophys. Geod.* 46: 677–690.

Sun, Y. and M.N. Toksoz (2006). Crustal structure of China and surrounding regions from P wave traveltime tomography, *J. Geophys. Res.* 111: B03310, doi:10.1029/2005JB003962.

Taner, M. T., F. Koehler, and R. E. Sheriff (1979). Complex seismic trace analysis, *Geophysics* 44: 1041–1063.

Tittgemeyer, M., F. Wenzel, K. Fuchs, and T. Ryborg (1996). Wave propagation in a multiple scattering upper mantle – observation and modeling, *Geophys. J. Int.* 127: 492–502

Virieux, J. (1988). P-SV wave propagation in heterogeneous media: velocity-stress finite-difference method, *Geophysics* 51: 889–901.

Yang, X., T. Lay, X. B. Xie, and M.S. Thorne (2007). Geometric spreading of Pn and Sn in a spherical earth model, *Bull. Seism. Soc. Am.* 97: 2053–2065.

Zhu, L., Y. Tan, D. V. Helmberger, and C. K. Sikia (2006). Calibration of the Tibetan Plateau using regional seismic waveforms, *Pure Appl. Geophys.* 1193–1213.

# GROUND TRUTH, MAGNITUDE CALIBRATION, AND REGIONAL PHASE PROPAGATION AND DETECTION IN THE MIDDLE EAST AND THE HORN OF AFRICA

Andrew A. Nyblade[1], Aubreya Adams[1], Richard A. Brazier[1], Yongcheol Park[1], and Arthur J. Rodgers[2]

Penn State University[1] and Lawrence Livermore National Laboratory[2]

Sponsored by National Nuclear Security Administration

Contract No. DE-FC52-05NA26602[1] and DE-AC52-07NA27344[2]
Proposal No. BAA05-07

## ABSTRACT

In this project, we have exploited unique and open-source seismic datasets to improve seismic monitoring across the Middle East (including the Iranian Plateau, Zagros Mountains, Arabian Peninsula, Turkish Plateau, Gulf of Aqaba, Dead Sea Rift) and the Horn of Africa (including the northern part of the East African Rift, Afar Depression, southern Red Sea, and Gulf of Aden). The data sets have been used to perform two related tasks. (1) We have determined moment tensors, moment magnitudes, and source depths for regional events in the magnitude 4.0 to 6.0 range. (2) These events have been used to characterize high-frequency regional phase attenuation and detection thresholds, especially from events in Iran recorded at stations across the Arabian Peninsula.

In the first part of this project, seismograms from earthquakes in the Zagros Mountains recorded at regional distances have been inverted for moment tensors, and source depths for the earthquakes have been determined via matching regional waveforms using a grid search algorithm and forward modeling of teleseismic depth phases. Early studies of the distribution of seismicity in the Zagros region found evidence for earthquakes in the upper mantle. But subsequent relocations of teleseismic earthquakes suggest that source depths are generally much shallower, lying mainly within the upper crust. For all of the events that have been studied, source depths lie within the upper crust. And the events all have thrust mechanisms with E-W or NW-SE striking nodal planes. In the second part of this project, the source mechanisms for these events have been used to characterize high-frequency (0.5–16 Hz) regional phase attenuation and detection thresholds for broadband seismic stations in the Arabian Peninsula, including International Monitoring System (IMS) stations and stations belonging to the Saudi Arabian National Digital Seismic Network.

To improve event locations, source mechanisms, and attenuation estimates, new regional P- and S-wave velocity models of the upper mantle under the Arabian Peninsula have also been developed using data from teleseismic events recorded at stations within the Arabian Peninsula and the Horn of Africa. These models show slower-than-average velocities within the lithsopheric mantle under the entire Arabian Shield. However, at sublithospheric mantle depths, the low-velocity region appears to be localized beneath the western side of the Arabian Shield.

## OBJECTIVE

The objective of this effort has been to determine ground truth source parameters (depth, moment, focal mechanism) for earthquakes in the Middle East. We have focused on events in the Zagros Mountains of Iran and used unique broadband waveforms from regional stations. Source moments are being used to calibrate coda wave moment magnitudes (Mayeda et al., 2003) and to model high-frequency regional body-wave amplitude spectra with the Magnitude-Distance Amplitude Correction (MDAC) methodology (Walter and Taylor, 2001). To help in this effort, we have also developed new velocity models of the upper mantle beneath the Arabian Peninsula.

## RESEARCH ACCOMPLISHED

### Introduction

In this project, we have exploited unique and open-source seismic data sets to improve seismic monitoring for the Middle East (including the Iranian Plateau, Zagros Mountains, Arabian Peninsula, Turkish Plateau, Gulf of Aqaba, Dead Sea Rift) and the Horn of Africa (including the northern part of the East African Rift, Afar Depression, southern Red Sea, and Gulf of Aden). Broadband waveform data sets have been used to perform three related tasks. (1) We have determined moment tensors, moment magnitudes, and source depths for regional events in the magnitude 3.0 to 6.0 range. (2) These events have been used to characterize high-frequency (0.5–16 Hz) regional phase attenuation and detection thresholds, especially from events in Iran recorded at stations across the Arabian Peninsula. (3) We have developed new velocity models of the upper mantle beneath the Arabian Peninsula. The results of this research enhance monitoring capabilities within the study region by improving our understanding of high frequency regional phase attenuation and how this attenuation affects detection thresholds, as well as the velocity structure of the uppermost mantle.

Towards meeting these objectives, seismograms from earthquakes in the Zagros Mountains recorded at regional distances have been inverted for moment tensors, which have then been used to create synthetic seismograms to determine the source depths of the earthquakes via waveform matching. The source depths have been confirmed by modeling teleseismic depth phases recorded on global seismographic network (GSN) and IMS stations. Early studies of the distribution of seismicity in the Zagros region found evidence for earthquakes in the upper mantle. But subsequent relocations of teleseismic earthquakes suggest that source depths are generally much shallower, lying mainly within the upper crust. All of the regional events studied nucleated within the upper crust, and most of the events have thrust mechanisms. The source mechanisms for these events have been used to characterize high-frequency (0.5–16 Hz) regional phase attenuation and detection thresholds for broadband seismic stations in the Arabian Peninsula, including IMS stations and stations belonging to the Saudi Arabian National Digital Seismic Network.

To improve event locations, source mechanisms and attenuation estimates, new regional P- and S-wave velocity models of the upper mantle under the Arabian Peninsula have also been developed using data from teleseismic events recorded at stations within the Arabian Peninsula and Horn of Africa. These models show slower-than-average velocities within the lithsopheric mantle under the entire Arabian Shield. However, at sublithospheric mantle depths, the low velocity region appears to be localized beneath the western side of the Arabian Shield.

### Background

The Arabian Shield consists of a late Proterozoic crystalline basement overlain by Tertiary and Quaternary volcanic rocks in some places. The breakup of the Arabian Plate from Africa initiated at about 30–5 Ma, with the formation of the Red Sea–Gulf of Aden rift system (Coleman and McGuire, 1988). Volcanism was widespread between 30 and 12 Ma, and an uplift of the Arabian Shield occurred at about 13 Ma (Coleman and McGuire, 1988). The volcanism and uplift are thought to be related to the presence of a hot upper mantle (Camp and Roobol, 1992). The uplifted Arabian Shield contains two major features: one is the

Makkah-Madinah-Nafud (MMN) volcanic line in the south and the other is the Ha'il-Rutbah Arch in the north (Figure 1). The MMN volcanic line, extending north-south, has been the major site of volcanism in Saudi Arabia over the past 10 Ma, and the Ha'il-Rutbah Arch has been the site of several periods of uplift (Camp and Roobol, 1992).

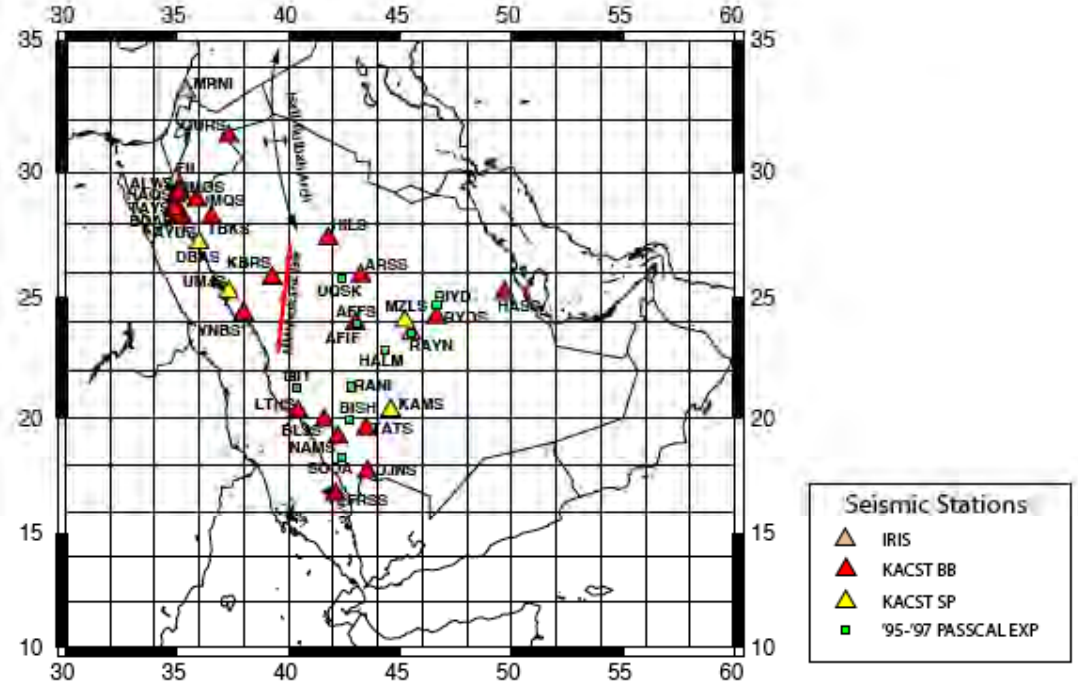


**Figure 1. Map showing seismic stations in the Arabian Peninsula used in this study. KACST stations belong to the Saudi Arabia Digital National Seismic network.**

The Zagros Mountain Belt, one of the world's most seismically active mountain ranges, marks the convergent boundary between the Arabian and Eurasian plates in southwestern Iran (Figure 2). The upper 11 km of the crust consists of folded sedimentary layers, while the lower 36 km of the crust are composed of faulted crystalline basement rock. The most prominent fault exposed at the surface is the Zagros Main Thrust, which marks the northern extent of seismicity associated with the Zagros Mountains and separates the Zagros Mountains from the Central Iranian Plateau. The Moho dips to the northeast from a depth of 40 km beneath the Persian Gulf to maximum depth of approximately 65–70 km beneath the Zagros Main Thrust (Hatzfeld et al., 2003). Early studies of the distribution of seismicity in the Zagros region found evidence for earthquakes in the upper mantle (Nowroozi, 1971; Bird et al., 1975). Subsequent recalculations of teleseismic earthquakes indicated that source depths were much shallower, lying within the upper crust (Maggi et al., 2000, 2002).

**Zagros Earthquakes**

Source depths and focal mechanisms for six well-studied events have been obtained (Tables 1 and 2). A grid-search method was used to determine the source parameters of each event. First, regional waveforms for each event were inverted for a moment tensor over a range of potential source depths. Synthetic seismograms were then computed using a reflectivity code for each source mechanism and compared to observed waveforms. In addition to the KACST and PASSCAL stations, data recorded at regional distances on open stations to the north and east were used, providing fairly good azimuth-ray coverage for each event. The quality of the visual fit between the synthetic and observed waveforms, along with the root-mean-square error, was used to determine the best-fitting focal mechanism and associated source depth. The velocity model used for the inversions is given in Table 3 and comes from Rodgers et al., (1999).

In addition, to help constrain focal depths, teleseismic depth phases from open stations in the 30 to 90 degree distance range were modeled using the focal mechanism obtained from the grid search at a particular depth. A local crustal model from Hatzfeld et al. (2003) was used for this modeling.

**Figure 2. Colored topography map of the Middle East showing the location of the main plates and the Zagros Mountains.**

The locations of the events are shown in Figure 3. Most of the events studied occurred within the central portion of the Zagros Mountains where there are the best constraints on crustal structure provided by receiver function and gravity studies. Figures 4a and 4b summarize graphically the results for two of the events, and serve to illustrate the quality of the waveform fits that we have obtained. Source depths for the events are within the upper crust.

**Table 1. Source Parameters for Well-Studied Events in the Zagros Mountains (event letters are the same as in Figure 3)**

| Ev # | Date | Time | Lat (N), Long (E) | EHB | ISC | | CMT | | This Study | |
|---|---|---|---|---|---|---|---|---|---|---|
| | | | | Depth (km) | Depth (km) | mb | Depth (km) | Mw | Depth (km) | M w |
| A | 11/13/98 | 13:01:10 | 27.79, 53.64 | 9 | 15.3 | 5.3 | f33 | 5.4 | 4-7 | 5.5 |
| B | 10/31/99 | 15:09:40 | 29.41, 51.81 | 15 | 38 | 4.9 | f33 | 5.2 | 4-5 | 5.4 |
| C | 3/1/00 | 20:06:29 | 28.39, 52.85 | 20 | 46.7 | 5.0 | f15 | 5.0 | 7-10 | 5 |
| D | 2/17/02 | 13:03:53 | 28.09, 51.76 | 15 | f15 | 5.5 | f33 | 5.3 | 2-6 | 5.2 |
| E | 7/10/03 | 17:06:38 | 28.36, 54.17 | 11 | 19 | 5.8 | f15 | 5.7 | 4-7 | 5.7 |
| F | 4/13/01 | 1:04:27 | 28.28, 54.87 | 20 | 28.7 | 4.9 | 26.1 | 5.1 | 8-11 | 4.9 |

International Seismic Centre (ISC) Catalog, Harvard Centroid Moment Tensor (CMT) Catalog, EHB (Engdahl et al., 2006); "f" indicates a fixed depth.

**Table 2. Moment Tensor Elements for Specified Focal Depths**

| Ev # | Depth (km) | Mxx | Mxy | Mxz | Myy | Myz | Mzz | Mo |
|---|---|---|---|---|---|---|---|---|
| A | 5 | 0.847e24 | 0.205e24 | -0.152e25 | 0.634e23 | 0.753e24 | -0.911e24 | 1.93E24 |
| B | 4 | 0.203e24 | 0.110e24 | -0.107e25 | 0.236e24 | 0.705e24 | -0.439e24 | 1.34E24 |
| C | 8 | 0.181e24 | -0.397e23 | -0.202e23 | -0.167e23 | 0.278e24 | -0.164e24 | 3.87E23 |
| D | 4 | 0.380e24 | 0.199e24 | -0.393e24 | 0.550e23 | 0.561e24 | -0.435e24 | 8.23E23 |
| E | 5 | 0.271e25 | -0.212e24 | 0.225e25 | -0.607e24 | -0.328e25 | -0.210e25 | 4.69E24 |
| F | 9 | 0.179e24 | 0.432e23 | 0.118e24 | 0.234e23 | -0.300e23 | -0.202e24 | 2.31E23 |

**Table 3. Velocity Model Used for Moment Tensor Inversion**

| Depth (km) | P-wave Velocity (km/s) | S-wave Velocity (km/s) |
|---|---|---|
| 1–4 | 4.00 | 2.31 |
| 4–20 | 6.22 | 3.59 |
| 20–38 | 6.44 | 3.72 |
| 38–42 | 7.30 | 4.21 |
| 42–74.5 | 8.04 | 4.48 |

**Table 4. Velocity Model Used for Modeling Teleseismic Depth Phases**

| Depth (km) | P-wave Velocity (km/s) | S-wave Velocity (km/s) |
|---|---|---|
| 1–11 | 4.700 | 2.714 |
| 11–19 | 5.850 | 3.378 |
| 19–46 | 6.500 | 3.753 |
| 46 | 8.000 | 4.620 |

A comparison of our results with previously reported magnitudes and source depths is provided in Table 1. The magnitude estimates obtained in this study are similar to those previously reported; however, the focal depths for a number of the events that we obtained are shallower than those reported in other catalogs.

The focal depth of earthquakes can affect the excitation of regional phases, particularly the guided Lg phase, which is composed of higher mode surfaces waves whose amplitudes are strongly depth dependent. The source parameters determined above can be used to infer how focal mechanism and depth might impact regional-phase S-wave generation and this might in turn impact P/S discriminants. Two nearby events (A and H) were recorded at station HILS on the northern Arabian Shield. Event A is the same event as in Table 1 and Figure 3. Event H was reported in Nyblade et al., (2006). These events had similar magnitudes (5.4 versus 5.7), and although both are thrust mechanisms, their strikes are slightly different. The high-frequency (0.5–5 Hz) response of these events is shown in Figure 5. Note that Lg is weaker with respect to the Pn for the deeper event (H), making the Pn/Lg ratio discriminant more explosion-like for this event. This suggests a possible depth-dependence of the Lg amplitude (and Pn/Lg ratio discriminant). Alternatively, the further event (H) may be located in a region of thicker crust, which leads to disruption of the crustal waveguide along the path to HILS. Both explanations would cause additional scatter in body-wave discriminants, compounding discrimination strategies.

**Body-Wave Tomography**

Upper mantle structure strongly impacts the propagation of regional Pn and Sn phases. We report velocity structure of the upper mantle reported from teleseismic P and S body-waves and from surface waves. To investigate upper-mantle structure under the Arabian Shield using body waves, we measured and inverted relative travel times from stations in Arabia. We augmented the KACST data with delay times measured from permanent stations in the region (RAYN, EIL and MRNI) and the 1995–1997 Saudi Arabian PASSCAL Experiment dataset. Figure 1 shows the locations of the seismic network used in this study. We computed travel time differences for two nearly colocated stations (AFFS and AFIF in Figure 1) between KACST and the PASSCAL networks in order to investigate possible biases between these data sets before combining all delay times from different seismic networks. We sorted events recorded on the common stations by back azimuth and distance and measured travel time residuals from arrival times subtracted from a theoretical travel time. The trends of the residuals with back-azimuth and distance are very similar and indicate no bias between the travel-time residuals for the common stations.

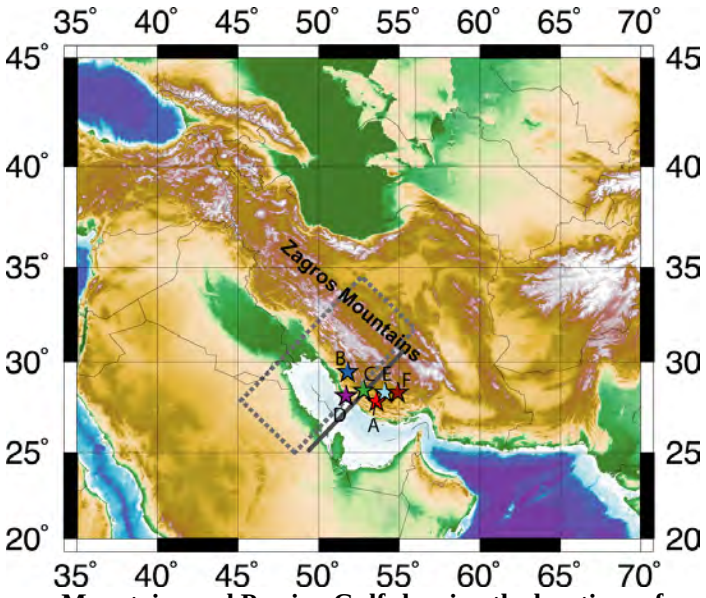


**Figure 3. Map of Zagros Mountains and Persian Gulf showing the locations of earthquakes studied. Letters correspond to the events in Table 1. The grey box shows the area where crustal thickness has been constrained using gravity data, and the white line shows where crustal thickness has been imaged using receiver functions.**

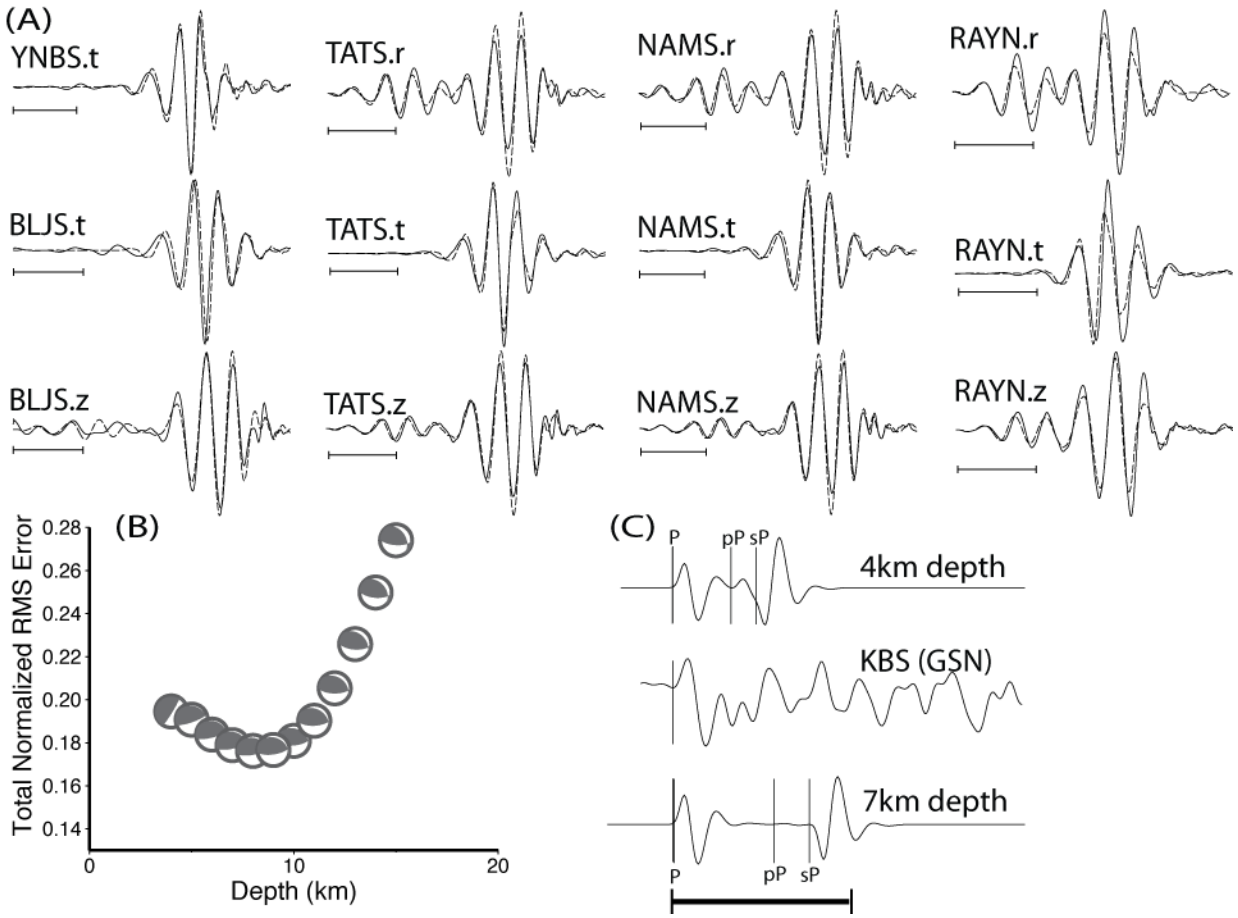


**Figure 4a. Results for earthquake A, illustrating the method used for obtaining source parameters and the quality of the waveform fits. (A) Long-period regional displacement waveforms**

**(solid line) and synthetics (dashed line) for a number of stations. The scale bar shows 100 seconds. (B) Plot of focal depth vs. error. (C) Short-period teleseismic waveforms (data and synthetics), showing depth phases. The scale bar shows 5 seconds.**

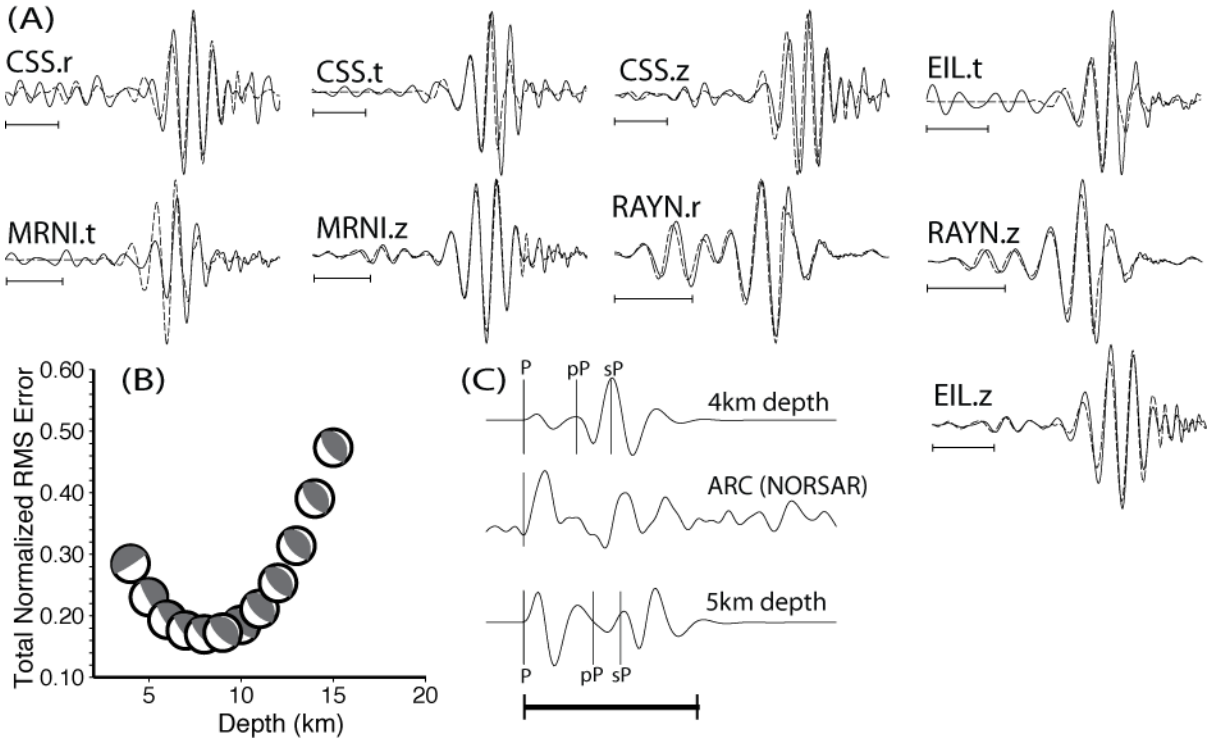


**Figure 4b. Results for earthquake B illustrating the method used for obtaining source parameters and the quality of the waveform fits. (A) Long-period regional displacement waveforms (solid line) and synthetics (dashed line) for a number of stations. The scale bar shows 100 seconds. (B) Plot of focal depth vs. error. (C) Short-period teleseismic waveforms (data and synthetics) showing depth phases. The scale bar shows 5 seconds.**

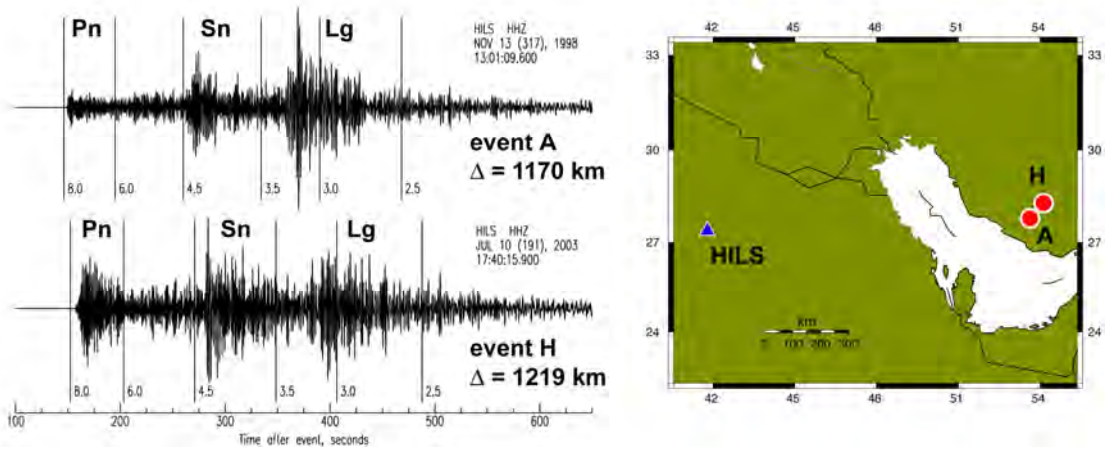


**Figure 5. (Left) Vertical component waveforms (filtered 0.5–5 Hz) for events A (top) and H (bottom) at station HILS (Al Hail, Saudi Arabia). (Right) These events are closely located with event H slightly farther away.**

For the datasets, we computed relative arrival-time residuals using a multichannel cross-correlation method (Crosson, 1990) and inverted for a three-dimensional velocity model using the method of VanDecar (1991). For the inversion, we parameterized travel-time slowness using a grid of knots composed of 34 knots in depth, 56 knots in latitude between 12.0° N, and 37.0° N and 56 knots in longitude between 29.5° E and 55.0° E. The horizontal knot spacing is one-third of a degree, and the vertical knot spacing is 25 km in the inner region of the seismic array (17.4° N–30.7° N, 35.5° E–48.5° E, and 0–200 km depth). We used the iasp91 model (Kennett and Engdahl, 1991) as the initial model for the inversion.

**Results for the P-Wave Tomography**

We used 401 earthquakes resulting in 3416 ray paths with P- and PKP-wave arrivals. The majority of the events are located in the western Pacific Rim between back azimuths of 15 and 150 degrees, but the events are distributed over a wide range of back azimuths. The waveforms were filtered with a zero-phase two-pole Butterworth filter between 0.5 to 2 Hz before the relative travel-time residuals were computed. The multichannel cross-correlation (MCCC) procedure was performed over a three-second window on the filtered data. A final model was selected by investigating the way in which changes in regularization levels (flattening and smoothing values) affect the reduction in travel-time residuals. To determine a preferred model, 2000 iterations of the conjugate gradient procedure are performed with several different pairs of flattening and smoothing values. For our preferred model, we have chosen a model with the values of 1600 for flattening and 3200 for smoothing. Figure 6 shows depth slices (a–d) and vertical cross-sections (e and f) through the P model. The first-order velocity variations seen in the S model are similar to the P model, and therefore we do not show the S-wave model here.

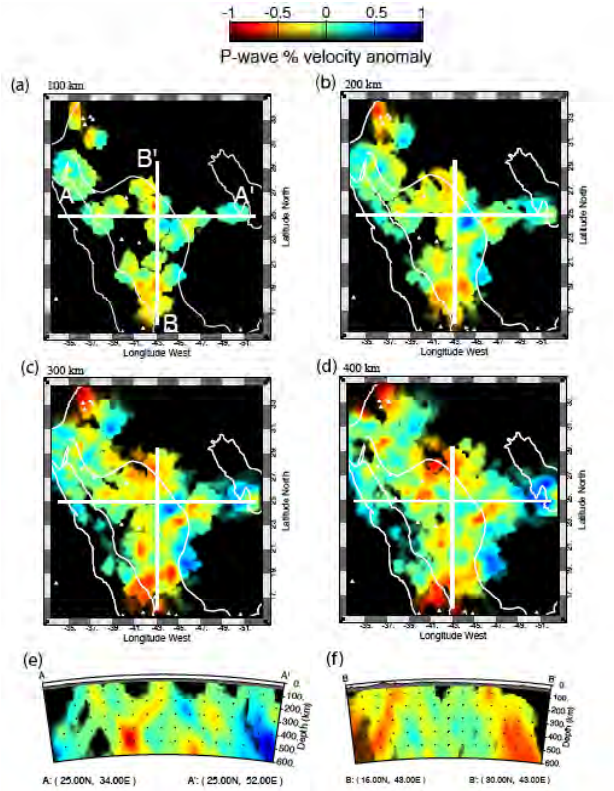


**Figure 6. Results of P-wave tomography. (a–d) Depth slices through the model at depths of 100, 200, 300, and 400 km. (e–f) vertical slices through the model along E-W (e) and N-S (f) profiles denoted with white lines in a–d.**

### Surface-Wave Tomography

The shear-wave velocity structure of the shallow upper mantle beneath the Arabian Shield has been modeled by inverting Rayleigh-wave phase velocity measurements between 45 and 140 s together with previously published Rayleigh-wave group velocity measurements between 10 and 45 s (Park et al., 2008). For measuring phase velocities, we applied a modified array method to data from several regional networks that minimizes the distortion of ray paths caused by lateral heterogeneity. The new shear-wave velocity model shows a broad low-velocity region to depths of about 150 km in the mantle across the Shield and a narrower low-velocity region at depths greater than 150 km localized along the Red Sea coast and Makkah-Madinah-Nafud volcanic line. The results are shown in Figure 7.

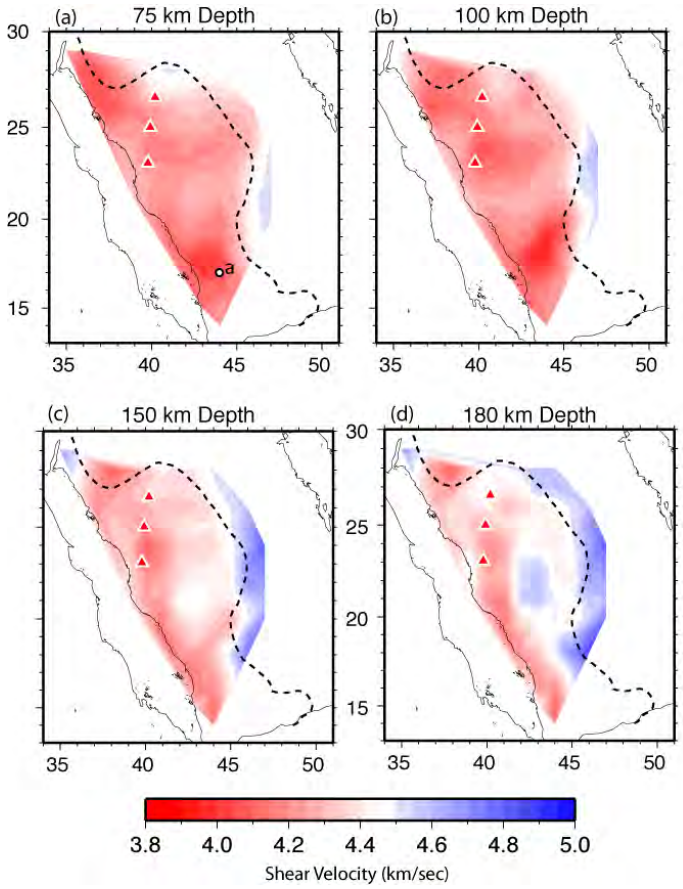


**Figure 7. S-wave model of upper-mantle structure from inverting Rayleigh-wave phase velocities. (a–d) Horizontal slices through the model are shown for depths of 75, 100, 150, and 180 km. The red triangles show the location of the Makkah-Madinah-Nafud volcanic line. The dashed line shows the outline of the Shield.**

## CONCLUSIONS

We have obtained focal depths and mechanisms for several earthquakes in the Zagros Mountains. The source parameters for these events can be used to calibrate coda wave magnitudes and to model high-frequency regional phase amplitude spectra with the MDAC methodology. We have inverted teleseismic data (body and surface waves) to obtain new velocity models of the uppermost mantle under the Arabian Peninsula. These models show slower-than-average velocities within the lithsopheric mantle under the entire Arabian Shield. However, at sublithospheric mantle depths, the low-velocity region appears to be localized beneath the western side of the Arabian Shield.

## ACKNOWLEDGEMENTS

The facilities of the Incorporated Research Institutions for Seismology (IRIS) Data Management System (DMS), and specifically the IRIS Data Management Center, were used for access to waveform and metadata required in this study. The IRIS DMS is funded through the National Science Foundation and specifically the GEO Directorate through the Instrumentation and Facilities Program of the National Science Foundation.

## REFERENCES

Bird, P., M. N. Toksoz, and N. H. Sleep (1975). Thermal and mechanical models of continent-continent convergence zones, *J. Geophys. Res*. 80: 4405–4416.

Camp, V. E. and M. J. Roobol (1992). Upwelling asthenosphere beneath western Arabia and its regional implications, *J. Geophys. Res.* 97: 15255–15271.

Coleman, R. G. and A. V. McGuire (1988). Magma systems related to the Red Sea opening, *Tectonophysics* 150: 77–100.

Crosson, R. S. (1990). Determination of teleseismic relative phase arrival times using multi-channel cross correlation and least-squares, *Bull. Seism. Soc. Am.* 80: 150–169.

Engdahl, E. R., J. A. Jackson, S. C. Myers, E. A. Bergman, and K. Priestley (2006). Relocation and assessment of seismicity in the Iran region, *Geophys. J. Int*. 222: 761–778.

Hatzfeld, D., M. Tatar, K. Priestley, and M. Ghafori-Ashtiany (2003). Seismological constraints on the crustal structure beneath the Zagros Mountain Belt (Iran), *Geophys. J. Int.* 155: 403–410.

Kennett, B. and E. R. Engdahl (1991). Travel times for global earthquake location and phase identification, *Geophys. J. Int.* 105: 429–465.

Maggi, A., J. Jackson, K. Priestley, and C. Baker (2000). A re-assessment of focal depth distributions in southern Iran, the Tien Sha and northern India: Do earthquakes really occur in the continental mantle? *Geophys. J. Int.* 143: 629–661.

Maggi, A., K. Priestley, and J. Jackson (2002). Focal depths of moderate to large earthquakes in Iran, *J. Seismol. Earthquake Eng.* 4: 1–10.

Mayeda, K., A. Hofstetter, J. O'Boyle, and W. Walter (2003). Stable and transportable regional magnitudes based on coda-derived moment-rate spectra, *Bull. Seism. Soc. Am*. 93: 224–239.

Nowroozi, A. A. (1971). Seismotectonics of the Persian Plateau Eastern Turkey, Caucasus, and Hindu-Kush regions, *Bull. Seism. Soc. Am.* 61: 317–342.

Nyblade, A., W. Walter, and R. Gok (2006). Developing and exploiting a unique seismic dataset from South African gold mines for source characterization and wave propagation, in *Proceedings of the 28th Seismic Research Review:Ground-Based Nuclear Explosion Monitoring Technologies*, LA-UR-0605471, Vol. 1, pp. 166–175.

Park, Y., A. A. Nyblade, A. J. Rodgers, and A. Al-Amri (2008). S wave velocity structure of the Arabian Shield upper mantle from Rayleigh wave tomography, *Geochem. Geophys. Geosyst.* 9: doi:10.1029/2007GC001895.

Rodgers, A. J., W. R. Walter, R. J. Mellors, A. M. S. Al-Amri, and U.-S. Zhang (1999). Lithospheric structure of the Arabian Shield and Platform from complete regional 256 waveform modelling and surface wave group velocities, *Geophys. J. Int*. 138: 871–878.

VanDecar, J. C. (1991). Upper mantle structure of the Cascadia subduction zone from non-linear teleseismic travel time inversion, Ph. D. thesis, Univ. of Washington, Seattle, WA.

Vernon, F. and J. Berger (1998). Broadband seismic characterization of the Arabian Shield, final scientific technical report, Department of Energy Contract No. F 19628-95-K-0015.

Walter, W. and S. Taylor (2001). A revised magnitude and distance amplitude correction (MDAC2) procedure for regional seismic discriminants, Lawrence Livermore National Laboratory technical report UCRL-ID-146882.

# ANALYSES AND SIMULATION OF 3D SCATTERING DUE TO HETEROGENEOUS CRUSTAL STRUCTURE AND SURFACE TOPOGRAPHY ON REGIONAL PHASES, MAGNITUDE DISCRIMINATION

Arben Pitarka[1], Don V. Helmberger[2], and Sidao Ni[1]

URS Group[1] and California Institute of Technology[2]

Sponsored by Air Force Technical Applications Center

Contract No. FA8718-07-C-0003
Proposal No. BAA08-39

## ABSTRACT

The main purpose of this study is the understanding of scattering and its effects through step-by-step numerical experiments and waveform modeling, with the goal of providing useful insights into ongoing research for the development of simple empirical models of scattering that can be used in reducing the scatter in measures of Lg and coda wave magnitude and for discrimination purposes as well. We are performing anelastic 3D finite-difference simulations of wave propagation in highly heterogeneous media for a range of source depths, receiver distances and source types. In the first stage of our study we investigated the effect of small-scale crustal heterogeneities on wave propagation scattering. During the second stage we investigated the effect of surface topography combined with crustal heterogeneities on wave propagation scattering. In our simulations of regional wave propagation we used a finite difference computer program using our computer cluster. The seismograms were calculated at up to 3.5 Hz for regional distances of up to 300 km. The topography elevation was simulated using correlated random variations along the free surface. Our simulations show that the surface topography increases the wave-path scattering effects. The combined effects of crustal heterogeneities and surface topography produce Lg, P, and S coda waves with significant energy even for explosion sources. The energy of Lg coda waves depends on the source depth. P/Lg ratios estimated at different frequencies indicate that this ratio could be a good discriminant between explosions and earthquakes when calculated at high frequencies. The wave-path scattering effects were also investigated by simulating observed high frequency source directivity effects, as well as fault zone wave trapping in highly fractured conditions from aftershocks of the Big Bear earthquake sequence.

## OBJECTIVES

Our objective is to analyze and evaluate the effect of scattering on the amplitude and frequency content of Pg, Rg, and Lg waves due to small-scale crustal heterogeneities and surface topography by three-dimensional (3D) finite-difference simulations and modeling of recorded waveform data. During this phase of our research we focused on the following topics:

1. Influence of scattering due to complex structure and surface topography on the variability observed in amplitude estimates of regional phases. We analyzed simulation results of regional wave propagation scattering, obtained with an efficient 3D finite-difference computer program executed on a computer cluster at the California Institute of Technology, using message passing interface (MPI) .
2. Influence of source emplacement conditions on scattering of P and S waves for explosion sources located inside and outside shallow basins.

## RESEARCH ACCOMPLISHED

Crustal heterogeneities of all scales and surface topography are shown to be very important factors influencing the scattered waves observed as coda arriving after the main wave phases. Some of their robust features such as amplitude and duration are related to the source itself, and location. Therefore different types of coda waves are being used for moment estimates for small event and source discrimination as well. The origin and the characteristics of the wave propagation scattering need to be investigated by both observational and numerical techniques. While analyses of recorded seismograms can reveal the degree of complexities in the crust and the effect of small- and large-scale perturbation on different wave phases, the numerical experiments can be used for isolating effects caused by the wave path, seismic source, and local structures. They can also be used to verify hypotheses that are at the foundation of several discrimination methodologies and complement studies of waveform analyses in regions with sparse station coverage.

The regional discriminants and magnitude methods rely mainly on the general feature of decreased S-phase amplitude and increase of P-phase amplitudes for explosion sources. However explosions produce anomalous large s-phase amplitudes that confound regional methods. It is therefore important to understand the factors that are at the origin of such behavior. In this study we investigate one factor: the effect of scattering due to random heterogeneities in the upper crust on the local and regional wavefield from explosion and earthquake sources.

In this study we apply a 3D staggered grid finite difference technique and a grid with variable spacing to simulate the effect of surface topography and shallow crustal heterogeneity on wave propagation scattering on both isotropic explosion and earthquake sources. Random fluctuations of wave speed and topography modeled with exponential averaging controlled by correlation lengths are used in generating crustal velocity models. In addition to simulated waveforms we analyzed smoothed envelopes of recorded waveforms from selected earthquakes and explosions in North Korea, recorded at regional stations with different wave-path scattering conditions. Our analyses show that the coupling between the surface and body waves, phase changes due to shallow wave propagation scattering, and local conditions in the source region significantly influence the amplitude of P and S coda waves as well as Rg waves. Such influence is frequency- and source-type dependent. Therefore, numerical experimention can help design efficient discriminantion procedures between earthquakes and explosions by using distant stations where the scattering removes the effects of Rg.

### Parameterization of Scattering Models

We have developed a regional seismic wave numerical modeling method to investigate wave scattering due to shallow crustal heterogeneity and free surface topography for explosion and earthquake sources. Our initial work has been focused on small-scale shallow crustal heterogeneity effects by using models with flat free surface. Now we have extended our study to more complex crustal structures that include complex surface topography.

The spatial perturbation of velocity in our 3D model is expressed as a percentage of the unperturbed shear modulus $\mu$. The random perturbations are intercorrelated using a spatial correlation length D. The perturbed shear modulus $\mu^*$ at each given grid node ‘k’ is calculated using the following equation:

$$\mu_k^* = \mu_k(1 + 0.35\, f_k)$$

where,

$$f_k = \frac{\sum_1^N \omega_i * rand_i}{W_k} \qquad W_k = \sum_1^N \omega_i \qquad \omega_i = \exp(-\tfrac{d_i}{D})$$

– $rand_i$: a spatial distribution of real random numbers ranging between -1 and 1.
– $d_i$: distance between the given node 'k' and adjacent nodes located within an ellipsoid centered at node 'k' with horizontal long axis D and short axis D/2.
– D: correlation length. D = 1.5 km.

The scattering parameters, such as the amount of perturbation and its correlation, were derived during the previous phase of this study. Velocity perturbation of up to 8% with a correlation length of 1.5 km was found to correctly reproduce the observed P and S coda waves' decay and the disappearance of their corresponding frequency-dependent radiation pattern. An example of scattering effect on observed P- and S-wave propagation, expressed as amplitude variation of the ground velocity envelope, is illustrated in Figure 1. This figure shows the amplitude variation of the ground velocity envelope as a function of frequency from the Mw4.5 070120 earthquake in South Korea. We used broad-band recordings at station CHC, CHJ, ULJ, and SES. The pure strike-slip mechanism of the earthquake and its recording at stations near the P wave nodal planes are ideal for analyzing regional scattered waves. Stations CHJ and CHC are close to P-wave nodal planes. The P wave scattering, expressed as the relative increase of amplitude of the P wave and its coda in the tangential component of motion at P-wave nodal stations, becomes significant at frequencies higher than 4 Hz. Note the relatively large amplitude of P coda waves on the tangential component at such frequencies. This indicates that high-frequency P- to S-wave conversions are significant. It is important to note that scattering effects due to small-scale perturbation in the shallow crust cause the increase in amplitude of high frequency P-wave coda in all three components. Because of their shorter wavelength, S waves are more susceptible to wave propagation scattering effects. As shown in Figure 1, for such waves, the amplitude difference between the three components that is controlled by the source radiation pattern is observed only at frequencies lower than 2 Hz. In general, at higher frequencies the amplitude of S wave coda is mainly controlled by scattering. Consequently it is the same for all three components. These observed features of P and S phases can help constrain scattering parameterization.

**Analyses of Scattering Effects on Observed Waveforms**

The origin of the high frequency scattering affecting mainly the P, Rg, and Lg coda waves (above 1 Hz) could be due to either deep or shallow crustal structure complexities along the wave path or in the source region (e.g., Dainty 1996; Wu et al., 2000, He et al., 2008). Lg waves show evidence of scattering from small-scale structures. Other causes of scattering could also be large-scale structural complexities such as crustal thinning or multipathing in the crust and large basins (e.g., Ni and Barazangi, 1983; Phillips et al., 2000).

Figure 3a shows smoothed envelopes of broad-band velocity seismograms from the 020416 earthquake in North Korea, recorded at station MDJ (Figure 2) and at a station located southwest of MDJ named STATION1. The epicentral distances of STATION 1 and MDJ are about 100 km and 400 km, respectively. The envelopes are calculated at the frequency bands of 0.8-2 Hz and 4-8 Hz. An interesting feature of the envelopes is the decay rate of P coda waves. At STATION 1 the decay rate is much higher than that at MDJ. Also in contrast with MDJ, at STATION1 the amplitude ratio between P and S waves does not change with frequency. These two observations suggest that in the considered region the wave propagation scattering is azimuthally dependent. Scattering is stronger along the path to MDJ, which is also the longest. As a consequence the S/P ratio at MDJ is strongly reduced at high frequencies in all three components.

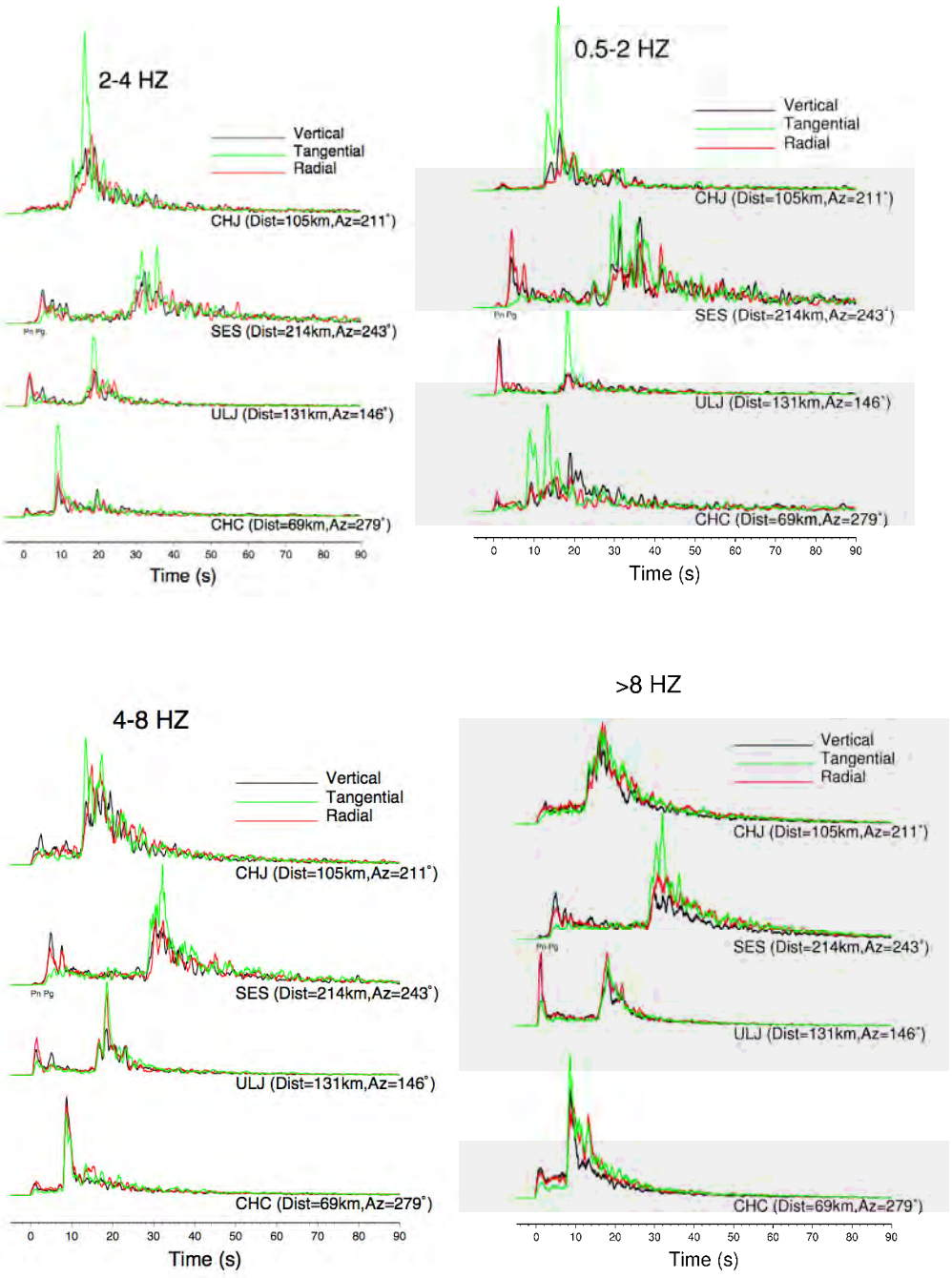


**Figure 1. Smoothed envelopes of broad-band velocity seismograms recorded at station CHJ, SES, ULJ, and CHC from the Mw4.5 070120 earthquake in South Korea. The envelopes are calculated at four frequency bands indicated on top of each panel. Color traces show different components. The epicentral distance and azimuth are indicated at each trace. Note the large amplitude of the P wave on the vertical and radial components at stations CHJ, SES, and ULJ, which are located near the nodal planes. The difference in the P wave seen among the three components is caused by the source radiation. It is preserved only at frequencies up to 4 Hz. In general, at frequencies higher than 4 Hz, the amplitude of P-wave coda become the same at all components. This is a clear indication of scattering effects in the shallow crust.**

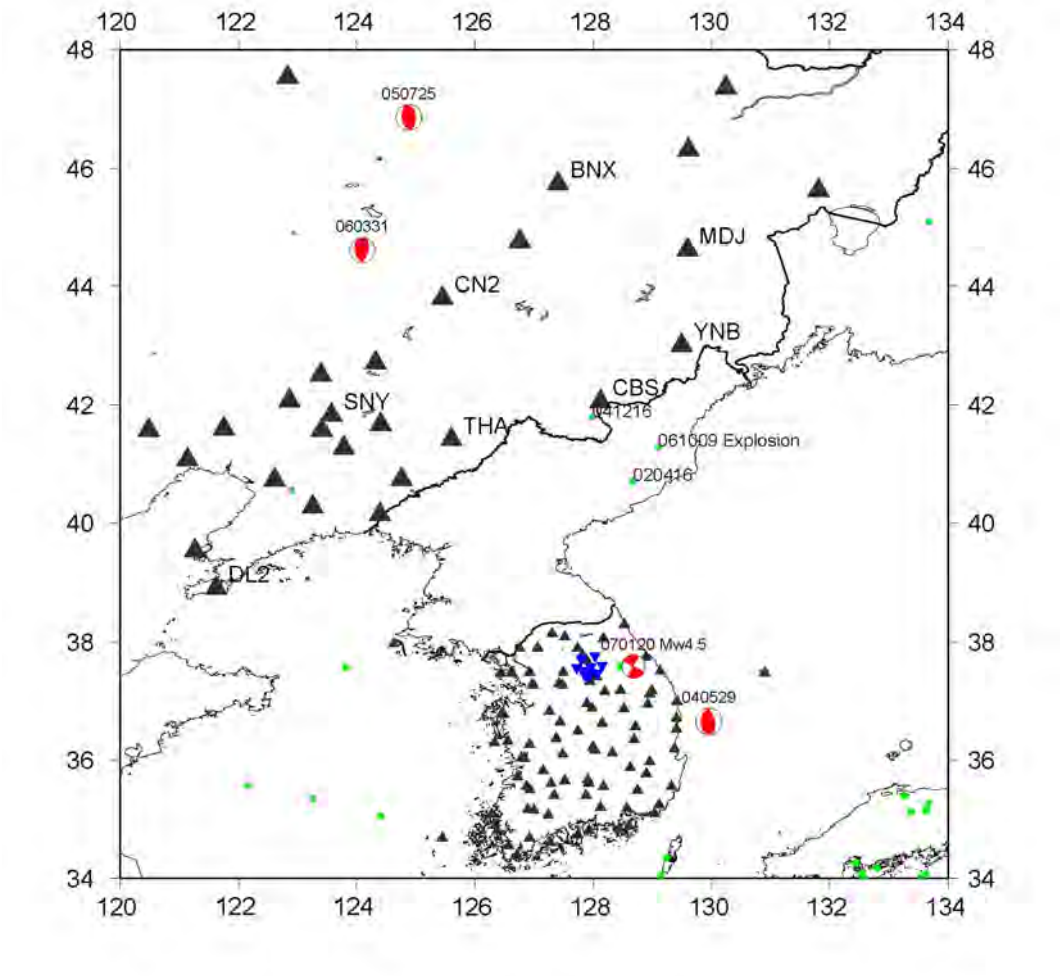


**Figure 2. Map indicating stations and events (M>4) in China, the Korea Peninsula and adjacent regions considered in this study. Triangles indicate broadband and short period stations of the China Seismic Network and Korean Seismic Network, and the blue inverted triangles indicate IMS stations (KSRS). The 061009 explosion and 020416 earthquake located in the Korean peninsula and analyzed in this study are shown by green dots.**

Figure 3b shows smoothed waveform envelopes for the 061009 North Korean explosion calculated at MDJ and STATION1. The explosion waveforms are rich in S wave energy, in particular at STATION1, which is closer to the source. The difference in wave scattering between the two stations remains visible even for the explosion source. which is much shallower than the earthquake. This suggests that the difference in scattering effects between the two stations is rather shallow and not strictly related to the source region.

The comparison of waveform envelopes between the earthquake and explosion is shown in Figure 4. At STATION1 with low wave path scattering the P/S coda waves amplitude ratio is the same for both earthquake and explosion. In contrast at MDJ the P/S ratio between the earthquake and explosion is very different. The P/S ratio for the explosion is much stronger. These observations suggest that at large epicentral distances for which the cumulative effect of wave scattering is enhanced, the P/S coda wave ratio could be a good discriminant between earthquakes and explosions.

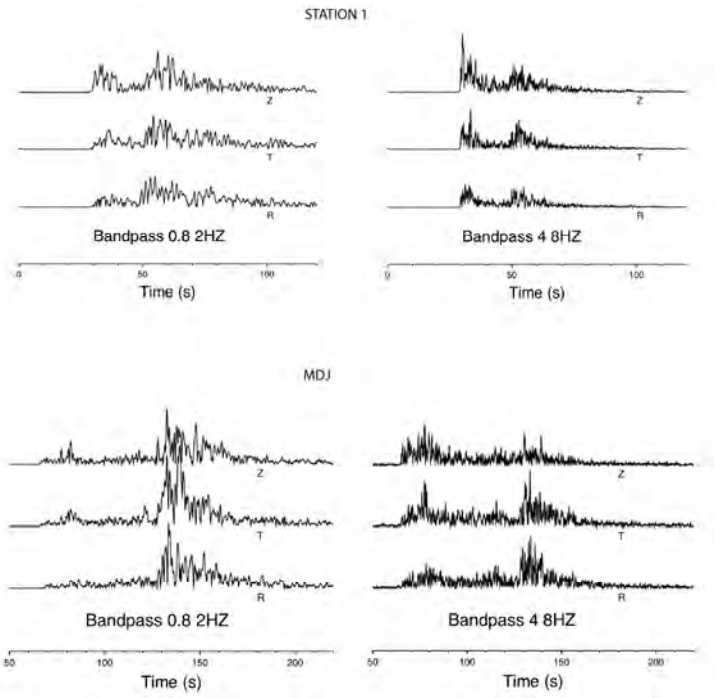


**Figure 3a. Smoothed envelopes of velocity seismograms from the 020416 earthquake in North Korea recorded at STATION 1 (top panels) and MDJ (bottom panels) in the frequency ranges 0.8–2 Hz and 4–8 Hz.**

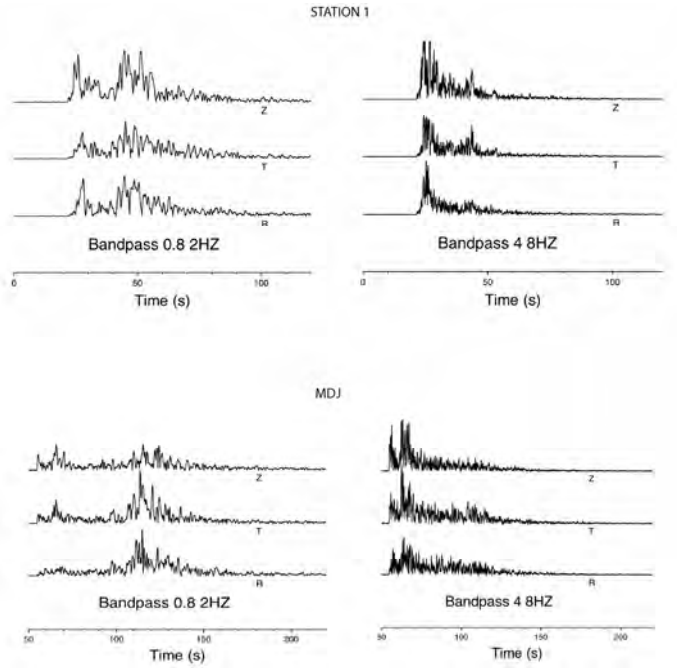


**Figure 3b. Smoothed envelopes of velocity seismograms from the 061009 North Korean explosion recorded at STATION 1 (top panels) and MDJ (bottom panels) in the frequency ranges 0.8–2 Hz and 4–8 Hz.**

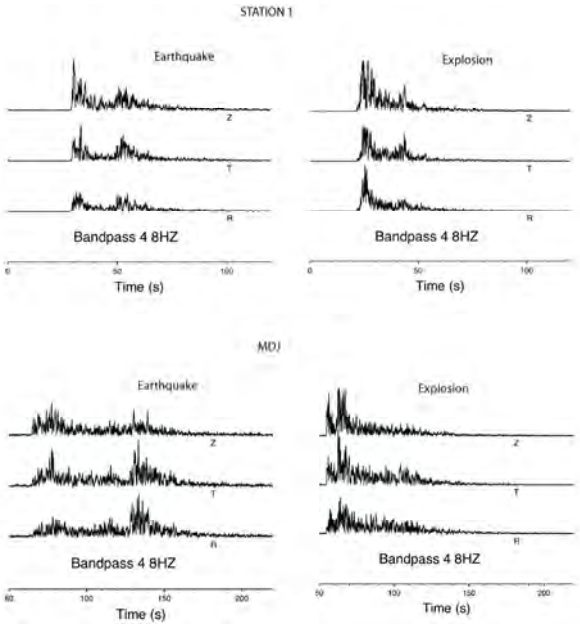


**Figure 4. Comparison of smoothed envelopes of velocity seismograms at STATION1 and MDJ from the 020416 earthquake (left panels) and 061009 explosion (right panels) in North Korea, band-pass filtered at 4–8 Hz. Note that along the short wave path to STATION1 P/S amplitude ratios for the earthquake and explosion are very similar. In contrast along the wave path to MDJ, which is longer, and with strong wave scattering, the P/S ratios between the earthquake and explosion are very different. At MDJ the P/S ratio for the explosion is much larger. This suggests that at large epicentral distances and in a strong scattering environment, the two types of sources discriminate very well.**

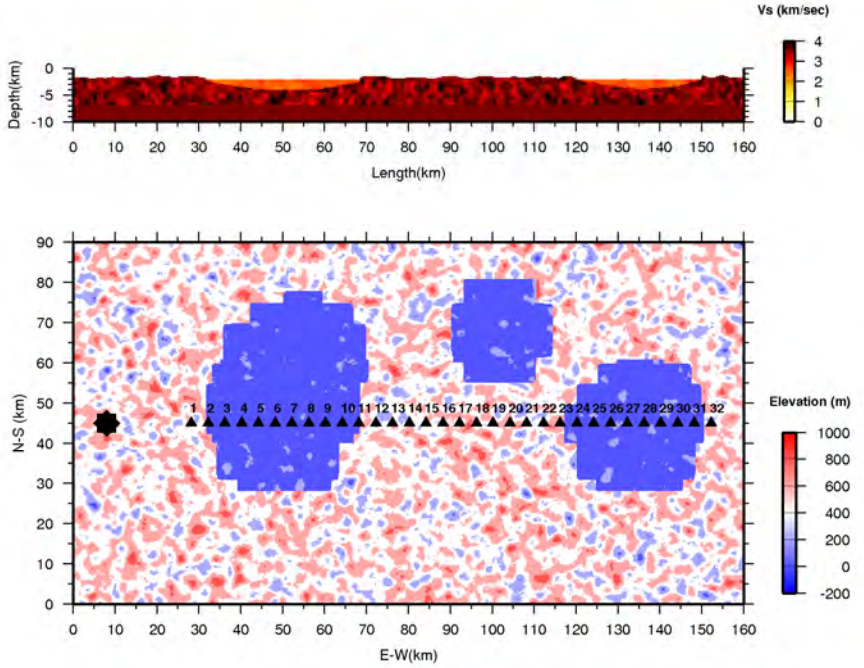


**Figure 5. Velocity model with smooth topography used in simulations of wave propagation scattering.**
**Top Panel: Cross section of the top 7 km of the velocity model along the source-station linear array. The velocity is randomly perturbed in the upper 5 km of the crust.**
**Bottom Panel: Topography elevation and stations (triangles) and epicenter (star) locations.**

**Simulated Scattering**

Numerical modeling can establish a link between the observed frequency-dependent effects of scattering and their physical explanation. During this second phase of our study we have examined combined effects of wave propagation scattering due to complexities in the shallow crust and surface topography. We have calculated synthetic seismograms for earthquake and explosion point sources using a parallelized 3D finite-difference code (Pitarka,1999). Our finite difference code solves the stress-velocity wave equations in a heterogeneous medium using staggered grids. The technique for generating the 3D velocity model on a regular grid with variable spacing allows for inclusion of small-scale complexities and surface topography as well. The technique we use to model free surface topography is an extension of the formalism that we have applied to modeling wave propagation in media with a curved free surface (Pitarka and Irikura,1996). The performance of our free-surface boundary condition technique at handling Lg coda waves for a flat free surface and very long distances was compared with that of the FK method of Saikia (1994) for a shallow source. Also, the technique has been validated against other standard and accurate techniques for modeling surface topography such as the 2D-Boundary Element Method (BEM) and the 2D-Discrete Wavenumber-Boundary Integral Equation method of Takenaka et al. (1996).

We looked at the relative contribution of wave-field scattering on different frequency bands of P, Rg and Lg coda waves due to surface topography and localized and highly heterogeneous small scale bodies embedded in a reference planar layered velocity model that was used in modeling regional wave propagation in the South Korea region (Kim, 1995). The small-scale variations of the velocity are randomly distributed along the top 5km of the crust. In addition to the small-scale fluctuations our velocity model includes several microbasins with sizes varying between 10-25 km and depth up to 4 km. The velocity fluctuations are in the range of 2-8% and their correlation length is 1.5 km. The elevation of surface topography varies between 0 and 800m. The correlation length of topography random variations is 3.5 km. The selected minimum grid spacing of 200 m ensures accurate wave propagation modeling up to 3.0 Hz. The 3D model occupies a volume of 160x90x20 km. The ground motion velocity was computed on a linear array of stations located on the free surface. The stations spacing is 20 km, and the maximum epicentral distance is 146 km. Several stations are located in basins.

Aiming at understanding scattering effects in relation to the source type we performed simulations for an explosion point source located at a depth of 400 m, and earthquake double-couple point sources located at a depth of 7 km. Since we are looking at indirect mechanisms of S wave generation, mainly wave-path scattering, we used the isotropic representation of the explosion source in our simulations. The source time function for both earthquake and explosion has a flat spectrum in the considered frequency range.

A cross section of the velocity model and free-surface topography used in the simulations is shown in Figure 5. Figure 6 shows the difference in waveform characteristics between the earthquake and explosion. We compared the vertical component of synthetic velocity seismograms calculated at a linear array of receivers for a strike slip earthquake located at a depth of 7 km. The strike angle of the fault is $90^o$ and the rake angle is $50^o$. It is obvious that shallow random complexities create coda waves with long duration. The S and Lg coda waves are very energetic even at short distances. The effects of the shallow heterogeneities on wave type conversions such as P to S and S to P as well as on Rg waves are impressive, especially for the explosion source that does not emit S waves. Our numerical experiment clearly shows that wave-path scattering alone caused by rough topography and crustal heterogeneities can produce Lg, P, and S coda waves with significant energy even for explosion sources. The Rg wave dominates the later phases in explosion seismograms. Their amplitude is larger than that of the direct P wave. However, at high frequencies (above 1 Hz) the Rg waves quickly attenuate with distance. Because of the Rg to Lg conversions caused by the surface topography, the amplitude of Rg waves is comparable with that of the P waves (see Figure 6b). As demonstrated by the comparison of smoothed envelopes of waveforms calculated at selected stations (Figure 7), P coda waves from the explosion remain strong. The cumulative effect of scattering caused by the surface topography and spatial structural heterogeneities contributes to the generation of P coda waves through P/S and S/P conversions. At high frequencies, the difference in the P/Rg ratio between the explosion and the earthquake source is significant. The P/Rg wave ratio could be a good discriminant when the earthquake is not very shallow and the explosion is not located near a complex boundary (e.g., Saikia, 1992).

**(a) 0.1–2.5 Hz** **(b) 1.0–2.5 Hz**

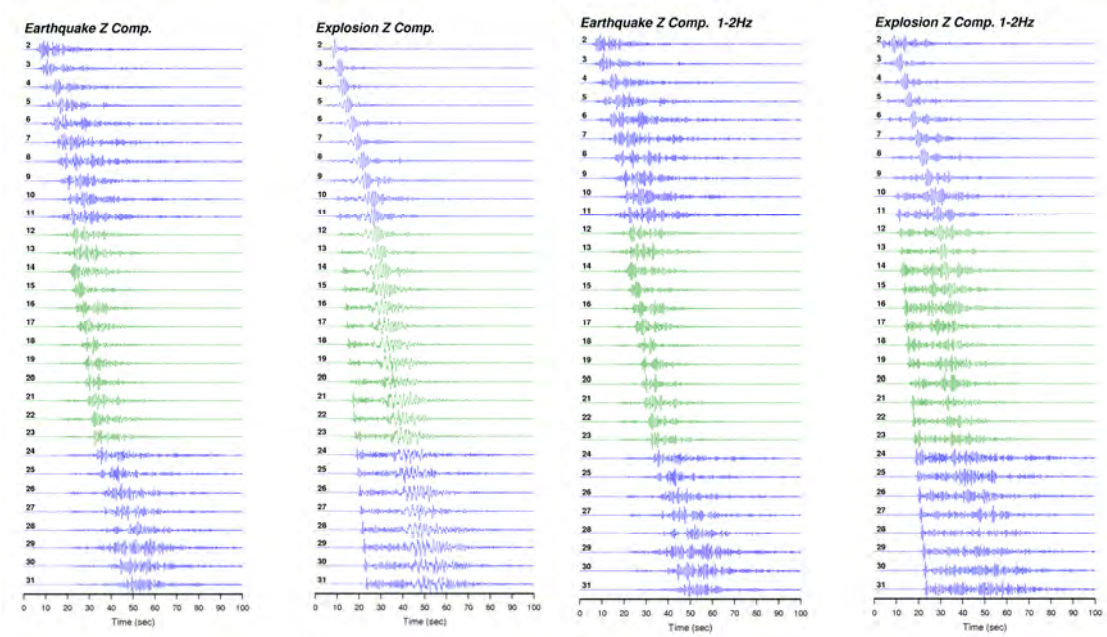


**Figure 6. Vertical component of synthetic velocity for a strike-slip earthquake with a source depth of 7 km (left panel) and an isotropic explosion source at a depth of 0.4 km (right panel). The synthetic seismograms are calculated with a 3D model that includes shallow crustal scattering effects. (a) Band-pass filtered at 0.1–2.5 Hz (b) Band-pass filtered at 1.0–2.5 Hz. All synthetics are scaled to their individual maximum amplitude in order to enhance the relative amplitude of P and S waves at each station. Note the impressive energy of S and Rg coda waves developed for an explosion source.**

**(a) 0.1–0.5 Hz** **(b) 1.0–2.5 Hz**

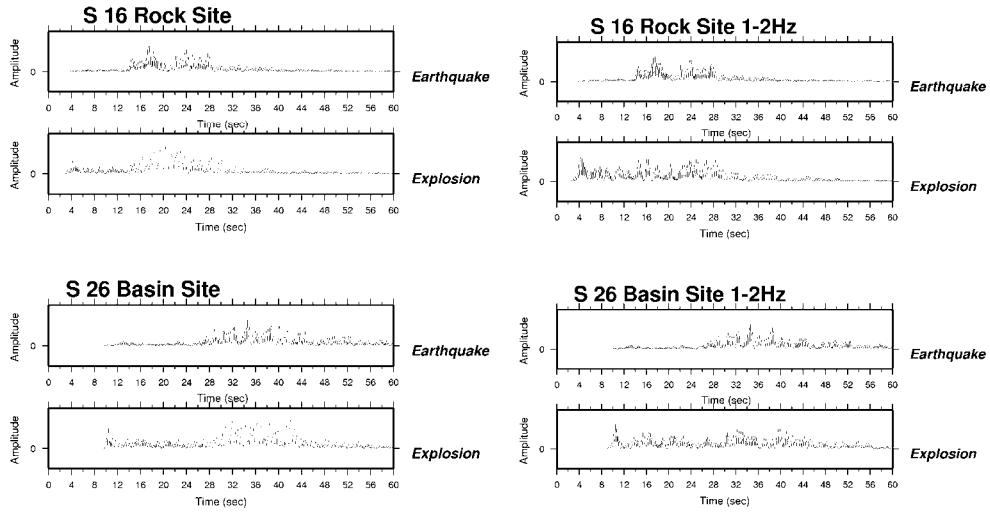


**Figure 7. Comparison of smoothed envelopes for the vertical component of synthetic velocity seismograms at a rock site (station 16) and basin site (station 26) for the earthquake and explosion sources. Note the relatively large P/S ratio of coda waves for the explosion. P/S ratio increases with the frequency, making it a good discriminant.**

**(a) 0.1–2.5Hz** **(b) 1.0–2.5 Hz**

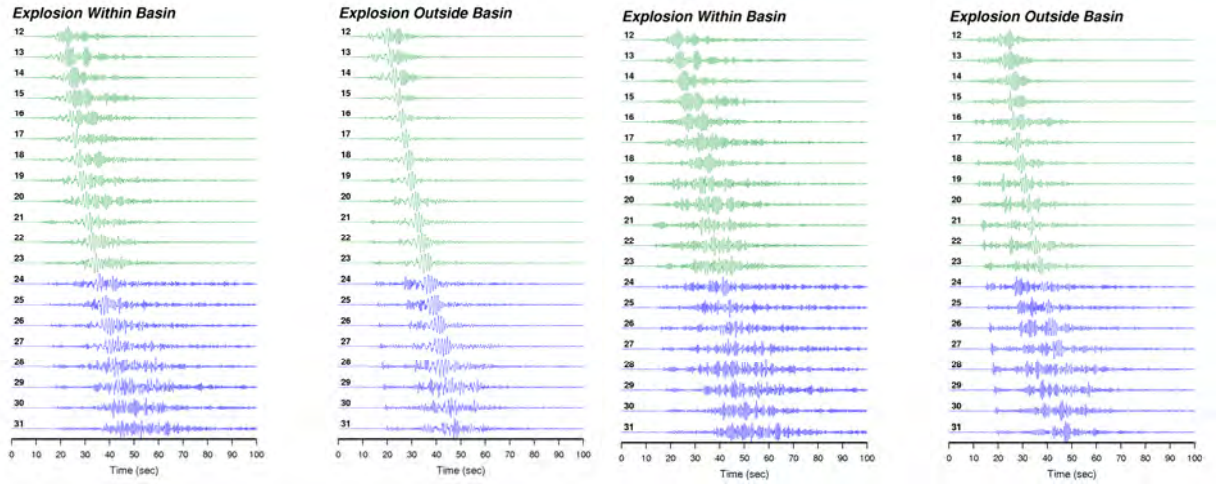


**Figure 8. Effect of the location of explosion source with respect to basin edge on wave scattering. Comparison of vertical component velocity seismograms for an explosion source located near the basin edge inside the basin (left panel) and outside the basin (right panel). (a) Band-pass filtered at 0.1–2.5 Hz (b) Band-pass filtered at 1.0–2.5 Hz. Note that because of the wave trapping within the basin, the S-wave coda for the explosion inside the basin are more pronounced. In contrast, the amplitude of P and P coda waves is reduced, especially at high frequencies.**

### Emplacement Effects

Figure 8 compares the simulated vertical component of velocity for explosion sources located near the basin edge, inside and outside a basin. The explosion outside the basin produces much larger P waves that are rich in high frequencies. In contrast the amplitude of the P wave and P coda waves is relatively small for the basin explosion. In this case the energy reduction of the P wave is caused by P to S conversions. Besides being attenuated in the basin sediments, the P waves do not develop much coda wave, as some of their energy that is reflected at the free surface leaks back to the underlying bedrock and deeper crust and probably is subject to trapping and intrinsic attenuation. As a consequence, the waveforms from the basin explosion look very similar to those from an earthquake. This is clearly seen in both Figure 9 and Figure 10 where we compare smoothed envelopes of synthetic waveforms in the frequency range 1.0–2.5 Hz. Our simulation suggests that P/Rg ratio for explosion sources is sensitive to the source emplacement.

## CONCLUSIONS AND RECOMMENDATIONS

Our numerical experiments with 3D velocity models that include surface topography, random velocity perturbations and microbasins, representing wave scattering in the upper 5 km of the crust, clearly show that wave-path scattering is a major contributor to S and Lg coda waves from explosions at regional distances. Explosion sources generate strong Rg waves. The energy of the Rg waves depends on distance and wave propagation scattering. Strong scattering and its cumulative effect at long distances breaks down Rg waves while still contributing to the creation of P coda waves. As a consequence, at regional distances and high frequencies, the P/Rg ratio is larger for explosions than for earthquakes. The amplitude of P waves and P coda waves from explosions depends on the source emplacement. Our simulations suggest that at large distances P waves generated from basin explosions located near the basin edge are relatively weak. Consequently, P/Rg ratios for such events could be very similar to earthquakes.

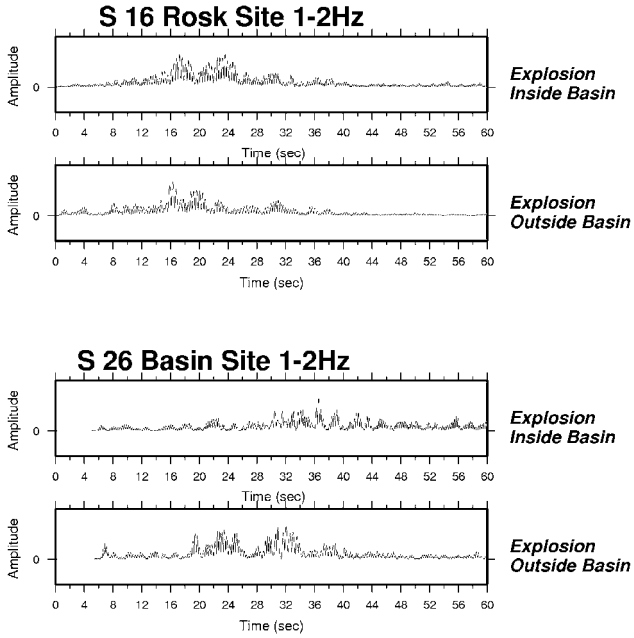


**Figure 9. Comparison of smoothed envelopes for the vertical component of synthetic velocity seismograms at a rock site (station 16) and a basin site (station 26) for explosion sources inside and outside the basin. Note that at longer distances (station 26) the two different source inplacements produce S coda waves with very different characteristics. The amplitude of S coda waves for the source inside the basin is reduced significantly.**

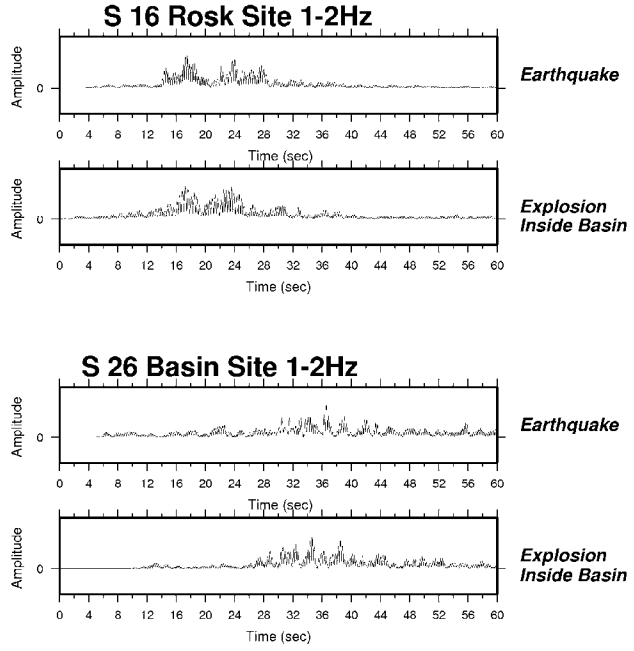


**Figure 10. Comparison of smoothed envelopes for the vertical component of synthetic velocity seismograms at a rock site (station 16) and basin site (station 26) for an earthquake source and explosion source located inside the basin. Note that for such a location of the explosion source and the considered frequency range, using P/Rg ratio to discriminate between an earthquake and an explosion becomes difficult.**

## REFERENCES


Dainty, A. (1996). The influence of seismic scattering on monitoring, in *Monitoring a Comprehensive Test Ban Treaty*. NATO Science Series. Springer: pp. 663–688.

Goff, J. A. and T. H. Jordan (1988). Stochastic modeling of seafloor morphology: Inversion of sea beam data for second-order statistics, *J. Geophys. Res*. 93: 13589–13608.

He, Y., X. Xie, and T. Lay (2008). Explosion-source energy partitioning and Lg-wave excitation: Contributions of free-surface scattering, *Bull. Seism. Soc. Am*. 98: 778–792.

Kim, W. and P. G. Richards. North Korean nuclear test: Seismic discrimination at low yield, *Trans. Am. Geophys. U*. 88: 158–161.

Mayeda, K. M., A. Hofstetter, J. L. O'Boyle, and W. R. Walter (2003). Stable and transportable regional magnitudes based on coda-derived moment rate spectra, *Bull. Seis. Soc. Am*. 93: 224–239.

Myers, C. S., J. Wagoner, L. Preston, K. Smith, H. Tkalcic, and S. Larsen (1996). The effect of realistic geologic heterogeneity on local and regional P/S amplitude ratios based on numerical simulations, in *Proceedings of the 28th Seismic Research Review: Ground-Based Nuclear Explosion Monitoring Technologies*, LA-UR-06-5471, Vol. 1, pp. 146–155.

Ni, J. and M. Barazangi (1983). High frequency seismic wave propagation beneath the Indian shield, Himalayan Arc, Tibetian Plateau, and surrounding regions: High uppermost mantle velocities and efficient Sn propagation beneath Tibet, *Geophys. J. Int*. 72: 655–689.

Phillips, W. S. and K. Aki (1986). Site amplification of coda waves from local earthquakes in central California, *Bull. Seism. Soc. Am*. 76: 627–648.

Phillips, W. S., H. E. Hartse, S. R. Taylor, and G. E. Randall (2000). 1 Hz Lg Q tomography in central Asia, *Geophys. Res. Lett*. 27: 3425–3428.

Pitarka, A. (1999). 3D elastic finite-difference modeling of seismic motion using staggered grid with nonuniform spacing, *Bull. Seis. Soc. Am*. 89: 54–68.

Pitarka, A. and K. Irikura (1996). Modeling 3D surface topography by finite-difference method: Kobe-JMA station site, Japan case study. *Geophys. Res. Lett.* 20: 2729-2732.

Saikia, C. K. (1994). Modified frequency-wave-number algorithm for regional seismograms using Filon's quadrature-modeling of L(g) waves in eastern North America, *Geophys. J. Int*. 118: 142–158.

Saikia C. (1992). Numerical study of quarry generated Rg as a discriminant for earthquakes and explosions: Modeling of Rg in southwestern New England. *J. Geophys. Res*. 97: 11057–11072.

Takenaka, H., B. L. Kennett, and H. Fujiwara (1996). Effect of 2-D topography and 3-D seismic wave field using a 2.5-D discrete wavenumber-boundary integral equation method, *Geophys. J. Int*. 124: 741–755.

Wu, Ru-Shan, S. Jin, and Xiao-Bi Xie (2000). Seismic wave propagation and scattering in heterogeneous crustal waveguides using screen propagators: I SH-waves, *Bull. Seismol. Soc. Am*. 90: 401–413.

Tan, Y., L. Zhu, D. V. Helmberger, and C. K. Saikia (2006). Locating and modeling regional earthquakes with two stations, *J. Geophys. Res*. 111: B01306, doi:10.1029/2005JB003775.

Xie, X., Z. Ge, and T. Lay (2005). Investigating explosion source energy partitioning and Lg-wave excitation using finite-difference plus slowness analyses method, *Bull. Seis. Soc. Am*. 95: 2412–2427.

Xie, X., T. Lay, and R. Wu (2005). Near-source energy partitioning for regional waves in 2D and 3D models, contributions of $S^*$-to-Lg and P-to-Lg scattering, in *Proceedings of the 27th Seismic Research Review: Ground-Based Nuclear Explosion Monitoring Technologies*, LA-UR-05-6407, Vol. 1, pp. 249–258.

# A NEW REGIONAL 3-D VELOCITY MODEL FOR ASIA FROM THE JOINT INVERSION OF P-WAVE TRAVEL TIMES AND SURFACE-WAVE DISPERSION DATA

Delaine T. Reiter[1] and William L. Rodi[2]

Weston Geophysical Corp.[1] and Massachusetts Institute of Technology[2]

Sponsored by Air Force Research Laboratory

Contract No. FA8718-04-C-0027
Proposal No. BAA04-67

## ABSTRACT

Accurate travel-time predictions for regional seismic phases are essential for locating small seismic events with the accuracy needed for nuclear monitoring decisions. Travel times calculated through a three-dimensional (3-D) Earth model have the best chance of achieving acceptable prediction errors, if the model is constrained by sufficient data. With this motivation, we have developed a self-consistent 3-D *P* and *S* velocity model of the crust and upper mantle in a large region of southern and central Asia to a depth of approximately 400 km. Our new model is the result of a nonlinear, joint body-wave/surface-wave inversion method applied to *Pn* travel times collected from the Engdahl, van der Hilst, and Buland (EHB) bulletin and group-velocity measurements provided by the University of Colorado and Lawrence Livermore National Laboratory. Consistency between the *P* and *S* velocities is achieved by imposing bounds on Poisson's ratio and by invoking a regularization constraint that correlates variations in *P* and *S* velocity from an initial model.

We have tested our new model for its predictive capabilities using data from a large database of ground-truth events, which were held out from the joint inversion. The tests include the relocation of the ground-truth events, using data sets of *Pn*-only and *Pn*/*Sn* arrivals, and the direct comparison of predicted *Pn* and *Sn* travel times to the ground-truth observations. Both types of tests indicate that our 3-D inversion model has much better predictive capability than either a 1-D global model or our initial model, which comprised a 3-D crustal structure overlying a 1-D mantle. Importantly, our *S* velocity model performed well in predicting *Sn* times, even though such data were not included in our joint inversion. This achievement relied on the use of anelastic corrections in surface-wave modeling, however, which raises the stakes on deriving good Q models for complex regions like southern Asia.

A final task in our project is to calculate the uncertainty of the new velocity model. We have begun to address this challenging task by developing numerical algorithms to compute two types of uncertainty measures. The first measure comprises slices of the posterior velocity covariance function for selected points in the inversion model. The second uncertainty measure translates model uncertainty to travel-time prediction uncertainty in the form of the posterior variance/covariance matrix of the travel-time prediction errors along a set of paths, such as those between a fixed event location to a network of regional stations.

## OBJECTIVES

The development and validation of accurate 3-D velocity models of the crust and upper mantle for regions of nuclear monitoring interest remains an important goal for nuclear monitoring organizations. Systematic biases caused by inadequately modeled Earth structures cause errors in the estimation of geophysical parameters such as the travel times and amplitudes of regional seismic phases. More accurate and reliable estimates of these quantities (especially in aseismic regions) will improve nuclear monitoring efforts to detect, locate, and discriminate regional events.

We have developed a joint 3-D inversion technique that incorporates both compressional-wave travel times and Rayleigh-wave group velocity measurements to determine the full *P* and *S* velocity structure of the crust and upper mantle. We have applied our algorithm to data from the broad region shown in Figure 1 to develop a new model, which we call *JWM* (for ***J***oint ***W***eston/***M***IT). In this paper we report on our efforts to validate the *JWM* model, as well as characterize its uncertainty using two new numerical approaches.

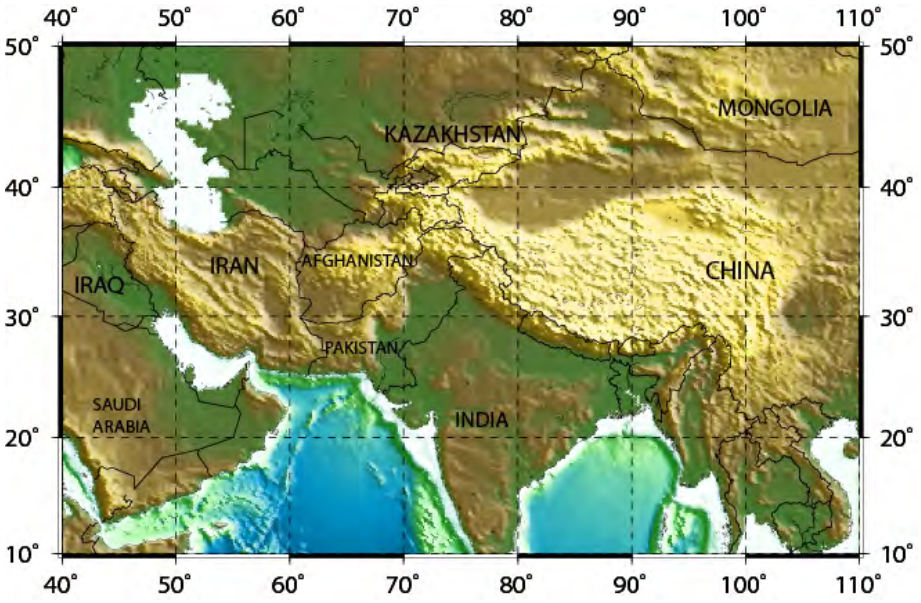


**Figure 1. Topographic map of study region, which encompasses most of central and southern Asia, as well as the eastern side of the Middle East.**

## RESEARCH ACCOMPLISHED

In Rodi and Reiter (2007) we provide a summary of the methodologies and data sets used in our joint inversion, and we refer the reader to that paper for more details on the development of the inversion model. During the past year we have incorporated a number of subtle, but important, changes to the inversion algorithm, data sets, and model parameterization and constraints. For example, we now incorporate anelastic corrections in our surface-wave dispersion modeling to help address discrepancies between the shear-wave models found using surface-wave measurements versus those from body-wave measurements. We compute these corrections using the relationships developed by Liu et al. (1976) and Yu and Mitchell (1979) and an attenuation profile (*Qp* and *Qs*) associated with the AK135 global reference model (Montagner and Kennett, 1996; Kennett et al., 1995). The attenuation profile is held constant everywhere in our model, except over the Tibetan Plateau, where we halve the crustal and uppermost mantle Q values to better agree with studies that indicate high attenuation in the crust for paths traversing the Plateau (e.g., Rodgers and Schwartz, 1998).

We have also expanded the travel time database used in the *P*-wave tomography. Our predominant source of arrival-time observations is the EHB bulletin from the years 1982–2004 (Engdahl et al., 1998). We have augmented the EHB bulletin picks over the Tibetan Plateau and southwestern China using data from temporary arrays, courtesy of Dr. Chang Li (pers. comm.; Li et al., 2006). As in Rodi and Reiter (2007) we compressed this data set by forming

summary events on a regular grid having 0.5-degree spacing in latitude and longitude and containing 13 nodes in depth between 0 and 200 km, with the depth spacing per node increasing from 5 to 20 km. The final database used in the body-wave tomography contains 104,065 arrivals for 3,689 summary events and 603 stations.

Another change we have implemented involves a slight modification of our 3-D model parameterization in the upper mantle. Previously we represented the upper mantle model from the bottom of the crust to the discontinuity at a 410-km depth with nine nodes in the vertical direction. We have doubled that sampling with the use of 17 vertical nodes in order to better represent any velocity gradients present in this depth interval.

Finally, we have adjusted the prior error levels and correlation lengths used in our geostatistical regularization.

**Joint Inversion Results**

In Figure 2, we show two vertical, or depth, slices through the most current version of the *JWM* model along great-circle paths. On the left is a slice across the Saudi Arabian Peninsula to the northeast across southern Iran and into eastern Kazakhstan. One feature in this slice is the high velocity area with respect to the background model beneath the Makran orogeny in southern Iran. The $V_P$ model shows these subsurface features most clearly, while the $V_S$ model only hints at it. There is also an interesting low velocity feature in both the $V_P$ and $V_S$ models beneath central Iran, which may have interesting implications for the active subduction processes occurring beneath the Eurasian continental collision zone. The slice on the right cuts across the Himalayan Front, stretching from northern India into central China. Here the *Vp* and *Vs* models are somewhat anti-correlated across the southernmost portion of the Tibetan Plateau, with a stronger low in *Vs* than in *Vp*. We find that the Poisson's ratio across the Plateau is strongly elevated, which agrees with some previous studies in the region (e.g., Owens and Zandt, 1997). However, in contrast with some travel-time based studies, we find fairly strong velocity lows in the uppermost mantle in the northern portion of the Tibetan Plateau.

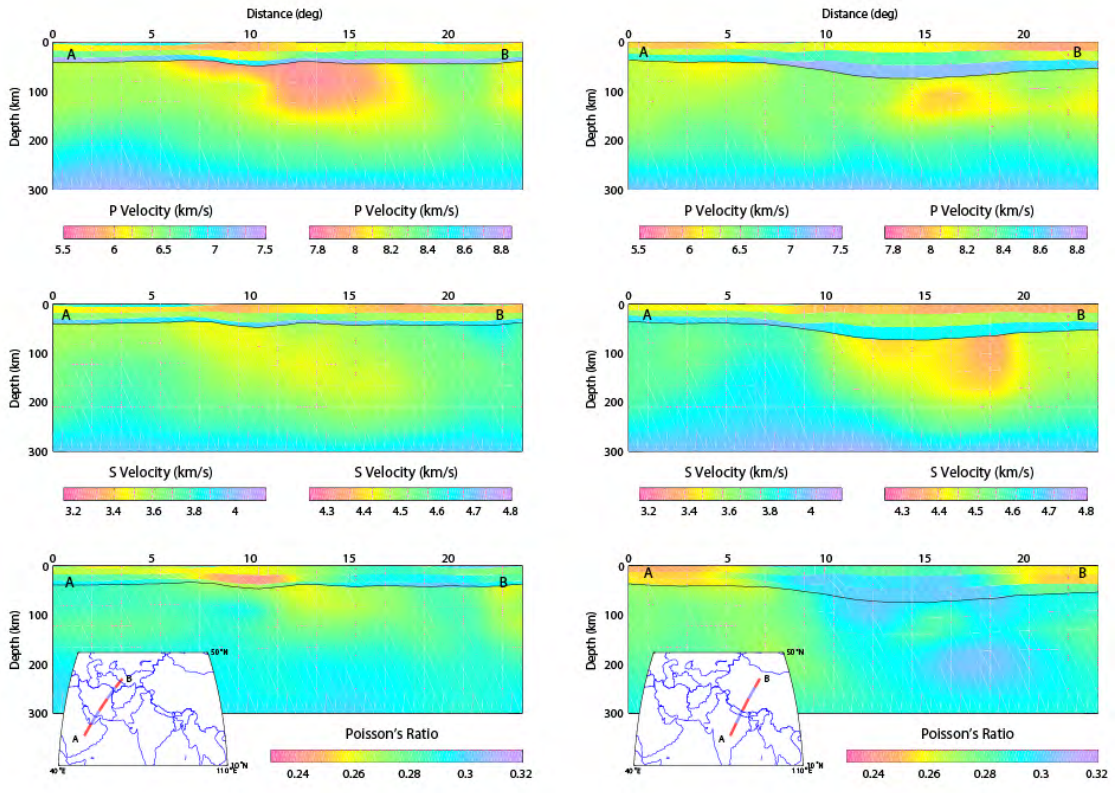


**Figure 2. Depth slices along two great-circle paths (see inset maps for path AB) in the *JWM* inversion model, including $V_P$ (top), $V_S$ (middle), and Poisson's ratio (bottom). Note that a different color scale is used for crust and upper mantle velocities.**

## Validation Exercises

We have employed two validation techniques to assess the performance of the *JWM* crust/upper mantle velocity model. First, we have assessed the ability of *JWM* to predict regional travel-time observations for a set of ground-truth (GT) events. Our GT database of explosions and shallow earthquakes was derived from several sources, including the EHB bulletin, the Group2 Reference Event List (REL; Bondár et al., 2004a) and a list developed by Dr. Bob Engdahl for an International Association of Seismology and Physics of the Earth's Interior (IASPEI) location workshop (Engdahl, 2006). In Figure 3a we show the events in our GT database that are within the resolved boundaries of the *JWM* model (10–50°N, 40–110°E). The GT database contains high-quality epicenters, but the Group2 events do not include a large number of regional *P* and *S* observations. Therefore, we cross-referenced the Group2 REL events to the EHB bulletin (Engdahl et al., 1998) to retrieve a larger set of regional observations. This filtering exercise produced a validation dataset of 180 explosions and 225 earthquakes, with 2,990 *Pg*, *Pb*, or *Pn* first arrivals and 1,796 *Sg*, *Sb*, or *Sn* arrivals. The great-circle paths of the *P* and *S* GT observations are shown in Figure 3b and 3c, respectively. It is notable that the region of the inversion model that is sampled by the GT data raypaths is quite limited, which illustrates the difficulty of validating a model in this manner.

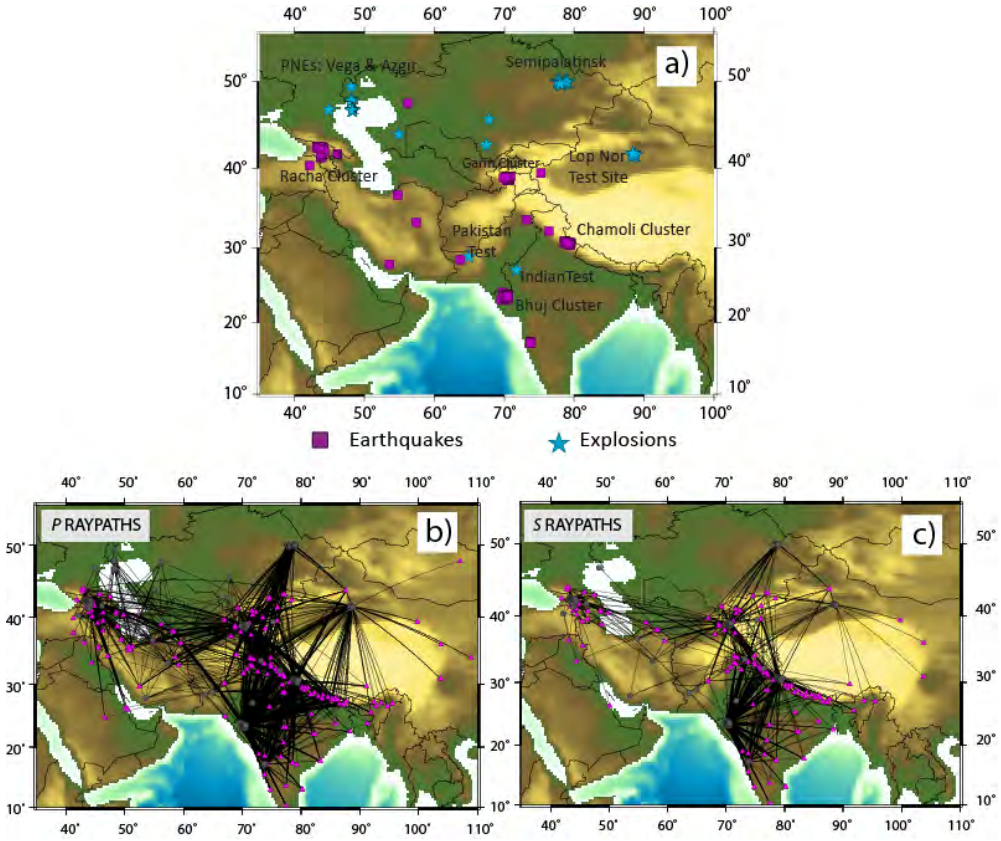


**Figure 3. Ground-truth epicenters (GT0-GT7) in the resolved regions of the *JWM* model. (a) explosions (blue stars) and earthquakes (purple squares) within our region; (b) great-circle raypaths for the EHB *P* observations associated with events in the GT dataset; and (c) great-circle *S* raypaths.**

We then predict the travel times of our regional GT observations through *JWM* using a 3-D finite-difference technique (Podvin and LeComte, 1991) and determine residuals with respect to the GT observed data. In Figure 4 we show the results of this exercise. To make it easier to see the trends in the data, we bin and average the residuals as a function of station-to-event epicentral distance. Figure 4 compares the residuals of the GT data relative to the AK135 reference model and to the 3-D *JWM* model. This validation, or 'prediction capability' test, demonstrates that we met the objectives of our study for the *P* travel times, but the *S* fits for JWM are not as good as we hoped they would be. One likely cause of the degraded fit of our model to the GT *S* data is the well-known '*S* discrepancy' between surface waves and body waves that other researchers have described (Baig and Dahlen, 2004; Montagner

and Kennett, 1996; Nolet and Moser, 1993). We note that the inclusion of anelastic corrections in the surface wave modeling has improved the *S* fits over previous versions of our inversion model. However, the corrections are just not quite enough to completely eliminate the negative bias that indicates our *S* model is perhaps 1%–2% too slow along the raypaths sampled by the GT *S*-wave data.

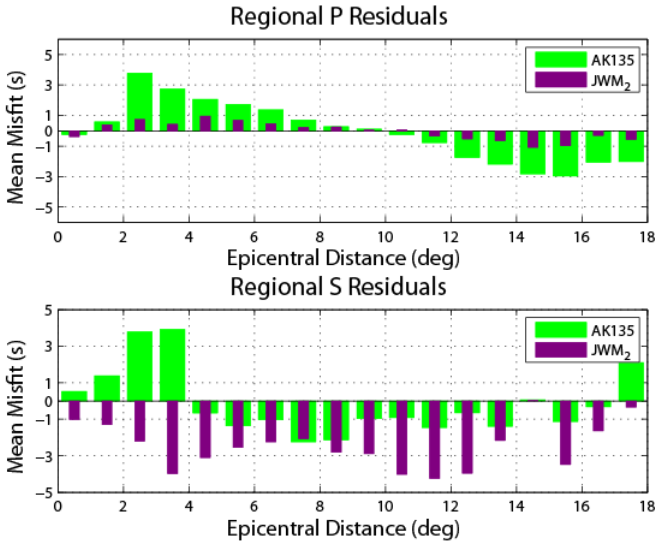


**Figure 4. Mean GT travel-time residual binned as a function of epicentral distance for the AK135 model (green bars) and the *JWM* model (purple bars). Top subplots show the *P* residuals, and bottom subplots show the *S* residuals (1,796 arrivals).**

In a second validation test we relocated a subset of events in our GT database to test the epicentral location accuracy of the *JWM* model. To avoid the most deleterious effects of poor network geometry on the solutions, we filtered the GT data to include only those events whose regional station distribution within our model has a secondary azimuthal gap less than 180°. Secondary azimuth gap (the largest azimuth gap when a single station of the network is removed) is a good proxy for the quality of the network coverage (Bondár et al., 2004b). This filtering reduced the testing data set to a list of 18 explosions and 54 earthquakes within our region, with 1,738 regional *P*-wave arrivals and 530 regional *S*–wave arrivals. The left side of Figure 5 shows the locations of our relocation events, color-coded according to the secondary azimuth gap of the regional arrivals.

We used the Grid-search Multiple-Event Location (GMEL) algorithm (Rodi, 2006) to relocate the events shown in Figure 5, first by including the regional *P* arrivals that fall within the confines of the model. Our GT relocation experiments were done with event depths fixed to their reported values. The subplot on the top right in Figure 5 compares the epicenter mislocations resulting with AK135 versus *JWM* travel-time predictions. Events that fall above the black unity line indicate 'wins' for the *JWM* model. The results show that *JWM* performs better than AK135 for all of the explosions and most of the earthquakes. On the bottom right of Figure 5 we show the comparison between AK135 and *JWM* for the case when both regional *P* and *S* arrivals are included. These results do not indicate a clear win for *JWM* over AK135 when the *S*-wave times are used to relocate the events. This is consistent with the decreased fits of the S model to the GT data, which reduces the effectiveness of the 3-D model to relocate better than the 1-D model. We note that a more detailed analysis of the individual events will likely yield more information about the relative performance of the 1-D and 3-D models in different sub-regions of our study area and how the performance might depend on network geometry.

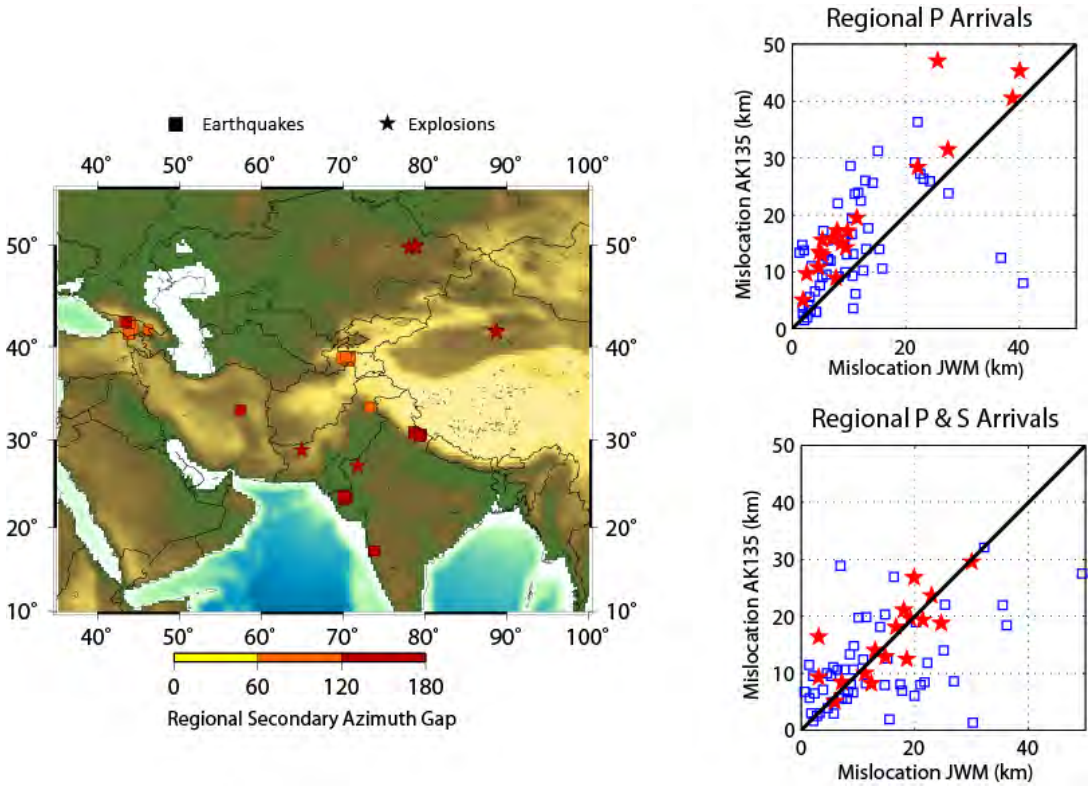


**Figure 5. Results from epicentral mislocation tests. Left: Map of events (54 earthquakes, 18 explosions) from our GT database that meet regional network criteria for the relocation exercise; they are color-coded by their regional secondary azimuth gap. Right: Epicenter mislocations for *AK135* versus *JWM* when either regional P arrivals (top) or regional P and S arrivals are used in the relocations. Events that fall above the black unity line indicate 'wins' for the *JWM* model.**

### Calculation of Model Uncertainty

Our joint inversion method is consistent with a Bayesian approach to model uncertainty, in that the regularization used in both the body-wave and surface-wave inversion steps can be related to a prior mean and covariance on the unknown velocity model. The prior mean is our initial background model, comprising a 3-D crustal structure over the 1-D AK135 mantle, while the prior covariance is given in terms of a geostatistical characterization of the error in the background model, parameterized by the variance and vertical and horizontal correlation lengths of velocity heterogeneity relative to the background. Formally, Bayesian inference defines a posterior probability distribution on the velocity model, which implies a posterior mean and covariance, and other statistical properties, of the velocity model. In a linear inverse problem, the poster mean is taken as the optimal Bayesian estimate of the true Earth model and the posterior covariance describes the uncertainty in that estimate. In a nonlinear inverse problem, like the body-wave and surface-wave problems we address, it becomes somewhat more problematical to define, and compute, an optimal estimate and its uncertainty.

We are implementing the Bayesian framework for model uncertainty under some approximations and restrictions. We adopt a standard approach to nonlinear geophysical inversion (see, for example, Tarantola, 1987) and take the optimal model estimate to be the "maximum a posteriori" (MAP) model, which minimizes the regularized objective function for the problem and, accordingly, maximizes the posterior probability density function of the model. We characterize the uncertainty in the MAP estimate with the posterior covariance, evaluated under a linear approximation to forward problem. The most significant approximation we are making, however, is a practical consequence of our separating the joint body-wave/surface-wave problem into alternating steps of body-wave and surface-wave inversion. That is, we evaluate model uncertainty in the separated problems, ignoring the model constraints we have imposed to couple them.

Under these restrictions, we are developing numerical algorithms to compute two types of uncertainty measures, each of which can be used for either prior or posterior uncertainty. The first algorithm computes 'slices' of the the operator that defines the covariance between the velocity at two arbitrary points. A slice of the operator yields the variance of the velocity at a fixed reference point and its correlation with other points. Figure 6 shows examples of these model covariance slices, computed for the JWM P-wave velocity inversion model. On the left side of Figure 6 we show prior (top) and posterior (bottom) covariance slices for a shallow reference point near the center of our study region (30°N, 75°E, 60 km depth). Note the de-correlation between the crust and upper mantle in the prior covariance image, which is an intentional constraint in our regularization. The posterior covariance incorporates the travel-time data, which consequently reduces the posterior covariance. The right side of Figure 6 corresponds to a different reference point near the southwest corner of our study region (15°N, 45°E, 120 km depth). The prior and posterior covariance plots are similar to each other in this case because there is a dearth of travel-time data to constrain the model at this point.

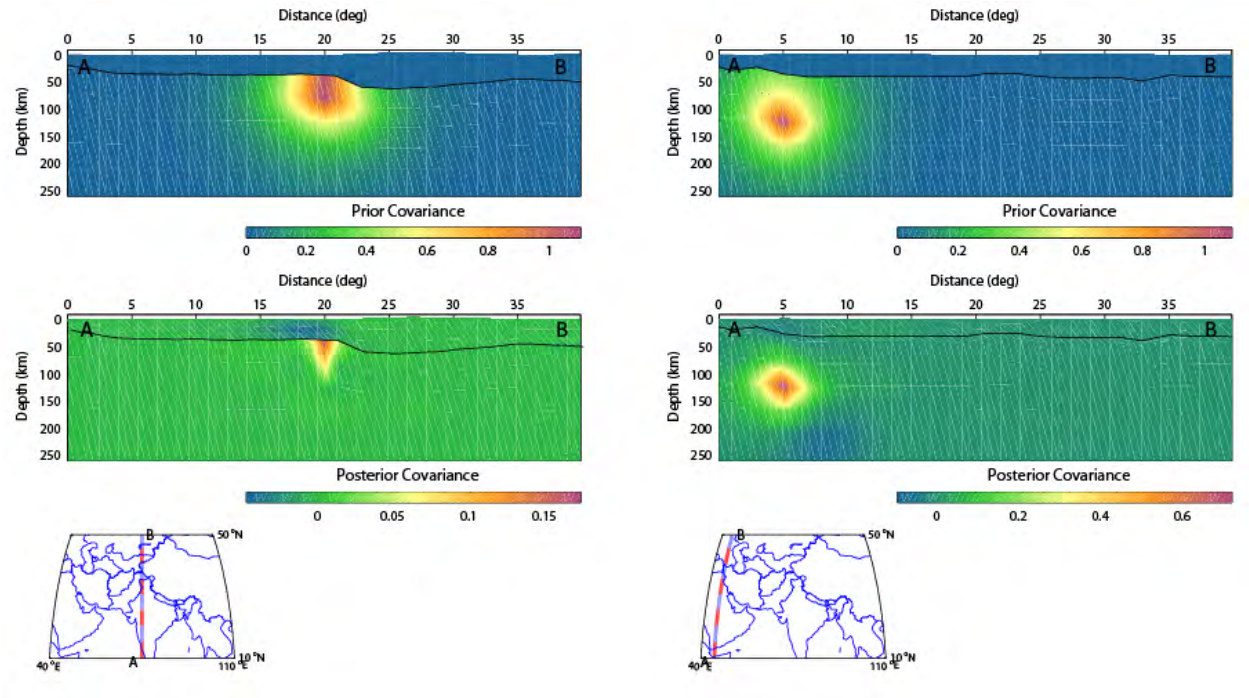


**Figure 6. Vertical cross-sections through prior (top) and posterior (middle) covariance slices for the JWM P-wave model. Slices are shown for a reference point in the middle of the study region (left) and a reference point near the southwest corner of the study region (right). The section passes through their respective reference points and project as the AB lines in the bottom maps. The units of covariance are squared per cent.**

The second uncertainty measure we compute is the variance/covariance matrix for the travel-time prediction errors along a set of paths; for example, from a fixed event location to a network of stations. This calculation allows us to translate the velocity uncertainty to travel-time prediction uncertainty. The algorithm for performing this translation is based on one developed for prior covariance matrices by Rodi and Myers (2007). To demonstrate this new capability, we mapped the covariance operator for the JWM P velocity model to the covariance matrix of P-wave travel-time prediction errors for an event in Iran (35°N, 58°E, 15 km). Twelve regional stations distributed from 1.8° to 17.5° recorded the event, as shown in Figure 7a. Figure 7b shows the prior and posterior standard-deviations of the travel-time predictions as a function of event-to-station distance, derived from the diagonal elements of the 12 by 12 covariance matrix.

The results in Figures 6 and 7 were based on the prior geostatistical parameters that were assumed in our most recent inversion. In particular, we assumed a 1% velocity standard deviation in both the crust and upper mantle. Rodi and

Myers (these Proceedings), however, find that larger velocity heterogeneity is more consistent with observed travel-time variability in Eurasia, such as 3% in the crust and 2% in the upper mantle. Based on these parameters, one would scale up the prior velocity covariances in Figure 6 by a factor of four and the prior travel-time standard deviations in Figure 7 by a factor of at least two. The impact of larger prior variances on posterior variances in Figures 6 and 7 is difficult to gauge since the posteriors depend also on the observational error variances assumed in the inversion, which would have to be reassessed if the priors are changed, an exercise underway. In any case, the posterior model variances will likely increase and translate to travel-time prediction error standard deviations noticeably larger than the rather small values seen in Figure 7b.

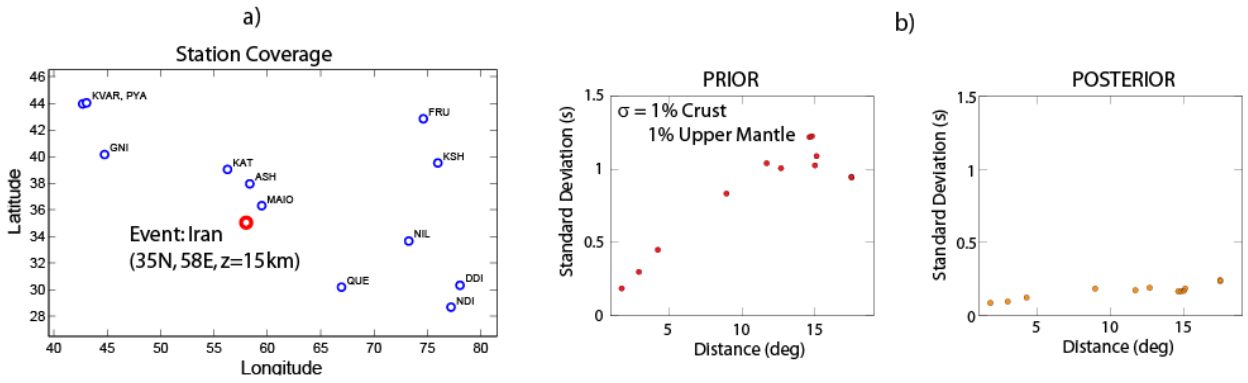


**Figure 7. Example of travel-time prediction error calculations. a) Regional station distribution for an event in Iran; b) travel-time prediction-error standard deviations for 12 *Pn* paths, plotted as a function of distance. A prior standard deviation on the *P* velocity of 1% in the crust and upper mantle was assumed, leading to a unrealistically small travel-time standard deviation of less than 0.5 second.**

## CONCLUSIONS AND RECOMMENDATIONS

We have completed the development of a new $V_P$ and $V_S$ model for central and southern Asia using a new joint inversion technique that incorporates P-wave travel times and Rayleigh-wave group velocity data. The forward modeling incorporated in our inversion algorithm utilizes fully 3-D ray tracing for the body-wave travel times, and a two-step procedure for the surface-wave dispersion data that includes 1-D dispersion modeling at a geographic point followed by 2-D ray tracing in the phase velocity maps. We numerically solve the inverse problem using a set of iterated inversion steps, applying a set of geostatistically based model constraints.

In location validation exercises the model has proved to be very successful at both predicting travel times and locating GT events with regional observations. The prediction of observed GT *S* travel times continues to be less than satisfactory for some paths such as those across the Tibetan Plateau, although it has been improved by including anelastic corrections in our surface-wave modeling.

We have begun to analyze the uncertainty of our inversion model in a Bayesian framework. The uncertainty analysis is restricted to the separate body-wave and surface-wave inverse problems and ignores the model constraints we have imposed to couple them. We have developed algorithms to compute prior and posterior variances on the velocity model itself and on travel times predicted by the model. Our initial calculations indicate that travel-time prediction errors for Pn paths in the well-resolved portion of our model are 0.25 seconds or less, but this result depends on the rather small prior velocity standard deviation we assumed (1%), which we are considering increasing to a more realistic value.

## REFERENCES


Baig, A. M. and F. A. Dahlen (2004). Traveltime biases in random media and the *S*-wave discrepancy, *Geophys. J. Int.* 158: 922–938.

Bondár, I., E. R. Engdahl, X. Yang, H. A. A. Ghalib, A. Hofstetter, V. Kirichenko, R. Wagner, I. Gupta, G. Ekström, E. Bergman, H. Israelsson, and K. McLaughlin (2004a). Collection of a reference event set for regional and teleseismic location calibration, *Bull. Seis. Soc. Am.* 94: 1528–1545.

Bondár, I., S. C. Myers, E. R. Engdahl, and E. A. Bergman (2004b). Epicentre accuracy based on seismic network criteria, *Geophys. J. Int.* 156: 483–496.

Engdahl, E.R. (2006). Application of an improved algorithm to high precision relocation of ISC test events, *Phys. Earth Planet. Interiors* 158: 14–18.

Engdahl E. R., R. van der Hilst, and R. Buland (1998). Global teleseismic earthquake relocation with improved travel times and procedures for depth determination, *Bull. Seis. Soc. Am.* 88: 722–743.

Kennett, B. L .N. Engdahl, E. R., and Buland R. (1995). Constraints on seismic velocities in the Earth from travel times, *Geophys. J. Int'l.* 122: 108–124.

Montagner, J.-P. and B. L. N. Kennett (1996). How to reconcile body-wave and normal-mode reference earth models, *Geophys. J. Int*. 125: 229–258.

Li, C., R. D. van der Hilst, and M. N. Toksöz (2006). Constraining *P* wave velocity variations in the upper mantle beneath Southeast Asia, *Phys. Earth Planet. Int*. 154: 180–195.

Liu, H.-P., D. L. Anderson, and H. Kanimori (1976). Velocity dispersion due to anelasticity; implications for seismology and mantle composition, *Geophys. J.R. Astr. Soc*. 47: 41–58.

Nolet, G., and T.-J. Moser (1993). Teleseismic delay times in a 3-D Earth and a new look at the *S* discrepancy, *Geophys. J. Int*., 114, 185-195.

Owens, T. J. and G. Zandt (1997). Implications of crustal property variations for models of Tibetan plateau evolution. *Nature* 387: 37–43.

Podvin P., and I. Lecomte (1991). Finite difference computation of traveltimes in very contrasted velocity models: a massively parallel approach and its associated tools, *Geophys. J. Int.* 105: 271–284.

Rodi. W. (2006). Grid-search event location with non-Gaussian error models, *Phys. Earth. Planet. Int*. 158: 55–66.

Rodi, W. and D. T. Reiter (2007). *SAsia3D*: A 3-D crust and upper-mantle velocity model of South Asia derived from joint inversion of *P*-wave travel times and surface-wave dispersion data, in *Proceedings of the 29th Monitoring Research Review: Ground-Based Nuclear Explosion Monitoring*, LA-UR-07-5613, Vol. 1, pp. 236–245.

Rodi, W.L. and S. C. Myers (2007). Modeling travel-time correlations based on sensitivity kernels and correlated velocity anomalies, in *Proceedings of the 29th Monitoring Research Review*: *Ground-Based Nuclear Explosion Monitoring*, LA-UR-07-5613, Vol. 1, pp. 463–471.

Rodi, W. L. and S. C. Myers (2008). Modeling travel-time correlations based on sensitivity kernels and correlated velocity anomalies, these Proceedings.

Rodgers, A. J., and S. Y. Schwartz (1998). Lithospheric structure of the Qiangtang Terrane, northern Tibetan Plateau, from complete regional waveform modeling: Evidence for partial melt, *J. Geophys. Res*. 103: 7,137–7,152.

Tarantola, A. (1987). *Inverse Problem Theory*, Elsevier.

Yu, G.-Y., and B. J. Mitchell (1979). Regionalized shear velocity models of the Pacific upper mantle from observed Love and Rayleigh wave dispersion, *Geophys. J. R. Astr. Soc*. 57: 311–341.

# SHORT-PERIOD SURFACE-WAVE DISPERSION FROM AMBIENT NOISE TOMOGRAPHY IN WESTERN CHINA

Michael H. Ritzwoller[1], Yingjie Yang[1], and Michael E. Pasyanos[2]

University of Colorado at Boulder[1], Lawrence Livermore National Laboratory[2]

Sponsored by National Nuclear Security Administration

Contract Nos. DE-FC52-05NA26607[1] and DE-AC52-07NA27344[2]
Proposal No. BAA05-48

## ABSTRACT

The goal of ambient noise tomography (ANT) is to improve the calibration of surface-wave propagation in aseismic areas, especially at periods shorter than 20 sec, which are hard to obtain from earthquake surface waves. In earlier work, we improved and optimized the method of ambient noise surface wave tomography for systematic application and applied it to broad-band seismic data obtained in Europe and the western part of the Middle East. The resulting phase and group speed measurements were documented in Ritzwoller et al. (2007).

Current work concentrates on the application of ANT in central Asia, especially western China, where significant data resources are available. The data are taken from about 180 broad-band seismic stations including the permanent Federation of Digital Seismographic Network (FDSN), two regional networks (KZ and KN), and three temporary US PASSCAL installations in and around China: HIMNT (YL), Namche Barwa (XE), and MIT-CHINA (YA). Cross-correlations are computed in daily segments and then stacked over a three-year period (2002-2004). Rayleigh wave phase and group speed dispersion curves from 8 sec to 60 sec period are measured using a phase-matched filter, frequency-time analysis technique. The dispersion measurements from our data set are combined with those from Zheng et al. (2008) (using the China National Seismic Network) to perform ambient noise tomography. The resulting group and phase velocity maps demonstrate significant correlation with known geologic features, such as sedimentary basins and lateral variation of crustal thickness.

## OBJECTIVES

The goal of this research is to obtain surface-wave dispersion measurements based on cross-correlations of ambient seismic noise and to produce a new data set of inter-station phase and group velocity measurements in Central Asia, especially western China, to complement that of Zheng et al. (2008), using the China National Seismic network. These new dispersion data are used to produce improved group and phase velocity tomographic maps, particularly at short periods (< 20 sec), which can provide new constraints on crustal structures.

## RESEARCH ACCOMPLISHED

### Introduction

In earlier work, we developed a new method to approach the surface-wave path calibration problem based on the use of long records of ambient seismic noise. This method, which we call “ambient noise tomography,” is based on the ability to estimate surface-wave Green functions by cross-correlating long sequences of ambient seismic noise (Shapiro and Campillo 2004; Shapiro et al., 2005). The details of this method are documented in Bensen et al. (2007). Dispersion measurements made on the estimated Green functions present significant advantages over traditional measurements made on recordings of waves emanated from earthquakes. Ambient noise tomography is particularly useful in calibrating surface-wave path effects at periods below 20 sec.

Previously, we applied this method to the large broad-band data set that has emerged through the growing Virtual European Broadband Seismic Network and regional networks in Europe and the western part of the Middle East (Yang et al., 2007; Richmond et al, 2007). Here, we shift our focus to Central Asia, where significant data resources are available. Under previous DOE/NNSA and Air Force support, we devoted substantial efforts toward developing Rayleigh and Love wave group speed data sets and tomographic maps at short and intermediate periods from earthquake data across Central Asia. These data sets have been widely distributed and used by the US nuclear monitoring community. Due to its substantial intra-continental seismicity, which results from the continental collision between India and Asia, Central Asia is particularly suited for classical earthquake surface-wave tomography (e.g., Ritzwoller and Levshin, 1998; Ritzwoller et al., 1998). However, at periods below about 20 sec, path coverage is suboptimal, and geographically variable, and the quality of the dispersion measurements degrades to appreciably shorter periods compared with longer periods.

Ambient noise tomography improves path coverage and resolution, especially at periods below 20 sec across much of Central Asia with the available data resources. We have processed all the available data sources in 2002, 2003, and 2004 in Central Asia and obtained inter-station surface-wave dispersion measurements. The new data set improves the path calibration of short-period surface waves.

### Data and Method

In Central Asia, between 2002 and 2004, there were significant data resources available, including the permanent FDSN, two regional networks, the Kazakh network (KZ) and Kyrgyz network (KN), and three temporary US

PASSCAL installations in and around China. The FDSN, regional networks, and PASSCAL data are all openly available now at the IRIS/DMC. The locations of the stations used in this study are shown in Figure 1. The names and the operation times of all FDSN station, regional network, and PASSCAL experiments are listed in Table 1. Any experiment that overlaps with another experiment in operation time is marked with a cross. These overlaps guarantee that dense path coverage in this study can be generated, as shown in Figure 1. Cross-correlations are run in each of the three years (2002–2004). The cross-correlations include those between stations within individual experiments and those across experiments and permanent installations. Letting $\leftrightarrow$ represent cross-correlation, we can depict the data processing symbolically as follows: FDSN$\leftrightarrow$FDSN, PASSCAL$\leftrightarrow$FDSN, and PASSCAL$\leftrightarrow$PASSCAL.

The data processing procedure applied here is similar to that described by Bensen et al. (2007) at great length. Continuous data are pre-processed before cross-correlation and stacking, which includes removal of instrument response, temporal normalization, and spectral whitening. The purpose of time normalization is to suppress the influence of earthquake signals, which is particularly important in the seismically active region of Central Asian. Cross-correlations are performed daily in the broad period band from 5 to 100 sec and then stacked over all time periods (three years). The correlation function contains both positive and negative time lags, resulting from noise propagating from the two opposite directions between a pair of stations. We use the symmetric component of the correlation as the empirical Green function (EFG) by averaging the positive and negative parts of the correlation. Examples of broad-band (5 to 30 sec) symmetric-component cross-correlations between a common station, LSA (Lhasa, China), and other stations are shown in Figure 2.

To evaluate the quality of cross-correlations, we calculate the signal-to-noise ratio (SNR) for each cross-correlation. If the SNR is larger than 15, Rayleigh wave group and phase speeds are then measured using a frequency-time analysis (Ritzwoller and Levshin, 1998; Lin et al, 2008). The inter-station dispersion measurements from cross-correlations are used to invert for the Rayleigh wave phase and group velocity maps using the method of Barmin et al. (2001).

**Ambient Noise Surface-Wave Tomography**

Zheng et al. (2008) performed ambient noise tomography in China using data from the China National Seismic Network. They obtained inter-station Rayleigh wave dispersion measurements between the 48 Chinese backbone stations at periods from 8 to 60 sec. Because most of the 48 stations are located in eastern China, the path coverage in western China is relatively sparse. To increase the density of path coverage and improve the resolution of tomography in western China, we combine the dispersion measurements from our data set with those from Zheng et al. (2008) to perform ambient noise surface-wave tomography. The tomography is performed for both phase and group speeds on a $1^o \times 1^o$ grid across western China and surrounding regions using the tomographic method of Barmin et al. (2001). Resolution is estimated simultaneously using the method described by Barmin et al. (2001) with modifications presented by Levshin et al. (2005). An example of path coverage and resolution is shown in Figure 3 for the 20-sec measurements. Results are similar for other periods.

Examples of resulting phase and group speed maps at two periods of 12 and 30 sec are shown in Figure 4. For comparison, maps of sedimentary and crustal thicknesses are plotted at the bottom of Figure 4. At the short periods (< 15 sec), surface waves are dominantly sensitive to shear velocities in the upper crust. Because the shear velocity of sediments is low, short-period low velocity anomalies are a good indicator of sedimentary basins. In the 12-sec Rayleigh wave speed maps, low velocities are correlated well with the locations of major basins, including the Tarim Basin, Qaidam Basin, Sichuan Basin, and Ordos Basin. At the intermediate periods of this study (25–60 sec), Rayleigh waves are primarily sensitive to crustal thickness and the shear velocities in the middle crust, lower crust, and uppermost mantle. At these periods, low velocities are usually observed in a region with thicker crust. In the 30-sec Rayleigh wave speed maps, low velocity is observed across Tibet where the crust is very thick (Figure 4f). Higher velocity is imaged in regions to the north and east of Tibet. The boundary between fast and slow velocities nearly coincides with the sharp topographic change.

## CONCLUSIONS

In this study, we use ambient noise data recorded at about 180 broad-band seismic stations, including the permanent FDSN, two regional networks (KZ and KN), and three temporary US PASSCAL installations in and around China: HIMNT (YL), Namche Barwa (XE), and MIT-CHINA (YA). Group and phase velocity dispersion measurements between stations are obtained at periods from 8 sec to 60 sec. These dispersion measurements are combined with those from Zheng et al. (2008) taken from the 48 stations of the China National Seismic Network to perform ambient noise tomography. The resulting velocity maps provide an improvement in the understanding of surface-wave dispersion in Central Asia, particularly at periods below about 20 sec. The group and phase velocity maps agree well with known geologic features, such as sedimentary basins and the lateral variation of crustal thickness.

## ACKNOWLEDGMENTS

All of the data used in this research were downloaded from the IRIS Data Management Center. In particular, the authors are deeply grateful to the research teams of the three PASSCAL experiments.

## REFERENCES

Barmin, M., M. Ritzwoller, and A. Levshin (2001). A fast and reliable method for surface wave tomography, *Pure Appl. Geophys.* 158: (8), 1351–1375.

Bensen, G. D., M. H. Ritzwoller, M. P. Barmin, A. L. Levshin, F. Lin, M. P. Moschetti, N. M. Shapiro, and Y. Yang (2007). Processing seismic ambient noise data to obtain reliable broad-band surface wave dispersion measurements, *Geophys. J. Int.* 169: 1239–1260.

Levshin, A.L., M.P. Barmin, M.H. Ritzwoller, and J. Trampert (2005). Minor-arc and major-arc global surface wave diffraction tomography, *Phys. Earth Planet. Ints.* 149: 205–223.

Lin, F., M.P. Moschetti, and M.H. Ritzwoller (2008). Surface wave tomography of the western United States from ambient seismic noise: Rayleigh and Love wave phase velocity maps, *Geophys. J. Int.*, doi:10.1111/j1365-246X.2008.03720.x.

Richmond, R, Ritzwoller, M. H., Villasenor, A., Yang, Y, Beck, S.L., Lerner-Lam, A, Levin, V., Shapiro, N.M, (2007). Ambient Noise Surface Wave Tomography Across Europe, AGU FALL MEETING, San Francisco, Dec. 10–14.

Ritzwoller, M., Y. Yang, R. Richmond, M. Pasyanos, A. Villasenor, V. Levin, A. Hofstetter, V. Pinsky, N. Kraeva, and A. Lerner-Lam (2007). Short period surface wave dispersion across the Mediterranean Region: improvements using regional seismic networks, in *Proceedings of the 29th Monitoring Research Review: Ground-Based Nuclear Explosion Monitoring Technologies*, LA-UR-07-5613, Vol. 1, pp. 226–235.

Ritzwoller, M. H. and A. L. Levshin (1998). Eurasian surface wave tomography: Group velocities, *J. Geophys. Res.*, 103: 4839–4878.

Ritzwoller, M. H., A. L. Levshin, L. I. Ratnikova, and A. A. Egorkin (1998). Intermediate period group velocity maps across Central Asia, Western China, and parts of the Middle East, *Geophys. J. Int.* 134: 315–328.

Shapiro, N. M., M. Campillo, L. Stehly, and M. H. Ritzwoller (2005). High-resolution surface-wave tomographyfrom ambient seismic noise, *Science* 307: 1615–1618.

Shapiro, N., and M. Campillo (2004). Emergence of broadband Rayleigh waves from correlations of the ambient seismic noise, *Geophys. Res. Lett.* 31: (7), 1615–1619.

Yang, Y., M. Ritzwoller, A. Levshin, and N. Shapiro (2007). Ambient noise Rayleigh wave tomography across Europe, *Geophys. J. Int.* 168 (1): 259–274.

Zheng, S., X. Sun, X. Song, Y. Yang, and M. H. Ritzwoller (2008). Surface wave tomography of China from ambient seismic noise correlation, *Geochem. Geophys. Geosyst.* 9: Q0502, doi:10.1029/2008GC001981.

**Table 1. Broadband seismic networks used in this study during 2002-2004. The network names are shown in rows and columns with the same order. A crossed block indicates the two networks overlap in time; i.e. inter-network cross-correlations can be performed.**

| Network (network Code) (appr. Operation time) | XW | YL | XE | YA | FDSN |
|---|---|---|---|---|---|
| HIMNT (YL) (Sep 2001-Dec 2002) | | × | | | × |
| Namche Barwa (XE) (Jul 2003-Dec 2004) | | | × | × | × |
| MIT-China (YA) (Sep 2003-Dec 2004) | | | | × | × |
| FDSN and Regional (G,PS,IC,II,IU,KZ,KN) | | | | | × |

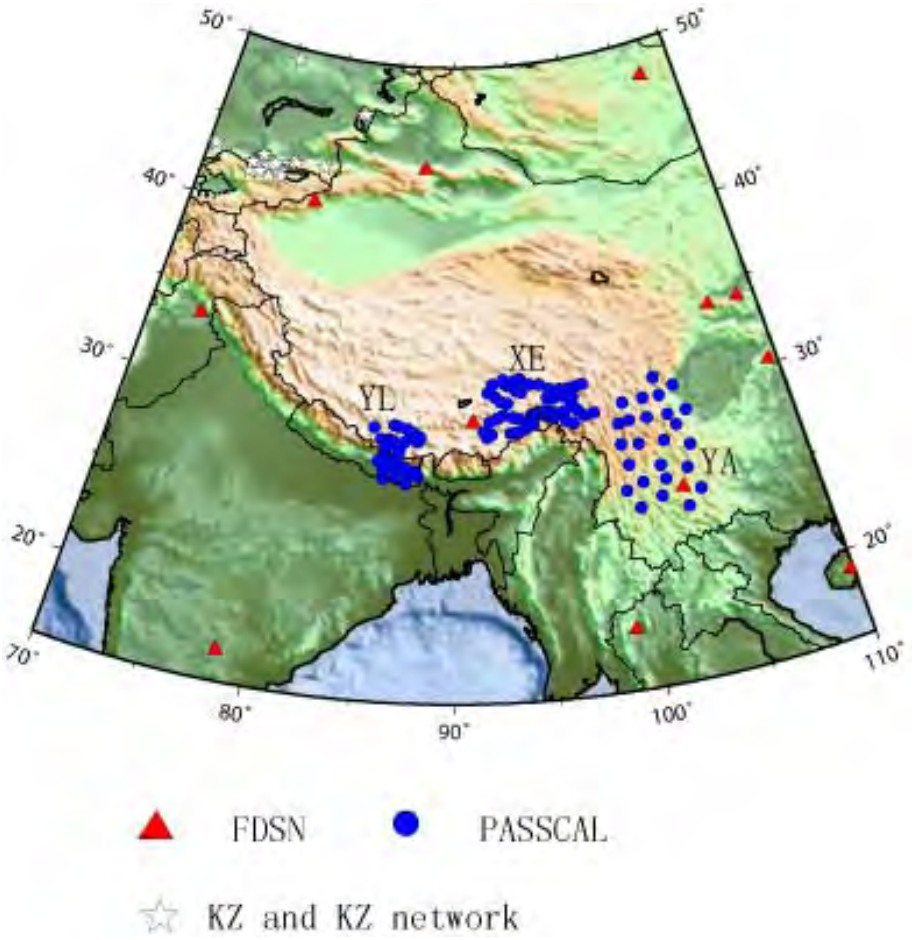


**Figure 1. Station distributions in W. China and surrounding regions. Stations include international stations (FDSN), regional networks (KZ and KN) and PASSCAL experiments (from west to east: YL, HIMNT; XE, Namche Barwa; YA, MIT-CHINA).**

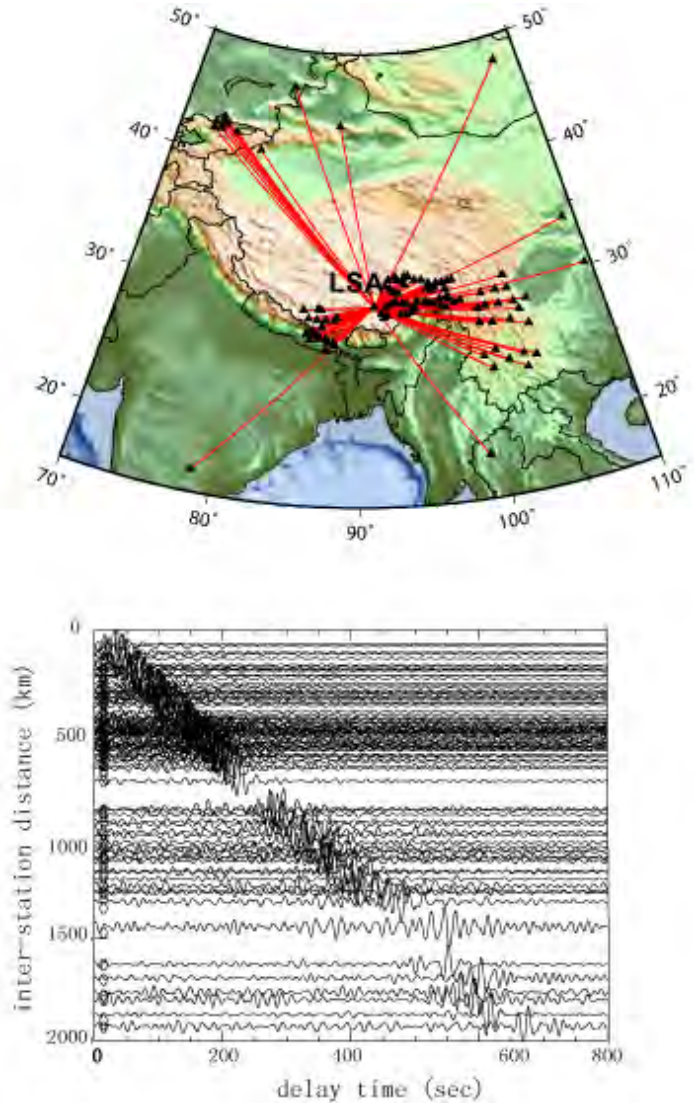


**Figure 2: An example of a cross-correlation record-section with inter-station paths plotted in the top diagram for cross-correlation with SNR > 15. The result is centered on station LSA (Lhasa, China) for the symmetric-signals, band-pass filtered from 10 to 30 sec.**

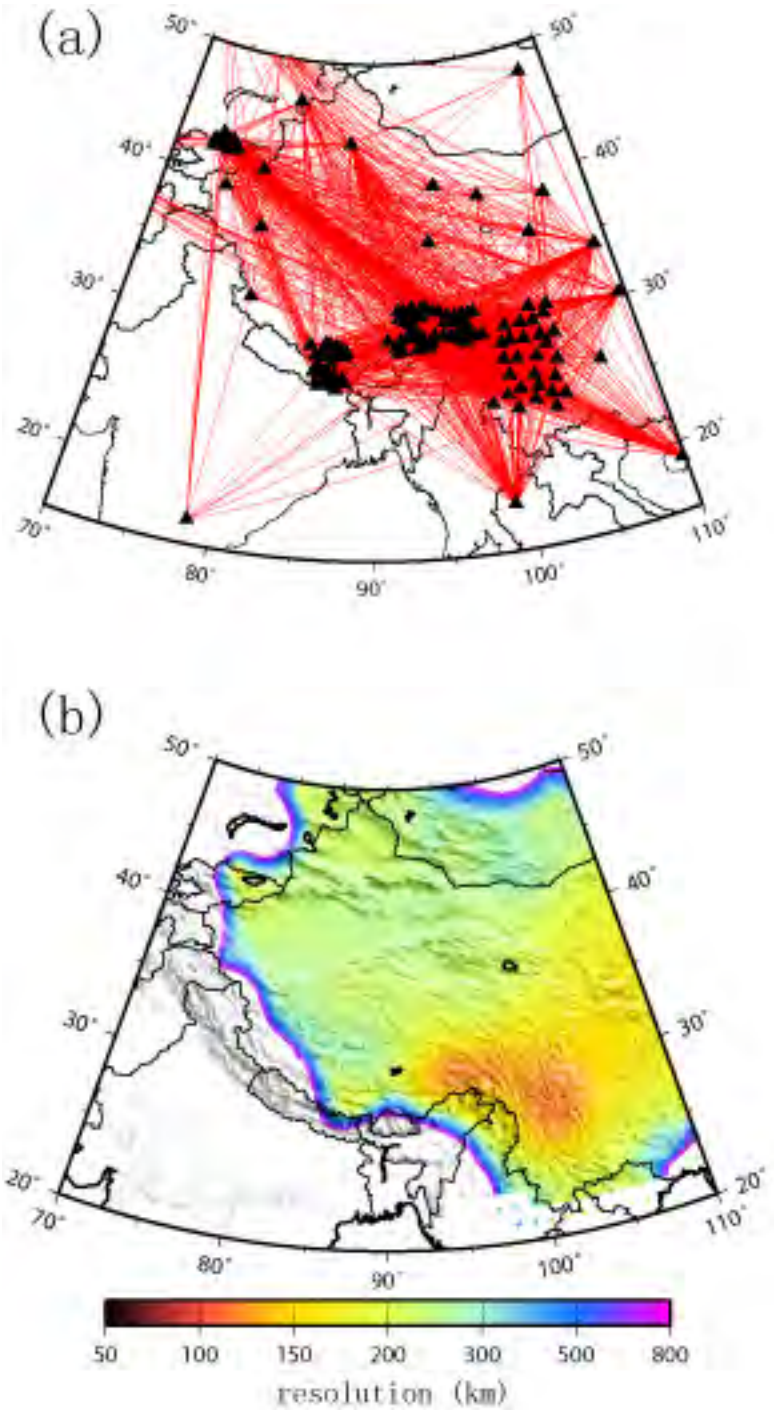


**Figure 3. (a) Path coverage and (b) resolution estimated for 20 sec period. Resolution is defined as the standard deviation of 2-D Gaussian fit to the resolution surface at each model node.**

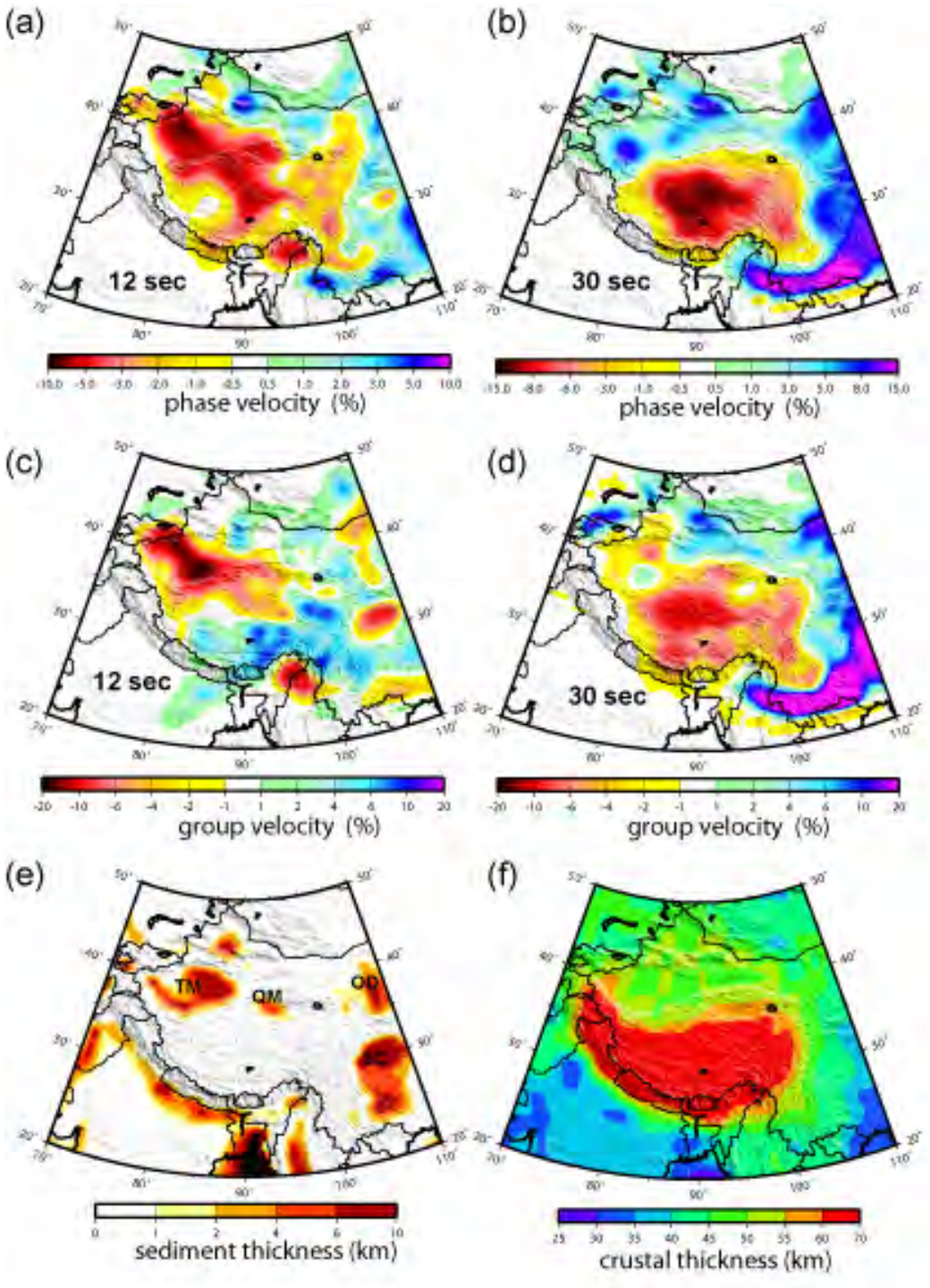


**Figure 4. (a-d) Rayleigh wave phase (top) and group (middle) velocity maps at 12 and 30 sec periods. The velocities are plotted as perturbation relative to the average values. (e) and (f) Maps of sediment thickness and crustal thickness (Laske and Masters, 1997). The major sedimentary basins are labeled: Tarim (TM), Daidam (QM), Sichuan (SC), and Ordos (OD).**

# SEISMIC SIMULATIONS USING PARALLEL COMPUTING AND THREE-DIMENSIONAL EARTH MODELS TO IMPROVE NUCLEAR EXPLOSION PHENOMENOLOGY AND MONITORING

Arthur J. Rodgers, Eric Matzel, Michael E. Pasyanos, Anders Petersson, Bjorn A. Sjogreen, Caroline Bono, Oleg Vorobiev, Tarabay H. Antoun, Ilya N. Lomov, William R. Walter, and Stephen C. Myers

Lawrence Livermore National Laboratory

Sponsored by National Nuclear Security Administration

Contract No. DE-AC52-07NA27344

## ABSTRACT

The development of accurate numerical methods to simulate wave propagation in three-dimensional (3D) earth models and advances in computational power offer exciting possibilities for modeling the motions excited by underground nuclear explosions. This presentation will describe recent work to use new numerical techniques and parallel computing to model earthquakes and underground explosions to improve understanding of the wave excitation at the source and path-propagation effects. Firstly, we are using the spectral element method (SEM, SPECFEM3D code of Komatitsch and Tromp, 2002) to model earthquakes and explosions at regional distances using available 3D models. SPECFEM3D simulates anelastic wave propagation in fully 3D earth models in spherical geometry with the ability to account for free surface topography, anisotropy, ellipticity, rotation and gravity. Results show in many cases that 3D models are able to reproduce features of the observed seismograms that arise from path-propagation effects (e.g., enhanced surface wave dispersion, refraction, amplitude variations from focusing and defocusing, tangential component energy from isotropic sources). We are currently investigating the ability of different 3D models to predict path-specific seismograms as a function of frequency. A number of models developed using a variety of methodologies are available for testing. These include the WENA/Unified model of Eurasia (e.g. Pasyanos et al 2004), the global CUB 2.0 model (Shapiro and Ritzwoller, 2002), the partitioned waveform model for the Mediterranean (van der Lee et al., 2007) and stochastic models of the Yellow Sea Korean Peninsula region (Pasyanos et al., 2006). Secondly, we are extending our Cartesian anelastic finite difference code (WPP of Nilsson et al., 2007) to model the effects of free-surface topography. WPP models anelastic wave propagation in fully 3D earth models using mesh refinement to increase computational speed and improve memory efficiency. Thirdly, we are modeling non-linear near-source shock wave propagation with GEODYN, an Eulerian Godunov finite-difference code (Antoun et al., 2001). This code accounts for shock wave propagation and a variety of effects, including cavity formation, rock fracture and plastic deformation. We are exploring the coupling of GEODYN to WPP to propagate motions from the near-source (non-linear) region to the (linear anelastic) region where seismic observations are made at local, regional and teleseismic distances. This effort has just begun and we show preliminary results in this paper. These simulation tools are supported by massively parallel computers operated by Livermore Computing.

## OBJECTIVES

Improvements in numerical methods to simulate wave phenomena in three-dimensional (3D) heterogeneous geologic materials, implementation of these algorithms on parallel computers and the inexorable increase of computational power offer exciting possibilities for the ability to simulate wave propagation for improving understanding of the nuclear explosion source and nuclear explosion monitoring. The objective of this study is to describe the development of new seismic wave modeling capabilities at Lawrence Livermore National Laboratory (LLNL) and articulate how these capabilities can improve understanding of observed seismic waves, particularly source excitation and propagation effects. Nuclear explosion monitoring based on seismic data ultimately relies on understanding the fundamentals of excitation of waves in the earth by the high-energy nuclear explosion source, shock-wave propagation in the near-source region and subsequent elastic wave propagation, including interaction with near-source geology and topography and path propagation. We are applying newly developed numerical methods and high performance computational resources to improve knowledge of observable effects on seismograms due to propagation in realistic 3D earth models and geologic materials.

## RESEARCH ACCOMPLISHED

This effort covers three areas of research: 1) simulation of regional distance (< 1500 km) seismograms at intermediate periods (0.02-0.1 Hz) with the spectral element method (SEM); 2) simulation of realistic free-surface topography with our Cartesian anelastic finite difference code (WPP); and 3) the simulation of non-linear shock wave phenomena in realistic geologic materials (GEODYN) and the coupling of non-linear motions to our linear anelastic code (WPP). All these efforts rely on massively parallel computer systems at LLNL.

### Simulations of Seismic Wave Propagation in 3D Models at Regional Distances and Intermediate Periods

Researchers in the academic and nuclear monitoring communities have vigorously developed 3D seismic velocity models based on various seismic tomographic methods. Computational methods for seismic wave propagation using parallel computers allow us to compute synthetic seismograms in 3D models for intermediate periods (≥ 10 seconds) at regional distances (< 1500 km). To do this, we are using the spectral element method (SEM) code SPECFEM3D (Komatitsch and Vilotte, 1998; Komatitsch and Tromp, 1999; Komatitsch et al., 2000). This code computes the response of the earth to arbitrary forcing in spherical geometry with fully 3D seismic velocity (including anisotropy) and density variations. The code also handles the effects of free-surface topography and bathymetry, ellipticity, rotation and self-gravitation. We have modified the code to handle a simple, but general 3D model format.

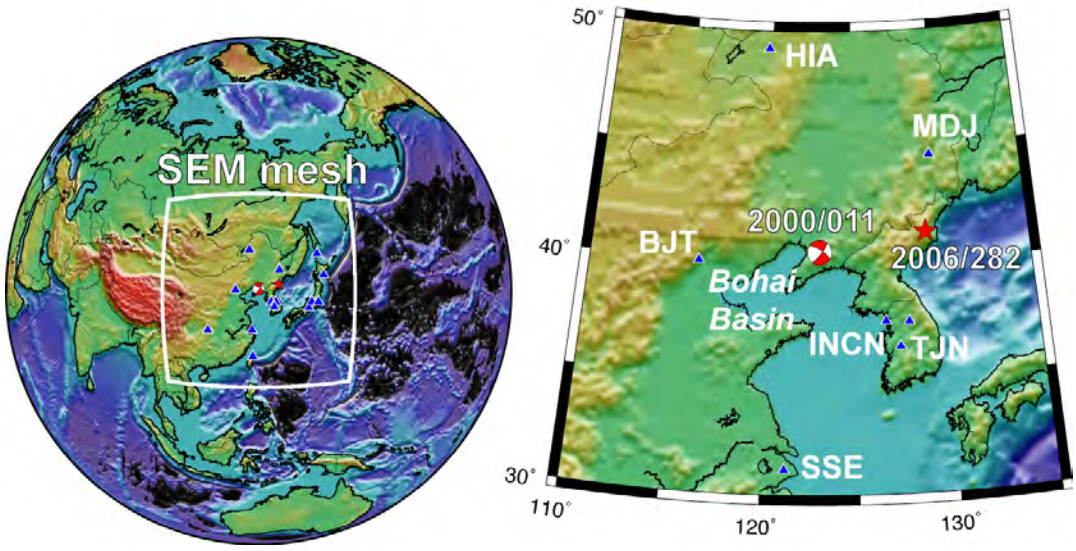


**Figure 1. (left) SPECFEM3D computational domain for regional simulations of events in East Asia. (right) Map showing the locations of the January 11, 2000 (2000/011) earthquake and October 9, 2006, (2006/282) North Korean nuclear explosion along with regional broadband stations that recorded the events**.

We have used this code to compute synthetics seismograms for the January 11, 2000, moderate ($M_W$ ~ 5) earthquake in the Korean Peninsula and the ($M_W$ ~ 4) October 9, 2006, North Korean nuclear explosion. Figure 1 (left) shows SPECFEM3D computational domain at the surface (white box) covering a 45° "chunk" (solid angle) of the earth. Figure 1 (right) shows a map of the events and recording stations for these two events. Focal parameters for the earthquake were obtained from waveform modeling using 1D methods.

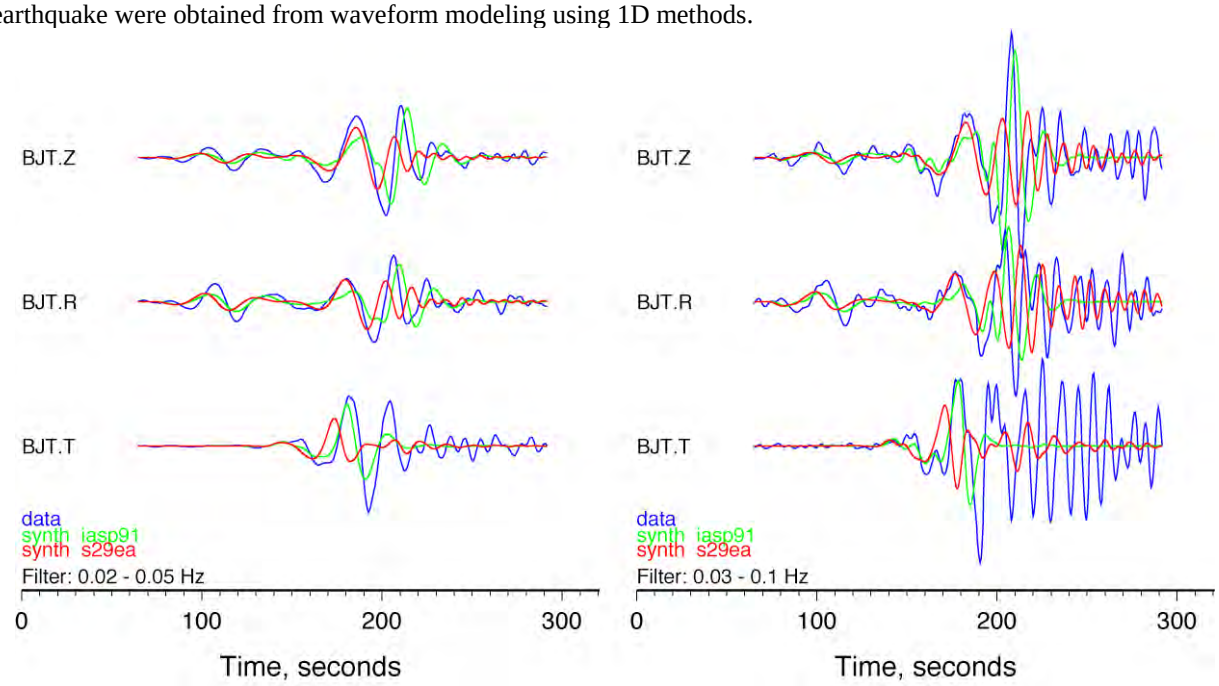


**Figure 2. Observed (blue) and synthetic seismograms for the 2000/011 earthquake at station BJT for the iasp91 (green) and *s29ea+CRUST2.0* (red) models filtered 0.02-0.05 Hz (left) and 0.03-0.1 Hz (right).**

Figure 2 shows the observed and synthetic waveforms for the 2000/011 earthquake at station BJT (Beijing, China) filtered in two different bands: 0.02–0.05 and 0.03–0.07 Hz (left and right, respectively). Synthetics were computed for two models: the iasp91 1D model (Kennett and Engdahl, 1991) shown as the green synthetics and the *s29ea+CRUST2.0* 3D model (Kustowski et al., 2008) shown as the red synthetics. Calculations resulted in seismograms that were resolved in the frequency band 0.0–0.12 Hz and took about 4 hours on 64 CPU's of a modest Linux cluster operated by the Ground-Based Nuclear Explosion Monitoring (GNEM) Program at LLNL. All calculations included the effects of surface topography, bathymetry and ellipticity. This event was moderately large ($M_W$ ~ 5.0) and had good signal-noise across a broadband. Note that for 0.02–0.05 Hz (20–50 second periods) the observed and synthetic waveforms are very simple with clear Pnl, Rayleigh and Love waves. At these periods the synthetics match the observed waveforms with the iasp91 model showing a slightly better fit to the phase and amplitudes of the data. However, including slightly higher frequencies (0.1 Hz or 10 seconds periods) the observed waveforms show much greater complexity, especially the surface waves. This complexity is likely due to interaction with the Bohai Basin (Figure 1). Note that the Rayleigh wave is strongly dispersed and the later part of the Love wave shows a long duration with little dispersion. The *s29ea+CRUST2.0* 3D model captures some of the more complex surface waveform, mostly in the Rayleigh wave. As expected at intermediate frequencies (0.02–0.07 Hz or 14–20 second periods) the observed waveforms are less complex.

This example (Figure 2) demonstrates the challenge for waveform-based monitoring of small-to-moderate sized events ($M_W$ 3.5–4.5). These events radiate very little long-period energy and are often observed where the surface waves only have signals above the noise for intermediate periods (e.g., 0.03–0.1 Hz or 10–33 seconds). For waveform analysis at intermediate periods seismologists require good constraints on the path-specific structure. We are performing calculations with a variety of available 3D models to determine the performance of models for predicting observed waveforms as a function of frequency content. It is important to quantify the performance of 3D

models so that they may be used as starting models for waveform-based tomography, such as adjoint methods (Tromp et al., 2005; Liu and Tromp, 2006).

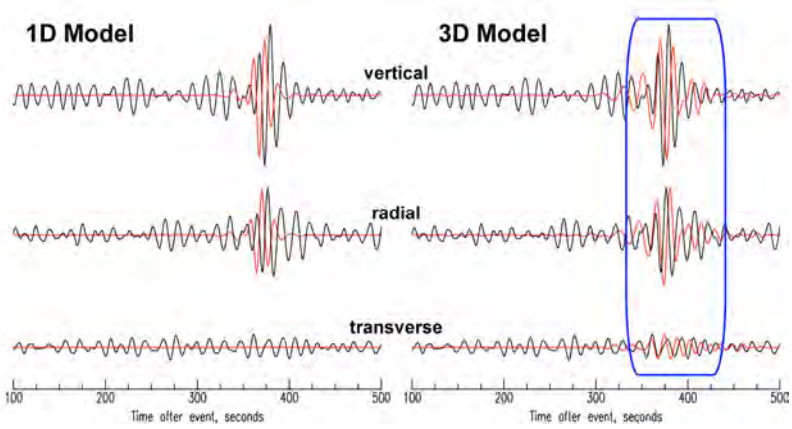


**Figure 3. Observed (black) and synthetic (red) three-component seismograms for the 1D iasp91 (left) and 3D CUB2.0 (right) models. Both data and synthetics are filtered 0.05-0.1 Hz (10-20 second periods).**

As another example of the effects of known 3D structure on intermediate period surface waves we show the observed and synthetic waveforms for the October 9, 2006, North Korean nuclear test at station BJT. The path to BJT passes through the northern edge of the Bohai Basin, similar to the path for the 2000/011 earthquake (Figure1). The synthetics for the 1D iasp91 and 3D *CUB2.0* model (Shapiro and Ritzwoller, 2002) are shown in Figure 3. While the signal-to-noise ratio of the transverse component at the expected time window of the surface wave is about 1:1 or slightly higher, the 3D synthetic predicts some energy that is not present in the synthetics for a 1D model. This illustrates how the refraction of surface waves by 3D structure, such as sedimentary basins, can cause rotation of energy from a purely isotropic source from the radial to the transverse component. Such wave propagation effects may bias estimates of source parameters for explosion sources such as seismic moment (and consequently explosive yield) and deviatoric moment tensor components.

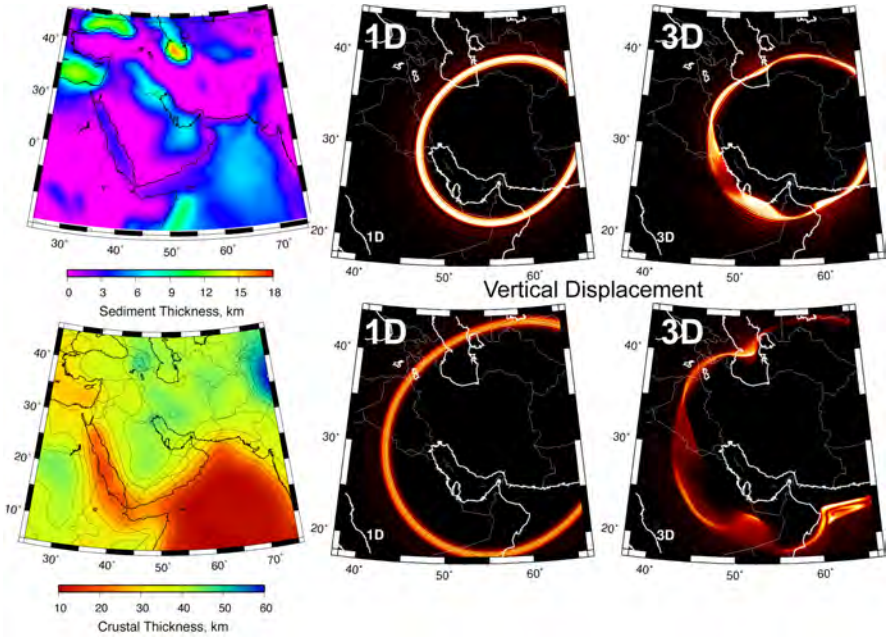


**Figure 4. WENA 3D model properties across the Middle East: sediment thickness (top left) and crustal thickness (bottom left). Snapshots of vertical ground displacements showing Rayleigh wave propagation for an isotropic source using an average 1D model (center) and the WENA 3D model (right).**

Finally, we performed large-scale simulations of regional seismic wave propagation in the Middle East using our anelastic finite difference code (WPP, described below). We modeled the $M_W$ 6.25, February 22, 2005, Kerman earthquake using an average 1D model and the 3D WENA model of Pasyanos et al. (2004). The WENA model represents 3D crustal and upper mantle structure with 1° resolution and reveals the known sedimentary and crustal structure of the Middle East (Figure 4, left). For simplicity of illustration, we compare the wave propagation excited by an isotropic source using the 1D and WENA 3D models (Figure 4, center and right, respectively). The vertical displacement wavefields are shown at two different time steps in the calculations. Notice the dramatic timing, amplitude and dispersion asymmetries in the 3D model compared to the 1D model. These effects are confirmed by observations of long-duration intermediate period surface waveforms for events in the Zagros Mountains and Iranian Plateau recorded in the eastern Arabian Peninsula along the Persian/Arabian Gulf coast.

Note that the simulations shown in Figure 4 required nearly 4 billion grid points for density, seismic velocities and quality factors covering a volume 3,000 km by 3,000 km by 400 km (depth) at 1,000-m resolution. The calculations took nearly 50,000 CPU-hours, taking nearly two days on 1,024 CPU's of the Thunder Linux cluster at LLNL. The simulations resulted in seismograms valid to 0.1 Hz (10 second periods).

**Simulation of Seismic Wave Propagation with Realistic Free Surface Topography**

LLNL recently developed a new parallel finite difference code for simulating anelastic wave propagation. The algorithm uses a node-center second-order discretization, described by Nilsson et al. (2007). The code, called WPP, is open source and available at https://computation.llnl.gov/casc/serpentine/index.html. Currently, the code handles fully 3D variations in seismic wave speeds and density, both acoustic and elastic wave propagation and attenuation with quality factors for P- and S-waves. The code allows for mesh refinement for memory and computational efficiency. As the resolvable frequency of seismic events increases, the corresponding wavelength of the seismic wave motion decreases requiring finer discretization and more grid points (and memory). For frequencies above about 0.5 Hz, effects of non-planar topography become increasingly important (Figure 5). We are currently extending the WPP code to accurately satisfy the free surface boundary conditions on realistic non-planar topography. This will be accomplished by using an energy conserving, summation-by-parts, finite difference discretization of the elastic wave equation on a curvilinear grid (Appelo and Petersson, 2008).

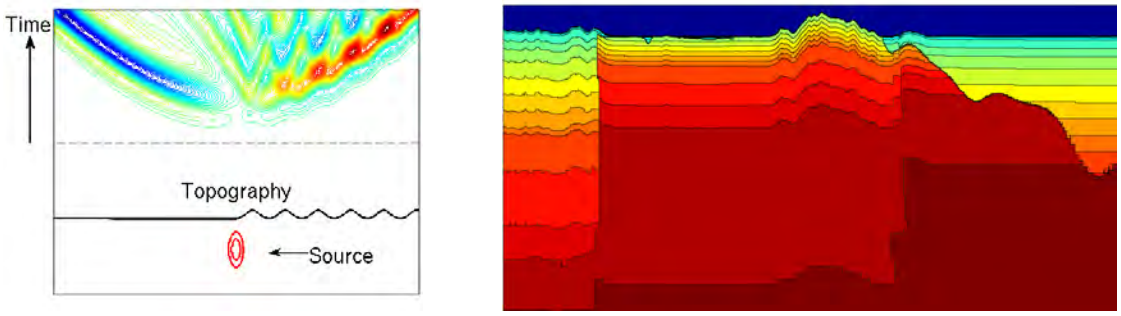


**Figure 5. (left) Vertical displacement time history along the surface due to an isotropic point source below the surface. Note the effects of topography on the right side of the domain. (right) Compressional velocity ($V_P$) in an east-west cross-section of the San Francisco Bay area going through Mt. Tamalpais. The scale goes from 5,000 m/s (dark red) to 0 m/s (dark blue). The cross section extends to a depth of 10 km below sea level.**

Since the curvilinear formulation involves about nine times more arithmetic operations per grid point than its Cartesian counterpart, the computational grid will be made Cartesian below some fixed elevation. As is visible in Figure 5 (right), the compressional wave speed ($V_P$) increases drastically with depth and is commonly about eight times larger below the Moho discontinuity (at about 30 km depth) than in sedimentary basins near the free surface. The propagation speed for shear waves has similar depth dependence, but the ratio between the two speeds depends on the material type (sediment, hard rock, etc.). Since the wavelength of elastic waves is proportional to the wave speed, structured mesh refinement (where the mesh gets coarser at depth) will be used to keep the grid size in approximate parity with the wavelength. Furthermore, since there is such a large change in wave speeds from the

surface to the bottom of the computational domain, mesh refinement will significantly reduce the total number of grid points and also allow the explicit time-stepping to use a much larger time step (improving computational efficiency). To guarantee stability of the time-stepping scheme in the presence of mesh refinement, we will use a newly developed energy conserving coupling of the solution across mesh refinement boundaries. For simplicity, only factor-of-two refinements are allowed and all mesh refinement boundaries must be horizontal. The latter restriction allows for a two-dimensional decomposition of the computational domain where each processor has a "pencil"-shaped domain from the topography at the top to the far-field boundary at the bottom. This layout allows for efficient load balancing on parallel machines and eliminates the need for expensive all-to-all communications.

The influence of topography is illustrated in Figure 6, where we show the response due to a vertically propagating shear wave impinging on a 3-D Gaussian hill. In this case, the material is homogeneous, a free surface boundary condition is imposed on the curved top surface, and periodic boundary conditions are used in the horizontal directions. The traces show displacement time histories at the surface along a densely sampled line passing through the center of the Gaussian hill. For a flat free surface, the horizontal component would only have one pulse corresponding to the arrival of the vertically propagation wave; the vertical component would be identically zero. In comparison, the curved topography induces reflected P- and S-waves, which also induce a vertical component to the motion.

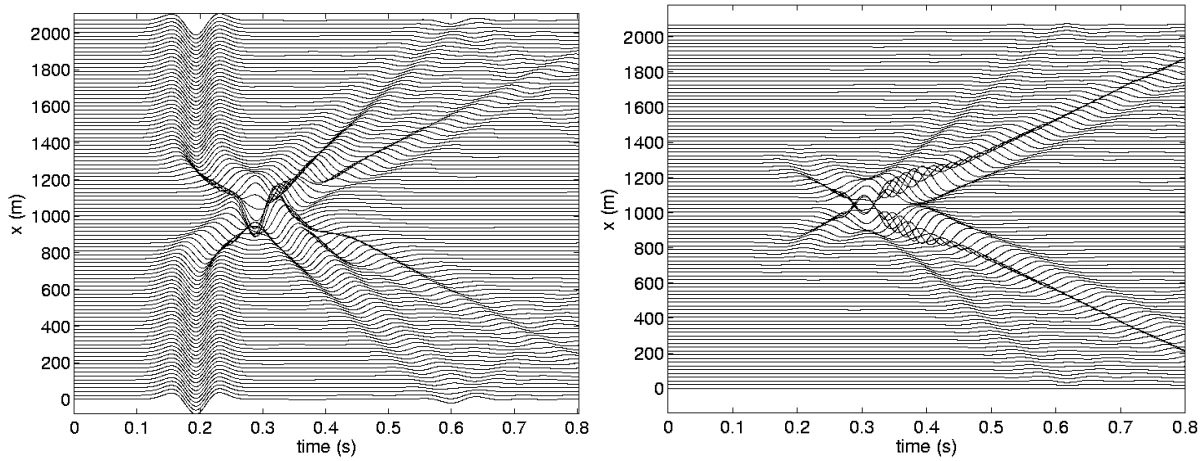


**Figure 6. Horizontal (left) and vertical (right) displacement time histories along a line through the center of the Gaussian hill.**

**Simulation of Non-Linear Hydrodynamics with GEODYN and Coupling to WPP**

The high energy density of chemical and nuclear explosions causes irreversible processes (e.g., vaporization, cavity creation and plastic deformation) in geologic materials near the source before stimulating seismic waves beyond the elastic radius. In order to simulate ground motions emerging from buried explosions, we must account for these processes including a complete thermodynmical treatment of the energy involved in these processes. Source emplacement conditions are known to have dramatic effects on the excitation of seismic waves that ultimately must be accounted for in yield estimates from seismic amplitudes and earthquake-explosion discriminants. The challenges of site-specific yield scaling relationships and the transportability of high-frequency regional discriminants can be traced to emplacement conditions and physical properties of geologic materials at the source.

The subject of this effort is to develop and illustrate a coupling approach between the non-linear GEODYN hydrodynamics code (Antoun et al., 2001) and the linear anelastic wave propagation code WPP, described above (Nilsson et al., 2007). GEODYN is a nonlinear Eulerian wave propagation code with adaptive mesh refinement (Antoun et al., 2001; Lomov and Rubin, 2003). The GEODYN code can handle large material deformations and phase transitions such as melting, vaporization, porous compaction and material damage. In the limit of low compressions and temperatures GEODYN can be applied to model linear waves in solid media, albeit at significant numerical cost over conventional anelastic finite difference methods. The code is not very efficient for handling linear waves since it carries around a lot of extra variables and performs calculations that are not needed for linear (elastic) wave propagation. WPP, on the other hand, cannot handle permanent deformations and uses a simple

scheme to model inelastic effects on the large scale (Liu and Archuleta, 2006). The purpose of this study (which has only just begun) is to couple the two codes to model the non-linear behavior of the near-source region with the full physics capabilities of GEODYN and pass these motions to WPP in an overlapping region in order to propagate the seismic waves to local, regional, and/or teleseismic distances. The basic idea of coupling is shown schematically in Figure 7.

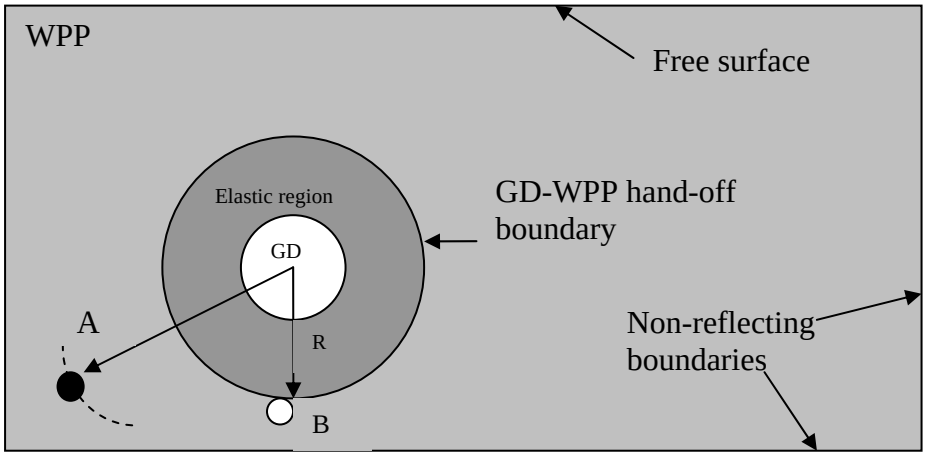


**Figure 7. Conceptual illustration of the coupling between the nonlinear source region from GEODYN (GD) to WPP. The GEODYN domain extends to radius R (dark gray region), while the WPP domain covers a larger entire volume.**

GEODYN can compute motions in 1D (spherically symmetric), 2D, 2.5D (2D axisymmetric) or fully 3D domains. Figure 7 describes a spherical source modeled in a 1D GEODYN calculation that was passed to a 3D WPP calculation. Material displacement inside the volume within the hand-off radius R was overwritten with pre-calculated 1D GEODYN data. One of the most important applications for GEODYN is the accurate simulation of ground motion due to underground explosions. Experimental data on spherical waves generated in situ by underground explosions published in open literature are scarce and are not always available with good geotechnical characterization of the emplacement rock. For this study, we chose to use data from a series of chemical high-explosive (HE) experiments in limestone performed in Kirghizia in 1960 (Murphy et al., 1997) to illustrate the code-coupling approach. The generic strength model described in Vorobiev (2008) was used in GEODYN to model 0.5% porous limestone. Experimental measurements of ground motion at different distances from the shot point were reported by Murphy et al. (1997). The explosions and motion recordings reported in this study were conducted in the subsurface in essentially rock whole-space conditions, making them ideal for our simulation experiments.

Figure 8 shows the vertical component displacement time histories calculated in 1D GEODYN (blue) and passed to WPP (red) at the boundary of the hand-off region (point B in Figure 7). The spatial resolution used in GEODYN was 6 cm and the space resolution used in 3D WPP was 1 m, allowing for resolution to about 100 Hz. Elastic constants used in WPP were chosen to match initial moduli for the generic limestone. Note that the amplitude and phase agree very well.

Figure 9 shows peak displacements as a function of range calculated by 1D GEODYN and 3D WPP codes. The 1D GEODYN calculations agree very well with experimentally measured values of peak velocity (crosses for point measurements taken from Figure 8 of Murphy et al., 1997). The peak displacements computed with WPP agree well with the GEODYN calculations when a fine grid spacing of 1 meter is used. However, the WPP peak displacements attenuate faster than 1/R when a grid spacing of 4 meters is used. This demonstrates that one must rigorously evaluate the numerical resolution of such calculations to be confident that numerical dispersion is minimized.

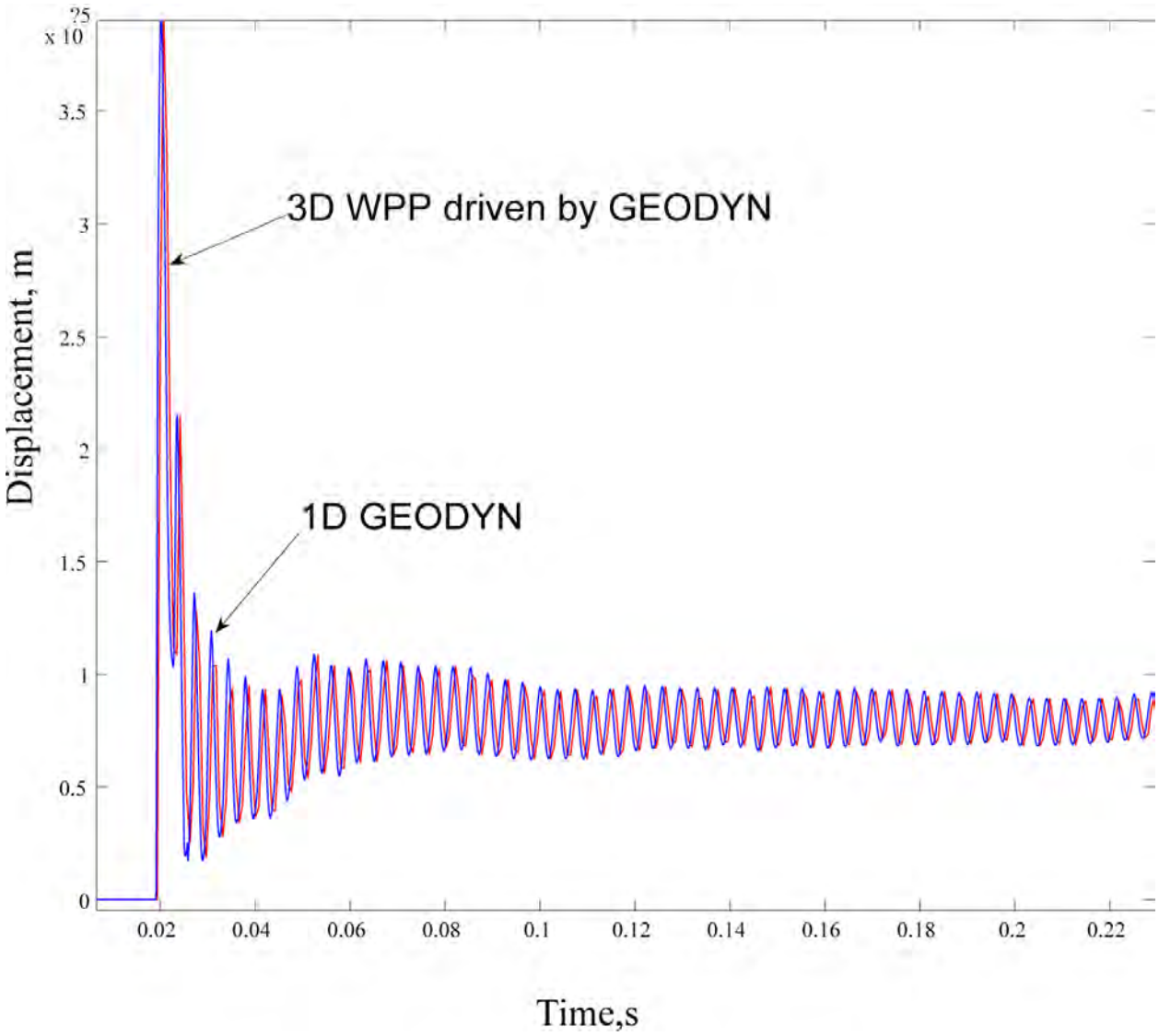


**Figure 8. Vertical component displacement time history at the boundary of the hand-off region (point B in Figure 7) for the 3D WPP (red solid line) and 1D GEODYN (blue dotted line).**

## CONCLUSIONS AND RECOMMENDATIONS

Recent development of numerical methods for simulation of the 3D seismic wave excitation and propagation, coupled with ever-increasing computational power are offering exciting new capabilities for improving knowledge of seismic wave phenomenology for nuclear explosion monitoring. In this study, we demonstrated several efforts underway at LLNL that promise to advance capabilities for various aspects of seismic wave simulation.

The SEM code, SPECFEM3D, models seismic wave propagation in spherical geometry including important effects (e.g., 3D heterogeneity, anisotropy, free surface topography, ellipticity). This code allows us to compute intermediate period seismograms (periods greater than about 10 seconds) at regional distance (up to about 1500 km). We are using this code to test current available 3D seismic models. This code will be used in another study to exploit finite frequency sensitivity kernels for seismic waveform tomography based on adjoint methods (Savage et al., these Proceedings).

We are improving our Cartesian anelastic finite difference code (WPP) to add the effects of free-surface topography. The method will rely on a summation-by-parts principle and has been proven in research codes. The production

version of the WPP (version 2.0) will include the effects of free-surface topography and other improvements. Note that WPP is an open source code and can be downloaded from LLNL.

The coupling of our non-linear hydrodynamics code, GEODYN, with WPP will allow us to simulate ground motions from underground nuclear explosions including an accurate representation of the important near-source effects of cavity formation, melting, yielding, plastic deformation, porous compaction, and material damage all in a consistent thermodynamic framework. While many details remain to be sorted out, we have made good progress in the short time that we have been working on this effort.

These efforts involve complex numerical codes running on massively parallel computers. LLNL has significant experience in parallel code development as well as the computational resources to enable simulations of relevance to the nuclear explosion source phenomenology and monitoring investigations.

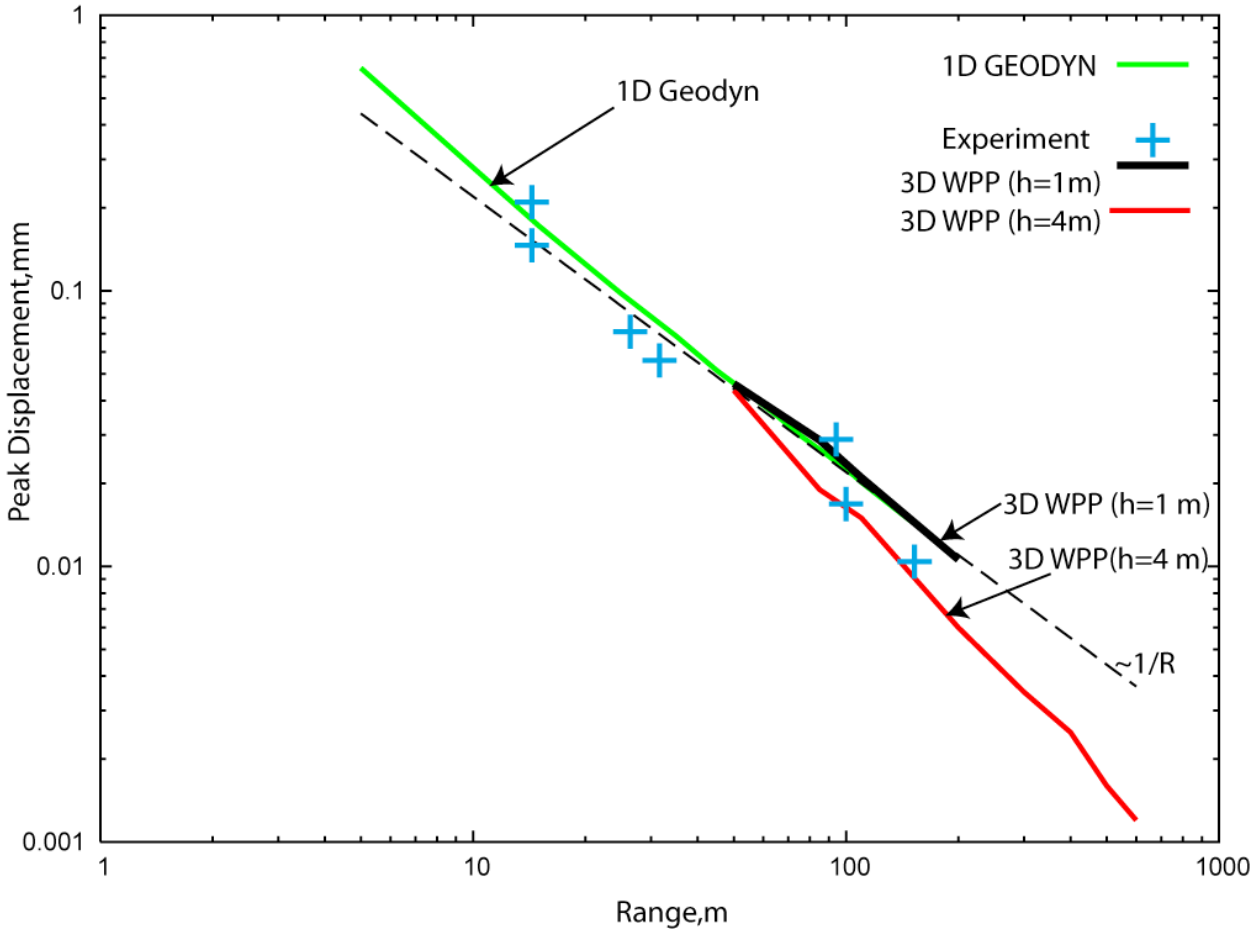


**Figure 9. Peak displacement versus range for a chemical HE source in a limestone whole-space: experimentally measured values (crosses) from Figure 8 of Murphy et al. (1997); calculated with 1D GEODYN (solid green line); and calculated with 3D WPP (red line for 4-m grid spacing and black line for 1-m grid spacing). These are compared with and the expected geometric spreading for a spherical wave in a homogeneous whole-space (1/R, fine dashed line).**

## ACKNOWLEDGEMENTS

SEM calculations were performed with the SPECFEM3D package developed by Jeroen Tromp, Dmitri Komatitsch and colleagues and distributed by the Computational Infrastructure for Geodynamics supported by the National Science Foundation (www.geodynamics.org). Calculations were performed on the GNEM Linux cluster, and we are grateful for support by Stan Ruppert and Jenny Aquilino. Larger calculations were performed on massively parallel systems operated by Livermore Computing. WPP was supported in part by Laboratory Directed Research and Development (project 05-ER-079). Some waveform data were obtained from the IRIS Data Management System, which is funded by the National Science Foundation.

## REFERENCES


Antoun, T. H., I. N. Lomov and L. A. Glenn (2001). Development and application of a strength and damage model for rock under dynamic loading, proceedings of the 38th U.S. Rock Mechanics Symposium, Rock Mechanics in the National Interest, D. Elsworth, J. Tinucci and K. Heasley (eds.), A. A. Balkema Publishers, Lisse, The Netherlands, 369–374.

Appelo, D. and N.A. Petersson (2008). A stable finite difference method for the elastic wave equation on complex geometries with free surfaces, *Communications in Computational Physics*, in press.

Kennett B.L.N. & Engdahl E.R. (1991). Travel times for global earthquake location and phase identification, *Geophys J Int*. 105: 429–465.

Komatitsch, D. and J.-P. Vilotte (1998). The Spectral Element Method: An efficient tool to simulate the seismic response of 2D and 3D geologic structures, *Bull. Seism Soc. Am*. 88: 368–392.

Komatitsch, D. and J. Tromp (1999). Introduction to the spectral element method for three-dimensional seismic wave propagation, *Geophys. J. Int*. 139: 806–822.

Komatitsch, D., J. Ritsema and J. Tromp (2002). The Spectral-Element Method, Beowolf computing and global seismology, *Science* 298: 1737–1742.

Kustowski B., Ekström G., and A. M. Dziewonski (2008). The shear-wave velocity structure in the upper mantle beneath Eurasia, *Geophys. J. Int.*, in press.

Liu, P.-C. and R. Archuleta (2006). Efficient modeling of Q for 3D numerical simulation of wave propagation, *Bull. Seism. Soc. Am*. 96: 1352–1358.

Liu, Q. and J. Tromp (2006) Finite-frequency kernels based on adjoint methods, *Bull. Seism. Soc. Am*. 96: 2383–2387.

Lomov, I. and M.B. Rubin (2003), Numerical simulation of damage using an elastic-viscoplastic model with directional tensile failure. *Journal De Physique IV*, 110, 281–286.

Murphy, J.R., Kitov, I.O., Rimer, N., Adushkin, V.V., Barker, B.W. (1997) Seismic characteristics of cavity decoupled explosion in limestone: An analysis of Soviet high explosive test data. *Journal of Geophysical Research* 102: (12), 27393–27405.

Nilsson, S., N. A. Petersson, B. Sjogreen and H.-O. Kreiss (2007). Stable difference approximations for the elastic wave equation in second order formulation, *SIAM J. Numer. Anal.* 45: 1902–1936.

Pasyanos, M., G. A. Franz, A. L. Ramirez (2006). Reconciling a geophysical model to data using a Markov chain Monte Carlo algorithm: An application to the Yellow Sea–Korean Peninsula region, *J. Geophys. Res*., Vol. 111, No. B3, B03313, 10.1029/2005JB003851

Pasyanos, M. E., W. R. Walter, M. P. Flanagan, P. Goldstein, and J. Bhattacharyya (2004). Building and testing an *a priori* geophysical model for Western Eurasia and North Africa, *Pure Appl. Geophys.* 161: 235–281

Shapiro, N.M. and M.H. Ritzwoller (2002). Monte-Carlo inversion for a global shear velocity model of the crust and upper mantle, *Geophys. J. Int.* 151: 88–105.

Tromp, J., C. Tape and Q. Liu (2005). Seismic tomography, adjoint methods, time reversal and banana-doughnut kernels, *Geophys. J. Int*. 160: 195–216.

van der Lee, S., S. Chang, M. Flanagan, H. Bedle, F. Marone, E. Matzel, M. Pasyanos, A. Rodgers, B. Romanowicz, and C. Schmid (2007). Joint Inversion for 3-Dimensional S-Velocity Mantle Structure Along the Tethyan Margin, in *Proceedings of the 29th Monitoring Research Review: Ground-Based Nuclear Explosion Technologies*, LA-UR-07-5613, Vol. 1, pp. 312–321.

Vorobiev. O. Y. (2008) Generic strength model for dry jointed rock masses, in press, *International Journal of Plasticity*, 10.1016/j.ijplas.2008.06.009.

# CALIBRATION OF 3D UPPER MANTLE STRUCTURE IN EURASIA USING REGIONAL AND TELESEISMIC FULL WAVEFORM SEISMIC DATA

Barbara Romanowicz[1], Aimin Cao[2], Paul Cupillard[1], Laurent Stehly[1], Ahyi Kim[1], Michael E. Pasyanos[3] and Douglas S. Dreger[1]

Berkeley Seismological Laboratory[1], Rice University[2], Lawrence Livermore National Laboratory[3]

Sponsored by National Nuclear Security Administration

Contracts No. DE-FC52-04NA25543[1] and DE-AC52-07NA27344[3]
Proposal No. BAA04-41

## ABSTRACT

We present progress in the development of a new approach to develop and evaluate earth models at the regional scale that utilizes full waveform seismograms.

We have implemented an approach which relies on a cascade of increasingly accurate theoretical approximations for the computation of the seismic wavefield, with the goal to develop a model of regional structure for a subregion of Southeast Asia (longitude 75 to 150 degrees and latitude 0 to 45 degrees). The selected area is highly heterogeneous, presenting a challenge for calibration purposes, but is well surrounded by earthquake sources and includes high quality broadband digital stations.

In previous years, we developed preliminary models based on successively more sophisticated theoretical approaches to time domain inversion of long period seismograms, in the framework of normal mode theory: 1) a 3D model based on the Nonlinear Asymptotic Coupling Theory (NACT), which includes the consideration of 2D kernels in the vertical plane containing source and receiver. This model was developed for a larger region (longitude 30-150 degrees and latitude -10 to 60 degrees); 2) a 3D model based on the "NBorn" approximation. This approach combines the 3D Born approximation with the path average approximation (PAVA) and allows to accurately account for large accumulated phase delays on paths that sample large scale smooth anomalies. The resulting model has a horizontal resolution of about 200 km.

In parallel, a regional version of the Spectral Element Method (SEM) code, in spherical geometry, RegSEM.1, was completed. This code uses Perfectly-Matched Layers (PMLs) at the borders of the region, and includes general 3D anisotropy, Moho and surface topography, ocean bathymetry, attenuation, and ellipticity. Because each SEM run (i.e., for one event) is time consuming, we proposed implementing an approach in which the wavefields for several events are computed simultaneously. This approach was introduced by Capdeville et al. (2005) and tested on synthetic data at the global scale, but never applied to real data or at a regional scale.

In the past year, we completed the codes and procedures that allow us to invert a collection of summed seismograms over the sub-region of Eurasia already considered for the NBorn inversion. Contrary to the NACT and NBorn cases, for which we collected teleseismic data, RegSEM, as currently implemented, requires sources and receivers to be included in the region of study. We thus collected an entirely new dataset, consisting of 96 events with $6.0 < Mw < 7.0$ observed simultaneously at 6 broadband global seismographic network (GSN) stations during the time period 1995 to 2007, with an epicentral distance between $5^o$ and $45^o$. We have completed the first successful tests of the method, which consisted of comparing the results of an inversion performed using a standard tomographic approach, where the waveform data correspond to individual source station paths, with an inversion using, as data, summed events at the six stations considered. The resulting 3D models are very similar, indicating that, at least at the wavelengths and periods considered, no substantial loss of information occurred in the event summation process. In these preliminary experiments, the short period cut off was 60 sec and the lateral resolution of the model was ~200km (spherical spline level 6). We present the results of these and other tests aimed at evaluating the potential and limitations of this method as we increase the frequency range to shorter periods, and experiment with different starting crustal models.

## OBJECTIVES

The primary objective of this research is to develop and apply an approach that utilizes increasingly advanced theoretical frameworks and numerical methods in order to obtain improved regional seismic structure calibration. Specifically, a large-scale regional Eurasian model has been developed from a large dataset of seismic waveforms using the path-average approximation (PAVA) and Non-linear Asymptotic Coupling Theory (NACT) (Li and Romanowicz, 1995), which are well-developed normal-mode based approaches. In these approaches, 1D and 2D waveform sensitivity is considered, respectively, in the vertical plane containing the great-circle path between source and receiver. We have refined this model in a smaller region using a linear implementation of Born single-scattering theory (Capdeville, 2005), which more accurately represents the 3D sensitivity of the seismic wavefield, for the inverse part of the problem, and using a non-linear modified 3D Born approximation for the forward part of the problem (Panning et al., 2008). Additionally, we have developed and implemented a regional version of the Spectral Element Method (RegSEM, Cupillard, 2008), a numerical approach that accurately models both wave propagation in a complex 3D earth (e.g., Faccioli et al., 1996; Komatitsch and Vilotte, 1998; Komatitsch and Tromp, 1999). Finally, we have implemented and tested a novel approach using RegSEM with stacked sources (Capdeville et al., 2005) to further speed computation.

A further objective of this research is to perform validation and improved calibration of the model described above using a variety of approaches and datasets, including ground truth datasets from the Knowledge Base. Specifically, we have been using broadband waveform modelling to tighten the crustal model on specific regional paths.

## RESEARCH ACCOMPLISHED

### Development of an "N-Born" Model.

In previous years, we developed a starting 3D upper mantle shear wave radially anisotropic model (Figure 1a) using NACT (Li and Romanowicz, 1995) from a global dataset of surface wave waveforms crossing the region of interest (longitude 30 to 150 degrees and latitude -10 to 60 degrees). This region is highly heterogeneous, presenting a challenge for calibration, but it is well surrounded by earthquake sources and a significant number of high quality broadband digital stations exist. We started from the existing waveform database that was collected at Berkeley over the last 10 years for the construction of global mantle tomographic models (Li and Romanowicz, 1996; Megnin and Romanowicz, 2000; Gung et al., 2003; Panning and Romanowicz, 2006), and added data from ~20 new events in the period up to to 2005. We now have 38826 3-component waveforms from 393 events recorded at 169 stations. The data has been processed using an automated algorithm, which removes glitches, and checks for many common problems related to timing, poor instrument response, and excessively noisy windows. A weighting scheme has been applied to insure even distribution of data across the region. This model is parameterized laterally in spherical spline level 6, which corresponds to lateral resolution of ~200 km. And the corresponding radially anisotropic model is parameterized in the spline level 5, which corresponds to a lateral resolution of ~400 km.

The next step in our study, finalized in 2007 (e.g., Cao et al., 2007ab), has been to perform an iteration of our 3D model using the "non-linear" Born approximation (N-Born), which is modified from the more standard 3D "linear" Born approximation by including a "Path Average" term (e.g., Panning et al., 2008). This term allows the accurate inclusion of accumulated phase shifts which arise in the case when the wavepath crosses a spatially extended region with a smooth anomaly of constant sign. The linear Born terms account for single scattering effects outside of the great circle path and are modeled according to the expressions of Capdeville (2005). With PAVA, multiple forward scattering is accounted for on the great circle.

Because the calculation of the 3D Born sensitivity kernels is very expensive computationally, we have selected a smaller subregion (longitude 75 to 150 degrees and latitude 0 to 45 degrees), where the lateral heterogeneities are more significant than the surrounding regions. In order to further reduce the length of the computation, we require that both events and stations must be within the large region (longitude 30 to 150$^{o}$ E and latitude -10 to 60$^{o}$ N) and only the ray paths along the minor arcs are selected. We calculated 3D Born sensitivity kernels for 162 events using the method of Capdeville (2005) and the computing facilities (Jacquard) of the National Energy Research Scientific Computing Center (www.nersc.gov). When we generate synthetics for the N-Born inversion, we use N-Born in the subregion and NACT outside of the subregion. The adopted damping scheme for isotropic and radially

anisotropic models is the same as that used in the NACT inversion. Figure 1 compares the isotropic part of the starting 3D (NACT) model and of the 3D "N-Born" model obtained after one iteration. The starting crustal model is CRUST2.0, and we invert for perturbations to the Moho topography together with volumetric perturbations in the upper mantle.

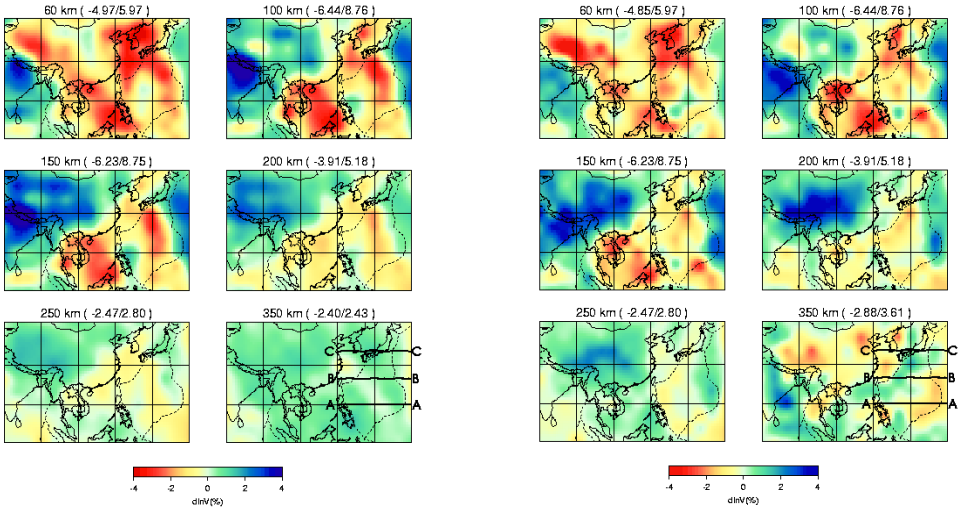


**Figure 1. a) Isotropic part of the starting NACT-derived 3D upper mantle model shown in a subregion (Lon 75 to 150 degrees and lat 0 to 45 degrees with map grid interval of 15 degrees). This model was derived using NACT in a somewhat larger region than shown, from a teleseismic waveform dataset. The lateral parameterization is in level 6 spherical splines which give a lateral resolution of ~200 km. Values are shown as percent perturbations from the isotropic velocity of the reference model, PREM (Dziewonski and Anderson, 1981). b) N-Born model (isotropic part) derived after one iteration, using the "non-linear" 3D Born approximation in the subregion shown.**

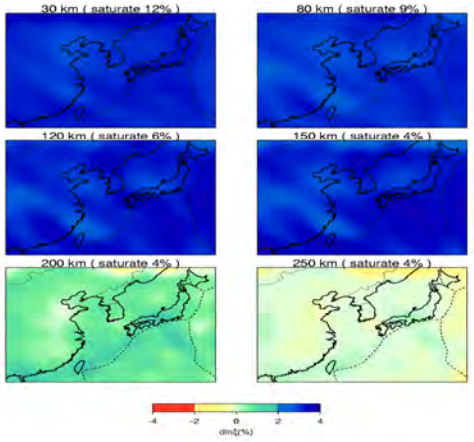


**Figure 2. Radially anisotropic part of the N-Born derived 3D upper mantle model of Figure 1. The lateral parametrization is in level 5 spherical splines (lateral resolution of ~400 km). The model is expressed in terms of relative variations in the parameter $\xi = (Vsh/Vsv)^2$.**

Both N-Born and NACT derived models can fit waveforms very well, with up to ~83% variance reduction (depending on the choice of damping), and the N-Born residual variance is even lower than that of NACT. While the models agree in general, there are some notable differences between them in detail. For example, beneath the Tibetan plateau, the N-Born model shows a stronger fast velocity anomaly in the depth range 150 km to 250 km,

which disappears at greater depth. This indicates that there is no delamination of lithosphere beneath the plateau, as has been suggested by some authors. Likewise, in the anisotropic part of the models, the largest differences are in the deeper layers.

**Implementation of RegSEM and a "Summed Events" Procedure**

In collaboration with researchers at Institut de Physique du Globe de Paris (IPGP), we have completed a regional version of the Spectral Element code (RegSEM, Cupillard, 2008). The regional SEM incorporates Perfectly Matched Layer (PML) boundary conditions on the lateral borders of the region, which effectively eliminate spurious reflections from the borders. Compared with previous versions, first of all, both Moho topography and surface topography have been included into the process of building the mesh. With reference to a Moho model, we are able to provide realistic velocity contrasts at the Moho discontinuity while introducing any 3D elastic mantle model. Second, anisotropy has been included in the present version of regional SEM (any anisotropic structure can be considered, but we currently have only included radial anisotropy). Finally, this new version of regional SEM has been fully optimized.

**Implementation of "Summed-SEM" Methodology**

The computation of the forward wavefield using SEM is very accurate, but heavy computationally. It takes 2 hours to compute the wavefield of a single seismic event down to 60 sec (i.e., at long periods) on a modest computer cluster (32 cpu's). To speed up computations and develop the capability of performing many iterations and reaching higher frequencies, we have implemented the approach of Capdeville et al. (2005), in which the wavefield corresponding to many events is computed simultaneously. To do so, all the seismic sources considered are shifted in time to a common origin time, and the wavefield generated by this composite source is calculated once. The observed waveforms, at each station, thus consist of the summed observed seismograms for all events, each of them appropriately shifted in time, and are compared to the predicted synthetic wavefield. While these "summed" waveforms do not have a physical meaning, i.e. there are no identifiable seismic phases, they retain sufficient information to allow retrieval of 3D structure, even in the presence of realistic background noise, at least at long wavelengths. This approach can reducecomputation time by one to several orders of magnitude, depending on the implementation. Capdeville et al. (2005) tested this approach in the framework of global tomography and a synthetic dataset. They showed that, even with realistic noise added to the synthetics, they can retrieve 3D upper mantle structure accurately from a single forward computation involving ~50 events observed simultaneously at ~150 stations worldwide. They used the C-SEM global code of Capdeville et al. (2002) for this development. In their tests, they used accurate numerically computed partial derivatives for the inversion. Their implementation turned out to be quite restrictive, as it is difficult in practice to find a sufficient number of events distributed adequately and observed with good signal to noise ratio at a fixed and large set of broadband global stations.

In the adaptation of this method to our regional case, we have proceeded with the RegSEM code (rather than C-SEM) and have relaxed the restriction of "all events observed by all stations", replacing the single summation over all events by a series of runs, each of which considers the sum of all events observed at a given station. The number of RegSEM runs is then equal to the number of stations considered in the region, which, in general, is significantly smaller than the number of events. In our case, we considered a smaller region within the sub-region of the previous N-Born computation, and initially considered six broadband stations within that region, for which data can be freely accessed from the IRIS Data Management Center (DMC), and collected data from about 100 events in the magnitude range 6–7, also included within this region. Figure 3 shows the region of study and the ray coverage for our initial summed event experiment. Here, we have relaxed the restriction of teleseismic observations. The epicentral distances range from 5 to $40^{o}$. In this case, we cannot perform any comparisons with the NACT or N-Born inversions, for which the theory breaks down at short distances, however, we can still perform comparisons with inversions obtained using the simpler Path Average (PAVA) approximation.

Figure 4 shows an example of comparison between "observed" versus RegSEM computed summed waveforms at station XAN, showing that, at these long periods, the starting model predicts the observed waveforms already quite well.

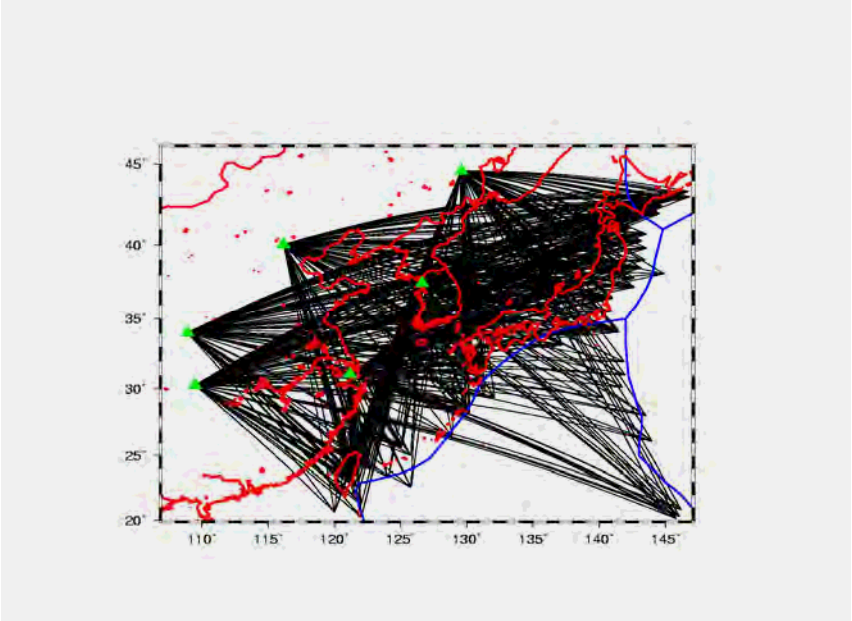


**Figure 3: Raypath coverage achieved in the "summed seismogram" experiment. The stations are indicated by green triangles.**

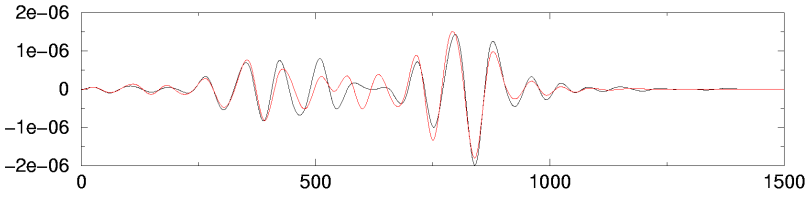


**Figure 4. Summed seismogram on the vertical component at station XAN. Black: observed trace, red: synthetic trace computed using RegSEM for the starting 3D model (NBORN) shown in Figures 1 and 2. Both observed and synthetic traces have been filtered with a cut-off period of 60 s.**

In order to reduce the computational time in the inverse step of the procedure, we also have opted, at least at this early stage, to compute partial derivatives approximately, using PAVA, in the inversion step of our procedure. We are assuming that, if our starting 3D model (the model derived using N-Born) is sufficiently accurate, these approximate partial derivatives will point us in the right direction and we will at the worst, need to compute a few more iterations to converge to the final model. Eventually, we can implement accurate numerical partial derivatives, whose calculation will also be faster, compared to conventional inversions, due to summation over events.

In order to test the summed event approach, we have first compared the results of an inversion obtained using, on the one hand side, the "summed event" seismograms at the 6 stations considered, and on the other, a "standard" approach, in which we have separately calculated the wavefield using RegSEM for all the events considered, and inverted the corresponding perturbations to the time domain waveforms, as we would do conventionally, using any of our previous inversion methods (PAVA, NACT, N-Born). The only difference in the latter is that now, the forward part of the modelling is computed using RegSEM, rather than mode perturbation theory. The synthetics have been computed down to 60 s period, and the observed seismograms have been filtered accordingly. Figure 5 shows a comparison of the isotropic models obtained using the conventional approach (single event-station paths) versus the summed approach. This figure also shows the inverted model obtained using the conventional approach, but instead of RegSEM synthetics, we use PAVA in both the forward and inverse steps. The two RegSEM models

are very similar indicating that the summed event approach works. A striking feature of the RegSEM models is the fast velocity anomaly south of Korea shallow depth (30 km), which is not present in any of the models developed with asymptotic mode perturbation theory., which shows low velocities throughout the ocean basins at this depth. The fast velocity seen in the RegSEM models is likely an artifact, due to the inaccurate crustal model, which does not incorporate the thick sediments present in that region. Since RegSEM models the crust much more accurately than our usual inversions based on mode perturbation theory, these kind of details start to matter, even at periods as long as this test case. Figure 6 shows the radially anisotropic part of the two RegSEM models (conventional procedure, and summed event procedure). Finally, Figure 7 shows the model obtained by conventional inversion of the same dataset, with the same starting model, but using the PAVA approximation in both the forward and inverse steps.

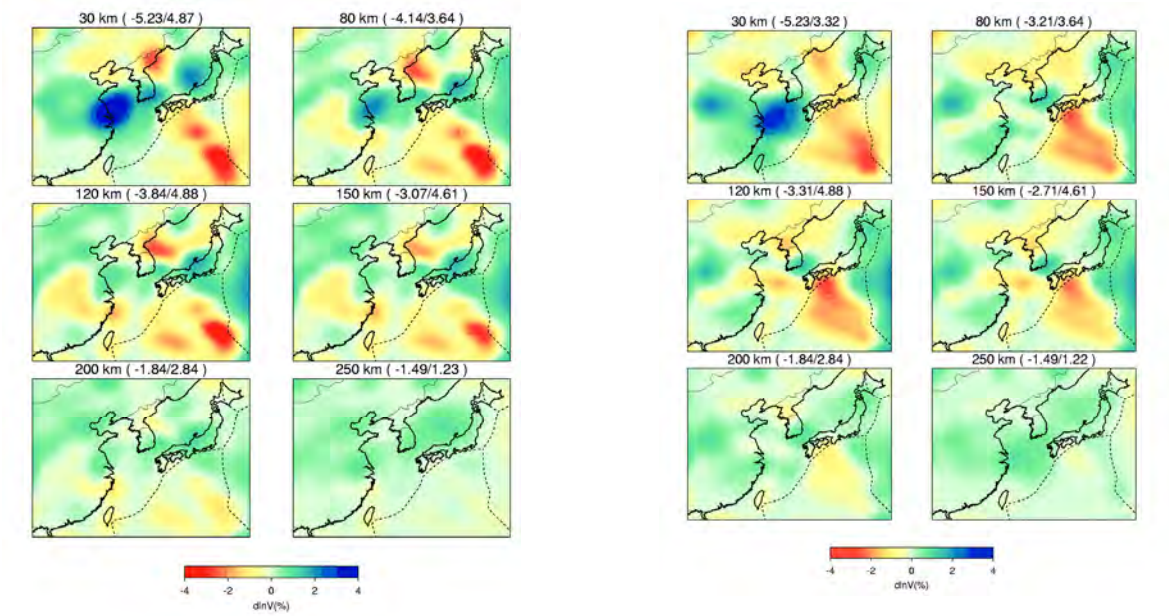


**Figure 5. Comparison of upper mantle models obtained after one iteration from the starting NBorn model, using waveform data on the path collection shown in Figure 4, RegSEM for the forward part of the computation, and PAVA for the calculation of partial derivatives. Left: conventional computation using individual source-station paths. Right: "summed-event" computation. The models differ in some details, which is not surprising given that**

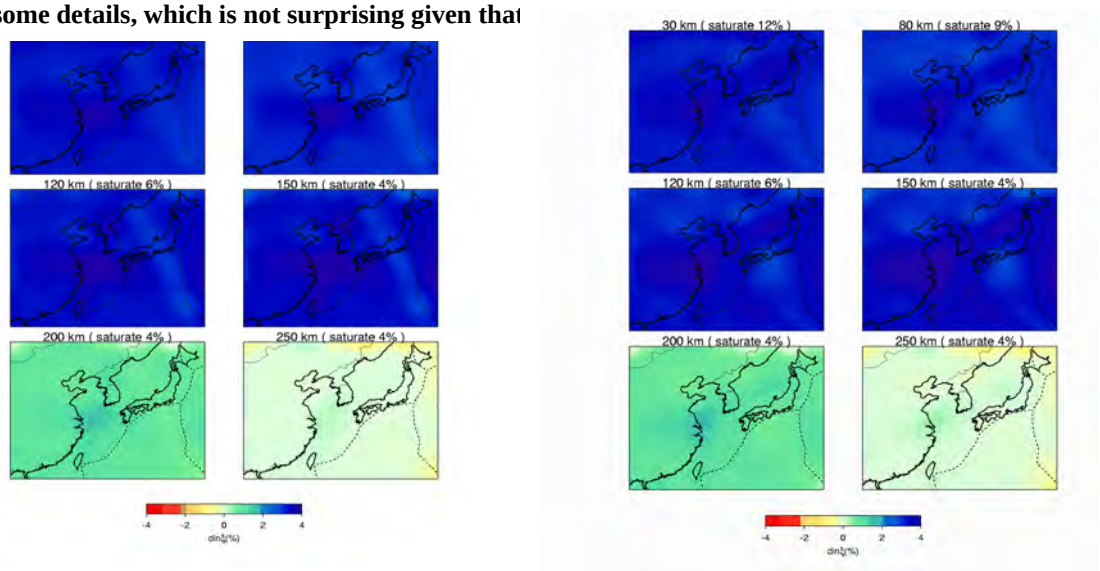


**Figure 6. Radially anisotropic part of the models shown in Figure 5. Left: computation on individual paths. Right: results of summed event inversion. Lateral variations are with respect to isotropy, bringing out the ubiquitous Vsh>Vsv structure at shallow depth.**

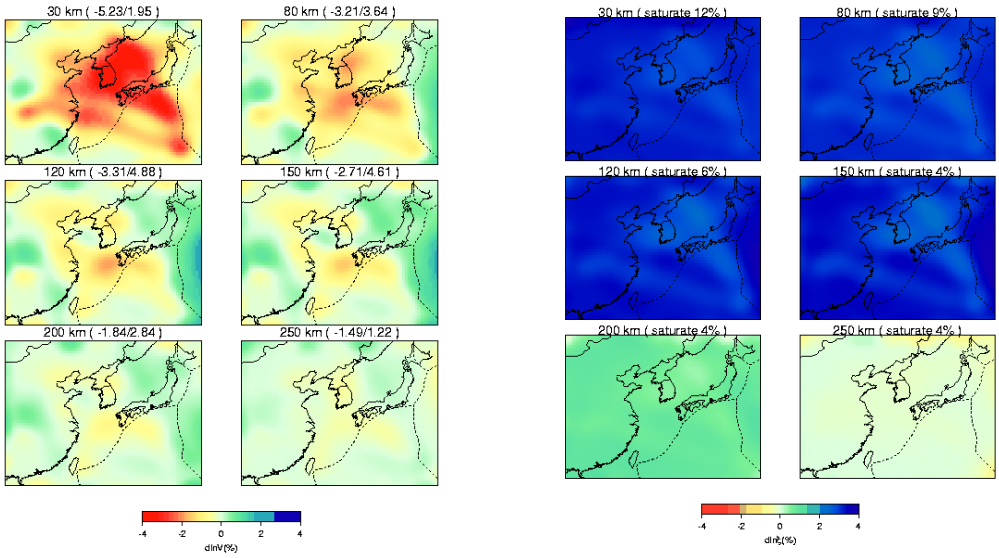


**Figure 7: Isotropic (left) and radially anisotropic (right) part of the 3D model obtained after one iteration from the same starting model as used to obtain Figures 5 and 6, and the same dataset, but using PAVA approximation in both forward and inverse steps, and individual source-station paths (no summed events). Here the shallow part of the model is different from those in Figures 5 and 6, as crustal effects are handled approximately through crustal corrections. This explains the very different structure obtained at 30 km depth.**

### Broadband Waveform Modeling on Specific Regional Paths

In parallel with the implementation of N-Born and summed RegSEM tomography, and in order to refine the starting crustal velocity input model beneath the region of our study, we have continued to perform forward waveform modeling with the method of frequency-wave number integration (FKI). Broadband seismograms are downloaded from IRIS and corrected to absolute ground velocity (cm/sec). We show 2 event locations of events 2000256 (9/12/2000, Mw6.1) and 2003107 (4/17/2003, Mw6.3), and the IRIS station distributions (Figure 8). We start with the 2000256 event, for which the continental ray paths are dominant, to obtain the 1D velocity structure between the source and each receiver. Broadband data are bandpass filtered at 0.005-0.05Hz. We used the Harvard Centroid Moment Tensor (CMT) solution for the source parameters, and the starting model is a 1D layered average crustal velocity structure derived from CRUST2.0. Using the best velocity model we can obtain (Figure 8), we compute Green's functions and perform the moment tensor analysis for two ranges of frequency (0.01-0.05Hz and 0.005-0.03Hz). Then, we select the event 2003107, for which we have similar ray paths as for event 2000256, to perform the moment tensor analysis using Green's function obtained from our 1D simulation (Figure 9). We find a moment tensor solution in good agreement with the CMT solution, whereas the solution obtained using the PREM reference model is very poor. While this example was chosen because we expect that we can use CMT solutions for M > 6 events as good references, this indicates that the additional regional modeling effort is worthwhile and will lead to better moment tensor solutions for smaller events in the area, when we extend the modeling to higher frequencies (0.02-0.05Hz).

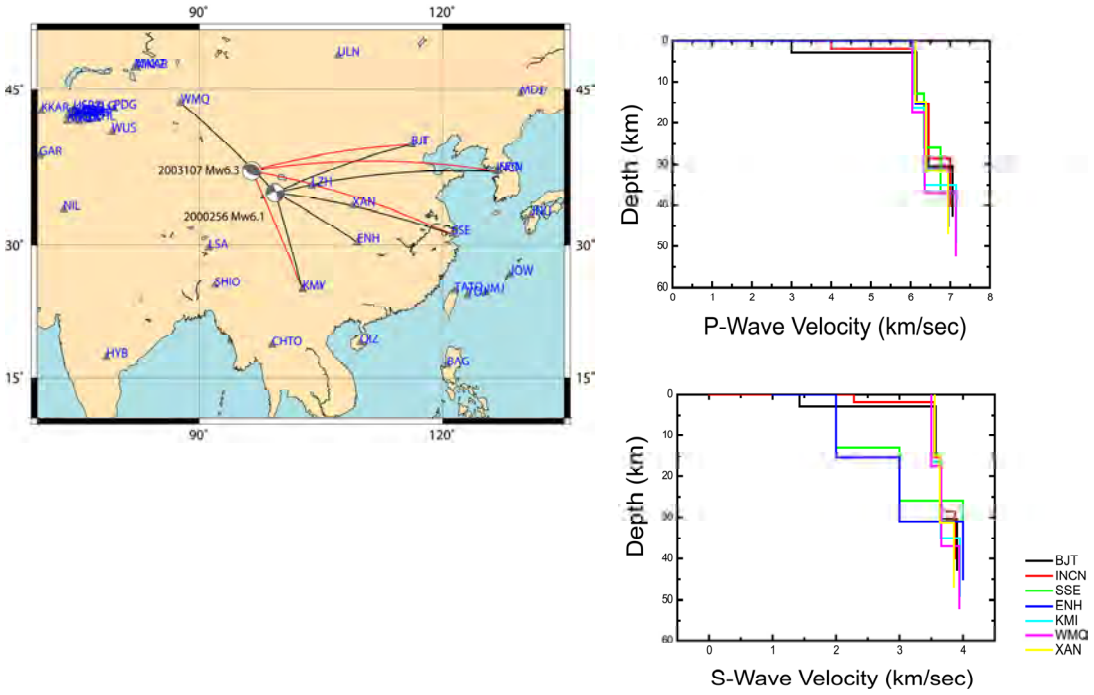


**Figure 8. Left: Event 2000256 (9/12/2000, Mw6.1), 2003107 (4/17/2003, Mw6.3) and IRIS station distributions. Source 2000256 (9/12/2000, Mw6.1) is used to obtain the velocity structures. Right: Best P-wave and S-wave velocity structures for the paths between event 2000256 and IRIS stations obtained from 1D forward modeling.**

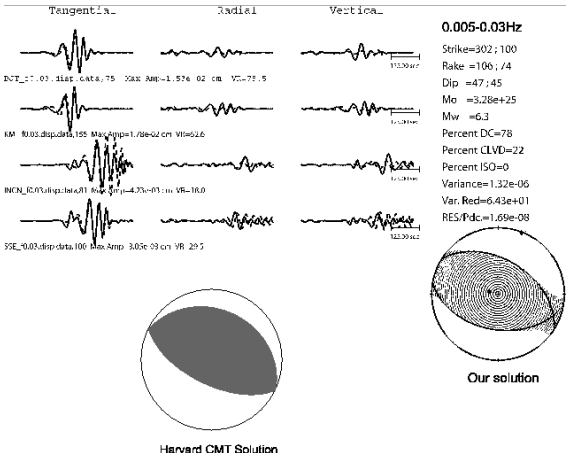


**Figure 9: Top: Moment tensor solution for event 2003107 in the 0.005-0.03Hz range using Green's function which were computed from the velocity model obtained using the 2000256 event (Figure 9). Bottom: Global CMT solution from Harvard University.**

Figure 10 shows another example, providing coverage of the region from the oceanic side. We note the significant lateral variations in S velocity in the top layer.

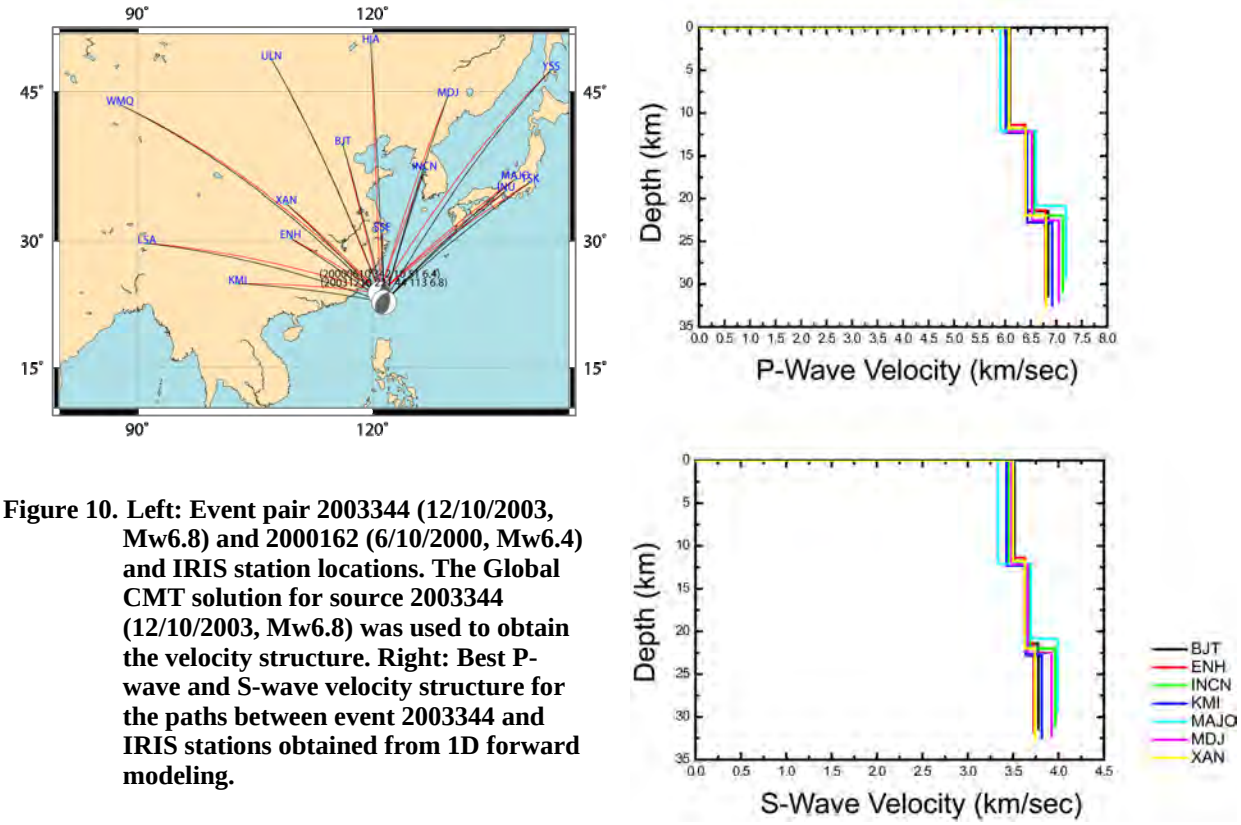


**Figure 10. Left: Event pair 2003344 (12/10/2003, Mw6.8) and 2000162 (6/10/2000, Mw6.4) and IRIS station locations. The Global CMT solution for source 2003344 (12/10/2003, Mw6.8) was used to obtain the velocity structure. Right: Best P-wave and S-wave velocity structure for the paths between event 2003344 and IRIS stations obtained from 1D forward modeling.**

## CONCLUSIONS AND RECOMMENDATIONS

Using better theoretical and numerical approaches in regional tomographic modeling is very important for adequate seismic path calibration. Here we show the progressive implementation of a cascade of theoretical approaches for waveform modeling, culminating in the use of the SEM for forward computations. Our initial tests of the summed seismogram approach using RegSEM synthetics are promising. Further testing involves iterating the model, progressively increasing the frequency range to higher frequencies, and implementing a more accurate crustal model, taking into account, in particular, variations in sediment thickness and the results of our forward modeling of broadband waveforms.

## ACKNOWLEDGEMENTS

We would like to acknowledge the contributions of Yann Capdeville at IPGP, who did extensive work on both the Born and SEM codes. Many computations were performed using computing resources obtained through a time allocation at the National Energy Research Scientific Computing Center from the DOE Office of Science Geosciences Division, for which we thank Dr. Nick Woodward of DOE.

## REFERENCES


Cao, A., M. Panning, A. Kim and B. Romanowicz(2007). Non linear 3D Born Shear Wave Tomography in Southeastern Asia, *EOS Trans*, AGU, 2007 Fall Meeting, Abstract S31E02.

Capdeville, Y., E. Chaljub, J. P. Vilotte, and J. P. Montagner (2002). Coupling the spectral element method with a modal solution for elastic wave propagation in global earth models, *Geophys. J. Int.* 152: 34–66.

Capdeville, Y., B. Romanowicz, and Y. Gung (2005). Towards global earth tomography using the spectral element method: a technique based on source stacking, Geophys. J. Int. 162: 541–544.

Capdeville, Y. (2005) An efficient Born normal mode method to compute sensitivity kernels and synthetic seismograms in the Earth, *Geophys. J. Int.* 163: 639–646.

Cupillard, P. (2008). Simulation par la méthode des éléments spectraux des formes d'onde obtenues par corrélation de bruit sismique, These de Doctorat, Institut de Physique du Globe de Paris.

Dziewonski, A. M. and D. L. Anderson (1981). Preliminary reference Earth Model, *Phys. Earth. Plan. Int*. 25: 4, 297–356.

Faccioli, E., F. Maggio, A. Quarteroni, and A. Tagliani (1996). Spectral-domain decomposition methods for the solution of acoustic and elastic wave equations, *Geophysics* 61: 1160–1174.

Gung, Y., B. Romanowicz, and M. Panning (2003) Anisotropy and lithospheric thickness, *Nature* 422: 707–711.

Komatitsch, D. and J. P. Vilotte (1998). The spectral element method: an effective tool to simulate the seismic response of 2D and 3D geological structures, *Bull. Seism. Soc. Am*. 88: 368–392.

Komatitsch, D. and J. Tromp (1999). Introduction to the spectral-element method for 3-D seismic wave propagation, *Geophys. J. Int.* 139: 806–822.

Li, X. D. and B. Romanowicz (1995). Comparison of global waveform inversions with and without considering cross branch coupling, *Geophys. J. Int.* 121: 695–709.

Li, X. D. and B. Romanowicz (1996) Global mantle shear velocity model developed using nonlinear asymptotic coupling theory, *J. Geophys. Res.* 101: 22,245–22,273.

Megnin, C. and B. Romanowicz (2000). The 3D shear velocity structure of the mantle from the inversion of body, surface and higher mode waveforms, *Geophys. J. Int.* 143: 709–728.

Panning, M. and B. Romanowicz (2006). A three dimensional radially anisotropic model of shear velocity in the whole mantle, *Geophys. J. Int*. 167: 361–379.

Panning, M., F. Marone, A. Kim, Y. Capdeville, P. Cupillard, Y. Gung, and B. Romanowicz (2006). Improvements in mode-based waveform modeling and application to Eurasian velocity structure, *Eos. Trans.* AGU, 87(52). Fall Meet. Suppl.

Panning, M., Y. Capdeville and B. Romanowicz (2008). Do first order 3D Born finite-frequency kernels improve modeling of surface waveforms?, *Geophys. J. Int.*, in press.

Romanowicz, B. (1987). Multiplet-multiplet coupling due to lateral heterogeneity: asymptotic effects on the amplitude and frequency of Earth's normal modes, *Geophys. J. R. Astr. Soc.* 90: 75–100.

Romanowicz, B., A. Cao, A. Kim, M. Panning, M. Pasyanos, and D. Dreger (2007). Calibration of 3D upper mantle structure in Eurasia using regional and teleseismic full waveform inversion, in *Proceedings of the 29th Monitoring Review: Ground-Based Nuclear Explosion Monitoring Technologies*, LA-UR-07-5613, Vol. 1, pp. 247–255.

Woodhouse, J. H. and A. M. Dziewonski (1984). Mapping the upper mantle: Three dimensional modeling of Earth's structure by inversion of seismic waveforms, *J. Geophys. Res.* 89: 5953–5986.

# GEOPHYSICAL MODELING IN EURASIA: 2D CRUSTAL P AND LG PROPAGATION; UPPER-MANTLE SHEAR WAVE PROPAGATION AND ANISOTROPY; AND 3D, JOINT, SIMULTANEOUS INVERSIONS

Charlotte A. Rowe, Monica Maceira, Michael L. Begnaud, Lee K. Steck, and W. Scott Phillips

Los Alamos National Laboratory

Sponsored by National Nuclear Security Administration

Contract No. DE-AC52-06NA25396

## ABSTRACT

New tomographic models have been developed to obtain improvements to travel-time predictions for a variety of crustal and upper-mantle seismic phases, and we approach the problem with both independent datasets and joint, simultaneous inversion of diverse geophysical parameters.

New Pg and Lg velocity models in Eurasia improve estimates of crustal travel times across the region. Inversion of Pg and Lg travel times improves RMS by ~30% compared to iasp91. Site terms for both phases show similar patterns and likely reflect thicknesses and velocities of sediments above the upper crust. Event terms are ~1 s, suggesting 5–10-km-average depth errors. Velocities are consistent with typical upper-crustal velocities set forth in the Department of Energy (DOE) Unified Model but suggest more geographic variability.

Upper-mantle shear wave (Sn) velocity tomography, including Sn gradient within the upper mantle, has been performed both with and without anisotropy. We use events that are GT25 and better, with depths of <50 km and path lengths between 400 and 1700 km. The 14,645 events recorded at 2,399 stations yielded 144,933 raypaths. Most arrivals were obtained from the International Seismological Centre (ISC), Annual Bulletin of Chinese Earthquakes (ABCE), and Earthquake Data Reports (EDR) catalogs. Crustal leg corrections assume 45-km average crustal thickness, 3.6-km/s velocity, and 52-degree incidence angles beneath station and source. The RMS reduction after inversion is ~56%. Sn velocities mirror those found for Pn; however, the Sn gradient appears to be weaker. Solving for anisotropy removes some high-frequency oscillations; the anisotropy appears to follow that found for Pn.

Motivated by the shortcomings of existing single-parameter inversion methods in accurate prediction of both seismic waveforms and other geophysical parameters, we have embarked on a simultaneous, joint inversion of disparate data types to obtain models that benefit from the comparative strengths of the different parameters and can provide improved constraint where a single data type may be lacking. We have jointly inverted Bouger gravity observations, surface-wave dispersion curves and receiver functions to obtain a self-consistent 3D shear velocity/density model with improved resolution for shallow geologic structures. Jointly inverting these datasets with seismic body wave (S) travel times provides additional constraints on the shallow structure and an enhanced 3D shear wave model for our study area in western China.

## OBJECTIVES

The goal of our work is to develop geophysical models that improve the seismic phase travel-time predictions over the models currently used. Several different seismic phases are used in routine event location, and the models we currently employ require significant travel-time corrections for accurate arrival prediction; these corrections are spatially varying and different for different phases. We aim to develop models and methods whose ability to predict travel times can significantly reduce the magnitude of empirical corrections needed for accurate event location.

## RESEARCH ACCOMPLISHED

We present progress to date for three distinct seismic modeling thrusts: (1) Pg (crustal, direct P-wave) phase propagation and Lg (crustal, shear body wave) phase propagation, (2) Sn (upper-mantle shear body wave) propagation, and (3) ongoing work towards joint, simultaneous inversion of Rayleigh (surface wave) group velocities, teleseismic P-wave receiver functions and Bouger gravity data from satellite observations, to determine 3D lithospheric shear-wave velocities. For Pg, Lg, and Sn, we are developing the models as two-dimensional (2D) velocity maps that can predict phase arrivals for any great circle path within the modeled region (e.g., Myers et al., this volume), with the addition of site corrections that are solved for simultaneously as we invert data for each of the phases modeled.

### Pg and Lg Modeling

The Pg phase is a compressional body wave that travels within the Earth's crust and is reported at local-to-regional distances in many seismic catalogs. The Lg phase is the analogous crustal shear wave. We use catalog arrivals from the Los Alamos National Laboratory (LANL) Ground-Based Nuclear Explosion Monitoring Research and Development (GNEMRD) seismic database to develop a 2D Pg model and a 2D Lg model for Eurasia. About 10% of the events in this database are classified as having epicentral uncertainty known to within 25 km of the true location (GT 25 km, GT25; e.g., Bondár). A time-distance plot (Figure 1) for Pg and Lg arrivals in our database shows contamination due to phase misidentification, data-entry typographical errors resulting in 60 s offsets, and bad arrival-time picks for both phase types.

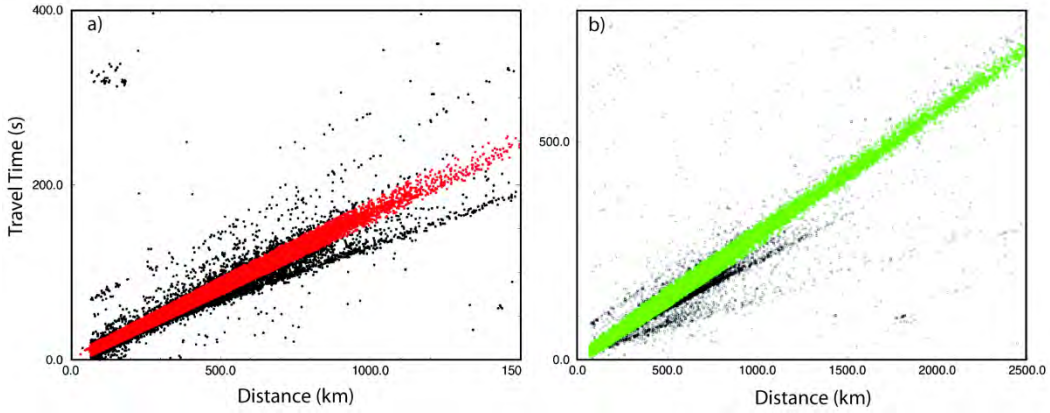


**Figure 1. Time-distance plot showing phase arrivals in the LANL seismic database. (a) full dataset, which exihibits contamination from 60-s data-entry errors, poor phase picks, and misidentified Pn phase. Red dots indicate arrivals used in our Pg tomographic inversion. (b) Lg arrivals for the same GT25 events. Black dots show all arrivals, including 60-s data-entry errors, poor picks and misidentified Sn arrivals; green dots show arrivals used in our Lg tomographic inversion. From Steck et al., 2008.**

For the Pg inversion, we have used 1,453,318 arrivals from 407,131 events recorded at 3,709 stations throughout Eurasia. For Lg, we use 1,049,125 arrivals from 266,751 events recorded at 3,084 stations (Steck et al., 2008). Data coverage is shown in Figure 2. To invert these datasets, we use a method analogous to Pn tomography, assuming a great circle path between source and receiver. Events used have depths of 33 km or less. Only path lengths between

0.5 and 14 degrees were used for Pg; path lengths of 0.7 to 25 degrees were used for Lg. In addition to solving for slowness along the great circle path, we also solve for both an event term and a site term to accommodate depth uncertainty and
near-receiver velocity effects, respectively. Site terms are damped so that they sum to zero. We use first-difference regularization over a 1×1 degree grid, and solve for slownesses using the LSQR conjugate gradient method (Paige and Saunders, 1982). We solve for slowness over a region from 0 to 89 degrees North latitude and –20 to 195 degrees East longitude.

We used checkerboard tests to test the ability of our data to resolve the study area. We examined checkerboard velocity anomalies using the available ray paths for 2-, 4-, and 10-degree squares with alternating velocity perturbations of +/-10%. Good resolution coverage is better for Lg than for Pg due to longer raypaths of Lg phases. The results of these resolution tests for both Pg and Lg are shown in Figure 3.

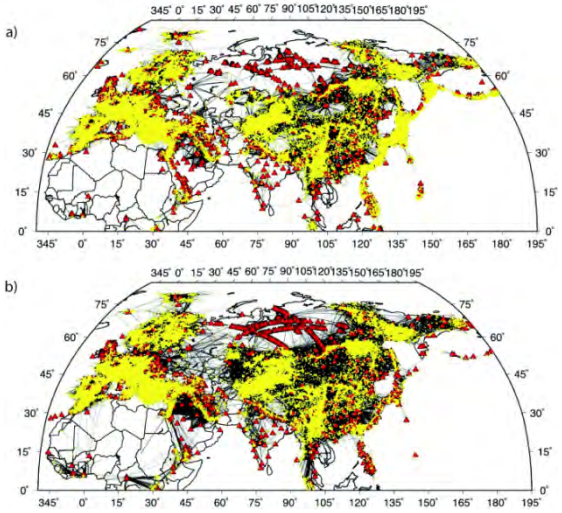


**Figure 2. Ray diagram showing data coverage for Pg (2a) and Lg (2b). Yellow dots indicate events, and red triangles are receiver locations. Black lines indicate great circle paths used in the tomography. From Steck et al., 2008.**

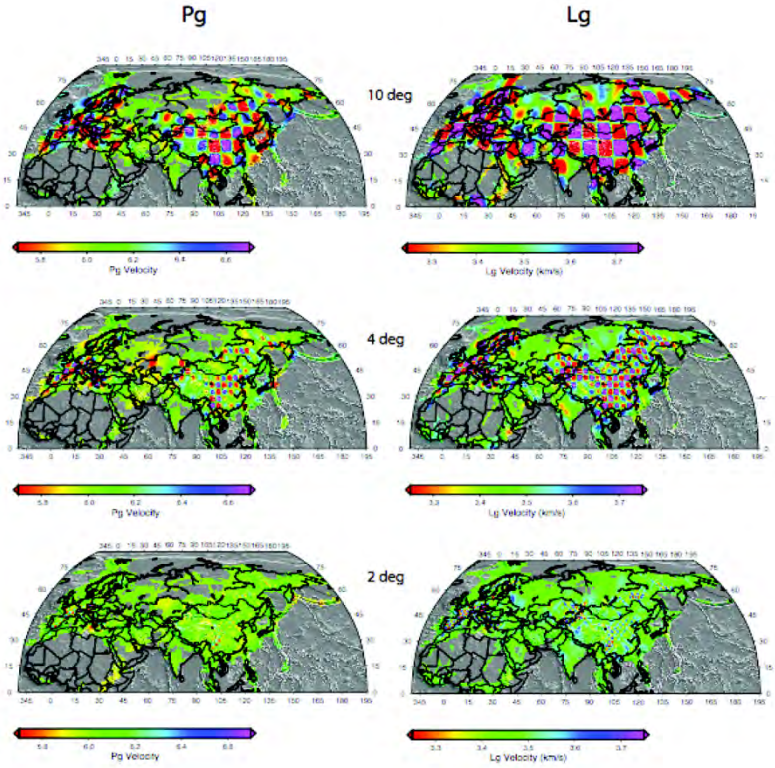


**Figure 3. Checkerboard Pg and Lg resolution tests for 2-, 4-, and 10-degree velocity perturbation grids. From Steck et al., 2008.**

For Lg, resolution is good throughout most of China and Mongolia as well as part of northeastern Russia and Kazakhstan. Europe, and Scandinavia are likewise well resolved. We also have some limited resolution for the Middle East and western India. Pg, on the other hand, has poorer resolution in all regions. At 2 degrees, only dense raypath regions are well resolved, including Western Europe and southcentral China.

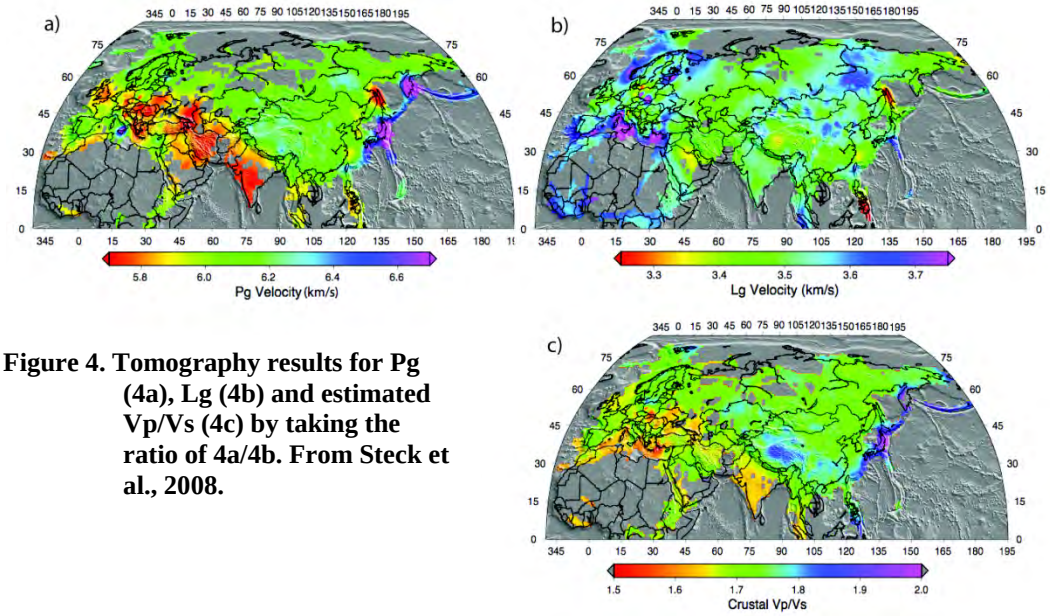


**Figure 4. Tomography results for Pg (4a), Lg (4b) and estimated Vp/Vs (4c) by taking the ratio of 4a/4b. From Steck et al., 2008.**

We show the inversion results in Figure 4. Pg appears fast in regions of convergence, such as the Pacific Rim. Most of Asia, from 80 degrees East to the continental margin, appears fast. The Middle East, India, Pakisan, and Kyrgystan appear slow, as do the Caspian Sea region and lower Volga. Scandinavia is average to fast, while most of Europe appears slow, except for Sicily, Spain, and central Turkey. Lg shows the bulk of Eurasia to be faster than average, with lower velocities manifested in parts of the Middle East, Gulf of Oman, Eastern Europe, central and northcentral Russia, Sakhalin Island, and Tibet. Vp/Vs ratios, computed by taking the ratio of the two tomographic maps, range from 1.7 near the Dead Sea to 1.9 in parts of Japan.

**Sn Velocity**

Following the technique of Phillips et al. (2007) that expanded on the Pn gradient method of Zhao (1993) and Zhao and Xie (1993), we have extended the Pn and upper-mantle Pn gradient tomography method to examine Sn and the upper-mantle Sn gradient for Eurasia. In our formulation, we will solve for great circle path Sn velocities as well as gradient and anisotropy, with static station and event correction terms (Begnaud et al., 2008). We depart from Phillips et al. by solving the gradient term in a nonlinear fashion, requiring an iterative approach. Our data consist of events that are GT25 and better. Sn arrivals from various global, regional, and local catalogs were merged (Begnaud et al., 2006). A vast majority of these data came from the ISC, ABCE (Lee et al., 2002), and Earthquake Data Report (EDR) of the National Earthquake Information Center (NEIC). We chose only events whose hypocentral depths are 50 km or less, and only arrivals having paths between 2.5 and 18 degrees were used; following culling of the data, which included a cursory 15-s residual trim relative to iasp91 and regularization with residual cutoffs, and limiting data range from 400 to 1700 km path lengths, our final data set consisted of 144,933 arrivals from 14,645 events recorded at 2,399 stations after discarding stations recording fewer than 10 events and events with fewer than 5 arrivals. Raypaths for our inversion are shown in Figure 5, indicating regions where we have good data coverage.

Our model was discretized in a 1-degree grid. Crustal thickness effects were estimated assuming 45-km average thickness, 3.6 km/s shear velocity, and a 52-degree incidence angle at both source and receiver. The event leg of the parameterization assumes the ray extends from the event depth to 45 km. We assumed a 4.55-km/s starting mantle velocity and 0.001/s starting mantle gradient. We regularized in both slowness and gradient using first differences. Damping from starting values used 30% of the smoothing value. We solved using the LSQR conjugate gradient approach (Paige and Saunders, 1982). Iterations continued until travel-time RMS change was less than 0.1 s; this was achieved in two iterations.

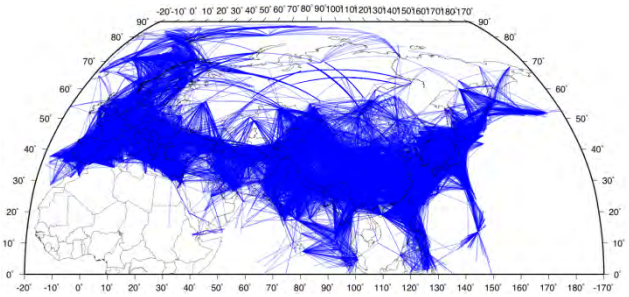

**Figure 5. Raypath coverage for Sn tomography. From Begnaud et al., 2008.**

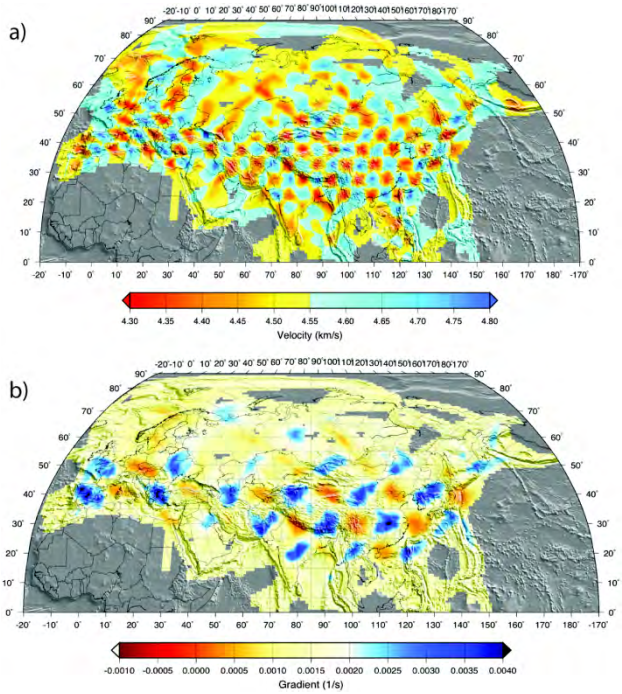


**Figure 6. Results of checkerboard tests for Sn velocity (6a) and upper-mantle shear velocity gradient (6b). From Begnaud et al., 2008.**

A further test of the data's resolving power was performed via the use of checkerboard velocity perturbations and velocity gradient perturbations. For the raypaths shown in Figure 5, we show the results of checkerboard tests in Figure 6. Upper-mantle S velocities were tested in 5-degree velocity cells using a 0.25 km/s anomaly from the starting model of 4.55 km/s, with 2.5 km/s Gaussian noise added. Resolution is good for much of Eurasia, although the Arabian Shield and Arctic are less well recovered. The upper velocity gradient was tested for 10-degree cells having 0.002/s perturbations from the starting value of .0015/s, with Gaussian noise of RMS 2.5 s added. The region showing resolution for gradient is roughly the same as for the Sn velocities.

Inversion results (Figure 7) show that Sn velocities generally exhibit the same patterns seen in Pn (e.g., Phillips et al., 2007), following expected variations for stable vs. tectonically active areas. The Sn gradient (Figure 7) is generally very low and even suggests negative gradients in areas such as eastern China and the Mediterranean, whereas it is relatively high in subduction zones and convergent plate margins (Tibet, Japan, and Korea) (Begnaud et al., 2008).

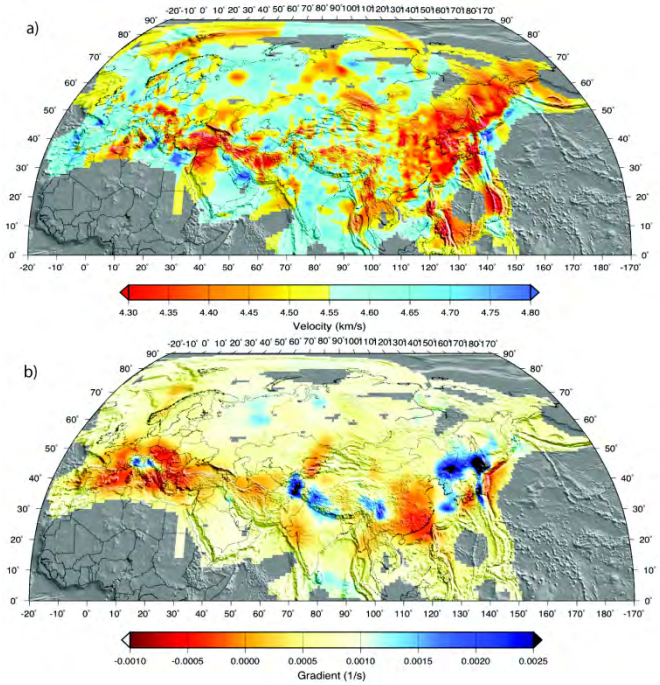


**Figure 7. Sn velocities (7a) and velocity gradient (7b) found in our study. The values depicted here result from solving without including an anisotropy term. Data-fit improvement following inversion was 56%. From Begnaud et al., 2008.**

When solving for upper-mantle gradient, the velocity seems to inversely adjust relative to gradient compared with solutions for velocity only (high gradients drive lower lid velocities). With few exceptions, station delays (Figure 8) follow known crustal thickness, with greater delays following mountain belts (the Himalayas, the Alps, the Appenines) and thicker lithosphere in platforms (Tibet, western China), while negative values are seen in areas of thinner lithosphere such as the Rhinegraben, east China, and the Mediterranean.

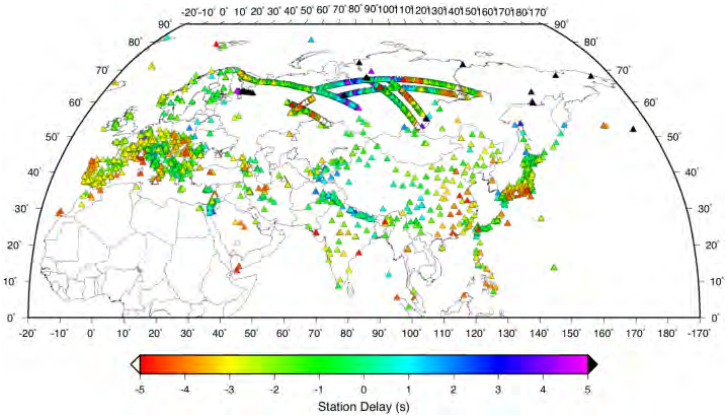


**Figure 8: Station delays. From Begnaud et al., 2008.**

Solving for Sn anisotropy removes some of the high-frequency patterns in the Sn velocity. The anisotropy patterns we see follow those found by Pei et al. (2007) for Pn anisotropy in their study of China. Figure 9 illustrates a closeup view of China-East Asia Sn anisotropy obtained in our study.

**Joint, Simultaneous 3D Tomography for Multiple Geophysical Datasets**

It is well known that derivation of geophysical models for a given observable, such as body wave models or surface wave models, may provide good predictors of behavior for the specific parameter modeled but often provides poor prediction for other parameters, even when we have empirical or theoretical knowledge of how the parameters relate to one another. Due to the nonunique properties of inversion methods, we may often find a solution for one data type, but we must acknowledge that, although it can predict behavior of that data type, the solution is ambiguous and other models may serve equally well.

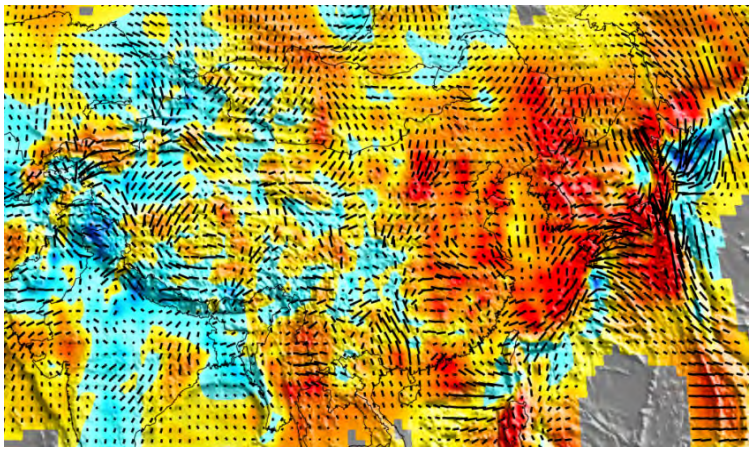

**Figure 9. Sn anisotropy. Black lines indicate direction and relative magnitude of the fast direction. Note the apparent signal parallel to the Songpan Ganzi fold belt and the strong signal parallel to the Japanese and Phillippine subduction zones. Anisotropy appears weak in the Indian craton, Bay of Bengal, and the stable Shanxi Plateau. From Begnaud et al., 2008.**

The materials whose properties we are modeling will influence not only the parameter in question but will also, at the same time, influence other geophysical parameters that we might also measure. Thus, a joint, simultaneous inversion of all pertinent and available data types for a region may provide us with a far more robust model than can be obtained by using only a single parameter. Moreover, the extent of our well-resolved model may be significantly expanded due to the variable coverage provided by different measurements, and its features may be better constrained due to the different resolving powers of different data types. For instance, it is becoming commonplace to derive seismic velocity models by jointly inverting surface wave dispersion values, which have the benefit of large regions of coverage but provide relatively little vertical control on impedance contrast interfaces, with seismic receiver functions, which by their nature are only point samples at the locations of seismic stations but which can provide detailed information about acoustic impedance interfaces at depth. The receiver functions by themselves are ambiguous in the depth-to-interface information, requiring some sort of a priori assumption of seismic velocities, but the surface wave modeling provides average velocities. These complementary characteristics can give us much greater confidence in the resulting inversion product. Inclusion of gravity data in the inversion provides increased resolution of shallow structures that are essentially invisible to the surface waves.

We have undertaken the 3D modeling of the Tarim Basin region using simultaneous joint inversion of surface wave dispersion (Maceira et al., 2005), teleseismic P-wave receiver functions (Ammon et al., 2004) and satellite gravity data obtained during the Gravity Recovery And Climate Experiment (GRACE) mission (Tapley, 2005). Recent adjustments to the inversion approach (Maceira and Ammon, 2008) include the use of Bouger gravity anomalies, as opposed to the free-air anomaly. This advance has proven to improve our resolution of the shallow structure, as topographic information is not included in the Bouger values. To invert for shear-wave velocities using the gravity data, we employ two empirical relationships to relate seismic velocity and density: for sedimentary rocks, the relationship developed by Nafe and Drake (1963) and for basement, Birch's Law (1961). A recent work by Brocher (2005) was tested (Maceira and Ammon, 2008) and found to provide no improvement to the fit for the GRACE gravity data for this region; clearly, additional work is warranted.

We parameterize the model as 1×1 degree boxes arranged in depth columns. Shear wave velocity values are treated as one-dimensional (1D) depth-dependent velocity profiles at the center of each cell, where we conisder fundamental mode group velocities and Bouger gravity anomalies computed against a background density model. Because the gravity values for any given cell are influenced by the surrounding cells, the model inversion uses a weighted factor of the values in neighboring cells, which we have determined is significant to three cell distances. We show the model parameterization in Figure 10.

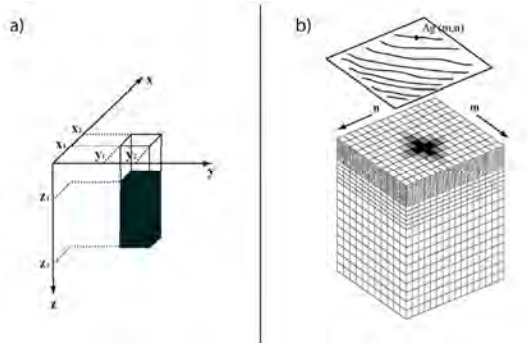


**Figure 10. Model parameterization. Each 1x1 degree cell is a column characterized by a stack of density prisms and a suite of 1D fundamental mode group velocities. (a) A single cell with its input geographic coordinate system. (b) For a given cell (black), the influence on the gravity value will include densities of surrounding cells. Weighting of these cells decreases with distance, as suggested by changes in their gray shading (from Maceira and Ammon, 2008).**

The new, jointly derived model can be best validated by showing improvements to predictions of independent data, which were not used in the development of the model. We have shown in previous presentations that the joint model provides a good simultaneous fit to the datasets used and that it agrees well with features known within the region studied. Our model requires slower velocities in the sedimentary basins than suggested by inversion of the surface wave data alone; this requirement is borne out through a comparison of waveform predictions using models derived from surface waves alone compared with the model derived in our joint inversion. Our test is focused on short periods, as these are the most influenced by shallow structure; moreover, improved fitting at short periods is needed if the monitoring community wishes to obtain reliable detections at lower thresholds (Taylor and Patton, 2006).

We demonstrate the method of Maceira (2006) applied to waveforms from 26 nuclear explosions. Displacement waveforms are passband filtered with center frequencies at 7, 10, 12, 16, and 20 seconds. Each bandpassed trace provided a particle motion window by multiplying the envelopes of the vertical and radial components, and a group velocity window, computed using minimum and maximum slowness values for the frequency of interest, calculated through both the joint 3D model and that derived solely from dispersion values. The measurement window is defined as the intersection of these two time windows. Amplitudes are measured only for the portion of the waveform found within the measurement window. If the particle motion and arrival time windows do not intersect, no measurement is possible.

We illustrate the results of both cases in Figure 11.

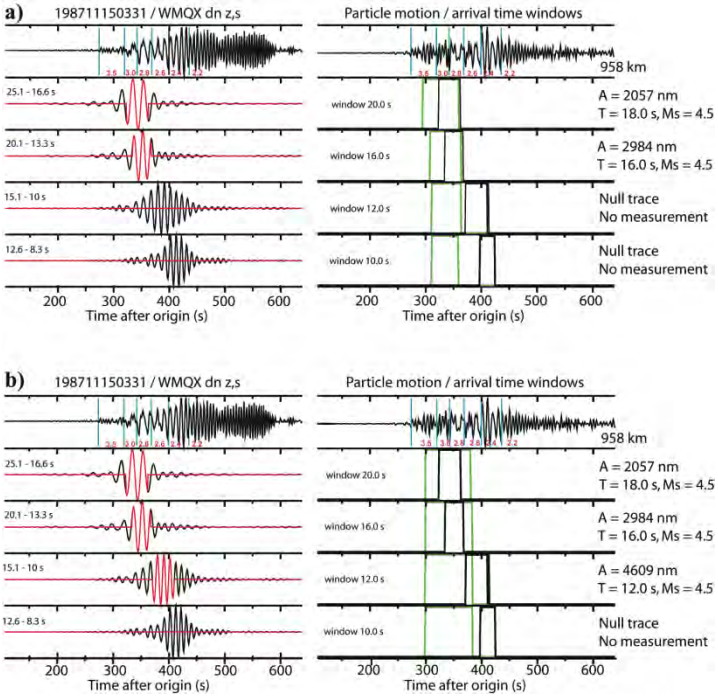


**Figure 11. Surface wave prediction comparing use of dispersion data (11a) with results using the combined datasets in joint inversion. Waveform matching is successful over shorter periods for predictions of the joint inversion (11b, left panel) compared with inversion from surface wave data alone (11a, left panel) due to better overlap of the group velocity window and particle motion window (green and black windowed boxes, respectively) for joint inversion (11b, right panel) compared with surface wave dispersion data alone (11a, right panel). From Maceira and Ammon, 2008.**

Calculations used from the joint 3D model were better able to predict the arrival of surface waves at short periods (compare the windows at 12 seconds). We found that in 73% of the cases the joint inversion 3D model was better able to predict surface wave arrivals at short periods than the model derived from dispersions alone.

Our method is being further refined through the addition of body wave travel-time data (S-wave arrivals) into the joint, simultaneous tomographic inversion. We begin by testing the method on a small piece of the test region; a time-distance plot for S-wave arrivals for the small study area is shown in Figure 12. Inclusion of these body wave travel times does not aid in resolution of deeper structure, as raypaths are limited to the crust and uppermost mantle; however, in the shallow part of the model, including the sedimentary basins, these data can significantly aid in resolution of more-detailed structure. Ray coverage for these data is shown in Figure 13. Although for the most part, these fine details will have little influence on longer-period surface wave modeling, we expect them to improve our capabilities at shorter periods, which are crucial for lower-magnitude threshold requirements.

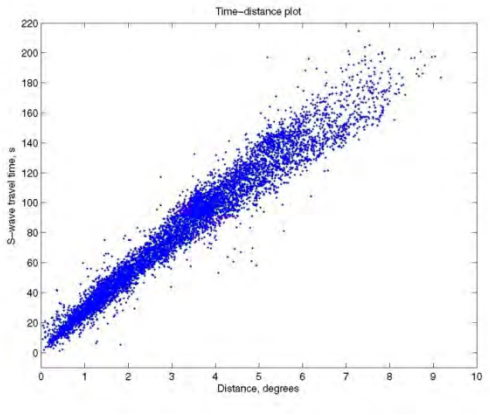


**Figure 12. Time-distance plot for S-wave arrivals used in preliminary test of joint inversion method with body-wave travel-time data. Although some scatter can be seen, in general, the well-behaved data should enhance resolution of shallow (crustal) structure in our inversion.**

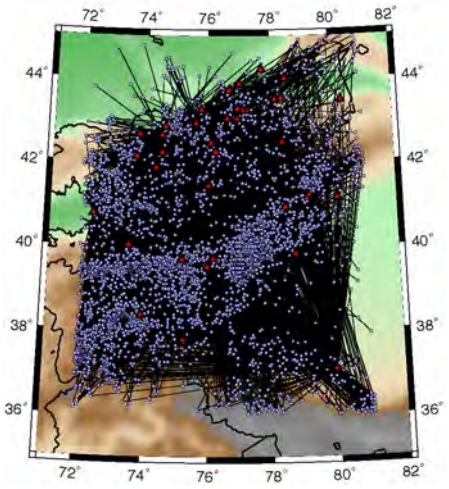


**Figure 13. S-wave raypaths integrated into a joint inversion test study. Red triangles represent seismic stations, and the blue dots are sources. This small pilot study images only the western half of the Tarim Basin.**

## CONCLUSIONS AND RECOMMENDATIONS

We continue to explore the various data types important to robust characterization of the Earth for seismic monitoring. Pg and Lg tomography leads to better understanding of the crustal influence on seismic travel times; crustal effects are increasingly important as we move toward near-regional and local monitoring. Because the increasing use of secondary phases is expected to become important in precise event location, we need data-driven models wherever possible to correctly predict travel times for these phases. The Sn tomographic analysis is likewise important for the use of Sn arrivals in location and to enhance our understanding between the well-studied Pn characteristics of Eurasia and the relationship with the Sn phases. Travel-time prediction may depend also on our correct accounting for travel-time anisotropy, which has been only superficially addressed for Pn and not examined by many researchers for Sn, due largely to the comparative lack of data for this phase. We have demonstrated a significant improvement in prediction capability of our 3D models when joint, simultaneous inversion of multiple datasets is performed. Increased resolution of shallow structures and sedimentary basins, arising from the inclusion of such parameters as Bouger gravity anomalies and/or seismic body wave arrival times, can aid us in our prediction of surface wave dispersion at shorter periods, which is essential to lowering the magnitudes at which our predictions are dependable.

**ACKNOWLEDGEMENTS**

D. F. Baker and M. Romero-Yeske performed data analysis, providing parameters used in these models. J. A. Chang and R. Stead provided important database support, without which these studies would not be possible. Our thanks to J. Benson and M. Wetovsky for editorial assistance.

**REFERENCES**

Ammon, C. J., W. Sevilla, R. B. Herrmann, and G. E. Randall (2004). Systematic inversion of receiver functions and surface wave dispersion for crustal structure in central Asia, in *Proceedings of the 26th Seismic Research Review: Trends in Nuclear Explosion Monitoring*, LA-UR 04-5801, Vol. 1, pp. 29–38.

Begnaud, M. L., L. K. Steck, and C. A. Rowe (2006). Improving seismic event locations in Asia by using catalog-scale empirical travel time correction surfaces, *EOS Trans. AGU* 87 (52), Fall Meet. Suppl., Abstract T51D-1550.

Begnaud, M. L., W. S. Phillips, C. A. Rowe, and L. K. Steck (2008). Sn velocity, gradient and anisotropic variations in the upper mantle of Eurasia (abstract), *Seismol. Res. Lett*. 79: 345.

Birch, F. (1961), The velocity of compressional waves in rocks to 10 kilobars, part 2, *J. Geophys. Res.* 66: 2199–2224.

Bondár, I., S. C. Myers, E. R. Engdahl, and E. A. Bergman (2004). Epicentre accuracy based on seismic network criteria, *Geophys. J. Int.* 156: 483–496.

Lee, W. H. K., H. Kanamori, P. C. Jennings, and C. Kissling (Eds.) (2002). *International Handbook of Earthquake and Engineering Seismology* (CD-ROM), Elsevier, New York.

Maceira, M. and C. J. Ammon (2008). Joint inversion of surface wave velocity and gravity observations and its application to Central Asian basins shear velocity structure, *J. Geophys. Res*. (in press).

Maceira, M. (2006). Surface waves, Earth structure, and seismic discrimination, Ph.D. thesis, Pennsylvania State University, State College, PA.

Maceira, M., S. R. Taylor, C. J. Ammon, X. Yang, and A. A. Velasco (2005). High-resolution Rayleigh wave slowness tomography of central Asia, *J. Geophys. Res*. 110: B06304, doi:10.1029/2004JB003429.

Nafe, J. E. and C. L. Drake (1963). *Physical Properties of Marine Sediments, in The Sea*, Vol. 3, M. N. Hill (Ed.). New York: Interscience, pp. 794-815,

Pei, S., J. Zhao, Y. Sun, Z. Xu, S. Wang, H. Liu, C. A. Rowe, M. N. Toksöz, and X. Gao (2007). Upper mantle seismic velocities and anisotropy in China determined through Pn and Sn tomography, *J. Geophys. Res*. 112: B05312, doi:10.1029/2006JB004409.

Phillips, W. S., M. L. Begnaud, C. A. Rowe, L. K. Steck, S. C. Myers, M. Pasyanos, and S. Ballard (2007). Accounting for lateral variations of the upper mantle gradient in Pn tomography studies, *Geophys. Res. Lett*. 34: L14312, doi:10.1029/2007GL029338, 2007.

Steck, L. K., W. S. Phillips, M. L. Begnaud, R. Stead, and C. A. Rowe (2008). Seismic tomography of Pg and Lg and its use for average upper crustal structure in Eurasia (abstract). *Seismol. Res. Lett*. 79: 305.

Tapley, B., J. Ries, S. Bettadpur, D. Chambers, M. Cheng, F. Condi, B. Gunter, Z. Kang, P. Nagel, R. Pastor, T. Pekker, S. Poole, and F. Wang (2005). GGM02 - An improved Earth gravity field model from GRACE, *J. Geodesy*, DOI 10.1007/s00190-005-0480-z.

Taylor, S. R. and H. J. Patton (2006). A probability of detection method for reducing short-period mb −Ms false alarm rates, *Bull. Seismol. Soc. Am*. 96: 1078–1090.

Zhao, L.-S. (1993). Lateral variations and azimuthal isotropy of Pn velocities beneath Basin and Range province, *J. Geophys. Res*. 98: B12: 22109-22122.

Zhao, L.-S. and J. Xie (1993). Lateral variations in compressional velocities beneath the Tibetan Plateau from Pn traveltime tomography, *Geophys. J. Int*. 115: 1070–1084.

# INITIAL STEPS TOWARD NEXT-GENERATION, WAVEFORM-BASED, THREE-DIMENSIONAL MODELS AND METRICS TO IMPROVE NUCLEAR EXPLOSION MONITORING IN THE MIDDLE EAST

Brian Savage[1], Arthur J. Rodgers[2], Jeroen Tromp[3], and Brian Covellone[1]

[1]University of Rhode Island, [2]Lawrence Livermore National Laboratory, and
[3]Princeton University

Sponsored by Air Force Research Laboratory and National Nuclear Security Administration

Contract No. FA8718-08-C-0009
Proposal No. BAA08-79

## ABSTRACT

In an effort toward improving current seismic-velocity models for the Middle East, the initial step of building a high-quality database of recordings from well characterized sources is essential. This high-quality database of recordings, or broadband waveforms, encompassing the region from the Mediterranean to the eastern edge of Tibet, will be the primary measure for evaluation and improvement in the iterative, waveform-based, adjoint-inversion process. Adjoint inversions, as with any waveform-based method, require precise estimates of the location, especially depth, and the faulting parameters or moment-tensor elements of the seismic sources. Imprecise locations and/or source terms will result in real changes in the amplitude and the phase of the incoming wave train; when close to a nodal plane, these changes can occur very rapidly with incoming azimuth. These errors will directly map into the resulting velocity model as uncertainty or biased values.

The initial database included about 250 well recorded, regional events in the Middle East from 1990 to 2007 with magnitudes $M_w > 5.5$. To reduce errors in the source-depth and faulting parameters, the events were evaluated using two complementary sets of data, a regional data set contained within the Middle East and a global teleseismic data set. Regional data were first utilized at long period, $\omega > 20$ s, using the waveform-based methods of Pasyanos et al. (1996) to determine the moment tensor elements. Then shorter periods, $\omega > 5$ s, were added, following Zhao and Helmberger (1994), to further assess errors in source depth and propagation effects by splitting apart the longer period surface waves from the shorter period, depth-sensitive *Pnl* waves. Problematic, or high-error, stations and paths were further analyzed to identify systematic errors with unknown sensor responses and complex wave propagation regions.

Teleseismic data were used in tandem with the regional seismic data to further assess the estimated moment tensor and place further constraints on the source depth. Synthetic seismograms were computed using a frequency wave-number integration scheme on the source and receiver sides and then time-shifted to account for direct *P*- and *S*-wave propagation. Data were then compared to synthetics, including source-side conversions, which are important to reducing error estimates of seismic-source depths.

## OBJECTIVES

Robust models of 3D velocity structure within the greater Middle East, from the Turkish Plateau to the eastern edge of Tibet (Figure 1), will increase our capability to locate events, discriminate between natural and man-made events, identify source depths, and determine magnitudes, as well as make practical error estimates. Improvement of current seismic-velocity models of the Middle East (1D and 3D) will be accomplished through an adjoint-tomography method to iteratively improve the models in three dimensions. The initial step toward any constrained tomography model is a well located and well characterized set of sources. Further, the adjoint-tomography method (Tape et al., 2007) needs full seismic waveforms as a measure of the misfit of the current model iteration. As such, an associated set of recorded, quality-controlled seismic data for each event is necessary to perform the inversion. Finally, the introduction of the etree model, a seamless way to represent 1D and 3D structural velocity models, will simplify the process during each iteration of synthetic waveform creation and velocity model improvement. In future years, an improved velocity model of the Middle East will be presented and distributed, built on the foundation of the seismic-waveform data set using the new 3D model representation.

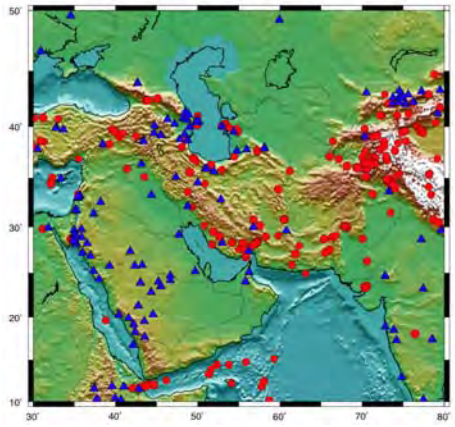


**Figure 1. Map of the available sources and stations in the Middle East.**

## RESEARCH ACCOMPLISHED

### Event Characterization

Earthquake source parameters in the Middle East, Mw > 5, were determined using two separate techniques: a teleseismic body-wave inversion method (Kikuchi and Kanamori, 1982) and a regional, full-waveform cut and paste (CAP) method (Zhao and Helmberger, 1994; Zhu and Helmberger, 1996). Both methods are sensitive to source-depth and faulting parameters and, to a lesser extent, to heterogeneous velocity structure, providing complementary event characterizations, including errors.

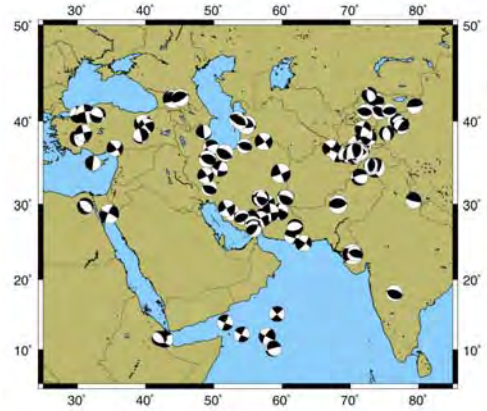


**Figure 2. Teleseimically determined focal mechanisms**

Initial results from the teleseismic body-wave inversion are shown in Figure 2. The teleseismic body-wave inversion uses a time-domain deconvolution to identify and solve for the faulting parameters of the largest signals in the recorded data. Depth, source duration, and, if desired, multiple subevents are solved for, using an iterative scheme to reduce misfit between the data and synthetics. A preliminary data set of 120 events for which there already existed local and regional data was analyzed for source-depth and faulting parameters, showing a good match between the data and synthetics.

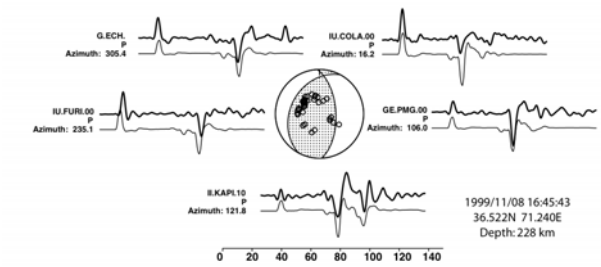


**Figure 3. Event 1999/11/08**

A second suite of events, with smaller magnitudes and thus smaller signal-to–noise, is also being examined, but with greater care. Determined depths, faulting parameters, and magnitudes show overall close agreement with previously published reports from the Harvard Global Centroid-Moment-Tensor Project (CMT) and the U.S. Geological Survey (USGS). In Figure 3, an example of a deep event from the eastern edge of Tibet shows a good match between the data (top) and the synthetics (bottom).

All direct and depth phases fit well in terms of timing and amplitudes. Figure 3 shows only a small subset of the data used to evaluate the faulting parameters and source depth for this event. Most events show good azimuthal coverage, with over 20 stations, on average, used in each event inversion. The results shown in Figure 3 indicate how sensitive the data and inversion are to changes in the faulting parameters when the depth phases, pP and sP, are included. P wave amplitudes for each station are all positive and about the same magnitude, but the depth phases show large variability against azimuth.

Faulting parameters were also determined using the CAP methodology (Zhao and Helmberger, 1994; Zhu and Helmberger, 1996 ), in which regional recordings are cut into windows around the faster, higher frequency Pnl components and slower, longer period surface waves. All cut windows are fit simultaneously, allowing equal weighting of phases that may be of different absolute amplitude. By emphasizing the faster, Pnl portion of the recorded data, sensitivity to source depth is substantially increased.

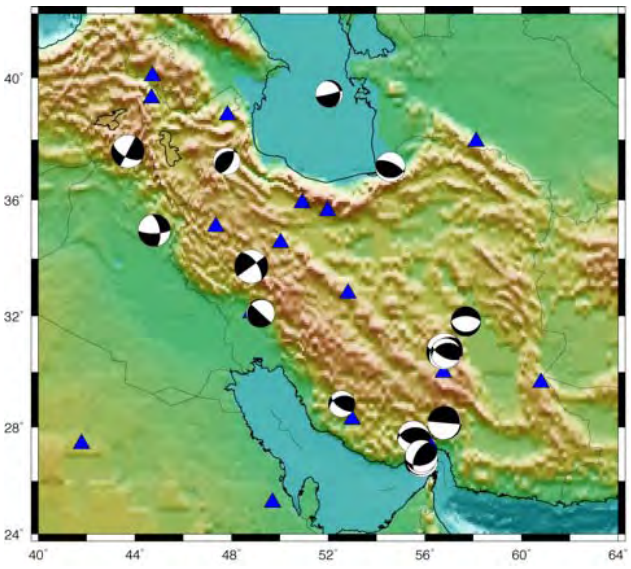


**Figure 4 - CAP determined focal mechanisms**

Shown in Figure 4 are preliminary results for 17 events for which faulting parameters and source depths could be determined using data solely from the Iranian National Seismic Network (INSN). Stations are plotted as blue triangles and focal mechanisms are plotted at the source. As with the teleseismic inversion, results compare well with the reported faulting parameters, including magnitude, which has a slight bias downwards of 0.16 in Mw. Depths determined for the suite of events have a much greater scatter, around 10 km, compared to those previously reported (Global CMT). This could be the result of either inadequate resolution from the long-period nature of the Global CMT or a complex velocity structure between the source and receiver. An example of the CAP method is shown in Figure 5. The first panel (A) displays the source location as a red circle and the stations used in the analysis as blue triangles. The second panel (B) presents solutions for a range of depths against the misfit, as well as any changes in focal mechanism or magnitude. The third panel (C) presents results for the best fitting solution at 8 km. Again, the Pnl window of the seismogram is sensitive to the source depth, where an increase will tend to separate the two large pulses on the Pnl radial and vertical components.

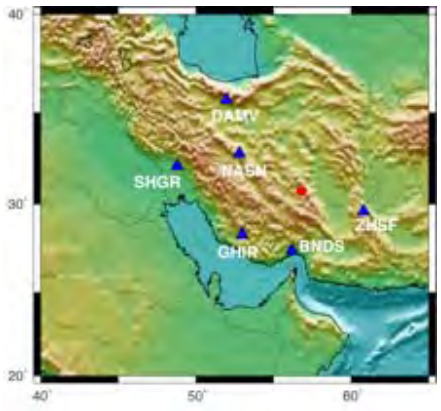


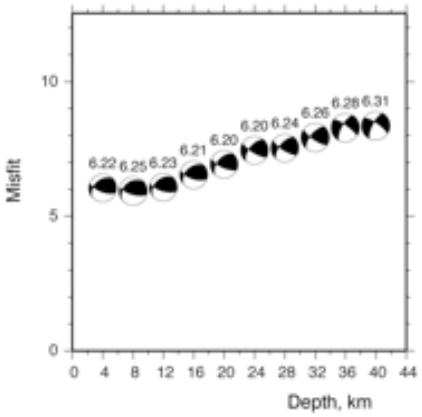


**Figures 5A (left) and 5B (right). Event Kerman, Iran**

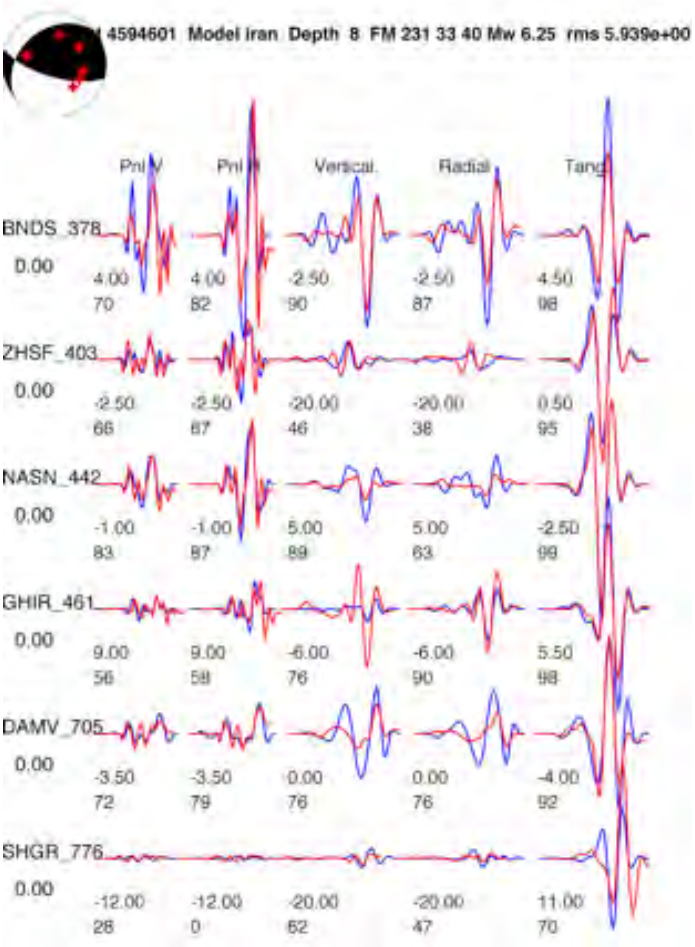


**Figure 5C. Event Kerman, Iran**

### 3D Velocity Model Representation

Models used in the adjoint tomographic inversion will be stored and accessed through the etree framework (Tu et al., 2004). This framework is currently being incorporated into the SPECFEM3D waveform simulation code (Komatitsch and Tromp, 1999), the numerical solver for the adjoint tomography. An etree is a compact representation of a 3D space allowing rapid access and variable resolution throughout the model. Figure 6 shows how quick access to elements within an etree is accomplished. The model on the left is divided into regions of variable resolution by powers of 2. The largest regions (h, m, and the regions containing i through l) are near the initial node of the etree, and regions of greater resolution are subdivided from there. The locations of the regions are encoded in compact notation for rapid access to material parameters, metadata such as units, and/or references from which the model is derived. Important motivations for using etree model representation are to build a framework within which models from a variety of references can be utilized to create synthetic seismograms and to improve these models within the adjoint framework.

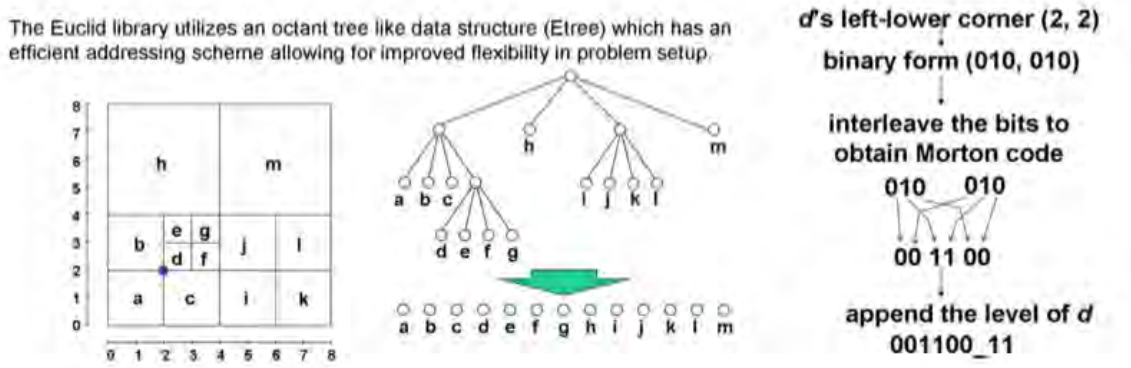


**Figure 6. Etree model representation**

Initial tests using a priori 3D models have shown dramatic improvements in fitting seismograms in the Middle East. An initial model to be evaluated is the Unified/WENA (Western Eurasia/North Africa) model (Pasyanos et al., 2004). Figure 7A shows sediment and crustal thickness within the model and how it affects the propagating wavefield. Crustal thickness in the Middle East varies between 30 and 40 km on land, with the exception of the eastern edge of Tibet, while it is less than 10 km in the Red Sea and oceanic environments. Conversely, there is little to no sediment throughout much of the Middle East but large basins of sediment in the Mediterranean, Black, and Caspian Seas, as well as in a large basin extending north from the Persian Gulf to the deltas of the Tigris and Euphrates Rivers. These rapid changes in crustal and sediment thickness can dramatically extend and twist the propagating wavefield.

Use of the Unified/WENA model against an 1D reference model in the Middle East is shown in Figure 7B. For the 1D model and an explosion source (left panel), a simple pulse of coherent energy travels radially outward from the source, with lighter colors indicating larger amplitudes. The Unified/WENA 3D model (right panel) for the same source produces a radically different wavefield. In regions of large basins and deep sedimentation, e.g., the Persian Gulf, the wavefield becomes extended in space and shows greater dispersion than in other regions, e.g., paths that propagate directly north and south into the Indian Ocean.

Effects of the 3D velocity structure can easily been seen by comparing data to 1D and 3D synthetics, as in Figure 7C. The data seismogram (black, top) has an extended, complex surface wave in comparison to the much simpler 1D reference synthetic (green, bottom). By using a 3D model—here, the Colorado University Boulder (CUB) global model (Shapiro and Ritzwoller, 2002)—the duration of the surface wave is now represented more fully, although there are still mismatches at high frequencies and overall amplitudes.

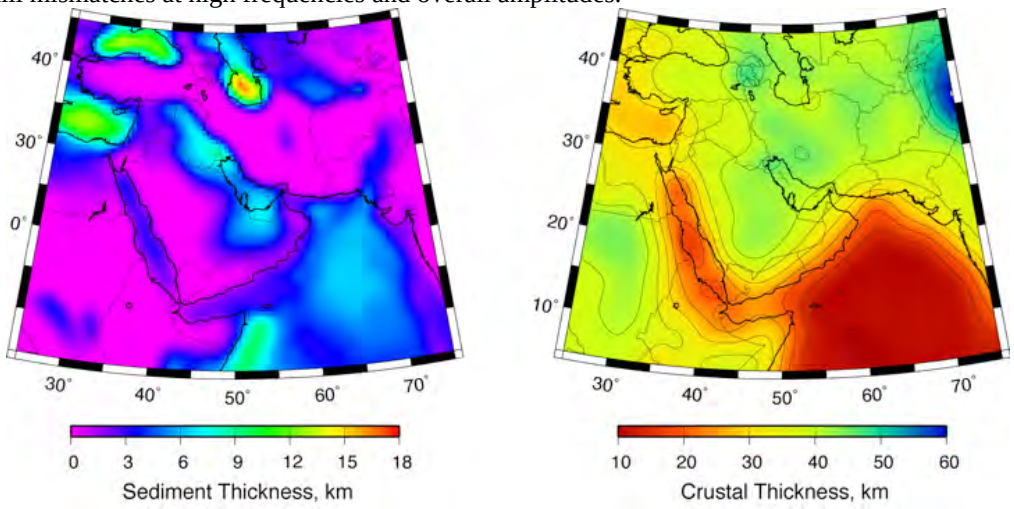


**Figure 7A. Unified/WENA Model**

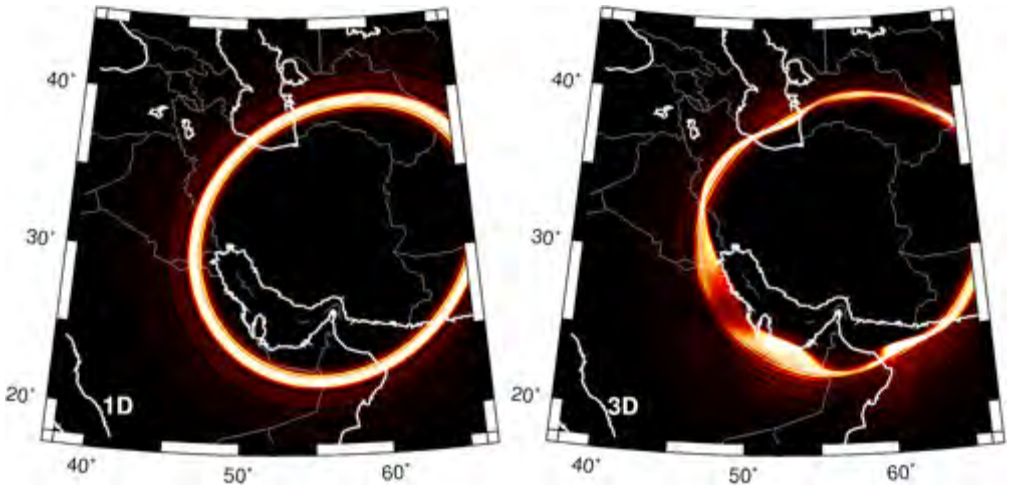


**Figure 7B. Wavefield distortion from 1D vs. 3D models**

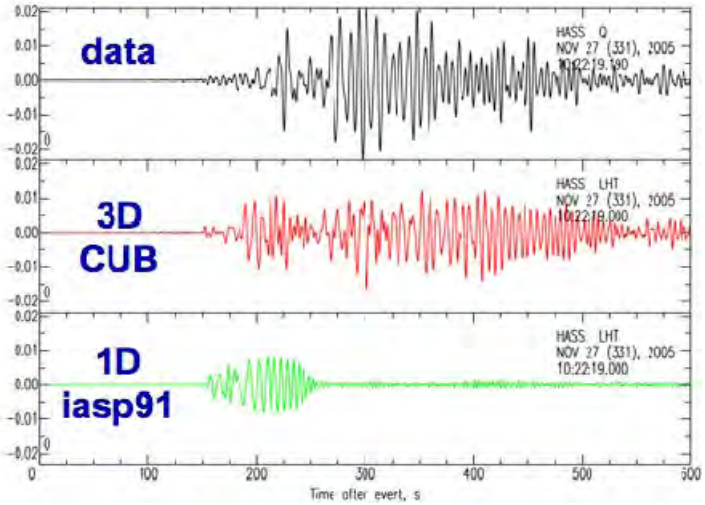


**Figure 7C. 3D velocity structure effects**

## CONCLUSIONS AND RECOMMENDATIONS

Foundations of a seismic-waveform database of the Middle East have been created. Initial work to characterize events in and around the Middle East has produced a large (> 100) and growing data set, constrained by teleseismic and regional waveform inversions. Both inversion methods provide robust estimates of source-depth and faulting parameters. When used jointly, each offers important verification of the other's result. Event characterization results from both inversions agree well with previously reported, routine determinations. Parallel work has also been undertaken to introduce the etree 3D model representation framework into the spectral-element, adjoint-tomography calculations. This new approach to 3D model representation will allow for more streamlined model handling and model updating during the inversion process. Initial testing of these 3D models has shown that they too meet the requirement to accurately depict recorded seismic data in the Middle East. For the best possible 3D velocity model results in the greater Middle East, we recommend that data from a wide range of sources be collected, quality checked, and added to the new waveform database, particularly seismic data from remote and/or sparsely instrumented areas.

## REFERENCES

Kikuchi, M. and H. Kanamori (1982). Inversion of complex body waves, *Bull. Seism. Soc. Am.* 72: 491–506.

Komatitsch, D. and J. Tromp (1999). Introduction to the spectral-element method for 3-D seismic wave propagation. *Geophys. Jour. Int.* 139: 806–822.

Pasyanos, M. E., D. S. Dreger, and B. Romanowicz (1996). Toward real-time estimation of regional moment tensors, *Bull. Seism. Soc. Am.* 86: 1255–1269.

Pasyanos M. E., W. R. Walter, M. P. Flanagan, P. Goldstein, and J. Bhattacharyya (2004). Building and testing an a priori Geophysical model for Western Eurasia and North Africa, *Pure and Applied Geophysics* 161: 2, 235–281.

Shapiro, N. and M. Ritzwoller (2002). Monte-Carlo inversion for a global shear-velocity model of the crust and upper mantle. *Geophys. J. Int.* 151: 88–105.

Tape, C., Q. Liu, and J. Tromp (2007). Finite-frequency tomography using adjoint methods -- Methodology and examples using membrane surface waves, *Geophys. Jour. Int.* 168: 1105–1129.

Tu, T., D. O'Hallaron, and J. López (2004). Etree: a database-oriented method for generating large octree meshes, *Engineering with Computers* 20: 117–128.

Zhao, L. S., and D. V. Helmberger (1994). Source estimation from broadband regional seismograms, *Bull. Seism. Soc. Am.* 84: 91–104.

Zhu, L., and D. V. Helmberger (1996). Advancements in source estimation techniques using broadband regional seismograms. *Bull. Seism. Soc. Am.* 86: 1634–1641.

# SURFACE WAVE DISPERSION MEASUREMENTS AND TOMOGRAPHY FROM AMBIENT SEISMIC NOISE CORRELATION IN CHINA

Xiaodong Song[1], Xinlei Sun[1], Sihua Zheng[2,1], Zhen Xu[1], Yingjie Yang[3], and Michael H. Ritzwoller[3]

University of Illinois at Urbana-Champaign[1], China Earthquake Administration[2], and University of Colorado at Boulder[3]

Sponsored by Air Force Research Laboratory

Contract No. FA8718-07-C-0006
Proposal No. BAA07-24

## ABSTRACT

We perform ambient noise tomography of China using the data from the China National Seismic Network and global and PASSCAL stations. The results so far are summarized below.

(1) Dispersion measurements and tomography. For most of the station pairs, we retrieve good Rayleigh waveforms from ambient noise correlations using 18 months of continuous data at all distance ranges across the entire region (over 5000 km) and for periods from 70 s down to about 8 s. We obtain Rayleigh wave group velocity dispersion measurements for periods 8 to 70 s and invert for Rayleigh dispersion maps for periods from 8 to 60 s. The dispersion maps correlate nicely with surface geology.

(2) Error estimates using bootstrap analysis. A major feature of the ambient noise method is that the whole process is completely repeatable with different time segments, which make it possible to evaluate the uncertainties. We adopt a bootstrap method to quantify the errors in the Rayleigh wave group velocity dispersion measurements and the tomographic maps. Most of the pairs show similar dispersion curves between different runs and small standard deviations, indicating good data quality and convergence of the Green's function. Group velocity for a long period generally has a larger error, which is consistent with the notion that the long period needs longer time to converge. The best retrieved periods are from 10 to 30 s with the optimal period of around 15 to 20 s. Pairs with large errors do not depend on the orientations of the paths or the locations of the stations. Rather, they are associated with a few stations with large average standard errors. The likely causes are missing data and poor instrumentation (or site conditions). Where ray coverage is good, there is only a subtle difference in tomography maps between different runs, suggesting that our solution is very stable.

(3) 3D structure. We invert the Rayleigh group and phase dispersion maps for 3D shear-wave velocity structure. The 3D model shows some remarkable features, including slow sedimentary layers of all the major basins in China at the shallow depth, Moho depth variation, fast (strong) mid-lower crust and mantle lithosphere in major basins surrounding the Tibetan Plateau (TP) (Tarim, Ordos, and Sichuan). These strong blocks thus seem to play an important role in confining the deformation of the TP to be a triangular shape. The Moho change from plateau to Tarim is very sharp; the change to the Sichuan Basin is gentler but still steep. The India lithosphere seems to terminate around the Bangong Nujiang Suture as indicated by the fast-slow velocity contrast in the mantle lithosphere, but it seems to extend further north under E. Tibet. A widespread, prominent low-velocity zone is observed in midcrust in the TP, providing strong support for the channel flow model. These slow velocities are generally connected and seem to reach to the surface near the margins of the TP, consistent with the thermal-mechanical modeling of the ductile extrusion of the Greater Himalayan Sequence.

## OBJECTIVES

The overall objective of this project is to obtain surface wave dispersion measurements from ambient seismic noise correlations of the Chinese backbone stations (China National Seismic Network, CNSN) and use these measurements to produce surface wave dispersion maps of China. More specifically, the objectives are (1) to obtain dispersion measurements between CNSN stations; (2) to obtain dispersion measurements between CNSN and the Federation of Digital Seismic Networks (FDSN), regional networks, and temporary stations; and (3) to obtain dispersion maps from these dispersion measurements.

## RESEARCH ACCOMPLISHED

### Method and Data

Recent theoretical and laboratory studies have shown that the Green's functions of a structure can be obtained from the cross-correlation of diffuse wavefields (e.g., Lobkis and Weaver, 2001; see also the review by Campillo, 2006). The basic idea is that linear waves preserve, regardless of scattering, a residual coherence that can be stacked and amplified to extract coherent information between receivers. The idea has now found rapid applications in seismology. In particular, surface waves have been found to be most easily retrievable from the cross-correlations of seismic coda (Campillo and Paul, 2003) or ambient noise (Shapiro et al., 2005; Sabra et al., 2005) between two stations. Both Rayleigh waves and Love waves can be retrieved. The new type of data has rapidly been used for tomographic mapping at regional or local scales and on continental scales. Most studies have focused on Rayleigh wave group velocity tomography from ambient noise. However, the method is applicable to Love waves and phase velocity measurements.

Ambient noise tomography (ANT) overcomes several important limitations of conventional methods based on earthquakes; i.e., uneven distribution of earthquake sources, uncertainty in earthquake location, and attenuation of short-period surface waves. Thus, the method is particularly useful for surface-wave path calibration and for tomographic mapping in aseismic regions, especially over short periods (below 30 s). In addition, the method can be applied any time without the need to wait for earthquakes and is completely repeatable, allowing the quantification of errors.

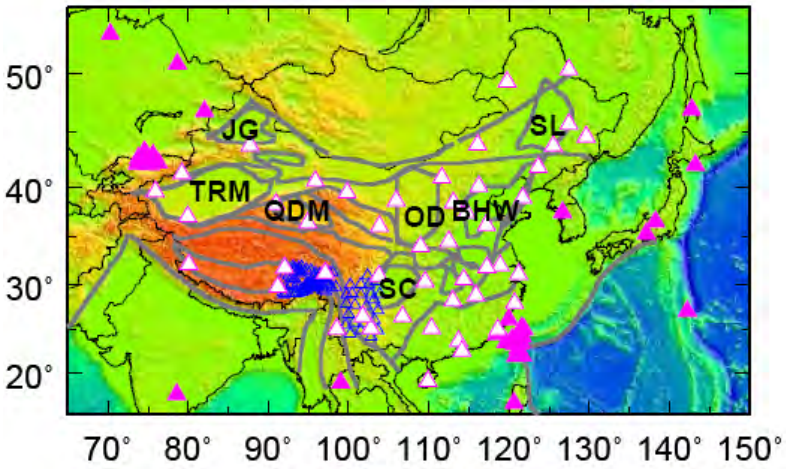


**Figure 1. Distribution of seismic stations used in this study, including CNSN stations (solid white triangles), global and regional stations in the surrounding regions (solid pink triangles), and PASSCAL stations (open blue triangle). Also plotted are major tectonic boundaries and major basins. The basins (labeled) include Tarim (TRM), Junggar (JG), Qaidam (QD), Sichuan (SC), Ordos (OD), Bohai Wan (BHW), and Songliao (SL) Basins.**

Our main stations are from the CNSN (Figure 1). The CNSN is the national backbone network, established around 2000, with a relatively uniform distribution across continental China. To increase data coverage, we also include some stations in the surrounding regions. We focus on Rayleigh wave group velocities in this study. We use 18 months of continuous data from 47 CNSN stations, 32 stations in surrounding regions, and 96 PASSCAL stations. All stations are broadband. The bandwidths of the CNSN stations are from 20 Hz to at least 120 s. We use the data-processing and imaging techniques described in great detail by Bensen et al. (2007). Below is a brief outline of our data procedure. First, we obtain the empirical Green's function (EGF) from ambient noise cross-correlation. Continuous data are preprocessed before correlation and stacking, which includes clock synchronization, removal of instrument response, time-domain filtering, temporal normalization, and spectral whitening. The purpose is to reduce the influence of earthquake signals and instrument irregularities and to enhance the strength and bandwidth of the ambient noise correlations. Second, if the signal-to-noise ratio (SNR) is sufficiently large, Rayleigh wave group speeds are measured using a frequency-time analysis (Ritzwoller and Levshin, 1998). Finally, the interstation dispersion measurements are used to invert for the Rayleigh wave group velocity maps, in exactly the same way as earthquake-based measurements.

**Dispersion Measurements and Tomography**

For most of the station pairs, we are able to retrieve good Rayleigh wave signals from the ambient noise correlations (Zheng et al., 2008). Figure 2 shows typical examples of EGFs and group velocity measurements of Rayleigh waves retrieved from ambient noise correlations. Our cross-correlations show clear arrivals at different settings (near the coast or well into the continental interior) and at both relatively low frequencies (20–50 s) and high frequencies (5–20 s). The EGFs can be retrieved over the entire region (at distances of over 5000 km) (Figure 2a).

We measured group velocity dispersion curves (Figure 2c) for station pairs with Rayleigh wave SNR >10. The SNR is defined as the ratio of the peak amplitude of the Rayleigh wave to the root-mean-square value of the background. The measurement is very stable. Clear dispersion can be commonly observed directly from the EGFs (Figure 2b). We found that the group velocity measurements can extend to periods of 10 s or shorter even for station pairs that are separated over thousands of kilometers. The group velocities of the HTA-BRVK path (Figure 2b,c), which samples the Tarim Basin, agree with a global 3D earthquake-based model (Shapiro and Ritzwoller, 2002) at longer periods but differ significantly at short periods (below 30 s). The slow group velocities at short periods are caused by the thick sediments of the Tarim Basin (see discussion below).

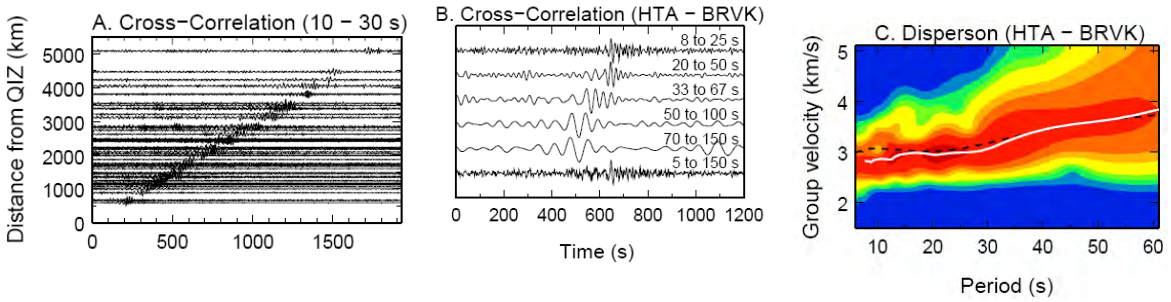


**Figure 2. Example of Rayleigh wave EGFs and dispersion measurements obtained from ambient noise correlations. (a) Symmetric component of the correlations between station QIZ (in Hainan Province, China) and other stations. The traces are band-pass filtered at relatively short periods (10-30 s). (b) EGFs filtered in different frequency bands. Long-period surface waves are clearly faster than short-period ones. The path is between HTA (bordering Tarim in the south) and BRVK (Borovoye, Kazakhstan). (c) Frequency-time analysis (Ritzwoller and Levshin, 1998) used to retrieve Rayleigh wave group velocity dispersion curve (white) for the HTA-BRVK path. The black dashed curve is the prediction from the 3D global shear velocity model of Shapiro and Ritzwoller (2002), which is used for phase-matched filtering in the data analysis and for comparison with measurements.**

We have obtained dispersion measurements with SNR >10 for periods 8–70 s (Figure 3, left). The best observed frequency band is 10–30 s with a retrieval rate of 50% to 80% of all the possible pairs. The ray paths provide good coverage of almost the entire Chinese continent except the southwestern margin of the Tibetan Plateau (Figure 3, right).

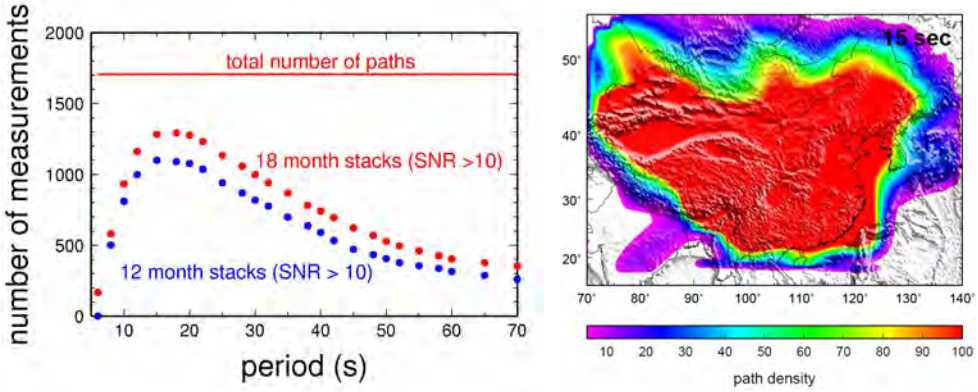


**Figure 3. Distribution of dispersion measurements for different periods (left) ray-density map for the period of 15 s (right). (Left) The total number of paths takes into account data availability for pairing up stations. The numbers of measurements obtained from 18 months of continuous (red dots) show improvement of about 20% over the numbers of measurements obtained using only 12 months of data (blue dots). (Right) The ray density is the number of rays inside a 1 degree by 1 degree cell. The rays are station pairs for which dispersion measurements have been obtained. The ray coverage is best for periods of 10 to 30 s. Coverages for shorter or longer periods deteriorate, but the spatial coverage patterns remain similar.**

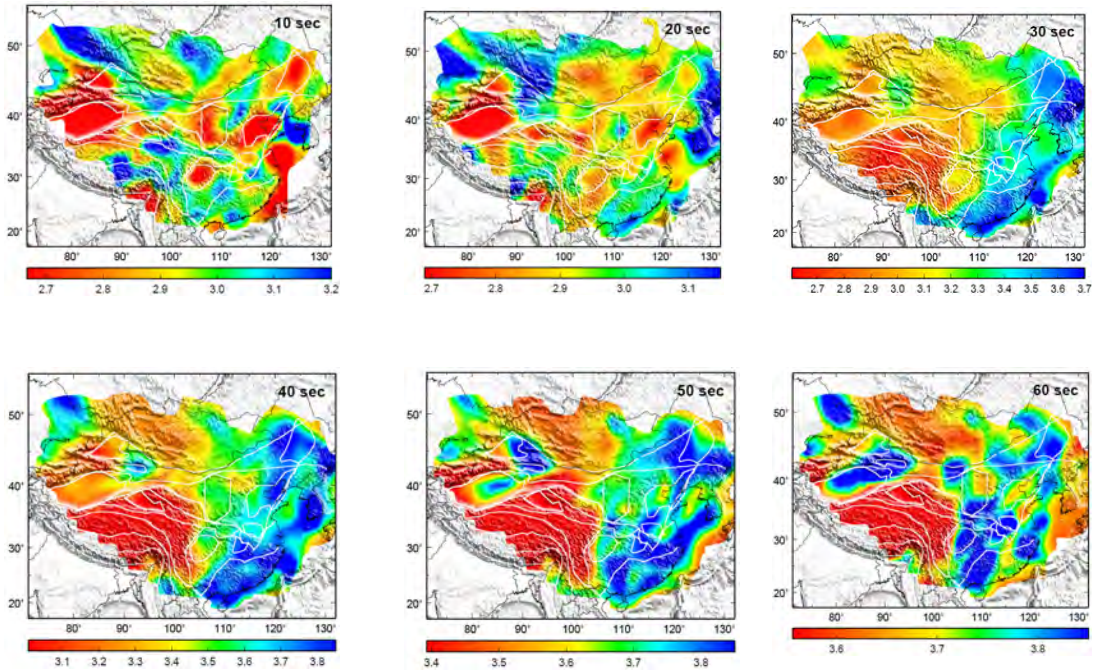


**Figure 4. Rayleigh wave group velocities obtained in this study. Shown are the maps at periods 10, 20, 30, 40, 50, and 60 s, respectively. Plotted in the background are major block boundaries and basin outlines (Figure 1).**

The ray coverage of our dispersion measurements is sufficient for us to invert for Rayleigh wave group velocity maps at periods from 8 s to 60 s (Figure 4). The results show remarkable features that correlate with large-scale geological structures of China. Major basins are well delineated with low velocities at short periods (8–20 s), including Bohai-Wan Basin (North China Basin), Sichuan Basin, Qaidam Basin, and Tarim Basin. The stable Yangtz Craton also shows up well with high velocities. At longer periods (25–50 s), the group velocity maps display striking bimodal distribution with high velocity in the east and low velocity in the west, which corresponds very well with the thinner crust in the east and much thicker crust in the west (e.g., Liang et al., 2004). The NNE-SSW trending boundary between fast and slow velocities (around longitude 108°E) coincides with the sharp topographic change and with the well-known Gravity Lineation.

A side-by-side comparison between a short period group velocity map and sediment thickness or between an intermediate period map and crustal thickness is presented in Figure 5. The correlations are quite striking if we compare the group velocities along a certain profile of interest (Figure 6). The selected profile along the latitude of about 39°N passes through three major basins: Tarim, Ordos, and Bohai-Wan (Figure 1). The thick sediments in these basins (Laske and Masters, 1997) correlate well with slow velocities at periods from 10 to 20 s (Figure 6a). The general trend of decreasing crustal thickness from west to east is well represented by increasing group velocities around 30 s (Figure 6b). However, the group velocity map displays more structure than the smooth crustal thickness curve from the global reference model (CRUST 2.0) (http://mahi.ucsd.edu/Gabi/rem.html), suggesting a more complex Moho. At the period of 50 s, the trend is no longer observable as the surface waves sample deeper into the mantle.

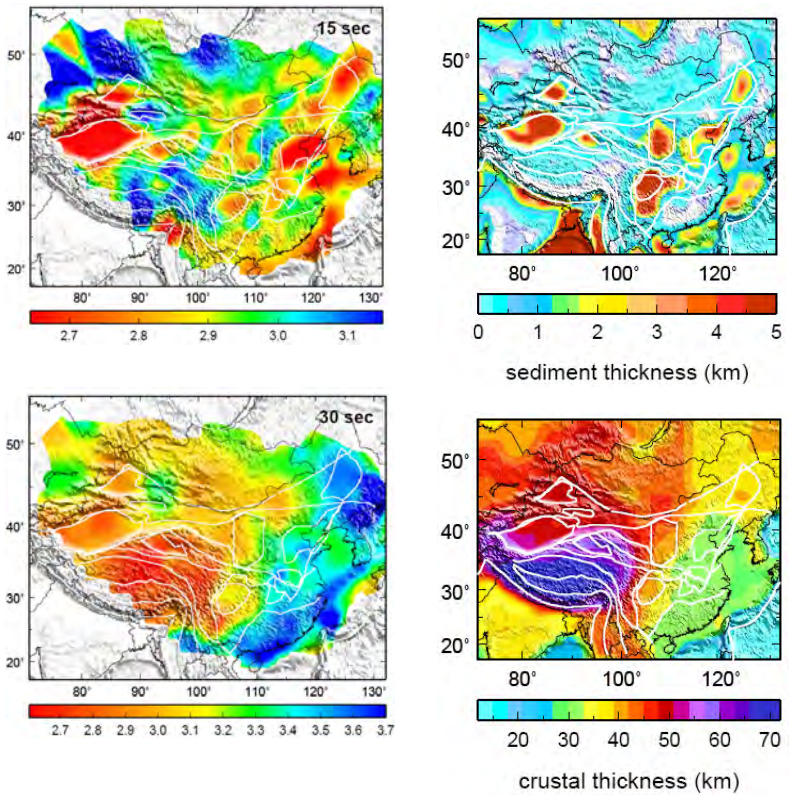


**Figure 5. Comparison of group velocities with sediment thickness (top) and crustal thickness (bottom). (Top) The group velocity map (left) is for 15-s Rayleigh waves. The major basins (including Tarim, Junggar, Qadaim, Sichuan, Bohai Wan, and Songliang, as well as the Southern North China and Jianghang basins in the east-central region) are well delineated by slow velocities. See Figure 1 for the location of the basins. (Bottom) The group velocity map is for 30-s Rayleigh waves. The major trend of crust thickening from the east to west (right) is well represented by the velocity decreases from east to west (left).**

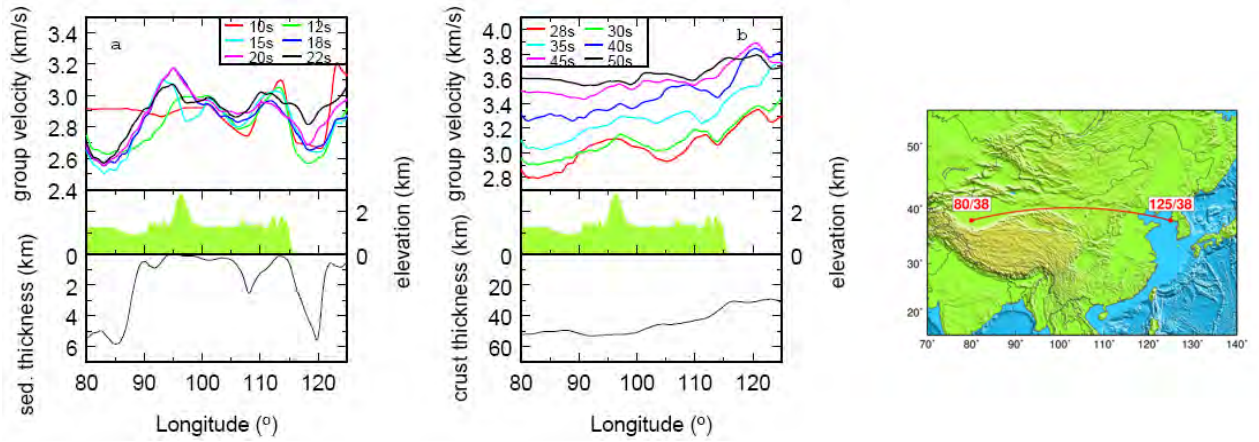


**Figure 6. Rayleigh wave group velocities are compared with sediment thickness (a) and crustal thickness (b) along a selected path. The selected path is along the great-circle path between (38°N, 80°E) and (38°N, 125°E), passing through three major basins (Tarim, Ordos, and Bohai Wan) (Figure 1). Plotted at the top are velocities for shorter periods (a) and for longer periods (b), respectively. Plotted at the bottom are sediment thickness (a) and crustal thickness (b), respectively. In the middle are surface elevations.**

**Validation and Error Analyses of Dispersion Measurements and Tomography**

Comparison of the tomographic maps with the geological features discussed above provides an important initial validation of the ANT methodology; i.e., the method provides models of group wave speeds that are consistent with well-known geological features and other geophysical observations. Furthermore, the complete repeatability of the ANT method makes it possible to directly validate the methodology and to evaluate the uncertainties of the dispersion measurements. Several methods have been proposed previously in this regard (see summary by Zheng et al., 2008). (1) Direct verification: Comparing the EGF with the surface wave generated by an earthquake along the same path. (2) Comparing the EGF obtained from ambient noise and that from seismic coda. (3) Temporal stability: Comparing the EGFs from the data observed at different time periods (e.g., different months). Furthermore, because the principal ambient noise sources are believed to come from the oceans, which are seasonal, the consistency of the correlations from different seasons gives a measure of the stability and error of the EGFs. (4) Spatial consistency: Comparing the EGFs for station-pairs along similar paths. The EGFs between a far-away station to two or more stations that are close to one another should be similar as the paths sample similar structures.

We have examined temporal and spatial consistency of our dispersion measurements and found that they are very consistent whenever the SNRs of the EGFs are high. Some examples are shown in Figure 7. The temporal comparisons include a station pair with an east-west path (BJT-BRVK) and another pair with a north-south path (XAN-CHTO) (Figure 7, top). We construct 23 dispersion curves using 12 months of data with different sliding windows or using 12 months of data over different seasons. For either pair, we find the standard deviation of these curves to be less than 2% for all periods and the standard deviation of the mean to be less than 0.5%. The spatial comparisons include two pathways (Figure 7, bottom), from GOM to GZH/SZN and from WMQ to SSE/NJ2. The group velocities between WMQ and SSE are quite similar to those between WMQ and NJ2 at all the observed periods (10 to 60 s). The group velocities between GOM-GZH and GOM-SZN are also similar at periods less than 40 s. At periods greater than 40 s, they are somewhat different but are within their temporal uncertainties.

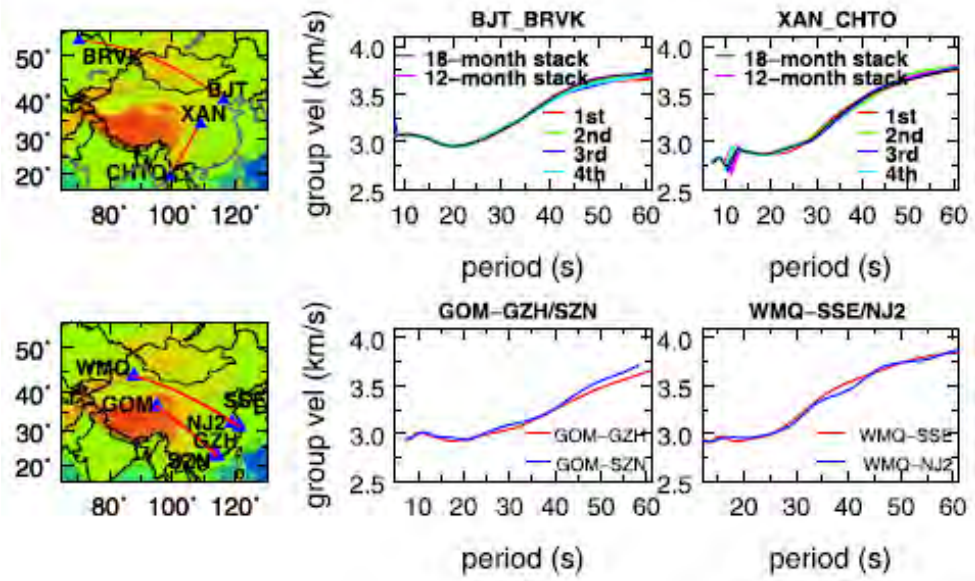


**Figure 7. Temporal (top) and spatial (bottom) consistency of dispersion measurements. (Top) Dispersion curves from different time windows. We select two pairs, BJT-BRVK along an east-west path and XAN-CHTO along a north-south path. For either pair, we calculate two sets of EGFs. For each calculation of the EGF, a total of 12 months of data are used. The 18-month stack (including all the data we collected) is plotted for comparison. One set uses seasonal data (red, green, blue, and cyan), i.e., data from the same season over a period of 4 years. The other set uses 12 months of data with a sliding time window of 10 days (total of 19 curves, all in magenta). (Bottom) Dispersion curves between a far-way station and two close stations. We select two pathways, one from GOM to GZH/SZN (distance about 2400 km) and the other from WMQ to SSE/NJ2 (distance about 3100 km). The distance between GZH and SZN is about 133 km, and that between SSE and NJ2 is 245 km.**

Figure 8 shows two examples of error estimates of the dispersion curves using the boostrap method. Most pairs show similar dispersion curves between different runs and a small standard deviation (generally less than 0.1 km/s), indicating good data quality and convergence of the Green's function. Group velocity for a long period generally has a larger error, which is consistent with the notion that the long period needs longer time to converge. There is only a subtle difference in tomography maps between different runs, suggesting that our solution is very stable (Figure 9). Standard deviation in the region with good ray coverage is small (generally less than 0.1 km/s), indicating a stable and reliable solution in well-sampled regions. The Rayleigh waves are best retrieved from 10 to 30 s with the best periods around 15 to 20 s. A pitfall of the model error estimates is that the standard deviations in the regions with poor ray coverage (at the margins) are also small, due to regularization in the tomographic inversion process. Our tomographic inversion includes regularization using a prior model. Thus, the inversions for the poorly sampled regions from different runs all converge to the prior model, giving an artifact of small errors.

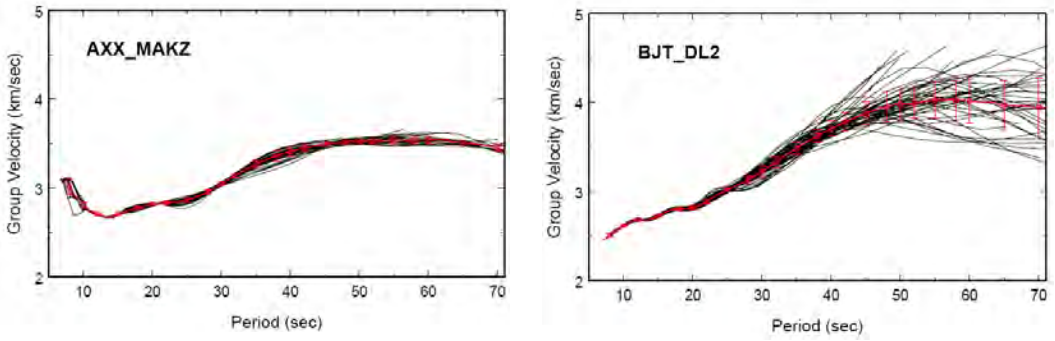


**Figure 8. Examples of error estimates of dispersion curves from bootstrap with a good pair (left) and a bad pair (right). Black curves are dispersion measurements for all the 50 runs. Red curves are the mean values. Error bars at different periods indicate the standard deviations. For the good pair (AXX-MAKZ), dispersion curves for different runs are very close to each other. The standard deviations are small throughout the whole periods. For the bad pair (BJT-DL2), dispersion curves spread out at long periods. The large standard deviations at long periods indicate large errors in the measurements.**

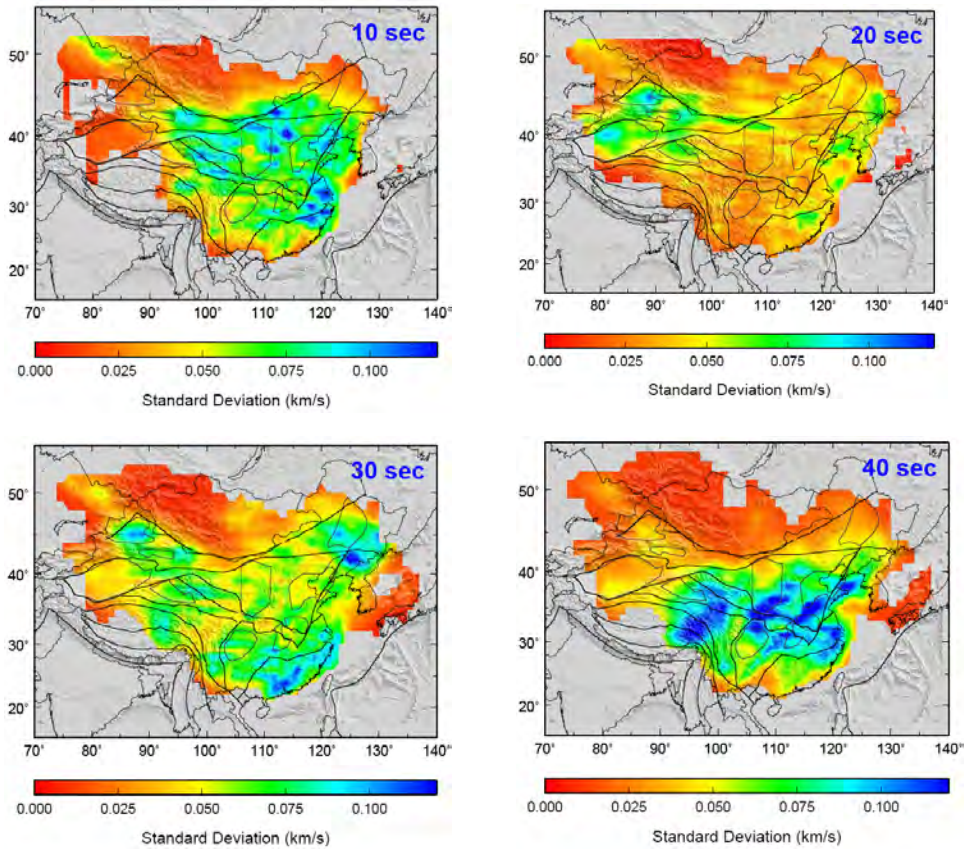


**Figure 9. Maps showing standard deviations of Rayleigh group velocity dispersion models at periods of 10 s (a), 20 s(b), 30 s(c), and 40 s (d). Color scales are the same in all the figures. The minimum standard deviation appears at about 20 s. As the period increases, the error also increases. Red color at the border region is an artifact from smoothing constraint and regularization. In the central part of China with best ray coverage, the small standard deviations indicate the robustness of the tomography results.**

Retrieval of the surface wave EGF relies on the stacking of cross correlation of continuous data for long-enough time series. The total length of data required for the Green's function to converge is empirical and highly frequency dependent: generally, the longer the period, the longer the time that is needed. Furthermore, the ambient noise source and station site conditions (including instrumentation stability) are uncertain. We have recently proposed a bootstrap method to quantify the errors in Rayleigh group velocity dispersion measurements and group velocity tomographic maps, based on the complete repeatability of the ambient noise correlation and tomography process (Xu et al., 2008).

Our bootstrap analysis uses the following steps. (1) We obtain the EGF using one month of data for each of the 18 months. (2) We select 18 random months among the months for which we have data. The selection process is a random sampling with replacement, as in any boostrap methods. We then obtain the stack EGF using the EGFs of these months for each and every station pair. Using these stacked EGFs, we measure dispersion curves for all station pairs and construct tomographic maps as usual. (3) We repeat step 2 50 times. (4) We obtain the mean and the standard deviation of the dispersion curve for each station pair from the 50 dispersion curves obtained in step 3. We regard the mean and the standard deviation as the group velocity estimate and the associated error. (5) Similarly, we obtain the standard errors of our tomographic models using the models obtained from the 50 iterations described in steps 2 and 3.

We found that the pairs with large variations do not have a preferred orientation or a particular geographical location (Figure 10, left). Rather, these pairs are generally associated with a few stations with large standard deviations. We derive an average standard deviation of the surface wave velocity for each station at each period by averaging over all the pairs associated with that station. Figure 10 (right) shows average standard deviations of dispersion measurements for individual stations over all periods. A few stations have standard deviations of greater than 0.19 km/s. The exercises provide a way to identify and sort out good and poor stations efficiently.

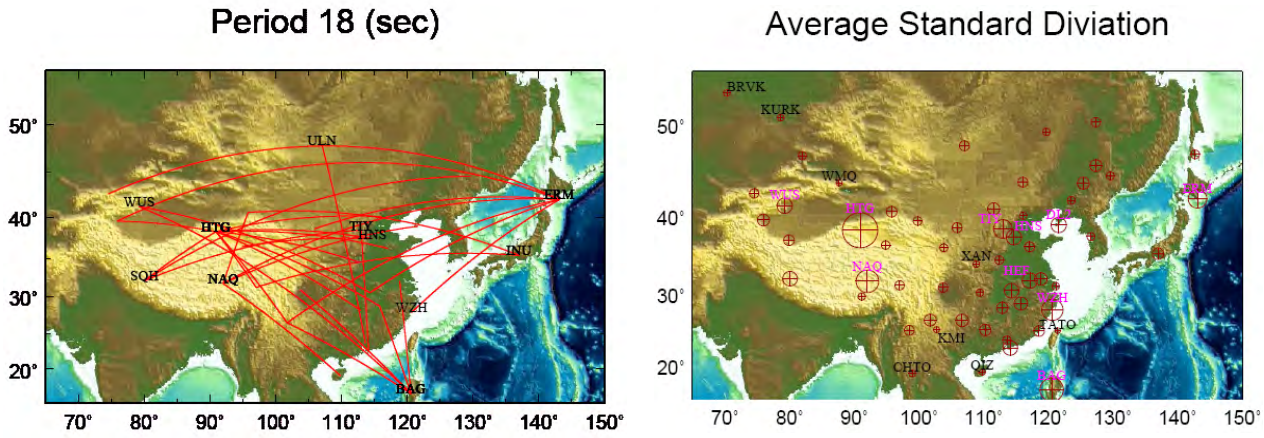


**Figure 10. (Left) Station pairs with standard deviations larger than 0.5 km/s. The bad pairs are generally associated with a few stations with large average standard deviations in the dispersion measurements (BAG, NAQ, HTG, ERM). (Right) Average standard deviations of dispersion measurements for individual stations plotted at the station sites. The size of the red cross or the open circle represent the size of the average standard deviation for the station. The larger the symbol size is, the larger the error is. Stations with average standard deviations smaller than 0.09 km/s are labeled in black, while stations with standard deviations larger than 0.19 km/s are labeled in pink.**

### 3D shear-wave structure

We combine our Rayleigh wave group and phase velocity maps (8–60 s) with longer-period dispersion maps from global earthquake-based measurements (Shapiro and Ritzwoller, 2002). We then invert the dispersion maps for 3D S

structures using programs by Bob Herrmann of St. Louis U. Preliminary results show some remarkable features for continental China and in particular the Tibetan Plateau (TP) (Figure 11), including slow sedimentary layers of all the major basins at the shallow depth, striking east-west contrasts in Moho depth variation and lithosphere thickness, fast (strong) mid-lower crust and mantle lithosphere in major basins surrounding the TP (Tarim, Ordos, and Sichuan) (in contrast, Qaidam Basin does not have such a "deep root"). These strong blocks thus seem to play an important role in confining the deformation of the TP to be a triangular shape. The Moho changes from plateau to Tarim and Sichuan Basins are quite sharp. The India lithosphere seems to terminate around the Bangong Nujiang Suture (BNS) as indicated by the fast-slow velocity contrast in the mantle lithosphere, consistent with many previous studies, but it seems to extend further north under E. Tibet. In northwest TP, slow anomalies extend from crust to great depth (200 km).

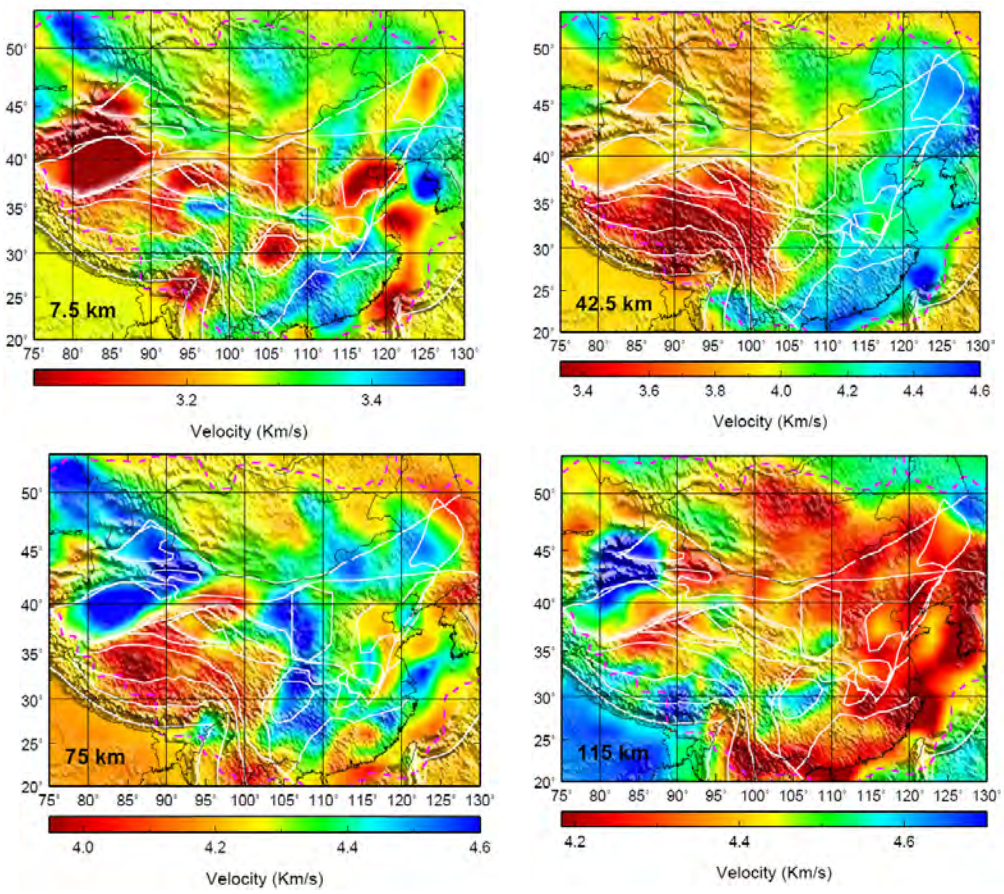


**Figure 11. Shear-wave velocity at 7.5 km (upper left), 42.5 km (upper right), 75 km (lower left), and 115 km (lower right).**

Extremely slow S velocities mark the mid-crust in much of the central, eastern, and southeastern TP. These slow velocities are widespread and often (but not always) connected in a laminar form. They seem to reach to the surface at certain localities in western, southern, northern, and southeastern margins. The mid/lower crust low-velocity zone provides support for the channel flow model that has been proposed for the outward growth and uplift of the TP (e.g., Clark and Royden, 2000) and for the extrusion of crustal materials to the surface (e.g., Beaumont et al., 2001).

## CONCLUSIONS AND RECOMMENDATIONS

We have obtained Rayleigh dispersion curves for periods of 8 to 70 s for ~10,000 new interstation paths from ambient noise correlation using correlations of 18 months of continuous data from CNSN, global and regional

permanent, and PASSCAL temporary stations. The best observed frequency band is 10–30 s with a retrieval rate of 50% to 80% of the station-pairs. We constructed new tomographic maps of China for periods from 8 to 60 s, which correlate with surface geology. Temporal and spatial analyses suggest that the dispersion measurements and tomography are robust. We proposed a bootstrap method, which allowed us to quantify the errors of each of our dispersion curves and the errors of the dispersion maps. For best periods (10–30 s) and for most regions, the Rayleigh waves have standard errors of less than 0.1 km/s. We have inverted the dispersion maps for 3D S model (down to about 200 km). The models show remarkable details of the crust and uppermost mantle, including major blocks, rapid changes in Moho, mid/lower crust low velocities in the TP, and variations in lithosphere velocities. We will add more PASSCAL stations, refine our error estimates of dispersions and tomographic maps, and conduct resolution tests of 3D structure.

## REFERENCES

Beaumont, C., R. A. Jamieson, M. H. Nguyen, et al. (2001). Himalayan tectonics explained by extrusion of a low-viscosity crustal channel coupled to focused surface denudation, *Nature* 414: 738–742.

Benson, G., M. Ritzwoller, M. Barmin, et al. (2007). Processing seismic ambient noise data to obtain reliable broadband surface wave dispersion measurements, *Geophys. J. Int.* 169: 1239–1260.

Campillo, M. (2006). Phase and correlation in random seismic fields and the reconstruction of the Green function, *Pure Appl. Geophys.* 163: 475–502.

Campillo M. and A. Paul (2003). Long-range correlations in the diffuse seismic coda, *Science* 299: 547–549.

Clark, M. K. and L. H. Royden (2000). Topographic ooze: Building the eastern margin of Tibet by lower crustal flow, *Geology* 28: 703–706.

Laske, G. and G. Masters (1997). A global digital map of sediment thickness, *EOS Trans. AGU* 78: F483.

Liang C., X. D. Song, and J. L. Huang (2004). Tomographic inversion of Pn travel-times in China, *J. Geophys. Res.* 109: B11304, doi. 10.1029/2003JB002789.

Lobkis, O. I. and R. L. Weaver (2001). On the emergence of the Green's function in the correlations of a diffuse field, *J. Acoust. Soc. Am.* 110: 3011–3017.

Ritzwoller, M. H. and A. L. Levshin (1998). Eurasian surface wave tomography: Group velocities, *J. Geophys. Res.*, 103: 4839–4878.

Sabra, K. G., P. Gerstoft, P. Roux, W. A. Kuperman, and M. C. Fehler (2005). Surface wave tomography from microseisms in Southern California, *Geophys. Res. Lett*.

Shapiro, N. M., M. Campillo, L. Stehly, and M. H. Ritzwoller (2005). High resolution surface wave tomography from ambient seismic noise, *Science* 307: 1615–1618.

Shapiro, N. M. and M. H. Ritzwoller (2002). Monte-Carlo inversion for a global shear velocity model of the crust and upper mantle, *Geophys. J. Int.* 151: 88–105.

Xu, Z., X. D. Song, S. H. Zheng, and M. H. Ritzwoller (2008). Bootstrap analysis on surface wave dispersion and tomography derived from ambient noise cross-correlation, IRIS Workshop, Skamania Lodge, Stevenson, WA.Zheng, S. H., X. L. Sun, X. D. Song, Y. J. Yang, and M. H. Ritzwoller (2008). Surface wave tomography of China from ambient seismic noise correlation, *Geochem. Geophys. Geosyst.* 9: Q05020, doi:10.1029/2008GC001981.

# STRONG MOTION STUDIES IN THE MINES OF KOLAR GOLD FIELDS

C. Srinivasan, Yesurathenam A. Willy, and C. Sivakumar

Sponsored by Air Force Research Laboratory

National Institute of Rock Mechanics

## ABSTRACT

Rockbursts are common phenomenon in mines during mining operations. A network of geophones was used to locate and assess the stability of mine workings. The important parameters needed to assess the damage potential and severity of a rockburst is its Richter's local magnitude. It was not possible from the records of geophone due to saturation effect. A strong-motion accelerograph has been installed and has recorded many rockbursts after closure of the mines. The Strong-motion accelerograms recorded due to rockbursts are therefore used to obtain a Wood-Anderson synthetic seismogram for getting accurate and reliable values of the local magnitudes. Using 100 typical strong motion accelerograms of rockburst in the mines of Kolar Gold Fields, the magnitudes have been computed. The maximum magnitude obtained from several rockbursts during the period has been found to be 4.29. Attenuation relationships for peak horizontal ground acceleration for short distances and low magnitudes have been used for the development of the attenuation relationship. Two step multi regressions have been made by analyzing the decay of individual magnitude classes with distance using it with the whole data set. The models used in the present study is

$$\log(A)=c_1+c_2\,M-c_4\,b\log(X+e^{c_3 M}) \qquad (1)$$

where A is the peak ground acceleration, X is the hypocentral distance, M is the local magnitude $M_L$ and $c_i$'s are regression coefficients. The discussions of the attenuation characteristics of the ground motion at shorter distances and low magnitudes have been discussed. The comparison of strong ground motion at similar distances using relationships developed from higher magnitudes reveals the difference in the observed peak ground horizontal accelerations with respect to the strain levels involved in the generation of the respective earthquakes.

## OBJECTIVES

The objective of this study is to use strong motion data to estimate the Richter's local magnitude and obtain attenuation relationships for peak horizontal ground acceleration for short distances and low magnitude in the mines of the Kolar Gold Fields.

## RESEARCH ACCOMPLISHED

A rockburst is defined as the sudden and some times violent release of accumulated energy when a volume of rock is strained beyond its elastic limit (Scott et al., 1997). Bennett et al. (1997) defined rockbursts more broadly as "any type of stress-release phenomenon which has been induced by mining activity and which results in the emission of seismic signals." Rockburst is a common phenomenon since the beginning of the 20th century in the mines of the Kolar Gold Fields, which is situated in Karnataka. Rockbursts have caused severe damages to buildings on surface and underground mine workings in several instances. One of the important parameters needed to assess the damage potential and severity of a rockburst is its Richter's local magnitude. However, it has not been possible from the records of conventional seismographs due to saturation effect. The rockbursts had been monitored using a seismic monitoring system since 1979. The Strong Motion Accelerograph has been able to record several rockbursts as it is in the close vicinity of the mines of the Kolar Gold Fields, which has formed the basis for the estimation of their local magnitudes.

The Richter's local magnitude of a seismic event is defined in terms of the maximum amplitude of the record on a standard Wood-Anderson seismograph (WAS) with a natural period of 0.8s, damping ratio of 0.8 of critical damping, and static magnification equal to 2,800 (Richter 1958, 1935). If A is the maximum trace amplitude in millimeters on a WAS at an epicentral distance of R km, the local magnitude ML is given by $\log A - \log A_0(R)$, where $\log A_0(R)$ is a correction factor for the attenuation of seismic waves with distance. For distances less than about 25 km, the standard WAS normally goes out of scale even for small-magnitude events. Therefore, several investigators (e.g., Trifunac and Brune, 1970; Kannamori and Jennings, 1978; Luco,1982; Uhrhammer and Bolt, 1991; etc.) have proposed to evaluate the local magnitude by synthesizing the response of WAS using Strong Motion accelerograms. Due to short distances for recording of strong-motion data, their use for computation of magnitude has the advantage that they are not much influenced by the propagation path effects.

To estimate the local magnitude using synthesized WAS records, Trifunac (1991) proposed a method based on the frequency dependent attenuation function due to Trifunac and Lee (1990), which has been used and found to be more suitable in several applications (Lee, 1991; Gupta and Rambabu, 1993, etc.). However, Richter's original definition only has been considered suitable for the estimation of magnitudes in the present study.

India has faced several devastating earthquakes in the past. The largest of these have originated in the Himalayan plate boundary region, which has remained a region of great scientific and engineering interest. Not surprisingly, considerable data and earthquake related literature are available about the northern part of India. On the other hand very little seismological information is available about Peninsular India (PI); this is taken here as south of 24◦ N latitude. This situation is changing, in response to the three recent devastating events: the Khillari (30.9.1993), Jabalpur (22.5.1997), and Kutch (26.1.2001) shocks. But the available quantified information is so sparse, engineers presently face a daunting problem in estimating ground motion levels for future events in PI. The present paper is motivated by this need, to have a simple approach to understand attenuation in PI from the engineering point of view. First, the database available from Kolar region is briefly reviewed.

### Peninsular India

The region of the Indian subcontinent south of 240N latitude is taken here as Peninsular India (PI). This landmass is far away from the Himalayan collision zone, which is a well known boundary between the Indian and the Asian plates. Nonetheless, it is recognized that Cambay and Rann of Kutch in Gujarat are among the very active regions of India. Leaving this region and the Andaman-Nicobar Islands, the remaining part of continental PI has reliably experienced some 400 earthquakes in a period of 600 years. This number will be much larger if all instrumentally recorded shocks of small magnitudes were also included. The seismicity of PI, from a seismological perspective has been discussed in the past notably by Chandra (1977), and Rao (1984). A catalogue of earthquakes of magnitude $\geq 3$ for PI has been compiled by Guha and Basu (1993). Seeber et al. (1999) have studied the seismicity of PI with particular reference to Maharashtra. They concluded that between 1960 and 1990 the seismicity of PI showed a

threefold increase. This was the period during which industrial development also increased several fold in PI. Thus, engineers have to recognize that the looming seismic risk to man-made structures in PI is more than what was previously believed.

**Seismological Model**

In regions lacking strong motion data, seismological models (Boore 1983) are viable alternatives and are used worldwide for deriving attenuation relationships (Atkinson and Boore 1995, Hwang and Huo 1997, Toro et al. 1997). Singh et al (1999) have used a seismological model for estimating ground motion in parts of PI, but no specific attenuation equation has been proposed by them. The theory and application of seismological models for estimating ground motion has been discussed in detail by Boore (1983; 2003).

**The Methodology**

To use the strong-motion accelerograms for computing the local magnitude, it is necessary first to synthesize the response of the WAS with a given accelerogram as input excitation. The WAS can be modeled as a single-degree-of-freedom system with natural period Tn=0.8s, fraction of critical damping $\zeta$=0.8 and static magnification Vs=2800. Thus, the displacement record, $x(t)$, of a WAS to a horizontal ground acceleration, $\ddot{z}(t)$, can be obtained by solving the following equation of motion:

$$\ddot{x}(t) + 2\zeta\omega_n \dot{x}(t) + \omega_n^2 x(t) = -V_S \ddot{z}(t)\,, \qquad (2)$$

where $\omega_n = 2\pi/T_S$ is the angular natural frequency of WAS. This equation has been solved using the algorithm due to Nigam and Jennings (1968) to compute the Wood-Anderson seismogram and to get its peak amplitude, $A_{synthetic}$, in millimeters. Figure 1 shows a typical example of the computed WAS seismograms along with the corresponding input strong-motion accelerograms. The magnitudes from the strong motion records are estimated using $A_{synthetic}$ as follows:

$$M_L^{SM} = \log A_{synthetic} - \log A_0(R)\,, \qquad (3)$$

where $\log A_0(R)$ is the Richter correction factor for recording at distances other than 100 km, and basically represents the attenuation of seismic waves with distance.

Luco (1982) pointed out that the use of the Richter's correction factor $\log A_0(R)$ is, in general, not suitable to describe the attenuation of strong-motion amplitudes in the near field, particularly near 20 km. He, therefore, proposed a modification in the Richter attenuation function for smaller distances. Jennings and Kannamori (1983) also suggested similar modifications in $\log A_0(R)$ for small R, but their failure to include the local geological site effects in the analysis resulted in a biased estimate of this attenuation. However, Luco (1982) as well as Jennings and Kanamori (1983) have found these modifications to be insignificant at very short distances within about 5 km. Trifunac (1991) has shown that the peak values of the response of WAS may occur at different wave periods depending upon the source-to-site distance, magnitude, and the geological condition at a site. Therefore, using the frequency-dependent attenuation function due to Trifunac and Lee (1990) and the knowledge of the frequency where most energy is concentrated in the strong-motion as filtered by the WAS, he has defined an attenuation function $\mathrm{Att}(\Delta_0)$ in place of the Richter function, where $\Delta_0$ is the hypocentral distance. This new attenuation function represents much faster decay of strong ground motion than the Richter's function for distances up to 35 km. Trifunac (1991) has also explained that the difference between the original Richter attenuation factor and $\mathrm{Att}(\Delta_0)$ is expected to approach zero at very small distances. In view of the above, the Richter attenuation factor is expected to be quite suitable without any modification or correction, as all the strong-motion data used in the present study are recorded within about 3.5 km of the epicentral distance. Figure 2 shows a typical rockburst recorded by the Strong Motion Accelerograph.

**Results and Discussion**

The methodology described in the above has been applied to compute the local magnitudes for 100 typical strong motion records obtained due to rockbursts in the Kolar Gold Field mines. All these events are distributed in all the

quadrants and distributed along the strike direction, which is in the north-south direction. The computed maximum amplitude of the synthesized Wood-Anderson seismograms and the corresponding strong-motion magnitudes are for both longitudinal and transverse components. The final magnitude is taken as the arithmetic mean of the magnitudes for both the components.

The distributions of the computed mean magnitudes are in the range between 0.67 and 4.68. It is seen that the available single station recording is able to record completely the rockbursts with a threshold magnitude of 2.0. This data can thus be of some predictive use by studying the temporal variation of b-value (Nuannin, 2006).

**Attenuation**

To work out the attenuation relation, as a first step, a linear regression analysis was carried out considering a simple relation. The attenuation of PGA with the distance was regressed to obtain the decay factor as given in the following equation. Figure 3 shows the plot of weak ground acceleration of rockbursts versus distance.

$$log\ (A) = b\ log\ (X) + c, \quad (4)$$

where, $A$ is acceleration, $X$ is the hypocentral distance, and $b$ and $c$ are the regression coefficient.

Strong ground motions are usually recorded on three orthogonal components. In this study, we are dealing with horizontal components. One must decide how the horizontal components are to be treated. Various ways of treating a horizontal component are, the largest of the two components or both components or the mean of both components or vectorial combination of both components or a random selection of components.

A method of combining components should be taken into consideration to ensure consistency. However recent studies reveal to use geometric mean of two horizontal components. In this study, the geometric mean of two components (horizontal components) is calculated and used for the regression.

Data having hypocentral distances less than one is removed since there was a drastic change in PGA values for the recording having less than one kilometer hypocenter distance.

Dataset finally used for the regression is shown in Figure 3 below.

The events were classified according to the magnitude ranges as $2.00 < M < 2.20$, $2.20 < M < 2.40$, $2.40 < M < 2.60$, $2.60 < M < 2.80$, and $2.80 < M < 3.00$. The individual decay factor, i.e., $b$, is given in Table 1. The average value of the decay parameter $b$ came out to be 0.103

**Table 1. B and C values computed using equation 2.**

| Magnitude Range | B | c |
|---|---|---|
| $2.00 < M < 2.20$ | 0.0360 | 0.724 |
| $2.20 < M < 2.40$ | 0.1220 | 0.885 |
| $2.40 < M < 2.60$ | 0.1280 | 1.100 |
| $2.60 < M < 2.80$ | 0.0954 | 1.310 |
| $2.80 < M < 3.00$ | 0.1350 | 1.520 |

Next, a general multiple regression analysis was performed for the whole data set by assuming the basic regression model as

$$\log (A) = aM - b \log (X) + c, \quad (5)$$

where M is the magnitude and a, b and c are the regression coefficients. Using the above equation, the value of the decay parameter while considering the whole data set came out to be 0.1135 (0.0054), (The figure in the bracket is the standard error of coefficient) which is much closer to the average value of each earthquake, that is 0.1030.

The regression model thus selected for the attenuation relation is considered as follows:

$$\log (A) = c_1 + c_2M - c_4\, b \log (X + \exp[c_3M]), \quad (6)$$

Where $c_1$, $c_2$, and $c_3$ are the regression coefficients, and b is the decay parameter. When the decay parameter is fixed as per the regression using Equation 5, $c_1$, $c_2$, $c_3$, $c_4$ (and b) come out to be as shown in table below.

| Coefficients | Value | Standard Error |
|---|---|---|
| $c_1$ | -1.25430 | 0.0545000 |
| $c_2$ | 0.93770 | 0.0162000 |
| $c_3$ | -3.1000 | 31.766500 |
| $c_4$ | 34.9123 | 2040.3784 |
| $b$ | 0.11350 | 0.0269000 |

From the regression it is found that the coefficient $c_4$ has a relatively larger error, so the regression is again carried out by removing coefficient $c_4$ and leaving the decay parameter b (renamed B) unconstrained. The results obtained are given in the table below. Figure 4 shows a typical earthquake recorded 100 km from the source to sensor.

| Coefficients | Value | Standard Error |
|---|---|---|
| $c_1$ | -1.3489 | 0.0280 |
| $c_2$ | 1.0095 | 0.3820 |
| $c_3$ | 0.1272 | 0.0689 |
| $B$ | 0.1956 | 0.0183 |

Finally, the equation obtained is as follows:

$$\mathbf{\log(a) = -1.3489 + 1.0095M - 0.1956 \log (X + e^{0.1272M})}$$

where '***a***' is in cm/sec$^2$. Standard deviation computed is 0.20.

## CONCLUSIONS AND RECOMMENDATIONS

Local magnitudes have been computed for strong-motion accelerograms of seismic events in the mines of Kolar Gold Fields for the first time using the above procedure. The events selected are from an epicentral distance of 0.15 to 3.6 km from the place where the strong motion recorder is installed. The local magnitudes computed are in the range of 0.67 to 4.68.

The peak ground accelerations of rockbursts have been used to obtain the attenuation relation for short distances and low magnitudes. The final equation obtained is

$$\text{Log}(a) = -1.3489 + 1.0095M - 0.195 \log (X + \exp[0.1272M]),$$

where **a** is in cm/sec$^2$. Standard deviation computed is 0.20.

## ACKNOWLEDGEMENTS

The authors are thankful to the Director of NIRM for giving permission to publish this paper. The Department of Science and Technology is thanked for providing the strong-motion accelerograph. We also thank Dr. I. D. Gupta, Joint Director, CWPRS, Pune for assistance in the local magnitude computation and Prof. M. L. Sharma, IIT,Roorkee for assistance in the attenuation regression analysis.

## REFERENCES

Bennett, T.J. and McLaughlin, K.L. (1997). Seismic Characteristics and mechanism of rockbursts for use in seismic discrimination, in *Proceedings of the fourth Symposium on Rockburst and Seismicity in Mines*, RASiM4, Poland, 61–66.

Chandra, U. (1977). Earthquakes of Peninsular India-A Seismotectonic Study, *Bull. Seismol. Society Am*. 67: (5), 1387–1413.

Guha, S. K., and Basu, P. C. (1993). Catalogue of earthquakes (M ≥ 3.0) in Peninsular India, 1993, Atomic Energy Regulatory Board, Tech. Document No. TD/CSE-1, 1–70.

Gupta, I. D. and Rambabu, V. (1993). Use of strong-motion accelerograms to evaluate the magnitudes of some significant earthquakes in the Koyna Dam Area, India, *Bull. Indian Soc.Eart. Tech.* 30: 4, 143–151.

Jennings, P.C. and Kannamori, H. (1983). Effect of distance on local magnitudes found from strong motion records, *Bull.Seis.Soc.Am.* 73: 1, pp.265–280.

Kanamori, H. and Jennings, P.C. (1978). Determination of local magnitude, ML, from strong-motion accelerograms. *Bull.Seis. Soc.Am*, 68: 471–485.

Lee, V.W. (1991), A note on computed magnitude MLSM from strong motion records. *Ins.Jour. of Soil Dyn. And Earthq. Eng.* 10: (1), 10–16.

Luco, J.E. (1982). A note on near source estimates of local magnitude. *Bull.Seis. Soc.Am*. 72: 941–958.

Nigam, N. C. and Jennings, P. C. (1968). Digital calculation of response spectra from strong-motion earthquake records. *Research Report, California Institute of Technology, Pasadena, USA.*

Rao, B. R., and Rao, P. S. (1984). Historical seismicity of peninsular India, *Bull. Seismol. Society Am.* 74: (6), 2519–2533

Richter, C. F. (1935). An instrumental earthquake scale, *Bull.Seis. Soc.Am.* 25: 1–32.

Richter,C. F. (1958). *Elementary Seismology*, Freeman and Co., San Francisco,USA.

Scott, D. F., Williams, T. J. and Friedel, M. J (1997). Investigation of a rockburst site, Sunshine Mine, kellog, Idaho, in *Proceedings of the fourth Symposium on Rockburst and Seismicity in Mines*, RASiM4,Poland, pp 311–315.

Seeber, L., Armbruster, J. G., and Jacob, K. H. (1999). Probabilistic assessment of seismic hazard for Maharashtra, Govt. of Maharashtra, Unpublished Report .

Trifunac, M.D. and Brune, J.H. (1970). Complexity of energy release during the Imperical Valley, California, earthquake of 1940. *Bull.Seis. Soc.Am*. 60: 137–160.

Trifunac, M.D. and Lee, V.W. (1990). Frequency dependent attenuation of strong earthquake ground motion. *Int. Jour. Soil Dynamics and Earthquake Engg.* 9: (1), 3–15.

Trifunac, M.D. (1991a). MLSM. *Int. Jour. Of Soil Dyn. And Earthq.Eng.* 10: (1), 17–25.

Trifunac, M.D. (1991b). A note on the difference in magnitudes estimated from strong motion data and from Wood-Anderson seismometer. *Int. Jour. of Soil Dyn. And Earthq.Eng.* 10: (8), 423–428.

Uhrhammer, R.A. and Bolt, B.A. (1991). " the Seismic magnitude of the 1989 Loma Prieta Main Shock determined from Strong-Motion Records", *Bull.Seis.Soc.Am.* 81: 5, pp 1511–1517.

Boore,D.M. and W.B. Joyner (1982). The empirical prediction of ground motion, *Bull.Seism.Soc.Am.* 72, S43–S60.

Fukushima, Y. and T. Tanaka (1990). A new attenuation relation for peak horizontal acceleration of strong earthquake ground motion in Japan, *Bull.Seism.Soc.Am*. 80: 757–783.

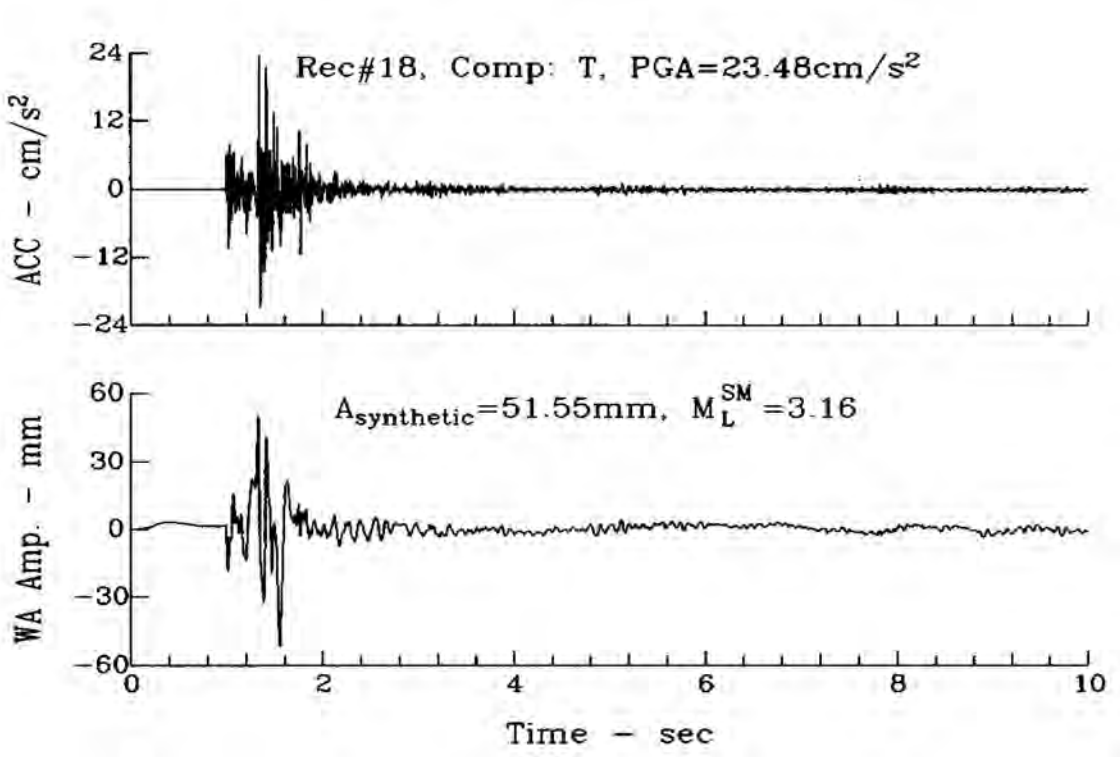


**Figure 1. Typical examples of Wood-Anderson records synthesized from strong- Motion Accelerogram**

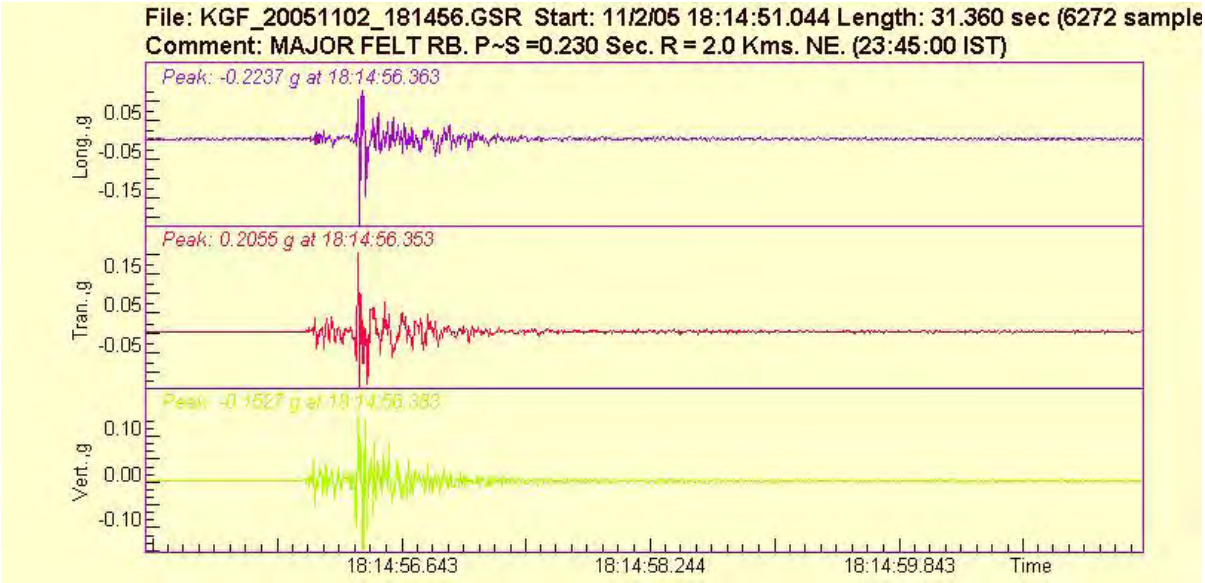


**record.**

**Figure-2. Typical rockburst recorded by strong motion accelerograph**

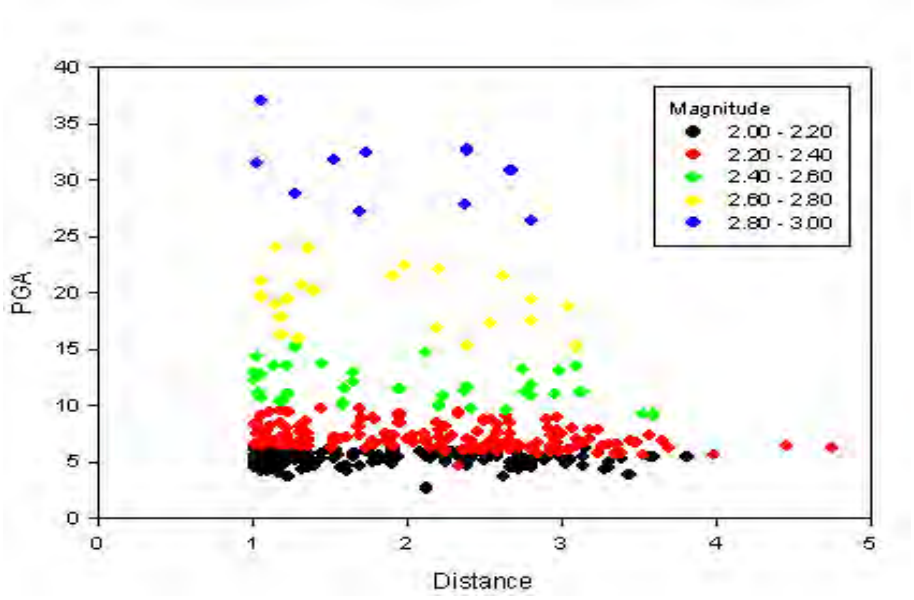


**Figure 3. Plot of peak ground acceleration of rockbursts versus distance.**

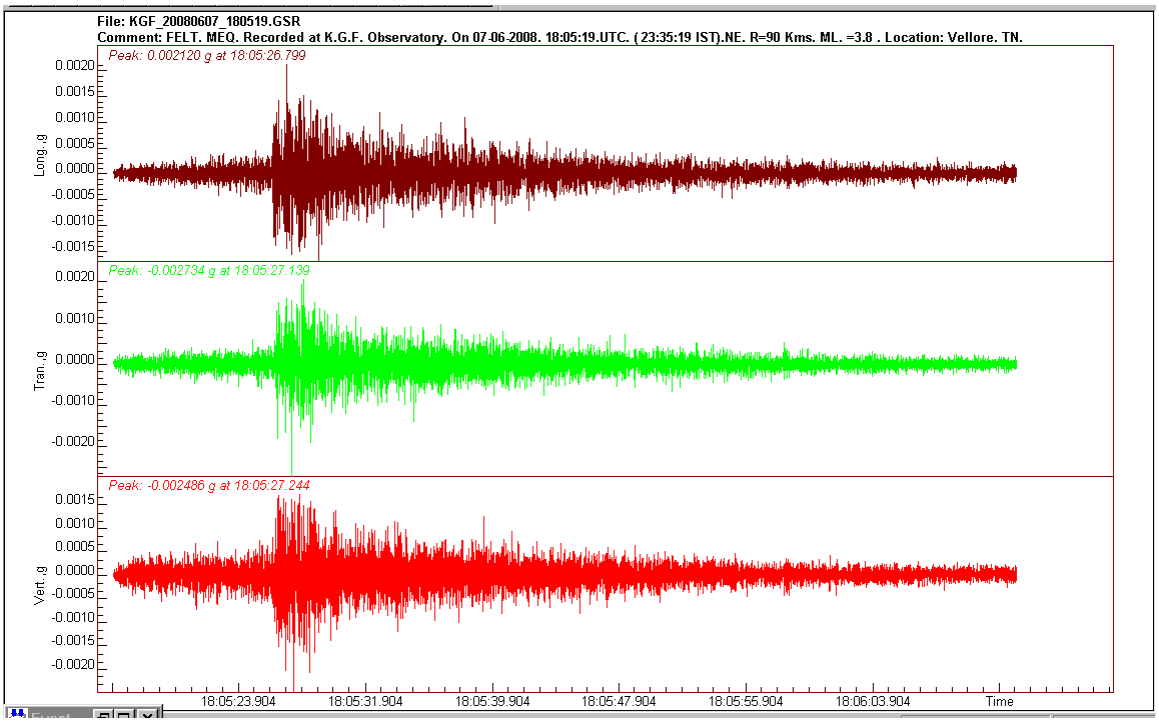


**Figure-4. Typical earthquake recorded by Strong Motion Accelerograph**

# SHEAR VELOCITY STRUCTURE IN NE CHINA AND CHARACTERIZATION OF INFRASOUND WAVE PROPAGATION IN THE 1-210 KILOMETER RANGE

Brian W. Stump[1], Rong-Mao Zhou[2], Tae-Sung Kim[1], Yun-Tai Chen[3], Zhi-Xian Yang[3], Robert B. Herrmann[4], Relu Burlacu[5], Chris Hayward[1], and Kristine Pankow[5]

Southern Methodist University[1], Los Alamos National Laboratory[2], Institute of Geophysics, China Earthquake Administration[3], Saint Louis University[4], and University of Utah Seismograph Stations[5]

Sponsored by Air Force Research Laboratory

Contract No. FA8718-05-C-0020
Proposal No. BAA05-38

## ABSTRACT

We continued the operation of the Southern Methodist University-Institute of Geophysics, China Earthquake Administration (SMU-IGPCEA) broadband seismic network through May 2008 using Program for the Array Seismic Studies of the Continental Lithosphere (PASSCAL) instrumentation. The operating network included three stations northwest of Beijing and 10 stations in Xiuyan, Liaoning Province, NE China. At the end of May, the PASSCAL instrumentation was returned to the U.S. During the 5.5-year operation, we collected approximately 600 Gb of miniSEED data. Most of the data have been archived at the Incorporated Research Insitutes for Seismology (IRIS) data center. This high-quality dataset has already provided us the opportunity to study the detailed velocity structure beneath the Huailai Basin and Haicheng in NE China using both teleseismic and regional signals. We are expanding our joint inversion of teleseismic receiver functions and surface wave phase velocities for crustal shear velocity structure from the Huailai Basin to the Huabei area using data from SMU-IGPCEA broadband seismic network with additional data provided by 48 broadband seismic stations in this region. Preliminary results show that the phase velocities under this region range from 3.2 to 4.0 km/sec over a period range of 10–90 sec. The joint inversion study will allow us to quantify the spatial variability of the shear velocity structure under this broader region in detail providing a better characterization of regional propagation paths.

Infrasound gauges originally destined for China were installed in three arrays in Utah. Data from these arrays are telemetered in real-time to the University of Utah. Each array consists of four infrasound sensors with approximately 100 m separation sampled at 100 samples/s. In the summer of 2007, a consortium participated in the design and installation phases of a 4-week experiment in northern Utah to record four rocket motor detonations at the Utah Test and Training Range at Hill AFB. These blasts were recorded on the existing dense distribution of Utah regional seismic stations, six infrasound arrays, the regional EarthScope transportable array (TA) stations, and a temporary field deployment of PASSCAL instruments with infrasound microphones distributed from 200 m to more than 200 km from the source. Balloon launches of rawinsondes were conducted near the shot time and tracked in order to experimentally quantify the temperatures and winds of the shallow atmosphere. The distance range of the observations includes the shadow zone where standard atmospheric models predict no infrasound arrivals (McKenna, 2005). The Utah infrasound network recorded infrasound signals in this shadow zone from the four rocket motor detonations. The preliminary analysis of observed infrasound signals shows arrivals at local (<100 km) and regional distances (140–210 km). Group velocities of local arrivals are estimated around at 350 m/s while those of regional arrivals are relatively slower (300 to 280 m/sec). The mean phase velocity in the local distance range is slightly slower (358.7 ±9.8 m/sec) compared to that at the regional distance range (385.5 ±7.6 m/sec). The Utah observations also document the focusing of infrasound energy around 50 km. These observed infrasound arrivals and amplitude anomalies at local distances are successfully modeled using the parabolic equation (PE) with the shallow atmosphere quantified by the balloon data. The PE results confirm that a shallow inverted atmospheric layer exists to a height of 1 to ~2 km and functions as a duct that traps infrasound energy at local distances and focuses energy at around 50 km.

## OBJECTIVES

The primary goal of the collaborative study between the SMU and the IGPCEA (formerly IGCSB) is to develop a database of seismic events in NE China, to refine crust and upper mantle structure in Yanqing-Huailai Basin and Haicheng area, to understand source characterization of natural and human-induced events, and to separate source and propagation path effects at regional distances.

A second objective of this project is the instrumental quantification of seismic and infrasound signals observed at regional distances. The focus in this case is on manmade and natural sources that generate both infrasound and seismic waves. Initially, plans called for infrasound gauges to be co-located with the seismometers deployed in NE China. After acquisition of the infrasound gauges, the deployment was made in the U.S., collocating infrasound gauges with seismometers operated in conjunction with University of Utah Seismograph Stations. These data are being used to assess atmospheric propagation path effects from known explosion sources.

## RESEARCH ACCOMPLISHED

### NE China

We continued the operation of the SMU-IGPCEA broadband seismic network through May 2008 using PASSCAL instrumentation. The deployment of the broadband seismic network operated by SMU and IGPCEA since November 2002 included 14 stations in and around Beijing, Huabei Province and 10 stations in the Haicheng area, Liaoning Province, China (Zhou et al., 2006). At the end of May the PASSCAL instrumentation was returned to the US. During the 5.5-year operation time period, we collected approximately 600 Gb of good-quality miniSEED data. Most of the data has been archived at the IRIS data center. This high-quality dataset has already provided us the opportunity to study the detailed velocity structure beneath Huailai Basin and Haicheng in the NE China area, using both teleseismic and regional signals (Zhou et al., 2006).

We are expanding our joint inversion of teleseismic receiver functions and surface wave phase velocities for crustal shear velocity structures from the Huailai Basin to the Huabei area using data from the SMU-IGPCEA broadband seismic network, supplemented by data provided by 48 broadband seismic stations that make up the Huabei Seismic Network, as illustrated in Figure 1. The new seismic work that is discussed in this paper focuses on preliminary analysis of this new dataset.

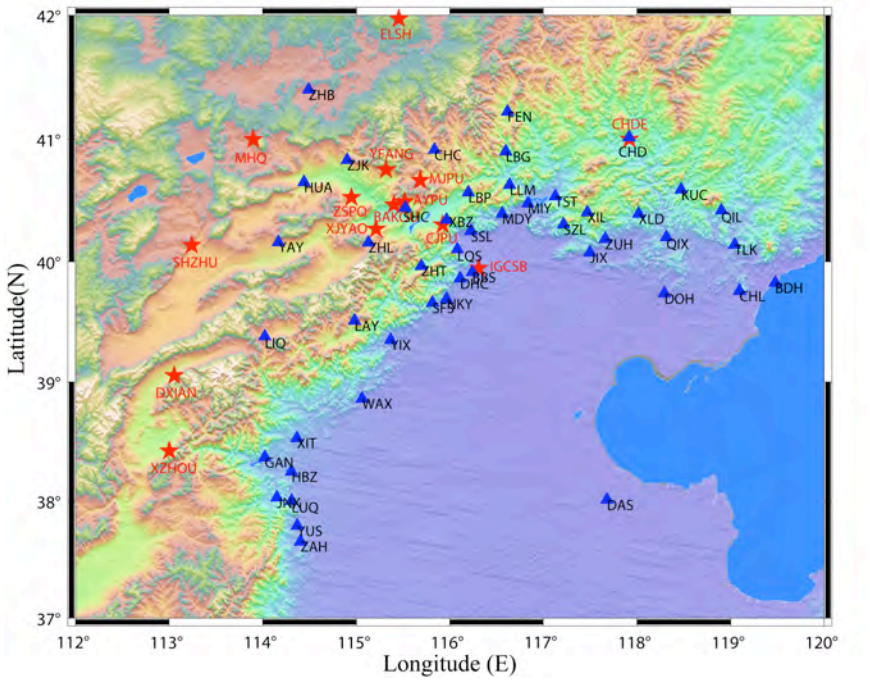


**Figure 1. Topographic map of the Huabei area, with broadband seismic stations (blue triangles: Huabei Seismic Network; red stars: SMU-IGPCEA stations in this region).**

Twenty-one teleseismic events with great circle epicentral distances in the range of $30^{o}$ to $80^{o}$ from 2004 to 2005 have been chosen for receiver function and surface wave analysis. Source parameters of these events were obtained from the Preliminary Determination of Epicenters (PDE) bulletins provided by the United States Geological Survey (USGS) National Earthquake Information Center (NEIC) and are listed in Table 1. Figure 2 is the map of the 21 teleseismic events (red dots).

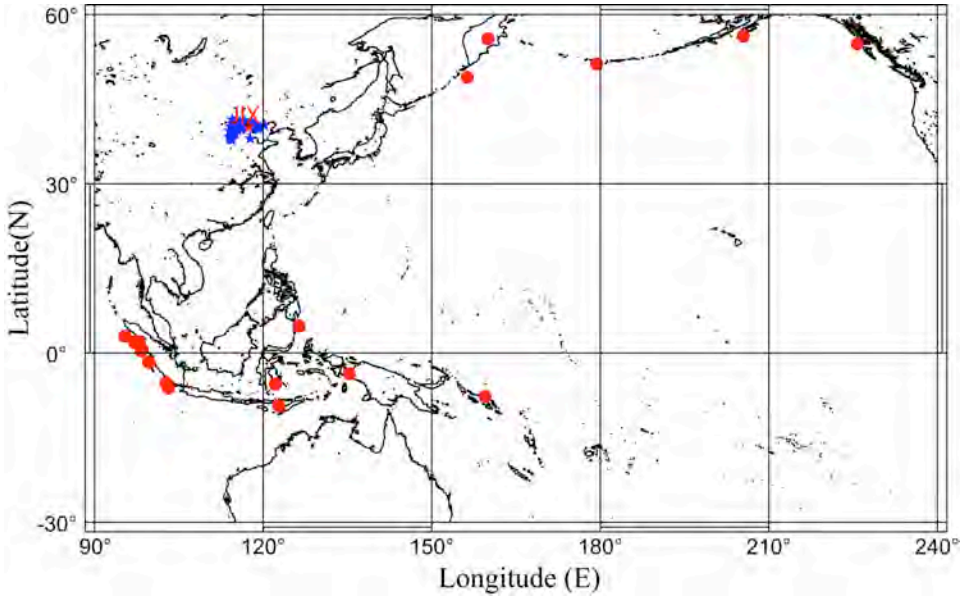


**Figure 2. Map of event locations (red dots) and broadband stations (stars).**

**Table 1. List of event parameters**

| Event Code | Date (Y-M-D) | Time (hhmmss.mm) | Latitude (°) | Longitude (°) | Magnitude | Depth (km) |
|---|---|---|---|---|---|---|
| 2004039 | 2004-02-08 | 085851.80 | -3.66 | 135.34 | 6.9 | 25 |
| 2004107 | 2004-04-16 | 215705.41 | -5.21 | 102.72 | 6.0 | 44 |
| 2004114 | 2004-04-23 | 015030.22 | -9.36 | 122.84 | 6.7 | 65 |
| 2004162 | 2004-06-10 | 151957.75 | 55.68 | 160.00 | 6.9 | 188 |
| 2004180 | 2004-06-28 | 094947.00 | 54.80 | -134.25 | 6.8 | 20 |
| 2004353 | 2004-12-18 | 064619.87 | 48.84 | 156.31 | 6.2 | 11 |
| 2005022 | 2005-01-22 | 203017.35 | -7.73 | 159.48 | 6.5 | 29 |
| 2005046 | 2005-02-15 | 144225.85 | 4.76 | 126.42 | 6.6 | 39 |
| 2005050 | 2005-02-19 | 000443.59 | -5.56 | 122.13 | 6.5 | 10 |
| 2005089 | 2005-03-30 | 161941.10 | 2.99 | 95.41 | 6.4 | 22 |
| 2005093 | 2005-04-03 | 005921.42 | 0.37 | 98.32 | 6.0 | 30 |
| 2005093-2 | 2005-04-03 | 031056.47 | 2.02 | 97.94 | 6.3 | 36 |
| 2005099 | 2005-04-09 | 151627.89 | 56.17 | -154.52 | 6.0 | 14 |
| 2005100 | 2005-04-10 | 102911.28 | -1.64 | 99.61 | 6.7 | 19 |
| 2005100-2 | 2005-04-10 | 172439.40 | -1.59 | 99.72 | 6.4 | 30 |
| 2005106 | 2005-04-16 | 163803.90 | 1.81 | 97.66 | 6.4 | 31 |
| 2005130 | 2005-05-10 | 010905.10 | -6.23 | 103.14 | 6.4 | 17 |
| 2005134 | 2005-05-14 | 050518.48 | 0.59 | 98.46 | 6.8 | 34 |
| 2005139 | 2005-05-19 | 015452.85 | 1.99 | 97.04 | 6.9 | 30 |
| 2005165 | 2005-06-14 | 171016.64 | 51.23 | 179.41 | 6.8 | 51 |
| 2005186 | 2005-07-05 | 015202.95 | 1.82 | 97.08 | 6.8 | 21 |

Receiver functions were extracted from all 21 events in Table 1 and Figure 2. Station JIX recorded 18 of 21 events, and the radial component receiver functions with Gaussian parameter, $\alpha = 1.0$, at JIX are presented in Figure 3 to illustrate the quality of the data and resulting receiver functions.

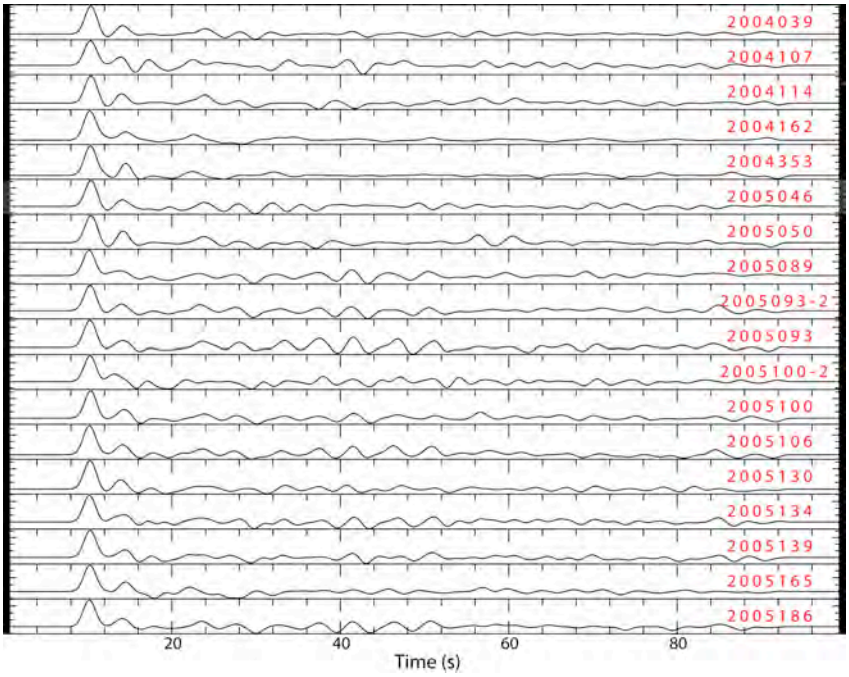


**Figure 3. Receiver functions from 18 events with Gaussian window parameters $\alpha = 1.0$, at station JIX.**

The phase velocities under this region are obtained using the fundamental mode Rayleigh waves extracted from raw data and the technique described by McMechan and Yedlin (1981). Figure 4 presents the averaged phase velocities in this region from analyzed events, and it ranges from 3.1 to 4.0 km/sec over period range of 10–90 sec.

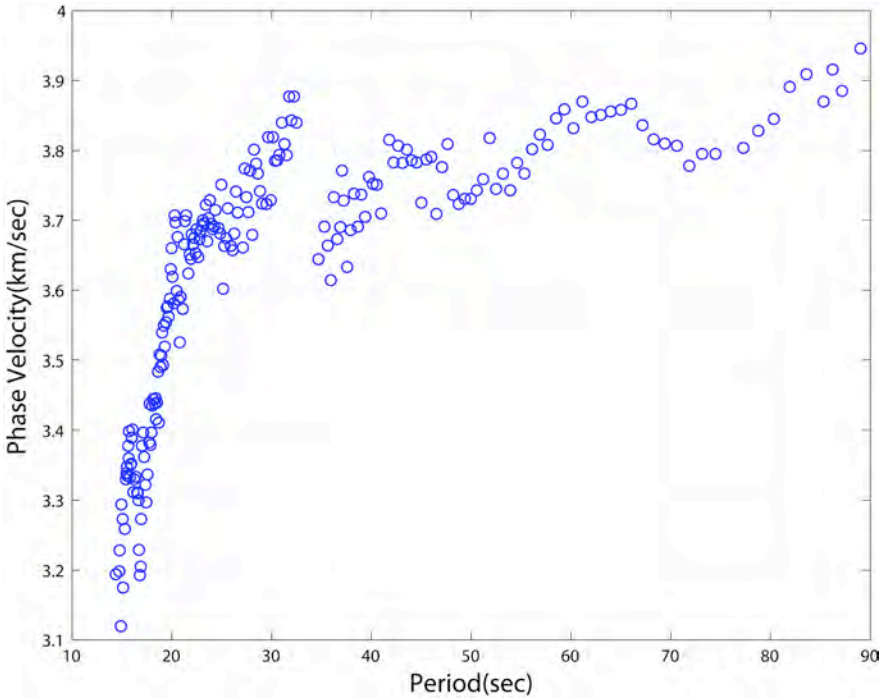


**Figure 4. Averaged phase velocities in this region.**

Work continues expanding the database from this new set of Chinese stations as well as the development of crust and upper mantle models based upon the new data source.

**Infrasound**

In the summer of 2007, a consortium participated in a 4-week experiment in northern Utah, designed to record regional seismo-acoustic signals including rocket motor detonations at the Hill AFB Utah Test and Training Range (UTTR) (Stump et al., 2007a; Stump at al., 2007b). The dense distribution of existing seismic stations, which is part of the regional network operated and maintained by the University of Utah Seismograph Stations (UUSS) and the temporarily installed seismic stations in Utah under the EarthScope National Science Foundation (NSF) project, were augmented 14 single acoustic stations and 6 acoustic arrays that our consortium deployed (Figure 5), including the 3 acoustic arrays supported under this contract. Equipment supplied by the PASSCAL program was used to make the infrasound measurements. This deployment of seismic and acoustic instruments at UTTR gives a unique opportunity to study the generation and propagation of local-to-regional seismic and low frequency acoustic energy from shallow sources. The seismic and acoustic stations were distributed in the 200 m to 210 km distance range. Rawinsondes were launched to measure the variation in temperature, wind speed, and wind direction from the surface up to 20 km.

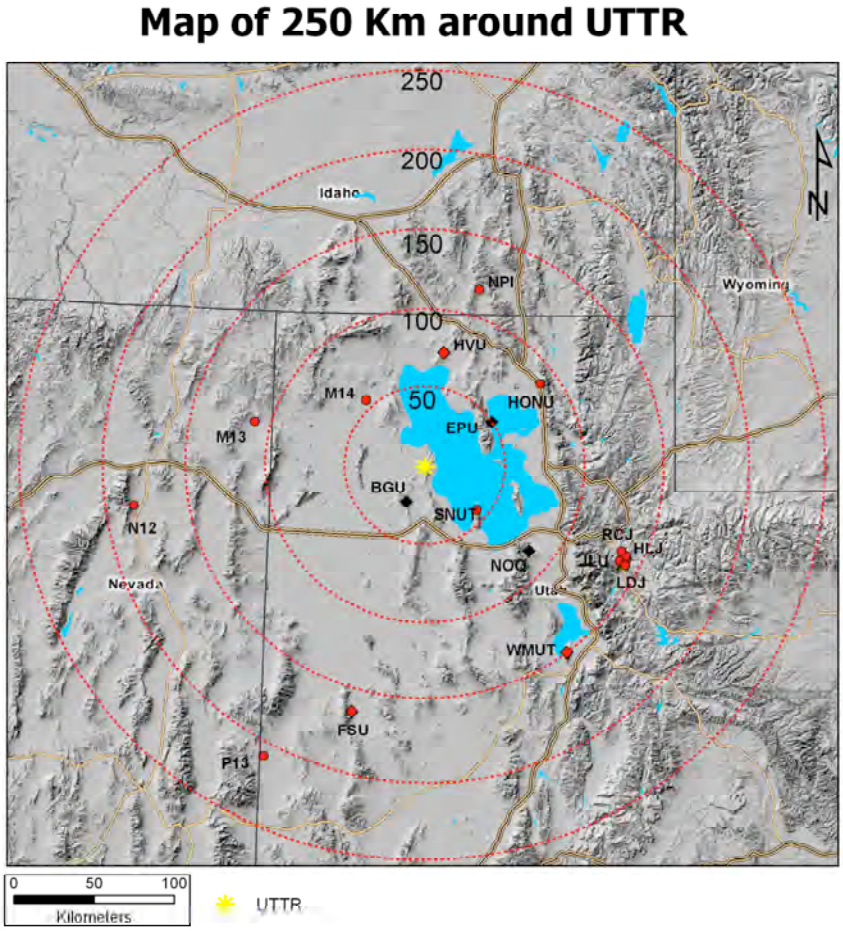


**Figure 5. Map of seismo-acoustic station distribution in Utah. The yellow star is UTTR. Solid black diamonds are permanent infrasound arrays supported under this project, red diamonds are temporary infrasound arrays, and red circles are locations of single infrasound gauges.**

During the 4-week deployment we recorded four rocket motor detonations (~50,000 TNT equivalent each), with duration magnitudes between 1.8 and 2.1 (UUSS). One example of a typical seismo-acoustic recording illustrates clear seismic arrivals with acoustic signals at station FSU (Figure 6). From the collocated seismo-acoustic sensors, it

was observed that rocket motor detonations generated air-to-ground coupling even at the maximum distance range of our experiment (~210 km).

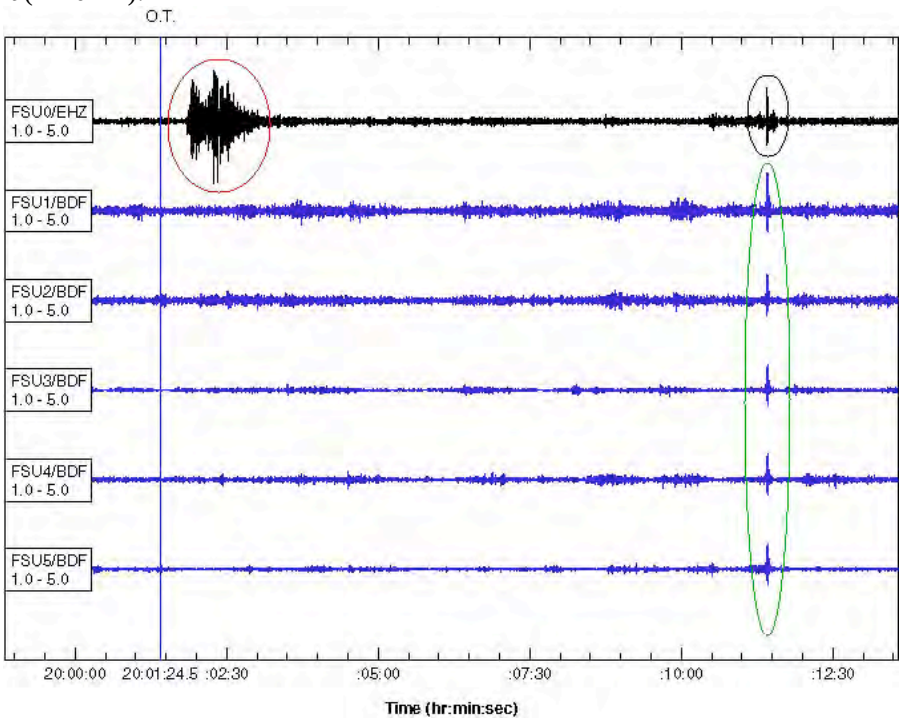


**Figure 6. Seismo-acoustic recordings at FSU from the first recorded rocket motor detonation on August 1, 2007, 20:01:24.5. Seismic signals (red circle) are illustrated with acoustic signals (green circle) as well as air-to-ground coupled seismic signal (black circle).**

Comparison of amplitude and waveforms at BGU from the four explosions illustrates that the seismic signals are repeatable while acoustic signals are not, even though the sizes and locations of sources are nearly the same (Figure 7). Waveforms at other stations are consistent with those from BGU. These observations suggest that the controlling factors on the infrasound amplitudes and waveforms are more than the size and location of sources and may require a time-varying atmospheric propagation path.

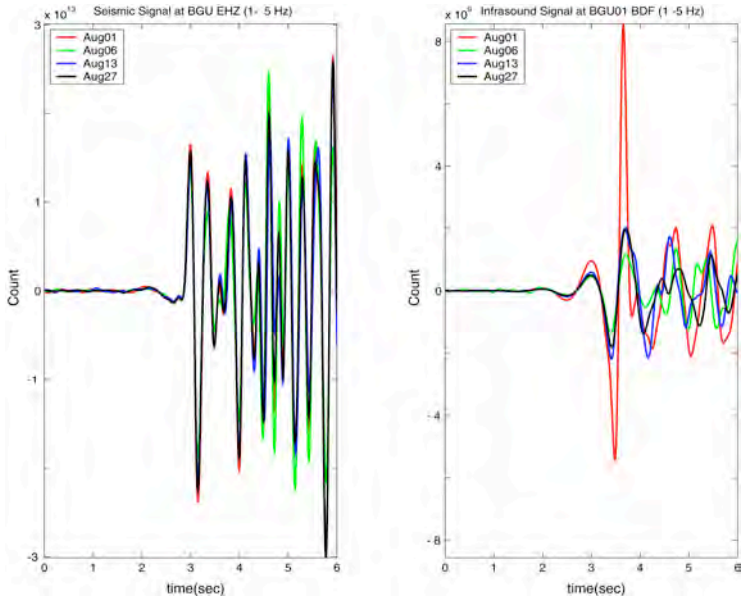


**Figure 7. Seismic signals (1-5 Hz) from the four detonations (left) are compared with acoustic signals (1–5 Hz, right) recorded at BGU.**

Record sections of acoustic signals from the four explosions are reproduced in Figure 8. We classify the infrasonic arrivals into two groups: (1) arrivals at a distance less than 100 km (local arrivals) and (2) those between 150 and 210 km (regional arrivals).

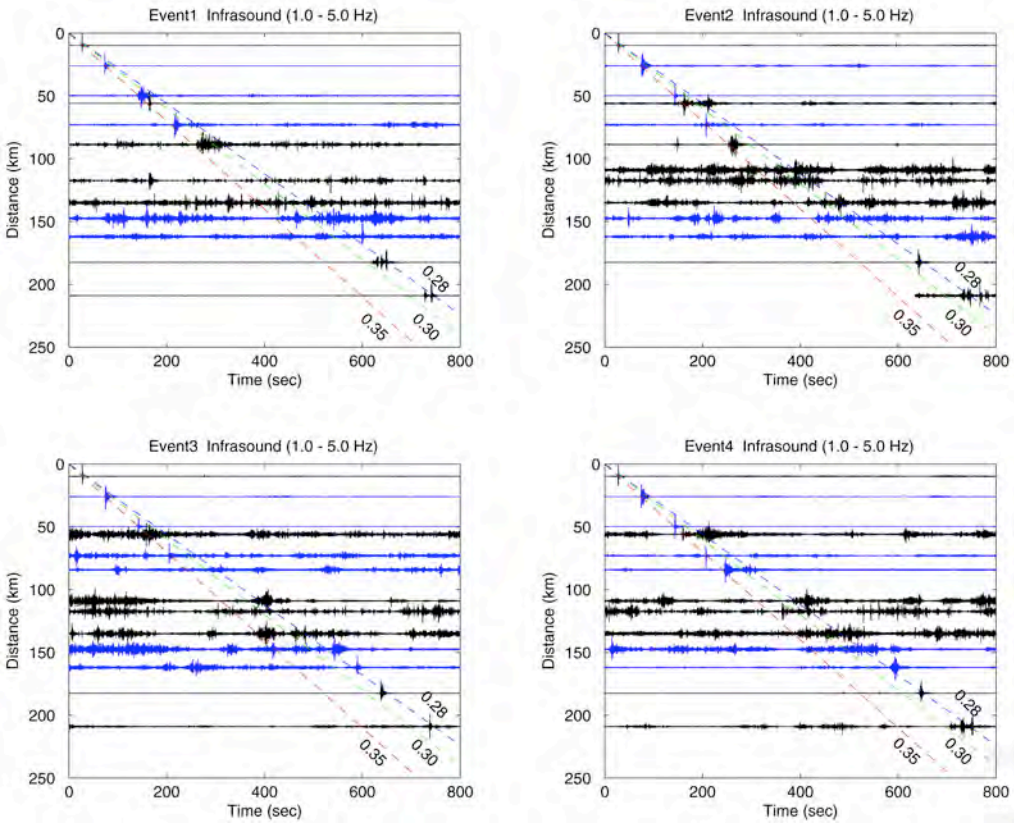


**Figure 8. Acoustic record section for the four detonations. Record sections consist of single stations (black) and array data (blue).**

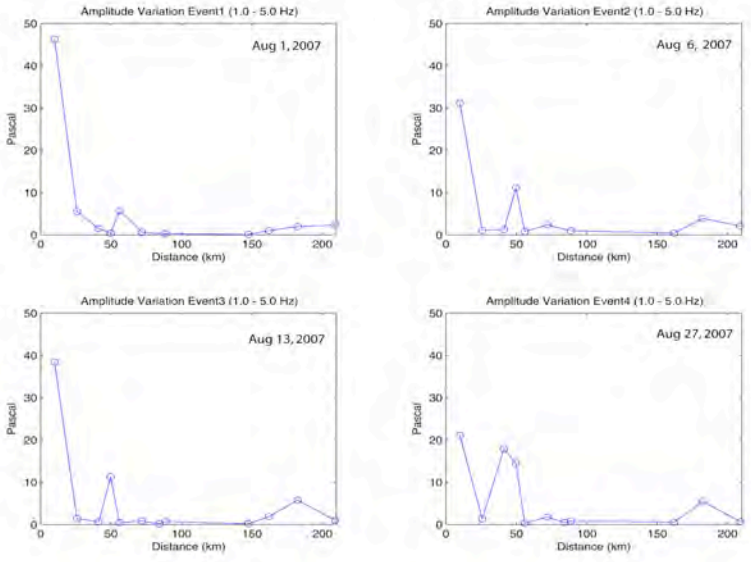


**Figure 9: Range effects of acoustic signals (1–5 Hz) from the four detonations. Maximum amplitude in the 1–5 Hz band is plotted.**

Estimates of group velocity at local distances are near 350 m/sec while those of regional distances vary from 280 to 300 m/sec. Using the acoustic arrays, mean phase velocity in the local distance range is 359 ± 9.8 m/sec, which is near the speed of sound at the surface, while that of the regional distance is 386 ± 7.6 m/sec, consistent with turning rays from the stratosphere or thermosphere. The backazimuth mean error estimate for all the explosions using data from the local distance range was 2.4$^{o}$, while that using regional distance data was 5.5$^{o}$. Figure 9 illustrates strong focusing and defocusing effects as a function of range. Higher amplitudes are observed at around 50 km although the exact location of the focus changes by as much as 10 to 20 km from day to day and thus can strongly impact the absolute amplitudes at a particular station for the four explosions.

The PE modeling method (Lingevitch et al., 2002) using local atmospheric profiles was used to investigate infrasound arrivals and amplitude variations in the local distance range. The software used for the modeling was InfraMAP (Norris and Gibson, 2006). The local atmospheric file was obtained using balloon launches of rawinsondes from an island in the Great Salt Lake at or near the detonation time. Figure 10 illustrates different 1-D velocity models that change as a function of propagation direction and time based on the empirical atmospheric data for the four days when the explosions were conducted.

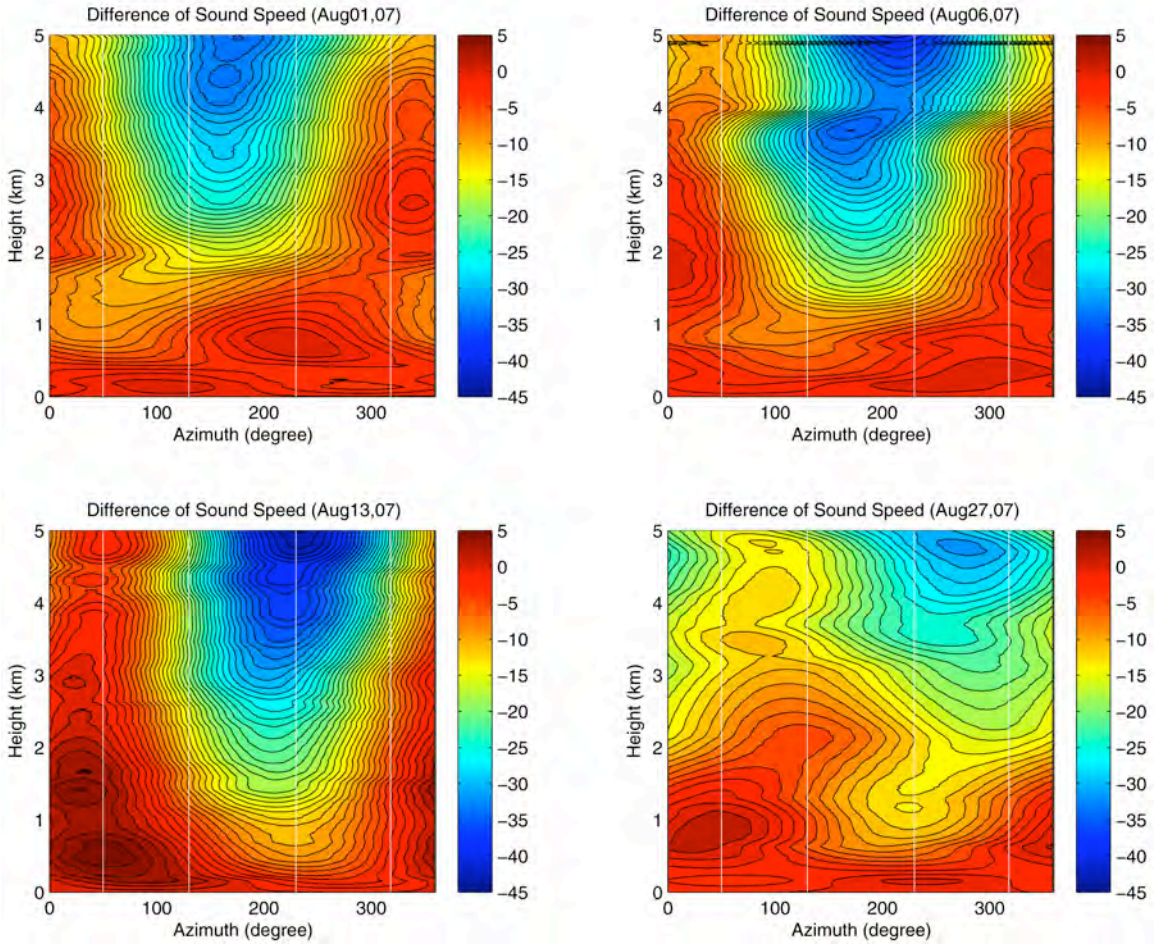


**Figure 10. Azimuthal and temporal variation of local atmospheric structure for the four explosion days based on rawinsonde launched at of near the explosion time. The color scale represents the difference between the speed of sound at a specific height and that of surface ($C_h$-$C_0$, unit: m/sec).**

PE modeling was performed at three different frequencies (0.25, 1.0, and 3.0 Hz) using the source-station specific directions and the1-D local atmospheric structure along that direction based on the rawinsonde data. One example of these PE solutions for the August 6, 2007, 20:00:00 hour GMT shows that there is a shallow duct (~2 km) for acoustic energy along the source to receiver azimuth of 45$^{o}$, while the calculations along the other two directions

(113° and 288°) do not predict trapped energy (Figure 11). These modeling results are consistent with the ranges and azimuths along which infrasound arrivals were identified in the local distance range, out to 100 km. For the three other shots, PE modeling produced predictions based on energy trapped in a shallow inverted layer between 1 and 2 km in height that were consistent with observations on these other days as well. The PE modeling suggests that observed acoustic arrivals at local distances (<100 km) and focusing of energy are related to the trapped acoustic energy between the surface and the shallow inverted atmospheric layer. For modeling the regional arrivals (150–210 km), the PE method and ray tracing with the G2S profile will be performed in a future study.

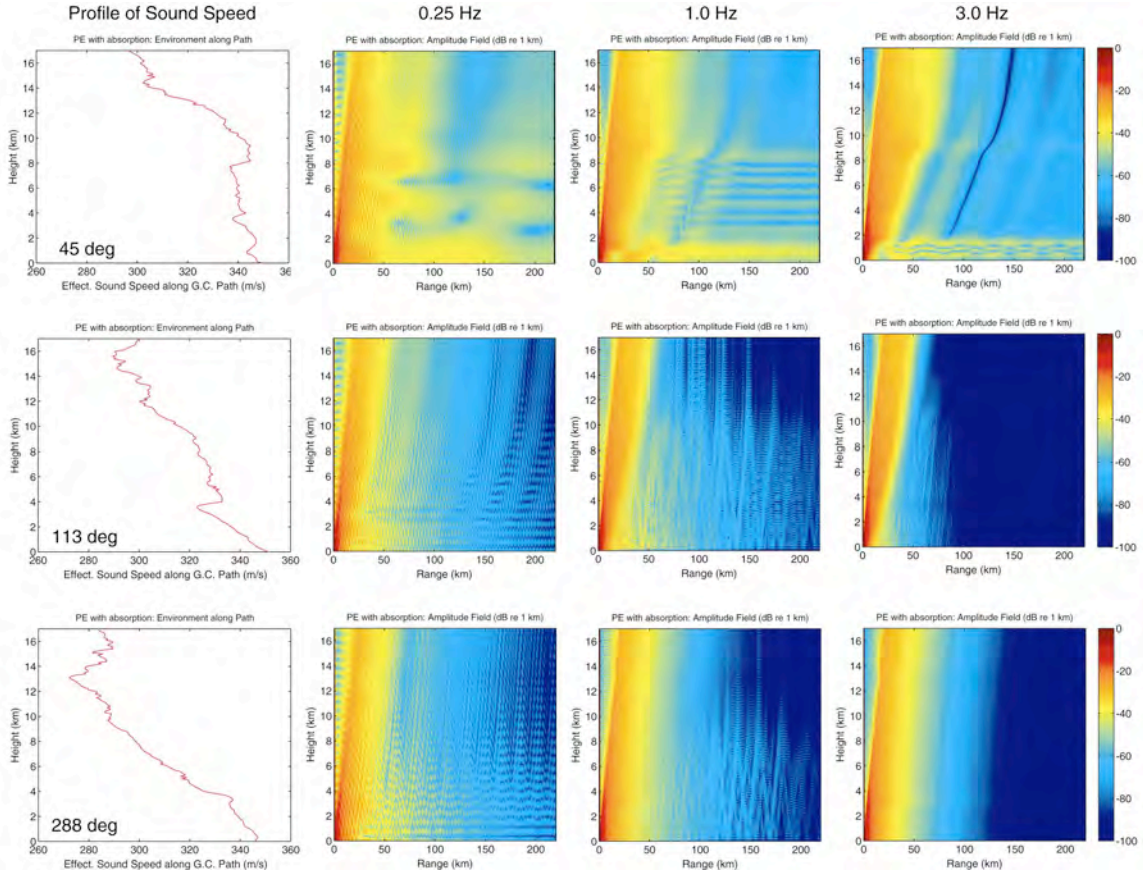


**Figure 11. One example of PE modeling for August 6, 2007, 20:00:00 hour. Sound profiles along the three azimuths of 45°, 113°, and 288° are displayed to the left. Energy estimates from the PE calculation as a function of range at frequencies of 0.25, 1, and 3 Hz are plotted to the right.**

## CONCLUSIONS AND RECOMMENDATIONS

### NE China

Seismic data from the Huabei Seismic Network in NE China are being used to improve crust and upper mantle models for NE China, supplementing data gathered from portable instrumentation deployed in the region as part of this project. Analysis of teleseismic body and surface waves from 21 events recorded by this network has been completed with the extraction of teleseismic receiver functions and phase velocity estimates across the network. Work continues to include this new data source in estimating the crust and upper mantle structure in the region.

### Infrasound

Preliminary data analysis of regional infrasound observations from four large explosions shows three major results: (1) Infrasound arrivals at local (<100 km) and regional distances (150–210 km) with group and phase velocity estimates constraining the propagation paths-local arrivals (<100 km) are related to the propagation in the near

surface and regional arrivals (150–210 km) are turning rays at higher altitude. (2) There were significant differences in amplitude and signal complexity of the observed seismo-acoustic signals for the four identical explosions detonated on four different days. (3) Modeling based on the PE method, using local atmospheric profiles based on empirical data, predicts trapped acoustic energy, which explains the infrasound arrivals and focusing of energy at local distance range (<100 km).

## REFERENCES

Lingevitch, J. F., M. D. Collins, D. K. Dacol, D. P. Drob, J. C. W. Rogers, and W. L. Siegmann (2002). Parabolic equations for atmospheric waves, research articles in *NRL Review, Acoustics*.

McKenna, M. H. (2005). Infrasound wave propagation over near-regional and tele-infrasonic distances, Ph. D thesis. Southern Methodist University.

McMechan, G. A. and M. J. Yedlin (1981). Analysis of dispersive waves by wave field transformation, *Geophysics* 46**:** 869–874.

Norris D. and R. Gibson (2006). User's guide for InfraMAP (Infrasound Modeling of Atmospheric Propagation), Version 5.1, BBN technical memorandum W2078.

Stump, B., R. Burlacu, C. Hayward, J. Bonner, K. Pankow, A. Fisher, and S. Nava (2007a). Seismic and infrasound energy generation and propagation at local and regional distances: Phase I—Divine Strake experiment, *Proceedings of the 29th Monitoring Research Review: Ground-Based Nuclear Explosion Monitoring Technologies*, LA-UR-07-5613, Vol. 1, pp. 674–683.

Stump, B., R. Burlacu, C. Hayward, K. Pankow, S. Nava, J. Bonner, S. Hock, D. Whiteman, A. Fisher, T. S. Kim, R. Kubacki, M. Leidig, J. Britton, D. Drobeck, P. O'Neill, K. Jensen, K. Whipp, G. Johnson, P. Roberson, R. Read, R. Brogan, and S. Masters (2007b). Seismic and infrasonic energy generation and propagation at local and regional distances: Phase I—Divine Strake experiment, Air Force Research Laboratory, AFRL-RV-HA-TR-2007-1188.

Zhou, R.-M., B. W. Stump, R. B. Herrmann, Y.-T. Chen, and Z.-X. Yang (2006). Broadband network operation and shear velocity structure beneath the Yanqing-Huailai Basin, NW of Beijing, in *Proceedings of the 28th Seismic Research Review: Ground-Based Nuclear Explosion Monitoring Technologies*, LA-UR-06-5471, Vol. 1, pp. 341–350.

# A 3D TOMOGRAPHIC MODEL OF SOUTH CENTRAL ASIA BASED ON Pn TRAVEL TIMES FROM GT EVENTS

Christopher J. Young[1], Sanford Ballard[1], James R. Hipp[1], Marcus C. Chang[1], Glenn T. Barker[1], Michael L. Begnaud[2], W. Scott Phillips[2], Lee K. Steck[2], and Charlotte A. Rowe[2]

Sandia National Laboratories[1] and Los Alamos National Laboratory[2]

Sponsored by National Nuclear Security Administration

Contract Nos. DE-AC04-94AL8500 and DE-AC52-06NA25396.

## ABSTRACT

Increasingly, nuclear explosion monitoring is focusing on detection, location, and identification of small events recorded at regional distances. Because Earth structure is highly variable on regional scales, locating events accurately at these distances requires the use of region-specific models to provide accurate travel times. Improved results have been achieved with composites of 1D models and with approximate 3D models with simplified upper mantle structures, but both approaches introduce nonphysical boundaries that are problematic for operational monitoring use. Ultimately, what is needed is a true, seamless 3D model of the Earth.

Towards that goal, we have developed a 3D tomographic model of the P velocity of the crust and upper mantle for the region of southcentral Asia centered around the Tibetan Plateau. Our model is derived from almost 140,000 Pn picks for more than 5300 events recorded at 563 stations from a Ground Truth (GT) dataset assembled by Los Alamos National Laboratory (LANL). Our starting model is the a priori model of East Asia developed by LANL, which is based on various global and regional studies. The topmost layers come from the Laske and Masters global sedimentary model from 1997. As our dataset lacks the resolution to improve this sedimentary portion of our model, we fix the velocity and depth of these layers, as well as the depths of the major mantle discontinuities (Moho, 410 km, 660 km). We invert for P velocities from the crust down through the upper mantle, along with source and receiver terms to account for the effects of event mislocation and fine-scale structure near the receiver not accounted for in the crustal model. Forward calculations are made using our own implementation of the Um and Thurber ray pseudo-bending approach (Ballard, 2008, these Proceedings) with full enforcement of Snell's Law in 3D at the major discontinuities. Because large portions of the model are underconstrained, we apply both damping and regularization to force the inversion to update the initial model only where good data coverage is available. We validate the model by performing several inversions with random portions of the dataset omitted and then testing the predictive capability of the model against those portions compared with AK135. We test the location performance of the model by relocating the GT events using our model and using AK135.

## OBJECTIVES

Our goal is to better predict Pn travel times for an area of south central Asia centered around the Tibetan Plateau. This is an area of high monitoring interest, as it encompasses the Indian, Pakistani, and Chinese test sites, as well as the former Soviet test site at Shagan River (now in Kazakhstan). It also spans several other countries that could be candidates for nuclear testing. Thus, locating events accurately in this region is tremendously important for tracking treaty compliance and nuclear weapon proliferation. To accomplish our goal, we have developed a three-dimensional (3D) P velocity model of the crust and upper mantle in this region. This is one of the most tectonically complex areas on the Earth, due to the collision of the Indian and Asian continents, which has led to the highest mountain ranges in the world, as well as the thickest crust and lithosphere.

## RESEARCH ACCOMPLISHED

### Dataset

Our data are drawn from an East Asia GT dataset collected over the past several years by Ground-Based Nuclear Explosion Monitoring Research and Development (GNEMRD) researchers at LANL. Considerable effort has gone into the collection of this dataset to draw on all possible sources of event catalogs for this region, and then to carefully screen them. Events are drawn from global catalogs from the NEIC (National Earthquake Information Center), and ISC (International Seismological Centre), as well as from various regional catalogs including the Annual Bulletin of Chinese Earthquakes (ABCE) (Lee et al., 2002). All events in the LANL GT set are assigned a GT level based on the Bondár criteria (Bondár et al., 2004), and for this project, only events with GT levels of 25 km or better were used. For each of these events, picks from the various catalogs were merged, removing redundant and/or outlier arrivals based on a preferred catalog hierarchy. Events without a priori GT information were relocated with the merged arrival set, comparing the results to the Bondár criteria (Begnaud et al., 2006). To focus on P velocity in the upper mantle, we chose to use only Pn phases and have limited source to receiver path lengths to be 25 degrees or less. This resulted in approximately 110,000 Pn picks for more than 5300 events recorded at 563 stations (Figure 1).

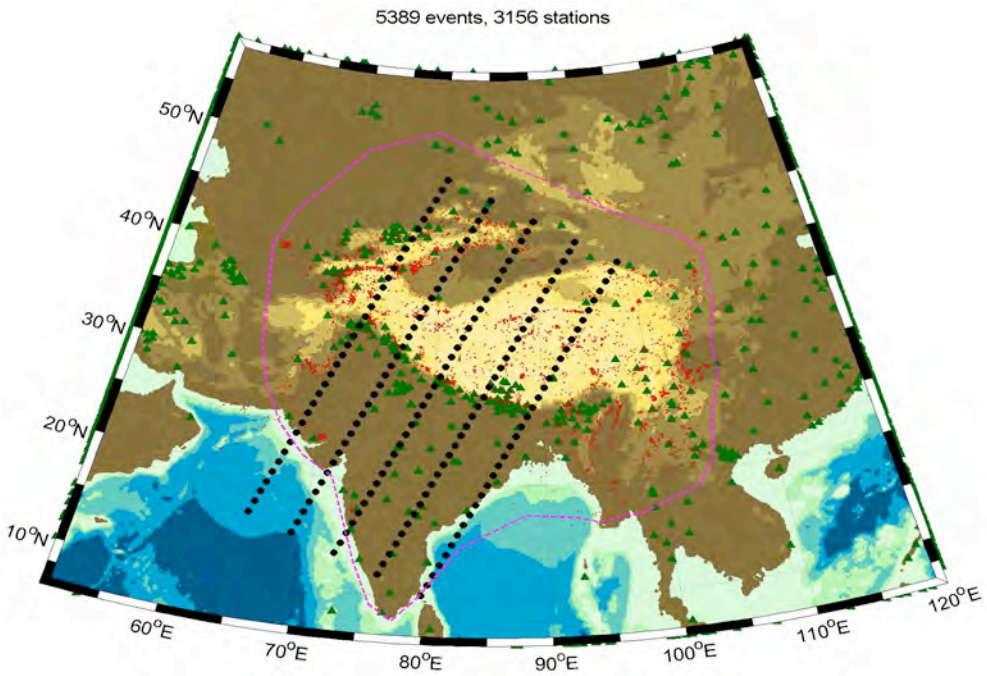


**Figure 1. Map showing the seismic events (red circles) and stations (green triangles) used in this study. The magenta dashed line shows the extent of the tomographic model we invert for, while the lines of black circles show the positions of cross sections through our model presented later.**

**Model Structure**

One of the areas in which we believe our model is an improvement over many of the previous tomographic models of the region is in the structure of the model. Many previous studies have used geographic grids that are regularly spaced in latitude and longitude. These types of grids are easy to construct and to use for interpolation (locating neighbor node positions within them is trivial), but they are inefficient because they compress northward as the longitude meridians converge. We instead use a grid that is truly equally spaced, regardless of latitude, as is shown in Figure 2. This grid is derived by progressive subdivision of an icosahedron with 12 nodes to a set of nodes with the desired spacing (see Ballard et al., 2008a, these Proceedings, for more details). As with a regular geographic grid, values at intermediate positions are found by interpolation of values at the neighbor nodes, but for this type of grid the neighbor nodes are found by a standard walking triangle search. To avoid the complications of dealing with ray paths that cross in and out of our model, we use a global grid, but the grid spacing is variable, being 1 degree in Eurasia and 2 degrees everywhere else in the world. The radial structure at each of these geographic node positions is represented with a standard set of layers that extend from the surface of the Earth to the center of the Earth: sediments, upper crust, mid-crust, lower crust, uppermost mantle, etc. The thicknesses (layers can pinch out), top and bottom depths, and top and bottom velocities of each of these layers can all change with geographic position, though we do assume that the velocity within a layer is fit by a linear gradient between the top and bottom values. Values at intermediate positions within layers are interpolated. Our model structure is described in more detail in the companion presentation by Ballard et al. (2008a, these Proceedings).

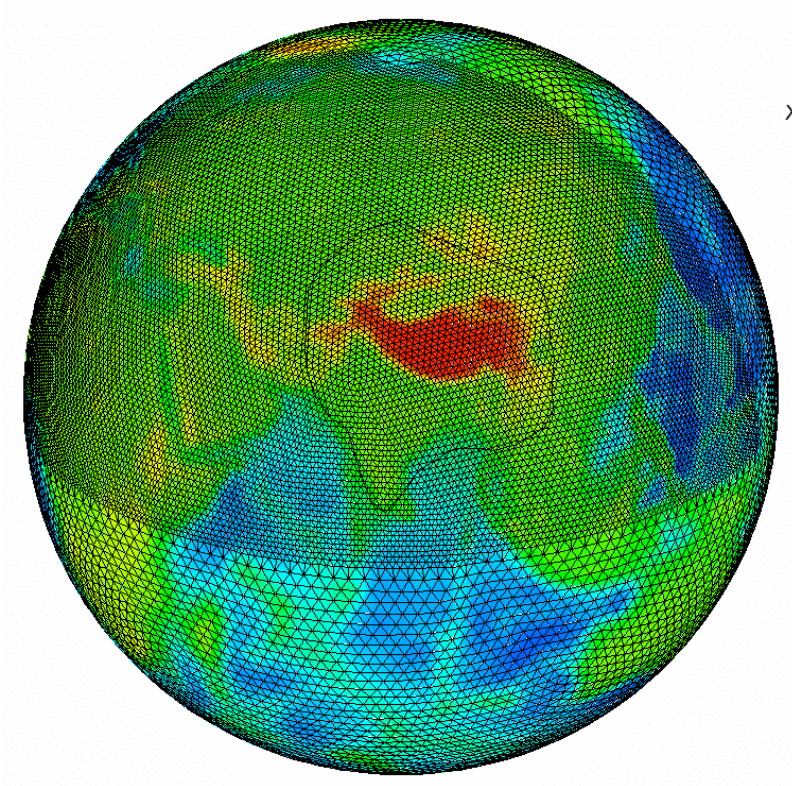

**Figure 2. Geographic grid for the tomographic model. Color is proportional to topography (red is high, green is medium, and blue is low). Each node marks the position of a layered profile extending from the surface to the center of the Earth. The black line around the Indian subcontinent and the Tibetan Plateau shows the portion of the overall model that will be updated by our tomographic inversion.**

**Starting Model**

As mentioned above, even though our goal is improved structure for a limited region of southern Asia, we have found it to be more straightforward to work with a global model. For a background, we use the crustal structure from the Laske, Master, and Reif Crust 2.0 model (Laske et al., 2008) on top of an AK135 mantle. For Europe, North Africa, and Asia, we use the a priori GNEMRD Unified Model created collaboratively by LANL and Lawrence Livermore National Laboratory (LLNL) (Begnaud et al., 2004; Pasyanos et al., 2004). This model has been shown to provide better Pn travel times than AK135 for Eurasia and North Africa (Flanagan et al., 2007), but not for southern Asia (Young et al., 2008), hence our motivation for this study. Shallow sedimentary layers are taken from Crust 2.0, while the deeper crustal layers are taken from various focused regional studies. The model also includes upper mantle structure from the 3SMAC model (Nataf and Ricard, 2004), but we choose not to use this because it is not based on seismic data. Instead, we use AK135 mantle structure.

**Limitations on the Inversion**

Based on the ray paths connecting our sources and receivers, we constructed the polygon shown in Figures 1 and 2 to limit the extent of our inversion. Only the velocities at the nodes within this polygon were updated. Further, we do not allow either the thicknesses or the depths of layers to change: only P velocities at the tops and bottoms of layers can be modified. We only include ray paths in the inversion that have 3/4 or more of their path lengths lying within our polygon. For such rays, observed times are always reduced by the travel time for the portion of the path external to the polygon before inversion. Because we are using Pn data only, we limit our inversion to rays that turn below the Moho but above the 410 km discontinuity. Hence, our inversion is limited to the crust and the portion of the upper mantle above the transition zone.

**Inversion Formulation**

Our inversion minimizes the travel time residuals formed by subtracting predicted Pn travel times from observed travel times. We assume that the travel time residual along a path from a source i to a receiver j can be calculated by multiplying the required slowness perturbations along the path by the lengths of the segments along the path, i.e.,

$$\Delta t_{ij} = \sum_{\ell} d_{\ell} * \Delta s_{\ell} \,, \tag{1}$$

where $d_{\ell}$ is the length of a path along the lth segment and $\Delta s_{\ell}$ is the slowness perturbation along that segment. With perfect data and perfect coverage of the entire model, this equation could be inverted directly to solve for the slowness perturbations (and hence the velocity structure). However, the data are never perfect, nor is the coverage, so a best model is solved for iteratively using a least-squares minimization of the residuals.

In tomographic inversions where the model is structured as a set of blocks, it is the path length through those blocks that provide the weights to be multiplied by the slowness perturbations to get the residuals. Because our model is represented by a set of nodes instead of blocks, the formulation is slightly different. We divide each path length into equal length subsegments 10 km long, then for each subsegment, we interpolate from the surrounding nodes to get the appropriate slowness to multiply times the subsegment length. Hence, in our formulation, we are solving for the slowness perturbation at the nodes, and the coefficients multiplying each of the node slowness perturbations are a combination of the path subsegment lengths and the weights of the nodes used for the interpolation. Because our data have noise, we cannot find a model that gives a zero residual everywhere but instead seek to minimize the squared residual:

$$\varepsilon = \left\| A\Delta s - \Delta t \right\|^2, \tag{2}$$

where $A$ is an *n* (number of observations) by *m* (number of nodes) matrix of node coefficients, $\Delta s$ is an *m* by 1 array of slowness perturbations, and $\Delta t$ is an n by 1 array of travel-time residuals.

Because portions of the model are under-constrained, we impose damping. In addition, we add horizontal and vertical smoothing (regularization) to produce models that are consistent with our geophysical intuition. Thus, the overall equation we invert is of this form:

$$\varepsilon = \left\| A\Delta s - \Delta t \right\|^2 + \lambda \left\| \Delta s \right\|^2 + \gamma \left\| L\Delta s \right\|^2 , \quad (3)$$

where $\lambda$ is the damping coefficient, $\gamma$ is the smoothing factor, and $L$ is the matrix of smoothing operators. To control the slowness adjustments in regions of the model where sampling is very poor, we use separate damping coefficients for each node slowness perturbation and make the damping coefficient for each inversely proportional to the ray coefficients, i.e., nodes with very little path sampling are highly damped, while those with high path sampling are damped very little.

**Travel-Time Prediction Calculation and Ray Paths**

Another area in which we believe this study improves over previous tomographic studies of the area is in our calculation of travel times and ray paths. For each iterative model, beginning with the starting model, we calculate true 3D ray paths using our own implementation of the Um and Thurber (1987) pseudo-bending methodology. Our implementation requires rays to honor Snell's Law at discontinuities (in this case the Moho), and it also avoids local minima by solving for a ray (refracted, diffracted, or reflected) in each layer, then finding the first refracting arrival. We have shown our implementation to be highly accurate (Young et al., 2008), but also computationally expensive, so we have designed a distributed computing framework to allow a set of rays to be run simultaneously on multiple processors. For our calculations for this model, we used a set of nine 16-processor PC-architecture machines for a total of 144 processors. For more on the ray bending algorithm implementation, we refer the reader to the companion paper by Ballard et al. (2008b).

**Travel-Time Prediction Improvement**

The ultimate goal of this project is to develop a model that can provide better Pn travel time predictions for our area. Our model shows clear improvements over the AK135 model for our dataset. Figure 3 shows mean and standard deviations of the observed minus prediction residuals for both models.

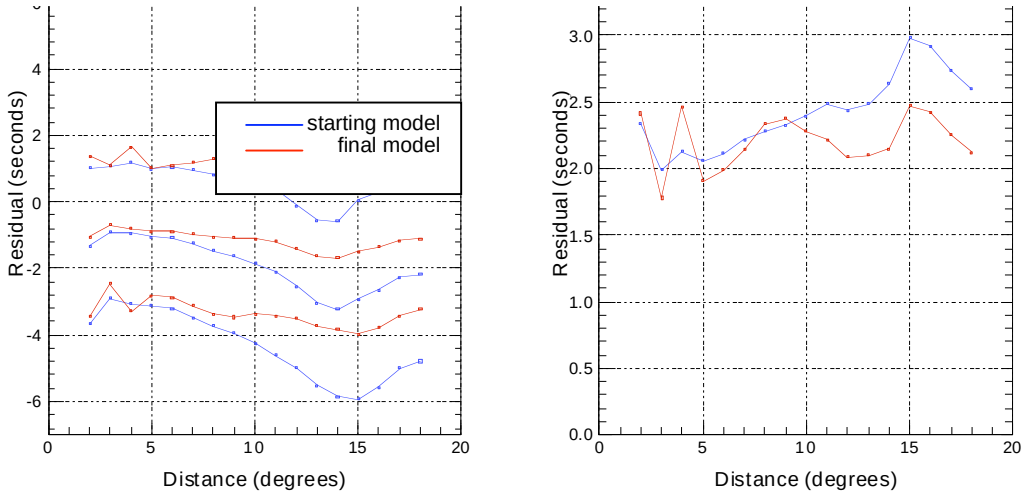


**Figure 3. (left) One degree station to event distance bins of mean plus and minus one standard deviation for starting model (red) and final model. (right) One degree station to event distance bins of standard deviation.**

The means of the residuals at all distances are negative for AK135, indicating that the data require a faster model. Further, the standard deviations are large (over 2 seconds), suggesting that there is considerable lateral heterogeneity in the region.

For our model, the overall RMS of the residuals has been reduced from 3.2 seconds to 2.5 seconds, an improvement of 22%. This suggests that we are modeling a substantial portion of the lateral heterogeneity in the region. The bulk of the improvement comes beyond 8 degrees, suggesting that it is the changes in the upper mantle portion of our model that are the most important. Our model decreases the bias, especially beyond 8 degrees, but does not remove it. We believe that the reason for this is that our damping coefficients were too strong, hence the model was unable to move far enough away from the starting model. In subsequent versions of the model, we plan to vary the damping coefficients to see if we can remove the bias entirely.

**Discussion of the Tomographic Model**

Figure 4 shows percent velocity changes from the staring model at the bottom of the lowermost crustal layer, at the top of the uppermost mantle layer, at 100 km, and at 200 km. To help interpret these pictures, at each depth we also show a map of the node ray hit count at each depth. Generally ray hit counts are good across the model for all depths, but there are lower hit counts at the edges of the model, especially in the crust where the ray paths are much more vertical than in the mantle.

Beginning with the shallowest structure and working downwards, we can see that overall the adjustments to the velocity at the base of the crust are much less than in the mantle. This suggests that the crustal portion of our starting model is doing a good job of fitting the data, as expected. Still, our results suggest that the crustal velocities beneath the Tibetan Plateau are lower than in the starting model, and that the velocities to the NW and SE of the plateau need to be higher to match the observations.

The strongest velocity changes are seen at 100-km depth, and they are predominantly velocity increases, which is consistent with the negative bias of the starting model seen in Figure 3. Velocities have been increased by 2% and greater throughout most of the region, with the exception of low-velocity regions near the Tarim Basin and in the southeast part of China. Both the positive and negative features seem to extend upward to the Moho and downward to 200 km, though not as strongly. Depth extent can be better assessed with the vertical cross sections shown in Figure 5 for the profiles shown in Figure 1. We can see a high-velocity region extending from the Indian subcontinent underneath the Tibetan Plateau, then being sharply truncated by low-velocity material at the Tarim Basin for slices that cross that basin farther to the east. Both these high and low-velocity anomalies extend from the top of the mantle down to at least 200 km. How much deeper they extend is not clear because of our poor ray coverage at depth.

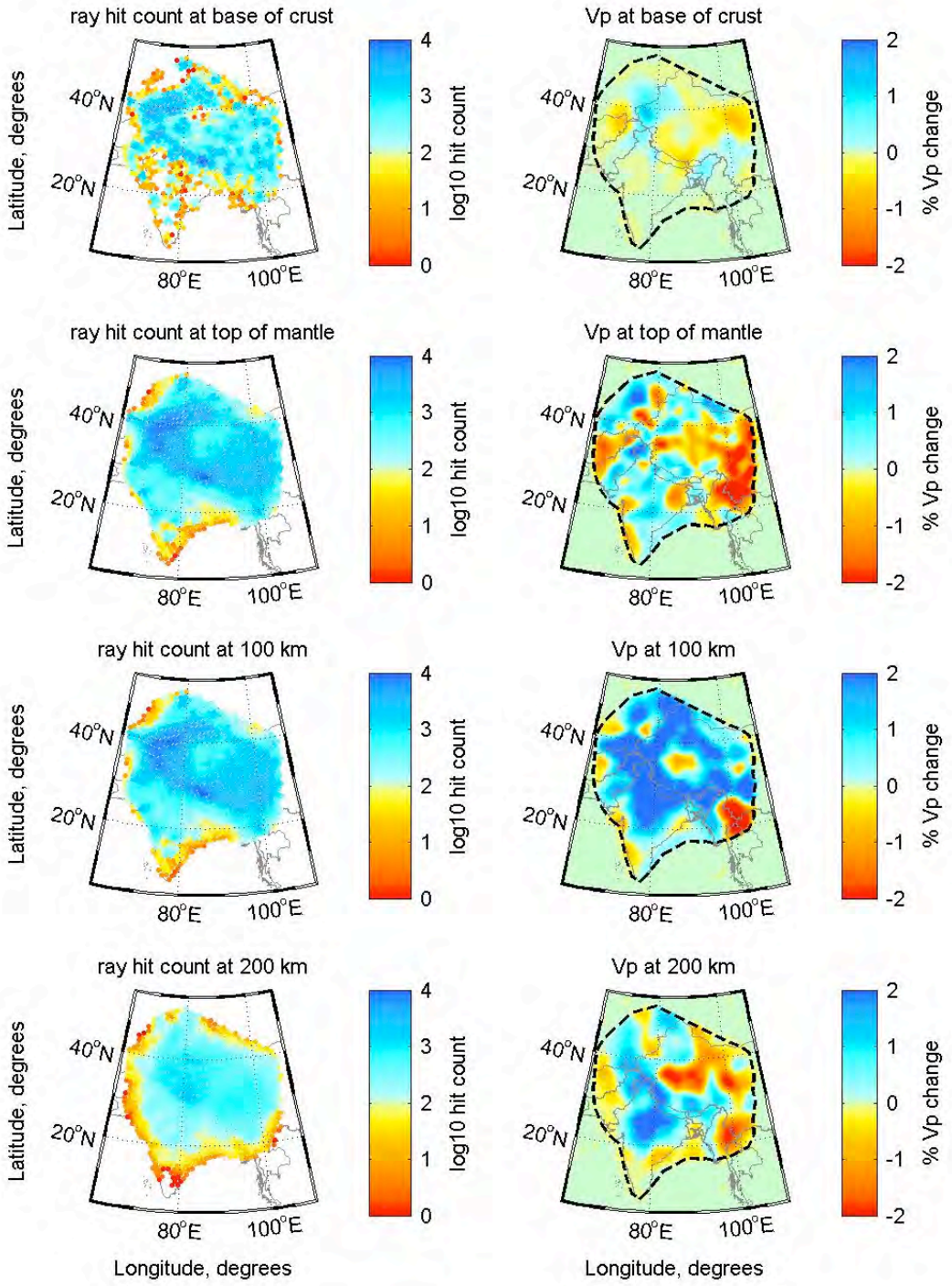


**Figure 4. (left side, top to bottom) Log10 ray hit counts for nodes at the base of the crust, the top of the mantle, the top of the 100-km-depth layer, and the top of the 200-km-depth layer. (right side, top to bottom) Percent P velocity change from starting model for the same nodes and depths.**

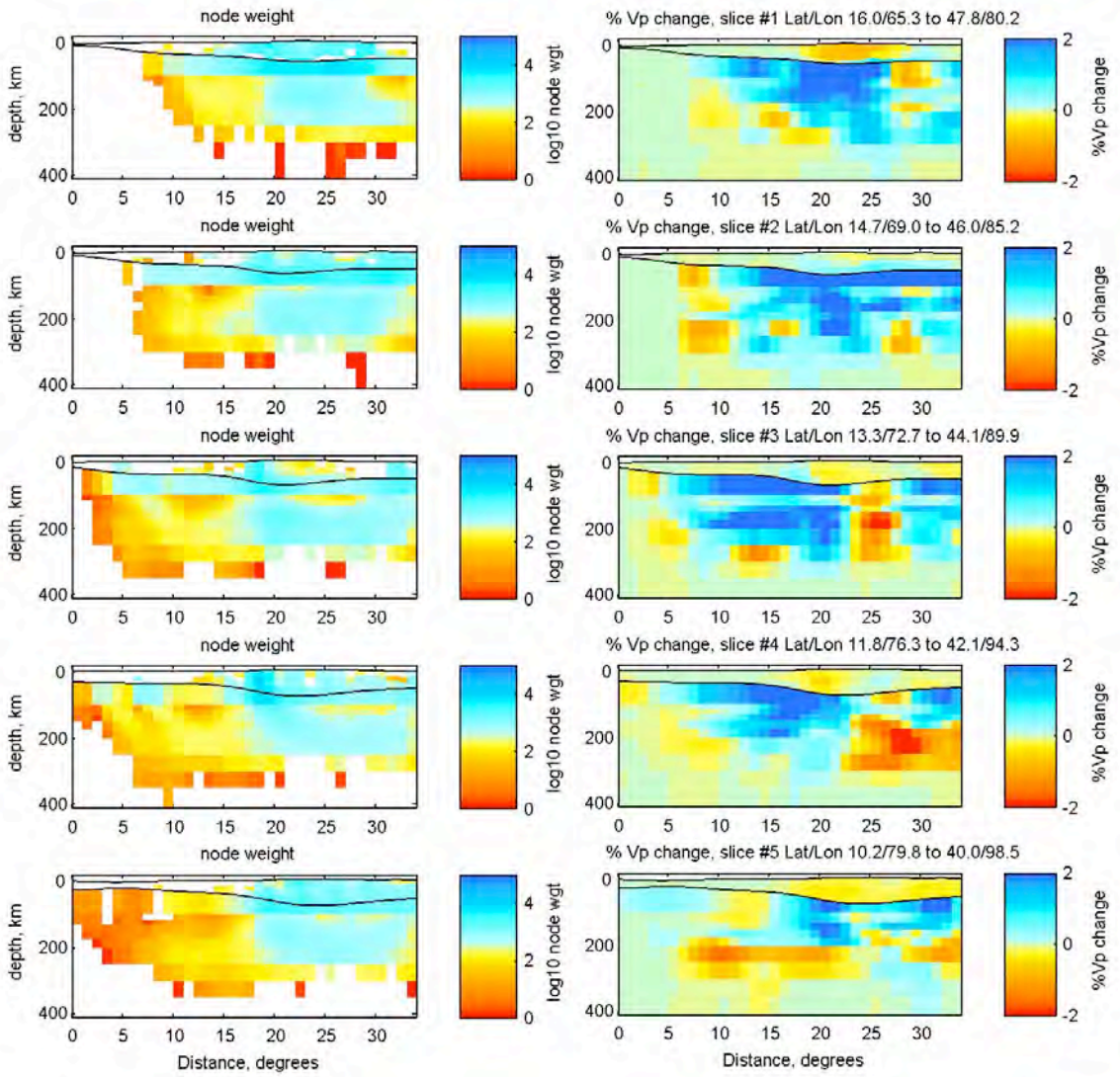


**Figure 5. (left side, top to bottom) Log10 ray hit counts for cross section slices shown in Figure 1. (right side, top to bottom) Percent P velocity change from the starting model for the same cross sections.**

## CONCLUSIONS AND RECOMMENDATIONS

We have developed a 3D model of the P velocity structure of the crust and upper mantle for a limited region of south central Asia. Our approach differs from previous efforts in several important ways. First, we utilize only high-quality GT data, collected by LANL GNEMRD researchers over the past several years. Second, our model is represented geographically with a grid of truly equally spaced nodes, and radially with a set of standard layers with variable properties. Third, we trace rays and calculate travel times using a 3D pseudo-bending approach that enforces Snell's law across discontinuities. The resulting model provides a 22% improvement in RMS travel-time residual over our starting model, which is taken from the LANL/LLNL a priori unified geophysical model that encompasses our region. Overall, our model is faster than the starting model, hence reducing the negative bias in residuals, but our model still has a negative bias, probably because damping is too strong. In future versions of the model, we plan to experiment with changing damping and regularization parameters to improve our model further.

## REFERENCES

Ballard, S., C. Young, J. Hipp, G. Barker, and M. Chang (2007). Computation of travel time through 3D velocity models for applications in real-time, global seismic event monitoring, *EOS Trans. AGU*, Fall Meet. Suppl.

Ballard, S., Hipp, J., and C. Young (2008a). Robust, extensible representation of complex earth models for use in seismological software systems, these Proceedings.

Ballard, S., Young, C., Hipp, J., G. Barker, and M. Chang (2008b). Implementation of a pseudo-bending seismic travel time calculator in a distributed computing environment, these Proceedings.

Begnaud, M. L., C. A. Rowe, and L. K. Steck (2004). Validating three-dimensional velocity models in China and East-Asia for use in regional seismic event location, *EOS Trans. AGU*, Fall Meet. Suppl.

Begnaud, M. L., L. K. Steck, and C. A. Rowe (2006). Improving seismic event locations in Asia by using catalog-scale empirical travel time correction surfaces, *EOS Trans. AGU* 87(52), Fall Meet. Suppl., Abstract T51D-1550.

Bondár, I., S. C. Myers, E. R. Engdahl, and E. A. Bergman (2004). Epicentre accuracy based on seismic network criteria, *Geophys. J. Int.* 156: 483–496.

Flanagan, M. P., S. C. Myers, and K. D. Koper (2007). Regional travel-time uncertainty and seismic location improvement using a three-dimensional a priori velocity model, *Bull. Seism. Soc. Am.* 97: 804–825.

Laske, G., G. Masters, and C. Reif (2008). Crust2.0: A new global crustal model at 2x2 degrees, http://mahi.ucsd.edu/Gabi/rem.dir/crust/crust2.html.

Lee, W. H. K., H. Kanamori, P. C. Jennings and C. Kissling (Eds.) (2002). *International Handbook of Earthquake and Engineering Seismology* (CD-ROM), Elsevier, New York.

Nataf, H. C. and Y. Ricard (2004). 3SMAC: An a priori tomographic model of the upper mantle based on geophysical modeling, *Phys. Earth Planet. Int.* 95: 101–122.

Pasyanos, M. E., W. R. Walter, M. P. Flanagan, P. Goldstein, and J. Bhattacharyya (2004). Building and testing an a priori geophysical model for Western Eurasia and North Africa, *Pure Appl. Geophys.* 161: 234–281.

Um, J. and C. Thurber (1987). A fast algorithm for two-point seismic ray tracing, *Bull. Seism. Soc. Am.* 77: 972–986.

Young, C. J., S. Ballard, G .T. Barker, M. L. Begnaud, C. A. Rowe, W. S. Phillips, and L. K. Steck (2008). Validating P wave travel times for a 3D model of East Asia using a pseudo-bending travel time calculation and a large GT data set, SSA 2008 Meeting, *Seismo. Res. Lett.* 79: 305.

# THREE-DIMENSIONAL SEISMIC IMAGING OF EASTERN RUSSIA

Haijiang Zhang[1, 2], Kevin G. Mackey[3], Kazuya Fujita[3], Clifford H. Thurber[1], Lee K. Steck[4], Charlotte A. Rowe[4], Steven Roecker[5], and M. Nafi Toksoz[2]

University of Wisconsin-Madison[1], Massachusetts Institute of Technology[2], Michigan State University[3], Los Alamos National Laboratory[4], and Rensselaer Polytechnic Institute[5]

Sponsored by National Nuclear Security Administration

Contract No. DE-FC52-06NA27325[1–3] and DE-AC52-06NA25396[4]
Proposal No. BAA06-77

## ABSTRACT

Eastern Russia is composed of a series of terranes which have been accreted to the Precambrian North Asian (Siberian) craton. In the southern part (Baikal and Amur regions), the terranes form a suture zone between the North Asian and North China cratons, which is being exploited by the present-day boundary between the Eurasian plate and the Amur block. The northern part (Magadan and eastern Yakutsk regions ) is composed of a series of terranes that accreted to the North Asian craton, primarily in the Mesozoic. This accretionary region is currently the location of the plate boundary between the North American and Eurasian plates. The complexities of accretion and subsequent intracontinental deformation likely result in a highly heterogeneous crust, a broad zone of deformation, and the formation of small blocks or microplates within the ancient suture and present-day plate boundary zones. We assembled catalog picks from ~13,000 events and ~100 stations for the Baikal and Amur regions in the period of 1970 to 2005. For the Magadan and Yakutsk regions, we assembled catalog picks from 3,170 events recorded at 56 stations. Each event has at least 8 P and S observations in order to reliably determine its location. Using the double-difference tomography method (Zhang and Thurber, 2003, 2006), our study for the first time provides a detailed seismic velocity model of the crust and upper mantle for this complicated area. The velocity models in Baikal and Amur regions, as reported in Zhang et al., (2007), show greater heterogeneities at shallow depths, as expected from the variable and complicated nature of the crust. Some Cenozoic and Quaternary rift-related basins around Lake Baikal such as the Upper Angara (northeast) and Tunka (southwest) basins correlate very well to strong low-velocity anomalies. The preliminary velocity models in the Magadan and Yakutsk regions also show strong heterogeneities in the crust. We also determined the Pn velocity model for eastern Russia using Hearn's Pn tomography code.

In our data set, many arrivals at larger distances are identified in the catalog as Pg or Sg phases, which are often observable because of their relatively large amplitudes. Without knowing detailed Moho depth variations, it is not possible to combine both Pn and Sn and Pg and Sg times together. Here we propose a simple way to use Pg and Sg times. From previous studies, the crustal thickness in this region is believed to be generally greater than 35 km. Therefore, in the starting velocity model we introduce an artificial lower-velocity region below 35 km. In this way, the ray paths will stay in the region above 35 km so that they correspond to Pg and Sg phases. During the inversion, we monitored each ray path to make sure it did not penetrate below 35 km. In this way, we can run separate inversions using first and secondary arrivals.

In our tomography algorithm, we use either the spherical-Earth finite-difference (SEFD) travel time method or the spherical pseudo-bending approach of Koketsu and Sekine (1998) to calculate travel times and trace rays. To improve the accuracy and efficiency of the ray tracing, we also adopt a hybrid approach. First, we utilize the FD method with a coarser grid interval to calculate an approximate ray path. Next we start bending this approximate ray path with the spherical pseudo-bending approach until it converges to the desired accuracy. In addition to event-pair differential times used in the double-difference tomography method, we also add station-pair differential times to the tomography algorithm to improve the resolution near the station region.

## OBJECTIVES

The objectives of this project are to investigate and develop new and improved methodologies for regional-scale three-dimensional (3D) seismic tomography using a combination of event- and station-pair arrival time differences, and to apply the new methods to the Michigan State University (MSU) and Los Alamos National Laboratory (LANL) Siberia database. The tomographic work proposed here will provide a more reliable velocity model for both the crust and upper mantle of the accretionary regions to the south and east of the Siberian craton. There are four main tasks in this project: (1) an extension of our development of double-difference (DD) seismic tomography to the use of station-pair residual differences, including the incorporation of a new method for resolution matrix calculation; (2) testing, refinement, and adaptation of a method for SEFD travel time calculations for use in DD tomography; (3) an extension of our Cartesian adaptive-grid DD tomography algorithm to spherical coordinates; and (4) collaborative work among the UW-Madison, LANL, and MSU groups to apply these analysis tools to the Siberia data set. In the 2nd year of this project, our focus is to assemble a data set for the Magadan and eastern Yakutsk regions, incorporate station-pair residual differences into the DD seismic tomography algorithm, and determine 3D P- and S-wave velocity models for the Magadan and eastern Yakutsk Baikal regions.

## RESEARCH ACCOMPLISHED

### Determining the Velocity Model for the Magadan and Eastern Yakutsk regions

Northeast Russia is composed of a large number of terranes of various affinities that have accreted onto the deformed margin of the North Asian (Siberian) Craton (Figure 1; e.g., Fujita et al., 1997; Nokleberg et al., 2000). The diverse nature of the terranes and the evolution of the region over time have resulted in a very heterogeneous crust with potentially abrupt changes in its characteristics. The North Asian Craton is composed of an Archean and Early Proterozoic metamorphic basement overlain by flat-lying Precambrian to Cenozoic sediments. Adjacent to the craton is a deformed margin consisting primarily of Paleozoic to mid-Mesozoic passive margin sediments, thickening to the east, which have been back-thrust onto the margin of the craton. Further east are a series of complexes and terranes that have accreted onto the margin of the North Asian Craton since the mid-Mesozoic. The Verkhoyansk Complex is composed of distal passive margin sequences and oceanic fragments that have been disrupted, deformed, and juxtaposed. The Kolyma-Omolon superterrane consists of a number of cratonal (Omolon, Prikolyma), continental margin (Omulevka), island arc (Alazeya, Khetachan), and oceanic terranes of diverse ages that amalgamated in the Early Mesozoic. In the far northeast of the study area is the Paleozoic to Early Mesozoic Chukotka passive margin terrane that may have formed along the margin of the North America Craton, rifted, and deformed when it collided with the Asian continent along the South Anyui Suture in the Cretaceous. In the south-central part of the study area is the Precambrian Okhotsk cratonal terrane. Southeast of the Okhotsk terrane and the Verkhoyansk complex is the Jurassic to Cretaceous Uda-Murgal island arc that accreted onto the Asian continent in the mid-to-late Cretaceous. Superimposed on all of the previously described units is the Okhotsk-Chukotka volcanic belt (Figure 1), a continental margin volcanic arc. Further complicating crustal and lithospheric structure in the region are a series of post accretionary extensional and compressional events that have affected the region since the Late Cretaceous, and the superposition and migration of the plate boundary between North America and Eurasia across northeast Russia in the Cenozoic (Fujita et al., 1990). In particular, Late Cenozoic rifting appears to have had significant impact on crustal and upper mantle structure.

We assembled catalog picks from 3,170 events recorded at 56 stations in the region bounded by latitudes $58^{o}$–$75^{o}$ and longitudes $115^{o}$–$165^{o}$ (Figure 2). Each event has at least 8 P and S observations in order to reliably determine its location. In total, we collected ~19,000 Pn+Pg arrivals and 24,000 Sn+Sg arrivals. Figure 2 also shows P and S ray path distributions. From travel time curves shown in Figure 3, we note there are some outliers in the catalog picks. We cleaned up the P and S times by removing outliers falling outside the major trend of the travel time curves. As a result, we obtained ~3,500 P and ~1,930 S first arrivals corresponding to 628 events. In comparison, there are ~12,690 Pg and ~18,600 Sg times from ~2,640 events because it is easier to pick Pg and Sg phases due to their relatively large amplitudes in the seismograms.

For eastern Russia, the crustal thickness is generally greater than 35 km. In order to use Pg and Sg times that are secondary arrivals, we intentionally add a lower velocity layer below 35 km so that the rays do not tend to penetrate deeper than 35 km. During the inversion, we monitored the maximum penetration depth for each ray path and removed it from the inversion if it penetrated deeper than 35 km. We constructed ~76,000 P and ~123,000 S event-pair differential times directly from catalog picks. For the starting model, we used a crustal model consisting

of 5 km of 5.3–5.8 km/s material overlying 15 km of 6.0 km/s material ("granitic"), and a 20-km thick lower crust of 6.8 km/s ("basaltic"). This yields a 40-km-thick crust which is underlain by 8.0 km/s upper mantle. The grid intervals in the horizontal directions range from 0.5° in the inner part to 2° around the edge of the model. In depth, the grid interval is 5 km. The initial root-mean-square (RMS) arrival time residual is 2.643 s. After 8 iterations of simultaneous inversion of the velocity model and locations, the final RMS arrival time residual is 0.826 s. Figure 4 shows the Vp and Vs models at selected depths.

**Pn velocity Tomography for Eastern Russia**

We collected 9,630 Pn travel times for 151 stations and 9,630 events from the MSU database (Figure 5). Each event has at least 3 Pn recordings. We followed Hearn's approach to invert Pn travel time residuals for lateral velocity variation within the mantle lid, event delays, and station delays (Hearn and Ni, 1994). The surface of the uppermost mantle is parameterized into a set of 0.5° by 0.5 ° cells. The initial RMS Pn travel time residual with respect to the average Pn velocity model of 8 km/s is 1.66 s and the final RMS Pn travel time residual is 1.12 s. Figure 6 shows Pn velocity variations of eastern Russia. Overall, the Siberian platform has higher velocities than the accretionary region.

**Differential Time Seismic Tomography Algorithm**

Zhang and Thurber (2003) generalized the DD location method of Waldhauser (2001) to determine 3D velocity structure and event locations jointly. The equations for the DD tomography algorithm are

$$r_k^i - r_k^j = \sum_{m=1}^{3} \frac{\partial T_k^i}{\partial x_m^i} \Delta x_m^i + \Delta\tau^i + \int_i^k \delta u \, ds - \sum_{m=1}^{3} \frac{\partial T_k^j}{\partial x_m^j} \Delta x_m^j - \Delta\tau^j - \int_j^k \delta u \, ds \quad (1)$$

where $r_k^i$ and $r_k^j$ are residuals from events i and j at station k, T's are travel times, x and $\Delta x$ are hypocenter coordinates and their perturbations, $\tau$'s are origin times, $\delta u$ is perturbation to slowness, and ds is an element of path length. Three types of data, absolute arrival times, catalog differential arrival times, and waveform cross-correlation (WCC) data, are used in the inversion. To combine these three types of data into one system, we apply a hierarchical weighting scheme during the inversion, similar to hypoDD (Waldhauser, 2001 ).

We can also consider a variant of Equation 1 in which we have two different, nearby stations recording a single event:

$$r_j^i - r_k^i = \sum_{m=1}^{3} \frac{\partial T_j^i}{\partial x_m^i} \Delta x_m^i + \int_i^j \delta u \, ds - \sum_{m=1}^{3} \frac{\partial T_k^i}{\partial x_m^i} \Delta x_m^i - \int_i^k \delta u \, ds \quad (2)$$

where now $r_j^i$ and $r_k^i$ are residuals from event i at stations j and k, and the origin time terms drop out since there is only one event involved. If the stations are sufficiently close, the location derivative terms in Equation 2 cancel, and what remains are slowness perturbation terms along slightly different paths. Phillips et al. (2005) explored the utility of this formulation for the determination of a 2D tomographic model. Their motivation was that, for advantageous geometries, the time difference for arrivals from one event to two stations can be insensitive to location accuracy. For example, for an event in line with (but not between) two stations, much of the ray paths are essentially in common, and the time difference is related to the properties sampled by the additional ray-path length to the more distant station as well as the medium directly under the closer station. This time difference will not change much if the source moves 10 km or even more. There is only a "dipole"-shaped area in between and perpendicular to the line between the two stations where the time differences are not stable and are very sensitive to location. Thus, the time differences provide strong constraints even if the ground truth (GT) levels of the events are poor.

The success of this simplistic approach leads us to propose the formal use of Equation 2 in a 3D tomographic inversion. There is a direct parallel between Equation 1 (DD tomography), in which event-pair time differences provide information about 3D structure in the vicinity of the sources, and Equation 2, in which station-pair time differences provide information about 3D structure in the vicinity of the stations. In the former case, we know that very precise differential times can be derived for closely spaced events, leading to very precise relative event locations and sharply defined structure in the source region. Similarly, we can expect that for closely spaced stations, relative times can be determined more precisely than individual absolute times. Tomography using station-pair residual differences is somewhat akin to teleseismic tomography, but with the sources contained within the model region.

For simplicity, we construct a 2D synthetic model (Figure 7) to show the properties of the inversions with different combinations of event- and station-pair differential arrival times, and/or absolute times. There are six clusters of earthquakes (circles) and each cluster has four closely spaced events with inter-event distances of less than 200 m. In the X- and Y-directions, the distances between clusters are 10 and 15 km, respectively. There are 36 stations around these events, with all the events observed at each station. As a result, there are 894 travel times in total for all the event and station pairs. The velocity is assumed to be constant at 5 km/s; thus, the rays between events and stations are all straight lines. The region is divided uniformly into 81 cells (or blocks). The model derivatives relative to slowness are just the path lengths crossing the cells.

Figures 8a and 9a show model resolution for location and slowness model parameters in the case of using event-pair time differences and station-pair time differences, respectively. These are shown for different combinations of weightings with absolute times. Event-pair and station-pair time differences are constructed for all possible event pairs and station pairs, respectively. For the case of using event-pair time differences (our original version of DD tomography) (Figure 8a), the systems with higher weighting on the differential data seem to better resolve event locations by having higher resolution values (~0.7 versus ~0.3). For slowness model parameters around the edge of the model, however, the systems having higher weighting on the absolute data have higher model resolution. This is mainly because the ray paths from event pairs outside the source region almost overlap so that the corresponding slowness model derivatives cancel out. This indicates that the absolute times are necessary to resolve the velocity model outside the source region. For the case of using the station-pair time differences (Figure 9a), both location and slowness model parameters have higher resolution for the systems having higher weighting on the differential data than those having higher weighting on the absolute data. When compared to the case of using event-pair differential times, using the station-pair time differences better resolves the structure near the station region.

We assume that the errors associated with both absolute and differential data (both event-pair and station-pair) are an uncorrelated Gaussian-distributed random process. The assumed standard deviations for the absolute and differential data are 80 and 20 ms, respectively. This simulates the scenario that the differential data are more accurate than the absolute data. These values would be representative of absolute catalog picks and differential catalog picks; using the even more precise cross-correlation differential times would obviously make the uncertainty contrast greater. Figures 8b and 9b show the model uncertainties for the cases of using event-pair, station-pair, and event- and station-pair time differences, respectively, including different combinations with absolute times. For the case of using event-pair time differences (Figure 8b), the model uncertainties estimated from the system having higher weighting on the absolute data are much larger, especially for event locations. We also notice that the slowness model cells closer to two model region edges (X=5 and 50 km) tend to have larger model uncertainties. This phenomenon results from the relatively smaller number of rays crossing through those cells. The characteristics of model uncertainties for the case of having higher weighting on the differential data (diff and diff+0.01*abs) are quite similar, with the system (diff+0.01*abs) having slightly larger uncertainties for some slowness model cells. We also observe that the model uncertainties, including event locations and slowness model parameters, are smaller for the systems having higher weighting on the differential times in the case of using station-pair time differences (Figure 9b). For the simple synthetic dataset analyzed, including a combination of absolute and differential data provides a better balance between good resolution and low uncertainty compared to using just absolute or differential data alone, as one might expect. We also conducted a resolution and uncertainty analysis in the case of using both event- and station-pair time differences. The results are very similar to the case of using station-pair time differences. This is mainly because the sources are so tightly clustered but the clusters are so far apart, whereas stations are more uniformly separated. The current synthetic model is too simple to represent the real case of proposed regional-scale tomography study where the inter-station and inter-event distances are quite variable and

relatively small compared to ray path lengths. However, this simple test does certainly show that including station-pair time differences helps to better resolve the velocity structure near the station region.

We successfully modified the double-difference tomography code to include the station-pair travel time differences. For the test, we applied it to the data set of Baikal and Amur regions. For this test, we constructed station-pair differences from all possible station pairs for each event. We started the inversion from the velocity model and event locations calculated using absolute and event-pair arrival time differences. The initial RMS station-pair travel time residual is 1.536 s and the final RMS residual is 0.653 s after four iterations of simultaneous inversion. Figure 10 shows the comparison of the velocity models using station-pair and event-pair time differences. The main features of the two velocity models are very similar, but the differences are up to 0.2 km/s. The mean horizontal and vertical location differences are around 1.5 km and 1.3 km, respectively. With the effect of origin times reduced, we expect the locations are more accurate using station-pair travel time differences.

## CONCLUSIONS AND RECOMMENDATIONS

We successfully modified the double-difference seismic tomography algorithm to include the station-pair travel time differences. The simple synthetic test showed that including station-pair travel time differences helps to better resolve the velocity structure near the station region. The application to the Baikal and Amur regions also showed the effectiveness of including station-pair travel time differences in resolving the structure in the crust.

We assembled a dataset for northeastern Russia comprising Pn+Pg and Sn+Sg picks. At larger epicentral distances, the Pg and Sg are secondary arrivals and could not be directly used in double-difference seismic tomography. To use Pg and Sg arrivals, we simply added an artificial low-velocity layer below the estimated Moho interface so that the rays only travel in the crust. The velocity model shows strong heterogeneity in the crust for northeastern Russia using Pg and Sg times. We plan to use the adaptive inversion mesh based on tetrahedral diagrams according to the data coverage.

## REFERENCES

Fujita, K., F.W. Cambray, and M.A. Velbel (1990). Tectonics of the Laptev Sea and Moma rift systems, northeastern USSR: *Marine Geology* 93: 95-118.

Fujita, K., D.B. Stone, P.W. Layer, L.M. Parfenov, and B.M. Koz'min (1997). Cooperative program helps decipher tectonics of northeast Russia, *Eos Trans. Am. Geophys. Union 78:*245,252–253.

Hearn, T. M., and J. Ni (1994). Pn velocities beneath continental collision zones: The Turkish-Iranian plateau, *Geophys. J. Int.* 117: 273– 283.

Koketsu, K., and S. Sekine (1998). Pseudo-bending method for three-dimensional seismic ray tracing in a spherical earth with discontinuities, *Geophys. J. Int.* 132: 339–346.

Nokleberg, W. J., L.M. Parfenov, J.W.H. Monger, B.V. Baranov, S.G. Byalobzhesky, T.K. Bundtzen, T.D. Feeney, K. Fujita, S.P. Gordey, A. Grantz, A.I. Khanchuk, B.A. Natal'in, L.M. Natapov, I.O. Norton, W.W. Jr. Patton, G. Plafker, D.W. Scholl, S.D. Sokolov, G.M. Sosunov, D.B. Stone, R.W. Tabor, N.V. Tsukanov, and T.L. Vallier (2000). Summary Circum-North Pacific tectono-stratigraphic terrane map, *US Geological Survey*, *Open-File Report*: 96-727, scale 1:10,000,000.

Phillips, W.S., C.A. Rowe, and L.K. Steck (2005). The use of interstation P wave arrival time differences to account for regional path variability, *Geophys. Res. Lett.* 32: L11301, doi:10.1029/2005GL022558.

Zhang, H., and C. H. Thurber (2003). Double-difference tomography: the method and its application to the Hayward Fault, California, *Bull. Seism. Soc. Am*, 93**:** 1875–1889.

Zhang, H., and C. Thurber (2006). Development and applications of double-difference tomography, *Pure and Applied Geophys.* 163: 373–403, doi:10.1007/s00024-005-0021-y.

Zhang, H., K. Mackey, K. Fujita, L. Steck, C. Rowe, C. Thurber, and S. Roecker (2007). High-Resolution Three-Dimensional Seismic Imaging of Baikal and Amur Regions of Eastern Russia, in *Proceedings of the 29th Monitoring Research Review: Ground-Based Nuclear Explosion Technologies*, LA-UR-07-5613, Vol. 1, pp. 333–342.

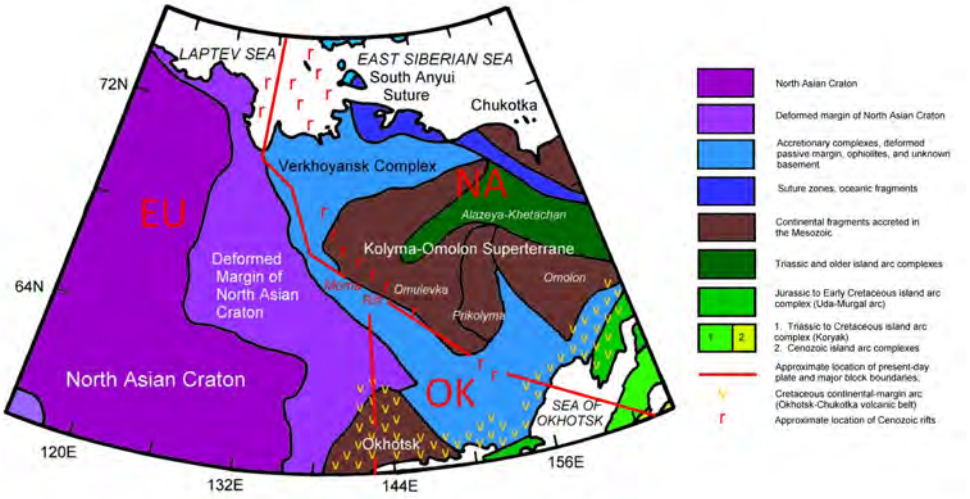


**Figure 1**. **Tectonic map of northeastern Russia**.

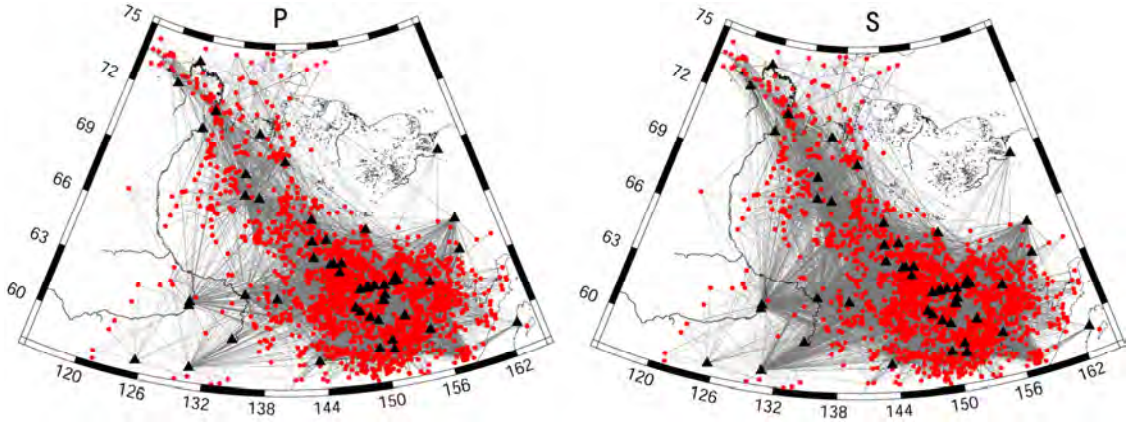


**Figure 2. Event-station path coverage for P-waves (left) and S-waves (right). Events are represented in red and stations are in black.**

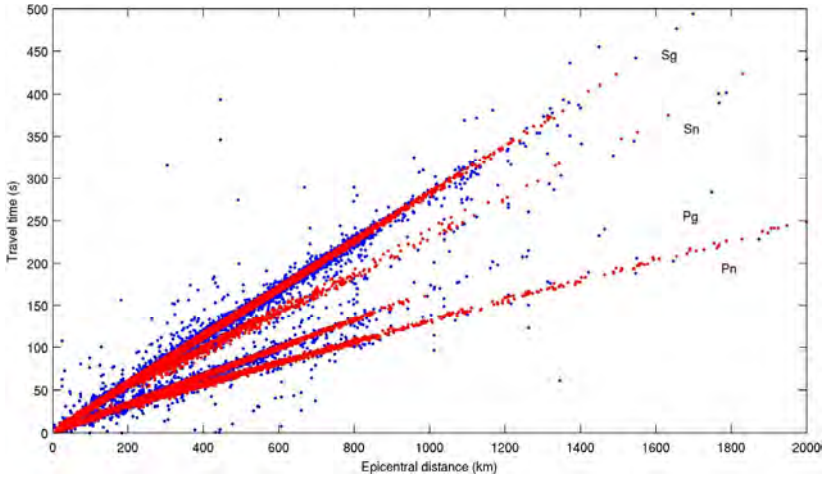


**Figure 3. Composite travel time curve. The blue color shows all the picks from the MSU database. The red color indicates the selected picks. The epicentral distance is calculated using original catalog locations.**

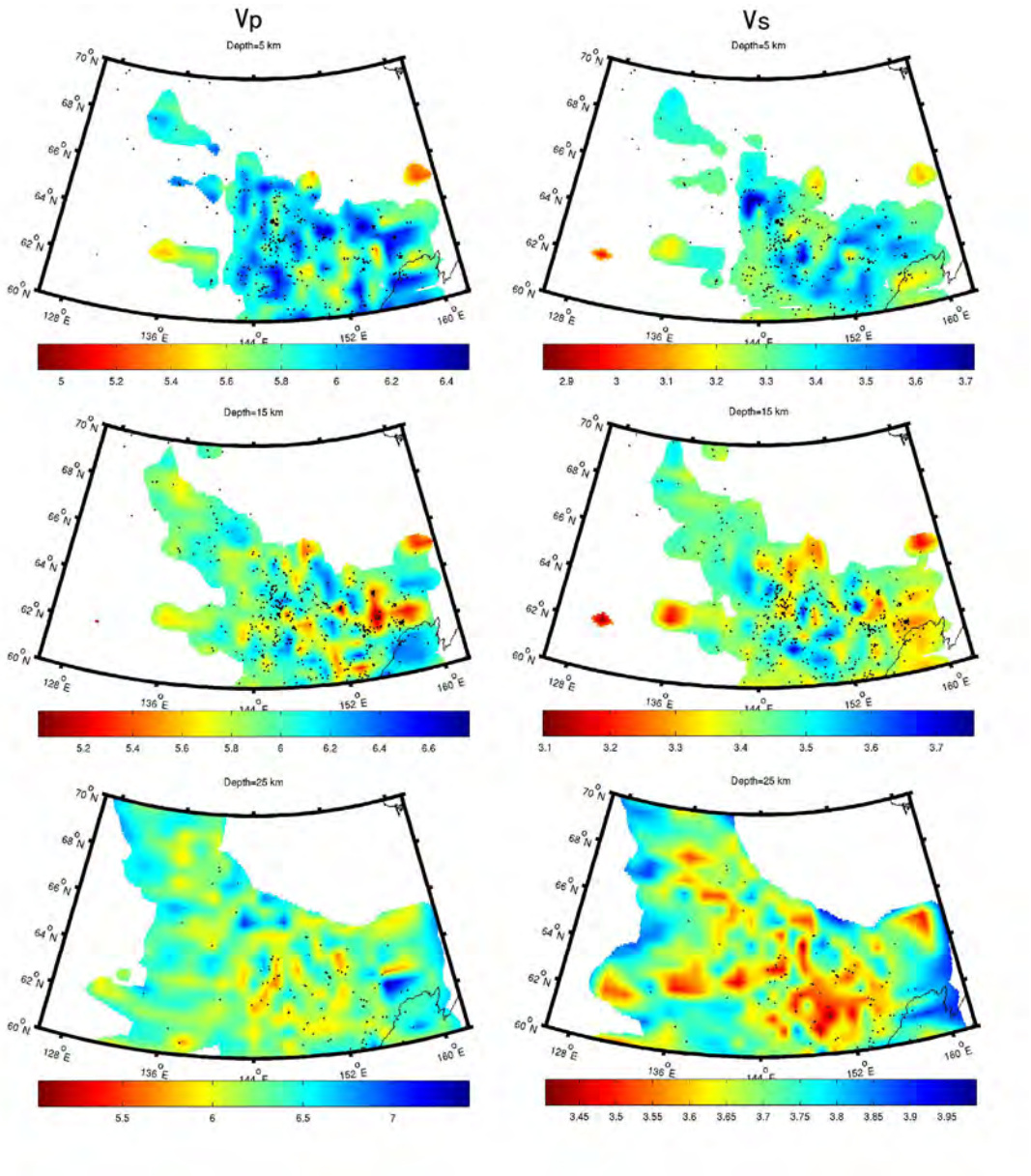


**Figure 4. Horizontal slices of Vp and Vs model at depths of 5, 15, and 25 km**.

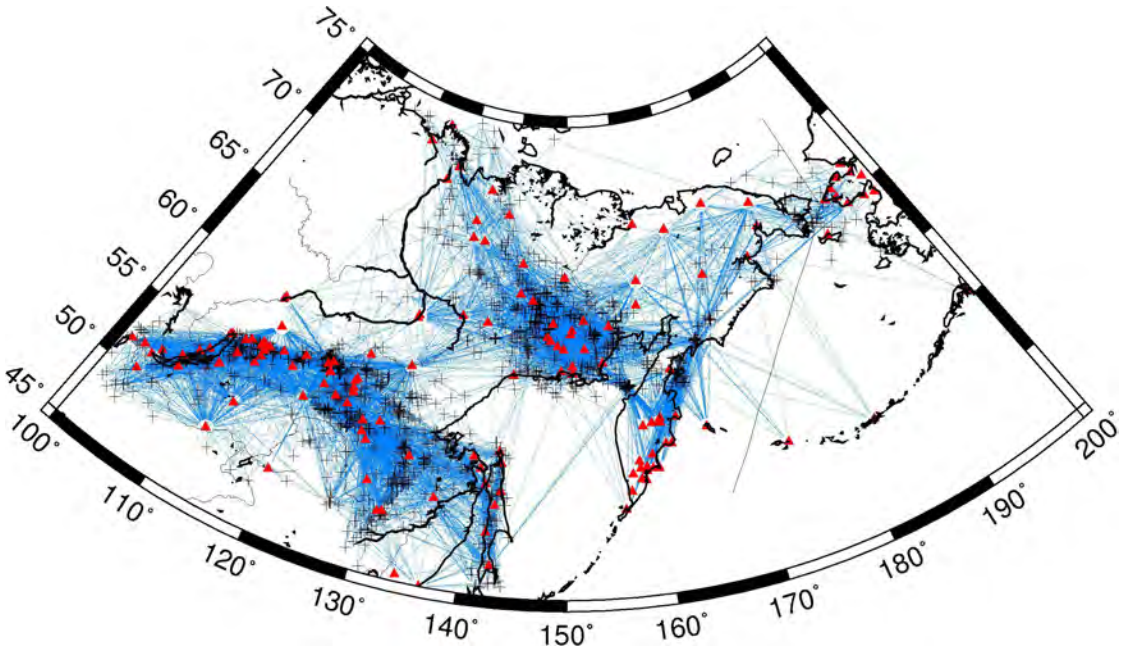


**Figure 5. Distribution of 9630 Pn ray paths (blue dashed line) from 1651 events (crosses) and 151 stations (red triangles) for eastern Russia.**

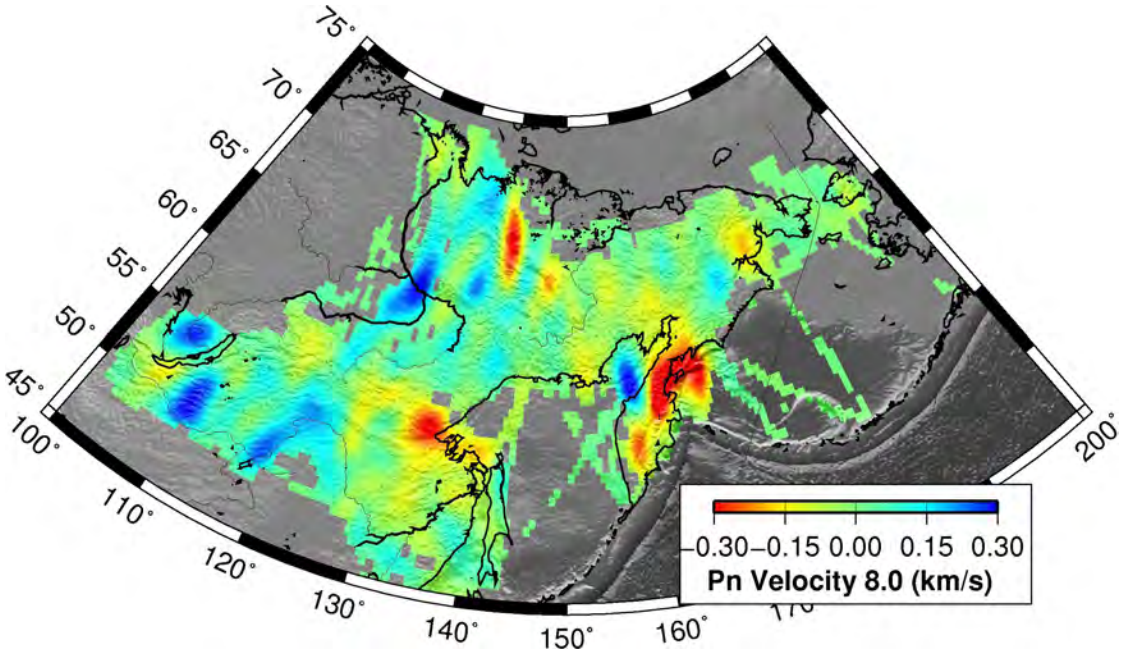


**Figure 6. Pn lateral velocity variations. Average Pn velocity is 8.0 km/s. Blue indicates higher velocity and red indicates lower velocity.**

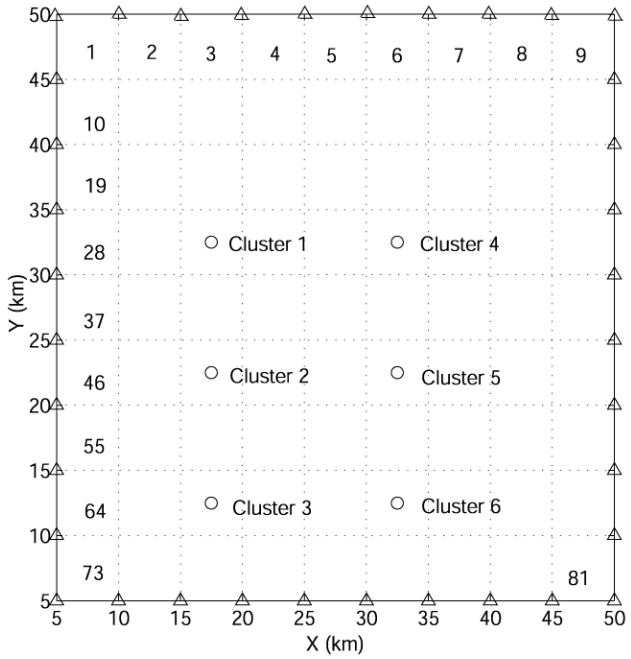


**Figure 7. Map of stations (triangles) and earthquake clusters (circles) for the synthetic example. Each cluster has 4 closely spaced events, with interevent distances among them less than 200 m. The velocity model is assumed to be a constant 5 km/s. The model region is divided into 81 cells uniformly, with numbers in the cells indicating the model parameter indices.**

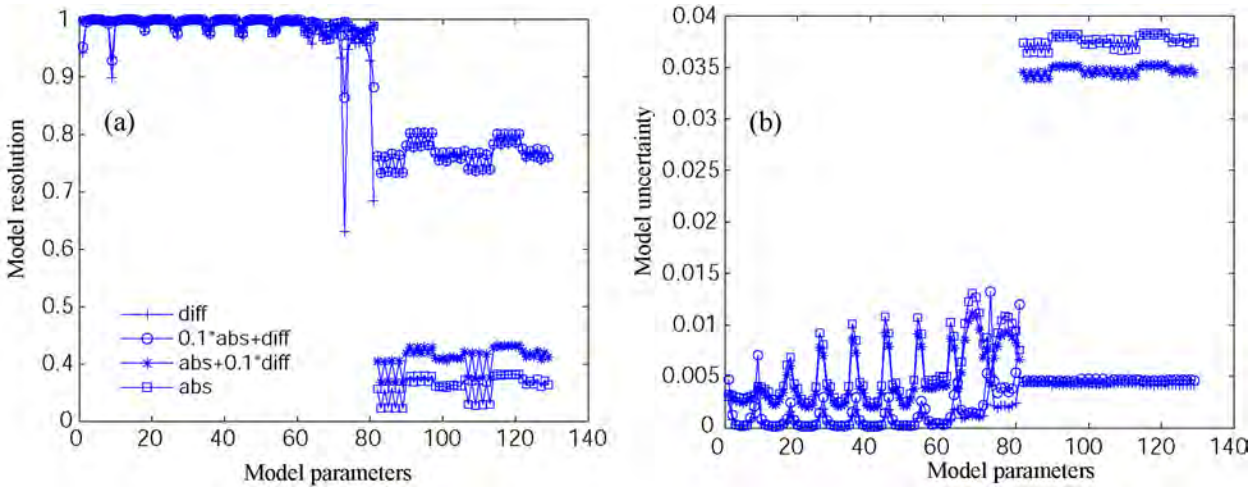


**Figure 8. Example of (a) resolution analysis and (b) uncertainty analysis for slowness (model parameters 1 through 81) and location (model parameters 82 through 129) model parameters. Including a combination of absolute and differential data provides a better balance between good resolution and low uncertainty compared to absolute or differential data alone.**

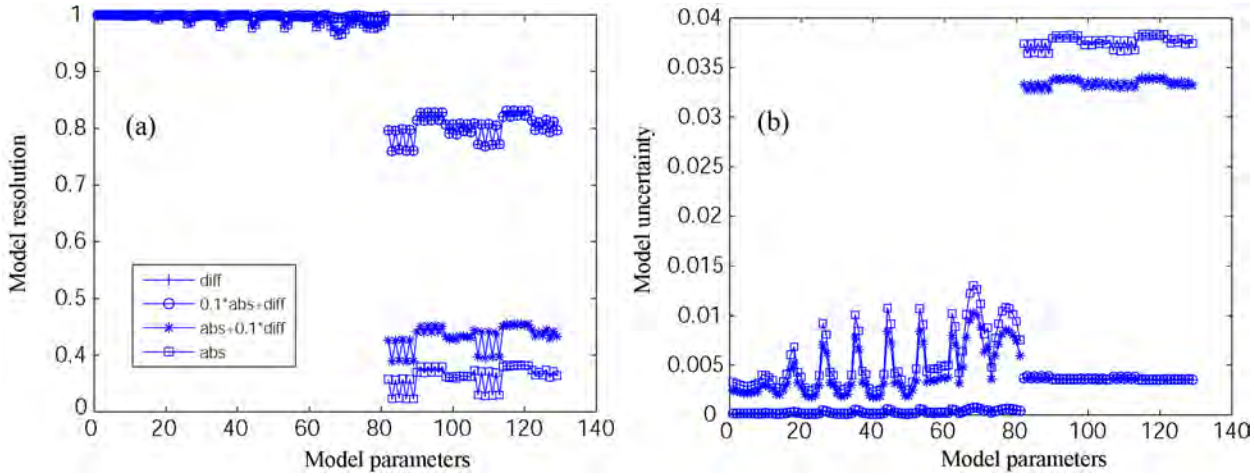


**Figure 9. Same as Figure 8 except for using station-pair time differences.**

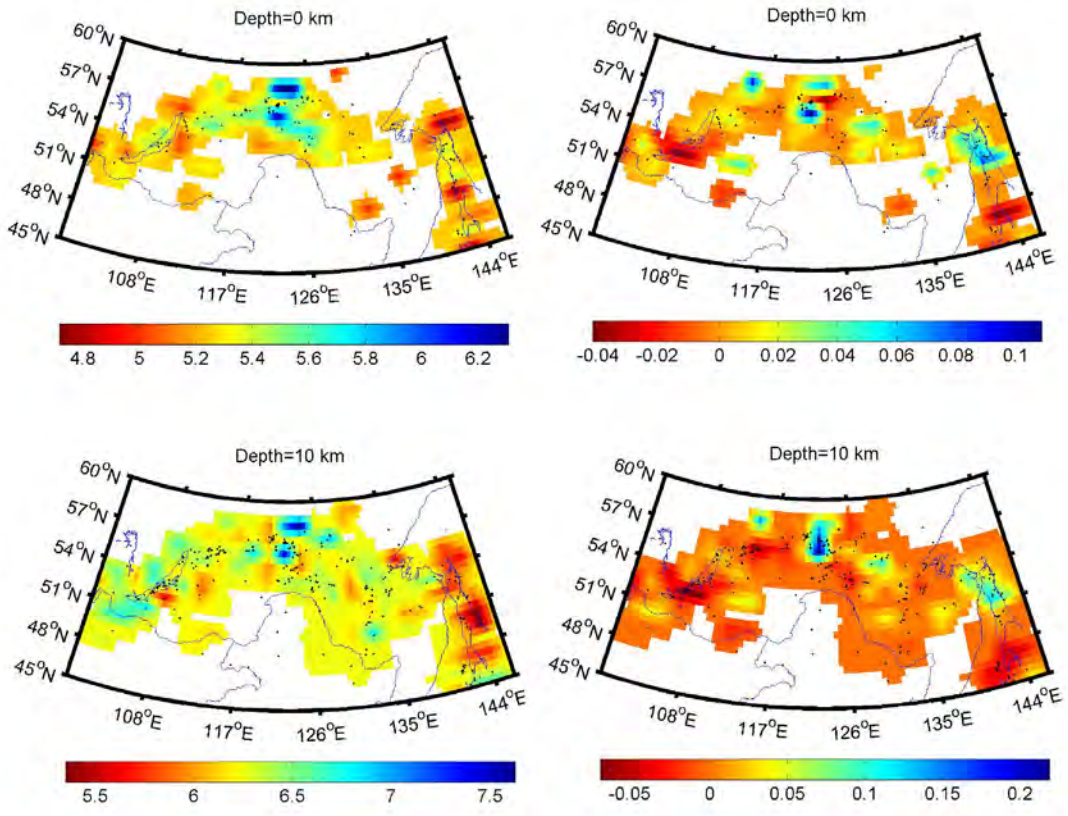


**Figure 10. Comparison of the velocity models using event-pair and station-pair time differences. (Left) Horizontal slices of the Vp model from the inversion using station-pair differences. (Right) Differences between velocity models derived from station-pair differences and event-pair differences.**

# REFINED LOCAL AND REGIONAL SEISMIC VELOCITY AND ATTENUATION MODELS FROM FINITE-FREQUENCY WAVEFORMS

Wei Zhang[2], Yang Shen[2], Li Zhao[3], and Xiaoping Yang[1]

Science Applications International Corporation[1], University of Rhode Island[2],
and Institute of Earth Sciences, Academia Sinica, Taiwan[3]

Sponsored by Air Force Research Laboratory

Contract No. FA8718-06-C-0014
Proposal No. BAA06-60

## ABSTRACT

In seismic tomography, the reference or starting models are commonly one-dimensional (1D) and the structural sensitivity kernels of seismic data are calculated without considering the finiteness of seismic waves in both time and frequency domains. These simplifications result in a theoretical limit, in addition to that from the data coverage, on the structural resolution in tomography inversions. In small-scale (such as the crustal) structural imaging, however, a higher resolution is desired, and the 1D reference model is no longer adequate; therefore, accurate modeling of wave propagation in three-dimensional (3D) reference models is necessary. To address this problem, elaborate numerical methods, such as the finite-difference and spectral-element methods, have been adopted to calculate the full-wave, finite-frequency, banana-doughnut, structural sensitivity kernels of seismic data.

The objective of this work is to develop refined local and regional velocity and attenuation models for selected areas of interest (AOIs) in Eurasia. We have carried out systematic tests to validate the finite-frequency sensitivity kernels computed by a staggered-grid, finite-difference method. These tests result in corrections in the calculation of the structural sensitivity kernels as well as an important finding that anomalies in S-wave speed have a significant contribution to P-wave traveltime perturbations (Zhang and Shen, 2008). Thus, current seismic tomography practices, in which P-wave traveltimes are assumed to be unrelated to S-wave velocity anomalies, may lead to systematic biases in inversion results. Furthermore, the different components of the same arrival at the same receiver have different traveltime and amplitude sensitivities to variations in the velocity structure (Shen et al., 2008). We have applied our finite-difference-based full-wave, finite-frequency approach to obtain a refined structural model in Eastern Turkey.

We continue the application of our finite-frequency approach in the refinement of the seismic velocity and attenuation models and focus on the Iran region. Our previous full-wave approach has been based on the finite-difference algorithm in a Cartesian coordinate system. However, the Iran region under current study is relatively large so that the Earth's curvature effect on wave propagation cannot be ignored. Thus, we developed an alternative finite-difference algorithm that solves the seismic-wave equation in the polar-spherical coordinate system on a non-staggered and non-uniform grid. We have also validated this algorithm by comparing its synthetic seismograms with those calculated by normal-mode summation. Our tomography study covers the region 39°E-66°E and 22°N-44°N, with a depth range of 0–700 km. Waveform records from regional events and stations were collected. For initial tomographic iterations, we selected 31 larger earthquakes at 16 stations belonging to the Iran National Seismic Network. Their source mechanisms are available from the Harvard CMT solutions, though we use the revised locations determined by Engdahl and Bergman (personal communication). We used the regional a priori 3D geophysical model of Pasyanos et al. (2004) as our starting model and applied the spherical finite-difference algorithm to compute the synthetic seismograms. Frequency-dependent anomalies in phase and amplitude are measured by the cross-correlation between synthetic and recorded seismograms. Full-wave, finite-frequency structural sensitivity kernels of these measurements are calculated by the spherical finite-difference scheme. The final 3D structural model for the Iran region will be obtained through a non-linear iterative process in which the inversion results from each iteration will serve as the reference model for the next iteration.

## OBJECTIVES

In this work we obtain Finite-Frequency Seismic Tomography (FFST) velocity models for Eurasia and use them as 3D reference models to refine crustal and shallow upper mantle velocity and attenuation models for focused AOIs by applying the fully 3D tomography approach.

## RESEARCH ACCOMPLISHED

### Development of Non-Staggered, Non-Uniform Grid Finite-Difference Algorithm in Spherical Geometry

In our research accomplished in the previous year, we focused on the 3D crustal structure in eastern Turkey and northern Iran and carried out a finite-frequency tomography inversion based on a 3D reference crustal model based on MENA 1.1 (Walter et al. 2000). We used a fourth-order staggered-grid finite-difference algorithm (Olsen 1994) to compute the synthetic seismograms in the layered crustal model with variable Moho depth. The crustal model has a minimum shear-wave speed of 1.1 km/s. In our finite-difference simulations, we used a uniform grid spacing of 300 m, resulting in reliable waveforms up to a nominal frequency of about 0.5 Hz.

Like most implementations of the finite-difference method, the staggered-grid finite-difference algorithm of Olsen (1994) we used in a previous study has been designed for rectangular geometry in the Cartesian coordinate system where the Earth's sphericity has been ignored. This is acceptable when the modeling area is small so that the paths of regional seismic waves are relatively short. In this year's research, however, we expanded our area of interest to the entire area of Iran and the surrounding region. As a result of the much larger modeling area, the paths of the seismic wave involved are often longer so that the effect of the Earth's curvature on seismic wave propagation needs to be taken into account. A simple approach to account for the Earth's sphericity is to make a so-called Earth-flattening transformation. It has often been applied in asymptotic treatment of wave propagation in the spherical Earth (Chapman and Orcutt 1985). However, the transformation is inexact, and the errors it causes in waveforms have not been quantitatively studied.

Here, we choose to develop an implementation of the finite-difference method in the polar spherical coordinate system so that the propagation of seismic waves in the 3D structure of a spherical Earth can be modeled accurately. We use the geocentric spherical coordinate (GSC) system in which the origin is located at the center of the Earth and the three coordinate variables are co-latitude θ, azimuth φ, and radius *r*. The conversion between the GSC system and the geocentric Cartesian system is

$$\begin{aligned} \theta &= \arctan\left(\frac{\sqrt{x^2+y^2}}{z}\right), \\ \varphi &= \arctan(y/x), \\ r &= \sqrt{x^2+y^2+z^2}. \end{aligned} \tag{1}$$

The elastic wave equation we solve can be written in the velocity-stress form:

$$\rho \mathbf{v}_{,t} = \nabla \cdot \boldsymbol{\sigma} + \mathbf{f}, \tag{2}$$

where the stress-rate tensor can be expressed via the Hooke's law

$$\dot{\boldsymbol{\sigma}} = \mathbf{C} : \{\frac{1}{2}[(\nabla \mathbf{v}) + (\nabla \mathbf{v})^{\mathrm{T}}]\}. \tag{3}$$

In the GSC system, these equations can be explicitly written as

$$\begin{aligned} \rho v_{\theta,t} &= \frac{1}{r}\sigma_{\theta\theta,\theta} + \frac{1}{r\sin\theta}\sigma_{\theta\varphi,\varphi} + \sigma_{\theta r,r} + \frac{1}{r}(3\sigma_{\theta r} + \sigma_{\theta\theta}\cot\theta - \sigma_{\varphi\varphi}\cot\theta), \\ \rho v_{\varphi,t} &= \frac{1}{r}\sigma_{\theta\varphi,\theta} + \frac{1}{r\sin\theta}\sigma_{\varphi\varphi,\varphi} + \sigma_{\varphi r,r} + \frac{1}{r}(2\sigma_{\theta\varphi}\cot\theta - 3\sigma_{\varphi r}\cot\theta), \\ \rho v_{r,t} &= \frac{1}{r}\sigma_{\theta r,\theta} + \frac{1}{r\sin\theta}\sigma_{\varphi r,\varphi} + \sigma_{rr,r} + \frac{1}{r}(2\sigma_{rr} - \sigma_{\theta\theta} - \sigma_{\varphi\varphi} + \sigma_{\theta r}\cot\theta), \end{aligned} \tag{4}$$

$$
\begin{aligned}
\dot{\sigma}_{\theta\theta} &= \frac{\lambda}{r}(v_\theta \cot\theta + \frac{1}{\sin\theta} v_{\varphi,\varphi} + v_r) + \frac{\lambda+2\mu}{r}(v_{\theta,\theta} + v_r) + \lambda v_{r,r}, \\
\dot{\sigma}_{\varphi\varphi} &= \frac{\lambda+2\mu}{r}(v_\theta \cot\theta + \frac{1}{\sin\theta} v_{\varphi,\varphi} + v_r) + \frac{\lambda}{r}(v_{\theta,\theta} + v_r) + \lambda v_{r,r}, \\
\dot{\sigma}_{rr} &= \frac{\lambda}{r}(v_\theta \cot\theta + \frac{1}{\sin\theta} v_{\varphi,\varphi} + v_r) + \frac{\lambda}{r}(v_{\theta,\theta} + v_r) + (\lambda+2\mu) v_{r,r}, \\
\dot{\sigma}_{\theta\varphi} &= \frac{\mu}{2r}(v_{\varphi,\theta} + \frac{1}{\sin\theta} v_{\theta,\varphi} - v_\varphi \cot\theta), \\
\dot{\sigma}_{\theta r} &= \frac{\mu}{2}(\frac{1}{r} v_{r,\theta} + v_{\theta,r} - \frac{1}{r} v_\theta), \\
\dot{\sigma}_{\varphi r} &= \frac{\mu}{2}(\frac{1}{r\sin\theta} v_{r,\varphi} + v_{\varphi,r} - \frac{1}{r} v_\varphi).
\end{aligned}
\tag{5}
$$

The free-surface boundary condition can also be expressed in the GSC system as

$$\sigma_{\theta r} = 0, \quad \sigma_{\varphi r} = 0, \quad \sigma_{rr} = 0. \tag{6}$$

One of the drawbacks of many finite-difference implementations in modeling seismic wave propagation is the requirement that the grid size be constant in all three spatial directions and everywhere in the modeling volume. When the seismic wave speed varies over a wide range, the efficiency of the finite-difference scheme is drastically reduced. This happens when the S-wave speed is very low near the surface, such as in a sedimentary basin, where a very small grid size is needed. If a uniform grid is required, then the same small grid size is used in the deeper part of the model where the wave speed is much higher and a small grid size may not be needed. To address this problem in order to increase the efficiency of the finite-difference algorithm, we developed a non-uniform grid approach in which the coordinates (θ, φ, *r*) of the uniform grid points are transformed to the coordinates of points on a non-uniform grid, denoted by (ξ, η, ζ), via the relations:

$$\theta = \theta(\xi), \ \varphi = \varphi(\eta), \ r = r(\varsigma). \tag{7}$$

The derivatives of these transformation relations can be calculated by the same differencing operator *D* used in the finite-difference algorithm

$$\theta_{,\xi} = D_\xi \theta, \ \varphi_{,\eta} = D_{,\eta}\varphi, \ r_{,\varsigma} = D_\varsigma r. \tag{8}$$

Therefore, the velocity-stress form of the elastic wave equations (4) and (5) become

$$
\begin{aligned}
\rho v_{\theta,t} &= \frac{1}{r}\xi_{,\theta}\sigma_{\theta\theta,\xi} + \frac{1}{r\sin\theta}\eta_{,\varphi}\sigma_{\theta\varphi,\eta} + \varsigma_{,r}\sigma_{\theta r,\varsigma} + \frac{1}{r}(3\sigma_{\theta r} + \sigma_{\theta\theta}\cot\theta - \sigma_{\varphi\varphi}\cot\theta), \\
\rho v_{\varphi,t} &= \frac{1}{r}\xi_{,\theta}\sigma_{\theta\varphi,\xi} + \frac{1}{r\sin\theta}\eta_{,\varphi}\sigma_{\varphi\varphi,\eta} + \varsigma_{,r}\sigma_{\varphi r,\varsigma} + \frac{1}{r}(2\sigma_{\theta\varphi}\cot\theta - 3\sigma_{\varphi r}\cot\theta), \\
\rho v_{r,t} &= \frac{1}{r}\xi_{,\theta}\sigma_{\theta r,\xi} + \frac{1}{r\sin\theta}\eta_{,\varphi}\sigma_{\varphi r,\eta} + \varsigma_{,r}\sigma_{rr,\varsigma} + \frac{1}{r}(2\sigma_{rr} - \sigma_{\theta\theta} - \sigma_{\varphi\varphi} + \sigma_{\theta r}\cot\theta),
\end{aligned}
\tag{9}
$$

$$
\begin{aligned}
\dot{\sigma}_{\theta\theta} &= \frac{\lambda}{r}(v_\theta \cot\theta + \frac{1}{\sin\theta}\eta_{,\varphi} v_{\varphi,\eta} + v_r) + \frac{\lambda+2\mu}{r}(\xi_{,\theta} v_{\theta,\xi} + v_r) + \lambda\varsigma_{,r} v_{r,\varsigma}, \\
\dot{\sigma}_{\varphi\varphi} &= \frac{\lambda+2\mu}{r}(v_\theta \cot\theta + \frac{1}{\sin\theta}\eta_{,\varphi} v_{\varphi,\eta} + v_r) + \frac{\lambda}{r}(\xi_{,\theta} v_{\theta,\xi} + v_r) + \lambda\varsigma_{,r} v_{r,\varsigma}, \\
\dot{\sigma}_{rr} &= \frac{\lambda}{r}(v_\theta \cot\theta + \frac{1}{\sin\theta}\eta_{,\varphi} v_{\varphi,\eta} + v_r) + \frac{\lambda}{r}(\xi_{,\theta} v_{\theta,\xi} + v_r) + (\lambda+2\mu)\varsigma_{,r} v_{r,\varsigma}, \\
\dot{\sigma}_{\theta\varphi} &= \frac{\mu}{2r}(\xi_{,\theta} v_{\varphi,\xi} + \frac{1}{\sin\theta}\eta_{,\varphi} v_{\theta,\eta} - v_\varphi \cot\theta), \\
\dot{\sigma}_{\theta r} &= \frac{\mu}{2}(\frac{1}{r}\xi_{,\theta} v_{r,\xi} + \varsigma_{,r} v_{\theta,\varsigma} - \frac{1}{r} v_\theta), \\
\dot{\sigma}_{\varphi r} &= \frac{\mu}{2}(\frac{1}{r\sin\theta}\eta_{,\varphi} v_{r,\eta} + \varsigma_{,r} v_{\varphi,\varsigma} - \frac{1}{r} v_\varphi),
\end{aligned}
\tag{10}
$$

with the free-surface boundary conditions for stress and velocity components (from equations 6 and 10):

$$
\begin{aligned}
\varsigma_{,r} v_{\theta,\varsigma} &= \frac{1}{r}(-\xi_{,\theta} v_{r,\xi} + v_\theta), \\
\varsigma_{,r} v_{r,\varsigma} &= -\frac{\lambda}{\lambda + 2\mu}\frac{1}{r}(\xi_{,\theta} v_{\theta,\xi} + v_\theta \cot\theta + \frac{1}{\sin\theta}\eta_{,\varphi} v_{\varphi,\eta} + 2v_r), \\
\varsigma_{,r} v_{\varphi,\varsigma} &= -\frac{1}{r\sin\theta}\eta_{,\varphi} v_{r,\eta} + \frac{1}{r} v_\varphi .
\end{aligned} \tag{11}
$$

We have implemented this spherical, non-uniform grid approach. A number of experiments have been conducted to validate the code by comparing the simulation results with the synthetics calculated by normal-mode summation. Figure 1 shows a few examples of the comparisons of the finite-difference and normal-mode synthetic seismograms. This alternative implementation of the finite-difference method enables us to efficiently and accurately model the propagation of seismic waves in a spherical Earth with 3D variations in seismic wave speeds. As a first application of this finite-difference algorithm, we use it to conduct a full-wave, finite-frequency tomography for the Iran region.

**Full-Wave, Finite-frequency Tomography for the Iran Region**

Iran is located in a seismically active region with frequent and widely distributed moderate-sized earthquakes (see Figure 2). Yet there has been a paucity of detailed investigation of the seismic structure of the crust and uppermost mantle in this region. Occasional seismic interests in this region included crustal studies using the Pn waves (e.g., Chen et al. 1980; Asudeh 1982; Hearn and Ni 1994; Ritzwoller et al. 2002) and uppermost mantle tomography studies (e.g., Ritzwoller and Levshin 1998; Ritzwoller et al. 1998; Maggi and Priestley 2005). In all the tomography studies, the Iran region is merely a portion of the larger model, and is characterized by a single swath of low-velocity region without internal structure. Therefore, a more focused study using local earthquakes and stations is necessary to obtain a refined 3D structure.

We selected the region between 22°N and 44°N and between 39°E and 66°E for our full-wave, finite-frequency tomography. For the reference or starting model, we chose the regional a priori 3D geophysical model of Pasyanos et al. (2004). This 3D model is constructed by combining the results from a number of published structural studies rather than from tomographic inversions. The resulting model includes density and the velocities and quality factors of P and S waves specified on a 1°x1° horizontal grid and at 24 depths from 0 to 660 km. Figure 3 shows a few map views and profiles of the 3D reference model.

We used the non-staggered grid finite-difference algorithm described in the previous section to compute the synthetic seismograms as well as the Fréchet kernels for tomography inversions. We stripped the water from the reference model by uniformly extending the structure right beneath the water up to the surface and imposed a minimum shear-wave speed of 1.2 km/s. Since most of the event-station paths are off the water/sediment covered areas (Figure 3), this approximation reduces computation with a minimum loss of accuracy in synthetic waveforms. A more refined grid can be applied to sediment-covered areas in following iterations of solution. In our finite-difference simulations, we used a time step of 0.12 s, a horizontal grid spacing of 0.02°, and a vertically variable grid spacing of 1–7.5 km, as shown in Figure 4, resulting in reliable surface waveforms up to a nominal period of about 15 s for event-station paths through the water/sediment covered areas and ~8 s for those elsewhere. For P waves, the period of reliable waveforms extends to 5 s.

We measured the frequency-dependent phase anomalies between the synthetic and recorded seismograms in several narrow frequency bands (0.0125–0.025, 0.025–0.05, 0.05–0.1, 0.1–0.2 Hz) and a broad frequency band (0.0125–0.2 Hz) by waveform cross-correlation. For the same arrival (say, Pn), we made measurements on all useful components of the three-component records, since the different components of the same arrival provide independent constraints on the Earth structure (Shen et al., 2008). Figure 5 shows an example of the band-pass-filtered observed and synthetic Pn and Rayleigh waveforms. We obtained over 2,400 high-quality measurements for the various arrivals, frequency bands, and components.

In order to compute the Fréchet kernels of the measurements with respect to the model parameters, we have adopted the strain Green tensor (SGT) database approach developed by Zhao et al. (2005; 2006). We have calculated the receiver strain Green tensors (RSGTs) for the 16 stations we have selected in the INSN network as well as the source strain Green tensors (SSGTs) for 31 events (see Zhao et al. 2006 for details of the Fréchet kernels using the RSGTs and SSGTs). The numerical calculations were carried out with 45 processors on the Linux cluster at URI/GSO. The resulting SGT database occupies a disk space of about 13 Terabytes. The Fréchet kernels for all the measurements can be efficiently calculated using the SGTs in the database in an iterative full-wave, finite-frequency 3D tomography for the Iran region.

Figure 6 shows an example of the sensitivity kernels for the Pn and Rayleigh waves in Figure 5. Note the sensitivities of the Pn traveltime to S wave speed. To a lesser extent, the Rayleigh wave phase is also affected by the P wave speed near the surface. Using numerical and analytical solutions, Zhang and Shen (2008) show that for finite-frequency waves, S wave-speed perturbations may have significant effects on P waveforms. At short source-receiver distances and near the source and receiver, the cross-dependence of P waveforms on S wave-speed is substantial. This finite-frequency effect has important implications for seismic tomography, particularly for regional and local earthquake tomography, in which the volume of interest is often within several 10 s of wavelength from receivers or both sources and receivers. Even for regions far from sources and receivers, neglecting this cross-dependence means that the estimates of the P wave-speed near the source and receiver are likely biased, and such errors may propagate into the rest of the model in tomographic inversions.

## CONCLUSIONS AND RECOMMENDATIONS

We have made great efforts in developing and validating finite-frequency sensitivity kernels for 3D velocity and attenuation reference models. We have implemented a non-staggered-grid finite-difference algorithm in spherical geometry which allows us to conduct full-wave, finite-frequency non-linear 3D tomography in a large region where the Earth's sphericity effect on seismic wave propagation cannot be neglected. We have calculated the strain Green tensors for the INSN stations and selected earthquakes. Using waveform cross-correlation, we measured over 2,400 body and surface wave phase anomalies relative to synthetic waveforms of an initial 3D reference model. We are applying the full-wave-field kernels to obtain a refined 3D model for the Iran region. Finally, substantial efforts are needed to further develop the method for large-scale 3D models and models with anisotropy.

## REFERENCES

Asudeh, I. (1982). Pn velocities beneath Iran, *Earth Planet. Sci. Lett*. 61: 136–142.

Chapman, C. H., and J. A. Orcutt (1985). The computation of body wave synthetic seismograms in laterally homogeneous media, *Rev. Geophys*. 23: 105–163.

Chen, C.-Y., W.-P. Chen, and P. Molnar (1980). The uppermost mantle P-wave velocities beneath Turkey and Iran, *Geophys. Res. Lett.* 7: 77–80.

Hearn, T. and J. Ni (1994). Pn velocities beneath continental collision zones: The Turkish-Iranian plateau, *Geophys. J. Int.* 117: 273–283.

Maggi, A., and K. Priestley (2005). Surface waveform tomography of the Turkish-Iranian plateau, *Geophys. J. Int.* 160: 1068–1080.

Olsen, K.B. (1994). Simulation of three-dimensional wave propagation in the Salt Lake Basin, Ph.D. Thesis, University of Utah, Salt Lake City, Utah, 157p.

Pasyanos, M. E., W. E. Walter, M.P. Flanagan, P. Goldstein, and J. Bhattacharyya (2004). Building and testing an *a priori* geophysical model for western Eurasia and North Africa, *PAGEOPH*, 161, 235-281.

Ritzwoller, M.H., M.P. Barmin, A. Villasenor, A.L. Levshin, and E.R. Engdahl (2002). Pn and Sn tomography across Eurasia to improve regional seismic event locations, *Tectonophysics* 358: 39–55.

Ritzwoller, M. H., and A. Levshin (1988). Eurasian surface wave tomography: Group velocities, *J. Geophys. Res*. 103: 4839–4878.

Ritzwoller, M. H., A. Levshin, L. Ratnikova, and A. Egorkin (1988). Intermediate-period group-velocity maps across Central Asia, western China, and parts of the Middle East, *Geophys. J. Int*. 134: 315–328.

Shen, Y., Z. Zhang, and L. Zhao (in press). Component-dependent Frechet sensitivity kernels and utility of three-component seismic records, *Bull. Seism. Soc. Am*.

Walter, W. R., M.E. Pasayanos, J. Bhattacharyya, and J. O'Boyle (2000). MENA 1.1 – An updated Geophysical regionalization of the Middle East and North Africa, UCRL-ID-138079, Lawrence Livermore National Laboratory Report.

Zhang, Z., and Y. Shen (in press). Cross-dependence of finite-frequency compressional waveorms to shear seismic wave-speeds, *Geophys. J. Int*.

Zhao, L., P. Chen, and T.H. Jordan (2006). Strain Green tensor, reciprocity, and their applications to seismic source and structure studies, *Bull. Seism. Soc. Am*. 96: 1753–1763, doi:10.1785/0120050253.

Zhao, L., T.H. Jordan, and K.B. Olsen, and P. Chen (2005). Fréchet kernels for imaging regional earth structure based on three-dimensional reference models, *Bull. Seism. Soc. Am.* 95: 2066–2080.

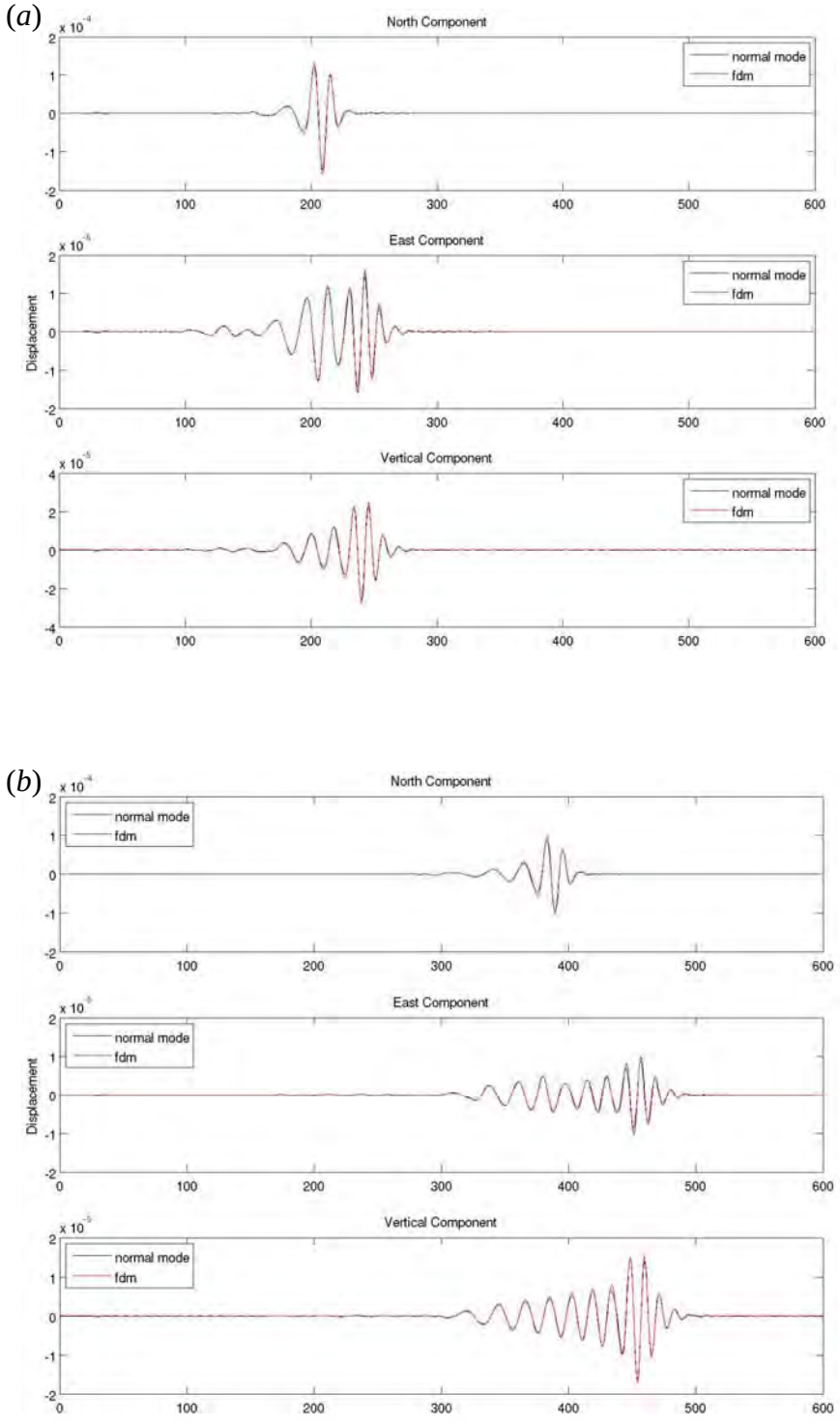


**Figure 1. Comparisons between two sets of 3-component synthetics calculated by the spherical finite-difference algorithm developed in this study and by normal-mode summation. These are for a surface source located on the equator with strike, dip and rake angles of 45°, 45° and 45°, respectively, and surface receivers to the east of the source at 5° (*a*) and 10° (*b*) distances.**

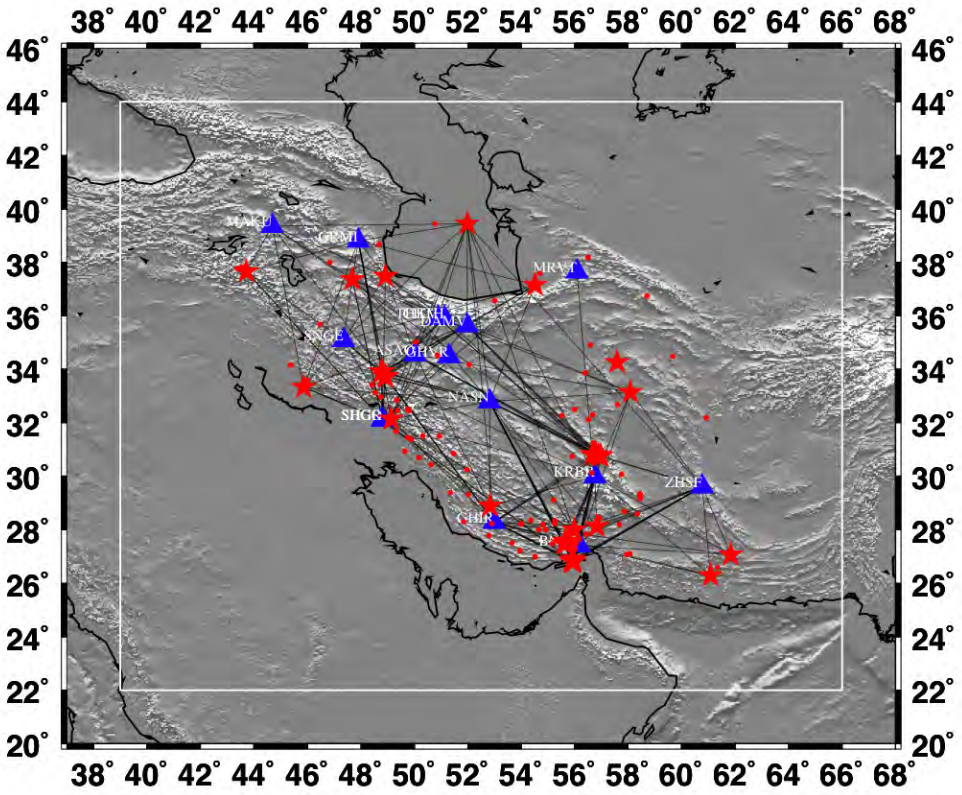


**Figure 2. Relief map of the Iran region under study. Red stars show the epicenters of the 31 selected earthquakes, and blue triangles show the INSN stations used in our tomography inversions. Small red dots mark the locations of the earthquakes, for which we have collected waveforms. Our modeling volume is in the area outlined by the rectangle and has a depth range of 0 to 700 km.**

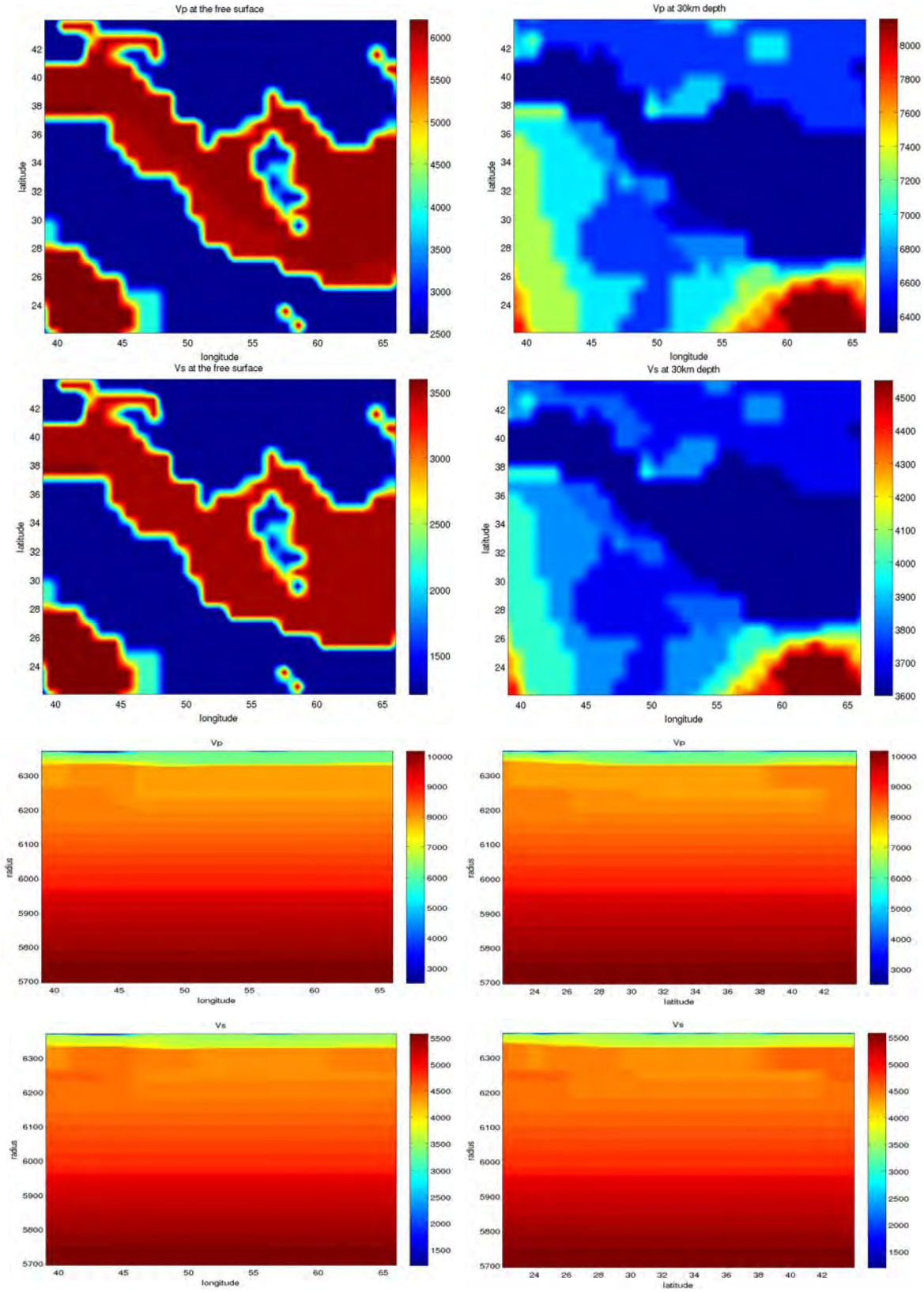


**Figure 3. Plots of the 3D reference model (Pasyanos et al. 2004). (1st row) Map views of Vp at 0 km and 30 km depths. (2nd row) Map views of Vs at 0 km and 30 km depths. (3rd row) Profiles of Vp along 34°N and 57°E. (4th row) Profiles of Vs along 34°N and 57°E.**

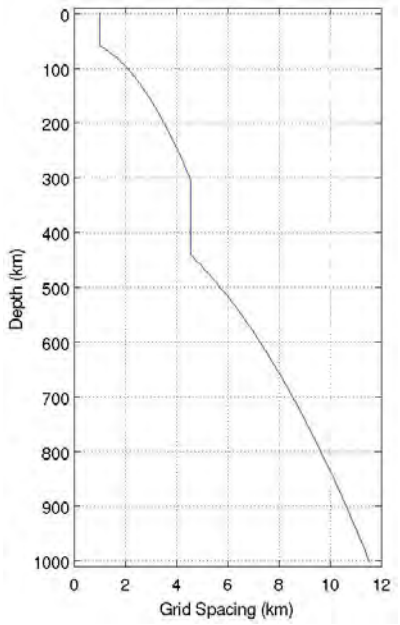


**Figure 4. Depth variation of the radial grid size used in the spherical non-uniform grid finite-difference simulations in the 3D reference model.**

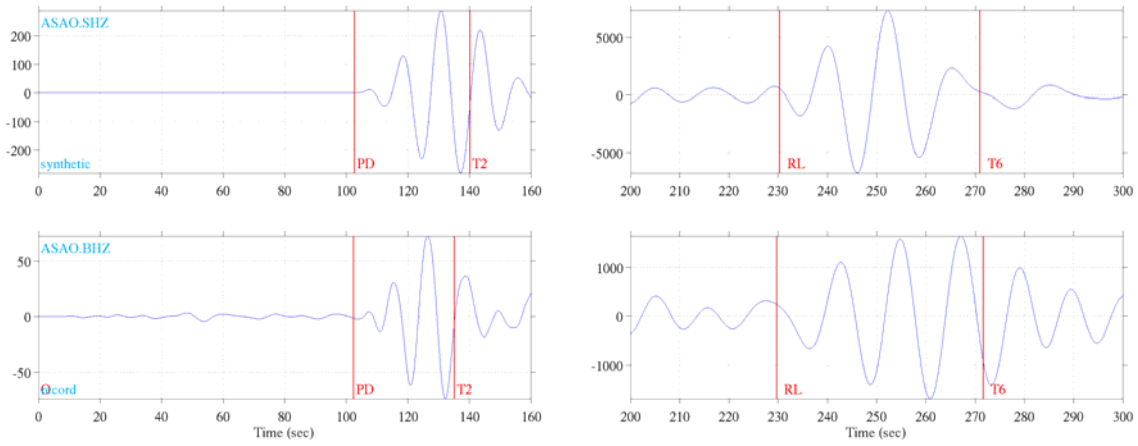


**Figure 5 Pn (left panels) and Rayleigh (right panels) waves from 14 May, 2005 earthquake ((Lat. 120.773, Long. 56.899) recorded on the vertical component at station ASAO (Figure 2). The synthetic waveforms calculated using the finite-difference code in a spherical coordinate system (top traces) are plotted for comparison. The waveforms have been band-pass filtered between 0.05-0.1 Hz. The vertical lines mark the time windows, within which cross-correlation measurements and corresponding sensitivity kernels (Figure 6) are calculated.**

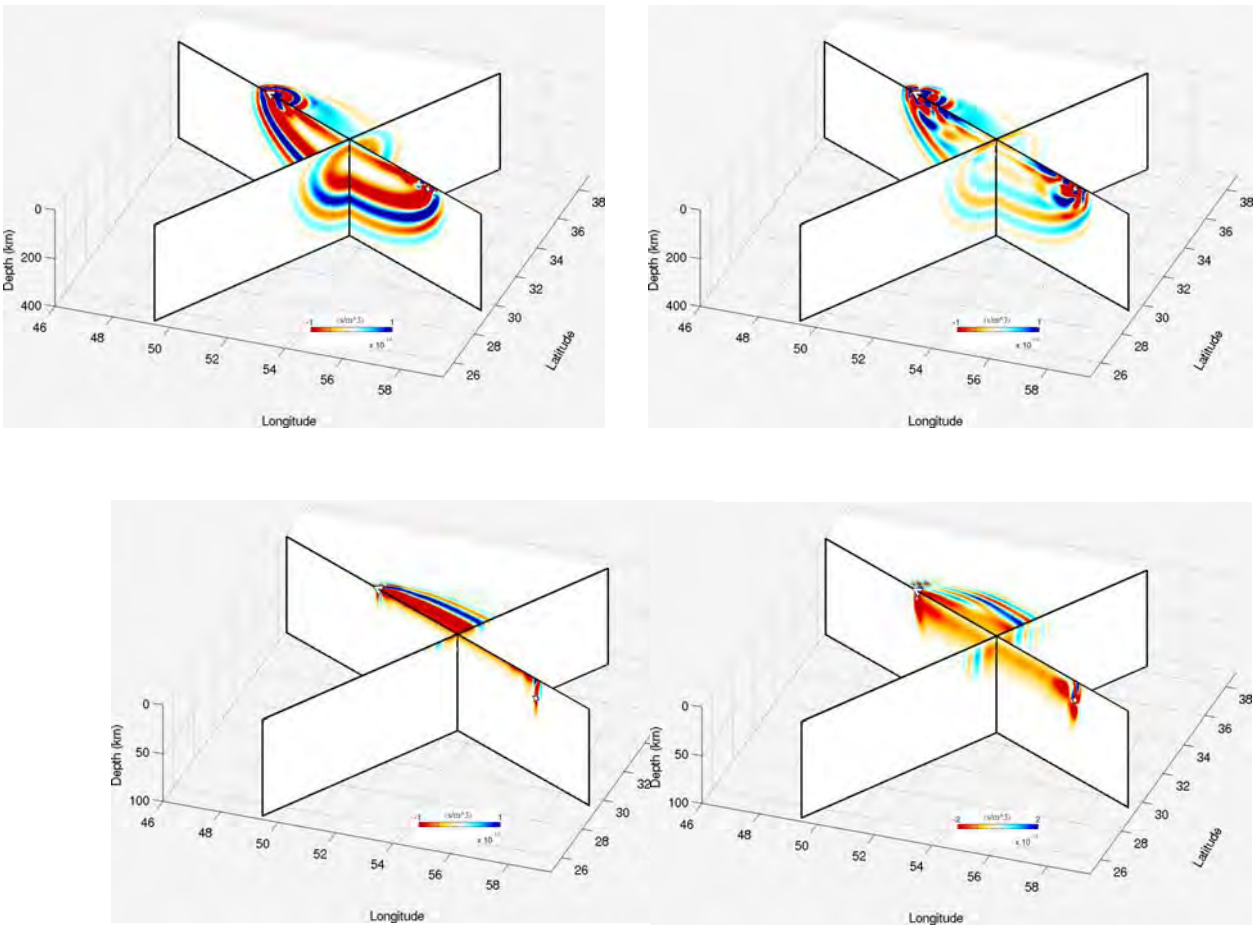


**Figure 6 (Top panels) Traveltime Sensitivity kernels of the Pn wave in Figure 5 to P wave-speed (left) and S wave-speed (right) perturbations. The kernels are so defined that low-velocity anomaly in the negative sensitivity region (red colors) results in a phase delay, while the same anomaly in the positive sensitivity region corresponds to an earlier arrival. (Lower panels) Phase sensitivity kernels of the Rayleigh wave in Fig. 5 to P wave-speed (left) and S wave-speed (right) perturbations. Note the vertical and color scales are different from those for the Pn wave.**

# Seismic Event Detection and Location

# NEXT GENERATION ROBUST LOW NOISE SEISMOMETER FOR NUCLEAR MONITORING

Igor A. Abramovich and Tao Zhu

PMD Scientific, Inc.

Sponsored by National Nuclear Security Administration

Contract No. DE-FG02-07ER84738

## ABSTRACT

Effective global monitoring of nuclear explosions calls for a worldwide network of seismic stations equipped with the next generation high quality digital seismometers for nuclear monitoring recording data in the 0.02–16Hz band. This project addresses these requirements: it is aimed at the implementation of the next generation, very low noise, broadband, wide dynamic range, extremely robust force-balanced digital seismometer for seismic monitoring of nuclear explosions. Successful completion of this project will serve vital national interests in greatly facilitating global compliance with nuclear non-proliferation and detection of possible violations of the Comprehensive Nuclear-Test-Ban Treaty by rogue states. The new seismometers should also be very competitive in various niches of the worldwide seismic market due to their valuable combination of high performance and exceptional ruggedness. The new generation seismometer uses improved electrochemical transducers built into three similar orthogonally mounted sensors, the latter based on conceptually new design ideas that, when implemented, will result in a drastic increase in signal to noise ratio. The principles of operation and detailed noise analysis of electrochemical motion sensors are presented along with the explanation of how such major noise reduction can and will be achieved. The new concept has shown to be promising based on test results of the experimental sensor prototypes. The new instruments should be easily and quickly deployable in field and stationary vault environments; they will be highly reliable and offer low cost of ownership since they require no maintenance: no mass locks; no mass position monitoring and/or mass centering over the full temperature range of -12 to +60C. The extremely rugged design will greatly reduce the probability of damaging such instruments during transportation and handling. The seismometer will incorporate a high-resolution, low-noise, very low power versatile 24-bit digitizer that will provide digital outputs with velocity-flat and optional acceleration flat and combined velocity/acceleration-flat response. The noise level of the proposed seismometers will be below the United States Geological Survey (USGS) New Low Earth Noise Model with the dynamic range of no less than 136dB over the 0.02 to the 16Hz frequency band. Maintaining the wide dynamic range, the uniform frequency response over the passband, and the considerably reduced noise will be greatly facilitated by the use of the efficient force-balancing electrodynamic feedback. In addition to the digitizer, each seismometer will also contain an ultra-low power microcontroller that will monitor gain and transfer function stability, provide for prompt, accurate temperature compensation over the full operating temperature range and perform on demand or periodical seismometer calibration. The complete digital seismometer is expected to consume less than 750mW.

## OBJECTIVES

Our current electrochemical sensors partially satisfy and all but one of the desired characteristics: their noise is at -170dB in the 0.05–8Hz band and thus has to be lowered by 15-20dB to be ~10dB below the NLNM in the broader (0.02 – 16Hz) band. Therefore, a radically new concept is needed that would lead to such significant noise reduction without sacrificing any of the original advantages of electrochemical sensors.

The ultimate objective of this project was to demonstrate the feasibility of the development of a novel force-balanced electrochemical seismic sensor with noise of at least 10dB below the USGS NLNM. Proof-of-concept prototype digital seismometers will be built and tested side-by-side with reference STS2 instruments.

***Objective:*** **Seismometer Noise.** Achieve the target noise levels shown in the Table below. Also included are the numbers anticipated to be achieved in the Phase II project:

| Passband | Target Noise Levels | |
|---|---|---|
| | Phase I | Phase II |
| 0.02-0.1Hz | -178 to -185dB♦ | -185 to -190dB♦ |
| 0.1 – 6Hz | -180 to -185dB* | --185 to -190dB* |
| 6 – 16Hz | -180 to -170dB• | (-185 -190) to -180dB• |

Notes: ♦ slightly bending upward toward longer periods; * practically flat; • sharper break toward higher frequencies similar to that observed in traditional seismometers.

***Objective:*** **Dynamic Range >136dB.** Demonstrate that implementation of the new design concept will not affect the instrument's dynamic range (our current production BB603 seismometers have a dynamic range of ~150dB).

***Objective:*** **Robustness.** Demonstrate that the targeted noise reduction will not require sacrificing of the inherent robustness of the electrochemical sensors. No mass locking mechanism should be used. Since electrochemical seismic sensors do not contain delicate moving mechanical parts they are extremely rugged. The newly proposed sensor promise to be even more rugged since it will have much smaller external inertial mass.

***Objective:*** **No Maintenance operation.** Demonstrate that the two signature features of electrochemical seismometers: no mass position monitoring/centering and ability to work with significant installation tilts will be preserved; the second feature is especially important for the borehole sensors.

***Objective:*** **Passband & Response.** Velocity-flat response in the required 0.02 – 16Hz band. The passband will be defined by the -3 dB corner frequencies with the ripple in gain of no more than +/- 1 dB from the mean gain values as measured from one octave above the lower corner frequency to one octave below the upper corner frequency

***Objective:*** **Digital Seismometer Power Consumption:** <750MW at 12Vdc. Of that amount the anticipated digitizer's share will be about two thirds.

## RESEARCH ACCOMPLISHED

### ELECTROCHEMICAL TRANSDUCER BASICS

A typical sensor (Figure 1) has a plastic housing filled with strong electrolytic solution: potassium iodide, *KI*, with a small addition of iodine, $I_2$. Electrolyte is contained between a pair of elastic membranes that significantly contribute to the sensor's transfer function. The transducer consists of four fine platinum mesh electrodes, two anodes, and two cathodes, separated by thin polymer mesh or laser-perforated mica spacers. The stack is tightly held together between two flanges. The motion of the fluid caused by an external acceleration is converted into an electrical signal via convective diffusion of the ions in the electrolyte. When a small dc offset is applied between the anodes and cathodes, the flow of ions of each type can be described by the following expression (Newman, 1973; Koryta and Dvorak, 1993).

$$\mathbf{j}_a = -D \cdot \nabla c_a + q_a \cdot c_a \cdot \mu \cdot \mathbf{E} \qquad (1)$$

Where D = diffusion coefficient; μ = mobility and $c_a$ = concentration of active ions; **E** = the electrical field vector. Since the strong electrolyte is an excellent conductor, the electric potential drops rapidly in the vicinity of the electrodes, and there is no electric field in the bulk of the fluid. Thus the second term in Equation 1 can therefore be ignored. Therefore, the application of a bias voltage results *only* in a concentration gradient. An acceleration, **a,** along the channel creates a pressure differential, **ΔP,** across the transducer, which forces the liquid to move with a velocity, **v**. This flow of electrolyte entrains ions and causes an additional charge transfer between the electrodes:

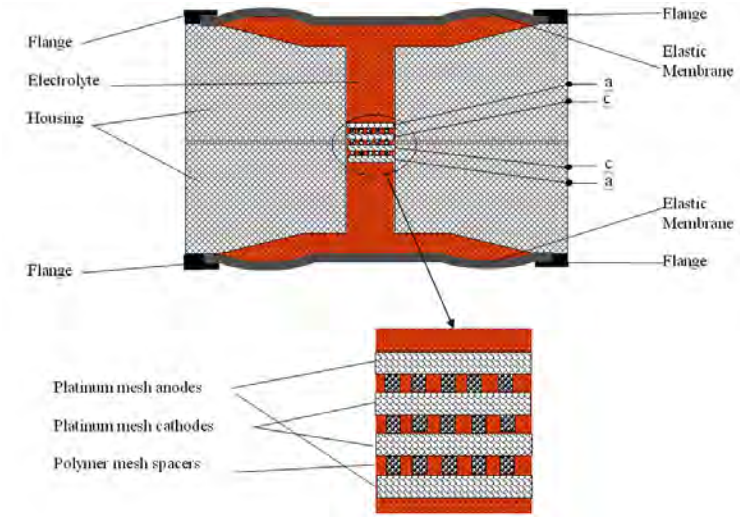


**Figure 1: Basic Electrochemical Seismic Sensor.**

$$\mathbf{j}'_{\mathbf{a}} = \mathbf{v} \cdot c_a \qquad (2)$$

The total current from active ions, in the presence of acceleration, can be expressed as:

$$\mathbf{j_a} = -D \cdot \nabla c_a + \mathbf{v} \cdot c_a \qquad (3)$$

Thus the transducer generates an electrical signal in response to acceleration.

A general expression describing noise in units of external acceleration:

$$\left\langle a^2 \right\rangle_\omega = \frac{2R_h kT}{(\rho L)^2} \qquad (4)$$

Where: $\rho$ = electrolyte density; $L$ = electrolyte effective length in the direction of the acceleration; $k$ = Boltzmann constant; $T$ = absolute temperature; $R_h$ = hydraulic impedance. The nominator in Equation 4 represents hydrodynamic thermal noise, similar to the Nyquist noise in electric circuits with the $R_h$ standing for the electric resistance $R$ (Van der Ziel, 1970). The total noise of a sensor agrees with Equation 4 only in the mid-frequency region. The elevated noise spectral density at both ends of the passband is due to at least two addition sources. The additional noise is unavoidable even when the two halves of the transducer are exactly symmetrical and thus their noise components add up to zero at the transducer differential output. These two sources are: fluctuation noise of the current flowing in the transducer; noise of the electronic amplifiers

The spectral density of fluctuation noise is described by the general equation:

$$\left\langle I^2 \right\rangle_\omega = 2qI \qquad (5)$$

Where $I$ = quiescent current of the transducer cell (Abramocvich and Daragan, 1992-94):

$$I = \frac{Dc_0 eS}{l}\left(1 - \exp(-\frac{qU_0}{kT})\right) \qquad (6)$$

$q$ = elementary charge in the cell. As two electrons participate in each elementary charge exchange reaction at the electrodes, $q = 2e$; $D$ = diffusion coefficient; $c_0$ = charge carriers equilibrium volumetric concentration; $U_0$ – voltage between and $S$ = effective area of the electrodes; $l$ = distance between the electrodes. Since each transducer consists of two independently working identical cells that are together characterized by the transfer function $W$, the following equation describes sensor fluctuation noise in units of acceleration:

$$\left\langle a^2 \right\rangle_\omega = 8eI \Big/ \left(W/\omega\right)^2 \qquad (7)$$

The practical method of increasing the signal-to-noise ratio is an addition of an inertial mass. For example, vertical and horizontal sensors of the PMD BB603 broadband seismometer are equipped with ~650g masses which results in noise below NLNM in the 0.06 – 8Hz. To account for the additional mass Equation 4 is modified:

$$\left\langle a^2 \right\rangle_\omega = \frac{2R_h kT}{\left(\rho L + M/S_s\right)^2} \qquad (8)$$

Where $M$ = external mass and $S_s$ = effective area of the sensor membrane. This is a simple, proven approach; it is easy to change/adjust $M$; the additional mass ("frame") is mounted in such a way that the membranes are not deformed. The frame carries a voice coil that transmits the feedback force to the membrane. Both qualitative and quantitative validity of Eq.10 have been confirmed experimentally. Evidently, further increase of the inertial mass would be impractical.

## PROPOSED DEVICE CONCEPT

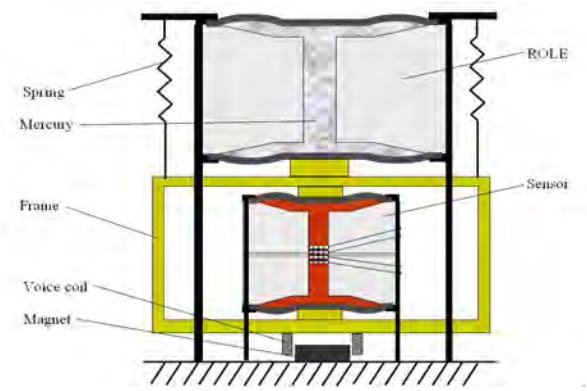


**Figure 2: HEX design concept.**

To achieve the required noise levels a radically new approach is necessary. While there is no known electrolyte with much higher density, a well known exceptionally heavy liquid exists: ***mercury*** (13.6 g/cm$^3$). The conceptual design of a sensor that we called Hybrid Electro-Chemical Sensor (HEX) is shown in Figure 2. A smaller electrochemical sensor has a frame with a voice coil moving around a magnet working in the force-balancing loop. The frame's top is firmly tied to the lower membrane of a larger sensor-like structure filled with mercury. The frame in such structure performs several functions: it carries the voice coil and thus transfers the balancing force to the sensor; it transfers pressure from the upper to the lower device; finally, it is attached to the suspension springs that balance the weight of the total oscillatory mass consisting of the frame itself, mercury and electrolyte. An external acceleration along the sensitive axis is transformed into pressure differential, $\Delta P_i$, between membranes in each of the two pairs: the large upper and the small lower. The following equation describes HEX noise:

$$\left\langle a^2 \right\rangle_\omega = \frac{2R_h kT}{\left(\rho_m h_m \dfrac{S_m}{S_s}\right)^2} \qquad (9)$$

Where $\rho_m$ and $h_m$ are respectively density and column height of mercury and $S_m$ = area of the ROLE membrane (we called the mercury-filled device 'ROLE' – short for '**ρ**-**L**-**E**nhancer': see $\rho$, $L$ terms in Equation 4).

Comparison of Equations 4 and 9 shows that the new concept not only capitalizes on the very high density of mercury, but achieves more than that: since the noise is inversely proportional to the ratio of the diameters of the two membranes it is possible to achieve an even larger increase in signal-to-noise ratio.

During Phase I research numerous vertical HEX sensors were built and tested. Initial tests were performed at PMD facility. A BB603 instrument specially tuned for the 0.02 – 16Hz band and with inertial mass increased to ~1.3kg was used as a reference. Most tests involved this reference and a pair of experimental sensors all placed on the same granite plate. The use of three instruments was necessitated by PMD noise calculation algorithm; all calculations were performed using DADiSP spreadsheet package. Many different configurations of HEX sensors were tested with various degrees of success. We encountered several unexpected phenomena. First off, our smallest diameter membrane that was promising the greatest gain in signal to noise ratio proved to be mechanically unstable. Several changes to the mold somehow improved its performance, however strong signals usually resulted in parasitic spikes. The strict time limits of the Phase I research did not allow us to manufacture another mold. Thus we had to make do with the larger size sensor membranes and therefore a limited $S_m / S_s$ ratio.

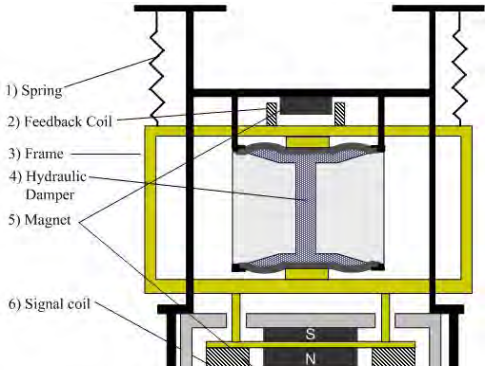


**Figure 3. Electrodynamic reference sensor with hydraulic Damper.**

Being understandably forced to test the preliminary prototypes at the PMD facility, we had to take into account the local background seismic noise. The area is mostly industrial, thus nightly and especially weekend nightly traffic is very scarce although a major street runs about ¾ miles away. PMD occupies a central part of a long, single storey industrial building. In a windless weekend night the long period noise in the passband of interest is at or slightly below -170db. The noise above several Hertz is always significant here though we could not tell whether it should be attributed more to the natural local background noise or to the noise of our instruments, whichever is higher. In order to find out the answer we built a special test instrument with inherently low noise at higher frequencies. An obvious and relatively simple solution would be using an electrodynamic transducer since its yield increases with frequency. At the same time we wanted this test instrument to share as much as possible its mechanical characteristics with an electrochemical sensor. A sketch of this force-balanced electrodynamic sensor is shown in Figure 2.

The inertial mass (frame, 3) is suspended on two springs, 1, and attached to the centers of the two membranes, similar to those used in standard electrochemical sensors. By measuring the time it takes for a known volume column of water to flow through a transducer, we determined experimentally the required diameter of the channel in the hydraulic damper, 4. The feedback coil, 2, is glued to the upper bar of the frame; the lower bar carries the pick-up coil, 6, which envelopes two very strong rare-earth magnets, 5.

To analyze the operation of such a hydraulically damped system let us start with the well-known generic equation of seismometer,

$$m \cdot \ddot{x} + D \cdot \dot{x} + K \cdot x = m \cdot \ddot{w} \qquad (10)$$

where: ***m*** = inertial mass; ***x*** = displacement of the inertial mass relative to the seismometer body; ***w*** = ground motion; ***D*** = damping coefficient; ***K*** = rigidity of the suspension.

In case of hydraulic damping this equation takes a slightly different form:

$$m \cdot \ddot{x} + K_s \cdot x + F_m = m \cdot \ddot{w} \qquad (11)$$

Where: $K_s$ = rigidity (rate) of the suspension spring, and $F_m$= the restoring force generated by the membranes. This force depends not only on the displacement ***x*** but also on the volume of the liquid in the buffer space under each membrane. This volume determines the initial position, $x_0$, of the membrane. Assuming small displacements, this force can be expressed as

$$F_m = 2K_m\left(x - x_0\right) \qquad (12)$$

where $K_m$ = rigidity (rate) of each membrane. Also,

$$\Delta x_0 = \frac{\Delta V}{S_m} \tag{13}$$

where: ***V***=volume of the liquid in the buffer space and $S_m$= effective area of the membrane. Now we can rewrite equation 8 in the following manner:

$$m \cdot \ddot{x} + K_s \cdot x + 2K_m\left(x - x_0\right) = m \cdot \ddot{w}. \tag{14}$$

In turn, $x_0$ is related to the displacement of the inertial mass:

$$\frac{dx_0}{dt} = \frac{dV}{dt} \cdot \frac{1}{S_m} = \frac{P}{R_h \cdot S_m} = \frac{K_m}{R_h \cdot S_m^2}\left(x - x_0\right) \tag{15}$$

Where: $P$ = pressure of the liquid and $R_h$= hydraulic impedance of the damper channel. For the sake of convenience we will rewrite equations 11 and 12 using Laplace operator $s$ that for harmonic signals equals $j\omega$:

$$m \cdot s^2 x + K_s x + 2K_m\left(x - x_0\right) = m \cdot s^2 w \tag{16}$$

$$s \cdot x_0 = \frac{K_m}{R_h \cdot S_m^2}\left(x - x_0\right), \text{ and thus} \tag{17}$$

$$x_0 = x \cdot \frac{K_m}{R_h \cdot S_m^2\left(s + \dfrac{K_m}{R_h \cdot S_m^2}\right)}\ . \tag{18}$$

And after substituting $x_0$ from equation 17 into equation 15,

$$x \cdot \left(m \cdot s^2 + K_s + \Gamma\right) = m \cdot s^2 w \tag{19}$$

Where: $\Gamma = 2K_m\left(\dfrac{s}{s + \dfrac{K_m}{R_h \cdot S_m^2}}\right)$. Looking at the expression in the parentheses, it is easy to conclude that at low frequencies, when $\omega$ is small, $\Gamma$ is reduced to $2R_h \cdot S_m^2 \cdot s$, and represents the damping factor. At higher frequencies, the $K_m / R_h \cdot S_m^2$ term becomes much smaller than $s$; $\Gamma$ reduces to $2K_m$, there is no additional damping in the system and the rigidities of the suspension spring and the membranes are added together.

Optimization of the damping is tightly connected with several additional critical parameters of the hydraulic device, in particular its possible contribution to the sensor noise.This hydraulic device plays several important roles in the system aside from the above described damping action. Indeed, the whole sensor is built around it: the inertial mass is suspended on its membranes; both pickup and feedback coils are mounted, in turn, on the inertial mass; the membranes provide proper centering of the whole oscillating system. The magnetic circuits are mounted on the damper assembly. Finally, it acts as an effective shock absorber during handling, transportation, and operation of the seismometer.

As mentioned above, the transducer directly measures the velocity of motion of the pickup coil relatively to the magnet that is attached to the seismometer base. Using Equation 16, one can find the relation between ground motion and this velocity:

$$x = \frac{m \cdot s^2 \cdot w}{m \cdot s^2 + K_s + \Gamma} \tag{20}$$

In the very low-frequency band (below 01Hz) this expression reduces to:

$$x = \frac{m \cdot s^2 \cdot w}{K_s + 2R_h \cdot S_m^2 \cdot s} \qquad (21)$$

Evidently, $s^2 \cdot w$ is ground motion acceleration. Then the corresponding pickup coil velocity, $V_c$, when s is so small that the second term in the denominator in Equation 12 can be neglected, will be expressed as follows:

$$V_c = s \cdot x \approx \frac{m}{K_s} \cdot s^3 \cdot w = \frac{m}{K_s} \cdot s \cdot a_{gnd} \qquad (22)$$

where $a_{gnd}$ = ground motion acceleration. Therefore, as expected, the pickup signal will be proportional to the ground motion frequency and inversely proportional to the rigidity of the suspension. The latter is a sum of the rates of suspension springs and membranes.

This sensor with inertial mass about 1.3kg performed rather well and indicated that during very quiet nights the background noise level at frequencies of several Hertz and higher was slightly below that of the HEX sensor. This result was rather surprising since, according to all calculations and general considerations, HEX sensor should have had a much lower noise at these frequencies. One of the contributors to this noise turned out to be a resonance peak at about 15–20Hz that had to be suppressed electronically. Other factors that will have to be investigated experimentally in Phase II will be combined noise from four membranes and hydraulic noise from the mercury-filled ROLE device. Evidently, we will have to optimize both geometries.

In March, 2008, we brought the best prototype HEX and the reference electrodynamic sensor to Albuquerque Seismological Laboratory (ASL) in Albuquerque for side-by-side testing against a high-gain STS2 seismometer. The recording was performed on Quanterra Q330 with two sampling rates: 1sps and 100sps. We selected a seemingly quietest period for noise evaluation using a PMD-developed algorithm based on data from three instruments. A superposition of three instrument-generated 1sps traces after correction for transfer function is shown in Figure 4 and noise curves calculated based on 100sps recordings in Figure 5.

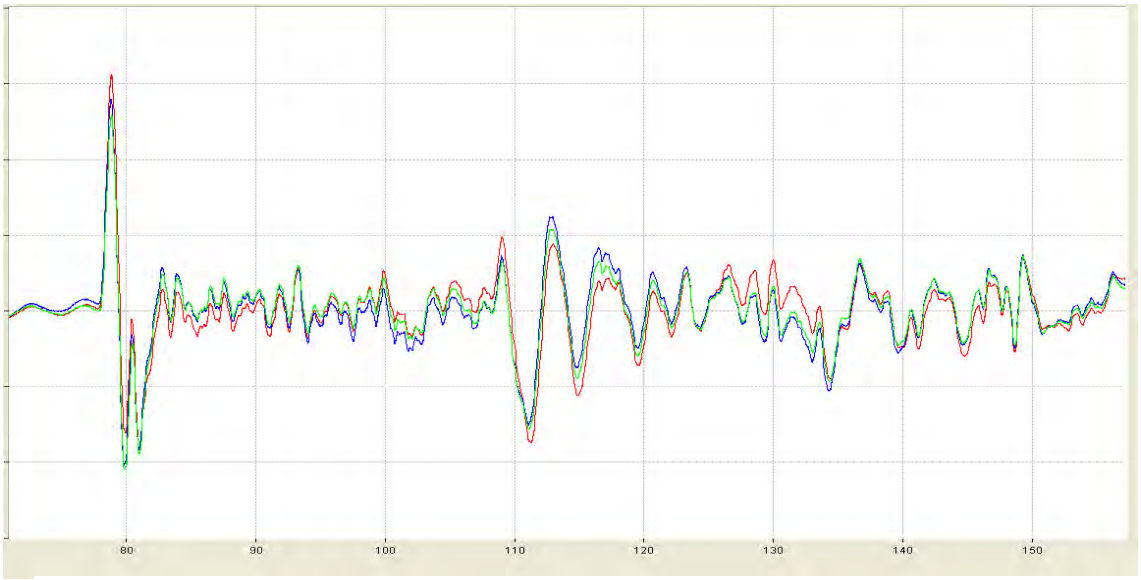


**Figure 4. Red-STS2; Blue – electrodynamic sensor, green – HEX sensor recorded at 1sps.**

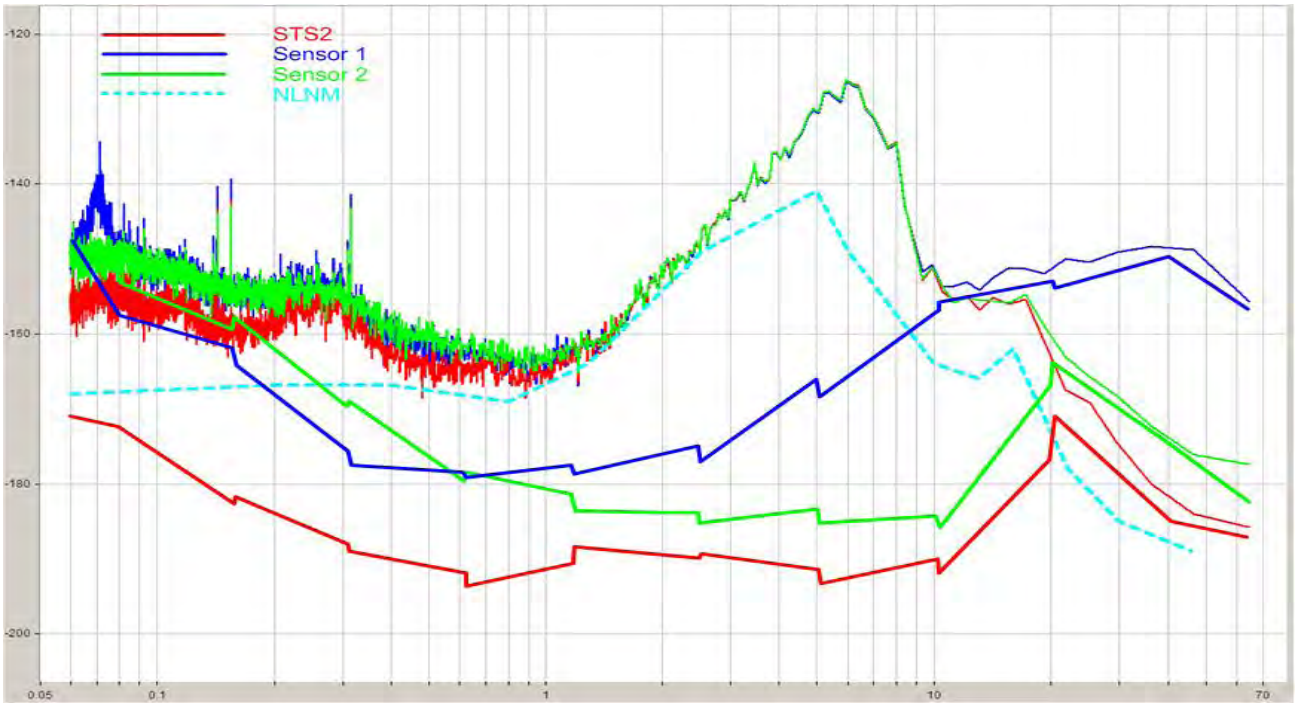


**Figure 5. Noise curves. Sensor 1 – electrodynamic; sensor 2 – HEX.**

Phase I objectives called for the following noise levels.

In the 0.02 to 0.1Hz passband noise curve was expected to go down from approximately -178dB to -185dB;
In the 0.1 to 6Hz band, the curve was expected to stay more or less flat within -180– -185dB margins;
Finally, from 6 to 16Hz the curve was expected to go up to approximately -170dB.

The prototype HEX sensor behaved in a way that we did not fully anticipate. Indeed, in the long period region, where we expected to encounter the most difficulties, the noise stayed below -180dB to between 1 to 20sec. The higher frequency noise went up from about 1sec. The seemingly sharp noise increase of both the HEX sensor and STS2 from 10s to longer periods should be explained by the imperfection of our noise cross-correlation calculation program: when one of the three sensors (in this case the electrodynamic sensor) has a significantly higher noise it obviously "pulls" with it two other test sensors, in this case the HEX and STS2. Therefore, the persistent ~6db differential between the STS2 and HEX after 10s may indicate that the latter indeed had a pretty low noise in this region, possibly to the desired levels.

The unexpected rise of the noise starting from about 1Hz and up can be partially explained by the smaller than intended $S_m/S_s$ ratio. Also this should suggest flaws in our mathematical model since the latter does not show noticeable frequency dependencies in the passband of interest. Had we been able to use the 25-mm-diameter sensor membrane, the whole curve would have shifted down by 6 to 10dB. But even in this case noise at 6Hz would be approximately -173 – -175dB or 7 to 10dB higher than desired. Fortunately, this mystery turned out to be easy to solve simply by looking at the noise curve of the electrodynamic sensor. The latter was supposed to have exceptionally low noise at higher frequencies and though it demonstrated a much better noise then HEX, starting at about 1Hz and up, the absolute noise levels were highly disappointing. We discovered the problem that was common for both test sensors on our return to PMD. All attention was paid to improving the transducers signal yield. Almost at the last moment it was decided to further enhance the low-frequency response of the test sensors by reducing their natural frequencies. Thus, we quickly designed and built astatizing suspensions, somehow similar to the original LaCost configuration. However, we evidently did not take into account the presence of another flexible member of the overall design: the membrane. When a signal is applied to the calibration input, it is easy to observe warping of the upper membrane (the one connected to the suspension system). Such warping is more detrimental at higher frequencies where, in particular, it results in several minor resonances that undoubtedly contribute to the

elevated noise. When we later replaced the “improved” suspension with a straight spring, the membrane moved along the direction of the axis of sensitivity without any noticeable parasitic warping. In addition, LaCost astatizing requires zero-length springs that we did not have in our possession.

## CONCLUSIONS AND RECOMMENDATIONS

Test results of the prototypes built during the Phase I effort, have proven the feasibility of the concept and of the proposed seismometer. A prototype instrument with noticeably reduced noise in comparison with the presently manufactured electrochemical seismometers exhibits the same ruggedness/robustness, passband, no maintenance operation (i.e., it does not require mass positioning and probably will not require the use of mass locks). Analysis of the field test results clearly points out the first step of the necessary improvements. At the exceptionally low noise levels required there is no doubt that several iterations of improvements and corrections will be needed. The most valuable lesson learned from the first experiments: do not do anything without very thorough evaluation no matter how “obvious” the results could be.

## ACKNOWLEDGEMENTS

We are extremely grateful to Dr. Bob Hutt and Mr. Leo Sandoval from ASL for their help in setting up and running the experiments.

## REFERENCES

Newman L. (1973). *Electrochemical Systems*, Prentice-Hall, Englewood Cliffs, NJ.

Koryta L and K. Dvorak (1993). *Principles of Electrochemistry*, J. Wiley, New York.

Van der Ziel A. (1970). *Noise; sources, characterization, measurement*, Prentice Hall.

Abramovich I. and S. Daragan, 1992–1994). *New Family of Inexpensive Broad Band Seismometers*, NSF SBIR Grant No. III-9360412.

# IMPLEMENTATION OF A PSEUDO-BENDING SEISMIC TRAVEL-TIME CALCULATOR IN A DISTRIBUTED PARALLEL COMPUTING ENVIRONMENT

Sandy Ballard, Chris Young, Jim Hipp, Glenn Barker, and Marcus Chang

Sandia National Laboratories

Sponsored by National Nuclear Security Administration

Contract No. DE-AC04-94AL8500

## ABSTRACT

Pseudo-bending is an algorithm for calculating seismic travel time through complex 3D velocity models. The algorithm was originally proposed by Um and Thurber (1987) and later extended by Zhao et al. (1992) to account for first order velocity discontinuities. We have modified Zhao's method of handling discontinuities by implementing a two-dimensional (2D) minimization algorithm that searches for the point on the velocity discontinuity surface where Snell's Law is satisfied. Further, our implementation reduces the likelihood that the pseudo-bending algorithm will return a local minimum by starting the ray calculation from several different starting rays. Specifically, interfaces are defined that include first order discontinuities plus additional interfaces at levels of the model where local minima might be generated. Rays are computed that are constrained to bottom in each layer between these interfaces. The computed rays might be reflected off the top of the layer, turn within the layer, or diffract along the interface at the bottom of the layer. The computed ray that is seismologically valid and that has the shortest travel time is retained.

The modifications we have made to the algorithm have made it more accurate and robust but have also made it more computationally expensive. To mitigate this impact, we have implemented our software in a distributed parallel computing environment, which makes possible the calculation of many rays simultaneously.

## OBJECTIVE

Our goal is to develop a practical, accurate, infinite frequency travel-time calculator through three-dimensional (3D) models of the distribution of seismic velocity in the Earth.

## RESEARCH ACCOMPLISHED

### Background

Three-dimensional models of the velocity distribution within the Earth are becoming increasingly available in the seismological research community and have the potential to significantly improve our ability to accurately and precisely locate seismic events around the world (e.g,. Flanagan et al., 2007). These 3D models are generally derived directly from observed travel times, using tomographic inversion techniques. Development of these models and use of the models in seismic-event location calculations, requires the ability to accurately compute predicted source-to-receiver travel times though the proposed 3D velocity structures. This is a complicated and computationally expensive task, and the many algorithms that have been proposed to accomplish it fall into three broad categories. Eikonal solvers (e.g., Vidale, 1988, 1990; Podvin and Lecomte, 1991; Rawlinson and Sambridge, 2004a, 2004b; and deKool et al., 2006) employ finite-difference techniques to propagate wavefronts through 3D velocity distributions defined on a 3D grid of points, thereby computing predicted travel times between a single point and an entire grid of points distributed within the medium. Ray shooters (e.g., Menke) systematically perturb an initial estimate of the ray take-off angle from a seismic source until the ray hits the seismic receiver, within some prescribed tolerance. Ray benders (e.g., Um and Thurber, 1987) start with an initial estimate of the ray geometry connecting the source and receiver and perturb the geometry of the ray until Fermat's principle of stationary time is satisfied all along the ray path. Though very different in approach to the problem, all of these techniques assume that the wave propagates from source to receiver with infinite frequency.

After reviewing several available algorithms, we chose to implement a version of the ray-bending algorithm described by Um and Thurber (1987), which was extended to include the effects of velocity discontinuities by Zhao et al. (1992) and Koketsu and Sekine (1998). We considered this algorithm superior to finite-difference eiknonal solvers for our intended applications because it provides direct, point-to-point travel times without interpolation off a grid and because it does not require calculation of full volumes of travel times for a small number of source-receiver pairs. We also consider it to be superior to ray shooters in that it will always find a solution, even in the presence of low-velocity zones, which can cause ray shooters to fail.

The algorithm is based on the fact that, along a valid ray path, the ray curvature is proportional to the component of the local velocity gradient normal to the ray path (Figure 1). The algorithm steps along an initial estimate of the path, perturbing the center point ($X_k$ in Figure 1) of three adjacent points on the path so that it satisfies this condition ($X_k$' in Figure 1). Zhao et al. (1992) and Koketsu and Sekine (1998) extended the algorithm to include the effects of planar and spherical velocity discontinuities, respectively. In this paper, we further extend the algorithm to allow discontinuities at arbitrary orientations. These modifications, described in detail in the next section, preclude the inclusion of the "enhancement factor" described by Um and Thurber (1987), and we have not included it in our implementation.

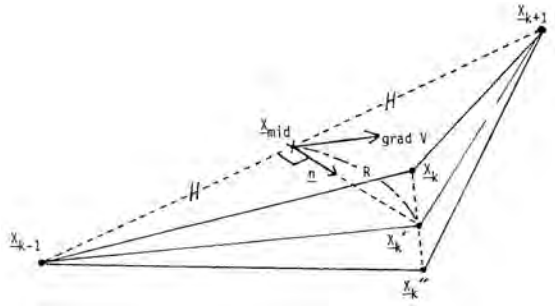


**Figure 1. Pseudo-bending algorithm (from Um and Thurber, 1987).**

A key feature of any system for computing travel time through 3D Earth models is the subsystem used to represent, and interpolate velocity values from, the 3D model itself. The system we use is described in detail in a companion paper (Ballard et al., 2008; these Proceedings) and is not reviewed here.

**Velocity Discontinuities**

Figure 2 depicts two media, $M_1$ and $M_2$, with velocity distributions $V_1(x, y, z)$ and $V_2(x, y, z)$, which may vary in three dimensions but which are first-order continuous internally. Surface S represents the smooth boundary between the two media such that the velocity may be discontinuous across S. The curve in Figure 2 represents the intersection of S with the plane of the figure, but S may dip into and/or out of the plane of the figure. Unit vector $\vec{n}$ is normal to S at X and does not necessarily lie in the plane of the figure. $P_1$ and $P_2$ are points in $M_1$ and $M_2$, respectively.; $\vec{x}_1$ and $\vec{x}_2$ are unit vectors that point from X toward $P_1$ and $P_2$ respectively.

In order for points $P_1$, X and $P_2$ to lie on a common ray path, Snell's Law must be honored at X, which requires that the following 3 conditions be satisfied:

$$C_1 = \frac{\sin\theta_1}{V_1} - \frac{\sin\theta_2}{V_2} = 0 \qquad (1)$$

$$C_2 = (\vec{x}_1 \times \vec{x}_2) \bullet \vec{n} = 0 \qquad (2)$$

and

$$C_3 = (\vec{x}_1 \times \vec{n}) \bullet (\vec{x}_2 \times \vec{n}) \le 0\,. \qquad (3)$$

In Equation 1, $V_i$ , $i$=1,2 is the arithmetic average of the velocity at $P_i$ and the velocity at X on the same side of S as $P_i$. Equation 2 requires that, $\vec{x}_1$ , $\vec{x}_2$ , and $\vec{n}$ be coplanar, implying that $\vec{n}$ lies in the plane of Figure 2 when Snell's Law is satisfied. Equation 3 prohibits $\vec{x}_1$ and $\vec{x}_2$ from residing on the same side of the line containing $\vec{n}$ (i.e., a nonphysical ray path). Figure 3 (a,b, and c) illustrates example distributions of Equations 1 through 3 displayed on a projection of S onto a spherical cap that passes through X.

While ray tracing, we are given points $P_1$ and $P_2$ on opposite sides of S and seek point X on S that satisfies Snell's Law, as expressed by the three conditions above. To find X, we implement a 2D search algorithm that minimizes

$$F = |C_1| + |C_2| + 10|C_3|\,. \qquad (4)$$

Experience indicates that the factor of 10 applied to $C_3$ improves convergence behavior. Figure 3d illustrates an example distribution of $F$ on a projection of S onto a spherical cap that passes through X.

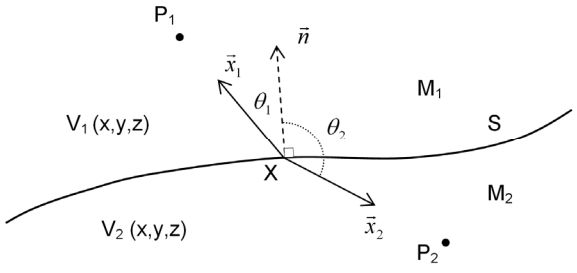


**Figure 2. Snell's Law applied at point X on surface S.**

**Phase Discrimination**

A problem that frequently arises when using the bending algorithm to predict travel times through realistic, regional to teleseismic scale, 3D models is that there exists more than one valid ray that connects a given source-receiver pair (Figure 4). Some of these rays represent different seismic phases, but even for a single phase there can be multiple valid rays that bottom at different levels in the Earth. Each of these represents a local minimum travel time but only once can represent the overall minimum path. To ensure that we get the desired ray, we specify a number of interfaces within the Earth and require the bender to compute rays that are constrained to bottom in each of the layers defined by those interfaces. We specify interfaces at all the velocity discontinuities with which a ray of a given phase must interact (Moho, 410, 660, etc.). We specify additional interfaces at levels within the Earth model that could potentially generate travel-time triplications, even though the velocity is continuous across these interfaces. The ray computed for each layer might be one that refracts within the layer, reflects off the interface at the top of the layer, or diffracts along the interfaces at the top and/or bottom of the layer.

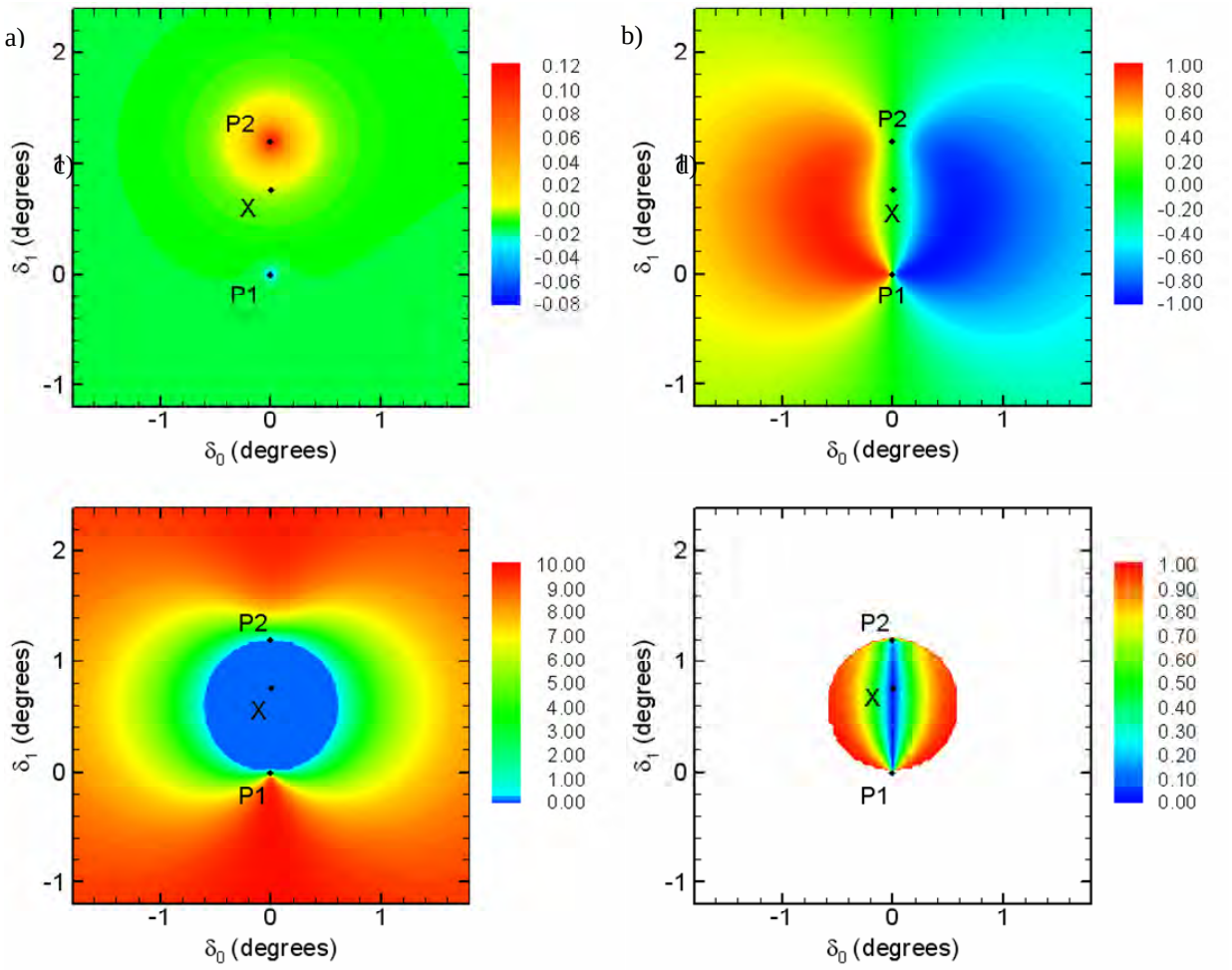


**Figure 3. Plots of (a) Equation 1, (b) Equation 2, (c) Equation 3, and (d) Equation 4 displayed on a projection of S onto a spherical cap that passes through X. Points P1 and P2 lie above and below the plane of the figures, respectively. In (d), portions of the map where Equation 3 is not equal to zero are blanked out.**

Not all of these rays are valid and hence can be discarded. In particular, rays that reflect off of, or diffract along, defined interfaces across which the velocity is continuous are not valid. If more than one valid ray is calculated from a given set of defined interfaces, the ray with the shortest travel time is retained.

A further advantage of this approach is that travel time for any desired phase can be computed by specifying the interfaces in the Earth with which the ray must interact (Figure 5). For example, to compute predictions for phase Pn, one would specify only the Moho and other interfaces in the mantle down to, but not including, the 660-km discontinuity, thereby constraining the computed ray to bottom somewhere in the mantle above the 660.

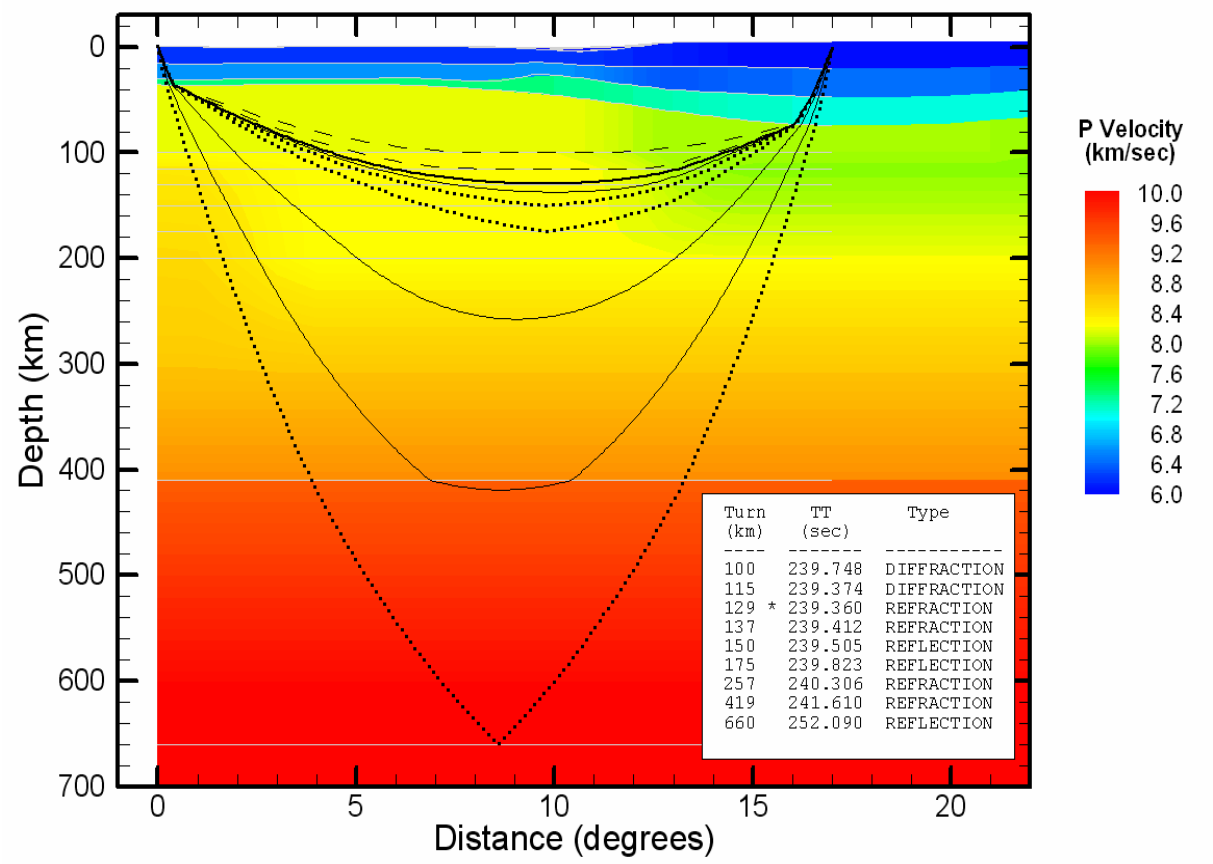


**Figure 4. Multiple valid seismic rays connect a given source and receiver, each constrained to bottom in a specified layer of the Earth model.**

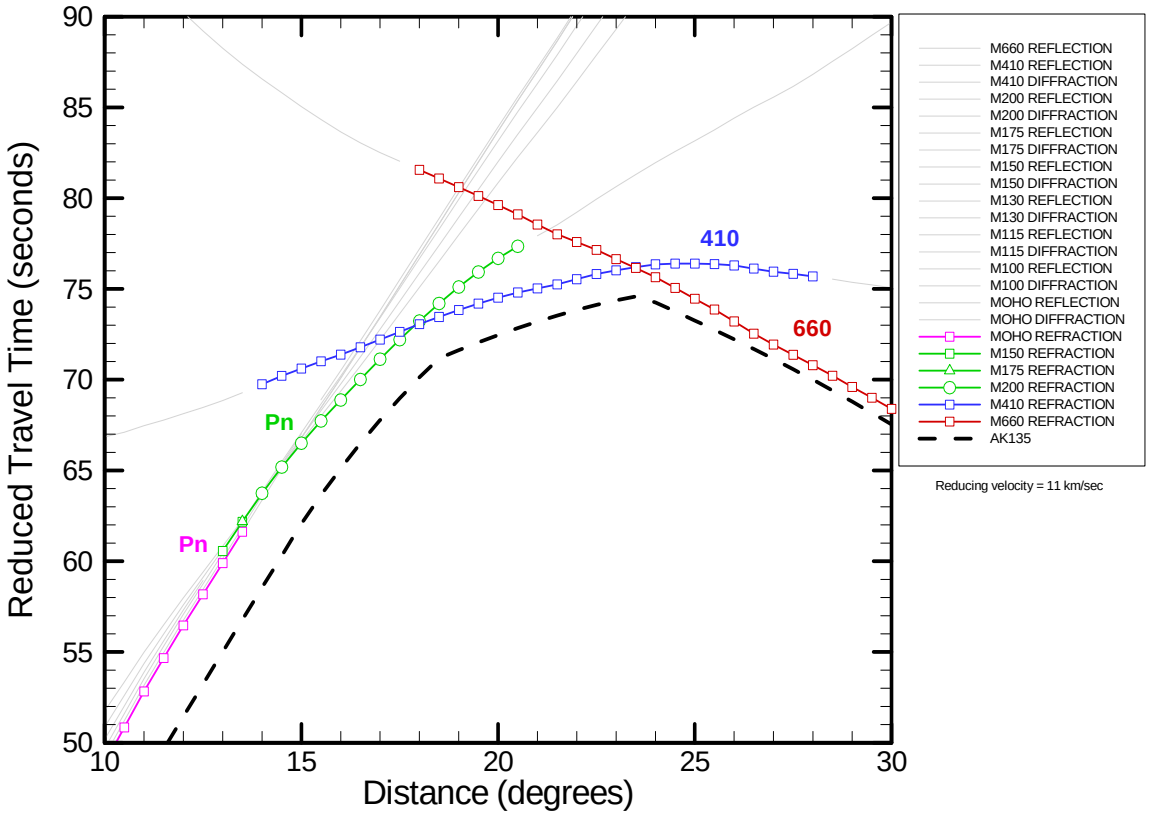


**Figure 5. Travel-time curves for a source-receiver pair in a 3D Earth model with velocity generally less than that of the AK135 model.**

### Algorithm Verification

We have verified the validity of the bender algorithm in two ways. First, we constructed a 3D version of the radially symmetric AK135 model (Kennett et al., 1995). The 3D version is deployed on a uniform, 1° triangular tessellation similar to the tessellations we use for more-complex 3D models (Ballard et al., 2008; these Proceedings), but the model is based on a spherical Earth with the same velocity discontinuities and radial velocity distribution as the AK135 model. Rays through the model computed with Bender are shown in Figure 6, and travel times computed with Bender and using the TaupToolkit software (Crotwell et al., 1999) are compared in Figure 7. The difference at all regional and teleseismic distances is at most a few hundredths of seconds, indicating that Bender is very accurate, even for long path lengths.

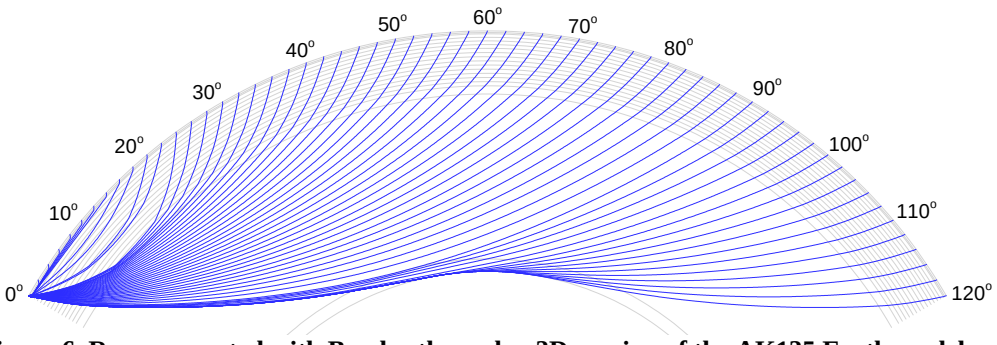


**Figure 6. Rays computed with Bender through a 3D version of the AK135 Earth model.**

To verify the validity of Bender travel times through Earth models with significant 3D velocity variations, we built a 3D model based on the a priori GNEMRD Unified Model (Begnaud et al., 2004; Pasyanos et al., 2004) and computed travel times through it using our Bender code and the FMM code (De Kool et al., 2006). Topography and bathymetry for the Unified Model were derived from ETOPO5, while shallow sedimentary layers were taken from the 1-degree-resolution sediment model of Laske and Masters (1997). The structure of crust and uppermost mantle is drawn from a variety of focused regional studies. The upper-mantle model (below 100 km) is taken from the a priori 3SMAC model (Nataf and Ricard, 1996).

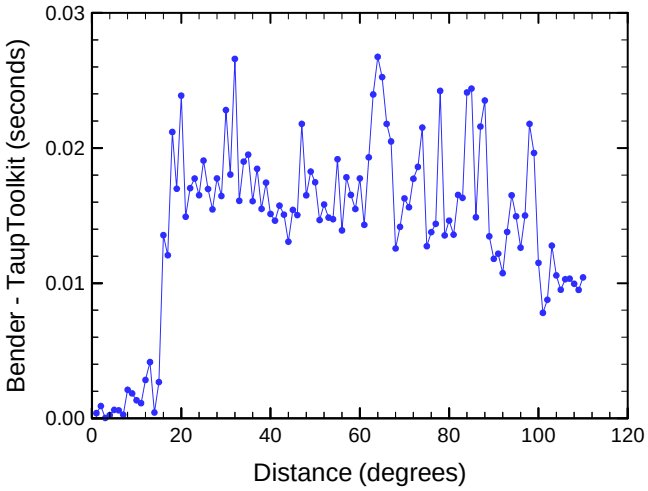


**Figure 7. Difference in travel time computed by Bender and Taup Toolkit through the AK135 velocity model.**

As with all finite-difference eikonal solvers, the FMM algorithm works by following a wavefront as it moves across a volume of grid points, updating the travel times in the grid according to the eikonal differential equation, using a second-order finite-difference scheme. We chose to use FMM for our comparison because it has a number of important features that make it well suited for making calculations in the regional-to-teleseismic distance ranges that we are interested in. First, the propagation grid is in spherical coordinates rather than Cartesian coordinates, so the sphericity of the Earth can be more readily represented. Second, interfaces are explicitly represented in the FMM grid, regardless of the propagation grid spacing. Thus, a finer propagation grid is not necessary to capture discontinuities with topography, like the Moho. Third, FMM allows calculation of secondary phases, so it can be used for non–first-arrival phases. Finally, finer grid spacing can be used near the source to better capture the highly curved wavefront and hence improve accuracy without drastically increasing the overall number of nodes.

For purposes of comparing travel times computed using Bender with those computed using FMM, we chose station NIL located in Nilore, Pakistan, at latitude 33.6506 N and longitude 72.2686 E. Even though the station is 0.629 km above sea level, we set the elevation to sea level for these calculations in order to avoid having to compute elevation corrections for the FMM results. Next, we specified a 40º × 40º grid of sources extending from 53º to 93º E longitude and 14º to 54º N latitude, with 0.25º grid spacing in both directions. All sources were positioned at 10 km below sea level. We computed travel times from these sources to the position of station NIL using both Bender and FMM. With Bender, it was possible to compute point-to-point travel times for these source-receiver pairs directly, but with FMM we had to first construct a 3D grid that extended from sea level to a depth of 1000 km in order to ensure that the depth of the grid exceeded the deepest bottoming depth of any rays we were interested in. In addition, the FMM grid had to be denser than 0.25º × 0.25º in order to achieve sufficient accuracy. To test the accuracy of the FMM results, we constructed two finite-difference grids, one 0.125º × 0.125º × 10 km and the other 0.0625º × 0.0625º × 5 km. Due to computer-memory limitations, we had to break the 3D grid into four quadrants, run FMM on each quadrant separately, recombine the results into a single grid, and finally subsample the FMM grids at the points of the 2D Bender grid. The difference in travel time between FMM and Bender, for the two different FMM grid resolutions, is illustrated in Figure 8. The difference in travel time decreased as a function of FMM grid resolution, and FMM travel time was virtually always greater than Bender travel time. From these observations we conclude that the Bender travel times are likely a better reflection of the actual travel time through the Earth model used in the calculations. It is entirely possible that FMM travel times would have been reduced, and approached the Bender travel times, had we been able to improve the resolution of the FMM grid even further. We were prevented from doing that by computer-memory limitations

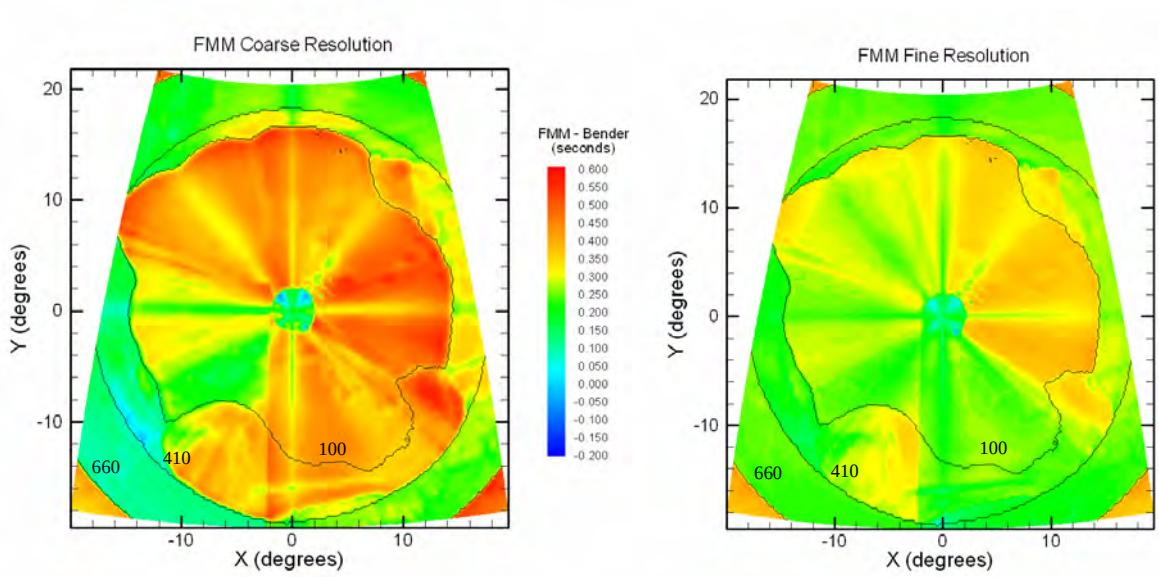


**Figure 8. FMM travel time minus Bender travel time for a 40º × 40º grid surrounding station NIL. On the left, the FMM travel times were computed on a 0.125º × 0.125º × 10 km grid; on the right, they were computed on a 0.0625º × 0.0625º × 5 km grid. Black contour lines indicate positions of sources where rays bottomed at depths of 100 km, 440 km, and 660 km, as determined by Bender.**

### Distributed Computing

The enhancements we have made to the pseudo-bending algorithm of Um and Thurber (1987), as modified by Zhao et al. (1992), have made it more robust and accurate but have also made it more computationally expensive. Our implementation typically requires approximately 0.5 seconds to compute one travel time on a single computer processor. To mitigate these negative performance impacts, we have implemented the software, which is written entirely in the Java programming language, in a distributed computing environment, using the Java Parallel Processing Framework (JPPF; www.jppf.org). This technology makes it fairly straightforward to run many travel-time calculations simultaneously on all available PC, Mac, Unix, and Linux computers. We are currently running our software on a cluster of nine 16-processor PC computers running the 64-bit Windows Server 2003 operating system. Combined with other PCs, Linux boxes, and Sun workstations, our system has almost 200 processors available for calculating travel times.

## CONCLUSIONS

We have implemented the pseudo-bending algorithm of Um and Thurber (1987), as modified by Zhao et al. (1992), for computing predicted travel times through 3D velocity models. We have modified Zhao's method of handling discontinuities by implementing a 2D minimization algorithm that searches for the point on the velocity discontinuity surface where Snell's Law is satisfied. Our implementation also significantly decreases the likelihood that the algorithm will return a ray that represents a local minimum by computing rays that bottom in many different specified layers in the model and returning the ray that yields the smallest travel time. We have validated our algorithm by comparing it with the TaupToolkit software (Crotwell et al., 1999) for radially symmetric 1D Earth models. We have also compared our results with travel times computed with the FMM finite-difference calculator (De Kool et al., 2006) and demonstrated that the Bender yields superior results with substantially fewer computer resources.

We are currently developing improved velocity models of the Earth using a tomographic inversion system that uses our Bender software as the forward travel-time calculator. Preliminary results for a study in southcentral Asia are reported in Young et al. (2008, these Proceedings).

## ACKNOWLEDGEMENTS

We thank Marthijn de Kool for his help in getting the FMM code running on our computers, and the GNEMRD researchers at Los Alamos National Laboratory and Lawrence Livermore National Laboratory for providing us with their a priori 3D geophysical model.

## REFERENCES

Ballard, S., Hipp, J., and C. Young (2008). Robust, extensible representation of complex earth models for use in seismological software systems, these Proceedings.

Begnaud, M. L., C. A. Rowe, and L. K. Steck (2004). Validating three-dimensional velocity models in China and East-Asia for use in regional seismic event location, EOS *Trans. AGU*, Fall Meet. Suppl.

Crotwell, H. P., T. J. Owens, and J. Ritsema (1999). The TauP toolkit: Flexible seismic travel-time and ray-path utilities, *Seism. Res. Lett*. 70: 154–160.

De Kool, M., N. Rawlinson, and M. Sambridge (2006). A practical grid based method for tracking multiple refraction and reflection phases in 3D heterogeneous media, *Geophys. J. Int*. 167: 253–270.

Flanagan, M. P., S. C. Myers, and K. D. Koper (2007). Regional travel-time uncertainty and seismic location improvement using a three-dimensional a priori velocity model, *Bull. Seism. Soc. Am.* 97: 804–825.

Hole, J. A. and B. C. Zelt (1995). 3D finite-difference reflection traveltimes, *Geophys. J. Int.* 121: 427–434.

Kennett, B. L. N., E. R. Engdahl, and R. Buland (1995). Constraints on seismic velocities in the Earth from traveltimes, *Geophys. J. Int*. 122: 108–124.

Koketsu, K. and S. Sekine (1998). Pseudo-bending method for three-dimensional seismic ray tracing in a spherical earth with discontinuities, *Geophys. J. Int.* 132: 339–46.

Laske, G. and T. G. Masters (1997). A global digital map of sediment thickness, *EOS Trans. AGU* 78: F483.

Menke, W. Case studies of seismic tomography and earthquake location in a regional context, http://www.ldeo.columbia.edu/users/menke/R3DPAPER/r3dpaper.pdf.

Nataf, H. C. and Y. Ricard (2004). 3SMAC: An a priori tomographic model of the upper mantle based on geophysical modeling, *Phys. Earth Planet. Int*. 95: 101–122.

Pasyanos, M. E., W. R. Walter, M. P. Flanagan, P. Goldstein, and J. Bhattacharyya (2004). Building and testing an a priori geophysical model for Western Eurasia and North Africa, *Pure Appl. Geophys*. 161: 234–281.

Podvin, P. and I. Lecomte (1991). Finite difference computation of traveltimes in very contrasted velocity models: A massively parallel approach and its associated tools, *Geophys. J. Int.* 105: 271–284.

Rawlinson, N. and M. Sambridge (2004a). Multiple reflection and transmission phases in complex layered media using a multistage fast marching method, *Geophysics* 5: 1338–1350.

Rawlinson, N. and M. Sambridge (2004b). Wave front evolution in strongly heterogeneous layered media using the fast marching method, *Geophys. J. Int*. 156: 631–647.

Um, J. and C. H. Thurber (1987). A fast algorithm for two-point seismic ray tracing, *Bull. Seismol. Soc. Am*. 77: 972–986.

Vidale, J. E. (1988). Finite-difference calculations of traveltimes, *Bull. Seism. Soc. Am*. 78: 2062–2076.

Vidale, J. E. (1990). Finite-difference calculations of traveltimes in three dimensions, *Geophysics* 55: 521–526.

Young, C. J., S. Ballard, J. R. Hipp, M. C. Chang, G. T. Barker, M. L. Begnaud, W. S. Phillips, L. K. Steck, and C. A. Rowe (2008). A 3D tomographic model of south central Asia based on Pn travel times from GT events, these Proceedings.

Zhao, D., A. Hasegawa, and S. Horiuchi (1992). Tomographic imaging of P and S wave velocity structure beneath northwestern Japan. *JGR* 97: B13, 19, 909–19,928.

# ROBUST, EXTENSIBLE REPRESENTATION OF COMPLEX EARTH MODELS FOR USE IN SEISMOLOGICAL SOFTWARE SYSTEMS

Sandy Ballard, Jim Hipp, and Chris Young

Sandia National Laboratories

Sponsored by National Nuclear Security Administration

Contract No. DE-AC04-94AL8500

## ABSTRACT

Models of geophysically important properties of the Earth, such as seismic velocity, Q and density, can become large and complex when those properties vary in three dimensions within the model. We have developed a system to represent the distribution of seismic properties in the Earth that can accommodate a wide range of local to global scale 3D Earth models with spatially variable resolution. A 2D grid of nodes is tessellated using either triangles or quadrilaterals and a profile is defined at each 2D grid node that extends from the center of the Earth to the surface. The surface of the model corresponds with the topographic/bathymetric surface of the Earth, which is referenced to the surface of the GRS80 ellipsoid. Each profile can be separated into a number of layers defined by interfaces across which geophysical properties may be discontinuous. Within the layers between interfaces, the vertical distribution of geophysical properties may be defined by a number of continuous sublayers, by arbitrary order polynomials or by various types of splines. Layer thicknesses can vary laterally and zero thickness layers and layer pinch-outs are accommodated. The distribution of nodes is very flexible, allowing model resolution to vary over a wide range in three dimensions. In this paper, we present detailed descriptions of the software algorithms used to construct, store and interpolate these models.

.

### Objective

Complex models representing the three dimensional distribution of seismological properties within extensive areas of the Earth are becoming ever more common in seismological endeavors. Notable examples include the global Crust 2.0 model (Laske et. al., 2008), the broad regional (Western Eurasia and North Africa (WENA) model (Pasyanos et al. 2004), and WINPAK3D model (India-Pakistan; Reiter et al, 2001). The prevalence of such models has come about in part as a result of the dramatic improvement in computational capabilities in recent years. Computer systems able to handle large (gigabyte), geographically extensive models that represent properties from deep in the Earth to its surface are now commonly available.

Unfortunately, the level of sophistication of model representation has not kept pace with the models themselves. Many models are still based on regularly spaced grids that lead to increasing densities of nodes towards the poles and deep within the Earth. These simplistic representations are employed not because they match the structure of the Earth, but because they are easy to implement and use. However, these representations are inherently inefficient and they are particularly ill-suited to global scale models. To develop global models that can be accessed and used quickly, a model representation is needed that is designed specifically to fit the real ellipsoidal, laterally and radially heterogeneous structure of the Earth. In this paper we describe an Earth model representation that enjoys global coverage in both radial and geographic dimensions, and variable resolution that reflects the state of knowledge of underlying parameters rather than ease of interpolation. As described in detail below, our representation involves a two-dimensional tessellation of triangles on the surface of a unit sphere, with radial profiles of Earth properties defined at points on the sphere where three or more triangles intersect. We also describe the types of information that must be stored in order to completely represent the model and methods for interpolating information from the model.

## RESEARCH ACCOMPLISHED

### Coordinate System

Before we can describe the model representation, we first define the Earth-centered coordinate system used to define the positions of points relative to the Earth. Points are defined by a unit vector, $\mathbf{x} = \{ x_0, x_1, x_2 \}$, with its origin at the center of the Earth, and radius, $r$, measured in km from the center of the Earth. As illustrated in Figure 1, this coordinate system is oriented such that $x_0$ points from the center of the Earth toward the point on the surface with latitude and longitude 0°, 0°; $x_1$ points toward latitude, longitude 0°, 90° and $x_2$ points toward the north pole.

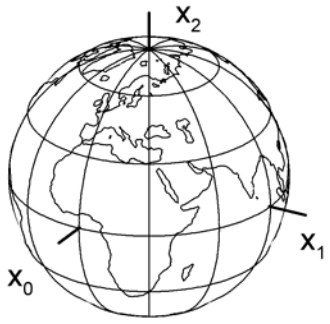


**Figure 1. Earth centered Cartesian coordinate system**.

### Earth Model Representation

The Earth model representation we describe here consists of a two-dimensional, multi-level tessellation of triangles which completely covers the surface of a unit sphere without gaps or overlaps. The highest level of the tessellation consists of large triangles which are subdivided into ever smaller triangles at lower levels of the tessellation. At the vertices of the triangles, which all reside at the surface of the unit sphere, Earth properties are defined along radial profiles that extend from the center of the Earth to its surface. We first describe how the tessellation is constructed, and then how to find an estimate of the value of an Earth property at an arbitrary point in the Earth by interpolating values stored in the model.

### Definitions

To facilitate description and manipulation of the tessellation, the following terms are defined:

- If vertex *V* is a corner of triangle *T*, then *V* is a *member* of *T* and *T contains V*.

- Given vertex $V_i$ that is a member of triangle $T$, then $V_j$ is the *next* vertex in $T$ if one arrives at $V_j$ by traversing the edge of $T$ that leaves $V_i$ in a clockwise direction as viewed from outside the unit sphere.
- Triangle $T$ has *edges*, $E_i$, $i$=1,3, where $E_i$ connects vertices $V_j$ and $V_k$, where $V_j$ is the next vertex in $T$ after $V_i$ and $V_k$ is the next vertex in $T$ after $V_j$. Note that given a vertex $V_i$, $E_i$ is the edge of $T$ that does not contain $V_i$.
- Triangle $N_i$ is the $i$'th *neighbor* of triangle $T$ if $N_i$ is the triangle on the other side of edge $E_i$.

Each vertex should maintain a *triangle membership list*, i.e., a list of the triangles of which it is a member.

Each triangle $T$ should maintain the following information:

1. References to the three vertices which are members of $T$
2. References to its three neighbors
3. References to three new vertices. These should default to null, but may be set to instantiated vertices if $T$ is subdivided, as will be described shortly.
4. A reference to a descendent triangle, if there are any. If $T$ is subdivided, as described later, the reference can refer to any of the triangles that are descendents of $T$.
5. A Boolean flag indicating whether or not $T$ is 'marked.' All triangles start out 'unmarked'.

**Tessellation Construction**

Construction of each level in the tessellation involves

1. Identifying the vertices involved in the given level of the tessellation.
2. Connecting the vertices together to define triangles that completely span the surface of the unit sphere.
3. For each vertex, populating its triangle membership list.
4. For each triangle, establishing which triangles are its neighbors.

The first level of the tessellation consists of a regular icosahedron, which is a convex regular polyhedron composed of twenty congruent, equilateral triangles that meet at twelve vertices (Figure 2). Using the coordinate system defined earlier, the coordinates of the twelve vertices of a regular icosahedron are given in Table 1.

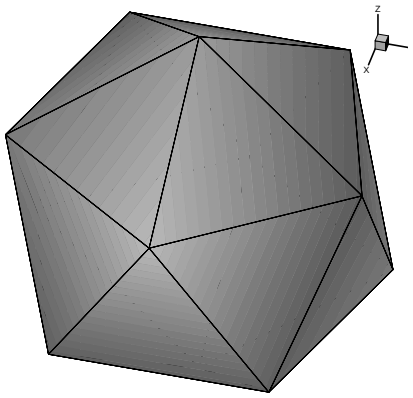


**Figure 2. A regular icosahedron consisting of 12 vertices and 20 congruent equilateral triangles.**

**Table 1 – Vertices of a regular icosahedron**.

| Vertex | $v_0$ | $v_1$ | $v_2$ |
|---|---|---|---|
| 0 | 0.000000000000000 | 0.000000000000000 | 1.000000000000000 |
| 1 | 0.894427190999916 | -0.000000000000000 | 0.447213595499958 |
| 2 | 0.276393202250021 | 0.850650808352040 | 0.447213595499958 |
| 3 | -0.723606797749979 | 0.525731112119134 | 0.447213595499958 |
| 4 | -0.723606797749979 | -0.525731112119134 | 0.447213595499958 |
| 5 | 0.276393202250021 | -0.850650808352040 | 0.447213595499958 |
| 6 | 0.723606797749979 | -0.525731112119134 | -0.447213595499958 |
| 7 | 0.723606797749979 | 0.525731112119134 | -0.447213595499958 |
| 8 | -0.276393202250021 | 0.850650808352040 | -0.447213595499958 |
| 9 | -0.894427190999916 | 0.000000000000000 | -0.447213595499958 |
| 10 | -0.276393202250021 | -0.850650808352040 | -0.447213595499958 |
| 11 | 0.000000000000000 | 0.000000000000000 | -1.000000000000000 |

These vertices are connected together to form 20 congruent, equilateral triangles as shown in Figure 3. The 20 triangles are numbered from 0 to 19 and the order in which the vertices are connected together is given in Table 2.

**Table 2 – Connectivity of initial tessellation.**

| Triangle | Vertex 0 | Vertex 1 | Vertex 2 |
|---|---|---|---|
| 0 | 0 | 2 | 1 |
| 1 | 0 | 3 | 2 |
| 2 | 0 | 4 | 3 |
| 3 | 0 | 5 | 4 |
| 4 | 0 | 1 | 5 |
| 5 | 2 | 7 | 1 |
| 6 | 3 | 8 | 2 |
| 7 | 4 | 9 | 3 |
| 8 | 5 | 10 | 4 |
| 9 | 1 | 6 | 5 |
| 10 | 1 | 7 | 6 |
| 11 | 2 | 8 | 7 |
| 12 | 3 | 9 | 8 |
| 13 | 4 | 10 | 9 |
| 14 | 5 | 6 | 10 |
| 15 | 7 | 11 | 6 |
| 16 | 8 | 11 | 7 |
| 17 | 9 | 11 | 8 |
| 18 | 10 | 11 | 9 |
| 19 | 6 | 11 | 10 |

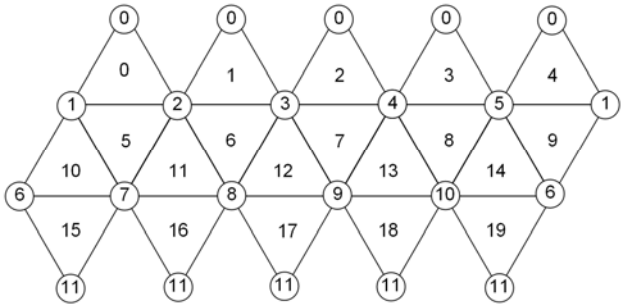

**Figure 3. Icosahedral net illustrating one possible node and triangle numbering scheme.**

As each triangle listed in Table 2 is instantiated, a reference to the triangle is added to each of its vertex's triangle membership list.

**Triangle Neighbor Identification**

Once a set of vertices have been combined into a set of triangles at a given level of the tessellation, and the vertices have updated their triangle membership lists, it is necessary to discover, for each triangle $T$ at the current level of the tessellation, references to the triangles $N_i$, $i$=1,3, that are the neighbors of $T$. This is accomplished by performing the following operations for each vertex $V_i$ in $T$ (see Figure 4):

1. Identify the other two vertices in $T$, $V_j$ and $V_k$, such that $V_j$ is the next vertex after $V_i$ and $V_k$ is the next vertex after $V_j$.
2. Mark each triangle in $V_j$'s triangle membership list that resides at the same level of the tessellation as $T$.
3. Search through the triangles in $V_k$'s triangle membership list. Exactly two triangles will be marked: the original triangle $T$, and the neighbor of $T$ that lies across the edge $E_i$, thereby allowing $N_i$ to be identified.
4. Unmark all the triangles which were marked in step 2.

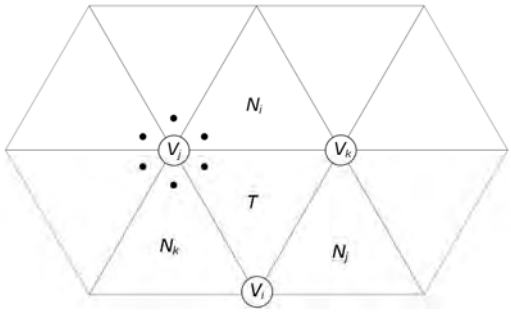


Figure 4 – Algorithm for identifying triangle $T$'s $i$'th neighbor, $N_i$. Triangles containing a black dot are triangles that have bee marked.

**Descendent Level Construction**

From a given level of the tessellation, a lower level can be constructed by subdividing some or all of the triangles of the given level into smaller triangles. Variable resolution is achieved by only subdividing a subset of the triangles at the higher level of the tessellation. Construction of a new, lower level from a given higher level is a three-step process.

Step 1

Visit each triangle $T$ at the lowest level of the tessellation. If it is determined that $T$ should be subdivided, then visit each edge $E_i$, of $T$. If there is not already a new vertex positioned in the middle of $E_i$, then

1. Instantiate a new vertex, $V_n$, in the middle of $E_i$,

2. Add a reference to $V_n$ to $T$'s list of new vertices
3. Add a reference to $V_n$ to $T$'s $i$'th neighbor, $N_i$'s list of new vertices.

After all the triangles at the current level of the tessellation have been visited, each triangle will have had 0, 1, 2 or 3 new vertices added to its list of new vertices.

Step 2

Each triangle $T$ at the current level of the tessellation is visited a second time and the number of new vertices added to its edges is identified. If three new vertices were added, then $T$ is divided into four new triangles, as illustrated in Figure 5a. If two new vertices were added, then there are two distinct ways that $T$ can be divided into three new triangles, as illustrated in Figure 5c and 5d. The choice can be made arbitrarily. If a single new vertex was added, then $T$ is divided into two new triangles as illustrated in Figure 5b. If no new vertices were added to $T$, then a new triangle is instantiated that has the same three vertices as $T$. It is necessary to create this new triangle, even though it has the same vertices as $T$, because the new triangle will ultimately reside on a different level of the tessellation and have different neighbors than $T$.

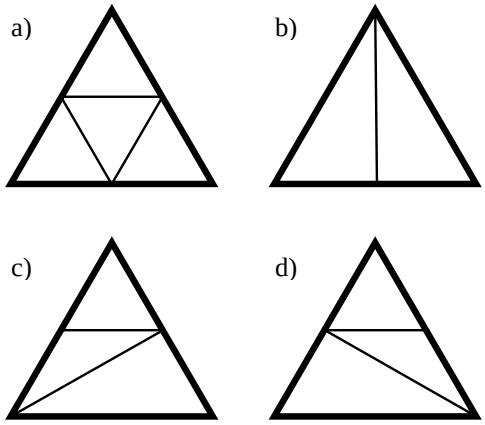


**Figure 5. An illustration of some of the ways in which a triangle can be subdivided into smaller triangles. a) three new vertices, b) one new vertex, c and d) two new vertices.**

One of the newly created triangles must be identified as the descendent of $T$. If $T$ was divided into three or four new triangles, then the center one should become $T$'s descendent. Otherwise there is either no choice to make, or the choice is arbitrary.

Once all the new triangles have been created and each old triangle's descendent identified, then all the new triangles are added to a new level of the tessellation. The third and final step of the creation of the new level of the tessellation is to determine each triangle's three neighbors as described above.

**Property Profiles at Vertices**

At each vertex of the tessellation, a radial property profile is defined which is comprised of some number of major layers. All property values within a major layer must be radially continuous but property values may be discontinuous across major layer boundaries. Examples of major property discontinuities within the Earth are sedimentary layer boundaries in the upper crust; boundaries between the upper, middle, and lower crust; the Moho, the 410 km discontinuity, the 660 km discontinuity, the core-mantle boundary (CMB), and the inner core boundary (ICB). The radial property distribution within a major layer can be constant, or it can vary. Currently, variations can be defined by a number of sublayers, by a polynomial in radius, or by a cubic spline. Support for other distributions could easily be added.

Property values within each layer, and the radii of the layer boundaries, may be different along profiles at adjacent tessellation vertices, and layers may pinch out to zero thickness. Since linear interpolation between adjacent profiles is employed, as described next, property values and interface radii will be laterally continuous.

**Model Interpolation**

Determining estimates of the property values and layer radii at an arbitrary position $X$ in the Earth consists of the following steps:

1. Finding the triangle $T$ in the tessellation such that $X$ resides in $T$ and $T$ has no descendents.
2. Determining the interpolation coefficients in geographic dimensions.
3. Computing the major layer radii along an interpolated profile at the geographic position of $X$ using the interpolation coefficients computed in step 2.

4. Identifying the layer in the interpolated profile in which the radius of *X* resides.
5. For each vertex $V_i$ of *T*, interpolating the value of the desired property at the radius of *X*, but constrained to be in the layer identified in step 4.
6. Computing the interpolated property values at *X* from the three property values calculated in step 5.

These steps are now described in more detail.

**Triangle Walking Algorithm**

To find the triangle in which *X* resides, a triangle walking algorithm is implemented (Lawson, 1977). This method is the standard approach of point searching a well-behaved, convex-everywhere, 2D mesh. We initialize *T* to be an arbitrary triangle at the highest level of the tessellation. For each edge $E_i$ in *T* we compute the scalar triple product $s_i = (V_k \times V_j) \bullet X$ , where $V_j$ and $V_k$ are the first and second vertices of $E_i$, respectively. *X* resides in *T* if $s_i \geq 0$ for $i = 1,3$ . If $s_i$ is negative for any $E_i$ in *T*, then *T* is set equal to the neighbor that resides on the other side of edge $E_i$ and the search continues. When *T* is identified such that $s_i \geq 0$ for $i = 1,3$ , *T* is checked to see if it has a descendent. If it does, then *T* is set equal to the descendent and the search continues. The search ends when *X* resides in *T* and *T* has no descendents.

The interpolation coefficients to be applied to the three vertices $V_i$, $i$=1,3 are

$$c_i = \frac{s_i}{S}, \quad i = 1,3 \tag{1}$$

where

$$S = \sum_{j=1}^{3} s_j \tag{2}$$

Next, we identify the 3 property profiles $P_i$ at vertices $V_i$, and instantiate an interpolated profile, *I*, at the geographic position of point *X*. Then we compute interpolated values for the radii of all the major layer boundaries in *I* using

$$r_j = \sum_{i=1}^{3} c_i r_{ij} \tag{3}$$

where $r_j$ and $r_{ij}$ are the radii of the *j*'th major layer boundaries in *I* and $P_i$, respectively. We then identify *m*, the index of the major layer in *I* in which the radius of *X* resides using bisection. Next, we interpolate property values $v_i$ at the radius of *X* in profiles $P_i$ using whatever interpolation algorithms are appropriate for the property distributions in layer *m* of profiles $P_i$. The interpolations should be constrained to layer *m*, i.e., if the radius of *X* is greater than the radius of the top of layer *m* in $P_i$, or less than the radius of the bottom of layer *m* in $P_i$, then $v_i$ is set to the value of the desired property at the top or bottom or layer *m* in $P_i$, as appropriate. Finally, we compute the interpolated value of the property at *X*

$$v_X = \sum_{i=1}^{3} c_i v_i \tag{4}$$

**Example Model**

To assess some of the advantages and disadvantages of the unstructured tessellations described here relative to more commonly encountered structured grids, we have constructed an unstructured version of the Crust 2.0 Model of Laske, et. al. (2008), which is represented with uniform, 2º latitude and longitude spacing. We built the unstructured tessellation in the manner described above, with the criterion that triangles were only subdivided if they:

- contained at least two of the original nodes from the Crust 2.0 Model;
- the geophysical parameter values at any two of the original nodes were different; and
- the triangle edges were larger than 2º.

Our triangles are no smaller than 2º and at low latitudes they either contain no original nodes, or all of the original nodes that they do contain are identical to each other. At high latitudes, where the Crust 2.0 Model is very highly sampled, many triangles do contain original nodes that are not identical in order to avoid violating the 2º minimum triangle size constraint. Figure 6 shows an orthographic projection of the globe, centered on the boundary between the Pacific Ocean and South America, illustrating the economies achieved over the oceans where the crustal structure is constant over broad areas.

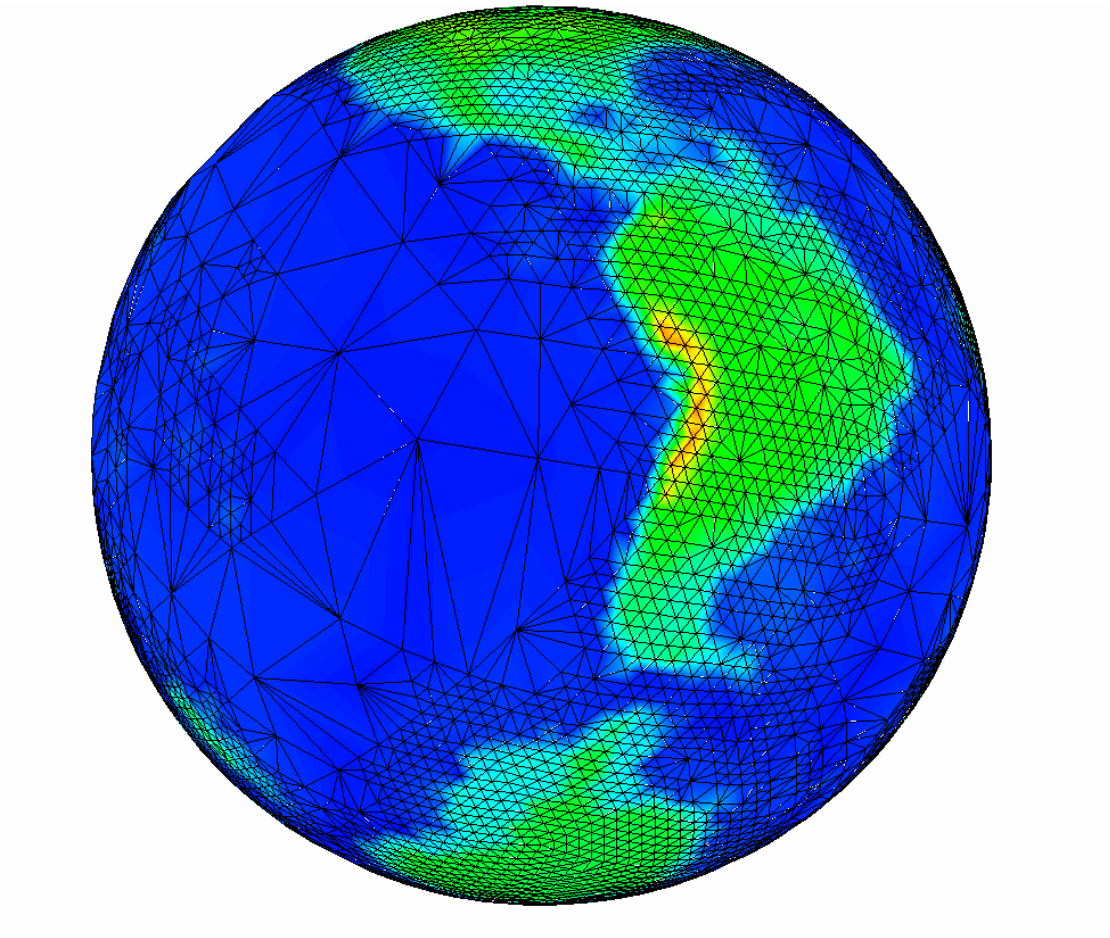

**Figure 6 – Orthographic projection of crustal thickness in the Eastern Pacific and South America.**

Figure 7 is an azimuthal equal angle projection of the area near the pole, illustrating that the triangular cells maintain approximately constant area, even at high latitudes, while the cells of the regularly spaced, 2º × 2º grid are characterized by very high aspect ratios.

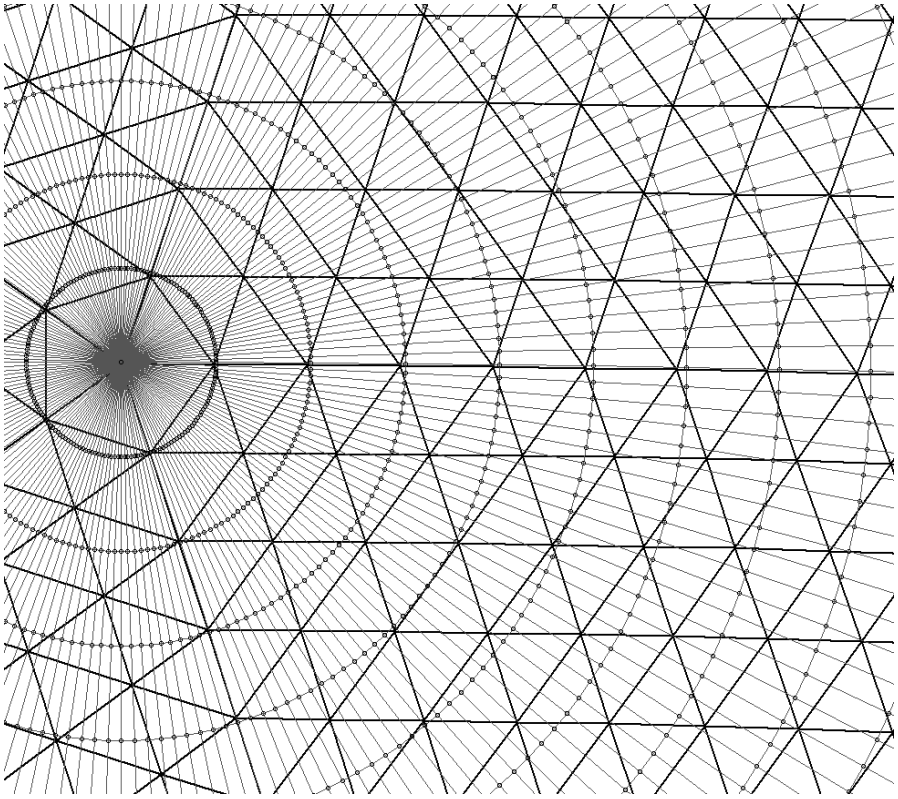

**Figure 7. Comparison of the unstructured triangular tessellation and the regularly spaced 2º × 2º original grid at high latitude. The North Pole is near the left edge of the image.**

Figure 8 illustrates that a 2º × 2º rectangular box near 60º latitude has half the surface area of a similar box at the equator and such a box near the pole has less than 2% of the surface area of the equatorial box.

## Conclusion

We have described a method for representing complex 3D Earth models based on a multi-level triangular tessellation of a unit sphere. At each triangle vertex, geophysical properties are defined along a radial profile that extends from the center of the Earth, through the triangle vertex and out to the topographic/bathymetric surface of the Earth. Construction of the tessellation starts with an icosahedron and proceeds by triangular subdivision. Variable resolution is accomplished by subdividing triangles into smaller triangles only where the distribution of the geophysical properties represented in the model warrants additional

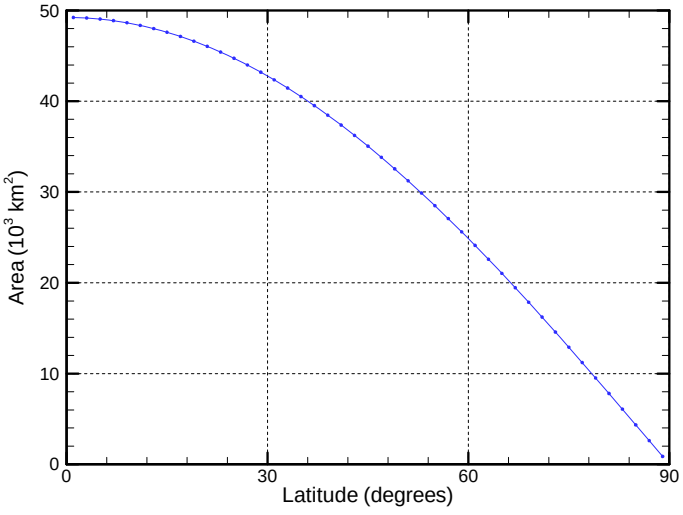


**Figure 8. Area at the surface of the Earth of a 2º × 2º rectangular box, as a function of latitude.**

resolution. Unlike structured, latitude-longitude grids, resolution need not increase arbitrarily at high latitudes, making this method of model construction particularly suitable for global scale models.

Efficient interpolation of geophysical properties at arbitrary points in the model is accomplished by implementation of a walking triangle algorithm which starts at the highest level of the multi-level tessellation and proceeds down through successively deeper levels until the desired position is reached.

**References**

Laske, G., G. Masters, and C. Reif (2008). CRUST 2.0: A New Global Crustal Model at 2x2 Degrees, http://igppweb.ucsd.edu/~gabi/rem.dir/crust/crust2.html.

Lawson, C. L. (1977). Software for $C^1$ surface interpolation, in Mathematical Software III, ed. Rice, J., Academic Press, New York.

Pasyanos, M. E., W. R. Walter, M. P. Flanagan, P. Goldstein and J. Bhattacharyya (2004). Building and testing an a priori geophysical model for western Eurasia and North Africa, *Pure Appl. Geophys.* 161: 235–281.

Reiter, D., W. Rodi, M. Johnson, C. Vincent, and A. Rosca (2001). A new regional 3-D velocity model of the India-Pakisan region, in *Proceedings of the 23rd Seismic Research Review: Worldwide Monitoring of Nuclear Explosions*, LA-UR-01-4454, Vol. 1, pp. 305–314.

# LOCATION IMPROVEMENTS IN EAST ASIA: TOMOGRAPHIC MODEL ANALYSIS AND UTILIZING PUBLIC DATA FOR GROUND TRUTH IDENTIFICATION

Michael L. Begnaud, Xiaoning Yang, Richard J. Stead, W. Scott Phillips, Charlotte A. Rowe, and Lee K. Steck

Los Alamos National Laboratory

Sponsored by National Nuclear Security Administration

Contract No. DE-AC52-06NA25396

## ABSTRACT

We continue to collect seismic catalog data from various sources and search that data for possible information to improve regional location in East Asia. Data collection and search efforts have greatly increased the availability of ground truth (GT) events and improved our ability to create detailed tomographic models for the area.

We have developed several regional phase tomography models for East Asia (see Rowe et al., 2008, these Proceedings) that display significant reduction in travel time residuals over starting models. Further analyses of these models are required to assess how such models will affect location accuracy and methods. We will determine how the tomography models reduce the travel time residuals for various stations within East Asia and what residual patterns remain after modeling. This will indicate whether any further location improvement can be expected by adding travel time correction surfaces to relocation methods in the area.

GT is usually collected through analysis of seismic, infrasound and satellite data or through direct on-site access. GT for areas where information is limited or denied must be derived from alternative sources. We obtained accurate and precise locations of two chemical explosions detonated in December 2007 in northern China through analysis of public information from the Internet and Google Earth™. The GT location of a multishot, delay-fired explosion detonated on December 20, 2007, is at 39.0529° N and 106.1155° E with a precision of GT1 or better. We located the epicenter of the second single-shot, contained explosion detonated on December 12, 2007, local time at 40.2671° N and 115.6955° E with a precision of GT0.3 or better. From seismic data recorded 48 km away, we determined the origin time of this explosion to be December 11, 2007, 19:00:18.91 UTC.

## OBJECTIVES

We continue to research ways to improve location and detection in East Asia through the gathering of GT information and the development of geophysical models to more accurately predict regional travel times. GT information is vital to calibration efforts in East Asia, as well as other areas of interest, and provides data that benefits other monitoring research efforts. New geophysical models are being created to obtain more accurate regional travel times (e.g., see Rowe et al., 2008, these Proceedings, and Myers et al., 2008, these Proceedings). These travel time models will greatly benefit the location calibration effort, with correction surfaces further improving the location accuracy.

The acquisition of new GT information is always beneficial to calibration efforts in monitoring research. We show that utilizing publicly available information on the Internet and through tools such as Google Earth™ can allow determination of GT points down to the sub-GT1 level.

## RESEARCH ACCOMPLISHED

### Reduction in Regional Travel Times Using Geophysical Models

Various models for East Asia have been produced by the monitoring community, both for geophysical interpretation and for travel-time calculation. Among these are Pn and Sn models (e.g., Begnaud et al., 2008; Hearn et al., 2004; Pei et al., 2007; Phillips et al., 2007) and the Pn Seismic Location Baseline Model (SLBM) (see Myers et al., 2008, these Proceedings). While these models tend to improve the residual misfit in arrival data, no model fits the data perfectly.

When attempting to remove regional travel-time residual trends, two-dimensional (2D) travel-time correction surfaces are generally used. These surfaces tend to remove the effects of local crustal structure, etc. from one-dimensional (1D) velocity models. Correction surfaces can also be applied to higher dimensional velocity and/or travel-time models.

We performed Pn travel-time tomography for Eurasia/North Africa as part of the National Nuclear Security Administration (NNSA) multilab SLBM effort. This effort used the "Unified" model that was developed by Los Alamos, Lawrence Livermore, and Sandia National Laboratories. The Unified model was the starting point for a tomographic inversion that solved for upper mantle slowness and gradient, as well as a crustal slowness modifier (see Myers et al., 2008, these Proceedings, for a full description) (Figure 1).

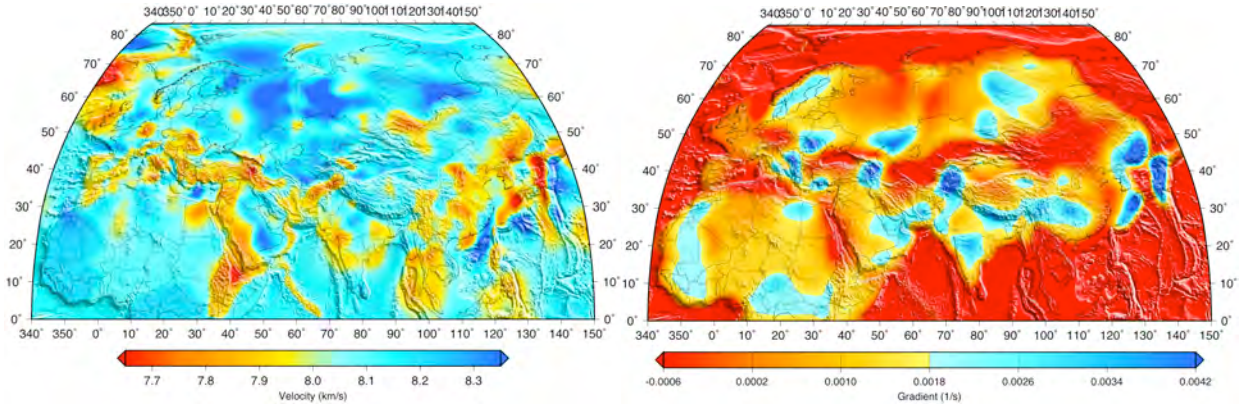


**Figure 1. Tomographic inversion results for Pn velocity and gradient using the SLBM Unified model as the starting model.**

For several stations in the western China region, we examined the resulting residuals when using the SLBM Pn tomographic model and a separate Sn tomographic model (Begnaud et al., 2008), looking for regional patterns and whether any such patterns were removed from the starting model by the tomographic inversion. For the Pn tomography (Figure 2), the stations all display highly variable residuals with little consistency in common areas. Using the SLBM tomographic model (Figure 1), residuals display more consistent values throughout the areas, with local and regional trends removed. Station WMQ has a variance reduction of 66% when using the tomography

model over the starting model. The Pn variogram for WMQ (Figure 3) before and after the inversion shows how the tomography stabilizes the residuals and reduces variability. The variogram for the starting model displays a possibly problematic correlation range (where the curve flattens out) while the variogram for the tomography is more realistic with an almost stationary curve.

After the inversion, residual patterns are still evident, though not as pronounced as in the starting model. Crustal velocity values were modified only with an overall modifier while crustal thicknesses (moho) were not varied at all. Any difference in the true crustal velocities or thicknesses could result in larger-scale residual patterns. In addition, the randomness of the resulting residuals after the inversion can be attributed to pick error. Travel-time corrections based on the tomography model are still warranted and should improve locations further than using the model alone.

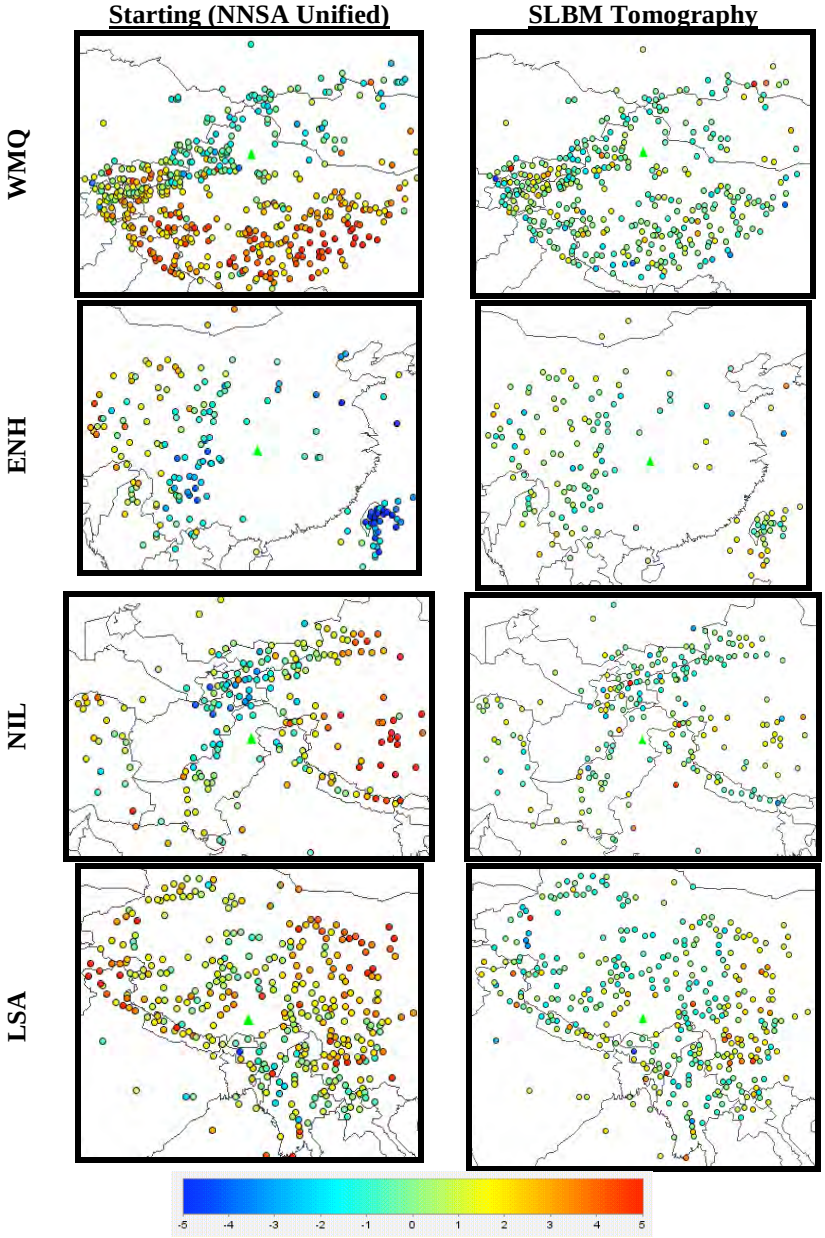


**Figure 2. Pn residuals (s) using the starting and final SLBM tomographic models for four stations in western China. Residuals were clustered at 0.5 deg. All stations display areas with highly variable residuals when using the starting model, typically corresponding to tectonic regions. The SLBM tomographic model results in more consistent residuals.**

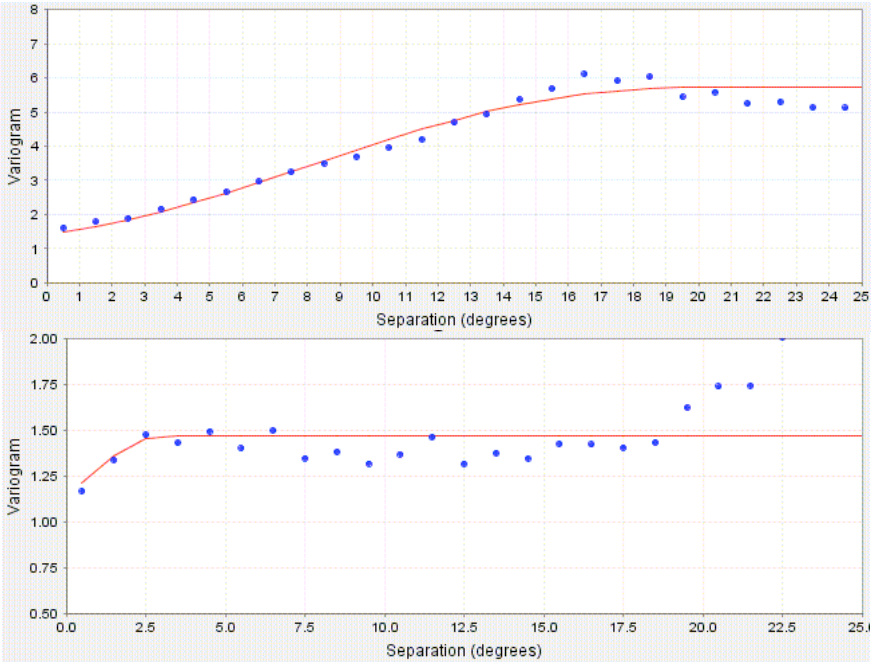


**Figure 3. Pn variogram plots for station WMQ. (top) Starting model. (bottom) After tomography. The curve-fit for the starting model appears problematic with a higher correlation range (where the curve flattens out) than expected. The curve fit after the tomography displays more realistic values and is more stationary.**

In addition to Pn models, we created an Sn tomographic model for Eurasia (Begnaud et al., 2008) (see Rowe et al., 2008, these Proceedings). The data for the Sn inversion had to be significantly culled as Sn is far more inconsistent than Pn for picking accuracy. Although the data for Sn are more variable than Pn, the tomographic model does remove the large biases observed in the Sn data (Figure 4). For station WMQ, the Sn variance was reduced by 53% and by 41% for station LSA.

The remaining Pn and Sn residuals after tomographic inversion still demonstrate the need for further 2D travel-time corrections. All stations display remaining residual patterns where the tomographic models need additional adjustment to match to observed travel times.

**Ground-Truth Collection Through the Internet and Google Earth™**

Accurate and precise GT information (time, location, size and type of seismic and infrasound events) is of vital importance to nuclear-explosion monitoring and the collection of new GT continues to be a major component of monitoring research (NNSA, 2004). GT is usually collected through analysis of seismic, infrasound and satellite data or through direct on-site access. GT can also be derived from alternative sources. Here, we demonstrate how we obtained accurate and precise GT (GT1 or better) from the Internet and Google Earth™ and the value of these resources in ground-truth collection especially in regions where information is limited or denied.

The GT that we collected concerns two chemical explosions detonated in northern China in 2007. One of the explosions is a multi-shot, delay-fired explosion designed to remove a mountaintop to expose the coal underneath. The other explosion is a single-shot explosion detonated as the source for a large-scale geophysical survey.

At the 2007 American Geophysical Union Fall Meeting, we learned that there would be a 5,000-ton, multishot, delayed-fired explosion on December 20, 2007, in northern China. On December 20, 2007, we started searching the Internet for information about this explosion using terms such as “China explosion.” Since the explosion was large enough, we obtained enough information including photographs of the mountain, where the explosion was conducted, and nearby buildings. Using this information, we were able to precisely locate the mountain and obtained the coordinate of the explosion at 39.0529° N and 106.1155° E with a precision of GT1 or better.

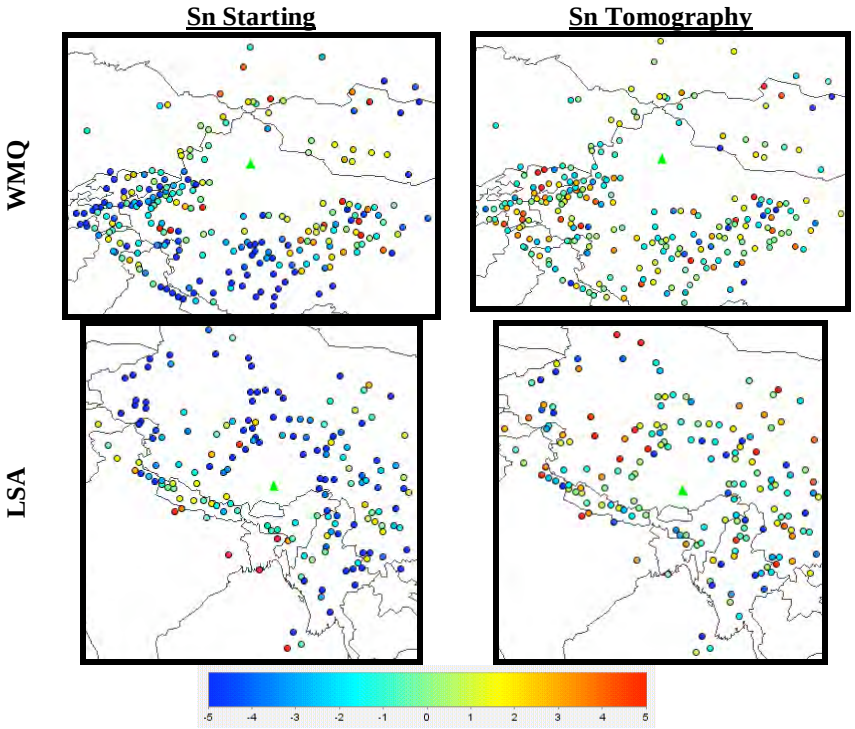


**Figure 4. Sn residuals (s) using a starting (constant velocity/gradient) and final tomographic model. Shown are two stations in western China. Residuals clustered at 0.5 deg. Although the data are more variable than Pn, the tomography model does remove the large residual offsets observed.**

When we searched the Internet about the December 20 explosion, we came across two news bulletins posted by the Anhui Seismological Bureau (ASB), a provincial bureau, and by the Institute of Geophysics, China Earthquake Administration (IGCEA) on their websites about another explosion conducted on December 12, 2007 (Dec122007). We will discuss in some detail in the following sections how we obtained precise GT location of this explosion.

**Information Collection from the Internet**

The ASB news bulletin, which was posted on November 27, 2007, mentioned that the anticipated explosion was part of a seismic experiment to be conducted at zero hours December 12, 2007, in Huailai region in northern China. The size of the detonation would be 50 tons of explosives. The bulletin posted by IGCEA provided more information about the experiment and the explosion. It stated that the experiment was designed to investigate, among others, the fine structure of the Earth's interior, regional travel time, strong ground motion, attenuation, coseismic electromagnetic effects, infrasound-seismic comparison and instrument calibration. No time, location or size of Dec122007 was disclosed in the IGCEA bulletin. Nevertheless, the bulletin included several photographs and figures related to the experiment. Figure 5 is a map of the experiment layout reproduced from IGCEA's bulletin. It shows the location of Dec122007, the locations of permanent and temporary seismic and infrasound stations and the regions where geomagnetic and strong-motion observations were made. From Figure 5, we estimated the location of Dec122007 to be at 40.2687° N and 115.6794° E. Since we do not know the error of the map, this location cannot serve as GT with confidence.

Based on the information from the two news bulletins about Dec122007, we decided to search the Internet again using refined terms such as "Huailai explosion." The search returned another news bulletin about Dec122007 posted on the website of the BIT Blast Ltd. (BIT Blast), the company that constructed and detonated Dec122007. More detailed information is revealed in this news bulletin. The bulletin stated that the location of Dec122007 was on a hill along a canyon near the village Longbaoshan in Huailai County of Hebei Province. In the surrounding area, there are orchards and a military explosive storage. According to the news bulletin, Dec122007 was detonated on December 12, 2007, at 03:00:20 local time (December 11, 2007, 19:00:20 UTC). The bulletin also confirms that the size of Dec122007 is 50 tons.

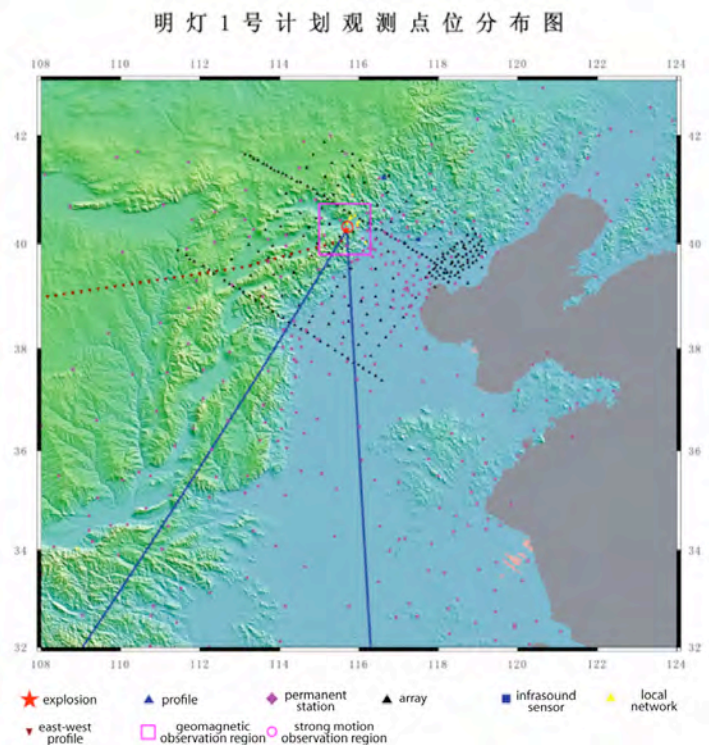


**Figure 5. A map from IGEAC's news bulletin showing the location of Dec122007 and the layout of the geophysical survey. The original map legend has been translated into English.**

**Location Using Google Earth™**

In addition to the text, the BIT Blast's news bulletin also includes several photographs of the test site. The photographs indicate that the company constructed Dec122007 by boring a horizontal tunnel on the side of a hill and excavating a chamber probably at the end of the tunnel for explosive emplacement. The photographs show the entrance to the tunnel and the road that leads up to the test site. The surface features near the test site revealed by the photographs make it possible for us to look for the exact location of Dec122007 in Google Earth™.

Google Earth™ is a virtual globe program that displays the Earth by superimposing satellite imagery, aerial photography, terrain data and maps (http://earth.google.com). According to Wikipedia (http://en.wikipedia.org/wiki/Google_Earth), for most parts of the world's continents, the spatial resolution of Google Earth™ images is 15 m or better. Most Google Earth™ images are one to three years old (http://earth.google.com).

We began our search for the test site in Google Earth™ by first locating Longbaoshan, the village mentioned in BIT Blast's news bulletin. Searching the Internet, we found a map of Huailai County, to which Longbaoshan belongs. Comparing the map with Google Earth™ images, we located the village in Google Earth™ (Figure 6).

Figure 7 shows another Google Earth™ image of Longbaoshan, this time looking south, along with the surrounding area. There are two canyons to the south of Longbaoshan and the Dec122007 test site could be in one of the canyons.

To locate the test site, we first estimated the orientation of the road that leads up to the test site so that we could look for road segments that have the similar orientation along the two canyons and branched-off roads in Google Earth™. Figure 8 is a photograph of the tunnel entrance from BIT Blast's news bulletin. From the shadows of different objects in the photograph, we estimated that the altitude of the Sun was about 24° and, with large uncertainty, the azimuth angle between the rock face above the entrance and the vertical plane containing the Sun was about 45° when the photograph was taken, assuming that the camera was properly leveled. The altitude and azimuth angles of

the Sun at a certain location and certain time can be found from various resources on the Internet (e.g., http://www.ga.gov.au/).

Using one of these tools, we calculated that at the Dec122007 test site and in late November to early December 2007, the Sun could have an altitude of about 24° at around 10:30 or 13:50. The azimuths of the Sun at these times are 155° and 206°, respectively. This means that the azimuth of the rock face shown in Figure 8 should be about 200° or 251°, again with large uncertainty. Figure 9 is another photograph from BIT Blast's news bulletin showing the road leading up to the tunnel entrance. The vertical rock fissure is visible in both Figure 8 and Figure 9. The road is at a steep angle with the rock face and appears to make a sharp left turn in front of the rock face. Taking into account the uncertainties in our estimates, we decided to investigate any road segments that are in the general west to northwest direction, and that make a left turn at the end of the segments. We identified a few road segments along the two canyons and in adjacent canyons that have the required characteristics. We then conducted detailed analysis comparing surface features shown in the photographs from BIT Blast's bulletin (Figure 9, Figure 10) with those in Google Earth™ images. Through laborious analysis and comparison, we identified the most likely location of the test site, which is marked by a red star in Figure 7.

**Figure 6. Longbaoshan as is shown in Google Earth™. The village is adjacent to a sand dune, which is a tourist spot.**

**Figure 7. Google Earth™ image of Longbaoshan and the surrounding area. Possible locations of the orchards and the explosive storage are labeled. The likely location of Dec122007 is marked by a red star (see text for details.)**

**Figure 8. A photograph of the tunnel entrance from BIT Blast's news bulletin.**

**Figure 9. The road leading up to the tunnel entrance from BIT Blast's news bulletin. Numbers in the figure mark some of the surface features that are recognized in the Google Earth™ image (Figure 11).**

Figure 11 is a Google Earth™ image of the probable test site looking in the northwest direction. Likely same surface features from previous figures are labeled with same numbers. Both the photograph shown in Figure 9 and the Google Earth™ image (Figure 11) were taken at times when the vegetation was green. The photograph shown in Figure 10 was taken in the winter when the vegetation became brown. Comparing the three figures, we found abundant similarities. The rock formation (1) has a patch of vegetation just to the right of the number "1" with similar shapes in all three figures. The rock face (3) has the same shape and a semicircular notch on the upper left (4) in all the figures. A piece of rock is seen inside the notch in all three figures as well. The rock face in Figure 11 has similar grass patches (5, 6) as those seen in Figure 9 and Figure 10. The horizontal extent of the rock face, estimated by analyzing the location of the green vehicle in Figure 10 relative to the rock face and the location of the photographer, is consistent with that measured in Google Earth™. A skinny tree (7) is seen in both Figure 9 and Figure 11. For some reason, the tree disappeared in Figure 10, possibly uprooted or broken by the explosion or the landslide afterwards.

In addition to the features marked by the numbers, there are other similarities as well. For example, Figure 9 shows that this segment of the road runs on the left side of the drainage. Figure 11 indicates the same configuration. There are also trees at same locations in different figures. The topography of the mountains in the background of the photographs is consistent with the topography in Google Earth™. We did not find apparent contradiction of features in the photographs and in the Google Earth™ image. The compelling evidence suggests that this location is likely the location of Dec122007.

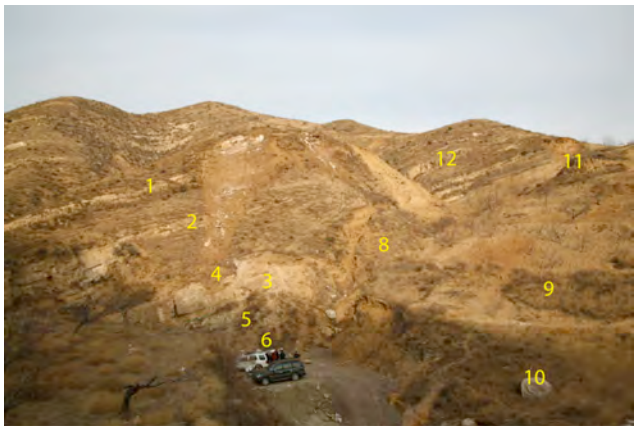


**Figure 10. A photograph of the Dec122007 test site after the explosion from BIT Blast's news bulletin. Minor landslides are seen on the side of the hill. Numbers in the figure mark some of the surface features that are recognized in the Google Earth™ image (Figure 11).**

**Figure 11. A Google Earth™ image of the likely Dec122007 test site. Numbers in the figure mark some of the surface features that can be seen in the photographs (Figure 9, Figure 10). The red star marks our location of Dec122007 using Google Earth™.**

Since we have no information about the length of the tunnel and only a rough estimation of the tunnel direction from Figure 8, we placed the likely location of Dec122007 at the location of the hilltop with a coordinate of 40.2671° N and 115.6955° E that we read from Google Earth™. The location is marked in Figure 11. Using the Google Earth™ measuring tool, we measured distance between the explosion location and the tunnel entrance to be about 80 to 90 m. Since the horizontal extent of the hill is only about 300 m at most, the precision of the location should be much better than GT0.3. The location that we measured from the map in IGCEA's bulletin (Figure 5) is about 1.4 km to the west of the Google Earth™ location. Using seismic data recorded about 48-km away at BJT, we estimated the origin time of Dec122008 to be December 11, 2007, 19:00:18.91 UTC, 1.09 seconds earlier than that reported in the BIT Blast's news bulletin.

Measured from the Google Earth™ image, the azimuth of the rock face above the tunnel entrance is about 250°. Comparing it with our estimates from the altitude and azimuth of the Sun when the photograph shown in Figure 8 was taken, it appears that the photograph was taken at about 13:50. If it was the case, the time stamp in the photograph could be the correct time if we replace "AM" with "PM." The angle between the road leading up to the rock face and the rock face is about 60°, consistent with our assessment of a steep angle from the photographs

(Figure 9). The existence of orchards and a possible explosive storage in the surrounding area of the test site (Figure 7) is consistent with the description in BIT Blast's news bulletin.

## CONCLUSIONS

Upper mantle tomographic models are being developed in East Asia for both Pn and Sn. The severe biases in starting models are generally resolved after the inversion, but residual patterns do remain and need to be accounted for in calibration procedures. Developing travel-time correction surfaces on top of these tomographic models will further improve seismic location efforts in East Asia.

Using the Internet and Google Earth™, we located two chemical explosions detonated in northern China in December 2007. The locations that we obtained can serve as GT1 or better for calibration purposes. The successful location of these explosions illustrates the possibility of using alternative means, in addition to the traditional seismic, satellite and direct-access methods, to obtain GT in regions where information is limited or denied.

## ACKNOWLEDGEMENTS

The authors wish to thank Leslie Casey in the Department of Energy office of NA22 for her support of the NNSA GNEMRD program over the years. J. A. Chang provided important database support, without which these studies would not be possible.

## REFERENCES

Begnaud, M. L., W. S. Phillips, C. A. Rowe, and L. K. Steck (2008). Sn velocity, gradient, and anisotropic variations in the upper mantle of Eurasia, *Seis. Res. Lett.* 79: 345.

Hearn, T. M., S. Wang, J. F. Ni, Z. Xu, Y. Yu, and X. Zhang (2004). Uppermost mantle velocities beneath China and surrounding regions, *J. Geophys. Res.* 109: B11301, doi:10.1029/2003JB002874.

Myers, S., S. Ballard, C. Rowe, G. Wagner, M. Antolik, W. Phillips, A. Ramirez, M. Begnaud, M. Pasyanos, D. Dodge, M. Flanagan, K. Hutchenson, G. Barker, J. Dwyer, and D. Russell (2008). A model and methods for regional travel-time calculation, these Proceedings.

*Nuclear Explosion Monitoring Research and Engineering Program, Strategic Plan* (2004). National Nuclear Security Administration, DOE/NNSA/NA-22-NEMRE-2004.

Pei, S., J. Zhao, Y. Sun, Z. Xu, S. Wang, H. Liu, C. A. Rowe, M. N. Toksöz, and X. Gao (2007). Upper mantle seismic velocity and anisotropy in China determined through Pn and Sn tomography, *J. Geophys. Res.* 112: B05312, doi:10.1029/2006JB004409

Phillips, W. S., M. L. Begnaud, C. A. Rowe, L. K. Steck, S. C. Myers, M. Pasyanos, and S. Ballard (2007). Accounting for lateral variations of the upper mantle gradient in Pn tomography studies, *Geophys. Res. Lett.* 34: L14312, doi:10.1029/2007GL029338, 2007.

Rowe, C., M. Maceira, M. Begnaud, L. Steck, and W. Phillips (2008). Geophysical modeling in Eurasia: 2D crustal P and Lg propagation; upper mantle shear wave propagation and anisotropy; and 3D, joint, simultaneous inversions, these Proceedings.

# SEISMICITY OF CENTRAL ASIA AS OBSERVED ON THREE IMS STATIONS

Ronald Brogan[1], Susan Nava[1], John Coyne[2], and Yan Jia[2]

ENSCO Inc.[1] and Comprehensive Nuclear-Test-Ban Treaty Organization[2]

Sponsored by Comprehensive Nuclear-Test-Ban Treaty Organization

Contract No. 2006-0289

## ABSTRACT

Four months of interactive seismic data analysis were conducted to describe the station characteristics of three International Monitoring System (IMS) seismic stations (MKAR, SONM, and BVAR) located in central Asia. Specific study objectives included the location of all local and regional seismic events observed on the three stations, including single station events; identification of seismic sources routinely observed at each station; background noise characterization; identification of any biases in station azimuth, time, and slowness, etc. Additionally, these data provided a baseline for a separate study for evaluation, tuning, and enhancement of automatic and interactive processing functions at the International Data Centre (IDC). During this project, notes were kept on the thresholds necessary at each station for a given event to be recorded at one of the other stations, trends in azimuth and velocity, and any timing errors.

A total of 120 days of data were reviewed (July 20–October 17, 2006; January 1–30, 2007). Over 9,000 events with at least one of the three stations at an epicentral distance less than 20° were human-analyst reviewed, including phase identification and event location. About six percent of the located events included arrival times from all three stations, while about 16% included data from at least two stations. Thirty-nine event clusters, based on geographic and temporal distribution, were identified. The three stations MKAR, SONM, and BVAR are all high-quality seismic arrays. Noise levels at the stations are generally acceptable for the period reviewed, except during the following conditions: (1) a 4.5-Hz intermittent noise source at MKAR, (2) periodic high-frequency bursts on portions of the SONM array, and (3) a monochromatic ring occasionally observed on BVAR. Trends in observed biases were catalogued for each station based on azimuthal distribution. The biases for each cluster were determined by averaging residuals for each measurement (time, azimuth, velocity) and comparing them with the iasp91 travel-time tables routinely used during production of the Reviewed Event Bulletin (REB). Seasonal variation of background noise observed at MKAR had some impact during analysis of the second dataset. Following completion of analysis of the second dataset, measures of the same residuals were conducted and examined relative to the values obtained from the first dataset.

## OBJECTIVES

The objective of this study was to interactively review several months of seismic data from three IMS seismic stations (MKAR, SONM, and BVAR) located in central Asia and subsequently characterize the dataset. Upon completion, these data would then be used as a baseline for a separate study for evaluation, tuning, and enhancement of automatic and interactive processing functions at the IDC. Here, we focused on (1) the location of all local and regional seismic events observed on the three stations of interest, including events located using only a single station; (2) identification of seismic sources routinely observed at each station; (3) background noise characterization; and (4) identification of waveform characteristics including any biases in station azimuth, time, and slowness, etc. Additionally, during this project, notes were kept on the thresholds necessary at each station for a given event to be recorded at one of the other stations, trends in azimuth and velocity (slowness), optimal filter bands for analysis, and any timing errors.

## RESEARCH ACCOMPLISHED

### Identification of Sources of Observed Seismic Activity

The first objective of this project was a four-month study period to locate all conceivable seismic events (including single station events) observable on three central Asian IMS seismic array stations: Makanchi, Kazakhstan (MKAR); Songino, Mongolia (SONM); and Borovoye, Kazakhstan (BVAR). Routine IDC analysis processing software, related configuration parameters, and database tables including automated seismic detections and events were provided. A total of 120 days of data were reviewed (July 20–October 17, 2006; January 1–30, 2007). The IDC provided dataset consisted of 364 seismic events (epicentral distance to one of the three stations <20°) with 9,566 associated detections. Data analysis for this study was performed by displaying the waveforms in a 5-minute window and manually scrolling page by page. In most cases, waveform filtering was performed on a nearly constant basis. Analyst Review Station (ARS) was the primary tool used for waveform review, phase identification, and location purposes. For routine frequency-wavenumber (F-K) processing, XfkDisplay and the multiband F-K module from the program Geotool were used. The surface solution from the location program was used when only one station observed the events. Geotool was used for spectral analysis and mapping of the clusters of seismic activity.

Over 9,000 events with at least one of the three stations at an epicentral distance <20° were located in the 4-month dataset (Figure 1). About 6%of the located events included arrival times from all three stations, while about 16% included data from at least two stations. Analyst review resulted in the location of 8,752 additional seismic events with 17,043 additional associated arrivals.

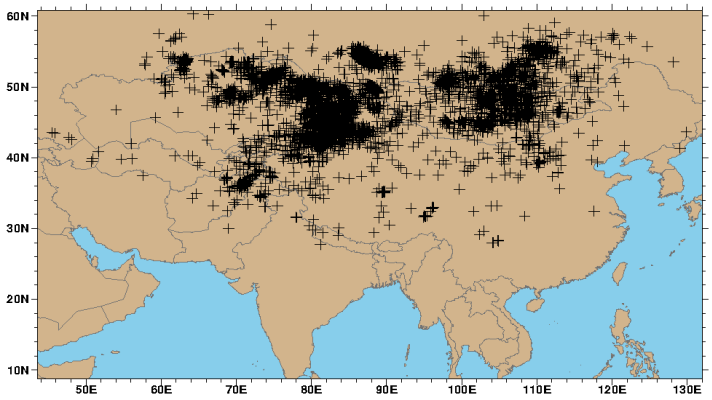


**Figure 1. Map showing the location of 9,116 seismic events (crosses) located during this study.**

Thirty-nine event clusters (both natural and man-made), based on geographic and temporal distribution, were identified (Figure 2; Table 1). The cluster definition was somewhat arbitrary and in general the size of the cluster area increases as a function of distance from the primary observing station. Of these clusters, 21 are proposed to be mining-related activity and 18 are proposed to be natural seismic activity. Attributes used to characterize clusters were temporal distribution, publicly available imagery, and waveform characteristics. We note that the clusters were

identified based on the seismic event distribution observed in the dataset from July 20–October 17, 2006, and that we did not attempt to identify new clusters in the smaller dataset from January 1–30, 2007.

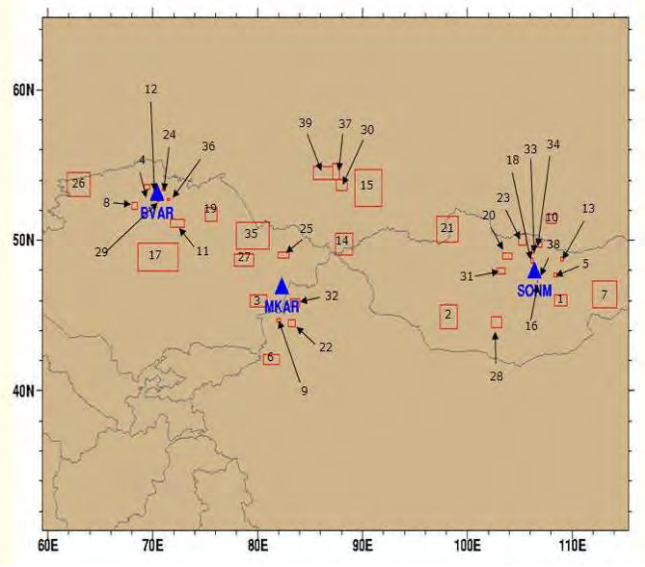


**Figure 2. Map of identified seismic event clusters (numbered boxes; numbers correspond to cluster number listed in Table 1) and the location of three IMS seismic stations.**

**Table 1. Identified Seismic Clusters**

| Cluster # | Count | Cluster # | Count |
|---|---|---|---|
| 1 | 72 | 21 | 236 |
| 2 | 23 | 22 | 51 |
| 3 | 38 | 23 | 25 |
| 4 | 26 | 24 | 29 |
| 5 | 67 | 25 | 39 |
| 6 | 2882 | 26 | 46 |
| 7 | 17 | 27 | 33 |
| 8 | 10 | 28 | 79 |
| 9 | 35 | 29 | 25 |
| 10 | 52 | 30 | 175 |
| 11 | 29 | 31 | 43 |
| 12 | 15 | 32 | 16 |
| 13 | 7 | 33 | 27 |
| 14 | 123 | 34 | 10 |
| 15 | 42 | 35 | 182 |
| 16 | 9 | 36 | 47 |
| 17 | 80 | 37 | 67 |
| 18 | 45 | 38 | 5 |
| 19 | 189 | 39 | 165 |
| 20 | 49 | | |

For each identified cluster, a brief discussion of the distinguishing characteristics of the seismic events was prepared. This included a table of seismic phase characteristics such as average time and azimuth residuals, average azimuth and slowness, and a plot of typical waveforms (Figure 3) for a representative event in the cluster. Histograms showing the time-of-day and day-of-week patterns were also prepared (Figure 4). Space limitations of this paper prevent providing characteristic summaries for all of the clusters. We present data from two clusters (Table 1, Clusters #5 and #6) here as representative of our findings.

Cluster 5 is located near Baga Nur, Mongolia, in an area of active surface mining. Table 2 shows the average time and azimuth residuals, average azimuth, slowness, and velocity for the 67 events in this cluster. F-K results were consistent, with the exception of Rg, possibly due to mixing with Sn phases. These events occur before the Pn/Pg crossover distance but all regional phases are present. Infrasound arrivals from IMS station I34MN were identified for several of these events. Cluster 6 is located in western China, ~150 km east of the border junction of China, Kazakhstan, and Kyrgyzstan, an active area of natural seismicity. Table 3 shows the average time and azimuth residuals, average azimuth, slowness, and velocity for the 2882 events in this cluster. Sn was the most prominent phase observed on MKAR for this set of earthquakes. In addition to the 2882 located events, countless other "lone Sn" events without discernable P-type phases were observed. The waveforms from this cluster are very similar amongst the numerous events and would be good candidates for waveform correlation analysis, which is beyond the scope of this study. A dominant noise source on station MKAR can be problematic for phase identification.

**Table 2. Phase-Specific Residuals for Cluster 5**

| Station | Phase | Count | Av. Time Res. (sec) ± 1 SD | Av. Azimuth (deg) ± 1 SD | Av. Azimuth Res. (deg) ± 1 SD | Av. Slowness (sec/deg) ± 1 SD | Av. Velocity (km/sec) |
|---|---|---|---|---|---|---|---|
| SONM | Pg | 65 | –0.66 ± 0 .19 | 94.92 ± 2.66 | –0.40 ± 2.66 | 17.46 ± 1.01 | 6.37 |
| SONM | Pn | 65 | 0.58 ± 0.26 | 96.82 ± 1.76 | 1.47 ± 1.76 | 14.52 ± 3.11 | 7.66 |
| SONM | Lg | 61 | –0.42 ± 0 .27 | 95.57 ± 1.89 | 0.25 ± 1.89 | 27.81 ± 2.01 | 4.00 |
| SONM | Sn | 65 | 1.56 ± 0 .70 | 95.44 ± 1.66 | 0.08 ± 1.66 | 24.07 ± 1.15 | 4.62 |
| SONM | Rg | 39 | 3.93 ± 1.93 | 94.03 ± 5.03 | –0.79 ± 5.03 | 26.84 ± 5.30 | 4.14 |

**Table 3. Phase-Specific Residuals for Cluster 6**

| Station | Phase | Count | Av. Time Res. (sec) ± 1 SD | Av. Azimuth (deg) ± 1 SD | Av. Azimuth Res. (deg) ± 1 SD | Av. Slowness (sec/deg) ± 1 SD | Av. Velocity (km/sec) |
|---|---|---|---|---|---|---|---|
| MKAR | Pn | 2501 | 0.00 ± 0.35 | 191.36 ± 5.10 | 2.08 ± 5.10 | 13.26 ± 1.63 | 8.39 |
| MKAR | Pg | 1960 | –0.72 ± 0.75 | 192.21 ± 4.62 | 1.97 ± 4.62 | 15.61 ± 1.36 | 7.12 |
| MKAR | Sn | 2871 | 2.29 ± 0.74 | 185.95 ± 3.08 | –3.55 ± 3.08 | 23.93 ± 0.89 | 4.65 |
| MKAR | Lg | 2722 | –1.51 ± 0.54 | 194.07 ± 3.64 | 4.45 ± 3.64 | 28.67 ± 1.63 | 3.88 |

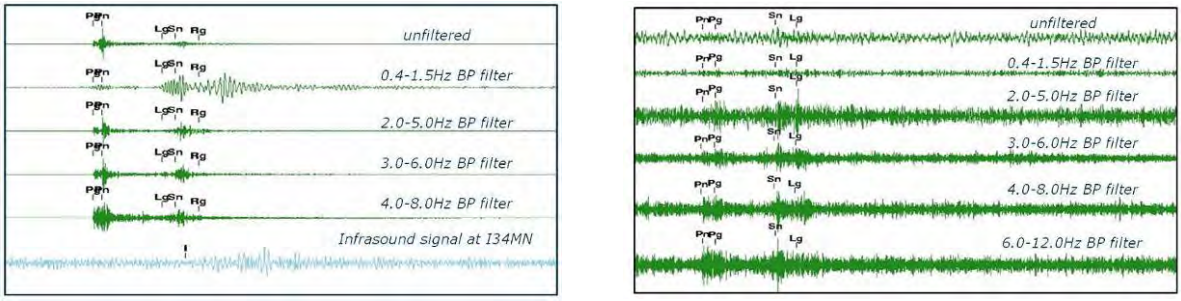


**Figure 3: Typical waveforms from seismic events in Cluster 5 (left) and Cluster 6 (right).**

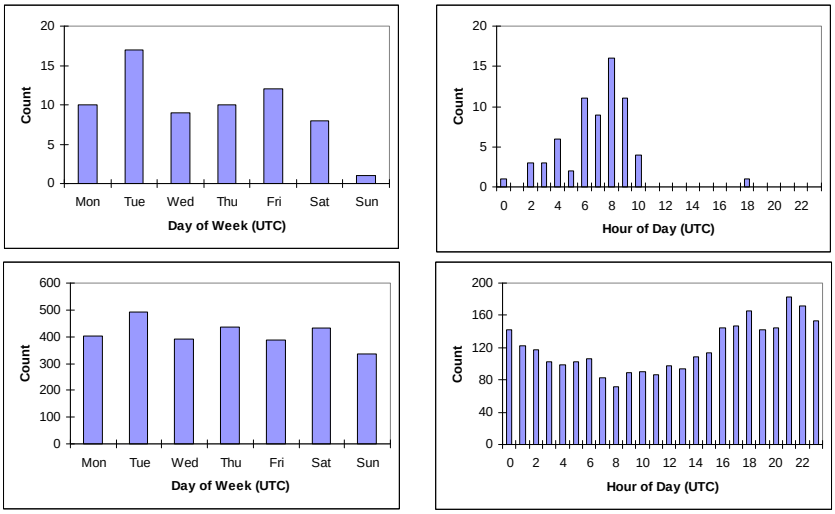


**Figure 4. Histograms of day of week and time of day for Cluster 5 (top) and Cluster 6 (bottom).**

**Station-Specific Observations**

In this section, we present observations on characterization of the background noise, identification of waveform characteristics including any biases in station azimuth, time, and slowness, etc., for each of the three stations studied.

*MKAR (Makanchi, Kazakhstan) Array*

In 2005, the IDC associated initial P-type arrivals from station MKAR with approximately 50% of Reveiwed Event Bulletin (REB) events (13,312 of 26,852). Signals are observed across the spectrum from low-frequency teleseismic to very high frequency local and regional events. A 2–5-Hz bandpass causal Butterworth filter was the primary filter used during the analysis of the July–October 2006 dataset. For the January 2007 dataset, a 1.5–3.0-Hz bandpass causal Butterworth filter was sufficient for observation of all seismic phases. Extremely high frequency events are commonly observed on MKAR waveforms, necessitating use of a suite of bandpass filters. Events from the southeast in an azimuth range between 110° and 140° possess very high frequency, sharp, clear Pn phases with high P/S ratios. Events located east of 95° east longitude have greatly attenuated S-type phases. For all seismic phases,

higher-than-expected velocities were observed from events located to the northwest. For local events (Δ <5°) location, a signal-to-noise ratio (SNR) >20 is typically required for 2+ station locations and an SNR >50 is needed for 3+ station locations. A prominent, intermittent noise source with a center frequency of 4.25 Hz was observed periodically (Figure 5, left).

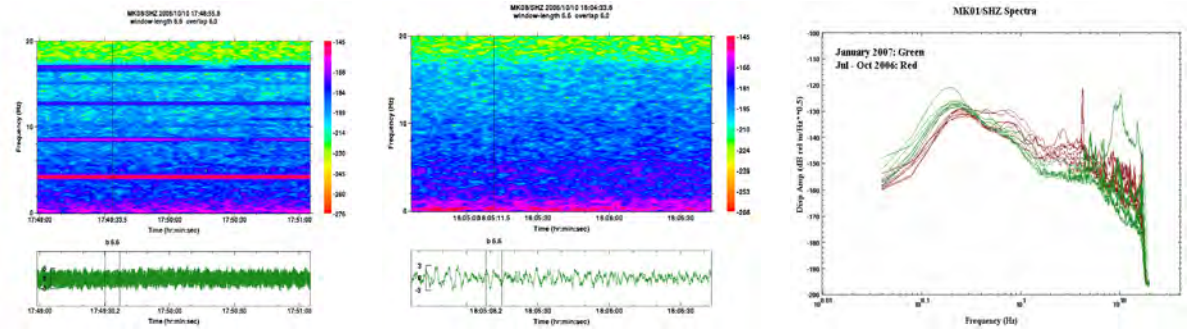


**Figure 5. Spectrograms of the element MK08 SHZ showing presence of persistent noise (left) and same element during a time period when the noise was absent (middle) and comparison of spectra from element MK01 SHZ during the two study periods (right).**

Figure 6 shows time residuals versus azimuth of each prominent regional phase observed at MKAR. Figure 7 shows azimuth residuals versus azimuth for each regional phase and Figure 8 shows velocity for the same phases.

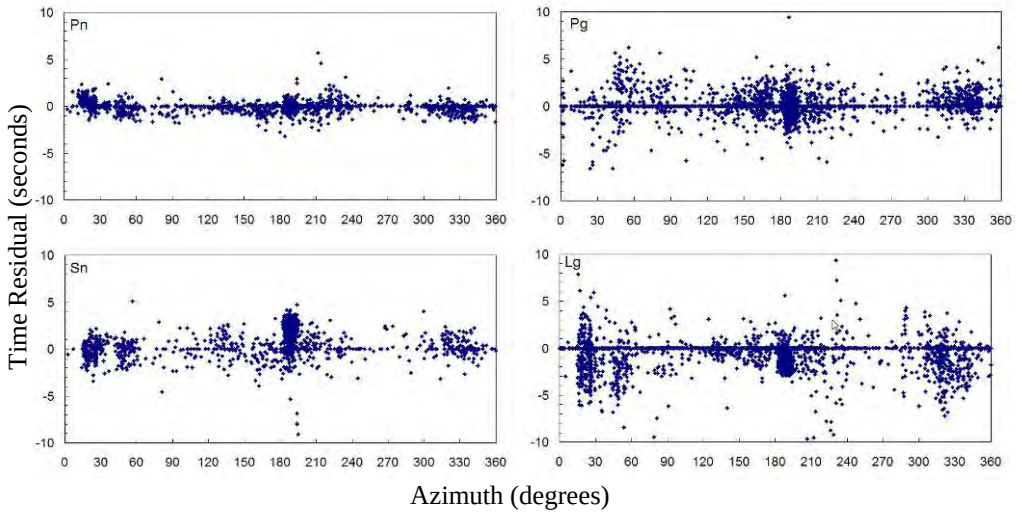


**Figure 6. Scatter plots of time residuals versus azimuth for each regional seismic phase observed at station MKAR for the combined datasets.**

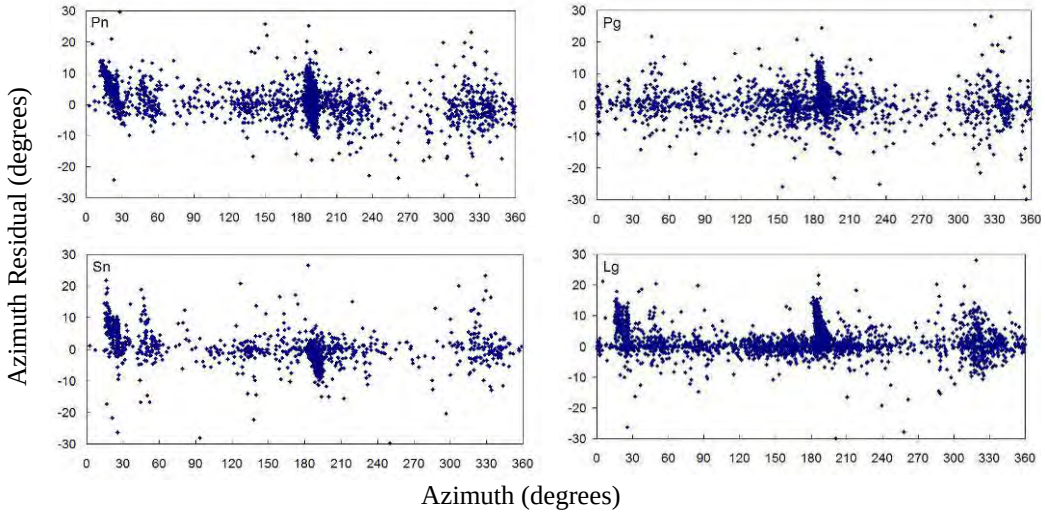


**Figure 7. Scatter plots of azimuth residuals versus azimuth for each regional seismic phase observed at station MKAR for the combined datasets.**

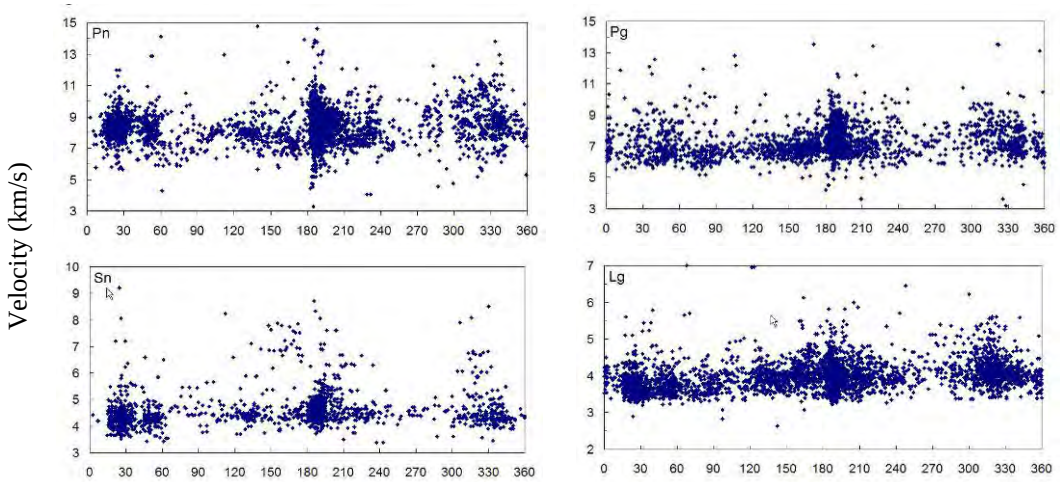


**Figure 8. Scatter plots of velocity versus azimuth for each regional seismic phase observed at station MKAR for the combined datasets.**

*SONM (Songino, Mongolia) Array*

In 2005, the IDC associated initial P-type arrivals from station SONM to approximately 56% of REB events (15,049 of 26,852). These statistics are partially misleading due to the large number of aftershocks following the December 26, 2004, Banda Aceh earthquake. For a more realistic assessment, initial P arrivals from station SONM contributed to 9,055 of 25,449 (35.6%) events in 2004. Local events are best observed with lower frequency filters (0.8–3.0 Hz) unless originating from the southwest. Lg arrivals from the north (290°–85° azimuth) often cannot be associated with P-type phases on station SONM. For local events ($\Delta$ <5°), an SNR >5 is typically required for 2+ station locations and SNR >120 is needed for 3+ station locations. During the study period, SONM exhibited random noise bursts on elements, predominantly on element SONA0 and its near neighbors in the array. The noise often looks like a seismic event with what appear to be clear P and S arrivals. An attempt to perform F-K analysis or polarization and achieve consistent results on these occurrences was nearly impossible. Figure 9 shows an example of one of these noise bursts.

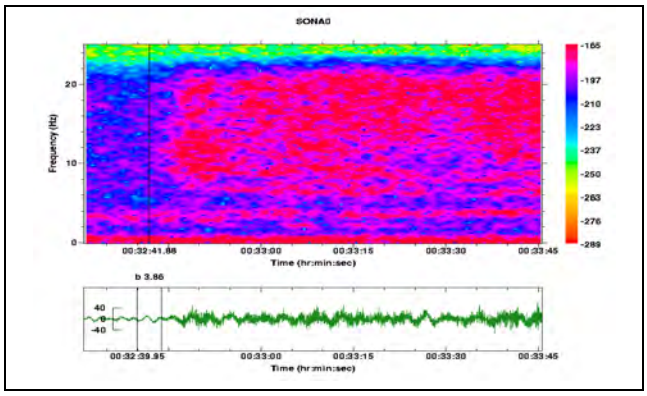


**Figure 9: SONA0 spectrogram for shown waveform.**

Figure 10 shows time residuals versus azimuth of each prominent regional phase observed at SONM. Figure 11 shows azimuth residuals versus azimuth for each regional phase, and Figure 12 shows velocity for the same phases.

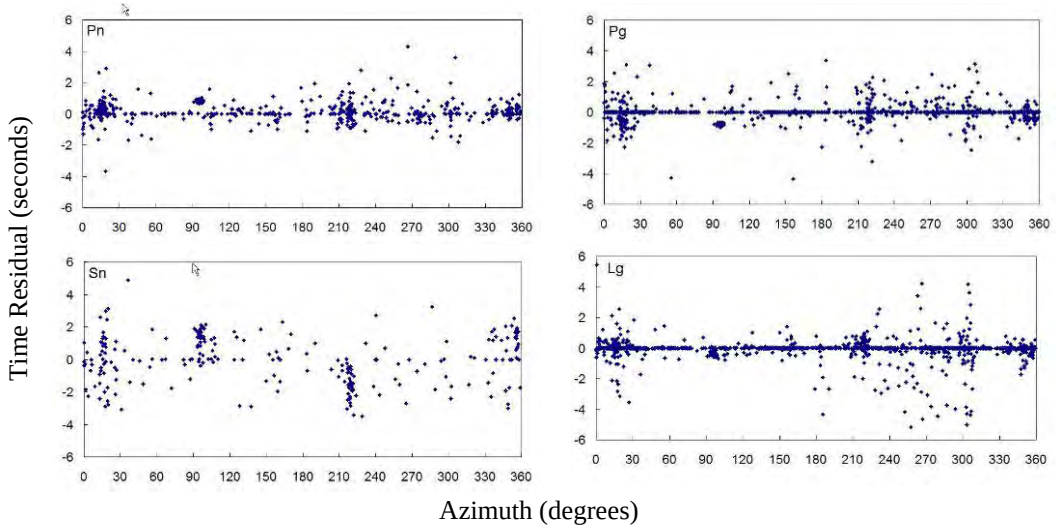


**Figure 10. Scatter plots of time residuals versus azimuth for each regional seismic phase observed at station SONM for the combined datasets.**

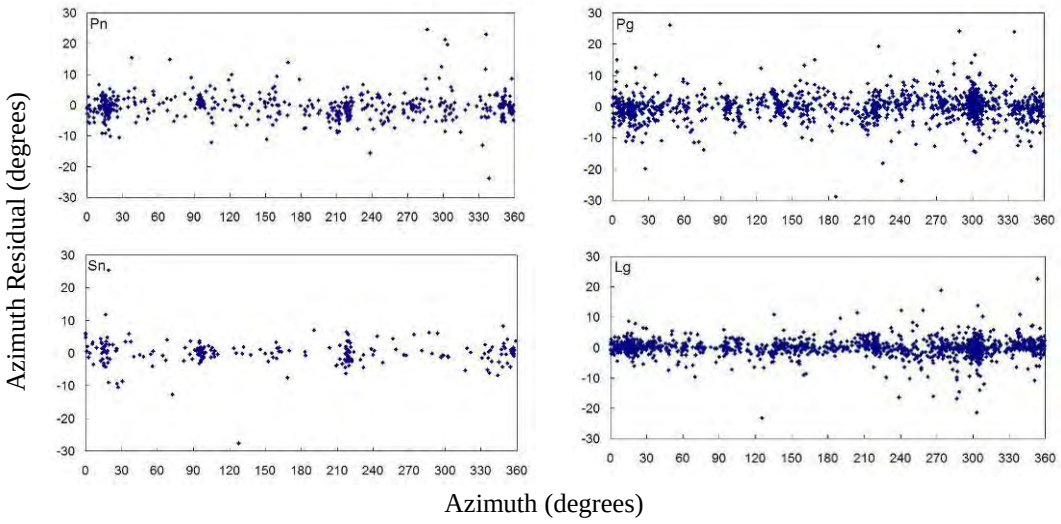


**Figure 11. Scatter plots of azimuth residuals versus azimuth for each regional seismic phase observed at station SONM for the combined datasets.**

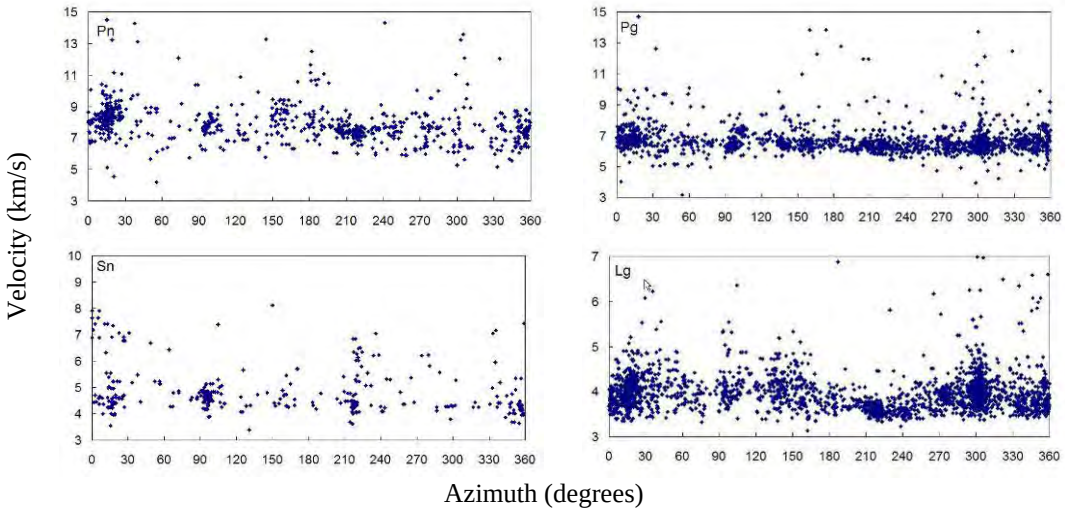


**Figure 12. Scatter plots of velocity versus azimuth for each regional seismic phase observed at station SONM for the combined datasets.**

*BVAR (Borovoye, Kazakhstan) Array*

In 2005, the IDC associated initial P-type arrivals from station BVAR to approximately 37% of REB events (9,997 of the 26,852). These statistics are not a full accounting of the station's contribution since it is not a primary station. Application of a 1–5 Hz causal Butterworth filter gave the best presentation of the data while preserving signal content from common events. Extremely high frequency events are common from only a few azimuths. BVAR was relatively free of random noise bursts as seen at station SONM. All regional phases have an azimuth residual 10°–15° degrees less than calculated station to event azimuth for events originating in the Hindu Kush area. For local events (Δ <5°), an SNR >10 is typically required for 2+ station locations and no 3+ station events were observed in the study dataset. A lower-frequency monochromatic ring (Figure 13) affected F-K analysis periodically. BVA0's east trace (BHE) was inoperative for the entirety of the analysis period.

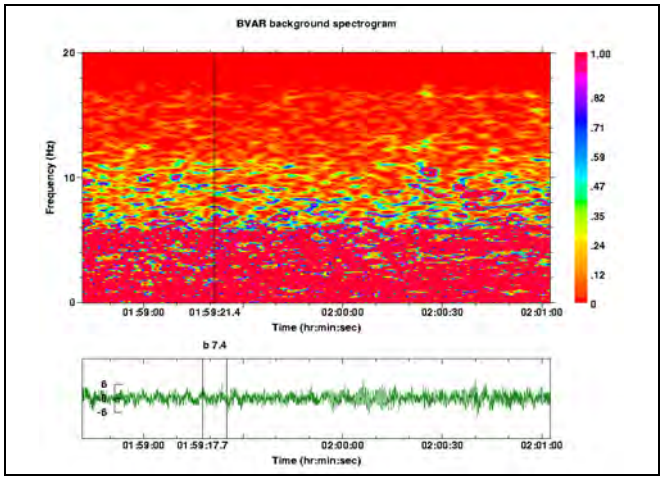


**Figure 13. Spectrum and spectrogram of the monochromatic background. The peak between 1 and 2 Hz complicates analysis since it is in the prominent band for signal observation.**

Figure 14 shows time residuals versus azimuth of each prominent regional phase observed at BVAR. Figure 15 shows azimuth residuals versus azimuth for each regional phase and Figure 16 shows velocity for the same phases.

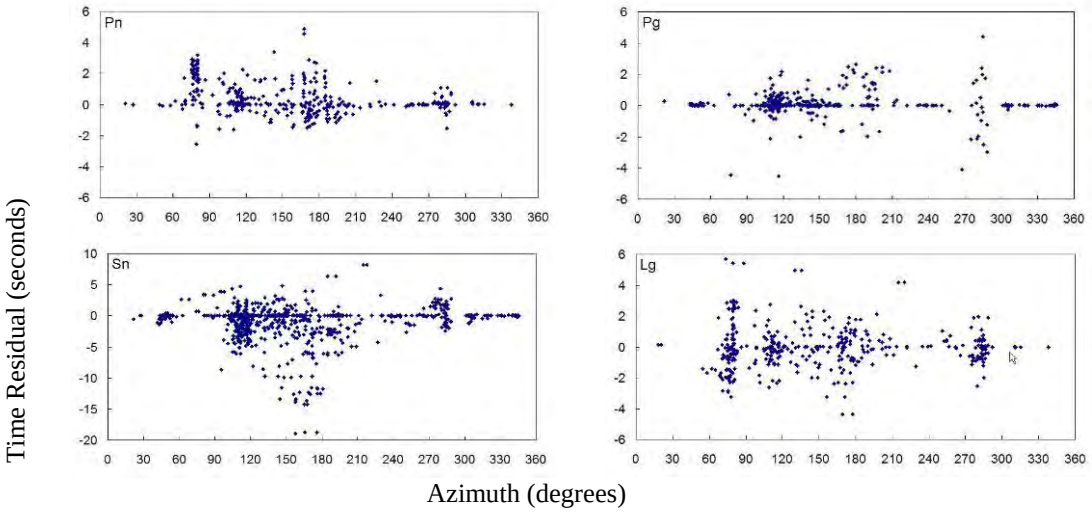


**Figure 14. Scatter plots of time residuals versus azimuth for each regional seismic phase observed at station BVAR for the combined datasets.**

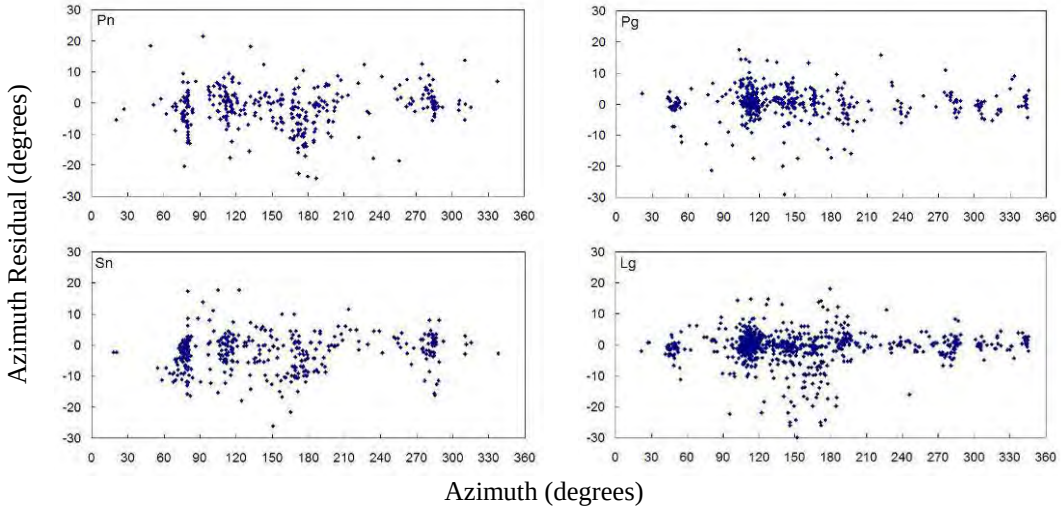


**Figure 15. Scatter plots of azimuth residuals versus azimuth for each regional seismic phase observed at station BVAR for the combined datasets.**

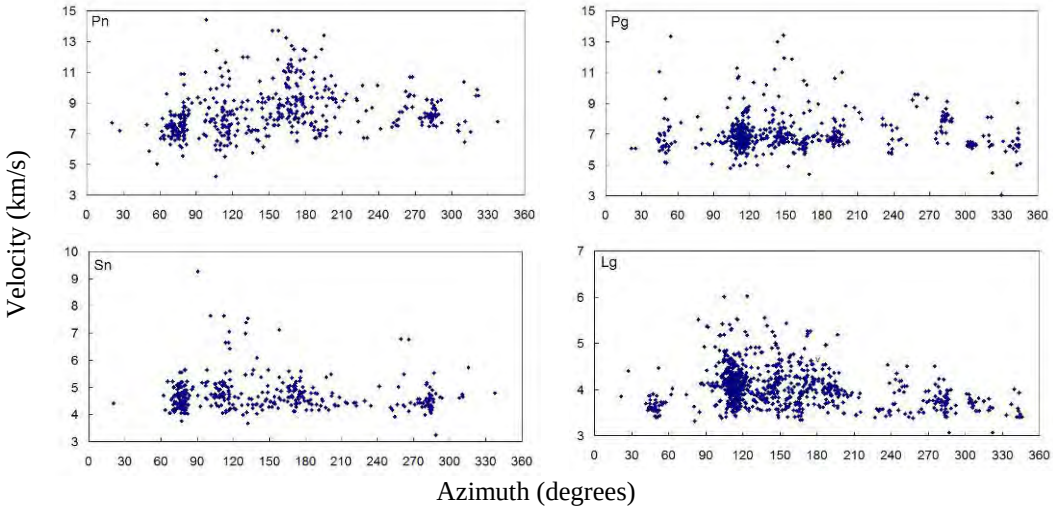


**Figure 16. Scatter plots of velocity versus azimuth for each regional seismic phase observed at station BVAR for the combined datasets.**

## CONCLUSIONS AND RECOMMENDATIONS

Over 9,000 events with at least one of the three IMS stations MKAR, SONM, and BVAR, located at an epicentral distance less than 20° were human-analyst reviewed, including phase identification and event location. About 6% of the located events included arrival times from all three stations, while about 16% included data from at least two stations. Thirty-nine event clusters, based on geographic and temporal distribution, were identified.

The three stations MKAR, SONM, and BVAR are all high-quality seismic arrays. Periodic noise on these stations affects phase identification. The most-prominent features of the dataset that impact routine analysis include the following observations. On station MKAR, regional phases from events located northwest of the station have F-K velocities much higher than are expected. On station SONM large numbers of "lone Lg" phases with no corresponding P-type phases are observed. Regional seismic phases observed on station BVAR from events located in the Hindu Kush area have an azimuth residual 10°–15° less than calculated station to event azimuth. The best frequency bands for general analysis of these stations are MKAR 2–5 Hz, SONM and BVAR 1–5 Hz. For the smaller events, manipulation of default F-K parameters is often necessary.

The final product of this study will provide a benchmark data baseline from which to tune automatic processes.

## ACKNOWLEDGEMENTS

The authors would like to thank Mr. Ivan Henson for contributing standalone versions of integral Geotool functions, that without, this work would still be in progress. A great deal of thanks to Ms. Elena Tomuta, Comprehensive Nuclear-Test-Ban Treaty Organization, whose assistance in configuring a very capable LINUX version of the software was invaluable.

# A LASER INTERFEROMETRIC MINIATURE SEISMOMETER

Dustin W. Carr, Gregory R. Bogart, Seth Goodman, Patrick Baldwin, and David Robinson

Symphony Acoustics, Inc.

Sponsored by National Nuclear Security Administration

Contract Number DE-FG02-08ER85108

## ABSTRACT

The threat of nuclear proliferation remains a critical issue in our society. Prevention requires knowledge, and there is no greater indicator of the capability and intent of a nation than observation of actual detonation tests being conducted. Ground-based monitoring systems have proven to be very capable in identifying nuclear tests, and can provide somewhat precise information on the location and yield of the explosive device. Making these measurements, however, currently requires very expensive and bulky seismometers that are difficult to deploy in places where they are most needed. A high-performance, compact device can enable rapid deployment of large scale arrays, which can in turn be used to provide higher quality data during times of critical need.

We are pursuing a design that is based upon a proven optical sensing modality, and will combine this interferometric transducer with a new mechanical system design in order to achieve the required sensor self-noise of 0.5 nano-g/$Hz^{1/2}$, with a total dynamic range of more than 150 dB. This will be accomplished in a form factor that is approximately 1 $cm^3$ per axis, and a power consumption below 30 mW. These metrics would represent substantial advancements over the existing state of the art.

Lower cost, smaller sensors will enable wide-scale deployment of sensor arrays, which will also greatly enhance our understanding of the earth and provide early-warning systems for earthquakes and tsunami. Slight variations in the sensor design will also find extensive use in oil and gas exploration.

## OBJECTIVES

High-performance seismic sensors have seen little advancement over many years, and for good reason. It is very challenging to produce a compact, robust sensor with self-noise that approaches the low noise model (LNM) of earth motion. This noise floor is comparable to detecting the vibration from a snowflake landing nearby. The approaches that have been taken towards solving this problem have led to large sensor components. The smallest high-performance seismometers on the market that can approach the LNM are about the same size and weight as a bowling ball. Fundamental physical limits for an accelerometer, however, would indicate that much smaller devices are feasible.

We can achieve significant advancement in the state of the art by using a novel optical design that has been developed at Symphony Acoustics, Inc. for use in a variety of physical sensors. For a low frequency accelerometer, this optical design offers several advantages over comparable sensors that utilize electrostatic, magnetic, piezoelectric, or piezoresistive sensing:

- The sensing modality is decoupled from the proof-mass system.
- The sensing components are very small.
- The optical signal can be electrically chopped, thus eliminating issues with 1/f noise in the sensing electronics.

Our optical interferometric design leverages advancements in optical components, packaging, and miniaturization that have been driven by consumer electronics, optical storage, and optical communications markets. We employ an elegant design that utilizes a mixture of low cost materials and processes and commercial off-the-shelf (COTS) components. The design proposed herein can thus readily scale to volume manufacturing with a substantial cost advantage over any existing sensors.

Some of the earliest work describing these sorts of applications for interferometric transducers can be found in the patent literature, wherein generic forms of accelerometers and microphones have been proposed. Uda (1987) describes a Fabry-Perot transducer, while Haritonidis et al. (1990) describes a micromechanical Michelson interferometer. Work by Greywall (1999) looked at specific implementations using simple silicon-nitride designs and was the first to consider the possibility of placing all of the components in a small package. Transducers based on grating light valves developed by Solgaard et al. (1992) were explored by Lee et al. (2004) and Hall et al. (2005). Fabry-Perot based micro-electromechanical system (MEMS) accelerometers were fabricated and studied by Waters et al. (2002). Tunable Fresnel lens structures have been made with considerable success at SINTEF by Sagberg et al., (2003). Work by the principal investigator of the proposed work, Carr et al. (2003), studied a different type of lateral-motion grating. Follow-on work to this wherein the transducer was incorporated in an accelerometer with 17 ng/Hz$^{1/2}$ noise limit was provided by Krishnamoorthy et al. (2008).

This paper describes the proposed work for a new contract that has not yet begun. We will thus focus on the background information in this section, and conclude with a brief description of the work plan.

### Fundamental Mechanical Considerations for Seismic Sensors

A seismic sensor is a device that detects ground motion by coupling the accelerations to an internal spring-mass system. Motion of the proof mass, *m*, is detected through a transducer that translates motion into an electrical voltage or current. In most, if not all, commercial devices, a feedback signal is fed into an actuator that holds the proof-mass in place, thus maintaining linearity and dynamic range. The discussion that follows herein is not entirely applicable to these closed-loop devices, because the dynamics of the feedback loop often dominate the considerations of both signal and noise. We are instead proposing a means for fabricating an open-loop freely moving proof mass system. Such an approach is enabled by the high dynamic range (150 dB) that is achievable with the optical detection system that we are proposing.

A good seismometer spring-mass system can be approximated very well as a linear device, with a Hooke's law spring constant *k*. This will have a fundamental mechanical resonance at a frequency of $\omega_0 = \sqrt{k/m}$. The resonant frequency is an important design parameter for two reasons. First, it is the transduction factor for converting an applied acceleration into a relative motion of the proof mass:

$$\Delta x = \frac{a}{\omega_0^{\,2}}. \tag{1.1}$$

Secondly, this frequency determines the bandwidth of the system. The exact useful bandwidth depends upon another parameter that measures the amount of mechanical damping in the system, which is the quality factor, or *Q*. For a system that is heavily underdamped, *Q*>>1, the operating bandwidth will typically extend from DC up to 1/3 to 1/2 of the resonant frequency, while an overdamped oscillator, *Q*<1, can have a bandwidth that extends up to the resonant frequency. These three parameters, mass, resonant frequency, and quality factor, determine all of the meaningful properties of the system, insofar as we neglect higher-order modes and cross-axis effects. We can now express the equation of motion in these terms

$$m\ddot{x} + m\frac{\omega_0}{Q}\dot{x} + m{\omega_0}^2 x = F_{ext} = ma_{ext}\,. \tag{1.2}$$

The second term is a mechanical resistance due to damping from any sources within the sensor system. This term is also responsible for thermal noise, just as resistance in an electrical circuit produces Johnson noise, as described by Gabrielson (1993). This is a white noise with a force spectral density given by

$$F_n = \sqrt{4k_B TR}\,(N/Hz^{1/2})\,, \tag{1.3}$$

wherein $k_B$ is the Boltzmann constant and $T$ is the temperature in Kelvin. By inspection of the equation of motion (1.2), we can see that the resistance is

$$R = \frac{m\omega_0}{Q}\,. \tag{1.4}$$

This noise force is applied directly to the proof mass, and thus results in an equivalent acceleration

$$a_n = \sqrt{\frac{4k_B T\omega_0}{mQ}}\,. \tag{1.5}$$

We will explore the magnitude of this noise source in combination with other noise sources in detail in the following section. As a point of reference, a system with a resonant frequency of 1 kHz, a mass of 1 gram, and a *Q* of 100, will have a thermal noise equivalent acceleration of about 3.2 ng/Hz$^{1/2}$, which is still 16 dB above the LNM.
The table below also gives some typical values for the amount of displacement in the proof mass when subjected to 1 g of acceleration.

**Table 1. Typical values of proof-mass displacement when subjected to a 1g acceleration.**

| Resonant Frequency | Displacement at 1g |
|---|---|
| 1 kHz | 250 nm |
| 100 Hz | 25 μm |
| 10 Hz | 2.5 mm |

If we take into account the thermal noise and the mechanical response, we can begin to understand why miniaturization and microelectromechanical systems (MEMS) technologies have had little impact to date upon low-noise seismometers. Silicon-based technologies are ill-suited for the problem. For a typical silicon wafer, with a thickness of 0.5 mm, the mass density is 0.13 grams/cm$^2$, which means that a significant fraction of a wafer would need to be consumed before we can approach even a mass of 1 gram. At the same time, if we reduce the frequency significantly below 1 kHz, we quickly run into very large displacements for micromechanical devices. This is why the best available accelerometers that utilize silicon MEMS remain 50 dB above the LNM.

**Fundamental Optical Transducer Design Considerations**

The basic operating principal involves the creation of an optical path whose length is varied when subjected to an external stimulus, such as pressure or acceleration. A Fabry-Perot type of interferometer can be used for consideration of the design issues in these types of transducers in general. This type of interferometer has two

parallel dielectric mirrors that bound an empty cavity as shown in Figure 1. Light that is incident upon the cavity will be partially transmitted according to the relation

$$T = \frac{1}{\left(1 + F \sin^2 \varphi/2\right)^2}, \tag{2.1}$$

wherein $F$ is determined by the reflectance of the two mirrors,

$$F = \frac{4R_0}{\left(1 - R_0\right)^2}. \tag{2.2}$$

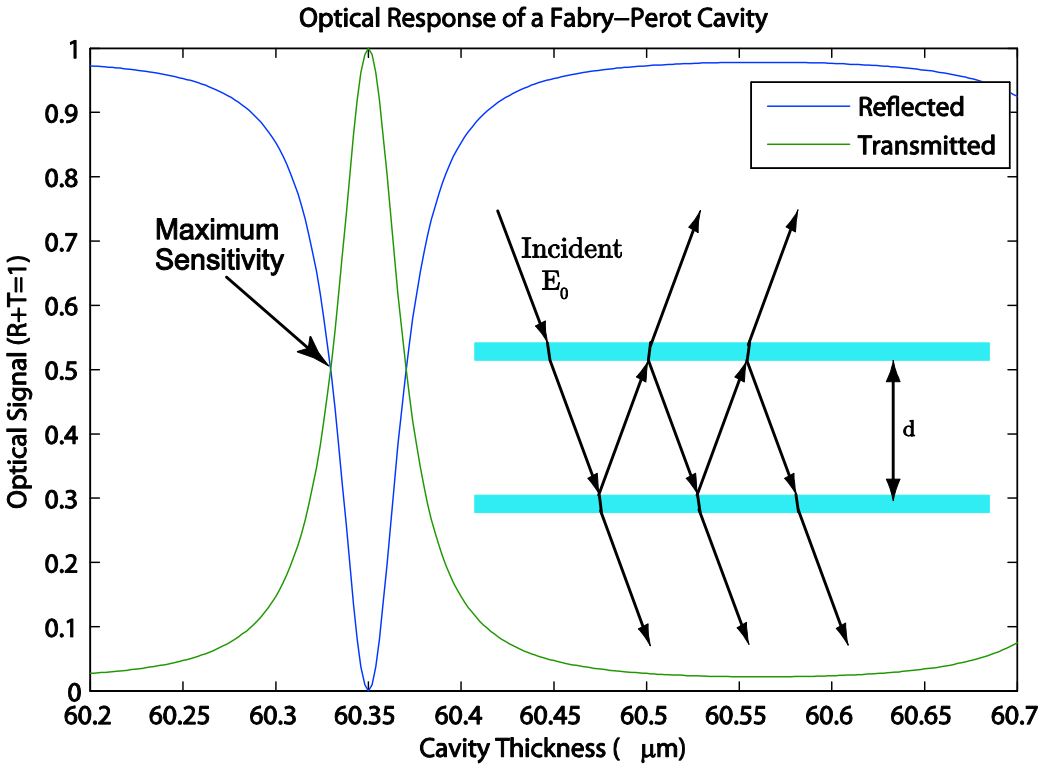


**Figure 1. A planar Fabry-Perot device consists of two dielectric mirrors as shown in the inset. Multiple reflections within the cavity defined by the two mirrors can produce a resonant condition where maximum transmission is achieved. The reflected and transmitted light can be collected, and will display a maximum sensitivity to changes in the cavity thickness at the point indicated.**

This assumes that the reflectance values of the two mirrors are equal. $\varphi = 4\pi d / \lambda$ is the phase that is picked up in a wave with wavelength $\lambda$ as it makes a roundtrip within the cavity of length $d$. Figure 1 shows a typical response for a cavity whose mirrors have a moderate reflectance. From this plot, we see that the slope has a maximum value at the points indicated. The slope sensitivity of the transducer is the change in optical power at the detector-per-unit change in cavity length. The maximum slope can be shown to be

$$S_{\max} = \frac{I\pi}{\lambda}\sqrt{F - 1}\frac{W}{m}, \tag{2.3}$$

where $I$ is the optical power.

From this we can start to see some of the potential benefit of the optical transducer. For illustration, a cavity with a reflectance of 0.7 on each side and an operating wavelength of 850 nm can achieve a relative sensitivity of 2%/nm. If we only consider laser relative intensity noise as the limit, we can still achieve a transducer noise floor that is below 1 pm/Hz$^{1/2}$, for a readily achievable intensity noise of -100 dB/Hz.

Theoretically, the true physical limit is going to be the photodiode shot noise. A differential detector can be designed that captures the reflected and transmitted signals, wherein the laser intensity noise is common to both and can thus be subtracted out, with the remaining noise limit being the photodiode shot noise.
The photodiode shot noise is given by the relation

$$n_{shot} = \sqrt{2eIB}\,\frac{A}{Hz^{1/2}}, \tag{2.4}$$

where $e$ is the electron charge, $I$ is the optical power that is incident upon the photodiode, and $B$ is the photodiode sensitivity in units of Amperes/Watt.
Dividing this by the slope sensitivity in (2.3) and converting to acceleration using (1.1), we can arrive at an expression for the shot noise equivalent acceleration

$$h_{shot} = \frac{l\,w_0^{\,2}}{p}\sqrt{\frac{2e}{BI_0(F-1)}}\,\frac{m}{s^2 Hz^{1/2}}. \tag{2.5}$$

In practical designs, there are unfortunately additional sources of noise that are not necessarily common between the reflected and transmitted signals in a conventional Fabry-Perot design. In particular, shifts in the laser wavelength are going to produce a signal that is not discernible from a shift in the cavity length. This wavelength noise is going to depend upon the cavity length, and so a shorter cavity results in a lower impact on the effective noise. To be exact, if we have a known wavelength noise spectral density of $\delta\lambda$ in units of m/Hz$^{1/2}$, then this will result in an equivalent displacement noise of

$$\eta_\lambda = \delta\lambda\,\frac{d}{\lambda}\,\frac{m}{Hz^{1/2}}. \tag{2.6}$$

Other design considerations, however, prevent this cavity from becoming arbitrarily short. A practical range would be somewhere between 10 and 100 μm. In order to achieve a noise level that is equivalent to the shot-noise limit, this means that the laser wavelength must be maintained to better than 1 part in $10^9$ per root Hz. While this is achievable in COTS diode lasers, it requires very careful design of the laser current control electronics. Given that the laser diodes have been optimized for applications that do not have this constraint, there is very little information on wavelength noise for COTS devices at the frequencies of interest for this application.

Note that laser wavelength noise is not related directly to the laser linewidth. The latter merely determines the coherence length of the laser, which is the distance that a wave packet can travel without the constituent waves falling out of phase. A shorter coherence length can result in a reduced signal amplitude in a transducer, but for cavity lengths around or below 100 μm, this is not a significant issue when quality laser diodes are utilized.

Because this source of noise typically has a strong 1/f component, it is very important to either reduce the wavelength noise through an active control technique, or somehow modify the design of the optical transducer such that it has less sensitivity to wavelength variation. Both of these approaches are being researched during this phase of the project.

Optical interference transducers have other mechanical advantages over their counterparts that use capacitive, piezoresistive, or piezoelectric sensing. First and foremost, the sensing mechanism is decoupled from the mechanical elements. Effectively, the motion of the structure being measured is “remote sensed.” An optical spot size that is as small as 10 μm can be used to interrogate the position. In other approaches, this is not typically the case. For instance, in a capacitively sensed device, the sensitivity will scale with the area of the electrodes, the distance between electrodes, and an applied voltage. The applied voltage in turn produces a force that must be accounted for in the design. All of these factors must be considered together in order to create an optimum design. In a

piezoelectric or piezoresistive device, appropriate materials must be used in the spring element, which is a significant manufacturing constraint.

The challenge in the optical design is that the response is only linear over a distance that is less than a quarter wavelength. There are many approaches for overcoming this limitation. The use of electrostatic actuators to compensate and pull the device to an optimum operating point has been proposed repeatedly. This approach introduces challenges that greatly reduce the potential benefits of the optical design when compared with other approaches. Introducing these actuators increases the complexity of the fabrication process, restricts the mechanical design space, and most importantly, creates a potential nightmare from a reliability standpoint. Laser wavelength can also be used as a control parameter, as a typical laser diode will have a wavelength that varies with the laser current. This is a more desirable design, as it allows the signal sensitivity to be directly controlled through the electronics. It does, however, require that the cavity length be sufficiently large (>50μm) (Figure 2).

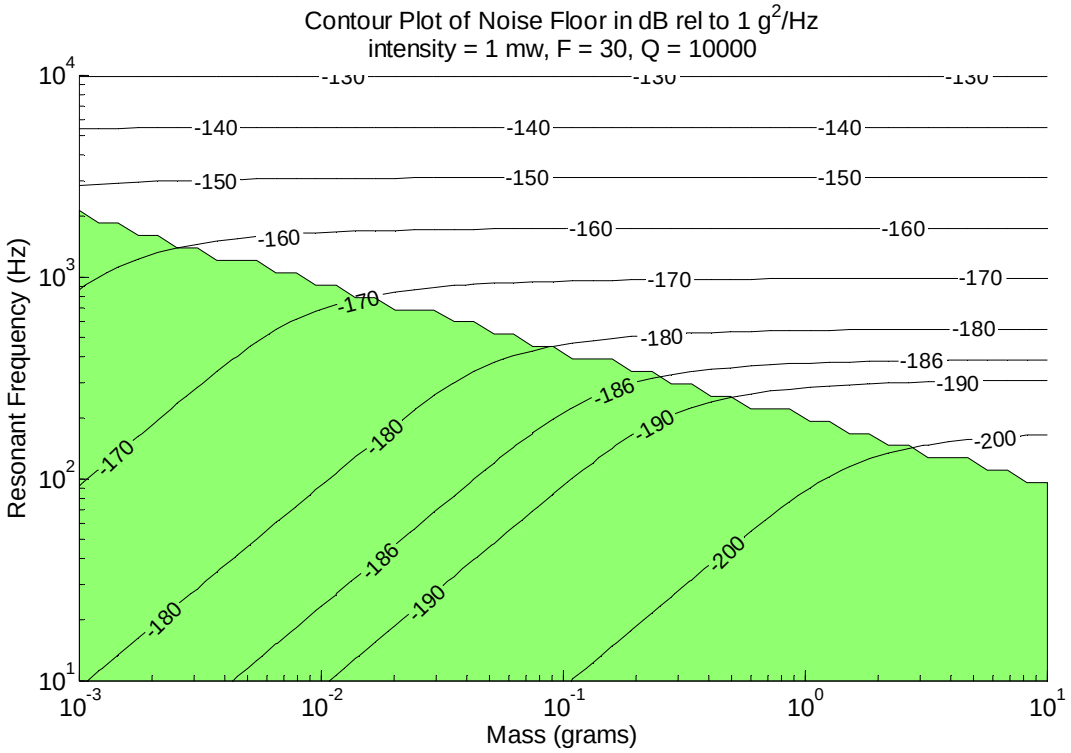


**Figure 2. Contours of constant noise floor as a function of the key design parameters, resonant frequency and mass. The target level for the broadband white noise is -186 dB/Hz, or 0.5ng/Hz$^{1/2}$. Within the shaded region, the device is limited by thermal noise. Outside of this region, the limit is photodiode shot noise.**

**Electronics Design Considerations**

Figure 3 is a block diagram of the electronics. There are a number of alternate topologies to produce an output corresponding to the difference between the two photodiode currents. Because the bandwidth of the system is relatively low and the dynamic range required is large, we choose to operate the photodiodes with zero bias, convert the photodiode currents to voltages with transimpedance amplifiers based on operational amplifiers (op amps) and produce a difference signal with a differential amplifier. Other approaches include a current proportioning differential transistor pair. The latter approach gives somewhat lower noise and automatically adjusts the relative gains of the two photocurrents to be equal, but it has potential linearity issues for this wide of a dynamic range.

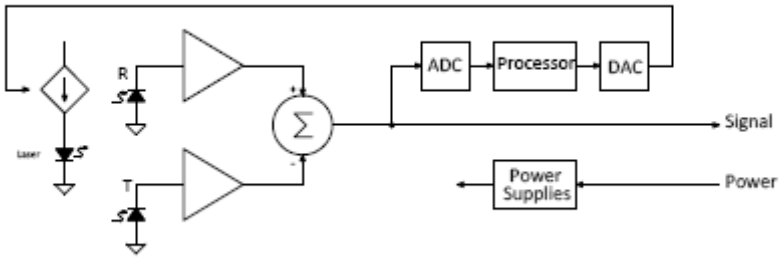


**Figure 3. Block diagram of the electronics used for laser control and signal extraction. The laser current is controlled with a DAC voltage. The reflected and transmitted light is collected at the photodiodes and transimpedance amplifiers convert the photocurrent to a voltage, and the seismic signal is the difference between the two. An analog to digital converter uses the signal and the measured capsule temperature to apply corrections to the laser current.**

We drive the Vertical Cavity Service Emitting Laser with a low-noise current source controlled by a microprocessor. Residual noise in the current source, plus intrinsic laser intensity noise, shows up as common to both photocurrents. These will cancel out to the extent that the total gain, optical plus electronic, is equal in the two signal paths. It is feasible to cancel the
laser-intensity noise far below the other noise sources without special measures.

Electronic noise in this system comes from a number of identifiable sources. All resistances have an associated thermal noise, or Johnson noise, which has a uniform (white) spectrum with voltage spectral density

$$V_n = \sqrt{4k_B TR}\,(V/Hz^{1/2}), \tag{3.1}$$

where $V_n$ is voltage noise spectral density, k is Boltzman's constant, T is absolute temperature and R is resistance. Op amps have equivalent input voltage and current noise sources, which are both white, as well as 1/f noise components of both voltage and current. The 1/f components are especially important for accelerometers, as the frequency range extends far below the 1/f noise corners of most op amps.

Noise sources attributable to the opto-mechanical system are shot noise, determined by laser optical power output (2.4), and the thermal noise equivalent of the proof mass (1.5). Both of these sources are white. Each of these individual noise sources has a transfer function from their position in the circuit to the output which is, in general, a function of frequency. Thus, the total noise at the output of the circuit depends both on topology and component values. Total dynamic range depends not only on the noise floor, but also on the largest usable signal. To make best use of a particular topology, it is critical to scale the signal properly inside this usable range to the extent practical.

Figure 4 shows the output noise spectrum of a novel differential circuit developed in our facility and its two primary components. The "electronic" white noise level is roughly equal parts of op amp voltage noise and resistor thermal noise. The 1/f component is entirely op amp 1/f voltage noise. On the same figure, the opto-mechanical white noise is made up of the shot noise inherent in the 1mW optical beam power and the thermal equivalent mass noise of the proof mass. The electronic white noise level is apparently 13dB below the opto-mechanical white noise, so it makes a negligible contribution. Below the 8Hz 1/f noise corner, 1/f noise dominates and neither the electronic nor opto-mechanical white noise components contribute.

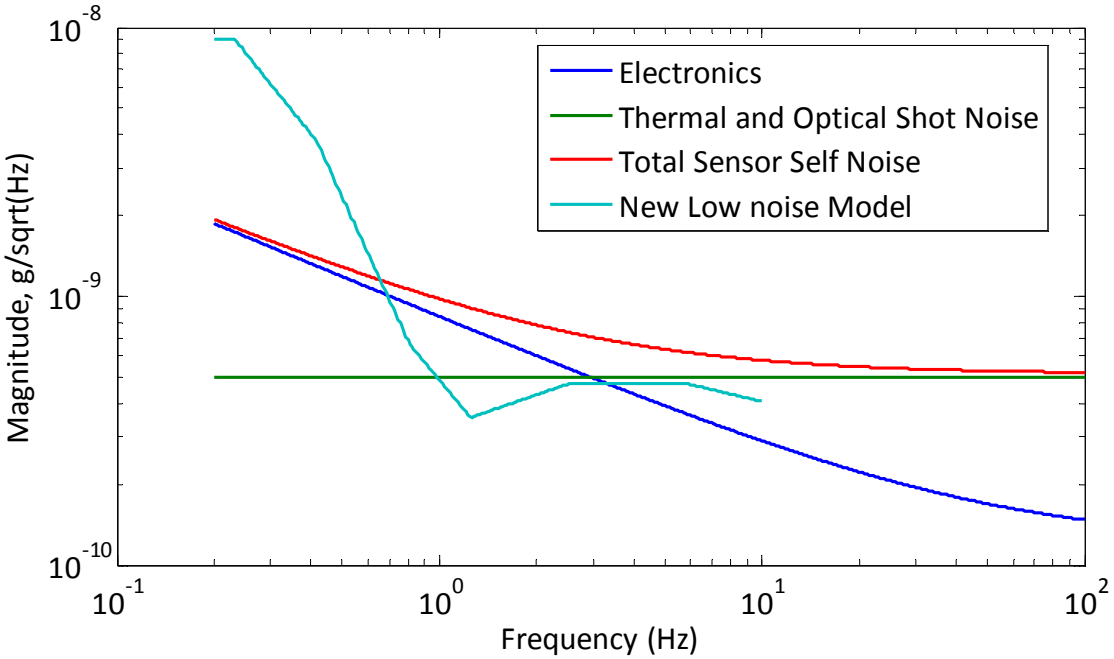


**Figure 4. Predicted noise contributions using our existing electronics design. The 1/f components in the electronics produce noise that is in excess of the LNM target between 3 Hz and 0.8 Hz. Many solutions exist for overcoming this limitation. Chopping of the laser electronics, substituting lower noise operational amplifiers, or small changes in the circuit topology are all areas to be researched.**

The proposed mechanical design has an acceleration scale factor that sets the high-frequency region of LNM at the same spectral level as opto-mechanical white noise. The LNM as described by Peterson (1993), with this scaling, is shown with the sum of electronic and opto-mechanical noise on Figure 4. This noise spectrum indicates that this initial design meets LNM everywhere except for the frequency range of 0.5-7Hz, where the 1/f noise dominates. The maximum signal size for this circuit is +5dBV, so the dynamic range is over 140dB.

For this topology, research work will involve reducing the 1/f noise power in the region where electronic noise is above LNM. Possible approaches are to modulate the signal out of the 1/f region by chopping the laser or by using chopper op amps. Other approaches are to create topology and/or component variations with noise spectra more suitable for the LNM. Increasing the light level by using a different laser, described in a previous section, also reduces electronic noise by decreasing the feedback resistance values in the transimpedance amplifiers.

## CONCLUSIONS AND RECOMMENDATIONS

Achieving LNM resolution in a seismic sensor is a very strong challenge. While we have built sensors with noise performance below 100 ng/Hz$^{1/2}$, extending this to 0.5 ng/Hz$^{1/2}$ is not trivial. The research to be carried out in phase one will cover the following:

1. Development of a robust mechanical design that will result in a sufficient range of motion and a thermal noise limit that is below the LNM target, combined with an optical design that will result in the required motion sensitivity.
2. Characterization of optical sources to identify lasers that have sufficient power (up to 10 mW) and low enough wavelength noise, and identify methods to mitigate the effects of wavelength noise.
3. Development of an electronics design that will not contribute significantly to the noise floor defined by the photodiode shot noise and the mechanical thermal noise, and have an overall power consumption below 30 mW per axis.
4. Assembly and testing of a compact single axis sensor capsule that will demonstrate the feasibility of the approach. The assembly of functioning sensors components is critical in determining the overall feasibility of this approach. The multi-physical nature of this design demands that we not rely on laboratory bench

demonstrations, but actually make self-contained sensors, thus allowing us to fully uncover the critical details involved in the technical approach.

## REFERENCES

Gabrielson, T. B. (1993). Mechanical-Thermal Noise in Micromachined Acoustics and Vibration Sensors. *IEEE Trans. Electron. Dev.* 40: pp. 903–909.

Uda, K. (1987). Pressure Sensitive Element. U.S. Pat. No. 4: 682,500

Haritonidis, J. H., S. D. Senturia, D. J. Warkentin, and M. Mehregany (1990). Optical Micropressure Transducer. U. S. Pat. No. 4,926,696

Greywall, D. S. (1999). Optical Interference Microphone. *Sens. Actuators.* 75: pp. 257–268.

Solgard, O. F.S.A. Sandejas, and D.M. Boom (1992). Deformable Grating Optical Modulator. *Opt. Lett.* 17: pp. 688–690,

Lee, W., N. A. Hall, Z. Zhou, and F. L. Degertekin (2004). Fabrication and Characterization of a Micromachined Acoustic Sensor With Integrated Optical Readout. *J. Sel. Topics. Quantum Electron.* 10: pp. 643–651,

Hall, N. A. B., Bicen, M. K. Jeelani, W. Lee, S. Qureshi, F. L. Degertekin, and M. Okandan (2005). Micromachined microphones with diffraction-based optical displacement detection. *J. Acoustical. Soc. Amer.* 118: pp. 3000–3009.

Waters, R. L and M. E. Aklufi (2002). Micromachined Fabry-Perot Interferometer for motion detection. *Appl. Phys. Let.* Vol. 81 pp. 3320–3322,

Sagberg, H., A. Sudbo, O. Solgaard, K.A.H. Bakke, and I.R. Johansen (2003). Optical Microphone Based on a Modulated Diffractive Lens. *IEEE Phot. Tech. Let.* 15: pp. 1431–1433,

Carr, D. W., J.P. Sullivan, and T.A. Friedmann (2003). Laterally Deformable nanomechanical zero-order gratings: Anomalous diffraction studied by rigorous coupled wave analysis. *Opt. Lett.* 28: pp. 1636–1638,

Keeler, B. E. N., D. W. Carr, J. P. Sullivan, T. A. Friedmann, and J. R. Wendt (2004). Experimental demonstration of a laterally deformable optical NEMS grating transducer. *Opt. Lett.* Vol. 29 pp. 1182–84.

Krishnamoorthy, U., D. W. Carr., G. R. Bogart, M. S. Baker, P. J. Clews, T. P. Swiler, and R. H. Olsson (2008). In-Plane MEMS-Based Nano-G Accelerometer with Sub-Wavelength Optical Resonant Sensor. *Sens. Act. A.* Vol. 145 pp. 283–290.

Peterson, J. (1993). Observations and Modeling of Seismic Background Noise. *OFR 93-322.*

# EVALUATION OF REGIONAL TRAVEL-TIME AND LOCATION IMPROVEMENT ALONG THE TETHYAN MARGIN USING A NEW THREE-DIMENSIONAL VELOCITY MODEL

Sung-Joon Chang [1], Megan P. Flanagan[2], Suzan van der Lee[1], Eric M. Matzel[2], and Michael E. Pasyanos[2]

Northwestern University[1] and Lawrence Livermore National Laboratory[2]

Sponsored by National Nuclear Security Administration

Contract Nos. DE-FC52-04NA25541[1] and DE-AC52-07NA27344[2]
Proposal No. BAA04-40

## ABSTRACT

For purposes of studying the lateral heterogeneity as well as predicting seismograms for this region, we construct a new 3-D S-velocity model by jointly inverting a variety of different seismic data. We jointly invert regional waveforms, surface wave group velocity measurements, teleseismic *S* and *SKS* arrival times, and crustal thickness estimates from receiver functions, refraction lines, and gravity surveys. These data types have complementary resolving power for crust and mantle structures, vertical and lateral variations, shallow and deep mantle features, local and global structure. Therefore, a joint inversion of these data sets might help unravel the complexity of this tectonically diverse area. These measurements are made from a combination of MIDSEA, PASSCAL, GeoScope, Geofon, GSN, IDA, MedNet, national networks, and local deployments throughout the study region which extends from the western Mediterranean region to the Hindu Kush and encompasses northern Africa, the Arabian peninsula, the Middle East, and part of the Atlantic Ocean for reference. The Moho depth result is broadly consistent with CRUST2.0, except in mid-northern Africa, where the crust from our joint inversion is about 5 km thinner. Fast velocity anomalies are found beneath the West African Craton, the Hellenic trench, the Apennines, the East European Platform, and the Arabian Platform at a 75–150 km depth, whereas low-velocity anomalies are located along the plate boundaries such as the mid-Atlantic ridge, Afar, the Anatolian Plateau, Iran, Afghanistan, western Mediterranean Sea, and the Red Sea. Based on the assumption that *P*-wave velocity anomalies in m/s scale are very close to *S*-wave velocity anomalies in m/s scale in our study area, we convert our *S*-velocity model to a *P*-velocity model with use of teleseismic *P* arrival times. Finally, our model is validated by performing travel-time predictions with a dataset of ground truth events. Our model generally produces better travel-time predictions than the iasp91 model. We expect that better travel-time predictions may be achieved by replacing the poorly resolved crust in our model with CRUST2.0 and refining the *P*-velocity model.

## OBJECTIVES

Our primary objective is developing a new 3-D *S*-velocity model for the Middle East and Mediterranean region, including North Africa, southern Europe, and Arabia that

1) is resolved in aseismic regions;
2) is resolved throughout the upper mantle (to 660 km);
3) resolves laterally varying crustal thickness;
4) contains laterally varying vertical velocity gradients;
5) is simultaneously compatible with multiple data sets;
6) utilizes several recent, unique waveform data sets; and
7) includes uncertainties of the model parameters.

These features would increase the model's ability to predict and calibrate regional travel times and waveforms, thereby providing improved event locations, focal mechanisms, and other event discriminants.

Secondly, we aim to convert the 3-D *S*-velocity model to a 3-D *P*-velocity model, using teleseismic *P*-arrival times.

Our third objective is to test both the *P*-and *S*-wave models' ability to predict regional *P* and *S* travel times, deflect wave paths and deform waveforms, and assess their effects first on the studied seismograms (travel times and amplitudes) and subsequently on the 3-D models derived from these data.

This report covers all the above-mentioned objectives.

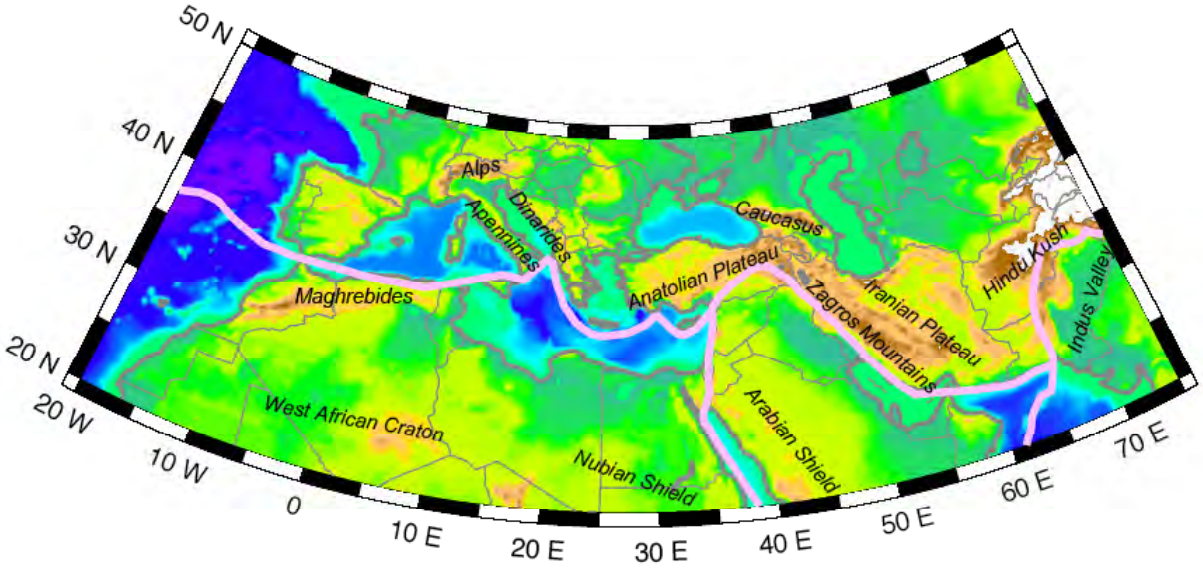


**Figure 1. Topographic map of the study region. The pink line is the NUVEL1-A (DeMets et al., 1990) representation of the Eurasia-Africa-Arabia plate boundary.**

The study region is centered around the Africa-Arabia-Eurasia triple junction (Figure 1), and extends west to the Africa-Eurasia-North America junction at the Azores, just off the map, and east to the Arabia-Eurasia-Indian Plate junction. The NUVEL1-A (DeMets et al., 1990) representation of these plate boundaries is shown by the pink line in Figure 1. The interaction of these five major tectonic plates with each other and with several microplates within an area of one quarter of the Earth's circumference yields this region rich with tectonic complexity. We plan to capture various renditions of this structurally complicated part of the world in one *S*-velocity model through the joint inversion of several different types of seismic data simultaneously; the new model will refine our understanding of the structure and tectonics in this region of the Earth. The data types we combine are constraints from independent studies on the depth to the Moho, fundamental-mode Rayleigh-wave group velocity measurements, waveform fits of regional *S* and Rayleigh waves, and arrival times of teleseismic *S* and *SKS* waves. We convert the resulting *S*-

velocity model to a *P*-velocity model with over 2.9 million teleseismic *P* arrival times. Then, we validate our model by performing travel-time prediction with a dataset of ground truth event.

## RESEARCH ACCOMPLISHED

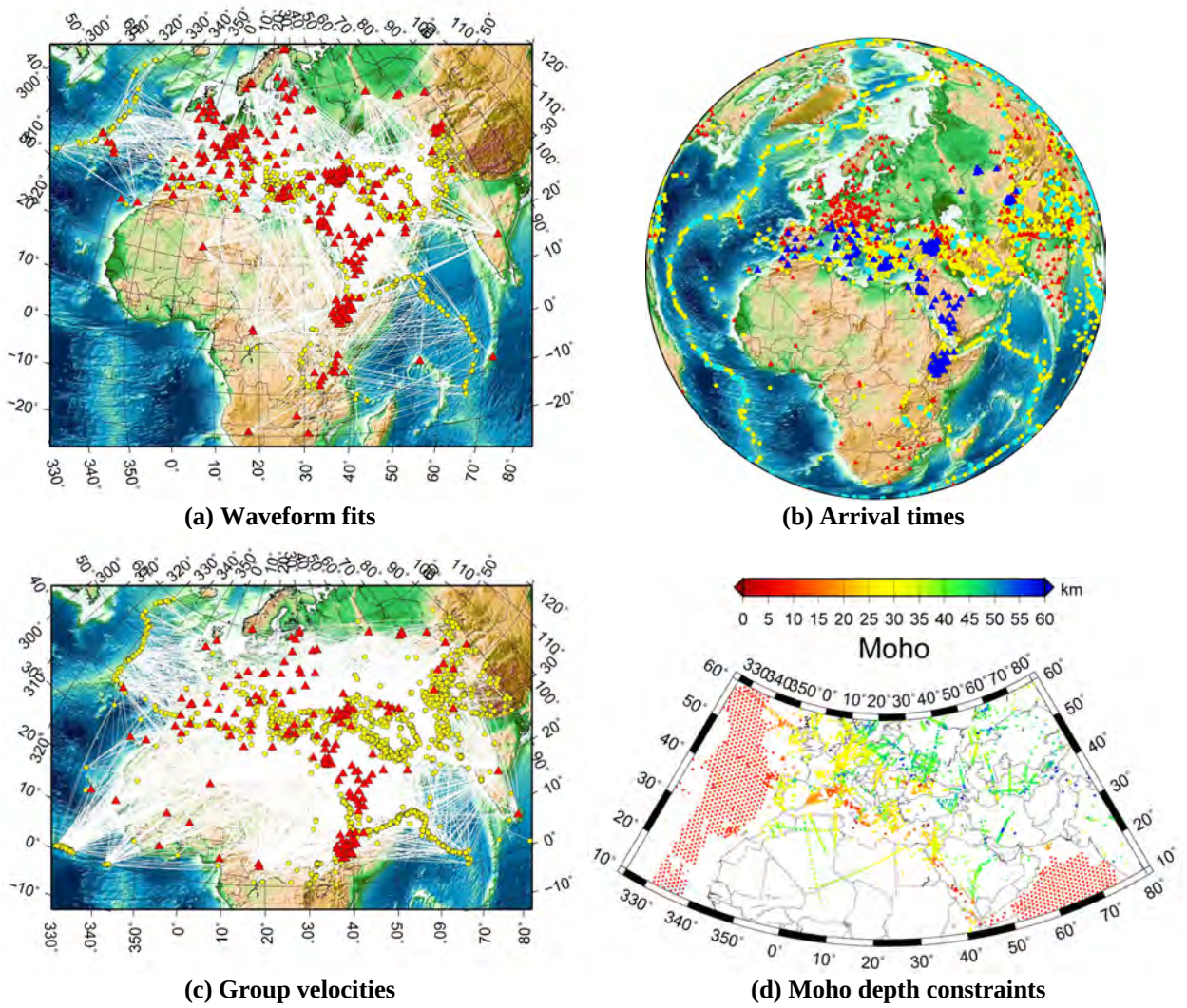


**(a) Waveform fits** **(b) Arrival times**

**(c) Group velocities** **(d) Moho depth constraints**

**Figure 2. Datasets used for the joint inversion. (a) Ray path coverage for regional waveform fits. Stations are illustrated as red triangles, and events as yellow circles. (b) Events and stations used for teleseismic *S* and *SKS* arrival time estimation. Cyan circles and blue triangles represent events and stations used for relative delay time estimation with MCCC, respectively. Yellow circles and red triangles are events and stations from the reprocessed ISC catalogue. (c) Great-circle wave paths for 45 s period Rayleigh waves. Stations are illustrated as red triangles, and events as yellow circles. (d) Map of the Moho depth distribution acquired from literatures. Artificial point constraints of 10 km depth are placed to the Atlantic and Indian Oceans where measurements are absent.**

### Regional Waveform Fits

We fit over 5,600 available waveforms from the Lawrence Livermore National Laboratory (LLNL) database and MIDSEA dataset (Marone et al., 2004) which sample the Mediterranean region, North Africa, the Middle East, Pakistan, and Afghanistan using the non-linear inversion procedure employed by partitioned waveform inversion studies (Nolet, 1990; Van der Lee and Nolet, 1997). We utilize events with magnitude larger than 4.0 and seismograms with epicentral distance from 5º to 50º. The great-circle wave paths for these seismograms are shown

in Figure 2(a). We have estimated path-averaged *S*-velocity structures for these paths using the same starting *S*-velocity model but a different crustal thickness (in 5 km increments) for each path, based on a priori reported estimates (Marone et al., 2004). The starting model often predicts significant phase differences relative to the data for both the *S*- and Rayleigh waves. The inversion procedure estimates the perturbations to the starting model by non-linear optimization (Nolet, 1990; van der Lee and Nolet, 1997). For the computation of synthetic waveforms we also need to know the source mechanisms of the events. We typically use the centroid moment tensors (CMT) from the Global CMT project, and hypocenters from Engdahl's reprocessed International Seismological Centre (ISC) database (Engdahl et al., 1998). The frequency content of the data and synthetic is different for each fit and generally falls within the band 0.006 to 0.1 Hz.

**Teleseismic *S* and *SKS* Arrival Times**

We obtained *S* and *SKS* phase arrival time data from two different sources. Both arrival times are adjusted for topography and Earth's ellipticity before inversion. First, we used high-quality relative arrival times of teleseismic *S* and *SKS* waves (Benoit et al., 2006; Park et al., 2007; Schmid et al., 2004) which are measured on broadband seismograms with use of multi-channel cross-correlation (MCCC; VanDecar and Crosson, 1990). Benoit et al. (2006), Park et al. (2007), and Schmid et al. (2004) used seismograms recorded in the Mediterranean, Ethiopia, amd Saudi Arabia, respectively. Moreover, we measured additional relative delay times at Turkey and central Asia. The number of *S* phase relative arrival times is over 5900 with epicentral distances of 30º–90º and the number of *SKS* phases is over 1,400 with distances of 87º–140º; over 73,00 in total. We set 0.5 s as uncertainty for weights during the inversion. Second, we obtained over 223,000 *S* phase arrival time data from the reprocessed ISC database (Engdahl et al., 1998) from 1964 to 2007. The epicentral distance range is 20º–80º. We set lower uncertainty of 2.5 s for the data because lots of outliers and systematic errors are found in this data set by Röhm et al. (2000). We illustrate location of stations and events for each of the two types of arrival time data in Figure 2(b).

**Surface Wave Group Velocities**

We have measured over 105,000 group velocities of fundamental-mode Rayleigh waves recorded at MIDSEA and other stations in the region and used them to update previous group velocity maps (e.g., Pasyanos, 2005). Figure 2(c) shows the great-circle wave paths for which we included fundamental-mode Rayleigh wave group velocities in our joint inversion. Compared to other data types we include, lateral coverage is best for this group velocity data set, though vertical coverage is provided mainly by the teleseismic arrival times and regional *S* and Rayleigh waveforms. The period for group velocities ranges from 7 to 100 sec.

**Crustal Thickness Constraints**

While the fundamental-mode Rayleigh-wave group velocities and regional *S* and Rayleigh waveforms have significant sensitivity to Moho depth, they cannot uniquely resolve Moho depth. We therefore include independent estimates of crustal thickness as point constraints in the joint inversion and thus compile such measurements from a large number of published studies. A partial list of these studies is provided in Marone et al. (2003) and part of these points stem from the database used for CRUST5.1 (Mooney et al., 1998). We have added new estimates of Moho depth from more recent studies and interactively resolved or removed conflicting data and outliers from the data set. Over 4,700 Moho depth constraints are mapped in Figure 2(d). The majority of this data set is from receiver function studies. Remaining points are from active-source studies and some are from gravity surveys. The active-source constraints were assigned relatively low errors and the Moho-depth estimates from gravity were assigned the largest errors. For the oceans we use a constraint of 10 km for Moho depth, but only for points also covered by data from our other data sets.

**Inversion Results**

We have developed software that handles the joint inversion of constraints from regional waveform fits, crustal estimates, group velocities, and teleseismic arrival times. The resolving power of the combined data is superior to that of each of the data sets alone. The joint inversion reduces the variance in the data sets by 38% for the teleseismic delay times, 55% for the Rayleigh-wave group velocities, 90% for the Moho point constraints, and 88% for the regional waveform fits.

Figure 3 shows the joint inversion results for Moho depth and velocity perturbations. The Moho map shows a good resemblance with the point constraints in Figure 2(d), but is much smoother because the regional waveforms and group velocity data, as well as regularization constraints in the joint inversion provide a smooth interpolation between the point constraints. The map is also broadly consistent with CRUST2.0, except in northern Africa, where the crust from our joint inversion is about 5 km thinner. Resolution tests indicate that our combined data sets can resolve the crustal thicknesses of CRUST2.0.

Fast-velocity anomalies are found beneath the West African Craton, the Hellenic trench, the Apennines, the East European Platform, and the Arabian Platform at 75–150 km depth, whereas low-velocity anomalies are located along the plate boundaries such as the mid-Atlantic ridge, Afar, the Anatolian Plateau, Iran, Afghanistan, western Mediterranean Sea, and the Red Sea. Fast-velocity anomalies are spread beneath the western Mediterranean Sea, Dinarides, the Aegean Sea, Turkey, and the Black Sea at a 500-km depth, which may indicate subducting slabs from the Apennine, the Calarian arc, and the Hellenic arc.

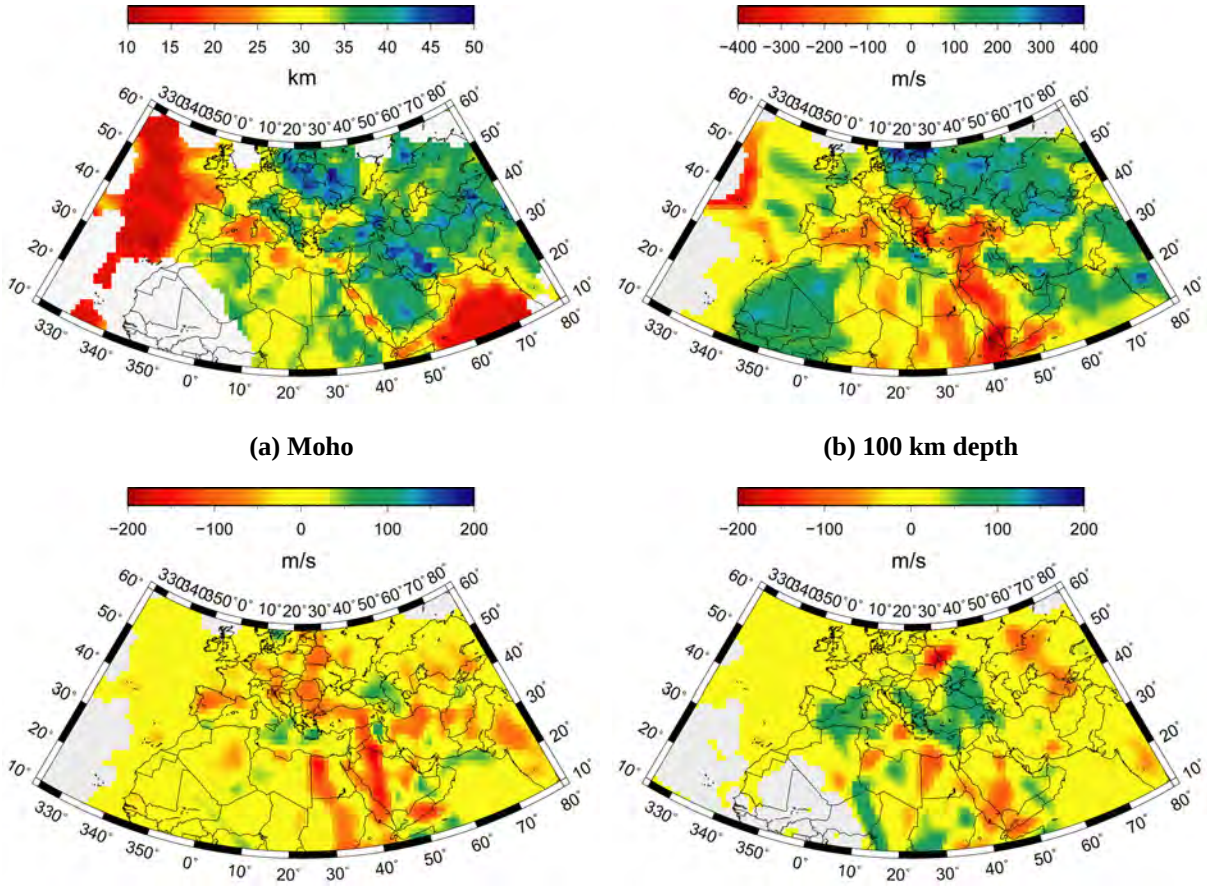


**(a) Moho** **(b) 100 km depth**

**(c) 300 km depth** **(d) 500 km depth**

**Figure 3. Moho and velocity perturbations resulting from our joint inversion. Moho map (a) and velocity perturbations at 100 km (b), 300 km (c), and 500 km depth (d) are illustrated.**

**Conversion of *S*-Velocity Model to *P*-Velocity Model**

One way to obtain a *P*-velocity model is to perform *P*-wave arrival time inversion using the equation,

$$\mathbf{G}_\alpha \mathbf{m}_\alpha = \mathbf{d}_\alpha , \quad (1)$$

where $\mathbf{G}_\alpha$ is the sensitivity kernel matrix for *P*-wave arrival times, $\mathbf{m}_\alpha$ is the 3-D *P*-velocity model vector, and $\mathbf{d}_\alpha$ is the teleseismic *P*-wave delay vector which is obtained by subtracting predicted arrival times through a reference model from observed arrival times. However, it is difficult to resolve shallow structure with teleseismic *P*-wave arrival time data because of poor resolution for shallow depth. Therefore, we have to find another way to get *P*-velocity model with *P*-wave arrival time data. It would be very promising in the inversion for *P*-velocity model if we can adopt the *S*-velocity model as a preliminary model, because the *S*-velocity model has good resolution for both shallow and deep structure due to our use of regional waveform fits, teleseismic arrival times, Rayleigh-wave group velocities, and Moho depth constraints.

We assume that *P*-wave velocity anomalies in m/s scale are very close to the *S*-wave velocity anomalies in m/s scale in our study area if temperature dominates the for cause of the velocity perturbations based on results in et al. (2004) in which similarity between *P*- and *S*-velocity anomalies is drawn with use of delay time ratio (see Figure 4a). Therefore, it is reasonable to adopt our *S*-velocity model as a starting model in performing a *P*-wave arrival time inversion (Schmid et al., 2008). By multiplication of the *S*-velocity model and *P*-wave sensitivity kernels, we can get predicted *P*-wave delays $\mathbf{d}_{\beta\to\alpha}$ by $\mathbf{m}_\beta$ as in

$$\mathbf{G}_\alpha \mathbf{m}_\beta = \mathbf{d}_{\beta\to\alpha} , \quad (2)$$

where $\mathbf{m}_\beta$ is the 3-D *S*-velocity model in m/s scale, and $\mathbf{d}_{\beta\to\alpha}$ is predicted *P* delays by $\mathbf{m}_\beta$. Then, teleseismic *P*-wave delays $\mathbf{d}_\alpha$ can be divided as

$$\mathbf{d}_\alpha = \mathbf{d}_{\beta\to\alpha} + \mathbf{d}_{res} , \quad (3)$$

where $\mathbf{d}_{res}$ is the residual *P* delay vector which means the difference between $\mathbf{d}_\alpha$ and $\mathbf{d}_{\beta\to\alpha}$. Therefore, Eq. (1) can be rewritten as

$$\mathbf{G}_\alpha (\mathbf{m}_\beta + \mathbf{m}_{new}) = \mathbf{d}_{\beta\to\alpha} + \mathbf{d}_{res} . \quad (4)$$

Eq. (4) is a linear equation, so we extract Eq. (2) from Eq. (4) to perform *P*-wave arrival time inversion for $\mathbf{m}_{new}$ using following equation,

$$\mathbf{G}_\alpha \mathbf{m}_{new} = \mathbf{d}_{res} . \quad (5)$$

A *P*-velocity model is finally obtained by adding $\mathbf{m}_{new}$ to the *S*-velocity model,

$$\mathbf{m}_\alpha = \mathbf{m}_\beta + \mathbf{m}_{new} . \quad (6)$$

The resulting *P*-velocity model with teleseismic *P* arrival time data in Figure 4(b) is shown at various depths in Figure 5. The results are similar to *S*-velocity perturbation results in Figure 3, which means *P*-velocity variations from the *S*-velocity model are small. But higher-velocity anomalies are found in the Alps, Hellenides, Turkey, and the Hindu Kush than in the *S*-velocity model.

**Model Evaluation**

Distributions of the travel-time residuals with respect to iasp91 and our joint inversion model (Joint Model) are shown in histogram form in Figure 6 for stations AJM, ELL, FRU, MAIO, NIL, PTO, QUE, and SVE. We report both the *L2* norm (mean, standard deviation, STD and variance reduction, VR) and *L1* norm statistics (median, scaled median absolute deviation, SMAD and SMAD reduction, SMADR). The SMAD provides an estimate of the spread of values which is less sensitive to outliers and so is often more appropriate in the presence of non-Gaussian errors. At most stations, SMADR is positive except for ELL, MAIO and QUE.

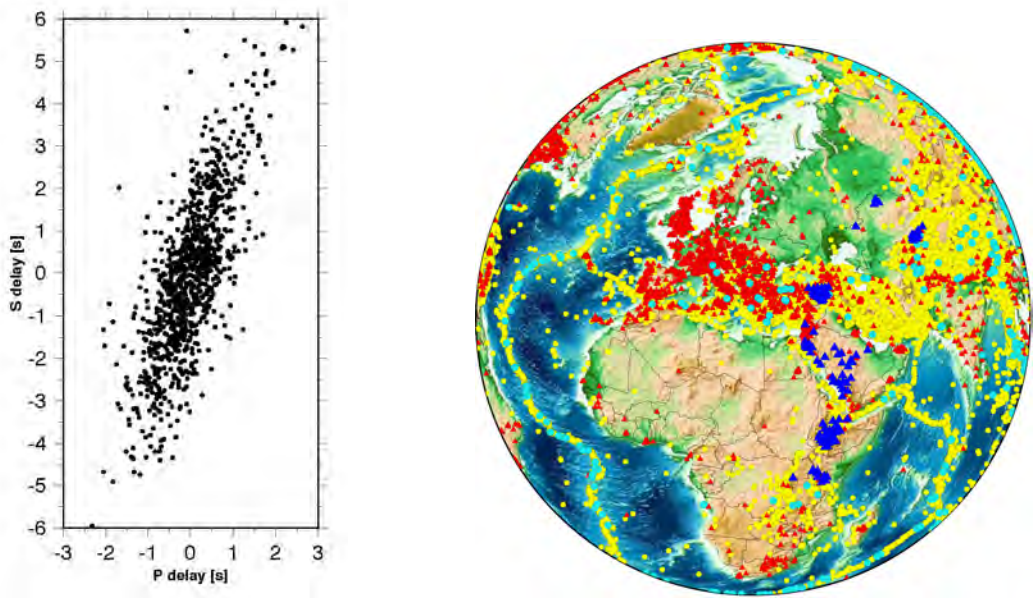


**(a)** **(b)**

**Figure 4. (a) *S* delays versus *P* delays (Schmid et al., 2004). (b) Events and stations used for teleseismic *P* arrival time estimation. Cyan circles and blue triangles represent events and stations used for relative delay time estimation with MCCC, respectively. Yellow circles and red triangles mean events and stations from the reprocessed ISC catalogue.**

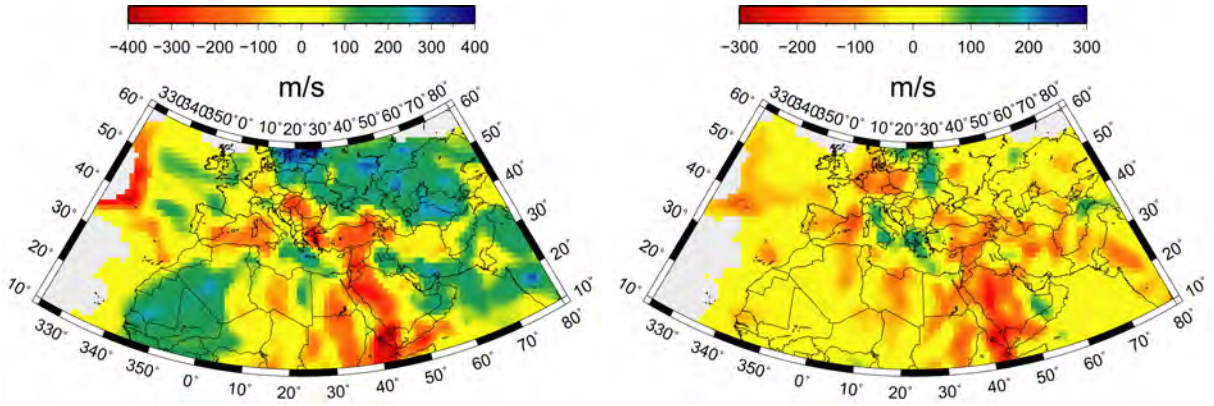


**(a) 100 km depth** **(b) 200 km depth**

**Figure 5. *P*-velocity perturbations at (a) 100 and (b) 200 km depth.**

Visually we can evaluate how well the joint inversion model (Joint Model) predicts the data geographically by computing 3D travel-time correction surfaces for some stations. To compute such model-based correction surfaces we subtract the iasp91-predicted time from the Joint Model-predicted time using 3D finite-difference algorithm. Example surfaces are shown in Figure 6 for the stations for a source depth of 10 km; we choose this depth as it represents the average focal depth of the GT25 events (epicenter mislocation of 25 km or less) selected. Color-coded residuals (data-iasp91) from events of focal depth 0 to 20 km are also plotted on top of the surfaces in Figure 6 to provide a visual assessment of the geographic agreement between Joint Model prediction and the data.

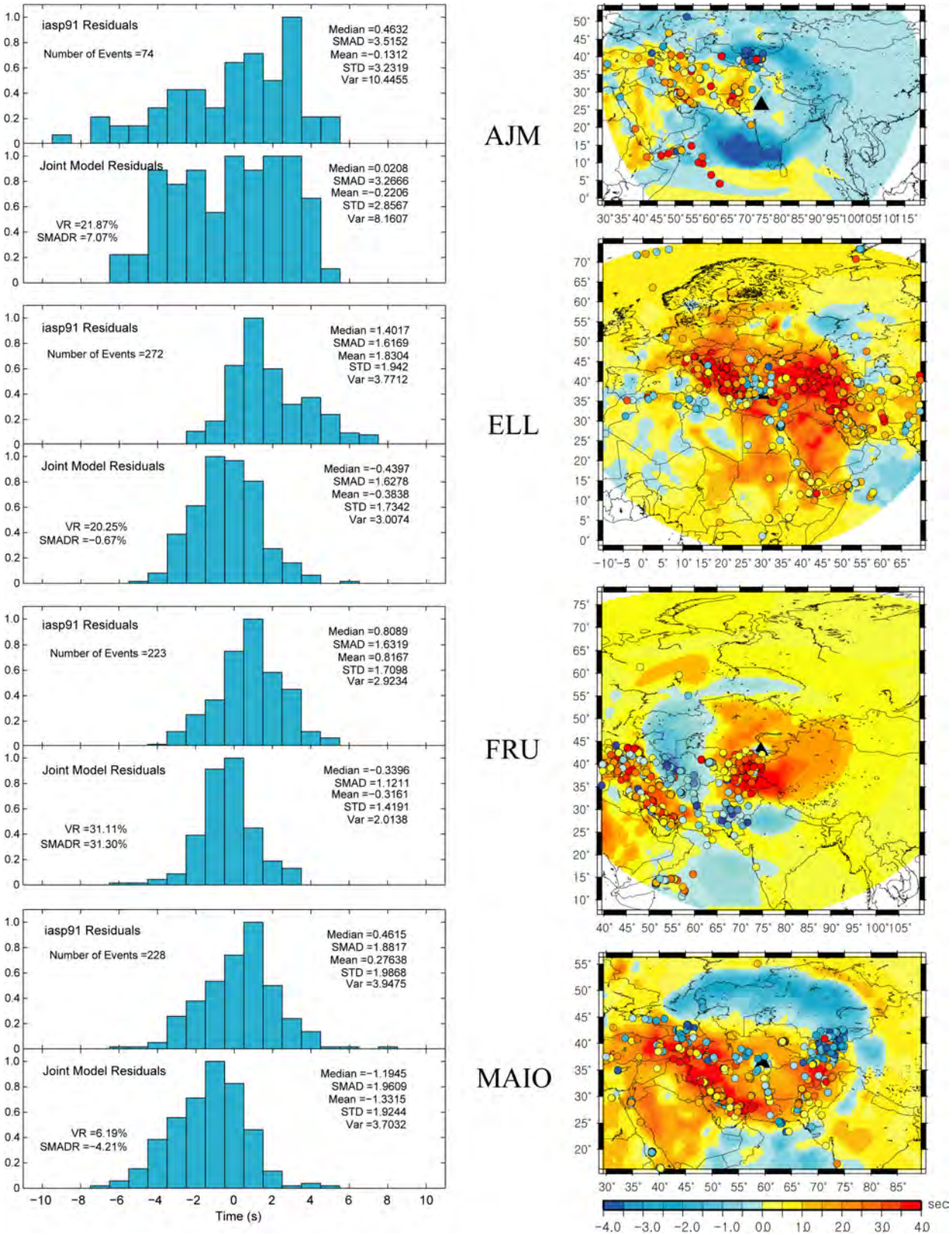
iasp91 Residuals
Number of Events =74
Median =0.4632
SMAD =3.5152
Mean =−0.1312
STD =3.2319
Var =10.4455
Joint Model Residuals
VR =21.87%
SMADR =7.07%
Median =0.0208
SMAD =3.2666
Mean =−0.2206
STD =2.8567
Var =8.1607
AJM
iasp91 Residuals
Number of Events =272
Median =1.4017
SMAD =1.6169
Mean =1.8304
STD =1.942
Var =3.7712
Joint Model Residuals
VR =20.25%
SMADR =−0.67%
Median =−0.4397
SMAD =1.6278
Mean =−0.3838
STD =1.7342
Var =3.0074
ELL
iasp91 Residuals
Number of Events =223
Median =0.8089
SMAD =1.6319
Mean =0.8167
STD =1.7098
Var =2.9234
Joint Model Residuals
VR =31.11%
SMADR =31.30%
Median =−0.3396
SMAD =1.1211
Mean =−0.3161
STD =1.4191
Var =2.0138
FRU
iasp91 Residuals
Number of Events =228
Median =0.4615
SMAD =1.8817
Mean =0.27638
STD =1.9868
Var =3.9475
Joint Model Residuals
VR =6.19%
SMADR =−4.21%
Median =−1.1945
SMAD =1.9609
Mean =−1.3315
STD =1.9244
Var =3.7032
MAIO
Time (s)
sec

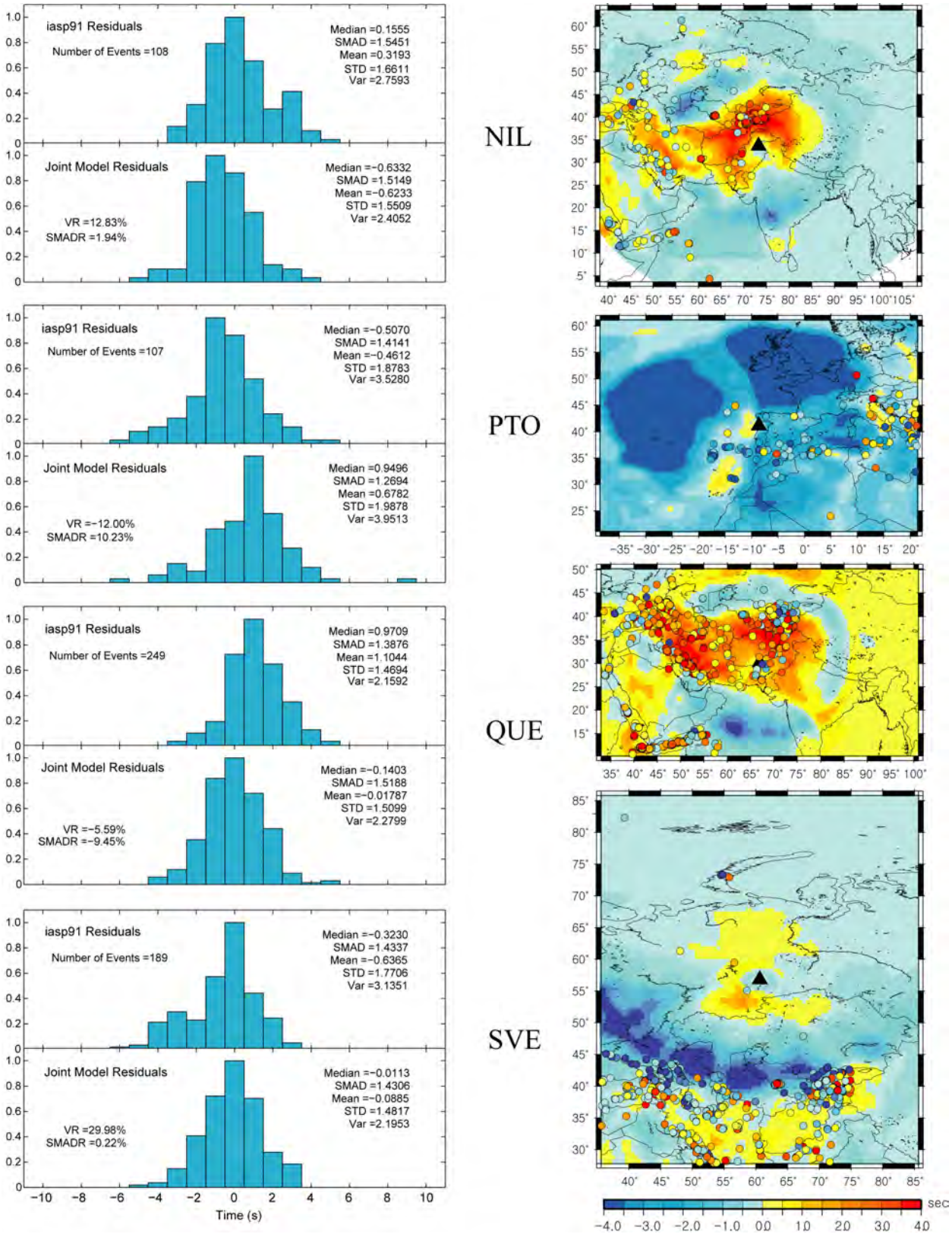


**Figure 6. Histograms of travel-time residuals for both models at stations AJM, ELL, FRU, MAIO, NIL, PTO, QUE, and SVE along with the travel-time residual surfaces (Joint Model-iasp91).**

## CONCLUSIONS AND RECOMMENDATIONS

Through a joint inversion of teleseismic *S*-wave arrival time delays, waveform fits of regional *S*- and Rayleigh waves, group velocity measurements of fundamental-mode Rayleigh waves, and independent constraints on Moho depth, we have achieved considerable variance reduction in each data set simultaneously. The new 3-D *S*-velocity model is converted to a *P*-velocity model with teleseismic *P* arrival times and the *P*-velocity model is used for travel-time prediction. Our model generally produces better prediction than the iasp91 1D model. SMADR is not reduced exceptionally at stations ELL, MAIO and QUE, but mean and median are closer to zero at station ELL and QUE in Joint Model residuals, which means our model succeeded in finding average velocity perturbations. Better refined results could be achieved by substituting our poorly resolved crust with CRUST2.0 and refining the *P*-velocity model.

## ACKNOWLEDGEMENTS

We acknowledge information gleaned from Dr. E. R. Engdahl from a personal communication in 2007.

## REFERENCES

Benoit, M. H., A. A. Nyblade, T. J. Owens, and G. Stuart (2006), Mantle transition zone structure and upper mantle *S* velocity variations beneath Ethiopia: Evidence for a broad, deep-seated thermal anomaly, *Geochem. Geophys. Geosyst*. 7: Q11013, doi:10.1029/2006GC001398.

DeMets, C. R.G. Gordon, D. F. Argus, and S. Stein (1990). Current plate motions, *Geophys. J. Int*. 101: 425–478.

Engdahl, E.R., van der Hilst, R. and Buland, R. (1998). Global teleseismic earthquake relocation with improved travel times and procedures for depth determination, *Bull. Seis. Soc. Am*. 88: 722–743.

Marone, F. S. Van der Lee, and D. Giardini (2003). Joint inversion of local, regional, and teleseismic data for crustal thickness in the Eurasia-Africa plate boundary region, *Geophys. J. Int*. 154: 499–514.

Marone, F., S. Van der Lee, and D. Giardini (2004). 3-D upper mantle *S*-velocity model for the Eurasia-Africa plate boundary region, *Geophys. J. Int*. 158: 109–130.

Mooney, W.D., G. Laske, and T.G. Masters (1998). CRUST 5.1: A global crustal model at 5° x 5°, *J. Geophys. Res*. 103: 727–747.

Nolet, G. (1990). Partitioned waveform inversion and 2-dimensional structure under the network of autonomously recording seismographs, *J. Geophys. Res*. 95: 8499–8512.

Park, Y., A. A. Nyblade, A. J. Rodgers, and A. Al-Amri (2007). Upper mantle structure beneath the Arabian Peninsula and northern Red Sea from teleseismic body wave tomography: Implication for the origin of Cenozoic uplift and volcanism in the Arabian Shield, *Geochem. Geophys. Geosyst*. 8: Q06021, doi:10.1029/2006GC001566.

Pasyanos, M. E. (2005). A varible-resolution surface wave dispersion study of Eurasia, North Africa, and surrounding regions, *J. Geophys. Res*. 110: B12301, doi:10.1029/2005JB003749.

Röhm, A. H. E., H. Bijwaard, W. Spakman, and J. Trampert (2000), Effects of arrival time errors on traveltime tomography, *Geophys. J. Int*. 142: 270–276.

Schmid, C., S. van der Lee, and D. Giardini (2004), Delay times and shear wave splitting in the Mediterranean region, Geophys. J. Int. 159: 275–290.

Schmid, C., S. van der Lee, J. C. Vandecar, E. R. Engdahl, and D. Giardini (2008). 3-dimensional S-velocity of the mantle in the African-Eurasia plate boundary region from phase arrival times and regional waveforms, *J. Geophys. Res*. 113: B03306, doi:10.1029/2005JB004193.

VanDecar, J.C., and R.S. Crosson (1990), Determination of teleseismic relative phase arrival times using multi-channel cross-correlation and least-squares, *Bull. Seism. Soc. Am*. 80: 150–169.

Van der Lee, S. and G. Nolet (1997). Upper-mantle S-velocity structure of North America, *J. Geophys. Res*. 102: 22,815–22,838.

# IMPROVED GROUND TRUTH IN SOUTHERN ASIA USING IN-COUNTRY DATA, ANALYST WAVEFORM REVIEW, AND ADVANCED ALGORITHMS

Eric R. Engdahl[1], Eric A. Bergman[1], Stephen C. Myers[2], and Floriana Ryall[2]

University of Colorado[1] and Lawrence Livermore National Laboratory[2]

Sponsored by National Nuclear Security Administration

Contract No. DE-FC52-03NA99516[1] and DE-AC52-07NA27344[2]
Proposal No. BAA03-19

## ABSTRACT

This research has the goal of developing in-country data sets that can be used to improve ground-based monitoring capabilities in southern Asia, in particular the region bounded by 20–44°N and 41–67°E, by providing information needed to develop and test more accurate travel-time models for seismic phases that propagate in the crust and upper mantle. We have also incorporated phase picks from an experienced analyst who reviewed waveforms of particular interest for specific events. These in-country arrival times and analyst-reviewed picks have been associated with known earthquakes reported by international agencies, combined with existing bulletin readings, and relocated using the Engdahl et al. (1998; EHB) methodology. Using in-country data, we have formed new events, mostly at lower magnitudes that were not previously included in standard global earthquake catalogs. This has resulted in a catalog of earthquakes in the region for the period 1923–2008 for events larger than about magnitude 2.5. Catalog events larger than about magnitude 4.0 have been highly reviewed. Events at lower magnitudes have been relocated with a standard procedure similar to the EHB procedure, but not all have been systematically reviewed.

The new catalog has been used to conduct a detailed analysis of historic and recently occurring event clusters (generally mainshock-aftershock sequences) using a multiple-event relocation technique and data sets of phase arrival times at distances from near-source to teleseismic. Absolute locations of such clusters are constrained using reference event information for one or more of the cluster events provided by local networks, aftershock deployments, or from non-seismic (e.g., InSAR or geological mapping) information. We have also developed a method for direct calibration of a cluster by using arrival time data only from local stations, with an appropriate crustal model, to locate the hypocentroid of the cluster. When both location and origin time can be calibrated for a cluster, we are able to estimate the unbiased travel times to all reporting stations. These estimates are the basis for improved models of the crust and upper mantle, which in the future will permit more accurate routine earthquake locations using regional seismic data.

We have performed hypocentroidal decomposition (HDC) calibration analyses on 27 earthquake clusters, containing 989 events, in the region. Of these, three clusters could not be calibrated at all. Twenty-two clusters contain at least one event with a calibrated location that meets GT5 criteria, a total of 549 GT5 events. We present a summary of the results of these calibration studies in the form of absolute travel-time information derived from the calibrated clusters, showing distance-dependence of travel times of different phases from different source regions. We also present summaries of empirical reading error determinations and of travel-time variability for different phases. Finally, we present a study of differences between arrival time picks made by an experienced analyst and those obtained from in-country and global bulletins.

## OBJECTIVES

This research seeks to improve the database of ground-truth information and velocity models useful for calibration in southern Asia with the following objectives: (1) Aggressive pursuit of in-country data acquisition, especially the collection of ground truth at GT5 level or better for events of magnitude 2.5 and larger recorded by dense local networks, including associated velocity models; (2) Expanded analyst review of relevant regional waveforms for ground-truth events by the comprehensive re-picking of phase arrival times from all available waveforms, with special attention to the regional phases Pg, Pb, Pn, Sg, Sb, and Sn; and (3) Application of advanced algorithms, specifically multiple event relocation, to refine and validate all available ground-truth data, to achieve the optimal selection of data for analysis, to better understand the uncertainties of the results, and to handle the error budget as realistically as possible.

## RESEARCH ACCOMPLISHED

### Compilation of Arrival-Time Data and Relocation of Seismicity

A comprehensive catalog of all instrumentally recorded events, magnitude 2.5 and greater, during the period 1923-2008, for the region bounded by 20–44°N and 41–67°E, has been assembled. Available bulletin arrival-time data from in-country seismic networks in the region, as well as phase picks from an experienced analyst who reviewed waveforms of particular interest for specific events, have been compiled and, where possible, associated with arrival-time data from known earthquakes reported by international agencies. However, with the in-country data we have also formed many new events, mostly at lower magnitudes that were not previously included in standard global earthquake catalogs. This combined catalog of more than 25,000 events has been relocated using the Engdahl et al. (EHB; 1998) methodology. Epicenters from the resulting catalog are plotted in Figure 1A and the stations reporting arrival time data for the period 1923–2008 in Figure 1B. Significant scatter in the distribution of seismicity is evident since many events at lower magnitudes are poorly located and are not azimuthally well constrained, especially in parts of the region where there are few stations.

A

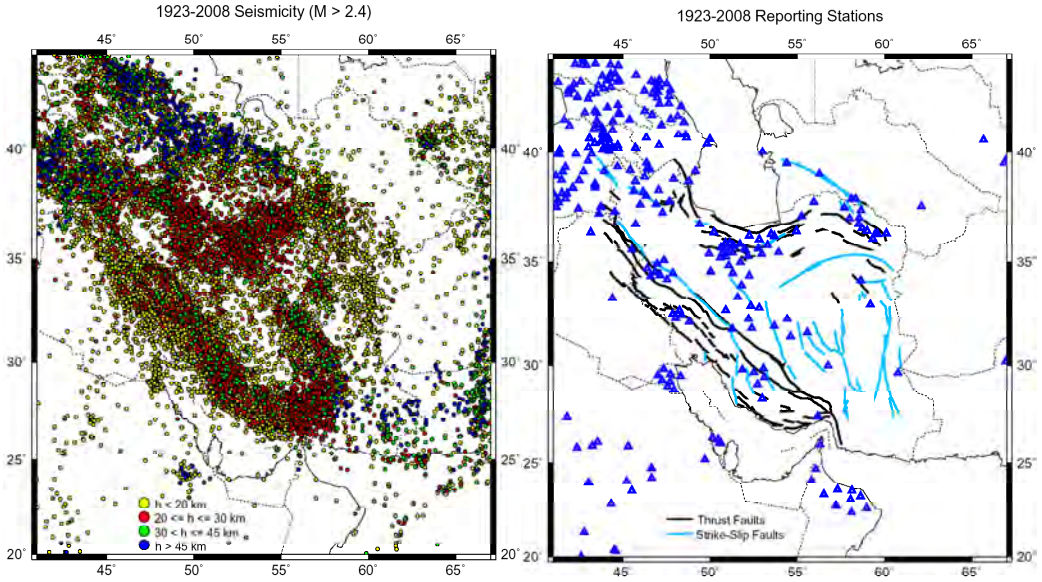


B

**Figure 1. A) Seismicity map of the study region color coded by depth based on the new catalog assembled in this project. B) Stations reporting arrival time picks.**

A

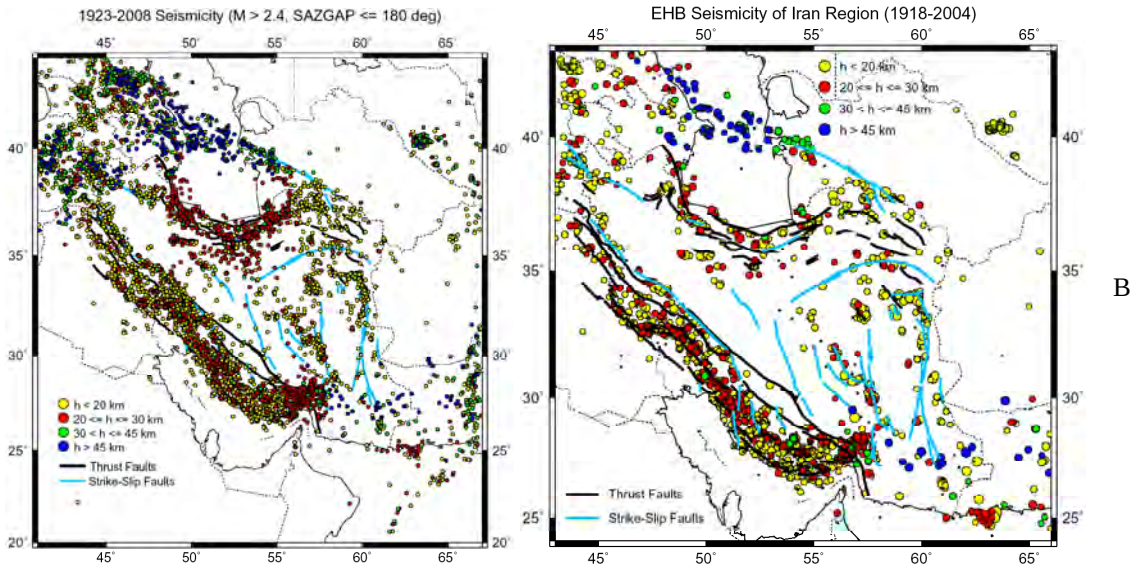


B

**Figure 2. A) Events meeting a secondary azimuth gap criteria of less than 180 degrees when applied to station distributions at all distances. B) For comparison, a figure reproduced from Engdahl et al. (2006) for events where the same secondary azimuth gap criteria is applied only to stations at teleseismic distances (> 28 degrees).**

In order to improve the location accuracy of the events shown in Figure 1A, we apply a modified EHB secondary azimuth gap criteria of less than 180 degrees when applied to event-station distributions at all distances. This reduces the database to over 7,000 events and significantly reduces the scatter. The seismicity distribution in the new map now shows a striking similarity to a map reproduced from Engdahl et al. (2006) showing events where the same secondary azimuth gap criteria are applied only to stations at teleseismic distances (> 28 degrees). However, the event depth distribution in Figure 1A requires further review (e.g., the depths in the Alborz region appear to be slightly overestimated).

### Analyst Reviewed Events

Waveforms at regional distances in this region are often complex. For many events, this makes arrival time picks are difficult to make, especially for smaller magnitude events, resulting in reported times that often differ from picks made by an experienced analyst.

A

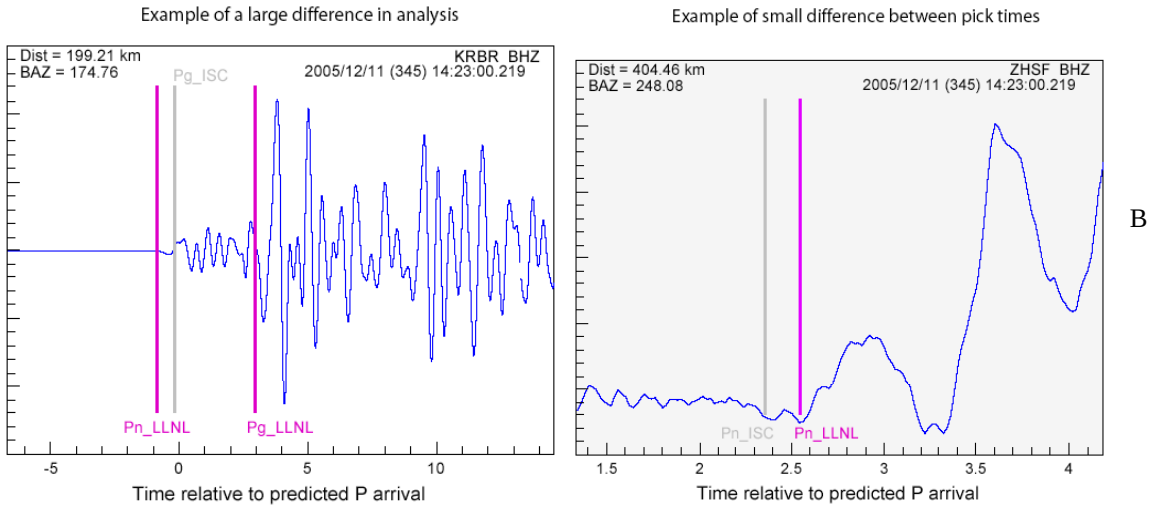


B

**Figure 3. Regional waveforms read by an experienced LLNL analyst. Note the difference in time scales. Examples of A) Large difference in reported pick times, and B) Small difference in reported pick times.**

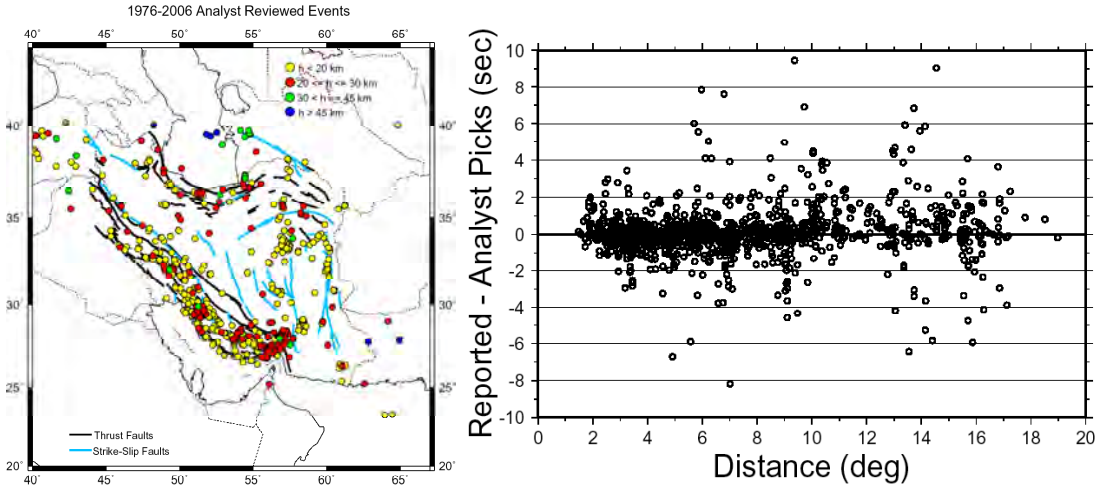


**Figure 4. A) Analyst reviewed events, and B) Reported minus analyst picks as a function of distance**.

Figure 3A is an example of a rather large late pick of the Pn phase by a regional network as it was reported to the International Seismological Centre (ISC) as compared to the obvious earlier pick made by an analyst. Figure 3B is an example of a Pn pick reported by a regional network that is slightly earlier than the analyst pick.

In Figure 4A are plotted all events for which an experienced analyst read arrival time picks from regional waveforms. The events sample a cross section of different tectonic regimes across the region. Figure 4B compares reported-versus-analyst pick times. In spite of the obvious outliers, the median (-0.06 s) and spread (0.51 s) are small, suggesting that more confidence can be placed in the picks reported by regional networks. However, analyst picks at distances of 12–17 degrees, at distances where there is increased complexity of waveforms due to multiple phase arrivals, appear to be slightly earlier than the reported picks.

**Empirical Reading Errors**

For each cluster analyzed in this study, we have conducted a careful "cleaning" exercise in which a robust estimate of the spread of residuals for each station-phase pair is made from the set of all observations of the given phase by the given station for the given cluster. We call this the "empirical reading error" for that station phase. The cleaning process consists of repeated estimates of empirical reading error, which is then used to identify outlier readings (typically starting with a 4.5σ cutoff), which are eliminated from the data set. This process is repeated with progressively smaller cutoff until the observed distribution of residuals satisfies a 3σ limit with the current estimate of empirical reading error. The number of samples available for this analysis varies for each station-phase pair, from 2 to the number of events in the cluster. Our estimate of empirical reading error includes traditional "picking error" but also includes all other effects which contribute to scatter of the residuals, including errors in relative location, unmodelled velocity variations in the source region, differences in practice among different analysts or the same analyst over time, changes or errors in timing equipment, other changes of instrumentation, and unreported changes in station location.

The number of station-phase pairs (in all clusters) for which we have determined empirical reading errors is summarized in Table 1.

**Table 1. Number of empirical reading errors**

| | P | S |
|---|---|---|
| Crustal | 195 | 106 |
| Regional | 1831 | 528 |
| Teleseismic | 8324 | 755 |

"Crustal" phases are Pg, Pb, Sg, and Sb. "Regional" phases are Pn and Sn. "Teleseismic" phases are first-arriving P and S. Histograms of the distributions of these phases are shown in Figure 5.

The occurrences of improbably small empirical reading errors (<0.15s) are dominated by cases in which there are only two or three samples of a station-phase pair that happen to be very close to each other. These distributions can be helpful in selecting a "default" reading error for cases in which it is not possible to make an estimate of empirical reading error from the distribution of residuals in a multiple-event analysis. However, the large range of empirical reading errors emphasizes the danger of assuming a single default picking error for all samples of the same phase in earthquake-location analysis, because data weighting normally depends on the assigned picking error. The problem is worse for smaller events with fewer observations. For a single-event location, there is no good solution other than using data for which a quantitative measure of picking error has been made at the same time as the pick itself.

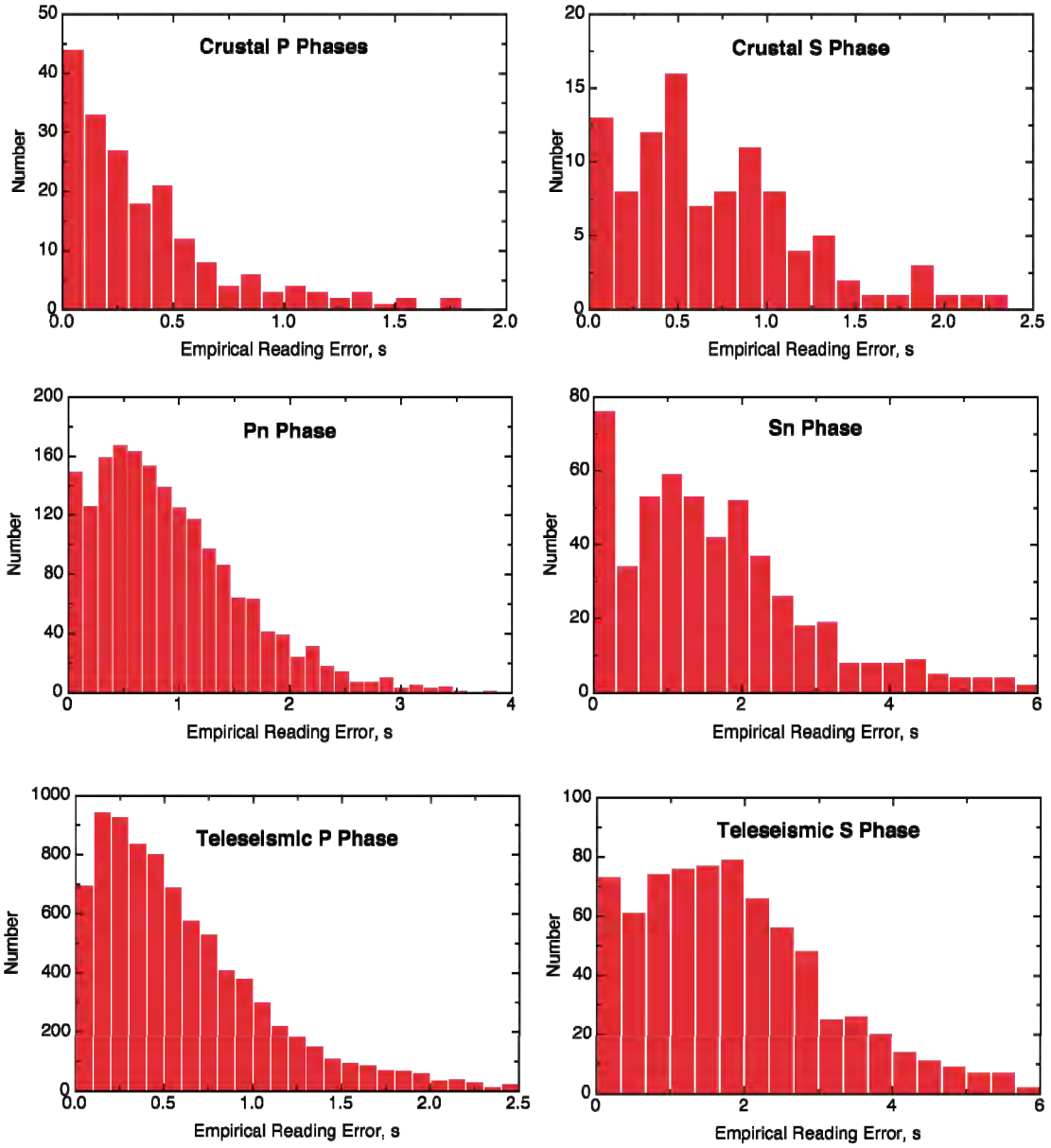


**Figure 5. Histograms of empirical reading errors for crustal, regional, and teleseismic P and S phases, from 27 earthquake clusters in the study region. Note that scales are different for each histogram.**

### Ground-Truth Data

Critical to our ground-truth data discovery and acquisition process are collaborative arrangements that have been made with key organizations in southern Asia. These arrangements are built on exchanges that are mutually beneficial to the parties involved, usually based on our applying advanced techniques to refine locations of the host country's natural seismicity in return for access to in-country ground-truth information. These arrangements provide a forum for gathering and assessing potential ground truth data, and collecting waveform and phase-reading data for events of interest from local and regional stations.

We are also in contact with several research groups developing ground truth locations from InSAR-detected ground displacement and other satellite-based location methods, as well as geological field work, that provide important constraints on earthquake location that are independent of seismic observations. Much new ground truth information is now being obtained from these sources as an ongoing activity.

### Location Calibration of Earthquake Clusters through Multiple Event Relocation

The HDC (Jordan and Sverdrup, 1981) method for location calibration yields improved accuracy for both the relative and absolute locations of clustered earthquakes. The gist of the method is to use a multiple event relocation method with regional and teleseismic phase arrival times to constrain relative locations of clustered earthquakes and then to calibrate the absolute location of the cluster by obtaining independent information on the absolute location of one or more members of the cluster. The HDC analysis includes further refinement of the data set by making empirical estimates of reading errors and using these estimates to help identify outliers. These steps yield significant improvements in accuracy and resolution for the relocations. Of course, the main benefit of HDC analysis is to largely remove the biasing effects (path anomalies) of lateral heterogeneity in the Earth, which permits much better resolution of the relative locations of cluster earthquakes.

We have recently extended the calibration process to take into account the uncertainties in calibration data in estimating an optimal calibration shift for the cluster. We also estimate a term to account for the inconsistency between multiple calibration events. Our final estimate of local accuracy for events in calibrated clusters includes all these sources of uncertainty, as well as the uncertainty in relative locations derived from the HDC analysis.

We have also developed a method for the direct calibration of a cluster by using arrival time data only from local stations, with an appropriate crustal model, to locate the hypocentroid of the cluster. We have found a number of cases in which no individual earthquake in the cluster is well-recorded enough to be treated as a calibration event, but the cumulative local-distance readings of all events do provide sufficient location accuracy to calibrate the hypocentroid directly at GT5 or better. Many of the clusters presented below have been calibrated in this manner.

### Summary of Calibrated Clusters

We have performed HDC calibration analyses on 27 earthquake clusters in the region that are summarized in Table 2. Not all clusters can be calibrated at GT5 or better levels of accuracy. Cluster boundaries and the locations of cluster events are plotted in Figure 6.

| Cluster Name | Centroid Latitude | Centroid Longitude | Centroid Depth | No. of Events | GT5 Events | GT3 Events | Direct Calib. | Indirect Calib. | Calib. Level | Seism. Calib. | InSAR Calib. | Location Calib. | OT Calib. |
|---|---|---|---|---|---|---|---|---|---|---|---|---|---|
| Alborz | 35.498 | 52.848 | 11.6 | 11 | 11 | 11 | Y | N | 1.6 | | | Y | Y |
| Ardebil | 38.093 | 47.891 | 9.9 | 16 | 0 | 0 | Y | N | 7.4 | | | Y | Y |
| Avaj | 35.552 | 49.035 | 7.9 | 17 | 16 | 1 | N | Y | 4.3 | 1 | | Y | Y |
| Baladeh | 36.345 | 51.399 | 8 | 25 | 22 | 20 | Y | N | 1.9 | | | Y | Y |
| Bam | 28.942 | 58.346 | 9.7 | 22 | 12 | 0 | N | Y | 3.4 | | 1 | Y | N |
| Bastak | 27.189 | 53.88 | 12.3 | 25 | 17 | 0 | N | Y | 3.5 | | 1 | Y | N |
| Darband | 37.731 | 57.299 | 11.5 | 44 | 41 | 17 | Y | N | 2.9 | | | Y | Y |
| Dasht-e-Bayaz | 33.824 | 59.455 | 11.1 | 101 | 44 | 0 | N | Y | 4.7 | 3 | 3 | Y | Y |
| Dinavar | 34.571 | 47.303 | 20 | 17 | 0 | 0 | N | N | | | | N | N |
| Dorud | 33.813 | 48.82 | 7 | 80 | 77 | 63 | Y | N | 1.8 | | | Y | Y |
| Firuzabad | 29.12 | 52.642 | 8.3 | 36 | 1 | 0 | N | Y | 13.3 | 1 | | Y | Y |
| Garmsar | 35.293 | 52.209 | 10 | 16 | 16 | 15 | Y | N | 1.3 | | | Y | Y |
| Ghir | 27.982 | 53.638 | 15.1 | 67 | 51 | 23 | N | Y | 2.8 | 2 | 1 | Y | Y |
| Igdir | 39.162 | 44.157 | 14.7 | 71 | 47 | 1 | Y | N | 3.1 | | | Y | Y |
| Jiroft | 28.336 | 57.141 | 23.7 | 60 | 0 | 0 | N | N | | | | N | N |
| Kahak | 34.47 | 50.89 | 15 | 15 | 15 | 6 | Y | N | 2.7 | | | Y | Y |
| Kerman | 30.065 | 57.611 | 12.8 | 55 | 0 | 0 | N | N | | | | N | N |
| Lagodekhi | 41.847 | 46.294 | 14.9 | 44 | 36 | 19 | Y | N | 2.4 | | | Y | Y |
| Nahavand | 34.477 | 47.854 | 17.7 | 25 | 0 | 0 | Y | N | 8.4 | | | Y | Y |
| Qeshm | 26.875 | 55.925 | 14.3 | 43 | 38 | 18 | N | Y | 2.6 | 2 | 1 | Y | Y |
| Rudbar | 36.773 | 49.377 | 10.7 | 37 | 1 | 0 | N | Y | 8.0 | 1 | | Y | Y |
| Sefidabeh | 30.681 | 60.5 | 8.4 | 7 | 7 | 6 | N | Y | 3.1 | 1 | 1 | Y | Y |
| Shusf | 32.10 | 60.006 | 6.7 | 7 | 4 | 1 | N | Y | 4.1 | | 1 | Y | N |
| Tabas | 33.315 | 57.147 | 10.1 | 30 | 14 | 2 | N | Y | 4.4 | 2 | | Y | Y |
| Urmieh | 38.445 | 45.23 | 13.3 | 26 | 25 | 0 | Y | N | 3.5 | | | Y | Y |
| Zarand | 30.691 | 56.828 | 11.5 | 49 | 44 | 7 | N | Y | 3.1 | 1 | 1 | Y | Y |
| Zirkuh | 32.991 | 60.123 | 11 | 43 | 10 | 0 | N | Y | 5.1 | 2 | | Y | Y |
| TOTALS | | | | 989 | 549 | 210 | 11Y | 13Y | | 10 | 8 | 24Y | 21Y |

**Table 2. Summary of ground-truth cluster data. The location of the hypocentroid in geographic coordinates and depth fixes the absolute hypocenters of cluster events. "Calibration level" is an estimate of the uncertainty of the calibration of the cluster hypocentroid, to which the uncertainty of the relative location (cluster vector) of individual events must be added in order to obtain the absolute location uncertainty for each event.**

A

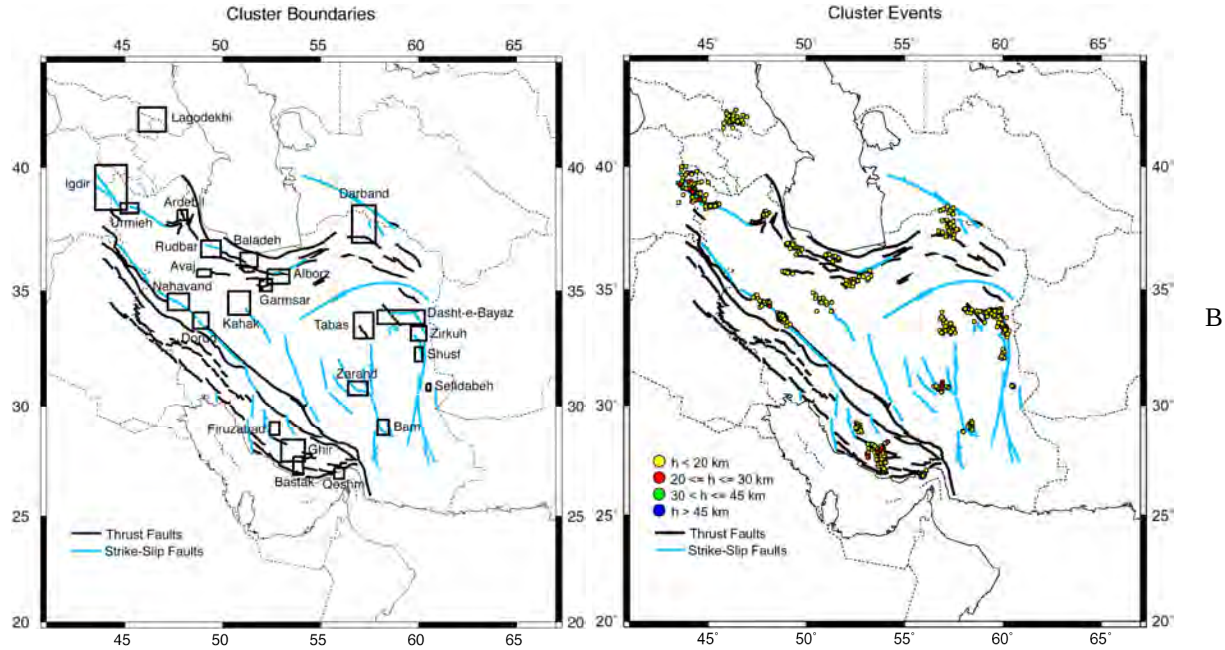


B

**Figure 6. Earthquake clusters studied for ground truth calibration. A) Boxes show the region covered by each cluster, with the name we have assigned. B) Distribution of cluster events color-coded by depth.**

### Summary of Travel-Time Anomalies

When both location and origin time can be calibrated for a cluster, we are able to estimate the unbiased travel times to all reporting stations. These estimates are the basis for improved models of the crust and upper mantle, which in the future will permit more accurate routine earthquake locations using regional seismic data. We use the calibrated cluster arrival time data to infer empirical path anomalies (relative to the global model ak135) from each cluster source region to surrounding seismic stations. The path anomalies can be the result both of variations in bulk velocity and differences in ray-path geometry caused by lateral heterogeneity.

We have combined the empirical path anomalies of all the clusters that are calibrated in both location and origin time to produce a summary plot of Pn/P arrivals as a function of epicentral distance (Figure 7).

A

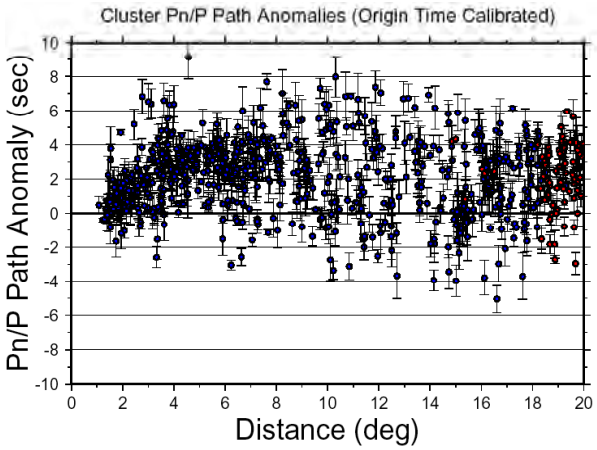


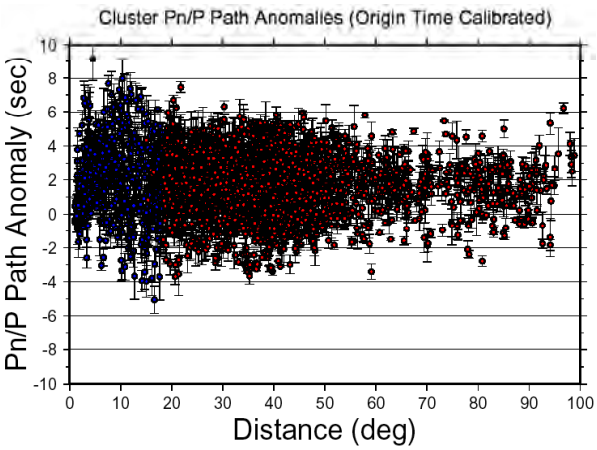


B

**Figure 7. Empirical path anomalies, relative to ak135, and spread for Pn (blue) and P (red) phases from 21 earthquake clusters that are calibrated both in location and origin time. A) Regional distances. B) Regional and teleseismic distances**.

The empirical path anomalies for individual clusters show evidence both for departures from the average earth model used for reference (ak135), and for lateral heterogeneity. When the path anomalies are combined however, most structure is lost in a cloud of impressive width, a range of 10–12 seconds for P phases over the regional and teleseismic distance range. Even here there is a suggestion of about 2-3 seconds baseline offset from ak135 in the study region. This can be accounted for with a crustal structure that is both thicker (40–45 Km Moho depth, vs. 35 km for ak135) and slower in bulk velocities. It is clear, however, that accurate earthquake location in this region will require the use of crustal models that are more specific to the source regions.

## CONCLUSIONS AND RECOMMENDATIONS

We have compiled a comprehensive catalog of all instrumentally recorded events, magnitude 2.5 and greater, that have occurred during the period 1923-2008 for the region bounded by 20–44°N and 41–67°E. The catalog includes substantial numbers of phase readings at in-country seismograph stations, as well as phase picks made by an experienced analyst who reviewed waveforms of particular interest for specific events. From this catalog we have acquired new or improved ground truth events and calibrated earthquake locations in the region, based on detailed multiple event relocation and the use of calibration data, both from local seismic network data and from InSAR and geological data. As new data have been acquired the quality and quantity of calibrated earthquake locations in this region has improved significantly.

## REFERENCES

Engdahl, E. R., R.D. Van der Hilst, and R.P. Buland (1998). Global teleseismic earthquake relocation with improved travel times and procedures for depth determination, *Bull. Seism. Soc. Am*. 88: 722–743.

Engdahl, E.R., J. A. Jackson, S. C. Myers, E. A. Bergman and K. Priestley (2006). Relocation and assessment of seismicity in the Iran region, *Geophys. J. Int*. 167: 761–778.

Jordan, T.H. and K.A. Sverdrup (1981), Teleseismic location techniques and their application to earthquake clusters in the south-central Pacific, *Bull. Seis. Soc. Am*. 71: 1105–1130.

# OPTICAL MEMS-BASED SEISMOMETER "WHIGS"

Dominique Fourguette[1], M. Volkan Ötügen[2], Liane M. Larocque[1], and Tindaro Ioppolo[2]

Michigan Aerospace Corporation[1] and Southern Methodist University[2]

Sponsored by National Nuclear Security Administration

Contract No. DE-FG02-08ER85099

## ABSTRACT

Low yield man-made seismic activity is difficult to detect and most often occurs in remote areas where seismic detection is weak. The Whispering Gallery mode-based seismometer (WhiGS) is an optical Micro-Electro-Mechanical System-based (MEMS) instrument. The seismometer is a three-axis instrument, is compact, has low power consumption and is capable of unattended operation.

WhiGS exploits morphology-dependent optical resonance shifts in small dielectric spheres (< 1 mm in diameter). These optical resonances, called whispering gallery modes (WGM), are extremely narrow, making the transducer highly sensitive to force (< $10^{-9}$ Newtons). The MEMS sensing element in this seismometer has demonstrated a Q-factor of $10^7$. As a result, the instrument will be capable of measuring accelerations as low as 10 nano-g.

This Phase I SBIR effort entails the development of the MEMS sensing elements and the complete design of a deployable 3-axis seismometer.

## OBJECTIVES

Michigan Aerospace Corporation, in collaboration with Southern Methodist University, is developing a compact WhiGs for monitoring man-made seismic activity. The sensing principle of the seismometer exploits the morphology-dependent optical resonance shifts of dielectric spheres to detect ground motion. These optical resonances are extremely narrow, making the transducer highly sensitive to ground motion. The small dielectric spheres are easily packaged into a small instrument capable of measuring accelerations as low as 10 nano-g.

In a typical seismometer the transducer element measures the relative displacement between the mass and the ground. The position of the mass relative to the ground is maintained, and a damper is used to minimize resonance. The transducer can be chosen to measure either relative mass displacement using a lever assembly or voltage output from a bridge, or relative mass velocity using magnetic induction. In the latter case, slow ground motion is difficult to detect as the induction is proportional to the relative mass velocity.

The present effort proposes to use a resonant micro-optical element as a transducer. The transducer uses morphology-dependent optical resonances described by Benner and Hill (1988), whispering gallery modes (WGMs) in this case, investigated by Guan et al. (2006), to measure minute shape variations in dielectric spheres squeezed between the mass and the instrument base. Recent studies at Southern Methodist University have shown that force resolutions of 5 x $10^{-3}$ N could be obtained by measuring WGM shifts in silica spheres. This resolution was improved to 1x$10^{-4}$ N using polymer spheres, and to 1 x $10^{-6}$ using hollow polymethyl methacrylate (PMMA) spheres, shown by Kozhevnikov et al. (2006) and Ioppolo et al. (2007). Current studies by the same team using 0.7 mm spheres of another polymer, polydimethylsiloxane (PDMS), indicate that a force resolution of $10^{-8}$ N is possible by exploiting the same sensing principle.

The Sensing Element

The optical MEMS sensing element, typically a microsphere (with diameters in the range 200 to 1000 μm), is weakly coupled to an optical fiber, as shown in Figure 1a. The optical fiber, which carries light from a tunable laser, serves as an input/output port for the microsphere. When the microsphere comes into contact with an exposed section of the fiber core, light is coupled into the outer layer of the sphere, (Figure 1b). Its resonances are observed as sharp dips in the transmission spectrum as depicted in Figure 1d. When the sphere is compressed (as in Figure 1c), the wavelength of the resonances shifts.

These optical resonances—the WGMs—are extremely narrow and hence are highly sensitive to any morphological change in the microsphere. Other micro-resonator geometries, such as micro-discs, can be used as sensing elements in place of the microspheres.

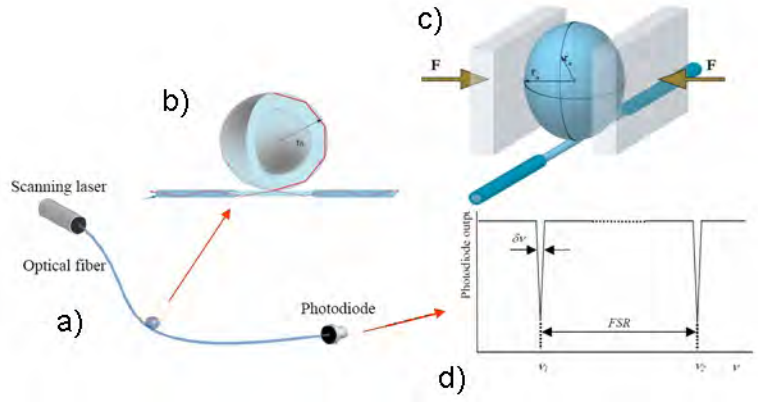


**Figure 1. Principle of the WGM pressure-induced wavelength shift $\delta\nu$.**

### Task 1: Whispering Gallery Mode Shifts in Spheres as Force Sensor

The first task is a computational and analytical analysis to determine the range of force/acceleration sensitivities and ranges for the sphere sizes and materials to be used in our sensor. For this, the analytical approach and finite element analysis (FEA) tools developed in our previous study will be used. These FEA tools are described in Nguyen et al. (2007). This objective entails the quantification of the precise effect of force and microsphere physical deformation on electromagnetic wave propagation in microspheres with the selected sizes and sphere material.

### Task 2: Preliminary Tests

The WGM characteristics of different-sized spheres (ranging from ~ 200 μm and 1 mm) will be investigated. The candidate material to be used for the spheres is PDMS (commercially known as Sylgard 184). Different percentages of additives (cure agents) will be used to obtain different elastic modulus values and optical characteristics in order to determine the force sensitivity ranges that can be achieved and their suitability for the seismometer to be developed. Polymer base-to-cure agent ratios of 50:1, 20:1 and 10:1 will be used at the first stage. The WGMs of the spheres will be interrogated using a distributed feedback diode laser with nominal wavelength in the infrared (~1.3 μm). The spheres will be calibrated in a vacuum chamber with a micro-cantilever beam force inducer. The deflection of the cantilever beam will be monitored using a Michelson interferometer setup. The vacuum chamber eliminates unwanted/uncontrollable aerodynamic forces that can affect the calibration process at such low force levels (in the order of nanonewtons). The effect of sphere size and additive ratio on the Q factors will also be investigated and methodologies to obtain higher Q values will be sought (beyond the currently achievable $Q \approx 10^7$). A small number of high-Q spheres will be produced to be used in the prototype seismometer.

### Task 3: Instrument Design

The third task of this effort will be the design of a seismometer prototype. This will include the design of the transducers and the mechanical design of the instrument. The design of the instrument will include the following considerations:

- The determination of the inertial mass and shape
- The sensitivity
- Resonant frequency
- The ability to measure 3 axes
- A damping mechanism to prevent long-term oscillations
- Electronics circuitry and noise

Figure 2 shows a schematic of the 3-axis seismometer. Each cylinder contains a suspended proof mass and one sensing element.

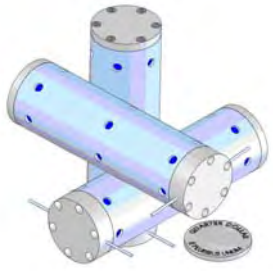

**Figure 2. Schematic of the 3-axis seismometer (a quarter is shown for reference).**

## RESEARCH ACCOMPLISHED

Support for this work was recently awarded and the research accomplished is in its early phase. The results presented in this section were obtained to establish the capabilities of such design.

### *Force Measurements Using WGMs in Spheres*

Figure 3 shows the resonant shift variation when a solid PMMA sphere (Figure 3a) and a hollow sphere (Figure 3b) are subjected to a measured force. In Figure 3a), the decompression measurement was conducted five days after the compression measurement. The dependence of λ on force is linear and shows no hysteresis. During the period between the two measurements, the sensor was left compressed at the maximum force indicated in the figure. No degradation was observed. Hollow PMMA spheres exhibit a significantly higher sensitivity, and the sensitivity is dependent on the wall thickness.

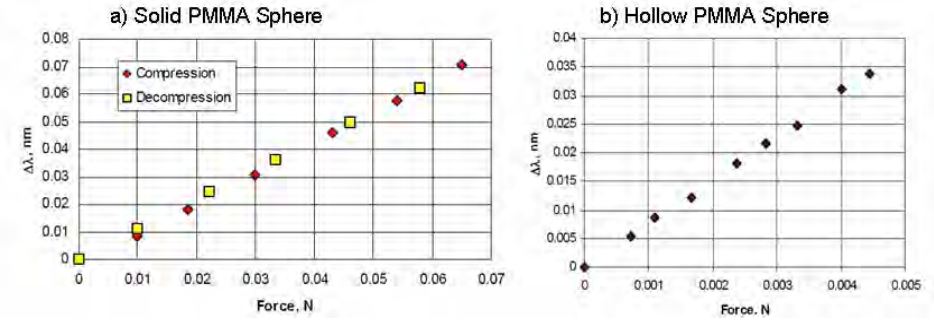


**Figure 3 Resonant shift variation with force: a) solid PMMA, (diameter D = 470 μm) and b) hollow PMMA sphere (diameter D = 960 μm).**

### *Preliminary Design*

Figure 4 shows a functional diagram of the sensing element used as a transducer. Light from a diode laser is coupled into a waveguide (optical fiber) which serves as the input/output conduit. Some of this light, in turn, is coupled into a polymer sphere placed on the waveguide. The laser frequency is scanned (dithered) in a very narrow bandwidth. The transmission spectrum is monitored at the output of the waveguide using a photodiode. The photodiode output, in turn, is fed into a proportional-integral-derivative (PID) controller that provides feedback into the diode laser and locks the laser wavelength to a given optical resonance (WGM) of the sphere. The laser current (which is proportional to its wavelength) is monitored externally, which provides the necessary information on the WGM shift. The feedback system allows for the monitoring of fast shifts in the WGM with a bandwidth limited by the dither frequency bandwidth of the laser (several tens of kHz). The output signal from the laser is transmitted to a remote receiver for further analysis.

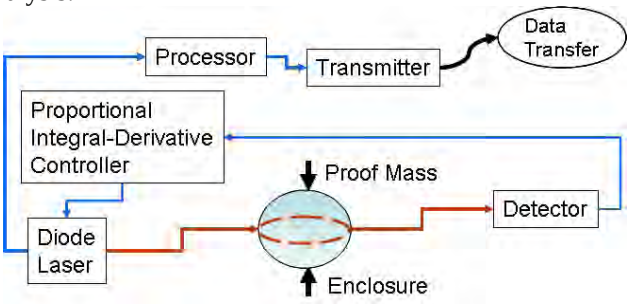


**Figure 4. Functional diagram for the sensing element.**

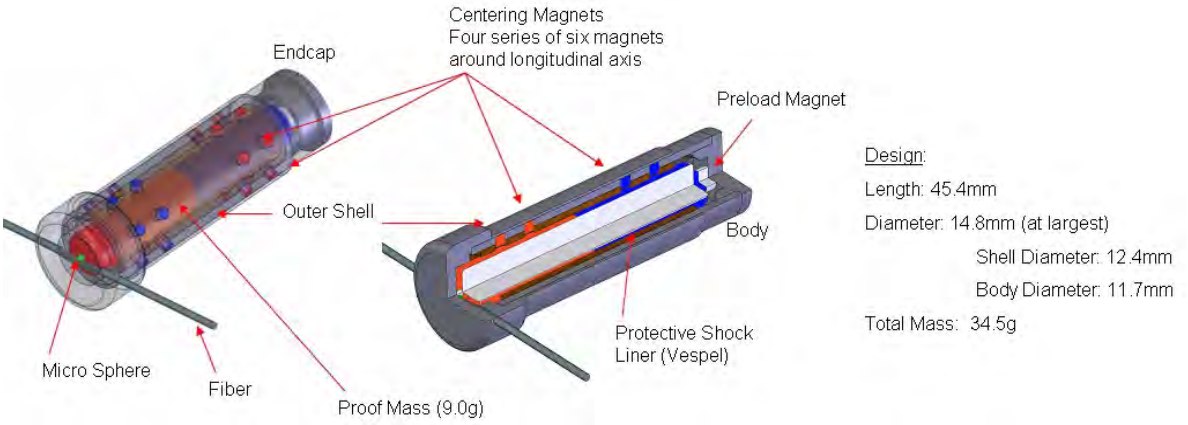


**Figure 5. Conceptual design of one arm of the seismometer.**

The baseline design for the each orthogonal horizontal axis is shown in Figure 5. The proof mass is suspended with magnets, and a preload magnet maintains the mass against the micro-sphere. The total mass for one arm of the instrument is less than 35 grams.

Other designs are being considered as part of a trade study.

## CONCLUSIONS AND RECOMMENDATION

The design and development of the seismometer are under way. Preliminary tests indicate that the high Q-factor of the whispering gallery modes enable a seismometer sensitivity in the nano-g range. Once the optimal mechanical design is selected, analytical work, modeling, and electronics design will be conducted to determine the seismometer characteristics.

## REFERENCES

Benner, R. E., and S. C. Hill (1988). Morphology-dependent Resonances. in *Optical effects Associated with Small Particles*, P. W. Barber and R. K. Chang, Eds., *Advanced Series in Applied Physics*, World Scientific.

Guan, G., S. Arnold, and M. V. Ötügen (2006). Temperature Measurements Using a Micro-Optical Sensor Based on Whispering Gallery Modes, AIAA Journal, Vol 44, No. 10, pp. 2385–2389.

Ioppolo, T., M. Kozhevnikov, M. V. Ötügen, and V. Sheverev (2007). Performance of a whispering gallery mode resonator-based micro-optical force sensor, Paper 2007-1262, 45th AIAA Aerospace Sciences Meeting and Exhibit, Reno, NV.

Kozhevnikov, M., T. Ioppolo, V. Stepaniuk, V. Sheverev, and V. Ötügen (2006). Optical force sensor based on whispering gallery mode resonators, Paper 2006-649, 44th AIAA Aerospace Sciences Meeting and Exhibit, Reno, NV.

Nguyen N., N. Gupta, T. Ioppolo and V. Ötügen (2008). Whispering Gallery Mode-Based Micro-Optical Sensors for Structural Health Monitoring of Composite Materialsm *J. Mat. Sci*, in review.

# ADVANCED WAVEFORM SIMULATION FOR SEISMIC MONITORING

Donald V. Helmberger[1], Arthur J. Rodgers[2], Sidao Ni[1,3], Shengji Wei[1], and Jeroen Tromp[1]

California Institute of Technology[1], Lawrence Livermore National Laboratory[2],
and URS Group, Inc.[3]

Sponsored by National Nuclear Security Administration

Contract No. DE-FC52-06NA27319[1] and DE-AC52-07NA27344[2]
Proposal No. BAA06-04

## ABSTRACT

Earthquake source parameters underpin several aspects of nuclear explosion monitoring. Such aspects are: calibration of moment magnitudes (including coda magnitudes) and magnitude and distance amplitude corrections (MDAC); source depths; discrimination by isotropic moment tensor components; and waveform modeling for structure (including waveform tomography). This project seeks to improve methods for and broaden the applicability of estimating source parameters from broadband waveforms using the Cut-and-Paste (CAP) methodology. The CAP method uses a library of Green's functions for a one-dimensional (1D, depth-varying) seismic velocity model. The method separates the main arrivals of the regional waveform into 5 windows: Pnl (vertical and radial components), Rayleigh (vertical and radial components) and Love (transverse component). Source parameters are estimated by grid search over strike, dip, rake and depth and seismic moment or equivalently moment magnitude, $M_W$, are adjusted to fit the amplitudes. Key to the CAP method is allowing the synthetic seismograms to shift in time relative to the data in order to account for path-propagation errors (delays) in the 1D seismic velocity model used to compute the Green's functions. The CAP method has been shown to improve estimates of source parameters, especially when delay and amplitude biases are calibrated using high signal-to-noise data from moderate earthquakes, CAP+.

In the last year, we have focused on several tasks:

(1) Building a High-Quality Catalog of Earthquake Source Parameters for the Middle East and East Asia. In East Asia we computed source parameters using the CAP method for a set of events studied by Herrmann et al., (2006) using a complete waveform technique. Results indicated excellent agreement with the moment magnitudes in the range 3.5–5.5. Below magnitude 3.5, the scatter increases. For events with more than 2–3 observations at different azimuths, we found good agreement of focal mechanisms. Depths were generally consistent, although differences of up to 10 km were found. These results suggest that CAP modeling provides estimates of source parameters at least as reliable as complete waveform modeling techniques. However, East Asia and the Yellow Sea Korean Paraplatform (YSKP) region studied are relatively laterally homogeneous and may not benefit from the CAP method's flexibility to shift waveform segments to account for path-dependent model errors. A more challenging region to study is the Middle East where strong variations in sedimentary basin, crustal thickness and crustal and mantle seismic velocities greatly impact regional wave propagation. We applied the CAP method to a set of events in and around Iran and found good agreement between estimated focal mechanisms and those reported by the Global Centroid Moment Tensor (CMT) catalog. We found a possible bias in the moment magnitudes that may be due to the thick low-velocity crust in the Iranian Plateau area.

(2) Testing Methods on a Lifetime Regional Data Set. In particular, the recent February 21, 2008, Nevada Event and Aftershock Sequence occurred in the middle of USArray, producing over a thousand records per event. The tectonic setting is quite similar to the Central Iran area and thus provides an excellent testbed for CAP+ at ranges out to 10°, including extensive observations of crustal thinning and thickening and various Pnl complexities. Broadband modeling in 1D, 2D, and 3D will be presented.

(3) Testing Shallow Crustal Structure and Sparse Network Source Inversions for Southern California. We conducted a detailed test of a recently developed technique, CAPloc, in recovering source parameters including location and depth based on tomographic maps. We tested two-station solutions against 160 well-determined events, which worked well except for paths crossing deep basins and along mountain ridges.

## OBJECTIVES

The objective of this study is to advance estimation of event source parameters using waveform modeling techniques. Principally we are applying the CAP methodology to regions of interest such as East Asia and the Middle East and evaluating the reliability of the method with real data, such as dense high-quality recordings from US Array, and synthetic data computed with 3D models. Time domain waveform modeling is a proven method for estimating seismic moment (and moment magnitude, $M_W$), focal mechanisms and depths and thus supports several aspect of nuclear explosion monitoring.

## RESEARCH ACCOMPLISHED

### Introduction

Extraordinary amounts of seismic recordings are presently being produced by the many arms of Earthscope and the world community. These data are being used both in traditional event-station analysis as well as station-to-station ambient noise measurements to generate short-period spectral models. The latter methods produce upper crustal shear-velocity models which can be related directly to short-period source studies such as the CAP method. The possibility of locating small events using sparse but entire 3-component records is becoming increasingly attractive where these various methodologies are combined. We are addressing such a synergy with a special study of the best recorded regional event to date (Wells event) and in Southern California, where over 250 events have been studied with the CAP method.

Some important issues are (1) How reliable is the CAP methodology in retrieving source information at larger ranges in complex tectonic regions, western U. S., Iran, etc., and how do these source parameters compare with other methods? and (2) Can we now determine self-consistent source parameters at all ranges by developing better 3D models and/or special path calibration?

In this short presentation, we will first discuss the Nevada event and then progress on modeling the Iranian events.

### Regional Analysis of the Wells Events (Nevada)

This sequence of events was extremely well recorded by the USArray (Figure 1) and produced an extraordinary set of crustal guided waves. Here, we examine the three-component data in terms of how well existing models perform in predicting the various regional phases, Rayleigh waves, Love waves, and Pnl waves. Previous events from this Basin-and-Range region recorded in southern California have been studied by Zhao and Helmberger (1996) and a 1D model produced by a joint-inversion of minimizing timing-delays and waveform fits, Song et al. (1996). Since this path is essentially the same as theirs to the present TriNet, we can expect good results as demonstrated below. Earthscope studies have greatly added 3D detail by using various analyses based on tomographic methods and noise-generated models. An example of a 2D cross-section along a particularly interesting azimuth is presented in Figure 1b, after Lin et al. (2008). They find relatively strong variation in the main crustal layer of up to 10%. As an introduction to the CAP method, Zhu and Helmberger (1996), we conducted a test against synthetic data. We generated synthetics from four models as displayed with 5% and 10% variation in velocities. These synthetics (now data) are then fit by the CAP method assuming an averaged 1D model where the Pnl are allowed to shift relative to the surface waves. These shifts simply correct for the timing issue. Note that the amplitudes display some disagreement caused by the receiver functions. We recover the mechanisms just fine with this shifting method. This method is applied to the Nevada data, where we perform the inversion as a function of range: 0 to 100 km, 100 to 200 km, etc. Note the stability of the inversion from 100 and beyond where the three fault parameters strike, dip, slip and Mw vary only a few percent, see Figure 2. Some results from the analyses of aftershocks is presented in Figure 3 along with preliminary results from inverting teleseismic waveforms for directivity effects of the main event by applying a wavelet inversion procedure, Ji et al. (2002). A more detailed picture can be constructed by calibrating the (.5–2s) periods for amplitude amplification factors, Tan and Helmberger (2007, 2008), and using the CAP+ procedures.

We used the solution from Figure 2 to predict the various phases at all stations in the array. Both the 10s Love waves and Rayleigh waves remained useful out to 11° although crossing basins produced some multi-pathing. In Figure 4, we display the delays along various paths in percentage of travel-time variation and simple mapping contours. Note

that many of the well-known geological features appear, i.e., Mooney et al. (2005). The delay map for the Rayleigh waves can be directly related to the velocity variation in the seismogenic zone (mid-crust), (Tan and Helmberger, 2008). Our results indicate slow-zones beneath the California-Nevada-Oregon corner and northern Utah-Colorado edge, and fast-zones to the northwest and southwest. These same features are apparent in noise-modeling, Lin et al. (2008). Thus, it appears that these delays can be predicted.

The simplest profile of Pnl's (Figure 5) occurred along the profile to Southern California, and the most interesting towards Washington. The apparent waveform periodicity of about 15s (southern profile) is caused by crustal multiples trapped between the surface and the Moho, see Helmberger (1983). Paths to the north have enhanced Pn (becoming P) caused by high-velocity fine structure at shallow upper mantle depths, Helmberger (1973).

To explain these interesting features, we have initiated numerical runs on existing models such as presented in Figure 1b. Some preliminary runs using 2D (finite-difference [FD], Helmberger and Vidale, 1988) and 3D (spectral-element [SEM], Komatitsch and Tromp, 1999) did not produce fits as good as presented in Figure 2. Part of the problem is that these models do not contain the shallow surface layer which controls the waveform surface wave shapes at these periods. There are, also, numerical issues involving element-sizes and grid-dispersion. We have conducted some 2D code testing against WK for these particular distances and frequencies, Figure 6. Although there are some amplitude differences at small ranges, the synthetics at larger distances look very good.

**Earthquake Source Parameters in East Asia and the Middle East**

As an initial test of the CAP methodology, we computed source parameters for a set of earthquakes in East Asia studied by Herrmann et al. (2007). Green's functions were computed using the same velocity model (mdj2). Results (Figure 7a) indicated that moment magnitudes, $M_W$, agree very well above about 3.5, while depths are more scattered with differences of up to 10 km. Focal mechanisms showed good agreement when 2-3 stations with good azimuthal coverage were available, but large differences were seen when the azimuthal coverage was poor or the signal-to-noise was low (such as for small events).

Applying 1D waveform modeling techniques to the Middle East is more challenging due to the great variability of sedimentary structure, crustal thickness and seismic velocity heterogeneity. We computed Green's functions for an average model of the region and estimated source parameters for a set of 17 earthquakes with Global CMT solutions, all with $M_W$ greater than about 4.5. These events were widely distributed throughout Iran and the mechanisms showed good agreement with the CMT double-couple solutions (Figure 7c). Comparison of the $M_W$ and depths from both methods is shown in Figure 7b. We found a bias in the $M_W$'s with the CAP method consistently resulting in higher values. This could be due to the use of a more realistic regional velocity model with lower average seismic velocity and thicker crust. Bias in the CMT $M_W$'s in Central Asia was reported by Patton and Randall (2002). They found a bias of 0.16 in $M_W$. We found a bias of twice as much; however this is sensitive to the seismic velocities at the event depth. A higher velocity would result in a smaller bias. Further work will be done to find an optimal average model for the entire region or sub-regions.

## CONCLUSIONS AND RECOMMENDATIONS

Cut-and Paste modeling for double-couple mechanisms, depth, and moment proves effective even in complex structures, although some bias in moment is still not resolved for the Iran area because of instrument troubles. There also seems to be a bias in depth estimates where CAP usually produces shallower focal depths. The latter estimates are controlled by using the body-wave depth phases included in the Pnl inversions.

Current 3D models for the western United States and the Middle East display great variability and roughly predict regional delays in short-period surface waves. However, these models need to be tested and refined to improve source inversion for small events, especially at shorter periods.

## ACKNOWLEDGEMENTS

The facilities of the Incorporated Research Institutions for Seismology (IRIS) Data Management System (DMS), and specifically the IRIS Data Management Center (DMC), were used for access to waveform and metadata required in this study. The IRIS DMS is funded through the National Science Foundation and specifically the GEO Directorate through the Instrumentation and Facilities Program of the National Science Foundation under Cooperative Agreement EAR-0552316. We also thank Bill Walter for velocity model (mdj2) information.

## REFERENCES

Ji, Chen, D. J. Wald, and D. V. Helmberger (2002). Source description of the 1999 Hector Mine, California earthquake. I. Wavelet domain inversion theory and resolution analysis, *Bull. Seismol. Soc. Am.* 92: 1192–1207.

Helmberger, Donald V. Helmberger (1973). On the structure of the low velocity zone, *Geophys. J. R. astr. Soc.* 34; 251–263.

Helmberger, D. V. (1983). Theory and application of synthetic seismograms, in *Earthquakes: Observation, Theory and Interpretation*, pp. 173–222, ed. Kanamori, *H., Soc. Italiana di Fisica*, Bologna, Italy.

Helmberger, Donald V. and John E. Vidale (1988). Modeling strong motions produced by earthquakes with two-dimensional numerical codes, *Bull. Seismol. Soc. Am.* 78; No. 1, 109–121.

Helmberger, D. V., D. Dreger, R. Stead, and H. Kanamori (1993). Impact of broadband seismology on the understanding of strong motions, *Bull. Seismol. Soc. Am.* 83: 830–850.

Herrmann, R., W. Walter, and M. Pasyanos (2007). Seismic Source and Path Calibration in the Korean Peninsula, Yellow Sea, and Northeast China, in *Proceedings of the 29th Monitoring Research Review: Ground-Based Nuclear Explosion Monitoring Technologies*, LA-UR-07-5613, Vol. 1, pp. 592–601.

Herrmann, R., Y. Jeon, H. Yoo, K. Cho, W. Walter, and M. Pasyanos (2006). Seismic source and path calibration in the Korean Peninsula, Yellow Sea, and Northeast China, in *Proceedings of the 28th Seismic Research Review: Ground-Based Nuclear Explosion Monitoring Technologies*, LA-UR-06-5471, Vol. 1, pp. 60–70.

Komatitsch, D. and J. Tromp (1999). Introduction to the spectral-element method for 3D seismic wave propagation, *Geophys. J. Int.* 139: 806–822.

Lin, F., M.P. Moschetti, and M.H. Ritzwoller (2008). Surface wave tomography of the western United States from ambient seismic noise: Rayleigh and Love wave phase velocity maps, *Geophys. J. Int.*, in press.

Mooney, Walter D., V. V. Rao, P. R. Reddy, G. S. Chulick, and S. T. Detweiler (2005). Comparison of the deep crustal structure and seismicity of North America with the Indian subcontinent, *Current Science* 88**:** No. 10, pp. 1639.

Ni, Sidao, A. Pitarka, and D. V. Helmberger (2008). Short-period synthetics for 3D models: Numerical vs. Analytical, *Seismological Res. Lett.* 79: No. 2, p.298.

Pasyanos, M.E., W.R. Walter, M.P. Flanagan, P. Goldstein and J. Bhattacharya (2004). Building and testing an a priori geophysical model for Western Eurasia and North Africa, *Pure Appl, Geophys.* 161: 235–281.

Patton, H. and G. Randall (2002). On the causes of biased estimates of seismic moment for earthquakes in central Asia, *J. Geophys. Res.* 107: B11, 2302, doi:10.1029/2001JB000351.

Song, Xi J., D. V. Helmberger, and L. Zhao (1996). Broad-band modeling of regional seismograms: the Basin and Range crustal structure, *Geophys. J. Int.* 125: 15–29.

Sun, Daoyuan, D. V. Helmberger, S. Wei, and L. Alisic (2008). MULTI-PATH DETECTORS I and II (Poster 80-81), EarthScope IRIS Annual Meeting/Workshop, Portland, OR, June 3–10, 2008.

Tan, Ying and D. V. Helmberger (2007). A New Method for Determining Small Earthquake Source Parameters Using Short-Period P Waves, *Bull. Seismol. Soc. Am.*, 97, No. 4, 1176–1195.

Zhao, L. S. and D. V. Helmberger (1996). Regional moments, energy levels, and a new discriminant, *Pure appl. Geophys.*

Zhu, Lupei and D. V. Helmberger (1996). Advancement in source estimation techniques using broadband regional seismograms, *Bull. Seismol. Soc. Am.* 86: 1634–1641.

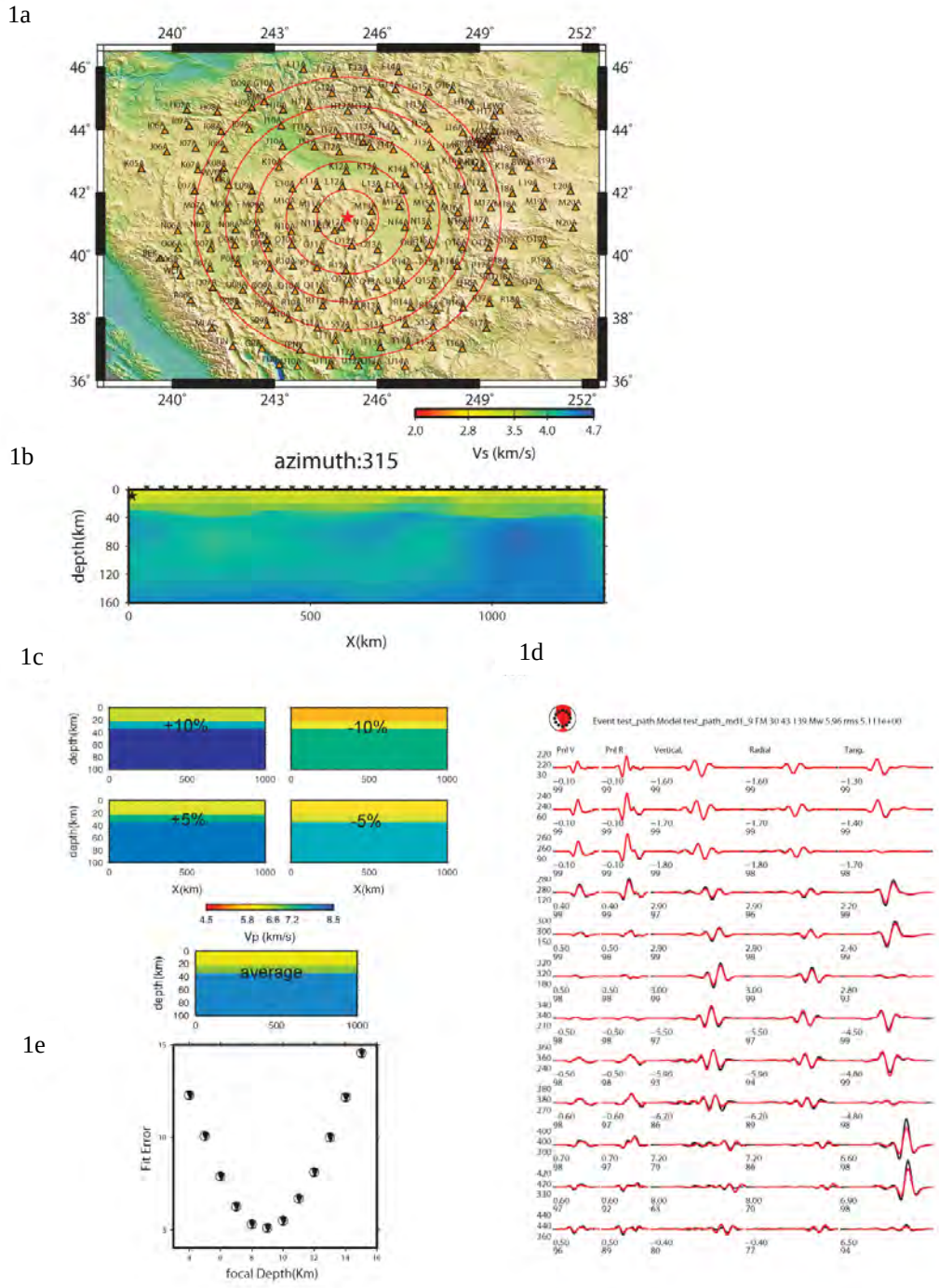


**Figure 1. (a) Display of USArray stations. Only the stations less than 5° are displayed here arranged in circles; 6 stations within 100km, 18 between 100 and 200 km, 32, 43, 87, etc. (b) A 2D velocity section (after Lin et al., 2008), starting from the Nevada Event source position with azimuth of 315°. (c) Upper four models are used to generate synthetic data and then the average model (lower one) is used to recover source mechanism. (d) CAP inversion using the average model. The length of Pnl traces is 35s and surface waves 70s, respectively. The dots on the focal plot indicates the sampling of mechanism. The fits are good and trial mechanism recovered. (e) Depth-mechanism-misfit indicates that the depth and mechanism are well-resolved.**

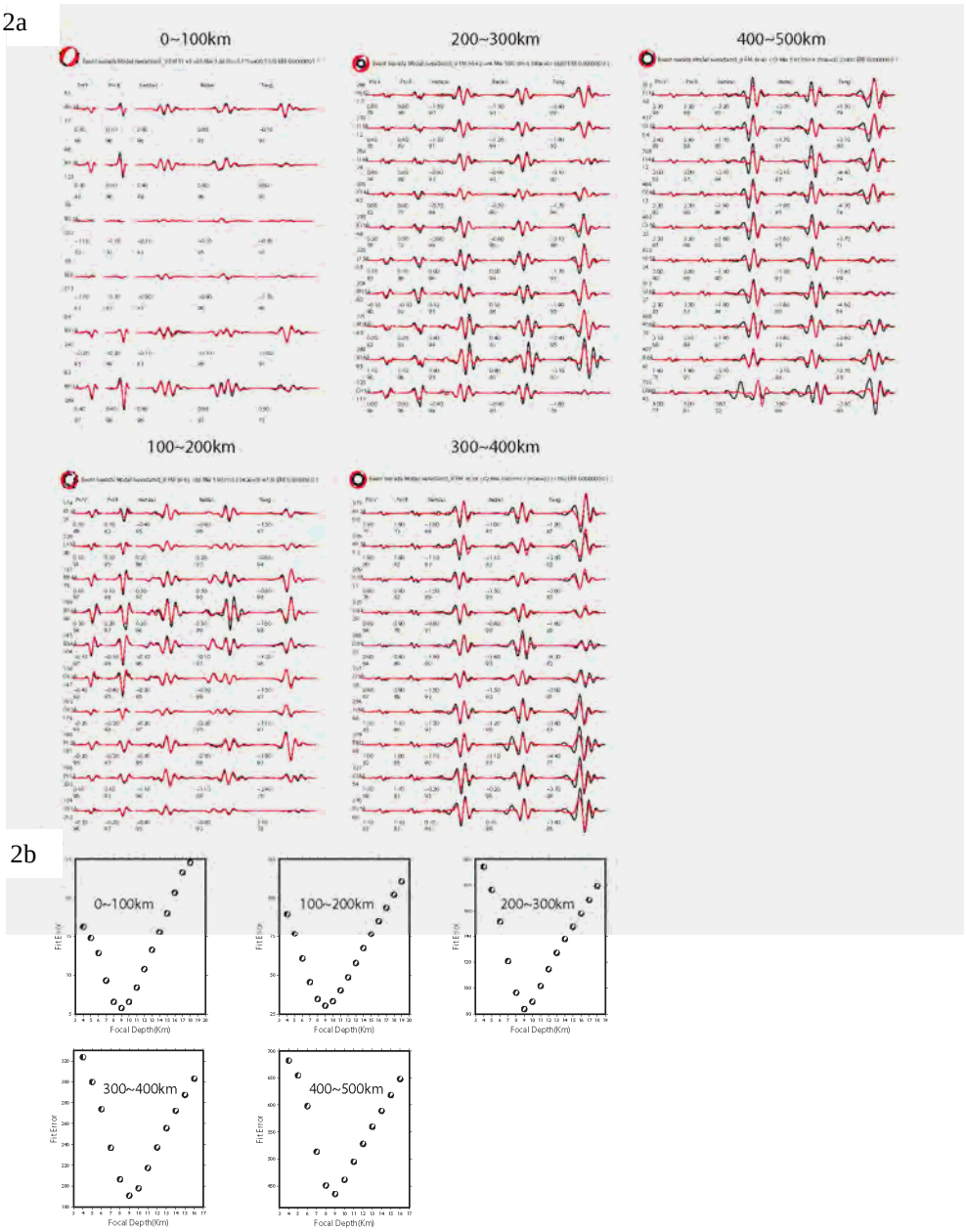


**Figure 2. According to the epicenter distance, data within five degrees are sorted into five groups. (a) Figure 2a shows 0 to 100km, etc. The "Cut and Paste" (CAP) modeling of Pnl and Surface waves have been done for each group of the data for the main Nevada Event. The name of the station is at the left of each seismogram, the number below the station name is the epicenter distance in kilometer, and above is the azimuth. The numbers on the lower left side of the seismograms are the time shifts(upper) and crosscorrelation coefficient in percent (lower). Positive time shifts mean that the synthetics have been shifted to the right. Pnl waves are filtered with bandpass (0.02~0.2Hz) and Surface waves are filtered with (0.02~0.1Hz). Only representative recordings have been included at the larger distances although all the data is used in the inversion. This earthquake features a mostly dip-slip mechanism (normal). The focal depth is estimated to be around 9km. Note the stability of the inversion where three fault parameters, strike, dip, slip and Mw vary only a few percent. The delays can be used to create a tomography image, Tan et al. (2008), discussed later. Figure 2b displays the corresponding depth resolutions. Since Pnl is included in the inversion, CAP has a good constraint on depth. The velocity model is from the Song et al. (1996) paper, featuring a 34km deep Moho in the Nevada area.**

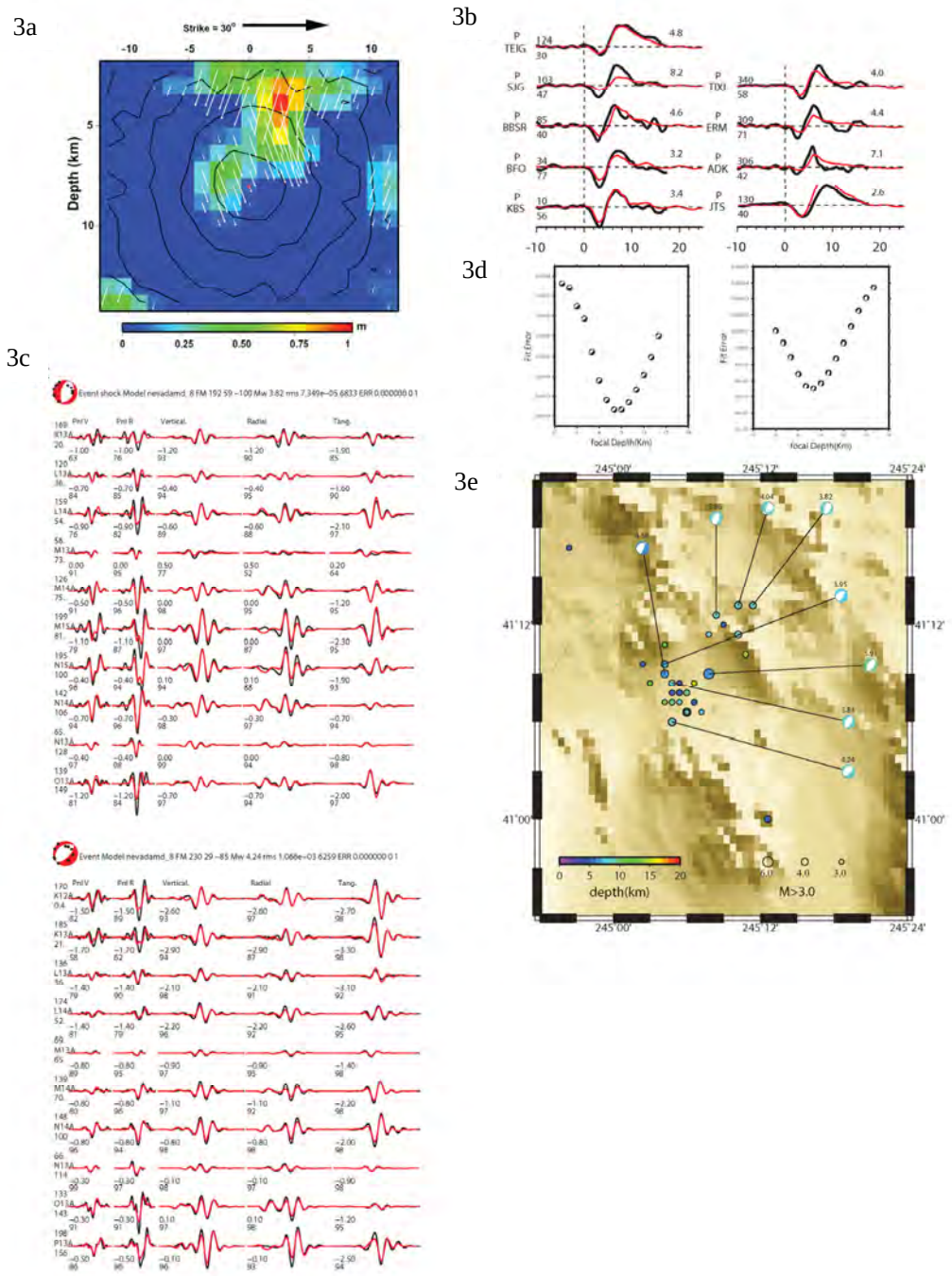


**Figure 3. (a) A preliminary distributed slip inversion for the main event. Slip contours (black) and slip model contours plotted for each 2.5 seconds. (b) Comparison between synthetic and data at teleseismic distance. The number on the left is the data amplitude in microns. Synthetic and data are shown with absolute amplitudes. Values on the right are azimuth(upper) and distance(lower). The rupture velocity is between 2~2.5km/s. Such inversions can be greatly improved by adding stations corrections, Ni et al. (2008) and regional data by including the CAP+ procedure. (c) The source mechanism of 7 aftershocks have been modeled. The waveform fits are given for two indicating some changes in strike. Including higher frequency in Pnl(up to 3Hz) still produces excellent fits and will be used in detailed inversions of the main event. Refer to Figure 2 for definition of numbers. (d) Depth resolutions corresponding to (c). (e) Aftershocks with their positions (NEIC). Only events with magnitude larger than 3.0 are shown.**

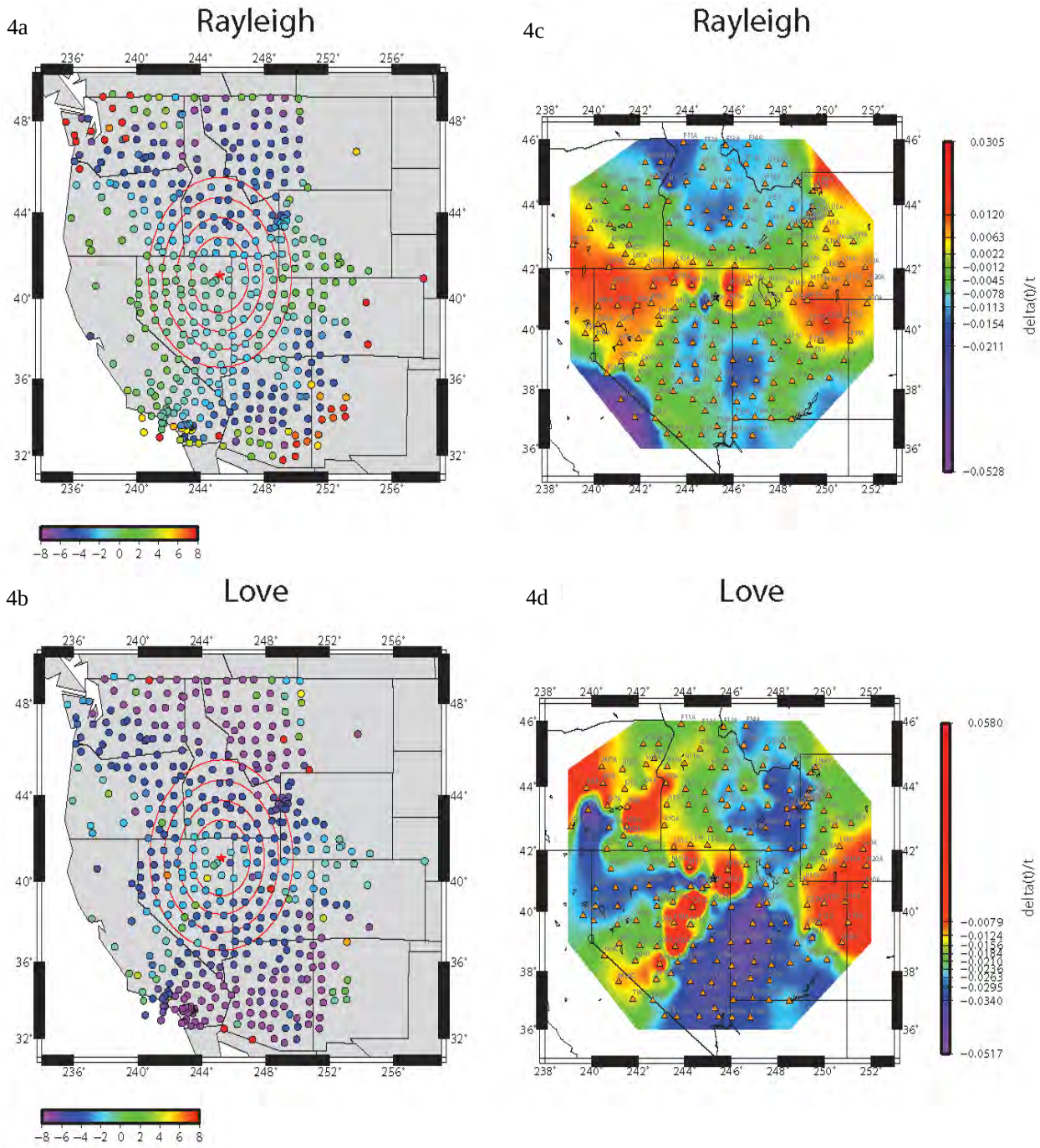


**Figure 4. Relative time shifts of surface waves between synthetic and data can used in locating events (CAPloc, Tan et al.(2006)) and are plotted in 4a and 4b. These shifts can be normalized by travel times and used to contour relative velocities, 4c and 4d.**

5a

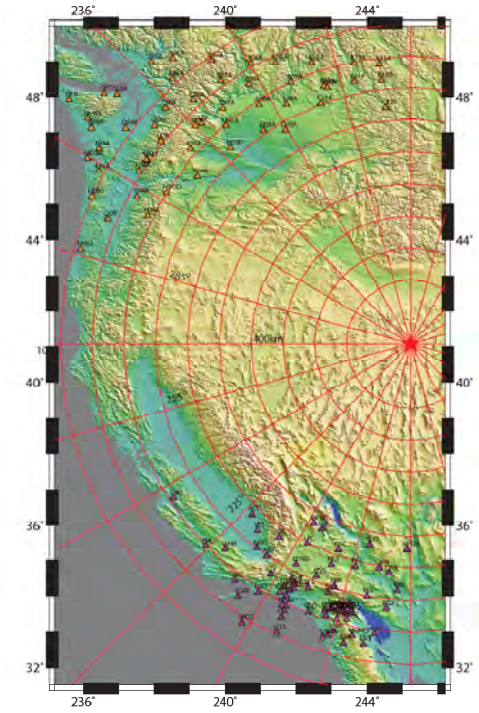


5b

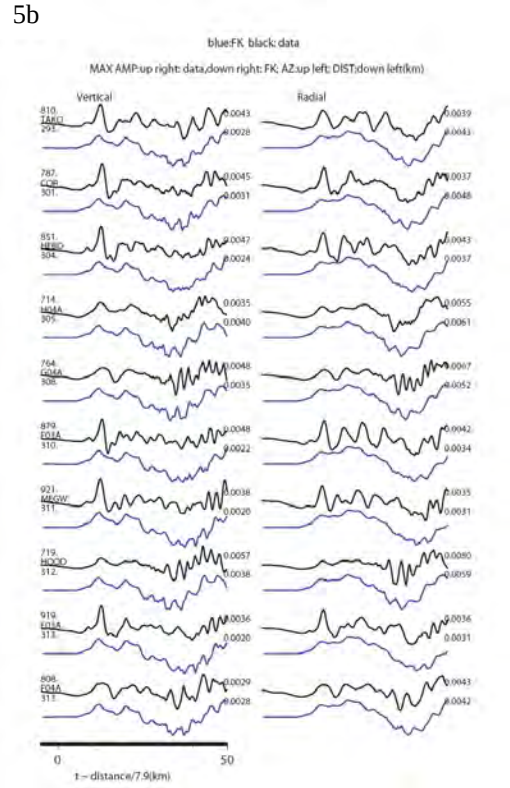


5c

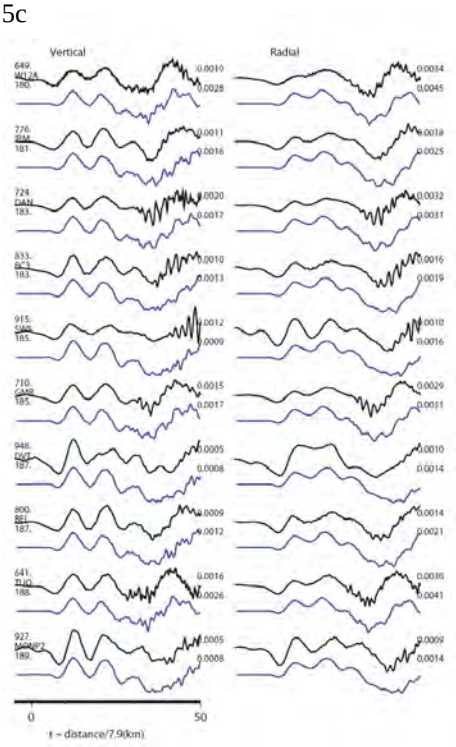


**Figure 5.**
**(a) Stations along specific azimuths(to the northwest and southwest) and epicenter distance.**
**(b) Record-section of Pnl portion of data and 1D synthetic in northwest direction. Data is in black and synthetic of 1D model in blue. The number on the right of each seismogram is peak amplitude in centimeter.**
**(c) Record-section of Pnl portion of data and 1D synthetic in the southwest direction. Many sections compare quite well out to about 900km, event with this simple model of a uniform mantle. The most interesting profile is displayed along the sector 290~330 degrees. In particular, note that the beginning portions of the Pnl wave train(H04A, G04A, etc.) are indeed Pn-like while some stations (COR, TAKO, F03A, etc.) are P-like (impulse) indicating significant mantle structure. These 3D effects are presently being investigated where the same set of stations display interesting multi-pathing of teleseismic signals (Sun et al., 2008).**

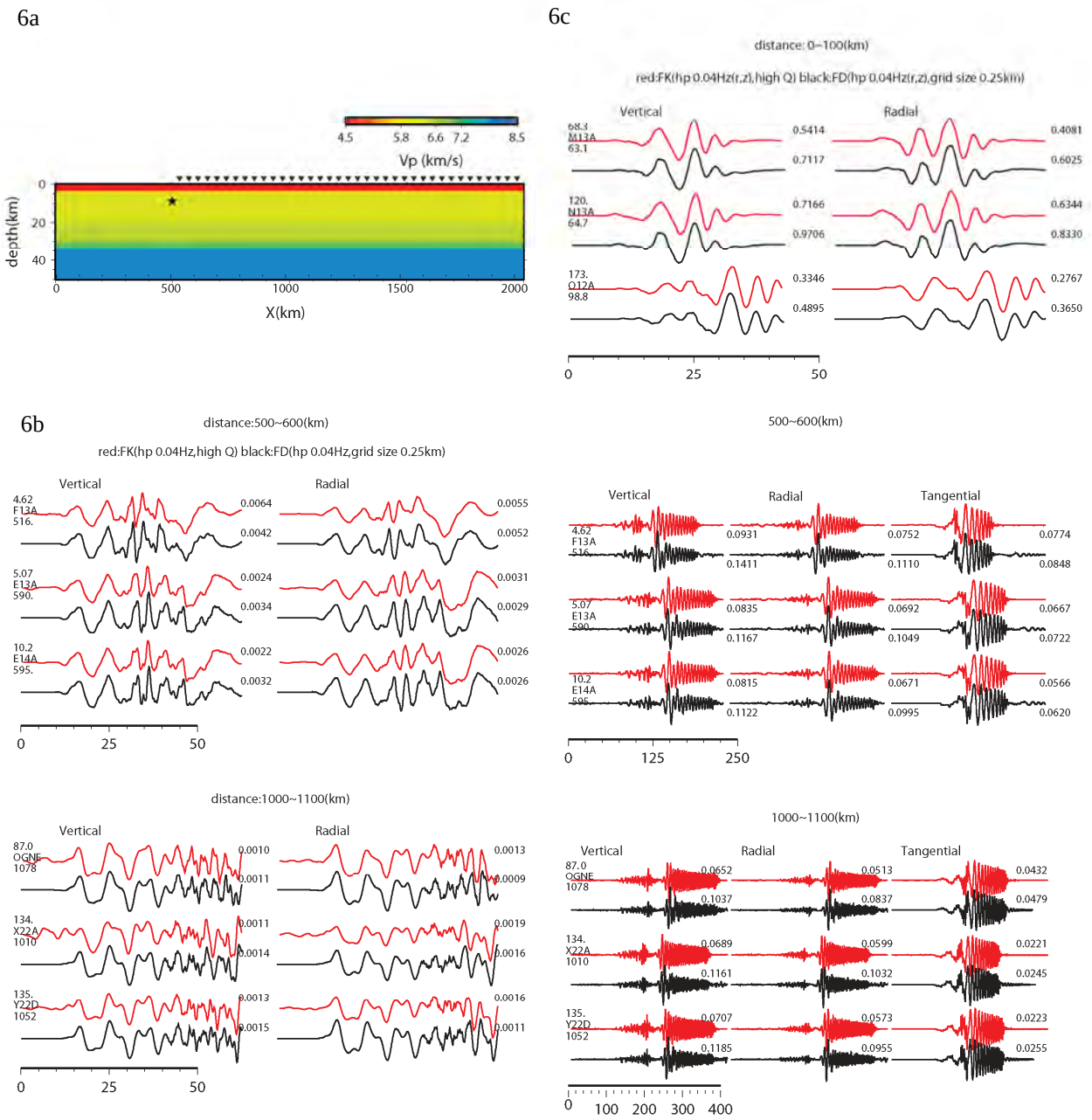


**Figure 6. Comparison of synthetics (FD vs. FK).**
**(a) Vp model for validated calculation.**
**(b) Synthetic seismograms comparison between FK (red) and 2D FD (black). Only Pnl-portion is plotted. The number on the right of each seismogram is the peak amplitude in centimeter. A highpass filter with corner frequency of 0.025Hz is applied to both synthetics.**
**(c) Surface wave comparison between FK and 2D FD. The number on the right of each seismogram is peak amplitude in centimeter. There two methods show high consistency up to distances beyond 1000km with a grid-size of 250m.**

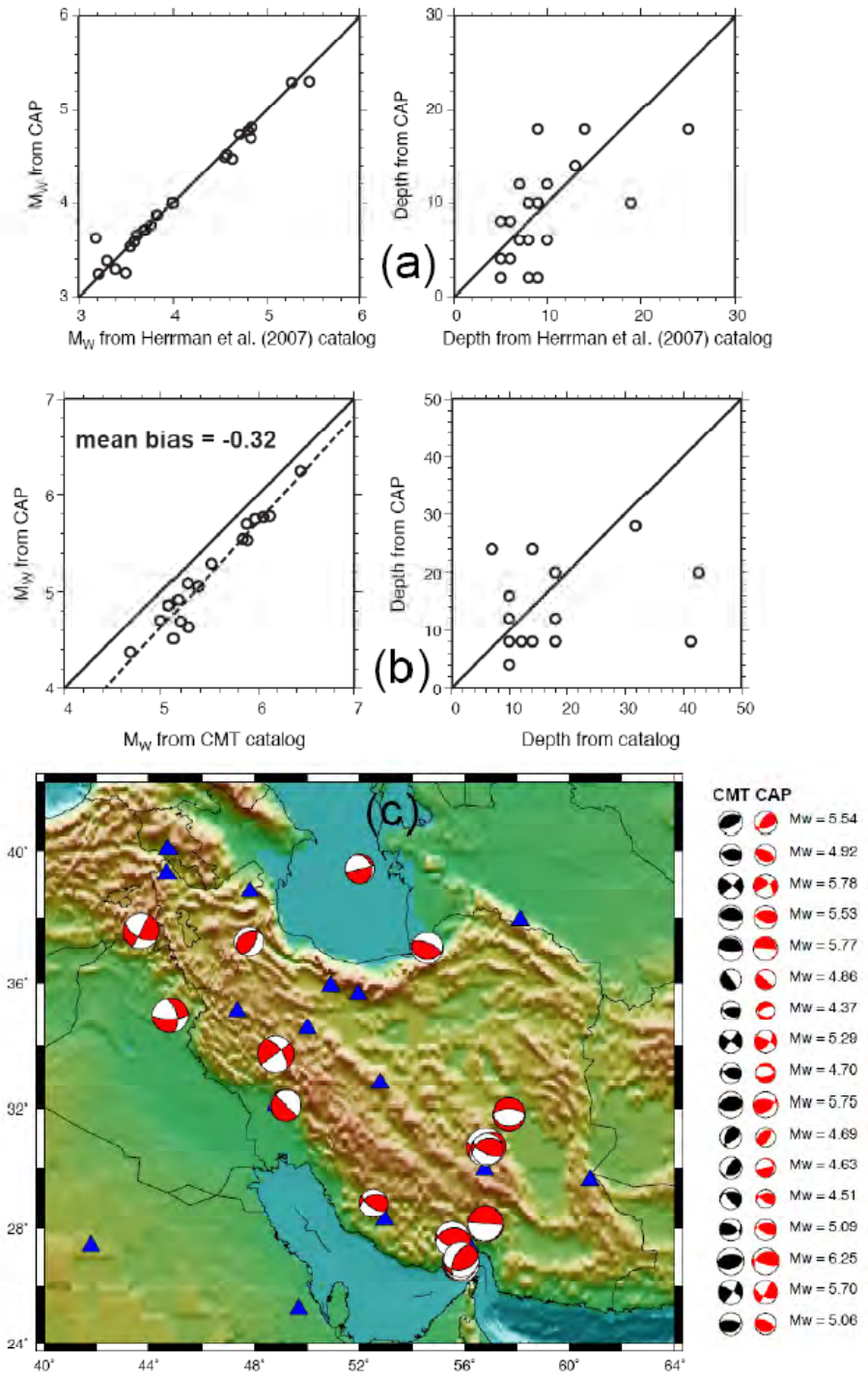


**Figure 7. Over 20 events distributed throughout the Korean Peninsula were analyzed with the CAP code both at local and regional distances (10 deg). Several 1D models were used but the most successful proved to be mdj2 (Bill Walter). The results with comparison with the Herrmann and Walter Catalog are given in Figure 7a. The results for the Middle East are given in Figures 7b and 7c and compared to the CMT solutions. The 1D model is an average of three provinces (Central Iran, Turkey-Iran, Arabian Platform) taken from the 3D model WENA (Pasyanos et al, 2004).**

# SEISMIC DETECTION USING MINI SEISMOMETER

Robert J. Leugoud

eentec

Sponsored by National Nuclear Security Administration

Contract No. DE-FG02-08ER85090

## ABSTRACT

The goal of this Phase 1 SBIR project is to develop a very small, versatile, rugged, low power, low noise, one or three-axis short-period seismometer. The total sensor size should be less than 1 cubic inch; and low power consumption and low sensor self noise below the USGS Low Earth Noise Model, with dynamic range at least 120 dB over a frequency band of 0.2 to 40 Hz. All commercially available high performance seismometers using various technologies are large, heavy and consume high power. The user must often face a difficult choice: use instruments with significantly lower performance characteristics, or reduce the size of the network. Our company, eentec, proposes a solution for this problem of designing a seismometer using a new technology of liquid inertial masses and electrochemical transducers. This overall approach will miniaturize a medium period seismometer while maintaining low self noise with low power consumption.

## OBJECTIVES

This project, if followed to its successful completion, would lead to the implementation of a state-of-the-art miniature, affordable, rugged, reliable, easily-installed high quality instrument, well suited for mass production and commercialization for use in many areas of seismic, civil engineering, geotechnical investigations, and many other areas were highly sensitive motion detection is required.

The seismometer resulting from our investigation is intended to meet the following requirements:

- miniature size—about 1 cubic inch
- power consumption below 100 mW for a basic analog sensor
- dynamic range—at least 120 dB
- high resolution in the required passband of 0.2 to 40Hz
- low self noise below the USGS Low Earth Noise Model (e.g., approximately 0.5 ng/sqrt[Hz]) while not sacrificing the high sensitivity required to be useful in the applications intended
- capable of operation at any selected orientation of its axis of sensitivity rugged and suitable in harsh field conditions

### *Overview of eentec Seismometer Technology*

The principle of operation is basically electrochemical in nature. The sensor element consists of a cylindrical channel with elastic membranes on the ends, and is filled with an electrolyte. A microporous ceramic plug containing platinum grid electrodes is within the channel. When translational motions are applied, a pressure differential occurs across the sensor cell, which causes the electrolyte to flow, and generates a current in the wire connected to the platinum grid.

***Overview of the Actual Physical Process***

The motion of the fluid caused by an external acceleration must be converted into an electrical signal to be useful. This is accomplished in the following manner.

When a small dc offset is applied between the anodes and cathodes, the flow of ions of each type is given by the following expression:

$$\mathbf{j}_a = -D \cdot \nabla c_a + q_a \cdot c_a \cdot \mu \cdot \mathbf{E} \qquad (1)$$

where D = diffusion coefficient, μ = mobility, $c_a$ = concentration of active ions, E = the electrical field vector. Since the strong electrolyte is an excellent conductor, the electric potential drops rapidly in the vicinity of the electrodes, and there is no electric field, E, in the bulk of the fluid. The second term in Eq. 1 can therefore be ignored. Thus, the application of a bias voltage results *only* in a concentration gradient. This is in contrast both to conductors, in which the current is driven by the external electric field, and to semiconductors, in which both the field and the concentration gradient determine the currents.

An external acceleration, **a,** along the channel creates a pressure differential, **ΔP,** across the transducer, which forces the liquid in motion with a velocity, **v**. This flow of electrolyte entrains ions and causes an additional charge transfer between the electrodes:

$$\mathbf{j}'_{\mathbf{a}} = \mathbf{v} \cdot c_a \qquad (2)$$

The total current from active ions, in the presence of acceleration, will thus be:

$$\mathbf{j}_{\mathbf{a}} = -D \cdot \nabla c_a + \mathbf{v} \cdot c_a \qquad (3)$$

The transducer thus generates an electrical signal in response to an input motion. The symmetric geometry of the transducer cell ensures its linear behavior over a wide range of input signals.

With a highly concentrated specially formulated electrolyte, the electric field is non-zero only in a narrow boundary layer adjacent to the electrodes. In this case, the electric current is fully determined by the diffusion**.**

These transducers are characterized by a very high conversion coefficient of mechanical motion into electrical signal. That is why the electronics noise plays a noticeably smaller role in the total signal-to-noise ratio than in the traditional electromechanical seismic motion sensors. In addition, this technology results in low power consumption, typically several times smaller than in any other active seismometers.

***The Current State of eentec's Technology***

Over the years eentec has taken the basic technology described above and slowly but surely refined and continually improved it. A number of significant advancements were introduced such as;

- introduction of a force balancing feature to improve the linearity of the older open loop designs
- improved construction material used in the sensor elements which significantly increased the ruggedness and long term field operation.
- improved membrane designs and electrolyte solutions leading to lower sensor self noise, currently at 140dB.
- coupled with the above, electronic improvements which enable the sensors to be manufactured at periods of 120 seconds.
- external mechanical improvements in the leveling legs, level bubble, and handle to facilitate easy of transport and installation in filed conditions.

***Some Benefits of eentec Technology Over Other Technologies***

High performance seismometer technology is still based on its roots of the mass and magnet technology used for over 80 years. Although the introduction of active seismometers that included electronics to increase their performance characteristics, their basic technology is still the mass and magnet. There are other technologies used for motion sensors such as piezo electric, monolithic miniature micromachined sensors (MEMS), formed from a silicon substrate, and opto-electric. However these other technologies are not currently used in high performance seismometer applications. The benefits that eentec has over other technologies are;

- sensitivity and dynamic range in the range of the mass and magnet technology but much better than the other technologies
- no mass centering required resulting in a large operational installation tilt for the sensor. This leads to lower cost and less complicated borehole and OBS sensor applications.
- no mass locks required for transport. With the current improvements detailed above the sensors are more rugged, easily and safely transported and deployed.
- inherently low power
- operational in high magnetic fields. Not influenced by magnetic environments.
- very little operational sensitivity to temperature changes over the operational temperature range on the sensor

**RESEARCH ACCOMPLISHED**

This research funding allows eentec the opportunity to more rapidly advance its technology to the next level. Taking advantage of the current state of the technology and the years of field experience and data obtained, we have a solid footing to make the advancements necessary to accomplish this projects goal.

*Evaluation of Pre-Phase I Preliminary Test Results*

We will initiate Phase I research with the analysis of data that will have been collected in tests of our present production units and conceptual prototype electrochemical instruments to determine the best directions to be taken to achieve the Phase I development objectives of the new technology.

The historical data will be run through the following revised models because the operation of a molecular electronic transducer cell is based on the convective diffusion of charge carriers and may be described by the following, generally non-linear, system of partial differential equations:

$$\frac{\partial \mathbf{v}}{\partial t} = (\mathbf{v}\nabla)\mathbf{v} = -\frac{\nabla p(t)}{\rho} + \nu \cdot \Delta \mathbf{v} \qquad (4)$$

$$\operatorname{div} \mathbf{v}(t) = 0 \qquad (5)$$

$$\frac{\partial c}{\partial t} + \mathbf{v}(t) \cdot \nabla c = D \cdot \Delta c \qquad (6)$$

where: (4) Navier-Stokes equation; (5) liquid incompressibility condition; (6) convective diffusion equation; where v = velocity of the electrolytic solution; *p* = pressure distribution; ρ = electrolyte density; ν = electrolyte viscosity; *c* = concentration of charge carriers; *D* = diffusion coefficient; *e* = elementary charge; This system of equations can only be solved with the proper boundary conditions. The solution cannot be found analytically and will require various computer simulations depending on the packaging of the system.

Also our current math models will be analyzed differently. Earlier we found solutions only for standalone equations of diffusion and hydrodynamics and never considered the relationship between them. Since eentec has acquired access to more powerful computers in the last several years, this will allow us to calculate the total math model including all equations involved.

*Development of the Improved Mathematical Model.*

Since the behavior of a sensor cell is described by non-linear differential equations, the accuracy of the calculated values of their coefficients has a decisive effect on the properties of its physical implementation. For example, a computer-generated dependence, based on our initial mathematical model, of the electrochemical cell sensitivity vs. the electrode geometry of the cell shows that relatively small deviations of the electrode mesh size may cause significant changes in the sensitivity. Also cell geometry of the electrochemical transducer defines its hydraulic impedance, the major parameter that affects the self-noise of the sensor. Basic increasing the size of the electrode assembly to ½ inch would give us 2 times lower noise ~1.5 $ng/\sqrt{Hz}$ while maintaining the dynamic range at the same 120 dB range. Analysis of the test data will result in the refinement of the mathematical model, which, in turn, will prompt the desirable modifications in the cell geometry and other parameters.

*Selection of Electrolytic Liquid for the Transducer Cell*

The selected configurations will require the use of electrolytic working liquid with a specific set of properties: density, viscosity, boiling and freezing temperatures, conductivity and permittivity. The advance knowledge of these parameters narrows the search field and saves time by eliminating excessive laboratory testing.

It should be noted that sensor cell self-noise is determined by the damping factor ($R_h$), which depends on the viscosity of the electrolyte, and the density (ρ) of working liquid:

$$\left\langle a^2 \right\rangle_{\omega} = \frac{2R_h kT}{(\rho \cdot L)^2} \qquad (7)$$

where $R_h$= transducer's hydraulic impedance; ρ = electrolyte density; L = electrolyte dimension along the sensitivity axis.

*Development and Optimization of the Membrane Design*

Fitting the sensor in 1 cubic inch requires reducing membrane diameter from the current 37mm to no more than 25mm. While changing sensor mechanical design will be a routine engineering task simulated on the computer, shrinking the membranes presents a much more difficult problem. Indeed, several important requirements must be met.

- Membranes should be sufficiently soft in order to provide for the sensor's adequate response at the lower frequency cutoff and at the same time sufficiently firm to support the combined column of liquids regardless of the sensor spatial orientation.

- Membranes must be designed to ***minimize their response to a pressure gradient across their diameter,*** such as would result from an external acceleration action along a perpendicular axis.

To meet the desired requirements, the specific design of the membrane will require a significant number of computer simulations. The low cut-off frequency of the sensor depends on the volumetric rigidity, $\boldsymbol{\mu}$, of the membrane:

$$\omega_l \propto \frac{Eh^2}{R_h S^3\left(1-\mu^2\right)} \qquad (5)$$

Where $E$ = Young's modulus; $h$ = thickness of the membrane and $S$ = membrane effective area.

It should be noted that the geometry, elastomer, and mold that will work with both of these items respectively would be included in the simulations required to complete this task.

*Electronic Circuit Design*

The transducer cell requires properly designed infralow-current electronic circuitry. In addition to its ability to condition and measure sub-nanoampere currents, the circuitry designed will have to meet the other specifications of the described devices: noise level, operating temperature range, etc. The circuits should also consume very little power so that the total power consumption would be less than 30 mW. The experimental circuit will have to be versatile enough to allow shaping of the required frequency response.

*Assembly and testing of prototype sensors*

After completion of all the modeling and simulations noted above, we plan to build at least 6 prototype sensors. These will initially be tested at our facility and then tested further at an outside facility by one of our consultants in the project. These results will lead us to further modify and improve the computer models and simulations created during the first phase.

## CONCLUSIONS AND RECOMMENDATIONS

The goal of the Phase I effort is to prove that the proposed technology can provide a sound foundation for producing and further enhancing the specifications and practical implementation of miniaturized, inexpensive, high performance short-period seismic sensors. In order to achieve this goal, the following technical objectives will be met (the corresponding Phase II target numbers are shown in parentheses):

1. Fabricate and test in the laboratory conceptual prototype of miniaturized electrochemical sensor with the following parameters;
2. Miniature size – about 1 cubic inch (1 cubic inch or less)
3. Dynamic range of 114 - 120 dB (≥132);
4. Passband of 0.2(0.07) to 40(50)Hz
5. Self-noise in the required passband: below 1 (0.5) ng/sqrt(Hz)
6. The sensor will be capable of operation at any selected orientation of its axis of sensitivity
7. Demonstrate that the cost of such sensor will be significantly less than that of traditional mechanical instruments;
8. Develop and test a miniature prototype rotational accelerometer with translational sensitivity <0.5% and a frequency band of 0.2 (0.07) to 40 (50) Hz.
9. Identify work to be performed in Phase II of this project.

There are several important improvements of the proposed sensors, which should be investigated during the Phase II project. They will result not only in the implementation of a more advanced sensor exceeding the proposed Phase I objectives but also in a more universal instrument such as, but not necessarily limited to the above mention strong/weak motion combination seismic sensor.

# A MODEL AND METHODS FOR REGIONAL TRAVEL-TIME CALCULATION

Stephen C. Myers[1], Sanford Ballard[2], Charlotte A. Rowe[3], Gregory S. Wagner[4], Michael S. Antolik[5], W. Scott Phillips[2], Abe L. Ramirez[1], Mike L. Begnaud[2], Mike E. Pasyanos[1], Doug A. Dodge[1], Megan P. Flanagan[1], Kevin D. Hutchenson[5], Glenn T. Barker[2], John J. Dwyer[4], and David R. Russell[4]

Lawrence Livermore National Laboratory[1], Sandia National Laboratories[2], Los Alamos National Laboratory[3], Air Force Technical Applications Center[4], and Quantum Technology Sciences, Inc.[5]

Sponsored by National Nuclear Security Administration

Contract No. DE-AC52-07NA27344[1], DE-AC04-94AL8500[2], DE-AC52-06NA25396[3], and FA8620-05-C-4301[5]

## ABSTRACT

This project develops a model and methods for routine computation of regional travel times for crustal events anywhere on the globe. To improve on existing methods, the travel time calculations must capture the effect of the three-dimensional (3D) earth, yet the computation must be exceedingly efficient. We achieve global coverage by defining a seamless global tessellation of nodes with spacing of approximately 1°. Three-dimensional crustal structure is captured by interpolating P- and S-velocity depth profiles at each node. Mantle structure is approximated by a linear velocity gradient (as a function of depth) at each node. The linear gradient parameterization in the mantle enables an analytical approximation for the diving Pn/Sn ray that allows computation of travel times in approximately 1 millisecond. Regional Pg and Lg propagation are approximated with a ray traveling horizontally along a mid-crustal layer. At local distance, P and S travel times are computed using the layered velocity structure under the station.

The starting model is a hybrid of the Lawrence Livermore National Laboratory (LLNL)/Los Alamos National Laboratory (LANL) unified model, which is a 3D geophysical compilation spanning Eurasia and North Africa, and CRUST2.0 elsewhere. These 3D models are adapted to the linear gradient parameterization using mantle velocities at the Moho and at 130-km depth. At 130-km depth the velocity of is predominantly derived from 2SMAC. We refine the Eurasian and North African portion of the model using a tomographic formulation that adjusts the average crustal velocity, Pn and Sn velocity, and the mantle gradient at each node. Our tomographic data consists of approximately 700,000 validated regional arrivals from events with known locations or locations meeting accuracy criteria. Pn tomography in the Eurasia/North Africa region reduces travel time residual variance by 78%, and additional (noncircular) tests confirm significant improvement in Pn travel time prediction accuracy. Improvement in epicenter accuracy is strongly dependent on network coverage, but improvement of 20%–30% is achieved for networks with azimuthal gap greater than 200°.

## OBJECTIVES

This project produces a laterally variable velocity model of the crust and upper mantle that is specifically designed for use in routine seismic location. At this time the Seismic Location Baseline Model (SLBM) is focused on travel time prediction at local and regional distances. Therefore, ray paths are wholly within the crust and upper mantle. Like any travel-time prediction method used in a location algorithm, the SLMB must return the following:

1. An accurate travel-time prediction
2. An uncertainty estimate of the travel-time prediction error

Because the SLBM is meant for use in routine location algorithms where networks can be dynamic and precomputation of travel times for all available data may not be possible, the SLBM must also do the following:

3. Compute the travel time on-the-fly, given regional- or local-distance station/event coordinates
4. Return the travel time in milliseconds, thus enabling the estimation of a location in a few seconds

Further, we aim to improve a starting model that is based on a geophysical compilation. The improvement is achieved using a ground-truth dataset and a tomographic technique that is tailored to optimize model parameters important to seismic location.

## RESEARCH ACCOMPLISHED

We meet the objectives outlined above by constructing one earth model that is used in the computation of all four regional phases. Further, we adapt several approaches for regional travel time calculation into one software package that provide a convenient travel time calculation utility for use in seismic location and other applications that require a fast and accurate calculation for crustal seismic events. In this paper, we report on methods for computing regional travel times for Pn, Pg, Sn, and Lg phases. We also report on Pn tomography results. Tomography for Pg, Sn, and Lg is in progress.

### Model Parameterization

We combine the laterally variable layer approach of Pasyanos et al. (2004) with the linear mantle gradient of Zhao and Xie (1993). Myers et al. (2007) provide model parameterization details, and we summarize here. Velocity vs. depth profiles are defined at nodes, and the profiles at the nodes are interpolated using an efficient code developed at Sandia National Laboratories (SNL) to determine velocity at any arbitrary location (lat,lon,depth). SNL has also developed a tessellation node structure on a spheroid with node spacing of approximately 1° (Figure 1). At present, the model development domain is Eurasia and North Africa, and nodes inside that domain capture the effects of 3D structure on travel times. Outside of the development domain nodes are set to a default velocity profile based on iasp91 (Kennett and Engdahl, 1991). We also have a version of the model that is CRUST2.0 with iasp91 in the mantle and core for the region outside of Eurasia and North Africa. This parameterization provides a seamless and extensible model. Expansion beyond Eurasia and North Africa does not require a change in the model parameterization itself, only modification of the velocity structure at previously defined nodes. Further, SNL has incorporated the GRS80 ellipsoid into the model, eliminating the need for the conventional ellipticity correction to travel time predictions.

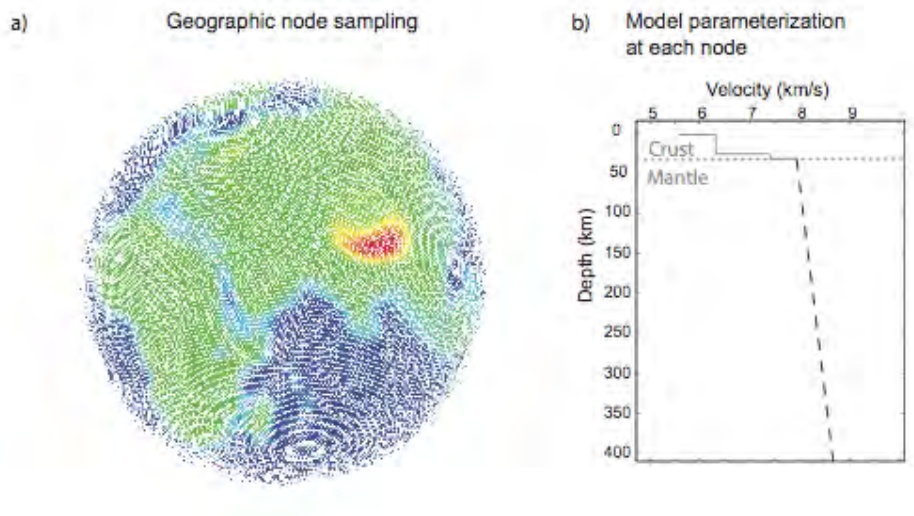


**Figure 1. Seismic Location Baseline Model (SLBM) global parameterization. (a) An example tessellation, with approximately 1° grid spacing. Color is based on approximate Moho depth. (b) An example velocity/depth profile as defined at each node. The mantle portion of the profile is specified by the velocity at the crust/mantle interface and a linear gradient.**

### Travel-Time Calculation, Pn and Sn

The travel-time calculation is based on the method described in Zhao (1993) and Zhao and Xie (1993). This calculation is similar to the widely used approach of Hearn (1984), with an additional term (γ) introduced to account for diving rays that may occur due to a positive velocity gradient with depth and Earth sphericity. The travel time calculation is

$$TT = \sum_{i=1}^{N} d_i s_i + \alpha + \beta + \gamma, \qquad (1)$$

where *d* and *s* are the distance and slowness (taken as 1/mantle MohoVelocity) in each of the *i* segments comprising the great-circle path between Moho pierce points near the event and station, α and β are the crustal travel times at the source and receiver, and γ is a term that accounts for the effect of both mantle velocity gradient and earth sphericity. Figure 2 shows the components of the ray path in a cross section.

We define α as

$$\alpha = \sum_{j=1}^{M} \left[ \sqrt{r_j^2 / v_j^2 - p^2} - \sqrt{r_{j+1}^2 / v_j^2 - p^2} \right], \qquad (2)$$

where *v* and *r* are the velocity and layer radius of the *M* crustal layers from the event to the Moho, and *p* is the ray parameter ($p = 1/v$, *v* evaluated at the ray bottoming depth).

We similarly define β as

$$\beta = \sum_{k=1}^{N} \left[ \sqrt{r_k^2 / v_k^2 - p^2} - \sqrt{r_{k+1}^2 / v_k^2 - p^2} \right], \qquad (3)$$

where *v* and *r* are defined as above for the *L* crustal layers from the station to the Moho. The same *p* is used in both Eqs. (2) and (3). Because the ray bottoming depth is a function of the pierce point, *p* is determined through an efficient, iterative process.

Per Zhao and Xie (1993),

$$\gamma = -\frac{c^2 Xm^3}{24 V_0} \quad , \tag{4}$$

where $X_m$ is the horizontal distance traveled in the mantle, c is a velocity gradient in the mantle that is normalized by the velocity at the crust mantle boundary plus an additional term to account for Earth sphericity (Helmberger, 1973), and $V_0$ is a regional average of Pn velocity over the entire study area.

We introduce spatially varying *c* into the model (Phillips et al., 2007), and we calculate γ by averaging c along each ray. $V_0$ remains an average Pn velocity over the whole model, which allows us to take advantage of linear tomographic inversion methods (see below). Tests suggest that the approximation to $V_0$ introduces negligible travel time error given Pn velocities ranging from 7.5 km/s to 8.3 km/s.

The Zhao (1993) method is applicable to events in the crust, making the approach well suited to nuclear explosion monitoring. However, seismic location algorithms may explore the possibility that an event occurred in the mantle, necessitating a consistent method of travel time predictions for mantle events. The following extends the travel time method to events in the shallow mantle, with the condition that $c^2h^2 << 1$ (h is the bottoming depth of the ray):

$$TT = \alpha + t_m \tag{5}$$

where α is the crustal travel time from the Moho to the station—as defined in Eq. (2)—and $t_m$ is the travel time in the mantle.

$$t_m = \frac{\left[ t_{Moho} \frac{x_m}{d} - \left( \frac{c^2 x_m^2}{24 V_0} \right) \right] \pm \left[ t_{Moho} \left( \frac{x_z}{d(1 + c_m z_m)} \right) - \left( \frac{c^2 x_z^2}{24 V_{0z}} \right) \right]}{2} \tag{6}$$

If the ray leaves the event upwards, then the second term in Eq. (6) is subtracted. If the ray leaves the event downwards, then the second term is added. The travel time is $t_{Moho}$ for a ray traversing the Moho from the event to the point where the ray enters the crust and propagates to the station. The horizontal distance is $x_m$ as measured at Moho radius by a ray that starts at the Moho then travels downward passing through the event and continuing to the station. The term $x_z$ is similar to $x_m$, but the horizontal distance for $x_z$ is measured at the radius of the event. The horizontal distance traveled in the mantle from the event to the Moho pierce point below the station is *d*, as measured at Moho radius. The mantle velocity gradient normalized by average Moho velocity is $c_m$, with the addition of a term to account for earth sphericity (Helmberger, 1973). The depth of the event below the Moho is $z_m$. The average model velocity at the depth of the event is $V_{0z}$.

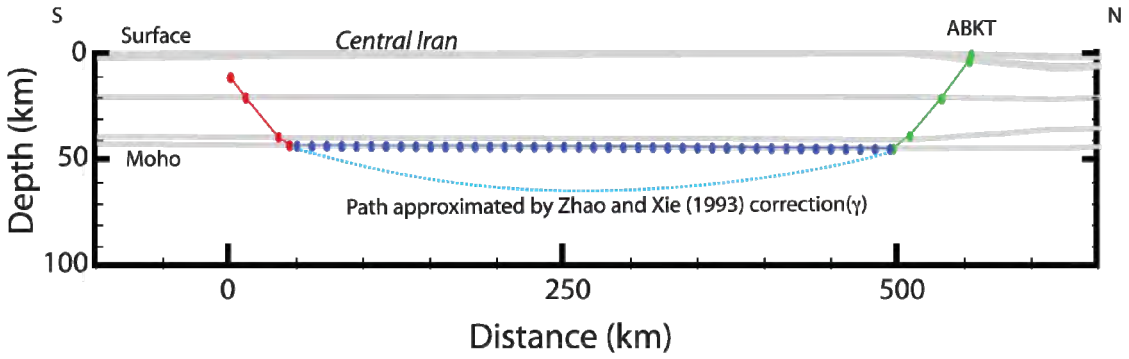


**Figure 2. Cross section extracted from the laterally variable SLBM model. The components of the Pn/Sn travel time calculation are also shown. The blue, red, green, and cyan colors correspond to the first, second, third, and fourth terms of Eq. (1).**

### Travel-Time Calculation, Pg and Lg

Both Pg and Lg phases are trapped in the crust, and both phases exhibit complex waveforms that require hundreds or thousands of rays to model. Further, the first arriving ray with sufficient energy to be observed is dependent on geologic structure and event-station distance. Therefore, it is difficult to physically model the observed travel time using conventional ray techniques. Empirically, Pg and Lg travel at horizontal velocities of approximately 6.0 km/s and 3.2 km/s, respectively, which is suggestive of propagation in the middle crust. Further, event depth can impart a static travel time delay, suggesting a component of propagation from the event to the middle crust then up to the station (for a shallow event). We capture this travel time behavior with a simple approximation, whereby

$$TT = \sum_{i=1}^{N} d_i s_i + \alpha + \beta, \qquad (7)$$

where $d_i$ is the distance traveled in the middle crust in each of $N$ ray segments, α and β propagate the phase to and from the middle crust, respectively. When the source is above the middle crust, then the calculation is almost the same as the Pn/Sn calculation Eq. (1), but the correction for a diving ray is not used. When the source is below the mid-crustal layer, we assume that the ray travels horizontally until Earth sphericity causes the ray to intersect the mid-crustal layer. While this approach by no means captures the physical complexity of Pg and Lg wave propagation, we find that it is suitable for estimating travel time.

The approach described above is suitable for regional travel time calculations. To compute travel times at local distances we approximate the velocity structure with a 1D model (velocity vs. depth) taken at the station of interest. We then use the τ-p approach of Buland and Chapman (1983) to compute travel times in the 1D structure. Using distinct approaches to compute local and regional Pg/Lg travel times necessitates a seamless hand off from one method to the other at the local/regional boundary. For events above the middle crust, we use $\tau$-$p$ if the ray bottoms above the middle crust (Figure 3, left). Mismatch between the local and regional calculations can occur due to differences in the velocity or depth of the middle crust for the local realization (1D) and regional (2D) models. At major tectonic transitions, such as ocean/continent boundaries, the mid-crustal depth and velocity do change rapidly with position, causing the only instances where a mismatch between local and regional travel-time calculations exceeding 0.1 second have been observed.

For events below the middle crust, we compute both the $\tau$-$p$ travel time and the travel time for a ray with slowness determined by the mid-crustal layer. The $\tau$-$p$ calculation is chosen if the ray (1) leaves upward

from the event, *and* (2) the local travel time is greater than the regional calculation. If either condition is not met, then the regional (mid-crustal refraction) calculation is used. These rules for choosing the local or regional calculation produce a piecewise continuous travel-time curve (Figure 3, right). Choosing the longer travel time ensures that the regional ray is (or is close to) geometrical. Figure 3 shows that both the effect of event depth (both locally and regionally) is captured and the effect of laterally varying structure is also captured (e.g., the bends in the regional travel-time curve for the left-hand side of Figure 3).

Tests of travel-time computation time are discussed in Myers et al. (2007). For both Pn/Sn and Pg/Lg computation time is approximately 1 millisecond.

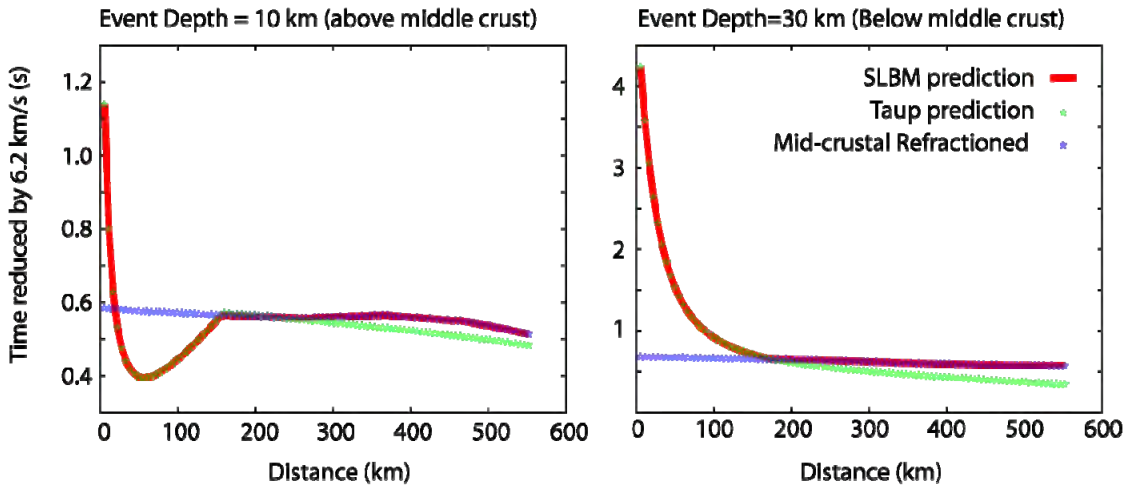


**Figure 3. SLBM Pg travel time as a function of distance (red) for an event above the mid-crustal layer (left) and below the mid-crustal layer (right). In both cases the $\tau$-$p$ travel time is shown in green and the mid-crustal refraction is shown in blue. Rules for choosing the local ($\tau$-$p$) and regional (refraction) travel-time calculation (see text) minimize the discontinuity of the SLBM calculation.**

**Dataset**

The dataset is, arguably, the most-important component of a tomographic study. The dataset must provide the ray-path coverage to constrain the model, and a dataset with small errors in event location and arrival-time measurements helps to improve model resolution. LLNL and LANL have combined ground-truth datasets for this study. Both national laboratories contribute global, regional, and local bulletins (some not widely available), as well as tens of thousands of arrival-time measurements made at the national laboratories. All event locations are evaluated against Bondar et al. (2004) epicenter accuracy criteria, and all picks are evaluated against an error budget that accounts for event mislocation, iasp91 prediction error, and arrival-time measurement error. Observations outside of the 99% confidence bounds for total error are removed. Figure 4 shows the node hit count for Pn rays throughout Eurasia, as well as the resulting tomographic "checkerboard" test for mantle-Moho velocity. The hit count is high (~10,000) throughout the Tethys collision belt (a roughly east-west band from the Pyrenees through the Himalayas). Node hit count to the north of the Tethys collision is also good, with regional bulletins and Soviet peaceful nuclear explosions (PNEs) providing data coverage. Node hit count is poorer south of the Tethys collision, and the starting model will not change significantly. While hit-count is a direct measure of data redundancy, Figure 4b shows that hit-count is also indicative of tomographic resolution.

**Tomography**

The Pn travel time-formula, Eq. (1) lends itself to tomography. The simple algebra results in a linear tomographic equation.

$$\begin{bmatrix} x_1^1 & \cdots & x_N^1 & -\frac{x_1^1 (Xm)^3}{24 V_O X m} & \cdots & -\frac{x_N^1 (Xm)^3}{24 V_O X m} & \sum_{p=1}^{Q} \frac{l_{1p}^1}{v_{1p}} & \cdots & \sum_{p=1}^{Q} \frac{l_{Np}^1}{v_{Np}} \\ \vdots & & & & \ddots & & & \vdots & \\ x_1^K & \cdots & x_N^K & -\frac{x_1^K (Xm)^3}{24 V_O X m} & \cdots & -\frac{x_N^K (Xm)^3}{24 V_O X m} & \sum_{p=1}^{Q} \frac{l_{1p}^K}{v_{1p}} & \cdots & \sum_{p=1}^{Q} \frac{l_{Np}^K}{v_{Np}} \\ & & & & \text{Re}\,gularization & & & & \end{bmatrix} * \begin{bmatrix} s_1 \\ \vdots \\ s_N \\ c_1^2 \\ \vdots \\ c_N^2 \\ a_1 \\ \vdots \\ a_N \end{bmatrix} = \begin{bmatrix} T^1 \\ \vdots \\ T^K \\ \text{Re}\,gularization \end{bmatrix}, \quad (8)$$

where

| | |
|---|---|
| *T* | = travel time |
| *s* | = Pn slowness |
| *x* | = Pn distance (or weight) for each model node |
| *c* | = normalized velocity gradient *v = vo(1+cz)* |
| *Xm* | = length of Pn path |
| *Vo* | = average Pn velocity |
| *v* | = velocity of a crustal layer |
| *k* | = index on K paths (travel-time observations) |
| *i* | = index on N model nodes (mantle path) |
| *j* | = index on N model nodes (crustal path) |
| *p* | = index on Q crustal layers |
| *a* | = scalar adjustment to the crustal slowness stack at each node |

This system of equations results in a stable inversion that does not require excessive iteration to convergence. The tomography equation solves for Pn slowness (*s*), mantle velocity gradient (*c*), and a scalar adjustment to crustal slowness (*a*). Solving for laterally variable mantle gradient is similar to the approach presented in Phillips et al. (2007). A significant difference between the formulation presented here and more-typical Pn-tomography formulations is the introduction of a scalar adjustment to the slowness of the crustal stack, as opposed to a static time term to account for errors in crustal travel time. Our goal is to produce a model that improves prediction of travel time along the whole ray path, and adjusting crustal slowness better meets our goal.

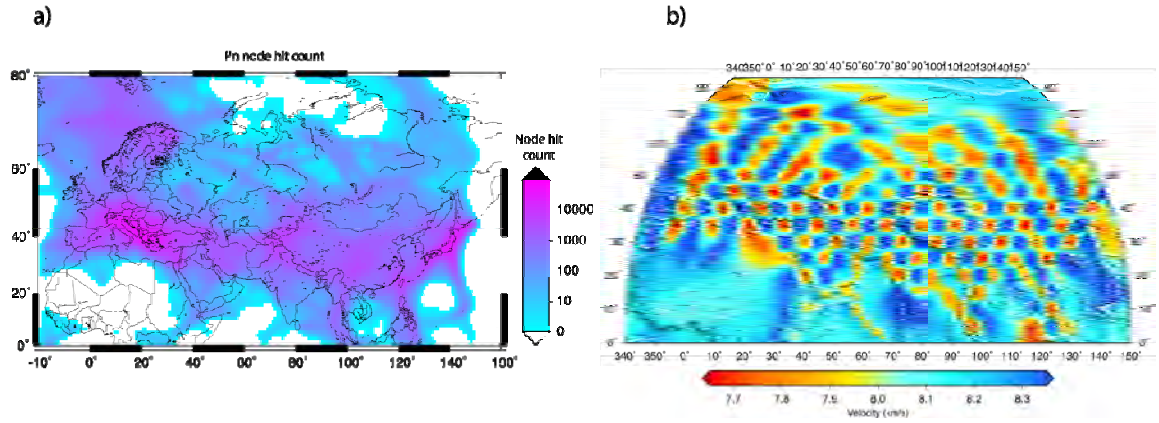


**Figure 4. (a) Node hit count for Pn rays. (b) Tomographic checkerboard test for the Pn dataset.**

Pn tomography results are presented in Figure 5. Across much of Eurasia and North Africa, starting model anomalies are enhanced and anomaly boundaries are altered by tomography. In the Scandinavian and Siberian shields, Pn velocity is higher than the starting model. Tomographic velocity is slower than the starting model across much of East Asia, and velocities are significantly reduced from the starting model in the Pacific subduction zones. Figure 5c shows that crustal velocities are not significantly changed from the starting model. The starting model features variable crustal thickness and laterally varying velocity. Further, smoothness constraints inhibit lateral variation of the crustal correction. Figure 5d shows that the P-wave velocity gradient varies considerably. The strongest gradients are seen in convergent zones, such as the Pacific subduction zones, Himalayan collision, and the Zagros Mountains and the Mediterranean subduction zones. Gradients are low in backarcs and moderate across large portions of the continental interior.

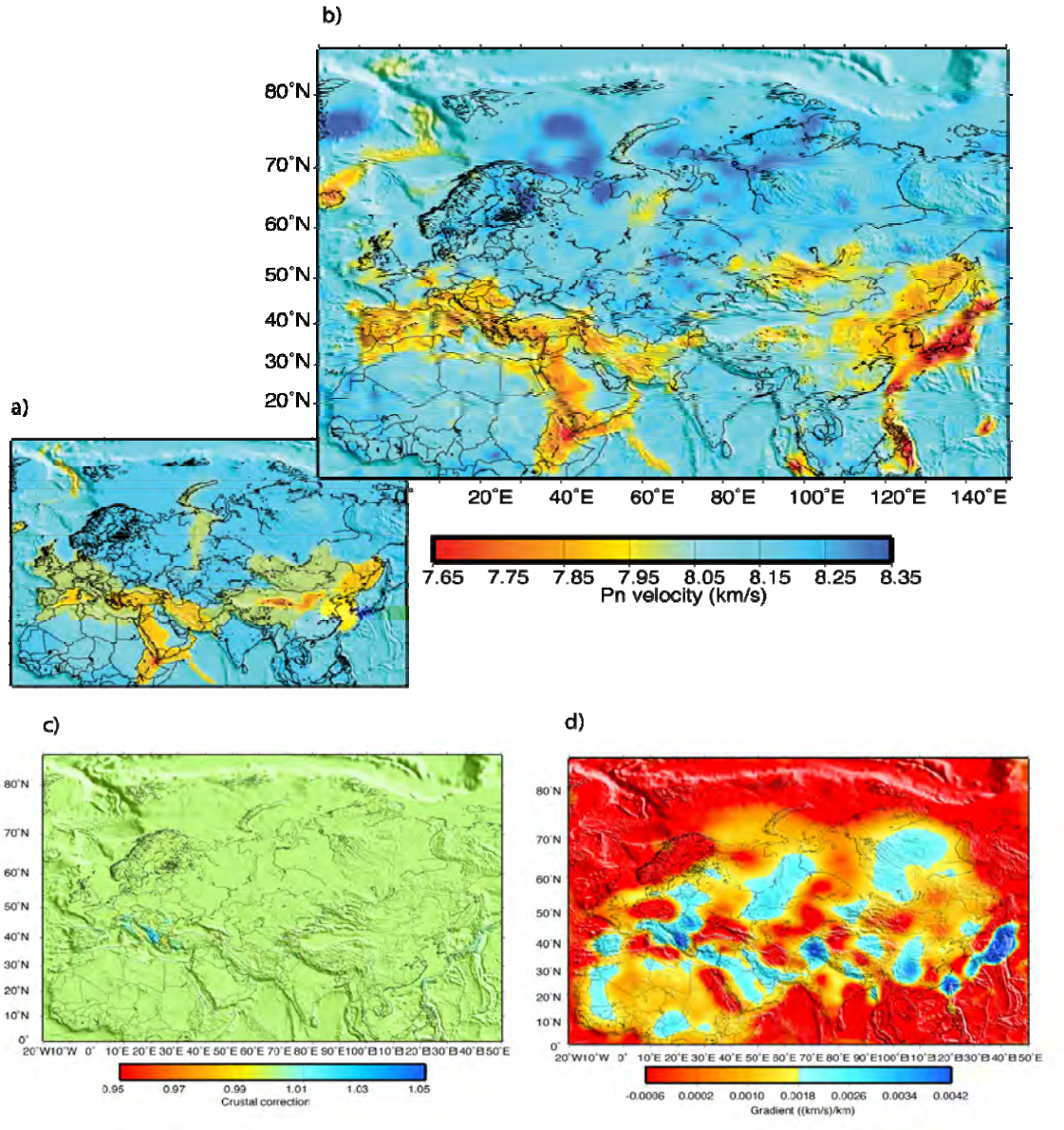


**Figure 5. Tomographic results. (a) Pn starting model. (b) Pn tomography model. (c) Pn tomography crustal correction (*a* in Eq. [8]). (d) Tomographic P-wave velocity gradient. See text for discussion.**

Figure 6 shows improvement of travel time prediction and epicenter estimation using the SLBM tomography. Figure 6a shows that *iasp91* model error (from Flanagan et al., 2007) is significantly higher at regional distance than at teleseismic distance (>~20°). SLBM tomography reduces Pn travel time prediction to approximately 1.25 seconds, making region travel time prediction error similar to teleseismic prediction error. Figure 6b reaffirms that model error does not significantly affect epicenter error when stations surround the event (Bondar et al., 2004). When network azimuthal gap increases, as is likely for a sparse regional network, SLBM tomography measurably improves epicenter accuracy. For azimuthal gap greater than 200°, SLBM improves epicenter accuracy by approximately 30%.

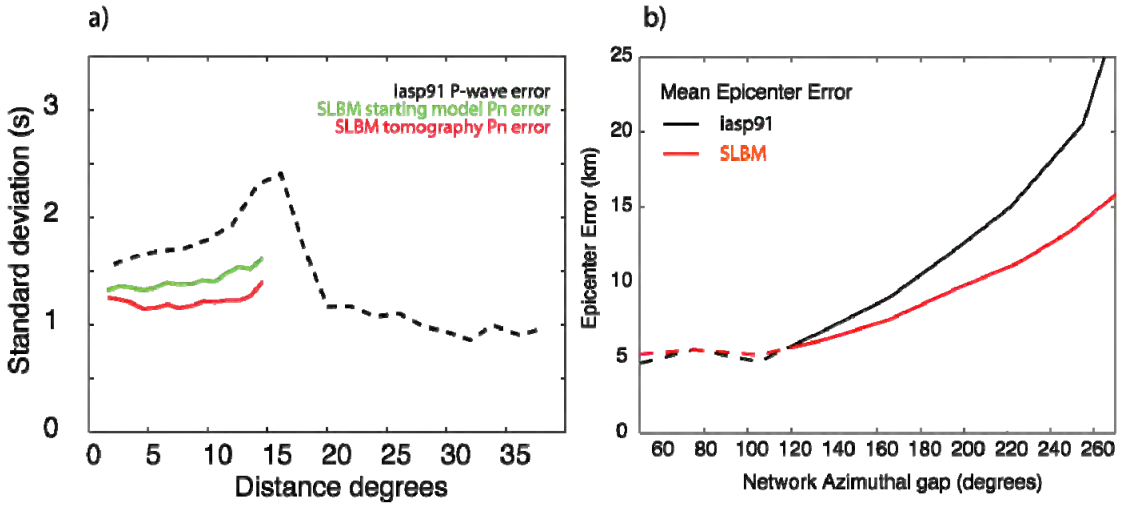


**Figure 6. Pn tomography validation results. (a) Travel-time error vs. event-station distance for the iasp91 (black), the SLBM starting model (green), and the SLBM tomography (red). (b) Mean epicenter error as a function of network azimuthal gap for iasp91 (black) and the SLBM tomography (red). See text for discussion.**

## CONCLUSIONS AND RECOMMENDATIONS

We describe the progress of the SLBM project to date. This project is distinct because it tailors the travel-time prediction algorithm and tomography results for use in routine seismic location algorithms. Emphasis is placed on travel-time prediction accuracy and computational efficiency of regional phases.

The tessellation model parameterization provides seamless global coverage. The use of a tessellation approach also allows fast interpolation of model parameters to extract the great-circle cross section of velocity structure that is needed to compute regional travel times. The current focus of the SLBM effort is Eurasia and North Africa, and model nodes outside of that area are set to a default velocity structure consisting of CRUST 2.0 (Bassin et al., 2000) with iasp91 for the mantle (Kennett and Engdahl, 1991). We note that the model is extensible, and a global calibration effort would entail updating node-centered velocity profiles (by whatever means), which does not require updates to the model tessellation or travel-time codes.

We make use of several approximations that result in a relatively simple algebraic form for travel-time calculations, Eq. (1). The algebraic form lends itself to a linear tomographic formulation, Eq. (8). LLNL and LANL have merged ground-truth databases to form a tomography dataset for this project. Pn ray coverage across Eurasia and North Africa is excellent (Figure 4). Pn tomographic results (Figure 5) are in general agreement with studies of the Eurasian subregions.

Tests of Pn tomography travel-time prediction show that Pn model error is reduced to approximately 1.25 seconds, and the error is relatively constant (stationary) with distance. Reducing regional travel-time prediction error to approximately the level of teleseismic error (~1 second) allows the joint use of regional and teleseismic data in event location without degrading epicenter accuracy. Epicenter accuracy improves by approximately 30% (relative to iasp91) for large network azimuthal gaps (i.e., when the stations are to one side of the event).

Tomographic efforts for Pg, Sn, and Lg are underway.

## ACKNOWLEDGEMENTS

This project would not be possible without the full support of Leslie Casey in the Department of Energy office of NA22. Steve Myers also wishes to thank Dave Harris for daily interactions and general technical discussions.

## REFERENCES

Bassin, C., G. Laske, and G. Masters (2000). The current limits of resolution for surface wave tomography in North America, *EOS Tran.s AGU* 81: F897.

Bondar, I., S. Myers, E. R. Engdahl, and E. Bergman, (2004). Epicenter accuracy based on seismic network criteria, *Geophys. J. Int.* 156: 483–496.

Buland, R. and C. H. Chapman (1983). The computation of seismic travel times, *Bull. Seismol. Soc. Am.*, 73: 1271–1302.

Flanagan, M.P., S.C. Myers, and K.D. Koper (2007). Regional travel-time uncertainty and seismic location improvement using a three-dimensional a priori velocity model, *Bull. Seismolog. Soc. Am*. 97: 804–825.

Hearn, T. M. (1984). Pn travel times in southern California, *Jour. Geophys. Res*. 89: 1843–1855.

Helmberger, D. V. (1973). Numerical seismograms of long-period body waves from seventeen to forty degrees, *Bull. Seism. Soc. Am*. 63: 633–646.

Kennett, B. L. N. and E. R. Engdahl, (1991). Traveltimes for global earthquake reference location and phase identification, *Geophys. J. Int.* 105: 429–465.

Myers, S. C., S. Ballard, C. Rowe, G. Wagner, M. Antolik, S. Phillips, A. Ramirez, M. Begnaud, M. Pasyanos, D. Dodge, M. Flanagan, K. Hutchenson, G. Barker, J. Dwyer, and D. Russell (2007). Tomography and methods of travel-time calculation for regional seismic location, in *Proceedings of the 29th Seismic Research Review: Ground-Based Nuclear Explosion Monitoring Technologies*, LA-UR-07-5613, Vol. 1, pp. 414–423.

Pasyanos, M. E., W. R. Walter, M. P. Flanagan, P. Goldstein, and J. Bhattacharyya (2004). Building and testing an a priori geophysical model for western Eurasia and North Africa, *Pure App. Geophys*. 161: 235–281.

Phillips, W. S., M. L. Begaud, C. A. Rowe, L. K. Steck, S. C. Myers, M. E. Pasyanos, and S. Ballard (2007). Accounting for lateral variations of the upper mantle gradient in Pn tomography studies, *Geophys. Res. Lett*. 34: doi:10.1029/2007GL029338.

Zhao, L.-S. (1993). Lateral variations and azimuthal isotropy of Pn velocities beneath Basin and Range province, *J. Geophys. Res*. 98:109–122.

Zhao and Xie (1993). Lateral variations in compressional velocities beneath the Tibetan Plateau from Pn traveltime tomography, *Geophys. J. Int*. 115: 1070–1084.

# ON THE CTBT MONITORING POTENTIAL OF USING LG-PHASE ARRIVAL TIMES AT LOCAL AND REGIONAL DISTANCE RANGES

Vladimir I. Pinsky[1], Eystein S. Husebye[2], Tatiana S. Matveeva[2], and Yury V. Fedorenko[3]

Geophysical Institute of Israel[1], Bergen Center of Computational Science, UNIFOB/UoBergen, Norway[2], Polar Geophysical Institute, Apatity, Russia[3]

Sponsored by University of Bergen and Geophysical Institute of Israel

## ABSTRACT

The prominent Lg wave is nearly always observed at local and regional distances. It is a surface wave propagating with almost constant group velocity around 3.5 km/s over a vast distance range of hundreds to thousands of kilometers. Thus, Lg propagation should in principle simplify epicenter location schemes, based on relative travel time equations. In our ongoing efforts to accomplish this we computed Hilbert or STA-envelopes and showed that in many recordings from Fennoscandia and Central Europe the Lg group velocities measured using the envelope peak arrival times are remarkably consistent. However, they tightly concentrate around 3.4 km/sec for the Baltic shield of Fennoscandia and around 3.2 km/sec for the much younger crust of Central Europe. These Lg picks were subsequently used in the Pinsky (2008) relative time location algorithms of "group beamforming" and "probabilistic beamforming" for refined epicenter locations in Balticum.

## OBJECTIVES

An often prominent phase arrival in local and regional seismic event recordings is the Lg-wave which propagates in the crustal wave guide. It was first reported in the seismological literature in 1952 by Press and Ewing. Analysis of Lg-records is popular for both ML-magnitude estimation and mapping attenuation (the Q-parameter) in the crust. Another obvious application of Lg-phase arrivals would be enhanced epicenter locations in view of the relatively high signal frequency of this phase and its slow propagation velocity at 3.5 km/sec.

To improve event locations we need mapping of the 3D velocity structure of the Earth and to collect so-called ground truth (GT) events for testing the adequacies of such approaches. Such models and GT-events are at present only available for limited areas. Hence, applying erroneous velocity models may result in biased epicenter solutions and, thus a remedy to avoid complicated 3D velocity models is an attractive challenge. Our approach here is for so-called model independent location schemes using a model of relative travel times and assuming homogeneous or simple 1D velocity environments for station clusters. An approach that is similar in principle to generalized beamforming has been introduced by Kværna and Ringdal (1996) for real-time seismic monitoring. These methods are attractive as they seemingly minimize velocity uncertainties in the Earth's interior but such uncertainties may penetrate into velocity models when we increase sizes of networks and cluster array apertures. In the scheme used in this study such uncertainty measures are incorporated in the final epicenter estimates (Pinsky, 2008). Below we briefly sketch the actual location approaches used.

## RESEARCH ACCOMPLISHED

### 1. Epicenter Location Method

Let us introduce "pseudo-slowness" $\boldsymbol{\beta}$ as a coefficient between the travel time difference $\boldsymbol{\tau_k - \tau_j}$ of a given seismic phase (P, S or Lg) for a pair of stations $\boldsymbol{Y}_k$ and $\boldsymbol{Y}_j$ and distance $\boldsymbol{R}$ difference $\boldsymbol{D_{kj}}$ from a given point (source) X on the Earth's surface. Then $\boldsymbol{D_{kj}}(X)=\boldsymbol{R_k(X) - R_j(X)}$ and we get the travel time difference equation:

$$[\tau(X,Y_k) - \tau(X,Y_j)] = \beta D_{kj}(X). \quad (1)$$

Then a travel-time equation for the pair of stations looks like:

$$t_k - t_j - [\tau(X,Y_k) - \tau(X,Y_j)] = t_k - t_j - \beta D_{kj} = \varepsilon_{kj}(X). \quad (2)$$

Equation 2 constitutes a "theoretical" stage of knowledge about arrival time differences $t_k - t_j$ in terms of Tarantola (2005). Measuring uncertainty $\boldsymbol{\varepsilon_{kj}}$ using a bell-shape "theoretical" function Ω (Pinsky, 2008), the robust location procedure yields in maximizing a probability density function (PDF) of the shape

$$F(X) = \sum w_{kj}\Omega(\varepsilon_{kj}(X)/\sigma), \quad (3)$$

where σ is a scaling coefficient, $w_{kj}$ is a weighting factor, and $\boldsymbol{X}$ is the unknown source. As an example of the bell-shape function Ω one may use the Gaussian: $\exp(-x^2/2)$ as in (Lomax, 2005) or a cosine function: $\cos(x)$, $(-\pi < x < \pi)$ as in (Pinsky, 2006).

From Equation 3 and using the notion of "pseudo-slowness" we get two location schemes avoiding previously known deterministic travel time models $\boldsymbol{\tau}$, namely the "group beamforming" and "probabilistic beamforming."

#### 1-A. *Group Beamforming.*

Group Beamforming (GB) is based on splitting a network into M sub-networks $W_m$ ,m=1,… M in which the pseudo-slowness $\boldsymbol{\beta} = b_m$ is a constant, when both stations of the pair belong to $W_m$. GB is achieved by jointly maximizing F(X)=F(X,B) in Equation 3 relative source coordinates $\boldsymbol{X}$ and the vector of pseudo-slowness values: $\boldsymbol{B}=\{b_1, b_2,\ldots, b_M\}^T$. For this purpose we are using direct grid-search over parameters $\boldsymbol{X}$ and $\boldsymbol{B}$. Because model parameters $\boldsymbol{B}$ are found jointly with event coordinates $\boldsymbol{X}$, the algorithm doesn't require a priori exact knowledge of the Earth model. If parameter vector $\boldsymbol{B}$ is considered known a priori from some Earth model or observations it will serve a role of parameter in PDF of $\boldsymbol{X}$ described by Equation 3. GB location fits well to the concept of Lg-waves energy propagation with constant velocity at large distance ranges. For example, let us presume that our Lg picks for Event #4 are subdivided in two groups of stations: one in Fennoscandina and another in Continental Europe having different average velocities of 3.2 km/s and 3.4 km/s, respectively. Application of the GB in such a case is

straightforward. We may also use the scheme with two constant pseudo-slowness parameters: 1/3.2 and 1/3.4 respectively.

**1-B.** ***Probabilistic Beamforming.***

Assume uncertainty of pseudo-slowness is described by the pdf ***f(x)*** for all station pairs. Then Equation 3 transforms into probabilistic beamforming (PB) scheme :

$$F(X) = \sum w_{kj} \int f(x)\Omega\{[t_k - t_j - xD_{kj}(X)]/\sigma\}dx \qquad (4)$$

Pinsky (2008) considers several variants of the PB formulation above. Here we shall limit ourselves to the case when the pseudo-slowness $\boldsymbol{\beta}$ is equally distributed in the interval ($\beta_1$, $\beta_2$) and does not take values outside this interval. Then the PDF of the source location Eq. (3) becomes:

$$F(X) = \sum_{k,j} w_{kj} \int_{b_1}^{b_2} \Omega[(t_j - t_k - xD_{kj})/\sigma]dx \qquad (5)$$

For Gausian ''theoretical" function $\Omega$ (x) = exp(-$x^2$/2 ) eq. (4) will transform to

$$F(X) = \sum_{k,j} \frac{w_{kj}}{D_{kj}} (F_N[(t_j - t_k - \beta_1 D_{kj})/\sigma] - F_N[(t_j - t_k - \beta_2 D_{kj})/\sigma]) \qquad (6)$$

where *FN(x)* is a standard normal probability distribution function. For the cosine "theoretical" function $\boldsymbol{\Omega(x)}$ = cos(***x***) eq.(4) will transform to:

$$F(X) = \sum_{k,j} \frac{w_{kj}}{D_{kj}} [\sin(D_{kj}(\beta_2 - \beta_1)/2)\cos(t_j - t_k - D_{kj}(\beta_1 + \beta_2)/2)] \qquad (7)$$

Choosing GB or PB depends on the case under consideration. The hybrid GB/PB schemes, when different PDFs are used for different station groups, are also practical. However, splitting the network might not be advantageous, because this way we reduce essentially the number of pairs and weaken constraints provided by the station pairs on the "opposite" sides of the epicenter. Hence, for using GB we need a good argument for splitting the network. In Pinsky (2008) for accurate location of nuclear tests the PB was used, because background experiments showed it to be more accurate. Choosing the pseudo-slowness range ($\beta_1$, $\beta_2$) depends on the range of epicenter-station distances. For example, if only regional+ local stations are involved, then for the P phase the range should not exceed 1/8.5 s/km from above and 1/6 s/km from beneath. Below we shall provide PB locations for four Baltic events using bulletin P arrivals and GB for event #4 using Lg picks.

## 2. Lg-Feature Extraction from Waveform Data

A prominent feature in SP seismograms at local and regional distances is the Lg-wave, which arrives well behind the Sn-wave train. Among the first to report on such observations were Press and Ewing (1952), who interpreted it as a surface shear wave propagating in the crustal wave guide. Their study triggered many investigations aiming at better understanding of Lg-wave propagation, amplitude decay with distance, crustal Q and so forth (e.g., see Nuttli, 1973; Campillo, 1990; Hansen et al., 1990; Mendi et al., 1994; Fedorenko et al., 1999; and Husebye et al., 2002). Despite the many efforts in modelling and understanding Lg-propagation, the practical usages of this `phase' are little explored. In particular the T=R/3.5+3.5 travel time line for the peak of energy propagation at regional distances may be used for robust epicenter locations as a supplement to the P arrival times in the envelope based location scheme by Pinsky, (2000). Also Husebye et al. (1998) reported Lg-phase arrival times in a consistent manner. From mode theory we have that the first and the next higher Lg-modes in the frequency range of 0.5 - 2.0 Hz have velocity minima at 3.40 +/- 0.10 km/sec so we intuitively expect that the energetic part (or peak amplitude) of the Lg-wave will travel with a group velocity around 3.40 km/sec as actually observed ( Panza and Calcagnile, 1974 and Mykkeltveit and Husebye,1981). In short, we will attempt to measure the Lg-phase arrival time at its peak amplitude in the envelope of the original waveform record. The envelope formation from the original waveforms are a smoothing operation and hence peak amplitude pickings can hopefully be made consistently which is otherwise not feasible using the original waveform records.

The first task here is that of checking whether a signal is present or not. This is achieved through a signal detector operation of the form STA/LTA > TH where STA is a short-term average (e.g., a root mean square [RMS] trace

power estimate) and LTA is the long term average defined in a similar manner. The threshold TH is given a value around 4.0 thus ensuring a moderate false alarm rate (Fedorenko et al., 2008). Anyway, the STA-operation transforms the original, pre-filtered waveform trace into a smooth envelope trace (a simplified form of the Hilbert transform operation) and will always be available as part of the signal detection operation. Our idea is to relate Lg-arrival time picks to the envelope peak amplitudes in the STA-envelopes usually identical to each other. After pre-filtering the original traces in a signal bandwidth around 0.5–2.0 Hz and resampling with a rate as low as 2 s/sec so we interpolate for picking times at the nearest 10th of a second. This is a simple and easy waveform operation to perform even in near real time. After experimenting with different envelopes and parameter settings we choose the STA-window length equal to 2.0 sec and updating every 0.5 sec for smoothing operation (example in Figure 1). For Lg-waves it is unclear whether their origin time is focal-depth dependent—at best weakly in view of their 'multiple reflections' generation mechanism. In the epicenter location schemes outlined above, we treat P- and Lg-arrival times independently thus avoiding this possible bias. It remains to demonstrate that introducing invariant and possibly focal depth independent Lg-phase travel times we may obtain enhanced source locations. We try to answer these questions through reanalysis of 4 Baltic region earthquakes. Regrettably, we have only Lg-recordings for the second Kaliningrad earthquake of 21 September 2004, which have been studied in detail by Husebye and Mantyenemi (2005) and Gregersen et al. (2007). Seemingly, up to 2005, only waveforms sampled at 1 s/sec were stored by IRIS and ORFEUS and similar agencies.

## 3. Events used in the Baltic Location Experiment

The four events used in the analysis are listed in Table 1 and are to our knowledge the largest earthquakes in the Baltic region since 1950. The two most recent ones took place close to the Russian city Kaliningrad (formerly Kønigsberg) in 2004, and despite a moderate magnitude of 5.0, caused considerably local damages (Gregersen et al, 2007; Husebye and Mantyenemi, 2005). These two earthquakes are of particular interest because 1) there was some dispute on exact epicenter location among the authors of the Gregersen et al. paper and 2) an abundance of digital records were available from many stations within a distance range of 2000 km for Event #4 (see Figure 2). The latter makes it feasible to test the relative merits of including Lg-readings in the epicenter location process. A puzzling feature here is that the two Kaliningrad earthquakes are often given nearly the same magnitude value, but the first one hardly produced any Lg-recordings.

The earthquake off-coast of Estonia was given much attention in 1976 as some newspapers suggested that this was an accidental nuclear explosion (Slunga, 1979). The one in 2002 to the south of Gotland (earthquake or explosion undecided), is also relatively strong ensuring many station reports but again hardly any digital records available. For the four events analysed, we have accepted P-arrival time readings as they appear in the International Seismological Centre (ISC) bulletins. The Swedish network readings were obtained from the local bulletin, Seismological Laboratory, Uppsala University. For the 1976 event, no waveform records were available but a relocation experiment using a better travel-time table and a different location scheme may be interesting. The same applies to Events #2 and #3 because no Lg-recordings were available. As mentioned, Event #4 is the exception with many Lg-recordings and corresponding Lg arrival-time data. This event is also by far the most interesting because, as far as we know, we are among the first to attempt using Lg-times in estimating the epicenter location for an earthquake.

## 4. Epicenter Relocation of Four Baltic Events using the Model-Free PB Method

First we used P picks from the ISC bulletins to relocate four Baltic events using the probabilistic beamforming scheme in the form of Equation 7. The parameters used for the location are: $\beta 1 = 1/100$ s/km, $\beta 2 = 1/7.5$ s/km, $\sigma = 2.5$ s.

The results of location are summarized in the Table 1. The Error column denotes the geometrical average of the two axes of the error ellipsoid estimated in the ISC, which appear to be too optimistic, because the scatter of epicenter location by different agencies essentially exceeds the error value. For example, for Event #4, the latitude varies from 54.7˚ to 55.04˚ and longitude varies from 19.08˚ to 20.19˚ (Gregersen et al., 2007). Besides, the two Kalinigrad events are most probably collocated; however, the distance between the ISC epicenter determinations is equal to 5 km. In this sense our PB locations, though falling out of the confidence area possess somewhat intermediate reasonable values.

## 5. Lg picking for Event N4

We took Lg picks obtained from the waveforms of Event N4 recorded at N=16+26+9=51 stations located in Europe, Scandinavia, and Finland, respectively (see Figure 2). The picks are presented in Figure 3 together with the travel-time curves. Occasionally, we picked STA-maxima (outliers) for the Sn-phase, but this is easily controlled by requiring the maximum reading to be within the 3.1–3.6 km/sec velocity window. Lg travel times are obtained as the differences between arrival times and the source origin time. Tables 2 and 3 document Lg pick velocities using location and origin time obtained by ISC and demonstrate together with the Figure 3 data, amazing stability of the velocity within different sub-networks. However, Lg velocities to the South of the Epicenter (Table 3) and to the North (Table 4) differ consistently and close to the mean values V=3.21 and V=3.38 km/s, respectively. The mean value difference of 0.17 km/s exceeds two standard deviations 2σ=0.16 km/s between them. The discrepancy is apparently seen also in Figure 3. Several outliers are also observed, such as at station KIF, which is 1,582 km away. Special effort to remove outliers for the best Lg velocity estimation is reflected in the tables.

**Table 1: Earthquakes in the low-seismicity area Baltic subjected to relocations using PB**

| Event | Date y/m/d | O.Time (h/m/s) | Latitude | Longitude | Error km | Deviation km | Nsta | Ml | Algorithm (Agency) |
|---|---|---|---|---|---|---|---|---|---|
| 1 | 1976/10/25 | 08/39/44.69 | 59.2030˚ | 23.5818˚ | 6.4 | 6.95 | 70 | 4.4 | ISC |
| | | | 59.2600˚ | 23.5800˚ | | | 70 | | PB |
| 2 | 2002/12/18 | 21/14.15.68 | 56.0585˚ | 18.0511˚ | 5.1 | 14.6 | 58 | | ISC |
| | | | 55.9324˚ | 18.0110˚ | | | 58 | | PB |
| 3 | 2004/09/21 | 11/05/03.00 | 54.8300˚ | 20.0400˚ | 2.34 | 5.8 | 544 | | ISC |
| | | | 54.8700˚ | 20.0900˚ | | | 242 | | PB |
| 4 | 2004/09/21 | 13/32/28.51 | 54.8254˚ | 19.9740˚ | 2.25 | 7.6 | 380 | | ISC |
| | | | 54.8854˚ | 20.0340˚ | | | 380 | | PB |

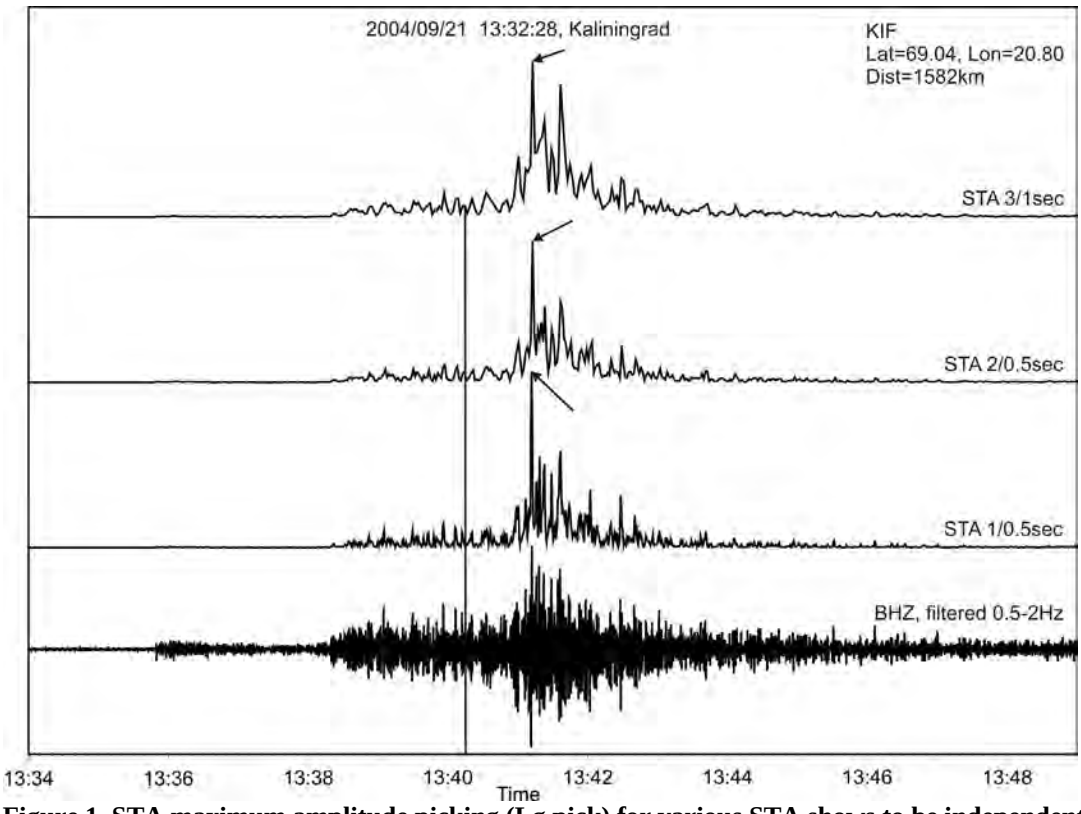


**Figure 1. STA maximum amplitude picking (Lg pick) for various STA shows to be independent of smoothing window parameters (duration/shift ) at station KIF. However, the Lg pick is anomalously late here (see also outlier point in Figure 3 at a distance of 1,582 km). The vertical line is the expected arrival time for the Lg phase in assumption that Lg velocity is 3.4 km/s.**

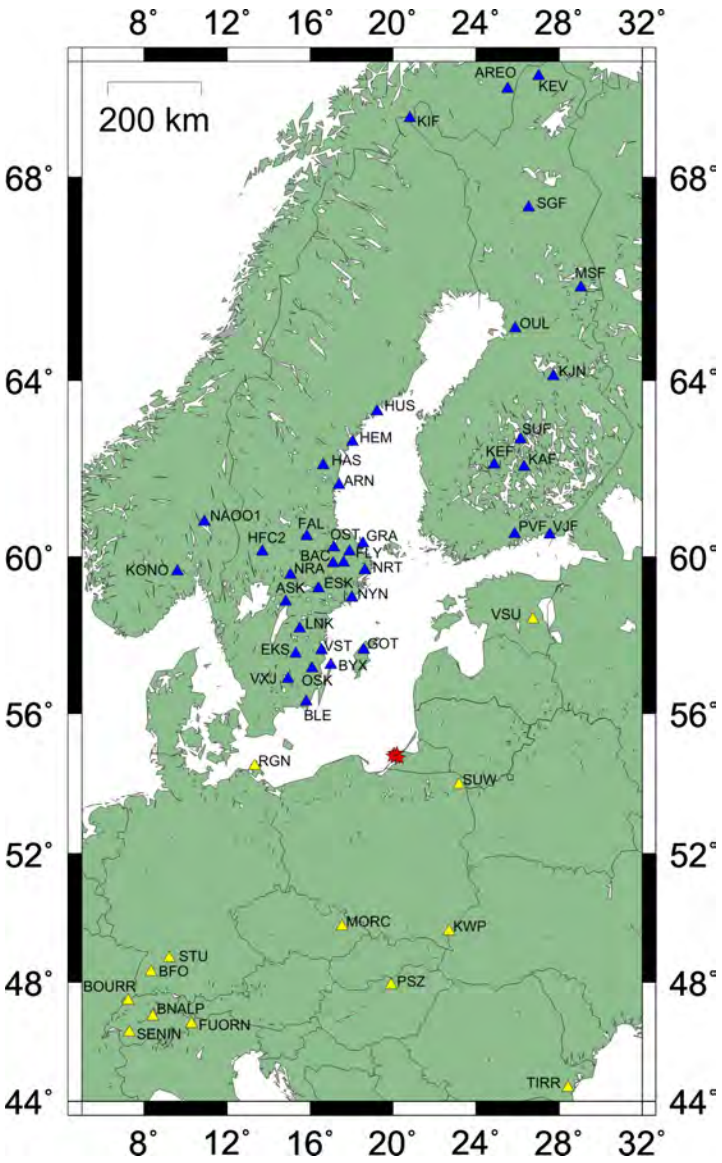


**Figure2. Scandinavian (SCAN), Finland (FIN) and Continental (EUR) group of stations ▲ used for Lg pickings of event #4. The set of stars depict different locations of the event.**

## 6. Model-Free PB and GB Relocations of Event N4 using Lg Picks

The relocations using Lg picks are summarized in Table 4, where PB of Equation 7 and GB with cosine target function $\Omega = \cos(x)$, $(-\pi < x < \pi)$ are applied for different network configurations comprised of EUR, SCAN, and FIN networks. For PB we have taken the pseudo-slowness interval determined by V1 =1/β2=2.5 km/s, V2 =1/β1= 4.2 km/s and the scatter parameter σ=4 s. For GB velocity, the lower limit was determined as V1= 1/β2=2.5 km/s and was changed incrementally in a grid-search with the step dV=0.1 km/s, NV=15, σ=4 s.

The latitude-longitude grid was 0.4˚X0.4˚ with a 0.02˚ interval. The locations obtained by GB in EUR+SCAN+FIN and EUR alone deviate from the ISC reference Lat=54.8254˚ Long=19.9740˚ by 8.5 and
11 km respectively, thus remaining within the latitude-longitude intervals given by epicenter locations from different agencies using P arrivals in the ISC bulletin (see above). As the result of the grid-search we get the pseudo-apparent

Lg velocity for each of the sub-networks as 3.1, 3.5, and 3.5 km/s, respectively at the maximum of the PDF (see Figure 4). These velocities slightly differ from the 3.2, 3.38, and 3.40 km/s velocities obtained as the result of the direct Lg group velocity computation. Using the Gaussian target function Ω =exp(-x2/2) provided a close and similar result.

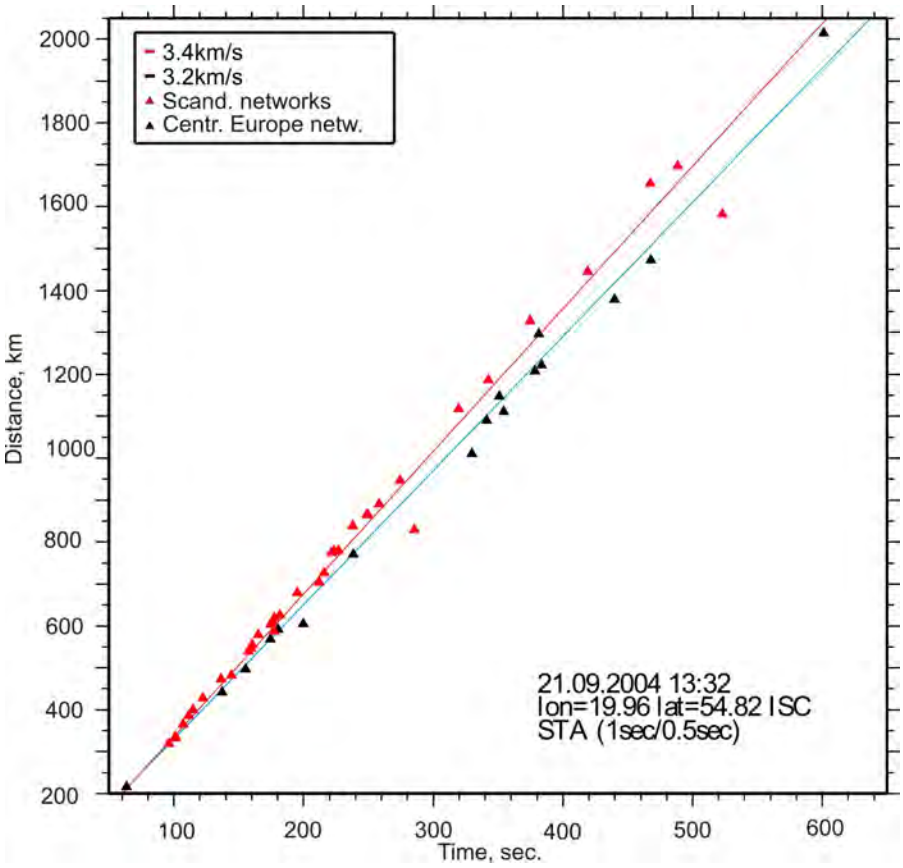


**Figure 3. Lg picks and the corresponding travel-time lines determined from the Fennoscandia and Central Europe groups of stations. The ISC epicentre location and origin time of the Event #4 are taken as reference for the travel time and distance calculations.**

**Table 2. Mean Lg group velocities and standard deviations relative to locations by different agencies for stations South to Epicenter. * notes that calculations were made excluding the outliers with velocities (for SUW and TIRR > 3.4 km/sec, for KWP and STU < 3.1 km/sec,)**

| Agency | Mean Velocity, km/sec | Std. deviation km/sec | Mean Velocity*, km/sec | Std. deviation* km/sec |
|---|---|---|---|---|
| IGF IASP | 3.23 | 0.12 | 3.23 | 0.07 |
| IGF AK | 3.24 | 0.11 | 3.23 | 0.07 |
| EMSC | 3.22 | 0.10 | 3.22 | 0.06 |
| ORFEUS | 3.17 | 0.14 | 3.15 | 0.09 |
| NEIC | 3.20 | 0.15 | 3.18 | 0.09 |
| ASS | 3.21 | 0.12 | 3.20 | 0.07 |
| GSRAS | 3.21 | 0.10 | 3.21 | 0.06 |
| MOS | 3.19 | 0.09 | 3.19 | 0.06 |
| ISC | 3.17 | 0.13 | 3.16 | 0.08 |
| IGF | 3.22 | 0.11 | 3.21 | 0.06 |
| Mean Instrumental | 3.21 | 0.11 | 3.20 | 0.07 |

**Table 3. Mean Lg phase velocities and standard deviations relative to locations by different agencies for stations North to Epicenter. * notes that calculations were made excluding the outliers with velocities (for KONO < 3.0 km/sec, AREO > 3.5 km/sec)**

| Agency | Mean Velocity, km/sec | Std. deviation km/sec | Mean Velocity*, km/sec | Std. deviation* km/sec |
|---|---|---|---|---|
| IGF IASP | 3.48 | 0.13 | 3.50 | 0.06 |
| IGF AK | 3.41 | 0.12 | 3.42 | 0.07 |
| EMSC | 3.36 | 0.12 | 3.38 | 0.08 |
| ORFEUS | 3.33 | 0.14 | 3.34 | 0.09 |
| NEIC | 3.34 | 0.13 | 3.36 | 0.09 |
| ASS | 3.35 | 0.13 | 3.36 | 0.08 |
| GSRAS | 3.40 | 0.12 | 3.42 | 0.07 |
| MOS | 3.30 | 0.12 | 3.32 | 0.08 |
| ISC | 3.32 | 0.13 | 3.33 | 0.09 |
| IGF | 3.36 | 0.13 | 3.38 | 0.08 |
| Mean Instrumental | 3.37 | 0.13 | 3.38 | 0.08 |

**Table 4**: **Relocation of Earthquake N4 using Lg picks, PB and GB algorithms**

| Algorithm | Network | Lat | Lon | $V_{EUR}$ | $V_{SCAN}$ | $V_{FIN}$ | PDF F(X) |
|---|---|---|---|---|---|---|---|
| GB | EUR+SCAN+FIN | 54.83˚ | 20.1˚ | 3.1 | 3.5 | 3.5 | 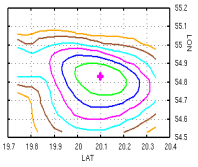 |
| GB | EUR | 54.83˚ | 20.14˚ | 3.1 | | | 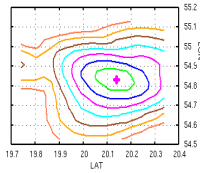 |
| PB | EUR+SCAN | 54.89˚ | 20.02˚ | | | | 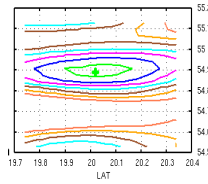 |
| PB | EUR | 54.83˚ | 20.04˚ | | | | 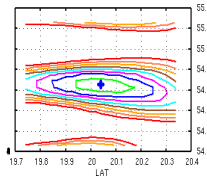 |

The epicenters given by PB are closer to the ISC solution, deviating by 8.5 and 4.4 km from the reference location, though the PDF patterns look worse due to the close local maxima and the elongated E-W shape. Note that using EUR stations alone provide better results, probably because of problematic association of stations from the different sub-networks. The SCAN and FIN networks alone or together are not useful for the epicenter location due to the poor azimuth constrain they provide.

## CONCLUSIONS AND RECOMMENDATIONS

The idea of this small chamber study was testing some alternative methods of earthquake location using a set of four interesting events, which occurred in Baltic region. On the other hand it was intriguing to verify how linearity of travel time of the Lg energy peak propagation would contribute to the earthquake location. There was only one event, the second Kaliningrad earthquake in the set, from which the Lg arrival times could be picked from the waveforms. However, even in this modest effort we obtained some interesting results.

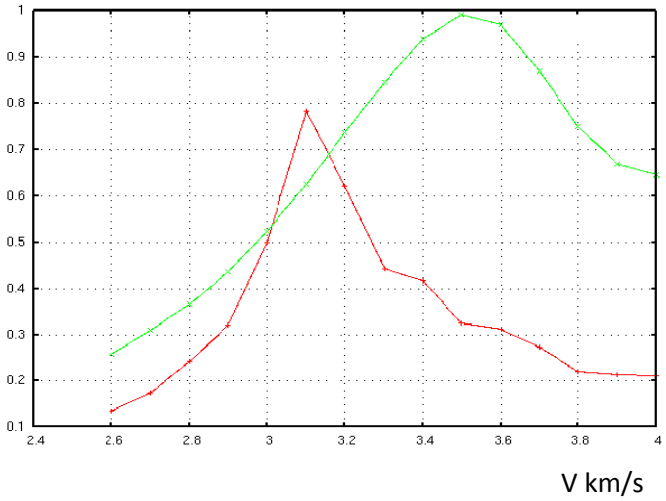


**Figure 4. Probability density distribution functions F(X,B) of apparent velocities for the EUR (red) and SCAN (green) groups of stations respectively. The epicenter X: Lat=54.83˚ Lon=20.1˚ is fixed.**

For epicenter location we have chosen the model-free robust GB and PB methods of Pinsky (2008), who demonstrated their effectiveness for a large set of nuclear test locations in regional and teleseismic distance ranges. The so-called pseudo-slowness notion introduced in PB and GB helps to accommodate uncertainties of velocity model when an explicit 3D model is not available. Therefore, we assumed that these methods might be helpful in large-scale heterogeneous conditions observed in the Baltic area. Besides, these relative time location methods are best suited for the case of travel times close to linear, as demonstrated by the Lg phase for Event #4. As the result of application of the PB to the P arrivals reported in the ISC bulletin for the four events we got epicentre locations which are reasonable and comparable to the reports of different agencies, yet out of the confidence area determined from the too optimistic Gaussian assumption.

Analysis of the Lg energy propagation revealed two apparent linear branches of the travel times as determined by more than 50 picks of the event: one for the continental stations with velocity V=3.2±0.07 km/s and the other for Scandinavian shield (Sweden and Finland) with V=3.38±0.08 km/s. Hence, the GB application, based on splitting the network into several sub-networks was straightforward as applied to the Lg picks and showed satisfactory results. The pseudo-apparent velocities determined independently as the result of the grid-search appeared rather close to those from the direct computation mentioned. The PB was applied to the Lg picks either and though the results are closer to those of the ISC, the solution looks less stable, because the assumption used about the even distribution of the pseudo-slowness is violated in this case. Note that the ISC epicentre location used as a reference is not a ground truth. Moreover, it gives almost one σ less Lg velocity than the average for velocity data from both Fennoscandian and Central European networks.

For complimenting the study we plan and recommend to 1) increase the waveform data set by available events; 2) elaborate on methods for jointly using P picks with the Lg picks for enhanced location; 3) consider hybrid PBGB methods; and 4) provide 3D modelling of travel times for events under consideration and the corresponding location experiments.

## ACKNOWLEDGEMENTS

We thank R. Bødvarsson for providing us with the Swedish network local bulletin and waveform data and Pasi Lindblom for the Finnish seismic network waveforms. The maps in this paper were prepared using GMT version 3.0 developed by Paul Wessel and H.F. Smith.

## REFERENCES


Campillo, M., (1990). Propagation and attenuation characteristics of the crustal phase Lg. *Pure Applied Geophysics* 132: 1–9.

Fedorenko, Yu., V. and Husebye, E.S., (1999). First break – automatic phase picking of P-and S-onsets in seismic records, *Geophys. Res. Lett.* 26: 3249–3253.

Fedorenko, Yu.,V., Husebye, E. S., and Matveeva, T. (2008). A 2-D seismic signal detector for stand alone 3-component stations. In E.S. Husebye (Ed), Earthquake Monitoring and Seismic Hazard Mitigation in Balkan Countries. Springer Verlag, Berlin, Germany, pp. 167–183.

Gregersen, S., Wiejacs, P., and Baltic Working Group (2007). The exceptional earthquakes in Kaliningrad district, Russia on September 21, 2004. *Phys. Earth Planet. Int*. 164: 63–74.

Hansen, R., Ringdal, F., and Richards, P. G. (1990). The stability of RMS Lg measurements and their potential for accurate estimation of the yield of Soviet underground nuclear explosions. *Bull. Seism. Soc. Am.* 80: 2106–2126.

Husebye. E.S. and Mantyniemi, P. (2005). The Kaliningrad, west Russia earthquakes on the 21st of September 2004 – surprise events in a very low-seismicity area. *Phys. Earth Planet. Int*. 153: 227–236.

Husebye, E. S., Fedorenko, Yu., V. and Beketova, E. B. (2002). Enhanced CTBT monitoring through modelling, processing and extraction of secondary phase information at high signal frequencies, in *Proceedings of the 24th Seismic Research Review—Nuclear Explosion Monitoring: Innovation and Integration*, LA-UR-02-5048, Vol. 1, pp. 292–301.

Husebye, E.S., Ruud, B.O. and Dainty, A.M., (1998). Robust and reliable epicentre determinations: Envelope processing of local network data. *Bull. Seism. Soc. Am*. 88: 284–290.

Kværna, T. and Ringdal, F. (1996). Generalized beamforming, phase association and threshold monitoring using a global seismic network. In E.S. Husebye and A. M. Dainty (Eds.), Monitoring a Comprehensive Test Ban Treaty. Kluwer Academic Publ., Dordrecht, NL, pp 447–466.

Lomax, A. (2005). A Reanalysis of the hypocentral location and related observations for the great 1906 California earthquake*, *Bull. Seism. Soc. Am*. 95: 861–877

Mendi, C.D. Husebye, E.S. and Ruud, B.O. (1994). The North Sea Lg-blockage puzzle. *Geophys. J. Int*. 130: 669–680.

Mykkeltveit, S. and Husebye, E.S., (1981). Lg wave propagation in Eurasia. In E.S. Husebye and S. Mykkeltveit (eds): Identification of Seismic Sources – Earthquake or Underground Explosion. D. Reidel Publ. Co., Dordrecht, NL, pp. 421–452.

Nuttli, O.W. (1973). Seismic attenuation and magnitude relations for Eastern North America. *J. Geophys. Res*. 78: 876–885.

Panza, G.F. and Calcagnile, G. (1974). Comparison of the multimode surface wave response in structures with and without a low velocity channel (Part I: Dip-slip sources on a vertical fault plane), *Pure Appl. Geophys*.112: 583–596.

Pinsky V. (2006). Using beamforming for the global network location. *Phys. Earth Planet. Int*, 158: 1, 75–83.

Pinsky, V. (2000). Prototype Autonomous Earthquake Locator for Regional Networks. *Geophys. Res. Letters* 27: 3549–3552.

Pinsky, V. (2008). Accurate location of seismic sources with and without ravel time model. . In E.S. Husebye (Ed), Earthquake monitoring &seismic hazard mitigation in Balkan countries (Nato scence series IV Earth & environmental sciences, Vol. 81) 197–216.

Press, F. and Ewing, M. (1952. Two slow surface waves across North America. *Bull. Seism. Soc. Am*. 42: 219–228.

Slunga, R., 1979. Source mechanism of a Baltic earthquake inferred from surface-wave recordings. *Bull. Seism. Soc. Am.* 69: 1931–1964.

Tarantola A. (2005). *Inverse problem Theory and Methods for Model Parameter Estimation*. SIAM, 333 p.

# FINITE-FREQUENCY SEISMIC TOMOGRAPHY OF BODY WAVES AND SURFACE WAVES FROM AMBIENT SEISMIC NOISE: CRUSTAL AND MANTLE STRUCTURE BENEATH EASTERN EURASIA

Yong Ren[2], Wei Zhang[2], Ting Yang[3], Yang Shen[2],and Xiaoping Yang[1]

Science Applications International Corporation[1], University of Rhode Island[2], and Tongji University[3]

Sponsored by Air Force Research Laboratory

Contract No. FA8718-05-C-0017
Proposal No. BAA05-34

## ABSTRACT

To improve seismic calibration for nuclear explosion monitoring, we use 3D sensitivity kernels of finite-frequency body and surface waves to develop models of the crustal and mantle structures beneath eastern Eurasia. We have collected and processed available broadband data from both permanent stations and temporary networks in eastern Eurasia. We obtained a regional P-wave velocity model for the mantle structures down to 1,500 km beneath the eastern Eurasia. We also carried out a detailed study of the P- and S-wave velocity structures in southeastern Tibet, which led to some interesting geological findings. Our P- and S-wave velocity models reveal a low-velocity anomaly in the crust and upper mantle to ~ 300 km depth beneath a north-south-trending rift zone in southeastern Tibet. This low-velocity anomaly is situated above a tabular, high-dipping-angle, high-velocity anomaly that extends into the upper-mantle transition zone. These results are evidence for the delamination of the mantle lithosphere and its causal relationship to the formation of the north-south trending rift in southeastern Tibet.

In order to improve models at shallow depths, we apply the finite-frequency methodology to the surface wave tomography using the ambient seismic noise. Unlike previous studies that calculated the dispersion curves from the estimated Green's functions to solve for phase or group velocity maps, we have developed a new approach using the 3D finite-frequency sensitivity kernels for the Green's functions. We have collected continuous data for stations in southeastern Tibet and computed the cross-correlations between all possible pairs of components from two stations. We constructed 3D sensitivity kernels for the estimated Green's functions derived from the cross-correlation of ambient noise, taking into account the effects of the surface topography. We will carry out a joint inversion of finite-frequency S-waves and estimated Green's functions, which are dominated by surface waves to resolve both the crustal and upper mantle structures.

## OBJECTIVES

The main objective of this research is to construct high-resolution P-and S-velocity models of the crust and mantle beneath eastern Eurasia using 3D finite-frequency sensitivity kernels for body and surface waves. For surface wave tomography, we will utilize Green's functions derived from the cross-correlation of ambient noise at pairs of stations. A joint inversion of finite-frequency S waves and estimated Green's functions will be carried out to obtain the crust and mantle structure. The results will be used to improve seismic calibration for nuclear explosion monitoring.

## RESEARCH ACCOMPLISHED

### Finite-Frequency Seismic Tomography of Body and Surface Waves

#### 1) Body Waves

To date, most global and regional tomographic studies are based on ray theory, where seismic waves are assumed to have an infinite frequency and the arrival time of a body wave phase depends only upon the wave speed along the geometrical ray path from the source to the receiver. However, because of wave front healing, scattering, and other diffraction effects, the travel time of a finite-frequency seismic wave is sensitive to a three-dimensional structure off the ray path. Based on the Born single-scattering approximation in conjunction with body wave ray theory, Dahlen et al. (2000) derived the formulation of the Born-Fréchet kernels for a seismic phase, which expresses the influence of velocity perturbations upon a finite frequency travel-time shift:

$$\delta t(\omega) = \int\int\int_{\oplus} K_b(\omega, \mathbf{x}) \frac{\delta c}{c}(\mathbf{x}) d^3\mathbf{x} \qquad (1)$$

where the quantity $K_b(\omega,\mathbf{x})$ is the Fréchet sensitivity kernel over the 3D Earth structure for a travel-time shift $\delta t$ measured by cross-correlation of an observed pulse with its synthetic one.

#### 2) Surface Waves

Similarly, a measured surface-wave phase delay $\delta\Phi$ is written as a linear volumetric integration over heterogeneities of shear-wave and compressional-wave speed perturbations ($\delta\beta/\beta$ and $\delta\alpha/\alpha$) in the three-dimensional Earth (Zhou et al., 2006):

$$\delta\Phi(\omega) = \int\int\int_{\oplus} K_\beta(\omega, \mathbf{x}) \frac{\delta\beta}{\beta}(\mathbf{x}) d^3\mathbf{x} \quad \text{, for Love waves, and} \qquad (2)$$

$$\delta\Phi(\omega) = \int\int\int_{\oplus} \left[ K_\beta(\omega, \mathbf{x}) \frac{\delta\beta}{\beta}(\mathbf{x}) + K_\alpha(\omega, \mathbf{x}) \frac{\delta\alpha}{\alpha}(\mathbf{x}) \right] d^3\mathbf{x} \text{ , for Rayleigh waves,} \qquad (3)$$

where $\omega$ is the angular frequency of surface waves, and $K_\beta$ and $K_\alpha$ represent the phase sensitivity kernels related to the perturbations in the shear and compressional wave speeds, respectively.

In both cases of body and surface waves, according to equations 1, 2, and 3, the general problem for the inversion, after parameterization of the model function on a spatial grid of nodes, can be expressed as follows:

$$d_i = A_{il} m_l \qquad (4)$$

where $d_i$ is the $i$th measured body-wave travel-time shifts and surface-wave phase delays, $A_{il}$ is the value of the integrated volumetric body-wave and surface-wave kernels, $Kd^3\mathbf{x}$, contributing to the $l$th node, and $m_l$ is the model parameter at the $l$th node.

**High-Resolution P and S Velocity Models in Southeastern Tibet**

We processed data from the Namche Barwa seismic experiment (Sol et al., 2007), which deployed a 50-station broadband array and a 20-element short-period array in southeastern Tibet during 2003–2004 (Figure 1). Data from the global seismographic network (GSN) station LSA, which is located close to this temporary network, are also included in this study. We used about 695 events that occurred during the operation period of the stations in 2003 and 2004, and with a magnitude greater than 5.5. With the multi-channel waveform cross-correlation method (VanDecar and Crosson, 1990), we measured differential travel times of teleseismic P and S waves between different stations for short, intermediate, and long periods: 0.5–2.0 Hz, 0.1–0.5 Hz, and 0.03–0.1 Hz for P waves, and, 0.1–0.5 Hz, 0.05–0.1 Hz, and 0.02–0.05 Hz for S waves. The P-differential travel times are measured on vertical component seismograms and those of S on traverse components. To avoid the ambiguity of long-period phase arrivals in the triplication range and the effects of the core-mantle boundary, we have considered only data with an epicentral distance of between 34° and 81°. Our final data set consists of ~ 36,313 P and ~15,043 S differential travel times, which are then utilized to invert for spatial variations in P- and S-wave velocity perturbations according to the 3-D finite-frequency kernel formulation (Dahlen et al., 2000; Hung et al., 2004; Yang et al., 2006).

Our results show the presence of a low-velocity anomaly in the crust and upper mantle down to a ~ 300-km depth beneath a north-south trending rift zone in southeastern Tibet (Figure 2) (Tapponnier and Molnar, 1977; Armijo et al., 1986; Yin, 2000). This low-velocity anomaly is situated above a tabular, high-dipping-angle, high-velocity anomaly that extends into the upper mantle transition zone. The Vp/Vs ratio of the high-velocity anomaly suggests that temperature variations are not the only cause and that a highly melt-depleted mantle is required. These results provide evidence for the mantle lithosphere delamination (Figure 3) and its link to north-south trending rifts in southeastern Tibet (Ren and Shen, 2008), contrary to previous studies that argued that the north-south trending rift zones in the Tibetan plateau are shallow features, formed by the eastward motion of the shallow crust decoupled from the mantle lithosphere by a low-viscosity lower-crust (e.g., Shen et al., 2001; Jiménez-Munt and Patt, 2006). Studies of an extended region in southern Tibet are thus needed to understand whether the mantle lithosphere delamination phenomenon is limited to the study area or occurs in a broad region where it plays an important role in the elevation and deformation of the Tibetan plateau.

**Surface-Wave Tomography using Ambient Seismic Noise**

Previous studies showed that the Rayleigh and Love Green's functions can be derived from the cross-correlation of ambient seismic noise on the three components (vertical, north and east) at pairs of stations, and that the ambient seismic noise tomography is an efficient method to image the crustal and shallow mantle structures with an improved path coverage and spatial resolution (Shapiro and Campillo, 2004; Sabra et al., 2005; Shapiro et al., 2005; Yao et al., 2006; Yang et al., 2007; Cho et al., 2007; Lin et al., 2008). In this project, we have applied the ambient seismic noise tomography to the region of southeastern Tibet to image the crustal and shallow upper mantle structures. But unlike previous studies that calculated the dispersion curves from the estimated Green's functions using an automated frequency-time analysis (FTAN) (Yao et al., 2006; Bensen et al., 2007; Yang et al., 2007; Cho et al., 2007) in order to solve for phase or group velocity maps, we are developing a new approach using the 3D finite-frequency sensitivity kernels for the Green's functions.

**1) Data collection from Ambient Noise Cross-Correlation**

We have collected and processed continuous data from about 70 stations deployed in the Namche Barwa seismic experiment during 2003–2004 (Figure 1, Sol et al., 2007). We have used all three components data (vertical, north, and east), and computed the cross-correlations between all possible pairs of components from two stations in order to obtain the estimated Green's functions. The raw data have been cut into 1-day-length waveforms, and the mean trend and instrument response are removed. All data are then bandpass filtered between periods of 4 s and 150 s, processed using the one-bit normalization, and stacked afterwards. Figure 4 shows an example of the cross-correlations (vertical-vertical, north-north, and east-east) between the Lhasa station LSA and the station ES11, bandpass filtered between 10s and 20s. The observed signals at both positive and negative correlation lag times

correspond to waves propagating in opposite directions between the stations. The Z-Z cross-correlation exhibits clearly the Rayleigh wave, whereas the N-N and E-E cross-correlations contain a combination of both Rayleigh and Love waves. The fact that surface wave waveforms are observed earlier on N-N and E-E cross-correlations than those on the Z-Z cross-correlation indicate effectively the presence of Love waves on the transversal components. The radial and transverse components, and thus first-order separation of Rayleigh and Love waves, can be obtained from the rotation of all possible combinations of cross-correlation of the three components (Lin et al., 2008). Figure 5 shows another example of the cross-correlations between the station LSA and all other stations for Z-Z, N-N, and E-E components, bandpass filtered between 10s and 20 s.

**2) Sensitivity Kernels for Green's Function from Ambient Noise Cross-Correlation**

In order to apply the finite-frequency methodology to the surface wave tomography using the ambient seismic noise, we have constructed 3D sensitivity kernels for the Green's function derived from the cross-correlation of ambient noise at pairs of stations. The kernels are calculated using the scattering integral method (Zhao et al., 2005; Zhang et al., 2007; Zhang and Shen, 2007). Because the Green's function derived from the cross-correlation of seismic ambient noise is the surface wave between pairs of stations, both the shallow velocity structure and surface topography may significantly affect the 3D sensitivity kernels. To assess the effects of surface topography on the sensitivity kernels, we put a band of random topography between the pair of stations. The topography is statistically characterized by a horizontal correlation length (a) and a height RMS (root mean square) fluctuation (ε) and has a Gaussian type autocorrelation function:

$$R(r) = \varepsilon^2 \exp^{-r^2/a^2}. \qquad (5)$$

Figure 6 shows an example of the 3D phase delay sensitivity kernels for a Green's function corresponding to the estimate from the cross-correlation of vertical records at two stations separated by 100 km in a modified ak135 model, in which the topography has a correlation length a=4 km and a height RMS fluctuation of 1 km. Our study shows that surface topography effect is most significant when the wavelength and the horizontal scale of surface topography are comparable (Zhang and Shen, 2007). This will occur if short-period waves are used. Thus in places with rough surface topography, the topographic effects must be taken into account in the use of short-period ambient noise.

**Other Work**

As shown in the previous report, we have obtained a regional P-wave velocity model for the upper 1,500 km beneath eastern Eurasia using the finite-frequency tomography methodology (Yang et al., 2006). We are collecting and processing additional data from the China National Seismic Network, which became available recently. The additional data will substantially improve the P-wave velocity model in this part of region. We will calculate travel-time corrections from the final P and S velocity models and relocate GT events with and without the corrections for model validation.

## CONCLUSIONS AND RECOMMENDATIONS

We have applied the finite-frequency sensitivity kernels of body and surface waves to develop the crustal and mantle structures beneath eastern Eurasia. For the body-wave tomography, we have assembled a large data set of broadband waveforms and used cross-correlation to measure P and S differential travel times. The data set is then inverted for spatial variations in P- and S-wave velocity perturbations according to the 3D finite-frequency kernel formulation. P and S-wave velocity models beneath southeastern Tibet provide evidence for a causal relationship between the mantle lithosphere delamination and the north-south trending rifts. For the surface wave tomography using ambient seismic noise, we have collected continuous data from southeastern Tibet, and have computed the cross-correlations between all possible pairs of components in order to obtain the estimated Green's functions. In parallel, we have calculated the 3D sensitivity kernels for Green's functions derived from the cross-correlation of ambient noise at pairs of stations and have estimated the effects of surface topography on the sensitivity kernels. Both P- and S-wave velocity models derived from the finite-frequency tomography of body and surface waves will be used to improve seismic calibration in Eurasia.

**ACKNOWLEDGEMENTS**

The data used in this work were obtained from the IRIS DMC. We thank the participants in the Namche Barwa seismic experiments and the Bhutan experiment for making their data available. Most figures in this paper were made with General Mapping Tools (P. Wessel and W. H. F. Smith).

**REFERENCES**

Armijo, R., P. Tapponnier, J. P. Mercier, and T. Han (1986). Quaternary extension in southern Tibet, *J. Geophys. Res.* 91: 13,803–13,872.

Bensen G. D., M. H. Ritzwoller, M. P. Barmin, A. L. Levshin, F. Lin, M. P. Moschetti, N. M. Shapiro, and Y. Yang (2007). Processing seismic ambient noise data to obtain reliable broad-band surface wave dispersion measurements, *Geophys. J. Int.* 169: 1239–1260, *doi: 10.1111/j.1365-246X.2007.03374.x.*

Cho, K. H., R. B. Herrmann, C. J. Ammon, and K. Lee (2007). Imaging the upper crust of the Korea Peninsula by surface-wave tomography, *Bull. Seism. Soc. Am.* 97 (1B): 198–207, doi: 10.1785/0120060096.

Dahlen, F. A., Hung, S.-H., and Nolet, G. (2000). Fréchet kernels for finite frequency traveltimes-I. Theory, *Geophys. J. Int*. 141: 157–174.

Hung, S.-H., Dahlen, F. A., and Nolet, G. (2000). Fréchet kernels for finite frequency traveltimes-II. Examples, *Geophys. J. Int*. 141: 175–203.

Hung, S-H ,Y. Shen, and L.-Y. Chiao (2004). Imaging seismic velocity structure beneath the Iceland hot spot: A finite frequency approach, *J. Geophy. Res.* 109: doi: 10.1029/2003JB002889.

Jimenez-Munt, I. and J.P. Platt (2006). Influence of mantle dynamics on the topographic evolution of the Tibetan plateau: Results from numerical modeling, *Tectonics* 25: TC6002, *doi:10.1029/2006TC001963*.

Lin F.-C., M. P. Moschetti, and M. H. Ritzwoller (2008). Surface wave tomography of the western United States from ambient seismic noise: Rayleigh and Love wave phase velocity maps, *Geophys. J. Int.* 173: 281–298, *doi: 10.1111/j.1365-246X.2008.03720.x.*

Ren, Y. and Y. Shen (2008). Tomographic evidence for a possible link between lithosphere delamination and the north-south trending rifts in Tibet, *J. Geophy. Res.*, under revision.

Sabra, K. G., P. Gerstoft, P. Roux, and W. A. Kuperman (2005). Extracting time-domain Green's function estimates from ambient seismic noise, *Geophys. Res. Lett.* 32: L03310, doi: 10.1029/2004GL021862.

Shapiro, N. M. and M. Campillo (2004). Emergence of broadband Rayleigh waves from correlations of the ambient seismic noise, *Geophys. Res. Lett.* 31: L07614, doi: 10.1029/2004GLL019491.

Shapiro, N. M., M. Campillo, L. Stehly, and M. H. Ritzwoller (2005). High-resolution surface-wave tomography from ambient seismic noise, *Science* 207: 1615–1618.

Shen, F., L. Royden, and B. C. Burchfiel (2001). Large-scale crustal deformation of the Tibetan plateau, *J. Geophys. Res.* 106 (B4): 6793–6816.

Sol, S., A. Meltzer, R. Burgmann, R. D. van der Hilst, R. King, Z. Chen, P. O. Koons, E. Lev, Y. P. Liu, P. K. Zeitler, X. Zhang, J. Zhang, and B. Zurek (2007). Geodynamics of the southeastern Tibetan Plateau from seismic anisotropy and geodesy, *Geology* 35: 563– 566, *doi:10.1130/G23408A.1*.

Tapponnier, P. and P. Molnar (1977). Active faulting and tectonics of China, *J. Geophys. Res.* 82: 2905– 2930.

VanDecar, J. C., and R. S. Crosson (1990). Determination of teleseismic relative phase arrival times using multi-channel cross-correlation and least squares, *Bull. Seismol. Soc. Am.* 80: 150–169.

Yang, T., Y. Shen, S. van der Lee, S. C. Solomon, and S. H. Hung (2006). Upper mantle structure beneath the Azores hotspot from finite-frequency seismic tomography, *Earth Planet. Sci. Lett.* 250: 11–26.

Yang, Y., M. H. Ritzwoller, A.L. Levshi, and N.M. Shapiro (2007). Ambient noise Rayleigh wave tomography across Europe, *Geophys. J. Int.* 168: 259–274.

Yao, H., R. D. van der Hilst, and M. V. de Hoop (2006). Surface-wave array tomography in SE Tibet from ambient seismic noise and two-station analysis –I. Phase velocity maps, *Geophys. J. Int.* 166: 732–744, *doi: 10.1111/j.1365-246X.2006.03028.x.*

Yin, A. (2000). Mode of Cenozoic east-west extension in Tibet suggesting a common origin of rifts in Asia during the Indo-Asian collision, *J. Geophys. Res.* 105: 21,745–21,759.

Zhang, Z., Y. Shen, and L. Zhao (2007). Finite-frequency sensitivity kernels for head waves, *Geophys. J. Int.* 171: 847–856, *doi:10.1111/j.1365-246X.2007.03575.x.*

Zhang, W. and Y. Shen (2007). Finite-frequency tomography using ambient seismic noise in the presence of surface topography, *AGU Fall Meeting Abstracts*, B1384.

Zhao, L., T. H. Jordan, K. B. Olsen, and P. Chen (2005). Frechet kernels for imaging regional earth structure based on three-dimensional reference models, *Bull. Seism. Soc. Am.* 95: 2066–2080.

Zhao, L. and T. H. Jordan (2006). Structural sensitivities of finite-frequency seismic waves: a full-wave approach, *Geophys. J. Int.* 165: 981–990, *doi:10.1111/j.1365-246X.2006.02993.x.*

Zhou, Y., F. A. Dahlen, and G. Nolet (2005). Three-dimensional sensitivity kernels for surface wave observables, *Geophys. J. Int.* 158, 142–168, *doi:10.1111/j.1365-246X.2004.02324.x.*

Zhou, Y., F. A. Dahlen, G. Nolet, and G. Laske (2005). Finite-frequency effects in global surface-wave tomography, *Geophys. J. Int.* 153: 1087–1111, *doi:10.1111/j.1365-264X.2005.02780.x.*

Zhou, Y., G. Nolet, F. A. Dahlen, and G. Laske (2006). Global upper-mantle structure from finite-frequency surface-wave tomography, *J. Geophys. Res.* 111: B04304, *doi:10.1029/2005JB003677.*

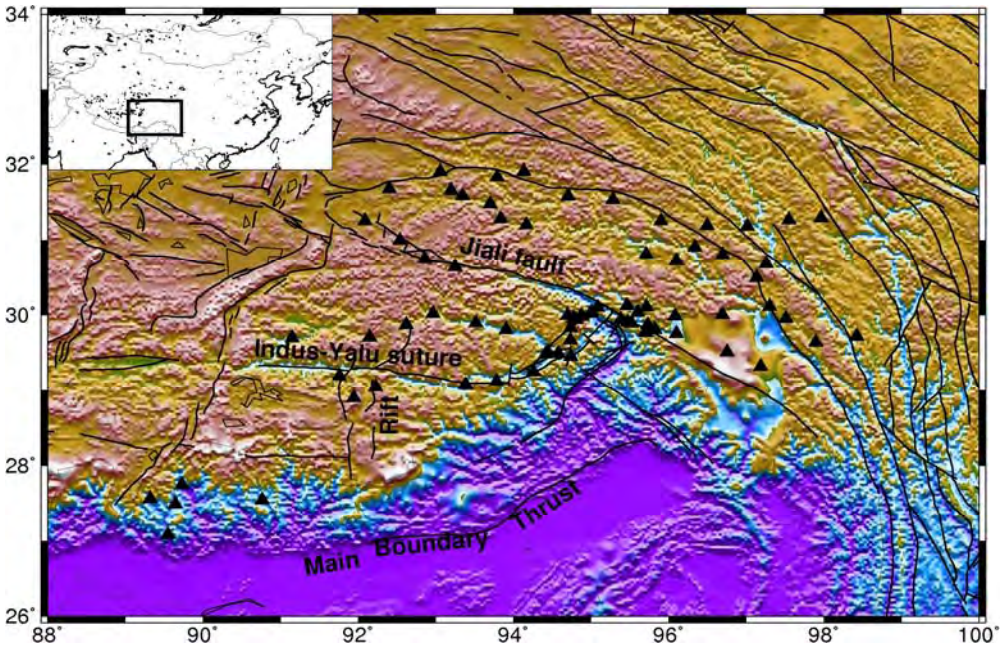


**Figure 1. Topographic map of southeastern Tibet with active faults in the region of the Himalayan Eastern syntaxis and the locations of the stations used in the study.**

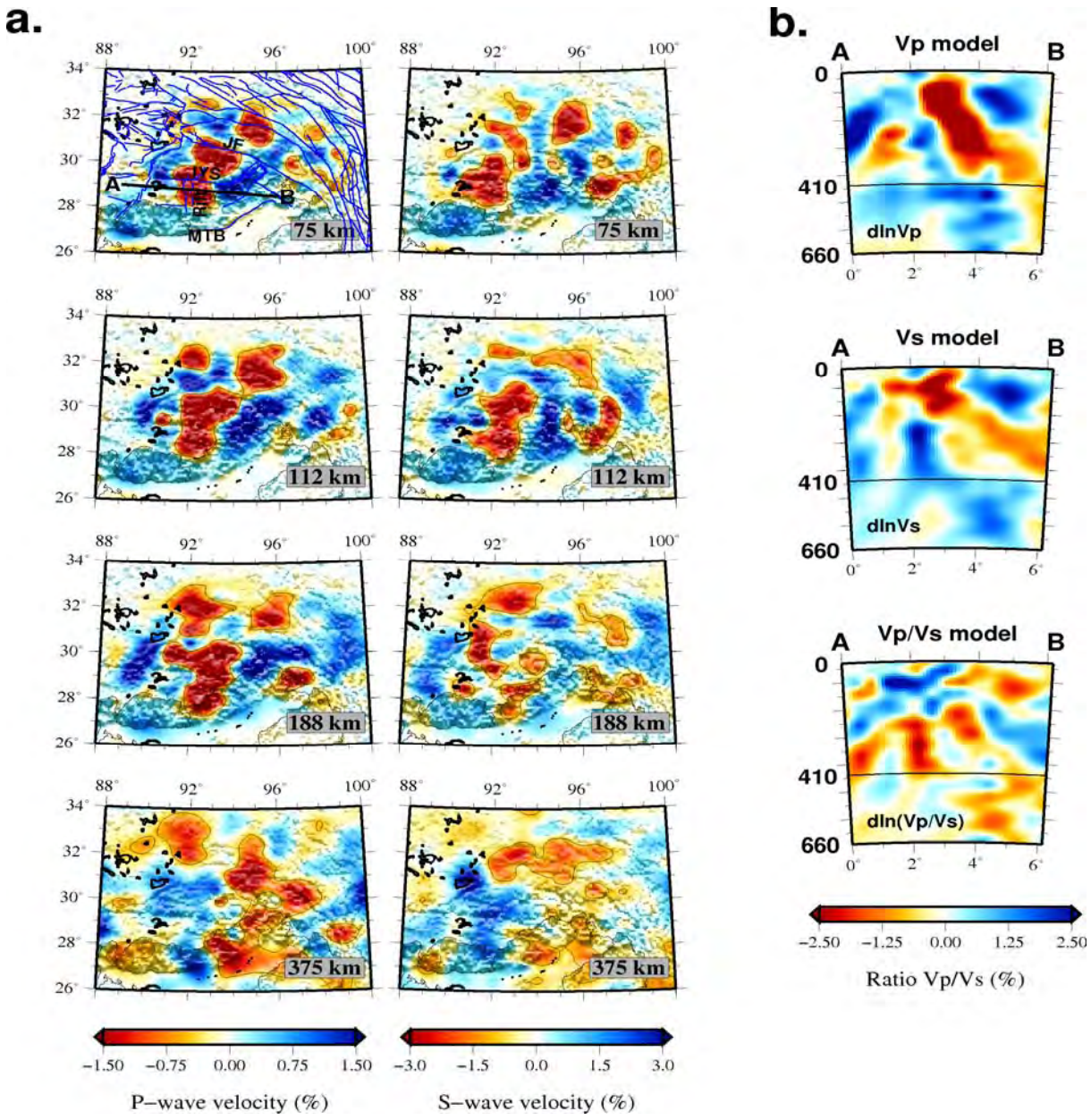


**Figure 2. (a). P- and S-wave velocity perturbations relative to the reference model (CRUST2.0 and iasp91) at different depths: 75 km, 112 km, 188 km and 375 km. (b). Cross-section A-B through P- and S-wave tomographic models, along the Indus-Yarlung suture and across the rift in southeastern Tibet. Topographic map of southeastern Tibet with active faults in the region of the Himalayan Eastern syntaxis and the locations of the stations used in the study.**

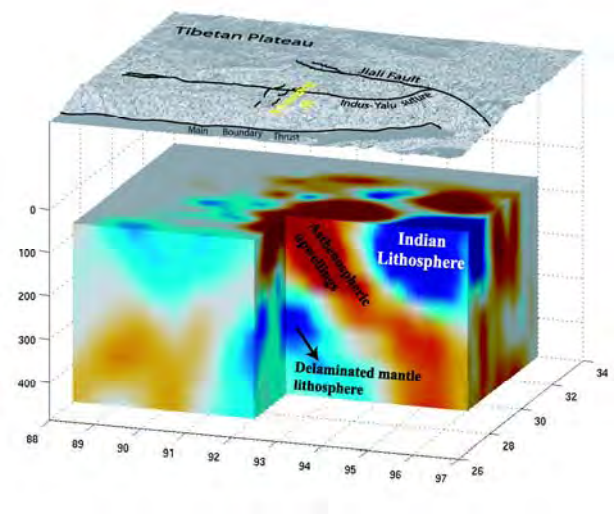


**Figure 3. Three-dimensional image of the P-wave velocity model with our interpretation of the observed structures in southeastern Tibet. The topography is not to scale.**

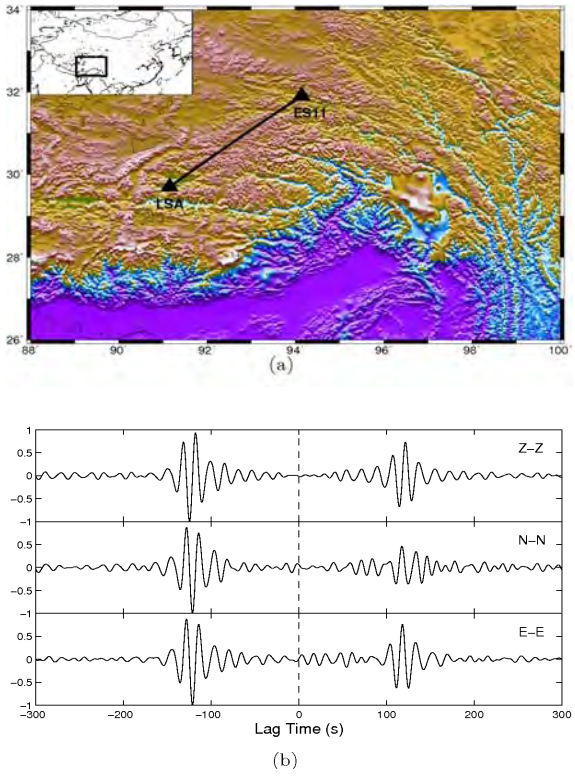


**Figure 4. (a). The path between the GSN station LSA (Lhasa, Tibet) and the station ES11. (b). The 10–20 s bandpass filtered cross-correlations observed between the station LSA and ES11, as showed in a). The labels Z-Z, N-N and E-E denote the cross-correlation between Vertical-Vertical, North-North and East-East components, respectively.**

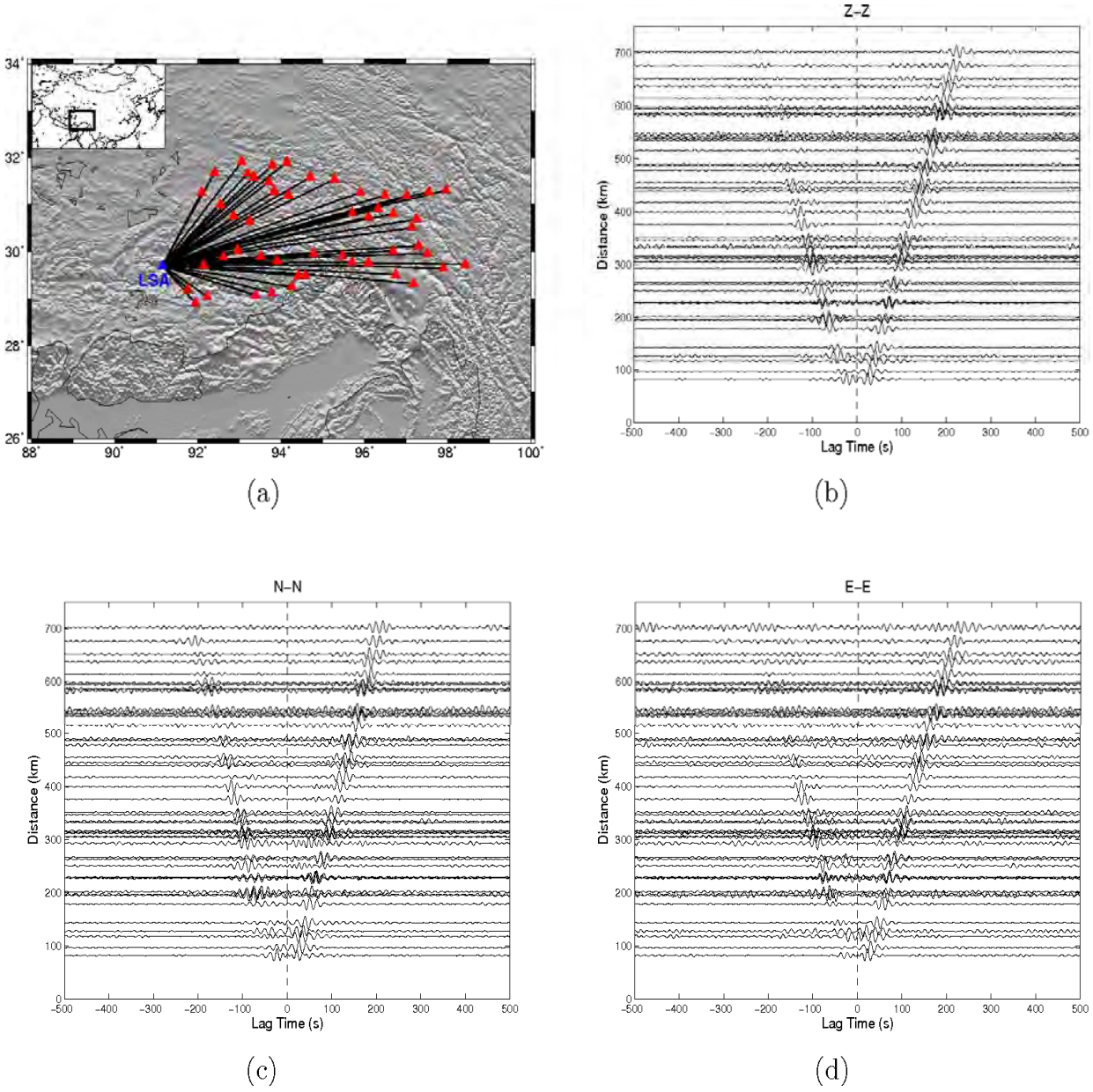


**Figure 5. (a). The path between the GSN station LSA (Lhasa, Tibet) and the stations deployed in the Namche Barwa seimic experipment. (b–d). The bandpass filtered (10–20 s) cross-correlations observed between the station LSA and other stations for Z-Z (Vertical-Vertical), N-N (North-North), and E-E (East-East) components.**

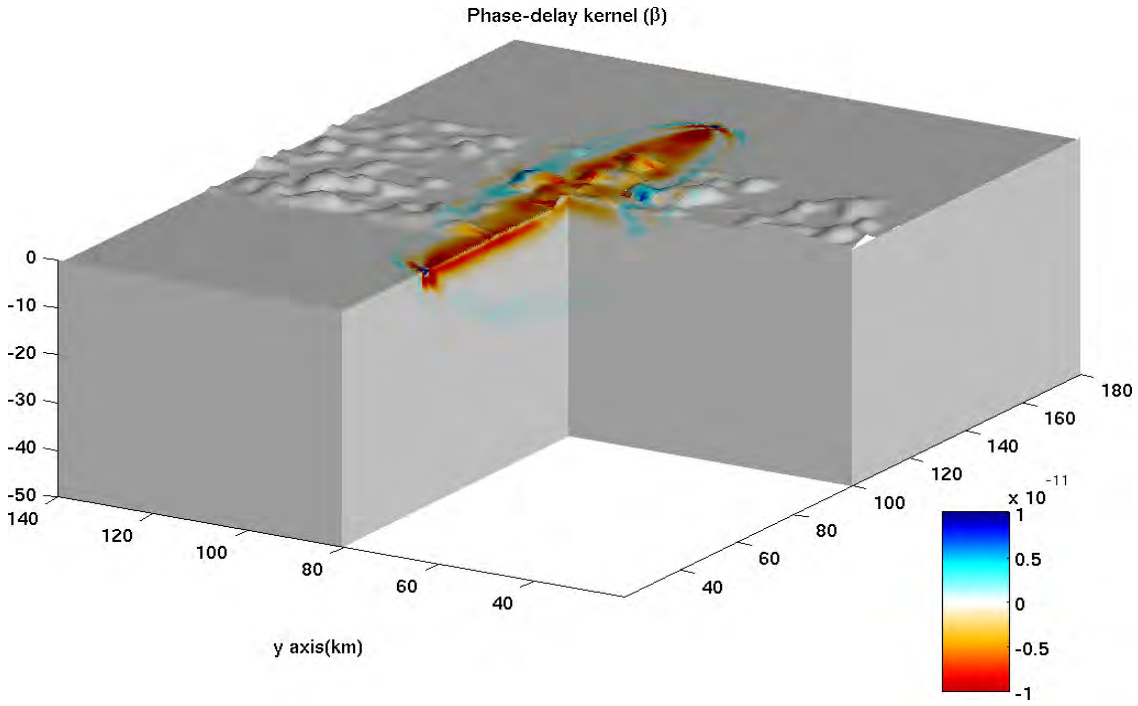


**Figure 6. Sensitivity kernels for a modified model ak135 with the topography having a correlation length a=4 km, RMS=1 km, and the center frequency of the source time function fc=0.5 Hz. The center wavelength is around 6 km, and the horizontal length of a single hill is around 8-9 km. The horizontal scale of the hill is greater than one wavelength. The topography-scattered waves cause some sensitivities at depth, and the kernels are distorted by the topography.**

# EXPANDING COHERENT ARRAY PROCESSING TO LARGER APERTURES USING EMPIRICAL MATCHED FIELD PROCESSING

Frode Ringdal[1], David B. Harris[2], Tormod Kværna[1], and Steven J. Gibbons[1]

NORSAR[1] and Lawrence Livermore National Laboratory[2]

Sponsored by Air Force Research Laboratory and National Nuclear Security Administration

Contract Nos. FA8718-08-C-0007[1] and DE-FC52-06NA27324
Proposal No. BAA08-39

## ABSTRACT

The objectives of this project are

- To investigate the limits of empirical matched field processing and other coherent array detection and parameter estimation methods as receiver aperture size increases from a few kilometers to many hundreds of kilometers.

- To investigate techniques for extending the geographical source-region footprint over which empirical matched field processing and other coherent calibrated methods apply.

Under a previous contract, we demonstrated the ability of empirical matched field processing to classify mining explosions by originating mine, using data from a single small-aperture array (ARCES) applied to mining events on the Kola Peninsula. In the current contract, we have chosen central Asia as our study region to assure programmatic relevance and to exploit the large belts of natural and man-made seismicity required for a test of our processing strategy. Data from suitable networks available for the study are from the four Kazakhstan arrays (MKAR, KKAR, ABKAR, BRVK) and the Kyrgyzstan network. Our overall approach will be to start with small apertures (the individual Kazakhstan arrays considered separately) to check the reproducibility of results we obtained for the European Arctic, then to extend the processing strategy first to a medium aperture (the Kyrgyzstan network; 200 km aperture) and then a large aperture (the four Kazakhstan arrays considered as a single coherent aperture; >1000 km). Simultaneously we will investigate methods to expand the source region footprint over which calibrations for coherent methods apply.

We have expanded our work on the dataset of mining explosions in the Kola Peninsula to investigate further the potential of the method and to validate the preliminary results obtained under a previous contract (BAA03-27). This validation has consisted of analyzing several hundred seismic waveforms from available local stations (Apatity and Lovozero) to make additional checks on the original ground truth information provided by the mining authorities. Cross validation also was introduced to avoid circularity in the data analysis. Through the use of empirical matched field processing we were able correctly to classify 539 of 549 explosions by originating mine among 10 closely spaced mines, using short segments (<10 seconds, filtered in the 2.5–12.5 Hz band) of Pn waves observed at the ARCES array. The mines are separated by as little as 3 kilometers and observed at a 340–410 kilometer range. Such classification performance is far superior to that obtained by traditional methods. Matched field processing should find application in screening mining explosions in Comprehensive Nuclear-Test-Ban Treaty monitoring applications and in studies of natural seismicity.

## OBJECTIVES

The objectives of this project are

- To investigate the limits of empirical matched field processing and other coherent array detection and parameter estimation methods as receiver aperture size increases from a few kilometers to many hundreds of kilometers.

- To investigate techniques for extending the geographical source-region footprint over which empirical matched field processing and other coherent calibrated methods apply.

We will begin by reanalyzing data from the European Arctic in order to reconfirm the potential of empirical matched field processing that has been indicated by our work under a previous contract. We then will proceed to study the central Asia region to assure programmatic relevance and to exploit the large belts of natural and man-made seismicity to test the applicability of the technique to diffuse seismicity.

## RESEARCH ACCOMPLISHED

### Introduction

Current operational seismic array processing methods for detection (beamforming) and parameter estimation (frequency-wavenumber analysis) have changed little since their introduction in the 1960s and 1970s. These methods rely upon a plane-wave assumption for predicting the spatial amplitude and phase structure of seismic waves incident upon an array aperture. Scattering and refraction in strongly heterogeneous seismic propagation media constrain the size of usable coherent processing apertures under the plane-wave assumption to a few wavelengths. This constraint severely limits the spatial resolution of beamforming and frequency-wavenumber (F-K) methods. In addition, the spatial correlation of ambient seismic noise constrains the minimum usable element separation. The combination of these constraints bounds the maximum number of usable sensors and places a fundamental limit on coherent processing gain through beamforming.

Existing beamforming and F-K estimation methods make some attempt to compensate for the non-ideal spatial structure of seismic waves. For example, it is common to apply an amplitude correction to estimated spatial covariance matrices when using the indirect approach to F-K spectrum estimation (i.e., by estimating the the spatial covariance function first, then evaluating its Fourier transform to obtain a wavenumber spectrum). Each element of the matrix is normalized by the square root of the diagonal elements in the same row and column. In direct methods (e.g., Kværna and Ringdal, 1986), it is now standard to integrate the F-K spectrum over a band of frequencies to stabilize the narrowband estimates that individually have high variance. That variance is controlled, in part, by the very small time-bandwidth product of signals in short analysis windows. However, it is likely that variance in the F-K estimate from frequency to frequency also is a function of wavefield scattering.

Recent advances in standardization of analysis windows and frequency bands for particular source regions have produced dramatic reductions in the variance of azimuth/slowness estimates derived from F-K spectra (Gibbons et al., 2005), at least in frequency bands (below 6–8 Hz) where the wavefield is approximately coherent across regional-array apertures. Finally, it is common to apply post-processing (i.e., post-F-K) vector slowness corrections (Schweitzer, 2001) to azimuth/slowness measurements in an attempt to remove frequency-dependent biases caused (presumably) by unmodeled wavefield refraction.

Recently, detection algorithms that exploit aperture-level calibrations have been developed that often substantially reduce detection thresholds in beamforming operations. Correlation detectors (Gibbons and Ringdal, 2006) and subspace detectors (Harris, 2006) use previously observed waveforms from events at specific sources in sensitive algorithms to detect subsequent events at those same sources. These algorithms rely upon the fact that the temporal and spatial structures of signals from these sources often are repeatable; past events constitute a spatio-temporal calibration across an array or network of sensors for future events. Such detectors simultaneously detect, locate, and identify events as being consistent with previous events at the same source location, with the same source time history and mechanism.

However, while the full exploitation of the spatial and temporal structure of the signal frequently leads to detectors one to two orders of magnitude more sensitive than simple power detectors (with conventional beamforming), such exploitation also presents two barriers to widespread application. Correlation methods generally have a source-region geographic footprint one to two wavelengths across (Harris, 1991), which can be ameliorated to some extent with the more general waveform representation of a subspace detector (Harris, 2006). Correlation methods correct incoherence across the receiver aperture, but trade it for incoherence across the source region; the reciprocity principle is at play in the correlation detection strategy. Correlation methods also are sensitive to source mechanism and time history, and can fail when these attributes differ from event to event.

The sensitivities of F-K methods and conventional beamforming to the plane wave assumption and of correlation methods to source variability leads us to consider another processing strategy based on temporally-incoherent, but spatially coherent signal processing extended with subspace techniques. Our general approach is to adapt narrowband empirical matched field processing, originally conceived for underwater acoustic applications (Baggeroer et al., 1993; Fialkowski et al., 2000) to the seismic monitoring task. Our processing agenda consists of (1) breaking the observed signal into narrow bands, (2) using empirical matched field methods to combine the near-monochromatic resultant waveforms coherently across an aperture to achieve processing gain, and (3) integrating the resulting power incoherently over the narrow bands to achieve a wideband result. We anticipate that this approach will ameliorate variations in source time history from event to event that defeat waveform correlation methods.

Matched field processing derives its name from the realization that conventional narrowband beamforming is a spatial matched filtering operation for plane waves, and that more general forms of spatial matched filtering are possible. In underwater acoustics, the velocity structure of the medium is far less variable than the seismic propagation medium and frequently known in detail. In such circumstances, it is possible to compute the detailed phase and amplitude structure of a narrowband wavefield incident on an array and apply the computed structure as the focusing kernel in a beamforming operation. This approach works well in the SOund Fixing And Ranging (SOFAR) channel waveguide and allows coherent processing across arrays to be expanded beyond the physical aperture limits implied by the assumption of a planar structure (locally the field is planar). A clever empirical approach to estimating the structure of the narrowband acoustic wavefield directly from observed wavefields was attempted (Fialkowski et al., 2000) but largely failed because of the spatial nonstationarity of the source.

**Reanalyzing Mining Data from the European Arctic**

Under a previous contract, DE-FC52-03NA99517 (Kværna et al., 2007), we demonstrated the ability of empirical matched field processing to classify mining explosions by originating mine, using data from a single small-aperture array (ARCES) applied to mining events on the Kola Peninsula.

We have continued our work on this data set for the mining explosions at the Kola Peninsula in order to further validate the preliminary results summarized by Kværna et al. (2007). This validation has consisted of analyzing over 500 seismic waveforms from available local stations (Apatity and Lovozero) to make additional checks on the original ground truth information provided by the mining authorities. We have also carried out classification tests using cross-validation to avoid issues of circularity.

We study the European arctic region (Figure 1) where the ARCES array, located in northern Norway, is 340–410 kilometers from two groups of mines in the Kola peninsula, Russia: the Olenegorsk (O1-O5) and Khibiny (K1-K5) groups. In monitoring for signals from distant nuclear events, the array observes thousands of mining explosions annually, which can be screened if attributed with a high level of confidence to their originating mines. However, the array, with a 3-kilometer aperture, is too small to resolve the individual mines. The array resolution (Rayleigh criterion) is determined by the separation of half-power (3 dB) points of the main lobe of the array wavenumber response. In Figure 1, the 3 dB points of the array response (at 4, 8, and 12 Hz) for first-arriving Pn waves are projected onto the array's geographic field of view; the array has been steered to one particular mine (K2). All 10 mines fall within the 3 dB contours even at 12 Hz.

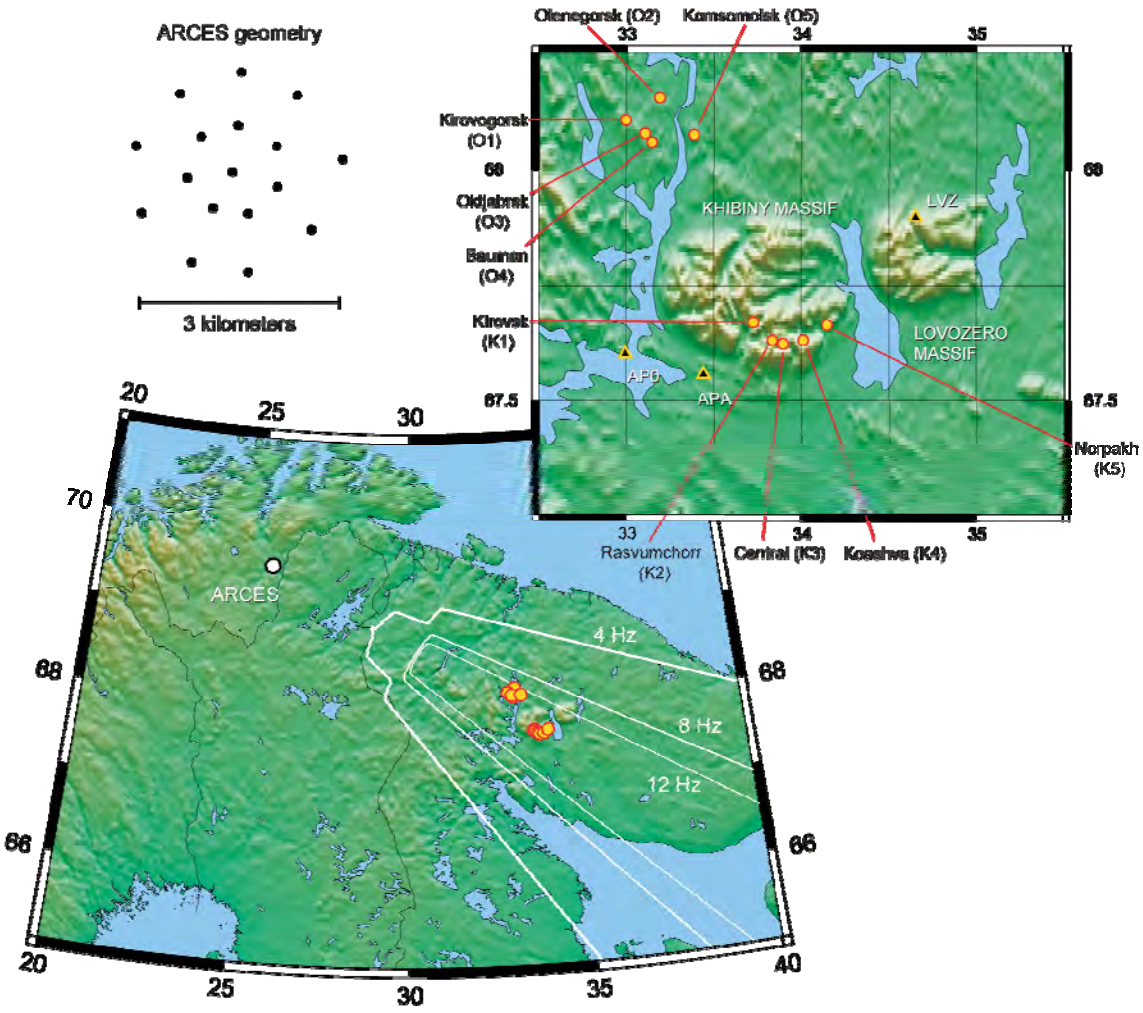


**Figure 1. The mines of the Khibiny and Olenegorsk regions are too close for explosions to be attributed to specific mines on the basis of wavenumber (F-K) spectrum direction estimates made from ARCES array (upper left) observations of Pn waves (Figure 2). ARCES resolution is indicated on the map at lower left, which shows the half-power contours of the array response at three frequencies when the array is steered to the Rasvumchorr mine (K2).**

We consider separating explosions from the 10 mines using only the first-arriving Pn wave. Figure 2 displays ARCES center station observations of 37 explosions originating at the Norpakh mine (K5). Note the large degree of signal variation, which complicates the use of correlation methods. For our analysis, we selected 549 explosions attributed to specific mines using reports from the mine operators, validated with data from stations (APA, LVZ) local to the mines.

The classical technique for estimating incident wave velocity and direction is the F-K spectrum,

$$P(\omega,\vec{k}) = \left| \int dt \sum_j r(t,\vec{x}_j) e^{i(\omega t - \vec{k}\cdot\vec{x}_j)} \right|^2 = \vec{\varepsilon}^{\,H} \vec{R}(\omega) \vec{\varepsilon} \qquad (1)$$

which maps the energy incident upon the array as a function of frequency $\omega$ and wavenumber (direction) $\vec{k}$ by computing a multidimensional Fourier transform of the signals $r(t,\vec{x}_j)$ recorded at the sensor locations $\vec{x}_j$. The F-K spectrum can be written as the indicated quadratic form between the steering vector

$\vec{\varepsilon} = \left[ e^{-i\vec{k}\cdot\vec{x}_1} \quad \cdots \quad e^{-i\vec{k}\cdot\vec{x}_N} \right]^T$, which expresses the spatial phase and amplitude structure of incident monochromatic plane waves, and the spatial covariance matrix $\vec{R}$, containing the cross-spectral information $R_{mn}(\omega) = (\int r(t,\vec{x}_m)e^{-i\omega t}dt)(\int r(t,\vec{x}_n)e^{i\omega t}dt)$ among the sensor waveforms.

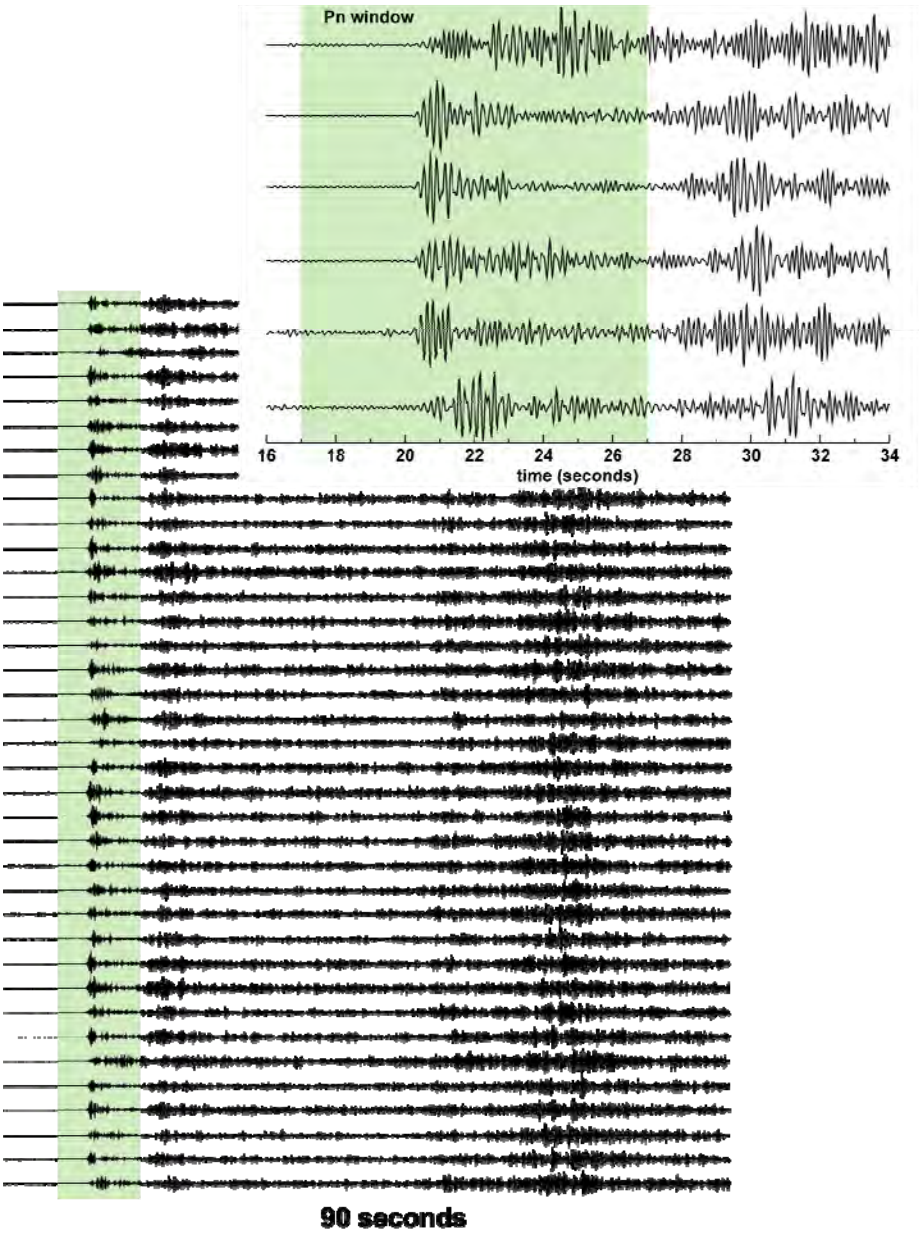


**Figure 2. The ensemble of events used to calibrate the Norpakh mine (K5). Note that the first-arriving P waves (see inset) show a degree of variation that makes classification by waveform correlation methods infeasible.**

It is common to integrate the energy over frequency to produce a map of total incident energy as a function of vector slowness, $\vec{s}$,

$$\widehat{P}(\vec{s}) = \int P(\omega, \omega\vec{s})d\omega \qquad (2)$$

This function aggregates energy incoherently across frequency, which is the basis for wideband estimation algorithms not sensitive to the specific temporal structure of signals.

The direction to the source of an observed signal is estimated by maximizing $\widehat{P}(\vec{s})$ over vector slowness. In practice, the wavefield often is strongly refracted leading to significant bias in direction estimates. It is common to compensate refraction effects with empirical corrections to the estimated slowness derived from events of known location (Schweitzer, 2001). This calibration approach effectively replaces the theoretical steering vector for a particular direction and velocity with a corrected vector, although one that still conforms to a plane wave signal.

Improvements in estimation accuracy result from improving the representation of the incident wavefield structure, embodied in the steering vectors. In underwater sound localization problems, matched field processing (Baggeroer et al., 1993) maximizes the quadratic form of Equation (1) over a manifold of steering vectors computed from detailed models of the oceanic sound velocity profile (SVP). Sufficiently accurate SVP models are not always available, which motivated attempts to develop steering vectors empirically (Fialkowski et al., 2000). In hydroacoustic applications, signal sources frequently are ships producing continuous waveforms modeled as narrowband random processes. When a single source is present, the steering vectors are obtained as the principal eigenvectors of sample covariance matrices estimated from array observations of the continuous wavefield.

In adapting the matched field processing approach to seismic applications, an empirical approach is required, since geophysical models of the propagation environment (the Earth) are not sufficiently detailed or accurate to predict wavefield structure, except at very low frequencies (< ~0.1 Hz). We are interested in improving performance at frequencies as high as 12 Hz. Since the typical seismogram consists of many different waves propagating in a multipath environment, we limit the observation window to a small portion of the waveform (approximately the first ten seconds) where we can be reasonably sure that a single wave is present. The short window raises the question of how to obtain suitably stable estimates of spectral covariance matrices. We solve this problem by assembling ensembles of events, such as that shown in Figure 2, from repeating sources (mines). The covariance matrices are computed as the ensemble average.

To provide a baseline for array performance consistent with the classical resolution limit, we classify the 549 explosions by originating mine first by maximizing $\widehat{P}(\vec{s})$ over the 10 plane-wave steering vectors appropriate to the great-circle azimuths to the mines. We refer to this approach as theoretical plane-wave (F-K) classification. We also perform the classification with calibrated plane-wave steering vectors, for which the directions and velocities have been chosen to maximize the ensemble power for each mine. We refer to this approach as empirical plane wave classification. Finally, we perform matched field classification using steering vectors obtained as the principal eigenvectors of the ensemble covariance matrices. In all cases, we estimate the energy in the 2.5–12.5 Hz frequency band, discretizing this band into 33 subbands of 0.3125-Hz width for the covariance calculations. We use a cross-validation approach to avoid circularity in the estimation process.

The three algorithms represent different choices for representing the narrowband spatial structure of the incident wavefield under the 10 source hypotheses. To assess the quality of the representations, we measure the normalized energy

$$\frac{\sum_j \vec{\varepsilon}_j^{\,H} \vec{R}(\omega_j)\vec{\varepsilon}_j}{\sum_j tr\{\vec{R}(\omega_j)\}} \qquad (3)$$

which ranges between 0 and 1 and is 1 only if the steering vectors represent 100% of the signal energy incident on the array. It is the fraction of energy captured by the specific representation.

Energy capture for one mine, Olenegorsk, under the 10 source hypotheses is shown in Figure 3. Both plane-wave classification methods have energy capture distributions centered about 0.2–0.3 for Olenegorsk events under the Olenegorsk origin hypothesis. The energy capture for the alternative hypotheses, which ideally should be 0, is lower for the empirical plane wave classifier than its theoretical counterpart, suggesting better classification performance for the calibrated classifier. Distributions for the matched field method show a very wide spread between the Olenegorsk hypothesis, for which energy capture averages about 0.8, and alternate hypotheses, predicting a high classification success rate.

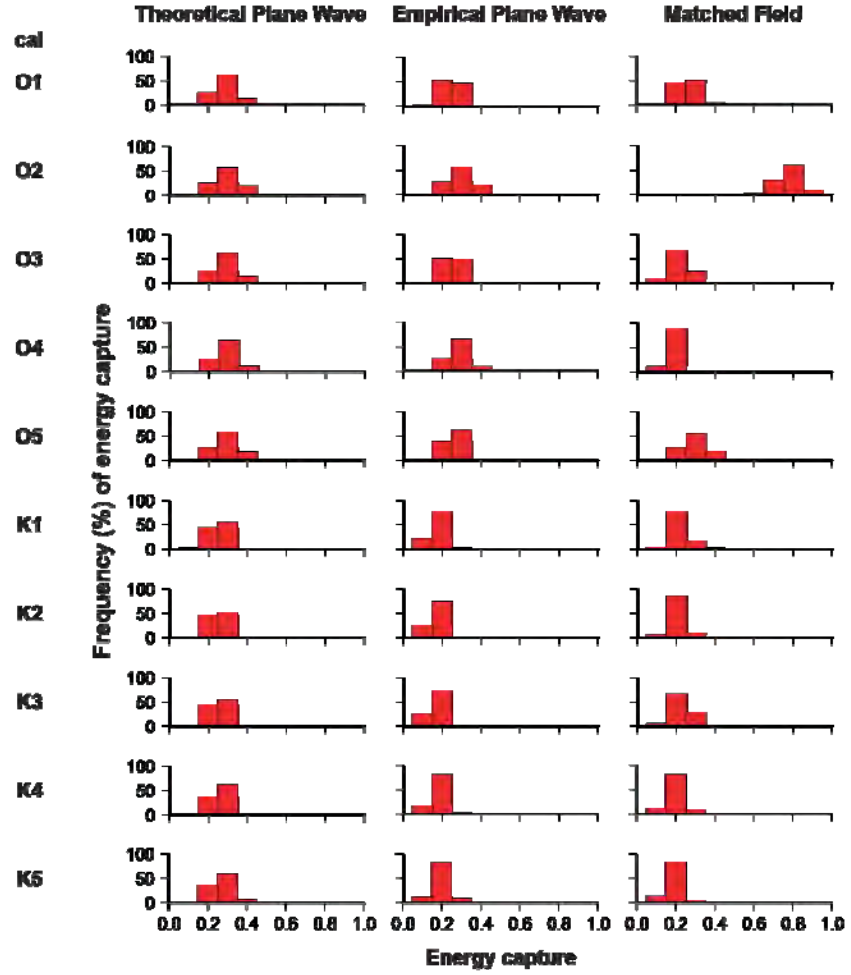


**Figure 3. Distributions of the matched field processing classification statistic (right) for the Olenegorsk (O2) mine population of 52 events under the 10 hypotheses about originating source (indicated at left) separate O2 unambiguously from the other mines. Frequency distributions for the theoretical plane-wave F-K classifier (left) are ambiguous. Distributions for the empirical plane wave F-K classifier show slightly improved separation between the two mining groups.**

Histograms of the relative frequency of classification for events from each mine obtained by maximizing $\widehat{P}(\vec{s})$ under the 10 hypotheses are shown in Figure 4. In the theoretical plane-wave case, a single mine, Rasvumchorr (K2), is assigned most of the events. Observed Pn azimuths generally are biased clockwise (to the south) for most events in this region. The Rasvumchorr mine is the southernmost mine, consequently the theoretical steering vector for this mine presents the best fit to the refracted wavefields. The empirical plane-wave classifier performs considerably better, generally assigning Olenegorsk group events to Olenegorsk mines and Khibiny events to Khibiny mines, probably as a consequence of calibrating wideband refraction effects. However, the empirical plane-wave classifier has large error rates when distinguishing among the 5 mines in each group. By contrast the matched-field classifier achieves nearly complete separation of the mines (1.8% misclassification rate).

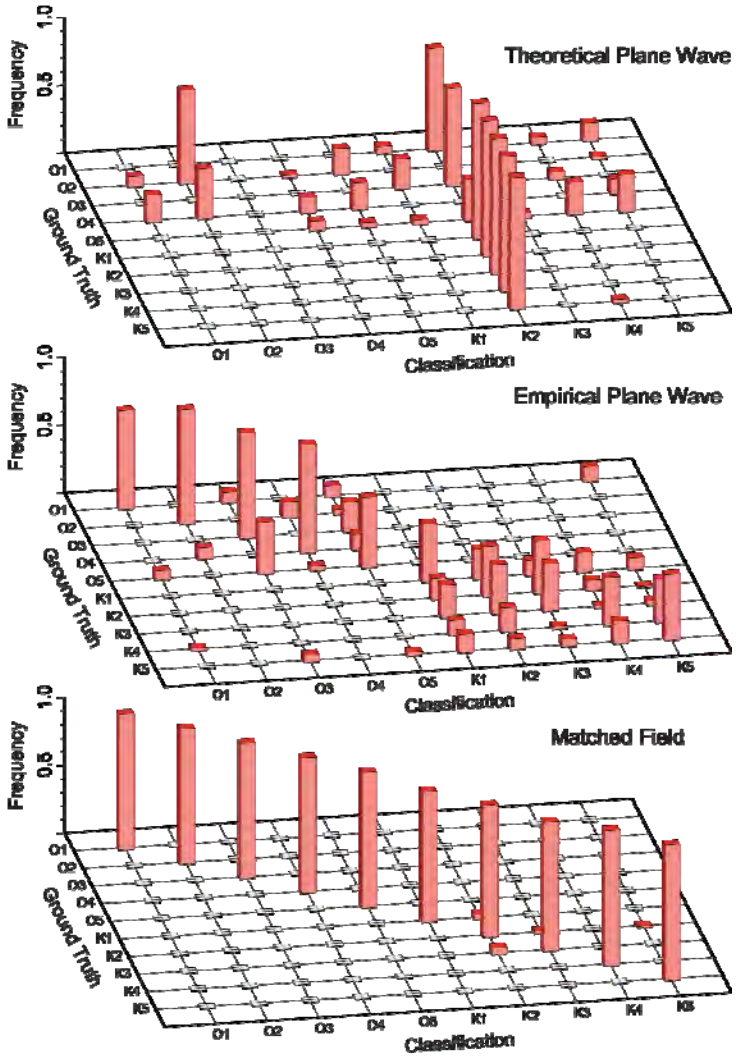


**Figure 4. Classification results for 549 events show that the theoretical plane-wave (F-K) spectrum is unable to resolve the mines, as expected. The empirical plane-wave algorithm largely separates the Olenegorsk group from the Khibiny group and begins to distinguish individual mines. The matched-field method separates all mines with a high (98.2%) degree of reliability.**

We interpret the matched field results to be a consequence of the rich scattering environment for wave propagation in the crust and upper mantle. Many of the mines are too closely spaced (just tenths of a degree apart in azimuth) to be resolved under free-space propagation conditions, which would offer only direct-path propagation. The highly heterogeneous environment creates multipath propagation. We suggest that explosions at the 10 mines illuminate the field of scatters in unique patterns, depending on their positions within that field, and that the seismic wavefields scattered toward the array across the broad scattering aperture differ significantly among the mines. Empirical matched-field calibration captures the detail of refracted and scattered wavefield structure across the array aperture, leading to superior performance in distinguishing the sources. Since mining explosions are usually distributed (ripple-fired) sources, source radiation pattern effects also may make a contribution to distinguishing the fields as energy is directed outward in a unique azimuthal pattern from each mine.

## CONCLUSIONS AND RECOMMENDATIONS

Empirical matched-field processing has already been demonstrated to hold considerable promise in separating and classifying closely spaced sources such as mining explosions. So far, the method has been tested only for one mining area (Khibiny/Olenegorsk on the Kola Peninsula) and one regional array (ARCES, northern Norway, at a distance of 400 km), albeit with outstanding results. A natural by-product of extending coherent processing to larger apertures will be a concomitant improvement in resolution. This effect will provide new tools for interpreting events by making it possible to assign them to very specific sources such as individual mines or aftershock sequences. The proposed methods will be well suited for implementation in an operational environment and may contribute significantly to the developent of a fully automated processing regime requiring less interaction by the human analyst.

We will, in this project, use central Asia as our main study region to exploit the large belts of natural and man-made seismicity required for a test of our processing strategy. Data from suitable networks available for the study are the four Kazakhstan arrays (MKAR, KKAR, ABKAR, BRVK) and the Kyrgyzstan network. Our overall approach is to start with small apertures (the individual Kazakhstan arrays separately) to check the reproducibility of results we obtained in the European Arctic, then to extend the processing strategy first to a medium aperture (the Kyrgyzstan network shown in Figure 5, with a 200-km aperture) and then to a large aperture (the four Kazakhstan arrays considered as a single coherent aperture; >1000 km). Simultaneously, we will investigate methods to expand the source region footprint over which calibrations for coherent methods apply.

We already have demonstrated that beamforming of correlation coefficient traces can be successfully applied across the Kyrgyzstan network (Figure 6), using as an example two events from an aftershock sequence. This is encouraging for the prospects of applying matched field processing to this network, since the matched field technique basically requires spatial coherence similar to the correlation technique for successful application.

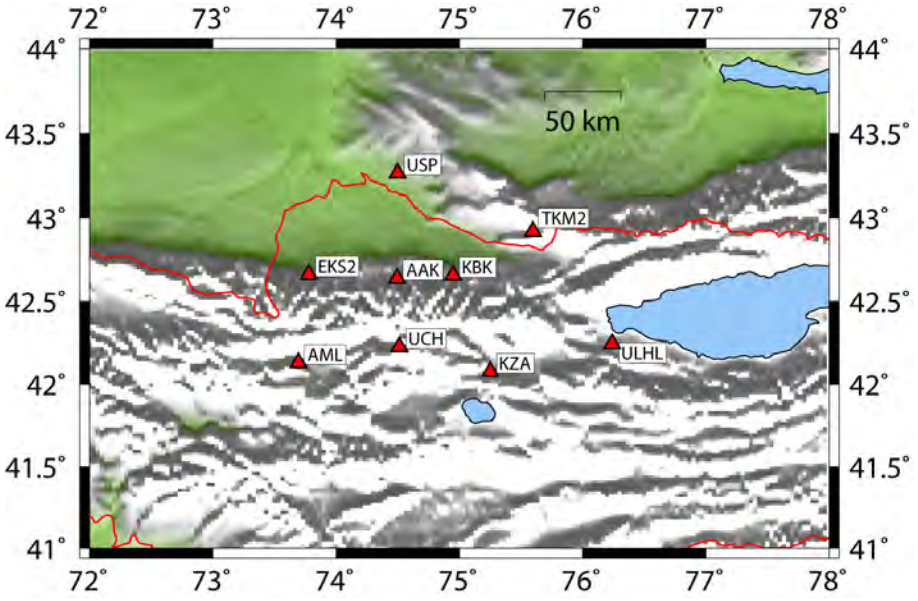


**Figure 5. Locations of 9 of the 10 stations of the Kyrgyzstan network (KNET). An additonal KNET station is located in southern Kazakhstan at coordinates 42.3ºN, 69.6ºE.**

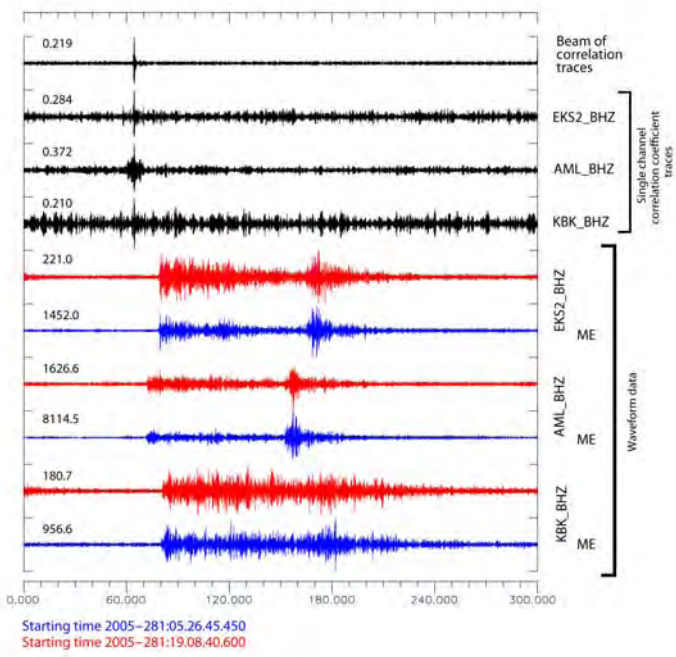


**Figure 6. Illustration of a positive correlation detection made over the KNET network. The master event (blue waveforms) has been cross-correlated with the detected event (red waveforms), resulting in the correlation traces (black). Note the significant signal-to-noise ratio gain on the beam (top trace).**

## REFERENCES

Baggeroer, A. B., W. A. Kuperman, and P. N. Mikhalevsky (1993). An overview of matched field methods in ocean acoustics, IEEE *J. Oceanic Eng*. 19: 401–424.

Fialkowski, L. T., M. D. Collins, W. A. Kuperman, J. S. Perkins, L. J. Kelly, A. Larsson, J. A. Fawcett, and L .H. F. Hall (2000). Matched-field processing using measured replica fields, *J. Acous. Soc. Am* 107: 739–746.

Gibbons, S. J., T. Kværna, and F. Ringdal (2005). Monitoring of seismic events from a specific source region using a single regional array: A case study. *J. Seismol* 9: 277–294.

Gibbons, S. J. and F. Ringdal (2006). The detection of low magnitude seismic events using array-based waveform correlation. *Geophys. J. Int*. 165: 149–166.

Harris, D. B. (1991). A waveform correlation method for identifying quarry explosions. *Bull. Seismol. Soc. Am.* 81: 2395–2418.

Harris, D. B. (2006). Subspace detectors: Theory. Lawrence Livermore National Laboratory report UCRL-TR-222758.

Kværna, T. and F. Ringdal (1986). Stability of various f-k estimation techniques. NORSAR Scientific Report: Semiannual Technical Summary No. 1—1986/1987. NORSAR, Kjeller, Norway, 29–40.

Kværna, T., S. J. Gibbons, F. Ringdal, and D. B. Harris (2007). Integrated seismic event detection and location by advanced array processing. Final scientific report. Contract No. DE-FC52-03NA99517. http://www.osti.gov/bridge/purl.cover.jsp?purl=/898306-G6b8PG/

Schweitzer, J. (2001). Slowness corrections—One way to improve IDC products. *Pure Appl. Geophys*. 158: 375–396.

# ADAPTIVE WAVEFORM CORRELATION DETECTORS FOR ARRAYS: ALGORITHMS FOR AUTONOMOUS CALIBRATION

Frode Ringdal[1], Steven J. Gibbons[1], and David B. Harris[2]

NORSAR[1] and Lawrence Livermore National Laboratory[2]

Sponsored by National Nuclear Security Administration

Contract No. DE-FC52-05NA26604[1] and DE-AC52-07NA28116[2]
Proposal No. BAA05-16

## ABSTRACT

Waveform correlation detectors compare a signal template with successive windows of a continuous data stream and report a detection when the correlation coefficient (CC), or some comparable detection statistic, exceeds a given threshold. Since these methods exploit characteristic details of the full waveform, they provide exquisitely sensitive detectors with far lower detection thresholds than typical STA/LTA algorithms. The drawback is that the form of the sought after signal needs to be known quite accurately a priori which limits such methods to instances of seismicity whereby a very similar signal has already been observed by every station used. Such instances include earthquake swarms, aftershock sequences, repeating industrial seismicity, and many other forms of controlled explosions. The reduction in the detection threshold is even greater when the techniques are applied to multiple channels since stacking can be performed on the correlation coefficient traces with a significant array-gain. A detected event that is co-located with the master event will record the same time-difference at every site in an arbitrarily spaced network which means that the correlation coefficient traces can be stacked coherently even when there is little or no similarity between the actual signals at the different sites.

The focus in the first year of the contract was testing limits of detection capability for almost co-located seismic events. It was demonstrated that the signal from a magnitude 3.5 earthquake could be used as a template to detect nearby events 3 orders of magnitude smaller using multi-channel correlation detectors. This is an improvement better than one magnitude unit for an ARCES-style regional seismic array and better than 1.5 magnitude units for a larger network where coherent array processing was not possible. In the second year, situations were considered where waveforms from closely spaced seismic events differed significantly, primarily due to complicated source-time functions. It was demonstrated that array-based waveform correlation could still be applied effectively by considering the CC trace alignment over the network, maintaining a low detection threshold and low false alarm rate. The application of correlation methods to expose and account for incorrect instrumental timing has been studied throughout.

In this third and final year of the contract, we have examined the size of the “correlation footprint” —how far apart two seismic events may be located and still be detected by correlation using a waveform template. Correlating high-frequency regional signals between sensors of regional arrays suggests through reciprocity that the single channel correlation distance is of the order of only a few hundred meters, and this is confirmed using sensors of the ARCES array for superbly constrained events in a Barents Sea seismic profile. Applying the full array increases the correlation distance to several kilometers, the array-gain resulting from the close alignment of the CC traces. Even a footprint of this size is still far too small for such correlation methods to classify extensive aftershock sequences effectively. We use aftershocks of a magnitude 6 earthquake near Svalbard to demonstrate the inadequacy of individual aftershocks as master events for the full aftershock sequence. No matched filter, constructed from waveforms of any individual aftershock, detected more than a small subset of the sequence. Incoherent correlation detectors can be constructed using multiple waveform envelopes from different seismogram transformations (e.g., different frequency bands, 3-C rotations, and beams) together with characteristic traces such as semblance and F-statistic for specified alignments. The incoherent detectors were demonstrated to be highly effective at identifying events that were clearly closely related to the mainshock, albeit undetected using a basic matched filter. The incoherent detectors are used to identify new master events and generate new waveform templates, and the classical correlation detectors are used to push down the detection threshold within the emergent clusters.

## OBJECTIVE

The overall objective of this three-year study is to develop and test a new advanced, automatic approach to seismic detection using waveform correlation, with special application to seismic arrays. The principal goal is to develop an adaptive processing algorithm. By this we mean that the detector is initiated using a basic set of reference ("master") events to be used in the correlation process, and then an automatic algorithm is applied successively to provide improved performance by extending the set of master events selectively and strategically. These additional master events are generated by an independent, conventional detection system. A periodic analyst review will then be applied to verify the performance and, if necessary, adjust and consolidate the master event set.

## RESEARCH ACCOMPLISHED

In the first year of this project, the primary focus was upon quantifying the improvement in detection capability provided by full-waveform correlation detectors. Inspired by the detection of very weak chemical explosions using the signals of stronger co-located events as templates (Stevens et al., 2006), Gibbons and Ringdal (2006) estimated (by sinking a template signal into increasing levels of background noise) that an improvement of approximately one order of magnitude was possible, with an even greater improvement afforded by the use of arrays. This result was confirmed for an actual example of natural seismicity at regional distances (Ringdal et al., 2006, Gibbons et al., 2007a) where the correlation detections made could be confirmed using data from a local seismic network. The signal from a magnitude 3.5 earthquake was used as a template to detect co-located events, using only array stations at distances of over 600 km from the epicenter. With a very low false alarm rate, earthquakes of magnitudes as small as 0.5 were detected using this system. It was pointed out that the improvement in detectability at a small aperture regional array was approximately 1.0 magnitude units, whereas the improvement at an equidistant array with very poor inter-site coherence was even greater: approximately 1.5 units. Traditional array processing methods fail with incoherent large aperture arrays, whereas the correlation detectors are equally effective over arbitrary network geometries.

In the second year, situations were considered in which waveforms from subsequent almost co-located events differed significantly (primarily due to variations in the source-time histories of the events). It was demonstrated (Ringdal et al., 2007) that multi-channel waveform correlation detectors were nevertheless able to classify such a sequence very effectively, provided that the alignment of the cross-correlation traces was consistent with the occurrence of co-located events. In this case, it was never sufficient only to detect individual local correlation maxima from a single channel correlation trace.

A consequence of the necessary alignment of the cross-correlation traces at all stations is that incorrect timing at one station or more should usually be detectable. Gibbons (2006) demonstrated how the detection of almost repeating mining-induced seismic events could be exploited to measure accurately a timing disparity on a distant single 3-component station. The principles involved are similar to those employed by Rubin (2002) who measured timing disparities from inconsistencies in high-precision earthquake catalogs, although the method employed here requires only waveform similarity without necessarily any knowledge of the source location.

This paper summarizes the principal activities in the third and final year. Firstly we explore the extent of the "correlation footprint;" first using an argument based around reciprocity, and then using recordings at an array station of multiple events in a seismic profile. Secondly, we consider a case study where a large earthquake is followed by an extensive aftershock sequence. It was immediately evident that the waveforms from the main event did not constitute an effective matched filter detector for aftershocks. We explore the possibility of an incoherent type of correlation detector which is able to associate potential master signal templates from the sequence such that the pool of waveform templates can be expanded strategically in order to detect and categorize a maximum number of the seismic events.

**Investigating the Size of the Correlation Footprint**

When assessing the applicability of waveform correlation detectors, it is of paramount importance to be able to estimate how far from the master event a subsequent event can be such that it can still be detected using the available signal template. We use the term “correlation footprint” to describe the region surrounding the master event location in which seismic events can be detected using this template. It is important to note that we are assuming the “best case scenario” for detectability, i.e. that the events have similar source mechanisms and similar source-time functions. Two seismic events which are essentially co-located may not correlate if these properties differ significantly.

The coherency of seismic signals over receiver arrays has been studied at great lengths since the signal semblance at various inter-site distances dictates how useful a given design of seismic array will be for detecting and estimating different classes of seismic signals. For example, a teleseismic signal dominated by low frequency energy can be highly coherent over a network with an aperture of many tens of kilometers, whereas higher frequency signals can be quite incoherent if the instruments are separated by more than a few hundred meters. Similar arguments are likely to apply to the source region and the size of the correlation footprint is likely also to be a function of the dominant frequency of the signal. Geller and Mueller (1980) suggest that well-correlating events are likely to be separated by no more than a quarter wavelength at the dominant wavelength. To examine the extent of the correlation footprint as a function of frequency band and signal duration, we would ideally have records of many hundreds of seismic events with precisely known locations over a very wide range of inter-event distances. The locations of earthquakes are seldom sufficiently well known, and it is expensive and logistically difficult to produce an event array of explosions from which a sufficient number of observations can be made. Mining explosions are often suitable for such studies (Harris, 1991) although these events are often associated with very differing and complicated source-time functions.

It can be informative to consider the reciprocal case, where the signal from a single event is recorded on closely spaced instruments of an array (an approach also taken by, for example, Menke, 1999). Figure 1 shows the signal recorded at the central element (ARA0) of the ARCES array from a surface explosion at a site in Finland at a distance of approximately 178 km (details of these events are provided by Gibbons et al., 2007b). At the sites in the A-ring (see Figure 1), with inter-site distances on the order of 150 m, a clear correlation peak indicates that the signals at these sites can easily be detected by a matched filter using the ARA0 signal as the template. Under our supposition of reciprocity, we assume that the signal from an event 150 m from the master event could probably be detected using this signal template. Figure 1 shows that the signal at the ARB1 site (a distance of 350 m) is also detected clearly using the ARA0 template, albeit with a lower value of the correlation coefficient, whereas the signals at the outer-ring sites (distances over 500 m), are too dissimilar for a matched filter detection. Similar calculations were repeated using the signals from all of the other elements as templates, and therefore covering a very large range of inter-site distances. For this regional event, with a 60-second-long template filtered from 2 to 8 Hz, the signal at a site at ARCES can be detected by correlation using the signal from a different site, provided the inter-site distance is less than about 500 m. This is consistent with the quarter wavelength argument of Geller and Mueller (1980).

In August 2007, a series of marine seismic profiles was shot in the Barents Sea under the name PETROBAR. One of these profiles is displayed in Figure 2 and was of great interest because most of the shots were reasonably well recorded by the ARCES array at a distance of less than 250 km. Unusually for such marine profiles, there are clear S-phases detected at the array. The signals are best observed in the 4-8 Hz frequency band and waveforms filtered in this range are displayed for a segment of a little over 26 minutes in Figure 3. The distance between the events is approximately 200 m, with an approximate 90-second delay between each shot. For the distance between the profile and ARCES, this allows a 60-second template to be extracted for each event, containing both P- and S-phases and coda, which is not contaminated with the signal from any other shots. Figure 3 also displays the single-channel cross-correlation traces calculated from the template as indicated. There is some variation between the different ARCES channels, but the primary observation is that, with only a single channel, the signal from one event can be used as a template to detect events up to 600 m away. This is consistent with the results from the reciprocity experiment described above. This calculation was repeated using every single event as a master event and the pattern remained largely unchanged. Although signals with an exceptionally low signal-to-noise ratio (SNR) usually resulted in a poorer detection capability, there was no obvious connection between the SNR of the master event signal and how many adjacent shots could be detected using the matched filter detector (Shelly et al., 2007, describe a correlation detection case study whereby the master event signals almost inevitably suffer from a low SNR).

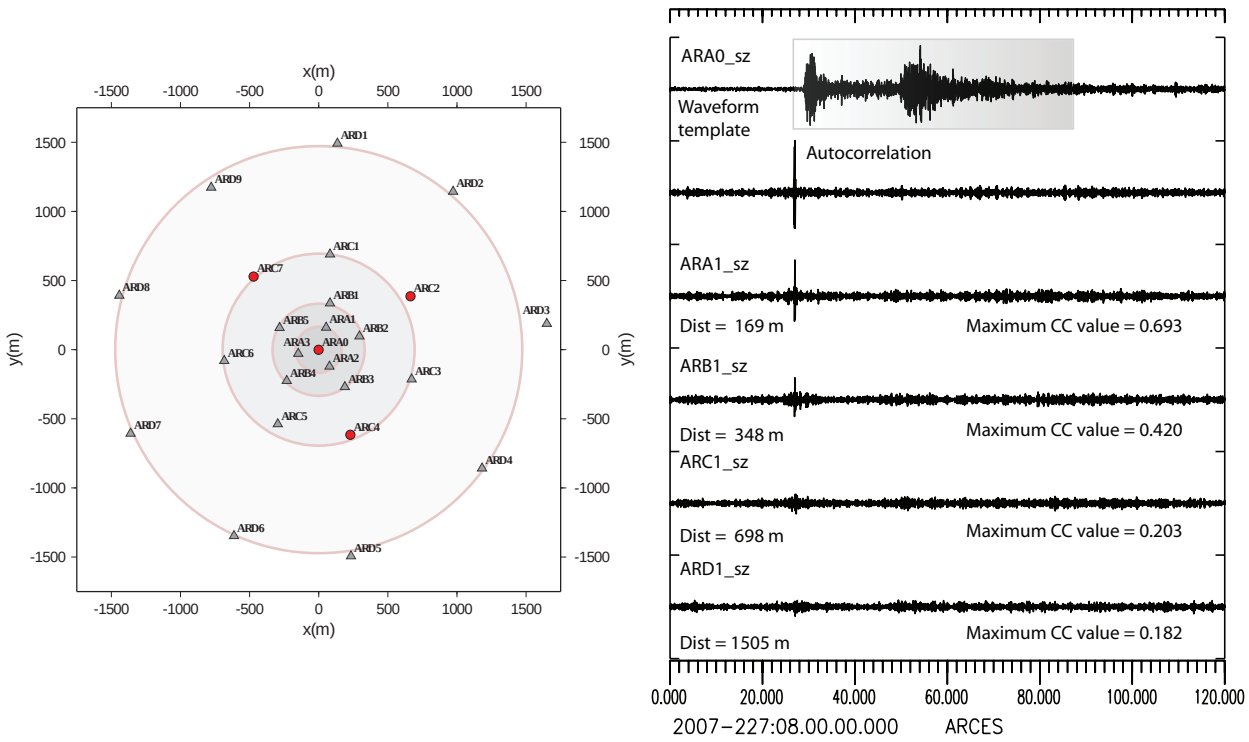


**Figure 1. (Left) Geometry of the ARCES seismic array. (Right) An attempt to detect, using single-channel waveform correlation, the seismic signal from a given event on various vertical sensors of the ARCES array using the signal recorded at the central ARA0 site as the waveform template. The length of the template is 60.0 seconds and all waveforms are filtered 2.0–8.0 Hz.**

The most important observation is that when the cross-correlation traces are stacked, the signals from events at several kilometers distance are detected from the given template. This result is non-intuitive and provides considerable motivation for the use of array-based waveform correlation detectors as opposed to detectors using only single stations. The preliminary investigations of Gibbons and Ringdal (2006) and Gibbons et al. (2007a) went only as far as to suggest that correlation trace stacking should improve the detectability of a co-located event with a lower SNR. That network stacking should increase the size of the correlation footprint is, however, consistent with an observation of Harris (1991) that statistically significant correlation coefficients were obtained between events at greater distances when a full-array was used than when only a single channel was used. Harris (1991) suggests that the quarter-length scale correlation footprint of Geller and Mueller (1980) could be replaced with a two-wavelength footprint.

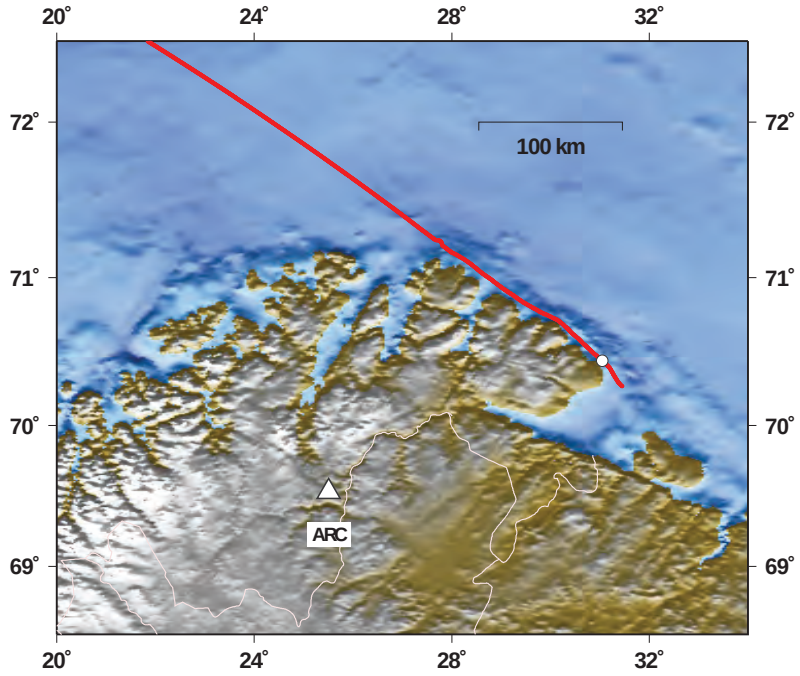


**Figure 2. Locations of shots in the PETROBAR 1 marine seismic profile in relation to the ARCES regional seismic array. The white circle shows the location of shot 121 with coordinates 70.444386°N, 31.053447°E and origin time 2007-221:03.02.32.523. For this part of the profile, shots are separated by approximately 200 m.**

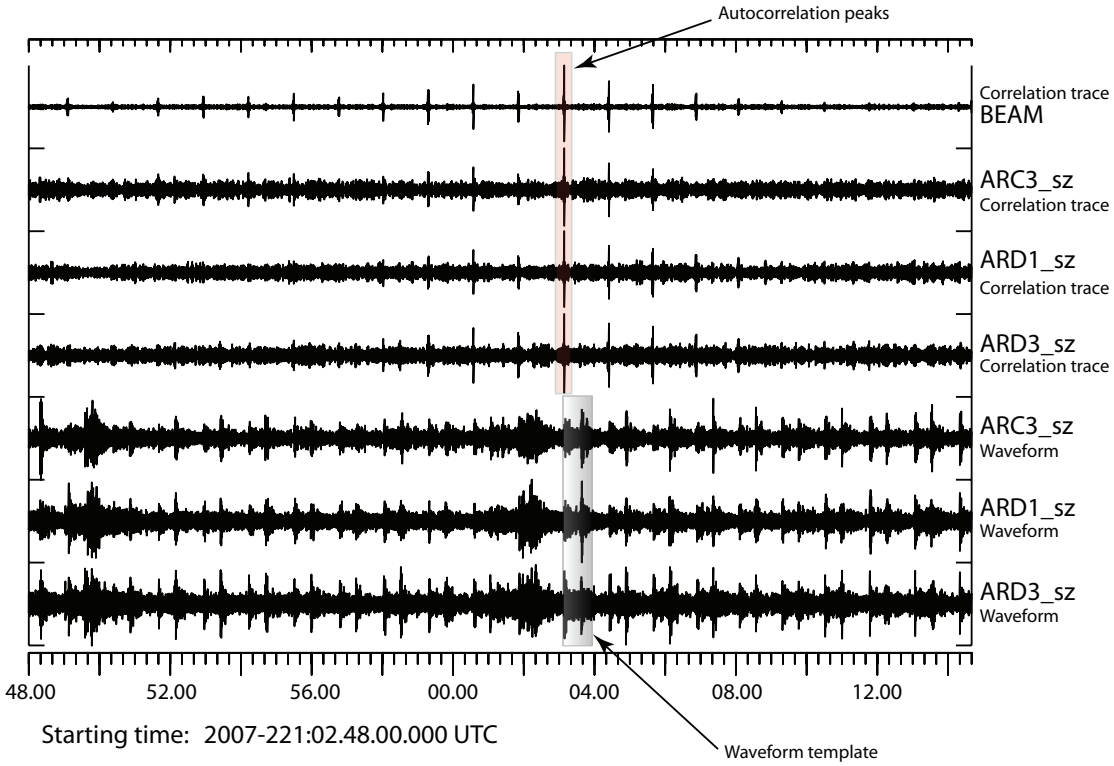


**Figure 3. Waveforms and cross-correlation traces with a template from the shot 121 signal.**

**Algorithms for Autonomous Calibration**

The classification of extensive aftershock sequences from large earthquakes is one of the most challenging problems faced by data centers engaged in the monitoring of nuclear explosions. The shear number of events requiring manual analysis and relocation can lead to significant backlogs in the compilation of event bulletins and the subsequent screening of unambiguous earthquakes. The identification and association of aftershocks should ideally be performed with as high a degree of automation as possible such that limited analyst resources are only necessary to provide checks on the results of the automatic processing.

On February 21, 2008, a magnitude 6 earthquake occurred in the Storfjorden region close to Svalbard. Whilst not large in a global perspective, this event illustrates beautifully the difficult task of aftershock identification. The aftershock sequence consisted of many hundreds of events within the first two days and a very much increased level of seismicity for several months afterwards. The simulated helicorder plot from the SPITS array (Figure 4, left) illustrates the largest events for February 23, 2008. The dynamic range at the SPITS array (Figure 4, right) saturated under the main event and the data is clipped on all channels. The signal at the ARCES array was not clipped and a template was extracted rapidly in an attempt to detect aftershocks using a correlation detector. It became evident that very few of the numerous aftershocks were being detected using this template, with essentially no convincing detections. Following the analyst review of the aftershocks in the first few days following the main event, matched filter detectors were initiated for a large number of master events. Many of these detectors were successful in detecting large numbers of other events and it became clear that a cluster analysis of the sequence would be possible using associations indicated by high values of the correlation coefficient.

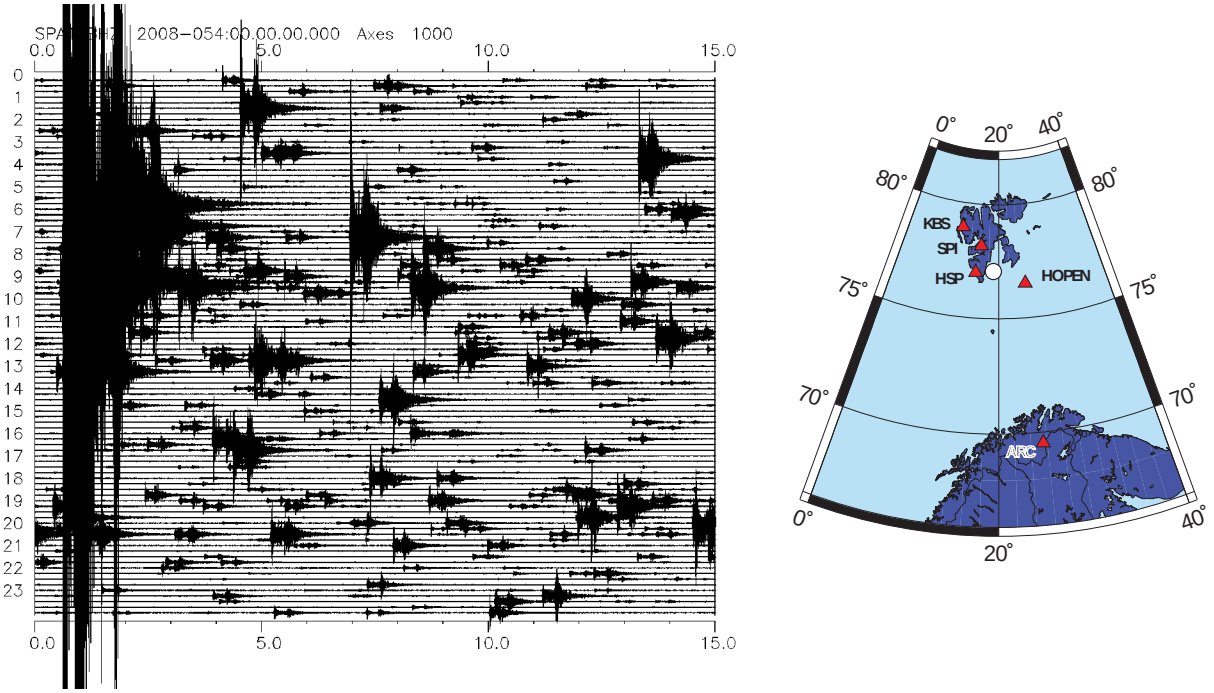


**Figure 4. (Right) Location of the M=6 Storfjorden, Svalbard, earthquake February 21, 2008 (white circle), in relation to the International Monitoring System arrays ARCES and SPITS and the 3-component stations KBS, HSP, and HOPEN. (Left) Simulated helicorder plot for February 23, 2008, filtered 2-8 Hz, on the SPA1_BHZ instrument of the SPITS array. Essentially all of the signals visible on this plot are aftershocks from this event.**

In performing this correlation analysis, we have, however, been completely dependent upon a bulletin of manually located events; our goal is to classify the sequence automatically. The preliminary automatic event bulletin (GBF: Ringdal and Kværna, 1989) upon which the reviewed bulletin is based is not accurate enough for an unambiguous association of events; errors in origin time and hypocentral location are too large even for the setting of time-windows for waveform correlation analysis. The fixed-window template method of Gibbons et al. (2005) is also not applicable.

This algorithm is designed for very small source regions (maximum length-scale of 2 or 3 km) for which numerous events have already been observed for the calibration of processing parameters. A preliminary examination of event location estimates for the Svalbard sequence indicates a source region aperture at least an order of magnitude larger than this. In addition, we would like to assume that our main shock has occurred in a location where no event has been observed previously, meaning that no calibration data are available.

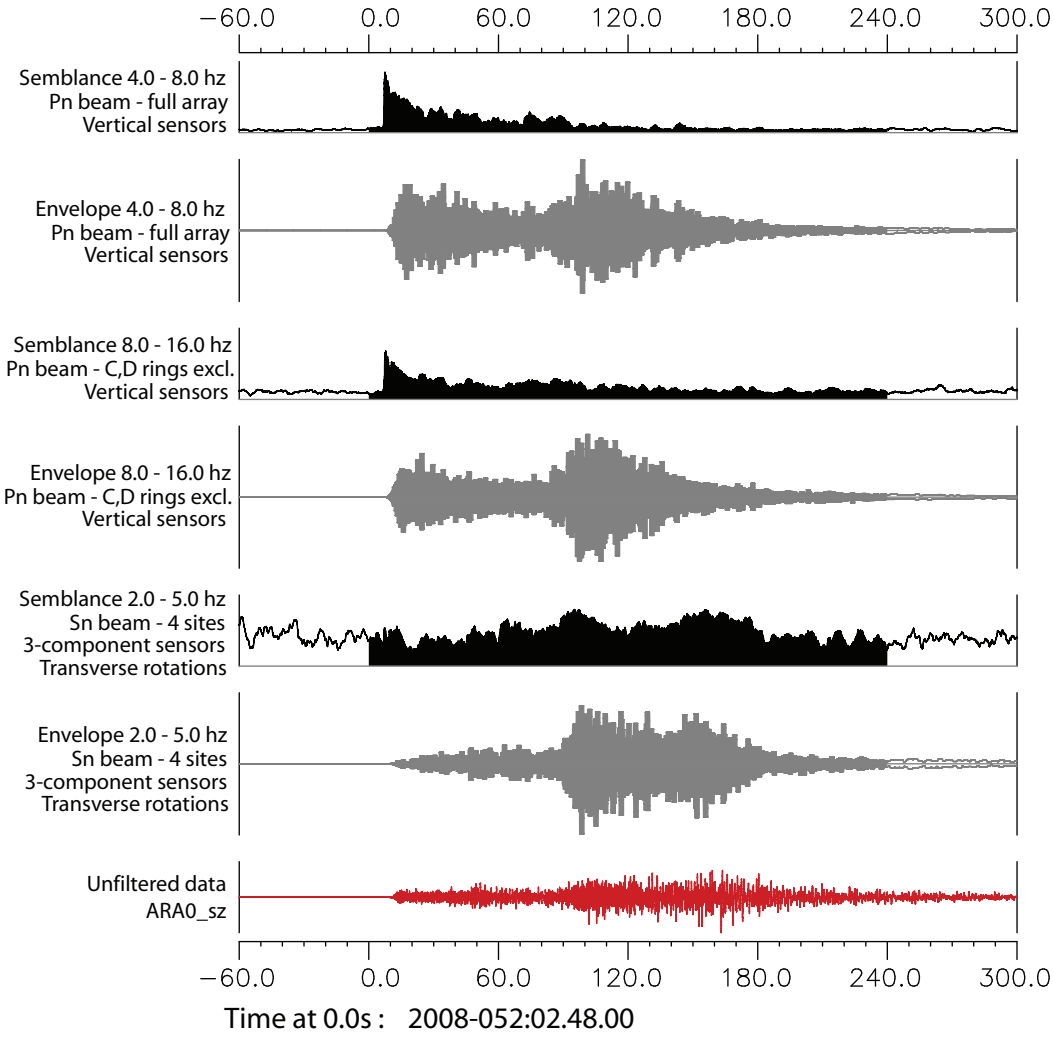


**Figure 5. Construction of an "incoherent matched filter detector" from ARCES waveforms from the February 21, 2008, Storfjorden main event. The small aperture of the ARCES array means that the variability of waveform envelopes between sensors is minimal and that there would therefore be very little advantage in stacking of correlation coefficient traces. However, the coherence of the waveforms can be exploited to form beams using time-delays corresponding to the slownesses of the various observed seismic phases. This emphasizes different sections of the seismograms at times characteristic of the source-receiver distance, although with far less sensitivity than that necessary for setting of the time-windows for f-k analysis prescribed in the algorithm of Gibbons et al. (2005). In addition to the envelopes of beams formed for different slowness vectors, different component rotations, and different frequency bands, we have the corresponding characteristic functions (semblance and the related F-statistic) that can also be correlated against the same functions evaluated for the incoming data stream. The semblance functions are greatest for the initial Pn-arrivals on the corresponding beams. The semblance function for the Sn beam on the transverse components suffers from the reduced number of instruments and non-optimal coherence of the Sn phase between these four widely spaced sensors.**

An alternative possibility is that of correlating characteristic functions of the waveforms against the corresponding transformations of the incoming data. Since we do not have "ripple for ripple" correspondence between the events we wish to associate, we need to correlate some "coarser" signature of the generated signals. Viable automatic detection and location schemes have been constructed that correlate waveform envelopes (see, for example, Withers et al., 1999) but we need to proceed with caution since the small aperture of our regional seismic array means that the waveform envelopes on the different channels show essentially the same features at the same times. The standard waveform correlation detector (a "coherent correlation detector") exploits details in the full wavetrain that are specific to the given site. For this reason, one would rarely apply beamforming prior to correlation since this would lose much of the available information about the signal's signature at each site - beamforming is applied after the correlation to much greater effect. However, since we wish to compare waveform envelopes, or some other signal attributes, (i.e. an "incoherent correlation detector") we should apply every possible transformation to the waveforms from a given event that are likely to result in a shape specific to that source region. The construction of part of the "incoherent template" at ARCES for the Svalbard event is displayed in Figure 5.

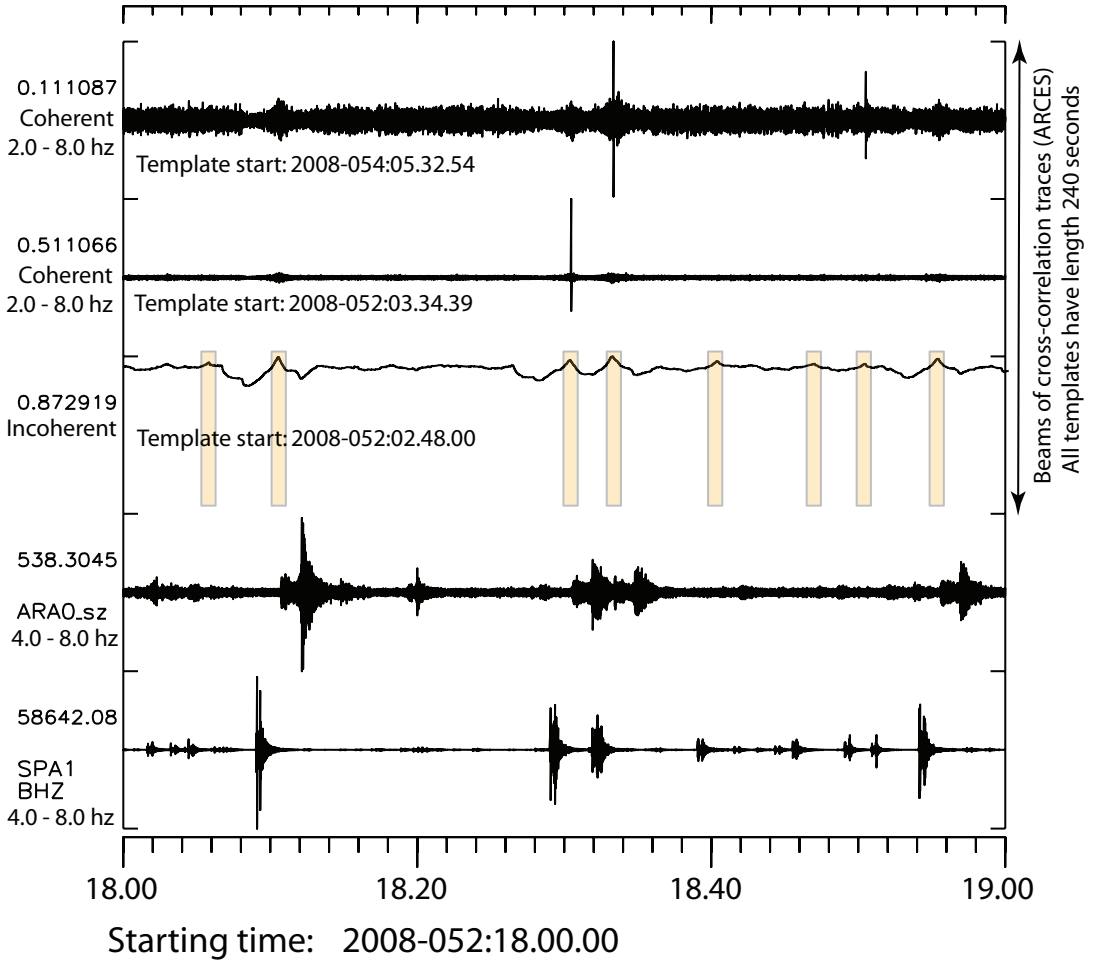


**Figure 6. Detections of aftershocks using the incoherent template illustrated in Figure 5 and using two standard correlation detectors. The template for the top trace detects two events during this one-hour interval, the template for the second trace detects one (different) event, and the incoherent template takes all three events plus 5 additional events. Data from the SPITS array in the lowermost trace confirms that each of the incoherent correlation detections does indeed correspond to a Svalbard aftershock. Note that the signals at the SPITS array arrive approximately 90 seconds prior to the ARCES detections due to the travel-time differences. The Svalbard aftershocks visible in the data that are not detected by the incoherent correlator occur within close succession of other Svalbard events, and such rapid sequences cannot be resolved using the four-minute templates at ARCES.**

Unlike the standard correlation detections, the peaks on the incoherent correlation trace beam are somewhat marginal (Figure 6) but, with a threshold carefully and empirically set, the detector has been demonstrated to identify essentially all of the major events in this sequence and with a very low false alarm rate.

The relationship between the three uppermost traces in Figure 6 suggests a system for the semi-autonomous readjustment of a waveform template pool for new master events. Signals from such events could be selected either for standard correlation detectors or, alternatively, as new templates to add to the basis for a signal subspace detector (Harris, 1989). A candidate template is any event that triggers a detection on the incoherent detector (probably verified by an analyst before accepting). The time of the corresponding event is searched for in the lists of correlation detections from the existing correlation detector pool. If an entry is found with a sufficiently high correlation coefficient, we can most likely ignore the new event since it seems that we already have a template that is likely to detect subsequent occurrences of this signal. If no entry in existing detection lists is found, or if there are detections that are marginal, it is probably sensible to include the new event as a waveform template in order to detect further occurrences of this signal, including those which are too weak for the incoherent method to detect.

## CONCLUSIONS AND RECOMMENDATIONS

Two major topics have been investigated in the third and final year of this contract.

Firstly, it has been demonstrated that the Geller and Mueller quarter wavelength argument is probably reasonable for the size of the correlation footprint for single channel matched filter detectors. Stacking the correlation coefficient traces over an array or network results not only in an improvement in detectability for weaker co-located events, but also an expansion of the size of the correlation footprint. For the regional signals in the PETROBAR-1 profile displayed here, the correlation distance for a single channel was of the order 500–600 m. When the full ARCES array was employed, this distance was increased to several kilometers.

Secondly, an extensive aftershock sequence has been studied whereby the signal from the main event did not constitute a suitable template for the detection of subsequent seismic events. Using various transformations of the signal from the main event (e.g., beamforming, filtering, rotation) we can construct a template of characteristic functions for the extended source region that constitutes an “incoherent correlation detector”. This detector successfully identified large numbers of the aftershocks with a very low false alarm rate. It is likely that the simultaneous running of an incoherent detector together with numerous standard correlation detectors will allow a more complete characterization of the aftershock sequence than would be possible if only the traditional matched filter detectors were to be used.

## ACKNOWLEDGEMENTS

We thank Dr. Oliver Ritzmann of the University of Oslo for providing the coordinates and origin times of the shots in the PETROBAR seismic profiles. We are grateful to Berit Paulsen of NORSAR for locating aftershocks of the February 21, 2008, Svalbard earthquake. Maps were created using GMT software (Wessel and Smith, 1995).

## REFERENCES

Geller, R. J. and Mueller, C. S. (1980). Four Similar Earthquakes in Central California, in *Geophys. Res. Lett*. 7: 821–824.

Gibbons, S. J. (2006). On the Identification and Documentation of Timing Errors: An Example at the KBS station, Spitsbergen, *Seism. Res. Lett*. 77: 559–571.

Gibbons, S. J., Bøttger Sørensen, M., Harris, D. B. and Ringdal, F. (2007a). The detection and location of low magnitude earthquakes in northern Norway using multichannel waveform correlation at regional distances, in *Phys. Earth Planet. Int*. 160: 285–309.

Gibbons, S. J., Kværna, T., and Ringdal, F. (2005). Monitoring of seismic events from a specific source region using a single regional array: A case study, in *J. Seismol.* 9: 277–294.

Gibbons, S. J. and Ringdal, F. (2006). The detection of low magnitude seismic events using array-based waveform correlation, in *Geophys. J. Int*. 165: 149–166.

Gibbons, S. J., Ringdal, F., and Kværna, T. (2007b). Joint seismic-infrasonic processing of recordings from a repeating source of atmospheric explosions, in *J. Acoust. Soc. Am.* 122: EL158–EL164.

Harris, D.B. (1989). Characterizing Source Regions with Signal Subspace Methods: Theory and Computational Methods, Lawrence Livermore National Laboratory report number UCID-21848.

Harris, D.B. (1991). A waveform correlation method for identifying quarry explosions, in *Bull. Seism. Soc. Am.* 81: 2395–2418.

Menke, W. (1999), Using waveform similarity to constrain earthquake locations, in *Bull. Seism. Soc. Am.* 89: 1143–1146.

Ringdal, F. and Kværna, T. (1989). A multi-channel processing approach to real time network detection, phase association, and threshold monitoring, in *Bull. Seism. Soc. Am.* 79: 1927–1940.

Ringdal, F., Gibbons, S. J. and Harris, D. B. (2006). Adaptive waveform correlation detectors for arrays: algorithms for autonomous calibration, in *Proceedings of the 28th Seismic Research Review, Ground-based Nuclear Explosion Monitoring Technologies*, LA-UR-06-5471, Vol. 1, pp 444–454.

Ringdal, F., Gibbons, S. J. and Harris, D. B. (2007). Adaptive waveform correlation detectors for arrays: algorithms for autonomous calibration, in *Proceedings of the 29th Monitoring Research Review: Ground-based Nuclear Explosion Monitoring Technologies*, LA-UR-07-5631, Vol. 1, pp 444–453.

Rubin, A. M. (2002). Using Repeating Earthquakes to Correct High-Precision Earthquake Catalogs for Time-Dependent Station Delays, in *Bull. Seism. Soc. Am.* 92: 1647–1659.

Shelly, D. R., Beroza, G. C., and Ide, S. (2007). Non-volcanic tremor and low-frequency earthquake swarms. *Nature* 446: 305–307.

Stevens, J. L., Gibbons, S., Rimer, N., Xu, H., Lindholm, C., Ringdal, F., Kværna, T., Murphy, J. R. (2006). Analysis and simulation of chemical explosions in nonspherical cavities in granite, in *J. Geophys. Res.* 111: B04306, doi:10.1029/2005JB003768.

Wessel, P. and Smith, W. H. F. (1995). New version of the generic mapping tools, *EOS Trans., Am. geophys. Un*. 76: 329.

Withers, M., Aster, R., and Young, C. (1999) An automated local and regional seismic event detection and location system using waveform correlation, in *Bull. Seism. Soc. Am.* 89: 657–669.

# MODELING TRAVEL-TIME CORRELATIONS BASED ON SENSITIVITY KERNELS AND CORRELATED VELOCITY ANOMALIES

William L. Rodi[1] and Stephen C. Myers[2]

Massachusetts Institute of Technology[1] and Lawrence Livermore National Laboratory[2]

Sponsored by National Nuclear Security Administration

Contract No. DE-FC52-05NA26603[1] and DE-AC52-07NA27344[2]

Proposal No. BAA05-14

## ABSTRACT

This project concerns the errors in predicted regional and teleseismic travel times resulting from velocity heterogeneity in the real Earth not represented in the reference Earth model used for travel-time calculation. We are developing techniques for calculating the covariances between such prediction errors associated with different event-station paths, based on a statistical characterization of the velocity heterogeneity and the theoretical travel-time sensitivity to the Earth's velocity structure for each path. This effort is motivated by previous discoveries that event location errors can be reduced when a locator uses the full covariance matrix for travel-time prediction errors, including off-diagonal elements to account for correlations. Moreover, a physical model for travel-time covariances potentially provides useful constraints in the construction of empirical travel-time correction surfaces. We have developed numerical algorithms that generate a covariance matrix for first-arrival P-wave travel times along paths to various station locations from a fixed event location. Calculations with various station geometries reveal a strong dependence of the travel-time variances and covariances on the spatial sampling of seismic rays. For example, we find that prediction-error variances are smaller for teleseismic P arrivals than for Pn arrivals since teleseismic rays travel a shorter, more vertical path in the upper mantle, whereas most of the Pn path is in the upper mantle where velocity heterogeneity is greatest. Our calculated travel-time variance vs. distance curve agrees well with empirical results for a Eurasian data set when the standard deviation of velocity heterogeneity decreases from 2% to 1% at the 410 km discontinuity. We further find that correlation between travel times can be parameterized by inter-station distance only when both stations observe the same travel-time branch, but distinct breaks in residual correlation occur at the cross-over of branches. Thus, our calculations show small travel-time correlation between a teleseismic P arrival and a Pn arrival at different stations, even when the stations are close to one another. Last, we are currently investigating the effects of finite frequency sensitivity kernels on travel-time correlation. In the preliminary work presented here, we estimate the spatial extent of finite-frequency kernels by computing delay times for paths off of the geometrical ray. We find that the sensitivity of 1-Hz Pn arrivals are sensitive to the entire velocity profile between the Moho and a maximum depth that reaches 200 km for an arrival at 15° distance, suggesting that prediction errors in regional and far-regional travel times will be correlated over distance separations well exceeding the correlation length of velocity heterogeneity.

## OBJECTIVE

To achieve accurate event locations and estimates of location uncertainty, seismic event location algorithms must account for two types of errors: *pick* errors in the measured arrival times of the seismic phases observed at various stations, and *model* errors incurred in predicting the travel times of observed station/phase combinations as a function of the event location. Model errors are attributable to velocity anomalies in the Earth that are not rendered in the velocity model used for travel-time prediction. When the observing stations are sufficiently close to one another, their model errors are expected to be correlated. While it is now standard practice for event location algorithms used in nuclear monitoring to assign error *variances* that include the contribution from model prediction errors, the algorithms generally set the error *covariances* to zero; correlations are ignored. Doing so can seriously degrade location accuracy when the distribution of seismic stations is far from uniform (Chang et al., 1983; Yang et al., 2004).

This project is investigating the phenomenon of correlated travel-time prediction errors from a physical point of view, making use of the principles of wave propagation through heterogeneous media and our knowledge of the statistical properties of the Earth's heterogeneity. Specifically, we are developing techniques to calculate covariance matrices of travel-time model errors by integrating travel-time sensitivity kernels with plausible correlation functions describing the Earth's velocity heterogeneity. This paper summarizes our approach and reports some numerical calculations designed to determine how travel-time prediction variances and correlations depend on the epicentral distance from an event. We also report a preliminary investigation into the importance of finite-frequency effects of travel-time covariances.

## RESEARCH ACCOMPLISHED

### Approach

Given a set of $n$ arrival time data from an event, one can decompose the data errors as (for $i = 1,\ldots,n$)

$$e_i = e_{\mathrm{p},i} + e_{\mathrm{m},i}, \tag{1}$$

where the first term is the *pick*, or measurement, error and the second term is the *model* error, or error in the travel time predicted by a reference velocity model. Typically, event location algorithms assume that the errors of both types have a zero mean and a diagonal $n \times n$ variance/covariance matrix, leading to a diagonal covariance matrix for the total errors. The errors for different $i$ are thus assumed to be uncorrelated. We are addressing the problem of calculating a full covariance matrix for model errors, having components $\sigma_{\mathrm{m},ij}$ defined by

$$\sigma_{\mathrm{m},ij} = \mathrm{E}[e_{\mathrm{m},i}\, e_{\mathrm{m},j}]. \tag{2}$$

E[ ] denotes the expectation operator.

To explain our approach to covariance modeling, we consider only P-wave arrivals. Let $v_0(\mathbf{x})$ denote the P velocity function for the reference model, and $v_E(\mathbf{x})$ denote the Earth's true (and unknown) velocity function. Then, model errors can be linked to the slowness difference, which we denote $m(\mathbf{x})$:

$$m(\mathbf{x}) = v_E^{-1}(\mathbf{x}) - v_0^{-1}(\mathbf{x}). \tag{3}$$

We assume that the travel-time dependence on slowness can be adequately approximated as linear, allowing us to express the model error in the $i$th datum as

$$e_{\mathrm{m},i} = \int d\mathbf{x}\; a_i(\mathbf{x})\, m(\mathbf{x}), \tag{4}$$

where $a_i(\mathbf{x})$ is the first-order sensitivity kernel of the $i$th travel-time prediction function, as evaluated at $v_0$. In the high-frequency limit, this kernel is concentrated along the geometrical ray connecting the event and station locations. For finite frequency, it is spatially distributed around this ray. In either case, we point out that the model error is a function of the event *and* station locations.

We consider $m(\mathbf{x})$ to be a Gaussian random field having zero mean and a specified covariance between any two points, described by a covariance operator $C(\mathbf{x}, \mathbf{x}')$:

$$\mathrm{E}[m(\mathbf{x})] = 0 \tag{5}$$

$$\mathrm{E}[m(\mathbf{x})\, m(\mathbf{x}')] = C(\mathbf{x}, \mathbf{x}'). \tag{6}$$

The covariance between two model errors is then given by

$$\sigma_{\mathrm{m},ij} = \int d\mathbf{x}\; a_i(\mathbf{x}) \int d\mathbf{x}'\; C(\mathbf{x}, \mathbf{x}')\, a_j(\mathbf{x}'). \tag{7}$$

Equation (7) implies that the extent to which two model errors are correlated depends on the spatial relationship between their sensitivity kernels in relation to the correlation structure of the velocity field.

## Covariance Modeling Algorithms

A flexible and numerically advantageous approach to characterizing nonstationary random fields is to specify the covariance operator indirectly through its operator inverse, which we denote $D$, such that

$$DC(\mathbf{x}, \mathbf{x}') = \delta(\mathbf{x} - \mathbf{x}'). \tag{8}$$

If we take $D$ to be a differential operator, then $C(\mathbf{x}, \mathbf{x}')$ is its Green's function. Following Rodi et al. (2003), we have implemented this approach with $D$ as (in spherical coordinates)

$$D = \frac{\mathrm{const}}{\lambda_1^2 \lambda_2 \sigma^2} \left[ \delta(\mathbf{x}) - \frac{1}{(2\ell - 3)} \left( \frac{\lambda_1^2}{r^2} \nabla_1^2 + \lambda_2^2 \frac{\partial^2}{\partial r^2} \right) \right]^{\ell}, \quad \ell \geq 2. \tag{9}$$

Here $\nabla_1^2$ is the horizontal Laplacian operator; $\lambda_1$ and $\lambda_2$ are horizontal and vertical correlation lengths, respectively; and $\sigma^2$ is the variance of the slowness. The order of the operator, $\ell$, controls how $C(\mathbf{x}, \mathbf{x}')$ decays as the distance between $\mathbf{x}$ and $\mathbf{x}'$ increases. We take $\ell = 2$, which leads to an exponential decay. In this approach, nonstationarity results from three effects: (1) a boundary condition at the Earth's surface, (2) de-correlation of velocity anomalies across interfaces, such as the Moho, and (3) allowing spatial dependence of $\sigma$, $\lambda_1$ and $\lambda_2$.

In previous years we developed two numerical methods for evaluating the double integral of equation (7), given that the inverse velocity covariance operator $D$ is specified. These algorithms are described in Rodi and Myers (2007).

## Distance Dependence of Travel-Time Covariance

To investigate the dependence of travel-time covariances on epicentral distance, we applied our numerical modeling approach to a north-south linear array of 70 stations equally spaced from 0.5° to 35° in epicentral distance from a nominal event location at 0°N, 0°E. The resulting $70 \times 70$ covariance matrix then reveals the dependence of travel-time variance on distance and of travel-time correlation on distance and distance separation between stations. The calculations were done using travel-time sensitivities implied by

Table 1: Geostatistical parameters for numerical examples

| | *Case A* | *Case B* |
|---|---|---|
| Velocity std. dev. ($\sigma$) | | |
| Crust | 3% | 3% |
| Mantle ($z \leq 410$) | 1.5% | 2% |
| Mantle ($z > 410$) | 1.5% | 1% |
| Horiz. correlation length ($\lambda_1$) | 300 km | 300 km |
| Vertical correlation length ($\lambda_2$) | | |
| Crust | 17.5 km | 17.5 km |
| Mantle | 60 km | 60 km |

geometrical ray theory, ignoring finite-frequency effects. Geometrical rays were evaluated with the *ak135* 1D Earth model (Kennett et al., 1995) and transformed to discrete sensitivities for a 3D model parameterization.

We performed the calculations under two assumptions about the geostatistical parameters of velocity heterogeneity, as listed in Table 1. The correlation distances are the same for both cases: $\lambda_1 = 300$ km, $\lambda_2 = 17.5$ km in the crust and 60 km in the mantle. The standard deviation of velocity variations in the crust was also common to both cases: $\sigma = 3\%$. The two geostatistical models differ in the standard deviation assigned to the mantle velocity. The first model (Case A) used $\sigma = 1.5\%$ throughout the mantle. Case B had $\sigma = 2\%$ in the upper mantle (above the 410-km discontinuity) and $\sigma = 1\%$ below 410 km.

Figure 1 shows the resulting standard deviations of travel-time model errors, derived from the diagonal elements of the $70 \times 70$ covariance matrix and plotted versus epicentral distance. Discontinuities in the travel-time standard deviation are evident at the same distances in both cases of geostatistical parameters. These discontinuities are directly attributed to discontinuities in ray parameter, which are controlled by the *ak135* model. From approximately 2° to 15° travel-time error increases consistently, but not strictly linearly. The rate of increase in the error diminishes with distances, as rays begin to average over several correlation lengths of velocity variations. At approximately 15°, rays begin to dive deeper into the upper mantle and travel more vertically, resulting in more averaging over the shorter correlation-length anomalies in the vertical dimension. Several breaks in the error structure are evident as rays dive below the 410-km velocity discontinuity and then the 660-km discontinuity. Error structure stabilizes at teleseismic distances ($\geq 24°$) when rays bottom in the lower mantle and the ray parameter remains continuous. Travel-time error is lower at teleseismic distance because vertically traveling rays in the more strongly heterogeneous upper mantle average over more wavelengths of geologic heterogeneity, recalling that we assumed the vertical scale of heterogeneity to be much smaller than the horizontal scale.

The red line in each panel of Figure 1 is an empirical travel-time error vs. event-station distance relation we inferred from observations in the LLNL ground-truth database of events for Eurasia and Africa (Ruppert et al., 2005). First-arriving P-waves were used for events meeting the GT criteria of Bondar et al. (2004) or whose location was constrained by non-seismic means (e.g., known explosions, mine collapses, earthquakes with InSAR signals). We used a methodology similar to Flanagan et al. (2007) to assess travel-time prediction (model) error. We began by selecting only stations with sufficient data for distance-dependent variance estimation (at least 10 arrivals in each 1° event-station distance bin). For each station, we assessed pick (random) error by computing the standard deviation of residuals for clusters of events within 20 km of one another. The random error for many event clusters was used to determine pick error as a function of station-event distance. We subtracted distant-dependent pick error variance from travel-time residual variance to estimate distance-dependent model-error variance. The final curve, shown in each panel of Figure 1, was obtained as an average of the model-error curve for stations throughout

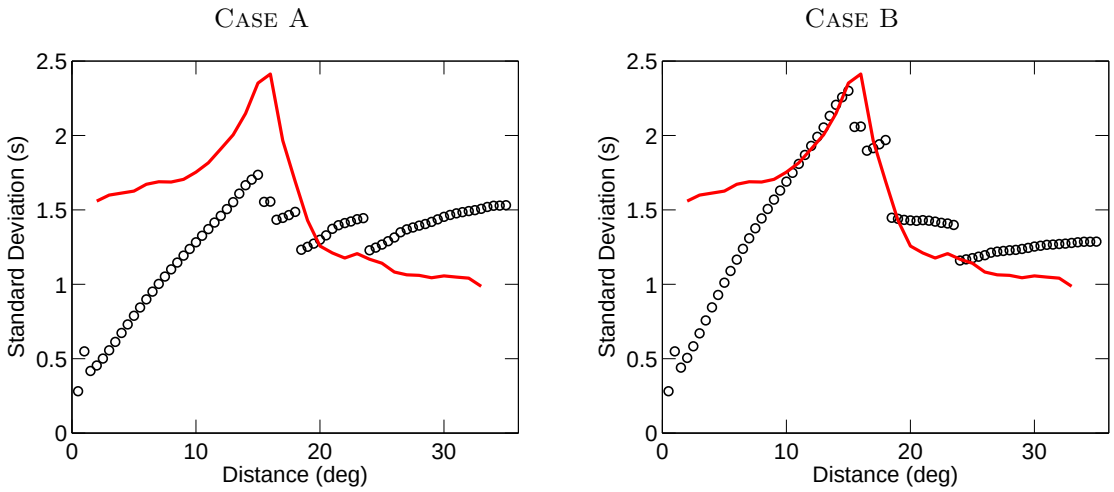


**Figure 1: Model-based standard deviation of travel-time prediction error as a function of epicentral distance, plotted as black circles and derived with two different geostatistical models of velocity heterogeneity (Cases A and B of Table 1). The cases differ in their assumption about the magnitude of mantle heterogeneity ($\sigma$), with the left panel assuming $\sigma = 1.5\%$ everywhere in the mantle, and the right panel assuming $\sigma = 2\%$ in the upper mantle ($z \leq 410$ km) and $\sigma = 1\%$ below 410 km. In each panel, the red line displays an empirically derived standard-deviation vs. distance curve.**

Eurasia and Africa. Comparing the left and right panels of the figure, it is clear that our Case B calculations of travel-time standard deviation are much more consistent with the empirically derived curve than are the Case A calculations, suggesting that a geostatistical model concentrating heterogeneity in the upper mantle is more realistic.

Figure 2 displays the model-based correlation matrix corresponding to the standard deviations shown in Figure 1. Only Case B is shown since the correlation matrices for the two cases were nearly identical. Analogous to the breaks in travel-time standard deviation, the correlation matrix, which is ordered by event-station distance, shows a roughly block-diagonal structure with the blocks delimited by the same cross-over distances and associated jumps in ray parameter. These results demonstrate that simple estimates of travel-time correlation based on the distance between stations do not adequately account for correlations between travel times near cross-over distances. If two stations straddle a break in ray parameter, then travel-time residuals are likely to be weakly correlated. This result has profound implications for both location algorithms and empirical methods (e.g., kriging) that make use of the travel-time residual covariance matrix.

## Travel-Time Correlation vs. Latitude and Longitude

In this example, we computed the travel-time covariance matrix for each of six station arrays, varying in distance from a nominal event location at 0°N, 0°E. Each array contained 169 stations in a $13 \times 13$ square with 1° spacing in latitude and longitude. The computations were done with *ak135* sensitivities for infinite-frequency travel times.

The results are shown in Figure 3. Each panel corresponds to one of the six arrays and plots the travel-time correlation coefficient between the center station (marked with a white dot) and the other stations of the array. The results show clearly the nonstationarity of travel-time model errors as a function of station location, evident as discontinuities in correlation coefficient with distance, as were seen in

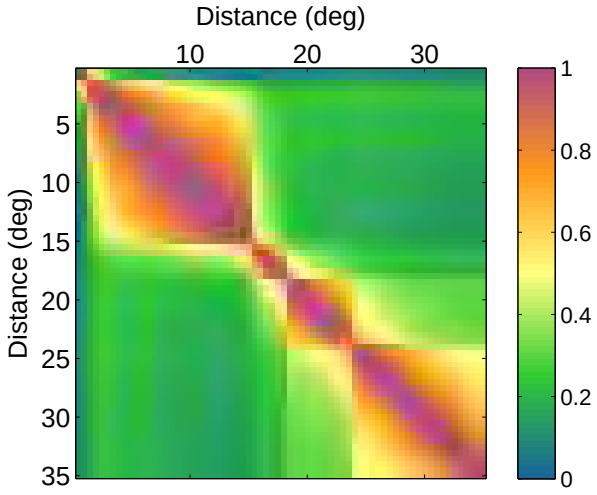


**Figure 2: Correlation coefficient between prediction errors at different epicentral distances and a common azimuth, computed with the Case B geostatistical parameters listed in Table 1.**

Figure 2. Figure 3 also allows us to see the azimuthal dependence of travel-time correlations. The azimuthal dependence, for each fixed distance, is not overtly nonstationary and appears to reflect the assumed horizontal correlation length of the velocity field (300 km).

**Finite-Frequency Effects**

Since arrival times are measured from seismograms having a finite bandwidth in frequency, their sensitivity to the Earth's velocity structure is distributed in a finite volume around the geometrical raypath. The theory of finite-frequency travel times has been developed by a number of authors (Marquering et al., 1999; Zhao et al., 2000; Dahlen et al., 2000; Hung et al., 2000). The resulting *banana-doughnut* sensitivity kernels have a spatial extent that can be related to the *delay-time* function given by

$$\tau(\mathbf{x}) = T(\mathbf{x}, \mathbf{x}_r) + T(\mathbf{x}, \mathbf{x}_s) - T(\mathbf{x}_r, \mathbf{x}_s), \tag{10}$$

where $\mathbf{x}_s$ denotes the source position and $\mathbf{x}_r$ the receiver position, and where the function $T(\mathbf{x}, \mathbf{x}')$ defines the (infinite-frequency) travel time between arbitrary points $\mathbf{x}$ and $\mathbf{x}'$. The maximum sensitivity of a banana-doughnut kernel for frequency $\omega$ occurs when

$$\tau(\mathbf{x}) = \frac{\pi}{2\omega}, \tag{11}$$

i.e. points at which the delay time is one-fourth the temporal period.

We have begun to consider whether finite-frequency effects would significantly alter our model-based travel-time covariances, even for the relatively high-frequency signals used in picking times for earthquake location. The effect would be potentially significant if the spatial extent of a travel-time sensitivity kernel were comparable to, or larger than, the correlation length of velocity heterogeneity. To quantify this, we have computed delay-time functions for regional and teleseismic paths, using *ak135* as the reference model for travel-time calculation.

Figure 4 shows maps of delay time versus geographic position for paths to four stations from a surface event at 0°N, 0°E. For each station, the minimum delay time with respect to depth is displayed as a

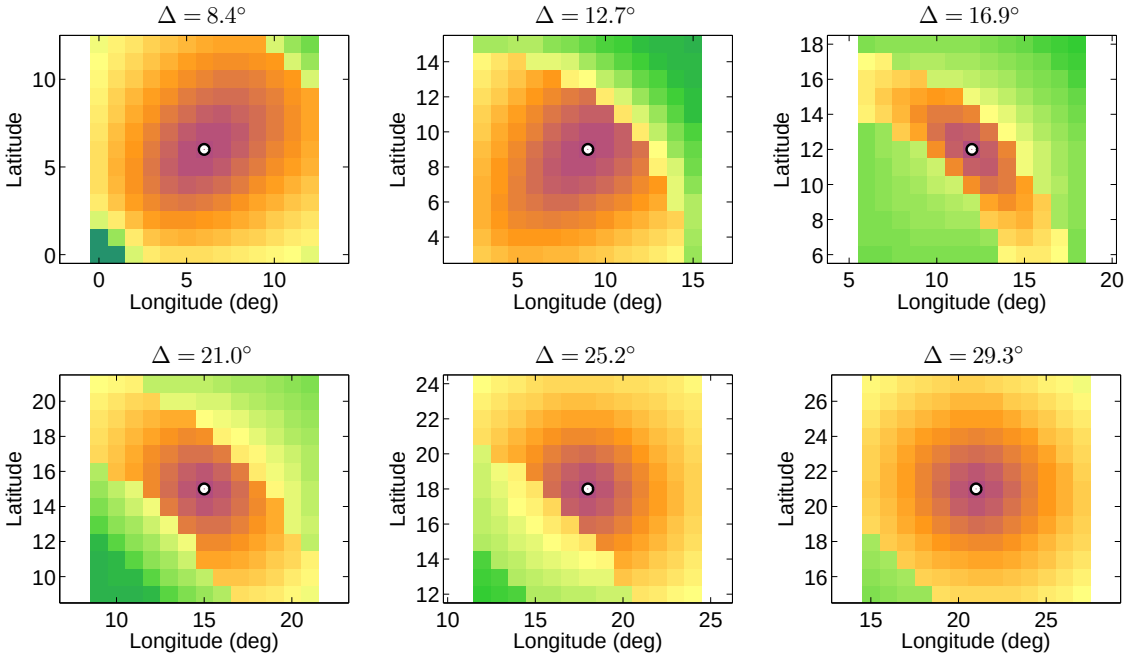


**Figure 3: Correlation coefficient between the travel-time prediction error at a fixed reference station location (white dot) and at station locations surrounding the reference point. The assumed event location is at 0°N, 0°E (southwest of the stations). For each panel, the distance of the reference station from the event location is indicated as Δ, with Δ increasing from the top-left panel to the bottom-right panel. The color scale for correlation coefficient is the same as in Figure 2.**

function of latitude and longitude. For a frequency of 1 Hz, the travel-time sensitivity peaks at a delay time of 0.25 s, so we may consider, as a rough rule of thumb, delay times of up to 0.5 s (yellow on the color scale) as defining the spatial extent of a travel-time sensitivity kernel. Under this criterion, we see that the lateral extent of the sensitivity kernels is roughly one-tenth the epicentral distance. For far-regional and teleseismic distances, this width becomes comparable to the horizontal correlation length of the velocity heterogeneity, at least as we have assumed it (300 km).

Figure 5 shows vertical sections through the delay time functions for various event-station distances. The left column spans regional distances from 11.5° to 15.5°. We see that up through an epicentral distance of $\Delta = 14.5°$ the 1 Hz travel time is sensitive to velocity structure from the Moho down to a depth that increases with distance, with the vertical extent of significant sensitivity ($\tau \leq 0.5$ s) eventually exceeding our assumed vertical correlation length of 60 km. Beyond 15°, the travel time begins to lose its sensitivity to the sub-Moho velocity and the sensitivity zone evolves into a more typical banana-doughnut shape localized around a geometrical ray (right column). Near cross-over distances, however, the sensitivity zone bifurcates (fourth panel down on right: $\Delta = 23.5°$). Although they lose their shallow sensitivity, the far-regional and teleseismic travel times still sense structure over a significant vertical extent.

## CONCLUSIONS AND RECOMMENDATIONS

Our past efforts have developed numerical techniques for computing covariances between travel-time predictions along different event-station paths, using a model-based approach that combines stochastic descriptions of velocity anomalies in the Earth with the theoretical sensitivity of travel times to those anomalies. The techniques provide a useful tool for the theoretical investigation of how travel-time covariances behave for different stochastic Earth models and different raypath geometries.

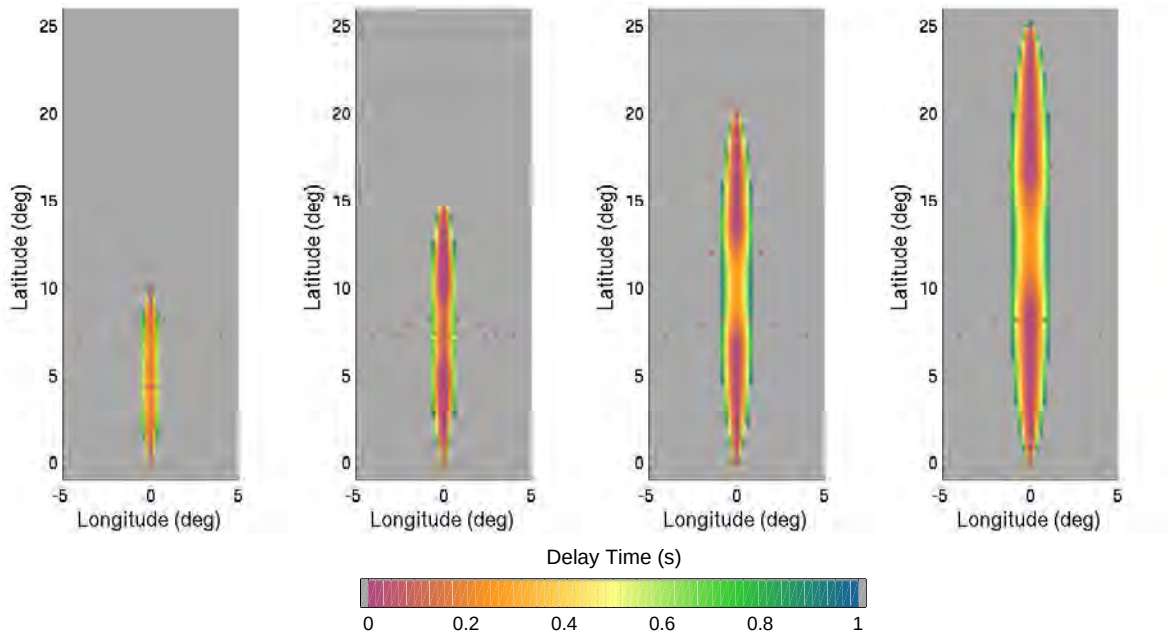


**Figure 4: Delay time, minimized over depth, as a function of latitude and longitude for four source-receiver paths with epicentral distances of 10°, 15°, 20°, and 25° (left to right).**

Applying the techniques with realistic assumptions about the statistical properties of velocity heterogeneity results in travel-time error vs. event-station distance plots that are in agreement with empirically developed curves (Figure 1). The often-noted decrease in travel-time error from regional to teleseismic distance is explained if the horizontal correlation length for velocity is greater than the vertical correlation length, and if the standard deviation of velocity decreases below the 410 km velocity discontinuity. Further, our calculations predict distinct breaks in residual correlation at the cross-overs between travel-time branches, the result of distinctly different ray paths for different branches. These breaks in travel-time correlation are exceedingly important for empirical travel-time calibration efforts and for proper estimation of the error covariance matrix that is used in seismic location.

We are currently investigating the effect of finite-frequency sensitivity kernels on travel-time covariances. Aside from the effect of velocity anomaly correlation, residuals along different paths will be correlated to the extent that their travel-time sensitivity kernels spatially overlap. Therefore, more spatially extensive sensitivity kernels are expected to result in greater residual correlation. In the preliminary work presented here we estimate the spatial extent of finite-frequency sensitivity kernels by computing delay times (relative to the geometric ray) for non-geometric paths. We find that the width of the sensitivity kernels for regional and teleseismic travel times, observed at a nominal frequency of 1 Hz, may be sufficiently large to affect travel-time correlations, especially for the far-regional Pn phase, whose sensitivity spans much of the upper mantle. This suggests that far-regional Pn residuals along similar event-station azimuths will be highly correlated, regardless of the correlation length of velocity heterogeneity.

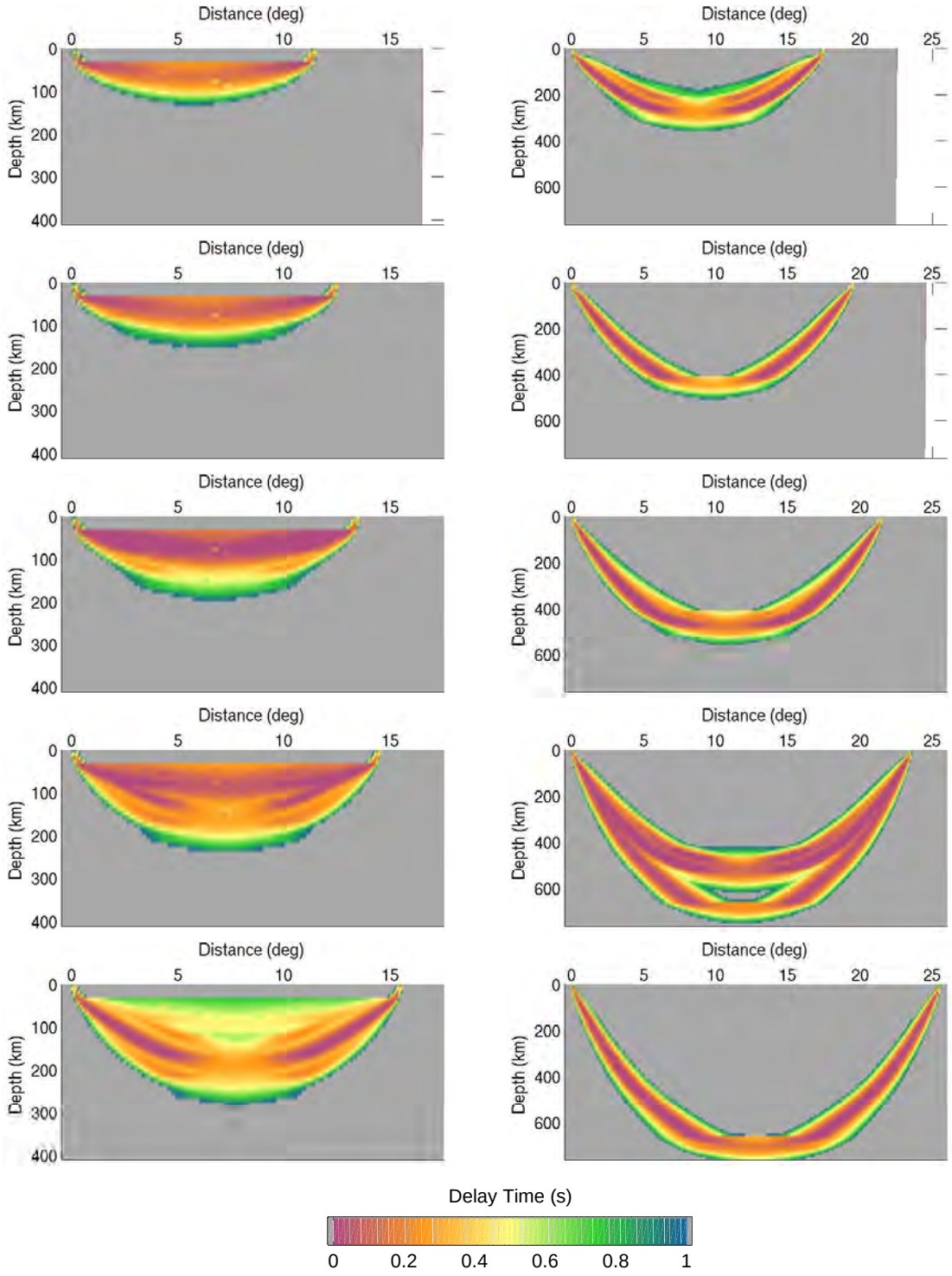


**Figure 5: Vertical cross-section through the delay-time functions for ten event-station paths. In the left column, the epicentral distance varies from 11.5° to 15.5° with a 1° increment. In the right column, distance varies from 17.5° to 25.5° with a 2° increment.**

## REFERENCES

Bondar, I., S. Myers, E.R. Engdahl and E. Bergman (2004). Epicenter accuracy based on seismic network criteria, *Geophys. J. Int.* 156: 483–496.

Chang, A.C., R.H. Shumway, R.R. Blandford and B.W. Barker (1983). Two methods to improve location estimates—preliminary results, *Bull. Seism. Soc. Am.* 73: 281–295.

Dahlen, F.A., S.-H. Hung and G. Nolet (2000). Fréchet kernels for finite-frequency traveltimes I. Theory, *Geophys. J. Int.* 141: 157–174.

Flanagan, M.P., S.C. Myers and K.D. Koper (2007). Regional travel-time uncertainty and seismic location improvement using a three-dimensional a priori velocity model, *Bull. Seism. Soc. Am.* 97: 804–825.

Hung, S.-H., F.A. Dahlen and G. Nolet (2000). Fréchet kernels for finite-frequency traveltimes II. Examples, *Geophys. J. Int.* 141: 175–203.

Kennett, B.L.N., E.R. Engdahl and R. Buland (1995). Constraints on the velocity structure in the Earth from travel times, *Geophys. J. Int.* 122: 108–124.

Marquering, H., F.A. Dahlen and G. Nolet, 1999. Three-dimensional sensitivity kernels for finite-frequency traveltimes: the banana-doughnut paradox, *Geophys. J. Int.* 137: 805–815.

Rodi, W. and S.C. Myers (2007). Modeling travel-time correlations based on sensitivity kernels and correlated velocity anomalies, in *Proceedings of the 29th Monitoring Research Review: Ground-Based Nuclear Explosion Monitoring Technologies,* LA-UR-07-5613, Vol. 1, pp. 463–471.

Rodi, W., S.C. Myers and C.A. Schultz (2003). Grid-search location methods for ground-truth collection from local and regional seismic networks, in *Proceedings of the 25th Seismic Research Review—Nuclear Explosion Monitoring: Building the Knowledge Base,* LA-UR-03-6029, Vol. 1, pp. 311–319.

Ruppert, S., D. Dodge, A. Elliott, M. Ganzberger, T. Hauk and E. Matzel (2005). Enhancing seismic calibration research through software automation and scientific information management, in *Proceedings of the 27th Seismic Research Review: Ground-Based Nuclear Explosion Monitoring Technologies,* LA-UR-05-6407, Vol. 2.

Yang, X., I. Bondar, J. Bhattacharyya, M. Ritzwoller, N. Shapiro, M. Antolik, G. Ekstrom, H. Israelsson and K. McLaughlin (2004). Validation of regional and teleseismic travel-time models by relocating ground-truth events, *Bull. Seism. Soc. Am.* 94: 897–919.

Zhao, L., T.H. Jordan and C.H. Chapman (2000). Three-dimensional Fréchet differential kernels for seismic delay times, *Geophys. J. Int.* 141: 558–576.

# A UNIFIED APPROACH TO JOINT REGIONAL/TELESEISMIC CALIBRATION AND EVENT LOCATION WITH A 3D EARTH MODEL

William L. Rodi[1], Delaine T. Reiter[2], and Stephen C. Myers[3]

Massachusetts Institute of Technology[1], Weston Geophysical Corporation[2], and Lawrence Livermore National Laboratory[3]

Sponsored by National Nuclear Security Administration

Contract No. DE-AC52-08NA28539[1,2] and DE-AC52-07NA27344[3]
Proposal No. BAA08-19

## ABSTRACT

This newly initiated project will develop and test a methodology for locating seismic events from combined data sets of regional and teleseismic arrival times, based on consistent travel-time predictions from a unified 3D Earth model. One focus of the project is to address the practical difficulty of raytracing in 3D models, which has been a serious impediment to the pursuit of 3D event location methods. We will investigate whether, for teleseismic travel-time prediction, approximate techniques, in particular linearization around rays calculated in a 1D reference model, are adequate for the purpose of event location as they are commonly assumed to be for the purpose of global tomography. A second focus of the project is tomographic calibration of a 3D model with combined regional and teleseismic data from earthquakes and ground-truth events. We will investigate the hypothesis that a joint regional/teleseismic calibration will lead to a noticeable improvement in location accuracy over the modest and inconsistent improvements 3D models have yielded to date. Additionally, we will consider whether travel-time prediction errors inferred from a tomographic uncertainty analysis can provide an appropriate weighting of various teleseismic and regional phases to optimize location accuracy even further. We plan to validate our methodology with catalog data from Asia, the Middle East and North Africa, using available regional crust/upper mantle models for these areas in conjunction with published 3D global models of the deeper mantle. Special attention will be given to south-central Asia, where Weston Geophysical and MIT are currently applying body-wave and surface-wave tomography to develop a regional model of the crust and upper mantle. This project will attempt to improve and extend the Weston/MIT model by adding teleseismic constraints.

## OBJECTIVE

The development of three-dimensional models of Earth structure continues to be an active field of seismology advancing along several fronts. A small sampling of these efforts include global travel-time tomography (e.g., van der Hilst et al., 1997; Antolik et al., 2003), global surface-wave dispersion tomography (e.g., Ritzwoller et al., 2002), regional models for Asia (Murphy et al., 2005; Li et al., 2006) and the Middle East (Pasyanos and Walter, 2002). An important question for nuclear monitoring is whether these, or improved, 3D Earth models can produce routine event locations with significantly reduced errors compared to 1D models when data at all event-station distances are used together.

The answer to this question would seem to be a definite *yes* when you consider that travel-time predictions from a 1D model like *ak135* (Kennett et al., 1995) differ from observed travel times systematically by up to 10 seconds at regional distances and a few seconds at teleseismic distances, more than enough to induce event mislocations of tens of kilometers. An example from our own work on tomography and location supports this view. Weston Geophysical Corp. and MIT are developing a new 3D crust and upper mantle model for southern Asia (see Figure 1) based on *Pn* travel times from the EHB database (Engdahl et al., 1998) and Rayleigh-wave dispersion in the period range 10-150 sec (see Reiter and Rodi, 2008). The inversion model, which we call *JWM*, constrains the *P* and *S* velocities only at depths less than 410 km, so we are validating *JWM* by relocating ground-truth events with local and regional arrival-time data. The results of two such tests are shown in Table 1, where mislocations are listed for the 1998/05/05 nuclear test in Pakistan and the 1998/05/28 nuclear test in India. We see that, even with a large number of regional phases, the locations based on *ak135* are in considerably more error than the locations derived from our 3D model. (These tests used only regional *P* arrivals (*Pn*) and the results shown are for constrained focal depth.)

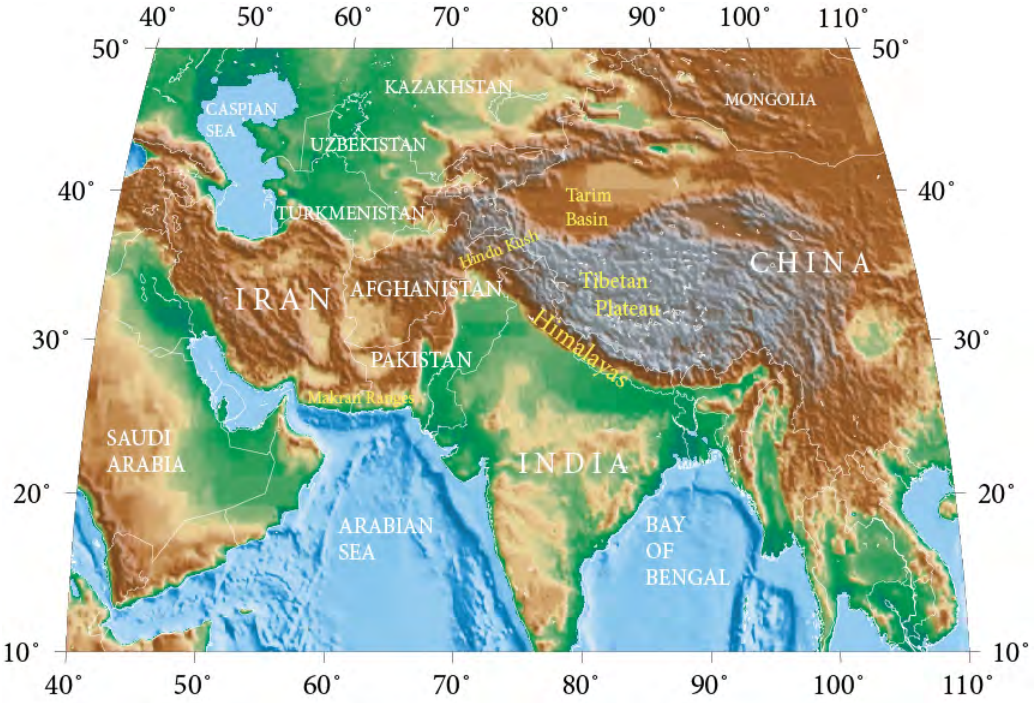


**Figure 1. Study region for the Weston/MIT regional tomography project, currently underway. The project is applying joint body-wave travel-time and surface-wave dispersion tomography to derive a self-consistent model for the *P*-wave and *S*-wave velocities of the crust and upper mantle. The inversion model (*JWM*) is described by Reiter and Rodi (2008).**

**Table 1: Location errors for the 1998 Pakistan and India nuclear tests, using regional arrival-time data.**

| *Event* | *Model* | *No. of data (for reg.)* | *Epicenter Error (km)* |
|---|---|---|---|
| Pakistan test | *ak135* | 35 | 12.6 |
| Pakistan test | *JWM* | 35 | 2.9 |
| India test | *ak135* | 27 | 37.2 |
| India test | *JWM* | 27 | 16.3 |

The results in Table 1 are very encouraging since events of monitoring interest are typically small and yield mostly regional observations. However, such events often yield teleseismic observations, too, as in the case of the North Korea test on 2006/10/08. Furthermore, the location of large events is also important for nuclear monitoring since well-located events, of any size, serve as reference events for calibration and modeling studies. Therefore, we also relocated the explosions in Pakistan and India with the addition of the many teleseismic P-wave observations available, using stations up to 50° from the events. We still used *JWM* for predicting Pn travel times but, since our model is constrained only to 410 km in depth, we used *ak135* for predicting teleseismic travel-times. We compared this mixed approach with purely *ak135* solutions. The results are in Table 2.

**Table 2: Location errors for the 1998 Pakistan and India nuclear tests, using regional and teleseismic data.**

| *Event* | *Model* | *No. of data* | | *Epicenter Error (km)* |
|---|---|---|---|---|
| | | *Reg.* | *Tel.* | |
| Pakistan test | *ak135* | 35 | 85 | 13.0 |
| Pakistan test | *JWM* | 35 | 85 | 16.6 |
| India test | *ak135* | 27 | 99 | 15.2 |
| India test | *JWM* | 27 | 99 | 5.9 |

When *ak135* is used for both regional and teleseismic times, the epicenter mislocation of the Pakistan test is about the same with or without teleseismic data (line 1 of Tables 1 and 2). However, when *JWM* is used for regional times and *ak135* for teleseismic, the mislocation increases significantly (line 2 of the tables). This degradation does not happen in the case of the India explosion, however (lines 3 and 4 of the tables), for which the addition of teleseismic data reduces the mislocation with either regional model. Notably, *JWM* still performs better than *ak135*. The conclusion we draw is that mixing a calibrated regional model with *ak135* (which is only calibrated in an average global sense) can make event locations worse, although not every time as we have seen.

Other studies have demonstrated improvement in regional event locations based on 3D crust/upper mantle models, although they have been restricted mostly to a priori, rather than tomographic, models (Ryaboy et al., 2001; Johnson and Vincent, 2002; Pasyanos et al., 2004; Flanagan et al., 2007). However, relatively little work has been on joint regional/teleseismic location with 3D models. In one of the few published studies, Yang et al. (2004) found that event locations obtained by combining regional and teleseismic data were only more accurate than locations found from the separate data sets *if* they corrected for a bias between the teleseismic and regional travel-time predictions, each made from a different 3D model (CUB1.0 for regional, J362 for teleseismic). The correction they inferred is small (0.79 sec), which is consistent with the fact that 3D crust/upper mantle effects on teleseismic travel times are relatively small (< 2 sec). But event small systematic shifts in teleseismic travel times can induce large location errors owing to the high apparent velocity of teleseismic arrivals.

It is clear to us that the most promising approach to event location with teleseismic and regional observations is to computer travel times consistently from a single model. Further, that model should be jointly calibrated with both regional and teleseismic data.

## RESEARCH PLANNED

This project will develop and test a self-consistent unified methodology for seismic event location and location calibration based on 3D Earth models. Some of the questions we will address are the following:

- Given a unified 3D model of the Earth, what numerical algorithms are best suited to the forward modeling of travel times for various seismic phases for use in event location? The phases we will be concerned with are the local, regional and teleseismic phases that are routinely available in earthquake catalogs such as the EHB database, and those potentially observable in monitoring applications.

- Using observations of the same phases from reference events and earthquake catalogs, or from temporary station deployments, what is the best strategy for calibrating the unified Earth model? An important issue here is whether regional models of the crust and upper mantle can be calibrated separately from lower mantle models, or whether a joint regional/teleseismic tomography is essential. Related to this, can a tomographic inversion for the crust and upper mantle include constraints from teleseismic data without varying the deeper mantle structure?

- Can a rigorous approach to model uncertainty provide automatic data weights for an event location algorithm, such that well-calibrated and weakly or un-calibrated travel-time predictions are combined optimally? Location algorithms used in nuclear monitoring currently employ estimates of "model errors" to perform this weighting. We will investigate whether more formal uncertainty estimates derived from tomographic calibration, including covariances between travel-time predictions along similar paths, can perform better.

We plan to address these questions using a variety of available 3D Earth models, including the *JWM* model referred to above, the WENA1.0 model developed at LLNL (Pasyanos et al., 2004), and global mantle models such as J362D28 (Antolik et al., 2003) and MITP07 (Li et al., 2008).

**Statement of the Problem**

The forward model in seismic event location employs a set of travel-time functions, each predicting the travel time of a seismic phase from any potential event hypocenter to an observing station. This prediction is based on wave propagation through a reference velocity model. Since the Earth's true velocity differs from the reference model, the forward model admits a prediction error (Billings et al., 1994).

Let $v_0$ denote the velocity of the reference model (focusing on just the velocity for *P* waves), and let $v_E$ be the Earth's true velocity. We can express the prediction error as

$$e(\mathbf{x}) = T(\mathbf{x};v_E) - T(\mathbf{x};v_0), \qquad (1)$$

where the travel-time function, $T(\mathbf{x};v)$, integrates $1/v$ along the raypath connecting the station to the hypocenter $\mathbf{x}$. Prediction errors add to the *observational* errors in arrival-time picks, and a difficult but important problem is to account for both kinds of error in locating an event.

Calibration is the task of reducing or correcting the prediction errors in travel times. One calibration approach that has been used in nuclear monitoring applications (e.g., Myers and Schultz, 2000) is the kriging, or geostatistical interpolation, of observed travel-time residuals from ground-truth events, which leads to a correction function or surface, $\Delta T(\mathbf{x})$, for a given station/phase. This method works well when all of the network stations have observed a GT event (or events) near an event of interest. The forward model used in event location is then taken as $T(\mathbf{x};v_0) + \Delta T(\mathbf{x})$. Model-based calibration, in contrast, attempts to correct the velocity model itself: replacing $v_0$ with an improved model $v_C \equiv v_0 + \Delta v$. The corrected model can be derived with travel-time tomography, applied to data similar to that used in kriging, but also can incorporate a variety of other constraints. An advantage of model-based calibration is that it allows the calibration of stations and seismic phases which have not been directly observed, as long as $v_C$ is defined for relevant portions of the Earth and, additionally, appropriate ray tracing techniques are available for the phases of interest.

The conceptual goal of this project can now be stated as follows. Given a globally defined 3D model, $v_C$, we wish to identify forward modeling and event location techniques which allow us to take advantage of all the travel-time data available for locating an event. Conversely, we wish to develop tomographic methods for calibrating $v_C$, given the available travel-time observations from ground-truth and other past events.

**3D Raytracing**

A critical choice in both event location and travel-time tomography with 3D Earth models is the choice of numerical technique to use for calculating travel times between sources and receivers. The choice involves somewhat different issues in location and tomography. First, an event locator requires travel-time calculations for arbitrary hypocenters as it searches for a best-fitting event location, while tomography is usually performed with event locations held fixed. Second, tomography needs the sensitivity of each calculated travel time to the velocity structure of the Earth, i.e. the ray trajectory connecting source and receiver, or its equivalent.

For travel-time calculation in a 1D reference model (e.g., *ak135*) the choice is straightforward since analytical solutions for travel times and rays, for any seismic phase (direct, refracted, diffracted or converted) are available and easily implemented in fast algorithms (Buland and Chapman, 1983). In contrast, travel-time calculation in 3D models presents many challenges.

Global travel-time tomography has generally been performed with a linearized approximation to the travel-time function. In this approximation, the slowness of the 3D model ($1/v_C$) is integrated along the raypaths computed in the reference model, $v_0$, with the reference model taken as 1D. We can identify the ray connecting a given station and a given event hypocenter, $\mathbf{x}_{ev}$, with a sensitivity kernel, $a(\mathbf{x},\mathbf{x}_{ev};v_0)$, that is concentrated along the ray trajectory. Then the linearized approximation to the travel time through $v_C$ can be written as

$$\begin{aligned} T(\mathbf{x}_{ev};v_C) &\approx T(\mathbf{x}_{ev};v_0) + \int d\mathbf{x}\, a(\mathbf{x},\mathbf{x}_{ev};v_0)\, [v_C^{-1}(\mathbf{x}) - v_0^{-1}(\mathbf{x})] \\ &= \int d\mathbf{x}\, a(\mathbf{x},\mathbf{x}_{ev};v_0)\, v_C^{-1}(\mathbf{x}). \end{aligned} \qquad (2)$$

We point out that this equation also applies to finite-frequency travel times, which Li et al. (2006) and others have used to model long-period body-wave observations. In this case, $a(\mathbf{x},\mathbf{x}_{ev};v_0)$ becomes a "banana-doughnut" sensitivity kernel (e.g., Dahlen et al., 2000) evaluated for the reference velocity model.

For the calculation of local and regional direct *P* arrivals, linearization is not adequate, as we will see in a moment. For this reason, Reiter and Rodi (2006) use the finite-difference ray tracing method due to Podvin and Lecomte (1991), as implemented in software by Lomax (2000). Reiter et al. (2005) augmented the Podvin-Lecomte (P-L) algorithm with a back-chaining algorithm to generate sensitivities of travel times with respect to the velocity parameters of the model. Since the P-L algorithm is written for flat-Earth models in Cartesian coordinates, we have integrated it into our tomography software with appropriate transformations between model parameterizations and sensitivities. Reiter et al. (2005) provide additional details of the ray tracing techniques we use for regional tomography.

We illustrate the importance of 3D ray tracing in modeling regional travel times using our *JWM* tomographic model. First, we compare travel times calculated through *JWM*, using the Podvin-Lecomte algorithm, to the travel times calculated through *ak135*. In each case, the times are calculated for the 76,000 event-station pairs in our tomography data set (extracted from the EHB catalog). The difference between the *JWM* and *ak135* times for these paths is plotted as a function of epicentral distance in the left panel of Figure 2. Not surprisingly, the models predict *Pn* times differing by several seconds.

Can *Pn* travel times through *JWM* be approximated with linearization around *ak135*, using Equation (2)? The right panel of Figure 2 shows the difference between the P-L calculated times ("Nonlin.") and the *ak135* linearized approximation ("Linear"). We see that the errors in the linearized times are as high as 25 sec. Much of this difference owes to the thick crust over much of the model region, exceeding 75 km thickness beneath the Himalayas. Therefore, large pieces of the *ak135 Pn* raypaths are incorrectly located within the *JWM* crust. While it might be possible to correct for this effect, or optimize the 1D model used to obtain the reference raypaths, the fact is that integrating a 3D velocity model along reference rays from a 1D model cannot accurately model *Pn* travel times through a complex, 3D Earth model.

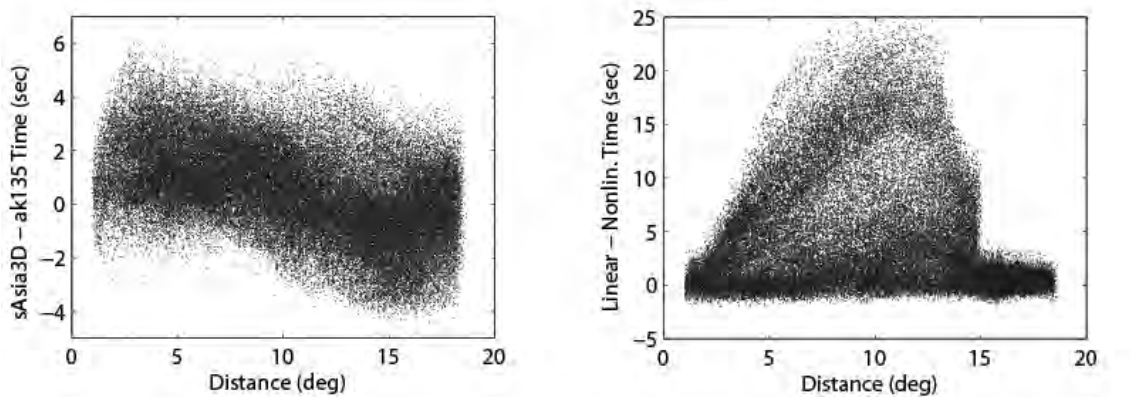


**Figure 2. Experiments with regional travel-time calculation performed with the 3D tomographic model *JWM* of Reiter and Rodi (2006). *Left*: Difference between calculated travel times for *JWM* and *ak135*. The *JWM* times were calculated with the Podvin-Lecomte (P-L) finite-difference algorithm. *Right*: Difference between calculated travel times from *JWM*, obtained two ways: "nonlinear" times obtained by the P-L method, and "linearized" times obtained by integrating the *JWM* slowness over *ak135* raypaths. In both panels, times are plotted for the 76,000 *Pn* paths used in the *JWM* tomography.**

However, it is interesting that the linearized travel times are not too bad for the longest *Pn* paths, i.e., beyond 14°, corresponding to rays bottoming between 210 and 410 km in the *ak135* model. This is because the crustal thickness variations affect these raypaths much less than for shorter epicentral distance, making Equation (2) more accurate. Also, the velocity differences between *JWM* and *ak135* in the mantle are smaller than in the crust.

Therefore, it is reasonable to ask whether the linearization approach would even more accurately predict travel times in the teleseismic distance range. This is a question we will investigate in detail as part of the proposed project. A preliminary look into the matter is offered in Figure 3. This figure is analogous to Figure 2, but the travel-time calculations were performed only for a line of stations emanating from station JYP (33°N, 75°E) along a great circle at an azimuth of -30° from north, out to near-teleseismic distances. To calculate teleseismic times in *JWM* with Podvin-Lecomte, *JWM* was extended below 410 km depth with the *ak135* velocity profile. The left panel of Figure 3 shows that the influence of the 3D structure in *JWM* on teleseismic times is less than 1 second, given this extrapolation at depth. The panel on the right, nonetheless, shows that the teleseismic travel times through *JWM* are accurately modeled by the linearized approach applied with *ak135* raypaths. It remains to be seen whether the presence of deep 3D structure alters this conclusion.

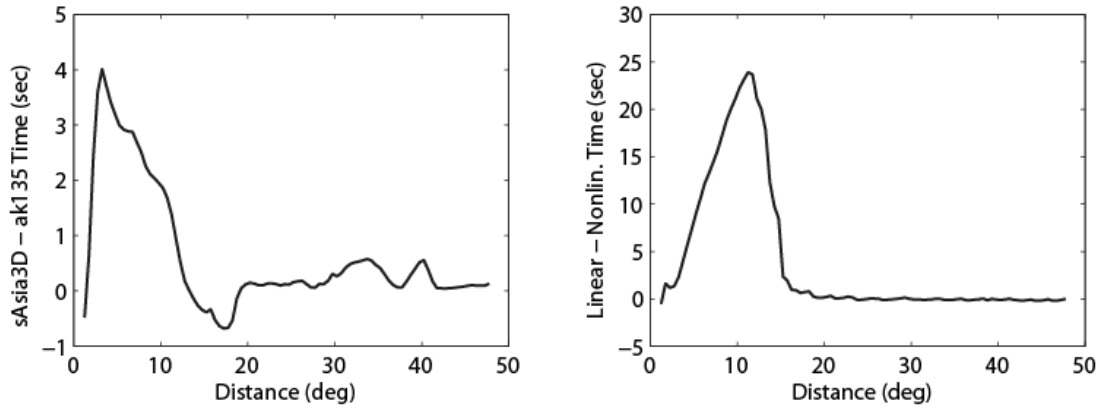


**Figure 3. Left: Difference between calculated travel times from *JWM* and *ak135*. Right: Calculation error of travel times from *JWM* by using linearization.**

**Event Location with a 3D Model**

The location validation effort in the Weston/MIT tomography project for southern Asia is using the grid-search location algorithm known as GMEL (Grid-search Multiple-Event Location), developed at MIT under previous projects and extended to 3D models in a previous joint project with Weston Geophysical Corp. GMEL uses travel-time predictions for either 1D reference velocity models or 3D reference models, using interpolation of pre-calculated tables in each case. A summary description of the numerical techniques used in GMEL is available in Rodi (2006). We plan to use GMEL in the proposed work, but we will investigate whether teleseismic travel times for 1D models *and* linearized travel times for 3D models can be efficiently calculated during the grid-search location process ("on-the-fly"). This will address an important implementation issue in the use of 3D models for event location and, if on-the-fly calculations are feasible, GMEL will be a more useful tool for the project.

Another previous effort we plan to take advantage of in the proposed work is a concurrent project on covariance modeling. Rodi and Myers (2006) presented a method for computing variances of, and covariances between, travel-time predictions from a reference model, based on a geostatistical description of the velocity anomalies in the Earth relative to the reference model. The numerical technique for doing this integrates travel-time sensitivities with a velocity model covariance function, $C(\mathbf{x},\mathbf{x}')$, that characterizes the velocity heterogeneity. Thus, the covariance between the travel-time predictions along two paths, *i* and *j*, is given by

$$\sigma_{ij}(\mathbf{x}_{ev}) = \int d\mathbf{x} \int d\mathbf{x}'\, a_i(\mathbf{x},\mathbf{x}_{ev};v_0)\, a_j(\mathbf{x},\mathbf{x}_{ev};v_0)\, C(\mathbf{x},\mathbf{x}'), \qquad (3)$$

where $a_i$ and $a_j$ are the sensitivity kernels for the two paths. An example of this calculation, taken from Rodi and Myers (2006), is shown in Figure 4.

We plan to implement the use of travel-time covariances in GMEL, and to extend the technique by replacing $C(\mathbf{x},\mathbf{x}')$ with the *a posteriori* covariance that results from performing travel-time tomography. This capability will accomplish a key part of our unified approach, with the data in an event location automatically and optimally weighted in correspondence to how well their travel-time predictions are calibrated.

## CONCLUSIONS AND RECOMMENDATIONS

Replacing a 1D Earth model with a global 3D Earth model for routine event location holds the promise of achieving much greater location accuracy, but it is an enormous undertaking when one considers all of the steps involved: model integration, calibration and validation, and efficient implementation for use in a locator. Moreover, it is an undertaking that is highly vulnerable to the one-step-forward, two-steps-back syndrome, with improvement on one front (e.g., better regional travel-time predictions) offset by regression on another (e.g., discrepancy between regional models, inconsistency with teleseismic predictions). The greatest benefit of our project will be a strategy for achieving the maximum effect from future efforts to develop and implement 3D Earth models for event location. Additionally we expect this project to have some concrete benefits beyond the methodology it develops. These include an improvement to the Weston/MIT model of the crust and upper mantle in southern Asia, incorporating teleseismic constraints, and an improved version of the EHB catalog for southern Asia.

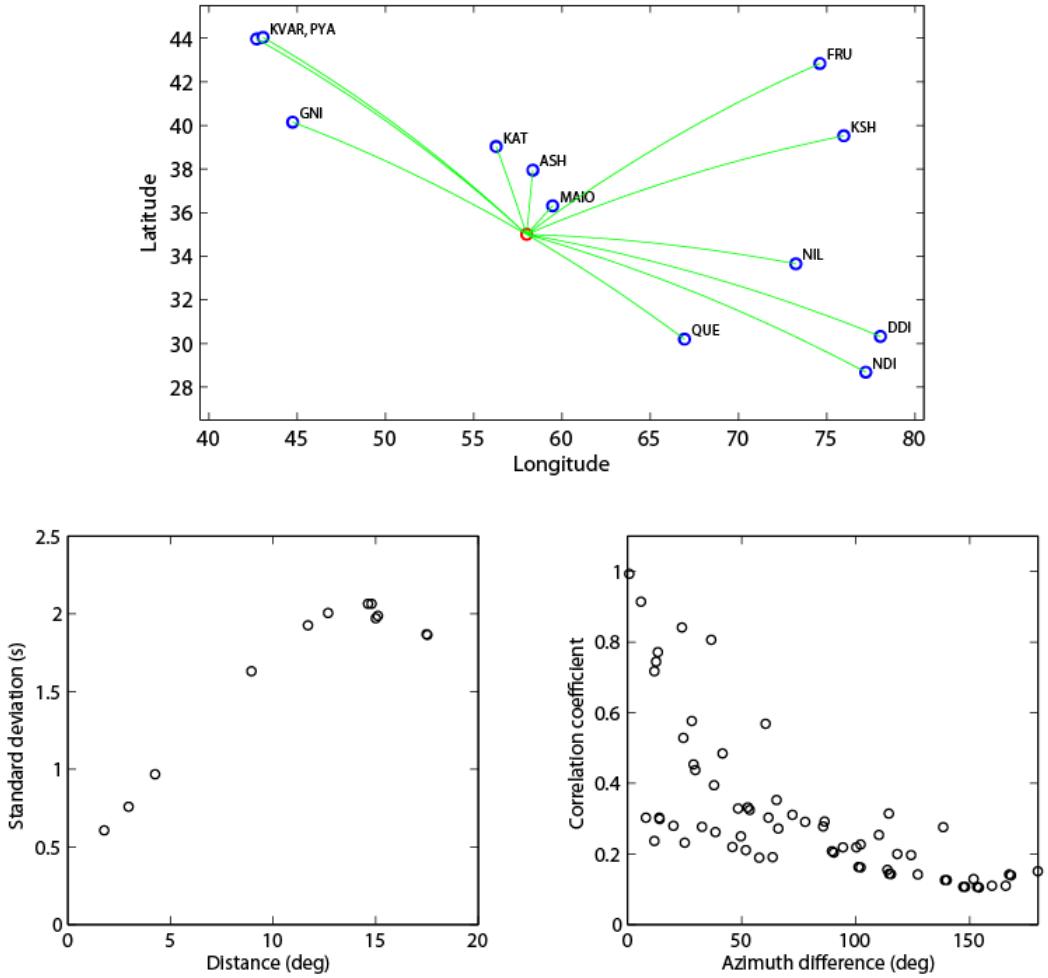


**Figure 4.** ***Top*** **- Diagram of the network geometry used for testing our numerical approach to modeling travel-time covariances among a set of stations. There are 12 stations at regional distances from an earthquake in northeastern Iran.** ***Bottom Left*** **- The standard deviation of the travel-time prediction error at each of the 12 stations, plotted as a function of epicentral distance.** ***Bottom Right*** **- Correlation coefficient between station pairs, plotted versus inter-station azimuth. The calculations assumed that velocity variations in the Earth have a standard deviation of 2% and correlation lengths of 300 km laterally and 100 km vertically.**

## REFERENCES

Antolik, M, Y.J. Gu, G. Ekstrom, and A. M. Dziewonski. (2003). J362D28: a new joint model of compressional and shear velocity in the Earth's mantle, *Geophys. J. Int.* 153: 443–466.

Billings, S. D., M.S. Sambridge and B.L.N. Kennett (1994), Errors in hypocenter location: picking, model and magnitude dependence, *Bull. Seism. Soc. Am*. 84**:** 1978–1990.

Buland, R., and C. H. Chapman (1983). The computation of seismic travel times, *Bull. Seis. Soc. Am.* 73**:** 1271–1302.

Dahlen, F.A., S.-H. Hung and G. Nolet, 2000. Fréchet kernels for finite-frequency traveltimes I. Theory, *Geophys. J. Int.* 141: 157–174.

Engdahl E.R., R. van der Hilst and R. Buland (1998). Global teleseismic earthquake relocation with improved travel times and procedures for depth determination, *Bull. Seism. Soc. Am.* 88: 722–743.

Flanagan, M. P., S. C. Myers, and K. D. Koper (2007). Regional travel-time uncertainty and seismic location improvement using a three-dimensional a priori velocity model, *Bull. Seis. Soc. Am*. 97: 804–825.

Johnson, M., and C. Vincent (2002). Development and Testing of a 3D Velocity Model for Improved Event Location: A Case Study for the India-Pakistan Region, *Bull. Seis. Soc. Am.* 92: 2893–2910.

Kennett, B. L. N., E. R. Engdahl, and R. Buland (1995). Constraints on the velocity structure in the Earth from travel times, *Geophys. J. Int.* 122: 108–124.

Li, C. R.D. van der Hilst and M.N. Toksöz (2006). Constraining P-wave velocity variations beneath Southeast Asia, *Phys. Earth and Planet. Int*. 154: 180–195.

Li, C., R.D. van der Hilst and E.Engdahl (2008). A new global model for *P* wavespeed variations in Earth's mantle, *Geochemistry, Geo- physics, and Geosystems*, in press.

Lomax, A., J. Virieux, P. Volant and C. Berge (2000). Probabilistic earthquake location in 3D and layered models: Introduction of a Metropolis-Gibbs method and comparison with linear locations, in *Advances in Seismic Event Location*, Thurber, C.H., and N. Rabinowitz (eds.), Kluwer, Amsterdam, 101–134.

Murphy, J.R., W. Rodi, M. Johnson, D.D. Sultanov, T.J. Bennett, M.N. Toksöz, V. Ovtchinnikov, B.W. Barker, D.T. Reiter, A.C. Rosca, and Y. Shchukin (2005). Calibration of International Monitoring System (IMS) stations in central and eastern Asia for improved seismic event location, *Bull. Seism. Soc. Am.* 95: 1535–1560.

Myers, S.C., and C.A. Schultz (2000). Improving sparse network seismic locations with Bayesian kriging and teleseismically constrained calibration events, *Bull. Seism. Soc. Am.* 90: 199–211.

Pasyanos, M. E., and W. R. Walter (2002). Crust and upper-mantle structure of North Africa, Europe and the Middle East from inversion of surface waves, *Geophys. J. Int*. 149: 463–481.

Pasyanos, M.E., W.R. Walter and M.P. Flanagan (2004). Building and testing an a priori geophysical model for Western Eurasia and North Africa, *Pure Appl. Geophys*. 161: 235–281.

Podvin, P., and I. Lecomte (1991). Finite difference computation of traveltimes in very contrasted velocity models: a massively parallel approach and its associated tools, *Geophys. J. Int*. 105: 271–284.

Reiter, D., and W. Rodi (2008). A new regional model 3-D velocity model for Asia from the joint inversion of *P*-wave travel times and surface-wave dispersion data, these Proceedings.

Reiter, D., and W. Rodi (2006). Crustal and upper-mantle P- and S-velocity structure in central and southern Asia from joint body- and surface-wave inversion, *Proceedings of the 28th Seismic Research Review, Ground Based Nuclear Explosion Monitoring Technologies*, LA-UR-06-5471, Vol. 1, pp. 209–218.

Reiter, D., W. Rodi and M. Johnson (2005). Development of a tomographic upper-mantle velocity model beneath Pakistan and Northern India for improved regional seismic-event location, *Bull. Seis. Soc. Am.* 95: 926–940.

Ritzwoller, M.H., and A.L. Levshin (1998). Eurasian surface wave tomography: Group velocities, *J. Geophys. Res*. 103: B3, 4839–4878.

Ritzwoller, M.H., N.M. Shapiro, M.P. Barmin and A.L. Levshin (2002). Global surface wave diffraction tomography, *J. Geophys. Res*. 107: doi: 10.1029/2002JB001777.

Rodi, W. (2006). Grid-search event location with non-Gaussian error models, *Phys. Earth. Planet. Int*. 158: 55–66.

Ryaboy, V., D.R. Baumgardt, P. Firbas, *et al.* (2001). Application of 3-D crustal and upper mantle velocity model of North America for location of regional seismic events, *Pure and Appl. Geophys*. 158: 79–103.

Van der Hilst, R.D., S. Widyantoro, and E.R. Engdahl (1997). Evidence for deep mantle circulation from global tomography, *Nature* 386: 578–584

Yang, X.P., I. Bondar, J. Bhattacharyya, *et al.* (2004). Validation of regional and teleseismic travel-time models by relocating ground-truth events, *Bull. Seism. Soc. Am*. 94: 897–919.

# INITIAL RESULTS ON RUGGED LOW POWER COMPACT SILICON MEMS SENSORS FOR USE IN NUCLEAR EXPLOSION MONITORING

Ian M. Standley[1] and W. Thomas Pike[2]

Kinemetrics Inc.[1] and Imperial College London[2]

Sponsored by Air Force Research Laboratory

Contract No. FA8718-06-C-0011
Proposal No. BAA06-16

## ABSTRACT

In this paper we present initial experimental results of our ongoing development of a family of high Q-factor in-plane microelectromechanical systems (MEMS) seismic sensors. Devices have been constructed that demonstrate all the required components of a MEMS seismic sensor, these include 11.5-Hz, high "Q", silicon spring mass systems, multiple electro-magnetic actuators integrated onto the proof mass, and a highly accurate displacement transducer based on our Linear Capacitive Array Transducer (LCAT). The performance of each of these elements is discussed in the paper. The difficulties encountered in the assembly of these devices and the progress in transferring this technology to a commercial MEMS fabrication is also discussed. The result of a separate study on the potential use of these devices in high shock conditions is also presented. The devices have been integrated with electronics, both to characterize the performance of the individual sensor elements but also to complete the overall system by providing force feedback to the sensor die to form a force-feedback sensor. We present our initial results on using simple proportional feedback electronics with the device to form a force-feedback accelerometer and show that the performance is closely simulated by our theoretical models.

## OBJECTIVES

The objective of this research program is to develop a silicon MEMS sensor suitable for use in Nuclear Explosion Monitoring Systems (NEMS). In Phase A we are developing a triaxial sensor model that we will fabricate and evaluate. This design would then be further optimized in Phase B of the development.

## RESEARCH ACCOMPLISHED

### Introduction

Our goal in Phase A of the project has been to complete the design and fabrication of the MEMS component of the sensor optimized for NEMS applications. The MEMS sensor integrates the proof mass and its suspension (Pike and Kumar, 2007), a displacement transducer, and a set of electromagnetic transducer coils.

To produce a working microseismometer (μSeis) this MEMS element is coupled with electronic circuitry that excites the displacement transducer, amplifies and demodulates the displacement signal, and then feeds back the correct signal to the coils to cause the device to operate as a force-balance acceleration or velocity sensor. Finally, both the MEMs elements and the associated electronics have to be held in a suitable mechanical package to allow the device to operate under field conditions.

For sensing Nuclear Explosions it has been suggested that the noise performance of ~1 nano-g/√Hz in the band from 10 Hz to 40 Hz is of considerable interest. These are the design levels used for the micro-seismometer (Standley & Pike 2007).

### Device Design Parameters

In this phase of the development, we have concentrated on the performance of a device based on a 20-mm x 20-mm die size and a natural frequency of 11.5 Hz sealed at ambient pressure with a Q-factor of approximately 275. This device includes enhancements to improve the shock resistance, and the same basic device structure was fabricated at both Imperial College and Innovative Micro Technology (IMT). This device uses a 200-micron period for the displacement transducer and assumes a spacing of the DT wafer of ~ 38 microns when sealed at ambient pressure. The design parameters are summarized in Table 1.

**Table 1. Device Design Parameters.**

| Device | Proof Mass Die Dimensions | Resonant Frequency/Hz | Q-Factor | Environment | DT Period /μm | Shock Resistance |
|---|---|---|---|---|---|---|
| 11.5-Hz Device | 20mm x 20mm x 0.5mm | 11.5 Hz | 275 | Ambient Pressure | 200 | Moderate |

In this paper we are reporting on devices fabricated at Imperial College that used a simpler geometry on the displacement transducer die which results in higher damping and a lower "Q". These devices were also not sealed. These changes were made for the initial devices to allow easier fabrication. Four devices have been fabricated and two have been evaluated.

### Measured Device Parameters

Two devices have been characterized and the results are presented in Table 2 below. The performance of the spring mass system was in excellent agreement with the design theory and the resonant frequency was within +/-5% of the design value. Figure 1 shows the open loop transfer function of Die 5 when it was driven by the calibration coil, the resonance can be clearly seen, and also the first spurious resonance which occurs at ~100 Hz. The first spurious mode is due to the finite mass of the suspension itself, which was minimized in this design, and predicted to occur at ~110 Hz (Pike and Standley, 2005, and Pike and Kumar, 2007).

**Table 2: Measured Device Parameters**

| Parameter | Die 4 | Die 5 | Target | Units | Comment |
|---|---|---|---|---|---|
| Resonant Frequency | 11.5 | 11.125 | 11.5 | Hz | Measured |
| Device "Q" | 63 | 40 | 275 | | Design Change |
| Mass | 0.229 | 0.229 | 0.245 | grams | Design Value |
| Motion 1g | 1.877 | 2.006 | 1.878 | mm | Calculated |
| Gain DT Mechanical | 38280 | 63360 | 71760 | V/m | Separation Dependent |
| Sensitivity Open Loop | 71.85 | 127.08 | | V/g | Calculated |
| Main Coil Resistance | 1100 | 1128 | 698 | Ohms | Measured |
| Main Coil Generator Const | 0.412 | 0.394 | 0.433 | N/Amp | Calculated |
| Integral Coil Resistance | Open | 1046 | 771 | Ohms | Measured |
| Integral Coil Generator Const | Open | 0.426 | 0.472 | N/Amp | Calculated |
| Calibration Coil Resistance | 630 | Open | 260 | Ohms | Measured |
| Cal Coil Generator Const | 0.086 | Open | 0.144 | N/Amp | Calculated |

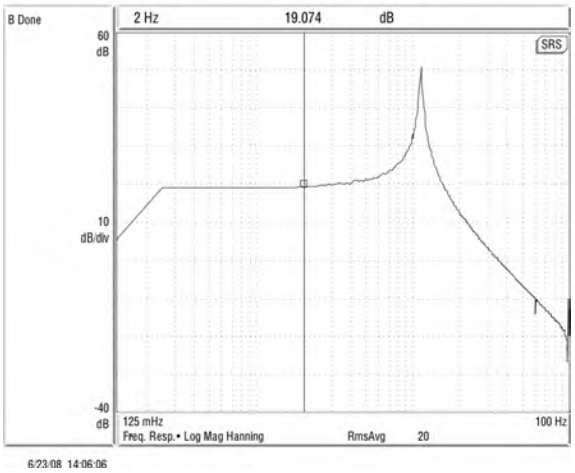


**Figure 1: Die 5 Open Loop Response**

The device "Q" in this case is about 40 and is limited by the Couette damping of the flat displacement transducer plate. The spacing on this device is closer than the design value of 38 microns, partly explaining the lower value compared with Die 4. Die 4 had a "Q" of 63, while test devices fabricated with no metallization but with the relieved areas on the displacement transducer wafer show "Q" values of several hundred under ambient pressure, in good agreement with the theoretical model. Previously we have reported that in a vacuum "Q"s in excess of 100,000 are obtainable (Standley & Pike 2007).

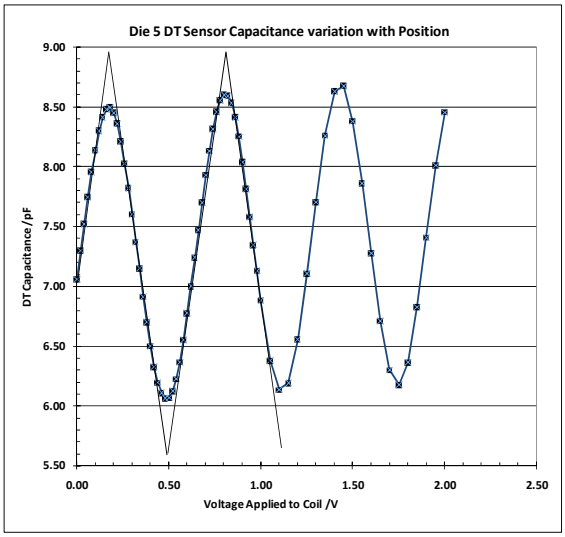


**Figure 2: Displacement Transducer Capacitance**

The capacitance values of the displacement transducer on Die 5 were measured as the proof that mass was moved by passing current through the main coil. Figure 2 shows the variation of the sensor capacitance as the displacement transducer is moved by applying a voltage to the main coil on the proof mass with the magnets present. The results show a nominal sensing capacitance of 3.5pF superimposed on a stray capacitance of approximately 5.5pF. The design value was a 3.3pF sensing capacitor with approximately 2pF of stray capacitance. The additional strays are likely due to the connections and cabling used in the test setup.

The Displacement Transducer circuit was then connected to die 5, and the proof mass moved by applying a voltage to both the Main and Integral coils of the device. The results are shown in Figure 3 and demonstrate the operation of the LCAT. The mechanical sensitivity of the displacement transducer was approximately 63kV/m compared with the predicted value of 72V/m. As the separation between the proof mass and the

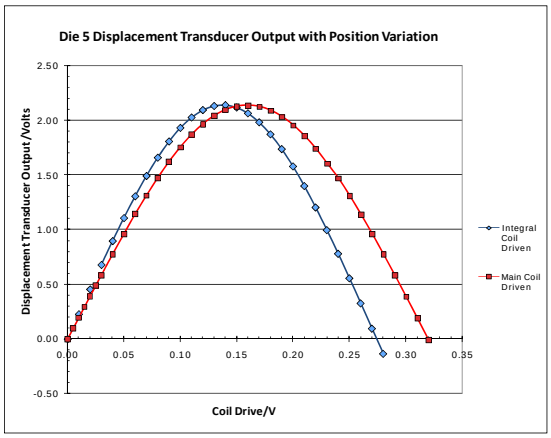


**Figure 3: Displacement Transducer Output**

Displacement Transducer in die 5 is probably below the nominal 38 microns, this suggests that the nominal mechanical sensitivity is ~50kV/m for this design. This suggests that stray capacitance and fringing fields are higher than our theoretical model. The theoretical noise figure is still well within our design limits with a theoretical displacement noise floor of ~0.225picometers/√Hz.

With the Displacement Transducer functional and the proof mass parameters measured, the generator constants of the electro-magnetic actuators could be determined. As shown in Figure 3, a certain voltage level is required to move the proof mass through a half period of the LCAT or 100 microns in this design. Knowing this and the spring constant of the proof mass suspension gives the force exerted, using the coil resistance, determines the current necessary to oppose this force and from this the Generator Constants can be calculated. As can be seen in Table 1 the Generator constants are between 5-10% lower than the design values, some of this is due to variation of the magnetic components, while about 5% can be explained by a slightly higher than designed separation of the magnetic pole pieces to ensure that they do not touch the device. The coil resistances were higher than designed due to a higher sheet resistance of the electro-plated layer. Process improvements should reduce this resistance in future devices.

**Die Packaging & Interconnection and Commercial Fabrication Results**

We still have some fabrication and packaging challenges with the devices fabricated at Imperial. Firstly, our yield is still low on the proof mass fabrication stage. This is a result of the relatively complex process required to make the devices and in particular the two layer metallization. Recently, the yield has improved and a way of repairing metallization faults has been developed. In the long term we are confident that our commercial MEMS fabrication partner can solve the yield issues.

The other remaining problems at the chip level concern the packaging. We have developed a process that allows us to electrically interconnect the proof mass wafer to the displacement transducer wafer and to control the spacing between the two wafers. We have not yet succeeded in sealing the three-wafer stack to isolate the devices from the surrounding atmosphere, we also are working on finding a better technology to machine the glass wafers so the cavities can be machined with good positional accuracy across a whole wafer. These tasks will the focus of a later fabrication run.

Our commercial MEMS partner (IMT) demonstrated all the essential elements of fabricating the proof mass including the following:

- Substrate Contact
- First Metal Layer
- High Temperature Insulator
- Second Electroplated Metal Layer
- DRIE etching of the proof mass and production of high “Q” spring mass systems

The yield on the initial wafer was low, but process and mask changes in the next phase should result in significant improvement.

The first wafer stack bonded at IMT cracked on the second bond and the cavity wafer delaminated from the proof mass and the DT. Also the spacing between the DT and the proof mass was too small so the proof masses could not move freely. Further process development is required to develop the frit bonding process, the vacuum gettering, and the wafer-to-wafer electrical interconnect.

### High Shock Testing

Seismometer suspensions are often exposed to high shock loading during transportation and deployment, particularly when utilized in drilling, automotive applications, space deployments, or military systems. High shock loading of suspensions can lead to failure due to fracture, delamination, or stiction. Additionally, for a suspension like that of the microseismometer, with a large range of travel and a low resonant frequency, the various components of the silicon suspension colliding with each other can lead to spallation damage and thus to a broken or severely compromised device. By completely embedding the suspension in a wax-like material which solidifies around the proof mass and springs, and thereby restrains them from motion, it should be possible to prevent any damage to these structures even in high shock environments. This encapsulating material would then be entirely removed via sublimation in order to return the suspension back to its original condition. Either heat or vacuum can be used to sublimate the encapsulant. To test this approach, impact trials of the suspension were carried out at a ballistic test range at Pendine in Wales. The impact velocity was about 310 m/s, impact angle between 88–108° creating a 'tail slap' with high in-plane acceleration. The in-axis peak acceleration was 20,000g at the front of the penetrator and around 10,000g at the rear of the penetrator. The lateral peak accelerations were measured at the rear of the penetrator and were 16,000g and 6,500g along the vertical and horizontal axes respectively. The compartment containing the suspensions was approximately in the middle of the penetrator. Suspensions were encapsulated within naphthalene and paradichlorobenzene (PDB) in a metal box. The sublimants were melted and poured into the boxes containing the suspensions. After the penetrator tests, these boxes were exposed to a $10^{-3}$ Torr vacuum, resulting in successful sublimation. Nine out of 12 suspensions that were encapsulated in naphthalene survived, as did 11 out of 12 suspensions that were encapsulated in PDB. In both cases, the sublimation was clean, resulting in suspensions with quality factors similar to those measured before the tests. This illustrates a potential method for protecting the silicon suspensions of the microseismometer against extremely high shocks prior to deployment.

### Configuration as an Accelerometer

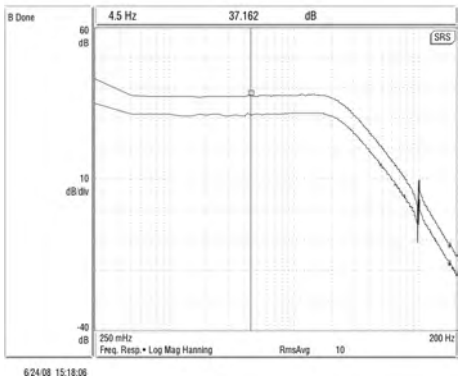


**Figure 4. Accelerometer Transfer Function**

The initial system testing of the device was performed by configuring the device as an accelerometer rather than a velocity sensor. This allowed initial evaluation of the performance of the device in a simple feedback circuit and allowed some other possible sources of error to be investigated before the more complex velocity feedback system is implemented. The device was configured as an accelerometer by driving the main coil from the displacement transducer through a resistor and capacitor in parallel. These two elements act as a proportional and differential feedback for the system. A 68nF capacitor was used in parallel to a 110k resistor. The output signal was taken from the top of the feedback resistor, passed through a unity gain buffer and then a final output stage that produced a differential output. The transfer function of the differential stage was actually unity due to the single ended to differential conversion scheme used. The circuit elements used were not optimized for this application as this topology was created by modifying a board designed to operate the device as a velocity sensor. The measured closed loop transfer function is shown in Figure 4. The measured sensitivity to acceleration was 40.3V/m/s^2 while PSPICE (Figure 5) predicted a slightly peaked response and a sensitivity of 42.4V/m/S^2. This difference is only about 5% showing the model is a good predictor of circuit performance. The die and magnet assembly used in the tests is shown in Figure 6. The mounting assembly and electronics are shown in Figure 7. The device was installed in Kinemetrics vault as shown in Figure 8. The seismometer was co-located with an STS-2 shown in the top right of the picture. The package was aligned with the Galperin Axis of the sensor aligned to true north to coincide with the North axis of the STS-2. The device was connected to a Q330 with pre-amplifiers enabled, and an STS-2 was connected to the other channel group of the Q330, also with pre-amplifiers enabled to allow comparisons of the data. The device was thermally insulated with several layers of thermal blanketing and foam to reduce temperature effects. The device was found to be sensitive to the vault noise and the tilts registered on the STS-2's horizontal axis. As the device is on the Galperin axis, it responds to both horizontal and vertical noise. Without another device to remove the horizontal signal, the horizontal noise is expected to dominate the device performance in this vault.

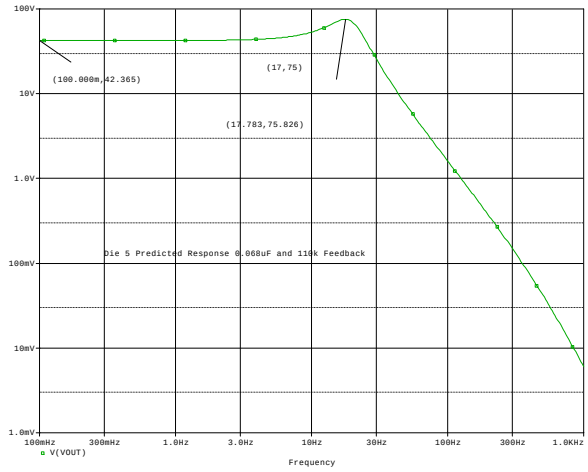


**Figure 7: Predicted Accelerometer Response**

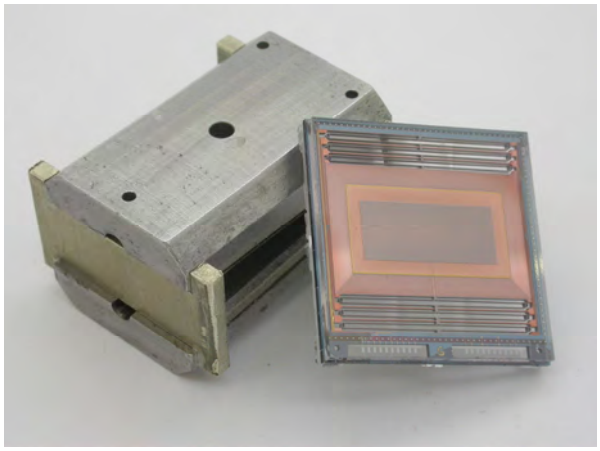

**Figure 5. Die & Magnet Assembly**

**Figure 6. Device and Electronics**

**Figure 8. Unit installed in Vault**

The device was run for over a week and several earthquakes were recorded. The noise analysis was performed on a 1.5 hour segment of data recorded in the late evening when no large seismic or other events were present and the cultural noise was at a minimum. The noise was processed in MatLab using a modified version of a United States Geologic Survey (USGS) Advanced National Seismic System program developed for accelerometer noise studies.

Figure 9 below shows typical vertical noise in the Kinemetrics vault during quiet periods. As can be seen we will need to look at periods of longer than 10 seconds for the ambient noise to be below our design limit. Figures 10 and 11 show the analysis of 90 minutes of the 20 sps samples from the Q330. As can be seen, the noise reaches a minimum between 10 and 30 seconds of about 13 nano-g/√Hz. This is currently considered to be an upper limit on the noise of the instrument. This is an order of magnitude higher that the design goal of < 1 nano-g/√Hz but already represents the lowest noise floor of a MEMS accelerometer presented to date.

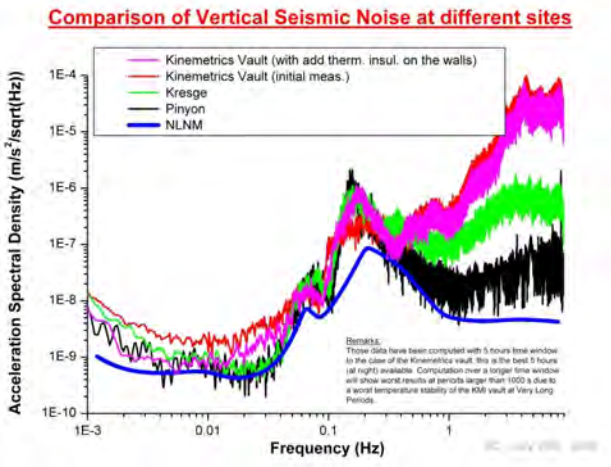


**Figure 9. Vertical Noise in Kinemetrics Vault**

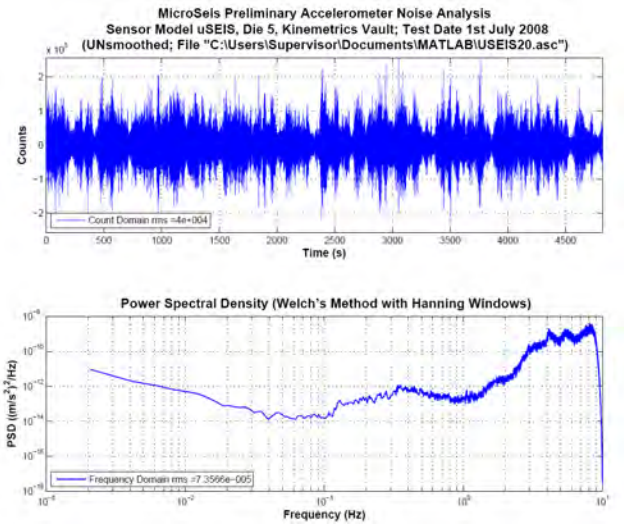


**Figure 10. Time Series and PSD of 20 sps Data**

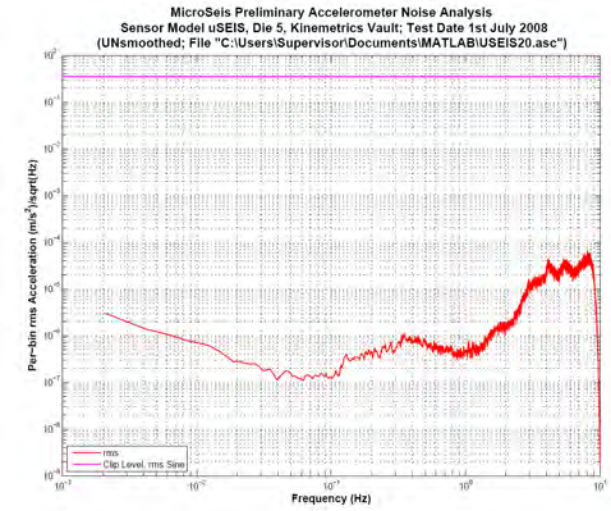


**Figure 11. Acceleration Noise Floor**

During the time the unit was in the vault it registered a magnitude 7.0 Mw earthquake east of the South Sandwich Islands on Monday June 30, 2008, at 06:17:43 UTC at 121 degrees from Pasadena. The event was recorded on the Q330 with pre-amps enabled. In figure 12 we see the top trace is the micro-seismometer acceleration output. The three signals below are from the co-located STS-2 signals for the E, N, and Z directions. The micro-seismometer output should be a vector combination of the N and Z signal converted to acceleration. These data have been filtered by the LPWWSS filter.

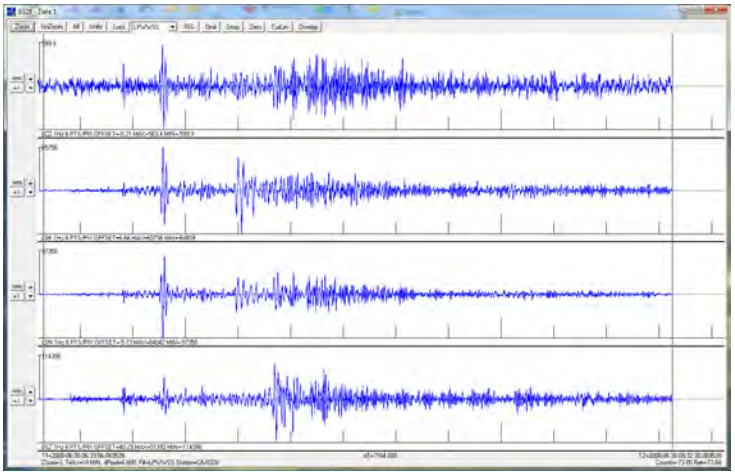

**Figure 12. Magnitude 7.0 Mw Sandwich Island Quake**

Further analysis was performed in MatLAB on the data. The data from the STS-2 was recombined to create a Galperin Axis pointed in the same direction as the Micro-seismometer. The acceleration data from the seismometer was then integrated to velocity and the results compared.

Figure 13 shows the data as a time series, Figure 14 shows the whole time series with the MEMS sensor data integrated compared to the calculated STS-2 U Axis. Figure 15 shows a small section on the same graph showing the correlation between the STS-2 and MEMS sensor data. This is an encouraging demonstration of the sensor performance.

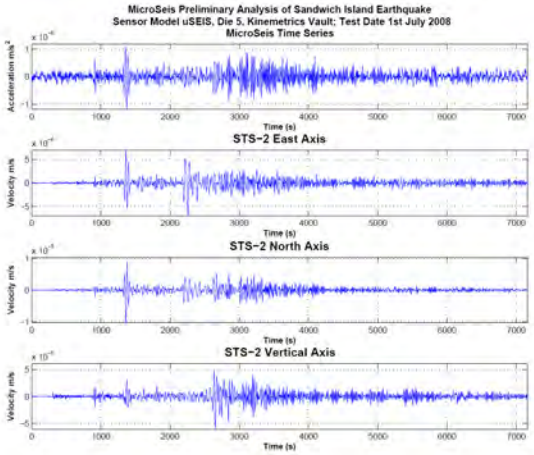


**Figure 13. Time Series of Event**

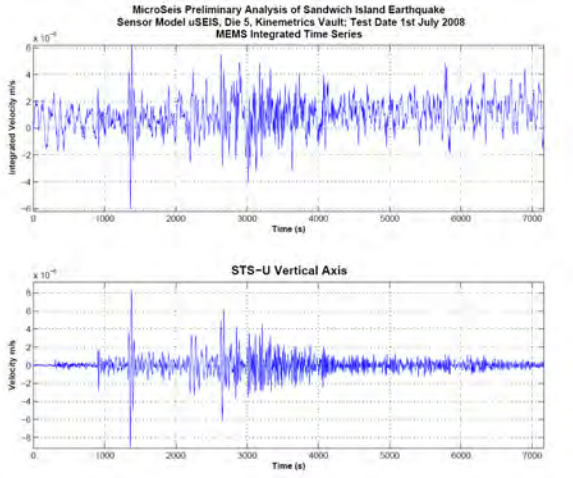


**Figure 14. Comparison of MEMS output converted to velocity to STS-2 Composite Axis**

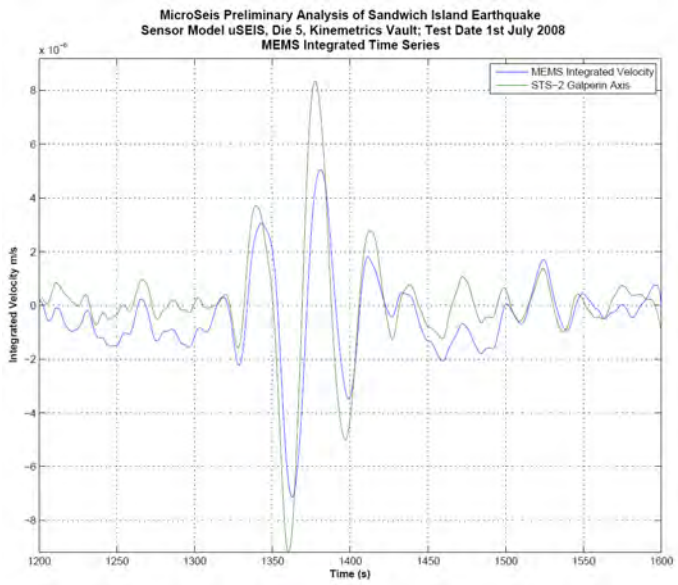


**Figure 15. Comparison of seven minute section**

## Temperature Sensitivity

Figure 16 shows a one day segment of data from the micro seismometer correlated with the temperature of the vault slab. This indicates that the offset is caused by temperature and amounts to about 375µg/°C or about 650ppm/°C of the gravity bias this is more than the expected 110 ppm/°C. Further modeling suggests that this is composed of both an exaggerated temperature sensitivity about four times higher than predicted coupled with a long term temperature independent drift. This temperature sensitivity will be investigated further as it both causes long term drift but is also likely to be responsible for the 1/f noise of the sensor being elevated at lower frequencies.

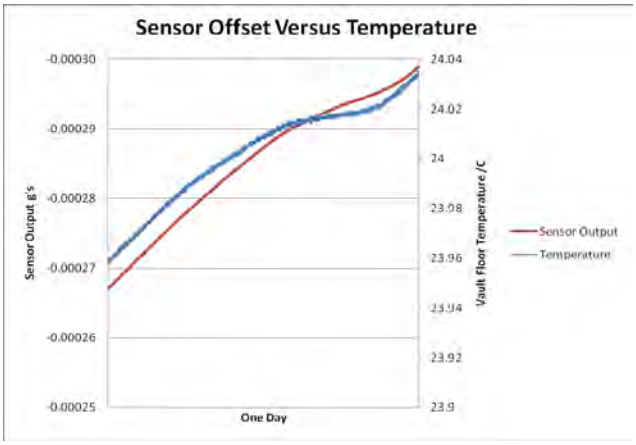


**Figure 16. Sensor Offset & Vault Temperature**

## CONCLUSIONS AND RECOMMENDATIONS

These tests have shown that we have produced all the necessary components of a broad-band seismometer on our silicon die. Only the "Q" differs significantly from the design target and this will be improved in future device lots when an etched displacement die will be used.

A commercial process to produce the proof mass wafers has been demonstrated, but more work is required to improve the yield and also to develop the vacuum sealing techniques for the wafer stack.

An overall packaging technique has been demonstrated that provides the electrical connections and required separation for device operation. The device has been integrated with simple feedback electronics and a demonstrated noise performance of ~13 nano-g/√Hz. It has also recorded several earthquakes with moderate fidelity.

The next stage will be to evaluate the performance of the device as a velocity sensor. The next phase of the development will utilize the lessons learned from this testing to improve device performance and yield. It is recommended that the next phase of the development at the commercial MEMS facility should also be undertaken at this time.

In conclusion, we believe we have made substantial progress in the development of a MEMS sensor for use by the Nuclear Explosion Monitoring community.

## ACKNOWLEDGEMENTS

We would like to thank the teams at Imperial and Kinemetrics who aided the authors in the design, fabrication, and testing of the devices: Sunil Kumar, Werner Karl, Trevor Semple, Toby Hopf, Sanjay Vijendran, John Stagg, and Ireck Briones. The team at IMT Inc, of Santa Barbara, California, led by Ian Johnston modified the process and performed the fabrication of the commercial devices.

## REFERENCES

Pike W. T. and S. Kumar (2007). Improved design of micromachined lateral suspensions using intermediate frames *J. Micromech. Microeng.* 17 pp 1680–1694.

Pike, W. T. and I. M. Standley (2005). Determination of the dynamics of micromachined lateral suspensions in the scanning electron microscope *J. Micromech. Microeng.* 15 (2005) S82–S88.

Standley, I. M., and W. T. Pike (2007). Progress in the development of rugged low power compact silicon MEMS sensors for use in Nuclear Explosion Monitoring, in *Proceedings of the 29th Monitoring Research Review: Ground- Based Nuclear Explosion Monitoring Technologies,* LA-UR-07-5613 ,Vol. 1, pp. 491–500.

# SEISMIC TOMOGRAPHY OF THE ARABIAN-EURASIAN COLLISION ZONE AND SURROUNDING AREAS

M. Nafi Toksöz[1], Robert D. Van der Hilst[1], Youshun Sun[1], Levent Gülen[1], Dogan Kalafat[2], Huseyin S. Kuleli[1], Chang Li[1], and Haijiang Zhang[1]

Massachusetts Institute of Technology[1] and Kandilli Observatory and Earthquake Research Institute, Bogaziçi University[2]

Sponsored by Air Force Research Laboratory

Contract No. FA8718-07-C-0001
Proposal No. BAA07-09

## ABSTRACT

The objectives of this study are to determine P-and S-wave velocity structures in the crust and upper mantle and to characterize seismic wave propagation in the Arabian-Eurasian collision zone and surrounding areas, including Iran, Arabia, Eastern Turkey, and the Caucasus. The Arabian-Eurasian plate boundary is a complex tectonic zone shaped by continent-continent collision processes. In recent years the number of seismic stations has increased greatly in the region because of expanded seismic networks in Azerbaijan, Turkey, Iran, and the Gulf countries. Unfortunately, the phase readings and waveform data cannot be obtained from a single data center. We are collecting the data through cooperation with individual network operators and the countries.

The travel-time tomography is carried out in three steps. First, obtain Pn and Sn velocities using local and regional arrival time data. Second, obtain the 3-D crustal P and S velocity models. Third, extend the model into the upper mantle and transition zone by combining local, regional, and teleseismic data and crust model constraints. We obtained the regional Pn velocity tomograms using 160,000 arrival times (including data from Iran) from 850 stations and 18,000 earthquakes. For Sn tomography, 75,000 phase readings were used. The Pn and Sn velocity variations agree quite well with some local differences. Pn velocities are very low under eastern Anatolia, northwest Iran, and the Lesser Caucasus. There are localized low-velocity anomalies. Velocities are low under the Iranian plateau. Pn velocities are high under the Arabian Platform, the Gulf, and the Zagros. In the north, high Pn velocities extend from the Black Sea to the Caspian and east to the Kara Kum Basin.

The upper mantle tomograms show the images of the subducted Neotethys slab. The slab geometry is quite complex, reflecting the history of the changes in plate motions and collision processes.

## OBJECTIVES

The objectives of this study are to determine P and S wave velocity structures in the crust and upper mantle and to characterize seismic wave propagation in the Arabian-Eurasian collision zone and surrounding areas, including Iran, Arabia, Eastern Turkey, and the Caucasus. The area of the study, shown in Figure 1, extends east-west from the Mediterranean to Central Asia and north-south from the Caspian to the Gulf of Aden and the Arabian Sea. The area covers all of the Arabian plate, the collision zone, and the areas in the Eurasian plate whose structure and tectonics are affected by the collision. The project will include data from countries whose seismic networks have expanded significantly in recent years, such as Turkey, Azerbaijan, Iran, Kuwait, United Arab Emirates (UAE), Oman, and Saudi Arabia. These locations provide data for high-resolution P and S wave travel-time tomography. Recent observations show that wave propagation and attenuation vary significantly even with small changes across the suture zone, indicating rapid spatial changes in crust and mantle properties.

A number of unanswered questions remain about the structure and processes in the upper mantle beneath the collision zone. The fate of the Neotethys plate subducted prior to the continental collision remains largely unknown. There are no intermediate and deep earthquakes under the Zagros-Bitlis suture zone, yet the subduction is too recent for the slab to reach thermal equilibrium and be assimilated. Some studies have suggested that the slab has recently broken off beneath the suture zone (Bird, 1978; Molinaro et al., 2005). In the Makran subduction zone in the south, seismicity and structure have been studied with the deployment of dense seismic networks (Yamini-Fard and Hatzfeld, 2006), confirming the Makran subduction, yet the nature of the transition from the subduction zone to the Zagros suture zone has not been fully resolved. High-resolution travel-time tomography would be a major step towards defining the present-day crustal and mantle structure of the Middle East region.

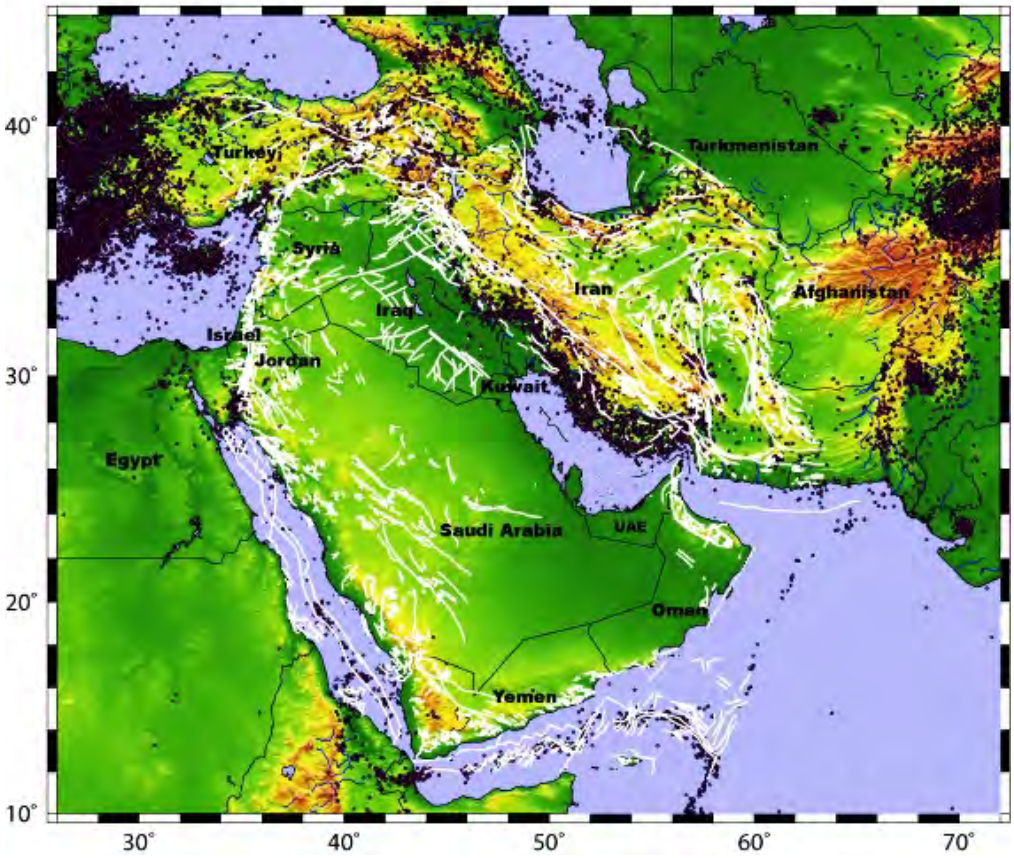


**Figure 1. Topographic map of the Middle East and surrounding regions. White lines denote the location of known faults, while the black dots represent the epicenter locations of earthquakes in the region.**

## RESEARCH ACCOMPLISHED

### Tectonic Setting

The Arabian-Eurasian plate boundary is extremely complex, and it is an ideal region to study a young (geologically) continent-continent collision belt. The current tectonics of the region are controlled by the collision and continuing convergence of the Arabian and Eurasian plates. The Arabian and Eurasian plates collided in the early Miocene, after the Neotethys Sea was subducted beneath Eurasia (Bird, 1978; Şengör and Yılmaz, 1981; Jackson and McKenzie, 1984; Dewey et al., 1986). Pre-, syn-, and post-collision tectonics produced very complex structures in the region. Over the last decade, a number of seismic studies have examined the crust and upper mantle structure beneath the Middle East to constrain the nature of the Arabian-Eurasian collision zone. Large-scale surface wave tomography studies have shown variable crustal thickness and upper mantle velocities (Ritzwoller and Levshin, 1998; Pasyanos et al., 2001; Villasenor et al., 2001; Pasyanos and Walter, 2002; Shapiro and Ritzwoller, 2002; Alinaghi et al., 2007; Reiter and Rodi, 2006). Regional-scale surface wave tomographic studies further highlight the complexity of the collision zone (Mindevalli and Mitchell, 1989; Rodgers et al., 1999; Mohktar et al., 2001; Maggi and Priestley, 2005) showing a thickened crust under the Caucasus and Zagros, and low shear velocity beneath the Turkish and Iranian plateaus.

Hearn and Ni (1994), Ritzwoller et al. (1998), Al-Lazki et al. (2003; 2004), and Phillips et al. (2007) found slow Pn velocities ($\leq$ 8 km/s) beneath the Anatolian plateau, northwestern Iran, the Greater Caucasus, and southwestern Arabia. The Pn velocities beneath northern Arabia and the Caspian region are faster than average (Al Lazki et al., 2004; Ritzwoller et al., 2002). This high degree of variability suggests that the Earth structure may be extremely complicated in the region.

Studies of the propagation and attenuation characteristics of regional waves (e.g., Pn, Sn, and Lg) provide additional evidence for strong heterogeneities. Surface wave studies show high shear wave attenuation beneath Iran, Anatolia, and the western part of the Arabian plate and relatively low attenuation in central and eastern Arabia (Seber and Mitchell, 1992; Sandvol et al., 2001; Cong and Mitchell, 1998; Jamberie and Mitchell, 2004). Sn and Lg waves are attenuated through much of the collision zone between the Arabian and Eurasian plates (Kadinsky-Cade et al., 1981; Rodgers et al., 1987; Mitchell et al., 1997; Cong and Mitchell, 1998; Gök et al., 2000; Sandvol et al., 2001; Al-Damegh et al., 2004). An Lg blockage exists across the Bitlis suture zone and across the Zagros fold and thrust belt.

The studies mentioned above present consistent results for the crust and uppermost mantle seismic properties on a regional scale. Significant variation in waveforms, observed particularly in short-period seismograms, over propagation paths that are close to each other, suggests structural variations over short distances at regional boundaries. Delineating these features requires seismic data from dense local and regional seismic networks. During this year we were able to increase the phase (arrival time) data significantly by adding readings from Iran and other regional networks.

### Travel-Time Data and Pn and Sn Tomography

An important task under this project is to collect arrival time data from seismic stations situated in more than 20 countries in the region. A significant number of these stations are in networks that are relatively new and whose data are not available from global data centers such as the Incorporated Research Institutions for Seismology (IRIS) or the International Seismological Centre (ISC). Figure 2 shows seismic stations in the region from which data may be obtained either through data centers or by bilateral arrangements. In the past year, Iran started to make available phase data from its networks. In Iran there are seven regional networks, deployed around major cities, with a total of 50 stations (Figure 3). Recently, Tehran University was designated as the central location that would collect and integrate data from the regional networks into a central database. Use of data from stations in Iran required the deciphering of nomenclature and the resolution of some apparent discrepancies between data from individual networks and the central database. We were able to obtain 100,000 P and 70,000 S arrival time recordings from local earthquakes for the time period between January 2006 and March 2008. Our database for the Pn tomography in the whole study region includes 160,000 arrival times from 850 stations and 18,000 earthquakes. The source-station ray paths are shown in Figure 4A. For Sn, the data are fewer, with 75,000 total phase readings. The ray paths are shown in Figure 4B.

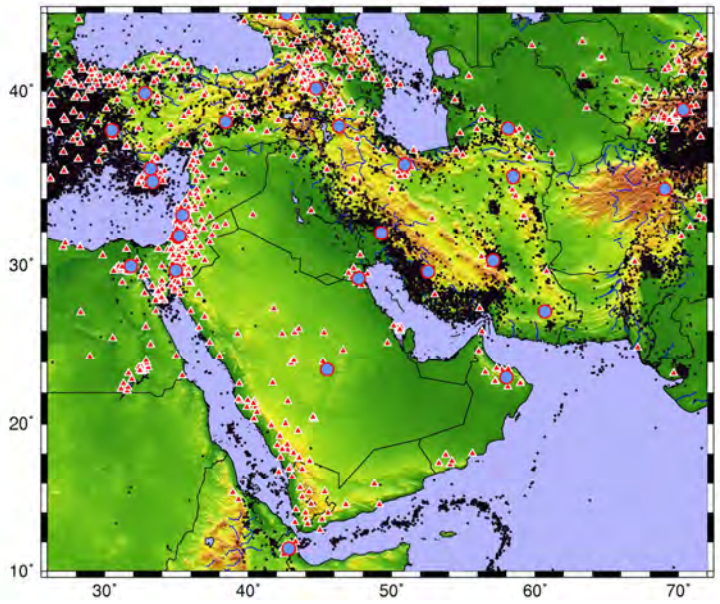


**Figure 2. Seismic stations (triangles) and events (black dots) in the region. Circles show broadband stations.**

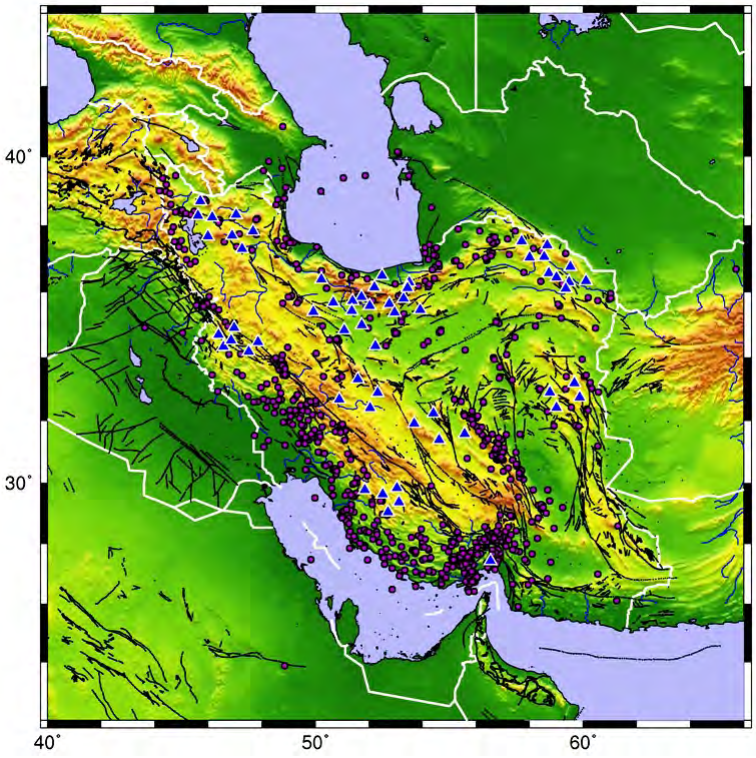


**Figure 3. Seismic stations (triangles) and events (dots) in Iran from January 2006 to March 2008.**

The Pn and Sn travel times (residuals) are inverted for lateral velocity variations using Hearn's approach (Hearn, 1996; Hearn et al., 2004), modified by Pei et al. (2007). Figure 5 shows the travel-time residuals before and after the Pn and Sn tomographic inversions. Figures 6A and 6B show Pn and Sn velocities, respectively. The general features of Pn velocities are similar to those of Philips et al. (2007), except that Figure 6A has finer spatial resolution. Pn

velocities are low under eastern Anatolia, northwest Iran, and the southern Caucasus. Isolated low-velocity anomalies exist along the Levant Fracture (Dead Sea Fault) Zone. A prominent low-velocity feature is observed just to the south of the Caspian Sea. The Iranian plateau is characterized by lower than average Pn velocity. Pn velocities are high under the Arabian platform, the Persian Gulf , and under the Zagros fold belt. Most likely these are the velocities associated with the top of the Neotethys lithosphere. In the north, the higher velocities are under the Black Sea, the Rioni and Kara Basins between the Greater and Lesser Caucasus, the southern Caspian, and the Kyzyl and Kara Kum Basins of Turkmenistan. These are most likely the remnants of the Paleotethys (Gülen, 1989). Sn velocities shown in Figure 6B are similar to Pn. In general, the regional features correlate quite well. Some isolated anomalies (e.g., Levant Fracture Zone) are very similar between the Pn and Sn.

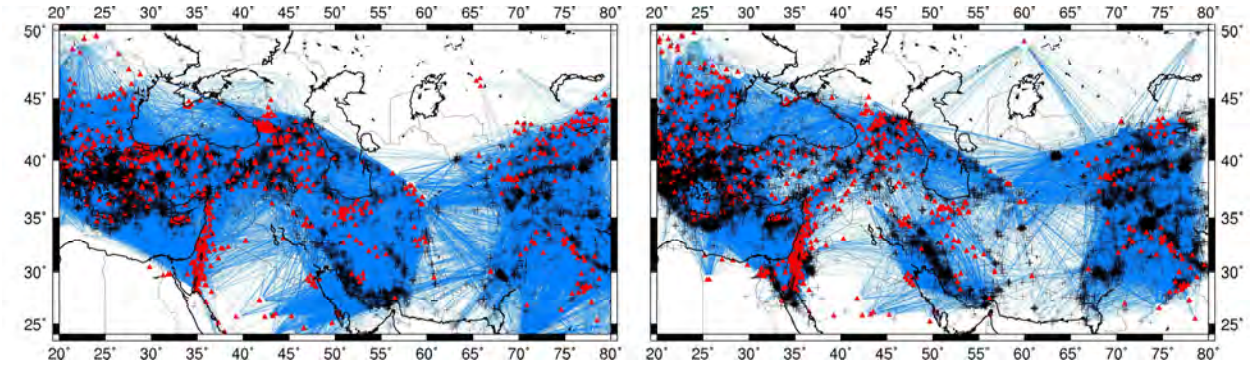

**Figure 4. (A) Left: Ray paths for Pn travel times. From 18,000 events recorded by 850 stations (red triangles), 160,000 Pn rays were obtained (black crosses). (B) Right: Ray paths for 75,000 Sn travel times.**

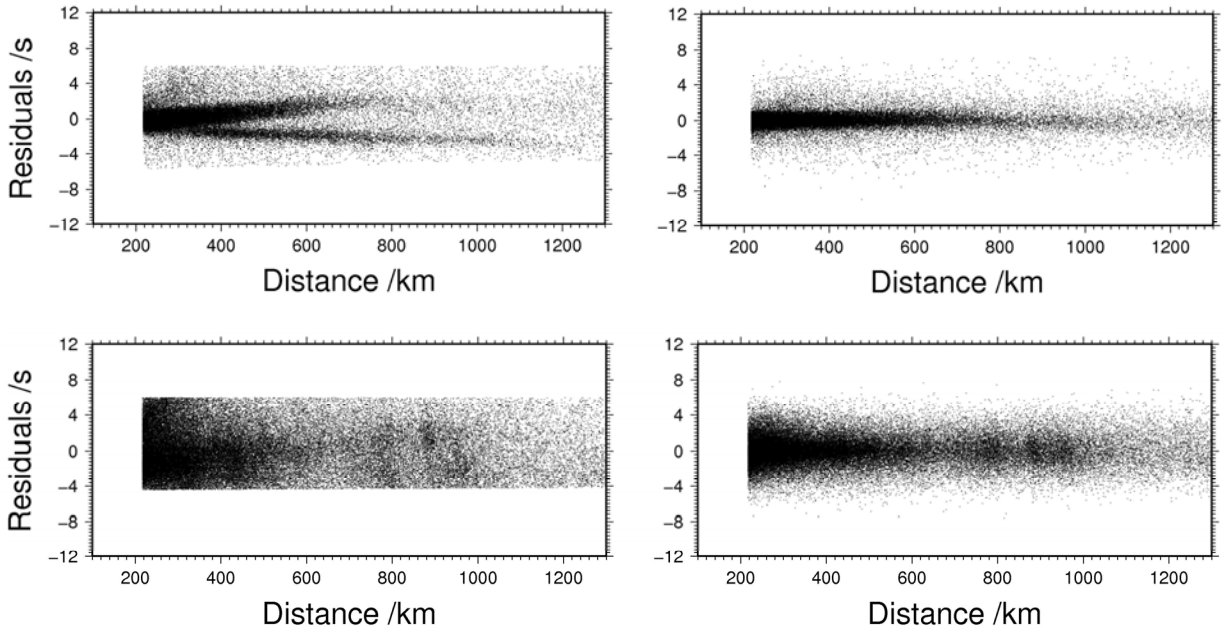


**Figure 5. (A) Top: Pn travel-time residuals before inversion (left) and after inversion (right). The standard deviation of travel-time residuals decreased to 1.26 s from 1.73 s. Bottom: Sn travel-time residuals before inversion (left) and after inversion (right). The standard deviation of travel-time residuals decreased to 1.89 s from 2.54 s.**

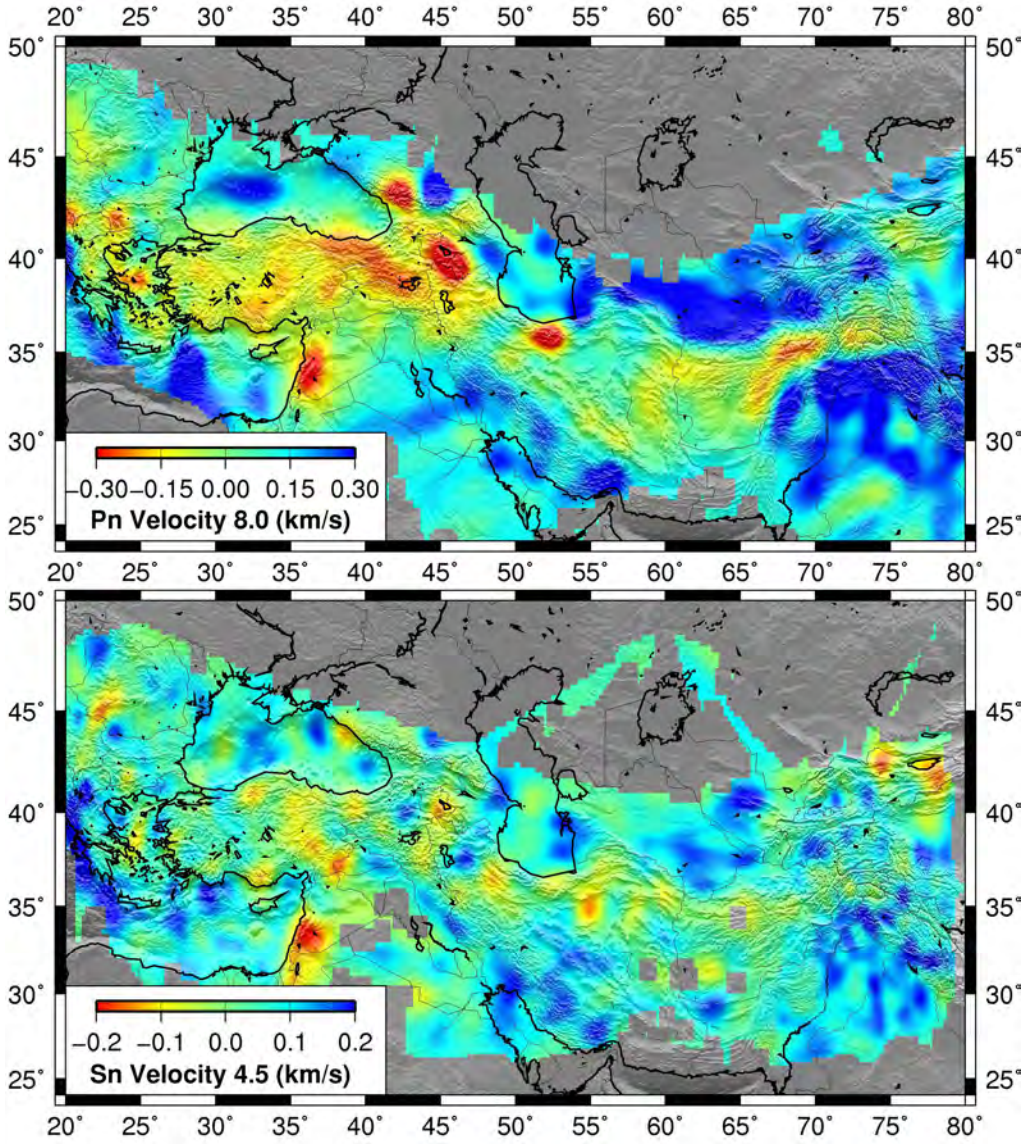


**Figure 6. (A) Top: Pn velocity lateral variations. Average Pn velocity is 8.0 km/s. (B) Bottom: Sn velocity lateral variations. Average Sn velocity is 4.5 km/s.**

**Upper Mantle Structure Beneath the Middle East**

We used teleseismic and local data for determining the velocity structure. The data used come from three sources: (1) the EHB (Engdahl, van der Hilst, and Buland, 1998) datasets, reprocessed from the ISC between 1964 and 2007; (2) picked arrival times from regional (temporary) seismic stations and arrays, including stations in Saudi Arabia and Ethiopia; and (3) the global PP-P differential travel-time dataset.

Travel-time residuals are then computed by subtracting travel times calculated based on the *ak135* reference model (Kennett et al., 1995). Although inversion is done for the whole mantle, a substantial number of stations of the EHB catalog are located within the Middle East region, and they provide key constraints on the subduction along the Zagros-Bitlis suture zone. In Figure 7, we show P-wave velocity variations beneath the Middle East in map view at four different depths. The coastlines and plate boundaries are shown for reference.

The model reveals the low-velocity anomaly beneath Ethiopia from 100 km down to 500 km depth. Another low-velocity anomaly is located beneath the northwestern part of the Arabian plate from 100 km to 300 km depth (Figure 7). These low-velocity anomalies extend to the transition zone and at the lower mantle, suggesting that they may be associated with deep mantle upwelling (Benoit et al., 2006).

The high-velocity anomalies associated with the Neotethys subducted lithosphere is clearly evident at velocity images at depths of 300, 500, and 700 km.

Cross sections across the collision zone (Figures 8A and 8B) provide other views of the convergence zone. The subducting slab is clearly visible under Makran and extends down to a 660-km discontinuity. Under the Persian Gulf and Zagros (Figure 8B), the slab geometry is more complete. This may be associated with changing velocities of the Arabian plate since the initial collision about 28 million years ago.

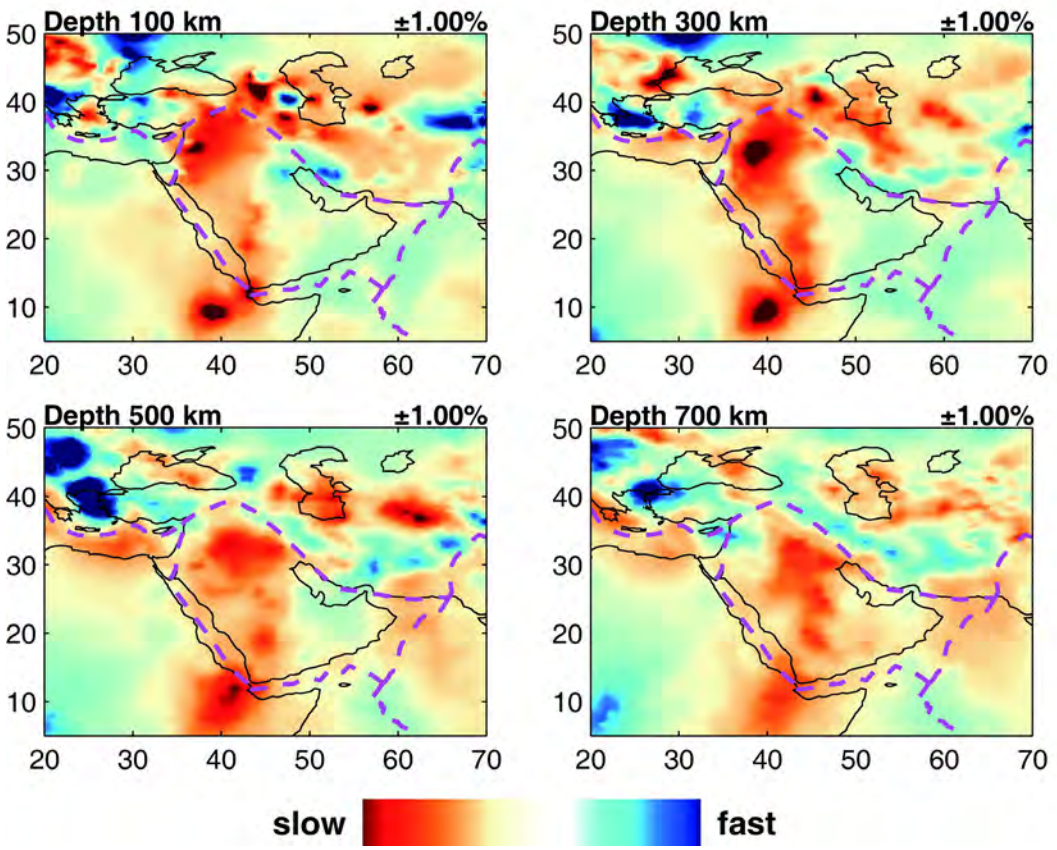


**Figure 7. P-wave anomalies beneath the Middle East at different depths as indicated on the left upper corner in each subplot. The blue and red represent high and low-velocity anomalies, respectively. The dashed purple lines are the plate boundaries, and the black lines are the coastlines.**

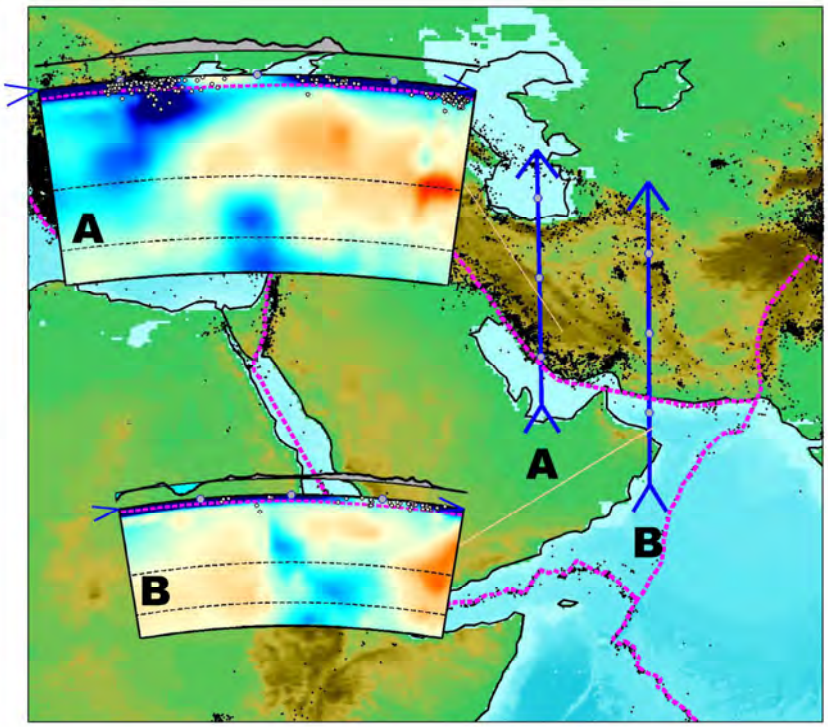


**Figure 8. Vertical cross sections showing the P-wave velocity anomalies down to 700 km depth. The color scale indicates 0.8% deviations with respect to the 1-D *ak135* model. The dashed lines indicate the 410 km and 660 km mantle discontinuities. The topography is shown on top of the cross section.**

## CONCLUSIONS AND RECOMMENDATIONS

Primary activities were dedicated to collecting P and S wave local/regional arrival time data from more than 750 stations in the study area. For the first time we were able to obtain arrival time data from 50 stations in Iran. Altogether, 160,000 Pn arrivals and 100,000 Sn arrivals were used to do a seamless tomography of the uppermost mantle on the Arabian Eurasian collision zone, and to obtain both the Pn and Sn velocities. The main features of the velocity models are as follows:

1. Pn and Sn velocities are similar in general. Measurable differences exist in some regions.

2. Pn (and Sn) velocities are lowest under eastern Anatolia, northwest Iran, and the southern Caucasus. Velocities under the Anatolian and Iranian plateaus are low.

3. Velocities are lower under Anatolia than under the Iranian plateau.

4. There are isolated low-velocity zones under the northern Dead Sea Fault.

5. Pn and Sn velocities are high under the Arabian Platform and under regions surrounding the Iranian and Anatolian platforms (e.g. Persian Gulf, Black Sea, South Caspian, and Kyzyl Kum and Kara Kum basins.

6. Upper mantle velocities obtained with regional and teleseismic arrival time data clearly delineate images of the subducted Neotethys slab.

7. Slab geometry varies significantly in different parts of the convergence zone. It is a typical oceanic subduction under Makran but becomes more complex under the northern parts of the collision zone.

Future work in the project will concentrate on obtaining travel-time data from additional stations, generating 3-D P and S wave velocity models for the crust, and redoing the upper mantle tomography with the new 3-D crustal model included. Evaluating the effects of velocity heterogeneities on the waveforms over local and regional distances will be an important part of the effort, as well as model evaluation with selected ground truth events.

## REFERENCES


Al-Damegh, K., E. Sandvol, A. Al-Lazki, and M. Barazangi (2004). Regional seismic wave propagation (Lg and Sn) and Pn attenuation in the Arabian Plate and surrounding regions, *Geophys. J. Int*. 157: 775–795.

Alinaghi, A., I. Koulakov, and H. Thybo (2007). Seismic tomographic imaging of P- and S-waves velocity perturbations in the upper mantle beneath Iran, *Geophysical Journal International* 169: 3, 1089–1102.

Al-Lazki, A., E. Sandvol, D. Seber, M. Barazangi, and N. Turkelli (2003). Pn tomographic imaging of mantle lid velocity and anisotropy at the junction of the Arabian, Eurasian, and African plates, *Geophys. Res. Lett.* 30: doi:10.1029/2003GL017391.

Al-Lazki, A. I., E. Sandvol, D. Seber, M. Barazangi, N. Turkelli, and R. Mohamad (2004). Pn tomographic imaging of mantle lid velocity and anisotropy at the junction of the Arabian, Eurasian and African plates, *Geophys. J. Int*. 158*:* 1024–1040.

Benoit, M. H., A. A. Nyblade, and J. C. Van Decar (2006). Upper mantle P wave speed variations beneath Ethiopia and the origin of the Afar Hotspot, *Geology* 34: 329–332.

Bird, P. (1978). Finite-element modeling of lithosphere deformation: The Zagros collision orogeny, *Tectonophysics* 50: 307–336.

Cong, L. and B. J. Mitchell (1998). Seismic velocity and Q structure of the Middle Eastern crust and upper mantle from surface wave dispersion and attenuation, *Pure Appl. Geophys.* 153: 503–538.

Dewey, J. F., M. R. Hempton, W. S. F. Kidd, F. Saroglu, and A. M. C. Şengör (1986). Shortening of continental lithosphere: The neotectonics of eastern Anatolia—A young collision zone, in *Collision Tectonics*, M. P. Coward and A. C. Ries (eds.) London: Geol. Soc. London, pp. 3–36.

Engdahl, E. R., R. D. van der Hilst, and R. Buland (1998). Global teleseismic earthquake relocation with improved travel times and procedures for depth determination, *Bull. Seism. Soc. Am*. 88: 722–743.

Gök, R., N. Turkelli, E. Sandvol, D. Seber, and M. Barazangi (2000). Regional wave propagation in Turkey and surrounding regions, *Geophys. Res. Lett.* 27: 429–432.

Gülen L. (1989). From plate tectonics to global domain tectonics, in *Crust/Mantle Recycling at Convergence Zones*, S. R. Hart and L. Gülen (eds.), NATO ASI Series, C258. Boston: Kluwer Academic Publishers, pp. 173–179.

Hearn, T. M., S. Wang, J. Ni, Z. Xu, Y. Yu, and X. Zhang (2004). Uppermost mantle velocities beneath China and surrounding regions, *J. Geophys. Res*. 109: doi:10.1029/2003JB002874.

Hearn, T. M. and J. Ni (1994). Pn velocities beneath continental collision zones: The Turkish-Iranian plateau, *Geophys. J. Int*. 117: 273–283.

Hearn, T. M. (1996). Anisotropic Pn tomography in the western United States, *J. Geophys. Res*. 101: 8403–8414.

Jackson, J. and D. McKenzie (1984). The active tectonics of the Alpine-Himalayan belt between western Turkey and Pakistan, *Geophys. J. R. Astron. Soc*. 77: 185–265.

Jamberie, A. L. and B. J. Mitchell (2004). Shear wave Q structure and its lateral variation in the crust of China and surrounding regions, *Geophys. J. Int*. 157: 363–380.

Kadinsky-Cade, J., M. Barazangi, J. Oliver, and V. Isacks (1981). Lateral variation in high-frequency seismic wave propagation at regional distances across the Turkish and Iranian plateaus, *J. Geophys. Res*. 86: 9377–9396.

Kennett, B. L. N., E .R. Engdahl, and R. Buland (1995). Constrains on seismic velocities in the Earth from travel times, *Geophys. J. Int.* 122: 108–124.

Maggi, A. and K. Priestley (2005). Surface waveform tomography of the Turkish-Iranian plateau, *Geophys. J. Int.* 160: 1068–1080.

Mindevalli, O. Y. and B. J. Mitchell (1989). Crustal structure and possible anisotropy in Turkey from seismic surface wave dispersion, *Geophys. J. R. Astron. Soc*. 98: 93–106.

Mitchell, B. J., Y. Pan, J. Xie, and L. Cong (1997). Lg code Q variation across Eurasia and its relation to crustal evolution, *J. Geophys. Res*. 102: 22,767–22,779.

Mokhtar, T. H., C. A. Ammon, R. B. Herrmann, and A. A. Ghalib (2001). Surface wave velocity across Arabia, *Pure Appl. Geophys.* 158: 144–1425.

Molinaro, M., H. Zeyen, and X. Laurencin (2005). Lithospheric structure beneath the southeastern Zagros Mountains, Iran: Recent slab break-off? *Terra Nova*, doi: 10.1111/j.1365-3121.2004.00575.

Pasyanos, M. E., W. R. Walter, and S. E. Hazler (2001). A surface wave dispersion study of the Middle East and North Africa for monitoring the comprehensive Nuclear-Test-Ban Treaty, *Pure Appl. Geophys.* 158: 1445–1474.

Pasyanos, M. E. and W. R. Walter (2002). Crust and upper mantle structure of North Africa, Europe, and the Middle East from inversion of surface waves, *J. Geophys. Int*. 149: 463–481.

Pearce, J. A., J. F. Bender, S. E. DeLong, W. S. F. Kidd, P. J. Low, Y. Güner, F. Şaroğlu, Y. Yılmaz, S. Maarbeth, and J. G. Mitchell (1990). Genesis of collision volcanism in eastern Anatolia, Turkey, *J. Volcanol. Geotherm. Res*. 44: 189–229.

Pei, S., J. Zhao, Y. Sun, Z. Xu, S. Wang, H. Liu, C. A. Rowe, M. N. Toksoz, and X. Gao (2007). Upper mantle seismic velocities and anisotropy in China determined through Pn and Sn tomography. *J. Geophys. Res.* 112: B05312, doi:10.1029/2006JB004409.

Reiter, D. and W. Rodi (2006). Crustal and upper-mantle P- and S-velocity structure in central and southern Asia from joint body-and surface-wave inversion, in *Proceedings of the 28th Seismic Research Review: Ground-Based Nuclear Explosion Monitoring Technologies*, LA-UR-06-5471, Vol. 1, pp. 209–218.

Ritzwoller, M. and A. Levshin (1998). Eurasian surface wave tomography: Group velocities, *J. Geophys. Res*. 103: 4839–4878.

Ritzwoller, M., A. Levshin, L. Ratnikova, and A. Egorkin (1998). Intermediate-period group-velocity maps across Central Asia, western China, and parts of the Middle East, *Geophys. J. Int*. 134: 315–328.

Ritzwoller, M. H., M. P. Barmin, A. Villasenor, A. L. Levshin, and E. R. Engdahl (2002). Pn and Sn tomography across Eurasia to improve regional seismic event locations, *Tectonophysics* 358: 39–55.

Rodgers, A. J., J. F. Ni, and T. N. Hearn (1987). Propagation characteristics of short-period Sn and Lg in the Middle East, *Bull. Seism. Soc. Am*. 87: 396–413.

Rodgers, A. J., W. R. Walter, R. J. Mellors, A. M. S. Al-Amri, and Y-S. Zhang (1999). Lithospheric structure of the Arabian Shield and Platform from complete regional waveform modeling and surface wave group velocities, Geophys. J. Int. 138: 871–878.

Sandvol, E., K. Al-Damegh, A. Calvert, D. Seber, M. Barazangi, R. Mohamad, R. Gok, N. Turkelli, and C. Gurbuz (2001). Tomographic imaging of Lg and Sn propagation in the Middle East, Pure and Appl.Geophys. 158: 1121–1163.

Phillips, W. S., M. L. Begnaud, C. A. Rowe, L. K. Steck, S. C. Myers, M. E. Pasyanos, and S. Ballard (2007). Accounting for lateral variations of the upper mantle gradient in Pn tomography studies, Geophys. Res. Lett., 34, L14312, doi:10.1029/2007GL029338.

Seber, D. and B. Mitchell (1992). Attenuation of surface waves across the Arabian Peninsula, Tectonophysics 204: 137–170.

Şengör, A. M. C. and Y. Yılmaz (1981). Tethyan evolution of Turkey: A plate tectonic approach, *Tectonophysics 75*: 181–241.

Shapiro, N. M. and M. H. Ritzwoller (2002). Monte-Carlo inversion for a global shear velocity model of the crust and upper mantle, *Geophys. J. Int*. 152: 88–105.

Villasenor, A., M. H. Ritzwoller, A. L. Levshin, M. P. Barmin, E. R. Engdahl, W. Spakman, and J. Trampert (2001). Shear velocity structure of central Eurasia from inversion of surface wave velocities, *Physics of the Earth and Planetary Interiors* 123: 169–184.

Yamini-Fard, F. and D. Hatzfeld (2006). Microseismicity and crustal structure of the Zagros-Makran Transition Zone (Iran): Evidence for a progressive transition from continental collision to oceanic subduction, in *Proceedings of the 2006 Gulf Seismic Forum.*

# THREE-AXIS SEISMOMETER

Luzhong Yin, Matthew Erdtmann, Larry Domash, and Jing Zhao

Agiltron, Inc.

Sponsored by National Nuclear Security Administration

Contract No. FG02-08ER85084

## ABSTRACT

Wide coverage and accurate detection of nuclear detonations are critical to prevent proliferation. Such applications require extremely high sensitivities on the order of approximately 0.5 ng/sqrt(Hz) on all three axes of acceleration, as well as robustness and cost effectiveness. Current sensors are too large or insensitive to be widely distributed in a sensor network. Agiltron, an innovator of microelectromechanical systems (MEMS) devices, has developed a new design of the Micro-Mechanical Tunneling Transducer based on the physics of atomic tunneling currents. The proposed seismometer device is extremely sensitive, will measure simultaneously in three axes, and has a very low noise floor and a very small form factor. This micromachined device is also amenable to low-cost manufacture in large quantities, once the processes have been established. Successful implementation of the proposed vibration or acceleration sensor will also be useful in other geophysical applications, such as updating (Global Seismographic Network), as well as in robotics, medical, and aerospace industries.

## OBJECTIVES

It is critical to precisely detect nuclear detonations in order to monitor covert testing and the proliferation of nuclear weapons. Such instruments must be widely deployed and so should be highly sensitive, extremely compact, and low in cost. MEMS accelerometers based on micromachined silicon are natural to consider because of the mature technology of MEMS accelerometers, which are commercially used, for example, in automotive collision and airbag sensors. But the commercial versions are designed to detect only very large g forces and are not sensitive enough for nuclear monitoring, which requires subnano-g responses.

Among MEMS accelerometer approaches, piezoresistive, piezoelectric, and capacitive transducers are well developed. but none has proven able to reach nano-g. Since the Nobel prize was awarded to Binnig and Rohrer in 1986 for building the first scanning tunneling microscope (STM), the use of tunneling current for sensors has been developed in many directions. The exponential dependence of tunneling current on proximity gives it an extremely high sensitivity. In particular, the possibility of producing a highly sensitive tunneling displacement transducer has been actively explored. Several years after the advent of the first tunneling transducers, various authors have demonstrated displacement resolutions approaching $10^{-4}$ $\mathring{A}\,Hz^{-1/2}$. This high sensitivity is independent of the lateral size of the electrodes because the tunneling current occurs between two metal regions located at opposite electrode surfaces. Due to their high sensitivity and miniature size, micromachined tunneling transducers (MMTTs) are excellent candidates for high-performance, compact, inexpensive seismometers.

In MMTT devices, mechanical-thermal noise is the main limiting factor. One of the methods to reduce the noise is to increase the inertial mass. However, the limitation on the total size of a sensor within 1 cubic inch puts a limit on this approach. Conventionally, silicon is used as the intertial mass material. We propose to use gold as the inertial mass, which could theoretically lead to a 70% reduction in mechanical-thermal noise. The total noise of the sensor will include the mechanical-thermal noise and electronic readout noise. Due to the high sensitivity of electron tunneling, the second noise source will be minimal. The combination of dense metal inertial mass with tunneling is an ideal path to MMTT.

An integrated multiaxis device to measure acceleration within a single chip would find applications in a variety of markets beyond nuclear proliferation monitoring. Until now, however, the complexity and cost of providing multiaxis inertial sensing on a single chip have precluded their development. A cost-effective, single-chip, multiaxis seismometer based on electron tunneling transducers on single chip would thus be highly desirable. We propose to develop a novel MEMS displacement sensor that can detect three-axis accelerations by multiple tunneling tips. Our design is simple and promises to be inexpensive.

## RESEARCH ACCOMPLISHED

### Three-Axis Tunneling Seismometer MMTT Design

The sensor structure is schematically shown in Figure 1. The seismometer consists of top, bottom and middle elements, the middle element being the structural element. The structural element has a square ring-shaped outer support frame 8. The spring 7 connects the frame 8 at the top. The spring 7 has four beams at two central axes of the top surface of the suspended mass 6, and connects to the center of the top surface of the suspended mass. The center of the mass is offset from the center of the spring 7. The spring 7 is made from a silicon wafer. The gold mass will be fabricated through electroplating and releasing procedure to attach on the springs to form the required suspended mass. The top element has four tunneling tips (1–4) to sense the displacement change of the suspended mass 6 on the middle element. The four tunneling tips (1–4) are located on the farther ends of four cantilever beams (5) on the top element. By controlling the voltages on four electrodes (51–54) located at the fixed end of the cantilever beams, the four tunneling tips will keep the distances constant to the proof mass 6.

Comparing with the originally proposed layout, in which the four tunneling tips could be rigidly fixed on the top element, the current independent tunneling tips adjustment system (control cantilever and its associated electrodes) provide the following advantages: (1) avoids the difficulty of the simultaneous adjustment of four tips on one plate to within tunneling current distance, (2) the higher frequency and flexibility of the control cantilever can facilitate close-loop control, and (3) the sensor's higher resolution is controlled by large proof mass (Rockstad et al., 1994) in the middle element.

To simplify the fabrication of the top element, z-axis direction shaped silicon tips will not be needed. A triangle shaped beam tip (as shown in Figure 1 on the top element) is sufficient for the tunneling tips. This is because tunneling will take place between the nearest atoms; therefore, a sharp tip is not essential.

Each of the top and bottom elements has four proof mass control electrodes (51–54, and 91–94), which are optional in the current layout. They connect to an optional low-frequency secondary feedback circuit to maintain the suspended mass 6 position within suitable range of the cantilevers. In the structure, the suspended mass 6 serves as a common counterelectrode for all tunneling tips and electrodes on top and bottom elements. The inner cavity between the top and bottom element is vacuum sealed.

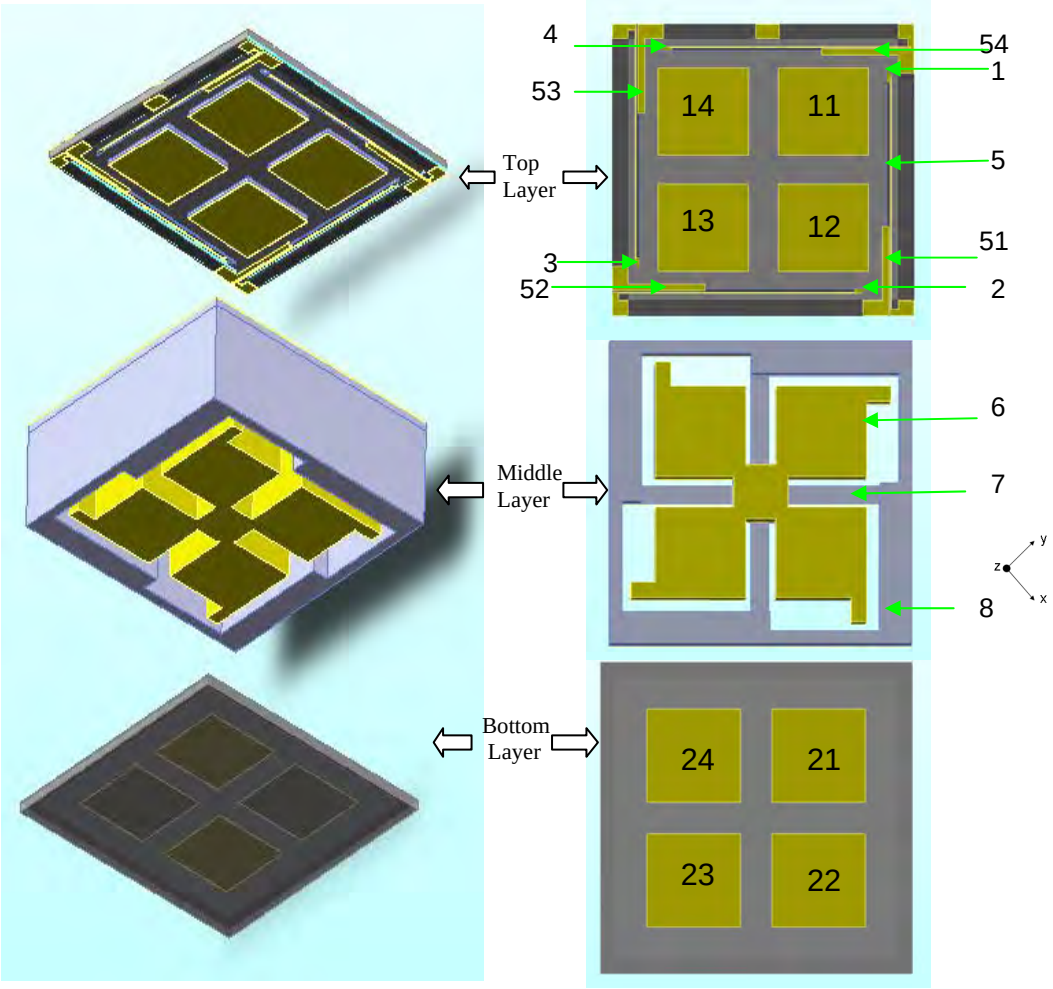


**Figure 1. Structure layout of the three-axis seismometer.**

The distances of the tunneling tips (1–4) to their counterelectrodes change in-phase when the suspended mass 6 is subjected to z-acceleration. The distances of the tunneling tips 2 and 4 to their counterelectrode change out-of-phase relative to each other when the suspended mass 5 is subjected to x-acceleration. Likewise, when subject to y-acceleration, the distances associated with tips 1 and 3 will move out-of-phase. By sensing these displacements, the current sensor is able to measure three-axis accelerations.

**Sensor Noise Analysis**

Thermal-mechanical noise: One of the key limitations of existing MEMS miniature high-sensitivity seismometer/accelerometers is thermal-mechanical noise. The Brownian equivalent acceleration noise for single mass is given as

$$g_B = \frac{1}{g}\sqrt{\frac{8\pi kTf_0}{MQ}} \quad (\mathrm{g}/\sqrt{\mathrm{Hz}})\,, \tag{1}$$

where k is Boltzmann's constant, T is the absolute temperature, $f_0$ is the natural frequency of the suspended mass, M is the suspended mass, and Q is the mechanical quality factor. For a two-mass system formed by a cantilever beam and the gold proof mass (as shown in Figure 1), the frame-equivalent rms thermal-mechanical noises at frequency $f$ contributed by the proof mass and the cantilever beam are given respectively by (Rockstad, et al., 1994):

$$g_{pB} = \frac{1}{g}\sqrt{\frac{8\pi kTf_{0p}}{m_p Q_p}}\text{, and} \tag{2}$$

$$g_{cB} = \frac{\left(2\pi f_{0p}\right)^2}{g}\sqrt{\frac{2kT\left[\left(1-\Omega_p^2\right)^2+\frac{\Omega_p^2}{Q_p^2}\right]}{\pi f_{0c}k_c Q_c\left[\left(1-\Omega_c^2\right)^2+\frac{\Omega_c^2}{Q_c^2}\right]}}, \tag{3}$$

where $\Omega_p = f/f_{0p}$, $\Omega_c = f/f_{0c}$ $Q_c$ and $Q_p$ are the mechanical quality factors of the cantilever and the proof mass respectively, $f_{0p}$ and $m_p$ are the proof mass natural frequency and mass, and $f_{0c}$ and $k_c$ are the natural frequency and stiffness of the cantilever. In the above the equations, the conditions of $f << f_{0c}$, that is, the frequency range of interest is much less than the natural frequency of the cantilever, and the proof mass natural frequency is small compared with that of the cantilever used. Equation (2) has the same formulation as in Equation (1), in which a large proof mass and a high Q (low damping) are helpful in achieving a low noise floor. Cantilever noise can be decreased by increasing the factor $\sqrt{f_{0c}k_cQ_c}$.

In the current work, we will use gold as the suspended mass. The density of gold is 8 times higher than that of silicon, which is used as suspended mass in current MEMS seismometers. To further decrease the mechanical-thermal noise, we will use our state-of-art high-vacuum packaging technology to the seismometer device, thereby minimizing squeeze-film damping. In our previous extensive thermal camera work (Zhao, 2007), we have successfully fabricated production devices with $10^{-4}$ torr vacuum stability. With this high-vacuum package, we have successfully observed Q >20,000 in Si MEMS devices.

We assume the use of a 5 × 5 × 0.5-mm gold suspended mass with a resonant frequency of 150 Hz and achieve Q ≈ 10,000. We can expect the equivalent thermal-mechanical noise to be ≈ 0.26 ng/sqrt(Hz) for the proof mass, which is better than the required 0.5 ng/ sqrt(Hz). Here we suppose the cantilever with a frequency of 16 kHz, with a mass of 9 micrograms. The thermal-mechanical noise of the cantilever beam vs frequency can be calculated as shown in Figure 2 (dotted line). As we can see from Figure 2, at lower frequencies (for example, smaller than 150 Hz), the dominant noise is from the proof mass. At that frequency range, the cantilever beam noise is about 0.039 ng/sqrt(Hz). Proof mass noise is shown in the dashed line, and the total noise is shown in the solid line in Figure 2. The dip at 150 Hz for cantilever thermal noise results from the noise being referred to the sensor case via the proof mass.

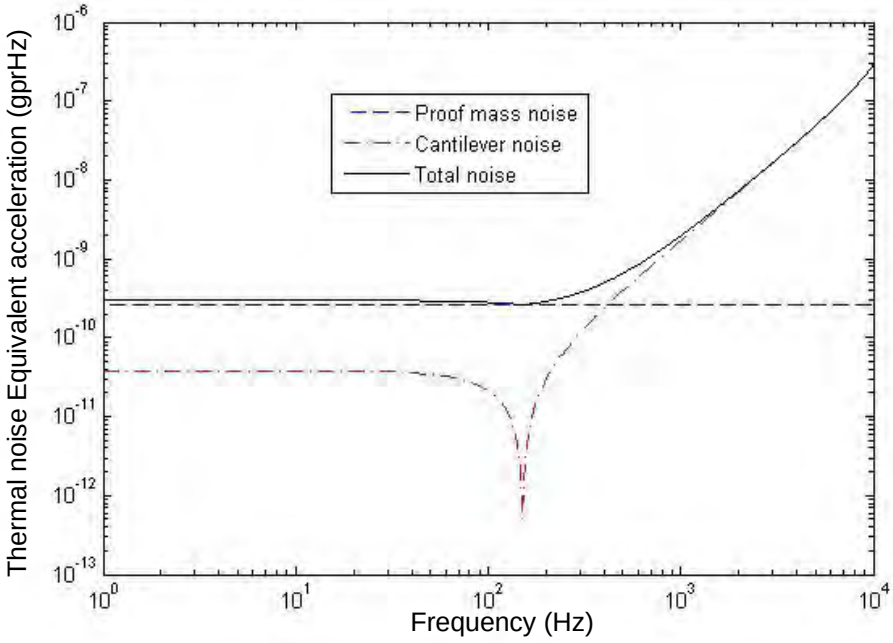


**Figure 2. Proof mass and cantilever thermal-mechanical noise vs frequency.**

Electronic readout noise: When a tunneling tip is close enough to its counterelectrode, a tunnel current $I_t$ is established by a small bias voltage $V_B$. The relationship between the tunneling gap and the tunneling current is given by

$$I_t \propto V_B \exp\left(-\alpha_I \sqrt{\Phi} s\right),$$

where $\alpha_I = 1.025\,\text{Å}\,\text{eV}^{-1/2}$ is the height of the tunnel barrier, and the bias voltage $V_B$ (typically about 100 mV is small compared with $\Phi$). For typical values of $\Phi$ and s (0.5 eV and 10 Å, respectively), the current varies by a factor of 2 for each Å change in electrode separation, which means sensitivity to less than one atom's dimensions. Because of this extreme sensitivity to position, the tip-to-substrate separation can be maintained constant to a high precision by close-loop control. The output of the feedback circuitry is then used as a measure of the tip's vertical separation. The tunnel transducer's sensitivity to position is superior to that of other compact transducers and is orders of magnitude better than standard compact capacitive sensors. In operation, feedback circuitry controls the vertical position of the tip to maintain the tunnel current constant. The small-signal displacement-to-current transfer constant is given by

$$\left|dI/dx\right| = I_t \alpha \sqrt{\Phi}\,.$$

The electrode gap is maintained so that the average tunneling current is 1.3 nA, with an applied bias voltage of 100 mV. The displacement-to-current sensitivity is then 9.4 A/m. With a resonant frequency of 150 Hz of the proof mass, the overall transfer constant is $1.05 \times 10^{-4}$ A/sqrt(Hz). For example, with this transfer constant and a JFET input preamplifier with an input current noise of the order of $10^{-15}$A/sqrt(Hz), this gives input noise $\approx 10^{-3}$ ng/sqrt(Hz).

Another source of noise is the shot-noise at tunneling (Gabrielson, 1993) is given as

$$i_s = \sqrt{2qI_t}\,,$$

where $q$ is the charge on an electron, and the shot-noise ≈ 0.09 ng/sqrt(Hz).

The total noise of the sensor is the square root of the sum of the squares of the above values, or about 0.31 ng/sqrt(Hz). From the above analysis, the electron tunneling readout method appears to meet the requirement for nano-g seismology.

**Large Dynamic Range**

Because proximity to a nuclear detonation is unknown, dynamic range is a key performance factor. The optional proof mass control electrodes (11–14 and 21–24) on the top element and the bottom element form a complementary electrostatic drive configuration. This configuration can greatly increase the dynamic range of the sensor with the use of a highly compliant spring 6. As the drive electrodes can provide only an attractive force, the electrodes' drive can provide the required servo rebalance force when the acceleration is such as to drive electrodes apart from one another. A typical electron tunneling accelerometer (Liu and Kenny, 2001) only has one set of drive electrodes on one side of the suspended mass. As a result, without acceleration, the elastic force provided by the springs must at least be equal to the rebalance force required to reposition the suspended mass to its servo null position upon application of full-scale acceleration. This will limit the dynamic range of the sensor. With our proposed complementary electrostatic proof mass position control configuration and close-loop control on each of the cantilever beams (5), the MMTT sensor can easily reach the dynamic range requirement of 120 dB.

Use of the complementary electrostatic drive configuration can also reduce the effect of the elastic suspension forces on the acceleration signal bias. This will be helpful to synch the electrical null with mechanical null positions. The complementary configuration allows use of highly compliant springs and a large mass, which is helpful for reaching the required high resolutions.

**Feedback and Control Design**

A scheme to control multiple-axis motion of the cantilevers 5 and the mass 6 is shown in Figure 5. When an external acceleration is applied on the suspended mass 6, the tunneling currents I1, I2, I3, and I4, which are respectively associated with tunneling tips 1, 2, 3, and 4, will change. Those currents through the amplifier convert to voltages V1, V2, V3, and V4. Those voltages are independently fed back to the electrodes (51–54), each of which is associated with one of cantilevers (5) to control the deflections of each tunneling tip.

The voltages (V1–V4) are also fed into an optional low-frequency secondary feedback circuit to maintain the suspended mass 6 position within suitable range of the cantilevers (5) through the synthesis circuit 1 to generate three components V1–V3, V2–V4, and V1+V2+V3+V4, and similarly for other components. Synthesis 4 gives the voltages needed to rebalance the z-translation force on all the top and bottom electrodes. All voltages are input to the Synthesis 5, which generates the final necessary voltage for each electrode to control the suspended mass 5 and return three error signals as the device output.

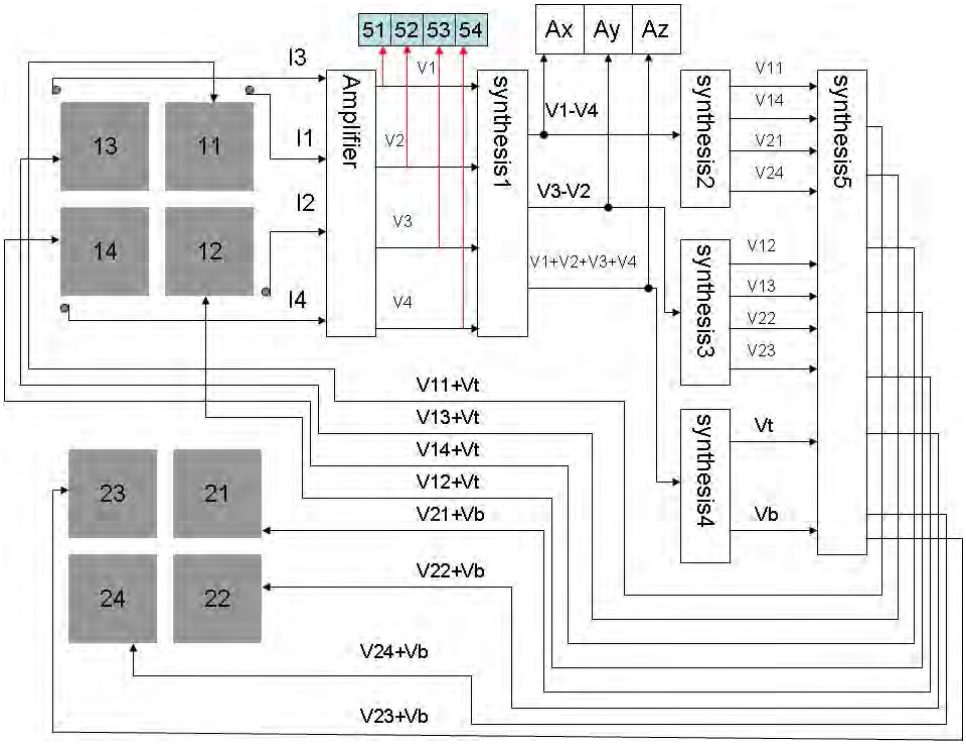


**Figure 3. Signal flow diagram.**

The advantage of feedback control is that the total sensor system can achieve much higher effective natural frequency and lower effective Q factor (GURALP; Liu and Kenny, 2001). The "stiffening" and "damping" added to the system by the electronic control does not add noise to the sensor, since the feedback forces are nondissipative. This can greatly enhance the performance of the seismometer.

**Sensor Package Concept**

The in-development three-axis MEMS seismometer is shown schematically in Figure 4. We estimate a noise floor smaller than 0.5 ng/sqrt(Hz), a dynamic range at least 120 dB over a frequency band of 0.2 to 40 Hz, a sensor size less than 1 cubic inch, and a power consumption below 100 mW. The MMTT sensor chip will be fabricated starting from a silicon-on-insulator (SOI) wafer. The chip will be mounted and wire bonded to a chip holder and vacuum packaged with a stainless steel lid. Coupled to controlling electronics, plug-in sensor units can be combined for easy integration into various deployment packages. The package is rugged and robust.

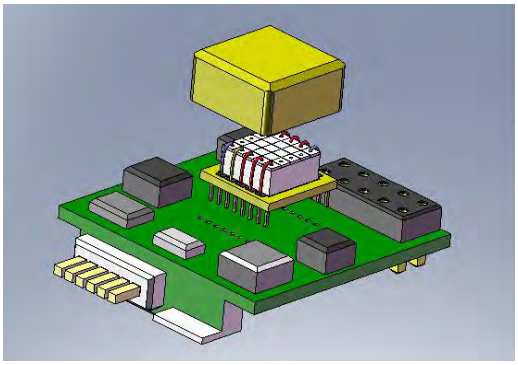

**Figure 4. Schematic package of the seismometer.**

## CONCLUSIONS AND RECOMMENDATIONS

The need exists for extremely miniaturized and low-noise seismometers for nuclear detonation monitoring with a self-noise less than 0.5 nanog/sqrt(Hz) and with the volume of 1 inch cube or lower. We have proposed to develop a Micro-Machined Tunneling Transducer to meet this requirement.

Agiltron's in-house MEMS expertise allows us to electroplate heavy metal gold to a silicon wafer to form a superior suspended mass in terms of decreasing thermal-mechanical noise. Agiltron's state-of-the-art high-vacuum packaging techniques will be used in the proposed seismometer, thus further decreasing the thermal-mechanical noise. Four independent controllable tunneling tips and complementary optional drive electrodes are used to sense and control the motion of the suspended mass. High sensitivity of the electron tunneling transducer effectively eliminates the electronic noise on the sensor. Complementary control electrodes for proof mass allow the sensor to work in a large dynamic range with ease. The combination of sensor and feedback control can help achieve higher effective natural frequency and damping without adding additional noise to the system. All these benefits translate into a low-noise, high-stability, qualified seismometer for monitoring nuclear detonation.

## REFERENCES

Gabrielson, T .B. (1993). Mechanical-thermal noise in micromachined acoustic and vibration sensors, *IEEE Trans. Electron Dev.* 40: 903–909.

Liu, C-H, T. W. Kenny (2001). A high-precision, wide-bandwith micromachined tunneling accelerometer, *J. Microelectromech. Syst.* 10: 425–433.

Rockstad, H .K., T. W. Kenny, J. K. Reynolds, W. J. Kaiser, and T. B. Gabrielson (1994). A miniature high-sensitivity broad-band accelerometer based on electron tunneling, *Sensors Actuators A.* 43: 107–114.

GURALP broadband seismometer, Guralp systems Ld, U.K.

Zhao, J. (2007). High sensitivity photomechanical MW-LWIR imaging using an uncooled MEMS microcantilever array and optical readout, *Infrared Technology and Applications XXXI*, B. F. Andresen, G. F. Fulop (Eds.) *SPIE* 5783: 1F-1

# Seismic Identification and Source Characterization

# SEISMIC SOURCE SCALING AND DISCRIMINATION IN DIVERSE TECTONIC ENVIRONMENTS

Rachel E. Abercrombie[1], Kevin Mayeda[2], William R. Walter[3], Gisela M. Viegas[1], and Katherine Murphy[2]

Boston University[1], Weston Geophysical Corporation[2], and Lawrence Livermore National Laboratories[3]

Sponsored by Air Force Research Laboratory

Contract No. FA8718-06-C-0024
Proposal No. BAA06-70

## ABSTRACT

The objectives of this study are to improve low-magnitude (concentrating on M2.5-5) regional seismic discrimination by performing a thorough investigation of earthquake source scaling using diverse, high-quality datasets from varied tectonic regions. Local-to-regional high-frequency discrimination requires an estimate of how earthquakes scale with size. Walter and Taylor (2002) developed the Magnitude and Distance Amplitude Corrections (MDAC) method to empirically account for these effects through regional calibration. The accuracy of these corrections has a direct impact on our ability to identify clandestine explosions in the broad regional areas characterized by low seismicity. Unfortunately our knowledge at small magnitudes (i.e., $m_b < \sim 4.0$) is poorly resolved, and source scaling remains a subject of on-going debate in the earthquake seismology community. Recently there have been a number of empirical studies suggesting scaling of micro-earthquakes is non-self-similar, yet there are an equal number of compelling studies that would suggest otherwise. It is not clear whether different studies obtain different results because they analyse different earthquakes, or because they use different methods. Even in regions that are well studied, such as test sites or areas of high seismicity, we still rely on empirical scaling relations derived from studies taken from half-way around the world at inter-plate regions.

We investigate earthquake sources and scaling from different tectonic settings, comparing direct and coda wave analysis methods that both make use of empirical Green's function (EGF) earthquakes to remove path effects. Analysis of locally recorded, direct waves from events is intuitively the simplest way of obtaining accurate source parameters, as these waves have been least affected by travel through the earth. But finding well recorded earthquakes with "perfect" EGF events for direct wave analysis is difficult, limits the number of earthquakes that can be studied. We begin with closely-located, well-correlated earthquakes. We use a multi-taper method to obtain time-domain source-time-functions by frequency division. We only accept an earthquake and EGF pair if they are able to produce a clear, time-domain source pulse. We fit the spectral ratios and perform a grid-search about the preferred parameters to ensure the fits are well constrained. We then model the spectral (amplitude) ratio to determine source parameters from both direct P and S waves. We analyze three clusters of aftershocks from the well-recorded sequence following the M5 Au Sable Forks, NY, earthquake to obtain some of the first accurate source parameters for small earthquakes in eastern North America. Each cluster contains a M~ 2, and two contain M~3, as well as smaller aftershocks. We find that the corner frequencies and stress drops are high (averaging 100 MPa) confirming previous work suggesting that intraplate continental earthquakes have higher stress drops than events at plate boundaries. We also demonstrate that a scaling breakdown suggested by earlier work is simply an artifact of their more band-limited data. We calculate radiated energy, and find that the ratio of Energy to seismic Moment is also high, around $10^{-4}$. We estimate source parameters for the M5 mainshock using similar methods, but our results are more doubtful because we do not have an EGF event that meets our preferred criteria. The stress drop and energy/moment ratio for the mainshock are slightly higher than for the aftershocks.

Our improved and simplified coda wave analysis method uses spectral ratios (as for the direct waves) but relies on the averaging nature of the coda waves to use EGF events that do not meet the strict criteria of similarity required for the direct wave analysis. We have applied the coda wave spectral ratio method to the 1999 Hector Mine mainshock ($M_w$ 7.0, Mojave Desert) and its larger aftershocks, and also to several sequences in Italy with M~6 mainshocks. The Italian earthquakes have higher stress drops than the Hector Mine sequence, but lower than Au Sable Forks. These results show a departure from self-similarity, consistent with previous studies using similar regional datasets. The larger earthquakes have higher stress drops and energy/moment ratios.

We perform a preliminary comparison of the two methods using the M5 Au Sable Forks earthquake. Both methods give very consistent results, and we are applying the comparison to further events.

## OBJECTIVES

The objectives of this study are to improve low-magnitude regional seismic discrimination by performing a thorough investigation of earthquake source scaling using diverse, high-quality datasets from varied tectonic regions. Local-to-regional high-frequency discrimination requires an estimate of how earthquakes scale with size. Walter and Taylor (2002) developed the MDAC method to empirically account for these effects through regional calibration. The accuracy of these corrections has a direct impact on our ability to identify clandestine explosions in the broad regional areas characterized by low seismicity. Unfortunately, our knowledge at small magnitudes (i.e., $m_b < \sim 4.0$) is poorly resolved, and source scaling remains a subject of on-going debate in the earthquake seismology community. Recently, there have been a number of empirical studies suggesting scaling of micro-earthquakes is non-self-similar (e.g., Kanamori et al.,1993, Abercrombie, 1995, Mayeda and Walter, 1996, Mori et al., 2003, Stork and Ito, 2004, Izutani and Kanamori, 2001, yet there are an equal number of compelling studies that would suggest otherwise (e.g., McGarr, 1999, Ide and Beroza, 2001, Imanishi et al., 2004, Prieto et al., 2004. It is not clear whether different studies reach different conclusions because they use different datasets and scaling varies with location, or because they use different methods. Sonley and Abercrombie (2006) show that small variations in the commonly used methods can lead to significant differences in results. Even in regions that are well studied, such as test sites or areas of high seismicity, we still rely on empirical scaling relations derived from studies taken from half-way around the world at inter-plate regions.

In summary, we address the following problems.

1. Do different studies obtain different results because they use different methods, or because they analyse different data sets? We will investigate whether coda and direct wave methods applied to the same datasets provide the same scaling.
2. Is scaling dependent upon the tectonic setting? We will investigate earthquakes from different tectonic settings and depth ranges, using the same coda and direct wave methods.
3. There have been few studies in intra-plate areas where seismicity is low and/or in regions where a clandestine test might occur. The MDAC method currently assumes earthquake source scaling that was derived exclusively from the western United States. Can we extrapolate or transport results from one region to others, or must we calibrate to each specific region? We will analyse earthquakes from both interplate (e.g., California) and intraplate (e.g., Eastern North America) regions to specifically address this question.

## RESEARCH ACCOMPLISHED

Our approach to obtaining improved source parameters for small earthquakes focuses on the direct and coda wave methods: to improve and investigate them both, and then to apply them to diverse data sets.

Locally recorded, direct waves from events have been least affected by travel through the earth, and so are thought to be the best candidate for obtaining accurate source parameters. But there are only a limited number of earthquakes that are recorded locally, by sufficient stations to give good azimuthal coverage. Even fewer of these have an equivalently well recorded, very closely located smaller earthquake that meets the stringent criteria required to be a good EGF to remove path effects. This EGF method is the preferred one for isolating the source, but concern about the quality of the EGFs is a major source of uncertainty in studies that use these methods. In contrast, coda waves average radiation from all directions so single-station records should be adequate and previous work suggests that the requirements for the EGF event are much less stringent. It is thus ideal in regions with sparse stations and events so that most events are only well-recorded by a single station. Our approach is to:

1. Develop an easy to apply coda wave spectral ratio method to obtain source parameters for large groups of earthquakes
2. Identify the mainshock – EGF earthquake pairs that meet stringent criteria for selecting the EGF, and obtain source parameters from the direct waves for this subset of events.
3. Use the direct wave results to confirm, and if necessary correct, the coda wave results.
4. Apply these methods to data sets from a range of tectonic environments.
5. Determine the implications of the determined source scaling results for both coda calibration and regional discrimination using MDAC and other similar means of source and path-corrected discriminants.

So far we have developed improved coda wave and direct wave methods that we will apply consistently to all the data sets. The new spectral-ratio method developed in this study makes the coda method much easier and simpler to apply, greatly extending the number of earthquakes that can be studied. The coda wave approach was published by Mayeda et al. (2007). We have applied the coda wave methods to several aftershock sequences in Italy

(Malagnini and Mayeda, 2008, Malagnini et al., 2008), and have begun to apply it in eastern North America. In the direct wave study, we have investigated the effects of the various analysis choices commonly made, and also developed criteria for assessing the quality of a particular EGF event. We have performed a very detailed direct wave EGF analysis of aftershocks of the Au Sable Forks earthquake (eastern North America), and obtained some of the best constrained source parameters for earthquakes in this tectonic setting. The direct wave analysis method and results are described by Viegas et al. (2008).

**Application of Coda Spectral Ratio Method: Apennines and Central California shear zone:**

Earlier in our study, we developed an EGF method using coda waves, and showed that it is stable and provides reliable results even if the EGF events have different focal mechanisms to the larger earthquakes, and are separated by as much as 25 km (published as Mayeda et al., 2007). We compared coda spectral ratios to direct spectral ratios and found that the coda wave ratios are much more stable, with little variation from station to station. We then applied the method to the Hector Mine (M7.1, 1999) earthquake and six large aftershocks in the central California shear zone. We now combine this method with a grid-search algorithm taken from MDAC (Walter and Taylor, 2002) to find the best fitting parameters for a group of earthquakes, as well as the fitting uncertainties. This algorithm is used to analyze network-averaged, coda-based spectral ratios, computed between the main event of a sequence, and all its available aftershocks.

We apply the coda spectral-ratio method to two sequences of earthquakes in the Apennines, an intra-plate setting (Figure 1), and again to the Hector Mine sequence to obtain consistent results, with error bars, for comparison. The San Giuliano sequence (2002) was characterized by two main events (both $M_w$ 5.7, and with similar, almost pure strike-slip mechanisms, depths, and source kinematics, see Vallee and Di Luccio, 2005). The main earthquakes were followed by a relatively small number of aftershocks at depths ranging between 10 and 20 km. Because of the low-level of observed ground shaking, both the main events were believed to be low-stress drop. The largest earthquake in the Colfiorito sequence (1997–1998, see Amato et al., 1998) was $M_w$6.0. The $M_w$7.1 Hector Mine earthquake was followed by a large aftershock sequence and we analyze six of the larger aftershocks, recorded at broadband stations.

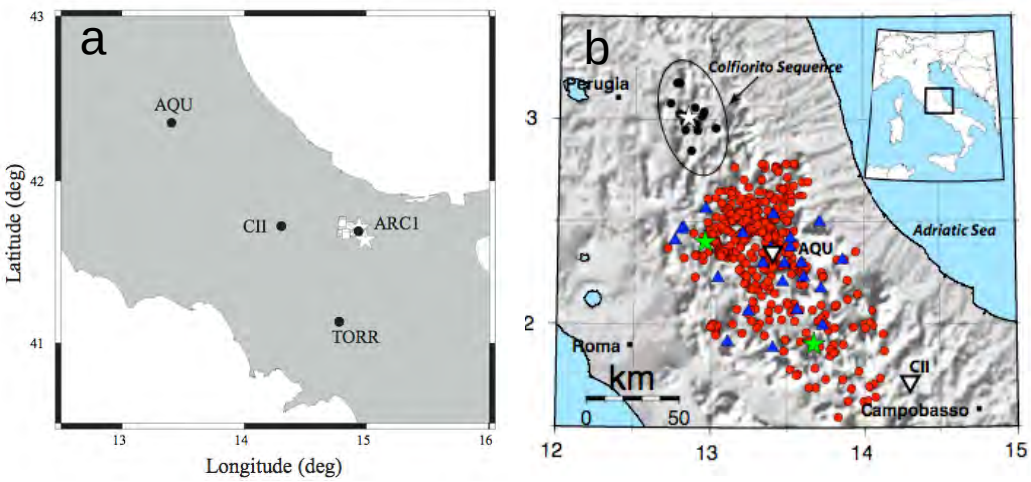


**Figure 1: Maps of (a) the San Giuliano and (b) the Colfiorito earthquake sequences. In (a) main shocks are indicated by white stars, aftershocks by white squares, and seismic stations by black solid circles. In (b) the earthquakes used are shown as black dots, and the stations as inverse white triangles.**

We follow the method described by Mayeda et al. (2007) to calculate coda spectral-ratios and fit them to obtain source parameters including seismic moment ($M_0$), corner frequency ($f_c$), and stress drop ($\Delta\sigma$). For each of the three seismic sequences analyzed in this study, the number of aftershocks is limited through a quality control performed on the available spectral ratios. Specifically, we define a 1.8 minimum bandwidth for each usable spectral ratio (log units, i.e., the ratio of the largest frequency to the lowest one must be larger than 63), and a minimum differential magnitude of 1.0. After this first screening, each average ratio is visually inspected to assure that bad data are not included in the analysis. Standard errors are obtained by looping through the entire set of available spectral ratios, using the technique described by Mayeda et al. (2007) in an iterative fashion. A different spectral ratio is used on

each iteration for the calculation of the scaling properties of the main shock, with respect to the specific aftershock to which the ratio is referred. At the end of the procedure, specific distributions are thus available for all the estimated parameters and so their standard errors can be given.

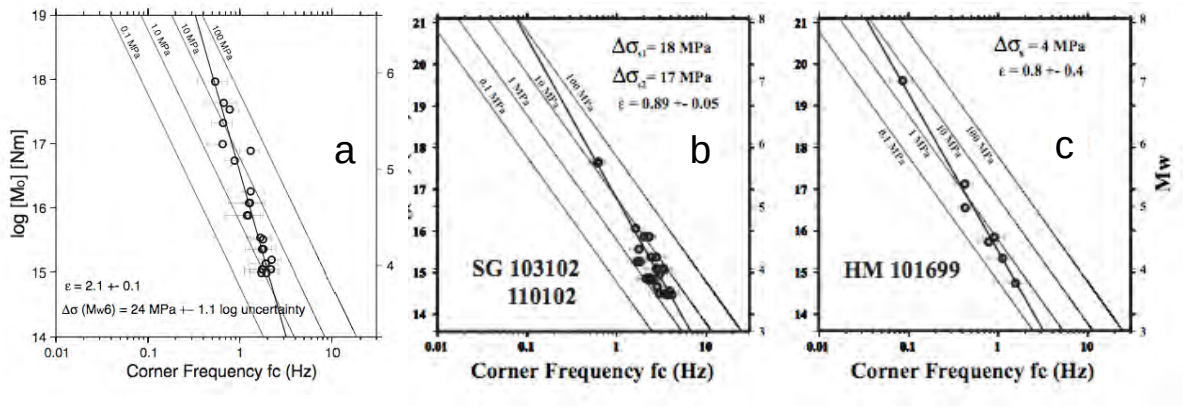


**Figure 2. Coda wave method results. Corner frequencies and stress drops for the (a) Colfiorito, (b) San Giuliano, and (c) Hector Mine earthquake sequences. All three sequences appear to show non-self similar scaling. The two intra-plate sequences have higher average stress drops than the Hector Mine earthquake sequence.**

Figure 2 shows the results of the analysis for the three sequences. The average stress drops of the two intraplate sequences (Figure 2a and b) are systematically higher than those of the Hector Mine sequence in a region with higher strain rate. None of the three sequences exhibit self-similar (constant stress drop) source scaling. The Colfiorito sequence shows a gradual decrease in stress drop with decreasing moment. The other two sequences are consistent with the same trend, or could also simply result from the largest earthquake having a higher stress drop than the aftershocks.

**Development of Direct Wave EGF Method and Application to Eastern North America:**

Analysis of earthquakes in stable, intraplate, low-seismicity regions is important to characterize these regions, but it is hard because of the sparcity of earthquakes and stations, and hence useful data. Relatively little is known about earthquake sources in intraplate regions, and often relationships based on minimal data, or simply extrapolated from interplate regions are assumed due to lack of local information. For example, Somerville et al. (2002) use the recordings of only three moderate-sized earthquakes to propose source scaling relationships for earthquakes in the Northeastern USA and other stable continental regions. Their results imply that earthquakes in the Northeastern USA have relatively high stress drops. This result was confirmed by Shi et al. (1998) who analysed almost 50 small earthquakes from the region. Their study included eight EGF pairs (Shi et al., 1996), but mostly individual earthquakes. They also found a decrease in stress drop with seismic moment, at small magnitudes (< M~3). This may indicate that earthquake source scaling is different in this intraplate region, or else may represent a limit to the resolution as was found earlier in the San Andreas Fault plate boundary region (e.g., Abercrombie and Leary, 1993). Shi et al (1998) were mostly limited by data availability to using regional recordings at single stations, and so to frequencies less than about 25 Hz.

In the last decade there has been a significant increase in the number of broadband seismic stations deployed in eastern North America, leading to a growing number of well-recorded earthquakes (M2-5). On April 20, 2002 an earthquake of magnitude $M_L$ 5.3 occurred in the northeastern Adirondack Mountains, Seeber et al. (2002). Following the mainshock, Lamont-Doherty Earth Observatory deployed digital portable seismographs to monitor aftershocks. The portable network spanned an area about 24 by 20 km with an average inter-station spacing of 4 – 6 km, smaller than the average source depth. Between April 22 and November 2002, 74 small aftershocks were detected and located in the epicental area of the mainshock. These data (200 samples/s) represent the best recorded earthquakes in the region to date, and so provide an unprecedented opportunity to investigate source parameters in this intraplate setting.

We calculate the source parameters using two methods commonly applied to direct waves recorded at local stations: spectral modeling of the individual three-component P and S waves (e.g., Abercrombie, 1995), and the EGF method

(e.g., Mori and Frankel, 1990, Abercrombie and Rice, 2005). Both methods require data with a high-frequency content to work well. Many studies consider the EGF method superior as it corrects for all path and site effects by using a smaller, collocated earthquake as an EGF. The EGF method cannot be used to calculate the seismic moment of the earthquakes, but this is the most reliable information that can be obtained from the individual spectral analysis. Using cross-correlation we identify three clusters of earthquakes with very similar waveforms that include the largest aftershocks recorded by the portable network. All clusters include an M≥2, and a number of M1-2 earthquakes, and two clusters also each include an M≥3 earthquake. We model the spectra obtained by dividing the spectrum of the large earthquake by the smaller one. We also use regional recordings (100 samples/s) to analyze the M5 mainshock using the largest aftershock (M3.7) as the EGF. These earthquakes are closely located, and the deconvolution produces a source time function, but clearly have a different focal mechanism, and so do not meet the criteria for selecting an EGF that we describe below. Unfortunately, no aftershocks well recorded regionally meet these criteria so we use the largest aftershock, and interpret our results with caution.

It is not clear in many studies how close the EGF events are to a perfect Green's function. They are typically too small to obtain focal mechanisms, and the location uncertainties are larger than the preferred separation between events. We select only events that are located within the uncertainties of the large event, and have a high degree of waveform similarity, determined by cross-correlation. As a further test, we transform all the spectral ratios back to the time domain, and we only use pairs where we are able to resolve a clear source pulse. If a source time function is observable in this way, then it demonstrates that the phase components of the spectra are also very similar. This test is similar to the investigation performed by Mori and Frankel (1990) to determine how closely located earthquake pairs must be for the EGF method to work well. Multitaper methods have long been preferred to calculate source spectra and spectral ratios as they better represent the frequency content of the waveforms than do cosine and other tapers (e.g., Park et al., 1987). Unfortunately, until recently multitaper codes only worked with amplitude spectra and so could not be used to perform the complex deconvolution. We use the multitaper approach recently developed by Prieto et al., (2008) to perform the full complex deconvolution so that we can use the same frequency analysis to obtain both the best spectra and retrieve the source time functions.

We correct the velocity seismograms for the instrument response, and then select time windows of 5 s (regional) and 0.75 s (local) that start 0.1 seconds before the P or S wave onset. We use the multitaper method from Prieto et al. (2008) to calculate the Fourier displacement amplitude spectra. We use seven weighted tapers and a time-bandwidth-product of 4. The algorithm also removes a noise peak centered at 60 Hz, if present. Figure 3 shows an example of the seismograms, spectra, and EGF analysis for two events in one cluster.

We first calculate source parameters using the individual spectra, to determine the seismic moments, and also to compare the results of this standard method with that of the preferred EGF method. Before modeling the individual amplitude spectra, we re-sample them on a logarithmic scale, so that the fits were not biased to the high frequencies. We use samples at intervals of $10^{0.02}$, and the amplitude value was the average of all the points in a neighborhood of $\pm 10^{0.01}$. We fit the displacement amplitude spectra with the omega-square source model with the sharper corner preferred by Boatwright (1980) and Abercrombie (1995) to obtain the seismic moment, corner frequency and attenuation Quality factor ($Q$). The travel time is calculated from the *S* minus *P* time. The displacement spectra are fit at bandwidths with signal to noise ratio above 3. We perform a grid search around the preferred parameters to investigate the uncertainties within a range of variance of fit of +5%. We take the mean of all available components and stations to calculate the final value. Following Abercrombie (1995) we assume the circular fault model of Madariaga (1976) to calculate source radius ($r$), and the solution of Eshelby (1957) for a circular crack to calculate stress drop ($\Delta\sigma$). We calculate the radiated seismic energy ($E_S$) by integrating the velocity-squared spectrum, using the data within the available bandwith and the best fitting model to extend the frequency range (Abercrombie 1995).

We then apply the EGF method to the earthquakes in the clusters we identified. We use the same amplitude spectra to calculate spectral ratios between the different events, and we also use the extension of the multitaper method to the complex spectra to deconvolve the spectral ratios back to the time domain and so obtain estimates of the source time functions. We only continued the analysis if we obtained a clear source pulse, justifying our choice of EGF event (see Figure 3). We resample the spectral ratios on a logarithmic scale (in the same way as the individual spectra) and we model the spectra ratios using the same source model as the individual spectra. We use reasonable constraints on the fitting parameters as a further constraint on the use of EGF pairs and ratios (Figure 3). We then calculate source parameters from the spectral fitting as for the individual spectra.

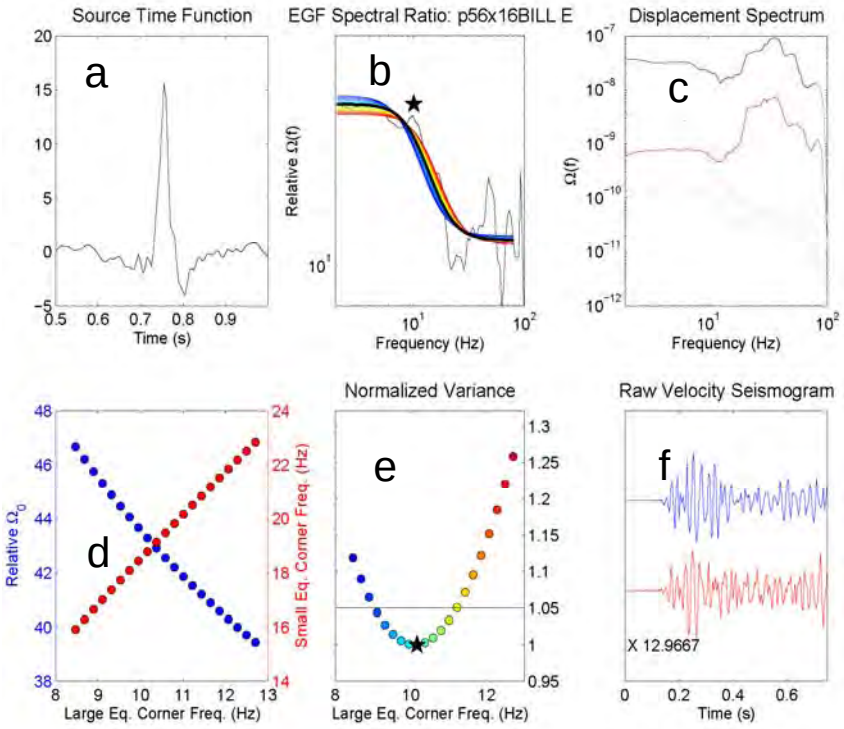


**Figure 3: Example of analysis to obtain parameters from spectral ratio. (a) shows the source time function, (b) the spectral ratio of the displacement spectra (black) and the fits (rainbow colors) within 5% increase of variance of the minimum. The star marks the corner frequency of the minimum variance fit. (c) the displacement spectra of the two earthquakes (solid) and their preceding noise (dotted). (d) the long period amplitude of the ratio, and corner frequency of small earthquake, as the corner frequency of the large earthquake is varied, (e) the variance of the fit, colors are the same as in (b), and (f) the raw P wave seismograms with the relative amplification of the smaller (red) earthquake used in the plot. In this example a M~3 is divided by a M~2, and the seismograms are highly correlated, we have a clear source time function, a tight parabola in variance, and two well resolved corner frequencies**

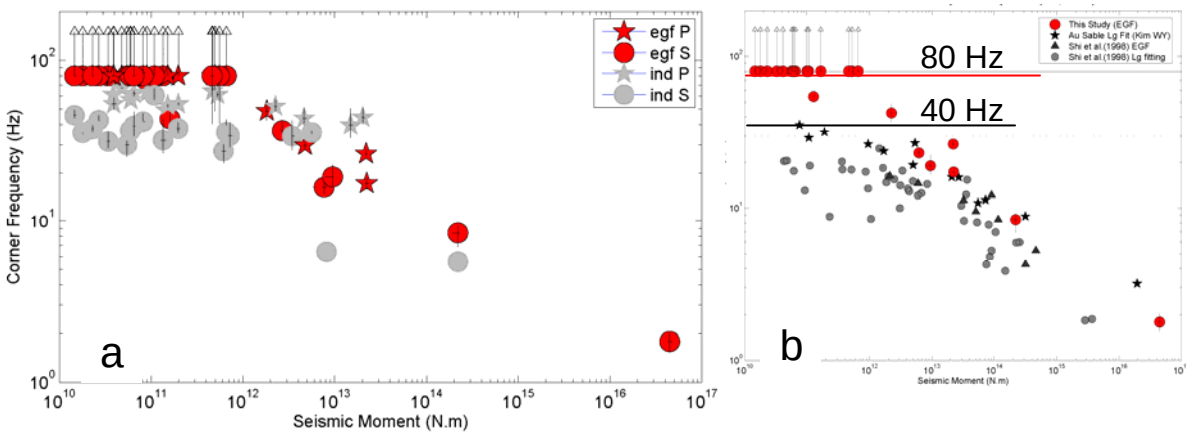


**Figure 4. Corner frequency measurements and comparison with previous work in eastern North America. (a) compares the EGF and individual fitting results for P and S wave measurements, averaged for each earthquake. The agreement is good for larger magnitudes, but the individual method underestimates the corner frequency when it nears the maximum frequency limit. (b) Comparison of our results with those of Shi et al. (1998). The concluded that scaling broke down below $M_0$~$10^{13}$ Nm, but comparison with our results implies that this is an artifact of their lower maximum frequency limit (40 Hz), and use of only individual fitting results for the smaller earthquakes.**

The smallest earthquakes have corner frequencies that are clearly outside the available bandwidth (>80 Hz). The EGF results are preferred because of their better correction for path and site effects. The individual fitting tends to underestimate the corner frequencies (and hence the stress drops) as they get close to the high frequency limit (Figure 4). The high stress drops we obtain are consistent with the previous studies which find relatively high stress drops for intraplate regions such as eastern North America. They are consistent with the results of Shi et al (1998) for their EGF events, but we do not see a breakdown in constant stress drop scaling at lower magnitudes, suggesting that this was an artifact of the limited bandwidth available to Shi et al. (Figure 4).

We obtain relatively high stress drops and apparent stress (proportional to the ratio of $E_S/M_0$), compared to previous studies, mostly in interplate environments (Figure 5). This is consistent with the hypothesis that faults in

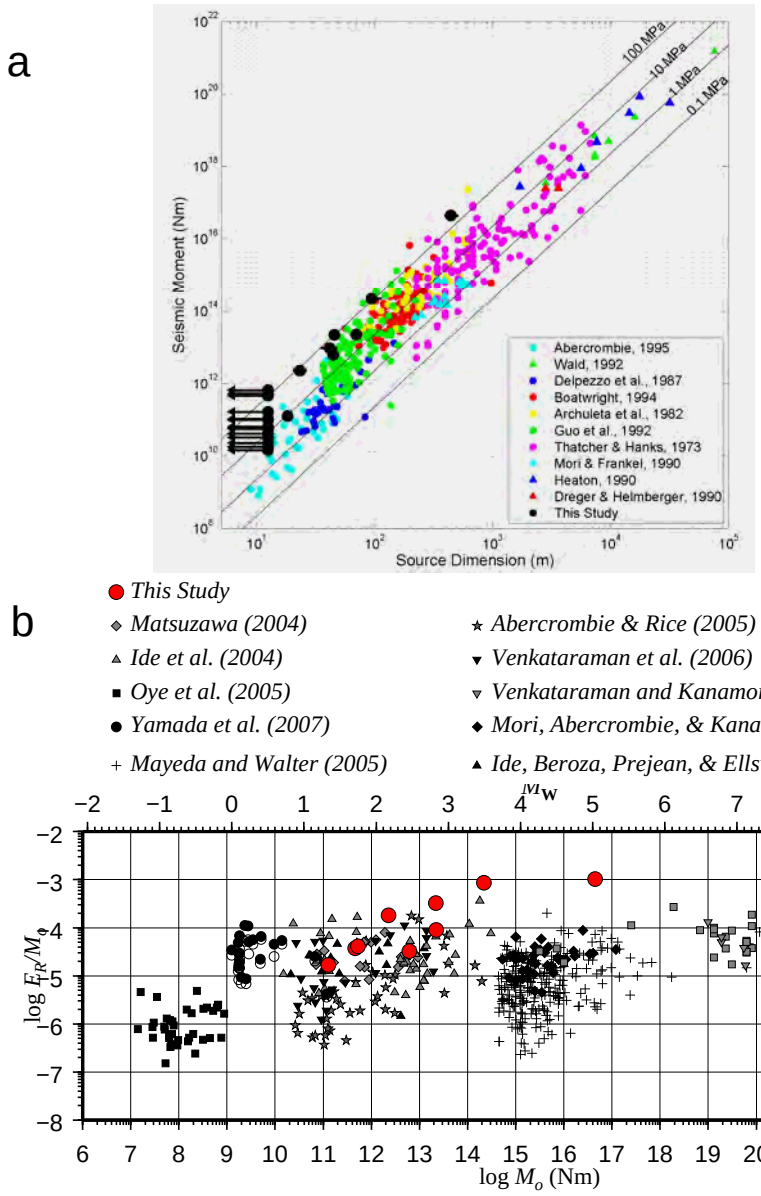


**Figure 5. Comparison of source parameters for the Au Sable Forks earthquake sequence with those from other studies, mostly at plate boundaries. The Au Sable Forks earthquakes have relatively high stress drops (a) and ES/M0 ratios (b) compared to those of earthquakes from continental plate boundary settings. (a) is after Tomic et al. (2008), the source model corrected version of Abercrombie and Leary (1993), and (b) is after Ide and Beroza (2001) and Yamada et al. (2007).**

intraplate settings with lower strain rates, lower cumulative deformation, and longer healing time between ruptures will be stronger than faster moving faults at plate boundaries. Our results also show some gradual decrease in stress drop and apparent stress with decreasing moment. Unfortunately, this is largely dependent on the uncertainties in the values for the two largest earthquakes. These are less reliable because of the lack of an acceptable EGF event.

**Coda Wave Analysis in Eastern North America:**

We calibrate the coda waves at regional broadband stations in eastern North America using the Au Sable Forks mainshock and largest aftershock. We then calculate the spectral ratio, and fit it, and obtain very similar results for corner frequency and stress drop to those for direct waves. This is encouraging, but we want to perform further testing because (1) we use the same EGF for both direct wave and coda wave, so we do not compare the effect of less stringent criteria for choosing EGF for the coda wave method, and (2) the EGF used for the direct wave work does not meet our preferred criteria. When we analyze the aftershocks of this, and other, sequences, we will compare using preferred EGFs for the direct wave analysis with using EGFs for the coda wave analysis that do not meet the requirements for the direct waves.

## CONCLUSIONS AND RECOMMENDATIONS

In summary, we have developed our preferred analysis methods for the direct and coda waves. We have applied the methods to different sequences of earthquakes, and begun to compare the methods directly. The next step is to study more earthquake sequences and rigorously compare the methods.

The coda wave analysis finds relatively high stress drops for two earthquake sequences in the intraplate setting of the Apennines, compared to earthquakes in the higher strain rate setting of western North America. These studies also show the non self-similar scaling that has been observed in previous studies using coda waves.

The direct wave analysis of the aftershocks of the Au Sable Forks earthquake confirms that earthquakes in eastern North America have very high stress drops (10–100 MPa). They also show that the sharp decrease in stress drop with decreasing moment at low magnitudes reported by Shi et al. (1998) is most likely an artifact of the limitations of their data. The stress drops and energy show some possible diversion from self-similar scaling, but uncertainties about the parameters for the largest earthquakes could be the cause.

The first preliminary comparison of the coda and direct wave methods for the Au Sable Forks earthquake (M5) finds very similar results by the two methods, which is encouraging but cannot be interpreted as a rigorous test.

The next stage of our analysis is to perform a more rigorous comparison of the coda and direct wave methods. We will perform coda wave analysis on the aftershocks of Au Sable Forks and other earthquakes of eastern North America. For the direct wave study, we will use earthquakes with EGFs that meet out preferred criteria. For the coda wave study, we will use the same EGF earthquakes, and also ones that clearly do not meet the direct wave criteria. We will also perform both direct and coda wave analyses on several sets of Californian earthquakes for tectonic comparison. In this way we will determine whether the results of the simpler, easier to apply, coda-wave ratio method really do represent average source parameters, or whether any corrections or systematic biases need to be considered.

## ACKNOWLEDGEMENTS

We thank Luca Malagnini for his contribution to the work on coda spectral ratios, German Prieto for developing the multi-taper code to obtain time-domain source time functions, and Won-Young Kim for providing the portable aftershock recordings of earthquakes in eastern North America, and information about his regional wave analysis.

## REFERENCES

Abercrombie, R. E. (1995). Earthquake source scaling relationships from -1 to 5 $M_L$ using seismograms recorded at 2.5 km depth, *J. Geophys. Res.* 100*:* 24,015–24,036.

Abercrombie, R. E. and Leary, P. C. (1993). Source parameters of small earthquakes recorded at 2.5 km depth, Cajon Pass, southern California: implications for earthquake scaling, *Geophys. Res. Lett.* 20: 1511–1514.

Abercrombie, R.E., and J.R. Rice (2005). Can observations of earthquake scaling constrain slip weakening?, *Geophys. J. Int.* 162: 406–424.

Amato, A., *et al*. (1998). The 1997 Umbria-Marche, Italy, Earthquake Sequence: A First Look at the Main Shocks and Aftershocks, *Geophys. Res. Lett.* 25: (15), 2861–2864.

Boatwright, J. (1980). A spectral theory for circular seismic sources: simple estimates of source duration, dynamic stress drop, and radiated energy, *Bull. Seismol. Soc. Am.* 70**:** 1–28.

Eshelby, J. D.(1957). The determination of the elastic field of an ellipsoidal inclusion and related problems, in *Proc. Roy. Soc. Lond., A*, 241: 376–396.

Ide, S. & Beroza, G. C. (2001). Does apparent stress vary with earthquake size, *Geophys. Res. Lett.* 28: 3349–3352.

Imanishi, K., W.L. Ellsworth, and S.G. Prejean (2004). Earthquake source parameters determined by the SAFOD Pilot Hole seismic array, *Geophys. Res. Lett.* 31: L12S09, doi:10.1029/2004GL019420.

Izutani Y. and Kanamori, H. (2001). Scale-dependence of seismic energy-to-moment ratio for strike-slip earthquakes in Japan, *Geophys. Res. Lett.* 28: 20, 4007–4010.

Kanamori, H., Mori, J., Hauksson, E., Heaton, T. H., Hutton, L. K., and Jones, L. M. (1993). Determination of of earthquake energy release and $M_L$ using TERRAscope, *Bull. Seismol. Soc. Am.* 83: 330–346.

McGarr, A. (1999). On relating apparent stress to the stress causing earthquake slip, *J. Geophys. Res.* 104: 3003–3011.

Madariaga, R. (1976). Dynamics of an expanding circular fault, *Bull. Seismol. Soc. Am.* 66*:* 639–666.

Malagnini, L., and K. Mayeda (2008). High-stress strike-slip faults in the Apennines: An example from the 2002 San Giuliano earthquakes (southern Italy), *Geophys. Res. Lett.* 35: L12302, doi:10.1029/2008GL034024.

Malagnini, L., L. Scognamiglio, A. Mercuri, A. Akinci, and K. Mayeda (2008). Source scaling for ground motion prediction in central Italy: Evidence for strong non-self-similar behavior, *Geophys. Res. Letts.*, submitted.

Mayeda, K., L. Malagnini, and W. R. Walter (2007). A new spectral ratio method using narrow band coda envelopes: Evidence for non-self-similarity in the Hector Mine sequence, *Geophys. Res. Lett.* 34: L11303, doi:10.1029/2007GL030041.

Mayeda, K., Hofstetter A., O'Boyle J. L., and Walter, W. R. (2003). Stable and transportable regional magnitudes based on coda-derived moment-rate spectra. *Bull. Seismol. Soc. Am.* 93: 224–239.

Mayeda, K., R. Gok, W. R. Walter, and A. Hofstetter (2005). Evidence for non-constant energy/moment scaling from coda derived source spectra, *Geophys. Res. Lett., 32*, L10306, doi:10.1029/2005GL022405.

Mori, J. and A. Frankel (1990). Source parameters for small events associated with the 1986 North Palm Springs, California, earthquake determined using empirical Green functions, *Bull. Seism. Soc. Am.,*80, 278 – 295.

Mori, J., R.E. Abercrombie, and H. Kanamori (2003). Stress drops and radiated energies of aftershocks of the 1994 Northridge, California, earthquake, *J. Geophys. Res.* 108, No. B11, 2545, doi:10.1029/2001JB000474.

Park, J., C. R. Lindberg, and F. L. Vernon (1987). Multitaper spectral analysis of high frequency seismograms, *J. Geophys. Res.* 92: 12,675–12,648.

Prieto, G. A., Parker, R. L., Vernon, F. L. (2008). A Fortran 90 library for multitaper spectrum analysis, *Accepted in Computers and Geosciences*.

Prieto, G. A., Shearer, P. M., Vernon, F. L., and Kilb, D. (2004). Earthquake source scaling and self-similarity estimation from stacking P and S spectra, *J. Geophys. Res.* 109: B08310, doi 10.1029/2004JB003084.

Seeber, L., W-Y. Kim, J. G. Armbruster, W-X. Du, A. Lerner-Lam, and P. Friberg (2002). The 20 April 2002 $M_w$5.0 earthquake near Au Sable Forks, Adirondacks, New York: A first glance at a new sequence, *Seism. Res. Lett.* 73: 480–489.

Shi, J., W. Y. Kim, and P. G. Richards (1996). Variability of crustal attenuation in the northeastern United States from Lg waves, *J. Geophys. Res*. 101: 25231–25242.

Shi, J., W. Y. Kim, and P. G. Richards (1998). The corner frequencies and stress drops of intraplate earthquakes in the northeastern United States, *Bull. Seism. Soc. Am.* 88: 531–542.

Somerville, P., N. Collins, N. Abrahamson, R. Graves, and C. Saikia (2002). Ground motion attenuation relation for the central and eastern Unites States. Final Report to NEHRP, U.S. Geological Survey.

Sonley, E. and R. E. Abercrombie (2006). Effects of methods of attenuation correction on source parameter determination, *American Geophysical Union Monograph, EARTHQUAKES Radiated energy and the physics of faulting*, eds. Abercrombie, McGarr, Di Toro and Kanamori.

Stork, A. L. and H. Ito (2004). Source Parameter Scaling for Small Earthquakes Observed at the Western Nagano 800-m-Deep Borehole, Central Japan , *Bull. Seismo. Soc. Am.* 94:1781–1794, DOI: 10.1785/012002214

Tomic, J., R. E. Abercrombie, and A. F. do Nascimento (2008). Source Parameters and Rupture Velocity of Small M≤2.1 Reservoir Induced Earthquakes, *J. Geophys. Int.*: in revision.

Vallee, M., and F. Di Luccio (2005). Source analysis of the 2002 Molise, southern Italy, twin earthquakes (10/31 and 11/01), *Geophys. Res. Lett.* 32, doi: 10.1029/2005GL022687.

Viegas, G. M., R. E. Abercrombie and W-Y. Kim (2008). Earthquake Source Scaling in the Northeastern United States, *J. Geophys. Res.*, in prep.

Walter, W. R. and S. R. Taylor (2002). A revised magnitude and distance amplitude correction (MDAC2) procedure for regional seismic discriminants: theory and testing at NTS, Lawrence Livermore National Laboratory Report, UCRL-ID-146882, http://www.llnl.gov/tid/lof/documents/pdf/240563.pdf

Yamada,T., J. J. Mori, S. Ide, R. E. Abercrombie, H. Kawakata, M. Nakatani, Y. Iio, and H. Ogasawara (2007). Stress drops and radiated seismic energies of microearthquakes in a South African gold mine *J. Geophys. Res.* 112*:* B03305, doi:10.1029/2006JB004553.

# DISCRIMINATION CALIBRATION ANALYSIS METHODS FOR REGIONAL STATIONS

Dale N. Anderson[1], Deborah K Fagan[1], Steven R Taylor[2], and Theresa M Mercier[1]

Pacific Northwest National Laboratory[1] and Rocky Mountain Geophysics, LLC[2]

Sponsored by National Nuclear Security Administration

Contract No. DE-AC05-RLO1830

## ABSTRACT

For event discrimination, operational implementation of a regional seismic station requires three sequential calibration analyses. 1) Magnitude, distance, and amplitude corrections (MDAC) made to observed regional amplitudes are necessary so that what remains in the corrected amplitude is mostly information about the seismic source-type. Corrected amplitudes can be used in ratios to discriminate between earthquakes and explosions. Calibration of MDAC can be accomplished with empirical Bayes estimation, which naturally provides metrics to determine when adequate calibration data have been acquired, and provides statistical assurance that the errors associated with MDAC calibration are negligible in future operational discrimination analysis. 2) MDAC-corrected amplitudes can then be used in ratios to discriminate between earthquakes and explosions. However, there remain source effects such as those due to depth, focal mechanism, local material property and apparent stress variability that cannot easily be determined and applied as amplitude corrections. We have developed a mathematical model to capture these near source effects as random (unknown) giving an error partition of three sources: model inadequacy, station noise and amplitude correlation. This mathematical model is the basis for a general multi-station regional discriminant. Calibration analysis for the standard error of the discriminant includes the calculation of the variances of model inadequacy and station noise, and amplitude correlation. 3) Likelihood-based seismic event identification analysis with MDAC discriminants requires estimated source population means and covariance matrices for the discriminants from each of the possible source types used in our analysis (e.g., deep earthquake, shallow earthquake, and explosion). Anderson et al. (2007) note that source population covariance matrices and the pooled covariance matrix are best estimated element-wise to fully utilize available calibration events. We propose an algorithm that may be used to mildly adjust an element-wise covariance matrix to ensure positive definiteness and non-singular behavior. The algorithm uses the Frobenius norm as the calibration metric because it minimally adjusts the variance terms of an element-wise covariance relative to the off-diagonal covariance terms to achieve a stable, positive semi-definite covariance matrix. Importantly, we show that it is not necessary to propagate the errors of MDAC parameter estimates to final event identification analysis.

## OBJECTIVES

Our objective is to develop efficient methods to calibrate a regional seismic station for event discrimination. The formulation of the discriminant from a station requires amplitude corrections based on MDAC, the correct calculation of the discriminant standard error, and the estimation of a stable covariance matrix that describes the discriminants mathematical relationship with other discriminants.

Corrections to regional phases to account for magnitude, distance, and amplitude are necessary so that what remains is fundamentally information about seismic source type. MDAC requires calibration data for a station, which may not be available for a time after it becomes operational. In order to incorporate the station into event identification processing, MDAC calibration can be performed using an empirical Bayes approach. The approach allows the station to be quickly assimilated into the network and also provides natural metrics for determining when adequate calibration data have been acquired.

Once amplitudes have been corrected with MDAC, there are still near source effects which have not been accounted for in the model, such as effects due to depth, focal mechanism, local material properties, or apparent stress variability. The uncertainty introduced by these effects needs to be accounted for in the statistical formulation of a regional amplitude discriminant. The mathematical model presented below partitions total uncertainty into three sources: amplitude correlation, model inadequacy, and station noise. The model inadequacy partition represents the near-source effects and is handled statistically as a random component in the model.

The event classification matrix (ECM) [Anderson et al. (2007)] implements likelihood based discrimination, which requires an estimate of population means and covariance matrices for each source type population of interest. In order to take advantage of all possible calibration data, covariance matrices may be estimated element-wise, which does not guarantee numerical stability for ECM calculations. We present an algorithm that adjusts the covariance matrix in a way to ensure positive semi-definiteness while minimally affecting the variance terms in the matrix.

## RESEARCH ACCOMPLISHED

### MDAC Calibration

The ratio of regional P and S wave amplitude measurements at high frequencies can discriminate between earthquakes and explosions (e.g., Walter et al. (1995); Taylor (1996); Bottone et al. (2002)). An issue with using these amplitudes in a practical application is how to remove the effects due to path, site and magnitude to emphasize the source differences. In Taylor and Hartse (1998), Taylor et al. (2002) and Walter and Taylor (2002) the MDAC technique corrects each regional phase (e.g., Pn, Pg, Sn, Lg) amplitude as a function of frequency in an attempt to make amplitudes independent of distance, magnitude, and station. MDAC is a simple physically based model that accounts for propagation effects such as geometrical spreading and Q, and corrects observed amplitudes assuming the scaling of an earthquake spectral model developed by Brune (1970). The idea of using an earthquake MDAC model to correct amplitudes is that spectra from an explosion will exhibit a poor fit to the model, which will be apparent in an observed discriminant. Because of complex explosion source phenomenology it is not necessarily obvious which combinations of regional phases will best separate earthquake and explosion populations. The MDAC technique allows the formulation of any combination of regional phases in any frequency band, so that a diversity of discriminants can be explored. The MDAC model partitions regional seismic spectra into component parts. The instrument-corrected regional phase spectra can be thought of as a convolution between the source-type and the path. In the frequency domain, this can be mathematically represented as

$$A(\omega,\Delta) = S(\omega)G(\Delta)P(\omega)B(\omega,\Delta) \ , \tag{1}$$

where S is the source spectrum, G is geometrical spreading, P is the frequency-dependent site effect, and B is the anelastic attenuation with function arguments epicentral distance Δ and angular frequency ω. Here we have split the path effect into three components: 1) a frequency independent geometrical spreading component, 2) a range-independent and frequency-dependent site effect, and 3) an anelastic attenuation component. The logarithm of both sides of Equation 1 gives

$$\log A(\omega,\Delta) = \log S(\omega) + \log G(\Delta) + \log P(\omega) + \log B(\omega,\Delta). \tag{2}$$

To remove distance and magnitude trends in the data, we correct the observed spectrum $\log A_O(\omega,\Delta)$ so that

$$Y = \log A_C(\omega,\Delta) = \log A_O(\omega,\Delta) - \log A(\omega,\Delta)\,, \tag{3}$$

where $A_C(\omega,\Delta)$ is the corrected spectrum. Equation 3 is used to calculate corrected MDAC amplitudes, denoted as Y, that are then used to construct discriminants. Specifically, from Equation 3, the corrected amplitude Y is a log observed amplitude minus MDAC—Y is the MDAC residual.

Referencing the development in Taylor and Hartse (1998), Taylor et al. (2002), and Walter and Taylor (2002), before MDAC is used in an operational setting, calibration earthquakes determine an average station site effect ($\Theta$) [=unitless], an attenuation parameter ($\gamma$)[=unitless], and the average stress drop parameter ($\sigma$) [=Passcals], which are embedded in source spectrum (S) and anelastic attenuation (B) terms. It is important to recognize that the fundamental sources of error for MDAC corrections are the model inadequacy affecting all stations and individual station noise. Once the parameters are estimated from calibration earthquakes, the MDAC equation is treated as a known physical correction.

From equation 3, $\log A_C(\omega,\Delta)$ can reasonably be modeled as Gaussian with zero mean and variance $\tau^2$. Here $\tau$ represents model uncertainty and station noise combined into one term, and only for earthquakes. The likelihood of n calibration earthquakes is

$$f\left[\text{data}\middle|\Theta,\gamma,\sigma,\tau\right] = \prod_j \prod_{i=1}^{n} f\left[\log A_{C_i}(\omega_i,\Delta), M_{o_i}\middle|\Theta,\gamma,\sigma,\tau\right], \tag{4}$$

where j indexes frequency, i indexes event, and $M_{oi}$ is the event moment. In application reasonable estimates and bounds can be placed on $\Theta$, $\gamma$, and $\sigma$ from geophysical knowledge. The Bayesian formulation of these estimates are simply represented as prior probability density functions (PDFs) $f(\Theta)$, $f(\gamma)$, and $f(\sigma)$. Here, use a Uniform(*l*, *u*) PDF in each case with *l* and *u* specified from geophysical knowledge. The prior PDF $f(\tau)$ is also modeled as Uniform. More sophisticated, physically based prior for MDAC parameters could be developed with further research. The full likelihood is now

$$f\left[\Theta,\gamma,\sigma,\tau,\text{data}\right] = f(\Theta) f(\gamma) f(\sigma) f(\tau) f\left(\text{data}\middle|\Theta,\gamma,\sigma,\tau\right) \tag{5}$$

and the posterior PDF is

$$f\left[\Theta,\gamma,\sigma,\tau,\middle|\text{data}\right] = c(\text{data}) f(\Theta) f(\gamma) f(\sigma) f(\tau) f\left(\text{data}\middle|\Theta,\gamma,\sigma,\tau\right), \tag{6}$$

where c(data) is a constant that ensures integration to unity. The uniform priors simply ensure that an MDAC parameter's range of possible values agree with physical basis. Several possible values for $\Theta$, $\gamma$, $\sigma$ and $\tau$ can be calculated, each derived from Equation (6), the posterior PDF. We recommend the mode of the posterior PDF as MDAC calibration values which are conceptually values of $\Theta$, $\gamma$, $\sigma$, and $\tau$ that are the most probable given the earthquake calibration data.

The data analyzed as an example are events at the Nevada Test Site (NTS) observed with combinations of four seismic stations: Kana, Utah, (KNB); Elko, Nevada (ELK), Landers, California (LAC) and Columbia College, California (CMB). Observed amplitudes are RMS measurements converted to pseudo spectra by application of Parseval's theorem [see Appendix B of Taylor et al. (2002)] with a 6 to 8 Hertz filter window (so that the number of frequencies is j = 1). KNB observed 43 earthquakes; these events are used to illustrate the Bayesian calculations of MDAC parameters for the Lg phase. Posterior PDFs are shown in Figure 1. Note the small amount of variability (spread) in the PDFs for $\Theta$ and $\gamma$. The slightly higher variability in the PDF for $\sigma$ is because the spectrum in this example was constrained by high-frequency amplitudes and the event moment. With lower frequency amplitudes included in the analysis, we expect the variability of the posterior PDF for $\sigma$ to be similar to that for $\Theta$ and $\gamma$. This will be demonstrated in a follow-on comprehensive analysis.

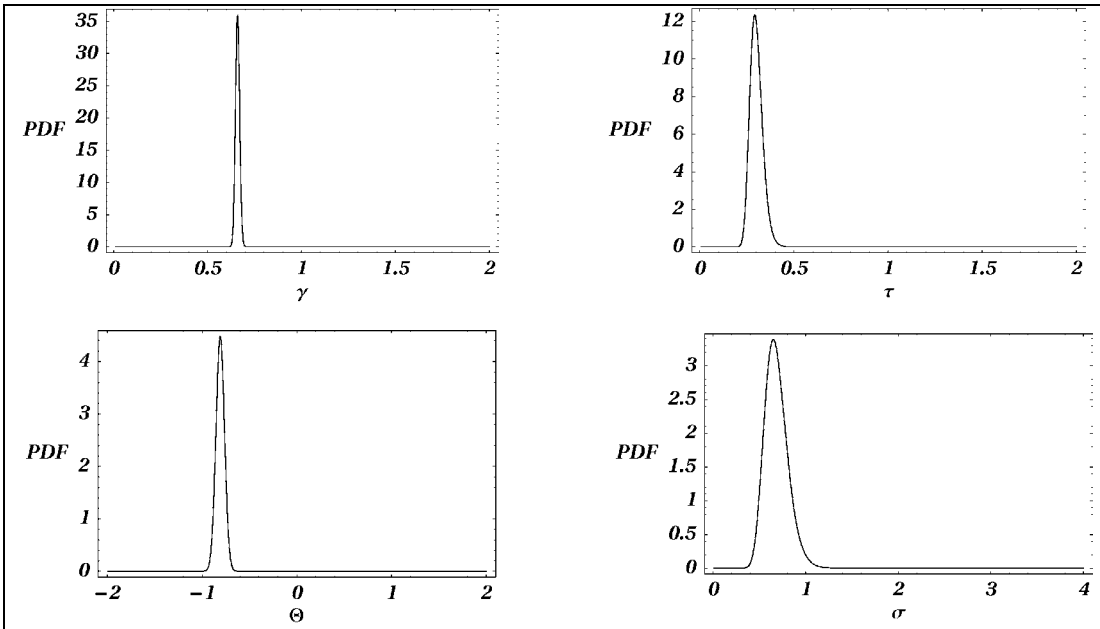


**Figure 1. Posterior PDFs for MDAC parameters. The posterior mode is used for the calibration value.**

**Discriminant Errors: MDAC Model Inadequacy and Station Noise**

The conceptual representation of the MDAC amplitude model is

$$Y = \log(\text{corrected amplitude}) = \textit{Bias}(\text{source - type}) + \textit{Event} + \textit{Noise}\ , \tag{7}$$

where *Bias*(source-type) is a source-type constant, *Event* is a zero mean random effect with variance $\tau^2$ that varies from event to event and represents model inadequacy from effects such as depth, focal mechanism, local material property and apparent stress variability, and *Noise* represents measurement and ambient noise, also with zero mean and variance $\sigma^2$. Note that in this section, calibration analysis partitions the variance $\tau^2$ in the MDAC calibration analysis above into two variance components *Event* ($\tau^2$) and *Noise* ($\sigma^2$). The MDAC approach results in a *Bias* term for earthquakes that is near zero, whereas for explosions the *Bias* is non-zero indicating discrimination potential. The error terms *Event* and *Noise* are modeled as equal for both explosions and earthquakes; therefore pooled data (amplitudes from explosions and earthquakes with their respective population means subtracted) are used in the calculation of $\tau^2$ and $\sigma^2$.

The station-averaged corrected amplitude $\bar{Y} = \underline{1}^T \underline{Y}/n$ has a standard error $\tau^2 + \sigma^2/n$, where n is the number of station amplitudes used in the average. Note that forming regional discriminants from station-averaged corrected amplitudes exactly parallels the methodology of the $m_b$ versus $M_s$ discriminant where both are station-averaged magnitudes. Omitting the term *Event* in Equation (7) implies that the corrected amplitude at a station is *Bias* plus station noise. As demonstrated with the following argument, this model formulation is fundamentally inconsistent with the realities of seismic observation. The standard error of $\bar{Y}$ with E removed from Equation (7) is $\sigma^2/n$ ($\tau^2 = 0$) and decreases as the number of stations n observing an event increases. This implies that if enough stations observe an event, this standard error effectively goes to zero and the average corrected amplitude quickly converges to Bias implying near-perfect discrimination capability. By not including the term *Event*, effects such as depth, focal mechanism, local material property and apparent stress variability are not accounted for in the theoretical model of amplitude, and clearly these effects cannot be removed by station averaging. The model given by Equation (7) captures these local source effects by admitting that they cannot be mathematically (theoretically) represented. Treating local source effects as a random effect *Event* compensates for them as a component in the standard error of a discriminant. Also, the lower bound of standard error $\tau^2 + \sigma^2/n$ is non-zero and therefore consistent with realistic seismic monitoring. Another important property of this model is that a corrected amplitude for a single event is correlated across stations. The correlation ($\tau^2/(\tau^2+\sigma^2)$) implies that large *Event* adjustment increases correlation

between stations because this random adjustment is applied to all stations observing an event, that is, the stations stochastically move together. Small *Event* adjustment implies the correction model is good and is conceptually equivalent to stations with incoherent noise. Small Event adjustment also implies $\tau^2$ is small and the standard error of $\bar{Y}$ is reduced further through station averaging.

The data used to illustrate the calculation of the variance components $\tau^2$ and $\sigma^2$ are events at and surrounding the Nevada Test Site (NTS). Events were observed with combinations of four seismic stations: Kanab, Utah (KNB); Elko, Nevada (ELK), Landers, California (LAC) and Columbia College, California (CMB). MDAC amplitudes from these stations are Pg and Lg amplitudes from pseudo spectral measurements with a 6 to 8 Hertz filter window. After applying data quality metrics (e.g., signal to noise and removal of events within 100 kilometers of a station), the data table consisted of 41 earthquakes (EQ) and 159 explosions (EX) for a total of 200 events. Moment magnitudes ranged from 2.6 to 6.1. Amplitude corrections for discrimination remove the effects of magnitude, source scaling and distance so that what remains in the corrected amplitude is fundamentally information about source type. Figure 2 demonstrates the removal of the effect of moment magnitude from the Pg and Lg amplitudes with MDAC. Also, Figure 2 shows the explosions and earthquake amplitudes before and after removal of population means – these centered data are used to calculation the variance components $\tau^2$ and $\sigma^2$, and additionally the correlation between amplitudes in a discriminant. The fit residuals are given in Figure 3 and the calculated variance components are given Table 1.

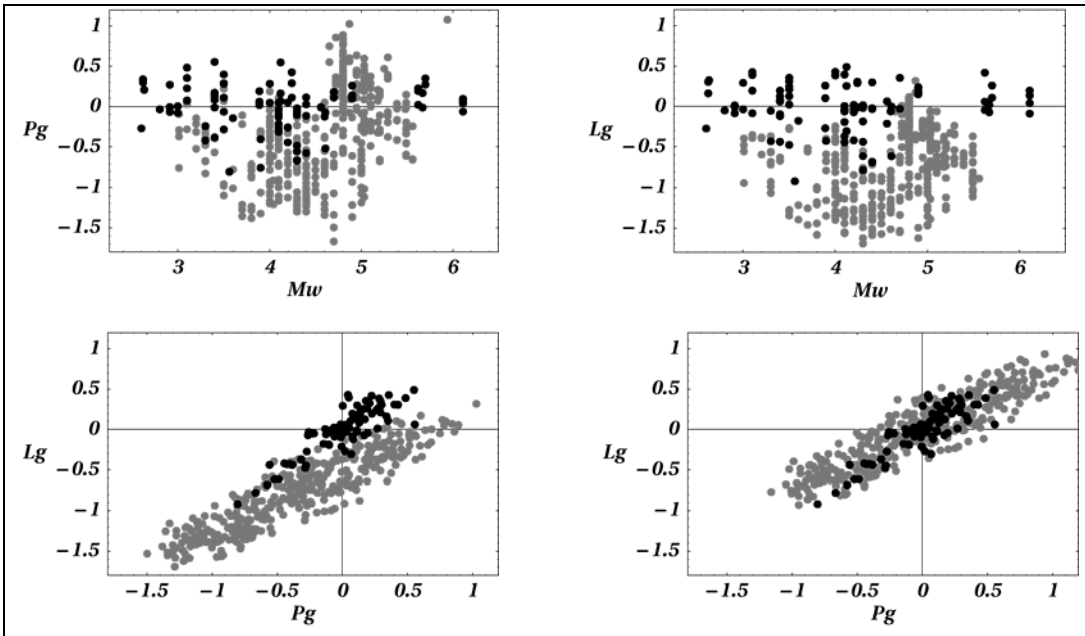


**Figure 2. Scatter plots of MDAC corrected amplitudes Lg and Pg versus moment magnitude Mw for earthquakes (dark) and explosions (light). MDAC corrects earthquakes to zero mean. Also, scatter plots of the MDAC corrected amplitudes Lg versus Pg for earthquakes (dark) and explosions (light). With the explosions mean centered, the pooled data are used to calculate the variance components $\tau^2$ and $\sigma^2$ for both populations.**

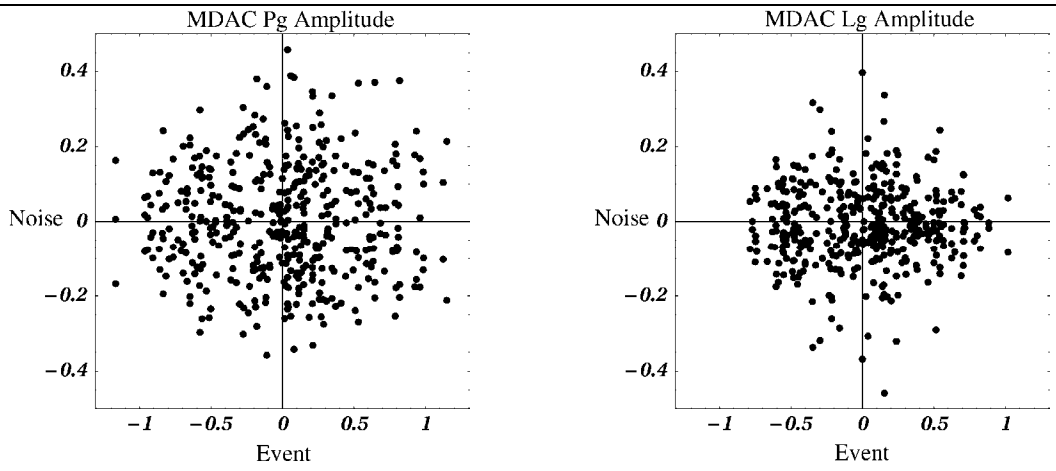


**Figure 3. Fitted model residuals for Event and Noise using pooled explosions and earthquake data. Residuals indicate reasonable agreement with model assumptions of uncorrelated terms Event and Noise.**

**Table 1. Calculated variance components $\tau^2$ and $\sigma^2$. From the pooled data presented in Figure 2, the calculated correlation between Pg and Lg is 0.95.**

| | Event ($\tau^2$) | Noise ($\sigma^2$) |
|---|---|---|
| Pg | 0.23 | 0.04 |
| Lg | 0.16 | 0.02 |

**Structured Covariance Matrix of Discriminants**

Seismic event identification using regularized discrimination requires estimated source population means and covariance matrices for the discriminants from each of the possible source types (e.g., deep earthquake, shallow earthquake, or explosion). Anderson et al. (2007) notes that the estimated source population covariance matrices denoted $S_k$, k = 1, 2... K, and the pooled covariance matrix, $S_0$, are estimated element-wise in order to take advantage of all available calibration data. Due to few calibration events or strongly correlated discriminants, one or more $S_k$ and/or $S_0$ may be singular. We present an algorithm inspired by Shaw and Geyer (1997) that may be used to adjust elements of singular covariance matrix estimates prior to regularized discriminant analysis (RDA).

Anderson et al. (2007) uses standardized discriminants Y to solve the seismic identification problem. We assume that the k populations are independent and, for the $k^{th}$ source population, $Y \sim MVN_p(\mu_k, \Sigma_k)$; where $\mu_k$ and $\Sigma_k$ are the source mean vector and covariance matrix, respectively, and p discriminants are used. The log likelihood function for $\mu_k$ and $\Sigma_k$, given the data y is

$$l(\mu_k, \Sigma_k | y) = -\frac{n}{2}\log|2\pi\Sigma_k| - \frac{n}{2}\mathrm{tr}\left(\Sigma_k^{-1} S_k\right) - \frac{n}{2}(\bar{y} - \mu_k)^T \Sigma_k^{-1}(\bar{y} - \mu_k), \quad (1)$$

where tr(·) denotes the trace operator and $S = \frac{1}{n}\left[\sum_{i=1}^{n}(y_i - \bar{y})(y_i - \bar{y})^T\right]$. Maximum likelihood estimators (MLEs) for $\mu_k$ and $\Sigma_k$ are $\bar{y}_k$ and $S_k$, respectively. These estimators are derived by setting the partial derivatives of equation (1) equal to zero and then solving for $\mu$ and $\Sigma$. The framework in Anderson et al. (2007) can be carried out as described if $S_k$ is non-singular. If $S_k$ is singular, however, a different estimator of $\Sigma_k$ is required. We desire an estimator, say $S^*_k$, that is positive semi-defnite, as "close" to $S_k$ as possible, and that the variance terms be minimally different from those in $S_k$ compared to the covariance terms.

We choose the Frobenius norm as the one to minimize, because as we demonstrate here, it is a norm which allows us to minimally alter the variance terms of S compared with the covariance terms. The Frobenius norm, denoted $\|\cdot\|$, is defined as the square-root of the sum of the absolute value of the matrix elements. Our optimization criterion becomes

$$\min_{Q}\|S-Q\| = \sqrt{\sum_{i=1}^{p}\sum_{j=1}^{p}\left|s_{ij}-q_{ij}\right|^2} \tag{2}$$

where Q is a p × p symmetric, invertible matrix.

Because S is a symmetric matrix, $S = S^T$, the eigenvalues of S are real and associated eigenvectors are orthogonal. Let the eigen decomposition of S be $V\Lambda V^T$, where $\Lambda$ is the diagonal matrix of ordered eigenvalues ($\lambda_i \geq \lambda_j$ for all i < j) and the columns of V are the corresponding eigenvectors. Likewise, let $Q = UCU^T$, where $C = \text{diag}\{c_1 \geq c_2 \geq ... \geq c_p\}$ and U is the matrix whose columns are the corresponding eigenvectors. We then want to minimize

$$\left\|V\Lambda V^T - UCU^T\right\|. \tag{3}$$

A linear algebra identity can be used to show that $\left\|V\Lambda V^T - UCU^T\right\| \leq \left\|V^2\right\| \|\Lambda - C\|$. Both $\Lambda$ and C are diagonal matrices, where the diagonal terms are sorted from highest to lowest and all of the elements are real. Therefore the diagonal vector $\boldsymbol{\lambda}$ has a set of positive, zero, and negative values, as does the vector $\mathbf{c}$. The Frobenius norm can be written as the sum of terms partitioned into positive, zero and negative terms so that

$$\|\Lambda - C\| = \sqrt{\sum_{i=1}^{m}\left|\lambda_i - c_i\right|^2 + \sum_{i=m+1}^{n}\left|\lambda_i - c_i\right|^2 + \sum_{i=n+1}^{p}\left|\lambda_i - c_i\right|^2}, \tag{4}$$

where $\{\lambda_1, \lambda_2, ..., \lambda_m\} > 0$, $\{\lambda_{m+1}, ..., \lambda_n\} = 0$ and $\{\lambda_{n+1}, ..., \lambda_p\} < 0$. By choosing

$$c_i = \begin{cases} \lambda_i & i = 1,2,\ldots,n \\ 0 & i = n+1, n+2, \ldots p \end{cases}$$

Equation 4 becomes $\|\Lambda - C\| = \sqrt{\sum_{i=n+1}^{p}\left|\lambda_i - c_i\right|^2}$ and consequently, $\left\|V\Lambda V^T - UCU^T\right\| \leq \left\|V^2\right\| \sqrt{\sum_{i=n+1}^{p}\left|\lambda_i - c_i\right|^2}$.

Our estimate of $S_k$ is then $Q = VCV^T = V\text{Diag}\{\lambda_1, \lambda_2, ..., \lambda_m, 0, 0, ..., 0\}V^T$.

The following example shows how the algorithm works. Figure 4 shows the original eigenvalues of the structured covariance matrix for a data set of deep earthquakes $S_{DEQ}$, which is singular. Figure 5 shows how $S_{DEQ}$ is adjusted to result in $S^*_{DEQ}$, a non-singular matrix. The white areas of Figure 5 indicate no change in the imposed structure. Notice that the diagonal elements are changed minimally, compared to the off-diagonal elements. This preserves the variance structure of the individual discriminants while minimally adjusting the covariance terms to achieve invertibility.

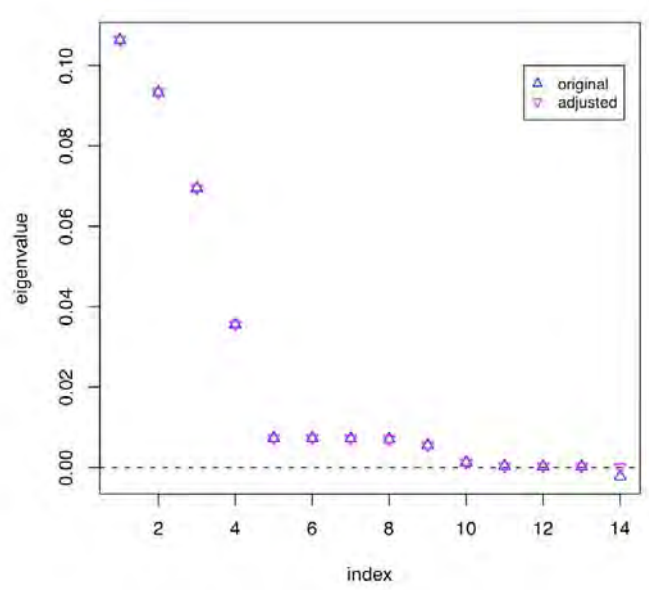


**Figure 4. Eigenvalues of the original covariance matrix $S_k$ and adjusted covariance $S^*_k$.**

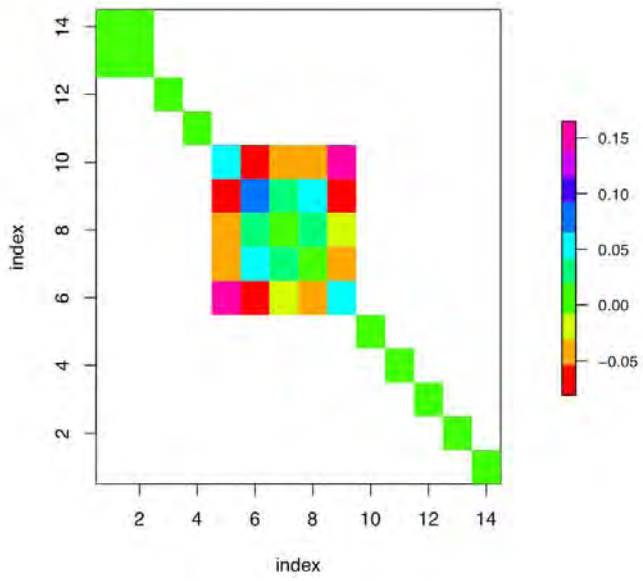


**Figure 5. Percent adjustment to $S_k$ to achieve invertibility.**

## CONCLUSIONS AND RECOMMENDATIONS

Three core conclusions can be stated from our analysis. First, MDAC parameters can be derived with sufficient precision to view the MDAC correction as fixed and deterministic in event identification analysis which implies it is not necessary to propagate the error from MDAC parameter estimation in event identification analysis. Further, reasonable physical constraints can be placed on MDAC parameters with Bayesian theory to aid in the calculation of MDAC parameters. We believe that no more than 100 well chosen earthquakes are necessary to calibrate the MDAC correction equation, and research and demonstration analysis for FY09 will verify this conjecture. Second, there are

two important sources of error when constructing a discriminant with MDAC correction amplitudes – the error due to MDAC model inadequacy and station noise. The calibration analysis for deriving these variance components is accomplished by embedding MDAC theory into a statistical random-effects linear model. The resulting standard error of a discriminant from this model correctly reduces station noise though averaging, but requires improvements to physical correction theory (an improved MDAC model) to reduce model inadequacy error. Third, the covariance matrices necessary to combine a diversity of discriminants in event identification analysis can be calculated with all available data by individually calculating each element of a matrix (variance and covariance elements). However, these calculations, while giving a symmetric covariance matrix, do not guarantee that the matrix is positive definite. We have demonstrated that with the Frobenius norm, a covariance matrix constructed element-by-element can be adjusted, with little impact on the variance terms, to achieve positive definiteness.

## ACKNOWLEDGEMENTS

The authors acknowledge the technical expertise and advice of Dr. Larry Chilton in the use of the Frobenius norm to achieve covariance matrix stability. We also thank Dr. Bill Walter of LLNL for providing the excellent measurements from the NTS dataset.

## REFERENCES

Anderson, D. N., D. K. Fagan, M. A. Tinker, G. D. Kraft, and K. D. Hutchenson (2007). A mathematical statistics formulation of the teleseismic explosion identification problem with multiple discriminants, *Bull. Seismol. Soc. Am.* 97: 1730–1741.

Bottone, S., M. Fisk, and G. McCartor (2002). Regional seismic-event characterization using a Bayesian formulation of simple Kriging. Bulletin of the Seismological Society of America 92: 2277–2296.

Brune, J. (1970). Tectonic stress and the spectra from seismic shear waves earthquakes. *J. Geophys. Res*. 75: 4997–5009.

Shaw F. H., and C. J Geyer (1997). Estimation and testing in constrained covariance component models, *BIOMETRIKA* 84: 1, 95–102.

Taylor, S. (1996). Analysis of high-frequency Pg/Lg ratios from NTS explosions and western U.S. earthquakes. *Bull. Seismol. Soc. Am*. 86:1042–1053.

Taylor, S. and H. Hartse (1998). A procedure for estimation of source and propagation amplitude corrections for regional seismic discriminants. *J. Geophys. Res*. 103: 2781–2789.

Taylor, S., A. Velasco, H. Hartse, W. S. Phillips, W. Walter, and A. Rodgers (2002). Amplitude corrections for regional seismic discriminants. *Pure. App. Geophys.* 159: 623–650.

Walter, W. and S. Taylor (2002). A revised magnitude and distance amplitude correction (MDAC2) procedure for regional seismic discriminants: Theory and testing at NTS. Technical Report LAUR-02-1008, Los Alamos National Laboratory, Los Alamos, New Mexico.

Walter, W., K. Mayeda, and H. Patton (1995). Phase and spectral ratio discrimination between NTS earthquakes and explosions part 1: Empirical observations. *Bull. Seismol. Soc. Am*. 85:1050–1067.

# A SUITE OF DISCRIMINANTS FOR GROUND-TRUTH MINING EVENTS IN THE WESTERN U.S. AND ITS IMPLICATIONS FOR DISCRIMINATION CAPABILITY IN RUSSIA

Marie D. Arrowsmith[1], Stephen J. Arrowsmith[2], Brian W. Stump[1], and Michael Hedlin[3]

Southern Methodist University[1], Los Alamos National Laboratory[2], and University of California San Diego[3]

Sponsored by National Nuclear Security Administration

Contract Nos. DE-FC52-03NA99510[1], DE-AC52-06NA25396[2], and DE-FC52-03NA99511[3]
Proposal No. BAA03-38

## ABSTRACT

The problem of identifying mining events has become an important one given the deployment of regional seismic stations in monitoring areas of interest, particularly in countries where mining efforts are significant to the economy. As with other types of regional events, signals from mining events are influenced by the propagation path and local site and receiver effects. Unique to mining explosions, however, are the complex source functions that are representative of the complicated firing sequences and spatial extent utilized in engineering blasts. Many factors contribute to the source function, including grid spacing, inter-row and inter-shot delay times, borehole depth, yield per hole, material casting, and total yield. During this four year study, we have developed a comprehensive database of ~150,000 waveforms featuring ~2500 mining events and ~1300 earthquakes. This database covers mines in the U.S. and in Russia; we have focused analysis on two regions: events associated with coal mines in Wyoming and regional earthquakes of the Western U.S., as well as mining events and nearby earthquakes in the Altai-Sayan (AS) region of Russia. Due to extensive collaboration with the largest coal mine in Wyoming and the nation, we have detailed shot information for ~1000 mining events, classified into six distinct blast types. We have limited information for events in the AS region based upon contacts with the AS Seismological Expedition.

We have applied three discriminants to data from 11 stations and one array in the Western U.S. The first discriminant, time-of-day (TOD), assesses the time an event occurs. In general, for our dataset, mining events occur between 9:00 am and 6:00 pm local time, while earthquakes are randomly distributed with respect to time. The second discriminant, amplitude ratios (AR), exploits spectral differences between regional phases due to source type. For the Western U.S dataset, results for Pg/Lg (6–8 Hz) are highly station centric. The largest type of mining events (cast blasts) shows some separation from earthquakes that are within distances of < 250 km from the mine; however, as the earthquake dataset expands spatially, discrimination performance degrades. The application of a 1D path correction improves results slightly, but due to dominating propagation effects, path calibrations are necessary to optimize this discriminant. The third discriminant, time frequency (TF), capitalizes on the unique spectral signature of ripple-fired mining events as a function of time. This discriminant separates the larger types of blasts at all stations. Smaller blasts presumably do not discriminate because of the shorter shot durations. We use a statistical method called classification and regression trees (CART) to combine these discriminants. CART yields an intuitive decision grid for classifying events based on the discriminant value for each of the three discriminants. In the AS region, we calculated these same discriminants at two stations for ~260 mining events. TOD results are similar to those in the Western U.S in that presumed mining events fall within working hours. The AR discriminant (Pg/Lg [6–8 Hz]) shows significant overlap of the earthquake and explosion population. Certain events do separate, but we have no information on what makes these events unique, if anything. Similar results are seen for the TF discriminant—there is overlap of populations, and although certain events can be identified as explosions, we cannot assess the reasons why we observe the overlap. We do not know if the discriminant itself fails, or if the majority of our data points are from smaller shots that have shorter durations. These unanswered questions illustrate the need for detailed ground-truth information. Future studies of mining event discrimination, particularly where large datasets are to be acquired, should involve a heavy degree of cooperation with mine operators in order to address ambiguities such as those identified in the AS study.

## OBJECTIVES

### Data Quality Control

As discussed in previous proceedings (e.g., Arrowsmith et al., 2007), we have developed a database of earthquakes and mine blasts at three mines in the U.S. and in the Altai-Sayan, Russia. We have continued our efforts in examining the extensive set of waveforms and include results from additional stations which have been analyst reviewed.

### Testing and Evaluation of Discriminants on a Large Dataset

We have identified three discriminants that can be easily applied to a large seismic catalog. The TOD discriminant characterizes events based both on typical working hours of mining operations and co-location with known mines. We have continued investigating amplitude ratios, using feature selection methods to identify potentially successful combinations. The time-varying spectral estimation method, described in detail in Arrowsmith et al. (2006), has also been applied to the dataset at multiple stations. We test the benefits and limitations of each discriminant on data in the U.S. and apply the results to data in Russia.

### Combination of Discriminants

In order to build upon the performance of the individual discriminants, we utilize a discriminant combination method—CART—to assess the results obtained at individual stations and for the entire analyst-reviewed dataset.

## RESEARCH ACCOMPLISHED

### Ground-Truth Database of Mining Explosions

Nearly ~150,000 waveforms comprise our dataset, consisting of ~2500 mining events and ~1200 earthquakes. In order to analyze discriminant performance, we have focused on a smaller portion of the large database, concentrating on the Black Thunder coal mine in Wyoming. Black Thunder is in a region of high mining activity known as the Powder River Basin (PRB); 40.6% of all U.S. coal production occurs in the PRB. Black Thunder is the largest producer in this region (and in North America), having produced 92,653,250 tons of coal in 2006 (Energy Information Administration, 2007). We have a working relationship with Black Thunder and thus have access to very detailed ground-truth data. This area is interesting to study because upper crustal seismicity in the region is distributed in several geologic environments, allowing us to investigate the role of path effects on the discriminants. We have concentrated our efforts on 11 stations and one array distributed azimuthally around the mine; each station has recorded hundreds of events, including many mining blasts (Figure 1).

Through cooperation with Black Thunder, we have obtained basic information such as origin time and blast types utilized by this mine for approximately 1000 events. We have additional detailed ground-truth data for 98 of these events, which includes information such as delay times between shots and rows, amount of explosive used, and number of rows in each blast. Jimeno et al. (1995) describe many of these parameters in detail and how they are applied to the blasting process. Additionally, we have records at two stations (RSSD and PD31) of seven single-fired explosions at Black Thunder that were collected as part of experiments in 1995 and 1997 (Stump et al., 2003). Of the various types of blasts in Figure 2, cast blasts are the largest and most likely to be observed at regional distances. In this type of blast, overburden above the coal seam is moved into an adjacent pit. Anandakrishnan et al. (1997) describe this process: an array of up to 1000 individual boreholes is filled with 5000 to 10,000 lbs of material and delay fired over several seconds. The explosive array is parallel to the free face of the mine and the time-delay procedure ensures that material closest to the free face is cast into the pit before subsequent rows are detonated. As much as 20 to 30 % of the overburden is cast into the pit and the remainder is dug with a dragline to expose the coal. At Black Thunder, overburden ranges from 100 to 230 feet in thickness and consists of unconsolidated sedimentary facies. There are four active pits at Black Thunder and four draglines are utilized to remove material that has been cast blasted. The “Truck Shovel” (TS) overburden explosions are similar to the cast blasts but material is cast such that it can be excavated with large truck shovels and hauled off. The coal shots are used to fracture the coal after it has been exposed so that a shovel can remove it and load it into haul trucks. Parting shots are used to remove small amounts of material between the two main coal seams currently being excavated. The latter two explosion types are generally small in total explosive charge and shorter in time duration.

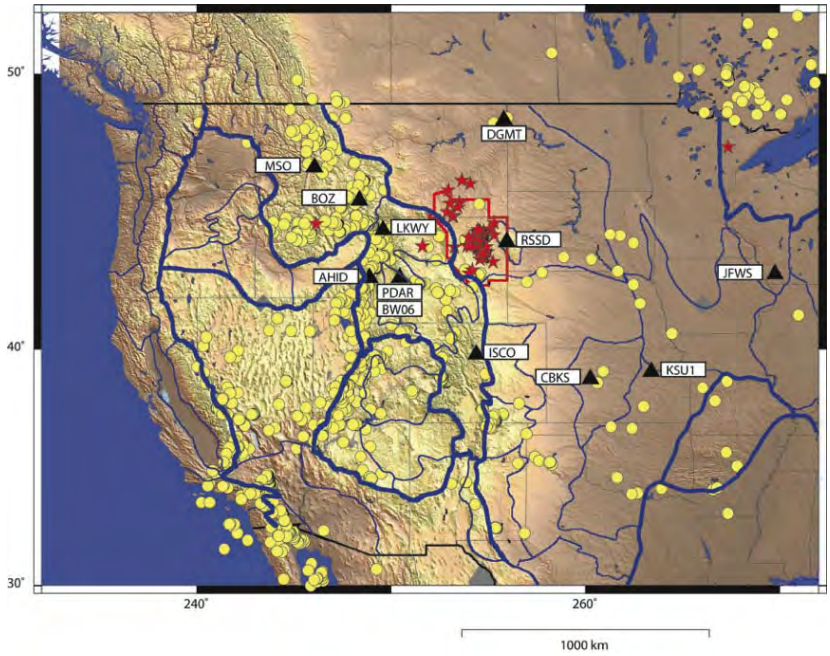


**Figure 1. Data featured for discrimination analysis. Earthquakes (yellow circles) and mining events (red stars) are interspersed throughout the Western U.S. and Interior Plains. Seismic stations (black triangles) used in the analysis are distributed around the main mining region, the Powder River Basin (red outline). Superposed on the high-resolution background topography are outlines (blue) of the major (thicker lines) and minor (thinner lines) geologic provinces of the U.S. Only sub-provinces within the Western U.S. and Interior Plains are shown.**

| Blast Type | Description | Min Yield (lbs) | Max Yield (lbs) |
|---|---|---|---|
| **Cast Overburden** | Overburden is casted and removed into adjacent empty pit. | 300,000 | 2,500,000 |
| Cast (Electric Delay) | Delays are controlled by electric delay detonators | | |
| Cast (Long Delay) | Interrow delay times are 300 seconds | | |
| **TS Overburden** | Blasts in overburden material to be excavated by shovels loading into trucks. | 100,000 | 600,000 |
| Extraction | Blasts in the main coal seam, which is 60 - 70 ft in thickness or in the upper coal seam, which is 10 ft in thickness. | 2,000 | 200,000 |
| **Parting** | Blasts of waste material layer between the upper and lower coal seam, ranging from 0 to 40 ft in thickness. | 200 | 500 |

| Location | Pit | Cut | Section | Loc. Code |
|---|---|---|---|---|
| | North | 22 | West | N22W |

| Explosives | | | |
|---|---|---|---|
| **No. Holes** | 132 | **Delay Time** | **Quantity** |
| **No. Rows** | 4 | 9 ms | 70 |
| **Hole Diameter** | 12.25 in | 200 ms | 66 |
| **Burden** | 48 ft | 500 ms | 66 |
| **Spacing** | 27 ft | 800 ms | 66 |
| **Avg. Hole Depth** | 188.1 in | 1100 ms | 66 |
| | | *Total Delays* | 653 |
| **Shot Type** | Cast OB | | |
| **Avg. Stemming Depth** | 35 Drill Cuttings | | |

| Type | Qty | Weight (lb) |
|---|---|---|
| SoftLoad | | 1,114,700 |
| 1-lb Primer | 264 | 264 |
| Det Cord | 32,000 | |
| Lead In (50' 100 ms) | 1 | |
| *Total Explosives Used* | | 1,114,964 |
| *Max Charge per 8 ms Delay (lb)* | | 10,302 |

| Miscellaneous | |
|---|---|
| **Temp** | 41 deg |
| **Cloud Cover** | Pt Cloudy |
| **Wind Speed** | 6 mph |
| **Wind Direction** | WNW |

Inter-row delay times (ms)

| Cast Blasts | TS Overburden | Coal Extraction | Parting |
|---|---|---|---|
| **300** | **300** | 300 | **42** |
| | 200 | 200 | |
| | 42 | 42 | |
| | 60 | **35** | |
| | | 7 | |

Inter-shot delay times (ms)

| Cast Blasts | TS Overburden | Coal Extraction | Parting |
|---|---|---|---|
| **9** | 20 | 42 | **42** |
| | **17** | 35 | 17 |
| | 9 | 17 | 9 |
| | | **9** | |

Total shot Duration (ms)

| | Cast Blasts | TS Overburden | Coal Extraction | Parting |
|---|---|---|---|---|
| *min* | 1044 | 424 | 18 | 72 |
| *max* | 1854 | 1638 | 1400 | 672 |
| *mean* | 1296 | 936 | 318 | 301 |

**Figure 2. Types of ground-truth data obtained from Black Thunder. Top panel describes types of shots the mine performs (color code will be used throughout the paper). Bottom, left panel describes a cast overburden shot pattern. Bottom, right panel summarizes timing information used for the different types of shots (bold numbers indicate the mode).**

**Discrimination of Mining Events in the Western United States**

*Time-of-day and location*

Using the entire U.S. event catalog, we followed the method described in Mackey et al. (2003) to visually examine the dataset based on TOD and event location. By clustering events into 1º x 1º bins, we observe the mining regions we have cataloged (in Arizona, Minnesota, and Wyoming) are predominantly daytime events; in other parts of the U.S., mixed daytime and nighttime events are seen. We also investigated the Western U.S. event catalog as a function of time-of-day and event type. Events categorized as mining events are constrained to working hours (roughly between 7 am and 6 pm), with the majority of events occurring between 11 am and 4 pm. One exception is an event occurring at hour 24, local time. Reviewing the ground-truth record for this blast shows that an origin time was not recorded by the blaster; a default value of 0:00:00 local time was noted in their records. The earthquake case shows a random distribution of events occurring both seasonally and as a function of TOD, which is an expected result. This discriminant, while simple, can be quite useful as a preliminary measure for categorizing or verifying events, particularly when the location and TOD characteristics are used together.

*Amplitude Ratios*

We reviewed and picked data from the 11 stations and the array shown in Figure 1 prior to measuring regional phase amplitudes. Due to poor signal-to-noise ratio (SNR), there were insufficient mining blast data from KSU1, JFWS, and LKWY to be used in the amplitude analysis. We used the magnitude and distance amplitude corrections (MDAC) methodology to make source and 1D path corrections and improve discrimination performance (Walter and Taylor, 2002).

We use the Mahalanobis distance, a multivariate statistical approach, to determine the best discriminant at each station. The Mahalanobis distance weighs the distance between two populations based upon the population variability. Using a feature selection method developed by Dr. Steven Taylor, we pre-selected 12 discriminants and determined the best amplitude ratio based upon the highest Mahalanobis distance. This analysis was performed for four cases: all earthquakes and all mining explosions; all earthquakes and only cast blasts; earthquakes within 250 km of Black Thunder and all mining explosions; and earthquakes within 250 of Black Thunder and only cast blasts. Results for all stations are shown in Figure 3.

| Station | Quakes All Mining | Quakes Cast Blasts | Quakes (250 km) All Mining | Quakes (250 km) Cast Blasts |
|---|---|---|---|---|
| AHID | Pn(6-8)/Lg(6-8) 0.4715 | Pn(6-8)/Lg(6-8) 0.4715 | Pg(6-8)/Lg(6-8) 17.8398 | Pg(6-8)/Lg(6-8) 17.8398 |
| BOZ | Pn(4-6)/Pn(1-2) 1.5441 | Pn(4-6)/Pn(1-2) 1.6742 | Pn(6-8)/Lg(6-8) 66.5964 | Pn(6-8)/Lg(6-8) 63.0015 |
| BW06 | Pg(6-8)/Lg(1-2) 0.5346 | Pg(6-8)/Lg(1-2) 0.8541 | Pg(6-8)/Pg(1-2) 53.2668 | Pg(6-8)/Lg(6-8) 36.7874 |
| CBKS | Pn(4-6)/Lg(4-6) 0.8514 | Pn(4-6)/Lg(4-6) 0.7638 | Pn(4-6)/Lg(4-6) 8.1918 | Pn(4-6)/Lg(4-6) 6.8957 |
| ISCO | Pg(4-6)/Pg(1-2) 0.9749 | Pg(4-6)/Pg(1-2) 1.0498 | Pg(4-6)/Pg(1-2) 9.4969 | Pg(4-6)/Pg(1-2) 9.4507 |
| MSO | Pg(6-8)/Pg(1-2) 1.5064 | Pg(6-8)/Pg(1-2) 1.5064 | Pg(4-6)/Pg(1-2) 6.0025 | Pg(4-6)/Pg(1-2) 6.0025 |
| PD31 | Pn(4-6)/Pn(1-2) 0.3442 | Pn(6-8)/Lg(6-8) 0.5673 | Pg(6-8)/Lg(1-2) 6.0651 | Pg(6-8)/Lg(1-2) 4.3922 |
| RSSD | Pg(6-8)/Lg(6-8) 21.3163 | Pg(6-8)/Lg(6-8) 23.2469 | Pg(6-8)/Lg(6-8) 285.8222 | Pg(6-8)/Lg(6-8) 123.7424 |

**Figure 3. The top discriminants at the nine stations used in the analysis. The top value in each column is the amplitude ratio and bottom value is the Mahalanobis distance for that discriminant.**

The best performing discriminants varies between stations, particularly in the performance metric (e.g., Mahalanobis distance). In general, high-frequency to low-frequency P/S ratios show the best performance, but there are deviations between stations. Additionally, Pg/Lg (6-8 Hz), which has been shown to be successful in other regions, is successful for some stations. Figure 4 shows this discriminant at all stations. As a result of low SNR at high frequencies for some stations, there is a lack of data points at stations, which makes a definitive conclusion about this discriminant difficult. Events that do discriminate from close-by earthquakes are predominantly cast blasts; smaller shots merge into the earthquake population. Despite some of the promising results seen at several of the stations for some of the events, the results are very station-centric. The application of MDAC does provide better separation, but we believe the diversity of regional geology (see Figure 1) is imprinted on the discriminant values.

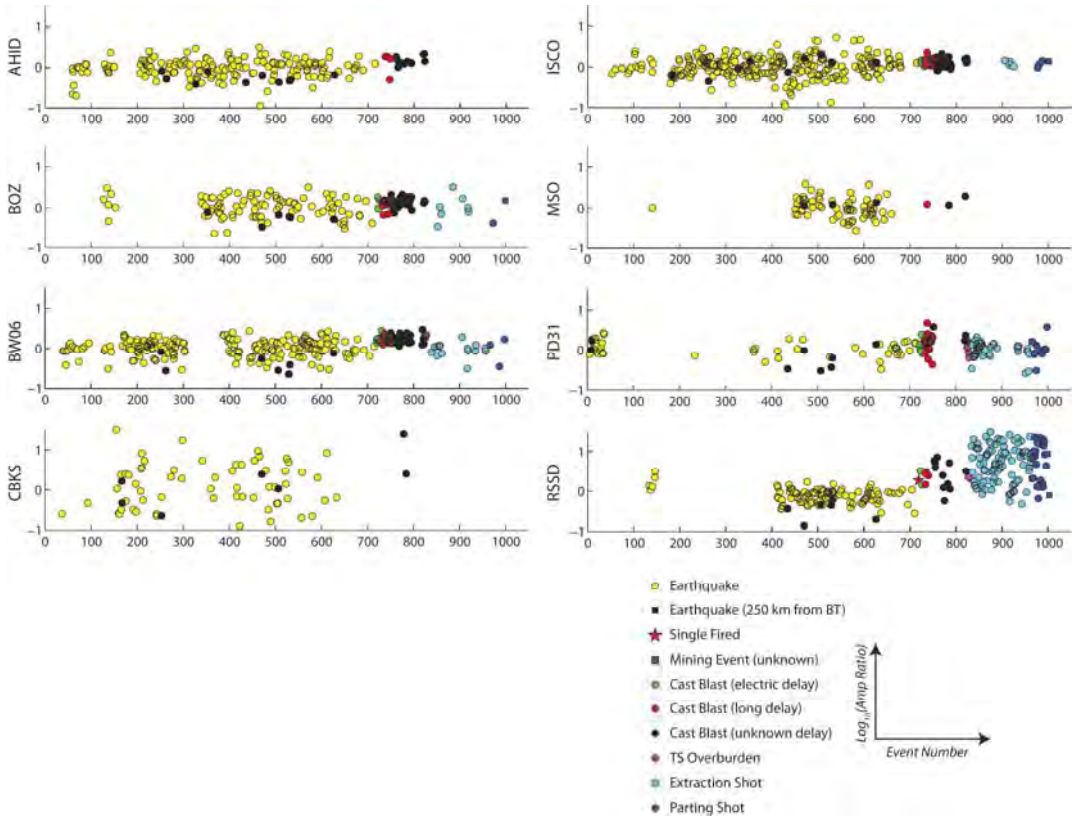


**Figure 4. MDAC corrected log (Pg/Lg [6-8 Hz]) discriminants (RSSD has not been corrected, as mining events are located before the crossover distance and the MDAC methodology is not applicable for events in this region). Data are plotted as a function as event number.**

*Time Varying Spectral Analysis*

For this discriminant we use an algorithm that has been developed for identifying delay-fired mining explosions (Arrowsmith et al., 2007). The discriminant measures the extent of time-independent spectral banding in each waveform in windows that begin at required first-arrival picks. Time-independent spectral banding, which consists of regularly spaced peaks and troughs in the frequency domain, is typically produced by delay-fired mining explosions and reflects periodicities in the nature of the source. In contrast, earthquakes and single-fired explosions do not typically contain a periodic source component. The characteristic function for time-independent spectral banding is the cepstrum of the 2D binary spectrogram, which measures periodicity in the spectral content of the waveform as a function of time. Thus, a binary spectrogram can be reduced to a single discriminant value, hereafter referred to as the cepstral mean.

The delay-fired event identification algorithm is applied to nine stations where a sufficient number of first-arrival picks were made. The resultant discriminants obtained for each station are shown in Figure 5. A common feature in the results is the clear separation between the large, delay-fired shots (cast blasts and TS overburden blasts) and the remaining event population (comprising earthquakes, extraction shots, and parting shots). The extraction shots and parting shots do not separate from the earthquakes, although there are a few exceptions. High values in the cepstral mean have been associated with inter-row delay times and total shot durations; inter-shot delay times are thought to not play a role since they are generally outside the bandwidth of the seismic observations. Figure 2 provides typical timing values for Black Thunder mining explosions. As expected, the larger blasts have the longest durations and larger inter-row delay times. Several of the extraction shots have longer durations and delay times, which may explain why there are outliers in the cepstral discriminant.

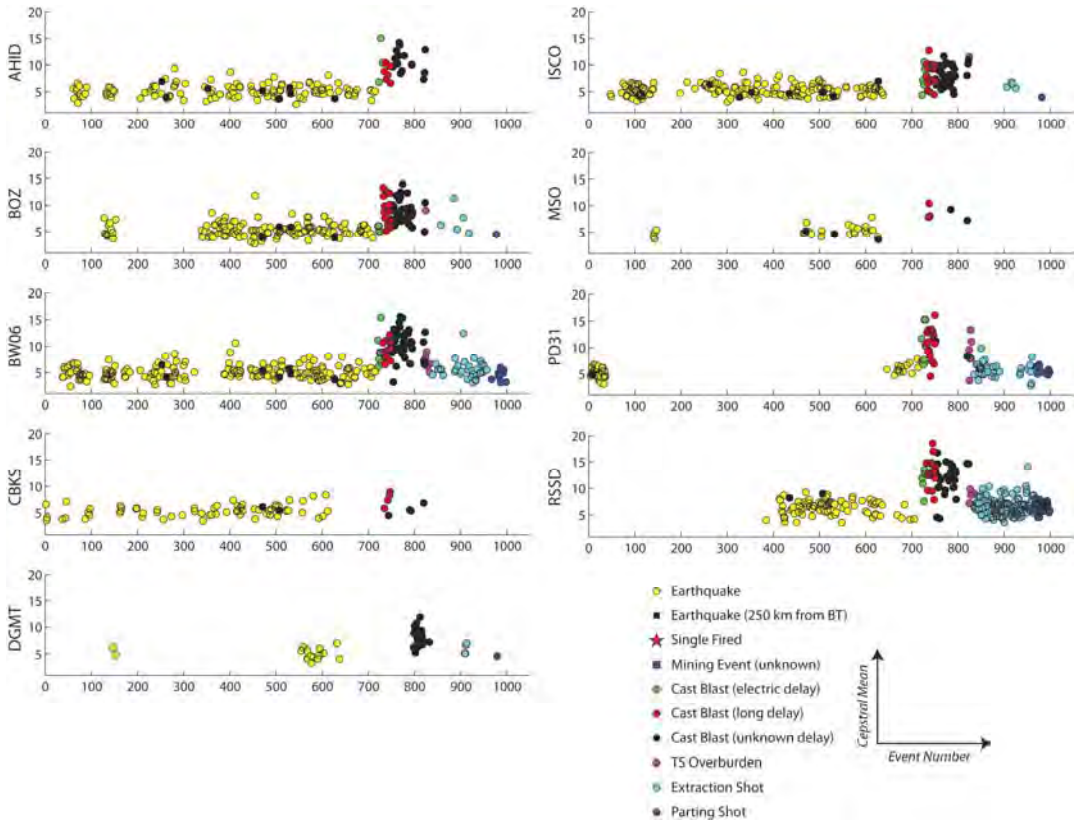


**Figure 5. Cepstral mean discriminant values plotted as a function of event number.**

*CART Analysis*

Combining discriminant measures has been shown to increase overall classification power; however, difficulty lies in combining multiple measures in a statistically sound way while accounting for problems such as missing data. In a comprehensive report, Dr. Dale Anderson and colleagues (1996) investigated eight classification methods for combining discriminants. After reviewing the methods using a comprehensive dataset of earthquakes and explosions, they found that CART met criteria related to treaty verification challenges; current discussions with Dr. Anderson about our dataset have also affirmed this method to be the most suitable for merging discriminant measures.

The classification tree considers each discriminant value, partitioning event types into homogenous regions. The process is iterative, and allows the tree to be branched or pruned based upon the number of discriminants, events, and probability levels achieved at each step in the iteration. We use a statistical software package called JMP, which has a CART module. In the example shown in Figure 6, a simple case from station RSSD is considered. Earthquake (blue) and cast blast (red) discriminant values are considered for three discriminants: TOD, Pg/Lg (6–8 Hz) amplitude ratio (Amp), and TF. Given the input data distribution assuming no discriminants are applied, the top-level box shows the probability of an event being an earthquake is 72% and 27% for a cast blast. The $G^2$ value is a measure of system entropy, and the goal throughout the tree-growing process is to minimize this value; the JMP routine allows us to do that by either maximizing the split statistic or maximizing the significance of the split. In the following example, we demonstrate the latter option. We can follow the tree based on whether we want to select explosions from the dataset (log(amplitude) $\geq$ 0.3925) or eliminate them from the dataset (log(amplitude) < 0.3925). For example, for the purpose of selecting explosions from background earthquakes, we choose the right path. This selects 53 probable events. The next best discriminant in this branch is TOD; by selecting events that have an hour greater than GMT of 18, we have a 97% probability of selecting a cast blast. Following the left branch of the tree, we can select events that are probable earthquakes and compare those against the values obtained in the right branch. The CART method provides a visually simple method of working with a number of discriminants, and can be tuned to handle additional discriminants (such as the presence of infrasound), as well as results for multiple stations.

Future work involves integrating data from all stations into a single blueprint that can be utilized for the different types of mining events seen in Figure 1, and applied to other regions.

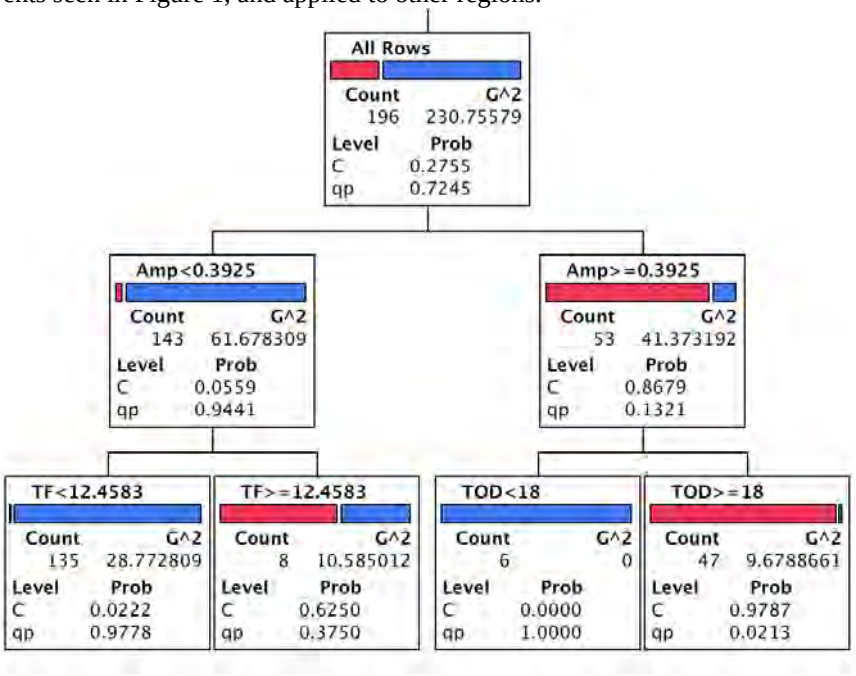


**Figure 6. Sample CART tree for station RSSD output from JMP.**

**Addressing Discrimination in the Altai-Sayan, Russia**

The AS (Figure 7) is an active mining region in Russia with numerous types of mines and quarries; approximately 40% of active surface coal mines in Russia are in the AS. The region also has a prevalence of natural seismicity due to the Asia-India collision zone to the south and the Baikal rift zone to the east. We have used this region to test the techniques developed in the Western U.S., as applied to a dataset where less is known about the ground-truth information from the mining explosions. The Altai-Sayans Seismological Expedition (ASSE) provided us with event lists (location, origin time, and $m_b$ converted from Russian K class) of 263 probable earthquakes and 843 probable mining explosions. We were not provided the criteria for how ASSE seismologists categorized event types. We analyzed data from five seismic stations (ZAL, KURK, MAKZ, TLY, and BRVK) using the event catalogs provided to us by the ASSE.

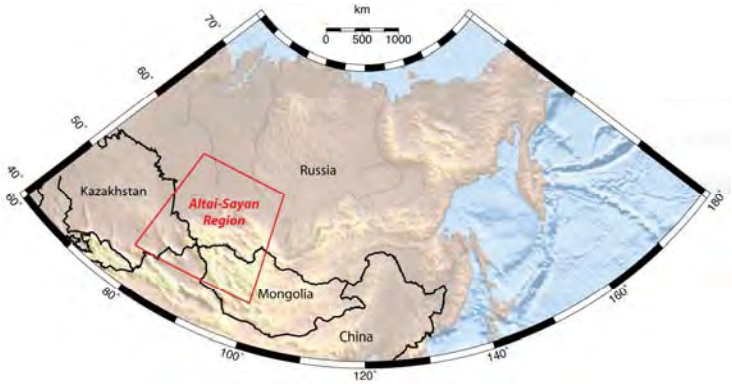


**Figure 7. The Altai-Sayan region (red) is located western Siberia and encompasses portions of Kazakhstan, Mongolia, and China.**

In a region where we have limited ground truth, one of the most important discriminants is the TOD information. Figure 8 shows the distribution of events with respect to month and hour for both mining explosions and earthquakes in the catalog. Mining events clearly occur during working hours, while the earthquakes exhibit no clear time-of-day dependence, providing confidence in the event bulletins supplied to us by the ASSE. These results also illustrate that TOD is not the sole criterion used by the ASSE in constructing the event bulletins, since the earthquakes occur also during working hours.

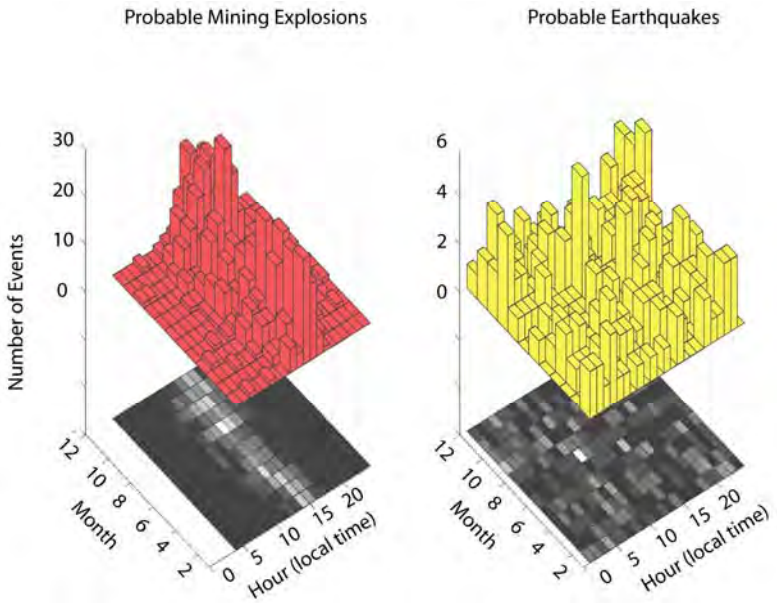


**Figure 8. Time-of-day distribution with respect to month and hour of day for the dataset for both probable mining events (left) and earthquakes (right). Surface reflections of the histograms show trends, where lighter colors indicate larger numbers of events.**

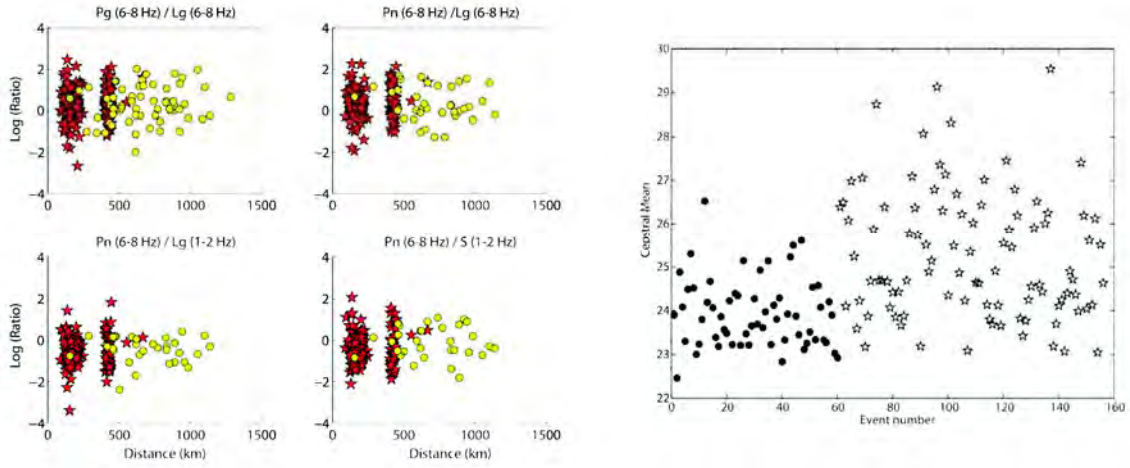

**Figure 9. Four log(amplitude ratios) (left) as a function of distance at station ZAL. Amplitude ratios are not corrected since instrument response problems are known at this station; however it is the closest station to the mining region. Data were analyst-reviewed and events with SNR > 2 are shown. The cepstral mean for this dataset is shown at right.**

Amplitude ratio discriminants (Figure 9) were not successful in separating waveforms from mining explosions from those generated by earthquakes in this region for multiple stations. There is large scatter in the explosion population (up to four log units), suggesting that different blasting types and timing patterns may be dominating the discriminant, since the propagation paths are very similar for each blast, although for certain discriminants the earthquake populations are similarly scattered; this phenomenon is seen for analyst-reviewed data of SNR quality at multiple stations. Without further ground truth, we cannot be sure what causes the failure of this discriminant. The time-frequency discriminant (Figure 9), which proved very successful in a multitude of geological regions within the Western U.S. and Interior Plains also does not work well in the AS region, again at multiple stations. Certain events have a high cepstral mean, and based upon the Western U.S. results, we can presume those are the largest blasts which emulate the cast or TS overburden shots we observe at Black Thunder. However, the majority of the mining events do not discriminate from the earthquakes and with a lack of information from the mines themselves, we cannot conclude definitively the reason why the discriminant behaves poorly.

## CONCLUSIONS AND RECOMMENDATIONS

In the Western U.S., we have gathered a large set of mining explosions from a region with prolific blasting activity. Due to a working relationship with a mining operator, we have detailed ground-truth for the dataset, which is crucial for understanding the behavior of waveform-based discriminants. A simple discriminant, time-of-day, is useful for verifying the event catalog and shows that mining events that are clustered in certain regions are confined to working hours. Amplitude ratios, which have been useful in other regions (high-frequency P/S), show mixed results in the Western United States. A number of factors come into play for this discriminant. The results are very station-centric, suggesting that sensitivities due to regional geology affect the discriminants. Attenuation studies in the Western U.S. by Phillips and Stead (2008) show strong variations in Lg amplitudes with relation to detailed crustal structure, implying that simple 1D path corrections are likely inadequate for the broad region of our study. Additionally, different event types seem to yield different discriminant results, with the larger cast blasts performing better. This result is also true for the time-frequency discriminant. Larger blasts discriminate very well, and station location seems to play no role in the success of the discriminant, consistent with the fact that this discriminant is strongly related to the distinctive spectral shape resulting from the long source duration. Smaller blasts merge with the earthquake population for this discriminant, and as there are many small blasts in the dataset, it would be easy to assume the discriminant was not working if we did not have the additional explosion features summarized in Figure 1. Being able to constrain the type of shot, as well as other types of information on the blasting configuration is invaluable in assessing discriminant success. Early work using the CART methodology to combine discriminant information gives a valuable and easy to use tool for synthesizing the multiple results we have obtained and assess the importance of multiple discriminants in characterizing the data set. The complete assessment of this tool is an ongoing study.

Applying these discriminants to the Russian dataset, which has very limited ground truth, yields much less promising results. The best performance comes from the time-of-day discriminant, which shows that mining events are constrained to working hours. Event locations are clustered in areas of known active mines. Both amplitude ratios and time frequency discriminants are largely unsuccessful, but this does not imply discriminant failure, just that we lack sufficient information to properly assess the results we see. Given these findings, we suggest the following recommendations: any future datasets in which mining explosions are specifically to be acquired should involve intense collaboration with mining operators; due to the regional imprint seen in the Western U.S. amplitude ratio values, understanding and correcting for path requires having a high-quality, highly station-sampled dataset. These results further motivate the development of detailed regional attenuation maps that can be used to correct regional amplitudes prior to discrimination analysis. The deterioration of the amplitude ratio discriminants with range found in the Western U.S. illustrates this effect.

## ACKNOWLEDGEMENTS

Much of the data from this experiment was provided by the Incorporated Research Institutions for Seismology Data Management Center and supplemented by Los Alamos National Laboratory (LANL) and Lawrence Livermore National Laboratory. Arch Coal allowed us access to Black Thunder mining blasts. Dale Anderson patiently answered questions about and guided us through the CART routine. LANL provided computing and office resources. Finally, Marv Wetovsky answered numerous editorial and grammatical questions, despite his busy schedule.

## REFERENCES

Anandakrishnan, S., S. R. Taylor and B. W. Stump (1997). Quantification and characterization of regional seismic signals from cast blasting in mines; a linear elastic model, *Geophys. J. Int.* 131: pp. 45–60.

Anderson, D.N, K. K. Anderson, D. N. Hagedorn, K. T. Higbee, N. E. Miller, T. Redgate, and A. C. Rohay, (1996),.Statistical Classification Methods Applied to Seismic Discrimination, *Pacific Northwest National Laboratory report PNNL-11192US*, pp. i–27.

Arrowsmith, M. D., S. J. Arrowsmith, B. Stump, and M. A. H. Hedlin (2007). Discrimination Capability for Mining Events in the Altai-Sayan Region of Russia and the Western United States, in *Proceedings of the 29th Monitoring Research Review: Ground-Based Nuclear Explosion Monitoring Technologies*, LA-UR-07-5613, Vol. 1, pp. 531–540.

Arrowsmith, S. J., M. A. H. Hedlin, M. D. Arrowsmith, and B. W. Stump (2007). Identification of delay-fired mining events using seismic arrays: Application to the PDAR array in Wyoming, USA, *Bull. Seism. Soc. Am.* 97: pp .989–1001.

Arrowsmith, S. J., M. D. Arrowsmith, M. A. H. Hedlin, and B. Stump (2006). Discrimination of delay-fired mine blasts in Wyoming using an automatic time-frequency discriminant, *Bull. Seism. Soc. Am.*. 96: pp. 2368–2382.

Energy Information Administration (2007). Annual Coal Report 2006, United States Department of Energy, DOE/EIA-0584.

Jimeno, C. L., E. L. Jimeno, and F. J. A. Carcedo (1995). Drilling and Blasting of Rocks, A.A. Balkema, Netherlands, pp. 179–190.

Mackey, K. G., K. Fujita, L. V. Gounbina, B. M. Koz'min, V. S. Imaev, L. P. Imaeva and B. M. Sedov (2003). Explosion Contamination of the Northeast Siberian Seismicity Catalog: Implications for Natural Earthquake Distributions and the Location of the Tanlu Fault in Russia, *Bull. Seism. Soc. of Am.* 93: 737–746.

Phillips, W. S. and R. J. Stead (2008), Attenuation of Lg in the western U.S. using the USArray, *Geophys. Res. Lett.*, Vol. 25, L07307, doi:10.1029/2007GL032926.

Stump, B. W., D. C. Pearson and V. Hsu (2003), Source scaling of contained chemical explosions as constrained by regional seismograms, *Bull. Seism. Soc. Am.* 93: pp.1212–1225.

Walter, W. R. and S. R. Taylor (2002). A Revised Magnitude and Distance Amplitude Correction (MDAC2) Procedure for Regional Seismic Discriminants: Theory and Testing at NTS, *Lawrence Livermore National Laboratory UCRL-ID-146882*, pp. 1–13.

# EMPIRICAL AND THEORETICAL SEISMIC ENERGY PARTITIONING FROM EXPLOSIONS UNDER DIFFERENT CONFINEMENT AND MEDIA CONDITIONS

Jessie L. Bonner[1], Brian W. Stump[2], William R. Walter[3], Xiaoning Yang[4], and Mark R. Leidig[1]

Weston Geophysical Corporation[1], Southern Methodist University[2],
Lawrence Livermore National Laboratory[3], and Los Alamos National Laboratory[4]

Sponsored by National Nuclear Security Administration

Contract Nos. DE-AC52-08NA28655[1,2]; DE-FC52-06NA27324[3]; and DE-AC52-06NA25396[4]
Proposal No. BAA08-97

## ABSTRACT

Some of the data-analysis results from the 2003 Arizona Source Phenomenology Experiments (SPE) were unexpected—explosions in slow-velocity limestone appear to be mainly isotropic under most emplacement conditions, while explosions in higher-velocity granite porphyry are marked by interesting source anisotropy. Even though the emplacement media were different, we did not expect to observe such prominent differences in the explosion phenomenology. While the SPE project was successfully completed, important questions remain regarding the fundamental physical mechanisms behind these differences, which could have important implications on explosion-generated *S*-wave models.

To improve our understanding of the physics behind the explosive-source phenomena, we are comparing the SPE data to that of other explosion experiments, including the Non-Proliferation Experiment (NPE). We are attempting to 1) develop a physical interpretation of the different SPE sources using comparative moment tensors analyses; 2) quantify the effects of spall, compensated linear vector dipole (CLVD), and other secondary sources; 3) characterize near-source, local, and regional *S*-wave phases, including prominent *SH* waves; 4) conduct moment tensor inversions of NPE explosions, including an overburied 177-kg calibration explosion, for comparison to the SPE explosions; and 5) examine the variability of regional phase partitioning from single-fired and production mining explosions in order to assess the transportability of regional discriminants. We have just started a two-year, multi-phase physical basis investigation aimed at developing a new explosion source model explaining the differences between the isotropic explosions in highly fractured limestone and anisotropic explosions in granite porphyry.

## OBJECTIVES

The 2003 Arizona SPE was conducted by Weston Geophysical, Southern Methodist University (SMU), Lawrence Livermore National Laboratory (LLNL), Los Alamos National Laboratory (LANL), and the University of Texas at El Paso (UTEP). The experiment included dozens of delay-fired mining blasts and 19 single-fired chemical explosions recorded by hundreds of seismic stations at local and near-regional distances. The single-fired explosions were detonated either in a *slow velocity, highly-fractured limestone* at a coal mine on Black Mesa, AZ or in a *faster-velocity granite porphyry* at a copper mine near Morenci, AZ. The results from prior research conducted by the SPE consortium are summarized in Table 1.

**Table 1. Summary of results from the SPE explosions.**

| Analysis | Slow-velocity limestone medium | Faster-velocity granite porphyry |
|---|---|---|
| **Moment Tensors** | Isotropic under all confining conditions | Strong anisotropy under all confining conditions |
| ***S*-wave Generation** | Large *SH* and direct *S*-wave arrivals with onset times that trace back to explosion origin times plus an offset | *S*-wave arrivals with onset times that trace back to explosion origin times |
| **Single Shot Regional *P/S* Discrimination** | Easily classified as explosions in 6-8 Hz *Pg/Lg* | Overlap with earthquakes for 6-8 Hz *Pg/Lg* |
| **Mining Blast Regional *P/S* Discrimination** | Classified as explosions, but separation from earthquakes is smaller than single-fired shots; Large variance between blasts | Classified as explosions with separations from earthquakes larger than single-fired shots; Large variance between blasts |

The 1993 NPE was conducted by the Department of Energy (DOE) and examined chemical-nuclear equivalence by detonating a kiloton of single-point, fully contained chemical explosives at the Nevada Test Site (NTS). When compared with nearby nuclear tests, the regional seismic records were found to be essentially identical, other than a different chemical/nuclear amplitude-yield scaling factor (e.g., Denny et al., 1997). Regional discriminants classified the NPE as a nuclear explosion (Walter et al., 1995). An additional highly over-buried NPE calibration explosion (NPE Cal) of 177 kg detonated at 390 m depth provided data from a source with no free surface non-linear interaction for comparison with the much larger NPE and its free surface interaction. The comparison of these two NPE shots could provide insight into possible depth of burial effects in the SPE data set.

Even though the SPE project was successfully completed, interesting phenomena arose from the analyses, and important questions remained. In this paper, we present initial work on answering many of these questions, including:

- Why are the source characteristics different for limestone and granite porphyry?
- What are the generating mechanisms of the larger vertical component and strong off-diagonal component(s) noted in the moment tensors of the Morenci copper mine explosions? Block motions? Asymmetries in damage? Can they be modeled with a compensated linear vector dipole (CLVD, Knopoff and Randall, 1970) source?
- What are the effects of the off-diagonal energy in the moment tensor on the generation and propagation of S waves?
- Can the scattering of *Rg* be isolated and the contributions to *S* waves quantified?
- Can near-source moment tensor investigations of the NPE and its highly over-buried calibration shot provide further constraints on depth-of-burial effects?
- Can a source model be developed for both SPE emplacement media so that both local and regional data can be explained?
- Can we explain the variance in the *P/S* ratios for the SPE shots and mine blasts at regional distances based on mining explosion practices/confinement/scaled depth of burial/etc?

## RESEARCH ACCOMPLISHED

### Comparison of Moment Tensors

We have compared the moment tensors for two under-buried SPE explosions at Black Mesa and Morenci (Figure 1). The results show that the absolute amplitudes and signal characteristics for these similar yield and depth explosions were almost the same on the $M_{zz}$ component. While the $M_{xx}$, $M_{yy}$, and $M_{zz}$ components for the Black Mesa shots are almost identical to each other, we note that the $M_{xx}$ and $M_{yy}$ components for the Morenci shot are greatly reduced compared to the corresponding $M_{zz}$ component. In fact, they are of similar amplitude to the off-diagonal component $M_{xz}$ for this shot. Conversely, there is no significant energy on the off-diagonal components for the Black Mesa shot. The explanation for these differences might be in the damage phenomenology as the Morenci shot cratered while the Black Mesa shot had a symmetric rubble mound (often called retarc, or crater spelled backwards). Another possible explanation is the different fracture generation and propagation phenomena that could result in different moment-tensor representations. We are continuing to examine near-source data from both mines to infer possible effects of fracture generation and propagation.

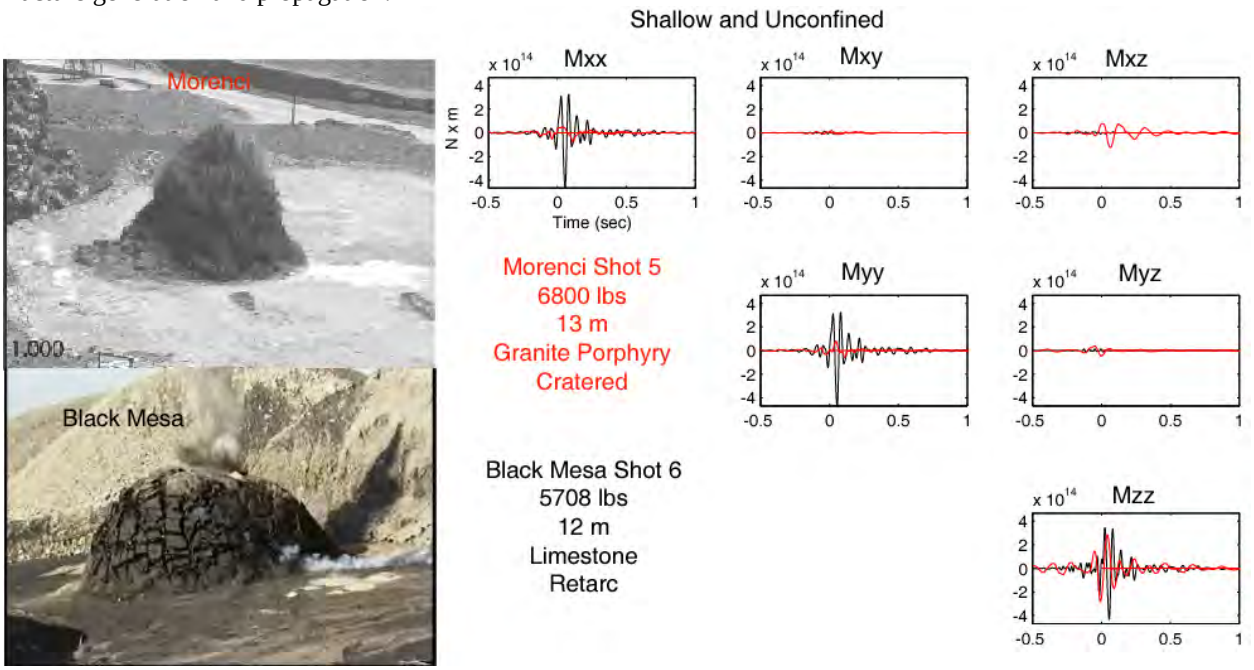


**Figure 1. Comparison of surface damage and moment tensors for two SPE explosions in different lithologies.**

### Examination of Spall

Spall is defined as the tensile failure of the near surface layers (Eisler and Chilton, 1964; Stump, 1985). For a contained explosion, the initial compressive shock wave reflects off the free surface as a tensile wave, which causes subsurface strata to fail in tension. Spall has been represented as a cylindrical source delayed in time from the explosion (Stump, 1985) or as a circular horizontal tension crack that opens and closes in the vertical direction (Stevens et al, 1991). To model the SPE explosions, we are extending the definition of spall to include both vertical and horizontal material cast.

Spall may have played an important role in the moment tensors for the unconfined SPE shots detonated near a free face (referred to as cast shots because the material was "cast" into the pit below). The cast shots have more complicated moment-tensor time histories (Figure 2). In addition, their moment tensors show an enhanced low-frequency (1-6 Hz) signal in the off-diagonal components, particularly in $M_{yz}$. This signal may have resulted from the material cast or horizontal spall effects.

We are working to quantify the effects of spall at both test sites using a forward modeling approach. Our emphasis is on modeling the data and moment tensors of unconfined near-free-face explosions and quantifying the contribution

of spall to the near-source seismic wavefield and to the generation of shear waves, especially *SH* waves, from these explosions. The depth of the equivalent spall source is not the same as the initial isotropic component of the explosion since the non-linear failure of the material dominates in the region above the contained explosion. In order to assess these effects on empirically determined moment tensors, we are conducting a forward modeling and inversion study.

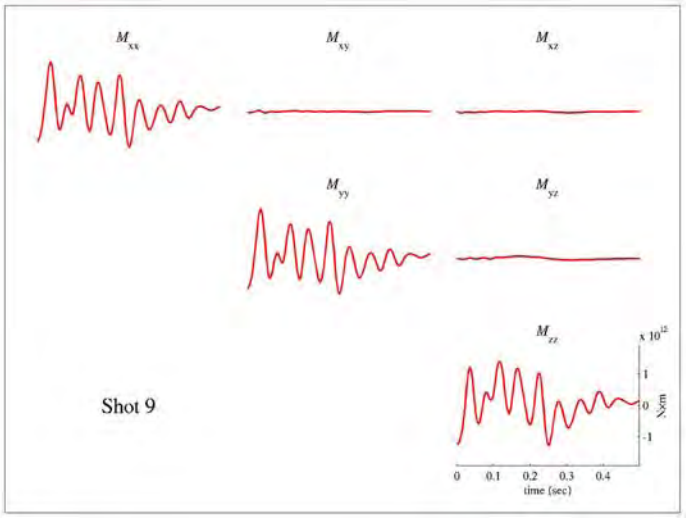


**Figure 2. Moment tensors from the inversion of a 1480-kg cast explosion at the Black Mesa coal mine. When compared to the moment tensor of an unconfined shot (such as in Figure 1), we note that the cast shot detonated near a vertical free face exhibits oscillatory behavior and low frequency energy on the off-diagonal $M_{yz}$ component.**

### *Rg* from a CLVD

It has long been recognized that underground explosions excite *Rg* waves efficiently. However, explosions in the field are not simple monopole (point isotropic) sources; rather, they are distributed sources in time and space, and emit non-spherical wave fields. Patton and Taylor (1995) proposed that the mechanism of *Rg* waves might involve a compensated linear vector dipole (CLVD, Knopoff and Randall, 1970), where the CLVD is the elastodynamic equivalent of an inverted conical volume source with its apex at the detonation point. The medium inside the cone deforms and fails as a result of tensile stresses caused by the downgoing shock wave reflected off the free surface. Spallation, which usually involves shallow, poorly-coupling geologic strata that open and close with no net displacement, is an example of such failure. Another example is driven block motions at depth, as envisioned by Masse (1981). This source might be more important for seismic wave generation than spall if it involves permanent deformations and couples better into the ground, since its centroid is located in more competent rock at depths greater than spall.

The source excites azimuthally independent Rayleigh waves and does not excite Love waves. Several interesting features characterize the Rayleigh-wave radiation from such a source, including excitation nulls in the Rayleigh spectra, which occupy the frequency range of *Rg* waves for source depths in the upper 300 meters of the crust. We generated *Rg* synthetics for a monopole ($M_{xx}=M_{yy}=M_{zz}=1$; $M_{xy}=M_{xz}=M_{yz}=0$) at 30 meters depth in the Morenci and Black Mesa velocity structures. We then generated *Rg* synthetics for a CLVD ($M_{xx}=-0.5$ $M_{yy}=-0.5$ $M_{zz}=1$; $M_{xy}=M_{xz}=M_{yz}=0$) source in the same structures at 20 meters depth (2/3 of the explosion centroid). The spectra for the *Rg* synthetics are shown in Figure 3 with CLVD excitation nulls at 4 Hz for the slower velocity structure and 7.5 Hz for the faster velocity structure. It appears that there is an excitation null between 2 and 4 Hz in the observed data from a 25-meter deep SPE shot at Black Mesa, but we do not observe a null in a 33-meter deep explosion at Morenci. We note that the Morenci synthetics suggest the null would be just outside our observed *Rg* frequencies, though.

A more detailed and thorough modeling study of the SPE data from the copper and coal mine single-fired explosions is being completed to determine if the CLVD source was a significant component of these explosions. To complete this task, we are using the methods defined by Patton et al. (2005) to match the amplitude and phase of a combined

monopole + CLVD source to the observed data. By determining the static moment for any CLVD source, we will have an important parameter needed for modeling the seismograms at regional distances.

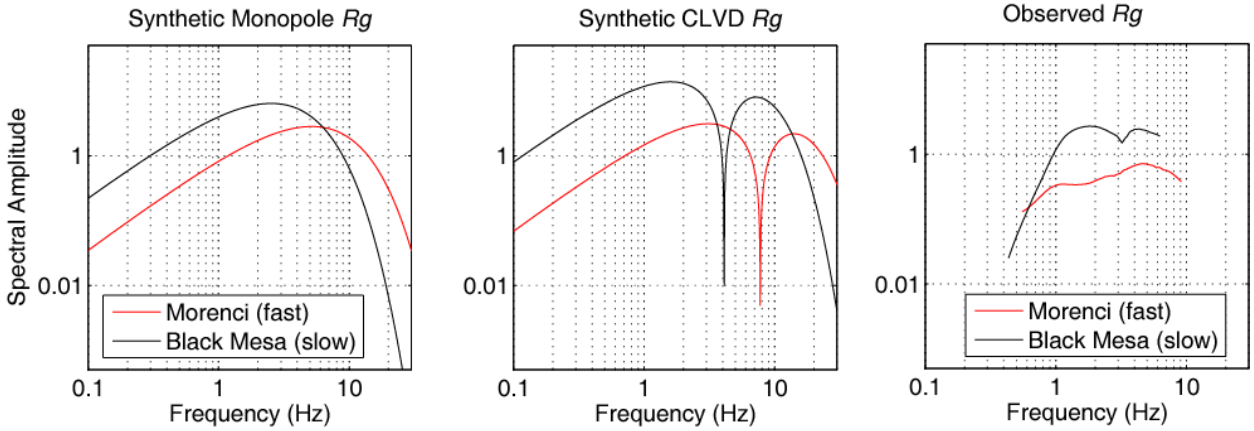


**Figure 3. Spectra for *Rg* generated from a synthetic monopole (left) in the velocity structures determined for Morenci (red) and Black Mesa (black). Also shown are the spectra for a synthetic CLVD source in the same media (middle) and the observed *Rg* spectra (right) for the deepest SPE shots.**

**Shear Wave Generation**

All available data from near-source, local, and near-regional distances are being combined in our analyses to quantify the shear wave generation and explain the origin of observed shear waves in different media. For the explosions in a granitic body, the shear energy includes both the direct shear arrivals and *Rg* at the local and near-regional distances recorded by the single-channel digitizers known as "Texans." The record sections presented in Figure 4 are from a 5076 kg Morenci shot, and have a frequency range of 0.7 to 20 Hz (Figure 4a) and 0.5 to 3 Hz (Figure 4b). The *Rg* energy is strongest at the lower frequencies, while the *P*-wave amplitudes are much larger than the shear amplitudes at high frequencies. There is significant shear energy with arrival times that are traceable back to the origin time.

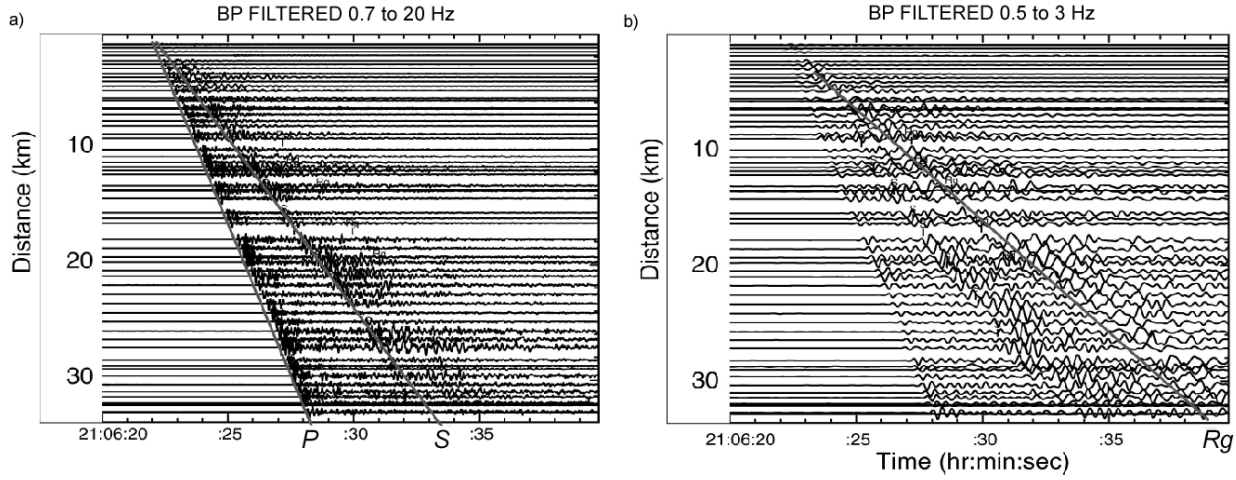


**Figure 4. Phase arrivals from SPE shots at the Morenci copper mine. a) Record section of Texan recordings showing *P*- and *S*-wave arrivals. b) Record section filtered to highlight the short-period Rayleigh waves (*Rg*).**

The SPE shots in limestone also generated significant shear-wave motion, as evidenced in Figures 5a and 5b. On the vertical-component "Texan" recordings (Figure 5a), the *P*-wave and *Rg* arrivals are easily identified and are traveling at apparent velocities of 2.7 km/s and 1 km/s, respectively. There are additional arrivals that we delineate

in the figure as possible direct *S*-wave arrivals. The apparent velocity for the phase is ~1.8 km/s. However, we note that tracing the arrival times of this phase back to the origin results in ~1 sec of offset from zero. Some may attribute this delay to near-source scattering, while others may argue that the delay is caused by secondary source effects (e.g., spall or CLVD).

Large amplitude *SH* waves were generated by the SPE explosions (Figure 5b). Similar arrivals have been noted in near-field recordings of nuclear explosions in Kazakhstan (Stevens, 2006) and chemical explosions in Alaska (Leidig et al., 2007). It is interesting to note that the largest amplitude *SH* waves are not associated with the largest yield explosions, but instead are observed in data from blasts in a topographic bench next to a free face.

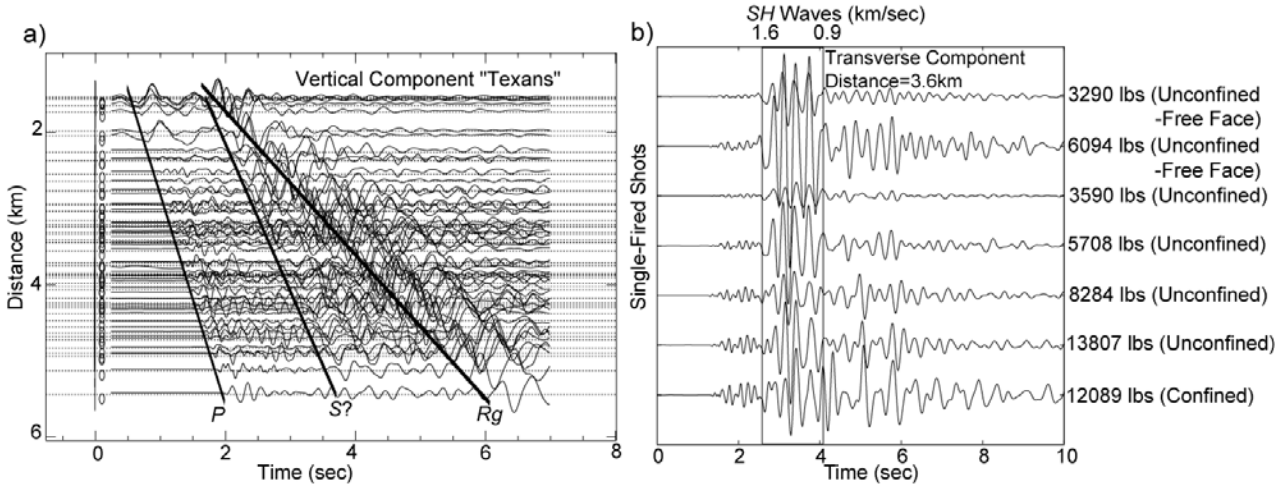


**Figure 5. Phase arrivals from SPE shots at the Black Mesa coal mine in northeastern Arizona. a) Record section of "Texan" recordings showing *P, Rg,* and a possible *S*-wave arrival. b) Transverse component recordings of seven SPE explosions at a single broadband station showing large amplitude *SH* (Love?) arrivals.**

The moment tensors for a free-face shot were shown in Figure 2. Although the amplitude of the $M_{yz}$ component in the 1–6-Hz frequency band is only a small fraction of the amplitude of the isotropic component in the same frequency band for the cast shots, it can generate large-amplitude shear waves. The deviatoric moment-tensor component of an explosive source, the causes of which include the non-spherical geometry of the source, the near-source region medium heterogeneity and/or anisotropy, and the secondary source effects such as CLVD and material cast can be important contributors in shear-wave generation even though the deviatoric component itself may be small. Synthetic seismograms (Figure 6) generated for the moment tensor results shown in Figure 2 show how small anisotropic behavior can generate strong *SH* waves.

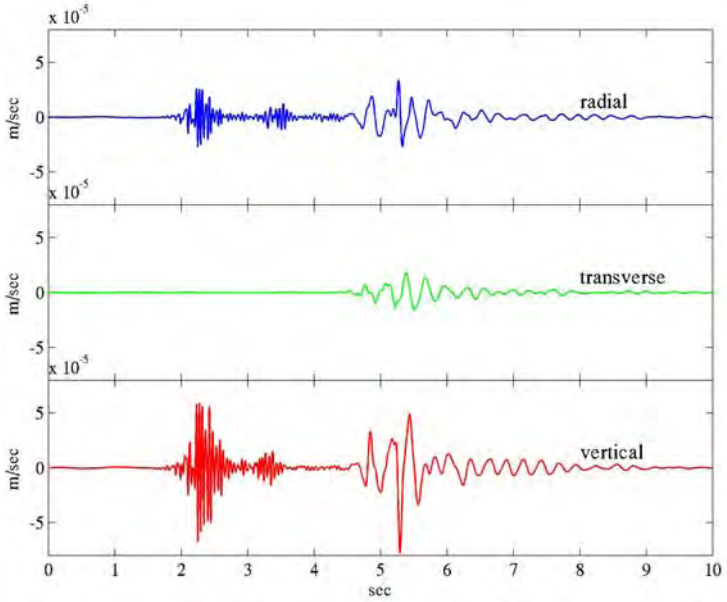


**Figure 6. Synthetic seismograms from the moment tensor shown in Figure 2. Receiver was 5 km from the source and at 0° azimuth from the *x* direction. Notice the large amplitude *SH* waves generated from this moment tensor solution even though the $M_{yz}$ component was not very large (barely perceptible on Figure 2).**

## Numerical Modeling

We are using the detailed velocity and attenuation models derived from the original SPE project coupled with the moment tensors to conduct numerical modeling of recorded near-source, local, and regional seismograms. We are using 1D, 2D, and 3D models, and including topography and stochastic properties of the media in order to quantify possible scattering effects. The goal of this modeling exercise is to determine how much of the local data can be related back to source effects and what characteristics of the local and regional data are due to path effects.

We present preliminary modeling results from the Morenci copper mine. The model (Figure 7) was developed by Kim and Stump (2005) using surface wave inversions and *P*-wave raytracing. The source is located at the origin, although a buffer is placed around the edges of the model during the numerical computations. We computed synthetics for both isotropic and anisotropic explosions documented by the Morenci moment tensor inversion (e.g., Figure 1). The results for the latter are presented in Figure 8 (black) and are compared to observed (red) data. As is expected, we are modeling the onset of *P* and *Rg* very well from these models. It is also interesting to note that the relative amplitudes of *P* and *Rg* in this frequency band (0.5 to 4 Hz) are similar for the observed and synthetic data. When a purely isotropic explosion was used, the relative amplitude ratios were dissimilar due to larger-amplitude P waves.

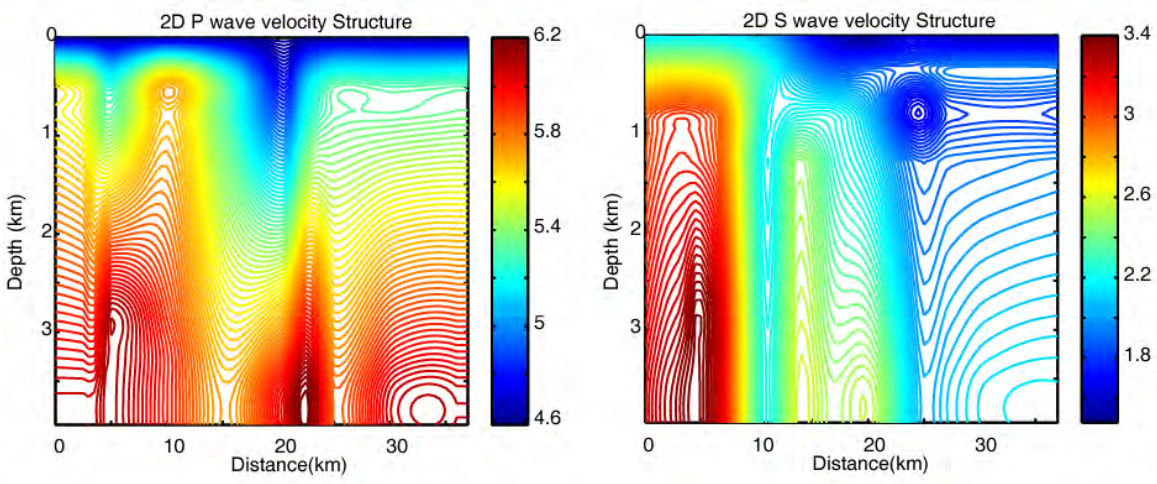


**Figure 7. An example of upper crustal *P*- and *S*-wave velocity structures for the Morenci mine being used in the numerical modeling studies.**

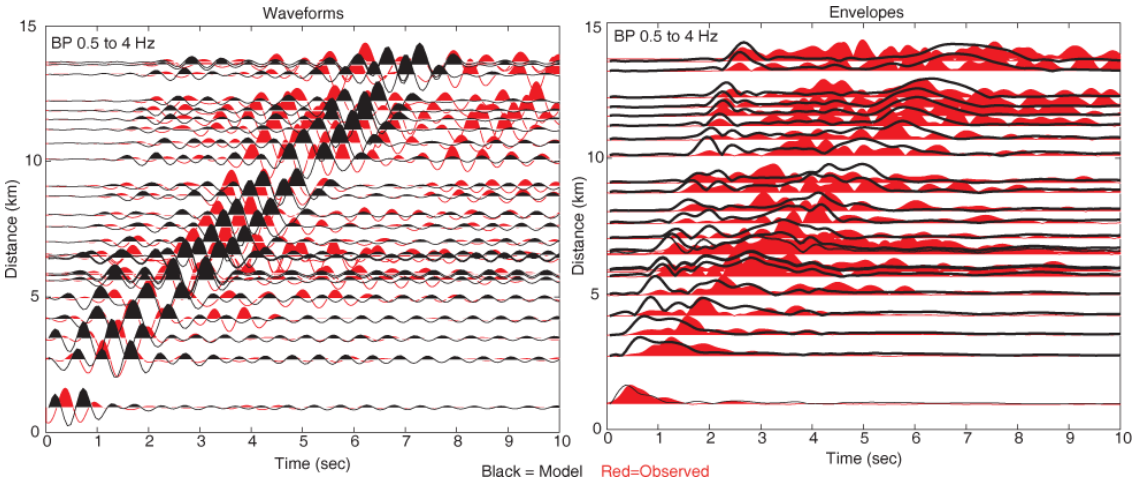


**Figure 8. Preliminary 2D modeling results for the crustal *P*- and *S*-wave velocity model shown in Figure 7. Left graph) Waveforms show our synthetics match some of the observed waveform characteristics. The waveforms were filtered between 0.5 and 4 Hz. Right graph) Envelope functions for the observed (red) and predicted (black) waveforms.**

## CONCLUSIONS AND RECOMMENDATIONS

Explosions recorded during the SPE project in a slow-velocity medium appear to be mainly isotropic under most emplacement conditions, while explosions in a higher-velocity medium are marked by interesting source anisotropy. We are completing analyses to determine the cause of this anisotropy, such as a variation in the damage phenomenology. Synthetic seismograms generated from moment tensors indicate that a small deviatoric component may result in significant shear, particularly *SH*, energy.

We have also initiated studies examining the source of *Rg* and shear waves. Comparing observed *Rg* spectra to synthetic CLVD *Rg* source spectra illustrates that the CLVD source may have played an important role in the explosive source. A delay in the origin time of shear waves from the Black Mesa explosions points to a secondary source such as a CLVD, fracturing, or spall. Similar analyses will continue to be conducted on the NPE data and data from other explosive source projects to aid in development of a comprehensive explosive source model.

## REFERENCES

Denny, M. D., P. G. Goldstein, K. Mayeda, and W. R. Walter (1997). Seismic results from DOE's Non-Proliferation Experiment: A comparison of chemical and nuclear explosions, In *Monitoring a Comprehensive Test Ban Treaty*, edited by E. S. Husebye and A. M. Dainty, 355–364, Kluwer Academic Publishers.

Eisler, J. D. and F. Chilton (1964). Spalling of the earth's surface by underground nuclear explosions. *J. Geophys. Res*. 69: 5285–5293.

Kim, T.S. and B. S. Stump (2005). Upper crustal velocity structure around the Morenci copper mine from *Pg* and *Rg* phases. SPE Final Report. 327 p.

Knopoff, L. and M. J. Randall (1970). The compensated linear-vector dipole: A possible mechanism for deep earthquakes, *J. Geophys. Res*. 75: 4957–4963.

Leidig, M., J.L. Bonner, R. Martin, and K. Murphy (2007). Possible effects of frozen rock on explosive coupling (Abstract). *Seism. Res. Letts*. 78: 252.

Masse, R. P. (1981). Review of seismic source models for underground nuclear explosions, *Bull. Seism. Soc. Am.* 71: 1249–1268.

Patton, H. J. and S. R. Taylor (1995). Analysis of *Lg* spectral ratios from NTS explosions: implications for the source mechanism of spall and the generation of *Lg* waves, *Bull. Seism. Soc. Am.* 85, 220–236.

Patton, H., J. Bonner, and I. Gupta (2005). *Rg* Excitation by Underground Explosions: Insights from Source Modeling the 1997 Kazahkstan Depth of Burial Experiments, *Geophys. J. Int*.

Stevens, J.L. T. G. Barker, S.M. Day, K.L. McLaughlin, N.Rimer, and B.Shkoller (1991). Simulation of teleseismic body waves, regional seismograms, and Rayleigh wave phase shifts using two-dimensional nonlinear models of explosion sources, in AGU Monograph 65, Explosion Source Phenomenology, Taylor, S., H. Patton, P. Richards, editors, ISBN 0-87590-031-3, pp. 239–252.

Stevens, J.L. (2006). Development and Future of Explosion Source Theory, in *Proceedings of the 100th Meeting of the Seismological Society of America*, *Seism. Res. Letts.* **77**: 2, 193.

Stump, B. W. (1985). Constraints on explosive sources with spall from near-source waveforms, *Bull. Seism. Soc. Am.* 75: 361–377.

Walter, W.R., K.M. Mayeda, and H.J. Patton, (1995). Phase and spectral ratio discrimination between NTS earthquakes and explosions, Part 1, Empirical Observations. *Bull. Seism. Soc. Am.* 85: 1050–1067.

# EXPLOSION SOURCE CHARACTERISTICS IN FROZEN AND UNFROZEN ROCK

Jessie L. Bonner[1], Mark R. Leidig[1], Katherine Murphy[1], Sara L. Dougherty[1], and Randolph J. Martin[2]

Weston Geophysical Corp.[1] and New England Research, Inc.[2]

Sponsored by Air Force Research Laboratory

Contract No. FA8718-04-C-0026
Proposal No. BAA04-66

## ABSTRACT

The Frozen Rock Experiment (FRE) was conducted in central Alaska in August 2006 to provide empirical data on seismically-estimated yield from explosions in frozen rock. Laboratory studies have demonstrated that frozen rock is significantly stronger than unfrozen rock, and it has been hypothesized that this increased strength, due to ice in the pores and cracks, can alter seismic yield. Central Alaska has abrupt lateral boundaries in discontinuous permafrost, and we detonated 3 shots in frozen, saturated rock and 3 shots nearby in unfrozen, dry rock ranging in size from 200 to 350 lbs. Approximately 125 accelerometers and seismometers were deployed specifically for this experiment at distances of 10 m to over 20 km. During the past year, we have conducted various studies (moment tensors, magnitudes, etc.) to characterize the explosions in frozen and unfrozen rock.

In order to conduct moment tensor inversions, a velocity and an attenuation model are required. We initially developed a 1-D model for central Alaska but found that the model could not account for azimuthally dependent velocities and did not explain observed surface-wave arrival times. We are currently developing a 3-D "block" velocity model using full waveform modeling in order to improve the preliminary moment tensor results. To develop an attenuation model for the upper crust of central Alaska, spectral amplitudes of *Rg* were extracted from complex waveforms using phase match filtering. The *Rg* amplitudes were then corrected for geometric spreading and regressed against distance to determine the attenuation coefficients at each period, which were then converted to $Q_{Rg}$ using the group velocity dispersion curves. We developed the relationship $Q_{Rg}(f) = 12.5f^{-0.39}$. When the attenuation coefficient data were inverted, *Q* values of less than 20 were required in the upper kilometer of the central Alaskan crust.

To model the sources, the *in-situ P*- and *S*-wave velocities of the frozen and unfrozen rock test sites were input into the Mueller-Murphy (MM; 1971) source model. The resulting source models predict that the explosions at the faster, frozen rock site should have a higher corner frequency ($f_c$~15 Hz) than an equivalent explosion at the slower, unfrozen site ($f_c$~10.5 Hz). MM also predicts a small overshoot to the explosions at the frozen rock site. Examinations of the observed spectra from the explosions match both the $f_c$ and overshoot predictions. The MM model predicts that the frozen-rock explosions should have slightly larger amplitudes at frequencies less than $f_c$; however, the observed data show that the amplitudes are approximately equivalent in this bandwidth. Denny and Johnson (1991) was used to predict $M_w$s for the explosions, and the resulting values closely matched the observed $M_w$s obtained from surface wave spectral amplitude modeling. Our results show that MM and Denny and Johnson (1991) source theories do an excellent job of modeling these small explosions when the *in-situ P*- and *S*-wave velocities of frozen and unfrozen rock are considered.

The *laboratory-determined P*- and *S*-wave velocities of the frozen and unfrozen rock test sites were used in the MM source model; however, the predicted corner frequencies were much higher than the observed data. The lab velocities are more indicative of deeper emplacement depths where there are fewer fractures and where any effect of the ice is predominantly-porosity related. We modeled a 1 kiloton explosion at a depth of 122 meters using the lab-determined velocities for frozen and unfrozen saturated rocks and found less than a 0.05 magnitude unit (m.u.) difference in their $M_w$s (unfrozen had larger $M_w$), which agrees with Rautian and Khalturin (2003), who observed less than 0.1 m.u. difference for explosions in the former Soviet Union in frozen and unfrozen media.

## OBJECTIVES

The consortium of Weston Geophysical, New England Research, and the University of Alaska, Fairbanks, conducted the Frozen Rock Experiments (FRE) in central Alaska to characterize the variations in ground motion scaling and coupling for explosions in frozen and unfrozen rock. We recorded the explosions on arrays of near-source and local stations deployed specifically for the experiment. The results are being interpreted to help understand possible biases in the estimation of seismic yield from explosions in frozen rock.

## RESEARCH ACCOMPLISHED

### Experiment Background

A critically important aspect of nuclear test monitoring is yield estimation. United States monitoring agencies must be able to accurately estimate yields for nuclear explosions detonated in regions of monitoring concern. If frozen-rock emplacement conditions create a circumstance favorable for biased yields, data must be available such that any bias can be accounted for when the yield is estimated. Prior studies (Mellor, 1971) have established that frozen-rock properties are considerably different from unfrozen-rock properties. Moreover, it has been hypothesized that these altered properties may be sufficient to cause significant variations in seismic coupling, which in turn, significantly alters seismic yield estimates.

Sammis and Biegel (2004) noted that an increase in low-temperature uniaxial strength is related to the ice in the initial pores and cracks. The ice increases the apparent coefficient of sliding friction on these initial cracks. Since the strengthening is strain-rate dependent, for nuclear explosions the full strengthening should occur in a small range near 0 °C. Increasing the seismic velocity and/or rock strength would cause reduced seismic amplitudes in the far-field for explosions in frozen rock, which would result in an underestimated yield.

### Experimental Setting

The objective of our project was to conduct nearly co-located explosions in frozen and unfrozen crystalline rock. To find a possible location for the experiment, we consulted the permafrost map of Alaska (Ferrians, 1965) for regions of discontinuous permafrost. One such location with frozen and unfrozen rock was a gold mine located 25 km north of Fairbanks, Alaska; however, test boreholes at this location proved that there was less than a 0.2°C difference between the unfrozen and frozen test sites (e.g., -0.1°C and +0.1°C, respectively). Discussions with property owners, miners, and drillers familiar with the ice stratigraphy in the region suggested that better sites with larger temperature contrasts were available for our study. One site that a local landowner proposed was in the Goldstream Valley, which is approximately 10 km north of Fairbanks, near the town of Fox, Alaska.

Gold was first discovered in the Fairbanks area in 1902 in the northern extents of Goldstream Valley. As a result, much of the Quaternary gravels and surficial deposits (Figure 1) that comprise the valley floor have been reworked with dredges through placer mining. One section that had not been dredged previously was an active gold mine with a working face that offered a cross-section of the geology in the valley floor. The top layer consisted of 5 meters of organic-rich, fine-grained glacial silt that had massive ground ice. This was followed by 5 meters of frozen gravels that overlie Paleozoic/Precambrian-aged quartz-pelitic schist, which the mine operators insisted was frozen based on how hard it was to “rip” for placer gold mining. The valley floor and mine pit are behind the shadow cast by the south rim of the valley for much of the year, allowing virgin ground to remain frozen and the reworked dredge piles to often refreeze. The gravels and frozen rocks in the valley grade into unfrozen, dry bedrock on its northern rim. Because this is a south-facing hill that receives plenty of sunlight throughout the year, it is not frozen. This is typical for this region of discontinuous permafrost in interior Alaska, where south-facing hills are unfrozen while north-facing slopes and valleys are typically frozen.

**Thermal Characterization in Goldstream Valley.** Test boreholes were drilled to a depth of 10 meters at the proposed frozen and unfrozen rock explosion sites. Each borehole was filled with 1.5-inch-diameter PVC pipe capped on both ends, backfilled with drill cuttings, and allowed to thermally equilibrate for 5–7 days. Vladimir Romanovsky at the University of Alaska, Fairbanks, installed thermistors in each hole allowing the temperatures to be measured at 1-meter depth intervals.

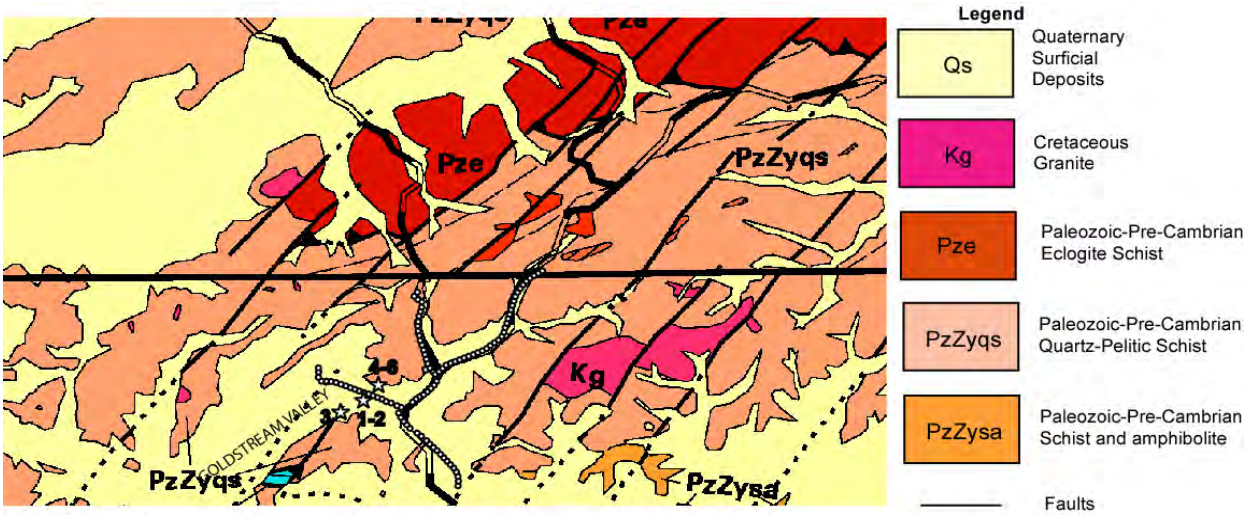


Geologic Map: Wilson *et al.*, 1998.

**Figure 1. Geologic map of the Frozen Rock Experiment test sites. The white stars show the location of the small explosions in frozen (1–3) and unfrozen (4–6) rock. Small white circles positioned on the roads near the test site represent geophones deployed to record the experiment (Map from Wilson et al., 1998).**

With the exception of seasonal thawing in the top meter, the proposed frozen test site (Shots 1–2) is below freezing, approaching a temperature of -1.35°C at the depth of explosives emplacement (approximately 8 meters). At the unfrozen test site, the rocks are above freezing at all depths in the borehole with a temperature at emplacement depth of +2.34°C. The relative differences between the temperatures at the frozen and unfrozen sites were larger, and the magnitude of the frozen-rock temperature colder than other sites we had examined during the experiment planning. Additionally, ice was visible in the fractures of the frozen rock at this location.

**Laboratory Velocity Analysis.** Rock samples from the test sites were sent to New England Research, Inc., for analysis. The physical rock properties of each sample were measured both saturated and dry at room temperature, and then the measurements were performed again when the samples were chilled to below -8 °C. Seismic velocities obtained from the laboratory analysis are presented in Figure 2.

Due to an unmapped metamorphic facies change between the two test sites, there are compositional differences in core samples taken from each test site as observed in thin section analyses (Figure 3). The rocks both have the same quartz, plagioclase, and mica matrix, which is foliated by the metamorphism. The grade of metamorphism is different with the unfrozen test site rock being schistose, while the frozen test site bedrock was gneissic (as will be so referenced for the rest of this paper). The difference in composition between the two samples are the large garnets observed in the unfrozen test site sample while only smaller garnets are observed in the frozen-rock sample.

Laboratory velocity analyses of these rocks (Figure 2) show that the differences in the mineral composition do not cause significant changes in the *P*- and *S*-wave velocities of the two samples. When the core samples from both test sites are saturated and cooled to -8°C, the *P*-wave velocity for the unfrozen test site sample—with large garnets—is approximately 0.1 km/s faster (e.g., 5.8 vs. 5.7 km/s) than the frozen test site sample at a wide range of confining pressures. At room temperature, the *P*-wave velocities for both saturated samples are similar (e.g., 5.4 vs. 5.2 km/s). Given that the unfrozen test site was dry, we also estimated the laboratory *P*- and *S*-wave velocities of a dry, unfrozen schistose sample, which was considerably slower at 4.1 and 2.8 km/s, respectively. All of these velocities are compiled in Table 1.

***In Situ* Velocity Analysis.** We conducted shallow geophysical investigations of both test sites. We used a 60-channel Geometrics system connected to a *P*-wave source recorded on three-component Mark-4 geophones. We picked the first breaks and inverted them for velocity structure for each test site. At the frozen test site, for which the working mine pit offers visual confirmation of the stratigraphy, we resolved the frozen gravel, which is highly

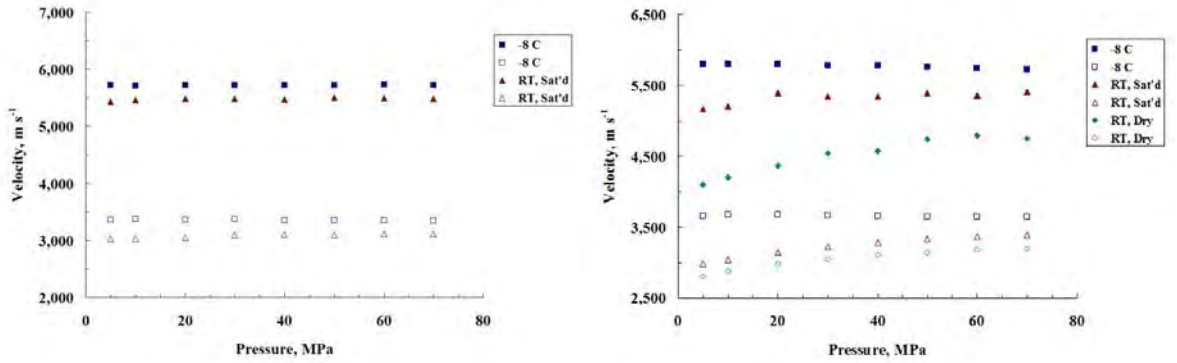


**Figure 2. *P*- and *S*-wave velocity estimates when the frozen test site rock sample (left) and unfrozen test site rock sample (right) were frozen (-8°C) and unfrozen (RT) in laboratory settings. Because the second test site was dry, we also include the lab-based velocities of the rock when unsaturated.**

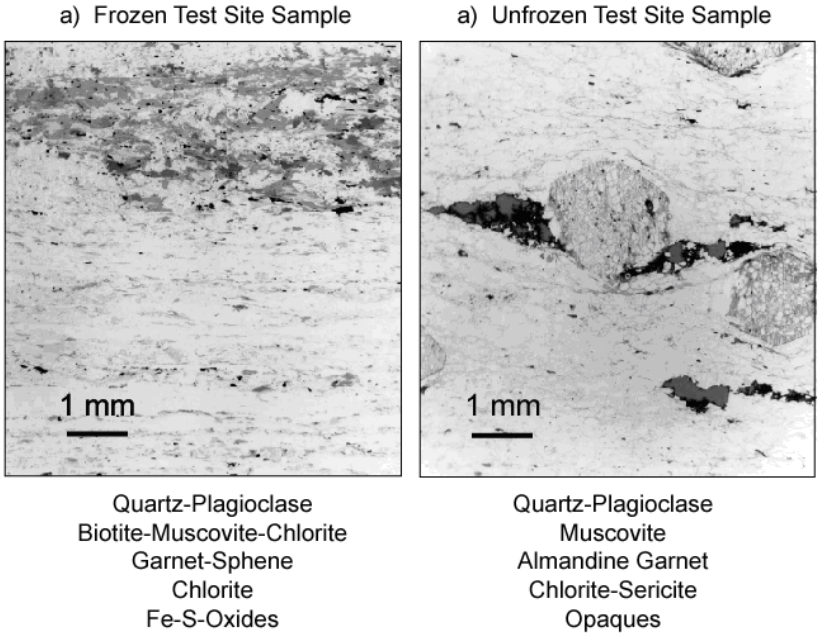


**Figure 3. Photomicrographs of core samples from the (a) frozen and (b) unfrozen rock test sites with the mineralogical constituents.**

**Table 1. Summary of Seismic Velocities for the Emplacement Media**

| Media | Laboratory | | *In Situ* | |
|---|---|---|---|---|
| | $V_p$ | $V_s$ | $V_p$ | $V_s$ |
| Gneiss: Frozen | 5.7 | 3.3 | 3.7 | 1.6 |
| Gneiss: Unfrozen | 5.4 | 3.0 | | |
| Schist: Frozen | 5.7 | 3.6 | | |
| Schist: Unfrozen | 5.2 | 3.0 | | |
| Schist: Unfrozen and Dry | 4.1 | 2.8 | 2.0-2.6 | 1.0-1.2 |

variable with *P*-wave velocities ranging from 1.6–2.5 km/s, and the fast bedrock (3.7 km/s). At the unfrozen test site, the dry bedrock *P*-wave velocity is only 2–2.6 km/s, and there was a velocity change near the middle of the explosives column with slower velocities above the bedrock. While drilling the boreholes at the unfrozen test site, we observed abrupt changes in the penetration rate at similar depths to our inverted interfaces.

We did not have direct *S*-wave refraction data, thus we attempted to invert the ground roll dispersion curves for each test site. The frozen test site shear-wave velocity is considerably faster than the unfrozen test site, with ground roll velocities ranging from 1.18 to 1.8 km/sec. The dispersion observed at the unfrozen test site is relatively flat and only ranges between 0.82 and 1.19 km/sec. Inversion of these dispersion curves (Herrmann, 2008) provided estimates of the shear-wave velocities at the depth of explosion emplacement of 1.6 km/sec and 1.0–1.2 km/sec for the frozen and unfrozen test sites, respectively.

**Explosion Detonation**

We detonated 6 explosions at the Goldstream Valley test sites on 24–26 August 2006. The yields ranged from 100 to 359 lbs of ammonium nitrate fuel oil (ANFO) explosives. Shots 1 (200 lbs), 2 (350), and 4 (200), 5 (350), and 6 (100) were all detonated in 10-meter boreholes loaded with at least 5 meters of stemming. Shot 3 (359) was detonated in a 15 meter borehole in frozen gravels. Because the event was the last shot on the first day, for safety reasons, we eliminated all unused boosters resulting in the increased yield as compared to Shots 2 and 5.

**Explosion Source Modeling**

Figure 4 provides an interesting snapshot of the differences in seismic waves produced by explosions in frozen-saturated and unfrozen-dry rock. The paths from the sources to this station at an epicentral distance of 22 km are essentially the same; thus the factor of 3 difference in the observed amplitudes is most likely related to coupling effects in the emplacement media. We note that the smaller amplitudes for the unfrozen shots were contrary to the expected result. The theory had suggested that the increased strength of the frozen-rock media would create smaller amplitudes on the seismic phases. The questions we had to answer were whether the observed differences were related to frozen vs. unfrozen effects and/or frozen vs. unfrozen-dry effects.

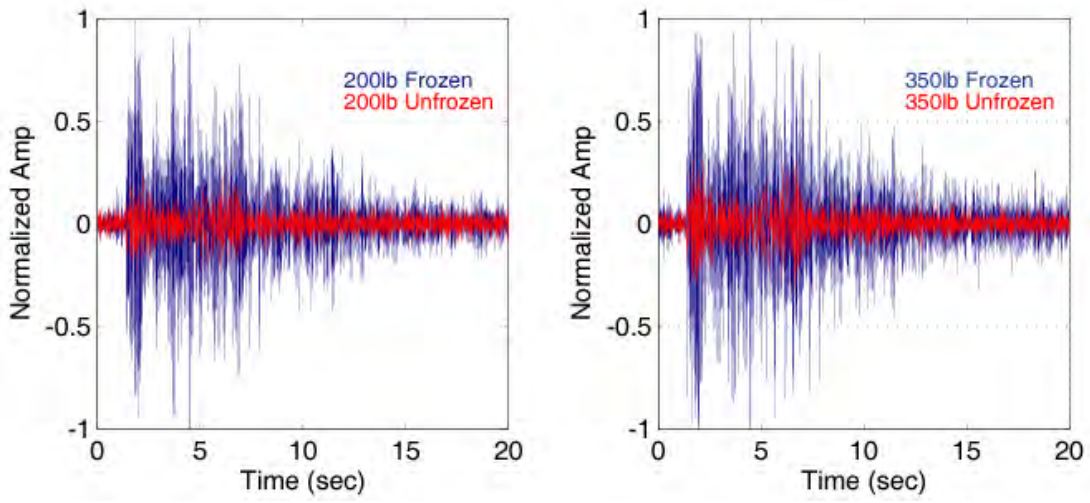


**Figure 4. Seismic waves from explosions in frozen and unfrozen rock recorded at a distance of 22 km from the explosions.**

To answer these questions, we attempted to model the observed spectra for the frozen and unfrozen test-site shots using the Mueller and Murphy (1971; MM71) explosion source model. MM71 was empirically developed based on nuclear explosions at the Nevada Test Site (NTS). It has been successfully applied to nuclear explosions at other test sites, mining explosions (Yang, 1997), and confined chemical explosions (Stump et al., 1999; Stump et al., 2003; Hooper et al., 2006). For our first attempt, we generated MM71 explosion-source spectra using the laboratory

velocities estimated from core samples (Table 1). The corner frequencies estimated for our small explosions with these fast laboratory velocities (e.g., $P$ > 4.1 km/s and $S$ > 2.8 km/s) were greater than 20–30 Hz for both test sites and did not offer a match to our observed data.

Next, we incorporated our in situ *P*- and *S*-wave velocities into the MM71 source and observed an improved correlation between the observed and theoretical spectra at near-source distances (Figure 5). The resulting source models predict that the explosions at the faster, frozen rock site should have a higher corner frequency ($f_c$~15 Hz) than an equivalent explosion at the slower, unfrozen site ($f_c$~10.5 Hz). MM71 also predicts a small overshoot to the explosions at the frozen-rock site. Examinations of the observed spectra from the explosions match the $f_c$ and overshoot predictions, although the predicted amplitude of the overshoot is smaller than observed. The MM71 model predicts that the frozen rock explosions should have slightly larger amplitudes at frequencies of less than $f_c$; however, the observed data show that the amplitudes are approximately equivalent in this bandwidth.

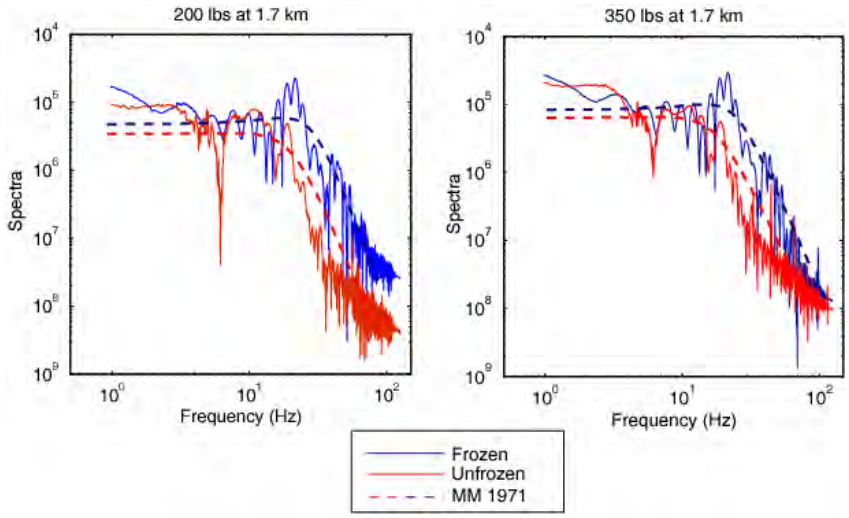


**Figure 5. Comparison of observed spectra (at 1.7 km) from explosions in frozen (blue) and unfrozen-dry (red) rock. Also shown are predicted MM71 reduced-velocity potential (RVP) spectra modeled from the *in situ* velocities at each test site.**

**Remaining Questions**

***What if the unfrozen test site had been saturated?*** We were unable to locate a saturated and unfrozen test site in hard rock within 20 km of our frozen, hard-rock site; thus an experimentally-confirmed answer to this question is unavailable at this time. Given how well the MM71 spectra modeled the observed data, we attempted to simulate the velocities at the unfrozen test site as if it had it been saturated. To do so, we enlisted the help of an excellent resource from Tatyana Rautian and Vitaly I. Khalturin entitled "Permafrost and Seismic Efficiency of Explosions," which was handed to us at the 2008 Seismological Society of America meeting by Dr. Paul Richards. It is a wonderful reference concerning frozen rock, including permafrost depths in the former Soviet Union, a summary of laboratory studies of frozen rock, aspects of explosive coupling, and attenuation in frozen media. It was compiled in 2003.

One of the studies highlighted in Rautian and Khalturin (2003) was by Dzhurik (1983), who studied the *in situ* seismic velocities in frozen and unfrozen hard rock (metamorphic and igneous) in East Siberia. Dzhurik used a hammer drop and geophones with far offsets of 200 meters to study *P*-and *S*-wave velocities in the upper 10 meters (appropriate for our test site). Using hundreds of measurements, Dzhurik was able to develop $V_p/V_s$ relationships for frozen-saturated, unfrozen-saturated, and dry-unfrozen rock (Figure 6). We plotted our two datapoints on Dzhurik's results, and then used the relationship for unfrozen- saturated rock ($V_p$=1.7+1.06$V_s$) to predict a range of possible velocities for our test site, had it been saturated. This interpretation is obviously no substitute for empirical explosion data; however, it may provide us with information to determine the feasibility of returning to Alaska for explosions in saturated-unfrozen rock

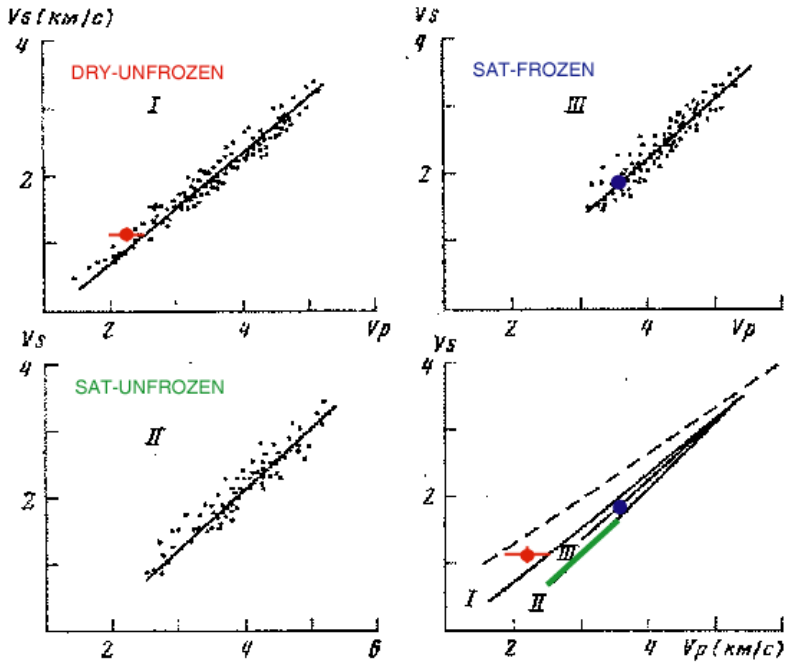


**Figure 6. $V_p/V_s$ ratios for frozen and unfrozen rock in Siberia (from Dzhurik, 1983). We plotted the *in situ* velocities of our test sites on these empirical relationships. We then used the linear relationship for II between our two data points to estimate the effect of saturation on our unfrozen test site (green line in lower-right subplot).**

Figure 7 shows the MM71 source RVP spectra for our two different test sites. Also shown are a series of predicted—based on the work of Dzhurik—RVP spectra, assuming that the unfrozen test site had been saturated. These RVP spectra suggest that saturated and unfrozen rock could have produced larger amplitude signals at frequencies below the corner frequency.

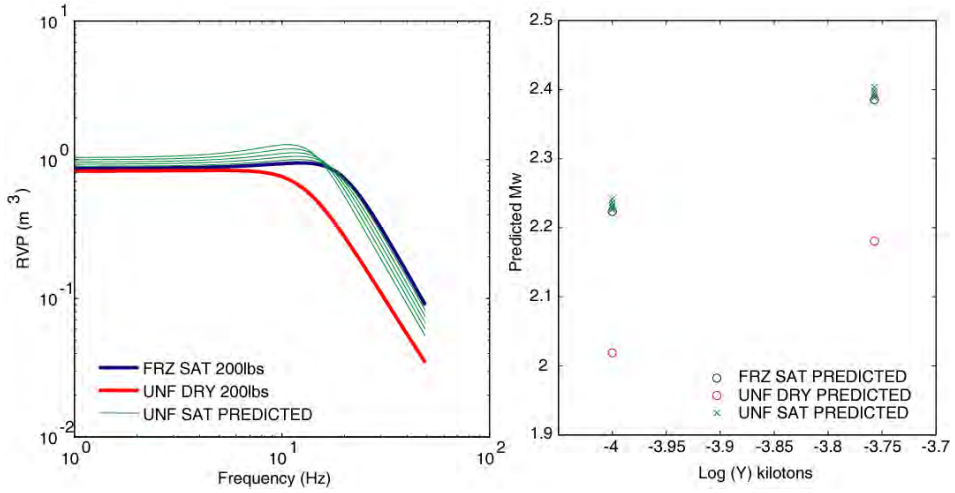


**Figure 7. (Left) RVP spectra for the frozen (blue) and unfrozen-dry (red) test site explosions in the Goldstream Valley. Also shown are possible RVP spectra, assuming the relationships of Dzhurik (1983) for unfrozen-saturated rock (green). (Right) Predicted moments (Denny and Johnson, 1991) for explosions in the various media.**

Denny and Johnson (1991) developed a model for the measured seismic moment ($M_o$) of explosions,

$$M_o = \frac{1}{311} M_t P_o^{0.3490} 10^{-0.0269GP}, \qquad (1)$$

where $GP$ is gas porosity and $P_o$ is overburden pressure ($P_o=\rho gh$). $M_t$ is the theoretical moment and is defined as

$$M_t = \frac{4}{3}\pi\rho\alpha^2 R_c^3, \qquad (2)$$

where $\alpha$ is the $P$-wave velocity and $R_c$ is the cavity radius estimated by:

$$R_c = \frac{1.47x10^4 Y^{\frac{1}{3}}}{\beta^{0.3848} P_o^{0.2625} 10^{0.0025GP}}. \qquad (3)$$

From the equations above, we can see that the measured moment for explosions in the Denny and Johnson (1991) model depends on the $P$-wave and $S$-wave ($\beta$) velocities and yield (Y). We used Equations 1–3 to estimate moment magnitudes ($M_w$) for the frozen and unfrozen rock explosions in Goldstream Valley. We then compared them to the moments obtained from spectral modeling of the surface wave amplitudes and found an almost 1:1 relationship between predicted and observed $M_w$. When the same techniques were applied to the possible saturated and unfrozen test site velocities from Dzhurik's (1983) data, the $M_w$s are not as large as expected (Figure 7; right). The $M_w$ would have probably been less than 0.1 magnitude unit larger had the unfrozen test site been saturated.

***How would this translate to a 1 kiloton explosion?*** It is beyond the scope of this project to try and predict the differences between a nuclear and chemical explosion in terms of the non-linear reactions and changes of state in frozen media. However, our successes with MM71 at modeling the near-source small explosion data could provide a valid framework to predict the spectra and moments for larger explosions (e.g., 1 kiloton at 122 meters depth) in permafrost. Since a larger explosion is likely to be buried deeper in less-fractured media, the laboratory velocities determined by New England Research (Table 1) were input in MM71 to model the emplacement media. The resulting reduced displacement potentials (RDP) for all five possible laboratory velocity combinations in Table 1 are presented in Figure 8. We see similar relative positioning of the potentials for frozen and unfrozen media as observed for the *in situ* velocities (Figures 5 and 7).

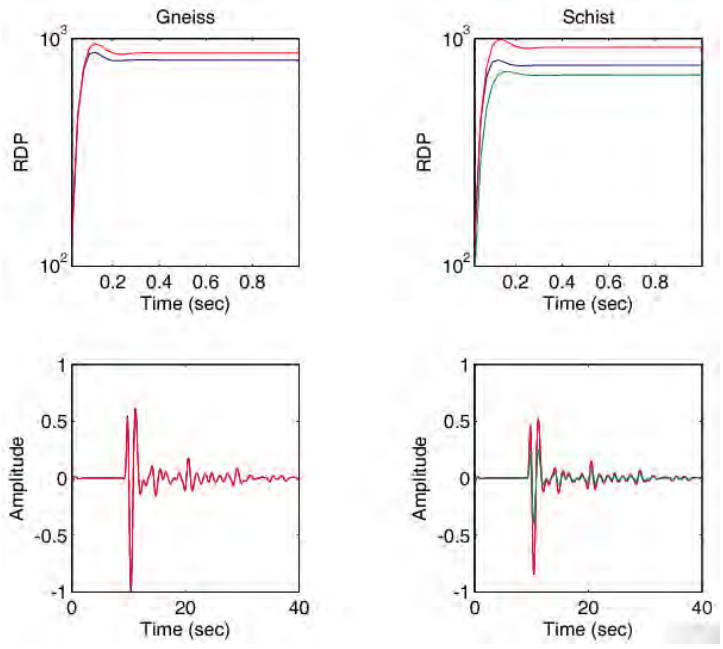


**Figure 8. (Top) Reduced displacement potentials (RDP) for a 1 kiloton explosion at 122-m depth for all five possible laboratory *P*- and *S*-wave velocity combinations in Table 1. (Bottom) Synthetic seismograms resulting from the convolution of the RDPs with teleseismic explosion Green's functions generated by Robert Herrmann's new Hudson96 program.**

Dr. Robert Herrmann generated teleseismic explosion Green's functions using his new Hudson96 modeling software (Herrmann, 2008) that were convolved with the RDPs in Figure 8 to produce synthetic seismograms. We then estimated $M_w$s using Denny and Johnson (1991) and $m_b$s using the synthetic *P*-wave amplitudes and

$$m_b = \log (A/T) + Q (D, h) , \qquad (4).$$

where Q (D, h) was obtained from the Veith-Clawson (1972) curves. The results presented in Figure 9 predict very small differences in magnitudes for frozen and unfrozen saturated rock explosions based on the MM71 model and laboratory velocities for gneiss and schist.

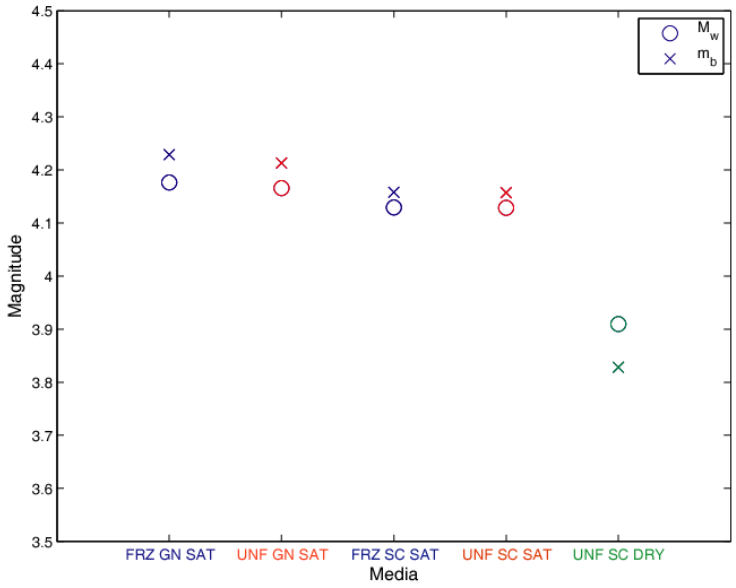


**Figure 9. Predicted $M_w$ and $m_b$ magnitudes for a 1 kiloton explosion in frozen and unfrozen gneiss (GN) and schist (SC) based on the MM71 source and teleseismic explosion Green's functions.**

***How do our results compare with Rautian and Khalturin?*** Our results suggest that there may not be significant magnitude variations between explosions detonated in frozen and unfrozen gneiss and schist as long as both are saturated. Rautian and Khalturin (2003) also attempted to address the possible coupling differences between explosions in frozen and unfrozen rock. First, they studied 23 Peaceful Nuclear Explosions (PNEs) that were detonated in permafrost regions. These included 8 in permafrost and 15 at depths below the base of the permafrost. They determined that the PNEs detonated in permafrost were about 0.1 magnitude unit larger than the shots below the permafrost. After considering the effects of depth, they report that "these data evidenced, that anyway, the permafrost does not affect seriously on magnitude effectiveness."

They also studied the nuclear explosions at Novaya Zemlya, but offered the surprising conclusion that most of the underground nuclear tests there were detonated deeper than the base of the permafrost. They determined that magnitude deviations between shots in and below the permafrost varied only between -0.01 and +0.04. They wrote, "so, again, there is no notable difference in magnitude efficiency, caused by permafrost."

Rautian and Khalturin (2003) also studied attenuation in frozen rocks as a possible source of amplitude bias. They concluded that the "frozen state of rock approximates its properties (velocities, moduli, strength) to that of hard rock (granite or so). It means, there is no reason to expect the high energy loss if the non-linear attenuation zone is in permafrost."

## CONCLUSIONS AND RECOMMENDATIONS

The Frozen Rock Experiment provides a unique dataset from small, nearly co-located explosions in frozen and unfrozen metamorphic rocks for which we have detailed laboratory and *in situ* characterizations of the emplacement

media. The characteristics of the explosions (corner frequency, overshoot, and isotropic moments) are modeled very well using the in situ velocity characteristics of the emplacement media and both the Mueller and Murphy (1971) and Denny and Johnson (1991) source models. The primary reason behind the differences in the explosions is related to the dry versus saturated-frozen emplacement media. Using Dzhurik's (1983) relationships between $V_p$ and $V_s$ for Siberian hard rock media, we predict a very small increase in amplitudes from the unfrozen-rock explosions had the media been saturated as compared to the frozen-rock explosions. Incorporating the laboratory velocities of our test site media into the Mueller-Murphy source, we predict little or no $m_b$ bias for explosive coupling in frozen and unfrozen media—unless the unfrozen media is dry. These results agree with Rautian and Khalturin (2003) who found no "notable" difference in magnitude efficiency for explosions detonated in permafrost.

## ACKNOWLEDGMENTS

We thank the following people for help on various aspects of this project: John Reeves, Aaron Ferris, James Britton, Jim Lewkowicz, Willie Zamora, Mike Johnson, Noel Barstow, Stephen Brown, Vladimir Romanovsky, Bob Grove, Roger Hansen, Dan May, Brenda and Stephen Birdsall, Dennis Conchlin, Bill Swan, John Betancour, Rich Schult, Anton Dainty, Robert Reinke, Yefim Gitterman, and last, but certainly not least, Robert Herrmann.

## REFERENCES

Denny, M. D. and L. R. Johnson (1991). The explosion seismic source function: model and scaling laws revisited, in H. J. Patton and P. G. Richards, Eds., Explosion Source Phenomenology, *Geophysics Monograph* 65, American Geophysical Union, Washington, pp 1–24.

Dzhurik, V. I. (1983). Issledovaniye uprugikh parametrov talykh i merzlych skal'nykh gruntov, *Inzhenernaya Geologiya* 1983(3): 45–54.

Ferrians, O. J, (1965). Permafrost map of Alaska: U.S Geological Survey Miscellaneous, *Geologic Investigations* Map I-445.

Herrmann, R. B. (2008). Computer Programs in Seismology software. St. Louis University.

Hooper, H., J. Bonner, and M. Leidig, (2006). Effects of confinement on short-period surface waves: observations from a new dataset. *Bull. Seism. Soc. Am*. 96: 697–712.

Mellor, M. (1971). Strength and deformability of rocks at low temperatures, Hanover, NH, Cold Regions Research and Engineering Laboratory (CRREL), U. S. Army Corps of Engineers, Research Report 294.

Mueller, R. A., and J. R. Murphy (1971). Seismic characteristics of underground nuclear detonations: Part I, Seismic scaling law of underground detonations, *Bull Seism. Soc. Am*. 61: 1675.

Rautian, T. G. and V. I. Khalturin (2003). Permafrost and seismic efficiency of explosions.

Sammis, C. and R. Biegel (2004). Mechanics of strengthening in crystalline rock at low temperatures: a preliminary assessment, in *Proceedings of the 26th Seismic Research Review: Trends in Nuclear Explosion Monitoring*, LA-UR-04-5801, Vol. 2, pp. 475–484.

Stump, B. W., D. C. Pearson, and R. E. Reinke, (1999). Source comparisons between nuclear and chemical explosions detonated at Rainier Mesa, Nevada Test Site. *Bull. Seism. Soc. Am.* 89: 409–422.

Stump, B. W., D.C. Pearson, and V. Hsu, (2003). Source scaling of contained chemical explosions as constrained by regional seismograms. *Bull. Seism. Soc. Am*. 93: 1212–1225.

Veith, K. F., and G. E. Clawson (1972). Magnitude from short-period *P*-wave data, *Bull. Seism. Soc. Am*. 62: 435–452.

Wilson, F.H., J. H. Dover, D. C. Bradley, F. R. Weber, T. K. Bundtzen, and P. J. Haeussler (1998). Geologic Map of Central (Interior) Alaska. *U.S. Geological Survey Open-File Report OF 98-133-A*: http://pubs.usgs.gov/of/1998/of98-133-a/

Yang, X., (1997). Mining explosion and collapse source characterization and modeling with near-source seismic data. Ph.D. Thesis, Southern Methodist University, Dallas, Texas.

# IMPROVING $M_s$ ESTIMATES BY CALIBRATING VARIABLE-PERIOD MAGNITUDE SCALES AT REGIONAL DISTANCES

Jessie L. Bonner[1], Robert B. Herrmann[2], Michael E. Pasyanos[3], Harley Benz[4], and David G. Harkrider[1]

Weston Geophysical Corporation[1], St. Louis University[2],
Lawrence Livermore National Laboratory[3], and the United States Geological Survey[4]

Sponsored by National Nuclear Security Administration

Contract Nos. DE-AC52-04NA25547[1,2] and DE-FC52-06NA27320[3]
Proposal No. BAA04-63

## ABSTRACT

During the final year of our project, we have calibrated the use of surface-wave magnitudes ($M_s$), measured at regional distances as a rapid and robust estimator of seismic moment. We have used the Russell (2006) variable-period surface-wave magnitude formula to convert $M_s$ to seismic-moment magnitude, $M_w$, at local to regional distances using global datasets. In this pilot study, the Russell $M_s$ technology was applied to 169 North American events with $3.2 < M_w < 6.5$ at distances ranging from 48 to 5,268 km. The technique uses a time-domain magnitude estimation procedure that employs zero-phase Butterworth filters to effectively measure Rayleigh-wave Airy phase amplitudes at local and near-regional distances (e.g., < 1000 km). This allows for surface wave magnitudes to be estimated within minutes of the initiation of a seismic event. Of the 7,370 event-station pairs, more than half (4,051) of the measurements were at distances < 1,000 km.

The $M_s$ estimates were regressed against moment magnitudes ($M_w$) estimated from *P*-wave modeling and/or Rayleigh- and Love-wave spectral amplitudes (Herrmann et al., 2008). $M_w$ can be estimated using the relationship: $M_w = 1.951 + 0.649\, M_s$. The observed scatter in the estimated $M_w$ was approximately ±0.2 magnitude units. The residuals between true and $M_s$-predicted $M_w$ have a definable faulting mechanism effect, especially when strike-slip events are compared to those with other mechanisms. Preliminary results suggest that our $M_s$:$M_w$ relationship for North America is also transportable to the Middle East and the Korean Peninsula.

We have also determined a methodology to estimate the $M_s$ detection thresholds for the Russell formula. Broadband noise estimates for any seismic station, which are typically in units of acceleration $m^2/s^3$ and decibels, can be converted to nanometers (nm) and input into the Russell equation for variable-period surface waves. We propagate these noise estimates at periods (T) between 8 and 40 s to distances ($\Delta$) between 1 and 40 degrees. The $M_s(T,\Delta)$ were estimated and contoured providing the optimal detection threshold for each station. We have estimated the $M_s(T,\Delta)$ for the stations of the Global Seismographic Network (GSN) using broadband noise estimates supplied by Berger et al. (2004).

## OBJECTIVES

Developing a methodology for calculating surface wave magnitudes that is valid at both regional and teleseismic distances, applicable to events of variable sizes and signal-to-noise ratios, calibrated for variable structure and propagation, and easy to automate in an operational setting, is an important monitoring goal. Our objectives are to create such a methodology, and to use it to lower $M_s$ estimation and detection thresholds. We hope that the method will provide a seamless tie between $M_s$ estimation at regional and teleseismic distances.

To accomplish our objectives, we developed the Matlab program EVALSURF (Bonner et al., 2006), which estimates variable-period (8 < T < 25 s; recently updated to 40 s) Rayleigh-wave magnitudes using the Russell (2006) and $M_s$(VMAX) measurement technique (Bonner et al., 2006) for comparison to the historical formulas of Marshall and Basham (1972) and Rezapour and Pearce (1998). The program uses the updated Lawrence Livermore National Laboratory group velocity models for Eurasia (Pasyanos, 2005) to identify, phase match filter, and extract the fundamental-mode Rayleigh waves for analysis. During the past year, we calibrated the use of surface wave magnitudes ($M_s$), measured at regional distances as a rapid and robust estimator of seismic moment. We have also determined a methodology to estimate the $M_s$ detection thresholds for European and Asian Global Seismographic Network (GSN) stations.

## RESEARCH ACCOMPLISHED

### Surface Wave Magnitudes

Many surface wave magnitude scales have been developed during the past century. They have either been based on empirical (Gutenberg, 1945; Vaněk et al., 1962; Marshall and Basham, 1972) or theoretical (Rezapour and Pearce, 1998; Stevens and McLaughlin, 2001) aspects of Rayleigh-wave propagation. Knowing how and when to apply these formulas has often been confusing, as some of these formulas were developed strictly for ~20-second surface waves at teleseismic distances. Others were developed for regional and teleseismic distances and variable periods (> 10 s). What was needed was a seamless relationship between estimating $M_s$ at regional and teleseismic distances for events of a wider range of magnitudes.

Russell (2006) addressed this need by developing a time-domain method for measuring surface waves with minimal digital processing, using zero-phase Butterworth filters. The method can effectively measure surface-wave magnitudes at both regional and teleseismic distances, at variable periods between 8 and 25 s. The magnitude equation is

$$M_{s(b)} = \log(a_b) + \frac{1}{2}\log(\sin(\Delta)) + 0.0031\left(\frac{20}{T}\right)^{1.8}\Delta - 0.66\log\left(\frac{20}{T}\right) - \log(f_c) - 0.43\,, \qquad (1)$$

where $a_b$ is the amplitude of the Butterworth-filtered surface waves (zero-to-peak in nanometers) and $f_c$ is the filter frequency of a zero-phase Butterworth band-pass filter with corner frequencies $1/T\text{-}f_c$, $1/T+f_c$. At the reference period $T$=20 s, the equation is equivalent to Von Seggern's formula (1977) scaled to Vaněk et al. (1962) at 50 degrees. For periods $8 \le T \le 25$, the equation is corrected to $T$=20 sec, accounting for source effects, attenuation, and dispersion. This technique is often referred to as $M_s$(VMAX) for **V**ariable-period, **MAX**imum amplitude magnitude estimates (Bonner et al., 2006).

The advantages of the $M_s$(VMAX) technique include

- The technique allows for time-domain measurements of surface-wave amplitudes, giving an analyst the ability to easily and visually confirm that the pick is correct and is an actual Rayleigh wave.
- It allows for surface-wave magnitudes to be measured at local and regional distances where traditional 20-s magnitudes cannot be used. These magnitudes are not biased with respect to teleseismic estimates.
- The application of narrow-band Butterworth-filtering techniques appropriately handles the Airy phase.
- The method is variable period and not restricted to near 20-s period, and the analyst is allowed to measure the surface wave magnitude where the signal is largest.

### $M_s$(VMAX) Methodology

To estimate $M_s$(VMAX), we apply a series of zero-phase 3rd-order Butterworth filters to the data with the corner frequencies $(1/T)$-$f_c$, $(1/T)$+$f_c$, where

$$f_c \le \frac{G\min}{T\sqrt{\Delta}} . \qquad (2)$$

For continental paths between 8 and 25 s, Gmin, which is based on dispersion effects, is set to 0.6. The center periods are placed at 1-second intervals between 8 and 25 s. We construct the envelope function of the filtered signal and measure the maximum zero-to-peak amplitude in a group velocity window between 2.0 and 4.0 km/s. An analyst then visually confirms that the correct waveform feature is being measured—a benefit of using a time-domain measurement. The procedure can be automated based on signal-to-noise requirements within the window. In Figure 1 we show examples of filter panels from an $M_w$=4.83 Montana earthquake recorded at station DUG at a near-regional distance of 509 km. Note the differences in the Rayleigh-wave amplitudes between 20-s periods, where traditional $M_s$ is measured, and 8–14 s periods.

We record the maximum amplitude in each of the 18 filter bands and then use Equation 1 to calculate a variable-period surface-wave magnitude. As a result, 18 different magnitudes are estimated for each station recording the event (Figure 2). We then search the variable-period filtered data (Figure 1) to determine the period of the maximum Airy-corrected amplitude. We use the magnitude calculated at that period as the final estimate. As an example, the period of maximum amplitude for the DUG recording occurred at T=10 s. We note that for this Montana event, all of the $M_s$(VMAX) estimates were made at periods of less than 18 sec. We do the same processing for all stations that recorded the event and then estimate a network $M_s$(VMAX) (4.42), the interstation standard deviation (0.13), and surface-wave magnitude "noise" floors at each station (see Figure 2).

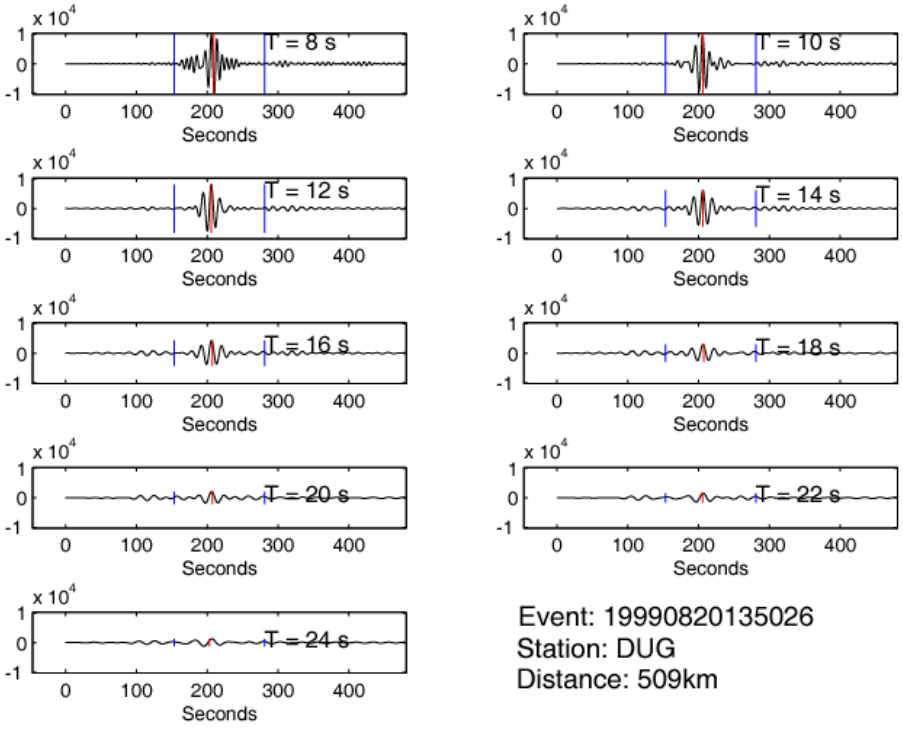


**Figure 1. Filter combs of Rayleigh waves at periods of 8, 10, 12,..,24 seconds for a Montana earthquake recorded at DUG. The first blue line is 4.0 km/s, while the second is 2.0 km/s. The red line marks the largest amplitude. Amplitudes are in nm.**

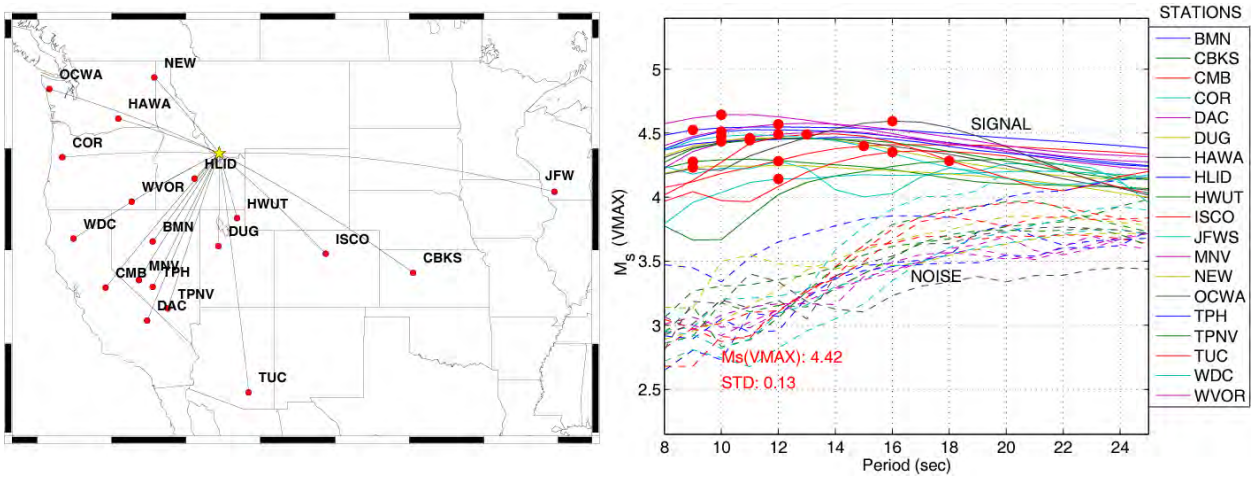


**Figure 2. $M_s$(VMAX) results for the Rayleigh waves recorded from a Montana earthquake. The solid lines represent signals while the dashed lines are pre-surface-wave noise levels. The station magnitudes were averaged to form a network $M_s$(VMAX) of 4.42 for this $M_w$=4.83 event.**

## Application in North America

We have used the $M_s$(VMAX) method to estimate surface-wave magnitudes for 169 events in North America. The events were part of a database of North American events for which Herrmann et al. (2008) measured an $M_w$, using either broadband waveform modeling and/or Rayleigh- and Love-wave spectral amplitudes. The events include most types of faulting focal mechanisms (Zoback, 1992). Figure 3 shows the geographic distribution of these events, which were $3.2 < M_w < 6.5$, and stations. $M_s$(VMAX) was estimated for stations at distances ranging from 48 to 5,268 km. Of the 7,370 event-station pairs, 4,051 of the measurements were at distances < 1,000 km.

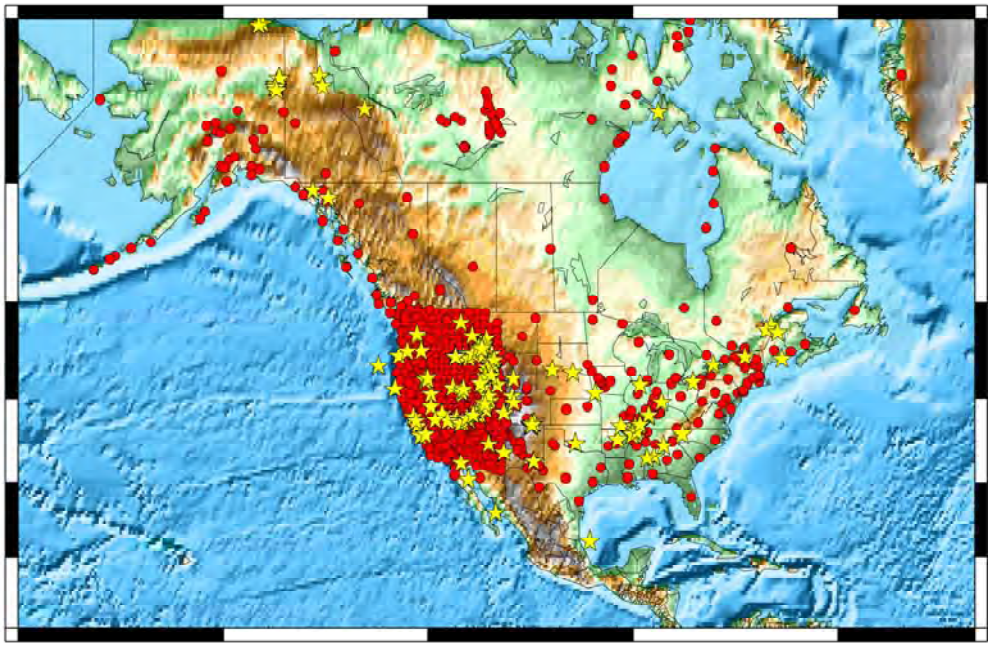

**Figure 3. Earthquakes (yellow stars) and stations (red circles) used in a pilot study to examine the effectiveness of using regional surface-wave magnitudes to estimate $M_w$.**

An example of the processing for the 21 February 2008 Wells, Nevada ($M_w$=5.88) event is shown in Figure 4. This event was located within the heart of Earthscope's Transportable Array, and thus was recorded on hundreds of stations within North America alone. Because the $M_s$(VMAX) technology can estimate unbiased surface wave magnitudes at epicentral distances as close as 50 km, we generated 506 surface-wave magnitude estimates for this event with only a very small azimuthal gap. Even though the focal mechanism for this normal fault event shows differences in the surface wave radiation patterns at 10, 15, 20, and 25 s (Herrmann et al., 2008), the radiation pattern of the $M_s$ estimates shows no significant radiation patterns. This is due in part to the fact that the variable-period methodology picks the surface-wave estimate at the largest amplitude and often migrates away from periods with radiation pattern nulls. We determined an $M_s$(VMAX) of 5.99 for the event.

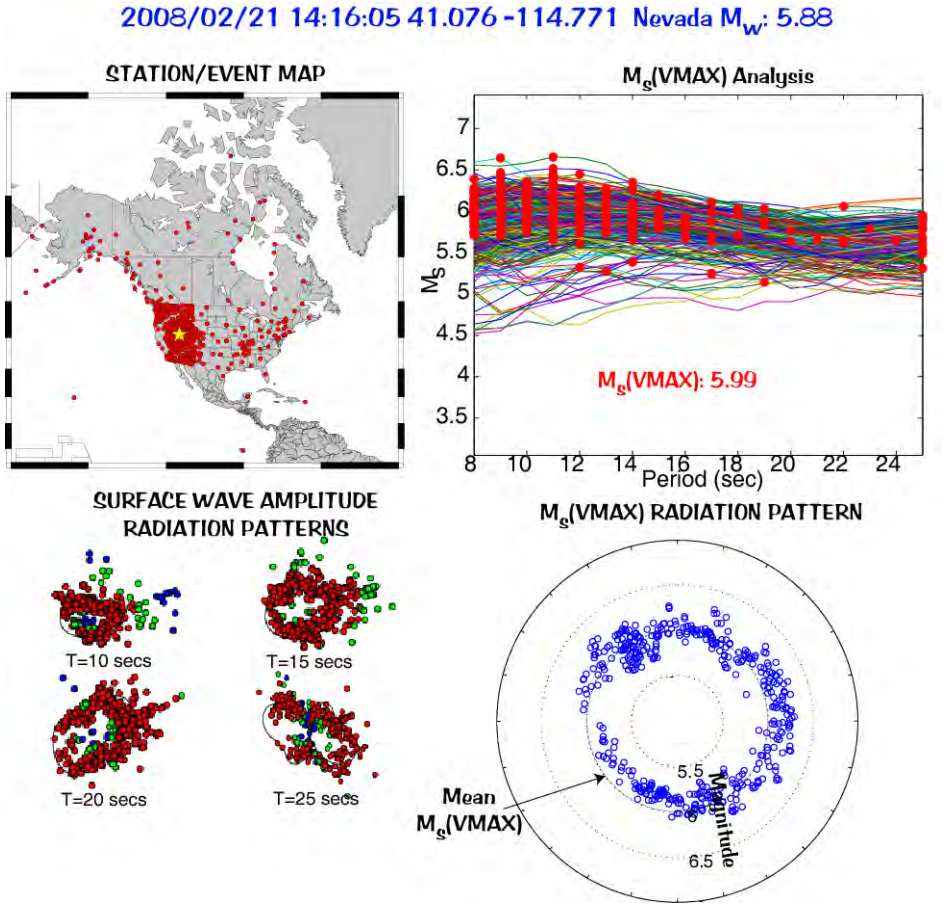


**Figure 4. $M_s$(VMAX) estimation for the 21 February 2008 Wells, NV earthquake. Shown are the stations used to estimate the variable-period surface-wave magnitude, the magnitude analysis at periods between 8-25 seconds, surface wave radiation patterns from Herrmann et al. (2008), and the $M_s$ estimates as a function of event-to-station azimuth.**

### Relationship Between $M_w$ and $M_s$(VMAX)

We derived a relationship between $M_w$ and $M_s$(VMAX) using the 169 North American earthquakes. The $M_s$ estimates were regressed (Figure 5) against moment magnitudes ($M_w$) and log $M_o$ estimated from *P*-wave modeling and/or Rayleigh- and Love-wave spectral amplitudes. $M_w$ can be estimated using the relationship: $M_w = 1.951 + 0.649\ M_s$. To demonstrate the observed scatter in the method, we show the residual $M_s$ estimates as a function of period and distance in Figure 6. With the exception of T=8 sec, where highly variable crustal structure is problematic, the residual surface-wave magnitude estimates are almost always within ±0.2 magnitude units of the mean value. And there are no significant distance trends observable in the data at periods greater than 10 sec.

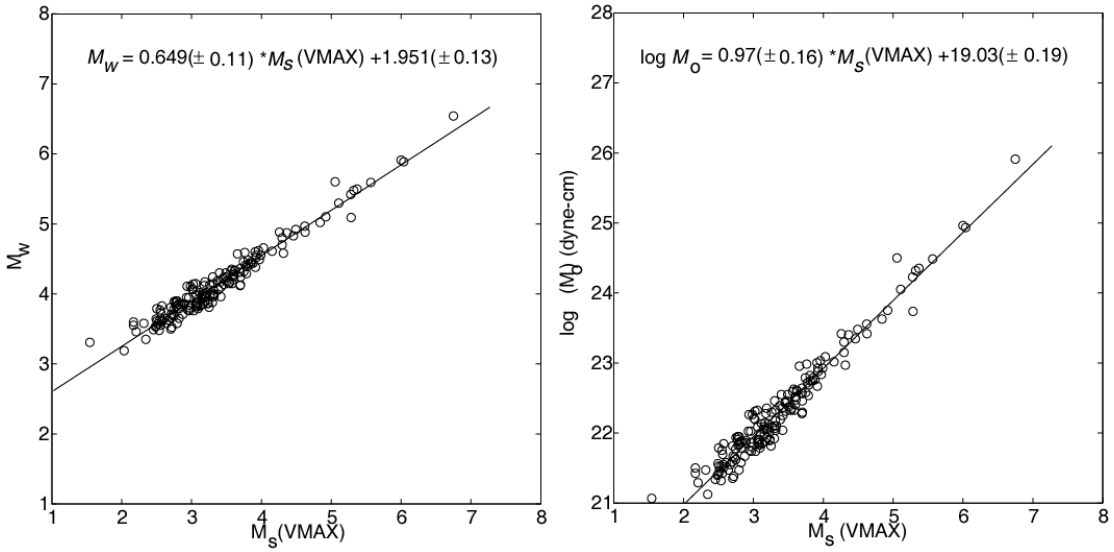


**Figure 5. Linear regressions of $M_w$ (left) and log $M_o$ (right) versus $M_s$(VMAX). The moments were determined from body wave modeling and/or Love and Rayleigh-wave spectral amplitudes (Herrmann et al., 2008).**

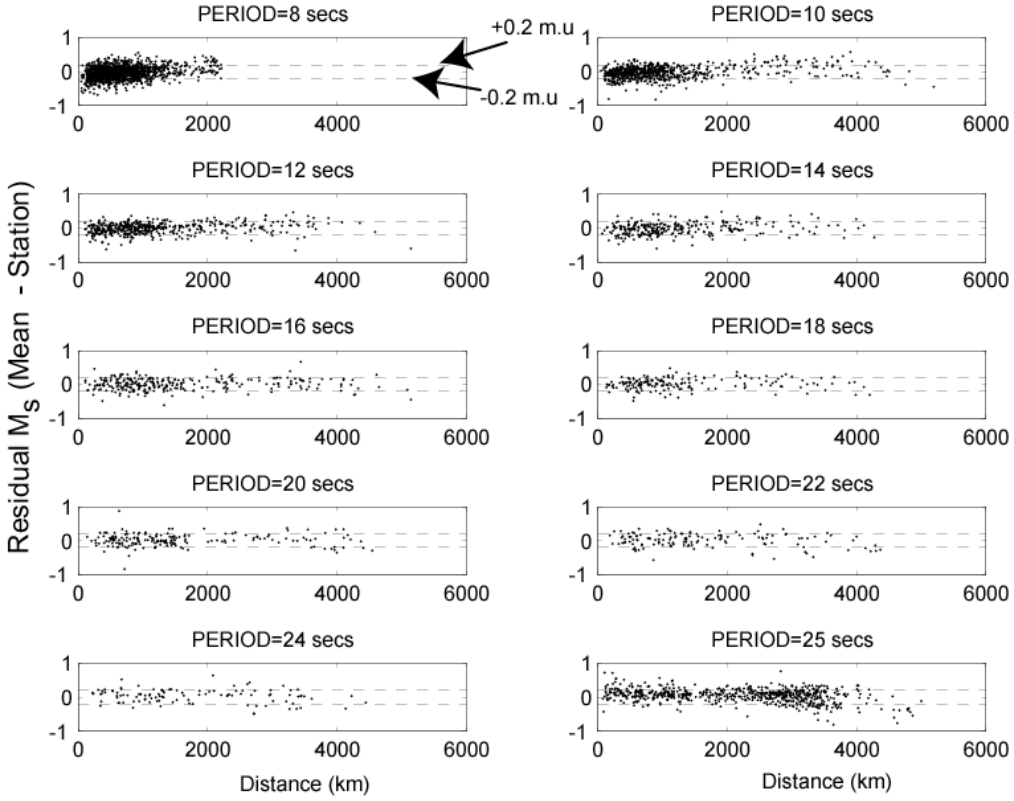


**Figure 6. Scatter in the estimated $M_s$(VMAX) estimates as a function of the evaluation period and distance.**

The scatter (Figure 7) between the observed and predicted $M_w$ shows mechanism dependence for normal and strike-slip faulting sources. Each focal mechanism was classified as either normal (NF) strike-slip (SS), thrust (TF), or oblique-slip variations of normal and thrust faults using the Zoback (1992) classification scheme. For normal faults,

the predicted $M_w$ is ~0.04 magnitude units larger than the observed $M_w$. A similar bias might be noted for thrust faulting as more estimates are obtained in the future. On the contrary, for strike-slip faults, the predicted estimate is ~0.07 magnitude units smaller than the observed $M_w$. The reason for these differences results from our $M_s$ estimates only being based on the Rayleigh waves. Strike-slip events contain a significant amount of their moment from energy in the Love waves, which are not considered in our technique. The results show there is little, if any, depth dependence on the predicted $M_w$s for events with crustal depths.

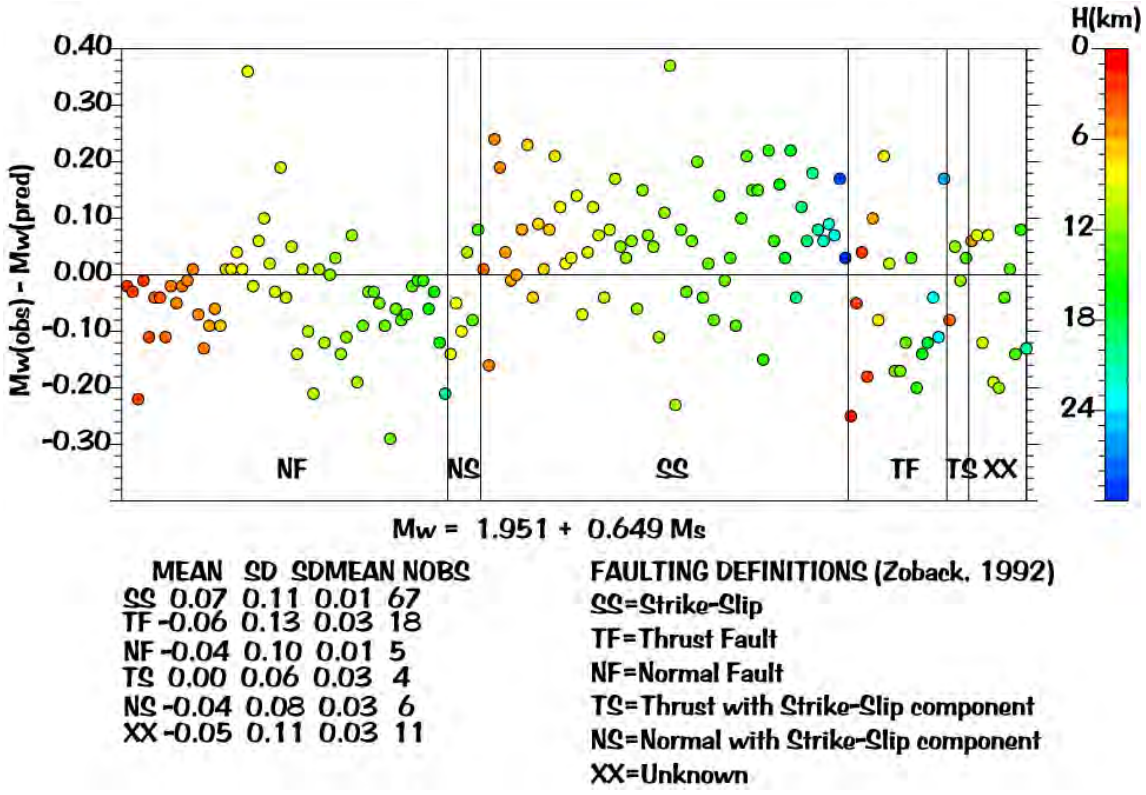


**Figure 7. The dependence of the $M_s$-predicted $M_w$ as a function of mechanism and depth. The mechanisms are based on the Zoback (1992) classification scheme. The residuals between the observed and $M_s$-predicted $M_w$ have a definable faulting mechanism effect, especially when strike-slip events are compared to those with other mechanisms.**

### Predicting $M_s$(VMAX) Detection Thresholds

Broadband noise estimates can be used to estimate the $M_s$(VMAX) threshold floor for any seismic station. Berger et al. (2004) compiled broadband ambient noise estimates for the GSN. Peter Davis (Executive Director, Project IDA at the University of California, San Diego) provided us with the noise estimates for the GSN stations. As an example, the left subplot of Figure 8 shows the 25$^{th}$ percentile noise estimate for station AAK compared to the low noise model for the GSN.

We converted these noise estimates, which were in units of acceleration $m^2/s^3$ and decibels, to nanometers (nm) and input them into Equation 1 for variable-period surface waves. We propagated these noise estimates at periods (T) between 8 and 25 s to distances ($\Delta$ between 1 and 60 degrees. The $M_s(T,\Delta)$ were estimated and contoured (right subplot of Figure 8). This colormap provides the optimal detection threshold for each station for a signal-to-noise ratio of 2. If the event has an $M_s$ smaller than these values at a particular distance or period, we will probably discard it due to the inability to verify that it is a Rayleigh wave because of the "noise-based" $M_s$ background level.

Using the GSN noise estimates (examples are shown in Figures 8 and 9), we determine the maximum distance in which we could record an $M_s$=2.5 and $M_s$=3.0. This distance is plotted as the radius of a circle centered on the station in Figures 10 and 11 for Europe and Asia. The blue circle shows the detection limits for the $M_s$(VMAX) technique, which considers periods between 8 and 25 s. The red circle shows detection distances if only periods between 17 and 23 s were considered, which is the traditional bandwidth for surface wave magnitude estimation. For $M_s$=2.5, the $M_s$(VMAX) technique has a mean detection distance of 9° compared with 7° for traditional 17–23-second measurements. For $M_s$=3.0, the mean detection distance is 26° for $M_s$(VMAX) and 22° for the traditional bandwidth.

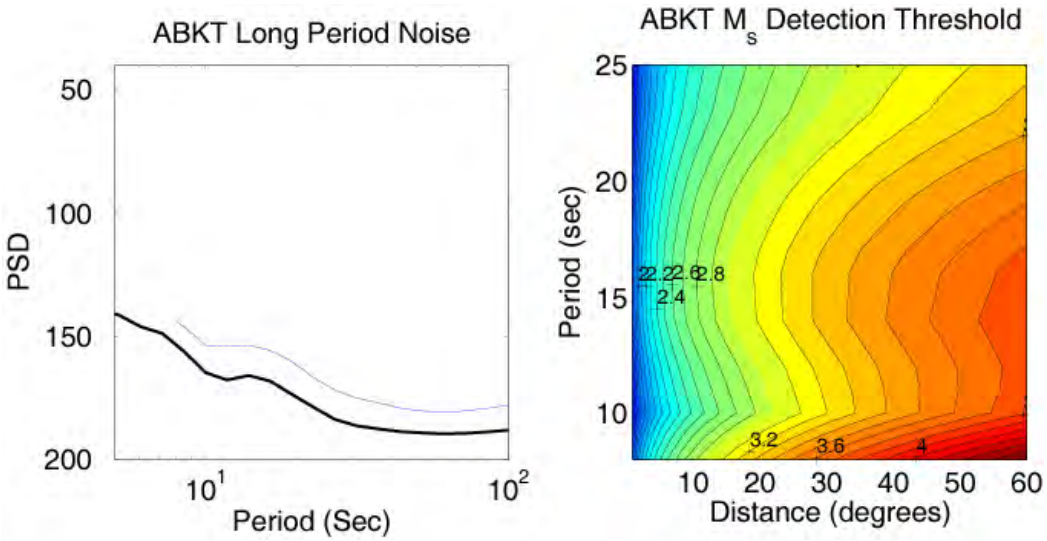


**Figure 8. $M_s$(VMAX) detection threshold for station ABKT. Left: Long-period noise estimates (blue line) for the station compared to the GSN low noise model (solid black line). Right: Detection magnitude thresholds contoured as a function of distance and period.**

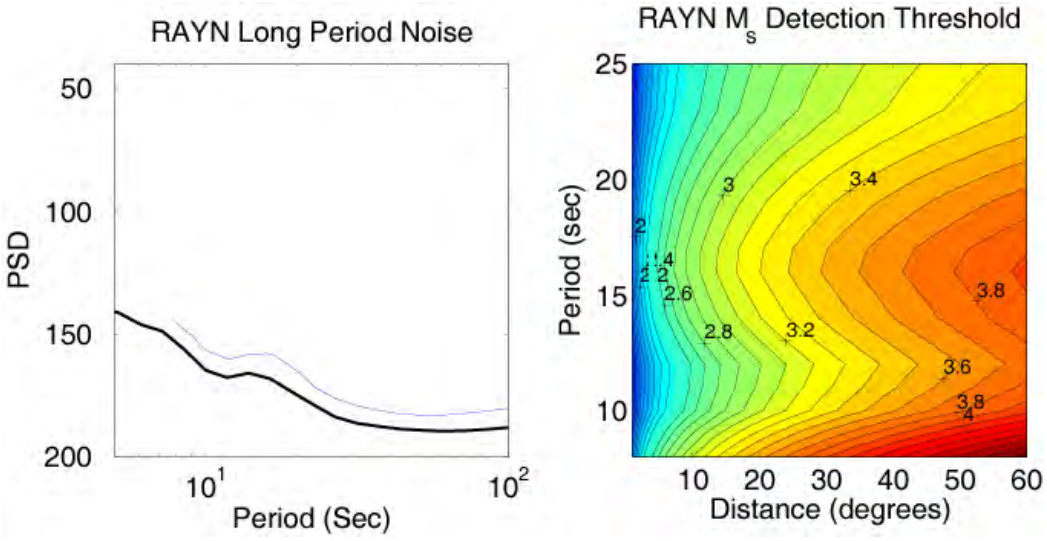


**Figure 9. $M_s$(VMAX) detection threshold for station RAYN. Left: Long-period noise estimates (blue line) for the station compared to the GSN low-noise model (solid black line). Right: Detection magnitude thresholds contoured as a function of distance and period.**

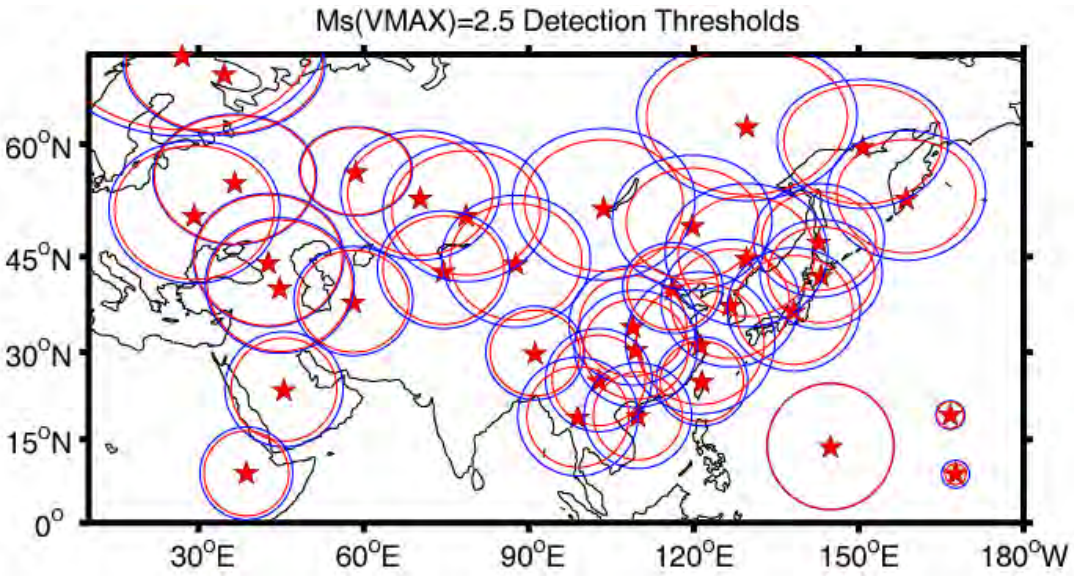


**Figure 10. Detection thresholds for Europe and Asian GSN stations for an $M_s$(VMAX)=2.5. The blue curve shows the detection threshold of *Ms*(VMAX) between 8- and 25-second periods. The red curve shows the detection thresholds only using 17–22-second surface waves, which is the traditional bandwidth for analysis.**

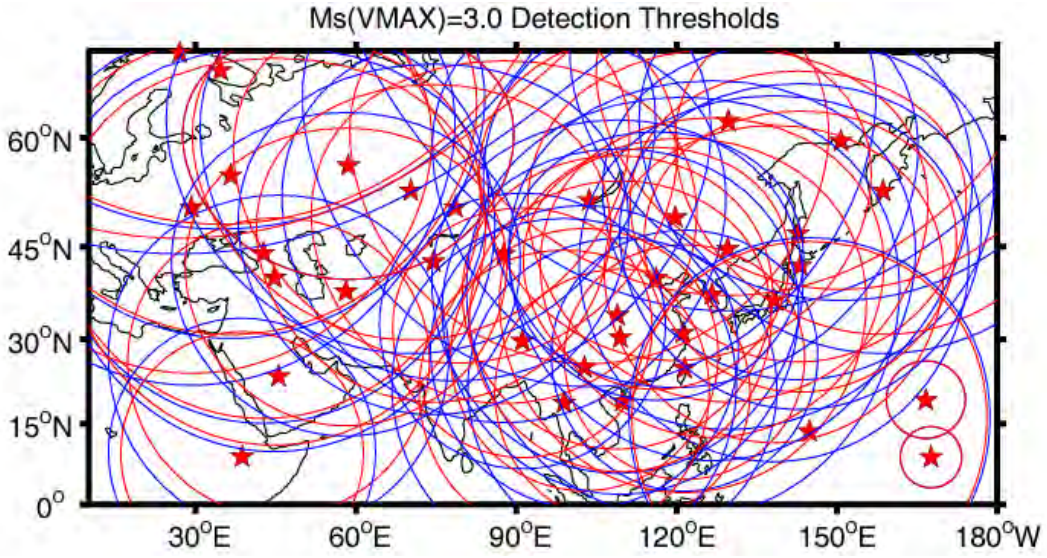


**Figure 1**

**Figure 11. Detection thresholds for Europe and Asia for an $M_s$(VMAX)=3. 0.**

## CONCLUSIONS AND RECOMMENDATIONS

The variable-period surface wave magnitude $M_s$(VMAX) continues to provide a better and more consistent estimate of source size, particularly for smaller events and at shorter distances. During the past year, we applied $M_s$(VMAX) to 169 North American events with $3.2 < M_w < 6.5$ at distances ranging from 48 to 5,268 km. The $M_s$ estimates were regressed against moment magnitudes ($M_w$) estimated from *P*-wave modeling and/or Rayleigh- and Love-wave spectral amplitudes. The resulting $M_s$:$M_w$ relationship has scatter on the order of ±0.2 magnitude units in the estimated $M_w$. The residuals between true and $M_s$-predicted $M_w$ have a definable faulting mechanism effect, especially when strike-slip events are compared to those with other mechanisms. This could have important

ramifications for the $M_s$:$m_b$ discriminant in regions where a particular mechanism dominates the seismicity. This exercise provides a tool for rapid $M_w$ estimation of events with $M_w$ > 3.5 for North America. Preliminary application of the same procedure to two other regions suggests that this $M_s$:$M_w$ relationship is also transportable to the Middle East and Korean Peninsula (Figure 12).

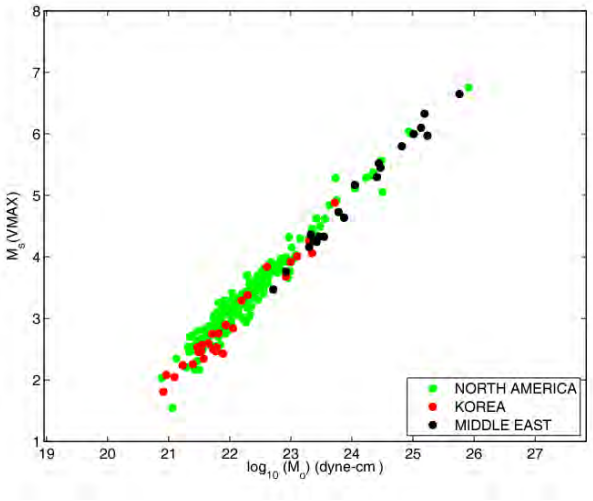


**Figure 12. Comparison of log $M_o$ versus $M_s$(VMAX) for earthquakes in North America (green), Korea (red) and the Middle East (black). Note that the Korean earthquakes are mostly strike-slip.**

## REFERENCES


Berger, J., P. Davis, and G. Ekstrom (2004). Ambient earth noise: a survey of the Global Seismographic Network, *J. Geophys. Res.* 109: B11307.

Bonner, J. L., D. Russell, D. Harkrider, D. Reiter, and R. Herrmann, (2006). Development of a Time-Domain, Variable-Period Surface Wave Magnitude Measurement Procedure for Application at Regional and Teleseismic Distances, Part II: Application and $M_s$—$m_b$ Performance. *Bull. Seism. Soc. Am.* 96: 678 – 696

Bonner, J., R. B. Herrmann, and H. Benz (2008). Rapid estimates of seismic moment using variable-period surface-wave magnitudes. *Seism. Res. Letts.* 79: 349.

Gutenberg, B., (1945). Amplitudes of surface waves and the magnitudes of shallow earthquakes. *Bull. Seism. Soc. Am.* 35: 3.

Herrmann, R. B., H. Benz, and C. Ammon (2008). Systematic moment tensor estimation for North America earthquakes. *Seism. Res. Letts.* 79: 349.

Pasyanos, M. E. (2005). A variable-resolution surface wave dispersion study of Eurasia, North Africa, and surrounding regions, *J. Geophys. Res.* Vol. 110, *No. B12, B12301* 10.1029/2005JB003749.

Rezapour, M., and R. G. Pearce, (1998). Bias in surface-wave magnitude $M_s$ due to inadequate distance correction. *Bull. Seism. Soc. Am.* 88: 43–61.

Russell, D. R., (2006). Development of a time-domain, variable-period surface wave magnitude measurement procedure for application at regional and teleseismic distances. Part I—Theory. *Bull. Seism. Soc. Am.* 96: 665–677.

Marshall, P. D. and P. W. Basham, (1972). Discrimination between earthquakes and underground explosions employing an improved $M_s$ scale. *Geophys. J. R. Astr. Soc.* 29: 431–458.

von Seggern, D., (1977). Amplitude distance relation for 20-Second Rayleigh waves. *Bull. Seism. Soc. Am.* 67, 405–411.

Stevens, J. L. and K.L. McLaughlin, (2001). Optimization of surface wave identification and measurement, in *Monitoring the Comprehensive Nuclear Test Ban Treaty: Surface Waves*, eds. Levshin, A. and M.H. Ritzwoller, *Pure Appl. Geophys.* 158: 1547–1582.

Vaněk, J., A. Zatopek, V. Karnik, Y. V. Riznichenko, E. F. Saverensky, S.L. Solov'ev, and N.V. Shebalin, (1962). Standardization of magnitude scales. *Bull. (Izvest.) Acad. Sci. U.S.S.R., Geophys. Ser.* 2: 108.

Zoback M. L.; 1992: First- and second-order patterns of stress in the lithosphere: the world stress map project, *J. Geophys. Res.* 97: 11703–11728.

# APPLICATIONS OF A NEXT-GENERATION MDAC DISCRIMINATION PROCEDURE USING TWO-DIMENSIONAL GRIDS OF REGIONAL P/S SPECTRAL RATIOS

Mark D. Fisk[1], Steven R. Taylor[2], Howard J. Patton[3], and William R. Walter[4]

Alliant Techsystems[1], Rocky Mountain Geophysics, LLC[2], Los Alamos National Laboratory[3], and Lawrence Livermore National Laboratory[4]

Sponsored by National Nuclear Security Administration

Contract No. DE-AC52-07NA28116
Proposal No. BAA07-46

## ABSTRACT

Using extensions of theoretical source models for earthquakes and explosions, Fisk (2006, 2007) provided a consistent model-based explanation of the frequency dependence of regional P/S discriminants at all major nuclear test sites as mainly due to larger systematic differences in P- and S-wave corner frequencies for explosions than earthquakes, as well as different spectral shapes. This project focuses on exploiting this new understanding to improve discrimination of earthquakes and explosions using regional data. The main objective is to develop and test an innovative processing and discrimination procedure, based on robust features of multi-dimensional spectral ratios for regional seismic phases, and using comparisons to source models. In this paper, two-dimensional grids of P/S spectral ratios for all combinations of frequencies of P- and S-wave spectra are shown to exhibit much greater differences in relative spectral amplitudes and shapes between explosions and earthquakes than considered before. The approach builds naturally upon the Magnitude and Distance Amplitude Correction (MDAC) technique (Taylor and Hartse, 1998; Taylor et al., 2002; Walter and Taylor, 2002), correcting the spectra for source, geometrical spreading, attenuation, and site effects. The analysis is first applied to underground nuclear explosions (UNEs) at the Semipalatinsk Test Site and regional earthquakes recorded by station WMQ (Urumchi, China). Measurements from the grids are considered that include a traditional Pn/Lg discriminant, a broadband cross-spectral ratio (high-frequency Pn and low-frequency Lg), and the root-mean-squared misfit to the MDAC model, under the hypothesis of a Brune (1970) earthquake source. The latter two, especially cross-spectral Pn/Lg, are shown to vastly improve discrimination performance over traditional Pn/Lg and to increase the applicability rate due to higher Lg signal-to-noise at lower frequencies. Similar analyses and improvements in discrimination performance are shown for UNEs at the Lop Nor Test Site in China and nearby earthquakes that were recorded by up to 19 regional seismic stations. Improvements are also demonstrated for earthquakes and UNEs at the Nevada Test Site (NTS), although geological differences between the test sites – mainly gas porosity of emplacement media – prompt the use of Lg spectral amplitudes at higher frequencies for NTS. Comparisons to source models may be used to confirm the physical basis of the discrimination results. The performance of various discriminants at test sites with different geology are discussed in the context of the theoretical source models.

## OBJECTIVES

The main objective is to develop and test an enhanced discrimination procedure, based on robust characteristics of multi-dimensional spectral ratios for regional seismic phases. The approach builds naturally upon the existing MDAC procedure by exploiting differences of relative spectral amplitudes and shapes due to source type that are currently not used, but are visually apparent. Another objective is to provide direct comparison of the empirical discrimination results to model calculations to confirm the physical basis and, in turn, to better understand source mechanisms that affect regional discriminants. Key tasks are to (1) compute 2D spectral ratios (Pn/Sn, Pn/Lg, Lg/Lg, etc.) for earthquakes and explosions at nuclear test sites, using spectra corrected for source, distance, and site effects; (2) compare the empirical spectra to theoretical predictions based on modified Brune (1970) and Mueller and Murphy (1971) [MM71] source models for P and S waves generated by earthquakes and explosions, respectively; (3) evaluate distinctive features of the 2D spectral ratios that capture model-based spectral differences of the event types and enhance discrimination performance; (4) quantify uncertainties of the corrected spectra for various regions, stations, and event types, as well as misfits of empirical and model 2D spectral ratio comparisons; (5) develop a robust discrimination procedure and evaluate its performance on broad sets of data; and (6) develop visualization techniques that allow the discrimination results and model comparisons to be assessed by a human analyst.

## RESEARCH ACCOMPLISHED

We have computed spectra of Pn, Pg, Sn, and/or Lg for explosions at the Semipalatinsk, Lop Nor, Novaya Zemlya, and Nevada Test Sites (STS, LNTS, NZTS, NTS, respectively) and regional earthquakes. We used phase-specific window lengths, with onsets prior to analyst picks of the regional phase arrivals to allow for a 10% cosine taper. We smoothed the log spectra using a moving 0.5 Hz window and corrected for instrument response. Using the MDAC approach, we then corrected the spectra for distance, site, and source terms, assuming a Brune (1970) earthquake source model. Details of the models and the parameters are provided by Fisk (2006, 2007) for the various test sites.

In the discrimination analysis below, we apply two hypothesis tests, based on the t-distribution, to assess whether an event is rejected as belonging to the explosion or earthquake populations. Let $\bar{R}$ denote station-averaged, MDAC-corrected log(Pn/Lg) in a given frequency band. An event is rejected as belonging to the explosion population if:

$$\frac{\bar{R} - \hat{\mu}_{R,\,EX}}{\sqrt{\dfrac{(N_{EX}-1)\hat{\sigma}^2_{R,\,EX} + (N_m - 1)\hat{\sigma}^2_m}{N_{EX}+N_m-2}\left(\dfrac{1}{N_{EX}} + \dfrac{1}{N_m}\right)}} < -t_\alpha(N_{EX}+N_m-2)\,, \qquad \text{(EQ 1)}$$

where $\hat{\mu}_{R,\,EX}$ and $\hat{\sigma}_{R,\,EX}$ are the mean and standard deviation of $\bar{R}$ estimated from $N_{EX}$ explosions in the multi-station training set, and $\hat{\sigma}_m$ is the standard deviation of $\bar{R}$ estimated from $N_m$ stations for the test event. Likewise, an event is rejected as belonging to the earthquake set if:

$$\frac{\bar{R} - \hat{\mu}_{R,\,EQ}}{\sqrt{\dfrac{(N_{EQ}-1)\hat{\sigma}^2_{R,\,EQ} + (N_m - 1)\hat{\sigma}^2_m}{N_{EQ}+N_m-2}\left(\dfrac{1}{N_{EQ}} + \dfrac{1}{N_m}\right)}} > t_\alpha(N_{EQ}+N_m-2)\,. \qquad \text{(EQ 2)}$$

In these expressions, $t_\alpha(N)$ is the (1–α)-percentile of the t-distribution with $N$ degrees of freedom. In the following applications, the significance level is set at $\alpha = 0.005$, unless otherwise stated. Events rejected by one test and not by the other are categorized as the latter event type. Events rejected by both or not rejected by either are categorized as *undetermined*. Using two criteria allows separate control of the error rates and clear definition of *undetermined*.

Figure 1 depicts locations of earthquakes, UNEs at STS and LNTS, and most regional seismic stations. Many STS UNEs up to 1989 were recorded digitally by WMQ (Urumqi, China) and BRV (Borovoye, Kazakhstan). For STS, we use WMQ recordings, which are better quality than BRV data. We also processed 74 earthquakes during 1995 to 2002, ranging from mb 3.2 to 5.9, and recorded at regional distances by WMQ. We chose the events over a broad region because there was only one earthquake during this time period within 280 km of STS. Many of the events since mid 1994, including ten LNTS UNEs, were recorded digitally by up to 19 regional stations. For LNTS, we processed all available regional recordings for the UNEs and a sample of 43 earthquakes (mb 3.5 to 5.4) in the box that contains LNTS in Figure 1. Fisk (2006) provides further information regarding these data and examples of the spectra and model comparisons.

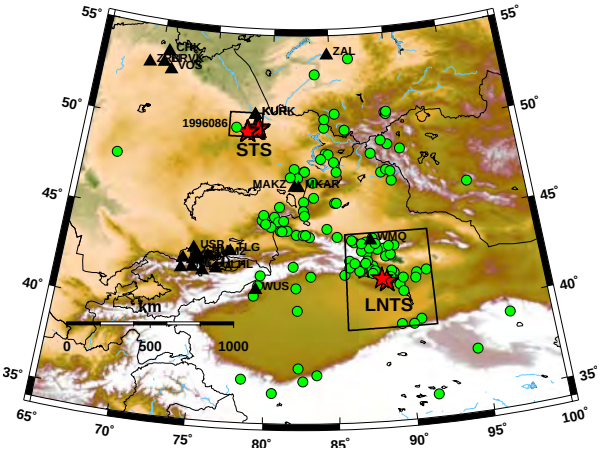


**Figure 1. Locations of UNEs (stars), earthquakes (circles), and most of the digital seismic stations (triangles) within 2000 km of STS and LNTS.**

### *Semipalatinsk Test Site*

Figure 2 shows Pn/Lg spectral ratios, corrected for site and distance effects, for the Soviet Joint Verification Experiment (JVE), a small UNE at Degelen, and a nearby earthquake on 1996/03/26 using WMQ data only (cyan) and averaging over 17 stations (green). Figure 2 also shows the Brune model prediction (gray curve) for the earthquake and MM71 model results for each UNE (black curves). The models represent the empirical Pn/Lg spectral ratios quite well, and explain the frequency dependence of P/S discrimination performance as mainly due to larger differences in explosion P and S corner frequencies and stronger spectral shapes, including overshoot, for explosions. Fisk (2006) shows similar frequency dependence for Pn/Lg and/or Pn/Sn at the Lop Nor and Novaya Zemlya test sites.

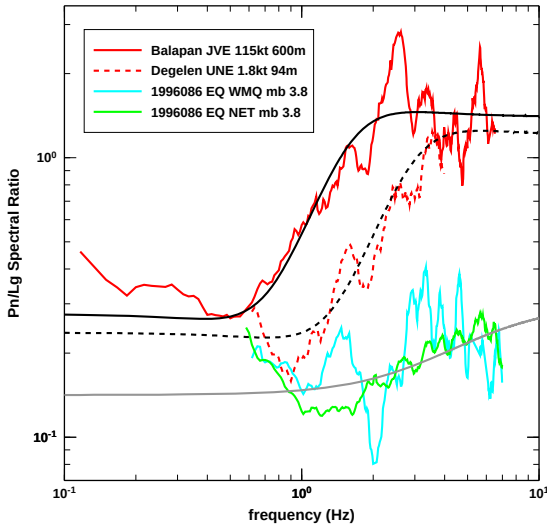


**Figure 2. Empirical and model Pn/Lg spectral ratios using WMQ data for the JVE, a small UNE at Degelen, and for a nearby earthquake using WMQ data only and averaging over 17 regional stations.**

Figure 2 not only illustrates a model-based explanation of why P/S discrimination performance is usually better at higher frequencies (i.e., near or above the Pn corner frequency for explosions, which depends on source size), but also that the earthquakes and explosions have different spectral shapes, that should be exploited to improve discrimination. To illustrate this, Figure 3 compares 2D empirical (left) and model (right) grids of Pn/Lg spectral ratios for the earthquake (top), the JVE at Balapan (middle), and a UNE at Degelen (bottom). The Pn and Lg spectra were corrected for Q, spreading, site effects, and a Brune source term (under the earthquake hypothesis), *a la* the MDAC approach. The 2D grids represent log Pn/Lg spectral ratios for all combinations of frequencies for the Pn and Lg spectra. The spectra are limited to signal-to-noise ratio (SNR) greater than 2. The grid for the earthquake (upper left in Figure 3) has values near zero and little variability over the usable bandwidth of Pn and Lg, as it should, if properly corrected. Alternatively, the grids for the explosions exhibit large departures from zero and spectral structure due to overshoot and spectral modulations. Plots on the

right side of Figure 3 show the model predictions of the 2D spectral ratios (corrected by the same Brune source terms as used for the corresponding empirical grids) for an earthquake and explosions in granite. Despite the variability using only WMQ, the model results exhibit similar behavior as the corresponding empirical grids.

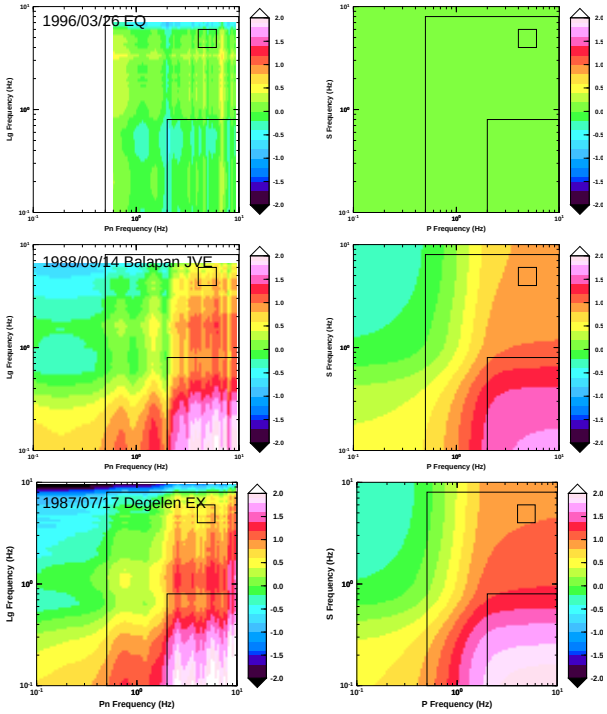


**Figure 3. Empirical (left) and model (right) 2D log Pn/Lg spectral ratios for an earthquake (top), the JVE (middle), and a UNE at Degelen (bottom). The grids were computed using only data from WMQ. The three rectangles indicate spectral bands used to measure Pn/Lg ratios for discriminant analyses.**

The three rectangles in each plot of Figure 3 are used to measure three types of discriminants. First, the small square represents a typical frequency band of 4–6 Hz for Pn and Lg, often used for a traditional P/S discriminant. Pn/Lg(6–8 Hz) did not improve performance much and there were fewer events with adequate SNR. Second, a cross-spectral ratio is computed as the average log Pn/Lg value for frequencies of Pn and Lg spectra in the 2–10 Hz and 0.1–0.8 Hz bands, respectively. The 2D grids over these frequencies exhibit far more distinction of UNEs and earthquakes than traditional high-frequency P/S. Third, the root mean square (RMS) value of the corrected 2D log Pn/Lg grids are computed over frequencies of 0.5–10 Hz for Pn and 0.1–8 Hz for Lg. This quantifies the misfit of the MDAC model (source, distance, and site terms), under the earthquake hypothesis, to the 2D empirical spectral ratio grid. We refer to these three types of measurements as *traditional*, *cross-spectral*, and *RMS-misfit* Pn/Lg ratios.

Figure 4 shows plots of these three types of log Pn/Lg measurements versus distance to WMQ (left) and mb (right) for earthquakes (circles and black square) and UNEs (stars). The plots show the residual dependence on magnitude and distance after applying the MDAC corrections. Pn/Lg(4–6 Hz) (top plots) provides some separation of explosions and earthquakes, but the overlap and variances limit discrimination performance. Some of the overlap and earthquake variance is due to diverse paths to WMQ. A kriged grid of the earthquake data (Figure 5) varies from –0.34 to 0.32, depending on the path, comparable to the mean separation of the earthquake and explosion populations. The lower four plots of Figure 4 show complete separation of the earthquakes and explosions. The cross-spectral Pn/Lg provides the best separation of the measurements examined. The earthquakes still have large variance, also due to path variations and other effects, but they are not nearly as significant because these new types of spectral ratios vastly increase the mean separation.

Figure 6 shows log Pn/Lg RMS-misfit versus cross-spectral measurements, with the same marker types as in Figure 4. The separation of earthquakes and explosions is remarkable, indicating that their characterization of source differences dominates the effects of path variations. The *RMS-misfit* quantifies how well the MDAC model, assuming a Brune earthquake source term, fits the data. It is generally expected to provide good discrimination, but it can also indicate earthquakes for which the model parameters (e.g., stress drop, Q, geometrical spreading) are inaccurate. Cross-spectral Pn/Lg highlights differences in source characteristics between explosions and earthquakes, based on their different relations of P and S corner frequencies and spectral shapes.

Applying the criteria in Eqs. (1) and (2) (with $N_m = 1$, using only WMQ) to traditional Pn/Lg(4-6 Hz) values, 6 of 28 UNEs (21.4%) and 59 of 72 earthquakes (81.9%) are categorized as *explosion-like* and *earthquake-like*,

respectively. The other events are *undetermined*. Poor performance for the UNEs is mainly due to the large earthquake variance, making it difficult to reject the earthquake hypothesis. Calibration of path effects is one way to reduce this variance and enhance performance.

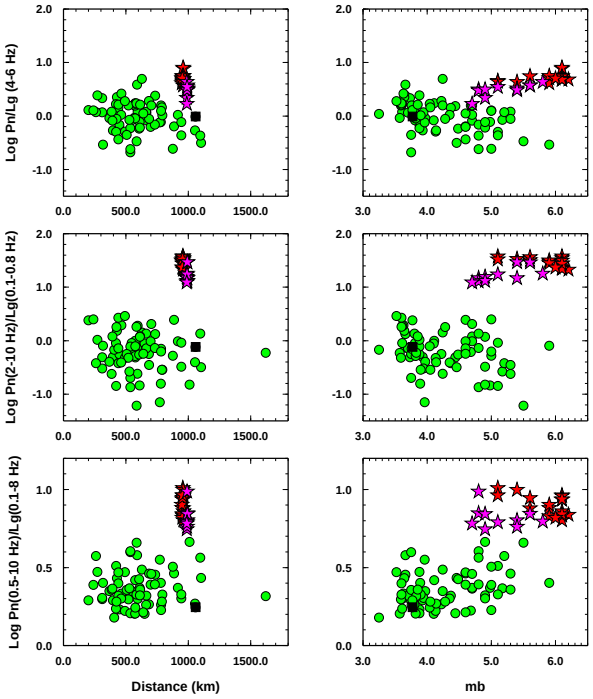


**Figure 4. Plots of traditional (top), cross-spectral (middle), and RMS-misfit (bottom) log Pn/Lg values versus distance (left) and mb (right) for earthquakes (circles) and UNEs (stars) at Balapan (red) and Degelen (magenta). The black square in each plot corresponds to the 1996/03/26 earthquake near STS.**

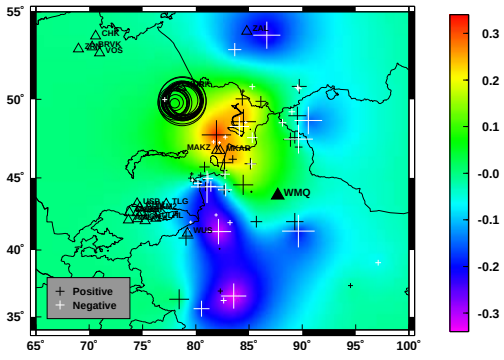


**Figure 5. Kriged grid of log[Pn/Lg(4-6 Hz)] for WMQ, based on 72 earthquakes. The markers (size and color) represent residuals to the grid for UNEs (circles) and earthquakes (crosses).**

Figure 7 shows results using cross-spectral Pn(2–10 Hz)/Lg(0.1–0.8 Hz) values. All 28 UNEs and 74 earthquakes are categorized properly, even at the 0.0005 significance level. This big improvement is due to the large difference of explosion and earthquake means. There are two more events with adequate SNR for Lg at 0.1–0.8 Hz than 4–6 Hz. For smaller events, even more should have adequate Lg SNR in the lower frequency band. Last, using RMS-misfit Pn(0.5–10 Hz)/Lg(0.1–8 Hz) values, all 28 UNEs and 72 of 74 earthquakes are categorized properly at the 0.005 significance level. The performance is much better than for the traditional high-frequency Pn/Lg and not quite as good as the cross-spectral Pn/Lg.

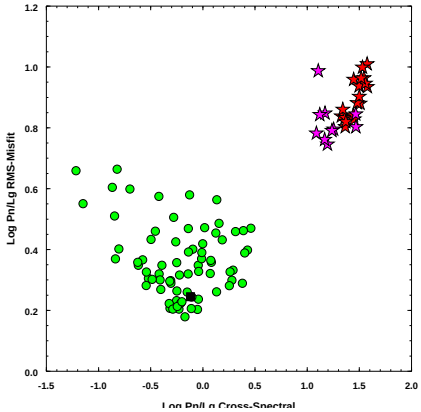


**Figure 6. Plot of RMS-misfit versus cross-spectral log Pn/Lg values for earthquakes and STS UNEs.**

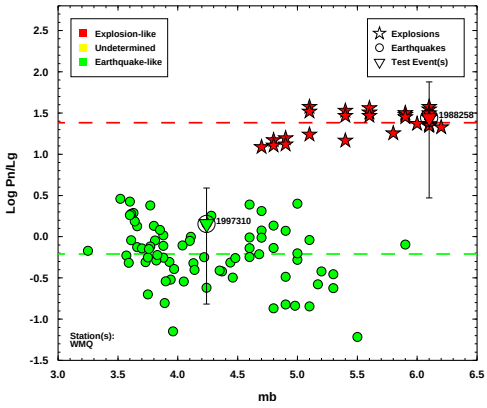


**Figure 7. Discrimination results for earthquakes and STS UNEs using cross-spectral Pn/Lg. Dashed lines show population means; 99.5% confidence intervals are shown for the Soviet JVE (1988258) and an earthquake (1997310). All events are categorized properly, even at the 99.95% confidence level.**

### *Lop Nor Test Site*

We performed similar analyses for LNTS events; Fisk et al. (2007) show plots like Figures 2 and 3. Figure 8 shows network-averaged Pn/Lg (left) and Pn/Sn (right) versus mb in the same frequency bands defined above. The square in each plot corresponds to the 1999/01/27 earthquake at LNTS. Traditional Pn/Lg and Pn/Sn (top plots) perform better than at STS because the paths for the earthquakes and UNEs are more similar and also due to averaging over many stations. Even so, as for STS, the cross-spectral discriminants (middle plots) exhibit a much better separation of explosions and earthquakes than traditional P/S. The variances are larger for smaller earthquakes because they were generally recorded by fewer stations with adequate SNR. The 1988/09/29 UNE was recorded at regional distance by only WMQ. Its discriminant values are all the highest of these events and tend to inflate the variances for the UNEs. No other LNTS UNEs have WMQ data for comparison. The plots for Pn/Lg and Pn/Sn are fairly similar for a given band, leading to similar discrimination results using either Pn/Lg or Pn/Sn. In the following, we focus on Pn/Sn.

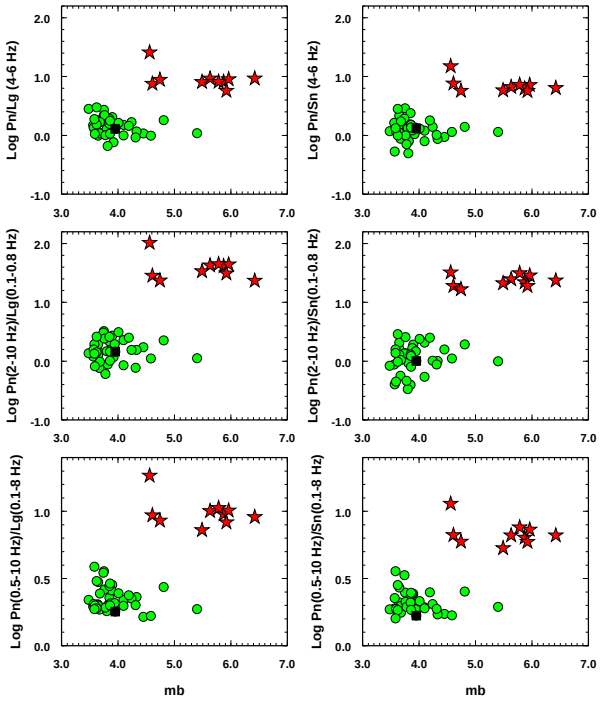


**Figure 8. Network-averaged log Pn/Lg (left) and log Pn/Sn (right) measurements versus mb for LNTS UNEs and earthquakes in three combinations of frequency bands, as in Figure 4.**

Applying Eqs. (1) and (2) to traditional Pn/Sn(4–6 Hz) values, all 10 UNEs and 41 of 43 earthquakes (95.3%) are categorized properly. Two events are *undetermined*. ($N_m$ ranges from 1 to 19 for the various events.) By most standards, this performance is very good. However, using cross-spectral Pn(2–10 Hz)/Sn(0.1–0.8 Hz) values for the same events, all events are categorized properly even at a very small significance level of 0.00005, a factor of 100 smaller than used for the traditional Pn/Sn. As for STS, this is a vast improvement in discrimination performance. Processing even smaller earthquakes and over a broader area would more clearly demonstrate the benefit, largely due to the increased separation of the earthquake and explosion means for cross-spectral P/S. Using RMS-misfit Pn(0.5-10 Hz)/Sn(0.1-8 Hz) values, all 10 UNEs and 40 of 43 earthquakes are categorized properly at the 0.005 significance level.

### *Nevada Test Site*

We now apply the spectral processing and discrimination methods to NTS. Unlike granite at STS and LNTS, the geology at NTS consists of tuff, rhyolite, and alluvium, with varying degrees of gas porosity (GP), especially above the water table at Yucca Flat. Walter et al. (2004) assembled a dataset for 151 events in the western U.S., including seismograms, origins from several bulletins, and regional phase picks by Ryall (2005). The UNEs range from ML 2.9 to mb 5.9 and include 40 at Yucca Flat, 18 at Pahute Mesa, and 11 at Rainier Mesa since mid 1979 that were recorded digitally by ELK (Elko, NV), KNB (Kanab, UT), LAC (Landers, CA), and/or MNV (Mina, NV). We also used 37 earthquakes at or near NTS, ML 2.6 to mb 5.7. We computed Pn, Pg, and Lg spectra and corrected for magnitude and distance, using MDAC parameters from Walter and Taylor (2002). Fisk (2007) lists the parameters and provides details of the events, including source and geological parameters for the UNEs (from Springer et al., 2002), and comparisons of empirical and model spectra. We used spectra for the 37 earthquakes, corrected for distance and magnitude, to estimate site corrections. We then applied the magnitude, distance, and site corrections to all of the events.

Figure 9 illustrates 2D grids of log Pn/Lg spectral ratios for earthquakes and UNEs. The spectra are limited to

SNR > 2, which is most restrictive on Pn spectra at lower frequencies. The grids for the earthquakes have values closer to zero and less variability than for the explosions, as they should after applying the corrections that include an earthquake source term. The rectangles in each plot of Figure 9 are used to measure various log Pn/Lg spectral ratios: (1) traditional measurements in the 4–6 Hz and 6–8 Hz bands; (2) the average log Pn/Lg value for frequencies of the Pn and Lg spectra in the 1-8 Hz and 4–10 Hz bands, respectively; and (3) the RMS value of the log Pn/Lg grids over the frequencies of 1-8 Hz for Pn and 0.2–10 Hz for Lg. The log Pn/Lg values were computed and averaged over LNN stations with available data. Figure 10 shows the measurements versus magnitude. The upper plots show that Pn/Lg (4–6 Hz) and Pn/Lg(6–8 Hz) provide useful separation of the explosion and earthquake populations. The lower left plot of Figure 10 exhibits complete separation.

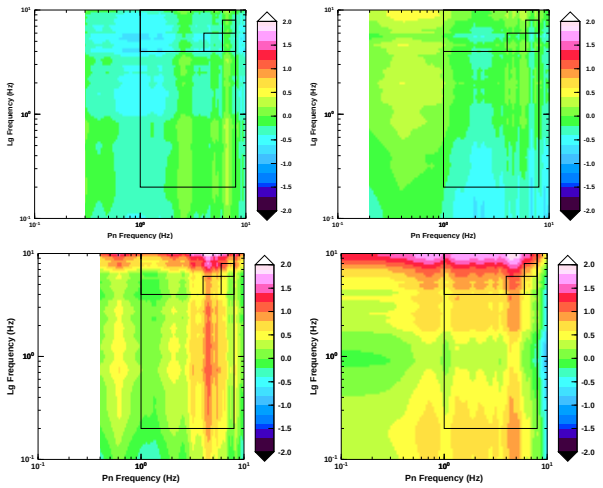


**Figure 9. Log Pn/Lg 2D spectral ratios, averaged over stations, for 2 earthquakes (top) and 2 UNEs (bottom). The rectangles depict spectral bands used to measure Pn/Lg ratios for discriminant analyses.**

We also considered cross-spectral measurements of log Pn[0.6–8 Hz]/Lg[0.1–1.0 Hz], as we did for LNTS and STS. The performance is good for UNEs in low GP media, but poor for ones above the water table at Yucca Flat, where GP is relatively high (10% to 25%; Springer et al., 2002). Taylor and Denny (1991) describe how an explosion in weak, porous rock has a shock wave that divides into a two-wave system, consisting of an elastic precursor followed by a plastic wave, causing a second effective corner frequency in the source spectrum. They found that Lg spectral amplitudes for such UNEs are especially depleted at higher frequencies. To model Lg spectral ratios for NTS UNEs in media of varying GP, they used the third-order source model (with $f^{-3}$ roll-off and two corner frequencies) of Denny and Goodman (1990). This physical understanding is why we use log Pn[1–8 Hz]/Lg[4–10 Hz], rather than a cross-spectral ratio (with Lg at lower frequencies). As illustrated in the upper larger rectangle in each plot of Figure 9, NTS UNEs consistently exhibit greater differences from earthquakes in this combination of frequency bands.

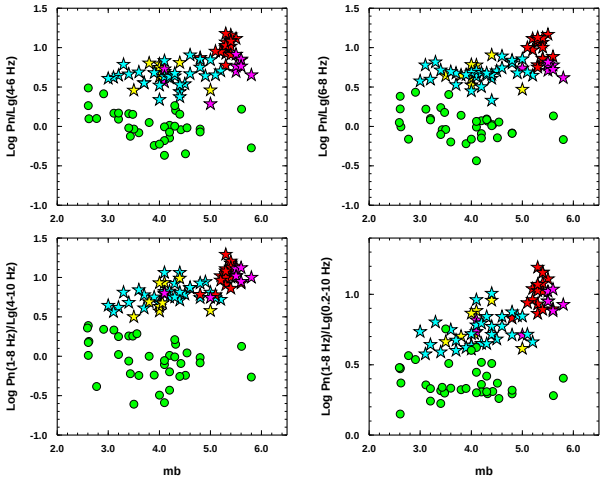


**Figure 10. Plots of log Pn/Lg ratios versus mb for NTS UNEs (stars, color-coded as in Figure 11 below), and earthquakes (circles) in four combinations of frequency bands. Average values are shown, except the lower right plot that shows RMS values.**

Figure 11 shows a plot of log Pn/Lg RMS-misfit versus log Pn[1–8 Hz]/Lg[4–10 Hz] values. The two types of measurements are highly correlated for the UNEs, indicating by either measure their inconsistency with the earthquake source model. The earthquakes with higher values of the RMS-misfit are typically ones farther from NTS, indicating that the MDAC corrections could be improved to reduce the variance of Pn/Lg data for the earthquake population. The site corrections, estimated from earthquake data that are predominantly at or near NTS, compensate to provide good overall corrections near the test site, but are less accurate away from NTS.

We apply Eqs. (1) and (2) to evaluate the performance of the various Pn/Lg discriminants. Here, $N_m$ ranges from 1 to 4, depending on data availability from various LNN

stations for a given event. The smallest (ML 2.9) UNE, WACO, has insufficient Pn SNR for all cases. For Pn/Lg (4–6 Hz), 66 of 69 (95.7%) UNEs and 28 of 37 (75.7%) earthquakes are categorized properly. Three earthquakes do not have adequate Pn SNR. The other two UNEs and 6 earthquakes are *undetermined*. For Pn/Lg(6-8 Hz), 66 of 69 (95.7%) UNEs and 31 of 37 (83.8%) earthquakes are categorized properly. Of the other two UNEs, one is *undetermined* and one (VILLITA) is mis-categorized as *earthquake-like*. One earthquake does not have adequate SNR and five are *undetermined*. Thus, the performance is somewhat better for 6-8 Hz than 4–6 Hz, except for mis-categorizing VILLITA. It is not mis-categorized if the significance level is reduced to 0.001, but then three UNEs and 10 earthquakes are *undetermined*.

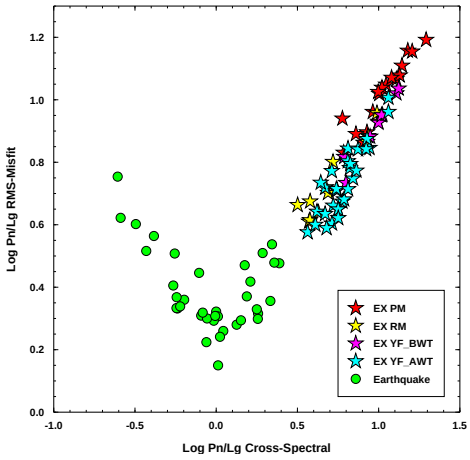


**Figure 11. RMS-misfit versus cross-spectral log Pn/Lg values for the NTS UNEs and earthquakes. The stars are color-coded for explosions at Pahute Mesa (PM), Rainier Mesa (RM), and below and above the water table at Yucca Flat (YF_BWT and YF_AWT).**

Using log Pn(1-8 Hz)/Lg(4–10 Hz), 68 of 69 UNEs (98.6%; all but WACO) and 34 of 37 earthquakes (91.9%) are categorized properly. The other earthquakes are *undetermined*. All three are relatively small, causing their Pn measurements to be biased high by noise, and they have measurements at only one station, resulting in larger uncertainties. Note that these three earthquakes were also *undetermined* or had insufficient data for the traditional 4–6 Hz and 6–8 Hz bands. The variance of log Pn(1-8 Hz)/Lg(4–10 Hz) values for the earthquake population is somewhat larger than for log Pn/Lg(4-6 Hz). However, the greater separation of earthquake and explosion means improves discrimination performance.

Using the RMS values of log Pn(1-8 Hz)/Lg(0.2–10 Hz), 66 of 69 explosions (95.7%) and 25 of 37 earthquakes (67.6%) are categorized properly. The other events are *undetermined*. Figure 11 shows large RMS values for some earthquakes (thus, they are *undetermined*) due to inconsistencies with the model, even though their average Pn/Lg values are very different from those of explosions. Thus, the RMS measurement is a useful indicator of model inconsistencies, which can be due to source type or various MDAC parameters.

Last, Figure 12 shows observed (cf. Walter et al., 2007) and model Pg and Lg spectra (left) and spectral ratios (right) for the 2006/10/09 UNE in North Korea. Noise effects seem to bias the Pg spectrum at low frequencies. This preliminary comparison suggests that our spectral analyses and modeling will perform quite well here, as at other test sites. Note that the model results, using MM71 for P waves and with shifted corner frequency for S waves (cf. Fisk, 2006, 2007), compare even better for Lg than Pg, similar to findings by Fisk (2007) for NTS.

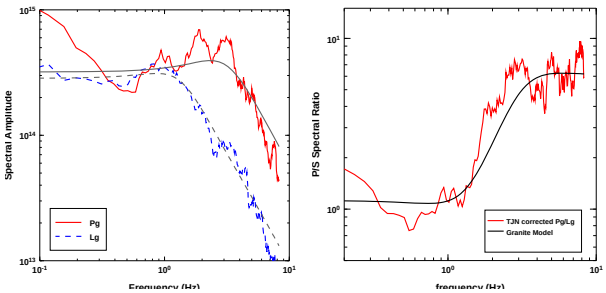


**Figure 12. Corrected Pg and Lg spectra (left) and Pg/Lg spectral ratio (right) computed from the TJN recording of the UNE in North Korea on 2006/10/09. Also shown are corresponding model calculations.**

## CONCLUSIONS AND RECOMMENDATIONS

The MDAC procedure (Taylor and Hartse, 1998; Taylor et al., 2002; Walter and Taylor, 2002), and recent advances by Fisk (2006, 2007) in modeling regional P and S wave spectra for explosions and earthquakes motivated the investigation of 2D grids of P/S spectral

ratios, as a function of all combinations of frequencies for P and S spectra, as a visual technique to assess better discriminants and to facilitate more replete comparisons to model calculations. The 2D P/S grids (shown above) illustrate some key features that are generally observed for a wide range of explosions and earthquakes, also at the test sites in India (Fisk et al., 2007) and North Korea. First, the Pn/Lg and Pn/Sn grids exhibit striking differences between earthquakes and explosions. Second, at hard-rock test sites the differences are most prominent for high frequency Pn and lower frequencies of Lg and Sn. This discriminant utilizes Pn and S-wave spectral content at frequencies mainly above or below the respective explosion P and S corner frequencies. Taylor et al. (2002) advocated cross-spectral P/S ratios. Now there is a model-based interpretation to substantiate their use and visual evidence to guide a more optimal choice of frequencies. Third, comparisons of model calculations to the empirical grids provide compelling evidence, beyond purely statistical metrics, confirming the physical basis of event identification results. The comparisons of the empirical and model grids (e.g., Figure 3) are compelling, not only in how they distinguish earthquakes and explosions, but also the unique signatures within the grids, including patterns and modulations. More detailed analysis of this spectral structure may perhaps be used to further enhance discrimination.

Using Pn/Lg(4–6 Hz) as a baseline case, 59 of 72 earthquakes and only 6 of 28 STS explosions were categorized properly. The other events were *undetermined*. The poor performance to confidently categorize explosions is mainly due to the larger variance of the earthquake population and the overlap of the explosion and earthquake populations when considering events over a wide range of locations. This observation, which is certainly not new, has motivated efforts to calibrate path effects by kriging, tomography, or other methods. Kriging, for example, has been shown to improve discrimination performance substantially. Using the cross-spectral Pn(2–10 Hz)/Lg(0.1–0.8 Hz) measure, all 28 STS UNEs and 74 earthquakes are categorized properly, even at 0.0005 significance (99.95% confidence). Its characterization of source differences dominates the variability from path effects. Further improvements could be obtained by kriging cross-spectral ratios to treat path effects, but this does not seem necessary. This is encouraging because efforts to calibrate path effects for application of P/S ratios to broad areas has been somewhat daunting. In addition to the improved performance, it is expected that many more events will have adequate SNR for Lg in the 0.1-0.8 Hz band than 4–6 Hz, increasing applicability of the cross-spectral discriminant. The benefit is marginal for the datasets used here because the earthquakes (mostly larger than mb 3.6) were originally selected under a previous study to calibrate a traditional Pn/Lg discriminant. Further work is needed to quantify this for smaller events.

The 2D grids and cross-spectral P/S measurements also improve discrimination performance over traditional bands at LNTS. In this case, the earthquakes were localized closer to the test site, and the events were typically recorded by numerous stations. In this case, all of the explosions and earthquakes were categorized properly even at the 0.00005 significance level. The performance is expected to degrade for earthquakes that are smaller, less well recorded, and/or farther from the test site. Nevertheless, this study illustrates the very significant improvement in performance that can be obtained over traditional P/S discriminants.

We also examined the performance of various measurements of 2D log Pn/Lg grids for NTS explosions and nearby earthquakes. The performance of analogous Pg/Lg measurements was not as good as for Pn/Lg, consistent with findings by Walter et al. (1995) and Fisk (2007). As for STS and LNTS, using a traditional Pn/Lg(4–6 Hz) spectral ratio as a baseline case, 95.7% of the explosions and 75.7% of the earthquakes were categorized properly at the 0.005 significance level. Using Pn(1-8 Hz)/Lg(4-10 Hz) values, 98.6% of the explosions and 89.2% of the earthquakes were categorized properly. One UNE (WACO) and three earthquakes could not be categorized, but neither could they be categorized using traditional Pn/Lg measurements. This is a noticeable improvement in performance over the baseline case, although not to the degree at STS for the following reasons. First, the performance of Pn/Lg(4–6 Hz) for NTS events is not as poor as for the STS case because the earthquakes are near NTS, so effects of path variability are much less. Second, there are up to four stations to average over for NTS events. Third, because of geophysical effects of porous rock on Lg from explosions, it was beneficial to use Lg spectral content at higher frequencies

(e.g., 4–10 Hz), especially for explosions above the water table at Yucca Flat. Despite the benefit, this range of frequencies is more similar to traditional high-frequency Pn/Lg. Note that discrimination performance is worse for explosions in media with higher gas porosity and cross-spectral Pn/Lg ratios seem to discriminate poorly for such events. These observations are consistent with the analysis and modeling results for STS and NTS by Taylor and Denny (1991).

Figure 11 suggests that the magnitude and/or distance corrections could be improved to reduce the variance of Pn/Lg for the earthquakes near NTS. In fact, one of the most useful aspects of the RMS-misfit measurements is to assess how well the MDAC model is fitting the spectra over a broad range of frequencies. Further improvements may also be obtained by combining the various spectral ratios in a multivariate test, as suggested by Figure 6. Valid treatment requires adapting the criteria to treat chi-square statistics. Further assessment of the methods is needed for additional and broader regional data.

## REFERENCES


Brune, J. N. (1970). Tectonic stress and the spectra of seismic shear waves from earthquakes, *J. Geophys. Res.* 75: 4997–5009.

Denny, M. D. and D. M. Goodman (1990). A case study of the seismic source function: Salmon and Sterling reevaluated, *J. Geophys. Res.* 95: 19,705–19,723.

Fisk, M. D. (2007). Corner frequency scaling of regional seismic phases for underground nuclear explosions at the Nevada Test Site, *Bull. Seism. Soc. Am*. 97: 977–988.

Fisk, M. D. (2006). Source spectral modeling of regional P/S discriminants at nuclear test sites in China and the Former Soviet Union, *Bull. Seism. Soc. Am*. 96: 2348–2367.

Fisk, M. D., S. R. Taylor, H. J. Patton, and W. R. Walter (2007). Next-generation MDAC discrimination procedure using multi-dimensional spectral analyses, in *Proceedings of the 29th Monitoring Research Review: Ground-Based Nuclear Explosion Monitoring Technologies*, LA-UR-07-5613, Vol. 1, pp. 551–560.

Mueller, C. S. and J. R. Murphy (1971). Seismic characteristics of underground nuclear detonations Part I: seismic spectrum scaling, *Bull. Seism. Soc. Am.* 61: 1675–1692.

Ryall, F. (2005). Analysis Summary of an Assembled Western U.S. Dataset, *Lawrence Livermore National Laboratory report, UCRL-TR-210751*.

Springer, D. L., G. A. Pawloski, J. L. Ricca, R. F. Rohrer, and D. K. Smith (2002). Seismic source summary for all U.S. below-surface nuclear explosions, *Bull. Seism. Soc. Am.* 92: 1806–1840.

Taylor, S. R. and M. D. Denny (1991). An analysis of spectral differences between Nevada Test Site and Shagan River nuclear explosions, *J. Geophys. Res.* 96: 6237–6245.

Taylor, S. R. and H. E. Hartse (1998). A procedure for estimation of source and propagation amplitude corrections for regional seismic discriminants, *J. Geophys. Res,* 103: 2781–2789.

Taylor, S. R., A. A. Velasco, H. E. Hartse, W. S. Phillips, W. R. Walter, and A. J. Rodgers (2002). Amplitude corrections for regional seismic discriminants, *Pure Appl. Geophys.* 159: 623–650.

Walter, W. R., E. Matzel, M. E. Pasyanos, D. B. Harris, R. Gok, and S. R. Ford (2007). Empirical observations of earthquake-explosion discrimination using P/S ratios and implications for the sources of explosion S-waves, in *Proceedings of the 29th Monitoring Research Review: Ground-Based Nuclear Explosion Monitoring Technologies*, LA-UR-07-5613, Vol. 1, pp. 684–693.

Walter, W. R., K. M. Mayeda, and H. J. Patton (1995). Phase and spectral ratio discrimination between NTS earthquakes and explosions. Part I: Empirical observations, *Bull. Seism. Soc. Am.* 85: 1050–1067.

Walter, W. R., K. D. Smith, J. L. O'Boyle, T. F. Hauk, F. Ryall, S. D. Ruppert, S. C. Myers, R. Abbot, and D. A. Dodge (2004). An Assembled Western United States Dataset for Regional Seismic Analysis, *Lawrence Livermore National Laboratory report, UCRL-TR-206630*.

Walter, W. R. and S. R. Taylor (2002). A Revised Magnitude and Distance Amplitude Correction (MDAC2) Procedure for Regional Seismic Discriminants: Theory and Testing at NTS, *Lawrence Livermore National Laboratory report, UCRL-ID-146882, LA-UR-02-1008*.

# IDENTIFYING ISOTROPIC EVENTS USING A REGIONAL MOMENT TENSOR INVERSION

Sean R. Ford[1,2], Douglas S. Dreger[1], and William R. Walter[2]

Berkeley Seismological Laboratory[1] and Lawrence Livermore National Laboratory[2]

Sponsored by National Nuclear Security Administration

Contract Nos. DE-FC52-06NA27324[1] and AC52-07NA27344[2]
Proposal No. BAA06-42

## ABSTRACT

The deviatoric and isotropic source components for 17 explosions at the Nevada Test Site, as well as 12 earthquakes and 3 collapses in the surrounding region of the western US, are calculated using a regional time-domain full waveform inversion for the complete moment tensor. The events separate into specific populations according to their deviation from a pure double-couple and ratio of isotropic to deviatoric energy. The separation allows for anomalous event identification and discrimination between explosions, earthquakes, and collapses. Confidence regions of the model parameters are estimated from the data misfit by assuming normally distributed parameter values. We investigate the sensitivity of the resolved parameters of an explosion to imperfect Earth models, inaccurate event depths, and data with a low signal-to-noise ratio (SNR) assuming a reasonable azimuthal distribution of stations. In the band of interest (0.02–0.10 Hz) the source-type calculated from complete moment tensor inversion is insensitive to velocity model perturbations that cause less than a half-cycle shift (<5 sec) in arrival time error if shifting of the waveforms is allowed. The explosion source-type is insensitive to an incorrect depth assumption (for a true depth of 1 km), but the goodness-of-fit of the inversion result cannot be used to resolve the true depth of the explosion. Noise degrades the explosive character of the result, and a good fit and accurate result are obtained when the SNR is greater than 5. We assess the depth and frequency dependence upon the resolved explosive moment. As the depth decreases from 1 km to 200 m, the isotropic moment is no longer accurately resolved and is in error between 50% and 200%. However, even at the most shallow depth the resultant moment tensor is dominated by the explosive component when the data has a good SNR. The sensitivity investigation is extended via the introduction of the network sensitivity solution, which takes into account the unique station distribution, frequency band, and SNR of a given test scenario. An example of this analysis is presented for the North Korea test, which shows that in order to constrain the explosive component one needs a certain station configuration. In the future we will analyze the bias in the source-type parameters due to error in the Green's function by incorporating a suite of suitable velocity models in the inversion.

## OBJECTIVES

We implement the time-domain full-waveform inversion of regional data for the complete moment tensor devised by Minson and Dreger (2008) after Herrmann and Hutcheson (1993) based on the work of Langston (1981). In general, synthetic seismograms are represented as the linear combination of fundamental Green's functions where the weights on these Green's functions are the individual moment tensor elements. The Green's functions for a one-dimensional (1-D) velocity model of eastern California and western Nevada (Song et al., 1996) are calculated as synthetic displacement seismograms using a frequency-wavenumber integration method (Saikia, 1994). The synthetic data are filtered with a 4-pole acausal Butterworth filter with a low corner of 0.02 Hz and a high corner of 0.05 Hz and 0.1 Hz for events with $M_W \geq 4$ and $M_W < 4$, respectively. At these frequencies, where dominant wavelengths are tens of kilometers, we assume a point source for the low-magnitude regional events investigated in this study. The point source assumption allows for linearization in the time-domain, which is where we carry out the least-squares inversion.

## RESEARCH ACCOMPLISHED

We analyzed events that were digitally recorded with a high signal-to-noise ratio by more than two regional broadband stations. Three-component data were collected from a total of 52 stations from the US National Seismic Network, IRIS/USGS, Berkeley Digital Seismic Network, Trinet, and the Lawrence Livermore National Laboratory (LLNL) network (Figure 1). All data is freely available from IRIS via the internet except the LLNL historic network data, which is available on compact disk (Walter et al., 2004). Not all stations recorded all events, and a total of 16 stations were used in the inversion of the explosion data, which are listed in Figure 1. We remove the instrument response, rotate to the great-circle frame, integrate to obtain displacement, and use the same filter as for the synthetic seismograms. The LLNL network (white triangles in Figure 1) was composed of Sprengnether instruments with limited long-period response, and for those data we used a passband of 10–30 seconds for both the data and synthetics.

We calibrated the algorithm by calculating the full moment tensor for the 1992 Little Skull Mountain event. We find a solution at all depths within 5 km of the reported depth. The depth that produces Green's functions that best fit the data is used in the final solution. Fit is quantified by the variance reduction (VR), which is a normalized variance given by

$$\mathrm{VR} = \left[ 1 - \frac{\sum_i (d_i - s_i)^2}{\sum_i d_i^2} \right] \times 100 \ ,$$

where $i$ are the displacements at all times for all components at all stations, and $d$ and $s$ are the data and synthetic, respectively.

We also allow the Green's functions calculated at a given distance to shift relative to the data to address small hypocentral errors and uncertainty in the velocity model used to compute the Green's functions. The shift that produces the best fit is used in the final solution. We limit the shift to less than 5 and 3 sec for high-pass corners of 0.05 and 0.10 Hz, respectively. The allowed time shift is large enough to make up for small hypocentral errors, but small enough to disallow cycle-skipping that could produce erroneous mechanisms. The sensitivity of the time shift relative to the assumed velocity model will be discussed later in the paper. The full moment tensor solution is decomposed to an isotropic and deviatoric component. We calculate the total scalar moment ($M_0$) as

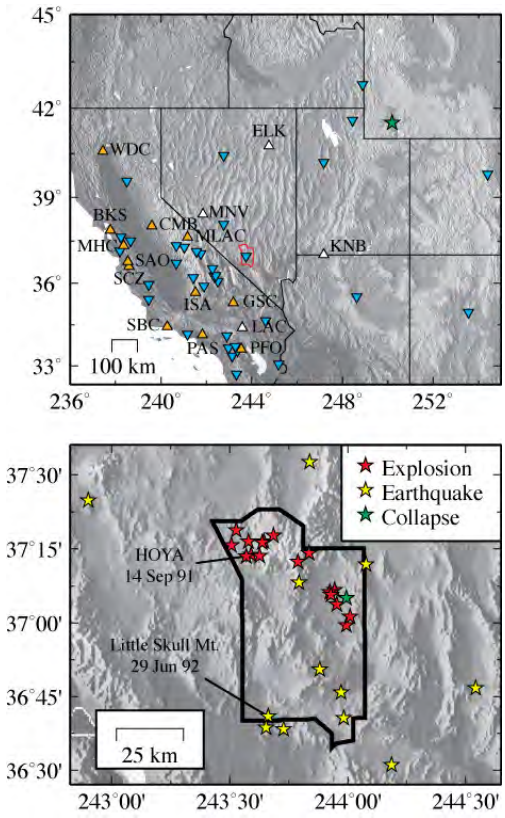


**Figure 1. Map of the Western US with stations (blue inverted triangles), earthquakes (yellow stars), explosions (red stars), and collapses (green stars) used in this study. The bottom panel is a blow-up of the Nevada Test Site (NTS) region with the NTS outlined in black and in the top panel in red.**

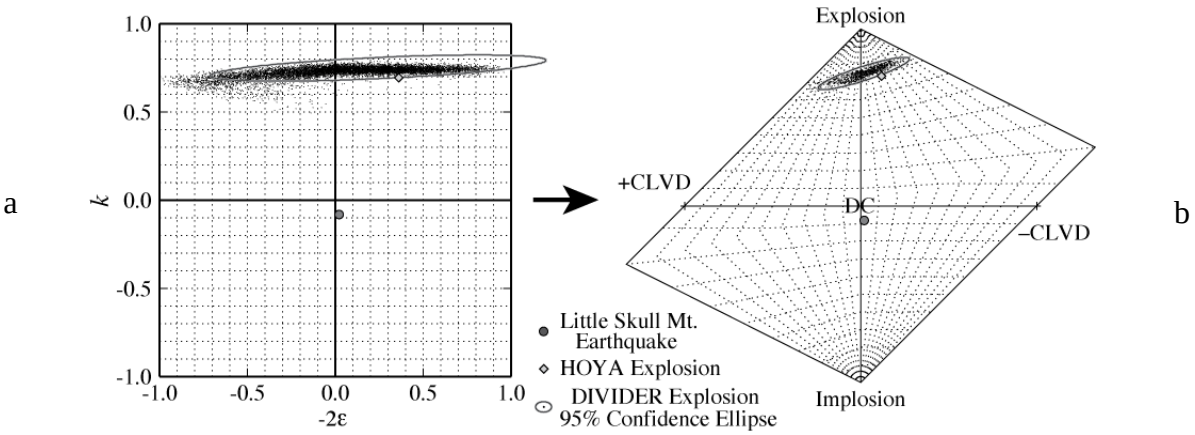


**Figure 2. Source-type plot for the Little Skull Mt. earthquake (dark grey circle), NTS test HOYA (light grey diamond), and bootstrap population of the NTS test DIVIDER (black dots) along with its 95% confidence region (grey ellipse). a) The source-type parameters ($k$, $-2\varepsilon$) given on a linear plot. b) The source-type plot of Hudson et al. (1989) with theoretical mechanisms plotted as well.**

defined by Bowers and Hudson (1999), where $M_0$ is equal to the sum of the isotropic moment ($M_{ISO}$ = ($M_{11}$+$M_{22}$+$M_{33}$)/3) and deviatoric moment ($M_{DEV}$), which is the largest deviatoric eigenvalue. For the Little Skull Mountain event we find $M_0 = 3.7 \times 10^{17}$ N-m ($M_W$ = 5.6), and the solution has a negligible isotropic moment ($M_{ISO}$ = $-0.31 \times 10^{17}$ N-m) so there is little change between the full and deviatoric solutions. The solution fits the data very well (Figure 2b) and is similar to the double-couple solution of Walter (1993), the deviatoric solution of Ichinose et al. (2003), and the full solution of Dreger and Woods (2002). With the same algorithm we calculate the full moment tensors of 17 nuclear test explosions at the Nevada Test Site (NTS) (Figure 1). In the case of explosions and collapses we calculate Green's functions at a depth of 1 km. The sensitivity of this assumption will be investigated later in the paper. An example of the analysis is given by the solution for the 1991 HOYA test, where the largest component in the decomposition is isotropic, and it contributes 70% of the total scalar moment.

**Source-Type Plot**

It is difficult to grasp the source-type from the standard focal mechanism plot for events with a large non-double-couple (DC) component. For example, one cannot discern the relative contributions of the isotropic and deviatoric components from the full focal mechanism for the HOYA explosion. In order to get at the tectonic contribution to the explosion, one could separate the deviatoric component into a DC and a compensated linear vector dipole (CLVD) that share the orientation of the major axis, but decompositions of this type are non-unique, where for example the DC and CLVD decomposition could be replaced by two DCs (see Julian et al. [1998]) for further decompositions). In an attempt to better characterize mechanisms, we follow the source-type analysis described in Hudson et al. (1989) and calculate $-2\varepsilon$ and $k$, which are given by $\varepsilon = \frac{-m'_1}{|m'_3|}$ and $k = \frac{M_{ISO}}{|M_{ISO}| + |m'_3|}$, where $m'_1$, $m'_2$ and $m'_3$ are the deviatoric principal moments for the N, P, and T axes, respectively, and $|m'_1| \le |m'_2| \le |m'_3|$. A measure of the departure of the deviatoric component from a pure DC mechanism, $\varepsilon$, is 0 for a pure double-couple and ±0.5 for a pure CLVD. A measure of the volume change is $k$, where +1 would be a full explosion and −1 a full implosion. For the Little Skull Mountain earthquake and the NTS explosion, HOYA, $-2\varepsilon$ and $k$ are given in Figure 2a. The earthquake is almost at the origin, which defines a pure DC, whereas the nuclear test is near where a theoretical explosion would plot. In order to estimate formal error in the fit, we create moment tensor populations by bootstrapping the residuals of the fit $n$times with replacement and then use those populations of size $n$ to calculate $-2\varepsilon$ and $k$, resulting in their own populations to which we fit normal distributions. Figure 2a shows the population of $n$ = 1,000 along with the 95% confidence region for the DIVIDER explosion. Increasing $n$ resulted in no change to the confidence regions.

Hudson et al. (1989) transform the parameters $-2\varepsilon$ and $k$ so that the displayed plot will have equal normal probability areas based on the assumption that the smallest principal moments can take any value between ± the largest absolute principal moment (Julian et al., 1998). The plot derived this way is the source-type plot, and it is

shown in Figure 2b for the parameters from the Little Skull Mt. earthquake and HOYA explosion. Figure 2b also shows the transformed bootstrap population for the DIVIDER explosion and its associated 95% confidence region. The transformation makes the assumption of normality in the error distribution valid as can be seen by the improved fit of an error ellipse to the bootstrap population between Figure 2a and b. The Hudson et al. (1989) plot is a superior way to display source-type and analyze error in the parameters. The error ellipses are not shown for the Little Skull Mt. earthquake or HOYA explosion examples because the error regions are too small to notice a difference due to the transformation.

We carry out similar analyses for 11 more earthquakes and three collapses (one cavity and two mine) and produce the source-type plot in Figure 3 along with the 95% confidence regions. The nuclear tests occupy the region where $k > 0.5$, the earthquakes cluster near the origin, and the collapses plot almost exactly at (1,-5/9), which is the location for a closing crack in a Poisson solid. Deviations from these trends will be discussed later.

**Sensitivity Analysis**

The relatively small area of the confidence regions given in Figure 3 and the excellent synthetic seismogram fit to the data as quantified by VR gives us great confidence that the assumed velocity model and depth are correct and the estimated moment tensor solutions are robust. However, these measures of goodness-of-fit assume the underlying model used to invert the data is correct. In the following section we will test these assumptions with synthetic data from a theoretical explosion ($-2\varepsilon=0$, $k=1$) created for two experimental geometries. The first geometry, referred to as 'Ideal,' is eight stations at distance increments between 100 and 300 km each separated by 45°. The second station geometry mirrors the analysis for the HOYA explosion. The synthetic data are filtered in the same two bands (20–50s and 10–50s) used in the analysis and when combined with the two geometries results in 4 scenarios.

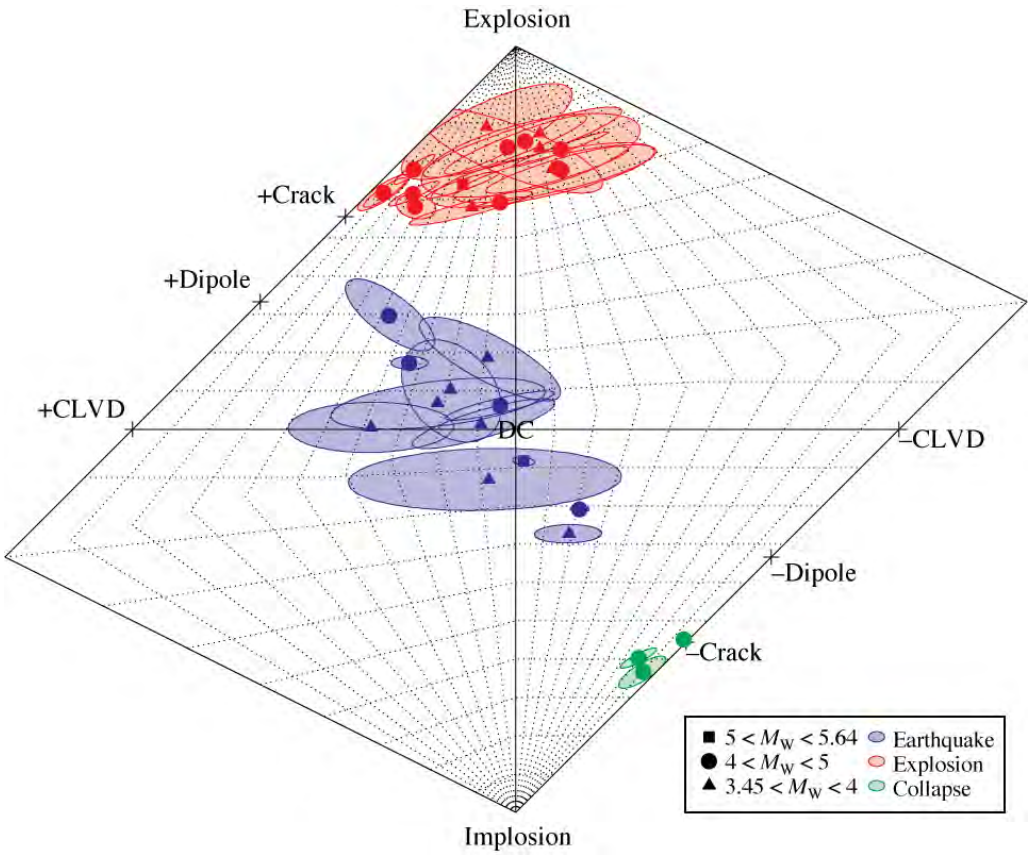


**Figure 3. Source-type plot of the 12 earthquakes (blue), 17 explosions (red), 3 collapses (green), and their associated 95% confidence regions (shaded). The magnitude of the event is given by the symbol. The abscissa measures the amount of volume change for the source and the ordinate measures the departure from pure DC. Theoretical mechanisms (crosses) are plotted for comparison.**

The error analysis presented above is due to a misfit of the data by the least-squares inversion. Part of the misfit may be due to nonstationary noise, and we test the sensitivity of the inversion to different SNRs. In order to best approximate real-world noise conditions, we derive the noise signal from data prior to the first arrival from the nuclear test METROPOLIS (10 March 1990) at station ANMO for all three components. The amplitude of this noise signal is bandpassed to match the synthetic data and multiplied by a factor so as to create a final synthetic signal with the desired SNR (ratio of synthetic data root-mean-square amplitude to noise root-mean-square amplitude).

The noise analysis has very little frequency dependence, so for clarity we only show results from the analysis in the 20–50 sec frequency band in Figure 4a. The Ideal configuration produces the best scenario where a large $k$ is retrieved (>0.3) when the SNR is greater than 2. For all scenarios $k > 0.5$ when SNR > 5. Typically, we use data with an SNR greater than 10; however, there are a few cases where the SNR is close to 3. An example of this type of data is for the DIVIDER explosion, which produced a signal that was right on the limit of acceptable SNR but still produced a well-fit solution.

Another source of error not incorporated into the formal error analysis is incorrectly calculated Green's functions due to ignorance of the true event depth. The method that produces the results presented above attempts to find an optimal depth for the earthquakes by perturbing the reported depth a few kilometers, performing the inversion, and finding the best-fit solution. For all explosions and collapses, the depth is fixed at 1 km. If this method were to be used for an event with an unknown source type, the depth could be an important source of error, as well as an important parameter for identification. We perform another synthetic test in which an explosion at 1 km is inverted with Green's functions calculated at varying depths.

The source depth analysis is not greatly affected by the two station configurations considered here, therefore we only show results for the HOYA configuration in Figure 4b. The result at an incorrect depth of 2 km is virtually indistinguishable from the true answer. When the source is moved to 3 km depth there is a small step decrease in $k$ due to a layer in the velocity model that begins at a 2.5-km depth. However, $k > 0.5$ for incorrect depths < 17 km with slightly more sensitivity in $k$ and a worse fit in the high-frequency band (10–50 sec) compared to the low-frequency band (20–50 sec). The relative insensitivity of the solution to mislocated depth for an explosion is different than is observed for DC events. Dreger and Woods (2002) show that the VR of the Little Skull Mountain earthquake solution is definitively maximized at the assumed true event depth. Thus, while the depth sensitivity of explosions is poor, the method is able to determine the depth of non-explosion sources, which also provides an important level of event screening.

Finally, we test how error in the assumed Earth structure is mapped through the Green's functions to error in the solution. We start with the well-calibrated Song et al. (1996) velocity model (Table 1) and perturb the velocities and depths of the layers using averaged parameters from another plausible velocity model (WestUS; Ammon, 1999) and a model from Southern California (SoCal; Dreger and Helmberger, 1990).

In order to produce a sensitivity test that best mimics our analysis, we use the time shift rule to filter the models. This means that we only allow velocity models that produce Green's functions where the time shift between data and synthetics that produces the best-

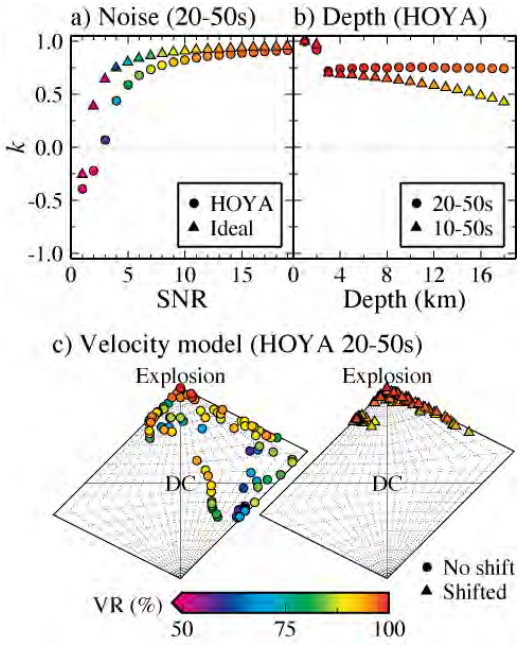


**Figure 4. Sensitivity analysis. a) Noise is added to the inversion of 20-50 sec synthetic data while velocity model and depth (1 km) are kept fixed for the HOYA (circle) and Ideal (triangle) scenarios. b) The inversion using the HOYA configuration is carried out assuming an incorrect depth while the velocity model is kept fixed for data in the 20–50-sec (circle) and 10–50-sec (triangle) band. c) The inversion using the HOYA configuration for 20–50 sec synthetic data is carried out for different three-layer velocity models where the data are not shifted relative to the Green's functions (left panel, circles) and allowed to shift less than 5 sec (right panel, triangles). The symbols are colored as a function of VR.**

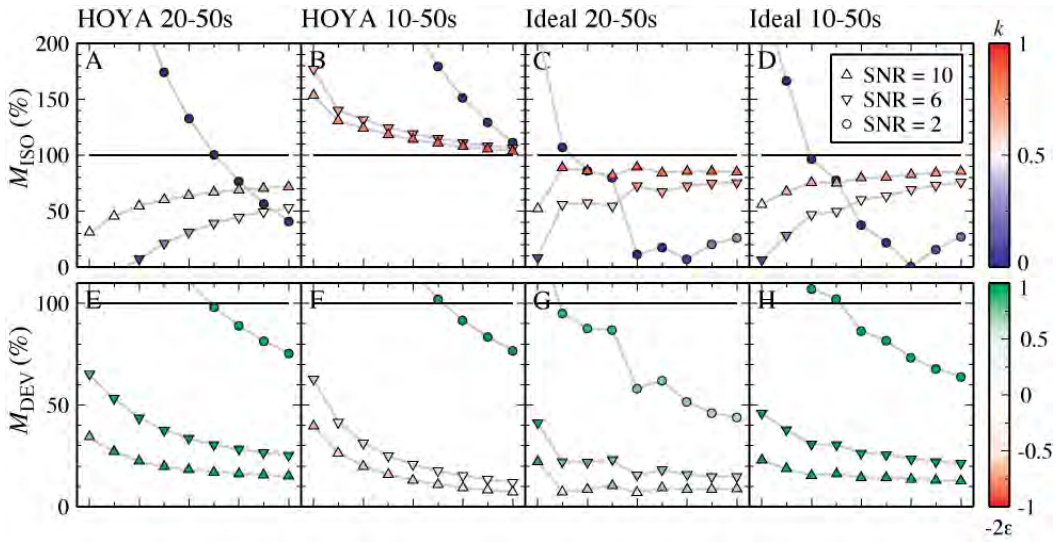


**Figure 5. Vanishing traction sensitivity. Synthetic data for a pure explosion ($k$=1) is inverted at depths less than 1 km for varying SNR and the four scenarios discussed in the text. a-d) Resolved $M_{ISO}$ for SNR values of 2 (circle) 6 (inverted triangle) and 10 (triangle) where the value for an inversion without noise (SNR=∞) is given by the black line (100%). $k$ is given by the color. e-h) Resolved $M_{DEV}$ for SNR values of 2, 6, and 10 with the same symbols, where the total scalar moment for an inversion without noise (SNR=∞) is given by the black line (100%), and $M_{DEV}$ should be 0. -2$\varepsilon$ is given by the color.**

fit solution is less than or equal to 5 or 3 sec from the theoretical arrival time for high-pass corners of 0.05 or 0.10 Hz, respectively. Primarily due to the velocity model filtering there is little difference among the scenarios so we only show source-type plots for the HOYA configuration in the 20–50-sec frequency band in Figure 4c. For this scenario the number of acceptable models is reduced to 88, and although not all possible combinations of model parameters are used, each parameter perturbation given is employed at least once.

Without shifting, there are a few velocity models that produce well-fit solutions (VR>90%) with mechanisms that are almost purely DC. However, when shifting is allowed, all velocity models produce good fits with highly explosive sources ($k$~>0.4).

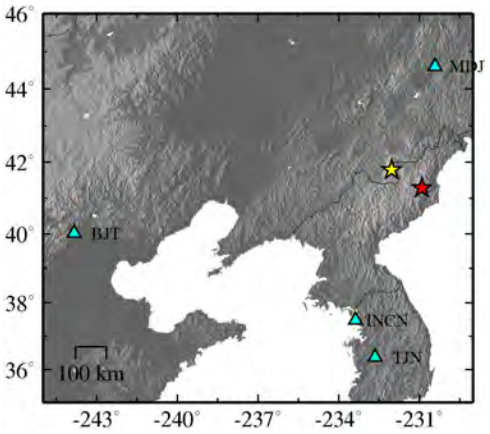


**Figure 6. Map of the YSKP with the North Korea test (red star) and nearby earthquake (yellow star) as well as the stations used in this study (blue triangles).**

## Free-Surface Effects

Another consideration is the ability to resolve displacements for explosions near the surface. Since tractions normal to the vertical vanish at the free surface, the excitation coefficients associated with those tractions must vanish (Julian et al., 1998). Therefore, at the free surface the moments of $M_{13}$, $M_{23}$, and the isotropic part of the $M_{ij}$ cannot be resolved. Given and Mellman (1986) showed that at a source depth of 1 km, the fundamental mode excitation functions associated with the moments listed previously effectively go to zero. We investigate the potential problems associated with vanishing traction at the free surface by inverting noisy data from a synthetic explosion source at depths between 200 and 1,000 m in a three-layer 1D velocity model using Green's functions calculated at those same depths.

The ability to resolve an explosive component is dependent on the station distribution, frequency, and SNR of the analysis, therefore Figure 5 shows all four scenarios. An explosive component ($k$>0.5) can be resolved under favorable noise conditions at a depth greater than 300 m for all scenarios, though with error in

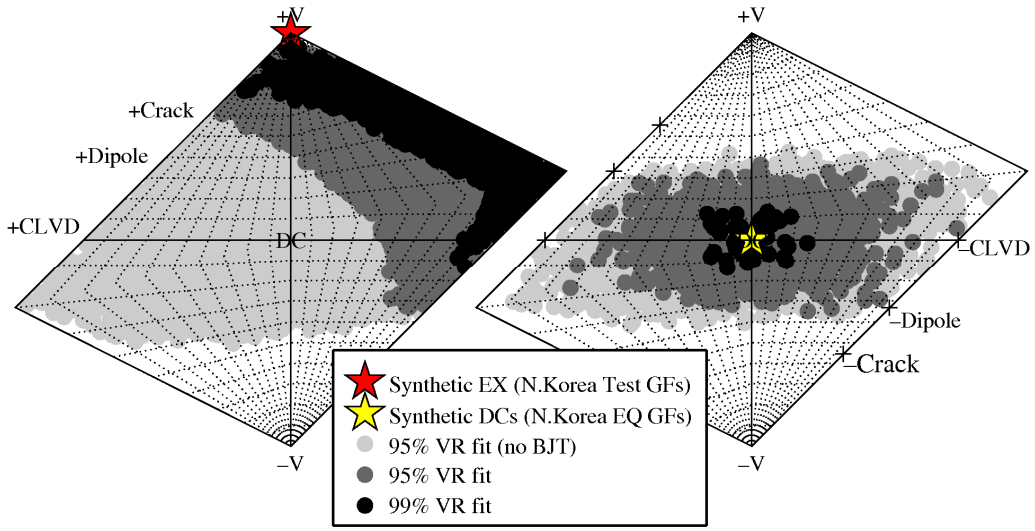


**Figure 7. Network sensitivity solutions for the North Korea explosion (left) and earthquake (right). The actual solution is given by the stars and other solutions for a given threshold VR are shown. The 95% VR fit is given with (dark gray) and without station BJT (light gray).**

$M_{ISO}$ between 50–150% (Figure 5a-d). The error is inversely proportional to the depth. For all scenarios, but the HOYA configuration at 20–50 sec (Figure 5a), favorable noise means SNR ≥ 6. The change in $M_{ISO}$ is due to a change in $M_{33}$ relative to the other dipole components, and this produces an erroneous deviatoric component. The moment of deviatoric component can be up to 50% of the theoretical isotropic moment (Figure 5e-h) and since it is related to the error in $M_{ISO}$ it is inversely proportional to the depth. At less than 200 m depth, the synthetic displacements become too small and the solution using these particular Green's functions is unreliable.

**Network Sensitivity Solution**

We extend the database of solutions by incorporating the North Korea test and a nearby earthquake that occurred on 16 December 2004 (Figure 6). We employ the records of four stations that recorded the events well in the period band of interest. We use the solutions to present a new way to estimate constraints on source-type. As discussed above, the ability to resolve a well-constrained solution is dependent on station configuration, data bandwidth, and SNR. The analysis presented in the previous section tried to assess error in those experimental conditions, but it is

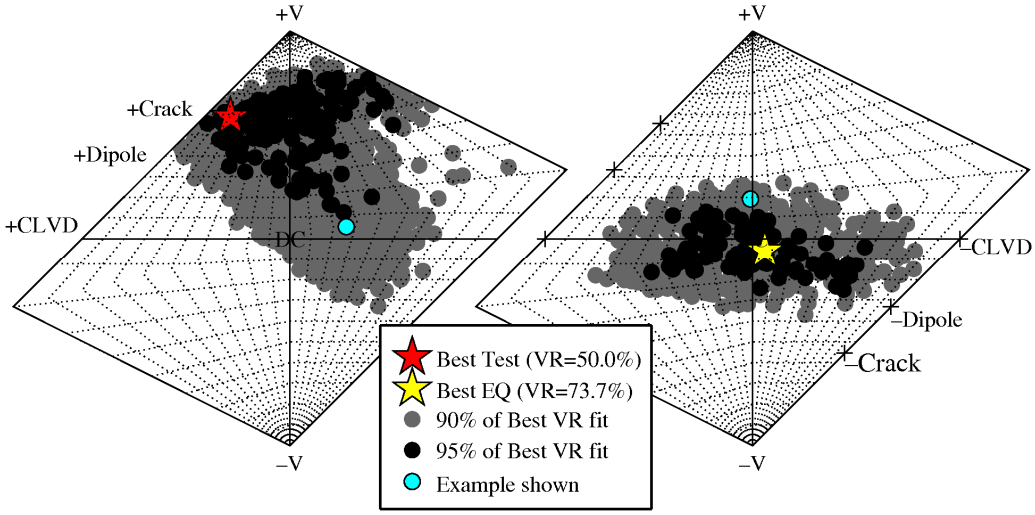


**Figure 8. Network sensitivity solutions for the North Korea explosion station configuration and Green's functions (left) and earthquake setup (right). The best solution is given by the stars and different levels of fit, as quantified by VR, are shown. The source-types of the solutions given in Figures 10 and 11 are also shown (blue circles).**

difficult to state steadfast rules for what source-types can be resolved for all conditions, when different conditions lead to different levels of confidence in the solution. Therefore, we calculate two types of forward confidence analyses, which we call network sensitivity solutions.

The first type of solution assumes a very large SNR and produces explosive or double-couple synthetics for a given station configuration using the Green's function employed in the inverse solution. In this case, the MDJ2 model is used to calculate the Green's functions. These model explosions and earthquakes are then compared with synthetic data produced by thousands of random seismic moment tensors that represent a uniform distribution of all possible moment tensors. A VR is calculated between the synthetics produced by the distribution of moment tensor and the perfect explosion or DC. In this way, we produce a source-type plot that shows solutions for a given threshold VR. Figure 7 shows the source-type plot constructed in this way for the North Korea test and nearby earthquake configurations. Without station BJT, most solutions fit the model explosive just as well as an explosion (Figure 7, left), whereas any source with an isotropic source greater than 50% does not fit the DC synthetics well (Figure 7, right). The use of this type of network sensitivity solution can give the user a feeling for what level of confidence can be expected in a given solution for the experimental setup employed.

The network sensitivity solution is also produced using the actual data in place of the synthetic explosion or DC. This plot can help the user understand the limits of confidence in the best solution. Figure 8 shows this type of network sensitivity solution for the same events as in Figure 7. The solutions are fairly well-constrained, but there

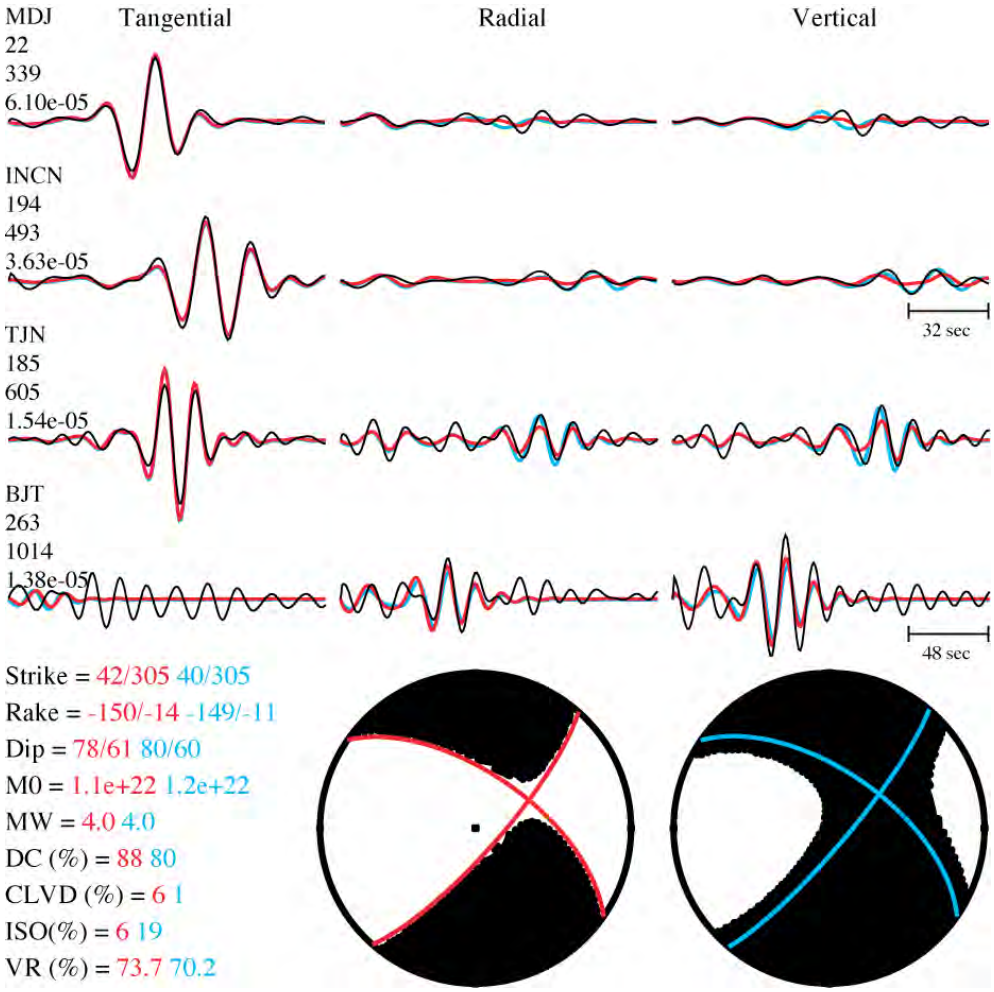


**Figure 9. Waveform fits and focal mechanism for the best-fit (red) and fairly-well fit (blue) solutions using data from the earthquake near the North Korea test. The station name, azimuth, distance, and maximum displacement in cm are given next to the traces. Information on the sources is also given.**

are some possible solutions with good VR that are near the DC section of the source-type plot, for the explosion data (Figure 8, left), and solutions that have some isotropic component, for the earthquake data (Figure 8, right). An understanding of what the VR means for these potentially confidence-busting solutions can be acquired by examining the data-fit. Figures 9 and 10 give the data fit for the best solutions (stars in Figure 8) and those for 'problematic' solutions with a high VR (blue circles in Figure 8). Visual inspection of the fits show that they are virtually indistinguishable and that both solutions may be possible given the data limitations. This is not so much a problem for the earthquake solution (Figure 9) since the percent DC is still relatively high, but the nuclear test solutions are fairly different (Figure 10).

## CONCLUSIONS AND RECOMMENDATIONS

The populations of earthquakes, explosions, and collapses separate in the source-type plot. These initial results are very encouraging and suggest a discriminant that employs the source-type plot parameters $(-2\varepsilon, k)$. Another advantage of the source-type plot is its display of 2-D error regions. In this way one can test a hypothesis that an event has a non-DC component. The source-type analysis can also be utilized to estimate model-based error as well. The error introduced by ignorance of the event location and Earth structure can be calculated with a Monte Carlo approach, where several solutions are computed for a-priori distributions of the hypocentral location and Earth model obtained from independent analyses.

We try to give some insight to the depth sensitivity of the method with Figure 4b, which shows that the use of this

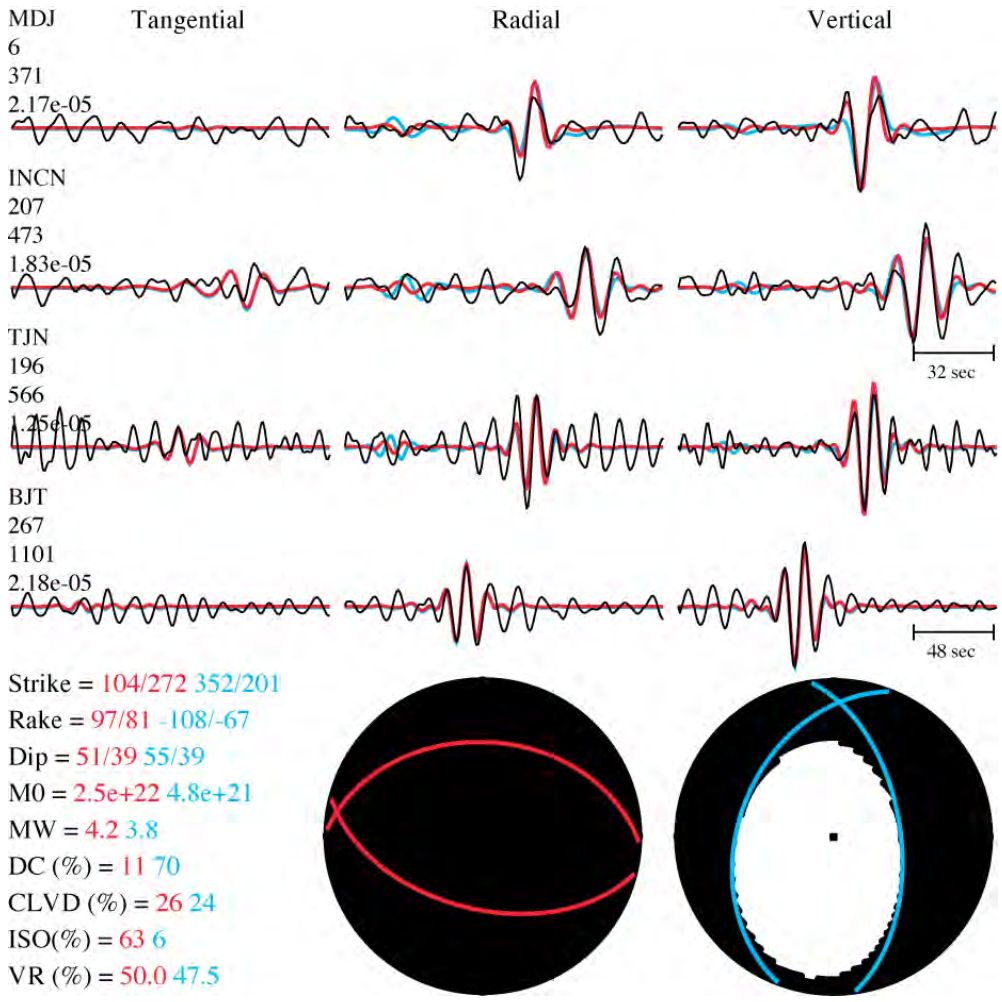


**Figure 10. Waveform fits and focal mechanism for the best-fit (red) and fairly-well fit (blue) solutions using data from the North Korea test. See Figure 9 for more information.**

method as a precise depth discriminant is not plausible for the frequencies used here, though sensitivity does increase for the higher-frequency band. These results are a demonstration of the fact that an isotropic radiation pattern has no sensitivity to takeoff angle, which depends on depth. As shown by Dreger and Woods (2002), there is limited resolution of the shallow depth of explosions using regional distance data. Although an explosive radiation pattern alone does not have depth sensitivity, the relative excitation of low-frequency body waves (Pnl) and Rayleigh waves does enable the method to discern the relatively shallower depths of explosions compared to earthquakes.

The velocity model analysis shown in Figure 4c suggests that the maximum-shift rule used in the analysis is a good proxy for evaluating the appropriateness of the velocity model. The level of departure of a given velocity model from the true model is station distribution, frequency, and SNR dependent. Therefore, it is a good idea to perform this style of sensitivity test to evaluate the amount of deviation a certain experimental setup will allow, because if the velocity model is poorly calibrated, then a good fit to the data can be obtained, but the solution may be inaccurate. The network sensitivity solution is a good way to accomplish this type of testing.

The change in moment due to the loss of traction at the free surface affects yield estimation, though event discrimination is still reliable at high SNR. A result of this change in moment is that the deviatoric moment becomes non-zero and could be significant at very shallow depths (Z<500 m) and low SNR (SNR<6). The moment manifests as a CLVD component, which means that interpretation of non-isotropic energy may be flawed for shallow events even with high SNR data. Though, as Figure 5 suggests, this effect is station configuration, frequency, and SNR dependent.

## ACKNOWLEDGEMENTS

We thank Jeff Stevens for discussions regarding free surface effects and Howard Patton for insights on the CLVD contribution to the explosion source. We also thank Bruce Julian for scripts to make the source-type plots.

## REFERENCES

Bowers, D. and J. A. Hudson (1999). Defining the scalar moment of a seismic source with a general moment tensor, *Bull. Seis. Soc. Am.* 89: (5), 1390–1394.

Dreger, D. and B. Woods (2002). Regional distance seismic moment tensors of nuclear explosions; seismic source mechanism through moment tensors, *Tectonophysics* 356: (1–3), 139–156.

Given, J. W. and G. R. Mellman (1986). Estimating explosion and tectonic release source parameters of underground nuclear explosions from Rayleigh and Love wave observations, Tech. rep., Sierra Geophysics Report No. SGI-R-86-126, Kirkland, WA.

Herrmann, R. B. and K. Hutchensen (1993). Quantification of MLg for small explosion, Tech. rep., Phillips Laboratory Report PL-TR-93-2070.

Hudson, J. A., R. G. Pearce, R. G., and R. M. Rogers (1989). Source type plot for inversion of the moment tensor, *J. Geophys. Res*. 9: (B1), 765–774.

Ichinose, G. A., J. G. Anderson, K. D. Smith and Y. Zeng (2003). Source parameters of Eastern California and Western Nevada earthquakes from regional moment tensor inversion, *Bull. Seis. Soc. Am*. 93: (1), 61–84.

Julian, B. R., A. D. Miller, and G. R. Foulger (1998). Non-double-couple earthquakes; 1. Theory, *Rev. Geophys* 36: (4), 525–549.

Langston, C. A. (1981). Source inversion of seismic waveforms; the Koyna, India, earthquakes of 13 September 1967, *Bull. Seis. Soc. Am*. 71: (1), 1–24.

Minson, S. and D. Dreger (2008). Improved seismic moment tensor inversion, *Geophys J. Int.*

Saikia, C. K. (1994). Modified frequency-wavenumber algorithm for regional seismograms using Filon's quadrature; modelling of Lg waves in Eastern North America, *Geophys. J. Int*. 118: (1), 142–158.

Song, X. J., D. V. Helmberger and L. Zhao (1996). Broad-band modelling of regional seismograms; the basin and range crustal structure, *Geophys. J. Int*. 125: (1), 15–29.

Walter, W. R. (1993). Source parameters of the June 29, 1992 Little Skull Mountain earthquake from complete regional waveforms at a single station, *Geophys. Res. Lett*. 20: (5), 403–406.

Walter, W. R., K. D. Smith, J. L. O'Boyle, T. F. Hauk, F. Ryall, S. D. Ruppert, S. C. Myers, R. Abbot, and D. A. Dodge (2004). An assembled western United States Dataset for regional seismic analysis, LLNL, UCRL-TR-206630.

# EXTENSION OF $M_S$(VMAX) TO GLOBAL PATHS

Jill M. Franks[1], Brian M. Pope[2], Richard A. Reed[2], Michael F. Jezard[1], Gordon D. Kraft[1], Siroos Motlagh[1], Steven J. LeClaire[2], Michael S. Antolik[1], Anne S. Henson[2], and Kevin D. Hutchenson[1]

Quantum Technology Sciences, Inc.[1] and Science Applications International, Corp.[2]

Sponsored by Air Force Technical Applications Center

Contract No. FA8620-05-C-4301

## ABSTRACT

Recent work with a prototype application for variable-period Rayleigh-wave magnitudes (Russell, 2006) has reported use of the $M_s$(VMAX) technique for periods between 8 and 25 seconds (Bonner et al., 2006a, 2006b, 2007). More recently, the technique has been extended to 40 seconds (Bonner, 2007). In all previous studies, the data were limited to continental paths and thoroughly reviewed.

This study has attempted to evaluate an operational scenario whereby all surface-wave paths are considered. Two groups of data have been utilized, twenty-seven (27) shallow events from the Asian continent and a larger (143 events) global event group with a broader depth range. All events have been reviewed by an analyst for validity. To obtain a better understanding of period and path effects, the data have been subdivided into three period ranges (8–17 seconds, 17–25 seconds, and 25–40 seconds) and separated by predicted group slowness into oceanic paths (*slow* < 32.25 sec/deg), continental paths (*slow* > 38.0 sec/deg), and mixed oceanic-continental paths (32.25 sec/deg ≤ *slow* ≤ 38.0 sec/deg).

Past studies have demonstrated the $M_S$(VMAX) technique works well for continental paths between 8 and 25 seconds (Bonner et al., 2006b, 2007). This study shows stable results for all paths (oceanic, mixed, and continental) between 8 and 25 seconds. Since the data have been shown to be path independent, the $M_S$(VMAX) technique may provide an automated replacement for $M_S$, allowing the inclusion of regional stations with Airy phases and reducing the analyst burden.

## OBJECTIVES

Our objective is to extend and evaluate the $M_S$(VMAX) magnitude calculation on a global scale, utilizing all available station paths, rather than being limited to continental paths. Extending the technique to all surface-wave paths is an important step towards automating the process in an operational monitoring environment, where manual analysis and calculation are not feasible for all events.

## RESEARCH ACCOMPLISHED

**Background.** Russell (2006) developed a magnitude equation, called $M_s$(VMAX), which was originally intended for surface wave paths through typical continental crust, however, it was unclear how well the original equation would extend beyond continental paths to other paths (oceanic or mixed continental-oceanic). The equation is

$$M_{s(b)} = \log(a_b) + \frac{1}{2}\log(\sin(\Delta)) + 0.0031\left(\frac{20}{T}\right)^{1.8}\Delta - 0.66\log(f_c) - 0.43$$

where $T$ is the period, $a_b$ is the amplitude of the Butterworth-filtered surface waves, $\Delta$ is the distance in degrees, and $f_c \le \frac{0.6}{T\sqrt{\Delta}}$ is the corner filter frequency of a third-order Butterworth band-pass filter with center period $T$ and bandwidth $2f_c$. The $M_s$(VMAX) method allows measurement of surface-wave magnitudes at both regional and teleseismic distances, while conventional $M_s$ measures magnitudes at teleseismic distances with periods between 17–23 seconds.

Methodologies using this approach have been presented by Bonner et al. (2006b, 2007). Differences between this and prior studies are the incorporation of all paths from an event and the use of an automated code to routinely process data. The automated results were subsequently reviewed; however, only automated measurements are presented. The interactive review of the measurements was used to evaluate outliers.

**Data.** The data used in this study consist of earthquakes obtained from the U.S. National Data Center (USNDC). The data were divided into two sets: 27 shallow events from the Asian continent and 143 globally-distributed events that contain a broader depth range and more path diversity (Figure 1). All events were reviewed by an analyst for validity prior to inclusion in this study.

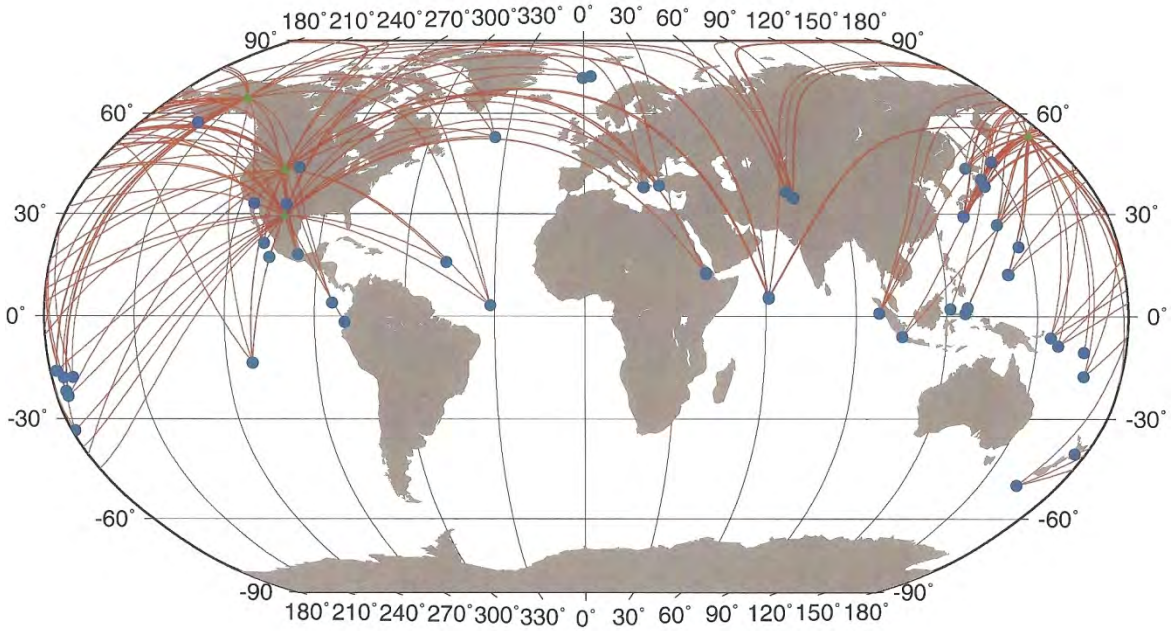


**Figure 1. Representative paths showing the inclusion of oceanic, mixed, and continental components.**

In order to better understand path and period-dependent effects, the data were partitioned into three period ranges: – 8–17 seconds, 17–25 seconds, and 25-40 seconds. These partitions were chosen based on the applicable period ranges of conventional $M_s$ (17–23 seconds) and to investigate the application of $M_s$(VMAX) to shorter (8–17 seconds) and longer periods (25-40 seconds). The 25–40-second period results are not presented in this study.

In addition, the data were also partitioned by predicted group slowness into three paths: oceanic paths (*slow* < 32.25 sec/deg), continental paths (*slow* > 38.0 sec/deg), and mixed oceanic-continental paths (32.25 sec/deg < *slow* < 38.0 sec/deg). This partitioning enabled determination of bias for the $M_s$(VMAX) calculations for each path and period range. The final slowness values used in the study were empirically determined using the data and paths.

All amplitudes were corrected to displacement using frequency/amplitude/response files. Contrary to conventional $M_s$ amplitudes measured on a long-period channel, the $M_s$(VMAX) amplitudes were measured on a decimated broad-band channel to provide a larger period range.

**Results.** Processing of the data used an automated code to perform all calculations following the methodology outlined by Bonner (2006a, b; 2007). The waveform data were windowed using the predicted Rayleigh arrival and representative noise using predetermined parameters. The predicted group-velocity limits used a recent surface-wave group velocity model (Pasyanos, 2005).

Following the processing methodologies of Bonner et al. (2006b, 2007), once the data were windowed, the largest signal amplitude at each center frequency was selected to calculate the magnitude. Results were automatically stored using a data model within a relational database.

The results were compared against the standard $M_s$ value. The Rayleigh phase amplitude for each waveform was determined by an analyst, selecting a peak-to-peak amplitude with a period in the 17 to 25 second range. An $M_s$ formula similar to the Prague formula (Vaněk et al., 1962) was used as the comparison.

Results from the globally distributed data showing the scatter and bias at the station level are shown for the three path types, oceanic, mixed oceanic-continental, and continental, and a combination of all three types in Figure 2. Development (Russell, 2006) and early work by Bonner (2006a, b; 2007) concentrated only on continental paths. Note the nearly constant 0.1 $M_s$ unit bias. Scatter may be acceptable for an operational mode.

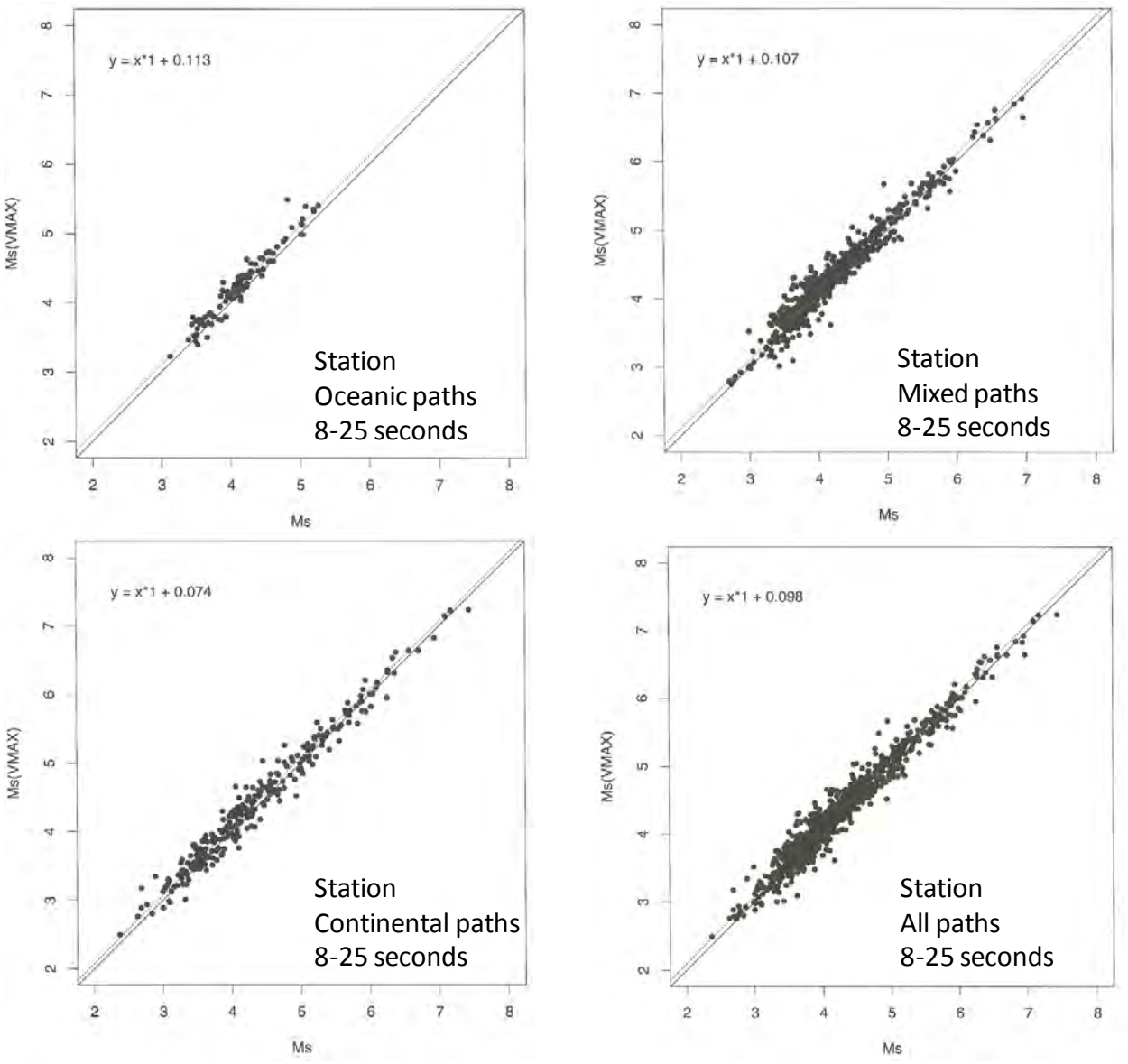


**Figure 2. Results showing the station-magnitude scatter and bias for each type of path and combined path for the investigated period range (8–25 seconds).**

We also investigated whether the bias contribution resulted from the shorter periods (8–17 seconds). To investigate this possibility, the paths were separated by period and path (Figure 3). No discernable bias is detectable. The results are consistent regardless of path and period.

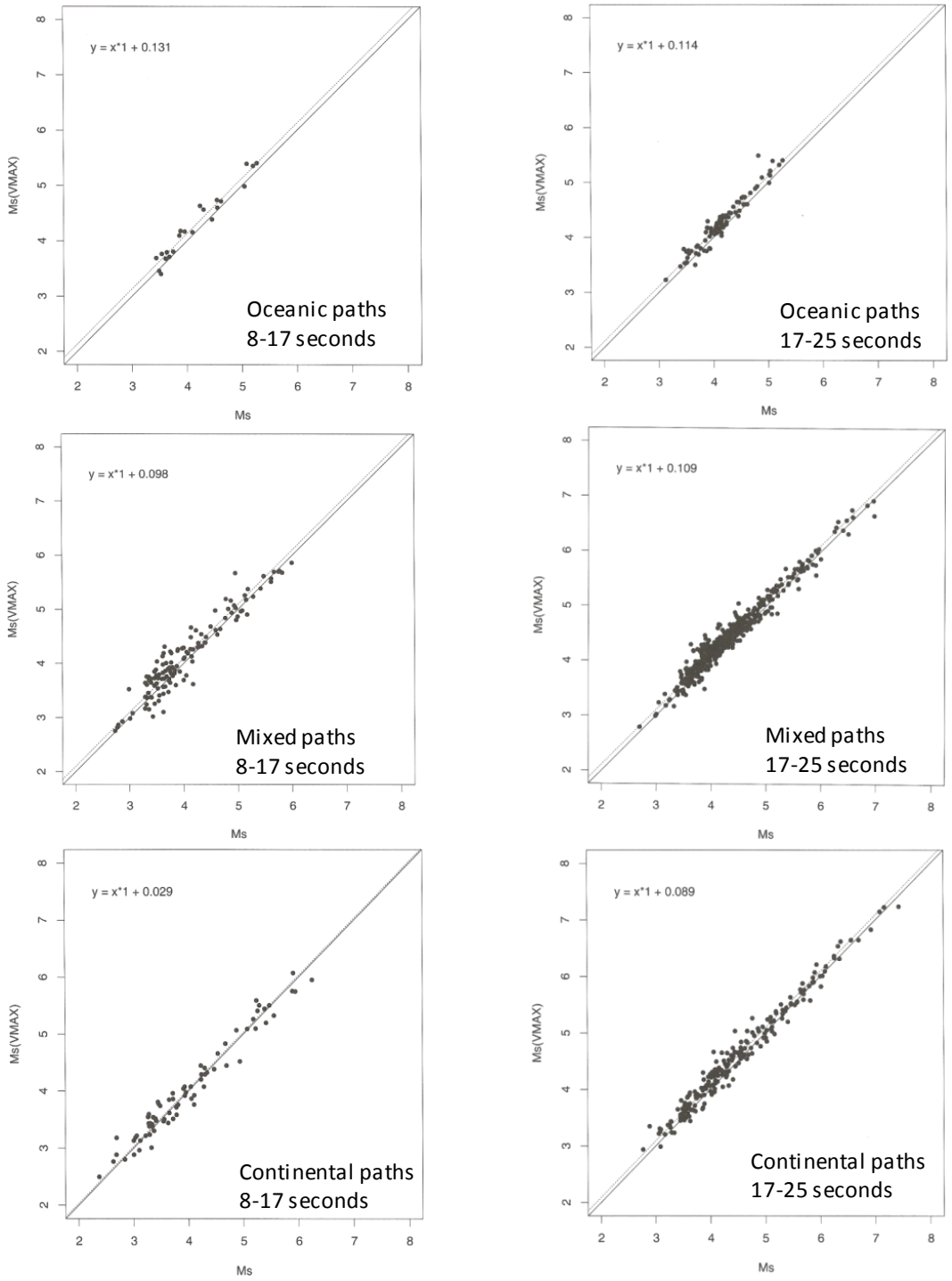


**Figure 3. Results showing the station magnitude scatter and bias for each type of path and separated by period ranges to include 8–17 seconds and 17–25 seconds.**

When the station magnitudes are combined into a network magnitude for each event, similar results are observed (Figure 4). The data show good agreement with a small bias of less than 0.1 $M_s$ units. Since the Russell (2006) magnitude equation was empirically determined, any real bias terms can be incorporated into the formula.

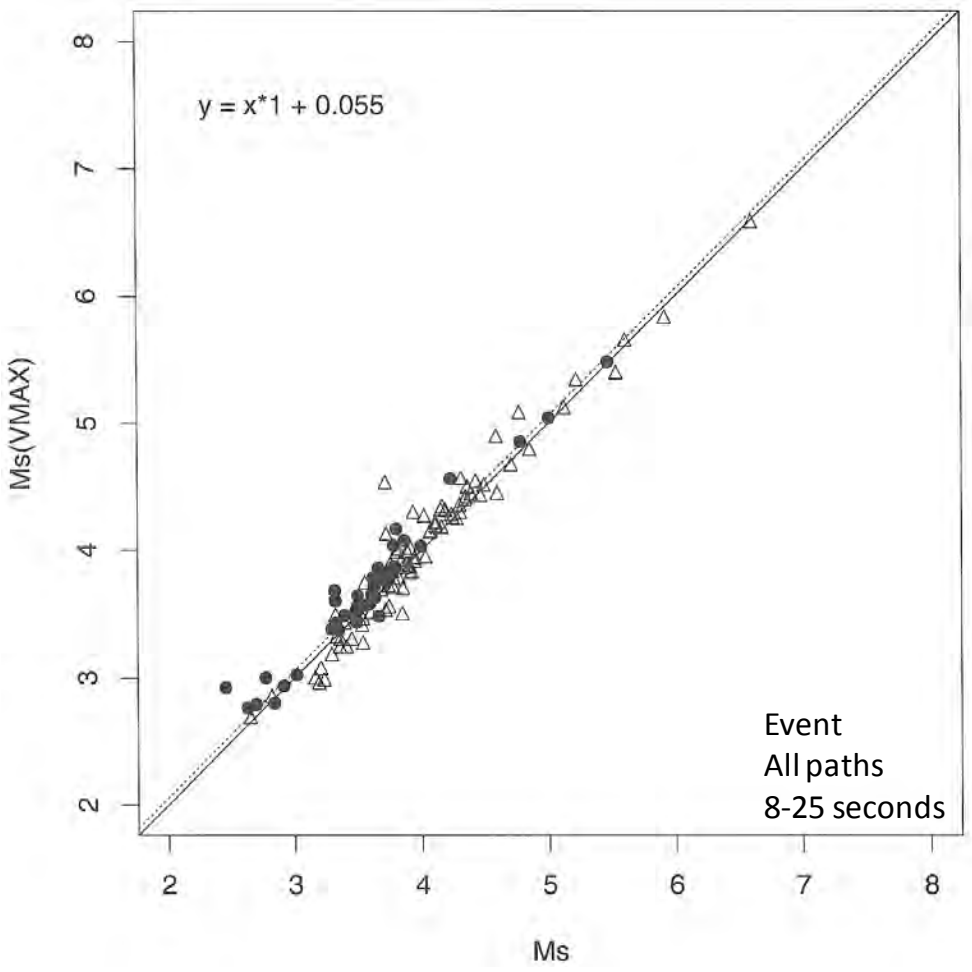


**Figure 4. Network magnitude results with all paths for the investigated period range (8–25 seconds). The solid circles (●) represent those event magnitudes where the number of $M_s$(VMAX) station contributions are equal to those for $M_s$. The triangles (Δ) represent the event magnitudes where additional station $M_s$(VMAX) measurements contribute to the event average.**

In Figures 2 and 3, the scatter plots show station-magnitude data, only a direct comparison between $M_s$ (VMAX) and $M_s$ is possible. However, the $M_s$(VMAX) technique is able to determine additional station contributions not obtainable using traditional $M_s$ techniques. Figure 4 separates those network averages to illustrate the additional $M_s$ (VMAX) station contributions. Stated differently, those network averages marked as solid circles (●) contain equal $M_s$ and $M_s$ (VMAX) stations in the network magnitude. The remaining network magnitudes (Δ) have additional station contributions in the averages, all from $M_s$ (VMAX). The additional contributions cover the entire magnitude range. This was an unanticipated result.

Obvious outliers were examined and removed from the data. Outliers were strictly a result of processing, not methodology. For example, when two events were closely spaced, the automated group-velocity windowing may have included both events. The methodology would pick the largest amplitude, whether it corresponded to the event of interest or not. Also, automated quality-control methodologies were not implemented on the selected data. A data spike, glitch, or flat spot creates ripples in the time domain from edge effects associated with the filtering process.

Any remaining outliers could not be removed. A likely scenario is a case of two overlapping signals, two simultaneously arriving signals from different events.

## CONCLUSIONS AND RECOMMENDATIONS

The $M_s$(VMAX) technique has been known to work well for continental paths between 8–25 seconds (Bonner et. al., 2006b, 2007). However this study shows stable results for oceanic and mixed oceanic-continental paths as well. Since the data were partitioned to ensure path independence, we have demonstrated the $M_s$(VMAX) technique is capable of functioning as an automated replacement for $M_s$. This allows the inclusion of regional stations with Airy phases, and stations for which a traditional $M_s$ may not be easily determined. Overall, the use of automated results should reduce the analyst burden of picking individual phases, only requiring checks when anomalies may be present.

## ACKOWLEDGEMENTS

The authors wish to thank the Air Force Technical Applications Center (AFTAC) for allowing the data to be used. Valid discussions were held between Team NDC, composed of QTSI and SAIC members, and AFTAC technical staff. In addition, Mr. Fredrick Ward (QTSI) assisted in investigating outliers and their cause.

## REFERENCES

Bonner, J. L., D. Russell, D. Harkrider, D. Reiter, and R. Herrmann (2006a). Development of a time-domain, variable-period surface wave magnitude measurement procedure for application at regional and teleseismic distances, Part II: Application and Ms-mb Performance, *Bull. Seism. Soc. Am.* 96: 678–696.

Bonner, J. L., M. Pasyanos, M. Leidig, H. Hooper, and D. Harkrider, (2006b). A comparison of different surface wave magnitude measurement procedures on a Eurasian dataset, in *Proceedings of the 28th Seismic Research Review: Ground-Based Nuclear Explosion Monitoring Technologies*, LA-UR-06-5471, Vol. 1, pp. 560–569.

Bonner, J.L., M. Pasyanos, M. Johnson, and D. Harkrider. (2007). Calibration of the $M_s$(VMAX) technique in Eurasia, in *Proceedings of the 29th Monitoring Research Review: Ground-Based Nuclear Explosion Monitoring Technologies*, LA-UR-07-5613,Vol. 1, pp. 541-550.

Pasyanos, M.E. (2005). A variable-resolution surface wave dispersion study of Eurasia, North Africa, and surrounding regions, *J. Geophys. Res.* 110: B12301.

Russell, D.R. (2006). Development of a time-domain, variable-period surface wave magnitude measurement procedure for application at regional and teleseismic distances, Part I: Theory, *Bull. Seism. Soc. Am.* 96: 665–677.

Vaněk, J., A. Zatopek, V. Karnik, N.V. Kondorskaya, Y.V. Riznichenko, E.F. Savarensky, S.L. Solov'ev, and N.V. Shebalin (1962). Standardization of magnitude scales, *Bull. Acad. Sci. USSR, Geophys. Ser*., no. 2, 108–111 (English Translation).

# MICRO-SEISMOMETERS VIA ADVANCED MESOSCALE FABRICATION

Neal A. Hall

Silicon Audio, LLC

Sponsored by National Nuclear Security Administration

Contract No. DE-FG02-08ER85106

## ABSTRACT

The Department of Energy's National Nuclear Security Administration (DOE/NNSA) seeks revolutionary innovations with respect to miniature seismic sensors for the monitoring of nuclear detonations. Specifically, the performance specifications are to be consistent with those obtainable by only an elite few products available today, but with orders of magnitude reduction in size, weight, power, and cost. The proposed innovation calls upon several advanced fabrication methods and read-out technologies being pioneered by Silicon Audio, including the combination of silicon microfabrication, advanced meso-scale fabrication and assembly, and the use of advanced photonics-based displacement/motion-detection methods. Successful implementation will result in a commercial product roughly the size of a common USB flash drive with the ability to address advanced national security needs of the DOE/NNSA. Additional commercial market sectors include military/defense, scientific/instrumentation, oil and gas exploration, and inertial navigation.

## OBJECTIVES

The DOE/NNSA seeks revolutionary innovations with respect to miniature seismic sensors for the monitoring of nuclear detonations. The specific sensor specifications solicited are as follows:

- Size—less than 1 $in^3$
- Power—less than 100 mW
- Sensor self-noise—below United States Geological Survey Low Earth Noise Model, or approximately 0.5 ng/√Hz
- Dynamic range at least 120 dB over a frequency band of 0.2 to 40 Hz.

The proposed design innovation calls upon several advanced fabrication methods and read-out technologies being pioneered by Silicon Audio, including advanced mesoscale fabrication of mechanical proof-mass elements, photonics-based displacement/motion detection, microscale optoelectronic integration, and the integration of new types of closed-loop sensing modalities for high stability and high dynamic range. In what follows, we first summarize basic design considerations for any proposed technology aiming to meet the aforementioned specifications. We then briefly summarize some of our prior research with optical based motion detection and micromachined sensors.

### Fundamental Design Considerations

A brief consideration of a few key design parameters for an accelerometer quickly reveals the challenges in achieving the noise specifications required by the DOE. For this purpose, a sufficiently accurate model for an accelerometer sensing structure is a simple spring-mass-damper system. Such a system is characterized by its mass, resonant frequency, and quality factor of resonance; $M$, $f_o$, and $Q$, respectively. Acceleration of this system results in an inertial force to the proof mass, which in turn results in a proof mass displacement proportional to the incoming acceleration. This displacement is measured in one of a number of ways (e.g., via capacitive, piezoresistive, or optical methods). There are two fundamental limits to the acceleration resolution of the sensor. The first is imposed by the resolution with which the proof mass displacements can be detected. This minimum detectable displacement (MDD) is expressed in m/√Hz and depends on the sophistication and design of the particular approach being used. The MDD is referred to input acceleration via the displacement sensitivity to acceleration of the system, which is expressed in m/(m/$s^2$) and equal[1] to $1/(2\pi f_o)^2$. This relation allows the MDD to be referred to a minimum detectable acceleration (MDA) via

$$MDA_d = MDD * (2\pi f_o)^2 . \qquad (1)$$

For example, in order to achieve a MDA of 0.5 ng/√Hz with a system with 50 Hz resonance, the displacement of the proof mass must be resolved with amazingly high resolution—50 fm/√Hz.

The second fundamental limit to the acceleration resolution of the sensor is Brownian motion (i.e., thermal mechanical noise) of the proof mass. The acceleration referred thermal noise limit can also be expressed in terms of the fundamental system parameters via the well-known relation shown below (Gabrielson, 1993):

$$a_{tm} = \sqrt{\frac{8\pi k_b T f_0}{MQ}} \qquad (2)$$

where $k_b$ is Boltzmann's constant and $T$ is the ambient temperature. With this as background, design parameters meeting the challenging noise requirement can be identified. Table 1 summarizes three designs for discussion, all with a 50-Hz resonance.

[1] This is obtained by recognizing that the inertial force is $F = M*a$, and the resulting displacement $\delta$ is equal to $F/K$ where $K$ is the system stiffness. The ratio $M/K$ is simply $1/(2\pi f_o)^2$, which results in the cited expression.

**Table 1. Summary of three mechanical designs**

| | *fo* (Hz) | M (kg) | Q | $a_{tm}$ g/sqrt(Hz) |
|---|---|---|---|---|
| **A** | 50 | 2.00E-06 | 100 | 1.63859E-08 |
| **B** | 50 | 2.00E-06 | 100,000 | 5.18166E-10 |
| **C** | 50 | 2.00E-03 | 100 | 5.18166E-10 |

Design A represents what has been demonstrated as the state-of-the-art in technologies based on micromachining (i.e., microelectromechanical [MEMS]). In fact, only a few research teams have rigorously demonstrated close to 20-ng/√Hz resolution from MEMS-based approaches. Most notably, T. Kenny and a research team at Stanford achieved 20-ng/√Hz resolution using electron-tunneling displacement sensing (capable of achieving 50 fm/√Hz) of a cantilevered proof mass combined with an electrostatic force rebalance architecture (Liu and Kenny, 2001).

The primary limitation in achieving a thermal noise level lower than 20ng/√Hz with any MEMS approach is the inherently small proof-mass. Doing so requires achieving very high resonance *Q*s (near 100,000 as summarized in Design B). This approach carries both vacuum packaging challenges and electronics design challenges, as all designs with a *Q* higher than unity must incorporate a closed-loop feedback system to realize the required flat frequency response (e.g., see Liu and Kenny, 2001; Standley and Pike, 2007). Primary challenges in achieving design type C include development of a robust, repeatable, and low-cost fabrication process for the larger mechanical proof mass elements and the integration of the proof mass structure with a high-fidelity motion detection technology. Silicon Audio is pioneering innovations to address both design types. In the remaining section, we present some preliminary work with micromachined sensors while highlighting one of several photonics based motion displacement technologies that can be integrated with theses sensors.

## RESEARCH ACCOMPLISHED

The device structure in Figure 1 is an example of an innovative optical-based sensor and has been described in more detail in Hall et al., 2008). A detailed characterization of the displacement sensing technique when used in an advanced microphone structure shows 20 fm/√Hz displacement detection resolution—limited by quantum shot noise at the photodetectors (Hall et al., 2007).

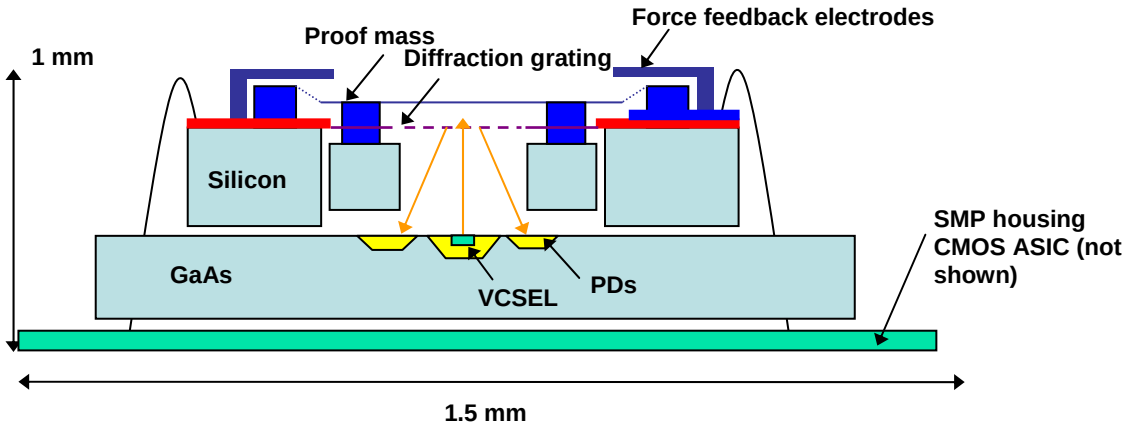


**Figure 1. Schematic of the complete sensor innovation. Light from a semiconductor laser, such as a vertical cavity surface emitting laser (VCSEL), illuminates a diffraction grating fabricated on silicon. A portion of the incident light reflects directly off the grating fingers, while the remaining light travels between the grating fingers to the proof mass and back, to accrue additional phase. A diffracted field results, consisting of a zero order and higher orders, whose angles remain fixed but whose intensities are modulated by the relative distance between the proof mass and grating with the sensitivity of a Michelson-type interferometer. (This figure first appeared in Hall et al., 2008.)**

Preliminary silicon micromachined proof mass structures are presented in Figure 2, and a measured dynamic impulse response of the proof mass displacement is presented in Figure 3, following application of a sharp electrostatic force pulse applied via the electrodes labeled in Figure 1. The Fourier transform of this measurement reveals a dynamic frequency response with a fundamental resonance of 220 Hz and *Q* equal to approximately 100 (for this test, the device was placed in a reduced atmosphere of 100 mtorr to emulate the type of conditions that can be achieved with wafer-level vacuum-packaging technologies). The structure has a 1.2-mg proof mass, from which one can infer a Brownian noise limit of 43.7 ng/√Hz for these proof-of-concept structures.

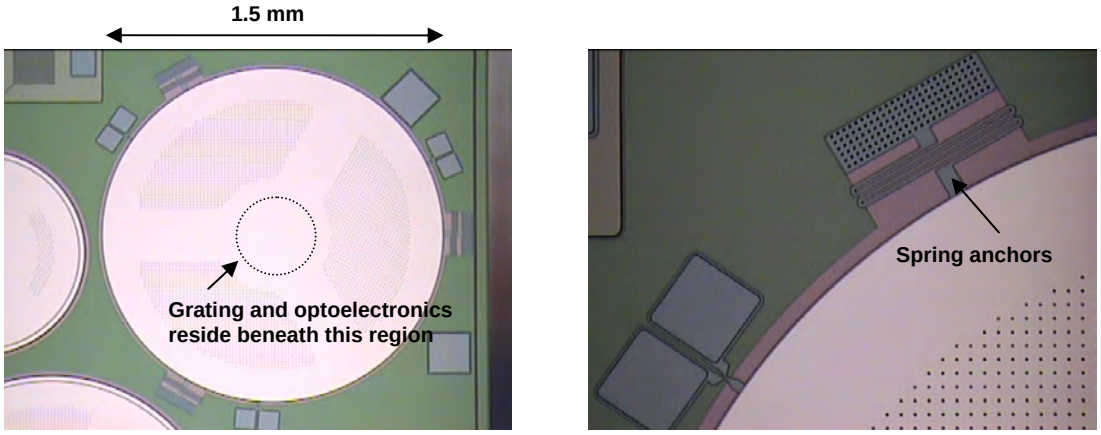


**Figure 2. Micrographs of fabricated silicon structures shown schematically in Figure 1. (Left) Full view of 1.5-mm-diameter structure. (Right) Zoomed-in view highlighting a polysilicon spring that anchors the bulk silicon proof mass to the silicon substrate. (This figure first appeared in Hall et al., 2008.)**

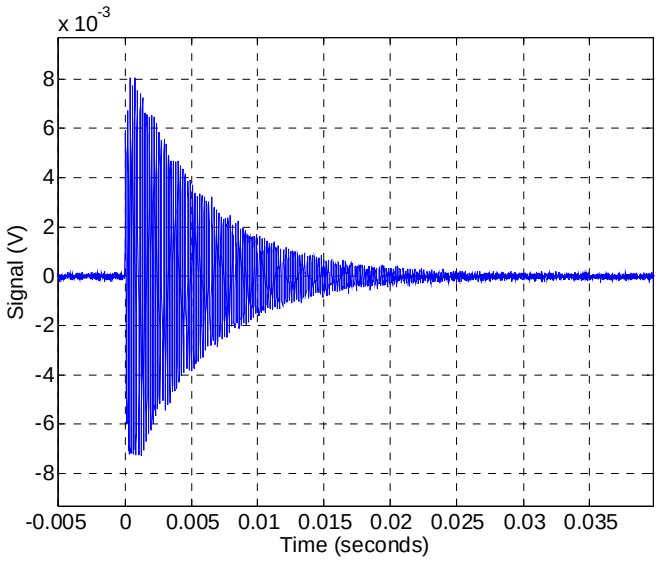


**Figure 3. Measured impulse response of the structure presented in Figure 2. (This figure first appeared in Hall et al., 2008.)**

## CONCLUSIONS AND RECOMMENDATIONS

In what is to come, we will be focusing on the application of both silicon micromachining and optical-based motion-detection principles to create high-performance seismometers that can meet the NNSA's performance requirements. Future challenges for the MEMS-based designs summarized above are rooted in vacuum-level packaging to increase resonance *Q* and lower thermal-mechanical noise. Although not discussed here, Silicon Audio is also pioneering advanced mesoscale proof mass structures and integration procedures that overcome the small mass limitations of silicon micromachined structures while at the same time introducing new and unique integration challenges.

## REFERENCES

Gabrielson, T. B. (1993). Mechanical-thermal noise in micromachined acoustic and vibration sensors, *IEEE Trans. Electron Dev.* 40: 903–909.

Hall, N. A., M. Okandan, R. Littrell, D. Serkland, G. Keeler, K. Peterson, B. Bicen, C. Garcia, and F. L. Degertekin (2008). Micromachined accelerometers with optical interferometric read-out and integrated electrostatic actuation, *J. Microelectromech. Syst.* (accepted for publication).

Hall, N. A., R. Littrell, M. Okandan, B. Bicen, and F. L. Degertekin (207).Micromachined optical microphones with low thermal-mechanical noise levels, *J. Acous. Soc. Am.* 122: 2031–2037.

Liu, C. H. and T. W. Kenny (2001). A high-precision, wide-bandwidth micromachined tunneling accelerometer, *J. Microelectromech. Sys.* 10: 425–433.

Standley, I. M. and W. T. Pike (2007). Progress in the development of rugged low power compact silicon MEMS sensors for use in nuclear explosion monitoring, in *Proceedings of the 29th Monitoring Research Review: Ground-Based Nuclear Explosion Monitoring Technologies.* LA-UR-07-5613, Vol. 1, pp. 491–500.

# REGIONAL EVENT IDENTIFICATION RESEARCH IN ASIA

Hans E. Hartse, George E. Randall, and Stephen J. Arrowsmith

Los Alamos National Laboratory

Sponsored by National Nuclear Security Administration

Contract No. DE-AC52-06NA25396

## ABSTRACT

Recent event identification efforts at Los Alamos National Laboratory (LANL) have focused on mining event ground-truth data collection in central Asia and testing far-local to near-regional discriminants using earthquakes, mining explosions, and single-charge chemical explosions. Our mining event efforts have identified over 20 mines and more than 1,000 mining explosions from around the former Soviet nuclear test site (KTS) in eastern Kazakhstan. Using the Kazakh National Data Centre (KNDC) bulletin from 2002 to 2007 and waveforms recorded at station KURK and array MKAR, we combined time-of-day seismic-event analysis, waveform cross correlations, seismic-event location methods, and image analysis to identify active mines. From our previous, but more limited studies, we had assumed mining explosions in eastern Kazakhstan occur only between about 8 AM and 8 PM local time. However, our latest study, using several thousand events, reveals that some mines shoot near midnight local time. Thus, we concluded that only during the hours of 21, 22, and 23 GMT (3, 4, and 5 AM local time) can we assume that the small events from this region are probable earthquakes.

Using this assumption, we selected 8 events within about 250 km of station KURK as earthquakes, and we selected about 250 mining explosions from three mines for discrimination analyses. In addition, we gathered all available depth-of-burial (DOB), hole-closing, and tunnel-closing single-charge chemical explosions that occurred at KTS from 1997 to 2000 and were recorded at KURK. The single-charge chemical events occurred within about 125 km of KURK. From published reports, we have flagged three of these events as fully contained. For the mining events, we do not know the shooting practices, such as delayed-firing along rows of shotholes.

Using the events described above, we tested spectral-ratio and phase-ratio body-wave amplitude discriminants. We find that contained, and even most partially contained single-charge explosions can be separated from earthquakes using a high-frequency (F>4 Hz) Pg/Lg ratio. For some mines, events do separate from the earthquakes at F>4, but for other mines, Pg/Lg ratios must be formed at F>7 before separation from earthquakes occurs. We also processed the mining events to detect spectral banding related to delay-fired shooting practices. Our cepstral analysis indicates that events from some mines have more pronounced spectral modulations than events from other mines.

## OBJECTIVES

Over the past year we have continued studies to collect mining-event ground-truth data in central Asia, focusing on a portion of eastern Kazakhstan surrounding the former Soviet nuclear test site (KTS). We have also collected waveforms from single-charge chemical explosions detonated at KTS in the late 1990s, and we have identified a few small earthquakes based on time-of-day analysis. We have therefore assembled seismograms of uncontained mining explosions, both contained and uncontained single-charge chemical explosions, and earthquakes. We have used these event types to test discriminants that can separate mining events both from earthquakes and from single-charge explosions at far-local to near-regional distances.

## RESEARCH ACCOMPLISHED

### Kazakh Mining Ground-truth Study

We have been expanding our seismic ground-truth data collection efforts for central Asia by identifying mines and mining explosions. Working with Kazakh National Data Centre (KNDC) bulletins (2002–2007), we combine time-of-day seismic-event analysis, waveform cross correlations, seismic-event location methods, image analysis, and seismic discrimination methods to identify active mines in the area between the International Monitoring System (IMS) array MKAR and the Global Seismic Network (GSN) station KURK. Most of the events within this area occur during daytime (Figure 1), are usually small (often recorded at only 1 or 2 stations or arrays), and therefore tend to be poorly located. Our goal is to tie event clusters to specific mine sites, and thereby establish ground-truth location and event type (earthquake or explosion) information.

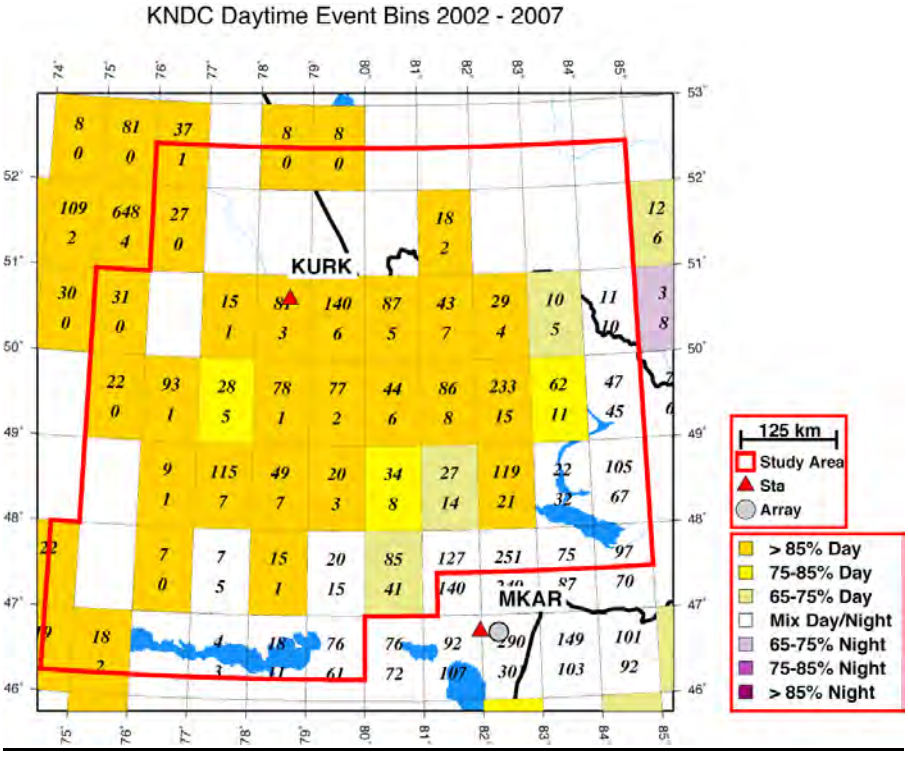


**Figure 1. Time-of-day seismicity for eastern Kazakhstan and surrounding regions. The primary event-information source is the KNDC web-published bulletin. Gold and yellow regions are dominated by daytime mining explosions. Within each bin, the upper number is the daytime event count and the lower number is the nighttime event count. We focused on the area within the red box between array MKAR and station KURK, which includes the former Soviet nuclear test site (KTS).**

Using KNDC locations as a guide, we assembled about 2,500 three-component, event-segmented waveforms from MKAR array-element MK31. After bandpass filtering between 1.5 and 5.5 Hz, we cross-correlated the first 20 seconds of each component's event record with every other event record from the same component (that is, broadband frequency (BHZ) was correlated with other BHZ records, etc). After stacking and normalizing the individual component correlations into three-component correlations, we assembled similar-event clusters based on peak correlation coefficients exceeding 0.4. From the relative timing offsets within a given cluster's correlation peaks, we time-shifted, aligned, and stacked the individual event waveforms to create a single, three-component record at stations MK31 and KURK, and we stacked MKAR seismic hazard zone (SHZ) array elements. These waveform sums become the reference waves of each event cluster. Figure 2 shows the stacked BHZ wave and several aligned individual waves at station MK31 for event cluster 310 (see Figure 3 for event cluster locations).

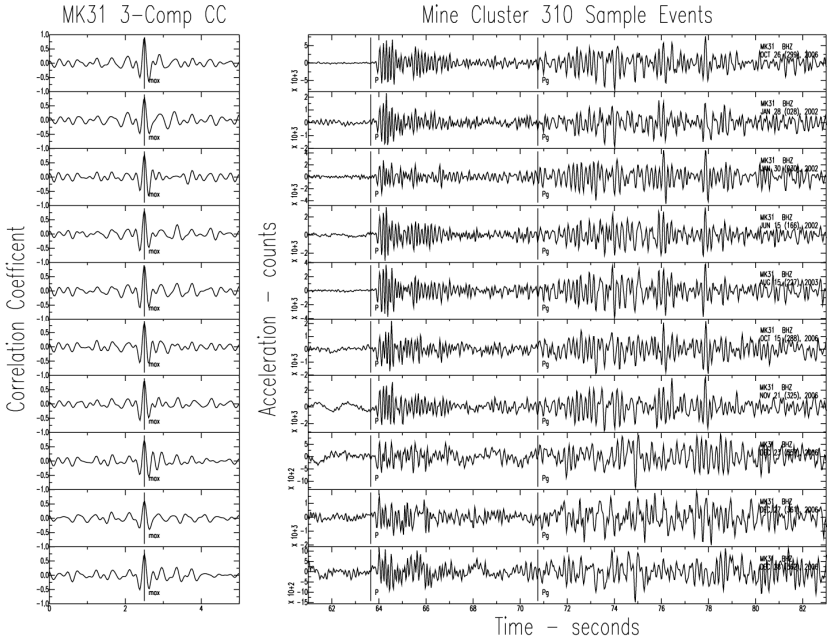


**Figure 2. Event cluster 310 sample waveform stack (top trace) and individual, vertical-component, time-aligned P-waves at MK31. The three-component cross-correlation results are shown at left, with autocorrelation at top left. Note improved S/N ratio on the stacked wave for Pn (first break).**

In all, we found 23 clusters, each with 5 or more events from probable mines, totaling for about 1,000 individual events. Event-station distances for the clusters are between about 75 and 550 km, and most event magnitudes are between about 1.0 and 3.5 mb (Figure 4). Although nearly all mining events occur during local daytime (about hour 2 GMT to hour 14 GMT, or 8 AM to 8 PM local time; Figure 4), we did find two clusters where events occur predominantly at night. Figure 5 contains a map and histograms from one of these event clusters. Events occur during probable work shift changes in the morning (2 GMT), in the evening (10 GMT), and at midnight (18 GMT). From previous studies (MacCarthy et al., 2008, Hartse et al., 2007) we had assumed unclustered, night events were earthquakes, but from our current study we have abandoned that assumption. For discrimination research, we now assume only events occurring during hours 21–23 GMT (3–5 AM local time) are earthquakes.

**Final Ground-Truth Event Selection**

Because we wanted to conduct discrimination studies involving the three event types—mining explosion, single-charge explosion, and earthquake—we selected data from station KURK. KURK has operated under the KZ and II network codes and has archived digital data available from the Incorporated Research Institutions for Seismology (IRIS) Data Management Center (DMC) going back to 1994.KURK therefore recorded nearly 20 single-charge chemical explosions from various locations around KTS, including (1) the 1997 DOB experiments (Glenn and Myers, 1997), (2) the Omega test series of tunnel explosions (Knowles, 2006), and (3) other hole-closing explosions (NNC RK, 1998).

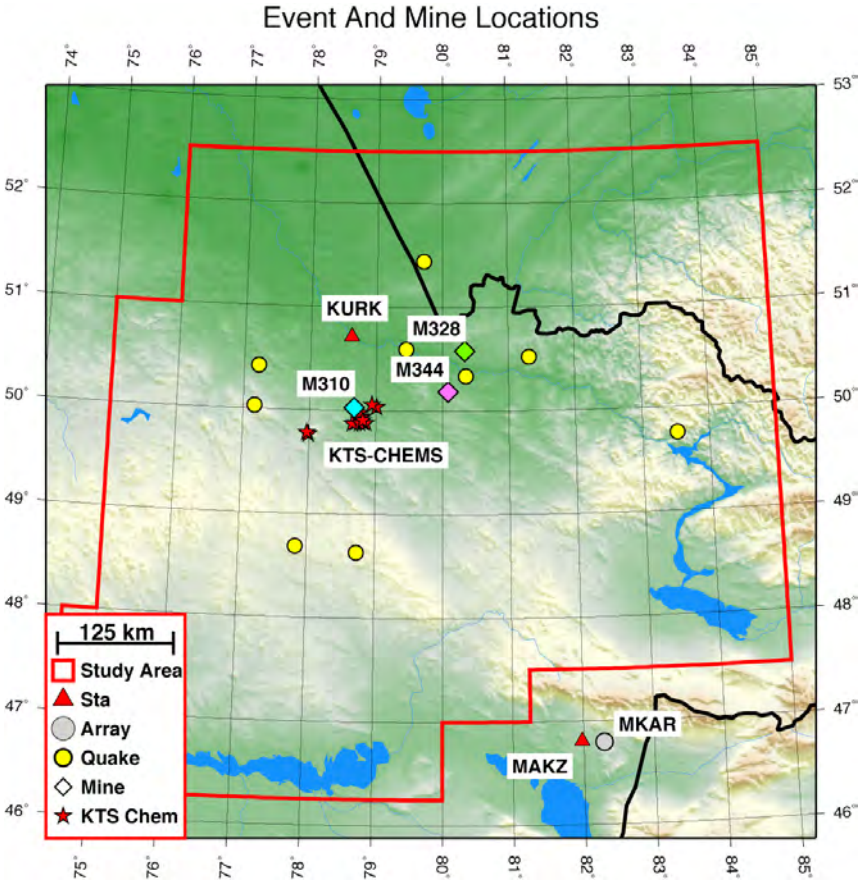


**Figure 3. Study area showing approximate mine locations (diamonds), single-charge chemical explosions (stars), and probable earthquakes (yellow circles). We estimated that the mine locations and the earthquake locations are from the KNDC; the KTS explosions are from published reports. About 250 individual mining events are represented by the 3 mine locations.**

KURK has also recorded many of the mining explosions, which we identified in our waveform similarity study as described above. Because of the low magnitudes of nearly all events in this area, for signal-to-noise purposes we limited the mining events to those occurring within local to near-regional distances of station KURK. We therefore selected about 250 events from three distinct mine clusters at distances of between about 100 and 150 km from the station (Figure 3).

Identifying ground-truth earthquakes around the relatively aseismic KTS is difficult. While there are plenty of seismic events, nearly all appear to be mining explosions. For the selection of earthquakes, we limited events to those within 250 km of KURK with origin times only from hours 21 to 23 GMT (see Figures 4 and 5). As described above, these were the only hours where we observed no waveform-clustered mining events. We also presumed any event within 350 km of KURK with mb larger than 4.0 was also an earthquake, regardless of origin time. Figure 3 shows the locations of the 9 presumed earthquakes we selected.

Summarizing, our final discrimination data set includes about 250 mining explosions, 18 single-charge chemical explosions, and 9 earthquakes, with nearly all events within 250 km of KURK. Figure 6 shows sample vertical-component waveforms from each event type.

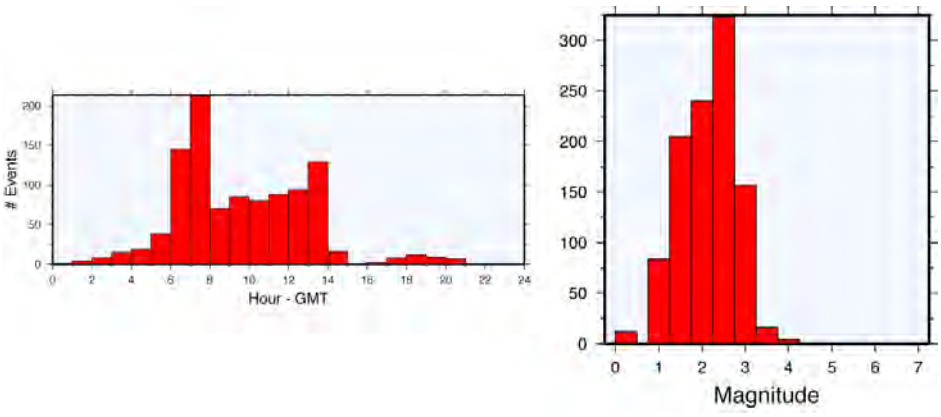


**Figure 4. Summary time-of-day and event magnitude histograms for 23 mining event clusters around KTS. Local daytime (8 AM to 8 PM) runs from 2 to 14 GMT.**

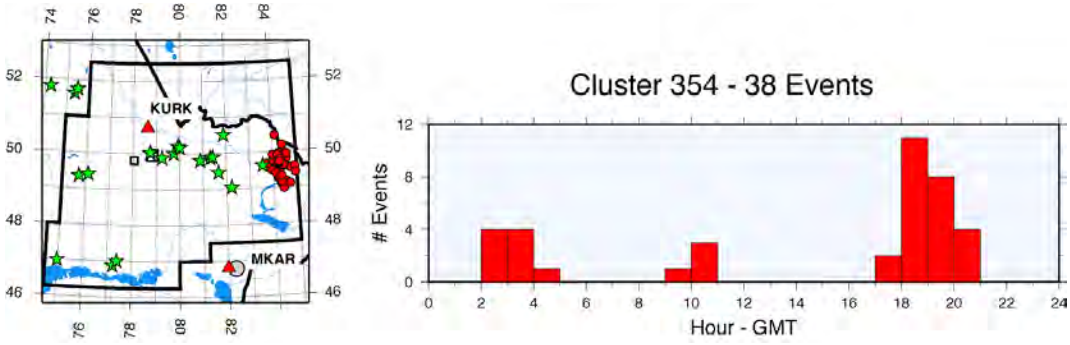


**Figure 5. Time-of-day histogram and event map for mine cluster 354; an example of night mining explosions. The map shows KNDC locations as red circles. Reported mines are green stars. Note that most events occur from hours 18 to 20 GMT, with local midnight at hour 18 GMT.**

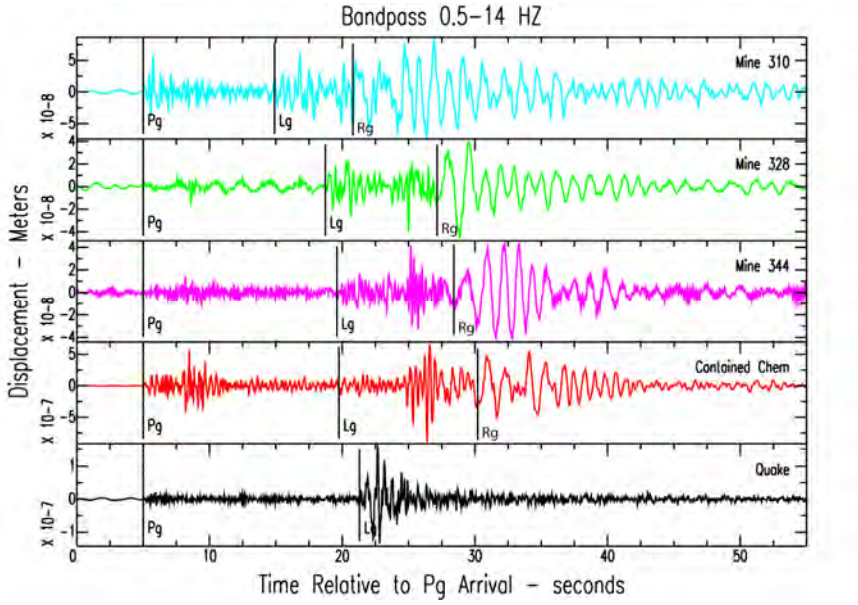


**Figure 6. Sample waveforms from each of three mines; a KTS contained, single-charge explosion; and a probable earthquake. Note the lack of Rg on the earthquake.**

**Seismic Event Discrimination Results**

Most events in our data set are within or only slightly beyond the crossover distance of KURK. Thus, we measured Pg and Lg body wave amplitudes [as root mean square (RMS) displacement in meters] and measured pre-phase and pre-event noise windows. Hartse et al. (1997) describes the measurement methods we followed. We formed Pg/Lg amplitude ratios and corrected the ratios for a distance trend prior to forming final ratio-versus-magnitude discrimination plots. We used only earthquake ratios to find the distance trends. We did not attempt any other corrections, as we currently hold only 9 earthquakes from the study area.

Figure 7 shows discrimination results from station KURK, comparing only the earthquakes and the KTS single-charge explosions. Most hole-closing and some tunnel explosions at KTS were shallow and not contained. We are confident that at least two DOB explosions were contained. These explosions vary in size from about 2 tons up to 100 tons. Only two uncontained explosions are within or near the earthquake population. The contained and the majority of the uncontained explosions separate from the earthquakes. Figure 7 demonstrates that small, single-charge explosions can be separated from earthquakes using a high-frequency P/S ratio at local to near-regional distances, even when containment is not complete.

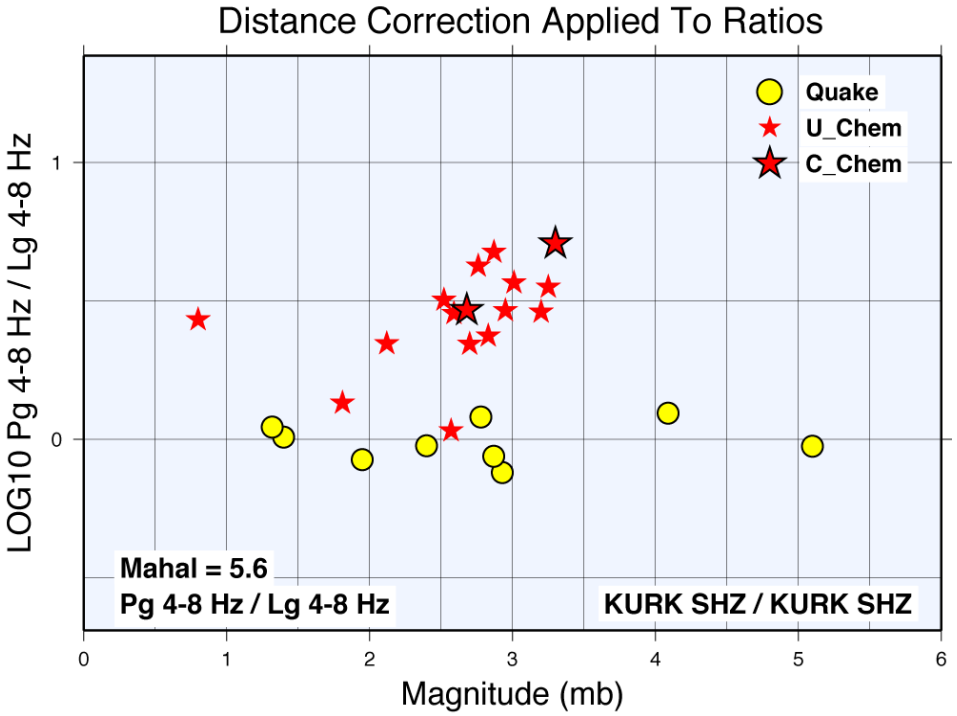


**Figure 7. Pg(4–8 Hz)/Lg(4–8 Hz) ratio versus magnitude for single-charge chemical explosions and earthquakes. As expected, the contained—and most uncontained—explosions separate from the earthquakes.**

Figure 8 uses the same ratios as Figure 7, but the events from the three mines are now included. We find that events from Mine 310 separate from the earthquakes, but the explosions from Mines 328 and 344 do not. This could be a function of the source-area geology, explosive emplacement depth, or shooting style. To test for evidence of multi-hole, delay-fired shooting, we applied the method of Arrowsmith et al. (2007) to derive a cepstral estimate for each earthquake and mining explosion (Figure 9). We obtained the cepstral results using the array elements at MKAR. The larger cepstral numbers indicate a greater probability of delayed shooting. At Mine 310 it therefore appears that delayed shooting is more common than at the other mines, but Mine 344 also has several events with larger cepstral numbers. On the discrimination ratio plots, we flag a mine explosion as “delayed” (diamonds with black borders) when the event cepstral number is above 10. Figure 8 shows that “delayed” shots at Mine 310 separate from earthquakes, but “delayed” shots from Mine 344 do not. We therefore conclude that delayed shooting by itself does not control the event separation seen on P/S ratio plots.

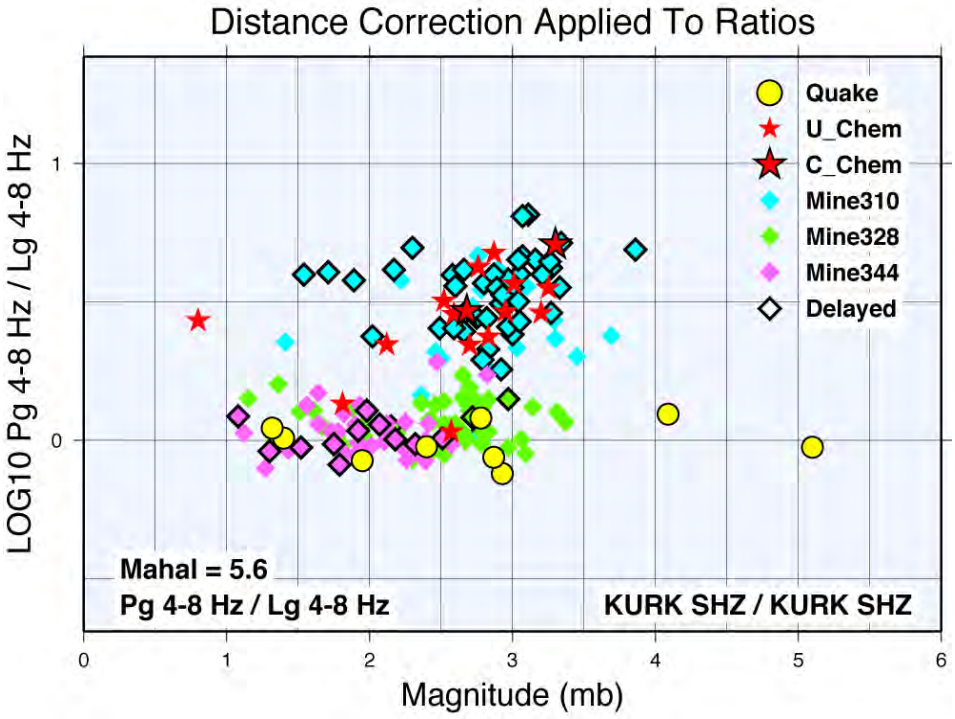


**Figure 8. Pg(4–8 Hz)/Lg(4–8 Hz) ratio versus magnitude for all explosions and earthquakes. Events from Mine 310 separate from earthquakes, but events from other mines do not.**

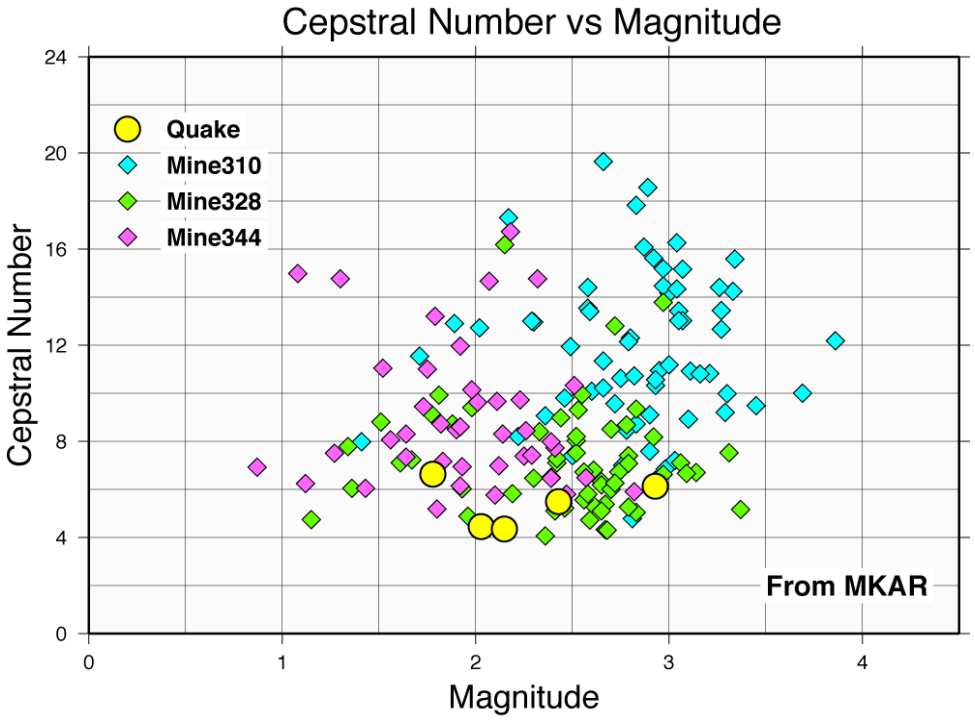


**Figure 9. Cepstral number versus magnitude for earthquakes and mining events. Larger numbers indicate probable delay-firing shooting practices. Delay firing at Mine 310 appears to be a more common practice compared to the other mines.**

Figure 10 shows that increasing the frequency band of the measured Pg and Lg amplitudes can improve separation of mining events from the earthquakes. For example, all events from Mine 344 are moved above the earthquake

population when the Pg/Lg ratio is formed at the 7–14 Hz band (compare Figures 8 and 10). The ratios from Mine 328 also begin to rise above the earthquake ratios. Because of the behavior of the anti-aliasing filters at KURK, the 40 samples per second data we used can only be measured to about 14 Hz, but these results suggest it may be possible to improve the separation of mining events from earthquakes by measuring appropriate data streams at even higher frequency bands.

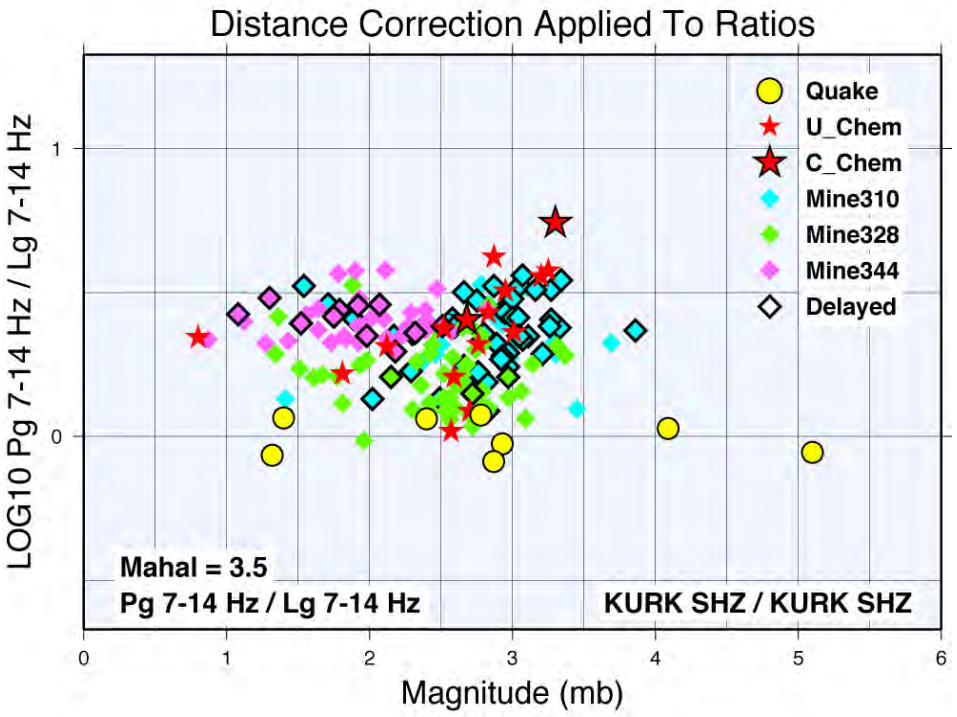


**Figure 10. Pg(7–14 Hz)/Lg(7–14 Hz) ratio versus magnitude for all explosions and earthquakes. Events from Mine 344 now separate from earthquakes. Compare to Figure 8, where the band is 4–8 Hz.**

The waveforms shown in Figure 6 show a strong Rg arrival for both mining and single-charge explosions relative to the direct Lg phase. This suggests that, within the appropriate group-velocity window, an Lg coda amplitude could be measured and placed into a ratio with direct Lg to form an earthquake-explosion discriminant. We determined that an Lg coda velocity window between 2.7 and 2.2 km/s captures the Rg arrival for these local to near-regional events, and we then measured RMS amplitudes in the 0.5–1.75 Hz band. The Lg/Lgcoda discrimination plot is shown in Figure 11. The "delayed" mining explosions have the same ratios as the mining explosions with small cepstral numbers. The earthquakes have no Rg, and true Lg coda was measured. Because most earthquakes were small and at distances greater than 200 km from KURK, only three had coda amplitudes that remained above background noise. But those three earthquakes are clearly separated from the explosions. One contained, single-charge explosion had a small direct-Lg amplitude and a large Rg arrival, resulting in separation from the mining events (lowest red star on Figure 11). The second contained, single-charge explosion and two other single-charge explosions are at the bottom of the mining event population. This suggests a possible discriminant for separating contained and uncontained explosions, but further information regarding the emplacement and containment of the single-charge events is necessary before conclusions can be reached.

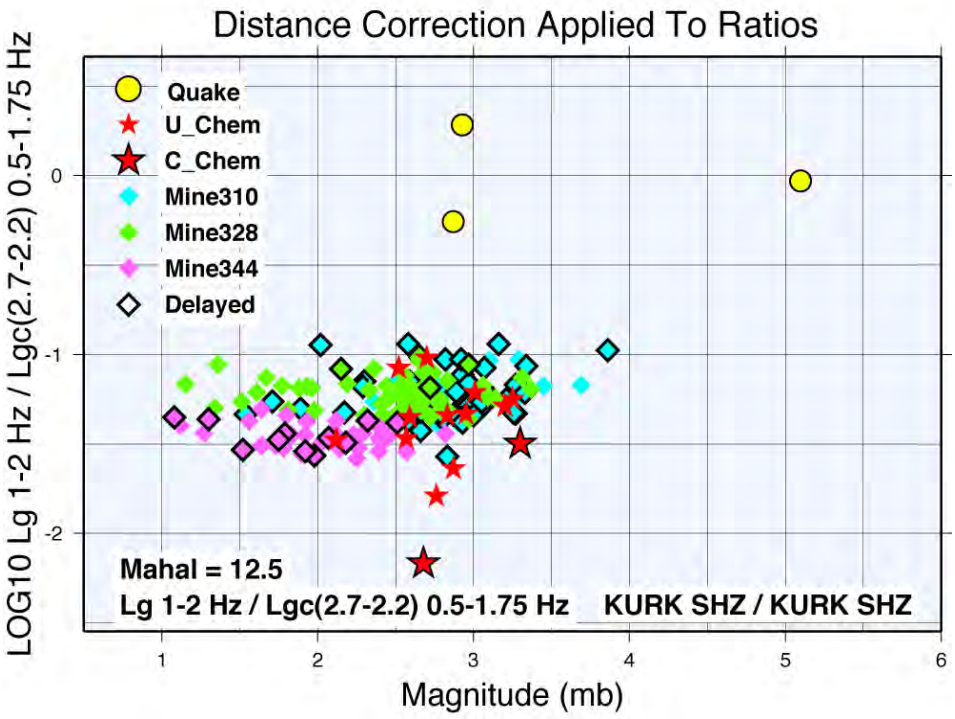


**Figure 11. Lg(1–2 Hz)/LgCoda(0.75–1.75 Hz) ratio versus magnitude for explosions and earthquakes. We measured the amplitude of the Lg coda over a velocity window between 2.7 and 2.2 km/s, which captured the Rg phase of the explosions (see Figure 6).**

## CONCLUSIONS AND RECOMMENDATIONS

We have an ongoing program to identify mining seismicity clusters and establish ground-truth mining event information from waveform correlations. For our eastern Kazakhstan study area, we have tied over 1,000 events to 23 distinct mining-event clusters. Event time-of-day analysis shows that mining explosions occur during all hours of the day in eastern Kazakhstan, except during the early morning hours (hours 21–23 GMT). We have identified 9 earthquakes near KTS and station KURK by assuming that early morning events are earthquakes. We have also assembled KURK waves from contained and uncontained single-charge chemical explosions detonated during experiments from the late 1990s at KTS. Using the earthquakes, single-charge explosions, and mining explosions from three mines near KURK and KTS, we have tested several discriminants. We find that (1) the high frequency (4–8 Hz) Pg/Lg ratio separates earthquakes from contained and even partially contained single-charge explosions, but this discriminant does not separate many mining explosions from the earthquakes; (2) increasing measurement frequency to above 7 Hz begins to separate mining explosions from earthquakes; (3) apparent delay-firing of mining events does not seem to influence the Pg/Lg discriminant performance; and (4) Lg/Lgcoda ratios that exploit the presence of the Rg phase may be useful for separating mining explosions from earthquakes and, possibly, contained explosions from uncontained explosions. We will continue to investigate discriminant measurement and correction methods in an attempt to improve performance in separating mining events from earthquakes and single-charge, contained explosions.

## ACKNOWLEDGEMENTS

We thank the entire LANL Ground-Based Nuclear Explosion Monitoring Research and Development (GNEM R&D) team for supporting efforts that make this work possible, and we especially thank Richard Stead, Julio Aguilar-Chang, and Diane Baker for their database assembly and maintenance efforts. We thank the IRIS DMC for rapidly filling data requests. We used data from operators and host institutions affiliated with the II and KZ networks.

## REFERENCES

Arrowsmith, S. J., M. A. Hedlin, M. D. Arrowsmith, and B. W. Stump (2007). Identification of delay-fired explosions using seismic array: application to the PDAR array in Wyoming, USA, *Bull. Seismol. Soc. Am.* 97: 989–1001.

Glenn, L. A., and S. C. Myers (1997). *Depth of burial experiments at Balapan,* LLNL report UCRL-JC-128313, 7 pp.

Hartse, H. E., S. R. Taylor, W. S. Phillips, and G. E. Randall (1997), A preliminary study of regional seismic discrimination in central Asia with emphasis on western China, *Bull. Seismol. Soc. Am.* 87: 551–568.

Hartse, H., G. Randall, X. Yang, and C. Rowe (2007). Regional event identification research in Asia, in *Proceedings of the 29th Monitoring Research Review: Ground-Based Nuclear Explosion Monitoring Technologies,* LA-UR-07-5613, Vol. 1, pp. 582-591.

Knowles, C. P. (2006). *The Omega test series,* Defense Threat Reduction Agency technical report DTRA 01-99-D-0047.

MacCarthy, J. K., H. E. Hartse, M. Greene, and C. Rowe (2008). Using waveform cross-correlation and satellite imagery to identify repeating mine blasts in eastern Kazakhstan, *Seismol. Res. Lett.* 79: 3, 393–399.

NNC RK (1998). *Report on seismic monitoring of test hole closures at Balapan,* Institute of Geophysical Research of the National Nuclear Center, Republic of Kazakhstan (no authors listed), 62 pp.

# INVESTIGATION OF REGIONAL SOURCE PROPERTIES OF THE UNDERGROUND NUCLEAR EXPLOSION IN NORTH KOREA

Tae-Kyung Hong[1] and Junkee Rhie[2]

Yonsei University[1] and Seoul National University[2]

Sponsored by Korea Meteorological Administration

Contract No. CATER-2007-5111

## ABSTRACT

We explore the source properties of the October 9, 2006, underground nuclear explosion (UNE) in North Korea from regional phases. The dense seismic stations deployed in South Korea, Japan, and China provided us unique regional observations of the UNE. The unique data set allows us to investigate the source properties by regional phases. The isotropic moment of UNE is estimated by $2.9 \times 10^{14}$ Nm from long-period waveforms. The source spectra of regional phases from the UNE are inverted. We determine the apparent moment, corner frequency, overshoot parameter, attenuation factors, and frequency power-dependence terms from the inversion. We present the inverted source spectra with comparison of theoretical source-spectral models. The inverted source spectra agree well with theoretical curves based on UNE source-spectral models. We find that the overshoot parameters of P phases are determined as close to those from theoretical UNE source-spectral models. On the other hand, the overshoot parameters of S are determined close to zero. The low overshoot parameters for S phases suggest that their excitation sources may be different from those of P phases. We analyze the source spectra of natural earthquakes at a nearby location for comparison with those of the UNE. We test P/S spectral-amplitude ratios for discrimination between UNE and earthquakes.

## OBJECTIVES

Despite a long-time monitoring of UNEs, the source-spectral properties of regional phases have not been fully understood due to lack of regional seismic observations. The October 9, 2006, UNE test in North Korea provides us a unique chance to investigate the source properties of UNE from regional phases. We study the source properties by inverting the source spectrum and overshoot parameter from regional waveforms. We also test the P/S spectral-amplitude ratio method for discrimination of UNE from natural earthquakes.

## RESEARCH ACCOMPLISHED

We investigate the source properties of regional phases from the UNE in North Korea. We compare the source properties between UNE and natural earthquakes. For the comparison, we also analyze a nearby earthquake with a magnitude of 4.2 that occurred in April 16, 2002. The magnitude of the earthquake is comparable to that of the UNE.

### Estimation of Moment

We collect seismic records from 48 broadband seismic stations deployed in South Korea, Japan, and China. The distances between the UNE and stations are 300–1100 km (Figures 1 and 2).

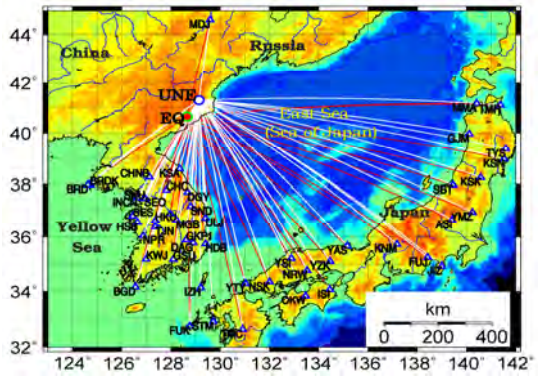


**Figure 1. Map of events (circles) and stations (triangles). The two events are the October 9, 2006, UNE and a nearby $m_b$ 4.2 earthquake (EQ).**

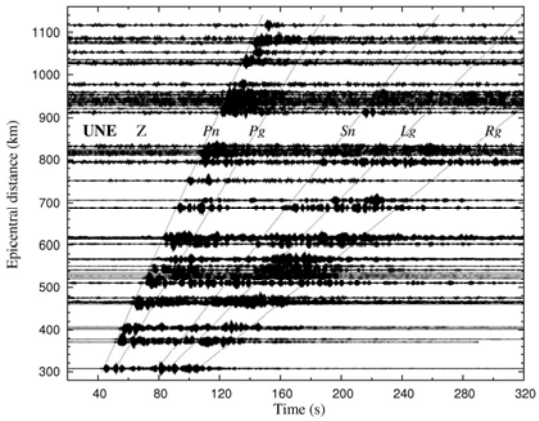


**Figure 2. Vertical seismograms of the UNE that are high-pass filtered above 2 Hz. Major regional phases are denoted.**

Long-period displacement waveforms are inverted for estimation of the moment of the UNE using the waveform inversion technique of Dreger and Helmberger (1993). We choose a frequency band in which signal-to-noise ratio is

sufficiently large. The waveforms of stations MDJ, DGY, CHC, and SEO in the frequencies of 0.05–0.1 Hz are analyzed for the inversion. The isotropic moment is estimated by $2.90 \times 10^{14}$ Nm (Figure 3). This estimate is approximately equivalent to $m_b$ of 4.4 (Patton and Walter, 1993). Also, the estimate is comparable to the regional observation of Hong et al. (2008).

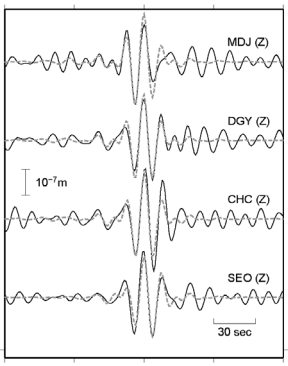


**Figure 3. Comparison of vertical displacement waveforms between observed (black) and synthetic (dotted gray) seismic records with estimated moment. The synthetic waveforms agree well with the observations.**

**Inversion of Source Spectra**

The amplitude of phase can be expressed by (Sereno et al., 1988; Taylor and Hartse, 1998; Xie and Patton, 1999):

$$A_i(f) = S(f) G(d_i) \exp[-\pi f d_i / (v_g Q_i(f))] e_i(f), \quad (1)$$

where $A_i(f)$ is the ground motion at station $i$ at the frequency of $f$, $S(f)$ is the source spectrum, $G(d_i)$ is the geometrical spreading term for the distance of $d_i$, $Q_i(f)$ is the attenuation factor on the ray path to station $i$, $v_g$ is the group velocity of the phase, and $e_i(f)$ is the cumulative effect of the other minor factors along the ray path. Here, the source spectrum model, $S(f)$, is different between UNE and natural earthquakes (see Sereno et al., 1988). We apply an inversion scheme that is modified from Xie and Patton (1999). In the inversion, we consider that the overshoot parameter is an unknown. Thus, we invert for the source spectra of regional phases by determining the moment, corner frequency, overshoot parameter, reference quality factors, and power-law frequency dependence terms. The detailed procedure is described in Hong and Rhie (2008).

From the inversion, we find that the Pn source spectrum of the UNE shows an apparent moment ($M_0$) of $6 \times 10^{14}$ Nm, corner frequency ($f_c$) of 5.4 Hz, and overshoot parameter ($\xi$) of 1.4. For Lg, we have $M_0 = 2 \times 10^{13}$ Nm, $f_c = 1.0$ Hz, and $\xi = 0.1$ (Figure 4). The estimated Pn overshoot parameter is close to those conventionally adopted, while the estimated Lg overshoot parameter is lower. On the other hand, the apparent moment and the corner frequency of Pn source spectrum of the earthquake are $M_0 = 2 \times 10^{15}$ Nm and $f_c = 5.8$ Hz. The Lg source spectrum of the earthquake shows $M_0 = 4.8 \times 10^{13}$ Nm and $f_c = 2.1$ Hz. The apparent moments of Pn and Lg spectra of the earthquake are estimated higher than those of the UNE.

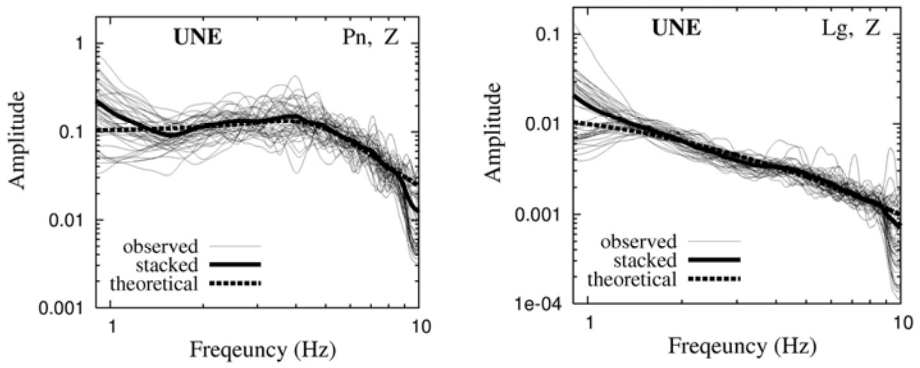


**Figure 4. Pn and Lg source spectra of the UNE. The Pn phase displays the characteristic overshooting feature, while the Lg phase decreases with frequency monotonically.**

### Pn/Lg Spectral-Amplitude Ratio

The Pn/Lg spectral-amplitude ratios of the UNE increase in the frequencies lower than the Pn corner frequency and increase in the frequencies higher than the corner frequency (Figure 5). This form is different from the spectral-amplitude ratio of the earthquake, which displays monotonic increase with frequency (figure is not presented). The observed P/S spectral-amplitude ratios of the UNE agree well with theoretical variation.

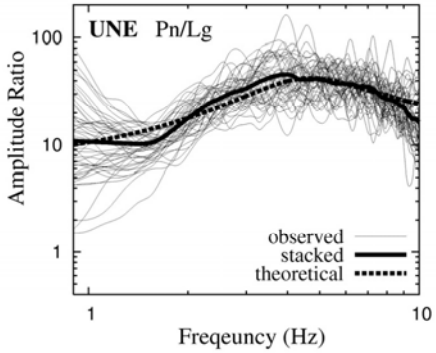


**Figure 5. Pn/Lg spectral-amplitude ratios of the UNE. The observed spectral-amplitude ratios agree well with the theoretical variation.**

## CONCLUSIONS AND RECOMMENDATIONS

Regional seismic records for the October 9, 2006, UNE in North Korea were inverted for investigation of source properties of regional phases. From a long-period waveform inversion, we estimated the isotropic moment of the UNE, which is given by $2.9 \times 10^{14}$ Nm. The source spectra of Pn and Lg phases were inverted with determination of apparent moment, corner frequency, and overshoot parameter. The dense observation allowed us to determine the overshoot parameter as an independent unknown. The estimated Pn overshoot parameter is estimated close to that conventionally assumed, while the Lg overshoot parameter is estimated lower. The observation suggests that the shear energy may be independent from the P-wave excitation source. The P/S spectral-amplitude ratios agree with theoretical expectation and appear to be useful for discrimination of UNE from earthquakes.

**ACKNOWLEDGEMENTS**

We are grateful to the Korea Meteorological Administration (KMA), the Korea Institute of Geoscience and Mineral Resources (KIGAM), the Incorporated Research Institutions for Seismology (IRIS), and the National Research Institute for Earth Science and Disaster Prevention (NIED) in Japan for making the seismic data available.

**REFERENCES**

Dreger, D. S. and D. V. Helmberger (1993). Determination of source parameters at regional distances with three-component sparse network data, *J. Geophys. Res.* 98: 8107–8125.

Hong, T.-K., C.-E. Baag, H. Choi, and D.-H. Sheen (2008). Regional seismic observations of the October 9, 2006, underground nuclear explosion in North Korea and the influence of crustal structure on regional phases, *J. Geophys. Res.* 113: B03305, doi:10.1029/2007JB004950.

Hong, T.-K. and J. Rhie (2008). Regional source scaling of the October 9, 2006, underground nuclear explosion in North Korea, *Bull. Seism. Soc. Am.*, (submitted).

Patton, H.J. and W.R. Walter (1993). Regional moment: Magnitude relations for earthquakes and explosions, *Geophys. Res. Lett.*, 20: 277–280.

Sereno, Jr., T. J., S. R. Bratt, and T. C. Bache (1988). Simultaneous inversion of regional wave spectra for attenuation and seismic moment in Scandinavia, *J. Geophys. Res.* 93: 2019–2035.

Taylor, S. R. and H. E. Hartse (1998). A procedure for estimation of source and propagation amplitude corrections for regional seismic discriminants, *J. Geophys. Res.* 103: 2781–2789.

Xie, J. and H. J. Patton (1999). Regional phase excitation and propagation in the Lop or region of Central Asia and implications for P/Lg discriminants, *J. Geophys. Res.* 104: 941–954.

# QUANTIFICATION OF ROCK DAMAGE FROM SMALL EXPLOSIONS AND ITS EFFECT ON SHEAR-WAVE GENERATION: PHASE I—HOMOGENEOUS CRYSTALLINE ROCK

Mark Leidig[1], Peter Boyd[2], Randolph J. Martin[2], James F. Lewkowicz[1],
Dorothy Richter[3], Robert Garfield[3], Jeffrey A. Reid[3], and Jessie L. Bonner[1]

Weston Geophysical Corporation[1], New England Research, Inc.[2], and Hager-Richter Geoscience, Inc.[3]

Sponsored by Air Force Research Laboratory

Contract No. FA8718-08-C-0044
Proposal No. BAA08-99

## ABSTRACT

We are currently conducting a one-year feasibility study to determine the most efficient way to characterize the damage from an explosive source and to identify the source(s) of shear wave generation. We hope to quantify crack nucleation and growth (Ashby and Sammis, 1990) as an *S*-wave generation mechanism in the far-field (Sammis, 2002) and to map the cone of damage (Patton et al. 2005; Stevens et al. 2003) above a source, modeled by a compensated linear vector dipole (CLVD). This study is being conducted at a quarry in Barre, Vermont, in a granite body that has a low fracture density and typically forms large blocks used for monuments.

In this study, we are detonating five small (< 200 lb) explosions at depths of approximately 9, 12, and 17 m each separated by at least 20 m so the damage zones do not overlap. We plan to use two different types of explosives in order to provide different fracturing in the rocks. An ammonium nitrate fuel oil (ANFO)-Emulsion mixture with a slow velocity of detonation (VOD) should produce larger length cracks while a molecular explosive with a high VOD should produce a large rubble zone near the borehole and cracks of smaller lengths.

We are quantitatively and qualitatively defining the damage around the source using coring, cross-borehole seismic tomography, and borehole televiewers before and after the explosions. We will also deploy a large network of accelerometers and seismometers from 5 m to 30 km from each blast. These stations will include near-source (<1 km) accelerometers and short-period seismometers that will record the physical characteristics of the primary seismic pulse created by the explosions. We will also deploy two linear arrays of intermediate and short-period sensors in order to track the *P*- and *S*-waves energy partitioning from the explosions with hopes of relating the observables back to the variation in damage caused by the explosions. The explosions are planned for July 2008.

## OBJECTIVES

Two of the proposed mechanisms for *S*-wave generation involve secondary processes related to the damage and deformations caused by the explosions. First, outside the cavity radius, there is a "shell" of fragmented rock. Sammis (2002) theoretically showed that the integrated effect of the nucleation and growth of the fractures in this shell can generate secondary seismic waves as large as the *P*-waves from the explosion itself.

A second proposed method is the CLVD, which is an elastodynamic equivalent of a conical source. In this case, it is an inverted cone with apex at the detonation point (Patton et al., 2005). Media within the cone deforms and fails as a result of tensile stresses caused by the downgoing shock wave reflected off the free surface. Spallation is an obvious example of such failure. Driven block motions at depth, as envisioned by Masse (1981), is another example that may have greater significance for seismic wave generation.

A problem for researchers trying to relate damage to *S*-wave generation is a paucity of detailed, readily available, damage-characterization data from explosions. Weston Geophysical Corporation and New England Research, Inc. plan to detonate small chemical explosions in relatively unfractured, homogeneous Barre granite in Vermont, USA. Barre granite has been a worldwide standard for homogeneous granite in commercial, monument, and industrial settings. The focus of the experiment will be to quantify the damage caused by these explosions and to provide a unique dataset that should have important ramifications for models of *P*- and *S*-wave generation from explosions in hard rock in areas of monitoring interest.

## RESEARCH ACCOMPLISHED

### Pre- and Post-Shot Characterization

We are currently implementing a three-phase experimental field project at a granite quarry in Vermont. Figure 1 shows a schematic of the planned experiment. First, the test-site rock rheology and fracture distribution will be thoroughly characterized through a series of boreholes drilled near the shot-point borehole. Next, a series of explosions at depths of burials ranging from approximately 9 to 17 meters will be detonated at the test site. Finally, post-deformation alterations to the *in situ* rock properties will be measured in order to provide a quantitative and detailed description of the rock damage caused by the explosions.

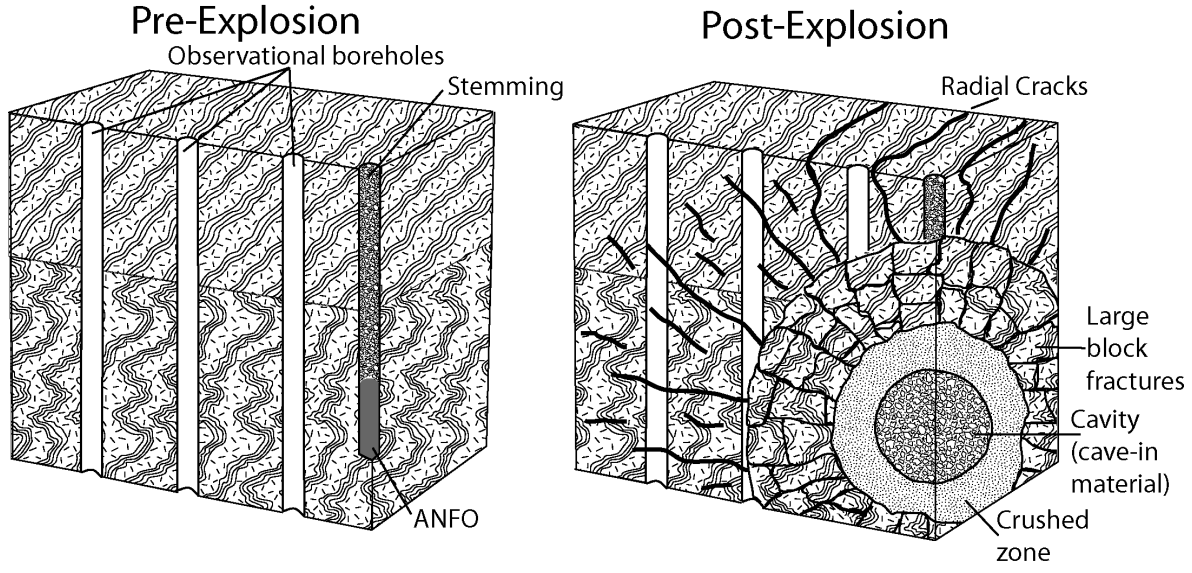


**Figure 1. Schematic of proposed experiment. A series of observational boreholes will be cored and logged to provide geotechnical data (left) before explosives are detonated (right). The boreholes will be cleared and re-logged. The information gained would be used to determine the characteristics of each damage zone.**

**In-situ Velocities.** An in-situ seismic velocity model will be developed using traditional seismic refraction and/or cross-borehole seismic velocities. Crosshole seismic surveys are used to obtain in situ properties of rock strata. Often used as part of a comprehensive geotechnical investigation, the crosshole seismic survey yields valuable information as to the strength and cohesiveness of the underlying bedrock, information that is critical to characterizing the pre- and post-shot media. We plan to drill two 4" boreholes on opposite sides of two explosion boreholes at the test site. These holes will be cased with PVC pipe and then a crosshole seismic velocity analysis conducted to measure the time for horizontally traveling *P*- and *S*-waves to travel from a source hole to a receiver hole. After the explosion, we will conduct another round of crosshole imaging to quantify the change in *P*- and *S*-wave velocities as a result of the explosions. Figure 2 provides a modeled crosshole response for our planned explosions.

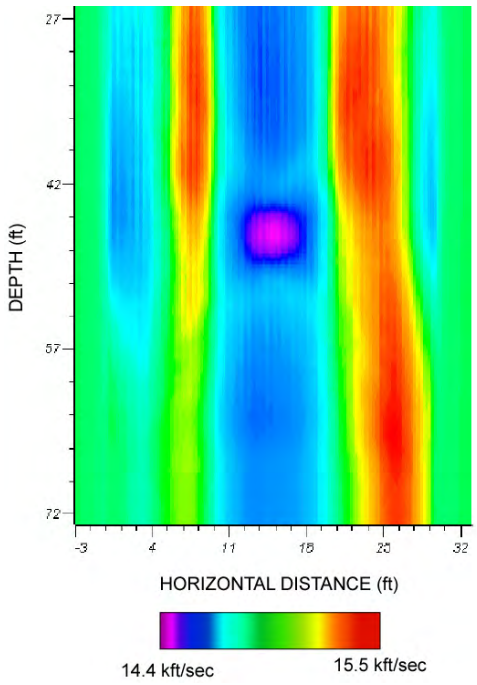


**Figure 2. Modeling the predicted response of an 1-m diameter rubble filled void (1200 fps) surrounded by a 1-m crushed zone (8500 fps) in a homogeneous 15,000 fps block. The observation holes are located 15 feet from the blast hole and the blast is located at a depth of about 40 feet. A geophone spacing of one-foot and a shot spacing of 2-feet are adequate to image the explosion effects.**

**Borehole Core Analysis.** A series of borehole cores have been recovered from the test site. Figure 3 shows an example of a 2.5-m section of core from the test site. The section core had to be broken with the coring machine due to a lack of natural fractures. The core samples are currently being studied using the AutoScan technology at New England Research, Inc. AutoScan has a capability of measuring permeability, electrical resistivity, and compressional and shear-wave velocity as a function of position on the core (Figures 4 and 5). After the explosions, additional core will be drilled through the shot point and at points just inside and outside the predicted cavity radius (e.g., Figure 1). The combination of the pre-and post-shot core data will allow us to test the spatial distribution of damage due to different boundary conditions.

**Figure 3. Section of core (2.5 meters in length) consisting of homogeneous granite with low fracture density from the test-site location.**

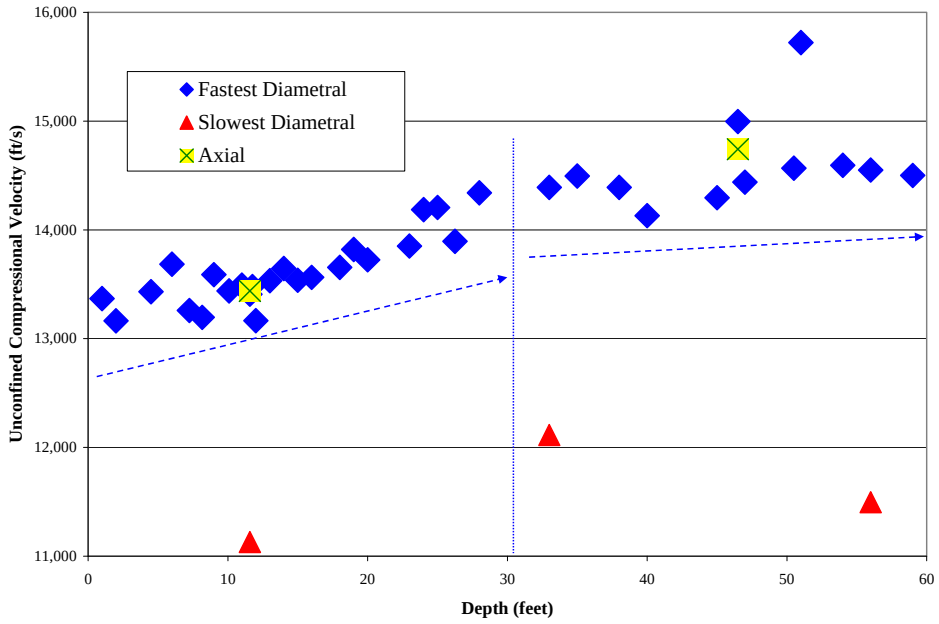


**Figure 4. Compressional wave velocity (feet per second), as a function of depth, in the corehole at the proposed location for Shot 2. Velocity increases with depth, and there appears to be a change in slope at approximately 30 feet. The increase in compressional velocity with orientation, at a single depth, can approach 25 percent.**

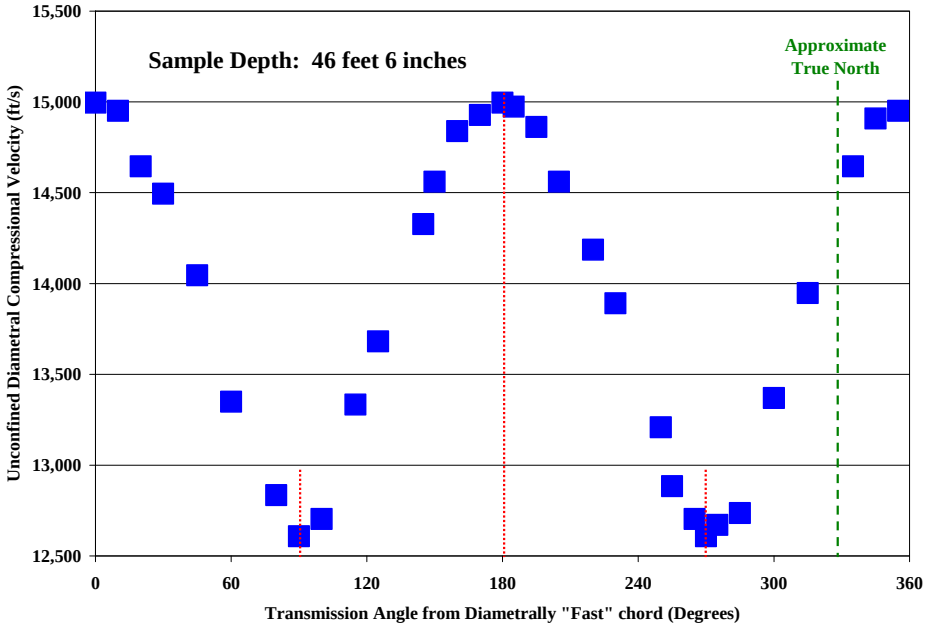


**Figure 5. Diametrally transmitted compressional wave velocity (in feet per second), as a function of chord orientation, in a core specimen recovered from a corehole at the Shot 2 location. The "Fast" chord is considered to define the orientation of the strike of the rift plane in the Barre granite. The strike of the rift plane appears to be oriented at approximately N30°E at this site, and it is considered to be near-vertical. The fastest compressional wave velocity is 19 percent greater than the slowest in this specimen.**

**Borehole Televiewer Analysis.** An optical or acoustic televiewer will be lowered in each borehole to obtain the fracture density, magnitude, and orientation. The acoustic televiewer transmits and records ultrasound pulses reflected off the borehole wall. The optical televiewer simply records a 360° picture of the borehole wall. Figure 6 shows images from an optical and acoustic televiewer of fractures in a borehole at our test site. Below 14.6 feet, there were only three rank-2 fractures, which are intermediate fractures that are distinct and continuous around the borehole with little or no apparent aperture. These fractures occurred at 21.1 (shown in Figure 6), 39.6, and 50.8 feet. Given the proposed depth of the explosion at this borehole location (12 meters or 39 feet), we may choose to detonate the explosives at a shallower depth to avoid this fracture. There was only one rank-3 fracture (e.g., major fractures that are distinct and continuous around the borehole with apparent aperture) in the imaged borehole, occurring at a depth of 7.7 feet.

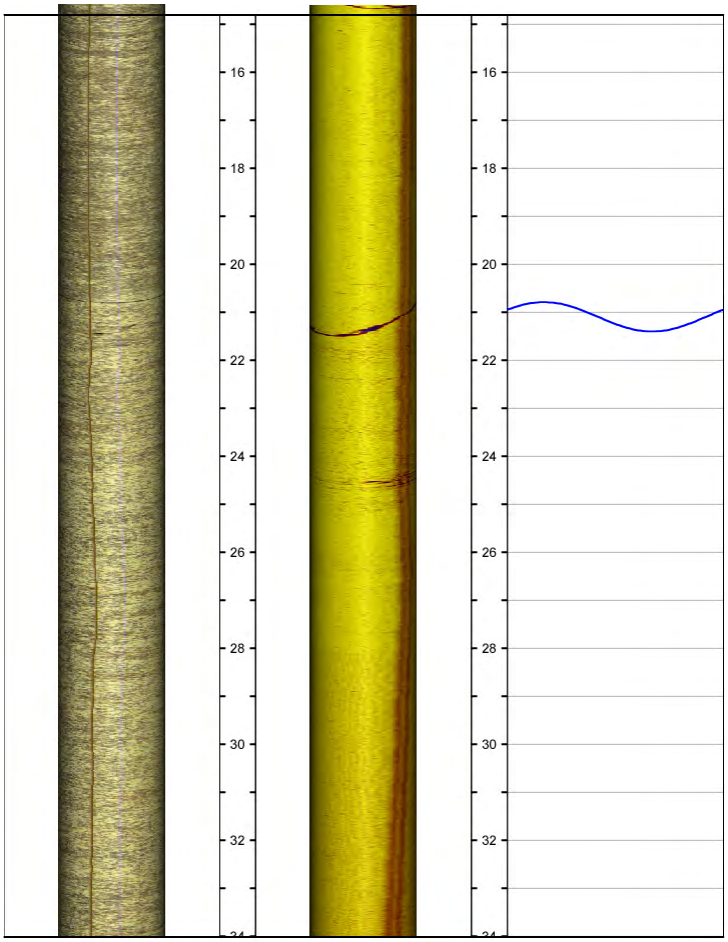


**Figure 6. Optical televiewer (left) and acoustic televiewer (middle) images of a portion of a borehole at the test site. In the section shown here, only one Rank-2 fracture was observed (right, at 21 feet).**

**Post-Shot Characterization**. After the test site has been completely characterized, the explosions will be conducted (see next section). Following detonation, we will re-open any boreholes that caved in or were damaged during the blasts, and the test-site physical properties will be examined again to determine the extent of the damage. New cores will be extracted for analysis. As shown in Figure 1, the borehole spacing will be devised to try and measure the radius of the cavity, pulverized rock, fragmented rock, and radial cracks. The televiewer will return images of the damage in each zone and quantify slip amounts along pre-existing and newly developed fractures. Surface mapping of faulting and radial cracks will be completed.

**Explosion Design**

Personal safety and structural integrity are the most important factors to consider when designing any explosion experiment. This damage experiment at the granite quarry in Vermont presented new challenges for design primarily due to two structures located less than 1 km from the proposed test site. The first is a cell phone tower located ~200 meters from the blast site, and the second is the vertical face high-wall of the active granite quarry (Figure 7) located ~550 meters from the blast site. Preliminary estimates of peak particle velocities (PPVs) from a fully-confined, 400-lb explosion were slightly above the United States Bureau of Mining vibration limits (USBM RI8507) at the cell tower and slightly below the regulations at the high wall.

**Figure 7. Near-vertical face of the Vermont granite quarry hosting the explosion experiments. The face shown here is less than 600 meters from the proposed test site. The face must not be damaged by vibrations from the planned explosions. All explosions will be conducted after work hours when quarry personnel are not in the pit.**

We attempted to locate another test site that was at a greater distance from the critical infrastructure in order to detonate the 400 lb explosions. We located a site at an abandoned aggregrate quarry pit more than double the distance from the cell phone tower and quarry free face. Coring operations commenced at this site in early May 2008 only to determine that the granite was unsatisfactory for our planned experiments. The granite had a higher fracture density than the original test site (hence, it was being used for aggregate rather than monument stone), and we cored into a large schist xenolith. The desire for greater homogeneity of the emplacement media and fewer fractures led us to return to the former site and evaluate detonation yields that would provide acceptable vibration limits at the two critical structures.

We predicted the PPVs for our explosions using the mining industry standard formula of

$$PPV\ (in/sec) = KxSD^{A} \qquad (1)$$

where A is an attenuation term that typically varies between -1.6 and -1.8, and SD is called the "scaled distance" and is defined by

$$SD = \frac{D}{\sqrt{W}} \qquad (2)$$

where D is distance and W is the explosive yield. K is a site vibration modifying factor for confinement, which varies from 24 for under-confinement to 605 for completely-confined. We used Equations 1 and 2 and K=605 to estimate the PPVs for 200-lb and 400-lb explosions at the cell tower and quarry face (Figure 8). The results show that the predicted PPVs for the 400-lb explosion are slightly above the USBM R18507 limits at frequencies greater than 10 Hz for the cell phone tower. And because the USBM vibration limits are more restrictive for lower frequency data, both explosions are predicted to vibrate above the limits at frequencies less than 10 Hz.

We have detonated three (3) 200-lb fully confined explosions in different emplacement media as part of our previous experiments (Bonner et al., 2005; Leidig et al., 2007). We plotted the PPVs for these blasts at stations between 0.2 and 11 km in Figure 8. All of the PPV data for our 200-lb shots fall below the predicted PPVs, which is due in part to the conservative choice of K=605 for the predictions. The observed data and the predictions suggest that detonating 200-lb explosions at the original test site (e.g., the site with monument-quality granite) will generate PPVs at the cell phone tower and quarry wall that are below USBM industry regulations.

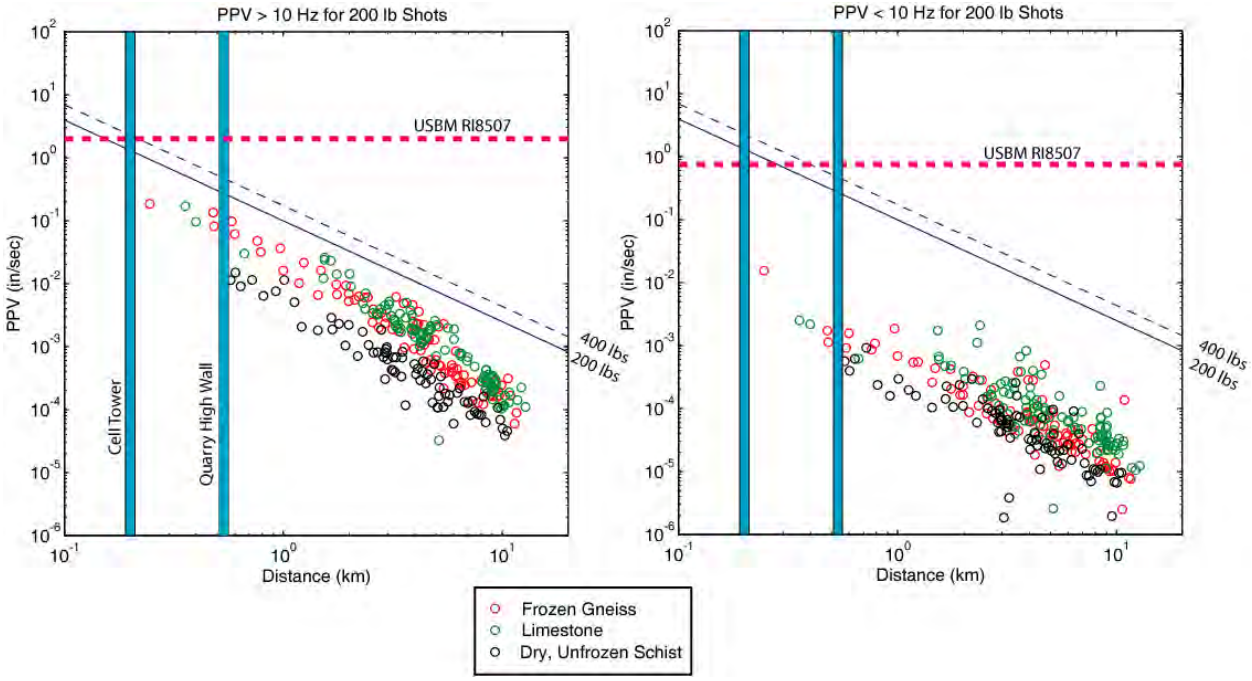


**Figure 8. Predicted and observed PPVs for explosions at frequencies greater (left) and less than (right) 10 Hz. Also shown are the USBM vibration limits, which are frequency dependent. The solid and dashed blue lines represent predicted PPVs based on Equations 1 and 2, while the circles are observed PPVs for three 200-lb explosions detonated during previous experiments in different emplacement media.**

Figure 9 shows the predicted layout for the five explosions (Table 1) in an image taken from near the base of the cell phone tower. To further ensure the safety of our planned operations, we are detonating three "calibration" explosions. Shot 1 will be a 50-lb ANFO explosion, while Shots 2 and 3 will be 100-lb single-fired shots. The PPVs from these "calibration" explosions will be recorded on Instantel accelerometers at the cell tower, the quarry high wall (top and bottom), and the nearest residential structure. The Instantels will provide us with rapid PPVs that can

be compared to Figure 8 in order to ensure that our homogeneous, low-fracture density media does not behave contrary to Equations 1 and 2. If the PPVs from Shots 1–3 are at or below the predictions, we will then load and detonate Shots 4 and 5, which are planned 200-lb shots located as far away from the cell tower as possible while remaining within the test pit.

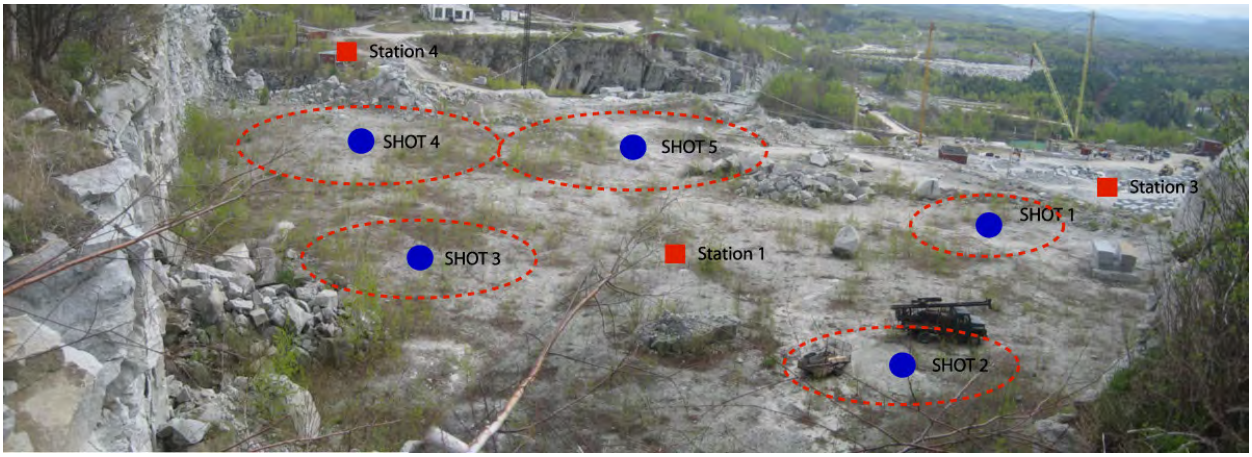


**Figure 9. Image of the test pit showing the planned locations of the shots. The blue circle shows the shot point, the red circles show the predicted elastic radii for the explosions, and the red squares represent near-source stations. Shots 1-3 will be detonated first and the PPVs recorded at critical infrastructure to ensure that the 200-lb Shots 4 and 5 will be at or below USBM safety regulations.**

**Table 1. Designed Explosions.**

| Shot | Projected Hole Depth (m) | Yield (lb) | Explosive Type |
|---|---|---|---|
| **1** | 9 | 50 | ANFO/Emulsion |
| **2** | 12 | 100 | ANFO/Emulsion |
| **3** | 12 | 100 | Composition B |
| **4** | 17 | 200 | ANFO/Emulsion |
| **5** | 17 | 200 | Composition B |

Also shown in Figure 9 are the predicted elastic radii for the planned explosions based on a Mueller-Murphy (1971) source model (see Figure 10). In designing the experiment, we separated the explosions by 1.5x the elastic radii or greater with the exception of Shots 4 and 5. Before drilling the Shot 5 blasthole, we may attempt to move the explosion a few meters west and away from Shot 4; however, this could result in damage to the access road to the pit.

The reason for the redundancy in the two 100-lb calibration shots is because we will load and shoot the holes differently. Our objective is to determine the effect of damage on *S*-wave generation; thus we plan to try and fracture the rock differently. We will detonate two different types of explosions. The first will be an ANFO/Emulsion mixture that is typically used in the mining industry that has a velocity of detonation (VOD) of ~4 km/sec. The second type of explosive used will be a molecular explosive (e.g., TNT or Composition B) with a velocity of detonation of ~8 km/sec. The two explosives will behave differently when detonated in the boreholes. Singh (1993) found that higher VOD explosives do less damage, fracturing, and over-breakage than lower VOD explosives. This is caused by the higher VOD explosives powderizing the material near the borehole due to the rapid, enormous pressures. The powderized rock subsequently hinders secondary gasses from significantly driving long cracks. The mining industry considers these phenomena as well as cost and logistics when choosing ANFO/Emulsion as their typical blasting agent for rock fracturing. By conducting a 100-lb calibration explosion of each type of blasting agent, we will have data to ensure that the detonation of the higher VOD explosives does not behave anomalously with respect to Equations 1 and 2, which were developed mainly with ANFO/Emulsion explosions.

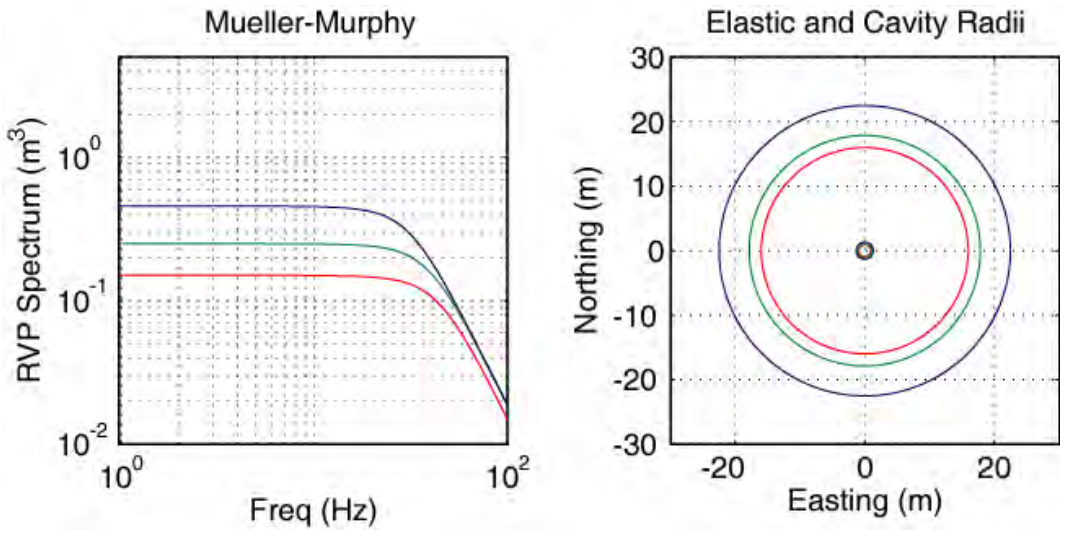


**Figure 10. Estimates of the corner frequencies (left) and elastic and cavity radii (right) for 50-lb (red), 100-lb (green) and 200-lb (blue) explosions. The smaller circles with radii of approximately 1 meter represent the cavity radii while the larger circles are the elastic radii. Note that for chemical explosions, the cavity is actually a rubble or powderized zone.**

**Seismic Networks**

We will record the explosions on an array of almost 160 accelerometers and seismometers. The near source instrumentation will consist of nine stations with high-g accelerometers and short-period seismometers within 1 km of the test site. One station will be installed in the middle of the explosions (Figure 11) to record the precise time of detonation and close-in phenomenology, such as spall, while the remaining close-in stations will be located to obtain complete azimuth coverage for moment tensor inversions. This array of sensors will be recorded at 500 samples per second.

Two linear arrays with a total of 19 three component seismometers and 120 vertical component geophones with "Texan" digitizers are going to be deployed to the northeast and southeast of the test site (Figure 11). The intermediate period seismometers will be installed at 3 km spacing with Texans placed along the same paths at 0.5 km spacing to increase sampling density. These sensors will record at 250 sps. The northeast array is oriented to follow the structural trend of the region, while the southeast array will lie oblique to the trend. Digital and analog video recordings will be made of the blasts to document any surface effects, although the explosions are designed to be fully contained and confined.

## CONCLUSIONS AND RECOMMENDATIONS

Our experiment to quantify damage from explosions and its effect on S-wave generation is planned for 12–13 July, 2008.

## ACKNOWLEDGMENTS

We wish to thank the following people for their contributions to this project to date: Donald Murray, Tim Rath, Charlie Sammis, Mike and Amy McGinley, Diane Baker, Noel Barstow, Robert Raistrick, Rick Schult, and Leigh House.

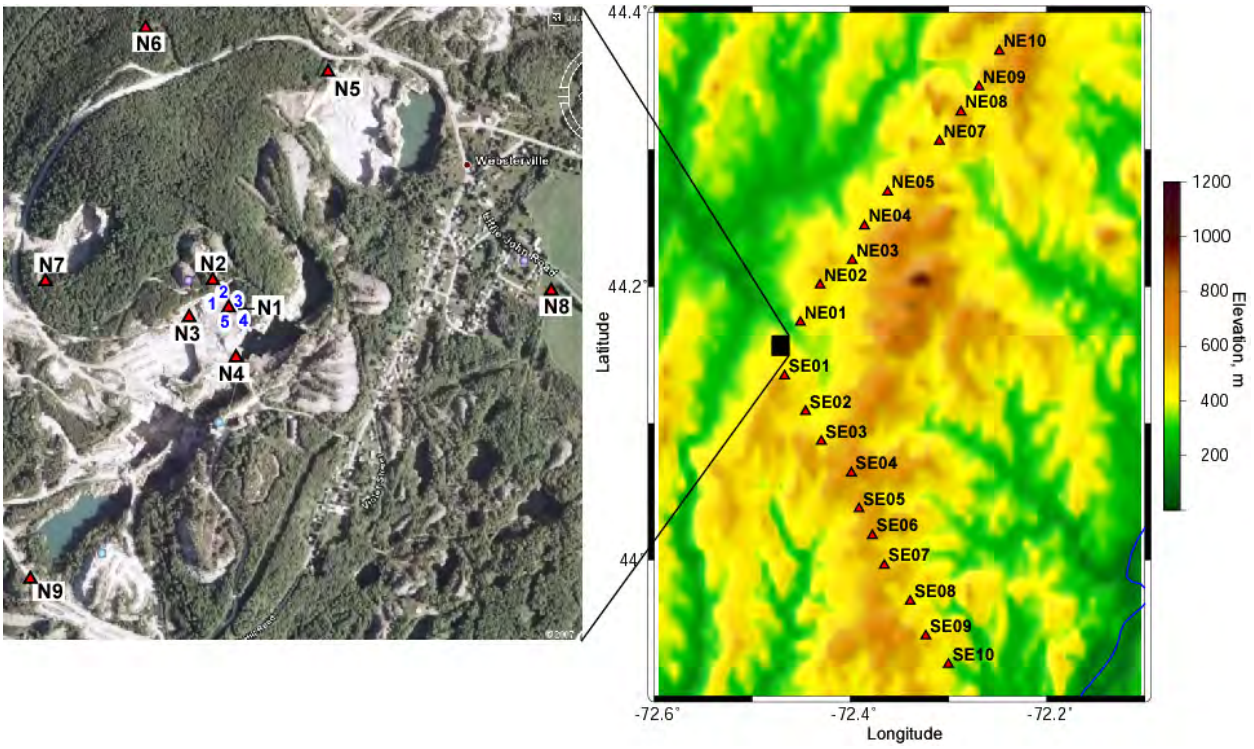


**Figure 11. Map of near source stations (left) relative to the explosions (blue numbers) and linear station arrays (right). The Texan sensors (not shown) will be placed along the path of the linear arrays to increase sampling density.**

## REFERENCES


Ashby, M. F. and C. G. Sammis (1990). The damage mechanics of brittle solids in compressions. *Pure appl. Geophys*. 133: 489–521.

Bonner, J.L., B.W. Stump, M. Leidig, H. Hooper, X. Yang, R. Zhou, T. S. Kim, W. R. Walter, A. Velasco, C. Hayward, D. F. Baker, C. L. Edwards, S. Harder, T. Glenn, C. Zeiler, J. Britton, and J.F. Lewkowicz, (2005). Source Phenomenology Experiments in Arizona. Final Report. 358 p.

Leidig, M., J.L. Bonner, R. Martin, and K. Murphy (2007). Possible effects of frozen rock on explosive coupling (Abstract*). Seism. Res. Letts*. 78: p. 252.

Masse, R. P. (1981). Review of seismic source models for underground nuclear explosions, *Bull. Seism. Soc. Am.* 71: 1249–1268.

Mueller, R. A., and J. R. Murphy, (1971). Seismic characteristics of underground nulear detonations: Part I, Seismic scaling law of underground detonations, *Bull Seism. Soc. Am*. 61: 1675.

Patton, H., J. Bonner, and I. Gupta, (2005). *Rg* Excitation by Underground Explosions: Insights from Source Modeling the 1997 Kazahkstan Depth of Burial Experiments. *Geophys. J. Int.* doi:10.1111/j.1365-246X.2005.02752.x

Stevens, J.L., G. E. Baker, H. Xu, T.J. Bennett, N. Rimer, and S.M. Day (2003). The physical basis of *Lg* generation by explosion sources, in *Proceedings of the 25th Annual Seismic Research Review on Nuclear Monitoring: Building the Knowledge Base*, LA-UR-03-6029, Vol. 1, pp. 456–465.

Sammis, C. G. (2002). Generation of High-Frequency *P* and *S* Wave Energy by Rock Fracture During a Buried Explosion: Its Effect on *P/S* Discriminants at Low Magnitude, in *Proceedings of the 24th Seismic Research Review—Nuclear Explosion Monitoring: Innovation and Integration*, LA-UR-02-5048, Vol. 1, pp. 542–551.

Singh, S., (1993). Damage causing potential of different explosives, in *Proceeding of the Ninth Annual Symposium on Explosives and Blasting Research*, California USA, pp. 325–337

# SMALL-EVENT YIELD AND SOURCE CHARACTERIZATION USING LOCAL P AND S-WAVE CODA SOURCE SPECTRA

Kevin Mayeda

Weston Geophysical Corporation

Sponsored by Air Force Research Laboratory

Contract No. FA8718-07-C-0010
Proposal No. BAA07-40

## ABSTRACT

The mission of the Air Force Technical Applications Center (AFTAC) requires accurate yield estimation for nuclear explosions. Historically, the focus has been on larger yield events ($m_b$ > ~4.5) using teleseismic body wave magnitudes and applying test-site-specific corrections for yield estimates. The regional coda methodology provides unprecedented stability and avoids test site bias because it is based upon absolute source spectra. Increasingly, however, there is interest in monitoring smaller events both for yield and source characterization. Unfortunately, these events may only be recorded with adequate signal-to-noise ratio at local distances from one station.

The project goals were to extend the well-established regional coda methodology to local distances using *S* and *P*-wave codas in regions of little-to-no calibration data and/or regions of high attenuation and lateral complexity. Previous studies show that local coda has a unique property of homogenizing its energy over a volume of the Earth's crust such that path corrections for distances less than ~200 km are not necessary, or minimal at worst. Our plan this year was to use existing datasets from a variety of active tectonic settings and source types with the aim of assessing performance under the assumption of little to no calibration data. We have compared S-wave coda path attenuation curves from a variety of regions to look for similarities and differences that could be correlated to the degree of tectonic activity. In general, we can make some preliminary statements. First, we find that central Italy exhibits the strongest attenuation (0.5 to 2.0 Hz), followed by Taiwan and western Iran for distances ranging between ~20 and 300 km. On the other hand, upstate New York, South Africa, and the Korean Peninsula appear to have the lowest attenuation, which is reassuring since both regions are the most tectonically stable. The San Francisco Bay Area is somewhere between the two.

This special feature may make it easier to define an a priori set of coda-calibration parameters that can be transported to new but geophysically similar regions. For example, it appears that tectonically similar regions have similar a coda path, envelope shape, and peak envelope velocity, which will allow us to derive average "local background" models then apply them to other regions for testing and evaluation, including cases to mimic an uncalibrated, single-station deployment.

## OBJECTIVES

The following outlines many of the questions and objectives that are being addressed in this study:

1) To what extent can an average local background coda model (e.g., path corrections, envelope shape, velocity, etc.) be developed and transported to a new area with no prior calibration? Specifically, can we transport these averaged parameters to a new, tectonically similar region? What are the associated errors?
2) For regional coda calibrations that lack local data and are unconstrained at these distances (e.g., central Asia, North Africa), can we seamlessly blend in the appropriate local background model?
3) Can local coda measurements in a heterogeneous region provide a stable yield estimate relative to direct wave measures?
4) Due to its inherent shorter window length, to what extent can the local *P*-wave coda be used and how do results compare with *S* coda? How does this compare with results from an ongoing regional *P*-wave coda study?
5) How much is gained by additional stations, or is one station enough?
6) For low seismicity regions, how can we obtain higher confidence estimates of site-response corrections? For example, can we use a single ground-truth source spectrum or calibration event? If so, what are the errors?
7) For highly attenuative regions, what is the minimum coda window length needed to maintain a stable amplitude estimate? What is the minimum magnitude threshold where we can still maintain stable estimates? Can we derive average detection threshold curves?
8) Can our local coda spectra be used for high-frequency seismic discrimination, for example, coda spectral ratios?
9) Can the spectral shape of the local, coda-derived source spectra provide depth-of-burial information?

## RESEARCH TO BE ACCOMPLISHED

In this project, we plan to demonstrate the capability of providing significantly lower uncertainties in yield and source estimation by extending the well-established regional narrowband coda methodology to local distances in regions of little to no calibration data using both *P* and *S*-wave codas. Furthermore, because of its stable nature, local coda-derived source spectra will be used to characterize a range of different event types (e.g., shallow and normal-depth earthquakes, mining-related explosions and their associated events, nuclear tests, rock bursts, and volcanic-related events). The motivation for using the coda comes from the fact that it has unique properties that, if exploited fully, can significantly improve our ability to monitor small events at local distances. For example, local high-frequency (>~0.5 Hz) *S*-wave coda has the unique property of homogenizing its energy over a volume of the Earth's crust such that path corrections for distances less than ~200 km are not necessary or minimal. Furthermore, the local coda averages over the focal sphere as well as the source-time function of the event, thus eliminating the need for dense seismic networks. Even in regions of strong lateral complexity, the local coda has been shown to be very stable, usually a factor of 4-to-5 times less variable than direct *S*-phases. This means that to achieve the same level of precision with the traditional direct phases, one would need a local network composed of ~16-to-25 stations surrounding the source, which in most cases would be unrealistic. Because the coda averages over the 3-D crustal heterogeneity as well as the source radiation pattern, it is ideal for small-event local monitoring with as few as one station. To demonstrate this, Figure 1 shows interstation magnitude results for Nevada Test Site (NTS) explosions recorded at near-regional distances (e.g., 200 to 300 km away). Here we compare the inter-station performance between $m_b(L_g)$, $m_b(Pn)$ and $m_b(L_g\text{coda})$ from Mayeda (1993). We observe that the coda-based $m_b$'s have the lowest standard deviation by roughly a factor of 4 to 5. This property makes it ideal for monitoring situations where station coverage is sparse.

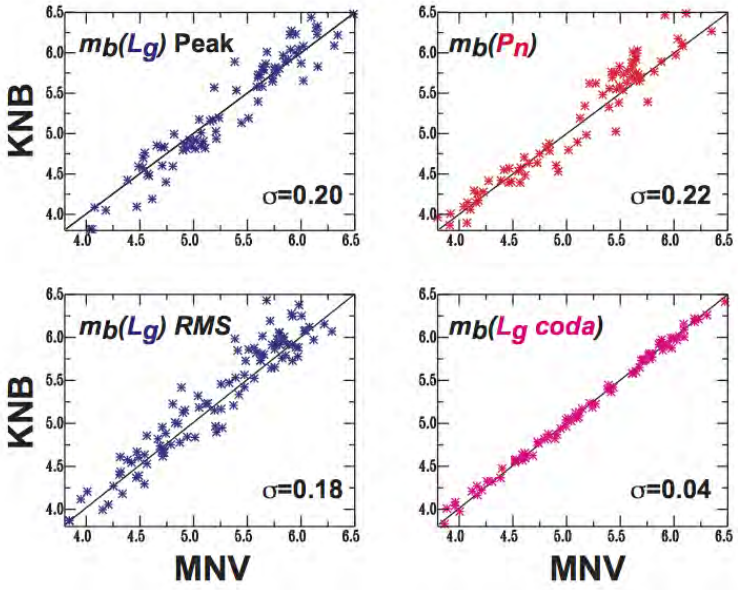


**Figure 1. Interstation comparisons of magnitude at two near-regional stations, KNB (Δ ~250 km) and MNV (Δ ~200 km) (from Mayeda, 1993). Note that the scatter in the coda-derived $m_b$'s (lower right) are a factor of 4-to-5 times smaller than the conventional regional magnitude measures using direct *P* and $L_g$.**

For regional applications of the coda methodology, path corrections can be significant and the Department of Energy (DOE) labs have a large effort in calibrating broad regions. However, for local monitoring, path effects on the coda are not as important. For example, Figure 2 illustrates a unique property of coda waves that has been the basis of numerous studies over the past several decades, namely that the coda approaches a homogeneous distribution in space and time behind the expanding direct-wave front (e.g., Aki, 1969; Aki and Chouet, 1975; Phillips and Aki, 1986). In this example we show three panels of three events that are recorded at station BKS and another station, SAO, located ~140 km to the southeast. The three events were chosen such that one was relatively close to BKS, the other roughly in between, and the last event was close to SAO. In all panels, we see that the coda envelope levels are approximately the same, independent of the source-station distance. This is in sharp contrast to the direct waves (*P*, *S*, and $L_g$), which differ significantly in amplitude because of attenuation, geometrical spreading, and radiation pattern. A way to help visualize this is to imagine the direct *S*-wave moving radially away from the source. Behind the *S*-wave front, there is a pool of scattered energy in its wake that decays at the same rate, irrespective of distance from the source. As stated to the principal investigator years ago by the late Kei Aki, "It's like a kind of magic!" Whether one believes in single or multiple scattering, isotropic or nonisotropic scattering (e.g., see review by Sato and Fehler, 1998), the observational evidence clearly shows that the crust tends to homogenize the coda energy at local-to-near-regional distances (e.g., Aki, 1969). This means that *ANY* seismic station within this region would provide a stable amplitude measure irrespective of its location relative to the source origin.

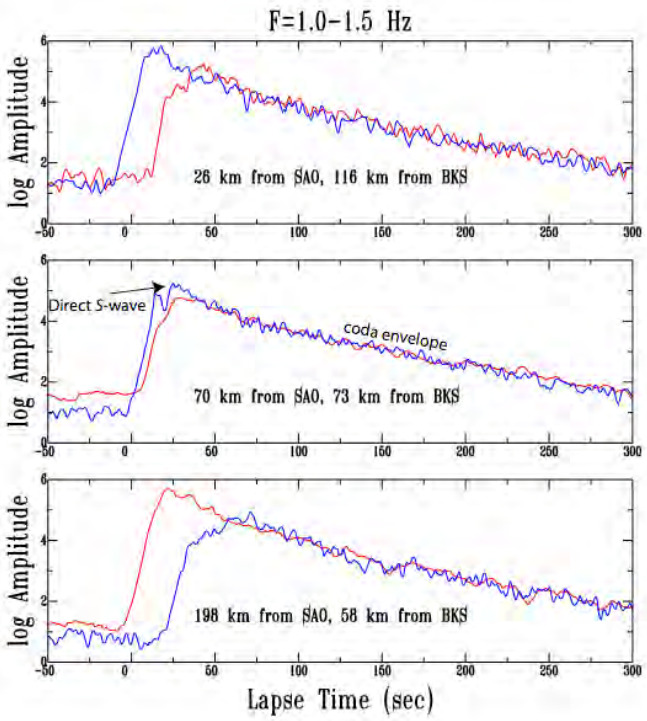


**Figure 2. Example envelopes (*f*=1.0–1.5 Hz) for three local earthquakes located in the San Francisco Bay region recorded at stations SAO (blue) and BKS (red), part of the Berkeley Digital Seismic Network (BDSN). At this range of distances, the scattered *S* waves or "coda" are homogeneously distributed in the crust (from Mayeda et al., 2005).**

As mentioned earlier, the motivation behind this study comes from the desire to estimate yield accurately and characterize the source, especially those that are small, or in regions of high regional attenuation. Ground-based nuclear explosion monitoring relies heavily on teleseismic and regional sensors that are sparsely distributed around the world, usually with station spacing on the order of ~1,000 km or more. Station distribution and regional attenuation will determine what size event can be reasonably recorded and processed. However, if local assets could be obtained, this would allow for much higher signal-to-noise ratio measurements. The size of the event, the emplacement conditions, and regional attenuation structure will dictate what calibration steps one would have to undertake. For example, in a highly attenuative region such as Iran, high frequency waves ($f$ >~2 Hz) would likely be missing from regional seismograms even at $M$ ~4. A local determination of the source spectra would provide a yield estimate and potentially depth-of-burial based on the location of the spectral peak in the coda-derived source spectrum. Likewise, if local monitoring were used in an on-site inspection, the background seismicity and duration of deployment will influence which calibration steps to follow.

Unlike yield estimates from magnitudes based on relative amplitudes from direct waves, estimating explosion yield from the coda has been developed around absolute source spectra (Figure 3).

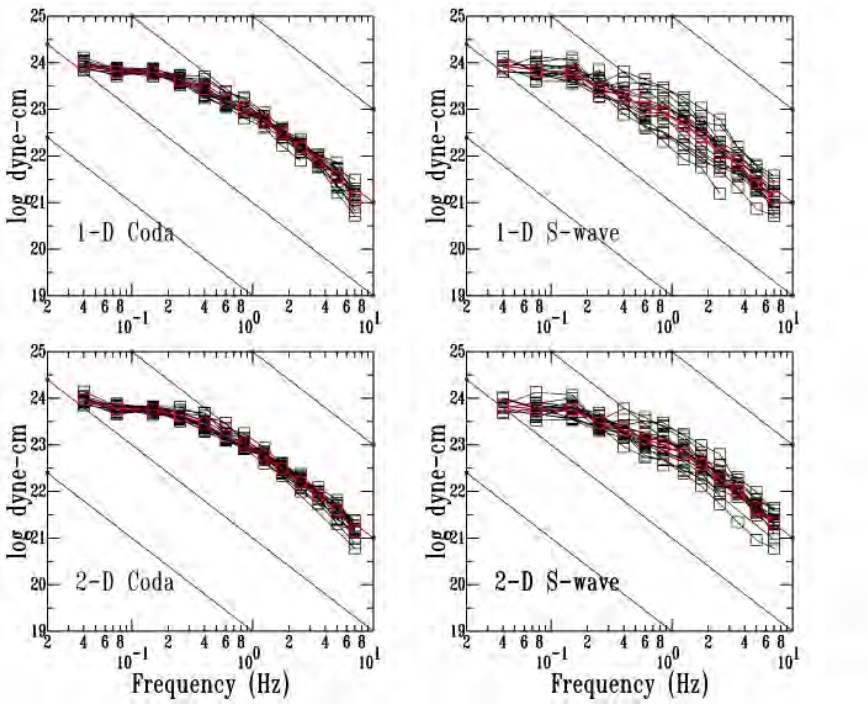


**Figure 3. Absolute source spectra (moment-rate spectra) for the $M_W$ 5.0 Napa earthquake of September 3, 2000. Top two panels show results assuming a one-dimensional (1-D), radially symmetric path corrections for coda and direct waves. Bottom panels show results using spatially varying two-dimensional (2-D) *Q*. Black lines represent individual station spectra, and red lines represent the average. Stations are situated at a variety of azimuths and range between a few tens of kilometers to over 400 km (from Mayeda et al., 2005). Notice that the coda-derived source spectra are remarkably stable in comparison with direct *S* and $L_g$ spectra.**

By using absolute spectra, we avoid potential regional biases, for example, those related to upper mantle and crustal differences (Sykes and Cifuentes, 1984). Currently, regional coda-derived amplitude-yield curves have been developed for different emplacement conditions. Local crustal structure can adversely affect the radiated energy and introduces large amplitude variability over short distances and azimuth ranges, especially at high frequency ($f$ > ~1 Hz). In sharp contrast, the path effects on coda are negligible for local distances and in fact benefit from the crustal heterogeneity because it provides the homogenization (e.g., see Figure 2). We anticipate that local coda data from a variety of regions behave similarly, thus facilitating the construction of average local background models.

For classic yield estimation using direct waves such as teleseismic $m_b$, regional biases can be imprinted on the estimated yield due to low upper mantle $Q$ (e.g., $t^*$ corrections for Central Asia and Novaya Zemlya). For the coda, the DOE national labs have developed a regional coda yield methodology that obviates the problem of regional bias by correcting the coda amplitudes all the way back to the absolute moment-rate spectra. The only corrections required are for the *S*-to-coda transfer function and site response, both of which are frequency dependent and could be obtained through geophysical analogy or with a single ground-truth event. To date, the coda methodology has been applied in numerous geophysically complex regions. We plan to expand upon the well-established coda methodology outlined in Mayeda et al. (2003) to test the feasibility of using well-studied, or ground-truth, regional and local-source spectra as calibration events for local stations in regions of interest. This "first of its kind" calibration procedure will be validated with data from a number of different local networks by leveraging existing data and calibration results.

The monitoring situation and region of study will dictate the calibration steps. For example, in an aseismic region, we are often faced with using geophysical analogy and transporting calibration results (e.g.,

velocity and attenuation structure) from a well-studied region to the new region of interest. The same might be true for an active region, but with no prior seismic data or calibration. On the other hand, and depending on the situation, a few or many sensors could be deployed in advance for calibration. This proposal is an initial "first-step," or scoping, study that will outline our steps to test local monitoring situations using both *P*- and *S*-wave codas. Future plans would involve characterizing a range of event types (e.g., shallow and normal-depth earthquakes, mining-related explosions and their associated events, nuclear tests, and volcanic-related events) and deriving a suite of local background models for a range of tectonic settings. For this pilot study, we will focus on active regions and test the transportability to another "active" region under the assumption of no a priori calibration data or information.

Since coda yield estimation for explosions is based upon calibration to the regional earthquake source spectrum, we will remain consistent and calibrate to earthquakes in each of our study regions. We point out that our proposed local *P*-wave coda research is not duplicative and in fact complements our ongoing regional-to-near-teleseismic *P*-coda research. One issue for the local *P*-wave coda is the short duration; however, as shown by Mayeda et al., (2003), *any* length of coda outperforms the direct arrival.

We plan to test the performance of the local background methodology, using narrowband coda envelopes in regions where calibration data may not be available from as few as one seismic sensor, perhaps clandestinely deployed within ~200 km of a monitoring region of interest. Specifically, we will compare amplitude variability between local *P* and *S* waves and their associated coda waves in a number of different regions (e.g., local data from the San Francisco Bay Area, Nevada Test Site, northern and central Italy, Yellow Sea and Korean Peninsula, Central Asia and others as needed, see Figure 4). Though most areas have ample data, we will mimic conditions where we have little-to-no ground truth and/or as few as one monitoring station. In doing so, we can compare against well-calibrated results and assess our performance.

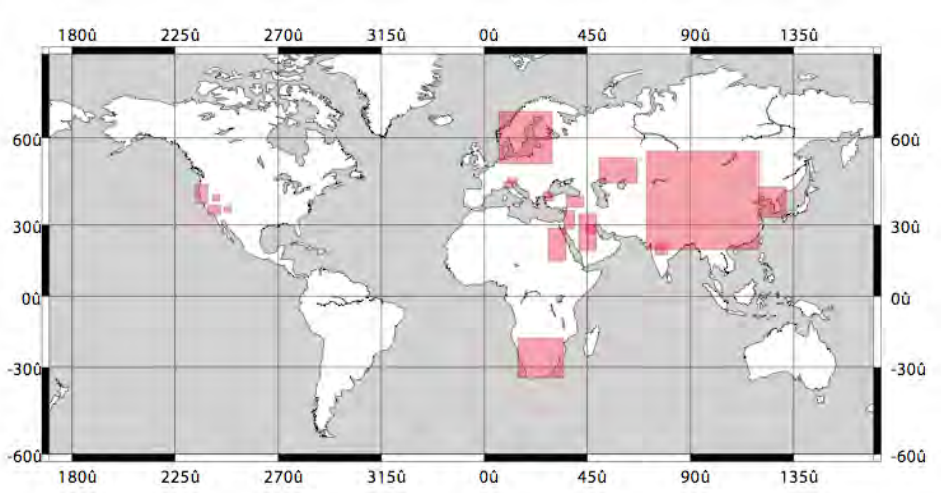


**Figure 4. Map of local and near-regional coda studies for which we have preliminary coda calibrations. In addition to these waveform and calibration data, we will leverage existing in-house seismic data from Los Alamos National Laboratory (LANL) and Lawrence Livermore National Laboratory (LLNL) databases to facilitate the construction of local coda background models for various tectonic provinces.**

This year we have compared coda path attenuation as a function of frequency for selected regions spanning local to near-regional distances, specifically, upstate New York (Au Sable Forks earthquake sequences and related regional events), western Iran, central Italy, San Francisco Bay area, Yellow Sea and Korean Peninsula region, and Taiwan.

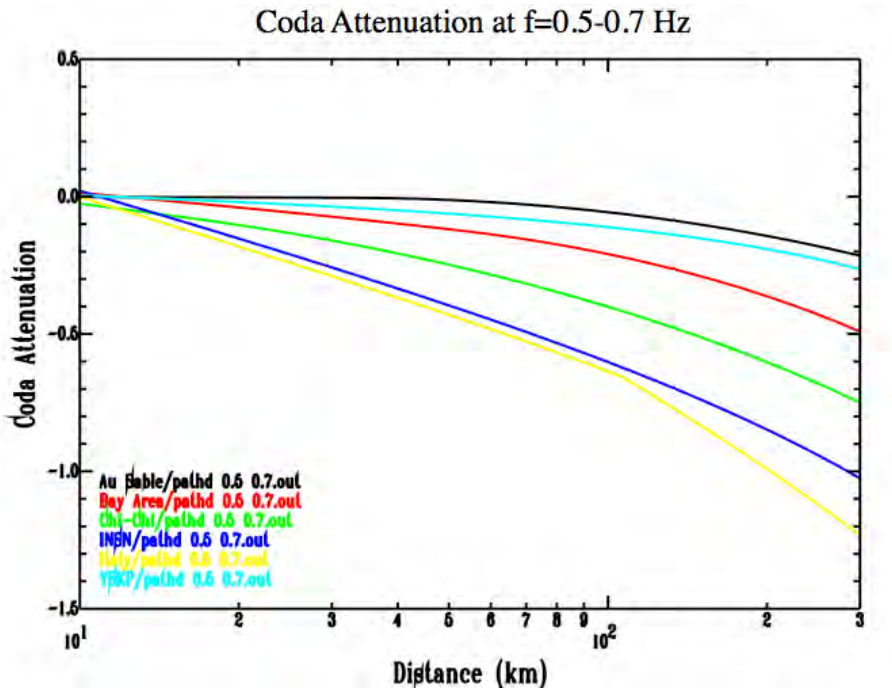


**Figure 5. Coda path attenuation for the 0.5–0.7 Hz band for six different regions. In general, we find that tectonically stable regions (e.g., Korea and New York) exhibit the lowest attenuation, whereas active regions (e.g., Iran and Italy) have much steeper decay.**

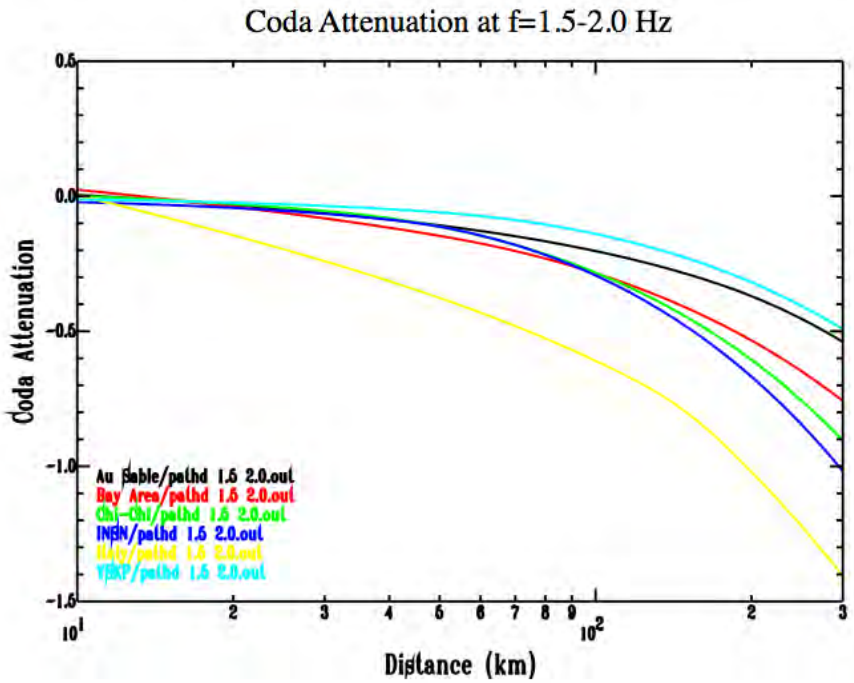


**Figure 6. Coda path attenuation for the 1.5–2.0-Hz band for six different regions. In general, we find that tectonically stable regions exhibit the lowest attenuation, although we find much larger variations in contrast to the 0.5–0.7 Hz band.**

In general, we can make some preliminary statements on similarities and differences between all the regions studied so far. First, we find that central Italy exhibits the strongest attenuation, followed by Taiwan and western Iran for distances ranging between ~20 and 300 km. On the other hand, upstate New York and the Korean Peninsula appear to have the lowest attenuation, which is reassuring since both regions are the most tectonically stable. The San Francisco Bay area is somewhere between the two.

## CONCLUSIONS AND RECOMMENDATIONS

For this project, we have been focusing on applying the coda methodology outlined by Mayeda et al., (2003) to local data, with an emphasis on transporting local background models to similar geophysical regions. Of course if a monitoring situation provides for ample seismic data, we would opt for a complete calibration, but our first assumption will be that data may be sparse or nonexistent. At these shorter distances, we have every reason to believe that the calibration will be easier because path corrections become much less important (e.g., Figure 2). Mayeda et al., (2003) started with the following empirical equation to describe the regional coda envelope:

$$A_c(f,t,r) = W_o(f)\cdot S(f)\cdot T(f)\cdot P(r,f)\cdot H\left(t-\frac{r}{v(r,f)}\right)\cdot\left(t-\frac{r}{v(r,f)}\right)^{-\gamma(r,f)}\cdot exp\left[b(r,f)\cdot\left(t-\frac{r}{v(r,f)}\right)\right],$$

where $W_o(f)$ is the *S*-wave source amplitude, $S(f)$ is the site response, $T(f)$ is the *S*-to-coda transfer function resulting from scattering conversion, $P(r, f)$ includes the effects of geometrical spreading and attenuation (both scattering and absorption), $H$ is the Heaviside step function, $v(r,f)$ is the peak velocity of the *S*-wave arrival, $\gamma(r,f)$ and $b(r,f)$ control the coda envelope shape, and $t$ is the time in seconds from the origin time. The following figures show results of empirical results for coda path corrections, peak envelope velocity, and coda shape parameter. As stated earlier, we plan to construct average background models then test them in geophysically similar regions and assess performance.

This preliminary result shown in Figures 5 and 6 are very promising because it suggests that "local background" path corrections can be constructed, and then applied to new, local regions of monitoring interest without prior path calibration. We should point out that the coda path correction, $P(r, f)$, has been modified since the Mayeda et al., (2003) study, which adopted a functional form that looks like the Brune source spectrum (Brune, 1970) (i.e., flat at short distances, then decreasing beyond a critical distance). The new formulation (curves shown in Figures 5 and 6) is being tested by the DOE labs and appears to significantly improve local-distance data. The formulation is modified from the Street et al., (1975) equation for geometrical spreading that transitions smoothly from spherical spreading of direct *S* waves to cylindrical spreading for $L_g$ waves beginning at a chosen critical distance. In the new formulation, the function is modified to allow for different spreading before the crossover distance and also provides for control on the curvature near the crossover. In addition to the background path parameters shown in Figure 5, we will derive average coda shape parameters, $b(r,f)$, and peak velocity $v(r,f)$ as a function of distance and test the extent to which average values can be applied to other geophysically similar regions. Again, we will assess the performance of the average background models by comparing directly with our ground-truth estimates, using region-specific calibrations, using the entire local dataset.

To date, we have compared coda attenuation parameters for six different regions for frequencies ranging between 0.5 and 8.0 Hz and have just completed path calibration for a seventh region, the volcanic region of Hawaii. We will continue to document other regions with which to compare and from which to draw final conclusions. We still need to look at coda shape parameters that should also be very region dependent, as evidenced by many local coda Q studies in the literature. At this point, we are on track with our proposed statement of work and are forging ahead.

We are now finished with shear wave calibration of Hawaii and will be focusing on combining the various regions and comparing their results to find correlations with the level of tectonic activity. This still leaves our local P-coda calibration study that will start in the latter part of 2008.

## REFERENCES

Aki, K. (1969). Analysis of the seismic coda of local earthquakes as scattered waves, *J. Geophys. Res*. 74: 615–631.

Aki, K. and B. Chouet (1975). Origin of coda waves: Source, attenuation and scattering effects, *J. Geophys. Res*. 80: 3322–3342.

Brune, J. N. (1970). Tectonic stress and spectra of seismic shear waves from earthquakes, *J. Geophys. Res.* 75: 4997–5009.

Mayeda, K. (1993). $m_b$(*Lg*Coda): A stable single station estimator of magnitude, *BSSA* 83: 851–861.

Mayeda, K., A. Hofstetter, J. L. O'Boyle, and W. R. Walter (2003). Stable and transportable regional magnitudes based on coda-derived moment-rate spectra, *BSSA* 93: 224–239.

Mayeda, K., L. Malagnini, W. S. Phillips, W. R. Walter, D. Dreger (2005). 2-D or not 2-D, that is the question: A northern California test, *Geophys. Res. Lett*., Doi:10.1029/2005GL022882.

Myers, S. C., W. R. Walter, K. Mayeda, and L. Glenn (1999). Observations in support of Rg scattering as a source for explosion S waves: Regional and local recordings of the 1997 Kazakhstan depth of burial experiment, *Bull. Seismol. Soc. Am*. 89: 544–549.

Phillips, W. S. and K. Aki (1986). Site amplification of coda waves from local earthquakes in central California, *Bull. Seism. Soc. Am*. 76: 627–648.

Sato, H. and M. Fehler (1998). *Seismic Wave Propagation and Scattering in the Heterogeneous Earth*. AIP Press series, Modern Acoustics and Signal Processing.

Street, R. L., R. Herrmann, and O. Nuttli (1975). Spectral characteristics of the Lg wave generated by central United States earthquakes, *Geophys. J. R. Astr. Soc.* 41: 51–63.

Sykes, L. R. and I. L. Cifuentes (1984). Yields of Soviet underground nuclear explosions from seismic surface waves: Compliance with the Threshold Test Ban Treaty, in *Proceedings of the National Academy of Sciences* 81: 1922–1925.

Walter, W. R., K. M. Mayeda, and H. J. Patton (1995). Phase and spectral ratio discrimination between NTS earthquakes and explosions. Part I: Empirical observations, *Bull. Seis. Soc. Am.* 85: 1050–1067.

Walter, W. R. and S. R. Taylor (2002). A revised magnitude and distance amplitude correction (MDAC2) procedure for regional seismic discriminants, Lawrence Livermore National Laboratory, Livermore report, UCRL-ID-146882.

# EXPLOSION SOURCE MODEL DEVELOPMENT IN SUPPORT OF SEISMIC MONITORING TECHNOLOGIES: NEW MODELS ACCOUNTING FOR SHOCK-INDUCED TENSILE FAILURE

Howard J. Patton

Los Alamos National Laboratory

Sponsored by National Nuclear Security Administration

Contract No. DE-AC52-06NA25396

## ABSTRACT

The traditional source model for long-period seismic waves from nuclear explosions consists of a monopole releasing tectonic strain. Tectonic release has been studied since the 1960's, and numerous studies have shown that linear superposition of monopole + double-couple sources can explain many observations of Rayleigh and Love waves. Free surface interactions and the dynamics of shock-wave rebound are responsible for modes of tensile failure which can also lead to permanent deformations affecting long-period excitation. Indeed, the vast majority of nuclear explosions worldwide were conducted under containment conditions that facilitated shock-induced, deep-seated tensile failure. A new source model, which is a superposition of monopole + tectonic release + shock-induced tensile failure, is proposed, the latter source represented by a compensated-linear-vector dipole (CLVD) with vertical axis of symmetry. This CLVD source does not excite Love waves. I draw upon the Toksöz-Kehrer (1972) model for tectonic release where $F$ is an index measuring long-period source strength of the release relative to monopole moment $M_I$. A new index $K$, analogous to $F$, is introduced, providing a relative measure of $M_{CLVD}$, the source strength of tensile failure. $M_{CLVD}$ vanishes for $K = 1$, and is $> 0$ in the case of extensional deformation along the vertical axis, e.g., $K > 1$.

Rayleigh waves from the CLVD destructively interfere with waves from the monopole, and polarity reversals occur on all azimuths for $K > \sim 3$ in Poisson media. Most Nevada Test Site (NTS) observations support $\sim 1 < K < 3$, and as such the new model predicts lower $M_s$ compared to the traditional model involving just tectonic release. This effect of tensile failure on $M_s$ improves $m_b$ - $M_s$ discrimination and suggests that anomalously large $M_s$ compared to $m_b$ for the North Korean test of 9 October 2006 is due to the absence of tensile failure on this explosion.

## OBJECTIVE

The objective is to develop new analytical explosion source models based on seismic moment tensor theory for further improvement and advancement of regional seismic discrimination and yield-estimation technologies. Such technologies rely heavily upon the source information contained in high-frequency shear (*S*) waves. The use of coda waves following regional *S* phases to estimate explosion yield is one example of an emerging technology offering great promise for improved nuclear monitoring. Unfortunately, an understanding of how explosions excite *S* waves is quite limited, and a widening gulf between theory and practice undermines our confidence to monitor broad areas at small yields. The new models will provide a physical basis for explosion-generated *S* waves and theoretical insights for advancing yield estimation and discrimination capabilities, thereby closing the gulf between theory and practice.

## RESEARCH ACCOMPLISHED

This project builds upon spherical (monopole) explosion source models developed in the 1970's. An important aspect of these models is the theory relating seismic amplitudes (in this case only compressional waves) directly to yield, depth of burial, and material properties of the source medium. Analytical relationships predicted by the theory draw upon empirical yield-scaling behaviors of key model constructs, such as the elastic radius. Furthermore, the analytical nature of these models facilitated their use since they were easy to implement by researchers, and as such they were widely applied to study the explosion source. Their application continues to this day, but with the recognition that a spherical point source is inadequate to explain *S*-wave generation.

Tensile failure is a source of asymmetry known to exist on most underground explosions, even those overburied for their yield. A kinematic description of shock-induced, deep-seated tensile failure is a CLVD with a vertical axis of symmetry in extension. A CLVD can generate *S* waves directly and indirectly through efficient excitation of short-period surface waves (Rg) and subsequent scattering into *P* and *S* waves close to the source. The research conducted in this project will introduce this source of asymmetry into spherical source models. The new model will require the development of scaling relationships like those for the elastic radius in the case of the spherical model, but for parameters of the tensile failure source, including centroid depth, source process time, and strength of the CLVD force system. A simple analytical form couched in seismic moment tensor theory will be adopted so that the model can be easily incorporated into researchers' preferred wave propagation codes for calculating synthetic seismograms.

In this first year of funding, the approach to model development was to start with a long-period description, such that a point-source approximation and step-function time dependence is valid. Rayleigh wave excitation was studied for an explosion source model involving a superposition of monopole, tensile failure, and tectonic release point sources. The relative strength of the CLVD compared to the monopole is given by an index *K*. Long-period Rayleigh wave amplitudes are reduced owing to destructive interference between an explosive monopole and a CLVD source with a vertical axis of symmetry in extension. The effect of tensile failure on $M_s$ is to enhance the explosion-like characteristics on a plot of $m_b$ - $M_s$. This model suggests that the $m_b$ - $M_s$ discriminant is so successful owing to the fact that nuclear tests were conducted under containment practices for which tensile failure is ubiquitous. The North Korean nuclear test of 9 October 2006 is a harbinger of poor $m_b$ - $M_s$ performance when tensile failure is suppressed. This work was submitted and accepted for publication in *Geophysical Research Letters* (Patton and Taylor, 2008).

*Inferred K for NTS explosions and comparisons with measured K values*. The *K* value is defined as follows

$$K = \frac{2M_{zz}}{M_{xx} + M_{yy}} \quad \text{or} \quad \frac{M_{CLVD}}{M_I} = \frac{2(K-1)}{K+2} \quad , \qquad (1)$$

where $M_{ii}$ are diagonal elements of the moment tensor, $M_{CLVD}$ is the moment of the CLVD source and $M_I$ is the monopole moment (see Patton and Taylor, 2008, for details). Note that $M_{CLVD}$ equals 0 for $K$ equal to 1. The Rayleigh-wave reduced excitation spectrum $A(\omega)$ (Patton, 1988) is of interest and serves as a surrogate for network-averaged $M_s$,

$$A(\omega) = (M_{xx} + M_{yy}) \cdot G_1(\omega) + M_{zz} \cdot G_2(\omega) \quad , \qquad (2)$$

where $G_1$ and $G_2$ are Greens functions and $\omega$ is the angular frequency. The degeneracy of long-period Rayleigh wave Greens functions for shallow sources is well known (*c.f.*, Patton, 1988):

$$G_2(\omega) \rightarrow -(2\nu/(1-\nu)) \cdot G_1(\omega), \qquad (3)$$

where $\nu$ is Poisson ratio. For a Poisson solid ($\nu = 1/4$),

$$G_2(\omega) \rightarrow -2/3 \cdot G_1(\omega). \qquad (4)$$

A low-frequency approximation of $A(\omega)$ in terms of the new source model is

$$A(\omega) \sim f(K) \cdot M_I \cdot G_1(\omega) \quad , \qquad (5)$$

where $f(K) = 6 \cdot (1 - \nu - K\nu)/(2 + K)(1 - \nu)$ . (6)

A CLVD with a vertical axis of symmetry in tension radiates Rayleigh waves uniformly in all azimuths just as the monopole does, but with opposite polarity. Destructive interference occurs between the sources for $K > 1$, constructive interference for $K < 1$. As $K$ increases above 1, Rayleigh-wave amplitudes decrease until $K$ reaches a value of 3 in a Poisson solid at which point polarity reversals occur at long-periods; amplitudes begin to increase for larger $K$ values. This CLVD source does not radiate Love waves.

Patton (1988) applied a method due to Romanowicz (1982) for decomposing Rayleigh-wave amplitude and phase observations into five azimuthal constituents (1, cosθ, sinθ, cos2θ, sin2θ) of the radiation pattern. The $A$ spectrum is extracted from the azimuth(θ)-independent constituent. Ekström and Richards (1994) employed a relative spectrum approach for explosion sources located in a small area and exploited the fact that low-frequency Greens functions vary little over plausible burial depths. This approach reduces the spectrum for different explosions to a scalar representing a gain factor with respect to an empirically-derived template $A_t(\omega)$. Figure 1 plots the logarithm of the gain factor log$A'$ against $m_b$ for 67 explosions, the vast majority located on Pahute and Rainier Mesas, recorded on seismic networks operated by Livermore and Sandia National Laboratories. The $m_b$ values are averages determined from regional and teleseismic estimates of $m_b(Pn)$ and $m_b(P)$.

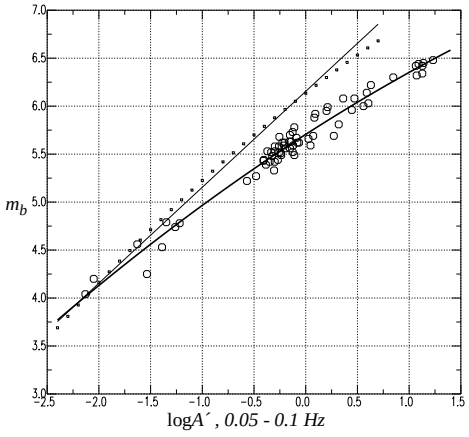


**Figure 1. Log$A'$ versus $m_b$ for 67 NTS explosions. Solid line is fit to observations. Dots are amplitudes measured off *RDP* for tuff medium, and thin line has a slope of 1.0.**

Observations in Figure 1 were subjected to regression analysis, and a quadratic model gave the best fit to the curvature or roll-over with increasing yield. The roll-over is not predicted by the Mueller-Murphy model (Mueller

and Murphy, 1971; MM71), as shown in the figure for calculations based on a reduced displacement potential (*RDP*) in tuff. These calculations were tied to the observations by assigning *RDP* amplitudes measured around 0.05 and 1 Hz for a 1-*kt* explosion log$A'$ and $m_b$ values of –2.1 and 4.05, respectively. MM71 predicts $m_b$ and $M_s$ scale close to 1:1 for yields less than ~1 *Mt*.

The simple relationship between the *A* spectrum and source parameters, $M_I$ and *K*, in Equation 5 above raises the question, what inferences about the source and a dependence of *K* on yield *W* can be made concerning the roll-over. To this end, I turned to fundamental source theory and the scaling results of Denny and Johnson (1991;DJ91). The interested reader is referred to the paper by Patton and Taylor (2008) for details. Very briefly, we deduced the general form of *K*'s dependence on yield for NTS explosions as follows: (a) adopted DJ91's formulas for $M_I$ (involves Equations 39 and 41 in their paper), (b) assumed nominal values for source region velocity, density, and gas porosity, and a nominal containment practice (e.g., depth of burial = $120 \cdot W^{1/3}$) for use in those formulas, (c) utilizing computed Greens functions for a Pahute Mesa velocity model, estimated the seismic moment of the empirical template used to obtain gain factors, and finally (d) adopted the $m_b$-*W* formulas of Vergino and Mensing (1990). Perturbations of the $m_b$-*W* formula for Pahute Mesa were tried, and in all cases the same general behavior of *K* was obtained.

The results are plotted in Figure 2 along with measurements of *K* values for 67 NTS explosions obtained from moment tensor inversions of regional data following the method of Patton (1988, 1991). The inferred yield dependence of *K* closely matches the measurements; however, the *K* values are too high, especially for $m_b > 5.0$. If the intercept of the $m_b$-*W* formula is larger than Vergino and Mensing's estimate, the fit to the measurements improves. There are other possibilities why the inferred *K* values are too high which are currently under investigation. The measured *K* values have large error bars, and work is underway to improve the moment tensor inversion method in order to reduce the error.

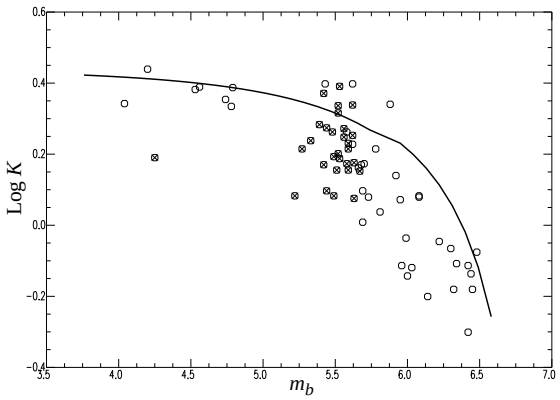


**Figure 2. Inferred dependence of *K* on $m_b$ (or yield; solid line) and measured *K* from moment tensor inversions. Twenty-nine Pahute Mesa tests above the water table are plotted with a circle-enclosed ×.**

For $m_b$ above 5.6, the rapid decrease in *K* suggests a connection with improved coupling for water-saturated shots. Shock waves impinging on the free surface are more forceful for shots below the water table, and spall mass and velocities increase dramatically compared to shots above, as empirical scaling relations for spall impulse show (Patton, 1990). *K* decreasing with yield may be telling us that the force of slapdown causes more compaction of the tuff matrix, closing voids, and reducing the static deformation of the CLVD source as yield increases. By the time yields reach 0.5-1 *Mt*, the deformation associated with deep-seated tensile failure is reduced to nearly zero. Kinematically speaking, the largest NTS explosions look virtually isotropic if the effects of tectonic release are ignored.

Most of the explosions with $m_b$ less than 5.0 in Figure 2 are located on Rainier Mesa and have emplacement depths somewhat deeper for their yield compared to explosions on Pahute Mesa. It is interesting that their measured *K* values are among the largest, even though "intuition" says that $M_{CLVD}$ should become smaller for explosions of a set yield as depth-of-burial increases. Individual measurements in Figure 2 are tentative until moment tensor inversion techniques

are improved to reduce the measurement error on an event-by-event basis. Still, the tendency for *K* to increase with scaled depth-of-burial (SDOB) for a number of overburied explosions suggests it might be real.

It is important to acknowledge the limits of our understanding of the phenomenology of tensile failure and the behavior of *K* as a function of SDOB. There is no argument that *K* must approach 1 as SDOB gets very large. Nevertheless, physical reasons may exist for *K* to increase over a certain range of SDOB before it starts to decrease.

While spallation per se is not the focus of the new source model, gravitational unloading of surface layers is a facilitator of shock-induced tensile failure at depth. Spallation and deep-seated tensile failure are remarkably robust phenomena, and observations suggest that the range where *K* decreases occurs at surprisingly large values of SDOB. For example, the 550 m 25-ton Balapan chemical explosion on 28 September 1997 with an SDOB of ~1450 scale meters did in fact spall, and has a *K* value of 1.1 (Patton et al., 2005). The 300-m 25-ton chemical explosion on 31 August 1997 with an SDOB of 770 also spalled and has a *K* value of 1.6. The change in *K* for these two shots fits intuition: *K* approaches 1 for very large SDOB. Still, the *K* value for the 300-m shot is quite large and its SDOB is far greater than the most overburied NTS explosion that we have processed to date (~400). The measured *K* value for that explosion is 2.8. Therefore, *K* does systematically decrease over the range of SDOB between 400 and 1,500 scale meters and approaches 1. However, the persistence of tensile failure and size of *K* values for such large SDOBs are indeed surprising.

Could *K* increase over a range of SDOB between nominal values of 120 and values as large as 400-scale meters? Perhaps, and the reason might be related to the dynamics of spall slapdown, as was proposed above for the decrease in *K* of very large Pahute Mesa explosions. Spallation is significantly weaker over ground-zero on overburied explosions compared to normal-buried explosions. Therefore, the impulse of slapdown should not cause a proportional amount of compaction as it does for normal buried explosions, especially at depths where the effects of cavity rebound are the strongest (App and Brunish, 1992), and the coupling of the CLVD source into the ground for NTS explosions is the best. Consequently, $M_{CLVD}$ might be proportionately greater for overburied explosions, at least for an intermediate range of SDOB above which mechanisms of deep-seated tensile failure should begin to “shut off” significantly, and *K* values decrease. Hydrodynamic simulations to test such hypothesis would be extremely valuable.

After better measurements from moment-tensor inversions become available, correlation studies will try to determine causes of variability in *K* in terms of emplacement conditions and material properties. Our ultimate goal is to develop a model to explain *S*-wave generation from explosions, and some preliminary signs suggest that shock-induced, deep-seated tensile failure does indeed play a role, as discussed in the next paragraph.

It is well-known that large-magnitude explosions discriminate extremely well using high-frequency *P/S* ratios. Taylor (1995) was among the first to note, "...that large NTS explosions ($m_b$ > 6) are characterized by the largest *Pg/Lg* ratios and are similar to signals expected for pure explosions." This is interesting in light of what was discussed about the yield dependence of *K*, where inferred and measured values approach 1.0 or less for large Pahute Mesa explosions. Following Taylor (1995), I made a cursory look at some high-frequency signals recorded at the Livermore network station ELKO about 400 km from Pahute Mesa. These signals are shown in Figure 3, where 3 of the 4 shots have estimates of *K* and the fourth is an over-buried explosion. While the *K* value has not been measured for this test, its SDOB is similar to Rainier Mesa explosions that have the largest *K* values measured to date. Figure 3 shows that the amplitudes of *Lg* waves compared to the *P* phases are dramatically different for Handley ($m_b$ 6.4) and Galveston ($m_b$ 3.7). Once better measurements of *K* are available for more NTS explosions, correlation studies will also investigate the dependence of *P/S* ratios on *K*.

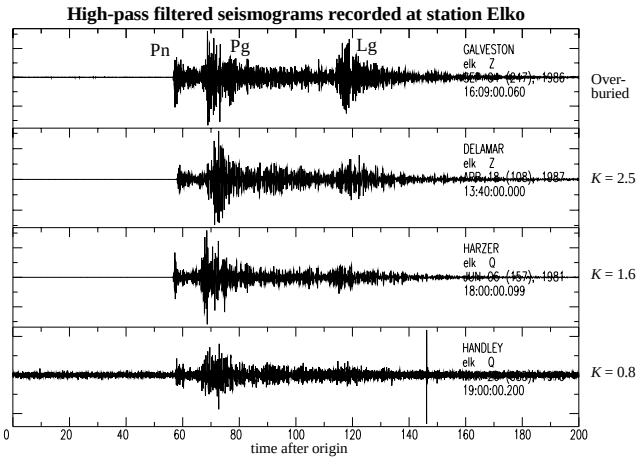


**Figure 3. Butterworth-filtered seismograms using 4-poles, and 1-pass, with a corner frequency of 2 Hz.**

<u>*Inferred K for STS explosions.*</u> *K* values for nuclear explosions at the Semipalatinsk Test Site (STS) will be inferred in the same way they were for NTS. Comparisons between *K* values for NTS and STS explosions are important to do because there are several expectations based on the model of shock-induced, deep-seated tensile failure.
(1) *K* values should be larger at STS on average. STS explosions are buried shallower for their yield compared to NTS explosions. Also, the mechanism of shear dilatancy plays a more significant role in hard rock media (Heuzé et al., 1991), and that should make *K* larger too. For some explosions, *K* values could become large enough for the CLVD to reverse the polarity of the *A* spectrum.
(2) *K* should not show as much yield dependence at STS. We posit that the reduction in *K* for NTS explosions is due to (a) compacting gas-filled pores in the media above the water table and (b) crushing displaced blocks that have been heaved upward by cavity rebound beneath the spall-parting depth. Both of these effects occur when the impulse of slapdown exceeds the strength of the tuff matrix. Since spall impulse increases with yield, *K* is expected to decrease as yield increases. On the other hand, there is essentially zero gas-filled porosity for STS explosions, and the granite matrix is stronger.

Ekström and Richards (1994; ER94) measured gain factors for the *A* spectrum on 71 nuclear explosions located at the Balapan test area. These gain factors, which they call $U_1$, are provided in Table 1 of their paper. To compare NTS results with those of EK94, the units of $U_1$ and of the abscissa in Figure 1 of this paper must be on a common scale. This common scale will be seismic moment in units of $10^{15}$ *Nm*. The relationship between $U_1$ and log*A´* can be ascertained by noting that $A(\omega) = 2U_1 \cdot G_1(\omega)$ . ER94 state on p. 133 of their paper that $U_1$ must be multiplied by 9.46 to convert into units of $10^{15}$ *Nm*. The seismic moment of the template *A* spectrum for NTS was determined to be $6.5\times10^{15}$ *Nm*. Thus the results in ER94 are related to the abscissa in Figure 1 by the formula $6.5 \cdot A' = 2 \cdot U_1$ , where $U_1$ has been multiplied by 9.46.

It is interesting to note that ER94 finds that 8 of the 71 tests have negative $U_1$ values, indicating that the *A* spectra for these STS explosions have reverse polarities. Reversed polarity *A* spectra have not been observed on NTS tests, and

these facts suggest that the *K* values for these 8 explosions are significantly larger than measurements of *K* for NTS explosions, just as anticipated in (1) above.

Figure 4 shows a plot of NTS and STS observations similar to the plot in Figure 1 except that the abscissa is now in terms of seismic moment in units of $10^{15}$ *Nm*. Plotted are just those STS explosions with normal polarity. The $m_b$'s are taken from Ringdal *et al.* (1992) and are based on the work of Blacknest seismologists. A subset of NTS observations in Figure 1, consisting of 29 shots above the water table on Pahute Mesa, are plotted for comparison. It is evident that the scatter is considerably larger for STS observations than it is for this subset of NTS shots. Indeed, the scatter of NTS observations is relatively small over the entire yield range in Figure 1.

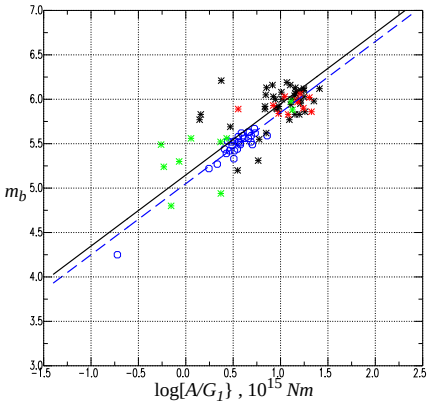


**Figure 4. *A*-spectrum gain factor plotted against $m_b$ for NTS and STS explosions. NTS gain factors and line fit are blue circles and a dashed line. The STS gain factors are color-coded by test area (NE, TZ, and SW), and the fit is a solid black line.**

The lines in Figure 4 are fits to the observations under the constraint that the slope equals 0.8. This value of slope was chosen because compilations of $m_b$ - $M_s$ observations support relationships of the form $M_s = 1.25m_b - B$ for NTS and STS, where *B* is a constant (Murphy, 2005). Clearly, the scatter of STS observations does not justify a quadratic fit used for NTS observations in Figure 1, and the subset of 29 explosions is adequately fit by a linear equation.

Using a linear approximation, we can write the following

$$m_b = L_1 \cdot \log[A/G_1] + L_2 \qquad (7)$$

and

$$m_b = m_1 \cdot \log W + m_2 \ . \qquad (8)$$

$L_1$ is constrained to equal 0.8, and $L_2$, $m_1$, and $m_2$ are free parameters determined from regressions. Plugging formulas for log[$A/G_1$] (Equation 5) and $m_b$ into Equation 7, substituting for $M_I$ using the equations in DJ91, and then solving for the index *K* yields

$$K = \frac{2(1-\nu)\cdot(3-\Im)}{\Im + \nu(6-\Im)} \qquad (9)$$

where $\Im = 10^{F_2} \cdot W^{F_1}$ , (10)

$$F_1 = 0.4385a + [(m_1 - L_1)/L_1] \ , \qquad (11)$$

and $F_2$ is a function of density, velocity, Poisson ratio ν, gas-filled porosity of the source medium, $h_o$, and parameters $L_1$, $L_2$, and $m_2$. Depth of burial follows the scaling rule $h = h_o \cdot W^a$ in meters.

It can be shown that *K* must decrease with yield if $F_1$ is positive. $F_1$ is a function of the exponent *a* and the yield scaling parameter $m_1$. The 1-Hz *P* waves from NTS and STS explosions do not yield scale similarly: an $m_1$ value of ~0.9 is generally found for NTS (Vergino and Mensing, 1990), and for STS, the value is ~0.75 (Ringdal et al., 1992).

Using these nominal values for $m_1$, the inferred yield scaling exponent $F_1$ for explosions at the two test sites and for two different containment rules are summarized in Table 1 below.

**Table 1: $F_1$ for NTS and STS Explosions Based on Different Containment Rules**

| *a* | NTS | STS |
|---|---|---|
| 1/4 | 0.235 | 0.047 |
| 1/3 | 0.271 | 0.084 |

$F_1$ is found to be positive for NTS, as we expected, and the same is true for STS, although it is much smaller. Thus, $K$ will decrease with yield at both test sites. The rate of decrease depends not only on the exponent $F_1$ but also on the size of the coefficient, $10^{F_2}$. Using nominal values for density, velocity, and gas porosity for the test sites, a ν of 1/4, $h_o$ and $m_2$ values of 100 and 4.45 for STS, and $L_2$ values of 5.05 and 5.15 from the fits in Figure 4, the coefficients on $\Im$ equal 0.21 and 0.30 for NTS and STS, respectively. Assuming cube-root containment practice, the inferred $K$ values are 1.65 and 2.1 for 100-*kt* explosions at NTS and STS. The rate at which $K$ decreases is lower for STS than it is for NTS. If the containment practice at STS is quarter-root, the rate of decrease is even less. These results are consistent with the expectations based on the physical model discussed at the beginning of this sub-section.

## CONCLUSIONS AND RECOMMENDATIONS

The first year of this project has witnessed good progress toward developing a new analytical explosion source model that will account for the generation of *P* and *S* waves. The model is built upon spherical source models developed almost 40 years ago, which served the monitoring community well but are recognized to be inadequate to explain *S*-wave generation. Our approach in developing a new model is to start with a long-period description, and future work will add increasing complexity to the source description in order to explain more observations for higher frequencies. To date, some interesting discoveries have been made from long-period predictions of the model:

(1) Interference between Rayleigh waves excited by the monopole and the CLVD, which is the kinematic representation of shock-induced, deep-seated tensile failure, reduces $M_s$ making explosions look more explosion-like on plots of $m_b$ - $M_s$.

(2) $m_b$ - $M_s$ observations for the North Korean test of 9 October 2006 can be explained if there was suppression of tensile failure. Indeed, this test may be one of the few examples of a source that is purely explosive with no significant secondary sources. Patton and Taylor (2008) show that its $m_b$ - $M_s$ observations are consistent with the MM71 model, while MM71 cannot explain $m_b$ - $M_s$ for the vast majority of other tests conducted worldwide.

(3) A long-period measure of the relative strength of tensile failure, $K$, decreases with yield for NTS explosions. The phenomenology of tensile failure and causes of the decrease suggest that $K$ for STS explosions should be larger on average than NTS explosions and should show less decrease with yield. Preliminary results appear to support both predictions.

## ACKNOWLEDGEMENTS

I have benefitted over the year from many helpful discussions and email exchanges with Dr. Steven R. Taylor.

## REFERENCES

App, F. N., and W. M. Brunish (1992). Modelling surface motion and spall at the Nevada Test Site, *LA-UR-92-0500*, Los Alamos National Laboratory Report, Los Alamos, NM.

Denny, M. D., and L. R. Johnson (1991). The explosion seismic source function: Models and scaling laws reviewed, in *Explosion Source Phenomenology, AGU Monograph, 65*, edited by S. Taylor, H. Patton, and P. Richards, 1–24.

Ekström, G., and P. G. Richards (1994). Empirical measurements of tectonic moment release in nuclear explosions from teleseismic surface waves and body waves, *Geophys. J. Int.* 117: 120–140.

Heuzé, F. E., T. R. Butkovich, O. R. Walton, and D. M. Maddix (1991). Explosion Phenomenology in jointed rocks: New insights, in *Explosion Source Phenomenology, AGU Monograph,* 65, edited by S. Taylor, H. Patton, and P. Richards, 253–260.

Mueller, R. A., and J. R. Murphy (1971). Seismic characteristics of underground nuclear detonations, Part I. Seismic spectrum scaling, *Bull. Seismol. Soc. Am.* 61: 1675–1692.

Murphy, J. R. (2005). Initial development of the IDC $M_s/m_b$ event screening criteria, IDC Technical Experts Meeting on Event Screening, Arlington, VA, October.

Patton, H. J. (1988). Source models of the Harzer explosion from regional observations of fundamental-mode and higher-mode surface waves, *Bull. Seismol. Soc. Am.* 78: 1133–1157.

Patton, H. J. (1990). Characterization of spall from observed strong ground motions on Pahute Mesa, *Bull. Seismol. Soc. Am.* 80: 1326–1345.

Patton, H. J. (1991). Seismic moment estimation and the scaling of the long-period explosion source spectrum, in *Explosion Source Phenomenology, AGU Monograph, 65*, edited by S. Taylor, H. Patton, and P. Richards, 171–183.

Patton, H. J., J. L. Bonner, and I. N. Gupta (2005). Rg excitation by underground explosions: insights from source modelling the 1997 Kazakhstan depth-of-burial experiment, *Geophys. J. Int.* 163: 1006–1024.

Patton, H. J., and S. R. Taylor (2008). Effects of shock-induced tensile failure on $m_b$ - $M_s$ discrimination: Contrasts between historic nuclear explosions and the North Korean test of 9 October 2006, *Geophys. Res. Lett*. 35: L14301, doi:10.1029/2008GL034211.

Ringdal, F., P. D. Marshall, and R. W. Alewine (1992). Seismic yield determination of Soviet underground nuclear explosions at the Shagan River test site, *Geophys. J. Int. 109*: 65–77.

Romanowicz, B. A. (1982). Moment tensor inversion of long-period Rayleigh waves: A new approach, *J. Geophys. Res.* 87: 5395–5407.

Taylor, S. R. (1995). Problems associated with *Pg/Lg* ratios from NTS explosions affecting seismic discrimination, Los Alamos National Laboratory Report LA-UR-95-3635, Los Alamos, NM.

Toksöz, M. N., and H. H. Kehrer (1972). Tectonic strain release by underground nuclear explosions and its effect on seismic discrimination, *Geophys. J. R. Astr. Soc.* 31: 141–161.

Vergino, E. S., and R. W. Mensing (1990). Yield estimation using regional $m_b(Pn)$, *Bull. Seismol. Soc. Am.* 80: 656–674.

# SEMI-EMPIRICAL YIELD ESTIMATES FOR THE 2006 NORTH KOREAN EXPLOSION

David H. Salzberg

Science Applications International Corporation

Sponsored by Air Force Research Laboratory

Contract number FA8718-08-C-0011
Proposal No. BAA08-60

## ABSTRACT

Science Applications International Corporation (SAIC) is testing a semi-empirical signal processing approach to estimate the yield of explosions. Under Air Force Research Laboratory contract FA8718-05-C-0019**,** SAIC developed a technique to combine the 'truth' of empirical observation with the flexibility of synthetics to generate 'empirical filters' that can be applied to the synthetic seismogram. Specifically, our approach is to design filters that transform the synthetic waveforms to match observed referenced waveforms. In the current project, the technique has been modified (and tuned) to provide yield estimates of interesting events. In particular, estimates of the yield of the North Korean Nuclear Test of Oct. 9, 2006, will be presented. The approach used is to compute semi-empirical synthetic waveforms based on a reference event, then use those synthetics to determine the appropriate scaling (yield) of the event of interest. The semi-empirical synthetics are created by computing a full waveform synthetic to the reference event then determining a filter that transforms the synthetic to the observed data, which is then applied to the new event. The empirical correction should include many of the non-modeled complexities information, particularly if the reference and new events are nearly co-located. As the North Korea event occurred in a seismically isolated region with no nearby earthquakes, more distant events must be used. An active source experiment for wide-angle reflection and refraction near the border in China provides some sort of propagation calibration. While the yield from the China experiment was small (1.2–1.5 tons), a good signal was recorded at the station MDJ for one particular explosion. This event, roughly ½ way between the North Korean Nuclear Explosion and MDJ, provides our reference event for our yield estimate of the North Korean Nuclear Explosion. In addition to computing the yield for the explosion, which we compute to be 850 tons (with an uncertainty of about 100 tons), we explore tradeoffs between the estimated yield and the assumed source depth of the nuclear explosions, the impact of variations of propagation models on the results, as well as yield vs. frequency.

Preliminary analysis indicates that the apparent yield does not vary significantly with the velocity model, but is highly dependent on the attenuation structure (Q), that the apparent yield increases significantly with depth (due to surface wave excitation) at lower frequencies, and higher frequencies produce a lower, but more stable yield estimate than the broad-band solutions.

## OBJECTIVES

The objective of this project is to use and extend SAIC's semi-empirical synthetic approach [Salzberg, 2005] to facilitate a proof of concept demonstration on yield estimation. While SAIC was able to estimate the yield of the North Korea Test of Oct. 6, 2006 to be about 460 tons, the accuracy of the estimate is unknown. In particular, the variability caused by uncertainty in the crustal model is explored. In addition, in the future, we will apply the technique to events with known yields, providing an understanding of the error bounds of estimates based on this approach.

## RESEARCH ACCOMPLISHED

### Yield estimate for North Korea

We have used a slight modification of our semi-empirical synthetic seismogram method of Salzberg [2005] to estimate the yield of the North Korea Nuclear test of Oct 9, 2006. The data used for the processing is from the seismic station, MDJ, which is located in Northeastern china, as shown in Figure 1. The reference data, used for calibration, was from a wide-angle refraction experiment. The 1.2–1.5-ton shot was set off 190 km south of MDJ, or about ½ way between the North Korean test and MDJ. While the data for the Chinese reference event is noisy, at higher frequencies bands, (> 1 Hz), the signal is clear (Figure 2). The signal for the North Korea Nuclear test has significant signal at all frequencies (Figures 3 and 4).

#### Method

The approach is to compute a semi-empirical synthetic, which is expressed as:

$$new(\omega) = \frac{reference(\omega)}{synthetic_{reference}(\omega)} \cdot synthetic_{new}(\omega) \qquad (1)$$

where *reference* and *new* refer to the observed waveforms, and *synthetic* refers to the synthetic waveform computed for a specific event range, depth, and mechanism. Thus, as we know the location of the nuclear and chemical explosions, the mechanism (assumed to be isotropic explosion), and the yield for the chemical shot, the formulation can be re-written to:

$$new(\omega) = \frac{reference(\omega)}{synthetic_{reference}(\omega) \cdot yield_{reference}} \cdot synthetic_{new}(\omega) \cdot yield_{new}, \qquad (2)$$

where the synthetics are computed for the same yield.

#### Application

As the separation between the reference event (Chinese experiment) and the North Korean explosion was significant (190 km, or ½ of the propagation distance, shown in Figure 1), and the frequency content of the data required high-frequency (>5 Hz) analysis, a coherent comparison was not feasible. Instead, the yield will be estimated by integrating (or summing) the energy envelopes, which is represented as:

$$Yield_{NK} = Yield_{CN} \cdot \frac{\sum O_{NK}}{\sum O_{CN}} \cdot \frac{\sum S_{CN}}{\sum S_{NK}} \qquad (3)$$

where *O* is the energy envelope for the observations of the two events, *S* is the energy envelope of the synthetics for the two events, the subscript *NK* refers to the North Korean test, and *CN* refers to the China experiment.

The primary issue that needs to be addressed is the background noise level in the Chinese reference event. The approach used is a Savitzky-Golay smoothing filter (Orfanidis, 1996) to characterize the noise. This technique is designed to remove impulsive noise from a narrow-band continuous signal. In our application, the narrow-band signal is the microseismic noise, and the impulse is our signal. So, the smoothing filter is designed to mimic the microseismic noise without perturbing the impulsive event signal.

The noise is then subtracted from the observed waveform for further processing. The results, shown in Figure 5, indicate that this approach can be used to minimize the longer period noise. The reduced long-period noise will allow for the processing at longer periods, as shown in Figure 6.

**Data Analysis**

The approach to analyzing the received energy in the signal is to sum the energy envelopes. The response is analyzed in a frequency dependent fashion by high-bass filtering the data with a varying corner frequency. The energy envelope is computed by:

$$A(t) = \left| s(t) + iH\left(s(t)\right) \right| \quad (4)$$

where A is the energy envelope, s is the observed seismogram, H is the Hilbert transform, and || is the absolute value.

The computation is shown in Figure 7; first, the energy envelope is computed. Then, the remaining noise is estimated (based on the pre-signal energy). The background noise is then subtracted from the energy estimate. The remaining signal is the observed energy from the event. This process is repeated for frequencies ranging from 0.1 to 5.0 Hz, with the results shown (for both the data and synthetics) in Figure 8.

**Computation of the Synthetic Seismograms**

Synthetic seismograms were computed using Herrmann's (2002) wavenumber integration software with a sample rate of 20 Hz to match the data at MDJ. Three velocity models were used: the first model was an arbitrary highly attenuating low-velocity model, the second was based on Herrmann's (2005) model for the Korean Peninsula, and the third model modified Herrmann's model to increase the attenuation in the shallowest layer to simulate Rg scattering. Qualitatively, all of the models produce more surface-waves than the observed signal. The basin model shows a classic dispersive chirp of about 45 seconds, whereas the high-Q version of the Herrmann model shows an unrealistically large Rg phase (Figure 9). Modifying the attenuation to account for scattering of the Rg (due to the tomography shown in Figure 1) gives a more realistic looking synthetic, again shown in Figure 9.

**Yield Estimates**

The sum of the energy envelopes is then computed in a manner identical to that performed on the data. Thus, for each model, we have measured all of the terms in the sum in the equation below.

$$Yield_{NK} = Yield_{CN} \cdot \frac{\sum O_{NK}}{\sum O_{CN}} \cdot \frac{\sum S_{CN}}{\sum S_{NK}} \quad (5)$$

The yields can be estimated using each model. The basin model shows a yield of about 900 tons at shallow depths and frequencies, increasing significantly at source depths below 2 km (which is the depth of the shallowest layer). The high-Q Herrmann model shows a very large yield at low frequencies, corresponding to the extremely large Rg phase observed. At higher frequencies, the yield is estimated to be about 1 kt. The low-Q Herrmann model (which is the preferred model) gives a yield of about 850 tons, with smaller variations (less than 100 tons), and is shown in Figure 10. It is worth noting that the corner frequency for both the reference event and the nuclear event are above the Nyquest frequency.

## CONCLUSIONS AND RECOMMENDATIONS

We have demonstrated that the semi-empirical technique seems to produce stable estimates of the yield of the North Korean explosion, provided a reasonable estimate of the attenuation is used. Even with unreasonable Q's, the yield apparently only varies by about 20% (850 tons to 1 kt).

## ACKNOWLEDGEMENTS

Discussions with Jesse Bonner were useful in characterizing both the corner frequency of the explosions and the appropriate value of Q for Herrmann's model. In addition, Michael Pasyanos recommended the use of Herrmann's (2005) model.

## REFERENCES

Herrmann, R. B. (2002). *Computer Programs in Seismology*, St. Louis Universtiy.

Herrmann, R. B., Y. S. Jeon, J. Yoo, K. H. Sho, W. R. Walter, and M. Pasyanos (2005) Seismic Source and Path Calibration in the Krean Peninsula, Yellow Sea, and North Each China, in *Proceedings of the 27th Seismic Research Review: Ground-Based Nuclear Explosion Monitoring Technologies*, LA-UR-05-6407, Vol. 1, pp. 42–51.

Orfanidis, S. J. (1996). *Introduction to Signal Processing*, Prentice-Hall, Englewood Cliffs, NJ, 1996.

Salzberg, D. H., K. E. Votaw, and M. E. Marshall (2005). Seismic source locations and parameters for sparse networks by matching observed seismograms to semi-empirical synthetic seismograms, in *Proceedings of the 27th Seismic Research Review: Ground-Based Nuclear Explosion Monitoring Technologies* LA-UR-05-6407, Vol. 1, pp. 454–462.

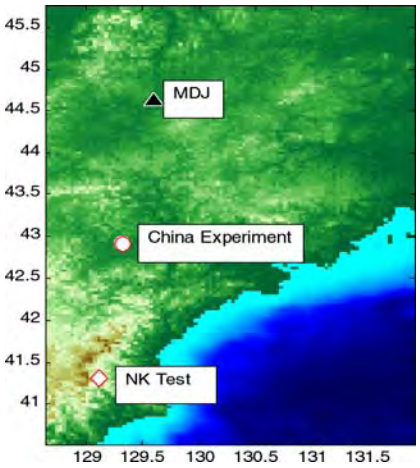


**Figure 1: A map showing the relative locations of the North Korea test, the China experiment, and the seismic station MDJ.**

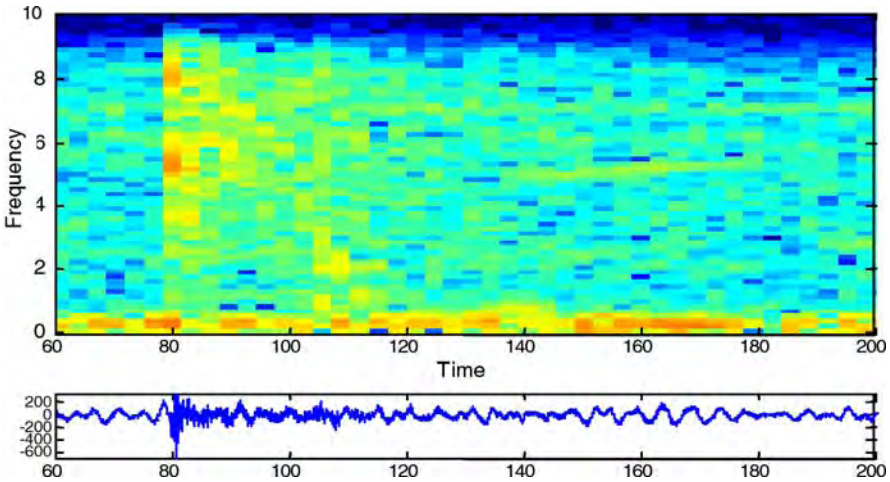


**Figure 2: Unprocessed waveform and spectrogram for the waveform from a wide-angle refraction/reflection experiment in North Eastern China. (1.2-1.5 t). This event is used as a reference event.**

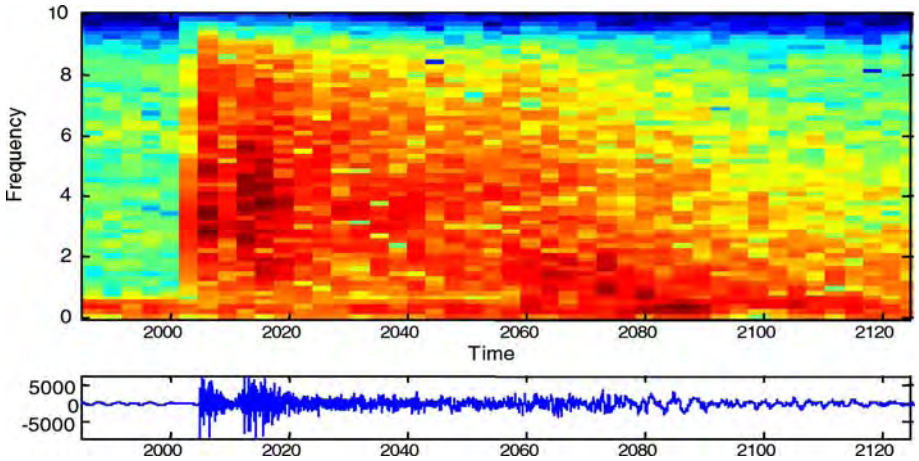


**Figure 3: Unprocessed waveform and spectrogram for the North Korean nuclear test.**

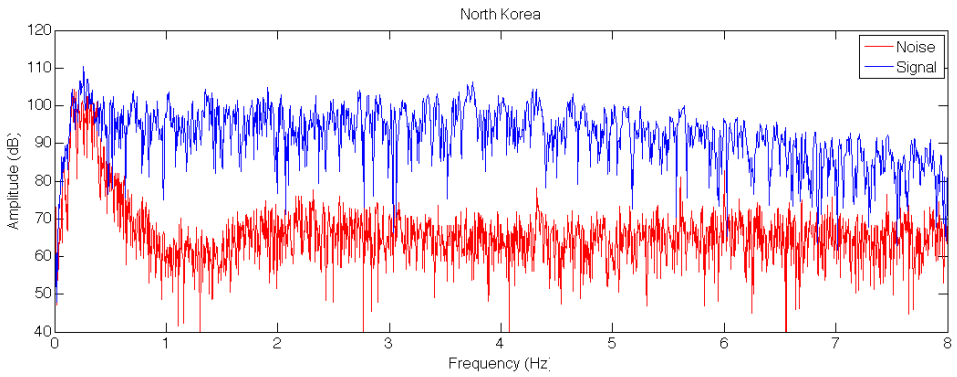


**Figure 4: Signal-to-noise ration for the North Korean Explosion recorded at MDJ.**

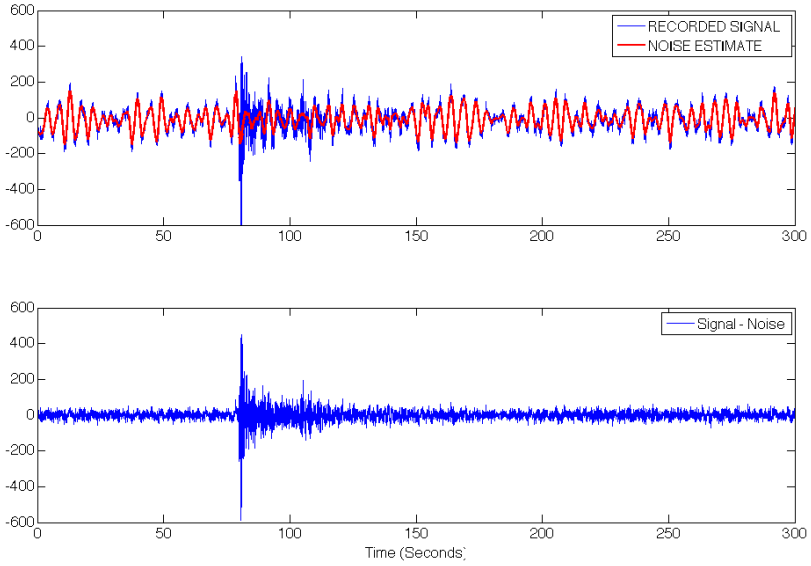


**Figure 5: Noise estimation (top) from the Savitzky-Golay smoothing filter, and the noise-reduced data (bottom).**

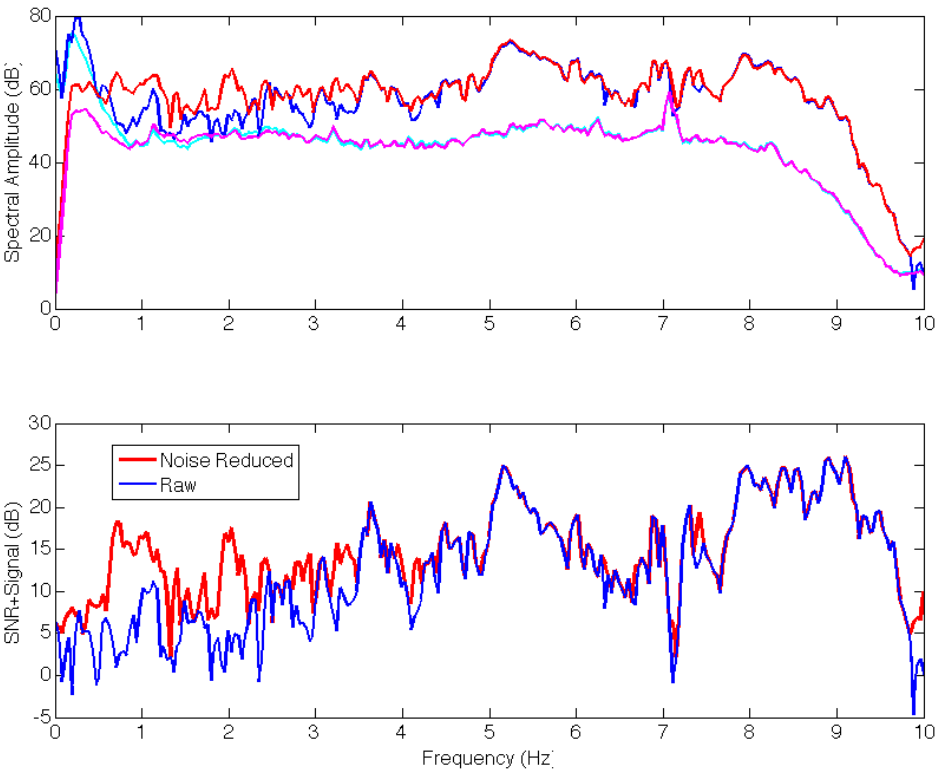


**Figure 6: The top shows a comparison of the signal and noise of the raw data (blue) and original noise (cyan) and the noise-reduced signal (red) and noise (magenta). The bottom figure showns the siffing SNR between the original and noise-reduced. The primary difference is the noise-reduced signal is clear down to ½ of a Hz, whereas the original is useful at frequencies about 3 Hz.**

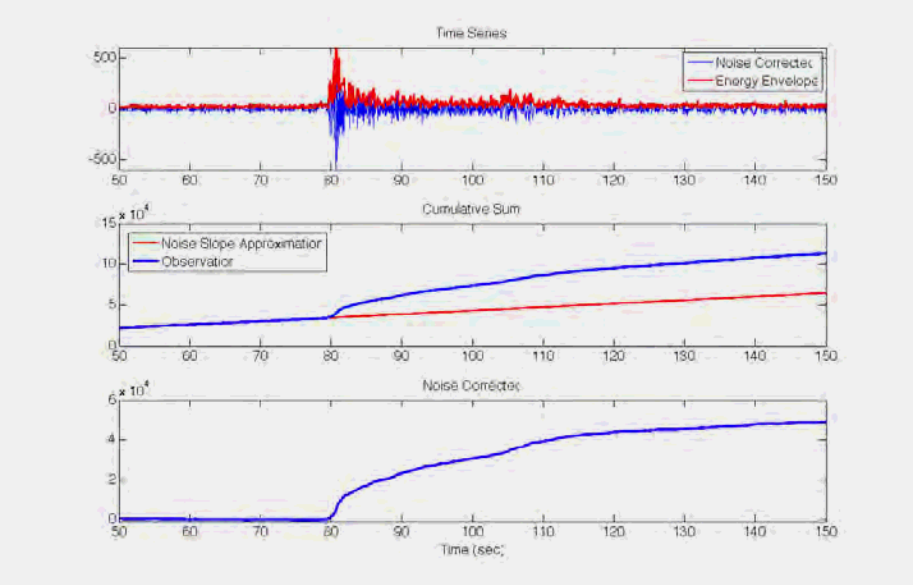


**Figure 7: The approach to computing the total received energy. First, the noise-corrected data is filtered then converted to energy envelope (top). Next, envelope is summed. The pre-signal sum gives us an approximation of the remaining noise (middle). The Pre-signal noise is then subtracted from the curve to give the received signal (bottom).**

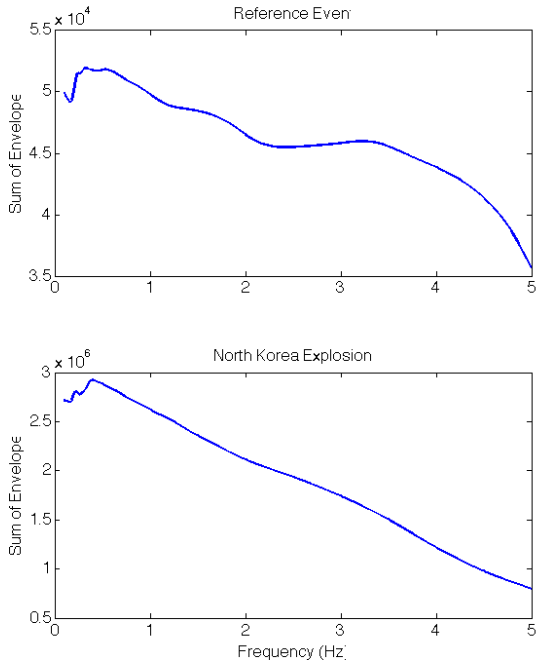


**Figure 8: The sum of the energy envelopes of the reference event (top) and the North Korean explosion (bottom).**

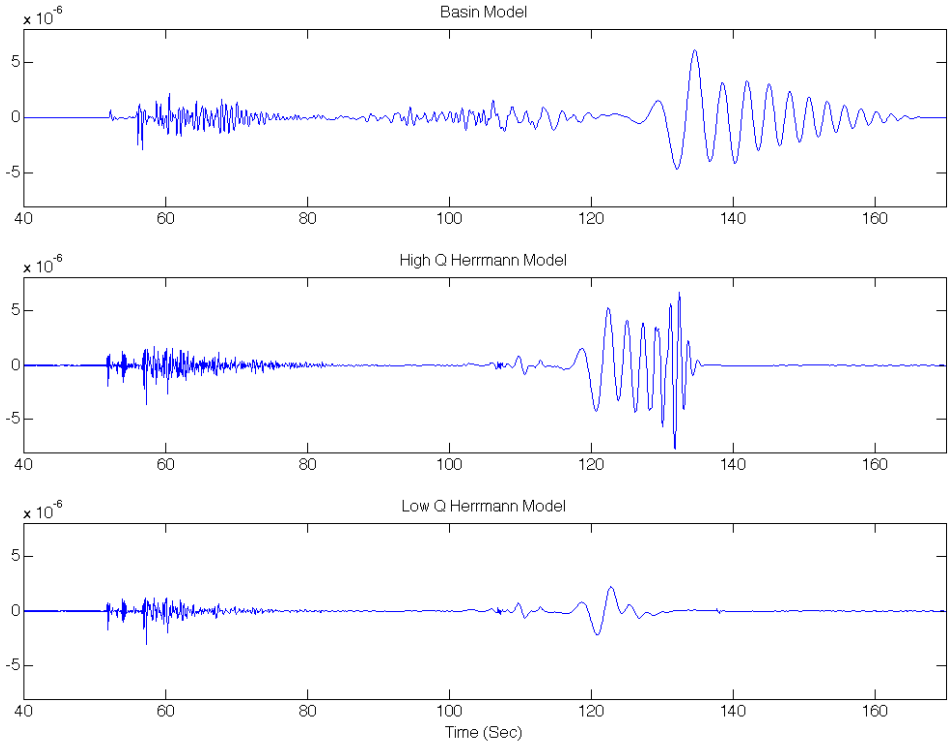


**Figure 9: Comparison of the synthetic for 800 m depth for the three velocity models.**

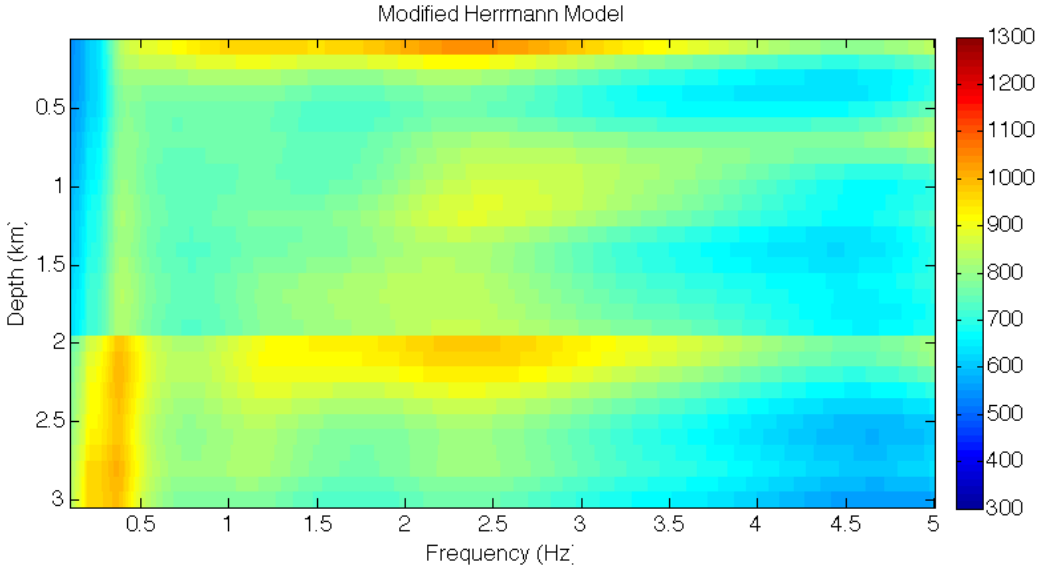


**Figure 10: Yield versus frequency and depth for our best model. This model is based on Herrmann's [2005] model as simplified and verified by LLNL. The model is modified to increase the attenuation (decrease the Q) to accurately reflect the scattering of Rg, as recommended by Bonner (personal communication). The results show that the probable yield 850 tons with an uncertainty of about 100 tons.**

# AN EXPERIMENTAL STUDY OF S WAVE GENERATION BY FRACTURE DAMAGE IN UNDERGROUND NUCLEAR EXPLOSIONS

Charles G. Sammis[1], Ronald L. Biegel[1], and Ares J. Rosakis[2]

University of Southern California[1] and California Institute of Technology[2]

Sponsored by Air Force Research Laboratory

Contract No. FA8718-08-C-0026
Proposal No. BAA08-82

## ABSTRACT

High-speed digital photography was used to observe the generation of S waves by explosions in fracture-damaged photoelastic Homalite plates. We found that either a preferred orientation of the pre-existing fractures or an anisotropic initial stress field produced significant S wave radiation in the far field. These experimental observations support theoretical predictions by Johnson and Sammis (2001).

## OBJECTIVES

The overall objective of this research program has been to understand and quantify the extent of fracture damage in the non-linear source region of an underground nuclear explosion and to assess its effect on the radiation of seismic energy to the far field. Of particular interest is the generation of high-frequency shear waves that may affect regional discrimination and yield estimation. The specific objective of this year's research has been to develop experimental techniques in Professor Ares Rosakis' high-speed digital photography laboratory at Caltech to directly observe the generation of S waves by fracture damage in photoelastic samples. We wish to explore the effects of the initial shear stress and the initial fracture density (damage) on the amplitude of the S-wave radiation.

## RESEARCH ACCOMPLISHED

The experimental apparatus shown in Figures 1 and 2 was developed by Xia et al. (2004) to observed a dynamic rupture on a fault plane in a 10-cm-square 1-cm-thick plate of Homalite, which is a transparent photoelastic polymer. When observed in transmitted polarized light as in Figures 1 and 2, gradients in shear stress can be measured.

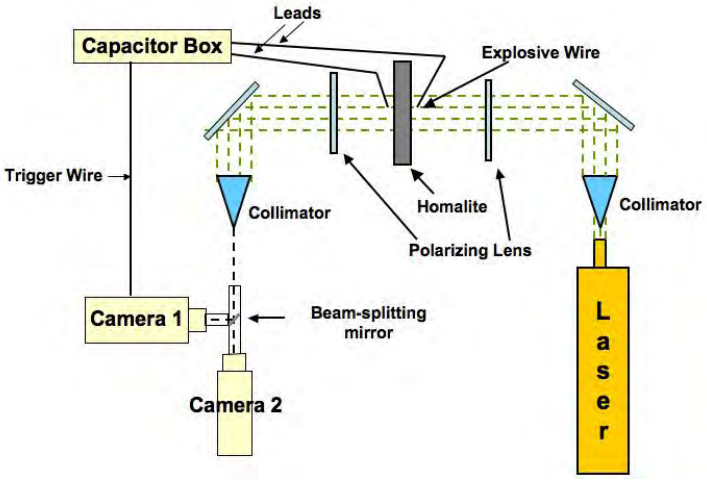


**Figure 1. Schematic of experimental apparatus used to image dynamic ruptures in photoelastic plates. A high-voltage pulse is applied to a wire through the sample which explodes to reduce the normal stress on a –cm-long patch, thereby nucleating a bilateral rupture on the fault plane. The voltage pulse also starts the high-speed digital camera.**

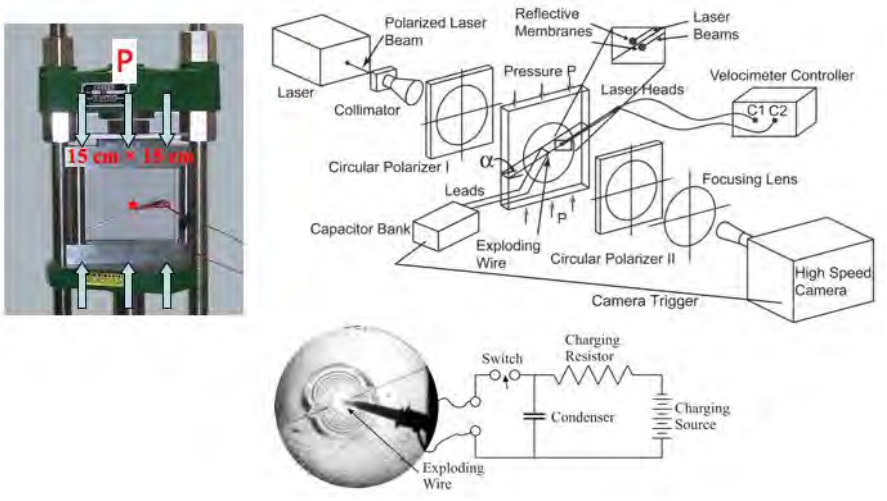


**Figure 2. Experimental configuration showing uniaxial loading frame and nucleation circuit.**

Figure 3 shows a damaged sample from the study by Biegel et al. (2008), in which we demonstrated that off-fault damage significantly reduces the rupture speed. The fracture damage was produced by scoring a grid onto both sides of the homalite sample with a razor knife and then dipping the sample into liquid nitrogen. The thermal shock produced a network of fractures which nucleate from the grid of scratches.

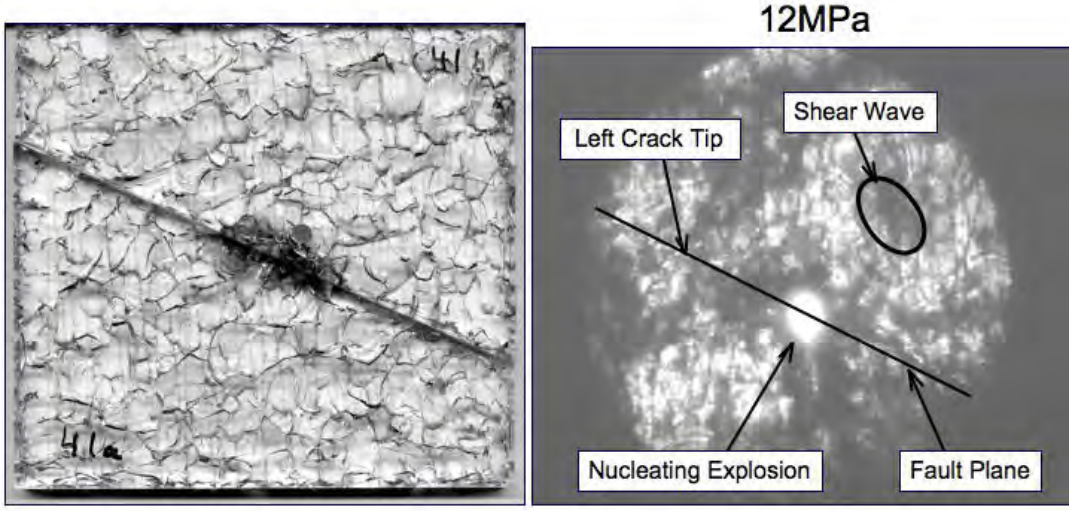


**Figure 3. Fracture damaged homalite plate from Biegel et al. (2008).**

In the present study, we drilled a hole in the center of the sample (with no fault plane) and scored a circular region centered on the hole, as shown in Figure 4. A hole was drilled in the center of the damaged region for the exploding wire.

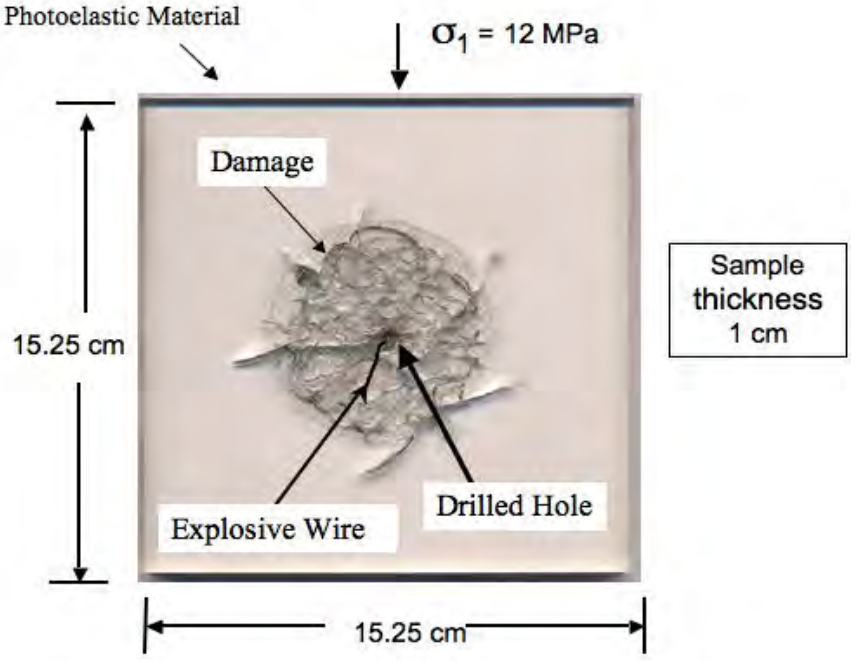


**Figure 4. Homalite plate with circular region of fracture damage.**

As illustrated in Figure 5, an explosion in the center of the damaged circle produced strong S waves.

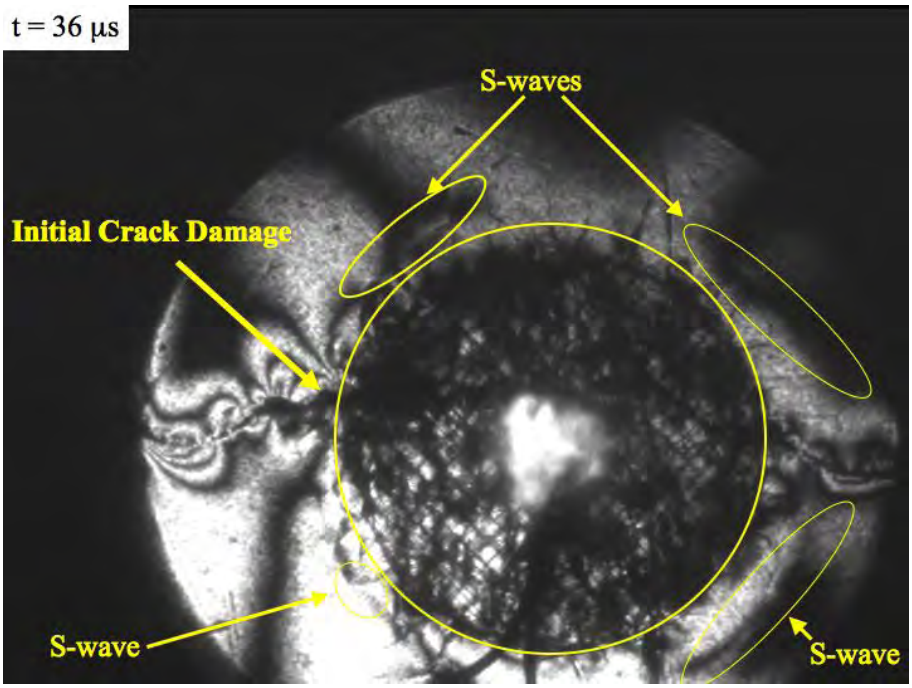


**Figure 5. Frame at 36 μs after the explosion from the high-speed digital movie using the sample in Figure 4.**

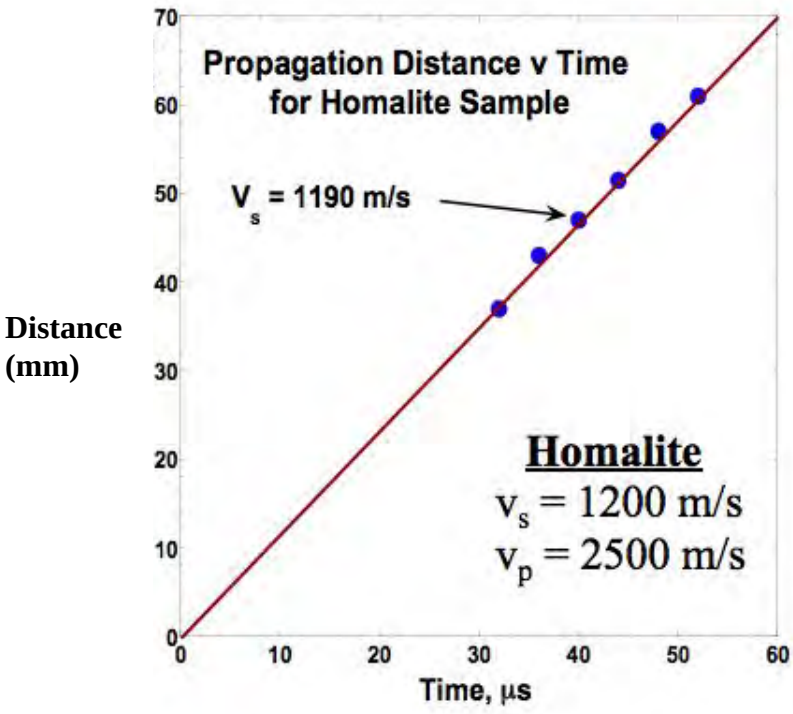


**Figure 6. Propagation distance of the S wave in the undamaged Homalite outside the damage zone as a function of time verifying that it is moving with the known S wave velocity in Homalite (1200 m/s).**

The only problem is that an explosion in an undamaged plate under uniaxial loading also produces S waves, as illustrated in the numerical simulation in Figure 7. However, we were able to show that S waves generated in a damaged circle were stronger than those generated in an undamaged plate at the same load, and additionally that S waves are also generated in a plate with oriented damage in the absence of a uniaxial load.

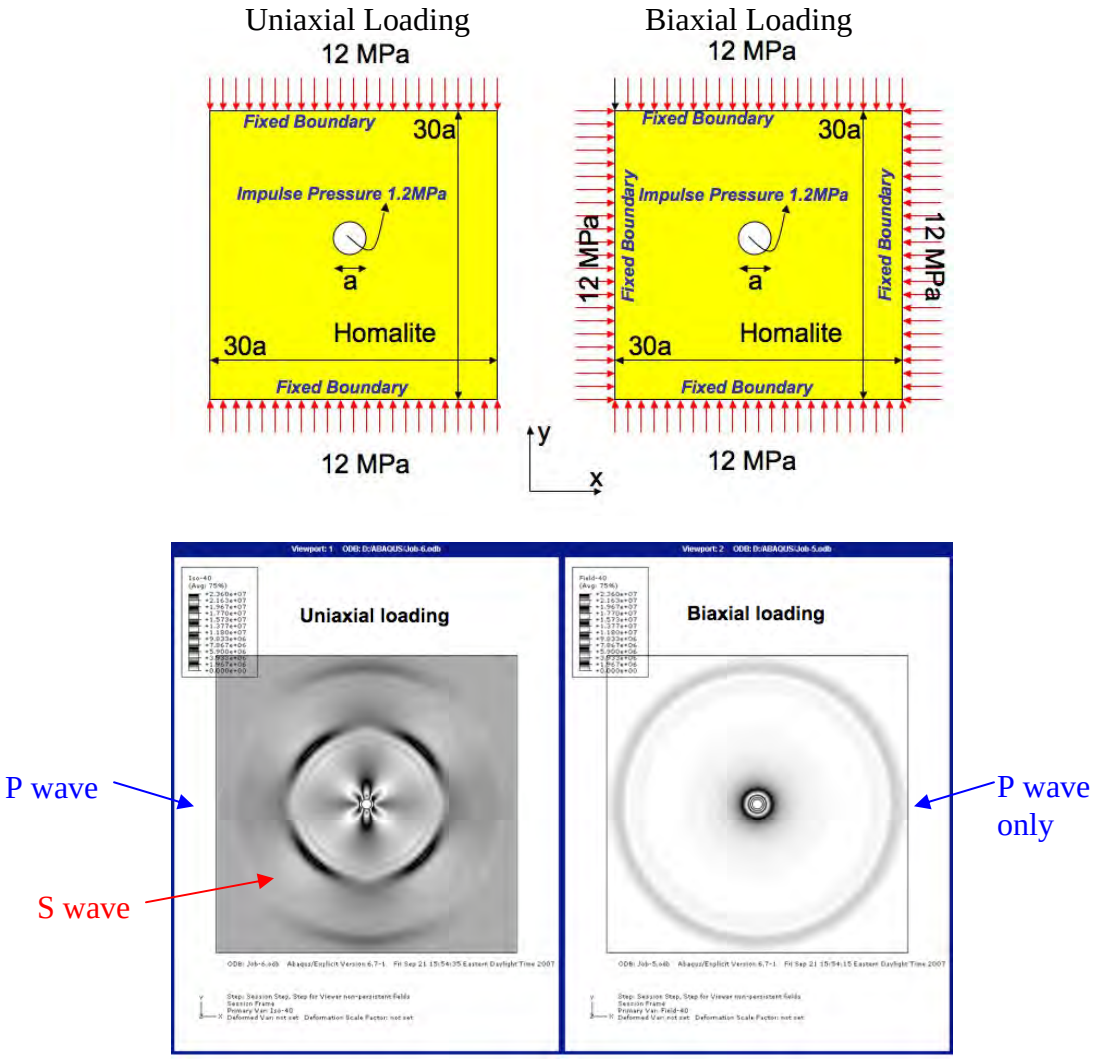


**Figure 7. Numerical simulation of an explosion under condition of uniaxial and biaxial loading. S waves are generated in the uniaxial case even in the absence of damage.**

## CONCLUSIONS AND RECOMMENDATIONS

Our main conclusion is that oriented damage in the source region of an explosion makes a strong contribution to the generation of S waves in the far field of an underground explosion as predicted by the theoretical calculations of Johnson and Sammis (2001). We are currently conducting experiments to quantify the enhancement in S-wave generation associated with damage in the non-linear regime of an underground explosion.

## REFERENCES

Biegel, R. L., C. G. Sammis, and A. J. Rosakis (2008). An experimental study of the effect of off-fault damage on the velocity of a slip pulse, *J. Geophys. Res.* 113: B04302, doi:10.1029/2007JB005234.

Johnson, L.R., and C.G. Sammis (2001). Effects of rock damage on seismic waves generated by explosions, *PAGEOPH* 158: 1869–1908.

Xia, K., A. J. Rosakis, and H. Kanamori (2004). Laboratory earthquakes: The sub-rayleigh-to-supershear rupture transition, *Science* 303: 1859–1861.

# mb BIAS AND REGIONAL MAGNITUDE AND YIELD

Richard J. Stead, Hans E. Hartse, W. Scott Phillips, and George E. Randall

Los Alamos National Laboratory

Sponsored by National Nuclear Security Administration

Contract No. DE-AC52-06NA25396

## ABSTRACT

Traditional seismic yield estimation is performed using body wave magnitude (mb) measured from compressional wave amplitudes recorded across the globe. Stability is obtained by averaging many measurements. These waves traverse the earth's mantle, and are affected by mantle properties, particularly under the source region, as other variations are averaged out. To monitor individual test sites during the testing era, test site corrections were obtained by various means, most notably the Joint Verification Experiment, and applied to obtain yield. To extend yield estimation to broad areas, we must apply an upper mantle correction on the fly. We have investigated two methods to map upper mantle bias over broad areas. The first estimates the bias at individual stations by inverting for corrections that best fit the collection of amplitudes measured at all stations. These measurements were taken from global monitoring agencies, including the International Data Centre (IDC) and National Earthquake Information Center (NEIC) bulletins, examined separately. We augment bulletin amplitudes by replicating monitoring agency measurement techniques for non-reporting or temporary stations in regions of particular interest, such as the Korean Peninsula, including State University of New York (SUNY) Binghamton's northeast China and Lamont's Sinpo deployments. The second method compares mb to magnitude derived from regional Lg coda, which is not affected by mantle properties, producing a map of the upper mantle effects across broad areas where earthquakes occur. The station-based technique retains near-site effects that the event-based technique does not, thus, resolving any differences between the two techniques is of great importance.

## OBJECTIVES

The North Korea explosion of October 9, 2006, resulted in a variety of yield estimates by numerous individuals and agencies across the globe. This situation created renewed interest in the technical details of yield estimation. A common means of estimating yield is through the use of magnitude-yield relations, and specifically the use of teleseismic P-wave magnitude, mb. However, magnitude bias has long been recognized as an issue in such work, and often a controversial one. Here, we describe a preliminary look into magnitude bias, updating some old techniques of investigating magnitude bias for use with modern data and databases, with measurements such as coda moment magnitudes, and specifically for the region of East Asia. We find significant potential for accurate determination of bias on a regional or even global scale, and present results to support this.

## RESEARCH ACCOMPLISHED

### Use of Reciprocity to Determine Bias

We extract a subset of events and stations from the United States Geologic Survey (USGS)-produced monthly Earthquake Data Reports (EDR) catalog, and invert these data to determine mb bias at stations. The data used are the individual station body wave magnitudes (mbs) reported in the EDR, during the period 1990–2005. We first examine the complete EDR station magnitude database to determine which stations report mb for a large number of events. We determine that a minimum of 500 events is reasonable to preserve good station statistics and not greatly reduce geographic coverage. This results in a total of 510 stations worldwide.

We then further reduce the data set by restricting the event-station distance to be in the range of 30 to 100 degrees. While mb is often reported at smaller ranges, the station measurements at these small ranges tend to have much greater scatter. We also eliminate any events having reported depths greater than 50 km. We do this out of concern that some stations may see a greater fraction of deep events relative to others, and that this could create a spurious bias, however we do not conduct any specific investigation to see if this is really a problem. We then limit the range of network mbs to between 4.7 and 5.7, which eliminates only about 5% of the data set. We use 5.7 as an estimate of the onset of mb saturation, and 4.7 as an estimate below which scatter and imprecision in magnitude increases. Note that these limits also help deal with data censoring (clipped data at high magnitudes and unreadable data at low magnitudes, problems that are addressed in these ranges using a non-linear maximum likelihood approach to determine network magnitude, but which is not amenable to linear inversion for bias). Finally, we limit the resulting set of events to those that were recorded at a minimum of 25 stations, so that particular events do not bias individual stations. The resulting dataset contains 510 stations, all of which recorded at least 100 events; 11,609 total events, all reported by at least 25 of the selected stations; and a total of 647,522 station magnitudes (about one quarter of the total number of EDR-reported station mbs).

As a final step before inversion, we eliminate all station magnitude outliers that are more than 1 magnitude unit different from the network mb. We then invert the station mbs using an LSQR conjugate gradient algorithm to simultaneously determine station bias and revised network-average mbs, under the constraint that mean station bias is zero across the dataset (and using the reported network mbs as the initial model for event mb, and 0 as the initial model for station bias). Use of an inversion technique is important, since the station biases feedback into the network mbs, and a simple mean station residual could often be a poor predictor of actual station bias (unless, of course, those means were determined using an iterative approach). The results are plotted on a global map in Figure 1, where the size of the symbols is proportional to the number of station mbs used for the station, and the color indicates the station bias. The inversion reduces station magnitude residuals by about 15% on average.

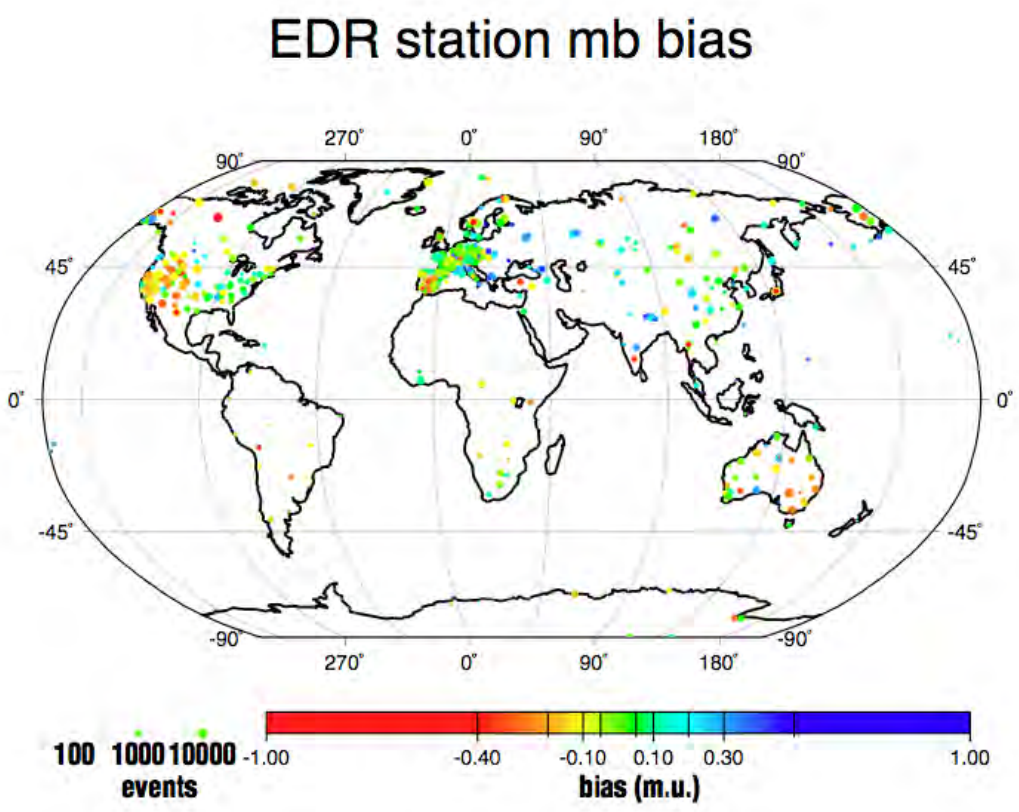


**Figure 1. EDR station mb bias.**

In general, expected features are present. For example, the prominent difference in bias between the eastern and western US is readily apparent. Several other areas of thin crust or active tectonics also show up with negative relative bias. And ocean island stations show large relative positive bias. However, a significant amount of scatter is also present, as is evident in some cases showing widely differing biases between nearly co-located stations. In particular, some of the large seismic arrays used by the Prototype International Data Center (PIDC) stand out relative to nearby stations. It is known that the USGS, in the past, has used available amplitudes, particularly from the PIDC, as mb amplitude measures, but they were unaware that these were not mb amplitudes. This may have the effect of seriously contaminating the EDR dataset and making it unsuitable for this kind of study without careful evaluation and editing. Indeed, a preliminary look at station residuals as a function of time indicates significant time dependence, but much more work would be needed to make such investigations conclusive. Nevertheless, the established bias at the Nevada Test Site (NTS) relative to Semipalatinsk is well reproduced, which is important for moving forward.

To avoid the question of inappropriate or inconsistently determined station magnitudes, we turn to the Reviewed Event Bulletin (REB) published by the PIDC and IDC. These station magnitudes are determined using a different algorithm from the USGS, but are very consistent. For this dataset, we use the REB from January 1995–May 2007. Given the relative consistency, and the smaller number of stations, we start with an initial limit of 100 events per station and 5 stations per event, and repeat the limit of 30 to 100 degrees in range and 50 km in depth. We revise the mb range to a minimum of 4.4 and a maximum of 5.8, which is more appropriate to this dataset, and eliminates approximately 5% of the of the dataset, as the narrower limit did for the EDR. This results in 158 stations, 15,593 events, and 249,506 station mbs for the inversion. The outlier limit of 1 magnitude unit is again applied, and then the inversion is done the same as for the EDR. The results are shown in Figure 2.

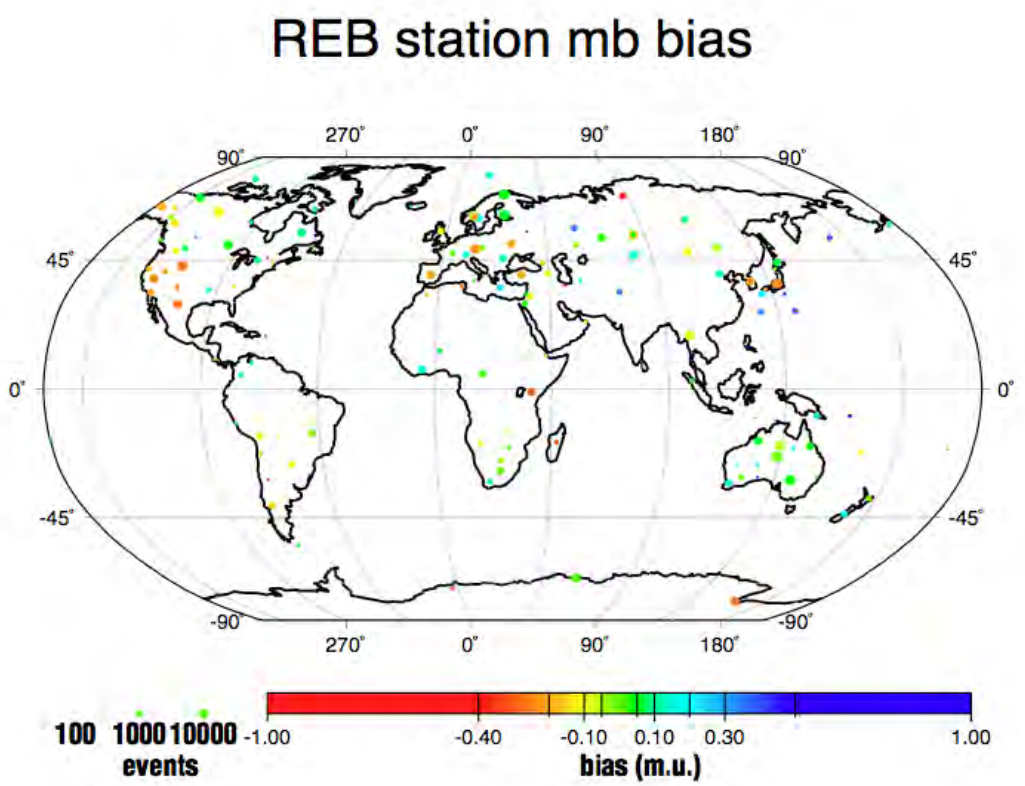


**Figure 2. REB station mb bias.**

The result for the REB station inversion is grossly similar to that for the EDR inversion, but with many fewer points (the REB uses a very restricted set of stations relative to the EDR). However, there is some evidence of improved consistency, particularly in Australia, which now is quite uniform and similar to other shield areas. This supports the inference above that a carefully vetted dataset extracted from the EDR could be as consistent. Such careful QC of EDR-reported station mbs could also allow the conservative limits on numbers of events and stations to be relaxed, greatly increasing the density of results.

We are interested in what station bias might reveal regarding magnitude bias in the vicinity of Korea. We acquired two PASSCAL datasets in the vicinity of Korea. One is the SUNY Binghamton northeast China project (1998–1999, 19 stations) and the other is Lamont's Sinpo site survey within North Korea (1995–1996, 3 stations). The Sinpo data should prove quite valuable for further studies of North Korea, see Figures 3 and 4. The northeast China dataset is also quite interesting and includes several regional chemical explosions that were done as part of the experiment. We have the full continuous data from all 22 stations. We select a number of events from global catalogs (EDR and REB, along with others) that would be at teleseismic range from these stations (30–100 degrees) and of sufficient magnitude to be well recorded. For this initial survey of the bias problem, we analyze data from three of the stations: one from the Sinpo dataset, HMP (Figure 3), and two from the northeast China dataset, FROG and CBAI. Teleseismic P for the selected events is then manually picked at each of these stations (Figure 4).

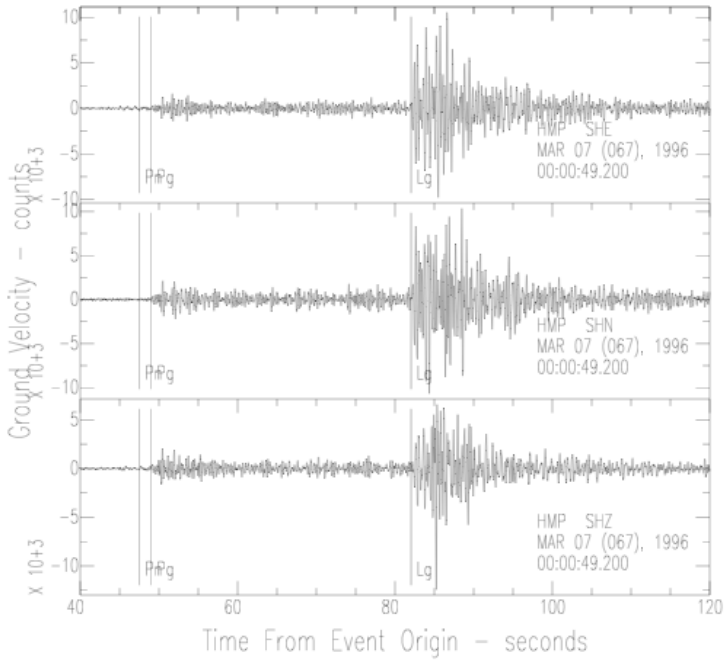


**Figure 3. Regional earthquake recorded at Sinpo station HMP in North Korea.**

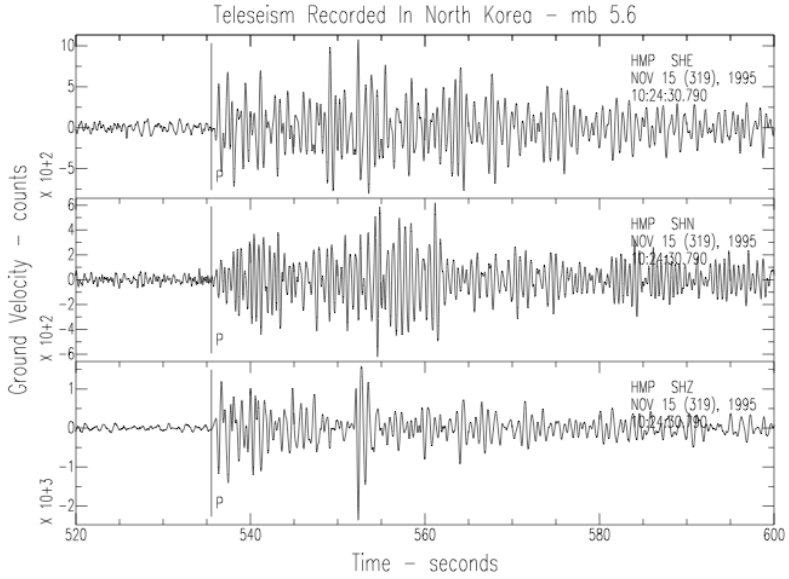


**Figure 4. Teleseismic earthquake recorded at Sinpo station HMP in North Korea.**

To use data from the PASSCAL studies in a global station magnitude inversion, we need to reproduce, as precisely and accurately as possible, the computation of station mb performed for a global bulletin. We select the USGS EDR primarily due to its greater number of stations. However, reproduction of the determination of station mbs for this bulletin is not a trivial exercise, and the development of this capability is important. Using available documentation (Dewey, et al., 2003, 2004) and a paper that attempted a similar reproduction (Granville, et al., 2005), we are able to reconstruct the EDR mbs reported at station MDJ in eastern China for a large number of teleseisms, and to within

+/- 0.1 magnitude units, which is the precision to which station mb is typically reported (see Figure 5). The steps in the algorithm we use to reproduce the EDR results are the following:

1. Select a segment of the vertical component from about 60 seconds before P to about 200 seconds after;
2. Correct the segment for instrument response to displacement in nm;
3. Filter the segment using a 1.05–2.65 Hz 2-pole Butterworth filter followed by a 0.5-6.5 Hz 2-pole Butterworth filter;
4. Select a window beginning at the P pick and extending 15 seconds into the P waveform;
5. Examine the large window for the maximum peak-to-trough amplitude, using a sliding window of 1.25 seconds;
6. Record half the maximum peak-to-trough amplitude and twice the time in seconds between the positive and negative extrema as the period;
7. Apply a correction to the observed amplitude which accounts for the amplitude attenuation introduced by the bandpass filters; and
8. Compute station mb, restricting the computation to signal-to-noise ratio > 2, using the Gutenburg-Richter formula for mb, along with the station-event distance and the Gutenburg-Richter attenuation correction.

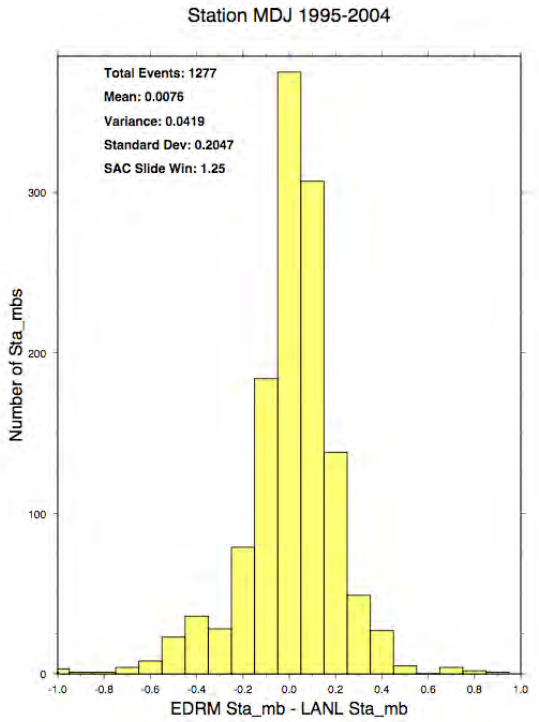


**Figure 5. Histogram of station mb measurements differences at MDJ between those reported in the EDR and those computed here.**

We apply this algorithm to the selected stations and record the station mbs. A cursory examination of these shows that CBAI has a strong bias for all results of nearly 1 magnitude unit, indicating an error in instrument response. We eliminate the station rather than attempt to determine the source of the error. We add the FROG and HMP data to the EDR dataset used for Figure 1, and re-invert. The results are shown in Figure 6. The dataset must be culled in a similar way to the original EDR selection, resulting in a loss of about half of the results.

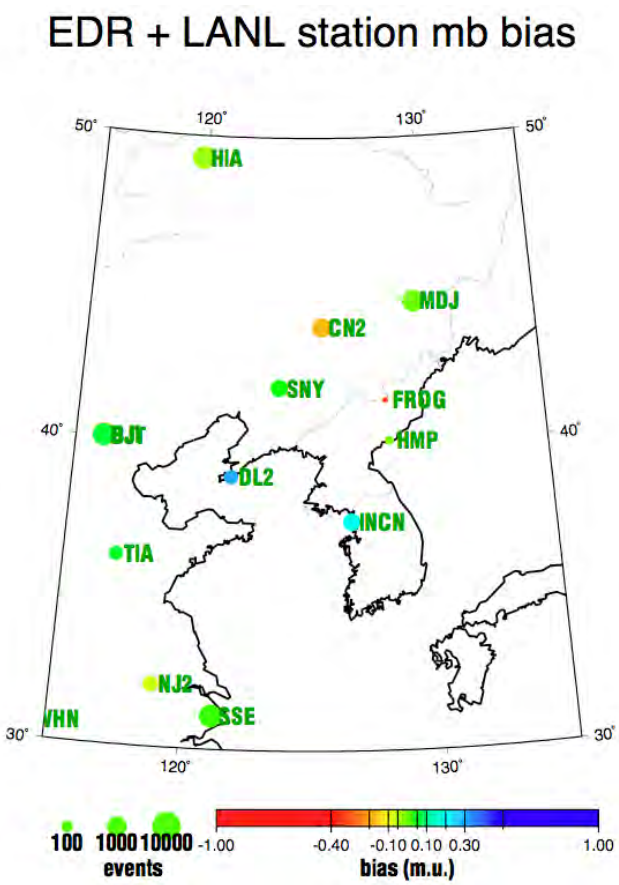


**Figure 6. EDR station mb bias, with addition of stations FROG and HMP.**

The remaining station mb values at HMP are sufficient, but those at FROG are very limited, and so FROG is probably undetermined. Interestingly, the results at HMP indicate that the station bias is somewhat shield-like, but it must be recognized that this result is highly preliminary and careful work is needed to improve the overall result. Clearly, the variation shown at DL2 and possibly CN2 from the EDR is too extreme, with stations like BJT/BJI showing different bias while nearly co-located are probably contaminated by bad station mbs, etc.

**Use of Independent Regional Measures to Determine Bias**

We now turn to the use of regional data as an independent estimate of event size, for a means of examining event bias. We select coda moment magnitudes (Mw) for this purpose. We have a large number of network coda Mw measurement available for Asia.

We first investigate the EDR network mbs. We select events that have both a coda Mw and a network mb from a global bulletin, subtract the two, and then use a Kriging algorithm (Schultz, et al., 1998) to produce a map of event bias. In this case we allow a larger range of mb than in the station inversion above, permitting a range of 3.8 to 5.8, and we allow somewhat greater depth, down to 100 km. This is necessary to keep the number of events sufficiently large for good kriging statistics, but knowing that kriging is robust against outliers. The total number of events is 6,417. We remove the mean, then decluster the data to a grid cell size of 1 degree, and then krig on the GRS-80 ellipsoidal earth, using an isotropic exponential blending function with a range of 10 degrees and a background variance of 0.4 and a non-bias constraint. The result is shown in Figure 7. The fine contours are 0.05 magnitude units of bias, the heavy contour is the limit of resolution at 0.2. Small circles are the events used. While the kriging algorithm ignores continental boundaries, we plot only the results within those boundaries, since the ocean basins generally do not produce accurate coda results. We restrict the range of bias plotted to between -0.5 and +0.4 to maintain a good range of color. Those regions outside this range are plotted in magenta.

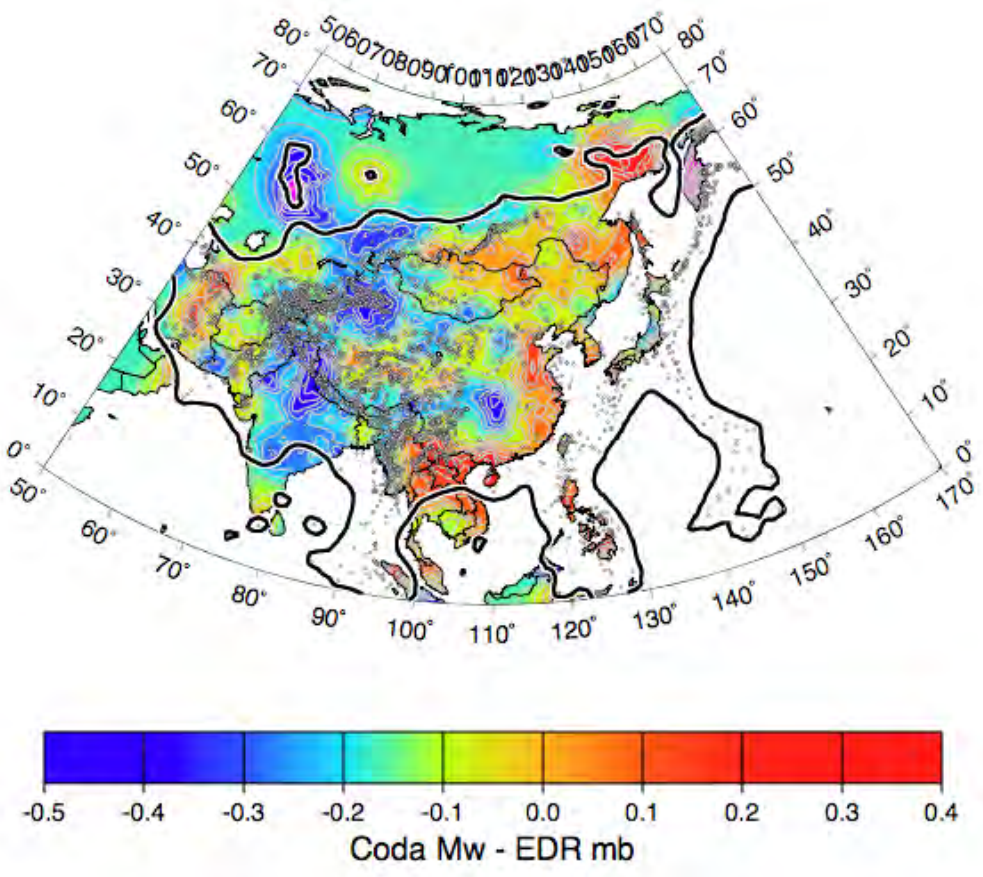


.

**Figure 7. Kriged EDR mb bias relative to coda Mw.**

The figure shows striking correlations with crustal and tectonic features. The thin crust of China's southern and eastern seaboard shows up as having relatively positive bias (Mw > mb), as do some areas of recent tectonic activity such as the central tectonic regions of Iran, and the region around Bhuj in India. These regions would be expected to have relatively high attenuation in the lower crust and upper mantle, consistent with relatively low mbs (more NTS-like). Stable continental regions have a relatively negative bias (mb > Mw), such as the interior of India and north-central Asia. Significant tectonic basins are relatively negative (Sichuan, Ordos, and Tarim basins). The lithosphere tends to be thick under these basins, possibly resulting in lower attenuation in the lower crust and upper mantle, resulting in relatively high mbs (more Semipalatinsk-like). The region around North Korea is interesting, showing a strong gradient from positive in the southwest to negative in the northeast. This is currently controlled by a rather small number of events, but may indicate some complexity in bias in this region, perhaps controlled by crustal thickness or the distribution of recent volcanism. The fact that Punggye would be in the region of relatively low attenuation (high mb) is interesting but certainly not conclusive at this point. The large variation in Iran is also a concern for further investigation. However, the overall strong correlation with tectonics across Asia indicates that this is a promising direction for further study.

Knowing that EDR mbs may have some issues, we proceed with REB mbs. Using the exact same selection criteria as used for the EDR study, and the exact same kriging parameters, we select 6,190 events and present the result in Figure 8.

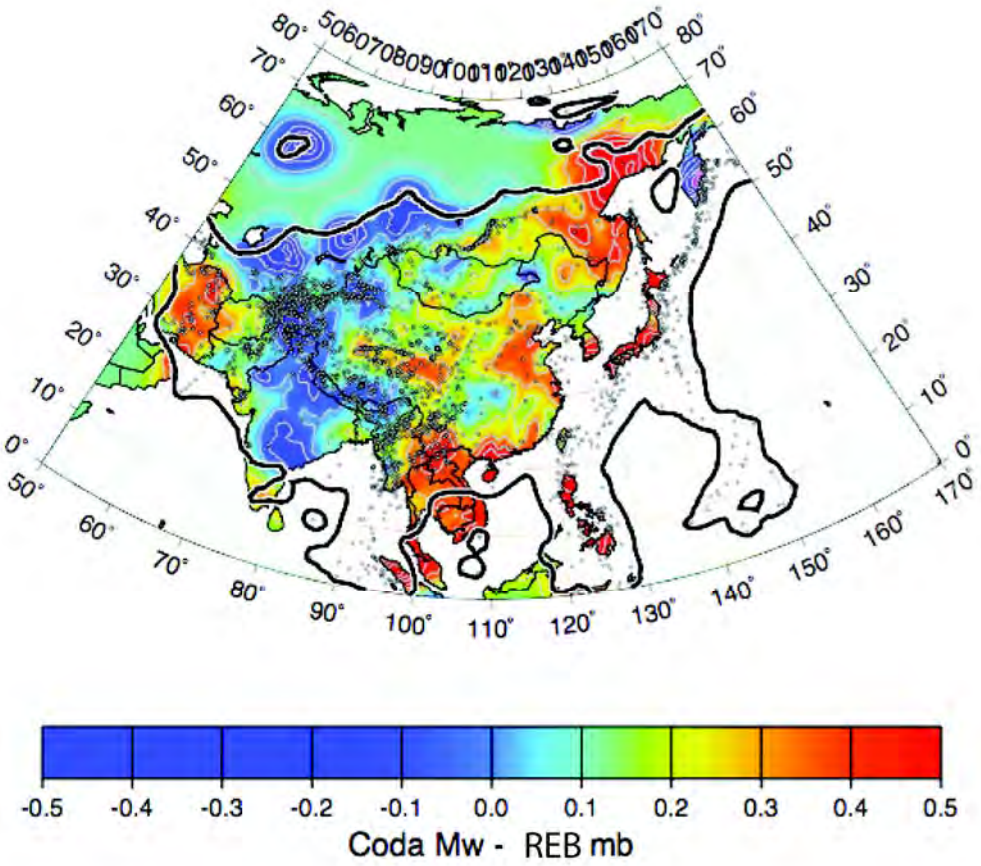


**Figure 8. Kriged REB mb bias relative to coda Mw.**

The resulting pattern is quite similar to the EDR result, but not identical. The coast of China appears negative again, as does central Iran and Bhuj. Central India, north-central Asia, the Sichuan basin and the Tarim basin are again negative. The Ordos basin is almost absent here relative to the EDR result, and the Sichuan basin is greatly diminished. This is undoubtedly due to the subset of stations used for the REB, which may be having some bias effect on the resulting network mbs. The gradient in the vicinity of North Korea appears to be a robust feature of both the EDR and REB mbs. It appears from the figures that the combination of network averaging of the station mbs by the bulletin authors, and the kriging is robust against any problems in individual station mbs in the EDR bulletin.

## CONCLUSIONS AND RECOMMENDATIONS

The results shown from this brief exploration of the mb bias problem indicate a number of promising directions for further work.

1. The station bias method shows excellent promise both to determine broad regional mb bias and mb bias at particular sites where stations exist. There are several aspects of this method to pursue:
   a) The station mbs should be studied, particularly as a function of time, to identify anomalous periods that can then be eliminated from the inversion.
   b) AFTAC station mbs should be used in an inversion similar to the EDR and REB inversions presented.
   c) The algorithms for AFTAC's and the REB's station mbs should be reproduced to the extent possible and applied to stations not represented in those bulletins, particularly the PASSCAL datasets used herein.
   d) Direct RMS amplitude measurements within narrow frequency bands and at a large number of global stations should be pursued, since these should be more stable than comparatively rough mb amplitude measures. In addition, the inversion can be extended in this case to simultaneously operate in multiple bands with the constraint that the amplitude as a function of frequency be linear (that is, that it is directly modeled as t*). A significant advantage to such an inversion is that t* might be directly determined at events as well as at stations.

2. The Mw bias method also shows excellent promise of determining good, regional maps of mb bias. Such maps might be useful for predicting bias in regions without events. There are again several aspects to pursue:
   a) Further constraints on event selection to improve stability and resolution.
   b) Re-computation of network mbs from station mbs, but with strong selection criteria on the station mbs, such as those discussed above.
   c) Use the map to predict station bias, and compare that to the results of the station bias study. Also, use it to correct station mbs before re-computing network mbs for use in the kriging.
   d) Explore the space of kriging parameters to see where the results are truly stable.

3. Investigate other independent constraints on event size, such as Nuttli's mbLg in place of coda Mw.

4. There is no reason to restrict the study to mb, other magnitude measures (Ms, for example), may show evidence of bias and should be explored.

## ACKNOWLEDGEMENTS

We acknowledge valuable information gleaned from personal conversations with Messrs. Dewey and Benz that aided us in reconstructing the EDR mbs reported at station MDJ in eastern China.

## REFERENCES

Dewey, J. W., P. S. Earle, and B. W. Presgrave (2003). Four decades of PDE mb, *SRL* 74: 2, 249.

Dewey, J. W., P. S. Earle, and B. W. Presgrave (2004). Quantifying year-to-year drifts in PDE mb and explaining their causes, *SRL* 75: 2, 275.

Granville, J. P., P. G. Richards, W.Y. Kim, and L.R. Sykes (2005). Understanding the differences between three teleseismic mb scales, *BSSA*, 95: 5, 1809–1824.

Schultz, C. A., S.C. Myers, J. Hipp, and C.J. Young (1998). Nonstationary Bayesian kriging: a predictive technique to generate spatial corrections for seismic detection, location and identification, *BSSA* 88: 1275–1288.

# WAVE PROPAGATION FROM COMPLEX 3D SOURCES USING THE REPRESENTATION THEOREM

Jeffry L. Stevens and Heming Xu

Science Applications International Corporation

Sponsored by Air Force Research Laboratory

Contract No. FA8718-08-C-0010
Proposal No. BAA08-57

## ABSTRACT

In spite of extensive prior research on the generation of seismic waves by underground nuclear explosions, it is still not possible to provide a complete explanation for the observed wavefields, particularly at regional distances. Spherically symmetric explosion models embedded in layered elastic media effectively model the P phases generated by explosions and the major characteristics of some reflected and transmitted phases. Nonlinear axisymmetric finite difference calculations of explosions, including gravity and the effect of the free surface, can model a more realistic explosion source that directly generated shear waves. These models explain more characteristics of explosion-generated seismic waves, including some aspects of regional shear phases. However, it is clear that linear and nonlinear near-source 3D effects are important in many cases. SH waves are commonly observed within a few kilometers of explosions, too close to have been generated by (simple) conversion of vertical and radial components, and often larger than those components. Furthermore, it has not been established what impact 3D effects have on discriminants and on explosion yield estimates. It is important, therefore, to be able to model and understand how 3D source and source region heterogeneity affect the seismic wavefield and what impact this has on parameters used for nuclear monitoring.

In this new project, we are implementing a technique that allows us to propagate the results of near-source 3D finite difference calculations to regional and teleseismic distances, and to use the results to investigate the impact of 3D near-source effects on regional and teleseismic phases, focusing in particular on the generation of SH phases by explosion sources. Our approach is to perform 3D explosion source region calculations, and then to propagate the wavefield to local, regional and teleseismic distances using layered earth Green's functions. We are interested in near-source heterogeneities in both the nonlinear and linear regimes, and therefore require both nonlinear and linear 3D codes to model the source region. In previous projects, we have used two nonlinear codes, STELLAR and CRAM, and the 3D linear elastic code TRES3D. STELLAR is an Eulerian 2D and 3D code well suited to performing near-source calculations, and CRAM is a 2D axisymmetric Lagrangian code that is capable of modeling the transition zone between the vaporized explosion cavity and linear elastic region, including the effects of gravity and the free surface. As part of this project, we are developing a 3D Lagrangian code with the material models and capabilities of CRAM, and we are developing the interface code to propagate 3D near source waveforms to regional and teleseismic distances using full waveform, modal and far-field body wave Green's functions.

The first part of this project has focused on the development of these numerical tools that will be used throughout the project. Our plans are to perform calculations for realistic near-source 3D heterogeneity in the nonlinear region; to propagate these calculations to local, regional, and teleseismic distances; and to compare results with explosion-generated waveforms.

## OBJECTIVES

The objective of this project is to investigate the generation of complex seismic waves by explosions in media with 3D heterogeneity using a method based on the exact representation theorem for propagating complex 3D-source calculations to local, regional, and teleseismic distances at which they are observed.

## RESEARCH ACCOMPLISHED

### Introduction

Source physics, near-source scattering, and propagation effects are all important to understanding seismic phases used in nuclear monitoring. Significant bodies of literature exist that address each subject individually. In addition to extending our understanding of source physics and near-source scattering to include the effects of realistic 3D heterogeneity, this new project links the progression of energy from its generation by the source, through the near-source region, and on into its partitioning among local, regional, and teleseismic phases. Distinguishing the far-field P and S waves enables us to quantify the effects of 3D structure on both P- and S-wave generation. Complete regional waveforms show how this energy is partitioned among the distinct phases important to event detection, identification, and magnitude estimation. How energy is distributed among surface wave modes determines Lg amplitudes and Rg amplitudes, including near-source conversions between these phases. Modal excitation of Lg as well as Rg has a significant depth dependence that is often neglected in nuclear monitoring studies (Baker et al., 2004), and these amplitudes can be disrupted further by near source effects and source region structure. This can either degrade or improve discrimination capability, depending on how well it is understood.

As an example of anomalous (but almost universally observed) SH waves from explosions, we present data from the Soviet Peaceful Nuclear Explosions (PNE) Quartz3 and Quartz4 (Figure 1, left). Figure 1 (right) shows an example of strong tangential component S waves from the Quartz 3 PNE. This 8.5-kiloton explosion was overburied by a factor of 3 relative to normal scaled depth, at a depth of 759 meters. This event should therefore be a good approximation to the ideal point, spherical explosion source. Nevertheless, it generated strong SH waves. Figure 2 shows an image of the source location. As indicated by the meandering river, the site is quite flat, so topography would be expected to have little effect on the seismic waves. Tangential component S at large distances would not be surprising, as the components gradually homogenize with distance; however, in this case the S waves exist strongly across the entire section, suggesting that they leave the source region as SH waves, rather than being rotated into that orientation by structure during propagation.

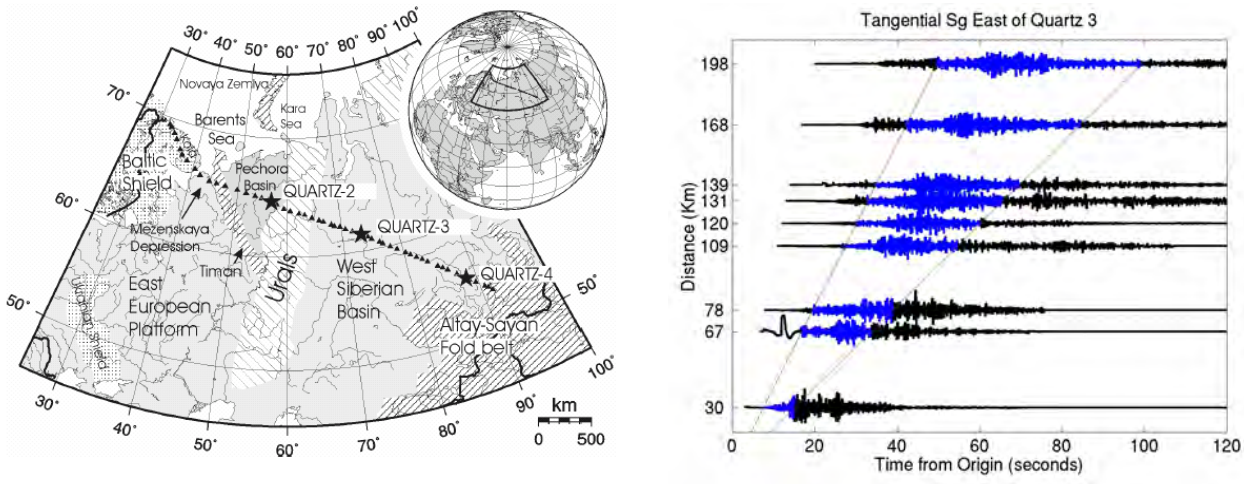


**Figure 1. Layout of stations from the Quartz3 and Quartz4 PNE (left) and tangential component S waves from Quartz3 (right). The blue part of the time series and the red lines delimit 4 to 2 km/s. Strong SH waves exist over the entire section.**

**Figure 2. Quartz3 location (left) and Quartz4 location (right). Each image is 24 km by 20 km. The explosion location is in the center of each figure. Both sites are quite flat. Granite can be seen at the surface at the Quartz 4 location.**

Quartz4 was a 10-kt explosion at slightly shallower depth (557 m) than Quartz3 but still overburied by a factor of 2. The explosion is in granite, and granite can be seen at the surface near the explosion site in Figure 2. Again, there is little apparent topography. Kitov (1997) states that "Geological structure for Quartz4 may be characterized as a homogeneous half-space covered by a thin (10 to 15 m) layer of soil." Figure 3 shows the three components of the Quartz4 seismograms at a station 31 km to the east. There is a strong SH wave on the tangential component and no obvious trace of it on either the vertical or radial component. Very similar observations were made for the deep U.S. explosion Rulison (Figure 3, right).

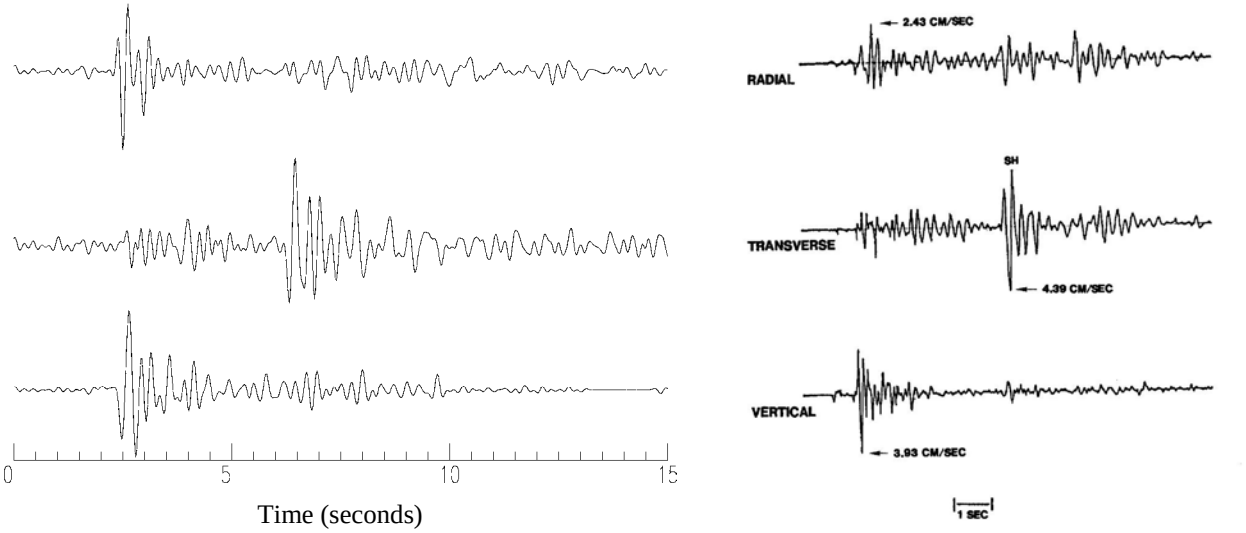


**Figure 3. Left: Radial (top), transverse (center), and vertical (bottom) seismograms from Quartz4 observed 31 km east of the explosion. Data have been bandpass filtered between 1 and 5 Hz. There is a strong SH phase on the tangential that does not exist on the radial or vertical components. Right: Similar figure showing seismograms at a distance of 23 km from the deep U.S. explosion Rulison (from Murphy and Archambeau, 1986).**

These examples (and many others) point to the need to understand 3D source effects. While it is not surprising to see SH waves from any single event, what is surprising is that they are always present and, at regional distances, scale with yield about as well as P waves. That is, while there are many mechanisms such as near-source scattering,

tectonic release, etc., that can generate SH waves, all of these effects should be highly variable from one event to the next. To address this question, we need to look at the types of 3D source effects that can exist, the range of variability that would be expected from them, and whether the predictions are consistent with observations.

**Source Region Calculations and Propagation Using the Representation Theorem**

Our approach is to perform 3D explosion source region calculations and then to propagate the wavefield to local, regional, and teleseismic distances, using layered-earth Green's functions. We are interested in near-source heterogeneities in both the nonlinear and linear regimes and therefore require both nonlinear and linear 3D codes to model the source region. In previous projects, we have used two nonlinear codes, STELLAR and CRAM, which are described briefly in Table 1 (we have also used the 1D nonlinear code SKIPPER, which is a spherically symmetric version of CRAM), and the 2D and 3D linear elastic code TRES3D.

**Table 1.** Numerical simulation tools to be used in this project

| Numerical Simulation Tools | |
|---|---|
| **STELLAR** | Eulerian finite-difference code. Used to simulate the early time history of the explosion shock. It handles material strength correctly, which is difficult for an Eulerian code. Uses a second-order accurate Riemann solver scheme. 1D, 2D planar and axisymmetric, and 3D. |
| **CRAM** | Lagrangian nonlinear finite difference code. Has been used extensively for axisymmetric explosion calculations. A 3D version of the code is being developed in this project. |
| **TRES3D** | Elastic finite difference code. 2D planar and axisymmetric, and 3D. |
| **Elastodynamic Representation Theorem** | The time-dependent displacements and stresses from 3D source region calculations are saved on a monitoring surface located outside the region of nonlinear response and/or 3D heterogeneity. A numerical implementation of the representation integral is then used to compute the corresponding far-field seismic radiation. |

In past projects, we have used these codes in the following ways:

1. Axisymmetric CRAM was used together with the representation theorem to propagate the results of nonlinear axisymmetric finite-difference calculations to regional and teleseismic distances (Day et al., 1987; Stevens et al., 1991; Stevens et al., 2004).
2. Axisymmetric STELLAR was used to calculate the early stages of an explosion. The solution at an appropriate time was overlaid onto CRAM to be propagated out to the linear, elastic region. The representation theorem was used to propagate the waveform to regional and teleseismic distances (Rimer et al., 1994). A similar technique was used to overlay results from the LANL code SOIL onto CRAM and propagate the results (Davis et al., 1992).
3. 3D STELLAR was used to calculate near-field waveforms from explosions in rectangular cavities (Stevens et al, 2006).
4. TRES3D was used to calculate the scattering from explosions in a region with 3D heterogeneity and topography (Stevens et al., 2004).

In the current project, we are doing the following: (1) using STELLAR to perform very near source nonlinear 3D calculations and TRES3D to perform linear elastic near-source and source region 3D calculations, (2) developing a 3D version of CRAM to model explosions from the source out through the very important nonlinear-to-linear transition region, and (3) completing the implementation of the elastodynamic representation theorem for full waveforms, modes, and body waves.

The technique for propagating numerical calculations using the representation theorem is to save displacements and stresses on a monitoring surface surrounding the nonlinear and/or heterogeneous region of the calculation and then to convolve these with a Green's function appropriate for the external region (Stevens et al., 1991). In the cases that we have done previously, 2D axisymmetric nonlinear finite-difference calculations were performed to model the nuclear explosion, and the stresses and displacements from the calculation were saved on a cylindrical surface in the elastic region outside the region of complex nonlinear behavior. We then invoked the representation theorem and integrated the stresses and displacements with an axisymmetric Green's function to calculate the displacement at any

point outside the calculation. We performed such calculations in 2D, using Green's functions for far-field body waves, for modes, and for full regional waveforms using wavenumber integration. The equations for the Green's functions for surface waves are given by Bache et al. (1982). The Green's functions for the complete seismograms are computed using a ring load source, from an algorithm based on the work of Luco and Apsel (1983) and Apsel and Luco (1983). The Green's functions for body waves are generated by a procedure similar to that described by Bache and Harkrider (1976), using a saddle point approximation to calculate a far-field plane wave for a given takeoff angle from a source in a plane-layered medium. Our objective in using multiple types of Green's functions is to gain as much insight as possible into the nature of the seismic wavefield generated by the source. An important part of the current project is to adapt these techniques to propagate seismic waves from 3D source calculations. Although any closed surface can be used for representation theorem integration, we use a cylindrical surface for axisymmetric problems and a rectangular surface for 3D problems.

**3D Implementation of the Representation Theorem**

The key to extending the axisymmetric representation theorem discussed above to 3D is to recognize that while the deformation in the source region may be arbitrarily complex, if the structure can be approximated as a plane-layered medium outside of the source region, then the known Green's function for a plane-layered medium applies (this also assumes that we can neglect the interaction of any backscattered waves returning to the source region after leaving it). Note that the representation theorem is exact. That is, no matter how complex the 3D motion is on the source region boundary, it will be correctly propagated by the representation theorem. The following benchmark test demonstrates the performance of the method by comparing the results with equivalent finite difference calculations and wavenumber integration seismograms.

The representation theorem states that displacement at an observation point is made up of contributions due to body forces throughout the source volume, plus contributions due to the traction and displacement on the source volume surface (Aki and Richards, 1980). In the three-dimensional numerical finite difference calculations, we save displacements and stresses due to the seismic source on a monitoring surface on the boundary of a rectangle (5 planar surfaces, excluding the upper surface), and calculate Green's functions from each point on the monitoring surface to the receiver. Thus the synthetic seismogram at the receiver point $X$ outside of the monitoring surface is obtained by integrating over the monitoring surface $s_M$

$$u_i = \oiint_{S_M} \left\{ G_j^i(\xi; X) * T_j^M(\xi) - u_j^M(\xi) * S_{jk}^i(\xi; X) n_k \right\} dA \qquad (1)$$

in the frequency domain, where $G_j^i(\xi; X)$ and $S_{jk}^i(\xi; X)$ are the Green's function and the stress tensor on the monitoring surface due to a unit impulsive force at $X$ in direction i, $T_j^M$ is the traction on the monitoring surface due to the seismic source, *u* is the displacement on the monitoring surface, and *n* is the normal to the monitoring surface. The operator * denotes convolution, and the summation convention is assumed.

Equation 1 is applicable to any Green's function for the exterior model, and so we can use a full waveform Green's function, far-field body wave Green's function, and/or modal Green's function, as we have discussed earlier for axisymmetric problems. We have implemented this technique for full waveform seismograms, calculating the Green's functions using wavenumber integration. We plan to implement the technique for body waves and modes later in this project.

The synthetic seismograms are computed using the following steps:

1. Displacements and stresses are saved on the monitoring surface during the finite-difference calculations.
2. If necessary, the monitoring solutions are resampled onto a coarse grid, as permitted by the required resolution. If there is a symmetry boundary, the entire monitoring surface is constructed first.
3. The finite-difference solutions at each point on the monitoring surface are transformed into the frequency domain.
4. The displacement and stress Green's functions due to the three orthogonal forces at the receiver location are calculated for each location on the monitoring surface in the frequency domain (using reciprocity).
5. Equation (1) is used to obtain the solution at the receiver in the frequency domain.

6. The solution is transformed back to the time domain.

Figure 4 shows an example of a test of this technique. In this test case, full waveform synthetics are generated from a 3D elastic finite-difference calculation in two ways: (1) by using the representation theorem to propagate the waveforms outside of the source region and (2) by direct calculation using the same finite-difference code. The comparison is very good, which shows that the representation theorem technique is working correctly and that we can effectively use the representation theorem to extend the size of the finite-difference calculation to any desired range, provided that the earth can be modeled as a plane-layered structure at points outside the monitoring surface. The technique also requires that the material properties at the boundary of the calculation match the plane-layered structure. We have implemented the technique for full waveform seismograms and plan to do the same for modal seismograms and far-field body waves as part of this project. The reason for implementing the other Green's functions is that the modal decomposition allows us to look at the effects on individual modes, and the far-field body wave representation provides the clearest picture of the P and S waves generated by the source.

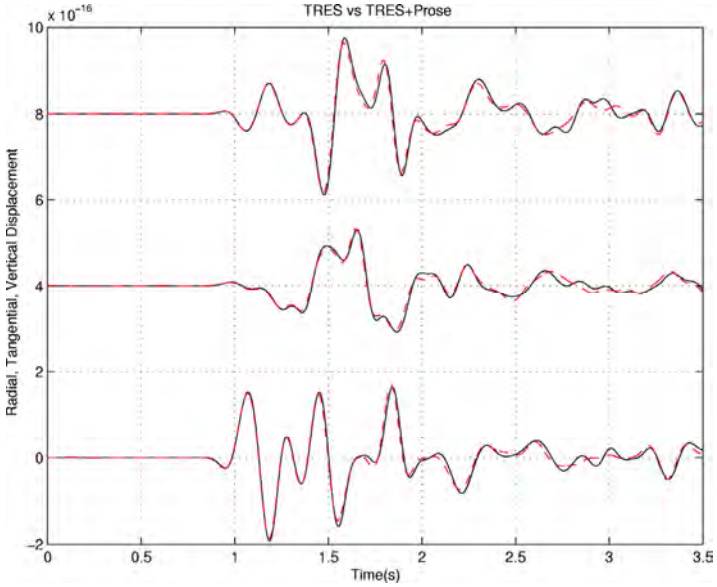


**Figure 4. Comparison between solutions using the finite-difference method (solid lines) and the solutions using the representation theorem (dashed line) at a distance of 2561 m. The three curves from bottom to top are the radial, tangential, and vertical components.**

The principal advantage of this approach is that it allows us to perform detailed calculations of the source region and then propagate the results to distances that would be impractical or impossible to include in the same numerical calculation. In addition to reducing cost and time, the hybrid method is also more accurate, as numerical dispersion increases with the size and duration of numerical calculations. A similar approach (in reverse) was used by Moczo et al. (1997) to calculate the effect of topography and near-surface structure on ground motion caused by a distant source. Wu et al. (2004, and earlier papers starting with Xie and Lay, 1994) used a similar concept by performing near-source finite-difference calculations followed by a calculation of slowness at large distances, which they then used to estimate the energy trapped in the crust versus lost to the mantle for different scattering scenarios. A significant advantage of the representation theorem approach described here is that we can also calculate waveforms at any location.

**Development of a 3D Nonlinear Finite Element Code**

A difficult task in this new project is development of a 3D nonlinear code with capabilities similar to our 2D axisymmetric finite-difference code CRAM. CRAM has a long history of successful calculation of explosions, and has well-tested material models. It also has the capability of including gravity and can model spall and other free-surface nonlinear interactions. For the current project, we are using a finite element code, as this is more easily adapted to complex 3D geometries. In particular, the cavity can be any shape, and the media can be nonlinear and heterogeneous.

We have implemented an explicit 3D Lagrangian finite-element algorithm that is capable of using multiple processors. All of the nonlinear material models from 2D CRAM have been implemented. The cavity is placed near the center of the grid and is enclosed by a spider grid that facilitates applying the pressure boundary condition and rezoning elements, as implemented in the 2D axisymmetric code, CRAM. Examples of the spider grid and outer grid are shown in Figure 5.

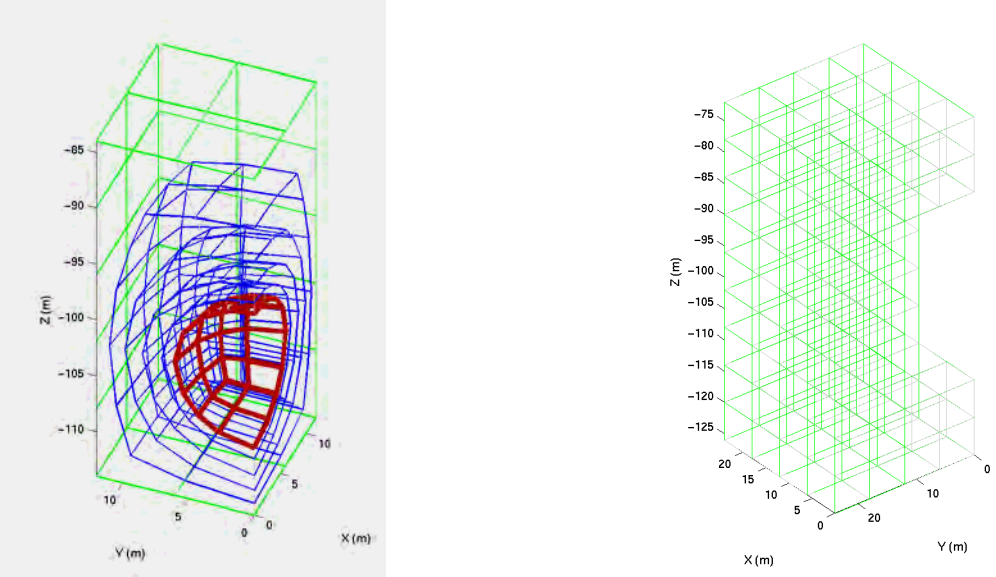


**Figure 5. Left: Schematic of one quadrant of the spider grid. The red grid lines represent the cavity boundary, the blue lines represent the tangential grid lines inside the spider grid, and the green lines represent the interface between the spider grid and the outer Cartesian grid. Right: The outer Cartesian grid enclosing the spider grid (left).**

In the numerical scheme, the wavefields in every element are computed, then the wavefields at each grid are computed by summing the contributions from each adjacent element (Ma and Liu, 2006). Since the one-point integration method is used for efficiency and flexibility, the resulting hourglass modes are damped, using both a viscous hourglass control scheme and a stiffness hourglass control scheme for large deformation. For grid stability due to strong shock-wave propagation, artificial viscosity is also necessary. Both linear and quadratic viscosity (extended from 2D CRAM) have been implemented.

**Benchmark Tests**

As a first benchmark test on the implementation of the finite element method, we calculate the dynamic response of a half-space to a pressure pulse applied to the wall of a spherical cavity with a 2-m radius buried 12 m deep in a linear elastic medium and compare this with the analytical results obtained using the point source theory of de Hoop (Jiang et al., 1994). The agreement is excellent and is the first step in validating the implementation of the finite-element algorithm (Figure 6).

As a second benchmark test, we calculate the dynamic response of a half-space nonlinear granite model (Stevens et al., 2003) to an explosion of 20 tons yield in a 5-m spherical cavity, buried at a depth of 102 m, using the new 3D CRAM and the existing 2D CRAM. Figure 7 shows a comparison of seismograms at the free surface. The results show that the 3D CRAM calculations are also in excellent agreement with the existing 2D CRAM calculations, demonstrating that both codes, though implemented by different numerical methods, are capable of accurately computing nonlinear wave propagation in rocks due to explosions in a cavity.

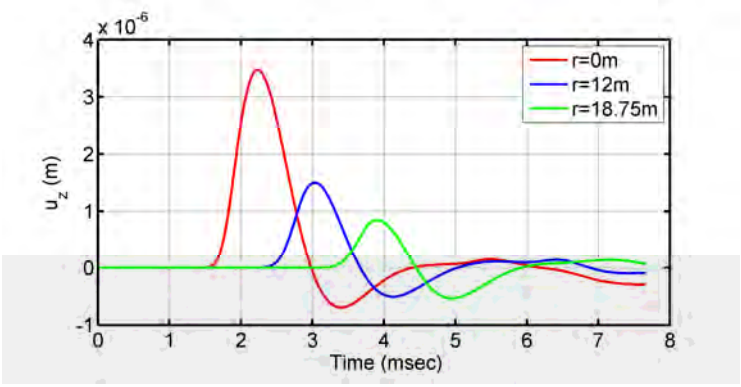


**Figure 6. Dynamic response of a half-space to a pressure pulse applied to the wall of a buried spherical cavity. The figure shows the vertical component of displacement versus time. The results are consistent with the analytical solutions (Jiang et al., 1994).**

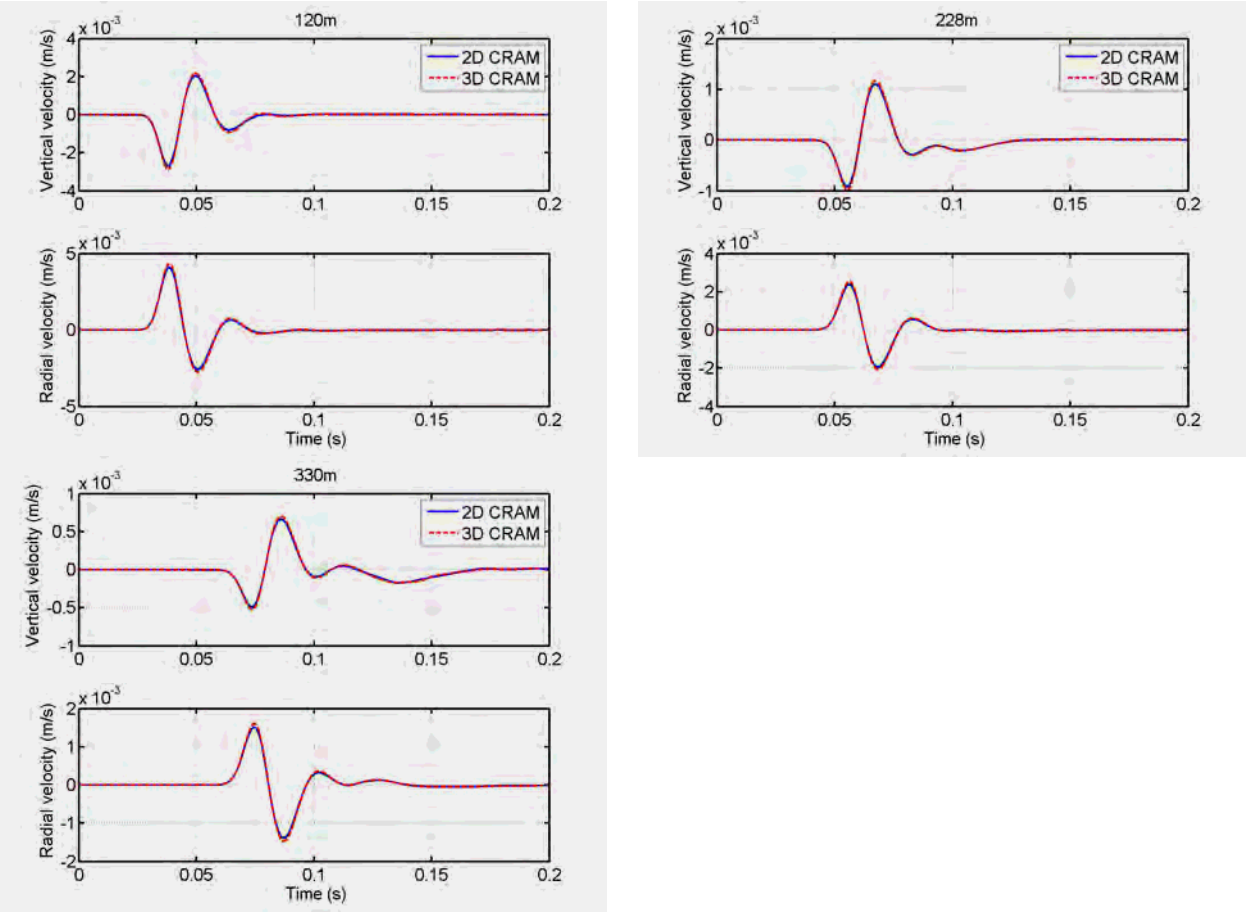


**Figure 7. Comparisons of seismograms at three surface locations—120 m (top left), 228 m (top right), and 330 m (bottom). The top row shows the vertical component; the bottom shows radial. Blue lines are calculated with 2D CRAM; red lines are calculated with 3D CRAM.**

### Explosions in Rectangular and Spherical Cavities

To illustrate the effect of a nonspherical cavity in three dimensions, we compare the waveforms from detonating the same yield of 20 tons in a spherical cavity (red in Figure 8, left) and a cubic cavity (blue), both cavities having the same volume. The recordings at the 4 surface stations are compared in Figure 8 (right). Stations 1 and 3 are located at a distance of about 8-10 times the cavity size (about 3 times the nonlinear region size). Although the cavity volume is the same, the differences between the seismograms generated by the two cavity shapes are clearly visible on the three components. The explosion in the rectangular cavity is found to cause more nonlinear deformation around the cavity and to generate shear waves shown in the tangential direction.

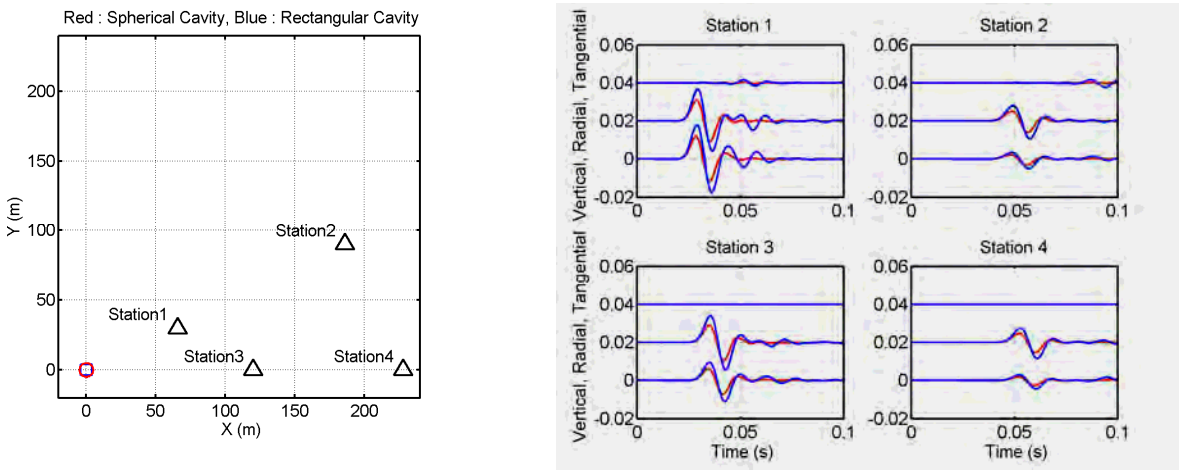


**Figure 8. Map view of cavity and stations (left). Comparison of velocity seismograms at 4 locations (right). Red and blue lines correspond to spherical and rectangular cavities, respectively.**

## CONCLUSIONS AND RECOMMENDATIONS

We are in the early stages of a new project to understand 3D effects on seismic radiation from underground nuclear explosions. We have partially completed development of a 3D version of CRAM, the Lagrangian code we have used previously for performing axisymmetric calculations of underground explosions. We have also implemented a procedure for propagating the results of 3D source region calculations to regional and teleseismic distances using the representation theorem to couple source region calculations to a wavenumber integration code. Our plans are to complete implementation of the numerical methods and then perform 3D calculations to understand and model the effects of 3D source region heterogeneity and the seismic response to that heterogeneity.

## REFERENCES

Aki, K. and P. G. Richards (1980). *Quantitative Seismology—Theory and Methods*. San Francisco: W. H. Freeman and Company.

Apsel, R. J. and J. E. Luco (1983). On the Green's functions for a layered half-space, Part II, *Bull. Seism. Soc. Am.* 73: 931–951.

Bache, T. C. and D. G. Harkrider (1976). The body waves due to a general seismic source in a layered earth model," *Bull. Seism. Soc. Am.* 66: 1805–1819.

Bache, T. C., S. M. Day, and H. J. Swanger (1982). Rayleigh wave synthetic seismograms from multi-dimensional simulations of underground explosions, *Bull. Seism. Soc. Am.* 72: 15–28.

Baker, G. E., J. L. Stevens, and H. Xu (2004). Lg group velocity: A depth discriminant revisited, *Bull. Seism. Soc. Am.* 94: 722–739.

Davis, C. G., W. E. Johnson, J. L. Stevens, N. Rimer, T. G. Barker, E. J. Halda, E. Bailey, and W. Proffer (1992). Seismic signals from asymmetric radiation-hydrodynamic calculations, Los Alamos National Laboratory report LA-12506-MS.

Day, S. M., J. T. Cherry, N. Rimer, and J. L. Stevens (1987). Nonlinear model of tectonic release from underground explosions, *Bull. Seism. Soc. Am*. 77: 996–1016.

Jiang, J., G. R. Baird and D. P. Blair (1994). Dynamic response of a half-space to a buried spherical source, *Geophys. J. Int.* 119: 753–765.

Kitov, I. O. (1997). Underground explosion seismic source function in various rock media as obtained from PNE local data, in upper mantle heterogeneities from active and passive seismology, K. Fuchs, Ed. Kulwer: 105–112.

Luco, J. E. and R. J. Apsel (1983). On the Green's functions for a layered half-space, Part I, *Bull. Seism. Soc. Am*. 73: 909–929.

Ma, S and P. Liu (2006). Modeling of the perfectly matched layer absorbing boundaries and intrinsic attenuation in explicit finite-element methods, *Bull. Seism. Soc. Am*. 96: 1779–1794.

Moczo, P., E. Bystricky, J. Kristek, J. M. Carcione, and M. Bouchon (1997). Hybrid modeling of P-SV seismic motion at inhomogeneous viscoelastic topographic structures, *Bull. Seism. Soc. Am*. 87: 1305–1323.

Murphy, J. R. and C. B. Archambeau (1986). Variability in explosion body-wave magnitudes: An analysis of the RULISON/GASBUGGY anomaly, *Bull. Seism. Soc. Am.* 76: 1087–1113.

Rimer, N., T. Barker, S. Rogers, J. Stevens, and D. Wilkins (1994). Simulation of seismic signals from partially coupled nuclear explosions in cylindrical tunnels, report DNA-TR-94-136, Defense Nuclear Agency, Alexandria, Va., August.

Stevens, J. L., S. Gibbons, N. Rimer, H. Xu, C. Lindholm, F. Ringdal, T. Kvaerna, and J. R. Murphy (2006). Analysis and simulation of chemical explosions in nonspherical cavities in granite, *J. Geophys. Res*. 111: B04306, doi:10.1029/2005JB003768.

Stevens, J. L., N. Rimer, H. Xu, G. E. Baker, and S. M. Day (2003). Near field and regional modeling of explosions at the Degelen test site, SAIC final report to DTRA, SAIC-02/2050, January.

Stevens, J. L., G. E. Baker, H. Xu, T. J. Bennett, N. Rimer, and S. M. Day (2004). The physical basis of Lg generation by explosion sources, SAIC final report submitted to the National Nuclear Security Administration under contract DE-FC03-02SF22676, December.

Stevens, J. L., T. G. Barker, S. M. Day, K. L. McLaughlin, N. Rimer, and B. Shkoller (1991). Simulation of teleseismic body waves, regional seismograms, and Rayleigh wave phase shifts using two-dimensional nonlinear models of explosion sources, AGU Geophysical Monograph 65: Explosion Source Phenomenology, S. Taylor, H. Patton, P. Richards, Eds., ISBN 0-87590-031-3, 239–252.

Wu, R. S., X. B. Xie, Z. Ge, and T. Lay (2004). Quantifying source excitation and path effects for high frequency regional waves, in *Proceedings of the 26th Annual Seismic Research Review: Trends in Nuclear Explosion Monitoring*, LA-UR-04-5801, Vol. 1, pp. 191–201.

Xie, X. B. and T. Lay (1994). The excitation of Lg waves by explosions: A finite difference investigation, *Bull. Seism. Soc. Am.* 84: 324–342.

# SHEAR WAVE GENERATION BY DECOUPLED AND PARTIALLY COUPLED EXPLOSIONS

Jeffry L. Stevens, Heming Xu, and G. Eli Baker

Science Applications International Corporation

Sponsored by Air Force Research Laboratory

Contract No. FA8718-06-C-0007
Proposal No. BAA06-46

## ABSTRACT

The objective of this project is to investigate the sources of shear wave generation by decoupled and partially coupled explosions, and the differences in shear wave generation between tamped and decoupled explosions. A perfectly spherical explosion at the center of a perfectly spherical cavity large enough to fully decouple the explosion would generate no shear waves, so all shear waves from decoupled explosions are due to asymmetries in and near the cavity, and to scattering and conversions. We quantify the effect of different sources of asymmetry through numerical modeling, and take advantage of unique features of different data sets to eliminate particular mechanisms and so constrain the possible sources of observed shear waves.

We present numerical calculations, and analytic solutions for different pressure functions, of the problem of shear wave generation by an explosion offset from the center of a spherical cavity, which causes the shock wave to vary in amplitude and arrival time around the cavity surface. The offset explosion has a dipole component and can generate significant shear waves with a modest offset from the center. The numerical calculations produce cavity reverberations that are strongest along the axis of the source offset. We develop a physically reasonable pressure function that models the pressure reverberations and show that it leads to longer duration waveforms with more low frequency content, again with a dominant dipole contribution.

We have shown previously that the radiation pattern of the near field, initial, shear-wave arrivals from the decoupled explosion Sterling could be reproduced by modeling that included the flat floor (due to melted and recrystallized salt) of the cavity. The observations also have substantial coda, which are not reproduced by the calculations. Similarity of coda waveforms with distance indicates their source is at or very near the cavity. Longer time modeling of the air shock evolution appears to produce a more realistic source function and provide a better match to the coda. We also assess the likelihood that fractures created by the tamped explosion that formed the cavity, Salmon, were re-opened by Sterling. Modeling of hydrofracture propagation driven by the Sterling explosion, by coupling stress wave dynamics in rock with fluid mechanics in the fractures, shows that the cavity pressure is insufficient to overcome the overburden to propagate fractures into rock, except for the area immediately below the explosion on the cavity floor.

We complete analysis and modeling of local records of a 27 Kt tamped and four smaller (0.01 to 0.35 Kt) water filled cavity explosions. We identify two distinct S-phases, neither of which has the 9 Hz bubble pulse peak that the decoupled explosions' coda and P spectra have, which is inconsistent with generation of the initial shear waves by P-wave scattering. Addition of a compensated linear vector dipole (CLVD) source of comparable moment to a spherical explosion source is necessary to reproduce the observed S-waves. Nonlinear source calculations indicate that neither an offset in the source or fracturing is a likely source of the shear waves.

The Israeli Oron decoupling experiment of 2006 consisted of one tamped and two partially decoupled explosions. The latter were strongly overdriven and have similar waveforms from 1 to 30 Hz, but have distinct differences at higher frequencies. The spectra of each event is very distinct. We use group velocities and particle motion to isolate P and S wave energy in local records, and find that for each event, the P and S spectra are similar, with one exception, the tamped explosion has a smaller S/P ratio at 30 to 50 Hz. This is consistent with S being primarily scattered from P, as is expected for these very shallow events in a low velocity medium. That conclusion is supported by the excellent fit to both P and S waves by point spherical explosion synthetics.

## OBJECTIVES

The objective of this project is to investigate the sources of shear wave generation by decoupled and partially coupled explosions, and the differences in shear wave generation between tamped and decoupled explosions. This is being accomplished through a program of data analysis and numerical modeling of decoupled and partially coupled explosions.

## RESEARCH ACCOMPLISHED

### Introduction

This project investigates shear waves from decoupled and partially coupled explosions, focusing on source mechanisms for shear waves, constrained by observations and numerical simulations. Although a nuclear explosion detonated at the center of a perfect spherical cavity large enough to decouple the explosion would generate no shear waves (other than conversions due to the earth's surface and scattering), in fact no cavity has perfect spherical symmetry, nor is the explosion exactly at the center, and shear waves have been observed from all decoupled explosions, even quite close to the source.

In this paper, we report on the completion of the analysis of three specific problems, previously discussed in Stevens et al (2007), and on preliminary analysis and modeling of a new data set. We present analytic and numerical solutions to the problem of shear waves generated by an explosion offset from the center of a spherical cavity. We complete the analysis and modeling of the Sterling explosion data, focusing on understanding the S-coda waveforms and spectra. We also complete the analysis and modeling of shear waves from nuclear explosions in water-filled cavities. Finally, we analyze and model P and S spectra from Israeli tamped and partially decoupled explosions.

### Shear Waves from a Non-Isotropic Explosion Source

In Stevens et al. (2007), we presented a general solution to the problem of shear waves generated by an explosion offset from the center of a spherical cavity. The offset causes a dipole component to the source which generates S waves and causes angular variation in P wave amplitude and shape. By conservation of momentum, the S waves must vanish at zero frequency but they may be a sizeable fraction of the P waves at frequencies of interest. We refine the model of the amplitude function, in particular its dependence on incidence angle, decay with time, and the effect of reverberations, the latter motivated by results of nonlinear axisymmetric calculation of an offset explosion in a spherical cavity.

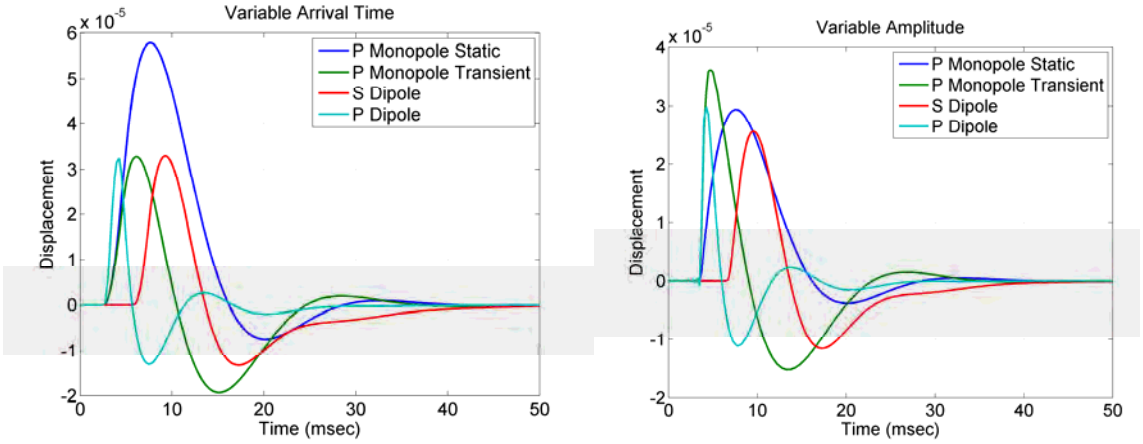


**Figure 1. Waveforms of the monopole and two dipole terms for the angle dependent arrival time with constant amplitude (left) and angle dependent amplitude variation (right), both for a point explosion source in a 17 meter radius cavity.**

We solve the general problem of the seismic wave field caused by a set of tractions applied to the inside of a spherical cavity. The solution includes terms that represent the response of the medium to the applied stress from the explosion and motion due to the response of the cavity wall. Both the applied pressure and the generated seismic wavefield can be expanded in vector spherical harmonics. The problem simplifies since the applied pressure is normal to the cavity wall. For the simple case where pressure has the same functional form at all points on the cavity

wall, differing only by start time, and has an exponential decay with time, the dipole term produces shear waves that are a significant percent of the P-wave size (Figure 1, left). Results are similar for the case where pressure is higher on the offset side, balanced by longer duration, lower amplitude pressure on the other side (Figure 1, right).

A nonlinear, axisymmetric, Eulerian calculation that simulates the explosion within the cavity and the air-rock interaction produces similar results, but with the addition of complex and persistent cavity reverberations. The calculation is for a 0.38 kiloton explosion in a 17 meter radius air-filled cavity, offset by 5 meters from the cavity center. The yield and cavity size correspond to the Sterling explosion, although we use a strong rock model to prevent the plastic yielding that occurs with salt. The calculation did not include gravity. Figure 2 shows the pressure field at 2.5 msecs, the pressure time histories at different points in the cavity, and P and S velocity waveforms.

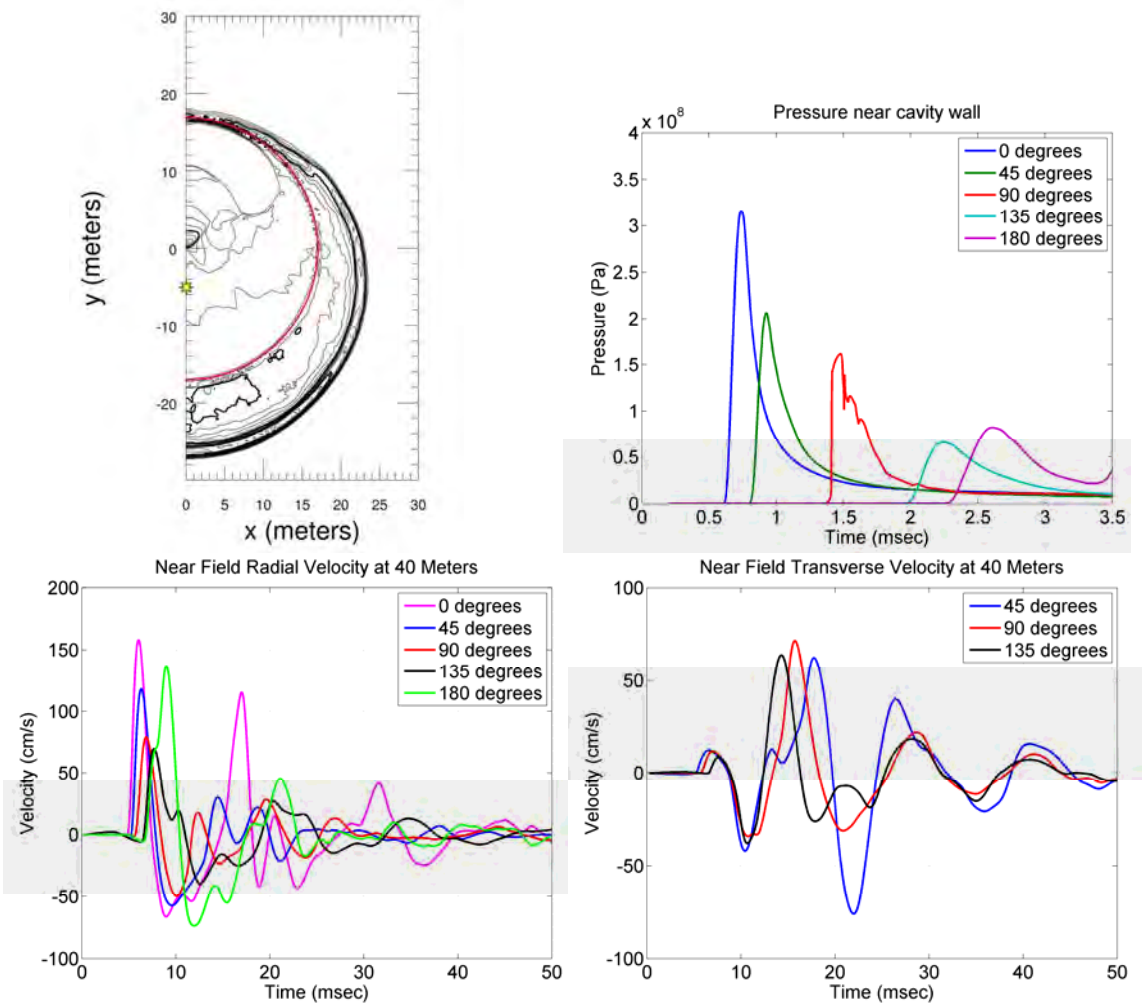


**Figure 2. Pressure contours at 2.5 msec (upper left). Red line on the contour plot shows the cavity wall; the yellow mark shows the explosion location. The first 3.5 msec of the pressure time histories at 5 points inside the cavity next to the wall (upper right). Zero degrees is in the direction of the explosion offset toward the bottom of the grid. Radial (bottom left) and vertical (bottom right) velocity waveforms low pass filtered at 200 Hz at a distance of 40 meters from the cavity center.**

These results motivate a model of pressure for the analytic solution that more accurately represents the reverberations within the cavity. Specifically, because the pressure pulses are stronger at the ends of the cavity and decline in amplitude with each reverberation, we model the pressure field as a series of transient pressure pulses on each half of the cavity with maximum amplitude at zero and π, varying as cos$\theta$. For a single pressure pulse on each side, the results are similar to the earlier examples. With multiple reverberations, however, the waveforms are longer

and have more low frequency content. Figure 3 shows an example with 10 reverberations, with the pressure decaying exponentially with time.

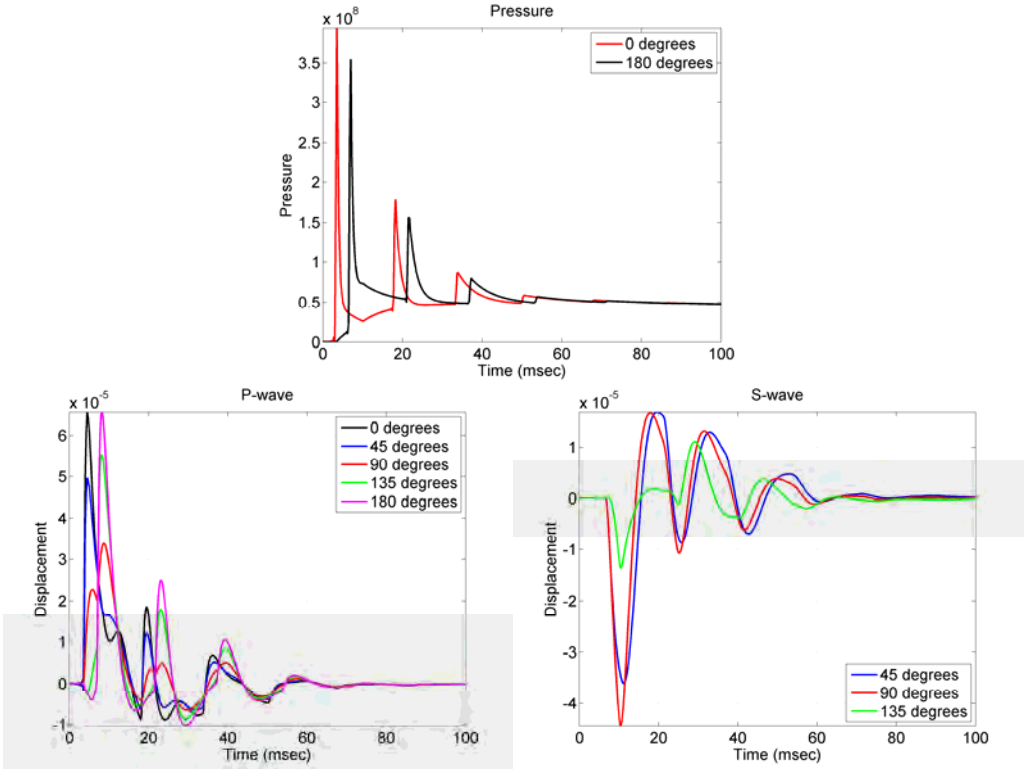


**Figure 3. Cavity pressure at 0 (the offset direction) and 180 degrees (top) and far field P and S waves generated by the pressure function.**

**Sterling Calculations**

Stevens et al. (2007) presented simulations of the Sterling explosion, reporting that near field waveforms, including the radiation pattern of the initial arrivals of near field shear waves, can be explained by the cavity shape and the asymmetry caused by varying impact of the explosion shock across different parts of the cavity. Those calculations were based on an initial state, determined using the Eulerian nonlinear code used in the offset source calculations. The calculation was run long enough to get the shock wave well into the surrounding material, and then the results of that calculation defined the initial conditions for a nonlinear Lagrangian finite-difference code that propagated the deformation out beyond the elastic radius. During the overlay the interior of the cavity is rezoned into a single zone with a constant pressure. Stevens et al. (2007) also report on hydrofracture calculations, which indicate that cracking is not likely the source of the observed shear waves. In particular, pressure within the Sterling cavity is not sufficient to open a single preexisting conical crack connecting to the outer bottom edge of the cavity, such as that proposed in the kinematic model of Langston (1983). In the case where cracks are allowed to form anywhere in the medium, the overburden greatly limits the extent of cracking, preventing generation of significant shear wave energy.

Here we address one further aspect of the problem, the reverberations within the coda. Stevens et al (2007) reported that stacks of coda from at, above, and below shot level records showed that the coda are similar at similar incidence, which indicated that the S-wave coda source is located at or very near the cavity. The coda shear waves also have a radiation pattern with incidence, different from that of the initial S-wave, suggesting a different mechanism from that of the initial S.

Figure 4 shows the near field P-wave observations, seismograms and spectra, made above, at, and below shot point, scaled to the most distant location by using Qp=200, and corrected for geometrical spreading. The time series and 30 Hz corner frequency of the observations are well matched by the nonlinear source calculation. The reverberations of the observed S-waves however, are not reproduced by the numerical model (Figure 5). Further, several studies have found that S source spectra are similar to those of P, but with the corner frequencies reduced by the S-to-P velocity

ratio (e.g., Fisk, 2007). For Sterling, the observed S spectra appear to have a much higher frequency corner. The apparent higher corner may be due to a broad resonance peak at 55 Hz. The results of the previous section bear on this result. The nonlinear source calculations took as initial conditions the stress and velocity at all grid points at a single instant, with the exception of the cavity itself, which was then modeled as a simple cavity with constant pressure. This proved very effective for modeling the initial P and S waves, but excluded cavity reverberations. The models presented in the previous section however, explain the observed long duration near field waveforms from Sterling as caused by vertically oriented cavity reverberations.

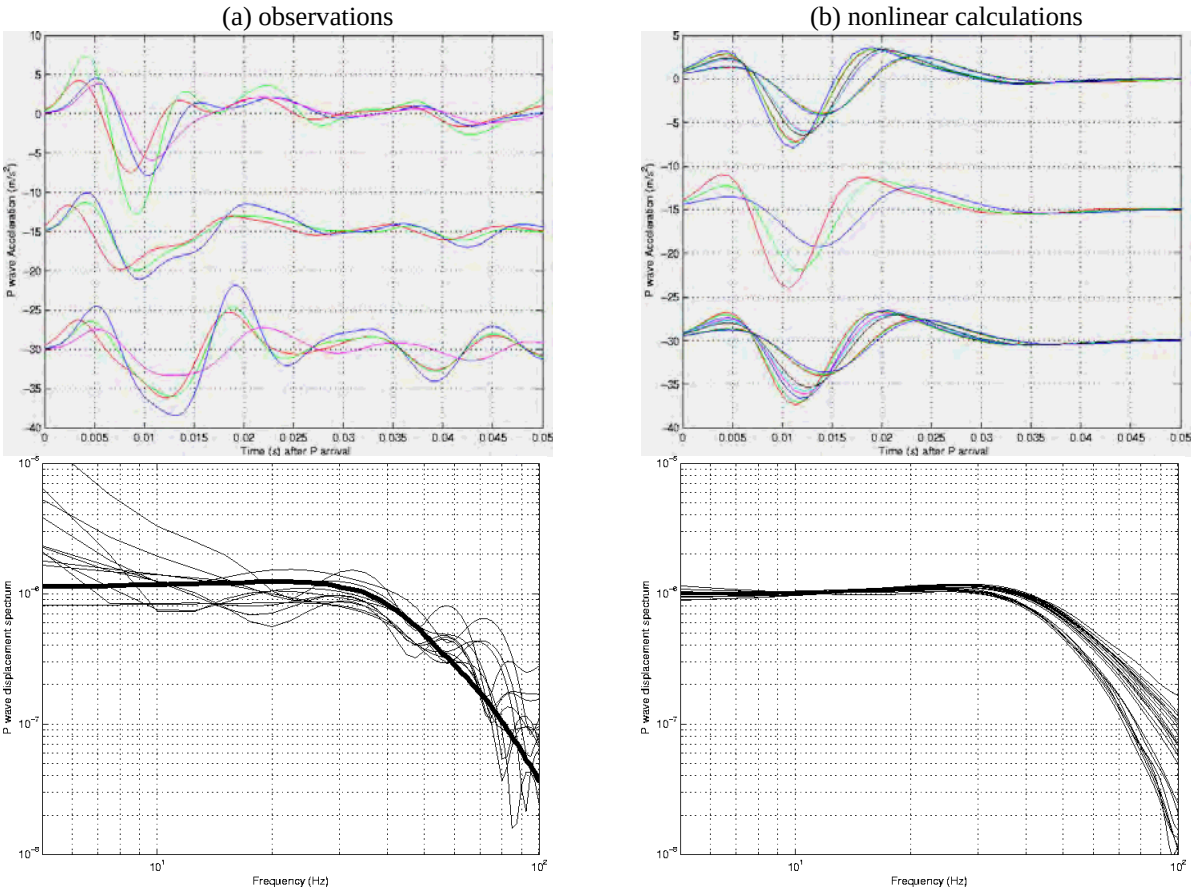


**Figure 4. Radial P waveforms aligned at their predicted arrival time and filtered from 3–100 Hz (top) and their spectra (bottom) from the observations (left) and nonlinear calculations (right). The top, middle, and bottom sets of seismograms correspond to receivers above, at, and below the shot level. In the observed spectra (bottom left), the thick line indicates the prediction for a spherically symmetrical case.**

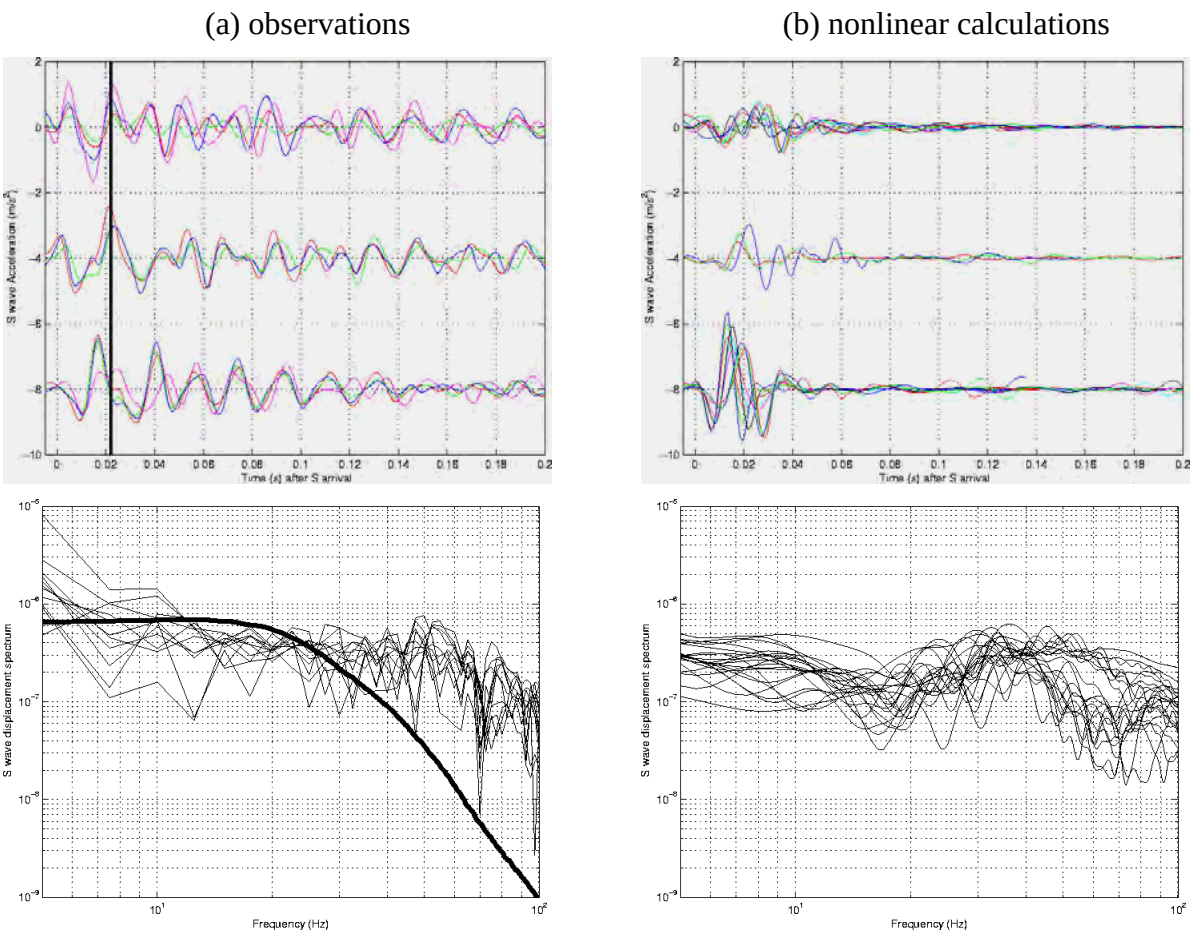


**Figure 5. Similar to Figure 4, but for tangential S waveforms. The solid line in the lower left figure shows the predicted spectrum from scaling the P spectrum by the S/P velocity ratio, which is clearly inconsistent with the data. The data can be explained by a vertical dipole source caused by cavity reverberations.**

**Explosions in Water-Filled Cavities**

In Stevens et al. (2007), we presented two independent sets of observations from a unique series of explosions, a tamped 27 Kt explosion at 597 m depth in salt at Azgir, followed by four very small explosions (yields 0.35, 0.10, 0.01, and 0.08 kt) in the water-filled, 32.5 m radius, cavity of the original explosion. These are effectively decoupled, in that the small explosions do not cause significant nonlinear deformation of the cavity, but provide large signals as the pressure is much greater in water than it would be in an air-filled cavity. We showed that the P, but not the S spectra of the decoupled explosions each have a 9 Hz bubble pulse resonance peak, indicating that the S waves were not scattered from P. The explosion depth precludes generation of 9 Hz Rg, so scattered Rg also cannot be the source of S. We also showed that the S travel time curve is consistent with direct generation of S at the source or near instantaneous scattering at the source.

Through further modeling and analysis of travel times and particle motion, we identify two distinct S phases (Figure 6, left). Particle motion of the second S phase is retrograde, consistent with identification as a higher mode surface wave. Equivalently, it is also consistent with shear waves trapped in the low velocity surface layer (the velocity model is provided in Stevens et al, 2007). The particle motion of the initial S wave is more complex, but for most records the motion transitions from linear in the P wave window to more circular in the S window. The travel time of the initial S wave is consistent with the direct arrival and the second is consistent with propagation along the surface. The S is not generated by a point spherical explosion, but requires an S wave source. Phase identification is consistent between events and over the range of distances observed (1 to 9 km).

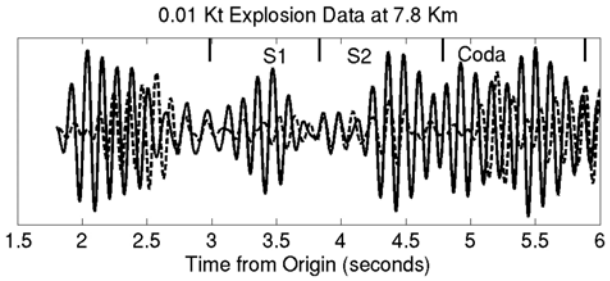


**Figure 6. Overlain vertical (solid) and Hilbert transformed radial (dashed) velocity records of the 0.01 Kt explosion at 7.8 km, filtered from 5 to 10 Hz (above). The first and second S arrivals (labeled S1 and S2) and the coda are delimited by vertical bars along the upper plot boundary.**

Neither of the shear waves have the bubble pulse peak, but the coda shares the bubble pulse peak with the P wave, demonstrating that a phase scattered at least partly from P will share that spectral feature, further indicating that neither S-wave is scattered from P (Figure 7).

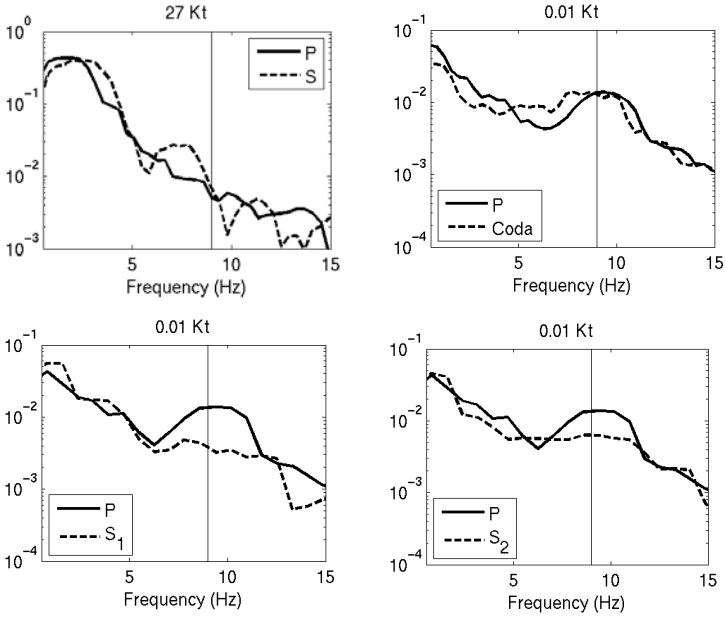


**Figure 7. Neither the P or S spectra of the tamped explosion (upper left) have a 9 Hz bubble pulse peak. The P (solid) and coda (dashed) spectra of the 0.01 Kt explosion both have the resonance peak (upper right). Neither the initial S (bottom left) or second S phase (bottom right) have the spectral peak. The results for other decoupled events are consistent.**

We estimate the relative size and depth of a CLVD component that is required to match the observations. We match the average of the vertical and radial component amplitudes, and for S, match the sum of the first and second S phase amplitudes. To first order, a CLVD with the same moment as the explosion provides a good match to the observed S-to-P ratio. There is some variability between even the decoupled explosion S-to-P ratios, so it is difficult to draw conclusions regarding second order differences between the decoupled and tamped explosions. Nonetheless, some of the details are interesting. When filtered from 5 to 10 Hz, the CLVD component required to match the observed decoupled explosion S-to-P ratios is significantly smaller than that of the tamped explosion, 41% of the total moment vs. 65%. When filtered from 4 to 8 Hz however, so the bubble pulse peak is excluded, the tamped explosion's CLVD moment relative to the spherical explosion moment is only slightly larger than the decoupled explosions'. Specifically, the CLVD then is, on average, 53% of the total moment of the decoupled explosions, vs 61% for the tamped. There is another difference between the decoupled and tamped events' S-waveforms that may reduce the difference further and shed light on their origins.

The initial S-wave of the tamped explosion is later than that of the decoupled explosions. This would occur if the tamped explosion's S-wave were generated at a shallower depth, as it would then excite slower modes. Figure 8 shows the sum of synthetics for a 597 m depth spherical explosion plus a CLVD of the same amplitude. The upper trace shows the case where the CLVD is at the same depth. The second trace shows the case where the CLVD is at half the depth. The S-wave energy is more strongly concentrated later in the seismogram in the second case. The earlier S arrival of the deeper CLVD source matches the earlier S of the 0.35 Kt event (third trace). All the

decoupled explosions have earlier S. The later arriving S due to greater excitation of higher modes by the shallower CLVD is consistent with the tamped explosion record (bottom).

Besides the effect on timing, a shallower source of the same moment yields larger amplitudes than a deeper source. This is due to greater excitation of the shallow modes and to the effect of depth on the cavity size, the latter of which isn't even reflected in the synthetics shown. This means that the moment of a shallow CLVD source necessary to match the observed S-to-P ratio of the tamped explosion is reduced. Resolution of the predicted amplitudes is limited by uncertainty in the details of the source structure and in the exact depth distribution of the tamped source. To first order however, we conclude that both the decoupled and tamped explosion records require an S-wave source of comparable moment to produce the observed S waves. The significant difference is that for the decoupled explosions, the source is at the spherical explosion depth, and for the tamped explosion, an S-wave source at half the depth provides a better match to the data.

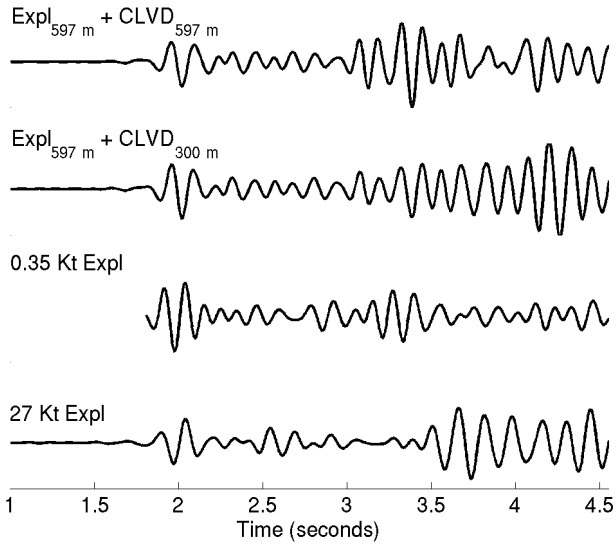


**Figure 8. Synthetic vertical seismograms at 7.8 km, filtered from 4 to 8 Hz for an explosion plus a CLVD source of the same moment at the same depth (top), and an explosion plus CLVD source of the same moment but at half the depth (second trace). The deeper CLVD source matches the earlier S of the 0.35 Kt event (third trace), while the shallower CLVD is consistent with the later S energy in the tamped explosion record (bottom).**

We performed several nonlinear source calculations to assess the effect of source asymmetries and fracturing, including calculations with the explosion at the top, center, and base of the cavity. Figure 9 shows the nonlinearly deformed areas in each of those cases. The hard anhydrite cap flattens the upper surface, and when the explosive is detonated at the base of the cavity, the deformation extends much further downward. Surprisingly however, the records of each are very similar to that of a spherical point explosion. Additional asymmetry of some sort is required to match the data, indicating that we are imposing more symmetry on the solution that actually exists.

We also performed fracture calculations. The first assessed the ability of the explosion to drive open pre-existing cracks connected to the cavity, where all the material about the cavity is fractured. In that case, with overburden pressure of about 130 bars and peak cavity pressure for the 0.35 Kt explosion at 269 bars, the dynamic region extends only 3 m into the salt and has no obvious preferred direction. The effect on the seismograms is not significant. We also performed a calculation with a horizontal crack radiating out from the cavity. As with the hydrofracture calculation, the peak cavity pressure of 269 bars overcomes the overburden of 130 bars, and so opens the crack outward 50m into the salt in the initial 300 ms and then closes to within 1 m of the cavity due to depletion of the cavity pressure. Again, however, the waveforms outside of the near field are similar to those of a spherical explosion source.

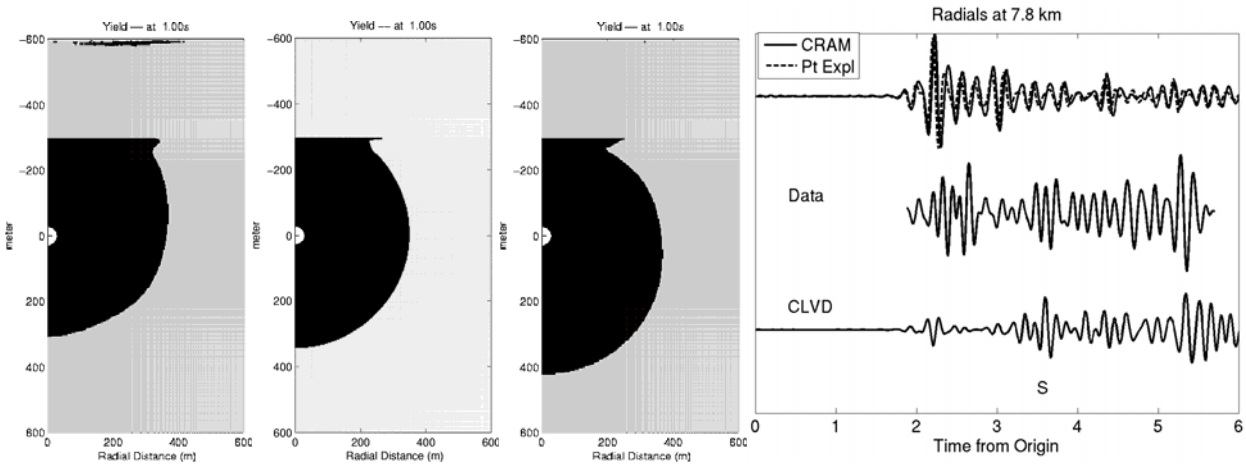


**Figure 9. Nonlinear yield region around the cavity for the 0.35 Kt explosion placed at the top, center, and bottom (left to right respectively) of the cavity. The rightmost plot shows radial seismograms at 7.8 km. The record from the calculation with the explosion at the center (upper trace, solid) is overlain with that from a spherical point explosion source (upper trace, dashed), and is compared with data (middle trace) and CLVD synthetics (bottom trace).**

### Israeli Decoupling Experiment

We have performed preliminary analysis and modeling of data from the Israeli decoupling experiment (Gitterman et al., 2007), which included three explosions, each of 1,240 kg of ANFO, one tamped at 30 m depth, one at the base of a 26.5 m deep, 4 $m^3$ cavity, and one at the base of a 60 m deep, 14 $m^3$ cavity. All were recorded on a common set of local to regional stations. We have identified the local P and S wave phases, investigated whether there are differences between those phases from the different events, and modeled the observations.

Although spectral differences exist between events, first order differences do not appear to exist between the P and S phases for a single event. Figure 10 shows the vertical P compared with the tangential S spectra for each event. For the most part, the S spectra is similar to the P, with the exception that there may be less S wave energy from 30 to 50 Hz from the tamped explosion.

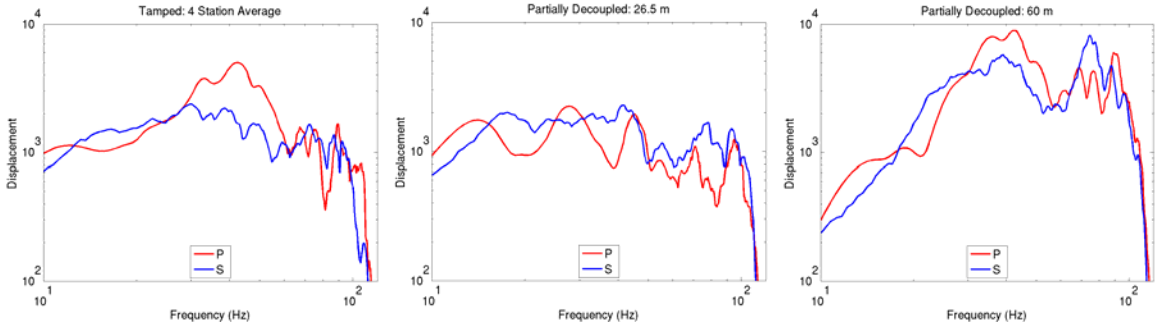


**Figure 10. Vertical P (red) and tangential S (blue) spectra from the tamped (left), and two partially decoupled explosions (center and right, 26.5 and 60 m depth respectively).**

Similar S to P spectra is consistent with conversion from P being the dominant source of S-waves. The velocity is very low at the source (Gitterman et al., 2007), so we expect pS to be trapped, plus the very shallow source depths will lead to strong S*, at least at the lower frequencies. Figure 11 compares spherical point explosion synthetics with the tamped explosion accelerometer records at 710 m from the source. Not only the P, but the large S arrival at approximately 0.6 seconds is well matched by the synthetics without shear wave generation at the source.

Figure 12 shows an example that confirms the additional shear wave energy observed from the partially decoupled explosions vs the tamped explosion in the 30 to 50 Hz range. It shows the vertical component records at the same station, 145.4 and 163.2 m, respectively, from the tamped (solid) explosion and the partially decoupled (dashed) explosion at 26.5 m depth. The records are integrated to velocity from the accelerograms. The waveforms are very

similar, with a slight decrease in amplitude for the partially decoupled explosion up to 30 Hz. Above 30 Hz however, there is a large arrival only from the decoupled explosion, at approximately 0.2 seconds after P.

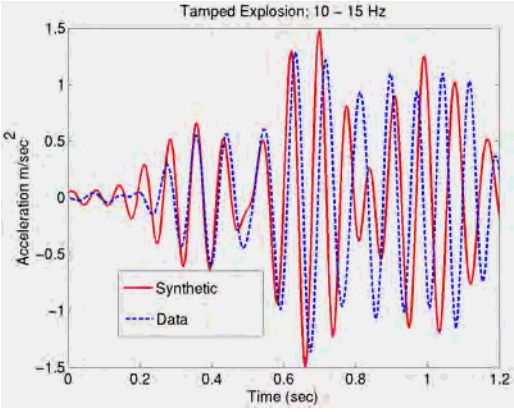


**Figure 11. Spherical point explosion synthetics (red) and tamped explosion acceleration records (blue) at 710 m.**

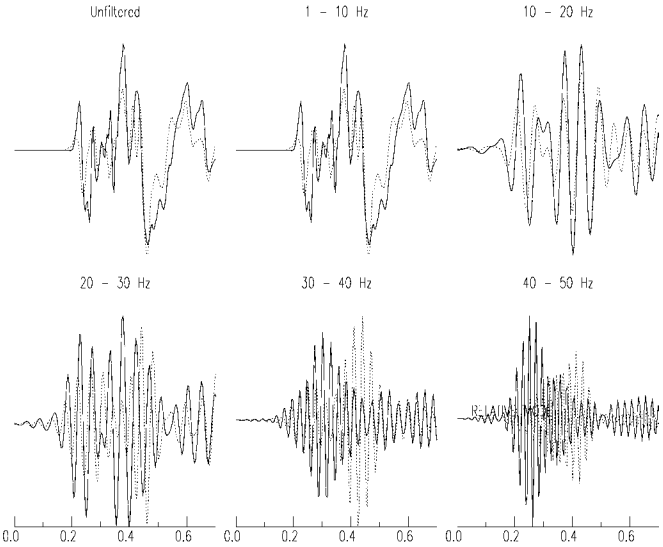


**Figure 12. Vertical component records of the tamped (solid) explosion and the shallower partially decoupled explosion, at 145.4 and 163.2 m respectively. Initial P arrivals are aligned at 0.2 seconds.**

## CONCLUSIONS AND RECOMMENDATIONS

We find that an explosion offset from the center of a spherical cavity generates significant S waves and can be modeled as a dipole source. Numerical simulations predict reverberations with a distinct orientation in cavity decoupled explosions. The long duration coda of the Sterling decoupled explosion near field records can be explained by these numerical and analytical results. We further analyze and model local records from the Azgir tamped and water-filled cavity explosions. We identify two distinct shear wave arrivals, neither of which has the prominent 9 Hz bubble pulse peak seen in the P-wave spectra, indicating the S-waves were not scattered from P. The coda waves do have the resonance peak, indicating that the lack of the peak in the S-waves is not likely due to attenuation. A spherical explosion source does not match the observed shear waves. Rather, a CLVD source of comparable moment is required. The S-arrival times from the decoupled explosions are better matched by placing the CLVD at the explosion depth. The tamped explosion shear waves arrive slightly earlier and are better matched by making the CLVD component shallower. Numerical simulations indicate that neither an offset source or fracturing is the likely source of shear waves from these explosions. Preliminary analysis of records from the Israeli decoupling experiment indicates that the shear waves are generated by conversion of P waves, with one exception. At 30 to 50 Hz, the partially decoupled explosions have relatively more S-to-P energy, indicating that there is an S source at those frequencies that is absent from the tamped explosion source.

## REFERENCES

Fisk, M (2007). Corner frequency scaling of regional Seismic phases for underground nuclear explosions at the Nevada Test Site, *Bull. Seism. Soc. Am.* 97: 977–988.

Gitterman, Y., R. Hofstetter, and V. Pinsky (2007). Depth-of-burial and decoupling explosion experiments in Israel: near-source and near-regional seismic energy generation, in *Proceedings of the 29th Annual Monitoring Research Review: Ground-Based Nuclear Explosion Technologies,* LA-UR-07-5613, Vol. 1, pp. 571–581.

Langston, C. A. (1983). Kinematic analysis of strong motion P and SV waves from the Sterling event. *J. Geophys. Res.* 88: 3486–3497.

Stevens, Jeffry L., Heming Xu, and G. E. Baker (2007). Analysis of shear wave generation by decoupled and partially coupled explosions, in *Proceedings of the 29th Annual Monitoring Research Review: Ground-Based Nuclear Explosion Technologies,* LA-UR-07-5613, Vol. 1, pp. 664–673.

# REGIONAL SEISMIC AMPLITUDE MODELING AND TOMOGRAPHY FOR EARTHQUAKE-EXPLOSION DISCRIMINATION

William R. Walter, Michael E. Pasyanos, Eric Matzel, Rengin Gök, Jerry J. Sweeney, Sean R. Ford and Arthur J. Rodgers

Lawrence Livermore National Laboratory

Sponsored by National Nuclear Security Administration

Contract No. DE-AC52-07NA27344

## ABSTRACT

We continue exploring methodologies to improve earthquake-explosion discrimination using regional amplitude ratios such as *P/S* in a variety of frequency bands. Empirically, we demonstrate that such ratios separate explosions from earthquakes, using closely located pairs of earthquakes and explosions recorded on common, publicly available stations at test sites around the world (e.g., Nevada, Novaya Zemlya, Semipalatinsk, Lop Nor, India, Pakistan, and North Korea). We are also examining if there is any relationship between the observed *P/S* and the point source variability revealed by longer period full waveform modeling (e.g., Ford et al., 2008). For example, regional waveform modeling shows strong tectonic release from the May 1998 India test, in contrast with very little tectonic release in the October 2006 North Korea test, but the *P/S* discrimination behavior appears similar in both events using the limited regional data available.

While regional amplitude ratios such as *P/S* can separate events in close proximity, it is also empirically well known that path effects can greatly distort observed amplitudes and make earthquakes appear very explosion-like. Previously we have shown that the Magnitude Distance Amplitude Correction (MDAC) technique (Walter and Taylor, 2001) can account for simple 1-D attenuation and geometrical spreading corrections, as well as magnitude and site effects. However, in some regions, 1-D path corrections are a poor approximation, and we need to develop 2-D path corrections. Here we demonstrate a new 2-D attenuation tomography technique using the MDAC earthquake source model applied to a set of events and stations in both the Middle East and the Yellow Sea Korean Peninsula regions. We believe this new 2-D MDAC tomography has the potential to greatly improve earthquake-explosion discrimination, particularly in tectonically complex regions such as the Middle East.

## OBJECTIVES

Monitoring the world for potential nuclear explosions requires characterizing seismic events and discriminating between natural and man-made seismic events, such as earthquakes and mining activities, and nuclear weapons testing. We continue developing, testing, and refining size-, distance-, and location-based regional seismic amplitude corrections to facilitate the comparison of all events that are recorded at a particular seismic station. These corrections, calibrated for each station, reduce amplitude measurement scatter and improve discrimination performance. We test the methods on well-known (ground truth) datasets in the U.S. and then apply them to the uncalibrated stations in Eurasia, Africa, and other regions of interest to improve underground nuclear test monitoring capability.

## RESEARCH ACCOMPLISHED

As part of the overall National Nuclear Security Administration Ground-Based Nuclear Explosion Monitoring Research and Development (GNEMRD) program, we continue to pursue a comprehensive research effort to improve our capabilities to seismically characterize and discriminate underground nuclear tests from other natural and man-made sources of seismicity. To reduce the monitoring magnitude threshold, we make use of local and regional body and surface wave data to calibrate each seismic station. Our goals are to reduce the variance and improve the separation between explosions and other event populations by accounting for the effects of propagation and differential source size and by optimizing the types and combinations of amplitude measurements used.

### Empirical *P/S* Observations

Empirical observations have shown clear differences between earthquake and explosion *P/S* amplitude ratios that can be exploited for nuclear explosion monitoring. These differences became apparent with the advent of widespread digital seismometry in the late 1980s and early 1990s, when a large number of different researchers found that at high frequencies, greater than around 2-4 Hz, the regional *P/S* amplitude ratios consistently discriminated explosions from earthquakes (e.g., Dysart and Pulli, 1987; Baumgardt and Young, 1990; Kim et al., 1993; Walter et al., 1995; Taylor, 1996; Hartse et al., 1997; Battone et al., 2002). For example, in Figure 1 we compare an earthquake and an explosion at each of four major test sites (rows), bandpass filtered in four different frequency bands (columns). Here we use closely spaced pairs of earthquakes and explosions recorded at the same station to minimize any path and site effects, and so the observed differences come from effects in the source region. There is a relative lack of S-waves in the explosions as the frequency increases. Note also there are interesting differences between the test sites, indicating that emplacement conditions (depth, media properties, geologic and tectonic conditions, topography, etc.) play a role in relative P- and S-wave generation.

Examination of *P/S* ratios at high frequencies has now been done all over the world. As we show in Figure 2, the characteristic pattern—that explosions have larger relative P-wave amplitudes than S-wave amplitudes—appears to hold everywhere, provided that we filter the data at a high enough frequency and that we compare events with very similar paths. One example in Figure 2 is the announced nuclear test by North Korea on October 9, 2006. In this case, the nearest earthquakes for comparison are around 100 km away, but we can bracket the test with earthquakes and clearly see that it is deficient in high frequency S-wave energy. This example shows the importance of accounting for path, as the S-wave energy in this case is partitioned into both Sn and Lg phases. The path of the recorded seismic energy crosses the Sea of Japan, a region of oceanic crust where Lg does not efficiently propagate. On can see that this earthquake, with a greater proportion of its path in the Sea of Japan, has stronger Sn than the other. It is important to correct for path effects and to consider *P/S* ratios for all the observable regional phases and avoid cases where one of the earthquake S-wave phases is attenuated to below the level of the noise and it appears explosion-like simply due to the path effects.

When similar-sized earthquakes and explosions are nearly co-located, we can understand the observed seismic contrasts, such as the relative P-to-S wave excitation, in terms of depth, material property, focal mechanism, and source time function differences. However, it is well known that path propagation effects (e.g., attenuation, blockage) and source scaling effects (e.g., corner frequency scaling with magnitude) can make earthquakes look like explosions and vice versa. We developed the MDAC technique (Walter and Taylor, 2001) to account for these

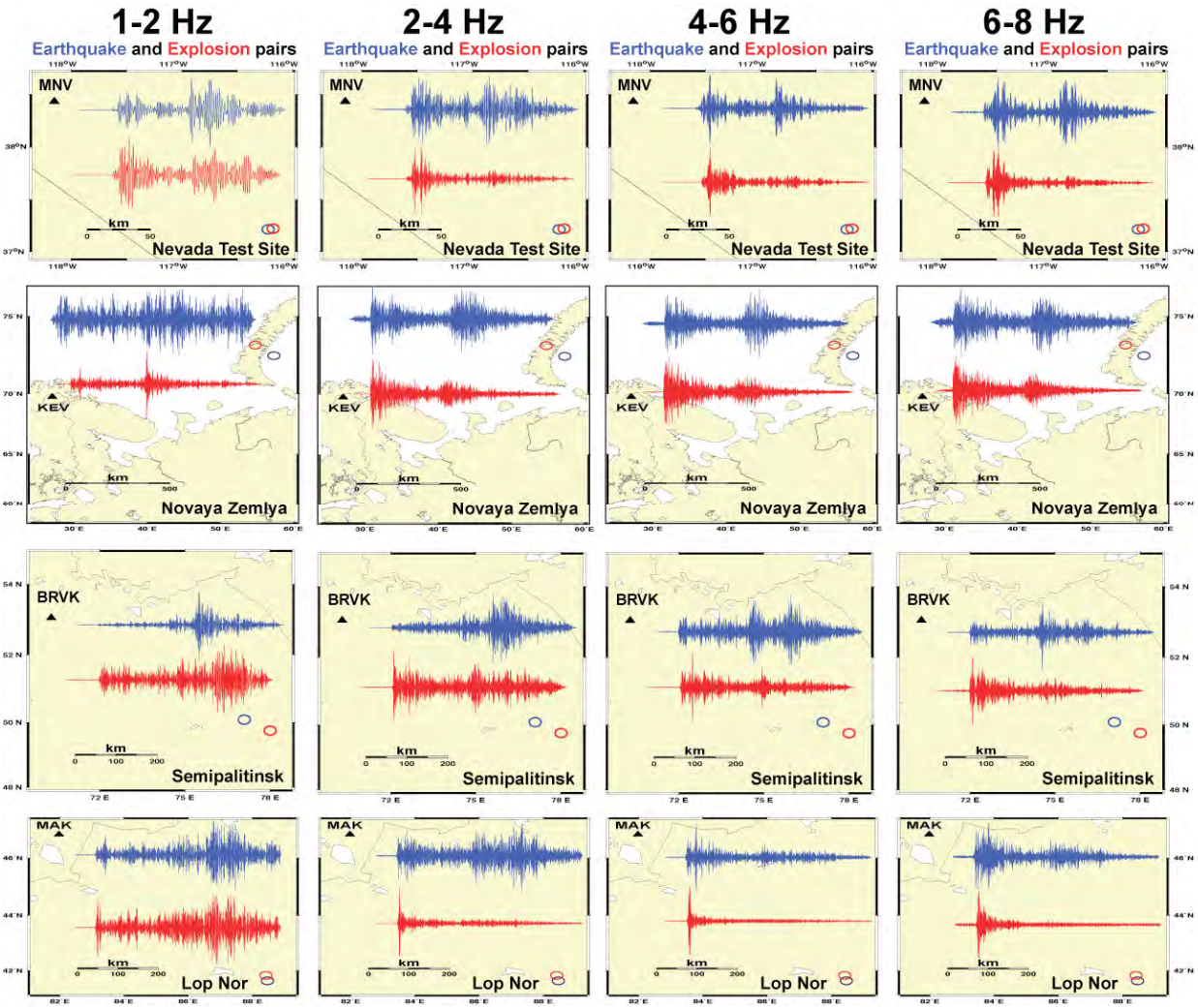


**Figure 1. An earthquake and explosion pair at four different test sites: Nevada, U.S.A.; Novaya Zemlya, Russia; Semipaletinsk former U.S.S.R. now Kazakhstan; and Lop Nor, China. The seismograms are bandpass filtered at four frequency bands (columns) illustrating significant differences in relative P and S wave amplitudes, with explosions have relatively less S-waves at higher frequencies.**

effects with proper calibration. We use the earthquakes alone to determine the MDAC parameters, such as geometrical spreading, frequency dependent Q, and the average apparent stress. After calibration, the MDAC formulation provides expected spectral amplitudes as a function of phase, frequency, magnitude and distance. These can then be subtracted from the actual observations. For earthquakes, the corrected data should exhibit a close-to-zero mean and no significant trends with magnitude and distance. Explosions should have significant non-zero mean residuals, leading to improved discrimination.

As shown in Figure 3, we applied MDAC to correct for path effects for earthquakes all around the Korean Peninsula, Yellow Sea, and northeastern China region recorded at stations MDJ and TJN, which are publicly available through data centers such as the Incorporated Research Institutions for Seismology (IRIS) and the Ocean Hemisphere Project Data Management Center (OHP-DMC). When ratios were available from both stations, they were averaged. We look at three different *P/S* ratios in four frequency bands. As Figure 3 shows, the North Korean test appears to discriminate progressively better at higher frequencies for all three types of *P/S* ratios. Due to event size, attenuation, background noise, and the need to be past the crossover distance to see Pn and Sn, not all measurements can be made for all phases and frequency bands. There are 167 earthquakes for 1–2 Hz Pg/Lg and fewer for the other ratios. In general, the number of measurements passing the signal-to-noise-ratio (SNR) thresholds (here 2 for P-waves and 1.3 for S-waves) diminishes as the frequency increases.

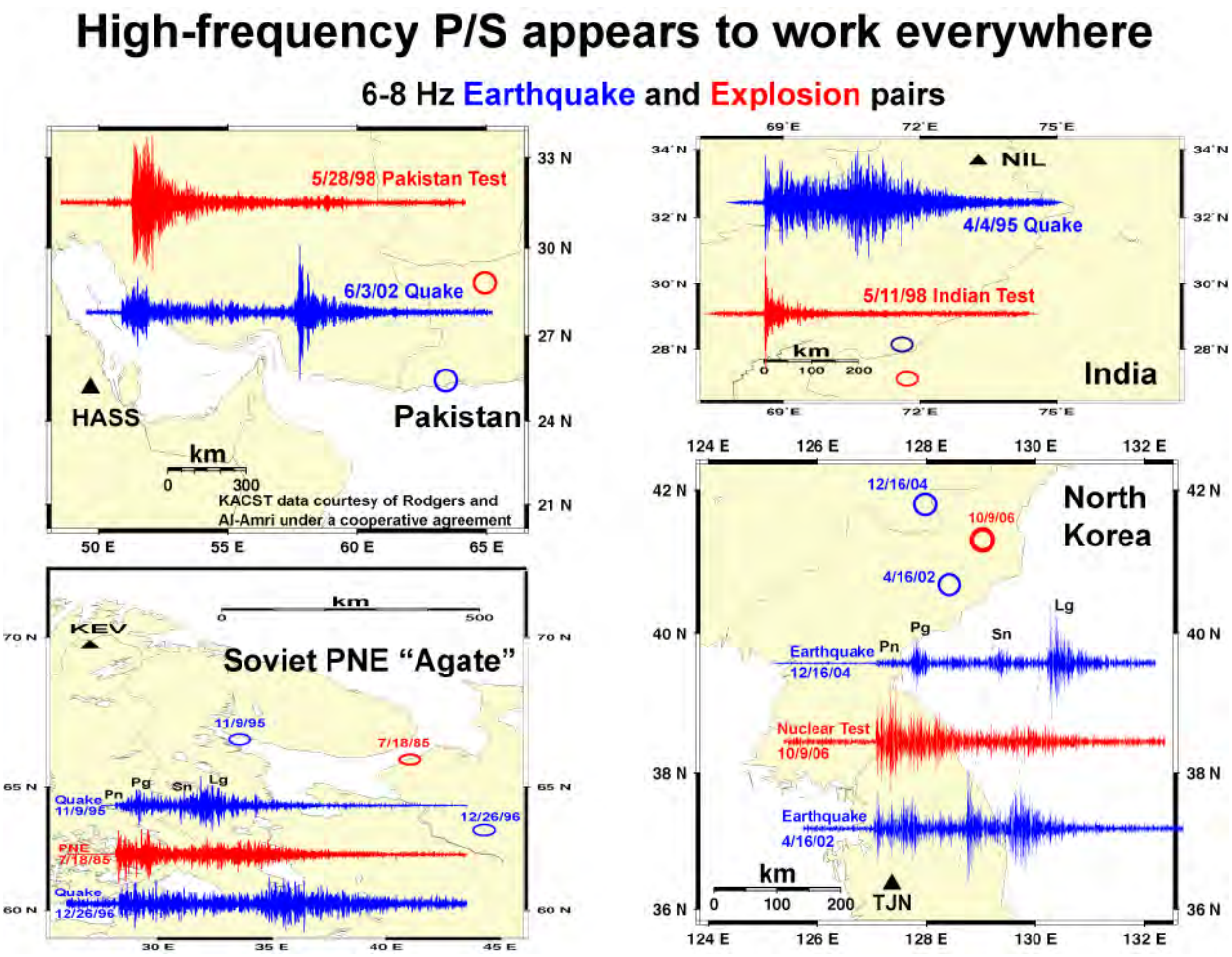


**Figure 2. Four examples of 6-8 Hz filtered seismograms of explosions compared to nearby earthquakes outside the major testing areas show the characteristic difference: explosions have larger *P/S* amplitude values.**

Practical considerations, such as whether we expect a new event in a particular area with a given magnitude to be detectable for a given phase and frequency, are critical for monitoring. Therefore it is good to see that there remains considerable discrimination capability in all three types of *P/S* ratios in the bands below 6–8 Hz, particularly the 2–4 and 4–6 Hz bands. As we have noted in prior MRR papers, it is possible to form multivariate combinations of ratios to enhance discrimination, and these can be tuned to optimize discrimination based on the bands you are likely to have to work with.

One type of ratio that has been considered from a practical viewpoint is the cross-spectral ratio (e.g., Taylor et al., 2002): comparing a higher frequency P-wave amplitude to a lower frequency S-wave amplitude. As shown in Figure 1 for Lop Nor or Figure 2 for India, some explosions do not have any visible S-waves at high frequency and the S-measurement is made on coda. Such explosion coda measures can work so long as one is sure a comparable-size earthquake would have produced measurable S-waves allowing discrimination. In a cross-spectral ratio, the S-wave band is chosen so that even explosion S-waves are detectable, and these have been shown to work well in some cases such as Lope Nor (e.g., Taylor et al., 2002). A complication with cross-spectral ratios occurs if the spectral decay at high frequencies is substantially different for explosions than for earthquakes: it can start to counteract the *P/S* difference and lead to poor discrimination. In Figure 4, we show an example of a 6–8 Hz Pn to 2–4 Hz Lg ratio for Nevada Test Site (NTS) data averaged over two stations, ELK and KNB. One can see that a number of the explosions do not discriminate at all. NTS explosions show a clear material property dependence (e.g., Walter et al., 1995) with explosions in weak, high-gas-porosity media having much stronger spectral decay than explosions in stronger, low-gas-porosity media when compared at the same station using the same path and site corrections, as shown in Figure 4.

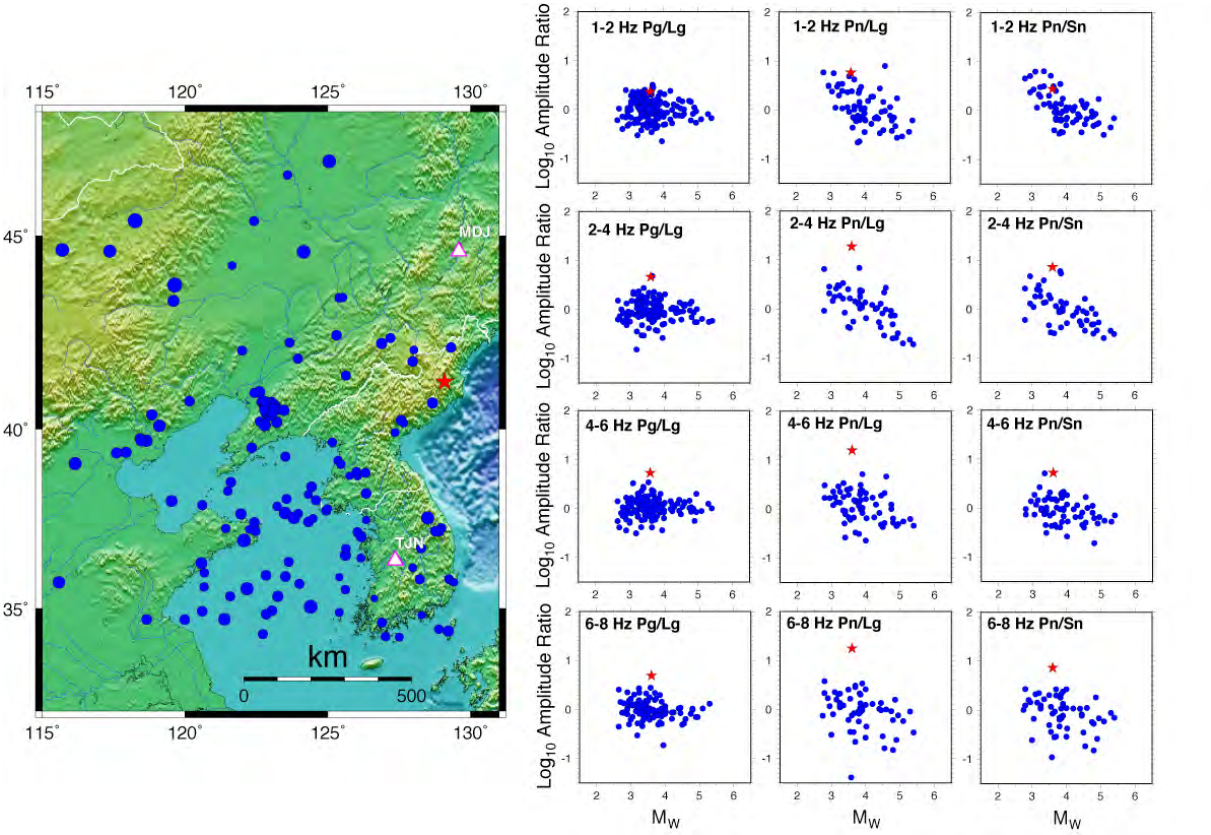


**Figure 3. The map shows earthquakes (blue circles) and the October 9, 2006, North Korean nuclear test (red star) observed at seismic stations MDJ and TJN. The scatter plots show the MDAC path corrected *P/S* ratios at each station (average when both available) for three different *P/S* ratios in four different frequency bands.**

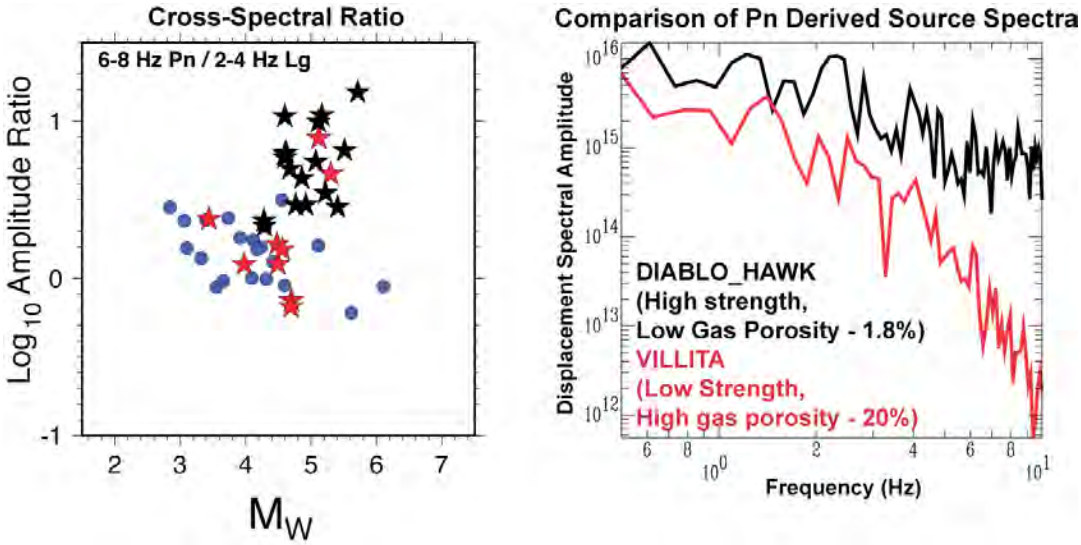


**Figure 4. Left: example cross-spectral ratio for NTS area data averaged for stations ELK and KNB. Right: NTS explosions show strong material property dependence of the P and S spectra. We separate the nuclear explosions into high-strength/low-gas-porosity (black) and low-strength/high-gas-porosity (red) populations, following the criteria in Walter et al. (1995) of $\log(\rho\alpha^2) = 0.093GP + 9.4$.**

In Figure 5, we show the same-frequency *P/S* ratios in different frequency bands for the ELK-KNB station averaged data color coded as in Figure 4 by media properties from Springer et al. (2002). At lower frequencies (0.5-4 Hz) there is some evidence that the material properties affect discrimination with the weak, high gas porosity events do not discriminate as well. At higher frequencies (6-16 Hz) there does not appear to be a significant difference though the dataset starts to get fairly small. Higher frequency *P/S* ratios (6 Hz and above) have become an important discriminant when they are available because of this apparent lack of material property dependence and good discrimination performance in all regions where good empirical data is available.

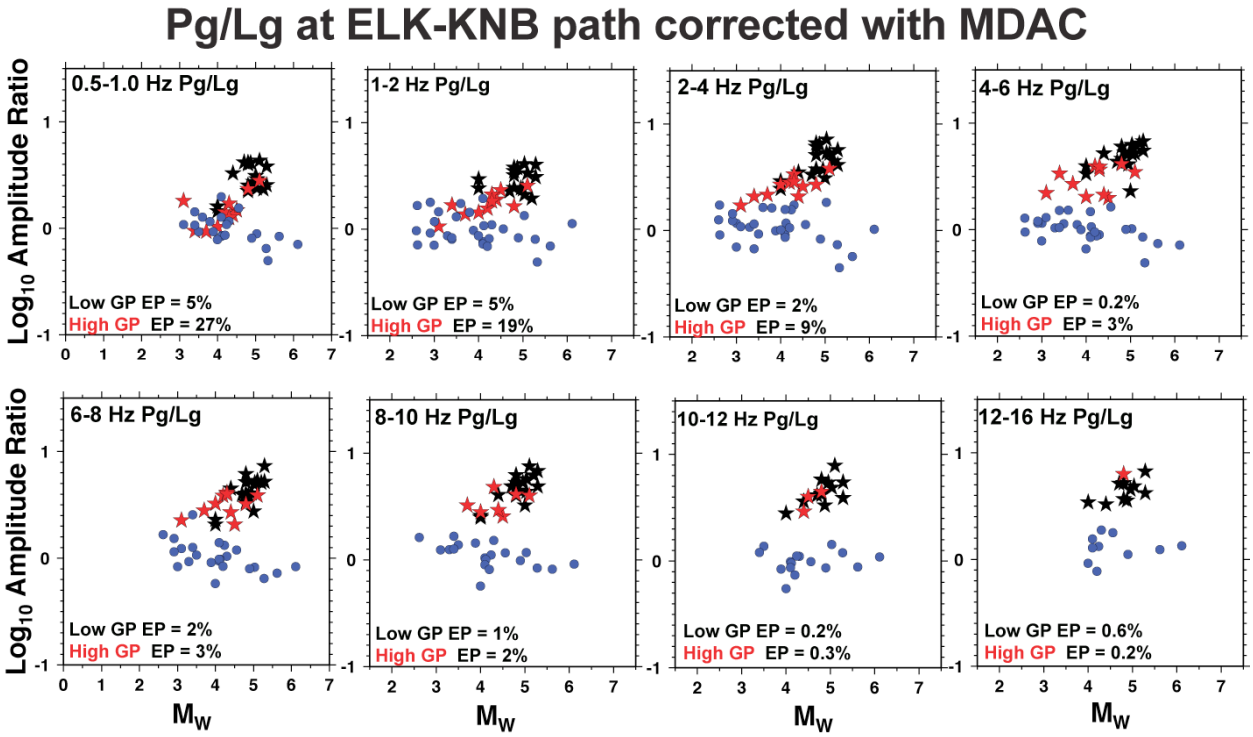


**Figure 5. Pg/Lg ratios for two-station (ELK-KNB), averaged, MDAC-corrected, NTS-region data. We separate the nuclear explosions into high-strength/low-gas-porosity (black) and low-strength/high-gas-porosity (red) populations, as in Figure 4. There is some evidence of a material property effect at low frequencies, but not at frequencies above 6 Hz. Note that discrimination performance in general continues to improve as frequency increases, at least to 12 Hz, but the number of events passing the SNR decreases significantly.**

### Are Long-Period Complexities Reflected in Short-Period Discriminants?

A remarkable feature of the high frequency *P/S* ratios for discriminating underground nuclear tests is that they seem to work about as well in cases where the long-period signals indicate that the explosions are complex as in cases where the long-period signals are very simple. For example, if we contrast the May 11, 1998, Indian test with the October 9, 2006, North Korean test, both show good high-frequency *P/S* discrimination in Figure 2. However, the Indian test shows significant Love waves and reversed Rayleigh waves (Walter et al, unpublished data; Selby et al., unpublished data), indicating a large amount of tectonic release and significant non-isotropic components of the moment tensor source. On the other hand, waveform modeling of the North Korean test shows almost no Love waves and a nearly pure isotropic moment tensor (e.g., Walter et al, 2007). Despite the complexities in the Indian test source, the S-waves disappear at frequencies of 1 Hz and higher, and the test easily discriminates from nearby earthquakes, as shown in Figure 2 and by Rogers and Walter (2002).

To better understand any connections between complexities in the long period signal and the high frequency discriminants, we are making use of the waveform modeling results of Ford et al., 2008 (see also Ford et al., these

Proceedings). For example, it has been proposed that the explosions can have a significant compensated linear vector dipole (CLVD) component as part of their interaction with the free surface and that this can impact surface wave magnitude and perhaps S-wave amplitudes as well (Patton and Taylor, 2008). In Figure 6, we compare Pg/Lg ratios in two frequency bands to the relative CLVD strength from waveform modeling. At the 1- Hz band there may be a correlation that is not apparent at the high frequencies. However, we are still assessing just how well resolved the relative CLVD components from the waveform model are before reaching any conclusions. We hope to have updated results to present at the meeting. Finally, we note that there is clear evidence from the coda that the absolute depth of burial has an affect on Rg excitation (e.g., Murphy et al., 2008), and to the extent the Rg scatters into Lg, which can be significant (Myers, personal communication), this also affects the 1–2 Hz Pg/Lg ratios.

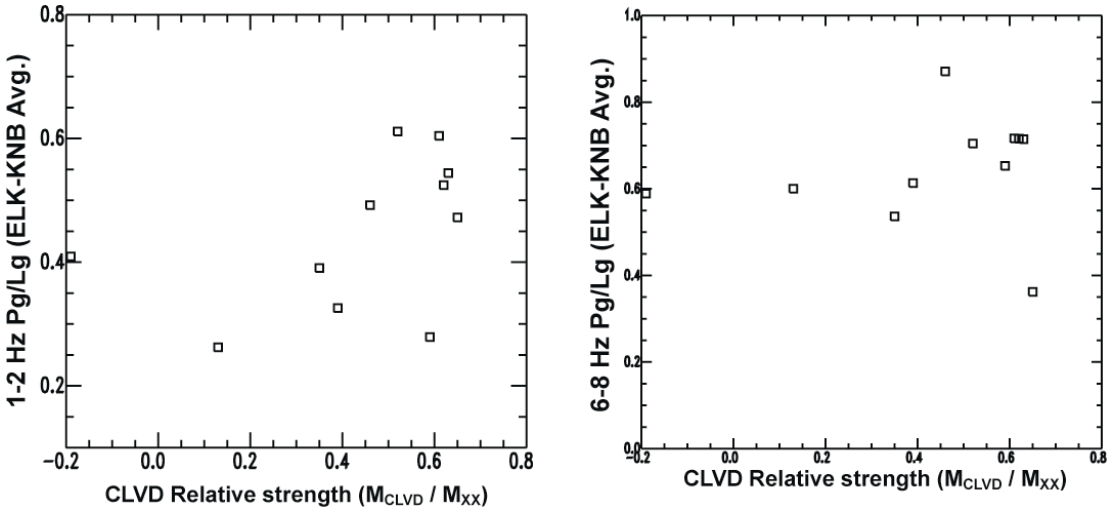


**Figure 6. We compare 1–2 Hz and 6–8 Hz Pg/Lg ratios for NTS explosions averaged from ELK and KNB to the relative CLVD strength determined from waveform modeling (Ford et al., 2008). Note there appears to be a correlation for low frequency (excepting METROPOLIS, which has a negative CLVD relative strength) but not for high frequency. Coda-derived spectra show a peak tied to absolute depth (Murphy et al., 2008), which appears related to Rg excitation and independent of scaled depth of burial (and spall/CLVD). Low-frequency Lg thus appears to be affected by both absolute depth Rg effects and relative depth spall/CLVD effects.**

**Amplitude Tomography**

In the MDAC corrections discussed so far, we have been using a single 1-D attenuation correction for a given station to a given region. However, it is well understood that in tectonically complex regions such as the Middle East, there can be very significant differences in the apparent attenuation of regional phase amplitudes over short distances. For example, Figure 7 shows a fairly dramatic example of large differences in the relative amplitude of 6-8 Hz Pn and Sn for two Zagros mountain events of about the same size and distance away. The top earthquake has the large Pn amplitude and weak Sn amplitude that we associate with explosions, particularly when compared with the other earthquake (e.g., Figure 1). To the extent these differences are due not to differences in source depth and mechanism but to propagation effects, we want to map them out and be able to correct for them. To do this, we are applying regional amplitude tomography techniques.

Crustal regional phase (Pg, Lg) amplitudes corrected for instrument and an assumed geometrical spreading (*A'*) can be written as a combination of source (S), path attenuation (R), and site (P) effects:

$$A'_{ij} = S_i * R_{ij} * P_j$$

Traditional amplitude tomographic techniques (e.g., Phillips and Stead, 2008) can then solve for each of these terms, with some tradeoffs between them. However, this results in source terms that can be significant. Given a new

event in a calibrated region, we want to be able to apply the tomographically derived apparent attenuation and get a predicted amplitude to use as a correction before forming a discriminant. What source term is associated with the new event? One way to make the source term more amenable for amplitude correction is to formulate it in terms of the MDAC (Walter and Taylor, 2001) modified Brune (1970) source term:

$$S_i = \frac{FM_o}{1+\frac{\omega^2}{\omega_c^2}} \quad where \quad \omega_c = \left(\frac{K\sigma}{M_o}\right)^{1/3}$$

where $F$ and $K$ are constants that depend on velocity, density, and average radiation patterns (see Walter and Taylor, 2001, for details), and where $\sigma$ is the apparent stress in the region. In this case, the source term in the tomography can be reformulated to solve for the change in moment from the assumed initial moment, where the initial moment comes from a calibrated coda moment technique (e.g., Mayeda et al., 2003) or other technique (e.g., waveform modeling). In this case, for a new event, the moment is first determined and then a 2D attenuation MDAC correction applied to get the predicted amplitude for an earthquake of that Mw and location, much as we have been using the 1D path correction in the MDAC methodology.

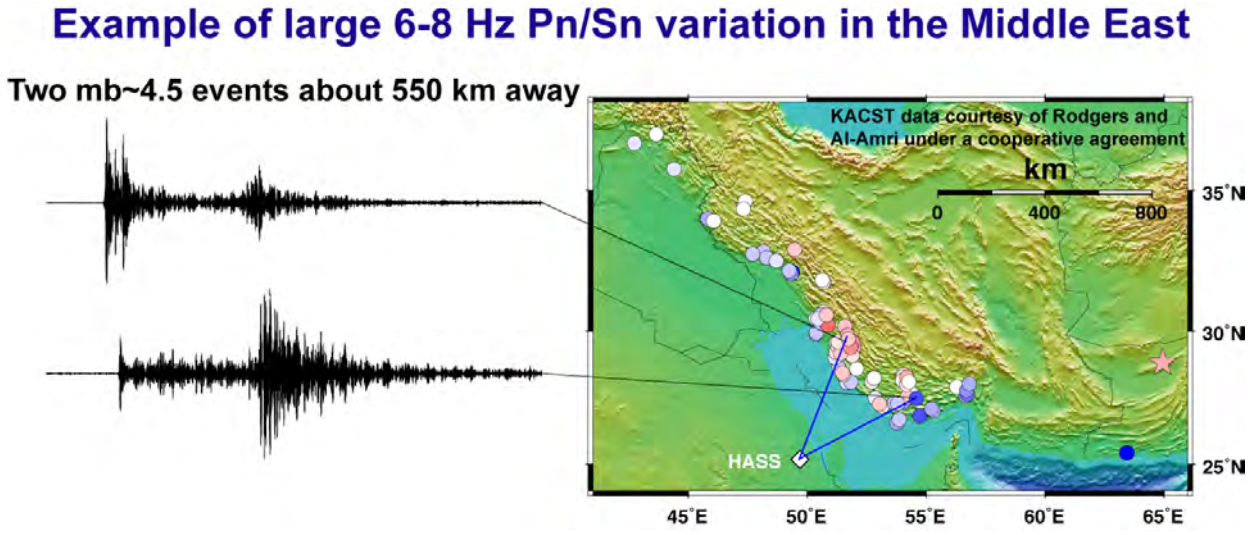


**Figure 7. An example of large *P/S* ratio differences for two events of similar size and distance that appear to be due to complex path effects. Top event looks explosion-like relative to the bottom event. We are exploring amplitude tomographic techniques to account for and correct 2-D path effects on regional amplitudes used in discriminants.**

Finally, if a good estimate of the source spectrum is available independently, through a coda technique or some other way, it is straightforward to use that for the source term directly and just solve for the path and site terms (e.g., Walter et al., 2007b). We are in the process of applying and testing these three variations of amplitude tomography in the Yellow Sea Korean Peninsula region (see Ford et al., these Proceedings) and in the Middle East. We plan to show some initial results at the meeting.

## CONCLUSIONS AND RECOMMENDATIONS

Regional discrimination algorithms require calibration at each seismic station to be used for nuclear explosion monitoring. We apply MDAC procedures to remove source size and path effects from regional body-wave phases. This allows comparison of any new regional events recorded at a calibrated station with all available reference data and models. This also facilitates the combination of individual measures at multiple stations to form multivariate discriminants that can significantly improve performance over single-station individual measures. We are working to quantify the performance of *P/S* ratio discriminants as a function of a number of factors, including frequency, phase type, source media properties, long-period moment tensor, and 2-D apparent attenuation patterns.

## ACKNOWLEDGEMENTS

We thank Stan Ruppert and Terri Hauk for loading and maintaining the Lawrence Livermore National Laboratory (LLNL) database. We thank Doug Dodge and Mike Ganzberger for developing and maintaining the LLNL software code RBAP, which was used to make the regional measurements. Regional phase-amplitude measurements were made using picks by the authors, as well as by former summer students Veronica Parker and Lindsay Lowe and by our expert analyst Ms. Flori Ryall.

## REFERENCES

Battone, S., M. D. Fisk, and G. D. McCarter (2002), Regional Seismic-Event Characterization Using a Bayesian Formulation of Simple Kriging, *Bull. Seism. Soc. Am.* 92: 2277–2296.

Baumgardt, D. R. and G. B. Young (1990). Regional seismic waveform discriminants and case-based identification using regional arrays, *Bull. Seism. Soc. Am.* 80: 1874–1892.

Brune, J. (1970). Tectonic stress and the spectra from seismic shear waves earthquakes, *J. Geophys. Res*. 75: 4997–5009.

Dysart, P. S. and J. J. Pulli (1987). Spectral study of regional earthquakes and chemical explosions recorded at the NORES array. SAIC technical report C87-03.

Ford, S. R., D.S. Dreger, and W. R. Walter (2008). Identifying isotropic events using a regional moment tensor inversion, submitted to *J. Geophys. Res.*

Hartse, H., S. R. Taylor, W. S. Phillips, and G. E. Randall (1997). A preliminary study of regional seismic discrimination in Central Asia with an emphasis on Western China, *Bull. Seism. Soc. Am*. 87: 551–568.

Kim, W. –Y., D. W. Simpson, and P. G. Richards (1993). Discrimination of earthquakes and explosions in the eastern United States using regional high frequency data, *Geophys. Res. Lett.* 20: 1507–1510.

Mayeda, K., A. Hofstetter, J. O'Boyle and W. R. Walter (2003). Stable and Transportable Regional magnitudes based on coda derived moment-rate spectra, *Bull. Seism. Soc. Am*. 93: 224–239.

Murphy, K. R., K. Mayeda, and W. R. Walter (2008). Lg-coda methods applied to Nevada Test Site events: spectral peaking and yield estimation, submitted to *Bull. Seism. Soc. Am.*

Patton, H. J. and S. R. Taylor (2008). Effects of induced tensile failure on mb-Ms discrimination: contrasts between historic nuclear explosions and the North Korean test of 9 October 2006., *Geophys. Res. Lett.*, in press.

Phillips, W. S. and R. J. Stead (2008). Attenuation of Lg in the western U.S. using the USArray, *Geophys. Res. Lett.* 35: L07307, doi:10.1029/2007GL032926.

Rodgers, A. J. and W. R. Walter, (2002). Seismic Discrimination of the May 11, 1998 Indian Nuclear Test with Short-Period Regional Data From Station NIL (Nilore, Pakistan), *Pure Appl. Geophys.* 159: 679–700.

Springer, D. L., G. A. Pawlowski, J. L. Ricca, R. F. Rohrer, and D. K. Smith (2002). Seismic source summary for all U.S. below-surface nuclear explosions, *Bull. Seism. Soc. Am.* 92, 1806–1840.

Taylor, S., (1996). Analysis of high-frequency Pg/Lg ratios from NTS explosions and Western U.S. earthquakes, *Bull. Seism. Soc. Am.* 86: 1042–1053.

Taylor, S., A. Velasco, H. Hartse, W. S. Philips, W. R. Walter, and A. Rodgers, (2002). Amplitude corrections for regional discrimination, *Pure. App. Geophys*. 159: 623–650.

Walter, W. R., K. Mayeda, and H. J. Patton (1995). Phase and spectral ratio discrimination between NTS earthquakes and explosions Part 1: Empirical observations, *Bull. Seism. Soc. Am.*, 85: 1050–1067.

Walter, W. R. and S. R. Taylor (2001). A revised Magnitude and Distance Amplitude Correction (MDAC2) procedure for regional seismic discriminants, Lawrence Livermore National Laboratory UCRL-ID-146882: http://www.llnl.gov/tid/lof/documents/pdf/240563.pdf

Walter, W. R., E. Matzel, M. E. Pasyanos, D. B. Harris, R. Gok and S. R. Ford (2007a), Empirical observations of earthquake and explosion discrimination using *P/S* ratios and implications for the sources of explosion S-waves, in Proceedings of the 29th Monitoring Research Review: Ground-Based Nuclear Explosion Monitoring, LA-UR-07-5613, Vol. 1, pp. 684–693.

Walter, W. R., K. Mayeda, L. Malagnini, and L. Scognamiglio (2007b). Regional body-wave attenuation using a coda source normalization method: application to MEDNET records of earthquakes in Italy, *Geophys. Res. Lett.* 34: L10308, doi:10.1029/2007GL029990.

# MRR 2008

## Proceedings of the 30th Monitoring Research Review: Ground-Based Nuclear Explosion Monitoring Technologies

## September 23–25, 2008

## Portsmouth, Virginia

## Volume II

Hydroacoustic Monitoring
Radionuclide Monitoring
Infrasound Monitoring
Data Processing and Analysis

Approved for Public Release; further dissemination unlimited.

National Nuclear Security Administration

AIR FORCE RESEARCH LABORATORY

LA-UR-08-05261

2008

MRR 2008 Proceedings of the 30th Monitoring Research Review: Ground-Based Nuclear Explosion Monitoring Technologies

To view these Proceedings online, visit
https://na22.nnsa.doe.gov/gnem/mrr2008.

Vol. II

## Previous Proceedings

| Year | Title of the Proceedings |
|---|---|
| 2007 | Proceedings of the 29th Monitoring Research Review: Ground-Based Nuclear Explosion Monitoring Technologies |
| 2006 | Proceedings of the 28th Seismic Research Review: Ground-Based Nuclear Explosion Monitoring Technologies |
| 2005 | Proceedings of the 27th Seismic Research Review: Ground-Based Nuclear Explosion Monitoring Technologies |
| 2004 | Proceedings of the 26th Seismic Research Review - Trends in Nuclear Explosion Monitoring |
| 2003 | Proceedings of the 25th Seismic Research Review - Nuclear Explosion Monitoring: Building the Knowledge Base |
| 2002 | Proceedings of the 24th Seismic Research Review - Nuclear Explosion Monitoring: Innovation and Integration |
| 2001 | Proceedings of the 23rd Seismic Research Review: Worldwide Monitoring of Nuclear Explosions |
| 2000 | Proceedings of the 22nd Annual DoD/DOE Seismic Research Symposium: Planning for Verification of and Compliance with the Comprehensive Nuclear-Test-Ban Treaty (CTBT) |
| 1999 | Proceedings of the 21st Seismic Research Symposium: Technologies for Monitoring the Comprehensive Nuclear-Test-Ban Treaty |

# Table of Contents - Volume II


## 4. Hydroacoustic Monitoring 713

4-01 **de Groot-Hedlin, C., D. Blackman, and C. Jenkins**
*Effects of Variability Associated with the Antarctic Circumpolar Current on Sound Propagation in the Ocean* 715

4-02 **Matsumoto, H., D. Bohnenstiehl, R. Dziak, R. Embley, and M. Park**
*Deployment of Autonomous Hydrophone Array in the Scotia Sea* 725

## 5. Radionuclide Monitoring 731

5-01 **Cooper, M., T. Bowyer, J. Hayes, T. Heimbigner, C. Hubbard, J. McIntyre, and B. Schrom**
*Spectral Analysis of Radioxenon* 733

5-02 **Farsoni, A., D. Hamby, C. Lee, and A. Elliott**
*Preliminary Experiments with a Triple-Layer Phoswich Detector for Radioxenon Detection* 739

5-03 **Haas, D., S. Biegalski, and K. Biegalski**
*Production of Samples of Individual Radioxenon Isotopes Through Neutron Irradiation of Stable Xenon Gas* 749

5-04 **Hennig, W., H. Tan, W. Warburton, A. Fallu-Labruyere, K. Sabourov, M. Cooper, J. McIntyre, and A. Gleyzer**
*Development of a COTS Radioxenon Detector System Using Phoswich Detectors and Pulse Shape Analysis* 758

5-05 **Hull, E., R. Pehl, J. Lathrop, P. Mann, R. Mashburn, B. Suttle, H. Miley, C. Aalseth, and T. Hossbach**
*P-Type Point Contact Germanium Detectors for Low-Level Counting* 768

5-06 **Hull, E., R. Pehl, J. Lathrop, P. Mann, R. Mashburn, B. Suttle, H. Miley, C. Aalseth, T. Bowyer, T. Hossbach, G. Rybicki, and J. Bucholtz**
*Mechanically Cooled Large-Volume Germanium Detector Systems for Nuclear Explosion Monitoring* 772

5-07 **Keillor, M., C. Aalseth, A. Day, J. Fast, E. Hoppe, B. Hyronimus, T. Hossbach, H. Miley, A. Seifert, and G. Warren**
*Design and Construction of an Ultra-Low-Background 14 Germanium Crystal Array for High Efficiency and Coincidence Measurements* 778

5-08 **Martin, G., K. Yocum, J. Colaresi, and H. Miley**
*Improving Germanium Detector Resolution and Reliability* 787

5-09 **McIntyre, J., S. Pratt, T. Bowyer, M. Cooper, J. Hayes, T. Heimbigner, C. Hubbard, H. Miley, and M. Ripplinger**
*Generation of Radioxenon Isotopes* 793

5-10 **Momayezi, M., B. Hurst, C. Wong, T. Heimbigner, M. Cooper, C. Hubbard, and J. McIntyre**
*Programmable Front-End Data Acquisition Module for Radio-Xenon Monitors* 802

5-11 **Wotawa, G. and A. Becker**
*The CTBTO/WMO Atmospheric Backtracking Response System and the Data Fusion Exercise 2007* 810

5-12 **Yocum, K., G. Martin, J. Colaresi, and H. Miley**
*Improvement in Ge Detector Cooling* 824

**6. Infrasound Monitoring** 835

6-01 **Arrowsmith, S. and R. Whitaker**
*InfraMonitor: A Tool for Regional Infrasound Monitoring* 837

6-02 **Arrowsmith, S., C. Hayward, B. Stump, R. Burlacu, I. Che, and G. Singh**
*Multi-Array Detection, Association and Location of Infrasound and Seismo-Acoustic Events in Utah* 844

6-03 **Brown, D., N. Brachet, and R. Le Bras**
*Enhancements to the CTBTO Operational Automatic Infrasound Processing System* 853

6-04 **de Groot-Hedlin, C.**
*Finite Difference Time Domain Modeling of Infrasound Propagation: Application to Shadow Zone Arrivals and Regional Propagation* 862

6-05 **Gibson, R., D. Norris, and D. Drob**
*Investigation of the Effects of Fine-Scale Atmospheric Inhomogeneities on Infrasound Propagation* 872

6-06 **Gitterman, Y. and A. Hofstetter**
*Infrasound Calibration Experiment in Israel: Preparation and Test Shots* 882

6-07 **Herrin, E., P. Golden, P. Negraru, M. McKenna, and R. Whitaker**
*Infrasound in the "Zone of Silence"* 894

6-08 **Walker, K., M. Dzieciuch, M. Zumberge, and S. DeWolf**
*A Portable Infrasonic Sensor Calibrator Down to at Least 8 HZ* 902

6-09 **Whitaker, R.**
*Infrasound Signals from Ground-Motion Sources* 912

**7. Data Processing and Analysis** 921

7-01 **Bahavar, M., B. Barker, T. Bennett, H. Israelsson, B. Kohl, Y. Kung, J. Murphy, and V. Oancea**
*Nuclear Explosion and Infrasound Event Resources of the SMDC Monitoring Research Program* 923

7-02 **Given, J., R. Le Bras, and Y. Kung**
*Determination of the Seismic Moment Tensor Using Surface Waves Recorded by the IMS Network* 932

7-03 **Hart, D., B. Merchant, and J. Harris**
*Progress on Component Evaluation for Nuclear Explosion Monitoring* 939

7-04 **Kim, W., H. Patton, G. Randall, and P. Richards**
*Improvements to a Major Digital Archive of Seismic Waveforms from Nuclear Explosions: Borovoye Seismogram Archive* 949

7-05 **Lewis, J., S. Ballard, C. Young, D. Carr, A. Gonzales, and B. Merchant**
*Merging Event Catalogs Using Agglomerative Hierarchical Clustering* 959

7-06 **Ringdal, F., T. Kvaerna, S. Mykkeltveit, S. Gibbons, and J. Schweitzer**
*Basic Research on Seismic and Infrasonic Monitoring of the European Arctic* 968

7-07 **Ruppert, S., D. Dodge, M. Ganzberger, T. Hauk, and E. Matzel**
*Enhancing Seismic Calibration Research Through Software Automation and Scientific Information Management* 978

**Appendices** 989

Acronyms, etc. 991

Guide to Seismic Phases 995

# Hydroacoustic Monitoring

# EFFECTS OF VARIABILITY ASSOCIATED WITH THE ANTARCTIC CIRCUMPOLAR CURRENT ON SOUND PROPAGATION IN THE OCEAN

Catherine de Groot-Hedlin[1], Donna K. Blackman[1], and C. Scott Jenkins[2]

Scripps Institution of Oceanography, University of California at San Diego[1],
Naval Surface Warfare Center, Indian Head Division[2]

Sponsored by Army Space and Missile Defense Command

Contract No. W9113M-05-1-0019

## ABSTRACT

A series of small depth charges was detonated along a transect from New Zealand to Antarctica over a period of three days in late December of 2006. Signals were recorded by hydrophones deployed near the source, and at a sparse network of permanent hydrophone stations operated by the International Monitoring System (IMS), at distances up to 9,600 km. Our purpose was to determine how well signal characteristics could be predicted by the World Ocean Atlas 2005 (WOA05) climatological database for sources within the Antarctic Circumpolar Current (ACC). Where recorded signal to noise ratios are high, travel times and signal dispersion are predicted to within two seconds under the assumption that propagation is adiabatic and follows a geodesic path. The deflection of the transmission path by abrupt spatial variations in sound speed at the northern ACC boundary is predicted to decrease travel times to the IMS stations by several seconds, depending on the path. The accuracy of source locations estimates based only on travel times depends on the monthly or seasonal database used to predict velocities and on whether we account for path deflection. The configuration of the IMS hydrophones limits source location accuracy within the ACC. Comparison of signal spectra for recordings near the source and at distance show that transmission loss is nearly uniform as a function of frequency.

## OBJECTIVES

Our objectives were to conduct a series of calibration shots within and to the south of the ACC that would generate acoustic signals at frequencies f > 30 Hz and to analyze the signals recorded at hydrophone stations operated by the IMS. The overall goal was to compare observed source-receiver travel times to the IMS hydrophone stations to those predicted by numerical models for paths crossing the Antarctic convergence zone and to use these results to determine the accuracy to which sources may be located within the ACC. A second goal was to compare observed vs. modeled transmission losses. The results of the second goal were reported last year; it was found that transmission loss is nearly uniform as a function of frequency for the shots examined in this study (de Groot-Hedlin et al., 2007; de Groot-Hedlin et al., 2008).

Acoustic propagation for sources within the ACC is complicated by the sharp temperature gradient at the northern boundary. The ACC boundary separates cold waters that flow eastward around Antarctica from warmer subtropical waters to the north. The abrupt spatial variation in temperature and salinity results in strong gradients in the speed of acoustic waves through the ocean, which in turn deflects the path of propagating acoustic waves near the northern boundary of the ACC (Heaney et al., 1999). Furthermore, south of the ACC boundary, the low-velocity oceanic "sound channel" axis, that is typically 100's to 1,000-m-deep shoals and the overlying higher velocity layer thins to nothing over a short distance, resulting in sea surface-limited propagation. Therefore, the detailed structure of the ACC boundary is strongly affected by seasonal temperature variations that extend to depths of over 1 km. Dushaw et al., (1999) showed that this type of seasonal variability produces considerable seasonal differences in acoustic travel times for paths through the North Pacific.

We conducted an experiment in December, 2006, to determine how well acoustic wave travel times and signal dispersion are predicted by models derived from the World Ocean Atlas 2005 (WOA05) global ocean climatology database. A series of small explosive sources provided acoustic signals along a single transect between New Zealand and Antarctica. The hydrophone stations are operated by the IMS that recorded the signals, allowing a comparison between observed and predicted signals. The recordings of the detonations provide ground-truth data, allowing us to compare the effect of lateral refraction on travel times and arrival estimates with predictions, and to estimate the effect of surface-limited propagation on source spectra. Thus, we may evaluate the accuracy of location estimates both for sources within the ACC and signals with propagation paths crossing the ACC.

The results reported here are initial steps in characterizing the effects of high temperature and salinity gradients near the ACC on acoustic propagation. Since our experiment was carried out over a time span of just a few days, we are not able to compare predictions with observations of a seasonal cycle, much less several seasons. However, these initial observations allow the scale of the differences between predictions and the data to be assessed, and we find that they are not negligible. In addition to specific comparisons based on the initial dataset, we assess the range in variability in signal characteristics that are predicted throughout the year, based on the long-term monthly/seasonal averages. Again, the predictions indicate that seasonal acoustic variability (travel-time, signal duration, coda shape) should be significant enough to be detectable and to affect determinations of source location.

## RESEARCH ACCOMPLISHED

*Signals Underwater Sound (SUS) Depth Charges*

Our experiment was conducted during the first part of a research cruise whose main effort was a separate study to be conducted in the northwest Ross Sea. The ship departed Lyttleton, New Zealand, and eventually arrived at McMurdo station in Antarctica. Over a period of three days during the first week of the cruise, explosive charges were detonated at six deployment sites. Water depths at the sites ranged from about 800 m to over 4 km. We used 1.8 kg SUS charges (M 59 mod1a) due to their ease of deployment in rough seas, which are common along the Southern Ocean crossing, and because SUS charges generate a high-energy signal over a broad frequency range. The sources were pre-set to detonate at depths of 305 m, 460 m, or 610 m.

Explosive charges were hand-dropped at each deployment site, starting from the shallowest detonation settings and working to the deepest. The ship speed slowed to approximately 1–2 knots during each set of deployments, which lasted from 20–30 minutes. A hydrophone was hand-deployed from the ship's deck to obtain a near-source (hundreds of meters) recording of the signal. Charge depths were confirmed using a semi-empirical equation relating the depth of the charge to the bubble pulse period for an underwater explosion far from either the free surface or the

sea floor. Several larger shots, using a combination of two or three 1.8-kg charges were tested at the last two deployment sites in an attempt to improve detections at the more distant stations and to vary the spectral content of the signal. Shot deployment sites were listed in Table 1 of de Groot-Hedlin et al., (2007); the geodesic paths from each site to the IMS hydrophones are shown in Figure 1.

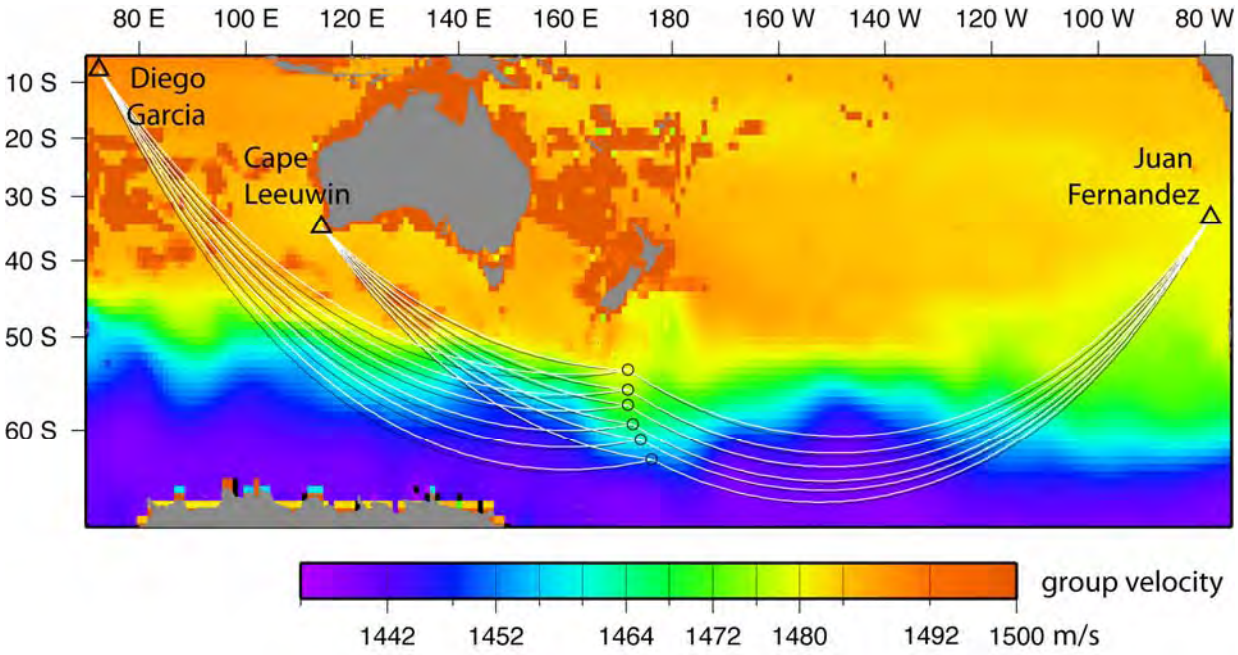


**Figure 1. Map showing shot locations (circles) and IMS hydrophone station locations (triangles), superimposed on a map of group velocities derived using average fall sound speed profiles for mode 1 at a frequency of 50 Hz. Geodesic paths (black) and laterally deflected sound paths (white) corresponding to minimum travel-time paths are shown from each shot to each IMS hydrophone.**

*Near-Source Hydrophone*

The near-source hydrophone deployed from the ship recorded the pressure signal of the explosive shots at a rate of 1,000 samples/s. A GPS time sync from the ship's navigation system was fed into the data logger to provide accurate timing. The depth of the near-source hydrophone depth was consistently shallow—from 4 to 6 m—due to the ship's forward motion and the relatively small 4-kg weight used to sink the hydrophone. As a result, signals measured at the hydrophone have two main propagation paths: the direct path and an amplitude-reversed echo from the water surface. Seafloor reverberations were recorded only at the first deployment site where water depths were shallowest *(about 810 m*); they were not evident in unfiltered data at the other stations, where seafloor depths ranged from 3,800–5,400 m. The surface reflection has a small time delay *dt* with respect to the direct path due to its slightly greater path length. The patterns of constructive and destructive interference caused by surface reflection had to be removed from the near-source spectra in order to compare signal spectra with those measured at the IMS hydrophone stations. The method for removing the effects of the surface echo from the source spectra is outlined in detail in de Groot-Hedlin et al., (2008). Here, we simply note that deconvolution adds a measure of uncertainly to the source spectrum estimates. We estimate an uncertainty of about 3 dB in the source spectrum estimates.

*Detections and Transmission Losses*

The shot locations provided several unblocked paths to arrays at three IMS stations: H01, located near Cape Leeuwin off the southwest coast of Australia, H08 near Diego Garcia island in the Indian Ocean, and H03 near Juan Fernandez island in the Pacific Ocean west of Chile. Background noise levels at each of the hydrophone stations did not vary significantly over the duration of the study. As illustrated in Figure 1, the Cape Leeuwin station (H01) was situated nearest the test shots, at a distance of approximately 5,000 km, as compared to approximately 8,000 km to H03N near Juan Fernandez and 9,600 km to H08S near Diego Garcia. The transmission paths are not entirely free of topographic blockages; for most paths, there is a ridge or plateau that projects at least partway into the sound channel and strips off the highest-order modes. All shots were recorded at H01 with the exception of the second set

of shots at site A2. Apparently, acoustic energy was scattered by shallow features along the Macquarie Ridge that are not resolved in the current global bathymetric database.

Only the first set of shots at site A1, near 53.8°N, 171.7°E, was clearly discernible at station H03N north of Juan Fernandez Island. Recordings of the shots at the remaining sites are difficult to distinguish from background noise levels. The receiver to source back-azimuth varies slightly as the shot locations progressed from north to south. This is sufficient to put H03N into an acoustic shadow zone created by Juan Fernandez Island for the shots at sites A2 through A6. Unfortunately, the southern triplet of the Juan Fernandez station was not in operation during our experiment. Signals were observed at station H08S, south of Diego Garcia for sites A2 through A6. The lack of arrivals for shots at site A1 is likely due to the longer transit over the shallow water depths of the Campbell Plateau south of New Zealand. The Chagos Archipelago blocked acoustic transmission to the northern triplet at Diego Garcia. Another IMS hydrophone station near Crozet Island was also not operational during the experiment, but it was almost certainly blocked by the Kerguelen Plateau anyway. Transmission losses were found to be fairly uniform over the 30-100 Hz band for propagation paths used in this experiment (de Groot-Hedlin et al., 2007).

*Comparison of Observed and Predicted Travel Times*

In this section we examine the effects of the temporal and spatial variability of sound speeds along propagation paths crossing the northern boundary of the ACC on predicted arrival times, and compare these with observations. Hydroacoustic phases are often represented as a suite of acoustic modes, which are derived from the Helmholtz equation that governs acoustic propagation at a given frequency. Each mode has a local velocity defined by the sound speed profile. In deep water with a well-defined sound speed minimum, low-order modes are associated with rays that propagate at shallow angles near the sound channel axis, and higher-order modes are linked to steeper rays that sample a greater vertical extent of the ocean. A common simplifying assumption is that propagation is adiabatic, that is, each mode propagates independently of the others, with a velocity and amplitude that varies slowly within the nearly range-independent waveguide. This assumption holds in a range-independent medium where the lower order modes are typically the highest amplitude arrivals at the end of the acoustic coda. However, in a more realistic environment, significant coupling of energy between modes occurs due to internal waves (Wage et al., 2005) or propagation through a polar front (Shang and Wang, 1999), resulting in the temporal spreading of acoustic arrivals.

Ocean sound speed profiles are derived from the World Ocean Atlas 2005 database, which gives salinity (Antonov et al., 2006) and temperature (Locarnini et al., 2006) values as a function of depth on a 1° grid. Sea floor depths are derived from ETOPO1, a global 1-minute gridded database of bathymetry and topography; the bathymetry is derived from satellite altimetry and ship depth soundings as described in Smith and Sandwell (1997). Sediment thicknesses are from Mooney et al., (1998). Sediment velocities are assigned a value of 1,550m/s at the seafloor, increasing by 1m/s per meter depth, in line with sea floor sediment velocity estimates from (Hamilton, 1980). The basement structure was assigned a velocity of 2,600 m/s.

Sound speeds along a path from site A3 to H01 are shown in Figure 2a for average October–December season profiles. Path variations in ocean temperatures, and hence sound speeds, are greatest above the sound channel axis. Ocean sound speed profiles along this path can be classified into three types. A polar channel exists to a range of approximately 2,500 km. Within this section, sound speeds reach a minimum near the surface; therefore, acoustic energy is surface limited—trapped between the surface and sound-speed gradients at depth. Propagation paths from the calibration shots to H01 cross the polar front at the northern boundary of the ACC near 50°S. A double channel extends from a range of about 2,500 km to 4,000 km; acoustic energy may become trapped within the surface duct within this region. The final segment consists of a single duct with a well-defined Sound Fixing and Ranging (SOFAR) channel.

Group velocities are shown in Figure 2b for several modes along this path for a 50-Hz source—where signal-to-noise ratio (SNR) is high. Because low-order modes propagate at depths near the sound speed minimum, the contrast in velocity is greatest across the ACC. A large contrast in sound speeds across the ACC boundary is linked with greater horizontal refraction there. Because higher order modes typically sample a greater vertical extent, they undergo greater interaction with the seafloor, and thus greater attenuation. Group velocities for high order, bottom-interacting modes are more poorly constrained than for low-order modes because sea-floor velocities are known only approximately.

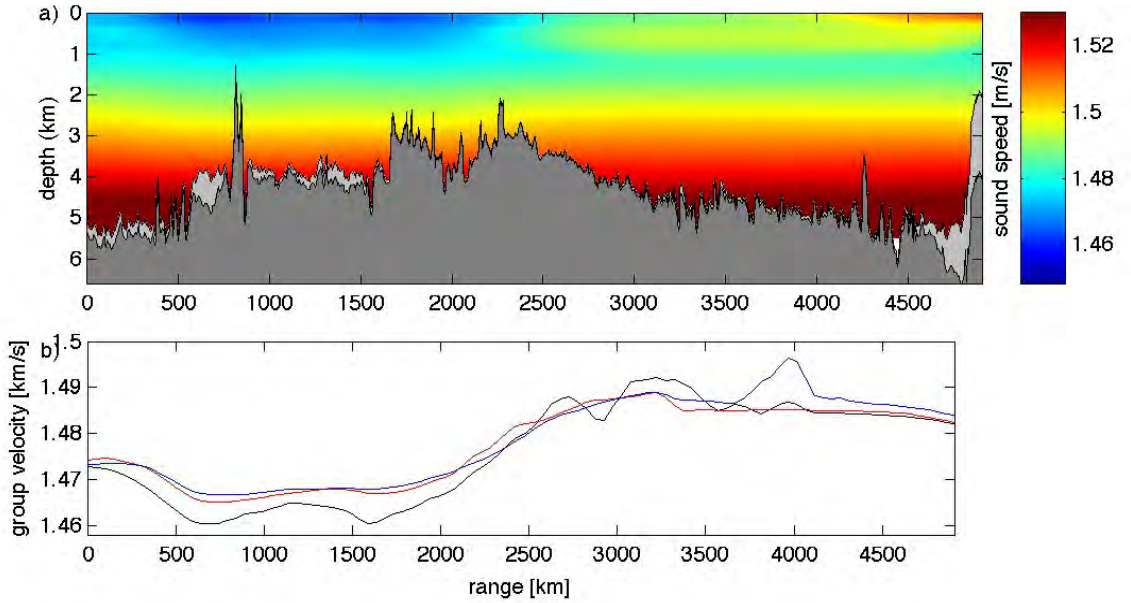


**Figure 2. a) Average fall (October-December) sound speed profile along the geodesic path from the first shot at site A3 to the hydrophone triplet at H01. Sound speeds are derived from the WOA05 database; bathymetry is from Smith and Sandwell (1997). Sediments, indicated in light gray, are underlain by a basement structure, shown in dark gray. b) Group velocities along the path for a 50-Hz source are shown for mode 1 (black), mode 4 (red), and mode 8 (blue).**

Figure 3 illustrates variations in the first 10 modes for a 50-Hz source at points along the propagation path near the source, within the double sound channel, and in the SOFAR channel. A comparison of mode shapes within the polar channel with those along the remainder of the path indicates that propagation of these acoustic modes is confined much closer to the surface within the ACC and are thus less subject to mode-stripping by bathymetric features. Modal degeneration occurs where adjacent modes have identical wave numbers. This occurs where modes become trapped in the upper duct of a double-channel feature and result in travel-time miscalculation (Shang and Wang, 1999), if the modes are assumed to be adiabatic. As shown in Figure 2b, the double-channel feature is associated with a significant variation in group velocity, particularly for higher-order modes. Seafloor depths near H01 are on the order of 1.6 km; thus, higher order modes interact with the seafloor at a frequency of 50 Hz for propagation near the IMS receiver.

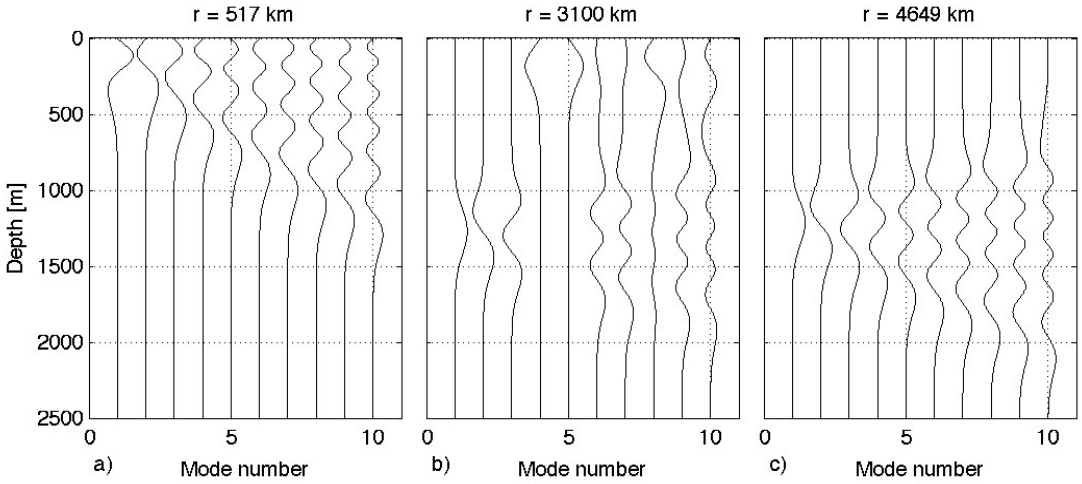


**Figure 3. Mode shapes at 50 Hz at several distances along the receiver path for the environmental model shown in Figure 2a. Mode shapes for a) the polar channel near the source, b) within the double sound channel, and c) within the SOFAR channel. All modes were computed for deep water profiles, with seafloor depths greater than 4,000 km.**

Travel times to a distant receiver are often computed under the assumptions that there is no significant lateral deflection of the travel path (e.g., Chapp et al., 2005), and that propagation is adiabatic, as discussed earlier. In this case, travel times may be computed by integrating the group velocities for a given mode along a geodesic path. The variation in the travel times for each mode gives an estimate of the duration of the arrival. The amplitude at the receiver at a given frequency is given by the formula in Jensen et al., (1994). The attenuation for each mode is given by the fraction of that mode's intensity within the attenuation seafloor, as in Heaney et al., (1991). Figure 4a shows predicted arrivals for the first 25 normal modes for adiabatic propagation from a 50-Hz source at a 300-m depth at site A3 to the first hydrophone within the H01 triplet. The environmental model and modal group velocities were illustrated in Figure 2a. Amplitudes are scaled with respect to the largest modal amplitude, mode 1 in this case. If propagation was adiabatic, the figure indicates that the recorded wavetrain would consist of a series of discrete pulses with mode 1 arriving last and having the largest amplitude.

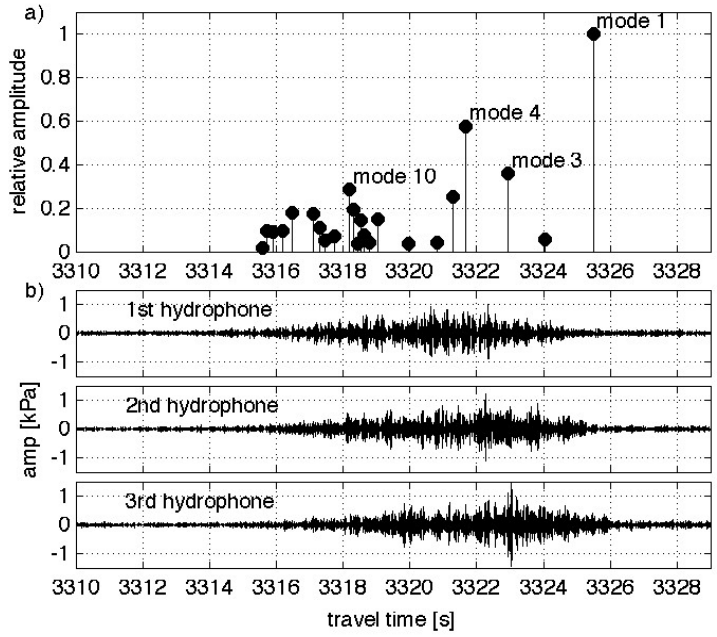


**Figure 4**. **a) Synthetic wavetrain (relative magnitudes are true; mode 1 is set to have an amplitude of 1 here) for adiabatic propagation from a 50-Hz source at a 300-m depth for the October-December average environmental model shown in Figure 2a, computed for the first hydrophone within the triplet at H01. The four highest amplitude modes are labeled. Mode amplitudes are normalized with respect to mode 1. b) Pressure (in kPa) recorded at each hydrophone within the array at H01 for a charge detonated at a300-m depth at site A3.**

For comparison, Figure 4b shows the wavetrains recorded on each hydrophone at H01 for the first charge at site A3, bandpassed from 45–55 Hz. The coda have a duration of less than 10 s, have a maximum amplitude near the center of the wavetrain, and end nearly a second early compared with the predicted maximum amplitude arrival associated with the first mode. The source had a duration of approximately 0.1 s as observed on the near-source hydrophone; therefore the lack of impulsive arrivals cannot be attributed to the source duration. Rather, the phase duration is attributable to mode dispersion; mode velocity increases with the increasing mode number, with an average group velocity of 1,480.2 m/s for the 25$^{th}$ mode, and 1,475.9 m/s for the first mode. The phase shape does not correspond to an energetic late arrival or discrete arrivals corresponding to individual modes as predicted by adiabatic mode theory, implying that significant mode coupling takes place along the propagation path. This suggests that picking acoustic arrival times based on the peak amplitude mode, as in Hanson et al., (2001), would lead to errors in source location as this choice relies on the adiabatic mode approximation. Although Figure 4 illustrates that the shape of the arrival is not correctly predicted by the adiabatic mode interpretation, the arrival onset and total duration of the arrival are predicted to an accuracy of approximately 2 s.

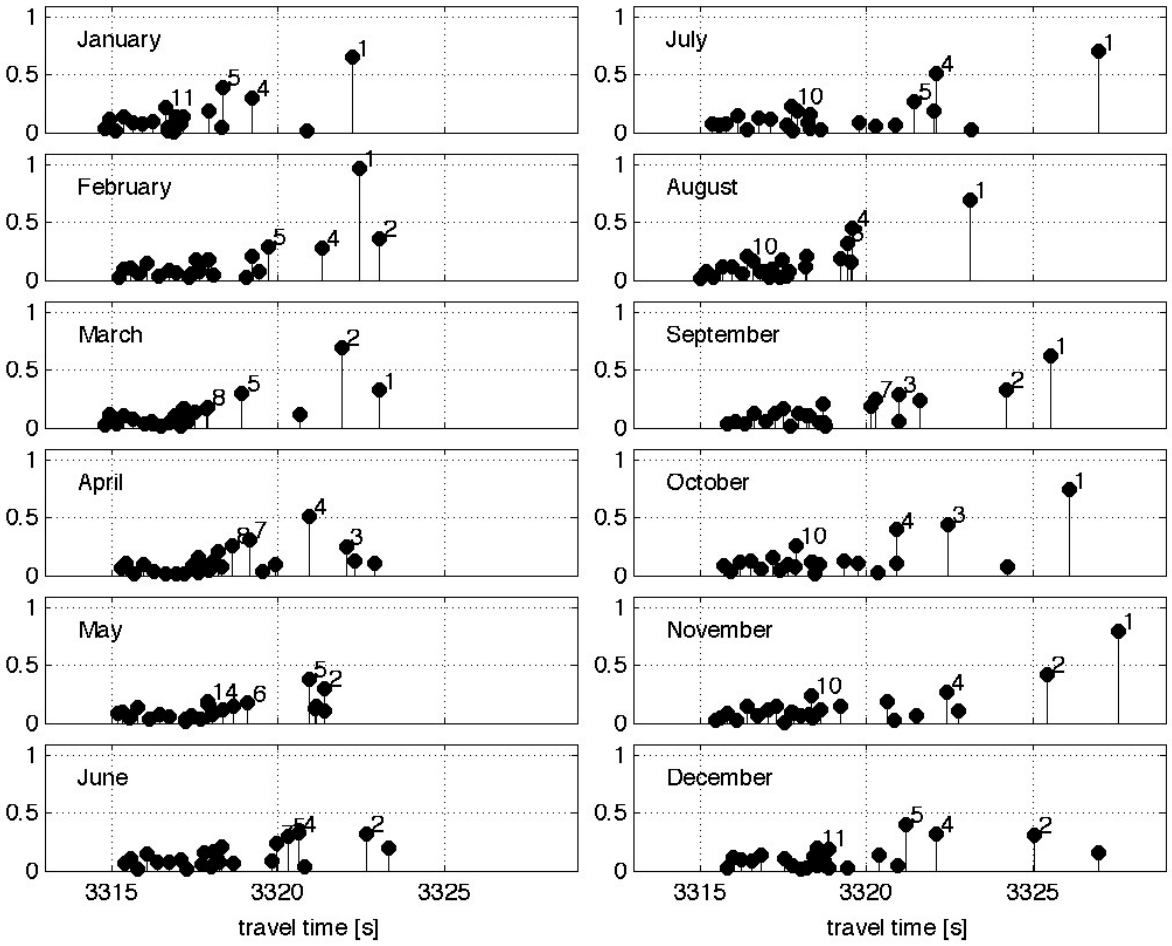


**Figure 5. a) Mode arrival times and amplitudes for adiabatic propagation from a 50-Hz source at a 300-m depth for site A3 to station H01, for the first 25 modes. The four highest amplitude modes are labeled for each month. Mode amplitudes are normalized with respect to the largest arrival over all months—mode 1 in February.**

Similar adiabatic mode computations were performed for the path from the first charge at site A3 to the first hydrophone at station H01 for each month of the year (Figure 5). Monthly temperature and salinity data from the WOA05 database are available to depths of 1,500 m and were extended to a depth of 5,500 m by merging them with the annual average data. A cosine taper was used to ensure smooth transitions between monthly and annual data. The coda onset times are predicted to vary little throughout the year, but the shape of the coda and degree of dispersion are predicted to change significantly. Early arrivals tend to be emergent, making it difficult to pick precise arrival onset times, and may undergo sea floor interaction. Increasing interaction with the sea floor leads both to enhanced attenuation and higher propagation speeds; thus, group velocities associated with the arrival onset may be poorly constrained. By contrast, the mode-1 travel time is predicted to vary significantly throughout the year, suggesting that small changes in the environmental model can lead to significant variations in predicted arrival times for the lowest-order modes, and hence the total phase duration. For example, the mode-1 arrival time and total coda duration is predicted to change by 5 to 6 s from December to January, indicating that monthly variations in sound-speed profiles lead to relatively large differences in computed travel times for this particular path. This implies that near-surface temperatures, which are sensitive to fluctuations in the weather, may affect computed acoustic travel times and durations in polar regions. Thus, the WOA05 climatology database, which is based on long-term averages, may be inadequate to compute arrival times for low-order modes to better than several seconds for sources within the ACC. More detailed ocean models are needed if greater accuracy is required.

These synthetic "wavetrains" were computed and compared to arrivals for 14 shots at sites A3–A6. In each case, the results confirmed that adiabatic mode theory correctly predicts several features of the arrivals. First, given equal charge sizes at a given site location, the shallowest ones—at 300 m depth—yield arrivals with the greatest signal strength at Cape Leeuwin. Secondly, the signal duration does not depend on either the charge depth or size. Thirdly, the duration increases for sources further to the south, indicating greater signal dispersion for longer propagation paths within the ACC. However, comparison of recorded waveforms with the synthetic wavetrain consisting of the first 25 modes confirms that the shape of the coda is not well predicted by adiabatic mode theory, again suggesting coupling between the modes along the propagation path.

The average group velocities along the propagation path vary from 1,475.9 m/s for mode 1 to 1,480.2 m/s for mode 25 at site A3, for a duration of 10 s at this site, decreasing to 1,467.4 m/s for mode 1 and 1476.4 m/s for mode 25 at site A6, for a total duration of 22 s. Thus, average along-path velocities depend on the source position; therefore, a single average acoustic velocity cannot be used to estimate travel time for sources within the ACC, as is done for sources further to the north (Blackman et al., 2004).

*Source Location Estimates*

In the previous section, travel times were computed for propagation along a geodesic path, which is the minimum-distance path between any two points. By Fermat's principle, the acoustic propagation path between two points is the least-time path, not the minimum-distance path. Thus, there can be significant deflection from a geodesic at polar latitudes due to large horizontal gradients in the modal velocities at the ACC boundary (Heaney et al., 1991). The deflection affects both travel times and back azimuths measured at the receiver, and thus impacts source location estimates. The degree of deflection at a given mode and frequency may be estimated using group velocities derived from the WOA05 database, which yields a smoothed representation of the actual spatial variations in velocity. A minimum-time raypath is then computed between any two given points using a perturbation method.

Figure 6 shows both the geodesic path and the deflected paths from each shot site to each IMS hydrophone station, superimposed on a map of the group velocities derived from October–December sound speed profiles for mode 1 at a frequency of 50 Hz. As indicated, there is a significant increase in group velocities from south to north across the ACC, thus ray-bending is significant. Ray-bending decreases the travel time to the Diego Garcia stations by 2.8 to 5.6 s, by 1.1 to 3.9 s to Juan Fernandez, and by 0.3 to 1.5 s to Cape Leeuwin, as compared to propagation along geodesic paths from each source to the receivers. The bending of the sound path deflects the back azimuths by $5.6^{o}$ from A1 to $8.7^{o}$ from A6 at Diego Garcia, by $5.7^{o}$ from A1 to $2.3^{o}$ from A6 at Juan Fernandez, and $1.1^{o}$ from A1 to $2.5^{o}$ from A6 at Cape Leeuwin. The contrast in group velocities across the ACC decreases somewhat at higher modes; thus, ray-bending is most significant for the lowest-order modes.

Back azimuths from multi-instrument stations can be computed to high precision by cross-correlating signals over a narrow frequency band and finding the best plane wave solution to the relative delay times. However, the degree of correlation decreases as the number of wavelengths between each hydrophone pairs increases. For the IMS stations, hydrophone pairs are each about 2 km apart, and cross-correlations are most effective at frequencies of 15 Hz or less. Low SNR at frequencies less than 20 Hz made this method infeasible for this experiment. Instead, azimuths measured from source to receiver were derived using cross-correlations of the envelopes of signal code between pairs of hydrophones within each station's triad. We estimated the azimuths over a number of frequency bands at each station to quantify the uncertainty in our estimates. Unfortunately, the azimuths derived in this way had an error of at least $7^{o}$ for each source-station pair, too large to use in deriving source locations.

Source location estimates were therefore derived using travel-time information only for shots that were recorded at two IMS stations; shots at sites A1 were recorded at both H01 and H03N; shots at A3 through A6 were recorded at both H01 and H08S; shots at site A2 were recorded at only one station. Arrival time picks were made at the end of the waveform because the lowest order modes arrive latest and are the most robust, i.e., the ones that undergo the least seafloor interaction. However, the drawback is that total travel times for the lowest-order modes vary seasonally, by up to 6 s as shown in Figure 5.

Source location estimates made using only travel time differences between pairs of observing stations are compared in Figure 6 for the cases where acoustic propagation is assumed to occur along geodesic paths, and where lateral diffraction is taken into account. In each case, the source locations were derived under the assumption that

travel-time differences are accurate to six seconds. Location estimates were derived from mode-1 group velocities for December, January, autumn (October through December) and winter (January through March). As shown, recordings made at Juan Fernandez and Cape Leeuwin yield source estimates that are more poorly constrained in latitude than in longitude, i.e., site A1, while the reverse is true for sources recorded at Cape Leeuwin and Diego Garcia (sites A3 through A6). Source location estimates for A1 have a precision of approximately 0.15° in longitude, or about 10 km, while source location estimates at A3 through A6 have a precision of approximately 0.5° in latitude, or about 55 km. The effects of seasonal variations in the WOA05 profiles make less difference in source location estimates than the effects of ray bending. In any scenario, the source location estimates for site A6 are biased southward with respect to the true location. The error at site A6 lies in differences of 6–10 s between observed and computed travel times to Cape Leeuwin. The error could arise from the misidentification of the end of the waveform due to the low SNR, or travel times could be overestimated if ocean models are inaccurate.

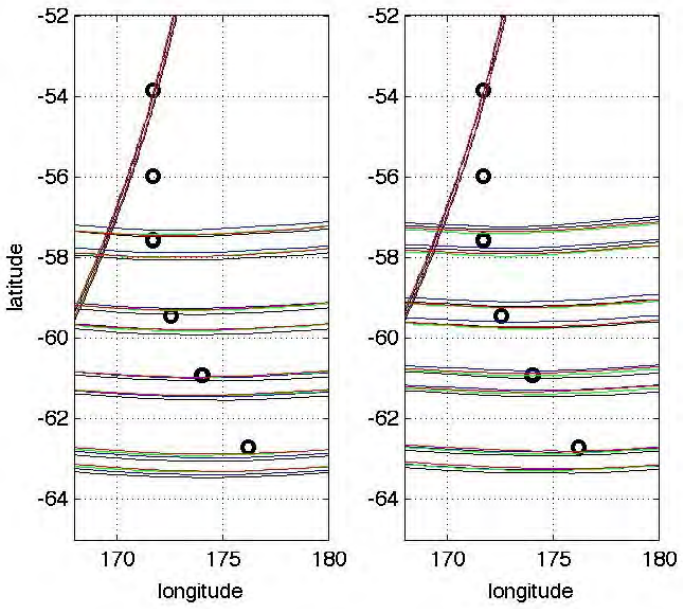


**Figure 6. Location estimates derived using travel differences between pairs of stations. Group velocities were derived from WOA05 profiles for December (blue), January (green), October-December (black) and January-March (red). The map at left shows source location estimates corresponding to propagation along geodesic paths, with actual source locations marked by circles. Source locations derived taking ray-bending into account are shown at right.**

## CONCLUSIONS AND RECOMMENDATIONS

The major findings of this study are the following:

1) Transmission losses are nearly uniform as a function of frequency for paths examined in this experiment. This was shown in de Groot-Hedlin (2007) and de Groot-Hedlin (2008).
2) Signal dispersion increases with the length of the propagation path through the ACC, in agreement with predictions. In this experiment, signal duration increased for shots furthest to the south. For instance, the distance from shot sites A3 through A6 to Cape Leeuwin increased from 4,900 km to 5,200 km, but the signal duration more than doubled from 10 s to 22 s. Since surface propagation varies throughout the year, there is a significant amount of seasonal variability in the signal duration.
3) Travel times computed under the adiabatic assumption were reasonably accurate for the source locations used in this study; at Cape Leeuwin where the SNR was high, there were 2 s between measured and predicted travel times and durations. However, travel times and signal dispersion are predicted to vary throughout year, especially for the lowest-order modes, which undergo surface-limited propagation within the ACC. More detailed ocean models are needed to obtain greater accuracy in travel times and durations.
4) Ray bending is predicted to alter the receiver to source azimuth by as much as 8.7° for travel paths that are highly oblique with respect to the boundary. This prediction could not be confirmed by observation in this study because of large errors in the estimated back azimuths at high frequencies; low SNR in the 5–15 Hz band precluded the use of more accurate waveform correlation methods.

5) Source location estimates made using travel times only are improved by taking ray bending into account but the receiver configuration is a larger source of localization error. Source location estimates are well constrained in longitude if arrivals are detected at Juan Fernandez and either Cape Leeuwin or Diego Garcia, but poorly constrained in latitude. Conversely, source-location estimates for signals detected at Cape Leeuwin and Diego Garcia are very poorly constrained in longitude and to only 55-km accuracy in latitude if travel time picks are accurate to 6 s. An accuracy of about 1 s in travel times measured at Cape Leeuwin and Diego Garcia would be required to estimate source locations to within 10 km in latitude. Alternatively, accurate receiver-to-source azimuths, if available, could be used to improve location accuracy, but the large deflections in the propagation path would have to be accounted for.
6) We were limited to an experiment conducted over three days. Further experiments conducted over the entire seasonal cycle and in other regions of the ACC would aid in characterizing seasonal variability in localization of travel times for sources in this area. Sources that generate broader spectrum signals, especially at the lower end of the frequency band measured at the IMS stations, would allow us to accurately estimate source azimuth using waveform cross-correlation methods, and thus aid in characterizing accuracy of source location estimates.

## ACKNOWLEDGEMENTS

Brian Dushaw provided helpful suggestions and provided the WOA05 monthly data and code to read the profiles. We thank Steve Cande and JoAnn Stock for allowing us to piggyback the experiment on their research cruise aboard the Nathanial B. Palmer, during which crew support for our work was excellent.

## REFERENCES

Antonov, J. I., R. A. Locarnini, T. P. Boyer, A. V. Mishonov, and H. E. Garcia (2006). *World Ocean Atlas 2005, Volume 2: Salinity.* S. Levitus, Ed. NOAA Atlas NESDIS 62, U.S. Government Printing Office, Washington, D.C., 182 pp.

Blackman, D. K., C. de Groot-Hedlin, P. Harben, A. Sauter, and J.A. Orcutt (2004). Testing low/very low frequency acoustic sources for basin-wide propagation in the Indian Ocean, *J. Acoust. Soc. Am.* 116: 2057–2066.

Chapp, E., D. R. Bohnenstiehl, and M. Tolstoy (2005). Sound-channel observations of ice-generated tremor in the IndianOcean, Geochem. *Geophys. Geosyst.* 6, Q06003, doi:10.1029/2004GC000889.

de Groot-Hedlin, C. D., D. K. Blackman, C. S. Jenkins (2007). Hydroacoustic propagation through the Antarctic Convergence Zone, in *Proceedings of the 29th Monitoring Research Review: Ground-Based Nuclear Explosion Monitoring Technologies,* LA-UR-07-5613, Vol. 2, pp. 697–706.

de Groot-Hedlin, C. D., D. K. Blackman, C. S. Jenkins (2008). Effects of variability associated with the Anatarctic Circumpolar Current on sound speed in the ocean, *Geophys. J. Int.*, submitted.

Dushaw, B. D. (1999). Inversion of multimegameter range acoustic data for ocean temperature, *IEEE J. Oceanic Engineering* 24: 215–223.

Hamilton, E. L. (1980). Geoacoustic modeling of the seafloor, *J. Acoust. Soc. Am*. 68: 1313–1340.

Hanson, J., R. Le Bras, P. Dysart, D. Brumbaugh, A. Gault, and J. Guern (2001). Operational processing of hydrocoustics at the Prototype International Data Center, *Pure Appl. Geophys.* 158: 425–456.

Heaney, K. D., W. A. Kuperman, and B. E. McDonald (1991). Perth-Bermuda sound propagation (1960): Adiabatic mode interpretation, *J. Acoust. Soc. Am.* 90: 2586–2594.

Jensen, F. B., W. A. Kuperman, M. B. Porter, and H. Schmidt (1994). *Computational Ocean Acoustics,* AIP, Woodbury, New York.

Locarnini, R. A., A. V. Mishonov, J. I. Antonov, T. P. Boyer, and H. E. Garcia (2006). *World Ocean Atlas 2005, Volume 1: Temperature.* S. Levitus, Ed. NOAA Atlas NESDIS 61, U.S. Government Printing Office, Washington, D.C., 182 pp.

Mooney, W. D., G. Laske and G. Masters, (1998), CRUST5.1: A global crustal model at 5°x5°. *J. Geophys. Res.* 103: 727–747.

Shang, E.C., and Y.Y. Wang (1999). Subarctic frontal effects on long-range acoustic propagation in the North Pacific Ocean, *J. Acoust. Soc. Am.* 105**:** 1592–1595.

Smith, W. H. F., and D. T. Sandwell (1997). Global seafloor topography from satellite altimetry and ship depth soundings, *Science* 277: 1957–1962, 26 Sept.

Wage, K. E., M. A. Dzieciuch, P. F. Worcester, B. M. Howe, and J. A. Mercer (2005). Mode coherence at megameter ranges in the North Pacific Ocean, *J. Acoust. Soc. Am.* 117: 1565–1581.

# DEPLOYMENT OF AUTONOMOUS HYDROPHONE ARRAY IN THE SCOTIA SEA

Haru Matsumoto[1], Del R. Bohnenstiehl[2], Robert P. Dziak[1], Robert W. Embley[3], and Minkyu Park[4]

Cooperative Institute for Marine Resources Studies[1], North Carolina State University[2],
National Oceanic Administration[3], and Korea Polar Research Institute[4]

Sponsored by National Nuclear Security Administration

Contract No. DE-AI52-08NA28654

## ABSTRACT

The remote area of the Atlantic Ocean near the Antarctic Peninsula and the South Scotia Sea is a region where acoustic surveillance by International Monitoring System (IMS) hydrophones is at best limited. Sound originating in this area is either blocked or hindered by the South Georgia Islands (SGI) and the associated seafloor ridge system, making the region a potential hydroacoustic blind spot for IMS stations. In the spring of 2008, we successfully completed the deployment of a hydrophone array consisting of six autonomous underwater hydrophones (AUHs) in the Scotia Sea area. The array configuration is optimum to study sound propagation through the Antarctic Convergence Zone (ACZ), as well as acoustic blockage and reflection caused by islands and associated seafloor topography. Regional seismo-acoustic signals and episodic harmonic tremor from large icebergs will be utilized as natural sound sources.

Since the acoustic data will not be available until the recovery cruise takes place in early 2009, this paper reports the progress we have made so far in evaluating International Data Centre (IDC) and National Earthquake Information Center (NEIC) earthquake data, as well as satellite-derived (NSIDC) information on the distribution of icebergs in the South Atlantic Ocean. We also describe the ice tremor and T-wave signals observed by a similar AUH array deployed near the Antarctic Peninsula in 2006–2007. This region is characterized by surface-limited propagation conditions similar to the Scotia Sea. Our focus is on the T-wave generated by an $m_b$ 7.0 earthquake along the South Scotia Ridge (61$^o$00.36'S, 34$^o$23.46 W) and the associated T-phase reflection from the SGI, as well as the characteristics of the ice tremor from iceberg uk213 during the time when it was positioned near Clarence Island (61$^o$19'S, 54$^o$16'W).

## OBJECTIVES

Monitoring underwater low-frequency sound is one of the critical components of the global nuclear explosion monitoring effort lead by the National Nuclear Security Administration, the Air Force Research Laboratory, and the Army Space Missile Defense Command. Their objective is to ensure that any nuclear weapon tests conducted in the ocean or near the surface above the ocean do not go undetected. One area where such a signal can be hidden from the eyes of the international community is the Scotia Sea in the south Atlantic. In the Scotia Sea propagation across the ACZ is poorly understood and the sound path to the IMS hydrophones is partially or completely blocked by the islands and associated seafloor ridge system that delineate the Scotia Plate.

With an array consisting of six AUHs successfully deployed in early 2008, a continuous recording of acoustic signals has begun in the Scotia Sea. The array will monitor the T-phases and ice tremors occurring in the Southern Ocean. Upon the recovery of hydrophones, which is scheduled in early 2009, our goals is to undertake a detailed study of acoustic signals received at the AUHs and IMS stations, investigating spectral characteristics and received levels affected by the ACZ, regional bathymetry and island blockages. Based on the acoustic data we will catalog source locations, source levels and origin times, along with associated arrival time and received signal level information. To assess our ability to accurately model the source level of signals originating in the remote southern ocean, the observational data will be compared with predictions derived from range dependant propagation models.

## RESEARCH ACCOMPLISHED

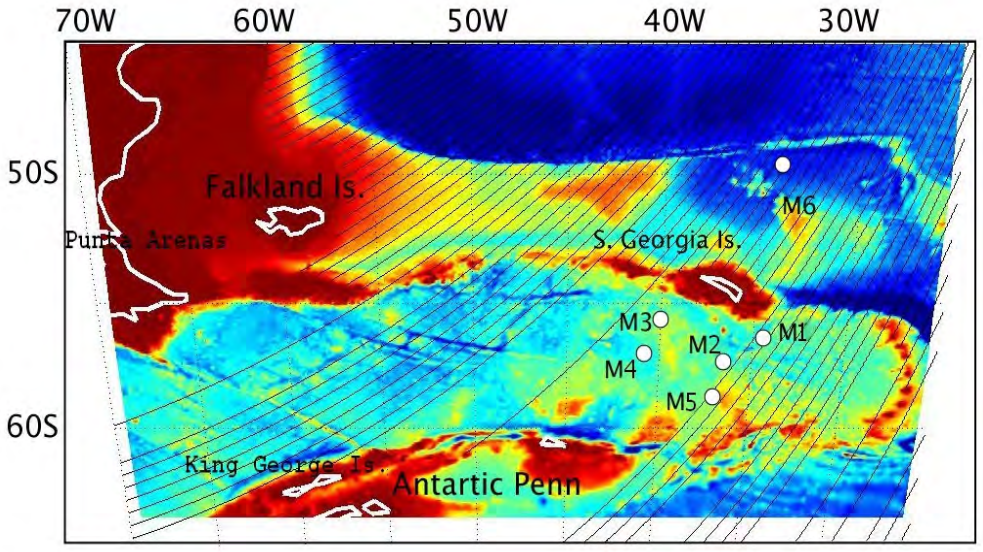


**Figure 1. 2007-2008 array configuration for detecting acoustic events and investigating propagation in the Scotia Sea area. Black lines show acoustic paths for Ascension Island, with a <500 m line-of-sight blockage criteria applied.**

In December 2007, as part of a collaboration between the Korea Polar Research Institute (KOPRI), the National Oceanic and Atmospheric Administration (NOAA), the Cooperative Institute for Marine Resource Studies (CIMRS) at Oregon State University and North Carolina State University (NCSU), a five-station AUH array (M1-M5, Figure 1) was deployed in the Scotia Sea region. With ship support from the British Antarctic Survey (BAS), we later deploy a sixth hydrophone to the north of SGI in April of 2008 (M6). When we recover all of the hydrophones in early 2009, the observation period will be approximately one year and the amount of acoustic records digitized at 250 Hz will be 16 GB per hydrophone (total of 96GB). As the data have not yet been recovered, this paper discusses the preliminary earthquake and iceberg data that we intend to use as sound sources in year two of this project. These data include seismic information from both the IDC and NEIC, and satellite derived information on the distribution of icebergs and sea ice obtained from the National Snow and Ice Data Center (NSIDC).

The five-AUH array configuration on the south side of SGI (M1 through M5) will allow us to accurately locate the acoustic events including seismic events below $m_b$ 3 originating from the south side of the island, namely the Scotia Sea, portion of the Drake Passage and the Weddell Sea. This area is acoustically blocked from the IMS hydrophones by the seafloor features associated with the SGI. We will first identify the sound sources by associating the spectral characteristics of the acoustic events at each hydrophone, and applying nonlinear least square technique to locate the sources based on travel times derived from GDEM (Generalized Digital Environmental Model) (Fox, 2001). Each hydrophone independently maintains the timing by an internal clock that is accurate to 1 sec/year. Source levels are then estimated based on propagation loss (Dziak 1997). A lone hydrophone on the north side of the SGI (M6) will allow us to examine the interference effect of SGI and associated seafloor features on the acoustic signals originating from the south of the island (e.g., earthquakes and ice tremors). This will be accomplished through comparisons with observations at the other hydrophone stations (M1-M5), which lie along unblocked paths from such sources.

Although in principle only three single-channel AUHs are needed to determine the locations and origin times of the events, two redundant hydrophones were added to improve the accuracy as well as insurance against possible instrument loss by the strong current of Antarctic Circumpolar Current (ACC) (Gabarato, 2003) and potential high concentrations of sea ice during the recovery. In the northern Weddell Sea during the austral winter, the area is partially covered by sea ice and the ice edge may extend as far north as 55°S. During the austral summer, the sea ice typically recedes to 65°S (Wolff, 2007). The mooring depth of all the hydrophones is 500 m below the surface (Figure 2A), which is shallower than the lower latitude hydrophone depth (typically 1,000 m). The 500-m hydrophone depth is not ideal but rather is a compromise between minimizing a risk of losing the system by large icebergs and keeping it close to the sound propagation layer near the surface in the high latitude waters.

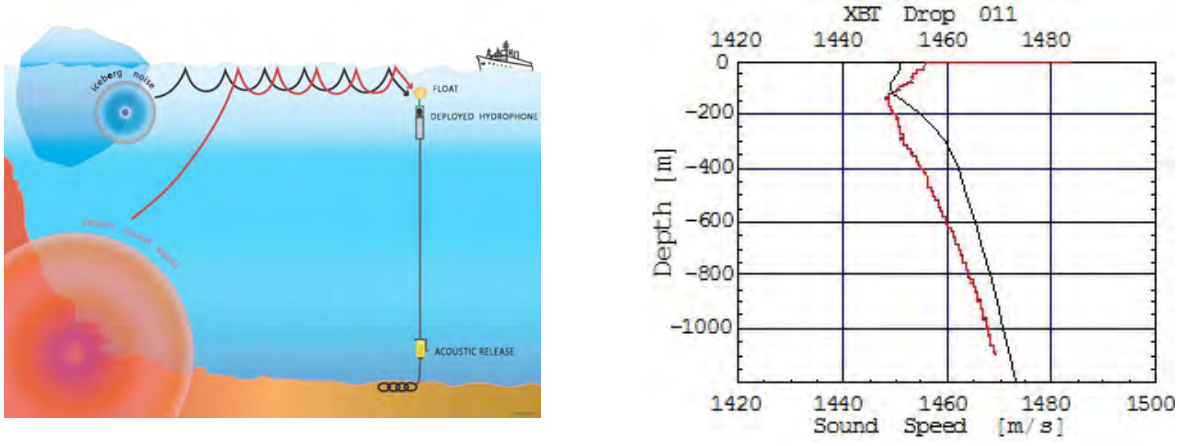


(A) (B)

**Figure 2. (A) Diagram of AUH mooring customized in the ACZ propagation study. The hydrophone is moored within this surface layer to take advantage of this relatively effective transmission. The spherical float (syntactic foam) is to keep the mooring line rigid while minimizing the drag force. The top 1000 m of the mooring line is made of a high tensile strength cable with low-flow-noise characteristics (Vectran®). The rest of the mooring lines are of Very Low Stretch (VLS) line. (B) The vertical temperature profile unique to the polar region makes the sound propagation "surface-limited." The sound speed (in red) is based on the XBT data taken at 57°28.5'S, 41°32.8'W on December 12, 2007 during R/V Yuzhmorgeologiya. Black solid line is based on typical temperature and salinity data from GDEM data set.**

During the deployment cruise, XBT casts were made at each mooring site to estimate the sound velocity profiles. Figure 2B shows one of the velocity profiles based on an XBT cast near the M4 mooring. In most propagation modeling environments, GDEM is sufficient. However, in the case of ACZ propagation within the Southern Ocean, sound speed profiles based on XBT data and GDEM indicate some differences (~4m/s), suggesting the need to incorporate additional water column data/field (e.g., Argo float and CTD data from other cruises) where available.

In 2006, a separate hydrophone array deployed for another experiment detected a series of ice tremors originated by the Clarence Island in the Bransfield strait near the Antarctic Peninsula (Figure 3). The signals originated from a 10x5 km iceberg (uk213), which was too small to be tracked by the NSIDC. The signal intensity was large enough to be heard by all the hydrophones in the area and the estimated sound intensity was equivalent to a $m_b$ 5.0 earthquake. The uk213 ice tremors resemble the "Variable Harmonic Tremor" described by Chapp et al. (2005), but they have a relatively short duration of 60–180 seconds. The uk213 tremors also exhibit harmonics with a much wider spectral range, up to 400 Hz, relative to those observed by the IMS hydrophones. The typical ice tremor bandwidth observed by the IMS hydrophones in the Indian Ocean was much narrower than this, including those described by Chapp et al.,(2005) which were less than 100 Hz. The ice tremors reported by Talandier et al. (2006) were less than 14 Hz. The uk213 tremors in the Bransfield also lack low frequency energy below 40 Hz. It appears that short-range propagation (~125 km) helped retain most of the high frequency components, which otherwise would be dissipated as the sound traveled over long ranges out to the open sea.

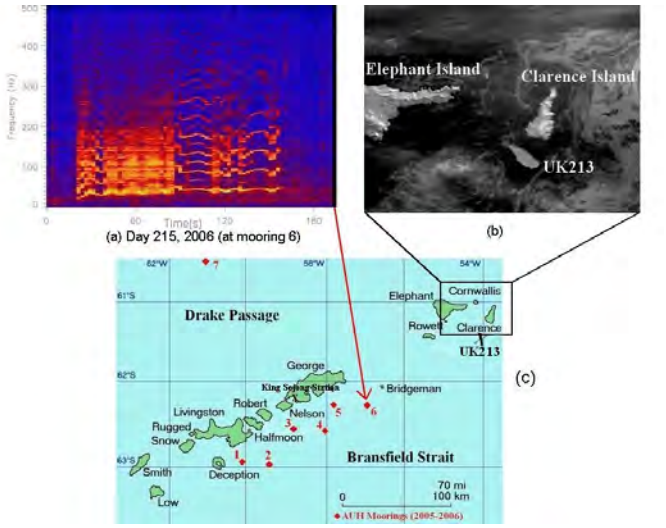


**Figure 3. (A) Harmonic tremor recorded by one of the NOAA/PMEL AUHs in the previous experiment (2006) in the Bransfield Strait (1kHz sampling rate). (B) Satellite image of uk213 iceberg (5km x 10km) on day 216, 2006. The iceberg was by Clarence Islands, at 61°20"S-54°W, 125km NE from the AUH 6. (C) Map of the South Shetland Islands Chain.**

On August 20, 2006, at 03:41:47 (UTC), an earthquake of $m_b$ 7.0 was detected in the area by the Global Seismic Network (GNS). Figure 4 shows the P-wave and T-wave that propagated 1,250 km from the epicenter and were recorded by the NOAA Bransfield AUH array. The epicenter was 61°00.36'S, 34°23.46'W at the boundary of the Scotia and the Antarctic plates. All AUHs recorded P-waves ($P_n$ phase) and T-waves generated by the earthquake including the AUH in the Drake Passage, although Elephant and Clarence Islands were directly in the line of sight from the epicenter. The third signal in Figure 4A arrived about 600 seconds later than the T-wave and was much weaker than the other two arrivals. Because of its relatively wide-band spectral content, the similarity of the spectral contents to the first T-wave and the timing of the arrivals (24 min 13 sec after the earthquake origin time), we believe that the third signal is a reflected T-wave off the steep slope of the South Georgia Island (Figure 4B), a phenomenon that also has been observed on the IMS signals in the Indian Ocean (e.g., Hansen and Bowman, 2006).

Relative to their low-to-mid latitude counterparts, all T-wave signals recorded by the Bransfield array are deficient in low frequency energy below 5 Hz. This observation is likely linked to the cut-off frequency of the shallow surface duct, a well-known phenomenon in ocean acoustics (Urick, 1983). However, we note that ice-generated signals recorded in the Indian Ocean at long ranges typically have fundamental harmonics < 5 Hz (Chapp et al., 2004). Consequently, the frequency-dependant coupling of ocean sounds may also be sensitive to the source depth.

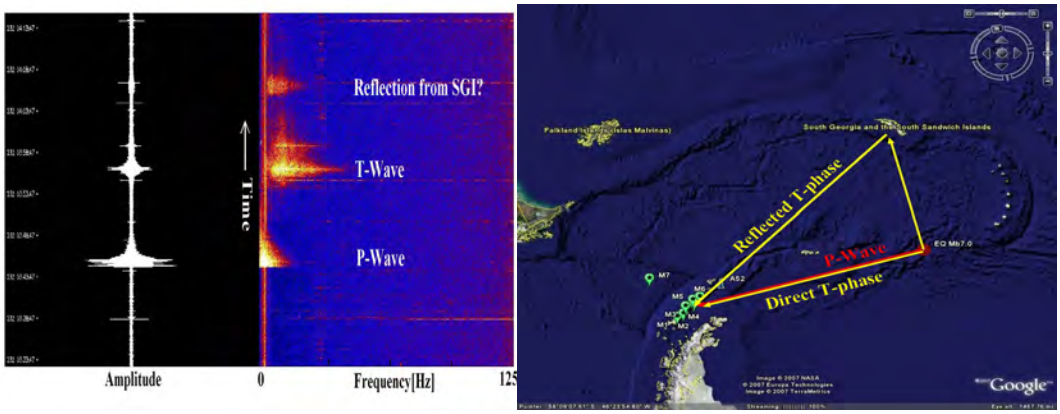


**(A)** **(B)**

**Figure 4. (A) $M_b$ 7.0 earthquake signals detected by the AUH 5 in the Bransfield Strait. (B) T-wave originated by Mb 7.0 earthquake in the S. Scotia Ridge was reflected by SGI arriving 600 seconds later after the direct T-wave arrival.**

As of July 2008, six large icebergs (>10NM on one side) have been registered by NSIDC in the Scotia Sea region based on satellite images. Figure 5A shows these iceberg locations indicated by blue triangles, which include A43F (53°21'S-36°13'W), A43K (58°51'S-42°43'W), B15D (55°01'S-42°24'W), uk248 (54°06'S-39°03'W), uk177 (59°05'S-45°01'W, and D18 (58°59'S-39°32'W). There are numerous other icebergs too small to be registered and tracked by NSIDC, but any one of these icebergs can potentially generate large ice tremor signals (Müller et al., 2005, Talandier et al., 2006) that we can utilize as the sound sources to study the sound propagation through the ACZ and interferences by bathymetry and island features. It also shows 111 accumulated earthquakes (red circles) registered since the Scotia Sea hydrophone deployment, January 1, 2008, through July 7, 2008, on the NEIC catalog. Earthquakes occurred mostly in the Scotia arc region where the South American plate is being subducted under the Sandwich microplate. Several T-phases originated in this arc region were large enough ($m_b$> 5.6) to be detected by the Ascension Island IMS hydrophone. None of the earthquakes that occurred in the south and southwest of the SGI were detected by the Ascension Island hydrophones, indicating that the earthquakes were either too small or that seafloor features were effective at blocking T-wave propagation across the SGI region.

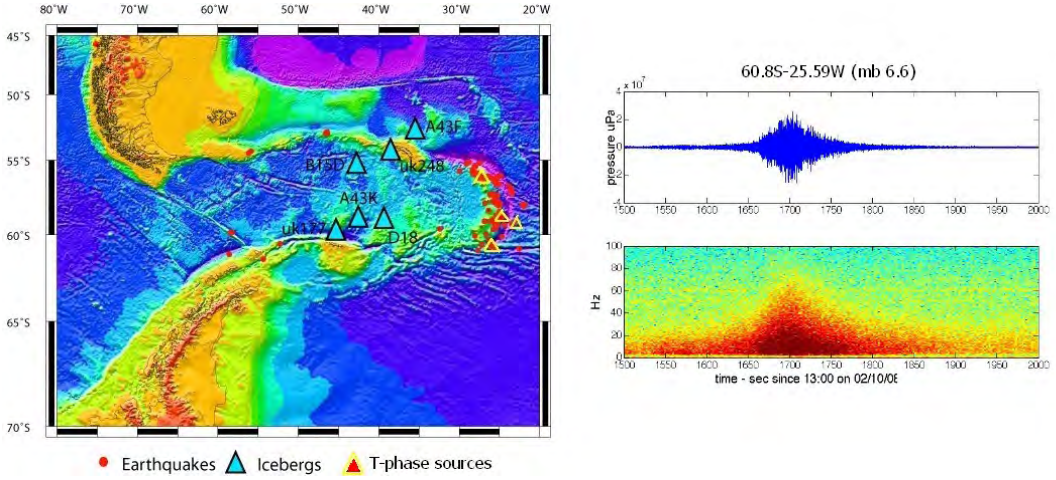


**Figure 5. Iceberg locations (blue triangles) as of July 07, 2008, from NSIDC and accumulated epicenters map (red circles) since January 1, 2008, based on the NEIC catalog. Four T-phase sources were identified during the same period by the Ascension Island IMS hydrophones (yellow triangles). One of the T-phases is displayed on the right-hand side. Most earthquakes are located near the arc. Several earthquakes were located near the Western Antarctic Peninsula area where the plate is old but volcanically is still active.**

## CONCLUSIONS AND RECOMMENDATIONS

- Successful deployment of all six hydrophones was accomplished in December 2007/April 2008. Recovery operations are planned for December 2008/April 2009, resulting in approximately one year of continuously recorded acoustic information.
- Preliminary analysis of the signal from the Scotia Sea detected by the IMS hydrophone is promising. NSIDC data indicate that there are numerous large icebergs located within and moving through the study area. We have identified several large earthquake sources with blocked and unblocked paths to the M6 hydrophone and the IMS station at Ascension Island.

## ACKNOWLEDGEMENTS

The authors thank Chris Hindley, Anthony Martin and crew of RRS J. C. Ross of the British Antarctic Survey for deploying one of our hydrophone moorings.

## REFERENCES

Garabato, A. C. N., D. P. Stevens, K. J. Heywood, (2003). Water mass conversion, fluxes, and mixing in the Scotia Sea diagnose by an inverse model, *J. Phys. Oceanogr*. 33: 2565–2587.

Chapp, E. D. R. Bohnenstiehl and M. Tolstoy, (2005). Sound-channel observation of ice-generated tremor in the Indian Ocean, *Geochem. Geophys. Geosys*. 6: 6.

Dziak, R. P. C. G. Fox, H. Matsumoto, and A. E. Schreiner, (1997). The April 1992 Cape Mendocino Earthquake Sequence: Seismo-Acoustic Analysis Utilizing Fixed Hydrophone Arrays, *Mar. Geophys. Res*. 19: 137–162.

Fox C. G., H. Matsumoto, and T. A. Lau, (2001). Monitoring Pacific Ocean seismicity from an autonomous hydrophone array, *J. Geophy. Res.* 106: B3, 4183–4206.

Hanson, J.A., and J. R. Bowman, (2006). Methods for monitoring hydroacoustic events using direct and reflected T-waves in the Indian Ocean, *J. Geophys. Res.* 111: B02305.

Müller, C., V. Schlindwein, A. Eckstaller, and H. Miller, (2005). Singing icebergs, *Science* 3: 1299.

Talandier, J., O. Hyvernaud, D. Reymond, and E. A. Okal, (2006). Hydroacoustic signals generated by parked and drifting icebergs in the Southern Indian and Pacific Oceans, *Geophys. J. Int.* 165: 817–834.

Upton, Z. M., J. J. Pulli, B. Myhre, and D. Blau, (2006). A reflected energy prediction model for long-range hydroacoustic reflection in the oceans, *J. Acoust. Soc. Am.* 119: 153–160.

Wolff, E.W. (2008). Whither Antarctic sea ice? *Science* 302: 1164.

Urick, R. (1983). *Principles of Underwater Sound*, 3rd Ed. McGraw-Hill, New York.

# Radionuclide Monitoring

# SPECTRAL ANALYSIS OF RADIOXENON

Matthew W. Cooper, Ted W. Bowyer, James C. Hayes, Tom R. Heimbigner,
Charles W. Hubbard, Justin I. McIntyre, and Brian T. Schrom

Pacific Northwest National Laboratory

Sponsored by National Nuclear Security Administration

Contract No. DE-AC05-RLO1830

## ABSTRACT

Monitoring changes in atmospheric radioxenon concentrations is a major tool in the detection of an underground nuclear explosion. Ground-based systems like the Automated Radioxenon Sampler /Analyzer (ARSA), the Swedish Unattended Noble Gas Analyzer (SAUNA) and the Automatic portable radiometer of isotopes Xe (ARIX), can collect and detect several radioxenon isotopes by processing and transferring samples into a high-efficiency β-γ coincidence detector. The high-efficiency β-γ coincidence detector makes these systems highly sensitive to the radioxenon isotopes $^{133}$Xe, $^{131m}$Xe, $^{133m}$Xe, and $^{135}$Xe.

The standard analysis of the 2-dimensional beta-gamma energy spectra uses regions of interest (ROI) to determine the amount of a particular radioxenon isotope present by summing the counts in region. This method relies on the peaks of interest falling within energy limits of the region. Some potential problems inherent in this method are the reliance on stable detector gains and a fixed resolution for each energy peak. In addition, when a high activity sample is measured, there will be more interference among the ROI, in particular within the $^{133}$Xe, $^{133m}$Xe, and $^{131m}$Xe regions.

A solution to some of these problems can be obtained through spectral fitting of the data. Spectral fitting is simply the fitting of the peaks using known functions to determine the number and relative peak positions and widths. By knowing this information it is possible to determine which isotopes are present. The area under each peak can then be used to determine an overall concentration for each isotope. Using the areas of the peaks, several key detector characteristics can be determined: efficiency, energy calibration, energy resolution, and ratios between interfering isotopes (Radon daughters).

## OBJECTIVES

Monitoring radioactive releases from nuclear explosions is a major component of the International Monitoring System (IMS) network (Hayes 1999, Bowyer 1999). Systems such as ARSA, SAUNA, and ARIX collect and detect several radioxenon isotopes by processing and transferring samples into a high-efficiency β-γ coincidence detector for analyses in support of treaty verification. The high efficiency β-γ coincidence detector makes these systems highly sensitive to the radioxenon isotopes $^{133}$Xe, $^{131m}$Xe, $^{133m}$Xe and $^{135}$Xe.

Standard radioxenon analysis uses ROIs in the beta-gamma energy correlation spectrum to determine radioxenon isotopic concentrations present. The ROI method relies on setting region energy limits such that the peaks of interest are fully encompassed. Some potential problems inherent in this method are the reliance on stable detector gains and a fixed resolution for each energy peak. Currently, the ARSA system uses 7 ROIs (Figure 1) while the SAUNA system uses 10 ROIs.

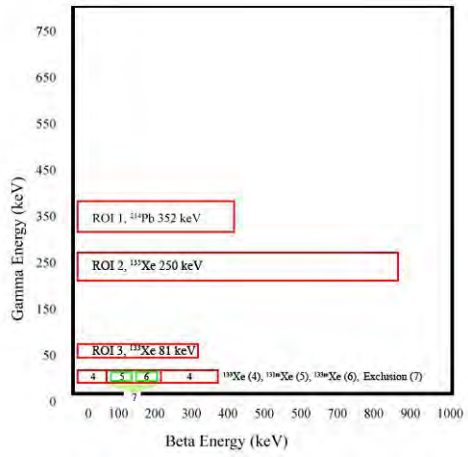


**Figure 1. Standard ARSA 7 ROI.**

The objective for spectral fitting is to supplement and/or replace the ROI beta-gamma energy correlation spectrum analysis method by fitting functions to the data. Several advantages are realized by using spectral fitting. First, detector gains and energy resolution can be checked by using an appropriate fitting algorithm, peaks can be found by differentiating the spectrum and looking for zero crossings. By performing a Gaussian fit to a peak, the centroid, sigma width, and pulse height are determined. The pulse height and width are used to calculate the peak area. The centroid of each peak is used for isotopic identification and to check for detector gain shifts. Changes in peak widths can indicate potential damage to a detector. A second advantage of spectral fitting is a reduced reliance on detector background measurements due to the ability to do a spectral background subtraction (often a linear fit). This in turn will reduce system setup time. Finally, an automated detector efficiency and energy calibration measurement can be made using spectral analysis. An automated method uses an algorithm to determine the peak position and then performs Gaussian fits to determine peak area and channel.

## RESEARCH ACCOMPLISHED

Fielded radioxenon systems have traditionally used the ROI beta-gamma energy correlation spectrum analysis method to make xenon concentration measurements. Pacific Northwest National Laboratory (PNNL) has made progress towards switching to a spectral analysis method instead. Although fielding a system using spectral analysis is still a considerable time away, a first attempt at an automated spectral fitting algorithm has been made based on the Cern ROOT data analysis framework (http://root.cern.ch/). However, for spectral fitting to be most effectively used, a nuclear physicist should perform and check the fits rather than rely on an automated algorithm. An automated fitting routine has been done at PNNL.

**Energy Calibration**

One of the first attempts to do spectral fitting at PNNL was in characterizing the beta-gamma coincidence detector. The first step in characterizing a detector is to determine the energy calibration. This is done by fitting multiple energy peaks and correlating the channel of the peak centroid with the corresponding energy from the literature. For a beta-gamma detector, the gamma energy calibration is initially determined using a $^{137}$Cs source, and a radioactive gas spike of $^{222}$Rn and $^{131m}$Xe. These sources give seven gamma- and x-ray energies ranging from 30 keV up to 662 keV. The seven gamma- and x-rays cover a good range of energies for the purpose of the detector.

A first step in performing a spectral fit is to subtract the background events. Accounting for background events is normally done by subtracting a background spectrum; however, it is also possible to fit a polynomial (Figure 2) to the sections of the spectrum that do not contain peaks. One assumption made when fitting the background is that there are no discontinuities present in the spectrum. By using a fit to subtract the background, measurement times are significantly reduced without a reduction in counting statistics.

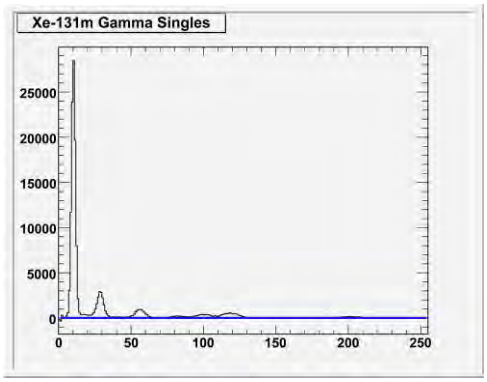


**Figure 2. A $^{131m}$Xe spectrum with both Radon daughters and $^{133}$Xe present, where the blue line is the linear background fit.**

Although background subtraction is not strictly necessary for determining the energy calibration and energy resolution of a detector, it is still best practice. Once the background is subtracted, a fitting algorithm can be run which performs Gaussian fits to those peaks present (Figure 3). Several limits are placed on the fitting algorithms to ensure a good fit. One limit is set based on the relative differences in expected energies. For example, $^{133}$Xe has a 30 keV X-ray and 80 keV gamma-ray so the peak position should reflect that relative difference. Other limits might include setting a range on the Gaussian peak area relative to the literature-listed intensities, the number of Gaussian fits, and Gaussian widths. Knowledge of general detector characteristics is invaluable when limiting fitting algorithms. For example, the energy resolution, or full width half maximum of the peak, as a function of energy is proportional to $1/\sqrt{E}$ .

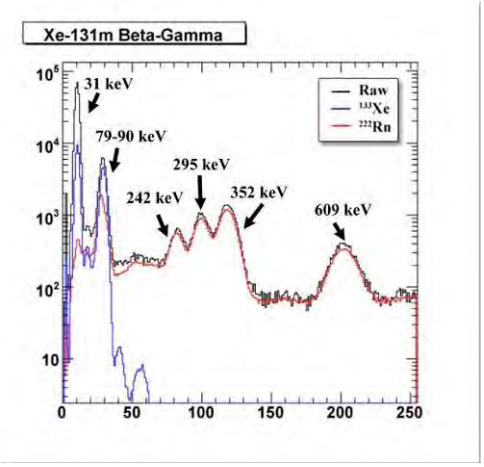


**Figure 3. A $^{131m}$Xe spectrum with multiple-fitting algorithms performed. Blue: $^{133}$Xe peak fits and in Red: $^{222}$Rn daughter peak fits.**

Once the energy calibration for the gamma-ray detector has been established, the energy calibration for the beta detector needs to be determined. Using a $^{137}$Cs source inserted along the beta detector it, becomes a relatively simple matter to measure the energy calibration. The 662 keV gamma-ray Compton scatters to produce a beta-gamma coincidence, which can be used to determine the beta-energy calibration (Figure 4). By fitting the diagonal line of constant energy (662 keV), a correlation between the gamma-energy calibration and beta-energy calibration can be defined, which in turn will determine the beta energy calibration. The energy calibration should be verified using the $^{131m}$Xe peak which has a 30 keV x-ray in coincidence with a 129 keV conversion electron (CE), giving a coincidence peak of known energy (Figure 5).

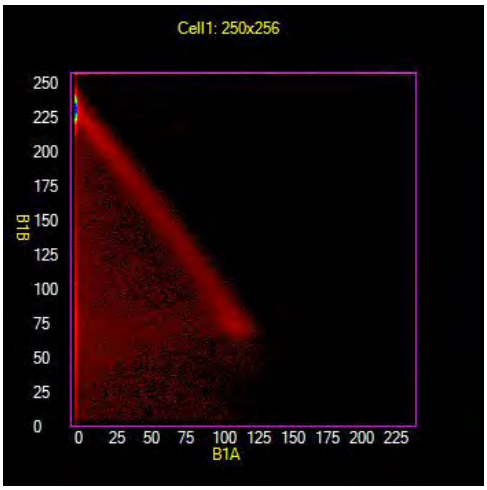


**Figure 4. Beta-gamma coincidence $^{137}$Cs spectrum.**

**Efficiency Measurement**

Once the detector energy calibration is known, the detector efficiency is determined. The detection efficiency for a given detector is the number of detected events divided by the number of total events. A general formula used in calculating the efficiency is shown in Equation 1:

$$\text{Number of Total Events} = \frac{Counts}{\varepsilon \cdot Br} \quad \textbf{(1)}$$

$\varepsilon = \text{efficiency}$

Where, $Br = \text{branching ratio}$

$Counts = \text{Number of counts in peak of interest}$

The first step is to use the $^{131m}$Xe data. By comparing the number of events detected in beta singles versus the number of events detected in beta-gamma coincidence, the gamma efficiency can be determined from Equation 2.

$$\frac{Counts_{\beta\gamma}}{\varepsilon_\gamma' \varepsilon_\beta' Br'} = \frac{Counts_\beta}{\varepsilon_\beta Br} \Rightarrow \varepsilon_\gamma' = \frac{Counts_{\beta\gamma}}{Counts_\beta} \quad \textbf{(2)}$$

In equation 2 the branching ratios are the same since there will always be an x-ray emitted in coincidence with the CE. The calculation also assumes ~100% detection efficiency of the 129 keV CE (partially due to an assumed low self attenuation) and a large detection solid angle (~ 99%). The 30 keV gamma-ray efficiency is then used in determining the beta efficiency for $^{133}$Xe. Using Equation 3, the ratio between the gamma singles and beta-gamma coincidence will yield the efficiency for the betas in coincidence with the 30 keV x-ray for $^{133}$Xe. Assuming this beta efficiency is the same as that for betas in coincidence with the 80 keV gamma-ray from $^{133}$Xe, it is possible to

determine the gamma efficiency at 80 keV. By using data collected from the Radon daughters ($^{214}$Pb) it is possible to determine the gamma detection efficiencies at 242, 295, and 352 keV.

$$\frac{Counts_{\beta\gamma}}{\varepsilon_{\gamma}^{'}\varepsilon_{\beta}^{'}Br^{'}} = \frac{Counts_{\gamma}}{\varepsilon_{\gamma}Br} \Rightarrow \varepsilon_{\beta}^{'} = \frac{Counts_{\beta\gamma}Br}{Counts_{\gamma}Br^{'}} \quad \textbf{(3)}$$

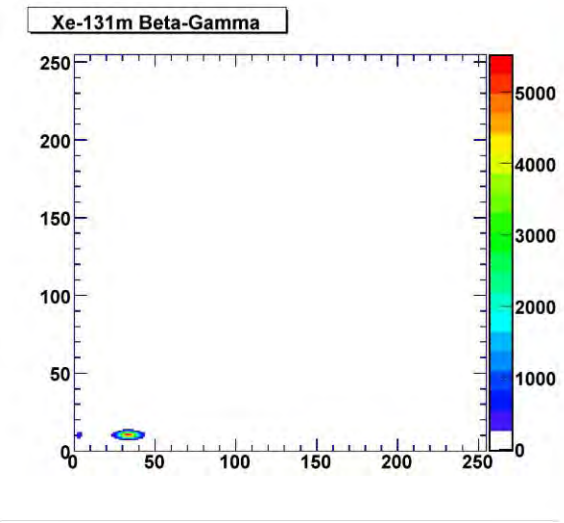


**Figure 5. Beta-gamma coincidence spectrum used for determining the gamma-detection efficiency at 30 keV.**

**Deconvolution**

Spectral fitting can also be used to perform deconvolutions. When multiple gamma rays are detected near the same energy, the resulting peak may fall within a single beta-gamma energy correlation spectrum ROI. However, when performing spectral fitting, it is possible to fit an asymmetrical peak with multiple Gaussian functions to resolve a more complex peak structure. This technique is often challenging and relies on knowledge of the nuclear structure for the isotopes detected. The majority of the nuclear structure is from the literature and can be imbedded into the isotopic identification and calculation. Several methods that can be used to determine if a peak is a multiplet, ranging from a wider peak than expected to actual peak structure (a shoulder on a peak). Once a multiplet peak has been identified, the number of Gaussian peaks used should be determined by matching the Gaussian width with the expected energy resolution at the particular energy (too many Gaussians will give a smaller width, while too few will give a wider width). Furthermore, the sum of the Gaussians should fit the overall peak of interest. Deconvolving a peak using spectral fitting is much easier to do in a manual fashion than automatically and is one of the reasons for spectral fitting being a supplement to the standard energy spectrum ROI method.

**Fermi-Kurie plot**

Given the difficulty in fitting a beta continuum, it is important to find an alternative method. A Fermi-Kurie plot (Krane 1988) is one method, which allows a beta spectrum to be plotted as a line. By plotting

$$\sqrt{\frac{n(T)}{\sqrt{T^2 + 2mc^2T(T+mc^2)}}} \text{ versus T,} \quad \textbf{(4)}$$

Where, $n(T) = \text{number of counts}$
$T = \text{energy - rest mass}$
$mc^2 = 511\,\text{keV}$

a nearly straight line is plotted which crosses the x-axis at the end-point energy for the beta decay. There is a corrective term (Fermi function) that has been neglected which corrects for low energy non-linearities. The corrective function takes into account the initial and final spin and polarity states.

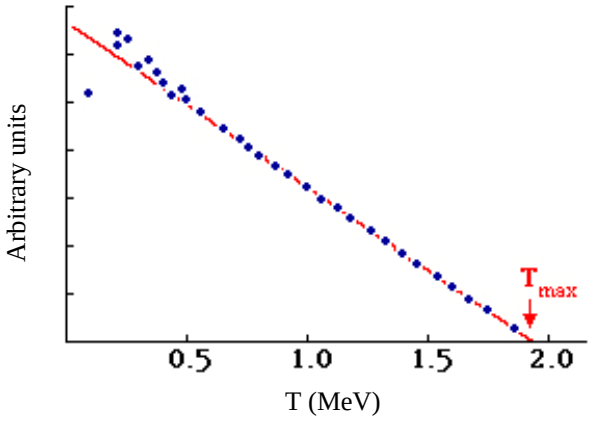


**Figure 6. Fermi-Kurie plot.**

## CONCLUSIONS AND RECOMMENDATIONS

Spectral fitting is a supplement and potentially a replacement for the standard energy spectrum ROI analysis technique for radioxenon measurements. The primary function used in spectral fitting is combining Gaussian and polynomial functions to fit an entire spectrum. The fitting is slightly more complex for a beta continuum given the smooth curve of the spectrum, but by using a Fermi-Kurie plot, the beta spectrum becomes linear and is easier to fit. Given the number of peaks, relative positions, widths, and end-point energies, it is possible to uniquely identify the isotopes present, number of decays detected, and thus the concentration for each isotope.

Although spectral analysis poses many advantages, additional work needs to be completed to successfully convert current analysis techniques to spectral fitting. Spectral analysis works best given good statistical data. Without relatively high statistics, the fitting algorithm begins to fail. This is an area that can be addressed by doing the fits manually; however, it would be best to have an algorithm do it automatically. The other area that should be addressed is to make multi-dimensional fitting algorithms (fit the beta-gamma coincidence data rather than the projected data). Multi-dimensional fitting would make the best use of the data collected and could be more effective at removing interference terms.

## REFERENCES

Hayes J. C, K. H Abel, T. W Bowyer, T. R Heimbigner, M. E Panisko, P. L Reeder, J. I McIntyre, R. C Thompson, L. C Todd, and R. A Warner (1999). Operations of the automated radioxenon sampler/analyzer—ARSA, Chapter 6. Radionuclide Monitoring in *Proceedings of the 21st Seismic Research Symposium: Technologies for Monitoring the Comprehensive Nuclear-Test-Ban Treaty*, LA-UR-99-4700 Vol. 1, pp. 249–260.

Bowyer, T. W., J. I. McIntyre, and P. Reeder (1999). High sensitivity detection of Xe isotopes via β-γ coincidence counting, in *Proceedings of the 21st Seismic Research Symposium: Technologies for Monitoring the Comprehensive Nuclear-Test-Ban Treaty*, LA-UR-99-4700, Vol. 2, pp. 2321–241.

http://root.cern.ch/http://root.cern.ch.

Kenneth S. Krane (1988). Introductory Nuclear Physics.

# PRELIMINARY EXPERIMENTS WITH A TRIPLE-LAYER PHOSWICH DETECTOR FOR RADIOXENON DETECTION

Abi T. Farsoni, David M. Hamby, Chee S. Lee, and Anthony J. Elliott

Oregon State University

Sponsored by National Nuclear Security Administration

Contract No. DE-FC52-06NA27322
Proposal No. BAA06-36

## ABSTRACT

The International Monitoring System (IMS) employs some special radiation detectors to monitor atmospheric or underground nuclear weapons tests around the world. These detectors should be able to detect ultra low concentrations of xenon radioisotopes in the atmosphere where the background level is relatively high. Exploiting the fact that the most interesting xenon radioisotopes ($^{133}$Xe, $^{133m}$Xe, $^{131m}$Xe, and $^{135}$Xe) emit a beta or conversion electron (CE) in coincidence with an X-ray or gamma-ray, these detectors have been designed and optimized to record coincidence events from the radioxenon isotopes. The IMS currently uses detection systems in which beta/CE and X-ray/gamma-ray are measured in separate detectors (as in the Automated Radioxenon Sampler/Analyzer [ARSA] system developed at Pacific Northwest National Laboratory [PNNL]). Although experimental results show that the ARSA system is able to detect very low concentrations of radioxenon, its complexity makes the beta and gamma-ray energy calibration very difficult.

Phoswich technology, accompanied by digital signal processing of photomultiplier tube (PMT) pulses, can simplify radioxenon detection. If well designed, like other current sensitive radioxenon detectors, a phoswich detector is also capable of detecting beta/gamma coincidence events using digital-pulse-shape analysis. We have designed a two-channel triple-layer phoswich detector for radioxenon detection. Each phoswich detector consists of three scintillation layers: a thin plastic (1.5mm) scintillator for detection of beta and CE, a $CaF_2$ layer (2mm) for X-ray detection and a NaI layer (25.4mm) for gamma-ray measurement. A two-channel FPGA-based Digital Pulse Processor, DPP2.0, (250 MHz, 12 bits) has been designed and constructed for capturing and transferring valid phoswich pulses to the PC. A graphical user interface (GUI) also has been developed to control the DPP2.0, digitally analyze phoswich pulses, and reconstruct the 2-D beta/gamma coincidence spectra.

In this paper, our digital pulse shape discrimination technique, the DPP2.0, and the GUI are introduced. At the end, our preliminary measurements with the prototypic phoswich detector are discussed.

## OBJECTIVE

To monitor atmospheric or underground nuclear weapons tests, special radiation detectors have been designed and employed for measuring the concentration of xenon radioisotopes in the atmosphere. In a high-level background environment, these detectors are capable of detecting very low amounts of radioxenon by employing a beta-gamma coincidence detection technique. Using this technique, the detection system updates the beta and/or gamma spectra only when the beta and gamma channels are triggered within a predefined time frame. The ARSA developed at PNNL is one such detection system which has two separate beta and gamma detection channels. The ARSA system has demonstrated detection of ultra-low concentrations of the fission product radioxenon isotopes in several field tests (McIntyre et al., 2001 and 2006). With four gas cells, the ARSA system employs 12 PMTs for detecting coincident beta and gamma rays. This number of PMT's in one compact system requires a continuous and very accurate calibration.

We have studied phoswich detectors as a simple alternative system for measuring xenon radioisotopes. A phoswich detector consists of two or more scintillation layers which are optically coupled to a single photomultiplier tube. Generally, the plastic scintillation layer, close to the front window, detects less penetrating radiations such as beta particles, whereas the last layer close to the PMT is intended to measure more penetrating radiations such as high-energy gamma rays. Then the energy deposition in each layer, either in coincidence or singles, can be measured by using digital-pulse-shape discrimination techniques.

Considering the radioxenon detection requirements and current available manufacturing capabilities, a prototypic planar triple-layer phoswich detector was designed, modeled, and constructed (Farsoni and Hamby, 2006). The phoswich detector consists of a plastic scintillator (1.5 mm) for detection of beta and conversion electrons, a $CaF_2$ crystal (2.0 mm) for X-ray detection and a NaI(Tl) crystal (25.4 mm) for measuring gamma rays. The xenon gas cell in the final system is a thin hollow disk, 2-mm thick and 76.2 mm diameter, surrounded by two identical triple-layer phoswich detectors. The gas cell is completed by an aluminum sleeve which also joins the two detectors. To digitally capture the PMT's anode pulses from the two phoswich detectors, a two-channel digital pulse processor was designed and constructed. We also developed a GUI for controlling our digital processor, detecting coincidence events, and reconstructing beta/gamma spectra from the phoswich detectors. This paper will cover our digital pulse shape discrimination technique, the two-channel digital pulse processor (DPP2.0), the GUI, and our preliminary experiments with the prototypic phoswich detector.

## RSSEARCH ACCOMPLISHED

### Digital Pulse Shape Analysis

Depending on how the incident radiation releases its energy within each layer of the phoswich detector, seven possible pulse shapes or types could be generated at the PMT's anode output (Farsoni and Hamby, 2006). Using the following equations, and by employing three digital trapezoidal filters (Figure 1), we are able to discriminate different pulse shapes or interaction scenarios as depicted in Figure 2:

Fast Component Ratio (FCR) = Fa / Fb  Equation 1

Slow Component Ratio (SCR) = (Fb-Fa) / (Fc-Fa)  Equation 2

Where

Fa = Max(Pulse∗F1)  Fb = Max(Pulse∗F2)  Fc = Max(Pulse∗F3)

Pulse: Detector Response,
F1: Triangular Filter (40 ns peaking time),
F2: Triangular Filter (300 ns peaking time),
F3: Triangular Filter (4000 ns peaking time).

In the equations above, " ∗ " is a digital convolution operator and Max() indicates the amplitude of filter response. A triangular filter is a special trapezoidal filter with Gap=0. By using three digital triangular filters, F1, F2, and F3, with appropriate peaking times, we can integrate different areas of an anode pulse. These filters also automatically perform baseline corrections. Fa, Fb, and Fc indicate the amplitudes of corresponding filter response or integration values of each area in a given pulse. In another words, Fa, Fb and Fc represent integration of each pulse 40 ns, 300 ns and 4000 ns after the trigger point, respectively. The fast scintillation component from BC-400 (with ~40-50 ns duration by our fast digital pulse processor) will appear primarily in the first area, represented by Fa, whereas the slower scintillation component from NaI(Tl) (~ 230 ns decay constant) will appear mostly in the second area, represented by Fb. Fc will cover the slowest scintillation component from the $CaF_2$ (~ 900 ns decay constant).

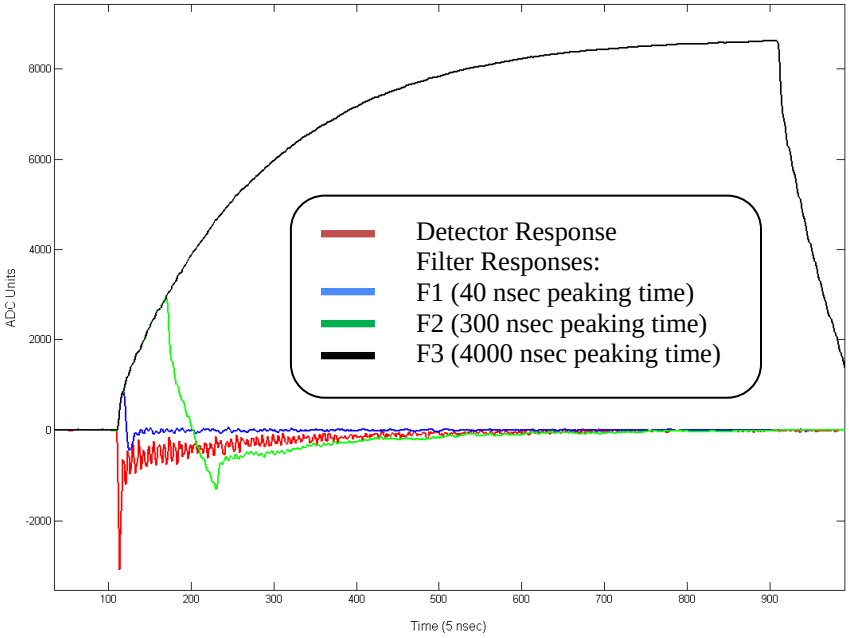


**Figure 1. Digital trapezoidal filters are employed for pulse shape analysis of phoswich pulses. The anode trace in this graph was captured with a sampling rate of 200 MHz and cutoff frequency of 95 MHz in the digital processor (analog low-pass filter).**

To discriminate between different pulse shapes, two ratios, FCR and SCR are calculated from each captured pulse. In Equations 1 and 2, the FCR and SCR range from zero to unity. Figure 2 shows a two-dimensional scatter plot of the FCR and SCR when the phoswich detector is exposed to a $^{137}Cs$ source. During this experiment, the $^{137}Cs$ source was shielded against beta and conversion electrons. Although the probability of occurrence of interaction scenarios are not same, by using this plot, the location of seven possible events or pulse shapes can be identified. Events from only BC-400 with high FCR are located in region1; these are mostly from Compton interactions from 662 keV of $^{137}Cs$. The value of FCR for $CaF_2$-only and NaI-only events is low (0.1-0.2) and similar, but with different SCR. Therefore, these events are located in regions 2 and 4, respectively. Combined events from BC-400 and $CaF_2$ fall in region 3. Region 5 accommodates combined events from BC-400 and NaI. Region 6 indicates combined events from NaI and $CaF_2$. Events falling in region 7 are assumed to have more than two components. Table 1 summarizes the origin of each event and the corresponding scintillation layer for each region when the phoswich is used for radioxenon detection. In Table 1, pulses in regions 6 and 7 have no useful information for radioxenon detection and therefore are rejected. Rejection of events in region 6 will reduce the Compton background for low-energy gamma-ray detection since these events have been involved in a Compton scatter in the $CaF_2$ and then absorption or another Compton scatter in the NaI or vice versa.

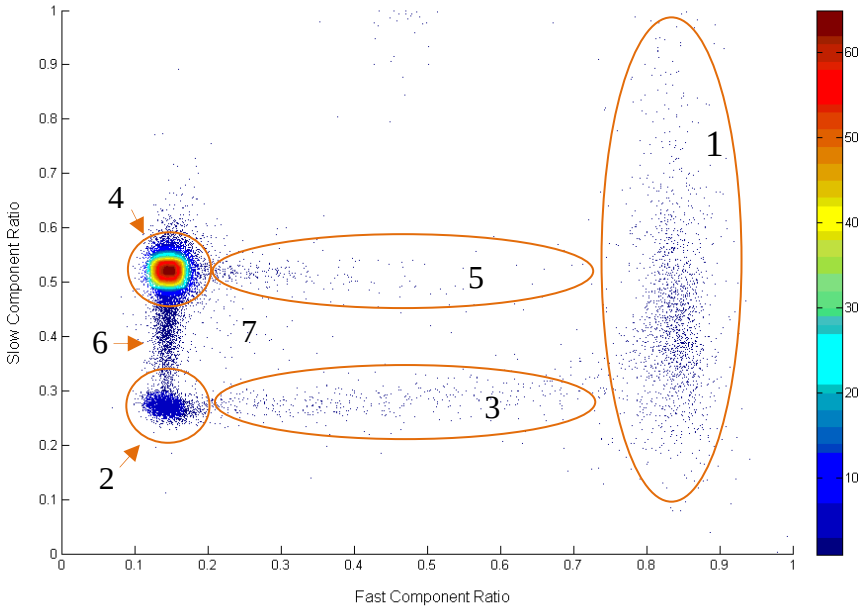


**Figure 2. Scatter of FCRs and SCRs from $^{137}$Cs. Seven marked regions correspond to seven pulse shapes, indicating how gamma rays interact with the three layers of phoswich detector. See Table 1 for more detail when this scatter plot is used for radioxenon detection.**

**Table 1. Seven pulse-type regions in Figure 2 and their corresponding layers and events when the phoswich detector is used for measuring xenon radioisotopes.**

| Region | Layer(s) | Event |
|---|---|---|
| 1 | BC-400 | Beta/CE |
| 2 | $CaF_2$ | X-Ray |
| 3 | $CaF_2$ + BC-400 | Coincidence X-Ray, Beta/CE |
| 4 | NaI | Gamma-Ray |
| 5 | NaI + BC-400 | Coincidence Gamma-Ray, Beta/CE |
| 6 | NaI + $CaF_2$ | Rejected |
| 7 | NaI + $CaF_2$ + BC-400 | Rejected |

Figure 3 shows two FCR/SCR scatter plots, once when the phoswich detector is exposed to $^{99}$Tc and again when exposed to $^{90}$Sr/$^{99}$Y. The beta particles from $^{99}$Tc always interact with the BC-400 (maximum energy of 293 keV). Therefore, region 1 is highly populated. In Figure 3b, some beta particles from $^{90}$Sr/$^{90}$Y have enough energy to pass through the BC-400 layer and interact with the $CaF_2$ layer. Therefore, regions 1 and 3 are more populated. There is a small fraction of events in region 2 which could be due to pulses with very small fast components. In both scatter plots, there is also a small fraction of events in region 4; these are assumed to be due to background gamma rays interacting in the NaI layer.

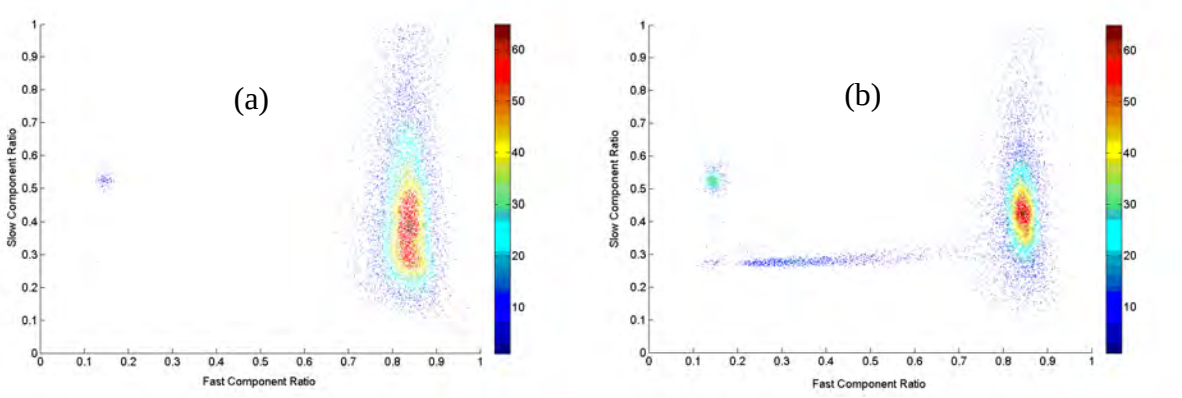


**Figure 3. Distribution of FCRs and SCRs from (a) $^{99}$Tc and (b) $^{90}$Sr/$^{90}$Y.**

**Two-Channel Digital-Pulse Processor**

A two-channel, high-speed (250 MHz) and compact (6.0 X 7.5 cm) DPP2.0 was designed and constructed for radoixenon analysis (Figure 4). The system benefits the new fast- and high-performance ADC's from analog devices (AD9230-250) with a sampling rate of 250 MHz and a resolution of 12 bits. The ADC consumes only 434 mW at its rated frequency. Such a very high sampling rate allows us to provide a more in-depth analysis of the signal pulses in which three timing components are possible. The ADC data bus uses the high performance Low-Voltage Differential Signaling (LVDS) standard. The offset and gain of each channel are controlled separately and digitally by our GUI software. The adjustable amplification gain for each channel ranges from -14 to +46 dB. A 3rd order, low-pass Bessel filter is used on board to attenuate high-frequency components in the signal pulses; the cut-off frequency of this filter is 95 MHz.

All the digital modules and functions such as trigger logic, circular buffer, digital trapezoidal filters, pile-up rejection, and coincidence detection are implemented in a 1500K gate-equivalent SPARTAN-3 FPGA from the Xilinx Incorporated. The on-board FPGA is automatically programmed via a high-speed USB2.0 port when the processor is connected to the PC. Once the FPGA is programmed (in about 30 msec), the high-speed USB2.0 interface is used either for controlling the processor or transferring data. The board is equipped with a 20-pin header interface to support a small LCD display for our future projects, when the board can be employed without using the PC.

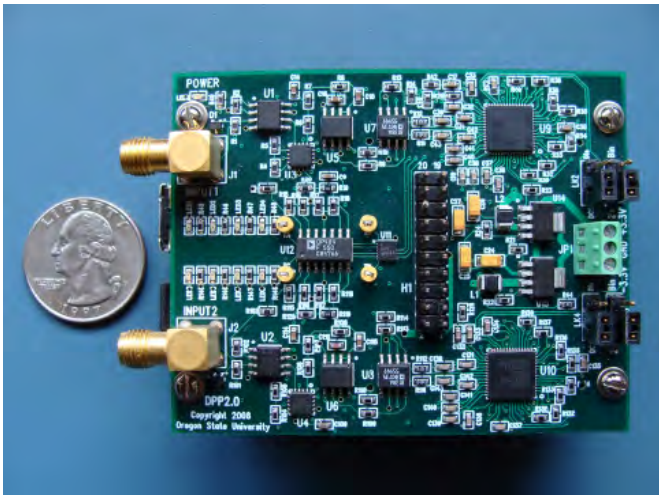


**Figure 4. The top side of high-speed (250 MHz, 12-bit) and compact (6.0 X 7.5 cm) 2-channel DPP2.0 designed in our laboratory.**

## Graphical User Interface

A GUI was developed to control the DPP2.0 and radioxenon measurements (Figure 5). The GUI is written in Python programming language and was developed with the wxPython GUI toolkit. Through the software interface, the user can specify data-collection time (either live or real time), trigger threshold, gain, offset, coincidence window, pulse-shape discrimination parameters, and energy calibration coefficients. All of these parameters can be set separately for each channel. At this stage, the GUI is intended for prototyping purposes.

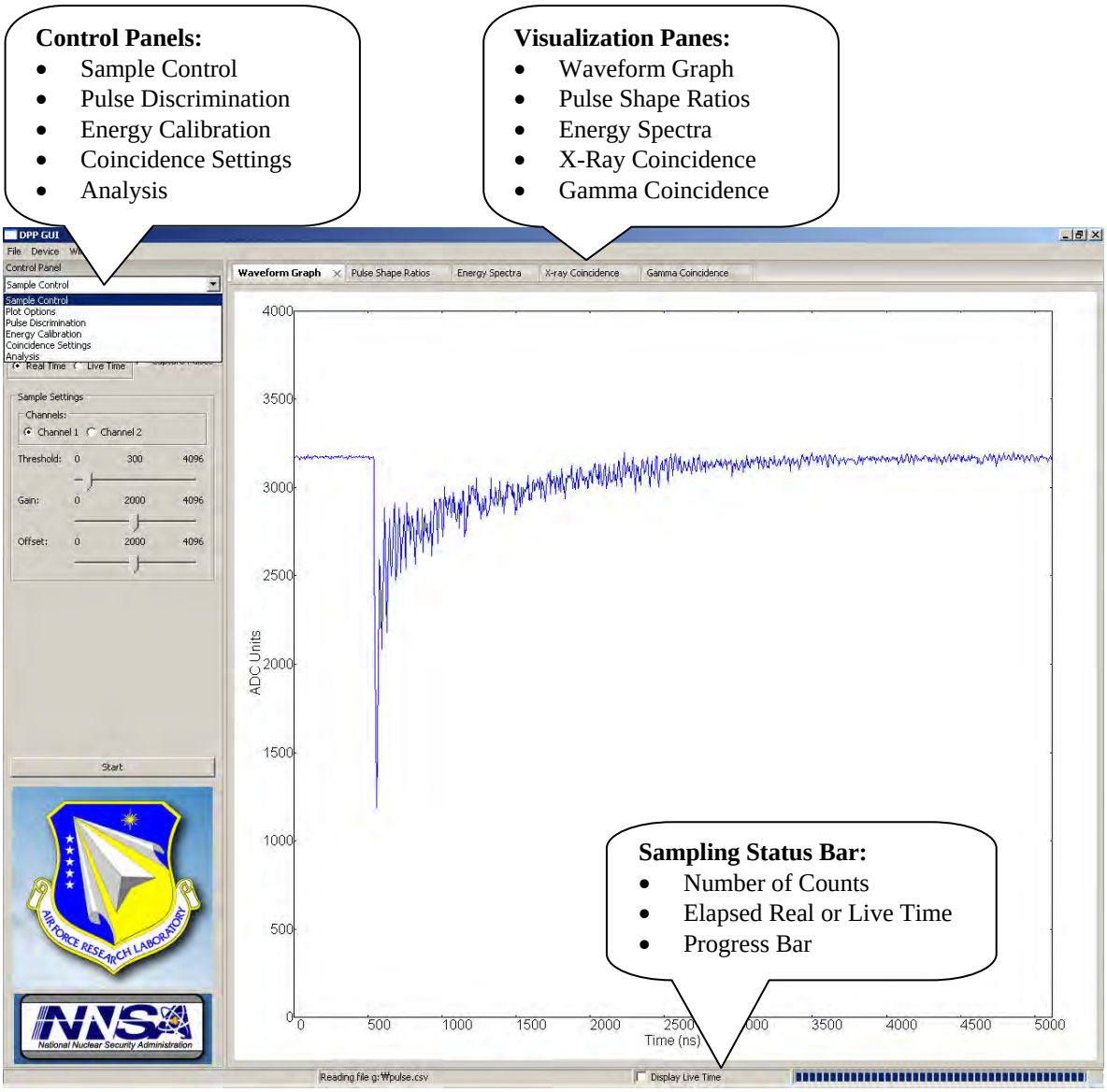


**Figure 5. A snapshot from the GUI for controlling the DPP2.0, pulse shape analysis and reconstructing beta/gamma coincidence spectra. The GUI is under development in our laboratory at Oregon State University.**

The user can direct the DPP2.0 to sample for a desired time (live or real) or number of counts through the software. During a sampling session, the GUI polls the FPGA for incoming data. When pulse data is received, the software

applies the three triangular filters to determine its FCR and SCR. Using the ratio information, the software tries to categorize the pulse into one of the five user-defined regions. Once the pulse type has been determined, the filter responses are used to calculate its energy content based on calibration coefficients for each of the different scintillator materials. Pulse type and energy are then used to produce energy histograms. The user may specify regions of interest on the histograms where the software calculates peak energy and full width half maximum (FWHM). To reduce memory usage on the host PC, the GUI discards the pulse waveforms, but saves the filter responses from each event. Hence, the effect of changing calibration and discrimination parameters can be observed without needing to begin a new sampling session. Filter widths and pre-processing parameters such as gain, offset, and threshold can also be set through the GUI, but those changes will only apply to future pulses. If further offline processing is desired, with MATLAB for example, the option to save pulse data to disk in comma separated values (CSV) format is available. The FPGA can also be reprogrammed from within the GUI if several variants of the FPGA code are to be tested. In the following, some key features of the GUI are given.

***Visualization Panes***

The GUI software has five visualization panes which are selectable via tabs along the top of the interface (see Figure 5).

***Waveform Graph.*** This pane acts as an oscilloscope for displaying individual anode pulses from each phoswich detector. By using this pane and monitoring the anode pulses, the gain and offset for each channel can be adjusted to optimize sampling conditions.

***Pulse Shape Ratios.*** This pane contains a scatter plot of FCR versus SCR for all pulses received in the sampling session.

***Energy Spectra.*** This pane contains three energy histograms corresponding to the energy spectra of three scintillator layers. These spectra are updated from events in regions 1, 2 and 4 shown in Figure 2.

***X-ray Coincidence***. This pane has two portions (not shown). The top portion of this pane contains a 2-D scatter plot of beta versus X-ray energy for pulses categorized as BC-400/$CaF_2$ coincidence events. The bottom section is a spectrum of beta energies for a specific X-ray gating energy range. This pane is provided to monitor coincidence events in the 30 keV region of the coincidence spectra.

***Gamma Coincidence***. This pane is identical to the X-ray coincidence pane, but it displays information for pulses categorized as BC-400/NaI coincidence events.

***Control Panel***

The left sidebar (see Figure 5) is the GUI control panel with six pages (see Figure 6 a through f), selectable via a drop-down list:

***Sampling Control (Figure 6a)***.In this panel, the user specifies the parameters for the sampling session. The session may be set to run for a specific real or live time, or until a certain number of pulses are acquired. For each channel of the DPP, threshold, gain, and offset can be set using sliders. The option is available to save captured pulse data to disk in CSVs format for offline processing.

***Plot Options (Figure 6b).*** This page has options to toggle the display of each channel's output and to set channel colors, rescaling the axes for the waveform graph and the pulse-shape ratio plot, and setting the update interval, which specifies how often the ratio plot and histograms are redrawn. Plots can also be exported as graphics and saved to disk via this page.

***Pulse Discrimination (Figure 6c).*** Here, the user can set the peaking time or the width of the fast-, medium-, and slow-pulse-shape discrimination filters. For a given peaking time of $T_p$, the resulting filter has $N = T_p.F_s$ taps with coefficients of -1 followed by N taps with coefficients of 1; $F_s$ is the sampling rate of ADC. The five pulse discrimination regions are also set here. For each region, the mouse can be used to select a rectangular area of the pulse-shape ratio plot where that type of pulse is expected.

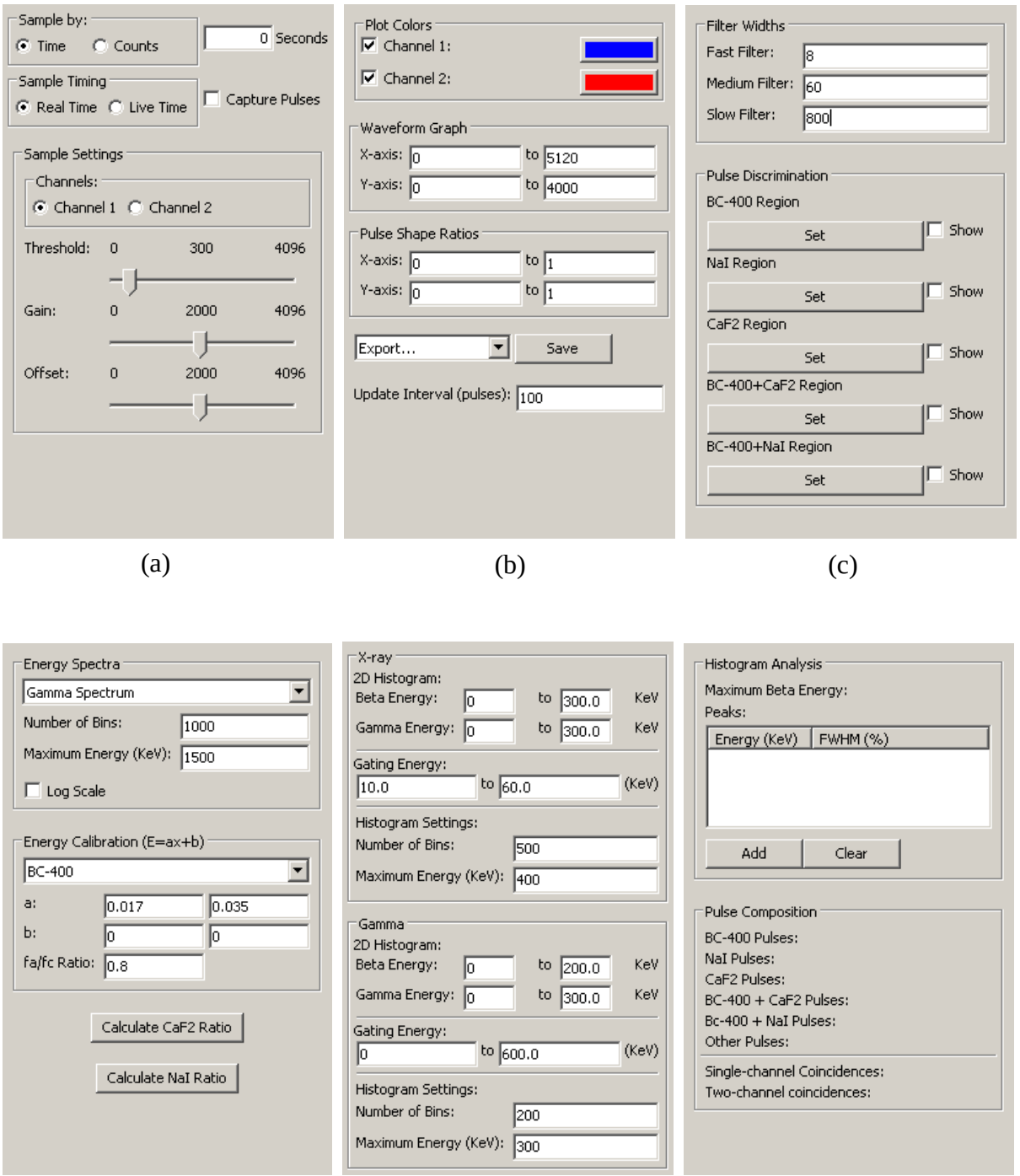


**Figure 6. Six control panels selectable via a drop-down list from the main screen (see Figure 5).**

***Energy Calibration (Figure 6d).*** This page contains controls for the histogram settings in the energy-spectra display pane. For each spectrum, maximum energy and number of bins can be specified, and the counts axis can be toggled between linear and logarithmic. The energy calibration coefficients can be set here, individually for each channel and scintillation layer. There are also two buttons in this panel to calculate the $CaF_2$ and NaI correction factors.

These correction factors are used to extract the fast component from a combined pulse, that of either $CaF_2$/BC-400 or NaI/BC-400.

***Coincidence Settings (Figure 6e).*** This page controls the two coincidence display panes. For each pane, the axes of the histograms can be rescaled and the number of bins in the energy spectrum can be set. The gating energy range for each coincidence spectrum can be set here.

***Analysis (Figure 6f).*** At the end of the sampling session, the analysis page is populated with information about pulse composition, coincidence occurrences, and maximum beta energy recorded. Here, regions of interest can be selected in the energy spectra and the software will calculate peak energy and full width half maximum.

***Other Features***

During sampling, the bottom status bar shows the number of pulses recorded, the amount of time (real or live) elapsed, and a progress bar. Dialogs are available from the top menu for reprogramming the FPGA. Saved pulse data can be re-imported to be reprocessed with different parameters such as filter width.

**Preliminary Measurements**

Because of the hygroscopic nature of the NaI, this crystal must be isolated from other parts of the detector by an optical quartz layer. Our radiation transport modeling (Farsoni and Hamby, 2006) showed that the 30 keV X-ray is significantly attenuated by the quartz. Thus, to compensate this effect, a $CaF_2$ layer was added to the phoswich design to detect 30 kev X-rays from xenon radioisotopes. Regarding its slow decay constant and relatively low-light yield, detection and discrimination of 30-keV X-ray pulses produced from this layer was challenging.

A source of $^{133}$Ba was used to find the optimum trigger parameters (e. g., duration of digital fast filter implemented in FPGA for triggering the system) in detecting and resolving X-ray and gamma rays. The $^{133}$Ba source emits X-rays (31 keV) and gamma-rays (81, 303, and 356 keV) with energies close to those of the xenon radioisotopes of interest (31, 80 and 250 keV). By processing events in regions 2 and 4 of Figure 2, the energy spectra from $CaF_2$ and NaI were obtained. The two energy spectra are depicted in Figures 7a and 7b, respectively.

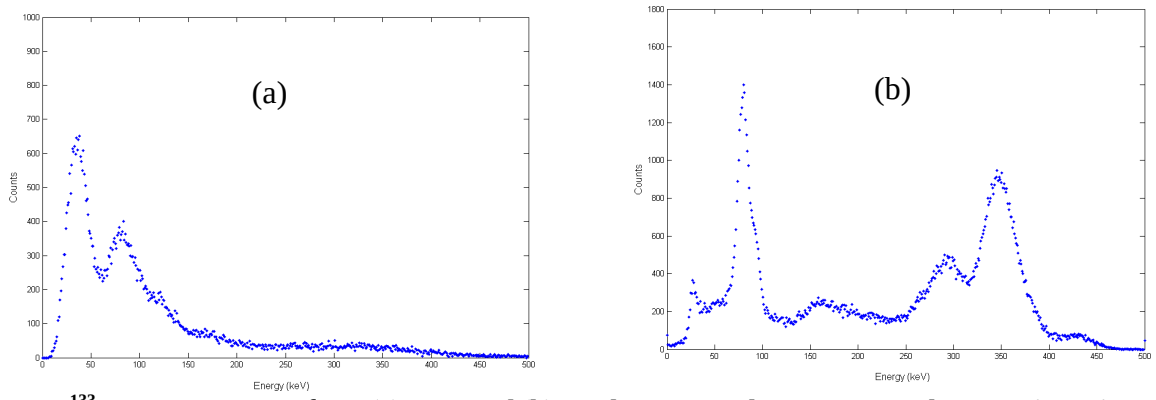


**Figure 7. $^{133}$Ba energy spectra from (a) $CaF_2$ and (b) NaI layers. For these spectra, only events in regions 2 and 4 of Table 1 were digitally processed, respectively.**

In the $CaF_2$ spectrum (Figure 7a), the FWHM for 30 keV X-ray peak is 55% and is well separated from the 81 keV gamma-ray peak. The 30 keV peak can be also seen in the NaI spectrum in Figure 7b; with a significant attenuation which was predicted by our MCNP modeling (Farsoni et al., 2007). The 81 keV peak in the NaI spectrum has a FWHM of 17%. Other gamma-rays with higher energies from $^{133}$Ba, such as 303 keV and 356 keV, are also prominent in this spectrum. There is also a peak from 276 keV gamma-ray which is overlapped with the 303 keV peak. At the time this paper was prepared, radioactive xenon gas was not available to test and characterize the phoswich detector for beta/gamma coincidence measurements.

## CONCLUSION

We have developed a two-parameter digital-pulse-shape analysis technique to discriminate different pulse shapes from the three layers of our phoswich detector. We have also designed and constructed a fast and compact two-channel DPP2.0 to digitally process the anode pulses from our two-channel triple-layer phoswich detector. All the digital modules and functions are implemented in a 1500K gate-equivalent SPARTAN-3 FPGA from the Xilinx Incorporated. A GUI has been developed to control the digital processor and to digitally analyze phoswich pulses. Features to be added in the GUI include concentration calculations using regions of interest, background stripping considering the memory effect, and triple coincidence display. The preliminary experiments with $^{133}$Ba showed that the use of $CaF_2$ in the phoswich design significantly increases the efficiency of the detector in measuring 30 keV X-rays from xenon radioisotopes. This experiment qualitatively demonstrated the digital pulse shape analysis technique and confirmed our previous MCNP modeling. Our future work includes use of commercially available radioxenon gas ($^{133}$Xe) to test and characterize the detection system for beta/gamma coincidence measurements. We are also currently working to produce a measurable amount of fission-product radioxenons by irradiating a highly enriched uranium foil in the Oregon State University's TRIGA reactor.

## REFERENCES

McIntyre, J. I., K. H. Able, T. W. Bowyer, J. C. Hayes, T. R. Heimbigner, M. E. Panisko, P. L. Reeder, and R. C. Thompson (2001). Measurements of ambient radioxenon levels using the automated radioxenon sampler/analyzer (ARSA), *J. Radioanal. Nucl. Chem.* 248: 3, 629–635.

McIntyre, J. I., T. W. Bowyer, and P. L. Reeder (2006). Calculation of minimum detectable concentration levels of radioxenon isotopes using the PNLL ARSA system, Technical Report, PNNL-13102 (March 2006).

Farsoni, A. T. and D. M. Hamby (2006). Study of a triple-layer phoswich detector for beta and gamma spectroscopy with minimal crosstalk, in *Proceedings of the 28th Seismic Research Review: Ground-Based Nuclear Explosion Monitoring Technologies*, LA-UR-06-5471, Vol. 2, pp. 794–792.

Farsoni, A. T., D. M. Hamby, K. D. Ropon, and S. E. Jones (2007). A two-channel phoswich detector for dual and triple coincidence measurements of radioxenon isotopes, in *Proceedings of the 29th Monitoring Research Review: Ground-Based Nuclear Explosion Monitoring Technologies*, LA-UR-07-5613, Vol. 2, pp. 747–756.

# PRODUCTION OF SAMPLES OF INDIVIDUAL RADIOXENON ISOTOPES THROUGH NEUTRON IRRADIATION OF STABLE XENON GAS

Derek A. Haas[1], Steven R. Biegalski[2], and Kendra M. Foltz Biegalski[2]

Pacific Northwest National Laboratory[1] and The University of Texas at Austin[2]

Sponsored by Army Space and Missile Defense Command

Contract No. W9113M-05-1-0017
Proposal No. BAA05-49

## ABSTRACT

The Spectral Deconvolution Analysis Tool (SDAT) software was developed to improve counting statistics and detection limits for nuclear explosion radionuclide measurements. SDAT utilizes spectral deconvolution spectroscopy techniques and can analyze both β-γ coincidence spectra for radioxenon isotopes and high-resolution HPGe spectra from aerosol monitors.

The deconvolution algorithm of the SDAT requires a library of β-γ coincidence spectra of individual radioxenon isotopes to determine isotopic ratios in a sample. In order to get experimentally produced spectra of the individual isotopes, we have irradiated enriched samples of $^{130}$Xe, $^{132}$Xe, and $^{134}$Xe gas with a neutron beam from the TRIGA reactor at The University of Texas. The samples produced were counted in an Automated Radioxenon Sampler/Analyzer (ARSA) style β-γ coincidence detector. The spectra produced show that this method of radioxenon production yields samples with very high purity of the individual isotopes for $^{131m}$Xe and $^{135}$Xe and a sample with a substantial $^{133m}$Xe to $^{133}$Xe ratio.

## OBJECTIVES

The goal of the experiment is to produce β-γ coincidence spectra of gaseous samples of each radioxenon isotope of interest in nuclear explosion monitoring. This experiment will take a new approach to creating radioxenon through neutron irradiation of stable xenon gas. The data is needed as a required library data set for the operation of the SDAT (Foltz Biegalski 2003, Biegalski 2005).

In order to produce the radioxenon isotopes of interest $^{130}$Xe must be activated to $^{131m}$Xe, $^{132}$Xe must be activated to both $^{133}$Xe and $^{133m}$Xe, and $^{134}$Xe must be activated to $^{135}$Xe. The irradiation is done in Beam Port 2 of The University of Texas at Austin 1.1 MW TRIGA reactor. The beam port is tangential to the core and has a neutron collimator. The thermal neutron equivalent flux emerging from the beam port is 1.24 x$10^{8}$ n $cm^{-2}$ $s^{-1}$ when the reactor is operating at 950 kW (Whitney 2006).

The gas is then transferred to a detector system very similar to that in the ARSA for counting (Bowyer 1999). The β-γ coincidence spectra that are produced are analyzed for purity and the effectiveness of the procedure is determined. For a more detailed explanation of the work, see the dissertation by Haas referenced here (Haas 2008).

## RESEARCH ACCOMPLISHED

### Results of $^{130}$Xe Irradiation

The production of $^{131m}$Xe through irradiation of enriched $^{130}$Xe is shown in Figure 1. The spectrum initially contained noticeable amounts of $^{133}$Xe and $^{135}$Xe. After three days of decay, the activity of $^{131m}$Xe has been reduced by less than half, but this constitutes more than seven half lives of $^{135}$Xe, effectively reducing it to background levels.

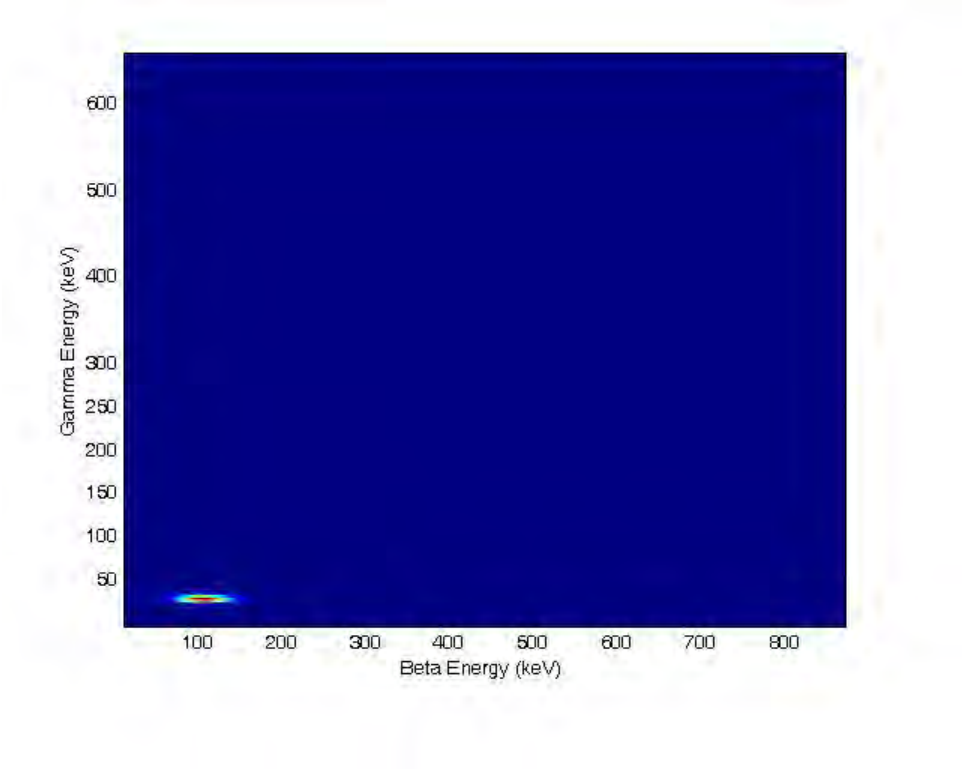


**Figure 1. Spectrum of a sample containing only $^{131m}$Xe—6.9-hour irradiation, 73.4-hour decay, 87.6-hour count**

The data in Figure 1 are analyzed and the initial ratio of $^{131m}$Xe/$^{133}$Xe by activity at the time the sample is placed in the detector is found to be 316, or a sample that is 99.7% $^{131m}$Xe by activity. If greater purity is needed, the sample can be allowed to decay further to increase the ratio, but this will also increase the effect of background counts on the sample.

### Results of $^{132}$Xe Irradiation

The irradiation of $^{132}$Xe results in both $^{133}$Xe and $^{133m}$Xe. Because $^{133m}$Xe has a shorter half life than $^{133}$Xe the optimum ratio of $^{133m}$Xe to $^{133}$Xe occurs immediately after irradiation. Figure 2 shows the spectrum produced when both $^{133m}$Xe and $^{133}$Xe are present.

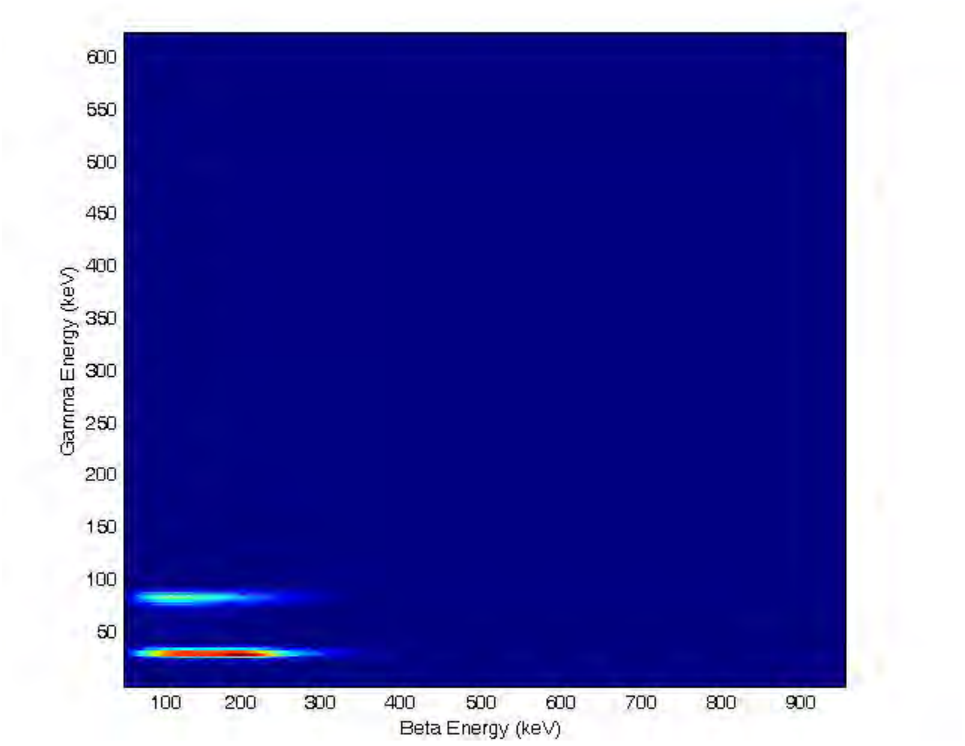


**Figure 2. Spectrum of a sample containing both $^{133}$Xe and $^{133m}$Xe—7.3-hour irradiation, 1.5-hour decay, 209.6-hour count.**

Figure 3 is a surface plot of the same data as Figure 2 and more obviously depicts the $^{133m}$Xe peak. Due to the greater probability that a $^{132}$Xe nucleus will be activated to the ground state than the metastable state of $^{133}$Xe, $^{133m}$Xe cannot be produced without simultaneously producing a greater activity of $^{133}$Xe using this method of radioxenon production.

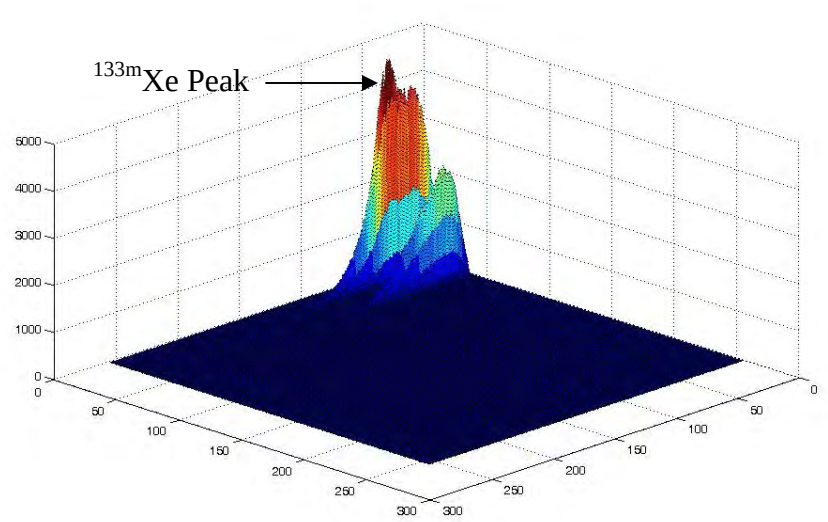


**Figure 3. Alternate view of mixed-sample spectrum—7.3-hour irradiation, 1.5-hour decay, 209.6-hour count.**

The procedure for this sample is to collect one mixed spectrum containing $^{133m}$Xe and $^{133}$Xe and one spectrum of the remaining $^{133}$Xe after the $^{133m}$Xe has decayed to background levels. A spectrum of $^{133}$Xe normalized to match the counts of $^{133}$Xe in the mixed spectrum can be subtracted from the mixed spectrum to yield a spectrum containing only $^{133m}$Xe.

Figure 4 shows the spectrum of $^{133}$Xe after the $^{133m}$Xe has decayed away. The count that produced this spectrum was started 9 days after the sample was produced. Since the expected initial activity of $^{133m}$Xe is around 25% of the expected initial activity of $^{133}$Xe, the activity of $^{133m}$Xe should be only a few percent that of $^{133}$Xe after four half lives. Also, the percentage of $^{133m}$Xe in the sample will decrease as the count is taken. Figure 5 shows a surface plot of the spectrum of $^{133}$Xe where the $^{133m}$Xe peak is visibly absent.

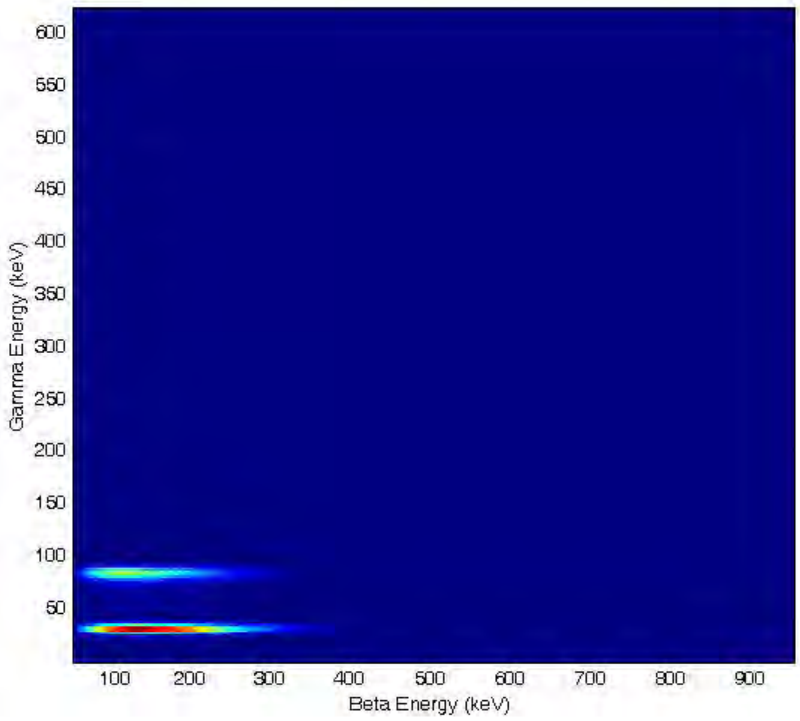


**Figure 4. Spectrum of a sample containing high purity $^{133}$Xe—7.3-hour irradiation, 211.1-hour decay, 330.2-hour count.**

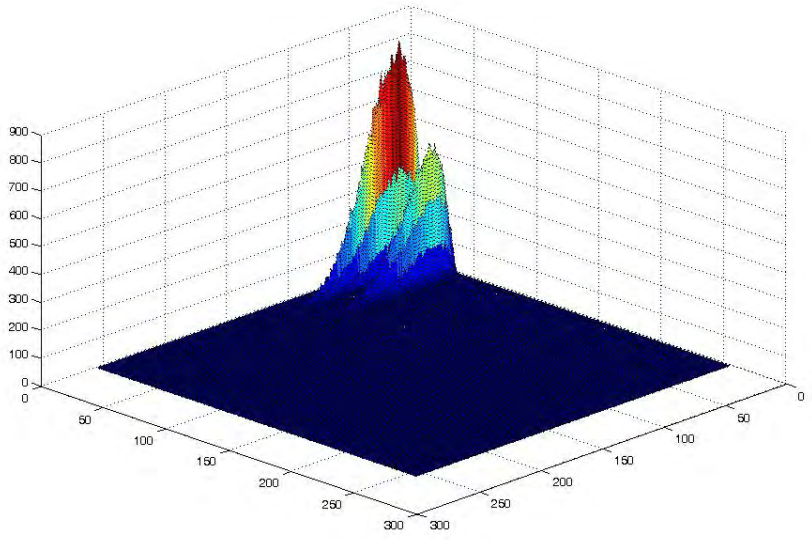


**Figure 5. Alternate view of $^{133}$Xe spectrum—7.3-hour irradiation, 211.1 hour decay, 330.2-hour count.**

The spectrum of $^{133}$Xe is normalized so that the 81 keV γ-peak has the same magnitude as the same peak in the mixed spectrum. Then the $^{133}$Xe spectrum is subtracted from the mixed spectrum, resulting in a sample consisting solely of $^{133m}$Xe. The result is shown in Figure 6.

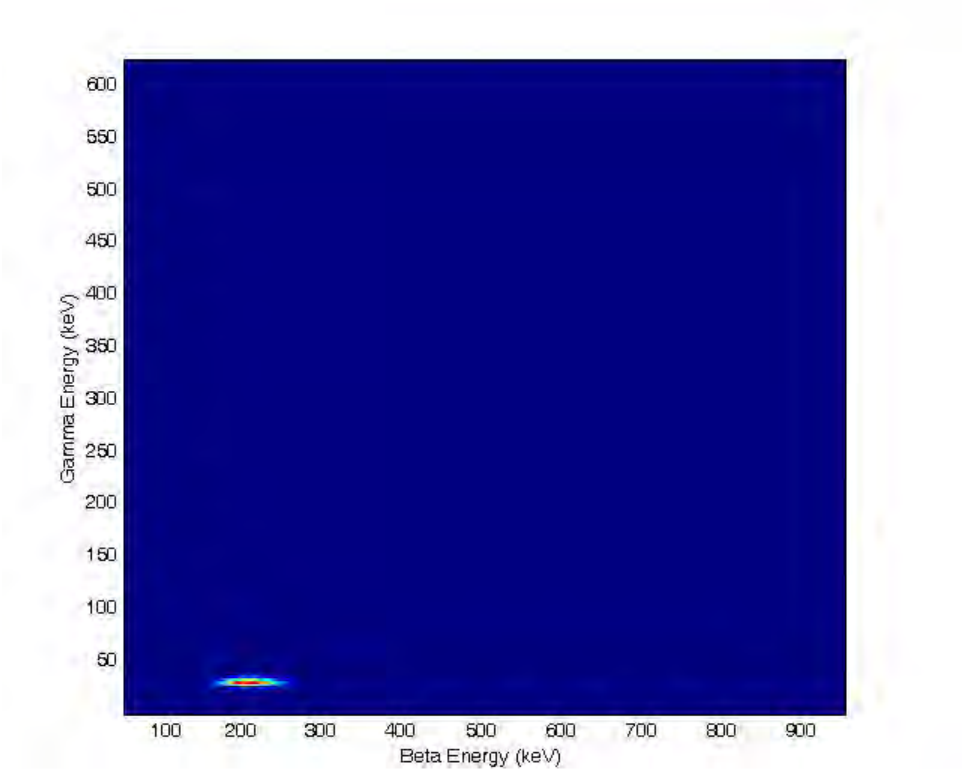


**Figure 6. Sample of $^{133m}$Xe resulting from subtraction of $^{133}$Xe from the mixed sample—7.3-hour irradiation, 1.5-hour decay, 209.6-hour count.**

The data in Figures 2 and 6 are analyzed to get the initial activity of each isotope. The 81 keV peak data is used to determine the activity of $^{133}$Xe. Of particular interest in evaluating the method of neutron irradiation of stable xenon gas is the ratio of $^{133m}$Xe to $^{133}$Xe that can be produced. The ratio found using an eight-hour irradiation is 0.31 by activity. This corresponds to a sample consisting of 23.6% $^{133m}$Xe and 76.4% $^{133}$Xe by activity.

### Results of $^{134}$Xe Irradiation

The most significant results of the enriched xenon irradiation are the spectra of isolated $^{135}$Xe. Because $^{135}$Xe has the shortest half life of the four radioxenon isotopes of interest, the spectra of $^{135}$Xe produced through the fission of uranium have an impurity of the other radioxenon isotopes. The spectrum produced through the irradiation of enriched $^{134}$Xe is shown in Figure 7.

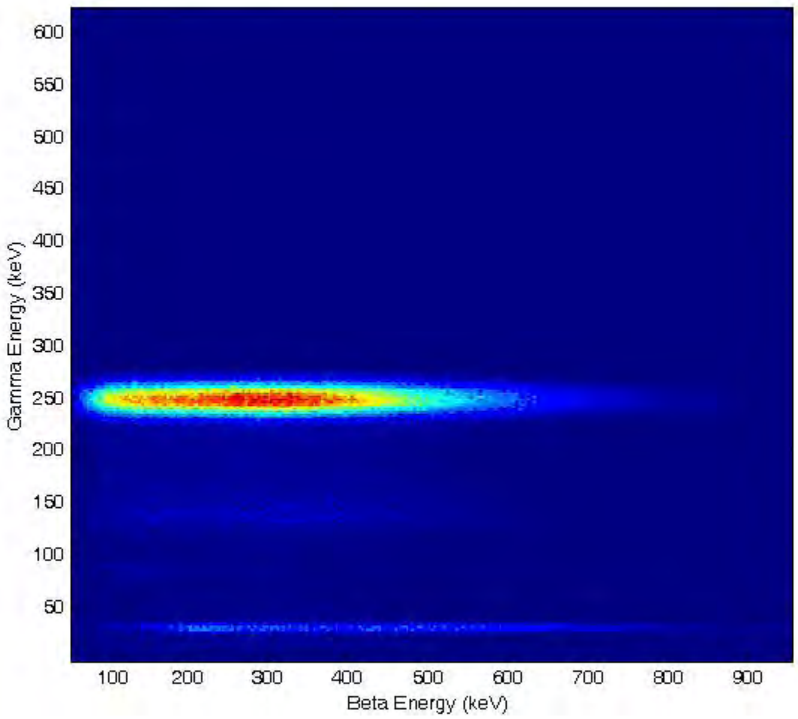


**Figure 7. Experimental $^{135}$Xe spectrum with trace amounts of $^{133m}$Xe and 133Xe—6.9-hour irradiation, 0.6-hour decay, 18.6-hour count**

The data from Figure 7 are analyzed with a longer count taken to provide more $^{133}$Xe counts. The 250 keV peak and 81 keV peak data were used to determine the activity of $^{135}$Xe and $^{133}$Xe, respectively. The same calculation can be done for the ratio of $^{135}$Xe to ($^{133}$Xe+$^{133m}$Xe) as was done for the ratio of $^{133m}$Xe to $^{133}$Xe. The sample of irradiated enriched $^{134}$Xe is found to be 99.1% $^{135}$Xe by activity when the sample is placed in the detector.

### Analysis of the Experimental Method in Context

The purpose for conducting these experiments was to produce spectra of the radioxenon isotopes that are of greater isotopic purity than those that have been produced in the past. In order to compare this method to others, we must find the activity of each isotope in each sample. Using the efficiency calculations from modeling and the counts-per-second data from the experiment section, we can determine the activity of the samples produced.

The sample of isolated $^{131m}$Xe is not as significant as the samples of the other isotopes due to the ability to wait for any sample of mixed radioxenon gas to decay until only $^{131m}$Xe remains. These data do prove, however, that the neutron irradiation of stable $^{130}$Xe can be used to produce samples of $^{131m}$Xe.

In order to compare this method to radioxenon production through the fission of $^{235}$U, we can derive the ratios of samples that can be extracted from the fission gases. The direct fission yields of $^{235}$U show that isotopic ratios

greater than those achieved through stable gas irradiation are possible with this method, but the build-in of $^{133}$Xe occurs quickly through the decay of $^{133}$I.

The production of radioxenon through the fission of $^{235}$U is modeled in ORIGEN-ARP2 to determine isotopic ratios from various reactor operation times (ORNL 2004). The results for the ratio of $^{133m}$Xe to $^{133}$Xe produced through fast separation of fission products are shown in Table 1 with the results from the stable gas irradiation experiment. Because separation is not a factor in the irradiation of stable gas, the ratio as a function of separation time is constant.

**Table 1. Initial Ratio by Activity of $^{133m}$Xe to $^{133}$Xe using Various Methods of Production**

| $^{133m}$Xe/$^{133}$Xe Ratio | Irradiation time (minutes) | | | | Ratio given by |
|---|---|---|---|---|---|
| Separation Time (hours) | 60 | 15 | 5 | 1 | Xe Irradiation Method |
| 0.5 | 0.115 | 0.164 | 0.186 | 0.196 | |
| 1 | 0.096 | 0.108 | 0.113 | 0.114 | |
| 3 | 0.078 | 0.080 | 0.080 | 0.080 | 0.31 |
| 5 | 0.074 | 0.075 | 0.075 | 0.075 | |
| 10 | 0.071 | 0.071 | 0.071 | 0.071 | |

The table above shows that even with a very short irradiation time, the ratio is not as high for the $^{235}$U method as for the xenon irradiation method. This calculation is also done to determine the ratio of $^{135}$Xe to the other radioxenon isotopes. This is shown in Table 2.

**Table 2. Initial ratio by activity of $^{135}$Xe to other radioxenon isotopes using various methods of production**

| $^{135}$Xe/($^{133}$Xe+$^{133m}$Xe+$^{131m}$Xe) Ratio | Irradiation time (minutes) | | | | Ratio given by |
|---|---|---|---|---|---|
| Separation Time (hours) | 60 | 15 | 5 | 1 | Xe Irradiation Method |
| 0.5 | 85 | 127 | 140 | 143 | |
| 1 | 67 | 84 | 88 | 89 | |
| 3 | 42 | 46 | 46 | 46 | 106 |
| 5 | 33 | 34 | 35 | 35 | |
| 10 | 21 | 22 | 22 | 22 | |

The two tables above show that the fast separation of the radioxenon isotopes may provide a method for achieving a higher initial ratio of the activity of $^{135}$Xe to the activities of the other radioxenon isotopes, but its application to the production of pure $^{133m}$Xe may be limited. The tables also show that the isotopic ratios produced using the irradiation of enriched stable xenon gas are significantly higher than those produced by systems that take hours to separate the radioxenon from other fission products.

## CONCLUSIONS AND RECOMMENDATIONS

The experiment to produce β-γ coincidence spectra of individual radioxenon isotopes through the neutron irradiation of enriched stable xenon gas has succeeded. Two of the four isotopes ($^{131m}$Xe and $^{135}$Xe) have been detected with greater than 99% purity. The production of an isolated sample of $^{133m}$Xe is not possible using these techniques, but a spectrum of the isotope has been produced through the subtraction of $^{133}$Xe. And a spectrum of $^{133}$Xe has been collected with trace amounts of $^{133m}$Xe and $^{131m}$Xe.

The data produced in this work will be used to further the field of underground nuclear explosion monitoring through the SDAT program. The application of this technique will allow the benchmarking of future detectors with samples of individual radioxenon isotopes as opposed to a mixture of all four. These benchmarks, along with improved data-analysis programs such as the SDAT will improve the sensitivity of global monitoring systems.

**ACKNOWLEDGEMENTS**

Thanks to Ted Bowyer, Justin McIntyre, and Matt Cooper of Pacific Northwest National Laboratory for their instruction on the setup and use of an ARSA style detector.

**REFERENCES**

Biegalski, S. R., K. M. Foltz Biegalski, and D. A. Haas (2005). Development of the spectral deconvolution analysis tool (SDAT) to improve counting statistics and detection limits for nuclear explosion radionuclide measurements, in *Proceedings of the 27th Seismic Research Review*: *Ground-Based Nuclear Explosion Monitoring Technologies*, LA-UR-05-6407, Vol. 2, pp. 770–778.

Bowyer, T. W., K. H. Abel, C. W. Hubbard, M. E. Panisko, P. L. Reeder, R. C. Thompson, and R. A. Warner (1999). Automated separation and measurement of radioxenon for the Comprehensive Test Ban Treaty, J. *Radioanal Nuc. Chem*. 1999. 235: (1-2), 77–81.

Foltz Biegalski, K. M., and S. R. Biegalski (2003). Deconvolution of Three-Dimensional Beta-Gamma Coincidence Spectra from Xenon Sampling and Measurement Units. in *Proceedings of the 25th Seismic Research Review—Nuclear Explosion Monitoring: Building the Knowledge Base*, LA-UR-03-6029, Vol. 2, pp. 542–551.

Haas, D. A. (2008). *Production of $\beta$–$\gamma$ Coincidence Spectra of Individual Radioxenon Isotopes for Improved Analysis of Nuclear Explosion Monitoring Data*. PhD Dissertation, The University of Texas at Austin.

Oak Ridge National Laboratory (ORNL). *Origen-ARP2*. 2004.

Whitney, S. C. (2006). *Light-Element Neutron Depth Profiling at the University of Texas*. MS Thesis, University of Texas at Austin.

# DEVELOPMENT OF A COTS RADIOXENON DETECTOR SYSTEM USING PHOSWICH DETECTORS AND PULSE SHAPE ANALYSIS

Wolfgang Hennig[1], Hui Tan[1], William K. Warburton[1], Anthony Fallu-Labruyere[1], Konstantin Sabourov[1], Matthew W. Cooper[2], Justin I. McIntyre[2], and Anshel Gleyzer[3]

XIA LLC[1], Pacific Northwest National Laboratory[2], and PhotoPeak, Inc[3]

Sponsored by National Nuclear Security Administration

Contract No. DE-FG02-04ER84121

## ABSTRACT

Several of the radioxenon detection systems developed for the International Monitoring System use beta/gamma coincidence detection to achieve high sensitivity. These systems, e.g., the Automated Radioxenon Sampler and Analyzer (ARSA) or the Swedish Automatic Unit for Noble gas Acquisition (SAUNA), currently use an arrangement of separate beta and gamma detectors to detect beta/gamma coincidence events characteristic of the different radioxenon isotopes. While they are very sensitive to small amounts of radioxenon, they also require careful calibration and gain matching of several detectors and photomultiplier tubes. An alternative approach is the use of a single phoswich detector in which beta-gamma coincidences are detected by pulse shape analysis (PSA). We previously reported the development of prototype phoswich well detectors, consisting of a fast plastic scintillator (absorbing betas) optically coupled to a slower CsI(Tl) scintillator (absorbing gammas). These detectors thus require only a single photomultiplier tube and an electronics readout channel. Beta/gamma coincidences create characteristic “fast/slow” signals that can easily be distinguished from “slow only” or “fast only” non-coincident interactions.

In this paper, we will describe the development of a commercial off-the-shelf (COTS) radioxenon detector system based on such phoswich detectors. The PSA functions were implemented using the digital signal processor in a set of commercial readout electronics that is also compatible with ARSA and SAUNA detectors. These functions detect coincidences in real time and accumulate 2D histograms in on-board memory. The acquisition and the PSA functions are operated through a C driver library that is called from a graphical user interface but can also be integrated into larger-scale acquisition and control software. Several phoswich detectors have been manufactured in a small-scale production run, and have been characterized for energy resolution, separation of coincidence events in 2D beta/gamma energy histograms, and detection efficiency using a variety of test sources, and for background count rates. In addition, a test pulser module has been developed to support monitoring and testing of the electronics for state of health during operation. The phoswich detector, readout electronics, and software are now available as a COTS product package (“PhosWatch”) that is currently being beta-tested at several radioxenon monitoring research laboratories.

## OBJECTIVES

Systems to measure the amount of radioactive xenon in the atmosphere, part of the International Monitoring System established by the Comprehensive Nuclear-Test-Ban Treaty to detect nuclear weapons testing, have been installed in several locations around the world. Several of these radioxenon detection systems, e.g., the ARSA or the SAUNA, use beta/gamma coincidence detection to suppress non-coincident background and achieve high sensitivity to the coincidence events characteristic of the radioxenon isotopes of interest (Reeder, 1998; Ringbom et al., 2003).

While these systems are very sensitive to small amounts of radioxenon, their complex arrangement of separate beta and gamma detectors also requires careful calibration and gain matching, which can make them cumbersome to operate. An alternative approach is the use of a single phoswich detector (Ely, 2003; Hennig, 2006-1; Farsoni et al., 2007) in which beta/gamma coincidences are detected by PSA. We previously reported the development of prototype phoswich well detectors (Hennig, 2007-1), consisting of a fast plastic scintillator cell containing the Xe gas and mainly absorbing beta particles and conversion electrons, optically coupled to and surrounded by a slower CsI(Tl) scintillator mainly absorbing X-rays and gamma rays. The phoswich detector thus requires only a single photomultiplier tube (PMT) and electronics readout channel. Beta/gamma coincidences create characteristic "fast/slow" signals that can easily be distinguished from "slow only" or "fast only" non-coincident interactions by PSA algorithms.

The objective of the work presented in this paper is to develop a COTS radioxenon detector unit based on phoswich detectors that can be used as a drop-in replacement for ARSA or SAUNA detector units. This objective consists of several tasks: 1) Manufacturing phoswich detectors in a small-scale production run and characterizing their performance. 2) Implementing the PSA functions in the digital signal processor (DSP) of the readout electronics (the DGF Pixie-4; Hennig, 2007-2) and integrating control of and output from PSA functions into the Pixie-4 user interface. 3) Developing a programmable coincidence pulse generator ("pulser") to support monitoring and testing of the electronics for state of health during operation. The research accomplished in each of these three tasks is described below.

## RESEARCH ACCOMPLISHED

### Detector Production and Characterization

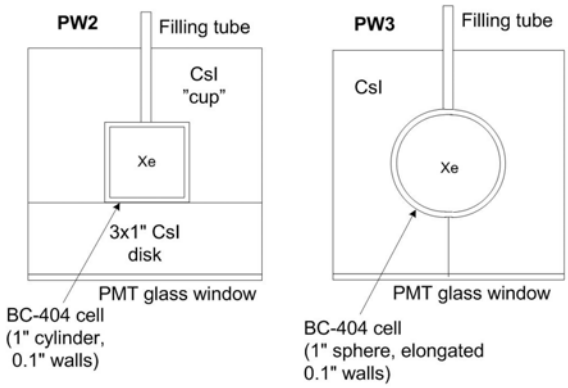


**Figure 1. Geometries of phoswich well detectors studied. Left: 1st well prototype (PW2). Right: 2nd well prototype and production detectors (PW3-PW7).**

At the time of this writing, a total of six phoswich well detectors have been built, named PW2-PW7. They all consist of a 1"-diameter BC-404 plastic cell enclosed in and optically coupled to a 3"-diameter CsI(Tl) crystal, but differ in detector geometry as shown in Figure 1. The geometry of the first well detector prototype PW2 is easier to manufacture, but due to the cut in CsI parallel to the PMT window, the light collection and thus energy resolution are degraded according to simulations (Hennig, 2006-2). The geometry of PW3-PW7, an elongated spherical cell embedded in a CsI crystal cut perpendicular to the PMT window, has the best light collection and resolution among all designs studied in simulations, though it is more difficult to manufacture. PW2, PW4, and PW5 use PMT model 9305KB (ElectronTubes, Inc), PW6-PW7 use PMT model R1307 (Hamamatsu). PW3 originally used PMT model

9305KB, but since this particular PMT performed poorly (low gain and noisy), PW3 was rebuilt with a new PMT and crystal and renamed to PW3a.

For each detector, acquisition parameters such as gain, HV bias, trigger thresholds and energy filter settings were first individually optimized for best performance. Detectors were then characterized by measuring resolutions at various energies with a number of test sources (see Table 1). It can be seen that PW2 achieves good resolutions at low energies, but at higher energies the resolutions degrade and the spectrum even shows double peaks. We attribute this to the different light-collection efficiency in the two sections of the CsI crystal, resulting in an estimated ~6% higher PMT signal amplitude from photons absorbed in the lower section of the CsI crystal than from photons absorbed in the upper section (Hennig, 2006-2). This amplitude difference adds in quadrature to other peak broadening effects (e.g., photostatistics), and thus becomes neglible at low energies, but not at high energies. PW3, the second prototype, achieved good resolution at high energies (~9% full width at half maximum [FWHM] at 662 keV), but with the original low gain, noisy PMT achieved only ~47% at 30 keV from $^{133}$Xe (small signal close to noise). PW4 and PW5, having preselected the PMT before assembly, combine the good resolution at high energy due to the better crystal geometry with the good resolution at low energy due to the low-noise PMT. PW6, PW7, and PW3a, using a different PMT and biasing system with even lower noise, achieve the best energy resolution of all detectors studied, except for low-energy beta lines.

**Table. 1. Energy resolution (FWHM) for various energies. Measurements with external sources use no PSA and measure only the energy deposited in CsI (Ec). Measurements with internal sources use PSA to extract the energy deposited in CsI by gamma-only events (Eco), the energy deposited in the plastic scintillator by beta-only events (Epo), and the energies deposited in either scintillator in coincidence events (Ecb and Epb). Numbers in () indicate non-optimal measurements as explained in the notes. Measurements with the rebuilt detector PW3a are still in progress.**

| Resolution (FWHM) | PW2 | PW3a | PW4 | PW5 | PW6 | PW7 | Notes |
|---|---|---|---|---|---|---|---|
| PMT model | 9305KB | R1307 | 9305KB | 9305KB | R1307 | R1307 | |
| Ec = 662keV (external $^{137}$Cs) | (12%) | 7.0% | 8.4% | 8.5% | 7.3% | 7.2% | PW2: two peaks, ~7% and ~9% |
| Ec = 120keV (external $^{57}$Co) | 16% | 11.4% | 13% | 14% | 12.7% | 11.6% | |
| Ec = 60keV<br>Ec = 26keV (external $^{241}$Am) | 18%<br>31% | 16%<br>28% | 17%<br>34% | 19%<br>32% | 17%<br>29% | 16%<br>27% | |
| Ecb = 20keV<br>Eco = 88 keV<br>Epb = 60 keV<br>Epo = 88 keV (internal $^{109}$Cd) | 39%<br>19%<br>44%<br>33% | (28%)<br>(20%) | -- | -- | 34%<br>17%<br>50%<br>43% | 32%<br>16%<br>47%<br>58% | PW3a: preliminary |
| Ecb = 609keV (internal $^{222}$Rn) | (12%) | | -- | -- | -- | 7.8% | PW2: two peaks, ~7% and ~9% |
| Ecb = 80keV (internal $^{133}$Xe) | 20% | | 21% | 21% | 17% | 16% | |
| Ecb = 30keV<br>Epb = 129keV<br>Epo = 160 keV (internal $^{131m/133}$Xe) | 35%<br>26%<br>29% | | 35%<br>--<br>-- | 34%<br>29%<br>29% | 30%<br>33%<br>33% | 28%<br>33%<br>34% | |

The photon energy resolutions of the "production detectors" PW4-PW7 are significantly better than resolutions reported for the ARSA detector, which achieves ~12% (FWHM) at 662 keV (Reeder, 2004) compared to ~8.5% for PW4 and PW5 and even 7.3-7.0% for PW6, PW7, and PW3a. For energies above 80 keV, the production detectors also match or exceed the resolutions obtained with Pacific Northwest National Laboratory's (PNNL's) redesigned β–γ detector, which in the preferred CsI(Na) variant achieves ~8.7% at 662 keV (Cooper, 2007-1). PW6, PW7, and PW3a even match or exceed the resolution of the SAUNA II detector, which achieves ~7.3% at 662 keV. However,

when comparing these resolutions it should be kept in mind that count rates and other experimental conditions can not be assumed to be the same for measurements performed at different times and institutions.

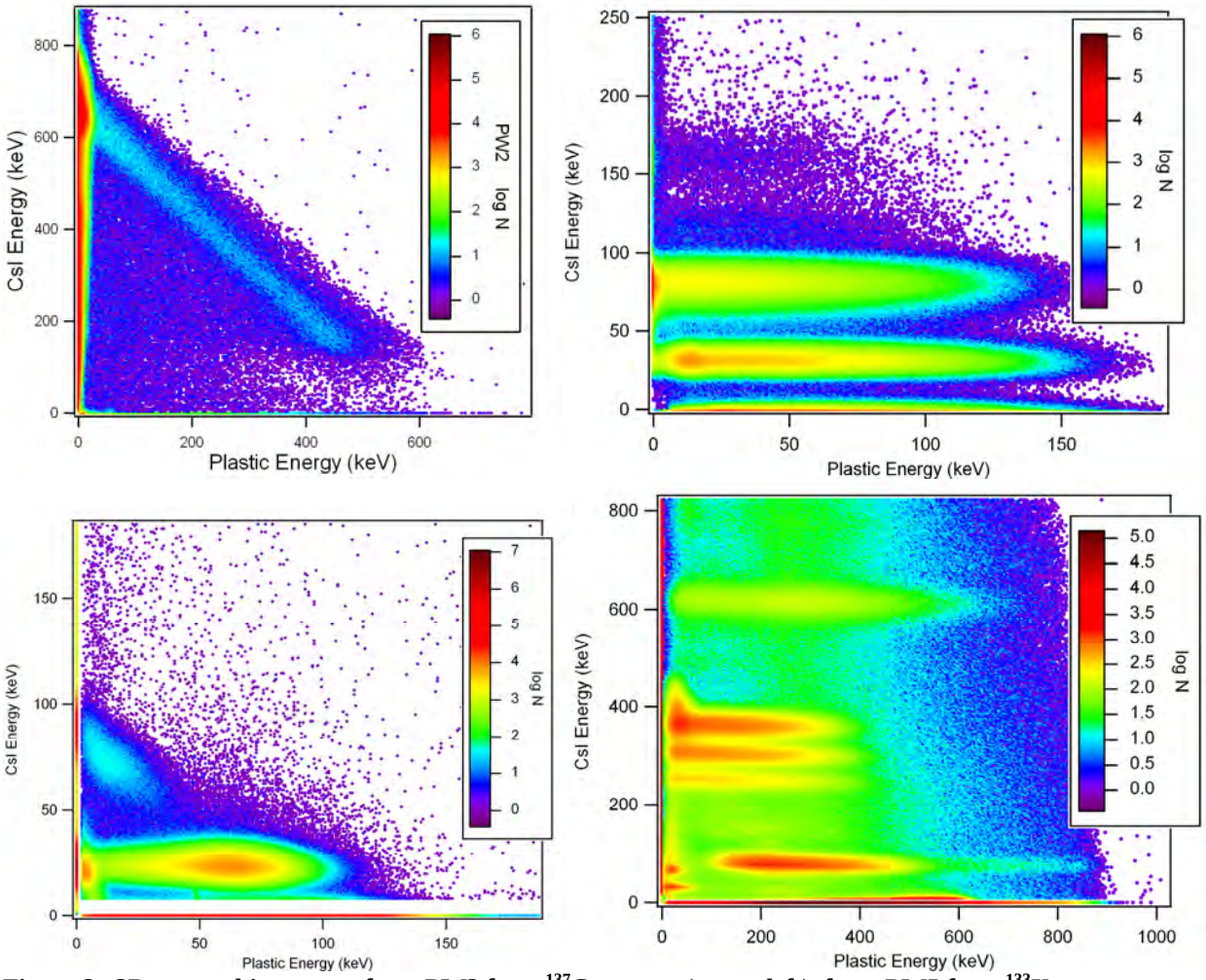


**Figure 2. 2D energy histograms from PW2 for a $^{137}$Cs source (upper left), from PW5 for a $^{133}$Xe source (upper right), from PW2 for a $^{109}$Cd source (lower left), and from PW7 for a $^{222}$Rn source with some residual $^{133}$Ba (lower right). In the lower spectra, non-coincident events have been contracted to the axes.**

Typical 2D histograms plotting the energy deposited in CsI (Ec) vs. the energy deposited in the plastic scintillator (Ep) are shown in Figure 2 for a variety of sources. Several issues are worth noting:

- All detectors achieve excellent linearity in the 2D spectrum, as indicated by the straight line of the $^{137}$Cs Compton scatter events. In contrast, some curvature can be observed in most ARSA or SAUNA 2D histograms, indicating non-linear effects in the energy measurement, e.g., due to PMT gain variations with deposited energy.

- The $^{109}$Cd measurements were performed with the source material deposited on a thin rod, inserted into the detector through the filling tube. Having similar decay energies and decay modes than $^{131m}$Xe, $^{109}$Cd can substitute for $^{131m}$Xe in test and calibration measurement. Since it is a solid source with a long decay time, it is much easier to handle. In addition, it has the advantage that repeated measurements are more consistent, since the amount of $^{109}$Cd in the source is the same in each measurement (except for the decay, which can be computed), whereas knowing the exact amount of $^{131m}$Xe in a test measurement is not trivial.

- In $^{222}$Rn measurements, there is also a rising diagonal line of events starting at Ec ~ 0 keV, Ep ~ 150 keV. The slope varies between detectors, but the "peaks" along the line—allowing for a different energy scale and for non-linearity at low energies commonly observed for heavy charged particles in plastic scintillators (Knoll, 2000)—match the alpha energies in the $^{222}$Rn decay chain. We thus conclude that these events are alpha particles, generating a slightly different pulse shape (slower decay) than electrons or photons when interacting with the plastic scintillator. The PSA algorithms, in their current form, interpret the slower decay as a contribution of a slow CsI pulse and thus compute a component in Ec proportional to the pulse height. Because Rn is removed from the sample in Xe monitoring measurements to minimize interference in the 80-keV line, there should then be no significant interference from alpha particles either. On the other hand, it is also possible to modify the PSA algorithms to detect and remove alpha pulses from the recorded data, e.g., by shape-matching fits, measuring the fall time or additional sums over characteristic intervals in the pulse.

- In systems with separate beta and gamma detectors, Ec and Ep are measured separately, and thus are zero if the PMT output is below the trigger threshold. In the phoswich system, Ec and Ep are computed from a single measurement. For non-coincident events, Ec (or Ep) is thus *computed* as zero, but plus/minus a noise contribution, resulting in a distribution of events around the Ec = 0 (or Ep = 0) axis (see upper plots in Figure 2). The width of this distribution sets a lower bound to the energy of coincidence events to be distinguished from non-coincident events. The width is about 5–8 keV for Ec and about 20–30 keV for Ep, comparable to the trigger thresholds in systems with separate beta and gamma detectors. Using the PSA event categorization as plastic only, CsI only, or a combination, these events can be contracted to the axes, creating a spectrum similar to the one from systems with separate detectors (lower plots).

In monitoring applications, the samples of radioxenon collected are very small, so the background count rate of the detector has to be as small as possible. In a lead enclosure (the lead wall thickness is 2" with an additional 0.5" inner lining with oxygen-free high conductivity [OFHC] copper), we measure an overall rate of 3–8 counts/s for PW2–PW5, of which ~0.05–0.08 counts/s are coincidences. PW6 and PW7 show higher background rates (~10 counts/s, of which ~0.5 counts/s are in coincidence), which is currently being investigated. All detectors reject over 99% of radiation from an external $^{137}$Cs source as non-coincident. The background rate in the ARSA detector is ~30 counts/s, of which ~0.1 counts/s are coincident, i.e., the background is higher in the ARSA detector than in PW2–5; however, the ARSA detector uses a much larger NaI crystal.

To determine the coincidence detection efficiency, a series of measurements was performed with PW4 and PW5 using $^{131m}$Xe, $^{133}$Xe and $^{222}$Rn at PNNL, and then analyzed following the procedure described in Cooper, 2007-2. We assume 98% beta efficiency (essentially the solid angle seen from the center of the Xe cell that is covered with aplastic scintillator, not a filling tube). The beta/gamma coincidence detection efficiency can be assumed to be (beta efficiency) times (gamma efficiency). From the $^{131m}$Xe data, we compute the gamma efficiency at 30 keV to be ~82%. Using this number and the $^{133}$Xe data, we compute the gamma efficiency at 80 keV to be ~65%. Using this number and the $^{222}$Rn data, we compute the gamma efficiency at 240 keV to be ~45–60%. The computed efficiencies have large uncertainties due to the limited statistics in the measurements and the methods to eliminate background and/or residual counts from previous sources, especially for the $^{222}$Rn measurements. However, numbers for PW4 and PW5 match to about 5% in most cases. Typical efficiencies measured on SAUNA detectors are ~75% gamma efficiency at 30 keV, ~85% gamma efficiency at 80 keV, ~65% gamma efficiency at 240 keV, but again it should be noted that measurement conditions vary. In particular, in the phoswich detector detection of low-energy X-rays is enhanced if they are in coincidence with beta particles since the latter creates a large PMT pulse that is easy to trigger on.

**Implementation of PSA Algorithms in On-Board DSP**

As described in (Hennig, 2006-1), the signals from the phoswich detector are read out with a Pixie-4 module and processed with PSA algorithms to extract Ec and Ep, and to categorize events as CsI only (i.e., gamma only), plastic only (i.e., beta only) or both (i.e., beta/gamma coincidence). The algorithms use three quantities measured for each pulse, as illustrated in Figure 3: a) an overall pulse integral E computed from a trapezoidal filter with three energy sums, b) an integral P-B over the initial portion of the pulse, and c) the pulse rise time (RT). For CsI only (or plastic only) events, Ec (or Ep) is equal to E times a scaling factor, and E is proportional to P-B. The proportionality factor $k_1$ (or $k_2$) is a gain independent detector constant that can be determined in calibration measurements. For coincident

events, the factors $k_1$ and $k_2$ are used together with measured quantities E and P-B to compute Ec and Ep for each event. To categorize events as CsI only, plastic only, or both, the computed values of RT, Ec, and Ep are compared against user defined thresholds.

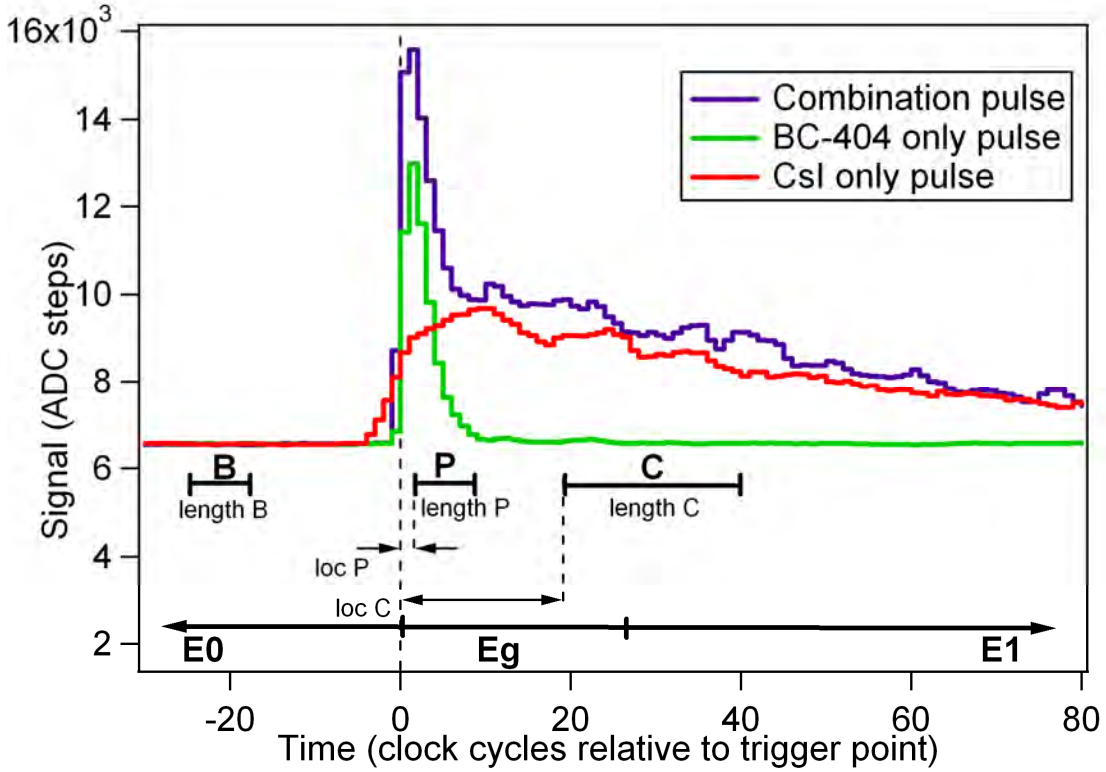


**Figure 3. Typical phoswich pulses and definition of filter sums in pulse shape analysis: There is a sum B over the baseline region, a sum P over the initial part of the pulse, and a sum C over the later part of the pulse. To measure an overall integral over the pulse, the trapezoidal filter implemented in the readout electronics uses the energy filter sums E0, E1, and Eg to compute the "energy" E. (P-B) and E are used to compute Ep and Ec, the energy deposited in the BC-404 (plastic) and CsI scintillators. Also measured is the pulse RT.**

In the past, for development purposes, the Pixie-4 measured E and acquired pulse waveforms, which are standard on-board pulse processing functions. P-B and RT were determined from the captured waveforms either by the on-board DSP with custom code or in offline analysis. Computation of Ec and Ep, event categorization, and accumulation of 1D and 2D spectra were always performed offline. Given the capabilities of the Pixie-4 and the desire to simplify and speed up operations on the host PC, all offline processing steps are now carried out in real time in the processing electronics, as illustrated in Figure 4. The standard functions of trigger detection, waveform capture, computation of energy filter sums, and pileup inspection are performed in field programmable gate arrays (FPGA) in parallel for four channels. For each channel that detected a valid pulse, the DSP uses the energy filter sums to compute E, analyzes the waveforms to compute P-B and RT, and computes Ep and Ec. RT, Ep, and Ec are then compared to user-defined thresholds to categorize the event. Measured and computed quantities are stored in on-board memory as event-by-event list mode data. The energies are also binned into a 2D spectrum (256 x 256 bins) and six 1D spectra (up to 8K bins); three spectra for each Ec and Ep of a) all events, b) only non-coincident events and c) only coincident events. The memory can be read out through the PCI bus in fast block transfers over 80 Mbyte/s. In order to limit readout dead time, the list data memory is divided into two blocks so that data from one block can be read out while the data acquisition continues and stores data in the second block.

In the simplest mode of operation, it is only necessary to start and stop data acquisition in the Pixie-4 according to the sample preparation schedule, and periodically read out the spectrum memory to feed spectra into the isotope

analysis routines of the main system software. For more control and flexibility, the list data can be read as well and used to re-compute energies and/or re-bin spectra with custom binning parameters at a later time.

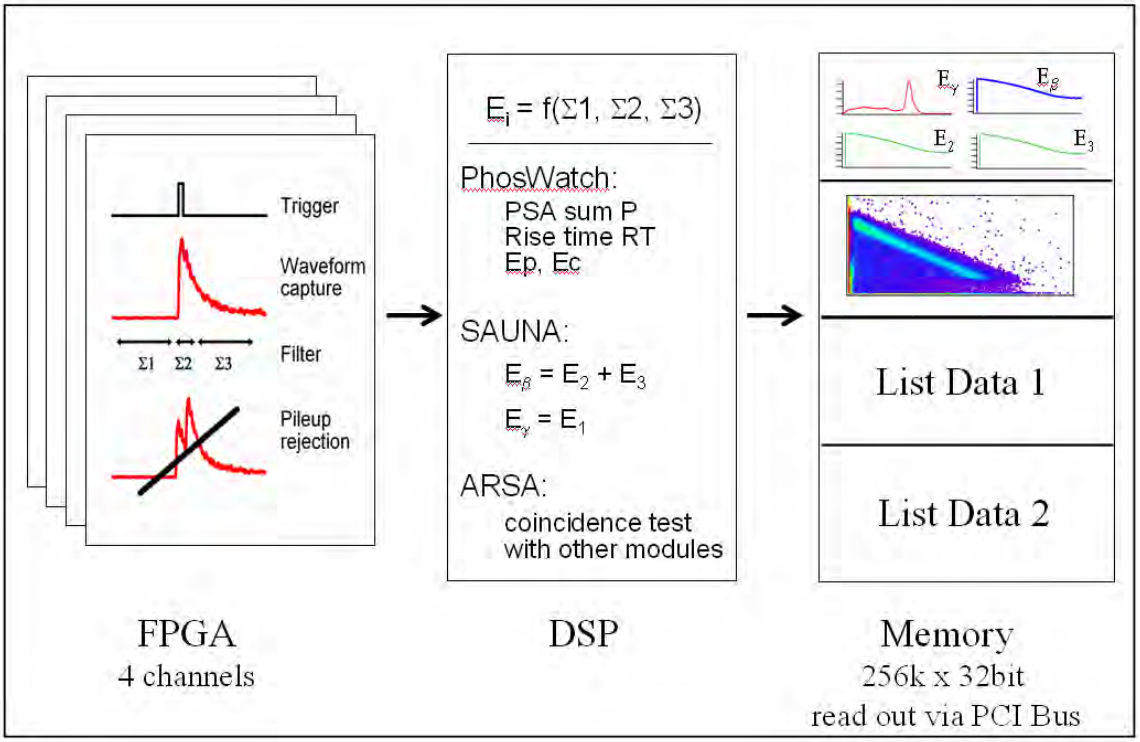


**Figure 4. Block diagram of processes in the Pixie-4. After digitization, pulses are detected in an FPGA that also computes energy filter sums. A DSP computes the energy E, analyzes the captured waveforms to compute PSA parameters, and computes Ec and Ep. Energy histograms and list mode data are stored in on-board memory and can be read out to the host PC in fast block transfers.**

The Pixie-4, being multi-channel COTS readout electronics for a wide range of applications, can also be used in radioxenon detector systems with separate beta and gamma detectors (or even for systems like SPALAX (Fontaine, 2004) with a single high-resolution HPGe gamma detector). With the standard software, the Pixie-4 computes pulse heights and accumulates 1D spectra for each channel, providing sufficient data to build 2D spectra offline. Adapting some of the phoswich code customization, we also developed DSP code to better support ARSA or SAUNA detector systems. For example, to accommodate the two beta channels and one gamma channel in the SAUNA detector, the DSP code has been modified to sum the pulse heights from the two beta channels, and accumulate in its on-board memory 1D spectra of the beta sum energy, the individual beta energies, and the gamma energy, as well as a 2D beta/gamma spectrum. This code can also be used with the redesigned beta/gamma detector developed at PNNL (Cooper, 2007-1) which has one beta and one gamma channel. For the ARSA detector, having a total of 12 channels and thus requiring three Pixie-4 modules, an accumulation of 2D spectra in a single module is not possible, but the modules can share triggers and hit patterns to make accept/reject decisions based on the coincidence between channels and modules. This can be used to limit the acquisition to only events of interest and thus helps to better parse through data offline and compute beta and gamma sum energies from different channels.

The above changes in the on-board processing require no changes in the standard Pixie-4 driver library, except that the 2D spectrum data have to be interpreted differently from the standard 1D data format. Minor changes are required in the user interface to enter input parameters such as the length of P or event categorization thresholds (normally constants). These changes have been applied to the standard Pixie-4 user interface as an add-on software option, which also provides functions to display spectra, fit peaks in 1D spectra and sum regions of interest in the 2D spectrum.

**Programmable Coincidence Pulse Generator**

The programmable coincidence pulse generator ("pulser") shown in Figure 5 is a CompactPCI/PXI module meant to support monitoring and testing of the electronics for state of health during operation, and to allow the development or testing of acquisition and analysis software without the need for a detector and gas sources. It features four high-speed digital to analog converters (DAC) controlled by an FPGA that can be configured from a host PC through a PCI interface. This allows it to output four arbitrary pulse shapes, independent to each other or in coincidence, depending on the FPGA configuration and host control settings. The pulser can be placed in the signal path between detector and readout electronics, passing through the detector signal or switching to a test signal according to host control commands. In addition, the pulser generates eight simple exponential decay pulses, can fan out incoming signals to multiple channels, and provides general-purpose I/O for trigger signals. Several pulser modules can be operated synchronously for systems with a large channel count. The PCI interface is the same as in the Pixie-4 modules, allowing integrated host control software for both the Pixie-4 and the pulser.

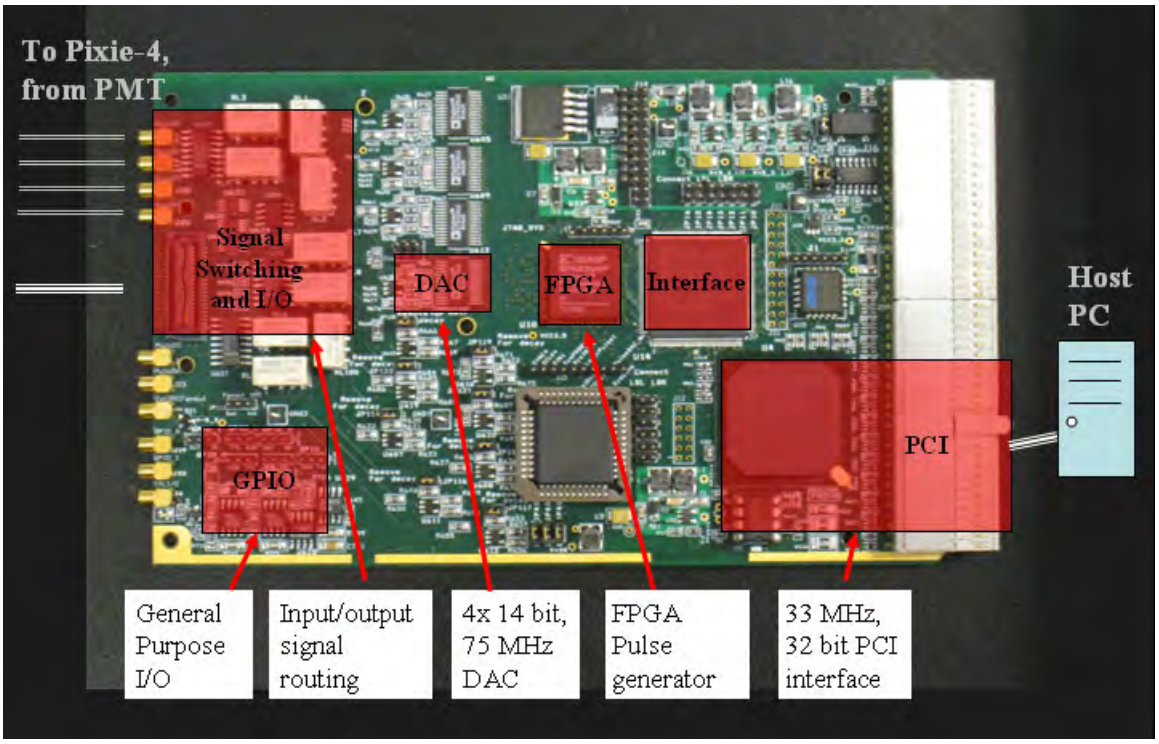


**Figure 5. Picture of the programmable coincidence pulse generator. An FPGA, programmed through PCI interface, generates four arbitrary waveforms for high-speed DACs and up to eight simple exponential decay pulses. Through FPGA-controlled switches, either pulser signals or external detector signals can be output to the Pixie-4 readout electronics.**

In a radioxenon monitoring system with a phoswich detector, one DAC channel of the pulser can thus be programmed to generate pulses with a fast and a slow component with varying amplitudes, simulating the phoswich detector response to exposure to radioxenon sources. During the acquisition, the host control software can periodically switch from detector signal to pulser test signal and verify that gains and threshold in the readout electronics are correct and that the test signal results are in the expected, reproducible test spectrum. In systems with separate beta and gamma detectors, several channels of the pulser can be programmed to generate coincident and non-coincident pulses from i) one or more plastic scintillators and ii) NaI or CsI scintillators, with pulse heights and count rates equivalent to the response to exposure to typical radioxenon sources.

## CONCLUSIONS AND RECOMMENDATIONS

In summary, we developed a COTS radioxenon detector unit, named "PhosWatch," consisting of a phoswich detector, readout electronics, and PSA functions to detect beta/gamma coincidences. Of the six phoswich detectors manufactured so far, most achieve energy resolutions, background rates, and detection efficiencies comparable to the existing detectors. In particular, detectors using the R1307 PMT achieve an excellent resolution of ~7.3%

FWHM at 662 keV. The readout electronics consists of the DGF Pixie-4, a general purpose multi-channel spectrometer module with an on-board DSP performing the PSA functions to compute beta and gamma energies and detect coincidences. It accumulates 1D and 2D radioxenon spectra ready for isotope analysis and additionally records event-by-event list mode data for optional detailed offline analysis. We also developed a programmable coincidence pulse generator to support monitoring and testing of the electronics for state of health during operation. Several PhosWatch units are currently being beta-tested at radioxenon monitoring research laboratories.

The PhosWatch is intended as a drop-in replacement for existing detector units with separate beta and gamma channels. Requiring only a single PMT and electronics readout channel, the key benefit of the PhosWatch is its simpler setup, calibration and operation than the existing detector units. Some of the existing systems already use (or test use of) Pixie-4 modules as readout electronics. Since all phoswich-specific functions are contained in the DSP code, these systems can be upgraded with a PhosWatch without making changes in the system control software interfacing to the Pixie-4 C library except for formatting of spectrum data and definition of PSA input parameters (which are mostly constants). Future efforts will include the production of several additional PhosWatch units and their long term evaluation at radioxenon monitoring research laboratories, as well as updating and improving on-board PSA algorithms according to the experiences during evaluation.

## ACKNOWLEDGEMENTS

We thank A. Ringbom for helpful information gleaned through private communications.

## REFERENCES

Cooper, M. W., J. I. McIntyre, T. W. Bowyer, A. J. Carman, J. C. Hayes, T. R. Heimbigner, C. W. Hubbard, L. Lidey, K. E. Litke, S. J. Morris, M.D. Ripplinger, R. Suarez, and R. Thompson (2007-1). Redesigned β-γ radioxenon detector, *Nuclear Instruments and Methods in Physics Research* A 579, 426–430.

Cooper, M.W., J. C. Hayes, T. R. Heimbigner, C. W. Hubbard, J. I. McIntyre, M. D. Ripplinger, and B. T. Schrom (2007-2). Automated QA/QC check for β-γ coincidence detector, in *Proceedings of the 29th Monitoring Research Review: Ground Based Nuclear Explosion Monitoring Technologies*, LA-UR-07-5613, Vol. 2, pp. 739–746.

Ely, J. H., C. E. Aalseth, J. C. Hayes, T. R. Heimbigner, J. I. McIntyre, H. S. Miley, M. E. Panisko, and M. Ripplinger (2003). Novel Beta-Gamma coincidence measurements using phoswich detectors, in *Proceedings of the 25th Seismic Research Review—Nuclear Explosion Monitoring: Building the Knowledge Base*, LA-UR-06-6029, Vol. 2, pp. 533–541.

Farsoni, A.T., D.M. Hamby, K.D. Ropon, and S.E. Jones (2007). A two-channel phoswich detector for dual and triple coincidence measurements of radioxenon isotopes, in *Proceedings of the 29th Monitoring Research Review: Ground Based Nuclear Explosion Monitoring Technologies*, LA-UR-07-5613, pp. 747–756.

Fontaine, J.-P., F. Pointurier, X. Blanchard and T. Taffary (2004). Atmospheric xenon radioactive isotope monitoring, *Journal of Environmental Radioactivity* 72: 129–135.

Hennig, W., H.Tan, W. K. Warburton, and J. I. McIntyre (2006-1). Single channel beta-gamma coincidence detection of radioactive Xenon using digital pulse shape analysis of phoswich detector signals, *IEEE Transactions on Nuclear Science* 53: (2) p. 620.

Hennig, W., H.Tan, A. Fallu-Labruyere, W. K. Warburton, J. I. McIntyre and A. Gleyzer (2006-2). Design of a phoswich well detector for radioxenon monitoring, in *Proceedings of the 28th Seismic Research Review: Ground Based Nuclear Explosion Monitoring Technologies*, LA-UR-06-5471, Vol. 2, pp. 801–810.

Hennig, W., H.Tan, A. Fallu-Labruyere, W. K. Warburton, J. I. McIntyre, and A. Gleyzer (2007-1). Characterization of phoswich well detectors for radioxenon monitoring, in *Proceedings of the 29th Monitoring Research Review: Ground Based Nuclear Explosion Monitoring Technologies*, LA-UR-07-5613, pp. 757–763.

Hennig, W., Y.X. Chu, H.Tan, A. Fallu-Labruyere, W. K. Warburton, and R. Grzywacz (2007-2). The DGF Pixie-4 spectrometer – Compact Digital Readout Electronics for HPGe Clover Detectors, *Nuclear Instruments and Methods in Physics Research* B 263, 175-178.

Knoll, G. F. (2000) *Radiation Detection and Measurement*, J Wiley & Sons, Inc. Chapter 8.

Reeder, P. L., T. W. Bowyer, and R. W. Perkins, (1998). Beta-gamma counting system for Xe fission products, *Journal of Radioanalytical and Nuclear Chemistry* 235: (1–2), 89–94.

Reeder, P. L., T. W. Bowyer, J. I. McIntyre, W. K. Pitts, A. Ringbom, and C. Johansson (2004). Gain calibration of coincidence spectrometer for automated radioxenon analysis., *Nuclear Instruments and Methods in Physics Research* A 521: 586–599.

Ringbom, A., T. Larson, A. Axelson, K. Elmgren, and C. Johansson (2003). SAUNA—a system for automatic sampling, processing and analysis of radioactive xenon, *Nuclear Instruments and Methods in Physics Research A* 508: 542–553.

# P-TYPE POINT CONTACT GERMANIUM DETECTORS FOR LOW-LEVEL COUNTING

Ethan L. Hull[1], Richard H. Pehl[1], James R. Lathrop[1], Peggy L. Mann[1], Ronnie B. Mashburn[1], Bruce E. Suttle[1], Harry S. Miley[2], Craig E. Aalseth[2], and Todd W. Hossbach[2]

PHDs Co.[1] and Pacific Northwest National Laboratory[2]

Sponsored by DOE Office of Science, Nuclear Physics SBIR Phase 2

Contract No. DE-FG-02-05ER84157

## ABSTRACT

Germanium detector arrays are needed for low-level counting facilities. The applications in such user facilities include the characterization of low-level radioactive samples. In addition, the same detector arrays can perform important fundamental physics measurements, including the search for rare-events like neutrino-less double-beta decay. Recently, relatively large detectors (~ 700 g) having relatively small (~ few mm) p+ contacts are being investigated as a possible detector basis for these detector arrays. A detector having a small, relatively low capacitance, p+ contact has been fabricated as a demonstration. The development and properties of the detector system are discussed.

## OBJECTIVES

Germanium detector arrays are useful in low-level counting facilities. The practical applications in such user facilities include the characterization of low-level radioactive samples. In addition, the same detector arrays can also perform important fundamental physics measurements, including the search for rare events like neutrino-less double-beta decay (Miley et al., 1991; Miley, et al., 1990; Majorana Collaboration White Paper, 2003; and Goulding et al., 1984). Coaxial germanium detectors having segmented outer contacts could provide the next level of sensitivity improvement in low background measurements. The segmented outer contact allows performance of advanced pulse-shape analysis measurements. These techniques can be used to discriminate between multiple Compton-scattered gamma-ray events and single-point beta-decay events. Because of their complexity, segmented coaxial detectors are expensive and available only after relatively long lead times. Improved detector segmentation techniques have shown promise toward making segmented p-type coaxial germanium detectors more readily available for low-level counting facilities (Hull et al., 2007). Recently, the Majorana collaboration and the dark-matter community have shown interest in relatively large volume p-type germanium detectors having a very small p+ contact (Barbeau et al., 2007). These detectors could serve as simpler—ultimately lower background—alternatives to the segmented coaxial detector approach for low-background counting. The small p+ contact makes the preamplifier signal exhibit pronounced charge collection signatures. These signatures enable a good deal of position resolution and background discrimination using only a single electronic channel. The fabrication complexity and manufacturability of these p-type point-contact detectors must be addressed for these detectors to be considered viable for a large detector array.

## RESEARCH ACCOMPLISHED

PHDs Co. has been investigating the viability of p-type point contact detectors. The pursuit has been a combination of experimental detector fabrication, cryostat fabrication, integration, and testing. The design of the p-type point contact detector allows a relatively large active germanium volume to be instrumented with a relatively small charge-collection contact. A diagram of the MJ70 detector is shown in Figure 1. The detector has a 72.2-mm diameter and is 37.3-mm long. The hole for the p+ contact is 1.5-mm in diameter and is 1.5-mm deep. The p-type bulk germanium depletes from the lithium-diffused n+ contact toward the small p+ contact. In principle, all the charge carriers created in the detector bulk should be collected at the central p+ contact. This detector design should have a capacitance of only ~ 1 pF at the small p+ contact when the detector is fully depleted.

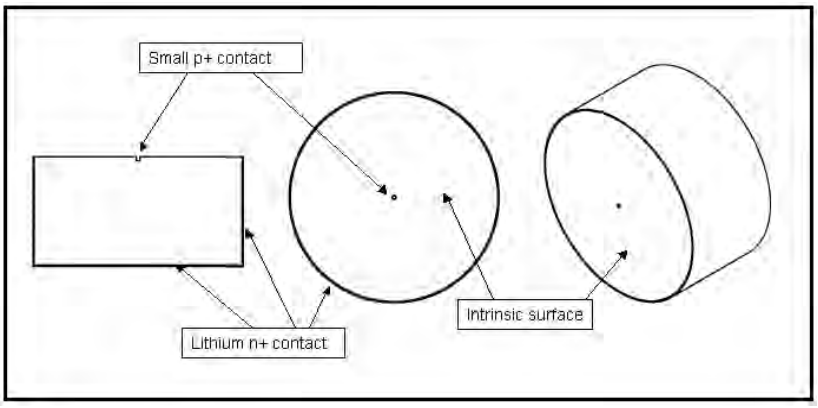


**Figure 1. The MJ70 detector is an example of a p-type point-contact germanium detector.**

The geometry of the MJ70 detector is similar to a closed-end coaxial detector except that the hole is very short and has a very small diameter relative to the other dimensions of the detector. This makes the capacitance of the detector relatively small, lending itself to relatively low-noise performance. The small p+ contact makes the charge collection process have very distinct features. Most of the charge signal is induced in the small p+ contact during the last few millimeters of charge-drift path toward the p+ contact. The current signal (the derivative of the charge signal) has very distinct spikes occurring when the carriers reach the contact. This feature allows discrimination between multiple gamma-ray interactions and single point-like beta-decay interactions. Because the bulk germanium is p

type, holes are collected on the small p+ contact, making the detector relatively insensitive to electron trapping problems that still exist today in detector grade germanium (Hull et al., 2005).

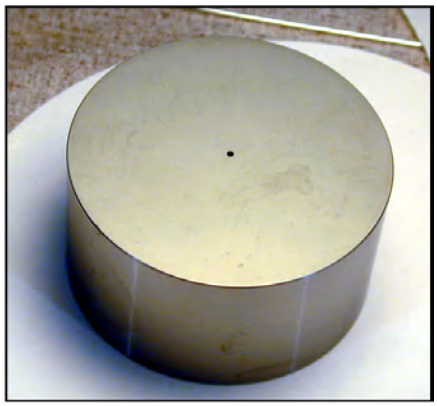

**Figure 2. The MJ70 detector as it was ground. The p+ contact is later fabricated in the small hole in the center of the intrinsic surface.**

PHDs Co. has developed, fabricated, and delivered the completed MJ70 prototype detector system. MJ70 is fabricated from a p-type germanium cylinder having a measured net electrically active impurity concentration of $6.3 \times 10^9$ /cm$^3$ above and $4.8 \times 10^9$ /cm$^3$ below the crystal. The crystal was ground to a 72.2-mm diameter and a 37.3-mm length. The hole for the p+ contact was ground to a 1.5-mm diameter and a 1.5-mm depth. The idea was to attempt to obtain reasonably good charge collection by fabricating a detector that approximates a hemisphere, having similar charge collection distances in all directions. The corners at the closed end were left square. Generally these corners are rounded off, beveled, or bulletized for coaxial detector fabrication to improve the charge collection from gamma rays interacting in these regions of the detector. In this case, the maximum detector mass is desired, and some poor charge collection in the corners may be tolerable as a tradeoff. The detector has a lithium diffused n+ contact around the outside of the detector and a very small metal evaporated nickel p+ contact for charge collection. A photograph of the crystal with the small hole is shown in Figure 2. The detector is held in a PHDs Co. MJX cryostat specifically made to hold, cool, and instrument these point-contact detectors. The MJX cryostat holding MJ70 is shown in Figure 3.

**Figure 3. The MJX cryostat holds, cools, and instruments p-type point contact detectors like MJ70.**

Numerous detector fabrication attempts were made. Problems with the intrinsic surface of the detector and the very small p+ contact were thought to be the main difficulty. In addition, the cryostat required several modifications. Finally, the detector depleted at a voltage of +1880 V and was operated at a voltage of +1980 V with minimal leakage current. The detector successfully cycled from the cryogenic temperature (~ 83 K) to room temperature and back again with no increase in the leakage current or degradation in the detector performance. The spectroscopy from the detector was quite reasonable given the geometry of the detector. Figure 4 shows a $^{60}$Co and $^{241}$Am spectrum from MJ70 using a peaking time of 5 microseconds. The functioning detector and cryostat were successfully delivered and operated at Los Alamos National Laboratory in June 2008.

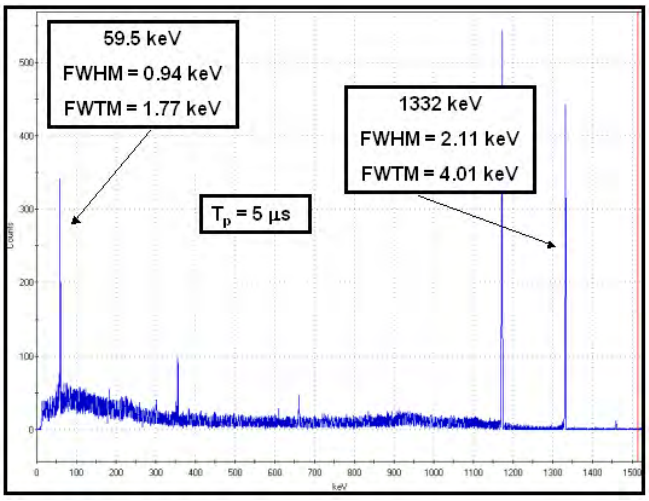


**Figure 4. The gamma-ray energy spectrum from MJ70 shows reasonable charge collection considering the geometry of the detector.**

## CONCLUSIONS AND RECOMMENDATIONS

From the point of view of detector fabrication, the p-type point contact detector design seems quite viable as a basis for large low-background counting arrays. PHDs Co. will continue the evaluation of this technology with the fabrication of other detectors having different aspect ratios compared to MJ70 to see how far the limits of charge collection can be pushed before the energy resolution is impacted.

## REFERENCES

Barbeau, P. S., J. I. Collar, and O. Tench (2007). Large-mass ultralow noise germanium detectors: performance and applications in neutrino and astroparticle physics. *Journal of Cosmology and Astroparticle Physics*, 09, 009.

Goulding, F. S., D. A. Landis, P. N. Luke, N. W. Madden, D. F. Malone, R. H. Pehl, and A. R. Smith (1984). Semiconductor detectors and double beta decay, *IEEE Trans Nucl. Sci*. NS-31: 285–299.

Hull, E.L., R. Pehl, J. Lathrop, P. Mann, R. Mashburn, B. Suttle, H. Miley, C. Aalseth, and T. Hossbach (2007). Segmentation of the outer contact on p-type coaxial germanium detectors, in *Proceedings of the 29th Monitoring Research Review: Ground-based Nuclear Explosion Monitoring Technologies.* LA-UR-07-5613, Vol. 2, pp. 764–770.

Hull, E. L., H. Miley, R. Pehl, C. Aalseth, and T. Hossbach (2005). Segmentation of the outer contact on p-type coaxial germanium detectors, in *Proceedings of the 27th Seismic Research Review: Ground-Based Nuclear Explosion Monitoring Technologies*, LA-UR-05-6407, Vol. 2, pp. 795–804.

Hull, E. L., R. Pehl, J. Lathrop, P. Mann, R. Mashburn, B. Suttle, H. Miley, C. Aalseth, and T. Hossbach (2005). Segmentation of the outer contact on p-type coaxial germanium detectors, in *Proceedings of the 27th Seismic Research Review: Ground-based Nuclear Explosion Monitoring Technologies*, LA-UR-05-6407, Vol. 2, pp. 795–803.

Majorana Collaboration White Paper (2003). The Majorana zero-neutrino double-beta decay experiment, LA-UR-2003-7709 and PNNL-14420, http://majorana.pnl.gov/MajoranaWhitePaper.pdf.

Miley, H. S., R. J. Arthur, R. L. Brodzinski, W. K. Hensley, J. H. Reeves, and F. T. Avignone (1991). Low background detectors for exotic physics experiments, in *Proceedings of the 4th International Workshop on Low Temperature Particle Detectors*.

Miley, H. S., F. T. Avignone, R. L. Brodzinski, J. I. Collar, and J. H. Reeves (1990). Suggestive evidence for the 2-neutrino double-beta decay of Ge-76, *Phys. Rev. Lett.* 65: 3092–95.

# MECHANICALLY COOLED LARGE-VOLUME GERMANIUM DETECTOR SYSTEMS FOR NUCLEAR EXPLOSION MONITORING

Ethan L. Hull[1], Richard H. Pehl[1], James R. Lathrop[1], Peggy L. Mann[1], Ronnie B. Mashburn[1], Bruce E. Suttle[1], Harry S. Miley[2], Craig E. Aalseth[2], Theodore W. Bowyer[2], Todd W. Hossbach[2], George C. Rybicki[3], and Jesse L. Bucholtz[3]

PHDs Co.[1], Pacific Northwest National Laboratory[2], and Air Force Technical Applications Center[3]

Sponsored by National Nuclear Security Administration

Contract No. DE-FC52-06NA27323

## ABSTRACT

Compact maintenance-free mechanical cooling detector systems are being developed to operate large-volume (~ 570 $cm^3$, ~ 3 kg, 140 % or larger) germanium detectors for field applications. These detector systems are necessary for remote long-duration liquid-nitrogen free deployment of large-volume germanium gamma-ray detector systems. The Radionuclide Aerosol Sampler/Analyzer (RASA) nuclear explosion monitoring systems will benefit from the availability of such detector systems by allowing the very largest available germanium detectors to be utilized for the highest sensitivity measurements. To reliably provide such detector systems, three fundamental technical issues are being investigated: temperature, vacuum, and vibration. Two prototype detector systems (RASA 1 and RASA 2) have been developed, fabricated, and tested. The cryostats have been demonstrated to cool very large (slightly greater than $10^+$-cm long and 10-cm diameter) detectors to temperatures as low as 50 K. The vacuum design has been demonstrated to show no measurable degradation over long time periods. The detector systems have been demonstrated to successfully instrument high-purity germanium detectors. Microphonic noise from the vibrating cooler has been completely eliminated in one case, serving as a demonstration of the total detector system viability. Microphonic noise remains the largest technical issue for these detector systems. The third generation, RASA 3, design incorporates mechanical changes to eliminate microphonic noise issues.

## OBJECTIVES

PHDs Co. is developing mechanically cooled detector systems for large-volume germanium detectors (~ 570 $cm^3$, ~ 3 kg, ~ 140 %, or larger). Maintenance-free Stirling-cycle mechanical coolers are being used. These coolers have operating lifetimes exceeding five years. The relatively large heat lift of these coolers quickly cools a detector to a very low operating temperature for gamma-ray measurements. Lower operating temperature improves the reliability of germanium detectors by lowering surface leakage currents (Pehl et al., 1973). These features will make liquid-nitrogen free operation of the largest (~200%) germanium gamma-ray detectors viable and convenient for nuclear explosion monitoring. The RASA detector system will benefit from the availability of such detectors (Bowyer et al., 1997; Miley et al., 1998).

Mechanical cooling of germanium detectors has historically been a difficult endeavor. The success or failure of mechanically cooled germanium detector systems arises from three main technical issues: temperature, vacuum, and vibration. These factors can affect one another. Previous years have seen analysis of these factors and their effects on detector performance (Hull et al., 2006), and the first prototypes thermally tested (Hull et al., 2007). This year, results are available from the study of the first prototype and a second-generation prototype with detectors in the detector systems. These endeavors include successful coaxial detector fabrication, detector-cryostat integration, cooling, and full- detector-system tests demonstrating operation with no measurable microphonic noise. The detector systems cool detectors to extremely low operating temperature (as low as 50 K), in a vacuum environment showing no measurable degradation with time. The remaining technical issue is microphonic noise from the vibrating cooler.

## RESEARCH ACCOMPLISHED

The second year of this project has seen several major accomplishments. The first prototype (RASA 1) was fully integrated and made to function with a p-type coaxial germanium detector. A detector fabrication technique was developed specifically to make the detectors for these detector systems. The fabrication technique has been repeatedly demonstrated to produce a functional germanium coaxial detector having good leakage current and reasonable noise characteristics. The RASA 1 detector, cooler, and front-end electronics have been integrated and function together as a single compact unit. A photograph of the complete RASA 1 detector system is shown in Figure 1. The detector is cooled to temperatures below 50 K when the cooler is operating at full power, ~ 200 W input power. After a few attempts, the detector was brought to working order after electronic interconnect issues were addressed. The detector is
70 mm in diameter and 70 mm long, and is made from p-type high-purity germanium. The detector depletes at 2,300 V and shows reasonably good charge collection at 2,400–2,500 V. The energy resolution was measured to be FWHM ~ 2.4 keV at 1332 keV using a peaking time of 5 μs. This measurement was made with the cooler switched off briefly. Initially, the resolution was on the order of 20 keV with the cooler running due to microphonic noise.

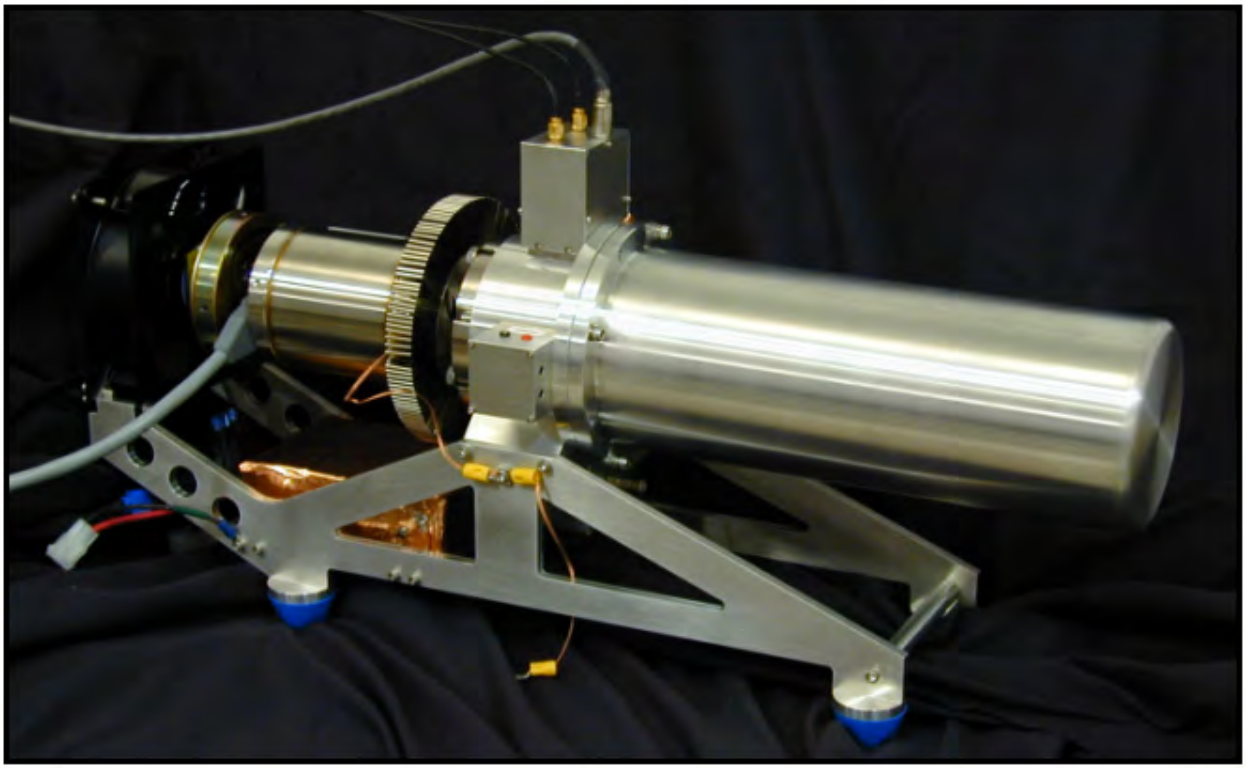

**Figure 1. The RASA 1 prototype holds, cools, and instruments a detector as large as 10-cm diameter and 10-cm long. Pictured here it holds a 70-mm diameter x 70-mm long coaxial detector.**

The microphonic noise issues were dealt with by making mechanical and electronic changes to the detector system at room temperature, pumping on the detector system with a turbo-molecular pump, verifying vacuum integrity with a helium leak checker, and cooling the detector system. The next day, the detector was biased, and the noise was measured. The most basic measurement was made by simply looking at the noise on an oscilloscope compared to known gamma-ray energies at a peaking time of 6 μs. This was determined to be the only method for troubleshooting the microphonic noise problems. Many tens of such thermal cycles were completed during the past year, each one taking several days. Some changes improved the microphonic noise; others made it worse. Fortunately, the cooler has no trouble with the repeated thermal cycles. The detector was also very robust. Overall, the detector was damaged only a handful of times as a result of these thermal cycles. The detector problems were usually the result of poor handling of the detector at room temperature. However, in most cases only a partial detector reprocessing cycle, taking less than one day, was sufficient to restore the detector. The most significant mechanical changes included improving the support of the detector while still maintaining a high thermal barrier between the cold surfaces and the room temperature surfaces. Vibration itself is not a problem. Rather, vibration of the sensitive JFET gate lead relative to other objects is the problem. Using this thinking, the internal parts were stabilized together to lessen the extent of the relative motion during cooler operation. A step that had a particularly good impact was the addition of a spring-loaded stabilization spider between the detector mount and the inside of the outer vacuum cap. After that step and several similar attempts, the microphonic noise was altogether eliminated from the gamma-ray energy spectrum from the detector in RASA 1. A 1332-keV resolution of full width at half maximum (FWHM) = 2.4 keV was observed with the cooler off or on. This measurement was made using a peaking time of 5 μs.

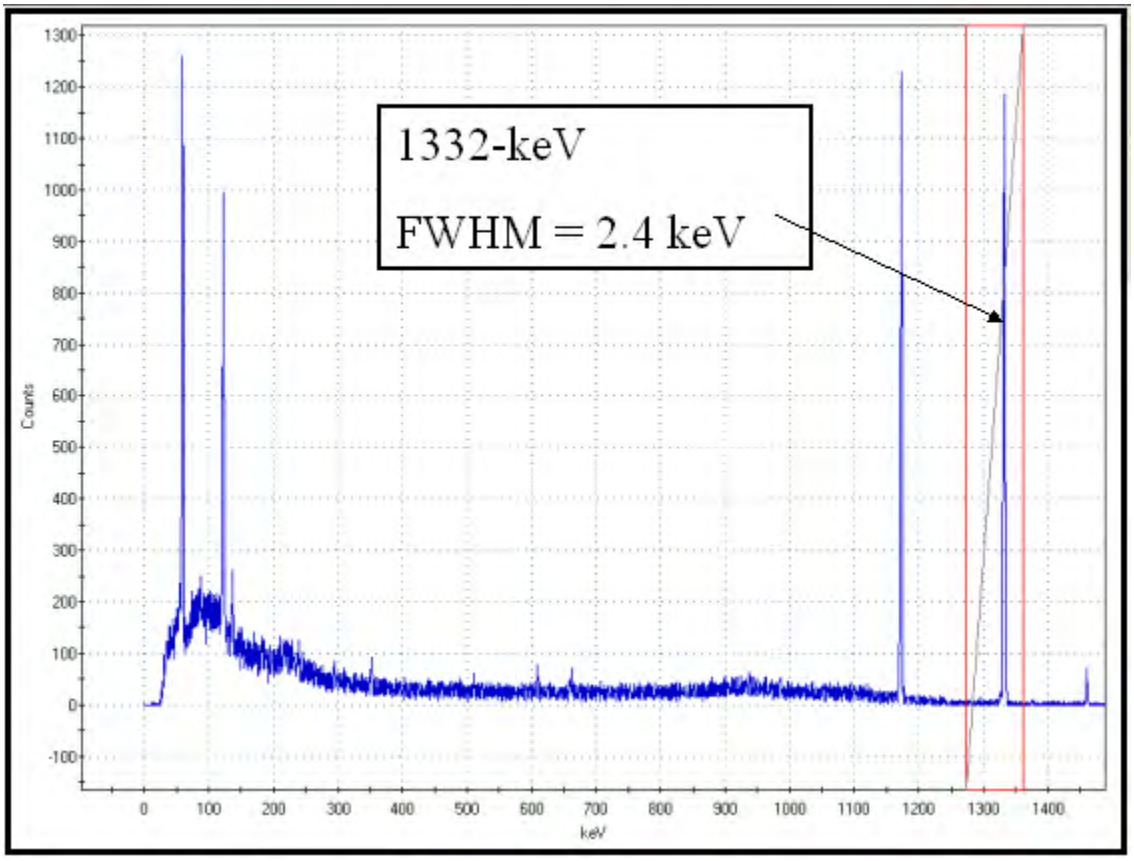


**Figure 2. This energy spectrum was accumulated from the detector in the RASA 1 detector system using a unipolar peaking time of 5 μs with the mechanical cooler operating at full power.**

Aside from the spectroscopy shown in Figure 2, the microphonic noise was analyzed on the oscilloscope. The signals from the detector preamplifier were shaped in a TC244 shaping amplifier using a peaking time of 6 μs. No microphonic noise was visible on the baseline. This was established with the 122-keV gamma-ray peak set to 6 V on the oscilloscope. This allows the baseline JFET channel noise to be easily observed on the 100- and 200-mV voltage scales. Channel noise from the JFET dominates when the cooler was not running at 6 μs. When the cooler was switched on, there is a brief burst of noise when it starts vibrating, then the noise almost immediately returns to the cooler-off level. This result, along with the spectroscopy was heralded as a great success initially. However, over a period of days, a small but significant amount of microphonic noise crept into the detector system. After a few days, the 1332-keV peak was significantly degraded to an FWHM ~ 3.5 keV. No changes were made to the detector system during that time. This result was repeated. Some part of the internal cryostat assembly must be loosening up over time with the cooler operating. The good microphonic noise results were always measured the morning following the cool-down of the detector. The insides of the cryostat may not have come completely to thermal equilibrium by that time. The detector was cold enough to operate well, but all the metal and ceramic parts may not have come to full equilibrium. It is not unusual for a detector to continue to creep down in temperature by a few degrees over the days following the cool-down. RASA 1 continues to be an excellent test unit for pursuing issues related to microphonic noise. The elimination of the microphonic noise from the energy spectrum and the excellent vacuum integrity of the detector system stand as proof that this detector-cryostat-cooler combination can ultimately serve as a viable detector unit for RASA detector systems.

During the pursuit of the microphonic noise issues with RASA 1, the RASA 2 prototype was designed. The RASA 2 was designed to accommodate all of the modifications and reworks required to make RASA 1 cool and operate a detector. In this case, the detector to be cooled came from a broken unit from another detector vendor. The RASA 2 design had to accommodate the different geometry of the detector and a rather different detector-mounting scheme, so RASA1 and RASA 2 were somewhat different in places. The detector system was assembled, and the detector was loaded into the detector system. The detector was suspected to be in working order. Indeed, the detector

recovered rather handily after overnight baking of the detector at 60°C while pumping with a turbo molecular pump. The detector takes full bias and has excellent gamma-ray energy resolution in the RASA 2 detector system when the cooler is turned off. The detector can be cooled as low as ~ 50 K inside the detector system. Unfortunately, the detector system exhibits rather poor microphonic noise performance at this stage of the development. At this time, the sources of microphonic noise are being addressed much in the same manner as they are being addressed with RASA1. The detector is cycled from room temperature to operating temperature and back again to allow testing of various mechanical and electronic component changes inside the cryostat.

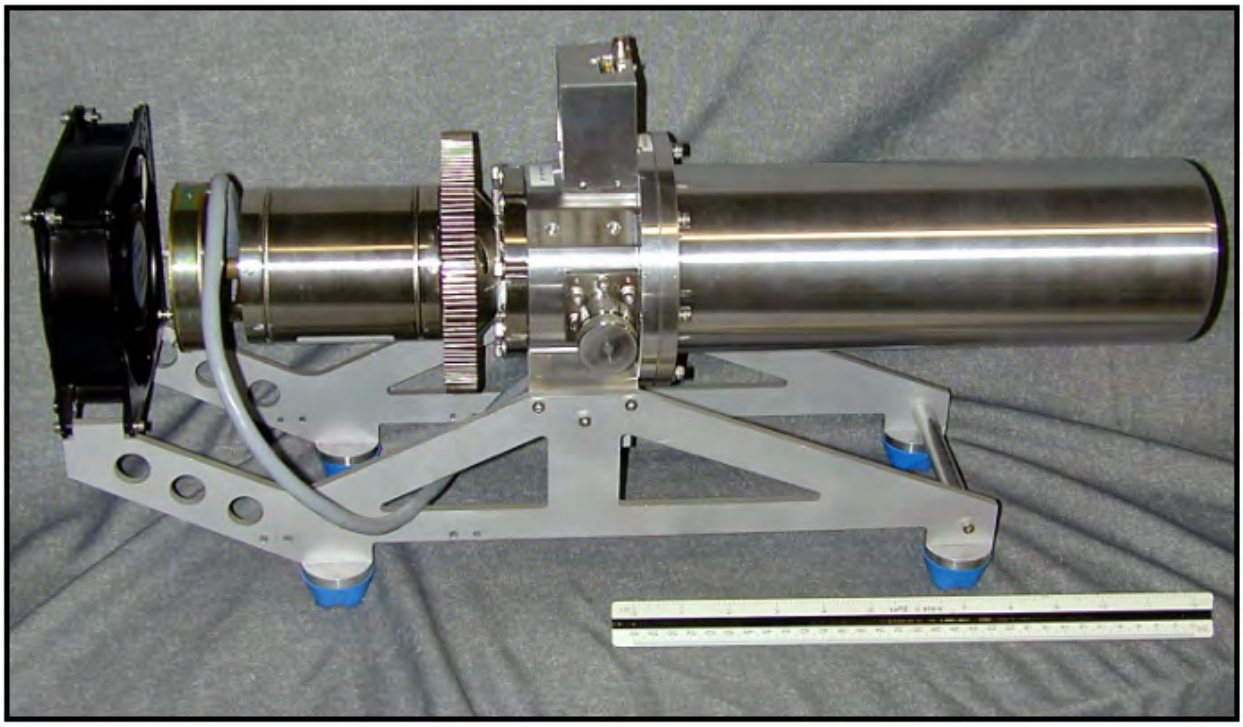

**Figure 3. The RASA 2 prototype is very similar to RASA 1. The detector system holds, cools, and instruments a coaxial detector that is 79 mm diameter and 106 mm long.**

The RASA 1 and RASA 2 developments have led to the design of a third-generation prototype, RASA 3. RASA 3 is being fabricated at this time. RASA 3 will preserve the vacuum and cryogenic designs of RASA 1 and 2 while improving the microphonic noise problems. RASA 3 has a cryostat design that addresses issues critical to the manufacturability of a germanium detector system using such a compact and powerful cooler. As in the RASA 1 and 2 design phases, care has been exercised to work with the AFTAC RASA users to insure the detector design works in harmony with the existing RASA detector system constraints.

## CONCLUSIONS AND RECOMMENDATIONS

The RASA 1 and RASA 2 prototypes have been designed, fabricated, and tested as demonstrations of a new integrated mechanical cooling detector system suitable for use with RASA stations. The third generation prototype, RASA 3, has been designed. Good technical progress has been made to overcome the problems associated with a compact, mechanically cooled germanium detector system. These new detector systems will have extremely long operating lifetimes with no maintenance requirements. At the end of this project, PHDs Co. will offer a new product line: the MCX mechanically cooled detector product line for use with RASA and similar remotely deployed detection systems.

## REFERENCES

Bowyer, S. M., H. S. Miley, R. C. Thompson, and C. W. Hubbard (1997). Automated particulate sampler for Comprehensive Test Ban Treaty verification (the DOE radionuclide aerosol sampler/analyzer), *IEEE Transactions on Nuclear Science* 44 3 (1): 551–556

Hull E. L. R. Pehl, J. Lathrop, P. Mann, R. Mashburn, B. Suttle, H. Miley, C. Aalseth, T. Bowyer, and T. Hossbach (2007). Mechanically Cooled Large Volume Germanium Detector Systems for Nuclear Explosion Monitoring, in *Proceedings of the 29th Monitoring Research Review: Ground-based Nuclear Explosion Monitoring Technologies*, LA-UR-07-5613. Vol. 2, pp. 770–779.

Hull, E. L., R. Pehl, J. Lathrop, R. Mashburn, H. Miley, C. Aalseth, and T. Hossbach (2006). Mechanically cooled large volume germanium detector system for nuclear explosion monitoring, in *Proceedings of the 28th Seismic Research Review: Ground-Based Nuclear Explosion Monitoring Technologies*, LA-UR-06-5471, Vol 2, pp. 821–830.

Miley, H. S., S. M. Bowyer, C. W. Hubbard, A. D. Mckinnon, R. W. Perkins, R. C. Thompson, and R. A. Warner (1998). A Description of the DOE Radionuclide Aerosol Sampler/Analyzer for the Comprehensive Test Ban Treaty. *Journal of Radioanalytical and Nuclear Chemistry* 235 (1–2): 83–87.

Pehl, R. H., E. E. Haller, and R. C. Cordi, (1973). Operational characteristics of germanium detectors at higher temperatures, *IEEE Trans. Nucl. Sci*. 20: 494.

# DESIGN AND CONSTRUCTION OF AN ULTRA-LOW-BACKGROUND 14 GERMANIUM CRYSTAL ARRAY FOR HIGH EFFICIENCY AND COINCIDENCE MEASUREMENTS

Martin E. Keillor, Craig E. Aalseth, Anthony R. Day, James E. Fast, Eric W. Hoppe, Brian J. Hyronimus, Todd W. Hossbach, Harry S. Miley, Allen Seifert, and Glen A. Warren

Pacific Northwest National Laboratory

Sponsored by National Nuclear Security Administration

Contract No. DE-AC05-RLO1830

## ABSTRACT

Physics experiments, environmental surveillance, and treaty verification techniques continue to require increased sensitivity for detecting and quantifying radionuclides of interest. This can be done by detecting a greater fraction of gamma emissions from a sample (higher detection efficiency) and reducing instrument backgrounds. A current effort for increased sensitivity in high resolution gamma spectroscopy will produce an intrinsic high-purity germanium (HPGe) array designed for high detection efficiency, ultra-low-background performance, and useful coincidence efficiencies. The system design is optimized to accommodate filter paper samples, e.g., samples collected by the Radionuclide Aerosol Sampler/Analyzer (RASA). The system will provide high sensitivity for weak collections on atmospheric filter samples, as well as offering the potential to gather additional information from more active filters using gamma cascade coincidence detection.

The current effort is constructing an ultra-low-background HPGe crystal array consisting of two vacuum cryostats, each housing a hexagonal array of 7 crystals on the order of 70% relative efficiency each. Traditional methods for constructing ultra-low-background detectors are used, including the use of materials known to be low in radioactive contaminants, the use of ultra pure reagents, clean room assembly, etc. The cryostat will be constructed mainly from copper electroformed into near-final geometry at Pacific Northwest National Laboratory (PNN)L. Details of the detector design, simulation of efficiency and coincidence performance, HPGe crystal testing, and progress on cryostat construction are presented.

## OBJECTIVES

This research will produce a high efficiency array of germanium crystals in an ultra-low-background system to provide improved gamma spectroscopy sensitivity. The system will be composed of two separate copper cryostats, each housing arrays of 7 HPGe crystals to provide high detection efficiency for large sized samples (e.g., filter paper media). The high detection efficiency serves to increase source counts for a given measurement, improving the high-leverage term in the $S^2/B$ figure of merit (FOM). The approach also combines the inherent excellent energy resolution of intrinsic germanium with ultra-low background detector construction and operation techniques to drive down the background term. For appropriate isotopes and measurement scenarios, additional sensitivity gains will be realized through the use of gamma-gamma coincidence techniques.

Measurements of atmospheric particulates collected on filter papers are one of the principal sample analyses that this effort is pursuing. The intention is to provide the highest sensitivity gamma spectroscopy measurement possible prior to radiochemical or other destructive processing of a sample. Filter papers collected by automated ground-based particulate samplers (e.g., RASA) or aircraft-based collectors are examples of potential samples. High interest samples (e.g., where other techniques have provided a tip-off) with initial negative results from field-based measurements are prime candidates for analysis. While a primary focus is currently on intact filter paper samples, the system will also provide an excellent measurement capability for chemically purified samples, and also has the potential to provide an outstanding gamma-gamma coincidence analysis of low-dose Neutron Activation Analysis samples.

### Design Philosophy

This system is designed to make the best possible use of the relatively small number of radioactive decays encountered in measuring a weak sample. This requires reducing backgrounds to the greatest extent possible so that sample activity is the dominant signal in the detector. Also required are the highest possible gamma detection efficiencies, meaning more of the emitted gammas are seen as signals in the detector. Finally, some isotopes have very specific nuclear decay signatures, and coincident gamma emissions, which can improve selectivity for these isotopes in a coincidence-capable detector.

Used all together, these methods can greatly enhance the sensitivity of a gamma spectroscopy system. Translated into design rules, they become three main focus areas for the instrument: ultra-pure materials, highly effective and low-background shielding, and array design to maximize the detection efficiency for both single and coincident gammas.

## RESEARCH ACCOMPLISHED

Significant progress has been accomplished toward construction of the first 7-crystal cryostat. The cryostat has been designed and extensive Monte Carlo modeling of the radiation detection performance is complete. New copper electroforming capability has been established, and parts for the first cryostat have been electroformed and machined into final form. Princeton Gamma Tech (PGT) has completed refurbishing eight existing PNNL HPGe crystals for this effort, and these crystals are being mounted and tested in a new mount design. A new revision of PNNL-developed low-background front-end electronics has been designed for this work and is being manufactured (Aalseth et al., 2004). This new instrument also represents significant complexity in data acquisition and analysis, and work proceeds to develop these necessary tools as well. Currently, the research team is working primarily on cryostat construction, vacuum and thermal testing. After successful testing, the first cryostat will be populated with HPGe crystals.

### System Design

The current system design was developed following PNNL's experience with the Multi-Element Gamma Array (MEGA) project (Kazkaz et al., 2003). The essential feature is to construct two HPGe 7-crystal arrays facing one another. In each array (see Figure 1), the crystals will be housed in a single cryostat / vacuum enclosure. Each crystal is mounted in an individual mounting package; this will reduce direct handling of the crystals, and allows relatively straightforward removal of a crystal for repair. The design of the crystal-mounting package draws on a number of recent designs in the double beta decay arena, and attempts to minimize materials between the crystals for improved detection of Compton scattered gamma-rays. Housing the array in a single enclosure also allows closer placement of the crystals, improving detection efficiency for the system. These two aspects, improved Compton-

scatter detection and better solid-angle coverage, are significant technical advantages over current cryostat designs, and make important contributions to the expected performance of the system. One drawback of the design is that failure of a single crystal requires the entire 7-crystal unit to be warmed and opened for repairs. The technical performance advantages of an array of crystals in a single enclosure over deploying crystals in separate cryostats far outweigh the increased risks when service is needed. Typical cryostats can go for many years without requiring such service.

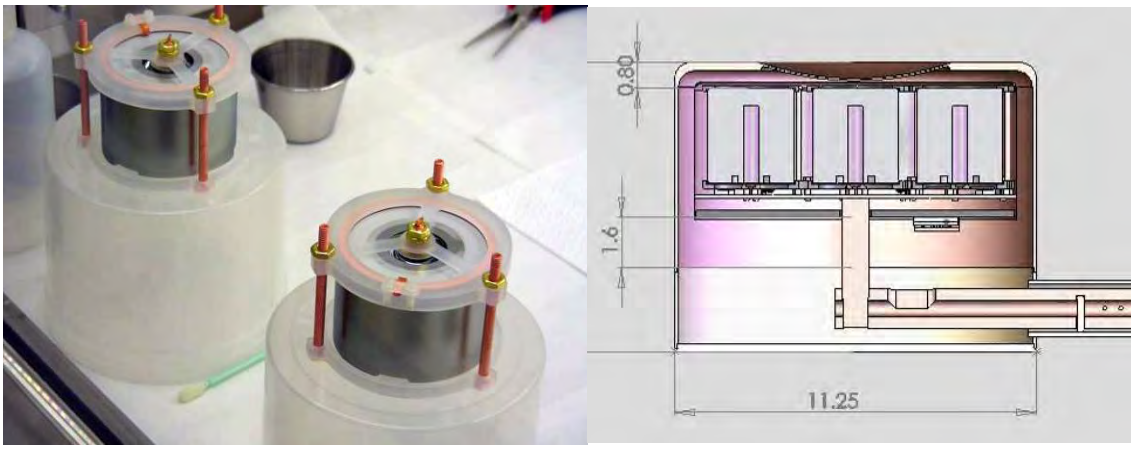


**Figure 1. The HPGe crystals are housed in individual crystal mounting packages that can be removed from the cold plate if repairs are necessary (left). The 7 crystals in their individual mounts will be bolted to the cold plate, and enclosed by a single copper IR shield. The system will also include an intermediate "floating" shield to enhance thermal performance. The design includes a thin copper entrance window to improve detection efficiency for lower energies (dished portion at the top of the figure on right).**

The two detector arrays will be housed in a lead shield depicted in Figure 2. The shield includes 16" of lead shielding, radon purge using boil-off nitrogen from the liquid nitrogen Dewar that cools the HPGe cryostats, and cadmium sheets exterior to the lead to reduce neutron events. The inner 2 layers of lead are low background lead or ultra-high-purity copper, depending on the location (depth) of the deployed system. An electric motor is used to roll the lead door out of the shield, allowing easy access for sample placement and detector maintenance.

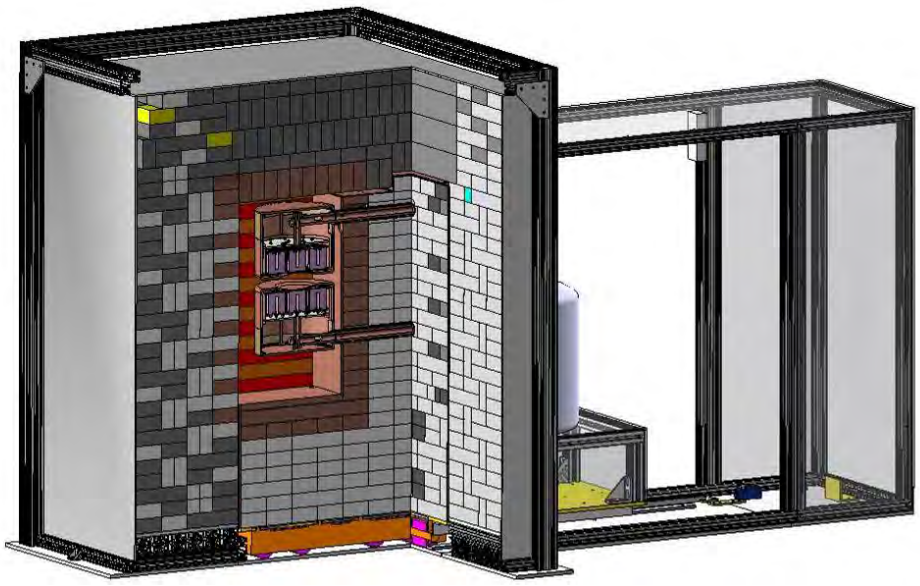

**Figure 2. Depiction of the two 7-crystal arrays in a 16" thick lead shield. The door of the shield opens to allow sample changes, as well as access for maintenance without un-stacking the lead.**

**Performance Modeling**

Simulations of the system detection efficiency performance and measurement of mixed fission products were conducted using the GEANT4 (G4) framework (Agostinelli 2003, Allison 2006). A diagram of the detector geometry is shown in Figure 3. The simulated geometry consists of two arrays of seven large p-type HPGe crystals looking head-on. Each crystal is 62 mm in diameter, 70 mm long, and has a dead layer of 0.25 mm. The actual dead-layer thickness of the crystals used will likely be a bit larger, reducing lowest-energy performance slightly. Each crystal array is surrounded by a 0.1-mm-thick IR shield, and a 5-mm-thick vacuum chamber wall with a 1 mm thick entrance window. A BGO Compton suppression detector was placed in the simulation surrounding the two crystal arrays for analysis of the potential benefit of such a future addition to the system. Decay particles were generated in a 100 mm square (about the size of a folded filter sample) 26 mm from the front of the crystals.

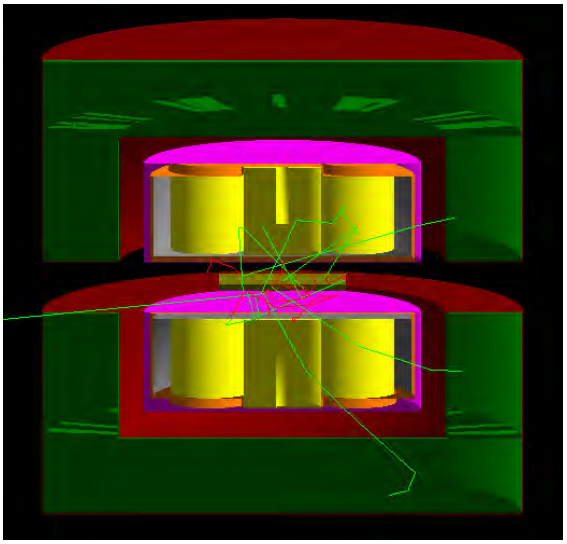

**Figure 3. The GEANT-4 geometry used for simulation of the 14-crystal array.**

Radioactive decay products for each isotope were generated based on the PNNL Coincidence Lookup Library (CLL) (Warren 2006). The CLL provides the cascade information for each isotope, such as probability of cascade and particle energies involved, based nuclear data from a version of the ENSDF database. The simulation package uses this cascade information to generate the decay particles for each isotope, including the generation of coincident gamma cascades.

The activity for each isotope was determined from a published series of ORIGEN2 calculations (Perkins 1997) of the time dependant fission product inventory subsequent to an HEU based nuclear explosion. The published tables were used as a starting point for a separate ORIGEN2 calculation that determined the average activity of each isotope from five to six days post-event. A sample size of $10^9$ fissions and a measurement period of 24 hours were assumed. A total of 80 fission products and 40 million decays were simulated in order to get a fair representation of the mixed fission product spectrum likely to be present.

After the number of decays for each isotope was determined, they were simulated independently through the detector model. The individual energy spectra collected were then summed to produce the mixed fission product spectrum. Isotopic-specific weighting was applied to a few specific isotopes for the summing process. For most isotopes, the weighting was 1.0. For the noble gas isotopes, the weighting was zero and for the iodine isotopes it was 0.333, except for I-132 which was set to 1.0. This weighting factor allowed the incorporation of the expected reduction in signals for the noble gases and most of the iodine isotopes due to chemical fractionation prior to collection by a particulate sampler. These singles histograms were analyzed using Genie (Canberra) and the coincidence histograms were analyzed using the PNNL-developed Multiple Isotope Coincidence Analysis (MICA) code (Warren et al., 2006).

Analysis of simulation results indicates that the RN Labs instrument should achieve roughly an order of magnitude improvement in sensitivity over measurement with a single ultra-low background crystal (during a 24-hour count). Table 1 presents the determination limit, $L_Q$, required to achieve a 10% result in a 24 hour measurement from day 5 to day 6, after an event. The table includes several high-yield fission products. In this analysis, the background from one of the “twin” detectors (Brodzinski et al., 1990) operating at ~ 1000 meters water equivalent (mwe) was used as an estimate for the background of each individual crystal in the 14-crystal array. The simulation results for one central crystal were used to calculate the single crystal value.

**Table 1. Determination limit comparison and estimated detection limit.**

| | | $L_Q$ for 10% (fissions) | | | $L_D$ (fissions) |
|---|---|---|---|---|---|
| **Isotope** | **Energy (keV)** | **Single Crystal** | **14 Crystal Array** | **Analysis Method** | |
| $^{95}$Zr | 756 | 1.6E07 | 1.4E06 | Super Sum | 1.4E05 |
| $^{99}$Mo | 739.5 | 1.2E07 | 1.7E06 | Summed Spectra | 1.9E05 |
| $^{103}$Ru | 497 | 8.9E06 | 9.2E05 | Super Sum | 1.4E05 |
| $^{131}$I | 364* | 2.3E06 | 2.8E05 | Super Sum | 5.0E04 |
| $^{132}$Te | 228* | 9.0E05 | 1.4E05 | Super Sum | 3.7E04 |
| $^{140}$Ba | 537 | 7.9E06 | 7.5E05 | Super Sum | 9.6E04 |
| $^{140}$La | 1596 | 4.7E06 | 6.8E05 | Super Sum | 4.1E04 |
| $^{141}$Ce | 145* | 3.8E06 | 7.9E05 | Summed Spectra | 1.7E05 |
| $^{143}$Ce | 293* | 3.5E06 | 5.0E05 | Super Sum | 9.6E04 |
| * Potential background continuum contributed by atmospheric $^{7}$Be has not been taken into account. | | | | | |

Table 2 presents a comparison of the projected system detection limits (from the far right column of Table 1) with a notional single crystal with a typical above-ground shielded background. For this comparison, the background from a commercial low-background detector installed in typical shielding at PNNL was used. The system does not have active anti-cosmic shielding or radon exclusion. Figure 4 shows a comparison of the surface detector background and postulated 14-crystal background at ~1,000 mwe. Detection efficiencies are based on the same single crystal simulation results for a central crystal of the RN Labs array.

**Table 2. Detection limits for high fission yield gamma emitters single crystal at surface vs. 14-crystal array at 1000 mwe.**

| | | $L_D$ (fissions) | | Improvement Factor |
|---|---|---|---|---|
| Isotope | Energy (keV) | Single Crystal | RN Labs | |
| $^{95}$Zr | 756 | 9.4E06 | 1.4E05 | 67 |
| $^{99}$Mo | 739.5 | 7.0E06 | 1.9E05 | 37 |
| $^{103}$Ru | 497 | 6.9E06 | 1.4E05 | 49 |
| $^{131}$I | 364 | 2.2E06 | 5.0E04 | 44 |
| $^{132}$Te | 228 | 9.8E05 | 3.7E04 | 26 |
| $^{140}$Ba | 537 | 5.6E06 | 9.6E04 | 58 |
| $^{140}$La | 1596 | 1.3E06 | 4.1E04 | 32 |
| $^{141}$Ce | 145 | 4.2E06 | 1.7E05 | 25 |
| $^{143}$Ce | 293 | 3.5E06 | 9.6E04 | 36 |

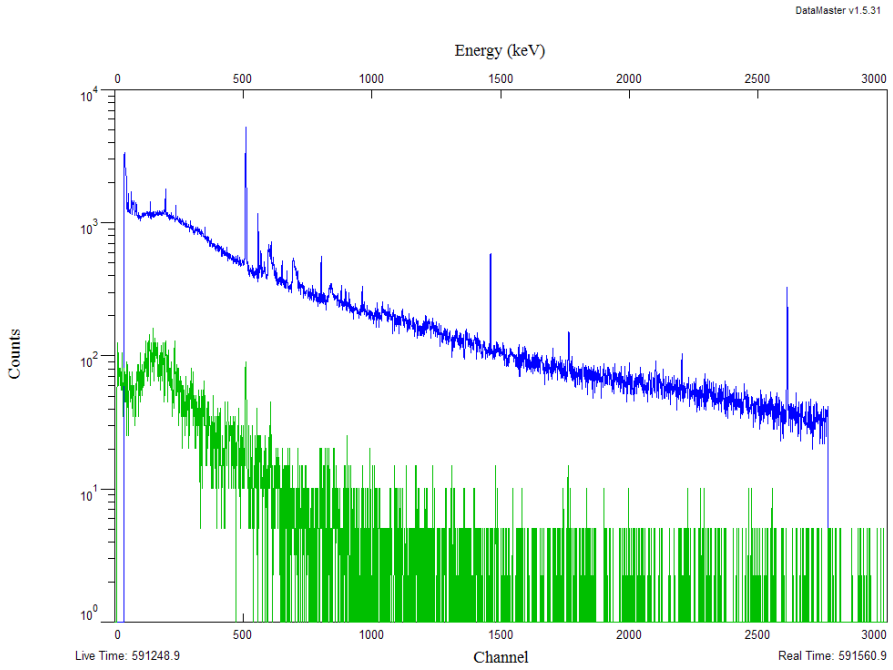


**Figure 4. A comparison between the background of a single shielded commercial low background detector, and potential background performance of this 14-crystal array.**

At this stage of our analysis, a few fission product isotopes have been identified that are detected with better sensitivity in coincidence mode than in singles mode by the 14-crystal instrument. Coincidence signatures for the same MFP measurement scenario used for singles mode analysis (24-hour count from day 5 to day 6) were investigated. In many cases, sensitivity gains realized by background reduction do not overcome the efficiency loss associated with detecting the coincident signature. This situation is exacerbated by the restricted count length—for isotopes with appropriate half-lives, longer count lengths would allow useful collection of data at very low background rates. Longer count times allow the sensitivity of the coincidence mode to overtake that of singles mode for additional mid- to long-lived isotopes.

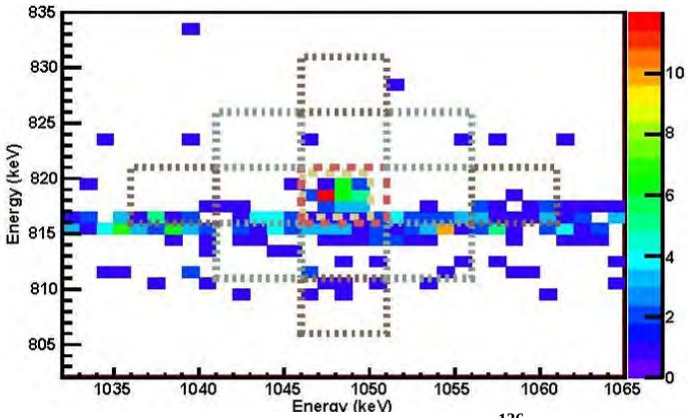


**Figure 5. Simulation results for detection of $^{136}$Cs using the coincident 815.5 and 1048 keV gamma-rays. This peak lies next to the Compton scatter ridge formed by full-energy deposition of the $^{140}$La 815 keV gamma, and Compton scatter of a coincident, higher energy $^{140}$La gamma (e.g., 1,596 keV). This plot is from a simulation of $10^9$ fissions.**

Figure 5 shows the 2-D coincidence plane for analysis of $^{136}$Cs. This figure represents simulation of $10^9$ fissions, resulting in a more sensitive determination of $^{136}$Cs than achieved with the singles analysis. In this case, the ridge running across the figure at 815 keV is associated with $^{140}$La, while the peak at the center is made up of $^{136}$Cs 818.5 – 1048 keV coincidence counts.

Europium-156 is another isotope that can be detected with higher sensitivity using coincidence techniques. In this case, the most intense gamma is emitted at 811.8 keV. As with $^{136}$Cs, this line is obscured in singles mode due to the strong $^{140}$La line at 815 keV. The $10^9$ fissions coincidence detection plane for the 646 and 1231 keV coincidence signature is shown in Figure 6. While this

signature isn't as dramatic the one in Figure 5, it represents a positive detect of $^{156}$Eu in the simulated data at near detection limits. Europium-156 is not detected in singles mode; in fact, the $^{156}$Eu activity would need to be elevated by roughly a factor of three above the simulated value to exceed the detection limit in singles mode.

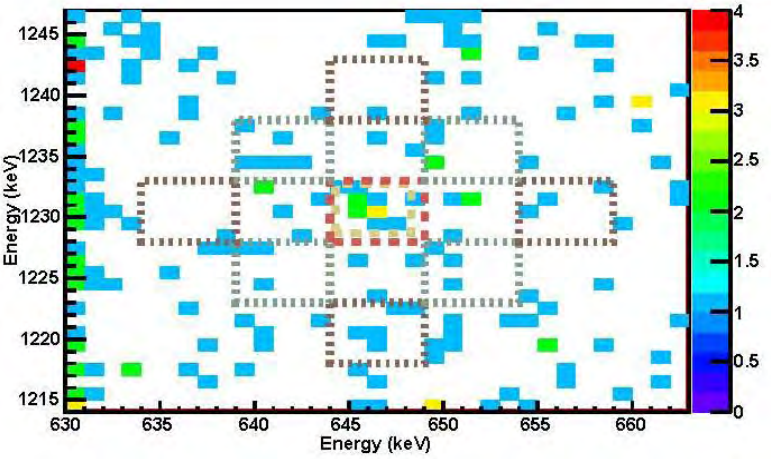


**Figure 6. Simulation results for detection of $^{156}$Eu using the coincident 646 and 1,231 keV gamma-rays. The isotope is detected slightly above the detection limit. This plot is from simulation of $10^9$ fissions.**

## Copper Electroforming and Assay

For over 20 years, PNNL has made improvements to the radio-purity and mechanical properties of electroformed copper. Recent inductively coupled plasma mass spectrometry analyses of this electroformed material have provided the lowest measured values of thorium impurities in copper. These techniques are being used to produce ultra-low-background cryostat parts for the current effort. Although copper electroforming is a long-standing capability at PNNL, electroforming baths with sufficient purity and capacity for the large parts required for this effort were not available at the beginning of the project. Two new large baths have been established and are working at full capacity to produce cryostat parts. These baths are capable of producing parts like pieces for the main body of the cryostat (~ 11" diameter), as well as long parts like the cross-arm and cold finger (~30" long). Figure 7 shows the cold finger for the first cryostat while it was being electroformed, as well as one of the large diameter parts for the cryostat.

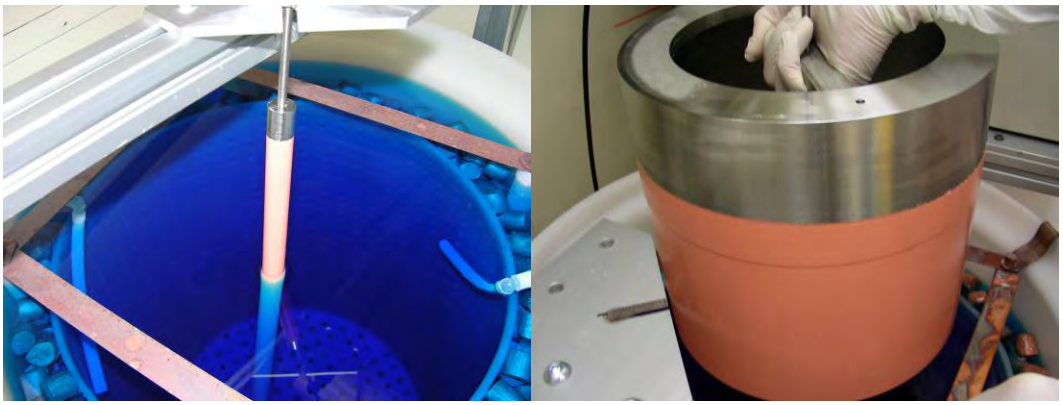

**Figure 7. Electroforming the cold finger and one of the large-diameter parts for the first cryostat. These photographs are from early in the electroforming process—both parts have since been completed and sent on for machining.**

### HPGe Crystals

Eight HPGe crystals have been received from PGT and have passed acceptance testing. These crystals were available at PNNL from prior projects, and were refurbished by PGT for this research. After acceptance testing, the crystals were removed from the delivery cryostat and kept in clean room conditions in a dry nitrogen storage cabinet. Storage periods ranged from a few weeks to several months. The crystals are being remounted into crystal packages shown in Figure 1, in preparation for populating the first 7-crystal array. A purchase order for additional new crystals for the 2nd cryostat has been placed with Canberra. The new crystal mounting technique has been successfully demonstrated. One of the main drawbacks to this method is the poor thermal coupling between the cold mass of the cryostat and the HPGe crystal. Typical single-crystal commercial cryostats will cool the crystal in less than 6 hours, while thermal equilibrium is not reached for ~48 hours in this new mount. While this is inconvenient in the event of repair work, thermal cycling of ultra-low-background systems is avoided as much as possible. Thus, this long cool-down period should not be a significant inconvenience for this system.

### Analog and Front-end Electronics

Semiconductor radiation detectors like HPGe produce signals too small to be observed without amplification. Typically, the first stage of amplification is placed only a few cm from the crystal, and is called the "Front-End" of the signal amplification and conditioning chain. Because it is close to the crystal, the radiopurity of this front-end is important. Because it contains active and passive electronic components, it is more challenging to purify of radioactive backgrounds than a bulk material like the copper used for the cryostat. Prior work has addressed this challenge by developing first a hand-assembled Low-background Front-End Package (LFEP), a second LFEP design that was suitable for production with standard electronics industry methods, and finally, a significantly smaller LFEP design that is to be used in this system. The evolution from a commercial front-end through the three LFEP designs can be seen top left-to-bottom right in Figure 8.

The LFEP works with the rest of the HPGe preamplifier to form a charge-integrating loop, converting the charge deposited in the HPGe by ionizing radiation into a voltage change that can be accurately measured by the digitizers described in the next section. For this work, custom 4-channel charge-integrating preamplifier boards have been prepared by Bridgeport Instruments to match the electrical characteristics of the LFEP units.

### Data Acquisition and Analysis

Data will be acquired from the 14 crystals and anti-cosmic shielding using X-Ray Instrumentation Associates (XIA) Pixie-4 cards, which provide four channels of digitization using 14-bit ADCs sampling at 75 MHz. This will allow digitization of event pulses received from all 14 crystals, if desired. Recording the pulse waveforms allows further background reduction through rejection of spurious pulses. This hardware platform offers ~13 ns time-stamps on all events and thus allows accurate reconstruction of coincident interactions in multiple crystals.

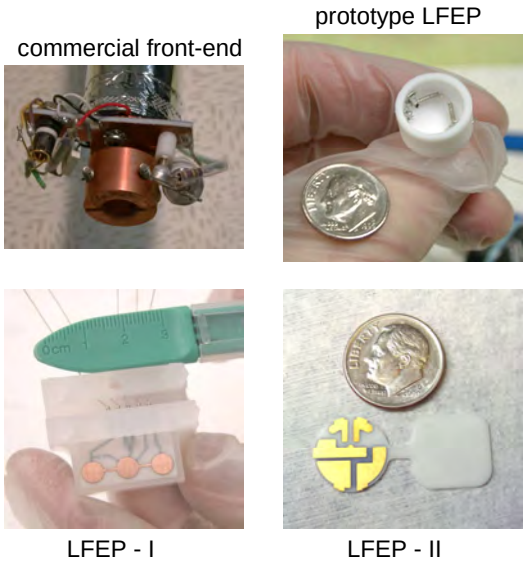


**Figure 8. Evolution of front-ends from commercial unit to current LFEP-II.**

### Production of Final Parts

Final parts for the first cryostat were machined over the summer; assembly and test of the cryostat is underway. Figure 9 shows the cryostat cross-arm and mandrel being turned to final dimensions on a lathe. In order to minimize surface contaminants, the machinists are required to wear gloves while handling the copper parts to improve cleaning results at later stages. Machine tool parts that contact the piece were also cleaned prior to work, and clean propylene glycol is

used to lubricate the surfaces during machining.

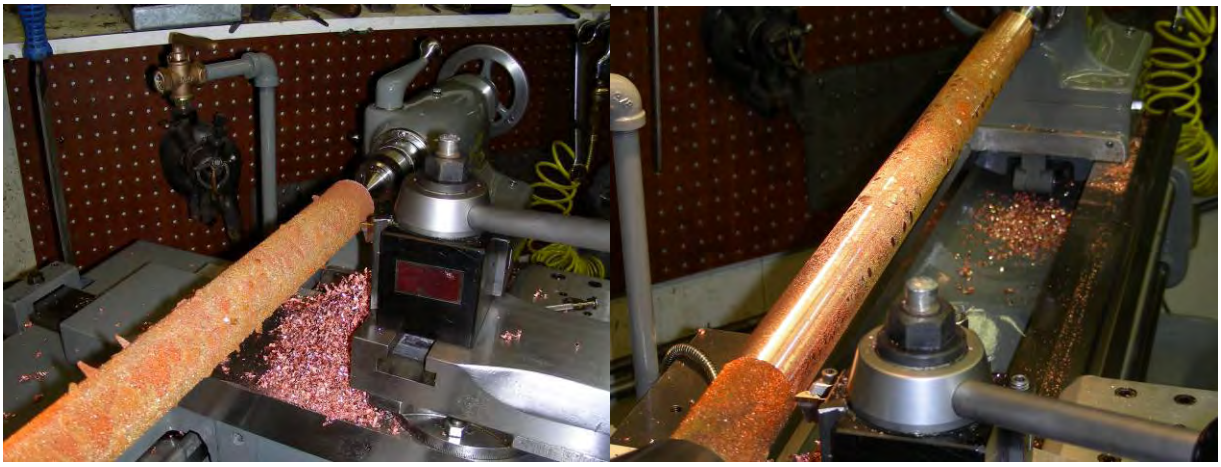

**Figure 9. Initial lathe turning of the cold finger for the first 7-crystal cryostat. Shavings are from truing the rod ends and starting to remove the nodule growths from the electroformed piece. Care must be taken during this stage to avoid tearing the nodules away and leaving pits that extend inside the finished diameter.**

## CONCLUSIONS AND RECOMMENDATIONS

Construction of the first of two ultra-low-background cryostats, each to house 7 HPGe crystals, is underway. Electroforming of parts for the 2nd cryostat is also in progress. Initial post-construction testing will include an assessment of vacuum and thermal performance, however test results are not available at the time of this writing. The crystals will be installed after successful check-out of the cryostat.

Simulation results for the system indicate that the potential to establish detection sensitivity levels in the range of mid $10^4$ fissions for samples measured fivedays post-event, with a 24-hour measurement and no chemical processing of the sample.

Achieving the lowest possible backgrounds is an important part of overall system performance. Accordingly, deployment to a shallow underground or deeper operating location (if available), will maximize the sensitivity performance of this system.

## REFERENCES

Aalseth, C. E., T. W. Hossbach, and H. S. Miley (2004). 2004 IEEE Nuclear Science Symposium Conference Record, V. 2, 1937–1938.

Agostinelli, S., J. Allison, K. Amako, J. Apostolakis, H. Araujo, and P. Arce (2003). Geant4—a simulation toolkit, *Nucl. Inst. Meth.* A 506: 250–303.

Allison, J., K. Amako, J. Apostolakis, H. Araujo, P. A. Dubois, and M. Asai (2006). Geant4 developments and application, *IEEE Trans. Nucl. Sci*. 53: 270–278.

Brodzinski R. L., H.S. Miley, H. J. Reeves, F. T. Avignone III (1990). Nucl. Instr. & Meth A, V 292, N 2, 337-342.

Kazkaz, K., C. E. Aalseth, T. W. Hossbach, V. M. Gehman, J. D. Kephart, and H. S. Miley (2003). 2003 IEEE Nuclear Science Symposium Conference Record, 2003, V. 1, 87–91.

Perkins, R. W. and U. P. Jenquin (1997). Pacific Northwest National Laboratory, PNNL-11554.

Warren, G. A., L. E. Smith, C. E. Aalseth, J. E. Ellis, A. B. Valsan, and W. Mengesha (2006). *IEEE Trans. Nucl. Sci*. 53: 351–355.

# IMPROVING GERMANIUM DETECTOR RESOLUTION AND RELIABILITY

Gregory N. Martin[1], K. Michael Yocum[1], James F. Colaresi[1], and Harry S. Miley[2]

CANBERRA[1] and Pacific Northwest National Laboratory[2]

Sponsored by National Nuclear Security Administration

Contract No. DE-AC52-08NA28650
Proposal No. BAA08-10

## ABSTRACT

High purity germanium (HPGe) detectors used in radionuclide assay systems such as Radionuclide Aerosol Sampler/Analyzer (RASA**)** systems must operate unattended for long periods of time. Currently, the performance and reliability of commercially available large (~100%) HPGe detectors are acceptable for the majority of laboratory applications. However, for remote systems designed for nuclear detonation detection and analysis, improved performance and reliability are required. The goals of this research include improving germanium detector reliability and resolution performance by developing new surface passivation techniques coupled with a unique detector contact arrangement. A major reliability improvement would be realized if germanium detectors were made less sensitive to storage and operational environments by improving the film coating used to passivate and protect the intercontact surface. This research is the investigation of two surface film techniques for passivating HPGe detector surfaces. Wet chemically grown oxide films and sputtered film coatings will in turn be applied to two standard P-type HPGe coaxial detectors. Each coating will be characterized to determine their surface chemistry passivating qualities as well as their inherent noise contribution to the overall system noise. The resolution of a germanium detector is a function of electrical noise and the inherent resolution of the detector element.

The electrical noise components which reduce the signal to noise ratio of a detector system are associated with detector leakage current, intercontact surface noise, contact noise and noise sources associated with preamplifier electronics. In particular, those noise components associated with the intercontact surface are leakage current and surface noise. We believe these two significant sources of noise can be reduced by using novel surface passivation techniques resulting in improved detector resolution. The techniques developed by this research will be applicable to new detectors and can also be applied as a retrofit to existing RASA units. This will improve the ability to obtain more sensitive and reliable detections of remote nuclear activity.

## OBJECTIVES

State of the art large-volume germanium photon detectors comprise a volume of high purity germanium, an $n^+$ hole blocking contact (lithium diffusion), a $p^+$ electron blocking contact (boron implant) and an intercontact surface. The performance of an HPGe detector depends on the electrical characteristics of each of its constituent components. The base material must be "detector grade" HPGe, meaning that it must have a sufficiently low concentration of electrically active impurities (net concentration of ~ $10^{10}$ $cm^{-3}$), have acceptable crystallography, and contain no appreciable concentration of deep levels usually associated with trapping and charge recombination centers. The electrical contacts which create the diode structure, and collect charge created by photon interactions, must be non-injecting and sufficiently robust to tolerate handling in a usual semiconductor manufacturing environment. Furthermore, the contacts must be completely tolerant of all stresses imposed as the detector is held in its vacuum cryostat. An intercontact surface is necessary for electrical separation of the detector contacts. It must allow very little reverse leakage current under the stress of as much as 5000 V of reverse bias. In addition the intercontact surface must create little electrical noise. Both surface leakage noise and passivant dielectric noise must not significantly deteriorate the system signal to noise ratio.

CANBERRA manufactures large HPGe coaxial detectors fabricated from both P-type HPGe and N-type HPGe. For the purpose of this research a CANBERRA version of the P-type coaxial detector configuration will be used. Our primary P-type coaxial detector product is the Standard Electrode Germanium (SEGe), which comprises a right circular cylinder with an outer wrap-around lithium $n^+$ contact and a boron implanted $p^+$ center or core contact. The intercontact surface is limited to a small annular region near the core by a unique wrap-around lithium contact. The ruggedness and stability of the contacts have been proven by their use on thousands of standard and special products provided by CANBERRA. Therefore, we will concentrate our reliability and performance improvement efforts on the intercontact surface. The geometry and contact configuration of the SEGe product is schematically represented by Figure 1.

Typically, HPGe detectors can develop poor resolution due to charge carrier injection current caused by contact imperfections or damage as well as surface leakage current caused by intercontact surface channels or carrier generation sites. The surface of single crystal germanium oxidizes readily when exposed to oxygen or water vapor, so it must be chemically passivated to prevent the uncontrolled growth of native oxide. Uncontrolled oxidation of germanium by exposing the surface to atmospheric oxygen and water vapor or to very fast oxidation from acid etches yields porous, low-density oxide films containing non-stoichiometric $GeO_x$ species. A poorly formed native oxide on the intercontact surface of a HPGe detector is unacceptable because such a native oxide layer often contains a significant density of electronic states. Native oxide layers containing empty states with energy levels in the germanium band gap can be positively charged which in turn accumulate electrons to the germanium surface region creating an inversion layer in P-type material or an accumulation layer in N-type material. Such effects in P-type germanium have been described by Brown (1953). Slow states in the oxide layer and fast states in the oxide/germanium interfacial layer have been investigated by Bardeen et al. (1956). Because electrons are attracted to the surface, band bending leads to the formation of weak field regions. More pronounced band bending inevitably creates conductive surface channels. The surface channel model was expanded to describe detector dead-layer effects by Dinger (1975). Hull and Pehl (1994) demonstrated how the temperature sensitivity of surface channels in HPGe can deteriorate detector performance. Furthermore, in the case of P-type material, inversion layers may lead to 1/f noise as reported by MacRae (1960).

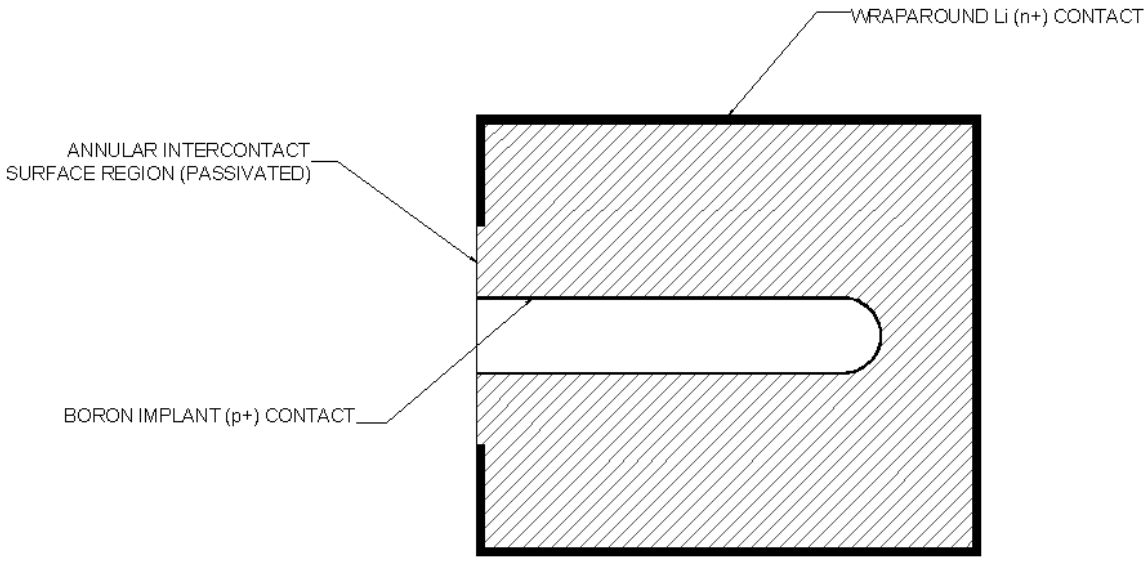


**Figure 1. Schematic representation of the CANBERRA SEGe detector element.**

As mentioned previously, it is imperative to chemically stabilize the intercontact surface of a germanium detector by passivation. Passivation in the world of HPGe detectors means to coat the intercontact surface using a high resistivity, low-loss dielectric containing a negligible density of electronic states. At CANBERRA, the intercontact surface of our SEGe detector is coated with a layer of $SiO_x$ where x is approximately 2. This coating is created by a well controlled evaporation of silicon monoxide, the methodology being a textbook subject described in many works such as the one by L. Holland (1970). The intercontact region is manufactured by first mechanically polishing the surface to remove gross damage left from the machining process. Microscopic damage is removed by a concentrated nitric acid based etch followed by water and methanol rinses. Subsequently, the intercontact surface is coated with a $SiO_x$ film approximately 100 nm thick using a silicon monoxide evaporation technique.

Although $SiO_x$ passivations have been an acceptable solution for our commercial detector products, some variability in reverse leakage currents as well as field-line distortion effects associated with intercontact surfaces have been observed. Some of the properties of evaporated silicon monoxide on germanium which result in deleterious surface effects have been investigated by Dinger (1976). The existence of weak-field regions and surface channels result from both fast electronic states (germanium surface) and slow electronic states ($SiO_x$ film, adsorbed gases). The charging of electronic states results in band-bending near the intercontact surface as well as field-line termination at the intercontact surface. The band-bending effect of an inversion layer created by positively charged oxide and surface states is represented by the energy-band diagram in Figure 2. Although these effects have been somewhat curtailed by the application of our unique wrap-around lithium $n^+$ contact, a more consistently neutral intercontact surface may be possible by improving or replacing the present $SiO_x$ passivation.

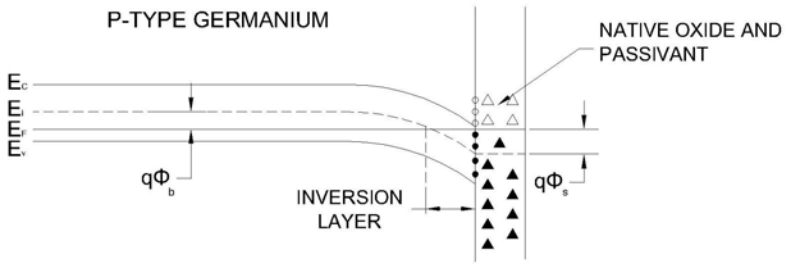


**Figure 2. Simplified energy diagram depicting an inversion layer on the surface of P-type HPGe including slow states (▲ neutral, △ positive) and fast states(● neutral, ○ positive). The vertical axis is relative energy (eV), the horizontal axis is displacement (arbitrary units), $E_C$ is the bottom of the conduction band, $E_V$ is the top of the valence band, $E_F$ is the material Fermi level, $E_I$ is the approximate intrinsic Fermi level, $\Phi_b$ represents bulk potential, $\Phi_s$ represents surface potential, and q is the electron charge. After Brown (1953) and Dinger (1975).**

Two large-volume (~100% relative) SEGe detectors will be manufactured using the $SiO_x$ passivant as described in the previous paragraphs. First, baseline data will be established by characterizing each detector using CANBERRA standard test procedures which include the measurement of relative efficiency, electronic noise analysis, resolution measurements, and peak shape measurements. Second, we will measure the reverse leakage current of each detector versus several operating temperatures using a mechanically cooled cryostat. In addition the electronic noise of both detector assemblies will be measured at each operating temperature. These tests should sufficiently characterize the temperature stability of the intercontact surface. The surface characteristics of high-purity germanium can be influenced both by the net impurity concentration at the intercontact surface and by local crystallography. To ensure that the results of the experiments are related to the passivants being tested rather than the characteristics of the specific germanium material, the same detector elements will be used throughout our development efforts.

To test our current passivation method for ruggedness, we will perform three basic tests. First, we intend to remove each device from its vacuum cryostat to perform 10 rapid thermal cycles from 87 K to approximately 300 K. We will then perform careful visual inspections of the devices to determine if cracking or flaking of the passivant is evident. Second, before the test devices are re-installed into their vacuum cryostats, we intend to "age" them at room temperature and atmospheric pressure for one month. We will re-install the devices into their respective vacuum cryostats then perform reverse leakage current and noise tests to determine if the devices survived. Third, we intend to perform three successive overnight vacuum pumping procedures at elevated temperatures (70 C to 100 C) , then we will repeat leakage current and noise tests.

The first new surface passivation to be evaluated will be a native oxide film grown on the detector interelectrode surface using a wet chemical oxidation (WCO) technique. Unlike the naturally occurring native germanium oxide which forms on clean germanium from exposure to atmospheric moisture and oxygen or the thick highly non-stoichiometric residual oxide left after most nitric-acid-based etches, oxide films produced by WCO techniques are very dense, homogenous and for the most part defect free. Germanium WCO techniques have been investigated by Gregory et al. (1988) who were successful in growing native $GeO_2$ with excellent stoichiometry. Gregory also found that the best films remained stable after samples were stored for one year at room temperature. Such films should behave as good passivants for detector interelectrode surfaces primarily because they contain a low density of electronic states which are a direct cause of surface channel formation. Furthermore, if WCO films are dense and continuous as suggested by Rutherford backscattering measurements and electron micrographs, they contain few interstices for the permeation of reactive gas species. By definition a native oxide is grown directly from the germanium surface with a resulting decrease in the density of unconsumed germanium bonds (dangling bonds) which act as charge generation sites. Limiting generation sites may reduce surface leakage temperature sensitivity and reduce surface noise.

Gregory found that using hydrofluoric acid with a trace of hydrogen peroxide creates a water insoluble phase of $GeO_2$ presumably by preventing the water / hydrofluoric acid soluble phase from accumulating on the germanium surface. For this research, native germanium oxide passivating films will be created using a similar WCO technique which will incorporate a hydrofluoric acid / oxidizer solution. Since a miniscule amount of oxidizer is used in all

WCO techniques (Gregory used less than 1% by volume $H_2O_2$ for his most successful attempts.), it is imperative to use a stable oxidizer, especially within a commercial laboratory environment. Hydrogen peroxide is generally very stable, however; it can be quickly decomposed by traces of transition metals unless artificially stabilized by the addition of compounds such as stannate salts. To avoid any variability in the growth of native germanium oxide due to unknown concentrations of hydrogen peroxide or the effects of stabilizing agents, we will attempt to substitute a more tolerant oxidizer. Several oxidation experiments will be needed to determine the acceptable oxidizer and ratio of the solution constituents, as well as reaction time and temperature. When we have grown acceptable oxides on the intercontact surfaces of both SEGe devices, we will remount the detectors into their electrically-cooled cryostats. The detectors will be evaluated in the same manner as for the standard $SiO_x$ passivation. Any additional tests required to demonstrate the ruggedness and stability of the oxide passivant will be performed as well. A subsequent progress report will include a summary of the successful film growth technique and test results.

Pioneering work done on the use of sputtered films for HPGe passivants was done by Hansen et al. (1980, 1986). Hansen stated that as passivants for HPGe detector surfaces, sputtered hydrogenated amorphous germanium (α-Ge:H) films demonstrate none of the drawbacks of films produced by silicon monoxide evaporations. Cathodic sputtering of germanium can be accomplished either by DC or AC techniques with AC techniques being more easily controlled especially at low power (~150 W). An argon / hydrogen atmosphere is used to create amorphous germanium films on crystalline germanium surfaces. Because of the innate random stoichiometry of amorphous films, the resulting unsatisfied germanium bonds in the film must be passivated with hydrogen. Also, the impact of ions and neutral atoms alike can break germanium bonds at the crystalline surface which require hydrogen passivation. Ions and neutrals impacting the device surface liberate oxides and other species resulting in a nearly clean surface albeit a damaged one. In addition to α-Ge:H, hydrogenated amorphous silicon (α-Si:H) is another consideration for creating passivant films. More stoichiometric oxide films other than those produced by silicon monoxide evaporations may be formed by adding oxygen rich chemical species such as boron trioxide ($B_2O_3$) to SiO to formulate a pure borosilicate glass which can subsequently be sputtered to deposit a passivating coating on germanium. Such a film may tolerate pump and bake temperatures exceeding 60 C which are needed to reduce the adsorbed gas load of detector / cryostat assemblies. Also, a more stable film with fewer electronic states than those created by evaporation techniques should produce less pronounced surface effects. Sputtering silicon-based glass requires more power than sputtering germanium which may damage the intercontact surface of a detector to a larger degree than a low-power germanium deposition. As done with sputtered germanium films, an argon / hydrogen atmosphere will be necessary to passivate damage sites. In turn, α-Ge:H, α-Si:H, and borosilicate films will be deposited on the intercontact surfaces of both test SEGe detectors for a total of six depositions. Each test passivant will be tested in the same manner as for the standard $SiO_x$ passivation. Again, additional testing may be required to demonstrate the ruggedness and stability of the passivant. A subsequent progress report will include a summary of the successful film deposition techniques and test results.

## RESEARCH ACCOMPLISHED

The contract period for this research began in the second week of June 2008. At the time of this writing no significant research has been accomplished.

## CONCLUSIONS AND RECOMMENDATIONS

Our research entails the characterization of several different films used as chemical passivants for the intercontact surface of HPGe photon detectors. We intend to compare the properties of grown native oxide films and sputter deposited films to the properties of a control technique comprising evaporated silicon monoxide films. Successful films must tolerate temperature cycling between room temperature and cryogenic temperatures, they must tolerate being exposed to room temperature at atmospheric pressure for long periods of time, and they must survive vacuum pump and bake cycles at temperatures exceeding 60ºC. Passivants must not contain an appreciable density of electronic states which can result in high surface leakage current or high surface noise; therefore, test detectors will be evaluated using standard procedures to determine surface leakage current and noise.

**ACKNOWLEDGEMENTS**

Our thanks to Ted Gallucci for contributing figure art work.

**REFERENCES**

Bardeen, J., R. E. Coovert, S. R. Morrison, J. R. Schrieffer, R. Sun (1956). Surface conductance and the field effect on germanium, *Physical Review* 104: p. 47.

Brown, W. L. (1953) N-type surface conductivity on p-type germanium, *Physical Review* 91: p. 518.

Chapman, B. (1980). *Glow Discharge Processes: Sputtering and Plasma Etching*, John Wiley & Sons, Inc..

Dinger, R. J. (1975). Dead layers at the surface of p-i-n detectors – a review, *IEEE Trans. Nucl. Sci*., NS-22: (1) p.135.

Dinger, R.J. (1976). Effect of evaporated dielectric materials on the surface of high purity germanium, *J.Electrochem. Soc.: Solid-State Science and Technology*, 123: 9, p. 1398.

Gregory, O. J., L. A. Pruitt, E. E. Crisman, C. Roberts, P. J. Stiles (1988). Native oxides formed on single-crystal germanium by wet chemical reactions, *J. Electrochem. Soc., Solid State Science and Technology*, April 1988, p.923.

Hansen, W. L., E. E. Haller, G. S. Hubbard (1980). Protective surface coatings on semiconductor nuclear radiation detectors, *IEEE Trans. Nucl. Sci.*, NS-27: 1, p.247.

Hansen, W. L., E. E. Haller (1986). Germanium detector passivated with hydrogenated amorphous germanium, U. S. Patent 4589006.

Holland, L. (1970). *Vacuum Deposition of Thin Film*s, Chapman & Hall Ltd.

Hull, E. L., R. H. Pehl, J. Xing, K. Komisaricik, J. Vanderwerp, D. Friesel, N. Madden, P.N. Luke, C. Cork, and D. Malone (1994). Temperature sensitivity of surface channels on high-purity germanium detectors, *1994 Annual Scientific and Technical Report-IU Cyclotron*, p.123.

Mac Rae, A. U., H. Levinstein (1960). Surface-dependent 1/f noise in germnaium, *Physical Review* 119: p. 62.

# GENERATION OF RADIOXENON ISOTOPES

Justin I. McIntyre, Sharon Pratt, Theodore W. Bowyer, Matthew W. Cooper, James C. Hayes, Tom R. Heimbigner, Charles W. Hubbard, Harry Miley, and Michael Ripplinger

Pacific Northwest National Laboratory

Sponsored by National Nuclear Security Administration

Contract No. DE-AC05-RLO1830

## ABSTRACT

With the continued population of the International Monitoring System (IMS) network and the certification of radioxenon laboratory systems, it has become necessary to calibrate and test these systems using as many of the radioxenon isotopes as possible. Several very promising techniques have been explored recently that allow for convenient production of Xe-133, Xe-131m, the short-lived isotope Xe-135, and even the difficult-to-obtain Xe-133m. IMS national and international laboratories have traditionally obtained Xe-133 from medical isotope suppliers. The activity of these medical dose samples is extremely high (~740 MBq) and requires very careful fume hood work to dilute down to appropriate levels (~10 Bq). By waiting for 10 or more half-lives it is possible to reduce the handling regime considerably, while also obtaining a strong Xe-131m signature due to its longer half-life (11.9 days). The short-lived isotope Xe-135 (9.14 hr) and the longer-lived parent nuclide Xe-133m (2.2-day half-life) are never present in these samples. To obtain these isotopes, another source or technique is required. This paper will discuss the two techniques developed and implemented at Pacific Northwest National Lab (PNNL) and show the results obtained from each technique. The first is an in-house method that allows for on-demand production of two of these isotopes, Xe-133 and Xe-135, using highly enriched uranium (HEU) and a modest flux neutron source. The second method uses a neutron activation of stable xenon.

## OBJECTIVES

The Automated Radioxenon Sampler/Analyzer (ARSA) and the Swedish Automatic Noble Gas Analyzer (SAUNA) systems were specifically designed to detect plumes of radioxenon that are a byproduct of fissioning transuranic elements (uranium and plutonium being the most relevant). The systems detect these isotopes via different collection platforms and a subsequent nuclear-detection platform that is virtually identical in form and function. This report confines itself to two in-house methods used to generate the radioxenon isotopes necessary to calibrate the nuclear detection system. The ARSA system is described in Bowyer et al., 1996; Bowyer el al., 1998; and Bowyer et al., 2002. The SAUNA system is described in Ringbom et al., 2003.

The use of radioactive xenon is instrumental for the calibration of the beta-gamma detectors in the ARSA and SAUNA systems (Reeder and Bowyer, 1998). For two of the isotopes (Xe-133 and Xe-131m) there are commercially available sources that have been successfully obtained from medical isotope production facilities. Typically costs for a vial containing 740 MBq of Xe-133 is about $15.00 and we receive a monthly shipment so that we always have Xe-133 on hand. As an added benefit, these samples of Xe-133 also contain trace quantities of Xe-131m. If the Xe-133 samples are allowed to age for several months the ratio of Xe-131m/Xe-133 becomes quite large (>>10) and it is possible to obtain the necessary detector efficiencies, energy calibration and resolutions for the Xe-131m isotope from these sources as well.

For the remaining two isotopes (Xe-133m and Xe-135) there is no such convenient source available because of the short half-lifes (2.2 days and 9.1 hours respectively). In addition Xe-133m has proven to be technically difficult to obtain in significant quantities and because it decays to Xe-133 and it is difficult to maintain significant ratios of Xe-133m/Xe-133 without a great deal of effort. In the past Xe-133m and Xe-135 have been obtained from neutron fissioning of microgram quantities of U-235 in the research reactor located on the campus of Washington State University at Pullman, Washington (Reeder et al., 2001). Shipping and handling requirements were difficult, and it was not possible to obtain the fission products from the irradiated samples for two days after irradiation. From the previous a ratio of Xe133m/Xe133 = 1/10 was the best that was obtained.

To overcome both the time delay and the administrative planning and coordination, we have developed two separate techniques here at PNNL to obtain three of the four radioxenon isotopes needed for detector calibration. The better of the two techniques used U-235, and was called the radioxenon generator (RXG). It produced very strong signatures of Xe-133 and Xe-135. The second technique used neutron activation to produce weak signatures of Xe-125m and Xe-133 and very little else. This method has however been coupled with isotopic enrichment of stable xenon isotopes and used with a nuclear research reactor by Derek Haas et al. of the University of Texas at Austin, Texas (Haas et al., 2008, these Proceedings).

## RESEARCH ACCOMPLISHED

The RXG uses the fissioning of U-235 while the second method used the direct neutron activation of stable xenon isotopes. Both techniques have yielded results but due to the low neutron effluence of the neutron sources used, the neutron activation method required much higher neutron sources and an additional isotopic separations step to be made a viable method. The U-235 fission method produced adequate quantities of Xe-133 and Xe-135 to be used for the detector calibration and was considered the superior approach.

### Radioxenon from Fissioning of U-235

The RXG is composed of 10.1 grams of $U_3O_8$ (uranium oxide) powder, with the uranium being 95% U-235. A diagram of the RXG is shown in Figure 1-A. The uranium-oxide powder is double sealed in 3-ply 3COM SBMF filter paper to prevent the oxide powder from being dispersed and to allow fission product gases to diffuse out. The sealed powder is then contained in a primary aluminum can that has several holes drilled in the sides to allow gas passage. This primary aluminum container is than wrapped in filter paper and placed in the secondary aluminum can that has an air-tight seal and a valve to keep the fission gases in. A layer of glass wool is placed on top to further prevent the spread of the uranium powder. The aluminum containment bottle was chosen both for reasons of safety

(quartz bottles may break if dropped), and low activation products. The gas samples are drawn out of the RXG using an evacuated gas bottle to volumetrically pump the fission gases out of the aluminum container.

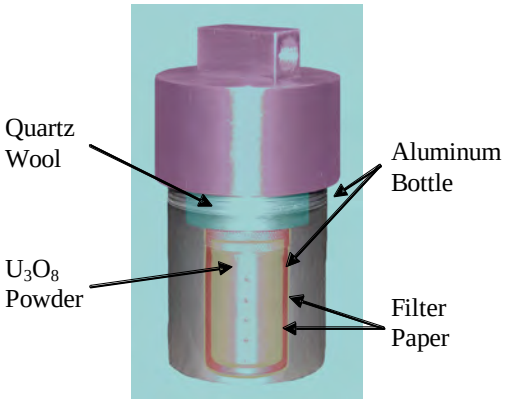


**Figure 1-A. Schematic of the RXG. The overall length is 10 cm with a diameter of 4 cm.**

To irradiate the uranium-oxide powder, two neutron sources were used with moderating material. During the irradiation of the sample, an 80-g PuBe source with a neutron flux of ~$8.8 \times 10^8$ neutrons/s and a 10 microgram Ca-252 source with a neutron flux of $2.8 \times 10^7$ neutrons/s were placed on either sides of the RXG (see Figure 1-B). The surrounding concrete of the source storage tube aids in the thermalization of the neutrons that are generated from the two sources. To further facilitate an increase in fission reactions, two plastic bottles filled with 385 g of polyethylene beads are placed on either side of the sources as moderators to increase the flux of thermal neutrons.

The neutron irradiation time was varied over a period of hours to several weeks and produced small amounts of Xe-133m, and much larger quantities of Xe-133 and Xe-135 along with several other noble gas isotopes (Kr-85m, its daughter product Kr-85, and Kr-88). The krypton isotopes decay away quickly and do not interfere with the primary isotopes of interest. An additional follow-on effort has been undertaken at Oregon State University with Dr. David Hamby's group to use very-fast irradiation times and the high neutron effluence of their nuclear research reactor to produce favorable Xe-133m/Xe-133 ratios. In this experiment, a flow-through cell will be constructed that quickly separates out the fissioning gases from the uranium metal and other parent fission isotopes (I-133 in particular) that lead to low Xe133m/xe-133 ratios.

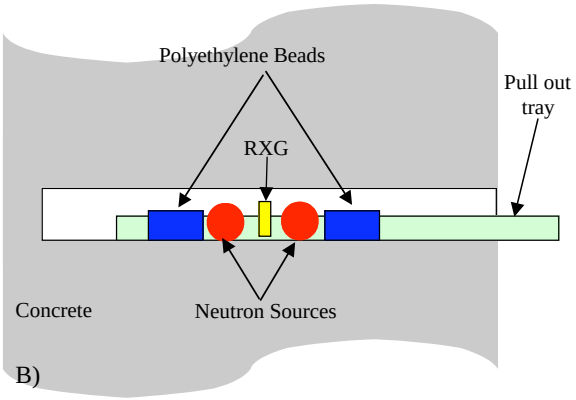


**Figure 1-B. Neutron source configuration for irradiation of the RXG (not drawn to scale). The pull out tray is 5 m long. The surrounding concrete is several meters thick.**

**Neutron Irradiation of Stable Xenon**

The irradiation of stable xenon provides another in-house technique that was pursued for the sake of availability and reduction in handling procedures. This technique used a simple plastic bottle filled with stable xenon gas to atmospheric levels. An irradiation was done using the same PuBe and Ca-252 neutron sources as was used for the uranium fissioning technique.

A quick look at the relevant isotopic abundances for stable xenon (Table 1) shows that Xe-132 and Xe-134 are the highest concentration isotopes of interest (Xe-132 + $n \rightarrow$ Xe-133 and Xe-134 + $n \rightarrow$ Xe-135) but they are not the most likely to capture a thermal neutron (*Health Physics and Radiological Health Handbook*, 1998). The neutron light isotopes of xenon (Xe-124, Xe-126 and Xe-129) are 1 to 3 orders of magnitude more likely to capture a thermal neutron. Table 1 shows the product of the thermal neutron cross-section a (column 4). It is clear from the isotopic abundance that the bulk of the strength is from the Xe-129 + $n \rightarrow$ Xe-130 reaction, which does not produce a nuclear decay. The next-highest activation is the Xe-132 + $n \rightarrow$ Xe-133 reaction followed by the Xe-124 + $n \rightarrow$ Xe-125m reaction.

**Table 1. A listing of the all the stable xenon isotopes along with pertinent information for each. Clearly Xe-124 has the highest thermal neutron cross-section followed by Xe-129. The production of Xe-129m actually comes from a (*n*,*2n*) reaction on Xe-130.**

| Xenon Isotope | % of Atmospheric Xenon | Thermal Neutron Cross Section (mb) | Product (% * Cross Section) | Metastable Component Half-Life |
|---|---|---|---|---|
| Xe-124 | 0.10 | 165,000 | 16,500 | None |
| Xe-126 | 0.09 | 3,500 | 315 | None |
| Xe-128 | 1.91 | 480 | 917 | None |
| Xe-129 | 26.4 | 22,000 | 580,800 | 8.89 days |
| Xe-130 | 4.1 | 450 | 1,845 | None |
| Xe-131 | 21.4 | 100 | 2,140 | 11.9 days |
| Xe-132 | 26.9 | 500 | 13,450 | None |
| Xe-134 | 10.4 | 265 | 2,756 | 290 ms |
| Xe-136 | 8.9 | 260 | 2,314 | None |

**Table 2. Data taken from *Table of Radioactive Isotopes*, edited by E. Browne, R. B. Firestone, and V. S. Shirley, 1986.**

| Isotope | Half-Life | Gamma-Rays (keV) | Beta (keV) | X-Rays (keV) | CE (keV) |
|---|---|---|---|---|---|
| Xe-122 | 20.1 hours | 148.6 (3.1%)<br>350.1 (7.8%) | IB<br>530 (<1.0%) | 28–33<br>(78.6%) | 5–24 (71%) |
| Xe-125 | 16.9 hours | 188.4 (54.9%)<br>243.4 (28.8%) | β+<br>1467 (0.69%) | 28–33<br>(100%) | 5–80 (120%)<br>155 (6.4%) |
| Xe-127 | 36.4 days | 172.1 (23.5%)<br>202.9 (68%)<br>375.0 (15.9%) | IB<br>457 (<1.0%) | 28–33<br>(54.6%) | 5–33 (69.3%)<br>90–125 (29.4%)<br>138–168 (84.2%) |
| Xe-129m | 8.89 days | 39.6 (7.5%)<br>196.6 (4.6%) | | 29–35<br>(126.5%) | 5–40 (215%)<br>162 (63.3%)<br>191–197 (60%) |

Predicted activations and branching ratios indicate that four of the isotopes (Xe-122, Xe-125, Xe-127, and Xe-129m) will generate conversion electrons that may interfere with the beta spectroscopy of the radioxenon

isotopes from fission. Table 2 shows the major gamma and beta signatures that each of the four new radioxenon isotopes emit. The short-lived isotopes and metastable isotopes have not been included as they have half-lives of 3 hours or less and so are very unlikely to have much strength after generation, emission, collection, processing and eventual counting in a beta-gamma cell. Two of the isotopes are known to be produced for medical purposes (Xe-127 and Xe-122) and are routinely generated at the Los Alamos Neutron Science Center (LANSCE) in Los Alamos National Lab and the Brookhaven LINAC Isotope Producer (BLIP) at Brookhaven National Lab in New York (*Isotopes for Medicine and the Life Sciences*, 1995).

## RESULTS AND ANALYSIS

Results have been obtained from both techniques as shown in this section. The fissioning of U-235 via neutrons produced the best results, and the radioactive gas has been used on both the ARSA and SAUNA systems for calibration purposes. The neutron activation method has the potential of providing very good results for individual isotopes (i.e., not a mix of three isotopes as seen from the RXG). However, it was clear from the results obtained at PNNL that a much higher neutron flux was necessary, and the use of isotopically purified xenon samples would provide unambiguous results.

### Results from Fissioning of U-235

The beta-gamma spectrum obtained from the RXG is shown in Figure 2. The x-axis is the beta distribution and the y-axis is the gamma ray distributions. The upper red distribution is from Xe-135, the beta end point corresponds to 910 keV, and the gamma ray is centered at 250 keV. The next-lower distribution is from Xe-133 at a gamma energy of 80-keV and a beta end point energy of 346 keV. The lowest distribution is the 30-keV x-ray region and it contains signatures from Xe-133, Xe-133m and Xe-135. It is difficult to cleanly separate these isotopes using this region of the spectrum, and special methods of analysis are required.

A beta-gated gamma spectrum is shown in Figure 3 that clearly shows Kr-85m, Kr-88, Xe-133, and Xe-135 and is typical when the sample is immediately put into the beta-gamma detector. These isotopes were produce after a 14-day neutron irradiation of the RXG. The short half-life radiokryptons (half-lifes <5 hours) and Xe-135 have reached secular equilibrium after a couple of days of irradiation, and the long irradiation time was chosen to maximize the Xe-133 yield. There are approximately 25 mBq of Xe-133, 0.7 Bq of Xe-133m, 50 Bq of Xe-135, 10 Bq of Kr-85m, and 0.6 Bq of Kr-88 in this sample. The daughter product, Kr-85, has a much longer half-life (10.9 years) and is a beta emitter (99.6% of the time), which yields no discernable beta-gamma coincidence in the nuclear detector. From simplistic fission yield and neutron-flux-rate calculations, these values should be 3 times higher, and it is currently believed that the uranium-oxide powder is holding up most of the fission gases. To increase the yield produced by the RXG, it may be advisable to use uranium-sterate, which allows emanation of fission gases more easily.

The short-lived radiokrypton isotopes provide additional gamma and beta energy points but are not needed for the calibration of the detector. In addition, neither the ARSA nor SAUNA system ever collect or analyze for these isotopes, as the systems were designed to capture and quantify xenon-only isotopes.

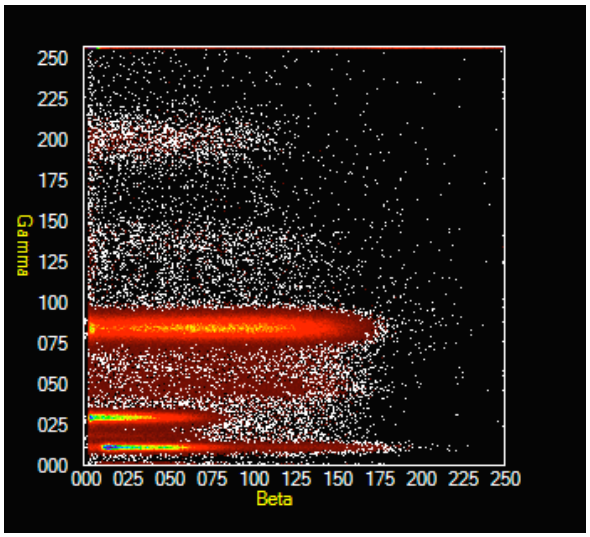


**Figure 2. Beta gamma spectrum of radioxenon and radio-krypton gases produced in the RXG. There is clear indication of Xe-135 (upper distribution at gamma channel 80) and Xe-133 (middle distribution at gamma channel 30). The 30-keV x-ray region (lowest distribution at gamma channel 12) shows both Xe-133 and Xe-135 beta + conversion electron distribution. There is also just a slight amount of Xe-133m. But most of the strength for this peak (~90 %) is from Xe-133 followed by Xe-135 (~6%).**

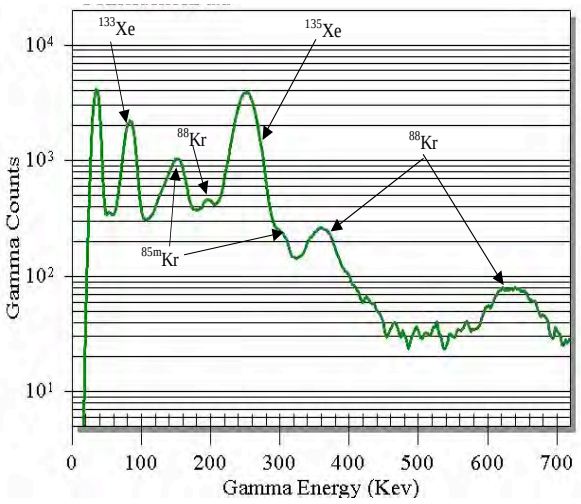


**Figure 3. Beta-gated gamma spectrum of radioxenon and radio-krypton gases produced in the RXG. The peak at 30-keV (peak on the far left) contains several x-ray and gammas from several of the isotopes. Most of the strength for this peak (~90%) is from Xe-133 followed by Xe-135 (~6%).**

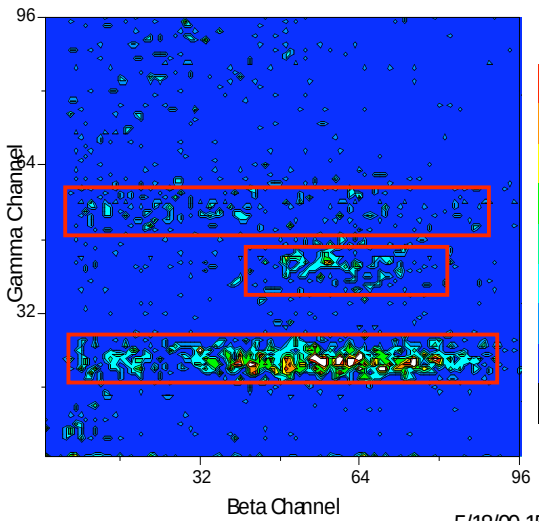


**Figure 4. This plot is the beta-gamma coincidence spectrum, which shows the three distributions in question. The top box is the 80-keV gamma region, the middle is the 60-keV gamma region, and the lowest box is the 30-keV gamma region.**

**Results from Neutron Activation of Stable Xenon**

A small flask of natural xenon (~10 $cm^3$) was placed next to the PuBe and Cf-252 neutron sources used in the previous U-235 irradiated RXG experiment. After 4 days of irradiation the flask was removed, and approximately 5 ml of gas was injected into a energy calibrated ARSA beta-gamma counting cells and counted for 4 days.

Figure 4 shows the beta-gamma coincidence plot, and three distributions highlighted by the red boxes can be seen. These distributions correspond to an x-ray energy of 30-keV and gamma energies of 60 and 80 keV. The 30-keV x-ray region was clearly the strongest of the three distributions and showed a definite peak along the beta axis, indicating a strong conversion electron component. The 60-keV region showed a clear peak in the beta distribution as well, with little to no characteristic beta distribution. The 80-keV distribution was clustered primarily at low energies and was indicative of the beta distribution from Xe-133.

Examination of the results after projecting the beta signal gated by appropriate γ energy cuts (Figures 5 and 6) shows the corresponding beta plus conversion electron distributions. The 1-D gamma-gated beta spectrum analysis show that the 60-keV peak is due to a Xe-125m conversion, emitting two iodine x-rays (one from the original electron capture decay and the other from the conversion process). This peak also bled into the 30-keV distribution, presumably from inefficiency of the NaI detector in detecting both the internal conversion x-ray and the conversion electron x-ray.

There seem to be two other conversion lines, corresponding to fission product radioxenon. The dataset is "sparse," however, and it is difficult to be quantitative. Comparing the 30- and 80-keV distributions, it seems likely that the 80-keV gated spectrum has a contribution from Xe-133. Most of the counts are at the lower end of the spectrum, as expected.

From these results it is clear that the activation of stable xenon will definitely complicate the analysis of the beta-gamma coincidence spectrum if large quantities are collected for a given sample. However, for calibration purposes, the technique does give several x-ray/gamma energies and several CE and beta endpoint energies.

Locally activated xenon offers a possible alternative to purchasing radioxenon from the National Institute of Standards and Technology (NIST) or producing fission product samples at the Pullman TRIGA reactor. Considering activation of Xe-124, the requisite 1-week activating and counting periods are problematic. Activating a greater amount of this isotope would require that activation would require either activation at Pullman or enriching the sample in Xe-124. Natural xenon contains only $9 \times 10^{-4}$ Xe-124, and it is only observed due to its high neutron cross-section and short lifetime (17 hours). Enriching the sample to ~100% would give a signature 1,120 times more intense. Unfortunately, this isotope is expensive: 500 ml of 25% Xe-124 would cost $4,600 after shipping and handling charges. A better choice might be a sample enriched in Xe-132, as it is makes up 27% of natural xenon gas. The irradiated sample would give both β particles and a conversion line at 199 keV. This would be a useful spike sample for Xe-133 and Xe-133m ARSA and SAUNA nuclear detector tests.

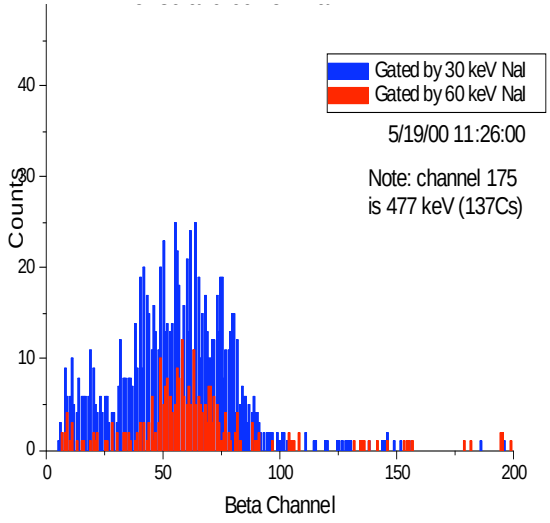


**Figure 5. The projected beta spectra from the 30- and 60-keV energy cuts. Note that the 60-keV spectrum does not extend to low pulse heights, and seems to be narrower than the 30-keV plot.**

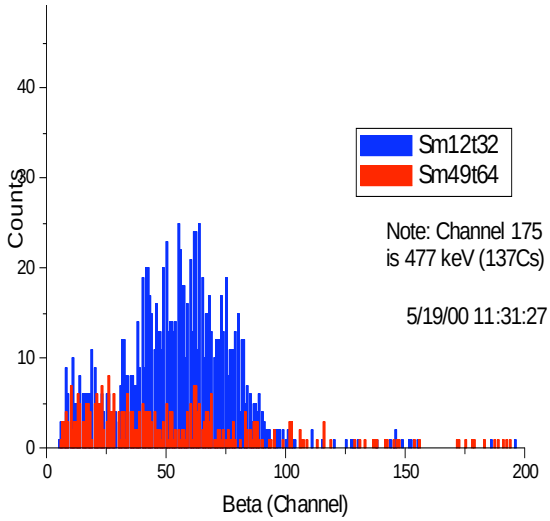


**Figure 6. This plot is the comparison of beta spectra from the 30- and 80-keV NaI energy cuts. Note that both spectra extend to low pulse heights, consistent with Xe-133. The broad peak in the 30-keV spectrum illustrates the difficulties that irradiated xenon may present.**

## CONCLUSIONS

The production of the fission-produced radioxenons has been successful, and a reliable supply of the short-lived Xe-135 has been demonstrated. Optimization of the process would be the next logical step, and it is foreseen that using other chemical forms of uranium along with more-intense neutron fluencies would significantly enhance this process. The production of short-lived krypton isotopes adds additional energy-calibration points that can be used when calibrating a beta-gamma coincidence detector.

The neutron activation has also been demonstrated and that it is possible, using existing equipment, to produce at least one of the four light radioxenons and Xe-133. The technique has also indicated that additional radioxenon

isotopes may show up in fielded ARSA and SAUNA units in the form of neutron-light radioxenon isotopes. It is important to include these neutron-light radioxenon isotopes as possible contaminants when extra peaks are detected in the beta-gated gamma spectrum. These isotopes have not been seen during the Freiburg tests of Phase II, nor have they been seen during the currently running Phase III tests. However, it is important for IMS analysts and others who will be responsible for the analysis of the radioxenon spectrum from all of the deployed systems to know of the potential signatures that these isotopes may have in some xenon collection units and not confuse the signatures with other fission-produced radioxenon isotopes.

## ACKNOWLEDGEMENTS

The authors would like to thank Dr. David Hamby and Mr. Anthony Elliot of Oregon State University for fruitful discussions of CANDU reactors and the irradiation of gram quantities of HEU.

## REFERENCES

Bowyer, T. W., K. H. Abel, W. K. Hensley, C. W. Hubbad, M. E. Panisko, R. W. Perkins, P. L. Reeder, R. C. Thompson, and R. A. Warner (1996). *Automatic Radioxenon Analyzer for CTBT Monitoring*, PNNL-11424, (December, 1996), Pacific Northwest National Laboratory, Richland, WA, also see http://www.ctbt.doe.gov.

Bowyer, T. W., C. Schlosser, K. H. Abel, M. Auer, J. C. Hayes, T. R. Heimbigner, J. I. McIntyre, M. E. Panisko, P. L. Reeder, H. Satorius, J. Schulze, and W. Weiss, *J. Environ. Radioact.* 59: 139–151.

Bowyer, T. W., K. H. Abel, C. W. Hubbard, M. E. Panisko, P. L. Reeder, R. C. Thompson, and R. A. Warner (1998). *J. Radioanal. Nucl. Chem.* 240: 109.

Haas, D., S. Biegalski, and K. Biegalski (2008). Production of samples of individual radioxenon isotopes through neutron irradiation of stable xenon gas, these Proceedings.

*Health Physics and Radiological Health Handbook* (1998). Third Edition, B. Shleien ed., Scinta Inc., pp. 7–42.

*Isotopes for Medicine and the Life Sciences* (1995). S. J. Adelstein and F. J. Manning eds. Washington D.C.: National Academy Press. pp 62–65.

Reeder, P. L. and T. W. Bowyer (1998). Xe isotope detection and discrimination using beta spectroscopy with coincident gamma spectroscopy, *Nucl. Instr. Meth. Phys. Res. A.* 408: 582–590.

Reeder, P. L., T. W. Bowyer, J. I. McIntyre, W. K. Pitts (2001). Determination of Xe-131m and Xe-133m in the presence of Xe-133g via combined beta spectroscopy and delayed coincidence, *J. Radioanal. Nucl. Chem.* 248: 617–622.

Ringbom, A., Larson, T., Axelson, A., Elmgren, K., Johansson, C., 2003. C. SAUNA—A system for automatic sampling, processing, and analysis of radioactive xenon. *Nucl. Instr. Meth. Phys. Res. A.* 508: 542–553.

# PROGRAMMABLE FRONT-END DATA ACQUISITION MODULE FOR RADIO-XENON MONITORS

Michael Momayezi[1], Brad Hurst[1], Chien P Wong[1], Tom R. Heimbigner[2], Matthew W. Cooper[2], Charles W. Hubbard[2], and Justin I. McIntyre[2]

Bridgeport Instruments, LLC[1] and Pacific Northwest National Laboratory[2]

Sponsored by Army Space and Missile Defense Command

Contract No. W9113M-07-C-0180
Proposal No. BAA07-48

## ABSTRACT

Detecting radioactive xenon isotopes in air is one of the methods employed in nuclear explosion monitoring. Using scintillator detectors, the xenon signal is distinguished from background via coincidence spectroscopy. The resulting detectors are complex instruments, with up to 12 scintillators, requiring specialized data acquisition (DAQ) electronics.

Bridgeport Instruments, in collaboration with Pacific Northwest National Laboratory is developing a compact, low-cost DAQ solution. The DAQ module produces raw data, such as energies, arrival times, triggers, etc in real time using digital signal processing embedded in FPGAs. These raw data are available immediately and can be combined in real time by an event builder to form complex events and to check for trigger patterns.

It is a unique characteristic of the DAQ module, that the event builder can be implemented by the customer in an open-source FPGA. In a similar manner, multiple DAQ modules can be connected to a backplane that contains programmable units, such as a trigger FPGA and a communication and control FPGA. All programmable logic on the backplane will be completely open-source.

With this approach we are creating a very versatile platform that uses proprietary code only to generate raw data from the scintillator detector pulses (energies, triggers, etc.). All other aspects, especially those that create a unique instrument from the combination of scintillator detectors are completely under customer control.

In this paper we present the architecture of this new nuclear instrumentation platform.

## OBJECTIVES

We aim to achieve two distinct goals: to create a commercially viable, general-purpose nuclear instrumentation platform and to create an implementation that will specifically serve the requirements of nuclear explosion monitoring via radio-xenon detection.

In particular we seek to create a platform that is partially open-source, allowing researchers and application engineers to add their own programming and thus create a unique instrument. The front-end modules will directly connect to scintillator detectors and compute raw data in real time. Such raw data include radiation-pulse energies, arrival times, trigger information, and even pulse-shape data. Raw data can be combined on the fly in an adjacent programmable unit, where more complex decisions and data formatting may take place, such as energy-sum triggers, trigger-pattern evaluation, and event building.

A number of front-end modules can be connected to a backplane, which will have completely open-source programming. The backplane is used to control a number of front-end modules and to combine and reformat data, before sending them to the host computer.

To interface with existing data acquisition computers, the front-end modules as well as the back plane will be able to communicate at least via USB and Ethernet.

Our second goal is to use this platform to implement new front-end data acquisition electronics for the Automated Radioxenon Sample/Analyzer (ARSA) radio-xenon detectors. That work will be discussed in a separate paper.

## RESEARCH ACCOMPLISHED

### The platform concept

The qMorpho has been designed to be an instrument on a PC board. The signal-processing (SP) FPGAs produce raw data, such as energies, etc., for each channel and an application engineer can program the open-source Communication and Control (C&C) FPGA to combine these data at will. This way, the application engineer can create a unique piece of instrumentation without having to divulge any proprietary or classified information to the hardware manufacturer.

The qMorpho data acquisition card can be thought of as a two-tiered system. The first tier is formed by two signal-processing (SP) FPGAs that absorb the signals from a total of four detectors. They operate by examining the digitized waveform of the detector signals and can therefore produce raw data almost as fast as theoretically possible. For each recognized pulse they produce a set of raw data that includes: 1) a trigger pulse indicating the arrival of a signal from the detector; 2) a trigger pulse indicating that the event has been accepted (i.e. it is not piled up or out of range); 3) a measure of its energy; 4) a measure of its arrival time; 5) a pile up measure; and 6) a pulse shape measure.

In standard configuration, the SP FPGAs will use these raw data to: 1) send trigger information to the C&C FPGA; 2) make energy, time and pulse-shape data available to the C&C FPGA; 3) accumulate statistics information in four counters per channel, measuring data acquisition time, accepted-event rates, input pulse rates, and trigger dead time; 4) accumulate one energy histogram for each channel; 5) accumulate list mode data; and 6) store individual event waveforms (oscilloscope function). In other words, in standard configuration the qMorpho acts like four independent DAQ channels providing triggering, energy histogramming, list mode, trace capture and even on-the-fly pulse shape analysis for particle discrimination, such as n/γ discrimination in liquid scintillators.

However, the true power of a multichannel DAQ system rests in its ability to combine the raw data event-by-event and in real time. Of course, users can only harness this power if they have programmatic access to the raw data. This is the key to creating a novel and unique radiation detection instrument.

In the past, scientists and engineers would use dedicated nuclear incident monitor (NIM) modules to create the raw data and use cabling and logic modules to realize a particular experiment. Now we can do better—in a much smaller space and at a much lower power consumption.

The C&C FPGA, which has access to all raw data, is open to custom programming. Almost arbitrarily complex trigger logic can be implemented with a few lines of verilog code. Secondary data sets, such as sum-energy histograms, or list mode data depending on coincidence time windows can be generated here. Data-formatting, zero suppression, and even event-building can be implemented here.

Just like its predecessor, the single-channel eMorpho, the four-channel qMorpho is supplied with an application programmer's interface (API) that is written in plain C with a minimal dependence on the operating system. The one notable exception is the single function that actually moves data across the physical interface. This design has made it possible to implement the eMorpho API on diverse platforms including Windows, Unix, Linux, QNX, as well as PIC and Rabbit 8-bit and 16-bit microprocessors using USB, UART/Ethernet or SPI physical interfaces.

**qMorpho Summary Description**

The first front-end module of this new nuclear instrumentation platform is the **qMorpho**. Based on the successful single-channel eMorpho, this unit is designed for operation with four independent scintillator detectors. For each detector there are two functional groups. One accepts the photomultiplier tube (PMT) signal directly from the PMT anode, and sends it through a switchable gain stage directly to a waveform digitizing ADC, without any pulse shaping. A signal-processing FPGA picks up the data stream from the ADC. Using digital signal processing, it analyses the digital image of the analog input pulse and computes the raw data such as energies, triggers, time stamps, pulse shapes, etc.

The second functional group consists of support elements, such as a 12-bit digital to analog converter (DAC) and a digital interface to control plug-on PMT HV-supplies (TwinBase), and a digital interface to the temperature sensor of the TwinBase. A set of general purpose I/O pins (GPIO) enhance the ability of the front-end section to interface with more sophisticated detector monitors and controls, e.g., for HV and power consumption. Finally, a set of trigger inputs and outputs facilitate integration and cooperation with secondary detectors.

There are three programmable units (all XC3S-400 FPGAs) on a qMorpho. Two of these equally share the task of computing the raw data for the four detectors.

**qMorpho analog sections**

The qMorpho can process data from four scintillator detectors simultaneously. For each detector, the analog signal is accepted directly from the PMT anode. The first amplifier is a current-to-voltage converter with a computer-controlled switchable gain. The available gain, expressed as a transimpedance (V/A = Ω), ranges from 100 Ω to 10,100 Ω. A differential-output OP-Amp presents this signal to a waveform digitizing ADC with an input voltage range of close to 1.0V. Hence, a full scale signal corresponds to a 10-mA peak anode current at the lowest gain and 0.10 mA at the highest gain. This range of maximum anode pulse currents is well matched to the characteristics and capabilities of the vast majority of photomultipliers.

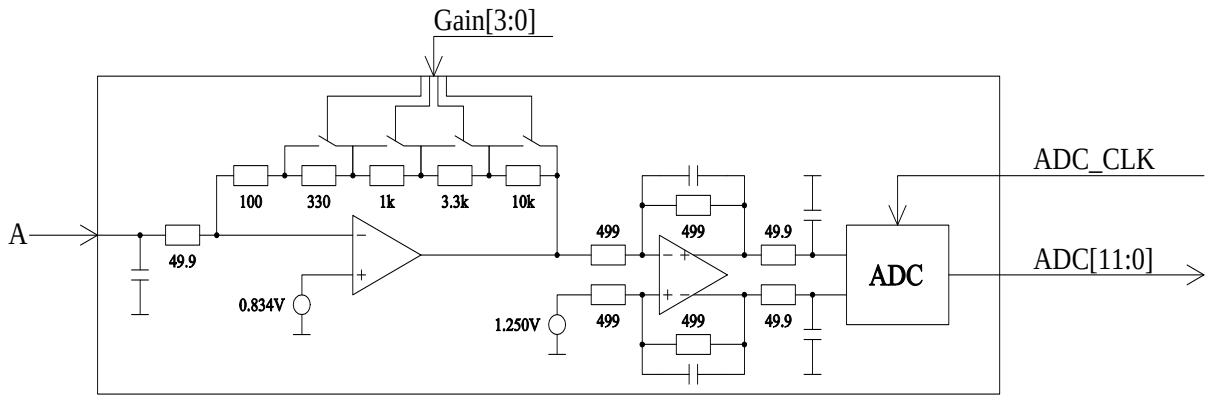


**Figure 1. qMorpho analog section, 1 of 4 channels. The qMorpho receives the PMT anode signal and converts it into a differential signal which is fed directly to the waveform digitizing ADC without integration or other pulse shaping. There are four identical analog channels.**

### qMorpho architecture

Figure 2 shows the architecture of the qMorpho DAQ card. Functionally, there are four independent acquisition channels, each serving one scintillator detector. The proprietary component of the digital signal processing is implemented in the two signal-processing FPGAs (SP0, SP1). The two connect to an open-source C&C FPGA, which can be accessed by a host computer through a number of different physical communication channels. At the minimum, these include a USB-1.1 interface, a UART/Ethernet interface as well as a connection to a 16-bit wide backplane data bus.

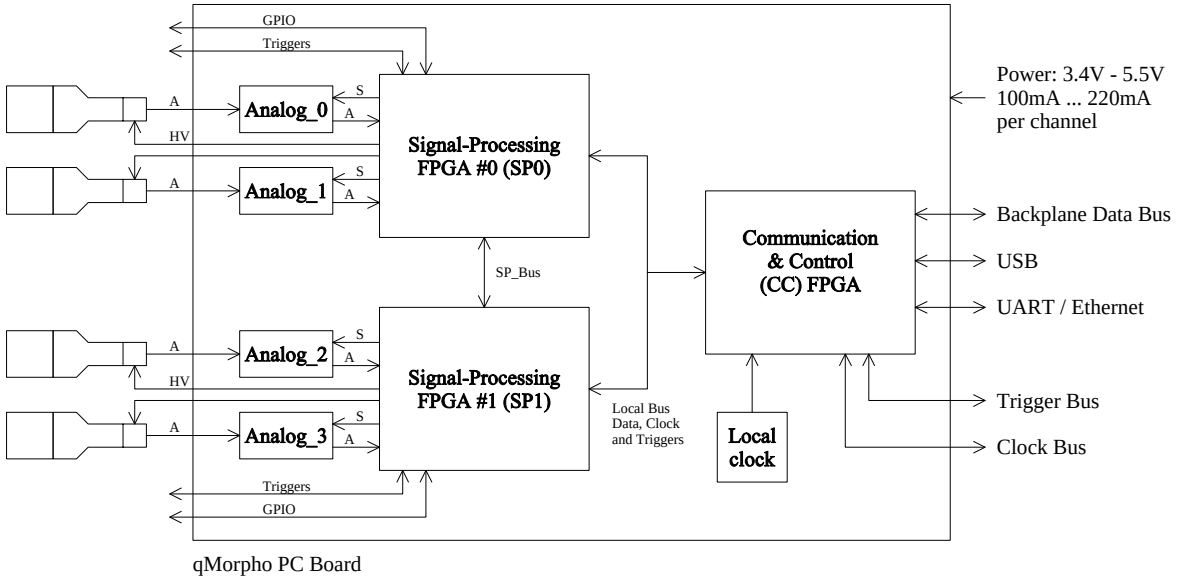


**Figure 2. qMorpho architecture.**

The signal-processing FPGAs generate triggers for each recognized scintillator pulse and send these to the C&C FPGA. The C&C FPGA can be used to validate events according to user-programmed trigger patterns and return validation triggers to the SP FPGAs. In a larger system, the C&C FPGA may pass the trigger information on to a backplane, where a dedicated trigger FPGA collects information from more than one qMorpho, makes its decision and returns validation triggers. The C&C FPGAs would then route the validation triggers down to the SP FPGAs.

The qMorpho has an onboard 24 MHz clock oscillator. A digital clock manager (DCM) in the C&C FPGA transforms the local clock into a 10_MSPS to 100_MSPS ADC sampling clock. Every operation on the card, with the exception of the USB micro-controller, is synchronous with the ADC clock. The C&C sends the ADC clock down to the SP FPGAs who supply the actual clock signals to the waveform digitizing ADCs.

Alternatively, the clock can be generated by a backplane and received by the qMorpho. The qMorpho can even act as a clock repeater, restoring clock amplitudes and duty cycles.

The qMorpho accepts power through a single input. The highest regulated voltage on the qMorpho board is 3.30 V. Using low-dropout regulators the qMorpho can accept input voltages from as low as 3.4 V up to 5.5 V. Power consumption can be below a 100 mA/channel when using 10-bit ADCs and rises to a maximum of 220 mA/channel when using 12-bit ADCS at 80 MSPS.

**qMorpho communication**

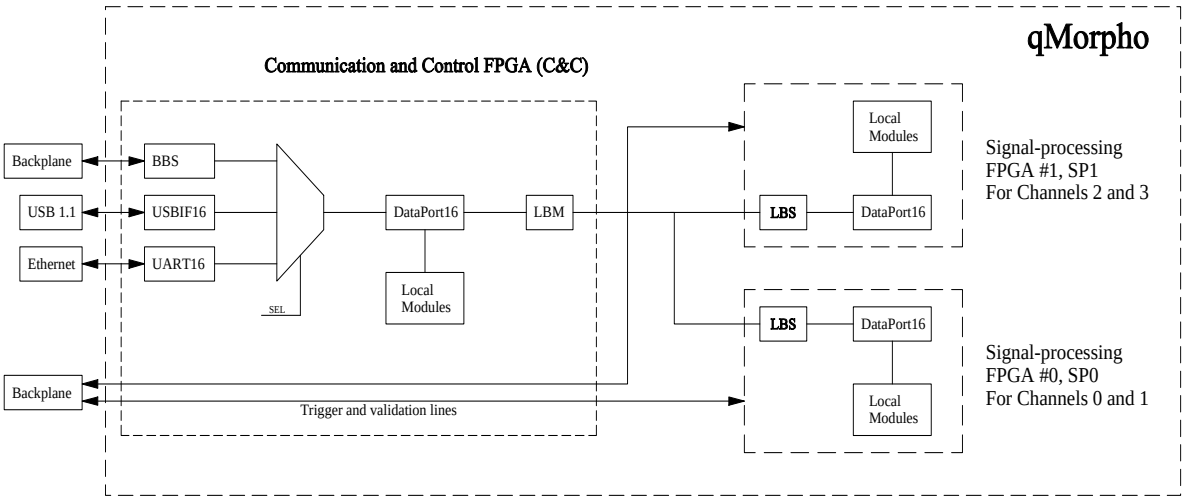


**Figure 3. Summary drawing of the qMorpho communication data paths. The C&C FPGA has access to all raw data generated by the signal processing FPGAs. The C&C FPGA is open-source and can be reprogrammed by application engineers to combine raw data as required, for instance to enforce complex trigger patterns, to build sum spectra, or in other ways create a unique instrument or**

All FPGAs on the qMorpho (and the associated backplane) use the same communication method. The central unit is the DataPort16. It receives 16-bit wide data and a set of control signals from an upstream interface module. For instance, figure 3 shows three interface modules able to communicate with the DataPort16 of the C&C FPGA: a backplane bus server, a USB interface and a UART/Ethernet interface. The C&C DataPort16 can direct the data flow to local data sinks and sources (timers, counters, version registers, etc.) or direct the data flow through a local bus master (LBM) onto the local data bus running between the three on board FPGAs. On the other end the signal-processing FPGAs connect to the local bus via a local bus server (LBS) that feeds into their DataPort16. The SP DataPort16 only connects to local modules which hold control/action registers and results from signal processing activities as shown in figure 4.

All communications start with writing data to the target FPGA. Every writing sequence begins with sending four 16-bit packet header words (PH) followed by a varying number of data words; i.e. the payload. The packet header information is used for routing the data to the intended recipient and to control the behavior of the target FPGA as well as the route-through devices. Table 1 illuminates the protocol being used.

| | **15** | | | | | | | **8** | **7** | | | | | | | **0** |
|---|---|---|---|---|---|---|---|---|---|---|---|---|---|---|---|---|
| **PH_0** | FS | | | R | WORDS | | | | SN | | | | | | | |
| **PH_1** | CM | | | | MA | | | | PAGE | | | | | | A | D |
| **PH_2** | | | | | | | | | | | | | | | | |
| **PH_3** | | | | | | | | | | | | | | | | |

**Table 1: Content of the four packet headers prepended to each data packet.**

Standard code makes use of only the first two packet headers, while the others are reserved for future use.
The 2-bit-wide field FS is used to select the target FPGA. SN is the slot number in a backplane-based system. CM is

the channel mask of addressed channels on the qMorpho. MA is the module address in whichever FPGA has been addressed. A and D are bits governing clearing the local address counter used for addressing data in the FPGA's modules. PAGE is the starting page (256-byte page size) for the next read operation. When using the UART/ Ethernet connection, WORDS determines how many words the unit will send back after receiving a read request. Setting the return bit (R) forces the unit to start sending data at the end of the write cycle. The packet header is followed by 28 data words.

### Writing to a qMorpho

Writing data to the qMorpho is straightforward. Four packet header words are loaded with the necessary routing information and transmitted first. They are then followed by 28 data words. Most often, the write is directed to one or more control register sets to program various aspects of the digital signal processing as well as the PMT high voltage and a built-in electronic pulser. The host is always writing 32 words in one try. When writing to the action registers (that control DAQ start and memory clearing) only the first four words of the payload are stored, and the rest are discarded.

Consider writing data via a backplane to a qMorpho. The C&C FPGA on the backplane will recognize from the FS mask that it is not the intended recipient of the data and will send them to the qMorpho residing in the slot number SN. A broadcast to all slots is achieved by using the special slot number 255.

The C&C FPGA on the addressed qMorpho can tell from the content of the FS field if it is the intended recipient or if data should be sent on to one of the SP FPGAs. If the data are meant for the C&C FPGA, they will be stored in a local module (mostly a set of registers). The module address is encoded in the 4-bit-wide field MA, which allows for 16 different modules.

If the data are meant for one or more channels in the SP FPGA, the qMorpho C&C FPGA uses the CM field to determine the target channels and accordingly sends the data to the intended SP FPGA(s). It is possible to send data to more than one processing channel at the same time by setting more than one bit in the CM field.

### Reading from a qMorpho

The method of reading from a qMorpho depends somewhat on the communication method used. For methods that provide a physical set of lines distinguishing reads from writes (R/W# line, or RX and TX lines) we first write to the qMorpho to select the target FPGA, target module, and the starting memory address. Then we issue the read command and read as many bytes as necessary. When operating through the UART (or an SPI) interface where there is only a Data_In and a Data_Out line, we write to the qMorpho as before but add the read (R) bit and the number of words to be read (WORDS) to the packet header as shown in Table 1. In this case the qMorpho will start sending data through the serial Data_Out automatically after the write cycle has been completed.

### qMorpho Communication Interface

The qMorpho is set up to accept communication through three different physical interfaces: The backplane bus, a USB 1.1 interface, and a UART. The first is used when the qMorpho is part of a larger system and is connected to a backplane or an equivalent system controller. Alternatively, the backplane bus interface can serves as a convenient interface to an embedded local microcontroller or single board computer. The second is a practical option for individual qMorpho cards controlled by a local host computer in the laboratory or in backpack-sized portable systems. The UART interface is used in conjunction with Ethernet-to-UART bridges where the Ethernet connection can be established through wired or wireless Ethernet modules at the user's discretion. Only the USB interface requires operating system dependent and proprietary driver software—the manufacturer's class driver. All other interfaces are open-source and can be manipulated as the application engineers see fit.

### The Signal-Processing FPGAs

The signal-processing FPGA provides identical real-time digital signal processing for all four channels. Implemented on a single silicon chip they deliver the functionality of many NIM modules. Figure 4 shows the

minimum setup as provided by the factory. Standard data acquisition capabilities include triggering, energy measurement, histogramming, oscilloscope function, list mode data and more.

At the same time, the qMorpho can power plug-on PMT HV-supplies (TwinBase) and the host can control the high voltage through registers in the SP FPGA. The host can also read the temperature of the TwinBase through the SP FPGA. Finally, there is a programmable pulser module for single and double pulses that can be used to drive an LED for optical gain measurements and gain stabilization.

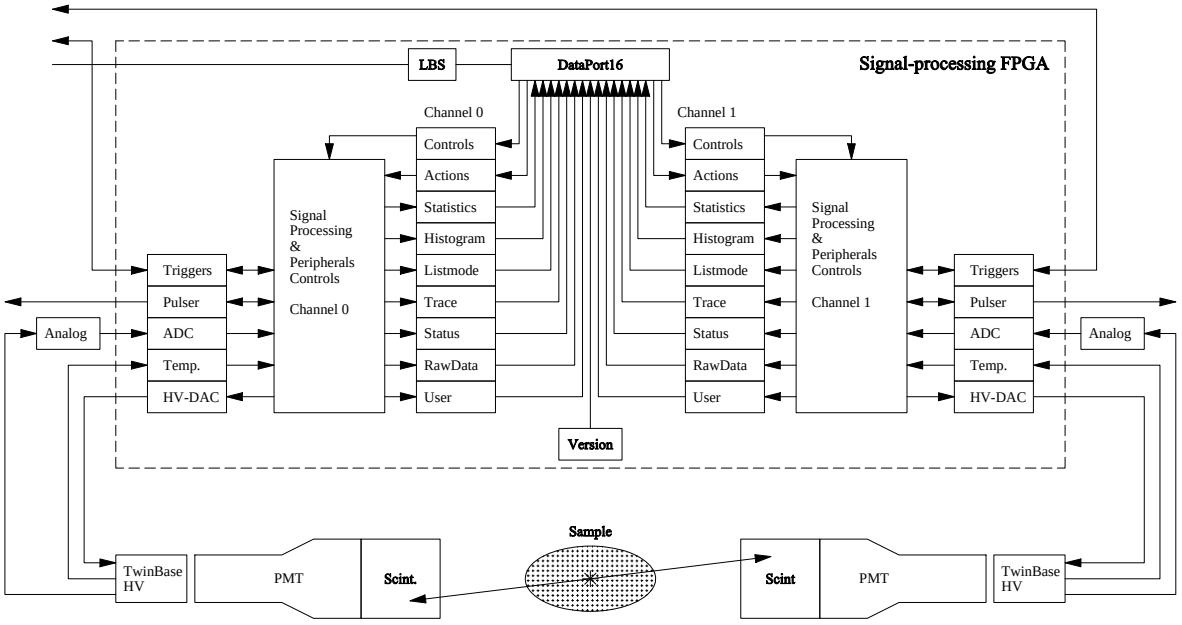


**Figure 4. Summary drawing of the qMorpho signal processing FPGAs.**

Factory-installed modules in the SP FPGAs will at least include the ones shown in Figure 4. The control register (28 words per channel) contain all the parameters required for the digital signal processing of the detector signals as well as the high voltage setting for the TwinBase plug on PMT high-voltage supplies. The action registers (4 words) contain bit-fields governing the data acquisition. These include one-time action, self-clearing bits for clearing histogram memory, resetting statistics counters and the like. The second action register carries continued-action bits such as those used to start and stop all kinds of data acquisition, for instance histogramming, oscilloscope function, and list-mode data acquisition. A user module provides memory for 1,024 data words provided by the host application. These three modules are write-only; all others are read only.

The statistics module consists of a set of counters collecting all the necessary information to accurately measure incoming pulse rates and the rate of accepted events. The histogramming module provides 8K x 32-bit histogramming memory for each channel. The list mode module can store energies and time stamps for 340 events before its buffer is full. The Trace module can record 1,024 waveform samples on a number of trigger conditions. It can shift the recorded waveform in memory to provide access to the pretrigger baseline. The status module reports the data acquisition status for the different DAQ types in a 16-bit status register. The RawData module reports event data (energies and time stamps) at the lower addresses followed by slower changing data such as DC-baselines and TwinBase temperatures. A host process (on the host computer, the backplane or in the qMorpho C&C FPGA) can choose to read all or just a subset of the RawData module.

For all registers and modules mentioned so far, there is one copy for each DAQ channel. The version module is the only one for which there is only one per SP FPGA. It reports information about the clock speed and firmware version.

## CONCLUSIONS AND RECOMMENDATIONS

In this paper we have described and documented our approach to providing a data acquisition solution that is general enough to become a commercial off-the-shelf (COTS) product, yet flexible enough to satisfy the particular requirements of the ARSA radioxenon stations. Our approach uses a judicious combination of proprietary and open-source firmware to allow scientists and application engineers to customize the instrument performance without having to share proprietary or classified information with the manufacturer. Its open-source control and communication FPGA allows application engineers to combine raw data, such as energies, triggers and time stamps, at will and in real time on an event-by-event basis. An operating-system independent application programmer's interface ensures that the qMorpho is compatible with almost every computer and microcontroller on the market. The qMorpho design is open-source where it matters, giving application engineers full control over how to combine the raw data from four independent nuclear radiation detectors, in real time and on an event-by-event basis. When operating with a backplane, application engineers can customize the operation and performance of larger detector arrays without having to rely on the manufacturer to provide custom programming.

## REFERENCES

Bowyer, T.W., K. H. Abel, C. W. Hubbard, A. D. McKinnon, M. E. Panisko, R. W. Perkins, P. L. Reeder, R. C. Thompson, and R.A. Warner (1998). “Automated separation and measurement of radioxenon for the Comprehensive Test Ban Treaty, *Journal of Radioanalytical and Nuclear Chemistry*, 235: 1-2: 77–81.

# THE CTBTO/WMO ATMOSPHERIC BACKTRACKING RESPONSE SYSTEM AND THE DATA FUSION EXERCISE 2007

Gerhard Wotawa and Andreas Becker

Provisional Technical Secretariat of the Preparatory Commission for the Comprehensive Nuclear-Test-Ban Treaty Organization

## ABSTRACT

Atmospheric Transport Modelling (ATM) is a Comprehensive Nuclear-Test-Ban Treaty (CTBT) verification technology that provides the required network processing capability for measurements at radionuclide stations (particulate as well as noble gas). The associated radionuclide source location analyses are a crucial element of the treaty verification system, since they can be compared and overlaid with localization information obtained from the waveform technologies.

Based on the 2003 cooperation agreement between the CTBTO Organization (CTBTO) and the World Meteorological Organization (WMO), a WMO Executive Council decision in 2007 and an exchange of letters between the CTBTO Executive Secretary and the Secretary General of WMO, the CTBTO Provisional Technical Secretariat (PTS) can now request ATM computations from WMO Centres in near-real-time in case of anomalous radionuclide measurements. Currently, nine WMO Centres in Europe (5), North America (1), Asia (2), and Australia (1) are participating. The system serves two purposes, namely (a) to supplement and add confidence to the PTS in-house computations, and (b) to form an ensemble modeling system that accounts for the inherent uncertainty of single models and individual meteorological analyses. The system is scheduled for entry into PTS provisional operations in September 2008.

The PTS and WMO have conducted a joint atmospheric backtracking exercise in December 2007. The exercise was triggered by a seismic event from the Standard Event List (SEL3) selected according to predefined criteria, and a forward simulation of the possible release of radionuclides at this event location was performed by the event selection team to obtain a subsequent measurement scenario at IMS radionuclide sites. The evolving measurement scenario was then communicated to the PTS Monitoring and Data Analysis Section, exactly according to the timelines laid down in the Operational Manual. The PTS subsequently notified WMO Centres according to the schedules of the new response system and performed interactive source location computations. The scenario went on for 10 consecutive days, and more and more hypothetical measurement data entered the system. The source location results were overlaid with the error ellipses from seismic events, and prototype data fusion bulletins were produced and attached to the PTS Secure Web Page. The exercise was considered very successful in three respects. First, the WMO response rate was very good, given the high complexity of the measurement scenario. Second, the PTS in-house procedures for interactive radionuclide source location analysis and data fusion worked, and the developed software proved to be fit for the purpose. Third, in the final data fusion bulletin, the PTS was able to narrow down the possible source region to three seismic events that were only 150 km and 24 hours apart. This by far exceeds the possibilities of source localization analyses based on radionuclide detections only, and proves that the data fusion concept works.

## OBJECTIVES

The objectives of the CTBTO Data Fusion Exercise 2007 were to (i) test the CTBTO-WMO atmospheric backtracking response system (ensemble backward modeling), (ii) validate the source location estimation algorithm in use at the PTS, (iii) validate the PTS capability to fuse a seismic event with a radionuclide event, and (iv) test and verify new PTS procedures and possible future products related to ATM and data fusion in a real-time, realistic scenario after a nuclear explosion.

## RESEARCH ACCOMPLISHED

### Introduction

As part of the automated processing, the PTS calculates source-receptor sensitivity (SRS) fields for all radionuclide samples (see Wotawa et al., 2003). This is done with 14-day backward runs utilizing the Lagrangian particle diffusion model FLEXPART (Stohl et al., 1998, 2005) fed with input data from the European Centre for Medium-Range Weather Forecasts (ECMWF). The SRS fields are used for the radionuclide network processing (source location estimates). They contain geotemporal information on the sensitivity of the measurement (sample) towards releases at all points on the globe. For a more comprehensive description, see the presentation from last year (Wotawa and Becker, 2007). Similar methods can be found in the relevant literature (see, e.g., Stohl et al., 2003; Seibert and Frank, 2004).

### CTBTO-WMO Response System

CTBTO/PTS and WMO have developed and tested a system where the PTS notifies WMO Regional Specialized Meteorological Centres (RSMCs) in case of anomalous radionuclide measurements. The RSMCs then send SRS fields calculated with their own models to the PTS. SRS fields are normally requested for the samples containing the relevant nuclides as well as for samples from neighbouring stations. These data supplement the PTS in-house computations. The response system has been tested and improved by means of two joint experiments in March 2003 (PTS, 2004) and January 2005 (Becker et al., 2007).

In December 2007, the PTS and the WMO conducted the third and so far most comprehensive atmospheric backtracking exercise. According to the plan, a computer model should be used to construct artificial measurements at RN stations of the International Monitoring System (IMS) after a hypothetical nuclear test. It was assumed that the final (79-station) network would already be in place. The release location would be the epicenter of a selected seismic event from the so-called Standard Event List (SEL3). The selection of the seismic event (according to predefined criteria) as well as the prediction of the related nuclear measurement scenario was to be done by a scenario selection team. The assumption was that $10^{15}$ Bq of a stable isotope would have been released during three hours starting from the time and location of the seismic event. The scenario selection team would then communicate the resulting hypothetical measurements to the Monitoring and Data Analysis Section of the PTS International Data Centre (IDC) exactly according to the timelines as specified in the IDC Operational Manual after Entry into Force of the treaty. The IDC would then issue “Requests for Support” to the WMO RSMCs. The RSMCs were expected to send their backtracking results to the IDC within 24 hours of each request. The IDC would then conduct its radionuclide network processing/source location analysis based on its own SRS fields and on the SRS fields contributed by the RSMCs. The IDC would try to fuse these results with the seismic event. Daily updated interactive source location and data fusion results would then be produced and attached to the IDC secure web page for access by the authorized users.

### Scenario for Exercise, Notification of WMO Centres

The scenario team selected a SEL3-event that occurred on 2 December 2007 at 20:21:48 UTC at longitude 29.79°, latitude 36.57° (see Figure 1). Based on this, the ATM forward simulations were performed to construct the measurement scenario (see Figure 2). According to the computations, the first radionuclide station (RUP61) was affected on 7 December 2007. The contaminated sample would have been analyzed and finally categorized by 10 December 2007. In the following nine days, more and more anomalous radionuclide samples were predicted to be encountered at the IDC. Assuming a minimum detectable concentration (MDC) of 0.1 mBq/m$^3$, 77 samples would have been reported as anomalous during this time period (Table 1).

The first notification message to WMO RSMCs was sent out on 10 December 2007, and the first set of RSMC SRS fields was received by 11 December. Further notifications were issued until 19 December 2007. In total, computations were requested for as many as 102 samples (Table 1). Despite this complex scenario, the centres responded reasonably well. All but one dataset were delivered to the IDC, and 87% of the data within the predefined timelines. Most centres responded considerably faster than the 24-hour limit (see Figure 3).

**PTS Source Location Analysis and Data Fusion**

SRS fields can be post-processed to determine possible source locations consistent with a given measurement scenario (Wotawa et al., 2003; Becker et al., 2007), or to predict a measurement scenario for a known source scenario (Wotawa et al., 2006). As part of the PTS source location analysis, the software tries all grid cells on a global 1° x 1°/3-hour grid as sole instantaneous source and calculates all resulting measurement scenarios. These scenarios are then correlated with the real observations. Grid cells (in space and time) with high correlation values ($r^2$) are source locations that would be consistent with the measurements. A detailed description can be obtained from the paper presented last year (Wotawa and Becker, 2007).

During the data fusion exercise for 2007, source location analyses have been done interactively with the software package WebGrape developed by the PTS (PTS, 2005). These analyses were performed based on the PTS SRS fields as well as on the fields contributed by the WMO Centres. As new measurements came in on a daily basis, the computations were updated accordingly. The procedure for the analysis was as follows: The data fusion officer first assumed that the source acted on the first day before the first measurement of the scenario (in our case this was the 6 December 2007). Then, the analysis was repeated going back one, two, and more days. It was assumed that the source acted in a 3-hour time interval (temporal resolution of SRS fields) on the day under consideration (see Figure 4). All results were saved and displayed for subsequent overlay with the available seismic events (data fusion).

The results of the radionuclide network processing (source location) mark a relatively large area as possible source region. This is especially true if no assumptions on the source date can be made. To narrow down the area to look at, we overlay (co-display) the possible source region with known seismic events. The co-display is done in space as well as time, since we only look at seismic events occurring on the same day for which the source location analysis is valid. As can be seen, this co-display can dramatically narrow down the region under scrutiny (see Figure 5).

During the CTBTO-WMO exercise 2007, daily source location computations based on PTS SRS fields and the incoming measurement data were conducted (see Figure 6). The computed possible source regions were fused with the SEL3/Reviewed Event Bulletin (REB) seismic events. As time passed by, only three events were found to fully coincide with a correlation maximum. All these events occurred on 2 December 2007, and the preselected (ground truth) event for the exercise was one of them. During the first few days, however, the possible source regions changed considerably from day to day (Figure 6). On day 2, the ground-truth event was even outside the correlation maximum. From day 4 onward, the results remained stable, with the three events within an area of higher correlation.

**WMO-Based Source Location and Fusion Results**

Besides the source location results based on the PTS SRS fields, the average correlations based on the contributions from the WMO RSMCs were computed as well (see Figure 7). The three seismic events under consideration were also marked as possible source locations by this analysis, but with a substantially lower correlation. On the other hand, the WMO-based analysis remained more stable over time, and the ground-truth event was part of the possible source region also on day 2.

The differences between the results of the participating centres were investigated and compared with the results from the experiments in 2003 and 2005. In total, the statistical comparison yielded a much better agreement as seen in the years before. An arbitrary chosen case during the exercise outperformed the best case of the experiment 2005 in terms of correlation and overlap (Figure 8). This indicates the increased experience gained in backtracking over the years.

**Prototype Products Produced for the Member States**

Throughout the 2007 exercise, the PTS produced daily prototype data fusion bulletins for the member states and made them available through the secure web page (see Figure 9). In these bulletins, the evolving measurement scenario and the related source location results were described and discussed, and several images were made available. As part of the discussion, seismic events that were co-located with correlation maxima in space and time were identified and listed. On the last experiment day, a summary bulletin was issued. Finally, the ground truth event was one of only three events during the period of interest that were co-located with a correlation maximum. All three events were only 150 km and less than 24 hours apart (spatial and temporal difference, respectively).

## CONCLUSIONS AND RECOMMENDATIONS

In December 2007, the first CTBTO-WMO Data Fusion Exercise was conducted. As ground-truth for the exercise, a SEL3 seismic event was selected, and a related radionuclide measurement scenario was computed by a scenario generation team. The measurement scenario was communicated to the PTS/IDC Monitoring and Data Analysis Section according to the timelines of the draft IDC Operational Centre. For 10 days in a row, the PTS sent out notification to WMO RSMCs to request computations of SRS fields. According to newly developed procedures, interactive source location analyses were conducted. The analyses considered PTS SRS fields as well as the SRS fields from WMO Centres. A data fusion between the source location results and the seismic events was conducted. A Data Fusion Bulletin was produced and put on the secure web page. As new measurements came in, the bulletin was updated every day. As a result, the exercise showed that the CTBTO-WMO response system works already reasonable well. It was shown once more that the source location algorithm used by the PTS does work within the constraints assumed. The PTS was able to identify three seismic events as potentially consistent with the monitoring results. These three events were only 150 km and 24 hours apart and included the ground truth event. Based on that fact, it is recommended that the response system be included in the provisional operations of the PTS as soon as possible. It is furthermore recommended that consideration be given to including data fusion in the list of products provided by the PTS to the National Data Centres of States Signatories.

## DISCLAIMER

This paper reflects the views of the authors but does not necessarily reflect the views of the CTBTO Preparatory Commission.

## REFERENCES

Becker, A., G. Wotawa, L.-E. De Geer, P. Seibert, R. R. Draxler, C. Sloan, R. D'Amours, M. Hort, H. Glaab, P. Heinrich, Y. Grillon, V. Shershakov, K. Katayama, Y. Zhang, P. Stewart, M. Hirtl, M. Jean, and P. Chen (2007). Global backtracking of anthropogenic radionuclides by means of a receptor oriented ensemble dispersion modeling system in support of Nuclear-Test-Ban treaty Verification, *Atmos. Environ.* 41: 4520, 4534.

PTS(2004). CTBTO-WMO experiment on source location estimation (July 2004). Technical report CTBT/PTS/TR/2004-1, Provisional Technical Secretariat of the CTBTO Preparatory Commission, Vienna International Centre, P.O. Box 1200, 1400 Vienna, Austria.

PTS (2005). A new tool for NDC analysis of atmospheric transport calculations. *CTBTO Spectrum Newsletter* 7: 19, 24 (http://www.ctbto.org/fileadmin/content/reference/outreach/spectrum_issues_singles/ctbto_spectrum_7/p19.pdf).

Seibert, P. and A. Frank (2004). Source-receptor matrix calculation with a Lagrangian particle dispersion model in backward mode, *Atmos. Chem. Phys.* 4: 51, 63.

Stohl, A., M. Hittenberger, and G. Wotawa (1998). Validation of the Lagrangian particle dispersion model FLEXPART against large scale tracer experiment data, *Atmos. Environ.* 32: 4245, 4264.

Stohl, A., C. Forster, S. Eckhardt, N. Spichtinger, H. Huntrieser, J. Heland, H. Schlager, S. Wilhelm, F. Arnold, and O. Cooper (2003). A backward modeling study of intercontinental pollution transport using aircraft measurements, *J. Geophys. Res.* 108: 4370.

Stohl, A., C. Forster, A. Frank, P. Seibert, and G. Wotawa (2005). Technical note: The Lagrangian particle dispersion model FLEXPART version 6.2, *Atmos. Chem. Phys.* 5: 2461, 2474.

Wotawa, G., L.-E. De Geer, P. Denier, M. Kalinowski, H. Toivonen, R. D'Amours, F. Desiato, J.-P. Issartel, M. Langer, P. Seibert, A. Frank, C. Sloan, and H. Yamazawa (2003). Atmospheric transport modelling in support of CTBT verification—Overview and basic concepts, *Atmos. Environ.* 37: 2529, 2537.

Wotawa, G., L.-E. De Geer, A. Becker, R. D'Amours, M. Jean, R. Servranckx, and K. Ungar (2006). Inter- and intra-continental transport of radioactive cesium released by boreal forest fires, *Geophys. Res. Lett.* 33: L12806, doi:10.1029/2006GL026206.

Wotawa, G. and A. Becker (2007). Atmospheric transport modelling and data fusion in support of CTBT verification, in *Proceedings of the 29th Monitoring Research Review: Ground-Based Nuclear Explosion Monitoring Technologies*, LA-UR-07-5613, Vol. 2, pp. 806–812.

**Table 1. Notification messages sent out during the CTBTO-WMO exercise 2007, number of detections encountered and number of SRS fields requested.**

| # | Request Day | Calculations requested | Detections >0.1 mBqm$^{-3}$ |
|---|---|---|---|
| 1 | 10-Dec-2007 | 5 | 1 |
| 2 | 11-Dec-2007 | 5 | 1 |
| 3 | 12-Dec-2007 | 7 | 3 |
| 4 | 13-Dec-2007 | 9 | 4 |
| 5 | 14-Dec-2007 | 8 | 5 |
| 6 | 15-Dec-2007 | 11 | 9 |
| 7 | 16-Dec-2007 | 14 | 11 |
| 8 | 17-Dec-2007 | 11 | 11 |
| 9 | 18-Dec-2007 | 16 | 16 |
| 10 | 19-Dec-2007 | 16 | 16 |
| | **SUM** | **102** | **77** |

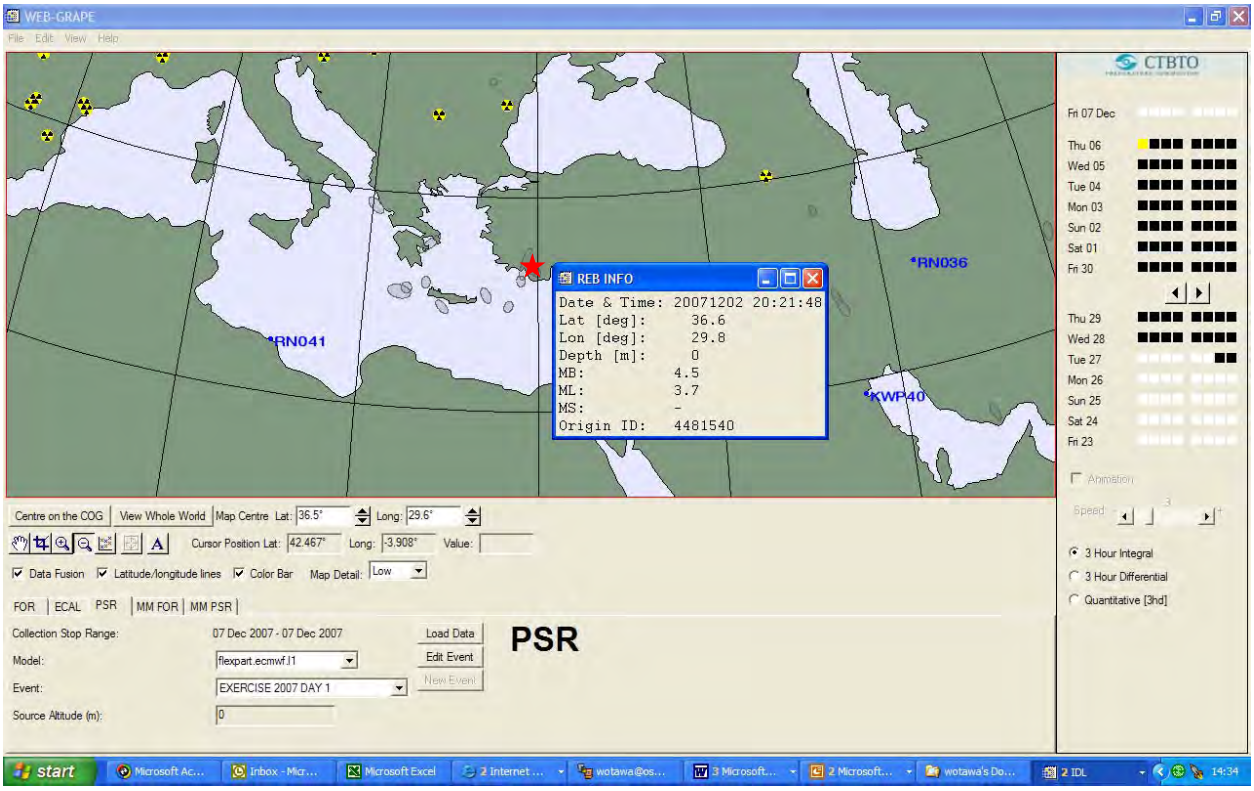


**Figure 1. Seismic event from the Standard Event List (SEL3) selected for the CTBTO-WMO 2007 data fusion exercise.**

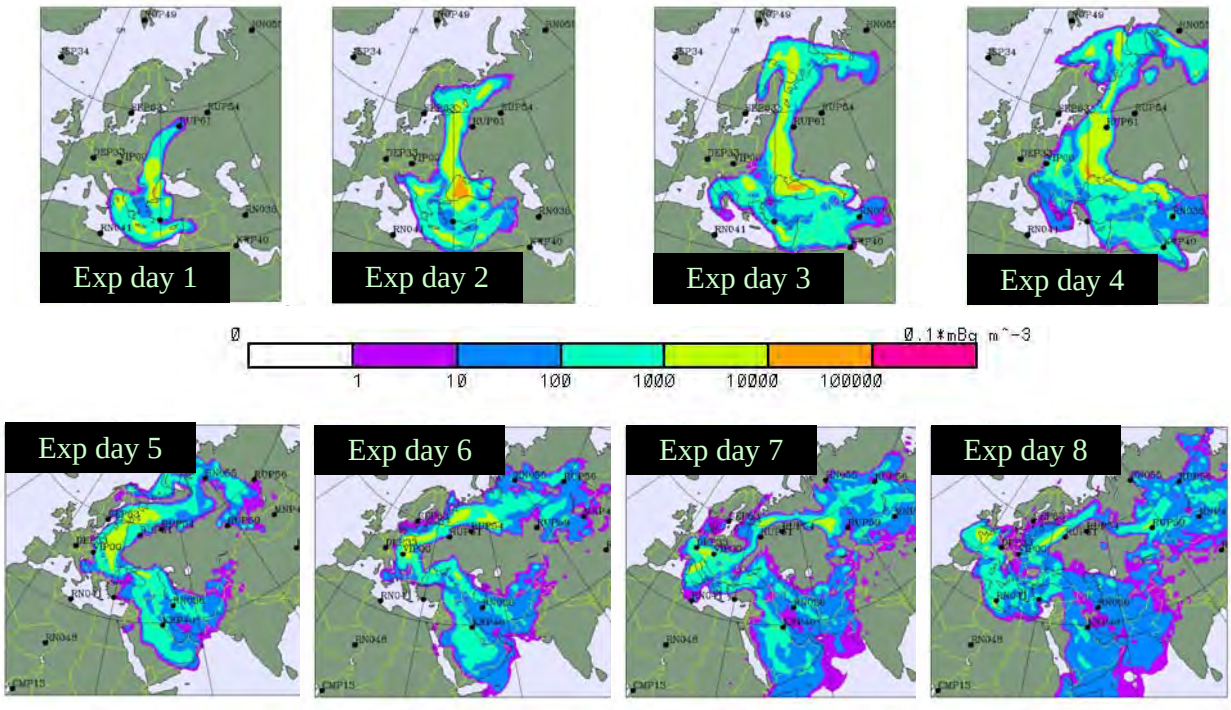


**Figure 2. Radionuclide plume caused by a fictitious release of $10^{15}$ Bq of a stable isotope at the selected seismic event location and event time. The plume reached the first radionuclide station (RUP61) on 7 December 2007 ("Exp day 1"). On the subsequent days, more and more stations were affected.**

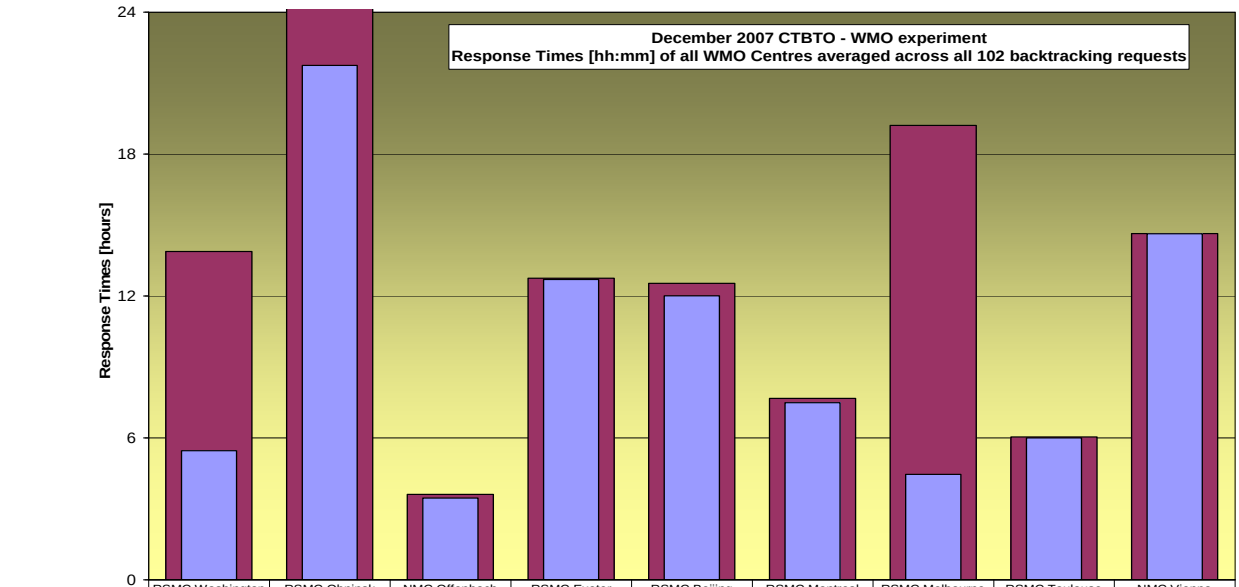


| | RSMC Washington | RSMC Obninsk | NMC Offenbach | RSMC Exeter | RSMC Beijing | RSMC Montreal | RSMC Melbourne | RSMC Toulouse | NMC Vienna |
|---|---|---|---|---|---|---|---|---|---|
| Final SRS file arrived | 13:52 | 25:21 | 3:36 | 12:45 | 12:32 | 7:40 | 19:12 | 6:02 | 14:38 |
| First SRS file arrived | 5:27 | 21:45 | 3:27 | 12:42 | 12:00 | 7:29 | 4:27 | 6:00 | 14:38 |

**Figure 3. Average response time of WMO Centres that participated at the 2007 exercise. The maximum response time foreseen was 24 hours.**

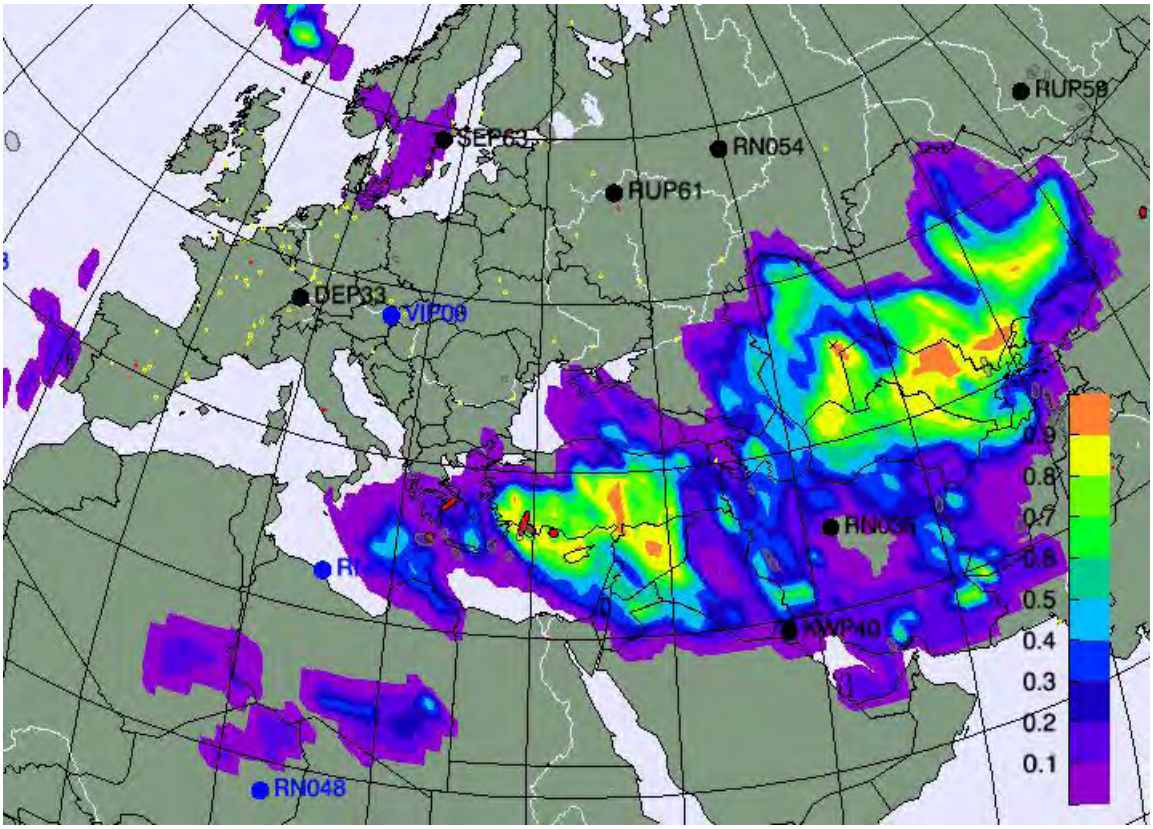


**Figure 4. Display of the Possible Source Region (in terms of correlation coefficients) for the measurement scenario encountered during the CTBTO-WMO 2007 data fusion exercise (days 1–5). For this image, we assume that the source acted during one 3-hour interval on 2 December 2007.**

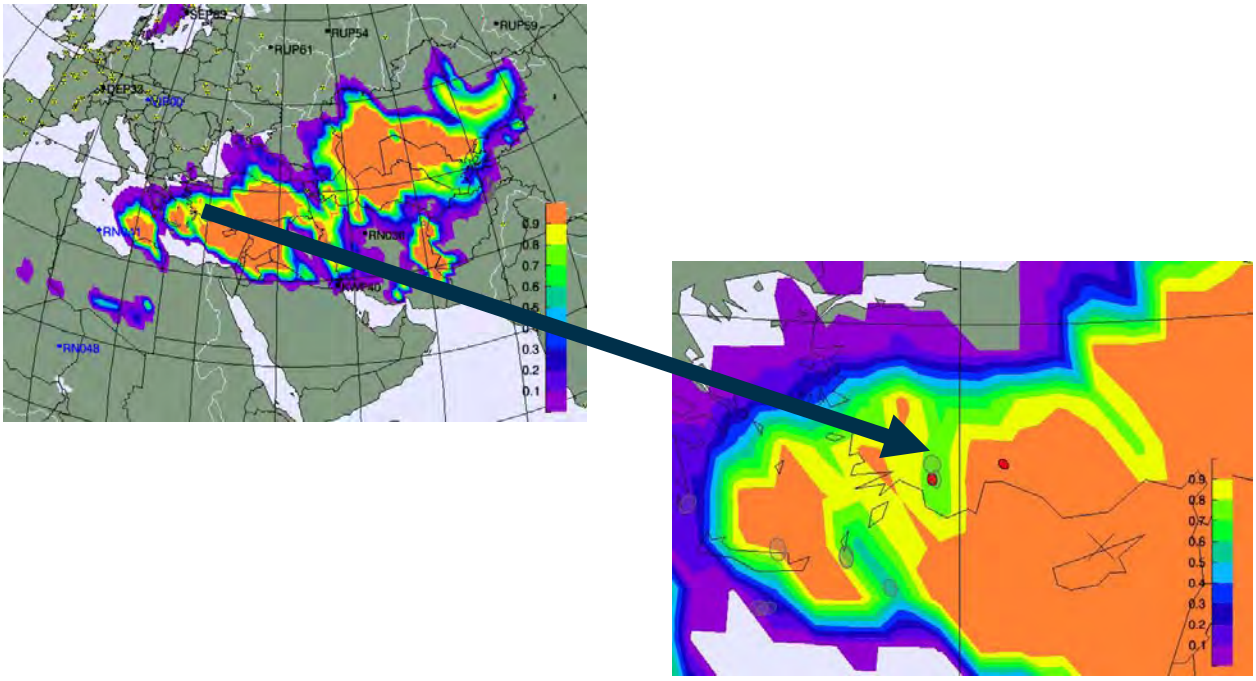


**Figure 5. Principle of data fusion between radionuclide and seismic events: The possible source region from the radionuclide network processing covers a large region, while the seismic localization information, including the error ellipse, is comparatively small. The red spots on the right image mark seismic events that occurred on the same day for which the possible source region is valid. The grey spots mark events occurring on another day. The co-display of radionuclide and seismic localization information (data fusion) can dramatically narrow down the area to look at. The analysis ends up with spotting a small number of seismic events that fit in space and time.**

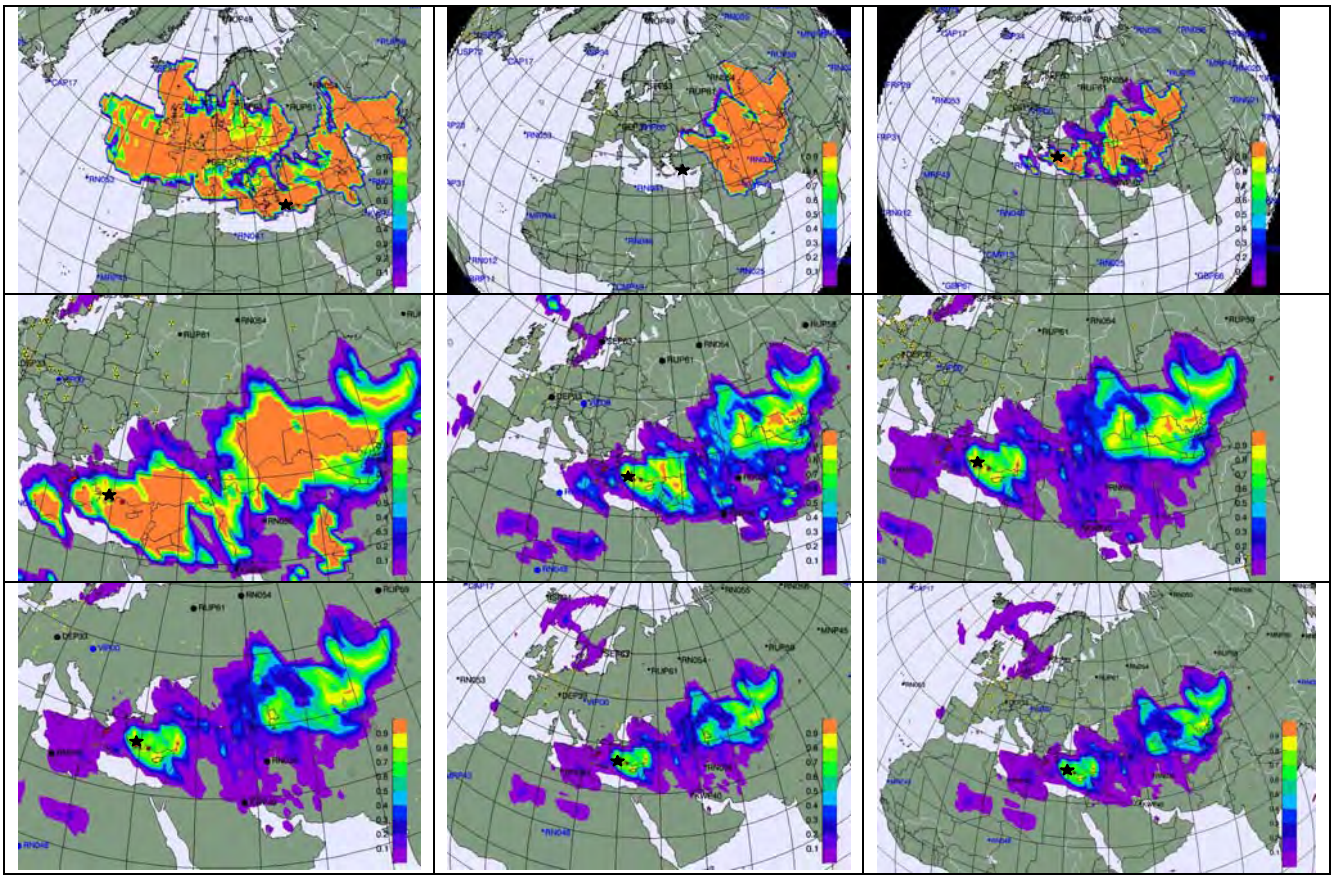

**Figure 6. Data Fusion results based on the PTS SRS data during the first nine days of the CTBTO-WMO exercise 2007 (from top left to bottom right). Results changed significantly for the first four days, based on the new measurements coming in, while staying stable from day 5 onwards. The ground truth location is marked black.**

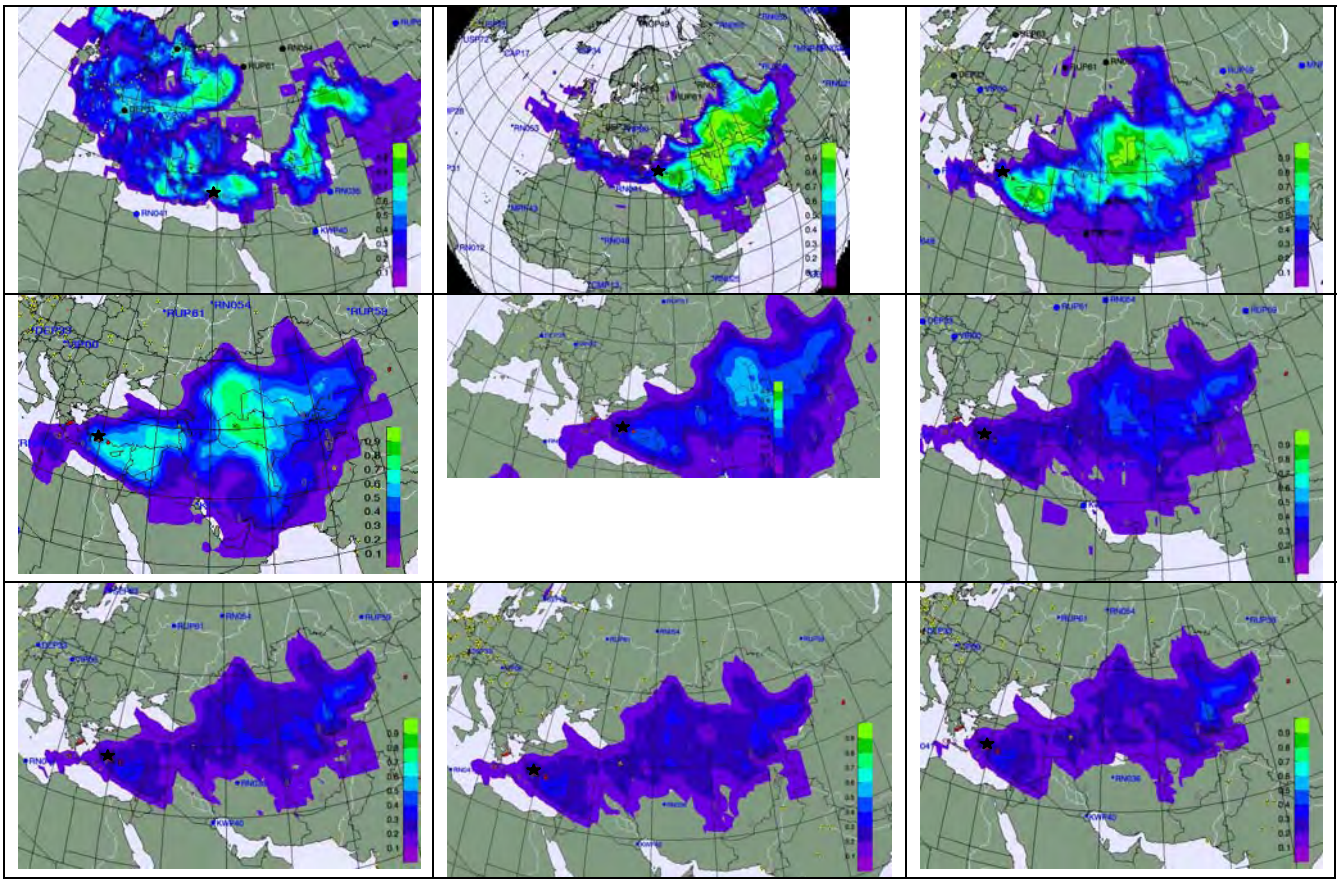

**Figure 7. Data fusion results based on the WMO SRS data (multimodel average correlation results) during the first 9 days of the CTBTO-WMO 2007 exercise (from top left to bottom right). Results changed for the first 3 days based on the new measurements coming in, while staying stable from day 4 onwards. The ground truth location is marked black.**

| Best congruent case in 2005 | | An average case in 2007 (1st detection of predicted scenario) | |
|---|---|---|---|
| RN Station Sample Overall Agreement / Overlap | NZP46; 26 January 2005; 6 UTC 50.90% / 42.11% | RN Station Sample Overall Agreement / Overlap | RUP61; 07 December 2007; 06 UTC 54.19% / 50.01% |

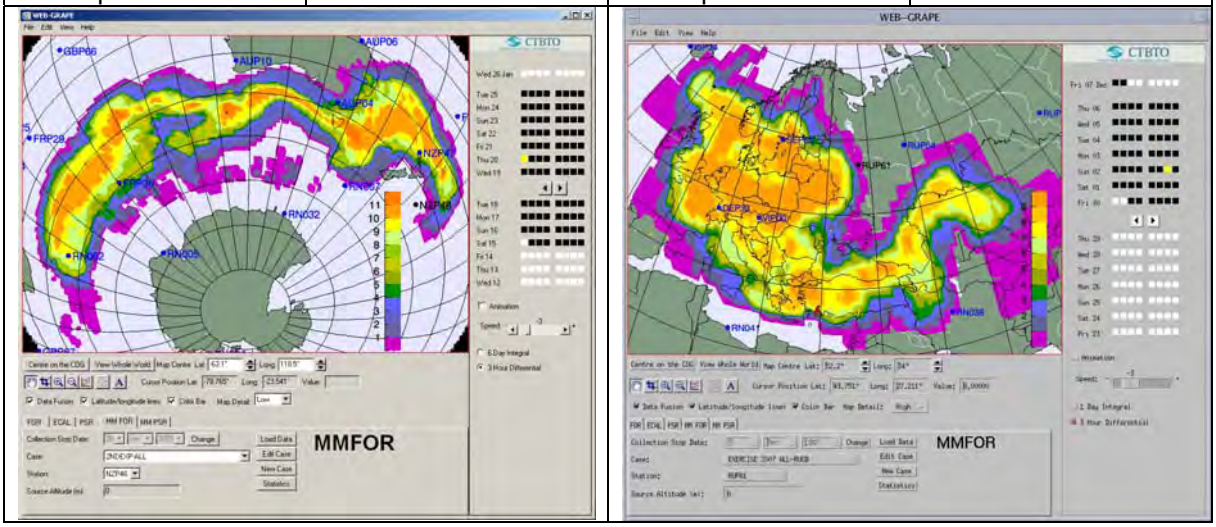


**Figure 8. Model agreement, January 2005 vs. December 2007 experiment. Comparison of the WMO centres overlap (Figure of Merit in Space) during January 2005 and December 2007 experiments. The left box shows the best congruent case of the 55 samples examined in January 2005 (Becker et al., 2007). The right box shows an arbitrarily chosen case with regard to the 102 backtracking requests examined during the December 2007 experiment. It is noticeable that this case outperforms the best case of January 2005 in terms of model agreement and overlap visualized for the three hours indicated in the calendar of the PTS post-processing software *WEB-GRAPE*.**

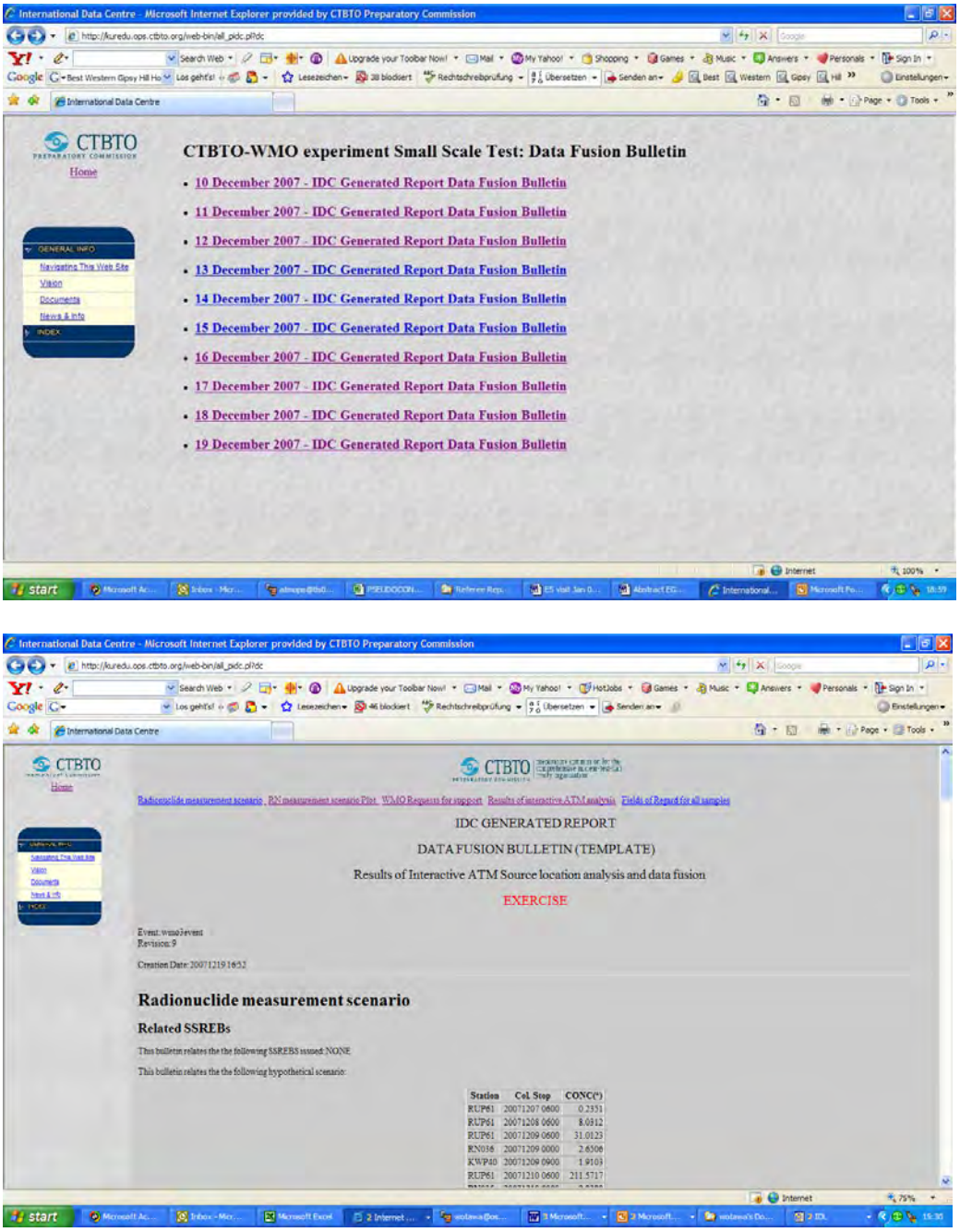





**Figure 9. A daily data fusion bulletin was issued by the PTS on its secure web page during the CTBTO-WMO 2007 Exercise (top). Every bulletin contained a description of the measurement scenario plus the related source location and data fusion results (bottom).**

# IMPROVEMENT IN GE DETECTOR COOLING

K. Michael Yocum[1], Gregory N. Martin[1], James F. Colaresi[1], and Harry S. Miley[2]

CANBERRA Industries, Inc.[1] and Pacific Northwest National Laboratory[2]

Sponsored by National Nuclear Security Administration

Contract No. DE-AC52-08NA28656[1]

## ABSTRACT

High purity germanium (HPGe) detector cooling technology used in remote radionuclide assay applications, such as the Radionuclide Aerosol Sampler/Analyzer (RASA) Mark IV, is continually evolving. Cryocooler improvements in recent years have resulted in reduced size, reduced maintenance, improved reliability, and enhanced HPGe detector performance compared to systems based on earlier generations of cooling devices. The Cryo-Cycle™ and Cryo-Pulse® 5 are two such HPGe detector cooler/cryostat systems that we are modifying and evaluating for use in the RASA. The modifications will enhance vacuum lifetime and integrity, improve performance, and resolve the need to procure and handle liquid nitrogen ($LN_2$). Both cryocoolers offer advantages over the existing generation of HPGe detector cooler/cryostats used in the RASA and other remote-sensing applications.

## OBJECTIVES

Improvements in HPGe detector cooling technology for use in remote radionuclide assay instruments such as the RASA Mark IV will be demonstrated. Our investigations involve modifying and testing two cryostat/cooler combinations available from CANBERRA Industries, Inc., Meriden, Connecticut. A Cryo-Pulse® 5 HPGe detector system incorporating a 4-watt pulse-tube cooler manufactured by Thales Cryogenics, Eindhoven, Netherlands, is being modified to incorporate ultra-high vacuum (UHV) design and fabrication techniques. An example of the Cryo-Pulse® 5 is shown in Figure 1. The detector chamber configuration is being modified to incorporate a low radiation background remote detector chamber (RDC) in place of the Slimline (SL) chamber shown in Figure 1. The low background RDC allows back shielding to be installed directly behind the detector to minimize streaming through the radiation shield penetration.

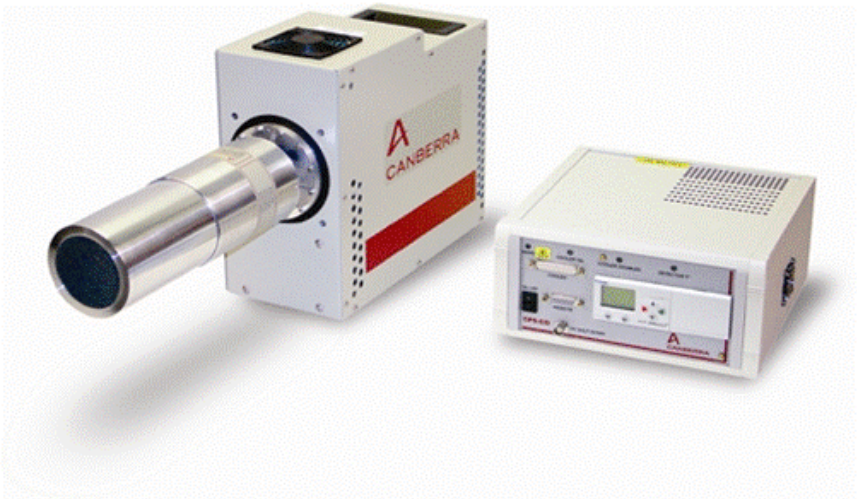


**Figure 1. Cryo-Pulse® 5 model CP-5SL (image from CANBERRA website http://www.canberra.com/pdf/Products/Detectors_pdf/CryoPulse5-DET-SS.pdf ).**

We will also investigate a Cryo-Cycle™ HPGe detector cooler comprising a closed-system nitrogen ($N_2$) reliquifier incorporating a 15-watt free-piston linear Stirling cooler manufactured by SunPower, Inc., Athens, Ohio. This hybrid system has the same footprint as a standard 30-liter $LN_2$ Dewar and receives dipstick HPGe detector cryostats like those commonly used in other $LN_2$-based systems. The dipstick cryostat for the RASA system will incorporate all-metal seals and a low-background RDC. The Cryo-Cycle™, shown in Figure 2, continuously condenses the $LN_2$ boil-off inside a closed Dewar to maintain a 22-liter reservoir of $LN_2$. Once charged, the system does not require additional $N_2$ except in the event of a long-duration power outage or to replace gas loss due to seal leakage. Make-up can be added by topping off with $LN_2$ or by adding $N_2$ gas. An $N_2$ gas generator will be integrated with the standard Cryo-Cycle™ to allow unattended operation in the RASA. In controlled environments such as the instrument bay inside RASA systems, the only maintenance required is semi-annual filter cleaning for both the Cryo-Cycle™- and Cryo-Pulse® 5-based systems. $N_2$ gas generator maintenance interval and lifetime have not yet been determined. Expected lifetimes for both cryocooler units are in excess of 50,000 hours. Both systems will be tested to validate spectroscopic performance, thermal performance, and vacuum performance for the RASA application. This research will demonstrate improved operational performance (better resolution) and improved operational reliability (less downtime) when compared to previous generations of mechanical coolers used in the RASA system.

**Figure 2. Cryo-Cycle™ shown with model 7500SL cryostat (from CANBERRA website http://www.canberra.com/pdf/Products/Detectors_pdf/CryoCycleCryostat-DET-SS.pdf )**

The contract period for this research began in the second week of June 2008. At the time of this writing, two weeks later, no significant research has been accomplished. We will therefore take this opportunity to discuss the nature of the challenges and the methods we will use to address them.

The RASA was developed at the Pacific Northwest National Laboratory (PNNL) in the 1990s to meet Comprehensive Nuclear-Test-Ban Treaty (CTBT) requirements for aerosol radionuclide measurements, as described by Bower et al. (1997) and Miley et al. (1998). Particulate air monitors are installed at each of the 80 radionuclide monitoring stations established worldwide by the International Monitoring System (IMS). The RASA draws approximately 24,000 $m^3$/day of air through six parallel filter media strips; every 24 hours the strips are combined and laminated between two continuous Mylar tapes to form a continuous strip of individual pouches, each representing a 24-hour sample. Each pouch is marked with a barcode containing identifying information. Perforations between pouches allow collection as a continuous reel or separation wherever desired. After a sample is collected and laminated, the pouch sits for 24 hours to allow decay of normal atmospheric short-lived radon daughters. It is then transported around an HPGe detector inside a shielded enclosure for a 24-hour measurement of gamma ray emissions. Software analysis of the data is performed, and the raw data and results are communicated to the International Data Centre (IDC) in Vienna. As the continuous tape of pouches exits the machine, it can be automatically reeled and stored, or specific pouches can be manually removed for transport to one of 16 IMS radionuclide laboratories for further analysis. The system operates unattended for 6-month intervals before routine preventative maintenance and replenishment of materials are required. Figures 3 and 4 show the RASA Mark IV pictorially and schematically.

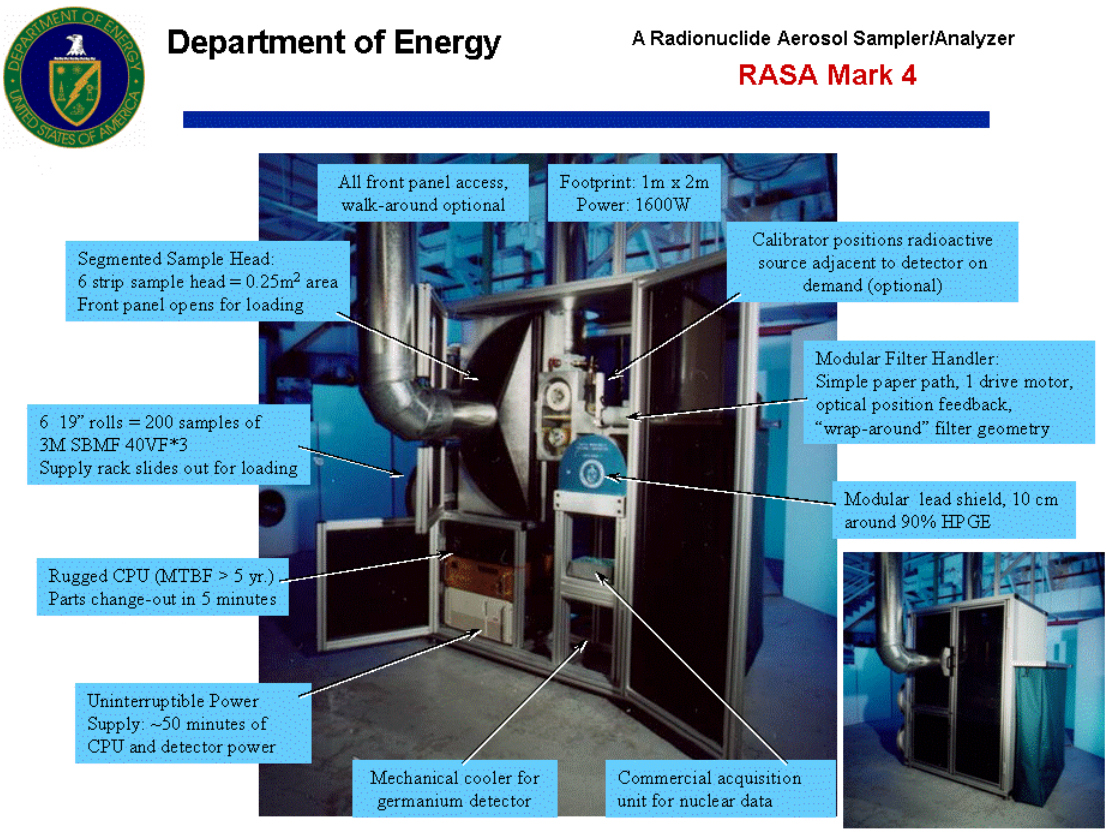


**Figure 3. RASA Mark IV.**

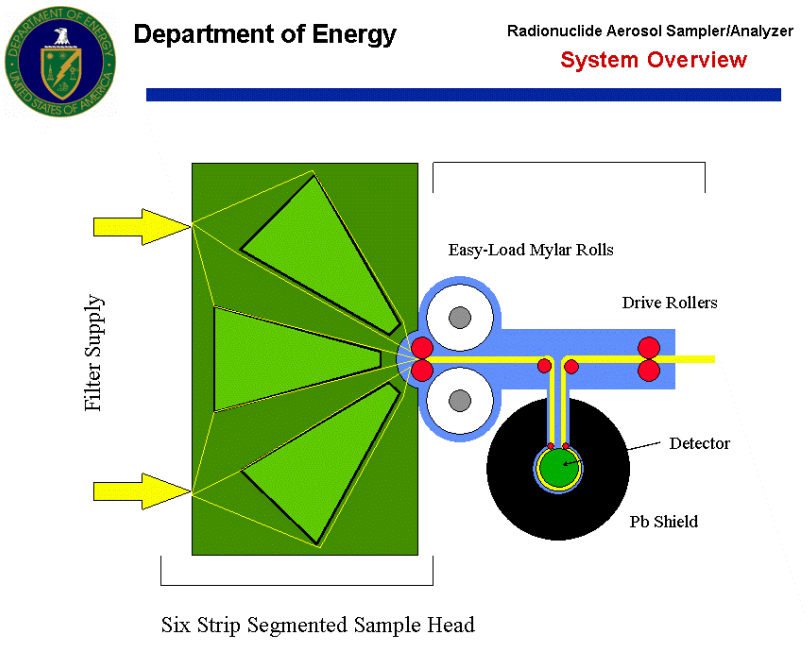


**Figure 4. Schematic diagram of the filter strip transport system in a RASA Mark IV.**

Radionuclide concentrations in air are quantified in microbecquerels per cubic meter ($\mu Bq/m^3$). The sensitivity of the RASA is defined as the minimum detectable concentration (MDC) of relevant fission-product radioisotopes it can measure. The Provisional Technical Secretariat (PTS) requires that the system be capable of measuring an MDC of 10 $\mu Bq/m^3$ for $^{140}Ba$ in the absence of radon and its daughters and an MDC of less than 30 $\mu Bq/m^3$ in operation (Zäringer et al., 2007). When measuring low radioisotopic concentrations, it is axiomatic that larger HPGe detectors (i.e., higher relative efficiency for $^{60}Co$, 1.33.MeV), lower background radiation, and better energy resolution lead to improved MDC. Given the existing configuration of the RASA, this translates realistically to detectors in the 100% efficiency range; hardware background radiation typical of industry-standard, ultra-low background materials; and resolution of less than 2.0 KeV for 1.33 MeV gammas. This performance level has been reached with the detectors previously provided to the RASA development effort by the vendors. Long-term mechanical cooler and cryostat performance, however, has been problematic.

Mechanically cooled HPGe detectors for the early generations of RASA application were procured from vendors in the mid- to late-1990s. These detector systems use mixed-refrigerant single-stage or auto-cascade closed-cycle Joule-Thomson (JT) coolers. To remove heat from the detector, the coolers rely on the expansion of gas mixtures or gas and fluid mixtures under high pressure through an orifice or series of orifices. Input power to the compressor is in the range of 0.5 to 1.0 kilowatts in order to provide a minimum cooling power of several watts at the roughly 100ºK temperature required for HPGe detector operation. Vibration from the large compressors and from the expanding gas often degrades detector performance. The expansion necessary to accomplish the low temperatures necessitates small JT expansion orifices that are prone to clogging. Water and oil contamination in the JT working fluid can freeze and cause clogging. The working gases are mixtures of flammable gases that can create hazardous situations when leakage occurs or maintenance is required to replace lost gas. Cooling power in JT coolers for HPGe detectors can be marginal. With time, the power is insufficient to overcome the cumulative effects of conductive and convective heat loads caused by vacuum degradation inside the detector chamber. Vacuum degradation is caused by gas permeation through elastomer vacuum seals and from hardware outgassing. For this reason, vacuum service is often required annually to re-evacuate detector cryostats. Molecular sieves used to establish and maintain high vacuum in detector cryostats are prone to outgassing during brief power outages. This then necessitates a 24–48 hr full thermal cycle to room temperature and back to operating temperature in order to clear detector contamination caused by the outgassing. Low cooling power also imposes constraints on cryostat configurations and detector size. Improvements in JT-cooled detector technology have been made, but all shortcomings for the RASA application have not been resolved.

Great strides have been made in alternative cooling technologies in the period since the first RASA systems were built, specifically with linear Stirling and linear Stirling-type pulse-tube coolers. Both types of cooler are inherently more efficient at high and low temperatures than the JT coolers used for HPGe detectors. Until recently, they had not been used to any large extent as HPGe detector coolers because of high cost, short lifetime, and high vibration. Events conspired in the 1990s to give rise to development efforts that removed or substantially lowered these hurdles. At the time, it was thought that many thousands of coolers would be needed to provide cooling for the electronics in cell phone and other communication network stations. This need has not yet fully materialized, but the prospect has led to substantial improvements in Stirling and pulse-tube cooler performance and price. Flexure bearings, gas bearings, magnetic and pneumatic stops, improved motor design, and improved manufacturing techniques have brought these coolers to the point that their costs are below $25,000, their lifetimes exceed 50,000 hours, and vibrations have been reduced, or at least offset, by the high cooling power available. Stirling and pulse-tube-cooled HPGe detectors are now available from major detector manufacturers in many different configurations. We believe that cooling systems based on the Cryo-Pulse® 5 direct-coupled, pulse-tube cooler and the Cryo-Cycle™ hybrid cooler now represent the best choices for the RASA application.

The Cryo-Cycle™ is referred to as a hybrid cooler for HPGe detectors because it uses an electrically powered mechanical Stirling cooler, and in this case an $N_2$ gas generator, to generate and indefinitely maintain a reservoir of $LN_2$ for cooling an HPGe detector. A 15-watt CryoTel GT Stirling cooler is attached to a closed $LN_2$ Dewar to reliquify boil-off gas and return it to the 22-liter $LN_2$ reservoir. The SunPower cooler incorporates a floating displacer with pneumatic axial centering system, gas bearings, a free-floating magnetic compressor piston, and a linear AC motor to reduce power consumption and eliminate the major causes of wear failures in Stirling coolers. Vibration is reduced by use of a tuned dynamic vibration absorber. Details of the design and references can be found at the SunPower website www.SunPower.com. To minimize the effect of vibration on detector performance, the

Stirling cooler is mounted on vibration isolators and coupled to the Dewar through a gas-tight, vibration-isolating coupling. A dipstick cryostat is inserted into the Dewar through a vibration-isolating gas-tight collar. The closed Dewar operates under 1–2 psig positive pressure relative to the surroundings. The footprint and function of the hybrid Dewar are similar to the standard 30-liter Dewar commonly used for HPGe dipstick cryostats.

Metal-sealed dipstick cryostats have a 40-year history of providing extremely long life and dependable germanium-detector performance. In recent years, some users have found that the administrative difficulties and logistical inconvenience of dealing with $LN_2$ outweigh the benefits of the metal-seal dipstick design. For remote unattended applications such as RASA, it can be seen that this is a legitimate consideration. However, the hybrid cooler removes the negative aspects of acquiring and handling $LN_2$, because the $LN_2$ is generated and confined inside a closed system. The operator and maintenance personnel never come in contact with it, and transport of $LN_2$ is not required. A major benefit of $LN_2$ is that it provides a 7-day reserve of cooling power. If any of the electrical cooling components fail, or if a power failure of long duration takes place, the 22-liter reservoir of $LN_2$ provides up to 7 days of cooling to the detector with no risk of a partial thermal cycle or warm-up. The detector is immediately available when power is restored. The modularity of the system ensures that, as long as the detector and Dewar are intact, the system will provide a 7-day buffer for replacement of a faulty component. In most cases, downtime is minimized, because the detector does not need to be warmed for repairs. Moreover, the interchangeability of dipsticks and Cryo-Cycle™ coolers allows independent replacement of either of the two most expensive components in the system. The Cryo-Cycle™, with an $N_2$ gas generator attached and a metal seal dipstick cryostat installed, is a closed system that is constantly maintained by electricity. The simplicity and proven track record of $LN_2$-cooled, long-life, metal-seal dipstick cryostats ensure the absolute highest level of dependability and performance.

The Cryo-Cycle™ is an off-the-shelf product for use with dipstick cryostats. The difficulties of integrating the Stirling cooler with the detector have been solved. There are no vibration, thermal, or vacuum issues to be addressed. For the RASA application, we will make improvements to the metal-seal dipstick design by developing a small-cross-section metal-seal end cap to be used on the RDC. As mentioned earlier, an RDC is preferred for the RASA because the detector chamber must reach inside a shielded enclosure. The RDC allows the most convenient method for back-shielding the detector. A long end cap that reaches through the shield penetration must include the back-shielding inside the cryostat vacuum space behind the detector. With an RDC, the back-shielding is installed outside the vacuum space behind the RDC. A diagram of a Cryo-Cycle™ RDC is shown in Figure 5. This can be compared to the photos of Slimline end caps shown in Figures 1 and 2. The RDC will contain standard-product ultra-low-background (ULB) hardware to reduce the amount of background radiation inside the shield. We will also use welded UHV electrical feedthroughs and a metal pinch seal on the vacuum pump-out port. Such a cryostat is expected to have a vacuum life in excess of 10 years. Finally, we will integrate an $N_2$-gas generator to completely remove the necessity for transporting and handling $LN_2$. An off-the-shelf high-purity $N_2$-gas generator will provide source gas for the initial charge of $LN_2$ and subsequent make-up $N_2$ gas. Excess $N_2$ gas can be used to maintain a purge in the shield cavity to reduce radon background. We believe that generation rate of several hundred cubic centimeters/minute of 99.995% pure $N_2$ gas should be sufficient, but this point requires further investigation, as does the maintenance interval for such generators.

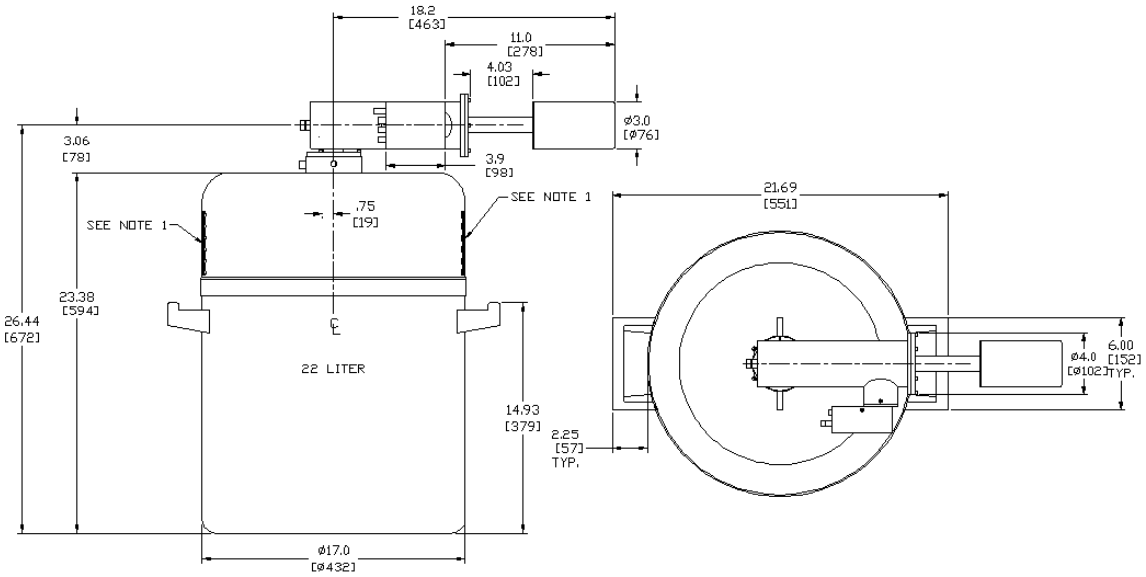


**Figure 5. Cryo-Cycle™ model CCHD RDC-4 (image courtesy of CANBERRA).**

Another approach we are pursuing for the RASA application is modification of a Cryo-Pulse® 5 to improve vacuum integrity and lifetime. The Cryo-Pulse® 5, shown in Figure 1, is a compact unit comprising a Thales 4-watt pulse-tube cooler directly coupled to a vacuum cryostat containing an HPGe detector. A separate controller is connected to the cooler by an electrical cable. The cooler/cryostat package with RDC is shown in Figure 6. The Thales cooler incorporates a moving-magnet linear helium compressor and a split pulse-tube cold head. The compressor makes use of dual, opposed permanent magnet pistons that are fully supported by flexures to prevent piston-to-cylinder contact and reduce wear. Stator coils are placed outside the helium pressure vessel, thereby removing a potential source of gas contamination. In addition, the external stator design eliminates the need for a glass or ceramic feedthrough in the pressure vessel. The pulse-tube cold head contains no moving parts, so wear is eliminated and vibration is reduced. These design choices remove the main causes of failure, wear and contamination, and improve reliability. Vibration is reduced by virtue of the canceling effect of the opposed pistons and by the lack of moving parts inside the cold head. The manufacturer states that the cooler has an expected life in excess of 50,000 hours. Details of the Thales cooler can be found at www.thales-cryogenics.com.

The Cryo-Pulse® 5 is available with detector sizes in excess of 100% relative efficiency and energy resolution of less than 2.0 keV for 1.33 MeV gammas. The ULB RDC is a standard option. End caps and RDC neck lengths are available in different sizes, with a 4-in.-diameter end cap accommodating detectors of up to 130% relative efficiency. An diagram of a Cryo-Pulse® 5 cryostat configuration usable in the RASA is shown in Figure 6.

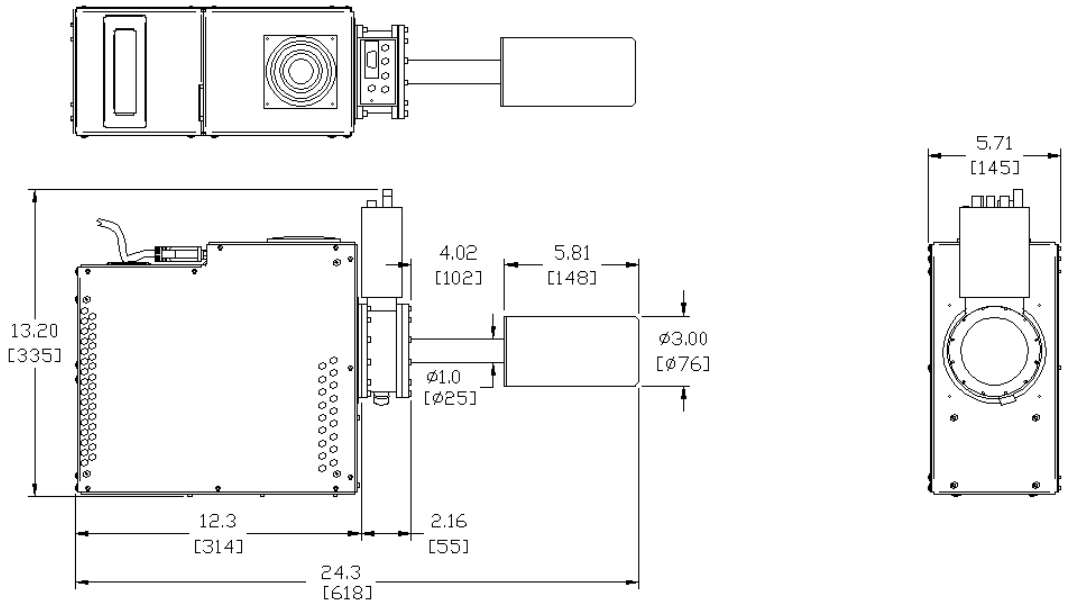


**Figure 6. Cryo-Pulse® 5 Model CP-5F with RDC (image courtesy of CANBERRA).**

The standard-product Cryo-Pulse® 5 so far discussed uses zeolite molecular sieves to maintain the detector vacuum when cold. As with all sieve-pumped cryostats, the unit is susceptible to partial thermal cycling in the event of a brief power outage. Because the sieves are closely coupled to the cooler cold tip, they are the first things to warm in the event of a power outage. As the sieves warm, they release large amounts of the gases they have captured. The gases then condense on the still-cold detector. If power is restored before the detector reaches room temperature, the detector is said to have partially thermal-cycled, and some gases remain adsorbed on the detector surface, causing leakage current and poor performance. In the event of a partial thermal cycle, the detector may be offline for 1–2 days during recovery.

The standard Cryo-Pulse® 5 has at least one elastomer seal on the vacuum pump-out port sealing plug. RDC-equipped cryostats also have an elastomer end-cap seal. The cryostat electrical feedthroughs are made of glass and sealed with epoxy. Elastomer, glass, and epoxy seals are all permeable to atmospheric gases to some small degree, and they are particularly permeable to helium. Because the partial pressure of helium in the atmosphere is low and the pulse-tube cooling power during cooldown is high, the lifetime of a Cryo-Pulse® 5 exceeds 5 years with normal use. But the demands of the RASA are such that a higher standard of reliability is required. We are currently designing a low-cross-section metal seal for the RDC end cap. A low cross-section is required to maximize the HPGe detector volume (i.e., the relative efficiency) that can be contained in a given end-cap outside diameter (OD). End-cap OD is in turn constrained by the bore diameter of the shield entry port. In the case of the RASA, this is an approximately 4-in. clearance. In addition to the end cap seal, we are replacing the electrical feedthroughs with welded UHV feedthroughs, such as Ceramaseal® UHV feedthroughs by CeramTec North America, Inc., Laurens, South Carolina. A metal pinch tube that forms a cold-weld metal bond when sealed will replace the pump-out port plug. Elimination of highly permeable seals will greatly enhance the vacuum integrity of the Cryo-Pulse® 5 but will not solve the problem of partial thermal cycling in the event of brief power loss. This risk can be mitigated by using an uninterruptible power supply (UPS) and/or back-up generator, but to completely eliminate the risk, we choose to use UHV cryostat design techniques.

The issues associated with gas loads in mechanically cooled HPGe detector cryostats have been elucidated in past proceedings of this conference by Hull et al. (2006, 2007). The intrinsic gas load inside a sealed vacuum cryostat results from leakage, diffusion, vaporization, and surface desorption. All these sources can be minimized by control of design, fabrication, cleaning, and assembly techniques. The most stringent application of these techniques is referred to as UHV technology. UHV denotes the vacuum pressure range below $10^{-9}$ torr. In order to achieve UHV,

the gas load must be severely reduced. Ekin (2006), O'Hanlon (2003), and Redhead et al. (1967) are only three of myriad references on the topic of applied UHV techniques. Since gas pressure inside the sealed vacuum cryostat is a function of the gas load and rate of gas removal by pumping, the battle is only half fought by controlling gas load. One or more pumping methods must be incorporated into the design in order to permanently remove evolved gases and ensure a long-lived working vacuum.

To minimize conductive and convective heat loads and reduce contamination of the HPGe detector junction surface, the working vacuum inside the detector cryostat must be maintained in the low $10^{-5}$ to $10^{-6}$ torr pressure range. We believe that chemical getter pumps and ion pumps are practical for compact detector cryostats because they permanently remove gas molecules from the vacuum space. Other types of pumps, such as cryopumps, turbomolecular pumps, and diffusion pumps, are impractical, primarily because of size or implementation constraints. Cryosorption pumps are impractical because they do not permanently remove gas molecules (with the possible exception of water molecules) from the vacuum space, thereby leaving the detector susceptible to partial thermal cycles. Chemical getter pumps, such as titanium sublimation pumps (TSPs) or non-evaporable getter (NEG) pumps, permanently remove reactive gases when they form chemical compounds on the getter surface. Noble gases are not affected. Alloys of vanadium and/or zirconium are used as the reactive media in NEG pumps manufactured by the SAES Getters Group (http://www.saesgetters.com/). In addition to irreversibly pumping many reactive gases, NEG pumps can possess high capacity for reversibly absorbing hydrogen. NEG pumps can be regenerated *in situ* by heating to several hundred degrees Celsius and diffusing the chemical reactants into the bulk of the media, thereby forming a fresh reactive surface layer. A TSP works by heating a filament of titanium that sublimes onto adjacent surfaces, forming a chemically reactive film. The lifetime of TSP filaments is short. Ion pumps remove gas molecules through several different mechanisms after the gases are ionized and accelerated by high voltage applied to the pump. Ionized gas molecules are removed from the vacuum by implantation into the electrodes, burial by metal sputtered from the electrodes, or by chemical reaction with metal sputtered from the electrodes.

In a UHV chamber, with NEG and/or ion pumps installed, the residual gas species and their partial pressures can be identified using a residual gas analyzer (RGA). Pressure can be measured with a modified Bayard Alpert ionization gauge tube or inverted magnetron cold-cathode gauge tube down to the $10^{-11}$ torr range. Even at these low pressures, knowledge of the exact nature of the residual gases inside the cryostat is important for predicting the lifetime of the pumps and the rate of long-term vacuum degradation. These residual gas species and their partial pressures can be identified using an RGA. We feel that, although we will be applying UHV techniques that have been successfully used on other products, it will still be important to determine the residual gas constituents in order to predict the optimum pumping methods and UHV materials to use. Investigations will be carried out using in-house RGA and UHV facilities to shed light on the nature of the residual gas environment in our modified Cryo-Pulse® 5. It may also be possible to carry out accelerated aging tests by observing the cryostat pressure over a period of weeks with the cryostat at elevated temperature.

## RESEARCH ACCOMPLISHED

The project work has just begun. We are currently in the design phase for the RDC end-cap low-cross-section metal seal. Information on small laboratory high-purity nitrogen generators is being gathered. Conceptual design is being carried out for the Cryo-Pulse® 5 UHV cryostat modifications.

## CONCLUSIONS AND RECOMMENDATIONS

Products based on Stirling hybrid cooler and pulse-tube cooler technologies show promise as improved HPGe detector coolers for the RASA system. Modification of the existing Cryo-Cycle™ and Cryo-Pulse® 5 products provides a means of avoiding the time and cost of full-scale efforts to develop new cooler technologies for this application. Integration of an $N_2$-gas generator with the Cryo-Cycle™ and incorporation of UHV seals and feedthroughs on the dipstick cryostat offer one solution. Enhancement of the Cryo-Pulse® 5 by application of similar and more rigorous UHV design principles to the cryostat hardware and vacuum maintenance methodology offers another solution. RGA analysis of the residual gases inside the cryostats can be beneficial with both products, especially the latter.

Our recommendation and intention are to pursue both solutions by building and testing modified versions of the two standard products. RGA analysis should be used to optimize UHV design.

## ACKNOWLEDGEMENTS

The authors thank Reuven Unger at SunPower, Inc., for many helpful discussions on the subject of mechanical coolers. Similar thanks go to Willem van de Groep at Thales Cryogenics for discussions on Thales pulse-tube coolers. Acknowledgements are also given to Jim Chester and Ted Gallucci for their preliminary design work and anticipated major involvement in the ongoing design and prototyping efforts.

## REFERENCES

Bower, S. M., H. S. Miley, R. C. Thompson, and C. W. Hubbard (1997). Automated particulate sampler for comprehensive-test-ban treaty verification (the DOE radionuclide sampler/analyzer), *IEEE Trans. Nuc. Sci.*, NS-44, vol.3, 551–556.

Ekin, J. W. (2006). *Experimental Techniques for Low-Temperature Measurement*, New York: Oxford University Press.

Hull, E. L., R. H. Pehl, J. R. Lathrop, P. L. Mann, R. B. Mashburn, B. E. Suttle, H. S. Miley, C. E. Aalseth, T. W. Bower, and T. W. Hossbach (2007). Mechanically cooled large-volume germanium detector systems for nuclear explosion monitoring, in *Proceedings of the 29th Seismic Research Review: Ground-Based Nuclear Explosion Monitoring Technologies*, LA-UR-07-5613, Vol. 2, pp. 770–778.

Hull, E. L., R. H. Pehl, J. R. Lathrop, G. N. Martin, R. B. Mashburn, H. S. Miley, C. E. Aalseth, T. W. Hossbach, and T. W. Bower (2006). Mechanically cooled large-volume germanium detector systems for nuclear explosion monitoring, in *Proceedings of the 28th Seismic Research Review: Ground Based Nuclear Explosion Monitoring Technologies*, LA-UR-06-5471, Vol. 2, pp. 822–831.

Miley, H. S., S. M. Bower, C. W. Hubbard, A. D. McKinnon, R. W. Perkins, R. C. Thompson, and R. A. Warner (1998). Automated aerosol sampling and analysis for the comprehensive-test-ban treaty, *IEEE Trans. Nuc. Sci.*, NS-45, vol.3, 1034–1039.

O'Hanlon, J. F. (2003). *A User's Guide to Vacuum Technology*, Hoboken: John Wiley and Sons.

Redhead, P. A., J. P. Hobson, and E. V. Kornelsen (reprint 1998). *The Physical Basis of Ultrahigh Vacuum*, New York: American Institute of Physics.

Zäringer, M., J. Bieringer, and C. Schlosser (2008). Three years of operational experience from Schauinsland CTBT monitoring station, *J. of Environmental Radioactivity* 99: 596–606.

# Infrasound Monitoring

# INFRAMONITOR: A TOOL FOR REGIONAL INFRASOUND MONITORING

Stephen J. Arrowsmith and Rod Whitaker

Los Alamos National Laboratory

Sponsored by National Nuclear Security Administration

Contract No. DE-AC52-06NA25396
Proposal No. BAA05-07

## ABSTRACT

With the recent increase of regional infrasound deployments, there is a need for tools that can be applied to networks of infrasound arrays in order to generate robust event catalogs. We present a new tool for regional infrasound monitoring that performs signal detection, association, and event location for networks of infrasound arrays. First, an algorithm for robust signal detection is presented, which utilizes an adaptive noise hypothesis, compensating for variable ambient noise. We show that the adaptive detection scheme performs significantly better than standard detection schemes in the presence of correlated noise. Next, we present a robust method for the association and location of infrasound events recorded at multiple arrays. A Matlab toolbox with a GUI interface, InfraMonitor 1.0, has been developed that incorporates this suite of algorithms for regional infrasound monitoring. An outline of the InfraMonitor 1.0 package is presented. A computer demonstration of InfraMonitor 1.0 will be available at the 2008 Monitoring Research Review meeting.

## OBJECTIVES

The objective of this work is to leverage new methodologies for regional infrasound monitoring, which have been recently developed at Los Alamos National Laboratory, by assimilating them into an integrated software package, which will be made available to the research community.

## RESEARCH ACCOMPLISHED

### Methodologies for regional infrasound monitoring

InfraMonitor 1.0 utilizes a new signal detection algorithm based on the F-statistic (Arrowsmith et al., 2008a, 2008b), which differs from the conventional F-detector in one key way: it adaptively accounts for real ambient noise. This adaptive approach is intuitively better since it is not based on an idealized assumption and therefore more closely matches the performance of human analysts.

An example showing the benefit of using an adaptive approach, which accounts for correlated noise (rather than assuming perfectly uncorrelated noise) is shown in Figure 1. This figure shows both conventional and adaptive F-detector results for a 15-minute record of data from the MSH1 four-element infrasound array in Washington State. During the 15-minute period analyzed, there was persistent correlated noise from a wind-farm located at a range of ~15 km from the array. Although this is quite an extreme case, due to the relatively large amplitude of the background noise source, a certain degree of correlated noise is typically present at any infrasound or seismic array. The example shows that the assumption of uncorrelated noise (made by the conventional detector) is clearly violated in this case, leading to virtually the whole record being detected. In contrast, the adaptive F-detector suitably compensates for the background noise, detecting purely transient high signal/noise ratio signals.

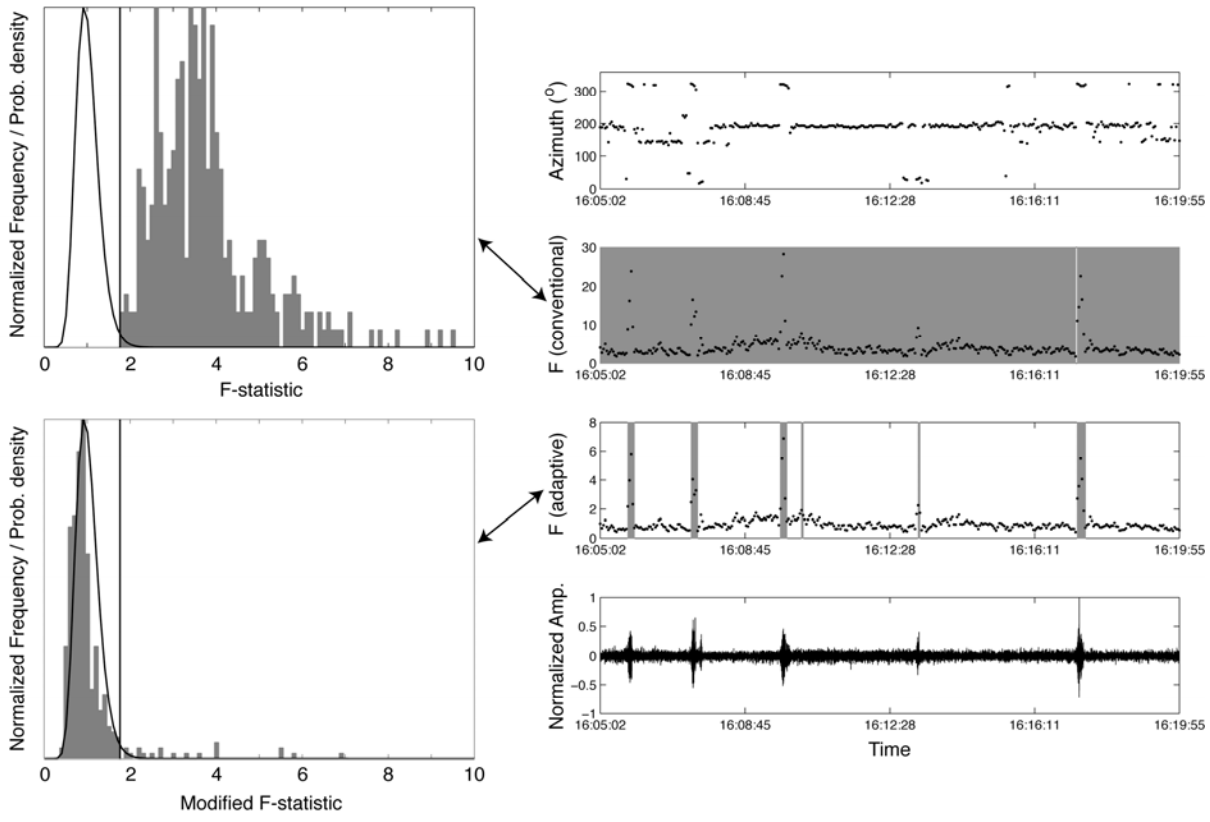


**Figure 1. Example illustrating the difference between a conventional detector and the new detector outlined in this study. Histograms of the F-statistics (top left), and scaled F-statistics (bottom left), in the 15-minute time window shown. Black curves denote the appropriate theoretical F-distribution, and vertical black lines denote a p-value of 0.01.**

A grid-search method for simultaneous signal association and event location has been developed and is outlined in detail by Arrowsmith et al., 2008a. The basis of the grid-search algorithm is illustrated in Figure 2. For each grid node, backazimuths, maximum interarray delay times, and minimum interarray delay times, are computed for each array (Figure 2). For each array, we have a set of observed arrival times $(\mathbf{t}_i)$ and backazimuths $(\Phi_i)$. We then loop over each grid nod, and search for sets of N arrivals (where N = number of arrays) that are consistent with predicted backazimuths (i.e., within a specified backazimuth deviation) and interarray delay times. A given event that is recorded at all N arrays may be associated with multiple grid nodes, which map out the possible event location for that event. The uncertainty in event location can be simply quantified by computing the standard deviations of the uncertainties in latitude and longitude respectively.

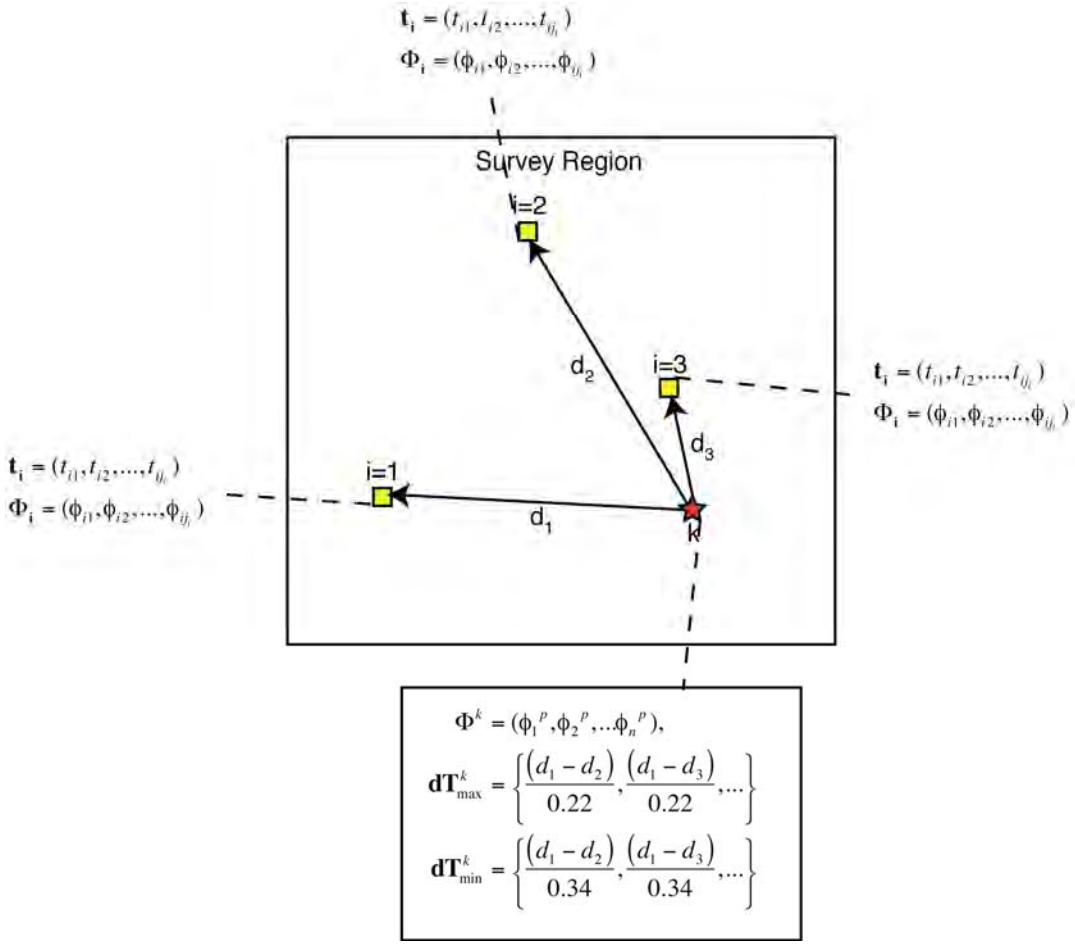


**Figure 2. Schematic illustrating the grid-search method used for simultaneous signal association and event location. Yellow squares represent arrays and the red star denotes a single grid node. The upper box denotes the survey region, which is parameterized with a set of grid nodes.**

**Integrated Software Package**

InfraMonitor 1.0 is a Matlab toolbox with a GUI interface that assimilates both the detection and the association/location algorithms outlined above. The software package is designed to seamlessly integrate the regional monitoring methodologies in order to enable the user to generate preliminary event catalogs, given waveform data from a network of infrasound arrays. This software package extends existing array-based tools such as MatSeis-InfraTool (Hart, 2004) and PMCC (Cansi, 1995) in three primary ways:

- Improved detector, which results in ~90% fewer detections from ambient noise in direct comparison tests.

- Signal Association and Event Location are fully integrated, allowing for generalized surveillance rather than a purely event-based approach.

- Command-line functionality allows for pipeline processing of large quantities of data (when the interactive interface is not practical).

Figures 3 and 4 illustrate the functionality of the InfraMonitor GUI interface for both detection and association/location of regional infrasound events.

A summary of the full InfraMonitor 1.0 processing scheme is outlined in Figure 5. The software reads array data from multiple arrays and processes the data to generate multiple detection bulletins. The full set of detection bulletins are then input into the association/location routine, which generates a preliminary event catalog for analyst review. The free parameters that must be specified in order to generate preliminary event catalogs are outlined in Table 1.

**Table 1. Free parameters that must be set in InfraMonitor 1.0**

| Free Parameter | Considerations |
|---|---|
| Time window | The processing time window should be set to the approximate signal durations of interest. |
| Overlap | An overlap between processing time windows allows us to better identify the continuous variation of slowness and backazimuth as a function of time. The limitation is computation speed. An overlap of 50% is recommended as an appropriate choice for most applications. |
| Adaptive window length (w) | The adaptive window length must be set long enough to obtain a sufficient sample distribution, but short enough to account for temporal variations in ambient noise. We have found that an adaptive window length of 1 hour is appropriate for typical infrasound data. |
| *p*-value | The *p*-value affects the numbers and signal-to-noise ratios of detections obtained. The value affects the tradeoff between the probability of detection $(P_d)$ and the probability of false alarm $P_f$. A p-value of 0.01 is typical and has been found to provide a good $P_d$ and low $P_f$. |
| Allowed backazimuth deviation $(\Delta\phi)$ | The allowed backazimuth deviation should be set sufficiently large to account for the effects of wind on measured backazimuths. A value of 5° is considered appropriate, based on observational studies. |
| Minimum group velocity | The minimum group velocity should depend on the phase-range of interest. Following Ceplecha et al. (1998), suitable values are the following: 0.33—Lamb wave, 0.30—Tropospheric return, 0.28—Stratospheric return, 0.22—Thermospheric return. |
| Maximum group velocity | The maximum group velocity should depend on the phase-range of interest. Following Ceplecha et al. (1998), suitable values are the following: 0.34—Lamb wave, 0.32—Tropospheric return, 0.31—Stratospheric return, 0.24—Thermospheric return |

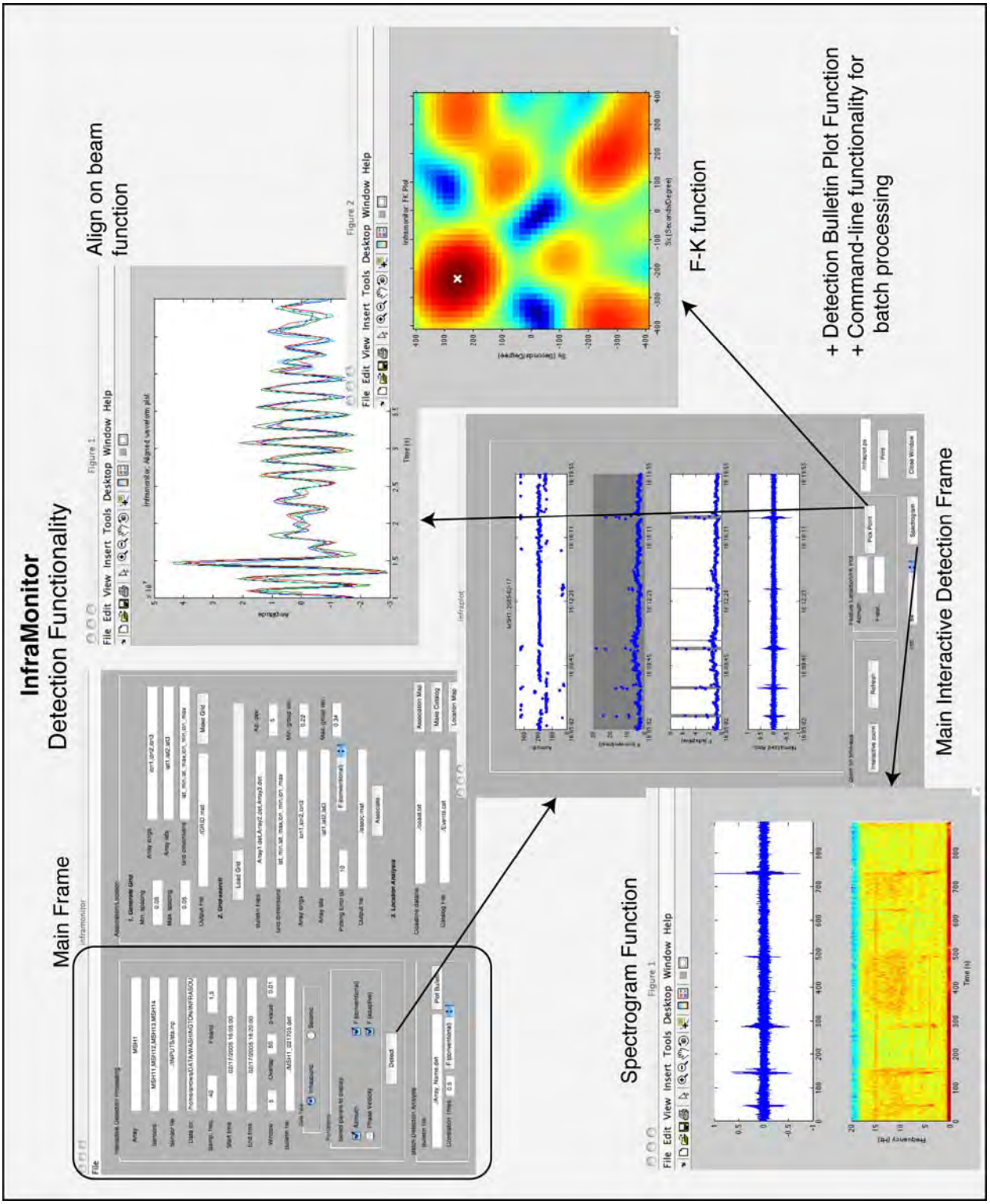


**Figure 3. Screenshots showing interactive detection functionality in InfraMonitor 1.0.**

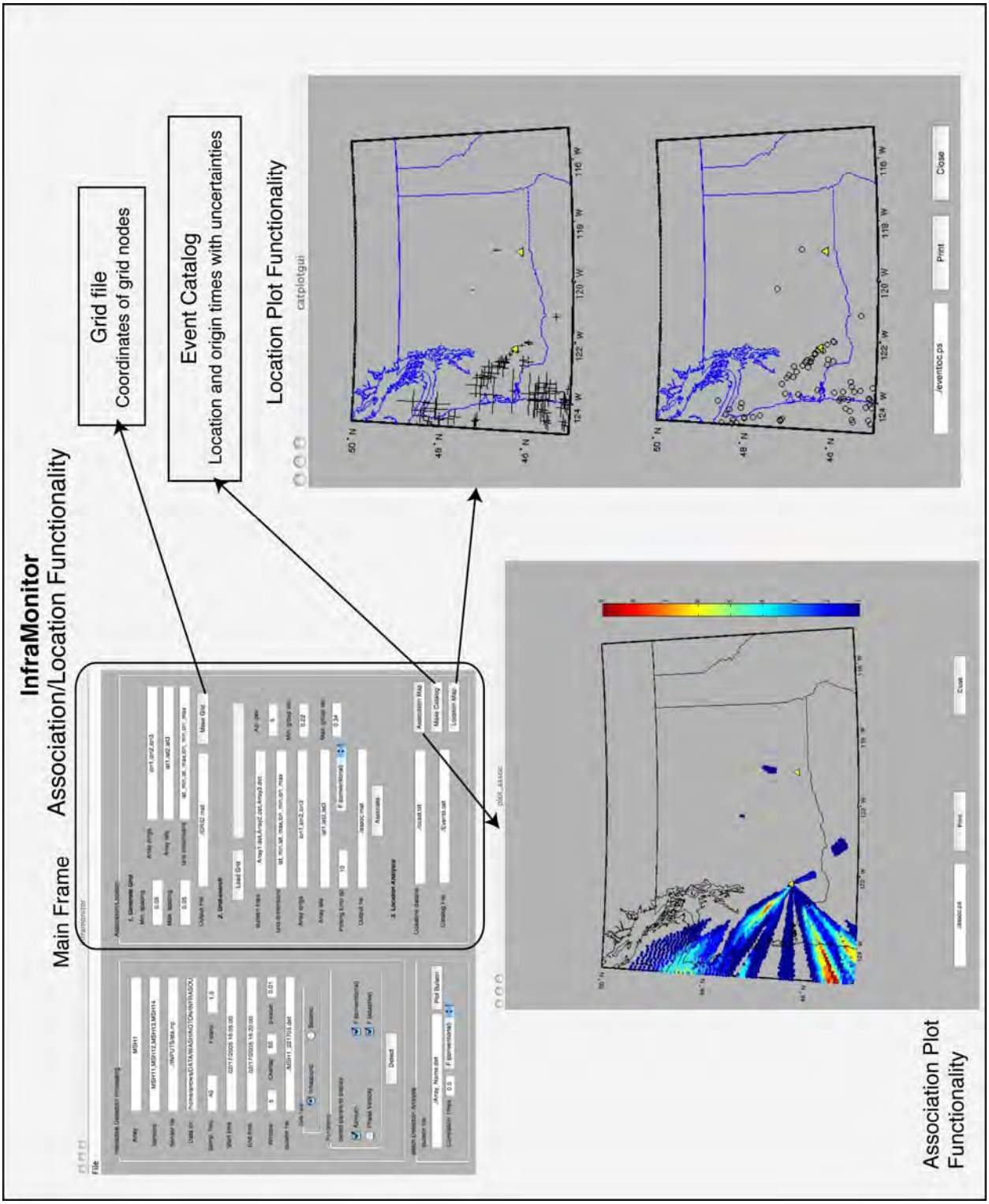


**Figure 4. Screenshots showing interactive association/location functionality in InfraMonitor 1.0.**

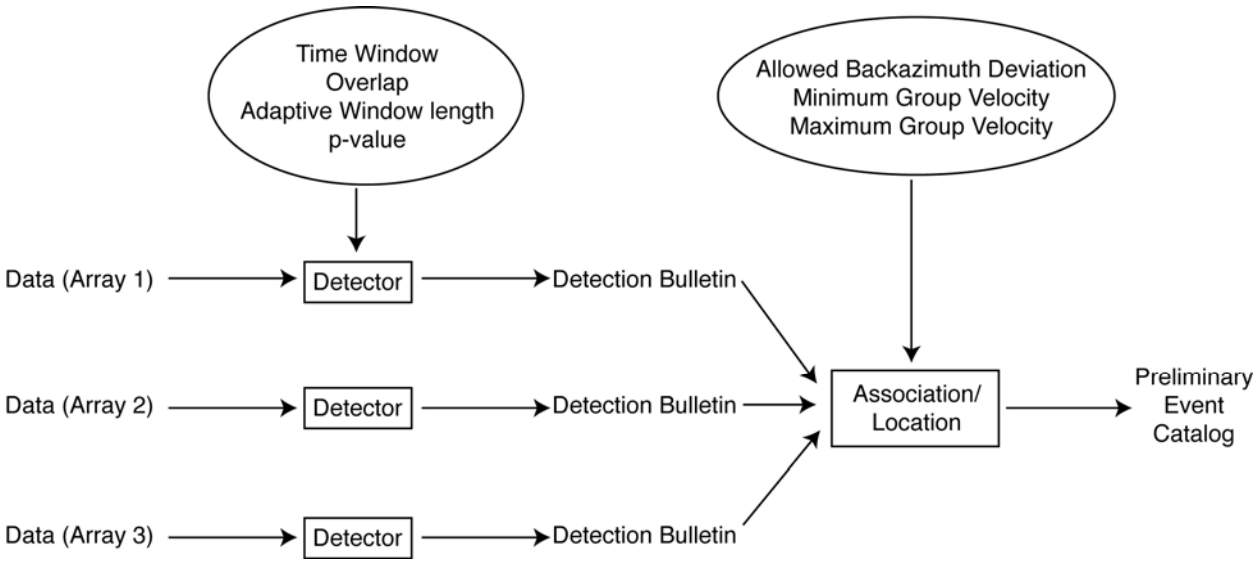


**Figure 5. Flowchart illustrating the processing scheme implemented into InfraMonitor 1.0. Input/Output products are denoted by open text, algorithms are denoted by boxed text, and free parameters are denoted by text enclosed by ellipses. For simplicity, the three-array case is shown, although InfraMonitor 1.0 can be applied to networks containing ≥2 arrays.**

## CONCLUSIONS AND RECOMMENDATIONS

This paper introduces a new research product that has been developed at Los Alamos National Laboratory for regional infrasound monitoring. New detection, association, and location algorithms are introduced and provide the framework for the integrated software package: InfraMonitor. We review the features of InfraMonitor 1.0 and outline the processing scheme underlying the software. This software provides an invaluable tool for researchers by generating preliminary infrasonic event catalogs for further study.

## REFERENCES

Arrowsmith, S. J., R. Whitaker, S. Taylor, R. Burlacu, B. Stump, M. Hedlin, G. Randall, C. Hayward, and D. ReVelle (2008a). Regional monitoring of infrasound events using multiple arrays: Application to Utah and Washington State, *Geophys. J. Int.*, submitted.

Arrowsmith, S.J., R. Whitaker, C. Katz, and C. Hayward (2008b). The F-detector revisited: An improved strategy for signal detection at seismic and infrasound arrays, *Bull. Seism. Soc. Am.*, in preparation.

Cansi, Y. (1995). An automated seismic event processing for detection and location: The P.M.C.C. method, *Geophys. Res. Lett.* 22: 1021, 1024.

Ceplecha, Z., J. Borovicka,W. G. Elford, D. O. ReVelle, R. L. Hawkes, V. Porubcan, and M. Simek (1998). Meteor phenomena and bodies, *Space Sci. Rev.* 84: 327–471.

Hart, D. (2004). Automated infrasound signal detection algorithms implemented in MatSeis – Infra Tool, Sandia report SAND2004-1889.

# MULTI-ARRAY DETECTION, ASSOCIATION AND LOCATION OF INFRASOUND AND SEISMO-ACOUSTIC EVENTS IN UTAH

Stephen J. Arrowsmith[1], Chris Hayward[2], Brian Stump[2], Relu Burlacu[3], Il-Young Che[4] and Gurpreet Singh[1]

Los Alamos National Laboratory[1], Southern Methodist University[2], University of Utah Seismograph Stations[3], and Korea Institute of Geosciences and Mineral Resources[4]

Sponsored by Air Force Research Laboratory and National Nuclear Security Administration

Contract Nos. DE-AC52-06NA25396[1] and FA8718-08-C-008[2-4]
Proposal No. BAA08-65

## ABSTRACT

The two main objectives of this work are to (1) develop an automated method for processing seismic and infrasound data from multiple seismo-acoustic arrays, and (2) to apply the method to a regional network of arrays for validation. The project involves development of automated techniques for detecting, associating, and locating infrasound signals at single and multiple arrays and then combining the processed results with similar automated procedures for seismic signals. This approach differs from most existing systems that typically depend on late association or data fusion after events are formed. Regional infrasound and seismo-acoustic events are automatically detected, associated and located using seismo-acoustic stations in Utah. We utilize the InfraMonitor toolbox, recently developed at Los Alamos National Laboratory (LANL), in collaboration with Southern Methodist University (SMU). The toolbox comprises an adaptive F-detector – which accounts for real ambient noise, and a robust signal association/event location algorithm. Seismic signals, obtained using a statistically based short-term average/long-term average (STA/LTA) detector, are associated with infrasound events obtained by InfraMonitor. A thorough ground-truth survey using satellite observations and independent data provides the basis for event identification. An analyst reviews automatic results in order to make a preliminary assessment of the number of false associations. We report on the numbers, distributions and sources of reviewed infrasound and seismo-acoustic events detected by Utah seismo-acoustic stations. Case studies of selected events provide examples of the infrasonic and seismo-acoustic records from regional events.

## OBJECTIVES

This project uses automatic detection, association, and location algorithms on regional seismo-acoustic array networks to build catalogs of seismo-acoustic events. To date, algorithms have been developed for robust detection, association, and location of infrasound and seismo-acoustic events. Each algorithm is designed for automatic near real-time application as part of a fully integrated seismo-acoustic monitoring system.

Validation of the method is done by applying it to one month's regional seismo-acoustic network data from Utah (Stump et al., 2007) and comparing automatic results with ground-truth information. We utilize direct ground-truth, Google Earth, and analyst review in order to assess the automatic results.

## RESEARCH ACCOMPLISHED

### Detection, Association, and Location Algorithms

Detections are perfomed with an F-detector (Blandford, 1974) modified to adapt to a variable scale parameter. This provides a detection null hypothesis that adapts to temporally variable ambient noise. First, F-statistics are computed for an adaptive time-window (*w*), using the standard formula outlined in Blandford (1974). F-statistics are then scaled by a constant c, such that the peak of the distribution of F-statistics in the time window *w* aligns with the peak of the theoretical central F-distribution with *2BT, 2BT (N-1)* degrees of freedom. This follows from work by Shumway et al. (1999) who showed that, in the presence of correlated noise, the F-statistic is distributed as

$$cF_{2BT,2BT(N-1)}. \qquad (1)$$

Infrasonic signal association and event location are performed simultaneously using a forward approach. A grid-search procedure is implemented over a dense set of grid nodes that span the geographic region of interest. For each grid-node we search for sets of N arrivals at N arrays that can be associated based on backazimuth and delay-time constraints. Constraints, (backazimuth deviation, $\Delta\phi$, and group velocities, $v_g$) , must be set depending on the grid spacing used, an expectation of the maximum backazimuth deviation from winds ($\Delta\phi$), and the range of infrasonic group velocities ($v_g$) suitable for a given region. Such constraints are chosen based on synthetic tests, as shown in the next section.

Seismic detection is performed on arrays using the same methodology described above. For single stations, we use a robust outlier detection on an STA/LTA power estimate. Briefly, STA/LTA is calculated on the time series power and the distribution of STA/LTA is transformed to a near-normal distribution using a Box-Cox power transformation. We then apply a standard robust outlier test to identify outliers that occur at >5 median absolute deviations from the median. We perform seismo-acoustic association using infrasound events to search for associated seismic arrivals.

For further details on the methodology developed as part of this project, the reader is referred to Arrowsmith et al. (2008).

### Synthetic Tests

We performed synthetic tests to assess network location resolution and the effect of grid search parameters (i.e., allowed group velocities and backazimuth deviations). Each synthetic test considers several defined event locations and origin time. From the event definition, synthetic arrival times and backazimuths are calculated for each array using pre-defined group-velocities and assuming backazimuths to be great-circle paths. The set of synthetic arrival times and backazimuths thus constitutes the input to the previously described grid-search procedure.

Figure 1 shows the results for synthetic events based on the actual locations of arrays in the Utah seismo-acoustic network. These arrays each consist of four Chaparral gauges with the average spacing between gauges close to 100 m. Details of the installation can be found in Stump et al., 2007b. Four pre-defined event locations are defined, one at the Utah Test and Training Range (UTTR) a known ground truth location and three at arbitrary locations outside the network. The figure illustrates that as the grid-search parameters are increasingly constrained, the location uncertainties collapse to the known event locations (Figure 1). Reducing the uncertainty by constraining the grid search is done at the expense of missing some associations due to errors in event time or backazimuth estimates. In

an operational monitoring scheme where the automatic stage is used to select events for analyst review, it is necessary to select sufficiently relaxed parameters to ensure that no events are missed. For the Utah network, this results in corresponding location uncertainties shown in Figure 1a. These observations must be considered when interpreting the results described below. Uncertainty estimates are strongly dependent upon the array geometry and the location of the event of interest.

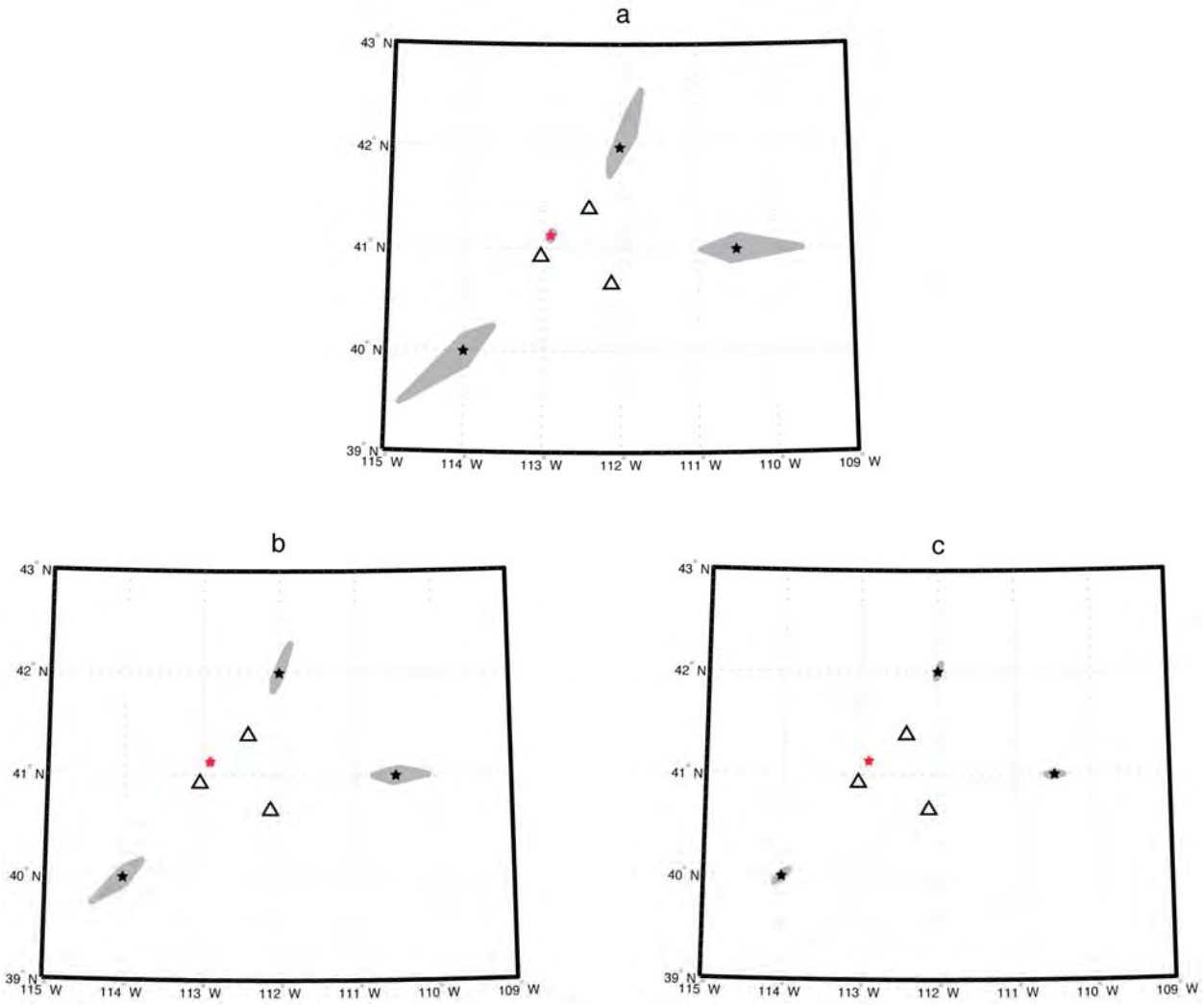


**Figure 1. Results of synthetic association/location tests for four pre-defined event locations (black stars). The grid search parameters used for each test are as follows: (a)** $\Delta\phi = 6°,\ v_g = 0.28 - 0.34\text{km/s}$ **, (b)** $\Delta\phi = 3°, v_g = 0.32 - 0.34\text{km/s}$ **, and (c)** $\Delta\phi = 1°, v_g = 0.299 - 0.301\text{km/s}$ **. Stars show input event locations (red denotes the location of ground-truth UTTR explosions) and gray regions highlight resultant event location uncertainties.**

**Application to Utah**

We have processed Utah seismo-acoustic network data for a period of ~1 month (07/24/07 – 08/28/07) using the previously described detection scheme with the following parameters: Processing window length = 10 s, Overlap = 50%, Frequency Band = 1–5 Hz, Adaptive Window Length (w) = 24 hours, Detection Threshold (p-value) = 0.01. These parameters are specifically tailored for the detection of relatively short, high-frequency arrivals. Such types of signals arise from a range of sources including explosions, mining events, rocket launches, earthquakes, bolides, and impulsive volcanic eruptions at local and regional distances. Our choice of parameters will filter out some

infrasound signals including large events with purely thermospheric arrivals (i.e., those with little high frequencies energy).

After applying the detector to the data, we obtain sets of arrivals at each array (EPU, BGU, and NOQ) in the Utah network (Figure 2). The following parameters are obtained for each arrival: start time, end time, backazimuth, phase velocity, F-statistic, c-value, and correlation. Clear spatial trends are observed in the arrivals at each array, as shown in Figure 2. For example, relatively large numbers of arrivals with Correlation~0.5 are observed from the east at each array.

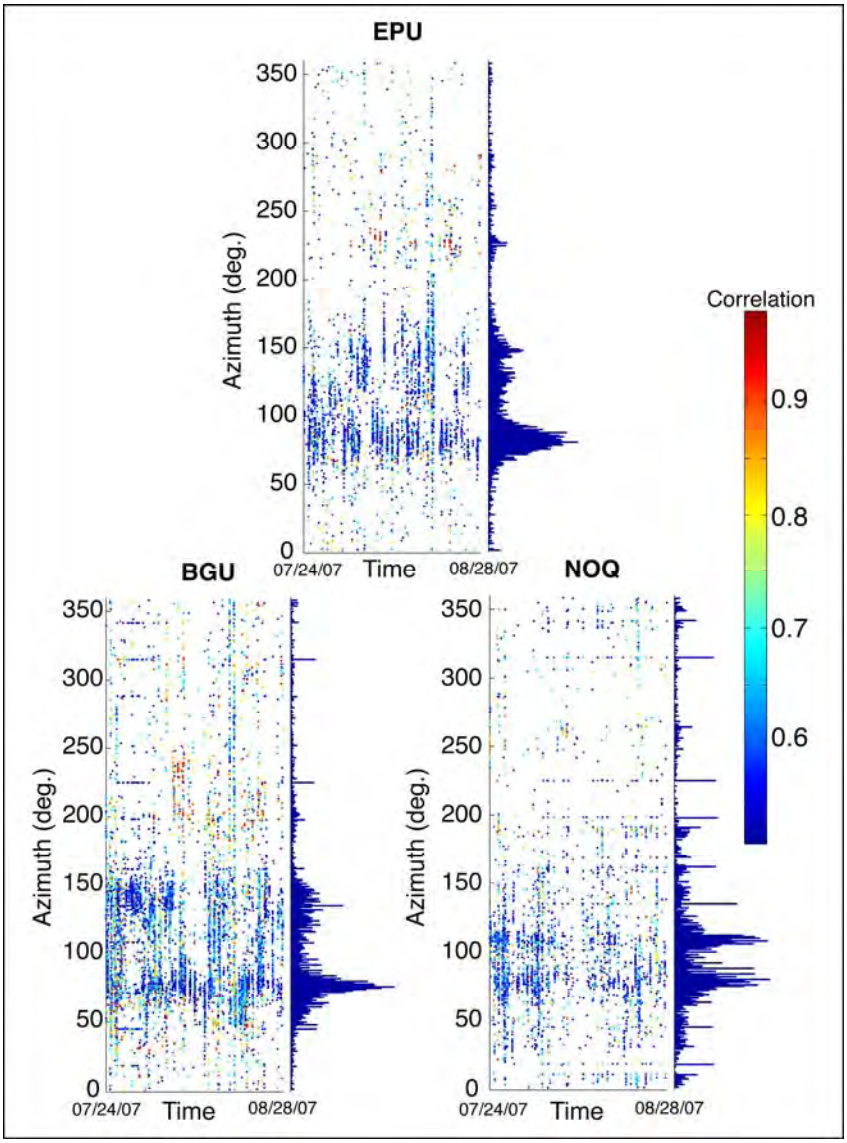


**Figure 2. Automatic detections obtained at the Utah seismo-acoustic network arrays. In each panel, detections are plotted with respect to time and backazimuth and color-coded by correlation. Some artifacts are observed, associated with lines of detections at constant azimuth, which arise from F-K processing of coherent signals with subsonic group velocities (i.e., winds). The histograms show numbers of detections from each 1-degree bin of backazimuth.**

The three sets of detections are then processed using the association algorithm previously described. We search for signals with group velocities that range from 0.28 to 0.34 km/s, thus ignoring any higher velocity thermospheric

arrivals that may not have been completely removed by the band-pass filter. The following parameters are used: Backazimuth deviation ($\Delta\phi$) = 6° and picking error ($E_p$) = 40 s. Large deviations in backazimuth are allowed in order to compensate for measurement uncertainty (e.g., Szuberla and Olson, 2004) and winds (e.g., Mutschlecner and Whitaker, 2005). The allowed start-time picking error is large due to the emergent nature of many infrasonic signals as well as possible temporal variations in the atmosphere. The result of this analysis is a set of triplets of associated arrivals at all three arrays (or "events"). In total, we obtain 287 events recorded at all three arrays during the period of study. Each event is associated with a set of N grid nodes, which delineates the possible source region for that event.

The final set of event locations is computed by taking the geographic means of the grid nodes associated with each event. The location uncertainties are taken to be the standard deviations of grid node locations in latitude and longitude respectively. The locations of all events recorded at all three of the arrays are shown in Figure 3. Four known rocket motor explosions, conducted at UTTR were automatically detected and located with a mean offset of 5.4 km (and standard deviation of 3.3 km), providing confidence in the automatic catalog. We also detect a number of unknown events, including relatively large numbers of events to the east of the network (possibly due to more sources in this direction or to dominant seasonal winds – which enhance detection of signals to the east of the network during the summer). However, due to the network geometry, which was intended primarily for studying local events, there is a large uncertainty in the range of these events (Figure 4).

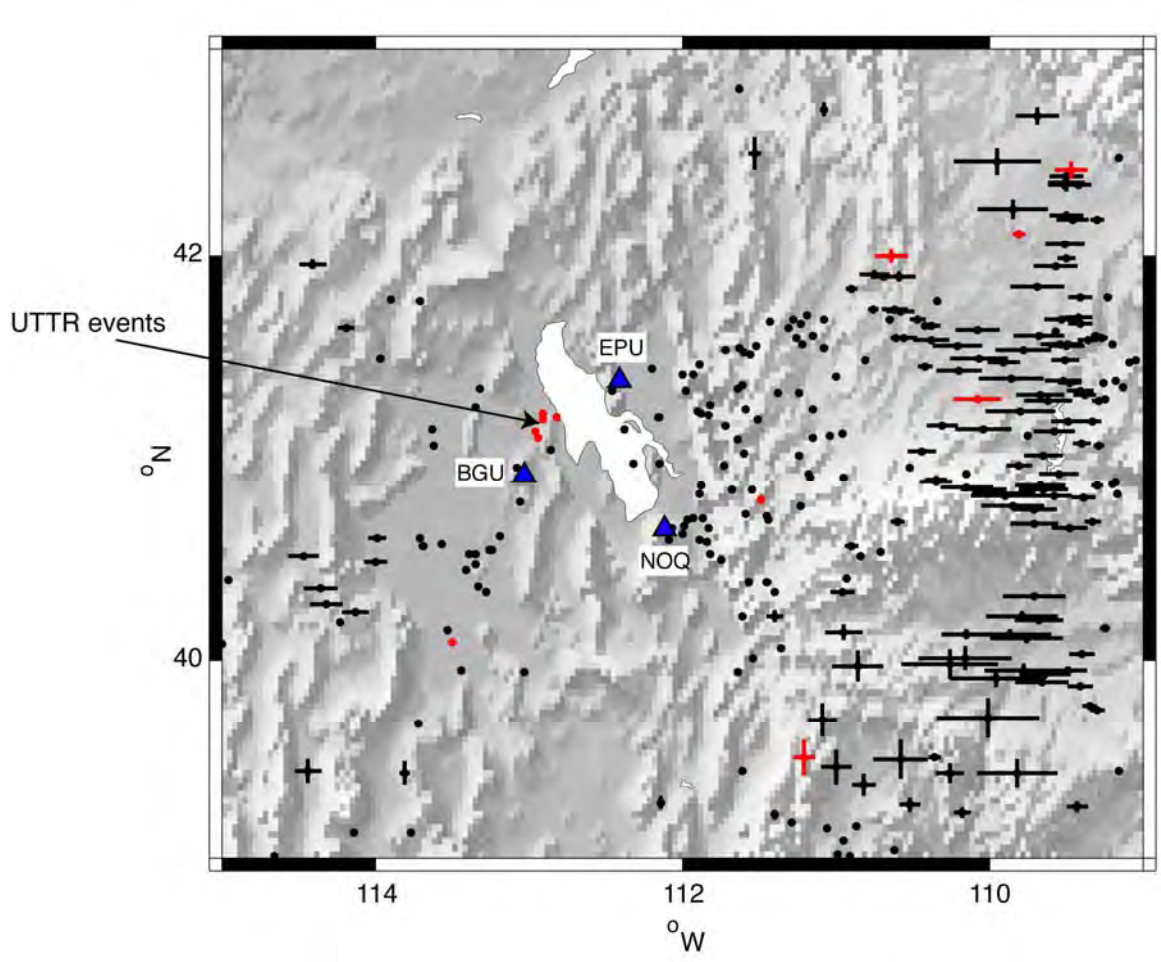


**Figure 3. Locations of infrasound (black) and seismo-acoustic (red) events with corresponding uncertainties in latitude and longitude. Blue triangles denote the locations of the three seismo-acoustic arrays.**

**Validation by Analyst Review, Ground-Truth, and Google Earth**

An analyst has reviewed all infrasound and seismo-acoustic events plotted in Figure 3. Of the 287 events, 70 were marked as excellent, with high signal/noise ratios observed on at least two arrays; 143 were marked as good, with clear signals observed at >=2 arrays, but relatively low signal/noise ratios; and 74 were marked as poor, with no obvious signals in the time series.

As noted earlier, four rocket motors were detonated at the UTTR during the ~1 month survey period. Each of these large events was detected and located by both infrasound and seismic instruments (Figure 3). Infrasound signals at all three arrays, from one of the explosions, are shown in Figure 4. Each explosion is associated with high-quality arrivals at each array, which are automatically associated and located within a mean distance of 5.4 km from the test site. Manually picking onset times, rather than using onset times of detections from the F-detector, should further reduce location errors.

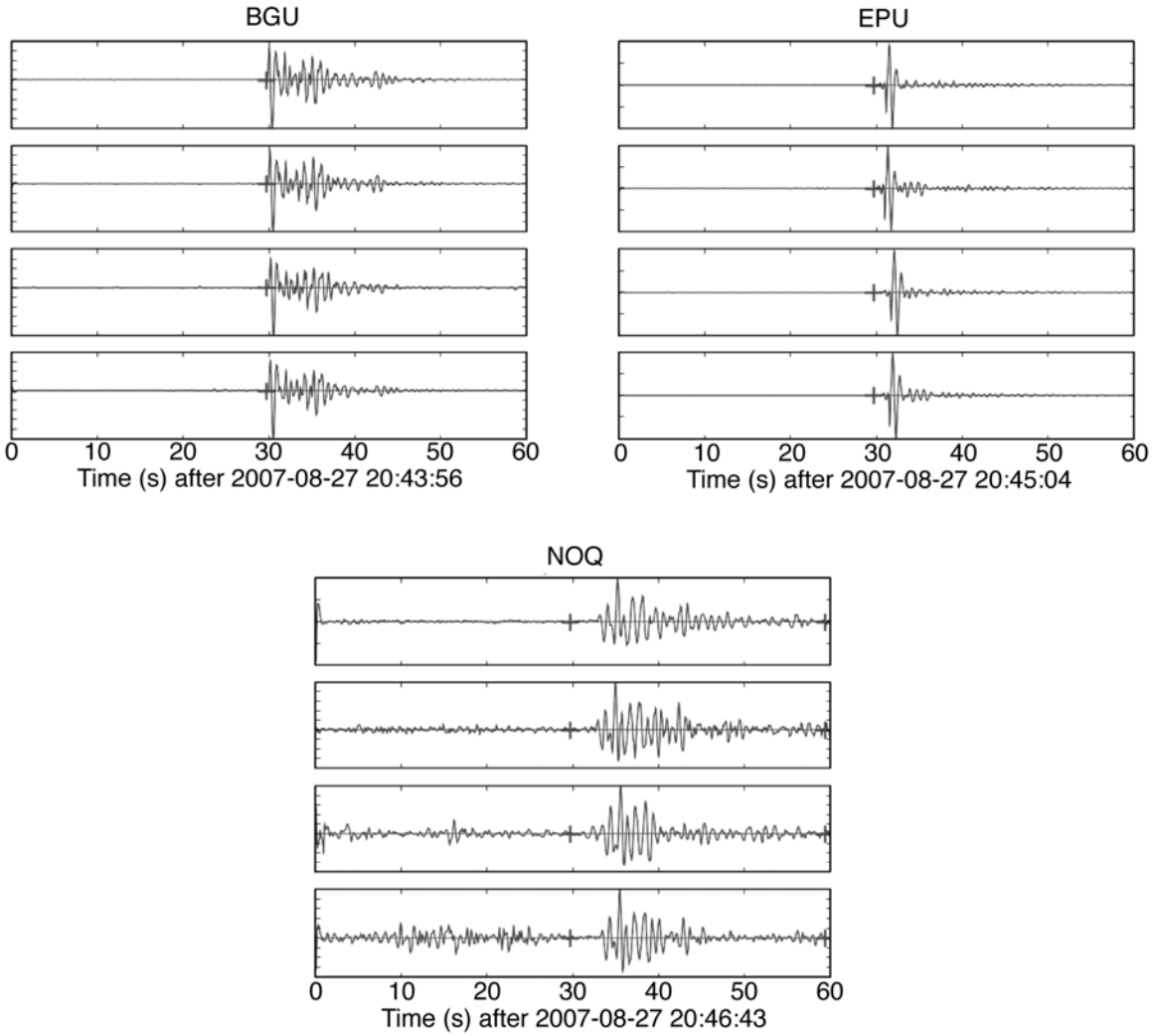


**Figure 4. Automatic waveform detection onset times for a UTTR explosion detected on August 27th, 2007. Automatic detection onsets associated with the event are located at 30 s on each panel. The waveform amplitudes are normalized to the maximum amplitude for each trace.**

For the purpose of obtaining additional ground-truth, we have uploaded the event locations into Google Earth, in order to search for tentative location associations (Figure 5). Events within a small radius of potential sources

identified in Google Earth are tentatively associated with that source, and flagged for further analysis (Figure 6). In addition to events occurring at or near the UTTR, we identified four surface-mine locations, numerous airports, and several events that are tentatively associated with an extensive oil and gas drilling field in Wyoming (Figure 5). At the time of writing, the majority of events remain unassociated, although ground-truth association work is at a preliminary stage. However, we note that a significant proportion of events occur in clusters, and that a large number of events are located on mountain peaks, suggesting that they may be associated with storms (common during July and August). Further research is required to investigate these events in more detail.

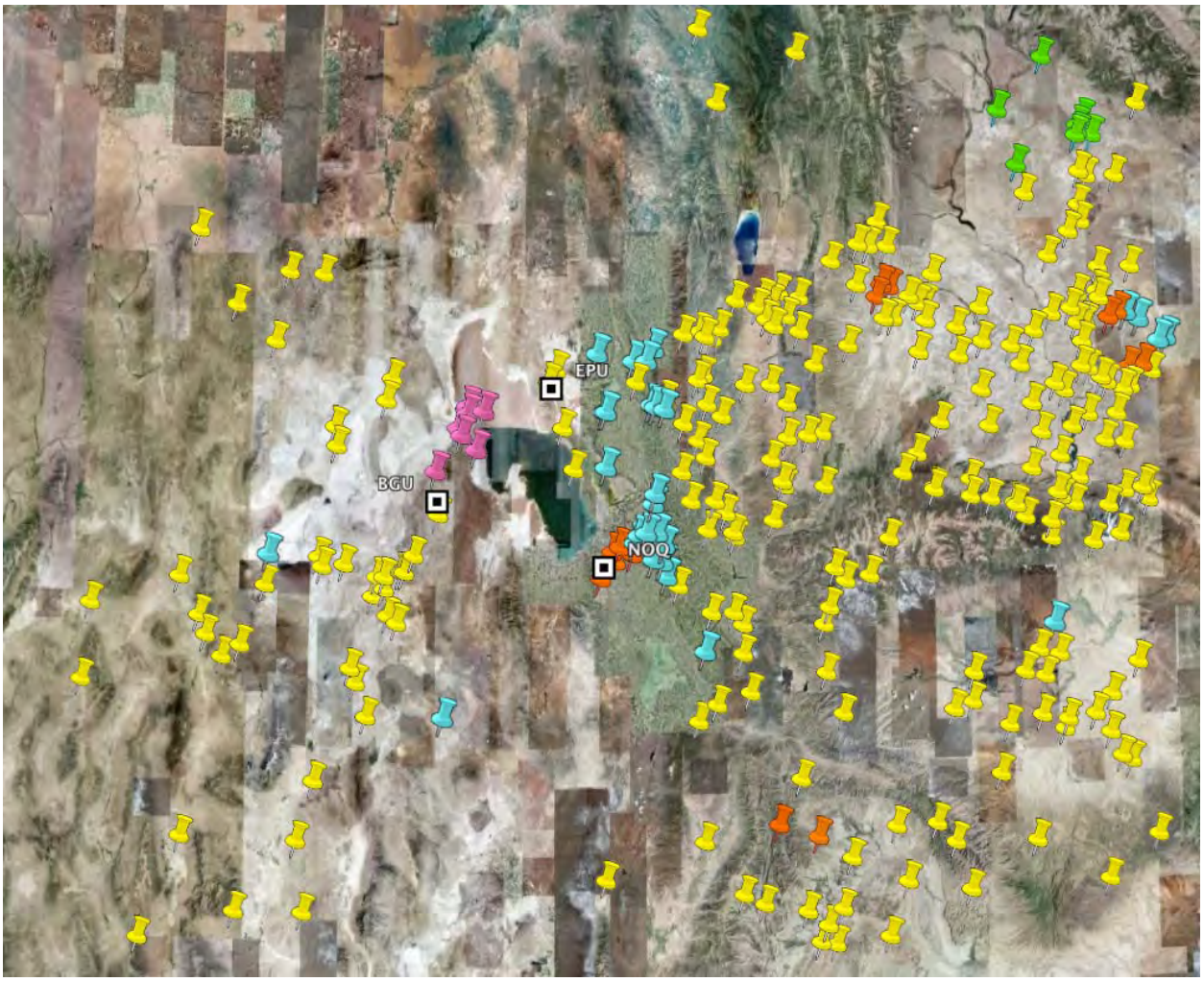


**Figure 5. Infrasound locations superimposed on satellite imagery from Google Earth. The colored pointers denote events that are unassociated (yellow), events tentatively associated with the UTTR (purple), events tentatively associated with mines (orange), events tentatively associated with airports (cyan), and events tentatively associated with drilling operations in the Upper Green Valley, Wyoming (green).**

## CONCLUSIONS AND RECOMMENDATIONS

This paper briefly outlines new methods for the detection, association, and location of infrasound and seismo-acoustic events. We focus on the application and assessment of these techniques using a test dataset: ~1 month of data from the three-array Utah seismo-acoustic network. During the period of survey, the detection, association, and location algorithms automatically find 287 infrasound events and 12 seismo-acoustic events. Of the 12 seismo-acoustic events, four are associated with known rocket motor explosions at the UTTR, and automatically located within an average distance of ~5 km from the ground-truth location. It must be emphasized that these results

are fully automatic; refinements by manual picking and correction for atmospheric winds are expected to improve results further. The algorithms outlined here are primarily designed to reduce the number of events that require analyst review to practical numbers. A preliminary analyst review and ground-truth survey using Google Earth has found that 70 of the 287 events are associated with high signal/noise signals. Of the remaining events, 74 may be mis-associations (i.e., ~25% of the total number of events), although some of these events are likely to be bona fide events with very low signal/noise ratios. We have tentatively associated events with surface mines, airports, and an extensive oil and gas field. Further work is required to more confidently associate events with these sources and to identify the origins of remaining sources.

In summary, the initial results presented here provide an encouraging preliminary validation of the detection, association, and location algorithms as follows:

- The Utah seismo-acoustic network produced an average of eight events per day.
- The automatic algorithm correctly assocated and located all four known ground-truth rocket motor explosion events.
- A comprehensive analyst review has confirmed that < 25% of the events are missassociations.
- A significant number of events have been tentatively associated with sources using Google Earth.
- The remaining un-associated events tend to form clusters, suggesting common origins.

**Figure 6. Zoom on Bingham mine (outlined by white line), showing infrasound events (orange pointers) that are tentatively associated with the mine.**

## ACKNOWLEDGEMENTS

Data gathered for the purposes of this project are supported by contract FA8718-05-C-0020 sponsored by the Air Force Research Laboratory. We thank Mark Debonis and Rod Whitaker for their contributions to this work.

## REFERENCES

Arrowsmith, S. J., R. Whitaker, S. Taylor, R. Burlacu, B. Stump, M. Hedlin, G. Randall, C. Hayward, and D. ReVelle (2008). Regional Monitoring of Infrasound Events using Multiple Arrays: Application to Utah and Washington State, *Geophys. J. Int.* Submitted.

Blandford, R.R. (1974). An automatic event detector at the Tonto Forest seismic observatory, *Geophysics* 39: 633, 643.

Mutschlecner, J. P., and R. W. Whitaker (2005). Infrasound from earthquakes, *J. Geophys. Res.* 110: doi:10.1029/2004JD005067.

Shumway, R.H., S.-E. Kim, and R.R. Blandford (1999). Nonlinear estimation for time series observed on arrays, *in Asymptotics, Nonparametrics and Time Series*, pp. 227–258, ed. Ghosh, S., Marcel Dekker, New York.

Stump, B., R. Burlacu, C. Hayward, J. Bonner, K. Pankow, A. Fisher, and S. Nava (2007). Seismic and infrasound energy generation and propagation at local and regional distances: Phase 1—divine strake experiment, in *Proceedings of the 29th Monitoring Research Review: Ground-Based Nuclear Explosion Monitoring Technologies*, LA-UR-07-5613, Vol. 1, pp. 674–683.

Stump, B., R. Burlacu, C. Hayward, K. Pankow, S. Nava, J. Bonner, S. Hoch, D. Whiteman, A. Fisher, T. S. Kim, R. Kubacki, M. Leidig, J. Britton, D. Drobeck, P. O'Neill, K. Jensen, K. Whipp, G. Johanson, P. Roberson, R. Read, R. Brogan and S. Masters (2007b). Seismic and infrasound generation and propagation at local and regional distances: Phase I – divine strake experiment, Final Report, AFRL-RV-HA-TR-2007-1188, Hanscom AFB, MA, 11 October 2007.

Szuberla, C.A. and J.V. Olson (2004). Uncertainties associated with parameter estimation in atmospheric infrasound arrays, *J. Acous. Soc. Am.* 115: 253, 258.

# ENHANCEMENTS TO THE CTBTO OPERATIONAL AUTOMATIC INFRASOUND PROCESSING SYSTEM

David J. Brown, Nicolas Brachet, and Ronan Le Bras

Comprehensive Nuclear-Test-Ban Treaty Organization

## ABSTRACT

The Preparatory Commission for the Comprehensive Nuclear-Test-Ban Treaty Organization (CTBTO) is exploring methods to enhance the current operational infrasound processing system at the International Data Centre (IDC) for infrasound data recorded by the International Monitoring System (IMS). Several enhancements are under development and are currently being tested.

The first enhancement is the incorporation of methods for determining signal amplitude. The following signal amplitudes are being determined for each infrasound detection: peak-to-peak amplitude, root mean squared (RMS) amplitude, and instantaneous amplitude as revealed by the analytic trace via the Hilbert Transform. Initial efforts consider a variety of frequency bands, with the utility in network processing being of primary importance.

A second enhancement is the incorporation of station noise characterization in terms of the power spectral density (PSD). This determines the noise field at each station for various times of day and as a function of season. This information is useful in determining network detection capability.

## OBJECTIVES

The objective of this work is to provide both CTBTO and external users of IDC data products with the ability to determine more accurate measures of IMS infrasound network capability.

This goal will be achieved through enhancements to the current automatic infrasound processing system that will

i. provide infrasound signal amplitudes, and

ii. provide a notion of the background noise characteristics at each station.

## RESEARCH ACCOMPLISHED

### Amplitude Determination

Signal amplitudes are being determined for each automatic infrasound detection using three different methods.

The peak-to-peak amplitude, RMS amplitude, and instantaneous amplitude as revealed by the analytic trace via the Hilbert Transform are being calculated for each arrival ID (**arid).**

The peak-to-peak amplitude is used typically in empirical infrasound amplitude attenuation laws (Whitaker, 1995; Blanc et al., 1997) and so provides a useful addition to the IDC Bulletin. The RMS amplitude, however, is a running average taken over a user-specifiable time interval and is more representative of the average signal strength than the peak signal strength, as revealed by the peak-to-peak amplitude. The RMS amplitude will, for example, assign small-to-modest amplitudes to short-duration spurious signals that consist of a single cycle or oscillation, since the neighboring uncorrelated data points will likely figure in the calculation and reduce the measure of the amplitude accordingly. The analytic trace amplitude is the formal definition of instantaneous wave amplitude, and its features may be useful. Assume $\mathbf{x}(t)$ is an infrasonic waveform and $\mathbf{H}(t)$ its Hilbert Transform (e.g., Bracewell, 1986). The analytic trace $\mathbf{A}(t)$ is written simply as the complex time-series $\mathbf{A}(t) = \mathbf{x}(t) + i\mathbf{H}(t)$, where $i$ is the unit complex number. The following identifications are then made:

a) instantaneous amplitude: $$A(t) = \sqrt{\mathbf{x}^2(t) + \mathbf{H}^2(t)} \quad (1)$$

b) instantaneous phase: $$\theta(t) = \arctan\left(\frac{\mathbf{H}(t)}{\mathbf{x}(t)}\right) \quad (2)$$

c) instantaneous frequency: $$f(t) = \partial\theta(t)/\partial t \quad (3)$$

Although the peak-to-peak amplitude is the preferred amplitude measure that is recorded in the amplitude table and thus will appear in the Bulletin, the two alternative amplitude measures are recorded for internal IDC use. The analytic trace amplitude, for example, may find application in a future microbarom classifier following Olson's microbarom analysis (Olson et al., 2000), whereas the RMS amplitude may find application in an infrasound detection 'measure-of-significance' value.

In a practical scheme, a band-pass filtered beam aligned with slowness appropriate for a given **arid** is formed, and each amplitude type determined. Two band-pass filters are typically used, viz: a Finite Impulse Response (FIR) filter, where the high- and low-corner frequencies are determined by the signal content as revealed by the pmcc detection algorithm; and a FIR filter in which the high and low corner frequencies are user specifiable.

As an example, amplitudes have been determined for an acoustic signal recorded at station IS26, located in Germany, from the Buncefield Oil Depot explosion in Hertfordshire, UK, in December 2005. The band-pass filtered data are shown in Figure 1.

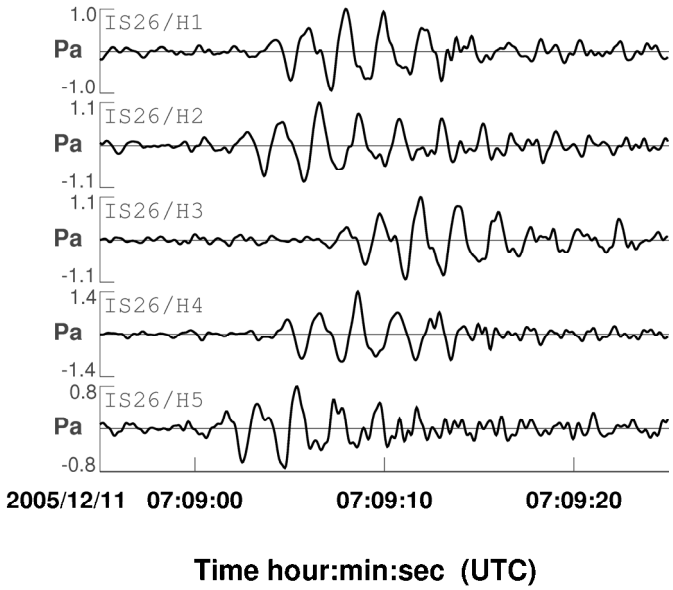


**Figure 1: Acoustic waveform recorded at station IS26, Germany from the December 2005 Buncefield oil depot explosion in Hertfordshire UK. Data have been band-pass filtered from 0.5 to 2.0 Hz.**

Figure 2 shows the time-aligned beam channel with the analytic trace (red) and a trace derived from the RMS amplitude channel (blue), assuming a 2 second sliding window, superimposed over the beam channel data.

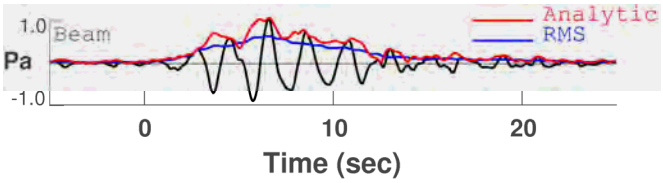


**Figure 2**: **Time aligned beam with analytic trace (red) and RMS Trace (blue) superimposed. The RMS amplitude trace was determined with a 2-second sliding window.**

For this signal, the peak-to-peak amplitude was found to be 1.90 Pa, analytic trace amplitude 1.04 Pa, and RMS amplitude 0.62 Pa. As one would expect, the analytic trace amplitude agrees exactly with the zero-to-peak amplitude at the maximum point of the signal. As can be seen from the figure, the averaging nature of the RMS amplitude may be useful in discarding less significant signals.

### Station Noise Characterization

Station ambient noise conditions are being represented by the PSD, which provides a measure of the differential power contained in the signal at each frequency. Implicit in the use of the PSD is that both the mean and autocorrelation of the sampled waveform are time independent, which is assumed to hold approximately true in general as the propagating acoustic signals are considered to be short-lived transitory phenomenon and will thus provide an only minor impact on the statistics.

PSDs are being determined for each station four times per day at hours 03:30, 09:30, 15:30, and 21:30 local station time. A one hour data interval is used in each case and, except for minor departures, the PSDs are being determined using the processing schema outlined in Bowman et al. (2005). In this scheme, the one-hour data interval is divided

into 21 three-minute intervals, each slightly overlapping the adjacent windows, and an average PSD determined. A Hanning-type window function is applied to each 3-minute interval to dampen spectral leakage and improve amplitude resolution.

Spectral information is recorded in a binary data file in two forms:

a. The base 10 logarithm of the power spectral data for each sensor for each station determined for each frequency picket in the sequence $\left\{\frac{n}{N}\Delta\right\}$; for $n = 0,\cdots,N/2$ where $N$ is the total number of sample points and $\Delta$ the sample rate. The sample rate is typically 20 samples-per-second, so with the 3,600 data samples in a 3-minute window, a PSD using 1800 frequency pickets is typically computed. As an example, the raw data for day 2007183 hour 21:30 on station IS22 (Port Laguerre, New Caledonia) is shown in Figure 3.

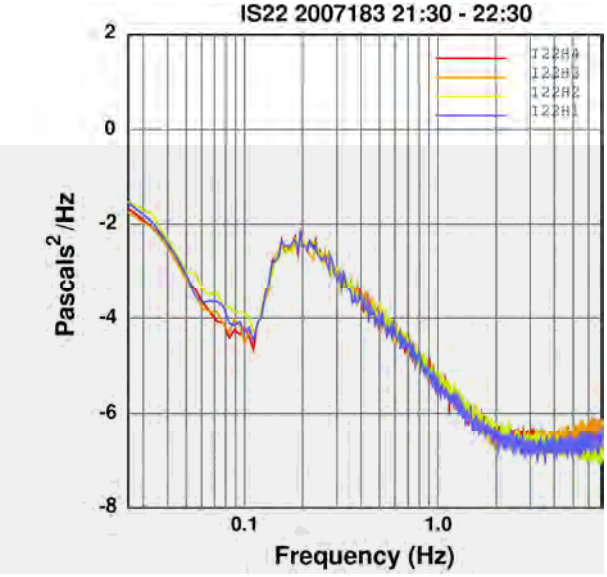


**Figure 3**: **Raw PSD data for station IS22 from 21:30 to 22:30 local time on day 2007183**

b. Monthly-averaged and smoothed logarithmic data for each station recorded at the frequency pickets $f_j = \log_{10}(\frac{\Delta}{N}) + \frac{1}{M}(\log_{10}(\frac{\Delta}{2}) - \log_{10}(\frac{\Delta}{N}))\left(j - \frac{1}{2}\right)$ for j = 1,…,M where M is typically 100. This choice of frequency picket facilitates linear abscissa on a log-log plot. The data are also smoothed with a 6th order 11-point Savitzky-Golay filter. Also recorded is the standard deviation for each data set. The mean and standard deviation data are updated each time new data become available. The monthly data for stations IS07 (Warramunga, Australia) and IS22 (Port Laguerre, New Caledonia) for July 2007 are shown in Figures 4 and 5, respectively.

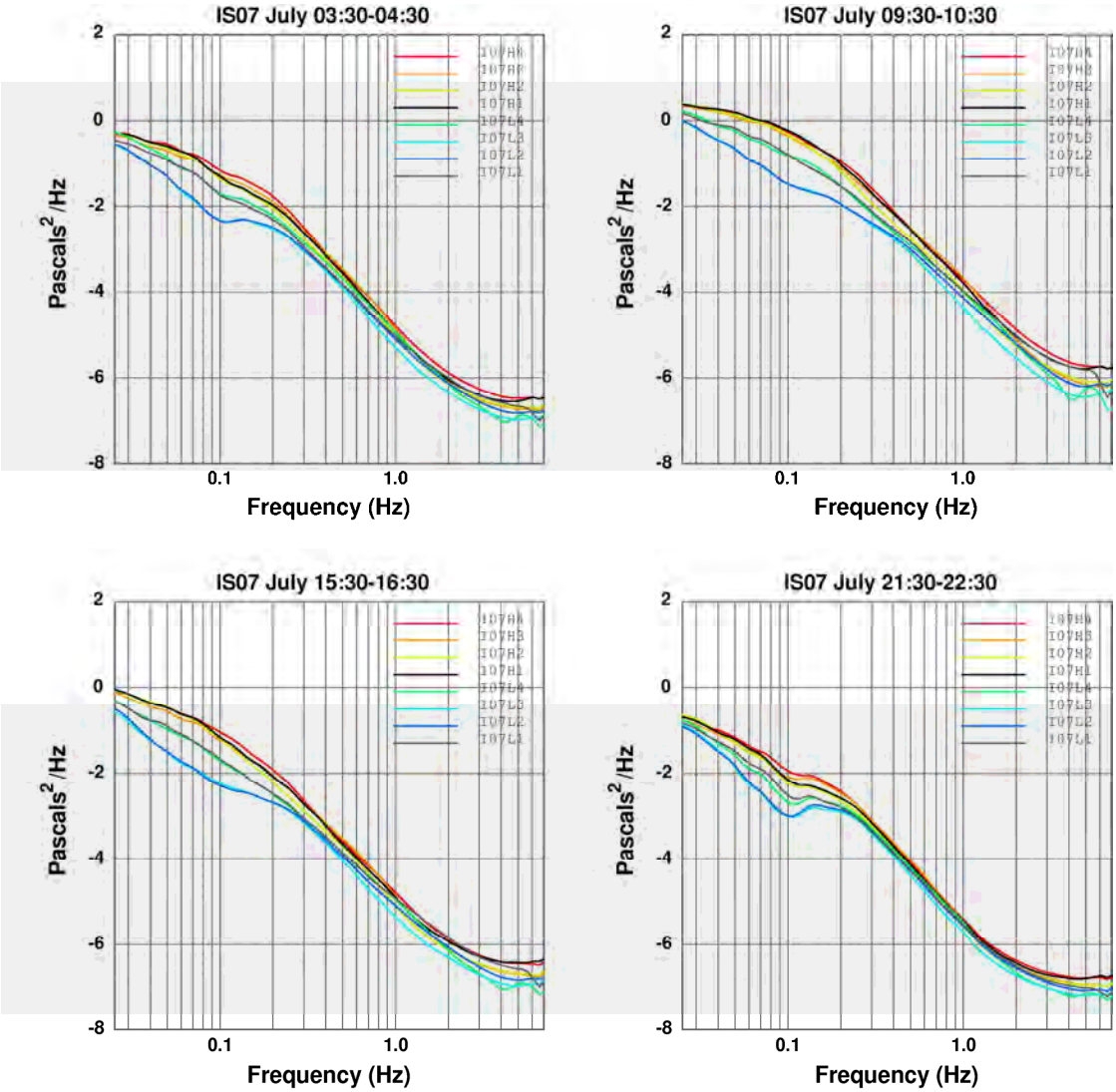


**Figure 4: The mean PSD data for station IS07 for the month of July 2007 taken at the four times: 03:30-04:30, 09:3-10:30, 15:30-16:30, and 21:30-22:30 local time. A 6$^{th}$-order, 11-point Savitzky-Golay filter has been used to smooth the data.**

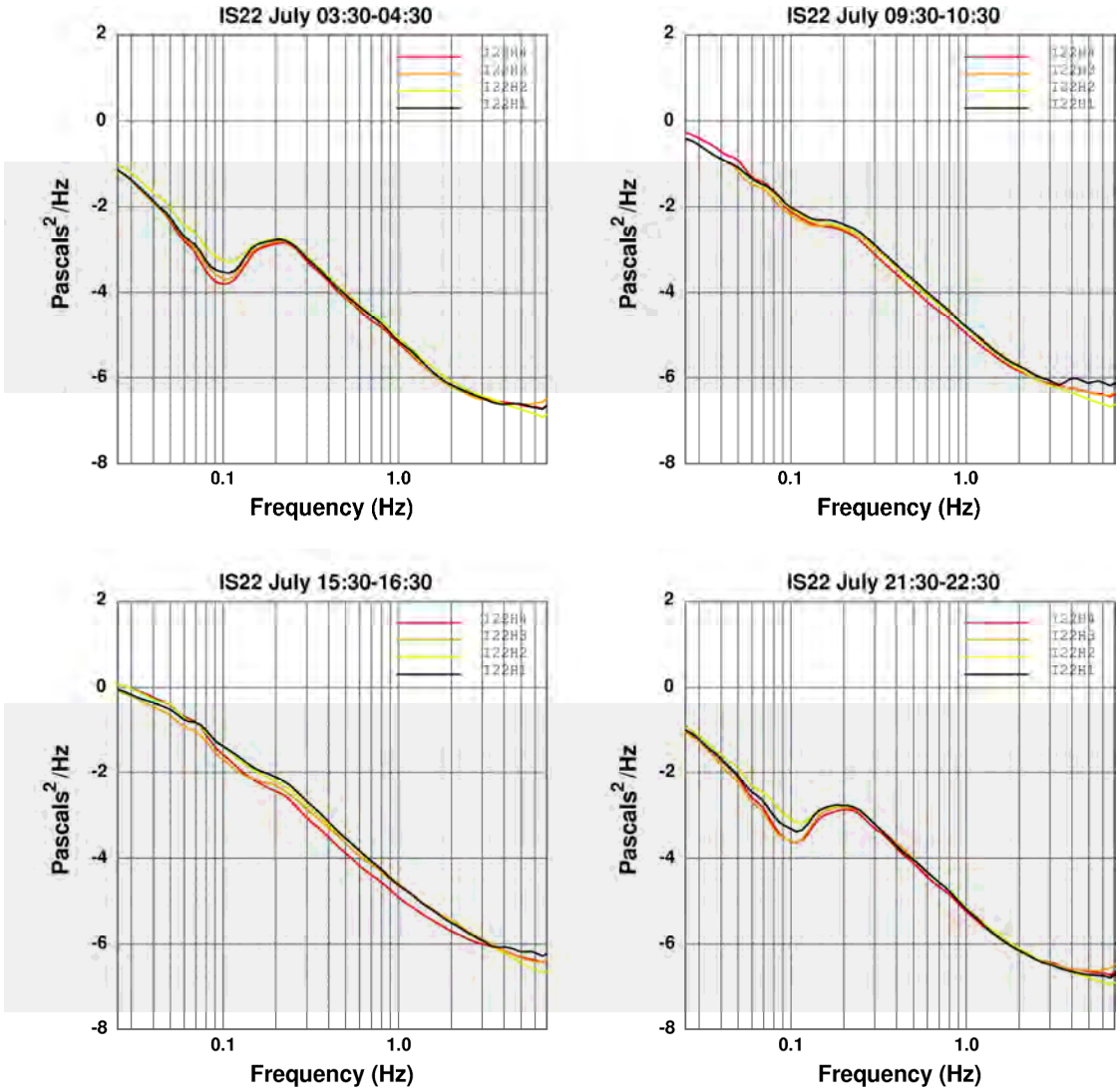


**Figure 5: The mean PSD data for station IS22 for the month of July 2007 taken at the four times: 03:30-04:30, 09:3-10:30, 15:30-16:30, and 21:30-22:30 local time. A 6th-order, 11-point Savitzky-Golay filter has been used to smooth the data.**

To provide an indication of the daily variation, spectral data for a single sensor, together with the mean $\mu$ and standard deviation, are presented for station IS07 and IS22 for the month of July 2007 in Figures 6 and 7, respectively.

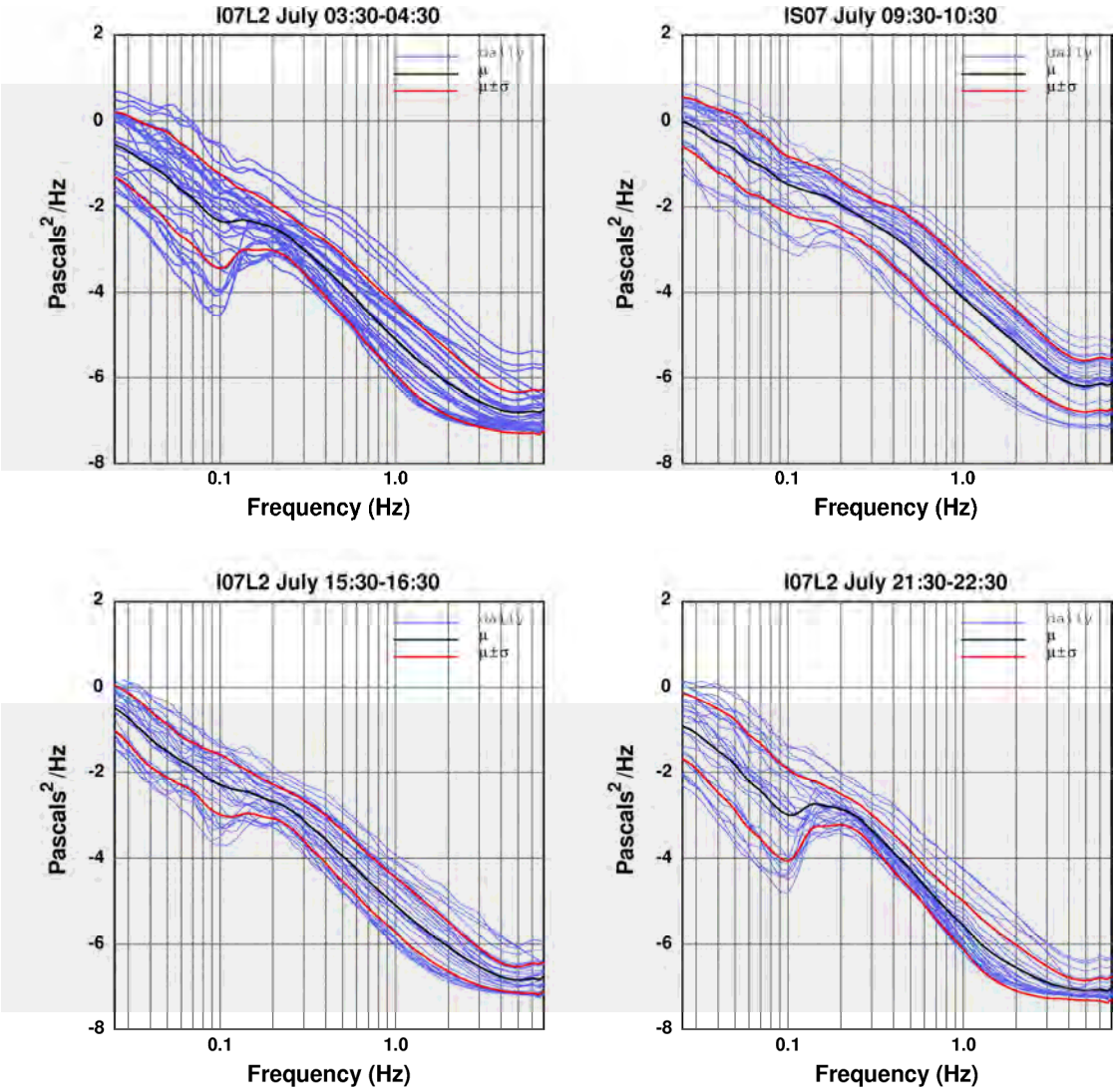


**Figure 6**: **Daily spectral data , the mean $\mu$ , and mean ± one-standard deviation $\sigma$ for sensor I07L2 for all days in July 2007 for the hours 03:30-04:30, 09:30-10:30, 15:30-16:30, and 21:30-22:30 local time.**

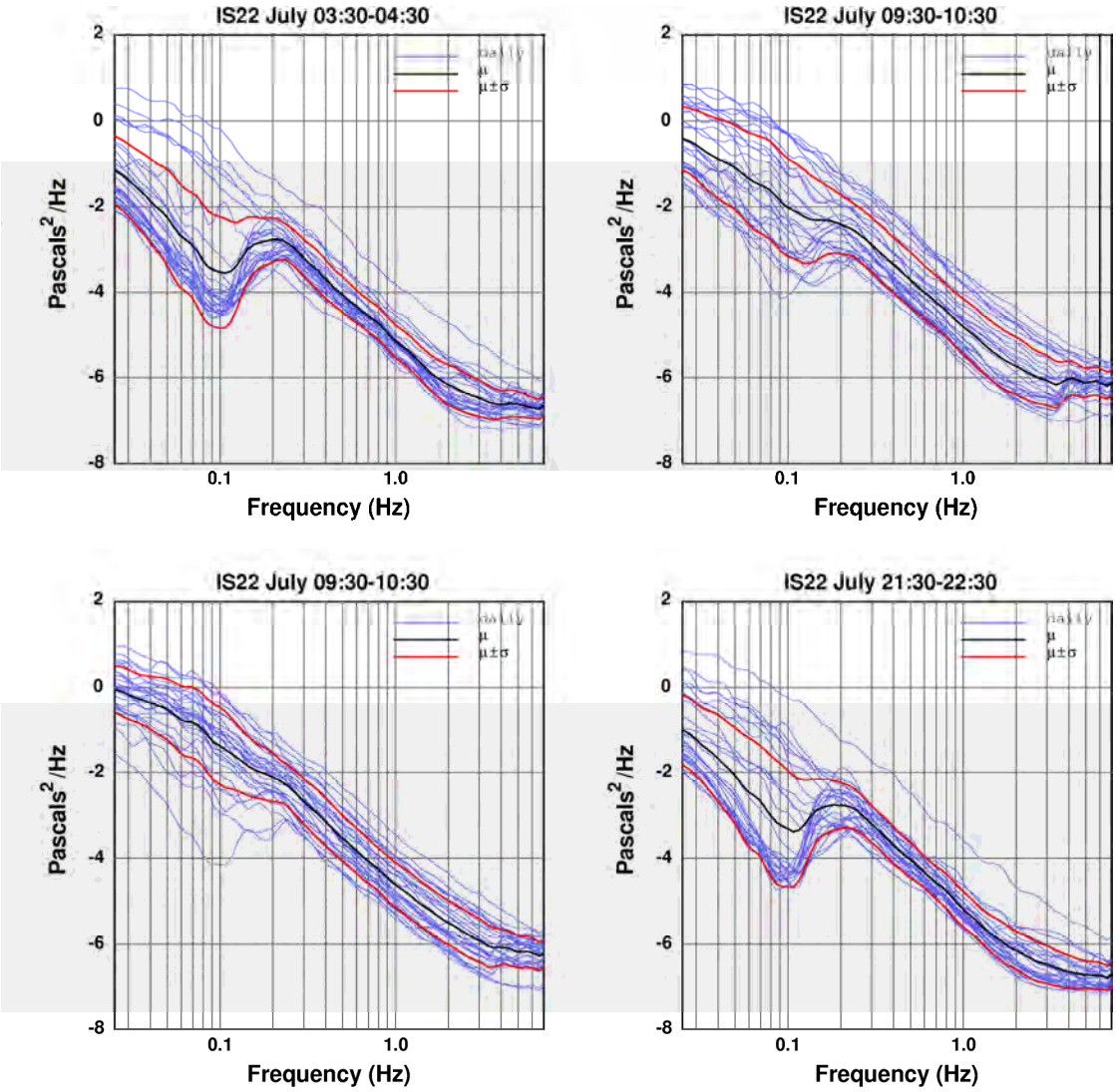


**Figure 7**: **Daily spectral data, the mean $\mu$, and mean ± one-standard deviation $\sigma$ for sensor I22H1 for all days in July 2007 for the hours 03:30-04:30, 09:30-10:30, 15:30-16:30, and 21:30-22:30 local time.**

The diurnal differences are quite obvious from these figures. Day-time convection has increased wind-noise to such a level that the microbarom peak is generally not visible during the day. Interestingly, the night-time hours seem to exhibit most variation, but neither station exhibits a situation in which no microbaroms are present, even if it is being masked by noise due to turbulence.

Spectral data are being written to binary files with the intention that users with access to IDC external data products be able to access them using conventional methods.

## CONCLUSIONS AND RECOMMENDATIONS

Amplitude and spectral information of the sort considered here provides a welcome addition to the IDC Bulletin, additionally providing external users of IDC data products vital knowledge concerning network performance.

## REFERENCES

Blanc, E., J. C, Millies-Lacroix, L. P. Issartel, and S. Perez (1997). Detection of nuclear explosions in the atmosphere. *Chocs* 17: 23–24.

Bowman, J. R., G. E., Baker, and M. Bahavar (2005). Ambient infrasound noise, *Geoph. Res. Lett* 32: L09803.

Bracewell, R. N (1986). The Fourier Transform and its applications, 2nd Edition. *McGraw-Hill, Reading, N.Y.*

Olson, J. V., C. R. Wilson, and C. A. L. Szuberla (2000). On the analysis of the spatial and temporal structure of natural infrasound signals in *Proceedings of the 22nd Annual Seismic Research Symposium*, New Orleans, LA.

Whitaker, R. W. (1995). Infrasonic Monitoring, in *Proceedings of the 17th Annual Seismic Research Symposium*, Scottsdale, AZ, September 12–15, pp. 997–1000.

# FINITE DIFFERENCE TIME DOMAIN MODELING OF INFRASOUND PROPAGATION: APPLICATION TO SHADOW ZONE ARRIVALS AND REGIONAL PROPAGATION

Catherine de Groot-Hedlin

University of California at San Diego

Sponsored by Army Space and Missile Defense Command

Contract No. W9113M-06-1-0003
Proposal No. BAA06-95

## ABSTRACT

The finite difference (FD) method yields solutions to discretized versions of the full acoustic wave equation for arbitrarily complex media. The method is reliable at all angles of propagation, including backscatter. This offers an advantage over other standard propagation methods in wide use, as it allows for accurate computation of acoustic energy levels in the case where significant scattering can occur near the source, such as may happen for an explosion near the surface, or underground. It also allows for the investigation of the penetration of infrasound energy into classical shadow zones, where ray theory predicts the upward refraction of sound. This fits in with nuclear monitoring goals, in that it allows for an improved understanding of the generation and propagation of infrasound energy from arbitrary sources, including underground and near-surface explosions.

The effects of 1) wind, 2) attenuation, and 3) gravity on infrasound propagation are examined separately, using finite-difference time-domain methods. The method is applied in 2-D Cartesian coordinates. The method, including the effects of wind, is applied to realistic problems in infrasound propagation, including the penetration of infrasound energy into “shadow” zones, as defined by ray theory. The effects of diffraction and topography are examined for sources near the surface. It is shown that the FD approach can be used to solve for sound intensities in complex models that may include high material contrasts and arbitrary topography.

## OBJECTIVES

A finite difference time domain (FDTD) method is sought for the numerically propagation of infrasound energy through realistic atmosphere properties, including variable winds, sound speeds, and density variations, and the interaction of the sound field with topography. The FDTD method yields the solution to a discretized version of the full acoustic wave equation for arbitrarily complex media, and can accurately handle propagation reliable at all angles of propagation, including backscatter. This offers an advantage over other standard propagation methods in wide use, as it allows for an accurate computation in cases where significant scattering can occur near the source, such as may happen for an explosion near the surface or underground. The effects of wind or gravity on infrasound propagation may also be incorporated into the infrasound propagation problem with relative ease using FD techniques. In this paper, a method to handle the inclusion of attenuation into the time-domain computations is investigated, as well as the effects of topography on infrasound.

The equation governing the effects of gravity, wind, and attenuation on the infrasound field are derived in this paper, and their effects on propagation through the atmosphere are demonstrated. The penetration of infrasound into a classical "shadow zone" is also demonstrated both for a model of a source above a flat surface with high impedance contrast, and also for the same source, above a rough surface with high impedance contrast. In this way, we examine the effects of topography on propagation of infrasound energy into a shadow zone.

## RESEARCH ACCOMPLISHED

Equations governing infrasound propagation through the atmosphere are derived here. The effects of gravity, wind, and atmospheric attenuation of the acoustic field are examined separately. Following that, the effects of topography on infrasound penetration into an acoustic shadow zone are shown. In each case, the methods are applied in 2-D Cartesian coordinates.

### *Linear acoustic propagation equations*

The equations governing propagation of sound in the atmosphere are
i) the conservation of momentum,

$$\rho \frac{D\vec{v}}{Dt} = -\nabla p + \vec{F}, \tag{1}$$

which relates the particle velocity, $\vec{v}$, to the total pressure, p, and density, ρ, and the external volume force per unit mass, $\vec{F}$;
ii) the conservation of mass,

$$\frac{D\rho}{Dt} = -\rho \nabla \bullet \vec{v}, \tag{2}$$

iii) and the equation of state,

$$\frac{Dp}{Dt} = c^2 \frac{D\rho}{Dt}, \tag{3}$$

where *c* is the total sound speed in the presence of acoustic perturbations. It's assumed in the equation above that infrasound propagation is isentropic, i.e., that entropy is constant. That is, it's assumed that attenuation is sufficiently small so that wave propagation dominates over diffusive propagation. This is a valid approximation for infrasound propagation within a realistic atmosphere.

The convective derivative (also known as the Lagrangian derivative) acting on a quantity G is defined as

$$\frac{DG}{Dt} = \frac{\partial G}{\partial t} + (\vec{v} \bullet \nabla)G, \tag{4}$$

where the derivative on the left represents the change of G with time in a frame moving with the fluid. The first term on the right side of Equation 4 represents the change in G at a point fixed in space. The second term, called the advective term, represents the change in G as the observer moves with the fluid at the velocity $\vec{v}$. For infrasound investigations, quantities are expressed in terms of a fixed point in space in order to compare computational results with observations made at stationary sensors.

Propagation of sound waves in the atmosphere introduces fluctuations in the pressure, density, and particle velocity values. The standard procedure in solving Eqs. 1 through 3 is to consider a perturbed solution of the form

$$p = p_O + p_S; \qquad \rho = \rho_O + \rho_S; \qquad \vec{v} = \vec{v}_O + \vec{v}_S, \qquad c^2 = c_o^2 + c_s^2; \tag{5}$$

where $p_o$, $\rho_o$, and $\vec{v}_O$ are the ambient values of pressure, density, and particle velocity in the absence of perturbations, and $p_s$, $\rho_s$, and $\vec{v}_S$ are perturbations caused by the passage of a sound wave. The pressure fluctuations cause slight fluctuations in the squared sound speed. Waveforms are derived by computing the pressure perturbations, $p_s$, as a function of time. Linear expressions for the particle velocity, $\vec{v}_S$, and pressure and density fluctuations, $p_s$ and $\rho_s$, are derived by retaining only first order terms in the pressure, velocity, and density. The zeroth order terms cancel because the ambient atmosphere is assumed to be in equilibrium.

***Linearized acoustic propagation, including gravitational effects***

In this sub-section, we consider solutions in a static medium, thus $\vec{v}_o$, denoting the wind velocity, is equal to zero. If the effects of gravity are included in the propagation equations, the external volume force per unit mass may be expressed as

$$\vec{F} = -(\rho_O + \rho_S)\vec{g} + \vec{f}, \tag{6}$$

where the gravity $\vec{g}$= [0,0,9.8m/s$^2$], and $\vec{f}$ represents all external forces other than gravity. Using Eqs. 5 and 6 in Eq. 1, and linearizing, yields

$$\rho_O \frac{\partial \vec{v}_S}{\partial t} = -\nabla p_S - \rho_S \vec{g} + \vec{f}. \tag{7}$$

under the assumption that there is no wind, and using the hydrostatic equation $\nabla p_O = -\rho_O \vec{g}$. Combining Eqs. 2 and 3 yields the following expression for pressure perturbations

$$\frac{\partial p_S}{\partial t} = \rho_O \vec{v}_S \bullet \vec{g} - \rho_O c_O^2 \nabla \bullet \vec{v}_S, \tag{8}$$

where the hydrostatic equation has again been used. Horizontal gradients in the ambient pressure and density, $p_o$ and $\rho_o$, are negligible in the horizontal direction. Equation 2 becomes

$$\frac{\partial \rho_S}{\partial t} + \vec{v}_S \bullet \nabla \rho_O = \frac{1}{c_O^2}\left[\frac{\partial p_S}{\partial t} + \vec{v}_S \bullet \nabla p_O\right]. \tag{9}$$

Combining the ideal gas law ($p_o = \rho_o RT$) with the hydrostatic equation, and the relation between sound speed and temperature ($c_o^2 = \gamma RT$ ) yields

$$\frac{d\rho_O}{dz} = -\frac{\gamma \rho_O g}{c_O^2} - \frac{2\rho_O}{c_O}\frac{dc}{dz}, \tag{10}$$

where $\gamma \approx 1.402$, $T$ is the temperature in degrees Kelvin and $R$ is the gas constant for dry air, $R = 287.04\ J\ kg^{-1}\ K^{-1}$. Using the hydrostatic equation for vertical pressure gradients and Eq. 10 for vertical density gradients, Eq. 9 can be expressed as

$$\frac{\partial \rho_S}{\partial t} = \frac{1}{c_O^2}\frac{\partial p_S}{\partial t} + \rho_O \vec{v}_S \bullet \left[\frac{(\gamma - 1)\vec{g}}{c_O^2} + \frac{2}{c_O}\nabla c_O\right]. \tag{11}$$

Equations 7, 8, and 11 are a complete set of equations, in a form amenable to FD time domain computations.

Note that Eq. 11 may also be expressed as (Gill, 1982)

$$\frac{\partial \rho_S}{\partial t} - \rho_O \vec{v}_S N^2 / \vec{g} = \frac{1}{c_O^2}\frac{\partial p_S}{\partial t}, \tag{12}$$

where the Brunt-Vaisala frequency N—or buoyancy frequency—is defined by

$$N^2 = g_z\left(\frac{(\gamma-1)g_z}{c_o^2}+\frac{2}{c_o}\nabla c_o\right). \tag{13}$$

The buoyancy frequency N is on the order of 1/300 Hz within the atmosphere. The equations suggest that the effect of buoyancy is negligible at the upper end of the infrasound range but becomes more significant with decreasing frequency. Results of computations are compared below for sources with peak frequencies of 0.2 Hz and 0.015 Hz, for $g_z = 0$ and $g_z = 9.8 m^2/s^2$. In each case the sound speeds are assumed to be uniform (i.e., an isothermal atmosphere) and exponentially decreasing density. The results confirm that gravitational effects are insignificant at higher frequency.

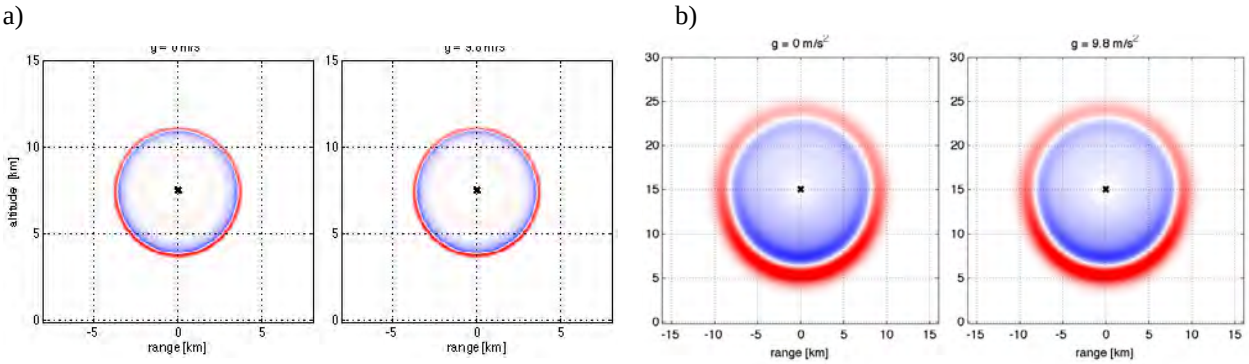


**Figure 1. Results shown above are for models with exponentially decreasing density. a) The source peak frequency is 0.2 Hz. There is less than 0.2% difference between the solution for g=0 and for g=9.8m²/s². B) The case for a source peak frequency of 0.015 Hz. There is less than 3.5% difference between the solution for g=0 and for g=9.8m²/s².**

***Linearized acoustic propagation, including wind and gravitational effects***

When wind is included, i.e., $\vec{v}_O \neq 0$, we use Eq. 4, the convective derivative to find

$$\rho_O\left(\frac{\partial \vec{v}_S}{\partial t}+\vec{v}_S\bullet\nabla\vec{v}_O+\vec{v}_O\bullet\nabla\vec{v}_S\right)+\rho_S\vec{v}_O\bullet\nabla\vec{v}_O=-\nabla p_S-\rho_S\vec{g}+\vec{f}, \tag{14}$$

for particle velocity. Re-arranging, and assuming that wind is invariant along path ($\vec{v}_O\bullet\nabla\vec{v}_O=0$, which is true for negligible turbulence) this becomes

$$\frac{\partial \vec{v}_S}{\partial t}=-\vec{v}_S\bullet\nabla\vec{v}_O-\vec{v}_O\bullet\nabla\vec{v}_S-\frac{1}{\rho_O}(\nabla p_S+\rho_S\vec{g}-\vec{f}), \tag{15}$$

*i.e.* wind shear is included in this formulation. The above result differs from Ostashev et.al. (2005) in that gravity is included and thus density perturbations must be computed.

The equation for pressure perturbations becomes

$$\frac{\partial p_S}{\partial t}+\vec{v}_S\bullet\nabla p_O+\vec{v}_O\bullet\nabla p_S=-\rho_O c_O^2\nabla\bullet\vec{v}_S-\rho_O c_S^2\nabla\bullet\vec{v}_O-\rho_S c_O^2\nabla\bullet\vec{v}_O \tag{16}$$

It's assumed that turbulence is insignificant (as in Ostashev et.al., 2005) so $\nabla\bullet\vec{v}_O$ is negligible. The hydrostatic equation is used to get the following form for pressure perturbations:

$$\frac{\partial p_S}{\partial t}=\rho_O\vec{v}_S\bullet\vec{g}-\vec{v}_O\bullet\nabla p_S-\rho_O c_O^2\nabla\bullet\vec{v}_S \tag{17}$$

The equation for density perturbations becomes

$$c_O^2\left[\frac{\partial \rho_S}{\partial t}+\vec{v}_S\bullet\nabla\rho_O+\vec{v}_O\bullet\nabla\rho_S\right]+c_S^2(\vec{v}_O\bullet\nabla\rho_O)=\frac{\partial p_S}{\partial t}+\vec{v}_S\bullet\nabla p_O+\vec{v}_O\bullet\nabla p_S \tag{18}$$

Winds are horizontal and the ambient density varies only with altitude, so $\vec{v}_O \bullet \nabla\rho_O = 0$. So, using the hydrostatic equation for $\nabla p_O$ and Equation 10 for the spatial density derivative $\nabla\rho_O$ and rearranging yields

$$\frac{\partial\rho_S}{\partial t} = \frac{1}{c_O^2}\left[\frac{\partial p_S}{\partial t} + \vec{v}_O \bullet \nabla p_S\right] + \rho_O\vec{v}_S \bullet \left[\frac{(\gamma-1)\vec{g}}{c_O^2} + \frac{2}{c_O}\nabla c_O\right] - \vec{v}_O \bullet \nabla\rho_S \qquad (19)$$

Equations 15, 17, and 19 are a complete set of equations for the propagation of infrasound energy, including gravity and wind, in a form amenable to FDTD implementation.

An example showing the sound field for realistic sound, wind, and density profiles (Figure 2a) is shown in Figure 2b, for a source at 100 km altitude, with a center frequency of 0.1 Hz. Densities and temperature profile data for a location near the I57US infrasound station were derived from the MSIS-90 atmospheric model, made available through *http://nssdc.gsfc.nasa.gov/space/ model/models/msis.html*. Wind data were derived from the Horizontal Wind Model (HWM) 1993 program (Hedin et.al., 1996). The results shown in Figure 3 are for the pressure field at 108 sec after the "explosion." As indicated, the pressure field is asymmetric due to the effects of wind, although the Mach numbers for this example are less than M=0.15 at all altitudes. The pressure field is shown in the panel at left, the pressure field normalized by $\rho_o^{-1/2}$ is shown in the panel at right. As indicated, the scaled pressure field is reasonably uniform with this scaling.

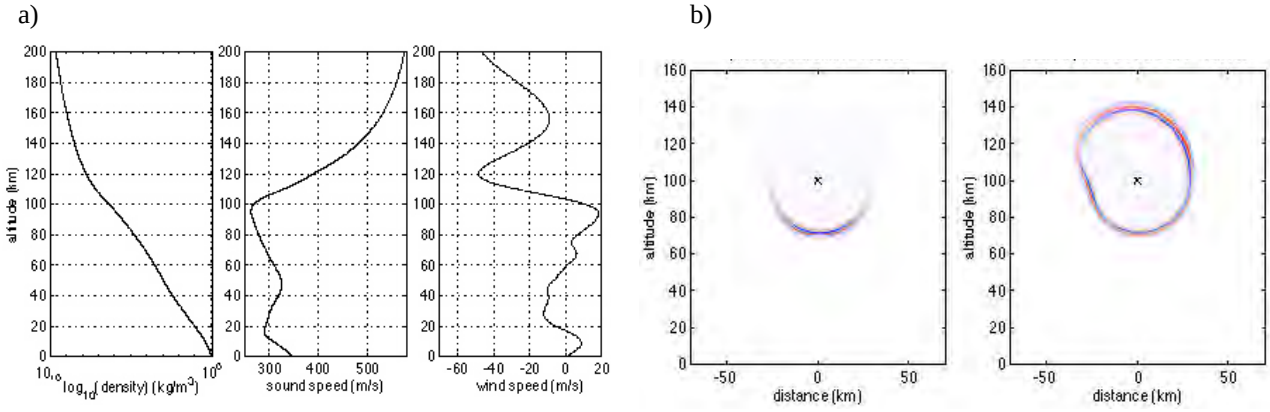


**Figure 2. a) Profiles for atmospheric density, sound speed, and wind speed. b) Pressure field (left) and the pressure field scaled by $\rho_o^{-1/2}$ (right) for a source with center frequency at 0.1 Hz and at an altitude of 100 km, for medium properties, as shown in Figure 2a.**

***Linearized acoustic propagation, including attenuation, wind and gravitational effects***

It has been shown that atmospheric attenuation is approximately proportional to the square of frequency (Sutherland and Bass, 2004; de Groot-Hedlin, 2008a). It can be shown (Batchelor, 1967), that the effects of atmospheric attenuation can be included by adding two terms to the equation for conservation of momentum: $\mu(\nabla^2\vec{v}_S + \frac{1}{3}\nabla(\nabla \bullet \vec{v}_S))$, where $\nabla^2\vec{v}_S$ is a vector with components $\nabla^2\vec{v}_s = [\nabla^2\vec{v}_{s,x}, \nabla^2\vec{v}_{s,y}, \nabla^2\vec{v}_{s,z}]$, and $\xi\vec{v}_S$. As shown in de Groot-Hedlin (2008a), the first term yields an amplitude decrease proportional to the square of frequency and the second is a constant as a function of frequency. Thus, the equation for the particle velocity becomes

$$\rho_O(\frac{\partial\vec{v}_S}{\partial t} + \vec{v}_S \bullet \nabla\vec{v}_O + \vec{v}_O \bullet \nabla\vec{v}_S) + \rho_S\vec{v}_O \bullet \nabla\vec{v}_O = -\nabla p_S - \rho_S\vec{g} + \mu(\nabla^2\vec{v}_S + \frac{1}{3}\nabla(\nabla \bullet \vec{v}_S)) + \xi\vec{v}_S + \vec{f} \quad . (20)$$

Equations 20, 17, and 19 are a complete set of equations for propagation of infrasound energy, including attenuation, gravity, and wind, in a form amenable to FDTD implementation.

An example comparing infrasound propagation with and without attenuation through a model with constant sound speed and exponentially decreasing density (i.e., an isothermal atmosphere) is shown in Figure 3. Attenuation is

proportional to the square of the frequency and is equivalent to that at an altitude of 110 km. Pressure waveforms are sampled at locations shown above and below the source and are compared in Figure 4, along with associated waveforms.

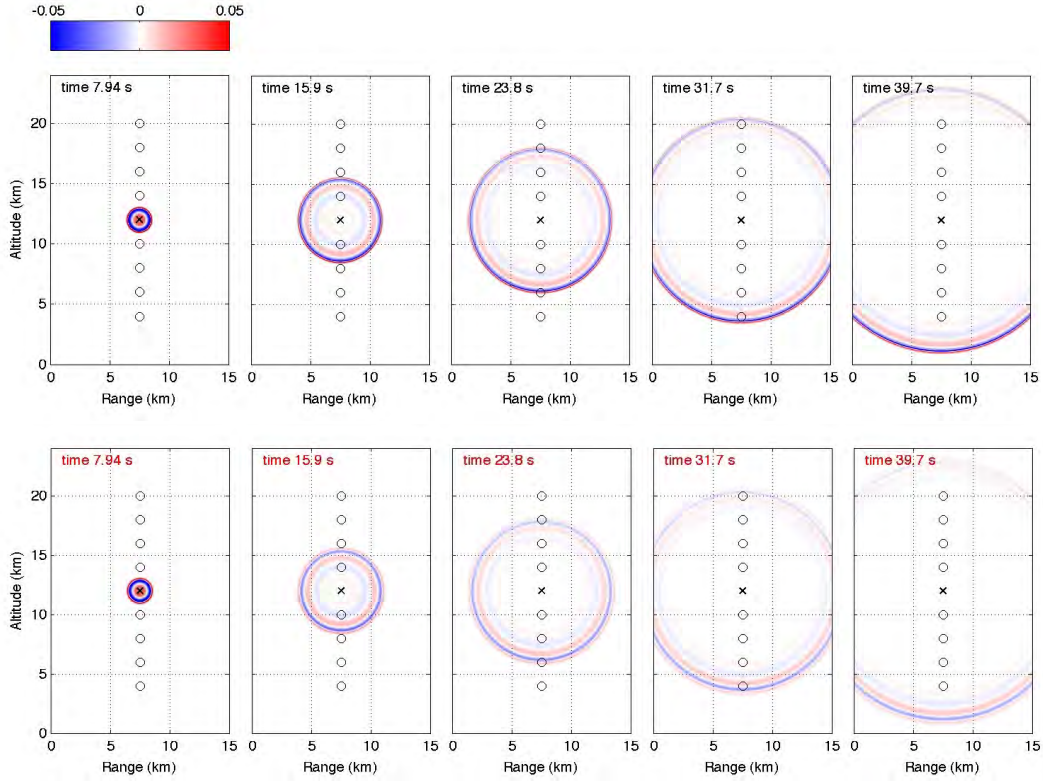


**Figure 3. (top) No attenuation. Waveforms are sampled at receiver locations shown by the circles. The source is indicated by an x. (bottom) same, but with attenuation equivalent to that at an altitude of 110 km.**

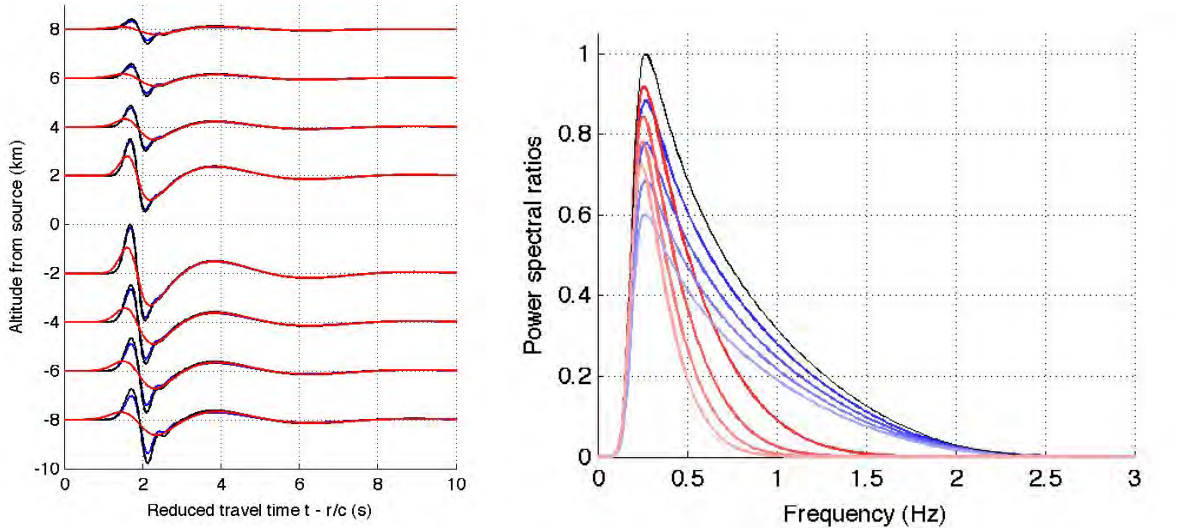


**Figure 4. (left) Waveforms are shown for no attenuation (black), constant attenuation (blue) and attenuation proportional to the square of the frequency (red, as shown in Figure 3b). (right) associated spectra, normalized with respect to peak power for waveforms propagated through non-attenuating media. Colored lines become lighter with increasing distance from the source.**

***Example of FDTD applied to penetration of infrasound into shadow zones***

Variations in wind velocities and temperature with altitude lead to the refraction of acoustic energy. During the day, temperatures and adiabatic sound speed typically decrease with altitude, causing sound to refract upward (Reynolds, 1873–1874). The effect of wind on refraction is often equal to or greater than that of temperature, so that sound is refracted downward in the direction of the wind and upward, away from the ground, in the opposite direction.

A first-order representation of acoustic "zones of silence" (ZoS) can be obtained using the high-frequency, ray-theory approximation as shown in Figure 5. Rays propagating through a moving atmosphere are computed using equations found in Garces (1998). Temperature decreases with altitude at a rate of 6.5$^{o}$C/km (the environmental lapse rate) and the wind profile was chosen to approximately offset the associated decrease in sound speed with altitude. Rays were launched at an altitude of 2 km at a variable interval angle such that the ray endpoints would fall at 0.5 km increments on the surface for a homogeneous velocity model (to correct for cylindrical spreading at the surface). Therefore, the distance between ray endpoints in Figure 5 (or the ray density per unit length) is a measure of the pressure amplitude, and shows the degree of focusing and defocusing due to velocity heterogeneity. Pressure amplitude is slightly greater to the far right (in the wind direction). To the left, pressure amplitude quickly decreases starting at x = -5 km and is effectively undetectable in the ZoS beginning at about x = -15 km. In nature, the first ZoS away from a near-surface source typically extends from several kilometers from the source to between 120 and 200 km, depending on stratospheric winds.

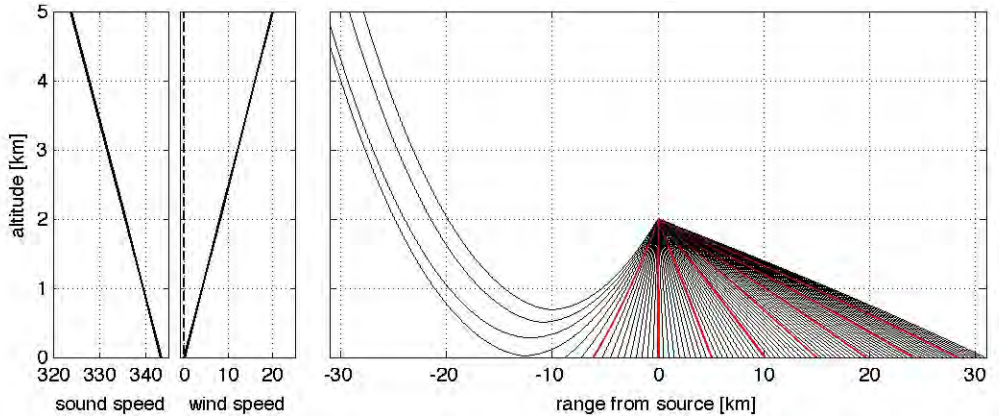


**Figure 5. A "zone of silence" (ZoS) illustrated by the high-frequency approximation of ray theory. The assumed adiabatic sound speed (m/s) and horizontal wind speed to the right (m/s) are shown in (a) and (b). The dashed line in (b) is out-of-plane wind speed (zero). Every tenth ray is red. Vertical exaggeration is 6.**

Ray theory relies on a high-frequency approximation to wave propagation. So its use assumes that sound speeds vary on a scale length much larger than the signal wavelength. This approximation starts to break down at infrasound frequencies under typical atmospheric conditions, where sound speed gradients of 4 m/s per km of altitude are common. A more complete description of infrasound propagation near the ground includes finite-wavelength effects like diffraction (Embleton, 1996), surface waves (Attenborough, 2002), scattering along rough topography, and also on temporal effects like turbulence and propagating gravity waves. These effects lead to a penetration of acoustic energy into the ZoS at amplitudes much greater than that predicted by ray theory (Embleton, 1996; Attenborough, 2002).

Zones of silence (ZoS) can be examined in better detail using numerical modeling algorithms that take dispersion, scattering, and other linear, full-wave effects into consideration. For instance, snapshots of the evolving pressure field are shown in Figure 6 from FD modeling using the same velocity model shown in Figure 5. The source (again at a 2-km altitude) consists of the superposition of a 0.9 Hz and a 0.2 Hz wavelet, multiplied by a cosine taper. Waveforms are shown at 5-km increments along the ground from -30 km to +30 km (Figure 7). The waveforms are scaled by the square root of the source-receiver distance to correct for spreading. Peak amplitudes are generally equal to the right, in agreement with the prediction from ray theory. However, the decrease in peak amplitude to the left is not as severe within the ZoS as predicted by ray theory. Lower frequencies are diffracted into the ZoS; the power spectra for each waveform show that 0.9 Hz energy decreases more rapidly than that around 0.2 Hz within the

ZoS. Therefore, ZoS predicted by ray theory may be completely penetrated by relatively lower-frequency infrasound, or exhibit frequency dependence with penetration distance. This is in line with observations: numerous studies have observed infrasound energy in classical shadow zones (e.g., Hedlin et al., 2008b; Ottemöller and Evers, 2008).

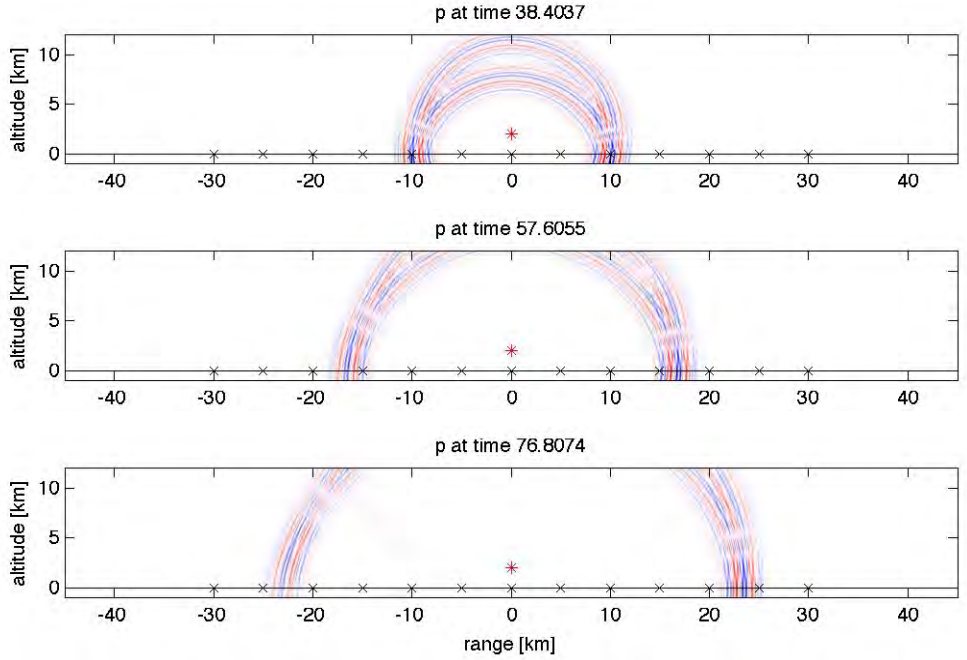


**Figure 6. Pressure snapshots at 38.4, 57.6 and 76.8 seconds, derived from FD numerical modeling. The wind and sound speeds are the same as for Figure 4. The source is at 2 km in altitude, marked by a red asterisk, and receiver locations are marked by an x.**

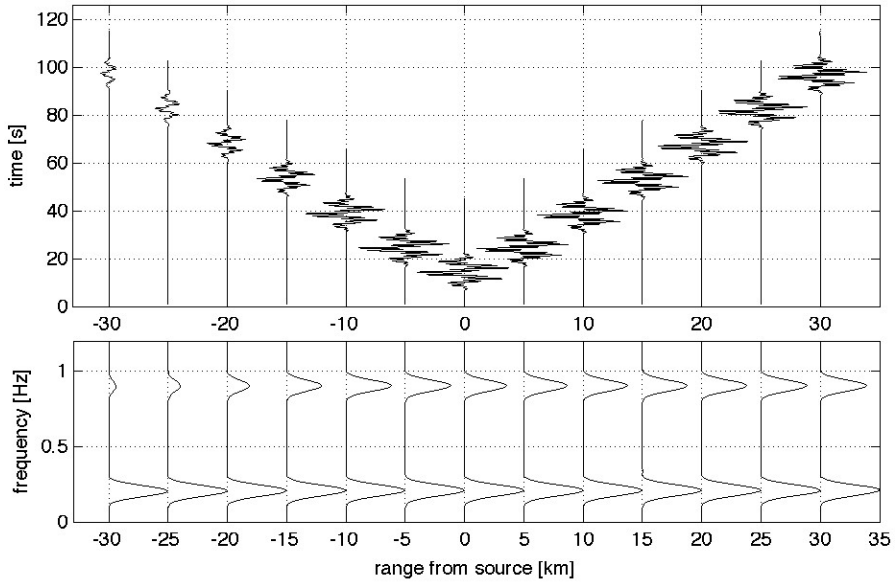


**Figure 7. (top) Waveforms predicted from FD modeling for a source near a flat surface. Waveforms are corrected for spreading at receivers located at 5-km intervals along the ground. (bottom) Power spectra are normalized by the level of 0.2 Hz energy.**

The FD algorithm was re-run, this time with variable topography to determine its effect on infrasound propagation into a shadow zone. The ground surface was modeled as a sine wave with a wavelength of 10 km, and a maximum height of 500 m. Receivers are located along the air/ground interface at an elevation of z=0 m, since the receivers all lie along the zero crossings of the sine wave. Several snapshots are shown in Figure 8 and the waveforms and spectra are shown in Figure 9. As shown, the introduction of topography complicates the response. The waveforms are amplified at some point (e.g., at -10 km and at +15 km) and diminished at others (-15 km and +10 km and +20 km). The higher frequencies are diminished more than the low frequencies. The results suggest that ZoS depends not only on atmospheric temperatures (hence, adiabatic sound speed) and temperatures, but is also a complicated function of frequency and topography. The addition of topography appears to further strip off high frequencies in comparison to the case for flat topography (Figures 6 and 7 above).

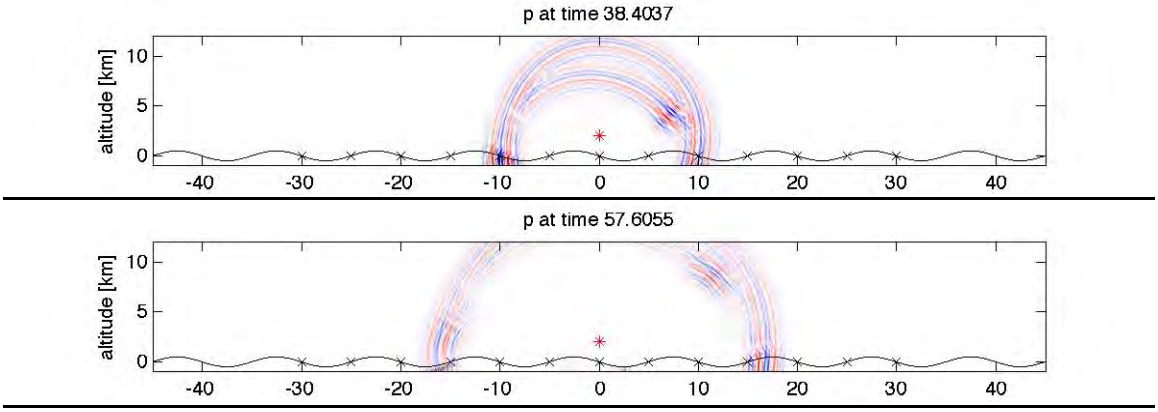


**Figure 8. Pressure snapshots at 38.4 and 57.6 seconds, derived from FD numerical modeling for the air/ground interface modeled as a sine wave. The wind and sound speeds are the same as for Figure 4. The source is at 2 km in altitude, marked by a red asterisk; receiver locations are marked by x. Receivers are at 0-km altitude, as in the previous example.**

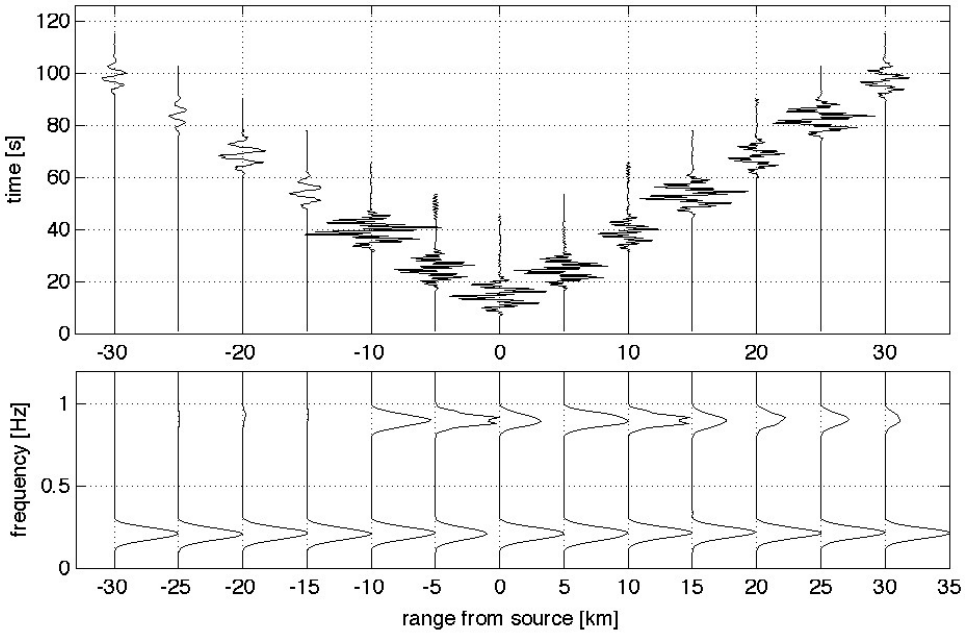


**Figure 9. (top) Waveforms predicted from FD modeling for a source near a sinusoidally varying surface. Waveforms are corrected for spreading at receivers spaced at 5-km intervals along the ground. (bottom) Power spectra are normalized by the level of 0.2 Hz energy.**

## CONCLUSIONS AND RECOMMENDATIONS

An algorithm has been developed to allow for the combined effects of wind and gravity on the infrasound field. The addition of attenuation into this code will be accomplished soon. The program is currently running slowly on a matlab platform. The plan is to convert it to fortran in the near future for considerable improvements in computational speed. After that, the code will be extended to three dimensions and tested against real data.

## REFERENCES

Attenborough, K. (2002). Sound propagation close to the ground, *Annu. Rev. Fluid Mech.* 34: 51–82.

Batchelor, G. K. (1967). *An introduction to fluid dynamics*, University Printing House, Cambridge.

de Groot-Hedlin, C. (2008a). Finite difference time domain synthesis of infrasound propagation through an absorbing atmosphere, *J. Acoust. Soc. Am*., [in press].

de Groot Hedlin, C. D., Hedlin, M. A. H., Walker, K. T., Drob, D. P., and Zumberge, M. A. (2008b). Study of infrasound propagation from the Shuttle Atlantis using a large seismic network, *J. Acoust. Soc. Am.* [in press].

Embleton, T. F. W. (1996). Tutorial on sound propagation outdoors, *J. Acoust. Soc. Am.* 100: 31–48.

Garcés, M. A., R.A. Hansen, and K. G. Lindquist (1998). Travel times for infrasonic waves propagating in a stratified atmosphere, *Geop. J. Int.* 135: 255–263.

Gill, A.E. (1982). *Atmosphere-Ocean Dynamics*, Academic Press, San Diego, CA.

Hedin, A. E., Fleming, E. L., Manson, A. H., Schmidlin, F. J., Avery, S. K., Clark, R. R., Franke, S. J., Fraser, G. J., Tsuda, T., Vial, F., and Vincent, R. A. (1996). Empirical wind model for the upper, middle and lower atmosphere, *J. Atmos. and Solar-Terr. Phys.* 58: 1441–1447.

Ostashev, V. E., D. K. Wilson, L. Liu, D. F. Aldridge, N. P. Symons, and D. Marlin (2005). Equations for finite-difference, time-domain simulation of sound propagation in moving inhomogeneous media and numerical implementation, *J. Acoust. Soc. Am.* 117: 503–517.

Ottemöller, L. and L. G. Evers (2008). Seismo-acoustic analysis of the Buncefiled oil depot explosion in the UK, 2005 December 11, *Geophys., J. Int.* 172: 1123–1134.

Reynolds, O. (1873-1874). On the refraction of sound by the atmosphere, *Proc. Roy. Soc. London* 22: 531–548.

Sutherland, L. C. and H. E. Bass (2004). Atmospheric absorption in the atmosphere up to 160 km, *J. Acoust. Soc. Am*. 115: 1012–1032.

# INVESTIGATION OF THE EFFECTS OF FINE-SCALE ATMOSPHERIC INHOMOGENEITIES ON INFRASOUND PROPAGATION

Robert G. Gibson[1], David E. Norris[1], and Douglas P. Drob[2]

BBN Technologies[1] and Naval Research Laboratory[2]

Sponsored by National Nuclear Security Administration

Contract Nos. DE-AC52-08NA28652[1] and DE-AI52-08NA28653[2].

## ABSTRACT

Recent infrasound observations and related research work in long-range sound propagation indicate that fine-scale atmospheric inhomogeneities contribute to refraction, scattering, and related phenomena that can result in anomalous infrasonic arrivals. Gravity waves, in particular, have been shown through physics-based modeling to be responsible for infrasonic arrivals, at regional ranges, that are not predicted by standard modeling techniques. Atmospheric turbulence can also cause scattering of infrasound that produces arrivals in shadow zones at local ranges from ground based sources.

We seek to improve understanding of the effects of gravity waves and other fine-scale atmospheric inhomogeneities, such as Kelvin-Helmholtz turbulent instability, on infrasound propagation. The approach is to build on recent advances in specifying the lower and middle atmosphere, state-of-the-art infrasound propagation calculation techniques, and existing stochastic models of gravity waves and turbulence. Atmospheric specification techniques are being developed that incorporate realistic models of gravity waves that are self-consistent with the background flow field and that include effects of altitude, latitude, longitude, and time-evolution over relevant scales.

The research effort includes systematic evaluation of the relevant atmospheric phenomena, improved atmospheric specification, advancement of the state-of-the art of modeling the interactions between fine-scale atmospheric inhomogeneities and infrasound, and model validation studies using ground truth datasets, focusing on local and regional ranges. Anticipated results of the work include new modeling tools to improve capability to predict infrasound arrivals and features relevant to phase classification at local and regional ranges.

## OBJECTIVES

The objective of this research effort is to improve understanding of the effects of gravity waves and other fine-scale atmospheric inhomogeneities on infrasound propagation. The improved understanding of the relevant atmospheric and infrasonic physics will result in enhanced capabilities for modeling infrasound features and waveforms.

It is evident that existing propagation modeling, coupled with state-of-the-art atmospheric characterizations, fails to adequately predict infrasonic arrivals in all circumstances. In particular, there have been numerous events for which infrasound arrivals are observed by sensors in regions that are predicted by standard modeling techniques to be in shadow zones. (e.g., Bhattacharyya et al., 2003; Kulichkov, 2004; Norris et al., 2006; Mutschlecner and Whitaker, 2006; Norris, 2006) This issue is relevant over both local and regional ranges.

Recent scientific work in gravity waves, atmospheric turbulence, long-range acoustic propagation, and infrasound has indicated that fine-scale atmospheric inhomogeneities contribute to refraction, scattering and related effects that result in unexpected infrasonic arrivals. Investigators use terms such as “leaky ducts” to explain infrasound propagation effects that are not fully understood scientifically. We endeavor to address this issue through systematic evaluation of the relevant atmospheric phenomena, advancement of the state of the art of modeling the interactions between fine-scale atmospheric inhomogeneities and infrasound, improved atmospheric specification, and model validation.

Specifically, the objectives are as follows:

- Review recent scientific progress in the understanding of gravity waves, their temporal and spatial variability, and their statistics, in order to develop an improved model of the characteristics of gravity waves that are relevant to infrasound propagation.
- Develop atmospheric specification techniques that incorporate realistic models of gravity waves in a manner that maintains self-consistency with the background flow field and that includes effects of latitude, longitude, and time-evolution over relevant scales.
- Exercise the improved gravity wave models with infrasound propagation models. Examine variability of infrasound predictions over a statistical ensemble of gravity wave realizations. Perform sensitivity studies to establish the effects of key atmospheric model variables on infrasound prediction.
- Improve understanding of additional classes of fine-scale atmospheric inhomogeneity, such as Kelvin-Helmholtz turbulence instability, and their effects in order to improve modeling of infrasound propagation at local ranges.
- Perform model validation studies using ground truth datasets, focusing on local and regional ranges.

In order to advance the state of the art for high-fidelity infrasound predictions in the presence of fine-scale inhomogeneities, it is necessary to develop propagation models and atmospheric characterizations that capture more of the fundamental physics that affect infrasound. This research effort primarily addresses improved atmospheric specifications that incorporate additional physical effects and the coupling of these specifications with physics-based propagation models. The resulting atmospheric characterizations will include an improved spectral gravity wave model assimilated with the background winds and temperature.

Propagation modeling will address the variability in the path of energy in the atmosphere by exercising models through multiple realizations of the environment. The fine-scale structure examined will include both atmospheric gravity waves and turbulence-driven inhomogeneities such as Kelvin-Helmholtz instability. Because atmospheric fine-scale structure is inherently turbulent, there is no deterministic model for the scalar and vector atmospheric fields associated with the turbulence; instead turbulence can be characterized by modeling the energy distribution across spatial scales using spectral formulations. These spectral models can then be used to generate representative realizations of variable fields. They also can be used directly in formulations that quantify their effect on scattering and related propagation phenomena.

The effort is anticipated to increase understanding of the regional and local propagation of infrasound through the dynamic atmosphere and also to improve the capability to predict infrasound arrivals and features relevant to phase classification. Research results are anticipated to include spectral-based atmospheric variability specifications; numerical modeling subroutines that enable improved propagation modeling via incorporation of effects of gravity waves and other fine-scale atmospheric structure phenomena; and a summary of model/data comparison results.

## RESEARCH ACCOMPLISHED

### Atmospheric Specification

The atmospheric structure responsible for the propagation of infrasound can change rapidly. Fine-scale atmospheric structures can be responsible for infrasonic refraction, advection, and scattering. Through recent research efforts, BBN Technologies (BBN) and the Naval Research Laboratory (NRL) have contributed to the current state of the art of infrasound modeling by developing and integrating propagation models and high-fidelity atmospheric specifications.

Global climatological models have largely been replaced in current infrasound modeling practice by the NRL Ground to Space (G2S) model of Drob et al. (2003, 2004), which was developed to provide background atmospheric information for the Nuclear Explosion Monitoring Research and Development program. The G2S data processing system combines operational numerical weather prediction (NWP) specifications with the upper atmospheric empirical models, NRLMSISE-00 and HWM-93 (Picone et al., 2002; Hedin et al., 1996). The near-real-time system incorporates 1ºx1º and 1ºx1.25º resolution global NWP input fields to the nearest 6-hour interval in the lower atmosphere.

Through a collaborative project involving NRL and BBN, the G2S system has recently been upgraded to include operational mesoscale (regional) NWP analysis products (with ~20 km horizontal resolution) in order to improve the temporal, horizontal, and vertical resolution in the 0 to 35 km region (Gibson et al., 2006). Regional atmospheric specifications from national and DoD weather centers have a high spatiotemporal resolution and accuracy compared to comprehensive global specifications. This is achieved by focusing additional efforts on the meteorological observations and atmospheric physics specific to a given geographic region. G2S-Mesoscale specifications also provide extra information at the surface by utilizing a terrain-following coordinate system, including high-resolution topography, and additional atmospheric boundary layer effects. In the current implementation of the G2S-Mesoscale model, the specification has 96 vertical levels, with the majority of levels in the first 25 km. These specifications are then interpolated to a regularly spaced latitude and longitude grid at 0.125° intervals.

However, these specifications are unable to resolve all fine-scale stochastic phenomena, e.g., atmospheric irregularities smaller than the model resolution, fine-scale structures above 35 km, and gravity wave fluctuations that cannot be deterministically measured or internally generated by the model. Fine-scale atmospheric structure not characterized by near-real-time atmospheric models such as G2S has been identified as a likely source of refraction and scattering effects that may play a significant role in infrasound propagation. In particular, gravity waves are of interest because their spatial scales are of the same order as infrasonic wavelengths.

### Propagation Modeling

The atmospheric specifications described above and a suite of infrasound propagation models (including 3-D ray-tracing, parabolic equation (PE), time-domain parabolic equation (TDPE), and normal modes) are currently integrated into the tool kit InfraMAP (Gibson and Norris, 2002; Norris and Gibson, 2004). InfraMAP (*Infrasonic Modeling of Atmospheric Propagation*) has been developed by BBN for use in the study of infrasound propagation and monitoring. InfraMAP can be applied to predict attenuation, travel times, bearings, amplitudes, and waveforms for infrasonic events. It also provides the ability to define a local network of stations and compute event localizations and associated error ellipses from station measurements and propagation predictions. The most recent version of InfraMAP includes TDPE waveform prediction capabilities based on either the Pierce blast wave or any user-defined waveform (Norris et al., 2005). The propagation models in InfraMAP have been used for a wide range of infrasound event analyses and validation studies.

Acoustic propagation through various types of inhomogeneous media have been studied (e.g., Ostashev, 1997), but fundamental issues have not been thoroughly investigated or validated for infrasound. Propagation through turbulence in the ocean and atmosphere has been treated using phase screen methods, which are computationally efficient but do not incorporate all of the relevant physics. The significance of the background internal wave spectrum in ocean acoustics has been studied and is well understood (e.g., Colosi, 2006). Much progress has been made in understanding propagation through locally homogeneous and isotropic turbulence in the atmosphere, but many problems still remain related to effects of turbulence intermittency and mesoscale anisotropic coherent

structures (Kallistratova, 2002). Understanding infrasound propagation through atmospheric internal gravity waves is an emerging scientific topic, as discussed below.

**Modeling Variability due to Gravity Waves**

Atmospheric properties vary in both space and time. Coherent spatial variability is observed at length scales from meters to thousands of kilometers, and temporal variability occurs over diurnal and seasonal time scales. The variability in wind and temperature makes modeling infrasound propagation difficult. Since the environment is dynamic and cannot be measured over the entire region through which the infrasonic signals propagate, stochastic modeling methods are necessary to account fully for the environment's influence on propagation.

The dominant source of variability affecting infrasonic propagation (beyond the synoptic-scale meteorology) is believed to be gravity waves, because their spatial scales are of the same order as infrasonic wavelengths. Gravity waves result from oscillations of air parcels displaced by buoyancy and restored by gravity. The oscillations have time scales ranging from minutes to tens of hours. Vertical length scales of gravity waves are in the range of 0.1 to 15 km, and horizontal scales can span from 10 to 1000 km. The multiscale nature of gravity waves presents a challenge to quantification of their properties. Owing to the important influences of gravity waves on the atmosphere's general circulation, vertical structure, and spatiotemporal variability, gravity wave dynamics is a significant atmospheric science research topic area. Recent research progress includes a better understanding of gravity wave source characteristics, evolution with altitude due to changes in wind conditions, and atmospheric stability (e.g., Fritts and Alexander, 2003). The development of high-fidelity physically-based gravity wave parameterizations is an active research area.

InfraMAP includes a baseline environmental variability model for predicting infrasound deviations due to atmospheric effects that are not resolved by the existing atmospheric specifications. The most basic variability model in InfraMAP uses a power-law wind perturbation spectrum, and it provides realizations of wind perturbation profiles. This spectrum is applicable primarily for small-scale turbulence, even though atmospheric turbulence covers a wide spectrum of spatial scales. A significant body of research has been carried out to define the spectral character of gravity waves. The spectral model of Gardner (1995, 1993) was selected for integration into InfraMAP's environmental variability module. This model is based on scale-independent diffusive filtering theory. A source spectrum is defined near the ground. As the spectrum is propagated up in height, attenuation is modeled by introduction of diffusive damping. The key spectral properties are increase in energy with height; shift towards larger length scales with height; and attenuation of smaller length scales with height.

Wind perturbations due to gravity waves are modeled in the spectral domain (Norris and Gibson, 2002), and both height and range-dependent gravity wave dependencies are modeled. The spectral model is used to generate multiple realizations of the perturbed environment, which in turn are used to quantify the statistical variability of the propagation. For ray-tracing, a Monte Carlo simulation may be executed where multiple rays are traced through the sum of mean and perturbed profiles. This simulation can be used to estimate moments of travel-time and azimuthal deviation. Atmospheric variability models have also been integrated into PE and TDPE models. Model predictions can be made through atmospheric "snapshots" of the inhomogeneities. These predictions capture the effects of the atmospheric variability on waveform metrics, such as amplitude, travel time, duration, and spectral content.

The Gardner spectral model is evaluated at four discrete heights, as shown in Figure 1 (Norris and Gibson, 2002). These heights capture the dominant gravity wave variability from the troposphere up to the lower thermosphere. Gravity waves are not fully developed below the troposphere. In the thermosphere, diffusion increases dramatically and gravity waves are damped out. Predicted standard deviations of wind perturbations are listed in the figure alongside the spectral heights.

Fourier inversion using random phase is applied to the spectra to generate realizations of wind perturbation profiles. A wind perturbation profile is generated for each of the five spectra. A composite profile is then computed by shading each profile spatially with a Gaussian filter and then summing them together, where Gaussian filter half-power points are set to the midpoint between each of the spectral heights. To model range-dependent variability, a dominant horizontal length scale is defined, and Gaussian weighting functions are used to combine the wind perturbation profiles.

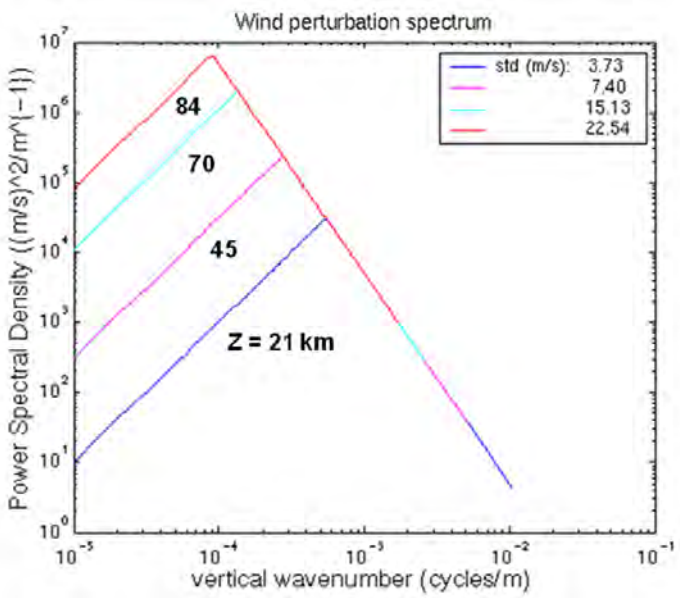


**Figure 1. Wind perturbation spectra from Gardner's gravity wave model evaluated at 5 discrete heights.**

Using our existing model, propagation variability studies have been conducted for various scenarios and event analyses. One finding has been that new propagation features can be seen with the introduction of range-dependence in the environmental variability models. Use of range-dependence in the gravity wave model more realistically models the horizontal scales associated with gravity wave observations. Modeling studies to date have indicated the presence of transient ducts that can significantly perturb travel times and signal velocities. These ducts form around localized minima in the sound speed, and their extent is determined by the horizontal correlation length of the gravity waves. Models of perturbed rays suggest that energy can get trapped within shallow transient ducts that form between gravity wave layers. One effect of this propagation mode is a reduction in the overall travel time and increase in signal velocity.

**Approaches to Improved Gravity Wave Modeling**

As reviewed above, existing approaches to modeling infrasound through gravity waves have relied on one-dimensional vertical wavenumber spectral models. This simplified model approach captures the vertical spatial scales in gravity waves as a function of height. We intend to extend this capability by accounting for additional dimensional variability, including horizontal wavenumber, which can be characterized using Gardner's spectral model. Given a spectral model, numerous parameters must be defined in order to apply it. For example, in the Gardner model, the parameters include peak spectral magnitude, dissipation rate, and dominant wavenumber. In work conducted to date, a single representative set of parameters was defined for use in all propagation scenarios. During this research effort, we will consider spatial and temporal dependencies in the parameter selection. For example, the peak energy parameter will be quantified from near-real-time atmospheric data for a given location or formulated based on latitude and Julian day. In addition, there exist more complex 2-D and 3-D spectral models that provide increased fidelity and insight into gravity wave structure (e.g., Ostashev et al., 2005). These models will also be considered for use during the research effort.

The baseline Gardner model does not account for the fact that gravity wave fields can vary dramatically with altitude, latitude, and season (e.g., Eckermann, 1995). This significant variability results from the corresponding changes in the background wind and static stability profiles. Thus there is a need to improve on the existing spectral approach used by Norris and Gibson (2002) to account for more realistic geophysical variability of the gravity wave spectra. Since the work of Gardner (1995, 1993), there have been a number of spectral gravity wave parameterization schemes that have sought to account for these additional effects. Development of these parameterizations is motivated by national efforts to improve general circulation modeling and numerical weather prediction of the lower and middle atmosphere.

The model of Gardner (1995, 1993) will be augmented by one that takes into account the refraction and reflection of a spectrum of gravity waves by arbitrary height-dependent winds and stratification. Models of this type have already been tested for other applications by the Middle Atmosphere Group at NRL. Wind shifting (refraction) of gravity wave spectral densities was parameterized and tested observationally by Eckermann (1995) based on a simple wind shifting model of Fritts and Lu (1993). That technique was extended by Warner and McIntyre (2001) to account more realistically for dissipation and spectral wave action conservation. A reasonable starting point for the current work, then, is the model of Warner and McIntyre (2001), which uses several idealizations that can be successively relaxed as the research results dictate.

The need to self-consistently account for gravity wave effects and variability by using as much observational data as possible is very important to both the understanding and the application of this problem. An over- or under-estimation of the gravity wave amplitudes and fluctuations in the background field will lead directly to an over- or under-estimation of scattered or refracted infrasound. Given extensive observational data, parameterizations of the refractive response of these energy spectra to background wind shear and stability changes can be extensively validated against data, as has been done in previous applications (e.g., Eckermann, 1995; Bacmeister et al., 1996). Extension of these studies to the current application and newer and more extensive observations of gravity wave spectral properties will be used to observationally constrain and validate our new spectral parameterizations and their response to environmental conditions specified by G2S. The result is anticipated to be realistic stochastic mesoscale variability at any given height and geophysical location.

All of the prerequisites for calculating the vertical and horizontal amplitudes of the random gravity wave perturbations (U, V, T, P, $\rho$) are provided by the available G2S specifications. We intend to develop and test subroutines needed to generate ensembles of random gravity wave perturbation fields that are dynamically self-consistent (to first order) with corresponding G2S atmospheric specifications. We are also undertaking development of subroutines that provide the stochastic gravity wave perturbation fields (u',v', t', p', and $\rho$') as a function of z, x, y and t given the corresponding G2S background atmospheric fields (u, v, t, P and $\rho$) over the same spatial domain z, x, y. These routines will account for the important seasonal, latitude, longitude dependence of the various auxiliary model parameters, such as the gravity wave spectrum lower cut off wave number (m*), which, together with the background atmospheric state, govern the nature and amplitude of the gravity wave spectrum.

This gravity wave fluctuation module, which we envision will ultimately be integrated into the G2S client software library, will provide a representation of the random gravity wave background field and its variability for infrasound propagation modeling, given current scientific understanding and modeling capabilities for gravity waves.

**Approaches to Modeling Turbulence Inhomogeneities**

There exists other fine-scale structure in the atmosphere, in addition to gravity waves, that has spatial scales on the same order as infrasound and which thus may influence infrasonic propagation. As part of this effort, we intend to explore the modeling of additional regions in the atmosphere where turbulent source mechanisms may affect propagating wavefronts. One source already identified is that generated by Kelvin-Helmholtz instabilities, or shear instabilities.

At altitudes of 10 to 15 km, a layer exists called the jet stream that is characterized by a stable, strong wind flow. The boundary between the jet stream and the more static fluid above it can become unstable. This instability results from the shear stresses between the two layers. The instability manifests itself through the generation of Kelvin-Helmholtz waves (Nappo, 2002). These waves are coherent perturbations of both scalar and vector fields in the boundary region. They start as rolling undulations and then evolve to a wave-like structure that eventually breaks down into vortices or billows. Kelvin-Helmholtz waves are often present within layers of moderate and severe clear air turbulence.

Because Kelvin-Helmholtz waves have very pronounced spatial features, spectral models do not capture the relevant structure that may affect infrasound. Therefore, as part of this effort, we intend to develop models that capture the dominant spatial features within the waves. For example, a wind perturbation model can be developed that provides a realization of the vector wind in the early, middle, and late phases of the evolving Kelvin-Helmholtz wave. This model can then be assimilated into the background atmospheric state, as provided by G2S, and then used in propagation modeling studies.

## Approaches to Improved Propagation Modeling

Fundamental understanding is needed of the physics of infrasound propagation through the inhomogeneous atmosphere. Much experimental and theoretical work has been done in the former Soviet Union on the interaction of low-frequency sound and infrasound with turbulence. In particular, many measurements have been conducted and reported, along with theoretical developments, by researchers at the Oboukhov Institute of Atmospheric Physics in Moscow. Some of these results are reviewed by Kulichkov (2004), who has observed "partial reflection (scattering)" of low-frequency acoustic or infrasonic pulses from fine-layered inhomogeneities in the middle atmosphere. These observations include "rapid variations" of infrasonic signals from a series of similar ground-based explosions timed at intervals of 10-30 minutes and observed at local or near-regional ranges. The signal variations, with time scales similar to the periods of internal gravity waves, and intermittent observations of signals in shadow zone regions are attributed to inhomogeneous coherent structure in the atmosphere (Kulichkov, 2004).

Further review of relevant investigations is presented by Kallistratova (2002). Scattering of sound from tropospheric gravity waves is discussed as a mechanism for explaining observed low-frequency signals. Quasi-regular inhomogeneities of temperature field and wind velocity or coherent structures that are "vertical, pancake and undulatory" all affect acoustic and infrasonic waves, and strong anisotropy of "pancake" structures in the stratosphere are particularly important for long-range propagation from explosions. "Horizontally stretched" anisotropic inhomogeneities can exist at both stratospheric and mesospheric heights and can theoretically explain observations by Kulichkov and his colleagues (Kallistratova, 2002). Kallistratova (2002) also emphasizes that it is necessary when considering nonlinear propagation phenomena to also consider the effect of turbulent fluctuations.

There have been a small number of theoretical papers dealing directly with the subject of infrasound in the inhomogeneous atmosphere (e.g., Chunchuzov, 2004; Ostashev et al., 2005, Chunchuzov et al., 2006). These authors point out that this subject involves combining two difficult topic areas: 1) three-dimensional spectra of temperature and wind velocity fluctuations due to gravity waves in a stably stratified atmosphere; and 2) a general theory of sound propagation refracted and scattered by anisotropic turbulence with both temperature and wind velocity fluctuations. While theoretical treatments exist, there has been limited progress toward validated numerical propagation calculation techniques for infrasound in turbulent structure.

Two modeling approaches will be undertaken in this effort with regard to assimilating the fine-scale atmospheric structure for use in propagation predictions: field realizations and random media formulations.

In the first approach, inverse Fourier transforms of the spectral models are taken to generate realizations of the variable fields. Random phases are added to the spectral bins so that each realization is different while as the same time maintaining the correct spatial scales and energetics. The variable fields generated are perturbation fields that reflect the temperature and wind deviations associated with the turbulence. They must be assimilated with the mean background fields to generate an overall solution of the atmospheric state. An example realization of wind fields, using our baseline technique and spectra derived from Gardner (1995, 1993), is shown in Figure 2 (Norris et al., 2006). The gravity waves are seen as thin layers of coherent wind anomalies. The total atmospheric wind realization is seen to be the sum of the mean G2S specification and fine-scale gravity wave structure.

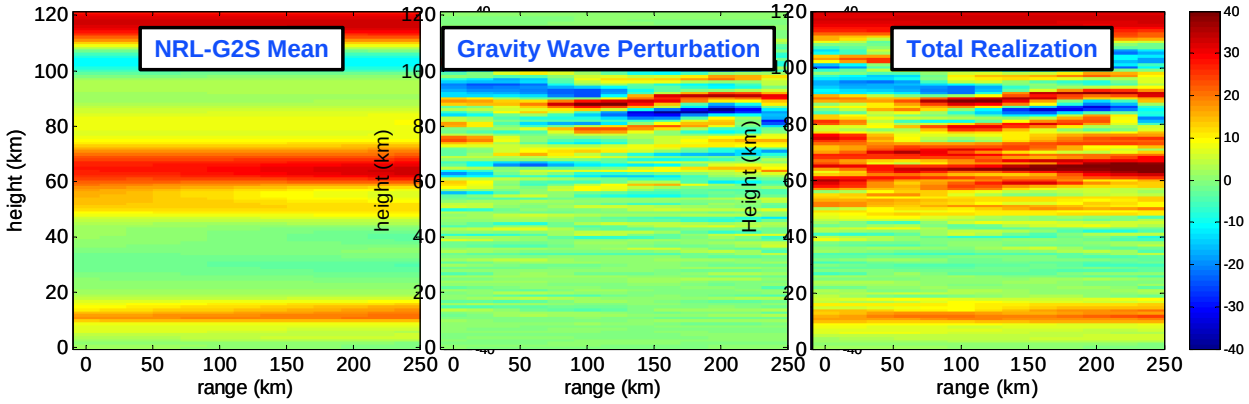


**Figure 2. Atmospheric specification showing the G2S mean wind fields (left panel), wind perturbations from gravity waves (middle panel), and resulting total realization (right panel).**

In this realization, the perturbed and mean fields are simply added. However, this approach ignores the interdependency between the background atmospheric state and locations of strong turbulent activity. We intend to improve upon this technique by accounting for the self-consistency required to combine the mean and perturbed fields. The self-consistency will be addressed by coupling the gravity wave model with the output of the background G2S model, as discussed in the previous section.

Improvements to propagation modeling techniques will be coupled with improvements to the gravity wave characterizations. The gravity wave model for infrasound can be improved significantly by including the geospatial and temporal dependence on the amplitude scale factor. Other issues to be examined include mean flow bias, maximum flow limits, anisotropy, horizontal correlation length, and zonal vs. meridianal flow dependence. Ultimately, by better defining the scales and amplitudes of the relevant environmental perturbations, better estimates of the stochastic properties of infrasound propagation are expected to be obtained.

The second approach to integrating the atmospheric models relies on well-developed theory of propagation through random media (Ostashev, 1997). By applying this theory, direct predictions of propagation variables can be made. The formulations require spectral models of the turbulence as input. We will use the spectral models as described above to directly predict the effects of fine-scale structure on the propagation. Variables that will be predicted include scattering cross section, scattering angle, coherence length, and mean pressure levels (Ostashev et al., 2005).

## CONCLUSIONS AND RECOMMENDATIONS

Model validation studies of infrasound observations using ground truth data have been conducted to build confidence in atmospheric specification procedures and calculation techniques and to identify areas where further refinements are required to achieve improved infrasound predictions. Substantial evidence for the importance of variability due to fine-scale inhomogeneity has been indicated by TDPE waveform predictions for several events observed at regional ranges (e.g., Norris et al., 2006; Norris, 2006). In several instances, conventional propagation modeling has failed to predict observed arrivals due to the lack of a stratospheric duct in the baseline atmospheric characterization; these observations exist in so-called “shadow zones.” However, modeled infrasound arrivals that considered stratospheric energy refracted or scattered from gravity waves agreed well in waveform shape, extent and arrival time with observations.

These results indicate the considerable benefit to regional monitoring that is to be gained by understanding gravity wave effects on infrasound. While implementation of our existing baseline gravity wave model enables prediction of certain infrasound features, there is significant additional understanding of the fundamental physics yet to be gained and additional model fidelity that is needed. It is anticipated that the dominant effects of gravity waves on infrasound are observed over regional paths. Local paths are also of significant interest as they are affected by turbulent instabilities and may represent the only observable energy for small events.

## REFERENCES

Bacmeister, J. T., S.D. Eckermann, P. A. Newman, L. Lait, K. R. Chan, M. Loewenstein, M. H. Proffitt, and B. L. Gary (1996). Stratospheric horizontal wavenumber spectra of winds, potential temperature and atmospheric tracers observed by high-altitude aircraft, *J. Geophys. Res.* 101: 9441–9470.

Bhattacharyya, J., H. Bass, D. Drob, R. Whitaker, D. ReVelle, and T. Sandoval (2003). Description and Analysis of Infrasound and Seismic Signals Recorded from the Watusi Explosive Experiment, in *Proceedings of the 25th Seismic Research Review—Nuclear Explosion Monitoring: Building the Knowledge Base*, LA-UR-03-6029, Vol. 2, pp. 587–596.

Chunchuzov, I. P. (2004). Influence of internal gravity waves on sound propagation in the lower atmosphere, *Met. Atmos. Phys.* 85: (1–3): 61–76.

Chunchuzov, I., S. Kulichkov, A. Otrezov, V. Perepelkin (2006). Acoustic pulse propagation through a fluctuating stably stratified atmospheric boundary layer, *J. Acoust. Soc. Am.* 117: (4), 1868–1879.

Colosi, J. A. (2006). Geometric sound propagation through an inhomogeneous and moving ocean: Scattering by small scale internal wave currents (L), *J. Acoust. Soc. Am.* 119: (2), 705–708.

Drob, D. P., J.M. Picone, and M.A. Garcés (2003). The Global Morphology of Infrasound Propagation, *J. Geophys. Res.* 108: doi:10.1029/2002JD003307.

Drob, D. P. (2004). Atmospheric Specifications for Infrasound Calculations, *Inframatics*, No. 5.

Eckermann, S. D. (1995). Effect of background winds on vertical wavenumber spectra of atmospheric gravity waves, *J. Geophys. Res.* 100: 14,097–14,112.

Fritts, D. C., and W. Lu (1993). Spectral estimates of gravity wave energy and momentum fluxes, II: Parameterization of wave forcing and variability, *J. Atmos. Sci.* 50: 3695–3713.

Fritts, D. C., and J. M. Alexander (2003). Gravity Wave Dynamics and Effects in the Middle Atmosphere, *Rev. of Geophys.* 41: 1, 1003.

Gardner, C. (1993). Gravity Wave Models for the Horizontal Wave Number Spectra of Atmospheric Velocity and Density Fluctuations, *JGR* 98; D1, 1035–1049.

Gardner, C. (1995). Scale-Independent Diffusive Filtering Theory of Gravity Wave Spectra in the Atmosphere, *The Upper Mesosphere and Lower Thermosphere: A Review of Experiment and Theory*, Geophysical Monograph 87, AGU.

Gibson, R., and D. Norris (2002). Development of an Infrasound Propagation Modeling Tool Kit, *Defense Threat Reduction Agency Technical Report DTRA-TR-99-47*, Alexandria, VA.

Gibson, R. G., D. P. Drob and D. E. Norris (2006). Advancement of Infrasound Propagation Calculation Techniques using Synoptic and Mesoscale Atmospheric Specifications, in *Proceedings of the 28th Seismic Research Review*: Ground-Based Nuclear Explosion Monitoring Technologies, LA-UR-06-5471, Vol. 2, pp. 900–909.

Hedin, A.E., E.L. Fleming, A.H. Manson, F.J. Scmidlin, S.K. Avery, R.R. Clark, S.J. Franke, G.J. Fraser, T. Tsunda, F. Vial, and R.A. Vincent (1996). Empirical Wind Model for the Upper, Middle, and Lower Atmosphere, *J. Atmos. Terr. Phys.* 58: 1421–1447.

Kallistratova, M. A. (2002). Acoustic Waves in the Turbulent Atmosphere: A Review, *Journal of Atmospheric and Oceanic Technology* 19: (8), 1139–1150.

Kulichkov, S.N. (2004). Long-range propagation and scattering of low-frequency sound pulses in the middle atmosphere, *Met. Atmos. Phys*. 85: No. 1–3, pp. 47–60.

Mutschlecner, J., and R. Whitaker (2006). *Infrasonic Signals from the Henderson, Nevada, Chemical Explosion*, LA-UR-06-6458.

Nappo, C.J. (2002). *An Introduction to Atmospheric Gravity Waves*, Academic Press.

Norris, D., and R. Gibson (2002). InfraMAP Enhancements: Environmental/Propagation Variability and Localization Accuracy of Infrasonic Networks, in *Proceedings of the 24th Seismic Research Review—Nuclear Explosion Monitoring: Innovation and Integration*, LA-UR-02-5048, Vol. 2, pp. 809–813.

Norris, D., and R. Gibson (2004). Advanced Tools for Infrasonic Modeling, *Inframatics*, No. 5.

Norris, D., R. Gibson, J. Bhattacharyya, and R. Whitaker (2005). Development of Advanced Propagation Models and Application to the Study of Impulsive Infrasonic Events at Various Ranges, in *Proceedings of the 27th Seismic Research Review: Ground-based Nuclear Explosion Monitoring Technologies*, LA-UR-05-6407, Vol. 2, pp. 838–844.

Norris, D., J. Bhattacharyya, and R. Whitaker (2006). Development of Advanced Propagation Models and Application to the Study of Impulsive Infrasonic Events, *Proceedings of the 28th Seismic Research Review: Ground-Based Nuclear Explosion Monitoring Technologies*, LA-UR-06-5471, Vol. 2, pp. 919–925.

Norris, D. (2006). Recent Advances in Predicting Infrasound using the Time-Domain Parabolic Equation Model (TDPE), *Infrasound Technology Workshop*, Fairbanks, AK.

Ostashev, V. E. (1997). *Acoustics in Moving Inhomogeneous Media*, E & FN Spon, London.

Ostashev, V. E., I. P. Chunchuzov, and D. K. Wilson (2005). Sound propagation through and scattering by internal gravity waves in a stably stratified atmosphere, *J. Acoust. Soc. Am.*, 118 (6): 3420-3429.

Picone, J., A. Hedin, D. Drob, and A. Aiken (2002). NRLMSISE-00 empirical model of the atmosphere: statistical comparisons and scientific issues, *J. Geophys. Res.* 107: 1468.

Warner, C.D., and M.E. McIntyre (2001). An ultrasimple spectral parameterization for nonorographic gravity waves, *J. Atmos. Sci.* 58: (14), 1837–1857.

# INFRASOUND CALIBRATION EXPERIMENT IN ISRAEL: PREPARATION AND TEST SHOTS

Yefim Gitterman and Rami Hofstetter

Geophysical Institute of Israel

Sponsored by Army Space and Missile Defense Command

Contract No. W9113M-07-C-0189
Proposal No. BAA07-52

## ABSTRACT

The Geophysical Institute of Israel (GII) started a new project of establishing a calibration infrasound dataset for the Eastern Mediterranean/Middle East region for improvement of monitoring capabilities of international network infrasound stations. The dataset is intended to characterize the infrasonic wave propagation in the region: travel times, spectra, amplitudes, dependence on source yield, and atmospheric conditions. To achieve these goals, a series of experimental surface shots will be conducted at Sayarim Military Range (SMR), located in southern Israel, Negev desert, including the main calibration explosion of 80 tons (TNT equivalent).

During the explosions numerous portable co-located infrasound and seismic systems will be deployed at near-source (0.1–1 km) (accelerometers), local (10–350 km), and regional distances (500–1500 km) in neighboring countries (during the main explosion). Tripartite arrays of low-frequency electret condenser microphones will be installed at close distances less than 100 km, and Chaparral sensors will be used for infrasound observations at larger distances.

Preliminary test explosions of broad yield range and various designs are planned during the first project year, on different days, including outdate ammunition detonations, conducted regularly at Sayarim Range, thus providing a wide range of atmospheric conditions. The test explosions are intended to fulfill a number of tasks: testing new infrasound recording systems; yield scaling signal amplitude/energy; testing charge design and preparations and conducting logistics for the big explosion; analyzing atmospheric effects on infrasound propagation in different azimuths, based on collected meteo-data about wind direction and velocity in different months; and validating safety estimations/conditions for successive increasing charges.

We collected GTI0 information and observations of acoustic phases at stations of the Israel Seismic Network and a few infrasound portable stations for a series of 7 experimental single shots (in the range of 0.4–1.2 tons) conducted by Israel Defense Forces (IDF) at Sayarim September 2007–February 2008. Just recently, June–July 2008, jointly with the IDF, we conducted another test series of 13 outdated ammunition detonations (in the range of 0.2–10 tons) and two special experimental project explosions of 1 ton each of pure different explosives (TNT and CompositionB). The two special experimental explosions, conducted close to and 10 minutes after an ammunition shot, were intended to estimate ammunition actual yield and also to check the feasibility of using one of such different explosives as a charge element for the large calibration explosion.

Analysis of signals recorded at seismic and acoustic channels of portable and permanent stations is presented, including charge scaling estimations, comparison of energy generation for different explosives, and examination of the influence of wind direction on parameters of infrasound phases. Results obtained from the test series will be used for elaboration of design and logistics of the main calibration explosion and selection of optimal experimental conditions and infrasound system locations.

## OBJECTIVES

Three major project objectives:

1. Conducting a surface calibration explosion of 80 tons at SMR (Figure 1), with deployment of a number of portable infrasound stations at local and regional distances up to 1500 km (jointly with ISLA, UH)
2. Establishing a calibration infrasound dataset for Eastern Mediterranean/Middle East region for improvement of monitoring capabilities of IMS infrasound stations
3. Characterizing the infrasonic propagation in the region: travel times, spectra, amplitudes, depending on source features and atmosphere conditions

A number of smaller test surface shots in different months are planned on the first stage with following goals:

- Testing new infrasound recording systems
- Yield scaling signal amplitude/energy
- Testing charge design and preparations/conducting logistics for the big explosion
- Analyzing the wide ranging effects of atmospheric conditions on infrasound propagation on different azimuths (based on collected meteorological data)
- Validating safety estimations/conditions for successive increasing charges

## RESEARCH ACCOMPLISHED

During the first year of the project, the research was focused on three areas: (1) selecting, purchasing, assembling, testing, and characterizing new recording infrasound systems—in order to document and characterize the regional propagation effects; (2) conducting and observing experimental and outdated-ammunition explosions; and (3) collecting available local meteorological information—in order to characterize atmospheric effects on infrasound propagation for recorded explosions. A great deal of administrative effort was spent on organizing tenders and selecting subcontractors for explosives supply and conducting experimental explosions.

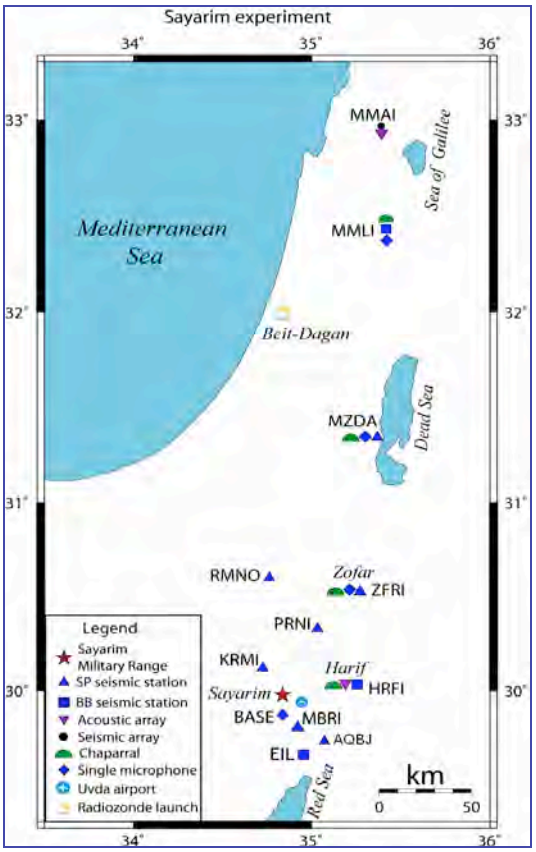


**Figure 1. Location of the Sayarim explosion site, stations of the Israel Seismic Network that recorded acoustic phases, and portable infrasound stations installed for observation of the project explosions.**

## New Infrasound Sensors

We selected two types of sensors for local infrasound observations of the explosions. We purchased five Chaparral M25 sensors from Chaparral Physics Inc. (an old Chaparral 2 model had been purchased previously). To provide more observation points along propagation paths, we purchased electronic components, assembled and tuned 12 much-cheaper low-frequency electret condenser microphones WM-54D5 (Figure 2,a). No data sheets or instrument response tests were found for these sensors, so we tried to quantify their response and their absolute and relative sensitivity. Appropriate recording systems, including A/D cards, amplifiers, global positioning system (GPS) devices, and PC-based data-acquisition software were developed. Laboratory calibration tests were conducted, in which a group of six microphones was run alongside a reference Chaparral 2 sensor (Figure 2,b).

Infrasound signals for calibration were produced by sharply opening or closing the building's exit door (located ~30 m from the laboratory room). Sample signal records and appropriate amplitude spectra are shown in Figure 3. The software jSTAR, developed at GII (Pinsky et al., 2007), was used for amplitude measurements and spectral calculation. Unlike Chaparral 2, microphones are used with an amplifier during calibration tests (and field observations), and their amplitudes are respectively corrected when comparing the sensitivity of the sensors.

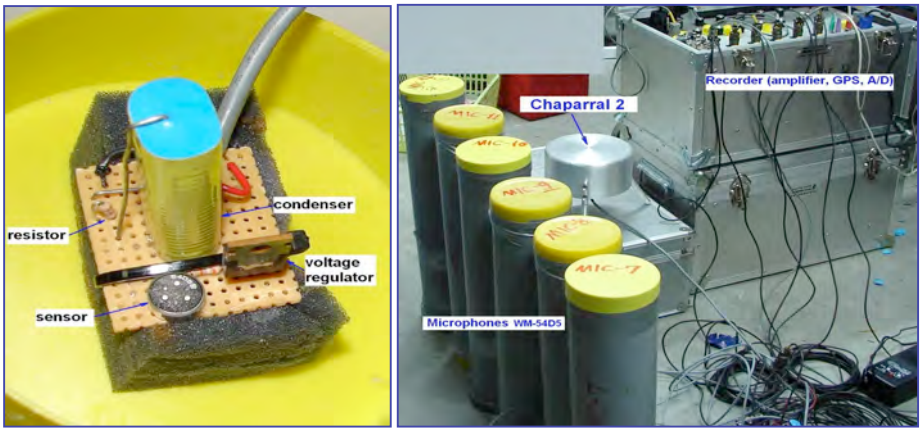


**Figure 2. Low-frequency microphones (cartridge WM-54D5) (a), placed in resonance boxes, were calibrated in the GII laboratory (b).**

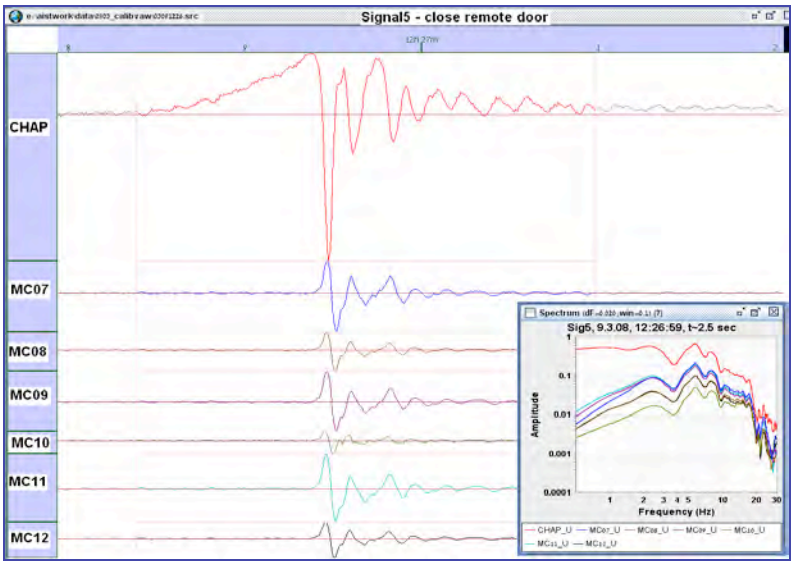


**Figure 3. Sample records of signals from six microphones and Chaparral 2, produced by closing the exit door.**

The results show large variation in sensitivity for different microphones (by 2 to 3 times), possibly caused by a large dispersion (~ 20%) of resistor and condenser values used in the microphone circuit, and another highly accurate electronic device should be tried to improve the sensor identity. The spectra clearly demonstrate different frequency responses from the microphones compared with the expected flat response of the reference Chaparral 2 sensor in the range of 0.1–30 Hz. We also compared signals from two co-located Sayarim ammunition shots that were recorded by both sensors at a remote location, and we calculated the amplitude spectra of the signals (Figure 4) and the spectral ratios of Chaparral signals to microphone signals as an estimation of the sensitivity ratio (SR) depending on frequency. These estimations generally correspond to the results of the laboratory calibration tests. We conclude that microphones represent well the amplitude and energy of signals for frequencies that are >3 Hz but significantly cut low-frequency energy for frequencies <1 Hz.

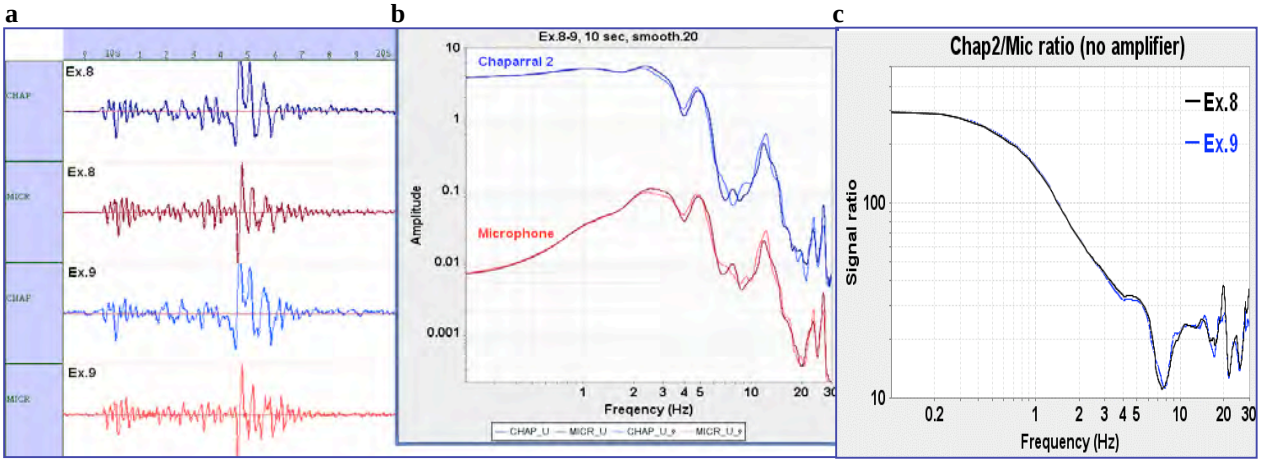


**Figure 4. Infrasound signals (in relative scale) from two similar Sayarim ammunition shots February 27, 2006, (with a delay of ~2 minutes and explosives of ~7 tons) recorded at Zofar(r ~73 km), (a) appropriate smoothed spectra, and (b) spectral ratios of Chaparral to microphone signals (c).**

### Collecting Atmospheric Data

Atmospheric conditions along the infrasound propagation path, especially the local altitude distribution of wind direction and velocity and their changes on different days, strongly affect acoustic signal amplitudes, duration, and propagation time (e.g., Garces et al., 1998; Stump et al., 2002). This effect is regularly observed at ISN stations (Figure 1) where clear acoustic phases from Sayarim ammunition detonations are observed at distances up to 150 km. Figure 5 shows a striking example of antipodal manifestation of acoustic phases of the same explosion at two SP stations located at the same epicentral distance but in opposite directions (October 27, 2003); this ratio was changed to the opposite on another day in another month (November 6, 2003).

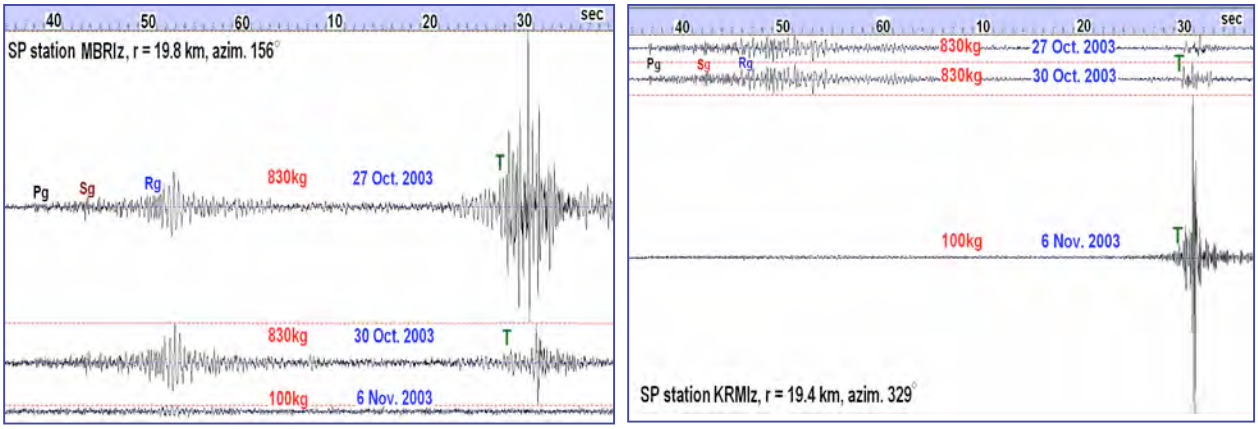


**Figure 5. Observations of diverse acoustic phases (T) from Sayarim surface single shots in 2003 at two ISN seismic stations (plotted in absolute scale; filter 1–5 Hz is applied).**

We collected archival meteorological information from the Israel Meteorological Service (IsMS) and processed the data. The information includes the data from a balloon-launched radiosonde system (at Beit Dagan, central Israel, see the map in Figure 1) measuring temperature and wind velocity and direction at altitudes up to 27 km. The data measured twice a day during 10 years (1971–1980) were averaged for different months. The average values were plotted as the function of altitude (Figure 6). Distinctive discrepancy is found for different months (seasons).

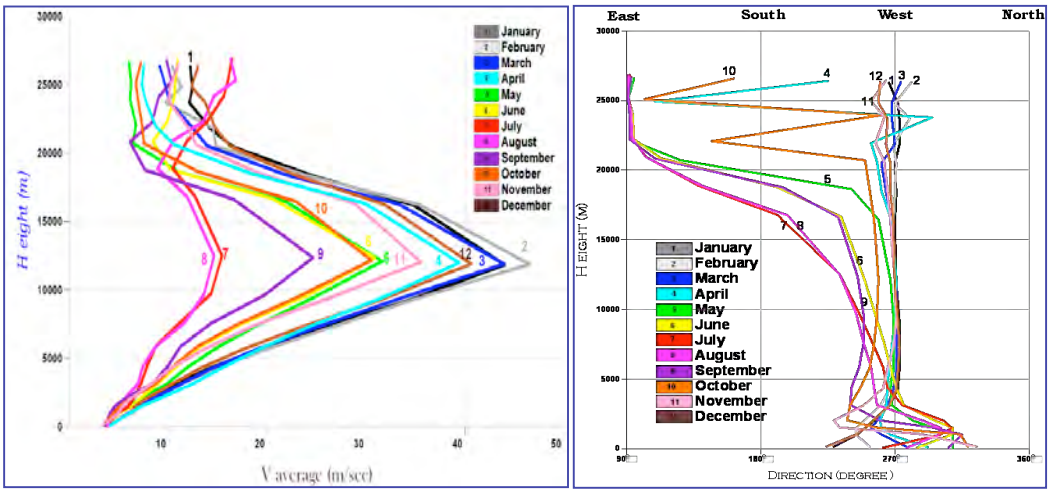


**Figure 6. Local altitude distributions of wind velocity and direction from IsMS radiosonde data in different months, averaged for 1971–1980.**

The IsMS can provide a full digital dataset of a balloon-launched radiosonde system (up to 25 km) for a specified day, at Beit-Dagan, central Israel. The private company Meteo-Tech conducts measurements of wind direction and velocity near the surface at the airport Uvda in the Negev, very close (~10 km) to Sayarim (see Figure 1). We purchased the data from IsMS and Meteo-Tech for specific days for which we provided infrasound observations, or clear acoustic phases were recorded at ISN stations for Sayarim explosions we collected ground truth (GT) information (Figure 7, Table 1). The data should assist in interpretation of observed variance of acoustic phases at the same station (see below) and will be used in the following for infrasound propagation modeling at local and regional distances.

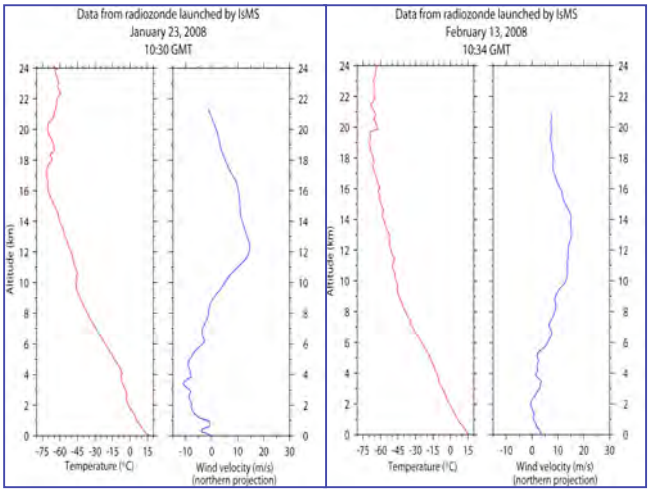


**Figure 7. Altitude distribution of temperature and wind velocity in a northern direction on days of observed explosions H6 and H7 (see Table 2). Note the clear differences in the wind curves.**

**Table 1. Meteorological data (by Meteo-Tech company), measured at Uvda airport at ~2 m above the surface.**

| Date yy/mm/dd | GMT time | Wind dir (back-azim),° | Wind speed, m/sec | Tempe-rature, C° |
|---|---|---|---|---|
| 07/09/05 | 10:40 | 0 | 3.7 | 32.7 |
| 07/09/10 | 09:20 | 15 | 5.4 | 29.0 |
| 08/01/14 | 12:00 | 11 | 5.2 | 10.3 |
| 08/01/16 | 13:40 | 9 | 4.3 | 12.2 |
| 08/01/21 | 13:40 | 3 | 5.1 | 13.2 |
| 08/01/23 | 12:00 | 282 | 6.0 | 14.2 |
| 08/02/13 | 13:10 | 33 | 1.7 | 16.6 |

**Series of Military Single Experimental Explosions Hashmonaim-3**

Aiming at achieving the objectives mentioned above, we collected GT0 information and observations for a series of experimental single surface shots (Hashmonaim-3) at SMR, conducted recently by the IDF jointly with teams from the USA and UK, and participated in two of them (H6 and H7), measuring accurate origin (detonation) time (O.T.) and GPS coordinates and deploying portable sensors. The explosions were of different charge, explosives, and design (Table 2, Figure 8), placed on a small playground about 30 × 30 m. O.T. values for unvisited shots were estimated from a location procedure in jSTAR software, based on seismic signals recorded at ISN stations around SMR.

**Table 2. Parameters of experimental surface explosions Hashmonaim-3 at SMR**

| Ex. # | Date yy/mm/dd | Origin time, GMT | Local coordinates | | Design | Charge, kg | |
|---|---|---|---|---|---|---|---|
| | | | X, km | Y, km | | actual | TNT equiv. |
| H1* | 07/09/05 | 10:34:00.6* | 183.18 | 429.45 | Tower of 20 kg ANFO packs, height ~2 m | 1800 | 1440 |
| H2* | 07/09/10 | 09:11:15.1* | | | | 1800 | 1440 |
| H3* | 08/01/14 | 11:48:26.6* | | | Cast TNT, hemispherical, on a wooden platform of height h~10 cm | 830 | 830 |
| H4* | 08/01/16 | 13:32:08.9* | | | | 830 | 830 |
| H5* | 08/01/21 | 13:25:31.6* | | | | 830 | 830 |
| H6** | 08/01/23 | 11:45:18.14** | 183.175 | 429.454 | | 830 | 830 |
| H7** | 08/02/13 | 11:01:56.59** | 183.200 | 429.449 | 36 mines (Composit.B), on 2 platforms, h~20 cm | 360 | 400 |

** visited, O.T. is measured * not visited - GT info from IDF, O.T. is estimated from ISN records.

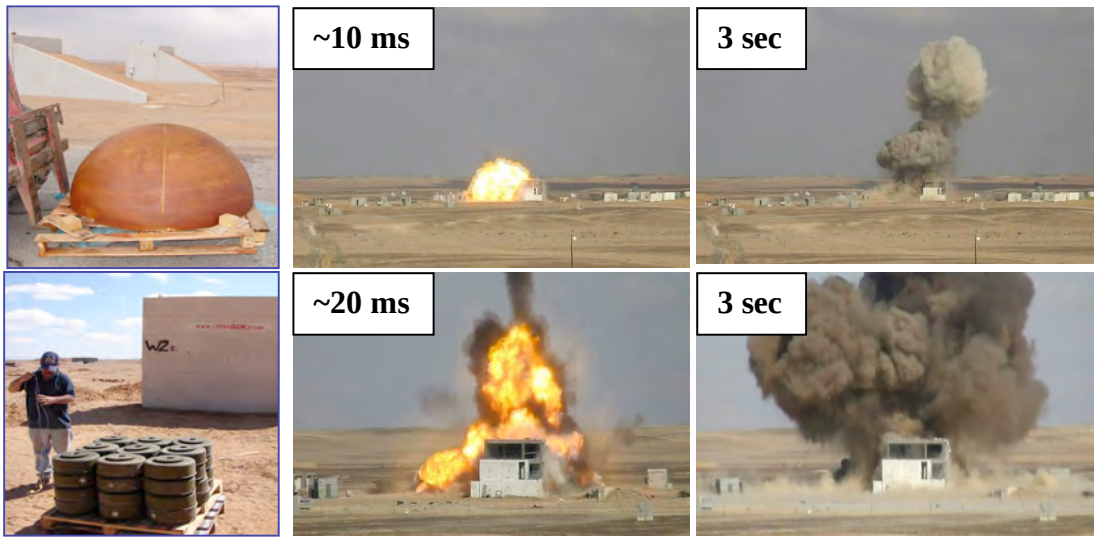


**Figure 8. View of the charges and snapshots from video records for two shots: H6 (above) and H7 (below).**

Video records of the shots provided visual observations of wind characteristics from movements of the dust column: a rather strong wind (~5 m/s) to the right (east-south) during H6 and almost still during H7 (Figure 8). These observations, confirmed later by the meteo-data (Table 1), helped to explain some differences in infrasound signals for the two shots (see below).

Near-source observations were also provided (Figure 9). For explosion H7, we installed, at close vicinity (64 m and 164 m), two accelerometers ETNA with GPS time (Figure 10,a). Strong air-shock phases were observed at both accelerometer records (velocity 424 m/s). The air-shock phases arrived within seismic signals and prevented measurements of peak ground acceleration (PGA) amplitudes and seismic energy in the near-source zone. For infrasound observations, five portable stations were installed before each explosion (H6 and H7). Usually a single microphone was used, complemented at St. 1 (Zofar) by Chaparral 2 sensor (the only Chaparral available at the moment); a tripartite microphone array was deployed at St. 2 (Harif) during explosion H7. Each station also included an SP vertical seismometer L4C (Figure 9).

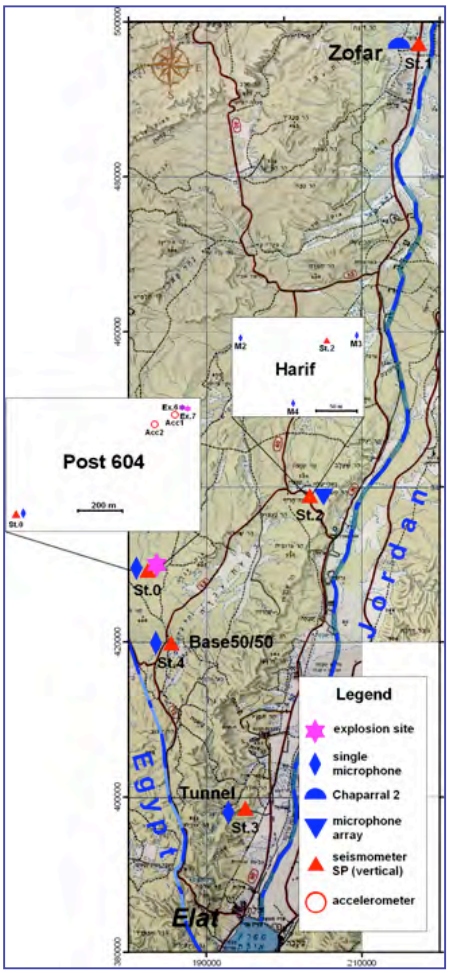


Figure 9. Location of explosions and portable stations during explosions H6 and H7.

The PC-based recording system (at 0.9 km) for measuring detonation time also included a microphone and an SP vertical seismometer (Figure 10,b). Acoustic signals were clipped but provided estimating infrasound (346 m/s); and seismic P-wave velocity was estimated (2140 m/s), characterizing subsurface sedimentary rocks.

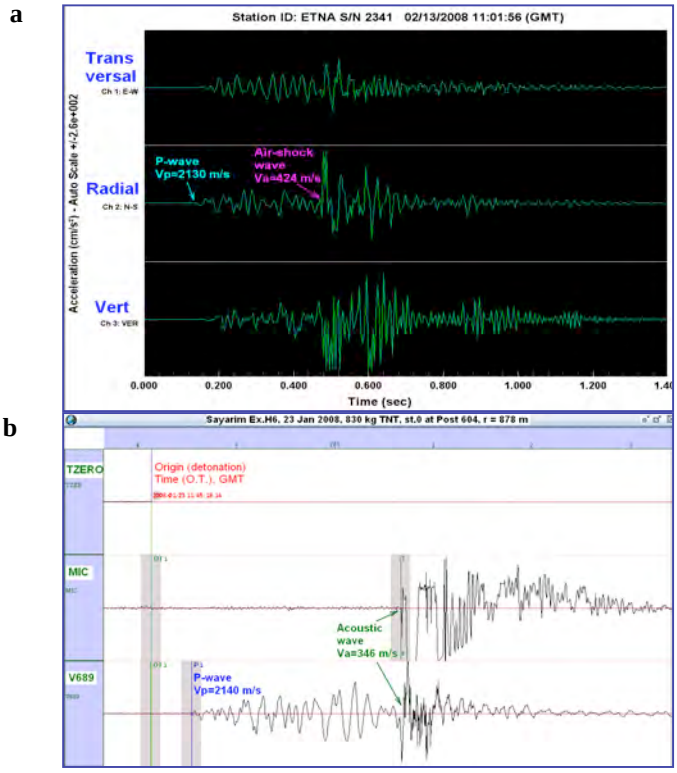


Figure 10. Near-source observations by accelerometer at r ~0.16 km during explosion H7 (a) and by microphone and seismometer at r ~0.9 km (explosion H6) (b).

Similar clear signals were recorded at a remote Zofar station for co-located microphone and Chaparral sensors (Figure 11). A waveform modulation, clearly visible in the spectra, is different from signals recorded at this location from previous Sayarim shots (see Figure 4,a), and the spectra again show the cutting of low-frequency energy (f <2 Hz) by microphone compared with Chaparral and maximum energy in the 3–5 Hz range.

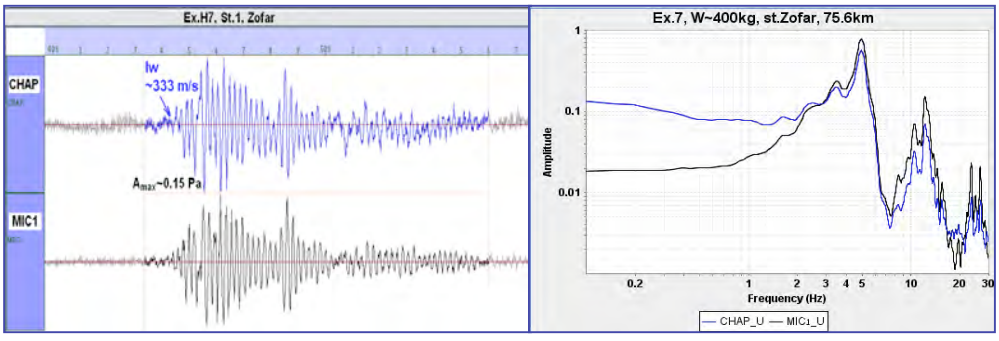


Figure 11. Infrasound phase Iw recorded at St. 1 (in relative scale) and appropriate spectra. Amplifier gain 40 dB was used for microphone recording.

Clear acoustic phases were recorded at several ISN network seismic stations located close to the Sayarim site, similar to many other observations (e.g., recent Stump et al., 2007; Gibbons et al., 2007). The same location of the series shots facilitated a comparison of seismic and acoustic phases at a fixed station. At all stations, seismic amplitudes clearly correspond to the charge size, whereas acoustic phases show a drastic variance of temporal structure and amplitudes from shot to shot and for different azimuths. Figure 12 shows sample records at SP MBRI and BB HRFI, located at similar distances from the shots but at different azimuths (see Figure 1), where distinctive acoustic phases for explosion H6 and H7 correspond in some way to the wind observations on the site and collected meteo-data (Figure 7, Table 1). The data provide a base for infrasound propagation modeling and verification.

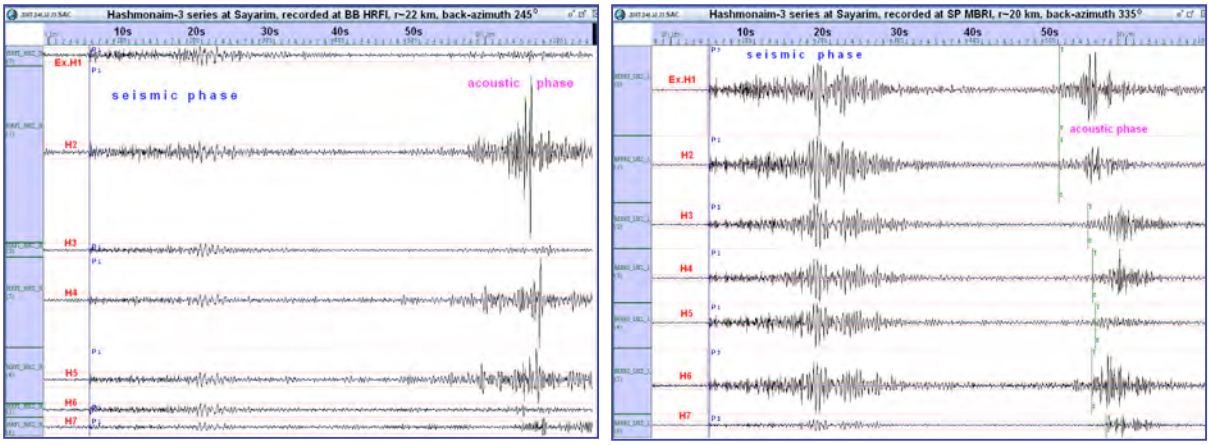


**Figure 12. Seismic and acoustic phases from the Hashmonaim-3 series observed at vertical channels of two ISN stations. All seismograms (1–10 Hz, in absolute scale) are aligned according to P-arrival time.**

### Series of Ammunition Detonations and Single Experimental Explosions in June and July 2008

In June and July 2008, we conducted, jointly with the IDF, another series of 13 tests of outdated ammunition detonations in the range of 0.2 to 10 tons (TNT equivalent) and two special experimental project explosions of 1 ton each of pure different explosives (TNT and CompositionB) (Table 3). We visited and documented the first eight shots, measured coordinates and O.T.; charge parameters for the next shots were informed by IDF.

**Table 3. Parameters of outdate ammunition and experimental surface shots at Sayarim, June–July 2008**

| Ex. # | Date | Origin Time, GMT | Coordinates | | Design | Total charge, ton |
|---|---|---|---|---|---|---|
| | | | X, km | Y, km | | |
| 1 | 23 June | 07:52:27.35* | 180.864 | 433.697 | Ammunition+chenamit emulsion 0.2 ton | 0.2 |
| 2 | | 12:24:45.3* | 180.830 | 434.016 | Ammunition+emulsion 6.0 ton | 6.05 |
| 3 | | 12:31:10.0* | 180.864 | 433.697 | Ammunition+CompB (18 mines) ~0.18 ton | 0.18 |
| 4 | 24 June | 08:52:50.4* | 180.870 | 433.722 | Ammunition+emulsion 4.9 ton | 4.94 |
| **5** | | **09:01:39.2*** | **180.831** | **434.039** | **Experiment: 1 ton TNT+CompB (2 mines)** | **1.02** |
| 6 | | 12:38:57.6* | 181.336 | 434.156 | Ammun.+emulsion 2.25 ton+mines 1.5 ton | 3.77 |
| 7 | 25 June | 10:27:48.1* | 180.867 | 433.719 | Ammunition+CompB (mines) 8.63 ton | 8.63 |
| **8** | | **10:37:05.4*** | **180.825** | **434.041** | **Experiment: 1 ton CompB+2 mines** | **1.02** |
| 9 | 30 June | ~07:00** | 180.83 | 434.02 | Ammunition+ emulsion ~0.25 ton | 0.25 |
| 10 | | ~09:15** | 180.87 | 433.72 | Ammunition+emulsion ~1 ton | 1.0 |
| 11 | | 12:27:30.7** | 181.34 | 434.16 | Ammunition+emulsion 6.25 ton | ~6.5 |
| 12 | 1 July | 11:53:14.6** | 180.83 | 434.02 | Ammunition+ emulsion 6.25 | ~6.5 |
| 13 | | 11:56:14.9** | 180.87 | 433.72 | Ammunition+emulsion 6.25 | ~6.5 |
| 14 | 2 July | 11:48:58.2** | 180.83 | 434.02 | Ammunition+emulsion 6.25 ton | ~6.5 |
| 15 | | 11:51:06.8** | 180.87 | 433.72 | Ammunition+emulsion 6.25 ton | ~6.5 |

* visited, O.T. is measured ** not visited - GT info from IDF, O.T. is estimated from ISN records.

The two experimental 1-ton explosions, each one conducted close to and 10 minutes after an ammunition shot (~300–350 m), were intended to estimate actual ammunition yield, which otherwise can not be counted up. Second, we wanted to check the effectiveness of the used 1-ton charges, consisting of reclaimed explosives pieces placed in two wooden boxes (see Figure 13), as an element of the large calibration explosion of 80 tons (planned of TNT and CompB). Finally, the two closely located shots with identical charge weight allowed comparisons of the generation of acoustic and seismic energy from these explosives, at different distances. Some preliminary comparison results for close locations are presented in Figure 14. As expected CompositionB produced larger amplitudes of acoustic (air-shock) and seismic waves (however, a stronger acoustic phase on a seismometer is found for the TNT charge, Figure 14b).

**Figure 13. Design of the experimental explosion #8 of 1 ton of Composition B (a), detonated ~10 minutes after the largest shot, explosion #7, in the series, in which outdated ammunition was destroyed by mines of 8.63 tons of Composition B (close to ~10 ton TNT equivalent) (b); as observed from a safe position at Post 604, at 5.3 km (c).**

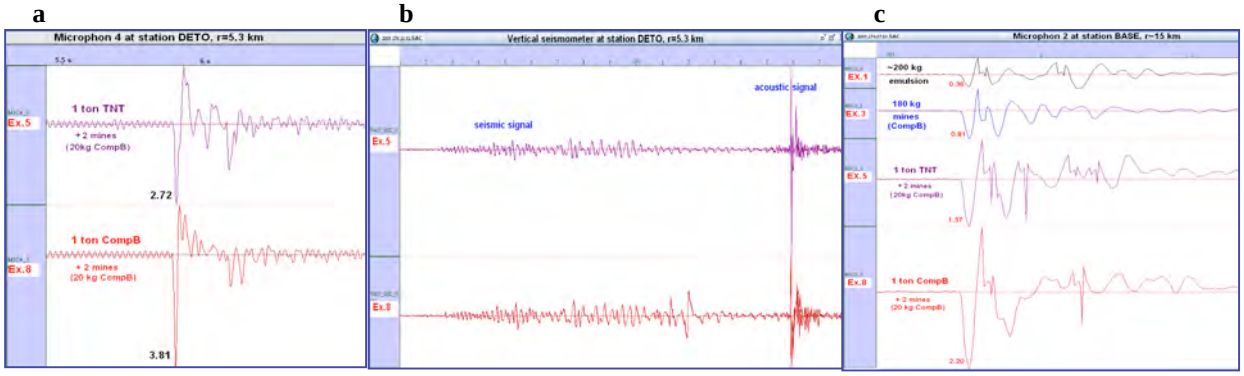


**Figure 14. Comparison of signals from two experimental 1-ton shots recorded at ~5 km by microphone #4 (a) and vertical seismometer (b), and signals from four small shots recorded by microphone #2 at ~15 km (b).**

A number of stations were installed at near-source, local, and regional distances for observation, infrasound, and seismic waves from the explosion series. Since the IDF uses radio signals to detonate large ammunition charges at a distance of 3–5 km, we could not use the old method of having an electric wire circle connected to the charge. Therefore, two accelerometers K2 were placed at ~150 m between a pair of ammunition and experimental explosions for measuring detonation time by a specially developed procedure (June 23–25 June only); another accelerometer Etna was placed at ~300 m. Strong seismic motions and air-shock wave arrivals were also recorded.

We used the same nearby station locations as before (Figure 9); three newly purchased and tested infrasound sensors, Chaparral M25, were installed at portable stations BASE, Harif, and Zofar. Two more new Chapparrals were placed jointly with single microphones at remote permanent ISN stations—MZDA (156 km) and MMLI (278 km)—where the records were transmitted on-line (Figure 1). Additionally, an infrasound array of three

microbarometers MB2000 was installed by Israel NDC at Mt. Meron (340 km), co-located with three elements (C1, C5, and C7) of IMS seismic array MMAI (Figure 1). A sample seismogram of an ammunition explosion is presented on Figure 15. Collection, processing, and analysis of the extensive dataset of records and meteo-observations will be continued.

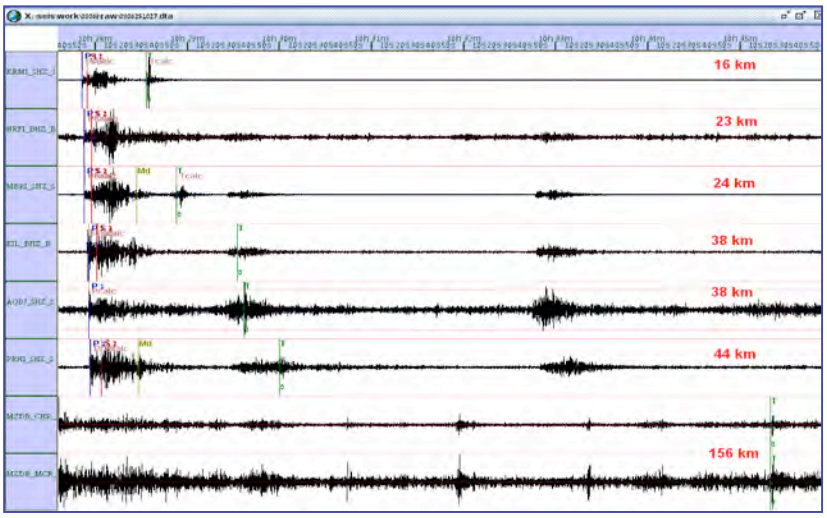


**Figure 15. Recording of the largest ammunition explosion, explosion #7, showing seismic and acoustic phases (T) at ISN stations and infrasound signals at a temporarily installed microphone (MZDB.MCR) and Chaparral M25 (MZDB.CHP) at station MZDA (156 km).**

## CONCLUSIONS AND RECOMMENDATIONS

1. Newly acquired infrasound recording systems were tested in laboratory and field experiment conditions and showed good performance. The tests included cheap microphone gauges suitable for observations in the 5–100 km range.
2. The extensive dataset collection from preliminary test explosions in the broad charge range of 0.2–10 tons allowed the analysis of yield scaling relationships based on amplitude and energy of seismic and infrasound signals.
3. The experimental explosions proved the feasibility of using 0.5-ton charge units, consisting of reclaimed explosives pieces placed in a wooden box, as an element of the large calibration explosion of 80 tons, planned of TNT and Composition B, when more Composition B is preferable to use (if available).
4. Collected meteo-data provided a base for infrasound propagation modeling. Numerous records of acoustic phases from repeating similar sources at the same location helped to estimate the effects of atmospheric conditions on infrasound propagation on different azimuths and verification of modeling results.
5. Acoustic signals observed closely from increasing charges will serve for validation of safety estimations.

## ACKNOWLEDGEMENTS

Thanks to Dr. I. Setter of IsMS for supplying valuable average meteo-data, to blast managers Y. Hamshidyan and E. Stampler of IDF's Experiment Division for conducting our experimental explosions and providing GT information, and to Dr. Y. Ben-Horin of NDC for organizing infrasound array deployment at Mt. Meron. We appreciate efforts of GII personnel: U. Peled for preparation and installation of portable stations and providing O. T. measurements and M. Kalmanovich and Dr. T. Meirov for preparing the presented maps and graphs.

## REFERENCES

Garces, M. A., R. A. Hansen, and K. G. Lindquist (1998). Traveltimes for infrasonic waves propagating in a stratified atmosphere, *Geophys. J. Int.*, 135: 28–34.

Gibbons , S. J., F. Ringdal, and T. Kvarna (2007). Joint seismic-infrasonic processing of recordings from a repeating source of atmospheric explosions in Northern Finland, *NORSAR Sci. Rep*. 2: 27–36.

Pinsky V., A. Polozov, D. Kadosh, A. Avirav, and R. Hofstetter (2007). New seismic system for acquisition and analysis in Israel. *Abstracts of XXIV General Assembly of IUGG*, July 2–13, 2007, Perugia, Italy.

Stump, B. W., S. M. McKenna, C. Hayward, and T-S. Kim (2002). Seismic and infrasound data and models at near-regional distances, in *Proceedings of the 24th Seismic Research Review—Nuclear Explosion Monitoring: Innovation and Integration*, LA-UR-02-5048, Vol. 1, pp. 572–581.

Stump, B., Burlacu, R., Hayward, C., Bonner, J., Pankow, K., Fisher, A. and S. Nava (2007). Seismic and infrasound energy generation and propagation at local and regional distances: Phase 1—Divine Strake experiment, in *Proceedings of the 29th Monitoring Research Review: Ground-Based Nuclear Explosion Monitoring Technologies*, LA-U-07-5613, Vol. 1, pp. 674–683.

# INFRASOUND IN THE "ZONE OF SILENCE"

Eugene T. Herrin[1], Paul Golden[1], Petru T. Negraru[1], Mihan McKenna[2], and Rodney Whitaker[3]

Southern Methodist University[1], US Army Engineer Research and Development Center-GSL[2], and Los Alamos National Laboratory[3]

Sponsored by Army Space and Missile Defense Command

Contract No. W9113M-06-C-0028
Proposal No. BAA06-62

## ABSTRACT

Two controlled source experiments were conducted in Nevada in 2006 and 2007 to study infrasound signal propagation at distances less than 300 km from the source. This area around a source is sometimes referred to as the "zone of silence" because, based on ray theory, no infrasound energy is expected to return to the ground. However, many observations of returned infrasound energy have been made at these distances.

In 2006, three temporary infrasound arrays were deployed at distances of 76, 108 and 157 from the source. In 2007, the site at 157 km was reoccupied, and data were also recorded at 288 km from the source. These arrays were supplemented with data from the permanent Nevada Infrasound Array (NVIAR), located 37 km from the source. In addition, meteorological data from balloon launched rawinsondes were collected in the path of the propagation.

Interesting results were derived from the travel time analysis. In 2006, the site at 76 km recorded both tropospheric and stratospheric arrivals, while at 108 and 157 km only stratospheric arrivals were recorded. In 2007, the site at 157 km recorded both tropospheric and stratospheric arrivals, while at 288 km both stratospheric and thermospheric arrivals were recorded. While stratospheric arrivals appear most frequently, atmospheric modeling with the InfraMAP software, did not predict these arrivals. Current modeling efforts focus on the tropospheric arrivals.

Amplitude variations at NVIAR for sources with the same yield varied more than an order of magnitude on two consecutive days. The site located 157 km from the source observed variations by a factor close to five. We therefore attempt to estimate the yields of the explosions using the predominant frequency content of the signals. The physical basis for such a method is found in an increased acoustic transit time of the explosion blast radius with increased yield. Past formulas were developed for old nuclear atmospheric explosions, but no extrapolation to the lower yields was ever performed. In the current work we use controlled sources with explosive yields of 2000–4,000 lbs. in order to verify the applicability of such a scale to lower yields. Preliminary results show that this is possible.

## OBJECTIVES

The primary objective of this research study is the propagation of infrasonic waves at distances up to 300 km from the source. This area, extending up to 300 km from the source has been called the "Zone of Silence" because classical ray theory does not predict any infrasound arrivals. However, under appropriate wind and temperature conditions, infrasound recordings in the "Zone of Silence" were reported several times (McKenna, 2005; Golden et. al. 2007).

## RESEARCH ACCOMPLISHED

Two controlled source experiments were carried out in 2006 and 2007 near Hawthorne, NV, where ammunition disposal operations take place on a regular basis. Shown in figure 1 is the location of the Nevada Seismic Array (NVAR) and the configuration of infrasound array. Also shown is the location of the disposal pits (dubbed New Bomb) and NVAR recordings of a typical disposal operation. In a typical operation day a suite of five explosions is recorded at NVAR, but the number of explosions in a day could vary from 3 to 10, depending on the nature of operation.

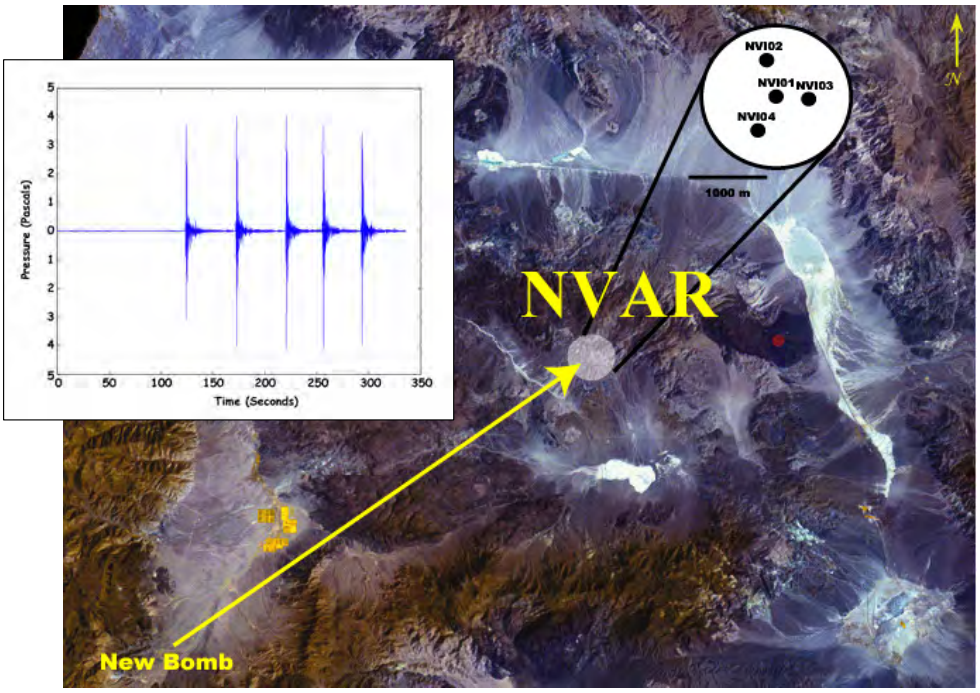


**Figure 1. Location of NVAR and the ammunition disposal site (New Bomb). Also shown are the NVIAR configuration and a typical NVIAR recording of the detonations.**

During the 2006 experiment, three 4-element temporary arrays were installed north of New Bomb, at distances of 76, 108 and 157 km. The array at 76 km was located within the village of Shurz NV (SHURZ), while the other 2 arrays were north and south of the city of Fallon, NV, designated Fallon north (FALN) and Fallon south (FALS), along State Highway 95. In the 2007 experiment, the site at FALN (157 km) was reoccupied, and a new temporary array was installed at 288 km from the source, north of Gerlach, NV (GERL). The locations of the temporary arrays and the individual layouts are shown in Figure 2. Each of the portable arrays consisted of 4 IML infrasound sensors located in line with the direction of propagation of the signals at separation distances of 50, 100, and 150 meters. The linear configuration was chosen to maximize the time delays across the array. In the 2006 experiment, data were collected for three days, while in the 2007 experiment, data was collected for four days.

In addition to the infrasound array data we collected meteorological data at the Hawthorne NV airport. We employed the National Severe Storms Laboratory (NSSL) to collect balloon launched rawinsonde meteorological data during our three experiment days. The rawinsondes were used to collect temperature, dewpoint, barometric pressure, GPS latitude, longitude, altitude, and wind speed and direction data.

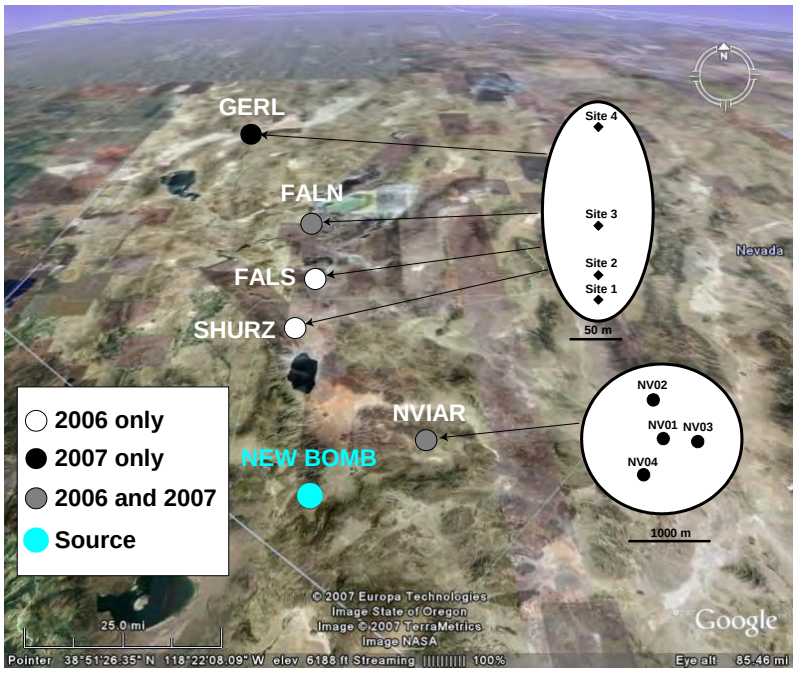


**Figure 2. Satellite image of the area of temporary infrasound arrays deployed for the experiments with plan layouts of each array.**

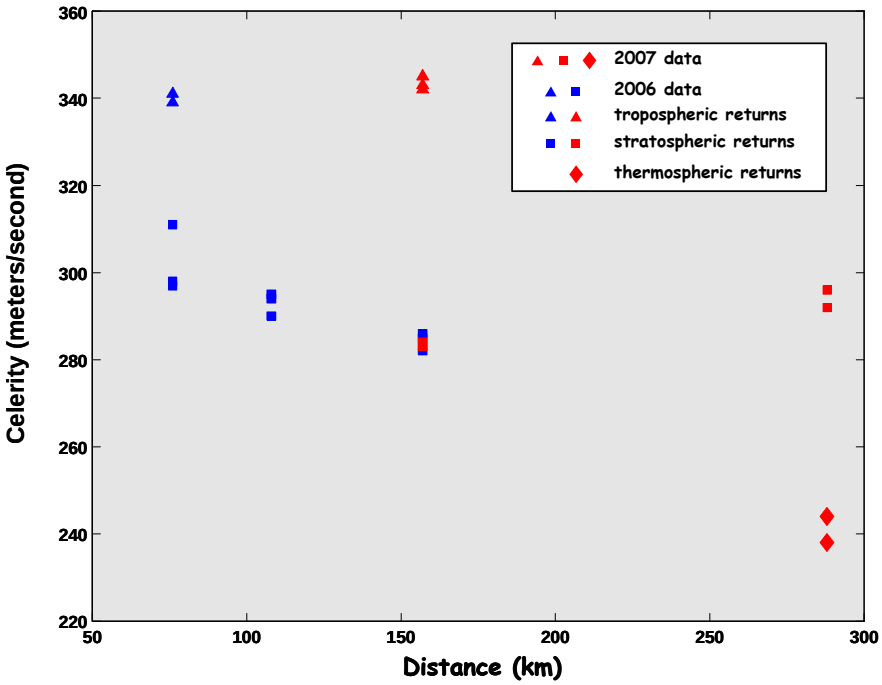


**Figure 3. Infrasound mean travel velocity (celerity) at each array for all observed arrivals.**

Interesting results were derived from the analysis of the travel time. Celerity (distance divided by the total travel time) was used as an indicator for the nature of recorded signals (Muntschlecner and Whiteker, 1999; Kulichkov et al., 2000). The celerity values are shown in Figure 3. In 2006, most of the recorded signals were stratospheric (celerities of 310–284 meters/second). Only SHURZ (76 km form the source) recorded a low tropospheric arrival (Figure 4) for the first two days of the 2006 experiment (celerities around 340 meters/second). In the 2007 tropospheric, arrivals were recorded at FALN during all days of the

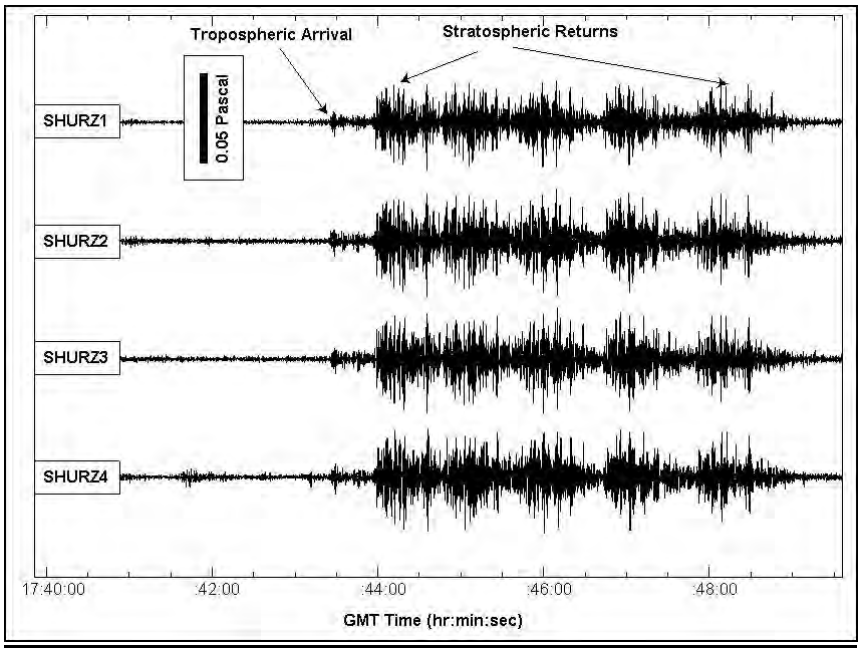


**Figure 4. Data recorded at SHURZ (76 km) during the 2006 experiment. Approximately 30 seconds before the arrival of the main wavetrain a low tropospheric arrival was recorded. Any other subsequent tropospheric arrivals would be masked by the much higher amplitude stratospheric signals.**

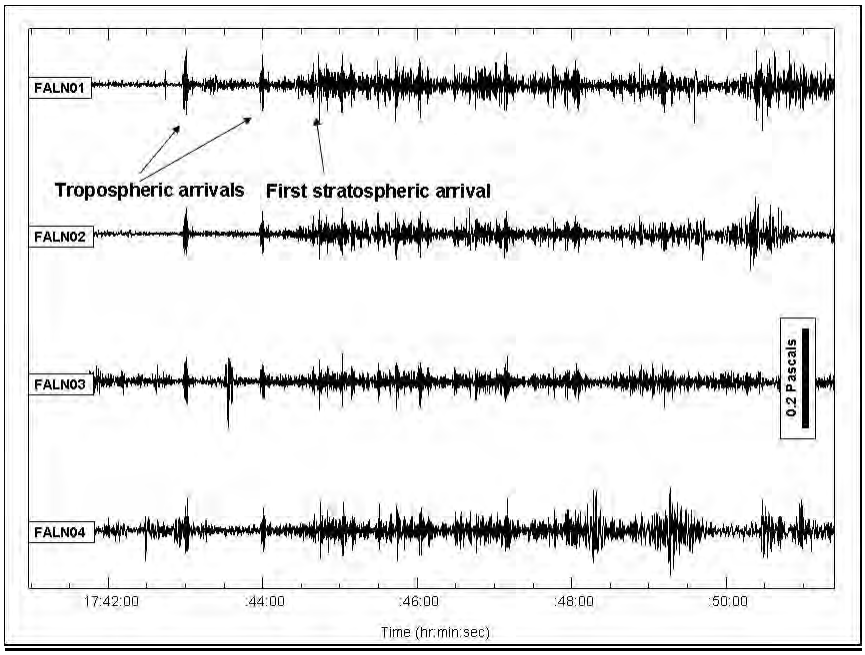


**Figure 5. Tropospheric and stratospheric signals recorded at FALN (157 km) during the 2007 experiment. After the tropospheric signals from the first two explosions, there is mixture of stratospheric and tropospheric signals.**

experiment. Figure 5 shows the FALN recording for Julian day 255. After the first two tropospheric signals, there is a wavetrain that is interpreted as a mixture of stratospheric and tropospheric signals. This combination of tropospheric and stratospheric signals was observed for the first three days of the 2007 experiment, while in the fourth day only tropospheric signals were observed. For the array at Gerlach (288 km), signals were observed for only two days of the experiment, while during the other two days of the experiment, the local noise conditions were significantly higher. GERL recorded a combination of stratospheric and thermospheric arrivals (celerities of 296 for stratospheric and 240 for thermospheric arrivals). The first thermospheric signal is recorded before the arrival of the last stratospheric signals (Figure 6). No tropospheric arrivals were observed at GERL.

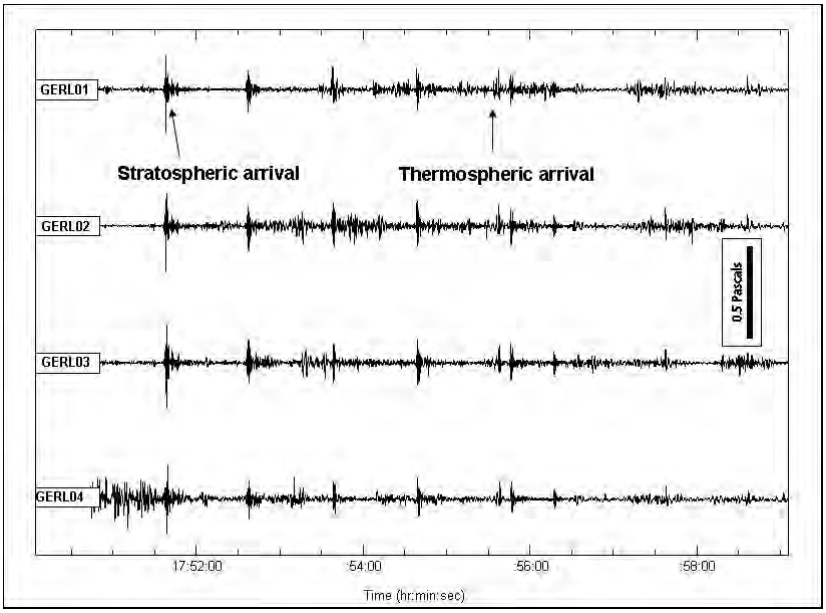


**Figure 6. Thermospheric and stratospheric arrivals recorded at GERL (288 km from the source). The first thermospheric arrival is observed after four stratospheric arrivals, before the last stratospheric signal.**

In addition, the carefully controlled explosive yields enable us to investigate various scaling relationships for yield. As we have observed in the past, amplitude variations more than one order of magnitude for infrasound signals recorded in similar conditions, we decided to use a relationship between the yield and dominant period of the signal. Such a relationship was developed from a suite of atmospheric nuclear explosions:

$$Y = 2.38 \cdot T^{3.34} \qquad (1)$$

Spectral estimates are typically obtained using Fourier-based methods which provide a relative measure of the energy at each frequency. For simple periodic signals the estimates might be accurate, but for real data with noise the Fourier methods provide a very poor estimate of the spectrum. Various windowing techniques were developed to reduce the variance of the spectral estimates (Blackman and Tuckey, 1959; Welch, 1967), but they tend to spread the energy over adjacent frequencies. An alternative way to obtain spectral estimates is the AR method (Priestly, 1981). The AR method is a parametric method, widely used in statistics and has direct applications in many areas of interest. The method provides an estimate of the spectrum and the fundamental (or system) frequencies of the time series. For a quick comparison of the methods Figure 13 shows the power spectrum estimate of a time series obtained with a simple periodogram, a windowing technique (Welch, 1967), and an AR method. By far the best estimator is the AR method.

An important problem in using AR methods is the order selection. The higher the order, the better the spectrum estimates will be, but the more difficult it is to interpret. In our case, the order selection was

performed empirically so that the potential noise bias on the frequency estimate is reduced. By adding noise before the arrival of the infrasound signal, and estimating the spectrum of signal and noise repeatedly, we found out that for orders higher than 16 the noise bias is significantly removed, even in the case of a signal with a low signal to noise ratio. The accuracy of the frequency estimates with an AR(16), for which the coefficients were determined with Burg's maximum entropy method (Burg, 1972), was tested with a bootstrap algorithm and it was found to be extremely reliable. The standard deviation of 5,000 realizations was determined to be below 0.15 Hz (Figure 7).

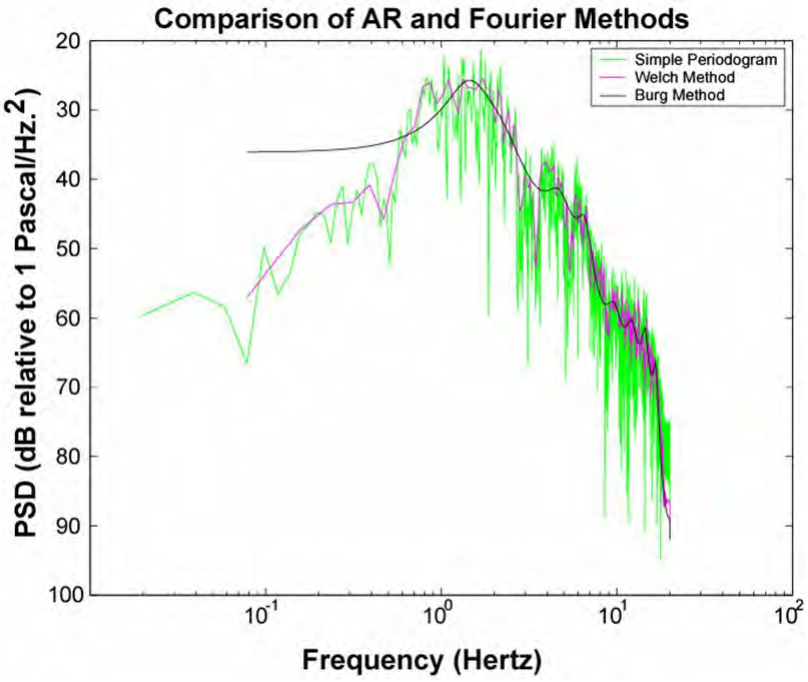


**Figure 7. Comparison of AR and Fourier methods.**

## CONCLUSIONS AND RECOMMENDATIONS

Infrasound modeling was performed with the InfraMAP software developed by BBN Technologies. Shown in figure 8 are the results of the modeling using the Naval Research Lab Ground-to-Space (NRL G2S) model for the 2007 data. The G2S model is supposed to include the local meteorological variations. The left plot shows the ray-tracing results, and the right shows the pressure amplitude field (in dB) obtained with the parabolic equation (PE) code. The locations of our arrays are shown on the left plot. On that particular day FALN recorded tropospheric and stratospheric signals, while at GERL we observed stratospheric and thermospheric signals. None of the actual arrivals are predicted with either of the method. Thermospheric rays are predicted to bounce at more than 350 km away from the source, while raytracing shows no stratospheric or tropospheric rays. These results are similar to the PE code.

Current modeling efforts focus on using the actual meteorological data acquired in the paths of the propagating signals to determine the presence of any potential duct in the troposphere that could have allowed the transmission of energy to greater distances. In addition, this controlled dataset will allow us to investigate the relationship between the celerity and the phase velocity (which in ray theory is supposed to be equal to the effective sound speed velocity in the place where that particular ray is turning).

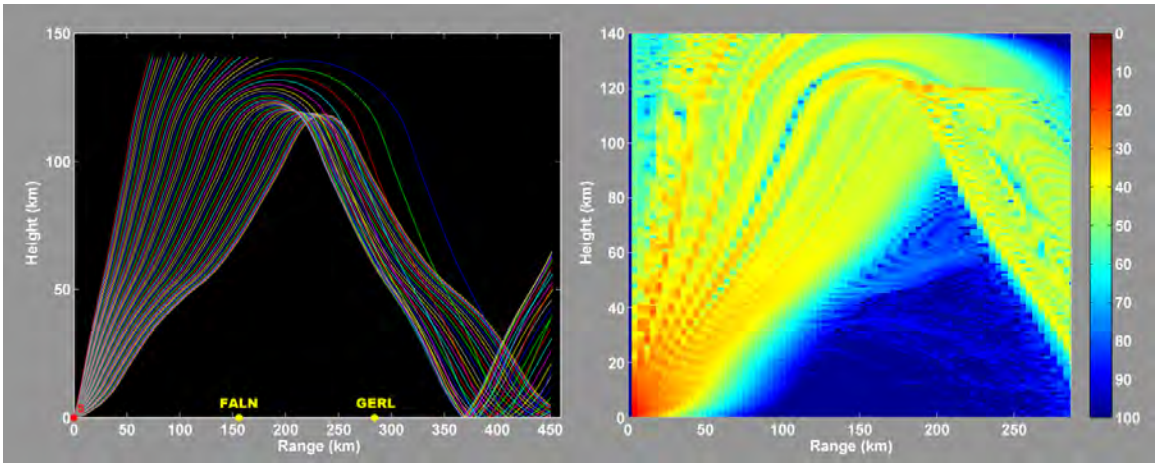


**Figure 8. Ray tracing (left) and PE calculations through the NRL G2S model for the 2007 data. The model is supposed to include the meteorological effects below 20 km.**

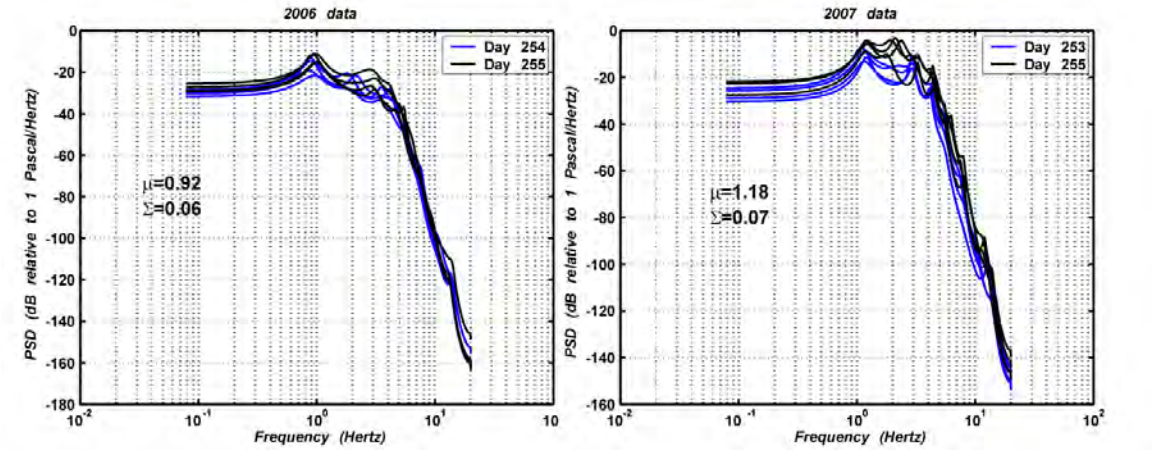


**Figure 9. AR estimates for different days for 2006 and 2007 data at NVAR.**

Frequency estimates for 2006 and 2007 datasets were obtained with an AR(16) method. Figure 9 shows the Power Spectral Density Functions for days in which the amount of ordnance disposed were the same in total weight (3,809 lbs.). However, the spectral estimates are different. The mean frequency estimate for the 2006 dataset (40 samples in total) is 0.92 Hz, while the mean for the 2007 (40 samples) dataset is 1.18. This difference is much larger than the error of the AR method, and therefore they can be attributed only to differences in the source. The logs from the disposal contractors indicate that though the total weight of the explosives was similar in the two years, the materials have different chemical characteristics (explosivity). In 2006, the total of 3,809 lbs. was composed of 1,800 lbs. HBX and 2,009-lb. grenades, while in 2007, the composition was 450 lbs. HBX, 1350 lbs. composition B and 2,009 lb.-grenades. HBX is the most energetic in this combination, and we believe that the higher frequency estimated for 2007 is due to less HBX. The operations at Hawthorne will be on going, and in the future there are scheduled detonations of HBX only. We will use these HBX only detonations as references for future investigations on the yield/dominant period relationship.

**AKNOWLEDGEMENTS**

We would like to thank Dr. Doug Drob at the Naval Research Laboratory for the NRLG2S data for the days of the experiments. We also thank the personnel at the ammunition disposal site in Nevada for their ongoing cooperation, in particular Ms. Suzanne Lehr for providing us with detonation logs.

## REFERENCES

Blackman R. B. and Tukey J. W. (1959). The Measurement of Power Spectrum rom the point of view of Communication Engineering, *Bell Systems Tech. Journal* 37: 185–282.

Burg J. P. (1972). The relationship between maximum entropy spectra and maximum likelihood spectra, *Geophysics* 37: 375–376.

Golden P., E. T. Herrin, and P. T. Negraru (2007). Infrasound in the zone of silence. Proceedings of the European Geophysical Union, Vienna, April 2008.

Kulichkov S. N., D.O. ReVelle, R. W. Whitaker and O. M. Raspopov (2000). On so called "Tropospheric" arrivals at the long distances from surface explosions in *Proceedings of the 9th Annual International Symposium on Long-Range Sound Propagation*, pp.229–237, NCPA Report No. DM0501-01.

McKenna, S.H. (2005). Infrasound Wave Propagation over Near Regional and Tele-infrasonic Distances, Southern Methodist University, PhD Thesis.

Muschlecner, J. P. and R. W. Whitaker (1999). Thermospheric Infrasound Signals, in *Proceedings of the 21st Seismic Research Symposium*: *Technologies for Monitoring the Comprehensive Nuclear-Test-Ban Treaty*, LA-UR-99-4700, Vol. 1, pp. 151–158.

Priestly M.B. (1981). Spectral Analysis and Time Series, Academic Press.

Welch P.D. (1967). The use of Fast Fourier Transforms for the estimation of power spectra: a method based on time averaging over short modified periodograms. Trans IEEE AU15, 70–73.

# A PORTABLE INFRASONIC SENSOR CALIBRATOR DOWN TO AT LEAST 8 HZ

Kris Walker, Matthew Dzieciuch, Mark Zumberge, and Scott DeWolf

Institute of Geophysics and Planetary Physics and University of California, San Diego

Sponsored by Army Space and Missile Defense Command

Contract No. W9113M-06-1-0002
Proposal No. BAA06-41

## ABSTRACT

An optical fiber infrasound sensor (OFIS) is a long compliant tube wrapped with two optical fibers that integrate pressure variation along the length of the tube at the speed of light via laser interferometry. Here we only present the initial results of research conducted under this contract due to delays in the construction of the Camp Elliott OFIS array. All the field work has been completed, but the remainder of the data analysis will be completed in the next two months and presented in the associated poster. In this paper, we show that M-sequences transmitted via an array of 18-inch subwoofers comprise a portable infrasound sensor calibrator, which also permits in situ evaluation of wind noise reduction filters. For example, a comparison of a 60-m OFIS with a Brüel & Kjær **(**B&K) microphone at a signal frequency of 50 Hz for a source ~240 m away shows that the OFIS reduced wind and other types of undesirable noise by 18 dB over the B&K microphone with a standard sponge wind screen. An 8-subwoofer array at a range of ~240 m yields a reliable calibration signal that smoothly decreases in power by a rate of 2.5 dB/Hz with decreasing frequency to 8 Hz, which is fairly remarkable given the 20 Hz rolloff frequency of the amplifier and speakers.

## OBJECTIVES

It is difficult to accurately calibrate infrasound sensors because of the difficulty in generating repeatable infrasound with small devices. Standard subwoofers are designed to have flat impulse responses down to ~20 Hz. Propane cannons or impulsive devices have difficulty generating infrasound below 5 Hz. A rotary speaker attached to a small building or covered truck may be an effective solution to this problem. The objective of this research is to develop an alternative calibration tool using commercially available subwoofers. Ideally, we seek a calibrator that can produce a signal in the 100-s to 20-Hz range. An array of subwoofers provides a larger source area, which can theoretically generate a lower-frequency signal. Furthermore, M-sequence technologies can be used to create a calibration signal at various frequencies where the energy transmitted by the source is power limited. Our objective is to develop and evaluate, with an OFIS sensor and collocated B&K microphone, an array of subwoofers that transmits M-sequences for infrasound sensor calibration.

The second objective of the research to be conducted under this contract is to develop a near real-time OFIS array infrasound signal tracking system with which we can directly compare, as a test, with a real-time sky video in the tracking of large aircraft.

## RESEARCH ACCOMPLISHED

The objectives to be completed under this research were partially dependent on the construction of the Camp Elliott OFIS array (funded by another source). The construction of the Camp Elliott OFIS array experienced a number of delays, including the discovery of sensor sensitivity to temperature in early 2007 (Walker et al., 2007) and the San Diego county firestorms and subsequent rains in late 2007. The array went online in April of 2008. Due to these delays, the calibrator and real-time tracking research are not yet complete. It is expected that they will be completed in the next two months and results included in the associated poster. However, some results are reported below for the calibrator part of this research.

### OFIS Sensor

The OFIS is a silicone tube wrapped with two fibers that integrates the pressure variation along the length of the tube in an effort to average out spatially incoherent wind noise (Figure 1; Zumberge et al., 2003). Because the pressure variation is averaged along the length of the tube, the instrument response is a function of the orientation of the OFIS, relative to the orientation of the signal wavefront, in a similar way as the variation of the response of a rosette wind filter as a function of elevation angle.

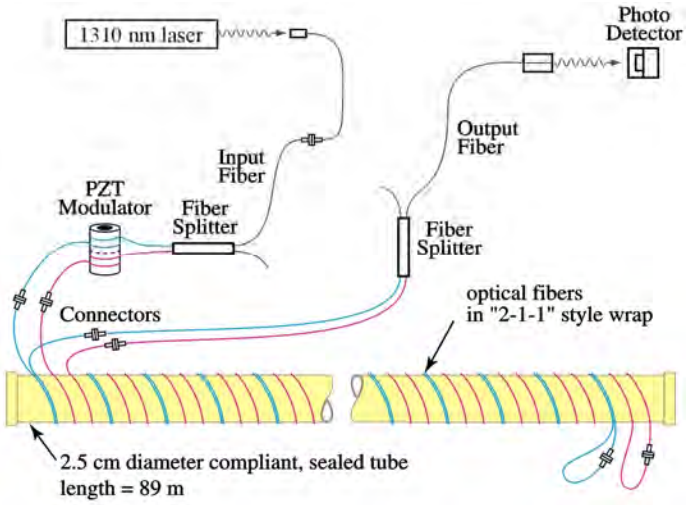


**Figure 1. Schematic of an OFIS.**

**Camp Elliott OFIS Array**

We installed five, 60-m OFIS arms at Camp Elliott (CEL), in north San Diego county near Miramar Marine Corps Air Station in early 2008. A sixth circular OFIS with a 7-m diameter was also installed at the center of the array. Each OFIS is buried beneath 6 inches of ¾-inch gravel. A Vaisala weather station, a 5-megapixel internet video camera, and a B&K microphone with sponge wind filter were also installed. Data from these sensors are streaming to our labs at the Institute of Geophysics and Planetary Physics (IGPP) in near real time (less than 2-s latency). A website displays filtered data at http://sail.ucsd.edu/~ofis/CEL/RT/. CSS3.0 data from this array will be archived daily at the RDSS beginning later in 2008.

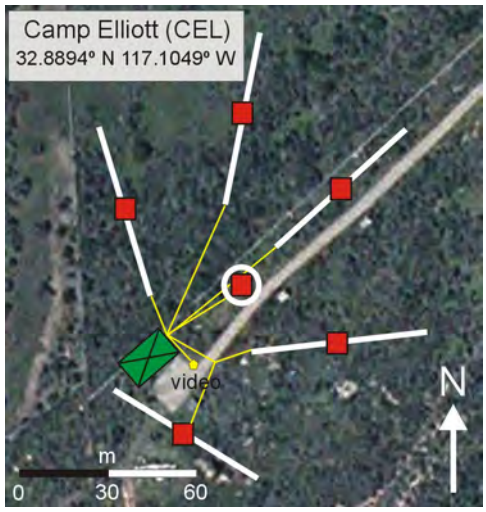


**Figure 2. Camp Elliott OFIS array (online April 2008).**

**M-Sequences**

An M-sequence is a random series of binary digits that has been extensively used in communication and imaging systems during the last 50 years. M-codes are periodic and can be generated with the use of a bit register and feedback law, often using modulo-2 addition of the last two bits in the register, shifting all values in the register by 1, and feeding that summed value to the front of the register (Figure 3a; Golomb, 1967). The period of an M-sequence is $2^N - 1$, where N is the length of the bit register (e.g., Figure 3b for N = 4). We then upsample the sequence (Figure 3c), scale it to –1/1 (Figure 3d), and use that "phase" function to modulate a sinusoid of a frequency $f_c$ (Figure 3e). Specifically, in Figure 3 we use a 4-bit register to generate the 15-bit sequence, which is used to modulate a 5-Hz signal at a rate of four carrier cycles per bit (Q = 4) to get a 12-s-long pseudo-random M-sequence.

In practice, one can determine the calibration signal power or signal-to-noise (SNR) by matched phase filtering. This demodulation technique is similar to cross-correlation and spiking deconvolution but yields better timing precision than the cross-correlation approach and is more stable than deconvolution. However, conceptually we can think of cross-correlation as the approach. If one transmits the input M-sequence calibration voltage to a recording system, one can cross-correlate that with the sensor recording. The maximum peak comes at some delay time that corresponds to the time it takes the signal to go from the source to the receiver (assuming timing on both recording systems is accurate). As an example, we calculate the autocorrelation of the M-sequence (Figure 3f). The SNR is calculated with

$$SNR = 20\log10\left(\max(autocorrelation)/noise(autocorrelation)\right).$$

The noise level can be obtained in a number of ways. We obtain it by taking the median of the absolute value of the autocorrelation function. The SNR for this 4-bit M-sequence is 29 dB. The SNR would be near infinite if the phase jumps used in this example were not precisely 180°. In our field experiments, the phase jumps are tuned to attenuate these side lobes. Furthermore, in the results shown below, the reference signal that we use in the phase-only filtering

is mathematically calculated rather than recorded at the source. Consequently, the time at which the peak in correlation occurs does not represent the travel time between source and receiver but represents the difference in time between the time the M-sequence generator was initiated at the source to the time it took the sequence generator to begin the next whole M-sequence period (pertinent to Figures 4–6). In other words, the program ignores the first transmitted fraction of the M-sequence when the reference signal is not used (since relative timing is not known).

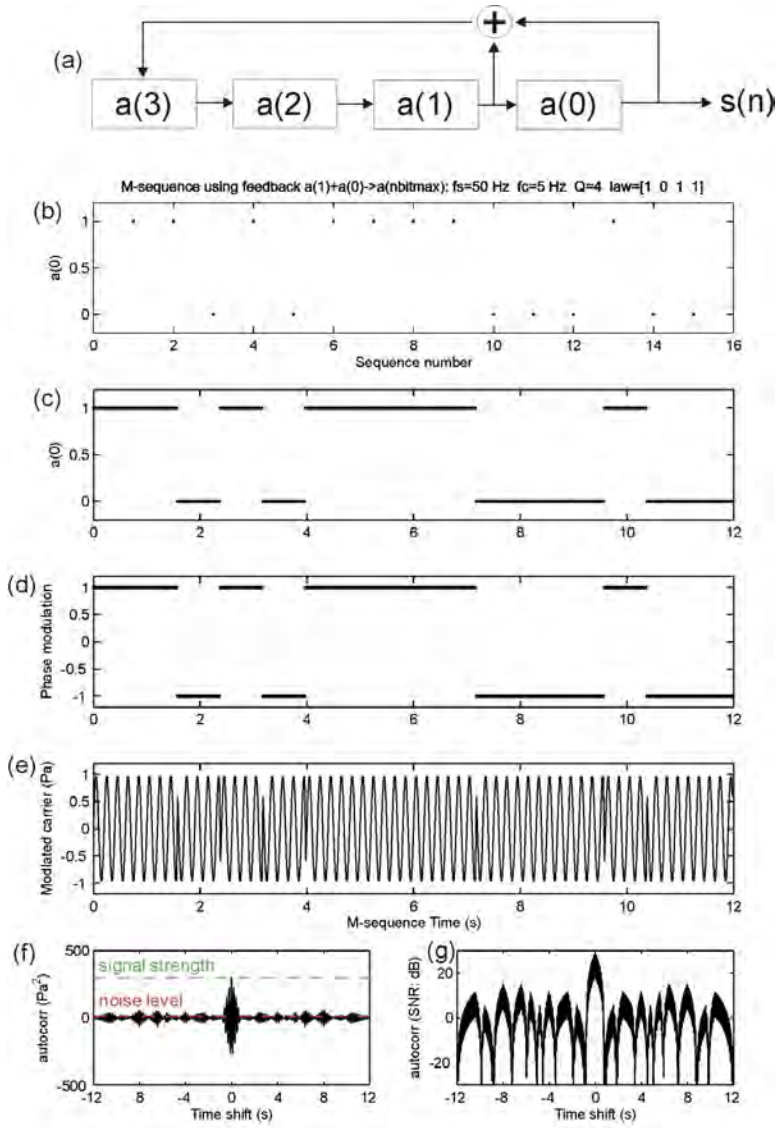


**Figure 3. M-code example from a 4-bit register to a pseudo signal-to-noise ratio (not using cross-correlation, but autocorrelation).**

### Hardware and Setup

In May 2007, we performed several M-sequence experiments with a single Yamaha 16-inch, 8-ohm subwoofer at a range of about 240 m from a 60-m OFIS and approximately collocated B&K microphone. The line between the center of the OFIS and the speaker array was at an angle of about 4° from the OFIS perpendicular. The subwoofer was connected to a Techron DC-coupled amplifier. An M-sequence circuit provided the input signal to the amplifier. Power was provided by a 3200-watt portable gasoline generator. The resulting input voltage to the subwoofer was

16.5 Vrms (33 watts) for frequencies between 5 and 50 Hz. These results were also discussed in Walker et al. (2007).

In August 2007, we performed several M-sequence experiments with an array composed of four Yorkville Elite Series cabinets located at the same position as in the earlier experiments. Each cabinet had two 1200-Watt, 4-ohm subwoofers for a total of eight subwoofers in the array. The cabinets did not have internal passive electronics. The subwoofers were connected to an American Audio V5000 Plus stereo amplifier in "subwoof mode," which has a theoretically flat response down to 20 Hz. An M-sequence circuit provided the input signal to the amplifier. Power was provided by a 3.2-kW portable gasoline generator. The subwoofers were tuned for peak performance by increasing the volume until the one of the limiting factors was encountered: (1) the breaker inside the cabinet was tripped or (2) the breaker inside the generator was tripped or the overload circuit protection system in the amplifier alarmed. There were three array configurations that we experimented with at a site located about 240 m away from a 60-m OFIS: (1) a horizontal line array, (2) a square array, and (3) a square array folded inward toward the sensors by about 45° and covered by ¾-inch plywood. Unfortunately, the B&K microphone was not available at the time of this experiment. However, we used an MB2000 and connected it to a 4-m porous hose that was pointing toward the array. The MB2000 was connected via a 300-m RG58 cable to a 16-bit digitizer. We calibrated and tested the MB2000 by pressing on the porous hose, and a large amplitude signal was observed. The MB2000 was first about 20 m in front of the speakers and subsequently moved to the previous location of the B&K microphone.

**Results**

*May 2007*

These experiments were implemented using a single subwoofer with a collocated OFIS and a B&K microphone with a sponge wind filter. The azimuth from the subwoofer to the OFIS center was 4º from the OFIS perpendicular, which means the signal wavefronts were approximately plane waves that impacted the entire 60-m OFIS and microphone simultaneously. Both sensors were sampled at 200 Hz. The 4-minute-long coded signal was impossible to observe by inspection in the 1-Hz, high-passed B&K microphone time series but is observed with a visual signal-to-noise ratio (SNR) of 5 dB in the OFIS recording (Figure 4a). The spectrograms for both sensors show that the signal was observed. The signal peak corresponding to the first arrival has an SNR of 34 dB for the B&K and 46 dB for the OFIS (Figure 4d; 12-dB difference). Due to the 4° azimuth deviation in the speaker array from the OFIS perpendicular, there is significant attenuation of a 50-Hz signal by the OFIS. Correction for this attenuation leads to a total SNR difference of 18 dB, which confirms that a 60-m OFIS is exceptionally sensitive to low-frequency sound and well attenuates wind noise and other sources of low-frequency sound that come from different directions that are not perpendicular to the length of the OFIS.

One application of this technique is to analyze each of the 24 coded signals separately and to measure the demodulated power and travel time of these signals. Since we hold the power input into the subwoofer constant, any demodulated power or travel-time fluctuations result from a change in the impulse response of the environment. Therefore, one can measure the coherence time of the atmosphere, changes in the velocity profile with time, or changes in the wind noise with time. We find a considerable degree of variability in the demodulated B&K signal power (Figure 4e), and a smoother variability for the OFIS recordings (Figure 4f). We performed the same experiment at $f_c$ = 20, 10, 5, and 1 Hz. We observed the coded signal for only the 50- and 20-Hz cases, running into the expected subwoofer rolloff at subaudible frequencies.

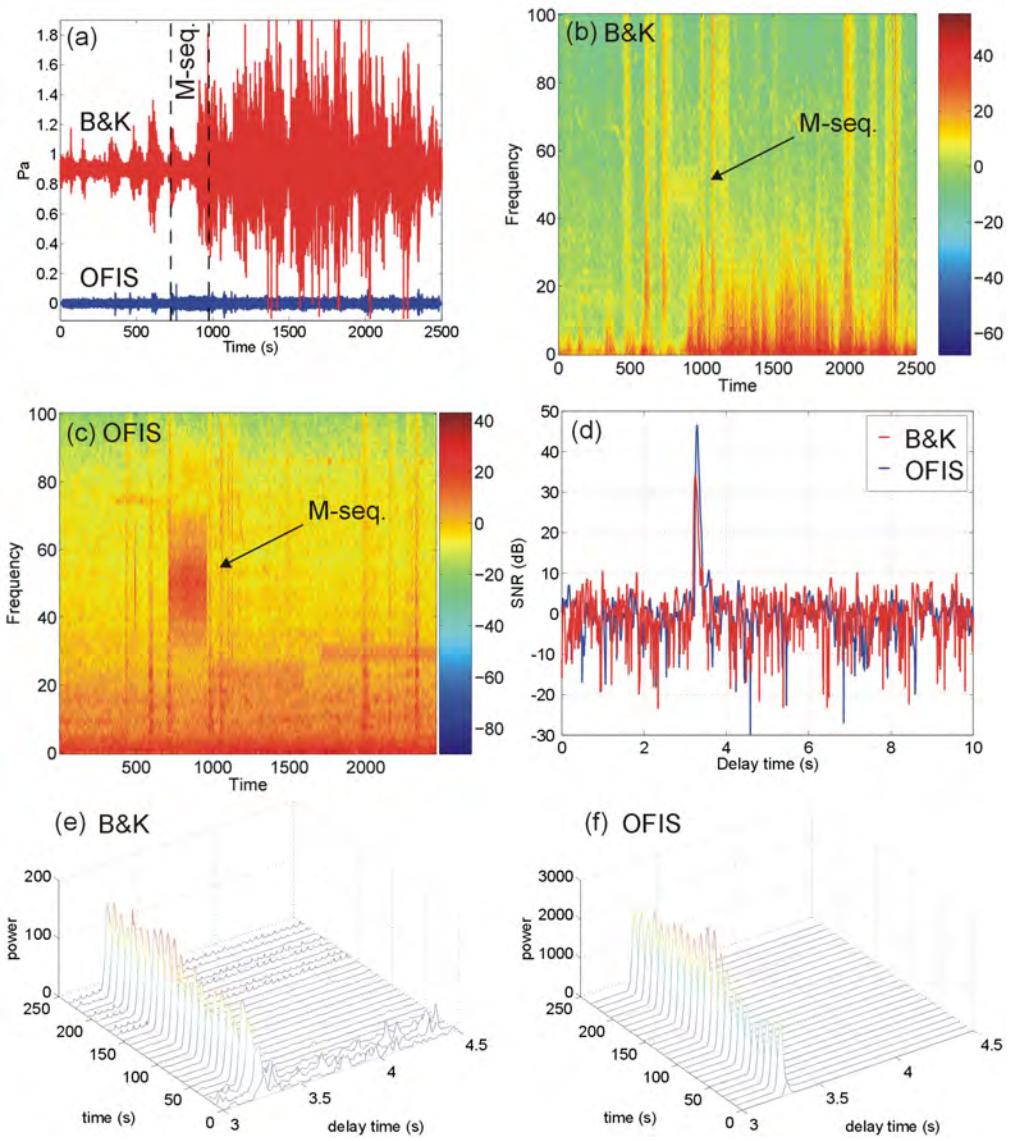


**Figure 4. M-sequence calibration technique using a 12-inch subwoofer at a 270-m distance from a tuned OFIS and a B&K microphone with sponge wind filter.**

*August 2007*

These experiments yielded much more information, although some of them were not ideal because the time windows were cut short because of breaker tripping. There were three speaker array configurations that we experimented with: (1) a horizontal line array, (2) a square array, and (3) a square array folded inward toward the source by 45,° with a ¾-in plywood covering the top. The output power of the array was measured by the MB2000 located 20 m in front of the array (20 Hz–0.02 Pa, 15 Hz 0.1 Pa, 10 Hz–0.008 Pa). The MB2000 theoretically has a high frequency rolloff of 27 Hz (3-dB attenuation point). There is only a 1-dB attenuation predicted between 15 and 20 Hz. The reason the 15-Hz frequency has a higher amplitude than the 20-Hz is likely related to the speaker and/or cabinet response.

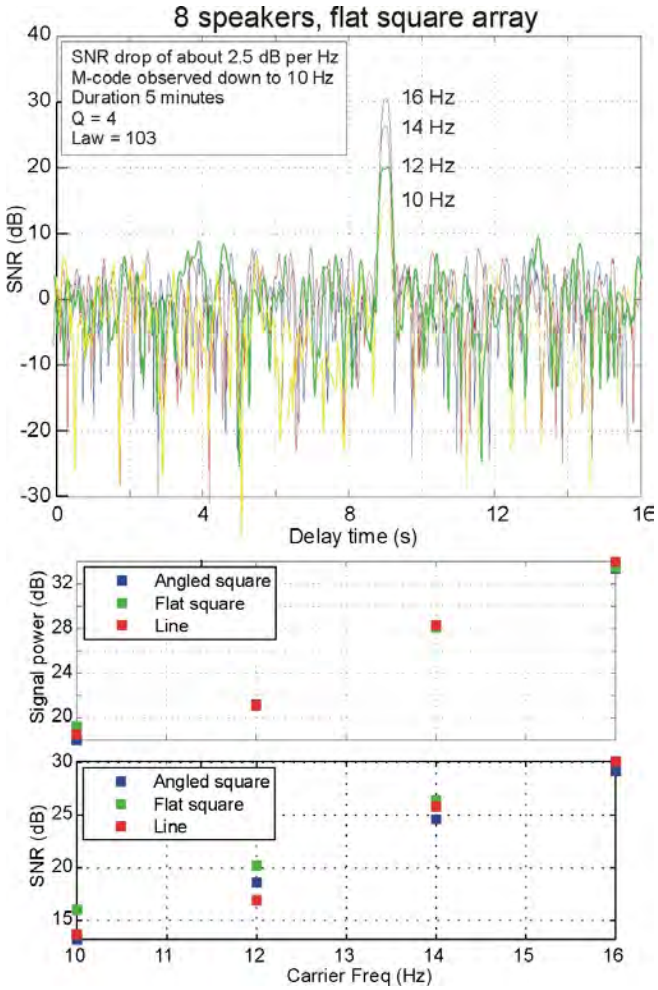


**Figure 5. Decrease in recorded calibration signal power with frequency for a square array (top) and other array configurations (middle and bottom). The signal power in this case is with respect to 1 rad$^2$ in OFIS interferometer units (subtract 28 dB with respect to 1 Pa$^2$).**

We ensonified the 60-m OFIS with a series of 5-min M-sequence time windows at different frequencies transmitted during the daytime by the square array (Figure 5). We found a decrease in the SNR by 2.5 dB per Hz between 10 and 16 Hz. Repeating this experiment on different array configurations did not significantly affect the recorded signal power, although the flat square seemed to give the best SNR for most frequencies.

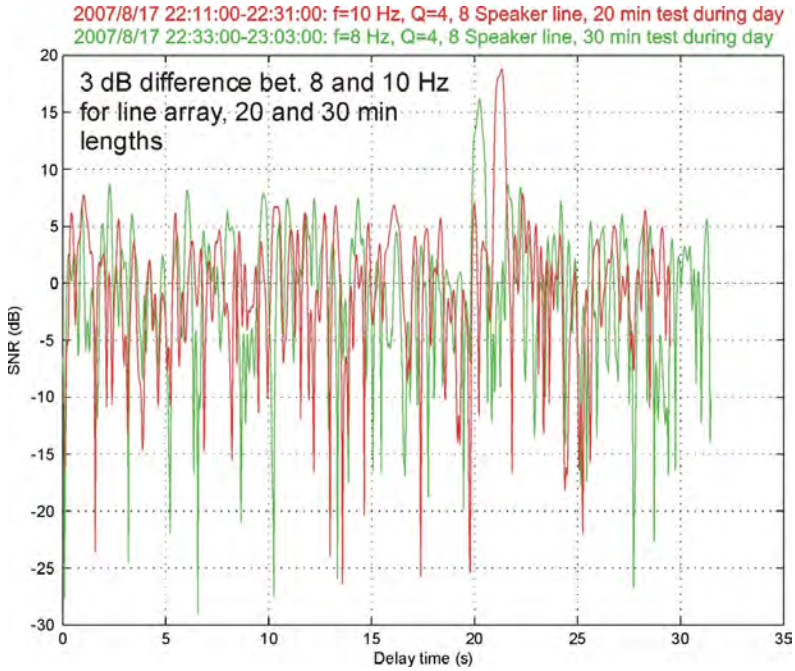


**Figure 6. Determining lowest reliable calibration signal frequency.**

Increasing the length of the M-sequence time window increases the SNR (Figure 6). We performed another daytime experiment with an M-sequence window of about 25 min for 6, 8, and 10 Hz. The lowest frequency for which we could observe a reliable signal was 8 Hz, which gave rise to an SNR of 16 dB and a recorded signal RMS amplitude of 0.002 Pa (40.0 dB SPL). We repeated this experiment at night when the atmospheric conditions were likely more conducive to long-range, near-surface sound transmission for 2-hour time windows. We could not see a 5-Hz signal, but we could see a 14-Hz signal with an increase in SNR of 21 dB over that obtained at 10 Hz during the day (the +2.5-dB/Hz rate estimated earlier only explains 10 dB of the 21 dB difference).

We moved the MB2000 to the previous location of the B&K microphone, which was collocated with the 60-m OFIS, and we performed another experiment to compare the wind-noise-reduction capabilities of an OFIS with respect to the adjacent MB2000, with 4 m porous hose pointing toward the array. An M-sequence of 2 hours ensonified the OFIS and MB2000 at 14 and 20 Hz. The OFIS recorded an SNR of 38 dB (14 Hz) and 48 dB (20 Hz). The power levels had roughly the same separation as well. Note that the 20-Hz SNR and power are much higher than the 14-Hz SNR, even though as mentioned earlier, the MB2000 located 20 m in front of the array recorded a 15-Hz signal that was about 5 times stronger than the 20-Hz signal. This discrepancy could be explained if the porous hose or the MB2000 sensor had an unexpected instrument response (Howard et al., 2007). The MB2000 at the location of the 60-m OFIS did not detect the 2-hour-long calibration signal at either 14 or 20 Hz. This result may have been impacted by the low dynamic range of the 16-bit digitizer. Repeating the experiment without the porous hose attached did not change this result.

A comparison was also made between the single Yamaha subwoofer/Techron amplifier and the subwoofer array/American Audio amplifier. The goal of this experiment was to determine the benefit of a subwoofer array over a single speaker. At 20 Hz and 50 Hz, the array yields a power level that is about 10 dB higher than the single speaker, approximately consistent with the gain predicted by octupling the power output by the single speaker (9 dB). This 9-dB gain could also be obtained with the single speaker by octupling the time window length of the M-sequence, providing the coherence time of the atmosphere remains longer than the time window. Comparison of the power levels between different frequencies within each source configuration shows that there is roughly 24 dB greater power received by the sensor. We tentatively interpret this to be due to the source radiating a greater level of energy at 50 Hz than 20 Hz. It appears that the SNR levels varied a bit more because the noise level fluctuated. The SNR increase at 20 Hz between one and eight speakers is about the same as the increase in power (~10 dB). However, the corresponding SNR increase at 50 Hz (1 dB) is remarkably small because the noise level increases by 12 dB from the 1-speaker to the 8-speaker experiments. It is unclear why the noise level increased by this much (it

was expected to have increased by only 4 to 5 dB). The timing of this noise correlates with the appearance of a secondary 20 dB (SNR) peak located 2.0 s after the first 50 dB (SNR) peak. This secondary peak could be explained by a reflection from the top of a 700-m-high atmospheric surface layer. However, at an SNR of 20 dB, the peak should have been observed in the single-speaker 50 Hz experiment 5 minutes prior to this time window, especially considering the noise for that single-speaker experiment was 12 dB less. Furthermore, there is no evidence of a burst of noise or airplane activity during this time window, which could have raised the noise floor. Our tentative conclusion is that there is some nonlinearity in the Yorkville eight-speaker array during our 50-Hz experiments that was not accounted for in our algorithm that calculated the M-sequence reference signal.

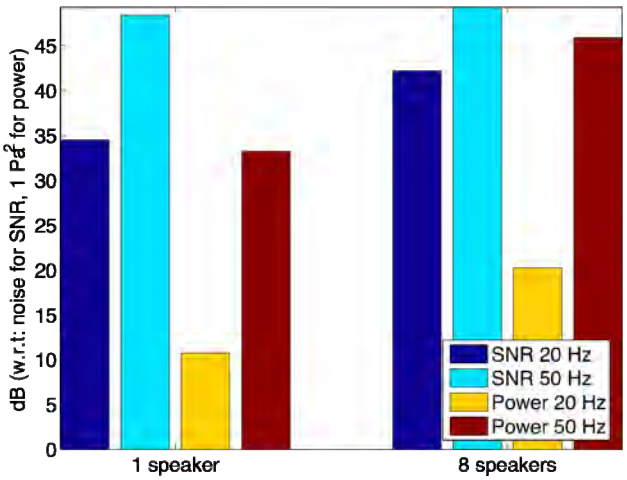


**Figure 7. OFIS recorded calibration SNR and power for a single-speaker and eight-speaker array for 5-minute M-sequence time windows during the late afternoon.**

## CONCLUSIONS AND RECOMMENDATIONS

The final analyses will be completed during the following months leading up to the MRR and will be presented on the associated poster.

Our results so far suggest that a single speaker has difficulty generating infrasound below 20 Hz with M-sequences at a range of at least 240 m. However, a square array of similar subwoofers that transmit M-sequences in phase is capable of generating infrasound down to at least 8 Hz in a predictable and repeatable manner at the same range. The technique can be used to calibrate infrasound sensors in situ (with or without large wind-noise-reduction filters). There are several techniques on how one can demodulate the M-sequence from the recording. Phase-only filtering is an optimum technique for this task because of its relatively good stability and temporal resolution.

Tests show that a 60-m OFIS records a 50-Hz calibration signal with an 18-dB improvement in SNR over that provided by a collocated B&K microphone with standard sponge wind screen. In terms of $1/n$ reduction in light wind noise, this means that a 60-m OFIS is equivalent to roughly 60 equally spaced microphones, or 1 microphone per OFIS meter.

## REFERENCES

Golomb, S. W. (1967) *Shift Register Sequences*. San Francisco: Holden-Day, Inc.

Howard, W., K. Dillion, and F. D. Shields (2007). Acoustical properties of porous hose wind noise filters, *J. Acoust. Soc. Am.* 122: 2985 [abstract].

Walker, K., M. Zumberge, and M. Dzieciuch (2007). OFIS experiments at Camp Elliott: Paving the way to infrasonic radar and a portable infrasonic sensor calibrator, these Proceedings.

Zumberge, M. A., J. Berger, M. A. H. Hedlin, E. Husmann, and S. Nooner (2003). An optical fiber infrasound sensor: A new lower limit on atmospheric pressure noise between 1 and 10 Hz, *J. Acoust. Soc. Am.* 113: 2474.

# INFRASOUND SIGNALS FROM GROUND-MOTION SOURCES

Rodney W. Whitaker

Los Alamos National Laboratory

Sponsored by National Nuclear Security Administration

Contract No. DE-AC52-06NA25396

## ABSTRACT

This report presents progress on an ongoing research project looking at near-field infrasound signals as a basis for discriminants between underground nuclear tests (UGT) and earthquakes (EQ). In an earlier program, infrasound signals from UGTs and EQs were collected at ranges of a few hundred kilometers, in the far-field. Analysis of these data revealed two parameters that had potential for discrimination purposes: signal duration and wind-corrected amplitudes. These far-field differences should be present in the near-field signals as well. To study the near-field signals, we are using computational techniques based on modeled ground motions from UGTs and EQs. One is the closed form numerical integration of the Rayleigh integral (RI), and the other is the application of a time-domain, finite-difference computational fluid dynamics (CFD) program, CAVEAT. This report summarizes recent progress in modeling these signals, showing comparisons of waveforms and power spectra from the two techniques. There is also a discussion of the effects of spatial and temporal zoning on the quality of the results. Application of Fourier techniques to the basic ground models is introduced as an analytic path to the radiation patterns of the ground-motion sources.

## OBJECTIVES

The objective of this research is to find differences in the near-field infrasound signals of UGTs and earthquakes that can be the basis for establishing discriminants between the two sources. Such differences in the near-field signal would likely survive to a longer range.

## RESEARCH ACCOMPLISHED

We have continued the numerical studies on modeling the near-field infrasound signal from the surface ground motion from underground nuclear tests (UGT) and earthquakes (EQ). The computational tools include numerical integration of the closed-form RI and the use of the time-domain, finite-difference code CAVEAT. CAVEAT was only mentioned in last year's MRR report but has been used more extensively this past year.

### CAVEAT Developments

CAVEAT is an established computational tool and has been applied to calculations of the time evolution of atmospheric nuclear explosions, including hydrodynamic outputs and optical signature outputs. CAVEAT is documented in Adessio et al. (1992). The following succinct description of the CAVEAT code is directly quoted from the abstract of the Adessio et al. (1992) report:

> CAVEAT uses an explicit time-marching, conservative finite-volume numerical technique in which all state variables, including velocity, are cell centered; values at vertices and cell faces are derived. The technique is a variation of the Godunov method that uses an approximate Riemann solver and accommodates arbitrary equations of state. Spatial differencing may either be first order (constant across the cell) or second order (linear variation across the cell) with a choice of limiters of the gradient in an attempt to preserve monotonicity. The formulation is spatially two-dimensional with options for Cartesian and curvilinear geometries, e.g., cylindrical (r,z). Discretization is achieved with a mesh of arbitrary quadrilateral cells whose vertices can move with time. Arbitrary mesh motion is supported by allowing transport of material between cells according to the arbitrary Lagrangian-Eulerian (ALE) technique. The computation is performed in two phases: a Lagrangian phase and a remapping phase in which conserved variables are transferred from the Lagrangian mesh to an arbitrary specified mesh. The dynamic mesh capability generally smoothes distortions in the mesh and can also result in higher resolution around features of interest, such as a shock discontinuity.

The report contains results for test cases of a shock tube, spherical blast wave, a pure advection problem, and a shock on wedge.

The initial calculations with CAVEAT used a separate ground motion acceleration model that was not the same as that used in the RI code. We have worked to correct this by using bi-cubic spline interpolations on the RI code computed velocity data as a function of range, r, and time, t. For a given event, the full set of surface velocities, $v(r,t)$ is written to an input file to CAVEAT. At the bottom of the CAVEAT mesh (grid), we employ the specified velocity boundary condition whose values at a specific time and range are interpolated from the $v(r,t)$ field using the bi-cubic spline algorithms from Press et al. (1990). In this manner the velocity data in the RI code and in CAVEAT can be made nearly the same. This scheme is quite general and efficient and applicable to other ground motion sources as well.

For the CAVEAT results reported here, we used cylindrical (r,z) coordinates with 500 mesh cells in each direction. The standard run was with radial and vertical steps of 30 m. The finer zone calculation was performed with mesh sizes of 15 m. The runs were made with an ALE coefficient of 0.9. The ambient atmosphere was from a Committee on Space Research (COSPAR) International Reference Atmosphere (CIRA) standard atmosphere.

We first show pressure contours for the standard and fine zone calculation (Figure 1), where the input velocity data were from the modeled accelerations for the Tortugas event in hole U3gg. In the CAVEAT results, we show the signal pressure that is the total pressure minus the ambient pressure, sometimes referred to as the perturbation pressure.

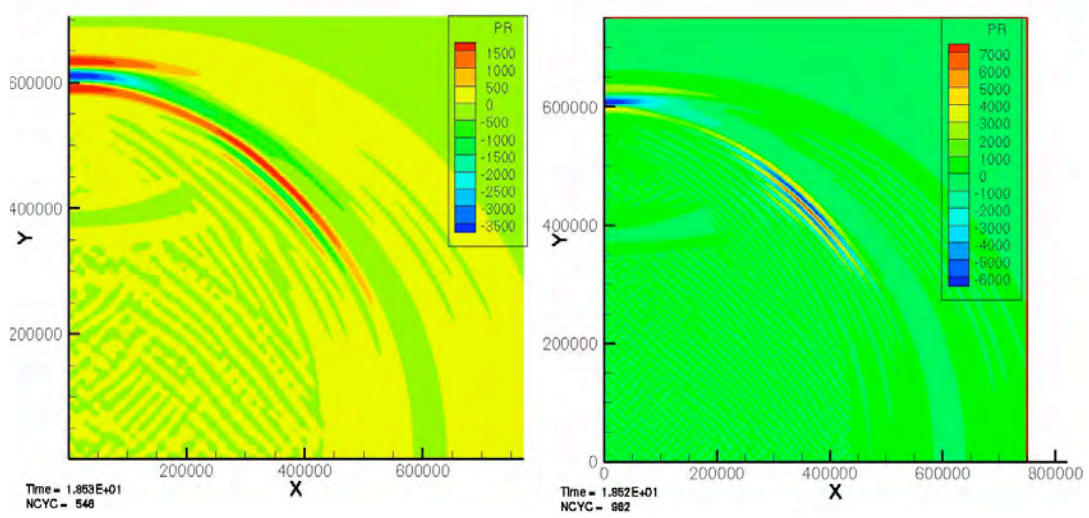


**Figure 1. Pressure contours for the standard CAVEAT run (left) and finer zone calculation (right) at 20 seconds. The x and y values are in centimeters, and pressure contours are in dynes/cm$^2$. Each calculation used 250,000 zones. Pressure contour values are shown in the upper right.**

The finer zone result shows more structure in the pressure field. From the contour legends we see that the finer zone result has larger (in absolute value) maximum and minimum pressures. By taking radial slices through the mesh at different elevation angles we can make additional comparisons. An example is shown in Figure 2.

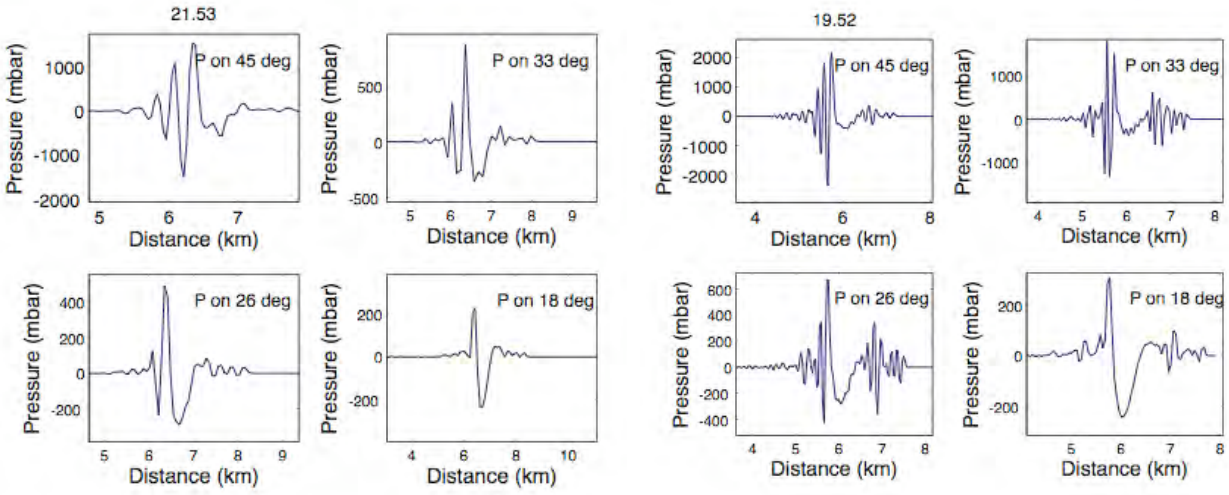


A B

**Figure 2. Radial slices through the Caveat mesh for the standard run (left 2 × 2 set, A) and for the finer zone run (right 2 × 2 set, B). The slices are at elevation angles of 18, 26, 33, and 45 degrees. The pressure unit "mbar" stands for "micro bar."**

The finer zone run generally has higher frequency structure and larger amplitudes, compare the 33-degree panels. To examine the impact of smoothing, we did a five-point running average on the pressure values on the 45-degree fine zone data (B set), and the result is quite similar to the 45-degree standard run result (A set). These results show the improved velocity model that has now been implemented into CAVEAT.

**Rayleigh Integral (RI) Code Developments**

For review, the RI is given by the following equation:

$$p(R_0,t) = \frac{\rho}{2\pi}\int \frac{a(r,(t-R/c))}{R} dA_s \,, \tag{1}$$

where a is the acceleration of the ground, r is a location on the ground (referenced to a center position), $dA_S$ is an element of area on the ground, R is the distance from the ground element to the observing point, t is time, ρ is the air density, c is the speed of sound in air, p is the air pressure, and $R_0$ is the observation location.

The RI code uses modeled ground motions for some 30 events. The parameters include the peak acceleration and temporal width of the initial acceleration pulse and the same for additional contributions from plastic or cavity rebound signals. A specified exponential decay with range is also applied.

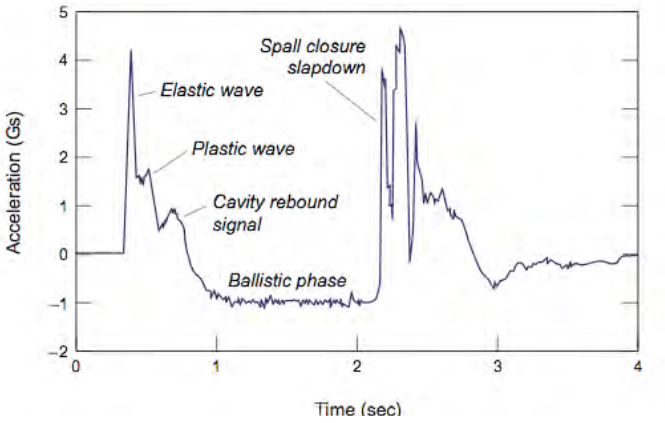


**Figure 3. An illustration of the characteristics of ground motion from a UGT.**

Figure 3 illustrates the features in UGT acceleration records. Some events have just the initial and slapdown contributions, such as Tortugas, U3gg, while others have additional contributions such as Duoro, U3lv. When the acceleration is the simple two-pulse shape, the velocity exhibits a simple form as well. This is illustrated in Figure 4. The acceleration is a classic two-pulse record, and the velocity has a well-defined linear portion due to the –1 g spall phase in the acceleration, Jones et al. (1993) and Huan and Walker (1980).

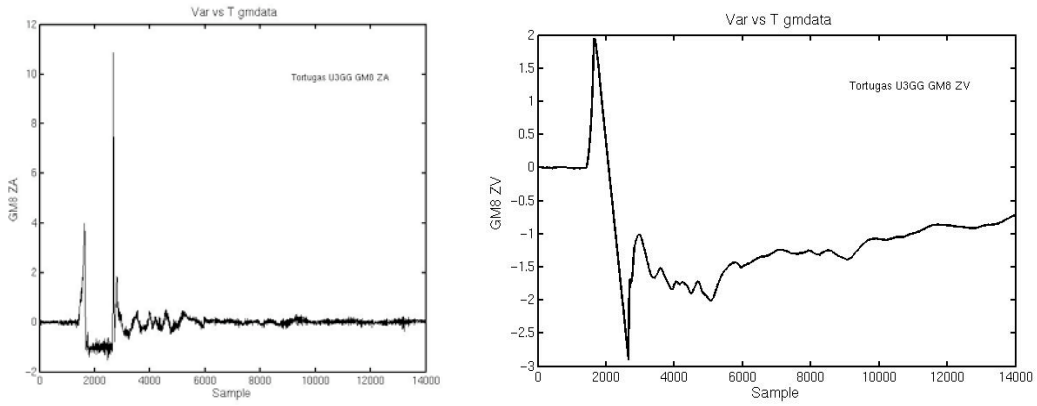


**Figure 4. A measured ground-motion acceleration record for Totugas (left) and the velocity record (right), where units are gs for acceleration and m/s for velocity. The horizontal axis is the sample number.**

If the acceleration record has contributions from other components, the behavior is more complicated, as is illustrated in Figure 5 for the Duoro event.

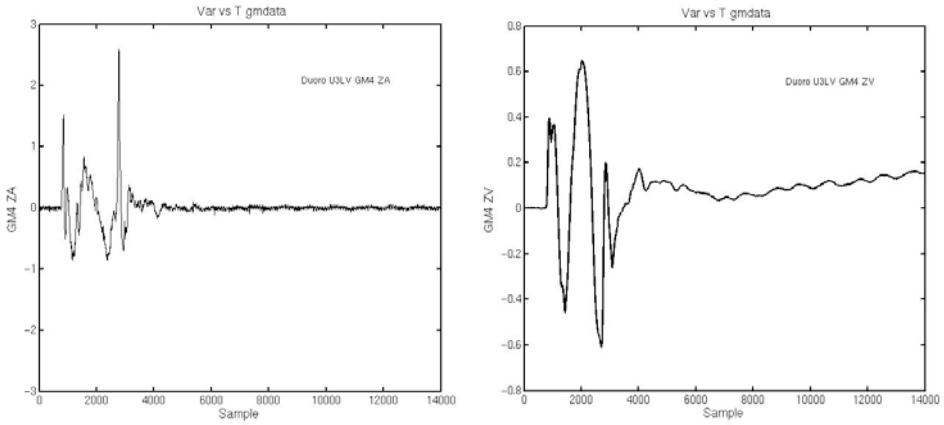


**Figure 5. The same as Figure 4 except for the Duoro event, which shows more-complicated behavior.**

We use the modeled ground motions from these two events to illustrate some results from the RI code. First, we show computed power spectra for the RI code calculation for an observer at an horizontal range of 5 km and a height of 4 km and for an observer at a horizontal range of 15 km and a height of 10 km. These are close to the same elevation angle. Figure 6 presents this comparison and shows good agreement.

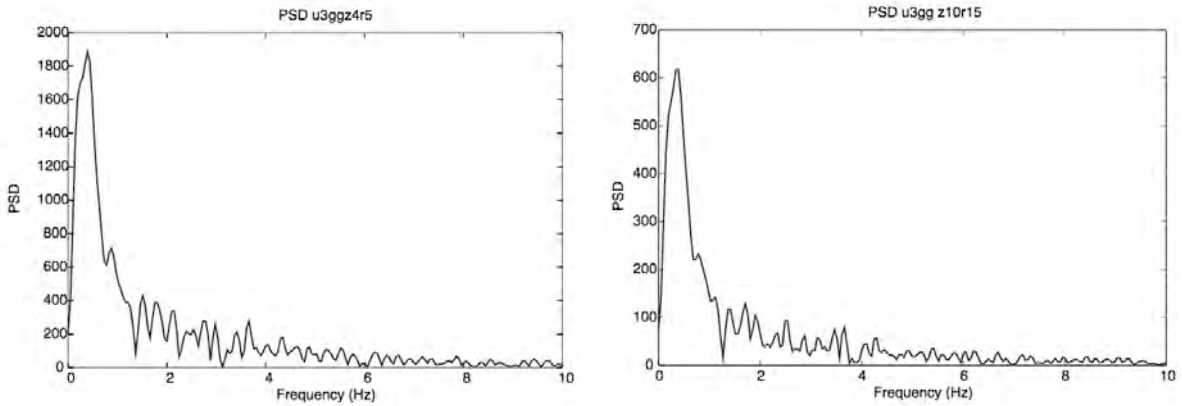


**Figure 6. Power spectra (relative units) for the Tortugas event, hole U3gg, for a height of 4km and a range of 5 km (left) and for a height of 10 km and range of 15 km (right). The results are reassuringly close. Frequency is on the horizontal axis.**

To illustrate the effects of the more complicated ground motion, Figure 7 shows the RI code power spectra for the Duoro event. As expected, the Duoro event has larger contributions at higher frequencies than does the Tortugas event, due to the more-complicated source acceleration.

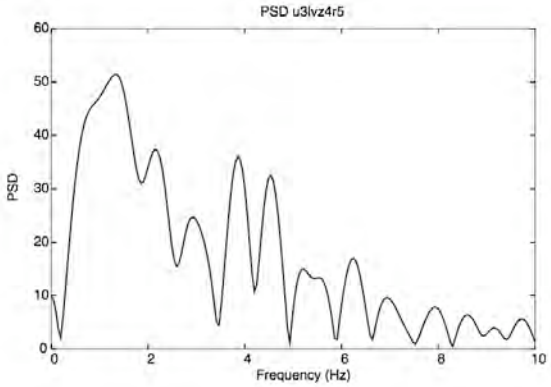


**Figure 7. RI code power spectra (relative units) for the Duoro event at a range of 5 km and a height of 4 km. Frequency is on the horizontal axis. Compare this result with that in the left panel of Figure 6.**

**Initial Comparisons of Two Techniques**

Below we show a comparison between the CAVEAT and RI codes for the Tortugas event, U3gg. CAVEAT advances in time so that, at a given time, we can take a snapshot of the pressure field in the computational domain. Then we can plot radial slices through that domain at different elevation angles. This is shown in Figure 8 with the left four plots from CAVEAT. The RI code provides a time history at a given observation location. When looking at the CAVEAT radial slices, one must remember that the pulse is proceeding to the right. Thus to properly compare the two code results one should flip the CAVEAT plot. With that in mind, one can see that the waveforms are quite similar in shape. The RI code result is at 45 degrees and shows a little better agreement with the CAVEAT profile at 26 or 18 degrees. This is probably due to refraction in a layered atmosphere as is used in CAVEAT while a uniform atmosphere is used in the RI code.

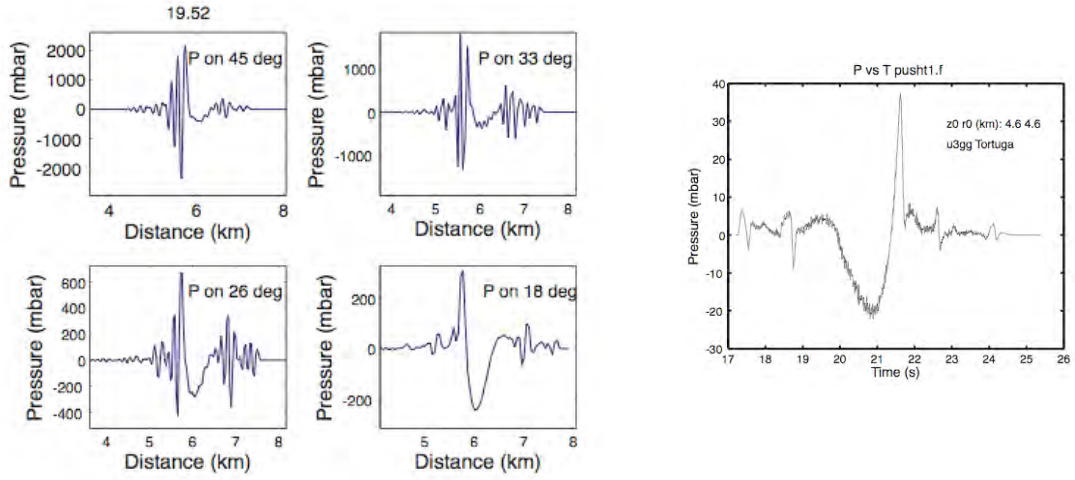


**Figure 8. A comparison of CAVEAT and RI code results for the Tortugas, U3gg, event. The left four panels are CAVEAT profiles at 20 seconds. The CAVEAT results are for the finer zoned calculation. The right plot is the RI code result at 45 degrees and range of 6.5 km. Due to a plotting error, the RI code pressures should be a factor of 10 larger.**

**Some Analytic Considerations**

1. An obvious direction in this work is that of a Fourier approach to the RI formulation. This is would serve as an easy way to compute the radiation pattern of ground-motion sources. A nice approach was given by Wecksung (1985) in an unpublished report and is summarized below for ease of reference, with some notational changes. The basic integral is given by

$$p(\vec{R},t) = \frac{\rho_0}{2\pi}\iint_A \frac{a(x,y,t-r/c)}{r}dxdy\,. \tag{2}$$

The area of motion is smaller than $R_0$, the distance from the center of the motion to the observation point. The source point on the ground is at $r_0 = r_0(x,y,0)$, and r is the distance from the source point to the observation point R. It is possible to use $1/R_0$ for the $1/r$ term in the integral and take it outside. Apply a change of variable of $\tau = t - r/c$ and take a temporal Fourier transform of Eq. (2) to get

$$\hat{p}(\vec{R},\omega) = \frac{\rho_0}{2\pi R_0}\iint_A \int_{-\infty}^{\infty} (a(x,y,\tau)dxdy)e^{-i2\pi\tau}d\tau e^{-i2\pi r/c}\,. \tag{3}$$

The normal acceleration, a, is related to the normal velocity, u, by

$$a(x,y,t) = \frac{\partial u(x,y,t)}{\partial t}, \tag{4}$$

and the integral over $a(x,y,t)$ becomes

$$\int_{-\infty}^{\infty} a(x,y,\tau)e^{-i\omega\tau}d\tau = i\omega\hat{u}(x,y,\omega), \tag{5}$$

where we have replaced $2\pi f$ with $\omega$ and $\hat{u}$ is the temporal Fourier transform of $u$. Then using Eq. (5), we can write

$$\hat{p}(\vec{R},\omega) = \frac{i\omega\rho_0}{2\pi R_0}\iint_A \hat{u}(x,y,\omega)e^{-i\omega r/c}dxdy\,. \tag{6}$$

At this stage the basic acceleration integral has been transformed, through a temporal Fourier transform, to a spatial Fourier transform of the normal velocity transform. Next, let $e$ be a unit vector in the direction of R, $\hat{e} = (\sin\theta\cos\phi, \sin\theta\sin\phi, \cos\theta)$. It is possible to write $\vec{r} = \vec{R} - \vec{r}_o$ and from that, have $r^2 = R^2 - 2\vec{R}\cdot\vec{r} + r_0^2$. A little simplification gives an approximate expression for r, $r \approx R - (x\sin\theta\cos\phi + y\sin\theta\sin\phi)$. Next, for the spatial transform of $\hat{u}$, write

$$U_\omega(\upsilon_x,\upsilon_y) = \iint_S \hat{u}(x,y,\omega)\exp[-i2\pi(x\upsilon_x + y\upsilon_y)]dxdy\,, \tag{7}$$

and with the approximate expression for $r$, Eq. (6) may be rewritten as

$$\hat{p}(\vec{R},\omega) = \frac{i\omega\rho_0}{2\pi R}\exp(-\frac{i\omega R}{c})U_\omega\left(\frac{-\omega\sin\theta\cos\phi}{2\pi c}, \frac{-\omega\sin\theta\sin\phi}{2\pi c}\right). \tag{8}$$

The acoustic intensity is related to the pressure by

$$I_\omega(\vec{R}) = \frac{\left|\hat{p}(\vec{R},\omega)\right|^2}{\rho_0 c}, \tag{9}$$

which leads to an expression for the far field intensity

$$I_\omega(\vec{R}) = \frac{\rho_0\omega^2}{4\pi^2R^2c}\left|U_\omega\left(\frac{-\omega\sin\theta\cos\phi}{2\pi c}, \frac{-\omega\sin\theta\sin\phi}{2\pi c}\right)\right|^2. \tag{10}$$

2. Below is given a simple and straightforward derivation of an expression for the maximum amplitude of a uniform piston. Let the piston displacement be given by

$$z = A\sin(2\pi ft), \tag{11}$$

where A is the amplitude of the motion, f is frequency, and t is time. Then the velocity is given by

$$V = 2\pi fA\cos(2\pi ft). \tag{12}$$

On axis, the solution for pressure from an uniform piston is proportional (Pierce 1989) to a difference of velocities at retarded times,

$$p(h) = \rho c\left[ V(t - \frac{h}{c}) - V(t - \frac{\sqrt{h^2 + R^2}}{c} \right] = \rho c\Delta V, \tag{13}$$

where h is the height above the center of the piston, R is the radius of the piston, $\rho$ is the air density, and c is the speed of sound. From Eq. (12), the $\Delta V$ term can be written as

$$\Delta V = Aa\left[ \cos(a(t - \frac{h}{c})) - \cos(a(t - \frac{\sqrt{h^2 + R^2}}{c})) \right], \tag{14}$$

where $a = 2\pi f$. We assume h >> R, then the square root term becomes

$$\frac{h}{c} + \frac{R^2}{2ch} = \frac{h}{c} + y \tag{15}$$

Let (t-(h/c)) = b, substitute Eq. 15 in Eq. 14, expand the second cosine term, cancel obvious terms and use the small angle approximations for sine and cosine to get

$$\Delta V = -Aa^2 y\sin(ab), \tag{16}$$

with a maximum of $Aa^2y$. Then Eq. (13) can be rewritten as (for the maximum value)

$$p(h) = \rho cAa^2 y = \frac{2\pi^2 A\rho f^2 R^2}{h}. \tag{17}$$

Evaluation then requires only the displacement amplitude, frequency, piston radius, air density and altitude. An equivalent expression to Eq. (17) was given, without derivation, in Banister (1979) but had been overlooked by the author.

**Some Additional Items**

Ground-motion data, from measured ground-motion data files, for the 30 modeled events have been extracted. The accelerations and velocities plots have been put into a draft report that can be supplied upon request. Power spectra are now routinely computed for any case calculated by the RI code. A postprocessor was written to extract radial slices from the CAVEAT mesh.

## CONCLUSIONS AND RECOMMENDATIONS

The improved velocity model from the RI code input to CAVEAT was implemented just before the deadline for the submission of this paper; only a few runs have been made. The mesh resolution in the CAVEAT runs needs further exploration. Initial comparisons of CAVEAT profiles with the RI code show some differences that need to be studied and understood.

## ACKNOWLEDGEMENTS

We thank Dr. George Randall for help with getting some Wells, NV, earthquake data and for performing some ground-motion calculations using the wavenumber integration program of Dr Robert Herrmann and part of his "Computer Programs in Seismology" (http://www.eas.slu.edu/People/RBHerrmann/CPS330.html).

## REFERENCES

Addessio, Frank L., John R. Baumgardner, John K. Dukowicz, Norman L. Johnson, Bryan A. Kashiwa, Rick M. Rauenzahn, and Charles Zemach (1992). CAVEAT: A computer code for fluid dynamics problems with large distortion and internal slip, Los Alamos National Laboratory technical report, LA-10613, Rev. 1.

Banister, J. R., A program for predicting ground motion induced air pressures (1979). Sandia National Laboratories report SAND 78-2361.

Jones, Eric M., Frederick N. App, and Rodney W. Whitaker (1993). Ground motions and the infrasound signal: A new model and the discovery of a significant cavity rebound signal, Los Alamos National Laboratory technical report LA-UR 93-861.

Lee, Huan and James J. Walker (1980). Model for ground motion and atmospheric overpressure due to underground nuclear explosions, Los Alamos Scientific Laboratory report LA-8554-MS.

Mutschlecner, J. Paul and Rodney W. Whitaker (2005). Infrasound from earthquakes, *J. Geophys. Res*. 110: D01108, doi:10.1029/2004JD0050067.

Pierce, Allan D. (1989). *Acoustics, an Introduction to Its Physical Principles and Applications*. New York: Acoustical Society of America.

Press, William H., Brian P Flannery, Saul Teukolsky, and William T. Vetterling (1990). *Numerical Recipes (Fortran Version)*. Cambridge University Press.

Wecksung, George W. (1985). Acoustic radiation patterns associated with the ground motion produced by a contained nuclear explosion, Amparo Corporation report (unpublished).

# Data Processing and Analysis

# NUCLEAR EXPLOSION AND INFRASOUND EVENT RESOURCES OF THE SMDC MONITORING RESEARCH PROGRAM

Manochehr Bahavar, Brian W. Barker, Theron J. Bennett, Hans G. Israelsson, Benjamin C. Kohl, Yu-Long Kung, John R. Murphy, Victoria Oancea

Science Applications International Corporation

Sponsored by Army Space and Missile Defense Command

Contract No. DASG60-03-C-0009

## ABSTRACT

The Research and Development Support Services (RDSS) project of the Space and Missile Defense Command (SMDC) provides a range of resources and services for use in nuclear explosion monitoring R&D. This presentation focuses on some recent enhancements to the infrasound, seismic, and hydroacoustic resources, which can be accessed from the RDSS website at http://www.rdss.info. In particular, ongoing developments and improvements are related to (1) the nuclear explosion database (NEDB) and (2) infrasound signals and associated source information.

The RDSS project has traditionally maintained an archive of information on source parameter data and waveforms from worldwide nuclear explosions. A major revision and update of the NEDB includes newly published or revised source information about historical explosions, access to additional or corrected waveform data for some explosions, and new data from more recent nuclear tests (viz., North Korea). New web tools for accessing the NEDB archive include GoogleMap visualization of alternative event locations, displays of recording station information (e.g., data availability and station parameters), seismic travel time residual displays, and new waveform display and retrieval options, which include options for simple prefiltering and signal rescaling during data review prior to download.

Identification of infrasound events for the RDSS infrasound database has continued. The effort is based primarily on seismic-event bulletins, volcanic activity reports, meteor observations, announcements on rocket launches and information appearing in the news media. The search for infrasound signals associated with events in these reports and bulletins is utilizing the automatic detection lists of International Monitoring System (IMS) stations augmented with the processing of waveform data from the SMDC waveform archive. The detectability at IMS infrasound stations I26DE (Freyung, Germany) and I18DK (Qaanaaq, Greenland, Denmark) of a large series of explosions in northern Finland to destroy ammunitions was also analyzed with regard to propagation conditions and station noise. During favorable conditions, low signal-to-noise ratio (SNR) signals were detected at the two stations, which are located at much larger distances than stations in Fenno-Scandia, for which infrasound signals have previously been reported for these events.

## OBJECTIVE

The RDSS project of the SMDC has the objective to support the nuclear explosion monitoring research and development community providing a range of data, state-of-the-art data access tools, and value-added datasets. This paper focuses on recent developments and enhancements to the seismic and infrasound resources, which can be accessed from the RDSS website. In particular, recent developments have been directed at (1) the nuclear explosion database archive and options for display and retrieval of the associated data resources, and (2) identification of infrasound events and association of the related signals.

## RESEARCH ACCOMPLISHED

### Nuclear Explosion Database

The SMDC NEDB has historically provided access to source parameter data and associated waveforms for worldwide nuclear explosions, online at www.rdss.info and documented in a series of reports (e.g., Yang et al., 2000). As described in Bahavar et al. (2007), access to those data is being upgraded; and, in some cases, events are being added or the associated source parameters are being updated utilizing new information sources (e.g., Springer et al., 2002; Khalturin et al., 2005; Bennett et al., 2006; DTRA, 2007; Kim and Richards, 2007). In addition to performing a range of QA/QC checks on the source data (e.g., comparisons with satellite imagery), station calibration and response information have been improved to make archived waveform data from the NEDB more useful to the research community. The focus of this paper is on (1) recent improvements to NEDB event documentation, (2) expanded event analysis options (e.g., display of station travel-time residuals), and (3) improved display, review, and retrieval of waveform data.

The NEDB includes source parameter data for some 2,154 announced or presumed nuclear explosions (1,628 underground, 518 atmospheric, 8 underwater) conducted by 8 countries in more than 43 distinct geographic regions (Figure 1). Access to the NEDB is provided under the Research Databases menu option at the RDSS home

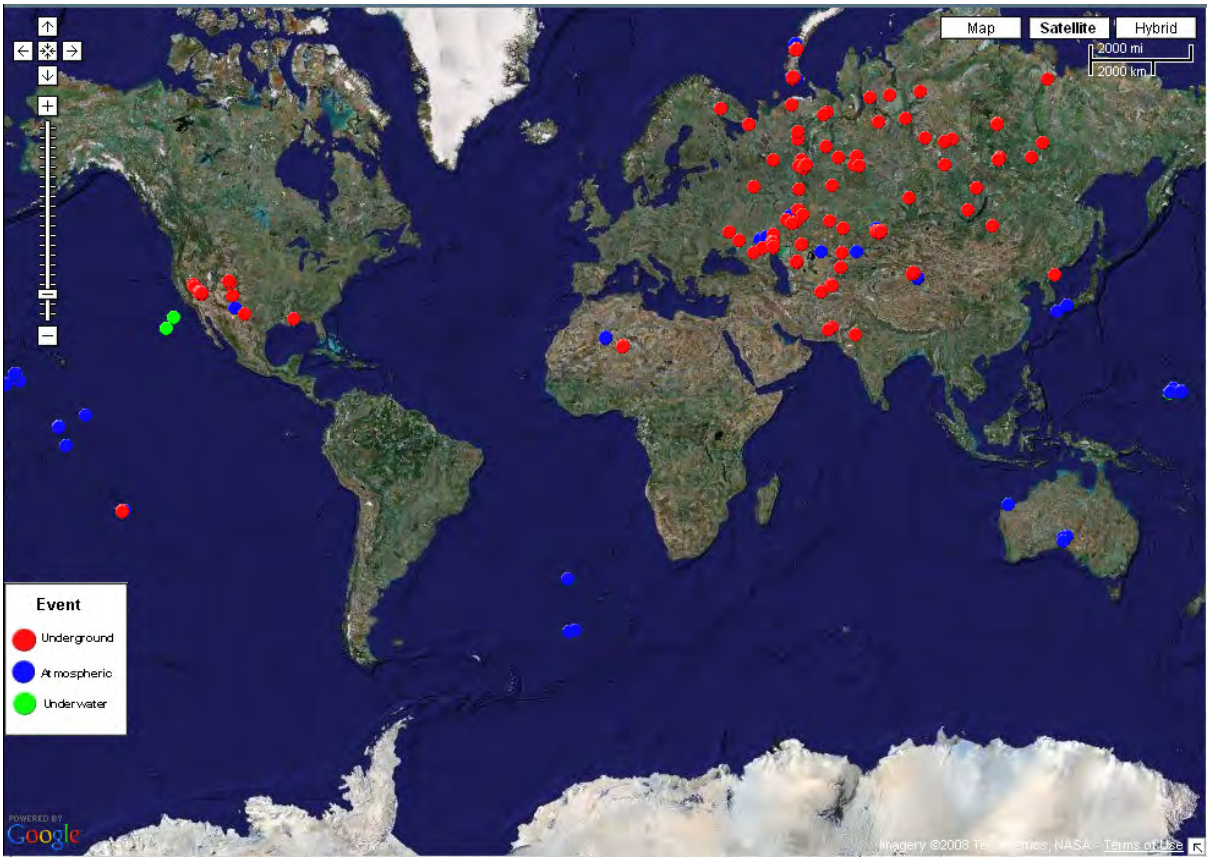


**Figure 1. Locations of 2154 announced or presumed nuclear explosions included in the NEDB.**

page using GoogleMap interaction, which enables comparisons between events or subsets of events, review of alternative source locations (e.g., the International Seismological Centre [ISC] or other seismic bulletins), assessment of relationships to terrain features visible in imagery, and analysis of seismic travel-time residuals.

Ground-truth information about explosion sources in the NEDB is quite variable and depends on many factors, including country of origin, age of the event, reliability and openness of documentation and record keeping, and region- or event-specific background knowledge. New emphasis has been placed on compiling the best available documentation regarding these nuclear explosions. As noted above, in some cases this information comes from newly published sources; in other cases review and cross-checking of previously reported source information has revealed discrepancies in the data, as noted previously (e.g., even recent reports such as Springer et al. (2002) include some errors in precision and accuracy). In compiling the revised NEDB, we have been attempting to provide the best available information for nuclear explosion source parameters along with the appropriate documentation to support the source description or allow the user to understand the uncertainties. This documentation is being provided in the form of event summary pages, accessible through links from the NEDB website.

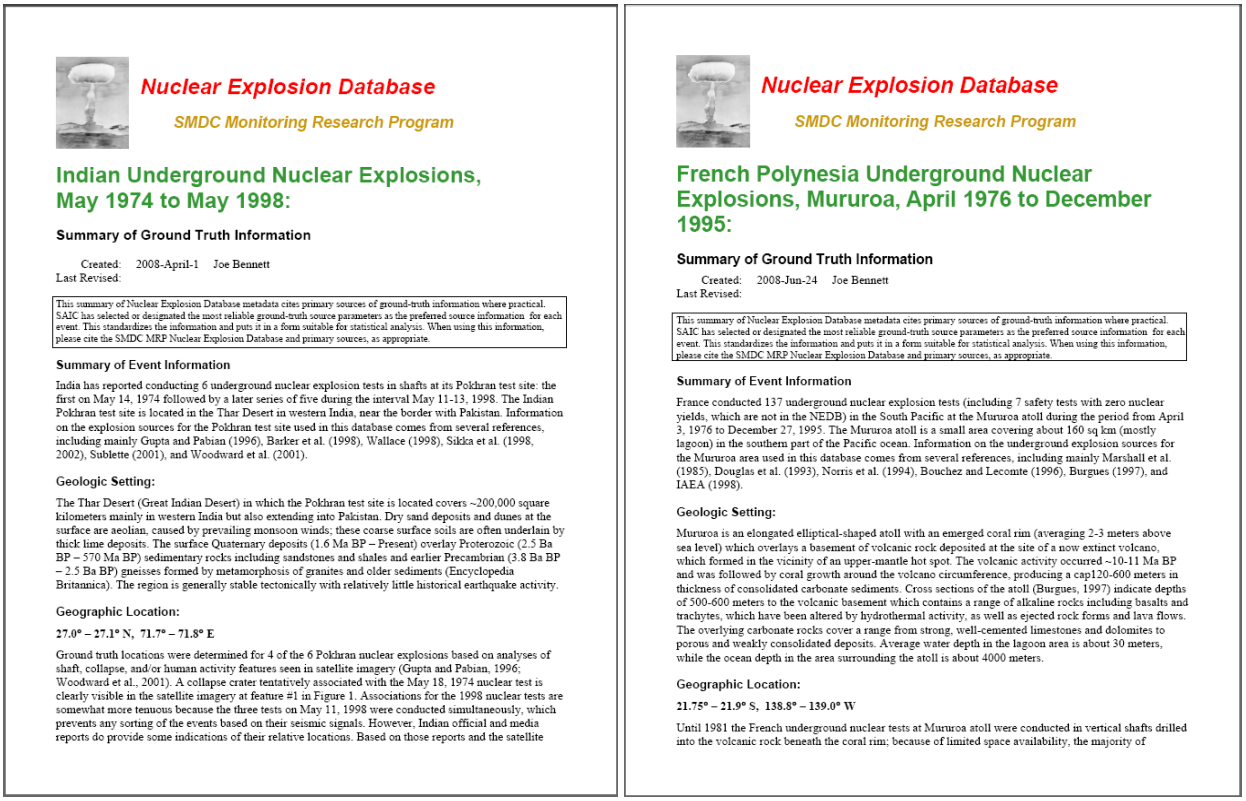

Nuclear Explosion Database

SMDC Monitoring Research Program

Indian Underground Nuclear Explosions, May 1974 to May 1998:

Summary of Ground Truth Information

Created: 2008-April-1 Joe Bennett
Last Revised:

This summary of Nuclear Explosion Database metadata cites primary sources of ground-truth information where practical. SAIC has selected or designated the most reliable ground-truth source parameters as the preferred source information for each event. This standardizes the information and puts it in a form suitable for statistical analysis. When using this information, please cite the SMDC MRP Nuclear Explosion Database and primary sources, as appropriate.

Summary of Event Information

India has reported conducting 6 underground nuclear explosion tests in shafts at its Pokhran test site: the first on May 14, 1974 followed by a later series of five during the interval May 11-13, 1998. The Indian Pokhran test site is located in the Thar Desert in western India, near the border with Pakistan. Information on the explosion sources for the Pokhran test site used in this database comes from several references, including mainly Gupta and Pabian (1996), Barker et al. (1998), Wallace (1998), Sikka et al. (1998, 2002), Sublette (2001), and Woodward et al. (2001).

Geologic Setting:

The Thar Desert (Great Indian Desert) in which the Pokhran test site is located covers ~200,000 square kilometers mainly in western India but also extending into Pakistan. Dry sand deposits and dunes at the surface are aeolian, caused by prevailing monsoon winds; these coarse surface soils are often underlain by thick lime deposits. The surface Quaternary deposits (1.6 Ma BP – Present) overlay Proterozoic (2.5 Ba BP – 570 Ma BP) sedimentary rocks including sandstones and shales and earlier Precambrian (3.8 Ba BP – 2.5 Ba BP) gneisses formed by metamorphosis of granites and older sediments (Encyclopedia Britannica). The region is generally stable tectonically with relatively little historical earthquake activity.

Geographic Location:

27.0° – 27.1° N, 71.7° – 71.8° E

Ground truth locations were determined for 4 of the 6 Pokhran nuclear explosions based on analyses of shaft, collapse, and/or human activity features seen in satellite imagery (Gupta and Pabian, 1996; Woodward et al., 2001). A collapse crater tentatively associated with the May 18, 1974 nuclear test is clearly visible in the satellite imagery at feature #1 in Figure 1. Associations for the 1998 nuclear tests are somewhat more tenuous because the three tests on May 11, 1998 were conducted simultaneously, which prevents any sorting of the events based on their seismic signals. However, Indian official and media reports do provide some indications of their relative locations. Based on those reports and the satellite

Nuclear Explosion Database

SMDC Monitoring Research Program

French Polynesia Underground Nuclear Explosions, Mururoa, April 1976 to December 1995:

Summary of Ground Truth Information

Created: 2008-Jun-24 Joe Bennett
Last Revised:

This summary of Nuclear Explosion Database metadata cites primary sources of ground-truth information where practical. SAIC has selected or designated the most reliable ground-truth source parameters as the preferred source information for each event. This standardizes the information and puts it in a form suitable for statistical analysis. When using this information, please cite the SMDC MRP Nuclear Explosion Database and primary sources, as appropriate.

Summary of Event Information

France conducted 137 underground nuclear explosion tests (including 7 safety tests with zero nuclear yields, which are not in the NEDB) in the South Pacific at the Mururoa atoll during the period from April 3, 1976 to December 27, 1995. The Mururoa atoll is a small area covering about 160 sq km (mostly lagoon) in the southern part of the Pacific ocean. Information on the underground explosion sources for the Mururoa area used in this database comes from several references, including mainly Marshall et al. (1985), Douglas et al. (1993), Norris et al. (1994), Bouchez and Lecomte (1996), Burgues (1997), and IAEA (1998).

Geologic Setting:

Mururoa is an elongated elliptical-shaped atoll with an emerged coral rim (averaging 2-3 meters above sea level) which overlays a basement of volcanic rock deposited at the site of a now extinct volcano, which formed in the vicinity of an upper-mantle hot spot. The volcanic activity occurred ~10-11 Ma BP and was followed by coral growth around the volcano circumference, producing a cap120-600 meters in thickness of consolidated carbonate sediments. Cross sections of the atoll (Burgues, 1997) indicate depths of 500-600 meters to the volcanic basement which contains a range of alkaline rocks including basalts and trachytes, which have been altered by hydrothermal activity, as well as ejected rock forms and lava flows. The overlying carbonate rocks cover a range from strong, well-cemented limestones and dolomites to porous and weakly consolidated deposits. Average water depth in the lagoon area is about 30 meters, while the ocean depth in the area surrounding the atoll is about 4000 meters.

Geographic Location:

21.75° – 21.9° S, 138.8° – 139.0° W

Until 1981 the French underground nuclear tests at Mururoa atoll were conducted in vertical shafts drilled into the volcanic rock beneath the coral rim; because of limited space availability, the majority of

**Figure 2. Examples of event summary reports accessible from the NEDB website**.

The content of the event summary reports includes information on source locations, origin times, emplacement depth or height, surface elevation, magnitude, yield, and geologic and geographic setting along with the pertinent references used as the bases for preferred and alternative explosion source data included in the NEDB.

One of the most basic of the nuclear explosion source parameters described in the NEDB is source location. In general, for the NEDB we have sought to determine ground truth rather than seismic bulletin locations, where that information was available. In some cases, the preferred locations come from government or other official sources (e.g., Springer et al., 2002; DTRA, 2007; IAEA, 1998); while in others the locations are based on indirect analyses, including comparisons with features seen in satellite imagery (e.g., Thurber et al., 1993, 1994; Woodward et al., 2001). As examples of the latter, Figure 3 shows results (Woodward et al., 2001) of satellite imagery analyses at the Indian Pokhran test site and the Pakistan Ras Koh mountain test site, respectively. Based on analyses of shaft, collapse, and/or human activity features seen in the satellite imagery, ground-truth locations were determined for the Pokhran tests in India as well as for the explosions at Ras Koh mountain in Pakistan.

**Figure 3. Satellite imagery analyses were used to establish ground-truth locations for nuclear explosions at the Indian Pokhran test site (below) and the Pakistan Ras Koh mountain test site (right), which are included in the NEDB as preferred solutions.**

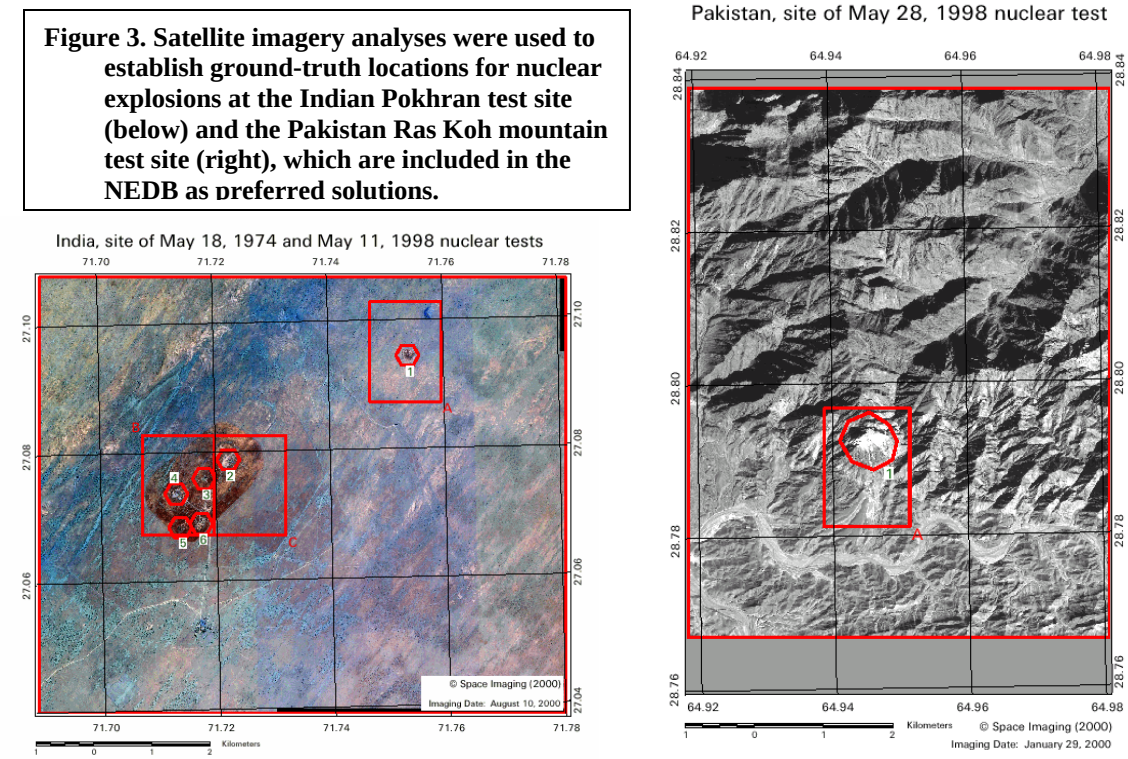


The NEDB website enables comparisons of these ground-truth source locations with surface features visible in the GoogleMap satellite imagery as well as with seismic bulletin locations (e.g., ISC). In addition, the website provides options for further review and analysis of ISC bulletin data in terms of travel time residuals for stations reported in the bulletin relative to the preferred ground truth explosion source locations. In particular, for all historical nuclear explosions from ISC bulletins, seismic travel-time residuals have been calculated for the reported station travel times relative to the times predicted for an iasp91 velocity model using the preferred ground-truth locations and origin times from the NEDB as the source. The results for the individual explosions can be easily displayed and compared using the website tools, which provide opportunities to investigate a variety of features in global and regional travel-time and velocity models.

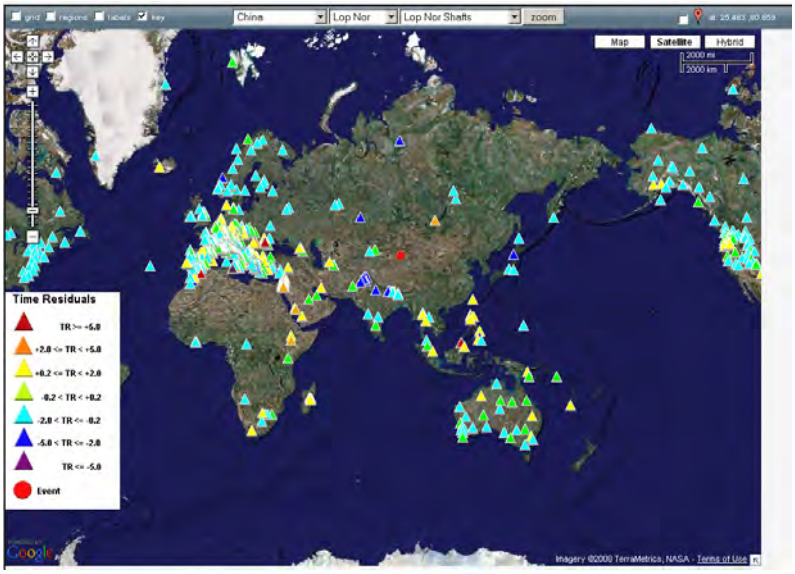


**Figure 4. Travel-time residuals at ISC bulletin stations (N ~700) relative to ground truth origin for 1996/06/08 Lop Nor China nuclear test.**

Figure 4 shows an example of the travel time residual display from the website for an underground nuclear test from the shaft area at Lop Nor China. Observed travel times tend to be somewhat fast or average in most of the world relative to the iasp91 model from this event; some of the most apparent slow areas in this plot are in the eastern Africa/Red Sea region, the Philippine islands, and parts of the western U.S. (Cascades area).

The NEDB website also provides an intuitive step-through process for accessing and retrieving digital waveform data from the RDSS archive, one of the most complete resources for digital waveforms from nuclear explosions. This archive includes more than 120,000 analyst-reviewed digital waveforms recorded at regional and teleseismic distances from the global network of seismic stations for 837 events from the NEDB. The options for previewing, selecting, and downloading waveforms from the website have recently been upgraded and simplified. The website now incorporates a simple and intuitive tool which provides for viewing waveforms, comparing signals between stations, and interactive display options (e.g., alternative filter choices, amplitude rescaling, time shifting) prior to selecting and downloading data. These new NEDB website waveform viewing options are illustrated in Figure 5 for the waveform data from the North Korean nuclear test of 2006/10/09.

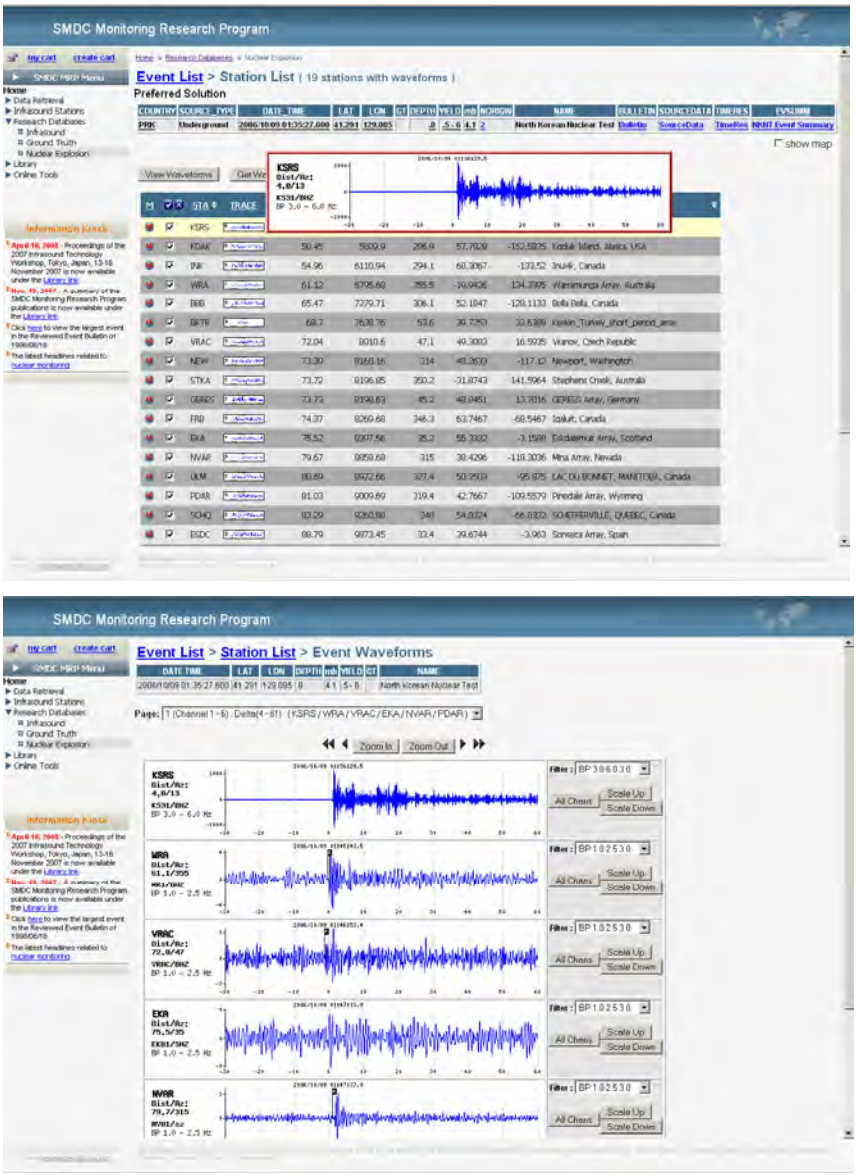


**Figure 5. NEDB waveform selection and downloading tools enable previewing and menu selection of station data (top), as well as some simple options for alternative filtering, amplitude rescaling, and time shifting of selected waveforms (bottom) prior to downloading.**

**Infrasound Database**

Identification of infrasound events for the RDSS Infrasound Database is based on a search of the International Data Centre (IDC) automated detection list and the RDSS waveform archive for signals that can be associated with recent events in seismic bulletins, volcanic activity reports, and media reports of events such as accidental explosions and bolides. Signal processing based on adaptations of Infratool and of the Maximum Cross-Correlation Method (MCCM) is used in this association. Modeling of atmospheric wave-propagation with InfraMap is also used in some cases. The search for candidate infrasound events has been focused on (1) mining events in Eurasia, (2) larger events with long paths and multi-station recordings of infrasound signals, and (3) cases with repeatable events during different times of the year for given source-station paths. Source data on infrasound events and their associated waveforms is also available to the nuclear explosion monitoring community in the research database provided at the SMDC RDSS website (www.rdss.info). Access to the Infrasound Database (IDB) is provided under the Research Databases menu option at the RDSS website.

The Infrasound Database contains information on events in the atmosphere for which there are associated microbarograph recordings. The database includes hundreds of events for different source types, including historical nuclear explosions, and contains, in addition to the associated waveform data, information on available source locations with related metadata and the available associated parametric data, such as arrival times of detected signals. The waveforms recorded at over 25 stations represent propagation along more than 500 distinct paths, with broad geographical coverage.

With the revival of infrasound as a monitoring technology, and the ongoing installation of the IMS infrasound network, an increasing number of infrasonic events, both natural (bolides, earthquakes) and man-made (planned and accidental explosions, rocket launches and re-entries, etc.) are being reported and recorded by a growing global network of sensors. Source locations are well-known for the explosions, and generally less well-defined for the bolides and rockets. The RDSS infrasound database provides a valuable resource for accessing and understanding the waveforms and effects of source and propagation on the measured signals.

The RDSS infrasound database is constantly being updated with additional waveforms. Over 800 infrasound-only or seismo-acoustic events were detected globally in 2007 (Figure 6). As seen in the figure, these new events provide a broad range of source locations and propagation coverage, supplementing the existing database.

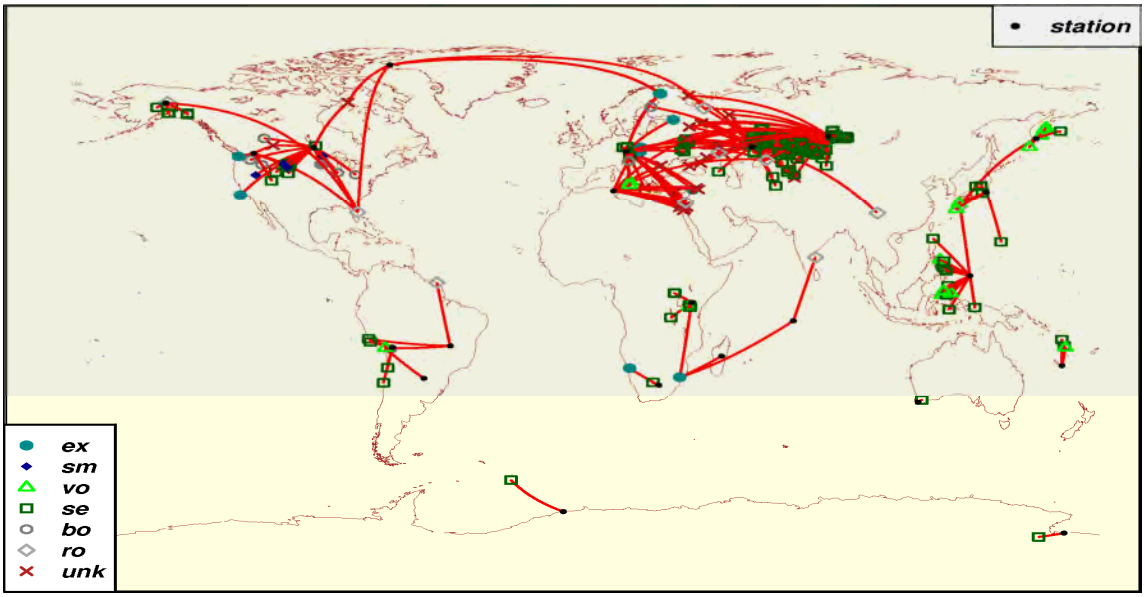


**Figure 6. More than 800 infrasound or seismoacoustic events detected in 2007 are candidates for inclusion in the RDSS infrasound database.**

Many of the events come from repeating sources (including mining events). Bahavar et al. (2007) reported infrasound and seismoacoustic observations from repeating mining events in south-central Russia and eastern Kazakhstan, and those have continued (Figure 7). Such repeating sources provide additional opportunities for a detailed study of a range of waveform processing tools, including alternative signal-detection methods.

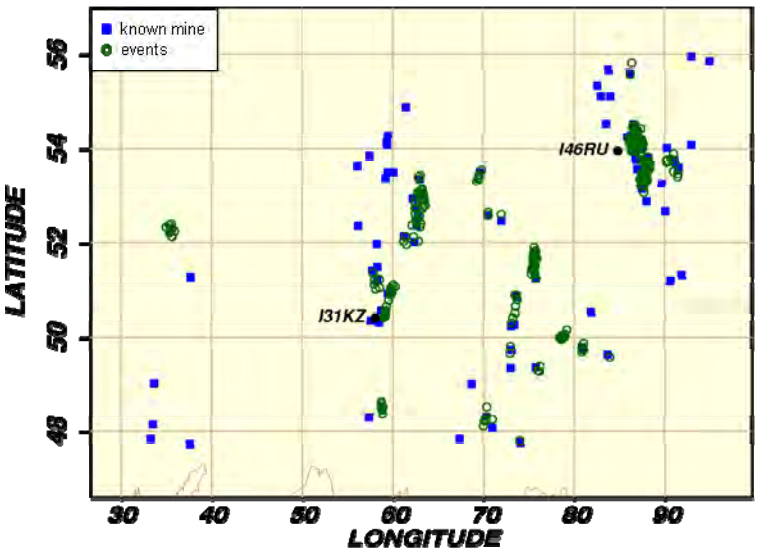


**Figure 7. Dozens of detected infrasound signals from seismoacoustic events associated with known mines in south-central Russia and eastern Kazakhstan were observed in 2007-2008.**

A valuable set of repeating events (under preparation for inclusion in the IDB) comes from sources in northern Finland. Suites of seismic events, confined to a small area in northern Finland, have occurred between mid-August and mid-September during the last several years (Ringdal et al., 2007). The events have been reported in the seismic bulletins of Helsinki University (http://www.seismo.helsinki.fi) and have been attributed to explosions carried out to destroy outdated ammunition (Ringdal et al., 2007). Seismic as well as infrasonic signals have been observed at the seismic array ARCES about 175 km due north of the source area (Ringdal et al., 2007). Events have also been recorded with high SNR at infrasound stations in Fenno-scandia at distances between 50 and 1,200 km (http://www.umea.irf.se). Data recorded at the two IMS infrasound arrays, I26DE (Freyung, Germany) and I18DK (Qaanaaq, Greenland, Denmark) located at about 2,500 and 3,000 km from the source area were analyzed for detections of events in the area between mid-August and mid-September in 2007. The map in Figure 8 shows the two IMS arrays, I18DK and I26DE, in relation to the source area. Data for all 46 events reported in the daily automatic bulletins of the Helsinki Seismological Institute (HEL) with local magnitudes between ML (HEL) = 0.9 and 1.5 have been analyzed.

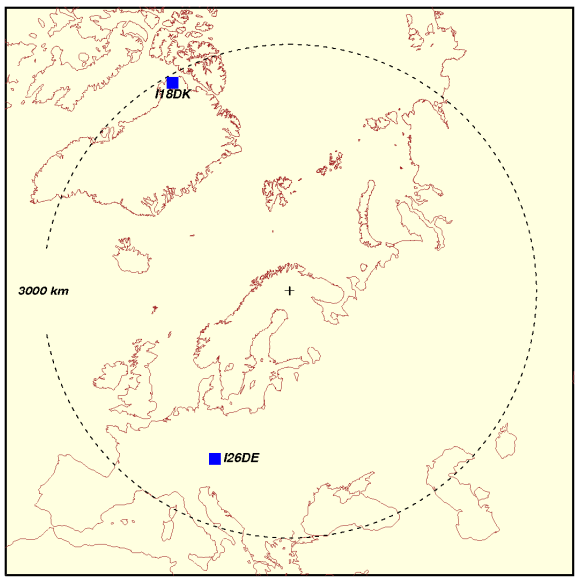


**Figure 8. Map showing the locations of the two arrays I18DK (Qaanaaq, Greenland, Denmark) and I26DE (Freyung, Germany) in relation to event area centered at 67.93N 25.80E (cross symbol in center).**

Automatic detections in the IDC detection list were associated with several events from this data set. The IDC detections are based on the Progressive Multi Channel Correlation, PMCC (Cansi, 1995), which is followed by phase categorization (Brachet et al., 2006 and Brachet et al., 2007), during which a detection is classified as signal (I) or noise (N) depending on duration, frequency content, and repetitiveness. Automatic IDC detections (both I and N phases) were associated with all 46 events; however, only a fraction of the events produced associated I detections at the two stations (7 at I18DK and 10 at I26DE). The infrasound data from these events have provided an opportunity to investigate alternative detection schemes at the two infrasound arrays based on frequency-wavenumber (fk) processing and the F-statistic. The results of comparing the alternative detection processing schemes indicates station-dependent differences which could be related to differences in the number of array elements at the two stations.

## CONCLUSIONS AND RECOMMENDATIONS

The NEDB for the SMDC RDSS has been updated to include newly published or revised information about historical nuclear explosions, access to additional or corrected waveform data for some explosions, and new data from more recent nuclear tests. Access to the data archive and documentation for the NEDB has been enhanced to include a range of search options and comparisons between events, alternative locations, and surface features visible in satellite imagery through an integrated GoogleMap tool. The website also provides an intuitive step-through process for accessing, displaying, and retrieving nuclear explosion digital waveform data from the NEDB archive. The waveform display options have been improved to make them more useful, more intuitive, and faster. For infrasound, comparisons of RDSS waveform archives with event bulletins (seismic and volcanic) and media reports have resulted in new infrasound events and their associated waveforms being added to the database. Infrasound signals from a repeating series of sources in northern Finland have provided a useful resource for comparing alternative infrasound signal-detection processing schemes.

## REFERENCES

Bahavar, M., B. Barker, J. Bennett, R. Bowman, H. Israelsson, B. Kohl, Y-L. Kung, J. Murphy, B. North, V. Oancea, M. O'Brien, and G. Shields (2007). Enhanced Resources of the SMDC Monitoring Research Program for Source Information and Data Acquisition, in *Proceedings of the 29th Monitoring Research Review: Ground-Based Nuclear Monitoring Technologies*, LA-UR-07-5613, Vol. 2, pp. 918–926.

Bennett, J., R. North, B. Kohl, J. Murphy, J. Stevens, I. Bondar, M. Fisk, M. Bahavar, B. Barker, H. Israelsson, and V. Oancea (2006). Analysis of IMS Data from the North Korean (DPRK) Nuclear Test of October 9, 2006, SAIC Report SAIC-06/2203.

Brachet, N., J. Coyne, and R. Le Bras (2006). Latest Developments in the Automatic and Interactive Processing of Infrasound Data at the IDC, Infrasound Technology Workshop.

Brachet, N., A. Ndiath, M. Fisseha, A. Kasmi, M. Ocal, K. Sitnikov, G. Turyomurugyend, and J. Coyne (2007). Smooth introduction of Infrasound Data into IDC Reviewd Event Bulletin, Part I: Procedure and Recent Developments, Infrasound Technology Workshop.

Cansi, Y. (1995). An automatic seismic event processing for detection and location, *Geophys Res Lett* 22: 1021–1024.

Defense Threat Reduction Agency (2007). Research and Development Enterprise, Nuclear Test Personnel Review Program, Related Historical Volumes from Atmospheric Nuclear Tests (http://www.dtra.mil/rd/programs/nuclear_personnel/atr.cfm).

International Atomic Energy Agency (1998). The Radiological Situation at the Atolls of Mururoa and Fangataufa – Main Report, STI/PUB/1028.

Khalturin, V., T. Rautian, P. Richards, and W. Leith (2005). A review of nuclear testing by the Soviet Union at Novaya Zemlya, 1955-1990, *Science and Global Security* 13: 1–42.

Kim, W.-Y. and P. Richards (2007). North Korean nuclear test: seismic discrimination at low yield, *Am. Geophys. Union EOS* 88: 160–161.

Ringdal, F., T. Kvaerna, S. Mykkeltveit, S. Gibbons, and J. Schweitzer, 2007, Basic Research on Seismic and Infrasonic Monitoring of the European Arctic, MRR, 2007.

Springer, D., G. Pawloski, J. Ricca, R. Rohrer, and D. Smith (2002). Seismic source summary for all U.S. below-surface nuclear explosions, *Bull. Seism. Soc. Am*. 92: 1806–1840.

Thurber, C., H. Quin, and P. Richards (1993). Accurate locations of nuclear explosions at Balapan, Kazakhstan, 1987 to 1989, *Geophys. Res. Letters* 20: 399–402.

Thurber, C., H. Quin, and R. Saleh (1994). Catalog of locations of nuclear explosions at Balapan, Kazakhstan, 1965 to 1985, *Bull. Seism. Soc. Am.* 84: 458–461.

Woodward, R., B. Kohl, and R. North (2001). Support System for Nuclear Explosion Monitoring Research and Development, in *Proceedings of the 23rd Seismic Research Review: Worldwide Monitoring of Nuclear Explosions*, LA-UR-01-4454, Vol. 1, pp. 219–228.

Yang, X., R. North, and C. Romney (2000). CMR Nuclear Explosion Database (Revision 3), CMR Technical Report CMR-00/16.

# DETERMINATION OF THE SEISMIC MOMENT TENSOR USING SURFACE WAVES RECORDED BY THE IMS NETWORK

Jeffrey Given[2], Ronan J. Le Bras[1], and Yu-Long Kung[2]

Comprehensive Nuclear-Test-Ban Treaty Organization[1] and Science Applications International Corporation[2]

Sponsored by the Comprehensive Nuclear-Test-Ban Treaty Organization

Contract No. 2006-1193

## ABSTRACT

The Provisional Technical Secretariat (PTS) of the Comprehensive Nuclear-Test-Ban Treaty Organization (CTBTO) has been ramping-up the installation of the International Monitoring System (IMS) consisting of a network of seismic, hydroacoustic, infrasound, and radionuclide stations, since its inception in March 1997. Data from this network are automatically processed at the International Data Centre (IDC) to produce, within a few hours, a series of automatic bulletins called the Standard Event Lists (SEL1, SEL2, SEL3). After analyst review and correction as necessary the Reviewed Event Bulletin (REB) is produced. Additional information about characterization of an event as an earthquake or otherwise is also available in the Standard Event Bulletin (SEB) shortly after production of the REB. The Comprehensive Nuclear-Test-Ban Treaty (CTBT) states that the IDC will apply standard event screening criteria to each event formed. The objective of this process is to filter out events that are considered to be consistent with natural or non-nuclear man-made phenomena, leaving a reduced set of events that may require further examination. In Annex 2 of the Protocol to the Treaty, the focal mechanism is listed as possible event screening parameters.

In order to provide a focal mechanism and increase the number of elements potentially useful as screening attributes, we have in the last two years implemented two methods for moment tensor (MT) inversion. One method is based on the P body waves and the other on surface waves. Implementation of these sophisticated inversion methods has led to improvements in the calibration of the broad-band seismic network, notably quality control of the instrument responses.

We report here on the results obtained from the implementation of the surface-wave MT inversion, which uses both Rayleigh waves and Love waves. We are presenting results of the application of this inversion scheme on selected events as well as statistics showing the results of automatic use of the method. Compared to using body waves, we find that using the surface waves allows us to lower the magnitude at which it is possible to obtain an automatic MT solution.

## OBJECTIVES

The objective of this project is to develop and integrate a Surface Waves Moment Tensor (SWMT) and moment magnitude $M_w$ (Hanks and Kanamori, 1979) measurement in the IDC processing system to take advantage of the broad-band data sent to the CTBTO IDC. For several reasons, this additional processing item will be of use to the IDC and the monitoring community in general:

- The focal mechanism for seismic events is mentioned in Annex 2 of the Protocol to the CTBT as a potentially useful attribute for event screening.
- The additional module will be of use in the prototype processing pipeline using the IMS network that can produce a timely bulletin useful as input for agencies charged with warning the general public about impending disasters such as tsunamis.
- The IDC automatic bulletins measure the size of events using the *mb* magnitude which is known to saturate for events larger than about magnitude 6.5 (e.g., Abe, K, 1995). It is therefore useful to develop other methods of assessing the size of large events in a timely manner. For large events, the focal mechanism also provides additional information for the tsunamigenic potential of the event.
- The method may be applied to data archived at the IDC and used to check the calibration of the IMS network at low frequencies for large events whose seismic moments have been estimated by publishing agencies (Harvard Centroid Moment Tensor, [CMT]) or the United States Geological Survey (USGS).

## RESEARCH ACCOMPLISHED

The fundamental mode surface waves $u_i(\omega,r_i,\theta_i)$ observed at the *i-th* receiver at point ($r_i$, $\theta_i$) generated by a moment tensor source located near the origin ($r = 0$) has the form in the frequency domain:

$$u_i^{R,Qt}(\omega, r_i, \theta_i) = T(|M|, \omega) S^{R,Q}(\omega) P^{R,Q}(\omega, \Delta t, \Delta r_i) E_{ijk}^{R,Q}(\omega, z) M_{jk} \qquad (1)$$

$E^{R,Q}$ are the vertical (Rayleigh, *R*) or tangential (Love, *Q*) excitation functions and depend on the frequency, the source region elastic structure, and the source depth. $T(|M|,\omega)$ is the source time function, which is assumed to be a function of the scalar moment. $P^{R,Q}(\omega, \Delta t, \Delta r_i)$ represents the propagation and is a function of the specific source-receiver path. $P^{R,Q}$ includes geometric spreading and the regional variation in attenuation and phase velocity. $S^{R,Q}(\omega)$ is the response at the receiver location. $\Delta t$ and $\Delta r_i$ are perturbations in origin time and epicentral distance around the initial estimate of the source origin parameters. $M_{jk}$ is the 9-element symmetric MT.

All source and path-specific parameters in Equation 1 are computed from earth models and parameters registered on a 1x1 degree grid.

The amplitude and phase spectra for the fundamental mode Rayleigh and Love waves are measured using a phase-matched filter approach to increase the signal-to-noise ratio in the measured spectra. This processing is an extension of the routine processing already used at the IDC to detect surface waves and measure $M_S$. The phase-matched filters are derived from a global map of phase-velocities specified with 1-degree resolution.

Two different dispersion models are available to design the phase-matched filters. One, from Stevens, et al. (2005) is based on a large tomographic inversion of Rayleigh wave phase and group velocities down to 20-s periods. The inversion directly inverts for the 1x1 degree earth structure. The resulting structure models are used to calculate both the Rayleigh and Love wave phase velocities. The second dispersion model is taken from Ekstrom, et al., (1997), which is also used in routine processing for the Global CMT project. Both models are essentially equivalent for

Rayleigh waves at periods longer than 35 s, since the CMT models were used as constraints in the tomographic inversion of Stevens, et al., 2005. For Love waves, the CMT phase velocities were derived directly from Love wave observations and are clearly more accurate. The Stevens et al. phase velocities extend down to 20 s periods, which may allow the method to be extended to smaller events.

In a routine operational setting, an initial source location and magnitude are generated by the automatic event detection system. Using the initial event parameters, a surface-wave detection and spectral measurement process determines where surface waves are observed and extracts the complex amplitude spectra corresponding to the fundamental mode Love and Rayleigh waves. A second process collects the spectra and, if there are enough observations of sufficient quality, a surface-wave MT is calculated.

The MT inversion uses an iterative least-squares method to determine the best-fitting MT and perturbation to the initial source location and origin time at a fixed depth. The inversion is repeated over the possible range of depths to determine the best fitting depth. The result is an MT solution, which can be interpreted as a combination of double-couples, and a revised hypocentral location.

The frequency range used for the inversion is selected based on the initial size of the event. The dispersion model used for the path propagation depends on the selected frequency range. For larger events, the CMT dispersion models are used and the periods are constrained to be greater than 50 s. For smaller events, the Stevens et al. Rayleigh-wave dispersion model is used and the Rayleigh-wave periods are constrained to be greater than 20 s. The current Love wave propagation phase corrections are not yet accurate enough to use the shorter-period Love waves in the inversion, and for all sources, the CMT Love-wave phase corrections are used for periods greater than 35 s. For observations at the shorter periods the source-receiver distance is further constrained.

**Recent Examples of Inversion and Comparison with the CMT Results**

The method has been tested on a number of recent events, including the aftershocks of the recent May 12$^{th}$, 2008, Eastern Sichuan earthquake which we present in this paper. Table 1 shows the results of the inversion on eight REB events and the comparison with the CMT results when these are available, which is the case for six of them. Although not part of the CTBTO IDC automatic processing pipeline, the off-line test was completely automatic in the sense that the data selection for the inversion was part of the process, and there was no second pass where an analyst checked on the results of the inversion and modified the input as necessary. The eight events are shown on a map in Figure 1. The various focal mechanisms vary from inverse along the SW-NE fault trend delineated by the aftershocks to strike-slip along the same trend. In spite of their variety, the focal mechanisms are compatible with a compression axis perpendicular to the trend of the fault. Note that the smallest event presented in the table (orid 4755448**)** and on the figure has an Mw magnitude of 4.7. The method has the potential of routinely producing MTs for events down to a magnitude of about 4.5 when appropriate data is available.

**Table 1. This table shows the results of the surface-waves MT inversion on eight REB events and the six CMT events for which a comparison was possible. The events are all aftershocks of the May 12$^{h}$ Eastern Sichuan earthquake. The MT components are in units of $10^{17}$ N-m.**

| | | | | |
|---|---|---|---|---|
| **12 May 2008 CTBTO (4750766 Mw 5.7)** | | | | |
| Epicenter | [32.13, 103.86] | **Mrr** | **3.71** | 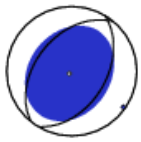 |
| Depth | 20 km | **Mtt** | **-1.10** | |
| | | **Mpp** | **-2.61** | |
| | | **Mrt** | **-0.22** | |
| Time | 20:08:33.6 | **Mrp** | **0.26** | |
| | | **Mtp** | **-0.72** | |
| **12 May 2008 CMT (Mw 5.6)** | | | | 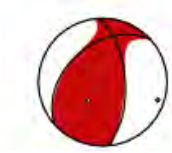 |
| Epicenter | [32.38, 104.08] | **Mrr** | **2.31** | |
| Depth | 28.4 km | **Mtt** | **0.46** | |
| | | **Mpp** | **-2.77** | |
| | | **Mrt** | **-0.68** | |
| Time | 20:08:53.6 | **Mrp** | **1.43** | |
| | | **Mtp** | **-1.47** | |
| **13 May 2008 CTBTO (4754479 Mw 5.8)** | | | | 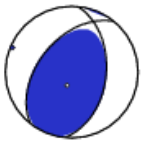 |
| Epicenter | [31.16, 103.34] | **Mrr** | **5.88** | |
| Depth | 20 km | **Mtt** | **-0.68** | |
| | | **Mpp** | **-5.21** | |
| | | **Mrt** | **-1.91** | |
| Time | 07:07:13.0 | **Mrp** | **0.58** | |
| | | **Mtp** | **-2.23** | |
| **13 May 2008 CMT (Mw 5.8)** | | | | |
| Epicenter | [30.88, 103.38] | **Mrr** | **4.85** | |
| Depth | 14.1 km | **Mtt** | **0.34** | |
| | | **Mpp** | **-5.19** | |
| | | **Mrt** | **-0.26** | |
| Time | 07:07:13.0 | **Mrp** | **1.27** | |
| | | **Mtp** | **-2.20** | |
| **13 May 2008 CTBTO (4755448 Mw 4.7)** | | | | |
| Epicenter | [32.34, 105.33] | **Mrr** | **0.008** | |
| Depth | 20 km | **Mtt** | **0.05** | |
| | | **Mpp** | **-0.06** | |
| | | **Mrt** | **0.00099** | |
| Time | 12:51:36 | **Mrp** | **-0.00079** | |
| | | **Mtp** | **-0.09** | |
| **14 May 2008 CTBTO (4750217 Mw 5.5)** | | | | |
| Epicenter | [31.47, 103.47] | **Mrr** | **-0.80** | |
| Depth | 10 km | **Mtt** | **1.95** | |
| | | **Mpp** | **-1.15** | |
| | | **Mrt** | **0.08** | |
| Time | 2:54:36.9 | **Mrp** | **-0.27** | |
| | | **Mtp** | **0.52** | |
| **14 May 2008 CMT (Mw 5.5)** | | | | |
| Epicenter | [31.32, 103.60] | **Mrr** | **-0.47** | |
| Depth | 12 km | **Mtt** | **1.92** | |
| | | **Mpp** | **-1.45** | |
| | | **Mrt** | **-0.46** | |
| Time | 2:54:36.9 | **Mrp** | **0.04** | |
| | | **Mtp** | **0.76** | |

| | | | | |
|---|---|---|---|---|
| **17 May 2008 CTBTO (4761579 Mw 5.9)** | | | | |
| Epicenter | [32.42, 105.08] | **Mrr** | **4.01** | |
| Depth | 10 km | **Mtt** | **-3.10** | |
| | | **Mpp** | **-0.91** | |
| | | **Mrt** | **-0.38** | |
| Time | 17:08:31.5 | **Mrp** | **-4.96** | |
| | | **Mtp** | **-2.03** | |
| **17 May 2008 CMT (Mw 5.7)** | | | | |
| Epicenter | [32.23, 105.10] | **Mrr** | **4.76** | |
| Depth | 14 km | **Mtt** | **-2.46** | |
| | | **Mpp** | **-2.29** | |
| | | **Mrt** | **-0.19** | |
| Time | 17:08:29.7 | **Mrp** | **0.45** | |
| | | **Mtp** | **-2.92** | |
| **19 May 2008 CTBTO (4765811 Mw 5.5)** | | | | |
| Epicenter | [32.97, 105.37] | **Mrr** | **.43** | |
| Depth | 40 km | **Mtt** | **1.74** | |
| | | **Mpp** | **-2.17** | |
| | | **Mrt** | **0.08** | |
| Time | 6:06:59.5 | **Mrp** | **0.24** | |
| | | **Mtp** | **0.22** | |
| **25 May 2008 CTBTO (4770155 Mw 5.9)** | | | | |
| Epicenter | [32.69, 105.43] | **Mrr** | **1.3** | |
| Depth | 10 km | **Mtt** | **6.44** | |
| | | **Mpp** | **-7.74** | |
| | | **Mrt** | **1.78** | |
| Time | 8:21:51.8 | **Mrp** | **-3.10** | |
| | | **Mtp** | **-2.31** | |
| **25 May 2008 CMT (Mw 6.0)** | | | | |
| Epicenter | [32.60, 105.48] | **Mrr** | **1.13** | |
| Depth | 15 km | **Mtt** | **11.30** | |
| | | **Mpp** | **-12.40** | |
| | | **Mrt** | **2.61** | |
| Time | 8:21:53.0 | **Mrp** | **-0.47** | |
| | | **Mtp** | **-6.22** | |
| **27 May 2008 CTBTO (4769576 Mw 5.45)** | | | | |
| Epicenter | [32.80, 105.66] | **Mrr** | **0.05** | |
| Depth | 10 km | **Mtt** | **0.12** | |
| | | **Mpp** | **-0.17** | |
| | | **Mrt** | **-0.45** | |
| Time | 8:37:55.7 | **Mrp** | **-1.03** | |
| | | **Mtp** | **-0.95** | |
| **27 May 2008 CMT (Mw 5.5)** | | | | |
| Epicenter | [32.75, 105.71] | **Mrr** | **-0.02** | |
| Depth | 15 km | **Mtt** | **0.37** | |
| | | **Mpp** | **-0.36** | |
| | | **Mrt** | **-0.87** | |
| Time | 8:37:55.2 | **Mrp** | **-1.26** | |
| | | **Mtp** | **-1.60** | |

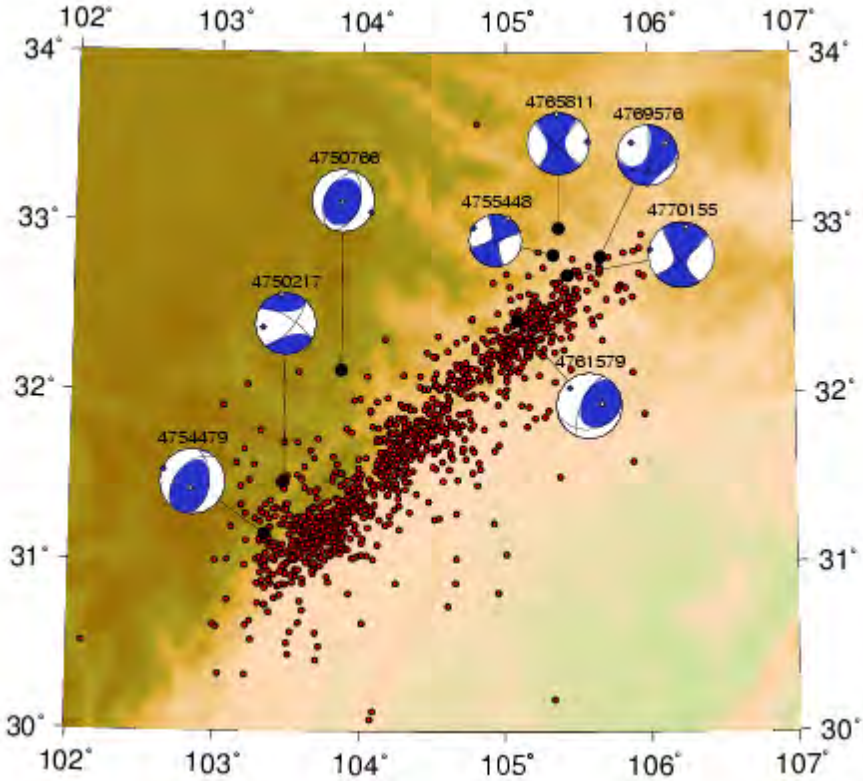


**Figure 1. This figure shows the locations (small red dots) of the May 12 2008, Sichuan aftershocks from 12 May to 3 June in the Reviewed Events Bulletin from the CTBTO IDC. The total number of aftershocks shown in the figure is 1,088. Also shown are the centroid locations (larger black dots) and the MTs for eight of the aftershocks (see Table 1) for which we have a surface-wave MT inversion result. The specifications of each of the MTs shown on this figure are listed in Table 1. To link the events presented in the figure to Table 1, refer to the unique number (orid number) on top of each focal mechanism.**

## CONCLUSIONS AND RECOMMENDATIONS

We have developed and integrated surface-waves MT inversion software into the IDC processing environment on an experimental basis. The inversion is integrated into a Web page where the user can toggle between several databases including an experimental database containing fast bulletins with events that occurred in the past 20 minutes, and the IDC archive database. At present, an experienced user can obtain a fast MT with a few mouse clicks and within a few minutes for events in these databases.

We are presently evaluating the method and the dispersion models used in the inversion. It is clear from the initial results that the method is routinely applicable to some events of magnitudes as low as 4.5 when it is possible to extract the frequency-amplitude information from the waveforms.

**ACKNOWLEDGEMENTS**

We thank Drs. Lassina Zerbo, IDC Director, and Jack Shlachter, IDC Coordinator, for allowing us to publish this research and for their support.

**REFERENCES**

Abe, K., (1995), Magnitudes and Moments of Earthquakes, in Global Earth Physics, A Handbook of Physical, AGU Reference Shelf 1:206, 213.

Ekström, G. , J. Tromp, and E.W.F. Larson (1997). Measurements and global models of surface wave propagation, *J. Geophys. Res.* 102: (B4), 8137–8157.

Hanks T.C. and H. Kanamori (1979). A moment magnitude scale. Journal of Geophysical Research 84 (B5): 2348–50.

Stevens, J. L., D. A. Adams, G. E. Baker, M. G. Eneva and H. Xu (2005), "Improved Surface Wave Dispersion Models, Amplitude Measurements and Azimuth Estimates," SAIC Final Report submitted to AFRL under contract DTRA01-01-C-0082, March

**Disclaimer**

The views expressed in this paper are those of the authors and do not necessarily reflect the views of the CTBTO Preparatory Commission.

# PROGRESS ON COMPONENT EVALUATION FOR NUCLEAR EXPLOSION MONITORING

Darren Hart, B. John Merchant, and J. Mark Harris

Sandia National Laboratories

Sponsored by National Nuclear Security Administration

Contract No. DE-AC04-94AL85000

,

## ABSTRACT

The Ground-Based Nuclear Explosion Monitoring Research and Development (GNEM R&D) program at Sandia National Laboratories (SNL) is regarded as the primary center for unbiased expertise in testing and evaluation of geophysical sensors and instrumentation for nuclear explosion monitoring. We had four main areas of interest to make progress on this year; this report will cover the advances made in these areas. First is the continued development and research of the three-component coherence technique of Sleeman et al. (2006). We have reverted back to synthetic testing to develop a firm understanding of the arithmetic limitations in processing to recover small value estimates of noise relative to large input signals. We explored the effects of digital quantization of the analog signal, as well as the limitations of the technique in the presence of high signal-to-noise input signals. The second area of interest is the upgrade of our suite of software used to analyze sensors and digitizer data (e.g., to calculate noise floor, time-tag accuracy). This past year has allowed us time to develop the new data model and relevant meta-architecture, proto-type existing algorithms in MATLAB with validation against existing tool sets, and develop sets of reusable modules (e.g., waveform editing tools and test description). Our third area of concentration over the past year focused on testing new components for both Provisional Technical Secretariat and the Air Force Technical Applications Center (AFTAC). Characterization reports were produced for two infrasound sensors, Chaparral Physics model 2.5 low-gain and the Inter-Mountain Labs model SS avalanche sensor as well as one data logger, Geotech Smart24. For the infrasound sensors tested, the test results allow us to conclude that both sensors had sufficiently quiet noise floor to be at or below the Acoustic low-noise model from 0.1 to 7 Hz, which make these sensors suitable to explosion monitoring. The characterization report on the Smart 24 documented meeting requirements for an International Monitoring System site. The final area of focus for the component evaluation (CE) project has been the maintenance and upgrade of our seismic and infrasound test-beds. Recent additions have included additional reference sensors for monitoring environmental conditions during infrasound testing as well as exploring the necessary requirements needed for an infrasound test chamber. This work directly impacts the Ground-Based Nuclear Explosion Monitoring mission by providing a facility, equipment, and personnel to give the operational monitoring agencies confidence in deployed instrumentation and capability for mission success.

## OBJECTIVES

Over the past year the Component Evaluation project of the GNEM R&D program at SNL has made reportable contributions in four areas. These areas are new component evaluation techniques and visualization methods, the upgrade of our existing methodology for the analysis, reporting and archiving of component evaluation test results, results of characterization testing of infrasound sensors and the upgrade and upkeep of test bed equipment for the Facility for Acceptance, Calibration, and Testing site.

### Introduction

AFTAC is tasked with monitoring compliance of existing and future nuclear test treaties. To perform this mission, AFTAC uses several different monitoring techniques to sense and monitor nuclear explosions, each designed to monitor a specific domain (e.g., space, atmosphere, underground, oceans, etc.). Together these monitoring systems, equipment, and methods form the United States Atomic Energy Detection System (USAEDS). Some USAEDS seismic stations may be included in the International Monitoring System (IMS). Each agency involved in the monitoring community has requirements which the system and components (sensors and data loggers) must pass before deployment and later certification. Historically, SNL has been involved in the testing of seismic systems to monitor for compliance with terms of nuclear weapon test ban treaties. With the recent addition of infrasound and seismo-acoustic stations, SNL has worked to develop the capability and procedures to perform the characterization of infrasound sensors, infrasound systems, and seismo-acoustic systems.

Over the past year Sandia has characterized more than 60 Chaparral Physics model 2.5 (CP2.5) low gain sensors. The CP2.5 sensors were characterized for sensitivity, amplitude response, linearity and self-noise. Two internal SAND reports (Hart, 2007a and 2007b) and one in progress detail the characterization of the individual sensors, here, we will summarize the results as related to the monitoring community. A second infrasound sensor, the Inter-Mountain Labs model SS infrasound sensor, was evaluated as a possible sensor for the monitoring community. The results were reported in Hart (2007c) and will be summarized here. Recently, we have started to investigate the effects porous-hose filters have on the characterized sensors. We find an unexpected filter response, at a lower frequency than expected. Sandia was also asked to evaluate the Geotech Smart24 data logger for qualification as a replacement to the Geotech DL24 data logger in US IMS stations. The results of testing the Smart24 data logger can be found in Hart (2008), the relevant aspects of bit-weight and timing accuracy and self-noise will be shown.

As part of a continuing effort to develop an improved technique to estimate a components (data logger, sensor, etc.) self-noise and relative response between three co-located and similar sensors or recording channels. The technique described by Sleeman et al. (2006) and results presented in Hart et al. (2007) on the three-component coherence algorithm were tested using synthetic data as input to verify and document the numerical limitations in calculation. Comparisons were made between the levels of coherent signal to incoherent noise to determine the maximum signal-to-noise ratio allowed by the technique. A second effect that was addressed is related to the digital sampling of the analog signal input. The resolution (24-bit versus 26-bit format) and rounding effects of digital sampling of the input signals as compared to double-precision float are shown.

SNL has developed and refined, over a number of years, several unique analysis techniques used in the evaluation of data loggers, and infrasound and seismic sensors. Due to the desire to increase the efficiency and traceability of our testing capability the component evaluation project is developing a new software tool for this purpose. At the current stage of development, a new underlying architecture has been developed with the intent of multi-platform compatibility, connection with research tools, traceability of testing with defined database schema, and an easy to use user interface.

## RESEARCH ACCOMPLISHED

### New Synthetic Test for Three Component Coherence

From our original paper, Hart et al. (2007), and continuing work that was presented at the annual fall meeting of the American Geophysical Union 2007 on the application of the three component coherence technique, two primary observations were made from our results. The first observation showed an accurate estimate of digitizer (i.e., Q330,

Q330HR and Smart24) self-noise was produced and matched the results of an independent self-noise estimator – Input Terminated Noise. Figures 1a and b illustrate for the Q330HR the accuracy of the estimation of noise for the three channels tested. The second observation was related to the results of processing of STS2 data. We observed a deviation in the self noise estimates for the three seismometers tested. The deviation from smooth noise is observed between 0.1 and 0.3 Hz. This band correlates in frequency with highest signal-to-noise ratio (SNR) of the power spectrum. Figures 2a, 2b, and 2c show these observations.

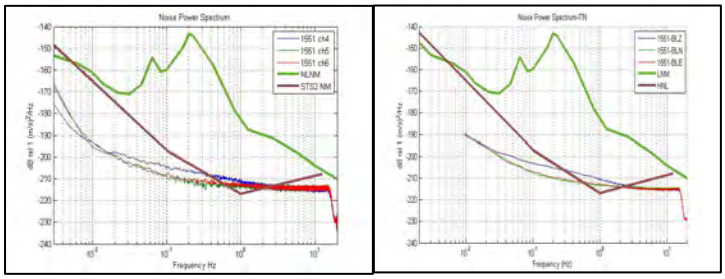

**Figures 1a and b. Self noise estimates for Q330HR channels 4-6, comparison results from 3C technique and ITN. The thick green line is the USGS low noise model. The thick brown line is the STS2 noise model. The thin blue, red and green lines are the noise estimates for the channels 4, 5 and 6 respectively.**

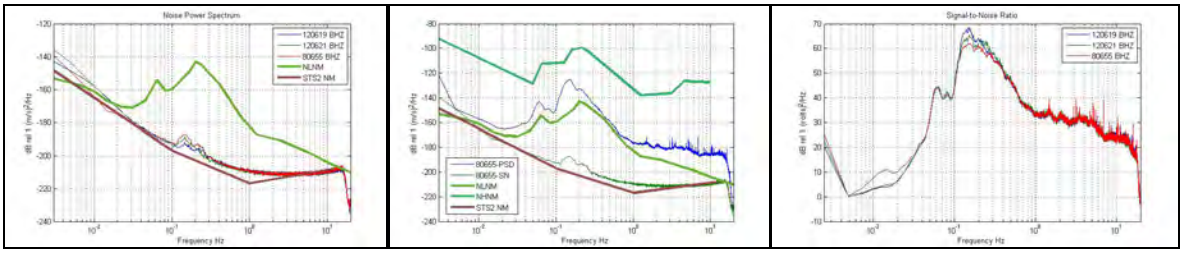

**Figures 2a, b, and c. Self noise estimates for three STS2 illustrating the observed deviation in noise between frequencies 0.1 and 0.3 Hz (a), this correlates to the peak in the background power spectrum (b) and the regions of highest signal-to-noise (c).**

To determine if the observed deviation was an artifact of the numerical limitations of the calculations we devised a set of tests using synthetic data in which we could vary the absolute level and level of separation between the noise and coherent signals. The tests consisted of generating four random sequences, three are used for the incoherent noise signals and the fourth is used as the coherent signal. We chose to use normally distributed, randomly generated, double precision numbers. The sequences ranged between approximately, ± 5.5. The absolute scaling ranged from -213 to 27 dB, while the SNR was varied from 0 to 240 dB. Assuming a purely linear system, we add each noise signal to the coherent signal to get the three new signals for processing with the 3C technique. The results are shown in Figure 3 and display 156 realizations of the technique. The graph is read from left to right for any one line type, at equal or greater scaling of the coherent signal to that of the three random sequences the 3C technique adequately resolves the power levels of the incoherent noise up seven orders of magnitude. At separations of SNR greater than seven, the estimated noise by the technique is greater than the actual noise levels.

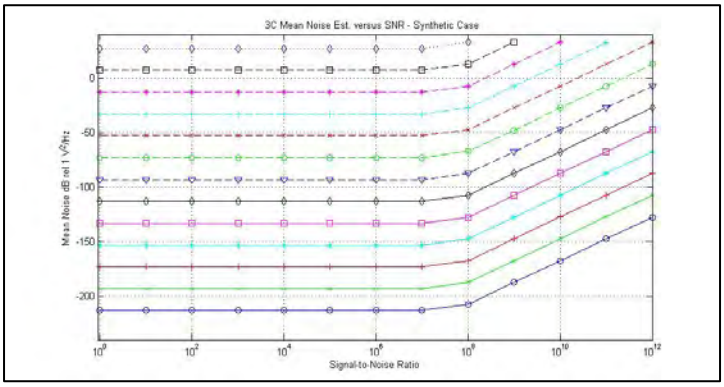


**Figure 3. Results of synthetic testing to determine numerical limitations of 3C technique showing 156 realizations each line common line type shows the results for a single absolute scale value, the effects of varying the separation of the combined coherent and incoherent signals.**

Varying the absolute level start which the analysis was done did not change the relative SNR level at which the technique started to break down, between 140 and 160 dB of SNR. To rule out the cause of the 140 dB limitation on the analog to digital conversion of the input signal, we devised another test to explore this. After the coherent and incoherent signals are combined, divide the series by the least-significant bit (LSB), then round the sequence to integer values and then multiple the series by the same LSB. Two different LSB were used to represent the 24-bit and 26-bit digitations. Figure 4 shows the results, on the left are results using floating point double precision correct extraction incoherent signal level of -133 dB across the 140 dB of SNR. The middle axes shows the results for the 24-bit LSB, with just over 1.5 dB of over-estimation of incoherent signal level, and the right axes showing results for 26-bit LSB with 0.2 dB over estimation. From this test we find that the digital conversion of the analog signal does not account for the band-limited deviation observed in the STS2 data, but one should consider the amount of over-estimates of noise when recording on 24-bit format. Through this synthetic test, we conclude that the 3C technique can produce reliable results when the scaling between the coherent and incoherent signals is less than 140 dB. Further thought will be given to deviating a suite of tests to understand these observations.

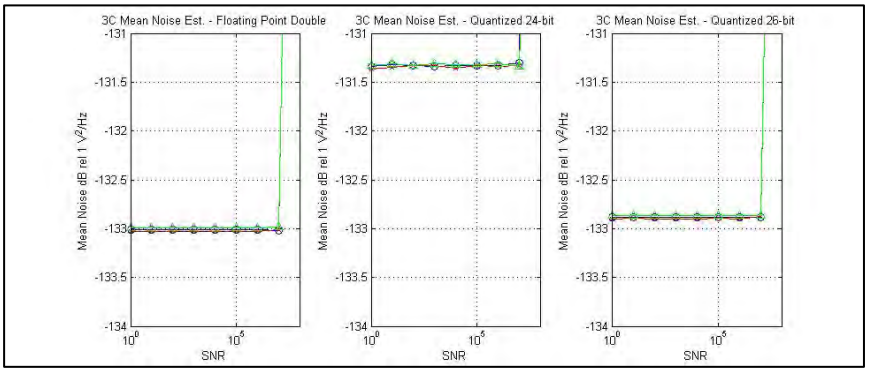


**Figure 4. Results of synthetic testing to determine limitations of 3C technique with respect to rounding effects; as pertaining to the digital conversion of an analog signal. Left axes shows results of using double-precision floating point, the middle axes shows results using 24-bit quantization and the right axes are results of using 26-bit quantization.**

**Characterization Geotech Smart24 Data-Logger with Active Fortezza Crypto Card Data Signing**

Over the spring of 2008 we have characterized the Geotech Smart24 data-logger with active data encryption as required for certain deployment applications. A complete characterization report can be fond in Hart, 2008a. Our characterization was done on two different configurations of the possible Smart24 Analog-to-Digital conversion boards, the first allows for maximum of 20 Vpp and second allows for a maximum of 40 Vpp. The 20Vpp ADC board had a serial number of 1360 and the 40Vpp ADC board had a serial number of 1724.

The overall performance of the Smart24 meets or exceeded the manufactures specifications for pass-band, dynamic range, bit-weight accuracy, and total harmonic distortion. The bit-weight accuracy was within 0.5% of nominal, RMS noise was below 1.5 μV for the 0.02 to 10 Hz band, maximum potential dynamic range was better than 131 dB, total harmonic distortion was better than -121 dB and channel-to-channel cross-talk was better than -122 dB. One area of issue was the time-tag accuracy, which fell just outside the manufactures specifications of ±10 μs at ~18 μs. Through working with the vendor we determined that configurations issues may exist between our test equipment and the Smart24 and are working to better understand the complexities of the interaction.

A follow up report on the application of a Smart24 matched with a Streckeisen STS2 low and high gain, Guralp CMG3T and a generic Geotech GS13 is currently underway. This will document the pass band is these sensors if matched with the Smart24.

**Characterization Inter-Mountain Labs Model SS Infrasound Sensor**

Our goal in testing the Inter-Mountain Labs infrasound sensors was to determine and document the performance of this sensor as pertaining to the monitoring community. Three sensors were evaluated, serial numbers 605368, 605408, and 605488, for the 0.1 to 10 Hz pass band, sensitivity, linearity between 0.007 and 11 Pa, amplitude response, and self-noise. The three sensors varied from there average 5 Hz sensitivity, mean sensitivity of 0.369 mV/Pa, by up to 5.3%. The sensors were linear in their sensitivity to within 1% between pressures ranging from

0.007 to 7.3 Pa. From our amplitude response verification test shown in Figure 5, we found the sensors to be flattest between 2 and 10 Hz and more than 3 dB of roll-off, relative to 5 Hz, at 1 Hz.

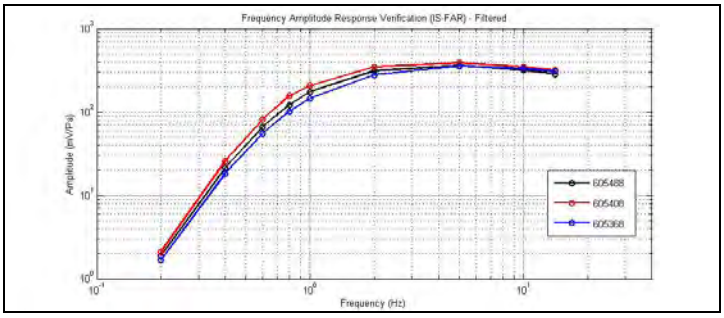


**Figure 5. Amplitude response model for the IML Model SS infrasound sensors.**

Using this response model, we correct self-noise power spectrum into units of Pa^2/Hz, shown in Figure 6. Plotting the noise of the IML sensor with the Acoustic Low Noise Model (ALNM), shows the IML sensor at or below the ALNM between 0.2 and 10 Hz, therefore this sensor would be capable of observing a broad range of signal levels due to its low noise characteristics.

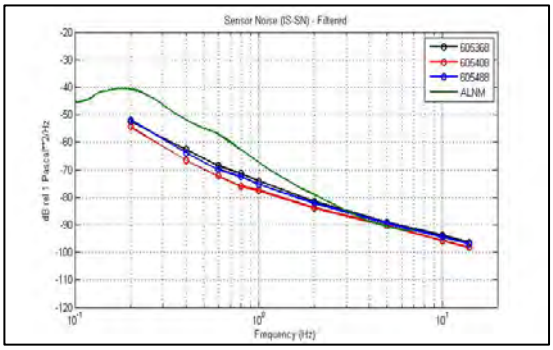


**Figure 6. Self-noise estimates for the Inter-Mountain Labs sensor, corrected using amplitude response model shown in Figure 5. ALNM is shown in green.**

**Characterization Chaparral Physics Model 2.5 Low Gain Infrasound Sensor**

One sensor type we have characterized a large number of prior to deployment is the CP2.5 low-gain. Typical characterization of these sensors includes sensitivity at 1 Hz, amplitude response between 0.02 and 5 Hz, linearity between 0.1 and 5 Pa, and noise characteristics of electronics and transducer. Typically, when a new set of CP2.5 sensors arrives for testing, we'll review the provided data sheets, and take relevant notes adding necessary information into a spreadsheet for reference. The sensors are tested and, where possible, we compare our results with those of the manufacture, noting any discrepancies. Two noteworthy observations have been made as a result of testing these sensors. The primary one being the 1 Hz sensitivity has been recorded as deviating from the manufactures specified value of 0.400 V/Pa (±5% for individual sensor sensitivities). Our testing has shown variability in 1 Hz sensitivities from 0.373 to 0.486 V/Pa, with our test results typically higher than those documented in the sensors data sheets. Table 1 shows a comparison between results of common tests: on average, we report a 25% higher sensitive and slightly less than half the frequency of the low frequency associated to the -3 dB roll-off point of the amplitude response.

**Table 1. Table comparing test results for 1 Hz sensitivity and the 3 dB corner frequency reported by Chaparral Physics in their data sheets and Sandia.**

| Serial Number | 1.0 Hz sensitivity (V/Pa) Chaparral | 1.0 Hz sensitivity (V/Pa) Sandia | 3 dB frequency - Chaparral | 3 dB frequency - Sandia |
|---|---|---|---|---|
| 061752 | 0.391 | 0.439 | 0.087 | 0.0459 |
| 061753 | 0.376 | 0.446 | 0.093 | 0.0436 |
| 061754 | 0.387 | 0.443 | 0.094 | 0.0435 |
| 061755 | 0.403 | 0.465 | 0.098 | 0.0457 |
| 061773 | 0.396 | 0.480 | 0.085 | 0.04 |
| 061778 | 0.411 | 0.472 | 0.088 | 0.0423 |
| 051756 | 0.392 | 0.392 | 0.1 | 0.0496 |
| 051757 | 0.396 | 0.445 | 0.095 | 0.0433 |
| **Average** | **0.394** | **0.448** | **0.0925** | **0.0442** |

The second observation is associated to the variability of the self-noise estimates of the individual chaparral sensors tested. The typical method for determining self-noise is done in one of two configurations. The first configuration is done to test for electronics noise, in which a relay is energized opening a circuit switching a fixed CR-circuit for the transducer element. The second configuration is done to measure transducer noise, in this case all the sensors pressure inlets are covered and the sensor is isolated in a chamber to dampen the effects of atmospheric influence. Figure 7 shows the results electronic noise tests for 61 different CP2.5 sensors. Typically, the sensors are below the ALNM at frequencies below 1.5 Hz and above the ALNM at frequencies above 1.5 Hz. This makes the CP2.5 not suitable for sites where their average background above 1 Hz is below -70 dB rel 1 Pa^2/Hz and another quieter sensors may be desired .

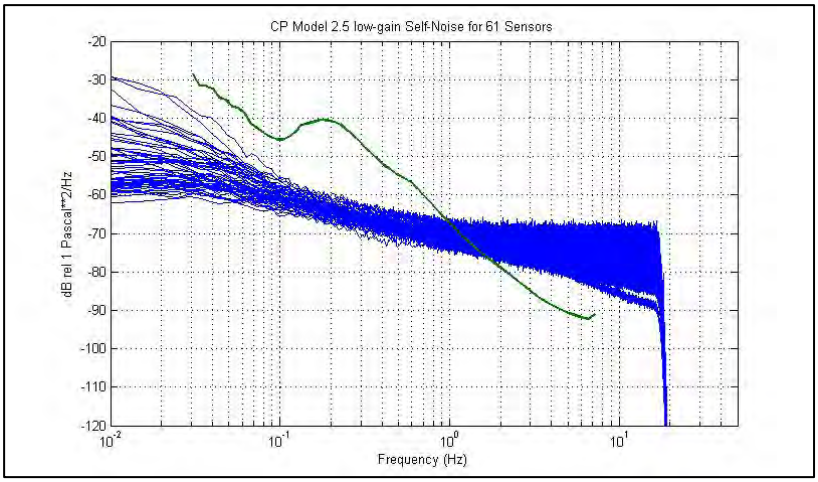


**Figure 7. Self-noise estimates for 61 Chaparral Physics model 2.5 low gain infrasound sensors. The ALNM shown as the green line. Sensors are typically at or below the ALNM from below 0.01 Hz to 1.0-1.8 Hz.**

As part of our tasking, we are looking for new ways of processing and visualizing the results from our testing. One new addition to our visualization capability has been to implement a similar analysis of our computed power spectral density (PSD) of sensors noise to that done by McNamara and Buland (2004) for ambient seismic background noise of the continental U.S. Instead of computing a single PSD for our analysis window, we compute several hundred for each analysis window. By statistical analysis of the power bins for each frequency, for the hundreds of compiled PSDs, yields probability density functions (PDFs) as a function of power. Comparison of related sensor self-noise PDFs show interesting artifacts related to sensor uniqueness and overall sensor quality. Figure 8 shows an example of the value of viewing sensors noise data as a PDF. The two plots (top and bottom) are of the same data, shown in different x-axis scales (top-logarithmic and bottom-linear). We can clearly see two dominant trends in the sensors noise characteristics at frequencies higher than 1 Hz, below 1 Hz the sensor's noise mergers into a single dominant feature of high probability. Using typical methods for noise analysis, one might only see the lower or upper noise features, masking the duality of the noise in this sensor. Further work will be done to migrate this technique into our routine analysis.

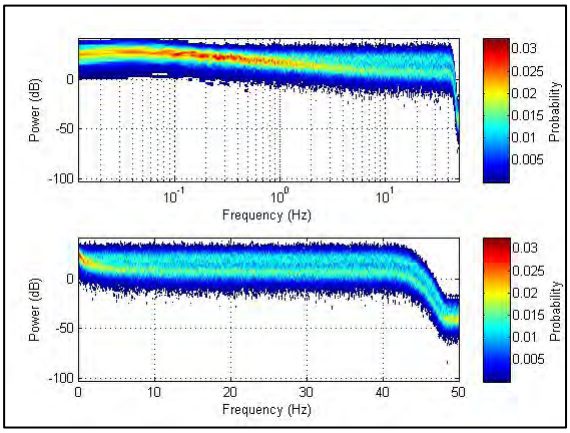


**Figure 8. Self-noise estimate for one Chaparral Physics model 2.5 low gain infrasound sensor shown as Probability Density Function (PDF) of power.**

**Characterization Porous Hose Filters used with Chaparral Physics 2.5 Infrasound Sensor Array**

As part of our on going effort to support operational needs of our customers, Sandia has built the capability to test and characterize the porous-hose filters used in some infrasound arrays for the monitoring purpose. The initial test configuration was designed around one deployment method for CP2.5 sensors. Each CP2.5 sensors inlet (each sensors has four inlets) is connected to a solid hose (1–3 feet in length), which is connected to environmental housing (EH). The outside of the EH then connects to a single inlet-to-double output Y connector. At each end of the Y connector a 50-foot porous hose is connected. At each sensor there are eight porous hoses aligned approximately $\pi/2$ radians apart from each other. The sites aperture is around 100 feet. A second CP2.5 sensor is co-located with the first, and has only a single short solid hose attached to one of its inlets, the other three inlets are left uncapped to reduce unwanted high frequency harmonics. A time segment was selected for processing and PSD were computed for the

two co-located sensors. To determine the relative amplitude response of the porous-hose filter system the two PSD were divided. We were expecting to see some sort of low pass filter characteristics, but what we saw was not anticipated. The filter can be characterized as low pass with little or no attenuation of acoustic signals with period longer than 50 seconds, while signals with shorter periods attenuated 15 dB at 0.1 Hz and ~25 dB at 1 Hz (Figure 9). With no correction for the amplitude reduction of the porous hose filter any analysis using amplitude measurements between 0.1 ands 10 Hz will under estimate the association.

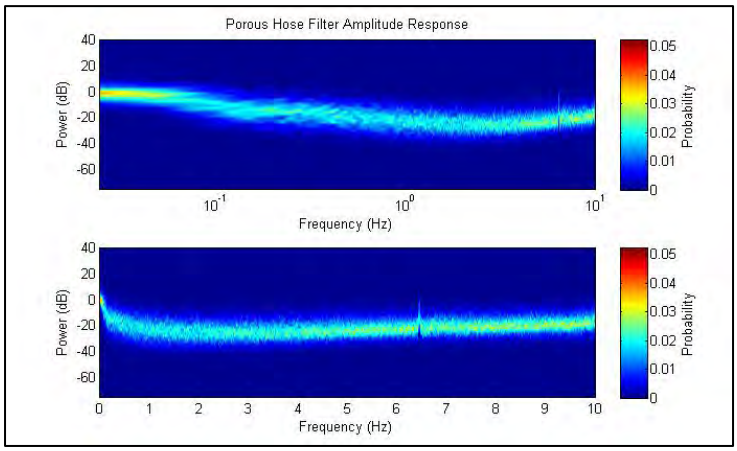


**Figure 9. Amplitude response of an 8-arm porous hose filter system. Filter can be characterized as low pass with little or no attenuation of acoustic signals with period longer than 50 seconds, while signals with shorter periods attenuated 15 dB at 0.1 Hz and ~25 dB at 1 Hz.**

**Component Evaluation Software Upgrade**

The current software used to analyze data collected from testing is called the Instrumentation Evaluation Software (IES) and was written for the component evaluation program in the late 1980's. The software was written as a collection of custom and distinct C utilities that perform the various aspects of the test analysis:

- Waveform file conversion
- Waveform time segmenting
- Manage sensor responses and apply responses to waveforms
- Compute PSD, THD, DC Accuracy, Coherency, Sine Fits, Time tag accuracy, etc

In order to run the analysis tools, the user must first load the waveform data recorded from the test and specify a time window to segment the waveform. The resulting segment is then stored in an ASCII file format that each of the analysis tools can read.

Each of the analysis tools must then be run individually and manually pointed to the cut waveform segment for that particular test. Once the analysis tool has been run, the results are presented to the user in the form of a graphical window. The user must then capture the results of that test either by transcribing values into a spreadsheet, printing the window, or capturing a screen shot to a file or embedded into a document. To be able to save the results (and later regenerate the test, if necessary), the user must retain a copy of the input waveform as well as all of the parameters that were used to generate the results. This typically results in a proliferation of various files saved in a folder on disk.

The major problems faced by the current set of analysis tools are that there is too much overhead involved in using the analysis tools and transferring the results of that analysis to a report. Also, the current methodologies in place for capturing the data and results for a test are inadequate.

Some of the goals of the proposed test analysis utility that could help to improve the Evaluators performance are to

- Streamline the analysis process to eliminate the need to shift from tool to tool.
- Ensure that the entire state of a test process is retained in a single easy to access location. This would also have the advantage of eliminating the clutter that is generated by having to store each stage of the analysis as a file on disk
- Provide users with the ability to return to a historical test and re-run the analysis with slightly different parameters (filter, window, etc). Possibly re-generate the updated report with a push of a button.
- Provide a mechanism for the results of the test analysis to be fed directly into a report.

One of the first steps in building a replacement for the IES tools was to ascertain what exactly the current analysis tools were doing. Towards that end, prototypes of the algorithms were implemented in MATLAB and the results

compared against those of the IES analysis tools. Verifying the functionality of the analysis tools is important to validate our understanding of the algorithms and to provide traceability in the results of any future analysis tools. Also, wherever possible, the implementation of the algorithms is being tied to an IEEE reference.

A database schema must be designed to capture and archive the state of the hardware being tested, the suite of tests to be run on each piece of hardware, and the results of each test. In the schema diagram in Figure 10, the schema is divided into four regions: Systems, Responses, Tests, and Models.

The System tables define the physical components that are to be tested and how those components are organized into subsystems. A component could be a seismometer, acoustic sensor, digitizer, meter, or even a cable. The Response tables define the response of a particular component in either pole-zero or FAP format. The Test tables provide a generic mechanism for capturing relevant information about any type of test by associating any arbitrary number of waveforms, parameters, and results. In addition, tests are associated with the particular component or subsystem that is being tested. Finally, the Model tables allow for capturing models that may be used for comparison within the testing system.

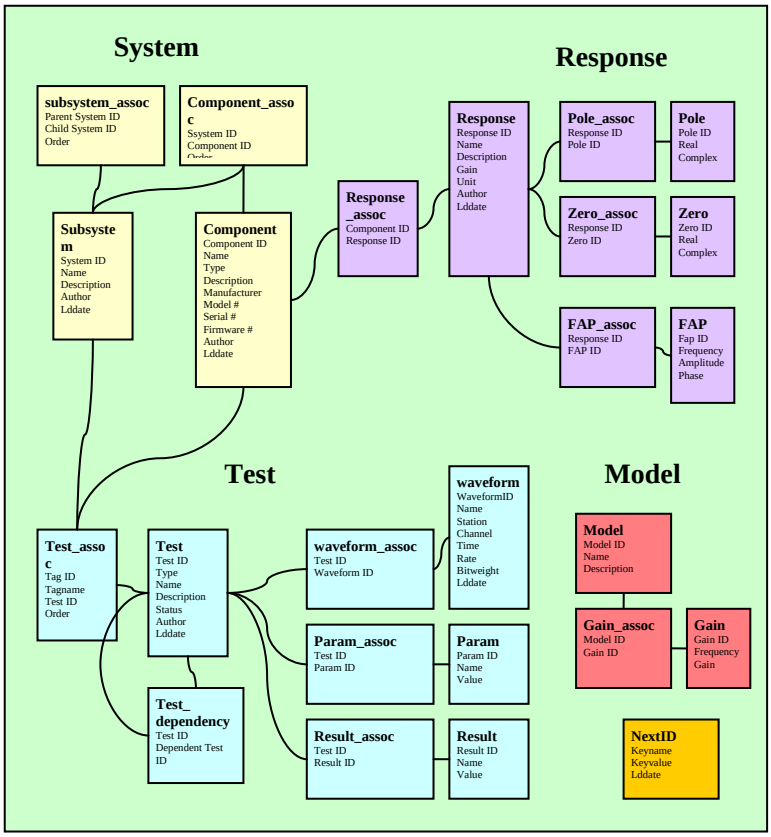


**Figure 10. Database Schema Diagram**

In addition to defining the database schema, the core set of functionality for the test system has been implemented, as described in the Object Model Diagram below (Figure 11). The object model lays out the bulk of the implementation: A database interface, waveform access, viewers for many of the objects, and signal processing algorithms. The bulk of the effort, however, is aimed at implementing the multitude of tests that are needed. A test interface is defined that supports the generic capability for the storage of the parameters, results, and waveforms within a test. Each test defines its own set of parameters, results, and waveforms as well as the computation that is necessary to complete the test analysis.

The implementations of the test interface are defined as plug-ins that can automatically register themselves at application startup time. The advantage of using this type of plug-in architecture is that the remainder of the application can interact with the test implementations just as generic tests. No prior assumption of a specific test is required. Also, the choice of possible tests that can be performed for each system or component is determined dynamically. Additional tests can be defined without making any changes to the system other than the specific implementation of the test.

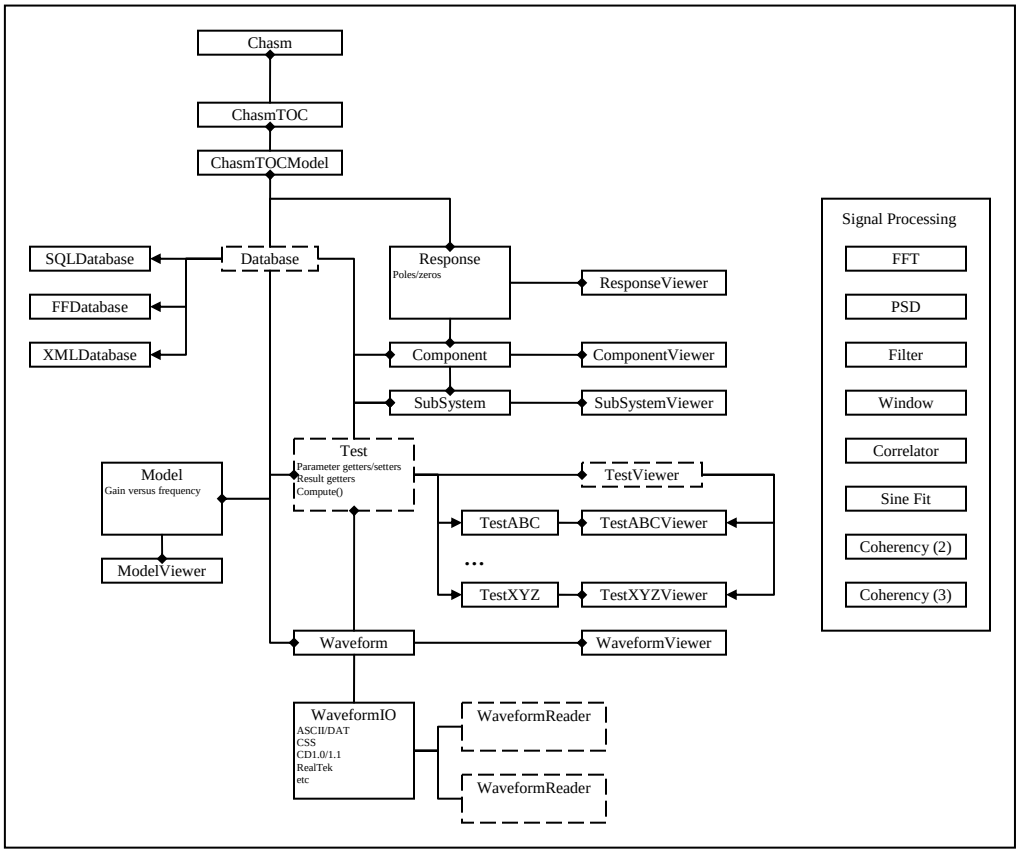


**Figure 11. Object Model Diagram**

## CONCLUSIONS AND RECOMMENDATIONS

Continuing work on three sensor coherence has allowed us to explore the numerical limitations of the technique with synthetic data. As well as, rule out possible causes for deviations observed in the self-noise estimates of STS2 seismometers. We continue to seek out new sensors technologies (primarily seismic and infrasound types) that may have value to the explosion monitoring community. New methods for the visualization of results from testing have led to the use of probability density functions to characterize self-noise of sensors, as well as to characterize the amplitude response of porous-hose filter system used at some monitoring infrasound stations. With continued support we hope to maintain an active role and add value to the nuclear explosion monitoring community.

## ACKNOWLEDGEMENTS

We would like to thank David Fee of the Hawaii Infrasound Laboratory for his help and contributions to getting the code together for producing the PDFs shown in this paper.

## REFERENCES

Hart, D. M. (2007a). Characterization of 12 Chaparral Physics Model 2.5 Infrasound Sensors June-October 2007, Sandia Report SAND2007-7064.

Hart, D. M. (2007b). Component and Sub-System Evaluation of the System Test and Evaluation and Monitoring Project 2C, Sandia Report SAND2007-9735.

Hart, D. M. (2007c). Evaluation of the Inter-Mountain Labs Infrasound Sensors July 2007, Sandia Report SAND2007-7020.

Hart, D. M., B. Merchant, and E. Chael (2007). Seismic and Infrasound Sensor Testing using Three Channel Coherence Analysis, in *Proceedings of the 29th Monitoring Research Review: Ground-Based Nuclear Explosion Monitoring Technologies*, LA-UR-07-5613, Vol. 2, pp. 935–944.

Hart, D. M. (2008). Evaluation of the Geotech Smart24 Data Acquisition System with Active Fortezza Crypto Card Data Signing and Authentication, Sandia Report SAND2008-3264.

McManara, D.E., and R.P. Buland (2004). Ambient Noise Levels in the Continental United States, Bull. Seism. Soc. Am.: 94, 1517–1527.

Sleeman, R., A. van Wettum, and J. Trampert (2006). Three-channel correlation analysis: A new technique to measure instrumental noise of digitizers and seismic sensors, *Bull. Seism. Soc Am.* 96: 258–271.

# IMPROVEMENTS TO A MAJOR DIGITAL ARCHIVE OF SEISMIC WAVEFORMS FROM NUCLEAR EXPLOSIONS: BOROVOYE SEISMOGRAM ARCHIVE

Won-Young Kim[1], Howard Patton[2], George Randall[2], and Paul Richards[1]

Lamont-Doherty Earth Observatory of Columbia University[1] and Los Alamos National Laboratory[2]

Sponsored by Air Force Research Laboratory

Contract No. FA8718-07-C-0004
Proposal No. BAA07-23

## ABSTRACT

We are in the second year of a three-year project to generate in modern form an easily usable archive of digital seismograms derived from regional waveforms recorded at the Borovoye Observatory (BRV), northern Kazakhstan, over a thirty-year period going back to 1966 and spanning the time when state-of-the-art sensors and dataloggers were introduced at this site by several different western groups. The BRV seismograms, which include multi-channel regional signals from 350 underground nuclear test explosions carried out in Eurasia, were made generally available to western scientists in 2001, but only as copies of the bits in the original digital waveforms. These copies contain large numbers of glitches and did not include instrument responses for approximately two-thirds of the events. In the first two years of this project, we are focusing on basic processing of the damaged waveforms to make them more easily usable by the removal of glitches and the inclusion of instrument responses (including absolute gains as well as poles and zeroes). In the third year we shall focus on a series of research projects with the restored waveforms. Our project is a joint effort by scientists at Lamont-Doherty Earth Observatory of Columbia University (LDEO) and at Los Alamos National Laboratory (LANL).

Three different sets of Soviet-style instruments and recording systems were used at BRV from 1966 to 1996. LANL scientists first processed the BRV regional signals for 210 nuclear tests (1,355 traces), mainly those for which instrument responses were available (the TSG system). In this project, LANL has also now processed the waveforms of the so-called SS system for 148 nuclear tests (1,215 traces), some of which were also recorded on the TSG system; and in late June 2008, LANL completed processing for waveforms in the archive from the SS and TSG systems (474 and 281 traces, respectively). A remaining main block of events, recorded on the KOD system (which was used in operations beginning in 1966 and operated continuously from 1967 to 1973) is planned for processing this year. The KOD system, which is based on three-component, short-period seismometers, is important as one of the few digital systems anywhere in the world in the late 1960s and early 1970s.

As part of the process of quality assurance, we are making measurements of signal amplitude where possible from the restored waveforms, to see if relative amplitudes of different parts of the seismogram (*P*, *Lg*, *Rg*, longer period surface waves, coda) meet expectations. We are also interpreting absolute amplitudes, for those underground nuclear explosions at the Semipalatinsk Test Site (STS), and in the Soviet Union's Peaceful Nuclear Explosion program, for which yield information is available. Although only 27 underground nuclear tests at the STS have officially announced yields (Mikhailov, 1996), additional yield information has been supplied in a variety of publications, and we have 62 STS underground nuclear tests for which yields have been reported.

## OBJECTIVES

We propose to generate in modern form an easily usable archive of digital seismograms derived from regional waveforms recorded at the Borovoye Observatory (BRV), northern Kazakstan, over a thirty-year period going back to 1966 and spanning the time when state-of-the-art sensors and dataloggers were introduced at this site in the summer of 1994. Specifically, we expect to process 1,200 to 1,400 digital waveforms from the Borovoye archive, for more than 200 underground nuclear explosions in Eurasia for which digital records are available but not yet in useful form due to problems with glitches and instrument calibration that have not yet been taken into account.

## RESEARCH ACCOMPLISHED

### Deglitching the Borovoye Archive

During 2007 and spring of 2008, Borovoye Archive waveform data from over 200 underground nuclear explosions have been deglitched by the LANL group. The locations of those explosions are plotted in Figure 1. Deglitched explosions include 73 explosions from Balapan, 59 from Degelen, and four explosions from Murzhik subregions of the STS; eight explosions from Lop Nor Chinese test site, and 53 PNEs (Peaceful Nuclear Explosions).

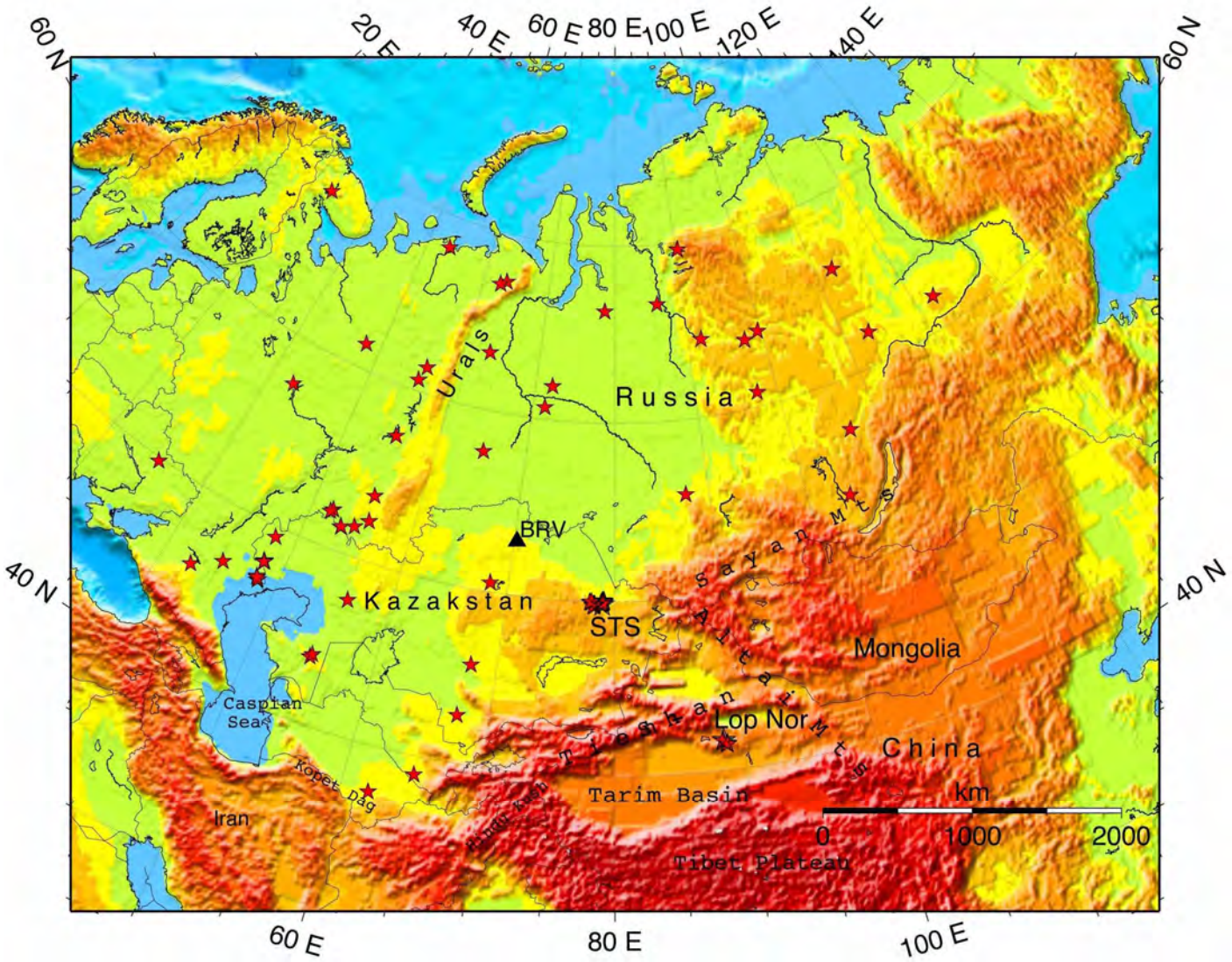


**Figure 1. Locations of underground nuclear explosions in Eurasia whose waveform data in the Borovoye Archive had been deglitched in this project by Spring 2008.**

An example of an extensive set of deglitched BRV archive seismograms, recorded on two systems (TSG, SS) from an underground nuclear explosion (UNE) at Balapan, on the STS, is plotted in Figure 2. This is a strong explosion with magnitude mb(P) = 6.0 and hence, many channels of the BRV archive records are clipped. The 24-channel STsR-TSG system produced seven useful channels, whereas all 10 channels of the STsR-SS system are useful (see Figure 2). A short-period, vertical-component record of the TSG system, sZ01, which is a low-gain channel with apeak amplitude of 510 counts, is on-scale. Other short-period channels, channels sZ06, sZ07, sN08, sE09 are all clipped. However, these records are still useful for picking accurate arrival times of the first arrival Pn phase (distance 695.6 km), as well as for quantitative analysis of amplitudes using coda waves (e.g., Mayeda and Walter, 1996). This explosion was also recorded by the SS system, which has low-gain long-period channels. Long-period channels, l02Z, l03N, l04E as well as a short-period vertical-component, s06Z are all on-scale. Short-period 3-component channels, s07Z, s08N, and s09E, are all clipped, but their long coda records (24 minutes from the origin time of the explosion), make the records still very useful. For instance, the P wave reflected from core-mantle boundary (PcP, arriving about 420 s after Pn) as well as the P wave reflected from the inner core boundary (PKiKP, arriving about 900 s after Pn) can be identified and used to study the nature of discontinuities in the Earth's deepest interior (e.g., Adushkin et al., 1997).

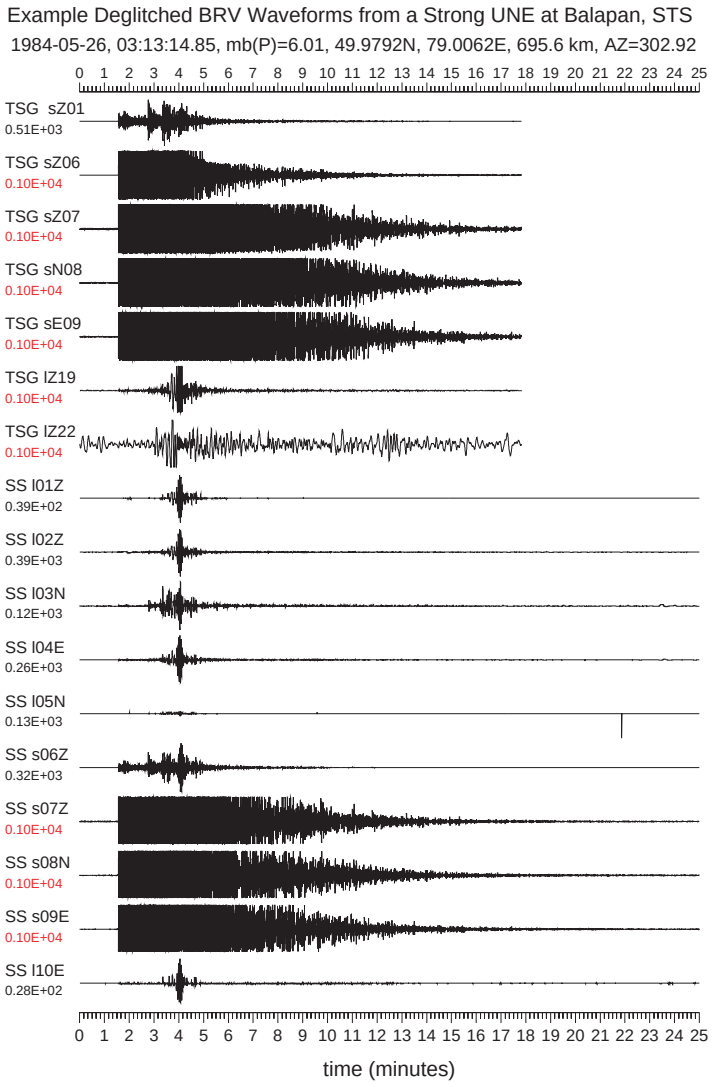


**Figure 2. Example of a set of deglitched BRV archive seismograms from an UNE at Balapan, STS. TSG = records from 24-channel STsR-TSG system, SS = 10-channel STsR-SS system. The first letter in the channel names, l or s, indicates long- or short-period records, respectively. The ground motion components (Z, N and E) are indicated by the second letter in the channel names for the TSG system and by the last letter in the SS system.**

**Calibration of Instrument Response and Gain of Borovoye Archive**

We have begun to calibrate instrument responses and gains of the deglitched BRV archive data. We are employing RMS (root-mean-squared) amplitude measurements of P or Lg wave trains to calibrate gains of the instruments used in the BRV archive. For a preliminary study, we have nine unclipped short-period vertical records from the SS system, channel sZ01 (= s01Z), and 28 unclipped short-period vertical records from the TSG system (KSVM, see Adushkin & An, 1990; Kim & Ekström, 1996). Measured RMS values from 37 short-period records from UNEs at Balapan, STS are listed in Table 1 and the first 12 traces are plotted in Figure 3. The KSVM recorder has a nominal gain of 48.6 counts/micron at 1.4 Hz, whereas the SKM-3 recorded in the SS system has a nominal gain of 200 counts/micron at 1.8 Hz (Kim et al., 2001).

**Table 1. Measurement of RMS (Lg), and some reported yields, are given here for unclipped short-period digital seismograms in the Borovoye archive from 37 UNEs at Balapan, STS.**

| Date | Origin Time | Lat. °N | Long.°E | mb(P) | log(RMS) | reported Y (kt) |
|---|---|---|---|---|---|---|
| 1975-10-29 | 04:46:59.82 | 49.9539 | 78.8739 | 5.61 | 3.04 | |
| 1976-04-21 | 05:02:59.70 | 49.9006 | 78.8308 | 5.12 | 2.57 | |
| 1976-08-28 | 02:56:59.99 | 49.9750 | 78.9264 | 5.74 | 3.08 | |
| 1976-12-07 | 04:56:59.85 | 49.9439 | 78.8392 | 5.80 | 3.15 | |
| 1977-05-29 | 02:57:00.01 | 49.9464 | 78.7717 | 5.75 | 3.09 | |
| 1977-06-29 | 03:07:00.35 | 49.9994 | 78.8667 | 5.20 | 2.51 | |
| 1978-06-11 | 02:57:00.08 | 49.9133 | 78.8019 | 5.83 | 3.11 | |
| 1978-07-05 | 02:46:59.97 | 49.9000 | 78.8667 | 5.77 | 3.10 | |
| 1979-02-01 | 04:13:00.17 | 50.0808 | 78.8533 | 5.29 | 2.84 | |
| 1984-03-29 | 05:19:10.66 | 49.9111 | 78.9269 | 5.86 | 3.25 | |
| 1984-04-25 | 01:09:05.99 | 49.9358 | 78.8506 | 5.90 | 3.27 | 76 |
| 1984-05-26 | 03:13:14.85 | 49.9789 | 79.0056 | 6.01 | 3.48 | 143 |
| 1984-07-14 | 01:09:12.99 | 49.9094 | 78.8772 | 6.10 | 3.43 | |
| 1984-10-27 | 01:50:12.93 | 49.9347 | 78.9281 | 6.19 | 3.40 | |
| 1984-12-02 | 03:19:08.85 | 50.0061 | 79.0089 | 5.77 | 3.30 | |
| 1984-12-16 | 03:55:05.07 | 49.9458 | 78.8086 | 6.12 | 3.39 | |
| 1984-12-28 | 03:50:13.09 | 49.8803 | 78.7039 | 6.00 | 3.34 | 113 |
| 1985-06-15 | 00:57:03.25 | 49.9086 | 78.8428 | 6.05 | 3.29 | |
| 1985-06-30 | 02:39:05.26 | 49.8644 | 78.6686 | 5.92 | 3.26 | 108 |
| 1985-07-20 | 00:53:16.91 | 49.9497 | 78.7839 | 5.89 | 3.28 | |
| 1987-03-12 | 01:57:19.57 | 49.9353 | 78.8289 | 5.31 | 2.61 | 11 |
| 1987-04-03 | 01:17:10.28 | 49.9181 | 78.7803 | 6.12 | 3.37 | |
| 1987-04-17 | 01:03:07.09 | 49.8778 | 78.6689 | 5.92 | 3.28 | 110 |
| 1987-06-20 | 00:53:07.09 | 49.9353 | 78.7442 | 6.03 | 3.34 | |
| 1987-08-02 | 00:58:09.27 | 49.8806 | 78.8747 | 5.83 | 3.24 | 80 |
| 1988-02-13 | 03:05:08.33 | 49.9367 | 78.8639 | 5.97 | 3.38 | |
| 1988-04-03 | 01:33:08.29 | 49.9083 | 78.9083 | 5.99 | 3.43 | |
| 1988-05-04 | 00:57:09.26 | 49.9494 | 78.7503 | 6.09 | 3.35 | |
| 1988-06-14 | 02:27:08.98 | 50.0189 | 78.9606 | 4.80 | 2.37 | |
| 1988-09-14 | 03:59:59.69 | 49.8778 | 78.8231 | 6.03 | 3.35 | 119 |
| 1988-11-12 | 03:30:06.26 | 50.0431 | 78.9689 | 5.24 | 2.74 | |
| 1988-12-17 | 04:18:09.29 | 49.8819 | 78.9247 | 5.83 | 3.19 | |
| 1989-01-22 | 03:57:09.02 | 49.9394 | 78.8194 | 6.10 | 3.27 | |
| 1989-02-12 | 04:15:09.34 | 49.9186 | 78.7111 | 5.86 | 3.19 | |
| 1989-07-08 | 03:47:00.03 | 49.8678 | 78.7803 | 5.55 | 2.85 | 33 |
| 1989-09-02 | 04:16:59.85 | 50.0058 | 78.9856 | 4.94 | 2.25 | 4 |
| 1989-10-19 | 09:49:59.81 | 49.9222 | 78.9083 | 5.86 | 3.19 | 75 |

The waveforms from most of the explosions are consistent, but there are some subtle differences. For instance, Sn phase from some explosions such as, 1979-02-01 and 1984-05-26, is stronger than those from other explorations as well as the Rg is less well excited on some explosions with smaller mb(P), such as 1976-04-21 and 1979-02-01. We calculated RMS Lg amplitude following the procedure given in Richards et al (1993) and Hansen et al. (1990). RMS Lg amplitude measurements for 37 explosions are compared with mb(P) given by Ringdal et al. (1992) in Figure 4. Regression of the measured RMS Lg values with mb(P) yields a standard deviation of 0.060 magnitude units and a slope of 0.89. We also compared the RMS Lg amplitude with a known yield of 11 UNEs as shown in Figure 4. The regression of RMS Lg amplitudes using BRV archive data with body-wave magnitudes or yields produced small scatter indicating that one may have confidence in both RMS Lg as a measure of source size, and in BRV archive instrument calibrations.

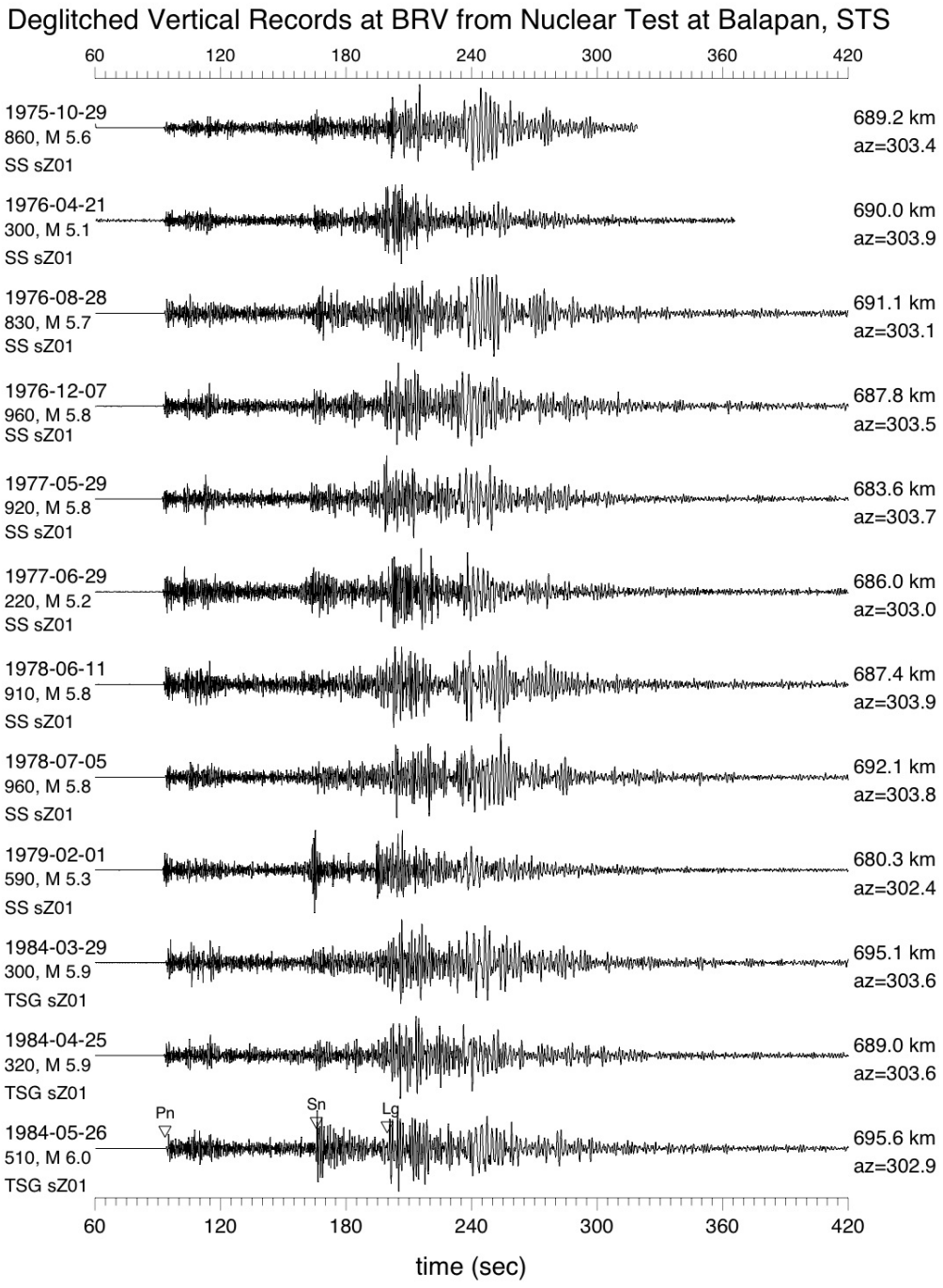


**Figure 3. Examples of BRV archive seismograms recorded by SS-SKM-3 and TSG-KSVM systems. Explosion id, peak amplitude in integer digital counts, magnitude, mb(P), and recording system and channel names, are indicated at the beginning of each trace.**

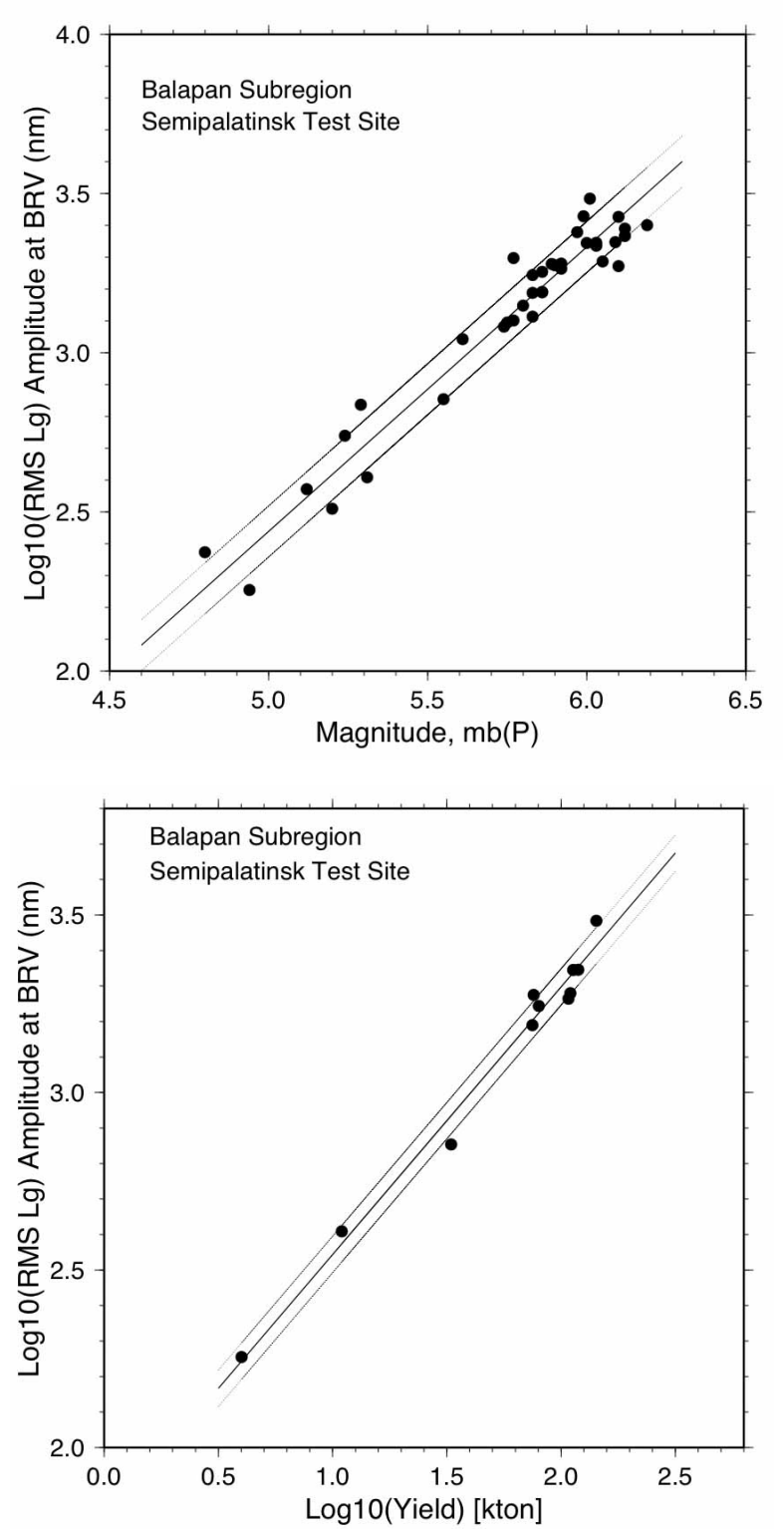


**Figure 4. (Upper panel) Comparison of log10(RMS Lg) measurements in nm at BRV with body-wave magnitude mb(P). RMS Lg amplitudes are obtained from unfiltered data with a single gaussian window centered at an Lg group velocity of about 3.3 km/s. Solid line is a fitted slope of 0.89 and an orthogonal rms misfit of 0.060 magnitude units. The dotted lines correspond to ±2 S.D. (Lower panel) Comparison of log10(RMS Lg) measurements in nm at BRV with a reported yield in kilotons for 11 UNEs. Solid line is a fitted slope of 0.75 and an orthogonal rms misfit of 0.041 magnitude units. The dotted lines correspond to ±2 S.D.**

**Repeating Underground Nuclear Explosions?**

Although UNEs may not be conducted at the same shaft except when two or more are carried out at almost the same time, two BRV archive records from nuclear tests at the Balapan subregion of STS are very similar (see Figure 5). However, the explosion on 1984-05-26 is a strong one with mb(P) = 6.01 and a reported yield of 143 kton, while the explosion on 1989-09-02 is a relatively weak one with mb(P) = 4.94 and a reported yield of 4 kton. Each of these two tests consisted of two separate explosive devices fired at almost the same time. The two records shown in Figure 5 have similar relative excitation of Pn, Sn, Lg, and Rg phases and are recorded by the same instrument at BRV.

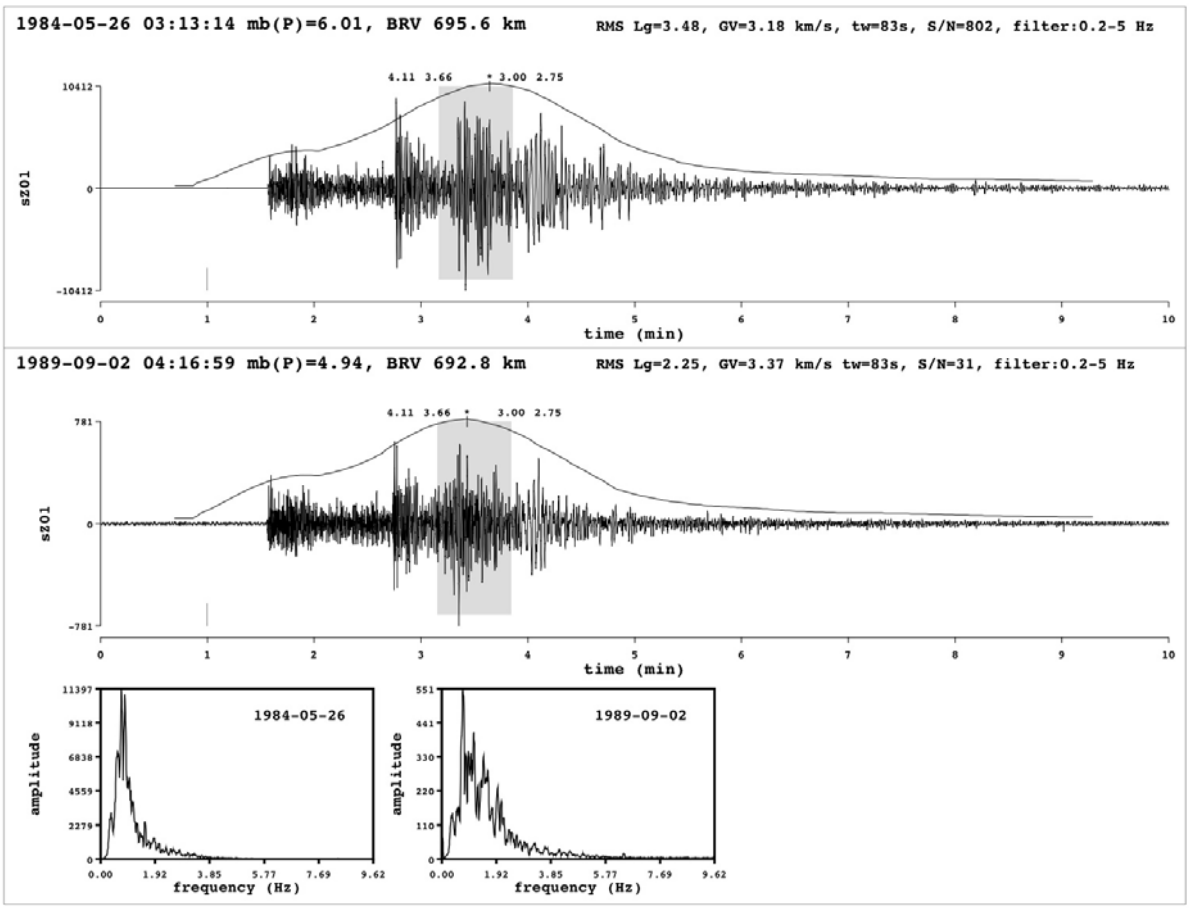


**Figure 5. (top trace) vertical record from an underground nuclear test of two explosive devices on 1984-05-26 (mb(P) = 6.01). Mean squared amplitude trace is plotted above the unfiltered raw data and its maximum is indicated by a star. Shaded area indicates the width of gaussian window with ±σ = 20 s centered at the Lg group velocity of 3.3 km/s.**
**(middle panel) vertical record from an underground nuclear test on 1989-09-02 (mb(P) = 4.94). The shafts for these two tests are located about 2–3 km apart and have the same azimuth to BRV.**
**(bottom panel) spectra of the two seismograms as recorded at BRV.**

**Summary of Work Flow in this Project**

We began this project with tar files for each of 350 underground nuclear tests in Eurasia from 1966 to 1996 containing the Borovoye digital seismogram archive, with glitches and lacking complete response information.

LANL processed regional signals for 210 nuclear tests (1,355 traces), mainly from the TSG system (but with some examples of SS and KOD records), prior to the beginning of this project. In 2007, LANL made this batch of already deglitched records available to Richards and Kim at Lamont.

In January 2008, LANL finished deglitching SS system waveforms from 148 tests (1215 traces), many of which had been recorded also on the TSG system, and this batch of waveforms was received at Lamont in February 2008.

In June 2008, LANL finished deglitching all the remaining waveforms in the SS and TSG systems (474 and 282 traces, respectively), and passed them along to Lamont in late June. These include records of nuclear tests at Novaya Zemlya. Figures above, in this paper, have used these deglitched records.

As of July 2008, there remain 709 traces recorded on the KOD system to be deglitched (by LANL) and to have their responses included (by Lamont). The KOD system is important as one of the very few digital datalogging systems in seismology in the 1960s and 1970s. It was first used in 1966 and ran continuously from 1967 to 1973. Information currently available to us on the response of this system is shown in Figure 6. We plan to make all of our processed waveforms openly available.

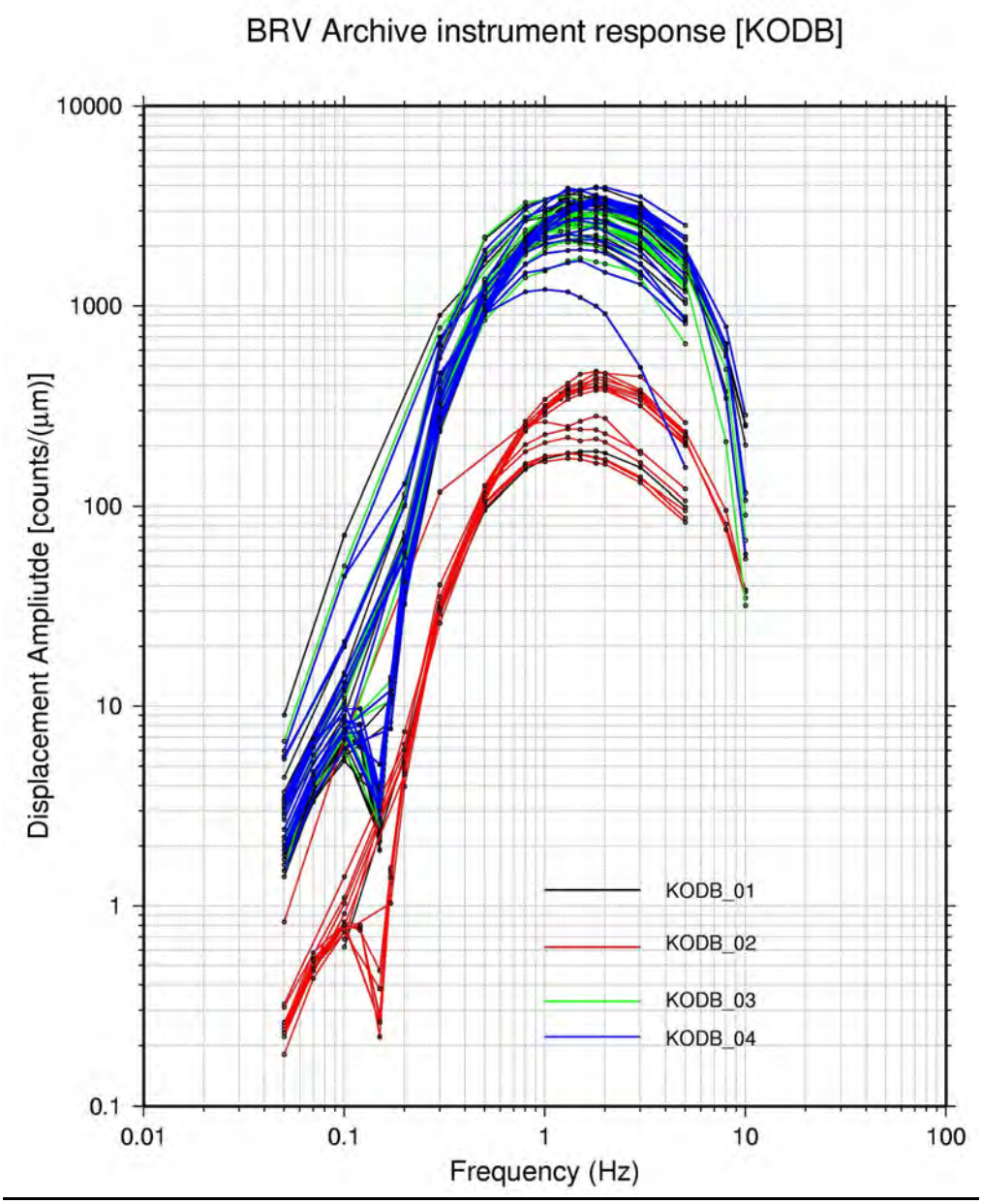


**Figure 6. Responses of the KOD system, used at Borovoye Geophysical Observatory from 1966 to 1973. The notch filter, apparent in some of these sampled amplitude spectra (which were measured many times, leading to the numerous responses shown here), was designed to reduce the effect of microseisms.**

## CONCLUSIONS AND RECOMMENDATIONS

We are about halfway through this three-year project, which entails much tedious work in the effort to remove glitches and to establish confidence in our knowledge of instrument responses—some of them established as far back as forty years ago. We would not do such work without the prospect of seeing benefits in an improved understanding of issues that are important in nuclear explosion monitoring.

Research based on these data cannot be completed until the whole archive is processed. We expect such research to be carried out in the third year of this project.

Ongoing studies, likely to benefit from an improved Borovoye digital waveform archive (and that can also help ensure that we have the correct gains and responses), are as follows:

- Yield estimation, using RMS Lg, Rg, and coda.
- Effects of source depth and shot-point geology, for example using PNEs from different regions.
- Discrimination using spectral ratios of seismic signals from earthquakes and UNEs, for example, at the Semipalatinsk and Lop Nor test sites (in shafts and tunnels—which may impose their own slight differences on observed spectra).
- Discrimination between regional seismic signals of nuclear explosions and mining blasts of various types. (Note that mining blast signals are being routinely acquired today by the well-instrumented modem BRVK station.)

## ACKNOWLEDGEMENTS

We thank the staff at the Institute for Dynamics of Geosphere, Moscow, Russia led by Drs. Vitaly Adushkin and Vladimir Ovtchinnikov, who copied the BRV waveform archive from old 35-mm tapes into modern media and performed extensive data reformatting work. We also thank staff at the Institute of Geophysical Research, National Nuclear Center, Republic of Kazakhstan led by Drs. Nadezhda Belyashova and Natalia Mihailova who provided us with ground truth data on shot-hole locations of Semipalatinsk test site.

## REFERENCES

Adushkin, V. V. and V. A. An (1990). Seismic observations and underground nuclear shot monitoring at Borovoye Geophysical Observatory, Izvestiya Akademii Nauk SSSR: Fizika Zemli, 47–59, No. 12, (also available in English as Physics of the Solid Earth, 1023–1031, #12 for 1990).

Adushkin, V.V., V.A. An, V.M. Ovchinnikov, and D.N. Krasnoshchekov (1997). A jump of the density on the outer-inner core boundary from the observations of PKiKP waves on the distance about 6 deg, *Transactions of the Russian Academy of Sciences*, 354, No. 3, 382–385.

Hansen, R., F. Ringdal and P. Richards (1990). The stability of RMS Lg measurements and their potential for accurate estimation of the yields of Soviet underground nuclear explosions, *Bull. Seism. Soc. Am*. 80: 2106–2126.

Kim, W-Y. and G. Ekström (1996). Instrument responses of digital seismographs at Borovoye, Kazakstan, by inversion of transient calibration pulses, *Bull. Seism. Soc. Am*. 86: 191–203.

Kim, W.-Y., P. Richards, V. Adushkin and V. Ovtchinnikov (2001). Borovoye Digital Seismogram Archive for Underground Nuclear Tests during 1966-1996, 41 pages, LDEO, April 2001.

Mayeda, K. and W. Walter (1996). Moment, energy, stress drop, and source spectra of western U.S. earthquakes from regional coda envelopes, *J. Geophys. Res*. 101: 11195–11208.

Mikhailov, V. N. (1996). USSR nuclear weapons tests and peaceful nuclear explosions, 1949 through 1990, Ministry of Atomic Enery and Ministry of Defense, Russian Federation, V. N. Mikhailov and I. A. Andryshin Eds, Russian Federation Nuclear Center, 63 pages.

Richards, P., W.-Y. Kim and G. Ekström (1993). RMS Lg studies of underground nuclear explosions in the U.S.S.R. and the U.S., Final Report, PL-TR-93-2227, Phillips Laboratory, Hanscom AFB, MA.

Ringdal, F., Marshall, P.D., and Alewine, R.W. (1992). Seismic yield determination of Soviet underground nuclear explosions at the Shagan River test site, *Geophys. J. Int.*, 109, 65–77.

# MERGING EVENT CATALOGS USING AGGLOMERATIVE HIERARCHICAL CLUSTERING

Jennifer E. Lewis, Sanford Ballard, Christopher J. Young, Dorthe B. Carr, Antonio I. Gonzales, and B. John Merchant

Sandia National Laboratories

Sponsored by National Nuclear Security Administration

Contract No. DE-AC04-94AL8500

## ABSTRACT

Many agencies construct catalogs of the hundreds of seismic events that occur daily around the world. The Ground-Based Nuclear Explosion Monitoring Research and Development (GNEMRD) program merges these catalogs together into a composite catalog containing multiple descriptions of the same seismic event, one from each catalog of interest. The merging process requires associating seismic events in individual catalogs (herein called *origins*), that are independent estimates of the same seismic event. In this paper we describe application of classical cluster analysis techniques that provide a straightforward and robust solution to this merging problem. The resulting algorithm is much simpler to tune than the rule-based methodology used by EvLoader, which is the application currently used to merge catalogs in the GNEMRD program.

For this study, we used a simple agglomerative hierarchical clustering technique to create clusters of similar origins where the various origins in a cluster represent different estimates of the seismic parameters of the same actual seismic event. Similarity between origins is calculated using a difference measure based on latitude, longitude, depth, time, and catalog author. Uncertainty in locations is accounted for by dividing distances between origins and differences in origin time by uncertainty estimates from the catalogs. To enforce the assumption that each catalog contains only a single origin for each event, origins from the same catalog are assigned infinite difference, regardless of other parameter values.

To evaluate our new method, we processed a dataset from December 2004 to May 2005 that contains approximately 65,000 origins from 34,000 events recorded in a total of 15 different catalogs including standard global catalogs (e.g., International Data Centre [IDC], PDE) as well as various regional catalogs. We compare our results with the results generated by processing with the existing rule-based algorithm used in the EvLoader software. The vast majority of the event groupings generated by the clustering algorithm are equivalent to the event groupings created by EvLoader. Some of the event groupings that are different arise from differences in how time versus depth across origins is interpreted, and we examine these in some detail. We conclude that the new agglomerative clustering methodology produces better results and is significantly easier to tune; hence, we plan to incorporate the new algorithm into EvLoader in the near future.

## OBJECTIVES

As seismic events occur around the world, different agencies construct catalogs containing information describing those events. The GNEMRD program takes these event descriptions, herein called origins, from multiple catalogs and combines them into one catalog with origins for common events grouped through an EVENT table. This process must ensure that the resulting event groupings do not contain more than one origin from the same originating catalog, and that the origins describing an event do in fact describe the same seismic event, which can be very challenging for poorly determined catalog origins.

Due to the volume of data collected on a daily basis, this process should be automated as much as possible. Most agencies that create these event groups from multiple catalogs use either an automated process or some combination of an automated process with some level of human interaction to resolve the cases the automated process was unable to handle properly.

EvLoader (Ballard and Lewis, 2004) is the current application used during integration of the multiple sets of information contained within the Air Force Technical Applications Center (AFTAC) Knowledge Base. EvLoader merges one or more events from a source EVENT table into a target EVENT table. All information linked to the source event is also merged. With EvLoader, origins in the source event can be merged with origins in the target event based on either EVID number or spatial/temporal correlation. While EvLoader yields correct results, it is essentially a rule-based application that is cumbersome to comprehend and maintain.

We propose an automated solution to this problem that uses an application of classical cluster analysis techniques, specifically a solution based on an agglomerative hierarchical clustering algorithm (Everitt et al., 2001; Romesburg, 1984). The resulting algorithm is much simpler to tune than the rule-based methodology used by EvLoader and generates clusters with errors at a rate of approximately 0.1% (errors are discussed in greater detail in the Validation section).

## RESEARCH ACCOMPLISHED

Clustering is a mathematical method for determining which subsets of objects in a dataset are similar enough to be clustered together (Everitt et al., 2001; Romesburg, 1984). To cluster objects, a similarity function must be defined that returns how similar any two objects in a set are. Objects in a set that are sufficiently similar can be grouped into the same cluster.

This mechanism of assigning similarity values to pairs of origins and then grouping origins that are sufficiently similar into an event (cluster) seemed well suited to an automated process for grouping origins into events. While assorted clustering techniques were explored, an approach based on agglomerative hierarchical clustering performed well for our initial attempt at automating a solution to this merging problem. Future work will explore alternate clustering techniques (i.e., min-cut) in order to ascertain which clustering approach is the most appropriate fit for this problem domain.

### Dissimilarity Function

A pivotal component to the clustering process is the mathematical function that assigns a similarity value to two objects. This function is continuous on [0, 1]. Two objects are identical if they have a similarity value of 1, and they are not at all similar if they have a similarity value of 0.

When determining how similar two origins are, the spatial and the temporal distances between two origins are used. Thus, lower distance values represent origins that are “closer” to each other (more similar) while higher distance values indicate origins that are “farther” from each other (less similar). This characteristic of how origin similarity is determined resulted in the use of a dissimilarity measure in place of a similarity measure; low dissimilarity values indicate origins that are similar while high dissimilarity values indicate origins that are not at all similar.

This dissimilarity function must assign a value used to determine if two origins have low enough dissimilarity to be contained in the same event. It must take into account the distance between the latitude and longitude of the two origins under consideration as well as their separation in time, and it must account for the uncertainties associated with these values. If two origins have the same catalog author, they are assigned infinite dissimilarity to mark them as completely dissimilar since they cannot be in the same event.

The dissimilarity function used is as follows:

$$D = \begin{cases} \infty & \text{, for } A_i = A_j \\ \sqrt{\left(\frac{\delta}{d\delta}\right)^2 + \left(\frac{t}{dt}\right)^2} & \text{, for } A_i \neq A_j \end{cases}, \qquad (1)$$

where

$D$ is the dissimilarity of two origins ($\infty$ = completely dissimilar, 0.0 = identical),
$A_i$ and $A_j$ are the catalog authors of the two origins,
$\delta$ is the horizontal separation of the two origins in degrees,
$d\delta$ is the sum of the lengths of the semi-major axes of the uncertainty ellipses surrounding the two origins, in degrees,
$t$ is the difference between the origin times of the two origins, in seconds, corrected for origin depth as described in the Adjustments to Data section, and
$dt$ is the sum of the origin time uncertainties of the two origins, in seconds.

Calculating the dissimilarity using this dissimilarity function results in values that are on the interval [0, $\infty$]. In order for these values to be useful in a clustering context, they must be scaled to values ranging from 0.0 (lowest dissimilarity) to 1.0 (completely dissimilar). Evaluation of initial results revealed that any dissimilarity value greater than 10 represented origins that could not possibly be in the same event grouping. Thus, all values generated by this dissimilarity function that were greater than 10 were simply set to a dissimilarity value of 1.0 to represent complete dissimilarity. All values less than or equal to10 were divided by 10 to produce a dissimilarity value ranging between 0.0 and 1.0.

One of the many benefits of this dissimilarity measure is how much information can be taken into account when calculating dissimilarity. Currently, the only origin data factored into this dissimilarity calculation are latitude, longitude, time, catalog author, origin time error, and semimajor axis of error ellipse information. However, if other information such as magnitude or event type needed to be utilized, this could easily be handled by modifying the dissimilarity function.

**Agglomerative Hierarchical Clustering Algorithm Summary**

When clustering a set of N origins, clustering begins with a set of N clusters, i.e. one for every origin. The agglomerative hierarchical clustering algorithm then assigns a dissimilarity value to each pair of origins in the set under consideration and stores these dissimilarity values in a dissimilarity matrix. For a set of five origins, the dissimilarity matrix might look something like the contents of Table 1.

**Table 1. Sample Dissimilarity Matrix for Five Origins.**

| | **1** | **2** | **3** | **4** | **5** |
|---|---|---|---|---|---|
| **1** | 0.00 | 0.04 | 0.30 | 0.02 | 0.01 |
| **2** | 0.04 | 0.00 | 0.09 | 0.07 | 0.40 |
| **3** | 0.30 | 0.09 | 0.00 | 0.08 | 0.90 |
| **4** | 0.02 | 0.07 | 0.08 | 0.00 | 0.15 |
| **5** | 0.01 | 0.40 | 0.90 | 0.15 | 0.00 |

The dissimilarity function returns 0.0 if two origins have no dissimilarity (are identical) and 1.0 if they have high dissimilarity (not at all similar). Recall that if two origins are from the same catalog, they are immediately assigned a maximum dissimilarity since they can never belong in the same cluster (event grouping). Notice that the matrix is symmetric because the dissimilarity of origin A with origin B is the same as origin B with origin A. Further, the diagonal terms themselves are the dissimilarities of each origin with itself (always 0.0). Thus, we only need to store the upper right or lower left portion of the matrix.

Once this matrix has been constructed, the clustering can begin. The first step in the clustering algorithm is to find the two origins that are the least dissimilar. In Table 1, this would be the dissimilarity value of 0.01 between origins 1 and 5. These origins are linked together in a cluster, and the dissimilarity matrix must be updated to contain dissimilarity information for this new cluster and the remaining origins. The dimension of the matrix (i.e., the number of rows and columns) will also be reduced by 1.

The dissimilarity between this new cluster (1,5) and the other origins (2, 3, and 4) can be computed based on the existing dissimilarity values between the origins in the original dissimilarity matrix, i.e. no new dissimilarities need to be computed. For example, when determining which dissimilarity to keep between cluster (1,5) and origin 2, the dissimilarity between origin 1 and origin 2 (0.04) and the dissimilarity between origin 5 and origin 2 (0.40) are considered. A variety of techniques exist that consider those two dissimilarities when yielding a new dissimilarity between (1,5) and origin 2 such as keeping the lowest dissimilarity, keeping the highest dissimilarity, or keeping the average. Analysis of our initial results revealed that keeping the average dissimilarity yields the best results, so the dissimilarity between (1,5) and origin 2 is set to 0.22 (the average of 0.04 and 0.40). Table 2 shows the results the resulting rebuilt dissimilarity matrix for our example.

**Table 2. Rebuilt Dissimilarity Matrix after Creating the (1,5) Cluster**

| | **2** | **3** | **4** | **(1,5)** |
|---|---|---|---|---|
| **2** | 0.00 | 0.09 | 0.07 | 0.22 |
| **3** | 0.09 | 0.00 | 0.08 | 0.60 |
| **4** | 0.07 | 0.08 | 0.00 | 0.09 |
| **(1,5)** | 0.22 | 0.60 | 0.09 | 0.00 |

If this process continues, every origin will eventually be combined into one all encompassing cluster, which is not the intended result. Thus, a dissimilarity threshold must be established that determines when no new clusters should be formed. This threshold is a value that represents the highest possible dissimilarity values that are allowed for origins within the same cluster. For the example in Table 2, if this threshold were set at 0.06, then all possible clusters would have been found since no remaining dissimilarity values are lower than 0.06. (Recall that lower dissimilarity values indicate higher similarity between origins.) The algorithm would have clustered five origins into four event clusters: (1,5), (2), (3), and (4). With a threshold set, this clustering process will continue to group origins into event clusters until all of the remaining dissimilarities in the dissimilarity matrix are greater than the dissimilarity threshold.

A dendrogram is a useful way to visualize which origins are grouped into clusters. The dendrogram in Figure 1 was generated from the results of clustering 77 origins into events. Events that contain only 1 origin are not represented in the dendrogram. Events containing more than one origin are represented by tree branch-like (or root-like) structures, where the lines tie together the least dissimilar two events, then the next least dissimilar event is tied to that line, and so on. The horizontal axis represents the dissimilarity value that existed between the origins when they were grouped into the same event cluster. Figure 1 demonstrates how origins with a range of dissimilarity values can still be clustered into events. Origins originally clustered into the event with EVID 29, had a higher dissimilarity value than the rest of the origins (between 0.00175 and 0.0020); this dissimilarity value was still low enough for those origins to be considered part of the same event. Origins originally clustered into the event with EVID 19 were much less dissimilar.

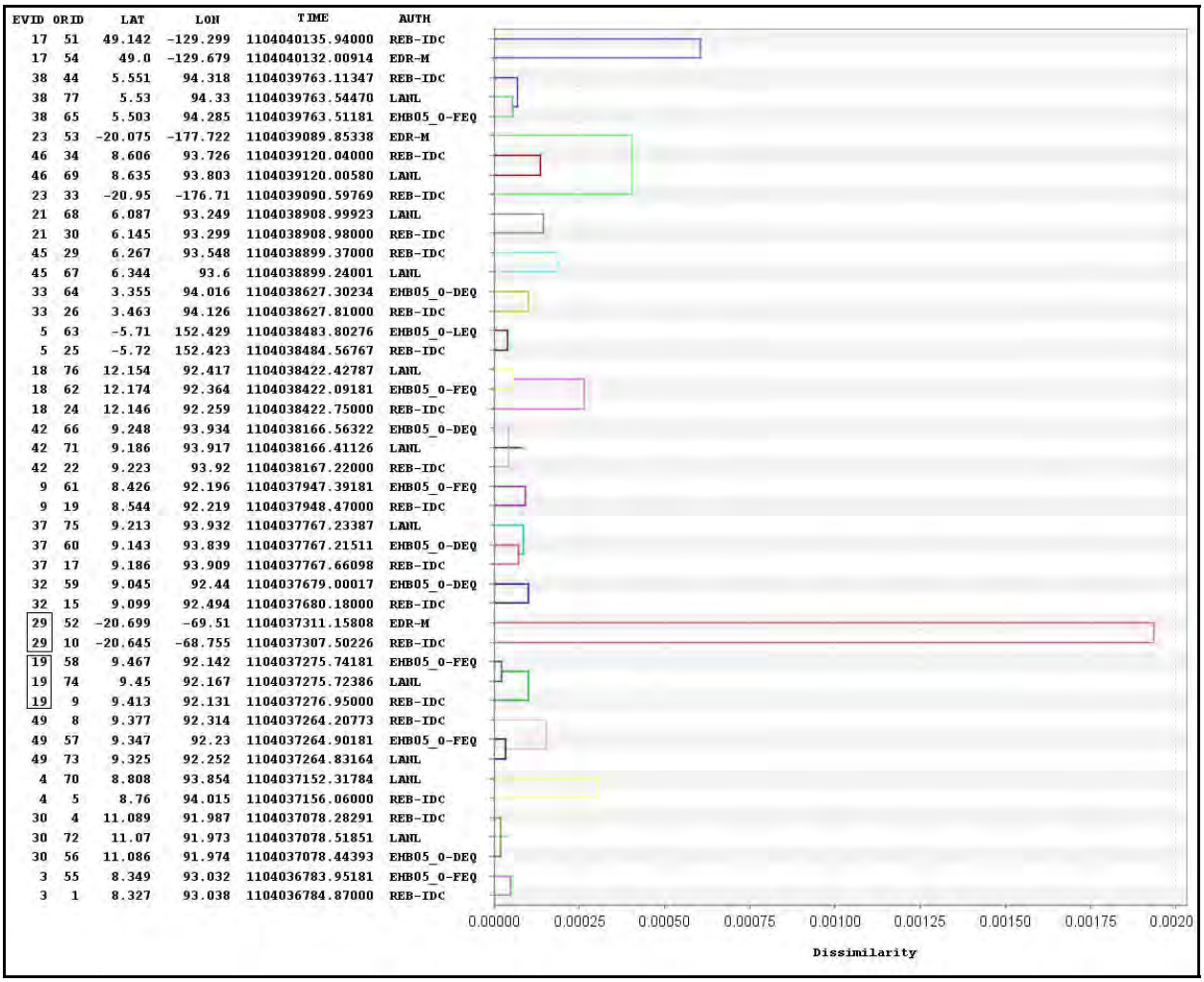

| EVID | ORID | LAT | LON | TIME | AUTH |
|---|---|---|---|---|---|
| 17 | 51 | 49.142 | -129.299 | 1104040135.94000 | REB-IDC |
| 17 | 54 | 49.0 | -129.679 | 1104040132.00914 | EDR-M |
| 38 | 44 | 5.551 | 94.318 | 1104039763.11347 | REB-IDC |
| 38 | 77 | 5.53 | 94.33 | 1104039763.54470 | LANL |
| 38 | 65 | 5.503 | 94.285 | 1104039763.51181 | EHB05_0-FEQ |
| 23 | 53 | -20.075 | -177.722 | 1104039089.85338 | EDR-M |
| 46 | 34 | 8.606 | 93.726 | 1104039120.04000 | REB-IDC |
| 46 | 69 | 8.635 | 93.803 | 1104039120.00580 | LANL |
| 23 | 33 | -20.95 | -176.71 | 1104039090.59769 | REB-IDC |
| 21 | 68 | 6.087 | 93.249 | 1104038908.99923 | LANL |
| 21 | 30 | 6.145 | 93.299 | 1104038908.98000 | REB-IDC |
| 45 | 29 | 6.267 | 93.548 | 1104038899.37000 | REB-IDC |
| 45 | 67 | 6.344 | 93.6 | 1104038899.24001 | LANL |
| 33 | 64 | 3.355 | 94.016 | 1104038627.30234 | EHB05_0-DEQ |
| 33 | 26 | 3.463 | 94.126 | 1104038627.81000 | REB-IDC |
| 5 | 63 | -5.71 | 152.429 | 1104038483.80276 | EHB05_0-LEQ |
| 5 | 25 | -5.72 | 152.423 | 1104038484.56767 | REB-IDC |
| 18 | 76 | 12.154 | 92.417 | 1104038422.42787 | LANL |
| 18 | 62 | 12.174 | 92.364 | 1104038422.09181 | EHB05_0-FEQ |
| 18 | 24 | 12.146 | 92.259 | 1104038422.75000 | REB-IDC |
| 42 | 66 | 9.248 | 93.934 | 1104038166.56322 | EHB05_0-DEQ |
| 42 | 71 | 9.186 | 93.917 | 1104038166.41126 | LANL |
| 42 | 22 | 9.223 | 93.92 | 1104038167.22000 | REB-IDC |
| 9 | 61 | 8.426 | 92.196 | 1104037947.39181 | EHB05_0-FEQ |
| 9 | 19 | 8.544 | 92.219 | 1104037948.47000 | REB-IDC |
| 37 | 75 | 9.213 | 93.932 | 1104037767.23387 | LANL |
| 37 | 60 | 9.143 | 93.839 | 1104037767.21511 | EHB05_0-DEQ |
| 37 | 17 | 9.186 | 93.909 | 1104037767.66098 | REB-IDC |
| 32 | 59 | 9.045 | 92.44 | 1104037679.00017 | EHB05_0-DEQ |
| 32 | 15 | 9.099 | 92.494 | 1104037680.18000 | REB-IDC |
| 29 | 52 | -20.699 | -69.51 | 1104037311.15808 | EDR-M |
| 29 | 10 | -20.645 | -68.755 | 1104037307.50226 | REB-IDC |
| 19 | 58 | 9.467 | 92.142 | 1104037275.74181 | EHB05_0-FEQ |
| 19 | 74 | 9.45 | 92.167 | 1104037275.72386 | LANL |
| 19 | 9 | 9.413 | 92.131 | 1104037276.95000 | REB-IDC |
| 49 | 8 | 9.377 | 92.314 | 1104037264.20773 | REB-IDC |
| 49 | 57 | 9.347 | 92.23 | 1104037264.90181 | EHB05_0-FEQ |
| 49 | 73 | 9.325 | 92.252 | 1104037264.83164 | LANL |
| 4 | 70 | 8.808 | 93.854 | 1104037152.31784 | LANL |
| 4 | 5 | 8.76 | 94.015 | 1104037156.06000 | REB-IDC |
| 30 | 4 | 11.089 | 91.987 | 1104037078.28291 | REB-IDC |
| 30 | 72 | 11.07 | 91.973 | 1104037078.51851 | LANL |
| 30 | 56 | 11.086 | 91.974 | 1104037078.44393 | EHB05_0-DEQ |
| 3 | 55 | 8.349 | 93.032 | 1104036783.95181 | EHB05_0-FEQ |
| 3 | 1 | 8.327 | 93.038 | 1104036784.87000 | REB-IDC |



**Figure 1. Sample dendrogram built from clustering 77 origins into events (only events with more than one origin shown)**

### Dataset Used

The origin dataset used by the clustering algorithm to generate event clusters and to check the accuracy of those clusters was a 7-month time segment of a much larger dataset collected by GNEMRD researchers at Los Alamos National Laboratory (LANL). This dataset contains predominantly global bulletin event information that LANL has collected from the following agencies:

- REB: the Reviewed Event Bulletin of the International Data Centre for the Comprehensive Nuclear-Test-Ban Treaty Organization, Vienna, Austria
- PDE: Preliminary Determination of Epicenters, the monthly version of event bulletins from the National Earthquake Information Center (NEIC)
- EHB: Engdahl, van der Hilst, and Buland which are refined origins from Engdahl et al., (1998)

In all, this dataset included origin information from 17 different catalogs, and event groupings had already been assigned and checked by LANL. Having an existing grouping provided a way to verify that the groupings generated by the clustering algorithm were indeed correct. For our test, we selected the November 2004–May 2005 timeframe

because it contains the December 26, 2004 Sumatra earthquake along with thousands of aftershocks spanning the next several months, thus providing a good test for our clustering algorithm.

This data were stored in database tables that conform to the National Nuclear Security Administration (NNSA) Core Schema (Carr, 2007).

**Adjustments to Data**

In order to accurately determine the dissimilarity between two origins, certain adjustments had to be made to the original data to accommodate missing uncertainty information. When no uncertainty information existed for the semimajor axis of error ellipse (SMAJAX column in the ORIGERR table), a default value of 20 km was used. When the origin time error uncertainty information (STIME column in the ORIGERR table) did not exist or was lower than a threshold of 10 seconds (an STIME threshold determined to be the best through analysis of the results of using a range of STIME values), an origin's STIME would be adjusted to be equal to the STIME threshold of 10 seconds.

Since some catalogs may have computed free-depth origins or may have fixed the origin depth at different values, we adjusted all origin times to 0 depth before calculating the dissimilarity between origins. This was accomplished by subtracting from the original origin time a correction term equal to the depth of the event, lengthened to account for an incidence angle of 30º, then multiplied by the integrated crustal slowness from the AK135 velocity model (Kennet et al., 1995).

**Validation**

One of the benefits of using origin data from a dataset that has already grouped those origins into events is that the event groupings generated by the clustering algorithm can easily be checked against the event groupings in the original dataset. The event groupings in the original origin data are represented in the form of the EVID column (in the ORIGIN table) that identified which event the origin belonged to, i.e., all origins in the same event have the same EVID.

Evaluation of our approach demonstrated that the number of event clusters found by the clustering algorithm was comparable to the event groupings that already existed in the LANL dataset when an appropriate dissimilarity threshold (dissimilarity values low enough to belong in the same cluster) was used as shown in Figure 2.

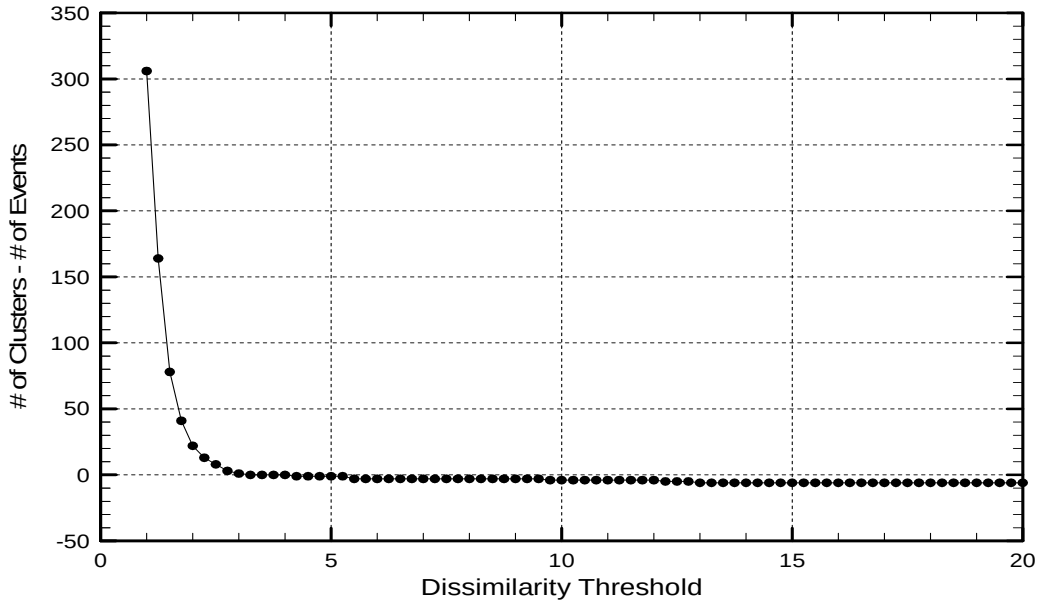


**Figure 2. Difference in the number of clusters found versus the number of events designated in the original dataset as a function of the dissimilarity threshold allowed within a given cluster.**

Figure 2 shows that once an appropriate dissimilarity threshold was determined, the clusters formed were comparable to the event groupings in the original data. The resulting clusters were checked to determine the following:

a) Clusters had more than one EVID in them. This would indicate that a cluster was formed that contained origins that were not originally grouped together.

b) Origins that were originally grouped in the same event were now in separate clusters. This would indicate that the algorithm determined that these origins should not be in the same event, while the original event grouping placed the origins in the same event.

Many of the errors found involved origin times that had been adjusted to depth 0; this could account for why the clustering algorithm found different event groupings than were present in the original dataset.

The clustering algorithm did not produce clustering results that were identical to the original event groupings found, although the number of generated clusters with errors was around 0.1% of the total number of clusters generated. The following types of errors were encountered: origins with low enough dissimilarity to be grouped in the same event cluster that had the same catalog author, origins that were originally in separate events that were placed in the same event cluster, and origins that were originally in the same event that were divided into separate events. The different types of errors found in the clustering results are discussed in greater detail below.

**Error Scenario 1: Origins with Low Dissimilarity and Non-Unique Authors**

In this scenario, multiple origins exist that have dissimilarities low enough to indicate that they could belong in the same event grouping. However, some of the origins have the same catalog author, which prevents grouping all of the origins into the same event. In some cases, the clustering algorithm did not always preserve the groupings present in the original dataset. Consider the following origin data:

| | LAT | LON | DEPTH | TIME | AUTH | STIME | SMAJAX |
|---|---|---|---|---|---|---|---|
| 1 | -1.8306 | 99.5737 | 0 | 1113135202.4700 | REB-IDC | 0.780000 adjusted: 10.0 | 32.200000 |
| 2 | -1.802 | 99.625 | 30 | 1113135207.0700 adjusted to depth 0: 1113135201.3118 | EDR-M | 0.380000 adjusted: 10.0 | 17.200000 |
| 3 | -1.51 | 99.798 | 38.7 | 1113135202.1800 adjusted to depth 0: 1113135195.0024 | EDR-M | 5.250000 adjusted: 10.0 | 55.407895 |
| 4 | -1.4674 | 99.8207 | 0 | 1113135196.6700 | REB-IDC | 1.150000 adjusted: 10.0 | 59.000000 |

The dissimilarity values for these origins are as follows (sorted from lowest to highest):

Origins 3 and 4: 0.0000956
Origins 1 and 2: 0.0001441
Origins 2 and 4: 0.0006088
Origins 1 and 3: 0.0006195
Origins 1 and 4: 1.0 (same auth)
Origins 2 and 3: 1.0 (same auth)

In the original dataset, origins 1 and 3 were in the same event and origins 2 and 4 were in the same event. However, based on the dissimilarity values, the clustering algorithm clustered together origins 1 and 2 as one event and origins 3 and 4 as another event.

**Error Scenario 2: Origins Originally in Separate Events Grouped into a Single Event**

The clustering algorithm would occasionally group origins that were originally in separate events into one event. Consider the following origin data:

| | LAT | LON | DEPTH | TIME | AUTH | STIME | SMAJAX |
|---|---|---|---|---|---|---|---|
| 1 | 11.2033 | 90.6702 | 0 | 1104059010.1300 | REB-IDC | 7.420000 adjusted: 10.0 | 63.000000 |
| 2 | 11.27864693 | 93.94496788 | 20 | 1104059031.5828 adjusted to depth 0: 1104059027.6011 | LANL:GT20070601 | 1.135997 adjusted: 10.0 | 33.956238 |
| 3 | 11.231 | 93.867 | 20 | 1104059031.8200 adjusted to depth 0: 1104059027.8383 | EHB05_O-FEQ | -1.000000 adjusted: 10.0 | 191.000000 |

The dissimilarity values for these origins are as follows (sorted from lowest to highest):

Origins 2 and 3: 0.0000460
Origins 1 and 3: 0.0013246
Origins 1 and 2: 0.0020136

In the original dataset, origins 2 and 3 were in the same event and origin 1 was in an event on its own. The clustering algorithm determined that these three origins should be grouped in the same event cluster since the dissimilarity values were low enough, and all of the authors were unique.

**Error Scenario 3: Origins Originally in the Same Event Divided into Separate Events**

In this final scenario, origins that had originally been part of the same event were separated into two different events. Consider the following origin data:

| | LAT | LON | DEPTH | TIME | AUTH | STIME | SMAJAX |
|---|---|---|---|---|---|---|---|
| 1 | 38.6051 | 27.4052 | 0 | 1105623537.5800 | REB-IDC | 1.36 adjusted: 10.0 | 18.5 |
| 2 | 39.25 | 27.98 | 10 | 1105623441.6000 adjusted to depth 0: 1105623439.60913 | EDR-M:ATH | -1 adjusted: 10.0 | -1 adjusted: 20.0 |

The dissimilarity value for origins 1 and 2 is 0.0053974. This dissimilarity value was higher than the dissimilarity threshold, which resulted in the clustering algorithm determining that these origins could not be part of the same event. Thus, it took two origins that had been part of the same event and separated them into two separate events.

## CONCLUSIONS AND RECOMMENDATIONS

Based on the results of comparing the clusters/event groupings generated by the clustering algorithm with the event groupings already present in the LANL data and the event groupings generated by EvLoader, this clustering approach holds promise for an automated means to discovering event groupings from origin data. The high level of flexibility offered by an easy-to-customize dissimilarity function allows the clustering application to take any relevant origin information into account when determining which origins are similar enough to belong in the same event.

## ACKNOWLEDGEMENTS

The authors wish to thank Julio Aguilar-Chang and Richard Stead at LANL for providing us with an excellent dataset to work with. Without such high-quality data to validate against, our job of verifying the degree to which the clustering algorithm was finding correct event groupings would have been a great deal more difficult.

## REFERENCES

Ballard, S. and J. Lewis (2004). DBTools: A suite of tools for manipulating information in a relational database, in *Proceedings of the 26th Seismic Research Review: Trends in Nuclear Explosion Monitoring*, LA-UR-04-5801, Vol. 2, pp 700–709.

Carr, D. (2007). National Nuclear Security Administration knowledge base database guide, Sandia National Laboratories technical report SAND2004-0961P.

Engdahl, E. R., R. van der Hilst, and R. Buland (1998). Global teleseismic earthquake relocation with improved travel times and procedures for depth determination, *BSSA* 88: 722–743.

Everitt, B. S., S. Landau, and M. Leese (2001). *Cluster Analysis*, Fourth Edition. Oxford University Press Inc.

Kennett, B. L. N., E. R. Engdahl, and R. Buland (1995). Constraints on seismic velocities in the Earth from travel times, *Geophys. J. Int.* 122: 108–124.

Romesburg, H. Charles (1984). *Cluster Analysis for Researchers*. Lulu Press.

# BASIC RESEARCH ON SEISMIC AND INFRASONIC MONITORING OF THE EUROPEAN ARCTIC

Frode Ringdal, Tormod Kværna, Svein Mykkeltveit, Steven J. Gibbons, and Johannes Schweitzer

NORSAR

Sponsored by Army Space and Missile Defense Command

Contract No. W9113M-05-C-0224

.

## ABSTRACT

This project represents a three-year research effort aimed at improving seismic and infrasonic monitoring tools at regional distances, with emphasis on the European Arctic region, which includes the former Novaya Zemlya test site. The project has three main components: a) to improve seismic processing in this region using the regional seismic arrays installed in northern Europe, b) to investigate the potential of using combined seismic/infrasonic processing to characterize events in this region and c) to carry out experimental operation, evaluation and tuning of the seismic threshold monitoring technique.

The recent upgrade of the Spitsbergen seismic array, which has included the installation of five new three-component seismometers, as well as an increase in the sampling rate from 40 to 80 Hz, has resulted in significant improvements in high-frequency signal characterization as well as S-phase detection. Our studies have shown a remarkably efficient wave propagation from events near Novaya Zemlya across the Barents Sea. Significant signal energy at frequencies of up to 30 Hz and above has been observed, even for seismic events below a magnitude 3 at an epicentral distance of more than 1,000 km. In order to investigate if this same efficient propagation could be observed at the ARCES array in northern Norway, we have recently installed additional recording equipment at the center broadband element of ARCES, with a sampling rate of 100 Hz. Our initial results are similar to those seen at Spitsbergen. We should note that the available high-frequency data so far does not include events to the east and northeast of the ARCES array, and the high-frequency propagation from the Novaya Zemlya region to ARCES is therefore still unknown. As more data are accumulated, we may be in a position to carry out a detailed study of the high-frequency propagation characteristics for additional paths in the region. Analysis of data from temporary seismic stations installed as part of the ongoing International Polar Year is expected to provide an important contribution to such a study.

We have continued our infrasonic studies, applying the data from the current array network in northern Europe. As a special case study, we have analyzed recorded infrasound signals from four confirmed rocket launches at the Plesetsk Cosmodrome in northwest Russia as well as infrasound signals from five possible (unconfirmed) launches from the same site. We have in particular attempted to obtain an understanding of the overall signal characteristics as well as the inherent variability among these signals. We have used available recordings both from the Apatity infrasound array and from the stations of the Swedish Infrasound Network. For two of the confirmed launches, we have sufficiently good quality recordings from three arrays (Apatity at a distance of 628 km, Kiruna and Jämtön, each at a distance of about 1,000 km). The backazimuths estimated during the wavetrains show some significant variations, with a deviation from the theoretical values by up to about 10 degrees. Particularly interesting is the azimuthal pattern at the Apatity array, which shows a clear trend of changing backazimuths with time, thus giving indications of a moving source. For the remaining two confirmed launches, we have only recordings from one array (Apatity), and again we see a time-varying trend, but in one of the cases the direction of change is reversed. This may be explained by differences in rocket takeoff directions relative to the Apatity station.

For the five unconfirmed events (which all occurred during one day: 23 January 2007) we see signal characteristics that are generally consistent with the observations of the confirmed launches, and it seems likely that they correspond to actual (unconfirmed) Plesetsk launches. We have calculated differential travel-times for onsets of the infrasound signals at the Jämtön and Kiruna stations relative to Apatity. The onsets were read visually from vespagrams and had a rather high uncertainty. We find that we cannot separate the source location for the unknown signals from the verified Plesetsk launches based on these differential travel times, and we therefore consider it likely that they could be rocket launches from this site.

## OBJECTIVES

The objective of the project is to carry out research to improve the current capabilities for monitoring small seismic events in the European Arctic, which includes the former Russian test site at Novaya Zemlya. The project has three main components: a) to improve seismic processing in this region using the regional seismic arrays installed in northern Europe, b) to investigate the potential of using combined seismic/infrasonic processing to characterize events in this region, and c) to carry out experimental operation, evaluation and tuning of the seismic threshold monitoring technique, with application to various regions of monitoring interest.

## RESEARCH ACCOMPLISHED

### Study of High-Frequency ARCES Recordings

We have carried out an initial investigation of recordings of high-frequency seismic waves at the ARCES array. This contribution describes initial results from these studies. We have analyzed in detail a number of seismic events at regional distances from ARCES, with epicentral distances ranging from 270 to about 1,300 km, and assessed the amount of high-frequency signal energy observed at the station. The events are listed in Table 1, and are shown on a map in Figure 1. In the following paragraphs, we discuss in some detail three of these events, which are quite typical in terms of the general characteristics observed for the waveforms. One is a presumed mining explosion in northern Sweden, and the other two are earthquakes south and north of Spitsbergen, respectively.

*Mining event in Malmberget/Aitik, Sweden (Event 4—Distance about 330 km).*

Figure 2 shows a spectrogram and waveform plot for a mining event in the Malmberget/Aitik area in northern Sweden. Malmberget is an underground iron ore mine, whereas Aitik is a nearby open-pit copper mine. The timing and size of the event are consistent with the explosion practice at Aitik, although we have not received confirmation from the mine authorities. We note a large amount of high-frequency energy for this event, up to the Nyquist frequency of 50 Hz. A particularly interesting observation is that the spectrogram shows distinct spectral lines, which is a characteristic feature for many ripple-fired explosions. It appears that the large bandwidth provided by the high-frequency recordings could be helpful in such cases to identify ripple-fired mining exposions.

**Table 1. Events selected for analysis. Magnitudes are those of the International Data Centre (IDC) Reviewed Event Bulletin where available, otherwise the generalized beamforming (GBF) values automatically calculated at NORSAR are used.**

| No | Date | Origin time | Lat | Lon | Dkm | Region | Magnitude |
|---|---|---|---|---|---|---|---|
| **1** | 2008/04/24 | 115-17:14:56.0 | 69.59 | 18.57 | 270.3 | Troms, Norway | 2.71 (GBF) |
| **2** | 2008/04/12 | 103-23:17:05.0 | 67.77 | 20.41 | 285.2 | Kiruna, Sweden | 1.82 (GBF) |
| **3** | 2008/04/12 | 103-23:19:21.0 | 67.77 | 20.41 | 285.2 | Kiruna, Sweden | 2.45 (GBF) |
| **4** | 2008/04/01 | 092-17:08:10.0 | 67.03 | 21.09 | 333.5 | Malmberget/Aitik, Sweden | 2.12 (GBF) |
| **5** | 2008/03/23 | 083-03:24:44.9 | 67.62 | 33.72 | 397.0 | Kola Peninsula, Russia | 2.53 (GBF) |
| **6** | 2008/04/11 | 102-06:02:55.1 | 67.90 | 15.09 | 458.8 | Steigen, Nordland, Norway | 3.6 (IDC) |
| **7** | 2008/04/10 | 101-06:20:00.1 | 77.02 | 18.59 | 863.0 | Storfjorden, Svalbard | 4.0 (IDC) |
| **8** | 2008/04/07 | 098-23:51:14.2 | 76.38 | 7.24 | 961.4 | Knipovich Ridge | 4.1 (IDC) |
| **9** | 2008/03/24 | 084-18:28:18.1 | 80.89 | 15.84 | 1292.5 | North of Svalbard | 3.8 (IDC) |

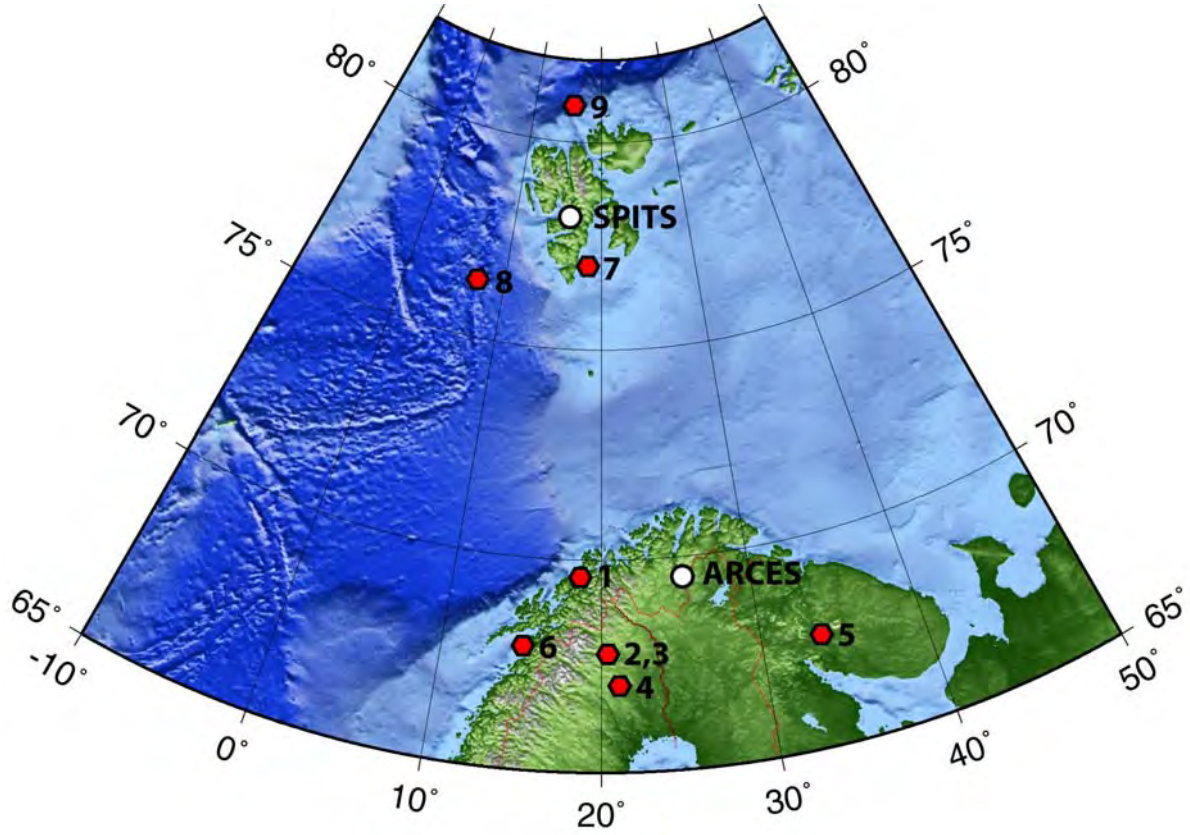


**Figure 1. Map of the European Arctic showing the location of the seismic events analyzed in this study, together with the location of the ARCES and Spitsbergen arrays.**

*Earthquake Storfjorden, Spitsbergen (Event 7—Distance about 860 km).*

This is an earthquake in a large aftershock sequence south of Spitsbergen. The main shock occurred on 21 February 2008 at 02.46.17 GMT. The magnitude of this earthquake was 6.2, making it the largest instrumentally recorded intraplate earthquake in Norway and surrounding areas. Figure 3 corresponds to one of the aftershocks occurring after the high-frequency system was installed at ARCES. The event magnitude is 4.0 as reported by the IDC. Like for the shorter epicentral distances, we note that there is significant signal energy even above 40 Hz. Again, the Pn and Sn phases are dominant. However, in the 1–2 Hz filter, there is a clear Lg phase about 1 minute after the Sn onset. This is surprising since the Barents Sea is generally considered as a region that has a distinct Lg blockage. This blockage is definitely seen for paths crossing the central Barents Sea (Baumgardt, 1990), but it appears from our observations that it is not quite so pronounced for paths covering the Western part of the Barents Sea. We have confirmed by vespagram analysis that this is indeed an Lg phase.

*Earthquake north of Svalbard (Event 9—Distance about 1290 km).*

This event, which is shown in Figure 4, is the event in our data set with the greatest epicentral distance (1,290 km) from the ARCES array. It is an intraplate earthquake, located on the continental slope north of Spitsbergen, with a travel path crossing the Svalbard archipelago as well as the western Barents Sea. Somewhat surprisingly, even this small earthquake (IDC magnitude 3.8) at such a large distance shows significant high-frequency signal energy in the 30-45 Hz band, especially for the Sn phase. This is clearly seen in Figure 4b and 4c. Furthermore, we again see evidence in Figure 4b of the Lg phase in the lowest frequency band (1–2 Hz).

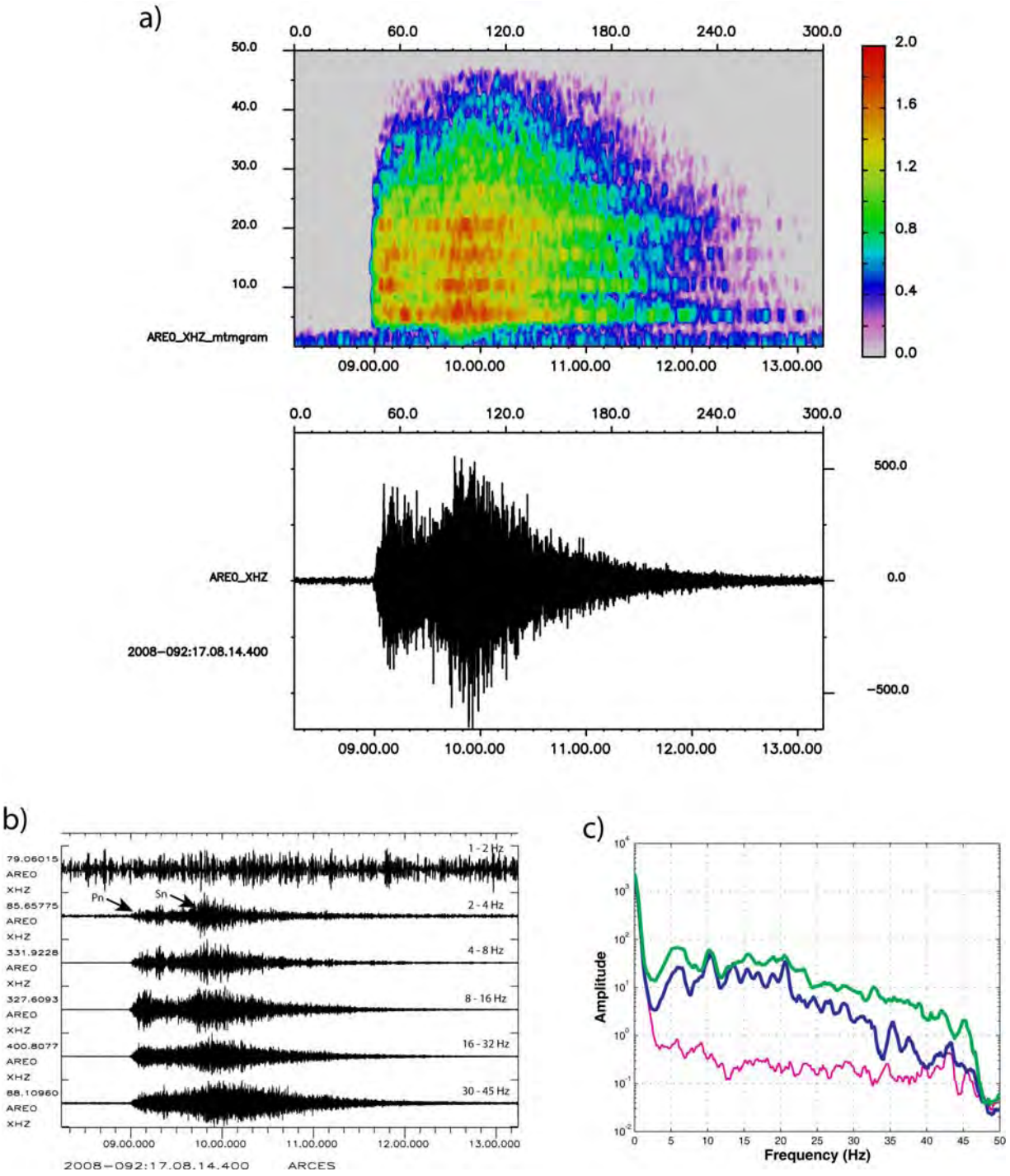


**Figure 2. This figure shows various displays representing the vertical component of the ARCES high-frequency seismometer for Event 4 (Malmberget/Aitik, Sweden, at a distance of about 330 km): a) displays of 5 minutes of spectrogram and waveform plot filtered with a 2.2 Hz high-pass filter, b) waveform plot filtered in 6 different frequency bands, with the main regional phases indicated, c) amplitude spectra of noise and phases indicated in the waveform plot: noise (magenta), Pn (blue), Sn (green). See text for details.**

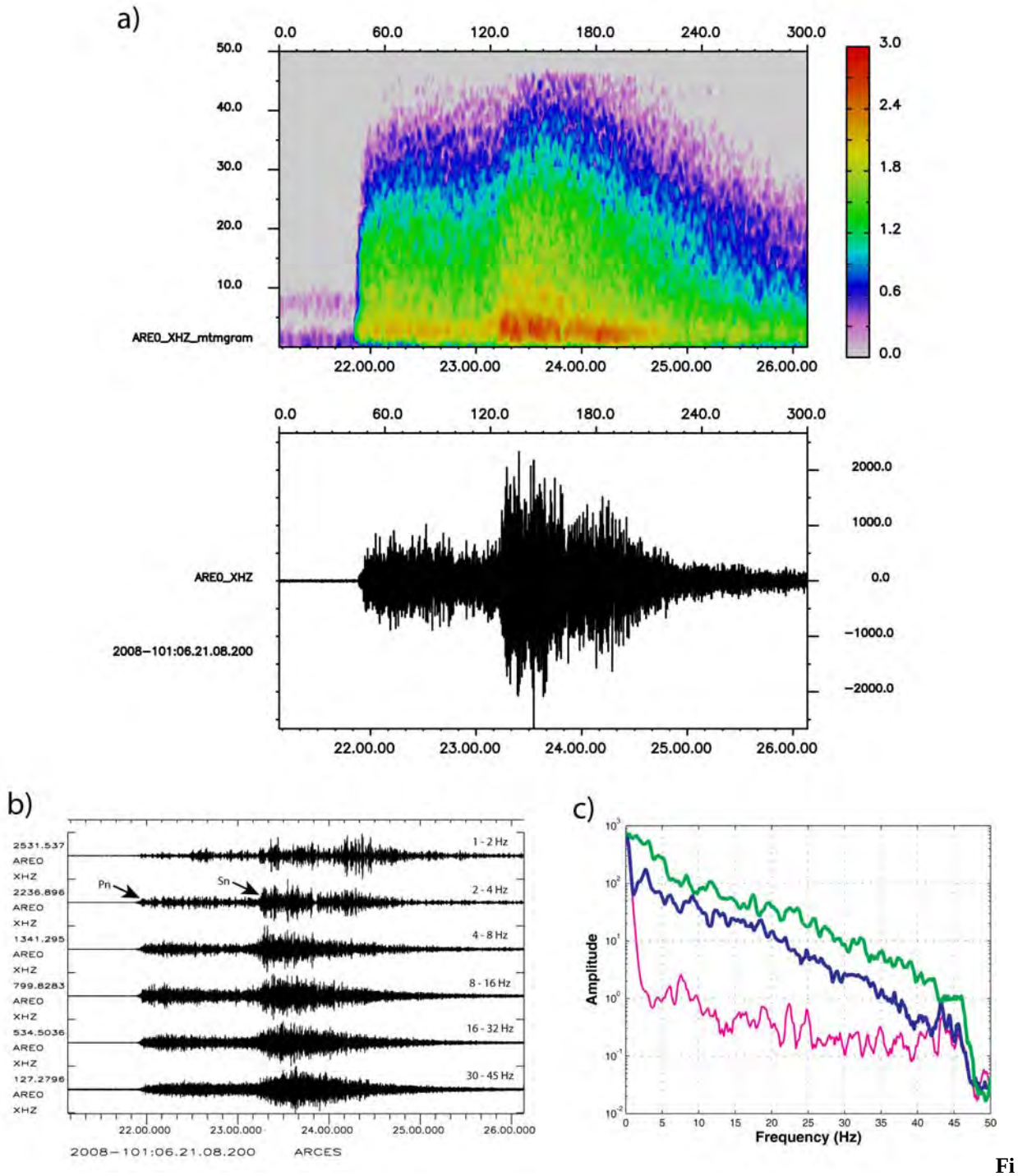


Fi

**Figure 3. This figure shows various displays representing the vertical component of the ARCES high-frequency seismometer for Event 7 (Storfjorden, Svalbard, Norway, at a distance of about 860 km): a) displays of 5 minutes of spectrogram and waveform plot filtered with a 2.2 Hz high-pass filter, b) waveform plot filtered in 6 different frequency bands, with the main regional phases indicated, c) amplitude spectra of noise and phases indicated in the waveform plot: noise (magenta), Pn (blue), Sn (green). See text for details.**

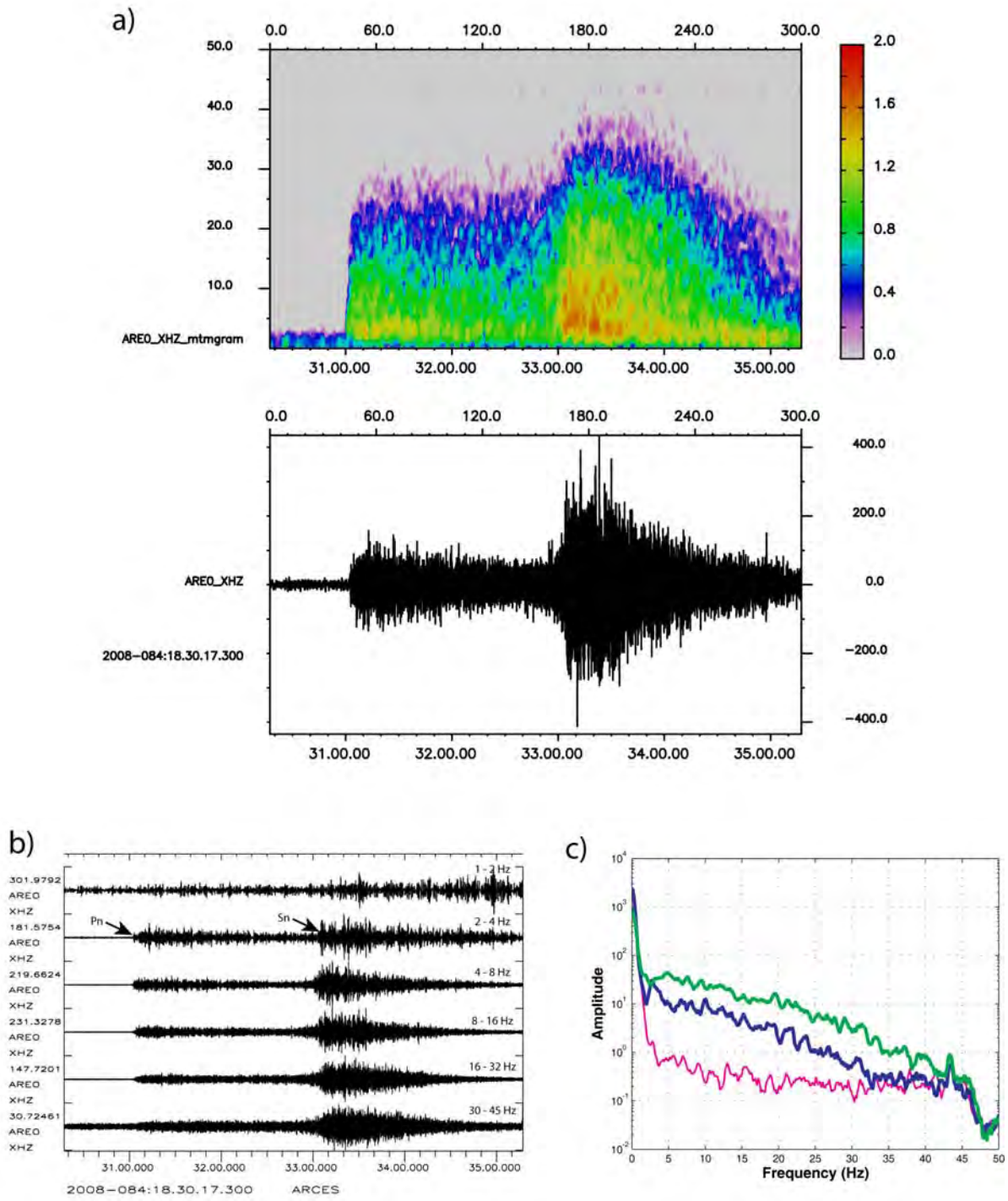


**Figure 4. This figure shows various displays representing the vertical component of the ARCES high-frequency seismometer for Event 9 (north of Svalbard, at a distance of about 1,290 km): a) displays of 5 minutes of spectrogram and waveform plot filtered with a 2.2 Hz high-pass filter, b) waveform plot filtered in 6 different frequency bands, with the main regional phases indicated, c) amplitude spectra of noise and phases indicated in the waveform plot: noise (magenta), Pn (blue), Sn (green). See text for details.**

We should note that the available high-frequency data so far do not include events to the east and northeast of the ARCES array, and the high-frequency propagation from the Novaya Zemlya region to ARCES is therefore still unknown. As more data are accumulated, we may be in a position to carry out a more detailed study of the propagation characteristics for additional paths in the region, and make a more systematic study of the benefits from combining the high-frequency observations from Spitsbergen and ARCES. Analysis of data from temporary seismic stations installed as part of a project under the ongoing International Polar Year is expected to provide an important contribution to such a study. This project is described by Schweitzer (2008) and involves the installation of 12 ocean-bottom seismometers, one new three-component broadband seismometer at Hornsund, Spitsbergen, one three-component broadband seismometer on the island of Hopen, and the installation of a small seismic array (13 three-component seismometers) on the Bear Island.

**Infrasound Recordings of Rocket Launches from Plesetsk, Russia**

The Plesetsk Cosmodrome is located about 800 km north of Moscow, with geographical coordinates 62.92 N 40.52 E. Plesetsk is used especially for military satellites placed into high inclination and polar orbits. However, global overviews on spaceflights, e.g., *http://en.wikipedia.org/wiki/2005_in_spaceflight,* show that geosynchronous satellites also are launched from this site. We have initially focused our attention on two launches, one on 19 June 2003 and another on 21 June 2005. See Table 2 for details.

**Table 2. Rocket launches at the Plesetsk Cosmodrome Observed at the Infrasound stations in Apatity, Jämtön and Kiruna**

| Launch Year/Date/Time | Rocket | Orbit | Mission/Function |
|---|---|---|---|
| **2003 19 June 20:00 GMT** | Molniya M (R-7 8K78M) | Highly elliptical (Molniya) | Communications Satellite |
| **2005 21 June 00:49 GMT** | Molniya M | Geosynchronous | Communications Satellite |

We have analyzed signals from these rocket launches recorded both at the Apatity infrasound array (Vinogradov and Ringdal, 2003) and by the stations of the Swedish Infrasound Network (Liszka, 2007). The Swedish network initially consisted of four infrasound stations: Kiruna, Jämtön, Lycksele, and Uppsala. The station in Uppsala was moved to Sodankylä, Finland, during the fall of 2006. Figure 5 shows the location of the infrasound stations currently in operation and the location of the Plesetsk Cosmodrome.

*Data Processing*

In order to get an overview of the signal characteristics, we have processed the infrasound data using vespagram analysis. Using a fixed apparent sound velocity of 0.333 km/s, we have calculated the resulting normalized beam power for a range of back-azimuths, where the maximum represents an estimate of the back-azimuth of the arriving signal. In our calculations we have used a window length of 10 seconds and a window step of 1.0 second. The Apatity infrasound data were processed in the 1–3 Hz frequency band, whereas the stations of the Swedish Infrasound network were all processed in the 2–5 Hz band. Figure 6 shows the results for the two Plesetsk rocket launches listed in Table 2 for the stations Apatity, Jämtön, and Kiruna. We observe the following general characteristics:

*Apatity*

- Some differences in waveforms between the 2003 and 2005 events.
- Quite similar azimuthal vespagrams, with a trend of changing back-azimuths versus time. Such observations are indicative of a moving source.
- Signal durations of almost 10 minutes. High signal-to-noise ratio (SNR) signals.
- Back-azimuths ranging between 145 and 137 degrees.

*Jämtön:*

- Quite similar waveforms and vespagrams for the 2003 and 2005 events.
- Signal duration of about 5 minutes. Moderate SNR signals.
- Back azimuths ranging between 91 and 102 degrees.

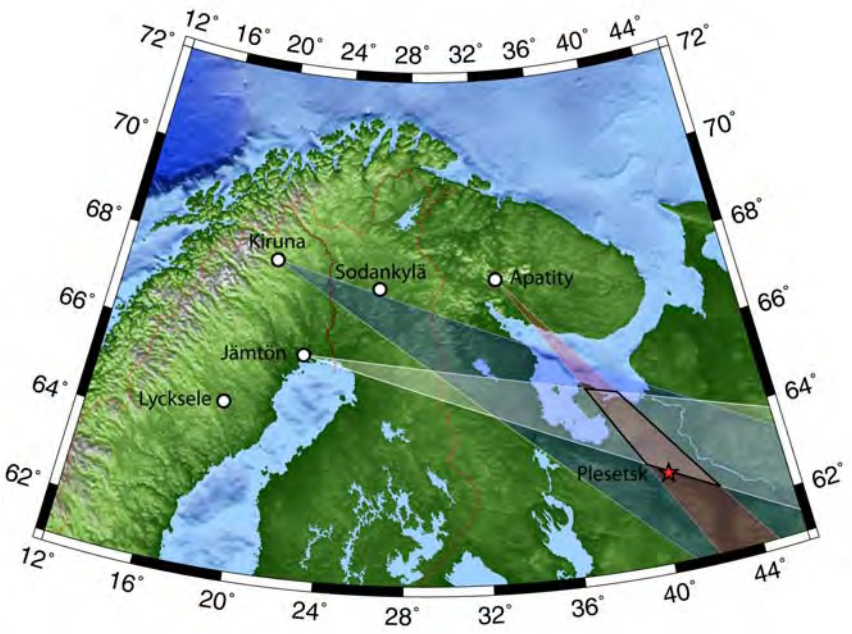


**Figure 5. Map showing the location of existing infrasound stations in Sweden, Finland, and Northwest Russia (filled white circles). The location of the Plesetsk Cosmodrome is shown by the red star. The azimuthal sectors from Kiruna, Jämtön, and Apatity represent the range of back-azimuth estimates during the wavetrain of infrasound signals from the 2003 and 2005 rocket launches.**

*Kiruna:*

- Quite similar waveforms and vespagrams for the 2003 and 2005 events.
- Signal duration of about 5 minutes. Low SNR signals with the influence of local noise.
- Back azimuths ranging between 101 and 118 degrees.

For two additional Plesetsk rocket launches in 2005 and 2007, we also have quite good recordings at the Apatity array. The 27 October 2005 signal is particularly interesting. It has characteristics similar to the 2003 and 2005 reference events, but with the exception that the trend of back-azimuthal change versus time is reversed. This may be explained by differences in rocket takeoff directions relative to the Apatity station.

In order to find how the direction estimates compare with the direction to the Plesetsk Cosmodrome, we have plotted azimuthal sectors from Apatity, Jämtön, and Kiruna spanning the range of azimuth estimates observed during the different infrasound wavetrains (Figure 5). It is interesting to note that the area of overlap between the different sectors includes the actual launch site. However, additional factors like atmospheric inhomogeneities, the wind field along the infrasound propagation path and the altitude and location of the infrasound source (the rocket) will most likely introduce biases in the azimuth estimates relative to the predicted Plesetsk direction.

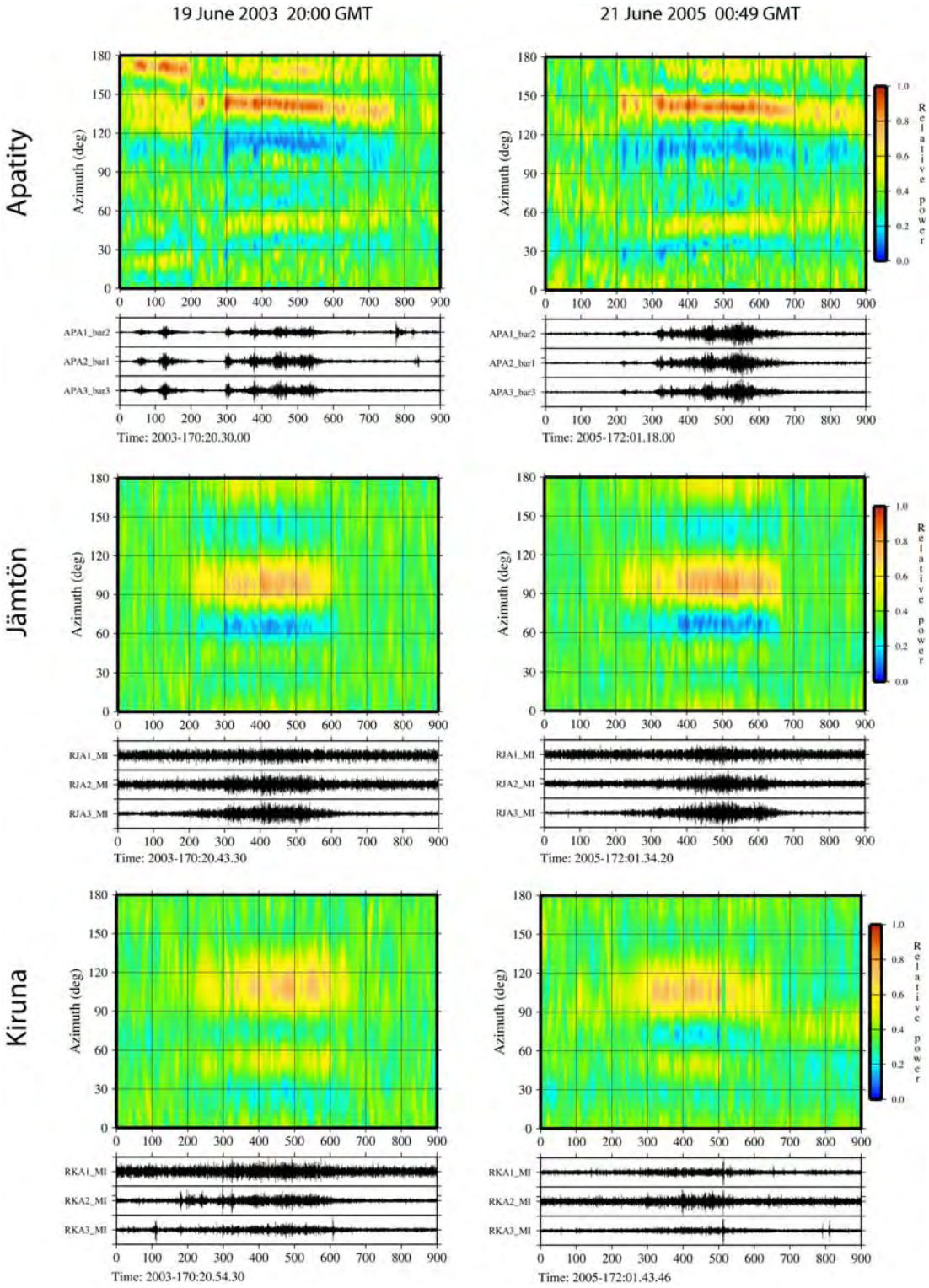


**Figure 6. Each panel shows the infrasound waveforms from Apatity, Jämtön, and Kiruna as well as the corresponding azimuthal vespagram of the signals from the 2003 and 2005 Plesetsk rocket launches given in Table 2.**

In addition to the confirmed rocket launches discussed above, we have also analyzed five unconfirmed events (which all occurred during one day—23 January 2007). For these events, we see signal characteristics that are

generally consistent with the observations of the confirmed launches, and it seems likely that they correspond to actual (unconfirmed) Plesetsk launches. We have calculated differential travel times for onsets of the infrasound signals at the Jämtön and Kiruna stations relative to Apatity. The onsets were read visually from vespagrams, and had a rather high uncertainty. We find that we cannot separate the source location for the unknown signals from the verified Plesetsk launches based on these differential travel times, and we therefore consider it likely that they could be rocket launches from this site.

## CONCLUSIONS AND RECOMMENDATIONS

Previous studies (e.g., Ringdal et al., 2007) have shown a remarkably efficient seismic wave propagation from events near Novaya Zemlya across the Barents Sea to the Spitsbergen array. By analyzing data from a newly installed high-frequency element in the ARCES array in northern Norway, we have found that similar propagation characteristics are observed for this array as well. We note that the available high-frequency data so far does not include events to the east and northeast of the ARCES array, and the high-frequency propagation from the Novaya Zemlya region to ARCES is therefore still unknown. As more data are accumulated, we recommend that a detailed study of the high frequency propagation characteristics for various paths in the region be carried out. We also recommend that data from temporary seismic stations installed as part of the ongoing International Polar Year be fully exploited in such a study.

The Swedish infrasound array network provides a useful supplement to the seismic and infrasonic arrays in Norway and Northwest Russia. We have continued our infrasonic studies, applying the data from the available array network in northern Europe. As a special case study, we have analyzed recorded infrasound signals from four confirmed rocket launches at the Plesetsk Cosmodrome in northwest Russia as well as infrasound signals from five possible (unconfirmed) launches from the same site. The backazimuths estimated during the wavetrains show some significant variations, with a deviation from the theoretical values by up to about 10 degrees. The azimuthal pattern at the Apatity array shows a clear trend of changing backazimuths with time, thus giving indications of a moving source. We plan to continue these studies.

We continue our work towards developing and evaluating a joint seismic/infrasonic bulletin for northern Fennoscandia and adjacent regions. This bulletin would be similar to the automatic seismic bulletin that we are currently providing on the NORSAR Web pages, but it would also contain infrasonic phase associations. Furthermore, we will experimentally attempt to generate an infrasonic event bulletin using only the estimated azimuths and detection times of infrasound phases recorded by stations in the Nordic network.

## REFERENCES

Baumgardt, D.R. (1990). Investigation of teleseismic Lg blockage and scattering using regional arrays, *Bull. Seism. Soc. Am.* 80: 2261–2281.

Liszka, L. (2007). Infrasound - A summary of 35 years of infrasound research, manuscript submitted for printing, 150 pp.

Ringdal, F., T. Kværna, S. Mykkeltveit, S. J. Gibbons, and J. Schweitzer (2007). Basic research on seismic and infrasonic monitoring of the European Arctic, in: *Proceedings of the 29th Monitoring Research Review: Ground-Based Nuclear Explosion Monitoring Technologies*, LA-UR-07-5613, Vol. 1, pp. 955–964.

Schweitzer , J. (2008). The International Polar Year 2007-2008 Project “The dynamic continental margin between the Mid-Atlantic Ridge system (Mohn’s Ridge, Knipovich Ridge) and the Bear Island region”. NORSAR Scientific Report: Semiannual Technical Summary No. 1 - 2008. NORSAR, Kjeller, Norway. pp. 53–63.

Vinogradov, Yu. and F. Ringdal (2003). Analysis of infrasound data recorded at the Apatity array, NORSAR Scientific Report: Semiannual Technical Summary No. 1 - 2003. NORSAR, Kjeller, Norway. pp. 68–77.

# ENHANCING SEISMIC CALIBRATION RESEARCH THROUGH SOFTWARE AUTOMATION AND SCIENTIFIC INFORMATION MANAGEMENT

Stanley Ruppert, Douglas A. Dodge, Michael D. Ganzberger, Teresa F. Hauk, and Eric M. Matzel

Lawrence Livermore National Laboratory

Sponsored by National Nuclear Security Administration

Contract No. DE-AC52-07NA27344

## ABSTRACT

The National Nuclear Security Administration (NNSA) Ground-Based Nuclear Explosion Monitoring Research and Development (GNEMRD) Program at LLNL continues to make significant progress enhancing the process of deriving seismic calibrations and performing scientific integration, analysis, and information management with software automation tools. Our tool efforts address the problematic issues of very large datasets and varied formats encountered during seismic calibration research. New information management and analysis tools have resulted in demonstrated gains in efficiency for producing scientific data products and improved accuracy of derived seismic calibrations.

The foundation of a robust, efficient data development and processing environment is composed of many components built upon engineered versatile libraries. We incorporate proven industry best practices throughout our code and apply source code and bug tracking management, as well as automatic generation and execution of unit tests, for our experimental, development, and production lines. Significant software engineering and development efforts have produced an object-oriented framework that provides database-centric coordination between scientific tools, users, and data. Over a half billion parameters, signals, measurements, and metadata entries are all stored in a relational database accessed by an extensive object-oriented multi-technology software framework that includes stored procedures, real-time transactional database triggers and constraints, and coupled Java and C++ software libraries to handle the information interchange and validation requirements. Significant resources were applied to schema design to enable management of processing methods and station parameters, responses and metadata. This approach allowed for the development of merged ground-truth (GT) datasets compiled by the NNSA labs and the Air Force Technical Applications Center (AFTAC) that include hundreds of thousands of events and tens of millions of arrivals. The schema design groundwork facilitated extensive quality control and revalidation steps. In support of the GT merge effort, a comprehensive site merge process was also accomplished this year that included station site information for tens of thousands of entries from NNSA labs, AFTAC, National Earthquake Information Center (NEIC), International Seismological Centre (ISC), and Incorporated Research Institutions for Seismology (IRIS). A core capability is the ability to rapidly select and present subsets of related signals and measurements to the researchers for analysis and distillation both visually (JAVA GUI client applications) and in batch mode (instantiation of multi-threaded applications on clusters of processors). Regional Body-Wave Amplitude Processor (RBAP) Version 2 is one such example. Over the past year RBAP was significantly improved in capability and performance. A new role-based security model now allows fine-grain access control over all aspects of the tool's functions enabling researchers to share their work with others without fear of unintended parameter alterations. A new, faster, and more-reliable geographic information system (GIS) mapping framework was added, as well as expanded powerful interactive plotting graphics. In addition, we implemented parent-child type projects to enhance calibration data management.

Our specific automation methodology and tools improve researchers' ability to assemble quality-controlled research products for delivery into the NNSA Knowledge Base (KB). The software and scientific automation tasks provide the robust foundation upon which synergistic and efficient development of Ground-Based Nuclear Explosion Monitoring Research and Development (GNEMRD) Program seismic calibration research may be built.

## OBJECTIVE

The NNSA GNEMRD Program has made significant progress enhancing the process of deriving seismic calibrations and performing scientific integration with automation tools. We present an overview of our software automation efforts and framework to address the problematic issues of improving the workflow and processing pipeline for seismic calibration products, including the design and use of state-of-the-art interfaces and database centric collaborative infrastructures. These tools must be robust and intuitive and reduce errors in the research process. This scientific automation engineering and research will provide the robust hardware, software, and data infrastructure foundation for synergistic GNEMRD Program calibration efforts. The current task of constructing many seismic calibration products is labor intensive, complex, expensive, and error prone. The volume of data as well as calibration research requirements has increased by several orders of magnitude over the past decade. The increase in the quantity of data available for seismic research over the last two years has created new problems in seismic research: data quality issues are hard to track, given the vast quantities of data, and quality information is readily lost if not properly tracked in a manner that supports collaborative research. We have succeeded in automating many of the collection, parsing, reconciliation, and extraction tasks individually. Several software automation tools have also been produced and have resulted in demonstrated gains in efficiency for producing derived scientific data products. In order to fully exploit voluminous real-time data sources and support new requirements for time-critical modeling, simulation, and analysis, continued expanded efforts to provide a scalable and extensible computational framework will be required.

## RESEARCH ACCOMPLISHED

The primary objective of the Scientific Automation Software Framework (SASF) effort is to facilitate the development of information products for the GNEMRD regionalization program. The SASF provides efficient access to, and organization of, large volumes of raw and derived parameters, while also providing the framework to store, organize, integrate, and disseminate derived information products for delivery into the NNSA KB.

These next generation information management and scientific automation tools are used together within specific seismic calibration processes to support production of tuning parameters for the United States Atomic Energy Detection System (USAEDS) run by the Air Force. The automation tools create synergy and synthesis between complex modeling processes and very large datasets by leveraging a scalable and extensible database centric framework. The requirements of handling large datasets in diverse formats, and facilitating interaction and data exchange between tools supporting different calibration technologies, has led to an extensive scientific automation software engineering effort to develop an object oriented database-centric framework using proven research-driven workflows and excellent graphics technologies as a unifying foundation.

The current framework supports integration, synthesis, and validation of the various different information types and formats required by each of the seismic calibration technologies. For example, the seismic location technology requires parameter data (site locations, bulletins) and time-series data (waveforms) and produces parameter measurements in the form of arrivals, gridded geospatially registered correction surfaces, and uncertainty surfaces. Our automation efforts have been largely focused on research support tools, RBAP and Knowledge-Base Automated Location Assessment and Prioritization (KBALAP). Furthermore, increased data availability and research requirements have driven the need for multiple researchers to work together on a broad area, asynchronously.

### Database-Centric Coordination Framework

As part of our effort to improve our efficiency we have realized the need to allow researchers to easily share their results with one another. For example, as the location group produces GT information, that information should become available for other researchers to use. Similarly, phase arrival picks made by any qualified user should also become immediately available for others to use. This concept extends to the sharing of information about data quality. It should not be necessary for multiple researchers to have to repeatedly reject the same bad data, or worse, miss rejecting bad data. Rather, once data are rejected because of quality reasons they should automatically be excluded from processing by all tools. We are implementing this system behavior using database tables, triggers, stored procedures, and application logic. Although we are at the beginning of this implementation, we have made significant progress over the last year with several kinds of information sharing using the new database centric coordination framework. These are discussed below.

Significant software engineering and development efforts have been successfully applied to construction of an object-oriented database framework that provides database-centric coordination between scientific tools, users, and data.

A core capability of this new framework provides is information exchange and management between different specific calibration technologies, and their associated automation tools, such as seismic location (e.g., KBALAP), seismic identification (e.g., RBAP), and data acquisition and validation (e.g., KBITS). A relational database (Oracle) provides the framework for organizing parameters key to the calibration process from both Tier 1 (raw parameters such as waveforms, station metadata, bulletins, etc.) and Tier 2 products (e.g., derived measurements such as GT, amplitude measurements, calibration, and uncertainty surfaces). Seismic calibration technologies (location, identification, etc.) are connected to parameters stored in the relational database by an extensive object-oriented multi-technology software framework that includes elements of schema design, PL/SQL, real-time transactional database triggers and constraints, as well as coupled Java and C++ software libraries to handle the information interchange and validation requirements. This software framework provides the foundation upon which current and future seismic calibration tools may be based. Interim results and a complete set of working parameters must be available to all research teams throughout the entire processing pipeline. Finally, our development staff has continually and efficiently leveraged our Java code library, achieving 45% code reuse (in lines of code) throughout several thousand Java classes. Source code control is managed by CVS (source code) and ER Studio (schema designs).

**Process Improvement**

Given the small size of our development staff, the ambitions of our researchers, and the heritage of many of our projects, our process has always been minimal. However, as the complexity and number of users of our system increased, the need for more discipline became apparent. For several years we have been using version control for our source code and have employed unit tests for selected high-risk modules. We have also maintained models of our database artifacts and briefly experimented with maintaining models of our code base. These experiments demonstrated that in our environment of rapidly changing requirements, modeling of source code, except on an as-needed basis, is not practical for us. Because the database does not evolve as rapidly as the code, it is tractable to maintain models of the database, and these prove to be useful both in the design of code and in the refactoring and extension of our database objects.

As the number of users of our applications has increased, it has become increasingly apparent that we must manage multiple system deployments, each with its own application servers and database. There is simply too much content on our production system to risk damage from code under development. Also, disruption to end users is a significant problem when developing on the production system. Accordingly, this year we established two additional CVS branches. One is for experimental development work, and the other is a release branch where we can do bug fixes on our deployed code without interference to ongoing code development. Each branch contains not only the source code, but all artifacts including data models and IDE configurations.

During the development of RBAP 2 we started tracking errors and features on a spreadsheet and discovered, among other things, that we were getting a significant number of regressions in the user interface code. Clearly, just maintaining unit tests for high-risk code wasn't enough. However, writing a comprehensive set of unit tests would take an amount of effort far greater than what we were devoting to fix regressions. Our compromise solution is to evaluate the utility of automated unit testing. Accordingly, we will soon install the JTest software product from Parasoft that helps automate the generation and execution of a comprehensive suite of unit tests and static analysis.

Another lesson we learned during the development of RBAP 2 was the usefulness of static analysis in eliminating actual or potential errors in the source code. By using automated tools we were able to detect and fix hundreds of problematic or erroneous code constructs. As a consequence, we have agreed on a process by which all code submitted to CVS by developers undergoes a set of static analyses and checks on formatting. When JTest is installed, the static analysis and unit tests will become mandatory upon check-in.

These changes are part of our effort to evolve a software development process with the right balance of agility and discipline for the environment in which we develop and in which our software is used.

**Automating Tier 1**

Corrections and parameters distilled from the calibration database provide needed contributions to the NNSA KB for the ME/NA/WE region and will improve capabilities for underground nuclear explosion monitoring. The contributions support critical functions in detection, location, feature extraction, discrimination, and analyst review. Within the major process categories (data acquisition, reconciliation and integration, calibration research, product distillation) are many labor intensive and complex steps. The previous bottleneck in the calibration process was in the reconciliation and integration step. This bottleneck became acute in 1998 and the KBITS suite of automated parsing, reconciliation, and integration tools for both waveforms and bulletins (ORLOADER, DDLOAD, UpdateMrg) were developed. The KBITS suite provided the additional capability required to integrate data from many data sources and external collaborations. Data volumes grew from 11,400 events with 1 million waveforms in 1998 to over half a billion raw parameters, measurements, and associated 100 terabytes of continuous data today (e.g., Ruppert et al., 1999; Elliott et al., 2006).

We receive enormous amounts of seismic data daily that must be properly processed. Previously, the movement and management of data were performed manually by our information technology (IT) staff and were extremely time intensive and inefficient. In response, we designed and implemented a distributed (multimachine), multiprocess solution to help automate the collection, movement, cataloging, reporting, viewing, and error processing of waveform segmentation data from multiple academic and government sources. The distributed processes are being written in Java, using encrypted data transfers, logging, an embedded Java relational database (Derby) for maintaining transfer metadata, and a monitoring interface for reporting and quality control. Also, the ability to easily query and view available continuous data was added to improve the efficiency of quality control and recording of metadata.

**Automating Tier 2**

As the data sources required for calibration have increased in number and source location, it has become clear that the manual, labor-intensive process of humans transferring thousands of files and unmanageable metadata cannot keep the KBITS software fed with data to integrate, nor can the seismic researcher efficiently and consistently find, retrieve, validate, or analyze the raw parameters necessary to effectively produce seismic calibrations in an efficient manner. Significant software engineering and development efforts were applied to address this critical need to produce software aids for the seismic researcher. The principal focus of these efforts has been on the development of two scientific automation tools, RBAP and KBALAP, for seismic location and seismic identification calibration tasks, respectively.

**RBAP Version 2**

The RBAP (Ruppert et al., 2007) has been extensively revised over the past year. Changes include:

- **Support for tiered projects:** Users can now create a parent calibration project, which defines the velocity model and MDAC parameters for a specific station and region. Subsequent child projects can then be created for the same station and region and MDAC corrected amplitudes calculated using the parent's calibrated parameters. This allows us to explore different source types in understanding discrimination.
- **An improved security model:** Now a minimum-privileged user is able to examine all aspects of any project without being able to change any data. Also, a project owner can now enlist multiple project group members who are able to add measurements without the risk of changing project parameters.
- **Improved scalability:** Computations have been reworked to use multiple producer-consumer threads with the number of threads scaling by available cores.
- **GIS overhaul:** The old GIS system has been replaced by a much higher-performance and more interactive system. Users may now drill-down from the map to view metadata behind measurements.
- **User interface improvements:** The user interface has been reworked to have a consistent look and feel throughout and the level of encapsulation in the GUI code has been substantially increased.
- **Discrimination capability:** Discrimination plots may now be easily produced for any station and any combination of phases and bands.
- **GT editing:** Users with appropriate database privileges may now view and manipulate GT etype information on a per-event basis.
- **Code Quality:** Thousands of code refactorings were performed to better meet industry best-practice standards and patterns.

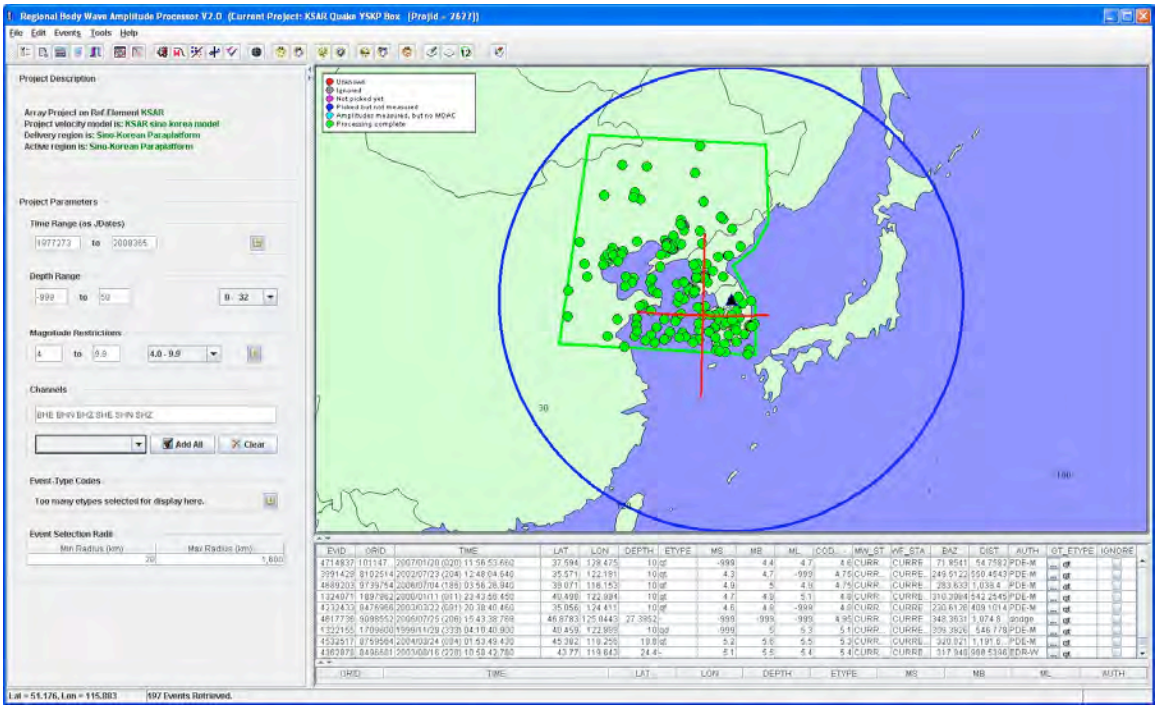

**Figure 1. A screenshot of the RBAP program, showing the project parameters in the left pane and a set of processed events displayed in the map and table.**

### Adding MDAC and Coda Magnitude Processing Module to RBAP

To supplement RBAP in source identification we are developing a waveform processing and signal analysis tool (WFT), which includes the ability to measure amplitudes and coda magnitudes. WFT was originally part of the Hydroacoustic Blockage Assessment Tool (HABAT) code (Matzel et al., 2005) used to discriminate explosion sources from earthquakes in the oceans. WFT has since been broken off into a standalone program with the ability to read, write, plot, and process seismic analysis code (SAC) and CSS format data from flat files or from the LLNL database and was used in the seismic inversion of 3D structure along the Tethyan margin (Flanagan et al., 2006). Along with the filtering, plotting and signal analysis routines derived from the original SAC algorithms, the WFT now includes two subprograms used in seismic discrimination studies: the Amplitude Measurement Tool (AMT) calculates spectral amplitudes, and the Coda Tool calculates coda magnitudes for calibrated regions. The AMT (Figure 2) makes raw and MDAC corrected amplitude measurements on flat file SAC waveforms. This code was designed specifically for use when the LLNL database is inaccessible, and allows us to work more easily with offsite collaborators. AMT performs all the basic RBAP amplitude calculations using the same MDAC parameter setup, it writes output to DiscrimData tables and can plot the results. The Coda Tool (Figure 3) allows anyone with a basic background in coda theory to read either database or flat file seismic data and calculate source magnitudes, given a regional calibration. Once data are read in, the user can calculate seismic data envelopes, calculate synthetics based on published theory (Mayeda et al., 2003), compute the spectral amplitudes, add site and path corrections, and compute the final coda Mw. We are currently extending the Coda Tool to create regional calibrations and to work directly with the LLNL database.

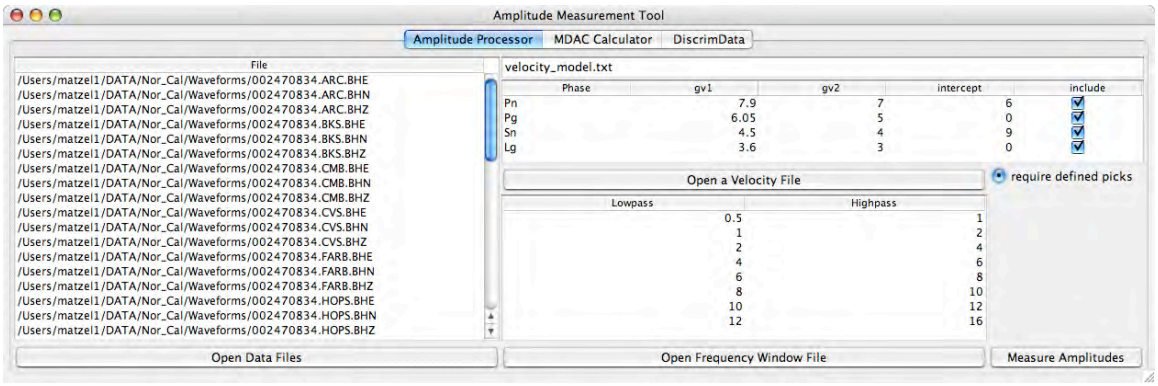


**Figure 2. A screenshot of the Amplitude Measurement Tool, which calculates spectral amplitudes for the seismic analysis code (SAC) and CSS flat files and applies MDAC corrections to the results.**

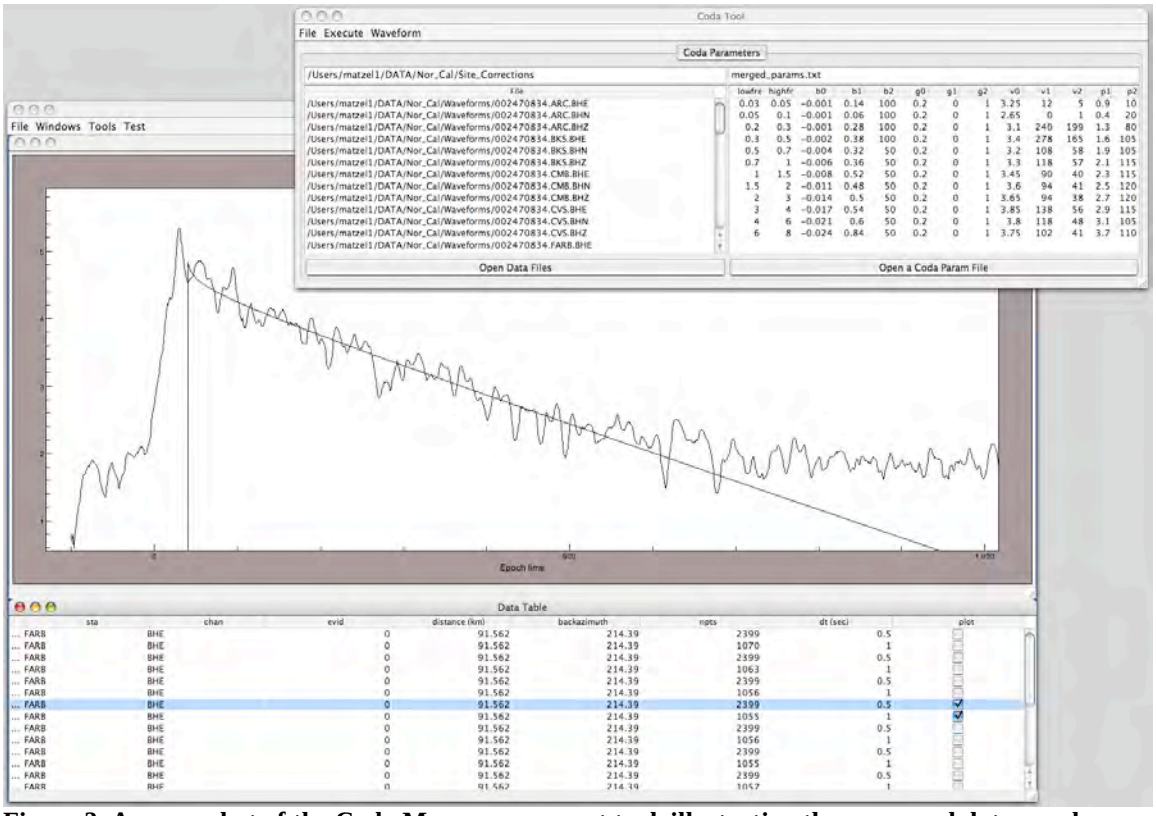


**Figure 3. A screenshot of the Coda Mw measurement tool, illustrating the measured data envelopes compared with synthetic envelopes.**

## The KBALAP Program

The KBALAP program is another Tier 2, event-centric automation effort in the GNEMRD program (Elliott et al., 2006). It is a highly interactive, graphical tool that uses a set of database services and a client application based on data selection profiles that combine to efficiently produce location GT. These data can be used in the production of travel time correction surfaces, and as part of the preferred event parameters used by other tools in our processing framework.

KBALAP's database services are responsible for evaluating bulletin and pick information as it enters the system for identifying origin solutions that meet predefined GT criteria without further processing and for identifying events

that would likely meet a predefined GT level if a new origin solution were produced using available arrivals. The database service is also responsible for identifying events that should have a high priority for picking based on their existing arrival distribution, and the availability of waveform data for stations at critical azimuths and distances.

The interactive portion of KBALAP has the following principal functions:
• Production of GT origins through prioritized picking and location
• Specification of GT-levels for epicenter, depth, origin time and etype
• Batch-mode location of externally produced GT information
• Production of array azimuth-slowness calibration data
• Easy review and modification of event parameters used by all GNEMRD researchers

Some key KBALAP features are listed below:
• Fast and efficient location
• Project management and collaboration
• Batch processing

**The Site Merge Effort**

Information about seismic station position and installed instrumentation is to a greater or lesser extent, fundamental to all the processing done within the GNEMRD Program. However, despite the importance of accurate information about seismic stations, in practice it is difficult to obtain a compilation of station information that does not include errors. There are many sources for these errors, including the following:
• Imprecise surveying/reporting by station operators
• Transcription errors
• Unrecorded station movements or equipment modifications

The situation is complicated even more by the fact that many different compilations have been produced using different sources and different assumptions, and these compilations are inconsistent with one another.

In the past, we have dealt with inconsistencies case by case. When a problem was identified, we would “fix” the offending data in our SITE table and go on. While this approach was problematic in a number of ways, given the limitations of the CSS SITE table and our need to build out other parts of our infrastructure, it was judged to be the best we could do. As the labs coordinate more in the process of producing calibration products for monitoring purposes, the need for a unified, consistent SITE table has become more apparent. Producing and maintaining such a table by integrating and reconciling our individual SITE tables is an even more difficult undertaking than simply maintaining an internal-use-only SITE table. Mainly this is because of the need to resolve conflicts in a way that is trackable, reproducible, and backed with documented decisions/assumptions.

We were tasked this year with performing the location GT merge between contributing laboratories. This effort depended critically on having a unified SITE table of the highest possible quality. This accelerated our work on producing a SITE merge, and we now have a system that we used to produce an integrated SITE table for the GT merge and as a replacement for our LLNL SITE table. Our merge process is implemented in Java and in PL/SQL and uses a number of tables to track metadata about the merge process. The codes allow for repeated contributions by the same author allowing, for example, updating of the merged SITE as new versions of the NEIC station book become available. The results and documentation will be provided to the relevant NNSA GNEMRD working groups for coordination and consideration.

Our approach to merging SITE data is to handle the position, elevation, operating epochs, station movements, array membership and possible code aliasing separately. We take this approach because there is no guarantee that a particular contributor’s information about a SITE will be uniformly better or worse than information from another source.

When SITE data come into the system, they are placed into a multiauthor site table (and supporting tables) that hold all the unmerged data. Before a new merge is executed, a process is run that identifies unresolved discrepancies (over a threshold value) in position and elevation. Any stations with unresolved discrepancies are added to

appropriate discrepancy tables. Although the merge can continue without resolving the discrepancies, these stations will not become part of the merged SITE table.

Discrepancies can be resolved in one of two ways: by making entries in a preferred table or by making entries in a rejected table. The reason column in each of these tables allows up to a 2000-character discussion of the reason for the decision. With this system, it is relatively easy to find out why a particular datum was or was not used, and if better information becomes available it is easy to change the first decision and redo the merge. The software also helps resolve position discrepancies by producing KML files that allow display in Google Earth of clusters of discrepant station position estimates.

We handle alternate station codes by excluding them from the merge process. After the merge is complete, duplicate entries are created for each alternate code, but with the original code replaced by the alternate code. In addition to the alternate codes provided by the NEIC, we identified a number of additional such codes by comparison of latitude, longitude, and elevation entries. These are treated in the same fashion as the NEIC alternate codes.

We have used our SITE merging system to combine SITE information from the most recent NEIC and ISC station books, the current NNSA GNEMRD SITE tables, and the Incorporated Research Institutions for Seismology (IRIS) SITE table (derived from dataless SEED volumes minus temporary deployments and California stations). There are about 39,000 entries in the multiauthor site table which produce more than 17,700 merged SITE entries. There are 376 preferred positions, 286 preferred elevations, 61 rejected positions, and 572 rejected elevations. The position overrides were determined mostly through a combination of inspection in Google Earth and residual analysis using GT events. Most of the elevation overrides were arrived at by comparison of reported elevations with elevations computed using the gtopo30 elevation model.

**Ongoing Work Related to the SITE Merge**

Although the code for producing the merged SITE is fully functional, we do not yet have an automated means of updating our production database when a new SITE table is produced. The problem is that if stations that exist in the current table are updated and their epochs change, it affects many other tables that have some dependence on SITE. This time we resolved those issues manually, but that process must be automated for future SITE updates. Also, it is apparent that we need to develop software tools that will allow a nontechnical user to make changes to the SITE table. The software must not only make changes to the production table(s), but must make appropriate entries in the metadata schema as well. For example, changing a station position must now require review of any justifications for the current position, and it must be required that the change be accompanied by a justification. After accepting the change, the system must update all tables affected by the change.

**Instrument Response Updates**

We are in the process of converting most of our SEED response files to the poles and zeros/finite impulse response (PAZFIR) format. The conversion is being done using code developed by George Randall of LANL. Each converted response is checked by comparing frequency-amplitude-phase spectra generated from the PAZFIR data to that generated from the SEED data. Those with an RMS difference of less than 1% (virtually all of the conversions) are retained. The remainder will stay as SEED for now.

Roughly 3,600 of our existing IRIS dataless SEED RESP files have been successfully converted, resulting in over 7,000 PAZFIR responses. In order to properly convert and validate responses, this effort involved writing C-shell, Java, and Matlab programs (that used Perl programs to perform the actual conversion). The principal effort remaining is to modify the conversion codes to move the converted responses into appropriate directories and to update the appropriate instrument rows.

**The GT Merge Effort**

The GT merge project involved the combination of GT data sets compiled by LLNL and LANL along with supporting and associated data from the labs and from AFTAC. The merge process also included extensive quality-control and revalidation steps. In all, over 230,000 events with over 20,000,000 arrivals were processed.

This process merges the GT25 and better datasets between contributing laboratories for use in both a tomographic inversion for *Pn* velocity of Eurasia and for computing first-*P* correction surfaces using the KBCIT software. The merge is intended both to resolve GT common between labs (choosing the better GT estimate when possible) and to perform an extensive set of quality control steps to the origin and phase data. We have developed a software system implemented in Java, Oracle relational database, and PL/SQL to perform this merge process (Flanagan et al., 2007).

The software brings together into a GTMERGE schema the GT data from both labs along with all supporting ORIGIN, ORIGERR, ASSOC and ARRIVAL data. All data are given new IDs unique within the GTMERGE schema, and events in common between labs are identified by spatial-temporal correlation. The Bondar-Myers-Engdahl-Bergman (BMEB) Epicenter accuracy criteria are used (Bondar et al., 2004). For those events in common, a set of ranking rules is applied to select the best non-BMEB GT. A small subset of the input GT that cannot be ranked is resolved manually.

The quality check (QC) steps performed by the software include the following:
- Enforcing common phase naming conventions
- Removing arrivals that are too early or too late to be of interest
- Removing phases not of interest
- Identifying and removing arrivals that are too discrepant to be useful
- Enforcing distance-dependent phase name conventions
- Choosing a “best” arrival for each EVID-STA-PHASE table

After QC is complete, the system evaluates all the BMEB GT for strict adherence to their criteria. All events that fail this check have a new origin solution computed using phase gathers appropriate to the GT level. If the new solution meets its criterion, then it is included in the final merge results. Otherwise, the event is rejected. When all GT have been re-evaluated, a new set of constrained origin solutions is computed using teleseismic P-arrivals. These “baselined” origins are the final product of the merge effort. The dataset produced by the merge effort includes about 97,000 distinct events with nearly 20,000,000 arrivals.

## CONCLUSIONS AND RECOMMENDATIONS

We present an overview of our software automation efforts and framework to address the problematic issues of consistent handling of the increasing volume of data, collaborative research efforts and researcher efficiency, and overall reduction of potential errors in the research process. By combining research-driven interfaces and workflows with graphics technologies and a database centric information management system coupled with scalable and extensible cluster-based computing, we have begun to leverage a high performance computational framework to provide increased calibration capability. These new software and scientific automation initiatives will directly support our current mission including rapid collection of raw and contextual seismic data used in research, provide efficient interfaces for researchers to measure and analyze data, and provide a framework for research dataset integration. The initiatives will improve time-critical data assimilation and coupled modeling and simulation capabilities necessary to efficiently complete seismic calibration tasks. This GNEMRD Program’s scientific automation, engineering, and research will provide the robust hardware, software, and data infrastructure foundation for synergistic calibration efforts.

## ACKNOWLEDGEMENTS

We acknowledge the assistance of the LLNL computer support unit in implementing and managing our computational infrastructure. We thank Jennifer Aquilino, Laura Long, and John Hernandez for their assistance in configuration and installation of our Linux cluster and workstations.

## REFERENCES

Bondar, I., S. Myers, E. Engdahl, and E. Bergman (2004). Epicenter accuracy based on seismic network criteria, *Geophys. J. Int.* 156: 483–496.

Elliott. A., D. Dodge, M. Ganzberger, T. Hauk, E. Matzel, and S. Ruppert (2006). Enhancing seismic calibration research through software automation and scientific information management, in *Proceedings of the 28th Seismic Research Review: Ground-Based Nuclear Explosion Monitoring Technologies*, LA-UR-06-5471, Vol. 2, pp. 967–975.

Flanagan, M, D. Dodge, and S. Myers (2007). GT merge processing documentation—Beta version, in University of California, Radiation Laboratory, 1–15 (in review).

Flanagan, M., E. Matzel, S. van der Lee, H. Bedle, M. Pasyanos, F. Marone, B. Romanowicz, C. Schmid, and A. Rodgers (2006). Joint inversion for three-dimensional velocity structure of the broader Africa-Eurasia collision region, in *Proceedings of the 28th Seismic Research Review: Ground-Based Nuclear Explosion Monitoring Technologies*, LA-UR-06-5471, Vol. 1, pp. 397–406.

Matzel, E., A. L. Ramirez, and P. E. Harben (2005). Model-based hydroacoustic blockage assessment and development of an explosive source database, in *Proceedings of the 27th Seismic Research Review: Ground-Based Nuclear Explosion Monitoring Technologies*, LA-UR-05-6407, Vol. 2, pp. 733–739

Mayeda, K., A. Hofstetter, J. L. O'Boyle, and W. Walter (2003). Stable and transportable regional magnitudes based on coda-derived moment-rate spectra, *BSSA* 93: 224–239.

Ruppert, S., T. Hauk, J. O'Boyle, D. Dodge, and M. Moore (1999). Lawrence Livermore National Laboratory's Middle East and North Africa research database, in *Proceedings of the 21st Seismic Research Symposium: Technologies for Monitoring the Comprehensive Nuclear-Test-Ban Treaty*, LA-UR-99-4700, Vol. 1, p. 243.

Ruppert, S., D. Dodge, M. Ganzberger, T. Hauk, and E. Matzel (2007). Enhancing seismic calibration research through software automation and scientific information management, in *Proceedings of the 29th Monitoring Research Review: Ground-Based Nuclear Explosion Monitoring Technologies*, LA-UR-07-5613, Vol. 2, pp. 965–974

# Appendices

# Acronyms, etc.

| Acronym | Definition |
|---|---|
| ACZ | Antarctic Convergence Zone |
| AFRL | Air Force Research Laboratory |
| AFTAC | Air Force Technical Applications Center |
| AK135 | seismic travel time model |
| ANFO | ammonium nitrate fuel oil |
| ARSA | Automated Radioxenon Sampler/Analyzer |
| BEM | boundary element method |
| BRV | Borovoye Observatory |
| CAP | cut and paste |
| CC | correlation coefficient |
| CDSN | Chinese Digital Seismic Network |
| CLVD | compensated linear vector dipole |
| CMT | Harvard centroid moment tensor |
| CNDSN | Chinese National Digital Seismic Network |
| COTS | commercial off the shelf |
| CRUST2.0 | crustal model (Bassin et al., 2000) |
| CTBT | Comprehensive Nuclear-Test-Ban Treaty |
| CTBTO | Comprehensive Nuclear-Test-Ban Treaty Organization |
| CU | University of Colorado |
| CUB2.0 | 3D global models (Shapiro et al., 2002) |
| CU-Boulder | University of Colorado, Boulder |
| DC | double couple |
| DD | double difference |
| DMC | Data Management Center (IRIS) |
| DOB | depth of burial |
| DoD | Department of Defense |
| DOE | Department of Energy |
| DOS | Department of State |
| DSP | digital signal processor |
| DSS | deep seismic sounding |
| EDR | Earthquake Data Reports - a USGS publication |
| EFT | earth-flattening transform |
| EGF | Empirical Green Function |
| EHB | Engdahl, E.R., van der Hilst, R. & Buland, R., 1998. Global teleseismic earthquake relocation with improved travel times and procedures for depth determination, Bull. Seismol. Soc. Amer., 88, 722-743 |
| ERL | Earth Resources Laboratory (MIT) |
| ETOPO | earth topographic (database) |
| ETOPO5 | terrain model |
| EventID | tool to implement event discrimination (Hartse et al., 1997; Walter et al., 1999) |
| FD | finite difference |
| FDTD | finite difference time domain |
| FE | finite element |
| FFST | finite-frequency seismic tomography |
| FFT | Fast Fourier Transform |
| F-K | frequency wavenumber |
| Fstat, F-stat | F-statistic |
| FSU | Former Soviet Union |
| FTA | frequency-time analysis |

| Acronym | Definition |
|---|---|
| FWHM | full width at half maximum |
| G2S | ground-to-space |
| GB | Gaussian beam |
| GBF | generalized beamforming |
| GII | Geophysical Institute of Israel |
| GIS | geographical information system |
| GMEL | Grid-search Multiple Event Location |
| GMT | generic mapping tool |
| GNEMRD | Ground-Based Nuclear Explosion Monitoring Research and Development Program |
| GRACE | gravity recovery and climate experiment |
| GSN | global seismographic network |
| GT | ground truth |
| GTx | ground truth information of accuracy x km |
| GUI | graphical user interface |
| HDC | hypocentroidal (or hypocentral) decomposition |
| HE | high explosive |
| HPGe | high purity germanium |
| HPXe | high-pressure xenon |
| Hz | hertz |
| IASPEI | International Association of Seismology and Physics of the Earth's Interior |
| iasp91 | standard earth model |
| IPGG | Institute of Petroleum Geology and Geophysics |
| IPGP | Institut de Physique du Globe de Paris |
| IDA | International Deployment of Accelerometers |
| IDC | International Data Centre |
| IDG | Russian Institute for the Dynamics of the Geospheres |
| IMS | International Monitoring System |
| InfraMAP | Infrasound Modeling of Atmospheric Propagation |
| InSAR | Interferometric Synthetic Aperture Radar |
| IRIS | Incorporated Research Institutions for Seismology |
| ISC | International Seismological Centre |
| JVE | Soviet Joint Verification Experiment |
| KB | Knowledge Base |
| KBCIT | Knowledge Base Calibration Integration Tool |
| KMA | Korean Meteorological Administration |
| KNDC | Kazakhstan National Data Center |
| LANL | Los Alamos National Laboratory |
| LDEO | Lamont-Doherty Earth Observatory |
| LLNL | Lawrence Livermore National Laboratory |
| LNM | low-noise model |
| LBS | local bus server |
| LVZ | low velocity zones |
| Matlab | commercial software application |
| MatSeis | seismic analysis package developed by SNL using Matlab |
| mb | body wave magnitude |
| MCMC | Markov Monte Carlo |
| MDAC | magnitude and distance amplitude corrections |
| MEMS | microelectromechanical systems |
| MIT | Massachusetts Institute of Technology |
| Ms | surface wave magnitude |
| MSE | mean squared error |

| Acronym | Definition |
|---|---|
| MSU | Michigan State University |
| MT | moment tensor |
| Mw | moment magnitude |
| NA-22 | Office of Nonproliferation Research and Development |
| NASA | National Aeronautics and Space Administration |
| NCSU | North Carolina State University |
| NEIC | National Earthquake Information Center |
| NEM R&D | Nuclear Explosion Monitoring Research and Development |
| NEMS | nuclear explosion monitoring system |
| NISN | North Iraq Seismographic Network |
| Nm | newton-meters |
| NNSA | National Nuclear Security Administration |
| NORSAR | Norwegian Seismic Array |
| NPE | Nonproliferation Experiment |
| NRL | Naval Research Laboratory |
| NSF | National Science Foundation |
| NTS | Nevada Test Site |
| NVAR | Nevada Seismic Array |
| PASSCAL | Program for the Array Seismic Studies of the Continental Lithosphere |
| PDE | preliminary determination of epicenters |
| PDF | portable document format |
| PE | parabolic equation |
| PNE | peaceful nuclear explosions |
| PNNL | Pacific Northwest National Laboratory |
| PPV | peak particle velocity |
| PSD | power spectral density |
| PSU | Penn State University |
| PTS | Provisional Technical Secretariat |
| Q | Seismic Q factor (reciprocal of attenuation) |
| RAS | Russian Academy of Sciences |
| RASA | Radionuclide Aerosol Sampler Analyzer |
| REB | Reviewed Event Bulletin - an IDC report |
| RF | receiver functions |
| RMS | root mean square (errors) |
| ROC | receiver operating characteristic |
| SAC | seismic analysis code |
| SAIC | Science Applications International Corporation |
| SBIR | Small Business Innovation Research |
| SCSN | Southern California Seismic Network |
| SEM | spectral element method |
| SLU | ST. Louis University |
| SMDC | Space Missile Defense Command (Army) |
| SMU | Souther Methodist University |
| SNL | Sandia National Laboratories |
| SNR | signal-to-noise ratio |
| SOFAR Channel | SOund Fixing And Ranging - primary sound channel in the ocean |
| SP | short period |
| SPE | source phenomenology experiments |
| STA/LTA | short-term average/long-term average |
| STS | Semipalatinsk Test Site |
| SUS | signal underwater sound |

| Acronym | Definition |
|---|---|
| T* (t-star) | A measure of the "damping" or attenuation along a path. T* is the ratio of the travel time along a ray path to the average Q (seismic "quality" factor) along it. |
| TOD | time of day |
| T-phase | hydroacoustic phase |
| UCSD | University of California, San Diego |
| UHV | ultra-high vacuum |
| UNE | underground nuclear explosions |
| UNR | University of Nevada, Reno |
| USAEDS | United States Atomic Energy Detection System |
| USBM | United States Bureau of Mines |
| USGS | United States Geological Survey |
| USNDC | United States National Data Center |
| UTEP | University of Texas at El Paso |
| VOD | velocity of detonation |
| WCC | waveform cross correlation |
| WSMR | White Sands Missile Range |
| WWSSN | World Wide Standardized Seismographic Network |

## Guide to Seismic Phases

The change of seismic velocities within Earth, as well as the possibility of conversions between compressional (P) waves and shear (S) waves, results in many possible wave paths. Each path produces a separate seismic phase on seismograms. Seismic phases are described with one or more letters, each of which describes a part of the wave path. Upper case letters denote travel through a part of the earth (e.g. P or S), and lower case letters denote reflections from boundaries. A complete, standardized nomenclature for seismic wave paths is available at the web site: http://www.isc.ac.uk/Documents/IASPEI/sspl.html. This information has also been published [Storchak, D.A., J. Schweitzer, P. Bormann (2003), "The IASPEI Standard Seismic Phase List", Seismol. Res. Lett. 74, 6, 761-772], and a pdf file of this publication is available from the same web site.

In the verification context, wave propagation in Earth is divided into *teleseismic* (distances greater than 2000 kilometers) paths and *regional* (distances less than 2000 kilometers) paths.

### Teleseismic Phases

In these plots, the seismic event is at the left, and seismic ray paths are shown to possible stations at several angular distances from the event.

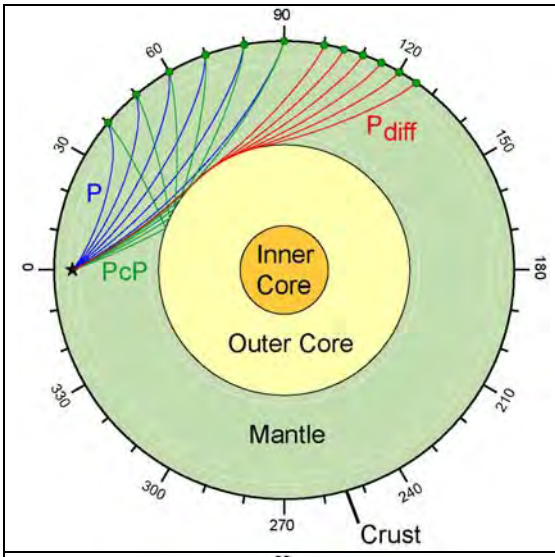


**P** A primary (compressional) wave that follows a simple path from event source to the station.

**PcP** A P wave that goes downward through the mantle (the first "P"), is reflected from the top of the outer core ("c") and goes upward through the mantle to the station (second "P").

**$P_{diff}$** A P wave that has been bent (diffracted) around the outer core boundary and arrives at a station in the ray "shadow" of the outer core.

**S** A secondary (shear) wave that follows a path similar to the P wave (not shown).

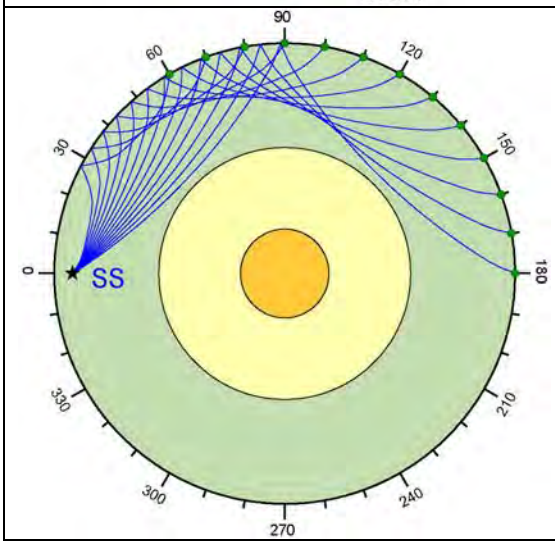


**SS** A shear wave that has traveled through the mantle ("S"), undergone one reflection from the underside of Earth's surface and traveled again through the mantle (second "S"). Unlike with most other reflected waves, there is no separate letter to denote the reflection at the surface; it is implicit.

**PP** A compressional wave that follows paths similar to those of SS (not shown).

| | | |
|---|---|---|
| 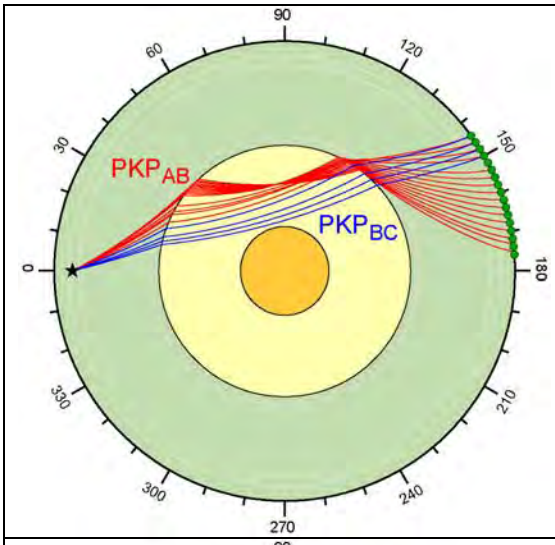 | **PKP** | A P wave that has traved through the mantle ("P"), been transmitted across the mantle-outer core boundary and traveled through the outer core ("K"), transmitted back across the outer core-mantle boundary and traveled as a P wave to the station ("P"). Because of the large difference between the P wave velocity in the mantle and the outer core, this wave is bent (refracted) strongly at the boundary. Seismic waves can follow slightly different paths (labeled $PKP_{AB}$, $PKP_{BC}$) and still arrive at about the same time. |
| 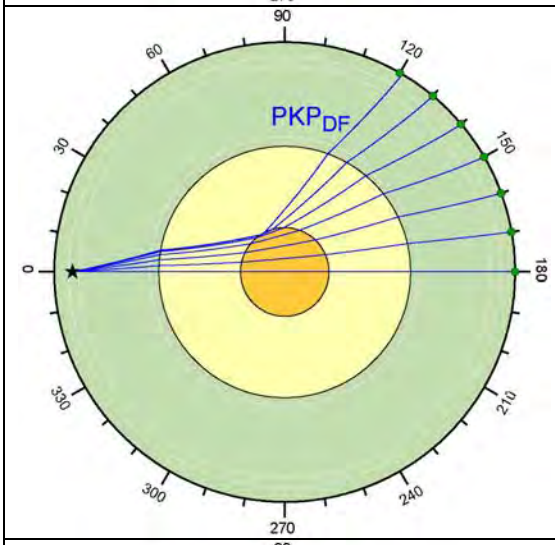 | **PKIKP** | A P wave that has traveled through the mantle ("P"), been transmitted across the mantle-outer core boundary ("K"), crossed the outer-core inner-core boundary and traveled through the inner core as a P wave ("I"), then followed a similar path in reverse to get from the inner core to the station (the second "KP"). An alternate name for this phase is $PKP_{DF}$ (shown in the path illustration). |
| 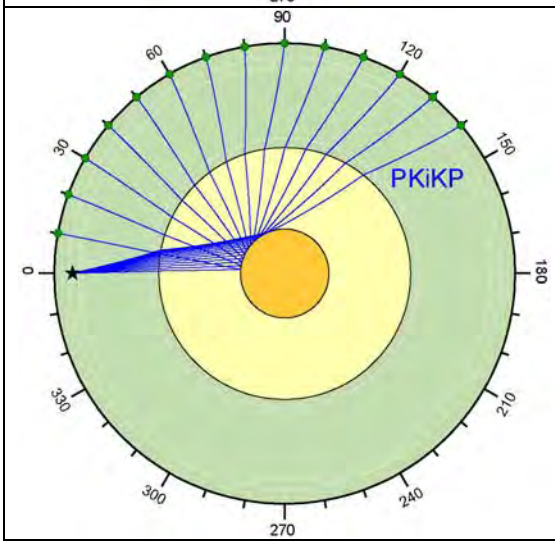 | **PKiKP** | This phase has followed a series of paths similar to the PKIKP phase, except it was reflected off the top of the inner core-outer core boundary (this is the "i" part of the path), rather than being transmitted through the inner core. |

Figures courtesy of Ed Garnero, Arizona State University (http://garnero.asu.edu/research_images/index.html)

**Depth Phases**

A number of "depth" phases are referred to in the proceedings. The paths of these phases are nearly the same as P waves. The depth phases all result from a reflection from the Earth's surface near the epicenter of the event. The time delay between the P wave and the depth phase is proportional to the depth of the event (hence the term "depth" phase).

**pP** A P wave that started out upward from the source ("p"), reflected off the Earth's surface, and traveled to the station as a P wave ("P").

**sP** An S wave that started out upward from the source ("s"), reflected off the earth's surface and also converted to a P wave, which then traveled to the station as a P wave ("P").

**pwP** Similar to the pP phase. A P wave that started out upward from the source ("p"), reflected off the ocean surface ("w" - water) and traveled to the station as a P wave ("P").

**Regional Phases**

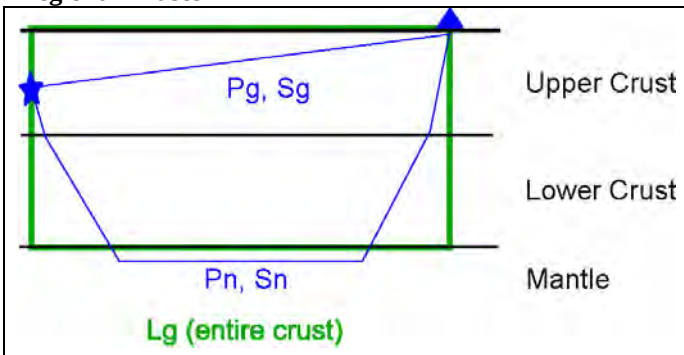


A highly simplified representation of the crust of Earth, which is seldom so simple and flat. Changes of crustal thickness and velocities can disrupt crustal phases, notably Lg.

**Pg (Sg)** At short event-station distances, an upgoing P (S) wave from a source in the upper crust (depicted here) or a P (S) wave bottoming in the upper crust. At larger distances the Pg phase includes arrivals resulting from multiple P-wave reverberations within the entire crust that propagate at a group velocity around 5.8 km/s.

**Pn (Sn)** A P (S) wave bottoming in the uppermost mantle or an upgoing P wave from a source in the uppermost mantle

**Lg** A wave group observed at larger regional distances and caused by superposition of multiple S-wave reverberations and S to P and/or P to S conversions inside the whole crust. The maximum energy travels with a group velocity around 3.5 km/s